

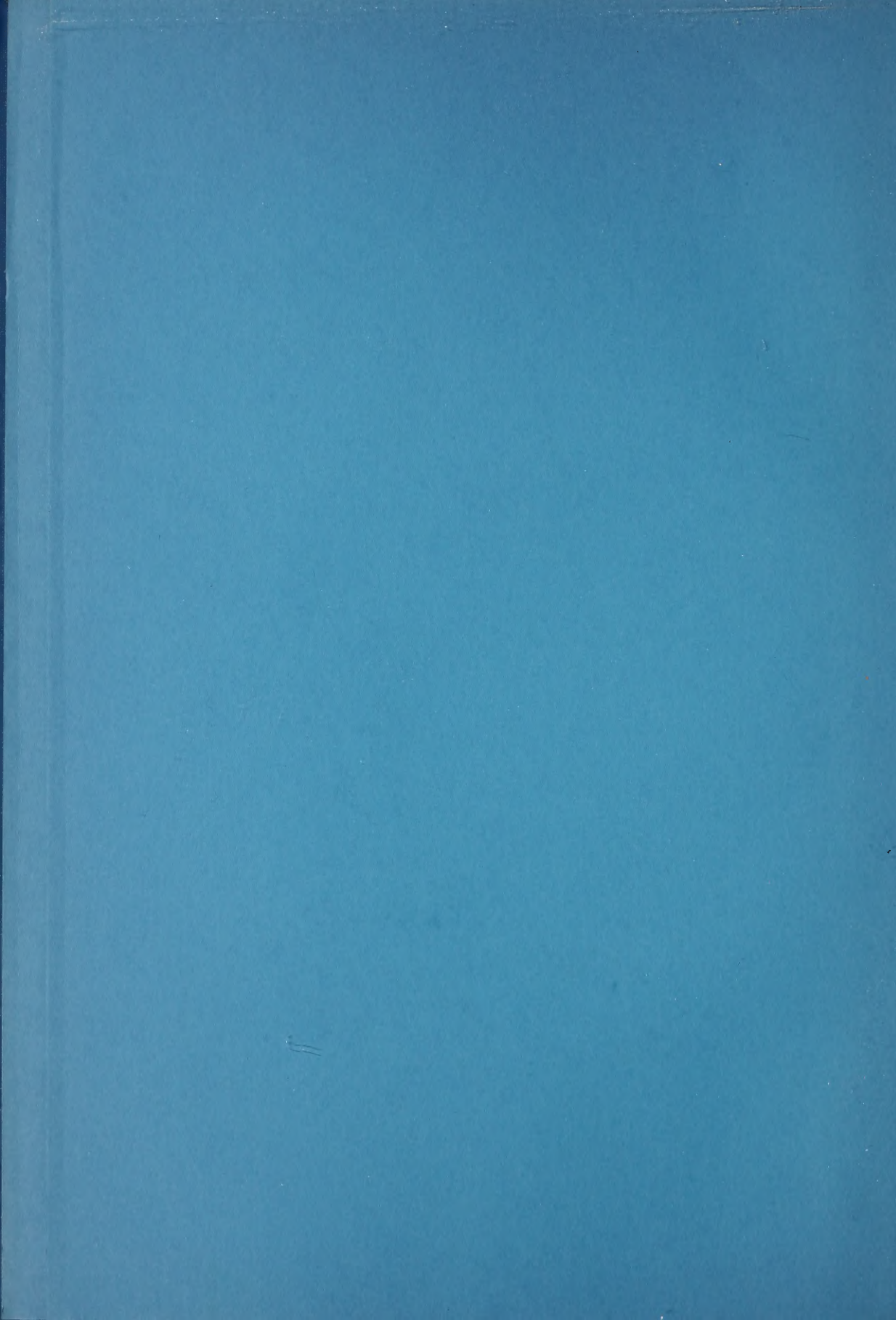
*Carnegie
Institution*

OF WASHINGTON

Year Book 75

1975-1976

Copy for Director's Office



*Carnegie
Institution*

OF WASHINGTON

Year Book 75

1975-1976





Library of Congress Catalog Card Number 3-16716
Champion Press, Inc., Baltimore, Maryland
Issued December 1976

Contents

| | |
|---|-----|
| Officers and Staff | v |
| Report of the President | 1 |
| Reports of Departments and Special Studies | 1 |
| Department of Embryology | 3 |
| Department of Terrestrial Magnetism | 105 |
| Hale Observatories | 273 |
| Department of Plant Biology | 347 |
| Geophysical Laboratory | 485 |
| Developmental Biology Research Group | 859 |
| Bibliography | 961 |
| Administrative Reports | 963 |
| Report of the Executive Committee | 965 |
| Abstract of Minutes of the Seventy-Eighth Meeting of the Board of Trustees | 967 |
| Financial Statement | 971 |
| Ten-Year Financial Summary | 973 |
| Report of Independent Public Accountants | 974 |
| Articles of Incorporation | 989 |
| By-Laws of the Institution | 993 |
| Index of Names | 999 |

Contents

| | |
|----------------------|------|
| Introduction | 1 |
| Chapter I | 10 |
| Chapter II | 25 |
| Chapter III | 40 |
| Chapter IV | 55 |
| Chapter V | 70 |
| Chapter VI | 85 |
| Chapter VII | 100 |
| Chapter VIII | 115 |
| Chapter IX | 130 |
| Chapter X | 145 |
| Chapter XI | 160 |
| Chapter XII | 175 |
| Chapter XIII | 190 |
| Chapter XIV | 205 |
| Chapter XV | 220 |
| Chapter XVI | 235 |
| Chapter XVII | 250 |
| Chapter XVIII | 265 |
| Chapter XIX | 280 |
| Chapter XX | 295 |
| Chapter XXI | 310 |
| Chapter XXII | 325 |
| Chapter XXIII | 340 |
| Chapter XXIV | 355 |
| Chapter XXV | 370 |
| Chapter XXVI | 385 |
| Chapter XXVII | 400 |
| Chapter XXVIII | 415 |
| Chapter XXIX | 430 |
| Chapter XXX | 445 |
| Chapter XXXI | 460 |
| Chapter XXXII | 475 |
| Chapter XXXIII | 490 |
| Chapter XXXIV | 505 |
| Chapter XXXV | 520 |
| Chapter XXXVI | 535 |
| Chapter XXXVII | 550 |
| Chapter XXXVIII | 565 |
| Chapter XXXIX | 580 |
| Chapter XL | 595 |
| Chapter XLI | 610 |
| Chapter XLII | 625 |
| Chapter XLIII | 640 |
| Chapter XLIV | 655 |
| Chapter XLV | 670 |
| Chapter XLVI | 685 |
| Chapter XLVII | 700 |
| Chapter XLVIII | 715 |
| Chapter XLIX | 730 |
| Chapter L | 745 |
| Chapter LI | 760 |
| Chapter LII | 775 |
| Chapter LIII | 790 |
| Chapter LIV | 805 |
| Chapter LV | 820 |
| Chapter LVI | 835 |
| Chapter LVII | 850 |
| Chapter LVIII | 865 |
| Chapter LIX | 880 |
| Chapter LX | 895 |
| Chapter LXI | 910 |
| Chapter LXII | 925 |
| Chapter LXIII | 940 |
| Chapter LXIV | 955 |
| Chapter LXV | 970 |
| Chapter LXVI | 985 |
| Chapter LXVII | 1000 |
| Chapter LXVIII | 1015 |
| Chapter LXIX | 1030 |
| Chapter LXX | 1045 |
| Chapter LXXI | 1060 |
| Chapter LXXII | 1075 |
| Chapter LXXIII | 1090 |
| Chapter LXXIV | 1105 |
| Chapter LXXV | 1120 |
| Chapter LXXVI | 1135 |
| Chapter LXXVII | 1150 |
| Chapter LXXVIII | 1165 |
| Chapter LXXIX | 1180 |
| Chapter LXXX | 1195 |
| Chapter LXXXI | 1210 |
| Chapter LXXXII | 1225 |
| Chapter LXXXIII | 1240 |
| Chapter LXXXIV | 1255 |
| Chapter LXXXV | 1270 |
| Chapter LXXXVI | 1285 |
| Chapter LXXXVII | 1300 |
| Chapter LXXXVIII | 1315 |
| Chapter LXXXIX | 1330 |
| Chapter LXXXX | 1345 |
| Chapter LXXXXI | 1360 |
| Chapter LXXXXII | 1375 |
| Chapter LXXXXIII | 1390 |
| Chapter LXXXXIV | 1405 |
| Chapter LXXXXV | 1420 |
| Chapter LXXXXVI | 1435 |
| Chapter LXXXXVII | 1450 |
| Chapter LXXXXVIII | 1465 |
| Chapter LXXXXIX | 1480 |
| Chapter LXXXXX | 1495 |
| Chapter LXXXXXI | 1510 |
| Chapter LXXXXXII | 1525 |
| Chapter LXXXXXIII | 1540 |
| Chapter LXXXXXIV | 1555 |
| Chapter LXXXXXV | 1570 |
| Chapter LXXXXXVI | 1585 |
| Chapter LXXXXXVII | 1600 |
| Chapter LXXXXXVIII | 1615 |
| Chapter LXXXXXIX | 1630 |
| Chapter LXXXXXX | 1645 |
| Chapter LXXXXXXI | 1660 |
| Chapter LXXXXXXII | 1675 |
| Chapter LXXXXXXIII | 1690 |
| Chapter LXXXXXXIV | 1705 |
| Chapter LXXXXXXV | 1720 |
| Chapter LXXXXXXVI | 1735 |
| Chapter LXXXXXXVII | 1750 |
| Chapter LXXXXXXVIII | 1765 |
| Chapter LXXXXXXIX | 1780 |
| Chapter LXXXXXXX | 1795 |
| Chapter LXXXXXXXI | 1810 |
| Chapter LXXXXXXXII | 1825 |
| Chapter LXXXXXXXIII | 1840 |
| Chapter LXXXXXXXIV | 1855 |
| Chapter LXXXXXXXV | 1870 |
| Chapter LXXXXXXXVI | 1885 |
| Chapter LXXXXXXXVII | 1900 |
| Chapter LXXXXXXXVIII | 1915 |
| Chapter LXXXXXXXIX | 1930 |
| Chapter LXXXXXXXI | 1945 |
| Chapter LXXXXXXXII | 1960 |
| Chapter LXXXXXXXIII | 1975 |
| Chapter LXXXXXXXIV | 1990 |
| Chapter LXXXXXXXV | 2005 |
| Chapter LXXXXXXXVI | 2020 |
| Chapter LXXXXXXXVII | 2035 |
| Chapter LXXXXXXXVIII | 2050 |
| Chapter LXXXXXXXIX | 2065 |
| Chapter LXXXXXXXI | 2080 |
| Chapter LXXXXXXXII | 2095 |
| Chapter LXXXXXXXIII | 2110 |
| Chapter LXXXXXXXIV | 2125 |
| Chapter LXXXXXXXV | 2140 |
| Chapter LXXXXXXXVI | 2155 |
| Chapter LXXXXXXXVII | 2170 |
| Chapter LXXXXXXXVIII | 2185 |
| Chapter LXXXXXXXIX | 2200 |
| Chapter LXXXXXXXI | 2215 |
| Chapter LXXXXXXXII | 2230 |
| Chapter LXXXXXXXIII | 2245 |
| Chapter LXXXXXXXIV | 2260 |
| Chapter LXXXXXXXV | 2275 |
| Chapter LXXXXXXXVI | 2290 |
| Chapter LXXXXXXXVII | 2305 |
| Chapter LXXXXXXXVIII | 2320 |
| Chapter LXXXXXXXIX | 2335 |
| Chapter LXXXXXXXI | 2350 |
| Chapter LXXXXXXXII | 2365 |
| Chapter LXXXXXXXIII | 2380 |
| Chapter LXXXXXXXIV | 2395 |
| Chapter LXXXXXXXV | 2410 |
| Chapter LXXXXXXXVI | 2425 |
| Chapter LXXXXXXXVII | 2440 |
| Chapter LXXXXXXXVIII | 2455 |
| Chapter LXXXXXXXIX | 2470 |
| Chapter LXXXXXXXI | 2485 |
| Chapter LXXXXXXXII | 2500 |
| Chapter LXXXXXXXIII | 2515 |
| Chapter LXXXXXXXIV | 2530 |
| Chapter LXXXXXXXV | 2545 |
| Chapter LXXXXXXXVI | 2560 |
| Chapter LXXXXXXXVII | 2575 |
| Chapter LXXXXXXXVIII | 2590 |
| Chapter LXXXXXXXIX | 2605 |
| Chapter LXXXXXXXI | 2620 |
| Chapter LXXXXXXXII | 2635 |
| Chapter LXXXXXXXIII | 2650 |
| Chapter LXXXXXXXIV | 2665 |
| Chapter LXXXXXXXV | 2680 |
| Chapter LXXXXXXXVI | 2695 |
| Chapter LXXXXXXXVII | 2710 |
| Chapter LXXXXXXXVIII | 2725 |
| Chapter LXXXXXXXIX | 2740 |
| Chapter LXXXXXXXI | 2755 |
| Chapter LXXXXXXXII | 2770 |
| Chapter LXXXXXXXIII | 2785 |
| Chapter LXXXXXXXIV | 2800 |
| Chapter LXXXXXXXV | 2815 |
| Chapter LXXXXXXXVI | 2830 |
| Chapter LXXXXXXXVII | 2845 |
| Chapter LXXXXXXXVIII | 2860 |
| Chapter LXXXXXXXIX | 2875 |
| Chapter LXXXXXXXI | 2890 |
| Chapter LXXXXXXXII | 2905 |
| Chapter LXXXXXXXIII | 2920 |
| Chapter LXXXXXXXIV | 2935 |
| Chapter LXXXXXXXV | 2950 |
| Chapter LXXXXXXXVI | 2965 |
| Chapter LXXXXXXXVII | 2980 |
| Chapter LXXXXXXXVIII | 2995 |
| Chapter LXXXXXXXIX | 3010 |
| Chapter LXXXXXXXI | 3025 |
| Chapter LXXXXXXXII | 3040 |
| Chapter LXXXXXXXIII | 3055 |
| Chapter LXXXXXXXIV | 3070 |
| Chapter LXXXXXXXV | 3085 |
| Chapter LXXXXXXXVI | 3100 |
| Chapter LXXXXXXXVII | 3115 |
| Chapter LXXXXXXXVIII | 3130 |
| Chapter LXXXXXXXIX | 3145 |
| Chapter LXXXXXXXI | 3160 |
| Chapter LXXXXXXXII | 3175 |
| Chapter LXXXXXXXIII | 3190 |
| Chapter LXXXXXXXIV | 3205 |
| Chapter LXXXXXXXV | 3220 |
| Chapter LXXXXXXXVI | 3235 |
| Chapter LXXXXXXXVII | 3250 |
| Chapter LXXXXXXXVIII | 3265 |
| Chapter LXXXXXXXIX | 3280 |
| Chapter LXXXXXXXI | 3295 |
| Chapter LXXXXXXXII | 3310 |
| Chapter LXXXXXXXIII | 3325 |
| Chapter LXXXXXXXIV | 3340 |
| Chapter LXXXXXXXV | 3355 |
| Chapter LXXXXXXXVI | 3370 |
| Chapter LXXXXXXXVII | 3385 |
| Chapter LXXXXXXXVIII | 3400 |
| Chapter LXXXXXXXIX | 3415 |
| Chapter LXXXXXXXI | 3430 |
| Chapter LXXXXXXXII | 3445 |
| Chapter LXXXXXXXIII | 3460 |
| Chapter LXXXXXXXIV | 3475 |
| Chapter LXXXXXXXV | 3490 |
| Chapter LXXXXXXXVI | 3505 |
| Chapter LXXXXXXXVII | 3520 |
| Chapter LXXXXXXXVIII | 3535 |
| Chapter LXXXXXXXIX | 3550 |
| Chapter LXXXXXXXI | 3565 |
| Chapter LXXXXXXXII | 3580 |
| Chapter LXXXXXXXIII | 3595 |
| Chapter LXXXXXXXIV | 3610 |
| Chapter LXXXXXXXV | 3625 |
| Chapter LXXXXXXXVI | 3640 |
| Chapter LXXXXXXXVII | 3655 |
| Chapter LXXXXXXXVIII | 3670 |
| Chapter LXXXXXXXIX | 3685 |
| Chapter LXXXXXXXI | 3700 |
| Chapter LXXXXXXXII | 3715 |
| Chapter LXXXXXXXIII | 3730 |
| Chapter LXXXXXXXIV | 3745 |
| Chapter LXXXXXXXV | 3760 |
| Chapter LXXXXXXXVI | 3775 |
| Chapter LXXXXXXXVII | 3790 |
| Chapter LXXXXXXXVIII | 3805 |
| Chapter LXXXXXXXIX | 3820 |
| Chapter LXXXXXXXI | 3835 |
| Chapter LXXXXXXXII | 3850 |
| Chapter LXXXXXXXIII | 3865 |
| Chapter LXXXXXXXIV | 3880 |
| Chapter LXXXXXXXV | 3895 |
| Chapter LXXXXXXXVI | 3910 |
| Chapter LXXXXXXXVII | 3925 |
| Chapter LXXXXXXXVIII | 3940 |
| Chapter LXXXXXXXIX | 3955 |
| Chapter LXXXXXXXI | 3970 |
| Chapter LXXXXXXXII | 3985 |
| Chapter LXXXXXXXIII | 4000 |
| Chapter LXXXXXXXIV | 4015 |
| Chapter LXXXXXXXV | 4030 |
| Chapter LXXXXXXXVI | 4045 |
| Chapter LXXXXXXXVII | 4060 |
| Chapter LXXXXXXXVIII | 4075 |
| Chapter LXXXXXXXIX | 4090 |
| Chapter LXXXXXXXI | 4105 |
| Chapter LXXXXXXXII | 4120 |
| Chapter LXXXXXXXIII | 4135 |
| Chapter LXXXXXXXIV | 4150 |
| Chapter LXXXXXXXV | 4165 |
| Chapter LXXXXXXXVI | 4180 |
| Chapter LXXXXXXXVII | 4195 |
| Chapter LXXXXXXXVIII | 4210 |
| Chapter LXXXXXXXIX | 4225 |
| Chapter LXXXXXXXI | 4240 |
| Chapter LXXXXXXXII | 4255 |
| Chapter LXXXXXXXIII | 4270 |
| Chapter LXXXXXXXIV | 4285 |
| Chapter LXXXXXXXV | 4300 |
| Chapter LXXXXXXXVI | 4315 |
| Chapter LXXXXXXXVII | 4330 |
| Chapter LXXXXXXXVIII | 4345 |
| Chapter LXXXXXXXIX | 4360 |
| Chapter LXXXXXXXI | 4375 |
| Chapter LXXXXXXXII | 4390 |
| Chapter LXXXXXXXIII | 4405 |
| Chapter LXXXXXXXIV | 4420 |
| Chapter LXXXXXXXV | 4435 |
| Chapter LXXXXXXXVI | 4450 |
| Chapter LXXXXXXXVII | 4465 |
| Chapter LXXXXXXXVIII | 4480 |
| Chapter LXXXXXXXIX | 4495 |
| Chapter LXXXXXXXI | 4510 |
| Chapter LXXXXXXXII | 4525 |
| Chapter LXXXXXXXIII | 4540 |
| Chapter LXXXXXXXIV | 4555 |
| Chapter LXXXXXXXV | 4570 |
| Chapter LXXXXXXXVI | 4585 |
| Chapter LXXXXXXXVII | 4600 |
| Chapter LXXXXXXXVIII | 4615 |
| Chapter LXXXXXXXIX | 4630 |
| Chapter LXXXXXXXI | 4645 |
| Chapter LXXXXXXXII | 4660 |
| Chapter LXXXXXXXIII | 4675 |
| Chapter LXXXXXXXIV | 4690 |
| Chapter LXXXXXXXV | 4705 |
| Chapter LXXXXXXXVI | 4720 |
| Chapter LXXXXXXXVII | 4735 |
| Chapter LXXXXXXXVIII | 4750 |
| Chapter LXXXXXXXIX | 4765 |
| Chapter LXXXXXXXI | 4780 |
| Chapter LXXXXXXXII | 4795 |
| Chapter LXXXXXXXIII | 4810 |
| Chapter LXXXXXXXIV | 4825 |
| Chapter LXXXXXXXV | 4840 |
| Chapter LXXXXXXXVI | 4855 |
| Chapter LXXXXXXXVII | 4870 |
| Chapter LXXXXXXXVIII | 4885 |
| Chapter LXXXXXXXIX | 4900 |
| Chapter LXXXXXXXI | 4915 |
| Chapter LXXXXXXXII | 4930 |
| Chapter LXXXXXXXIII | 4945 |
| Chapter LXXXXXXXIV | 4960 |
| Chapter LXXXXXXXV | 4975 |
| Chapter LXXXXXXXVI | 4990 |
| Chapter LXXXXXXXVII | 5005 |
| Chapter LXXXXXXXVIII | 5020 |
| Chapter LXXXXXXXIX | 5035 |
| Chapter LXXXXXXXI | 5050 |
| Chapter LXXXXXXXII | 5065 |
| Chapter LXXXXXXXIII | 5080 |
| Chapter LXXXXXXXIV | 5095 |
| Chapter LXXXXXXXV | 5110 |
| Chapter LXXXXXXXVI | 5125 |
| Chapter LXXXXXXXVII | 5140 |
| Chapter LXXXXXXXVIII | 5155 |
| Chapter LXXXXXXXIX | 5170 |
| Chapter LXXXXXXXI | 5185 |
| Chapter LXXXXXXXII | 5200 |
| Chapter LXXXXXXXIII | 5215 |
| Chapter LXXXXXXXIV | 5230 |
| Chapter LXXXXXXXV | 5245 |
| Chapter LXXXXXXXVI | 5260 |
| Chapter LXXXXXXXVII | 5275 |
| Chapter LXXXXXXXVIII | 5290 |
| Chapter LXXXXXXXIX | 5305 |
| Chapter LXXXXXXXI | 5320 |
| Chapter LXXXXXXXII | 5335 |
| Chapter LXXXXXXXIII | 5350 |
| Chapter LXXXXXXXIV | 5365 |
| Chapter LXXXXXXXV | 5380 |
| Chapter LXXXXXXXVI | 5395 |
| Chapter LXXXXXXXVII | 5410 |
| Chapter LXXXXXXXVIII | 5425 |
| Chapter LXXXXXXXIX | 5440 |
| Chapter LXXXXXXXI | 5455 |
| Chapter LXXXXXXXII | 5470 |
| Chapter LXXXXXXXIII | 5485 |
| Chapter LXXXXXXXIV | 5500 |
| Chapter LXXXXXXXV | 5515 |
| Chapter LXXXXXXXVI | 5530 |
| Chapter LXXXXXXXVII | 5545 |
| Chapter LXXXXXXXVIII | 5560 |
| Chapter LXXXXXXXIX | 5575 |
| Chapter LXXXXXXXI | 5590 |
| Chapter LXXXXXXXII | 5605 |
| Chapter LXXXXXXXIII | 5620 |
| Chapter LXXXXXXXIV | 5635 |
| Chapter LXXXXXXXV | 5650 |
| Chapter LXXXXXXXVI | 5665 |
| Chapter LXXXXXXXVII | 5680 |
| Chapter LXXXXXXXVIII | 5695 |
| Chapter LXXXXXXXIX | 5710 |
| Chapter LXXXXXXXI | 5725 |
| Chapter LXXXXXXXII | 5740 |
| Chapter LXXXXXXXIII | 5755 |
| Chapter LXXXXXXXIV | 5770 |
| Chapter LXXXXXXXV | 5785 |
| Chapter LXXXXXXXVI | 5800 |
| Chapter LXXXXXXXVII | 5815 |
| Chapter LXXXXXXXVIII | 5830 |
| Chapter LXXXXXXXIX | 5845 |
| Chapter LXXXXXXXI | 5860 |
| Chapter LXXXXXXXII | 5875 |
| Chapter LXXXXXXXIII | 5890 |
| Chapter LXXXXXXXIV | 5905 |
| Chapter LXXXXXXXV | 5920 |
| Chapter LXXXXXXXVI | 5935 |
| Chapter LXXXXXXXVII | 5950 |
| Chapter LXXXXXXXVIII | 5965 |
| Chapter LXXXXXXXIX | 5980 |
| Chapter LXXXXXXXI | 5995 |
| Chapter LXXXXXXXII | 6010 |
| Chapter LXXXXXXXIII | 6025 |
| Chapter LXXXXXXXIV | 6040 |
| Chapter LXXXXXXXV | 6055 |
| Chapter LXXXXXXXVI | 6070 |
| Chapter LXXXXXXXVII | 6085 |
| Chapter LXXXXXXXVIII | 6100 |
| Chapter LXXXXXXXIX | 6115 |
| Chapter LXXXXXXXI | 6130 |
| Chapter LXXXXXXXII | 6145 |
| Chapter LXXXXXXXIII | 6160 |
| Chapter LXXXXXXXIV | 6175 |
| Chapter LXXXXXXXV | 6190 |
| Chapter LXXXXXXXVI | 6205 |
| Chapter LXXXXXXXVII | 6220 |
| Chapter LXXXXXXXVIII | 6235 |
| Chapter LXXXXXXXIX | 6250 |
| Chapter LXXXXXXXI | 6265 |
| Chapter LXXXXXXXII | 6280 |
| Chapter LXXXXXXXIII | 6295 |
| Chapter LXXXXXXXIV | 6310 |
| Chapter LXXXXXXXV | 6325 |
| Chapter LXXXXXXXVI | 6340 |
| Chapter LXXXXXXXVII | 6355 |
| Chapter LXXXXXXXVIII | 6370 |
| Chapter LXXXXXXXIX | 6385 |
| Chapter LXXXXXXXI | 6400 |
| Chapter LXXXXXXXII | 6415 |
| Chapter LXXXXXXXIII | 6430 |
| Chapter LXXXXXXXIV | 6445 |
| Chapter LXXXXXXXV | 6460 |
| Chapter LXXXXXXXVI | 6475 |
| Chapter LXXXXXXXVII | 6490 |
| Chapter LXXXXXXXVIII | 6505 |
| Chapter LXXXXXXXIX | 6520 |
| Chapter LXXXXXXXI | 6535 |
| Chapter LXXXXXXXII | 6550 |
| Chapter LXXXXXXXIII | 6565 |
| Chapter LXXXXXXXIV | 6580 |
| Chapter LXXXXXXXV | 6595 |
| Chapter LXXXXXXXVI | 6610 |
| Chapter LXXXXXXXVII | 6625 |
| Chapter LXXXXXXXVIII | 6640 |
| Chapter LXXXXXXXIX | 6655 |
| Chapter LXXXXXXXI | 6670 |
| Chapter LXXXXXXXII | 6685 |
| Chapter LXXXXXXXIII | 6700 |
| Chapter LXXXXXXXIV | 6715 |
| Chapter LXXXXXXXV | 6730 |
| Chapter LXXXXXXXVI | 6745 |
| Chapter LXXXXXXXVII | 6760 |
| Chapter LXXXXXXXVIII | 6775 |
| Chapter LXXXXXXXIX | 6790 |
| Chapter LXXXXXXXI | 6805 |
| Chapter LXXXXXXXII | 6820 |
| Chapter LXXXXXXXIII | 6835 |
| Chapter LXXXXXXXIV | 6850 |
| Chapter LXXXXXXXV | 6865 |
| Chapter LXXXXXXXVI | 6880 |
| Chapter LXXXXXXXVII | 6895 |
| Chapter LXXXXXXXVIII | 6910 |
| Chapter LXXXXXXXIX | 6925 |
| Chapter LXXXXXXXI | 6940 |
| Chapter LXXXXXXXII | 6955 |
| Chapter LXXXXXXXIII | 6970 |
| Chapter LXXXXXXXIV | 6985 |
| Chapter LXXXXXXXV | 7000 |
| Chapter LXXXXXXXVI | 7015 |
| Chapter LXXXXXXXVII | 7030 |
| Chapter LXXXXXXXVIII | 7045 |
| Chapter LXXXXXXXIX | 7060 |
| Chapter LXXXXXXXI | 7075 |
| Chapter LXXXXXXXII | 7090 |
| Chapter LXXXXXXXIII | 7105 |
| Chapter LXXXXXXXIV | 7120 |
| Chapter LXXXXXXXV | 7135 |
| Chapter LXXXXXXXVI | 7150 |
| Chapter LXXXXXXXVII | 7165 |
| Chapter LXXXXXXXVIII | 7180 |
| Chapter LXXXXXXXIX | 7195 |
| Chapter LXXXXXXXI | 7210 |
| Chapter LXXXXXXXII | 7225 |
| Chapter LXXXXXXXIII | 7240 |
| Chapter LXXXXXXXIV | 7255 |
| Chapter LXXXXXXXV | 7270 |
| Chapter LXXXXXXXVI | 7285 |
| Chapter LXXXXXXXVII | 7300 |
| Chapter LXXXXXXXVIII | 7315 |
| Chapter LXXXXXXXIX | 7330 |
| Chapter LXXXXXXXI | 7345 |
| Chapter LXXXXXXXII | 7360 |
| Chapter LXXXXXXXIII | 7375 |
| Chapter LXXXXXXXIV | 7390 |
| Chapter LXXXXXXXV | 7405 |
| Chapter LXXXXXXXVI | 7420 |
| Chapter LXXXXXXXVII | 7435 |
| Chapter LXXXXXXXVIII | 7450 |
| Chapter LXXXXXXXIX | 7465 |
| Chapter LXXXXXXXI | 7480 |
| Chapter LXXXXXXXII | 7495 |
| Chapter LXXXXXXXIII | 7510 |
| Chapter LXXXXXXXIV | 7525 |
| Chapter LXXXXXXXV | 7540 |
| Chapter LXXXXXXXVI | 7555 |
| Chapter LXXXXXXXVII | 7570 |
| Chapter LXXXXXXXVIII | 7585 |
| Chapter LXXXXXXXIX | 7600 |
| Chapter LXXXXXXXI | 7615 |
| Chapter LXXXXXXXII | 7630 |
| Chapter LXXXXXXXIII | 7645 |
| Chapter LXXXXXXXIV | 7660 |
| Chapter LXXXXXXXV | 7675 |
| Chapter LXXXXXXXVI | 7690 |
| Chapter LXXXXXXXVII | 7705 |
| Chapter LXXXXXXXVIII | 7720 |
| Chapter LXXXXXXXIX | 7735 |
| Chapter LXXXXXXXI | 7750 |
| Chapter LXXXXXXXII | 7765 |
| Chapter LXXXXXXXIII | 7780 |
| Chapter LXXXXXXXIV | 7795 |
| Chapter LXXXXXXXV | 7810 |
| Chapter LXXXXXXXVI | 7825 |
| Chapter LXXXXXXXVII | 7840 |
| Chapter LXXXXXXXVIII | 7855 |
| Chapter LXXXXXXXIX | 7870 |
| Chapter LXXXXXXXI | 7885 |
| Chapter LXXXXXXXII | 7900 |
| Chapter LXXXXXXXIII | 7915 |
| Chapter LXXXXXXXIV | 7930 |
| Chapter LXXXXXXXV | 7945 |
| Chapter LXXXXXXXVI | 7960 |
| Chapter LXXXXXXXVII | 7975 |
| Chapter LXXXXXXXVIII | 7990 |
| Chapter LXXXXXXXIX | 8005 |
| Chapter LXXXXXXXI | 8020 |
| Chapter LXXXXXXXII | 8035 |
| Chapter LXXXXXXXIII | 8050 |
| Chapter LXXXXXXXIV | 8065 |
| Chapter LXXXXXXXV | 8080 |
| Chapter LXXXXXXXVI | 8095 |
| Chapter LXXXXXXXVII | 8110 |
| Chapter LXXXXXXXVIII | 8125 |
| Chapter LXXXXXXXIX | 8140 |
| Chapter LXXXXXXXI | 8155 |
| Chapter LXXXXXXXII | 8170 |
| Chapter LXXXXXXXIII | 8185 |
| Chapter LXXXXXXXIV | 8 |

President and Trustees

PRESIDENT

Philip H. Abelson

BOARD OF TRUSTEES

William McChesney Martin, Jr.
Chairman

Frank Stanton
Vice-Chairman

William T. Golden
Secretary

Robert O. Anderson¹

J. Paul Austin¹

Lewis M. Branscomb

John T. Connor

John Diebold

Michael Ference, Jr.

Carl J. Gilbert

Hanna H. Gray

Crawford H. Greenewalt

William C. Greenough

Caryl P. Haskins

William R. Hewlett

Henry S. Morgan

William I. Myers²

Walter H. Page

Robert M. Pennoyer

Richard S. Perkins

William M. Roth

Robert C. Seamans, Jr.

Charles H. Townes

Juan T. Trippe

James N. White

Garrison Norton

Charles P. Taft

Trustees Emeriti

¹ Elected April 1976.

² Died January 30, 1976.

Former Presidents and Trustees

PRESIDENTS

| | | | |
|-------------------------|-----------|-----------------------|-----------|
| Daniel Coit Gilman | 1902-1904 | John Campbell Merriam | 1921-1938 |
| Robert Simpson Woodward | 1904-1920 | Vannevar Bush | 1939-1955 |
| Caryl P. Haskins | | 1956-1971 | |

TRUSTEES

| | | | |
|-----------------------|---------|--------------------------|---------|
| Alexander Agassiz | 1904-05 | Robert A. Lovett | 1948-71 |
| Lord Ashby of Brandon | 1967-74 | Seth Low | 1902-16 |
| George J. Baldwin | 1925-27 | Wayne MacVeagh | 1902-07 |
| Thomas Barbour | 1934-46 | Keith S. McHugh | 1950-74 |
| James F. Bell | 1935-61 | Andrew W. Mellon | 1924-37 |
| John S. Billings | 1902-13 | John Campbell Merriam | 1921-38 |
| Robert Woods Bliss | 1936-62 | Margaret Carnegie Miller | 1955-67 |
| Amory H. Bradford | 1959-72 | Roswell Miller | 1933-55 |
| Lindsay Bradford | 1940-58 | Darius O. Mills | 1902-09 |
| Omar N. Bradley | 1948-69 | S. Weir Mitchell | 1902-14 |
| Robert S. Brookings | 1910-29 | Andrew J. Montague | 1907-35 |
| Vannevar Bush | 1958-71 | William W. Morrow | 1902-29 |
| John L. Cadwalader | 1903-14 | Seeley G. Mudd | 1940-68 |
| William W. Campbell | 1929-38 | William I. Myers | 1948-76 |
| John J. Carty | 1916-32 | William Church Osborn | 1927-34 |
| Whitefoord R. Cole | 1925-34 | James Parmelee | 1917-31 |
| Frederic A. Delano | 1927-49 | Wm. Barclay Parsons | 1907-32 |
| Cleveland H. Dodge | 1903-23 | Stewart Paton | 1916-42 |
| William E. Dodge | 1902-03 | George W. Pepper | 1914-19 |
| Charles P. Fenner | 1914-24 | John J. Pershing | 1930-43 |
| Homer L. Ferguson | 1927-52 | Henning W. Prentis, Jr. | 1942-59 |
| Simon Flexner | 1910-14 | Henry S. Pritchett | 1906-36 |
| W. Cameron Forbes | 1920-55 | Gordon S. Rentschler | 1946-48 |
| James Forrestal | 1948-49 | David Rockefeller | 1952-56 |
| William N. Frew | 1902-15 | Elihu Root | 1902-37 |
| Lyman J. Gage | 1902-12 | Elihu Root, Jr. | 1937-67 |
| Walter S. Gifford | 1931-66 | Julius Rosenwald | 1929-31 |
| Cass Gilbert | 1924-34 | William W. Rubey | 1962-74 |
| Frederick H. Gillett | 1924-35 | Martin A. Ryerson | 1908-28 |
| Daniel C. Gilman | 1902-08 | Henry R. Shepley | 1937-62 |
| Patrick E. Haggerty | 1974-75 | Theobald Smith | 1914-34 |
| John Hay | 1902-05 | John C. Spooner | 1902-07 |
| Barklie McKee Henry | 1949-66 | William Benson Storey | 1924-39 |
| Myron T. Herrick | 1915-29 | Richard P. Strong | 1934-48 |
| Abram S. Hewitt | 1902-03 | William H. Taft | 1906-15 |
| Henry L. Higginson | 1902-19 | William S. Thayer | 1929-32 |
| Ethan A. Hitchcock | 1902-09 | James W. Wadsworth | 1932-52 |
| Henry Hitchcock | 1902 | Charles D. Walcott | 1902-27 |
| Herbert Hoover | 1920-49 | Frederic C. Walcott | 1931-48 |
| William Wirt Howe | 1903-09 | Henry P. Walcott | 1910-24 |
| Charles L. Hutchinson | 1902-04 | Lewis H. Weed | 1935-52 |
| Walter A. Jessup | 1938-44 | William H. Welch | 1906-34 |
| Frank B. Jewett | 1933-49 | Andrew D. White | 1902-16 |
| Samuel P. Langley | 1904-06 | Edward D. White | 1902-03 |
| Ernest O. Lawrence | 1944-58 | Henry White | 1913-27 |
| Charles A. Lindbergh | 1934-39 | George W. Wickersham | 1909-36 |
| William Lindsay | 1902-09 | Robert E. Wilson | 1953-64 |
| Henry Cabot Lodge | 1914-24 | Robert S. Woodward | 1905-24 |
| Alfred L. Loomis | 1934-73 | Carroll D. Wright | 1902-08 |

Under the original charter, from the date of organization until April 28, 1904, the following were *ex officio* members of the Board of Trustees: the President of the United States, the President of the Senate, the Speaker of the House of Representatives, the Secretary of the Smithsonian Institution, and the President of the National Academy of Sciences.

OFFICE OF ADMINISTRATION

1530 P Street, N.W., Washington, D.C. 20005

Philip H. Abelson *President*

James W. Boise *Bursar; Secretary-Treasurer, Retirement Trust;
Executive Secretary to the Finance Committee*

Marjorie H. Walburn *Assistant to the President*

Sheila A. McGough *Publications Officer; Editor*

Kenneth R. Henard *Assistant Bursar; Assistant Treasurer,
Retirement Trust*

Joseph M. S. Haraburda *Assistant to the Bursar*

Richard E. Hewitt *Administrative Officer for Services*

Marshall Hornblower *Counsel*

STAFF MEMBERS IN SPECIAL SUBJECT AREAS

Ellis T. Bolton
Roy J. Britten
Tatiana Proskouriakoff

DISTINGUISHED SERVICE MEMBER IN SPECIAL SUBJECT AREA

Barbara McClintock

RESEARCH ASSOCIATE AT LARGE

Harry E. D. Pollock

Carnegie Institution of Washington adheres in all phases of its operations, including employment and educational programs, to a policy barring discrimination on the basis of race, religion, color, national or ethnic origin, or sex. In its educational programs it admits qualified students as fellows without regard to race, religion, color, national or ethnic origin, or sex to all the rights, privileges, programs, and activities generally accorded or made available to fellows at the Institution. It does not discriminate on the basis of race, religion, color, national or ethnic origin, or sex in administration of its educational policies, admissions policies, fellowship programs, and other Institution-administered programs.

Report OF
THE *President*

ELECTRONICS REVOLUTION

Earlier in the century, this country experienced a long era of sustained growth in many aspects. There was a steady increase in level of education, life expectancy, and standard of living. Growth of all kinds was welcomed, including industrial expansion and population increase. A feeling of progress, of achievement, of well-being was everywhere. As a corollary, a striving for excellence and the search for understanding were widely admired.

Today the mood of this country has turned pessimistic and negative. Those who are so inclined can find much evidence to support these views. Growth in the use of energy in the form of oil was suddenly curtailed in 1974. Growth in consumption of the kind seen in the 1950s and 1960s will not occur again. That part of the standard of living that is based on large-scale consumption of energy is not likely to improve during this century.

However, those who prefer optimism have reason for hope. Human ingenuity in solving problems is great. And native intelligence has been amplified enormously by the use of knowledge accumulated through research. An important product of research and a basis for hoping for a bright new future is the vitality of the continuing electronics revolution. This revolution has been in progress for about 60 years. Lately its tempo has increased greatly. Until recently its importance was overshadowed by changes brought about by the large-scale expansion in the use of energy. But the electronics revolution promises to be more important, of more enduring consequence, than the earlier Industrial Revolution.

Some of the great changes brought about by this revolution have gone on comparatively unnoticed; at the start they were evolutionary rather than sudden and drastic. The telephone, which we take for granted, was invented 100 years ago. Nearly every decade since then, the quality and scope of service have steadily improved while the cost (measured in constant dollars) is now a tiny fraction of what it was 50 years ago.

Numerous applications of electronics gradually affected individuals and almost every component and activity of society. Americans listen to commercial radio an average of nearly four hours daily. Television has come to most homes. During the last few years the accelerated tempo of change has led to an increased impact on society. For example, there is the rapidly burgeoning acceptance of the citizen's band radio, the worldwide use of the telephone, and the current astonishingly low prices at which hand-held computers and electronic watches are being sold. Less evident to the individual but in total more important to society are new and increasing applications of electronics to process control for industry, to research equipment, to merchandising, to banking, to management, to national defense, and to a host of other activities.

This revolution, which is destined to have great long-term consequences, is quite different in nature from the earlier Industrial Revolution. The Industrial Revolution was based on the profligate use of energy (mainly fossil fuels). Much of its technology was crude, with only a modest scientific or theoretical base. In large measure what the Industrial Revolution did was to make available and to employ large amounts of mechanical energy. History may well describe the past century as the Era of Brute Force.

In contrast, the electronics revolution represents one of the most noble intellectual achievements of mankind. Its development has been the product of the most advanced science, technology, and management. In many applications electronics requires little energy. Indeed, one factor that guarantees enduring impact for the electronic revolution is that it is sparing of energy and materials.

With electronics one can control the disposition of large amounts of energy and force, but the relationship is much like the use of the brain in directing the effort of muscles. In some aspects, electronics can be more subtle, more nimble, more dependable than the brain. In other applications, electronics serves as a great extender of human capabilities by rapidly carrying out routine but complex calculations, thus freeing the mind to make intuitive judgments and short cuts to new insights.

In laboratories devoted to extending the electronics revolution, the use of powerful investigative tools based on electronics is speeding new developments. Ultimately, there must be limits to what can be done. However, the barriers are not yet obvious, and it is clear that the revolution has some distance to go. What has been accomplished and something of what is possible may be found in the history and potential of certain solid-state devices. Writing about integrated circuits formed on silicon chips, Robert N. Noyce has commented:

The cost reductions resulting from higher levels of integration have been remarkable. The individual diffused transistor sold for a price of approximately one dollar in 1961, a few years after its introduction. Today, a 1024 bit memory including over six thousand transistors sells for about one dollar a few years after its introduction, representing a cost reduction of about 6000:1 in 15 years. The resulting effect on equipment costs can be seen in the electronic calculator, which has been reduced in cost by a factor of 500:1 in the last 8 years, creating a substantial new market unforeseen only 10 years ago.

Noyce and others are confident that the performance of silicon chips will be improved by at least a factor of 10. Already a tiny device has the computing power that earlier required a roomful of tubes and other electronic components.

One of the factors assuring a bright future for electronics is its high degree of social acceptance. There have been sporadic attacks on various electronic devices such as computers, but the intensity of criticism has diminished. In comparison to the level of criticism of chemical products or the environmental concerns associated with nuclear and fossil fuel energy, objections to electronics have been few. Broadly available items such as the hand-held computer, electronic watch, and citizen's band radio enhance the public's feeling of participating in the benefits of electronics while not bringing with them discernible side effects. In future, electronics will provide many new tools for humanity.

There are, of course, limitations to what electronics can do. It cannot supply the basic human needs of food, clothing, and shelter. But it can increase the efficiency of the processes by which these requirements are met. It can contribute to economies in the use of energy, for example, by improving the engine efficiency of automobiles through ignition control. Better electronic communications will lessen the need for business travel. Solar panels of improved cost and efficiency may be developed, making them an important energy source.

Just as electronics is increasingly changing the ways in which industry and commerce are conducted, it has also altered and continues to change the tools for scientific research, sometimes drastically, and the new tools are creating great research opportunities.

The use of electronic instrumentation has very much affected the conduct of research at the Carnegie Institution. In astronomy, it has increased the volume of the measurable universe by as much as a factor of 50. In the physical and biological sciences, electronics has expanded the time horizon and vastly increased the sensitivity and accuracy of many measurements. Human response time is of

the order of 1/10 to 1/5 second, but electronics enables humans to conduct experiments with time spans as short as a picosecond (10^{-12} second).

Two examples may be cited to illustrate the increased sensitivity and ease of analytical determinations. At one time the analysis of a silicate rock required a sample of about a gram and the processing occupied about a week's time. A skilled chemist might complete a dozen determinations in a week. Today, using the electron microprobe, one can analyze a sample of perhaps 10^{-10} gram in about 10 minutes.

Another example involves the analysis of a mixture of organic chemicals such as those found in petroleum. The original work to determine the composition of a crude oil, the Ponca City crude, required the fractionation of many barrels of oil—about a million grams—and efforts of many workers extending over about two decades. Today such an analysis can be performed in a few hours employing a sample containing a tenth of a gram.

Of comparable importance is the use of small but powerful on-line computers. These greatly facilitate the accumulation and interpretation of data and free investigators from dull bookkeeping tasks.

Many of these tools are production models of major instrument makers such as Hewlett-Packard. But leaders in research do not necessarily wait for some one else to produce a new device. Indeed, they often become leaders by being first to develop and exploit a new tool. Developing new tools and using them has been a tradition and practice at Carnegie installations.

In the past, most new research instruments used at the departments of the Institution were totally designed by them. The current practice is to combine commercially available electronic packages such as amplifiers or minicomputers with home-designed components to make a new device with unique capabilities.

Any account of the electronics revolution, however brief, would be incomplete without mention of the key role that three Carnegie trustees have had and are continuing to have in it. William Hewlett's company has made enormous contributions. Scientists and engineers worldwide are impressed with the quality and usefulness of the many instruments that Hewlett-Packard has innovated. Lewis Branscomb has had a long association with electronics, and as Vice-President and Chief Scientist for IBM he is helping guide the development of new products for that company. Charles Townes, who received the Nobel Prize for his research in quantum electronics that led to the maser-laser principle, continues creative work. His current radio telescope studies of molecules in space and his infrared work are advancing the frontiers of astronomy.

EVOLUTION OF THE INSTITUTION

On the surface the Institution appears much as it did six years ago. The five major departments retain their names and most of the staff members. However, there have been substantial changes. Four new directors have taken over, research programs have evolved, new equipment has been obtained, and major facilities have been constructed.

DEPARTMENT OF PLANT BIOLOGY

The changes at Plant Biology are particularly satisfying. Under Winslow R. Briggs the department has become what some consider the world's best center for plant research. He has built on solid foundations laid by his predecessor. For many years, C. Stacy French had conducted a small though well-regarded department. During his tenure, French attracted fellows and guest investigators,

many of whom were or became leaders in the field. He also provided leadership in creation and use of new instruments for plant research.

As the time for French's retirement approached, special thought was given to the opportunities inherent in plant biology. It was obvious that advances in plant biology might provide great benefits to a world seeking solutions to its problems of food and energy. The great agricultural research stations could be expected to conduct excellent studies on existing crops. For Carnegie, the optimal opportunities for research lay in long-term fundamental studies of plant biology that carry with them the potential for breakthroughs. Such new knowledge could be expected ultimately to lead the way to better plants and to better management of existing species.

For some years the biology of plants did not enjoy so intense a study as that devoted to other related sciences. The substantial funds available for medically oriented research had led to great advances in molecular biology and biochemistry. The emphasis was on studies of microorganisms or animals. But these large-scale efforts developed concepts, techniques, and powerful equipment applicable to plant research.

Briggs was fully aware of the possibilities. He was attracted also to the abundant opportunities for interaction with biology professors and students at Stanford University. It was clear, though, that to create an establishment commensurate with the opportunities would require extensive renovation of the laboratories and new construction. The necessary planning, design, and construction were completed with minimal disruption of research efforts. The resultant modern facilities are functional, versatile, and attractive to staff, fellows, and guest investigators. In addition to standard laboratory equipment for biochemical studies, the department has controlled plant growth chambers capable of maintaining a broad range of environments. The department shares a mobile laboratory with Stanford (complete with minicomputer) that facilitates *in situ* studies in diverse climatic areas. Special equipment is available at the laboratory for observations on the photosynthetic processes at time spans as short as 10^{-6} second. Other equipment is designed to measure the absorption spectra or action spectra of intact plant materials or of membrane preparations. The output of such devices is electronic, and they are programmed and their output is processed by an in-house computer that has time-sharing capabilities.

The research program at the department includes major activities that continue from the past—studies of the mechanisms of photosynthesis and physiological ecology. Briggs has brought a new program involving himself and others in the study of membranes. Membranes have a role in photosynthesis, and the temperature behavior of lipids of membranes is relevant to physiological ecology. Thus the three major thrusts of the department interact well together.

One measure of the overall quality of the department is its attractiveness to Stanford biologists and to guest investigators from elsewhere. In his current annual report Briggs lists the many people who are now finding the department a satisfying place for scholarship.

HALE OBSERVATORIES

Astronomers of the Hale Observatories continue to be pathfinders in the study of the universe and its contents. They are concerned with providing answers to basic questions: the age of the universe, the formation and evolution of galaxies and stars, and the nature of bizarre physical processes in x-ray sources, neutron stars, and black holes. These profound problems have justified the Institution's largest construction project in several decades—the new observa-

tory at Las Campanas with its 2.5-meter Irénée du Pont telescope. Staff astronomers are at the forefront in developing new instruments for measurement of the faintest and most remote objects that can be detected. Because optical astronomy can provide enormous amounts of detailed information about chemical composition, temperature, pressure, density, strength of gravity, electric fields, and magnetic fields in particular regions of stars, earth-based telescopes will continue to have a central role. Hale staff have interacted with observers studying other portions of the electromagnetic spectrum. They have also been leaders in developments that have extended the reach of telescopes.

New electronic devices detect and count individual photons. The ability of telescopes to detect dim and very distant objects is limited by a faint but ever-present airglow in the earth's atmosphere: That is, even when the telescope is pointed to areas of the sky where there are no stars, some light is received. With electronic detectors, it is possible to subtract the airglow effect when spectra are being recorded. The use of such electronic detectors extends the distance to which humans can measure the universe. By such means it will be possible to detect light from an object so distant that the light that reaches us began its journey 15 billion years ago.

For the Hale Observatories, one of the big developments of the past six years has been the creation of a major observatory in the southern hemisphere.

The Mount Wilson Observatory of the Carnegie Institution was the world's leader in astronomy for nearly four decades with its 1.5-meter and 2.5-meter telescopes. With the inauguration in 1948 of the 5-meter telescope on Palomar Mountain by the California Institute of Technology, a new powerful tool was made available to Carnegie staff through an arrangement in which Mount Wilson and Palomar were operated as a unit in what came to be called the Hale Observatories. With the passage of time, the telescopes at Mount Wilson lost some of their value because of an increase in scattered light from the metropolitan region.

If the Institution were to provide its share of facilities to the Hale Observatories, it would be necessary to add something new. The southern skies held relatively unexploited opportunities, and surveys showed that viewing conditions in north-central Chile were particularly favorable. Initial efforts to obtain outside support for a 5-meter telescope proved disappointing. However, a gift by Henrietta Swope and a later gift from the Crawford Greenewalts provided impetus to the building of an observatory on Las Campanas in the Norte Chico district of Chile. Facilities there include a 0.55-meter telescope owned and operated by the David Dunlap Observatory of the University of Toronto, the 1-meter Swope telescope, and the 2.5-meter Irénée du Pont telescope.

Into the du Pont telescope have gone the products of the genius of two of the world's most experienced designers and engineers—the optical skill of the late Ira S. Bowen and the mechanical expertise of Bruce Rule. The 2.5-meter du Pont telescope is smaller than, for example, the 5-meter Hale at Palomar, so it takes longer to collect the same amount of light. But its capabilities are unique among telescopes of its size. The du Pont telescope optics employ principles of design that make it possible to expose photographic plates 51 centimeters square, or 12 times the usable area of those employed with the 5-meter at Palomar. The focal length is the same as the Hale 5-meter, so the du Pont can reach objects as faint and distant as any other instrument on earth, although requiring more time. But because of the enormous size of the photographic plates in the du Pont telescope, it will be uniquely able to perform crucial astronomical surveys. It can perform surveys three times faster than the huge 5-meter Hale telescope by scanning much greater areas of the cosmos.

Spectrographic observations are crucial to studies of stellar chemical composition and evolution. To provide maximum efficiency for spectrographic analysis of light from the south polar region of the sky, a radically new coudé system has been designed that requires only three reflections of light instead of the usual five. Since at each reflection a considerable amount of light is lost, the new design will substantially increase the effectiveness of the instrument.

Another feature of the du Pont telescope is its electronic control system that employs programmable microprocessors. These devices represent some of the latest advances in electronics. The microprocessors of the telescope's electronic control system are used to set the telescope accurately and quickly, move the dome and the windscreen automatically, provide correct rates for driving the telescope, and assist the astronomer with data acquisition. Automated controls and sensing devices will permit much of the observing to be done remotely, with the astronomer in the control room. An integrated closed-circuit television system permits guiding on very faint objects.

With its exceptionally wide field for direct photography, the du Pont telescope is well adapted for searching for distant quasars. It is also well adapted for studying objects that are closer. Observers in the southern hemisphere have the advantages of studying regions of the sky that have not been so thoroughly examined as those of the northern. In particular, the Greater and Lesser Magellanic Clouds present special opportunities. They are our nearest galactic neighbors, and they contain very old stars, but they also contain very young ones. The Magellanic Clouds are very active regions of star formation.

The new telescope is becoming operational at a time of great challenges and opportunities for astronomy. The subjects are truly cosmic—events at the far reaches of the universe, events at the beginning of time, the creation and evolution of galaxies, the birth and death of stars.

GEOPHYSICAL LABORATORY

During the early years of this century, the easily available oil and mineral resources were heavily exploited. Most of the oil that was formed during hundreds of millions of years was consumed. At the beginning of this century, the copper ore being mined contained about 3% of the metal. Currently the average grade is about 0.7%. The degree of exhaustion of the high grades of various elements differs, but the overall picture is similar to that of copper.

Man will continue to turn to the earth as an essential source of raw materials. However, it will be necessary to employ much more advanced knowledge and technology to the processes.

The Geophysical Laboratory has been a leading source of new information about the earth. The late W. W. Rubey, one of the founders of modern geology and a trustee of the Institution, evaluated the work of the Laboratory in an article published in 1974 as part of a survey of major developments in earth sciences occurring in the last 50 years. In discussing advances in knowledge about the petrology of igneous and metamorphic rocks, Rubey cited the Geophysical Laboratory as having made perhaps the most far-reaching contributions through applications of principles of physical chemistry. He summarized his discussion of the Institution's work by saying

It is probably fair to state that the science of petrology has been made over by the results of experimental work at the Geophysical Laboratory and by [N. L.] Bowen's theory. Perhaps an even greater contribution of the Laboratory is one that extends beyond petrology into many

other fields of science. This is the demonstration that problems of seemingly hopeless complexity may be divided into simpler, more tractable parts and brought into the laboratory for analysis and solution.

In general terms the objectives of the Geophysical Laboratory are much the same as they were nearly 70 years ago. However, the specific research programs are entirely different, and they are carried out using different equipment. Indeed, a history of the laboratory would necessarily emphasize a continuing change of equipment, techniques, and interpretations, with many of the new tools invented and developed there. Especially during the past decade, there has been heavy and increasing use of electronics to better understand the processes involved in the formation and evolution of the earth.

Various kinds of analytical tools, such as the electron microprobe, Mössbauer equipment, chromatography coupled with electronic detectors, spectrophotometry, and micro x-ray crystallography, have shortened the time for determinations by factors of a hundred or more while diminishing the size of sample required by many orders of magnitude—in some instances by factors of more than a million.

Much of the analytical equipment utilizes dedicated minicomputers to program the analytical procedure and to record and analyze the results. Another important use of electronics is in the storage and retrieval and processing of the vast amounts of information produced by numerous workers. The rocks of the earth are many and they have been generated by a variety of processes from differing starting materials. Over the years many tens of thousands of chemical analyses have been performed on rocks in laboratories around the world. Information of this sort is now so voluminous and so widely dispersed as to make its retrieval and reduction by conventional methods grossly inefficient. Chayes has designed a computerized information system that efficiently scans a model data base containing 16,000 multicomponent analyses, and he is planning a much larger and more sophisticated world data base for igneous petrology.

Over the years, the Geophysical Laboratory has been a leader in the invention and application of high-pressure techniques for the study of minerals. Using a device that permitted accurate control of pressure and temperature, Yoder made many pioneering studies at pressures of 10 to 15 kilobars during the 1950s and 1960s. This pressure corresponds to a depth of 30 to 45 kilometers and to the region of many rock-forming processes. In 1960 Boyd and England developed a solid media press routinely capable of pressures of 50 kilobars. This device has been widely copied and used. During the last several years Mao and Bell have redesigned and extended the range of the diamond press that was originally developed by Van Valkenberg and others at the National Bureau of Standards. This year they were able to achieve a pressure of 1200 kilobars and to make routine measurements at 900 kilobars. They have accordingly been able to study behavior of minerals at pressures of the core-mantle boundary (2000–2500 km deep).

DEPARTMENT OF TERRESTRIAL MAGNETISM

Over the years a central thread of the work of the department has been the physics of the earth and its environs. In the early days, a major effort was devoted to study of the earth's magnetic field first by expeditions, including those of nonmagnetic ships, and then at magnetic observatories. The program was of considerable practical importance, but after the accumulation of several decades of data, scientific interest in the work diminished. These magnetic studies were halted when Merle Tuve returned to the department as director following his

very successful war work with the proximity fuze. Geophysical investigations of seismicity, radioactive dating, and cosmic rays were initiated, and some ionospheric studies were continued. A long-enduring program in low energy nuclear physics was carried out. In addition, a dynamic effort in biophysics was successfully launched and maintained. Interest shifted from the ionosphere to the new science of radio astronomy and to development of the Carnegie image tube for astronomical observations.

These broad programs of the department continued to progress following Tüve's retirement in 1966. The biophysics group made many fundamental contributions to molecular biology [see Roberts in *Year Book* 74]. Eventually, however, as the study of molecular biology matured, the DTM's biophysics program lost some of its distinctiveness. With reluctance the biophysics program was phased out.

In 1975 George W. Wetherill succeeded Ellis T. Bolton, who had followed Tuve as director. Wetherill was trained in physics, and his research had included geophysics. His current work on physics of the origin and evolution of the solar system fits well with other research activities in the department.

As the success of DTM's program has shown, a training in physics is particularly useful as a preparation for problem solving. Since the department is for the most part staffed by physicists, it is not surprising that they have invented, developed, or adapted many items of electronic equipment.

For example, two developments conceived by the radio astronomy group are still in routine use at radio observatories. The development of the multichannel line spectrometer only two years after the discovery of emission from interstellar neutral hydrogen enabled radio astronomers to study the entire frequency spectrum of a region without retuning the receiver for each frequency. The development of a traveling feed for large transit radio telescopes greatly increased the sensitivity of these instruments. Also, image intensifiers developed under the Carnegie image tube program were distributed to 34 observatories, and their worldwide use opened a new era in observational astronomy.

The DTM geophysics group has long been recognized for its development of instrumentation. In the last ten years two significant new instruments have allowed acquisition of much valuable new seismic data.

In the mid-1960s, Sacks designed a broad frequency band, high dynamic range seismograph system that for the first time allowed near-source recording of long-period seismic waves. These seismometers are now produced commercially, and special features of the magnetic tape recorder which enable stable low-speed recording have been copied by other seismologists as well as having been incorporated into commercial recorders.

Toward the end of the 1960s, Sacks, working with Dale Evertson from the University of Texas, developed a bore hole strainmeter, and it has now been demonstrated that this device reliably records earth strain at a sensitivity several orders of magnitude better than other strainmeters. Major use of this instrument is being made in the Japanese earthquake prediction program.

In the field of isotope geochemistry, the DTM group was one of the first to make use of minicomputers for automatic control and data acquisition in the operation of mass spectrometers. This development increased the efficiency and reproducibility of mass spectrometric operation enormously, and permitted the reduction of quantities of data which would otherwise have been prohibitively large. More than anything else, this made it possible to achieve the precise isotope ratio measurements needed to carry out the investigations of the sources of oceanic basalts by Hart and his collaborators.

DEPARTMENT OF EMBRYOLOGY

Few departments have changed as completely during the tenure of a director as did Embryology under James D. Ebert. When he came to the Institution in 1956, the department was located in crowded quarters in the Johns Hopkins Medical School. From his predecessors Ebert inherited a world famous collection of human embryos, a monkey colony, and a program largely geared to primate embryology. Though the department enjoyed a high standing in its field, the challenges inherent in the study of morphology of embryos had diminished. Ebert gradually changed the thrust of the research and moved the department to a new building on the Homewood Campus of Johns Hopkins. Today there are practically no vestiges of the earlier program. While the study of development remains a general goal, the approach to it is largely in terms of molecular biology. A typical major effort is one devoted to study of the structure, arrangement, and evolution of genes.

In his last report as director of the department, Ebert has described some of the changes that occurred during his tenure. A new director, Donald D. Brown, took over on October 1, 1976. It is too early to guess the direction in which the department will move. But evolve it will, for the new director has drive and enthusiasm, and his tastes are somewhat different from those of his predecessor. Moreover, the exterior environment is changing, and with it new opportunities will emerge.

The Year in Review

GEOPHYSICAL LABORATORY

Considerable information is available from geophysical, geochemical, petrological, and geological observations at or near the surface of the earth. But one of the most challenging and tantalizing mysteries is the nature of the deep interior of the earth.

The Geophysical Laboratory has been particularly active in furnishing the foundations for intelligent speculation by determining the behavior of minerals at temperatures and pressures prevalent in the interior of the earth. During recent years the Laboratory has been a leader in two such major programs. Boyd has led what now amounts to a sizable international effort to exploit the potential of nodule suites propelled upward in kimberlite pipes. These mineral assemblages, which may contain diamonds, originated at depths of about 200 km. In this year's report are presented the results of examination of nodules from South Africa, Siberia, and Colorado. These and earlier such studies were facilitated by the pioneering research at the Laboratory that produced geothermometers and geobarometers applicable to conditions at the site of origin of diamonds.

Another major program is being conducted by Mao and Bell in their experiments with minerals under great pressures (about 1000 kilobars) in their new diamond cell apparatus. One of the first steps in developing a physical model of the earth's deep mantle and core is to determine the physical properties of minerals and mineral assemblages likely to be there. Among the principal candidates are close-packed oxides and metals including SiO_2 , MgO , iron oxides, and metallic iron. For work employing the new cell, MgO and ϵFe were chosen. Both phases had been studied earlier by shock wave techniques, and it was useful to correlate those results with findings from static pressure measurements. Compressibility of MgO and ϵFe was measured in the new study at 900 kilobars. It was found that no phase changes occurred above 130 kilobars. There was agreement between the shock wave and static results. The data serve to set constraints on potential mineral properties to an equivalent depth in the earth of 2000 to 2500 km.

Exploration for ore minerals in 1900 was a simple matter. Prospectors roamed the hills and inspected outcrops of rocks. Later, economic geologists established empirical procedures based on observations that better guided deeper exploration.

They observed, for example, that many ores are found in relation to geologic structures. They also noted that such ores seemed to have been emplaced as a result of motion of fluids through permeable regions associated with breakages in the rock. A record of processes that have occurred is left in the rocks; because the fluids react chemically during passage. The nature of the reaction is, of course, governed by the chemical content of the fluids and the physical conditions at the time of the reaction. Economic geologists have long used the products of such reactions as a guide for seeking ore, but there has been no solid theoretical base for systematizing field observations.

This year Frantz and Mao made considerable progress toward such a theoretical framework. They developed a general mathematical model to predict quantitatively the mineral sequences that occur by mechanisms known as intergranular diffusion and infiltration, and this year they solved the equations describing the thickness of zones and the relative directions of movement of the zone boundaries. Of particular importance, their theory aids in deducing the direction of transport of the various species in solution. The model accommodates variable permeabilities, diffusion constants, infiltration rates, and any number of components.

The model has yet to be applied to natural ore deposits; but they did show its application to the system $\text{CaO-MgO-SiO}_2\text{-H}_2\text{O-CO}_2$. The mineral zone sequences were found to be entirely dependent on the mobilities of the various diffusing species. The lack of data on diffusion constants will, for the moment, retard application of the theory. Eventually, however, it will be necessary to observe only the minerals in the end zones and the thickness of the zones. By combining these data with the diffusion constants determined in the laboratory, it will be possible to predict the mineral content and thickness of the intermediate zones.

The behavior of minerals containing the abundant oxides (SiO_2 , Al_2O_3 , MgO , Na_2O , CaO , and FeO) is extremely important to the understanding of earth processes. These common minerals have valuable but limited usefulness as indicators of earlier events in the evolution of igneous rocks. A basaltic lava can arise from a broad range of original ingredients. In contrast, trace elements can, in principle, provide much sharper diagnostic tools and they are also of interest because of potential economic value. The behavior of a given trace element is partly governed by the major components of the rocks or magmas with which it is associated. If one or more of the elements present have ionic radius and valence similar to that of the trace element, the trace element can readily enter a crystal structure as proxy for the abundant element. When the radii and charge differ, substitution becomes more difficult and complex. A particularly interesting set of trace elements are the rare earths. For the most part these have the same valence (3) but their ionic radii differ systematically. For more than a decade it has been known that the rare earths are fractionated differently when magmas are formed or are partially crystallized. But few attempts have been made at calibrating trace element partitioning within the range of natural abundances. Mysen has now developed a general method for measuring their fractionation. In one application he studied the partitioning of samarium between olivine, orthopyroxene, and a hydrous silicate liquid, using the number of beta-tracks generated by samarium-151 as a measure of the amount of samarium present in the various phases. By this means he was able to determine accurately the concentration of samarium at levels as low as parts-per-billion.

Mysen found that only approximately 1 ppm Sm can enter olivine and orthopyroxene before the activity coefficients of samarium become dependent on the samarium concentration. That is, the trace element concentration range of be-

havior according to Henry's law is limited; the range is 25% larger in orthopyroxene than in olivine. This concentration range in both minerals increases about 15% per 100°C. He also found the crystal-liquid partition coefficients to increase with pressure; yet increasing temperature results in increased partitioning of samarium into the olivine relative to liquid, whereas the partitioning decreased in orthopyroxene relative to liquid. These results are already leading to a more definitive understanding of what constitutes trace element behavior. The determination of partition coefficients between crystals and between crystals and liquid under known conditions will provide a novel method, presumably independent of major components, for ascertaining the conditions of formation of igneous rocks.

DEPARTMENT OF TERRESTRIAL MAGNETISM

During the past decade we have learned a great deal about the origin and evolution of the earth. We are now reasonably certain that the solar system was formed 4.6 billion years ago. The oldest rocks that have been dated on earth are about 3.7 billion years old. From that time to the present, rocks of different ages were formed, attesting to a restless, changing earth. What of the gap between 4.6 b.y. and 3.7 b.y.? If the earth were our only source of specimens, we could not hope to learn much about the hiatus. But space exploration has brought information from other bodies such as meteorites, Mercury, Mars, and especially the moon. As a result of a detailed examination of lunar samples, events on the moon from 4.6 b.y. to 3.7 b.y. ago are now fairly well known. The moon, though a comparatively small body, was at least partially molten very early. It is generally agreed that the necessary heat was derived from gravitational impacts. A large body such as the neighboring earth must have had a similar history, with early melting. The lunar samples also provide information about large-scale impacts that occurred about 4.0 b.y. ago. Thus there is now a reservoir of information about the solar system that merits study and interpretation. Wetherill has devoted considerable attention to this matter and has arrived at a model for the accretional history of the solar system that is somewhat different from the currently accepted view.

It is commonly believed that a very rapid, 10^3 to 10^4 year time-scale is a rather firm constraint on the formation of the moon, and by inference, of the terrestrial planets as well. The principal observational basis for this is the evidence for very early chemical differentiation of the moon, coupled with thermal history calculations that purport to show that this requires rapid accretion to prevent the limited gravitational energy of accretion from being wasted by radiation into space. If true, such a constraint would be very useful in limiting the range of permissible speculation. If false, it would be an obstacle to understanding what really happened.

The problem is that all serious quantitative theories of planetary accretion lead to time-scales of approximately 10^8 years, a discrepancy of 4 or 5 orders of magnitude (the principal contributors in this area are V. S. Safronov and his colleagues at the Institute for the Physics of the Earth in Moscow). Safronov and Ruskol (his wife) have pointed out that the presence of large (about 100 km) accreting bodies could overcome the thermal problem if the heat were buried below the large craters resulting from their impact. Unfortunately, a quantitative application of Safronov's theory leads to an initially cool moon.

During the past year Wetherill has pursued this problem, using a stochastic

simulation of the solar system based on earlier work by Öpik and Arnold. This leads to much larger bodies and higher velocities than those found by Safronov, and consequently much greater accretional energy—now primarily the kinetic energy of heliocentric motion of the bodies rather than the gravitational energy resulting from falling into the gravitational “potential well” of the moon. These differences arise from the “lumpiness” of the planetesimal distribution and particularly the presence of the biggest lump, the embryo of Venus accreting nearby. From this point of view, the initial temperature of the moon and planets would be high on any accretional time scale, and the range of permissible thermal and petrological models greatly increased.

Since the beginning, much of the research of the Department of Terrestrial Magnetism has been strongly oriented toward global problems of the earth and its history. Today a major program at the department is the study of the earth's mantle, using the most advanced techniques of geochemistry and geophysics.

In the first few years of the “plate tectonic revolution” it seemed likely that continents were a superficial feature of the earth, riding along on lithospheric plates similar to those in oceanic regions. This view has been changing, as a consequence of several developments: (1) Surface wave dispersion down to the wavelength-limited depth of 200 km showed the absence of a low velocity zone under South America. (2) Sacks and Okada have shown that beneath continents Q and seismicity are high down to 350 km but decrease below that depth. (3) Isotopic and geochemical data on mantle-derived continental rocks show that heterogeneities are preserved on a time-scale long compared to that of rates of continental drift.

Because of these developments it is now believed that continental lithospheres are fundamentally different from those below oceans, and some workers doubt that there is any asthenosphere at all beneath continents.

This year Sacks and Snoke report direct evidence for a lithosphere-asthenosphere boundary under South America at a depth of 400 ± 30 km associated with a transition zone only a few kilometers thick. This evidence is in the form of a seismic arrival that comes in between the p and s arrivals, which is interpreted as resulting from an incident s phase converted to compressional waves at a boundary. Unlike other models, this one fits all aspects of the data, such as amplitude ratios of the different components. First-motion studies show the polarity of the boundary—low velocity below, high velocity above. Thus the bottom of a continent has been found, replacing the Moho, which has been known to be superficial since acceptance of sea floor spreading and continental drift a decade ago.

In some astrophysical work, Ford, Peterson, and Rubin report very high resolution spectra of an elliptical galaxy, spectra of such quality that at first glance one would think they were those of a star rather than a galaxy. Previously, high resolution spectra had been obtained for spirals in which the high abundance of excited gas results in prominent emission lines. In contrast, these emission lines are absent in the gas-poor elliptical galaxies; these new spectra are absorption spectra, resulting from the integrated absorption of the stars in the galaxy. From these spectra, velocity fields, a preliminary mass model, and a mass/light ratio as a function of radius have been calculated. This development opens up for observation the chemical and dynamical history of elliptical galaxies, a prerequisite for progress in understanding the reasons galaxies occur in two such different forms. This development resulted from taking advantage of the high spatial and spectral resolution of the 4-meter Carnegie image tube spectrograph at Kitt Peak Observatory. The spectrograph is also being used to study absorp-

tion spectra of other galactic features, such as the stars in the central bar of barred spiral galaxies.

HALE OBSERVATORIES

Earlier in this report I discussed the approaching completion of the Las Campanas Irénée du Pont telescope and described some of its novel features. Obviously, design and construction of such an instrument places heavy burdens on staff, on some more than others. But the new construction in Chile was only one of the tasks to be addressed. The other Hale telescopes must be continually maintained and upgraded. Electronic control systems have evolved. In addition, the use of electronics at the observing end of the telescope continues to increase, and Hale staff are necessarily involved in the design, development, testing, and use of such equipment. Added to all this are time-consuming tasks such as allocation of observing time and dealing with 60 or more guest investigators.

In spite of all these burdens, which are borne by a relatively small staff, the Hale Observatories are remarkably productive of advances in astronomy.

The new electronic devices create opportunities, and these are being exploited. A major new frontier has been created by instruments that can count individual photons. Sky background can be subtracted so that very distant, faint objects that had been inaccessible can now be studied.

There are now available digital or linear photoelectric devices capable of precise photometry on large numbers of picture elements within an optical image. Such devices are equally important in the focal plane of a telescope and at the output end of a spectrograph that is attached to the telescope. But the photographic plate, especially with the most modern emulsions of high information content and optimum color sensitivity, continues to be improved and is indispensable, particularly for wide-angle recording.

At the Hale Observatories, Sandage and Kristian, using the photographic method, and Gunn and Oke, using an image tube, are reporting the discovery of impressive numbers of new faint clusters of galaxies. Such clusters are important because the brightest galaxy in a cluster has a standard luminosity very nearly the same for any cluster. From this information the relative distances to such clusters can be derived, and if the redshift of several galaxies in each cluster can be measured with the spectrograph, new points in the Hubble diagram of redshift versus distance can be plotted.

Not only are dozens of distant clusters of galaxies being found, but the production of spectra and the measurement of redshifts of galaxies in them is proceeding at a record rate. For this work Sandage, Kristian, and Westphal are using an SIT (silicon intensifier target) Vidicon on a prism spectrograph at the 5-meter telescope, while Gunn and Oke are using the SIT-Vidicon with a grating spectrograph.

Most of the new redshifts being measured are greater than $z = 0.2$ and a substantial fraction have $z > 0.4$. Each of these galaxies is of small angular extent, and most are much fainter than the uniform light of the sky (airglow and zodiacal light) that overlies them. Spectroscopy involves subtracting electronically the spectrum of the sky from that of the object plus sky. The principal limitation now is not measuring the spectra but finding faint candidates and positioning them on the slit. Observing depends upon low-level closed-circuit TV systems for these operations, which formerly involved the much more difficult technique of making blind offsets from nearby stars.

Sandage has made an important discovery of substantial quantities of dust in regions lying above the galactic plane. Though the finding itself was serendipitous, it illustrates the benefits of intensive, long-term observational programs of the kind the Hale Observatories can sponsor. During the last five years while looking for remote clusters of galaxies, Sandage surveyed extensively the sky in the region of the north and south polar gaps. During that survey he noted occasional high latitude fields that have bright nebulous regions often in patterns correlated over distances of degrees. He was able to show that these structures are reflection nebulae whose illumination comes from our galactic plane.

Schmidt has analyzed spectroscopic and photometric observations of a complete sample of quasi-stellar sources in the 6-cm National Radio Astronomy Observatory survey. The value of V/V_{\max} , which measures the position of an individual source within the available volume, appears to be correlated with the radio spectral index. Sources with steep radio spectra have a mean V/V_{\max} around 0.7, similar to values found previously for quasars in the 3C catalogue of radio sources and the revised 4C catalogue, most of which have steep radio spectra. This implies that the space density of these quasars rises steeply with redshift (declines with cosmic time) by a factor of around 1000 to a redshift of 2.5. In contrast, quasars with flat or inverted radio spectra have a lower mean value of V/V_{\max} around 0.52 ± 0.05 (m.e.), consistent with a uniform distribution in space.

Searle is making a comparative study of the chemical history of the globular cluster systems of the Galaxy, of M31, and the Magellanic Clouds. A more sensitive method of determining the metal abundance in individual red giants belonging to a cluster has been developed. In this report year Searle and Zinn calibrated the new system and began a program to determine the metal abundance of all globular clusters for which color-magnitude arrays are available. They are especially interested in remote clusters and other stellar systems on the fringes of the Galaxy.

In a related investigation Searle has obtained low resolution spectrophotometric scans of 70 of the globular clusters in M31. So far all the observations appear to be consistent with the idea that the M31 globular clusters differ from one another in one parameter only—presumably the metal abundance. However, there are differences between the globular clusters of M31 and the Galaxy, and those of the Magellanic Clouds. There are also important differences between the clusters of the Small and Large Clouds.

DEPARTMENT OF PLANT BIOLOGY

In the past ten years very powerful techniques have been developed to study the structure and action of DNA. Substantial contributions to this important effort have been made by Carnegie staff. The work of Britten and others at DTM and of Brown and others at Embryology has been outstanding. Their work has largely been devoted to animal DNA.

These techniques are now being applied to plants by Thompson and colleagues at Plant Biology. Thompson reports this year on an analysis of the sequence organization of pea DNA. The pea genome has a pattern much like that of the toad *Xenopus*, with single-copy DNA sequences less than 3000 nucleotides long interspersed with repetitive sequences. It is already clear that the study of plant DNA will be a powerful tool in the elucidation of evolutionary relationships in plants. A typical question is the origin of C_4 photosynthesis in *Atriplex* (saltbush) and the DNA sequence comparison between C_3 and C_4 species of that genus.

Using techniques available for examining DNA, Rogler, a fellow, and Thompson have made a useful contribution to knowledge of crown gall tumors and to the controversial topic of recombinant DNA.

Wounded plant tissue infected with *Agrobacterium tumefaciens* will, under appropriate conditions, form tumors that have several physiological properties in common with mammalian cancer. These properties include non-self-limiting growth on synthetic medium devoid of hormones and the inability to differentiate into organized, functional tissue in response to treatments causing such differentiation in normal cultured cell lines. Crown gall tumor cells retain these properties when cultured in the absence of the inciting organism and, when grafted into healthy plants, produce tumorous overgrowths.

Recently it was discovered that all pathogenic strains of *Agrobacterium tumefaciens* contain one or more large plasmids¹ and that loss of the plasmid results in loss of virulence.² On the other hand, transformation with plasmid DNA results in acquisition of virulence by the strain acquiring the plasmid. These two lines of evidence strongly support the hypothesis that the plasmid is a necessary genetic element for virulence in *Agrobacterium*.

Rogler and Thompson have described changes in plasmid DNA sequences in *Agrobacterium* during either the loss or the acquisition of virulence. In their report they discuss an instance in which a large deletion in the plasmid genome is associated with loss of virulence. They also present evidence that acquisition of virulence may involve replacement of a preexisting avirulent plasmid with a virulent plasmid derived from another strain of *Agrobacterium*.

Rogler and Thompson do not attempt to relate their findings to the current controversy over DNA work—perhaps wisely so. One can choose to view the results with alarm or with equanimity. Today much recombinant DNA work uses plasmids of *Escherichia coli*. The fact that a change in a plasmid of another bacterium gives rise to crown gall tumors argues for caution when producing new kinds of plasmids in *Escherichia coli*. A contrary view is that the pathogenicity of *Agrobacterium tumefaciens* arose naturally and doubtless is the result of innumerable experiments performed by nature. It may well be true, as some argue, that among the countless experiments on DNA performed by nature everything and every possible combination has already been tested.

The physiological ecology group continues to make good progress in understanding the factors that enable plants to cope with stress and thus to exist under extreme conditions of temperature, moisture, light intensity, and other variables. The general approach is to combine field observations using mobile equipment with laboratory studies. When plants having unusual characteristics are noted in nature, their photosynthetic machinery can be studied in the laboratory.

In the current report, Mooney, Björkman, Ehleringer, and Berry describe some of their efforts in studying the native flora of Death Valley, California. Although Death Valley is often identified as one of the hottest and driest environments on earth, these extremely high air temperatures (exceeding 50°) occur only in the summer. In winter, relatively cool temperatures (20°C) predominate, and in spring and fall air temperatures are often around 30°C. Consequently,

¹ Zaenen, I., N. van Larebeke, H. Teuchy, M. van Montagu, and J. Schell, *J. Mol. Biol.*, **85**, 109–127, 1974.

² van Larebeke, N., O. Engler, M. Holsters, S. van den Elsaker, I. Zaenen, R. A. Schilperoort, and J. Schell, *Nature*, **225**, 169–170, 1974.

Watson, B., T. C. Currier, M. P. Gordon, M. D. Chilton, and E. W. Nester, *J. Bacteriol.*, **123**, 255–264, 1975.

Death Valley provides a broad variety of thermal environments and a unique opportunity to study the ways plants adapt to these seasonal thermal regimes.

Utilizing the mobile laboratory, the photosynthetic capacity of plants was measured during the winter (January), spring (March), summer (late May), and fall (October) seasons. Plants studied included a winter annual (*Camissonia claviformis*), a summer active herbaceous perennial (*Tidestromia oblongifolia*), and two evergreen shrubs (*Larrea divaricata* and *Atriplex hymenelytra*).

Under natural conditions the two evergreen shrub species were photosynthetically active throughout the year, although their maximum photosynthetic rates were considerably below those of the two that hold their leaves for a short period. The two herbaceous species, *Tidestromia* (C₄) and *Camissonia* (C₃), have extremely high maximum photosynthetic rates; yet their physiological activities are restricted for the most part to a single season.

The C₃ winter-active annual *Camissonia* germinates following heavy winter rains and can, under certain conditions, complete its entire life cycle in six weeks. This short-lived species has a remarkable capacity to capture sunlight and fix carbon. *Camissonia* converts incident photosynthetically active radiation (400–700 nm) to chemical energy with an efficiency of 8.5%. This is possible because of the lack of light saturation at midday irradiances, a feature that is also characteristic of *Tidestromia*. The *in situ* midday photosynthetic rate of *Camissonia* was higher than the rate measured for such productive crop species as corn, sorghum, and sugar cane.

Earlier studies had identified *Tidestromia oblongifolia* as a plant with a high rate of photosynthesis at elevated temperatures. During the year Björkman, Boynton, and Berry participated in studies to determine the thermal stability of key components of the photosynthetic machinery responsible for the marked differences in temperature tolerances between thermophilic higher plant species such as *T. oblongifolia* and cool-temperate plants such as *Atriplex sabulosa*. As reported last year, the two C₄ species differ in their high temperature stability in several respects, including the maintenance of semipermeability of the cell membranes, respiratory activity, and photosynthetic activity. While onset of high-temperature damage differed by about 10°C in the two plants, photosynthesis was affected at considerably lower temperatures than either respiration or membrane semipermeability.

This year they studied the effect of temperature on the quantum yield for photosynthesis by intact leaves with its effect on photosystem I and II activities; ribulose 1,5-diphosphate carboxylase activity (the C₃ enzyme for CO₂ fixation); phosphoenolpyruvate carboxylase activity (the C₄ enzyme for CO₂ fixation); and heat coagulability of soluble proteins as a measure of irreversible denaturation. It is clear that the best fit with thermal inhibition of photosynthesis in both cases is with system II activity. In addition, however, there were interesting differences in heat stability of the C₃ enzyme from the two plants, suggesting that not just lipids but proteins may differ between plants adapted to high temperatures and those adapted to low temperatures.

DEPARTMENT OF EMBRYOLOGY

James D. Ebert, the retiring director, leaves this department after having brought it successfully through a major era of evolution from classical embryology to a new form of developmental biology heavily based on molecular biology.

The two major classes of studies at this department are (1) broad-ranging

fundamental research on DNA—its structure in chromosomes and its behavior as genetic material and (2) researches aimed at better understanding of the structure, behavior, and interactions of membranes. The investigations of DNA are progressing very well and the department has compiled an impressive record of achievements in this field. The studies of membranes are a newer, evolving activity in the department which have already been fruitful and which have great potential. The staff investigators (Fambrough, Muller, and Pagano) are young and have been brought together fairly recently. Of the three, Fambrough has been at the department longest and has accumulated an impressive record of accomplishment in studies of nerve-muscle interactions with emphasis on the acetylcholine (ACh) receptors in skeletal muscle fiber membranes. In a series of articles Fambrough and his students and colleagues report on the appearance of ACh receptors during muscle development, the production and incorporation of ACh receptors into the surface membranes of myotubes and their subsequent degradation, the clustering of ACh receptors at newly formed neuromuscular junctions both *in vitro* and *in vivo*, the number and distribution of ACh receptors in adult rat skeletal muscle fibers, and the time course of change in these parameters following denervation. They are continuing to explore physiological aspects of receptor function, examining further the biosynthesis and degradation of ACh receptors and obtaining more accurate estimates of ACh receptor density on denervated muscle fiber membranes.

In this year's report, Fambrough and his student Peter Devreotes present a model for the major events in receptor metabolism. The protein subunits that are to form the ACh receptor are synthesized inside the muscle cells and are rapidly assembled into receptor units in the cytoplasm of the muscle cells where they constitute a "precursor pool." The average residence of a new receptor in the precursor pool is 2 to 3 hours. Receptors are transferred from this pool to the surface by an energy-requiring process and are then able to function. The average half-life of an ACh receptor in the plasma membrane is 22 hours. Receptors are degraded by an energy-requiring process that involves the internalization of the receptor and transport to secondary lysosomes and then proteolytic destruction.

In his continuing professional development, Pagano illustrates one of the principles on which the Institution is based: Andrew Carnegie's advice that the Institution seek out talented individuals and support them.

Ebert followed this course in choosing and fostering Pagano. Four years ago, when this young scholar came to the department, his background was that of a physical chemist who had worked with some nonliving model membrane systems. He has since acquired substantial experience in cellular biology, and he and his colleagues have been using artificially generated lipid vesicles to perturb membrane components in living cells. In the report of the director they present findings on the interactions of phosphatidyl choline vesicles with murine lymphocytes, and the physiological consequences of these interactions. Pagano and postdoctoral fellows Huang and Ozato have shown that the pathways of vesicle-cell interactions enumerated in previous reports (vesicle-cell fusion, adsorption, and lipid exchange) are exquisitely sensitive to the molecular composition and physical properties of the artificial vesicles. In the lymphocyte system, the resulting membrane perturbations lead to altered surface properties and greater proliferative activity of these cells when stimulated by various mitogens and antigens.

Muller, the most recently added staff member, is tackling the major question of how single nerve cells are organized into a nervous system. He is especially looking at the pathways neurons take to reach their targets. For this purpose he

has been studying activities in the nervous system of the leech. This creature has a very simple nervous system, yet its neurons behave in many ways like the neurons of higher animals.

Neurons in this segmented worm are grouped 350 together to form essentially identical ganglia that are linked in a chain by axon bundles; each ganglion mediates the reflexes and controls the behavior of its segment. It has been possible to monitor electrical activity from within single sensory and motor neurons with microelectrodes and to correlate the physiological activity of functionally identified neurons with their characteristic shape and position within each ganglion. By recording from pairs of neurons, one can trace synaptic connections, which have been found to be surprisingly uniform and in that sense predictable between specific neurons.

In his current report, Muller describes the structural details of chemical synapses, delineates their arrangement on sensory neurons, and explores the sprouting of sensory neuron terminals.

Staff members active in DNA research include Brown, Dawid, Reeder, and Suzuki. In a series of investigations inspired by Brown and Dawid, this group together with fellows and guest investigators have made a significant impact in developmental, molecular, and evolutionary biology. Studies of "developmental genetics by gene isolation" have led to new and brilliantly successful approaches to fundamental questions in development. The department has originated and exploited techniques for gene purification. Studies of "gene anatomy"—the structure and arrangement of genes—have resulted in new insights into the mechanism by which multiple tandem genes evolve together.

Brown has a long-term goal of reassembling the macromolecules that enable DNA to be transcribed with fidelity in the living cell. In this way he hopes to elucidate the control mechanisms of animal genes. For this purpose he and his colleagues are now concentrating on the family of genes from *Xenopus* which code for the small RNA molecule of ribosomes termed 5S RNA.

This year Brown's group reports progress along several lines. The "transcription unit," that is, the region of the *Xenopus* DNA that is transcribed into 5S RNA in the living cell, is relatively simple—only 120 base pairs long. Moreover, the form of RNA polymerase that transcribes this gene in vivo has been identified. The fact that the mature RNA transcript does not appear to be derived from a higher molecular weight precursor is especially important: It means that the true initiation site of transcription from 5S DNA is known. Therefore, one can detect faithful transcription when it occurs in vitro.

Three different kinds of 5S DNA have been cloned in *E. coli* by means of the new recombinant DNA methodology, thereby providing an order of magnitude more material to work with and permitting the careful examination of a single repeating unit of a tandem gene family. The "restriction maps" of these cloned DNAs—the sites where they are cleaved by certain restriction enzymes—are described by fellows Jeffrey Doering and Scott Emmons. Emmons is attempting to develop an assay for proper transcription. Fellow Nina Federoff is exploring DNA sequencing methods to determine the exact nucleotide sequence in the spacer regions of 5S DNA, particularly those regions adjacent to the initiation site of the gene.

DNA structure continues to hold the attention of several staff members and fellows. Reeder and Dawid, along with fellow Peter Botchan, report on the structure of nontranscribed spacer regions in *Xenopus* ribosomal DNA, based on studies using cloned fragments of rDNA generated with the restriction endonuclease EcoRI. Fellow Peter Wellauer and Dawid, a staff member, have under-

taken the first stages of a study of the ribosomal DNA of *Drosophila*; Dawid and his colleagues are cloning *Xenopus* mitochondrial DNA; and Carnegie fellow Ohshima and staff member Suzuki are attempting to clone the silk fibroin gene.

In all these studies, the department has adhered to the safety standards proposed by the Asilomar Conference on Recombinant DNA.

EDUCATION

To an unprecedented extent this country has become a nation of the here-and-now with a great part of its efforts and resources devoted to instant gratification. One of the few but important investments we make for the future is in education. For most people, formal education stops at graduation from college or before; comparatively few of these go on for advanced degrees in the sciences to form the cadre from which our future leaders in science and technology will emerge. But of the cadre only a fraction achieve creativity. After twelve years of primary and secondary schools and four years of university, most young people have mastered the memorizing of facts, have developed some judgment and some synthetic abilities, and have arrived at a personal identity. But the effort needed to become a creative scientist and to establish a professional identity is far more demanding than the struggles of adolescence. Among other things, what is involved is a metamorphism from a fact-accumulating to an idea-producing organism—a change from depending on the direction of others to confidently relying on one's own judgments and initiatives. The last two predoctoral years and the first three postdoctoral years are the critical period. During that time only those few who achieve the metamorphism are launched on a productive career. There is evidence to show that a crucial factor in the outcome is the intellectual environment in which the young scholar is immersed. At the Carnegie Institution we have diligently sought, and I believe we have succeeded in providing, optimum circumstances for the metamorphism of our fellows. In turn we feel that our fellowship program is one of the best kinds of investment that the Institution and the nation makes for the future.

Each year the departments of the Institution makes contributions to knowledge that win for them continuing recognition as leaders in their fields. At the same time staff members enjoy a high reputation for innovation. This aura of success attracts young scholars, many of whom seek to associate with experts in their chosen fields and to savor the excitement and intellectual growth that a creative group fosters. Since the departments can choose from among many excellent candidates, the quality of our predoctoral and postdoctoral fellows is excellent. They merit careful tuition and fostering, and they get them.

An important factor is the Institution's policies with respect to staff and fellows. Staff members are expected to participate actively and personally in research and teaching. They do not sit at command posts in offices while others work for them. They devote almost all their time to scholarly activities with few interruptions for administrative activities. Thus they are highly available for discussions. Since the ratio of staff to fellows is about one to one, the young scholars can have all the consultation and instruction they want. The situation is a modern version of the ideal enunciated nearly a century ago of professor and student sitting on a log discoursing together.

Optimal intellectual growth of fellows is promoted by another policy of the Institution. They are encouraged to pursue projects of their own choosing, and

they are given the kind of back-up in equipment and supplies that is enjoyed by staff members.

The precise patterns of training differ from department to department, reflecting the needs and opportunities of the respective fields of inquiry. However, some general patterns prevail throughout the Institution, and these are outlined and illustrated in an essay on education in the Department of Embryology that was prepared for this report by the retiring director, James D. Ebert. His comments follow:

For the past two decades training has been an integral part of the department's program. It was clear in 1956, as the department prepared to embark in new directions in molecular developmental biology and genetics, that even if ample funds and space were available immediately to undertake all the tasks that had been set, the scientific talent was not. The world's pool of able developmental biologists then was small. President Haskins and the director agreed that the catalysis provided by young minds—graduate students and postdoctoral fellows—would be a vital ingredient in the shaping of these new fields.

The wisdom of that decision has been demonstrated repeatedly. A glance at today's staff tells a part—but only a small part—of the story. Director-designate Donald Brown and staff members Igor Dawid, Douglas Fambrough, Ronald Reeder, and Yoshiaki Suzuki all joined the department initially for training. Thus, students become teachers and they, in turn, set standards of excellence for new generations of students to follow.

Douglas Caston, Professor and co-Director of the Developmental Biology Center at Case Western Reserve University, emphasized this point recently when he wrote "The experience I gained as a fellow [at Carnegie] has been the major force in shaping not only my personal career but in my helping junior colleagues shape their careers."

The department's purpose in offering its training program is to encourage the development of research scientists. First consideration is given to students who appear likely, by their intellectual gifts and intentions, to contribute to the advancement of the field whether in biology or in medicine. The previous training of applicants, whether in embryology, molecular biology or genetics, pediatrics or physics, may be of secondary importance, preference being given to the most promising students. Thus the department's program has had a profound impact not only in molecular developmental biology but in the clinical and mission-oriented fields that draw from the same spring. Caston is a molecular development biologist, yet his experience is matched by that of Glenn Rosenquist, one of the nation's leading students of cardiology and birth defects, now Professor of Pediatrics at the University of Nebraska Medical Center, who wrote "The two years I spent at Carnegie Institution were probably the most important years of my entire career."

Although over the years opportunities have been provided for the training of undergraduate students of exceptional promise, most of the department's teaching has been focused on graduate students and postdoctoral fellows. It is at the graduate and postgraduate levels that the department's unique resources—both human and scientific—can have their greatest impact. Several generations of fellows have written about the department's unique intellectual climate. The department provides well-organized and well-equipped laboratories where, in Dorothea Rudnick's words, "Everything peripheral [is] taken care of." In such an environment the most promising young people can be afforded the

opportunity to exercise and extend their abilities, enabling them to take their critical steps toward independence.

A listing of the department's graduate students and postdoctoral fellows constitutes a veritable "Who's Who" of developmental biology. Even a cursory glance reveals Carnegie fellows teaching and carrying forward their research at Harvard, Princeton, Brown, and Rockefeller Universities; at Virginia, Emory, Case Western Reserve, and Washington University, St. Louis; at the Universities of California (Berkeley), Kyoto, Tokyo, and London. They are working actively in departments of biology, in schools of medicine, and in an enormous variety of both basic and clinical research institutions.

Thus far we have emphasized the "products" of training, that is, the students themselves. Yet there is another factor to be considered: The greatness of the department's contribution to science can itself be attributed in part to its insistence that teaching and research are inextricably interwoven. We spoke earlier of the catalysis provided by young minds. The truth of that observation is reiterated year after year in the department's Annual Reports. The interaction between staff member and student is truly reciprocal, with students being an intimate part of some of the department's greatest achievements. The classic demonstration of the role of the nucleolus in the synthesis of ribosomal RNA was provided by a staff member, Brown, working with a fellow, Gurdon. Similarly, two fellows, Yoshiaki Suzuki and Patrick Gage, worked closely with Brown in the isolation and characterization of the gene for silk fibroin. Fambrough's far-reaching studies of the acetylcholine receptor sites in muscle have been advanced through the contributions of graduate students Hartzell and Devreotes. Fellow Peter Wellauer, working with Brown, Dawid, and Reeder, has led the way in elucidating gene structure.

The crucial nature of the intellectual climate needed for the training of young investigators is emphasized in our earlier expression "steps toward independence." Each student or fellow must be considered an individual. It is difficult, some may say impossible, to teach another individual how to do research except by example. There must be a special interplay between student and preceptor. The student or fellow must be afforded an ample opportunity to, in the words of former fellow Malcolm Steinberg, now Professor of Biology at Princeton University, "follow his own nose." Steinberg went on to say "The trail I picked up as a fellow in the Department of Embryology has broadened into a significant field of investigation now pursued by many scientists the world over." Turning again to the clinical side, Gilbert Greenwald, Professor of Obstetrics and Gynecology at the University of Kansas Medical Center, wrote "The freedom that I had to pursue a number of my own ideas gave me the confidence to think that I could embark on my own career as an independent and . . . imaginative investigator. I believe the last point is the most important objective to be gained from any postdoctoral experience.

LOSSES . . .

I am sorry to report that William I. Myers died in January. For 27 years the board of trustees benefited from the insight and knowledge he acquired during a career of distinguished service in government and education.

As one of President Roosevelt's top agricultural aides from 1933 to 1938, Dr. Myers established and headed the Farm Credit Administration. He also

served as president of the Federal Farm Mortgage Corporation and the American Farm Economics Association. In addition, he was director of the Federal Surplus Relief Corporation and the Commodity Credit Corporation.

In 1938 Dr. Myers accepted the chairmanship of the Department of Agricultural Economics at Cornell University. He became dean of the department in 1943 and held that post until his retirement in 1959. He was director of the Eisenhower Exchange Fellowships from 1953 to 1969 and was a trustee of the Agricultural Development Council from 1954 to 1971. He was also a trustee of the Rockefeller Foundation (1941-1957) and later served on its Board of Consultants for Agricultural Sciences until 1965.

At home in New York State, he was part of the Science and Technology Foundation and a member of the Council of Economic Advisers and a director of the Association for Crippled Children and Adults of New York. Dr. Myers was a director or trustee of six companies as well as Marine Midland Banks, Inc., and the New York State Gas and Electric Corporation.

Another loss to the Institution is Berwind P. Kaufmann, the last director of the Department of Genetics (1960-1962), who died in September 1975. After distinguishing himself as a professor at Southwestern College and at the University of Alabama, he joined Carnegie Institution in 1936 and remained with us until our research in genetics was phased out in 1962.

At the department, Dr. Kaufmann's cytological and cytogenetic research made important contributions to the field, among them the pioneering discovery that chromosomes contain double spiral bands and the first demonstration of interchange between X and Y chromosomes. His studies indicated the association of RNA with a histone-type protein and of DNA with a tryptophane-rich protein many years before confirmatory biochemical data were obtained. He also studied the effects of radiation, especially on chromosomes, and was a member of the National Academy of Sciences' Committee on Genetic Effects of Atomic Radiation.

After retiring from the Institution, Dr. Kaufmann continued his genetics research at the University of Michigan, Ann Arbor, as professor of zoology and botany and senior research scientist. He was made professor emeritus when he retired from the University in 1967.

I must also report with sorrow the death in January of Rudolph Minkowski, a staff member of the Hale Observatories from 1937 to 1960. A native of Germany, he fled to this country in 1935 and became an American citizen in 1940.

Throughout his career he collaborated with another German-born Observatories' astronomer, Walter Baade. Together they studied supernovae, which they divided into two types on the basis of long sequences of supernovae spectra first obtained by Minkowski. With Baade, he became interested in radio astronomy, and in the 1950s was the first to identify and interpret correctly a radio source, the remnant of a long-dead supernova in the constellation of Cassiopeia. For years Dr. Minkowski supervised the National Geographic Society-Palomar Observatory Sky Survey.

Dr. Minkowski received the Bruce Medal of the Astronomical Society of the Pacific in 1961 and an honorary doctorate from the University of California, Berkeley, in 1968. After his retirement from Hale, he worked at the University of California's radio astronomy laboratory.

The decision this year by an exceptionally gifted scientist and administrator to leave the Institution is, inevitably, cause for regret. Yet our sense of loss is

assuaged by our pride in the accomplishments of James D. Ebert during the twenty years he was director of the Department of Embryology. And we look forward to Dr. Ebert's contributions to developmental biology at the Marine Biological Laboratory, Woods Hole, Massachusetts, where he is the first full-time president and director.

Since his appointment as director in 1955 by the late Vannevar Bush, Dr. Ebert has guided the Embryology laboratory through a metamorphosis that took it from a place in the forefront of classical embryology to a leading role in molecular developmental genetics.

Among the outstanding achievements of the Department during Dr. Ebert's administration are his own work on the cellular and molecular basis of heart development in embryos, and his studies on the graft-versus-host reaction, the relation of viruses to tumor formation, and the regulation of DNA synthesis. Moreover, his leadership and encouragement created a stimulating and supportive environment in which the research of his colleagues and students also flourished.

In addition to its standing as a foremost research center, the Department of Embryology has become, under Dr. Ebert's guidance, internationally known for its advanced training program in developmental biology.

Dr. Ebert's contributions to the scientific community go beyond his research and his service to his "home" institution. He is professor of biology and professor of embryology at The Johns Hopkins University, and he has lectured as a visiting professor at other institutions in the United States and abroad. He is the first chairman of the Assembly of Life Sciences of the National Academy of Sciences; past president of the American Institute of Biological Sciences, the American Society of Zoologists, and the Society for the Study of Development and Growth. He is a trustee of the Board of Scientific Overseers of the Jackson Laboratory, a member of the Corporation of Woods Hole Oceanographic Institution, and he is on the board of visitors of ten universities. He has served as a consultant to the U.S. Department of Health, Education and Welfare. And he has been the editor or a member of the editorial board of half a dozen biological journals.

. . . AND GAINS

It is our privilege to welcome to the Institution this year two men of outstanding achievement in their fields. Robert O. Anderson and J. Paul Austin were elected trustees at our annual meeting of the board on April 30.

Robert O. Anderson, chairman of the board and chief executive officer of Atlantic Richfield Company, has held those positions since 1965. His experience in the business world is extensive and varied. He joined the American Mineral Spirits Co. in his native Chicago soon after his graduation from the University of Chicago in 1939. Within two years he had set up his own corporation, Malco Refineries, Inc., which later became Hondo Oil and Gas Co. and merged with Atlantic Richfield in 1963. At that time Mr. Anderson became one of the directors of Atlantic Richfield.

Although the focus of Mr. Anderson's business career has been in the petroleum industry, he has been involved in such diverse enterprises as mining, milling, and general manufacturing. In addition, he operates his own livestock company in Lincoln County, New Mexico. His experience is further broadened by being a

trustee of three universities, and a director of the First Chicago Corporation and the First National Bank of Chicago. His participation in cultural, civic, and charitable organizations includes chairmanships with the Aspen Institute for Humanistic Studies and The Lovelace Foundation.

J. Paul Austin, chairman of the board and chief executive officer of the Coca-Cola Company, has enjoyed a distinguished career with that firm since 1949. Joining the legal department of the Company in that year, Mr. Austin transferred to the Coca-Cola Export Corporation the following year and became the Corporation's president in 1959. In 1962 he was elected the tenth president of the Coca-Cola Company, in 1966, its chief executive officer, and in 1970, chairman of the board.

Mr. Austin also holds directorships with other well-known companies, among them Morgan Guaranty Trust Co. of New York; Dow Jones and Co., Inc.; and the General Electric Co. He is a trustee of numerous organizations, including the United States Council of International Chambers of Commerce, the National Industrial Conference Board, the Rand Corporation, the Twentieth Century Fund, and the California Institute of Technology. He is also a regent of the Smithsonian Institution.

Mr. Austin was born in Georgia in 1915 and received his A.B. (1937) and LL.B. (1950) degrees from Harvard University. He served with the U.S. Navy in the Pacific during World War II, achieving the rank of lieutenant commander. He was awarded the Legion of Merit.

When James Ebert moved to Woods Hole, we were especially fortunate to have Donald D. Brown to take over the direction of the Department of Embryology. Since 1961 when he was brought to the department as a promising fellow by Ebert, Brown has matured in the Carnegie environment, becoming a pioneer in developmental biology and molecular genetics and a gifted teacher.

Brown attended Dartmouth College and received the M.S. (in biochemistry) and the M.D. degrees from the University of Chicago in 1956. After interning at Charity Hospital, New Orleans, he embarked upon a research career, first as a research associate in the National Institute of Mental Health (1957-1959) and then as a special fellow of the National Cancer Institute in the Service de Biochimie Cellulaire, Institut Pasteur, Paris. After a year as fellow at the Department of Embryology, he was appointed staff member.

A leader in developing techniques for the recombination of animal genes with bacterial DNA molecules, Dr. Brown was one of the first to isolate animal genes—from the South African clawed toad *Xenopus laevis*. He has also studied the fibroin gene of the larval silkworm *Bombyx mori*. In recognition of these accomplishments he was chosen by the National Academy of Sciences to receive the U.S. Steel Foundation Award in Molecular Biology (1973) and was awarded the V. D. Mattia Lectureship of the Roche Institute of Molecular Biology (1975). In 1976 he received the Distinguished Alumni Award from the University of Chicago Medical School and an honorary D.Sc. from the University of Chicago.

A frequent contributor to scientific journals, Dr. Brown became editor of *Developmental Biology* in 1975. He has been president and treasurer of the Society for Developmental Biology and is a member of the National Academy of Sciences and a fellow of the American Academy of Arts and Sciences. Concurrent with his work at Carnegie, Dr. Brown is part-time professor of biology at The Johns Hopkins University.

The following honors have been awarded to Staff Members during the year:

L. Thomas Aldrich of the Department of Terrestrial Magnetism was re-elected General Secretary of the American Geophysical Union.

Peter M. Bell of the Geophysical Laboratory received the Exceptional Scientific Achievement Medal of the National Aeronautics and Space Administration.

Donald D. Brown of the Department of Embryology was honored by his *alma mater* with the Distinguished Alumni Award of the University of Chicago Medical School and a D.Sc. degree from the University of Chicago. He also received the V. D. Mattia Lectureship of the Roche Institute of Molecular Biology and gave the John M. Prather Lectures in Biology at Harvard University.

Jesse L. Greenstein of the Hale Observatories received several awards, including the Distinguished Public Service Medal of the National Aeronautics and Space Administration, a Medal of the University of Liège, and the Gold Medal of the Royal Astronomical Society.

James E. Gunn, Hale Observatories, was the first George Ellery Hale Visiting Professor at the University of Chicago.

Elburt F. Osborn was given the 29th Albert Victor Bleining Award by the Pittsburgh Section of the American Ceramics Society.

The Institution has been fortunate in the generosity of its friends and associates. Gifts from staff, former staff, and trustees, as well as other individuals and organizations, have added \$1,909,000 to the funds for research over the past six years. Some of the recent donors are the late Dr. Vannevar Bush, Mr. William Golden, Mr. and Mrs. Crawford H. Greenewalt, Mr. William McChesney Martin, Jr., Mr. John C. Meyer, Mr. Henry S. Morgan, Mr. Walter H. Page, Dr. George W. Preston, and Mr. Orley H. Truman.

FACULTY, FELLOWS, AND STUDENTS

1975-1976

DEPARTMENT OF EMBRYOLOGY
Baltimore, Maryland*Director*

James D. Ebert

Director Designate

Donald D. Brown

*Staff Members*Igor B. Dawid
Douglas M. Fambrough
Kenneth J. Muller
Richard E. Pagano
Ronald H. Reeder
Yoshiaki Suzuki*Fellows*Peter Botchan
Diana Card
S. T. Carbonetto
Jeffrey Doering
Scott Emmons
Nina Fedoroff
Paul Geshelin
Elizabeth Godwin
Leaf Huang
Yasumi Ohshima
Keiko Ozato
Aileen K. Ritchie
Alex Sandra
Masatoshi Takeichi
Katherine Tepperman
Harvey Wahn
Peter K. Wellauer*Students*Peter Devreotes
John Gardner
Carol Kaushagen
Jose RamirezGEOPHYSICAL LABORATORY
Washington, D.C.*Director*

Hatten S. Yoder, Jr.

Carnegie Institution Distinguished Professor

Elbert F. Osborn

Emeritus

Emanuel G. Zies

Staff Members

Peter M. Bell
Francis R. Boyd, Jr.
Felix Chayes
John R. Cronin
Gordon L. Davis
David H. Egger
Larry W. Finger
John D. Frantz
P. Edgar Hare
Thomas C. Hoering
T. Neil Irvine
Thomas E. Krogh
Ikuo Kushiro
Ho-Kwang Mao
Yoshikazu Ohashi
Douglas Rumble III
David Virgo

Fellows

Richard J. Arculus
Nicholas T. Arndt
Timothy M. Benjamin
John M. Ferry
Anthony A. Finnerty
Toshitsugu Fujii
John I. Hedges
Frank E. Huggins
Gifford H. Miller
Bjørn O. Mysen
Howard R. Naslund
Frank S. Spear
Juergen Trochimczyk
Rosemary J. Vidale
E. Bruce Watson
Bernard J. Wood

Students

Julia A. Dill
Dora Y. Lee
Catherine A. McCammon

HALE OBSERVATORIES
Pasadena, California

Director

Horace W. Babcock

Associate Director

J. Beverley Oke

Staff Members

Halton C. Arp
Eric E. Becklin
Edwin W. Dennison
Jesse L. Greenstein
James E. Gunn
Robert F. Howard
Jerome Kristian
Robert B. Leighton
Guido Münch
Gerry Neugebauer
S. Eric Persson
George W. Preston
Bruce H. Rule
Allan R. Sandage
Wallace L. W. Sargent
Maarten Schmidt
Leonard T. Searle
Stephen A. Schectman
Arthur H. Vaughan, Jr.
James A. Westphal
Harold Zirin

Staff Associates

Robert J. Brucato
Michael W. Werner

Fellows

A. Ger de Bruyn
Eduardo Hardy
Mark Hartoog
François Schweizer
Christopher P. Wilson
Hirokazu Yoshimura
Robert J. Zinn

Carnegie-Chilean Fellow

Maria Teresa Ruiz

Student Observers

Steven V. W. Beckwith
Kirk Borne
Todd Boroson
France Cordova
David J. Diner
Jonathan H. Elias
Richard F. Green
Paul Hickson
John G. Hoessel
John P. Huchra
Steven Kent
John Kormendy
Barry J. Labonté
Philip Massey
Jorge Melnick
Daniel Nadeau

William C. Friedhorsky
Douglas M. Rabin
Russell O. Redman
Anneila I. Sargent
William L. Sebok
David Sholle
Richard J. Terrile
Edwin L. Turner
Barry E. Turnrose
Richard Wade
Theodore B. Williams
Steven P. Willner

DEPARTMENT OF PLANT BIOLOGY
Stanford, California

Director

Winslow R. Briggs

Staff Members

Joseph A. Berry
Olle Björkman
Jeanette S. Brown
David C. Fork
Malcolm A. Nobs
William F. Thompson

Emeritus

C. Stacy French
William M. Hiesey

Fellows

Michael Blatt
Steven J. Britz
James Collatz
John Cross
Ulrike Dohrmann
James Ehleringer
Algirdas J. Jesaitis
George Johnson
Aaron Kaplan
John Mackenzie
Bruce E. Mahall
Norio Murata
Michael Murray
Charles E. Rogler
Ulrich Schreiber
Diana Stein
Alan Stemler
Heather Strong Belford

Students

Brian Anderson
Robert D. Brain
Daniel Cosgrove

William Curtis
Mary Enama
Thomas Payne
Richard Preisler
Karen Swift

DEPARTMENT OF
TERRESTRIAL MAGNETISM
Washington, D.C.

Director

George W. Wetherill

Distinguished Service Member

Merle A. Tuve

Emeritus

Scott E. Forbush

Staff Members

L. Thomas Aldrich
George E. Assousa
Louis Brown
Dean B. Cowie
W. Kent Ford, Jr.
Stanley R. Hart
Albrecht W. Hofmann
David E. James
Alan T. Linde
Nancy R. Rice
Richard B. Roberts
Vera C. Rubin
I. Selwyn Sacks
Norbert Thonnard
Kenneth C. Turner

Research Associates

Tom I. Bonner
Mordechai Magaritz
J. Arthur Snoke
Kiyoshi Suyehiro

Fellows

John R. Bannister
Charles L. Bennett
Arturo Cuyubamba
Gregory S. DeWitt
John R. Evans
Antonio Flores
George H. Pepper
Charles J. Peterson
R. Sundar Rajan
Michael Schneider
Christine M. Seber
Stuart J. Weidenschilling
David J. Whitford

Reports of Departments and Special Studies

Department of Embryology

Department of Terrestrial Magnetism

Hale Observatories

Department of Plant Biology

Geophysical Laboratory

Developmental Biology Research Group

Department of Embryology

Baltimore, Maryland

James D. Ebert

Director

Donald D. Brown

Director-Designate

Carnegie Institution of Washington Year Book 75, 1975-1976

Contents

| | |
|---|----|
| Introduction | 7 |
| Developmental Genetics by Gene Isolation: The Dual 5S DNA System in <i>Xenopus</i> .. | 12 |
| Preparation of 5S DNA recombined with the plasmid PMB9 | 12 |
| Restriction enzyme maps of two cloned fragments of <i>X. mulleri</i> oocyte-type 5S DNA | 14 |
| Characterization of a new 5S DNA from <i>X. mulleri</i> | 15 |
| Reconstruction of 5S RNA transcription | 16 |
| Sequencing studies on <i>Xenopus</i> 5S DNA | 17 |
| The Structure of Ribosomal DNA from <i>Xenopus</i> | 20 |
| Studies of Human X-chromosome DNA | 22 |
| Chromosomal Proteins and the Control of Gene Function | 23 |
| Isolation and characterization of amplified nucleoli | 24 |
| The subunit organization of mouse satellite chromatin | 27 |
| The Polarity of Ribosomal DNA in <i>Xenopus</i> | 28 |
| Determination of polarity with DNA exonucleases | 28 |
| Determination of polarity using rDNA transcription complexes | 29 |
| Ribosomal DNA in <i>Drosophila melanogaster</i> | 30 |
| Purification of <i>Drosophila</i> rDNA | 31 |
| Analysis of EcoRI fragments of <i>Drosophila</i> rDNA | 32 |
| Length heterogeneity in the spacer region | 35 |
| Arrangement of length heterogeneity | 35 |
| Distribution of rDNA repeat lengths on the X and Y chromosomes of <i>D. melanogaster</i> | 36 |
| Structural and Functional Studies of Fibroin Genes | 36 |
| Physical purification of the gene coding for silk fibroin | 37 |
| Cloning of fibroin gene plasmid | 37 |
| Accentuated expression of fibroin genes in vivo and in vitro | 38 |
| Biogenesis of Mitochondria | 45 |
| Cloning of <i>Xenopus laevis</i> mitochondrial DNA | 46 |
| Maps of <i>X. laevis</i> and <i>X. mulleri</i> mtDNA: restriction sites, the D-loop and the rRNA genes | 46 |
| Mapping of 4S genes on <i>X. laevis</i> mtDNA | 48 |
| Mapping studies with mtDNA from <i>Drosophila melanogaster</i> | 49 |
| Mapping and sequence comparisons of goat and sheep mtDNAs | 50 |
| Phospholipid-Cholesterol Dynamics in Mammalian Cells | 52 |
| Interactions of phospholipid vesicles with murine lymphocytes: vesicle-cell adsorption and fusion as alternative pathways of uptake | 53 |
| Evidence for a stable vesicle-cell adsorption | 53 |
| Vesicle-cell fusion and lipid exchange | 56 |
| Interaction of Phospholipid vesicles with murine lymphocytes: vesicle-cell adsorption leads to altered surface properties and enhanced proliferative response | 57 |
| Enhancement of proliferation by lipid vesicle pretreatment | 58 |

| | |
|--|-----|
| Alterations in lectin-induced agglutinability and lectin-binding in vesicle-treated cells | 59 |
| Alteration of cell surface properties by vesicle adsorption | 60 |
| Studies of membrane adhesion | 61 |
| Vesicle to cell adhesion | 62 |
| Cell to cell adhesion | 63 |
| Distribution of lipophilic fluorescent probes in intact cells | 66 |
| Membrane Transplantation by Fusion | 67 |
| Mechanism of Syngeneic Response Induced by Lectins | 73 |
| Studies on Skeletal Muscle and Neuronal Plasma Membranes | 76 |
| ACh receptor biosynthesis | 78 |
| Autoradiographic analysis of receptor degradation | 81 |
| Effect of muscle activity on receptor turnover | 83 |
| Organization of muscle plasma membrane in vivo | 84 |
| Studies on the mobility of extrajunctional ACh receptors in plasma membrane ... | 85 |
| Preparation of a fluorescent derivative of α -bungarotoxin | 86 |
| Properties of fluorescent α -bungarotoxin | 86 |
| Use of FITC- α -bungarotoxin as a probe in studying membrane structure | 87 |
| Turnover of plasma membrane proteins | 87 |
| Studies on neuronal plasma membranes | 88 |
| Signaling in the Nervous System: Synapses of Specific Neurons in the Leech | 90 |
| Chemical synapses in the leech | 90 |
| Structural details of the synapse | 90 |
| The arrangement of synapses on sensory neurons | 91 |
| Sprouting of sensory neuron terminals | 91 |
| An electrical synapse in the leech | 95 |
| Interruption of the Rohde neuron | 96 |
| The Collection of Human Embryos | 97 |
| Developmental stages in human embryos | 98 |
| Development of the nervous system | 98 |
| The Bluntschli Collection | 98 |
| Staff Activities | 99 |
| Bibliography | 102 |
| Personnel | 103 |

INTRODUCTION

In *Pentimento**, Lillian Hellman wrote, "Old paint on canvas, as it ages, sometimes becomes transparent. When that happens it is possible, in some pictures, to see the original lines: a tree will show through a woman's dress, a child makes way for a dog, a large boat is no longer on an open sea. That is called pentimento because the painter 'repented,' changed his mind. Perhaps it would be well to say that the old conception, replaced by a later choice, is a way of seeing and then seeing again."

There have been three conceptions of the Department of Embryology: the conception of Franklin P. Mall and George Streeter (1913–1940), the vision of George W. Corner (1940–1955), and of the writer (1956–1976). Now there will be another. By the time this report is in the hands of its readers, the Department's fifth Director, Donald D. Brown, will be charting its course.

The departmental canvas is a large one, painted and repainted over more than six decades, not just by four directors, but by perhaps twenty "masters" and ten times that number of their students. Here and there, especially in the older sections, the paint is transparent, and one can see and see again the classic works for which the Department is justly renowned.

The Department was, for five decades, the world's leading center for the study of the human embryo. It pioneered in the development of primates for research, having the earliest successful breeding monkey colony. Using these animals, large strides were made toward understanding menstruation and cyclic changes in the ovaries and uterus, laying much of the groundwork for more recent advances in family planning.

Earlier studies, culminating in Ramsey's classic works, set the standard for

research on the primate placenta. Burns' studies of sex transformation similarly provided a standard in the field of sex differentiation. Although the techniques of cell culture were born in the neighboring Department of Anatomy of the Johns Hopkins Medical School, they came of age in the Department of Embryology especially in the contributions of M. R. and W. H. Lewis and, later, Irwin Konigsberg.

During the past two decades the field of developmental biology has been reshaped, as students of development began to perceive that it should be possible to understand the factors regulating the synthesis of specific products and their assembly during the shaping of a new organism. The Department of Embryology has played a part—at times a key part—in this reshaping process. However, the paint in these newer sections of the canvas is not yet transparent enough for the viewer—especially one as biased as the writer—to make out all of the landmarks. A few do stand out in bold relief. Donald Brown pioneered in the isolation and characterization of animal genes and their immediate products, the ribonucleic acids. His study with Carnegie Fellow John Gurdon of an anucleolate mutant strain of the South African clawed toad *Xenopus* constitutes a modern classic, offering decisive proof of the role of the nucleolus in the synthesis of ribosomal RNAs. By further exploitation of the anucleolar mutant, Brown was able to map the genes encoding these RNAs. He and his co-workers then proved that during oogenesis the genes for ribosomal RNAs are amplified into about 900 copies. His research then evolved to the point where it became possible for him to isolate the genes coding for the 28S and 18S ribosomal RNA fragments—the first genes to be isolated from any eukaryotic cell. A further extension of these techniques

**Pentimento: A Book of Portraits*, 1973, Little, Brown & Co., Boston.

culminated in the isolation and characterization of the genes coding for 5S ribosomal RNA.

Brown and his co-workers then turned to the question of whether the amplification of specific genes can be demonstrated in specialized cell types. Together with Suzuki, he isolated the messenger RNA coding for the silk protein fibroin in the larval silkworm *Bombyx mori*. Using this mRNA as a probe, Brown was able to show that the fibroin gene is not amplified in the cells of the silk glands as compared to other cells, thereby providing strong evidence that the amplification of specific genes is not a generalized mechanism of cell differentiation. Brown's and Suzuki's studies have provided what may be the most complete account thus far available of the waxing and waning of gene action during development.

The group's continuing investigations have made a significant impact in developmental, molecular, and evolutionary biology. Studies of "developmental genetics by gene isolation" have led to new and brilliantly successful approaches to fundamental questions in development. The Department has pioneered in the development and exploitation of techniques for gene purification, genes of known function having been characterized with the long-term goal of reconstructing their controls in vitro. Studies of "gene anatomy," the structure and arrangement of genes, have resulted in new insights into the mechanism by which multiple tandem genes evolve together.

It was just a decade ago, in his now-classic articles in *Journal of Molecular Biology* and *Proceedings of the National Academy of Sciences*, that Igor Dawid proved that the so-called cytoplasmic DNA of amphibian oocytes, long an enigma to embryologists, is in fact mitochondrial. In cooperation with a series of able postdoctoral fellows and students, he has explored in depth the mitochondrial genes (mtDNA) and their products, the mitochondrial ribosomal RNAs (mt-rRNAs) and transfer (mt-tRNAs).

Cell and tissue interactions are the hallmark of development. The differentiation of most cells requires, at one or more points in their life histories, interactions with their neighbors, and failures in close range tissue interactions may result in alterations in the normal patterns of development. The question has been posed in a general way as follows. How does the microenvironment make its impact on cell function *via* the cell membrane? Genes direct the synthesis of the components of cell membranes, and must, in turn, be regulated by signals *from* the cell membrane.

A better understanding of the role of the microenvironment demanded the capability to analyze cell differentiation in vitro. Of the Department's achievements in cellular developmental biology in the 1960s one stands out: Konigsberg's clonal analysis of myogenesis. His was the first clonal study of any differentiating cell. We are indebted to T. T. Puck of the University of Colorado, who first developed the "feeder layer" technique, enabling him and others to clone a number of established cell lines. It was Konigsberg, however, who modified the technique and applied it significantly in developmental biology. It deserves special mention, too, that two other members of the Department, Coon and Kaighn, followed Konigsberg's initial success with uncommonly important clonal analyses of chondrocytes and liver, and that a former Carnegie Fellow, Tokindo Okada, has used his experience in the Department to great advantage in his studies of "transdifferentiation" of pigmented retinal to lens cells.

Another significant advance in cell biology came in DeLanney and Ebert's description of the graft-versus-host reaction.

But single "major discoveries" do not tell the whole story. Equally important is the steady flow of consistent, reproducible findings that, over the years, illuminate an entire subject. For nearly two decades the Department was the Nation's, indeed the world's,

leading center of research on the development of the heart, with the work of DeHaan, Rosenquist, and Ebert being especially noteworthy.

Finally, mention must be made of the studies of a number of contributors, notably Kaighn, Lee, Hay, and Yoshikawa-Fukada, on the interplay of tumor viruses and differentiating cells. Their findings provided many of the "building blocks" in our current understanding of viral oncogenesis. Yoshikawa-Fukada's first description of the viral oncogenic sequences, lost sight of at times because of the flood of related findings in the cancer virus field, nonetheless marked her as an innovating spirit.

1975-1976

In recent years, no single research program has attracted more attention to the Department than Douglas Fambrough's continuing exploration of the acetylcholine receptors in skeletal muscle fiber membranes. Acetylcholine (ACh) receptors are of special interest to Fambrough and his colleagues, both as membrane glycoproteins and as elements figuring prominently in neuromuscular interactions. In a series of definitive articles, they have reported on the appearance of ACh receptors during muscle development, the production and incorporation of ACh receptors into the surface membranes of myotubes and their subsequent degradation, the clustering of ACh receptors at newly formed neuromuscular junctions both *in vitro* and *in vivo*, the number and distribution of ACh receptors in adult rat skeletal muscle fibers, and the time course of change in these parameters following denervation. They are continuing to explore physiological aspects of receptor function, examining further the biosynthesis and degradation of ACh receptors and obtaining more accurate estimates of ACh receptor density on denervated muscle fiber membranes.

In this year's report, Fambrough and

his student Peter Devreotes discuss in detail their model for the major events in receptor metabolism. Its main features can be summarized briefly. The protein subunits of which the ACh receptor is composed are synthesized with the usual protein synthesizing mechanisms of the cells and are rapidly assembled into receptor units resembling those in the plasma membrane. These newly synthesized receptors occur upon some membrane systems in the cytoplasm of the muscle cells and are collectively referred to as the "precursor pool." The average residence of a new receptor in the precursor pool is 2-3 hours. Receptors are transferred from this pool to the surface by an energy-requiring process and are then able to function. The average half-life of an ACh receptor in the plasma membrane is 22 hours. Receptors are degraded by an energy-requiring process which involves the internalization of the receptor and transport to secondary lysosomes and then proteolytic destruction. Interested readers will find the evidence supporting these conclusions in the body of the report, along with indications of the group's new directions, including a foray into the membranes of neurons.

Richard Pagano and his associates are also focusing attention on the cell membrane, their work being concerned with the possible dynamic role which membrane phospholipids and cholesterol may play in the regulation of cell behavior. During the past several years they have utilized artificially generated lipid vesicles to perturb membrane components in living cells in a controlled and systematic way. In the present report they offer findings on the interactions of phosphatidylcholine vesicles with murine lymphocytes, and the physiological consequences of these interactions. Pagano, and postdoctoral fellows Huang and Ozato, have shown that the pathways of vesicle-cell interactions, enumerated in previous reports (vesicle-cell fusion, adsorption and lipid exchange) are exquisitely sensitive to the molecular composition and physical properties

of the artificial vesicles. In the lymphocyte system, the resulting membrane perturbations lead to altered surface properties and an enhanced proliferative activity of these cells, when stimulated by various mitogens and antigens.

In a separate line of research, Carnegie Fellow Masatoshi Takeichi has explored some of the adhesive properties of a fibroblastic cell line and reports on his attempts to identify and characterize membrane proteins which participate in this phenomenon. Parallel studies on the adherence of lipid vesicles of known composition to cells are also discussed.

The importance of cellular interactions is illustrated strikingly in Kenneth Muller's studies of synapses in the leech. The role that a neuron assumes in the nervous system is dependent upon the connections that it makes with other neurons or with peripheral targets. Therefore, an essential step both in determining the forces that act initially to organize the nervous system and in characterizing the mechanisms by which a neuron handles, or integrates, information is to ascertain the relationship between a neuron's function and the arrangement of its synapses. A related problem in neurobiology has been to determine the extent that a neuron's shape and other properties are intrinsic, or whether its contacts or associations with other neurons are essential for certain aspects of its growth and maintenance.

The nervous system of the leech *Hirudo medicinalis* has been particularly favorable for study of the physiological role and functioning of specific neurons, largely because its organization is relatively simple. Neurons in this segmented worm are grouped 350 together to form essentially identical ganglia that are linked in a chain by axon bundles; each ganglion mediates the reflexes and controls the behavior of its segment. It has been possible to monitor electrical activity from within

single sensory and motor neurons with microelectrodes and to correlate the physiological activity of functionally identified neurons with their characteristic shape and position within each ganglion. By recording from pairs of neurons one can trace synaptic connections, which have been found to be surprisingly uniform and in that sense predictable between specific neurons.

In his current report, Muller describes the structural details of chemical synapses, delineates their arrangement on sensory neurons, and explores the sprouting of sensory neuron terminals. He also describes the unexpected discovery of an electrical junction between unpaired Rohde neurons in neighboring ganglia.

Brown and his colleagues are now concentrating on the family of genes which code for the small RNA molecule of ribosomes termed 5S RNA. The "transcription unit," that is the region of this DNA which is transcribed into RNA in the living cell, is relatively simple—only 120 base pairs in length. Moreover, the form of RNA polymerase which transcribes this gene in vivo has been identified. The fact that the mature RNA transcript does not appear to be derived from a higher molecular weight precursor is especially important: It means that the true initiation site of transcription from 5S DNA is known. Therefore, one can detect faithful transcription when it occurs in vitro. Using this system Brown hopes to reassemble the macromolecules which enable this DNA to be transcribed with fidelity in the living cell. In this way he hopes to elucidate the control mechanisms of an animal gene.

This year his group reports progress along several lines. Three different kinds of 5S DNA have been cloned in *E. coli* by means of the new recombinant DNA methodology, thereby providing an order of magnitude more material to work with and permitting the careful examination of one single repeating unit of a tandem gene family. The "re-

striction maps" of these cloned DNAs, i.e., the sites where they are cleaved by certain restriction enzymes, are described by Fellows Jeffrey Doering and Scott Emmons. The latter is attempting to develop an assay for proper transcription. Fellow Nina Fedoroff is exploring DNA sequencing methods to determine the exact nucleotide sequence in the spacer regions of 5S DNA, particularly those regions adjacent to the initiation site of the gene.

DNA structure continues to hold the attention of several Staff Members and Fellows. Reeder and Dawid, along with Fellow Peter Botchan, report on the structure of nontranscribed spacer regions in *Xenopus* ribosomal DNA, based on studies using cloned fragments of rDNA generated with the restriction endonuclease EcoRI. Fellow Peter Wellauer and Dawid have undertaken the first stages of a study of the ribosomal DNA of *Drosophila*, Dawid and his colleagues are cloning *Xenopus* mitochondrial DNA, and Carnegie Fellow Ohshima and Staff Member Suzuki are attempting to clone the silk fibroin gene.

In all of these studies, the Department has adhered to the safety standards proposed by the Asilomar Conference on Recombinant DNA.

Mention has already been made of the contributions of several fellows and students. Peter Wellauer, whose time in 1975–1976 was shared between California Institute of Technology and this Department, will return to Switzerland to a new position in the Swiss Cancer Research Institute in Lausanne. Scott Emmons will continue his postdoctoral training at the University of Colorado. Leaf Huang has taken up his new responsibilities in the Department of Biochemistry of the University of Tennessee, and Katherine Tepperman will join the University of Cincinnati's faculty. Keiko Ozato will move to the Johns Hopkins School of Medicine–Good Samaritan Hospital.

Continuing in the Department are Diana Card, a Fellow of the Muscular Dystrophy Associations of America, Inc., with Fambrough; Peter Botchan and Harvey Wahn, with Reeder; USPHS Fellows Jeffrey Doering and Nina Fedoroff with Brown; Paul Geshelin and Yasumi Ohshima, with Suzuki; Alex Sandra, with Pagano; Elizabeth Godwin, with Dawid; and S. T. Carbonetto, with Muller and Fambrough.

This brief listing of postdoctoral fellows brings me full circle to my starting point in 1956. In his autobiography, *Anatomist at Large*, George Corner wrote that the secret of his success was his ability to place himself under wise leaders. His words ring true for me as well. I would emphasize still another ingredient: the catalysis provided by young minds—fellows and students. When President Haskins and I began to chart the Department's course in 1956, a vital principle emerged. It was clear that even if ample funds and space were available immediately to undertake all the tasks we had set for ourselves, the scientific talent was not. The pool of able developmental biologists then was small. It was agreed, therefore, that training would henceforth be an integral part of the Department's program. The wisdom of that decision is demonstrated by a glance at today's staff—Brown, Dawid, Fambrough, Reeder and Suzuki all joined the Department initially for training. Thus the reshaping of the Department has been gradual, not cataclysmic. As I wrote in 1956 (*Year Book* 55, p. 270), the Department may be likened to an organism. Although there has been considerable change or turnover within its parts, as a whole it enjoys stability. We achieve what Rudolph Schoenheimer called a condition of stability with flux—working toward a better understanding of the mechanisms of development, using for that purpose whatever methods become necessary.

DEVELOPMENTAL GENETICS BY GENE ISOLATION: THE DUAL 5S DNA SYSTEM IN *Xenopus*

D. D. Brown, J. Doering, S. Emmons, N. Fedoroff, and E. Jordan

In *Year Book 74* (p. 12) we described our reasons for concentrating on the family of genes which code for the small RNA molecule of ribosomes termed 5S RNA. The "transcription unit," that is, the region of this DNA which is transcribed into RNA in the living cell, is relatively simple—only 120 base pairs in length. The form of RNA polymerase which transcribes this gene in vivo has been identified by Roeder as form III. The mature RNA transcript does not appear to be derived from a higher molecular weight precursor. This observation is especially important because it means that we know the true initiation site of transcription from 5S DNA and therefore can detect faithful transcription when it occurs in vitro. Using this simple system we hope to reassemble the macromolecules which enable this DNA to be transcribed with fidelity in the living cell. In this way we hope to elucidate the control mechanisms of an animal gene.

In this report we summarize progress made along several lines. Three different kinds of 5S DNA have been cloned in *E. coli* by means of the new recombinant DNA methodology (see *Year Book 74*). This approach provides an order of magnitude more material to work with and permits us to examine carefully a single repeating unit of a tandem gene family. We describe the "restriction maps" of these cloned DNAs, i.e., the sites where they are cleaved by certain restriction enzymes (Doering and Emmons). Various schemes are being investigated to develop an assay for proper transcription (Emmons). DNA sequencing methods will determine the exact nucleotide sequence in the spacer regions of 5S DNA, particularly those regions adjacent to the initiation site of the gene (Fedoroff). We have two new species of *Xenopus* obtained from the collection of

M. Fischberg of Geneva, Switzerland. We have purified partially the principal 5S DNA component from each of these. Although we will not describe these experiments in this report, we have a specific purpose for isolating the genes from different species which encode the same function. The spacer regions that separate the genes have diverged considerably in their nucleotide sequences. Control regions within these spacers are likely to be conserved. By comparing the nucleotide sequences in comparable regions of 5S DNA isolated from different species we can identify possible control regions.

PREPARATION OF 5S DNA
RECOMBINED WITH THE PLASMID
PMB9

D. D. Brown and E. Jordan

We have used exclusively the plasmid PMB9 for recombining with, and cloning, *Xenopus* 5S DNA. This circular plasmid has a molecular weight of 3.5×10^6 (5400 base pairs). It has a single site for several restriction enzymes into which foreign DNA can be introduced and joined. We have used the plasmid site that is cleaved by the enzyme HindIII for insertion because three different *Xenopus* 5S DNAs also have HindIII sites. This enzyme leaves at each end four nucleotide single-stranded regions that are complementary and can be joined by ligase.

Xenopus laevis oocyte-type 5S DNA has a single HindIII site once per repeat, and *Xenopus mulleri* oocyte 5S DNA has irregular HindIII sites which occur on the average about once every four repeats. The newly isolated 5S DNA from *Xenopus mulleri* also has a single HindIII site per repeat. The scheme for insertion is as follows. The plasmid is digested to completion with HindIII. The 5S DNA is digested either

completely or partially with HindIII, depending upon whether monomers or multimers are to be inserted. The plasmid and 5S DNAs are mixed and joined with T4 ligase. The bacteria are transformed with the recombined DNA. Those bacteria which incorporate a plasmid can be selected by their resistance to colicine or tetracycline. Grunstein and Hogness (*Proc. Nat. Acad. Sci.* 72, 3961, 1975) devised a simple screening test to detect bacteria that contain a specific inserted gene. Many individual colonies are grown on a filter paper disc and their DNA is immobilized on the paper after alkaline denaturation. The filter is then hybridized with iodine-125 labeled 5S RNA. Only the clones that contain 5S DNA hybridize with the 5S RNA and become radioactive. The radioactive clones are located by exposing the filters to x-ray film. Individual clones are grown up for analysis. Figure 1 demonstrates one such screening experiment.

This method of colony hybridization not only simplifies the identification of bacteria that contain 5S DNA sequences, but it avoids growing large amounts of bacteria that might contain unknown DNA sequences. Such bacteria remain on the agar plate and are autoclaved. Since 5S DNA occurs as a tandem gene family, no other DNA molecules are likely to be inserted into a plasmid with the 5S DNA fragment. These considerations are important because of our continuing concern with safety precautions, especially when there is a possibility of cloning unknown animal DNA fragments. The colony isolation method described above minimizes this possibility. In addition we have introduced a "chemical" containment step during the isolation of recombinant DNA. When we grow *E. coli* cultures containing a recombined plasmid, we kill the bacteria before isolating their plasmid DNA. This step is achieved simply by adding small amounts of chloroform to the cultures just before harvesting. No viable bacteria remain after five minutes of chloroform treatment.

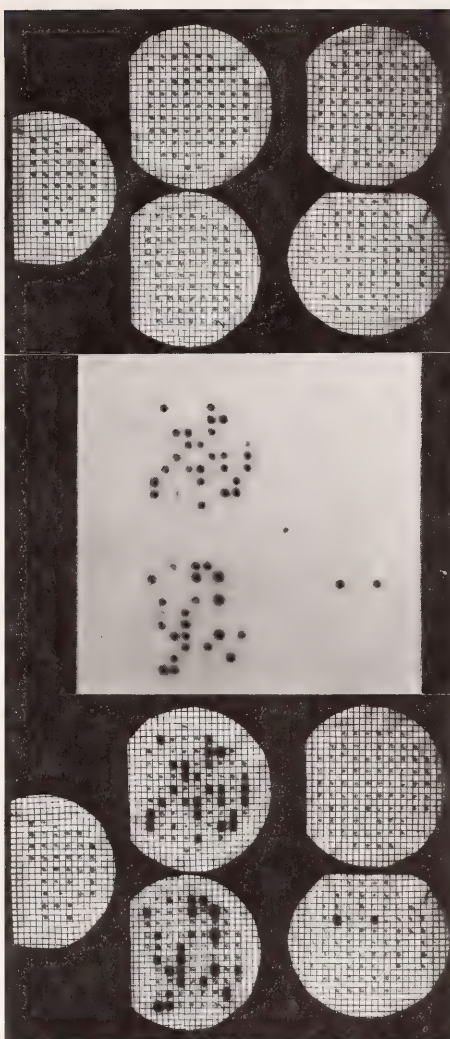


Fig. 1. Autoradiograph of bacterial colonies that had been hybridized with ^{125}I -labeled 5S RNA. Tetracycline-resistant colonies (containing the plasmid or plasmid plus 5S DNA insert) were grown on the filter paper, treated with alkali to denature DNA, neutralized, dried, and hybridized with the radioactive RNA. The excess radioactivity was removed, and the labeled colonies containing 5S DNA molecules were detected by autoradiography. Top, a photograph of three filter papers with dried colonies. The middle filter contains bacteria that had been transformed with PMB9 recombined with *X. laevis* oocyte-type 5S DNA. Bacteria on the other two filters were transformed with PMB9 recombined with *X. mulleri* oocyte-type 5S DNA. The film itself is shown in the middle panel, and it has been placed over the filters to show which ones contain the 5S DNA insert (bottom panel).

The Structure of X. laevis Oocyte-Type 5S DNA

A model for one repeating unit of *X. laevis* oocyte-type 5S DNA (XLo) was first published in *Year Book 74*. This model is refined and corrected in Fig. 2. The A+T-rich spacer region was placed erroneously at the 3' end of the transcription unit (the 5S RNA gene). We know that there is a short A+T-rich region adjacent to the 3' end of the gene from the experiments of R. D. Brown (*Year Book 74*). However, the recent sequencing studies by Claude Jacq and George Brownlee at the Medical Research Council Laboratory of Molecular Biology in Cambridge, England, have shown that the principal A+T-rich spacer region is at the 5' end of the transcription unit. Our current model (Fig. 2) incorporates this change in orientation. The A+T-rich 15-mer oligonucleotides that comprise most of this region are designated by short dotted lines. Their exact location and number are unknown. Jacq and Brownlee also partly sequenced an interesting region called the "pseudogene," which differs from the gene sequence by only six bases in the region from residue 45 to residue 100. The terminal 20 nucleotides are completely different; sequencing of the first 44 nucleotides is incomplete. The recognition site for the restriction enzyme HaeIII (Fig. 2) occurs in a part of the pseudogene which is analogous to a corresponding region in the gene. The other HaeIII sequence found in the gene is missing in the pseudogene. The function of the pseudogene is unknown.

RESTRICTION ENZYME MAPS OF TWO CLONED FRAGMENTS OF *X. mulleri* OOCYTE-TYPE 5S DNA

J. Doering and S. Emmons

The restriction enzyme HindIII cuts *X. mulleri* oocyte-type 5S DNA (Xm₀) occasionally yielding fragments which are heterogeneous in length. Fragments from a complete HindIII digest of Xm₀ were cloned by the methods described above in *E. coli* HB101 using the plasmid PNB9. Two of these cloned fragments were selected for detailed study.

Xm₀3 is a 2700 base-pair fragment. It is cut by the restriction enzyme HpaII into four fragments, the smallest of which is present in two copies. To determine the order of these fragments, Xm₀3 was end-labeled using α -³²P-labeled ATP and T4 polynucleotide kinase. The labeled DNA was digested with the enzyme and the fragments run on a gel. Radioactive terminal fragments were identified by autoradiography. The order of the remaining fragments was deduced from the sizes of partial digestion products (Fig. 3). The pattern of fragments obtained after double digestion with HpaII and HaeIII was indistinguishable from that obtained with HaeIII alone, indicating that all HpaII sites are very close to HaeIII sites. This implies that HpaII cleaves only within the gene sequence itself, since the recognition sequence for HpaII occurs next to an Hae site in *X. mulleri* oocyte-type 5S RNA. The restriction map in Fig. 3 was constructed using

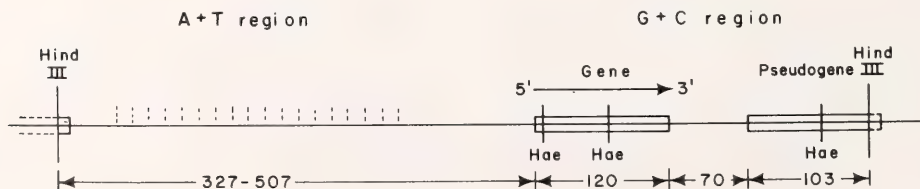


Fig. 2. Model of one repeat of *X. laevis* oocyte-type 5S DNA. Restriction enzyme sites are included. The numbers refer to base pairs.

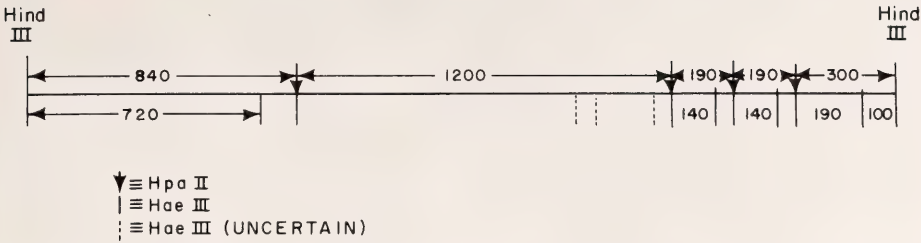


Fig. 3. Restriction map of one *X. mulleri* oocyte-type cloned fragment (Xm₀₃). The numbers refer to base pairs. Some cleavage sites are tentative. They are shown as dotted lines.

end-labeled fragments, partial digests, and HaeIII digests of each HpaII fragment.

Xm₀₁ is an 800 base-pair fragment containing one HpaII site, one HhaI site, and six HaeIII sites. A map is being constructed using the methods described above.

CHARACTERIZATION OF A NEW 5S DNA FROM *X. mulleri*

J. Doering

In the search for the 5S DNA coding for the somatic-type 5S RNA, new 5S DNA-containing satellites were isolated from both *X. laevis* and *X. mulleri*. The new *X. laevis* 5S DNA was found to code for a 5S RNA different from both the oocyte and somatic types (Year Book 74, p. 13).

The kind of 5S RNA gene carried by the new *X. mulleri* 5S DNA is still unknown. Table 1 lists some characteristics of Xm-new DNA compared with those of the oocyte-type 5S DNA from *X. mulleri*. The partially purified new 5S DNA from *X. mulleri* (Xm-new) is cut by the restriction enzyme HindIII into homogeneous 900-base-pair fragments (Fig. 4). Higher molecular weight DNA is also present after digestion, but only the 900-base-pair fragments hybridize with 5S RNA. Fragments from a complete HindIII digest of Xm-new were cloned by the methods described above. The Xm-new DNA from one clone has been subjected to detailed study.

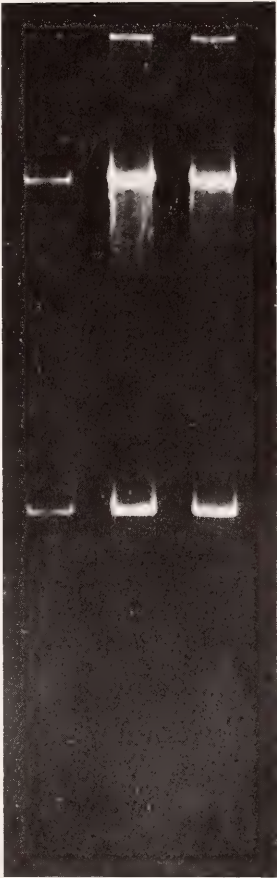


Fig. 4. Electrophoresis in a 2% acrylamide, 0.5% agarose composite gel of HindIII digests of Xm-new 5S DNA (left), purified from the animal's DNA, PMB9 containing one Xm-new 5S DNA insert (middle), and a mixture of these two samples (right). Electrophoresis is from top to bottom.

TABLE 1. Characteristics of the Newly Isolated 5S DNA from *X. mulleri* Compared to *X. mulleri* Oocyte 5S DNA

| | Oocyte-5S DNA | New 5S DNA |
|--|---------------|----------------|
| Density (g/cm ³) | 1.695 | 1.712 |
| Average no. of repeats | 9000 | 700 |
| Repeat length (base pairs) | 1400 | 900 |
| Length heterogeneity | great | not detectable |
| Strand separation in alkaline CsCl | yes | yes |
| 5S RNA coding strand | light | light |
| Restriction Enzyme Sensitivity (cuts/repeat) | | |
| EcoRI | resistant | resistant |
| HindIII | less than one | 1 |
| HpaII | variable | 3 |
| HhaI | variable | 2 |
| HaeIII | variable | > 5 |

The cloned Xm-new DNA has a biphasic melting curve, and both regions are high in G+C content. HaeIII, which cuts DNA at the sequence 5'-GGCC-3', digests about one-third of the 900-base-pair fragments into pieces of less than 40 base pairs. This suggests that the spacer has a short repeating sequence that contains a repetitive HaeIII cleavage site. The spacer region of cloned Xm-new DNA has little, if any, homology with Xm₀3 DNA by hybridization criteria. While *E. coli* RNA polymerase was found to transcribe the noncoding strand of *X. laevis* oocyte-type 5S DNA preferentially, the enzyme transcribes both strands of cloned Xm-new DNA about equally.

A restriction enzyme map of the cloned Xm-new DNA is being constructed in preparation for sequencing studies to determine what type of 5S gene the new DNA carries.

RECONSTRUCTION OF 5S RNA TRANSCRIPTION

S. Emmons

Our efforts to devise a system in which to detect and study 5S RNA transcription in vitro (*Year Book* 74, p. 19) have continued over the past year. The immediate aim is to develop a sensitive and specific assay for the initiation of transcription at the beginning of the 5S RNA gene.

For this purpose we have available to us a number of small (one hundred to a few hundred base pairs), well-characterized DNA "restriction fragments" cut from various regions of 5S DNA by restriction enzymes. Some of these fragments carry the initiation site for 5S RNA transcription, being produced by a cut before the gene region and a cut within the gene region. We envisage that these fragments may be used in one of two ways in transcriptional studies. First, they may be used as hybridization probes to determine whether a population of RNA transcriptions contains any molecules whose 5' ends are identical to the 5' end of 5S RNA. In this method, RNA transcripts are hybridized to the restriction fragment and treated with a single-strand-specific ribonuclease. RNA molecules resulting from a correct initiation event will give rise to an RNA fragment equal in length to the known length of the gene region carried on the restriction fragment. This RNA fragment could be identified by gel electrophoresis and nucleotide sequencing. In the second method, the DNA restriction fragment is used as a template for RNA polymerase or for RNA-synthesizing extracts. Since the fragment ends within the gene, correct initiation of transcription again results in an RNA fragment of known length.

Both of these approaches have been attempted using the (approximately) 450 base-pair fragment produced by

the restriction enzyme HaeIII from *X. laevis* oocyte 5S DNA. This fragment carries all of the A+T-rich spacer, the hypothetical promotor region(s) before the gene, and the first eight nucleotides of the gene itself (Fig. 2). To determine whether this fragment could be used as a hybridization probe, attempts were made to hybridize it with ^{125}I -labeled 5S RNA. For this purpose, the fragment was denatured and bound to nitrocellulose filters, and RNA annealed to it under conditions favoring the stability of the very short hybrid (1 M NaCl, 0°C). Under these conditions a 13-nucleotide-long oligomer (produced from 5S RNA by ribonuclease T1) annealed to 5S DNA, but shorter oligonucleotides did not, and ^{125}I -5S RNA did not anneal to the restriction fragment. It is presumed that this is because the RNA was not at a high enough concentration. Unfortunately, higher concentrations are not obtainable easily in an assay using a mixture of transcripts, so it is concluded that if restriction fragments are to be used as hybridization probes they must carry more than the first eight nucleotides of the gene.

The 450-nucleotide HaeIII fragment from *X. laevis* has also been used as a template in transcription studies. A protein extract of *X. laevis* ovaries was prepared following procedures of Roeder (*J. Biol. Chem.* 249, 241–248, 1974; personal communication), and its RNA polymerase activity analyzed using various templates. This extract was found to be relatively inactive on *Xenopus* 5S DNA fragments, compared with poly dAT and with *E. coli* plasmid fragments. No activity at all (conversion of precursor to TCA insoluble material) could be observed even with high concentrations of the 450 nucleotide fragment. In one experiment, the reaction mixture was nevertheless fractionated in a system (homochromatography on DEAE paper) that would have revealed the presence of an eight nucleotide oligomer, but none was seen.

The 5S gene system of *Xenopus* re-

mains an optimal one for attempts to reconstruct eukaryotic transcription in vitro. Purified 5S DNAs from several species are available as templates, and the structure of these DNAs is being studied intensely. Two classes of genes, expressed in different tissues (somatic and oocyte) exist, allowing an analysis of the mechanisms operating to control their expression. In addition, the primary transcription product in this system is small and of known sequence.

SEQUENCING STUDIES ON *Xenopus* 5S DNA

N. Fedoroff

We have focused on the introduction and development of direct DNA sequencing techniques. DNA sequencing methodology has been evolving rapidly over the past few years. The approach that has proved most fruitful is identification of the terminal nucleotide in successively shorter fragments having one fixed end. With technical improvements in oligonucleotide fractionation procedures, the number of nucleotides that can be ordered in a single analysis has increased steadily. Several laboratories are engaged in developing and improving different methods for generating the requisite fixed-end fragments and identifying terminal nucleotides.

Our immediate interest is in the nucleotide sequence of the spacer region adjacent to the 5' terminal portion of the 5S RNA gene in *Xenopus*, since this is likely to contain a control region for transcription. All of our studies so far have been done on a single repeating unit of *X. laevis* oocyte-type 5S DNA. Quantities sufficient for sequencing studies have been obtained by integration of the DNA into bacterial plasmids as described in previous sections. The distribution of restriction endonuclease HaeIII sites within this DNA, shown in Fig. 2, makes the region of interest accessible to direct sequencing in several ways.

We have, for example, used two dif-

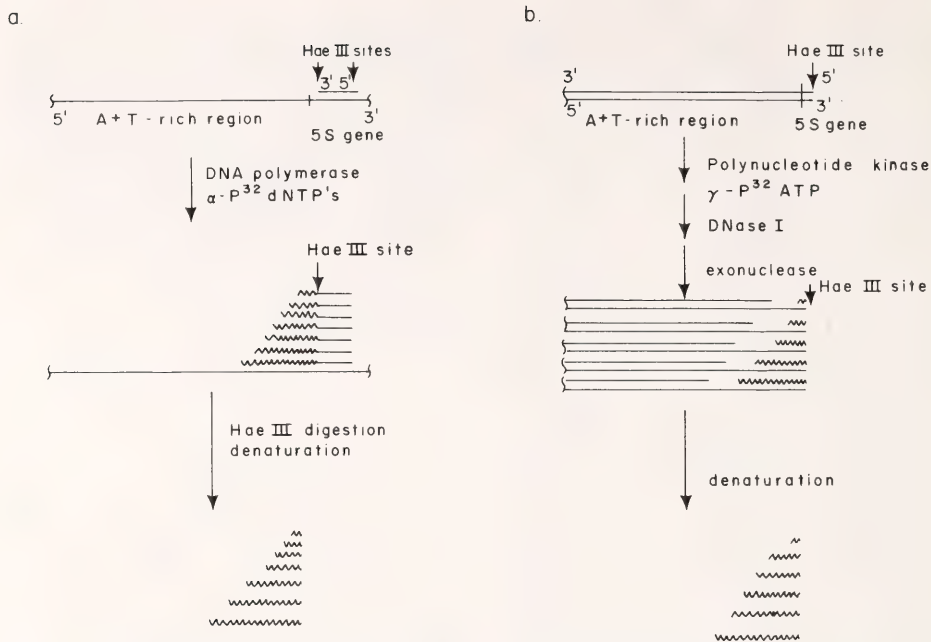


Fig. 5. Two schemes for direct DNA sequencing applied to the region adjacent to the initiation site of 5S DNA. A series of labeled DNA fragments (wavy lines) are generated which have a unique 5' terminus and a known 3'-end; that is, the nucleotide at the 3'-end is known to be A, T, G, or C. These different-sized fragments are separated by polyacrylamide gel electrophoresis. (a) The Sanger-Coulson method. (b) A modification developed in this laboratory. Details are given in the text.

ferent procedures to generate fragments which have a common 5' terminus and which extend over the region adjacent to the gene (Fig. 5). Figure 5a represents a direct application to 5S DNA of the scheme developed by Sanger and Coulson (*J. Mol. Biol.* 94, 441-448, 1975). The strand of 5S DNA containing the 5S RNA sequence (non-coding strand) is used as a template for *E. coli* DNA polymerase I. The HaeIII fragment extending from residue 9 to residue 66 of the 5S RNA sequence (Fig. 2) is used as a primer for the enzyme. The strand of the fragment complementary to 5S DNA (coding strand) is annealed to the template extended with DNA polymerase in the presence of α - P^{32} -labeled nucleotides. This generates a population of labeled fragments that begins at residue 8 of the 5S gene and extends into the adjacent spacer region (Fig. 5a). The identity of

the terminal nucleotide in the labeled fragments is determined by the following procedure. The extended primer-template complex is purified and aliquots are reincubated with DNA polymerase in the presence of either one or three unlabeled nucleotides. Under the conditions used, the labeled fragments are degraded until they terminate at the single included nucleotide, or extended until they terminate just prior to the single omitted nucleotide. For example, the reaction mixture containing TTP will yield only those oligonucleotides terminating in T residues. Since all fragments have a common 5' end, the position of T residues in the sequence can be deduced directly from the length of the T-terminated fragments. Separation of oligonucleotides that differ in length by a single residue is carried out by electrophoresis in high-percentage de-

naturing polyacrylamide gels.

One difficulty with this approach is inherent in the organization of the 5S DNA. As described in an earlier section, each repeating unit of *Xenopus laevis* oocyte 5S DNA contains both a gene and a very similar sequence, termed the "pseudogene" (see Fig. 2). The gene and pseudogene differ by approximately four nucleotides within the segment covered by the primer molecule. The primer, therefore, hybridizes to both regions, and the extended primer molecules represent sequences adjacent to both gene and pseudogene. One way around this difficulty is to determine the sequence of the short fragment released by digesting the extended template-primer complex with HaeIII as shown in Fig. 5a. Since the pseudogene lacks this HaeIII site, the radioactive fragments will be released from primer molecules on gene sequences but not pseudogene sequences. In principle, this permits determination of at least the first 50 residues of the spacer sequence adjacent to the gene before the longer fragments extended from the pseudogene interfere. Using this approach, we have obtained useful sequence information over a 30-nucleotide region beginning between 10 and 20 nucleotides from the first intragenic HaeIII site. The first 10 to 20 nucleotides are recovered in very low yield or not at all because of differential labeling and probably also because of differential degradation of short oligonucleotides.

We have developed an alternative procedure for generating the same population of labeled fragments that includes the region which is adjacent to the gene. In this procedure, illustrated in Fig. 5b, the population of labeled oligonucleotides is derived directly from the HaeIII fragment of 5S DNA which contains the A+T-rich spacer region and extends to the 8th residue of the gene sequence (Fig. 2). The coding strand of the fragment is labeled at the 5' end using α -³²P-labeled-ATP and

polynucleotide kinase. Label is introduced in only one of the two strands, essentially as described by Maniatis *et al.* (*Proc. Nat. Acad. Sci., U.S.A.* 72, 1184, 1975). A larger HaeIII fragment containing a HindIII site is labeled at both ends and cleaved with HindIII. The two resulting fragments, each labeled in only one strand, are recovered separately. The labeled fragment of interest is then nicked internally with DNase I at a low level. The nicks are enlarged into gaps by the 3' to 5' exonuclease activity of either the T4 DNA polymerase or snake venom phosphodiesterase. The gapped complex is equivalent to the extended primer-template complex in Fig. 5a, and subsequent steps in the sequencing procedure are identical. The fragments are extended with DNA polymerase in the presence of either one or three of the cold nucleotides and the lengths of the specifically terminated fragments are determined on a gel. As with the previous method, we observed a differential loss of short oligonucleotides. Using a fragment of known sequence (the intragenic HaeIII fragment), we have been able to derive an accurate sequence to within about 20 nucleotides from the 5' end of the molecule. Another difficulty we have encountered is that certain nicks introduced by DNase I appear to be relatively resistant to one or the other of the exonucleases used.

In general, the strengths and weaknesses of these enzymatic approaches are those discussed by Sanger and Coulson. The principal advantage of this method is that each terminal nucleotide is identified separately and each sequence is, in effect, determined twice within the same experiment. A shortcoming of this method is in sequencing runs of the same nucleotide, since a run is usually represented only by the oligonucleotide terminating just before the run and the oligonucleotide containing all members of the run.

In addition to the enzymatic methods

described above, we are using a chemical sequencing method for DNA which has been developed in the laboratory of W. Gilbert. In this procedure, termi-

nally labeled DNA fragments are cleaved chemically at specific bases, followed by the gel electrophoretic separation described above.

THE STRUCTURE OF RIBOSOMAL DNA FROM *Xenopus*

R. H. Reeder, P. Botchan, and I. B. Dawid

The nontranscribed spacer regions in *Xenopus* rDNA are heterogeneous in length; the physical basis for this length heterogeneity was described in *Year Book 74* (pp. 19–36). The studies of spacer structure involved the use of cloned fragments of rDNA generated with the restriction endonuclease EcoRI. EcoRI cuts each repeating unit of rDNA (gene plus spacer) into just two fragments—one containing only gene sequences and a second fragment that contains all of the nontranscribed spacer region plus some gene region on either end. Four of these spacer containing fragments (each with a different length spacer) have been cloned using a bacterial plasmid as vector. These cloned EcoRI fragments were used for the heteroduplex mapping experiments reported last year and have also been used in the restriction mapping described here. The structure of one of the fragments, Xlr14, is shown in Fig. 6.

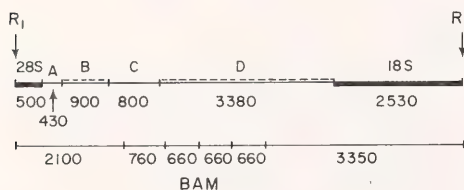


Fig. 6. Structure of the cloned rDNA fragment Xlr14. This fragment was generated by cleavage with EcoRI. As shown on the upper map, it contains some transcribed gene region on each end and all of the nontranscribed spacer region in the middle. The location of regions A, B, C, and D were defined from heteroduplex mapping. The dotted lines indicate regions that contain repeating sequences. The lower map shows the location of BAMHI cutting sites on the same fragment. Molecular weights are in base pairs.

Measurement of heteroduplexes formed between long and short cloned spacers led to the conclusion that each spacer contains two regions, each composed of a short repeating nucleotide sequence. One such region (region B in Fig. 6) is near the 28S sequence and the other (region D) is near the 18S sequence. Regions B and D appear to be separated from each other by a non-repetitious sequence (region C). In order to gain more insight into the structure of the nontranscribed spacer, we have begun to dissect these cloned fragments with other restriction enzymes.

The procedure we have used for mapping restriction cuts is as follows. Cloned spacer-containing fragments were labeled at both ends of the molecule using polynucleotide kinase to put a ³²P atom on the 5' end of each DNA chain. The label at the 28S end can be eliminated by restriction with endonuclease HindIII, which cleaves once, 500 bases from the 28S end. If the fragment now labeled only at the 18S end is partially cleaved with a restriction endonuclease, an overlapping set of fragments is created, all possessing the same ³²P labeled 18S termini. If the partial digestion products are then electrophoresed on a 1% agarose gel and their positions determined by autoradiography, the order of the terminal digestion products can be determined by subtracting the molecular weight of one partial product from the molecular weight of the next largest partial product. This procedure has been used for ordering the fragments produced by endonucleases SmaI, from *Serratia marcescens*, and BAMHI, from *Bacillus amyloliquefaciens*. Results of

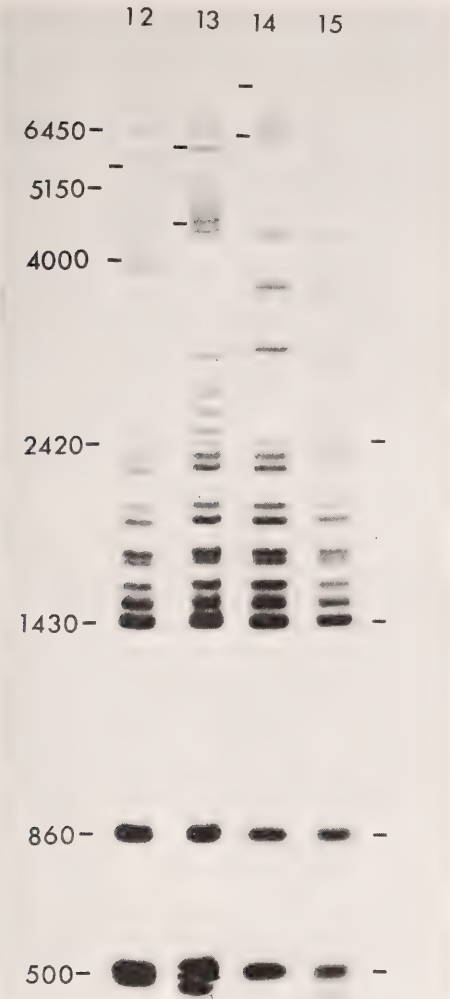


Fig. 7. Autoradiographs of partial SmaI digests of four cloned spacer containing fragments. Four EcoRI-generated spacer fragments (Xlr12, 13, 14, and 15) were end-labeled with polynucleotide kinase, digested with HindIII to remove the 28S end, and then partially digested with SmaI. After electrophoresis on 1% agarose the gels were dried and autoradiographed. The bands at 5150 and 6450 are from ColE1 plasmid carrier. Molecular weights are in base pairs.

SmaI partial digests on four cloned spacer-containing fragments are shown in Fig. 7 (the 500-base-pair terminally labeled fragment has not been separated out and appears as the bottom-most band). The SmaI diges-

tions reveal that the fragments produced from the 18S end of all clones are identical up to a point 2420 base pairs from the 18S end. At this point the location of SmaI sites diverges sharply among the different clones. The location of the divergence boundary agrees well with previous estimates of the gene-spacer boundary made from RNA-DNA heteroduplex measurement. Therefore, it appears that the nontranscribed spacer region shows some divergence close up to the gene-spacer interface. Within the transcription region, however, no sequence variation has been found among the four clones.

SmaI also appears to recognize a repeating sequence in region B. The clearest example is Xlr12 in Fig. 7 where SmaI produces a series of finely spaced bands starting at 4000 bases from the 18S end.

Mapping of the restriction fragments produced by BAMHI reveals that this enzyme recognizes sites only within the spacer region of all four clones. With three of the four clones BAMHI produces a fragment of about 3300 base pairs containing the 18S end, and from the same clones a fragment of about 2100 base pairs containing the 18S end. Internal to these terminal fragments is a region of expanding size which accounts for most of the size heterogeneity of the four clones. The internal spacer fragments vary from about 500 base pairs on the smallest clone to a 660 base-pair fragment that tandemly repeats itself five times on the largest clone. The exact order of BAMHI fragments on cloned Xlr14 is shown in Fig. 6.

Further restriction analysis has been done on the 2100 base-pair BAMHI fragment containing the 28S end. This fragment overlaps region B (Fig. 6) which has been shown by electron microscopy to contain a highly repeating sequence 100 base pairs or less in size. Digestion of the BAMHI fragment with either of the restriction endonucleases

HpaII, RII, SmaI, HHA or HaeIII reveals that all recognize a higher order repeating sequence of about 250–300 base pairs in length. Since all these enzymes recognize either the sequence 5' CCCGGG 3' or a simple variation of this, it is possible that the basic small repeat in this region is closely related to this sequence. In summary, the restriction analysis when combined with the electron microscopy reported last year indicates that: (a) the length heterogeneity of the clones is largely confined to one region of the spacer,

near the 28S end (region *D*; Fig. 6); (b) the spacer is composed of a short repeating sequence that is probably 100 base pairs or less in size; (c) the *D* region and possibly the *B* region also exhibit a higher order repeating structure superimposed upon the smaller sequence repeat. The latter two observations are characteristic of all "satellite" DNAs so far analyzed with restriction enzymes. The interest in this case is that the satellite is regularly interspersed between repeated gene sequences.

STUDIES OF HUMAN X-CHROMOSOME DNA

B. Migeon

We have begun attempts to isolate the human X-chromosome or portions of it. The X-chromosome in mammals is subject to a control mechanism termed heterochromatinization in which all but one X-chromosome in a cell are in a condensed, inactive form in interphase cells. Although there has been much speculation, little is known about the molecular basis for this

unique form of gene regulation.

In metaphase, inactive X-chromosomes (although indistinguishable from their active homologues by all chromosome staining techniques) can be identified because they replicate very late during DNA synthesis and are the last chromosomes to terminate replication. The inactive X is also identifiable in interphase nuclei because of

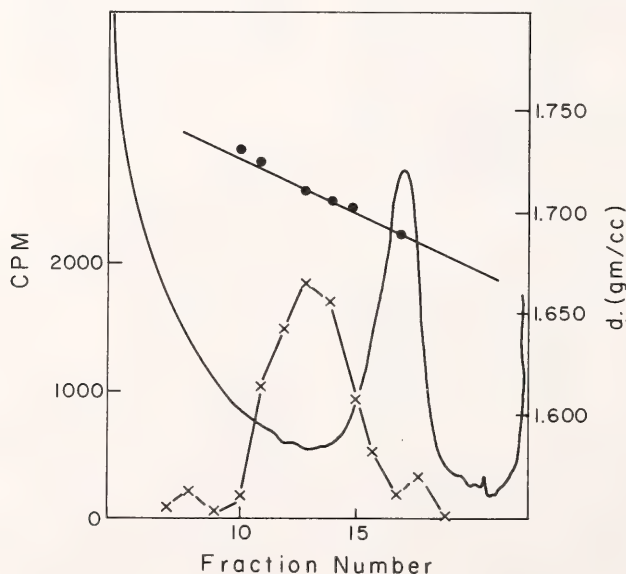


Fig. 8. BrdU-labeled DNA from isolated chromosomes centrifuged to equilibrium in CsCl. The purified chromosome fraction of human lymphocytes that had been stimulated to divide with a mitogen was labeled with ^3H -BrdU for 1 hr and chased for 3 hr. cts/min (x—x) A_{260} (—).

its highly condensed state at a time when the majority of DNA from other chromosomes is dispersed. It may be possible to isolate this highly condensed X (or Barr body) from interphase cells, but this requires a highly specific assay for X-chromosome DNA.

As a preliminary step we have initiated experiments designed to obtain X-specific DNA sequences that may provide the essential probe for the Barr body isolation. We are attempting to isolate X-specific DNA from the *inactive* X-chromosome because the timing of its replication enables us to label the X-DNA selectively with bromodeoxyuridine (BrdU). The newly synthesized DNA has a greater buoyant density and can be separated on that basis from other chromosomal DNA.

We have established short-term cultures of leukocytes from the peripheral blood of human females and exposed these cells to a one-hour pulse of ^3H -BrdU (S.A. 1 Ci/mM) during the terminal period of DNA synthesis. After several hours cells that had incorporated BrdU into DNA reach metaphase and are blocked at that stage with colchicine. The next step is to purify chromosomes from interphase cells in the culture. Chromosomes are separated from contaminating interphase nuclei by velocity sedimentation in a sucrose gradient. The fractions con-

taining chromosomes—but no nuclei—are pooled, and the DNA is extracted. Only late replicating DNA incorporates the BrdU, thereby altering the buoyant density of DNA and permitting the separation of the BrdU-substituted DNA from the unsubstituted DNA by cesium chloride density gradient centrifugation.

The BrdU-labeled DNA can be a template for the synthesis of complementary RNA and the cRNA obtained can be hybridized *in situ* to human metaphase chromosomes to determine its specificity.

Examination of chromosomes from cultured cells obtained just prior to cell lysis has revealed that under the conditions used, BrdU is incorporated into the chromosomal DNA—and that most of the label is confined to the X-chromosome. However, under these conditions, only a few metaphase cells have labeled chromosomes. We have been able to obtain a small amount of BrdU-labeled DNA isolated as a satellite of the main band (Fig. 8). The quantity, however, has so far been insufficient to use as template for cRNA synthesis.

We are attempting to increase the field of specifically labeled DNA and decrease the small amount of contamination released from breakdown of interphase nuclei.

CHROMOSOMAL PROTEINS AND THE CONTROL OF GENE FUNCTION

*R. H. Reeder, A. Bokhon'ko, and H. L. Wahn
with the assistance of E. Hogan*

We have continued to improve the method for isolating nucleoli from *Xenopus* oocytes so that we can recover not only the amplified ribosomal DNA as chromatin but also several enzymatic activities associated with it. We have demonstrated both RNA polymerase I activity previously known to be associated with rDNA as well as an enzymatic activity that relaxes superhelical turns in DNA. Some evi-

dence suggests this latter activity may be involved in transcribing rDNA.

In *Year Book 74*, pp. 27–28, we presented evidence that at least some fraction of the rDNA in *Xenopus* cultured cells is in subunit configuration with chromosomal proteins. This year we expanded this observation by demonstrating that the A+T-rich satellite DNA of mouse is also organized with proteins in the same subunit fashion.

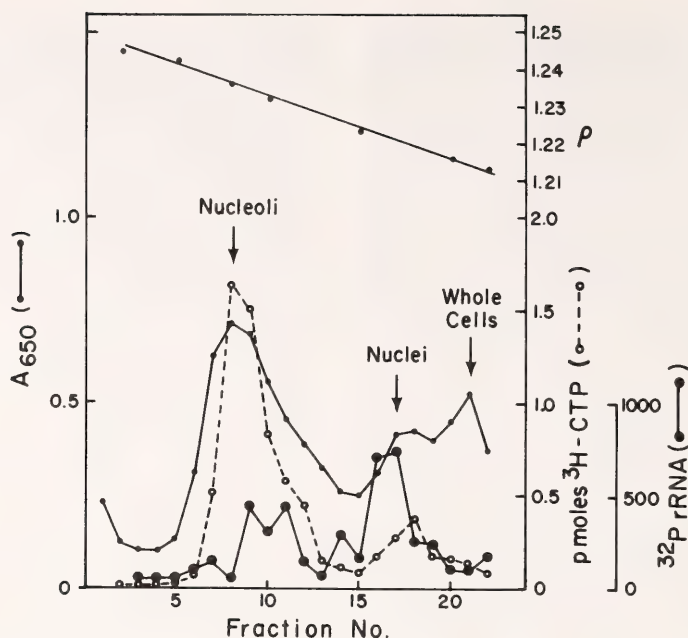


Fig. 9. Isolation of amplified nucleoli on a metrizamide density gradient. A homogenate of immature *Xenopus* oocytes was used to pour a metrizamide density gradient as described in the text. Fractions were analyzed for light scattering, A_{650} (•—•); ribosomal DNA hybridization (●—●); and RNA polymerase activity (○—○).

ISOLATION AND CHARACTERIZATION OF AMPLIFIED NUCLEOLI

H. L. Wahn and R. H. Reeder

We have improved the previous method for isolating amplified nucleoli by the addition of a density gradient separation as the final step. Immature pigment-free oocytes were isolated essentially as described in *Year Book 73* (p. 28). The oocytes were then homogenized in a solution of metrizamide and the homogenate used to pour a linear metrizamide density gradient. Metrizamide is an inert tri-iodinated benzamido derivative of deoxyglucose which can be used to form gradients that cover the entire density range of biological macromolecules. Since metrizamide is non-ionic, the gradients do not dissociate nucleoli or other cellular organelles and they can be isolated in an apparently native state.

Figure 9 shows the result when a metrizamide density gradient was used

to fractionate a whole oocyte homogenate. Examination of each fraction by phase contrast microscopy revealed that nucleoli were banded at a relatively high density location well separated from contaminating nuclei. Measurement of light scattering at 650 nm (metrizamide absorbs ultraviolet light) showed a peak of scattering that coincided with the location of nucleoli in the gradient and which coincided with a peak of rDNA as measured by hybridization with radioactive rRNA. If nucleoli were rebanded in a second-round metrizamide gradient, it was possible to reduce bulk chromosomal DNA contamination to less than 10% of the total DNA found in the nucleolar peak (as judged by analytical ultracentrifugation analysis).

Nucleoli isolated by this method have all the characteristics expected for nucleoli that are active in rRNA synthesis. As seen in Fig. 10 they show RNA polymerase activity. This RNA polymerase is sensitive to actinomycin D and resistant to high concentrations

of α -amanitin. Therefore, it has the properties of the template requiring polymerase I or nucleolar polymerase. In addition, these isolated nucleoli exhibit the normal morphology characteristic of active nucleoli when analyzed by electron microscopy, and they contain both 40S and 30S rRNA precursor.

However, when nucleoli are re-banded on a shallow metrizamide gradient, it is apparent that not all are equally active in transcription. Figure 10 shows another gradient in which RNA polymerase activity and rDNA amount were measured in each fraction. The more dense nucleoli have a much higher polymerase to rDNA ratio than do the less dense nucleoli. Although we do not yet know the basis for this subfractionation of nucleoli, it has

proved very useful in helping to determine which proteins are associated with transcriptionally active rDNA.

Figure 11 shows an SDS-acrylamide gel electrophoresis of total nucleolar proteins from each fraction across a second-round metrizamide gradient. The distribution of RNA polymerase activity and rDNA is also shown for the same gradient. Our next major task is to sort out these proteins, subtract those which are involved only in ribosome assembly, and determine the function and location of those proteins which bind to the rDNA. Some proteins, such as the four major histones, have distributions that appear to coincide with the distribution of rDNA. Several other protein bands, however, follow the distribution of RNA polymerase activity and these are of prime interest for future study.

One highly interesting protein that distributes with the polymerase activity is an enzyme that relaxes supercoiled DNA. To assay for this enzyme, nucleolar fractions were incubated with supercoiled Col E1 plasmid DNA and the DNA was electrophoresed on a 1% agarose gel. A densitometer trace of the stained gel is shown in Fig. 12. Some of the supercoiled DNA has been completely relaxed while some of it has been trapped at intermediate levels of supercoiling, giving rise to a series of discretely spaced bands in the gel. The relative level of DNA-relaxing enzyme was assessed by measuring the amount of completely supercoiled DNA left after incubation for a standard time interval. The distribution of relaxing activity across a metrizamide gradient is shown in Fig. 10. It is clear that the relaxing enzyme tracks with RNA polymerase activity and not with the rDNA distribution. This suggests that the relaxing enzyme may be an integral part of the transcription machinery. It seems unlikely that the presence of this relaxing enzyme is due to the presence of DNA replication, since these nucleoli are in a replication dead end. They have previously replicated their DNA weeks to months before iso-

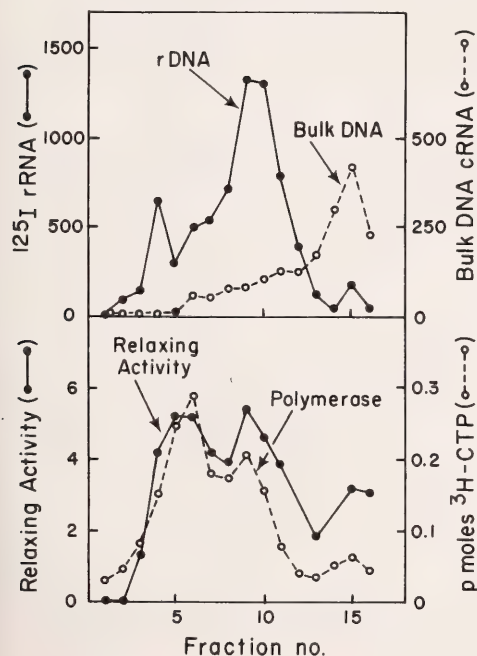


Fig. 10. Association of RNA polymerase-relaxing and DNA-relaxing activities with nucleoli. Nucleoli were banded in a second-round metrizamide density gradient, and fractions were assayed in various ways. Upper panel: Ribosomal DNA hybridization (●—●). Bulk chromosomal DNA hybridization (○—○). Lower panel: DNA-relaxing activity (●—●). RNA polymerase activity (○—○).

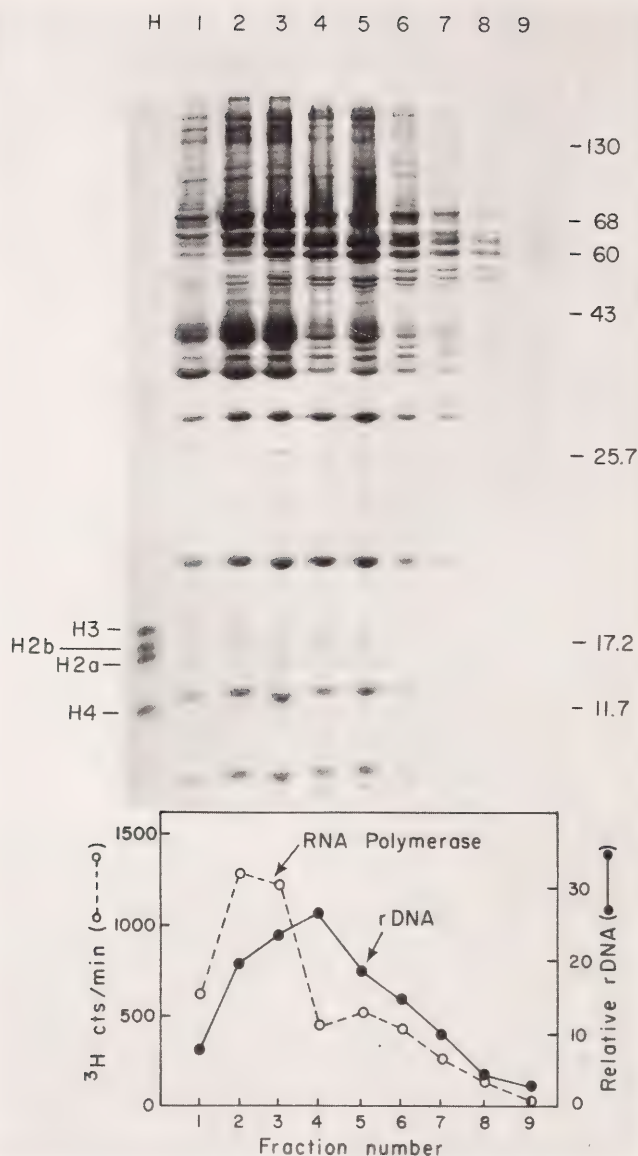


Fig. 11. SDS-acrylamide gel electrophoresis of proteins from nucleoli banded in metrizamide. Nucleoli were banded in a second-round metrizamide gradient, and protein from each fraction was electrophoresed on a 15% acrylamide-SDS gel. Aliquots of each fraction were also assayed for RNA polymerase activity (○—○) and ribosomal DNA location (●—●). Lane H shows acid-extracted *Xenopus* histones. Molecular weights are in daltons $\times 10^{-3}$.

lation and they will never enter the replication cycle again. Furthermore, we cannot detect any significant DNA polymerase activity associated with these nucleoli even after adding an exogenous template.

Since amplified rDNA is most likely present as circular molecules, it is quite reasonable that a relaxing enzyme might be necessary for some phase of transcription. Initiation by RNA polymerase requires localized

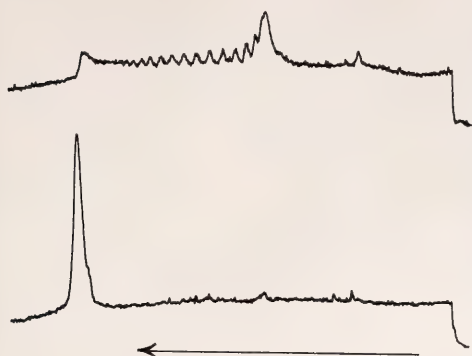


Fig. 12. Assay of nucleolar DNA relaxing enzyme. Supercoiled ColE1 plasmid DNA was incubated in the presence (upper trace) and in the absence (lower trace) of nucleoli purified through metrizamide. The ColE1 DNA was then electrophoresed on a 1% agarose gel, and the DNA was located by staining with ethidium bromide. Direction of electrophoresis is from right to left. Supercoiled ColE1 (major peak in lower trace) has a higher mobility than relaxed circular ColE1 DNA (major peak in upper trace). The intermediate bands differ from each other by integrals of one supercoil turn.

strand separation of the DNA and therefore must introduce superhelical strain into the DNA. It is also possible that chain elongation causes similar physical changes in DNA structure, especially if the polymerase must dislodge histones as it transcribes the gene. Therefore, an enzymatic activity that would release physical strains placed on the DNA by transcriptional processes would be required to return the DNA to its normal state.

THE SUBUNIT ORGANIZATION OF MOUSE SATELLITE CHROMATIN

A. Bokhon'ko

Most of the DNA in a eukaryotic chromosome is complexed with histones to form subunits resembling

beads on a string. This structure can be observed with the electron microscope and can be demonstrated in several indirect ways. One property of this subunit organization is that DNA contained within the bead is more resistant to endonuclease attack than is DNA between the beads. Thus, limited digestion of chromosomes with nuclease cleaves the DNA into small fragments that are multimers of about 200 base pairs of DNA. An example of this phenomenon is shown in Fig. 13. In this experiment mouse liver nuclei were briefly digested with nuclease, and the DNA was deproteinized and electrophoresed on an acrylamide gel. An oligomeric series of bands is observed, resulting from histone protection in the chromatin subunits.

It is of interest to know if there are any specific DNA sequences that are exempt from this type of subunit organization. Last year we presented evidence that some fraction of the ribosomal genes were so organized and suggested that histones may be present on actively transcribed sequences. This year we have used similar techniques to examine the A+T-rich satellite sequences in mouse DNA. This DNA is located in highly condensed centromeric heterochromatin and appears never to be transcribed in the cell.

The experiment is shown in Fig. 13. After brief digestion of mouse liver nuclei with micrococcal nuclease the protected DNA fragments were electrophoresed on an acrylamide gel. The gel was then sliced and the DNA in each slice was hybridized with radioactive RNA transcribed *in vitro* from purified mouse satellite L-strand. The hybridization essentially follows the distribution of the bulk DNA, and we conclude that mouse satellite is also organized in a similar subunit fashion.

Together, these results increase the likelihood that histones are associated with all of the chromosomal DNA regardless of its function.

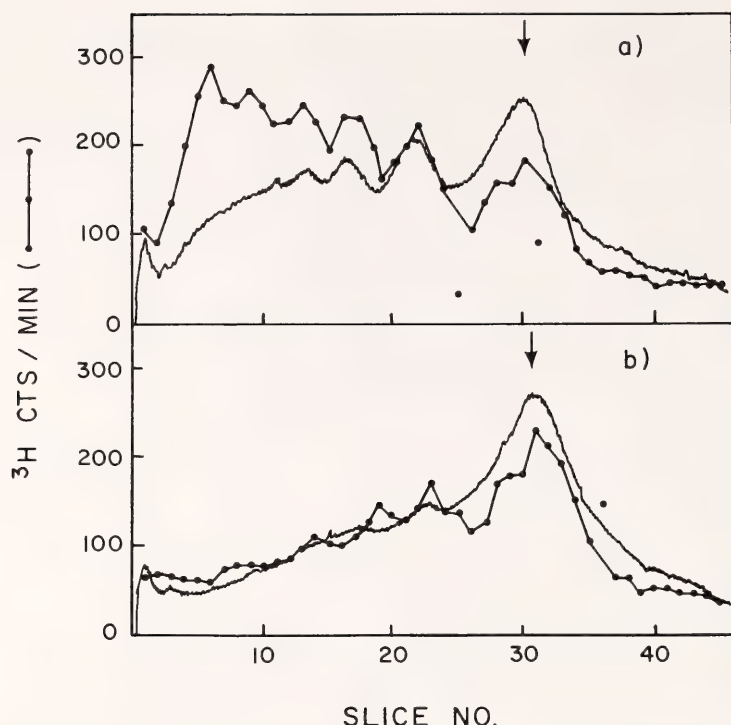


Fig. 13. Hybridization of mouse satellite cRNA to micrococcal nuclease fragments from mouse liver nuclei. Mouse liver nuclei were partially digested with micrococcal nuclease, and the DNA fragments were purified and electrophoresed on a 6% acrylamide gel. The gel was sliced and the DNA in each slice was hybridized with ^3H cRNA transcribed in vitro from the L-strand of purified mouse satellite DNA. The bulk DNA was located by staining with ethidium bromide. (a) Fragments from nuclei digested for 5 min. (b) Fragments from nuclei digested for 20 min. The arrow indicates the position of the presumed monomer at approximately 170 base pairs.

THE POLARITY OF RIBOSOMAL DNA IN *Xenopus*

I. B. Dawid, R. H. Reeder, P. K. Wellauer, T. Higashinakagawa
in collaboration with O. L. Miller, Jr.*

Ribosomal RNA (rRNA) in *Xenopus* and other eukaryotic nuclei is transcribed as a precursor molecule containing both 18S and 28S RNA regions and transcribed spacer segments. The question of whether the 18S or the 28S region is closer to the 5' end of the precursor has been answered in opposing ways (Year Book 69, 565; Year Book 72, 38; Year Book 73, 45; and Year Book 74, 20). We have undertaken a re-investigation of this question which leads to the strongly supported conclusion that the 18S RNA sequence is closer to the 5' end (transcription origin) of the precursor than is the 28S

RNA sequence. This order of sequences is almost certainly correct for rRNA precursor molecules of other eukaryotes as well. Transcription in the direction of small-to-large rRNA is a general feature of genomes, including prokaryotes, eukaryotic nuclei, chloroplasts and mitochondria. A model of a segment of *Xenopus laevis* ribosomal DNA with the correct polarity of the precursor is shown in Fig. 14.

DETERMINATION OF POLARITY WITH DNA EXONUCLEASES

The first test of polarity in rRNA that we describe depends on the

*University of Virginia.

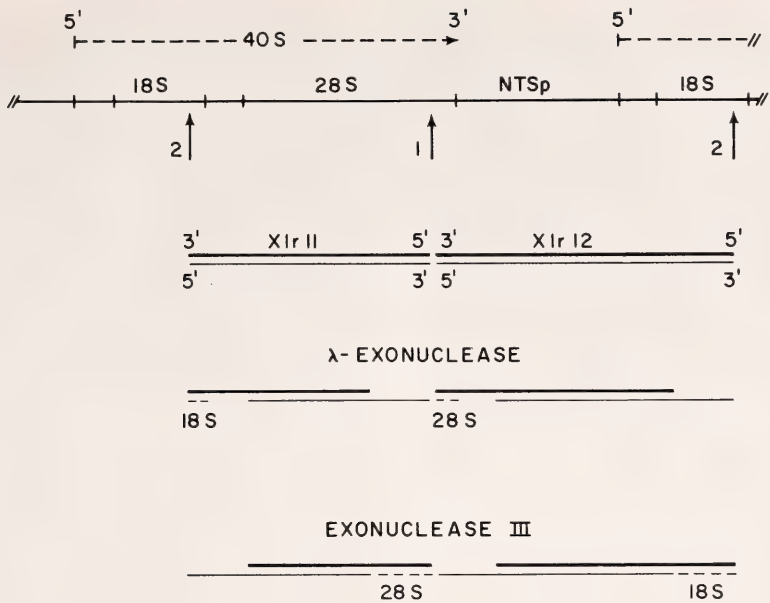


Fig. 14. Determination of rDNA polarity with DNA exonucleases. The figure is described in the text.

availability of fragments of rDNA whose ends have been mapped with respect to the rRNA (see Fig. 14) and of DNA exonucleases with known specificities. Exonuclease III from *E. coli* (specific for 3' ends) and lambda exonuclease (specific for 5' ends) were donated by former fellows of our Department, John Chase and John Morrow, respectively. The principle of the experiment is illustrated in Fig. 14. At the top we show a model of a segment of rDNA with the polarity that is supported by the experiments reported here. EcoRI cleaves each repeat twice, creating two types of fragments. Such fragments have been cloned in *E. coli* and two particular ones are named Xlr11 and Xlr12. In Fig. 14 the coding strand is the "heavier" line and the polarity of each strand is indicated in agreement with the polarity of the RNA. Such rDNA fragments were partially digested with each of the two exonucleases until about 20% of the DNA was hydrolyzed. The models in Fig. 14 illustrate the resulting molecules. Lambda exonuclease digestion of Xlr11 removes the anti-coding

strand in the 18S region, thereby exposing 18S sequences on the coding strand. At the other end of Xlr11 the same exonuclease digests the coding strand only. The resulting DNA fragment with single-stranded tails is therefore expected to hybridize with 18S rRNA only, as indicated in the figure by dotted line. Similar models for the other fragments and both exonucleases are shown in Fig. 14. When the opposite polarity is assumed in the rRNA, the predictions for exonuclease III and lambda exonuclease are simply interchanged. We consider the conclusion from these experiments to be firm because the specificities of the two exonucleases have been well established and because the test involves four separate experiments (two fragments, two exonucleases) all of which give highly consistent data in support of the same polarity.

DETERMINATION OF POLARITY
USING rDNA TRANSCRIPTION
COMPLEXES

The second test of polarity makes use of the fact that ribosomal gene trans-

cription complexes can be spread for viewing in the electron microscope. This technique was first developed by O. L. Miller, Jr., at the University of Virginia, and this experiment was done with his collaboration. The nascent rRNA chains in such transcription complexes are seen to be short at one end of the complex (the 5' end of the precursor) and to increase in length until they are released at the other (3') end. To determine which end the 18S rRNA sequence was near, we digested transcription complexes with the restriction enzyme EcoRI which cuts rDNA at two known locations within the transcribed region.

The cut transcription complexes were then spread for electron microscopy, and we measured the distances from cut sites to either termination (3' end) or initiation (5' end) sites.

The experiment is diagrammed in Fig. 15. In panel (a) a full-length transcription complex is shown at top with the location of EcoRI sites indicated, assuming the 18S sequence is proximal to the 5' end of the precursor. Below are shown the four types of transcription complex fragments that would result from this model. Four types of cut ends are generated because proteins on the rDNA block the EcoRI sites with a certain probability so that only partial digestion is achieved. Panel (b) shows the predicted fragments if the opposite polarity is assumed.

Measurement of 100 EcoRI cut transcription complexes yielded results that agreed well with model (a) and strongly disagreed with model (b). This supports the conclusion that the 18S sequence is proximal to the 5', or initiation, end of the rRNA precursor.

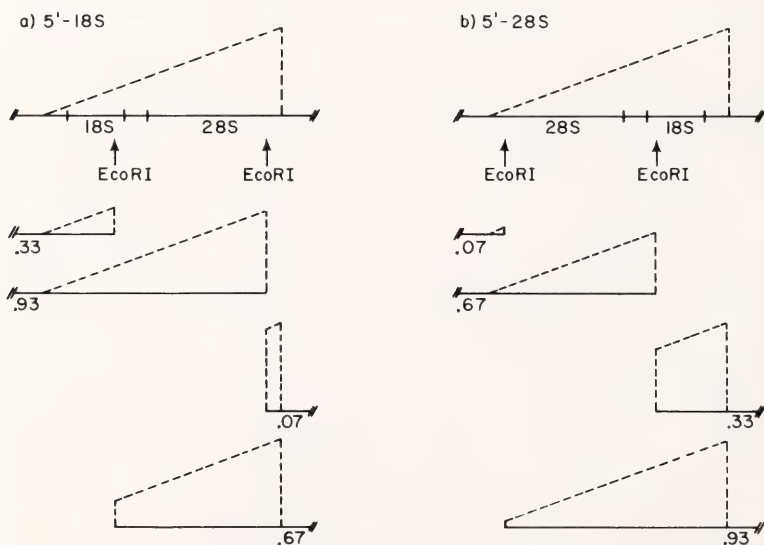


Fig. 15. Determination of rDNA polarity using EcoRI on transcription complexes. The figure is described in the text.

RIBOSOMAL DNA IN *Drosophila melanogaster*

P. K. Wellauer and I. B. Dawid
in collaboration with K. D. Tartof of the Institute for Cancer Research Philadelphia,
and with the assistance of M. Rebbert

The genes that code for the large ribosomal RNA (rRNA) molecules occur in multiple copies. The ribosomal DNA (rDNA) forms clusters of redun-

dant genes in the nuclei of all organisms studied. Since the rDNA of many species has special physical properties, it may be isolated and characterized. The rDNA of *Xenopus laevis* was the first eukaryotic gene to be purified (Year Book 67, 401), and this DNA has since been characterized extensively (see Year Book 74, p. 19, and this Year Book). In spite of the fact that *Xenopus* rDNA had been isolated some time ago and the isolation of rDNA from other organisms seemed technically feasible, few reports on the purification and detailed characterization of rDNAs have appeared in the literature. It is clear that the properties of rDNA are of great interest, and that generalizations about the structure and evolution of this DNA can be based only on the comparison of results with several organisms. We decided to study rDNA in *Drosophila melanogaster* because this organism offers the advantage of producing many known mutants that affect the ribosomal locus, and because it shows the interesting phenomena of compensation and magnification of rDNA.

PURIFICATION OF *Drosophila* rDNA

In contrast to *X. laevis*, *Drosophila* rDNA is not a density satellite, i.e., the buoyant density of rDNA is very close to the density of the average DNA. We achieved purification of the rDNA in two different ways. In the first procedure *Drosophila* DNA, purified from embryos, was centrifuged in cesium sulfate in the presence of 0.2 moles of mercury ions per mole of nucleotide. The rDNA was located by hybridization with rRNA, the corresponding region of the gradient pooled, and the DNA centrifuged in cesium chloride in the presence of actinomycin D. Again, rDNA was pooled and centrifuged in cesium sulfate with mercury at a ratio of 0.08. The rDNA pooled from this third gradient was usually "pure," which means that we estimate its purity above 80% (see below).

The second method for rDNA purifi-

cation is based on the R-loop procedure developed by White and Hogness of Stanford University. When native DNA and RNA are annealed in high concentrations of formamide at the right temperature, the RNA invades the duplex and displaces one of the DNA strands. The resulting complex is suitable for mapping by electron microscopy and also for preparative purposes, since the RNA/DNA hybrid is more dense than native DNA. Thus, *Drosophila* DNA was incubated with rRNA and centrifuged in cesium sulfate. The rDNA region, which was slightly more dense than the main band of DNA, was pooled and centrifuged again in the same way. The

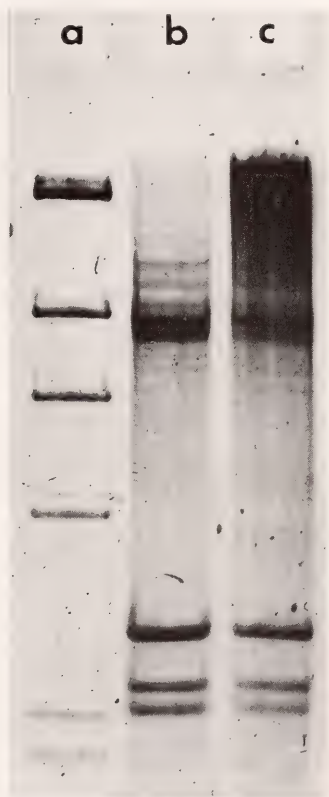


Fig. 16. Electrophoretic patterns of *Drosophila* rDNA digested with the restriction endonuclease *Sma*I. Electrophoresis is from top to bottom; the gels were stained with ethidium bromide and photographed in ultraviolet light. Lane a, marker fragments from a *Hind*III digest of lambda DNA; lane b, partially purified rDNA containing 10–20% rDNA; lane c, rDNA purified by the mercury–actinomycin D method.

resulting rDNA was pooled and the RNA removed. The product was effectively pure rDNA of high molecular weight.

The purity of rDNA is most easily checked by digestion with the restriction endonuclease *Sma*I. Figure 16 shows that rDNA is cleaved into one class of fragments of about 8.5 kb (kilobases or kilobase pairs); this class is heterogeneous because of length heterogeneity in the rDNA repeating units (see below). Further, there are discrete fragments of 2.8, 2.3 and 2.2 kb. Since *Sma*I sites are rare in main-band DNA, contaminating DNA is largely uncleaved and appears in the

gel as a broad band moving more slowly than the 8.5-kb fragment set. This is easily seen in Fig. 16*b*, which shows the pattern given by an *Sma*I digest of partially purified rDNA. By comparison, lane *c* of Fig. 16 shows little if any contaminating material.

ANALYSIS OF *Eco*RI FRAGMENTS OF *Drosophila* rDNA

The restriction endonuclease *Eco*RI cleaves rDNA into a number of fragments (Fig. 17*a*). Predominant bands of 16.5 and 11 kb are seen. In addition, there are bands of intermediate size,

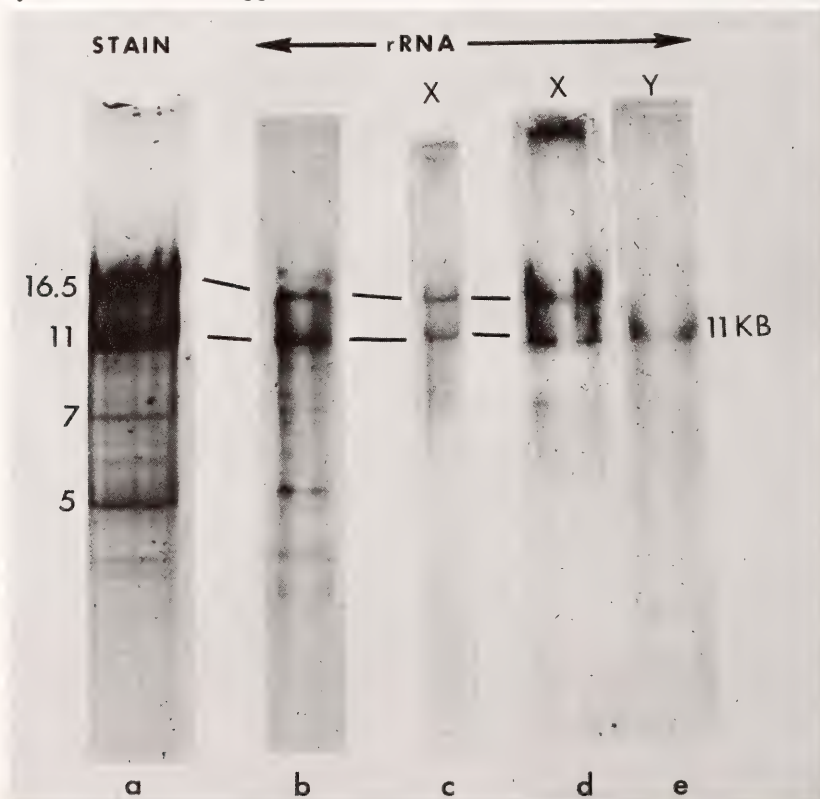


Fig. 17. Electrophoretic patterns of *Drosophila* rDNA digested with the restriction endonuclease *Eco*RI. Lane *a*, from wild-type male and female flies stained with ethidium bromide. Lane *b*, purified wild-type rDNA was digested and separated by electrophoresis, and the DNA fragments were transferred to membrane filters as described in Southern (*Journal of Molecular Biology* 98, 503-517, 1975), and hybridized with labeled rRNA. The figure shows the autoradiogram of the hybridized filter. Lanes *c* and *d*, autoradiograms of rDNA patterns from DNA isolated from flies that carried a *bobbed* mutation on their Y chromosome so that at least 95% of the rDNA is derived from the X chromosome. Lane *e*, rDNA pattern from flies of the genotype *sc*^{*l*}-*sc*^{*8*}/Y in which the nucleolus organizer is deleted from the X chromosome.

and many bands smaller than 11 kb, among which two bands at 7.4 and 5.4 kb are relatively abundant.

Electron microscopy was used to analyze the structure of EcoRI fragments of rDNA. We first summarize the results and then illustrate some of the evidence for it. The fragments of 11 kb and larger are the results of a single EcoRI cut in the 18S RNA region of each rDNA repeating unit. The 11-kb fragments have a structure similar to that of *Xenopus* rDNA: The 18S and 28S rRNA regions are separated by a short spacer segment that is likely to be transcribed (Sp1 in Fig. 18B) and by a longer spacer segment that must contain mostly nontranscribed sequences (Sp2 in Fig. 18B).

The 16.5-kb fragments contain a rather unexpected type of structure: In addition to the regions found in the 11-kb fragments there is a spacer segment that is inserted within the 28S gene region. We call this spacer the "insertion." Figure 18A shows that this insertion is located 1.13 kb from the end of the 28S gene. In *Drosophila* as in other insects, 28S rRNA as isolated has a break about in the middle. The position of this break is seen in the maps of

Fig. 18 as a gap, suggesting that the break is generated from the original continuous transcript by the removal of about 140 bases. It is important to note that the position of the spacer insertion and the position of the gap are separated by 740 base pairs. The insertion occurs in different size classes. The most abundant class is a long insertion that is present in the 16.5-kb type of repeating unit. Other insertion sizes account for the EcoRI fragments found in the gel between the 11- and 16.5-kb positions. Remarkably, the insertions occur in size classes that are multiples of a basic size of close to 0.5 kb. Whether the larger insertions are actually repetitions of the 0.5-kb sequence is not known. EcoRI fragments smaller than 11 kb are produced by additional cuts in some repeating units of rDNA.

Before we discuss the implications of these structures we show some of the evidence for them in Fig. 19. The figure shows hybrid molecules between single strands of rDNA EcoRI fragments and rRNA. In the DNA fragments that contain insertions, one 28S rRNA molecule hybridizes with its complementary sequences on both sides of

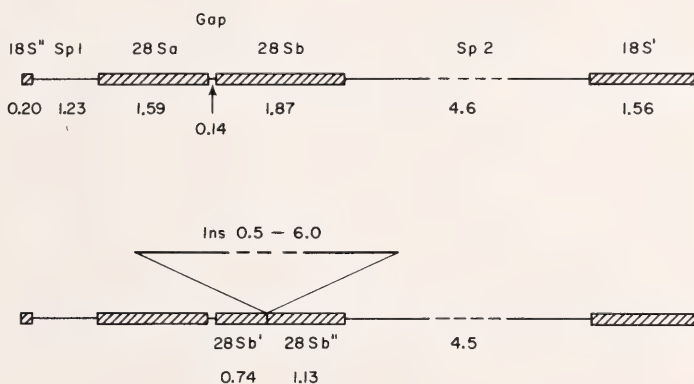


Fig. 18. Models of EcoRI fragments of *Drosophila* rDNA. These fragments constitute complete repeats. The EcoRI site is in the 18S RNA region. Sp1 is likely to be transcribed; Sp2 is mostly nontranscribed. The gap in the 28S RNA region is the position where an interruption occurs in the 28S RNA. Sp2 is shown as a broken line, since length heterogeneity occurs in this region. Model B shows the 11-kb fragment; the numbers are the sizes of the different regions in kb. Model A shows the class of fragments that contain an insertion of spacer sequences within the 28S gene region. Those regions not labeled in model A have the same length as in model B. The insertion occurs in size classes from 0.5 to 6.0 kb and in multiples of 0.5 kb.

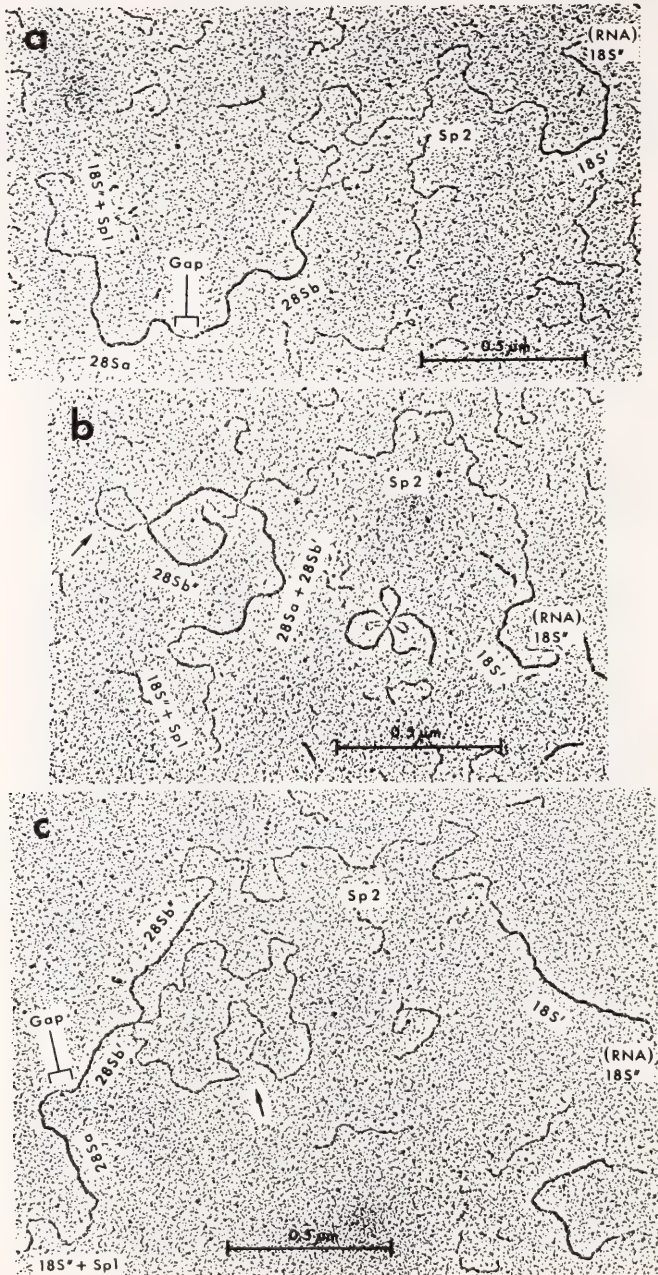


Fig. 19. Electron micrographs of hybrid molecules between EcoRI fragments of *Drosophila* rDNA and rRNA. Hybrids were prepared for electron microscopy by the formamide modification of the Kleinschmidt technique. The various regions are indicated and are explained in the legend to Fig. 18. Insertions are indicated by arrows. (A) 11-kb EcoRI fragment. (B) EcoRI fragment with a 1.5-kb insertion. (C) EcoRI fragment with a 5.0-kb insertion.

the insertion so that the insertion forms a loop. Such molecules, which were frequent, show most clearly that the position of the strand interruption in the 28S RNA and the position of the insertion in the gene are distinct. In Fig. 19 we show one 11-kb repeat and two insertion repeats, one from the major (16.5-kb) class and another molecule with a 12.5-kb repeat that has a 1.5-kb insertion.

These observations raise the question of whether, and if so how, the rDNA repeats with insertions are transcribed. To produce intact 28S rRNA there would have to be transcription from gene sequences on both sides of the insertion with subsequent ligation of the products by a hypothetical RNA ligase. Or, the RNA polymerase would "jump" across a loop of DNA, as the RNA does in the hybrids of Fig. 19. Such a mechanism has not been described in any system. Alternatively, the genes with insertions may not be transcribed, or transcription may end at the insertion point (we assume that transcription begins to the left of the 18S region and proceeds towards the 28S region. In the latter case RNA transcripts would arise from the insertion-carrying genes, but they could not produce complete 28S rRNA and would be nonfunctional. One would then ask why the inserted genes have been conserved during evolution. At present we cannot choose among these alternatives and cannot answer the questions raised by the observations.

LENGTH HETEROGENEITY IN THE SPACER REGION

In addition to the length differences in the insertion there is also length heterogeneity in spacer 2 (Fig. 18), which corresponds to the "standard" nontranscribed spacer of *X. laevis* rDNA. This length heterogeneity is less extreme than in *Xenopus*, with most spacers falling into a fairly narrow distribution. Nevertheless, we

have obtained unequivocal evidence for the existence of heterogeneity by examination of heteroduplex molecules. EcoRI fragments of rDNA were separated on gels, and 11-kb, 16.5-kb, and intermediate fragments were isolated. These fragments were denatured and allowed to reassociate. Many of the duplex molecules that formed had single-stranded deletion loops in the spacer region. Especially in those molecules where only a single loop appeared we may conclude that the spacers of the two strands which formed the duplex differ in length.

Drosophila rDNA has two regions in which length heterogeneity occurs: the insertion, which comes in multiples of 0.5 kb and accounts for most of the heterogeneity; and the nontranscribed spacer, which varies in length in a narrow range without detectable size classes.

ARRANGEMENT OF LENGTH HETEROGENEITY

We have tried to resolve whether rDNA repeats without insertions and with insertions of different length occur in clusters, or whether they are interspersed along the chromosome. High molecular weight rDNA was isolated, denatured, hybridized with rRNA, and inspected in the electron microscope. The results demonstrate that repeats of different length are interspersed. Repeats of 11 kb may occur next to 11-kb, 16.5-kb, or intermediate length repeats, and the same is true for all classes of repeats. A statistical evaluation of 85 pairs of adjacent repeats shows that the frequencies with which different types of repeats are nearest neighbors are close to those expected from a random assortment of the different length classes. In some cases a tendency toward clustering of similar repeats was seen, and we cannot decide whether the distribution is fully random or not. But it is clear that extensive scrambling of different repeat sizes occurs in *Drosophila* rDNA,

as it does in the rDNA of *Xenopus* (Year Book 74, p. 22).

DISTRIBUTION OF rDNA REPEAT LENGTHS ON THE X AND Y CHROMOSOMES OF *D. Melanogaster*

In *D. melanogaster* the rDNA is clustered in one nucleolus organizer each on the X and the Y chromosome. About 200 repeats of rDNA compose each wild type nucleolus organizer. To test the structural properties of rDNA derived from the two genetic loci we digested DNA from the appropriate stocks with EcoRI, separated the fragments by electrophoresis, and hybridized the fragments with rRNA by the method of Southern. Figure 17 shows some of the results. While in resolution the hybridized gels do not match the stained gel of purified wild type rDNA, it is clear that the X chromosome carries both major classes of repeat length (11 kb and 16.5 kb), while the Y chromosome carries the 11-kb fragment but not the 16.5-kb fragment. Minor fragments occur on both chromosomes but are not well displayed in Fig. 17 c to e.

These observations raise some intriguing questions about the evolution of tandem repetitive gene families and about the "correction mechanism" pos-

tulated to operate during this evolution (see Year Book 74, p. 19). There is prior genetic evidence against recombination between the X and the Y chromosomes. The absence of 16.5-kb fragments on the Y chromosome supports this evidence: If such recombination occurred, one would expect the 16.5-kb fragments to spread to the Y chromosome unless some unknown mechanism prevents these repeats from occurring on the Y chromosome. If, however, the X and the Y are genetically isolated, how are the similarities between them maintained? These similarities are extensive, since rRNA transcribed from either chromosome is very similar and probably identical, and the 11-kb fragments and some other features of gene organization are closely similar in X and Y rDNA. If there were no genetic exchange, one would have to postulate that selective pressures maintain all these features on the two separate chromosomes. It appears to be difficult to adhere to such a hypothesis in its strict form. However, we would like to raise the possibility that selection plays a larger part in the maintenance of homogeneity in tandem gene families than had been believed. *Drosophila* rDNA seems highly suited for experiments that will aid in understanding these processes.

STRUCTURAL AND FUNCTIONAL STUDIES OF FIBROIN GENES

Y. Suzuki, Y. Ohshima, P. Geshelin, and P. E. Giza

We wish to know how a tissue-specific gene is transcribed in that tissue at a given time. More practically, our long-term goal is to understand fibroin gene control by reproducing its function in vitro with the purified gene and other necessary components. Each gene system has certain advantages and disadvantages for this kind of study. The fibroin gene system in the posterior silk gland of *Bombyx mori* has the advantages that (1) the coding sequence is extremely simple, internally repetitious, and of high G+C con-

tent; (2) the gene comprises a high proportion of the genome; (3) its expression is temporally regulated, and fibroin mRNA comprises an unusually high proportion of cellular RNA at certain developmental stages; and (4) isolated nuclei also synthesize the mRNA in high proportion. Making use of these advantages, we have been employing three approaches toward our goal: (1) development of methods for purifying fibroin genes, (2) development of methods for cloning genes, and (3) transcriptional analysis of fibroin

genes in vivo and in vitro. Some of our progress is summarized below.

PHYSICAL PURIFICATION OF THE GENE CODING FOR SILK FIBROIN

P. Geshelin

In order to characterize the manner in which silk fibroin synthesis is controlled, we need to isolate the DNA that codes for the protein. Single-copy genes from various organisms are being isolated in several laboratories at present using one of two general methods. In the first, a small amount of whole-organism DNA is partially purified by proved physical methods, enzymatically attached to plasmid DNA, and grown in infected bacteria. After the clone(s) of bacteria that contain the sought-after sequences are selected (usually by hybridization to the corresponding messenger RNA), the gene is replicated many times over by growth of the clone(s). In the second method the tiny amount of desired DNA is isolated physically from a huge amount of DNA from the whole organism by hybridizing messenger RNA to the sheared DNA and separating the DNA-RNA hybrids from the rest of the DNA by utilizing the physical properties of the RNA. One makes use of the higher density of the RNA, compared to DNA. This density differential can be increased by binding substances to the RNA before hybridization. Alternatively, the RNA can be covalently bound to a solid support (i.e., agarose beads) before hybridization, and the DNA not annealed to it after hybridization may be simply washed away.

Attempts are under way to isolate silk fibroin DNA by a modification of these physical methods. Messenger RNA coding for silk fibroin will be covalently bound to mercury atoms by procedures developed by Ward and co-workers (*Biochemistry* 14, 2447-2457 and 2458-2469, 1975). The messenger RNA will then be mixed with whole-cell DNA and placed at the melting temperature of the DNA in high

formamide. Because RNA-DNA duplexes are more stable than DNA-DNA, especially in the solvent formamide, the RNA displaces the minus or coding strand of DNA from the helix over the region to which the RNA is homologous, forming a triple-stranded structure termed an R-loop. These R-loops will then be separated from the rest of the nucleic acid by affinity chromatography on sulhydryl agarose, which selectively binds the mercury atoms.

This new method could have several advantages over previous procedures for purifying single-copy genes. First, one will get both strands of the silk fibroin DNA, in contrast to the methods involving melting and annealing, which yield only the coding strand. Second, affinity chromatography theoretically offers much greater resolution between mercurated and non-mercurated nucleic acids than does density centrifugation between DNA and RNA. Finally, since the resolution of the separation technique does not depend on DNA size, one can strive to isolate whole-gene DNA with large flanking sequences thought to contain important control sequences.

CLONING OF FIBROIN GENE PLASMID

Y. Ohshima and Y. Suzuki

The fibroin gene exists as a single copy per haploid complement. However, the gene is so large (about $12-14 \times 10^6$ daltons) that it comprises 0.004% of the *B. mori* genome. In order to be able to carry out the structural and functional analyses of the gene, we need to have large amounts of it in a pure form. Therefore, we are trying to obtain an *E. coli* clone that carries a recombinant plasmid including the whole fibroin gene with some adjacent DNA. Such plasmid DNA, when it is isolated, can be produced in milligram quantities and will be of crucial importance for our experiments.

The plasmid we have chosen is tetracycline-resistant Col E1 type plasmid PMB9. It has a molecular

weight of 3.5×10^6 and carries a replication function in the presence of chloramphenicol and one restriction site each for the endonucleases EcoRI and HindIII. In order to recombine this plasmid with a large DNA molecule containing the full-size fibroin gene and some extra sequences (about 25×10^6 daltons) we employ the dA-dT joining method. Covalently closed DNA of PMB9 was isolated and made into linear forms by EcoRI. For poly(dA) or poly(dT) addition we use terminal deoxynucleotidyl-transferase from calf thymus in the presence of 1 mM CoCl_2 (in either the presence or the absence of MgCl_2). We have succeeded in adding the single-stranded tail of poly(dA) or poly(dT) directly to EcoRI ends of the plasmid DNA without pretreatment of the DNA by lambda exonuclease. Most of the dA or dT incorporation was found co-sedimenting with the plasmid DNA in a neutral or an alkaline sucrose gradient. When observed under the electron microscope, 80–90% of the ends of the plasmid DNA have a single-stranded tail.

For the fibroin gene part, in order to obtain the adjacent control regions as well as the whole coding sequence in a plasmid we must start with a high molecular weight preparation of *B. mori* DNA, since the gene is extraordinarily large. We isolated a large quantity of DNA with a molecular weight of $15\text{--}30 \times 10^6$ from frozen silk glands. After two successive CsCl-gradient bandings in the presence of actinomycin D, we obtained a DNA preparation in which fibroin gene DNA assayed by hybridization with ^{125}I -mRNA was enriched by 40-fold (the gene concentration is about 0.2%). With this DNA we propose to make poly(dT) tail additions to the poly(dA)-tailed PMB9 DNA followed by transformation of *E. coli*. *E. coli* clones carrying the fibroin gene-PMB9 plasmid will be selected by tetracycline resistance and hybridizability with ^{125}I -mRNA of high specific activity (about 1×10^4 cpm/ng).

ACCENTUATED EXPRESSION OF FIBROIN GENES IN VIVO AND IN VITRO

Y. Suzuki and P. E. Giza

We have developed a direct chemical method for quantitating fibroin mRNA in RNA mixtures (*Year Book* 73, p. 20). Using this method we have measured the amount of fibroin mRNA in the posterior silk gland of *B. mori*. Fibroin mRNA accumulates throughout the fifth instar, ultimately comprising as much as 4.4% of the total cellular RNA toward the end of the instar. The number of fibroin mRNA molecules accumulated by the end of the fifth instar was 5.8×10^4 molecules/gene, about 5-fold higher than the number of rRNA molecules (1.1×10^4 molecules/gene). This observation has led us to estimate the rates of fibroin mRNA and rRNA accumulation at various stages of the instar. As shown in Table 2, it was found that (1) the rate of mRNA accumulation is almost constant throughout the stage, whereas that of rRNA changes as much as 30-fold, and (2) mRNA accumulation relative to gene number is proceeding at a higher

TABLE 2. Rates of Accumulation of Fibroin mRNA and rRNA during the Fifth Instar

| Time Intervals* | rRNA | Fibroin mRNA |
|-------------------|--------------------|--------------|
| | molecules/gene/min | |
| Ecdysis – 1st day | 1.8 | < 1.2 |
| 1st day – 2nd day | 6.6 | 10 |
| 2nd day – 4th day | 2.6 | 7.9 |
| 4th day – 6th day | 0.3 | 7.4 |
| 6th day – 7th day | 0.2 | 9.3 |

*Every 24-hr period after the fourth ecdysis was designated as 1st day, 2nd day, etc. The quantitation of the RNAs was done at ecdysis and at the end of 1st, 2nd, 4th, 6th and 7th days. The difference in amount of RNA between two time points was divided by the total number of genes and the time elapsed (24 hrs or 48 hrs in minutes). The number of genes was calculated from the amount of DNA present at the middle of the two time points, with the further assumption that each haploid complement of DNA contains 240 rRNA genes and 1 fibroin gene.

rate than that of rRNA not only at later stages of the instar but throughout the instar except on the 1st day. The most exaggerated situation is seen on the 7th day of the instar. At this stage new rRNA synthesis almost ceases while mRNA accumulation continues actively. These results as well as the consideration of the high proportion of fibroin genes in the genome have prompted us to try to detect fibroin mRNA in pulse-labeled RNAs by our direct chemical method.

The calculated proportion of fibroin mRNA synthesized and accumulated for different labeling periods of 10 to 720 min at various stages of the fifth instar and the preceding fourth moulting stage are summarized in Table 3. As expected from the exaggerated situation found on the 7th day of the instar, fibroin mRNA was detectable even by a 10-min pulse, and occupied as much as about 4% and 6% of the total cellular RNA pulse-labeled on the 7th and 8th day of the instar, respectively (Table 3). These are the highest proportions of transcription ever found for a single mRNA species. The proportion of mRNA becomes even greater with longer pulses, and reaches as high as 24% of the total RNA labeled in a 240-min pulse, indicating that fibroin

mRNA is much more stable than other heterogeneous RNAs. When 30-min pulses were given at various stages of the fifth instar as well as the fourth moulting stage, it was found that fibroin mRNA was not detectable during the moulting stage, but in contrast, as the fifth instar proceeded the proportion of mRNA increased from 1.2% up to 7.5% (Table 3). These observations indicate that the synthesis of RNAs of non-fibroin mRNA type is active at the earlier stages, decreasing drastically toward the end of instar, since it was already shown that the rate of fibroin mRNA accumulation is constant throughout the stage (Table 2). As for the moulting stage, we cannot determine whether fibroin genes are inactive or whether their transcription is not detectable simply because of a rapid and selective degradation of fibroin mRNA.

From the proportion of fibroin mRNA (Table 3) and rRNA (not shown) synthesized in a 4-hr and a 12-hr pulse in the 7th day we calculated rates of each RNA synthesis per gene. The ratio of the rates of fibroin mRNA synthesis to that of rRNA synthesis was about 50 to 1 both for the 4-hr and 12-hr pulses. This result indicates that fibroin mRNA is being synthesized

TABLE 3. Proportion of Fibroin mRNA to Total Cellular RNA Synthesized during Short-Pulse Periods*

| Stage† | Time of Pulse Labeling | | | | |
|-----------------|------------------------|--------|--------|---------|---------|
| | 10 min | 30 min | 90 min | 240 min | 720 min |
| | Proportion (%) | | | | |
| Fourth moulting | ... | <1.7 | ... | ... | <0.5 |
| Fifth instar | | | | | |
| 1st day | ... | ... | ... | ... | 0.6 |
| 2nd day | ... | 1.2 | ... | ... | 1.8 |
| 3rd day | ... | 2.0 | ... | ... | ... |
| 4th day | ... | 3.0 | ... | ... | 4.6 |
| 6th day | ... | 4.8 | ... | ... | 10 |
| 7th day | 3.9 | 7.5 | 12 | 24 | 27 |
| 9th day | 5.9 | ... | ... | ... | ... |

*Pulse-labeling experiments were done in the middle of the day.

†Defined as in Table 1.

‡Not determined.

about 50 times more rapidly than rRNA. Because the ratios are the same between the two time points, we infer that rRNA and fibroin mRNA have similar stabilities during these labeling periods and that the ratio of transcription for these genes would also be near 50 during shorter labeling periods at this stage.

Because of this accentuated expression of fibroin genes *in vivo*, we have tried to isolate and characterize silk gland nuclei aiming at transcription *in vitro* (*Year Book* 74, p. 36). The nuclear isolation method has been applied to the determination of the distribution of unlabeled and newly synthesized fibroin mRNA in the cell. The results are shown in Table 4. More than 80% of the long lived mRNA which was identified by A₂₆₀ oligonucleotide profile after T₁ RNase digestion was found in the cytoplasm, and only 8% in the nuclei. With our current nuclear isolation method we must admit the possibility of contamination of cytoplasmic RNA in our nuclear preparations. Therefore, we conclude that most, if not all, of the long-lived mRNA is localized in the cytoplasmic fraction. The result also indicates that with our current method we can eliminate about 90% of unlabeled fibroin mRNA from the nuclear preparation. The newly synthesized fibroin mRNA (in 30 min) was found about equally in the cytoplasmic fraction (47%) and the nuclear fraction

(51%). This indicates that it takes less than 30 min to transport fibroin mRNA from the nucleus to the cytoplasm.

RNA synthesis with disrupted and isolated nuclei using endogenous RNA polymerase was carried out at 25 °C. The incorporation of ³H-UTP or α-³²P-UTO was almost linear for 30 min, and then slowed, but a slight increase was still observed at 120 min. The labeled RNA was usually extracted after 30 min incubation for characterization. RNA transcribed *in vitro* was hybridized to *B. mori* DNA fractionated by Act D/CsCl (Fig. 20). The hybridization conditions were such that only transcripts of repetitive sequences, which include fibroin mRNA because of its internal repetitive nature, hybridized. As shown in Figure 20, a prominent hybridization peak is seen at fractions 9 to 11. This peak is presumed to be rRNA since it was competed for by cold rRNA. A small and heterogeneous peak at fractions 16 to 19, which is the region for fibroin genes, was competed for by unlabeled pure fibroin mRNA (see Table 5). It was also observed that virtually all of the counts hybridized were competed for by total posterior gland RNA. These results indicate that similar repetitive sequences are transcribed both *in vivo* and *in vitro*.

The RNA labeled *in vitro* for 30 min was fractionated by a Bio-Gel A-50m column (Fig. 21a) and compared with the RNA labeled *in vivo* for 30 min

TABLE 4. Localization of Fibroin mRNA in Cytoplasmic and Nuclear Fractions

| Fractions | Newly Synthesized mRNA* (%) | Long-Lived, Unlabeled mRNA† (%) |
|---------------------|-----------------------------------|---------------------------------------|
| Cytoplasmic sup (a) | 47 | 84 |
| Sucrose sup (b) | 2 | 8 |
| Nuclear pellet (c) | 51 | 8 |

Homogenate of posterior silk glands from the 7th day of the fifth instar was washed and centrifuged three times in the presence of NP40, and the combined supernates were designated as cytoplasmic sup (a). Crude pellet thus obtained was centrifuged through 2.2 M sucrose, and the supernate (b) and nuclear pellet (c) were obtained.

*Posterior silk glands were labeled *in vivo* for 30 min with ³H-uridine and subjected to the fractionation mentioned above, and radioactive fibroin mRNA was quantitated by T₁ RNase fingerprint method.

†The long-lived, unlabeled mRNA was quantitated by A₂₆₀ oligonucleotide profile after T₁ RNase digestion.

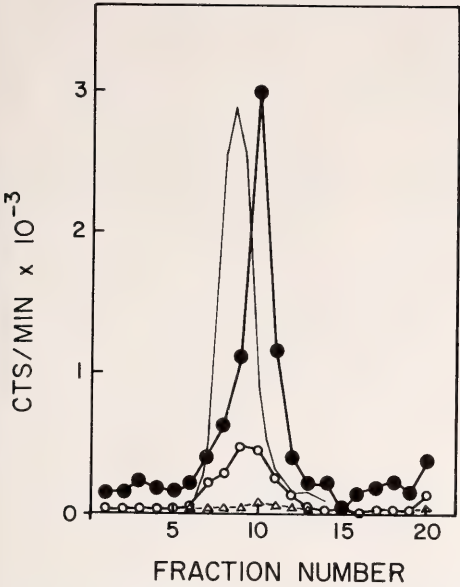


Fig. 20. Hybridization of RNA synthesized in vitro to *B. mori* DNA fractionated by Act D/CsCl and competition of the hybridization by unlabeled posterior silk gland RNA. The RNA was labeled with 500 μ Ci of α - 32 P-UTP (23.7 Ci/mmole) in vitro for 30 min in disrupted nuclei (170 μ g of DNA). Aliquots equivalent to 5% of whole nuclear preparation from a pair of posterior silk glands were hybridized to *B. mori* DNA (200 μ g/gradient) in the presence or absence of competitor at 50°C for 17 hr in 50% formamide-4 \times SET. No competitor added (\bullet); competitor RNA equivalent to 20-fold excess of posterior-gland nuclei added (\circ — \circ); competitor equivalent to 200-fold excess of posterior-gland nuclei added (Δ — Δ).

(Fig. 21b). Comparison of Fig. 21a and Fig. 21b reveals that the radioactivity profiles from Bio-Gel columns are similar for RNA labeled in vitro and in

vivo. However, there is a higher proportion of lower molecular weight RNAs labeled in vitro than in vivo. More than 55% of the radioactivity of the RNA in vitro was found in the region larger than 28S (Fig. 21a).

The void volume fraction shown in Fig. 21a, which contained 14% of the total radioactivity, was recovered and an aliquot was subjected to RNase T₁ digestion for characterization. The sample was estimated to contain about 15% fibroin mRNA (Fig. 22c). Therefore, we conclude that about 2.1% of the total transcripts synthesized in vitro by disrupted nuclei in 30 min was fibroin mRNA of apparent full-size length. This is the highest value ever found for a single mRNA species and is about two orders of magnitude higher than that of globin mRNA sequences synthesized in vitro. The hybridization assay was used to confirm the presence of mRNA sequences. An aliquot of the void volume fraction of Fig. 21a was hybridized to DNA in the fibroin gene region (Fig. 23). The hybrid was recovered from filters 10 to 15, digested with T₁ RNase, and the digest was subjected to a DEAE-Sephadex A25 column (Fig. 22d). Figure 22d demonstrates the existence of fibroin mRNA sequences in the RNA in vitro, and a comparison of Fig. 22c (15% pure fibroin mRNA) with Fig. 22d (40% pure) indicates that mRNA was selected by the hybridization procedure.

Nucleoplasmic RNA polymerase II is known to be sensitive to low concentrations of α -amanitin and is possibly the

TABLE 5. Inhibition of Fibroin mRNA Synthesized in vitro by Low Dose of α -Amanitin

| System of RNA Synthesis | Hybridization to Partially Purified Fibroin Genes | |
|-----------------------------------|---|------------------------|
| | Without Cold Fibroin mRNA | With Cold Fibroin mRNA |
| Complete (a) | 474 cpm | 124 cpm |
| Complete + α -amanitin (b) | 156 cpm | 112 cpm |

Nuclei containing 150 μ g of DNA were incubated with 80 μ Ci of 3 H-UTP for 30 min in the absence (a) or presence (b) of 0.2 μ g/ml of α -amanitin. For assay 2.0 mg of *B. mori* DNA was fractionated by Act D/CsCl, and 10% aliquots of the fractions containing fibroin genes were used for hybridization. For the hybridization 2.5% aliquots of each reaction mixture (a or b) were used in the absence or presence of unlabeled fibroin mRNA (5.1 μ g/ml). Hybridization was done at 50°C for 2.5 hr in 5 ml of 50% formamide-4 \times SET.

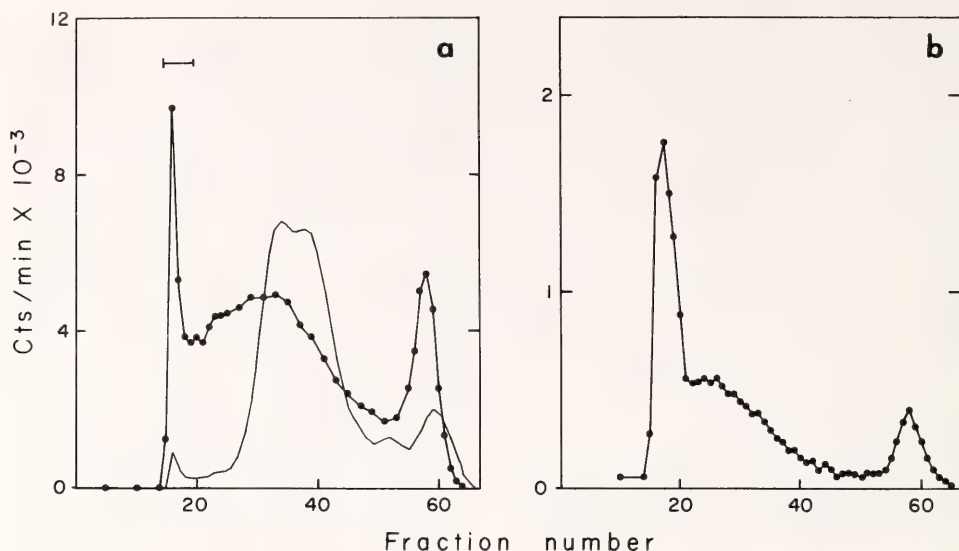


Fig. 21. Bio-Gel fractionation of the RNAs synthesized in vitro by disrupted nuclei (a) and in vivo (b) in 30 min. (a) On the 7th day of the fifth instar disrupted nuclei were isolated from the posterior silk glands. An aliquot of the nuclei containing about 200 μ g of DNA was incubated with 250 μ Ci of α -³²P-UTP (10 Ci/mmole) and other ingredients in 1.0 ml volume at 25°C for 30 min. The RNA products were applied to a 2.6 \times 66 cm column of Bio-Gel A-50m, 5.5-ml fractions were collected, and 0.5-ml aliquots were counted after TCA precipitation. (b) A larva was injected with 2.5 mCi of ³H-uridine on the 7th day of the fifth instar and incubated at 25°C for 30 min. The RNA was extracted from the posterior gland and fractionated as in (a). cts/min/0.5ml (●—●); A₂₆₀ monitored by a Gilson spectrophotometer (—).

polymerase form that is involved in transcription of the nuclear precursors to mRNAs. Therefore, we wondered whether fibroin mRNA synthesis in disrupted nuclei is sensitive to low doses of α -amanitin. RNA synthesis was carried out for 30 min in the presence or absence of 0.2 μ g/ml of α -amanitin. The drug inhibited 21% of RNA synthesis in vitro. Each product was hybridized to partially purified fibroin genes in the presence or absence of unlabeled pure fibroin mRNA as a competitor (Table 5). Fibroin mRNA, as defined by labeled RNA that hybridized to fibroin DNA and was competed for by excess cold fibroin mRNA, was not synthesized in the presence of α -amanitin, thus providing the first direct evidence that RNA polymerase II is the form that transcribes structural genes in the living cell.

We wanted to test the ability of the disrupted nuclei to initiate RNA synthesis in vitro. Incorporation of γ -³²P-ATP was carried out for 30 min. The RNA was fractionated on a Bio-Gel A-50m column (Fig. 24). Aliquots of fractions 14 to 19 were pooled and subjected to the following analysis. The sample was digested with RNase T₁ and the digest was divided into two. One part was directly fractionated by a DEAE-Sephadex column (Fig. 25a). The other was digested further with alkaline phosphatase and then subjected to a DEAE-Sephadex column (Fig. 25b). In Fig. 25a, digests having negative charges of 5.5, 6.5, 7.5 and so on were observed. These are tentatively identified as ³²ppp^Ap^Gp, ³²ppp^Ap^Xp^Gp, ³²ppp^Ap^Xp^Xp^Gp and so on. The ³²P-radioactivity shown in Fig. 25a was mostly sensitive to alkaline phosphatase (Fig. 25b). This result excludes

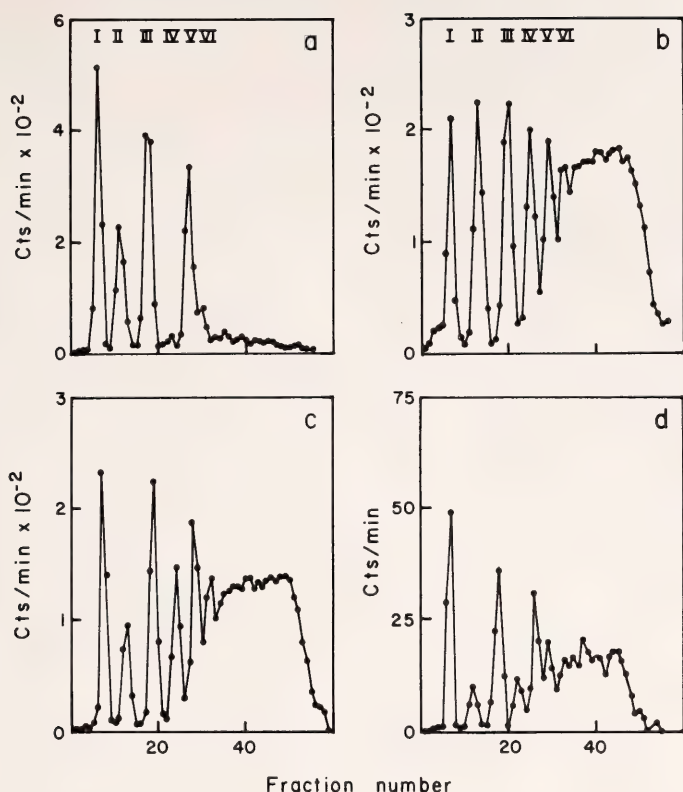


Fig. 22. RNase T_1 "fingerprints" of various RNAs labeled with α - ^{32}P -UTP. (a) Pure fibroin mRNA from the posterior glands labeled in vivo for 24 hr during the 6th day of the fifth instar. (b) High molecular weight RNA (void volume fraction of a Bio-Gel A-50m column) from animal's carcass labeled in vivo for 24 hr during the 6th day. (c) An aliquot of crude fibroin mRNA fraction (the void volume fraction shown by the bracket in Fig. 21) synthesized in vitro in disrupted nuclei. (d) Other aliquot of the void volume fraction of Fig. 21 was hybridized to fibroin genes (Fig. 23), and purified. ^{32}P cts/min (●—●).

the unlikely possibility that a strange structure like $\text{A}(5')\text{ppp}^{32}(5')\text{G}_p$ or $\text{A}(5')_{\text{ppp}}^{32}(5')\text{X}_p\text{G}_p$ is the product. Fractions 20 to 54 were also pooled, and analyzed. Hydrolysis of an aliquot of the sample by 0.3N KOH gave a single peak at a negative charge of 4.3 (Fig. 25c), which we tentatively identify as $^{32}\text{ppp}^{\text{A}}\text{ppp}$. Therefore, ^{32}P was not incorporated into internal positions. Digests having negative charges of 5, 6, 7, etc., were obtained by pancreatic RNase digestion (Fig. 25d) together with an unidentified peak having -3.8 charge. By T_1 RNase digestion we found digests having negative charges of 5.5, 6.5, 7.5, etc. (Fig. 25). There was

a small peak cochromatographing with 5'-ATP marker and a large peak having -4.3 charge which we could not identify (Fig. 25e). Although there are some unidentified products in the digests, we conclude that most of the γ - ^{32}P -ATP was incorporated at the 5' end of RNA molecules in the void column fraction, which contained 15% fibroin mRNA, as well as in the lower molecular weight region of the Bio-Gel column (Fig. 24). These observations that the disrupted nuclei retain their ability to reinitiate RNA synthesis strengthen the usefulness of the system for the study of fibroin gene regulation in vitro.

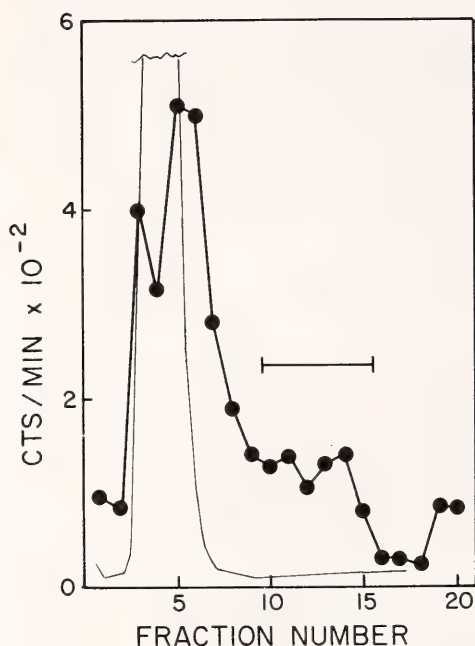


Fig. 23. Hybridization of crude fibroin mRNA synthesized in vitro to partially purified fibroin genes. *B. mori* DNA (2.0 mg) was fully sheared, actinomycin D (1.0 mg) was added, and the refractive index was adjusted to 1.3842. The mixture was centrifuged at 32,000 rev/min at 20°C for 66 hr in a Spinco 50.2 rotor, and fractions were trapped on filters. The void volume fraction of Fig. 21a was hybridized to the DNA filters in 50% formamide-4 × SET at 50°C for 20 hr, and the RNA hybridized to fibroin gene region shown by the bracket was recovered for RNase T₁ "fingerprint" analysis (Fig. 22d). In order to obtain enough counts the hybridization and elution of the hybrid RNA was repeated. cts/min (●—●); A₂₆₀ (—).

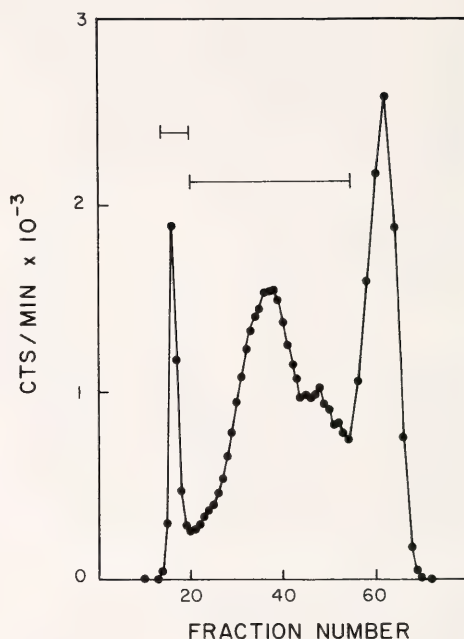


Fig. 24. Incorporation of γ -³²P-ATP into RNA synthesized in vitro by disrupted nuclei. Nuclei containing 150 μ g of DNA were incubated with 500 μ Ci of γ -³²P-ATP (18.7 Ci/mmol) and other ingredients in 1.0 ml volume at 25°C for 30 min. The RNA was phenol-extracted, precipitated twice with ethanol, passed through a 0.9 × 66 cm column of Sephadex G25, precipitated again twice with ethanol, and fractionated by a 2.6 × 66 cm column of Bio-Gel A-50m. Out of 5.5-ml fractions each 1.0-ml aliquot was counted after TCA precipitation. Fractions shown by the brackets were pooled and subjected to analyses shown in Fig. 25.

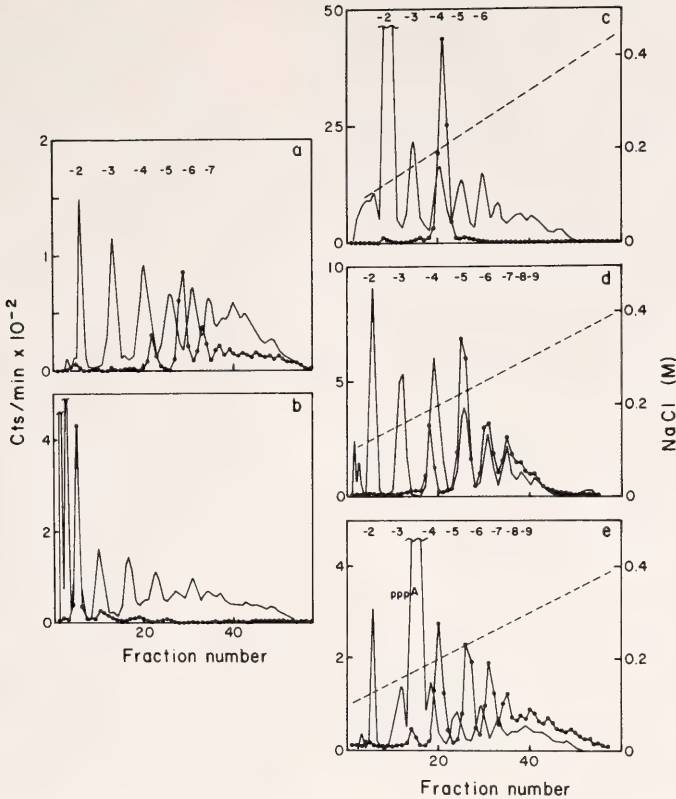


Fig. 25. Characterization of the RNA synthesized in vitro labeled with $\gamma^{32}\text{P}$ -ATP. Aliquots of fractions 14–19 of Fig. 24 were pooled; *E. coli* tRNA was then added as a carrier, precipitated with ethanol twice, and the precipitate digested with T_1 RNase and divided into two. One was applied directly to a DEAE-Sephadex column (a), and the other was digested further with alkaline phosphatase (b). Aliquots of fractions 20–54 of Fig. 24 were pooled, and *E. coli* tRNA was added and precipitated with ethanol twice. Aliquots were subjected to digestion with 0.3 *N* KOH (c), pancreatic RNase (d), and T_1 RNase (e). All the digests were fractionated on DEAE-Sephadex A25 columns with an NaCl gradient 0.10–0.40 *M* in the presence of 7*M* urea. Before application to the column the digest for (c) was neutralized and carrier oligonucleotides were added. Cold 5'-ATP was added as marker to the digest for (e). ^{32}P cts/min (●—●); A_{260} (—); $[M]\text{NaCl}$ (---).

BIOGENESIS OF MITOCHONDRIA

*I. B. Dawid, E. A. Godwin, C. K. Klukas, J. L. Ramirez, S. Ohi, and W. B. Upholt
with the assistance of M. Rebbert*

We have continued our studies on the structure of mitochondrial DNA (mtDNA) in several animal cells with the aim of obtaining comparative maps of different mtDNAs (see *Year Book 74*, p. 46). Ultimately, we would like to know what functions are coded for by mtDNA; how these functions are arranged on the DNA; how the primary

sequence and the overall anatomy of mtDNA changes in evolution; and what kind of evolutionary forces and mechanisms operate on this DNA.

MtDNA codes for two specific ribosomal RNAs (rRNAs), a set of transfer RNAs (tRNAs), and several poly(A)-containing RNAs that may be messenger RNAs. The rRNAs and

tRNAs have been well characterized in a number of organisms. Our aim has been to map the location of the regions coding for these RNAs in the mtDNA of *Xenopus laevis* and *X. mulleri*. We have also studied the location of the D-loop, which marks the replication origin. Experiments have been initiated to study nonribosomal RNAs in *Xenopus* mitochondria. A mapping study of *Drosophila melanogaster* mtDNA has been completed during this year. A detailed comparison of the mtDNAs of the goat and sheep has been carried out.

The major results of these experiments are as follows. The mt-rRNA genes in *Xenopus* and *Drosophila* as well as in Hela mtDNA are located next to each other on the H-strand with a gap of 120 to 160 nucleotides between them. In *X. laevis* and Hela this gap carries the gene sequence for a mitochondrial 4S RNA, and one 4S RNA gene is located immediately beyond the ends of the rRNA genes. A total of 15 to 16 genes for 4S RNA are distributed widely over the H-strand. These features are again similar to the situation in Hela mtDNA as reported by Wu and her colleagues (*Journal of Molecular Biology*, 71, 81-93, 1972). We further determined the polarity of the mt-rRNA in *Drosophila* and *Xenopus*: transcription proceeds from the smaller to the larger RNA. Transcription in the direction small-to-large rRNA is now recognized to be generally true for rRNA genes. In both *X. laevis* and *X. mulleri* the D-loop begins at a distance of about 800 base pairs from the end of the rRNA genes and replication is directly away from the rRNA genes.

We reported previously (*Year Book* 71, p. 22; *Year Book* 70, p.44) that the primary sequence of mtDNA changes quite rapidly in evolution. Our recent observations show that the overall anatomy of the mtDNA molecule is highly conserved over long evolutionary distances.

CLONING OF *Xenopus laevis* MITOCHONDRIAL DNA

I. B. Dawid, W. B. Upholt, and J. L. Ramirez
with the assistance of M. Rebbert

To aid structural studies of *X. laevis* mtDNA, we prepared hybrid plasmids between mtDNA and suitable vectors and grew these plasmids in *E. coli* (see *Year Book* 74, pp. 16 and 20). In this work we adhered to the safety standards proposed by the Asilomar Conference on Recombinant DNA. The restriction endonuclease EcoRI cleaves *X. laevis* mtDNA into two fragments, one of 15 kb and one of 2 kb (kb is kilobases or kilobase pairs). The small fragment was linked to the kanamycin-resistant vector PCR11 (PCR11 is 12.6 kb); the larger fragment was linked to the tetracycline-resistant vector PMB9 (PMB9 is 5.3 kb). After growth in *E. coli* the recombinant plasmids were isolated, digested with EcoRI, and the mitochondrial fragments were purified. Both cloned fragments were shown to be identical with the EcoRI fragments of frog mtDNA by gel electrophoretic analysis of the patterns obtained by digestion with other restriction enzymes. These cloned mtDNA fragments were then used in mapping studies in addition to fragments isolated directly from frog mtDNA.

MAPS OF *X. laevis* AND *X. mulleri* mtDNA: RESTRICTION SITES, THE D-LOOP, AND THE rRNA GENES

J. L. Ramirez and I. B. Dawid

In *Year Book* 74, pp. 46-47, we showed maps for these two mtDNAs which contain the locations of EcoRI sites, the SmaI site in *X. mulleri* mtDNA, and the D-loop positions. We now add the positions and the polarity of the rRNA genes (Fig. 26).

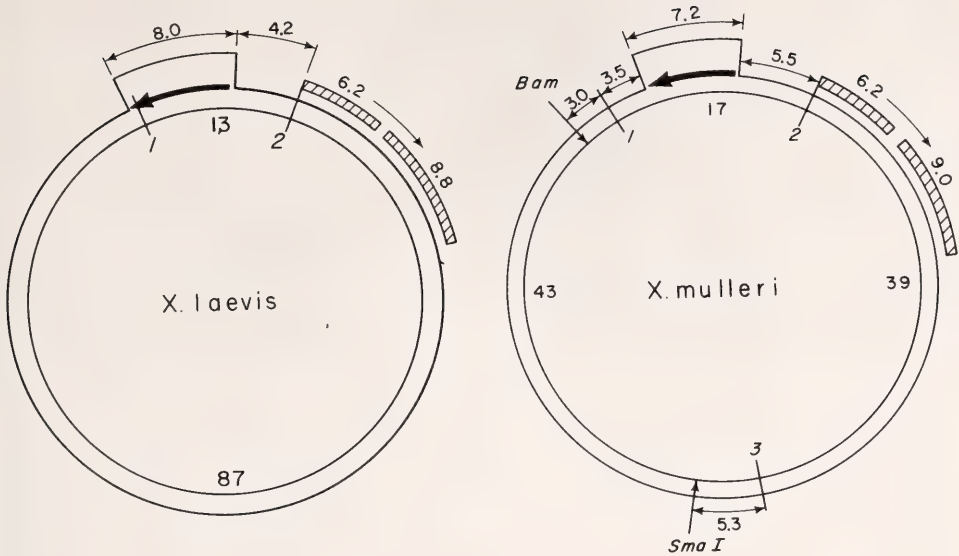


Fig. 26. Maps of *X. laevis* and *X. mulleri* mtDNA. EcoRI sites are numbered in italics inside the circles. Other restriction sites are labeled. The rRNA genes and the D-loops are shown, and the polarity of transcription and replication is indicated with an arrow pointing in the 5'-to-3' direction on the growing RNA or DNA strand. Distances are given as percent of total genome, which is 17,100 base pairs. The H-strand is shown on the outside, the L-strand on the inside.

The mapping of the rRNA genes was done in the following way. We know that the two genes are located next to each other with a gap of about 120 bases separating them (*Year Book 72*, p. 45). EcoRI fragments of *X. laevis* mtDNA were annealed with mt-rRNA, and the hybrid molecules were inspected in the electron microscope. The rRNA/DNA hybrid regions were close to the end of the larger EcoRI fragment, with the small mt-rRNA located at the end. This position for the rRNAs was confirmed by "R-loop mapping," a method developed by White and Hogness of Stanford University. In this method, native DNA and RNA are annealed under conditions in which the RNA invades the DNA duplex and displaces one of the strands. A loop is clearly visible in the electron microscope. To determine the relation of the

rRNA genes and the D-loop, the DNA is fixed with glyoxal to preserve the D-loop, then digested with EcoRI, and finally hybridized with large rRNA before examination in the electron microscope. Figure 27 shows such a molecule which established the relative positions of the D-loop and the rRNA genes in *X. laevis* mtDNA. The *X. mulleri* map was derived in an analogous way and is also shown in Fig. 26.

The polarity of the mt-rRNA was determined by digestion of EcoRI fragments of the DNA with specific exonucleases, followed by hybridization of the resulting single-stranded tails with rRNA. The result is incorporated into the models of Fig. 26. The direction of replication was deduced from the observation of a number of "expanded D-loop molecules" in *X. mulleri* mtDNA, and is also shown in the maps.



Fig. 27. Electron micrograph and tracing of an *X. laevis* mtDNA molecule with the D-loop in the "H-form" (D) and an R-loop formed by the large rRNA (R). Note that the R-loop has a "whisker," i.e., a portion of the RNA is displaced by the DNA strand and forms a single-stranded tail.

MAPPING OF 4S RNA GENES ON *X. laevis* mtDNA

S. Ohi, W. B. Upholt and I. B. Dawid

In *Year Book 74*, p. 47, we described our initial experiments on the mapping of mitochondrial 4S RNA genes of *X. laevis*. The covalent attachment of ferritin to 4S RNA was achieved by the method of Wu and Davidson (*Journal of Molecular Biology* 78, 1, 1973); ferritin-4S RNA complexes were hybridized to separated strands of mtDNA, and the hybrids were analyzed in the electron microscope.

The H-strand of mtDNA carries the genes for the mt-rRNAs and a majority of the 4S RNA genes. The rRNA regions were used as reference points in the mapping. The result of the measurements of these hybrid molecules is shown in Fig. 28. At least 15 and possi-

bly 16 sites for 4S RNA were found on the H-strand. The more remarkable positions are those between and immediately flanking the rRNA genes: Hela cell mtDNA has 4S RNA positions at the analogous points, as determined by Wu and her colleagues (*J. Mol. Biol.* 71, 71-93, 1972). The remaining 4S RNA sites are distributed widely over the H-strand. This wide distribution is also similar to the situation in Hela mtDNA.

Our results with the L-strand of *X. laevis* mtDNA are incomplete. There is, however, tentative evidence for 5 or 6 sites on this strand. If these results can be confirmed in future experiments, we would have evidence for 20 to 22 sites for 4S RNA on *Xenopus* mtDNA. This number would come close to the expected number of tRNAs required for a complete protein synthesizing "machine" that depends fully on endogenous tRNAs.

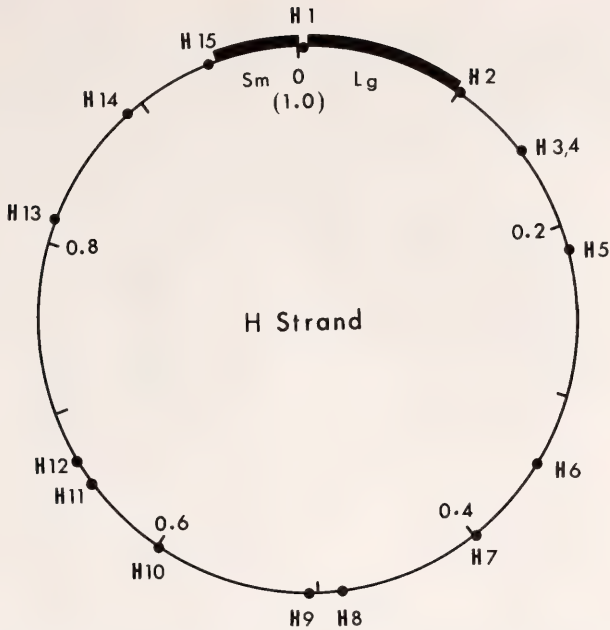


Fig. 28. Map of 4S RNA sites on the H-strand of *X. laevis* mtDNA. Closely adjacent sites are only then considered to represent two sites if both sites were seen repeatedly to be occupied by ferritin on the same DNA strand. Site 10 may be a doublet site, but it has been observed only twice out of 158 molecules examined as a doublet and is not considered certain. Comparison with Fig. 26 shows that the D-loop position is from about 0.82 to 0.90 on this map. Thus, position H14 may be within the D-loop, but this is not certain.

MAPPING STUDIES WITH mtDNA FROM *Drosophila melanogaster*

C. K. Klukas and I. B. Dawid

mtDNA and mt-rRNA from *Drosophila* have been isolated and characterized (Year Book 74, pp. 49–53). The circular mtDNA molecule has a molecular weight of 12×10^6 , i.e., it consists of 18,400 base pairs. About 25% of this molecule has a very high content of adenylic and thymidylic acids and can be visualized as an early melting region by electron microscopy. The mt-rRNAs have molecular weights of about 300,000 and 530,000.

We have mapped the positions of the cleavage sites of the restriction endonucleases HaeIII and HindIII relative to each other and relative to the early melting region. The map was constructed from electron microscopic measurements of partially denatured

total and partial restriction digestion of the DNA, and from gel electrophoretic analysis of the DNA with each enzyme separately and both enzymes together. Figure 29 shows the results.

We next mapped the location of the rRNA genes relative to restriction sites by electron microscopy of RNA/DNA hybrids. The assignment of positions to the rRNA genes was confirmed and refined by a quantitative hybridization experiment in which the small and the large rRNA were separately hybridized to HindIII and HaeIII fragments of mtDNA. The resulting map shows the two rRNA genes located in close proximity and separated by a gap of 160 nucleotides.

The polarity of the rRNA was determined in an analogous way to the method outlined for *X. laevis* mt-rRNA. As in the case of *Xenopus* the direction of transcription in *Drosophila* mtDNA is from the smaller to the larger rRNA.

Both the close proximity of the two rRNA genes and the polarity of the RNA are highly conserved in the evolution of animal mtDNAs, since the identical arrangement is found in frogs and fruit flies.

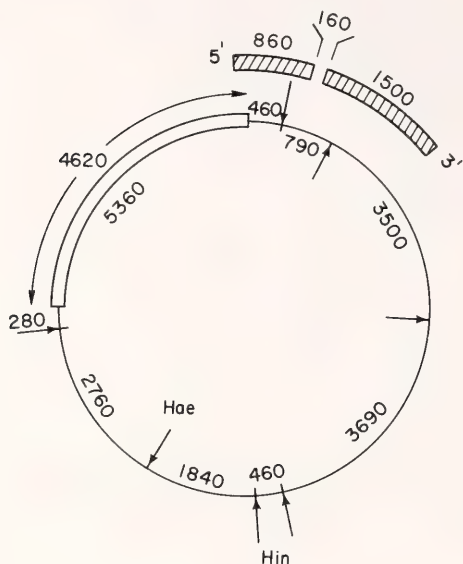


Fig. 29. Map of *D. melanogaster* mtDNA. The cleavage sites of HaeIII and HindIII are indicated by arrows, and the early melting region is indicated by an open section of the circle. The rRNA genes are indicated and are separated by a gap of 160 nucleotides. The direction of transcription, i.e., 5' to 3' polarity of the RNA, is shown. Distances are given in base pairs. The total genome size is 18,400 base pairs.

MAPPING AND SEQUENCE COMPARISONS OF GOAT AND SHEEP mt DNAs

W. B. Upholt

A detailed comparison of sheep and goat mtDNA was initiated with the aim of observing the differences in the mtDNAs of closely related animals (*Year Book* 74, p.48). This study should give information about the least conserved regions of the mtDNA rather than the most conserved ones, which

are best studied in more distantly related species (see *Year Book* 70, p. 44).

The analysis of restriction fragments of sheep and goat mtDNA was carried further. Endonuclease HaeIII yields 27 to 30 fragments from these mtDNAs. From a consideration of conserved fragments it follows that sheep and goat mtDNAs have diverged to the extent of 7% to 11% of their sequences. In the course of these studies the interesting fact was observed that the mtDNAs from individual sheep and goats differed from each other with respect to the HaeIII fragment pattern and therefore with respect to primary sequence. Figure 30 shows the electrophoretic separation of these fragments from the mtDNA of two goats and three sheep. No two patterns are exactly alike. The sheep patterns are all rather similar to each other, the two goats differ substantially, and the sheep and goat patterns are very different. On the basis of these experiments and with certain assumptions, one may calculate a sequence divergence of 0.5% to 1% among the sheep mtDNAs and about 2% between the DNAs of the two goats.

Detailed maps were constructed for the cleavage sites of endonucleases EcoRI and HindIII on both sheep and goat mtDNAs. The two goats differed with respect to EcoRI and HindIII sites, a fact that emphasizes the considerable difference in sequences of the two DNAs. The position and lengths of the goat and sheep D-loops were determined and are also shown on the maps of Fig. 31. Several EcoRI HindIII sites were conserved between sheep and goat, but some of the sites differ. The D-loops are at analogous positions on the two mtDNAs, but the lengths of the loops are different. We reported last year that a region of high evolutionary change overlaps one end of the D-loop (the left end in Fig. 31). This region where the two D-loops differ in length and the area immediately beyond it have been studied in more detail by electron microscopic heteroduplex mapping. We confirm the earlier conclusion that this region shows a high

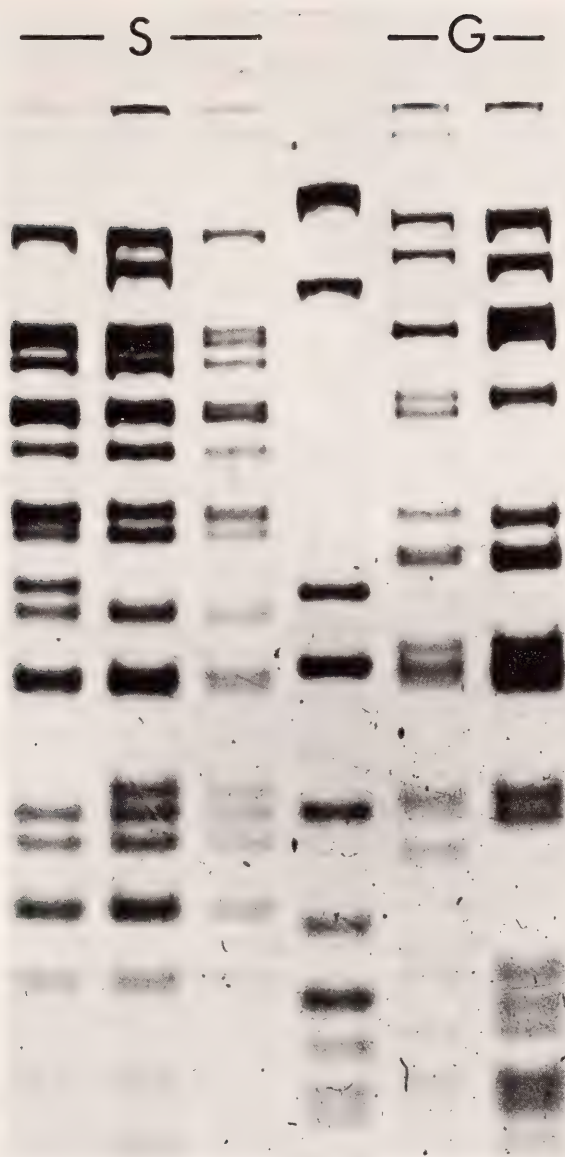


Fig. 30. HaeIII fragments of sheep and goat mtDNA. The direction of electrophoresis is from top to bottom. Fragment sizes range from just under 2000 to 200 base pairs. Smaller fragments occur but are not shown in this figure. mtDNA fragments from three individual sheep (S) and two goats (G) are displayed; the unmarked lane contains HaeIII fragments of the plasmid PSC101. Differences in the band patterns of individual sheep and goats are apparent.

rate of evolutionary change and further suggest that it contains a duplication of about 150 base pairs. Thus, the segment of DNA overlapping and

adjacent to the D-loop may show a high rate of base mutation and also a tendency to rearrangements on a larger scale.

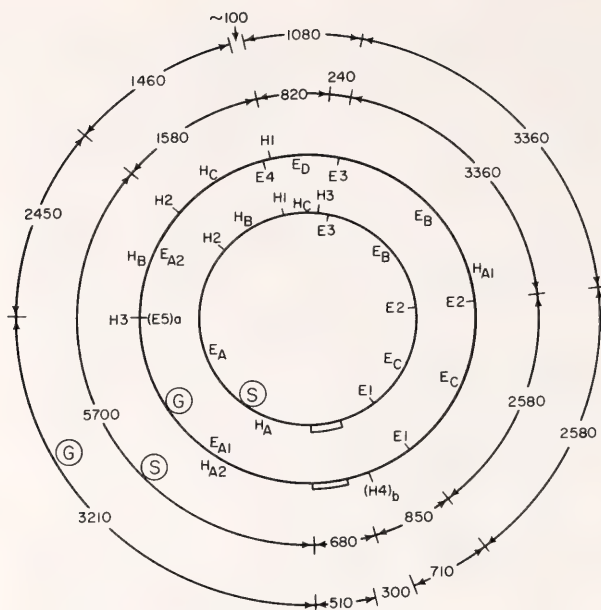


Fig. 31. Maps for sheep (S) and goat (G) mtDNAs. EcoRI sites are labeled *E* and numbered; HindIII sites are labeled *H*; fragments are labeled with capital letters. Subscripts refer to sites or fragments that are present in one of the two goat mtDNAs only. The position and length of each D-loop are indicated. The lengths of the different regions in the molecules are shown on the outer circles in base pairs.

PHOSPHOLIPID-CHOLESTEROL DYNAMICS IN MAMMALIAN CELLS

*R. E. Pagano, L. Huang, K. Ozato and M. Takeichi
with the technical assistance of E. Asch, E. Somerville and D. Duncan*

Work in this laboratory is concerned with the possible dynamic role that membrane phospholipids and cholesterol may play in the regulation of cell behavior. During the past several years we have been developing a technique utilizing artificially generated lipid vesicles, which permits a controlled and systematic perturbation of these membrane components in living cells. In the present report we emphasize our recent findings on the interactions of phosphatidyl choline vesicles with murine lymphocytes and the physiological consequences of these interactions. We show that the pathways of vesicle-cell interactions, enumerated in previous reports (vesicle-cell fusion, adsorption, and lipid exchange) are ex-

quisitely sensitive to the molecular composition and physical properties of the artificial vesicles. When lymphocytes are the "recipient" cells, the resulting membrane perturbations lead to altered surface properties and an enhanced proliferative activity of these cells, when stimulated by various mitogens and antigens.

In a separate but related line of research, Takeichi has explored some of the adhesive properties of a fibroblastic cell line and reports on attempts to identify and characterize membrane proteins that participate in this phenomenon. Parallel studies on the adherence of lipid vesicles of known composition to cells are also discussed.

Finally, a critique of the use of small

hydrophobic fluorescent probes to monitor changes in the physical state of the lipids in natural membranes is presented.

Details of our studies on each of these topics are presented in separate sections below.

INTERACTIONS OF PHOSPHOLIPID VESICLES WITH MURINE LYMPHOCYTES: VESICLE-CELL ADSORPTION AND FUSION AS ALTERNATIVE PATHWAYS OF UPTAKE

L. Huang, K. Ozato, and R. E. Pagano

The various mechanisms by which unilamellar lipid vesicles interact with cells and the subsequent modification of cell behavior that would result have been the subject of recent investigations from this and other laboratories. In *Year Book 74* (p. 53) we showed that the incorporation of lecithin into dioleoyl lecithin (DOL) vesicles were primarily via vesicle to cell fusion and lipid exchange processes. The interaction of dimyristoyl lecithin (DML) vesicles with these cells was also studied, and exhibited an enhanced uptake when the temperature of vesicle-cell incubation was below the thermotropic

phase transition temperature ($T_c \approx 25^\circ\text{C}$) of DML. While the detailed mechanisms for DML uptake were not explored, this peculiar temperature dependence suggested an additional pathway for vesicle incorporation. In the present study with mouse thymic lymphocytes, we identify this pathway as vesicle-cell adsorption. Furthermore, in a survey of the uptake of various lecithin vesicles by thymocytes, it is shown that these lipid vesicles can be classified according to whether they are incorporated principally by vesicle to cell fusion or a stable vesicle to cell adsorption.

Evidence for a Stable Vesicle-Cell Adsorption

In an EM autoradiographic survey of thymocytes treated with a variety of [^3H] lecithin vesicles, we observed two distinct patterns of silver grain distributions in treated cells. In the case of EYL (egg yolk lecithin) or DOL vesicles, most of the exogenous lipid label appeared inside the cell, while for DML or DPL (dipalmitoyl lecithin) vesicle-treated cells, relatively large amounts of radioactivity appeared to reside at the cell surface. Typical examples of such autoradiograms are shown in Fig. 32 for cells treated with EYL vesicles

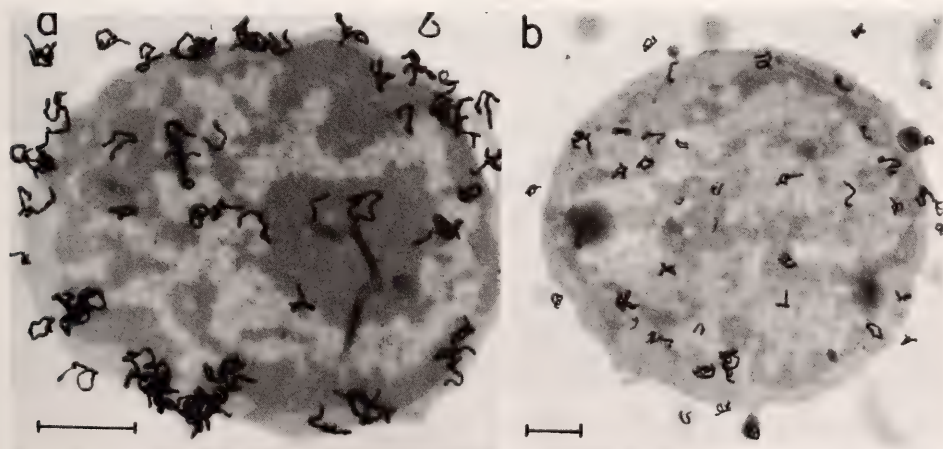


Fig. 32. Electron microscope autoradiographs of mouse thymocytes treated with (a) [^3H] DML vesicles (2°C , 60 min), $\times 14,000$ and (b) [^3H] EYL vesicles ($22\text{--}23^\circ\text{C}$, 30 min), $\times 7,700$. Bar is $0.1\ \mu\text{m}$.

(30 min at 22–23 °C) and DML vesicles (1 hr at 2 °C). Similar autoradiograms were also obtained for thymocytes treated with these lipids at 37 °C. Thin layer chromatographic (TLC) analysis of the extracted lipids from these cells revealed that most (~90%) of the radiolabel was still in lecithin, indicating that the grains seen in the autoradiograms represent the approximate location of the exogenously introduced lecithin and not some degradation product. This qualitative observation of two classes of grain distribution was confirmed in a statistical analysis of a large number of autoradiograms of treated cells and is summarized in Table 6. The accumulation of silver grains at the surfaces of DPL or DML (vs. EYL or DOL) vesicle-treated cells is readily apparent, both from calculations of the percentage of grains found near the cell surface and from the ratio of the normalized grain densities.

It should be noted that all vesicle-cell incubations were carried out at 22–23 °C except in the case of DML. In this instance, incubations were carried out at 2 °C to avoid complications which might arise from the phase transition of the DML vesicles. A suggestion of the complex uptake behavior which results from this transition is seen in Fig. 33, where the temperature dependence of DML and EYL uptake by thymocytes is compared. Each data point in this figure represents the lipid uptake by cells following a 60-min incubation at a given temperature. For EYL vesicles, the lipid uptake increased mono-

tonically with temperature between 0°C and 37°C. In striking contrast, the lipid uptake from DML vesicles showed a peculiar temperature dependence, exhibiting a sharp maximum at about 20°C and minima at about 15° and 24°C. Furthermore, the uptake at 0°C was greater than at 37°C. DML uptake was always larger than EYL uptake; for example, about 1.5 µg of EYL vs. 4 µg of DML were taken up by 10⁷ cells at 37°C.

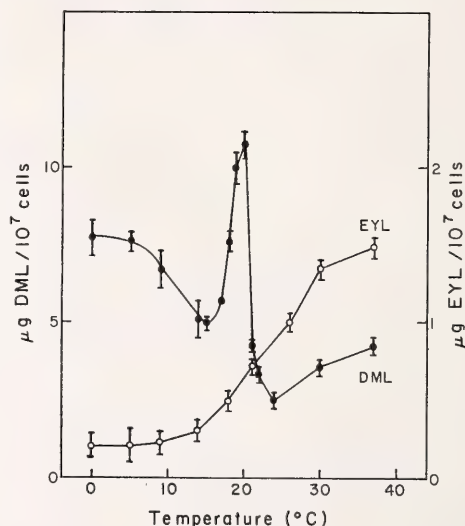


Fig. 33. Temperature dependence of [³H] EYL (1 mg/ml, 1 × 10⁶ cpm/mg) and [¹⁴C] DML (1 mg/ml, 4 × 10⁵ cpm/mg) uptake by mouse thymocytes. 10⁷ cells/ml were incubated 60 min with vesicles in Gey's balanced salt solution.

The existence of two types of lecithin vesicle-cell interactions suggested by the data above was confirmed in ul-

TABLE 6. Distribution of Autoradiographic Grains over Mouse Thymocytes Treated with [³H] Lecithin Vesicles

| Lipid Type | Treatment | | Total Silver Grains Counted | Percent Grains in Surface Compartment* | (Surface Grain* Density) ± S.E.M. |
|--------------------|------------|------------|-----------------------------|--|-----------------------------------|
| | Time (min) | Temp. (°C) | | | (Interior Grain Density) |
| ³ H DML | 60 | 2 | 565 | 69 | 8.1 ± 1.0 |
| ³ H DPL | 30 | 22–23 | 342 | 71 | 8.6 ± 1.2 |
| ³ H EYL | 30 | 22–23 | 348 | 27 | 1.5 ± 0.2 |
| ³ H DOL | 30 | 22–23 | 133 | 25 | 1.4 ± 0.2 |

*See Pagano, Ozato, and Ruyschaert, elsewhere in this report, for description of analysis.

trastructural studies of vesicle-treated cells. Thymocytes incubated with EYL or DOL vesicles at temperatures between 2 ° and 37 °C showed smooth cell surfaces identical to those of untreated control cells. A typical example of the surface of an EYL-treated cell is shown in Fig. 34a. In the DPL-treated cells (Fig. 34b), many of the intact vesicles had apparently adsorbed to the cell surface. These vesicles ranged in size from about 250 Å to about 650 Å in diameter, possibly reflecting heterogeneity in the applied vesicle population. Furthermore, the distribution of adsorbed vesicles on the cell surface was not uniform. Micrographs obtained from cells treated with DML vesicles also showed evidence of adsorbed material at their surfaces. However, the DML vesicles were apparently ruptured or collapsed in the 2 °C treatments (Fig. 34c), while large masses of amorphous material were seen ad-

sorbed to cells treated at 37 °C (Fig. 34d). From the ultrastructural studies shown in Fig. 34 and the autoradiographic data (Fig. 32; Table 6) showing an accumulation of [^6H] DPL or [^3H] DML at the surfaces of treated cells, it is concluded that the adsorbed materials seen in Fig. 34b, c, d actually represent native or modified applied vesicles. In the case of DML, intact vesicles were rarely seen adsorbed at the surface of treated cells. The presence of collapsed or ruptured vesicles and amorphous material suggests a reorganization of the vesicle membranes. This modification of vesicle morphology could be a consequence of an inherent bilayer instability in this relatively short chain lecithin. Our findings of an enhanced uptake of DML by thymocytes near or below the phase transition temperature (T_c) or DML (Fig. 33) and the ultrastructural evidence presented in Fig. 34c and d suggest an en-

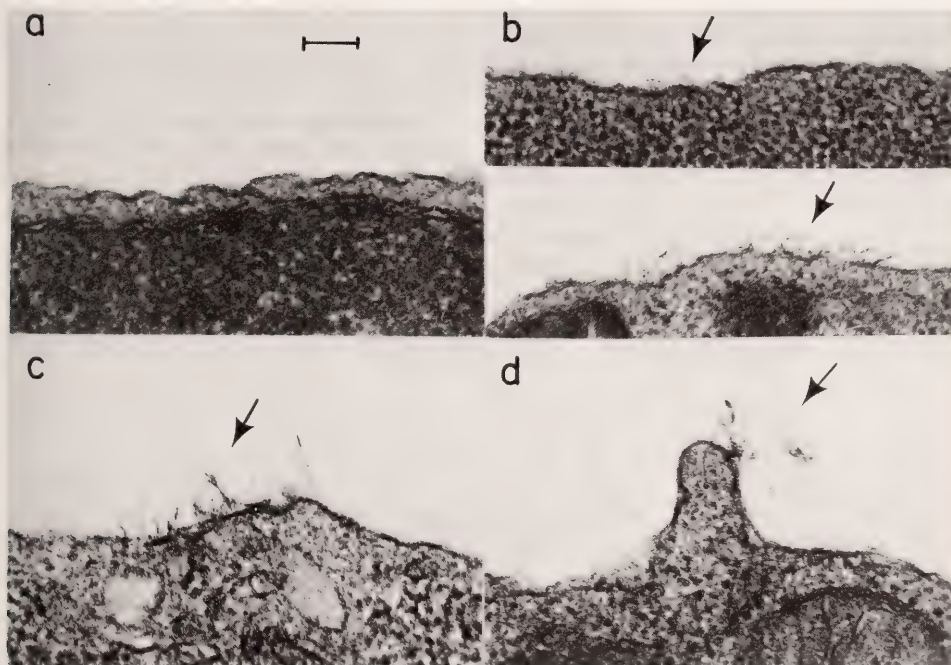


Fig. 34. Transmission electron micrographs of mouse thymocytes treated for 30 min with vesicles comprised of (a) EYL (22–23°C), (b) DPL (22–23°C), (c) DML (2°C) and (d) DML (37°C) $\times 78,000$. Bar is 1 μm . Intact vesicles (b), collapsed or ruptured vesicles (c), and amorphous material (d) are seen at arrows.

hanced adsorption of DML at these temperatures. Such an enhancement could be due to the increase in bilayer thickness below the T_c of the lipid.

Vesicle-Cell Fusion and Lipid Exchange

Since the EM autoradiographic data as well as the micrographs presented in Fig. 34a suggested an absence of vesicle-cell adsorption for DOL and EYL vesicles, other possible mechanisms for the uptake of these vesicles have been investigated. In *Year Book 74* (p. 62) we suggested that EYL vesicles were incorporated by thymocytes principally by a vesicle-cell fusion mechanism. This suggestion was based in part on the finding that when thymocytes were treated with [^{14}C] EYL vesicles containing trapped [^3H] inulin, both components became cell associated at identical rates, consistent with the uptake of "intact" vesicles. Additionally, the uptake of EYL vesicles was insensitive to NaN_3 and cytochalasin-B, two known inhibitors of endocytosis in other cell types. During the past year, further direct evidence for the fusion of EYL vesicles with thymocytes was obtained. Cells

were treated with EYL vesicles containing high specific activity [^3H] inulin under various conditions. EM autoradiography was then used to examine the intracellular distribution of the vesicle marker in treated cells. Statistical analysis of a large number of autoradiograms showed approximately 75% of the trapped [^3H] inulin was *randomly* distributed in the cytoplasm and nucleoplasm of the treated cells, suggesting that the contents of EYL vesicles were released into the cells by fusion.

In order to explore the possibility of lipid exchange between vesicles and cells, thymocytes with endogenously (^3H -palmitate) labeled lipids were incubated with [^{14}C] EYL unilamellar vesicles for 1 hr at 37°C . Following this incubation, the vesicles were separated from the cells and subjected to molecular sieve chromatography on Sepharose 4B. Each fraction was examined for both ^{14}C - and ^3H -cpm. The results of such an experiment are given in Fig. 35. The ^{14}C -cpm showed one broad symmetrical peak, typical of unilamellar lipid vesicles. Three ^3H -cpm peaks were observed. The first peak eluted at the exclusion volume of the column and probably represents

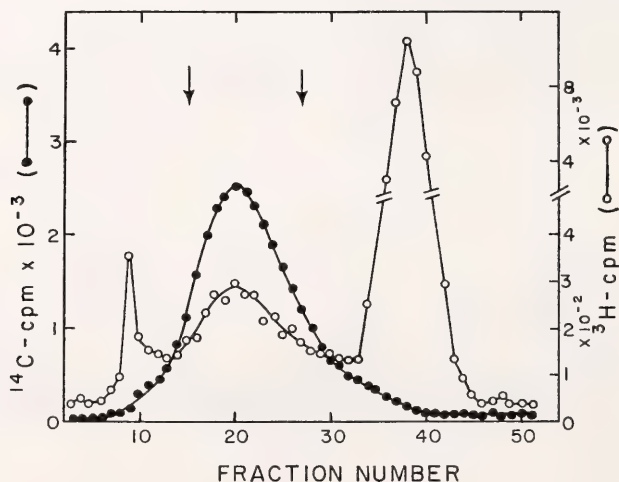


Fig. 35. Elution profile of [^{14}C] EYL vesicles on Sepharose 4B following incubation (1 hr at 37°C) with mouse thymocytes. Endogenous cell lipids were labeled with [^3H] palmitic acid. Fractions between arrows were analyzed for lipid composition.

unremoved whole cells or fragments. The third and major ^3H -cpm peak eluted at the end of the column volume; its radioactivity was chloroform-methanol nonextractable and presumably represents some secreted metabolic products of small molecular weights. The second ^3H -cpm peak precisely cochromatographed with the unilamellar ^{14}C -vesicle peak. Between fractions 15 and 27 (Fig. 35, arrows) a total of 3×10^3 ^3H -cpm was found. In control experiments in which the [^{14}C] EYL vesicles were incubated with a balanced salt solution previously in contact with the ^3H labeled cells, a total of only 5×10^2 ^3H -cpm was found in these fractions. Practically all ($\sim 90\%$) of both the ^3H -cpm and ^{14}C -cpm in these fractions was chloroform-methanol extractable; TLC analysis shows more than 80% of the ^3H -cpm was lecithin. These results demonstrate that transfer of cellular lipid to the vesicles, always present in excess, can occur in addition to EYL vesicle-cell fusion. In this experiment, although lecithin was a minor lipid ($\sim 30\%$) in the endogenously labeled thymocytes, it constituted a major fraction ($\sim 80\%$) of the cell lipids transferred to the vesicles. This indicates an apparent specificity in the vesicle-cell lipid transfer process. From the data in Fig. 35, the number of lecithin molecules per EYL vesicle, and a lower limit for the specific activity of the cellular lecithin, it was calculated that no more than two cellular lecithin molecules were transferred per 100 EYL vesicles. If it is assumed that the transfer of cell lipids to vesicles is accompanied by an equal amount of transfer of vesicle lipids to the cells, it is further calculated that only 1–2% of the total EYL uptake (37°C) is due to the lipid exchange process.

Thus we conclude that the major pathways of lecithin vesicle uptake by mouse thymocytes are (1) a stable vesicle to cell adsorption in the cases of DML or DPL and (2) vesicle-to-cell fusion for EYL (or DOL) with a minor contribution due to lipid exchange.

Since all these processes require an initial vesicle-to-cell contact, it follows that for DML and DPL this contact is further developed into a state of stable adsorption, while for EYL or DOL it leads to subsequent fusion. We speculate that the physical properties of the lipid vesicles, dictated by the fatty acyl composition of the vesicle lecithin, ultimately determine the predominant pathway for vesicle uptake.

INTERACTION OF PHOSPHOLIPID VESICLES WITH MURINE LYMPHOCYTES: VESICLE-CELL ADSORPTION LEADS TO ALTERED SURFACE PROPERTIES AND ENHANCED PROLIFERATIVE RESPONSE

K. Ozato, L. Huang, and R. E. Pagano

In order to delineate the relationship between cell surface properties and membrane lipid composition, we have explored the use of unilamellar lipid vesicles to perturb the surface of mouse lymphocytes, stimulated by various mitogens to undergo blast transformation. This approach seemed particularly hopeful, since previous studies from this and other laboratories using other cell types had demonstrated that vesicle lipids could be incorporated into cells by vesicle-to-cell fusion and lipid exchange processes. We first made a detailed study of the interactions of a variety of lecithin vesicle types with mouse lymphocytes and confirmed the existence of these pathways of vesicle uptake (Huang, Ozato, and Pagano; this report). Surprisingly, in certain types of lipid vesicles, a previously unreported mechanism of vesicle uptake was also found, namely, a stable vesicle-to-cell adsorption. We report here on the ability of lipid vesicles to modify the agglutinability and lectin binding of lymphocytes. Most significantly it is shown that vesicle pretreatment can also enhance the proliferative activity of stimulated cells. The extent of these modifications of cell

behavior depends on the lipid vesicle type and is correlated directly with the ability of vesicles to adsorb to the cell surface.

Enhancement of Proliferation by Lipid Vesicle Pretreatment

Cortisone-resistant thymocytes (CRT) were briefly (30 min) treated with unilamellar lipid (lecithins or 1:2 lecithin: cholesterol) vesicles and subsequently cultured in a serum- and lipid-free medium containing a mitogenic dose of Con A ($1 \mu\text{g}/\text{ml}$). The proliferative activity of these cultures was periodically examined using the criteria of increased $[\text{H}]$ TdR incorporation and increased number of total cells and lymphoblasts. Figure 36 shows the time course of DNA synthesis in CRT, activated by Con A, for both DML vesicle pretreated and, for control, untreated cells. In both cultures $[\text{H}]$ TdR incorporation reached a peak on day 3. The pretreated cells showed

obviously higher DNA synthesis than control at every time point tested, with the largest differences ($2-3\times$) occurring at days 3 and 4 in culture. By the fifth day, DNA synthesis in both cultures had practically ceased. The degree of enhancement of the mitogenic response by DML varies from experiment to experiment ($2-5\times$ control) but was always the largest of the lipid vesicles tested. The level of the DML effect was dependent on the temperature of the vesicle pretreatment with pretreatment at 2°C giving about a twofold larger effect than vesicle-cell incubations carried out at $22-23^\circ\text{C}$. Table 7 compares the effect of different lipid vesicle pretreatments on the level of DNA synthesis in Con A-stimulated CRT. Each of the vesicle pretreatments also resulted in an increase in total cells as well as lymphoblasts in the culture. The degree of enhanced proliferation depended on the type of lipid vesicle used, with DML always giving the largest stimulation and EYL the least.

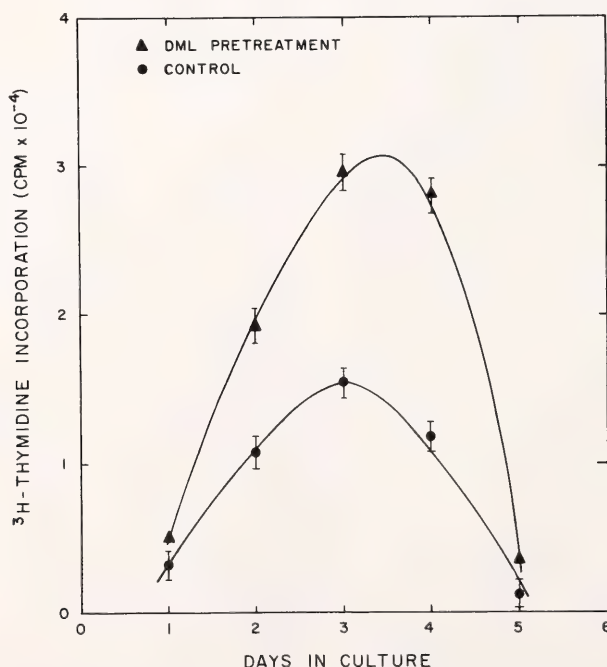


Fig. 36. Time course of DNA synthesis in cortisone-resistant thymocytes stimulated by Con A ($1 \mu\text{g}/\text{ml}$).

TABLE 7. Effects of Lipid-Vesicle Pretreatments on Cortisone-Resistant Thymocytes Stimulated with Con A

| Lipid Vesicle Pretreatment* | Temperature of Pretreatment (0°) | Typical Experiment (cpm/culture × 10 ⁻³ † | Total/Culture × 10 ⁻⁶ | Lymphoblast/Culture × 10 ⁻⁴ |
|--|----------------------------------|--|----------------------------------|--|
| EYL | 22-23 | 11.5 ± 0.9 | 3.0 ± 0.1 | 6.1 ± 0.2 |
| DOL | 22-23 | 11.4 ± 0.8 | 3.0 ± 0.2 | 6.0 ± 0.3 |
| 1:1 EYL:Chol | 22-23 | 14.6 ± 1.2 | 3.1 ± 0.2 | 6.3 ± 0.3 |
| DPL | 22-23 | 29.0 ± 1.5 | 3.7 ± 0.3 | 9.0 ± 0.5 |
| DML | 22-23 | 18.3 ± 1.1 | 3.6 ± 0.3 | 8.7 ± 0.4 |
| DML | 2 | 37.8 ± 1.3 | 4.4 ± 0.3 | 14.3 ± 0.8 |
| Control: no vesicles | ... | 10.5 ± 0.4 | 2.8 ± 0.1 | 5.2 ± 0.3 |
| Control: no mitogen | ... | 0.4 ± 0.0 | 1.7 ± 0.0 | 0.0 |
| Control: DML or DPL vesicles; no mitogen | 22-23 | 0.9 ± 0.0 | 1.6 ± 0.0 | 0.0 |

*Optimum lipid concentration of vesicle suspension was 0.5 mg total lipid/ml cell suspension, except for 1:1 EYL:Chol vesicles (1.0 mg/ml).
† Mean of triplicate cultures ± standard deviation.

The observed order was DML (2-5 ×) > DPL (2-3 ×) > 1:1 EYL:Chol (1.5-2.5 ×) > EYL ≅ DOL (1.2-2 ×) > untreated cells.

Cells pretreated with lipid vesicles and subsequently cultured in the absence of mitogen did not exhibit significant DNA synthesis 72 hr after culture. Additional experiments in which cells were continuously cultured in the presence of lipid vesicles at sufficiently low concentrations (0.1 mg/ml) to prevent toxicity even for periods of incubation up to 72 hr, also showed no significant enhancement of DNA synthesis levels. Thus it is concluded that none of the lipid vesicles tested were themselves mitogenic for T-cells.

The effects of lipid vesicle pretreatment on spleen cell cultures stimulated by a B-cell mitogen, bacterial lipopolysaccharide (LPS), were also studied. In nearly every case lipid-vesicle pretreatment of B-cells resulted in a significant enhancement of their proliferative activity when stimulated by LPS. Again, a graded enhancement in DNA synthesis, depending on the vesicle lipids used, was observed in the same order as that found in T-cells. Lipid vesicle pretreatment of spleen cell cultures was not itself mitogenic.

Alterations in Lectin-Induced Agglutinability and Lectin-Binding in Vesicle-Treated Cells

The lectin-induced agglutinability of normal thymocytes pretreated with lipid vesicles was assayed quantitatively by measurements of the total particle number in cell suspensions incubated with and without Con A. As shown in Table 8 pretreatment of thymocytes with lipid vesicles prior to incubation with Con A significantly enhanced the agglutinability of the treated cells. Furthermore, the degree of enhanced agglutinability was dependent on the vesicle type and showed exactly the same order as that found in the proliferation studies, that is, DML > DPL > 1:1 EYL:Chol > EYL ≅ DOL > no treatment. Vesicle pretreatments themselves did not induce thymocyte agglutination in the absence of lectin. In control and EYL or 1:1 EYL:Chol vesicle pretreated cells, α-MM (but not galactose) could almost completely reverse Con A-induced agglutination. However, the agglutination was only partially reversed for DML or DPL pretreatments. These effects of vesicle pretreatments on lectin induced agglutination were consistently observed for

different lectin concentrations (5–50 $\mu\text{g/ml}$). The effect of vesicle pretreatments on the binding of radiolabeled Con A to normal thymocytes was also studied. In Fig. 37, the binding of [^{125}I] Con A (1 $\mu\text{g/ml}$; 60 min at 2 °C) to normal thymocytes pretreated with various lipid vesicles is compared. The binding of [^{125}I] Con A to 1:1 EYL:Chol, EYL or DOL vesicle pretreated cells was indistinguishable from that of untreated control cells, both in terms of the total as well as the α -MM inhibitable portion of the binding. In the case of DML or DPL vesicle pretreatments, however, the binding was significantly enhanced. Cells pretreated with DPL vesicles always showed greater total [^{125}I] Con A binding than DML-pretreated cells, while the opposite order was found when the α -MM inhibitable portions were compared. Binding studies carried out at 37 °C showed increased lectin binding and an identical trend with respect to the ability of different vesicle types to modify that binding. The binding of [^3H] Con A to vesicle-treated cells studied at higher lectin concentrations (50 $\mu\text{g/ml}$) also showed a striking enhancement of overall and α -MM inhibitable binding of DML and DPL vesicle-pretreated cells.

TABLE 8. Effect of Lipid-Vesicle Pretreatment on Lectin-Induced Agglutinability of Thymocytes

| Vesicle Pretreatment | Agglutination Index* Con A (10 $\mu\text{g/ml}$) | |
|---------------------------|--|----------------|
| | – α -MM | + α -MM |
| None | 76.5 \pm 1.7† | 1.0 \pm 0.0 |
| DML (2°C) | 93.0 \pm 2.4 | 25.8 \pm 0.2 |
| DML (22–23°C) | 91.8 \pm 1.5 | 12.3 \pm 0.1 |
| DPL (22–23°C) | 89.7 \pm 1.8 | 31.6 \pm 0.1 |
| 1:1 EYL:Chol (22–23°C) | 87.7 \pm 2.0 | 2.4 \pm 0.0 |
| DOL (22–23°C) | 85.0 \pm 0.3 | ND‡ |
| EYL (22–23°C) | 84.4 \pm 0.8 | 1.2 \pm 0.0 |

*Defined as
$$1 - \frac{\text{Particle no. in presence of Con A}}{\text{Particle no. in presence of Con A}} \times 100$$

†Mean \pm standard deviation.

‡Not determined.

Alteration of Cell Surface Properties by Vesicle Adsorption

In the foregoing studies (Huang, Ozato, and Pagano) on the mechanism of lecithin vesicle uptake by lymphocytes, it was shown that DML or DPL, but not EYL or DOL, vesicles become associated with lymphocytes principally through a stable vesicle-to-cell adsorption process. Thus, those lipid vesicles which have the most significant effect on the mitogenic response and on lectin binding and agglutination are those which adsorb to the cell surface. This correlation suggests that the alteration of lymphocyte surface properties may be a direct consequence of vesicle-to-cell adsorption.

The stable adsorption of vesicles to cells could lead to an enhanced binding of mitogen to vesicle-treated cells, in those cases in which mitogen binds directly to lipid. Thus, the enhanced Con A binding observed in DML or DPL pretreated cells may be a result of direct interaction between Con A and adsorbed vesicles. The finding that a significant fraction of Con A binding is noninhibitable by α -MM, particularly in DPL treated cells, supports the idea that some fraction of the binding might represent a direct association of lipid with Con A. In further support of this notion is a recent study (van der Bosch and McConnell, *Proc. Nat. Acad. Sci. U.S.A.*, 72, 4409–4413, 1975) demonstrating a strong interaction of Con A with DPL vesicles, which results in vesicle-vesicle fusion.

The adsorption of vesicles to cells, as well as the postulated vesicle-lectin interactions, can also be used to explain the differential effects of vesicle treatments on lectin-induced agglutinability. Thus, in the presence of Con A, agglutination could be mediated both by cell-bound Con A and Con A bound to cell-associated vesicles. In this regard it is interesting to note that the agglutination of DPL or DML vesicle pretreated thymocytes could not be fully reversed by α -MM (Table 8). This

may be due to the large residual Con A binding found in cells treated with these vesicles (Fig. 37).

The present findings demonstrate an enhanced proliferation in stimulated T cells and B cells following incubation with various unilamellar lipid vesicles. This observation is particularly significant, since T and B cells respond to different specific mitogens and may have different triggering mechanisms. The stable adsorption of lipid vesicles to lymphocytes may provide a common element by which the enhancement in these different cell types can take place. Thus, the enhancement of cell proliferation following vesicle treatment may be due to the increased mitogen binding resulting from vesicle-to-cell adsorption and the subsequent utilization of mitogen in vesicle-treated cells.

In conclusion, our results suggest a direct correlation between the surface

localization of exogenous lipids resulting from vesicle to cell adsorption and their ability to modify lymphocyte cell surface properties such as agglutinability and lectin binding. It is further suggested that vesicle-to-cell adsorption can have profound physiological consequences in treated cells—namely, enhancement of the proliferative activity of stimulated lymphocytes.

STUDIES OF MEMBRANE ADHESION

M. Takeichi and R. E. Pagano
with the assistance of W. Duncan

The adhesive properties of cells are among the more important factors controlling cell behavior and morphogenesis in multicellular organisms. While many investigators have attempted to elucidate the mechanisms of cell adhesion, the molecular basis of this phenomenon remains unclear. In

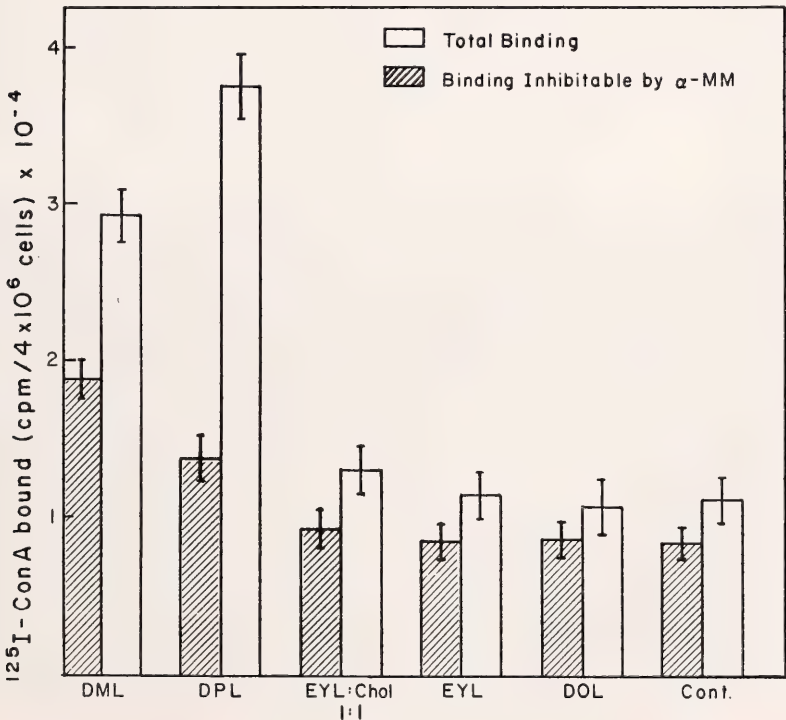


Fig. 37. Effect of different lipid vesicle pretreatments on the binding (1 hr at 2°C) of [¹²⁵I] Con A (1 μ g/ml) to normal thymocytes.

the present study of membrane-membrane interactions, we describe the adhesive properties of Chinese hamster V79 fibroblasts to each other as well as to artificial lipid vesicles, and we present a preliminary characterization of some of the cell surface molecules that may play a role in the adhesion process.

Vesicle to Cell Adhesion

Elsewhere in this report we have documented the formation of a stable adsorption between unilamellar phosphatidyl choline vesicles comprised of dimyristoyl lecithin (DML) or dipalmitoyl lecithin (DPL) in vesicle-treated lymphocytes. Such a stable vesicle-to-cell adhesion appears to be a general phenomenon and has also been found to occur in the V79 fibroblast cell line. The characteristics of this vesicle-to-

cell adhesion phenomenon are described below.

Monolayer cultures of V79 cells were dissociated into single cells with chelating agents (EDTA; E cells) or a combination of EDTA followed by trypsin treatment (ET cells). The dispersed cells were then incubated with [^3H] DML vesicles for 1 hr at 2 °C, washed and analyzed for the incorporation of radioactive phospholipid. Figure 38 shows the dependence of DML uptake on vesicle concentration. Between concentrations of 0.005 and 5.0 mg/ml of applied DML vesicles, the DML uptake increased monotonically from about 0.1 to 8.7×10^9 molec DML/cell. Furthermore, the technique used to dissociate the cells from the culture dish prior to vesicle-cell incubation had a marked effect on the amount of DML which became cell associated, with E cells taking up about an order of magnitude

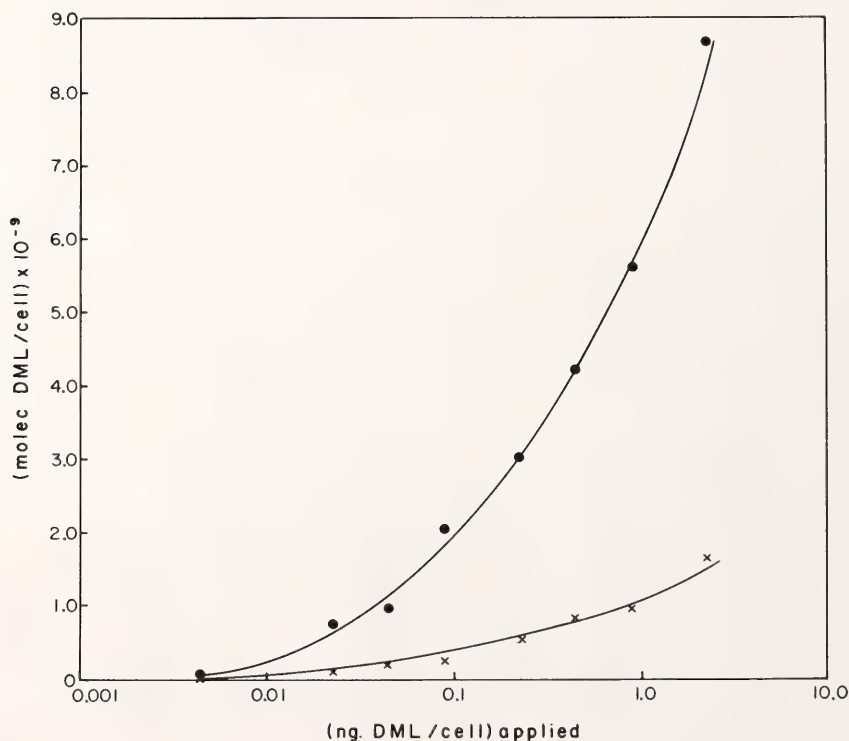


Fig. 38. Concentration dependence of DML uptake by V79 cells in suspension. Cells were dissociated with EDTA (o—o) and subsequently treated with trypsin (x—x) prior to incubation with vesicles.

more exogenous phospholipid than ET cells. The presence of the divalent cations (Ca^{++} or Mg^{++}) in the vesicle suspension had no effect on the amount of DML uptake in E or ET cells.

EM autoradiographs of E cells and ET cells (Fig. 39) treated with [^3H] DML vesicles (1 mg/ml) for 1 hr at 2 °C clearly show that the radiolabeled DML is confined primarily to the cell surface, consistent with the stable adhesion of this vesicle type of cell. Additionally, it is seen that the amount of radiolabel found associated with ET cells is considerably less than for E cells, in agreement with the data in Fig. 38. In preliminary experiments, a protein homogenate of E and ET cells incubated with [^3H] DML vesicles was subjected to SDS-polyacrylamide gel electrophoresis. The distribution of [^3H] DML in the gel suggests that a few of the protein bands had a high affinity for the radiolabeled DML. Thus, it is concluded that the adsorption of intact DML vesicles may involve some trypsin-sensitive material at the cell surface. A further characterization of this material is in progress.

Cell to Cell Adhesion

Monolayers of V79 cells were dissociated into single cells with chelating agents or proteases, and the ability of these cells to reaggregate was determined. Cells dispersed with EDTA (E cells) possess strong reaggregability in the absence of divalent cations, which was enhanced in the presence of Ca^{2+} (Fig. 40a). Cells dispersed with crystalline trypsin in Ca^{2+} - and Mg^{2+} -free medium or with trypsin in the presence of EDTA (TE cells) had no ability to reaggregate in any medium tested (Fig. 40c). Cells dispersed with crystalline trypsin in the presence of Ca^{2+} (TC cells), however, totally retained the reaggregability in a Ca^{2+} containing medium but showed no indication that there may be two pathways for cell-to-cell aggregation, a Ca^{2+} -independent and a Ca^{2+} -dependent one. The function of Ca^{2+} -dependent adhesion sites seems to be protected from trypsin digestion by the presence of Ca^{2+} (Fig. 40b vs. 40c). Mg^{2+} at physiological concentration could not substi-

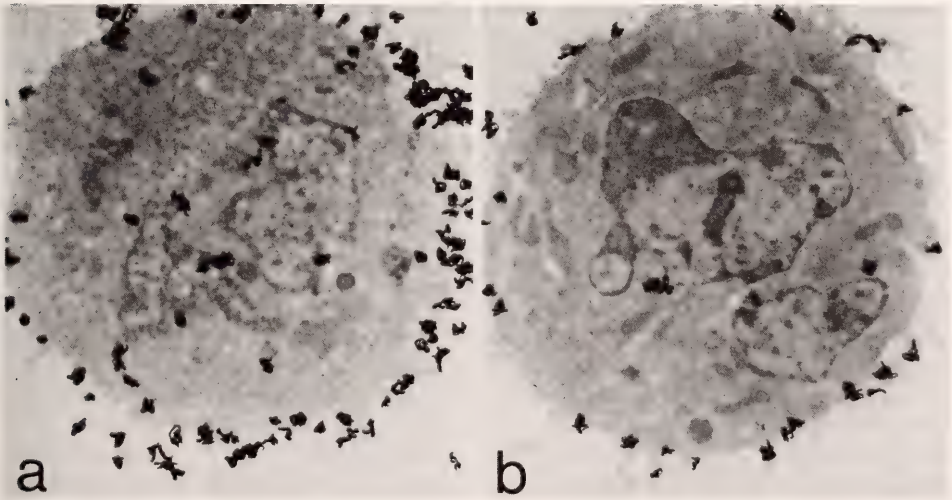


Fig. 39. EM autoradiographs of V79 cells incubated with [^3H] DML vesicles (1 hr at 2°C). (a) EDTA-dissociated cell. (b) EDTA-dissociated and trypsin-treated cell.

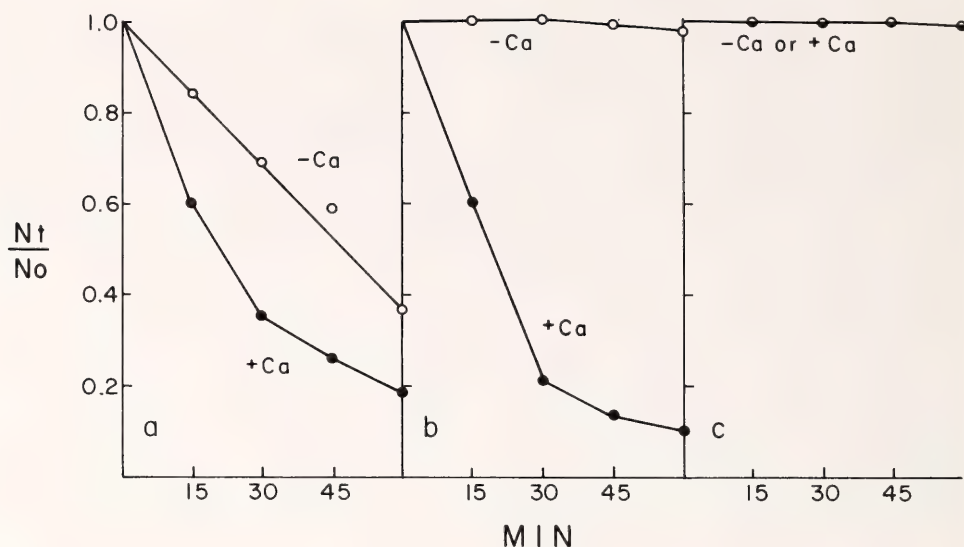


Fig. 40. Reaggregation of cells dissociated with 1 mM EDTA (a), 0.01% trypsin + 0.1 mM Ca^{2+} (b), and 0.01% trypsin + 1 mM EDTA (c) in the medium with or without 1 mM Ca^{2+} . The extent of aggregation was represented by an index Nt/N_0 , where N_0 is the initial particle number in cell suspension and Nt is the total particle number at the time t of incubation.

tute for Ca^{2+} in the phenomenon described above.

Additional experiments were carried out to compare the adhesive properties of cells to a noncellular substrate with the cell-to-cell adhesion described above. Ca^{2+} (but not Mg^{2+} or Mn^{2+}) was totally ineffective in promoting the adhesion of cells to gelatin-coated plastic substrate. Furthermore, reagents that inhibit cell-to-substrate adhesion (e.g., cytochalasin B, colcemid, and tetracaine) did not significantly affect the Ca^{2+} -dependent cell-to-cell adhesion. TC and TE cells were not markedly different in their adhesiveness to noncellular substrates. These observations suggest that a Ca^{2+} -dependent mechanism observed for cell-to-cell adhesion is absent in cell-to-substrate adhesion.

In order to explore the possibility that changes in cell-to-cell adhesiveness correlate with modifications of cell surface proteins, the surface proteins of intact fibroblasts were labeled with ^{125}I using lactoperoxidase, and the protein species subsequently examined by SDS-polyacrylamide gel electro-

phoresis. While a number of proteins are labeled with ^{125}I in all three cell types (Fig. 41a), several iodinated bands were more intensely labeled in E cells than the others, suggesting that one of the cell surface proteins could be related to the Ca^{2+} -independent adhesiveness of cells. The difference in iodinated bands between TC and TE cells, however, was clear and simple. One protein whose molecular weight (MW) is in a range of 140K to 150K was predominantly found in TC cells. No other qualitative difference in iodinated bands was observed between these two types of cells. The above 140–150 MW band was also present in E cells.

The correlation of the presence of 140–150 MW protein with the ability of cells to aggregate in Ca^{2+} was also found in another experiment. TE cells did recover the Ca^{2+} -dependent adhesiveness after several hours of incubation in normal cell culture medium. This recovery could be completely inhibited by the addition of cycloheximide to the medium. Interestingly, the recovery of cell adhesiveness

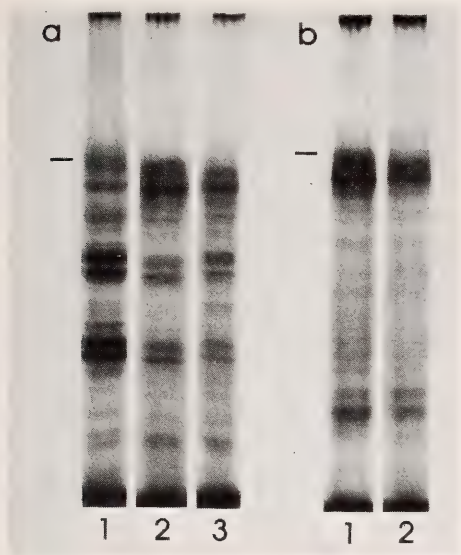


Fig. 41. Autoradiograph of [¹²⁵I]-labeled cell-surface proteins electrophoresed in 7.5% SDS-polyacrylamide gel. (a) E cells (1), TC cells (2), and TE cells (3). (b) TE cells cultured for 6 hr in the medium without (1) and with (2) 100 µg/ml cycloheximide. Iodination was carried out in Ca²⁺-free medium at 5°C (a) and at 20°C (b). The difference in the pattern of iodinated bands between (a) and (b) is due to the different temperature used for the iodination. Bars indicate the position of 140–150K molecular weight region. Top is cathode.

directly correlated with the appearance of the 140–150 MW protein at the cell surface of TE cells (Fig. 41b).

Evidence was also obtained suggesting that the 140–150 MW cell-surface protein can interact with Ca²⁺. This is supported by the finding that the radiolabeling of this protein was sensitive to the presence of Ca in the iodination medium. Thus, the 140–150 MW protein in TC cells could be iodinated only in the absence of Ca²⁺ (Fig. 42a vs. 42c), while the labeling of the other proteins in TC cells and all the proteins in TE cells were unaffected by the presence or absence of Ca²⁺ (Fig. 42b). This effect of Ca²⁺ might be equivalent to another effect of Ca²⁺ to protect the 140–150 MW protein from trypsin digestion. These phenomena suggest that the 140–150 MW protein undergoes a

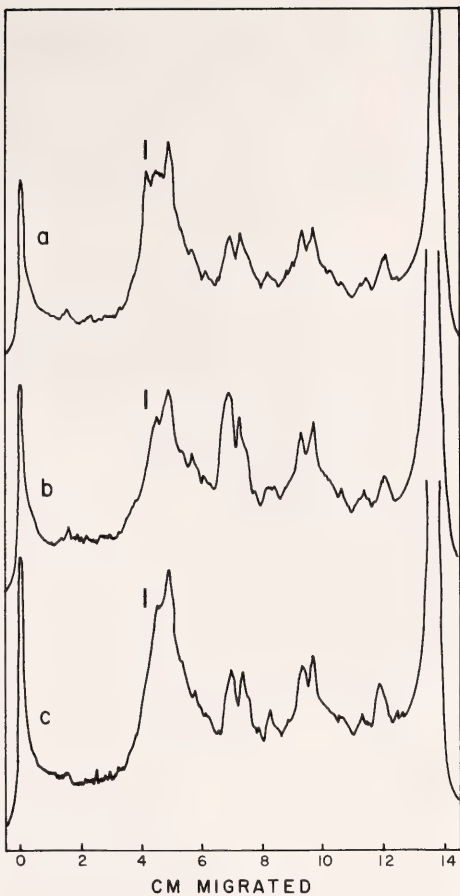


Fig. 42. Densitometer traces of autoradiographs of [¹²⁵I]-labeled cell-surface proteins electrophoresed in 7.5% SDS-polyacrylamide gel. (a) TC cells iodinated in the absence of Ca²⁺; (b) TE cells iodinated in the absence or presence of Ca²⁺; (c) TC cells iodinated in the presence of Ca²⁺. Bar indicates the position of 140–150K molecular weight region in each figure.

conformational change or alters its molecular state in the cell membrane as a result of an interaction with Ca²⁺.

In summary, these observations suggest a correlation of the appearance of the 140–150 MW surface protein with the Ca²⁺-dependent mechanism for cell adhesion. The ability of this protein to interact with Ca²⁺ is consistent with the possible participation of this protein in a Ca²⁺-dependent cell adhesion mechanism. Future experi-

ments will focus on the isolation and purification of this protein to determine its role in cellular adhesion processes.

DISTRIBUTION OF LIPHILIC FLUORESCENT PROBES IN INTACT CELLS

*R. E. Pagano, K. Ozato, and J. M. Ruyschaert**

The use of small lipophilic fluorescent molecules for probing the physical state of lipid bilayer model membranes has been the subject of investigation by "membranologists" for a number of years. Such probes partition into the hydrophobic phase of the lipid bilayer and can be used to detect, by fluorescence changes, subtle changes in the molecular packing of the lipid molecules in the vicinity of the probe. Recently, such probes have been used to monitor the membranes of intact living eukaryotic cells; however, no direct examination of the location of these molecules in whole cells has been made. We report here on the intracellular distribution of three such fluorescent probes, 1,6-phenyl-1,3,5-hexatriene (DPH), perylene, and 2-p-toluidinyl-6-naphthalene sulfonate (TNS), in murine thymocytes, using radiolabeled probes and the technique of EM autoradiography.

DPH, perylene and TNS were radiolabeled by tritium gas exposure method of Wilzbach and subsequently purified by crystallization from the appropriate organic solvents. Labeling of mouse thymocytes was performed with a $2 \times 10^{-6} M$ solution of each of the probe molecules dispersed in 0.15 M KCl. One volume of cell suspension ($0.5\text{--}2 \times 10^7$ cells/ml) was mixed with one volume of probe suspension and incubated for 60 min at 25 °C. The labeled cells were then washed twice, fixed in glutaraldehyde, and processed for electron microscope autoradiography by standard methods.

*Free University of Brussels.

Micrographs of thymocytes treated with [^3H] fluorescent probes were taken at 14,000 \times , and the outline of individual cells and location of grains traced on paper. Each traced cell was then divided into two compartments and the number of silver grains in each compartment determined. A cell-surface compartment was defined by a zone two half distances (HD) wide and centered over the cell-surface membrane contour. The remaining portion of the cell defined the internal compartment. The HD determined by Salpeter for the electron microscope autoradiographic conditions used in the present study (^3H ; 100-nm sections; Ilford L4 purple interference color; Microdol-X development) was 160 nm. For each cell, the areas of these compartments were measured. Grain densities were obtained by dividing the number of grains in each compartment by the area of that compartment. The ratio of surface grain density to interior grain density and the average \pm SEM were then calculated. The results of these measurements for each of the probes tested are summarized in Table 9. It is readily seen, both from the percentage of silver grains found in the surface compartment and from the ratio of surface to internal compartment grain densities, that in DPH and perylene the probes are largely internalized in the treated cells while most TNS is confined to the cell surface.

The cell population used for these studies was contaminated with a small fraction ($\sim 1\%$) of red blood cells and thus permitted a simultaneous analysis of the distribution of each of the probes in this cell type. The data obtained for [^3H] DPH is given in Fig. 43 and shows a symmetrical distribution of the radioactivity about the cell membrane, with approximately 80% of the grains found within a distance of ± 0.3 microns of the membrane surface. Similar data were obtained for [^3H] TNS and [^3H] perylene.

These autoradiographic findings are consistent with the known physical

TABLE 9. Distribution of Autoradiographic Grains over Mouse Thymocytes Treated with [³H] Fluorescent Probes

| Probe | Total Grains Counted | Percent Grains in Surface Compartment | (Surface Grain Density) | ± S.E.M. |
|-------------------------|----------------------|---------------------------------------|--------------------------|----------|
| | | | (Interior Grain Density) | |
| ³ H TNS | 302 | 69 | 11.4 ± 1.3 | |
| ³ H DPH | 990 | 16 | 2.0 ± 0.3 | |
| ³ H Penylene | 918 | 27 | 2.4 ± 0.1 | |

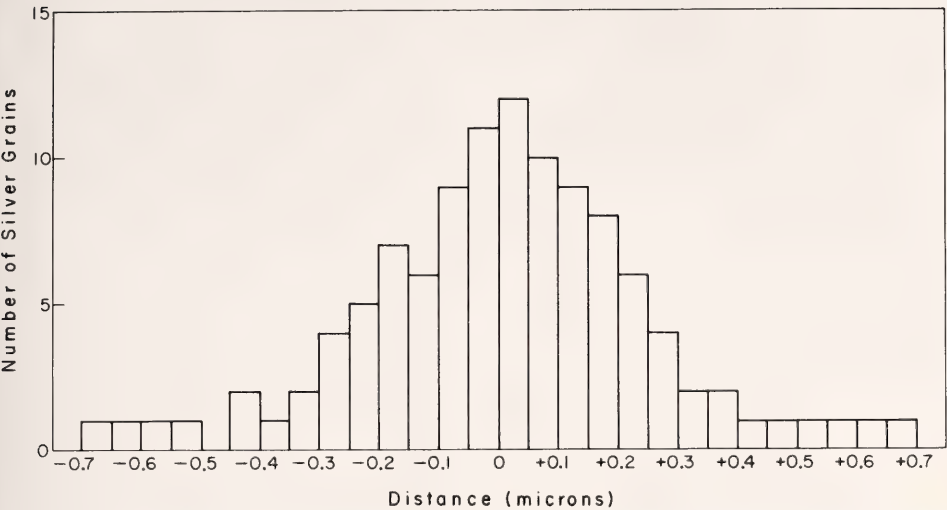


Fig. 43. Distribution of autoradiographic silver grains in murine red blood cells, treated with [³H] DPH. Number of grains found is plotted vs. their distance in microns from the cell surface (+, outside; -, inside).

properties of the fluorescent probes used, and suggest that except for TNS or cells such as the erythrocyte, considerable ambiguity may arise in inter-

preting fluorescence data obtained with whole cells containing various intracellular membranes into which these probes can partition.

MEMBRANE TRANSPLANTATION BY FUSION

L. Huang and A. K. Ritchie

The goal of this work is to establish methods by which one can transfer a membranous protein molecule with a well-defined function to the plasma membrane of cells normally devoid of such function ("membrane transplantation") and to study the physiological

function of the protein in its altered environment. Since most hydrophobic proteins require a lipid environment for their function, the transplantation process can best be accomplished by using the lipid membrane as a carrier for the pro-

tein. Joining the carrier membrane with the receiving membrane, a fusion process, should then transfer the protein molecules to their target membrane. One approach is to solubilize and isolate protein molecules and to reconstitute them into lipid vesicles. The reconstituted vesicles can then be used for fusion with the recipient cell. An alternative method is to fuse intact membrane vesicles, isolated from a source very much enriched with a protein, directly with the plasma membrane of the recipient cell. The molecule used in this study is the nicotinic acetylcholine receptor (AChR), an integral membrane protein responsible for the selective ion permeability found in the postsynaptic membrane of some nerve and muscle cells. We hope to introduce chemosensitivity toward cholinergic agonists in recipient cells. The ACh receptor is a convenient protein, since in addition to its well-defined functional activity it can also be tagged in a highly specific and relatively irreversible manner with ^{125}I - α -bungarotoxin.

We have isolated AChR from the electroplax of *Torpedo californica*. The electroplax contains membrane that is extremely rich in nicotinic acetylcholine receptors. Tissue from the electroplax (stored at -70°C) was homogenized in a buffered isotonic salt solution, centrifuged ($100,000g \times 30$ min at 4°C), then successively washed in a high and low salt concentration before solubilization by 2% triton X-100 (1 hr at room temperature). All solutions contained 0.02% NaN_3 and 5 mM EDTA to minimize bacterial contamination and protein degradation and were kept at 4°C where possible. Partial purification and detergent exchange were achieved by sedimenting the AChR into a sucrose density gradient containing 1% Na cholate. AChR sedimented as a 10S peak, occasionally with faster sedimenting shoulder. This preparation had about $0.2 \mu\text{moles}$ of α -bungarotoxin binding sites/g protein which is about 20-fold less than that reported for *Torpedo* AChR purified by

affinity chromatography. The partially purified AChR was then mixed with dioleoyl lecithin (DOL) which had been predispersed in 2% Na cholate solution. The final concentration of lipid was 10 mg lipid/ml in 1.5% cholate, 100 mM NaCl, 5 mM EDTA, 0.02% NaN_3 and 10 mM Tris, pH 7.4. The clear mixture was then exhaustively dialyzed against six changes of the buffered salt solution at 4°C for 72 hours. The solution became slightly turbid after dialysis. Thin-section transmission electron microscopy revealed the presence of very uniform unilamellar vesicles with an average diameter of 500 Å (Fig. 44a). If the DOL-cholate dispersed solution was dialyzed without protein, similar vesicles of smaller size (average diameter 400 Å) were found (Fig. 44b). The homogeneity and efficiency of vesicle formation was also demonstrated by the presence of a single peak on Sepharose 4B gel chromatography which represented 99% of the radioactivity when using tritium labeled DOL. The reconstitution of the AChR into vesicles was determined by velocity sedimentation in a detergent free sucrose density gradient. AChR was always associated with the ^3H -DOL vesicles which floated at the top of the gradient (Fig. 45a). If vesicles were first ruptured by 2% triton X-100, dissociation of AChR from the lipids occurred (Fig. 45b) with the lipids remaining at the top of the gradient and receptor migrating to its usual 10S position. The amount of receptor which could be incorporated into the vesicle fraction increased linearly then saturated as the protein/lipid ratio reached 45 ng protein/mg lipid. About two α -bungarotoxin binding sites per vesicle were found under saturation conditions. Such a low saturation level of reconstitution may be due to the differential affinity of AChR and other contaminating proteins for the hydrophobic sites in the lipid vesicles. We expect much higher efficiency for reconstitution when pure AChR is used. The reconstituted vesicles were also tested for ^{125}I - α -bungarotoxin ac-

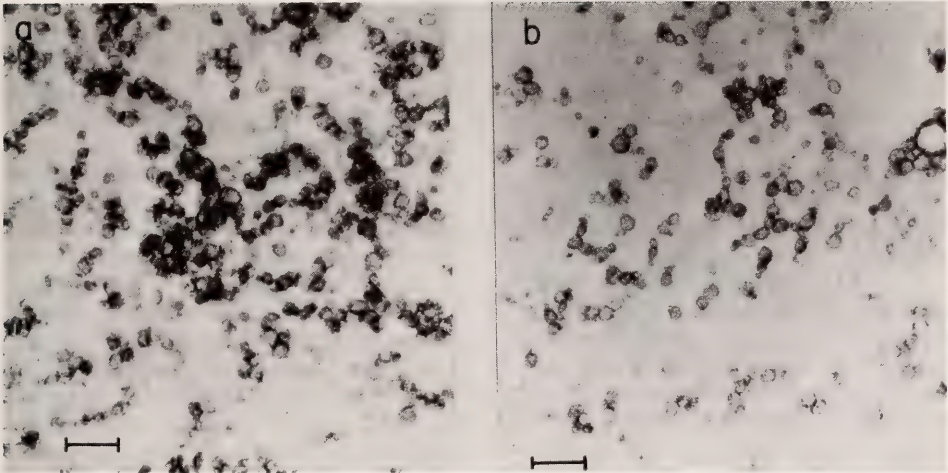


Fig. 44. Reconstituted vesicles prepared by dialysis method. (a) Vesicles containing AChR and DOL. (b) Vesicles containing DOL alone. Bar is 2,000Å.

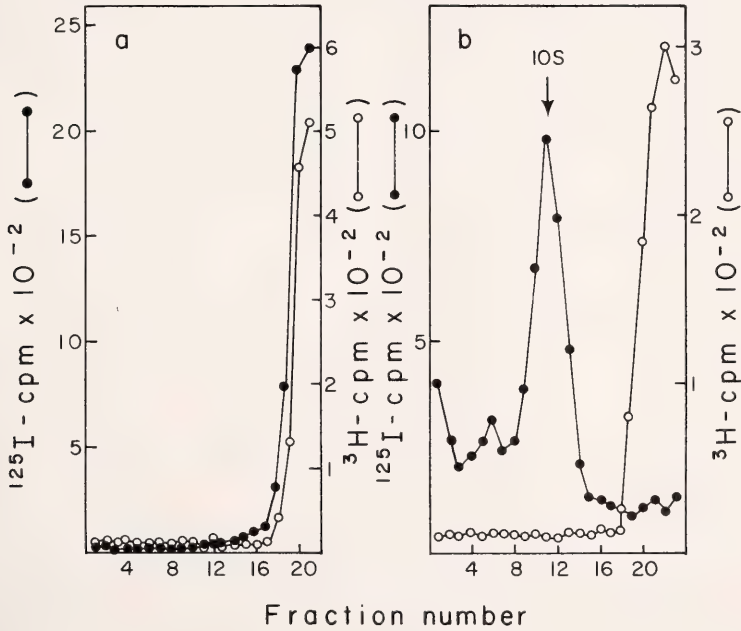


Fig. 45. Velocity sedimentation profiles of ¹²⁵I-α-bungarotoxin labeled AChR and ³H-DOL in the reconstituted vesicles in (a) detergent-free linear sucrose density gradients (5–20% w/w), and (b) similar gradient but containing 1% triton X-100. Fractions of 0.22 ml were collected from the bottom of the gradient. These receptors were prelabeled by treatment of the crude triton extract with 0.1 μg/ml ¹²⁵I-α-bungarotoxin prior to reconstitution. Free ¹²⁵I-α-bungarotoxin was separated from toxin receptor complexes on a BioGel P60 column.

tivity in the presence or absence of triton X-100. About 80% of the total AChR in the vesicle population was available for binding when vesicles were not ruptured by detergent, i.e., most of the reconstituted receptors had their toxin-binding sites facing the exterior of the vesicle.

Simple adsorption of the receptor to the exterior of the lipid vesicle seems unlikely, since co-migration of lipid and receptor on a triton-free sucrose gradient failed to occur when dialyzed receptor was mixed with preformed vesicles. We have also attempted to distinguish between incorporated receptor and loosely adsorbed receptor by testing for sensitivity to chymotrypsin digestion. Chymotrypsin digestion (0.1 mg/ml) of receptor extracted with triton from *Torpedo* or from cultured chick myotubes and of dialyzed *Torpedo* receptor results in a shift of 10S material to a 3S position on the sucrose gradient. On the other hand, receptors on the surface of cultured chick skeletal myotubes or on reconstituted vesicles remain as 10S material after digestion by chymotrypsin. Thus, receptors associated with vesicles occupy a protected position (i.e., failure to be degraded to 3S material) similar to the receptors in the membrane of intact chick myotubes. The comparable experiments on *Torpedo* membranes are still in progress. These results encourage us to believe that the reconstituted receptor is an integral part of the vesicle membrane and not merely adsorbed to its surface.

When the reconstituted AChR vesicles were incubated with Chinese hamster V79 cells for 45 min at 37 °C, extensive uptake of AChR by the cells was found with no evidence of cytotoxicity. The intact cell-associated AChR remained available for specific ^{125}I - α -bungarotoxin (the binding was inhibited by 10^{-4}M curare and formed a receptor toxin complex that migrated as 10S on sucrose gradients). The vesicle-treated cells acquired about 5×10^4 α -bungarotoxin binding sites per cell. An autoradiograph of a sparsely

plated culture dish of V79 cells that had been treated with reconstituted vesicles then labeled with ^{125}I - α -bungarotoxin revealed that most of the grains were directly over cells. This is in contrast to the random labeling of the dish when cells were treated with dialyzed receptors. An EM autoradiograph of vesicle-treated cells that had been labeled with ^{125}I - α -bungarotoxin further showed that the ^{125}I -label was randomly distributed over the cell surface. The persistence of the surface location of AChR in these cells was also examined. Vesicle-treated cells that were incubated for various times in complete growth medium at 37 °C still retained over 70% of their original activity when tested for toxin binding after 10 hr of incubation. If vesicle-treated cells were labeled with ^{125}I - α -bungarotoxin and subsequently incubated at 37 °C, those cells also retained over 70% of their radioactivity after 10 hr (Fig. 46). About 43% of the radioac-

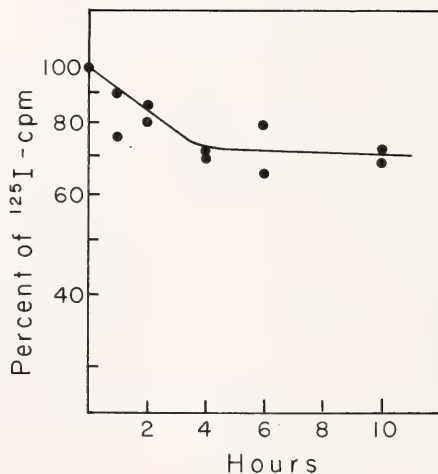


Fig. 46. The persistence of labeled receptor on the surface of V79 cells containing transplanted AChR. Monolayer cultures of V79 cells were incubated for 45 min at 37°C with reconstituted AChR. The cells were washed three times with Gey's medium, then labeled with ^{125}I - α -bungarotoxin. The washed cultures were then incubated at 37°C for the indicated amount of time. The percentage of ^{125}I - α -bungarotoxin remaining on the culture is plotted against the incubation time.

tivity that was lost from the cells into the medium after 10 hr of incubation was receptor-toxin complex, while 57% was low molecular weight material (included on a Bio-Gel P60 column) similar to the receptor- ^{125}I - α -bungarotoxin degradation product that results from the metabolism of the internalized membrane of cultured chick myotubes. Thus, the specific α -bungarotoxin binding activity of AChR can be transplanted to the surface of V79 cells previously devoid of any toxin-binding ability, and such activity remains on the cells for relatively long periods of time.

The uptake of receptor by V79 cells treated with vesicles was time dependent (Fig. 47a) but independent of the temperature of incubation. This is in marked contrast to the uptake of labeled lipid by the same cultures. The uptake of labeled lipid was dependent on both the time and temperature of incubation and consistent with the kinetics observed using vesicles formed by other methods. The amount and nature of lipid uptake was the same

whether pure lipid vesicles or vesicles containing receptor were used. Only 0.1% of the receptor was associated with the cells after 45 min of incubation at 0°C , whereas 0.33% of the lipids were associated with the cells under the same conditions (Table 10). When the study was repeated with vesicles containing prelabeled receptors, then the percentage of incorporation was higher, since this assay measures internalized receptors as well as the externally available receptors. In this case the percentage of incorporation of the lipid (0.26%) and that of the receptor (0.2%) at 0°C were nearly the same. The discrepancy between the amount of lipid uptake and the receptor uptake becomes very large at 37° due to the absence of any enhancement of receptor uptake at the higher temperature. The mechanism responsible for the temperature-dependent portion of lipid uptake (a process involving vesicle fusion) is thus different from the process involving receptor uptake. It is not clear to us at this time how the receptor is being transplanted.

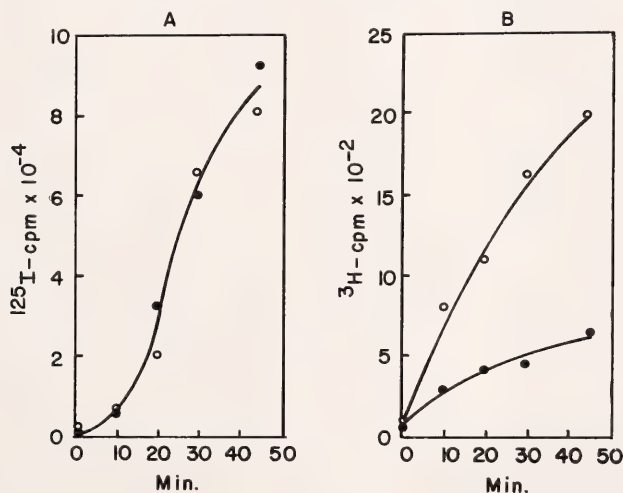


Fig. 47. The uptake of AChR and ^3H -DOL by V79 cells. A confluent 35-mm dish of V79 cells was incubated with reconstituted vesicles at 0° (●—●) and 37°C (○—○) for the indicated times. Each dish was treated with vesicles containing 8 mg/ml of DOL and $0.36 \mu\text{g/ml}$ of protein, then washed three times with Gey's medium. The plates were then incubated with $0.1 \mu\text{g/ml}$ of ^{125}I - α -bungarotoxin for 30 min at room temperature. The cells were washed six times with Gey's medium, then extracted with 1% triton and counted by liquid scintillation (for ^3H ; Fig. 47B) and/or a Gamma well counter (for ^{125}I ; Fig. 47A).

TABLE 10. Uptake of Lipid and ACh Receptor by V79 Cells Treated with Vesicles Containing the Reconstituted Receptor

| | Temp. (°C) | ³ H-DOL incorporation into cells as percent of the total ³ H-DOL applied | Receptor incorporation into cells as percent of the total applied |
|---|------------|---|---|
| *Receptor and ³ H-DOL vesicles | 0 | 0.33 | 0.1 |
| | 37 | 1.1 | 0.1 |
| † ¹²⁵ I- α -bungarotoxin receptor and ³ H-DOL vesicles | 0 | 0.26 | 0.2 |
| | 37 | 0.66 | 0.2 |

*Cells were treated for 45 min at 37 °C with vesicles containing unlabeled receptors. The cultures were then washed three times with Gey's medium and incubated for 30 min at room temperature with 0.1 μ g/ml ¹²⁵I- α -bungarotoxin. Cultures were washed 6 \times 5 min, then extracted with 1% triton X-100.

†Cells were treated in the same manner as above except that the vesicles contained receptors that had been prelabeled with ¹²⁵I- α -bungarotoxin prior to reconstitution.

We have also attempted to introduce the AChR into the plasma membrane of V79 cells by treating these cells with membrane fragments isolated from the *Torpedo* electroplax. A membrane fraction containing 10^{-2} moles of α -bungarotoxin binding sites/g protein was obtained by sedimenting a crude membrane preparation on a discontinuous sucrose density gradient. Thin-section electron microscopy of this fraction showed closed membrane vesicles of very heterogeneous size distribution (0.1–2 μ in diameter). A suspension of this material was incubated with a monolayer of cultured V79 cells in the presence of UV-inactivated Sendai virus or lipid vesicles comprised of 90% phosphatidyl choline and 10% phosphatidyl glycerol or phosphatidyl serine. Some toxin binding activity was observed, but this method did not appear to be as promising as the use of the reconstituted vesicles to transplant membrane proteins.

Finally, we have tried to test our reconstituted vesicles and V79 cells treated with the reconstituted vesicles for some indication of functional activity by the receptor (i.e., ion permeation specifically induced by a cholinergic agonist). The most satisfactory method of testing the vesicles for ²²Na ion flux was a 1-ml P60 Bio-Gel column in which vesicle-associated ²²Na could be

completely separated from free ²²Na in 1 min. When reconstituted receptor vesicles were tested, they demonstrated an uptake of ²²Na which was saturated within 10 min. This influx, however, was not enhanced by the presence of carbachol, a cholinergic agonist. Attempts to test the V79 cells that had been treated with vesicles for AChR activity by electrophysiological techniques were also negative. These cells had resting potentials of about –25 mV but did not respond to bath or iontophoretic application of ACh. There was no change in the ACh sensitivity of cultured chick myotubes similarly treated with reconstituted receptor after blockade of endogenous receptors with α -bungarotoxin. There are a number of possibilities for our failure to detect receptor functional activity: (1) The receptor, although retaining its α -bungarotoxin binding capacity, may have lost its ability to function as an ionophore due to some denaturation or degradation of the protein. (2) The isolated receptor may be lacking some other necessary component that was discarded or inactivated in the isolation process. (3) The receptor may have been transferred but was not situated in the membrane in an integral manner that allowed it to function as an ionophore. Limited success by other investigators in restoring both crude and purified AChR into artificial

membranes and vesicles, although with only intermittent success, leads us to believe that the first possibility is the most likely reason for our failure.

Experiments are in progress to determine the conditions necessary for restoring functional activity to the receptor. The mechanism by which

transplantation occurs will also be of primary importance, using either the ACh receptor as a marker—provided that functional activity can be restored—or some other membrane protein. Our preliminary data indicate that this is a promising method of membrane transplantation.

MECHANISM OF SYNGENEIC RESPONSE INDUCED BY LECTINS

K. Ozato and J. D. Ebert

In *Year Book 74*, pp. 90–92, we demonstrated that the modification of the lymphocyte surface by lectins renders the cells responsive to syngeneic lymphocytes, as revealed by the proliferation of T cells stimulated by spleen cells bearing the same histocompatibility antigens. A syngeneic response can be obtained when either responding cells or stimulating cells are pretreated with native or succinyl-Con A (N-Con A or S-Con A).

During the past year we attempted a more analytical study of this syngeneic response. Two directions of research were undertaken. We first undertook to determine the characteristics of the cellular stimulus produced by syngeneic spleen cells. We have obtained data that suggest that the response is characteristic of T cells. Congenital athymic mice (nu/nu) provide a lymphocyte population deficient in T cells. The spleen cells from nu/nu mice did not respond to syngeneic cells. Further, in an allogeneic situation, they did not manifest the Con A pretreatment effect that usually augments the mixed lymphocyte reaction. Con A coating of either responding cells or mitomycin-C treated spleen cells failed to respond in nu/nu mice. Since we first observed the syngeneic response in a pure T-cell population, we now believe that the response is a pure T-cell specific phenomenon.

The analysis of the stimulating population has been carried out by treating the cells with antibodies against specific surface components of

T cells or B cells. Goat antimouse Ig or AKR anti CBA θ were used for elimination of B cells and T cells, respectively. Antibody treatment was carried out before the cells were coated with Con A. The effect of antibodies was studied when both responding cells and stimulating cells were coated with Con A. As shown in Table 11 (a and b) when stimulating spleen cells were treated with anti-Ig, the response was effectively suppressed, whereas anti- θ antibody treatment did not affect the response. This finding indicates that stimulatory function depends on the presence of B cells. We have tested the possible participation of adherent cells (mostly macrophages). Spleen cell populations that are deleted of adherent cells by passing the cells through plastic petri plates still manifest their stimulatory function.

Then how do responding T cells interact with stimulating cells (probably B cells)? Do B cells release a factor into the medium? Do stimulating cells somehow enable Con A molecules to associate with T cells more effectively? Stimulating and responding cells must either be in contact or be "very close neighbors," for the culture fluid in which stimulating cells have been grown does not stimulate. Moreover, when stimulating cells and responding cells are cultured separately, using nucleopore filter membranes, the syngeneic response is not observed. The role of stimulating cells does not appear to be to provide physical support of Con A molecules on the surface,

TABLE 11(a). Effect of Anti- θ or Anti-Ig on Con A-induced Syngeneic Response CRT vs. [N-Con A]-Syngeneic Spleen

| Treatment | ³ H-TdR Uptake on Day 3 (cpm $\times 10^{-3}$ /culture) | |
|---------------------------------------|--|----------------|
| | B10.D2 | CBA |
| Medium RPMI | 27.2 \pm 3.0 | 18.3 \pm 1.4 |
| Normal Serum AKR (1/20) | 30.3 \pm 2.4 | 16.7 \pm 1.0 |
| Normal Serum Goat (1/20) | 32.4 \pm 2.6 | 16.2 \pm 1.3 |
| Rabbit C' (1/15) | 15.6 \pm 1.6 | 17.6 \pm 1.5 |
| AKR Anti- θ (1/20) | 25.3 \pm 3.0 | 18.8 \pm 1.0 |
| AKR Anti- θ (1/40) | 38.0 \pm 2.5 | 16.0 \pm 0.7 |
| AKR Anti- θ (1/40) + C' (1/15) | 29.3 \pm 3.0 | 17.2 \pm 2.0 |
| Goat Anti-Ig (1/20) | 0.8 \pm 0.1 | 0.8 \pm 0.1 |
| Goat Anti-Ig (1/40) | 0.2 \pm 0.0 | 1.0 \pm 0.0 |
| Goat Anti-Ig (1/40) + C' (1/15) | 0.4 \pm 0.0 | 0.3 \pm 0.0 |

Spleen cells pretreated with mitomycin C were then treated with antibodies for 45 min at 37°C in the presence or absence of complement (C'). The parentheses indicate the dilution of the antiserum. After washing the cells to remove killed cells as well as unbound antibodies, cells were further treated with N-Con A at 50 μ g/ml at 37°C for 30 min. They were then mixed with responding cells (cortisone-resistant thymocytes) in a 1:1 ratio (2×10^6 cells) in 0.5 ml. The response was measured by ³H-TdR uptake on day 3.

TABLE 11(b). [N-Con A-CRT] vs. Syngeneic Spleen

| Treatment | ³ H-TdR Uptake on Day 3 (cpm $\times 10^{-3}$ /culture) | |
|---------------------------------------|--|----------------|
| | C57BL/10 | CBA |
| Medium RPMI | 12.7 \pm 0.5 | 12.3 \pm 0.7 |
| Normal Serum AKR (1/20) | 10.3 \pm 0.8 | 11.5 \pm 0.8 |
| Normal Serum Goat (1/15) | 14.4 \pm 1.1 | 10.0 \pm 0.8 |
| Rabbit C' (1/15) | 13.0 \pm 0.6 | 10.0 \pm 0.8 |
| AKR Anti- θ (1/20) | 11.4 \pm 0.7 | 9.0 \pm 0.1 |
| AKR Anti- θ (1/40) | 10.9 \pm 0.3 | 13.5 \pm 1.3 |
| AKR Anti- θ (1/40) + C' (1/15) | 12.0 \pm 1.0 | 8.9 \pm 0.9 |
| Goat Anti-Ig (1/20) | 0.3 \pm 0.0 | 4.3 \pm 0.7 |
| Goat Anti-Ig (1/40) | 0.9 \pm 0.1 | 4.7 \pm 0.3 |
| Goat Anti-Ig (1/40) + C' (1/15) | 0.2 \pm 0.0 | 3.0 \pm 0.1 |

Stimulating spleen cells were treated with antibodies in the same manner as (a), after which they were mixed with responding cells that had been treated with N-Con A (50 μ g/ml).

for when stimulating cells are killed by fixation or by freezing and thawing after they were coated with Con A, the response is completely abrogated (Table 12). However, treatment with metabolic inhibitors or the microfilament disrupting agent, cytochalasin B, did not affect the response. Thus we may suggest that the intact cell membrane of stimulating cells is required. It is an interesting possibility that membrane components may be exchanged between responding cells and

stimulating cells and that Con A molecules are transferred from stimulating cells to responding cells or vice versa. We are now studying the fate of Con A molecules, using ¹²⁵I-Con A bound to either stimulating cells or responding cells to test this possibility.

Another goal of our research has been to delineate the role of lectins. If the response is entirely dependent on stimulating cells, the role of Con A or other lectins must be to enhance the "physical contact" of responding and

TABLE 12. No Syngeneic Response from Fixed "Stimulating" Cells

| Treatment of Stimulating Cells | ³ H-TdR Uptake on Day 3 (cpm × 10 ⁻³ -) | |
|--------------------------------|---|---|
| | I. Responding Cells: Coated with N-Con A | II. Stimulating Cells: Coated with N-Con A |
| 1. No treatment | 18.5 | 15.6 |
| 2. Glutaraldehyde (2.5%) | 0.2 | 0.0 |
| 3. Ethanol | 0.3 | 0.3 |
| 4. Acetone | 0.1 | 0.1 |
| 5. Freezing and thawing | 0.2 | 0.1 |
| 6. Cytochalasin B (40 μg/ml) | 23.7 | 18.4 |
| 7. Dinitrophenol (2 mM) | 22.4 | 19.2 |
| 8. Sodium azide (50 mM) | 23.1 | 17.8 |

Stimulating cells (mitomycin-C treated) were treated with various reagents for 15 min at room temperature (2 to 4) or treated for 45 min at 37°C (5 to 8). Freezing and thawing were repeated twice. In column II, Con-A pretreated cells were used. The response of cortisone-resistant thymocytes was measured on day 3.

stimulating cells. If so, any lectin that can agglutinate lymphocytes should give the same effect. Among lectins we have tested, similar syngeneic response was observed with two other lectins, namely, leucoagglutinin (purified form of phytohemagglutinin)

(Fig. 48), and lentil lectin (a gift from John Cebra at Johns Hopkins University). Although wheat germ agglutinins agglutinate lymphocytes, they do not induce the syngeneic response. Binding to a sugar does not seem to be a specific requirement. The ability to

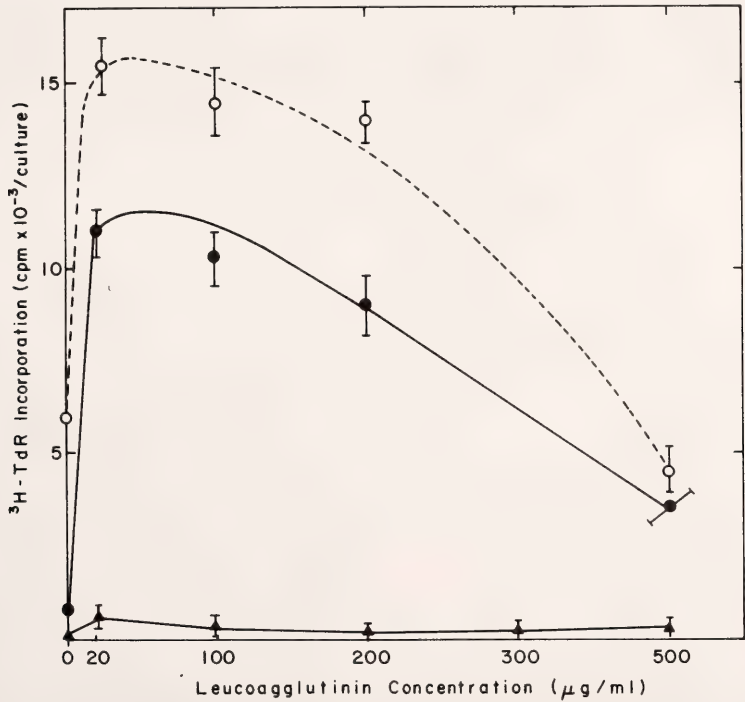


Fig. 48. CBA cortisone-resistant thymocytes were cultivated with syngeneic (CBA) (●—●) or allogeneic (B10.D2) (○—○) spleen cells pretreated with leucoagglutinin at the concentrations indicated at 37°C for 30 min. As controls, spleen cells (Δ—Δ) were cultured alone.

produce a syngeneic response appears to be limited to those lectins that have mitogenic properties in T cells. It is therefore conceivable that such lectins

not only effect a physical association between cells but also provide a stimulus to the responding cells.

STUDIES ON SKELETAL MUSCLE AND NEURONAL PLASMA MEMBRANES

*D. M. Fambrough, R. E. Pagano, P. N. Devreotes, K. Tepperman, D. J. Card, and S. Carbonetto
with the technical assistance of A. Mabin, W. Duncan, and H. W. Chen*

The acetylcholine (ACh) receptor is a major glycoprotein in the muscle plasma membrane of the neuromuscular junction and a minor component of extrajunctional plasma membrane. The ACh receptor has been our point of focus in studies on the differentiation and organization of skeletal muscle plasma membrane, and it has become clear that the number and distribution of ACh receptors in skeletal muscle (which vary with the developmental and physiological state of the muscle) are regulated largely by regulation of ACh receptor metabolism. Our studies of the metabolism of extrajunctional ACh receptors have led us to propose a model for the major events in receptor metabolism, illustrated in Fig. 49.

The main features of the model are as follows. The protein subunits of which the ACh receptor is composed are synthesized by the conventional protein synthesizing mechanisms of cells and are rapidly assembled into receptor units resembling those in the plasma membrane. These newly synthesized receptors occur upon some membrane system(s) in the cytoplasm of the muscle cells and are collectively referred to as the "precursor pool." The average residence time of a new receptor in the precursor pool is 2–3 hr. Receptors are transferred from this pool to the surface by an energy-requiring process and are then able to function. The average half-life of an ACh receptor in the plasma membrane is 22 hr.

HYPOTHETICAL "LIFE-CYCLE" of ACETYLCHOLINE RECEPTORS

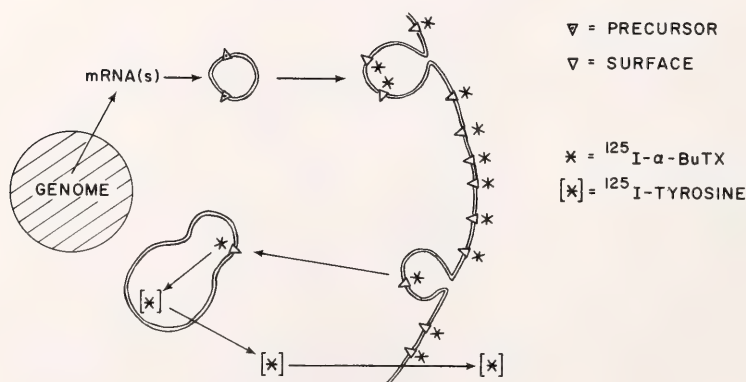


Fig. 49. Hypothetical "life cycle" of acetylcholine receptors in cultured chick skeletal muscle. The figure depicts a cross section through a myotube with receptors symbolized as triangles in membrane profiles. Arrows indicate processes consistent with data on receptor metabolism. Symbols for precursor and surface receptors and for $^{125}\text{I}-\alpha\text{-bungarotoxin}$ and $^{125}\text{I}\text{-tyrosine}$ are indicated on figure.

Receptors are degraded by an energy-requiring process that involves the internalization of the receptor and transport to secondary lysosomes and then proteolytic destruction.

This model for ACh receptor biosynthesis and turnover was developed mostly on the basis of data from experiments involving the use of α -bungarotoxin and [125 I] labeled α -bungarotoxin as probes for ACh receptors. The strategies for using these probes to measure the accumulation of receptors in plasma membranes, the incorporation of newly synthesized receptors into plasma membranes, and the degradation of receptors have been described in previous *Year Books*. Some of the details of the models were based upon data from studies involving inhibitors of various cellular processes. In *Year Book 74* (pp. 68–73) we described the application of two new techniques to the study of ACh receptor metabolism: electron microscope autoradiography and the "density shift" technique. EM autoradiographic studies during the past year have provided quantitative supporting data for the degradative aspects of the model of receptor metabolism. The density shift technique has made it possible to label ACh receptors directly and thus to verify the kinetics of receptor biosynthesis and incorporation into plasma membranes.

Now that we can confidently measure many steps in the metabolism of extrajunctional ACh receptors, we have begun to investigate the manner in which external stimuli influence the number and distribution of ACh receptors in skeletal muscle fibers via their influence upon receptor metabolism. The two classes of stimuli postulated to affect receptor metabolism are (1) hypothetical "trophic" factors released by motoneurons onto muscle fibers and (2) muscle activity (which is normally driven by the activity of motoneurons but can be artificially driven by electrical stimulating). So far we have only investigated the effect of artificially driven or suppressed muscle activity on

the metabolism of extrajunctional receptors. These studies suggest that muscle activity leads to a reduction in the number of receptors because of a decrease in the rate of receptor biosynthesis or incorporation into plasma membranes.

The organization of ACh receptors into dense clusters at postsynaptic sites may involve active "gathering" of extrajunctional receptors or merely stabilization of receptors implanted in the plasma membrane at the site of nerve-muscle interactions. From an experimental point of view, one can pose the question: Can preexisting extrajunctional receptors be accumulated into postsynaptic receptor arrays? To investigate this question and also to gain some insight into the number and distribution of receptors on embryonic skeletal muscle during differentiation and synapse formation, we have begun a study of the chick anterior latissimus dorsi muscles. We are also developing techniques to determine whether or not ACh receptors on muscle are free to move in the plasma membrane.

We consider the ACh receptor both a functional entity of great interest in its own right and also an example of a membrane glycoprotein. In this latter frame of reference, we are interested to know whether the kinetics of turnover of ACh receptors are typical of or identical to the kinetics of turnover of other membrane proteins. To investigate this matter we have been attempting to label a set of membrane proteins by the lactoperoxidase iodination technique and then to study the turnover of this class of proteins. Some progress and the definition of some difficulties are summarized in the report.

Our interest in excitable cells has extended to neurons, and as a first approach to studies of membrane metabolism and control of membrane properties in neurons we have selected chick sympathetic neurons. This choice was based largely upon the work of Greene and collaborators, who have demonstrated the specific binding of α -bungarotoxin to such cells. We are

currently testing whether or not α -bungarotoxin binds to ACh receptors in cultures of such neurons and whether the binding is strong enough to permit us to develop strategies similar to those used to study the metabolism of skeletal muscle ACh receptors.

ACh RECEPTOR BIOSYNTHESIS

P. N. Devereotes

Purification of the plasma membrane and its proteins poses a major technical difficulty to membrane biologists. The total plasma membrane protein usually represents only about 1% of the cell protein, and specific membrane components may represent only a small fraction of this total. In their investigations of membrane proteins, therefore, membrane biologists have turned to specific markers or specific chemical modification techniques to tag these proteins. Marking methods generally label membrane components exposed on the outer surface of the membrane *after* synthesis and *after* insertion into the plasma membrane. Accordingly, attempts to study biosynthesis and turnover of membrane components have been indirect, including our studies of ACh receptor metabolism with the use of α -bungarotoxin. Criticism is usually raised that the degradation or turnover of the bound marker rather than the native protein itself is being studied. Attempts have been made to study biosynthesis and turnover directly by labeling the membrane components with radioactive amino acids. With this approach, however, the advantages gained through the specificity of the marker must be sacrificed. Marker specificity can be retained in direct labeling experiments if receptors are directly labeled not with radioactive amino acids but with amino acids that change a physical property of the receptors—their density.

A specific and nearly irreversible marker for acetylcholine receptors is

[125 I] mono-iodo- α -bungarotoxin. In addition, α -bungarotoxin receptor complexes can be sedimented through dense sucrose-deuterium oxide gradients. As will be demonstrated below, receptors synthesized from [2 H, 13 C, 15 N] amino acids and complexed with α -bungarotoxin can be separated from normal density α -bungarotoxin-receptor complexes on such gradients.

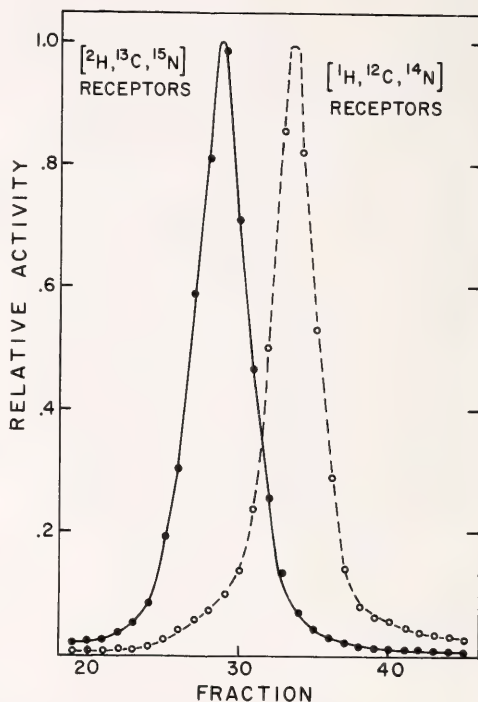


Fig. 50. Density-shifted receptors from differentiating cells. Twenty large-muscle cultures were grown for 24 hr in normal medium. At that time, there were very few myotubes in culture, and the myoblasts were fed with medium containing [2 H, 13 C, 15 N]-amino acids. After the cells had fused in the density-labeled medium, the surface receptors were complexed with [125 I] mono-iodo- α -bungarotoxin. The complexes were then extracted into 25% cholate, 10-mM Tris and mixed with a marker of [131 I] mono-iodo- α -bungarotoxin-receptor complexes prepared from myotubes grown in normal medium. A 0.4-ml aliquot of the mixed extract was carefully layered over a 25–40% sucrose-deuterium oxide gradient containing 1% triton, 1mM EDTA-PMSF, 10 mM Tris, pH 7.8. Centrifugation was for 2 days in a Beckman SW41 rotor at 36K at 4°C. Gradients were pumped into scintillation vials and the activity of each isotope determined.

So far, the most reliable method of preparing a sample of pure density labeled [¹²⁵I] mono-iodo- α -bungarotoxin-receptor complexes is to allow cells to differentiate in medium containing [²H, ¹³C, ¹⁵N] amino acids. with [¹²⁵I] mono-iodo- α -bungarotoxin and extracted in nonionic detergents. Nearly complete separation of these receptors from [¹H, ¹²C, ¹⁴N]-receptors has been obtained, as shown in Fig. 50. Over 90% of the acetylcholine receptors extracted from cells that have differentiated in [²H, ¹³C, ¹⁵N] amino acid medium are of altered buoyant density.

An estimate of the apparent density shift between [¹H, ¹²C, ¹⁴N]-receptors and [²H, ¹³C, ¹⁵N]-receptors can be obtained by measuring sedimentation rates of the respective complexes with α -bungarotoxin in shallow gradients of different average densities. The average density of the gradients was varied by substitution of D₂O for H₂O. It can

be shown that for shallow gradients the logarithm of the distance traveled by a given protein versus time is a straight line. For a given protein, the slope of this line is a function of the average density of the gradient medium. In fact if λ is the slope, then

$$\lambda = k(1-\rho_o/\rho)$$

where k is a constant dependent on molecular weight, rotor speed, and temperature; ρ is the density of the protein; and ρ_o is the average density of the medium. Plots of λ versus ρ_o , therefore, intersect the ρ_o axis at ρ . This kind of analysis has been carried out for [¹H, ¹²C, ¹⁴N]- and [²H, ¹³C, ¹⁵N]-receptors. As shown in Fig. 51, the apparent density of [¹H, ¹²C, ¹⁴N]-receptors is 1.26 and that of [²H, ¹³C, ¹⁵N]-receptors is 1.33. When corrections are made for detergent binding to the α -bungarotoxin receptor complexes (detergent binding causes, in part, the

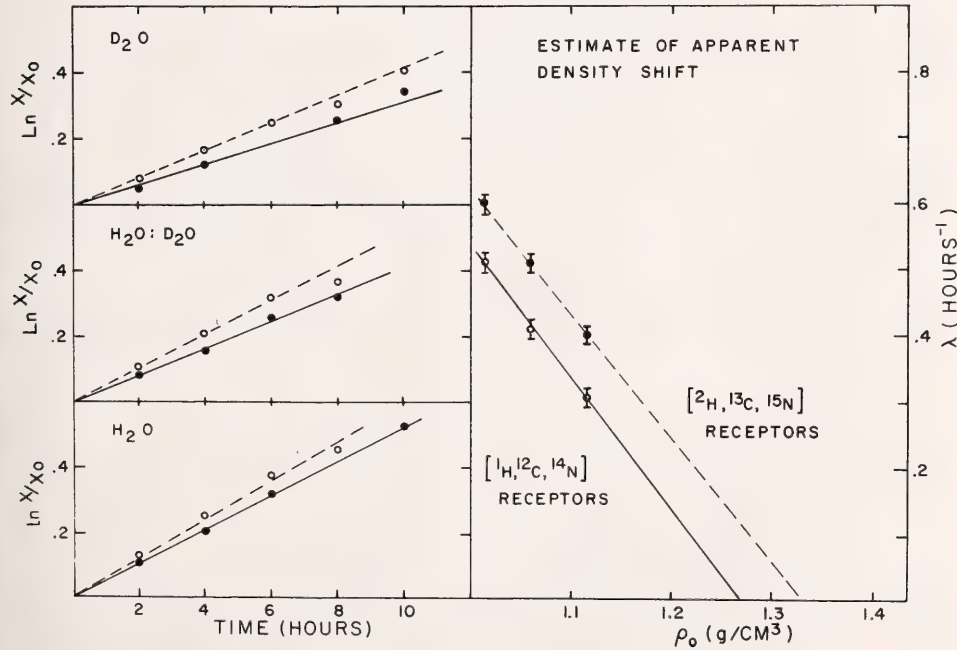


Fig. 51. Estimate of density shift. Identical aliquots of the same mixed extract described in the legend to Fig. 49 were layered onto identical gradients and centrifuged for different times. Gradients for each series were 5–20% sucrose in H₂O, 50% D₂O or D₂O containing 1% triton, 10 mM Tris. Gradients were collected into scintillation vials, and the position of the two bands determined at each time for the three different series. X_o and X refer to the distance from the center of the rotor to the meniscus and the position of the band, respectively. Lambda is the slope of the straight lines shown on the left. Experiment was repeated twice.

anomalous low density of the receptor), a density shift of 0.08 g/cm^3 is calculated. This corresponds to a shift of approximately 6%. The maximum attainable shift (calculated from the amino acid composition of purified receptors from *Electrophorus electricus*) is about 8.5%. Since the calculated shift is a *minimum* estimate, a substantial fraction of the amino acids of the receptor must be substituted by [^2H , ^{13}C , ^{15}N]-amino acids.

As has been described in the previous section, the model for acetylcholine receptor biosynthesis suggests that receptors undergo a 3-hr transit time before being inserted into the plasma membrane. This feature of the model has been derived from observations using puromycin and cycloheximide to block protein synthesis. When protein synthesis is inhibited, new receptors are incorporated into the surface for about 3 hr and then incorporation stops, suggesting that the pool of pre-synthesized receptor has been depleted. Direct evidence of a 3-hr transit time for receptors can be obtained by the density shift technique. Density-shifted [^2H , ^{13}C , ^{15}N]-receptors should begin to appear in the cell surface about 3 hr after their synthesis.

The experiment was carried out as follows. The existing surface receptors were first blocked by an overnight exposure to unlabeled α -bungarotoxin. After rinsing away the unbound α -bungarotoxin, myotubes were incubated in medium containing [^2H , ^{13}C , ^{15}N]-amino acids. New receptors then appear on the surface of the myotubes as a linear function of time (in these experiments, the heavy medium may have had a slightly deleterious effect on the cultures at late times) and can be labeled at subsequent times with [^{125}I] mono-iodo- α -bungarotoxin. After extraction into nonionic detergents, these [^{125}I] mono-iodo- α -bungarotoxin-receptor complexes were mixed with a marker of [^{131}I] mono-iodo- α -bungarotoxin-receptor complexes extracted from myotubes grown in normal medium. The mixed extract

was then centrifuged through sucrose-deuterium oxide gradients to determine the fraction of [^2H , ^{13}C , ^{15}N]-receptors. These density-shifted receptors represent the fraction of newly appearing receptors that were synthesized after addition of dense amino acids to the medium. As shown in Fig. 52 new receptors begin to appear on the surface without a lag; however, [^2H , ^{13}C , ^{15}N]-labeled receptors appear at the maximum rate only after a lag of about 3.5 hr. Small amounts of [^2H , ^{13}C , ^{15}N]-receptors appear at 2 and 3 hr; after 3.5 hr most of the newly appearing receptors are density shifted.

Since most receptors only appear on the surface at the maximum rate 3.5 hr after their biosynthesis, it is suggested that newly synthesized receptors undergo a 3-hr transit time within the cell. Since small amounts of receptors appear at 2 and 3 hr, however, it is suggested that the intracellular transport of receptors is not a strictly linear, assembly-line process. Newly synthesized receptors and receptors already in transport can become, to a certain extent, intermixed and inserted at random into the plasma membrane. Alternatively, the small amounts of receptor appearing at 2 and 3 hr after synthesis might be in a subpopulation of myotubes in which the transit time is shorter than average.

It has also been learned from these experiments that acetylcholine receptors are not "unmasked" during the development of the cultures. Most of the newly appearing receptors are synthesized a few hours before incorporation into plasma membranes. Furthermore, as evident from the experiment described in the legend to Fig. 50, the acetylcholine receptors expressed during differentiation of myoblasts into multinucleated myotubes are newly synthesized. It is unlikely, therefore, that presynthesized receptors are stored within myoblasts and expressed during differentiation.

The density shift technique for acetylcholine receptors has enabled us to confirm several aspects of the model

for acetylcholine receptor biosynthesis *without* purification of the receptor or the plasma membrane. We are using density labeling technique to measure the kinetics of incorporation of isotop-

ically substituted amino acids into the receptors undergoing intracellular transport and to measure directly the half-life of receptors once they become members of the surface population.

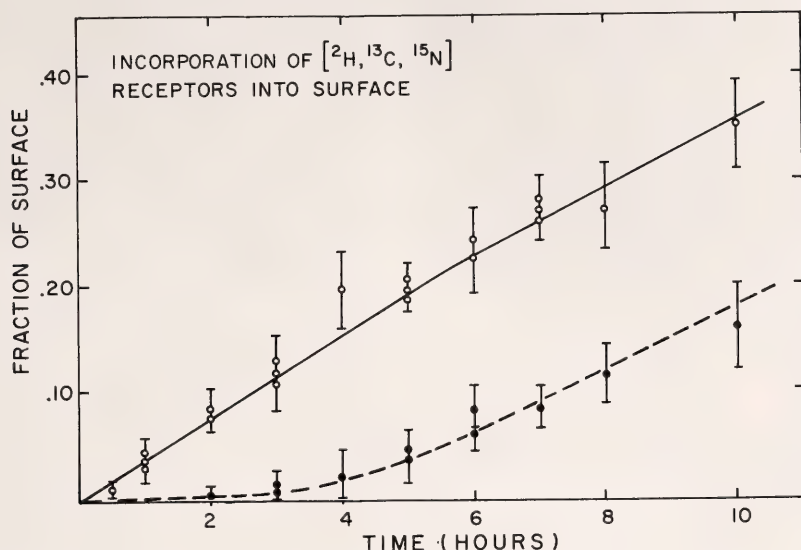


Fig. 52. Appearance of density-labeled receptors on surface membrane. Three-, four-, or five-day-old cultures of myotubes were saturated with unlabeled α -bungarotoxin ($0.2 \mu\text{g}/\text{ml}$ for about 15 hr). After rinsing away unbound α -bungarotoxin, the medium was replaced with medium containing [^2H , ^{13}C , ^{15}N] amino acids. After incubation for the indicated times at 37°C , sets of cultures were cooled at 4°C and saturated with [^{125}I] mono-iodo- α -bungarotoxin. The [^{125}I] mono-iodo- α -bungarotoxin-receptor complexes were then extracted in 2.5% cholate, 10 mM Tris, mixed with a marker of [^{131}I] mono-iodo- α -bungarotoxin-receptor complexes prepared from myotubes grown in normal medium. Samples were layered in thin bands on 10–20% sucrose-deuterium oxide gradients containing 1% triton, 10mM Tris. After centrifugation for 1 day in a SW41 rotor at 36K at 4°C , gradients were collected into scintillation vials. Total receptors (○). Amount of material running to the position of [^2H , ^{13}C , ^{15}N]-receptors (●—●) was determined by curve fitting. Different ratios of "heavy" and "light" peaks were added together by a computer program which used, for the shape of each peak, the shape of the marker on each gradient. These curves were matched to the data and could be fit within 5%. Similar results could be obtained by counting the area outside the marker peak and expressing it as a fraction of the total area.

AUTORADIOGRAPHIC ANALYSIS OF RECEPTOR DEGRADATION

P. N. Devreotes and D. M. Fambrough

The rate of appearance of radioactivity in the medium after [^{125}I]-mono-iodo- α -bungarotoxin is bound to ACh receptors is a measure of receptor degradation. Our data on the mechanism of degradation of receptors are consistent with a model (Fig. 49) in which receptors are internalized and then de-

graded. For example, homogenates of myotubes labeled with [^{125}I] mono-iodo- α -bungarotoxin have little or no capacity for degradation; and degradation is inhibited by 2,4-dinitrophenol and is very temperature sensitive, having a Q_{10} of 8. After a brief "pulse" incubation of myotubes with [^{125}I] mono-iodo- α -bungarotoxin, the rate of release of [^{125}I] mono-iodo-tyrosine into the medium (due to degradation of the [^{125}I] labeled α -bungarotoxin initially bound to surface ACh receptors) requires about 90

min to reach a maximum (Fig. 53). During this time some of the labeled toxin-receptor complexes must move into a small compartment of receptors earmarked for degradation. Since the lag time is equivalent to about one hour of degradation and since receptors are normally degraded at about 3% per hour, the compartment should contain about 3% as many receptors as there are surface receptors. We have looked for the subcellular location of this hypothetical compartment, using electron microscopy autoradiography. In these studies the location of radioactiv-

ity on and within cultured muscle cells was determined as a function of time after brief exposure of cells to [125 I] α -bungarotoxin. The large secondary lysosomes of the muscle cells were found to accumulate radioactivity up to a plateau level of slightly over 2% of total cellular radioactivity (Fig. 53). This accumulation occurred with kinetics consistent with a model of degradation in which the transport of [125 I] α -bungarotoxin-receptor complexes to lysosomes and their hydrolysis in lysosomes results in the production of [125 I]-tyrosine.

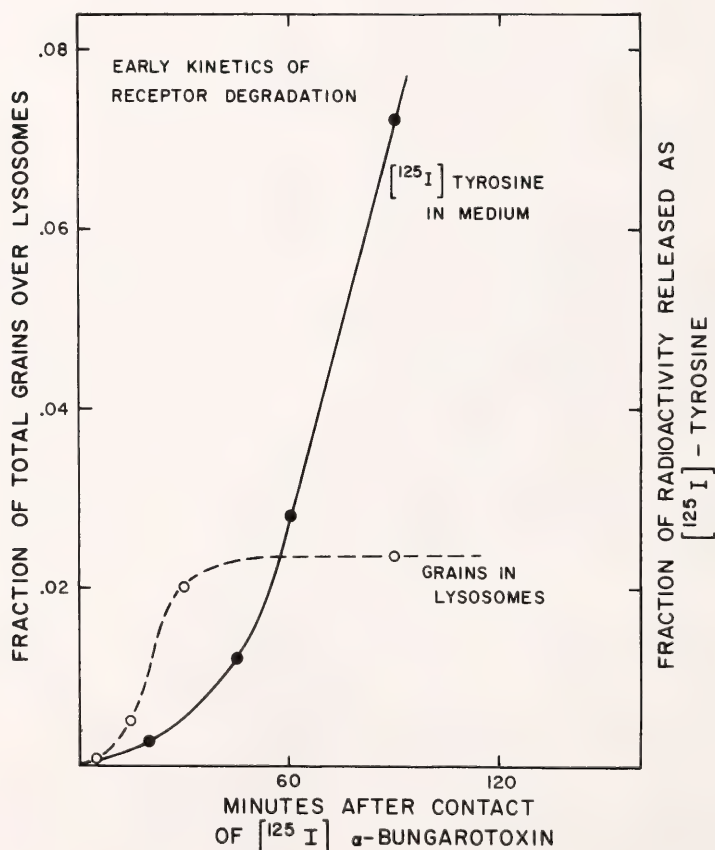


Fig. 53. Kinetics of transport of radioactivity to secondary lysosomes (○—○) and kinetics of liberation of iodo-tyrosine from chick muscle cultures (●—●) after brief exposure of muscle to 125 I- α -bungarotoxin. Data obtained from electron microscope autoradiographs and from chromatographic analysis of culture medium.

EFFECT OF MUSCLE ACTIVITY ON RECEPTOR TURNOVER

D. J. Card and D. M. Fambrough

Recent experiments have shown that muscle activity is important in regulating extrajunctional chemosensitivity of skeletal muscles. Acetylcholine sensitivity of muscle increases following denervation and decreases upon reinnervation. Electrical stimulation of denervated or cultured embryonic muscle can lead to a decline in extrajunctional ACh sensitivity; on the other hand, an increased sensitivity to ACh can be produced after blockade of spontaneous contractions in cultured cells by tetrodotoxin (a selective inhibitor of voltage-sensitive sodium current). These changes in ACh sensitivity reflect changes in the number of extrajunctional ACh receptors. Thus, the changes should be understandable in terms of the incorporation of receptors into the muscle membrane and their subsequent degradation.

Experimental strategies for measuring incorporation of new ACh receptors into unstimulated cultured chick skeletal muscle fibers and the degradation of receptors thereafter have already been reported by this laboratory. We were able to reproduce the observation of Shainberg and Nelson that tetrodotoxin induced a twofold increase in ACh receptor number within 24 hr of application to active cell cultures. However, a quantitative assessment of the synthesis and degradation of ACh receptors in active vs. quiescent cultured cells is difficult because it is nearly impossible to control or to quantitate the amount of activity of the cultured cells. After 4 to 5 days in culture, muscle cells usually begin to develop spontaneous contractions, but not all the muscle cells contract. Also, the time of onset of spontaneous contractions differs greatly between cultures, so not all 5-day or even all 11-day cultures are spontaneously active. It has not been possible to electrically stimu-

late and drive every cell or even most cells in a culture dish.

This laboratory has previously reported measurements of degradation rates of extrajunctional receptors from denervated mouse extensor digitorum longus (EDL) muscle. Because EDL muscle is easily activated by electrical stimulation, it was used to study the effects of muscular activity on degradation of receptors. After mid-thigh resection of the sciatic nerve, the lower leg (including the EDL muscle) is denervated. The time course of development of extrajunctional ACh receptors after denervation is tabulated in Table 13. In our studies on receptor degradation, muscles denervated for at least 5 days were used.

TABLE 13. Accumulation of ACh Receptors Following Denervation of Mouse EDL

| Days After Denervation | ACh Receptor Sites* (molecules \times 10 ⁶ /mg muscle) |
|------------------------|--|
| 0 | 2.0 |
| 1 | 2.0 |
| 2 | 2.1 |
| 3 | 3.5 |
| 4 | 8.8 |
| 5 | 12.5 |
| 7 | 15.6 |
| 9 | 17.6 |
| 14 | 14.1 |
| 21 | 13.6 |

*Measured as α -bungarotoxin binding sites.

The degradation rate of extrajunctional receptors was inferred from measurements of the rate at which [¹²⁵I]-labeled α -bungarotoxin bound to these receptors was degraded with concomitant release of radiolabeled degradation products from the muscle fibers. We have not yet characterized released radioactive species, but this has been done with denervated rat diaphragm. Metabolic inhibitors such as cycloheximide and dinitrophenol and reduced temperature decreased the degradation rate, as expected. The perfusion chamber used in the degradation measurements was similar to that reported last year, but instead of

mounting the muscle on a screen it was tied and stretched between two platinum electrodes (used for electrical stimulation) mounted on a Plexiglas strip. Oxygenated Trowell T-8 medium was dripped over the muscle and was continuously aspirated out of the muscle chamber into test tubes; the radioactivity of the perfusate was then measured in a gamma counter. The half-life of ACh receptors in the plasma membrane averaged 27 hr under these conditions. After several hours, the muscle was stimulated at 50 stimuli per sec for 1 sec every 10 sec for 8 hr. The degradation rate of receptors decreased rapidly to 78% of the value before stimulation. Thus stimulation of the denervated EDL muscle increased the half-life of the receptors in the plasma membrane to approximately 34 hr.

Degradation rate for extrajunctional ACh receptors does not appear to change during the first two weeks of denervation (Table 14). Also the stimulation-induced reduction in rate is independent of the length of the denervation period. Since chemosensitivity declines during electrical stimulation without any acceleration of degradation, it follows that electrical stimulation must repress the biosynthesis or incorporation of new receptors into plasma membranes.

TABLE 14. Degradation Rate of Receptors from Muscle Denervated 5-13 Days

| Denervation Time (days) | Receptors Degraded/Hour (%) |
|----------------------------|--------------------------------|
| 5 | 2.75 |
| 6 | 2.38 |
| 7 | 2.15 |
| 12 | 2.34 |
| 13 | 2.01 |

The effects of muscle activity on ACh receptor biosynthesis and incorporation into plasma membranes are not known. We are attempting to perfect a strategy for the high time-resolution measurement of incorporation rate of new receptors into extrajunctional membranes of denervated adult muscles.

ORGANIZATION OF MUSCLE PLASMA MEMBRANE IN VIVO

D. J. Card

Acetylcholine receptors are found over the entire surface of embryonic skeletal muscle fibers in vivo. These sites gradually disappear after innervation, as clusters of acetylcholine receptors form in the postsynaptic membrane. The junctional receptors may result from the organization of some of the extrajunctional receptors into a much more compact spatial arrangement. In assessing the role of extrajunctional acetylcholine receptors as components of newly forming synapses, it is necessary to know whether junctional receptors appear before, during, or only as a result of, formation of functional neuromuscular synapses. We are studying muscle morphology and acetylcholine receptor number and distribution at different developmental stages of the chick anterior latissimus dorsi (ALD) muscles to learn the time of nerve outgrowth, synapse formation, appearance of junctional receptors, and disappearance of extrajunctional receptors.

Muscles were removed from the embryos, fixed in 2% glutaraldehyde, 100 mM cacodylate buffer, sliced into 1-micron sections and then stained with toluidine blue. In order to study receptor binding sites the muscles were incubated for 1 hr in a solution of [125 I]- α -bungarotoxin (0.5 μ g/ml), washed several hours and then fixed in 2% glutaraldehyde, 100 mM cacodylate buffer. Following this treatment, the total number of acetylcholine receptors was measured, and single muscle fibers were dissected for autoradiography.

Some preliminary observations based upon light microscopy and autoradiography and on the binding of [125 I]-mono-iodo- α -bungarotoxin follow. Initially (5-6 days incubation) the presumptive anterior latissimus dorsi (ALD) muscle was composed of loosely organized, undifferentiated cells. However, after 9 days, muscle cells and

nerve bundles were evident. Autoradiographs of single ALD muscle fibers (6–9 days of incubation) show radioactive label (ACh receptors) dispersed uniformly over the muscle surface. No receptor aggregations were present. After 13–15 days incubation the ALD muscle fibers looked morphologically similar to post-hatch muscles, except that fiber size was smaller and ACh receptors were scattered over the cell surface. Some areas of each muscle fiber from 13 to 15 days development appeared to have a high receptor density, but these observations have not been quantified.

At 16 days the ALD had well-defined clusters of ACh receptors spaced every 120–170 microns along each muscle fiber, with many ACh receptors still scattered outside the clusters. The spacing of the dense clusters of ACh receptors, presumably junctional receptors, agrees favorably with morphological, electrophysiological, and cholinesterase data obtained by others (Gordon, Perry, Ruffery and Vrbova, *Cell Tiss. Res.* 155: 13–25, 1974; Bennett and Pettigrew, *J. Physiol.* 241: 515–545, 1974).

Total number [¹²⁵I]-α-bungarotoxin binding sites was measured in muscles from embryonic day 6 to 2 days post-hatch (Table 15). Most of the [¹²⁵I] is present as receptor-[¹²⁵I]-α-bungarotoxin complexes as judged by sucrose gradient velocity sedimentation of detergent extracts. It is not clear yet when functional synapses are formed. However, Gordon and her collaborators and Bennett and Pettigrew have reported morphological nerve contacts

TABLE 15. [¹²⁵I]-α-Bungarotoxin Binding to Embryonic Chick ALD Muscles at Different Developmental Ages

| Developmental Age (days) | Muscle Weight (mg) cpm/muscle |
|--------------------------|-------------------------------|
| 6 | 7,000 |
| 11 | 15,300 |
| 13 | 9,800 |
| 16 | 7,700 |
| 19 | 3,200 |
| 20 | 3,000 |
| +2 | 1,300 |

and acetylcholinesterase staining at days 9 to 15. The number of ACh receptors per mg muscle is also highest at that time. As extrajunctional binding sites disappear, the number of total ACh receptors/per mg muscle also decreases.

STUDIES ON THE MOBILITY OF EXTRAJUNCTIONAL ACh RECEPTORS IN PLASMA MEMBRANE

R. E. Pagano and D. M. Fambrough

The principal objective of this study, which is aided by a generous grant from the Whitehall Foundation, is to examine the general role of membrane fluidity in membrane organization and function. This problem will be tackled by measuring the lateral (translational) mobility of acetylcholine receptors in skeletal muscle fibers, and by studying the effects which a variety of membrane perturbants (local anesthetics; exogenous phospholipid and cholesterol treatments) have on this mobility. Quantitative fluorescence microscopy will form the basis for determining protein (ACh receptor) mobility. The measurement will be made by complexing fluorescent-labeled α-bungarotoxin with ACh receptors on muscle fibers. A small area of fluorescent cell surface will then be bleached with a short pulse of bright light, and the rate at which unbleached molecules from adjacent areas of the cell surface migrate into the bleached area will be quantified by measuring the fluorescence intensity from that area as a function of time.

During the first year of this study, some of the necessary background work for carrying out our experiments was completed. Fluorescent-labeled α-bungarotoxin was prepared using fluorescein isothiocyanate (FITC), and the preparation was well characterized. It was shown that incubation of mono-FITC-bungarotoxin, with skeletal muscle at 1 μgm/ml results in highly fluorescent neuromuscular junctions as judged by fluorescence microscopy. The rate of FITC-α-bungarotoxin binding was also com-

pared with that of iodinated α -bungarotoxin, and found to be about 50-fold slower than the radioactive species—inconsequential for our experiments. Preliminary experiments further demonstrated that FITC- α -bungarotoxin receptor complexes on skeletal muscle are readily bleachable and that reversal of this process is a very slow process.

Preliminary experiments were carried out to test the feasibility of manipulation of cultured muscle cell lipids, using artificial phospholipid vesicles as agents for introducing foreign phospholipids into the cell surface. Cells treated at 2°C with dimyristoyl phosphatidyl choline (DMPC) vesicles showed a significant accumulation of CMPC in their surface as evidenced by high resolution electron microscopy autoradiography. Furthermore, lipid analyses showed little degradation of the exogenously supplied lipid. Thus, it is concluded that significant amounts of perturbing foreign phospholipids can be introduced into the cell surface. Their effect on ACh receptor mobility remains to be tested.

Preparation of a Fluorescent Derivative of α -Bungarotoxin

Native α -bungarotoxin binds extremely tightly to acetylcholine receptors on cultured skeletal muscle cells and is routinely used as a potent, very selective, and virtually irreversible inhibitor of receptor function. The radioactive derivative, mono-iodo- α -bungarotoxin, retains the potency of the native toxin.

During the past year we have developed methods for the production of fluorescent derivatives of α -bungarotoxin and have determined the toxicity of the most useful fluorescent derivative. In essence the method involves the interaction of purified α -bungarotoxin with fluorescein isothiocyanate in the cold at pH 9.0 in sodium carbonate-bicarbonate buffer. An eight-fold molar excess of FITC is used and the reaction proceeds slowly, first

forming a mono-FITC- α -bungarotoxin and later, further derivatized forms. The unreacted FITC is then separated from the FITC- α -bungarotoxin by chromatography on Bio-Gel P-4 and any unreacted α -bungarotoxin is removed from the FITC- α -bungarotoxin by ion-exchange chromatography on CM-Sephadex C-50. It has been found that the mono- and di-FITC bungarotoxin are also separable from each other in Bio-Gel P-4, the di-FITC α -bungarotoxin being retarded by the column. When mono-FITC α -bungarotoxin is fractionated on Sephadex C-50, using a gradient of NaCl in 3.3 mM phosphate buffer pH 7.2, it is eluted far ahead of unreacted α -bungarotoxin and thus quantitatively freed of this contamination.

Properties of Fluorescent α -Bungarotoxin

The purified mono-FITC α -bungarotoxin binds to acetylcholine receptors with a very high affinity. After incubation of muscles in a solution containing about 1 μ g/ml FITC α -bungarotoxin, followed by rinsing to remove unbound toxin, the acetylcholine receptors at the neuromuscular junctions are complexed with FITC- α -bungarotoxin and appear as vividly fluorescent structures when examined by fluorescence microscopy. This interaction is essentially irreversible, and these fluorescent structures maintain their fluorescence for more than 6 months at 10°C in a dilute buffer solution.

The relative rates of interaction of FITC- α -bungarotoxin and of radioactive iodinated α -bungarotoxin have been compared by mixing these two toxin derivatives in different concentration ratios and then measuring the amount of iodinated α -bungarotoxin that bound to cultured skeletal muscle. Such competition curves have been carried out on three preparations of FITC- α -bungarotoxin, and all suggest that the speed of binding is reduced 50-fold for the fluorescent derivative. Thus, higher concentrations are re-

quired to saturate the acetylcholine receptors in a short incubation period. Even so, 10^{-7} M FITC- α -bungarotoxin will saturate the receptors in cultures of skeletal muscle in about 20 minutes.

Use of FITC- α -Bungarotoxin as a Probe in Studying Membrane Structure

Following our original proposal we have developed the FITC- α -bungarotoxin as an easily bleachable fluorescent tag for cholinergic receptors. Preliminary experiments using microscopic equipment at the Leitz and Zeiss showrooms in New Jersey and New York and qualitative experiments done with our yet incomplete fluorescence microscopy set-up at Carnegie demonstrate that fluorescent FITC- α -bungarotoxin-receptor complexes on skeletal muscle fibers are readily bleached and that the bleaching is mainly irreversible or only very slowly reversible. Also, stable fluorescence measurements can be made when appropriate filters and light chopping are employed. Thus the main prerequisite for a fluorescent probe to use in executing our proposed experiments on the mobility of receptors in plasma membranes has been met.

TURNOVER OF PLASMA MEMBRANE PROTEINS

K. Tepperman

The model for the turnover of the ACh receptor of muscle cells raises the question of the relationship of the receptor to other plasma membrane proteins. The study of ACh receptor turnover is aided by the availability of the specific probe α -bungarotoxin. Since other membrane proteins are not so easily identified, new approaches to studying turnover of populations of proteins are being devised. One approach is to covalently label surface proteins by enzymatic iodination and to follow loss of radioactivity from specific proteins. Another approach, developed by Robert Schimke, is to allow

the cells to incorporate different radioactive isotopes of leucine on two successive days and to look at the ratio of the different isotopes for each of the membrane proteins. We are using both of these approaches to study the turnover of plasma membrane proteins of cultured muscle cells.

In *Year Book 74*, p. 78, we reported preliminary observations on enzymatic iodination of muscle cells. At that time the total material on iodinated tissue culture dishes was extracted in SDS and run on polyacrylamide gels, resulting in approximately 15 radioactive bands. It is difficult to determine which of these proteins are actually part of the membrane and which proteins may be less intimately associated with the surface. In the past year, several methods for dissociating loosely bound proteins from membranes were explored. One currently in use is treatment of cells with low ionic strength medium, followed by homogenization and centrifugation to obtain a membrane pellet. When this pellet is used for SDS gels, the resulting pattern of iodinated polypeptide chains is much simpler than when total material is used. The number of radioactive bands is reduced to approximately seven, and one of the major bands in the original preparation, one with a molecular weight of about 230,000 daltons, is among those which are lost, suggesting that this protein is not an integral membrane protein.

Preliminary results using surface iodination for turnover studies have suggested that most of the proteins that are accessible to iodination are degraded at the same rate. In these experiments, sets of cultures are iodinated, then incubated at 37 °C for different periods of time. After extraction, equivalent amounts of radioactivity from different chase periods are loaded onto gels. Densitometer traces of autoradiographs of the gels show that different bands have essentially the same relative amounts of radioactivity. Experiments are now in progress in which [131 I]-bungarotoxin is bound to cells

that have been treated with lactoperoxidase and [^{125}I]. This is done to provide an internal measure of the rate of ACh receptor turnover with which to compare the loss of [^{125}I]-label from other membrane proteins of the cells. Initial results are compatible with the idea that turnover of the iodine-labeled proteins occurs at the same rate as turnover of the ACh receptor.

In the iodination experiment, several points have been raised which require further clarification. Although published reports on lactoperoxidase iodination of cells generally indicate little labeling of lipids, when muscle cells are iodinated, approximately 35% of the radioactivity in a membrane fraction is chloroform methanol extractable, indicating that lipids have been labeled. Thin-layer chromatograms have been done which show that the label is present in a variety of lipid fractions. Another result of the iodination experiments is that during the course of incubation following iodination, the radioactivity lost from the cells can be fractionated into three components by column chromatography on Bio-Gel P-2. One fraction probably represents nonspecifically associated iodide, which comes off the cells and the tissue culture dishes during the incubation. Another fraction is iodotyrosine, which probably results from internalization and degradation of labeled proteins. A third fraction, excluded by the P-2 columns, may represent proteins or other material that is lost from the cells.

Another approach to studying turnover of populations of proteins is the double isotope method of Schimke. In his reports using this method, he generally finds a correlation between turnover rates of proteins and their molecular weights. Preliminary results using this method with cultured muscle cells show that the correlation for the major polypeptides of a crude membrane preparation holds. However, experiments are in progress which will study this question on plasma membranes specifically. Also,

the effects of various treatments designed to remove all but integral membrane proteins will be studied to determine whether the molecular weight correlation with turnover rate still holds. Such a correlation is contraindicated by the iodination results.

STUDIES ON NEURONAL PLASMA MEMBRANES

S. Carbonetto

Much of our work on the plasma membrane during differentiation of skeletal muscle has relied upon the use of α -bungarotoxin and its radioactive derivatives that bind selectively to the acetylcholine receptor molecule in muscle cells. Similar information about formation of neuronal plasma membranes has been unobtainable due to lack of a suitable ligand. This report deals with our initial studies on a neuronal preparation that apparently binds α -bungarotoxin with high affinity.

Sympathetic ganglionic chains have been dissected out of 11 to 12 day old chick embryos, dissociated in 0.25% trypsin, washed and plated onto collagen-coated culture dishes in Eagles MEM plus Nerve Growth Factor (2 units/ml; Burroughs Wellcome). Within 24 hr neurons become attached to the surface of the plate and begin to send out processes. Intracellular electrophysiological recordings from these cells after three days indicate that neurons have resting membrane potentials of 30 mV, and can be stimulated to generate action potentials (Fig. 54). Furthermore, when cultured chick sympathetic neurons are incubated with [^{125}I]- α -bungarotoxin and analyzed by light microscope autoradiography, grains appear over the neuron soma and down to the tip of the processes but are absent over non-neuronal cells in the culture (Fig. 54). Washing the culture for 28 hr at 14 °C after [^{125}I]- α -bungarotoxin binding only slightly reduced the density of grains over neurons. In one experiment

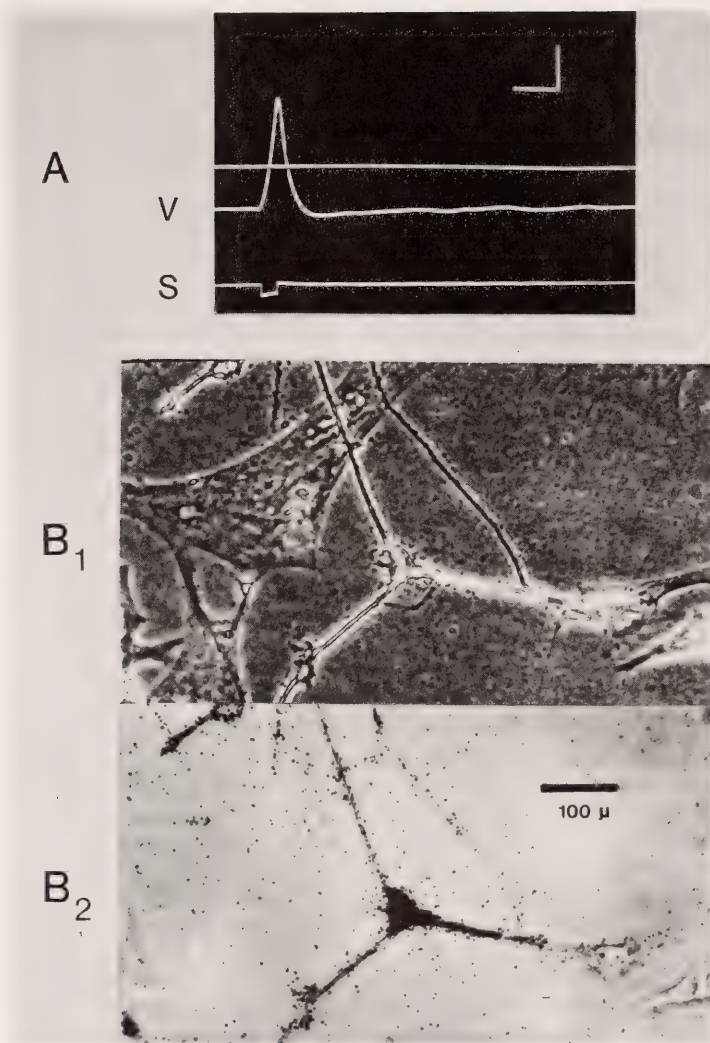


Fig. 54. (A) Intracellular recording from a chick sympathetic neuron in culture. The voltage record, *V*, shows an action potential evoked by a stimulating pulse, *S*, applied to the surface of the neuron by an extracellular microelectrode. The uppermost trace is at 0 mV. The calibration is 50 mV; 20 msec. (B) Autoradiograph of cultured chick sympathetic neurons incubated with ^{125}I - α -bungarotoxin. When viewed with phase optics the neuron and several nonneuronal cells are visible in the field (*B*₁). With bright field illumination (*B*₂) only exposed emulsion grains are visible and these cover the neuronal cell body and its neurites. There is no localization of grains over any of the nonneuronal cells.

$10^{-3}M$ d-tubocurarine prevented the association of radioactivity with the cells.

These preliminary data suggest that chick sympathetic neurons in culture

exhibit properties of well-differentiated neurons and also may specifically bind α -bungarotoxin. Experiments are in progress to determine the association and dissociation kinetics of

bungarotoxin binding to neurons and also to localize the appearance of the grains by EM autoradiography. We are testing whether these neurons contain functional acetylcholine receptors by

electrophysiologically monitoring their response to iontophoretically applied acetylcholine and testing if such response can be blocked by application of bungarotoxin.

SIGNALING IN THE NERVOUS SYSTEM: SYNAPSES OF SPECIFIC NEURONS IN THE LEECH

*K. J. Muller and S. T. Carbonetto
with the technical assistance of B. Thomas*

The role that a neuron assumes in the nervous system is dependent upon the connections it makes with other neurons or with peripheral targets. Therefore, an essential step both in determining the forces that act initially to organize the nervous system and in characterizing the mechanisms by which a neuron handles, or integrates, information is to ascertain the relationship between a neuron's function and the arrangement of its synapses. A related problem in neurobiology has been to determine whether a neuron's shape and other properties are intrinsic or whether its contacts or associations with other neurons are essential for certain aspects of its growth and maintenance.

The nervous system of the leech *Hirudo medicinalis* has been particularly favorable for study of the physiological role and functioning of specific neurons, largely because its organization is relatively simple. Neurons in this segmented worm are grouped 350 together to form essentially identical ganglia that are linked in a chain by axon bundles; each ganglion mediates the reflexes and controls the behavior of its segment. It has been possible to monitor electrical activity from within single sensory and motor neurons with microelectrodes and to correlate the physiological activity of functionally identified neurons with their characteristic shape and position within each ganglion. By recording from pairs of neurons one can trace synaptic connections, which have been found to be surprisingly uniform and in that sense

predictable between specific neurons. Last year we described studies under way that provided a morphological description of sensory and motor neurons and of the distribution of their synapses within the ganglion (*Year Book 74*, p. 85). These investigations, using the enzyme horseradish peroxidase (HRP) as an intracellular marker for both light and electron microscopy, were to lay the groundwork for our determining any structural basis for physiological changes that we had previously produced with selective lesions of the leech nervous system (*J. Physiol. (Lond)* 242, 289, 1974), as well as for charting the course of regenerating neurons. An additional feature of HRP as an intracellular marker is that although it diffuses extensively within an injected neuron, it does not pass between electrically coupled neurons, as do smaller markers used by others. Neuron terminals that make electrical contacts are therefore sharply demarcated even within an intricate meshwork of neuron processes.

CHEMICAL SYNAPSES IN THE LEECH

K. J. Muller and B. Thomas

Structural Details of the Synapse

A good picture of the normal, fully developed synapse is requisite for the study of the distribution and formation of synapses. Because the chemical synaptic transmission that one can record in the leech central nervous sys-

tem resembles that in other invertebrates and vertebrates, it is not surprising that in the electron microscope customary synaptic features—the presence of presynaptic vesicles, membrane densities and a widened, uniform intercellular cleft—serve to delineate the synapse. In the leech, synapses are made almost exclusively in the center of the ganglion in the region called the neuropil rather than on cell bodies that form layer or cortex around the ganglion. Sections through the neuropil manifest a variety of synaptic profiles, but careful analysis reveals that most result from different planes of section through the same structural configuration (Fig. 55). Typically, agranular vesicles (~50 nm diameter) are clustered near a ridge of presynaptic density that apposes a pair of conjoint postsynaptic profiles across a cleft about 30 nm wide. Larger (~100 nm) dense-core vesicles and mitochondria are also found in the presynaptic terminal. Identified mechanosensory neurons that have been injected with the HRP for an intracellular marker have branched processes that exhibit similar features (Fig. 56). This indicates, in accord with their physiology, that these neurons are presynaptic. The same processes are also postsynaptic to other neurons. In contrast with the sensory neurons, the large longitudinal (L) and annulus erector (AE) motoneurons that act to shorten the animal and to erect its annular rings into ridges, respectively, are seen in the electron microscope to be solely postsynaptic within the neuropil. Physiologically these are neurons upon which the mechanosensory neurons synapse. One class of apparently presynaptic terminals (Fig. 59, white arrow) has been found that does not readily fit the pattern of terminals that contain agranular vesicles: These terminals, which contain small granular vesicles (~50 nm diameter) and extremely dense, eccentric cored large vesicles (~100 nm), are generally found to be cells that stain with the dye Neutral Red and are widely regarded

to contain serotonin as a transmitter. What are in fact the membrane specializations at synapses made by such neurons remains to be determined.

The Arrangement of Synapses on Sensory Neurons

One remarkable pattern in the organization of the leech nervous system is that synapses of mechanosensory neurons are clustered upon fingerlike swellings or enlargements. Their lineaments are sufficiently similar within a modality, e.g., touch, pressure or stimulus, but different between them to permit a reliable distinction to be made between sensory modalities solely on the basis of the shapes and distribution of synaptic terminals viewed in the light microscope. A possibility raised by the differences in the shapes of synapse clusters is that, as with certain vertebrate motor neurons, the morphologies of terminals are intrinsic to the presynaptic neurons and are not dependent upon the type of postsynaptic target. This will be discussed in the next section.

From a functional standpoint, the separation of clusters from one another and the difference in synaptic inputs to them suggest that clusters may sometimes act autonomously. But this means a single neuron that synapses onto two neurons in two spatially separate regions could produce differential postsynaptic effects. We have reported such differential actions (*J. Physiol. (Lond)* 238, 357, 1974), and studies are under way to determine if independence of clusters from one another can account for these and other integrative phenomena.

Sprouting of Sensory Neuron Terminals

The paired connectives that link adjacent ganglia to form the leech nerve cord are axonal pathways that are virtually free of synapses. Certainly the mechanosensory neurons, which synapse in their own neuropil and in adjacent ganglia, run directly between

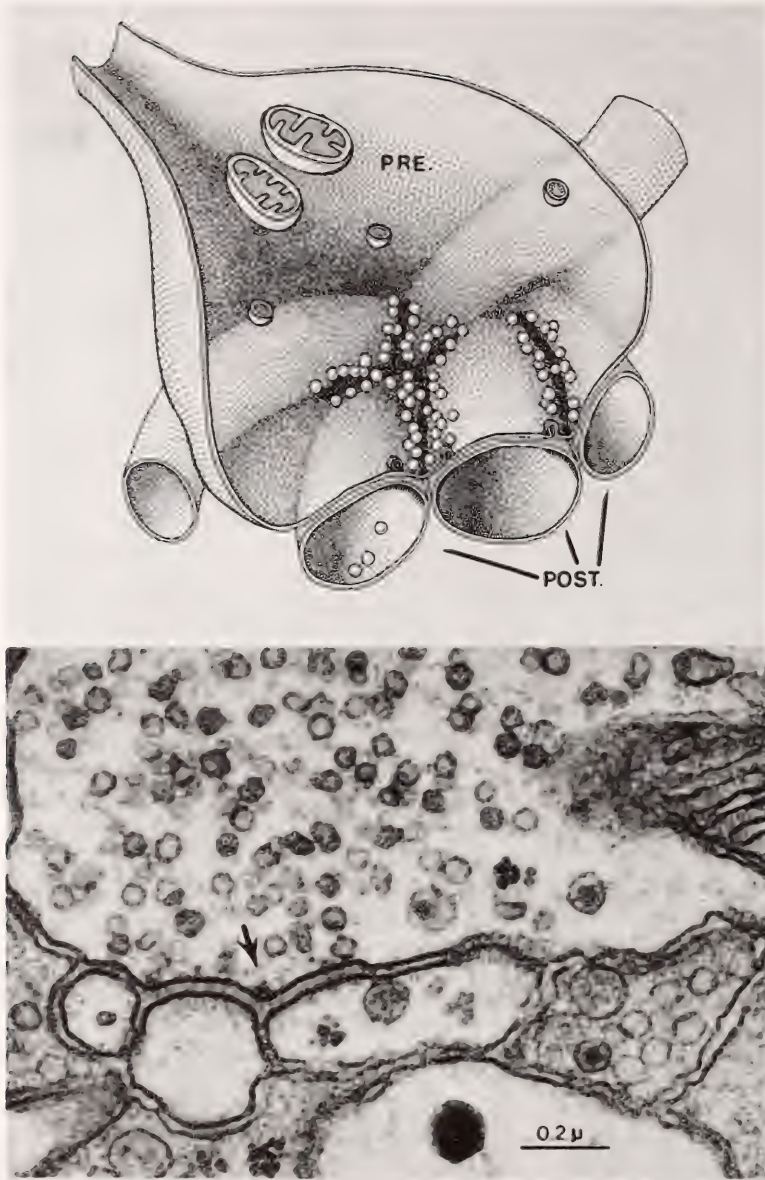


Fig. 55. *Top*: General scheme of synaptic specializations in the leech, based on serial sections. The presynaptic terminal contains numerous 50-nm agranular vesicles (only those clustered next to the plasma membrane are shown) and is separated from postsynaptic processes by extracellular space widened to about 30 nm. Lateral to a dense band along the inner surface of the presynaptic membrane, an occasional vesicle fuses with the membrane. *Bottom*: A band in such a terminal, cut in cross section, is indicated by an arrow.

ganglia without branching and synapsing until they pass the connective. It was recently reported that crushing a leech connective can cause synapses to

form within the connective at the crush. This presents us with a system that promises to make it possible to examine the formation *de novo* of

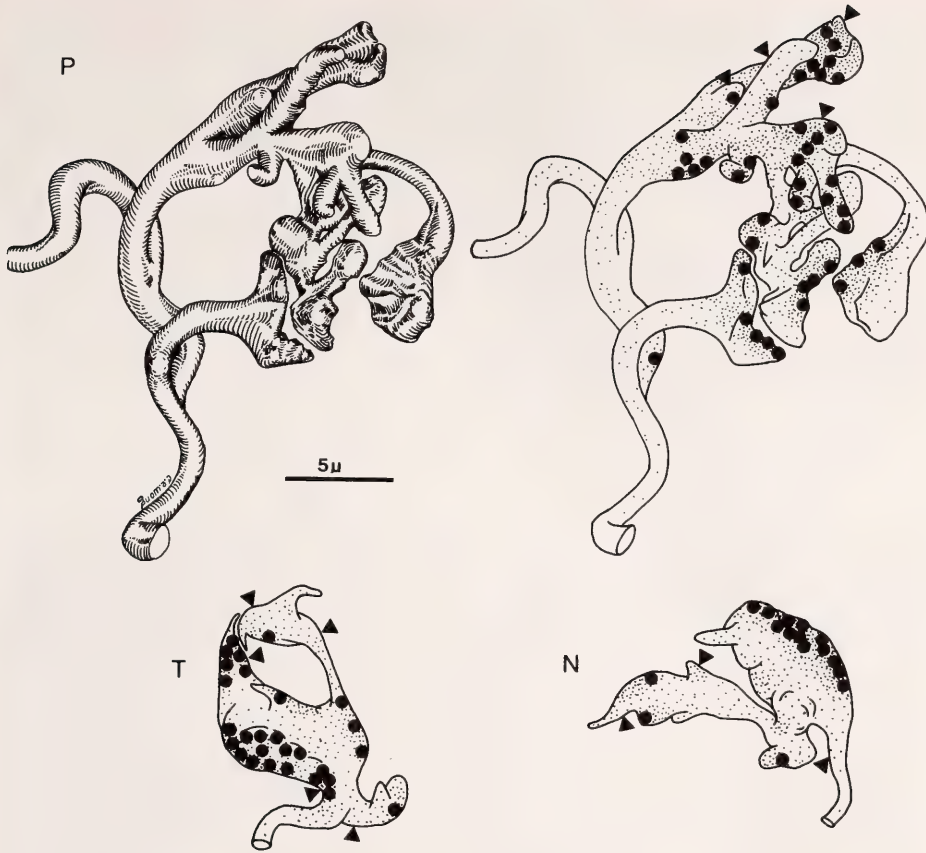


Fig. 56. Sites of synapses of the pressure, *P*, touch, *T*, and nociceptive, *N*, sensory cells culled from serial electron micrographs of regions like those indicated by arrowhead in Fig. 57 a and b. Three-dimensional reconstructions of injected neurons (upper left) were projected (upper right) and stippled to indicate approximate distributions of synaptic vesicles within the irregular fingers that arise from secondary processes. Points of contact onto pairs of postsynaptic processes are indicated by large dots; at the triangles the sensory neuron is postsynaptic.

synapses made by functionally identified neurons whose developed synapses have now been well described.

We have found that in animals whose connectives have been severed or crushed between a pair of ganglia several months previously and not permitted to regenerate, the crushed portion of sensory axons has in some cases sprouted a profusion of branches at the site of the cut or crush (Fig. 57). The branching unfortunately occurs within a mass of scar tissue that becomes dense after staining for specific neuron processes, so comparisons were

made with a cleaner, *in vitro* system developed by others. In culture, neurons also sprout at the crush, but scar tissue is not present to obscure the details of branching (Fig. 57). We have seen no qualitative differences *in vivo* and *in vitro* with the light microscope. This system provides an ideal chance to examine the growth of new processes and the requirements for synapse formation. In the light microscope, we can now say that sensory neurons form swellings that look like presynaptic terminals along and at the ends of new branches, and that such branches form

not only at a crush or cut *between* ganglia, but even at free cut end. In operated animals a comparison has not yet been made between modalities, but the shapes of enlarged fingers along new branches of touch-sensitive (T) cells do resemble normal T-cell presynaptic terminals. In culture a clear distinction cannot be made between the new T-cell arbors and the new branches of pressure-sensitive (P) neurons. The complex and distinctive cluster of enlarged fingers of the P cell within the neuropil (see Fig. 57) has not developed

at the crush for periods up to 3 weeks—a time sufficient for regeneration across the cut. It is now necessary to examine the sequence of growth and to determine if some of the regeneration we have seen might involve a fusion of a growing axon with the old, distal stump. Whether it is a loss of its target, direct damage to its axon, or the presence of new targets that fosters a neuron's sprouting is testable with a variety of lesions, particularly in culture.

It remains unclear whether some en-

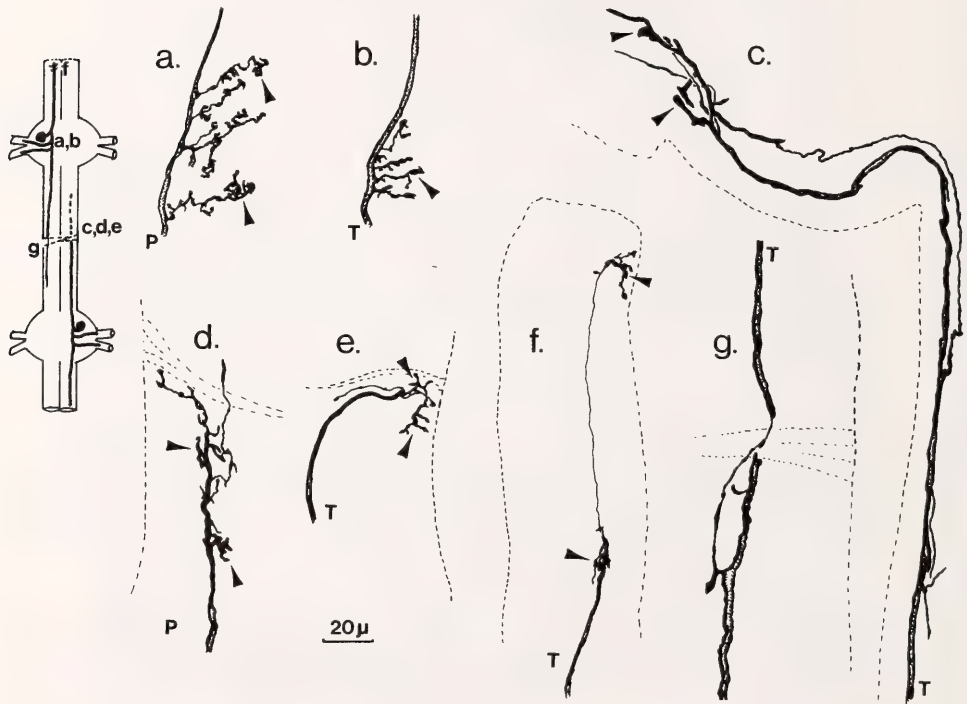


Fig. 57. Experimentally induced sprouting of the sensory neuron axon in the connective. A crush or cut was made between two ganglia as shown at left. Sensory neurons were injected at their cell bodies with HRP, stained with diaminobenzidine, and their processes traced from whole mount using *camera lucida*. (a) and (b): Normal secondary branches of pressure, P, and touch, T, neurons within the ganglion neuropil. Arrowheads indicate where synapses are typically clustered, for comparison with swellings along new branches in the connective (c) to (f). (c): Sprouting where the connective was cut 100 days previously. (d) and (e): Crush between ganglia maintained in culture for 24 days, P, and 13 days, T. (f): Crush at end of connective rather than between ganglia (24 days in culture). (g): Regeneration across cut at 24 days in culture. Note the fewer sprouts. T and P placed at ends nearest cell body; dashed line, edge of connective and lesions.

largements at early stages might represent growth cones. One likely prospect is that such enlargements will become synaptic terminals in a new neuropil formed at the site of the crush as reported in the connective of another species of leech. We have not yet observed structures that can be clearly identified as synapses, but the presence of large dense-core and small agranular vesicles at ends of branches of identified sensory neurons suggests that synapse formation may be in its early stages. In this case, the structures that make synapses take shape before synapses are made and would appear to dictate the association of synapses that are peculiar to sensory cells.

AN ELECTRICAL SYNAPSE IN THE LEECH

K. J. Muller and B. Thomas

Both types of neuronal synapses—chemical and electrical—are readily detected physiologically with microelectrodes in the leech. Yet in leech ganglia electron microscopy has failed to provide us with a clear example between neurons of gap junctions, the putative sites of electrical transmission. The reason for our failure remains obscure, but it is likely that the actual extent of synaptic membrane is limited and that the separation between membranes is, as at other invertebrate gap junctions, wider than at

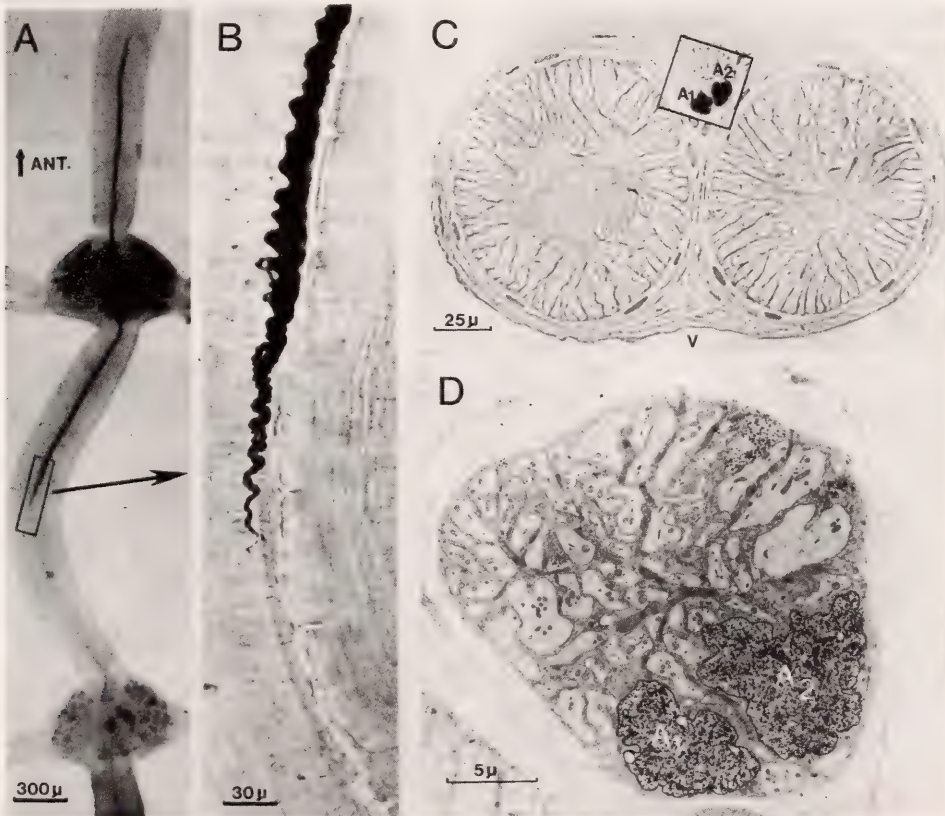


Fig. 58. Rohde fibers extend to meet in the connective. (A) Rohde neuron injected in the cell body in one ganglion reaches halfway to the next. The region of overlap with the uninjected Rohde cell in the lower ganglion is included in (B). When both are injected and a cross section taken through such a region, axons of the two cells (A_1 and A_2) can be resolved. (C) light micrograph; and (D) corresponding electron micrograph of boxed region in (C). The axons run in the small, unpaired nerve (Faivre's nerve).

gap junctions in vertebrates. It was therefore unexpected when an electrical junction was discovered between unpaired neurons in neighboring ganglia, neurons that were reportedly syncytial. The junction across which dye molecules as large as Procion yellow (MW about 500) can readily pass but not horseradish peroxidase (MW about 40,000) occurs between "giant" Rohde fibers in the middle of the unpaired connective (Fig. 58). The electrical coupling between adjacent Rohde neurons is so strong that no junction was thought to exist between them, yet it is *only* at this mid-connective region that the two neurons meet and synapse. Visible in the electron microscope is the extensive arborization of the two cells into fine, connecting processes, rather than an extensive contact along a septum (Fig. 59). The details of the contact between the neurons is still under intensive examination, but the region of overlap along the connective is nearly 200μ and the extent of the many contacts is nearly as great. Also peculiar to this region of apposition are numerous terminals

(Fig. 59, white arrow) containing small and large granular vesicles of the sort that have been shown by others to be inhibitory upon leech muscle. Such an inhibitory action upon the fine Rohde fiber collaterals could have pronounced and perhaps directional effects upon electrical transmission between Rohde fibers. This possibility is currently under physiological and anatomical investigation using selective stimulation and marking techniques.

Interruption of the Rohde Neuron

The discovery that Rohde neurons contact each other across an electrical junction that is physically separate from the neuropil and is permeable enough for some large molecules to pass has presented us with an unusual opportunity to examine the interdependence of the two neurons.

For example, by crushing or severing a connective near one ganglion, the distal portion of one Rohde axon is isolated from the soma. Can it then be maintained through its synapse? Or does the interruption stimulate the

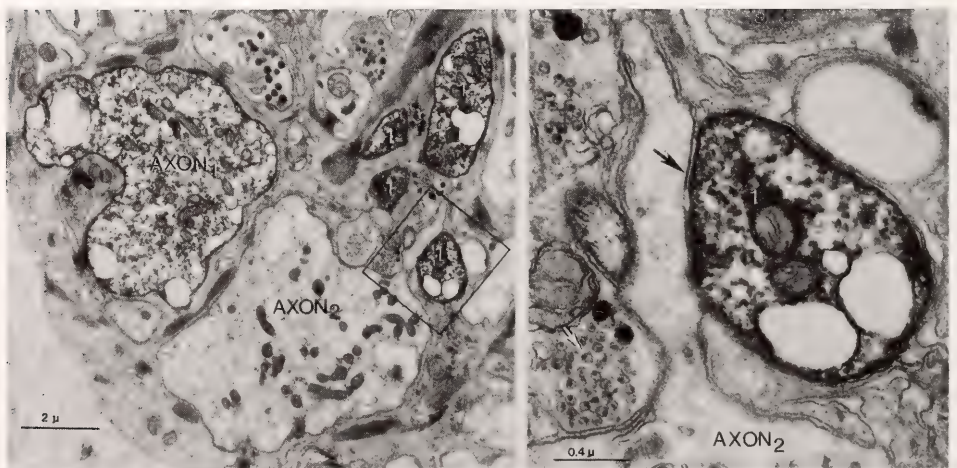


Fig. 59. The electrical synapses between Rohde filters in the connective. The principle axons (1 and 2) branch profusely as they terminate (left). The cells contact each other principally along their branches (right) at areas of narrowed extracellular space (black arrow) 3–4 nm wide as at gap junctions in some other invertebrates. Terminals containing small granular vesicles (white arrow) are seen in close association with the branches. Only neuron 1 has been injected with HRP, but axon 2 is recognizable by its size and location.

other intact Rohde fiber to grow beyond the synapse until it can reestablish *functional* contact with the adjacent Rohde neuron? Our results are preliminary, but where we have been able to examine this problem, we have found in an animal operated upon 79 days previously that the undamaged neuron does grow beyond the synapse. The neighboring Rohde neuron, its axon severed and unable to reestablish contact, has undergone a massive and unusual arborization within the ganglion while eliminating much of its large axon (Fig. 60). Whether the new processes are making functional con-

tacts is not clear, but it is noteworthy that the level of spontaneous synaptic and impulse activity that can be recorded from such cells is elevated, while the basic features of the nerve impulse are preserved.

A study of the role that this synapse can play in the structure and metabolism of the interacting cells is in progress using ganglia in culture. Here, by selectively destroying one neuron and thereby eliminating principal target tissue, the relative importance of intrinsic and extrinsic stimuli to growth and synapse maintenance in the nervous system may be weighed.

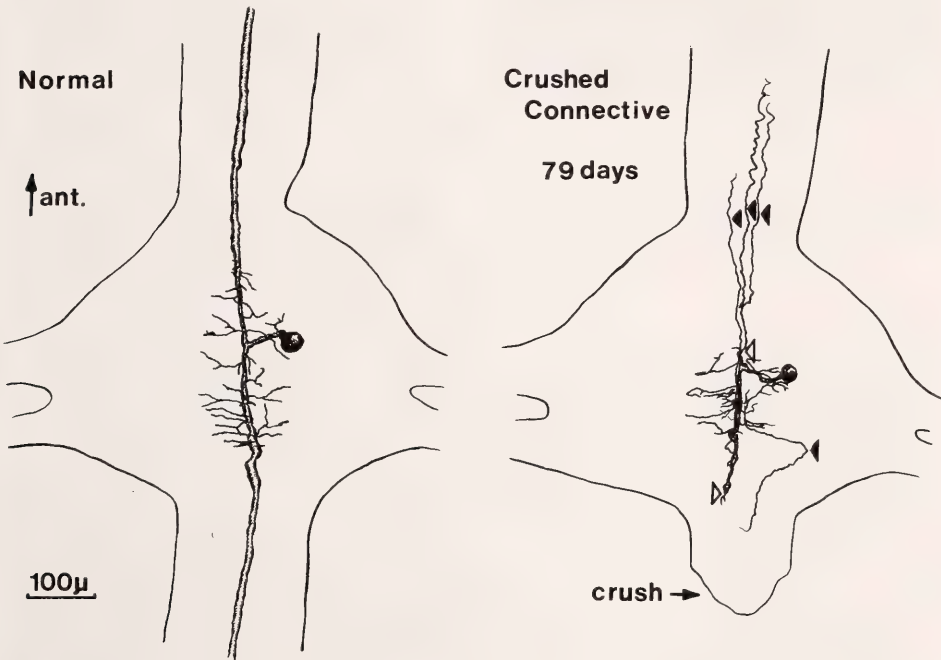


Fig. 60. Plasticity of the Rohde interneuron. The connective between ganglia was crushed in an animal 79 days prior to injection of the neuron, identified by the location of its soma and the size and shape of its action potential. The principal axon has disappeared beyond the open triangles, even within the anterior connective that was untouched, and new sprouts have appeared (black triangles) that reach toward the connective but only slightly beyond the ganglion.

THE COLLECTION OF HUMAN EMBRYOS

Ronan O'Rahilly and Ernest Gardner

The Carnegie Embryological Collection was opened formally at the Uni-

versity of California in Davis on 21 November 1975. Drs. Ronan O'Rahilly

and Ernest Gardner were in attendance, and speakers included Drs. J. D. Ebert, Elizabeth M. Ramsey and Arthur T. Hertig. Dr. Ramsey presented a book on the Carnegie monkey colony, and Dr. Hertig later donated the binocular dissecting microscope he had used in his searches for early human embryos. Dr. George W. Corner was unable to be present. The University was represented by Deans Allen G. Marr, C. John Tupper, and William R. Pritchard. Carnegie President Philip H. Abelson visited the laboratories on the following day.

All inquiries concerning the collection, as well as requests for permission for publication, should be addressed to Professor R. O'Rahilly, Carnegie Laboratories of Embryology, University of California, Davis, California 95616.

DEVELOPMENTAL STAGES IN HUMAN EMBRYOS

Work continues on the revision of stages 10 to 23 (R. O'Rahilly), on the tabulation of the timing and sequence of developmental events in staged human embryos (R. O'Rahilly), and on the establishment of a computer catalogue (Alexander Barry).

Development of the Nervous System

Work continues on the developmental neurobiology of primates (E. Gardner and associates). A chapter on "The developmental anatomy and histology of the human central nervous system" is awaiting publication in the *Handbook of Clinical Neurology*, edited by Vinken and Bruyn. Articles on "The

Dandy-Walker and Arnold-Chiari malformations," "The prenatal development of the human eye," and "The timing and sequence of events in the development of the limbs in the human embryo" were published. An account of "The nerve supply and conducting system of the human heart at the end of the embryonic period proper" is due to appear in the *Journal of Anatomy*. Studies of the developing anterior falcate artery are being undertaken by Dr. F. Muller.

THE BLUNTSCHLI COLLECTION

Renewed interest has been shown in the comparative collection of the late Professor Hans Bluntschli of Bern. It was established on expeditions to Amazonia in 1912 and to Madagascar in 1930, and was acquired by the Carnegie Institution in 1950. The Bluntschli collection comprises insectivores (tenrecs), prosimians (lemurs), and platyrrhines (New World monkeys), as shown in Table 16. During the past year, the Bluntschli microscope slides were studied by Dr. F. Muller (Basel) and by Prof. F. Strauss (Bern).

Professor Strauss had worked with Professor Bluntschli in Switzerland and is donating further material relevant to the collection. Professor David B. Meyer has been studying the comparative development of the eye. Theses (for the M.Sc. degree) on "Embryonic limb development in the rhesus monkey (*Macaca mulatta*)" by G. Stone and on "Staging of the early embryonic brain in the baboon (*Papio* sp.) and rhesus monkey (*Macaca mulatta*)" by R. Davignon have been approved.

TABLE 16. Chief Insectivores and Primates in the Carnegie Collection

| BLUNTSCHLI COLLECTION | | | | |
|--|--------------------------------|--------|-------|---------|
| INSECTIVORA | Chiarelli's (1972) Decimal Key | | | |
| Centetes (Common tenrec) | | | | |
| Hemicentetes (Banded tenrec) | | | | |
| Ericulus (Hedgehog tenrec) | | | | |
| | Suborder | Family | Genus | Species |
| PROSIMII | | | | |
| Microcebus (Mouse lemur) | 1. | 4. | 1. | 1 |
| Avahi laniger (Woolly lemur) | 1. | 5. | 2. | 1 |
| PLATYRRHINAE | | | | |
| Saguinus fuscicollis (Hapale; Mystax bluntschlii) (Tamarin) | 2. | 1. | 4. | 3 |
| Aotes trivirgatus (Nyctipithecus vociferans) (Owl-faced or night monkey) | 2. | 3. | 1. | 1 |
| Alouatta seneculus (Mycetes auratus) (Red howler-monkey) | 2. | 3. | 6. | 3 |
| Saimiri sciurea (Chrysothrix nigrivittata) (Squirrel monkey) | 2. | 3. | 7. | 1 |
| Cebus apella (C. macrocephalus) (Hooded or brown capuchin) | 2. | 3. | 8. | 1 |
| Cebus albifrons (C. gracilis) (White-fronted capuchin) | 2. | 3. | 8. | 3 |
| Lagothrix lagotricha (L. infumatus) (Brown woolly monkey) | 2. | 3. | 11. | 1 |
| HARTMANN COLLECTION | | | | |
| CATARRHINAE | | | | |
| Macaca mulatta (Macacus rhesus) (Rhesus macaque) | 3. | 1. | 1. | 9 |
| MALL COLLECTION | | | | |
| CATARRHINAE | | | | |
| Homo sapiens | 3. | 5. | 1. | 1 |

STAFF ACTIVITIES

International conferences and symposia in which members of the Department participated during the year included three in Scotland ("The Synapse," in St. Andrews, sponsored by the Scottish Electrophysiological Society; "Genetic Engineering," in Glasgow, the Second Tenovus Symposium of the Nucleotide Group, Chemical and Biochemical Societies; and the annual symposium of the British Society of Developmental Biologists, also in Glasgow). The annual symposium of the Japanese Society of Developmental Biologists at Osaka also proved to be attractive. Others attended symposia

held before and during the meeting of the Federation of European Biochemical Societies in Paris, one on "Organelle Biogenesis" and another on "Structure of the Eukaryotic Genome." Similar topics, "Genetic Function of Mitochondrial DNA" and "The Organization and Expression of Chromosomes," were treated in Bari, Italy, and in Berlin, respectively. Also deserving mention was the Institut de la Vie's Conference on "Teratogenesis" in Martinique, and the Symposium on "Biochemistry of Cell Surfaces" held at the Fogarty Center of the National Institutes of Health, Bethesda.

Among the other conferences engaging the interest of members of the group, the following should be mentioned: the Cold Spring Harbor Symposium on "The Synapse"; the annual Symposium of the Society of General Physiologists, on the subject "Biogenesis and Turnover of Membranes"; a related symposium on "Membrane Receptors" at Duke University; a meeting sponsored by the Neurosciences Research Program (Boston) on "Depolarization-Release Coupling Systems in Neurons"; Gordon Research Conferences on "Developmental Biology" and "Molecular Pharmacology"; and the ICN-UCLA Symposium on "Molecular Mechanisms in the Control of Gene Expression."

Lectures were presented on a number of campuses, including Albert Einstein College of Medicine, California Institute of Technology, Case Western Reserve University, Columbia University, Cornell Medical College, DePaul University, Harvard University, Hershey Medical Center, Middlebury College, Rockefeller University, University College, London; and the Universities of Alberta, Arizona, and Bern; California at Davis, Irvine, Los Angeles, San Diego, and San Francisco; Chicago, Cincinnati, Connecticut, Iowa, Kyoto, Maryland, Michigan, Pennsylvania, Rochester, Tokyo, Utah, and Virginia; Vanderbilt University, Washington University, and Yale University.

Special presentations included The John M. Prather Lectures in Biology at Harvard, the Mitsubishi Lecture in Tokyo, and a Lowell Lecture in Boston.

Members of the group also spoke at hospitals and research centers, among them the Radiation Effects Research Foundation in Hiroshima, Japan; the Beatson Institute for Cancer Research, Glasgow; the Roche Institute for Molecular Biology; Oak Ridge Associated Universities; Sloan-Kettering Institute; National Institutes of Health; and the Muscular Dystrophy Research Laboratories at Newcastle-upon-Tyne.

Members of the Department took part in meetings of learned societies, including, in addition to those already mentioned, the American Association for the Advancement of Science, American Association of Anatomists, American Society of Biological Chemists, American Society for Cell Biology, American Philosophical Society, Biophysical Society, Federation of American Societies for Experimental Biology, National Academy of Sciences, Society for Developmental Biology, Society of Neurochemistry, Society for Neuroscience, and Tissue Culture Association.

Advisory and consultative services included Editor-in-Chief of *Developmental Biology* and membership on the editorial boards of *Anales del Desarrollo*, *Cell*, *Excerpta Medica* (section on Human Developmental Biology), *Current Topics in Developmental Biology*, *Oceanus*, and *Quarterly Review of Biology*.

Members of the staff also acted in these capacities: Chairman, Assembly of Life Sciences, National Academy of Sciences-National Research Council; Member of the Board of Governing Trustees and the Board of Scientific Overseers, Jackson Laboratory; Trustee, President, and Director, Marine Biological Laboratory; Member of Corporation, Woods Hole Oceanographic Institution; Trustee of International Medical Congress, Ltd., and member of its program committee planning the Fifth International Congress on Birth Defects.

Other posts occupied by members of the Department include the following: in the American Institute of Biological Sciences, member, Council of Past Presidents and member, Finance Committee; in the Institut de la Vie, Chairman, World Committee on the Formative Weeks of Human Life; in the National Academy of Sciences, member, Committee on Energy; in the National Institutes of Health, member, Board of Scientific Counselors, National Institute of Child Health and

Human Development, member, Gerontology Research Center Resources Advisory Committee, member, Physiological Chemistry Study Section, and member, Cell Biology Study Section; and in the Society for Developmental Biology, Past-President.

Members of the Department served on several visiting committees, including those for the Departments of Biology at Harvard University, Massachusetts Institute of Technology, and Princeton University; the Department of Molecular Biology and Biochemistry at Harvard; and the External Advisory Committee of the University of Chicago's Cancer Research Center.

Special service was rendered as co-Chairman of the "Cluster on Developmental Biology" of the President's Panel on Biomedical Research.

Staff members taught courses at the Marine Biological Laboratory as well as at Johns Hopkins (in the Departments of Biology, Biophysics, Pediatrics and Physiological Chemistry).

Seminars

The roster of speakers at the seminars organized by the Department to serve all those working in developmental biology in the region included: Aftab Ahmed, National Naval Medical Center; S. T. Carbonetto, University of North Carolina; James Darnell, Rockefeller University; Sarah Elgin, Harvard University; Walter Gilbert, Harvard University; Robert Grainger, Yale University; Alan F. Horwitz, University of Pennsylvania; Karl Illmensee, Institute for Cancer Research, Philadelphia; Lionel Jaffe, Purdue University; Stuart Kauffman, University of Pennsylvania; M. S. Letinsky, University of California at Los Angeles; D. K. Morest, Harvard Medical School; Josh Sanes, Harvard Medical School; Susumu Tonegawa, Basel Institute for Immunology; Herman Vandenburg, University of Pennsylvania; David Ward, Yale University; and K-W Yau, Stanford University.

BIBLIOGRAPHY

- Adler, W. H., *see* Ozato, K.
- Albright, J. F., J. W. Deitchman, S. A. Hassel, and K. Ozato, Differential antibody production by adherent and nonadherent spleen cells transferred to irradiated and cyclophosphamide-treated recipient mice. *J. Reticuloendothelial Soc.*, 17, 195-209, 1975.
- Biroc, S. L., and R. H. Reeder, Iodination of *Xenopus laevis* histone F2a1 in chromatin. *Biochemistry*, 15, 1440-1448, 1976.
- Bokhon'ko, A., and R. H. Reeder, The subunit structure of mouse satellite chromatin. *Biochem. Biophys. Res. Comm.*, 70, 146-152, 1976.
- Brown, D. D., Genome organization in higher organisms, *Federation Proceedings*, 35, 11-12, 1976.
- Brown, D. D., *see also* Brown, R. D., Carroll, D., and Thomas, C.
- Brown, R. D., and D. D. Brown, The nucleotide sequence adjoining the 3' end of the genes coding for oocyte-type 5S ribosomal RNA in *Xenopus*. *J. Mol. Biol.*, 102, 1-14, 1976.
- Carroll, D., and D. D. Brown, Adjacent repeating units of *Xenopus laevis* 5S DNA can be heterogeneous in length, *Cell*, 7, 477-486, 1976.
- Carroll, D., and D. D. Brown, Repeating units of *Xenopus laevis* oocyte-type 5S DNA are heterogeneous in length, *Cell*, 7, 467-475, 1976.
- Dawid, I. B., *see* Leister, D. E., and Wellauer, P. K.
- Deitchman, J. W., *see* Albright, J. F.
- Devreotes, P. N., and D. M. Fambrough, Synthesis of acetylcholine receptors by cultured chick myotubes and denervated mouse extensor digitorum longus muscles. *Proc. Nat. Acad. Sci.*, 73, 161-164, 1976.
- Devreotes, P. N., and D. M. Fambrough, Turnover of acetylcholine receptors in skeletal muscle, *Cold Spring Harbor Symp. Quant. Biol.*, 40, 237-251, 1976.
- Ebert, J. D., "Katsuma and Dan and the Quiet Revolution," in *Development, Growth and Differentiation*, Vol. 18, pp. i-ii, 1976.
- Ebert, J. D., *see also* Ozato, K.
- Fambrough, D. M., *see* Devreotes, P. N., and Ritchie, A. K.
- Gardner, E., and R. O'Rahilly, Neural crest, limb development, and thalidomide embryopathy, *Lancet*, 1, 635-637, 1976.
- Gardner, E., R. O'Rahilly, and D. Prolo, The Dandy-Walker and Arnold-Chiari malformations, *Arch. Neurol.*, 32, 393-407, 1975.
- Gardner, E., *see also* O'Rahilly, R.
- Hassel, S. A., *see* Albright, J. F.
- Huang, L., and R. E. Pagano, Interaction of phospholipid vesicles with cultured mammalian cells. I. Characteristics of uptake. *J. Cell Biol.*, 67, 38-48, 1975.
- Huang, L., *see also* Pagano, R. E.
- Leister, D. E., and I. B. Dawid, Mitochondrial ribosomal proteins in *Xenopus laevis*/*X. mulleri* interspecific hybrids, *J. Mol. Biol.*, 96, 119-123, 1975.
- O'Rahilly, R., The prenatal development of the human eye, *Exp. Eye Res.*, 21, 93-112, 1975.
- O'Rahilly, R., and E. Gardner, The timing and sequence of events in the development of the limbs in the human embryo, *Anat. Embryol.*, 148, 1-23, 1975.
- O'Rahilly, R., *see also* Gardner, E.
- Overton, C. G., *see* Weinberg, E. S.
- Ozato, K., Review of J. Klein, "Biology of the mouse histocompatibility-2 complex. Principles of immunogenetics applied to a single system." *Science*, 190, 978, 1975.
- Ozato, K., W. H. Adler, and J. D. Ebert, Synergism of bacterial lipopolysaccharides and concanavalin A in the activation of thymic lymphocytes, *Cellular Immunology*, 17, 532-541, 1975.
- Ozato, K., J. D. Ebert, and W. H. Adler, Pretreatment of thymocytes by phytohemagglutinin inhibits the binding of ³H-Concanavalin A, *J. Immunol.*, 115, 334-339, 1975.
- Ozato, K., and J. D. Ebert, Concanavalin A potentiates syngeneic response in murine lymphocytes, *J. Exp. Med.*, 143, 1-14, 1976.
- Ozato, K., J. D. Ebert, and W. H. Adler, The differentiation of suppressor cell populations as revealed by studies of the effect of mitogens on the mixed lymphocyte reaction and on the generation of cytotoxic lymphocytes, *Cell Immunol.*, 22, 323-333, 1976.
- Ozato, K., *see also* Albright, J. F.
- Pagano, R. E., and L. Huang, Interaction of phospholipid vesicles with cultured mammalian cells. II. Studies of mechanism, *J. Cell Biol.*, 67, 49-60, 1975.
- Pagano, R. E., *see also* Huang, L.
- Prolo, D., *see* Gardner E.

- Reeder, R. H., *see* Biroc, S. L., Bokhon'ko, A., and Weinberg, E. S.
- Ritchie, A. K., and D. M. Fambrough, Ionic properties of the acetylcholine receptor in cultured rat myotubes. *J. Gen. Physiol.*, 65, 751-767, 1975.
- Ritchie, A. K., and D. M. Fambrough, Electrophysiological properties of the membrane and acetylcholine receptor in developing rat and chick myotubes, *J. Gen. Physiol.*, 66, 327-355, 1975.
- Shutt, R. H., *see* Weinberg, E. S.
- Suzuki, Y., Fibroin messenger RNA and its genes, *Adv. Biophys.*, 8, 83-114, 1975.
- Thomas, C. and D. D. Brown, Localization of the genes for silk fibroin in silk gland cells of *Bombyx mori*, *Developmental Biology*, 49, 89-100, 1976.
- Weinberg, E. S., C. G. Overton, R. H. Shutt, and R. H. Reeder, Histone gene arrangement in the sea urchin, *Strongylocentrotus purpuratus*, *Proc. Nat. Acad. Sci., U.S.A.* 72, 4815-4819, 1975.
- Wellauer, P. K., and I. B. Dawid, Structure and processing of ribosomal RNA: A comparative electron microscopic study in three animals, *Brookhaven Symposia in Biology*, 26, 214-223, 1974.

PERSONNEL

Year Ended June 30, 1976

(including those whose services began or ended during the year)

Research Staff

Donald D. Brown, Biochemistry,
Director-designate
Igor B. Dawid, Biochemistry
James D. Ebert, Director
Douglas M. Fambrough, Biochemistry
Kenneth J. Muller, Neurobiology
Richard E. Pagano, Biophysics
Ronald H. Reeder, Biochemistry
Yoshiaki Suzuki, Biochemistry

Research Associates (extramural)

Bent G. Böving, Detroit, Michigan
Robert L. DeHaan, Atlanta, Georgia
Ernest Gardner, Davis, California
Arthur T. Hertig, Boston, Massachusetts
Irwin R. Konigsberg, Charlottesville,
Virginia
Ronan O'Rahilly, Davis, California
Elizabeth M. Ramsey, Washington, D.C.

Postdoctoral Fellows and Grant-Supported Associates

Peter Botchan, U.S. Public Health Service
Grant (Reeder)
Diana Card, Fellow of the U.S. Public
Health Service; Fellow of Muscular
Dystrophy Associations of America, Inc.

S. T. Carbonetto, Fellow of Carnegie
Institution of Washington
Jeffrey Doering, Fellow of the U.S. Public
Health Service
Scott Emmons, Fellow of the National
Cystic Fibrosis Research Foundation
Nina Fedoroff, Fellow of the U.S. Public
Health Service and Carnegie Institution
of Washington
Paul Geshelin, Fellow of the U.S. Public
Health Service
Elizabeth Godwin, U.S. Public Health
Service Grant (Dawid)
Leaf Huang, Fellow of Carnegie Institution
of Washington and the U.S. Public
Health Service
Yasumi Ohshima, Fellow of Carnegie
Institution of Washington
Keiko Ozato, Joint Fellow of Carnegie
Institution of Washington and Marine
Biological Laboratory
Aileen K. Ritchie, Fellow of Muscular
Dystrophy Associations of America, Inc.
Alex Sandra, U.S. Public Health Service
Grant (Pagano)
Masatoshi Takeichi, Fellow of Carnegie
Institution of Washington
Katherine Tepperman, Fellow of the U.S.
Public Health Service
Harvey Wahn, U.S. Public Health Service
Grant (Reeder)

Peter K. Wellauer, Fellow of the National
Cystic Fibrosis Research Foundation

Students

Peter Devreotes, Graduate, Johns Hopkins
University
John Gardner, Graduate, Johns Hopkins
University
Carol Kaushagen, Graduate, Johns
Hopkins University
Jose Ramirez, Graduate, Johns Hopkins
University

*Visiting Investigators and
Extramural Collaborators*

W. H. Adler, Baltimore, Maryland
George Brownlee, Cambridge, England
John W. Chase, Boston, Massachusetts
Hayden G. Coon, Bethesda, Maryland
Michael Edidin, Baltimore, Maryland
J. W. S. Harris, London, England
Uel J. McMahan, Boston, Massachusetts
R. M. Ruyschaert, Brussels, Belgium
Christian Thomas, Brussels, Belgium
Witold Wozniak, Poznan, Poland

Clerical and Technical Staff

Elaine S. Asch, Senior Technician
Judith M. Bernstein, Secretary
James H. Blackwell, Custodian

Leo Blackwell, Recorder
Paul Blackwell, Custodian (part-time)
Julian L. Certain, Librarian (part-time)
Huei-Wen Chen, Technician
Jeffrey Ciemny, Recorder
William J. Cleary, Recorder
William H. Duncan, Senior Technician
Ernestine V. Flemmings, Laboratory
Helper
Kate Francis, Secretary
Paul Giza, Technician
Richard D. Grill, Photographer
Virginia S. Hicks, Laboratory Helper
Mary E. Hogan, Technician (part-time)
John E. Jones, Custodian
Eddie D. Jordan, Senior Technician
Carrie Kahn, Technician (part-time)
Catherine R. Lane, Librarian (part-time)
Alice H. Mabin, Laboratory Helper
Thomas F. Malooly, Business Manager
Rudolph Matthews, Recorder
Judy Miller, Recorder
Thomas F. Miller, Custodian
Ann N. Murphy, Secretary
Joyce I. Patterson, Laboratory Helper
John Pazdernik, Jr., Building Engineer
Betty Lou Phebus, Bookkeeper-Technician
Martha L. Rebbert, Senior Technician
Adrienne Robinette, Secretary
Bessie H. Smith, Laboratory Helper
Delores V. Somerville, Senior Technician
John L. Wiser, Machinist

*Department
of Terrestrial Magnetism*

Washington, District of Columbia

George W. Wetherill

Director

Contents

| | |
|---|-----|
| Introduction | 109 |
| Galaxies and Stars | 118 |
| Evidence for motion of the Galaxy | 118 |
| A search for extragalactic extinction | 119 |
| The statistics of galaxy alignments | 121 |
| Kinematic studies of NGC 3351, 3115, and 1275 | 122 |
| An illustration of galaxy redshifts | 127 |
| The irregular galaxy WLM and its surroundings | 130 |
| The nucleus of M31 | 133 |
| Star counts in globular clusters | 134 |
| Neutral hydrogen supernova remnant study | 136 |
| Type I supernovae: Interpretation of optical spectra | 139 |
| The 21-cm receiver for the Instituto Argentino de Radioastronomía | 143 |
| 820-MHz survey of the Southern sky | 144 |
| Image tube systems | 145 |
| Activities of the Instituto Argentino de Radioastronomía | 147 |
| The Earth and the Solar System | 149 |
| Gas-solid interactions in the solar nebula | 149 |
| Interplanetary bodies and solar system history | 151 |
| The role of large impacting bodies in the formation of the earth and moon | 152 |
| Late (4.0 b.y.) bombardment of the moon and terrestrial planets | 157 |
| The earth-crossing Apollo objects | 164 |
| Particle tracks and micro-impact features in grains from gas-rich meteorites | 170 |
| Cosmic-ray research | 176 |
| Rb-Sr mantle isochrons | 176 |
| Part I: Continental regions | 177 |
| Part II: Oceanic regions | 191 |
| Geochemistry of late Cenozoic volcanic rocks from the Nevado de Toluca area, Mexico | 207 |
| Preliminary Rb/Sr data on the minimum age of the central Andean Precambrian basement complex | 213 |
| Volcanoes, Q , and seismicity in western South America | 216 |
| Determination of the lithosphere-asthenosphere boundary using converted waves | 223 |
| Shallow seismicity in subduction zones | 229 |
| A model for laterally heterogeneous velocity structure at the base of the mantle | 233 |
| Single site phase velocity determinations | 240 |
| Maximum entropy spectral analysis | 243 |
| Atomic Physics and Properties of Materials | 249 |
| Diffusion in silicate melts and glasses | 249 |
| Diffusion measurements using fast deuterons for <i>in situ</i> production of radioactive tracers | 259 |
| Observation of x radiation characteristic of a united atom | 263 |
| Bibliography | 268 |
| Personnel | 270 |

INTRODUCTION

It has become a rather tiresome cliché to contrast the universal genius or "Renaissance man" of former years with today's specialist. Concentration of one's work into limited areas of knowledge is often blamed for the frequent inability of scientists to grasp adequately the relationships between their work and that of others, and to achieve the unifying syntheses which are the goal of intellectual endeavor. Worse yet, in the political and entertainment world simple mention of the titles of specialized research projects results in serious scholars becoming sources of public amusement or objects of public ridicule.

In this context it is sometimes forgotten that there is a unifying countercurrent upon which even the most specialized scientists are borne. The mainstream of twentieth century physics and chemistry has been the development of a universal theory of matter, applicable to all times and all places. In addition to blurring the boundary between physics and chemistry almost to the point where the difference is unrecognizable, this development has been of profound importance to all of natural science. Astronomy, geology, and biology have lost their taxonomic and descriptive flavor.

For a time those in the vanguard of this development felt it necessary to identify their activity (often in a somewhat superior tone) as geophysics or geochemistry rather than geology, or as astrophysics rather than astronomy. (Even between these so-called interdisciplinary fields there is a certain hierarchy. I once annoyed a famous solar spectroscopist by introducing him to a class of chemistry students as an astrochemist; upon gaining the floor he firmly reestablished his identity as an astrophysicist.) Although these distinctions are still made, they are less useful, and possibly

as part of the current vogue for nostalgia, there are now many scientists primarily concerned with thermodynamics of multiphase systems who proudly describe themselves as geologists, and experts in nuclear reactions who would object to being called anything but astronomers. In many universities, if you really want to learn thermodynamics you will attend lectures in the geology department, and if you really want to learn fluid mechanics you will go to meteorology or oceanography; and the genuine physics and chemistry departments find themselves only one among many and not always the best. Thus the battle is over; physics and chemistry are now the cornerstone of all science. The earth is now treated as a chemical and mechanical system; stars and galaxies are to be understood only through knowledge of plasmas, nuclear reactions, and molecular chemistry.

However, even though physicists and chemists have reproduced themselves within geology and astronomy departments to the point where their progeny are now dominant, it is also apparent that the unity in the basic approach to science which has now been achieved has not been as fully exploited as it could be, and that many of the old barriers remain, even though they are more often surmounted today than in the past.

The reasons for the continued existence of these obstacles are manifold. To a significant extent they are a consequence of practical problems basically of a nonscientific nature. In a university, lecture courses have to be taught, and students have to be accredited as bona fide geologists, astronomers, or meteorologists if they wish to find employment. The department needs to be sure it gets at least its fair share of university positions, funds, and space. The need to deal with these

problems can unite the faculty of a department more effectively than their mutual scientific interests, and it deflects their attention from what might become mutually stimulating scientific interaction with those in other departments. In another area, the sheer size of the federal funding structure requires agencies such as the National Science Foundation to be compartmented into "disciplines," even though this word has lost most of the significance it formerly possessed. Program directors and the associated peer reviewers can impose severe penalties on those scientists who stray too far from what may be regarded as the most fundamental and important subjects for research even though they may simply be the most fashionable at the moment within a limited group of scientists.

We have been given the opportunity to be remarkably free of these essentially nonscientific pressures to identify with a particular professional group. Our more informal mode of instruction avoids the problem of repeatedly "covering" a prescribed body of knowledge. Our endowed research support and our freedom from government influence is much greater than that available to our colleagues elsewhere, and historically there has been within the Department a tradition of extending our research beyond the point which a reviewer might well regard as the limits of our competence. Freedom from duties associated with a professorial position and the obligation to serve on institutional and federal committees also can provide us with the time and tranquility necessary to look inward to the Department, to understand and value the work of one another, and to contemplate in greater depth the meaning of our work and its relationship to that of others. With this unusual opportunity comes the responsibility to break away from artificial boundaries associated with our professional origins and to build a research community dedicated to viewing the earth, solar system, stars, and galaxies

as a continuous and unified field of scientific investigation. Although at greater risk, workers elsewhere have taken steps to achieve this. The principal barrier to our success in this effort should be only our finite abilities.

The reader of this report can judge the extent to which we have accepted this responsibility. Some changes from previous reports can be seen. There are no longer organized reports of "sections" of astrophysics, geophysics, and atomic physics. The report has been subdivided into units only in order to make it easier to read. The boundaries between these units are intentionally arbitrary. New work has begun in an area of science transitional between our previous work in astronomy and earth science. This is the study of the solar system and its history, as revealed by the most primitive material available, the meteorites, and by theoretical investigations ultimately based upon observations of the earth, the moon, and the planets. Of course, all of this could be viewed as a façade; a perceptive reader will note that to a large extent the same people are working on the same problems as before. A cynical reader could conclude that all of the foregoing is a pretense and that things will always be the same. That is not our intention. Only time will tell.

CURRENT RESEARCH IN THE DEPARTMENT

There is a natural hierarchy in the organization of the universe. On the largest scale there are the clusters of galaxies, galaxies, and their constituent stars and interstellar material. Within the stars are formed the elements that are the matter from which new stars and planetary systems are in turn formed. The formation of new stars and planetary systems is controlled by the physical and chemical structure of the interstellar medium. It is the structure of the interstellar medium that defines the initial and boundary conditions for the formation of planetary bodies such as the earth

and moon. These conditions largely determine the nature and magnitude of the processes which have occurred during subsequent earth history, and which have resulted in the present chemical and physical state of our planet. Underlying and unifying all are the fundamental properties of matter as learned from atomic and nuclear physics.

At all levels in this hierarchy we are confronted with mysteries. Although the earth has been extensively studied, one need go only a few tens of kilometers beneath its surface to arrive at the frontier area of current research. The formational solar system has tended to be treated as a magical wonderland where one qualitative speculation is as good as another. Although much progress has been made in understanding stellar evolution during the past several decades, there does not exist at the present time any usable quantitative theory for understanding either the beginning or the end of a star's life. In the area of galactic evolution we are at best emerging from a descriptive stage where masses, velocity fields, and chemical abundances are measured for various types of objects including "peculiar" ones in the expectation that before too long these data will form the basis for a more general understanding of galaxies. The strong coupling between the nature and history of galaxies, stars, and planets results in this imperfection of understanding in one area affecting our ability to understand another. Some sort of simultaneous attack on the unknown is needed. We are obviously too small to undertake this mighty task. However, in working simultaneously at several of these frontiers along with other scientists throughout the world we are in an excellent position to contribute to the solving of these problems and to the understanding of their relationship to one another.

GALAXIES AND STARS

During the past year investigations of the universe at the galactic scale

have made use of the all-sky sample of ScI galaxies which was established by Ford, Rubin, and Thonnard in their study of the anisotropy of the Hubble expansion. This work has now been completed, with the conclusion that the observed anisotropy has its origin in motion of both our Galaxy and the Local Group of galaxies, relative to the more distant sample galaxies, at a velocity of about 450 km s^{-1} . The conflict between this result and the reported isotropy of the 3°K relic black body radiation remains as a problem to be resolved theoretically or observationally.

Now that optical spectra and radio observations exist for such an all-sky sample, they can be used for the investigation of other fundamental problems. Rubin and Thonnard have in this way explored the possibility that between the members of the group of nearby galaxies there is an excess of extragalactic matter, analogous to the interstellar material within a galaxy. Such material would be expected to lie within the plane defined by these nearby galaxies, and should lead to excess extinction in the direction of this plane, compared with the perpendicular direction. No significant excess extinction is found. It is concluded that the density of this intergalactic material is similar to the average density of the universe, and that no significant portion of the missing matter required to cause the universe to be gravitationally closed was found in the form of this "intergalactic medium."

In past exploration of the nature of the various types of galaxies, principal attention has been directed toward observation of spiral galaxies, their velocity fields and masses being determined by observation of bright emission lines of the gas that is abundant in these galaxies. The velocity fields of the underlying stars that form the bulk of the mass of galaxies have been relatively little studied in the spirals and in the equally important gas-free elliptical galaxies. Ford, Peterson, and Rubin report on the use of absorption lines

originating in the stars. Velocity fields and mass and angular momentum models have been obtained for two objects, a barred spiral galaxy and an early-type galaxy. It is found that the rotation over the radial extent of the bar is that of a solid body, but whether the stars are permanently associated with the bar or the bar is a density-wave phenomenon passing through the stellar distribution cannot be determined from the data. Overall the dynamics of the barred galaxy are very similar to those of a normal galaxy. For the first time, high resolution spectra of an elliptical galaxy are available to provide a sound observational basis for constructing a realistic dynamical model. In addition, investigations of a peculiar colliding pair of galaxies discovered by Minkowski 20 years ago show that the galaxies are still approaching one another, and the evidence for an earlier explosive event in one of the galaxies cannot be explained by the presence of the other galaxy.

The all-sky sample of galaxies has also been used by the same workers to illustrate the good general agreement of both optical and 21-cm measurements of redshifts when measured on the same galaxies.

Ford, Peterson, and Rubin also report on the more detailed structure of the nearby Andromeda galaxy, M31. They find evidence that the angular momentum vector of the nucleus may be tilted with respect to the plane of the disk of the galaxy. If this is the case, this will be an important fact to be included in attempts to understand the general principles of the dynamics of galaxies. Other interpretations are possible. However, future observations should permit these alternatives to be tested.

Thonnard reports 21-cm observations of neutral hydrogen in the irregular galaxy WLM, which lies in proximity to the Magellanic Stream. He finds that this galaxy, although containing relatively few stars, contains almost as much neutral hydrogen as the Large Magellanic Cloud, and that this hydro-

gen is located within WLM rather than being a portion of the adjacent Magellanic Stream.

Turner has carried out a Monte Carlo study of the statistics of galaxy alignments in order to understand the significance of reported observations of such alignments. He finds that the probability of such alignment by chance is surprisingly high, and that a fair number of such alignments should occur even in the absence of a genetic or dynamic association between the aligned galaxies.

Peterson has continued his work on globular clusters, and reports new star counts and comparisons with dynamical models for 27 clusters. Globular clusters are perhaps the oldest type of object available for investigation and may predate the galaxy with which they are associated. Their structure may therefore still bear a record of the earliest events of galactic history. These data provide constraints which must be satisfied by theories of galactic evolution.

Going to more recent events in the history of the Galaxy, new results on supernovae are described. An understanding of these explosion events is essential to understanding the terminal stages of stellar evolution, element formation, x-ray sources, pulsars, neutron stars, cosmic ray sources, and possibly the initiation of the formation of new stars. Consequently there has been considerable recent interest in the development of supernova models. Such models require observational data against which they may be tested. Assousa reports calculations which may explain why in his previous work neutral hydrogen was found in only a few of the supernova remnants studied. Use of remnant expansion velocities from other workers permits calculation of the mass of the objects studied and shows good agreement between the predicted and the observed neutral hydrogen mass.

Assousa, Ford, Peterson, and Rubin describe new spectra of extragalactic type I supernovae and their compari-

son with generated synthetic spectra. They conclude that these spectra appear to be dominated by transitions in ionized iron, which could possibly be produced by radiative excitation during the explosive event.

In the area of instrumentation, much effort of both the scientific and technical staff (Ecklund, Little, Thonnard, and Turner) is going into the construction of a modernized 21-cm receiver for use on the 30-meter radio telescope at the Instituto Argentino de Radioastronomía. It is expected that this will permit much higher quality observations of Southern sky high velocity clouds and spiral galaxies than has hitherto been possible. Digital equipment for an 820-MHz survey of the Southern sky is also under construction.

Ford continues his work with image tube systems, in addition to his collaborative use of the present "Carnegie Image Tubes" in the current investigations described earlier in this report. Two new spectrographic image tube systems have been constructed in our shop. In addition, facilities are under development for analysis and evaluation of the new generation of digital imaging devices as they become available.

A brief report is also given of the activities of the Instituto Argentino de Radioastronomía, with which we at DTM have been closely associated since its beginning. In spite of severe economic difficulties, a significant program of instrument development and observation has continued. Of particular significance has been the near completion of a low velocity neutral hydrogen survey which reveals the large-scale structure of this material over most of the Southern sky.

THE EARTH AND THE SOLAR SYSTEM

At the interface between astronomical science and earth science lies investigation of the formation of the solar system. The processes are adjuncts of star formation. Many of the facts

against which theories can be tested are based on measurements of rocks, particularly meteorites.

In this area of science there is a severe need for the development of theories sufficiently quantitative to be testable and communicable. There needs to be developed a community of scientists who have enough respect for the work of one another to seriously attempt to understand its details, criticize what they believe to be wrong, and build upon what is of value. Unfortunately such a community does not exist at present; rather too frequently, investigations are pursued in splendid isolation from one another, and while there is much disagreement, there is too little effort to understand the origin of these differences.

Weidenschilling has made significant progress in development of a quantitative model of the dynamics of particles of various sizes moving in a gaseous disk of the type generally believed to have been present during the early stages of planet formation. This builds upon and extends earlier work of Whipple. He shows that there is a strong dependence on particle size which may influence the rate at which the initial ≈ 1 -km bodies are formed and possibly also the chemical composition of these bodies.

Somewhat later in the formation of the solar system these earlier condensations must somehow or other have coagulated to form planets. There has developed in the past five years or so a common belief that the time scale for this accumulation must have been very short, on the order of 10^3 to 10^4 years. There exists at present no quantitative dynamical theory which predicts such a rapid time scale. Perhaps the principal reason for widespread acceptance of this short time scale has been the evidence that at least much of the moon was heated above its melting point essentially at the time of its formation, leaving insufficient time for the slow buildup of temperature by the decay of long-lived radioactive elements and therefore requiring the trapping of

gravitational energy associated with rapid accretion. In 1969, V. S. Safronov, working at the Institute of the Physics of the Earth in Moscow, published a theory of early terrestrial heating in which a calculated distribution of large impacting bodies during accretion "buried" a sufficient quantity of their interplanetary kinetic energy beneath the accreting surface of the earth to heat much of the interior to near its melting temperature. We were fortunate in having the opportunity of hearing Safronov explain this work further at a recent DTM seminar.

When applied to the moon, however, this theory still fails to provide the necessary initial temperature, primarily because in the case of the earth the interplanetary kinetic energy is augmented by acceleration during the fall of the body into the earth's gravitational field. This effect will be much less for the smaller moon.

During the past year a variant of Safronov's theory has been developed (Wetherill) using techniques previously employed by the author for the study of the evolution of meteorite orbits. This leads to a considerably greater fraction of the accreting bodies being large (>200 km in radius) and of high velocity (~ 8 km/s). Both of these result in much greater burial of kinetic energy during the formation of the moon, and thereby provide a mechanism for obtaining initial high lunar temperature even if the time scale is as large as that given by quantitative dynamical theories ($\sim 10^8$ yr).

Application of the same and similar techniques to two other solar system problems are reported. These are the causes of the late heavy bombardment (4.0 b.y. ago) which produced the crater-saturated surface of the moon (and probably other planets as well) of that age and the role played by present earth-crossing interplanetary bodies (Apollo objects) as sources of chondritic meteorites.

Extension of realistic theoretical investigations into early solar system history, both here and elsewhere, may

be expected to clarify considerably our thinking with regard to these problems, but taken alone, are not likely to be able to distinguish between alternative hypotheses. Fortunately they do not have to be taken alone, as there are available samples of meteoritic rocks which in various senses have preserved relic information concerning the earliest history of the solar system and quite likely of some presolar events as well. In addition, at least some meteorites have been affected by more recent events prior to their impacting the earth, and these must be disentangled somehow from the primordial effects in order to be well understood. A promising opening into this area was found by Brownlee and Rajan several years ago in the discovery of submicron impact craters on the surfaces of meteorite grains. When combined with the occurrence of solar flare tracks in the same grains, this leads to an analogy between the surface of the meteorite parent body and the lunar regolith (soil), for which such phenomena have been extensively studied. Rajan and his collaborator Poupeau of C.N.R.S., France, report a continuation of this work, directed toward an understanding of similarities and differences between the lunar regolith and the inferred regolith surfaces of the parent bodies of meteorites of various kinds.

Lunar studies show that the probability of a grain found on the surface being cratered increases as the regolith matures, as a consequence of being continually impacted, turned over, and mixed. These new results show the meteoritic data lie on the extrapolation of this lunar trend and correspond to very immature regoliths. This correlation suggests a common dynamical mechanism that is operative on all regoliths. On the other hand, glassy splashes are absent from meteorite grains, although they are quite abundant even on immature lunar soils, an effect which is not yet understood.

Other extraterrestrial research reported here concerns measurement of reversals of the sun's poloidal magnetic

field as inferred from ionization chambers operated continuously by the Department since 1937 (Forbush). This time scale of almost three decades is long compared with that of changing emphases in the field of high energy physics with which cosmic-ray research was associated in 1937, but it represents less than two cycles in the variations of the sun's poloidal field. The success of these measurements is a tribute to the value of making observations on the time scale peculiar to the phenomena being studied rather than on the basis of changing fashion.

Since the beginning much of the research of this Department has been strongly oriented toward global problems of the earth and its history. This continues to be the case. Currently major emphasis is being placed upon using geochemical and geophysical techniques to learn as much as possible concerning the nature of the earth's mantle.

During the past year, much of the time of those working in isotope geochemistry (Brooks, James, and Hofmann, in collaboration with Hart, now at M.I.T.) has been devoted to taking stock of the isotopic data developed here and elsewhere in recent years, and attempting to understand its implications regarding the earth's mantle beneath the oceans and the continents.

A compilation of all the data of sufficient quality shows that in both these regions the initial isotopic composition of the strontium mantle-derived rocks is not uniform. The initial $^{87}\text{Sr}/^{86}\text{Sr}$ ratios of rocks from both oceanic islands and continental areas are usually distinctly higher than the much more uniform values found in mid-ocean ridge basalt. Such elevated Sr isotope ratios have commonly been interpreted as indicating either a crustal origin of the rocks or at least crustal contamination. This interpretation is particularly untenable for oceanic rocks; arguments are presented against this being the case for most of these continental rocks as well.

A key point in these arguments is that in a given region the data indicate not only higher initial Sr isotope ratios but a correlation between the $^{87}\text{Sr}/^{86}\text{Sr}$ ratio and the Rb/Sr ratio. Thus a "pseudoisochron" is obtained which resembles the more familiar whole-rock isochrons which are used for age determinations and are based on the present $^{87}\text{Sr}/^{86}\text{Sr}$ ratio of the rocks rather than their initial ratio. This correlation is interpreted as indicating that the present rocks possess not only a "memory" of some mean Rb/Sr ratio of their source as indicated by their initial Sr isotope ratio but that some information concerning the time scale for the variation of this Rb/Sr ratio in the mantle source has also been preserved. Thus "pseudoisochrons" are in fact mantle isochrons and may possess real time significance, even though obscured by scatter in the data resulting from the superposition of later events. More specific models are proposed for the chemical development of these mantle source regions. The seismic evidence for the great thickness of the continental lithosphere and the possible complete absence of continental asthenosphere is incorporated into these models, and it is hypothesized that the continental mantle isochrons are the result of more or less closed system evolution of an ancient heterogeneous continental lithosphere, with a typically higher Rb/Sr ratio than the more depleted asthenosphere sources of ocean ridge basalts. In the oceanic islands, there is not thick lithosphere of this kind, and it is proposed that the deeper mesosphere plays an analogous role in the formation of these rocks.

In addition to this synthesis of isotopic data obtained during the past several years, some new results are also reported. Whitford and his collaborator Bloomfield in the Institute of Geological Sciences in London are working on orogenic volcanic rocks from Mexico which are situated on old, typically continental crust adjacent to a convergent plate boundary. The rocks are compared with typical island arc

volcanics from the Sunda arc of Indonesia. The Mexican rocks appear to be geochemically distinct from those of the island arc. They are richer in SiO_2 and Na_2O and are characterized by higher atomic $\text{Mg}/(\text{Mg} + \text{Fe}^{2+})$ ratios. Although this work is still in progress, the isotopic data now obtained together with the high $\text{Mg}/(\text{Mg} + \text{Fe}^{2+})$ ratios suggest a mantle origin for the Mexican rocks.

James has obtained a minimum Rb/Sr whole-rock age of 1012 ± 52 m.y. for rocks from the central Andean basement complex near Arequipa, Peru. This is the oldest age measurement reported from this basement complex and suggests a similar or older age for the mantle lithosphere underlying this region, which is believed to be the source of those rocks exhibiting the mantle isochrons discussed earlier in this introduction.

These geochemical results are related to geophysical data in the same area. Sacks, Snoke, and Linde summarize their work on the distribution of volcanism, mantle anelasticity, and seismic activity in South America. They find that in southern Peru and Chile there is an anelastic zone (low Q) between the subducting oceanic plate and the >300 km thick continental lithosphere. This is correlated with seismic activity in the downgoing plate and presence of volcanoes, indicating partial melting of the mantle in this region. Farther to the north in Peru, the low- Q zone is absent, the subducting slab has low seismicity, and volcanoes are absent. It appears that the development of a well-defined seismic plane in the subducting slab of oceanic lithosphere near its interface with the rocks above requires these overlying rocks to be hot and partially molten.

Both geophysical and geochemical data indicate more and more that old continental areas are underlain by lithospheres hundreds of kilometers thick, and thus despite the occurrence of continental drift on moving plates, continents are not an extremely super-

ficial feature of the earth. This gives rise to the question of whether a lower boundary to the continental lithosphere exists at all, and if so, if it can be detected. Conventional techniques, using surface waves, have no resolution below about 200 km depth. Sacks and Snoke describe seismic arrivals in Peru, northern Chile, and Argentina which they have been able to model only as converted phases arising from a nearby horizontal transition zone at a depth of 400 km. Furthermore, these data indicate the seismic shear velocity is lower below the interface, which leads to the interpretation that a boundary between the thick continental lithosphere and an underlying asthenosphere has been found.

Sacks, Rodriguez, Snoke, and Linde report results from the long-term collaboration between DTM and the University of San Agustín in Arequipa, Peru. These data show that there is an earthquake-free shallow (<50 km thick) region on the continental side of the trench extending for about 80 km. This same feature is found elsewhere, e.g., in the Aleutians. The explanation offered for this phenomenon is that although the rocks in these regions are of normal strength they are subjected to a superposition of stresses (a compression resulting from the relative plate motion and a tension caused by the curvature of the plates at the trench) which leads to the region being nearly stress free.

These results in observational seismology have been supported by several interesting theoretical studies. In 1974 Sacks reported anomalies in the amplitudes of seismic phases that have traversed the earth's core, and he showed that these are correlated with certain regions on the core-mantle boundary. Thus in some unclear way these results were maps of "geographic" regions on the core-mantle interface. Snoke and Sacks now propose a velocity model that fits these data. In this model the anomalous regions consist of cells ~ 150 km in dimension

which multiply scatter the seismic signals traversing them along near-grazing ray paths. The size and velocity variations required are of a magnitude compatible with their being small convection cells. These cells are believed to occur in clusters in those areas of the lowermost mantle corresponding to the anomalous regions found earlier.

Sacks, Snoke, Evans, and their collaborators King and Beavan at Cambridge University report a technique for the measurement of seismic phase velocity at a single site. Conventionally, determination of the phase velocity requires a widely spaced network that measures travel times through the network as a function of frequency. The large spacing required limits the seismic wavelength that can be used and hence limits determination of the earth structure to relatively shallow depths (≤ 200 km). It is now found that a vertical seismometer and a volume strainmeter operating at a single site can, at least in principle, be used to determine phase velocity without any intrinsic upper wavelength limit and without uncertainties introduced by local heterogeneities and tilts.

Seber, James, Snoke, and Linde have investigated the application of maximum entropy spectral analysis to seismic data. This has the potential advantage that in contrast to the more usual Fourier analysis this technique is well suited to extract the spectral content from noisy or incompletely recorded signals. Calculations using simulated signals bear out this expectation to a considerable extent, but some puzzling results were found which will require further investigation.

ATOMIC PHYSICS AND PROPERTIES OF MATERIALS

Hofmann and Magaritz have considerably extended earlier work on cation diffusion in natural melts. In addition

to increased understanding of the role played by diffusion in natural systems, these new results display effects that must be relevant to the fundamental atomic and molecular structure of silicate liquids.

Measurements of diffusion rates in basaltic melts show that diffusive mixing distances in a partially molten mantle may be expected to be on the order of hundreds of meters in 10^9 yr. These results are used to test a model for the development of "hot spot" sources of oceanic islands which has been proposed by others and for which mixing by processes other than diffusion is not expected. The limited diffusion lengths appear to preclude the development of enriched regions sufficiently large to be of geochemical importance.

Measurements of diffusion in Sr and Ba obsidian glass also indicate the extent of diffusive transport as a geochemical mechanism. These results show that at metamorphic temperatures of 700°C , transport distances may be limited to 20 cm in a million years. This shows that large widely spaced whole-rock samples may not indicate a reliable age of metamorphism when used for Rb-Sr dating, and that small-scale ($\sim\text{cm}$) sampling may be required to ensure the isotopic equilibration required to establish an age.

These workers give examples of the wide applicability of these diffusion data to problems of trace element geochemistry, igneous petrology, and to the microscopic structure of liquids.

Hofmann and Brown have developed a new technique for measurement of cation diffusion in basaltic melts wherein the radioactive tracer is initially located in a sharply defined zone within the sample rather than being located on the surface. This is accomplished by bombardment of basaltic glass with 40-Mev deuterons for the formation of radioactive species such as ^{22}Na , ^{46}Sc , and ^{56}Co within the sample. This approach minimizes convective mixing during the subsequent melting

of the sample and eliminates evaporation of volatile tracers such as sodium from the surface. This technique is found to be highly successful and has been used to confirm and extend the measurements found using the earlier technique.

Brown and Pepper continue their investigations of fundamental problems in atomic structure. These are approached by study of the x rays produced when heavy ions collide at energies of a few Mev. From the theoretical point of view it is not clear how the transient "molecule" formed by the two ions at the moment of their collision should be treated, and there are a number of experimental results that still require explanation.

These workers report the most clear example of the formation of a "united atom" in which both nuclei temporarily

combine as a single center of charge. The L and M x-ray bands characteristic of such an atom are clearly observed, and the limits of these bands change exactly as predicted when the atomic number of the target is changed.

In another experiment it is found that when praseodymium is bombarded with potassium atoms, the praseodymium L shell x-ray lines are found as expected, as a consequence of transfer of electronic vacancies from the K shell of the potassium ion. However, the remarkable thing is that only two of the several possible L lines are seen. The exchange is selective. This is believed to represent a form of charge exchange not observed before, and it is suggested that it is a consequence of rotational coupling that occurs while the two colliding nuclei are relatively distant from one another.

GALAXIES AND STARS

G. E. Assousa, E. T. Ecklund, W. K. Ford, Jr., C. A. Little, C. J. Peterson, V. C. Rubin, N. Thonnard, K. C. Turner, and M. A. Tuve

Collaborators

B. Balick, B. F. Burke, J. W. Erkes, J. Graham, C. K. Kumar, J. Oort, M. S. Roberts, and R. E. White

EVIDENCE FOR MOTION OF THE GALAXY

W. K. Ford, Jr., V. C. Rubin, and N. Thonnard

During the past year we completed our study, made in collaboration with Dr. J. A. Graham from Cerro Tololo Inter-American Observatory and Dr. M. S. Roberts from the National Radio Astronomy Observatory*, of a sample of Sc I galaxies, which was undertaken to investigate the isotropy of the Hubble expansion (Rubin *et al.*, 1976a,b). As discussed in detail in last year's report (*Year Book 74*, p. 113), we have detected an anisotropy, in the sense

that galaxies on one half of the sky have velocities that are small for their magnitudes; galaxies on the remaining half of the sky have velocities that are large for their magnitudes. From the extensive observational and statistical study making use of optical magnitudes, optical velocities, 21-cm magnitudes, 21-cm velocities, and diameters and maximum velocities of the rotation curves, we conclude that a motion of the Galaxy and of the Local Group of galaxies relative to the sample is the only interpretation consistent with all of the observations. The Galaxy is moving approximately edge on, with the leading edge in the anti-center direction. The velocity of the center of the Galaxy is $V_{GM} \sim 450 \pm 125 \text{ km s}^{-1}$; as observed at the sun (and

*Operated by Associated Universities, Inc., under contract with the National Science Foundation.

therefore including the rotation of the sun about the center of the Galaxy) the velocity is $V_o \sim 600 \pm 125 \text{ km s}^{-1}$.

Alternative explanations of the observed effect which we have considered but rejected include the following: (1) Galaxies on one half of the sky are intrinsically fainter than those on the other half. (2) Galaxies observed beyond the central region of our Galaxy are less obscured than those observed in the anticenter direction. (3) The Hubble expansion increases by 20% across the sky for galaxies in the distance range $3500 < V_c < 6500 \text{ km s}^{-1}$.

After correction for the motion of the observer, the random motions of galaxies are small [$\sigma(\Delta v) < 200 \text{ km s}^{-1}$], and the Hubble flow is very uniform [$\sigma(\Delta H/H) < 0.04$]. This result thus supports the similar earlier conclusions of deVaucouleurs (1958) and Sandage and Tammann (1975). The conflict with the observed isotropy of the 3°K relic radiation, which implies $V_o < 300 \text{ km s}^{-1}$, remains unresolved.

References

- deVaucouleurs, G., Further evidence for a local supercluster of galaxies: rotation and expansion, *Astron. J.*, **63**, 253, 1958.
 Rubin, V. C., W. K. Ford, Jr., N. Thonnard, M. S. Roberts, and J. A. Graham, The motion of the Galaxy and the Local Group determined from the velocity anisotropy of distant Sc I galaxies. I. The data, *Astron. J.*, **81**, in press, 1976a.
 Rubin, V. C., N. Thonnard, W. K. Ford, Jr., and M. S. Roberts, The motion of the Galaxy and the Local Group determined from the velocity anisotropy of distant Sc I galaxies. II. The analysis for the motion, *Astron. J.*, **81**, in press, 1976b.
 Sandage, A. R., and G. A. Tammann, Steps toward the Hubble constant. V. The Hubble constant from nearby galaxies and the regularity of the local velocity field, *Astrophys. J.*, **196**, 313, 1975.

A SEARCH FOR EXTRAGALACTIC EXTINCTION

V. C. Rubin and N. Thonnard

Knowledge of the type and quantity of intergalactic material is of interest

because it can help determine the total amount of matter in the universe and place limits on the amount of material outside the galaxies. Attempts to determine this have involved searching in the direction of galaxy clusters for excess reddening of galaxies, changes in the number density of distant galaxies, and excess luminosity in the space between galaxies. We have extended the approach used by Rubin *et al.* (1976) in determining the extinction within our Galaxy to search for excess extinction between the galaxies in the direction of the supergalactic plane, the flattened disk of nearby galaxies (radial velocities less than 2000 km s^{-1}) of which we are an outlying member.

Because we are located in the supergalactic plane, if extragalactic matter is distributed in this plane, our line of sight to more distant galaxies passes through this layer of obscuring matter. Taking a uniform sample of distant galaxies that have a small spread in intrinsic luminosity (Sc I's with $3500 < V < 6500 \text{ km s}^{-1}$) and correcting the observed magnitudes and velocities for all known systematic effects, one can form a parameter called the Hubble Modulus. When we examine the Hubble Modulus as a function of supergalactic latitude, any systematic change can be interpreted as a variation due to the change in path length through the obscuring material for galaxies at different latitudes. We find no variation in extinction as a function of supergalactic latitude, which implies that we have detected no intergalactic material.

An analysis by Takase (1972) of the corrected colors for 650 galaxies in the *Reference Catalogue of Bright Galaxies* marginally showed that elliptical and S0 galaxies within 10° from the supergalactic plane are reddened with respect to galaxies at supergalactic latitudes greater than 30° by approximately 0.04 magnitude at blue wavelengths. G. deVaucouleurs *et al.* (1972) repeated this analysis and included colors for 262 additional galaxies observed at the 91-cm

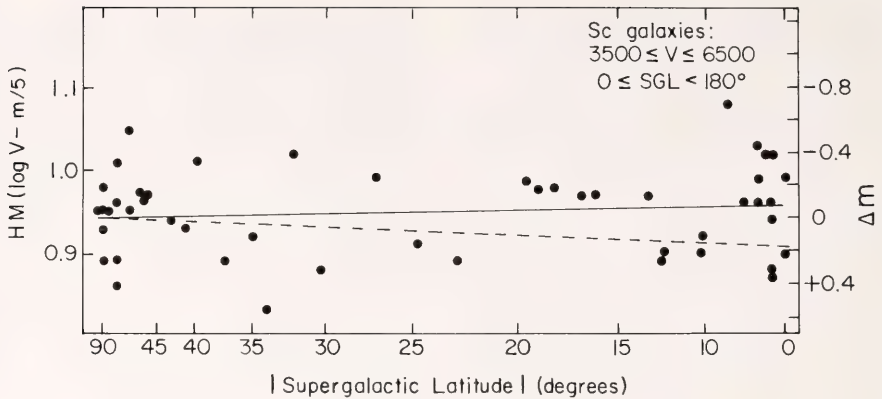


Fig. 1. Hubble Modulus for 49 Sc I galaxies at supergalactic longitude less than 180° as a function of the absolute value of supergalactic latitude. Solid line is least-squares fit to data giving total change from SG pole to SG equator of -0.07 ± 0.10 magnitudes. Dashed line is from de Vaucouleurs *et al.*, (1972), using galaxy colors, and gives a total change from SG pole to SG equator of $+0.18 \pm 0.05$ magnitudes.

McDonald reflector. Their results also marginally indicate excess reddening in the supergalactic plane for both elliptical and spiral galaxies and furthermore indicated a greater effect in the direction of the Virgo cluster.

If one assumes that the excess reddening is due to wavelength-dependent intergalactic absorption and that the reddening mechanism for galaxies in the supergalactic plane is the same as in the galaxy, then the excess reddening seen by Takase implies an excess extinction of $+0.16$ magnitude between the supergalactic plane and the pole. However, we see the not significant difference of -0.12 ± 0.08 magnitude. In Fig. 1 we plot the Hubble Modulus against the argument of the empirical reddening law derived by deVaucouleurs. The solid line is a least-squares solution to the data, while the dotted line is the effect found by deVaucouleurs *et al.*, converted from colors to blue magnitudes. Their results indicated a total extinction of $+0.18 \pm 0.05$ magnitude toward the supergalactic plane, whereas we see

-0.07 ± 0.10 magnitude. Our results imply an upper limit to the density of intergalactic material in the Local Supercluster of $10^{-31} \text{ g cm}^{-3}$, which is approximately the same as the minimum average density of the universe and therefore would at most only double the density. Therefore, the "missing matter" needed to close the universe is not in intergalactic space in a form that can cause significant extinction.

References

- deVaucouleurs, G., A. deVaucouleurs, and H. G. Corwin, Jr., Intergalactic extinction in the Local Supercluster. I. Selective extinction, *Astron. J.*, **77**, 285, 1972.
- Rubin, V. C., W. K. Ford, Jr., N. Thonnard, M. S. Roberts, and J. A. Graham, The motion of the Galaxy and the Local Group determined from the velocity anisotropy of distant Sc I galaxies. I. The data, *Astron. J.*, **81**, in press, 1976.
- Takase, B., Intergalactic reddening of galaxies, *Publ. Astron. Soc. Japan*, **24**, 295, 1972.

THE STATISTICS OF GALAXY ALIGNMENTS

K. C. Turner

From time to time in the astronomical literature, processes are inferred on the basis of the alignment of various objects. For example, a number of galaxies are found to lie along a straight line. Such alignments have been offered as evidence for the ejection of small galaxies by large ones. Quantitative estimates of the unlikelihood of such arrangements, however, have been very rare and not of high quality. An attempt to understand the probability structure of such alignments was begun some two years ago.

Extensive Monte Carlo calculations to determine the probability of finding m objects lying within a given distance of a straight line when there are N objects in a square field have been completed (see *Year Book 73*, pp. 886-887.) This approach has been necessary because the problem is quite intractable analytically. (A recently published attempt at such a calculation [Barnothy, 1974] is incorrect). Figure 2 illustrates

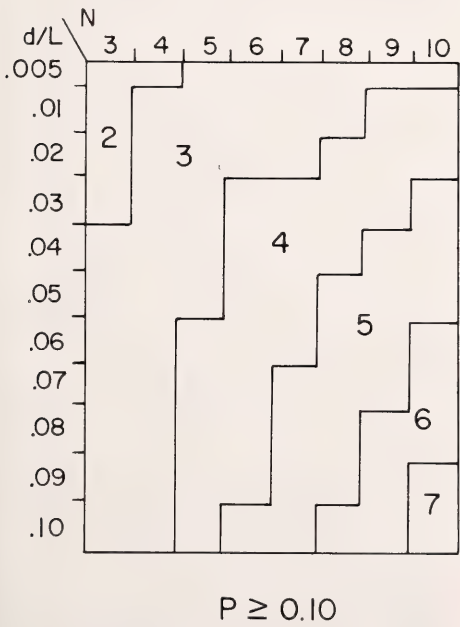


Fig. 2. Contours of N for $P \geq 10\%$.

the general nature of the results. Given the number of objects, N , and the ratio of the half width of the line to the side of the square field, the areas where one may find m objects aligned with probability greater than 10% are labeled with the value of m . Thus, for example, in a field of nine objects, the odds are greater than 1 in 10 that one can find five objects lying within 5% of the field size of some straight line. Figure 3 is a similar representation at the 1% probability level.

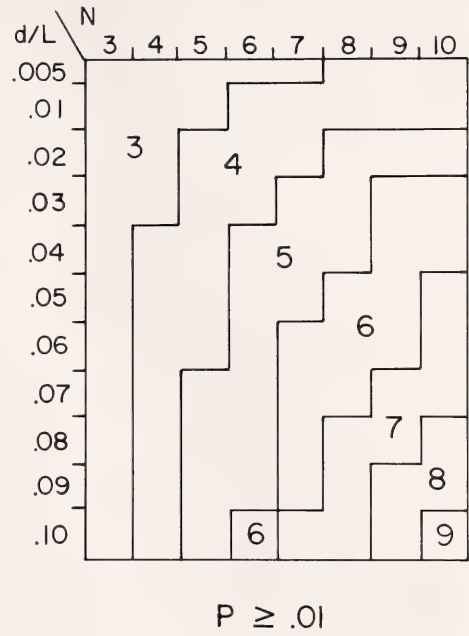


Fig. 3. Contours of N for $P \geq 1\%$.

Tables produced by these calculations have been used to make estimates of the likelihood that the alignments of galaxies proposed by Arp (1972 and references therein) as evidence for the expulsion of QSOs and galaxies from galactic nuclei are merely coincidences. In all cases examined, the probability of finding such alignments by chance has exceeded 10^{-3} . Figure 4 illustrates one such case, the region of NGC 520, a peculiar galaxy represented by the square. All quasi-stellar objects in the Parkes Catalog in this region are plotted as open circles if

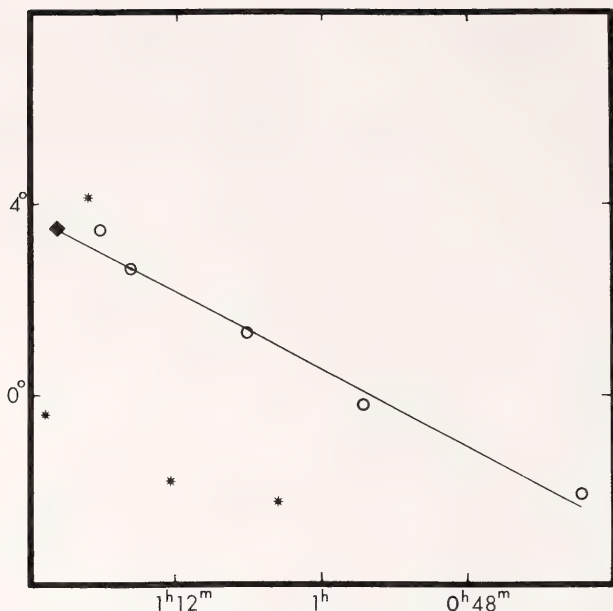


Fig. 4. Quasi-stellar objects near NGC 520.

they lie near Arp's suggested line of ejection and as filled points if they are far from the line. The field contains ten objects, six of which are near the line. The ratio of line width to the side of the area searched (calculated from distance of the farthest open circle to the line) is 0.03. The probability of finding such an arrangement by chance is 0.013 (If we eliminate the farthest point, we can reduce the accuracy ratio to 0.02, but then only five of the ten points lie on a line, and the probability becomes 0.048.)

References

- Arp, H. C., Ejection of small compact galaxies from larger galaxies, *IAU Symp. No. 44*, D. Reidel Publ. Co., New York, p. 380, 1972.
 Barnothy, M. F., The NGC 520 chain of quasars, *Astron. J.*, 79, 8, 1974.

KINEMATIC STUDIES OF NGC 3351, 3115, AND 1275

W. K. Ford, Jr., C. J. Peterson, and V. C. Rubin

A fundamental question of cosmology concerns the arrangement of mat-

ter in the universe. Is most of the mass of the universe contained in galaxies, or is there a sizable fraction of mass outside the galaxies? A second question concerns the significance of the division of galaxies into two major types. Why do some galaxies have flattened disks, contain gas, dust, and young stars in significant quantities, and usually exhibit spiral structure; while other galaxies are spheroidal, dust and gas free, generally structureless, and contain principally older, evolved stars? Answers to these questions can be approached by (1) statistical examination of large galaxy samples, and (2) studies of masses of fairly nearby typical galaxies (deduced from a detailed study of their velocity fields). It is the latter approach which has occupied part of our research efforts over the past few years.

During the last decade, significant progress has been made in observing the velocity fields and hence the masses of spiral galaxies, as measured from the emission lines in their spectra. These emission lines arise in the excited gas in each galaxy. Although the gas constitutes in general only a small

percentage of the mass of the galaxy, it is assumed that the gas is in dynamical equilibrium in the gravitational field of the stellar population, and can thus be used as a tracer of the underlying velocity pattern.

For gas-free stellar populations such as are found in the bars of barred spiral galaxies or in elliptical or S0 galaxies, velocity data are almost nonexistent and mass data are meager. During the past year, we have directed our observations toward these difficult objects, and have obtained spectra of sufficiently high quality so that we could measure the velocities of the stellar populations from the absorption lines in the integrated galaxy spectra. We report here on studies of three such galaxies: NGC 3351, a barred spiral galaxy in which for the first time it has been possible to measure the velocities of stars in a bar; NGC 3115, an E7/S0 galaxy that had been studied earlier but with contradictory results; and NGC 1275, an exceedingly peculiar galaxy whose nature has long been a puzzle.

Motions of the Stars and the Excited Gas in the Barred Spiral Galaxy NGC 3351

Although numerous studies of motions in barred spiral galaxies have been made, such studies have been restricted to the motions of the excited gas in the nuclei and in the outer spiral arms. Because of the difficulties in determining accurate velocities from stellar absorption features, no velocities for the stars in the bars had been obtained. We have now completed a study of the velocities of both the stars and the gas in the barred spiral NGC 3351, and so for the first time can describe the motions of the stars in the bar of a galaxy of this type.

NGC 3351 is one of the few bright barred spirals in the Northern sky (Fig. 5a). It is a particularly good candidate in which to search for noncircular motions of the stellar population in the bar because the galaxy is oriented on the sky with the bar only a few de-

grees from the line of sight. A spectrum taken at the 4-m telescope with the spectrograph slit aligned along the bar is shown in Fig. 5a (right). Prominent absorption lines arising from the stellar population in the bar are marked. A careful inspection of the spectrum reveals that each galaxy line is redshifted $\sim 800 \text{ km s}^{-1}$ (due to the systemic velocity of the galaxy) from a corresponding but generally weaker line at $V = 0 \text{ km s}^{-1}$. The latter lines arise from the scattered solar spectrum in the night-sky radiation. It is the high resolution of the spectrum that permits us to resolve the galaxy features from these night-sky features and to obtain accurate measures for the galaxy lines. Velocities measured along the bar indicate that the stars are moving in circular orbits around the nucleus, with velocities that increase linearly with distance from the nucleus. There is no evidence of large-scale stellar streaming motions in the bar.

Measures of both stellar and gas features in the galaxy lead to the following conclusions:

1. The nuclear region contains a ring of HII regions $r \sim 340 \text{ pc}$, which is rotating with $V_{\text{rot}} = 126 \pm 16 \text{ km s}^{-1}$ and contracting to the nucleus with $V_c = 34 \pm 11 \text{ km s}^{-1}$.

2. The stars in the bar ($r \leq 3 \text{ kpc}$) are rotating with constant angular velocity $80 \pm 20 \text{ km s}^{-1} \text{ kpc}^{-1}$. The bar is thus a quasi-stationary feature in this galaxy. There is no evidence for large-scale streaming motions of the stars in the bar, nor evidence of excited gas in the bar.

3. Beyond the region of the bar, the velocities of the HII regions within the outer ring reach a maximum of $V_{\text{rot}} \sim 220 \text{ km/s}$ at $R \sim 3\text{--}5 \text{ kpc}$ and then begin to decrease.

4. A simple mass model for the galaxy gives a total mass and angular momentum consistent with values found for normal spiral galaxies. Thus in NGC 3351 there is no indication that the presence of the bar, so prominent in optical photographs, distorts the

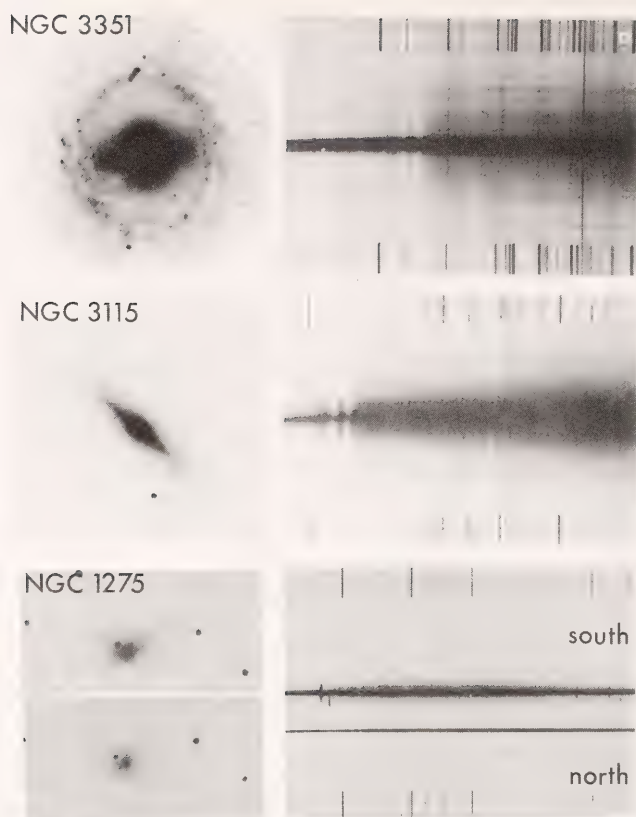


Fig. 5. Absorption line spectra from three different types of galaxies; all spectra taken with the Kitt Peak 4-m spectrograph, which incorporates a Carnegie image tube. (a) NGC 3351, a barred spiral galaxy. Spectrum of the bar shows prominent galaxy absorption lines displaced to red from corresponding lines in the night sky. (b) NGC 3115, a spheroidal (E7/S0) galaxy and a spectrum along the bar. Note the variation in velocity along the disk, indicated by the curvature in the absorption lines. Galaxy photograph courtesy of S. Strom, KPNO. (c) The peculiar galaxy NGC 1275 and a spectrum crossing the nucleus. To the south, prominent absorption lines are seen which are obscured to the north. This is attributed to the presence of an intervening galaxy. Emission lines from both galaxies (at different velocities) are seen to the north (bottom of spectrum).

large-scale gravitational field in the galaxy. The surprising result from this study is that NGC 3351 has a velocity field that appears normal, much like that of a typical nonbarred spiral galaxy.

The Rotation Curve of the E7/S0 Galaxy NGC 3115

NGC 3115 is a nearby galaxy originally classified as an elliptical. More recent photographs have revealed a flattened disk embedded in a spheroidal system (Fig. 5b). Because of its relatively high surface brightness, its large angular extent, and the presence

of a disk, it is a prime target for a study of the dynamics and kinematics of an elliptical galaxy, albeit a nontypical one. Earlier spectroscopic studies attempted to determine the rotation of these galaxies. An early one by Minkowski (1960) indicated a minimum in the circular velocities at large distances from the nucleus; a more recent study by Williams (1975) failed to reveal the minimum, but his data showed a large scatter in the measured velocities.

We have obtained two spectra of very high resolution along the major axis of the galaxy (Fig. 5b), using the 4-m

Mayall telescope with Carnegie image tube spectrograph. Measurement of the positions of 14 absorption features of CaII, FeI, H, MgI, and CrI as a function of distance from the nucleus gives rotation curve data with extremely small statistical errors (Fig. 6). The central angular velocity is $17.5 \pm 1.0 \text{ km s}^{-1} \text{ arcsec}^{-1}$. The velocity curve rises rapidly, but beyond 20 arcsec it remains level at $V \simeq 270 \text{ km s}^{-1}$. Although we intend to obtain additional observations at greater distances from the nucleus before making a final mass model, we can draw some preliminary conclusions based on an extremely simple model. A spheroid of axial ratio $c/a = 0.4$ and density distribution given by $\rho = 9 \times 10^{10} [1 + r/0.2]^{-2.1}$ will reproduce the flat rotation curve outside of the nucleus. An additional nuclear mass of some $10^9 M_{\odot}$ is implied by the shape of the rotation curve and the velocity dispersion: The mass out to $r = 5 \text{ kpc}$ is about $7 \times 10^{10} M_{\odot}$. The projected surface density of the adopted spheroid gives a mean surface brightness as a

function of distance from the nucleus which is too bright near $r = 5 \text{ kpc}$ compared with the observed surface brightness (Strom *et al.*, 1976). Hence the mass-to-light ratio of the integrated starlight must increase by a factor of 3 or 4 from $r = 1$ to $r = 5 \text{ kpc}$ in the disk. We will attempt to use this variation, together with the observed radial gradient in color, to model the dynamical and chemical history of the galaxy.

The distance of NGC 3115 is uncertain. It does not appear to be a member of any clearly definable group of galaxies, and its systematic velocity of 395 km s^{-1} (corrected for the motion of the sun and Galaxy in the Local Group of Galaxies) is too small to give an accurate distance estimate by use of the Hubble law. Minkowski (quoted by Williams 1975) gives a distance of $D = 6.6 \text{ Mpc}$ based on the apparent brightness of the globular clusters associated with the galaxy. We have adopted a distance of $R = 10 \text{ Mpc}$ for our calculations.

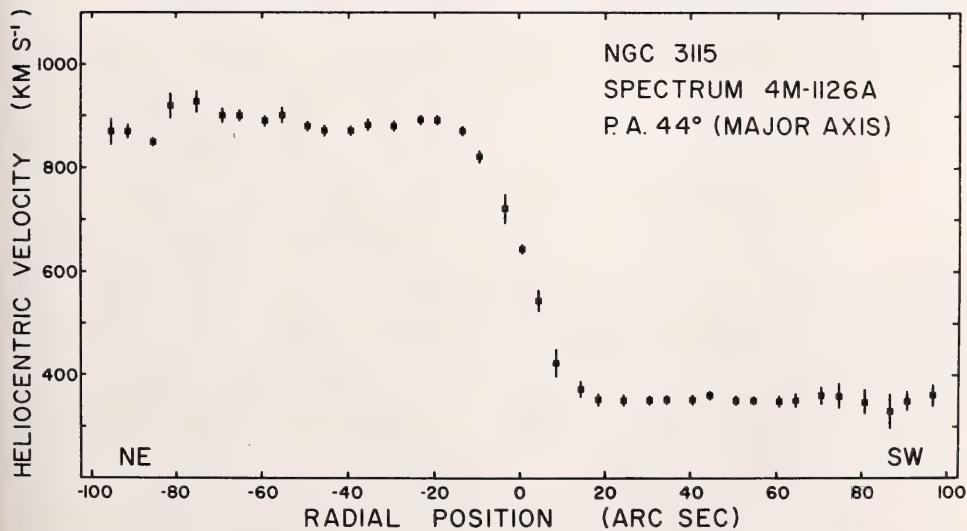


Fig. 6. The observed velocity in the E7/S0 galaxy NGC 3115 as a function of distance from the nucleus. Each data point represents the mean velocity over a radial range of 5'' from measurements of stellar absorption lines due to CaII, CaI, FeI, MgI, CrI, and H.

The Peculiar Galaxy NGC 1275

NGC 1275 (Perseus A) is one of the most peculiar objects in our region of the universe. Twenty years ago, Minikowski (*Year Book* 54, p. 25) discovered in its spectrum two sets of emission lines, one set with a redshift of $V \sim 5200 \text{ km s}^{-1}$ and a second with $V \sim 8200 \text{ km s}^{-1}$. Since that time NGC 1275 has been interpreted as either an exploding galaxy or a collision between two galaxies. In order to study the underlying stellar population and the excited gas in NGC 1275, an extensive body of spectroscopic and photographic material has been obtained at the 2.1-m and 4-m telescopes of Kitt Peak National Observatory. Analysis of this material in collaboration with Professor J. H. Oort leads to the following conclusions:

1. The luminosity profile of the stellar continuum (see Fig. 7) shows that

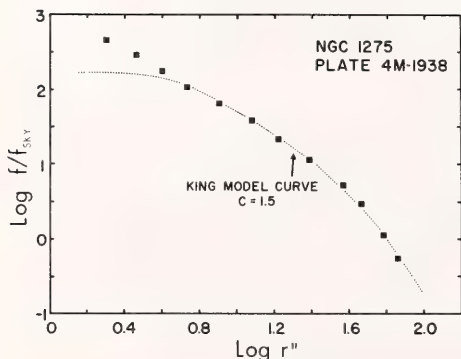


Fig. 7. The luminosity profile of the continuum light from NGC 1275, from an east-west trace. The plate is a 144-min exposure at the prime focus of the 4-m Mayall telescope, N_2 -baked 0.98 emulsion + $\lambda 6558$ filter; FWHM 92Å. In the passband of this plate and filter combination, there is no light from emission in either velocity system in the galaxy. The ordinate is the logarithm of the surface brightness, f , of the galaxy in units of the surface brightness of the sky. The abscissa is the logarithm of the radius in seconds of arc. The dashed line is a profile from the dynamical models of King (1966) with concentration parameter $C = 1.5$. The surface brightness (solid squares) diverges from the model curve at small radii ($r < 4''$) due to an unresolved component in the nucleus of the galaxy.

the main galaxy is spheroidal (Fig. 5c). A strong absorption line spectrum is seen at $V = 5200 \text{ km s}^{-1}$, which agrees with the velocity of the extensive filamentary material surrounding the galaxy. South of the nucleus is a strong A-type absorption line spectrum; to the north the Balmer lines are obscured. Emission lines of H, O, and N are also seen (Fig. 5c).

2. Emission patches at $V = 8200 \text{ km s}^{-1}$ over the northern part of NGC 1275 are associated with obscuration that hides the stellar continuum of the underlying galaxy. The pattern of velocities in the high-velocity system (Fig. 8) shows a fairly smooth transition from velocities near 8100 km s^{-1} in the east to velocities of 8400 km s^{-1} in the west. This pattern is consistent with that expected from a late-type galaxy rotating with a maximum velocity of $V_{\text{max}} = 150 \text{ km s}^{-1}/\sin(\text{inclination angle})$. In addition, the emission line ratios seen in this high velocity gas are typical of large, low-density HII regions observed at large distances from the nucleus in late-type galaxies. No stellar absorption lines have been found associated with this system. This high-velocity gas is in front of the low-velocity system.

NGC 1275 is at the center of the Perseus cluster of galaxies. A count of galaxies in the central region of the cluster suggests that the probability of finding a spiral galaxy within $30''$ of the nucleus of NGC 1275 has the reasonably high value of $1/30$.

3. NGC 1275 is a strong radio source as well as a strong infrared and strong x-ray source. This plus the optical appearance of the low-velocity filamentary material, reminiscent of the Crab Nebula supernova remnant in our own Galaxy, implies that the object has undergone a violent event in the past. The A-type stellar spectrum indicates that a burst of stellar formation was associated with this event. It is likely that the time scale required for the dispersal of material into the low-velocity filament system is longer than the time scale over which the two

NGC 1275 HIGH VELOCITY SYSTEM

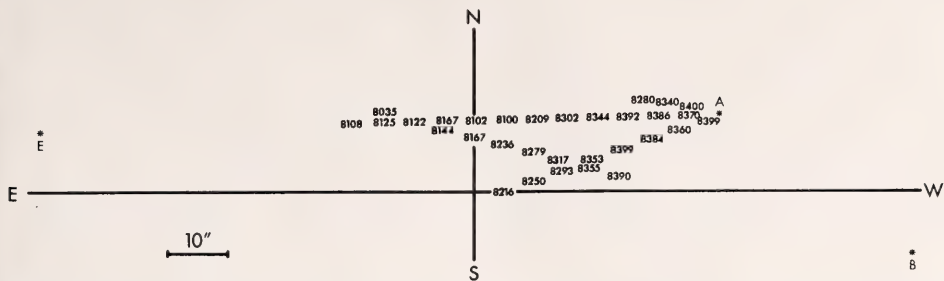


Fig. 8. Observed velocities in the high velocity system in the galaxy NGC 1275. The coordinate system is centered at the nucleus of the early-type galaxy. High velocity gas is seen only in the northern section of this peculiar object. The smooth variation in observed velocity from east to west is consistent with that expected from an almost edge-on galaxy, rotating with a maximum velocity near 200 km s^{-1} .

galaxies may have been in gravitational interaction (the two objects are still approaching each other); thus, the presence of the second galaxy cannot have triggered the explosion in the underlying galaxy. Hence our interpretation of the NGC 1275 phenomenon requires both an explosive event in the elliptical galaxy and a high-excitation late-type intervening galaxy. While it is unlikely that the two main galaxy masses are interacting, it is still possible that an energetic nuclear source in the underlying elliptical may be the source of excitation for the high-excitation spectrum observed in the late-type galaxy.

Moderately peculiar galaxies are commonplace in the universe. Severely peculiar galaxies are less so, but the attempt to understand them has led some astronomers to question whether yet unknown laws of physics govern their behavior. Our observations of NGC 1275 show that individual properties, i.e., the luminosity profile of the underlying galaxy, the observation of the northern part, the velocity and line-intensity pattern of the high velocity system, all can be understood in terms of previously known characteristics of galaxies. Such is the progress of astronomy. Only when detailed studies reveal characteristics that are outside the realm of previously observed prop-

erties of galaxies can we properly appeal to an unknown physics.

References

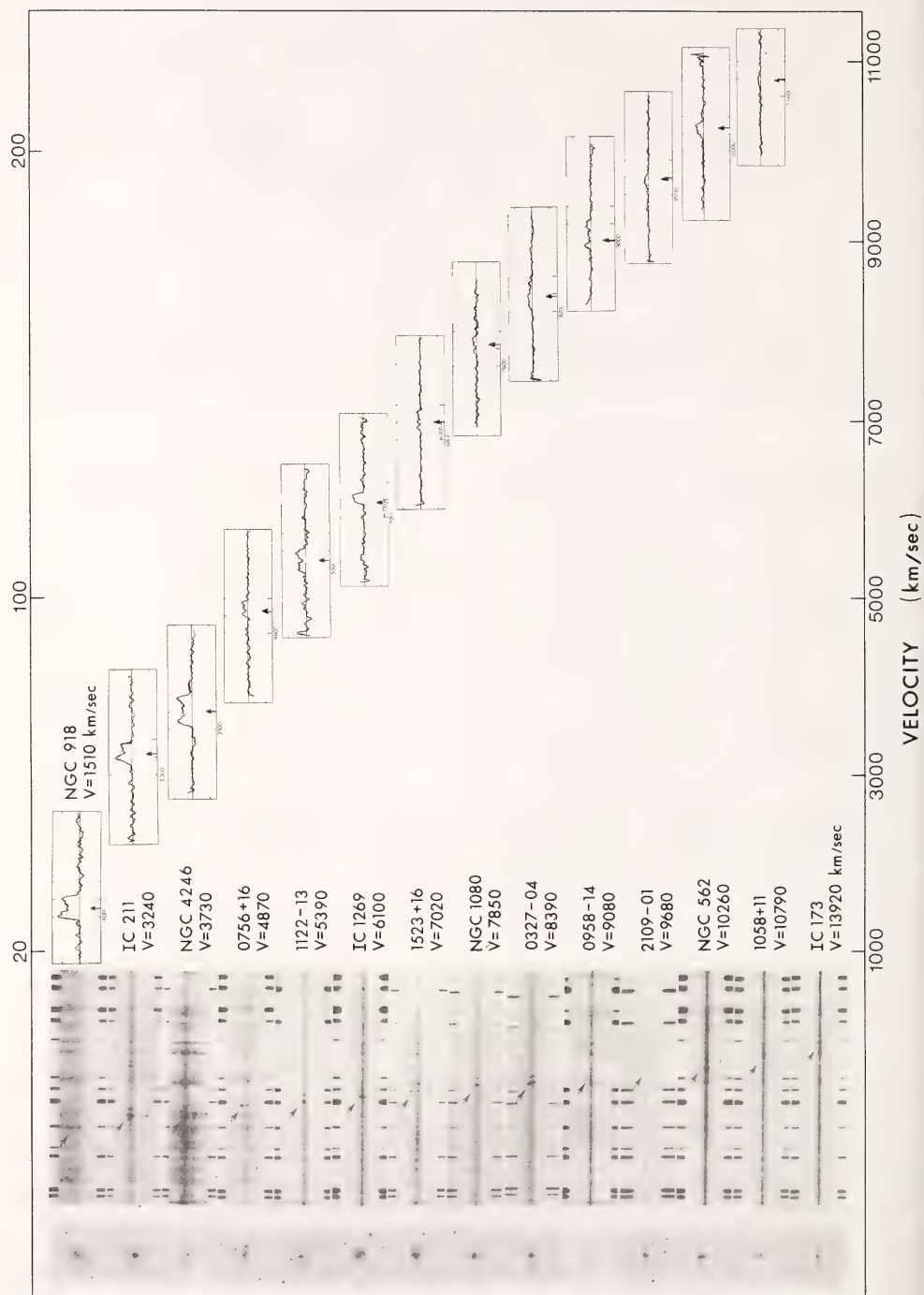
King, I. R., The structure of star clusters III. Some simple dynamical models, *Astron. J.*, 71, 64, 1966.
Minkowski, R., Problems of extragalactic spectroscopy, *Ann. Astrophys.* 23, 385, 1960.
Strom, S. E., K. M. Strom, J. W. Goad, F. J. Vrba, and W. Rice, Color and metallicity gradients in E and S0 galaxies, *Astrophys. J.*, 204, 684, 1976.
Williams, T. B., The rotation curve of NGC 3115, *Astrophys. J.*, 199, 586, 1975.

AN ILLUSTRATION OF GALAXY REDSHIFTS

W. K. Ford, Jr., C. J. Peterson, V. C. Rubin, and N. Thonnard

In connection with the observing program to study the radial velocities of high-luminosity spiral galaxies, we have obtained optical and 21-cm radio spectra of a homogeneous sample of galaxies. Figure 9 has been constructed to illustrate the effect of increasing redshift with distance, using both the optical $H\alpha$ and the 21-cm hydrogen lines. Photographs of the galaxies, all at the same scale, are copied from the National Geographic Society-Palomar Observatory Sky Survey prints.

DISTANCE IN MILLIONS OF PARSECS ($H = 50$ km/sec per Mpc)



The optical spectra of the Northern Hemisphere galaxies were obtained with the 84-inch (2.1-meter) reflector of Kitt Peak National Observatory, and spectra of the Southern galaxies with the 60-inch (1.5-meter) reflector at the Cerro Tololo Inter-American Observatory near La Serena, Chile. A two-stage Carnegie image tube was incorporated into each spectrograph. The spectra are reproduced here as negatives; dark features indicate emission. Wavelength increases toward the right. In each spectrum, the horizontal band is the spectrum from the integrated starlight in the nucleus. The superimposed emission knots arise from the hot gas in the nucleus and in regions of ionized gas surrounding young massive stars in the spiral arms. The principal emission line is $H\alpha$, indicated by the arrow.

The $H\alpha$ emission arises when an electron in an excited atom makes a transition from the $n = 3$ to the $n = 2$ orbit. The wavelength of the emitted light, 6563\AA , corresponds to 6.563×10^5 cm. In contrast, the neutral hydrogen emission at 21 cm (a wavelength 3×10^5 larger than that of $H\alpha$) occurs when the electron in the hydrogen atom reverses its spin with respect to the spin of the nucleus. Because neutral hydrogen is a significant component of the interstellar material and hence of the total mass of an Sc I galaxy, the 21-cm line can be observed in these galaxies even though the spin reversal in an individual atom is a rare event.

The theoretical resolving power of a telescope is a measure of the diameter of the telescope in units of the wavelength of the observed light; the size of the 84-inch (2.1-m) is $2.1 \text{ m} / 6.563 \times 10^5 \text{ cm} = 3 \times 10^6$ $H\alpha$

wavelengths. In practice, however, the limiting resolution is set by the turbulence of the atmosphere, and the resolving power is generally about $1''$, or 2×10^5 . To observe a galaxy at a wavelength of 21 cm with the equivalent resolving power would require a telescope of $21 \text{ cm} \times 2 \times 10^5 = 40 \text{ km}$, or about 25 miles. Lacking this, we have used the largest single telescope at the National Radio Astronomy Observatory, the 300-foot (91-m), which gives a resolving power of $91 \text{ m} / 21 \text{ cm} = 4 \times 10^2$, or only 1/500th that of the 84-inch telescope. Hence, instead of resolving $1''$ in the galaxy, the radio telescope integrates over about $10'$ of the sky.

With the 300-ft transit telescope equipped with a new low-noise cooled receiver, we have obtained spectra of program galaxies with velocities up to $V = 10,800$, or $\Delta\lambda/\lambda = 0.036$. The galaxy with the largest redshift, $1058+11$, is the most distant one thus far for which the 21-cm emission line has been detected. The galaxy velocity V is adopted as the midpoint of the intensity profile; the arrow beneath each profile marks the optical velocity. In general, the optical and the 21-cm velocities agree well. Where they do not, the difference might represent a difference in the velocity of the excited hydrogen in the nucleus compared with the mean velocity of the neutral hydrogen throughout the galaxy. More likely, the velocity difference reflects uncertainties in the optical and 21-cm velocities. The general agreement of the two velocities over a wavelength range of 3×10^5 is a stringent test of the wavelength invariance of the Doppler expression.

The final adopted velocity V for each galaxy is listed in Fig. 9. With a value

Fig. 9. A new illustration of the Hubble recession of the galaxies, showing both optical and radio spectra for 13 spiral galaxies. The galaxy photographs are reproduced from the *National Geographic Society-Palomar Observatory Sky Survey*. The optical spectra were taken with an image tube spectrograph on the 84-in (2.1-m) reflector at Kitt Peak National Observatory or the 60-in (1.5-m) reflector of the Cerro Tololo Inter-American Observatory near La Serena, Chile. The 21-cm observations were taken with the 300-ft (91-m) transit telescope of the National Radio Astronomy Observatory. With increasing distance from the observer, the emission line of $H\alpha$ in the optical spectra and the 21-cm line in the radio spectra are shifted farther toward longer wavelengths (right).

for the expansion parameter of $H = 50$ km s⁻¹ Mpc⁻¹, the distance of each galaxy is found from $V/50$. These distances are indicated at the top of Fig. 10. Because the value of H is still uncertain, the indicated distances will have to be changed if the value for H is revised.

THE IRREGULAR GALAXY WLM AND ITS SURROUNDINGS

N. Thonnard

Irregular galaxies frequently have neutral hydrogen envelopes that are considerably larger than their optical image. Recently, a large band of extragalactic neutral hydrogen, a few degrees wide and extending nearly 180° across the sky, was discovered by Mathewson *et al.* (1974). They named it

the Magellanic Stream, as one end of it was in the direction of the Magellanic Clouds. It was soon realized that many irregular galaxies were close to the stream, and it was even suggested that some of the concentrations in the stream might be "proto-galaxies" that had not yet formed stars. Observations made in 1973 with the 100-foot CIW-IAR* radio telescope in Argentina (*Year Book 73*, pp. 918-919) of WLM a low surface brightness irregular galaxy, similar in many respects to the Large Magellanic Cloud but much smaller in angular size—indicated that the neutral hydrogen extent is considerably larger than the optical image. In addition, a large concentration of neutral hydrogen at approximately the

*Carnegie Institution of Washington-Instituto Argentino de Radioastronomía.

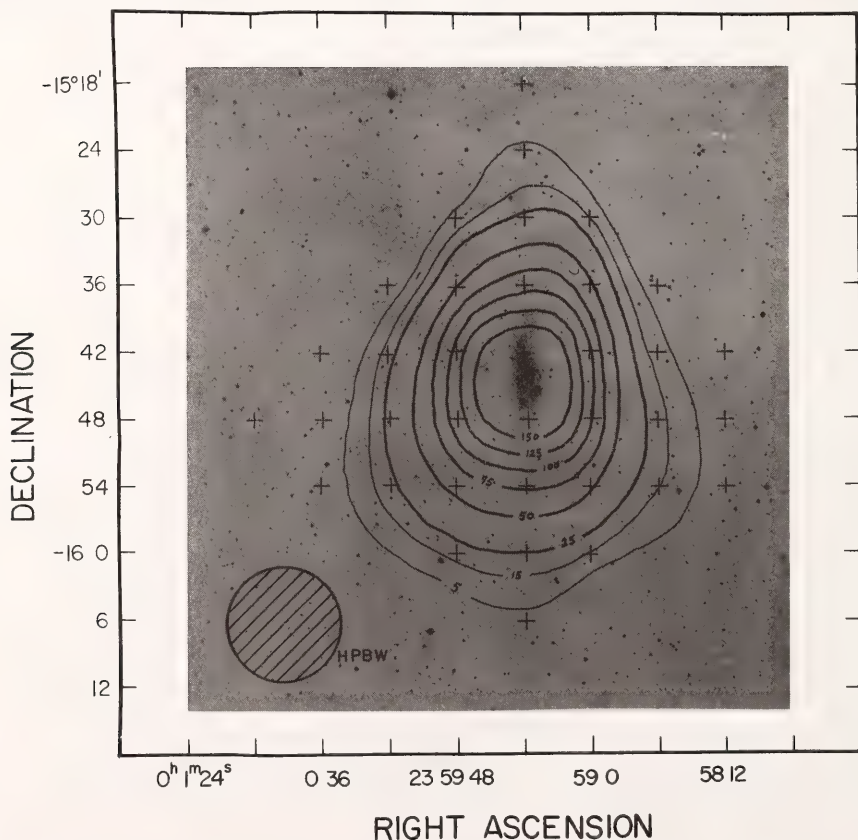


Fig. 10. Contours of neutral hydrogen integrated flux density in Jy km s⁻¹ superimposed on the optical image of WLM.

systemic velocity was seen in the vicinity of WLM, which in retrospect was realized to be part of the Magellanic Stream. To study the neutral hydrogen structure of WLM and to attempt to understand its relationship with the Magellanic Stream, it was decided to make higher resolution and higher sensitivity observations with the facilities of the National Radio Astronomy Observatory (NRAO).

The WLM galaxy was mapped with the 300-foot transit telescope at NRAO on a 6×6 arcmin grid. Figure 10 is a contour map of the integrated neutral

hydrogen distribution of the galaxy superimposed on a high-contrast copy of the National Geographic Society-Palomar Observatory Sky Survey blueprint. Note the large extent of the neutral hydrogen contours compared with the optical image, especially at the southern end of the galaxy. At the northern end, there is some suggestion that the hydrogen contours are distorted westward in the same sense as the "kink" in the optical image. Profiles from cuts through the major and minor axes are shown in Fig. 11a and Fig. 11b. The rotation of WLM can

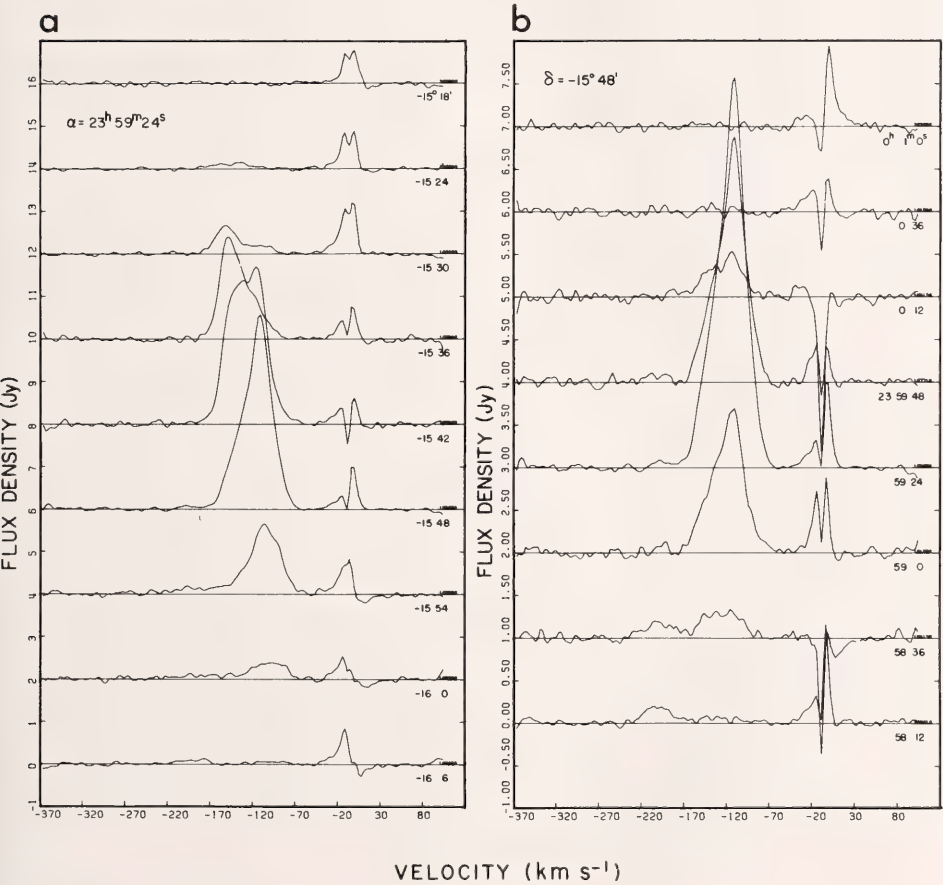


Fig. 11. (a) Velocity profiles along the major axis of WLM. The declination is indicated at the right of each profile. (b) Velocity profiles along the minor axis of WLM. The right ascension is indicated at the right of each profile. Note that the intensity scale is twice as sensitive as in Fig. 12a.

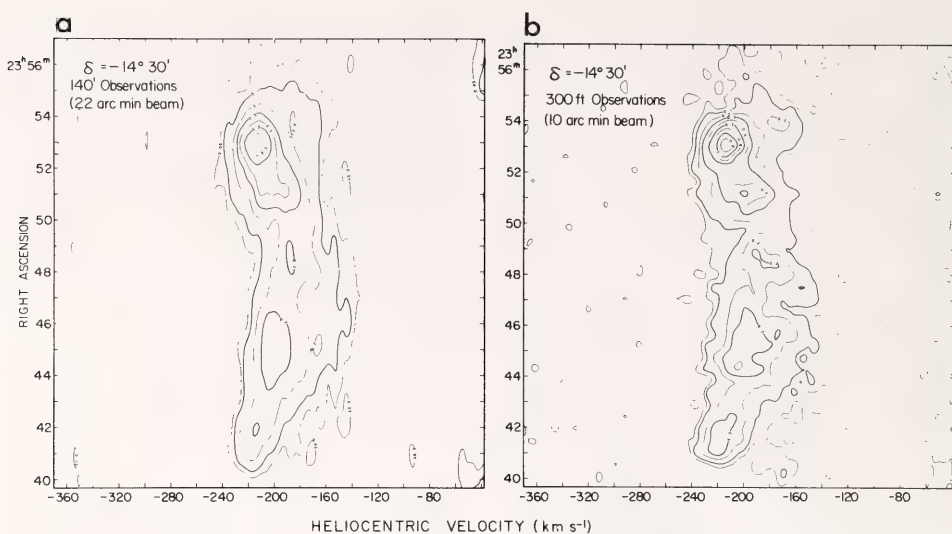


Fig. 12. (a) Position-velocity map at $\delta = -14^\circ 30'$ in the vicinity of WLM observed with the 140-ft telescope. (b) Identical map, but observed with the 300-ft telescope. The intensity scales were normalized on the broad feature at $23^h 45^m$.

readily be seen in the velocity shift of the profiles from approximately -80 km s^{-1} to -190 km s^{-1} along the major axis. The weak signals at $\sim -200 \text{ km s}^{-1}$ seen at the southern and western edges are due to the eastern edge of the Magellanic Stream; the peaks at zero velocity are from neutral hydrogen in our own galaxy.

The total neutral hydrogen integrated flux density for WLM is $446 \text{ Jy}^* \text{ km s}^{-1}$. Using a distance of 2 Mpc to WLM, (Ables, 1974) the total neutral hydrogen mass is $4.2 \times 10^8 M_\odot$. From the velocity width of the profiles and approximate inclination for the galaxy derived from the neutral hydrogen contours, the total mass of WLM is $3 \times 10^9 M_\odot$. Therefore, WLM is about half as massive as the Large Magellanic Cloud but contains more than three fourths as much neutral hydrogen as the LMC, indicating it is a rather normal irregular galaxy.

A $5^\circ \times 3^\circ$ region around WLM was also mapped with the NRAO 140-foot

telescope on a 15×15 arcmin grid to see the fine structure of the Magellanic Stream and determine its relationship with the galaxy. One cut in right ascension was also made with the 300-foot telescope to determine the minimum size of some of the features. The analysis of these observations is just beginning, but the remarkable similarity between Fig. 12a and Fig. 12b indicates that most features are completely resolved with a 20-arcmin beam. Even for the "hot" spot at $\alpha = 23^h 53^m$, one can estimate from the difference in peak signal between the two telescopes that its angular dimensions are not much smaller than approximately 30 minutes of arc. Therefore, the hydrogen in the Magellanic Stream in the vicinity of WLM is of much lower concentration and of much larger angular extent than in the galaxy itself.

References

- Ables, H. D., private communication, 1974.
 Mathewson, D. S., M. N. Cleary, and J. D. Murray, *The Magellanic Stream, Astrophys. J.*, **190**, 291, 1974.

*1 jansky (Jy) = $10^{-26} \text{ W m}^{-2} \text{ Hz}^{-1}$.

THE NUCLEUS OF M31

W. K. Ford, Jr., C. J. Peterson, and V. C. Rubin

There are very few galaxies sufficiently close so that their nuclear regions can be studied in detail. M31, the Andromeda Nebula, is a major exception. The limiting resolution generally available on earth, 1", subtends 3 pc on M31. (In our Galaxy, at the position of the sun, a sphere of radius 3 pc contains only about ten known stars; at the nucleus of M31, a comparable region contains about 10^6 stars.) High-resolution photographs of M31 can supply details of galactic structure with high spatial resolution. Above the atmosphere, still higher resolution can be obtained; a recent Stratoscope balloon flight photographed the nucleus of M31 with a resolution of 0''.2 (Light, Danielson, and Schwarzschild 1974). A major result of these observations is an indication that the position angle of the major axis of M31 is not constant with distance from the nucleus but apparently rotates with increasing nuclear distance. If this apparent change in the

major axis arises from the presence of absorbing clouds and lanes near the nucleus, then it has no important relevance to the dynamics of M31. However, if the observations reflect a true tilt of the angular momentum vector of the nucleus with respect to the disk, this fact may be an important piece in the puzzle of what relation the nucleus bears to the structure and dynamics of the outer disk of a fairly normal galaxy.

Because the earlier observations cover only a limited range in r , we have obtained a sequence of direct narrow-band red photographs of the nucleus of M31 with a Carnegie image tube at the Ritchey-Chrétien focus of the 4-m telescope with a large spatial scale (6''/7 mm). We have fitted ellipses to the isophotes to determine the alignment of the major axis as a function of radius. In Fig. 13, we show our data together with previous measures. In the region from $r = 0''.2$ to $r \approx 1000''$, the position angle of the major axis decreases uniformly from $PA \sim 70^\circ$ to $PA \approx 40^\circ$.

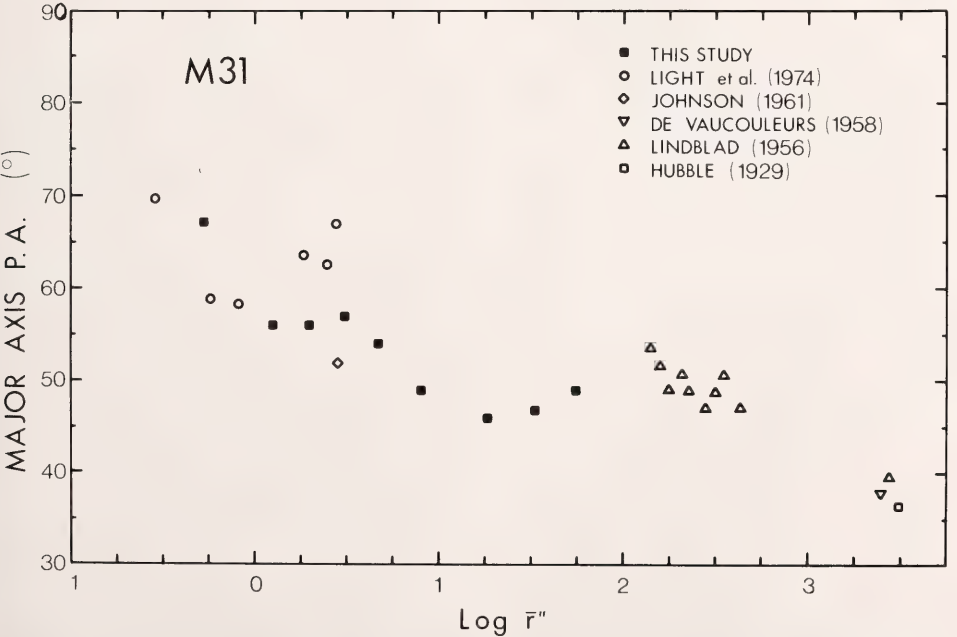


Fig. 13. The alignment of the major axis as a function of radius for the Andromeda Nebula.

It is not possible to deduce the cause of this variation from our results. However, from a similar set of observations in a different spectral region it would be possible to separate dynamical effects from absorption effects because of the wavelength dependence of absorption.

References

- Johnson, H. M., The nucleus of M31, *Astrophys. J.*, 133, 309, 1961.
 Light, E. S., R. E. Danielson, and M. Schwartzchild, The nucleus of M31, *Astrophys. J.*, 194, 257, 1974.

STAR COUNTS IN GLOBULAR CLUSTERS

C. J. Peterson

A resurgence of interest in globular clusters has occurred in the last few years. A primary factor has been the totally unexpected discovery (Clark *et al.*, 1975; Canizares and Neighbors, 1975) that several clusters are the sources of variable x-ray emission. The role of the globular clusters in the study of the Galaxy is important: The numerous cluster color-magnitude diagrams that have recently become available have permitted a reassessment of the scale of the Galaxy (Harris 1975), and other spectroscopic and photometric studies are being interpreted in terms of the evolution of the chemical abundances in the Galaxy.

As part of a long-term study of the globular cluster system (*Year Book 74*, pp. 133–135), star counts have been obtained in 27 clusters, using available photographic material in the plate collections of David Dunlap Observatory, Hale Observatories, and Ray White at Steward Observatory. The derived distribution of stars (log surface density versus log radius) is shown in Fig. 14 for four representative clusters. The observed data has been fitted with theoretical curves from self-consistent dynamical models (King 1966); these model curves depend on three param-

eters. The core radius r_c is the radius at which the observed surface density has dropped to one half the central value; it is closely related to the binding energy of the cluster. The tidal or limiting radius r_t defines the "edge" of the cluster; this limit is imposed upon the cluster by the gravitational tidal field of the Galaxy during the closest approach of the cluster to the Galactic Center. A third parameter indicates the brightness scale of the cluster and may be either the central surface brightness m_0 or the total brightness of the cluster m_t . The lack of correlation between r_c , r_t , and either scale factor m_0 or m_t shows that three parameters are indeed necessary to define the structure of any given cluster.

The statistical distributions of these data quantities, as well as their correlations with other cluster properties and with the spatial position in the Galaxy of the clusters, are the result not only of the formative process of the Galaxy but also of the subsequent dynamical evolution of the clusters individually and within the framework of the Galaxy as a whole. In principle, therefore, these data hold clues to distinguish between the two models that have been proposed for the origin of the cluster system. The first, proposed by Peebles and Dicke (1968), suggests that the clusters formed very early in the history of the universe. At a later epoch galaxy formation occurred and in that process the clusters became spatially associated with the much more massive galaxies. The alternative hypothesis suggests that the clusters formed coevally with the initial collapse of the material that was to form the Galaxy. Neither theory, however, has advanced to the point where either general or specific predictions of cluster properties have been made.

Any theory of the formation and evolution of the cluster system must be consistent with the following properties of the cluster system:

1. The three structural parameters do not correlate with each other or with

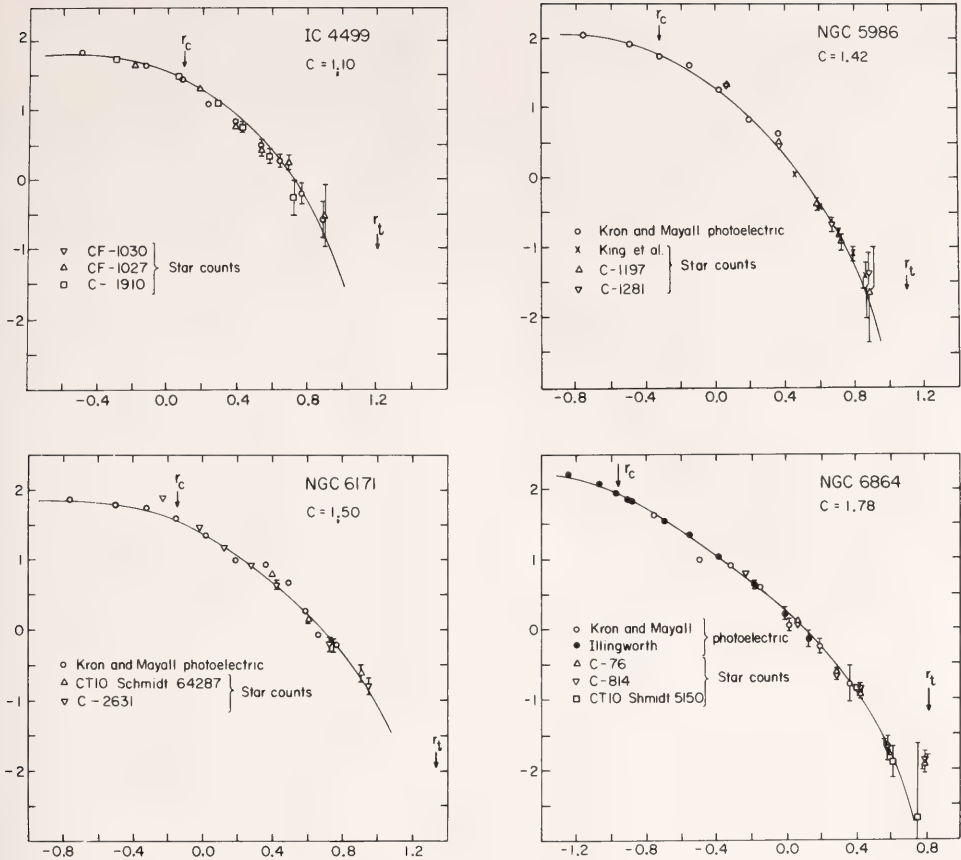


Fig. 14. Surface density profiles for a representative set of four globular clusters. The data represents star counts and concentric aperture photoelectric photometry. The ordinate is the logarithm of the surface density (stars per unit area in arbitrary units), and the abscissa is the logarithm of the radius in minutes of arc. The solid line in each figure is a theoretical surface density profile from the dynamical models of King (1966). Core and tidal radii are indicated as well as the concentration class ($c \equiv \log r_t/r_c$) for each cluster.

other cluster properties (e.g., color, metallicity, HR diagram morphology) which are related to the stellar population of the cluster.

2. There is no correlation between the concentration class (defined as $c = \log r_t/r_c$) of a cluster and its position in the Galaxy. There is, however, a general tendency for clusters with large core radii (i.e., weakly bound clusters) to be absent from the center of the Galaxy. This is not unexpected, as these weakly bound clusters would be preferentially disrupted near the center of the Galaxy by the strong galactic

gravitational tidal field. Because the limiting radius r_t is set by the tidal field of the Galaxy, larger clusters tend to be found farther from the Galactic Center.

3. As the radial extent of a cluster is set by the tidal field of the Galaxy at that point in the cluster orbit where the gravitational forces are strongest, this datum (r_t) can be used to determine the closest approach of the cluster to the Galactic Center. This gives a fifth orbital parameter which, when combined in a statistical analysis with the three components for the present

position of the cluster and its observed line-of-sight velocity, yields the distribution of orbital eccentricities for the cluster system (Fig. 15). This distribution is consistent with an isotropic velocity distribution (i.e., the dependency on velocity of the phase space distribution function $f(\bar{r}, \bar{v})$ goes only as $|\bar{v}|^2$); this result has one immediate consequence of great importance. As the clusters range to great distances from the Galaxy, they are the best objects to use for the study of the effect of the total gravitational field of the Galaxy. With this conclusion, more stringent limitations can be applied to the theoretical analysis of the positions and velocities of the clusters which will yield a more accurate estimate for the total mass of the Galaxy.

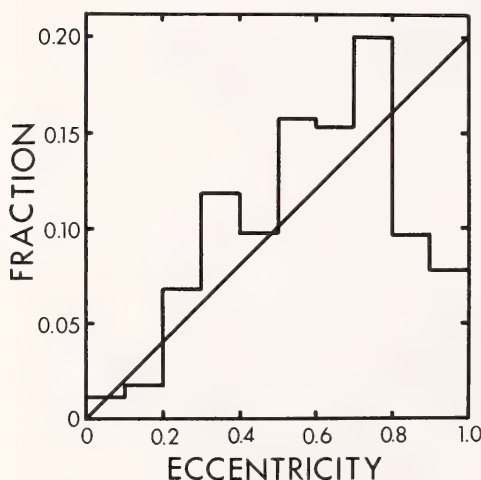


Fig. 15. A histogram showing the distribution of orbital eccentricities computed from the data for 61 globular clusters. The straight line is the distribution of eccentricities expected if the phase space distribution $f(r, v)$ for the clusters is isotropic in velocity.

References

- Canizares, D. R., and J. E. Neighbors, Observation of a bright variable x-ray source in a globular cluster, *Astrophys. J. (letters)*, 199, L97, 1975.
- Clark, G. W., T. H. Markert, and F. K. Li, Observations of variable x-ray sources in globular clusters, *Astrophys. J. (letters)*, 199, L93, 1975.
- Harris, W. E., Distance to the galactic center measured from globular clusters, *Bull. Amer. Astron. Soc.*, 7, 436, 1975.
- King, I. R., The structure of star clusters. III. Some simple dynamical models, *Astron. J.*, 71, 64, 1966.
- Peebles, P. J. E., and H. R. Dicke, Origin of the globular star clusters, *Astrophys. J.*, 154, 891, 1968.
- ### NEUTRAL HYDROGEN SUPERNOVA REMNANT STUDY
- G. E. Assousa
- The survey of old galactic supernova remnants (SNR) at 21 cm reported earlier (Assousa and Erkes, 1973; Assousa, Balick, and Erkes, 1974) was carried out to study interaction of SNRs with the interstellar medium, and in particular to test the hypothesis that SNRs accrete a shell of interstellar material during the last phase of their evolution. This is the phase of the SNR's history during which the remnant expands while conserving momentum but not kinetic energy. The onset of this phase is characterized by a shock velocity of 200 km/s (Woltjer, 1972) and ends when the shock velocity becomes comparable to the random interstellar gas motions, i.e. ~ 10 km/s.
- Although in principle, estimates of the mass accreted by the SNR can be made on the basis of the Sedov-Oort Solution (Woltjer, 1972), it could not be calculated without knowing both the SNR's radius and its expansion velocity.
- Until recently, only two large remnants, Cygnus Loop and HB21, with filament expansion velocities below 200 km/s., had been measured. To date we could only verify the existence of expanding fragmentary neutral hydrogen shells in the vicinity of two remnants: HB21 (Assousa and Erkes, 1973) and S147 (Assousa, Balick, and Erkes, 1974). We have obtained their

masses and expansion velocities. We found marginal evidence for a shell associated with the Cygnus Loop (Assousa, Balick, and Erkes, 1974) and W41 (Assousa, 1975). A detailed study of 3C396.1, W50, CTB 63, W63, CTB 1, HB 3 and HB 9, and PKS 0607+17 shows no evidence for any shell structure. The remaining objects CTB 72, CTA 1, CTB 13, VRO 4205.01, and OA 184 have been partially analyzed, but even for these objects, with the exception of VRO 4205.01, there appears little evidence for HI which we are able to detect with present instrumental sensitivity (peak-to-peak noise 0.3° K).

The absence of these shells, initially puzzling, becomes understandable, at least for some remnants, with the availability of filamentary velocity data (Lozinskaya, 1975). Knowledge of

these velocities and the radii of the SNR allows us to make the mass estimates. Table 1 lists in columns 1 through 9 the object name, longitude and latitude of object, distance to object (R) in kpc, filament or shell velocity (V) in km/s; radius (r) in pc; interstellar density (ρ_0) in H atoms/cm³, accreted mass (\mathfrak{M}) in \mathfrak{M}_\odot , age (t) in 10³ yr, and initial explosion energy (E_0) in 10⁵⁰ ergs.

Given R and V , the interstellar medium density ρ_0 is uniquely defined by the Sedov (adiabatic-energy conserving phase)–Oort (isothermal-momentum conserving phase) solution (Woltjer, 1972) for an initial explosion energy of 1×10^{50} ergs. The family of solutions for $\rho = 0.01, 0.1, 1.0$, and 10.0 H atoms/cm³ is given in Fig. 16. Examination of the mass column shows

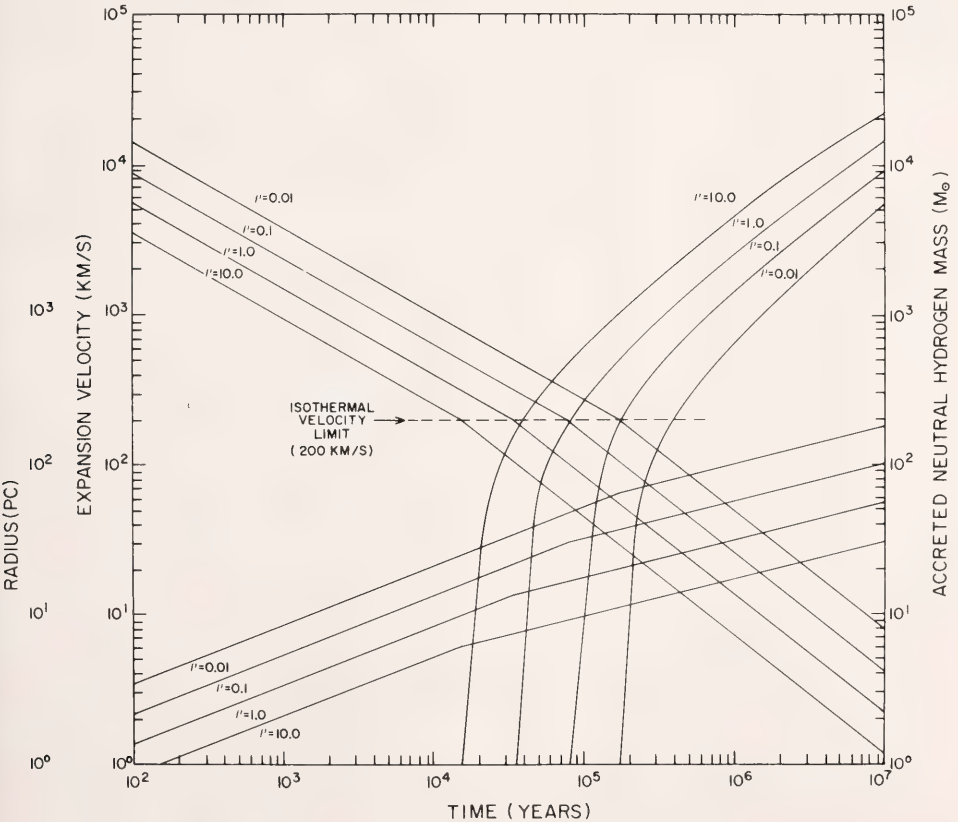


Fig. 16. The evolution of a 1×10^{50} erg SNR. The family of curves represents the expansion velocity vs. time (double-slope lines, decreasing), radius vs. time (double-slope lines, increasing), and accreted mass vs. time for a range of ISM densities.

TABLE 1. Observed and Calculated Parameters for Supernova Remnants

| Object | l_z/b_z | R (kpc) | V (km/s) | | | r (pc) | | | ρ_0 (cm ⁻³) | | | $M(M_\odot)$ | | | $t(10^3 \text{ yr})$ | | | $E0(10^{50} \text{ ergs})$ | | |
|-------------|------------|-----------|------------|-----|--------|----------|-----|-----|------------------------------|----------|-----|--------------|------------|-----------|----------------------|---------|----------|----------------------------|-----|---|
| | | | L | S | M | L | S | M | L | S | M | L | S | M | L | S | M | L | S | M |
| Cygnus Loop | 74.0/-8.6 | 0.7 | 120 | ... | 120 | 20 | 20 | ... | 0.1-1.0 | ... | 0.5 | ... | N.D. | 165 | 70→50 | ... | 90 | 0.3-3.0 | 1.5 | 1 |
| HB21 | 89.1/ 4.7 | 1.0 | 20-25 | 25 | 25 | 17 | 26 | ... | 3-5 | 2.5 | 1.0 | ... | 4000 | 1300 | 260→190 | ... | 450 | 0.2 | 3.2 | 1 |
| HB9 | 160.5/ 2.8 | 1.1 | 70 | ... | 70 | 21 | ... | ... | 1 | ... | 0.8 | ... | N.D. | 350 | 120-90 | ... | 140 | 1 | ... | 1 |
| VRO42.05.01 | 166.2/ 4.3 | 4.0 | 35(15) | ... | 35(15) | 28 | 1 | ... | ... | 0.3(1.3) | ... | ... | N.D. | 400(2250) | 400-300 | ... | 420(800) | 1 | ... | 1 |
| S147 | 180.0/-1.7 | 1.0 | 90* | 25 | 75 | 26 | 40 | 1 | 0.3 | 1.0(0.3) | ... | 1500 | 1275(1275) | 120-85 | ... | 450-720 | 3.0 | 1.0 | 1 | 1 |

l = data obtained from Lozinskaya, 1975.

S = data obtained from survey.

M = data obtained from Sedov-Oort plot.

N.D. = no shell detected.

*We observe no HI filaments that justify this velocity.

good agreement with measured and estimated mass where available and shows a mass too low to be detected for the remaining objects, consistent with our results. The list represents objects observed in the survey for which velocities are available.

Lozinskaya (1975) has suggested that a homogeneous class of objects expanding into a medium of variable density may account for the observed properties of a sample of remnants she has studied. Our observations are consistent with this suggestion. More precisely, we see that 10^{50} ergs is a good estimate of the initial energy.

We thus summarize that present observational data for old galactic SNRs may have arisen from nearly identical initial conditions (presupernova mass and SN kinetic energy 10^{50} ergs) but expanded into regions of varying interstellar medium densities.

References

- Assousa, G. E., Search for shell structure in association with old galactic supernova remnants in neutral hydrogen and formaldehyde, *Carnegie Inst. Wash. Year Book* 74, 126, 1975.
- Assousa, G. E., B. Balick, and J. W. Erkes, Supernova remnants, *Carnegie Inst. Wash. Year Book* 73, 899, 1974.
- Assousa, G. E., and J. W. Erkes, An expanding shell of hydrogen surrounding the supernova remnant HB 21, *Astron. J.*, 78, 885, 1973.
- Lozinskaya, T. A., Supernova remnants as optical nebulae, *Sov. Astron.*, 19, no. 1, 21, 1975.
- Woltjer, L., Supernova remnants, *Ann. Rev. Astron. Astrophys.*, 10, 129–158, 1972.

TYPE I SUPERNOVAE: INTERPRETATION OF OPTICAL SPECTRA

G. E. Assousa, W. Kent Ford, Jr., C. J. Peterson,
and V. C. Rubin

Supernovae (SN) represent an end-stage of stellar evolution. An under-

standing of this phenomenon is critical for the determination of the rates at which SNs contribute to the synthesis of elements, to cosmic rays, and to the energy released into the interstellar medium.

Observationally one is hampered by the relatively low rate of SN production. Ilovaisky and Lequex (1972) estimate on the basis of a galactic survey of supernova remnants a rate of (50 ± 25) years/SN.

For the optical astronomer the spectra of SNs and their evolution with time, following initial detection, provide one observational handle. An understanding of the nature and the time-behavior of these spectra may not provide direct evidence of heavy-element (more massive than oxygen) synthesis. It may do so indirectly by identifying those elements which give rise to the spectrum. Simultaneously, it provides information regarding the physical conditions in the SN which give rise to these lines.

To date, the problem of line identification remains only partially solved. This is particularly true for supernovae of type I (SNI). This problem is aggravated by the lack of data in the literature. While many spectra of supernovae exist and have been used for classification of their spectral type, most spectra have never been published. Published spectra exist for only about 10% of recorded supernovae (Oke and Searle, 1974).

There are, of course, difficulties in obtaining supernovae spectra. Few are bright at the time of discovery. Their rapid decline in brightness severely limits the time over which spectra may be easily acquired; in addition, nearly one half of the possible observation time is lost due to the brightness of the moon-lit sky. The development of fast image tube systems in the past decade has made practical the recording of spectra of faint supernovae. As part of a continuing program on the study of extragalactic systems, two of us (VCR and WKF) have made a practice of securing spectra of supernovae whenever

possible (Rubin and Ford, 1967; Ford and Rubin, 1968).

Here we present the spectra of three supernovae, SN 1970j in NGC 7619, SN 1971 l in NGC 6384, and SN 1971 μ in MCG 5-26-14.

Based on the present and other available data on the spectra of SNIs, we have generated synthetic spectra that closely resemble the observed spectra.

The original spectra and microdensitometer tracings are shown in Figs. 17 through 19. In Fig. 20, the spectrum of SN 1971 l (C-47) at 18 days after maximum has been replotted. The bottom plot is a synthetic spectrum composed of emission time of FeII, CaII, NaI, H α , H β , H γ , H δ , and the HeII P α line at 4686 Å. There are 48 lines due to FeII, 2 lines each for CaII and NaI, 4 lines for HI, and a single line for HeII. The wavelength is the rest frame of the galaxy. The lines have been Gaussian-broadened to reflect a velocity dispersion of 3000 km/s. For all except HeII, the relative strengths of the lines were obtained from the relative line widths in the Nova DQ Hercules (Mustel, 1974). The HeII contribution was arbitrarily chosen at twice H α . Al-

though the C-47 spectrum is in density, the marked similarity of the actual and synthetic spectra is very striking. In the synthetic spectra the FeII is the dominant contributor. Kirshner *et al.* (1973) have shown that the peak at 4600 Å gradually shifts with time. A reasonable interpretation is that the HeII 4686 line becomes more prominent with time, becoming considerably stronger than the FeII.

Improved spectral fits may be obtained by including other lines expected to be present, such as SiII, but the improvement remains small.

We are thus led to conclude that spectra of SNIs are primarily dominated by FeII transitions. We have not attempted to devise a complete model to determine the physical conditions in the SN which give rise to this result. A radioactive excitation mechanism by resonance transitions at 2500 Å, followed by permitted transitions to lower metastable states as suggested by Wampler and Oke (1967) for identifying the FeII lines in the QSO 3C273 is physically plausible for SNIs.

But, regardless of the mechanism, the presence of Fe in SNI appears inescapable.

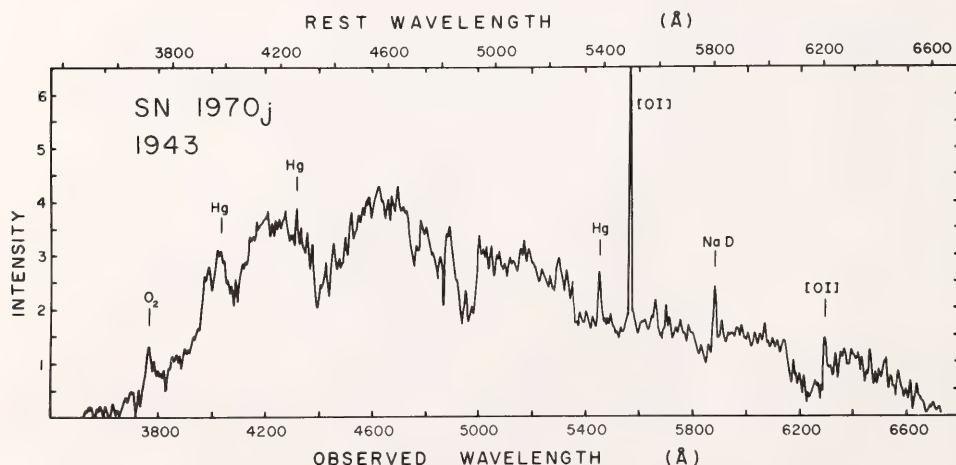


Fig. 17. Spectrum of supernova 1970j in the galaxy NGC 7619 at 1 day before maximum light. The bottom scale gives the observed wavelength; the top scale gives the wavelength in the rest frame of the galaxy. No corrections have been made for change of instrumental sensitivity with wavelength. Original dispersion is 57 Å/mm.

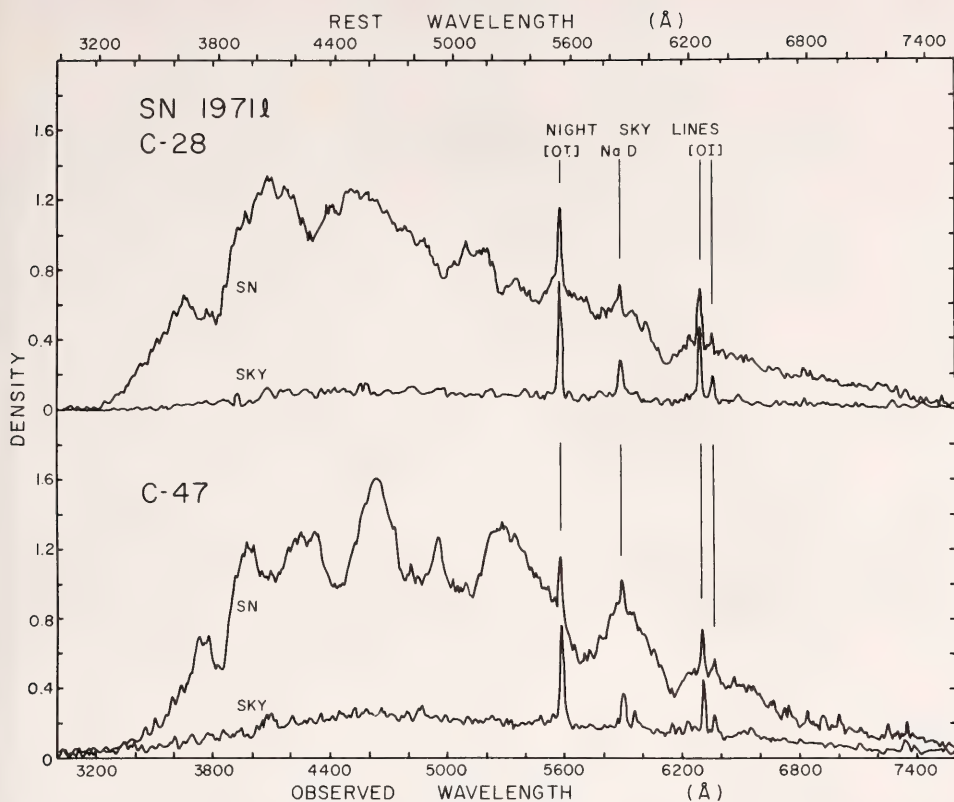


Fig. 18. Spectra of supernova 1971 in the galaxy NGC 6384. Spectrum C-28 was obtained on 29 June 1971 at maximum light (Barbon *et al.*, 1973). Spectrum C-47 was obtained 18 days later on 17 July 1971. Because no calibrations exist for these photographic spectra, the data are presented in terms of density. The top and bottom scales are galaxy rest-frame and observed wavelengths, respectively. No corrections have been made for change of instrumental sensitivity with wavelength. Original dispersion is 300 Å/mm.

References

- Barbon, K., F. Ciatti, and L. Rosino, Observations of five supernovae 1970–71, *Memoria della Società Astronomica Italiana*, 44, 65, 1973.
- Branch, D., and B. Patchett, Type I supernovae, *Mon. Notic. Roy. Astron. Soc.*, 161, 71, 1973.
- deVaucouleurs, G., and A. deVaucouleurs, *Reference Catalogue of Bright Galaxies*, (Austin: University of Texas Press), 1964.
- Ford, W. K., Jr., and V. C. Rubin, The spectrum of the 1968 supernova in NGC 2713, *Proc. Astron. Soc. Pac.*, 80, 466, 1968.
- Ilovaisky, S. A., and J. Lequex, A study of galactic supernova remnants, *Astron. Astrophys.*, 20, 347, 1972.
- Kirshner, Robert P., J. B. Oke, M. V. Penston, and L. Searle, The spectra of supernovae, *Astrophys. J.*, 185, 303, 1973.
- Mustel, E. R., Analysis of the physical conditions inside the envelope of DQ Hercules 1934, *Vistas in Astronomy*, vol. 16, (A. Beer, ed., Pergamon Press, New York), pp. 260–269, 1974.
- Oke, J. B., and L. Searle, The spectra of supernovae, *Ann. Rev. Astron. Astrophys.*, vol. 12, 315–329, 1974.
- Rubin, V. C., and W. K. Ford, Jr., The spectrum of the 1967 supernova in NGC

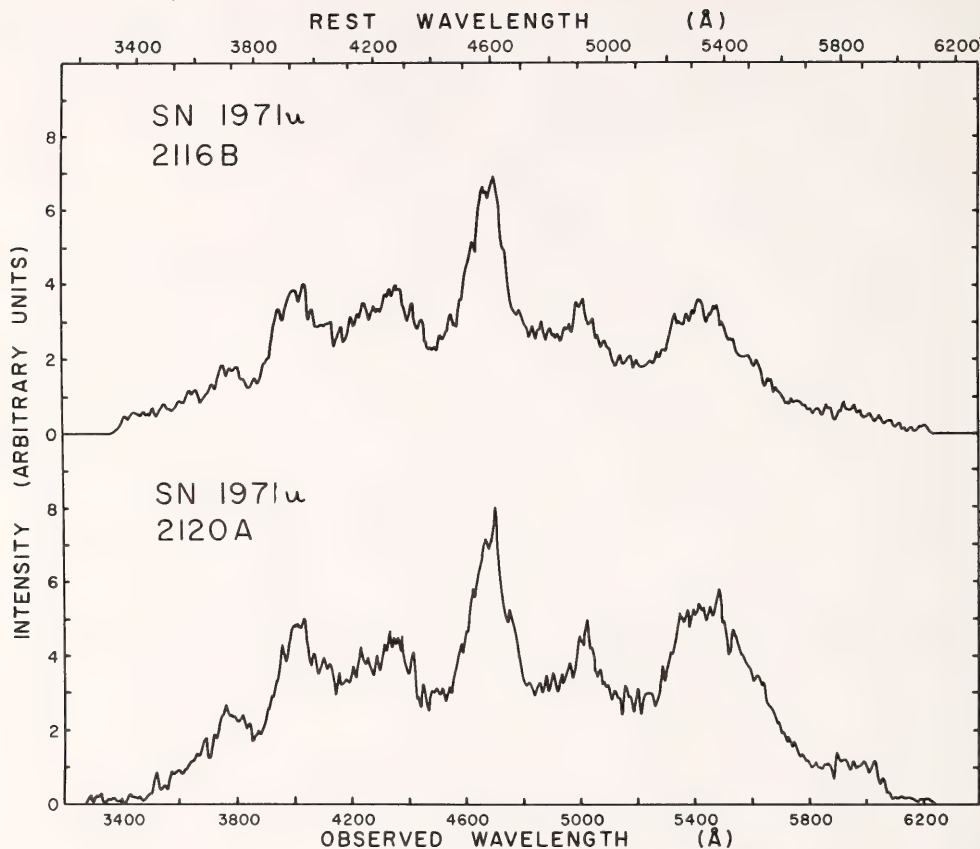


Fig. 19. The spectra of supernova 1971u in the anonymous galaxy MCG 5-26-14. Spectra 2116 B and 2120 A were obtained on successive nights (16 and 17 December 1971, respectively) and are consistent with type I SN spectrum at 15 ± 2 days after maximum light. The contributions from the night sky have been removed from both spectra. As in the previous two figures, no corrections have been applied for instrumental sensitivity with wavelength. The bottom scale gives the observed wavelength; the top scale gives the observed wavelength; the top scale gives the wavelength in the rest frame of the Galaxy. Original dispersion is 109 Å/mm .

3389 and H-alpha velocities in the Galaxy, *Proc. Astron. Soc. Pac.*, 79, 322, 1967.

Rubin, V. C., W. K. Ford, Jr., N. Thonnard, M. S. Roberts, and J. Graham, The motion of the Galaxy and the Local Group

determined from the velocity anisotropy of distant Sc I galaxies, I. The Data, *Astron. J.*, in press, 1976.

Wampler, E. J., and J. B. Oke, The emission line spectrum of 3C273, *Astrophys. J.*, 148, 695, 1967.

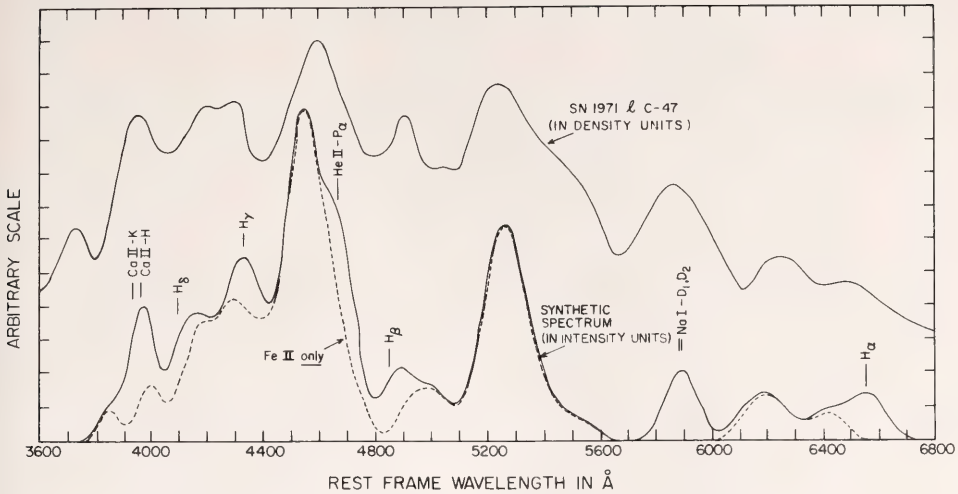


Fig. 20. The SN 1971 *l* spectrum at 18 days after maximum (top) and the synthetic spectrum (bottom). The lines used in obtaining the spectrum were broadened with a Gaussian assuming a velocity spread of 3000 km/s. Positions of the NaI, CaII, and H α , β , γ , δ , lines are indicated. The presence of the Balmer lines produces minor changes in the shape of the spectrum. The HeII line at 4686 clearly has the effect of redshifting the 4600 Å peak. The dashed spectrum is due to FeII alone. All wavelengths are in the rest frame of the Galaxy.

THE 21-CM RECEIVER FOR THE INSTITUTO ARGENTINO DE RADIOASTRONOMÍA

*E. T. Ecklund, C. A. Little, N. Thonnard, and
K. C. Turner*

The joint proposal to modernize the 21-cm receiver at the IAR and to undertake an investigation of high-velocity clouds and southern spiral galaxies at the neutral hydrogen line was funded as of November 1, 1975, by the National Science Foundation and the Agencia Ejecutiva Argentina. We have already had a four-week visit in January by Ing. E. Filloy, the chief engineer of the IAR, during which we finalized all of the details in the receiver design.

Most of the components for the front-end of the receiver have been received or are on order. A block diagram of the receiver front-end package is shown in Fig. 21. The parametric

amplifier has been received, and using the noise figure and/or losses in the other components, we expect a total receiver-noise temperature of 56°K. This leads us to expect a system temperature of 70°K on the sky. The use of dual frequency conversion allows a large separation between signal and image frequencies and simplifies the design of band rejection filters.

Figure 22 is a block diagram of the "back end" of the receiver. By utilizing an on-line computer for phase detection and integration, we hope to avoid many nonlinearities and temperature-dependent effects which proved troublesome in the old system. In addition, we will be able to automatically calibrate the system gain and baseline every few seconds, thus eliminating several other possible instability problems. All components for the digital part of this system are now on hand, and their assembly into a working system is under way.

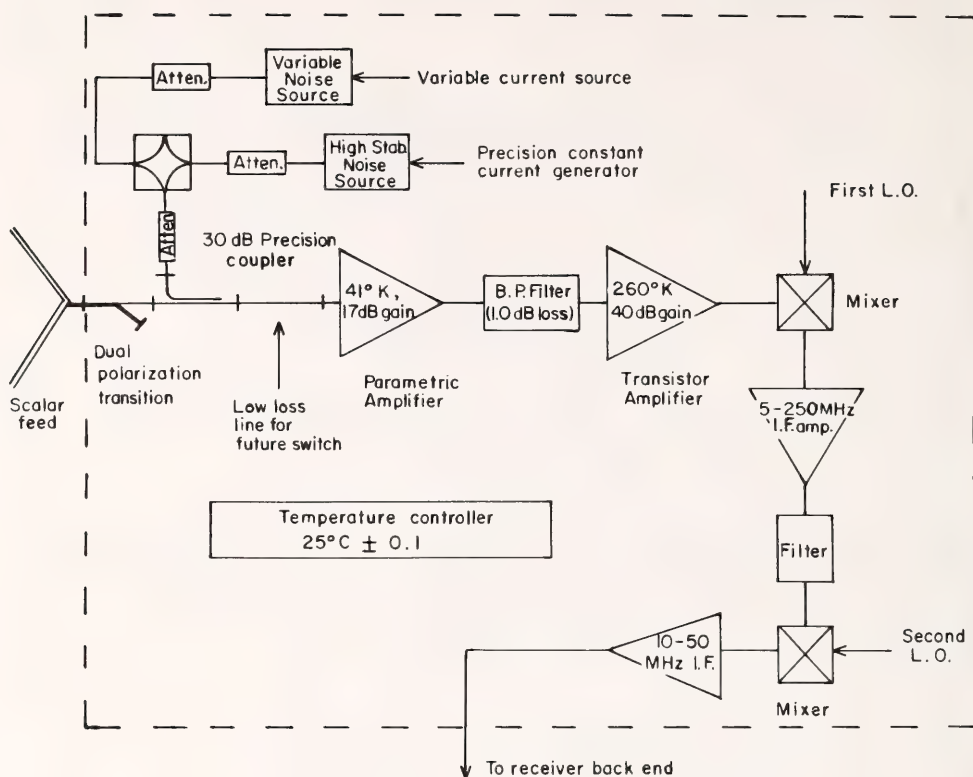


Fig. 21. Front end for the new 21-cm receiver at the IAR.

820-MHz SURVEY OF THE SOUTHERN SKY

N. Thonnard and K. C. Turner

A recent development in radio astronomy, pleasing both aesthetically and scientifically, is the possibility of constructing maps of the whole sky with respectable angular resolution (i.e., $\sim 1^\circ$). Such pictures are revealing structures so large in angular size as to be heretofore unobservable.

One such survey of local neutral hydrogen by Heiles and his collaborators at the University of California, Berkeley, is now being completed at the IAR in cooperation with our Argentine colleagues.

We are presently designing a system to produce such an all-sky picture of

the continuum radiation at 820 MHz in a cooperative program with members of the IAR and Professor H. Weaver's group at Berkeley. The northern portion of the survey already exists down to declination -7° by Berkhuijsen (1972), done at Leiden. The southern portion will be done at the IAR, and a central region overlapping both halves to ensure proper calibration of scales will be done at the Berkeley Hat Creek Observatory. Both polarizations of the incoming radiation will be measured.

Design and construction of the back-end and data-acquisition systems will be done at DTM, while the Berkeley group will be responsible for the front-end system. All of the digital equipment has already been acquired and is now being assembled. A KIM-1 microprocessor based system made by

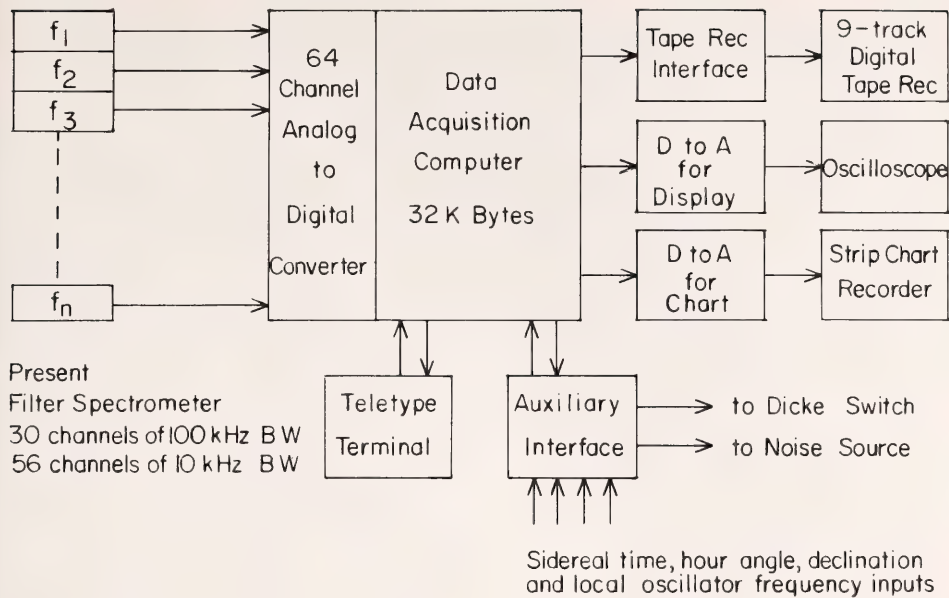


Fig. 22. Phase detection, integration, and control system for line spectrometer at the IAR.

MOS-Technology will serve as the central control for the system. The availability of such sophisticated data handling systems at very low prices makes possible much more adequate control of the gain and baseline offset of the receiver, as these parameters can be measured automatically every few seconds.

Reference

Berkhuijsen, E. M., A survey of the continuum radiation at 820 MHz between declinations -7° and $+85^\circ$. I. Observations and reductions, *Astron. Astrophys. Suppl.*, 5, 263, 1972.

IMAGE TUBE SYSTEMS

W. K. Ford, Jr.

The combination of the Carnegie Image Tube and the III-aJ recording emulsion continues to be used to produce astronomical data of high quality.

The tubes, which are manufactured by RCA (Type C33063EP3), were originally developed with the support of grants from the National Science Foundation. These improved versions of the original Carnegie Tube are now in operation at a number of observatories including Kitt Peak, Cerro Tololo, and Las Campanas.

During this report year two image tube systems for spectroscopic work were built in the Department of Terrestrial Magnetism's shop. One of these systems was designed in collaboration with Drs. Searle and Brucato of the Hale Observatories for use with a Bowen-type f/1.4 Schmidt camera on the Boller and Chivens spectrograph at the new Irénée du Pont Telescope at Las Campanas. The second system was built for use on the DTM spectrograph at Lowell Observatory. It replaces the early Carnegie Image Tube System (incorporating RCA tube type C33011) that has been in regular operation at Lowell Observatory, especially by Drs. Rubin and Ford, since 1966.

We anticipate that much of our astronomical work in the next few years will continue to be done with photographic recording of the image intensifier output. In spite of the problems of accurate photometric calibration of the plates on one hand and the great progress that is being made with direct recording of data with digital sensors on the other, there are some types of observations for which the size (or number of picture elements), stability, and efficiency of the present intensifier systems still give an overwhelming advantage. Therefore, we are undertaking a modest renovation and modernization of the DTM scanning microphotometer. The principal mechanical improvement is the replacement of the old traveling stage with a precision transverse stage of one micron resolution and driven by a stepping motor. Also, the card-punch recording of the data is being replaced by a digital magnetic tape recorder. These changes will ease the task of extracting relative intensity information from the plates.

The intensifier-image dissector scanners at Lick Observatory and at the Kitt Peak National Observatory and the Silicon Intensified Target (SIT) systems at Hale, Kitt Peak, and Cerro Tololo Observatories are operating successfully and are yielding photometric astronomical data with sky background subtraction. However, these types of systems appear to fall short in performance over what might be achieved with some silicon detectors now in the development stage. In these detectors an image is read out serially point by point by moving photogenerated charge laterally through the bulk silicon of the device to an output gate. The charge can be accumulated during an exposure or integration period and then moved by manipulating in appropriate phase the potential applied to metallic electrodes insulated from the bulk silicon. These structures are generally described by the generic term charge coupled devices, or more frequently simply CCDs.

The basic advantage of the CCD over more conventional camera tubes that astronomers seek to exploit is the inherent geometrical stability, compactness, and long-term stability of sensitivity. There are two broad approaches: the photon-in mode, analogous to the silicon target vidicon; and the electron-bombardment mode, analogous to the SIT vidicon. The photon-in mode has the advantage of high quantum efficiency, a high signal-to-noise ratio for high signal levels, and probably a higher dynamic range than conventional camera tubes. The relative lack of problems associated with electron beam-landing on the target should simplify obtaining quantitative information. The electron-in, or event-counting, mode may eventually offer advantages at very low light levels with the quantum efficiencies associated with photoemissive surfaces. The commercial development of prototypes of both these devices is proceeding along several competitive lines.

As a result of the long program of development and evaluation of image tube systems at DTM we are in a good position to analyze and evaluate the characteristics of some of the more promising of these devices. In particular, the data handling system we have used with our image dissector scanner can be adapted to measuring the performance of the CCDs as they become available. This preliminary evaluation can be done without the expensive development of a full data handling system. As a step toward making some initial tests at DTM and in order to provide some on-line data compression for spectroscopic applications, Ford and Thonnard, assisted by a very capable summer student, Mr. Charles Bennett, have designed and built a fast arithmetic logic unit to operate with our signal averaging device. This unit allows us to sum repetitive scans of an image, thereby improving the signal-to-noise ratio and at the same time reducing the total number of picture elements that

need to be stored at the expense of reduced resolution in one dimension.

ACKNOWLEDGMENTS

We thank the Directors of the Cerro Tololo Inter-American Observatory, Kitt Peak National Observatory, and National Radio Astronomy Observatory for making telescope time available, and the Director of the Hale Observatories for granting permission to reproduce the National Geographic Society-Palomar Observatory Sky Survey prints. One of us (CJP) wishes to thank Drs. R. Racine and S. van den Bergh of David Dunlap Observatory and H. Swope of Hale Observatories for their hospitality during visits to these institutions. We also wish to thank the Office of Naval Research for the continuing loan of the lead ballast used in the counterweights of our Derwood telescope (Contract No. N0014-71-C-0211).

ACTIVITIES OF THE INSTITUTO ARGENTINO DE RADIOASTRONOMIA

For the IAR as well as for most of the Argentine observatories, 1975 was a difficult year because of the economic situation. Nevertheless, some major projects have been carried out. One of them was the relocation of the 21-cm line receiver to a new control building. Except for the necessary interruption during the movement of the receiver, observations have continued an average of 16 hours a day.

The joint project between CIW and IAR for the new 21-cm receiver was started after the agreement between the Agencia Ejecutiva Argentina and the National Science Foundation was finalized. Under this agreement the Consejo Nacional de Investigaciones Científicas y Técnicas de la República Argentina will support the expenses for three round trips to Washington,

each of one month duration. These trips are intended for personnel of the IAR to cooperate in the design, assembly, testing, and data processing for the joint project.

Five parametric amplifiers at 21 cm have been received from the Netherlands Foundation for Radioastronomy. These amplifiers were used in the Westerbork Synthesis Radiotelescope during its earlier observations. They are going to be used in the near future in the radio interferometer of the IAR, which is planned as an aperture synthesis instrument.

The scientific staff has increased this year with two young members: Drs. T. E. Gergely and M. Zales de Caponi, both of whom received the Ph.D. at the University of Maryland.

Since July, E. Bajaja has been the Director of the IAR.

Technical Activities

The main task of the Technical Department this year was the installation of the 21-cm receiver in the new building. This building was built between the two 30-m dishes and equipped with an effective air conditioning system. There is enough room for the receivers and for the operation facilities.

The electrical wiring, cable ducts, air conditioning, lighting, and appliances were ready around March. The movement of the receiver started in April. At the same time, some parts were replaced with new ones designed and built at the IAR; for example, the low frequency section of the LO and the old SOLA AC regulators were replaced by small units with harmonic rejection and better stability. A complete set of interconnected boxes allows easy maintenance of the whole system; and individual power distribution was added to each rack. Some of the old IF amplifiers were replaced by new ones with better stability. A more reliable temperature controller was installed in

the filter boxes, and some of the chassis were rewired and readjusted. First tests of the system started in June, and in July the receiver was put into normal operation.

The new set-up is much more reliable, and stability has been improved by a factor of 5, allowing a better front-end adjustment. The system-noise temperature is about 180°K.

At the end of the year some work was also done on the second 30-m dish, such as painting, and construction of cable ducts, interconnection house, and part of the electrical installation.

Summary of Current Research

E. Bajaja, F. R. Colomb, and R. Moras have extended their observations at intermediate galactic latitudes and are now analyzing the results of the region $200 \leq l \leq 315$; $-10 \geq b \geq -32$.

Bajaja, Colomb, G. Dubner, and T. Gergely are completing the study of four supernova remnants: G 296.3+10, G 261.9+5.5, G 327.6+14.5 and G 330.7+15. Other supernova remnants of small angular diameter have also been observed.

Colomb, W. Pöppel, and C. Heiles of the University of California continued the observations for the hydrogen survey at low velocities ($-50 \leq V \leq 50$

km/s) of the Southern Hemisphere. They completed about 60% of the observations and produced a radio map of the Southern sky every 2° in δ .

Colomb and I. Mirabel observed emission profiles in the direction of 23 southern pulsars.

Bajaja, Colomb, and Pöppel began observations of spiral and irregular galaxies with $m < 9$. Thirty wide filters ($\Delta V = 25$ km/s) and the multichannel integrator have been used in this program.

Pöppel and M. Franco observed the region $0 \leq l \leq 20$; $-3^\circ \geq b \geq -17^\circ$ every 1° in l and b , and continued with the analysis of the region $348^\circ \leq l \leq 372^\circ$; $3^\circ \leq b \leq 17^\circ$ (*Atlas of Galactic Hydrogen*, Pöppel and Vieira, CIW, 1974).

Pöppel and D. Vota completed the observation of the galactic clusters NGC 5460, Rn 106, and G 394.

E. Arnal completed the observations of the galactic clusters NGC 2243, 3688, 2345, 2204, 4755, 3680, 6611, and 6994, IC 2391, Mel 227, and A (Blanco) as a general survey of HI in the direction of galactic clusters.

Gergely and Arnal completed the observations of the globular clusters B46, B67a, B87, and B63.

Arnal completed the observations of the association CMaOB1.

Gergely and Mirabel completed the observations of globular clusters with known reddening.

THE EARTH AND THE SOLAR SYSTEM

L. T. Aldrich, C. Brooks, J. Cleary, J. R. Evans, M. Feigenson, S. E. Forbush, S. R. Hart, A. W. Hofmann, D. E. James, A. T. Linde, M. Magaritz, S. Rajan, I. S. Sacks, M. Schneider, C. M. Seber, J. A. Snoke, K. Suyehiro, D. J. Whitford, and S. Weidenschilling

Collaborators

C. Aguirre, J. Bannister, R. J. Beavan, K. Bloomfield, M. Bracamonte, R. Cabre, A. Cuyubamba, G. L. Davis, S. del Pozo, D. W. Evertson, A. Flores, L. Gélinas, A. A. Giesecke, N. Girardin, G. C. P. King, Y. Motoya, L. Ocola, H. Okada, G. Olafsson, R. W. Page, G. Poupeau, A. Rodriguez B., D. Simoni, R. Stefansson, S. Suyehiro, L. Tamayo, J. G. Williams, Y. Yamagishi, and E. Zinner

GAS-SOLID INTERACTIONS IN THE SOLAR NEBULA

S. J. Weidenschilling

It is widely believed that the planetary system was formed from matter in a cloud of gas and dust which surrounded the sun. The origin and structure of this solar nebula are disputed, but it is generally depicted as a rotating, flattened disklike structure. It is reasonable to assume that it was somewhat centrally condensed, with the gas pressure and density in the central plane decreasing with distance from the axis. Such a pressure gradient would partially support the gas against the sun's gravity, requiring its rotation rate at any radius to be less than the local Kepler orbit velocity.

Solid bodies are not supported by the pressure gradient; in the absence of gas, they would pursue Kepler orbits. A balance of gravitational, centrifugal, and drag forces requires that a particle always have some velocity relative to the gas. The radial component of its motion is always in the direction of increasing pressure, i.e., inward. We define the "stopping time," t_e , as the time for a particle's velocity to be reduced by a factor e by drag in the absence of other forces; t_e depends on the properties of the particle and the gas, and on the velocity. The particle motion is characterized by the ratio of t_e to the orbital period, t_p . Two limiting cases were examined quantitatively by Whipple (1973);

1. Small body ($t_e/t_p \ll 1$). The particle is constrained to move with the an-

gular velocity of the gas. It feels a residual central attraction. In a frame rotating with the gas, it falls directly inward. The terminal velocity increases with particle size.

2. Large body ($t_e/t_p \gg 1$). The particle pursues a Kepler orbit, which is perturbed by drag. It loses angular momentum and spirals inward. The larger the body, the smaller is the effect of drag.

In the limits of very large and very small bodies, the radial velocity approaches zero. Somewhere between these cases (when $t_e/t_p \sim 1$), it must reach a maximum, as shown schematically in Fig. 23. This case, potentially the most interesting, had not been examined in detail before the present study. In general, the equations of motion for the strongly perturbed case must be solved numerically. However, some interesting properties of the solution can be shown analytically:

1. There is an upper limit to the radial velocity, which depends only on the nebular structure. It is independent of the drag law and the particle properties.

2. The radial and transverse components of the "wind" velocity felt by the particle are uniquely related. They also depend only on the nebular structure.

3. If the gas is assumed ideal, the maximum radial velocity is independent of the gas density. The results for any case are therefore insensitive to the nebular mass.

The particle properties and drag law determine the velocity components corresponding to a given particle size. The

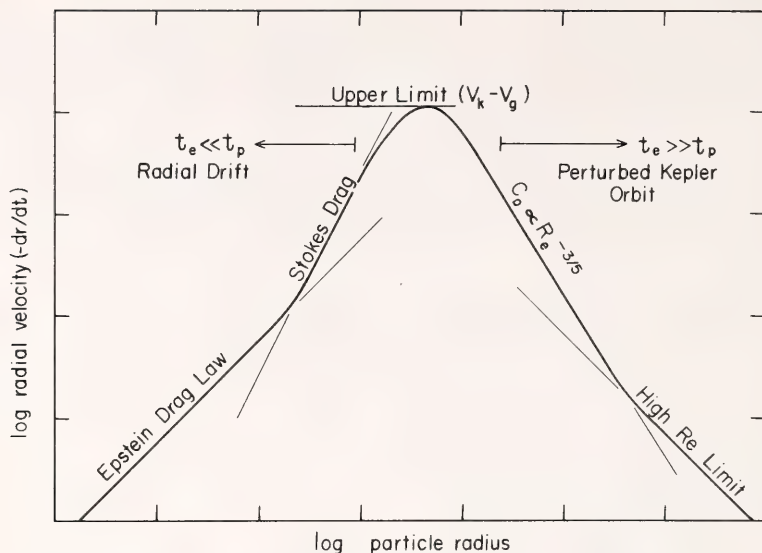


Fig. 23. Radial velocity as a function of particle size (schematic). The shape of the curve depends on the drag laws, but the value of the upper limit does not.

solution is complicated by the fact that any of four drag laws may be applicable, depending on the Reynolds number and the ratio of mean free path to particle size. Each drag law must be tried until a self-consistent solution is found. I have written a computer program that performs this task, solving the equations of motion numerically. The velocity components can be determined for a (spherical) particle of any size and density in a nebula of arbitrary structure. Results to date must be considered preliminary, but the following conclusions appear to be justified for a wide range of "reasonable" nebular models:

(1) The maximum radial velocity can be large. In the inner nebula, it may exceed 100 m/s^{-1} at 1AU, decreasing by about an order of magnitude in the outer part. (2) These velocities generally correspond to particle of radii $\sim 10\text{--}100 \text{ cm}$ (Fig. 24). (3) Characteristic lifetimes for spiraling into the sun can be very short for such particles, ranging from a few tens of years in the inner nebula to 10^4 years in the outer part. The loss of solids from any region,

or mixing between regions, could have been significant, depending on the particle size distribution. (4) For small particles ($t_e \ll t_p$), larger and/or denser bodies are removed more rapidly. For large particles ($t_e \gg t_p$), the opposite is true. Fractionation by composition, e.g., Fe from silicates, could occur in either direction. The rate of mass loss is greatest in the inner nebula; Mercury's high Fe content may be explainable by this effect. (5) Radial and transverse velocities are strongly dependent on particle size. It is generally assumed that gas drag would damp their relative motions. However, if the particles vary in size, they may have large relative velocities because of the gas. It is not clear whether the growth of large bodies would be aided or hindered. High relative velocities would inhibit gravitational instability (Goldreich and Ward, 1973), but if particles stick together on impact, the increased rate of collisions might be conducive to growth.

These and many other consequences remain to be investigated in greater detail.

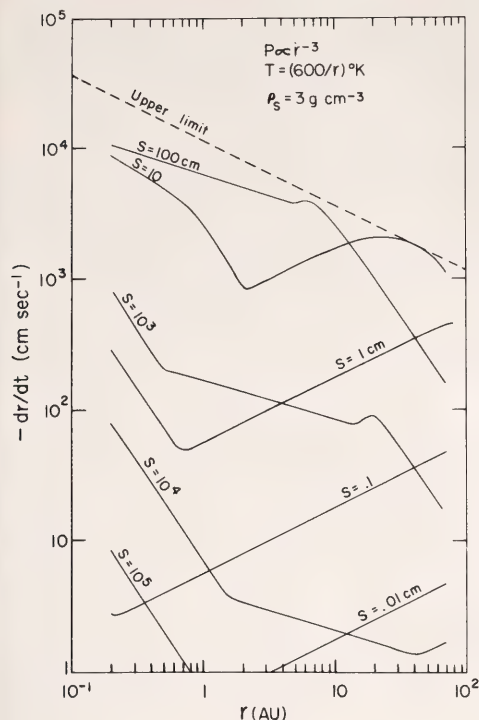


Fig. 24. Radial velocities of particles of various radii (S) as functions of location in a typical model nebula. Particle density = 3 g cm^{-3} . Nebular gas pressure varies as r^{-3} , density as r^{-2} .

References

- Goldreich, P., and Ward, W. R., The formation of planetesimals, *Astrophys. J.* **183**, 1051, 1973.
- Whipple, F. L., Radial pressure in the solar nebula as affecting the motions of planetesimals, *NASA SP-319*, 355, 1973.

INTERPLANETARY BODIES AND SOLAR SYSTEM HISTORY

George W. Wetherill

Studies of the solar system and its origin have been primarily directed toward the largest bodies—the sun and the planets. However, during the past few decades it has become increasingly clear that equally significant information can be obtained from the smaller bodies of the solar system: the satel-

lites of the planets including our moon, and the asteroids, comets, meteoroids, and meteorites. The small size of these bodies has permitted their record of primordial events in solar system history to be preserved to a much greater extent than is the case for hot and internally active planets. The interplanetary orbits of comets and many asteroids produce a cratering record on the moon and planets which reveals their size and number throughout the history of the solar system. Study of meteorites and lunar samples permits direct chemical investigation of the record of events dating back to the formative period of the solar system. Recent evidence for presolar grains in meteorites (Clayton and Mayeda, 1975) provides a link between planetary formation and the presolar galactic history of the matter from which it was formed.

Interpretation of the data obtained from studies of these small bodies requires understanding of their sources in the solar system and the evolution of their orbits. Very significant advances in these areas have followed the development of new techniques for tracing their orbital evolution over billions of years (Öpik 1951, Arnold 1965), for understanding the detailed structure of the asteroidal regions (Williams 1969, 1971), and for calculation of the development of the swarm of interplanetary bodies which preceded the formation of the planets themselves (Safronov 1969). Examples of application of these achievements are given in the following three subsections, which deal with the role of interplanetary bodies in distinct periods in solar system history: (1) the formation of the planets and the moon (4.5 billion years ago); (2) the late heavy bombardment of the moon and terrestrial planets which produced the heavily cratered terrains preserved on the lunar highlands, Mercury, and Mars (4.0 billion years ago); and (3) the earth-crossing Apollo objects that have dominated the cratering record of the earth and moon during the past three billion years.

The Role of Large Impacting Bodies in the Formation of the Earth and Moon

Introduction. Over the years many processes have been suggested which involve the existence of large ($\geq 10^{24}$ g, ~ 500 km radius) planetesimals during the formation of the solar system. These include lunar-sized meteorite parent bodies (Urey, 1959), capture theories for the formation of the moon (Gerstenkorn, 1969; Singer, 1972), disintegrative capture by passage of bodies within the earth's Roche limit (Öpik, 1972; Smith, 1974; Mitler, 1975), impact heating of the earth (Safronov, 1969) and moon (Ruskol, 1974), tilting of the earth's rotation axis by a small number of large impacts (Safronov, 1960), formation of the moon by "splashes" resulting from grazing impacts with the earth (Hartmann and Davis, 1975; Cameron and Ward, 1976), predifferentiation of lunar planetesimals (Kaula and Bigeleisen, 1975), and the existence of large post-accretional residual bodies needed to produce the late heavy bombardment which continued for ~ 600 m.y. after the end of the accretion of the planets (Wetherill, 1975b). An evaluation of the plausibility and relative importance of these processes requires a theory that predicts at least semiquantitatively both the size and the velocity distribution of the planetesimals that accumulated to form the terrestrial planets and the moon. Considerable progress toward such a theory has been made by Safronov (1969) and his co-workers (Zvyagina *et al.*, 1973). Other, less comprehensive treatments of this problem have been given by Marcus (1965, 1969), Hallam and Marcus (1974), Hartmann and Davis (1975), and Weidenschilling (1974). A characteristic of these theories is that accumulation of the planetesimals into the terrestrial planets and the moon by random encounters is slow (10^5 to 10^8 years) compared with the time scale of $\sim 10^3$ yr proposed for accumulation from a gaseous solar nebula rather than from a protoplanetary swarm of

planetesimals (Cameron, 1973). Serious difficulties with the latter type of theory have been discussed (Safronov, 1975). In spite of these difficulties, gravitational accretional heating associated with very rapid accumulation has been the starting point of most discussions of the geochemical and geophysical evolution of the moon, and it is commonly stated that such dynamically unlikely rapid accretion is required if one is to understand the evidence for early chemical differentiation of the moon.

As discussed by Safronov (1969), appreciable accretional heating does not require rapid accretion, provided that a sufficiently large number of the accumulating bodies are massive and energetic enough to deposit a significant quantity of energy deep beneath the accretional surface and thereby to preclude loss by surface radiation into space.

Calculation of the size distribution of the largest bodies is not readily amenable to coagulation theory (Safronov and Zvyagina, 1969) even though considerable insight is provided by this approach to the size distribution of smaller bodies, especially when the combined effects of accumulation and fragmentation are considered (Zvyagina *et al.*, 1973). One reason for the failure of the theory for the largest accumulating bodies is that for these bodies the gravitational field of the growing body can augment its effective cross section in such a way that the cross section becomes nearly proportional to the fourth power of its radius rather than to the geometrically determined square of the radius. This effect is partially included in the only solutions to the coagulation equation which have been reported, i.e., for a coagulation kernel linear in the mass and hence proportional to the cube of the radius. This approximates the situation over much of the mass range but not at the uppermost end of the range, in which a small difference in radius might, at least in principle, lead to a great difference in the rate at which

the radius increases. Numerical examples of such "runaway accretion" have been given by Hartmann and Davis (1975).

Safronov (1969) has made use of runaway accretion to predict a "second largest mass" in the earth's accumulation zone of 10^{-3} earth masses, i.e., 6×10^{24} g. In the present work a variant of this model is proposed which leads to the second largest body being more massive, and thereby also implies significantly greater accretional heating of the moon.

Runaway accretion. The rate of growth of the ratio of the radii of the two largest bodies ($R = r_1/r_2$) is by the elementary rules of differentiation:

$$r_1 \frac{dR}{dt} = R \left[\frac{dr_1}{dt} - R \frac{dr_2}{dt} \right] \quad (1)$$

In a simple accumulation model in which a body of radius r sweeps up smaller bodies with relative velocity \bar{V} ,

$$\frac{dr}{dt} = \frac{\rho_c(t)}{\rho_p} \bar{V} \left(1 + \frac{Ve_z}{V_2} \right) \quad (2)$$

where $\rho_c(t)$ = the spatial density of mass in the form of smaller bodies, ρ_p = the density of the larger body, and Ve = the escape velocity of the larger body.

In Safronov's accretion theory the mean relative velocity is related to the escape velocity of the largest body by use of the dimensionless ratio θ :

$$\bar{V}^2 = \frac{Ve_p^2}{2\theta} \quad (3)$$

$$\text{and} \quad \theta = \frac{GM_p}{R_p \bar{V}^2} \quad (4)$$

where G is the gravitational constant, and the subscript p refers to the escape velocity, mass, and radius of the largest body in the earth's zone. Safronov, following earlier work of Gurevich and Lebedinskii (1950), presents calculations that support his conclusion that θ varies slowly (i.e., by a factor of ~ 2), while M_p increases by a

factor of $\sim 10^{12}$ during accretion. This implies that the mean relative velocity "keeps step" with the growth in radius and escape velocity during accumulation. The numerical value of θ depends on the balance between acceleration by mutual perturbations by planetesimals and dissipation of energy in collision of planetesimals. Under a variety of conditions in which accretion occurs after loss of most of the nebular gas (appropriate to earth's zone), the value of θ is estimated to range from about 7 down to about 1. Therefore, the mean velocity with which smaller bodies collide with the largest body is always less than its escape velocity. Calculations such as those reported by Marcus (1969) using experimental data of Gault *et al.* (1963) then lead to the conclusion that at these velocities the largest bodies will grow in radius rather than fragment. Smaller bodies may either accrete or erode, depending upon their mass.

Substitution of θ into (2) permits (1) to be developed to:

$$\frac{dR}{dt} = \sqrt{\frac{2}{3} \frac{\pi G}{\theta \rho_p}} \rho_c(t) \left\{ (2\theta - R)(R - 1) \right\} \quad (5)$$

where G is the gravitational constant.

For constant θ , the solution of (5) may be written as:

$$R = \frac{1 + 2\theta \left\{ \frac{R_0 - 1}{2\theta - R_0} \right\} \exp\left(\frac{2\theta - 1}{2\theta + 1} \lambda t^*\right)}{1 + \left\{ \frac{R_0 - 1}{2\theta - R_0} \right\} \exp\left(\frac{2\theta - 1}{2\theta + 1} \lambda t^*\right)} \quad (6)$$

where R_0 is the initial value of R ,

$$\lambda = (2\theta + 1) \rho_c(o) \left[\frac{2}{3} \frac{\pi G}{\theta \rho_p} \right]^{1/2}$$

and t^* is a time-like variable:

$$t^* = \frac{1}{\rho_c(o)} \int_o^t \rho_c(t) dt.$$

Equation (6) shows that the extent of the runaway accretion is limited, as discussed earlier by Safronov (1969). As t becomes indefinitely large, $R \rightarrow 2\theta$, which is therefore the maximum ratio of the final radii. For nonzero values of the initial radius

$$R < 2\theta \quad (7)$$

The final ratio of the masses of the two largest bodies is therefore less than $(2\theta)^3$. By use of $\theta = 5$ and assuming t^* to be infinite, Safronov obtained the result mentioned earlier, that the second largest body in the earth's zone had a mass of $\sim 6 \times 10^{24}g$.

As will be seen later, in this case the number of bodies surviving to the terminal stages of growth of the moon will be too small to produce much accretional heating.

However, there is no reason to suppose that θ must be as large as 5. In fact, Safronov (1969, Table 8, Chapter 7) gives $\theta \approx 2$ during the stage of planetesimal growth prior to the time in which most of the mass is in a single largest body, the planetary embryo. This value limits the mass ratio to less than 64. It is very difficult to know the correct value of θ to be used at this stage, as direct knowledge of the appropriate dissipation to be assumed in protoplanetary planetesimal collisions is not available. However, the values assumed by Safronov to obtain $\theta \approx 2$ appear plausible. During later stages of growth of the planetary embryo, Safronov shows that the value of θ increases to ~ 5 , implicitly assuming that the remaining planetesimals cross the orbit of only one dominant planetary embryo, moving in a circular orbit. Insofar as this assumption is correct, this is a consequence of the fact that successive encounters with the embryo will always occur at the same value of the mean geocentric velocity, provided that no perturbations by a third body occur between these successive encounters. This in turn is a consequence of the conservation of energy in these encounters in the geocentric reference frame, related to the constancy of the

Tisserand criterion and the Jacobi integral in the restricted three-body problem.

The fact that when the earth has reached $\sim 10\%$ of its final mass, bodies with geocentric velocities of 2.5 km/s will cross the orbit of Venus invalidates the above assumption. The case where a small body is crossing the orbit of both Earth and Venus has been investigated both by analytical and Monte Carlo techniques, and it has been found that Venus-crossing results in θ decreasing to the range 2 to 0.5 during the final stages of planetary accretion, rather than increasing to ~ 5 , as is obtained when this effect is not considered. This leads to mean velocities of ~ 8 km/s for objects crossing the orbits of both Earth and Venus. Results of calculations of the masses of the second largest body are given in Table 2.

Elimination of the residual planetesimals. These lower values of θ lead to much larger objects in the zone of Earth and Venus during the final stages of accumulation. In the case of runaway accretion the overwhelming dominance of the planetary embryo was established by the much more rapid growth of the largest body. For these lower values of θ , this dominance is established by an alternative effect: the greater stability of the embryo during the regime of fragmentation which exists during the final stage of accumulation of the embryo. This fragmentation primarily results from two processes: disruption following approach within the Roche limit of the Earth or Venus, or collisional fragmentation.

The largest residual planetesimals ($\sim 10^{26}g$) will probably be immune to destruction by collision and are likely to be continuing to accrete until they are disrupted by tidal forces. Their mass is greater than that of the present moon, which is near equilibrium with respect to accretion vs. erosion by cratering (Gault *et al.*, 1963; O'Keefe and Ahrens, 1975, 1976) at an average impact velocity about twice as great. At a

TABLE 2.

| A. Mass of the Second Largest Body When the Earth Embryo is 2×10^{27} g Initial Mass Ratio at $M_1 = 10^{21}$ g: | | | |
|--|------------------------|------------------------|------------------------|
| θ | 1.16 | 2.20 | 8.00 |
| 1 | 1.1×10^{27} g | 4.2×10^{26} g | 2.0×10^{26} g |
| 2 | 4.0×10^{26} | 7.4×10^{25} | 3.9×10^{25} |
| 3 | 1.9×10^{26} | 2.4×10^{25} | 1.2×10^{25} |
| 4 | 1.1×10^{26} | 1.1×10^{25} | 5.5×10^{24} |
| 5 | 7.2×10^{25} | 6.4×10^{24} | 2.9×10^{24} |
| B. Mass of the Second Largest Body When the Largest Body is 4×10^{27} g | | | |
| 1 | 2.2×10^{27} g | 6.4×10^{26} g | 5.0×10^{26} g |
| 2 | 7.0×10^{26} | 1.3×10^{26} | 7.7×10^{25} |
| 3 | 3.0×10^{26} | 4.3×10^{25} | 2.3×10^{25} |
| 4 | 1.6×10^{26} | 2.0×10^{25} | 1.0×10^{25} |
| 5 | 1.1×10^{26} | 1.1×10^{25} | 5.5×10^{24} |

mean impact velocity of 8 km/s, bodies less than $\sim 2 \times 10^{24}$ g in mass will be subject to fragmentation rather than continuing to accrete. The lifetime for collisional destruction of these bodies by smaller residual bodies in the zone of Earth and Venus may be estimated by methods used earlier (Wetherill, 1967) to be in the range of 10^6 to 10^7 years. Smaller bodies of mass less than 10^{22} g will be very short lived ($<10^5$ yr), and a collisional mass distribution may be expected to be established among these smaller bodies. The population of small bodies will be maintained by supply of $\sim 10^{23}$ g bodies resulting from Roche limit destruction of bodies $<10^{24}$ g in mass. Fragments will be removed from this population of fragmental material by accretion onto those bodies large enough to accrete (i.e., $\leq 2 \times 10^{24}$ g), which will ultimately be only the Earth and Venus embryos. Therefore, the final result will be the same as was the case for the alternative of runaway accretion. All the mass will be in the planetary embryos (except for a small fraction accelerated to Jupiter-crossing). The difference will be that large bodies, up to $\sim 3 \times 10^{26}$ g in mass will have had a transient existence during the final stages of accretion. The time scale for sweep-up of all the bodies will be somewhat extended by the higher ve-

locities during the final stages but will still be $\sim 10^8$ yr.

Heating of the moon by impact of large planetesimals. As discussed earlier (Safronov 1969, Ruskol 1974, Wetherill 1975a), large high-velocity impacts will deposit their kinetic energy beneath the lunar surface, which will be buried by fallback of crater ejecta into the transient cavity. This trapping of energy will be particularly pronounced for the largest impacts inasmuch as in this case most of the fragmented material will fail to escape the cavity because of the large gravitational energy required.

In an accreting body, the heat trapped in this manner will be further buried by deposition of newly accreted material onto the floor of the crater, thereby minimizing the radiation into space which limits the temperature in most accretion models (i.e., Hanks and Anderson, 1969; Mizutani *et al.*, 1972). This effect has been estimated by a simple model in which the depth of burial of the heat increases as a result of accretion and decreases by conduction of heat to the surface.

Under the conditions of accretion, the dominant mode of heat transfer to the surface will not be ordinary lattice conduction but mixing of previously buried material to the surface by subsequent impacts. The appropriate

value of "eddy conductivity" to be used is quite uncertain. Values of $\sim 2 \text{ cm}^2/\text{s}$ are calculated by Safronov (1969), and similar values can be estimated from the work of Blake and Wasserburg (1976) carried out in a different context. Use of this value indicates that bodies with radii larger than $\sim 40 \text{ km}$ in radius, i.e., with masses $\leq 10^{21} \text{ g}$ will have a large fraction of their kinetic energy permanently trapped beneath the accreting surface. At first the fraction of impact melt produced in any single impact will not be large. Much of the melted material will be mixed with pulverized unmelted crater debris; it will merely heat it slightly and produce little igneous differentiation. However, the cumulative effects of further impacts will cause the temperature of the multiply reworked debris to approach and exceed the melting point. Very close estimates are difficult, but preliminary calculations suggest that during the addition of the final half of the moon's mass (outer 360 km) about 10% of the impacting mass was in the form of bodies more massive than 10^{20} g . This leads to an average kinetic energy trapped within the outer 360 km of $\sim 8 \times 10^9 \text{ ergs/g}$. This is about 40% of the energy required to produce complete melting of this region. If these figures are correct, the outermost portion of the moon will be heterogeneously melted and differentiated at the end of accretion. The individual large accreting bodies will be sufficiently energetic to completely melt many times their own volume of material, which has already been heated much of the way toward melting point. Regions which by chance failed to be impacted by a very large body would contain only small regions of total melt and much fine material mixed with quenched glass. The resulting state of primordial differentiation may be quite different from a "magma ocean" resulting from uniformly distributed heat sources.

In the alternative model, in which runaway accretion causes the second largest body to be much smaller, it seems unlikely that lunar heating

would be sufficient to account for the evidence for primordial lunar differentiation, especially if the larger bodies are still destroyed by encounters within the Roche limit. The resulting trapped energy in the outer 360 km is estimated to be $\sim 3 \times 10^7 \text{ ergs/g}$, sufficient to melt only $\sim 0.1\%$ of this region. Because of many uncertainties in these calculations, the absolute values of these numbers should probably not be taken too seriously. However in the alternative model, the much smaller number of large bodies, impacting at less than half the velocity, must inevitably result in much smaller quantities of trapped energy.

Concluding remarks. This rather sketchy account of a chain of events within the framework of the Safronov accretion theory should at least show that significant primordial differentiation of the moon could have occurred even on a long $\sim 10^8$ time scale. The subsequent magmatic evolution of a heterogeneously melted and differentiated moon will be more complex than that of the "magma ocean." Although this complexity may be an inconvenience, in no way does complexity or simplicity bear on the question of whether the moon was uniformly or heterogeneously differentiated. The possibility of heterogeneous differentiation was not introduced as an *ad hoc* complexity to complicate the lives of petrologists; it is merely a probable consequence of an equally simple, and dynamically more plausible, model of accretion. It may be that exploration of the petrological consequences of this variant may result in its seeming more satisfactory than the magma ocean, or vice versa. This remains to be done; some speculations bearing on this have been presented (Wetherill 1975a).

Primordial heating of the terrestrial planets would also result from this mechanism. The differences in the initial temperatures between the larger bodies such as the earth and the moon would be less than in the case of heating by the very rapid accretional mod-

els that have been published (e.g., Hanks and Anderson, 1969). This arises from the fact that in the theory presented in this work the energy input depends primarily upon the kinetic energy of the heliocentric planetesimals, the acceleration by the gravitational field of the accreting planet being of secondary importance. However, somewhat higher initial temperatures may be expected for the earth, if only as a consequence of all the impacts being caused by heliocentric bodies rather than largely geocentric bodies, as is the case for a coaccreting moon. Insofar as planetesimals in the range of $10^{25} - 10^{26}$ g are still accreting prior to tidal disruption, significant heating and even igneous differentiation of their interiors are possible but difficult to estimate with any degree of certainty.

As mentioned in the introduction, numerous other authors have invoked large bodies in connection with various problems of lunar origin. The accretional model outlined herein can, when more fully worked out, lead to fairly definite predictions concerning the size distribution, orbits, and evolution of large bodies in the early solar system. In this context these suggestions by others represent processes which are possible, rather than being contrived, as has sometimes been alleged. It remains to be seen to what extent they are probable rather than simply possible.

It is also of interest to inquire into the ultimate fate of the large bodies that were initially present in the inner solar system. Most of them simply accreted to form the moon and terrestrial planets. A small percentage of them were ejected from the solar system. However, the Monte Carlo calculations mentioned earlier indicate that if Mars was present during the accretion of the earth, about 1% of the earth planetesimals remaining after the growth of the earth was essentially complete would be removed from earth-crossing by Mars perturbations. Most of these would have been deep Mars-crossers in

orbits similar to the present Amor objects and returned to earth-crossing on a time scale of $\sim 2 \times 10^8$ years. The role of these bodies in the late heavy bombardment of the terrestrial planets has been discussed elsewhere (Wetherill 1975b). Of greater interest are the smaller number ($\sim 10\%$) of these which evolve into shallow Mars-crossers with lifetimes comparable to the age of the solar system. Of the $\sim 10^{26}$ g which remained when the growth of the earth was 98% complete, perhaps 10^{23} g was "implanted" into these long-lived orbits. If Mars accumulated on the same time scale as the earth, those bodies would be outnumbered by similar residua from the formation of Mars. On the other hand, the formation of Mars is difficult to understand unless it represents an "aborted" earth-size planet, the growth of which was terminated by the early heavy bombardment of Jupiter planetesimals, as suggested by Saffronov (1969) and Weidenschilling (1975). In this case the Mars residua would have been destroyed before the implantation of the earth planetesimals, and this region of the asteroid belt would now be largely populated with residual material from the formation of Earth and Venus. The differentiated meteorites, such as the basaltic achondrites, are likely to arise from this region of the asteroid belt, and it is possible that these objects are fragments of earth planetesimals that have now returned home after an absence of 4.5 billion years. When viewed from this standpoint it is possible that the dynamic and chemical heterogeneity of the present asteroid belt is a consequence of this region of the solar system being a "sink" for residual material from both the inner and the outer solar system.

Late (4.0 b.y.) Bombardment of the Moon and Terrestrial Planets

Introduction. Prior to the recent program of manned and unmanned exploration of the moon and terrestrial planets, there was a tendency to sepa-

rate earth history into two discrete and nonoverlapping periods of time. These were the last $\sim 3.5 \times 10^9$ yr, revealed by the terrestrial geological record, and the primordial nebular and accretional periods, 4.6×10^9 years ago. Evidence concerning the latter was inferred from theoretical considerations and observational and meteoritic data. It was commonly believed that the cratered surface of the moon represented bombardment during the terminal phase of this primordial period.

Following the Apollo 14 mission to the Fra Mauro region of the moon and dating of these rocks at $3.9\text{--}4.0 \times 10^9$ years, it became apparent that the period of intensive lunar cratering and mare basin formation continued long after the completion of the $\sim 10^8$ -year formational period of the moon and planets. In addition to the "early heavy bombardment" which more or less accompanied the accretion of the planets, there was a "late heavy bombardment" which continued for hundreds of millions of years and may well have been episodic in character (Tera *et al.*, 1974).

The Mariner 10 spacecraft photographed $\sim 40\%$ of the surface of Mercury to a resolution of 10 km and selected regions to a resolution of 200 m. Photogeological study of these data indicates a remarkable similarity between the impact flux on Mercury and the moon (Murray *et al.*, 1975). Both planets contain densely cratered regions containing more than 200 craters/ 10^6 km² larger than 10 km in diameter. The lunar regions of this kind represent a steady-state crater population, whereas Mercury contains both steady-state regions of this kind and poorly understood "intercrater" terrains in which a high density of craters larger than 50 km in diameter appears to be superimposed on an older relatively uncratered surface (Trask and Guest 1975). Both planets contain ringed impact basins and associated ejecta deposits ranging up to ~ 1000 km in diameter. In both cases postbasin surfaces have crater densities of ~ 120 craters/ 10^6 km² greater than 10 km

diameter. Finally, both planets contain younger basin-filling surfaces presumably of volcanic origin with lower crater frequencies of ~ 40 craters/ 10^6 km² greater than 10 km in diameter. Although the Martian crater record is obscured by erosional and depositional processes, photogeological studies suggest a similar impact history for that planet (Wilhelms, 1973; Chapman, 1974; Soderblom *et al.*, 1974).

These similarities between the three planetary bodies could be coincidental or could be the result of their experiencing a very similar impact flux history. If the latter is the case, the relatively lightly cratered postbasin surfaces with crater counts of $\sim 120/10^6$ km² represent a "marker horizon" throughout the inner solar system corresponding to a time of 3.9 ± 0.1 b.y. ago, as indicated by the lunar radiometric chronology.

The purpose of this work is to quantitatively explore alternative models for the interplanetary flux during the first $\sim 10^9$ years of solar system history in order to evaluate whether any of these are compatible with the hypothesis of a uniform flux history for these planets. The other consequences of these models must also be examined in order to understand the extent to which they can be reconciled with other features of the solar system, its origin, and history.

Size distribution of the impacting bodies. Insofar as the crater density is not so high as to represent a steady state between crater production and destruction (Gault 1970), the size distribution of craters can be used to infer the size distribution of the impacting bodies. Although the most densely cratered regions of the lunar highlands are in such a steady state, the more lightly cratered plains regions such as the Fra Mauro and Cayley plains are well below a steady-state density.

Detailed investigations of lunar crater size distributions (Neukum *et al.*, 1975) show that the pre-Imbrium, plains, and mare surfaces contain the same size distribution of craters. This

distribution cannot be described by a single-power law exponent over the entire range of crater sizes. For the largest craters (>10 km diameter) the slope of the distribution is rather flat and approximately corresponds to a cumulative distribution:

$$N = N_0 D^{-\alpha}$$

where α is in the range 1.4 to 1.6. This is in agreement with the results of previous authors (Shoemaker *et al.*, 1962; Baldwin, 1963) and represents a projectile mass distribution in which the total mass is strongly concentrated in the largest projectiles.

If the size range of bombarding projectiles is continued to include the Imbrium planetesimal, this concentration of mass in the largest bodies is at least equally pronounced. The projectile mass required to produce the large mass craters can be estimated by combining mare crater counts (Shoemaker *et al.*, 1962) with a reasonable energy-scaling law based on nuclear explosions and which relates diameter to impacting mass:

$$D = 0.115 M^{1/3}$$

where D is the crater diameter in meters, M is the impacting mass in grams, and an impact velocity of 15 km/s is used. This calculation gives 3×10^{19} g as the total flux since the filling of the mare basins. The integral flux on the Fra Mauro and Cayley plains formations is about three times as great, corresponding to a mass flux of $\sim 10^{20}$ g. A similar calculation for the mass of the Imbrium planetesimal gives a mass of $\sim 10^{21}$ g. In the same way, the mass of the Orientale projectile comes out to be $\sim 2 \times 10^{20}$ g. Therefore, up to and including projectiles of Imbrium size (~ 50 km in radius), the large projectiles are characterized by the fact that the largest body has a mass greater than that of the remaining objects.

This is not the kind of size distribution expected for objects that are in a steady state resulting from mutual collisional comminution. It more closely

resembles the end product of an accretional process in which larger bodies have grown at the expense of smaller ones. In the treatment of specific models for the sources of the late heavy bombardment, one relevant consideration should be whether or not a collisional mass spectrum should be expected under the conditions assumed for the model.

Insofar as there is some proportionality between the quantity of impact breccias and the extent of impact resetting of measured ages, a mass distribution dominated by a few large impacts will produce an episodic age distribution. Therefore the ~ 30 -fold decrease in mass flux between the time of the Imbrium impact and the older mare surfaces need not be entirely explained in terms of a uniformly decaying mass flux but will be in a major way a consequence of a statistical fluctuation in this flux. Therefore, to a certain extent episodicity will result simply from the "lumpiness" of the size distribution. This effect in itself is insufficient to produce *simultaneous* episodes on several planets. However, approximate simultaneity of the cessation of the late heavy bombardment could result from a flux decreasing with a characteristic half-life of ~ 50 m.y.

Relative bombardment rates on the moon and terrestrial planets. The hypothesis that the density time scale of the lunar craters can be extended to the other terrestrial planets requires that there have existed one or more populations of bodies in the inner solar system which had a nearly equal probability of impacting a given area on any of the planets. Candidate populations will be characterized by their orbital element and mass distributions and by their total mass.

The two principal classes of orbits which should be considered are those of bodies in heliocentric orbit and those orbiting as satellites of a terrestrial planet. Apart from the possibility that a constant crater density may arise by coincidence, the latter class must

evolve into heliocentric orbits in order to impact planets other than the one they are initially orbiting. No detailed discussion of this evolution from planetocentric to heliocentric orbits exists, although treatments of tidal evolution of satellites (reviewed by Kaula, 1971) and geocentric swarms (Ruskol, 1960, 1963, 1972; Ruskol *et al.*, 1975; Kaula and Harris, 1975) are relevant to this problem. This class of initial orbits will not be discussed here. However, this possibility should not be forgotten.

The evolution of various classes of heliocentric interplanetary orbits has been discussed previously (Wetherill 1974). This treatment included a discussion of the modifications made in the Monte Carlo techniques which permitted an adequate statistical sample of impacts on small bodies such as the moon and Mercury. The results of these calculations are given in Table 3.

The first two entries in this table represent bodies evolving from initial orbits similar to those required to explain the orbital distribution of the Prairie Network fireballs, and the observed time of fall and radiants of chondritic meteorites (Wetherill 1968, 1971). Such orbits can evolve from those of short-period comets. The second entry in Table 3 is such an object, Comet Temple 2. These data are nor-

malized so that the lunar impact probability per unit area is assigned the value of unity. The impact probability per unit area on the four terrestrial planets is seen to agree with the lunar value within a factor of about 3. This result is largely independent of the large difference in the efficiency with which these bodies impact the planets, shown in the third column. Objects initially in orbits similar to those of the first entry will very frequently strike an inner planet; 24% of them will hit the earth. In contrast, those in orbits similar to that of the second entry will more often be perturbed into Jupiter-crossing and ejected by that planet into interstellar orbits. Only a fraction of a percent of these bodies will impact a terrestrial planet.

The next three entries represent initial orbits that penetrate more deeply into the inner solar system, penetrating the perihelia of Venus or Mercury. The orbits calculated are those of actual bodies in the present solar system, but this is done only for illustrative purposes and not to suggest that these modern objects have any relation to the late heavy bombardment. The objects with the smaller perihelia will cause a greater crater density on Mercury than on the moon and Mars. Strictly speaking, these initial orbits are not consistent with a uniform flux history. How-

TABLE 3. Relative Impact Probability/Unit Area*

| | Initial Orbit | | Earth Impacts (%) | Mercury | Venus | Earth | Mars |
|---|---------------|------------|-------------------------|--------------------|-------|-------|------|
| | Aphelion | Perihelion | | | | | |
| 1 | 1.01 | 4.00 | 24.0 | 0.30 | 0.94 | 2.26 | 1.15 |
| 2 | 1.36 | 4.67 | 0.11 | 0.69 | 1.26 | 1.78 | 0.71 |
| 3 | 0.34 | 4.18 | 6.0 | 4.21 | 2.37 | 1.23 | 0.37 |
| 4 | 0.19 | 1.97 | 18.5 | 7.50 | 1.97 | 1.08 | 0.45 |
| 5 | 0.70 | 3.61 | 5.2 | 1.60 | 2.34 | 1.34 | 0.27 |
| 6 | 1.27 | 1.89 | 27.8 | 1.08 | 2.58 | 2.82 | 11.9 |
| 7 | 0.98 | 0.99 | 45.0 | 1.05 | 3.02 | 3.99 | 0.96 |
| 8 | 0.67 | 0.82 | 29.6 | 1.08 | 2.44 | 1.36 | 0.18 |
| 9 | 0.33 | 0.41 | <0.01 | $>1.5 \times 10^4$ | ... | ... | ... |

*Normalized to Moon = 1.0.

ever, an admixture of such orbits with others with perihelia nearer to that of the earth (the first two entries) would lead to an approximately uniform flux history as an average result.

The last four entries represent initial orbits of sufficiently low eccentricity to cross the orbit of only one planet. It might be thought that this would greatly favor impacts on that planet. To some extent this is true. The Mars-crossers are about ten times more likely to strike Mars (per unit area) than the moon. Mercury-crossers only very rarely evolve into even Venus-crossing before they strike Mercury. The results for these two planets are largely a consequence of these small planets having insufficient mass to readily "pump" the eccentricity to high enough values to cross another planetary orbit. In contrast, the larger terrestrial planets, Venus and the earth, perturb bodies into highly eccentric orbits that have a good chance of striking the moon or any of the terrestrial planets.

The general result of these calculations is that planetary perturbations tend to spread interplanetary bodies throughout the inner solar system, resulting in a comparable flux on the moon and terrestrial planets. There are exceptions to this; those which initially cross only Mercury are a particularly striking exception. Nevertheless, it will usually be difficult to confine an interplanetary population primarily to a particular planet, and many distributions of initial orbits will lead to a similar flux on the moon and Mercury.

To compare crater densities on the various planets it is necessary to consider the impact velocity as well. These have been calculated by the same techniques used to obtain the data of Table 3. Examples of these calculated velocity distributions are given in Figs. 25 and 26. Those orbits with initial perihelia well beyond Mercury will impact Mercury with about two to three times the velocity they impact the moon. When this result is combined with the size distribution discussed in

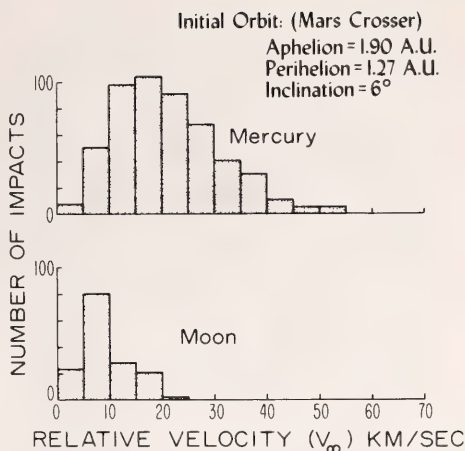


Fig. 25.. Distribution of impact velocities on the moon and Mercury for a swarm of bodies initially in Mars-crossing orbit. The velocity is given as V_{∞} , i.e., prior to the additional acceleration resulting from the gravitational field of the planet. For small planets like these this effect is small.

the previous section, it turns out that the effect of velocity is to increase the crater density by a factor of about 2.5. For objects such as those given in the first two entries of Table 2, this effect offsets the factor of 2 to 3 lower impact probability on Mercury relative to the moon, which arises from the rather ineffectual "Earth and Venus barrier" these bodies must surmount. This velocity effect is less pronounced for orbits that are initially Mercury-crossing, as shown in Fig. 26. These bodies produce a greater flux on Mercury than on the moon. The effect of velocity is thus seen to partially offset the effect of the initial perihelia, tending to result in more uniform crater densities.

Storage places. Much of the earlier discussion of this problem has centered on the question of whether there are places in the solar system in which large bodies can be "stored" for hundreds of millions of years prior to their impacting the moon or planets. Typical lifetimes, given by Monte Carlo calculations, characterizing the stability of various types of initial orbits, are given in Table 4. It may be seen that two regions of the solar system will store

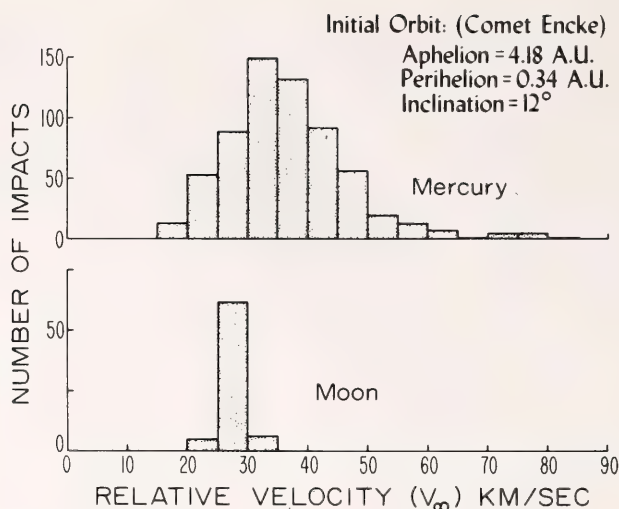


Fig. 26. Distribution of impact velocities for bodies initially in orbits equal to that of periodic Comet Encke.

bodies for the required length of time. They are the inner Mars-crossing edge of the asteroid belt and the outer portion of the solar system in the vicinity of Uranus and Neptune.

Breakup within the Roche limit. There are no known storage places which lead to a simultaneous sharp peak in the flux on the moon and terrestrial planets. Insofar as the photo-geological and radiometric age data do indicate a peak flux or "cataclysm" at ~ 3.9 b.y. and possibly at other discrete earlier times, some other explanation must be found. Several authors have proposed the breakup of a large body in the asteroid belt at that time. This is possible but improbable.

There is another, more probable way in which ~ 200 -km bodies in earth-

crossing orbits may be fragmented. As discussed by Öpik (1951), secular perturbation of the argument of perihelion will cause planet-crossing orbits to evolve on a time scale of $\sim 10^4$ years into orbits that intersect those of the crossed planets. Collisions with the planets can occur during the time interval for which this intersecting condition exists. Quantitative evaluation of the problem leads to the well-known collision formula of Öpik that forms the basis for subsequent Monte Carlo calculations of orbital evolution. The same formula can be used to calculate the probability of close encounter within a given distance of a planet simply by use of the encounter radius rather than the planetary radius. The probability of encounter within a dis-

TABLE 4. Typical Lifetimes of Planet Crossing Orbits

| Type of Orbit | Approximate Half-Life (10^6 yr) |
|--|---------------------------------------|
| Earth crosser, aphelion ~ 3 A.U. | 40 |
| Earth crosser, aphelion ~ 4.50 A.U. | 10 |
| Mars crosser, perihelion ~ 1.2 A.U. | 200 |
| Mars crosser, perihelion ~ 1.5 A.U. | 1200 |
| Jupiter crosser | 1 |
| Saturn crosser | 2 |
| Uranus crosser | 100 |
| Neptune crosser | 200 |

tance of R_e planetary radii is simply R_e^2 times the probability of impact. A consequence of this is that close planetary encounters do not in any sense constitute an improbable or *ad hoc* assumption but are a natural consequence of the same dynamical processes that have produced the observed craters on the moon and planets.

When a small body passes sufficiently close to a planet, differential gravitational attraction by the planet will generate a stress field within the body which, if strong enough, can lead to its disruption. Roche (1847) considered this problem for the case of a self-gravitating liquid satellite and obtained the result:

$$R_e = 2.44 (\rho_0/\rho)^{1/3}$$

When the encounter distances (in planetary radii) are less than R_e , disruption will occur; ρ_0 and ρ are the densities of the planet and the small body, respectively. This expression must be modified in the case of a solid body with nonzero rigidity. The latter problem has been treated by Jeffreys (1947), Öpik (1950, 1966), and Sekiguchi (1970). This earlier work has been reviewed and extended by Aggarwal and Oberbeck (1974). The latter authors show that a 200-km radius body with a reasonable tensile strength of 10^7 dynes/cm² will undergo tensile failure along a complete plane passing through the center of the body within an encounter distance of $1.18 (\rho_0/\rho)^{1/3}$ planetary radii. For a "rocky" body with $\rho = 3$ encountering the earth ($\rho_0 = 5.5$) this distance is 1.44 planetary radii, whereas for a predominantly "icy" body with $\rho = 1$, the corresponding encounter distance will be 2.08 planetary radii. Somewhat smaller distances will be found for Venus encounters. Because of these assumptions, very close approaches are required for disruption. Under these circumstances the number of disruptive encounters will be similar to the number of Earth or Venus impacts. Because of the greater surface area of Earth or Venus, impacts with these planets are much

more frequent than lunar or Mercury impacts (Table 3). Consequently a large body is more likely to undergo a disruptive encounter with Earth and Venus and to distribute fragments to the moon and Mercury than it is to impact these smaller planetary bodies directly. For the observed mass distribution law (equation 8), and disruption into ~ 100 fragments of more or less equal mass, lunar impacts of $\sim 10^{21}$ g fragments of a 10^{23} g body will outnumber direct impacts of 10^{21} g bodies by a factor of about 5. Therefore, even in this extreme case, disruption can be expected to produce episodes of heavy bombardment distributed throughout the inner solar system.

The discussions given lead to the conclusions that a modest total mass of $\sim 10^{23}$ g will suffice to produce the late heavy bombardment, that storage places with sufficiently long lifetimes exist, and that there is at least one mechanism for producing simultaneous episodes of bombardment in the inner solar system.

In work presented elsewhere a discussion of alternative specific models for the late heavy bombardment is presented (Wetherill 1975b). The most satisfactory of these are derivation of the impacting bodies from residual planetesimals in the vicinity of Uranus and Neptune, possibly the proto-cometary cloud, and derivation from residual Mars-crossing bodies. Both of these models are compatible with probable concentrations and size distributions of mass in these regions of the solar system 4 billion years ago. In both cases Roche limit disruption provides a mechanism for producing a simultaneous late heavy bombardment similar to that suggested by the cratering record.

The Mars-crossing source has the property of requiring a different cratering time scale for Mars than for the moon and Mercury. A difficulty with the Mars-crossing model is the requirement of a rather special initial distribution of Mars-crossing orbits to obtain the sharp cut-off in lunar bom-

bardment about 3.9 billion years ago. Further detailed treatment of the Uranus-Neptune source requires development of new theoretical techniques for proper handling of dynamical problems in the outer solar system.

Concluding remarks. The central question of whether it is dynamically permissible to extend to other planets the late heavy bombardment observed and dated on the moon can be answered. The answer is yes: Bodies in a wide class of orbits will have very similar probabilities for impacting the moon and terrestrial planets; there are at least two "storage places" that are sufficiently long-lived; the mass requirements are not excessive; and there is a dynamically plausible mechanism for producing simultaneous episodes of heavy bombardment on all the terrestrial planets.

Attention can then be shifted from the question of whether this hypothesis of simultaneous late heavy bombardment is permissible to the much more difficult question of whether or not it actually occurred.

Positive evidence for the hypothesis may some day come from radiometric dating of impact-related rocks from other terrestrial planets. At present the only bodies in the solar system other than the earth and the moon which can be dated in this way are the parent bodies of the meteorites. As reviewed elsewhere (Wetherill, 1974), there is considerable uncertainty concerning the location of these parent bodies in the solar system. It seems likely that at least most differentiated meteorites—achondrites, irons, and stony-irons—are of asteroidal origin, even though skepticism on this matter would prove difficult to refute. The projectiles of the late heavy bombardment should have spent much of their time in the asteroid belt and thereby increased the impact rates on the parent bodies of these differentiated meteorites, and this should be reflected in the meteorite age measurements.

Even if it occurred, this increased impact rate in the asteroid belt may

not have been very pronounced because of the high background collision rate in this region of the solar system. For example, there are at present about 30 asteroids equal to or larger than the Imbrium planetesimal ($R \cong 50$ km). If the late heavy bombardment involved an additional 100 projectiles of this size, the number of such bodies would be increased by only a factor of 4. The duration of the bombardment would be ~ 30 –100 m.y., and the integral flux on the asteroids would represent primarily impacts unrelated to the late heavy bombardment. It may also prove difficult to distinguish between impact metamorphism and melting, and similar rocks resulting from internal heating of the meteorite parent bodies. At present there is some evidence for differentiated meteorite ages in the vicinity of 3.8 b.y. (e.g., Burnett and Wasserburg, 1967; Papanastassiou *et al.*, 1974). However, it is premature to say whether these data argue for or against a simultaneous late heavy bombardment in the inner solar system.

The Earth-Crossing Apollo Objects

The study of meteorites is central to geochemical research. The remarkable similarity in the concentration of the abundant nonvolatile elements (e.g., Mg, Si, Fe, Na, Al, Ca) in carbonaceous and chondritic meteorites and the sun shows that the chondrites represent solar system material that has undergone only limited chemical processing. Therefore, it is likely that chondritic ratios such as K/Rb, Fe/Ni, and Mg/Fe represent an approximation to fundamental solar system values for these quantities rather than being more or less random numbers associated with special types of rocks. Also, the partition of trace elements between silicate, metal, and sulfide phases in meteorites is a principal basis for the geochemical classification of the elements as lithophile, chalcophile, and siderophile. The primitive nature of meteorites is indicated by their $\sim 10^8$ yr I-Xe formation intervals, and therefore the

age of the solar system can be inferred from the $\sim 4.6 \times 10^9$ yr age of most meteorites. Consequently, it is quite likely that isotopic inhomogeneities such as those found in neon (Black and Pepin, 1969), oxygen (Clayton and Mayeda, 1975), and magnesium (Lee and Papanastassiou, 1974) can be attributed to nebular or even presolar system phenomena.

For these and other reasons, our understanding of solar system history depends heavily on meteoritic data. Invaluable as these data have been, their full importance cannot be realized until we identify the actual bodies in the solar system of which the meteorites are fragments. Our understanding of this problem has advanced considerably during the past decade. To a large extent these advances have made more clear the intricacies of the problem and have shown that simple solutions, whether or not they are "generally accepted," may be incorrect or at least inconclusive. The present status of the general problem has been reviewed (Wetherill 1974). It is concluded therein that the present sources of meteorites are probably multiple: It is plausible that both comets and asteroidal bodies of several kinds contribute to the flux of meteorites on the earth.

During the past year attention has been focused on a particular class of potential meteorite source, the kilometer-sized interplanetary bodies known as Apollo objects. These are earth's nearest neighbors in space; one will pass within the orbit of the moon about once in 50 years. The name of the first of these bodies to be discovered, 1862 Apollo, has been used to give the name "Apollo objects" to the entire class. The common association of the term "asteroid" with this class may be misleading. Rather than being related to the true asteroids, primarily confined to orbits between Mars and Jupiter, these Apollo "asteroids" may actually be the exposed nonvolatile cores of comets, remaining after their icy mantles have

been evaporated by solar radiation (Öpik, 1963).

There is no doubt that both Apollo objects and their fragments impact the earth. Their elliptical orbits extend into the asteroid belt, and while in this portion of their orbits they cannot escape collisions with the asteroidal collision debris present in that region (Wetherill, 1967). The larger collision fragments derived from the Apollo objects will typically have velocities less than 100 m/s relative to the body of which they are fragments (Gault *et al.*, 1963). They will travel in orbits very similar to that of their Apollo object source, and therefore the orbits of the fragments will also cross the orbit of the earth. Precession of the argument of perihelion will cause orbits that cross earth's orbit to evolve on a time scale of $\sim 10^4$ years into orbits which intersect earth's orbit. The earth will be actually present at the point of intersection a calculable fraction of the time, and an impact with the earth will result. Whether or not we have meteorites in our collections which are fragments of Apollo objects depends upon whether the total annual number of fragments impacting the earth is sufficiently large to ensure their being represented among the ~ 2000 meteorites that have been found. In addition, it is necessary that the fragments have sufficient strength to survive passage through the earth's atmosphere at the entry velocities of typical meteorites (11–20 km/s).

In contrast, fragments of most belt asteroids cannot impact the earth. Whereas the Apollo object fragments when produced are already in earth-crossing orbit, fragments of typical asteroids ejected at ~ 100 m/s following collisions will remain in the asteroid belt. Only if they are ejected at very high velocity (~ 5 km/s) will they be placed directly into earth-crossing. However, any reasonable partition of this kinetic energy into internal degrees of freedom will melt or pulverize the fragment, and it will no longer re-

semble typical relatively unshocked meteorites. The absence of lunar rocks in our meteorite collections contributes empirical evidence for this conclusion. Special mechanisms have been proposed which may permit removal of a small quantity of collision fragments from the asteroid belt without these shock effects. The most promising of these involve proximity of the asteroid to an orbit that is resonant with the motion of Jupiter (Williams, 1973; Zimmerman and Wetherill, 1973). These also constitute promising meteorite sources, particularly for differentiated meteorites such as irons.

In recognition of their *prima facie* candidacy as meteorite sources a quantitative evaluation of the mass yield, lifetime, and orbital characteristics of meteorites derived from Apollo objects was carried out a few years ago (Wetherill and Williams, 1968). This work showed that if the mass yield is calculated from the approximately 20 *observed* Apollo objects alone, it is much too low. Estimates were given of the number of unobserved similar objects required in order for the mass yield to be adequate to produce a major part of the observed meteorite flux. Although the fairly large number required could not be ruled out on observational grounds, an assumption that there actually were so many would have been excessively conjectural.

Extension of an approach first used by Whipple (1967, 1973) now shows that the total number of these bodies larger than about 500 meters in radius is about an order of magnitude higher than most previous estimates. This approach makes use of the fact that no Apollo object has been accidentally discovered twice, even though the mode of discovery approximates a random search procedure. This would obviously be an improbable result if there were only a few more bodies than actually observed. More quantitatively, this fact has been inverted to estimate the most probable number of Apollo ob-

jects. This procedure requires establishing an upper limit on the number of Apollo objects; otherwise the most probable number would be arbitrarily large. Rather good upper limits can be set in two ways. Shoemaker *et al.* (1975) have used completeness of search calculations to show that it is unlikely there are more than 1200 of these bodies. Impacts of these bodies will produce lunar and terrestrial craters about 10 km in diameter. The small number of these craters on surfaces 3 billion years in age shows that Shoemaker's upper limit is if anything too high. Thus bounded, the inverse problem can be solved, with the result that it is 95% probable there are more than 200 of these bodies; a value compatible with all the evidence is about 600. This is in agreement with the recent estimate of 800 ± 400 given by Shoemaker *et al.* based on completeness of search.

Use of this higher abundance, together with more recent results on asteroid diameters and cratering mechanics leads to a revision of the estimates of meteorite yield given previously. The total quantity of earth-impacting Apollo fragmentation debris in the meteorite size range ($10^2 - 10^6$ g) is now estimated to be about 2×10^8 g/yr. This is in good agreement with estimates of the actual impact rate, as determined by observations of fireballs with the Prairie Network (McCroskey, 1968) and lunar seismometry (Duennebier *et al.*, 1975). Thus, provided these fragments have sufficient strength to penetrate the atmosphere, it may be that most meteorites are derived from these bodies.

If so, what kind of meteorites are they likely to be? Good spectrophotometric data have been obtained on one Apollo object, 1685 Toro (Chapman *et al.*, 1973). They indicate a surface composition similar to the most abundant class of meteorites: the metamorphosed ordinary chondrites. Albedo and lower resolution spectral data suggest this is

the case for several other Apollo objects.

Discrepancies exist between the observed distribution of meteorite radiants and time of fall and that predicted for fragments of Apollo objects. Possible but by no means assured ways to remove these discrepancies have been studied and discussed (Wetherill, 1976).

The short ($\sim 10^7$ yr) dynamical lifetime of Apollo objects requires a source to maintain the supply throughout solar system history. Various possible asteroidal sources have been investigated. Several mechanisms for removing kilometer-sized asteroid fragments from the asteroid belt are qualitatively acceptable. However, quantitatively these mechanisms fail by at least an order of magnitude. An adequate theory of asteroidal origin requires a mechanism by which $\sim 5\%$ of all the Apollo-sized fragments being produced in the asteroid belt undergo the necessary ~ 5 km/s velocity change to cause them to become earth-crossing. No such efficient mechanisms are known at present. An alternative is that most Apollo and many Amor objects are the cores of comets that have lost their volatiles by solar heating (Öpik, 1963). Observational evidence exists that there actually are a sufficient number of such cores, and it is believed that this is a likely possibility. The principal uncertainty in relating chondritic meteorites to comets is the possibility that the Apollo material does not have the mechanical strength characteristic of ordinary chondrites.

If the foregoing chain of reasoning is followed, then ordinary chondritic meteorites are fragments of comets. In spite of the fact that this conclusion does not fit well with our present thinking regarding the chemical history of the early solar system, these investigations indicate that there is a problem to which this conclusion may be a solution.

References

- Aggarwal, H. R. and V. R. Oberbeck, Roche limit of a solid body, *Astrophys. J.*, **191**, 577–588, 1974.
- Arnold, J. R., The origin of meteorites as small bodies, 2, the models; 3, general considerations, *Astrophys. J.*, **141**, 1536–1547, 1965.
- Baldwin, R. B., *The Measure of the Moon*, U. Chicago Press, p. 488, 1963.
- Black, D. C., and R. O. Pepin, Trapped neon in meteorites—II, *Earth Planet. Sci. Lett.*, **6**, 395–405, 1969.
- Blake, M. L., and G. J. Wasserburg, Cratering and cosmogenic nuclides, *Geophys. Res. Lett.*, **2**, 477–479, 1976.
- Burnett, D. S., and G. J. Wasserburg, Evidence for the formation of an iron meteorite at 3.8×10^9 , *Earth Planet. Sci. Lett.*, **3**, 137–147, 1967.
- Cameron, A. G. W., Accumulation processes in the primitive solar nebula, *Icarus*, **18**, 407–450, 1973.
- Cameron, A. G. W., and W. R. Ward, The origin of the moon. In *Lunar Science*, **7**, pp. 120–122, Lunar Science Institute, Houston, 1976.
- Chapman, C. R., Cratering on Mars: 1. Cratering and obliteration history, *Icarus*, **22**, 272–291, 1974.
- Chapman, C. R., T. B. McCord, and C. Pieters, Minor planets and related objects X. Spectrophotometric study of the composition of (1685) Toro, *Astron. J.*, **78**, 502–505, 1973.
- Clayton, R. N., and T. K. Mayeda, Genetic relations between the moon and meteorites, *Proc. 6th Lunar Sci. Conf.*, pp. 1761–1769, Pergamon Press, New York, 1975.
- Duennebier, F., J. Dorman, D. Lammlein, G. Latham, and Y. Nakamura, Meteoroid flux from passive seismic experiment data, *Proc. 6th Lunar Sci. Conf.*, pp. 2417–2426, Pergamon Press, New York, 1975.
- Gault, D. E., Saturation and equilibrium conditions for impact cratering on the lunar surface: criteria and implications, *Radio Science*, **5**, 273–291, 1970.
- Gault, D. E., E. M. Shoemaker, and H. J. Moore, Spray ejected from the lunar surface by meteoroid impact, *NASA TN* 1767, 39, 1963.
- Gerstenkorn, H., The earliest past of the earth-moon system, *Icarus*, **11**, 189–207, 1969.

- Gurevich, L. E., and A. I. Lebedinskii, Formation of the planets, *Izvestia Akad. Nauk USSR, Seriya Fizich.*, 14, 765-799, 1950.
- Hallam, M., and A. H. Marcus, Stochastic coalescence model for terrestrial planetary accretion, *Icarus*, 21, 66-85, 1974.
- Hanks, T. C., and D. L. Anderson, The early thermal history of the earth, *Phys. Earth Planet. Int.*, 2, 19-29, 1969.
- Hartmann, W. K., and D. R. Davis, Satellite-size planetesimals and lunar origin, *Icarus*, 24, 504-515, 1975.
- Jeffreys, H., The relation of cohesion to Roche's limit, *Mon. Notic. Roy. Astron. Soc.*, 107, 260-262, 1947.
- Kaula, W. M., Dynamical aspects of lunar origin, *Rev. Geophys. Space Phys.*, 9, 227-248, 1971.
- Kaula, W. M., and P. E. Bigeleisen, Early scattering by Jupiter and its collision effects in the terrestrial zone, *Icarus*, 25, 18-33, 1975.
- Kaula, W. M., and A. W. Harris, Dynamics of lunar origin and orbital evolution, 363-371, *Rev. Geophys. Space Phys.*, 13, 1975.
- Lee, T., and D. A. Papanastassiou, Mg isotopic anomalies in the Allende meteorite and correlation with O and Sr effects, *Geophys. Res. Lett.*, 1, 225-228, 1974.
- Marcus, A. H., Positive stable laws and the mass distribution of planetesimals, *Icarus*, 4, 267-272, 1965.
- Marcus, A. H., Speculations on mass loss by meteoroid impact and formation of the planets, *Icarus*, 11, 76-87, 1969.
- McCrosky, R. E., The distribution of large meteoritic bodies, *Smithsonian Astrophys. Observ. Spec. Rep.*, 280, 13 pp., 1968.
- Mitler, H. E., Formation of an iron-poor moon by partial capture, or: yet another exotic theory of lunar origin, *Icarus*, 24, 256-268, 1975.
- Mizutani, H. T., T. Matsui, and H. Takeuchi, Accretion process of the moon, *The Moon*, 4, 476-489, 1972.
- Murray, B. R. G. Strom, N. J. Trask, and D. E. Gault, Surface history of Mercury: Implications for terrestrial planets, *J. Geophys. Res.*, 80, 2508-2514, 1975.
- Neukum, G., B. König, and J. F. Arkani-Hamed, A study of lunar impact crater size distributions, *The Moon*, 12, 201-229, 1975.
- O'Keefe, J. D., and T. J. Ahrens, Shock effects from a large impact on the moon, *Proc. 6th Lunar Sci. Conf.*, 2831-2844, 1975.
- O'Keefe, J. D., and T. J. Ahrens, The high speed ejecta from a meteorite impact and planetary accretion (abstract), *EOS*, 57, 274, 1976.
- Öpik, E. J., Roche's limit; Rings of Saturn, *Irish Astron. J.*, 1, 25-26, 1950.
- Öpik, E. J., Collision probabilities with the planets and the distribution of the interplanetary matter, *Proc. Roy. Irish Acad.*, 54A, 165-199, 1951.
- Öpik, E. J., Survival of comet nuclei and the asteroids, *Advan. Astron. Astrophys.*, 2, 219-262, 1963.
- Öpik, E. J., Sun-grazing comets and tidal disruption, *Irish Astron. J.*, 7, 141-161, 1966.
- Öpik, E. J., Comments on lunar origin, *Irish Astron. J.*, 10, 190-238, 1972.
- Papanastassiou, D. A., R. S. Rajan, J. C. Huneke, and G. J. Wasserburg, Rb-Sr ages and lunar analogs in a basaltic achondrite; implications for early solar system chronologies, In *Lunar Science V*, pp. 583-585, Lunar Sci. Institute, Houston, 1974.
- Roche, E. A., Académie des Sciences et Lettres de Montpellier, Mémoires de la Section des Sciences, 1, 243-262, 1847.
- Ruskol, E. L., The origin of the moon I, formation of a swarm of bodies around the earth, *Sov. Astron. AJ*, 4, 657-668, 1960.
- Ruskol, E. L., On the origin of the moon II, the growth of the moon in the circumterrestrial swarm of satellites, *Sov. Astron. AJ*, 7, 221-227, 1963.
- Ruskol, E. L., The origin of the moon III, some aspects of the dynamics of the circumterrestrial swarm, *Sov. Astron. AJ*, 15, 646-654, 1972.
- Ruskol, E. L., On the origin of the moon, In *Proceedings of the Soviet-American Conference on Cosmochemistry of the Moon and Planets*, pp. 638-644, Nauka, Moscow, 1975.
- Ruskol, E. L., E. V. Nikolaev, and A. S. Syzdykov, Dynamical history of coplanar two-satellite systems, *The Moon*, 12, 11-18, 1975.
- Safronov, V. S., Accumulation of the earth-group planets, *Voprosy Kosmogonii*, 7, 59-65, 1960.
- Safronov, V. S., *Evolution of the Proto-planetary Cloud and Formation of the Earth and Planets*, Nauka, Moscow, translated for NASA and NSF by Israel

- Program for Scientific Translations, (1972); 1969.
- Safronov, V. S., Time scale of the formation of the earth and planets and its role in their geochemical evolution, In *Proceedings of the Soviet-American Conference on the Cosmochemistry of the Moon and Planets*, Moscow, June 4-8, 1974, pp. 624-629, Nauka, Moscow, 1975.
- Safronov, V. S., and E. V. Zvyagina, Relative sizes of the largest bodies during the accumulation of the planets, *Icarus*, 10, 109-115, 1969.
- Sekiguchi, N., On the fissions of a solid body under influence of tidal force; with application to the problem of twin craters on the moon, *The Moon*, 1, 429-439, 1970.
- Shoemaker, E. M., R. J. Hackman, and R. E. Eggleton, Interplanetary correlation of geologic time, *Adv. Astronaut. Sci.*, 8, 70-89, 1962.
- Shoemaker, E. M., E. F. Helin, and S. L. Gillett, Populations of the planet-crossing asteroids. Abstract of paper presented at the International Colloquium of Planetary Geology in Rome, Italy, September 22-30, 1975.
- Singer, S. F., Origin of the moon by tidal capture and some geophysical consequences, *The Moon*, 5, 206-209, 1972.
- Smith, J. V., Origin of the moon by disintegrative capture with chemical differentiation followed by sequential accretion, *Lunar Science*, V, 718-720, Lunar Science Institute, Houston, 1974.
- Soderblom, L. A., C. D. Condit, R. A. West, B. M. Herman, and T. J. Kreidler, Martian planetwide crater distributions: Implications for geologic history and surface processes, *Icarus*, 22, 239-263, 1974.
- Tera, F., D. A. Papanastassiou, and G. J. Wasserburg, Isotopic evidence for a terminal lunar cataclysm, *Earth Planet. Sci. Lett.*, 22, 1-21, 1974.
- Trask, N. A., and J. E. Guest, Preliminary 'geologic-terrain map of Mercury, *J. Geophys. Res.*, 80, 2461-2477, 1975.
- Urey, H. C., Primary and secondary objects, *J. Geophys. Res.*, 64, 1721-1737, 1959.
- Weidenschilling, S. J., A model for accretion of the terrestrial planets, *Icarus*, 22, 426-435, 1974.
- Weidenschilling, S. J., Mass loss from the region of Mars and the asteroid belt, *Icarus*, 26, 361-366, 1975.
- Wetherill, G. W., Collisions in the asteroid belt, *J. Geophys. Res.*, 72, 2429-2444, 1967.
- Wetherill, G. W., Time of fall and origin of stone meteorites, *Science*, 159, 79-82, 1968.
- Wetherill, G. W., Cometary vs. asteroidal origin of chondritic meteorites, In *Physical Studies of the Minor Planets*, T. Gehrels, ed., 447-460. NASA SP-267, 1971.
- Wetherill, G. W., Solar system sources of meteorites and large meteoroids, *Ann. Rev. Earth Planet. Sci.*, 2, 303-331, 1974.
- Wetherill, G. W., Possible slow accretion of the moon and its thermal and petrological consequences, pp. 184-188, Conf. on origin of mare basalts and their implications for lunar evolution, Lunar Science Institute, Houston, Nov. 17-19, 1975, 1975a.
- Wetherill, G. W., Late heavy bombardment of the moon and terrestrial planets, *Proc. 6th Lunar Sci. Conf.*, 1539-1559, Pergamon Press, 1975b.
- Wetherill, G. W., The role of large bodies in the formation of the earth and moon, In press, *Proc. 7th Lunar Sci. Conf.*, Pergamon Press, 1976.
- Wetherill, G. W., and J. G. Williams, Evaluation of the Apollo asteroids as sources of stone meteorites, *J. Geophys. Res.*, 73, 635-648, 1968.
- Whipple, F. L., The meteoritic environment of the moon, *Proc. Roy. Soc. London*, 296A, 304-315, 1967.
- Whipple, F. L., Note on the number and origin of Apollo asteroids, *The Moon*, 8, 340-345, 1973.
- Wilhelms, D. E., Comparison of Martian and lunar multi-ringed circular basins, *J. Geophys. Res.*, 78, 4084-4095, 1973.
- Williams, J. G., Secular perturbations in the solar system, Ph.D. dissertation, U. California, Los Angeles, 1969.
- Williams, J. G., Proper elements, families, and belt boundaries, In *Physical Studies of the Minor Planets*, ed. T. Gehrels, 177-181, NASA SP-267, 1971.
- Williams, J. G., Meteorites from the asteroid belt? *EOS*, 54, 233, 1973.
- Zimmerman, P. D., and G. W. Wetherill, Asteroidal source of meteorites, *Science*, 182, 51-53, 1973.
- Zvyagina, Y. V., G. V. Pechernikova, and V. S. Safronov, A qualitative solution of the coagulation equation taking into account the fragmentation of bodies, *Astron. Zh.* 50, 1261-1273, 1973.

PARTICLE TRACKS AND MICRO-IMPACT FEATURES IN GRAINS FROM GAS-RICH METEORITES

G. Poupeau* and R. S. Rajan

Introduction

Gas-rich meteorites are extraterrestrial breccias made of single crystals and lithic fragments once exposed to free space before compaction, as evidenced by the presence in individual grains of tracks from solar flare, iron group nuclei (Lal and Rajan, 1969; Pellas *et al.*, 1969) and solar wind ^4He (Poupeau *et al.*, 1974). From the anisotropy of solar flare irradiation effects in single crystals, it was inferred that the irradiation occurred in a regolith on the surface of a parent body (Poupeau and Berdot, 1972; Rajan, 1974). From analogy with the lunar soil samples, we should expect that impact features such as microcraters and glassy splashes will also be found on crystal surfaces of gas-rich meteorites. This expectation was indeed confirmed (Brownlee and Rajan, 1973) when such features were found on solar flare irradiated glass balls of the gas-rich howardite Kapoeta. Similar observations have recently been reported for carbonaceous chondrites (Goswami *et al.*, 1976). Radiometric studies of individual clasts from a few gas-rich meteorites have shown that these breccias could have been compacted as early as ~ 3.5 AE ago in the case of Kapoeta (Papanastassiou *et al.*, 1974; Rajan *et al.* 1976), ~ 3.7 AE for Malvern (Rajan *et al.*, 1975) to ~ 4.3 AE for Bununu (Rajan *et al.*, 1975). Fission track evidence also suggests that the carbonaceous chondrite Murchison was probably compacted ~ 4.2 AE ago (Kothari and MacDougall, 1975).

So far, extensive studies of the solar flare tracks/microcraters record in single grains of extraterrestrial re-

golith have been limited to the lunar soils (Poupeau *et al.*, 1975; Poupeau and Johnson, 1976) and the carbonaceous chondrite Murchison (Goswami *et al.*, 1976). We are extending these studies to a number of gas-rich meteorites, with the main purposes of (1) defining the micrometeorite mass distribution over different geological times as inferred from microcrater measurements, and (2) studying the temporal variations of the micrometeorite flux relative to the solar flare flux and ultimately, in collaboration with E. Zinner, to the solar wind flux. The solar wind record can be studied in single grains with the help of an ion probe (Zinner *et al.*, 1976). Finally, the combined study of glassy splashes as well as microcraters and tracks on single meteoritic grains should give some insight into the regolith dynamics of their parent body.

In this report we present results of a search for microcraters and other impact features (glassy discs/splashes) as well as the measurement of the cosmic-ray track records in the gas-rich meteorite Kapoeta.

Sampling and Experimental Procedures

Gas-rich meteorites are known in several groups of stony meteorites: ordinary and carbonaceous chondrites as well as achondrites such as howardites and aubrites. We have selected for our work, on the basis of their high content of solar wind gases and abundance of track-rich grains, one meteorite from some of these groups: the howardite Kapoeta and the aubrite Khor Temiki. For comparison, we have also included the carbonaceous chondrite Murchison. The samples of Kapoeta and Murchison were single fragments and weighed ~ 0.5 and ~ 0.8 grams, respectively. Our sample of Khor Temiki is an aliquot of a 92–150 μm sieved powder previously used by Eberhardt *et al.* (1965) for rare gas analysis.

In order to study the impact record of micrometeorites on single grains, we

*McDonnell Center for the Space Sciences of Washington University, St. Louis, Missouri 63130. On leave from Centre National de la Recherche Scientifique, Paris, France.

have disaggregated the fragments of Kapoeta and Murchison into their original grains. It is very important that during this process the "external" surfaces of the crystals and chondrules are preserved. Although gentle crushing may partly preserve the external surface of crystals, we have increased the recovery of original surfaces by thermally induced disaggregation.

For this purpose at DTM we have designed and built an automated device for gentle disaggregation of the meteorite samples. The sample is first evacuated to $\sim 1 \mu$ and filled with deionized water. The tube containing the sample is then alternately cycled between liquid nitrogen and water at 45°C . A schematic diagram of the device is shown in Fig. 27. The method is very effective in recovering grains with their original surfaces intact for grains greater than 50μ , as deduced from scanning electron microscope (SEM) observations.

The Khor Temiki powder was prepared by Eberhardt *et al.* (1965) from gentle crushing of a fragment of this meteorite. The low degree of compaction of this meteorite allows an easy separation of its constituent crystals. It has been shown from the presence of

both solar wind ^4He and solar flare VH-ion tracks in single crystals that original surfaces have in fact survived the crushing process at least partially (Poupeau *et al.*, 1974).

Impact features on the surface of extraterrestrial grains consist of microcraters and a variety of glassy splashes (cf. Blanford *et al.*, 1974). The presence of microcraters, in either meteorites or lunar material, seems to be limited to grains irradiated by the solar flares (Brownlee and Rajan, 1973; Goswami *et al.*, 1976; Poupeau and Johnson, 1976). On the contrary, it has been shown that in lunar soils, glassy splashes were present on almost all crystals (Poupeau and Johnson, 1976). We therefore applied different procedures for the search of microcraters and glassy splashes on meteoritic crystals. For glassy splashes, a series of crystals chosen randomly among those exhibiting euhedral to nearly euhedral shapes were observed in an SEM. For microcraters, as the abundance of solar flare irradiated grains is usually rather low, a selection had to be made on the basis of nuclear track data. Therefore, series of crystals were mounted in epoxy, polished, and etched. Only crystals having solar flare

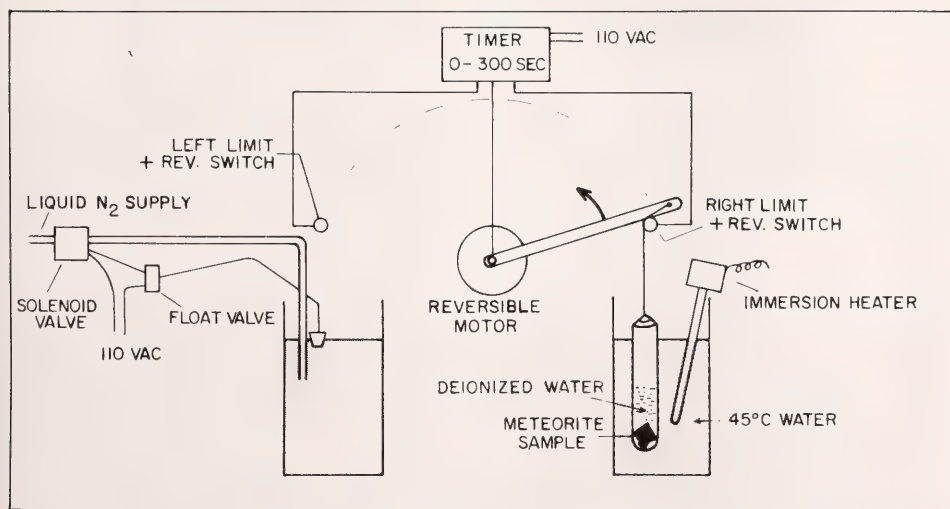


Fig. 27. An automated device for gentle disaggregation of meteorites (and lunar samples).

tracks were extracted from the epoxy and their remaining external surface studied for microcraters in an SEM.

Results and Discussions

We have studied for impact features ~70 crystals and glassy objects from the three meteorites Kapoeta, Khor Temiki, and Murchison. The search for microcraters and glassy splashes was carried out under a standard 5000 \times magnification scan (Poupeau *et al.*, 1975) in order to make a meaningful comparison with the results from the lunar samples. The results are reported in Table 5, where they are compared with other available lunar and meteoritic data. All our measurements (including the data on lunar soils) have been obtained on crystals in the ~100–150 μm range.

Of the 45 crystals studied from Kapoeta, Khor Temiki, and Murchison, none had any detectable microcraters. Brownlee and Rajan (1973) had found microcraters in 2 out of the 9 glassy spherules from Kapoeta. We scanned 16 more spherules, but no additional microcraters ($\geq 0.2 \mu\text{m}$) were detected.

Lunar and meteoritic microcraters present the same general morphology illustrated in Fig. 28. Figure 28(a and b) shows cratered glass balls from the lunar breccias 15086 and Kapoeta, respectively. The largest microcraters found in the meteoritic spherule (Fig. 28b) have diameters of 9 and 6 μm , respectively Brownlee and Rajan, 1973). One of the above craters is shown in Fig. 28(d), and a crater found in a lunar glass sphere from the regolith breccia 15086 is shown for comparison in Fig. 28(c). Both craters on Fig. 28(c and d) present characteristic spall zones surrounding the central pits. Submicron craters in both lunar and meteoritic grains are typically characterized by raised rims around the pits (Fig. 28, e and f). By analogy to the lunar soil studies, we have classified the thin discs of $\leq 2 \mu\text{m}$ diameter (the "pancakes" of Blanford *et al.*, 1974) from the thicker glassy splashes on the surface of crystals (Fig. 28f). No glassy discs have yet been found on any meteoritic crystal, but some are possibly present on the surface of glassy spherules.

Thicker glassy splashes are definitely present on glassy spherules in

TABLE 5. Cosmic-Ray Tracks, Microcraters, and Glassy Discs on Crystals from Lunar Soils and Gas-Rich Meteorites

| Sample | Mineral Phase | Fraction of Crystals with: | | | | |
|-----------------------------------|---------------|---|--------|-------------------------|----------------------------|--------|
| | | Track Densities ≥ 10 ⁶ /cm ² | (N)† | Microcraters ≥ 0.1μm | Glassy Discs ≥ 2μm dia. | (N)* |
| <i>Lunar Soils</i> ⁽¹⁾ | | | | | | |
| 12033 | F† | 0.03 | (156) | 0 | 0.07 | (14) |
| 14141 | F | 0.35 | (60) | 0.14 | 0.74 | (19) |
| Mature Soils | F | ≥ 0.8 | (>200) | 0.35–0.67 | ≥ 0.90 | (>200) |
| <i>Meteorites</i> | | | | | | |
| Kapoeta | F, Py† | 0.13 | (65) | 0 | 0 | (15) |
| | "glass" balls | 0.20 | (15) | 0.08 | ~0.04 | (25) |
| Khor Temiki | Py | 0.12 ⁽²⁾ | (1203) | 0 | 0 | (15) |
| Murchison | 01† | | | 0 | 0 | (15) |
| | 01 | 0.01–0.05 ⁽³⁾ | (3000) | ~0.001 | N.D. | (20) |

* (N) = total number of observed crystals.

[†]F = Feldspar; Py = pyroxene; Ol = olivine; N.D. = not determined.

(1) Poupeau and Johnson, 1976.

(2) Poupeau *et al.*, 1974.

(3) Goswami *et al.*, 1976.

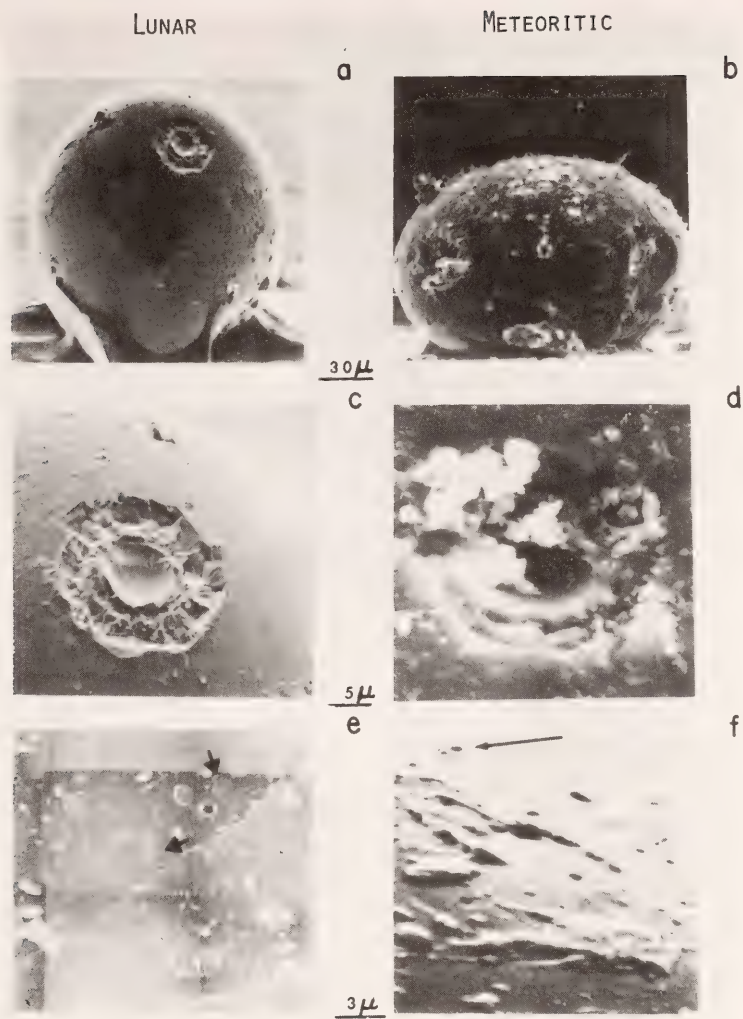


Fig. 28. Microcraters and glassy splashes on meteoritic and lunar glassy spherules and crystals, as observed under a scanning electron microscope (SEM). (a),(c) Glassy spherule from the Apollo 15 regolith breccia 15086. (b),(d) Glassy spherules from Kapoeta meteorite. (e) A feldspar crystal from the lunar soils. Flat glassy discs ("pancakes") are indicated by arrows. (f) A glassy splash on the surface of a spherule from Kapoeta. A submicron crater is indicated by the arrow.

Fig. 28(e). On crystal surfaces, we have not yet found any features that can be unambiguously attributed to glassy splashes. This may be in part due to the large background of adhering grains on the crystal surface, many of which are in fact embedded.

Our track density ($\equiv P$) measurements on 40 feldspar grains from a single centimeter-sized fragment give

well-defined peak in the range of $1.5 \pm 0.8 \times 10^6/\text{cm}^2$, containing 29 crystals. The above peak is well understood as due to the stopping iron nuclei from the galactic cosmic rays during the cosmic-ray exposure age of the meteorite. An example of such a crystal is shown in Fig. 29(c). Six crystals had ρ values in the range of $2.4\text{--}4.0 \times 10^6/\text{cm}^2$, which is possibly due to a some-

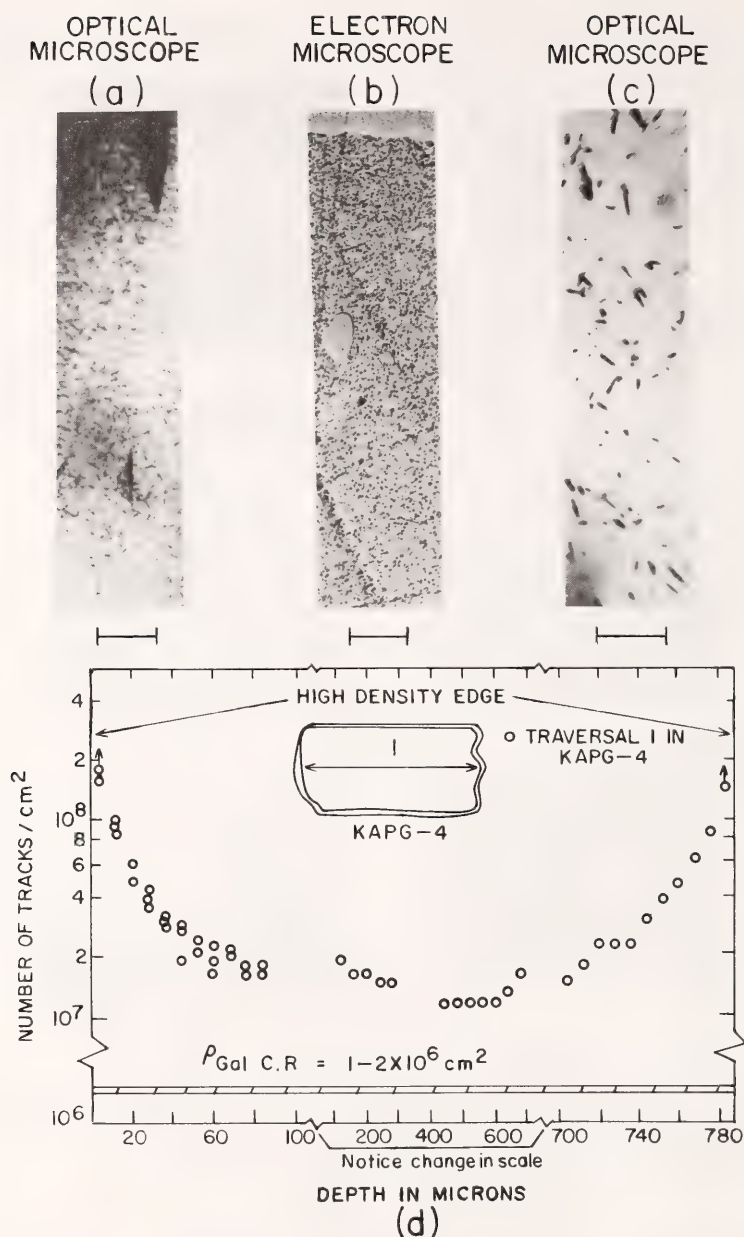


Fig. 29. Cosmic-ray tracks in Kapoeta feldspars. (a),(b) "Track-rich" crystals with track density gradients from the edges, as viewed under an optical (a) or in a transmission electron microscope (b), using a C-Pt replica technique (Rajan, 1974). The scale bars are 10μ and 2μ and track density values at the edges are $\sim 2 \times 10^8/\text{cm}^2$ and $\sim 2 \times 10^9/\text{cm}^2$. (c) Crystal with a low homogeneous track density, accumulated from galactic cosmic rays during the cosmic-ray exposure age of the meteorite. The track density is $\sim 2 \times 10^6/\text{cm}^2$.

what closer location to the preatmospheric surface. The remaining five crystals have significantly higher

track densities, indicative of a precompaction irradiation history. While one crystal had $\rho = 1.5 \times 10^7/\text{cm}^2$, the re-

maining four crystals were "track-rich", i.e., they had track density at the edges of $\geq 10^8/\text{cm}^2$ and had characteristic steep gradients toward the center of the crystal, with ρ values at the center of the crystal being $\sim 2 \times 10^7/\text{cm}^2$. An example of a track-rich grain is shown in Fig. 29 (a and b), and the measured track-density profile across the crystal is shown in Fig. 29(d), indicating the dramatic gradient.

Finally, we removed the track-rich crystals from the epoxy mounts and observed their remaining external surfaces under an SEM. No microcraters larger than $0.15 \mu\text{m}$ (our detection limit) were found in any of these four crystals.

It is known from lunar soil studies that for a grain to be cratered, being track-rich is a necessary but not sufficient condition (Poupeau and Johnson, 1976). The probability of a track-rich grain being cratered increases with the maturity of the soil, being essentially zero for immature soils, evolving in a complex way, and approaching unity for very mature soils. Interestingly, from the present work we find that the meteorites lie on the extrapolation of the same trend line exhibited by lunar soils. Such a correlation would be significant when confirmed with more observations on meteorites and would suggest a common dynamical mechanism operative on all the regoliths. However, we do not yet understand the scarcity of glassy splashes on meteoritic grains, since they are quite abundant even on rather immature lunar soils (see Table 5).

References

- Blanford, G. E., R. M. Fruland, D. S. McKay, and D. A. Morrison, Lunar surface phenomena: solar flare track gradients, microcraters and accretionary particles, *Proc. 5th Lunar Sci. Conf.*, 3, 2501, 1974.
- Brownlee, D. E., and R. S. Rajan, Discovery of micrometeorite craters on chondrule-like objects from Kapoeta, *Science*, 182, 1341, 1973.
- Eberhardt, P., J. Geiss, and N. Grogler, Ueber die Verteilung der Uredelgase im meteoriten Khor Temiki, *Tschermaks Mineral. Petrogr. Mitt.*, 10, 535, 1965.
- Goswami, J. N., I. D. Hutcheon, and J. D. MacDougall, Microcraters and solar flare tracks in crystals from carbonaceous chondrites and lunar breccias, *Proc. 7th Lunar Sci. Conf.*, in press, 1976.
- Kothari, B. K., and J. D. MacDougall, *Meteoritics*, 10, 428, 1975.
- Lal, D., and R. S. Rajan, Observations on space irradiation of individual crystals of gas-rich meteorites, *Nature*, 223, 269, 1969.
- Papanastassiou, D. A., R. S. Rajan, J. C. Huneke, and G. J. Wasserburg, Rb-Sr ages and lunar analogs in a basaltic achondrite: implications for early solar system chronologies, *Lunar Science V* (C. Watkins, ed.) Lunar Science Institute, Houston, 583, 1974.
- Pellas, P., G. Poupeau, J. C. Lorin, H. Reeves, and J. Audouze, Primitive low-energy particle irradiation of meteorite crystals, *Nature*, 223, 272, 1969.
- Poupeau, G., and J. L. Berdot, Irradiation ancienne et recente des aubrites, *Earth Planet. Sci. Lett.*, 14, 381, 1972.
- Poupeau, G., and J. Johnson, Micrometeorite and solar flare maturation of lunar soils, *Earth Planet. Sci. Lett.*, in press, 1976.
- Poupeau, G., T. Kirsten, F. Steinbrunn, and D. Storzer, The records of solar wind and solar flare in aubrites, *Earth Planet. Sci. Lett.*, 24, 229, 1974.
- Poupeau, G., R. M. Walker, E. Zinner, and D. A. Morrison, Surface exposure history of individual crystals in the lunar regolith, *Proc. 6th Lunar Sci. Conf.*, 3, 3433, 1975.
- Rajan, R. S., On the irradiation history and origin of gas-rich meteorites, *Geochim. Cosmochim. Acta*, 38, 777, 1974.
- Rajan, R. S., J. C. Huneke, S. P. Smith, and G. J. Wasserburg, ^{40}Ar - ^{39}Ar chronology of isolated phases from Bununu and Malvern howardites, *Earth Planet. Sci. Lett.*, 27, 181, 1975.
- Rajan, R. S., J. C. Huneke, S. P. Smith, and G. J. Wasserburg, ^{40}Ar - ^{39}Ar chronology of individual clasts from the Kapoeta howardite and the origin of howardites, submitted to *Earth Planet. Sci. Lett.*
- Zinner, E., R. M. Walker, J. Chaumont, and J. C. Dran, Ion probe analyses of artificially implanted ions in terrestrial samples and surface-enhanced ions in lunar sample 76215,77, *Proc. 7th Lunar Sci. Conf.*, 1976.

COSMIC-RAY RESEARCH

Scott E. Forbush

Cosmic-ray diurnal anisotropy and the reversals of the sun's poloidal magnetic field. Variations with a "period" of two solar cycles in the cosmic-ray diurnal anisotropy component in the asymptotic direction 128° east of the sun which are related to the reversals of the sun's poloidal magnetic field have been discussed in previous annual reports. The component of the diurnal anisotropy in the asymptotic direction 90° east of the sun varies with geomagnetic activity and exhibits a solar cycle variation. Together these two components account for essentially all the variations of the annual means of the diurnal anisotropy from 1937 to 1974, as was reported by Forbush at the 14th International Cosmic-Ray Conference in Munich, August 1975. These results could only have been derived from data covering the long interval since 1937; such data are available from three stations with Carnegie Institution of Washington ionization chambers. Nevertheless, this interval is less than that covered by two "cycles" in the variation of the sun's poloidal magnetic field. Thus, it is desirable to extend the observational series for at least another two or three years (circa 1978), which fortunately is being achieved by the unselfish, whole hearted, gratuitous cooperation of individuals at three stations,

Observations and reduction of data. Cosmic-ray ionization chambers were operated throughout the report year at Huancayo, Peru; at Fredericksburg, Virginia, U.S.A.; and at Christchurch, New Zealand. It is anticipated that by the end of 1976 the scaling and reduction of records will again be on a current basis.

Cooperation in operation of cosmic-ray meters. Appreciation is expressed to the U.S. Geological Survey and the U.S. Department of the Interior and its staff at the Fredericksburg Geomagnetic Center for efficient operation of the

cosmic-ray meter there during the past report year, and to the Government of Peru and the Director and staff of the Instituto Geofísico del Peru for making cosmic-ray records from Huancayo available. Appreciation is also expressed to the Director and staff of the Geophysical Observatory at Christchurch, New Zealand, for the excellent maintenance of the equipment there and for the fine records obtained.

RB-SR MANTLE ISOCHRONS

C. Brooks, D. E. James, S.R. Hart,
and A. W. Hofmann

INTRODUCTION

The use of isotopic abundances of strontium in volcanic rocks as tracers of the source composition has long been an important geochemical tool for the study of the earth's mantle. Because of their uniquely low $^{87}\text{Sr}/^{86}\text{Sr}$ ratios, it has been shown, for example, that the mid-ocean ridge volcanics must tap a mantle source that is different from virtually all other volcanic rocks including those found on oceanic islands. A difficulty encountered in the interpretation of the isotopic data is that these other groups of volcanic rocks, though nearly always higher in $^{87}\text{Sr}/^{86}\text{Sr}$ than mid-ocean ridge basalts, tend to have much more variable isotope ratios, thus obscuring the isotopic distinction even between crustal and mantle derived material.

In the two sections of this report we attempt to obtain additional information by using both the $^{87}\text{Sr}/^{86}\text{Sr}$ ratio and the Rb/Sr ratio of these rocks in conventional isochron diagrams. Because isolated occurrences of apparent Rb-Sr isochrons with "ages" greatly in excess of the age of the volcanic eruptions have been reported before, we undertook a systematic search of the literature and our own data for such

pseudoisochrons. We found that pseudoisochrons are indeed very common in individual groups of volcanic rocks. Moreover there is a well-defined single pseudoisochron for a world-wide sampling of oceanic tholeiitic basalts.

We believe that these pseudoisochrons are inherited from the mantle and that the volcanic rocks therefore contain much more specific information about the local and world-wide evolution of the mantle than had been realized. For example, the world-wide Rb-Sr isochron age of 1.6 ± 0.2 b.y. for tholeiites from oceanic islands and mid-ocean ridges may date a major event in the evolution of the earth's mantle. Similarly, the more variable and mostly younger ages derived from isochron correlations for more localized groups of continental volcanic rocks are interpreted as inherited from old subcontinental lithosphere.

To account for this heterogeneous structure of the mantle we propose a model for the mantle whereby diapirs or "blobs" rise from the lower mantle (mesosphere) through a partially molten upper mantle (asthenosphere) until they encounter the completely solid uppermost mantle (lithosphere). In oceanic regions the lithosphere is relatively thin (100 km or less), and the blobs rise directly to the surface to form oceanic islands. The world-wide mantle isochron for these rocks is generated by mixing of mesosphere and asthenosphere in different proportions, and the age of 1.6 b.y. may date the chemical fractionation and segregation of these largest-scale heterogeneities of the mantle. In continental regions the lithosphere is thicker (up to 400 km), and the mesospheric material does not necessarily penetrate directly to the surface. Rather, much of it remains near the base of the lithosphere and is gradually incorporated by the slowly thickening lithosphere which grows by freezing out of partially molten asthenosphere. Continental volcanism is caused by reactivation of this heterogeneously accreted lithosphere, and

the mantle isochrons contain a record, possibly distorted, of the accretion history of this lithosphere.

PART I: CONTINENTAL REGIONS

In this report we discuss apparent Rb-Sr isochron relationships of volcanic (and a few intrusive igneous) rocks, believed to be derived from the subcontinental mantle. Most of the rocks included in this discussion are basalts and andesites, but others are more exotic rock varieties, mostly of strongly alkalic affinity (phonolites, nephelinites, syenites, ijolites, and shoshonites). The intrusive rocks include two suites of granites from California. In most cases the age of the continental crust is greater than 10^9 years, so it is reasonable to expect that at least some of the underlying lithosphere is also quite old. In contrast with the results reported in Part II (for oceanic volcanic rocks), we have not averaged any of the data by geographical (or any other) groupings because we do not attempt to show (nor would we expect to find) any meaningful world-wide correlations, except perhaps that from a statistical point of view rocks with high Rb/Sr ratios would tend to have high $^{87}\text{Sr}/^{86}\text{Sr}$ ratios.

The terminology adopted is as follows: *Lithosphere* is the rigid outer shell of the earth which includes the crust and upper mantle; *asthenosphere* is mobile (probably incipiently melted) mantle material underlying the lithosphere; *mesosphere* is the rigid mantle material underlying the asthenosphere and constituting the bulk of the mantle. *Subcontinental mantle* is a general term used primarily to mean lithospheric mantle but not necessarily excluding asthenosphere and mesosphere. *Undepleted* refers to a mantle system with Rb/Sr and Sr-isotopic ratios compatible with closed system evolution for 4.5 b.y. *Enriched* and *depleted* refer to systems in which present Rb/Sr ratios are higher and lower, respectively, than those required for closed system evolution. Thus, the typ-

ical mid-ocean ridge tholeiite comes from partially depleted mantle and is therefore much lower in K, Rb, Sr, Ba, and Rb/Sr ratio than tholeiites of otherwise similar composition from oceanic islands and from continental regions. *Homogeneous* implies that chemical composition is uniform from place to place, provided that the sample is large enough to average out mineral scale compositional variation. *Heterogeneous* is used to refer to compositional variations on any scale. A *mantle "age"* refers to the time of some geological event in the mantle, such as the development of large-scale heterogeneities.

Pseudoisochrons. Because mantle-derived magmas in continental areas have traversed some 30–40 kilometers of ancient radiogenic sialic crust, the high and variable Sr-isotope ratios observed in these magmas are commonly ascribed to crustal contamination (e.g., Bell and Powell, 1970; Compston *et al.*, 1968; Compston, 1974; Doe *et al.*, 1969; Ewart and Stipp, 1968; Faure *et al.*, 1972; Green and Ringwood, 1967; Halpern *et al.*, 1974; Hedge, 1966; Hurley *et al.*, 1966; Kudo *et al.*, 1971; Laughlin *et al.*, 1972; Manton, 1968; Montigny *et al.*, 1969; Pushkar, 1968; Pankhurst, 1969; Scott *et al.*, 1971). It is also possible, however, that these higher Sr ratios are primary, inherited from subcontinental mantle possessing higher and more variable abundances of radiogenic Sr. The observed range in values would reflect lateral and/or vertical heterogeneities within this mantle. The recent literature increasingly favors the latter possibility, mostly due to studies of alkalic rocks (e.g., Powell and Bell, 1974), and volcanics of western U.S.A. where subcontinental lithosphere and asthenosphere are apparently playing a major role in surface-reaching magmatism (Hedge and Noble, 1971; Leeman, 1974, 1975; Leeman and Manton, 1971; Mark *et al.*, 1975; Peterman *et al.*, 1970). The possibility that the Sr-isotopic ratios are inherited directly from subcontinental mantle is

further strengthened by the presence of ubiquitous pseudoisochrons. (We note here that we use the term pseudoisochrons or mantle isochron for any positively correlated array of data, as long as this correlation is statistically significant. In the conventional usage of the term isochron, one usually requires the data to define a straight line within the limits of analytical error. The implication of our more relaxed usage is that the initial $^{87}\text{Sr}/^{86}\text{Sr}$ need not be perfectly correlated for all samples).

Prior to discussing the data upon which this paper is based, it is essential to distinguish between the simple isochron plot and the pseudoisochron plot utilized throughout our data presentation. The isochron diagram for a group of igneous rocks plots their individual $^{87}\text{Sr}/^{86}\text{Sr}$ composition as measured today (termed present-day ratios) versus their respective Rb/Sr ratios. The pseudoisochron diagram, however, plots the *initial* $^{87}\text{Sr}/^{86}\text{Sr}$ ratios of the samples versus their respective Rb/Sr ratios. In other words, on a pseudoisochron plot the $^{87}\text{Sr}/^{86}\text{Sr}$ of the samples have been individually "corrected back" to their time of crystallization, using independent information for the age of crystallization. Ideally, a group of volcanics 100 m.y. old would define a line on an isochron diagram whose slope corresponds to an age of 100 m.y. The same volcanics on a pseudoisochron plot, however, should define a horizontal line (i.e., zero age) whose intercept is the unique $^{87}\text{Sr}/^{86}\text{Sr}$ composition of the parent magma. When these volcanics do *not* plot as a horizontal array on the pseudoisochron plot, then there is a hint that some precrystallization history in $^{87}\text{Sr}/^{86}\text{Sr}$ has been preserved in the rocks. If the data actually define a good linear array, the hint is strengthened, and there is a strong possibility that the information given in the pseudoisochron plot pertains directly to the source region of the volcanics. For many volcanic rock associations of continental regimes this source region is the mantle. Therefore,

we searched the literature for pseudoisochrons with the aim of evaluating the possible preservation of mantle isotopic properties in surface-reaching igneous rocks.

The results of the literature survey are given in Table 6 and Table 7. Here, each measured $^{87}\text{Sr}/^{86}\text{Sr}$ ratio has been corrected for the true age of the rock, and the whole-rock initial $^{87}\text{Sr}/^{86}\text{Sr}$ ratios then plotted vs. Rb/Sr on a pseudoisochron diagram. Correlation theory and regression analysis indicate that most of these pseudoisochrons have slopes significantly different from zero at confidence levels up to 95% (in some cases up to 99.9%) and that they define excess "ages" ranging from 70 m.y. to more than 3000 m.y. Some examples are shown in Fig. 30.

For the most part the pseudoisochrons come from young volcanic terranes in which no age correction of the measured present-day Sr isotopic composition is necessary. Noteworthy are the numerous examples from western U.S.A., where pseudoisochrons are observed in rock associations of widely differing chemical composition. Furthermore, pseudoisochrons are not restricted to young volcanics. Examples are also encountered in plutonic and hypabyssal rocks of Mesozoic age (the California batholith, the Jurassic dolerites of Antarctica), Caledonian basic igneous rocks of Scotland (Haddo House mass), and in ancient, layered, mafic intrusions (Usushwana Complex of South Africa).

There are a variety of mechanisms that could produce the pseudoisochrons given in Table 6. These mechanisms can be divided into crustal and mantle types. The crustal-related processes simply involve mixing of mantle-derived magmas with crustal material of higher $^{87}\text{Sr}/^{86}\text{Sr}$ (crustal contamination). The criteria for evaluating this process as a potential means of raising the $^{87}\text{Sr}/^{86}\text{Sr}$ of mantle-derived magmas are well illustrated in studies of young island arc volcanics (Ewart and Stipp, 1968; Pushkar, 1968). In these studies,

a hyperbolic relationship between $^{87}\text{Sr}/^{86}\text{Sr}$ and Sr concentrations is taken to be indicative of contamination. Clearly, however, many forms of disequilibrium melting or mixing of heterogeneous mantle may produce similar curves and otherwise be indistinguishable from crustal contamination. Hence such relationships cannot be considered diagnostic.

On the other hand, there is often independent evidence against crustal contamination of mafic volcanics. We include in this category such pertinent features as:

1. Limited range of Sr isotopic composition of the volcanic rocks despite the very large range in isotopic composition of the supposed contaminating materials.

2. Limited range of Sr isotopic composition in many volcanic associations despite a wide range in Sr concentrations.

3. Persistence of normal rock compositions (e.g., tholeiites) despite significant variability in isotopic composition and hence presumed wide variation in the nature and quantity of contaminant required.

4. Constancy of composition of differentiates, irrespective of the nature and amount of the supposed contaminant.

5. Lack of correlation between thickness or age of continental sialic crust and the $^{87}\text{Sr}/^{86}\text{Sr}$ ratios observed at the surface.

6. High "initial" $^{87}\text{Sr}/^{86}\text{Sr}$ ratios that ought not to be influenced by crustal contamination, assuming linear mixing relations.

7. Lack of geographic correlation of isotopic compositions for many tectonic environments.

8. Lack of correlation between Sr and Pb isotopic ratios.

9. $^{206}\text{Pb}/^{204}\text{Pb}$ ratios in basalts and rhyolites which commonly show the same range of values.

10. Paucity of included material such as crustal xenoliths.

TABLE 6: Pseudoisochrons of Rb/Sr versus Initial ($^{87}\text{Sr}/^{86}\text{Sr}$) for Some Igneous Associations of Continental Affinity

| Location | Identity ¹ | Apparent Age (M.Y.) | $\left(\frac{^{87}\text{Sr}^2}{^{86}\text{Sr}_0} \right)$ | N ² | r ³ | Ref. ⁴ |
|--------------|---|---------------------|--|----------------|----------------|-------------------|
| U.S.A. | Absaroka Volcanic Field; Andesites | 3340 ± 1540 | 0.6987 ± 33 | 4 | 0.84(2) | 18 |
| U.S.A. | W. Grand Canyon; Hawaiites | 1300 ± 290 | 0.7025 ± 4 | 12 | 0.86(3) | 13 |
| U.S.A. | W. Grand Canyon; Alkali Basalt Series | 1100 ± 240 | 0.7025 ± 3 | 20 | 0.75(4) | 13 |
| Scotland | Haddo House Mass; Quartz and Olivine Norites | 1160 ± 210 | 0.7049 ± 11 | 9 | 0.90(3) | 16 |
| Brazil | Parana Basin; Mesozoic Basalts and Dolerites | 1020 ± 280 | 0.7011 ± 16 | 4 | 0.93(4) | 7 |
| U.S.A. | Colorado Plateau; Basalts | 960 ± 240 | 0.7028 ± 3 | 9 | 0.84(3) | 12 |
| U.S.A. | Snake River Plain; King Hill Basalts | 940 ± 210 | 0.7089 ± 10 | 6 | 0.92(3) | 14 |
| Scotland | Arnage Mass; Quartz and Olivine Norites | 830 ± 180 | 0.7054 ± 8 | 8 | 0.89(3) | 16 |
| S. Africa | Archaeon Ushwana Complex; Mafic Rocks | 815 ± 390 | 0.7014 ± 8 | 10 | 0.59(2) | 4 |
| Spain | Jumilla, Alkalic Complex; Jumillites | 780 ± 390 | 0.7117 ± 16 | 6 | 0.70(1) | 19 |
| Gondwanaland | Snake River Plain; Craters of the Moon Basalts | 620 ± 60 | 0.7055 ± 3 | 10 | 0.97(4) | 14 |
| U.S.A. | Tasmania, Africa, Antarctica; Jurassic Dolerites | 520 ± 80 | 0.7059 ± 8 | 30 | 0.75(4) | 3,6,9 |
| Antarctica | Jurassic Dolerites | 470 ± 90 | 0.7064 ± 10 | 25 | 0.73(4) | 3,6 |
| U.S.A. | Absaroka Volcanic Field; Shoshonites | 470 ± 50 | 0.7032 ± 2 | 6 | 0.98(2) | 18 |
| Peru | Arequipa Volcanics; Andesites, Dacites | 440 ± 70 | 0.7061 ± 2 | 16 | 0.82(4) | 10 |
| Uganda | Napak Alkalic Complex; Nephelinites, Ijolites | 380 ± 340 | 0.7031 ± 1 | 8(1) | 0.41(1) | 1 |
| Peru | Barroso Volcanics; Andesites, Dacites | 310 ± 50 | 0.7045 ± 3 | 8 | 0.91(4) | 10 |
| U.S.A. | Columbia River Group; Basalts, Andesites, Dacites | 290 ± 80 | 0.7032 ± 4 | 6 | 0.86(3) | 8 |
| U.S.A. | California; Mesozoic Granites ($^{87}\text{Sr}/^{86}\text{Sr}_0 > 0.706$) | 277 ± 47 | 0.7030 ± 3 | 9(2) | 0.91(4) | 11 |
| U.S.A. | Basin and Range; Basalts | 200 ± 70 | 0.7029 ± 4 | 11 | 0.54(1) | 12 |
| U.S.A. | N.W. Great Basin; Basalts | 190 ± 80 | 0.7033 ± 2 | 13(1) | 0.58(2) | 15 |
| U.S.A. | Navajo Alkalic Province; Trachybasalts, Lamprophyres | 170 ± 110 | 0.7062 ± 6 | 11 | 0.44(1) | 19 |
| U.S.A. | Leucite Hills; Lamproites, Orendites | 150 ± 80 | 0.7056 ± 4 | 17 | 0.41(1) | 19 |
| U.S.A. | California; Mesozoic Granites ($^{87}\text{Sr}/^{86}\text{Sr}_0 > 0.706$) | 115 ± 29 | 0.7055 ± 4 | 11 | 0.80(3) | 11 |
| New Zealand | East Arc, North Island; Basalts, Andesites | 110 ± 20 | 0.7046 ± 2 | 35 | 0.71(4) | 5,20 |
| U.S.A. | Cascades, Glacier Peak; Basalt, Andesites, Dacites | 110 ± 90 | 0.7034 ± 3 | 6 | 0.49(1) | 2,8 |
| U.S.A. | Cascades, Mt. Lassen; Basalts, Andesites, Dacites | 100 ± 50 | 0.7036 ± 2 | 10 | 0.58(2) | 2,8,17 |
| Uganda | Budeda Alkalic Complex; Ijolite Series | 80 ± 50 | 0.7032 ± 2 | 8(1) | 0.57(1) | 1 |
| U.S.A. | Bearpaw Mountains Alkalic Complex; Syenites, etc. | 80 ± 40 | 0.7069 ± 4 | 7(1) | 0.64(2) | 19 |
| Uganda | Toror Alkalic Complex; Phonolites, Nephelinites, etc. | 70 ± 5 | 0.7034 ± 1 | 4(1) | 0.99(4) | 1 |

The data have been statistically validated by (1) calculating the Pearson correlation coefficient (r) which defines the "goodness-of-fit" of the data about a regression line, and (2) testing the slope of the fitted line for significance against zero. The regression treatment used to obtain slopes and intercepts was that of York (1966), in which the errors in the age and initial ratio are calculated solely from the data scattering and are given at 1 standard deviation (following Brooks *et al.*, 1972).

¹Unless stated, volcanic associations are Tertiary or younger.

²Number of samples regressed; (N) indicates number of samples excluded from regression analysis.

³Pearson correlation coefficient; (N) indicates at what level of confidence the fitted regression line differs from zero. (Given in increments of standard deviation).

⁴For reference list, see Table 7.

TABLE 7. Reference Key to Table 6

| Key No. | Reference |
|---------|--------------------------------|
| 1 | Bell and Powell (1970) |
| 2 | Church and Tilton (1973) |
| 3 | Compston <i>et al.</i> (1968) |
| 4 | Davies <i>et al.</i> (1970) |
| 5 | Ewart and Stipp (1968) |
| 6 | Faure <i>et al.</i> (1972) |
| 7 | Halpern <i>et al.</i> (1974) |
| 8 | Hedge <i>et al.</i> (1970) |
| 9 | Heier <i>et al.</i> (1970) |
| 10 | James <i>et al.</i> (1976) |
| 11 | Kistler and Peterman (1973) |
| 12 | Leeman (1970) |
| 13 | Leeman (1974) |
| 14 | Leeman and Manton (1971) |
| 15 | Nobel <i>et al.</i> (1973) |
| 16 | Pankhurst (1969) |
| 17 | Peterman <i>et al.</i> (1970a) |
| 18 | Peterman <i>et al.</i> (1970b) |
| 19 | Powell and Bell (1970) |
| 20 | Stipp (1968) |

In a detailed study on the cause of high $^{87}\text{Sr}/^{86}\text{Sr}$ ratios in Cenozoic andesites and dacites of southern Peru, criteria of this nature led us to reject crustal contamination as a plausible mechanism for either the high $^{87}\text{Sr}/^{86}\text{Sr}$ ratios or the pseudoisochrons observed there (James *et al.*, 1976). This conclusion is especially remarkable when it is noted that the Andean crust through which these magmas have passed is about 70 km thick, thicker than any other known crustal section in the world save that of the Himalayas.

Based on this synthesis, we advocate that the hitherto durable and facile crustal contamination explanation for high $^{87}\text{Sr}/^{86}\text{Sr}$ in continental volcanic rocks be considered improbable, and that other possible mechanisms leading to the observed isotopic compositions be evaluated. We believe that these mechanisms are all mantle related, implying that both the high Sr ratios and the pseudoisochrons are the result of mantle processes. This viewpoint is supported by the observation that some pseudoisochrons and high $^{87}\text{Sr}/^{86}\text{Sr}$ ratios are observed in oceanic regions where little or no possibility of sialic contamination exists (Brooks *et al.*, 1976).

Mantle-related processes that could lead to Rb-Sr pseudoisochrons include: (1) mixing of heterogeneous mantle material; (2) selective melting of heterogeneous mantle material of the same or different age; and (3) disequilibrium melting of homogeneous mantle in which individual mineral phases are in isotopic disequilibrium.

Distinguishing between these possibilities is difficult, as none of the proposed mechanisms leads to a uniquely identifiable compositional property in the rocks, other than that of Pb and Sr isotopic variation; nonetheless, it is important to inquire whether the pseudoisochrons do contain meaningful age and isotopic information about the mantle.

One means of evaluating pseudoisochrons is to determine whether they involve identifiable mixing-line chemistry. Rb-Sr variation diagrams and plots of $^{87}\text{Sr}/^{86}\text{Sr}$ versus $1/\text{Sr}$ can be used for this purpose. Examination of such plots for the data used to build Table 6 reveals that a good pseudoisochron is commonly accompanied by a good positive correlation between ($^{87}\text{Sr}/^{86}\text{Sr}$) and $1/\text{Sr}$ but no correlation at all between Rb and Sr. The absence of a Rb-Sr correlation is inconsistent with simple magma mixing. Thus, while we cannot discount mixing of heterogeneous mantle material, the data in general seem to preclude simple two-component magma mixing as an important factor in most pseudoisochrons. The volcanics of Peru are among the few examples that display good correlations between ($^{87}\text{Sr}/^{86}\text{Sr}$) and $1/\text{Sr}$, and Rb and Sr (James *et al.*, 1976). In this case, the pseudoisochrons could result either from mixing or selective melting of a heterogeneous source region of uniform age or from disequilibrium melting of homogeneous mantle.

Selective withdrawal of magma from mantle material that is heterogeneous (and of uniform or nonuniform age) will result in the generation of pseudoisochrons that do not necessar-

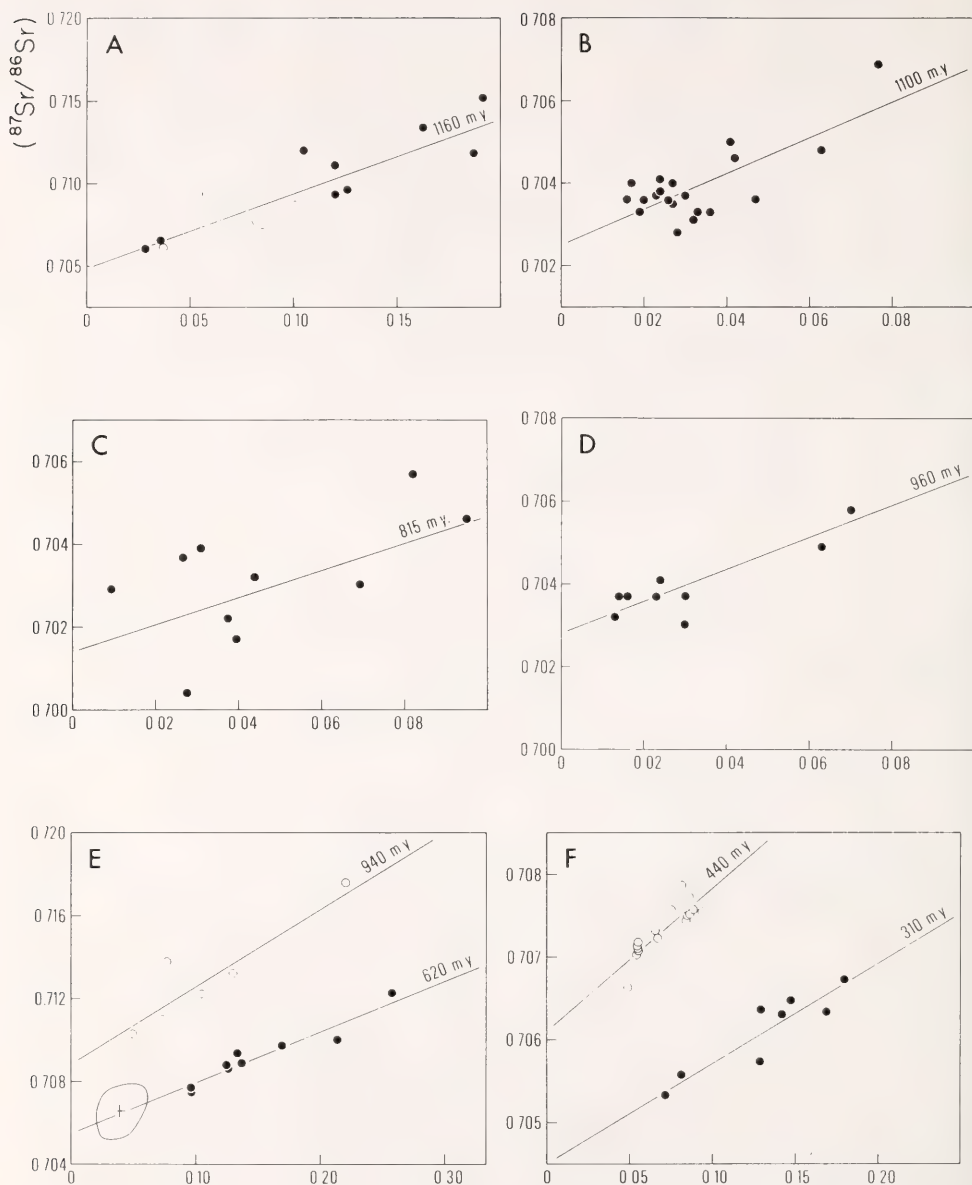


Fig. 30. Rb-Sr mantle isochrons (initial $^{87}\text{Sr}/^{86}\text{Sr}$ versus Rb/Sr) for some representative igneous rock associations of continental affinity (for more detail, see Table 6). (A) Quartz and olivine norites from the Arnage (open circles) and Haddo House (closed circles) igneous masses, Scotland. (B) Alkali basalt series of the Western Grand Canyon, U.S.A. (C) Mafic rocks of the Archean Usushwawa Complex, South Africa. (D) Colorado Plateau basalts, U.S.A. (E) Snake River Basalts, U.S.A. Closed Circle, Craters of the Moon basalts; Open circle, King Hill basalts. The field is for olivine tholeiites ($N = 34$) with the cross showing the average composition. (F) Peruvian Cenozoic volcanics, Southern Peru. Closed circle, Barroso volcanics; open circle, Arequipa volcanics.

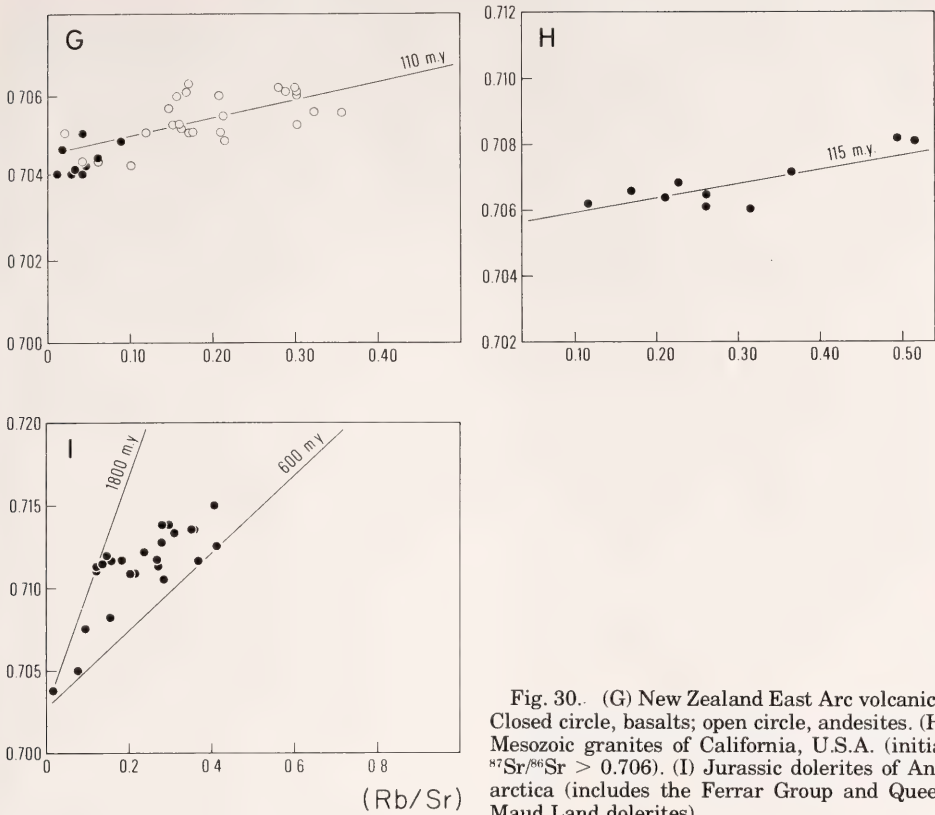


Fig. 30. (G) New Zealand East Arc volcanics. Closed circle, basalts; open circle, andesites. (H) Mesozoic granites of California, U.S.A. (initial $^{87}Sr/^{86}Sr > 0.706$). (I) Jurassic dolerites of Antarctica (includes the Ferrar Group and Queen Maud Land dolerites).

ily reflect the average age of the source region; however, we cannot avoid the conclusion that such pseudoisochrons reflect a long history of isolated isotopic evolution of the subcontinental mantle. Thus, whatever the specific origin of pseudoisochrons, they do imply a significant age for mantle heterogeneities, and for this reason we refer to them as *mantle isochrons*, a general term designed to emphasize the unique nature of the ancient isotopic imprint borne to the surface in mantle-derived magmas.

Accepting that pseudoisochrons are mantle isochrons places major constraints on the nature of the mantle source regions. First, the age information embodied in mantle isochrons demands the existence of mantle that has long preserved a distinct chemical

identity. This in turn demands that the mantle source region be sufficiently immobile as to be static and resistant to reworking and mixing processes during most of its history. Second, the elevated Sr-isotopic ratios indicated by the mantle isochrons suggest that the mantle source region is not chemically depleted. Third, the wide range in observed Sr-isotopic composition requires that the mantle be grossly heterogeneous, probably on both regional and local scales (Hofmann, 1975; Hofmann and Hart, 1975).

What sort of mantle fits these requirements? Asthenosphere most probably does not, leaving either subcontinental lithosphere or mesosphere as the likely source region. The linear arrangement of continental island arc volcanoes associated with magmatic

activity derived from above subducted lithosphere would seem to preclude mesosphere as a likely direct source, even though its nature and composition are probably compatible with the mantle isochrons. Is continental lithosphere compatible with these requirements, however? In the following section we will show that there is a substantial amount of evidence that allows an independent case to be built for thick, ancient, heterogeneous and chemically undepleted continental lithosphere with an isotopic composition consistent with that implied by mantle isochrons.

Nature of continental lithosphere. Most of our knowledge concerning the nature of continental lithosphere comes from three sources: seismic studies, heat-flow measurements, and the analysis of ultramafic nodules believed to be samples of lithosphere rafted to the earth's accessible regions in mantle-derived magmas. These broad areas are so interdependent that it is impractical to isolate the individual contributions originating in each. Consequently, in this discussion we synthesize the evidence from these sources by treating successively the questions of thickness of continental lithosphere, chemical composition of lithosphere (and the resulting implications for heat flow), isotopic heterogeneity of lithosphere, and the age of lithosphere.

Although there is no consensus among geophysicists on the thickness of continental lithosphere, with estimates ranging between about 200 and 400 km (Dziewonski, 1971; Kanamori, 1970; Jordan, 1975; Okal and Anderson, 1975; Sipkin and Jordan, 1975; Toksöz and Anderson, 1966), the lack of agreement is largely one of definition and not substance. In particular, the lower estimates of lithosphere thickness are based on the determination of the *minimum* depth below which oceanic and continental velocity structures need not differ. But depths so calculated provide no information on actual lithosphere thickness; that

thickness is determined by the depth at which shear-wave velocities or Q decrease rapidly or discontinuously to asthenospheric values. By this criterion, few seismic studies successfully identify the base of the lithosphere. They do show, however, that lithosphere beneath cratons may be at least 300–400 km thick (Alexander and Sherburne, 1973; Goncz and Cleary, 1976); that is, the continental mantle is subsolidus to that depth, exhibiting no significant low velocity or low Q zone at lesser depths. While there may be a low-velocity channel at greater depths, the poor resolving power of the seismic data precludes its unequivocal identification. One important study of Q beneath the Andes of South America, however, clearly demonstrates the existence of a low-rigidity (and probably low-velocity) channel at a depth of 350 km beneath a high-rigidity lithosphere (Sacks, 1969; Sacks and Okada, 1974). This result is of considerable general importance because the Andean orogen evolved atop the ancient South American shield, and the integrity of the underlying lithosphere appears to be intact (James, 1971).

Additional evidence favoring thick continental lithosphere comes from an analysis of global heat-flow data by Pollack and Chapman (Pollack and Chapman, 1976; Chapman and Pollack, 1975). Although the results of their study are not conclusive, they indicate that the lithosphere beneath ancient continental interiors may attain thicknesses in excess of 300 km. This estimate is based upon regional variation in geothermal gradient and the corresponding depths at which the geotherm intersects an empirically postulated temperature of incipient melting. Pollack and Chapman (1976) take the temperature at the lithosphere-asthenosphere boundary to be 0.85 the temperature of dry melting of peridotite. This value is obtained empirically by considering the thickness of oceanic lithosphere as a function of varying oceanic geothermal gradients. The general form of continental geo-

thermal gradients inferred from heat flow is corroborated by the results of geochemical studies in which experimentally determined phase relationships and mineral compositions of coexisting pyroxenes as functions of temperature and pressure are applied to nodules to obtain estimates of their equilibration temperatures and pressures (e.g., Boyd and Nixon, 1975). The persistence of subsolidus temperatures to great depth is further attested to by the absence of interstitial glass in ultramafic nodules (e.g., Kudo *et al.*, 1972). The Pollack and Chapman model, as in most previous thermal models (Clark and Ringwood, 1964; Sclater and Francheteau, 1970), assumes that the continental lithosphere is somewhat depleted in heat-producing elements. Yet, one of the principal conclusions to be drawn from the interpretation of mantle isochrons is that continental lithosphere is essentially undepleted. Since chemical composition is the input to the thermal model, our conclusion must be consistent with both the observed heat-flow data and with what is known about the composition of continental lithosphere as revealed by studies of ultramafic nodules found in kimberlites and basalt (see Ringwood, 1975, pp. 100–114 for general discussion and extensive bibliography).

Kimberlites crystallize from volatile-rich magmas that appear to have originated at depths greater than 200 km (Dawson, 1972; Boyd and Nixon, 1970; Ringwood and Lovering, 1970; Ringwood, 1975). They apparently ascended rapidly, and in so doing incorporated many ultramafic xenoliths which are believed to represent samplings of different depth zones of the mantle (Wagner, 1928; Dawson, 1972; Harris *et al.*, 1972; Harris and Middlemost, 1969; MacGregor, 1975; Boyd and Nixon, 1975; Lovering and Tatsumoto, 1968). Although there is debate about the source region of the kimberlite magma and no assurance that it lies in the lithosphere, there is general consensus that many of the

xenoliths are subsolidus mantle fragments showing little reequilibration to lower temperature and pressure assemblages (MacGregor, 1968; Boyd and Nixon, 1975; Dawson, 1972; O'Hara *et al.*, 1975). The nodule compositions can therefore be used as guides to real mantle compositions. Studies of nodules in kimberlite indicate that the subcontinental mantle has high Rb/Sr ratios, correspondingly high $^{87}\text{Sr}/^{86}\text{Sr}$ ratios, and is otherwise undepleted in its basaltic fraction (Rhodes and Dawson, 1975; Barrett, 1975; Ridley and Dawson, 1975; Hutchinson and Dawson, 1970; O'Hara *et al.*, 1975). The undepleted character of the mantle from which the nodules were derived is attested to by the dominance of the fertile garnet peridotite (especially the sheared variety) over other more depleted nodules (O'Hara *et al.*, 1975). Thus, nodule studies corroborate our conclusions based on Sr-isotopic compositions and argue for the existence of a continental lithosphere that is far from depleted and which, under favorable thermal conditions, would be a ready source of basaltic magma.

Steady-state thermal models based on undepleted mantle compositions can be constructed that are entirely consistent with measured heat flow and postulated geothermal gradients. Consider, for example, a surface heat flux for a continental craton of 1.05 heat flow units (HFU), a standard 40-km crust which produces 0.43 HFU, and a lithospheric mantle 310 km thick that consists of undepleted peridotite containing 1000 ppm K, 0.06 ppm U, and 0.23 ppm Th. Crustal heat production and steady-state heat flow are taken from Sclater and Francheteau (1970), and are consistent with the relationship between heat flow and surface heat production proposed by Roy *et al.* (1968). K/U and U/Th ratios are taken from Clark and Ringwood (1964). This mantle material will contribute 0.38 HFU to the steady-state heat flux, leaving 0.24 HFU to be derived from below 350 km, a deep-mantle contribution that is only about one half the

value assumed in the static earth model of Clark and Ringwood. Our thermal model, in which most surface heat flow originates in the lithosphere rather than at greater depth, results in slightly lower geothermal gradients for the same surface heat flux; this in turn forces the point of incipient melting to even greater depths, thereby making thick continental lithosphere even more feasible. This example illustrates that steady-state thermal models based on undepleted mantle compositions are entirely consistent with observed heat flow and postulated geothermal gradients.

The study of ultramafic nodules provides evidence not only that the continental lithosphere is chemically undepleted but that it is ancient, isotopically enriched, and grossly heterogeneous. Kimberlite nodules typically show $^{87}\text{Sr}/^{86}\text{Sr}$ ratios that vary between 0.703 and 0.710 (average, 0.707) (Barrett, 1975; Allsopp *et al.*, 1969; Mitchell and Crocket, 1971; Ridley and Dawson, 1975; Hutchinson and Dawson, 1970; Harris *et al.*, 1972). The consistent and wide variation in isotopic ratio cannot be attributed to contamination and must reflect mantle inhomogeneity (Barrett, 1975; Ridley and Dawson, 1975). Furthermore, the existence of isotope disequilibrium between mineral phases in individual nodules suggests that the heterogeneity is present even on the scale of mineral grains (Kudo *et al.*, 1972; Paul, 1971; Compston and Lovering, 1969; Steuber and Ikramuddin, 1974; Burwell, 1975; Barrett, 1975; Peterman *et al.*, 1970; Harris *et al.*, 1972; Dasch and Green, 1975).

The high average $^{87}\text{Sr}/^{86}\text{Sr}$ ratio suggests significant prehistory for continental lithosphere, long isolated from less enriched asthenosphere. More direct evidence that the subcontinental mantle is very old comes from Sr and Pb isotope studies on ultramafic nodules. Measurement of apparent ages indicates mantle ages up to 3 b.y. or more (Burwell, 1975; Manton and Tatsumoto, 1971; Paul, 1971; Steuber and Ikramuddin, 1974; Dasch and

Green, 1975; Cooper and Green, 1969; Harris *et al.*, 1972). Other studies showing wide variation in Sr isotopic ratios between nodules provide indirect evidence that parts of the mantle have remained in isotopic isolation over very long periods of time (Barrett, 1975; Kudo *et al.*, 1972; Compston and Lovering, 1969). Thus while no single geochemical study yet provides definitive evidence of ancient mantle, the integrated result of all studies argues for an aged and heterogeneous subcontinental lithosphere.

Implications. Because continental lithosphere exists at relatively low, subsolidus temperatures, it is protected from transport into subduction zones by the buoyancy of the overlying continental capping; as a result, parts of the lithosphere may be as old as the coupled sialic crust (e.g., early Precambrian for continental cratons). Any sections of lithosphere that are not depleted will, by virtue of their sheltered existence, possess distinctive isotopic compositions that result from both regional and local variation in Rb/Sr ratios. If this ancient lithosphere participates in younger magmatism, then those volcanic products will contain isotopic evidence of the source region's "pre-history." This evidence, manifest as mantle isochrons, raises two major questions: first, how does this lithosphere form, and second, how does such lithosphere, isolated for long periods of time, become involved in young magmatism?

The range in initial $^{87}\text{Sr}/^{86}\text{Sr}$ of mantle-derived magmas (Table 6 and Figure 30) provides strong evidence that the continental lithosphere is characterized by a degree of regional isotopic heterogeneity that is more pronounced than that observed in other mantle provinces. Specifically, the subcontinental mantle has Sr isotopic ratios ranging from as low as 0.703 to more than 0.710, a range of values nearly identical to that found for mantle-derived ultramafic nodules. By comparison, ocean-ridge basalts, taken to represent oceanic asthenosphere,

display a quite limited range of values (about 0.7027) (Hofmann and Hart, 1975), indicating that this asthenosphere is comparatively homogeneous isotopically as might be expected in rapidly convecting, partially molten material. On the other hand, oceanic islands, taken to represent at least part mesosphere, exhibit a considerable range in Sr-isotopic values (from about 0.703 to 0.706), which suggests that the mesosphere has substantial regional isotopic heterogeneities, although not as pronounced as those of continental lithosphere (Brooks *et al.*, 1976; and Sun and Hanson, 1975).

The upper limits of these ranges in $^{87}\text{Sr}/^{86}\text{Sr}$ ratios lead to an important inference concerning the relative enrichment of the different mantle provinces. Continental lithosphere consistently has Sr-isotopic values that are significantly higher than those of oceanic asthenosphere, indicating that some parts of the subcontinental mantle are considerably more enriched in radiogenic components and LIL (large-ion-lithophile) elements than suboceanic mantle. Mesosphere, as manifest in oceanic islands, can be regarded as a nondepleted base to oceanic and continental regions alike, locally possessing a degree of enrichment in radiogenic components comparable to but possibly somewhat smaller than that of continental lithosphere.

Our review of mantle isochrons and related Sr-isotopic data indicates that continental lithosphere is in part both more enriched and more heterogeneous in its radiogenic components (and LIL elements) than other mantle provinces. Such lithosphere enrichment and heterogeneity could result from a variety of processes operating either individually or in concert, and possible models include:

(i) Thermal accretion by "freezing" of enriched asthenosphere. Since lithosphere begins its formation soon after crustal formation, the lithosphere under old continental areas may have started its formation at a time when the asthenosphere was enriched or

nondepleted (as contrasted with its present state of chemical depletion).

(ii) Trapping of an enriched asthenosphere boundary layer (formed by progressive crystallization of the lithosphere with concomitant concentration of LIL elements into the partial-melt zone of the asthenosphere directly beneath the lithosphere boundary).

(iii) Upward percolation of a LIL-element and volatile-rich phase (not miscible with the silicate partial melt) from mesosphere or asthenosphere into the subcontinental lithosphere.

(iv) Diapiric rise of LIL-element enriched mantle diapirs or blobs from the mesosphere, which underplate and become incorporated into the thickening subcontinental lithosphere. The mechanism of rise of diapirs from a buoyant mantle layer has been considered at length by Ramberg (1972). The formation of oceanic island volcanism by ascent of chemically distinct blobs or plumes forms a background to our model and has been discussed by Schilling (1975).

Model (i) would produce a zoned lithosphere grading from enriched at the top to depleted at the base (since present-day asthenosphere is depleted). Derivation of continental magmas from such a lithosphere might reflect this zoning, with magmas formed at the greatest depths (youngest lithosphere) carrying a depleted signature. There is no convincing evidence, however, for the existence of significant quantities of "depleted" magmas in continental regions, and hence operation of this model requires either that no magmas are derived from this depleted zone of the continental lithosphere, or that such magmas reequilibrate with shallower, more enriched lithosphere.

Model (ii) has been proposed by Kay (1975) for the formation of heterogeneities in the suboceanic mantle; however, consideration of the rates of diffusion of LIL-elements in silicate melts (Hofmann, 1975; Hofmann and Hart, 1975), shows that any such en-

riched boundary-melt layer will be very thin (~ 10 m) and quantitatively insignificant for the later production of enriched magmas. The main difficulty in this model (for both oceanic and continental regions) arises because lithosphere accretes at a velocity larger than the scale lengths of LIL-element diffusion in silicate melts, so that the steady-state composition of the lithosphere would be close to that of the asthenosphere from which it forms, and only trivial amounts of "enriched" partial melt could result from this process.

Model (iii) requires a mobile phase that is *not* miscible in the partial melt phase of the asthenosphere at the pressures and temperatures characteristic of the asthenosphere. Such a phase might be a hydrous, carbonate-rich fluid that separates from the mesosphere and rises buoyantly through the asthenosphere to be trapped against the advancing lithospheric front. Later partial melting of lithosphere containing this enriched phase could produce magmas showing enriched characteristics. In extreme cases, this enriched phase might progress directly through the lithosphere, forming members of the kimberlite-carbonatite suite at the surface. While this model has many plausible characteristics (and is closely related to model iv with which it could operate in conjunction), we note that it also implies the presence of kimberlite-carbonatite magmas throughout the geologic record. They are in fact rare in Precambrian time, a time when presumably thinner crust and lithosphere would have greatly enhanced the likelihood of such magmas reaching the surface.

Model (iv) involves a convecting mesosphere containing thermal or chemical heterogeneities (Anderson, 1975), such that blobs or plumes of material can become separated, rise through the asthenosphere and become plastered-on and slowly incorporated into the thickening subcontinental lithosphere. This mesospheric material

is presumed to be enriched in the LIL-elements *relative to asthenosphere* so that the resulting subcontinental lithosphere will be a heterogeneous combination of frozen-out asthenosphere and included mesosphere-derived blobs. This model is attractive because it can be applied equally well in oceanic regions to explain the existence of oceanic islands (variously related to hot spots or plumes) which invariably are built of volcanic material enriched in LIL-elements and Sr and Pb isotopes relative to the depleted, asthenosphere-derived spreading-ridge basalts.

In oceanic regions, the mesospheric blobs or plumes (a plume may be simply a more or less continuous train of blobs) do not necessarily go through a two-stage process of lithosphere underplating and subsequent remelting. Instead, they may diapirically penetrate the thinner oceanic lithosphere and directly supply the partial melt leading to ocean island volcanism. If the blobs do not penetrate the lower boundary of oceanic lithosphere, they will produce heterogeneity similar to that of the continental lithosphere. By this concept, then, oceanic regions provide us with a recent (< 200 m.y.) record of the continuous upward migration of enriched blobs from the mesosphere, a process which has been going on under continents for billions of years.

The main difference between mantle isochrons of oceanic and continental regimes is that higher Rb/Sr and $^{87}\text{Sr}/^{86}\text{Sr}$ ratios are found for continental volcanics. This implies that there must be an additional fractionation (increase) of Rb/Sr ratio associated with the two-stage continental case (underplating and subsequent remelting) relative to the single-stage oceanic case (direct penetration). We explain this as follows: At some point in the rise of mesospheric blobs, they become partially molten; this silicate melt, with a higher Rb/Sr than the initial value of the blob, becomes partially segregated

from the crystalline residue as the blob ascends and is plated onto the bottom of the continental lithosphere. Later partial melting of this material will favor the previously partially segregated melt, leading to a second stage of Rb/Sr enrichment. The relatively high $^{87}\text{Sr}/^{86}\text{Sr}$ ratios observed in continental volcanics (relative to oceanic-island volcanics) arise because of the isotopic aging that follows the initial Rb/Sr fractionation. Cases of more or less complete melt-crystal segregation prior to or during the underplating stage would result, on further cooling, in an eclogite solid (frozen melt) and ultramafic residue. The eclogite nodules commonly brought to the surface in kimberlitic rocks may be evidence for such a segregation process.

The combined weight of the evidence discussed in this paper suggests that continental lithosphere accretes through a combination of processes (i) and (iv). Such a model provides a satisfactory explanation for mantle isochrons from both continental and oceanic regions. A schematic view of this model is given in Fig. 31A, and although it is recognized that some aspects of the other models discussed may be of local importance, we have restricted our figure to a portrayal of the main features of continental lithospheric growth.

The data of Table 6 show that mantle isochrons are associated with a number of specific tectonic environments where ancient lithosphere can become reactivated and involved in partial melting processes. These environments are created where, (1) subcontinental lithosphere overlying a subduction zone is activated by proximity to that zone; (2) continental-scale rifting forms fractures that penetrate deep, unloaded lithosphere; and (3) a continent-bearing plate over-rides an oceanic rise or plume.

Schematic representation of these reactivation environments is illustrated in Fig. 31B.

Recognition that ancient lithosphere can play a major role in younger magmatism in these tectonic environments allows us to formulate hitherto untreated models of magma genesis.

As an example of subduction zone reactivation, consider the well-studied Cenozoic volcanic rocks of the Andean region of southern Peru. These provide documentation of the role of ancient continental lithosphere in producing both high $^{87}\text{Sr}/^{86}\text{Sr}$ ratios and well-defined mantle isochrons in subduction zone environments (James *et al.*, 1976). Here, the ancient lithosphere of the South American shield extends beneath the Andes to a depth of at least 200 to 300 km and forms, throughout the depth range over which magma is generated, a continuous lithosphere-lithosphere boundary with the descending Nazca plate. The model which most plausibly explains the isotopic and trace element data is one in which andesitic magma is produced by subduction zone melting of the ancient South American lithosphere. The isotopic imprint of that aged lithospheric mantle material is preserved in the mantle isochrons and anomalously high $^{87}\text{Sr}/^{86}\text{Sr}$ ratios of the young volcanics of the Andean region.

The rifting-related reactivation environment is represented by the alkalic complexes of Africa and the Jurassic tholeiitic flood basalts (and dolerite sheets) associated with the break-up of Gondwanaland. The latter define mantle-isochrons both on a local (Antarctica) and regional (Antarctica, Tasmania, and Africa) scale (Table 6), and document the existence of very undepleted mantle in these regions. Mantle isochrons are also common in regions where a continent appears to have over-ridden an ocean rise or mantle plume. Our examples all come from western U.S.A., where many rock associations have mantle isochron ages in the range 600 to 1000 m.y. This particular region is probably the most complex of those discussed, and despite

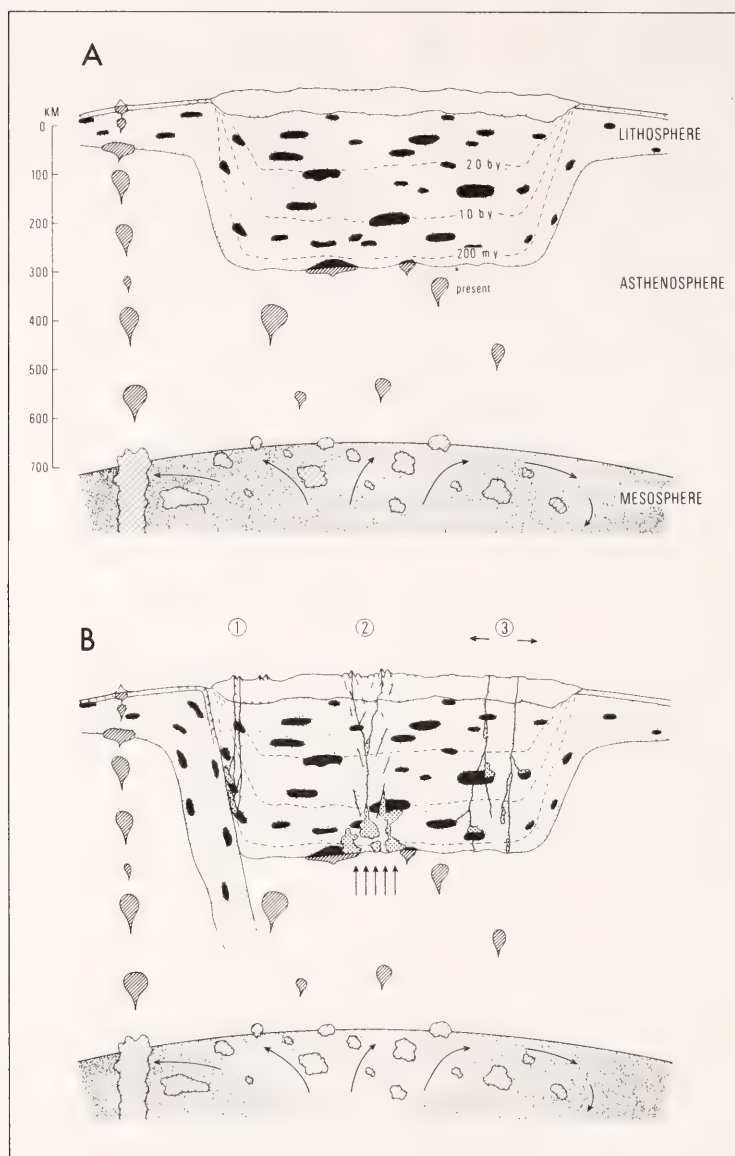


Fig. 31. Diagram showing development (A) and subsequent reactivation (B) of blob-enriched continental lithosphere (vertical exaggeration about 5 = 1). (A) Blobs are released from mesosphere by buoyancy and convection, ascend through convecting asthenosphere, and penetrate through either under-plate thickening continental lithosphere or oceanic lithosphere. Ascending blobs (diagonally ruled pattern) may be partially molten, with some segregation of liquid occurring before they become subsolidus in the lithosphere (solid pattern). Dashed "age" lines in lithosphere represent progressive positions of the boundary representing accretion of lithosphere from asthenosphere. Note that oceanic lithosphere is shown to be younger than 200 m.y. An oceanic "plume" is indicated schematically as a continuous train of blobs. (B) Various reactivation environments, where partial melts (stippled pattern) are formed in continental lithosphere: (1) above a subducting oceanic plate; (2) over a thermal or upwelling anomaly in the asthenosphere (plume or overridden ridge, arrows); and (3) during continental rifting (initial stage shown without causal mechanism).

numerous studies a definite pattern of ancient lithosphere consumption is not yet forthcoming. However, the possible participation of the lithosphere in the magmatism of the region is discussed in the literature (Hedge and Noble, 1971; Leeman, 1974, 1975; Leeman and Manton, 1971; Mark *et al.*, 1975; Peterman *et al.*, 1970).

An important aspect of Table 6 is that mantle isochrons are not restricted to young volcanics but are also encountered in young hypabyssal and plutonic intrusives (Jurassic dolerites of Antarctica; California Mesozoic batholiths), metamorphosed basic rocks of early Palaeozoic age (Caledonian basic-igneous Province, Scotland), and in ancient layered-intrusions (Usushwana complex of South Africa). These examples are encouraging because they demonstrate that mantle isochrons are not necessarily masked by either differentiation or metamorphism, thereby considerably extending their usefulness as petrogenetic indicators.

One consequence of the mantle isochron model is that crystallization ages determined on basic igneous rocks by the Rb-Sr whole-rock technique can be in excess of the true age by many hundreds of millions of years. This problem of inherited age is more serious for younger rocks, and there are well-documented instances of conflicts between stratigraphic age and Rb-Sr age in the literature (e.g., Compston, 1974; Cormier, 1969).

Effective use of the mantle isochron concept requires knowledge of actual crystallization ages (so that the measured isochron can be divided into its pre- and postcrystallization components), and determination of isochron parameters on rocks that have been subjected to minimal postmelting processes (fractional crystallization, wall-rock contamination, etc.). The concept of Rb-Sr mantle isochrons as we have presented it provides a new tool for understanding the petrogenesis of mantle-derived igneous rocks.

Acknowledgments

This study has been supported in part by the National Science Foundation (Grant No. GA 36094) and the National Research Council of Canada (Grant No. A 5581 to C.B.). One of us (C.B.) gratefully acknowledges the Carnegie Institution of Washington for providing financial support and research facilities during his sabbatical year.

PART II: OCEANIC REGIONS

Introduction

Tatsumoto (1966) showed that basalts from oceanic areas preserved a correlation between U/Pb ratio and lead isotopic ratio, and concluded that this correlation, presumably inherited from the mantle source of the basalts, suggests a mantle in which U/Pb heterogeneities have existed for a billion years or more. A similar general correlation was noted between $^{87}\text{Sr}/^{86}\text{Sr}$ and Rb/Sr for oceanic basalts (Hart, 1971; Allègre, 1972). Recently, this systematic Rb-Sr isochron correlation was emphasized by Sun and Hanson (1975), who showed that Sr isotope data for alkali basalts (and nephelinites) from 14 oceanic islands defined a correlated array which, if interpreted as an isochron, suggested an age for mantle heterogeneities of about 2000 m.y. We were impressed with these relationships and undertook a careful screening of published data to look at the Rb-Sr systematics of *both* tholeiitic and alkali basalts from oceanic regions. We found striking regularities in almost all cases and present these results because of their importance in constraining the space and time evolution of mantle chemistry.

Compilation of Data

The data were compiled from the literature, using only those analyses of relatively high precision which could

be confidently normalized to an Eimer and Amend standard value of 0.7080. For some islands the published $^{87}\text{Sr}/^{86}\text{Sr}$ was not accompanied by Rb/Sr data. In these cases, powders of the original sample were requested (and are here acknowledged with thanks), and the Rb/Sr ratio was measured using conventional x-ray fluorescence techniques. In other cases, unpublished data were made directly available to us, and these are also gratefully acknowledged.

During the oceanic-island compilation, we attempted to retrieve data for basaltic rocks only, because differentiation effects might distort the Rb-Sr systematics. This screening, together with the identification of association (tholeiitic or alkali basalt) was based on published assignments; for some islands earlier literature was searched for chemical analyses and descriptions as an aid to proper evaluation. The rock types from some islands were classed as transitional, possessing chemical compositions between tholeiite and alkali basalt. Such rocks were grouped with the alkali basalts in order to keep the potentially "primitive" tholeiitic association as uncluttered as possible.

Results and Treatment

$^{87}\text{Sr}/^{86}\text{Sr}$ -Rb/Sr analyses were retrieved for 167 alkali basalts and 109 tholeiites. There are three principal ways in which correlations between Rb/Sr and $^{87}\text{Sr}/^{86}\text{Sr}$ can be evaluated: (1) On a local scale using individual data. Wherever the number of samples permits, intra-island (or island group) relationships can then be examined. (2) On a regional scale using individual data. The islands from a given ocean can be grouped and the relationships between the individual data examined. (3) On a regional scale using averaged data. The data for each island (or island group) can be averaged to give a single representative data point, and the relationships between these aver-

age data points examined. Obviously treatments (2) and (3) will provide the same result only if each island is represented by a comparable number of individual analyses. However, many islands are represented by a few analyses, and a few islands by many analyses, and it is the latter that then dominate the relationships obtained by use of treatment (2). This is well portrayed in a trial comparison of the Pacific and Indian Ocean tholeiites. The averaged island data are well correlated ($r = 0.90$) and form an 1100-m.y. isochron. The individual data however are uncorrelated ($r = 0.12$) and do *not* define an isochron. In this example, the difference is due to the sample weight of the Hawaiian Islands ($n = 30$), an island group that displays no internal correlation between Rb/Sr and $^{87}\text{Sr}/^{86}\text{Sr}$ on even an intra-island scale. The manner in which the data are treated is essential to the discussion that follows, and we are confident that the average island treatment (3) provides an insight to the regional Rb-Sr systematics of mantle-derived volcanics that otherwise would be lost in the more conventional individual-data treatments. Consequently we will use only treatments (1) and (3) in our appraisal of the data.

The averaged data for the oceanic islands (or island groups) are given in Table 8, together with the number of samples and the appropriate source(s) of the data. When plotted on an Rb/Sr versus $^{87}\text{Sr}/^{86}\text{Sr}$ (isochron) diagram (Fig. 32) the *averaged* data show two striking features: Tholeiites and alkali basalts occupy distinct and essentially nonoverlapping fields; and each field indicates a pronounced positive correlation between $^{87}\text{Sr}/^{86}\text{Sr}$ and Rb/Sr. The tholeiite data appear more closely correlated than the alkali basalt data, as there are four alkali-basalt data points which appreciably extend that field toward higher Rb/Sr ratios. We note that two of these island points (Gough and Rodriguez) contain only one and two individual analyses, respectively,

TABLE 8. Average Rb/Sr and $^{87}\text{Sr}/^{86}\text{Sr}$ for Basalts from Oceanic Islands (or Island Groups) and the Ocean Floors

| Location | Rb/Sr | $^{87}\text{Sr}/^{86}\text{Sr}$ | N^* | Graph No.† | Data Sources‡ |
|--------------------------------------|-------|---------------------------------|-------|------------|---------------|
| <i>Oceanic island tholeiites</i> | | | | | |
| Bouvet | 0.016 | 0.70369 | 4 | 1 | 1 |
| Hawaiian Islands | 0.017 | 0.7038 | 30 | 2 | 2,3,4,5,6 |
| Iceland | 0.014 | 0.70307 | 13 | 3 | 1,7,(A) |
| Kerguelen | 0.033 | 0.7048 | 5 | 4 | 8 |
| Kolbeinsey | 0.009 | 0.70290 | 1 | 5 | 1 |
| Reunion | 0.033 | 0.7042 | 8 | 6 | 8,9,(B) |
| Samoa | 0.049 | 0.7053 | 5 | 7 | 10,11 |
| St. Pauls | 0.039 | 0.7045 | 7 | 8 | 8,12 |
| <i>Ocean floor tholeiites</i> | | | | | |
| Indian | 0.015 | 0.70314 | 8 | 9 | 13,14 |
| Pacific | 0.011 | 0.70265 | 15 | 10 | 13,15 |
| Atlantic | 0.008 | 0.70264 | 13 | 11 | 13,(A) |
| <i>Oceanic island alkali basalts</i> | | | | | |
| Amsterdam | 0.045 | 0.7039 | 4 | 12 | 8 |
| Ascension | 0.066 | 0.7028 | 4 | 13 | 1,16 |
| Azores | 0.046 | 0.7035 | 26 | 14 | 1,17,18 |
| Canary | 0.032 | 0.7033 | 7 | 15 | 1,5 |
| Cape Verdes | 0.028 | 0.7031 | 4 | 16 | 19 |
| Crozet | 0.060 | 0.7041 | 2 | 17 | 8 |
| Easter | 0.019 | 0.7030 | 7 | 18 | 20,(C) |
| Eniwetok | 0.048 | 0.7038 | 2 | 19 | 21,(C) |
| Gough | 0.059 | 0.7033 | 1 | 20 | 16 |
| Guadeloupe | 0.024 | 0.7033 | 4 | 21 | 20,(C) |
| Hawaiian Islands | 0.028 | 0.7033 | 32 | 22 | 4,5,6,(D) |
| Iceland | 0.040 | 0.7032 | 10 | 23 | 1,7,(A) |
| Jan Mayen | 0.074 | 0.7036 | 9 | 24 | 1,22 |
| Kerguelen | 0.069 | 0.7052 | 4 | 25 | 8 |
| Madiera | 0.036 | 0.7031 | 1 | 26 | 5 |
| Rodriguez | 0.077 | 0.7038 | 2 | 27 | 9,(B) |
| Samoa | 0.067 | 0.7054 | 14 | 28 | 11,23 |
| St. Helena | 0.034 | 0.7030 | 18 | 29 | 10,24 |
| Tahiti | 0.047 | 0.7042 | 9 | 30 | 20,(C) |
| Tristan de Cunha | 0.062 | 0.7052 | 7 | 31 | 1,5 |

*N = number of samples averaged.

†Reference number for figures.

‡See Table 9.

and that the Jan Mayen point may be anomalous because of the possibility that the island is built on continental crust.

When individual samples are examined, only two islands, Kerguelen and Samoa, show an intraisland correlation with a positive slope (Fig. 33). The other islands show either horizontal data arrays (constant $^{87}\text{Sr}/^{86}\text{Sr}$, variable Rb/Sr, e.g. Iceland, Tristan da

Cunha, the Azores), equidimensional fields with significant variation in both directions (e.g., St. Helena, Hawaii), or correlations with a negative slope (Canary Islands, Jan Mayen, Cape Verde Islands). We find it interesting that the only two islands which internally show positively correlated data are the two which have the highest average $^{87}\text{Sr}/^{86}\text{Sr}$ (and Rb/Sr) and we shall return to this point.

TABLE 9. Reference Key to Table 8

| Key No. | Reference |
|---------|--|
| 1 | O'Nions and Pankhurst (1974) |
| 2 | Hart (1973) |
| 3 | Heier, Compston, and McDougall (1965) |
| 4 | Powell and DeLong (1966) |
| 5 | Bence (1966) |
| 6 | Lessing and Catanzaro (1964) |
| 7 | Hart, Schilling, and Powell (1973) |
| 8 | Hedge, Watkins, Hildrett, and Doering (1973) |
| 9 | McDougall and Compston (1975) |
| 10 | Hedge (1966) |
| 11 | Hedge, Peterman, and Dickinson (1972) |
| 12 | Girod, Camus, and Vialeth (1971) |
| 13 | Hart (1976) |
| 14 | Subbarao and Hedge (1973) |
| 15 | Subbarao (1972) |
| 16 | Gast, Tilton, and Hedge (1964) |
| 17 | White, Hart, and Schilling (1975) |
| 18 | Hart and Brooks (1974) |
| 19 | Klerkx, Deutsch, and DePaepe (1974) |
| 20 | Peterman and Hedge (1972) |
| 21 | Hedge and Peterman (1970) |
| 22 | Lussia, Berdou, Polve, and Vidal (1973) |
| 23 | Hubbard (1971) |
| 24 | Grant, Powell, Walther, and Burkholder (1976) |
| (A) | S. R. Hart (unpublished data) |
| (B) | C. Brooks (unpublished data) |
| (C) | C. E. Hedge (unpublished data) |
| (D) | M. A. Lanphere, G. B. Dalrymple, and D. A. Clague (unpublished data) |

To decide if the positive correlations shown in Figures 32 and 33 are statistically significant, the data of Table 8 have been appraised by calculating the correlation coefficient r , and testing the slope of the fitted line for significance against zero. The regression treatment used to obtain slopes and intercepts was that of York (1966); the errors in the "age" and initial ratio are calculated solely from the data scatter and are given at 1 standard deviation (following recommendations of Brooks *et al.*, 1972). While it is convenient to express the slopes of these correlated arrays as ages, we emphasize here that these "ages" need not have time significance. This point is discussed in considerable detail later in the paper.

The statistical parameters relevant to oceanic islands are presented in Table 10. The significance levels of the correlation coefficients range from 95% (e.g., for Samoa and Kerguelen) to greater than 99.99% (e.g., for the complete tholeiite suite including ridge basalts, and for the high-density portion of the alkali-basalt field). We find these correlations remarkable and suggest that these data provide important and hitherto unused constraints relating to processes of oceanic magmatism.

Discussion

Possible causes for the positive isochron correlations presented in the previous section include surficial weathering and contamination by crust, sediments, or sea water; and inheritance of these isochron parameters from a heterogeneous and aged mantle.

We believe direct weathering is ruled out because of the fresh and unaltered nature of most of the samples involved. Other contamination processes might include mixing of low $^{87}\text{Sr}/^{86}\text{Sr}$ magma of direct mantle derivation (ridge basalts) with more radiogenic material represented by sediments or oceanic crust which has interacted with sea water. Oceanic sediments may have $^{87}\text{Sr}/^{86}\text{Sr}$ values as high as 0.717 and Rb/Sr values greater than 1.0 (Dasch, 1969; Biscay and Dasch, 1971; Church, 1971). Only limited data exist for altered oceanic crust, but material has been analyzed with Rb/Sr ratios of 0.15–0.25 (Dasch *et al.*, 1973; Hart, 1969), and presumably $^{87}\text{Sr}/^{86}\text{Sr}$ ratios could rise to values as high as sea water (0.709). Thus, both sediments and altered oceanic crust could provide a mixing component that would produce positive correlations of the kind shown in Fig. 33. This mechanism has been described in detail in earlier papers and generally dismissed as a significant effect in the petrogenesis of oceanic basalts (Tatsumoto, 1966; Powell and DeLong, 1966; Gast *et al.*, 1964; Grant *et al.*, 1976). The fact that

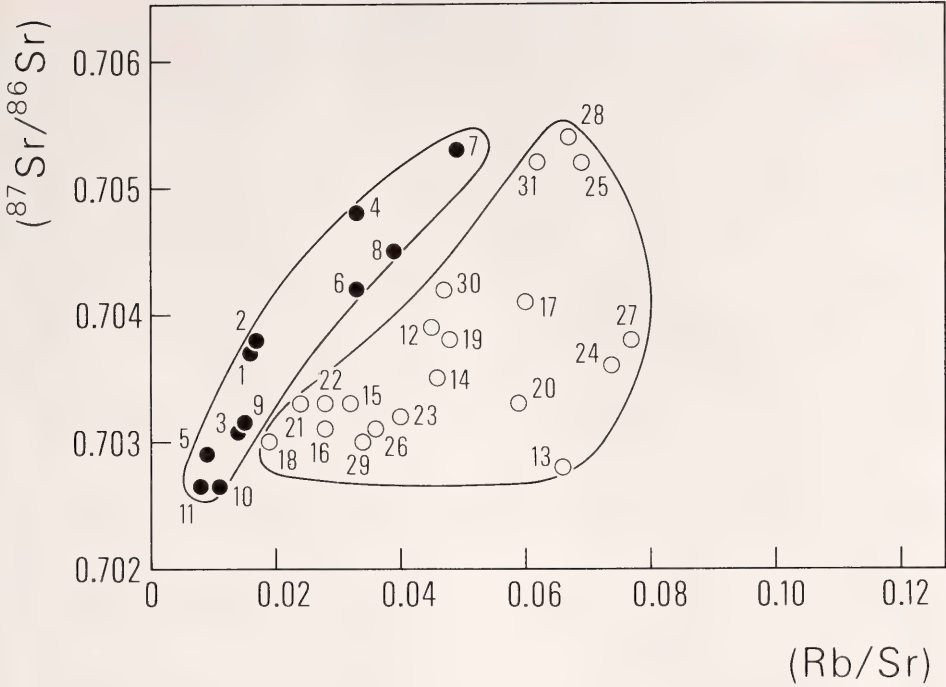


Fig. 32. $^{87}\text{Sr}/^{86}\text{Sr}$ -Rb/Sr isochron plot of tholeiites (filled circles) and alkali basalts (open circles) from oceanic islands. Each point represents an average of available data on individual samples from a given island or island group. Numbers refer to the data index in Table 8.

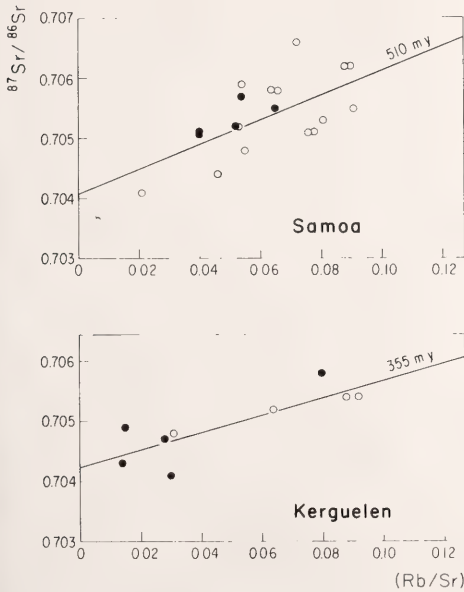


Fig. 33. Isochron plot of data for individual samples of tholeiite (filled circles) and alkali basalt (open circles) from the Samoa Islands and Kerguelen Island. Best-fit regression lines and slope values are shown.

the lead isotope regression line for oceanic basalts is distinctly different from the regression line for oceanic sediment (and sea water) also argues against such a contamination mechanism (Sun and Hanson, 1975; Chow and Patterson, 1962; Church and Tilton, 1973; Meijer, 1976). Furthermore, the marked uniformity of $^{87}\text{Sr}/^{86}\text{Sr}$ values for some islands (O'Nions and Pankhurst, 1974; Hart *et al.*, 1973), and the general lack of a positive isochron (mixing-line) correlation between individual intra-island samples also argues against a sediment-crust contamination model. As we have discussed, only Samoa and Kerguelen show intra-island "isochrons," whereas these might be expected to be ubiquitous under the operation of a contamination model. Some islands do show correlations of negative slope, as would be expected from contamination processes involving carbonate.

The conventional interpretation of oceanic island strontium (and lead)

TABLE 10. Mantle Isochrons of Rb/Sr versus Present-Day
 $^{87}\text{Sr}/^{86}\text{Sr}$ for Basalts of Oceanic Regions

| Location Identity | Age (m.y.)* | ($^{87}\text{Sr}/^{86}\text{Sr}$)* | N† | r‡ |
|--|-------------|--------------------------------------|----|---------|
| <i>Oceanic Islands</i> | | | | |
| Alkali basalts: all averaged island data | 600±210 | 0.7025±4 | 20 | 0.56(3) |
| Alkali basalts: all data except points 3,20,24 and 27 | 1190±150 | 0.7017±3 | 16 | 0.91(4) |
| Tholeiites: all averaged island data | 1430±180 | 0.7025±2 | 8 | 0.96(4) |
| Tholeiites: all averaged island data plus MORB§ | 1570±150 | 0.7023±2 | 11 | 0.97(4) |
| Kerguelen, tholeiites: individual data | 485±210 | 0.7041±4 | 5 | 0.80(1) |
| Kerguelen, alkali basalts: individual data | 248±20 | 0.7045±1 | 4 | 0.99(2) |
| Kerguelen, all basalts: individual data | 355±90 | 0.7042±2 | 9 | 0.83(2) |
| Samoa, tholeiites: individual data | 466±(250) | 0.7044±3 | 5 | 0.74(1) |
| Samoa, alkali basalts: individual data | 584±200 | 0.7039±6 | 14 | 0.65(1) |
| Samoa, all basalts: individual data | 510±150 | 0.7041±4 | 19 | 0.62(2) |

*Errors given at 1σ

†Number of samples regressed.

‡Pearson correlation coefficient. Value in parentheses indicates at what level of confidence the fitted regression line differs from zero (given in increments of standard deviation).

§MORB indicates mid-ocean ridge basalts.

isotope variations ascribes these to derivation from an isotopically heterogeneous mantle (a review of this model is given by Hofmann and Hart, *Year Book* 74, p. 195, 1975). We consider this the most tenable model at present, and advance it here to explain the "isochron" correlations shown in Fig. 32. We view these positive "isochron" correlations as being inherited by oceanic basalt during derivation from a heterogeneous suboceanic mantle.

Rb-Sr coherence during basalt genesis. Figure 32 shows that oceanic island tholeiites and alkali basalts have a similar range of $^{87}\text{Sr}/^{86}\text{Sr}$ values and suggests that the separation of data fields is due to higher Rb/Sr ratios in the alkali basalts. On the average, the alkali basalts of Table 8 have Rb/Sr ratios about a factor of 2 higher than the tholeiites (whereas the average tholeiite $^{87}\text{Sr}/^{86}\text{Sr}$, 0.7037, is essentially identical with the average alkali basalt $^{87}\text{Sr}/^{86}\text{Sr}$, 0.7038).

We believe this is a significant observation and propose that the observed Rb/Sr and strontium isotope ratios of the tholeiites are directly representative of the mantle source but that the alkali basalts are displaced toward higher Rb/Sr ratios relative to

the mantle source. The following discussion is an attempt to justify this proposition.

While it is generally accepted that a basalt will inherit the strontium isotopic composition from its source (Hofmann and Hart, *Year Book* 74, pp. 195-210), it is less obvious that a basalt will also preserve the Rb/Sr ratio of that source (because of the effect of partial melting and fractional crystallization processes). This will happen only if the partial melting process leaves no residual mantle phase which is a significant carrier of Sr and Rb, and if all fractional crystallization occurring after melting involves only phases that are poor in Rb and Sr or that do not fractionate Rb relative to Sr. In the case of tholeiites, which involve large degrees of melting, phases that carry Rb or Sr (such as phlogopite and amphibole) will probably not persist after melting, so we would expect the partial melt to have the same Rb/Sr ratio as the original source material. Phlogopite has been shown to have a field of stability well above the wet solidus of peridotite (Bravo and O'Hara, 1975; Modreski and Boettcher 1973; Forbes and Flower, 1974; Boettcher *et al.*, 1975; Holloway and Eggler, this

Year Book). However, the phlogopite content of the mantle must be quite small (probably less than 1%: Hofmann and Hart, *Year Book* 74, pp. 195-210), and phlogopite will be consumed during a large degree of melting even if its upper stability limit exceeds the temperature at which melting occurs.

Amphibole may also be stable during hydrous melting of peridotite (Boettcher *et al.*, 1975; Allen and Boettcher, 1973). However, it is less effective than phlogopite at fractionating Rb/Sr during large degrees of melting. For example, for 25% melting of amphibole peridotite, where one half of an original 20% of amphibole persists after melting, the Rb/Sr ratio of the liquid will be only slightly higher (6%) than that of the starting material (using partition coefficients from Philpotts and Schnetzler, 1970). For clinopyroxene, the partition coefficients of Rb and Sr are sufficiently small ($D_{Sr} \sim 0.08$, $D_{Rb} \sim 0.003$) (Hart and Brooks, 1974; Shimizu, 1974), that residual clinopyroxene produces negligible (<3%) fractionation of Rb/Sr during melting. Arguments similar to these led Gast (1968) to the conclusion that tholeiites formed by large degrees of melting (15-25%) would contain most of the Rb and Sr (and many other trace elements) of the original mantle source.

Gast (1968) also showed that fractional crystallization is relatively ineffective in fractionating Rb from Sr. Only crystallization of plagioclase will be effective in changing the Rb/Sr ratio, as the partition coefficients of Rb and Sr in olivine and pyroxene are too low to cause any significant fractionation of Rb from Sr. However, limits can be placed on the extent of plagioclase fractionation by noting that most oceanic basalts have little or no detectable europium anomaly (Schilling, 1971; Sun and Hanson, 1975b). A detectable europium anomaly (5-10%) will be produced by crystallization of 15-25% of plagioclase, which in turn will generate an increase in the Rb/Sr

ratio of the liquid of from 25-60% (using partition coefficients appropriate to a 75-80% plagioclase (Philpotts and Schnetzler 1970). We conclude that in the case of oceanic tholeiites, the extruded basalt very closely represents the $^{87}Sr/^{86}Sr$ and Rb/Sr ratios of the mantle source.

Alkali basalts, on the other hand, which are thought to be derived by relatively small degrees of partial melting (Gast, 1968; Green, 1973), may offer more possibility of leaving behind residual phases such as phlogopite (Bewick, 1976) or amphibole. In these cases, using reasonable values for partition coefficients (Philpotts and Schnetzler, 1970) and phase proportions, major changes in Rb/Sr ratios can be brought about. For example, if a 3% melt fraction is derived from a source containing 15% amphibole and 10% clinopyroxene and the amphibole provides all of the melt (i.e., 12% amphibole and 10% cpx remain after melting), the Rb/Sr ratio of the melt will be 35-65% higher than that of the original source (the range is due to selection of two different sets of partition coefficients from Philpotts and Schnetzler (1970). Phlogopite is surprisingly ineffective at fractionating Rb/Sr at low degrees of melting because of the competing effect of clinopyroxene (residual clinopyroxene raises the melt Rb/Sr, whereas phlogopite lowers it). A 3% melt fraction of a source containing 1% phlogopite and 20% clinopyroxene (where 0.5% phlogopite and 2.5% clinopyroxene enter the melt) will have a Rb/Sr ratio about 10% higher than the source material. Note that liquids derived from a mantle source containing only phlogopite as a Rb-Sr carrier will have Rb/Sr ratios *lower* than the source.

These model calculations are not intended to include all possible variations of parameters but only to suggest approximate magnitudes of certain limiting cases. To explain the higher Rb/Sr ratio in alkali basalts than in tholeiites (Fig. 32) we suggest that am-

phibole, not phlogopite, is a necessary residual phase during alkali basalt genesis. For melts derived from depths greater than the stability limit of amphibole, reequilibration between such melts and shallower amphibole-bearing mantle may be required.

Alternative explanations for the Rb/Sr and Sr isotopic pattern in tholeiites and alkali basalts. In the preceding section, we gave our preferred interpretation of the pattern observed in Fig. 32. Some other conceivable explanations are: (i) Alkali basalts and tholeiites come from chemically different mantle sources. (ii) Alkali basalts have undergone more fractional crystallization of plagioclase (or clinopyroxene) than tholeiites. (iii) Basalt derivation from the mantle does not occur under conditions of chemical equilibrium between melt and residue (O'Nions and Pankhurst, 1974). (iv) Tholeiites and alkali basalts are generated sequentially by fractional melting from the same source material (Beswick, 1976).

Explanation (i) is difficult to reconcile with the fact that many islands erupt both tholeiites and alkali basalts and that the strontium isotope ratios of both are generally very similar. Compare in Table 8, for example, the isotope ratios of tholeiites and alkali basalts from Iceland (0.7031 vs. 0.7032), Samoa (0.7053 vs. 0.7054), Kerguelen (0.7048 vs. 0.7052), and the Hawaiian Islands (0.7038 vs. 0.7033).

Explanation (ii) would require about 30% more plagioclase crystallization in alkali basalts than in tholeiites. Plagioclase crystallization of 30% would lead to a consistent and easily observable europium anomaly of some 15–20% alkali basalts relative to tholeiites (presuming oxygen fugacities and resultant REE partition coefficients to be the same in both cases). In addition, there should be a significant "plagioclase" effect in the major-element data and norms of alkali basalts relative to tholeiites, and this is also not observed (CaO and Al_2O_3 con-

tents of oceanic tholeiites and alkali basalts are quite similar). Extreme and unrealistic amounts of clinopyroxene crystallization would be required to produce significant changes in Rb/Sr ratios; the ratio is increased only 50% after 99% crystallization.

Explanation (iii) is not consistent with the relative coherence of trace element patterns and the observed constancy of major element composition in various basalt types (Yoder, 1976). Disequilibrium melting has also been considered on the basis of existent diffusion data (Hofmann and Hart, *Year Book* 74, pp. 195–210), and judged to be highly unlikely.

Explanation (iv), as proposed by Beswick (1976), depends on the persistence of a minor phase, phlogopite, through a first stage of extensive partial melting (tholeiite production). By retaining K and Rb in residual phlogopite, this first melt would have a lower Rb/Sr (and higher K/Rb) ratio than the bulk source. The reserve of K and Rb stored in phlogopite is then released during alkali basalt production, giving rise to a higher Rb/Sr (and lower K/Rb) ratio in the melt. As noted above, the persistence of a *minor* refractory phase is difficult to reconcile with an equilibrium involving large degrees of melting. No one, to our knowledge, has yet studied a peridotite system containing 1% phlogopite or less, where residual phlogopite remains after, say, 20% of partial melting. Beswick's model also requires a considerably higher K/Rb partition coefficient for phlogopite-melt (~ 3) than has yet been reported (Philpotts and Schnetzler, 1970).

In summary, the alternative explanations outlined in this section all appear unsatisfactory, and we conclude that small degrees of melting with amphibole as a residual phase during alkali basalt genesis is the best explanation for the differences in Rb-Sr between tholeiites and alkali basalt.

Comparison of Rb-Sr and U-Pb systematics. First, while tholeiites have the same range of $^{87}\text{Sr}/^{86}\text{Sr}$ as alkali

basalts, it appears that tholeiites show a smaller range in $^{206}\text{Pb}/^{204}\text{Pb}$ than alkali basalts (Tatsumoto, 1966; Sun and Hanson, 1975a,b; Church and Tatsumoto, 1975; Sun and Jahn, 1975). This may in part reflect the fact that no lead isotope data are available for tholeiites from the high $^{87}\text{Sr}/^{86}\text{Sr}$ islands such as Samoa and Kerguelen. Second, the alkali basalts invariably have higher U/Pb ratios than the tholeiites. Furthermore, the *observed* U/Pb ratios of alkali basalts are higher than the inferred U/Pb ratios of the mantle source (these can be calculated from the lead isotope ratios), whereas the observed U/Pb ratios of tholeiites are similar to the inferred U/Pb ratio of the source (Tatsumoto, 1966; Allègre, 1969). Thus the lead isotope systematics provide strong evidence for a fractionation of U relative to Pb during the derivation process of alkali basalts, and this supports the arguments presented above for an increase in Rb/Sr ratio during alkali basalt genesis.

Finally, for many islands the lead isotope ratios appear to exhibit significant variations, whereas the strontium isotope ratios appear almost constant. For example, Iceland shows a 4% spread in $^{206}\text{Pb}/^{204}\text{Pb}$ ratio (Sun and Hanson, 1975a; Sun and Jahn, 1975), but only a barely detectable variation in $^{87}\text{Sr}/^{86}\text{Sr}$ (O'Nions and Pankhurst, 1974; Hart *et al.*, 1973). This effect may be largely one of experimental precision in the isotope measurements. The spread in Pb ratios on Iceland requires a 35% range in source U/Pb ratio (averaged over 1.5 billion years); a 35% range in Rb/Sr ratio would produce over the same time interval a spread of $^{87}\text{Sr}/^{86}\text{Sr}$ of only 0.7029–0.7031. This is close to the observed spread of Sr isotope ratios for young Icelandic tholeiites but is only barely significant in terms of analytical precision.

Rb-Sr mantle isochrons. If the tholeiite correlation of Fig. 32 is inherited from a mantle source, what meaning can be attached to the parameters of this correlation? One model would

invoke a mantle that is heterogeneous on a scale larger than the scale sampled by individual island magmatism, with the magmas essentially sampling a continuum of mantle Rb/Sr systems. The correlation of Fig. 32 thus would be in a sense a *mantle isochron*, and the slope could have definite age significance. If the mantle heterogeneities developed at a discrete time (two-stage process), then the slope of the tholeiite correlation shown in Fig. 32 suggests an age of about 1.6 ± 0.2 billion years for this process. If the development of the Rb-Sr heterogeneity was a continuous or multiphasic process, then any "age" inferred from the slope is simply some average age for the process as a whole (it is possible to construct mathematical models of such processes in such manner that subsequent mixing of the appropriate reservoirs will give rise to linear trends or "isochrons" [Church and Tatsumoto, 1975]).

Another model would consider a mantle that has only two discrete compositions, one at each end of the tholeiite trend shown in Fig. 32, with intermediate points representing various mixtures of the two compositions. For example, the mantle that supplies MORB (asthenosphere) is relatively uniform and distinct isotopically (Hofmann and Hart, 1975), and could be the lower end-member. A uniform mesosphere might be the upper end-member, with mixing of these two taking place during mantle convection and diapirism. In this case, the slope of the mixing line can only be interpreted directly as an *age* if the system from which the two end-members developed had a uniform strontium isotopic composition. A simple test for such a binary mixing process might be a linear relationship between $^{87}\text{Sr}/^{86}\text{Sr}$ and the reciprocal of Sr concentration (no such linear relation is apparent in our data). However, such a test is valid only if it is applied to mixtures of melts rather than mixtures of mantle source material. The Sr concentration of melt extracted from a mixed mantle source

will vary inversely with the degree of melting, and any significant variation in the degree of melting would perturb the expected inverse mixing relationship between isotopic composition and concentration.

At this point, it is important to note that many oceanic islands have lead isotopic compositions that define linear trends (Sun and Hanson, 1975a, b; Sun and Jahn, 1975). These trends are subject to the same uncertainty of interpretation as the Rb-Sr trend of Fig. 32. They may be secondary isochrons, implying the age of a geological event, or they may be mixing lines. Ages calculated from the slopes of these lead isotope trends are in remarkable agreement with the Rb-Sr "age" of the tholeiite trend in Fig. 32. For basalts from sea mounts and spreading ridges in the N.E. Pacific, the Pb isotope trend gives an age of 1.75 ± 0.1 b.y. (Church and Tatsumoto, 1975). Alkali basalts from oceanic islands fall along this same trend, with a Pb isotope age of about 2 b.y. (Sun and Hanson, 1975a).

We feel this general concordance of U-Pb and Rb-Sr systematics is not fortuitous but is strong evidence against a *random* mixing process—i.e., any mixing process in which the end-members started with uncorrelated isotopic parameters. Granted this point, then there is little essential difference between binary (or multicomponent) mixing models and a two-stage model with a continuum of subsystems: both result in trends that have definite *age* significance. The difficulty lies in distinguishing these two-stage models from continuous or multistage models in which the trends no longer have a specific age interpretation.

At present, the simplest model seems to be that of mixing between relatively radiogenic mantle (mesosphere) and unradiogenic mantle (asthenosphere), with the isochrons for both Pb-Pb and Rb-Sr systems having a distinct age significance. A definitive test of these models will depend on further refinement of U-Pb and Rb-Sr data, comparison with other decay schemes (Lu-Hf or

Sm-Nd), and analysis of materials from similar tectonic settings in the past geologic record.

Scale of mantle heterogeneities. We have previously indicated that two island groups display significant positive intra-island Rb-Sr isochron correlations, and we would like to suggest that they are also derived from aged heterogeneous mantle. Two facts then need explanation: Why do only these two island groups retain a "mantle isochron", and why is the apparent age of these isochrons younger (360–510 m.y.) than that of the oceanic island ensemble as a whole (1200–1600 m.y.) and younger than both intra-island and inter-island Pb-Pb isochrons? Our ideas on this are admittedly speculative, but we suggest that the heterogeneities in the mantle exist on variable size scales, and that the more extreme mantle compositions (note that Samoa and Kerguelen are both the most radiogenic end-members of the trends in Fig. 32) may only exist as smaller volumes. Magmatism in a given island group can thus sample a finite variety of compositions from a mantle in which the heterogeneities exist on a smaller scale. At the same time, the limited size of these heterogeneities may allow for some isotopic reequilibration between the various systems, and thus the "age" which would be detected by magmatic sampling would be in some sense partially "reset". This reequilibration or internal redistribution may take place by severe shear during diapirism or during the final magmatic stage, keeping in mind that diffusive transport distances for Sr in silicate melts can be of the order of 50 meters per 10 m.y. (Hofmann, 1975; see also Hofmann and Magaritz, this report).

Rb-Sr model calculations show that redistribution of Sr can lead to partial rotation of isochrons, with relatively little disturbance of the linear aspect of the data array (Farhat, 1975). Pb-Pb isochrons will not be rotated by this mechanism, as internal redistribution of Pb in these cases will simply move subsystems up or down the existing

isochron. An analogy could be drawn here between the behavior of mineral isochrons and whole-rock isochrons during the metamorphism of an igneous pluton (the mineral systems are smaller than the whole-rock systems and may undergo isotopic reequilibration leading to clockwise rotation of Rb-Sr mineral isochrons and convergence of points on mineral Pb-Pb isochrons). Further evaluation of these concepts can be made when Pb isotope data become available from Samoa and Kerguelen.

The mantle isochrons discussed here are compatible with the model outlined in the preceding companion report by Brooks *et al.* for the development of a heterogeneous subcontinental lithosphere by the incorporation or underplating of ascending plumes or blobs. The main difference is that there is no old lithosphere in oceanic regions, and the blobs or partial melts derived from mesosphere penetrate the oceanic lithosphere directly, thus generating oceanic island magmatism.

Summary and Conclusions

Rb/Sr ratios and $^{87}\text{Sr}/^{86}\text{Sr}$ ratios, when averaged by ocean basin (for mid-ocean ridge basalts) and by oceanic island or island group, yield significant positive correlations on an Rb/Sr isochron diagram. The correlation for tholeiitic basalts is especially strong, and we interpret it as a mantle isochron that may date a major event (or events) of mantle differentiation, such as the segregation of a chemically isolated asthenosphere 1.5–2.0 b.y. ago. Alkali basalts show greater scatter and are displaced toward higher Rb/Sr ratios relative to the tholeiites. We attach no *direct* age significance to the alkali-basalt correlation because these basalts are derived by much smaller degrees of partial melting than are tholeiites, so that the probability of significant fractionation between Rb and Sr (and therefore change of Rb/Sr ratio) is much greater.

The Rb-Sr mantle isochron for tholeiites is identical in age (1.6 ± 0.2 b.y.) to ages (so-called secondary isochrons) of oceanic rocks based on the isotopic composition of lead (1.8 ± 0.1 b.y.). This is an important finding, as it strengthens the conclusion that the isochron ages represent real geological events rather than the result of random mixing processes of no age significance.

Although we do not argue that the data could not also be explained by a continuous or multiepisodic differentiation and remixing event, the simpler, first-order explanation, if correct, may date an event of fundamental importance in the earth's history that is not easily recognized from the surface geological record.

We conclude by stating that the apparent coherence of strontium isotope ratio and Rb/Sr ratio in basaltic magmas lends strong support to the currently popular ideas of a mantle in which chemical heterogeneities have existed on a long time scale (billions of years). This coherence can be a powerful tool in mapping mantle heterogeneities and in understanding their time evolution.

Acknowledgments

We acknowledge the valuable criticisms and suggested improvements of D. J. Whitford and C. Allègre. We also gratefully acknowledge the following people for providing either data or sample powders: W. Compston, P. Pushkar, C. E. Hedge, M. P. Groton, J. B. Gill and M. A. Lanphere. M. Strobel provided invaluable assistance with statistical theory and relevant computer programs. This study has been supported in part by the National Research Council of Canada (Grant No. 5581 to C.B.).

References

Alexander, S. S., and R. W. Sherburne, Crust and upper mantle structure in continental South America and its role in global tectonics, *Comptes Rendus* No. 18,

- Part 1, IUGG, p. 85, Intern. Assoc. of Seis. and Phys. of the Earth's Interior, Programs of the Scientific Assembly, Lima, Peru, Aug. 20-31, 1973.
- Allègre, C. J., Comportement des systèmes U-Th-Pb dans le manteau supérieur et modèle d'évolution de ce dernier au cours des temps géologiques, *Earth Planet. Sci. Lett.*, 5, 261, 1969.
- Allègre, C. J., Géochronologie isotopique et développement de la croûte terrestre au cours des temps géologiques, in *Structure et Dynamique de la Lithosphère*, p. 373, C. J. Allègre and M. Mattauer, eds., Paris, Hermann, 1972.
- Allen, J. C., and A. L. Boettcher, Phase relations and the stability of amphiboles in an olivine nephelinite at high pressures, *Trans. Am. Geophys. Union*, 54, 481, 1973.
- Allsopp, H. L., L. O. Nicolaysen, and P. Hahn-Weinheimer, Rb/K ratios and Sr-isotopic compositions of minerals in eclogitic and peridotitic rocks, *Earth Planet. Sci. Lett.*, 5, 231-244, 1969.
- Anderson, D. L., Chemical plumes in the mantle, *Geol. Soc. Am. Bull.*, 86, 1593-1600, 1975.
- Armstrong, R. L., A model for the evolution of strontium and lead isotopes in a dynamic earth, *Rev. Geophys.* 6, 175-199, 1968.
- Barrett, D. R., The genesis of kimberlites and associated rocks: Strontium isotopic evidence, in *Physics and Chemistry of the Earth*, 9, pp. 637-654, L. H. Ahrens, J. B. Dawson, A. R. Duncan, and A. J. Erlank, eds., Elmsford, N. Y., Pergamon Press, 1975.
- Bell, K., and J. L. Powell, Strontium isotopic studies of alkalic rocks: The potassium-rich lavas of the Birunga and Toro-Ankole regions, East and Central Equatorial Africa, *J. Petrol.*, 10, 536-572, 1969.
- Bell, K., and J. L. Powell, Strontium isotopic studies of alkalic rocks: The alkalic complexes of eastern Uganda, *Geol. Soc. Amer. Bull.*, 81, 3481-3490, 1970.
- Bence, A. E., The differentiation history of the Earth by Rb-Sr isotopic relationships, Ph.D. thesis, Mass. Inst. of Technology, 1966.
- Beswick, A. E., K and Rb relations in basalt and other mantle derived materials: Is phlogopite the key? *Geochim. Cosmochim. Acta*, 40, in press, 1976.
- Biscaye, P. E., and E. J. Dasch, The rubidium, strontium, strontium-isotope system in deep-sea sediments: Argentine basin, *J. Geophys. Res.*, 76, 5087-5096, 1971.
- Boettcher, A. L., B. O. Mysen, and P. J. Modreski, Melting in the mantle: phase relationships in natural and synthetic peridotite-H₂O and peridotite-H₂O-CO₂ at high pressure, *Phys. Chem. Earth*, 9, pp. 855-867, L. H. Ahrens, J. B. Dawson, A. R. Duncan, and A. J. Erlank, eds., Elmsford, N.Y., Pergamon Press, 1975.
- Boyd, F. R., and P. H. Nixon, Kimberlite diopsides, *Carnegie Inst. Wash. Year Book* 68, p. 324, 1970.
- Boyd, F. R., and P. H. Nixon, Origins of the ultramafic nodules from some kimberlites of northern Lesotho and the Monastery Mine, South Africa, in *Physics and Chemistry of the Earth*, 9, pp. 431-454, L. H. Ahrens, J. B. Dawson, A. R. Duncan, and A. J. Erlank, eds., Elmsford, N.Y., Pergamon Press, 1975.
- Bravo, M. S., and M. J. O'Hara, Partial melting of phlogopite-bearing synthetic spinel- and garnet-lherzolites, in *Phys. Chem. Earth*, 9, pp. 845-854, L. H. Ahrens, J. B. Dawson, A. R. Duncan, and A. J. Erlank, eds., Elmsford, N.Y., Pergamon Press, 1975.
- Brooks, C., S. R. Hart, and I. Wendt, Realistic use of two-error regression treatments as applied to rubidium-strontium data, *Rev. Geophys. Space Phys.*, 10, 551-577, 1972.
- Brooks, C., S. R. Hart, A. Hofmann, and D. E. James, Rb-Sr mantle isochrons from oceanic regions, *Earth Planet. Sci. Lett.*, in press, 1976.
- Burwell, A. D. M., Rb-Sr isotope geochemistry of lherzolites and their constituent minerals from Victoria, Australia, *Earth Planet. Sci. Lett.*, 28, 69-78, 1975.
- Chapman, D. S., and H. N. Pollack, Global heat flow: A new look, *Earth Planet. Sci. Lett.*, 28 23-32, 1975.
- Chow, T. J., and C. Patterson, The occurrence and significance of lead isotopes in pelagic sediments, *Geochim. Cosmochim. Acta*, 26, 263-308, 1962.
- Church, S. E., Strontium isotope and alkali element geochemistry of selected sediments from the northeast Pacific Ocean, *Geochim. Cosmochim. Acta*, 35, 1300-1305, 1971.
- Church, S. E., and M. Tatsumoto, Lead isotope relations in oceanic ridge basalts from the Juan de Fuca-Gorda ridge area, northeast Pacific Ocean, *Contrib. Mineral. Petrol.*, 53, 253-279, 1975.

- Church, S. E., and G. R. Tilton, Lead and strontium isotopic studies in the Cascade Mountains: Bearing on andesite genesis, *Geol. Soc. Amer. Bull.*, **84**, 431–454, 1973.
- Clark, S. P., Jr., and A. E. Ringwood, Density distribution and constitution of the mantle, *Rev. Geophys. Space Phys.*, **2**, 35–88, 1964.
- Compston, W., The Table Hill volcanics of the Officer Basin, Precambrian or Paleozoic? *Geol. Soc. Australia J.*, **21**, 403–411, 1974.
- Compston, W., and L. F. Lovering, The strontium isotopic geochemistry of granulitic and eclogitic inclusions from the basic pipes of Delegate, eastern Australia, *Geochim. Cosmochim. Acta*, **33**, 691–699, 1969.
- Compston, W., I. MacDougall, and K. Heier, Geochemical comparison of the Mesozoic basaltic rocks of Antarctica, South Africa, South America, and Tasmania, *Geochim. Cosmochim. Acta*, **32**, 129–149, 1968.
- Cooper, J. A., and D. H. Green, Lead isotope measurements on lherzolite inclusions and host basanites from western Victoria, Australia, *Earth Planet. Sci. Lett.*, **6**, 69–76, 1969.
- Cormier, R. F., Radiometric dating of the Coldbrook group of southern New Brunswick, Canada, *Can. J. Earth Sci.*, **6**, 393–398, 1969.
- Dasch, E. J., Sr isotopes in weathering profiles, deep-sea sediments and sedimentary rocks, *Geochim. Cosmochim. Acta*, **33**, 1521–1552, 1969.
- Dasch, E. J., and D. H. Green, Strontium isotope geochemistry of lherzolite inclusions and host basaltic rocks, Victoria, Australia, *Amer. J. Sci.*, **275**, 461–469, 1975.
- Dasch, E. J., C. E. Hedge, and J. Dymond, Effect of sea water interaction on strontium isotope composition of deep-sea basalts, *Earth Planet. Sci. Lett.*, **19**, 177–183, 1973.
- Davies, R. D., H. L. Allsopp, A. J. Erlank, and W. I. Manton, Sr-isotopic studies on various layered intrusions in southern Africa, *Geol. Soc. S. Africa Sp. Pub.* **1**, 576, 1970.
- Dawson, J. B., Kimberlites and their relationship to the upper mantle, *Trans. Roy. Soc. London*, **A271**, 297–311, 1972.
- Doe, B. R., P. W. Lipman, C. E. Hedge, and H. Kumsawa, Primitive and contaminated basalts from the southern Rocky Mountains, U.S.A., *Contrib. Mineral. Petrol.*, **21**, 142–156, 1969.
- Dziewonski, A. M., Upper mantle models from “pure-path” dispersion data, *J. Geophys. Res.*, **76**, 2587–2601, 1971.
- Ewart, A., and J. J. Stipp, Petrogenesis of the volcanic rocks of the central North Island, New Zealand, as indicated by a study of $^{87}\text{Sr}/^{86}\text{Sr}$ ratios, and Sr, Rb, K, U, and Th abundances, *Geochim. Cosmochim. Acta*, **32**, 699–736, 1968.
- Farhat, J. S., Geochemical investigation of the early Archean rocks of the Minnesota River Valley, Ph.D. dissertation, Univ. of California, Los Angeles, 1975.
- Faure, G., R. L. Hill, L. M. Jones, and D. H. Elliot, Isotope composition of strontium and silica content of Mesozoic basalt and dolerite from Antarctica, unpublished manuscript presented at SCAR Symposium, Oslo, Norway, Aug. 6–15, 1972.
- Forbes, W. C., and M. F. J. Flower, Phase relations of titan-phlogopite, $\text{K}_2\text{Mg}_2\text{TiAl}_2\text{Si}_4\text{O}_{20}(\text{OH})_4$: a refractory phase in the upper mantle? *Earth Planet. Sci. Lett.*, **22**, 60–66, 1974.
- Gast, P. W., Trace element fractionation and the origin of tholeiitic and alkaline magma types, *Geochim. Cosmochim. Acta*, **32**, 1057, 1968.
- Gast, P. W., G. R. Tilton, and C. Hedge, Isotopic composition of lead and Sr from Ascension and Gough Islands, *Science*, **145**, 1181–1185, 1964.
- Girod, M., G. Camus, Y. Vialette, Sur la présence de tholéiites à l’île Saint-Paul (Ocean Indien), *Contrib. Mineral. Petrol.*, **33**, 108, 1971.
- Goncz, J. H., and J. R. Cleary, Variations in the structure of the upper mantle beneath Australia, from Rayleigh observations, *Geophys. J. Roy. Astron. Soc.*, in press, 1976.
- Grant, N. K., J. L. Powell, J. D. Walther, and F. R. Burkholder, The isotopic composition of Sr in lavas from St. Helena, South Atlantic, in press, 1976.
- Green, D. H., Experimental melting studies on a model upper mantle composition at high pressure under water-saturated and water-undersaturated conditions, *Earth Planet. Sci. Lett.*, **19**, 37–53, 1973.
- Green, D. H., and A. E. Ringwood, The genesis of basaltic magmas, *Contrib. Mineral. Petrol.*, **15**, 103–190, 1967.
- Green, T. H., and A. E. Ringwood, Genesis of the calc-alkaline igneous suite, *Contrib. Mineral. Petrol.*, **18**, 105–162, 1968.

- Green, T. H., and A. E. Ringwood, High pressure experimental studies on the origin of andesites, *Oreg. Dept. Geol. Mineral Ind. Bull.*, 65, 21–32, 1968.
- Halpern, M., U. G. Cordani, and M. Berenholc, *Rev. Brasil. Geociencias*, 4, 223, 1974.
- Harris, P. G., and E. A. K. Middlemost, The evolution of kimberlites, *Lithos*, 3, 77–88, 1969.
- Harris, P. G., R. Hutchinson, and D. K. Paul, Plutonic xenoliths and their relation to the upper mantle, *Phil. Trans. Roy. Soc. London*, A271, 313–323, 1972.
- Hart, S. R., K, Rb, Cs content and K/Rb, K/Cs ratios of fresh and altered submarine basalts, *Earth Planet. Sci. Lett.*, 6, 295–303, 1969.
- Hart, S. R., Dredge basalts: Some geochemical aspects (abstr.), *Trans. Amer. Geophys. Union*, 52, 376, 1971.
- Hart, S. R., Submarine basalts from Kilauea rift, Hawaii: Nondependence of trace element composition on extrusion depth, *Earth Planet. Sci. Lett.*, 20, 201–203, 1973.
- Hart, S. R., LIL-element geochemistry, leg 34 basalts, in *Initial Reports of the Deep Sea Drilling Project*, 34, in press, 1976.
- Hart, S. R., and C. Brooks, Clinopyroxene-matrix partitioning of K, Rb, Cs, Sr, and Ba, *Geochim. Cosmochim. Acta*, 38, 1799–1806, 1974.
- Hart, S. R., J. G. Schilling, and J. L. Powell, Basalts from Iceland and along the Reykjanes Ridge: Sr isotope geochemistry, *Nature Phys. Sci.*, 246, 104–107, 1973.
- Hedge, C. E., Variations in radiogenic strontium found in volcanic rocks, *J. Geophys. Res.*, 71, 6119–6126, 1966.
- Hedge, C. E., R. A. Hildreth, and W. T. Henderson, Strontium isotopes in some Cenozoic lavas from Oregon and Washington, *Earth Planet. Sci. Lett.*, 8, 434–438, 1970.
- Hedge, C. E., and D. C. Noble, Late Cenozoic basalts with unusually high Sr/Rb and $^{87}\text{Sr}/^{86}\text{Sr}$ ratios from the southern Great Basin, western United States, *Geol. Soc. Am. Bull.*, 82, 3503–3510, 1971.
- Hedge, C. E., and Z. E. Peterman, The strontium isotopic composition of basalts from the Gorda and Juan de Fuca Rises, northeastern Pacific Ocean, *Contrib. Mineral. Petrol.*, 27, 114, 1970.
- Hedge, C. E., Z. E. Peterman, and W. R. Dickinson, Petrogenesis of lavas from Western Samoa, *Geol. Soc. Amer. Bull.*, 83, 2709–2714, 1972.
- Hedge, C. E., N. D. Watkins, R. A. Hildreth, and W. P. Doering, $^{87}\text{Sr}/^{86}\text{Sr}$ ratios in basalts from islands in the Indian Ocean, *Earth Planet. Sci. Lett.*, 21, 29–34, 1973.
- Heier, K. S., W. Compston, and I. McDougall, Thorium and uranium concentrations, and the isotopic composition of strontium in the differentiated Tasmanian dolerites, *Geochim. Cosmochim. Acta*, 29, 643–659, 1965.
- Hofmann, A. W., Diffusion of Ca and Sr in a basalt melt, in *Carnegie Inst. Wash. Year Book* 74, pp. 183–189, 1975.
- Hofmann, A. W., and S. R. Hart, An assessment of local and regional isotopic equilibrium in a partially molten mantle, in *Carnegie Inst. Wash. Year Book* 74, pp. 195–210, 1975.
- Hubbard, N. J., Some chemical features of lava from the Manu'a Islands, *Pacific Sci.*, 25, 178, 1971.
- Hurley, P. M., H. W. Fairbairn, and W. H. Pinson, Rb-Sr isotopic evidence in the origin of potash-rich lavas of western Italy, *Earth Planet. Sci. Lett.*, 5, 301–306, 1966.
- Hutchinson, R., and J. B. Dawson, Rb, Sr, and $^{87}\text{Sr}/^{86}\text{Sr}$ in ultrabasic xenoliths and host-rocks, Lashaine Volcano, Tanzania, *Earth Planet. Sci. Lett.*, 9, 87–92, 1970.
- James, D. E., Plate tectonic model for the evolution of the central Andes, *Bull. Geol. Soc. Am.*, 82, 3325–3346, 1971.
- James, D. E., C. Brooks, and A. Cuyubamba, Andean Cenozoic volcanism: Magma genesis in the light of strontium isotopic composition and trace-element geochemistry, *Geol. Soc. Am. Bull.*, 87, 592–600, 1976.
- Jordan, T. H., The continental tectosphere, *Rev. Geophys. Space Phys.*, 13, 1–12, 1975.
- Kanamori, H., Velocity and Q of mantle waves, *Phys. Earth Planet. Inter.*, 2, 259–275, 1970.
- Kay, R., Chemical zonation of the oceanic mantle (abstr.) *Trans. Amer. Geophys. Union*, 56, 1077, 1975.
- Kistler, R. W., and Z. E. Peterman, Variations in Sr, Rb, K, Na, and initial $^{87}\text{Sr}/^{86}\text{Sr}$ in Mesozoic granitic rocks and intruded wall rocks in central California, *Geol. Soc. Amer. Bull.*, 84, 3489–3512, 1973.
- Klerkx, J., S. Deutsch, P. DePaepe, Rb, Sr content and Sr isotopic composition of strongly alkalic basaltic rocks from the Cape Verde Islands, *Contrib. Mineral. Petrol.*, 45, 107–118, 1974.
- Kudo, A. M., K. I. Aoki, and D. G. Brookins, The origin of Pliocene-Holocene basalts of

- New Mexico in the light of strontium-isotopic and major element abundances, *Earth Planet. Sci. Lett.*, **13**, 200–204, 1971.
- Kudo, A. M., D. G. Brookins, and A. W. Laughlin, Sr-isotopic disequilibrium in lherzolites from the Puerco Necks, New Mexico, *Earth Planet. Sci. Lett.*, **15**, 291–295, 1972.
- Laughlin, A. W., D. G. Brookins, and J. R. Carden, Variations in the initial strontium ratios of a single basalt flow, *Earth Planet. Sci. Lett.*, **14**, 79–82, 1972.
- Leeman, W. P., The isotopic composition of strontium in late-Cenozoic basalts from the Basin-Range province, western United States, *Geochim. Cosmochim. Acta*, **34**, 857–872, 1970.
- Leeman, W. P., Late Cenozoic alkali-rich basalt from the western Grand Canyon area, Utah and Arizona: Isotopic composition of strontium, *Geol. Soc. Amer. Bull.*, **85**, 1691–1696, 1974.
- Leeman, W. P., Radiogenic tracers applied to basalt genesis in the Snake River Plain–Yellowstone National Park region—evidence for a 2.7 b.y.-old upper mantle keel, *Geol. Soc. Amer. Abstr.* 7–7, 1165, 1975.
- Leeman, W. P., and W. I. Manton, Strontium isotopic composition of basaltic lavas from the Snake River Plain, southern Idaho, *Earth Planet. Sci. Lett.*, **11**, 420–434, 1971.
- Lessing, P., and E. J. Catanzaro, $\text{Sr}^{87}/\text{Sr}^{86}$ in Hawaiian Lavas, *J. Geophys. Res.*, **69**, 1599–1601, 1964.
- Lovering, J. F., and M. Tatsumoto, Lead isotopes and the origin of granulite and eclogite inclusions in deep-seated pipes, *Earth Planet. Sci. Lett.*, **4**, 350–356, 1968.
- Lussiaa-Berdou-Polve, M., and P. Vidal, Initial Sr isotopic composition of volcanic rocks from Jan Mayen and Spitsbergen, *Earth Planet. Sci. Lett.*, **18**, 333–338, 1973.
- MacGregor, I. D., Mafic and ultramafic inclusions as indicators of origin of basaltic magmas, *J. Geophys. Res.*, **73**, 3737–3745, 1968.
- MacGregor, I. D., Petrologic and thermal structure of the upper mantle beneath South Africa in the Cretaceous, in *Physics and Chemistry of the Earth*, **9**, pp. 455–466, L. H. Ahrens, J. B. Dawson, A. R. Duncan, and A. J. Erlank, eds., Elmsford, N.Y., Pergamon Press, 1975.
- Manton, W. I., The origin of associated basic and acid rocks in the Lebombo-Nuanetsi igneous province, southern Africa, as implied by strontium isotopes, *J. Petrol.*, **9**, 23, 1968.
- Manton, W. I., and M. Tatsumoto, Some Pb and Sr isotopic measurements of eclogites from the Roberts Victor Mine, South Africa, *Earth Planet. Sci. Lett.*, **10**, 217–226, 1971.
- Mark, R. K., C. L. Hu, H. R. Bowman, F. Asaro, E. H. McKee, and R. R. Coats, A high $^{87}\text{Sr}/^{86}\text{Sr}$ mantle source for low alkali tholeiite, northern Great Basin, *Geochim. Cosmochim. Acta*, **39**, 1671–1678, 1975.
- McDougall, I., and W. Compston, Sr-isotope composition and K/Rb ratios in some rocks from Reunion and Rodriguez, Indian Ocean, *Nature*, **207**, 252–253, 1965.
- Meijer, A., Pb and Sr isotopic data bearing on the origin of lavas from the Mariana Arc System, *Geol. Soc. Amer. Bull.*, in press, 1976.
- Mitchell, R. H., and J. H. Crocket, The isotopic composition of strontium in some South African kimberlites, *Contrib. Mineral. Petrol.*, **30**, 277–290, 1971.
- Modreski, P. J., and A. L. Boettcher, Phase relations of phlogopite in the system $\text{O}_2\text{--H}_2\text{O}$ to 35 kilobars: a better model for micas in the interior of the earth, *Am. J. Sci.*, **273**, 385, 1973.
- Montigny, R., M. Javoy, and C. J. Allègre, Le problème des andésites: Étude du volcanisme quaternaire du Costa Rica (Amérique centrale) à l'aide des traceurs couples $^{87}\text{Sr}/^{86}\text{Sr}$ et $^{18}\text{O}/^{16}\text{O}$, *Soc. Géol. Fr. Bull.*, **11**, 794–799, 1969.
- Noble, D. C., C. E. Hedge, E. H. McKee, and M. K. Corringa, Reconnaissance study of the strontium isotopic composition of Cenozoic volcanic rocks in the northwestern Great Basin, *Geol. Soc. Amer. Bull.*, **84**, 1393–1406, 1973.
- O'Hara, M. J., M. J. Saunders, and E. L. P. Mercy, Garnet-peridotite, primary ultrabasic magma and eclogite: Interpretation of upper mantle processes in kimberlite, in *Physics and Chemistry of the Earth*, **9**, pp. 571–604, L. H. Ahrens, J. B. Dawson, A. R. Duncan, and A. J. Erlank, eds., Elmsford, N. Y., Pergamon Press, 1975.
- Okal, E. A., and D. L. Anderson, A study of lateral inhomogeneities in the upper mantle by multiple ScS travel-time residuals, *Geophys. Res. Lett.*, **2**, 313–316, 1975.
- O'Nions, R. K., and R. J. Pankhurst, Petrogenetic significance of isotope and trace-element variations in volcanic rocks from the Mid-Atlantic Ridge, *J. Petrol.*, **15**, 603, 1974.

- Oversby, V. M., and P. W. Gast, Isotopic composition of lead from oceanic islands, *J. Geophys. Res.*, 75, 2097–2114, 1970.
- Pankhurst, R. J., Strontium isotope studies related to petrogenesis in the Caledonian basic igneous province of northeast Scotland, *J. Petrol.*, 10, 115, 1969.
- Paul, D. K., Strontium isotope studies on ultramafic inclusions from Dreiser Weiher, Eifel, Germany, *Contrib. Mineral. Petrol.*, 34, 22–28, 1971.
- Peterman, Z. E., I. S. E. Carmichael, and A. L. Smith, $\text{Sr}^{87}/\text{Sr}^{86}$ ratios of Quaternary lavas of the Cascade Range, northern California, *Geol. Soc. Amer. Bull.*, 81, 311–318, 1970a.
- Peterman, Z. E., I. S. E. Carmichael, and A. L. Smith, Strontium isotopes in Quaternary basalts of southeastern California, *Earth Planet. Sci. Lett.*, 7, 381–384, 1970b.
- Peterman, Z. E., B. R. Doe, and H. H. Prostka, Lead and strontium isotopes in rocks of the Absaroka volcanic field, Wyoming, *Contrib. Mineral. Petrol.*, 27, 121–130, 1970.
- Peterman, Z. E., and C. E. Hedge, Related strontium isotopic and chemical variations in oceanic basalts, *Geol. Soc. Amer. Bull.*, 82, 493–499, 1971.
- Peterman, Z. E., C. E. Hedge, R. G. Coleman, and P. D. Snively, Jr., $\text{Sr}^{87}/\text{Sr}^{86}$ ratios in some eugeosynclinal sedimentary rocks and their bearing on the origin of granitic magma in orogenic belts, *Earth Planet. Sci. Lett.*, 2, 433–439, 1967.
- Philpotts, J. A., and C. C. Schnetzler, Phenocryst-matrix partition coefficients for K, Rb, Sr, and Ba, with applications to anorthosite and basalt genesis, *Geochim. Cosmochim. Acta*, 34, 307–322, 1970.
- Pollack, H. N., and D. S. Chapman, On the regional variation of heat flow, geotherms, and lithospheric thickness, submitted to *Tectonophysics*, 1976.
- Powell, J. L., and K. Bell, Strontium isotopic studies of alkalic rocks. Localities from Australia, Spain, and the western United States, *Contrib. Mineral. Petrol.*, 27, 1–10, 1970.
- Powell, J. L., and K. Bell, Isotopic composition of strontium in alkalic rocks, in *The Alkaline Rocks*, p. 412, H. Sorenson, ed., New York, Wiley & Sons, 1974.
- Powell, J. L., and S. E. Delong, Isotopic composition of strontium in volcanic rocks from Oahu, *Science*, 153, 1239–1242, 1966.
- Pushkar, P., Strontium isotopic ratios in volcanic rocks of three island arc areas, *J. Geophys. Res.*, 73, 2701–2714, 1968.
- Ramberg, H., Mantle diapirism and its tectonic and magmatic consequences, *Phys. Earth Planet. Inter.*, 5, 45–60, 1972.
- Rhodes, J. M., and J. B. Dawson, Major and trace element chemistry of peridotite inclusions from the Lashaine Volcano, Tanzania, in *Physics and Chemistry of the Earth*, 9, pp. 545–558, L. H. Ahrens, J. B. Dawson, A. R. Duncan, and A. J. Erlank, eds., Elmsford, N. Y., Pergamon Press, 1975.
- Ridley, W. I., and J. B. Dawson, Lithophile trace element data bearing on the origin of peridotite xenoliths, ankaramite, and carbonatite from Lashaine Volcano, N. Tanzania, in *Physics and Chemistry of the Earth*, 9, pp. 559–570, L. H. Ahrens, J. B. Dawson, A. R. Duncan, and A. J. Erlank, eds., Elmsford, N. Y., Pergamon Press, 1975.
- Ringwood, A. E., *Composition and Petrology of the Earth's Mantle*, 618 pp., Hightstown, New Jersey, McGraw-Hill Book Co., 1975.
- Ringwood, A. E., and J. F. Lovering, Significance of pyroxene-ilmenite intergrowths among kimberlite xenoliths, *Earth Planet. Sci. Lett.*, 7, 371–375, 1970.
- Roy, R. F., D. D. Blackwell, and F. Birch, Heat generation of plutonic rocks and continental heat-flow provinces, *Earth Planet. Sci. Lett.*, 5, 1–12, 1968.
- Sacks, I. S., Distribution of absorption of shear waves in South America and its tectonic significance, in *Carnegie Inst. Wash. Year Book* 67, pp. 339–344, 1969.
- Sacks, I. S., and H. Okada, A comparison of the anelasticity structure beneath western South America and Japan, *Phys. Earth Planet. Inter.*, 9, 211–219, 1974.
- Schilling, J. -G., Sea-floor evolution: rare earth evidence, *Phil. Trans. Roy. Soc. London*, 268, 663, 1971.
- Schilling, J. -G., Azores mantle blob: Rare-earth evidence, *Earth Planet. Sci. Lett.*, 25, 103–115, 1975.
- Sclater, J. G., and J. Francheteau, The implication of terrestrial heat flow observations on current tectonic and geochemical models of the crust and upper mantle of the earth, *Geophys. J. Roy. Astron. Soc.*, 20, 509–542, 1970.
- Scott, R. B., R. W. Nesbitt, E. J. Dasch, and R. L. Armstrong, A strontium isotope evolution model for Cenozoic magma genesis,

- eastern Great Basin, U.S.A., *Bull. Volcanol.* 2-35, 1-26, 1971.
- Shimizu, N., An experimental study of the partitioning of K, Rb, Cs, Sr., and Ba between clinopyroxene and liquid at high pressure, *Geochim. Cosmochim. Acta*, 38, 1789-1798, 1974.
- Sipkin, S. A., and T. H. Jordan, Lateral heterogeneity of the upper mantle determined from the travel times of ScS, *J. Geophys. Res.*, 80, 1474-1484, 1975.
- Steuber, A. M., and M. Ikramuddin, Rubidium, strontium, and the isotopic composition of strontium in ultramafic nodule minerals and host basalts, *Geochim. Cosmochim. Acta*, 38, 207-216, 1974.
- Stipp, J. J., The geochronology and petrogenesis of the Cenozoic volcanics of North Island, New Zealand, unpublished Ph.D. thesis, Australian National University, Canberra, Australia, 1968.
- Subbarao, K. V., The strontium isotopic composition of basalts from the East Pacific and Chile Rises and abyssal hills in the eastern Pacific Ocean, *Contrib. Mineral. Petrol.*, 37, 111, 1972.
- Subbarao, K. V., and C. E. Hedge, K, Rb, Sr, and $^{87}\text{Sr}/^{86}\text{Sr}$ in rocks from the Mid-Indian Ocean Ridge, *Earth Planet. Sci. Lett.*, 18, 223-228, 1973.
- Sun, S. S., and G. N. Hanson, Evolution of the mantle: Geochemical evidence from alkali basalt, *Geol.*, 3, 297-302, 1975a.
- Sun, S. S., and G. N. Hanson, Origin of Ross Island basanitoids and limitations upon the heterogeneity of mantle sources for alkali basalts and nephelinites, *Contrib. Mineral. Petrol.*, 52, 77, 1975b.
- Sun, S. S., and B. Jahn, Lead and strontium isotopes in post-glacial basalts from Iceland, *Nature*, 255, 527, 1975.
- Tatsumoto, M., Genetic relationships of ocean basalts as indicated by lead isotopes, *Science*, 153, 1094-1101, 1966.
- Toksöz, M. N., and D. L. Anderson, Phase velocities of long-period surface waves and structure of the upper mantle: 1. Great-circle Love and Rayleigh wave data, *J. Geophys. Res.*, 71, 1649-1658, 1966.
- Wagner, P. A., The evidence of the kimberlite pipes on the constitution of the outer part of the earth, *S. African J. Sci.*, 25, 127, 1928.
- White, W. M., S. R. Hart, and J. G. Schilling, Geochemistry of the Azores and the Mid-Atlantic Ridge: 29°N to 60°N, in *Carnegie Inst. Wash. Year Book* 74, 224-234, 1975.
- Yoder, H. S., Jr., Generation of basaltic magma, National Academy of Sciences, in press, 1976.
- York, D., Least-squares fitting of a straight line, *Can. J. Phys.*, 44, 1079-1086, 1966.

GEOCHEMISTRY OF LATE CENOZOIC VOLCANIC ROCKS FROM THE NEVADO DE TOLUCA AREA, MEXICO

D. J. Whitford and K. Bloomfield*

Introduction

Orogenic igneous rocks are characterized by a wide diversity of compositions ranging from island arc tholeiites through a spectrum of calc-alkaline to high-K calc-alkaline (or shoshonitic) varieties. Although they are usually associated with zones of lithospheric subduction, they occur in a variety of tectonic environments, from purely intraoceanic island arcs such as the Tonga-Kermadec island chain to continental margins such as the Andes of South America. It is the purpose of this report to outline the geochemistry of a suite of orogenic igneous rocks from a continental margin, to compare these rocks with those from a typical island arc, and to outline some of the geochemical implications and limitations on petrogenetic models.

The major and trace element and Sr isotopic compositions of a representative suite of volcanic rocks have been determined. The rocks, which range in age from Miocene to Recent, are from an area of approximately 2500 km² centered on the volcano Nevado de Toluca (Bloomfield and Valastro, 1974). This volcanic ruin lies within the Mexican volcanic belt approximately 80 km west-southwest of Mexico City. It is situated on old, typically continental crust, approximately 40 km thick (Cummings and Schiller, 1971). The volcano, which has been built up on a series of Tertiary and Mesozoic vol-

*Overseas Division, Institute of Geological Sciences, London.

canics and sediments, consists of an eroded central strato-volcano composed mostly of andesitic and dacitic flows with lahar and fluvial deposits, often capped by pumice on the lower slopes (Bloomfield and Valastro, 1974).

Analytical Techniques

Major elements have been determined by electron microprobe on directly fused glasses following the methods of Nicholls (1974a). The trace elements Rb, Sr, Zr, and Y were determined by x-ray fluorescence spectrometry on pressed powders following the methods of Norrish and Chappell (1967). Major and trace element analyses were performed at the Research School of Earth Sciences, Australian National University.

The Sr isotopic composition of the lavas was determined at DTM on a 6-inch automated mass spectrometer. All $^{87}\text{Sr}/^{86}\text{Sr}$ ratios have been normalized to an $^{86}\text{Sr}/^{88}\text{Sr}$ ratio of 0.1194, and all analyses have been corrected to an E and A SrCO_3 standard $^{87}\text{Sr}/^{86}\text{Sr}$ ratio of 0.70800. Repeated analysis of the E and A standard during the time in which the analyses were performed yielded an average $^{87}\text{Sr}/^{86}\text{Sr}$ ratio of 0.707934 ± 0.000044 (2σ of population).

Major and Trace Elements

Results. Selected representative analyses are listed in Table 11. The lavas exhibit many features characteristic of orogenic igneous rocks, including generally low concentrations of TiO_2 and MgO and high concentrations of Al_2O_3 . Concentrations of K_2O , Rb, and Zr and the FeO-MgO relationships indicate calc-alkaline affinities (Jakobs and Gill, 1970), which are typical of the volcanic rocks of continental margins.

However, in many important respects they differ from typical island arc volcanics such as those found in the western Pacific. The Mexican rocks are distinctly richer in SiO_2 , Na_2O , and MgO relative to FeO. In these respects, they are similar to some Recent volcanics from the Andes (Noble *et al.*, 1975). Some of these differences are summarized in Figs. 34 and 35.

Figure 34 illustrates the frequency distribution of SiO_2 concentrations in both the Mexican lavas and a representative suite of typical island arc lavas from Indonesia (Nicholls and Whitford, 1976). The Mexican rocks have SiO_2 concentrations ranging from 55% to 70% with a mode of about 67%. Basalts ($< 52\%$ SiO_2) are totally absent. This contrasts with the Indonesian rocks, which have a mode of approximately

TABLE 11. Selected Representative Major and Trace Element Analyses

| | 157-72 | 133A-72 | 91-72 | 183-72 | 134-72 | 161-72 | 9-72 |
|--------------------------|----------|----------|----------|----------|----------|----------|----------|
| $^1\text{SiO}_2$ | 55.1 | 57.6 | 59.4 | 62.4 | 64.1 | 66.2 | 67.0 |
| TiO_2 | 0.74 | 0.96 | 0.84 | 0.90 | 0.68 | 0.57 | 0.50 |
| Al_2O_3 | 16.4 | 16.2 | 17.1 | 16.7 | 18.3 | 16.9 | 16.8 |
| ^2FeO | 7.43 | 6.49 | 6.08 | 5.08 | 4.21 | 3.62 | 3.41 |
| MO | < 0.12 | < 0.12 | < 0.12 | < 0.12 | < 0.12 | < 0.12 | < 0.12 |
| MgO | 7.94 | 6.86 | 4.86 | 4.04 | 2.20 | 1.97 | 1.96 |
| CaO | 8.18 | 6.66 | 6.05 | 5.11 | 4.44 | 4.10 | 3.97 |
| Na_2O | 3.31 | 3.62 | 4.11 | 3.71 | 4.55 | 4.57 | 4.47 |
| K_2O | 0.82 | 1.68 | 1.55 | 2.07 | 1.50 | 2.14 | 1.98 |
| Mg/Mg + Fe^{2+} | 0.66 | 0.65 | 0.59 | 0.59 | 0.48 | 0.49 | 0.50 |
| ^3Rb | 15.7 | 34.6 | 28.4 | 48.2 | 14.2 | 51.3 | 42.9 |
| Sr | 366 | 541 | 537 | 448 | 518 | 570 | 516 |
| Zr | 100 | 182 | 142 | 244 | 158 | 158 | 161 |
| Y | 59 | 23 | 21 | 25 | 17 | 16 | 15 |

¹All values in wt % normalized to 100% total.

²Total Fe expressed as FeO.

³All trace element concentrations expressed as ppm.

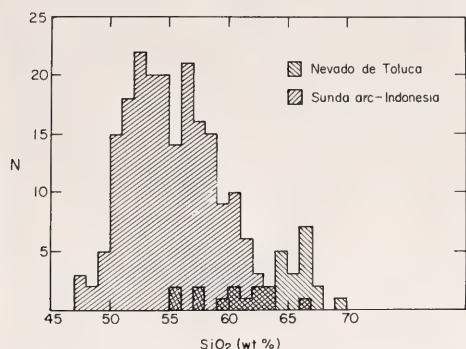


Fig. 34. Histograms of SiO_2 (wt %) contents of analyzed lavas from the Nevado de Toluca area and from the Sunda arc of Indonesia (Nicholls and Whitford, 1976).

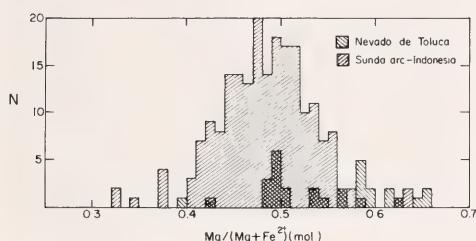


Fig. 35. Histograms of the atomic ratio $\text{Mg}/\text{Mg} + \text{Fe}^{2+}$ in analyzed lavas from the Nevado de Toluca area and from the Sunda arc of Indonesia (Nicholls and Whitford, 1976). Before calculation of $\text{Mg}/\text{Mg} + \text{Fe}^{2+}$, ferrous iron in all analyses was adjusted to $\text{FeO} = 0.85 \sum \text{FeO}$ (total Fe as FeO). This relationship is similar to that determined for basaltic to andesitic liquids equilibrated at oxygen fugacities of the wüstite-magnetite buffer (Fudali, 1965); similar oxygen fugacities are believed to prevail in the upper mantle (Boettcher, 1973).

55% SiO_2 . In this respect the Mexican volcanics are very similar to the Cenozoic lavas from Peru (D. E. James, personal communication).

Figure 35 shows the frequency distribution of the atomic ratio $\text{Mg}/\text{Mg} + \text{Fe}^{2+}$ in both the Mexican and Indonesian rocks. Although the division is not as well defined as in Fig. 34, the Mexican rocks are, on average, more mafic in terms of the ratio $\text{Mg}/\text{Mg} + \text{Fe}^{2+}$ than those from Indonesia. Experimental data for the partitioning of Fe^{2+} and Mg between olivine and coexisting silicate liquid (Green and Ringwood, 1967;

Roeder and Emslie, 1970; Nicholls, 1974b) indicate that liquids in equilibrium with olivine of supposed upper mantle peridotite must be highly magnesian ($\text{Mg}/\text{Mg} + \text{Fe}^{2+} \geq 0.61$) (Nicholls and Whitford, 1976). Depending upon both total pressure and water content, experimental evidence indicates that these equilibrium liquids may have up to 60% SiO_2 (Nicholls, 1974b). These results suggest that despite being relatively silicic, rocks such as 157-72 and 133A-72 (Table 11) may represent unfractionated partial melting products of the mantle.

The magnesian character of the Mexican volcanics together with the Y abundances, which suggest heavy rare earth concentrations 7–30 times chondritic abundances, also argues against any single-stage petrogenetic model involving partial melting of quartz eclogite (Nicholls and Whitford, 1976, and references therein).

Sr Isotopes

Table 12 lists the concentrations of SiO_2 , K_2O , Rb, and Sr together with the ratios K/Rb, Rb/Sr, and $^{87}\text{Sr}/^{86}\text{Sr}$. Sr exhibits a significant spread in isotopic composition, with $^{87}\text{Sr}/^{86}\text{Sr}$ ratios ranging from 0.70321 to 0.70446. Because of uncertainties about the absolute ages of the older samples, no corrections have been applied for the ^{87}Sr that has accumulated since eruption. Assuming an extreme age of 25 m.y. for the oldest samples, the Rb/Sr ratios are sufficiently low that the differences between the measured and calculated initial ratios lie within the uncertainties of the isotopic analyses.

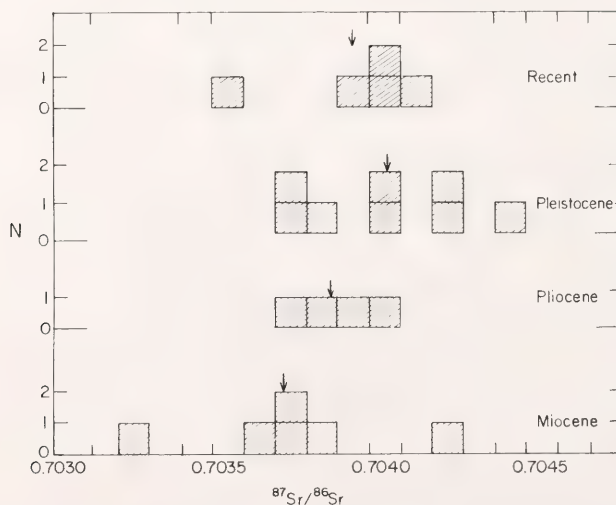
It is important to note that rocks which are related in both space and time have significantly different isotopic compositions. The $^{87}\text{Sr}/^{86}\text{Sr}$ ratios are plotted as histograms according to age in Fig. 36. On average, there is a poorly defined overall decrease in $^{87}\text{Sr}/^{86}\text{Sr}$ ratio with increasing age.

The observed range of isotopic compositions is similar to that observed in volcanic rocks from many other island

TABLE 12. Trace Element and Sr Isotopic Results

| Age | Sample | SiO ₂ (%) | K ₂ O(%) | Rb | Sr | K/Rb | Rb/Sr | ⁸⁷ Sr/ ⁸⁶ Sr* | ±2σ |
|-------------|---------|----------------------|---------------------|------|------|------|--------|-------------------------------------|---------|
| Miocene | 91-72 | 59.4 | 1.55 | 28.4 | 537 | 453 | 0.0529 | 0.70374 | 0.00009 |
| | 221-72 | 61.0 | 1.57 | 30.7 | 667 | 425 | 0.0460 | 0.70385 | 0.00010 |
| | 172-72 | 63.5 | 1.79 | 20.4 | 500 | 728 | 0.0408 | 0.70420 | 0.00009 |
| | 125-72 | 64.0 | 1.90 | 38.1 | 621 | 414 | 0.0614 | 0.70368 | 0.00008 |
| | †107-72 | 64.3 | 2.02 | 39.6 | 609 | 423 | 0.0650 | 0.70372 | 0.00011 |
| | †116-72 | 64.6 | 1.57 | 25.7 | 754 | 507 | 0.0341 | 0.70321 | 0.00005 |
| | 45-72 | 65.4 | 1.87 | 46.6 | 432 | 333 | 0.108 | ... | ... |
| | 147-72 | 69.0 | 2.50 | 50.5 | 542 | 411 | 0.0930 | ... | ... |
| Pliocene | 208B-72 | 64.6 | 1.70 | 26.7 | 478 | 529 | 0.0559 | 0.70376 | 0.00005 |
| | 162-72 | 65.4 | 2.20 | 163 | 668 | 112 | 0.244 | .70385 | 0.00007 |
| | 161-72 | 66.2 | 2.14 | 51.3 | 570 | 346 | 0.0900 | 0.70401 | 0.00005 |
| | 47-72 | 67.0 | 2.24 | 57.8 | 445 | 322 | 0.130 | .70391 | 0.00006 |
| Pleistocene | 157-72 | 55.1 | 0.82 | 15.7 | 366 | 434 | 0.0429 | 0.70381 | 0.00009 |
| | 186-72 | 55.1 | 1.15 | 20.5 | 657 | 466 | 0.0312 | 0.70378 | 0.00005 |
| | 132A-72 | 57.0 | 2.37 | 32.8 | 1330 | 600 | 0.0247 | 0.70419 | 0.00005 |
| | 133A-72 | 57.6 | 1.68 | 34.6 | 541 | 403 | 0.0640 | ... | ... |
| | 181-72 | 60.8 | 1.67 | 36.3 | 540 | 382 | 0.0672 | 0.70420 | 0.00007 |
| | 236-72 | 62.0 | 1.76 | 36.1 | 593 | 405 | 0.0609 | 0.70421 | 0.00007 |
| | 183-72 | 62.4 | 2.07 | 48.2 | 448 | 357 | 0.108 | ... | ... |
| | 134-72 | 64.1 | 1.50 | 14.2 | 518 | 877 | 0.0274 | 0.70446 | 0.00005 |
| | †10-72 | 65.3 | 1.97 | 39.0 | 681 | 419 | 0.0573 | 0.70379 | 0.00008 |
| | 44-72 | 66.1 | 1.99 | 41.2 | 525 | 401 | 0.0785 | ... | ... |
| | †53-72 | 66.7 | 1.92 | 40.7 | 516 | 392 | 0.0789 | 0.70409 | 0.00009 |
| Recent | †96-72 | 66.9 | 2.04 | 42.2 | 503 | 401 | 0.0839 | 0.70400 | 0.00005 |
| | 89-72 | 60.9 | 1.71 | 30.3 | 644 | 469 | 0.0470 | ... | ... |
| | †VIII/A | 63.1 | 1.58 | 30.1 | 528 | 436 | 0.0570 | 0.70358 | 0.00005 |
| | †VIII/5 | 66.1 | 1.89 | 41.9 | 512 | 374 | 0.0818 | 0.70400 | 0.00012 |
| | †27-71 | 66.1 | 1.92 | 42.2 | 528 | 378 | 0.0799 | 0.70412 | 0.00011 |
| | †108-72 | 66.6 | 2.05 | 42.3 | 550 | 402 | 0.0769 | 0.70397 | 0.00004 |
| | †9-72 | 67.0 | 1.98 | 42.9 | 516 | 383 | 0.0831 | 0.70408 | 0.00005 |

†Samples used in Fig. 39.

*Corrected to *E* and *A* ⁸⁷Sr/⁸⁶Sr = 0.70800.Fig. 36. Histograms showing the frequency distribution of ⁸⁷Sr/⁸⁶Sr ratios in the volcanic rocks from the Nevado de Toluca area. Average values are indicated by arrows.

arcs and continental margins including the Cascades, most of the northwestern Pacific arcs, and Japan (Whitford, 1975, and references therein). Despite some similarities in major and trace element composition, the Mexican rocks have $^{87}\text{Sr}/^{86}\text{Sr}$ ratios generally lower than those from the Andes (James *et al.*, 1974a, 1974b).

Figure 37 is a plot of $^{87}\text{Sr}/^{86}\text{Sr}$ versus $^{87}\text{Rb}/^{86}\text{Sr}$ in the analyzed lavas from Nevado de Toluca. Overall, there is clearly no correlation. However, if only those samples from the immediate vicinity of the volcano itself are chosen, there is a significant positive correlation (Fig. 38). Using the method of York (1966), an "age" of 430 ± 97 m.y. is indicated ($\lambda^{87}\text{Rb} = 1.39 \times 10^{-11} \text{ yr}^{-1}$). It may be significant that the age of approximately 400 m.y. is similar to that observed by James *et al.* (1974b) for the Arequipa and Barroso volcanics of Peru. The fact that the rocks from Nevado de Toluca have been erupted within an area of approximately 100 km² over a time interval of up to 25 m.y. obviously has important implications in terms of magma genesis and eruption. This theme has been developed in some detail in the report by Brooks *et al.* (this Year Book). Apart

from this relationship, the Mexican lavas show no correlation between $^{87}\text{Sr}/^{86}\text{Sr}$ and either major or trace elements.

Discussion

Without knowledge of the nature of the deep crust beneath Nevado de Toluca, quantitative evaluation of the possible importance of crustal melting and/or assimilation is not possible. However, it is clear that the relatively low $^{87}\text{Sr}/^{86}\text{Sr}$ ratios in the volcanics and their high Sr concentrations place very severe limitations on such models and that the ultimate origin of these rocks lies in the mantle. Despite higher $^{87}\text{Sr}/^{86}\text{Sr}$ ratios in many of the Recent volcanics from Peru, James *et al.* (1974b) were forced to the similar conclusion that crustal processes were not primarily responsible for the observed geochemical variations.

This immediately raises the question of why volcanic rocks from at least some continental margins differ from those of island arcs. Assuming that the process of subduction and the subducted lithosphere itself are similar in each environment, the differences in the erupted rocks must therefore re-

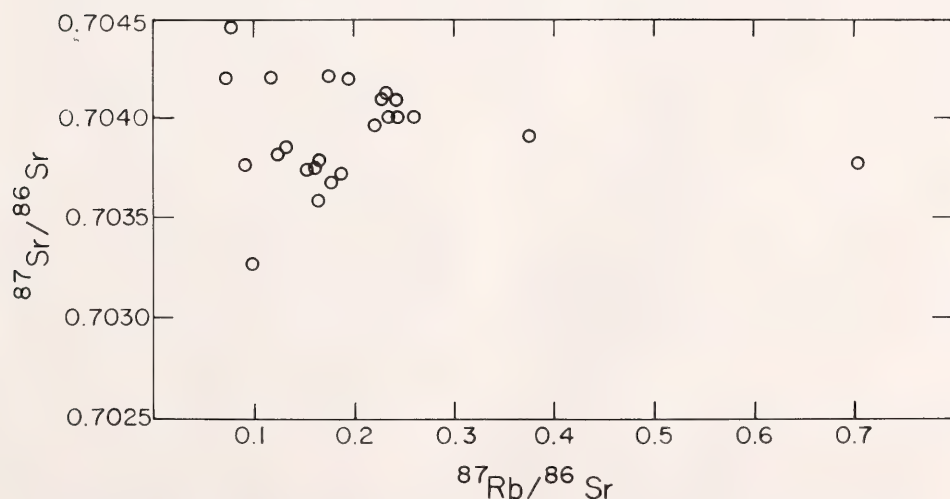


Fig. 37. Plot of $^{87}\text{Sr}/^{86}\text{Sr}$ vs. $^{87}\text{Rb}/^{86}\text{Sr}$ in all analyzed lavas from the Nevado de Toluca area.

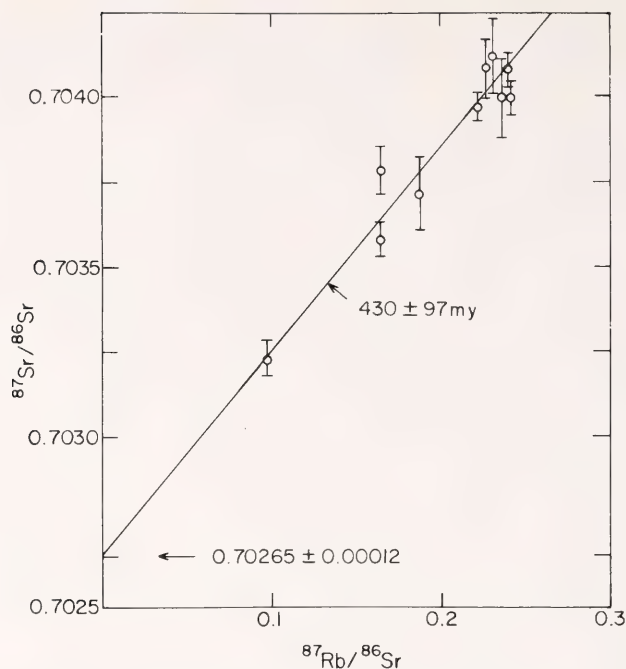


Fig. 38. Plot of $^{87}\text{Sr}/^{86}\text{Sr}$ vs. $^{87}\text{Rb}/^{86}\text{Sr}$ for lavas from the immediate vicinity of the volcano Nevado de Toluca. Two σ error limits in the isotopic determinations are also plotted.

flect differences in the chemistry and/or the physical state of the mantle wedge above the subducted lithosphere. Sacks and Okada (1974) showed that the mantle wedge above the subducted lithosphere beneath the Andes is itself lithospheric rather than asthenospheric. The possibility of lithospheric thickening beneath older continental areas has been invoked by Brooks *et al.* (this *Year Book*) as an explanation for certain Sr isotopic effects such as the existence of initial isochrons similar to that shown in Fig. 38. Although presently unconstrained, lithospheric thickening beneath continents offers a solution to the problem of generating differences between the mantle source regions beneath island arcs and some continental margins

Conclusions

1. Late Cenozoic calc-alkaline volcanic rocks from the Nevado de Toluca area of Mexico display features such as low concentrations of TiO_2 which are

characteristic of orogenic igneous rocks. However, they differ from typical island arc rocks in having generally higher concentrations of SiO_2 and Na_2O and higher $\text{Mg}/\text{Mg} + \text{Fe}^{2+}$ ratios.

2. The Mexican volcanics have relatively low $^{87}\text{Sr}/^{86}\text{Sr}$ ratios, ranging from 0.7032 to 0.7045. There are significant differences in $^{87}\text{Sr}/^{86}\text{Sr}$ ratios between spatially and temporally related rocks. Miocene to Recent rocks from the Nevado de Toluca volcano itself have an apparent age of 425 m.y.

3. The low $^{87}\text{Sr}/^{86}\text{Sr}$ ratios and the higher $\text{Mg}/\text{Mg} + \text{Fe}^{2+}$ ratios in at least some of the volcanics suggest an ultimate origin within the mantle. Differences between continental margin and island arc volcanic rocks may reflect lithospheric thickening beneath older continental regions.

References

Bloomfield, K., and S. Valastro, Late Pleistocene eruptive history of Nevado de To-

- luca volcano, Central Mexico, *Geol. Soc. Am. Bull.*, 85, 901–906, 1974.
- Boettcher, A. L., Volcanism and orogenic belts—the origin of andesites, *Tectonophysics*, 17, 223–240, 1973.
- Cummings, D., and G. I. Schiller, Isopach map of the earth's crust, *Earth Sci. Rev.*, 7, 97–125, 1971.
- Fudali, R. F., Oxygen fugacities of basaltic and andesitic magmas, *Geochim. Cosmochim. Acta*, 29, 1063–1075, 1965.
- Green, D. H., and A. E. Ringwood, The genesis of basaltic magmas, *Contrib. Mineral. Petrol.*, 15, 103–190, 1967.
- Jakés, P., and J. Gill, Rare earth elements and the island arc tholeiitic series, *Earth Planet. Sci. Lett.*, 9, 17–28, 1970.
- James, D. E., C. Brooks, and A. Cuyubamba, Strontium isotopic composition and K, Rb, Sr geochemistry of Mesozoic volcanic rocks of the Central Andes, in *Carnegie Inst. Wash. Year Book 73*, pp. 970–983, 1974a.
- James, D. E., C. Brooks, and A. Cuyubamba, Andean Cenozoic volcanism: magma genesis in the light of Sr isotopic composition and trace element geochemistry, in *Carnegie Inst. Wash. Year Book 73*, pp. 983–997, 1974b.
- Nicholls, I. A., A direct fusion method of preparing silicate rock glasses for energy dispersive electron microprobe analysis, *Chem. Geol.*, 14, 151–157, 1974a.
- Nicholls, I. A., Liquids in equilibrium with peridotitic mineral assemblages at high water pressures, *Contrib. Mineral. Petrol.*, 45, 289–316, 1974b.
- Nicholls, I. A., and D. J. Whitford, Primary magmas associated with Quaternary volcanism in the western Sunda arc, Indonesia, in *Volcanism in Australasia*, pp. 77–90, R. W. Johnson, ed., N. Y., Elsevier Publ. Co., 1976.
- Noble, D. C., H. R. Bowman, A. J. Hebert, M. L. Silberman, C. E. Heropoulos, B. P. Fabbi, and C. E. Hedge, Chemical and isotopic constraints on the origin of low-silica latite and andesite from the Andes of central Peru, *Geology*, 3, 501–504, 1975.
- Norrish, K., and B. W. Chappell, X-ray fluorescence spectrography, in *Physical Methods in Determinative Mineralogy*, pp. 161–214, J. Zussman, ed., N. Y., Academic Press, 1967.
- Roeder, P. L., and R. F. Emslie, Olivine liquid equilibrium, *Contrib. Mineral. Petrol.*, 29, 275–289, 1970.
- Sacks, I. S. and H. Okada, A comparison of the anelasticity structure beneath western South America and Japan, *Phys. Earth Planet. Inter.*, 9, 211–219, 1974.
- Whitford, D. J., Strontium isotopic studies of the volcanic rocks of the Sunda arc, Indonesia, and their petrogenetic implications, *Geochim. Cosmochim. Acta*, 39, 1287–1302, 1975.
- York, D., Least squares fitting of a straight line, *Can. J. Phys.*, 44, 1079–1086, 1966.

PRELIMINARY Rb/Sr DATA ON THE MINIMUM AGE OF THE CENTRAL ANDEAN PRECAMBRIAN BASEMENT COMPLEX

D. E. James and C. Brooks

Introduction

The Andean volcanic arc obscures both figuratively and literally the Precambrian basement of that part of South America. It is generally accepted, however, that the orogenic belt in Peru is underlain at least in part by the westward extension of the Brazilian shield (e.g., Stewart, *et al.*, 1974; Isaacson, 1975), although this has not been established for adjacent northern Chile (Gonzales-Bonorino and Aguirre, 1970). The basement complex (see Fig. 39), consisting primarily of granitic gneisses and migmatites, is best exposed to the west of and on the westernmost flank of the Cenozoic volcanic belt (Cobbing and Pitcher, 1972; Isaacson, 1975). There is little evidence to suggest that much of the central Andean volcanic arc is underlain by ancient sialic crustal remnants, although the gneiss massif cannot constitute the whole of the lower crust as Cobbing and Pitcher speculate—if for no other reason than that the crust was probably less than half its present thickness 100 m.y. ago (James, 1971).

In studies reported in earlier *Year Books* we have concerned ourselves with the Peruvian coastal gneiss complex only enough to show that it cannot have contributed in any significant way to the contamination of the

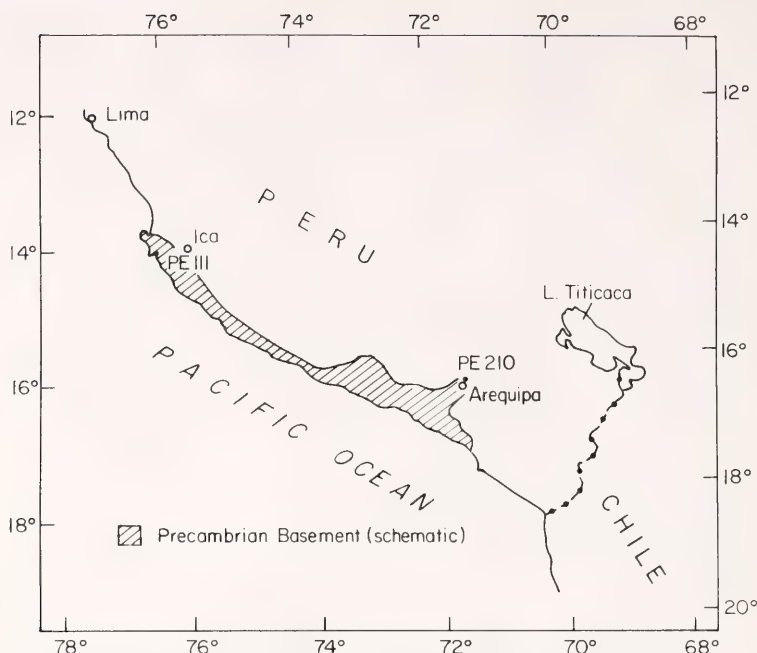


Fig. 39. Map giving schematic outline of region in which the coastal Precambrian gneiss complex crops out in southern Peru. Sample localities are shown for the two samples analyzed in this study.

Mesozoic and Cenozoic volcanic rocks. This neglect, however, is not to deny the considerable interest we have in knowing the age and composition of the basement complex. Its age is of particular importance because it bears upon the question of the age of the lithospheric mantle that underlies that part of the South American continent. We have proposed (James *et al.*, 1976) that the anomalous isotopic character of the late Cenozoic magmas of the central Andes is inherited from ancient subcontinental lithosphere with a composition significantly different from that of other parts of the mantle. The only practical means available for placing age constraints on mantle rocks of the continental lithosphere is to determine the history of the oldest rocks exposed at the surface.

The Rb-Sr measurements given below are ultimately to be used in conjunction with zircon age measurements not yet completed. We consider the Rb-Sr ages to be minimum or

metamorphic ages. Ages were obtained by cutting slabs about 1 cm thick and 15 cm across from the samples perpendicular to the banding and measuring Rb and Sr concentrations (by x-ray fluorescence) and $^{87}\text{Sr}/^{86}\text{Sr}$ ratios in each individual band.

Results

The results of the analyses are plotted in Fig. 40. Sample PE 210 is from the Charcani gneiss exposed in the Rio Chili River valley near Arequipa, Peru, which represents one of the most easterly exposures of the Peru coastal gneiss complex. Its Rb-Sr age of 1012 ± 52 m.y. is significantly greater than the K/Ar ages of about 650 m.y. obtained by Stewart *et al.* (1974) for two gneiss samples from the same general region of Arequipa. It is remarkable that PE 210 still retains a 1 b.y. age despite the fact that the outcrop from which it was collected is tightly sandwiched between opposing flanks of Misti and Chachani, two of the largest

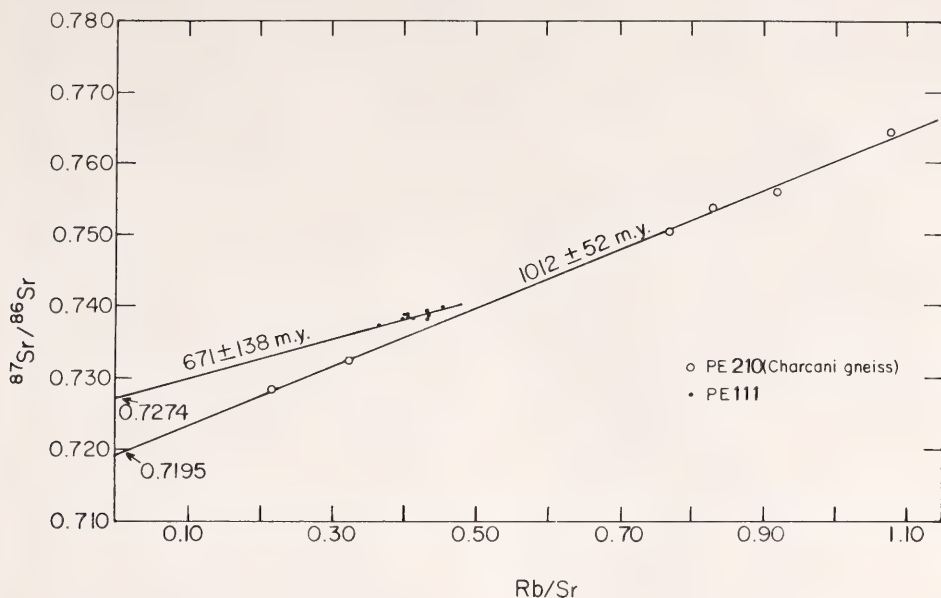


Fig. 40. Plot of $^{87}\text{Sr}/^{86}\text{Sr}$ vs. Rb/Sr for gneiss slab sections. Age and errors calculated using York regression. Solid dots are for PE 111, open circles for PE 210.

andesitic strato-volcanoes of southern Peru. This Rb-Sr age further pushes back the minimum age of the central Andean basement complex.

Sample PE 111 is from a coastal outcrop south of Pisco on the Paracas Peninsula. The outcrop is cut by veins and dikes of basaltic material, indicating that the gneiss was intimately involved with Mesozoic or Cenozoic magmatism. The scatter in the Rb-Sr data may be due in part to the effects of this later magmatism. We calculate an age of 671 ± 138 m.y. from the best-fit line through the data but place little reliance on this result. The basis of our skepticism is found in the considerable data scatter and in the progressive change of initial $^{87}\text{Sr}/^{86}\text{Sr}$ with position in the slab (Fig. 41). The points on the isochron diagram that tend to lie below the best-fit line come from one end of the slab; points that lie above the line come from the other end of the slab, irrespective of Rb/Sr ratio. This correlation could, for example, be caused by mixing of the gneiss material with injected material that is isotopically dis-

tinct. Such an interpretation is suggested by prominent veining found in the outcrop and in the sample itself. Whatever the explanation, the slab is not in isotopic equilibrium for a given age from one end to the other. Because of this, the Rb-Sr age measurements on PE 111 are necessarily suspect, and hence the difference in isotopic age between PE 111 and PE 210 is not necessarily real.

References

- Cobbing, E. J., and W. S. Pitcher, Plate tectonics and the Peruvian Andes, *Nature*, 240, No. 99, 51–53, 1972.
- Gonzales-Bonorino, F., and L. Aguirre, Metamorphic facies series of the crystalline basement of Chile, *Geol. Rundschau*, 59, 979–994, 1970.
- Isaacson, P. E., Evidence for a western extracontinental land source during the Devonian period in the central Andes, *Geol. Soc. Am. Bull.*, 86, 39–46, 1975.
- James, D. E., Plate tectonic model for the evolution of the central Andes, *Geol. Soc. Am. Bull.*, 82, 3325–3346, 1971.

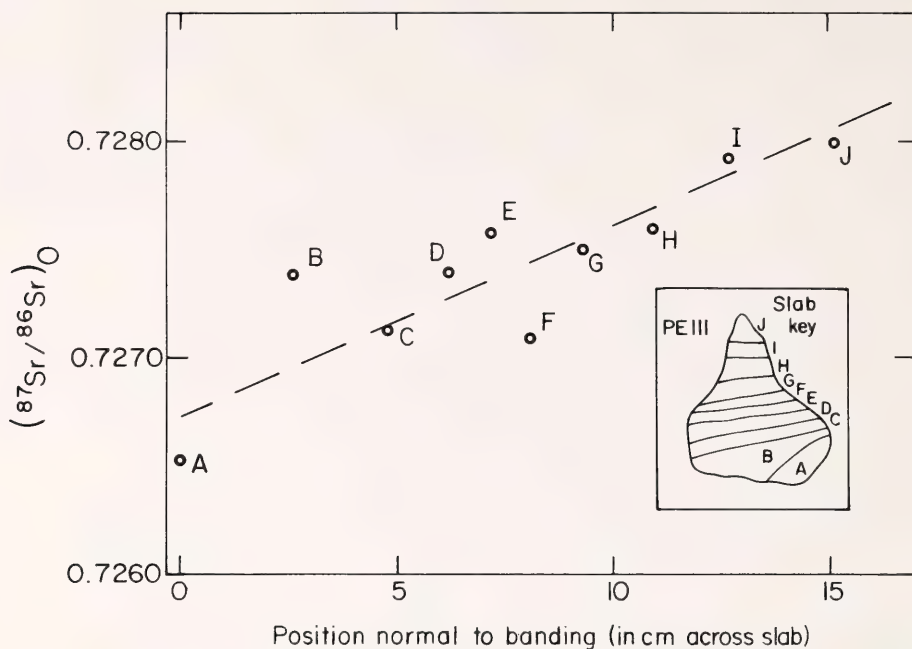


Fig. 41. Plot of initial $^{87}\text{Sr}/^{86}\text{Sr}$ vs. position in the slab. Slab cross section is shown in inset. Letters key layers analyzed to the $^{87}\text{Sr}/^{86}\text{Sr}$ initial ratios. Abscissa is in centimeters from center of layer A along a line normal to the layering (see inset).

James, D. E., C. Brooks, and A. Cuyubamba, Andean Cenozoic volcanism: Magma genesis in the light of strontium isotopic composition and trace-element geochemistry, *Geol. Soc. Am. Bull.*, 87, 592–600, 1976.

Stewart, J. W., J. F. Evernden, and N. J. Snelling, Age determinations from Andean Peru: A reconnaissance survey, *Geol. Soc. Am. Bull.*, 85, 1107–1116, 1974.

VOLCANOES, Q, AND SEISMICITY IN WESTERN SOUTH AMERICA

I. S. Sacks, J. A. Snoke, and A. T. Linde

Introduction

Subduction zones are regions where oceanic plates, generated at mid-ocean ridges, plunge into the asthenosphere under an adjacent oceanic or continental plate. This interaction generates a

characteristic pattern of seismic and volcanic activity as well as a clearly recognizable anelasticity structure. We have studied the distribution of these features along the extensive subduction zone of western South America, using their expression in the Japan region as a reference for normal distribution. Regions of anomalous anelasticity structure are also found to have diffuse seismicity and an absence of volcanoes.

The study of the anelasticity structure of various parts of the earth has been our major focus for a number of years (see *Year Book 72*, pp. 226–233; *Year Book 74*, pp. 256–266). In particular, from broadband seismographs installed in South America and in Japan, we have learned that there is a thick, low absorption (high-Q) keel beneath the South American continent. This has been confirmed by a technique using converted shear to compressional energy, which is described in the following paper. From the study in the Japan region (Sacks and Okada, 1974), we learned, inter alia, that the subduc-

tion of a cool oceanic lithosphere can reduce the amount of partial melt in the adjacent asthenosphere. This causes relatively rapid thickening of the continental lithosphere and reduces the thermal gradient in the downgoing lithosphere. A possible manifestation of these effects in the subduction zone of western South America is described in this report.

Anelasticity. The absorptive part of seismic energy propagation may be used to calculate an anelasticity structure of a region. The effect of an absorptive medium on seismic waves is to attenuate the amplitudes at higher frequencies more than at lower. Seismographs with a wide frequency range (Sacks, 1966) are used and allow accurate absorption ($1/Q$) determinations to be made. Records from local seismographs, though of smaller bandwidth, are used to expand the coverage. Spectral ratio techniques (e.g., Sacks, 1968) are used throughout to avoid dependence on the source spectra of the

earthquakes used for the study. Anelasticity is often used as a sensitive indicator of the lithosphere (high- Q , or low absorption) and the asthenosphere (low- Q , or high absorption).

Anelasticity studies of the upper mantle have been made for regions beneath Japan (Katsumata, 1960; Utsu, 1966; Sacks and Okada, 1974), Fiji (Isacks *et al.*, 1968; Barazangi and Isacks, 1971), South America (Sacks, 1969, Sacks and Okada, 1974), and New Zealand (Mooney, 1970). The anelasticity structure of a typical subduction zone consists of a high- Q ($Q_p \approx 1000$) lithosphere overlying a low- Q ($Q_p \approx 200-500$) asthenosphere, which in turn overlies the dipping subducted oceanic lithosphere with Q_p of 1000 near the surface and 3000 or more at depth. The lithosphere beneath Japan is about 70 km thick, whereas that beneath South America is in excess of 300 km. The study leading to these conclusions is fully described in Sacks and Okada (1974), and the gross anelasticity structures are shown in Fig. 42.

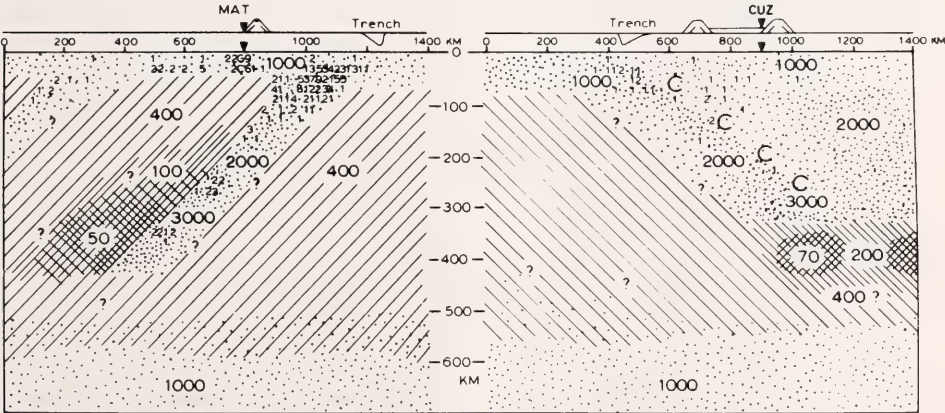


Fig. 42. The Q_p -structure beneath Japan (left) and South America (right). Dots indicate areas of high Q (1000–3000); slant lines, intermediate Q -values (300–500); and cross-hatching, low Q -values (50–100). The small numbers in the dotted region indicate earthquake hypocenters. The region above the dipping seismic plane is of intermediate Q in Japan, whereas in South America it has high Q . The high- Q slab in Japan is continuous down to the deepest earthquakes; in South America there is a substantial decrease in Q below 350 km even though there are earthquakes 600 km deep. In northern Chile and southern Peru, a distinct low- Q region, marked C, overlies the dipping plane.

In some regions, such as northern Chile and southern Peru, the gross anelasticity structure is similar to that beneath Japan except for the much thicker lithosphere beneath South America. In these regions, a low- Q zone was found between the high- Q subducting lithosphere and the high- Q continental lithosphere. Intermediate depth (200–300 km) earthquakes occurring in the subducting slab were found to have low- Q paths to the broadband seismograph at Toconce, which is 210 km from the coast in northern Chile. However, paths to the same seismograph originating at, or penetrating to, the same depth but staying wholly within the continental lithosphere have high Q . Fig. 43 shows these seismic ray paths. Paths to a coastal seismograph at Antofagasta have high Q from the same intermediate depth subduction zone earthquakes which had low Q at Toconce. Therefore, there must be a low- Q region between the subducting lithosphere and the continental lithosphere. It is difficult to determine the thickness of this low- Q zone; it is less than 100 km but probably not less than 40 km. This zone has a Q_p of about 400, which is in the range of asthenosphere values found elsewhere, e.g., Japan. The low- Q zone can be traced from

Puno in southern Peru to Peldehue in central Chile. Seismograms from these stations show the same absorption distribution as those from Toconce in northern Chile.

Beneath central Peru, which has similar seismic station coverage, we have not been able to find an equivalent low- Q zone. All paths from earthquakes at depths less than 300 km to the broadband seismograph at Cusco (340 km from the coast) have high Q . This seems to be true also for the Huancayo seismograph farther to the northwest. These paths are considered in greater detail in Sacks (1969). The anelasticity structure described above is in agreement with the areal distribution of absorption given by Barazangi *et al.* (1975).

In summary, south of Cusco (i.e., southern Peru and northern Chile) there is a low- Q zone between the subducting lithosphere and the continental lithosphere; Q values in this zone are similar to those found in the asthenosphere. In the region north of Cusco, no low- Q zone between the high- Q subducting and continental lithospheres has been found, presumably because such a zone is either very thin or nonexistent.

Seismicity. The seismicity of subduction regions is characterized by a dipping seismic plane some tens of kilometers thick, which is thought to delineate the upper surface of the subducting lithospheric plate. There are no earthquakes in the asthenosphere on either side of this subducting plate. Earthquakes do occur in the continental lithosphere above the subduction. The seismicity is not uniform along the subducting plate; regions of low or zero seismic release are found. In some regions, such as New Hebrides, the deeper part of the subducted slab appears to be detached (Barazangi *et al.*, 1973). This is suggested to be the case beneath South America as well (Sacks and Okada, 1974; Snoke *et al.*, 1974, and others). However, Isacks and Barazangi (1973) interpret the subducting plate to be continuous, though

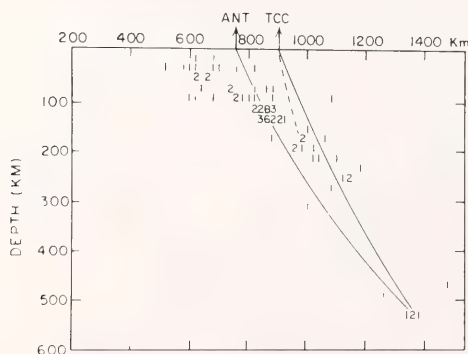


Fig. 43. A seismicity section 50 km wide, normal to the trench in northern Chile. The numbers indicate earthquake locations (according to CGS) and the arrows show the position of two seismographs whose records were compared. TCC (Toconce) arrivals from 200–250 km events show asthenosphere-type Q -values.

having zero seismicity, in the depth range 350–500 km.

For regions in which the subduction is not clearly delineated by the seismicity, an alternative method developed by Okada (1974) may be used to detect the upper surface of the descending plate. This technique relies on the efficient conversion of near vertical shear waves, *ScS*, into compressional waves at an inclined interface. Figure 44 shows the ray paths giving rise to the phase *ScSp*. The time difference between *ScSp* and *ScS* gives a locus of possible conversion points in the earth, indicated by the shaded line in Fig. 45, which also shows an example of the phase. The amplitude ratio *ScSp*/*ScS* is used to determine the depth, indicated by a circle, at which the conversion of shear-to-compressional energy takes place (Snoke and Sacks, 1975; Okada, 1976). This method has been confirmed in areas where the subducting plate is clearly delineated by earthquakes, e.g., Japan and southern Peru (Okada, 1974).

At Peldehue in central Chile, clear *ScSp* arrivals originate from the

deeper part (150 km) of the dipping seismic plane. The interpretation of the Arequipa (southern Peru) records indicates an interface that coincides well with that delineated by seismicity. Farther north, however, this is no longer the case. The Naña (central Peru) seismograms show clear *ScSp* arrivals (Fig. 45), which also indicate the probable conversion point. This conversion point lies on an extension of the shallow seismicity (near the trench) which seems to disappear below 100-km depth. This suggests that the subduction has a dip angle similar to the other regions discussed (southern Peru to central Chile) but is of low seismicity.

There is considerable seismic activity in what we have interpreted to be the continental lithosphere. This is interpreted by some, e.g., Stauder (1975) and Isacks and Molnar (1971), to be subducting oceanic lithosphere with a dip of about 15°. The *ScSp* observations and the trend of shallow seismicity persuade us that this is not the case.

Volcanism. Volcanoes generally occur in subduction regions at some

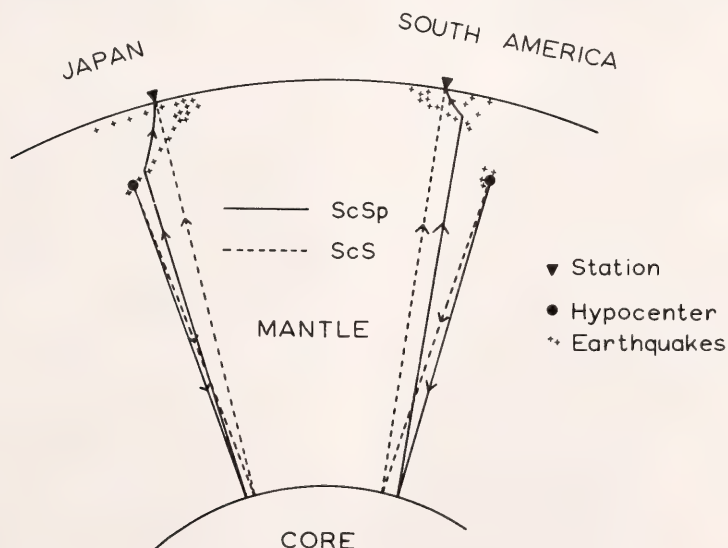


Fig. 44. A schematic model showing the paths of the *ScSp* phase (solid line) and the *ScS* phase (dotted line). The shear energy reflected from the earth's core, *ScS*, is efficiently converted to compressional energy at the dipping interface.

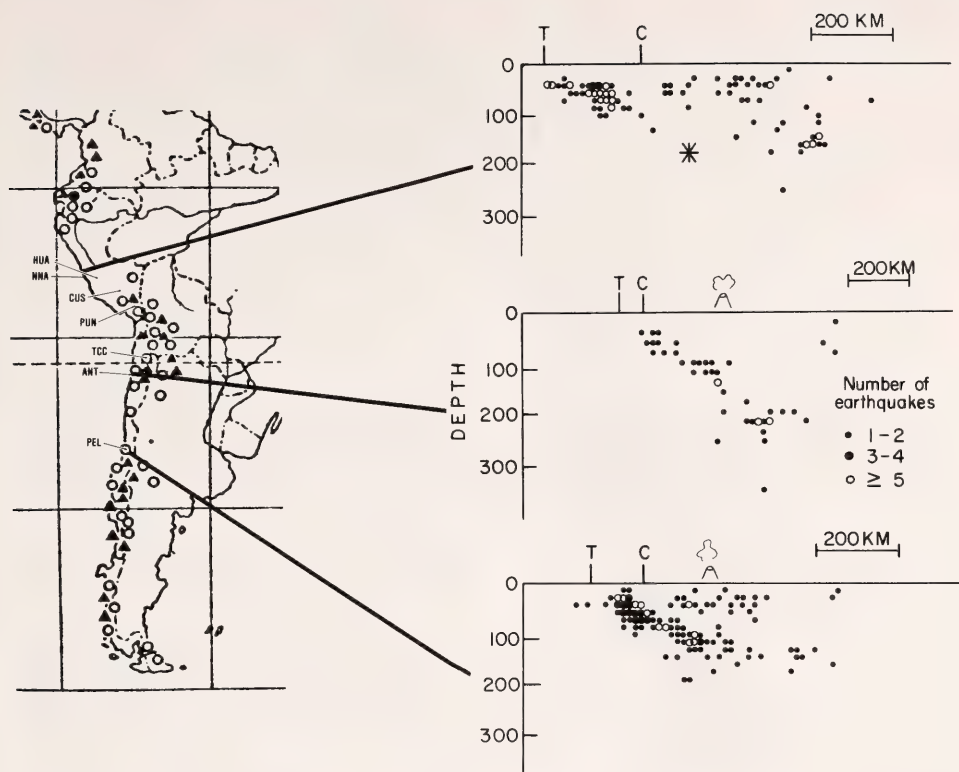


Fig. 46. Recent volcanism and seismicity of western South America. The circles on the map indicate extinct volcanoes; the triangles, recent volcanism (reproduced from Fig. V.11, p. 105, in *The Earth's Crust and Mantle* by F. A. Vening Meinesz, 1964). The three seismicity sections of CGS hypocenters on the right side of the figure are taken normal to the trench and are of equal width. *T* and *C* stand for trench and coast, respectively. The asterisk indicates the conversion point for the *ScSp* phase recorded by the NNA (Naña) seismograph. The seismograph stations mentioned are indicated.

indicating temperatures high enough to cause partial melting, between the subducting plate and the thick (greater than 300 km) continental keel. Most of the seismicity in these regions (see lower two seismicity sections in Fig. 46) is confined to the subducting plate, although there is also considerable activity in the continental block. Volcanoes occur, and the seismic plane is about 150 km beneath them, as is the case in other regions such as Japan.

In central Peru, however, the low-*Q* zone (sliver of asthenosphere) is small or absent, and the subducting slab is not characterized by seismicity below about 100 km. There is no recent volcanism in this region (see Fig. 46). Note that there are earthquakes at

depths of 150 km, but these occur inland far from the subducting slab (as determined in the studies discussed above) and are considered to be in the continental lithosphere.

It appears that the contact of hot and therefore weak material (characterized by low values of *Q*) with the subducting lithosphere provides the boundary conditions that give rise to a well-defined seismic plane and the generation of magma.

We conjecture further that in the case of an interaction of a subduction zone with a thick continental lithosphere, the cooling effect of the down-going oceanic lithosphere in the asthenosphere between it and the continental lithosphere can eventually

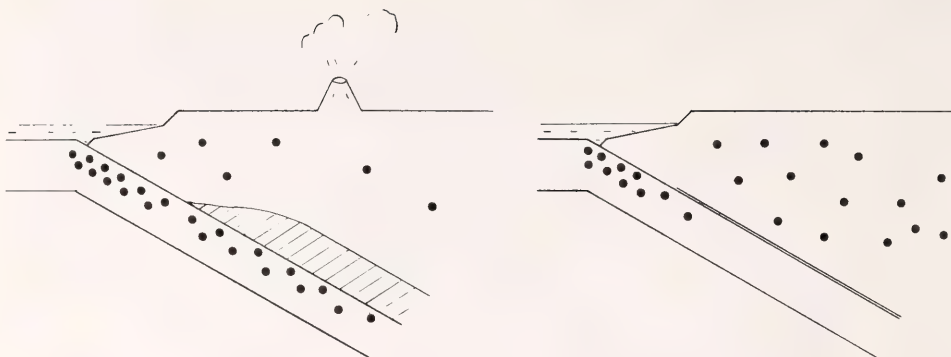


Fig. 47. Schematic drawing indicating the key features in the Chile-southern Peru region (left diagram) and the central Peru region (right diagram). The shaded zone indicates asthenosphere. Where this exists, the earthquakes (dots) are mainly confined to the subducting slab, and volcanoes occur above the 150–175 km deep earthquakes. Where asthenosphere is absent, as in central Peru, volcanoes do not occur and the seismicity is more dispersed.

freeze out that asthenosphere. There is then direct contact between the subducting lithosphere and the continental lithosphere which inhibits volcanism and causes diffuse or low seismicity. Of the 58°-long subduction zone south of the equator in western South America, 25° is already devoid of active volcanism.

Acknowledgments

This research was supported in part by National Science Foundation Grant No. DES 72-01295A02.

References

- Barazangi, M., and B. Isacks, Lateral variations of seismic-wave attenuation in the upper mantle above the inclined earthquake zone of the Tonga island arc: Deep anomaly in the upper mantle, *J. Geophys. Res.*, **76**, 8493–8516, 1971.
- Barazangi, M., B. Isacks, J. Oliver, J. Dubois, and G. Pascal, Descent of lithosphere beneath New Hebrides, Tonga-Fiji and New Zealand: Evidence for detached slabs, *Nature*, **242**, 98–101, 1973.
- Barazangi, M., W. Pennington, and B. Isacks, Global study of seismic wave attenuation in the upper mantle behind island arcs using P waves, *J. Geophys. Res.*, **80**, 1079–1092, 1975.
- Isacks, B., and M. Barazangi, High-frequency shear waves guided by a continuous lithosphere descending beneath South America, *Geophys. J. R. Astron. Soc.*, **33**, 129–139, 1973.
- Isacks, B., and P. Molnar, Distribution of stresses in the descending lithosphere from a global survey of focal-mechanism solutions of mantle earthquakes, *Rev. Geophys. Space Phys.*, **9**, 103–174, 1971.
- Isacks, B., J. Oliver, and L. R. Sykes, Seismology and the new global tectonics, *J. Geophys. Res.*, **73**, 5855–5899, 1968.
- Katsumata, M., The effect of a seismic zone upon the transmission of seismic waves, *Kenshinjiho (Q. J. Seismol.)*, **25**, 89–95 (in Japanese), 1960.
- Mooney, H. M., Upper mantle inhomogeneity beneath New Zealand: Seismic evidence, *J. Geophys. Res.*, **75**, 285–309, 1970.
- Okada, H., Geophysical implications of the phase $ScSp$ on the dipping lithosphere underthrusting western South America, *Carnegie Inst. Wash. Year Book* **73**, pp. 1032–1039, 1974.
- Okada, H., Ph.D. thesis, Hokkaido University, Sapporo, Japan, in preparation, 1976.
- Sacks, I. S., A broad-band large dynamic range seismograph, in *Geophys. Monogr.* **10**, Am. Geophys. Union, pp. 543–553, 1966.
- Sacks, I. S., Q for P -waves in the mantle, *Carnegie Inst. Wash. Year Book* **66**, pp. 28–29, 1968.
- Sacks, I. S., Distribution of absorption of shear waves in South America and its tectonic significance, *Carnegie Inst. Wash. Year Book* **67**, pp. 339–344, 1969.

Sacks, I. S., and H. Okada, A comparison of the anelasticity structure beneath western South America and Japan, *Phys. Earth Planet. Inter.*, 9, 211-219, 1974.

Snoke, J. A., and I. S. Sacks, Determination of the subducting lithosphere boundary by use of converted phases, *Carnegie Inst. Wash. Year Book* 74, pp. 266-273, 1975.

Snoke, J. A., I. S. Sacks, and H. Okada, A model not requiring continuous lithosphere for anomalous high-frequency arrivals from deep-focus South American earthquakes, *Phys. Earth Planet. Inter.*, 9, 199-206, 1974.

Stauder, W., Subduction of the Nazca plate under Peru as evidenced by focal mechanisms and by seismicity, *J. Geophys. Res.*, 80, 1053-1064, 1975.

Utsu, T., Regional differences in absorption of seismic waves in the upper mantle as inferred from abnormal distributions of seismic intensities, *J. Fac. Sci. Hokkaido Univ., Ser. 7 (Geophys.)*, 2, 359-374, 1966.

Vening Meinesz, F. A., *The Earth's Crust and Mantle (Developments in Solid Earth Geophysics, Vol. 1)*, Am. Elsevier, New York, 1964.

DETERMINATION OF THE LITHOSPHERE-ASTHENOSPHERE BOUNDARY USING CONVERTED WAVES

I. S. Sacks and J. A. Snoke

Introduction

There is considerable evidence for a thick lithosphere under South America. A study of surface-wave dispersion across the shield area by Alexander (1972) showed an absence of a low-velocity zone down to at least 200 km, which implies that the lithosphere extends to at least that depth. Sacks and Okada (1974) found that there is a Q reversal at about 350 km depth under the continent and that the Q at a given depth above 350 km is approximately the same as in the downgoing plate. They concluded that the lithosphere extended to about 350 km depth. Also, the seismicity is absent between depths of about 350 km and 500 km, which is consistent with the theory

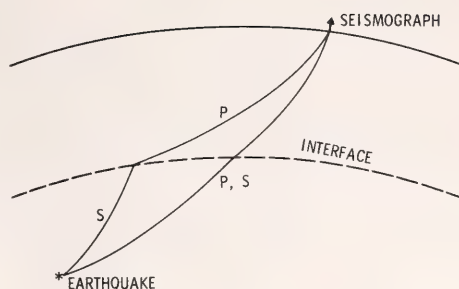


Fig. 48. Ray paths of direct S, direct P, and sp.

that this depth range contains weak (asthenospheric) material incapable of supporting the stress concentrations necessary for earthquakes.

In this report we describe a technique to determine the depth of the lithospheric-asthenospheric boundary by utilizing the fact that the asthenosphere probably has a partial melt, so that there is a significant rigidity contrast at the boundary, leading to relatively efficient conversion of incident shear waves to transmitted compressional waves (Fig. 48; see also Sacks, 1968 and Jordan and Frazer, 1975).

Data

Arrivals intermediate between P and S were observed at the Carnegie broadband stations (Sacks, 1966) CUZ in Peru and TCC in northern Chile, and at stations employing mechanical, horizontal seismographs at Antofagasta (ANT) in northern Chile, and in Argentina at La Plata (LPA), Zonda (ZON), La Quiaca (LQA) and Jujuy (JUY). The data are summarized in Table 13, and station locations and the epicentral regions of analyzed earthquakes are shown in Fig. 49. Examples of the arrivals are shown in Figs. 50 and 51. The arrivals were observed at epicentral distances of 4° to 13° from events in the depth range 526-650 km. The locations of epicenters and seismographs are such that it is impossible that the intermediate arrivals result from conversions at interfaces related to subduction.

TABLE 13. List of Observed Arrivals between *P* and *S*. Locations from USCGS/NOAA. $\delta T = T_{\text{arrival}} - T_p$.

| Date (d-m-y) | Mag. | Depth (km) | Station | Back azim. | Dist. (deg.) | Comp. | δT (s) |
|-----------------------|------|---------------|---------|---------------|-----------------|-------|-------------------|
| 6-7-59 ₍₁₎ | 6.75 | 600 | LQA | 137 | 6.06 | NS | 24 |
| 6-7-59 ₍₂₎ | 6.9 | 600 | JUU | 125 | 4.13 | EW | 24 |
| | | | | | | NS | 22 |
| | | | LQA | 140 | 5.76 | EW | 22-26 |
| | | | | | | NS | 25 |
| | | | | | | EW | 22 |
| 28-12-59 | | 650 | ZON | 53 | 8.04 | NS | 21.5 |
| | | | LPA | 327 | 8.13 | NS | 30 |
| | | | | | | EW | ... |
| 19-8-61 | 7.0 | 649 | ANT | 357 | 12.85 | NS | 42.5 |
| 29-9-62 | 6.5 | 575 | ZON | 46 | 6.33 | EW | 20.30 |
| 8-12-62 | 5.9 | 620 | ZON | 40 | 7.36 | NS | ... |
| | | | | | | EW | 28 |
| | | | | | | NS | 15 |
| 9-12-64 | 5.9 | 586 | ZON | 51 | 6.24 | EW | 29 |
| 5-3-65 | 5.5 | 573 | ZON | 47 | 6.52 | EW | 19, 29 |
| 13-5-65 | 5.1 | 589 | ZON | 21 | 7.25 | NS | ... |
| | | | | | | NS | 24.5 |
| | | | | | | EW | 15 |
| 30-7-65 | 4.5 | 526 | TCC | 98 | 4.17 | EW | 15 |
| 20-12-66 | 5.7 | 586 | ZON | 28 | 9.78 | NS | 14.5 |
| | | | ZON | 44 | 7.24 | EW | 24.5 |
| | | | | | | NS | ... |
| 9-9-67 | 5.9 | 578 | ZON | 53 | 6.18 | NS | 24 |
| 12-1-72 | 5.9 | 580 | CUZ | 0 | 6.67 | UD | 23 |
| | | | | | | NS | 24 |
| | | | | | | EW | ... |



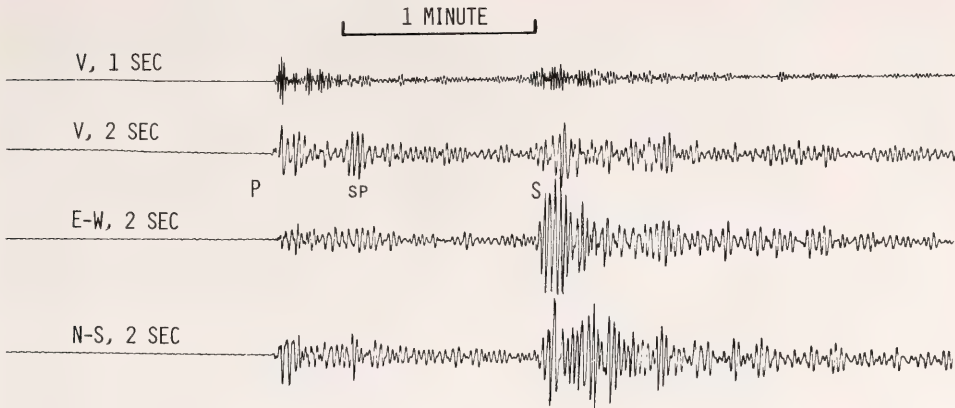
Fig. 49. Location map showing seismograph stations and the epicentral regions (hatched zones) of analyzed earthquakes. The arrival at CUZ was for a northern (Peru-Brazil) earthquake; all observations at other stations were for southern earthquakes.

Figure 52 has tracings of the waveforms for the intermediate arrival (labeled *sp*) and direct *S* for an event as recorded at TCC. The similarity of the two waveforms suggests that the phase was radiated as a shear wave. The intermediate arrival has relatively more high frequencies than does direct *S* (Fig. 50), from which we infer that the phase traverses the low-*Q* zone below 350 km (Sacks and Okada, 1974), with a steeper path through that region than does direct *S*. The amplitude of the arrival is largest on the vertical component of the seismogram (Fig. 50) but is in all cases much smaller than direct *S* at long periods.

These arrivals were not observable on WWSSN seismograms because of the high magnification and limited dynamic range and frequency response of these seismographs.

Theory and Interpretation

The only model we have found consistent with the data is that the inter-



CUZCO 12 JAN 1972 $H = 580 \text{ KM}$ $\Delta = 6.68^\circ$ $M = 5.9$

Fig. 50. Three-component, filtered *P*, *sp*, and *S* arrivals for an earthquake as recorded by the Carnegie broadband seismograph CUZ. The upper trace is the vertical component filtered at 1-s period. The other traces are vertical, E-W (transverse horizontal), and N-S (radial horizontal) filtered at 2-s periods. The *sp* arrival is strongest on the vertical and weakest on the transverse, as predicted. The shorter periods ($\leq s$) are attenuated in the low-*Q* region below the lithosphere for *S* and *sp*.

mediate arrivals are *sp* phases for which the *S*-to-*P* conversion occurs at an approximately horizontal interface at about 400 km depth (Fig. 48). Previous studies (e.g., Jordan and Fraser, 1975) of *sp* or *Sp* have considered only *S*-to-*P* conversion at the Moho discon-

tinuity, in which case the arrival is observed as an immediate precursor to direct *S*.

The variation of the displacement amplitude ratio at *sp* to *S* with epicentral distance is shown in Fig. 53 (vertical component) and Fig. 54 (horizontal

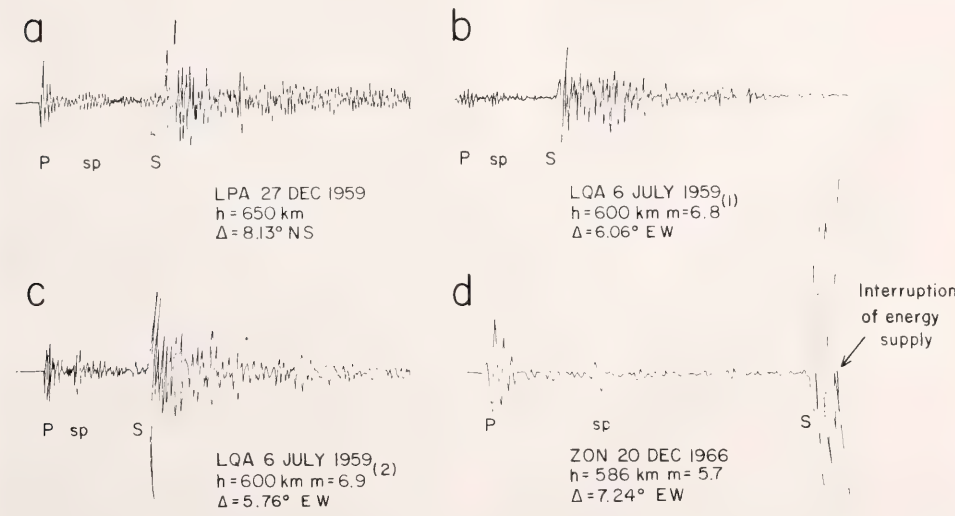


Fig. 51. Tracings of *P*, *sp*, and *S* arrivals for earthquakes as recorded by mechanical seismographs at ZON, LQA, and LPA. (See Fig. 50 for station locations.) Note that the clear *sp* arrival on record *d* has the same polarity as *S*.

TCC E-W 30 JULY 1965 $\Delta=4.17$ 

Fig. 52. Tracings of filtered (at 2.5-s period) *sp* and *S* arrivals for an earthquake as recorded by the Carnegie broadband station TCC. The waveforms are very similar, and the polarity is the same.

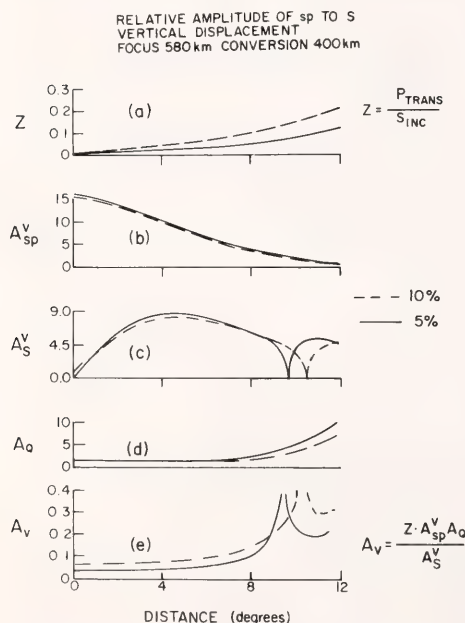


Fig. 53. (a) The transmission coefficient for *P* transmitted with an incident *S* vs. epicentral distance for *sp*. (b) and (c) vertical displacement amplitude for *sp* and *S*, respectively, based on geometrical spreading. (d) Relative attenuation of *S* to *sp* below the conversion depth at 400 km assuming $Q_S = 50$ and a period of 2.5 s. (e) The relative amplitude of *sp* to *S* for vertical displacement. The focus is at 580 km, and 5% and 10% enhancements for V_{400-}/V_{400+} are included.

radial component). (The *sp* amplitude should be zero on the horizontal transverse component.)

The ratios are calculated using ray theory and include the effects of geometrical spreading, *S*-to-*S* and *S*-to-*P* conversion at the interface (for enhancements of both 5% and 10% of the velocities above the interface), relative attenuation below the interface, and the free-surface conversion of amplitudes into ground displacement. For this example of a focal depth of 580 km and a conversion depth of 400 km, there is a cutoff at about 12° . The relative amplitude is larger on the vertical (Fig. 53e) than on the radial (Fig. 54e) but is always much less than unity. (Including earthquake radiation-pattern effects may change the amplitude ratios somewhat.)

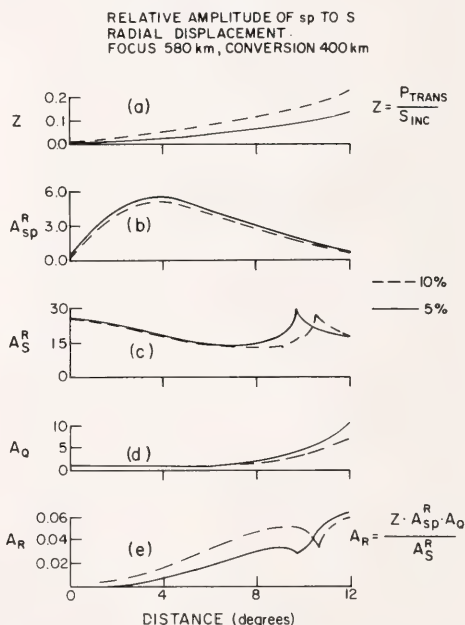


Fig. 54. Same as in Fig. 53 but showing the relative radial displacement amplitudes instead of the vertical.

The amplitude ratios would be approximately the same if one assumed instead a 5% or 10% decrease in the velocities above the interface, and for our data set, one cannot determine the di-

rection of the velocity change at the interface on the basis of travel time alone (Fig. 56). It is important geophysically to know which it is: A decrease above the interface could imply that the usual 400-km discontinuity is a sharp discontinuity rather than the more usually modeled gradual (over 60-km) velocity increase with depth, while an increase above the interface would lead to the interpretation that the interface is the boundary between the continental lithosphere and the underlying asthenosphere.

The polarity of the outgoing P wave for an S -to- P refraction depends on the sign of the velocity change at the conversion interface. The sign of the velocity change can be determined by comparing the waveforms, or even the directions of first-motion, of the sp and the direct S on radial-component seismograms. Enhanced velocities above the interface result in in-phase waveforms and hence in first-motions in the same direction; enhanced velocities below the interface result in opposite polarity waveforms and hence in first-motions in opposite directions. The first-motions and waveforms from Figs. 52 and 51d are in phase, indicating that the interface is a velocity reversal which we interpret to be the lithosphere-asthenosphere boundary.

From the plot $\delta T = T_{sp} - T_P$ vs. epicentral distance (Fig. 55) we determine that a one-second increase in δT results from an increase in focal depth of about 12 km at short epicentral distances, or about 7 km for larger epicentral distances. Keeping the focal depth fixed and decreasing (increasing) the conversion depth gives similar results for increases (decreases) in δT .

Figure 56 has curves of δT vs. epicentral distance for different velocity-depth models. Compared with the normal J-B model, a model with a sharp increase-with-depth of the velocities instead of the normal 400-km discontinuity gives essentially identical results. A model with velocities above the interface enhanced by 5% (10%) gives similar δT 's by up to 3 (6) seconds. For

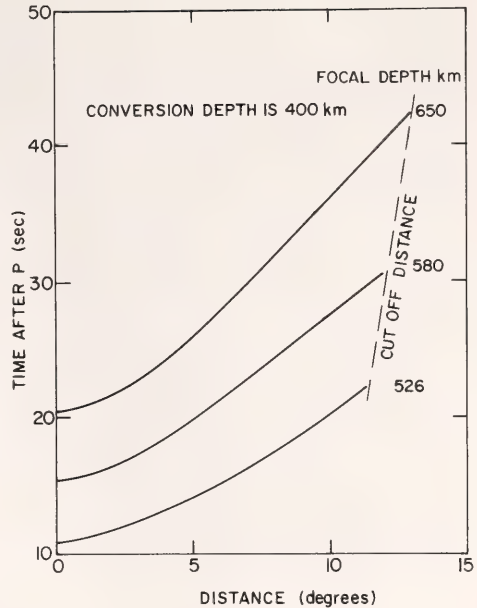


Fig. 55. The calculated difference in sp and P arrival times is plotted vs. epicentral distance for a conversion depth at 400 km and focal depths at 526, 580, and 650 km. The long-distance cutoff is indicated by a dashed line. The J-B model is used.

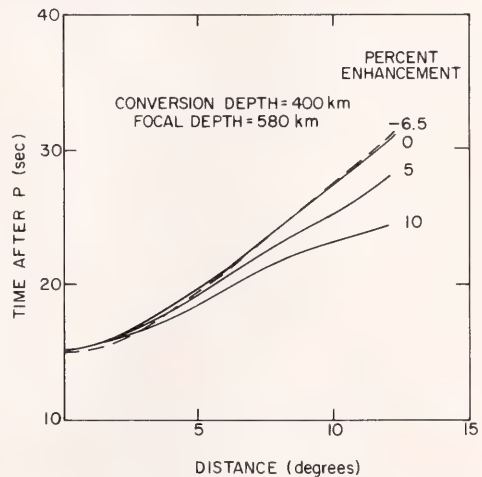


Fig. 56. Differential travel times as in Fig. 55 for a focal depth of 580 km and a conversion depth of 400 km for different velocity-depth models. Indicated are the percentages of the velocity contrasts for the velocity above the interface relative to those below.

our data these differences are not significant.

Figure 57 is a plot of the observed δT minus the calculated δT (using the normal J-B model) vs. epicentral distance. It should be noted that the data include events for focal depths of 526–650 km and for epicentral distances of 4° – 13° and are at a large range of azimuths. The observations suggest a probable conversion depth of 400 ± 30 km.

An indication of the thickness of the transition zone can be obtained from the high-frequency content of the arrivals. From Fig. 50 we see that the arrival is clearly recorded at periods as small as 2 seconds, so that to a 10-km wavelength the discontinuity is sharp. Hence the transition zone must be only a few kilometers thick.

Concluding Remarks

Anelasticity and surface-wave studies, the seismicity and the *sp* studies provide conclusive evidence that there is a thick lithosphere under South America. The *sp* arrivals provide a high-resolution technique to determine the lithosphere-asthenosphere boundary. Our results show that the

bottom of the lithosphere is approximately horizontal under a substantial part of the continent; the depth of the boundary is within a few tens of kilometers of 400 km; and the transition zone is at most a few kilometers thick with a velocity contrast of 5%–10%.

Preliminary investigations of other geographical regions indicate that *sp* and *Sp* arrivals exist and that conversion depths correlate with other evidence for the lithosphere-asthenosphere boundary in those regions.

Acknowledgments

This research was supported in part by National Science Foundation Grant No. DES 72-01295A02.

References

- Alexander, S. S., Crust-mantle structure of shields and their role in global tectonics, *Trans. Am. Geophys. Union*, 53, 1043, 1972.
- Jordan, T. H., and L. N. Frazer, Crustal and upper mantle structure from *Sp* phases, *J. Geophys. Res.*, 80, 1504–1518, 1975.
- Sacks, I. S., A broad-band large dynamic range seismograph, in *Geophys. Monogr.*

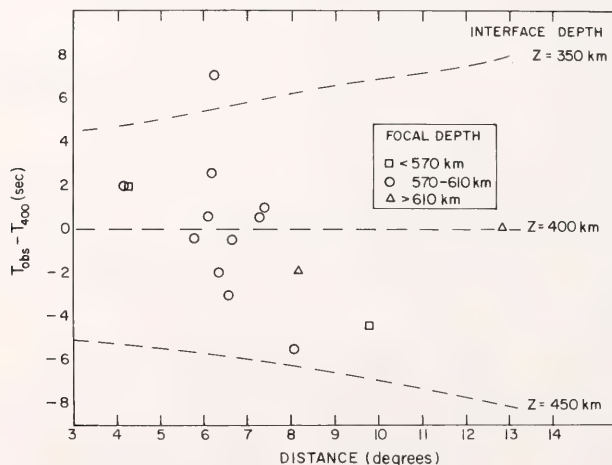


Fig. 57. Plot of observed δT minus calculated δT vs. distance for a conversion depth of 400 km. Also included are lines corresponding to $\delta T_{\text{observed}} = \delta T_{\text{calculated}}$ for conversion depths of 350 and 450 km. An interface depth of about 400 km is preferred. The normal J-B model was used to obtain the calculated δT .

10, Wash., D. C., Trans. Am. Geophys. Union, pp. 543–553, 1966.

Sacks, I. S., Converted waves from the interface at a depth of 410 km. *Carnegie Inst. Wash. Year Book* 66, pp. 32–35, 1968.

Sacks, I. S., and H. Okada, A comparison of the anelasticity structure beneath western South America and Japan, *Phys. Earth Planet. Inter.*, 9, 211–219, 1974.

SHALLOW SEISMICITY IN SUBDUCTION ZONES

I. S. Sacks, A. Rodriguez B.*,
J. A. Snoke and A. T. Linde

Introduction

The study described here is one of the results of long-term collaboration between this department and the Characato Observatory of the University of San Agustín in Arequipa.

The seismicity of subduction regions is characterized by a dipping seismic plane, some tens of kilometers thick, which is thought to delineate the upper surface of the subducting lithospheric plate. There are no earthquakes in the asthenosphere on either side of this subducting plate. Earthquakes do occur in the continental lithosphere above the subduction. The seismicity is not uniform along the subducting plate; regions of low or zero seismic release are found.

In this report we describe and interpret the shallow seismicity under southern Peru using high-resolution data from a net operated by the University of San Agustín in 1965 (James *et al.*, 1969). The hypocenters (Figs. 59, 60) delineate a 30° dipping Benioff zone but also indicate intraplate activity. Of particular interest is the existence of an aseismic wedge between the shallower earthquakes in the subducting lithosphere and those in the continental lithosphere. We show below that this aseismicity can be explained quite simply on the basis of the elastic forces involved in the tectonics.

*Characato Geophysical Observatory, San Agustín University, Arequipa, Peru.

Data

During 1965 the Characato Observatory of the University of San Agustín operated a net of nine high-sensitivity seismographs in southern Peru. The locations of these stations, as well as some others used for this study, are shown in Fig. 58.

The method used to locate the earthquakes recorded by the Arequipa net is discussed in detail by James *et al.* (1969). Stable hypocenters for the local earthquakes were determined by an iterative method utilizing both the *P* and the *S* arrival times. In this method the origin time is determined independently from the spatial location parameters at stations at which *S* is observed, and a least-squares iteration procedure is applied to only the three spatial parameters.

Figures 59 and 60 show vertical distributions of shallow (<100 km) earthquakes located by the Arequipa net. For comparison, Fig. 61 is a vertical seismicity cross section for the same geographical area as in Fig. 60, but using earthquake hypocenters located



Fig. 58. Location map of seismograph stations used in this study. The stations in the Arequipa net are CUS, PUN, CRV, ONG, SHP, ATI, SGP, AYE, and ARE. Also used, but not shown, were ANT (Antofagasta, Chile) and LPB (La Paz, Bolivia).

by USCGS/NOAA for the period 1964–1974.

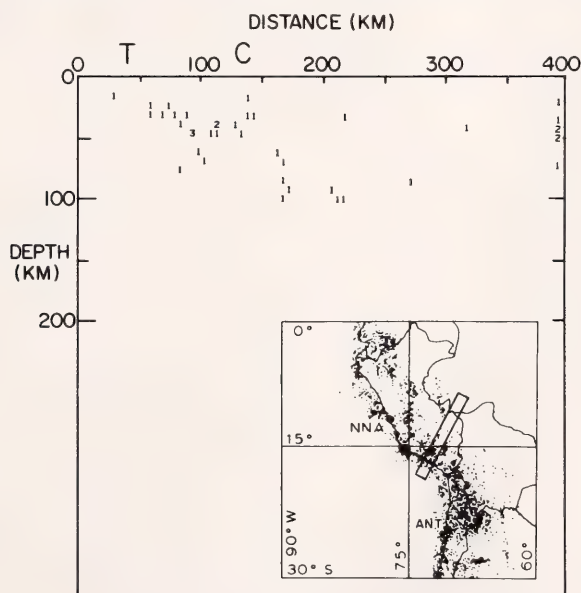
In addition, bathymetric data (Getts, 1975), as shown in Fig. 61, indicate a curvature in the ocean floor on both sides of the trench.

The Aseismic Wedge

The seismicity cross sections in Figs. 59 and 60 indicate that between the trench and the west there is an aseismic wedge of about 80 km in lateral extent and about 50 km in maximum depth. This feature can also be seen on the cross section using USCGS/NOAA locations (Fig. 61), but because of the smaller data set and less reliable locations one could not propose the existence of this wedge on the basis of the USCGS/NOAA data alone.

A model that is consistent with the observations is illustrated in Fig. 63. It is proposed that the hatched area labeled "low stress zone" in Fig. 63C corresponds to the aseismic wedge. The relative plate motion leads to drag at

the upper boundary of the downgoing plate and compressive stress in the oceanic and continental plates far from the subduction (Fig. 63a). (The compressive stresses in these regions are consistent with the focal mechanisms found by Stauder, 1975; Mendiguren, 1966). Counteracting the compression near the subduction zone is tension caused by the downwarping of the continental lithosphere due to the drag of subduction (Fig. 63b). The curvature of the interacting plates at the trench can be seen from the bathymetry (Fig. 62). The tension can be explained by beam-bending theory (e.g., Sokolnikoff, 1956), according to which, near the upper surface of a (convexly) bent plate there is a tension inversely proportional to the radius of curvature. A superposition of the stresses indicated in Figs. 63a, 63b results in a low-stress zone (hatched regions in Fig. 63c). Earthquakes occur in regions of high or rapidly varying stress, so that the lower-stress zones in Fig. 63c are also seismically quiet regions. That this is a



USCGS/NOAA 1964–1974

Fig. 61. Vertical cross section of the seismicity down to 100 km as located by USCGS/NOAA from 1964 to 1974. The events are for the same area as Fig. 60. Even though the data are for a period eleven times as long as the Arequipa net data, there are only one-fourth the number of events.

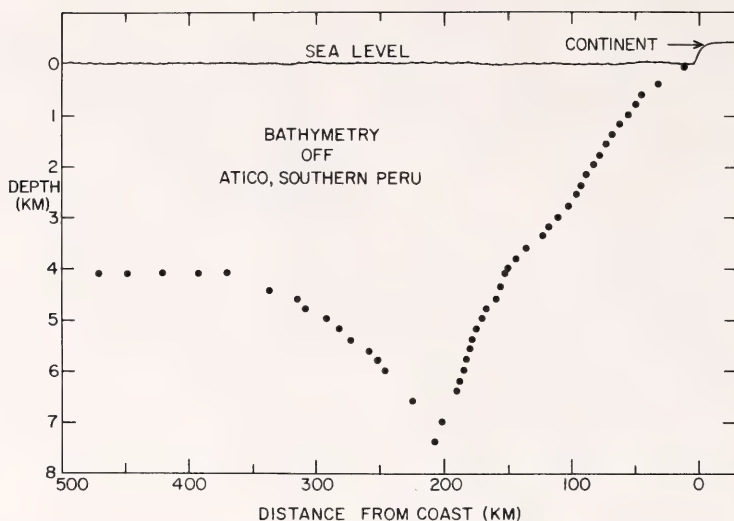


Fig. 62. The bathymetry off Atico, southern Peru. The vertical scale is 50 times the horizontal scale. The curvature of both the oceanic plate (left of trench) and the continental plate is apparent.

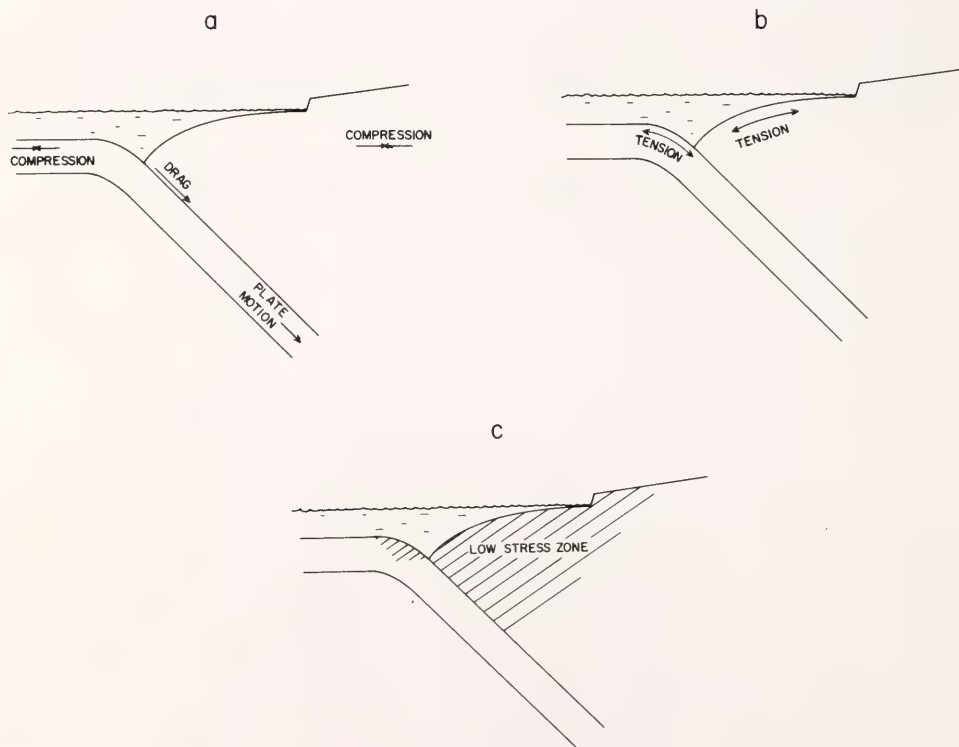


Fig. 63. Our model for explaining the aseismic wedge. (a) Stresses due to relative plate motion inferred from fault-plane solutions and frictional drag. (b) Tension due to downwarping of the plates at the trench due to the drag of subduction. (c) The superpositions of the stresses from a and b result in low-stress (hatched) regions as shown.

global phenomenon can be seen from high-precision seismicity studies such as were made in the Aleutians (Engdahl and Sleep, 1976), which also show a shallow aseismic wedge.

Shallow earthquakes are therefore not expected between the trench and a region fairly well inland. In most subduction regions, the coast (*C* in Figs. 59, 60) is earthquake free.

Acknowledgments

This research was supported in part by National Science Foundation Grant No. DES 72-01295A02.

References

- Engdahl, R. E., and N. H. Sleep, Seismicity and stress beneath the central Aleutian Arc, *Trans. Am. Geophys. Union*, 57, 329, 1976.
- Getts, T., Preliminary contour map, Hawaii Institute of Geophysics, unpublished, 1975.
- James, D. E., I. S. Sacks, E. Lazo, L. and P. Aparicio G., On locating earthquakes using small networks, *Bull. Seis. Soc. Am.*, 59, 1201-1212, 1969.
- Mendiguren, J. A., Focal mechanism and pressure axis direction in Central America and South America, *IJSEE Bull.*, 3, 1-20, 1966.
- Sokolnikoff, I. S., *Mathematical Theory of Elasticity*, McGraw-Hill, New York, 1956.
- Stauder, W., Subduction of the Nazca Plate under Peru as evidenced by focal mechanisms and by seismicity, *J. Geophys. Res.*, 80, 1053-1064, 1975.

A MODEL FOR Laterally HETEROGENEOUS VELOCITY STRUCTURE AT THE BASE OF THE MANTLE

J. A. Snoke and I. S. Sacks

Introduction

Sacks and Beach (1974) showed that the core phase *PKPAB* (Fig. 64), which has near-grazing incidence at the mantle-core boundary, has an

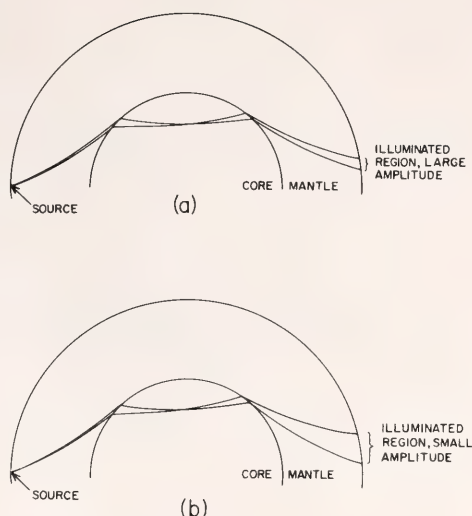


Fig. 64. Ray paths for the phase *PKPAB* leading to large-amplitude (a) and small-amplitude (b) arrivals due to scattering in the lower mantle near the core-departure crossing.

amplitude anomaly that correlates with the regions of the core-mantle boundary crossings. Regions of high and normal transmission were identified, and a correlation was found between these regions and the isostatic anomalies in the earth's gravity field as determined from satellite orbits. We have used a ray-theory approach to model regions at the base of the mantle to determine the characteristics of the velocity structure that gives rise to large-amplitude *PKPAB* arrivals.

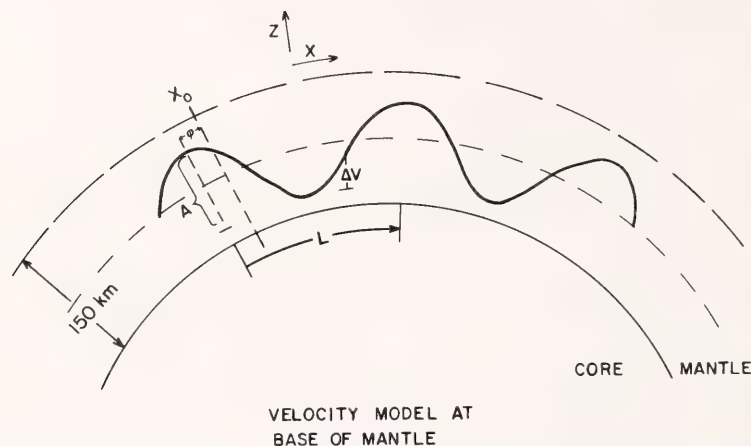
It was suggested by Sacks and Beach that there are two types of regions at the base of the mantle: regions with small convection cells (*A* in Fig. 65) and regions that are involved in large-scale (whole mantle) convection (*B* in Fig. 65). In this report we describe, for the *A*-type region, a velocity-structure model that leads to results consistent with the observed amplitude anomalies.

The Model

Figure 66 shows the velocity-structure model used for the bottom 150 km of the mantle at either the core-entry or core-departure region for



Fig. 65. Models for the lowermost mantle. (A) Nonconvecting whole mantle. If the whole mantle does not convect, the lower viscosity region (Sacks, 1972) at its base probably will, the convection cell being bounded at the top by static material with a higher viscosity. (B) Whole-mantle convection (or plumes).



$$V(x, z) = V_0(z) \left\{ 1 + \frac{A}{2} \left[1 + \cos \left(2\pi \frac{x - x_0}{L} + \phi \right) \right] \right\}$$

Fig. 66. The velocity model for the lowest 150 km of the mantle used in this study. x_0 is fixed relative to the source. The minimum velocity at a given depth z is $V_0(z)$, and the maximum is $V_0(z)(1+A)$.

the core phase *PKPAB*, the phase that has the amplitude anomaly when it crosses a type-A region. Figure 67 is a comparison of our model and the structure inferred by the small-scale convection cells.

Our model superimposes a cosine lateral (x) variation on a normal velocity-depth model (the B 1 model developed by Jordan and Anderson, 1974). In our model the lateral variation is independent of depth in the lowermost 150 km of the mantle. The parameter x_0 is kept fixed relative to the source, so there are three variables in the model (Fig. 66): A is the maximum deviation of the velocity from the nor-

mal value at a given depth (all deviations are positive); L , the "wavelength" of the cosine, is a measure of the lateral extent of a cell; and ϕ , the "phase" of the cosine, gives the lateral position of the cells relative to the source. Only two-dimensional structure was considered, and only great-circle paths were calculated directly. The simulation of the third dimension is discussed below.

For each model run A , L , and ϕ were fixed for either a core-entry or core-departure crossing. Then ray paths were calculated to include all *PKPAB* arrivals with epicentral distances greater than 158° . Relative amplitudes were calculated by comparing the

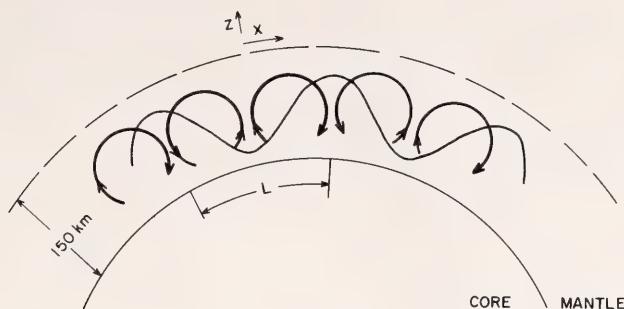


Fig. 67. Comparison of our velocity model and the convection cells it is intended to simulate. The velocity variations in the model are independent of the depth.

change in epicentral distance for a given change in departure angle from the source (Fig. 64). The two-dimensional ray-tracing routine is based on a method developed by Jacob (1970).

In a laterally homogeneous medium, the ray parameter $p = dT/d\Delta$ is constant along a ray path, where T is the travel time and Δ the epicentral distance between any two points along the ray path. Lateral heterogeneities result in variations in p . Rays traveling to a single point at the earth's surface can come from a region at the base of the mantle of extent d , which can be determined if the variation in p is known. We simulate off-great-circle paths by which a ray travels from earthquake to seismograph by assuming that the deviations off the great circle are similar to those along it—that is, by superimposing, with a suitable weighting, runs of a range in ϕ of $\delta\phi = 360d/L$.

The lateral position of the cells relative to the source is probably not determinable, so we average over ϕ . Hence our model is not strictly deterministic, and the comparison with data must be on a probabilistic or statistical basis.

The observed AB amplitudes are defined relative to the $PKBDF$ amplitude for the same earthquake-seismograph pair (Fig. 68). The DF branch has approximately normal incidence at both

core-mantle crossings, which makes it far less sensitive than the near-grazing AB rays to any lateral velocity structure at the base of the mantle. Our criterion for large AB amplitude is that it be 1.5 times the size of the corresponding DF amplitude. Our comparison with the data will be on the basis of the percentage of large amplitudes and the ability of the model to predict the observed frequency dependence of the amplitude anomaly.

Results

For each run, the lateral heterogeneities cause multiple arrivals at most epicentral distances (Fig. 69). Sufficiently small steps in departure angle were taken to ensure that no aliasing occurred. The difference in arrival times of the multiple arrivals is small enough (<0.2 s for a 1.5% heterogeneity model) that, for periods considered, the arrivals can be added coherently. We considered models with $L = 40$ km, 150 km, and 600 km; and $A = 0.008$, 0.015, and 0.03. The analysis will be described in detail for the model we found to be most successful: $A = 0.015$ and $L = 150$ km. (The rejected models and the criteria for their rejection will be discussed later.) So far we have analyzed in detail applications of the model to only the core-departure region.

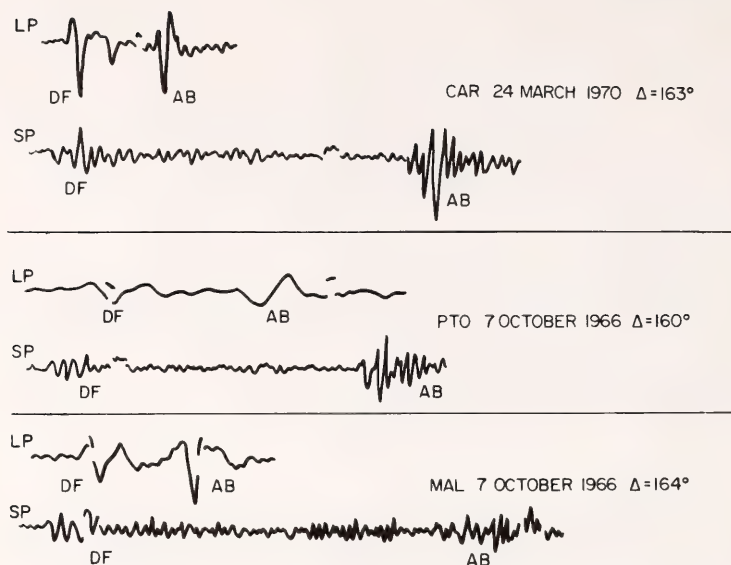


Fig. 68. Tracings of *PKPAB* and *PPBDF* arrivals from long-period and short-period seismograms illustrating the possible frequency dependences for large *AB*-amplitude anomalies. For the top pair the *AB* amplitude is large on only the short-period record; for the middle pair it is large on both, and for the bottom it is large on only the long-period record. For an explanation in the context of our model, see text and Fig. 74.

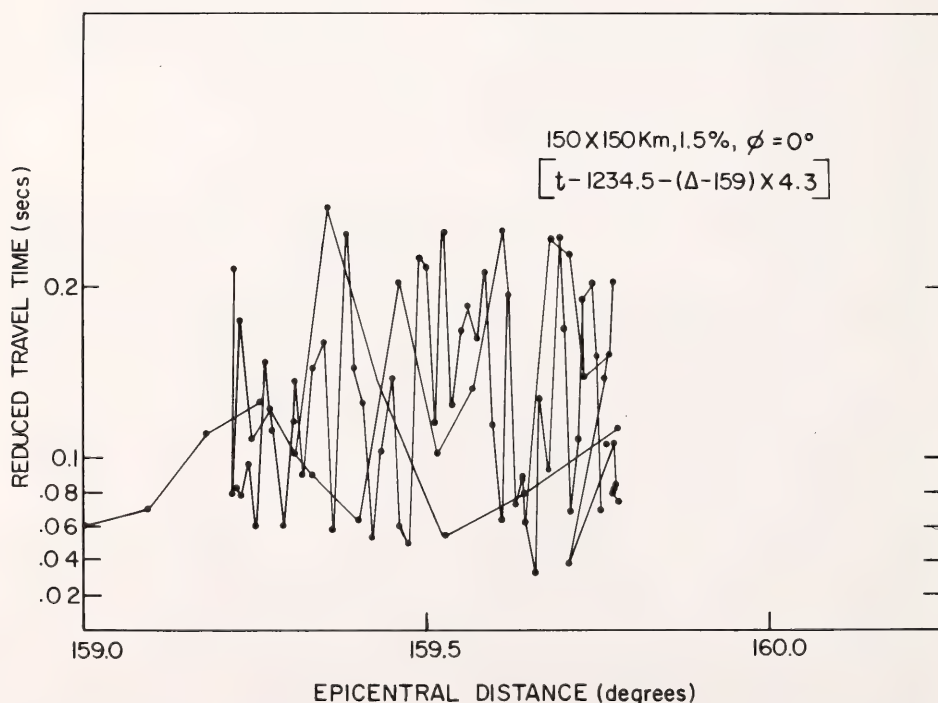


Fig. 69. Plot of part of the travel-time curve for a model run with $L = 150$ km, $A = 0.015$, and $\phi = 0^\circ$. The circles are model-derived points, and the lines connecting the circles indicate the continuous variation in the input ray parameter $p = dT/d\Delta$. Note that the scatter in arrival time is < 0.2 sec.

Figure 70 contains a summary of the model data. Plotted are the large-amplitude regions at epicentral distances for ϕ ranging from 0° to 330° in 30° steps. For each run (a fixed ϕ) one sees there are brightly illuminated regions as well as small-amplitude regions, as is required by energy conservation. Some of those bright regions are less than 0.1° ; others are as large as a half degree. For different ϕ s the patterns are similar, but the position of the bright regions shifts. For these runs the standard deviation in the change in the ray parameter p was 0.04 s/degree, which implies a source region at the base of the mantle of extent $d \approx 200$ km. Following our technique for simulating off-great-circle paths, this results in a range in ϕ to be superimposed of $\pm 240^\circ$. The resulting model probability for large amplitudes is 34% , and this result is insensitive to the central value of ϕ .

In the data analysis, event-seismograph pairs were selected so that the data set included a large area at the core-entry crossing for the rays for a given core-departure region (Fig. 71). The data therefore include rays

with traversal regions of both type A and type B on the core-entry side. Assuming that the model results for the core-entry side will be similar to our results for the core-departure side and that the two types of regions have approximately equal probability, we get an additional 11% in expected large-amplitude arrivals and thus an overall expectation of 45% . The observed large-amplitude-arrival probability for type A regions is 48% (Fig. 72).

A model with $L = 600$ km and $A = 0.015$ led to a 7% probability of large amplitude arrivals, and a model with $L = 40$ km and $A = 0.015$ led to a probability approximately the same as the model with $L = 150$ km and $A = 0.015$. The probability for $L = 600$ km can be increased by increasing A , but in order to get results comparable with the other model, A must be large enough to cause measurable shifts in the travel times, which are not observed. Hence we reject $L = 600$ km.

The other two models give different predictions for the size of the illuminated (large-amplitude) regions on the earth's surface (Fig. 73). The $L = 150$ km model is capable of explaining the

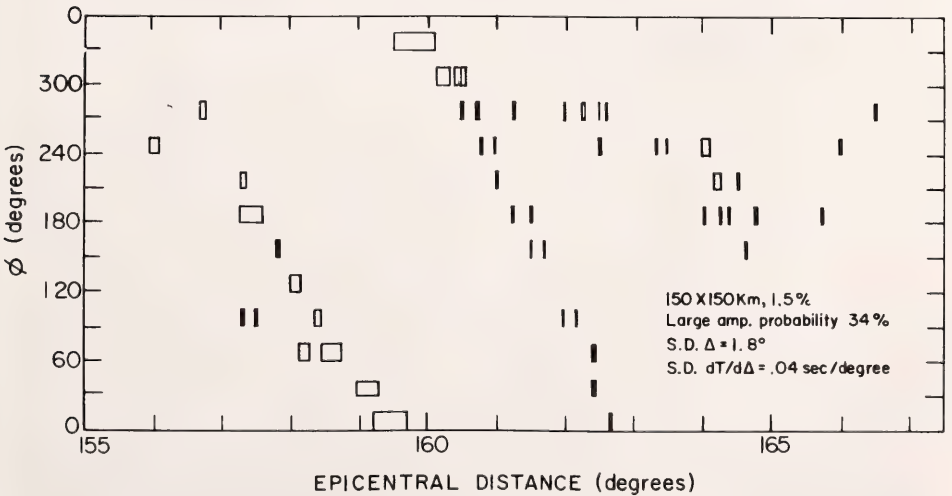


Fig. 70. Results of model runs for $A = 0.015$ and $L = 150$ km and different values of ϕ . Large-amplitude arrival regions on the earth's surface are indicated by rectangles. Regions smaller than 0.1° are filled rectangles. See the text for the method of determining the large-amplitude-arrival probability.

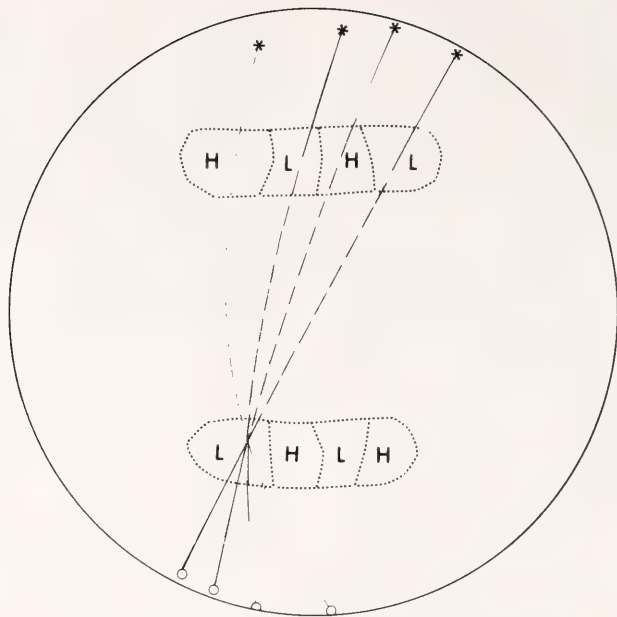


Fig. 71. Technique used to resolve the ambiguity of the two core crossings. The dotted lines indicate areas at the base of the mantle whose transmission properties are being investigated. *L* indicates low-amplitude transmission, and *H* indicates high amplitudes. Circles are seismographs; asterisks, earthquakes; full lines show mantle paths; and broken lines, paths in the core. The average amplitude for the *L* region sampled is $(LL + LH + LL + LH)/4$. If the adjacent *H* region was sampled, the average would be $(HL + HH + HL + HH)/4$, which is clearly larger.

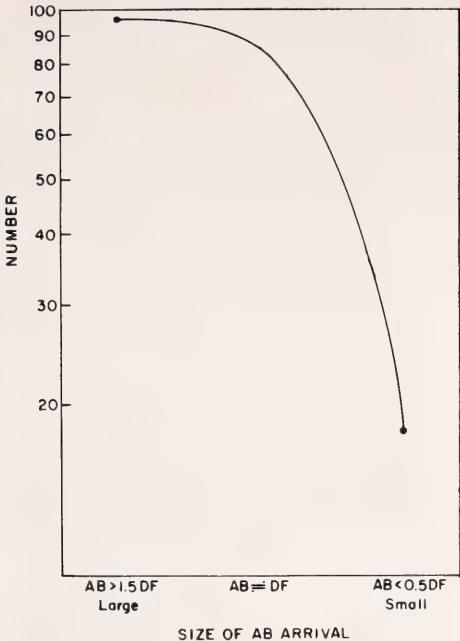
different types of observations (Fig. 68; see also Fig. 74): (1) where the amplitude of the *AB* is large on the short-period but not on the long-period seismograms (because the extent of the illuminated region is small compared to the wavelengths for which the long-period seismometer is sensitive), and (2) where the amplitude is large on both short-period and long-period instruments (because the extent of the illuminated region is above the threshold for the long-period seismometer). For the $L = 40$ km model there are no illuminated regions larger than 0.1° in length (Fig. 73). We can therefore rule out the $L = 40$ km model because it cannot explain the observations for which the *AB* arrivals are large on both long-period and short-period seismograms (e.g., Fig. 68).

Model runs for the *PKPDF* branch using the same parameterization as for

the *PKPAB* branch produced results that were essentially the same as for the laterally homogeneous ($A = 0$) case.

Concluding Remarks

We have shown, therefore, that in some regions at the base of the mantle cells of $150 \text{ km} \times 150 \text{ km}$ with a maximum lateral velocity variation of 1.5% can explain the observed amplitude anomaly of *PKPAB* arrivals. The possibility of convection occurring is proportional to the cube of the cell size, so it is encouraging for the convection model that smaller cells are not required to fit the seismic data. The limits on the cell size and velocity variations obtained from this study impose constraints that will be invaluable in studies of convection and heat flow at the core-mantle boundary.



Acknowledgments

This research was supported in part by National Science Foundation Grant No. DES 72-01295A02.

References

Jacob, K. H., Three-dimensional seismic ray tracing in a laterally heterogeneous spherical earth, *J. Geophys. Res.*, 75, 6675-6689, 1970.
Jordan, T. H. and D. L. Anderson, Earth structure from free oscillations and travel times, *Geophys. J. R. Astron. Soc.*, 36, 411-459, 1974.
Sacks, I. S., Viscosity and *Q*, *Carnegie Inst. Wash. Year Book* 71, pp. 227-229, 1972.
Sacks, I. S. and L. Beach, Lateral heterogeneity at the base of the mantle—an indication of whole mantle convection, *Carnegie Inst. Wash. Year Book* 73, pp. 1020-1032, 1974.

Fig. 72. Number versus size of the PKBAB amplitude arrival for a type-A (small-scale convection) region for the core-departure crossing of the PKPAB rays. The percentage of large arrivals is 48.

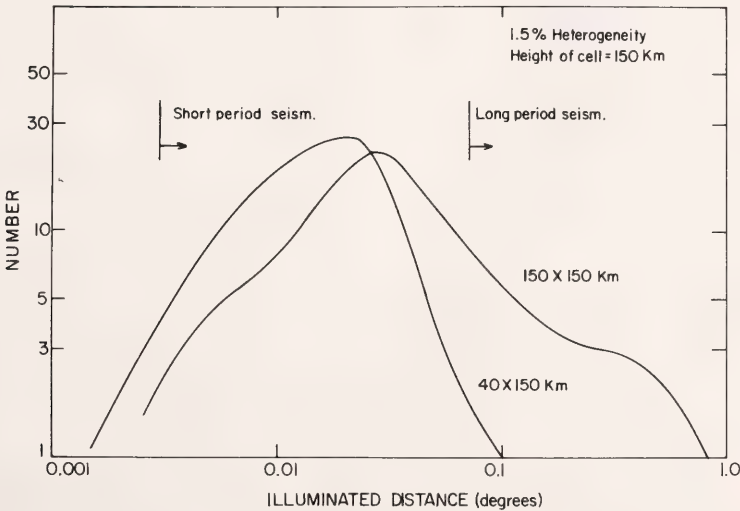


Fig. 73. Number versus size of the illuminated (large-amplitude) region on the earth's surface for $L = 150$ km and $L = 40$ km. Also shown are the lower limits of the sensitivity of the WWSSN long-period and short-period seismometers for an arrival to be recorded as large. The fact that there are observed large amplitudes on long-period seismograms rules out $L = 40$ km.

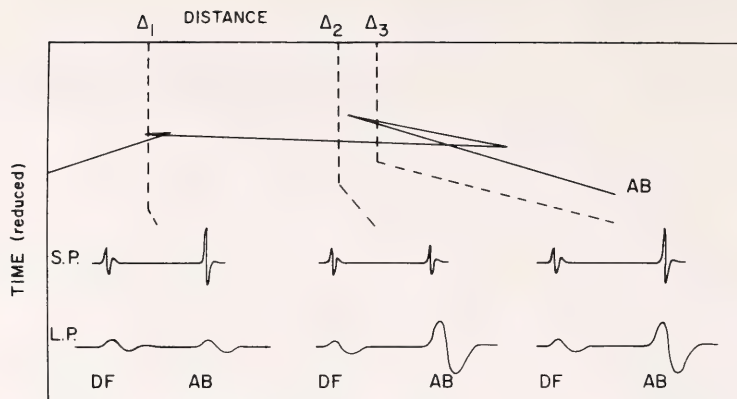


Fig. 74. Explanation for the observed frequency dependence of the large AB amplitudes (see Fig. 68 for examples). A large amplitude on only short-period records (Δ_1) occurs for a triplication over an epicentral distance range of less than 0.1° . A large amplitude on only the long-period record (Δ_2) results from diffractive scattering from the caustic. Such arrivals were not considered in this study. Large amplitudes on both short-period and long-period records (Δ_3) result from a triplication over an epicentral distance range greater than 0.1° in extent.

SINGLE SITE PHASE VELOCITY DETERMINATIONS

I. S. Sacks, J. A. Snoke, J. R. Evans, G. C. P. King, and R. J. Beavan**

The lithosphere beneath oceans is generally less than 120 km thick. Evidence is mounting that beneath large, old continental areas, such as South America, the lithosphere is very much thicker. Anelasticity studies by Sacks and Okada (*Year Book* 72, pp. 226–233) and the interpretation of converted *sp* phases (Sacks and Snoke, this *Year Book*) indicate that the lithosphere beneath South America must be about 400 km thick and that it overlies asthenosphere which has much higher absorption (lower *Q*).

A method to determine subcrustal velocity structure utilizes surface-wave phase velocities (see Fig. 75). Phase velocities are traditionally obtained by using sets of widely spaced seismometers which record simultaneously. The velocity determination follows then from measurements of the travel times of different frequencies over known distances. For low-frequency (long-

wavelength) waves, the separation of the instruments must be large to permit satisfactory resolution, and even at shorter wave lengths, large spacing is an advantage as it prevents velocity estimates being contaminated by multipathing resulting from lateral refraction and diffraction. The best results for phase velocity using these methods are obtained only when two or more stations lie close to a greater circle including the seismic epicenter (Brune and Dorman, 1963).

The lithosphere asthenosphere boundary is characterized by a velocity reversal and beneath large, old continents this boundary may be as deep as 400 km (see Sacks and Snoke, this *Year Book*). Because of the long-period limitations in the determination of phase velocities by the technique described above, Alexander (1972) was able to show only that there is no velocity reversal under the shield area in South America above 200 km.

We describe a method whereby it is, in principle, possible to determine the phase velocity of any seismic wave from the simultaneous measurement of the wave amplitude (or its time derivative) and its spatial derivative (strain or tilt) at the same site. Mikumo and

*Department of Geodesy and Geophysics, Cambridge University, Cambridge, England.

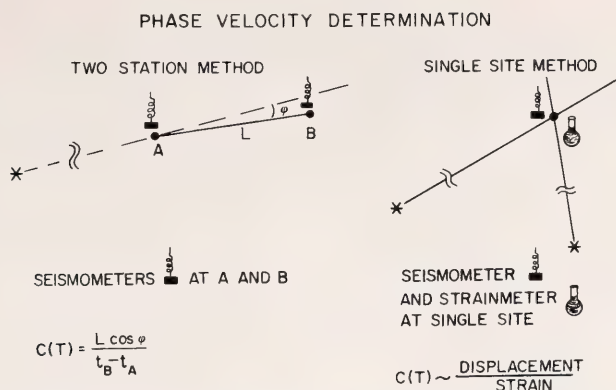


Fig. 75. Sketch illustrating the two methods for determining the phase velocity: the single-site method discussed in this report and the traditional two-site method. T , the period, $= 2\pi/\omega$.

Aki (1964) have previously used this technique for the combined analysis of records from a *horizontal* seismometer and a horizontal strainmeter at a single station. For the five earthquakes studied they found good agreement between measured and predicted phase velocities for body waves and in some cases for surface waves.

Rodgers (1968) has shown that for long periods (>100 s) horizontal acceleration and tilt cannot easily be separated instrumentally, and recent work by King *et al.* (1976) indicates that near-station crustal inhomogeneity may give rise to strain-strain and strain-tilt interactions. Thus, records from long-period horizontal strainmeters are heavily contaminated by tilt and strain. Records written by vertical seismometers do not suffer this defect. We rederived (Sacks *et al.*, 1976) the principle of single-site velocity determination, taking into account the strain-coupling effects noted by King *et al.* and using vertical acceleration. Our discussion is presented for Rayleigh waves and assumes that the ellipticity of particle motion at the surface is independent of frequency. (The validity of this assumption may be tested if there is a site-calibrated horizontal seismometer at the same site.)

In this report we present and discuss a method for phase velocity determination employing a vertical seismometer

and a volume strainmeter. The derivation for this case and for the more general case of a vertical seismometer and a linear strainmeter are to be found in Sacks *et al.* (1976).

From Sacks *et al.* (1976) the phase velocity c as a function of angular frequency, ω , can be written

$$\tilde{c}(\omega) = Y\tilde{W}(\omega)/\omega, \quad (1)$$

where Y is a constant (assuming the ellipticity to be independent of frequency) and

$$\tilde{W}(\omega) = \tilde{u}_3(\omega)/\tilde{D}(\omega), \quad (2)$$

where \tilde{u}_3 is the vertical displacement and \tilde{D} the dilatation. The \sim indicates that the quantity is averaged over areas of extent large compared to the size of the local heterogeneities but less than or equal to the wavelengths of interest. If the region were uniformly layered, $u_3 = \tilde{u}_3$ and $\tilde{D} = D$ so that \tilde{W} from Equation 2 would be given in measured quantities. However, if there are local heterogeneities, King *et al.* (1976) have shown that, to a good approximation

$$u_3(\omega) = \tilde{u}_3(\omega) \quad (3)$$

and

$$D(\theta, \omega) = A(\theta)\tilde{D}(\omega), \quad (4)$$

where θ is the back-azimuth of the Rayleigh wave. Hence from Equations 2-4, Equation 1 can be rewritten in terms of the measured quantities u_3 and D :

$$\tilde{c}(\omega) = YA(\theta)W(\theta, \omega)/\omega, \quad (5)$$

where

$$W(\theta, \omega) = u_3(\omega)/D(\theta, \omega). \quad (6)$$

There is therefore an azimuthally dependent factor $A(\theta)$ in the expression for the phase velocity due to the presence of local heterogeneities. Figure 76 is a sketch of $\log_{10}\tilde{c}(\omega)$ vs. ω for different azimuths based on Equations 5

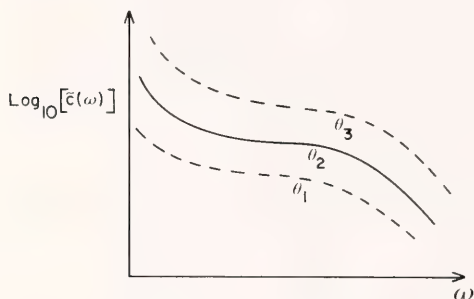


Fig. 76. Sketch to show the expected relationship of $\log_{10}[\tilde{c}(\omega)]$ versus ω for Rayleigh waves arriving from three different directions θ_1 , θ_2 , and θ_3 . The curves are shifted vertically relative to each other by the presence of local heterogeneities, but their shape remains unchanged.

and 6. If the region is uniformly layered the curves for different azimuths should superimpose. The presence of local heterogeneities, on the other hand, would result in the curves being displaced from one another. Hence determining the phase velocity for Rayleigh waves from a number of different azimuths allows an estimate of the local heterogeneity. (An alternative technique for determining the site effects using tidal observations was described by King *et al.*, 1976.)

The shape of the curves in Fig. 76 is independent of $A(\theta)$. By normalizing these curves at some frequency and averaging over determinations for a number of different azimuths, it should

be possible to reduce the effects of signal-generated noise in the determination of the spectral shape of the phase velocity. If $c(\omega)$ can be determined at any frequency ω_0 by other methods (such as from crustal refraction), Equation 5 can be rewritten as

$$\tilde{c}(\omega) = \tilde{c}(\omega_0)W(\theta, \omega)/W(\theta, \omega_0) \quad (7)$$

Hence the phase velocity can be determined for all frequencies without knowing the ellipticity or $A(\theta)$.

Single-site phase velocity determinations have two main advantages: There is no inherent limitation in the maximum period such as is caused by finite station spacing using the traditional techniques; and phase velocities can be averaged for any azimuth, which will increase the precision of the velocity determinations, particularly at longer periods. This technique will be particularly useful in studies of the structure of continental lithospheres with thicknesses up to 400 km.

The implementation of this technique requires seismometers (accelerometers) and strainmeters with high sensitivity at long (>400 s) periods. Suitable strainmeters have already been developed at the Department of Terrestrial Magnetism (see *Year Book* 68, pp. 448-452; *Year Book* 69, pp. 426-430; *Year Book* 70, pp. 336-340; *Year Book* 71, pp. 321-325; *Year Book* 72, p. 326; *Year Book* 73, 1058-1060; *Year Book* 74, pp. 287-291). A suitable seismometer is being developed.

Acknowledgments

This research was supported in part by National Science Foundation Grant No. DES 72-01295A02.

References

- Alexander, S. S., Crust-mantle structure of shields and their role in global tectonics, *EOS. Trans. Am. Geophys. Union*, 53, 1043, 1972.

- Brune, J. N., and J. Dorman, Seismic waves and earth structure in the Canadian Shield, *Bull. Seis. Soc. Am.*, 53 (1), 167–209, 1963.
- King, G. C. P., W. Zurn, R. Evans, and D. Emter, Site correction for long-period seismometers, tiltmeters, and strainmeters, *Geophys. J. Roy. Astron. Soc.*, 44, 405–411, 1976.
- Mikumo, T., and K. Aki, Determination of local phase velocity by intercomparison of seismograms from strain and pendulum instruments, *J. Geophys. Res.*, 69, 721–731, 1964.
- Rodgers, P. W., The response of the horizontal pendulum seismometer to Rayleigh and Love waves, tilt and free oscillations of the earth, *Bull. Seis. Soc. Am.*, 58, 1364–1406, 1968.
- Sacks, I. S., R. Evans, G. King, J. Beavan, and J. A. Snoke, Single site phase velocity measurement, to appear in *Geophys. J. Roy. Astron. Soc.*, 1976.

MAXIMUM ENTROPY SPECTRAL ANALYSIS

C. Seber, D. E. James,
J. A. Snoke, and A. T. Linde

Introduction

Spectral analysis of seismic waves is used to investigate a wide range of problems in seismology. This is because a great deal of information contained in a seismogram is not readily observable in the time domain but can be observed in the frequency domain. Frequency domain information for both body waves and surface waves had been used by us previously to study earthquake mechanisms and earth structure (*Year Book 69*, pp. 447–464, and *Year Book 70*, pp. 343–344). For body waves generated by earthquakes, we calculated spectral amplitudes as functions of frequency to investigate the nature of rupture processes in the earth (e.g., fault length, speed of rupture propagation along the fault, fault offset); for dispersed surface waves, period was plotted vs. time to obtain dispersion curves that yielded information on the velocity structure of the

earth's crust and the upper mantle beneath the central Andes.

In nearly all previous work, both by us and by others, frequency domain information was obtained by Fourier analysis. The advantages of the Fourier technique are many, including the fact that it is completely understood theoretically and has a fast computer algorithm. Because of these obvious advantages, most workers have been content to ignore, or at least tolerate, the manifest disadvantages of the technique, notably that it gives poor resolution of spectral peaks, especially at long periods, and that it makes arbitrary and predetermined assumptions about the behavior of the signal outside the interval in which it is being analyzed. To understand these limitations better, we must first recognize that any block of data is by necessity only a finite subset of an infinite data set. Therefore, any scheme of spectral analysis necessarily results only in a "spectral estimate." To keep the error of this spectral estimate within tolerable limits using Fourier analysis, it is usually necessary that the length of data be many times longer than the greatest period of interest. Even when this is possible, however—and it commonly is not—Fourier analysis often cannot yield satisfactory results because it assumes that the signal outside the data block is either zero or a periodic duplication of the data within the block to be analyzed. These inherent weaknesses in Fourier techniques led Burg and others in the late 1960s to discard such convenient devices and to seek a more flexible approach to spectral analysis. (For a more complete and particularly lucid summary of the rationale for discarding Fourier techniques and applying the maximum entropy methods instead, see McGee 1969.)

Maximum entropy spectral analysis as formulated by Burg (1967, 1968) results from applying entropy considerations to spectral determinations so that information is carried from the time domain (e.g., seismogram) to the

frequency domain with a minimum of distortion. The method is particularly powerful in that it avoids the Fourier assumptions about the nature of the signal outside the analyzed region; instead, no a priori assumption is made, and an estimate of the signal outside the known interval is based only upon information (entropy) extracted from the data themselves. (Entropy is used in the sense of statistical entropy as defined by Shannon and Weaver [1949] and may be considered to be equivalent to information. Since we wish the spectral estimate to exhibit as much information as is fully consistent with the data and no more, we state that [McGee, 1969]: "The most reasonable spectral estimate for any set of data is that estimate which exhibits maximum entropy and yet fully agrees with the available data."). The maximum entropy method (MEM) has been shown to give improved spectral resolution compared to Fourier analysis (FA) for many kinds of signals.

The theoretical basis for MEM is given by Burg (1967, 1968), McGee (1969), Claerbout (1976), Seber (1976), and many others. A recent review of the technique is given by Ulrych and Bishop (1975), who also evaluate the optimum filter length criterion of Akaike (1969, 1970). Our computational methods are based on algorithms given by Ulrych and Bishop.

Most previously published work on MEM has involved simple synthetic signals such as sine waves or superimposed sine waves with various amounts of added random noise. Results from these studies have shown that: (1) MEM produces highly peaked spectra compared to FA for short record segments (one half to two cycles) of continuous sine waves, giving frequencies that are correct to within a few percent. The addition of noise to the signals does not significantly degrade the result. The largest single effect on calculated frequency appears to be the starting phase of the input signal (Chen and

Stegen, 1974). (2) For superimposed sinusoids of different frequencies, MEM resolves the frequencies far better than FA (Fig. 77). If the sinusoids have equal amplitude, the power spectra should have equal areas under the curves. MEM appears to err in this regard by as much as a factor of 2. The theoretical reason for this is not known, and as a consequence amplitude instability has been a major reason MEM has not been more widely used for spectral analysis. We note, however, that FA produces even greater errors for these simple signals.

It is the purpose of this study to test MEM on synthetic seismic signals to evaluate the applicability of the method to problems in seismology. We have analyzed both body waves and dispersed surface waves and obtained results that show sufficient promise to warrant further investigation.

Synthetic Seismic Signals

Body waves. Difficulties in the Fourier frequency analysis of body waves often arise because the signal of interest may be affected by either earlier or later arriving phases. The problem is to determine the spectral content of the complete signal, uncontaminated by other arrivals. Because MEM works well on short pieces of information relative to Fourier techniques, it might prove a more effective tool for extracting frequency information from signals suffering interference from earlier or later arrivals. Moreover, the prediction potential of MEM might allow one to predict frequency content of the interfering signal so that it could be subtracted from the signal of interest. Another technique that might be considered (Ulrych *et al.*, 1973) is using MEM to extend the given short signal to a length where Fourier analysis can be used successfully. This seems to have been done with considerable success. Where phase information is of interest this would be especially useful, since phase

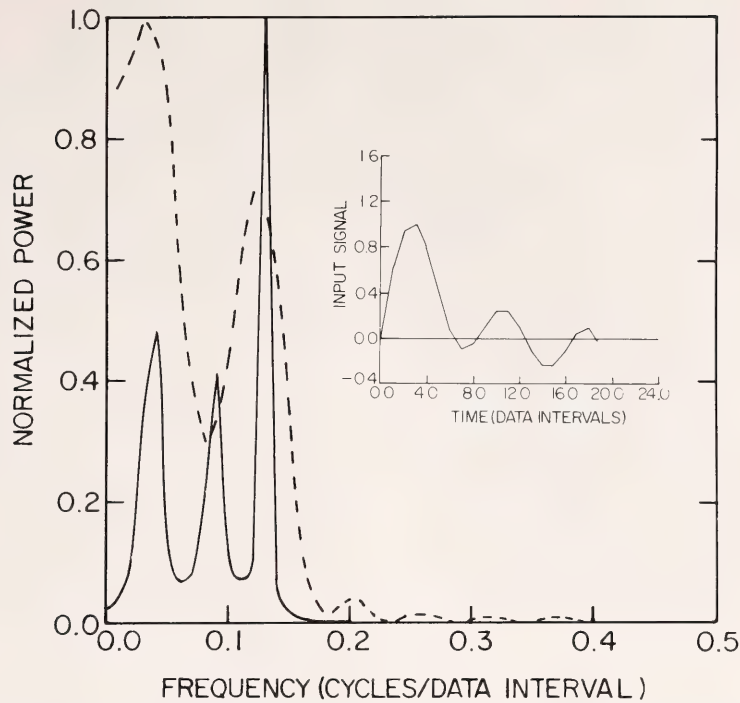


Fig. 77. Burg power spectrum and periodogram of signal shown in inset. Input signal consists of 20 points at 1-s intervals of a time series made up of three superimposed equiamplitude sine waves with frequencies of 0.04, 0.08, and 0.12 Hz. Adapted from Ulrych *et al.*, 1973.

information is available in the Fourier transform but is lost in MEM.

Simple radiated pulse. Brune (1970) gives an expression for the radiated pulse for a simple earthquake model. From many studies using real data, it has been shown that the shape of the displacement amplitude in the frequency domain for an earthquake is reasonably well approximated by Brune's empirically derived model. This model has simple analytical expressions in both the frequency and time domains and provides a straightforward comparison of the relative accuracy of FA and MEM for signals of the kind encountered in seismology.

Brune's model is defined by a function, $f(t)$, for a finite time interval such that $f(t) = te^{-t}H(t)$ where

$$H(t) = \left\{ \begin{array}{ll} 0 & t < 0 \\ 1 & t > 0 \end{array} \right\}.$$

The Fourier power spectrum is given by

$$P_b(\omega) = \frac{1}{(1 + \omega^2)^2} \{ 1 - e^{-b} [2(1 + b) \cos b\omega + 2b\omega \sin b\omega] + e^{-2b} [(1 + b)^2 + b^2\omega^2] \}$$

where b is the length of the signal in the time domain. No truncation corresponds to the limit $b \rightarrow \infty$.

Figure 78 shows a Brune's model pulse with various points of truncation. The maximum entropy spectrum agrees very closely with the theoretical spectrum (see Fig. 79). Truncating the signal on the left (reducing the number of zeros) had no significant effect on the spectrum. With just one zero value preceding the signal onset, MEM was still able to detect the discontinuity and give a good spectrum.

The effects of successive truncations on the right side of the signal are shown in Fig. 78. For a -1 to 4 second record, MEM was significantly better than Fourier analysis. A signal truncated at point 61 (see Fig. 78) gives a MEM spectrum that compares very favorably with theory. Similarly, signals from points 15 to 25 (3 s) and from points 15 to 31 (5 s) and from points 15 to 25 (3 s) also give very good spectra, although they are not as accurate at higher frequencies. The 15-21 (2 s) segment produces a spectrum that deviates significantly from the spectrum of the full signal. It was observed that the zero frequency amplitude was inversely proportional to the length of the window. This seems to indicate a high degree of amplitude stability.

The MEM results can be compared to those obtained using Fourier analysis. At a 5-s truncation, there is a strong effect on the spectrum which progres-

sively worsens with increasing severity of truncation (see Fig. 78).

We conclude that the MEM gives a very good estimate of the true spectral content even if the pulse is severely truncated. This result is encouraging and indicates that MEM may be useful in estimating the spectral content of truncated seismic signals.

Sine wave convolved with instrument response. Linde and Sacks (1971) have described the spurious spectral amplitudes in the long-period part of the spectrum that result from having to analyze long-period body-wave arrivals of essentially one cycle. Studying a sine wave convolved with instrument response, they found that increasingly severe truncations resulted in increasing emphasis of long-period amplitudes, even though the amplitude of the truncated part of the signal was small (see Fig. 79).

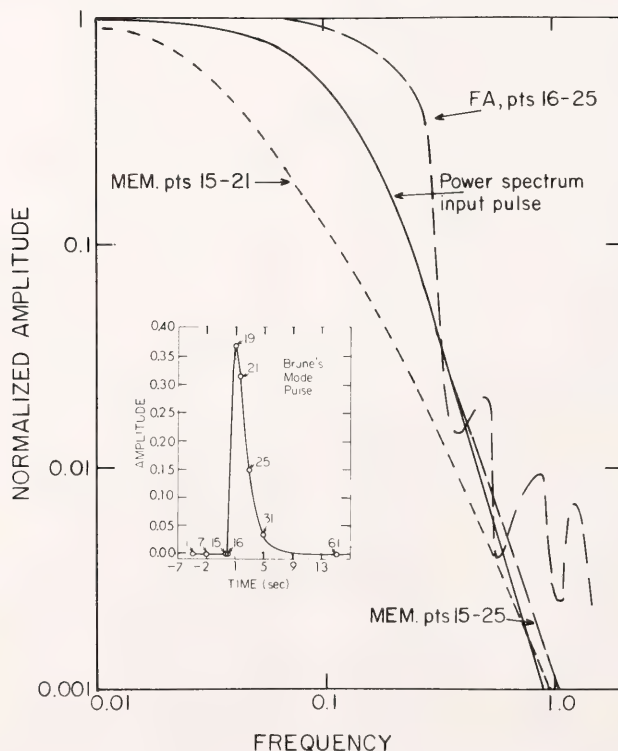


Fig. 78. Maximum entropy and Fourier power spectra of Brune's model pulse (see inset) for various truncation points indicated in inset. Point intervals over which signal has been analyzed are indicated on the figure. MEM and FA denote maximum entropy method and Fourier analysis, respectively.

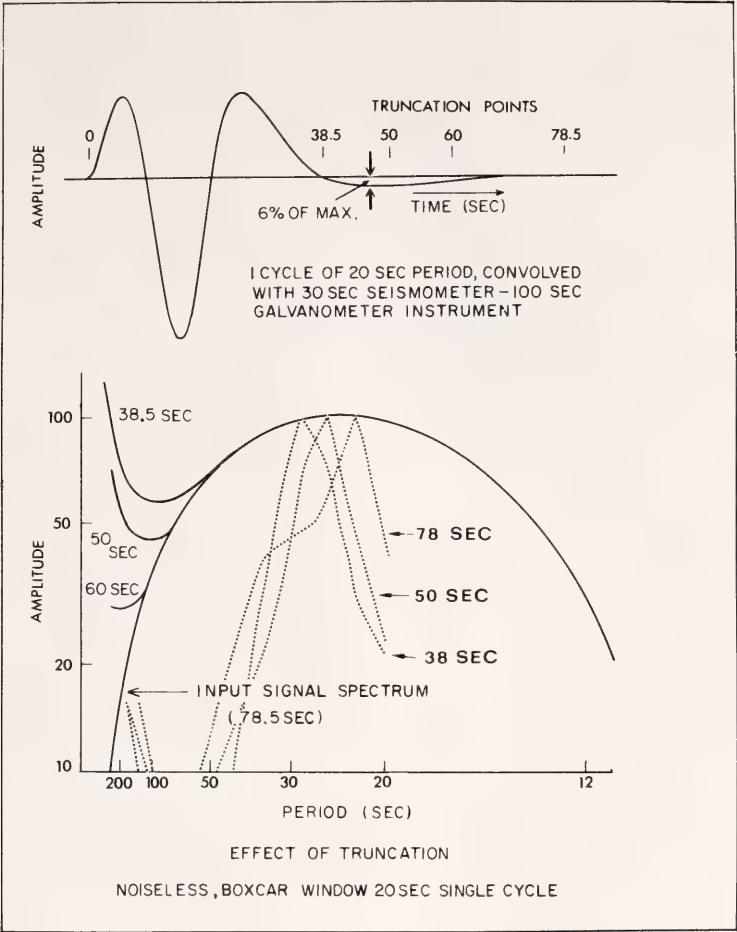


Fig. 79. Normalized maximum entropy power spectra (dashed lines) and Fourier amplitude spectra (solid lines) showing the effect of truncation in the time domain (upper figure) of a noiseless 1-cycle 20-s sine wave convolved with a 30-s seismometer, 100-s galvanometer instrument. Successive truncation at shorter and shorter times drastically affects the long-period end of the Fourier spectrum but results mostly in a shift in the peak frequency for the maximum entropy spectra. The input signal spectrum is the theoretical Fourier spectrum.

When this signal is essentially of infinite length, the area under the curve is zero (i.e., the zero frequency term will be zero) but truncation results in a positive area (i.e., positive zero-frequency term). Erroneous low-frequency amplitudes are further magnified when multiplied by the transform of the instrument response, which is large at very low frequencies. It was hoped that MEM would not produce these spurious effects for the long-period part of the spectrum. As

can be seen in Fig. 79, MEM makes a good estimate of the frequency of the convolved sine wave but does not produce zero amplitude at very long periods. Hence, multiplication by the instrument correction causes an erroneous rise in amplitude at the long-period end of the spectrum. We note, however, that the amount of spurious long-period signal is not due to truncation effects but seems to remain roughly constant regardless of the amount of truncation. We are unable to

explain these spurious amplitudes at long periods, since for single sine waves MEM has no difficulty in recognizing zero area under the curve. As a further test of MEM on more complex signals with zero spectral amplitude at zero frequency, we also analyzed a double Brune pulse. The double pulse has the property that its Fourier transform at zero frequency is zero. The function $f(t)$ is given by $f(t) = \{te^{-t} - a^2te^{at}\} H(t)$. It begins discontinuously in the time domain and dies off exponentially as $t \rightarrow \infty$. Once again MEM gives similar incorrect results in the low frequency range, tending to a nonzero amplitude plateau rather than to zero.

Surface waves. All modern analytical techniques used to obtain dispersion curves for surface waves require that some form of filtering (in either the time or the frequency domain) be applied to the record. These techniques are generally satisfactory for short periods but are incapable of high resolution at long periods. This is to say that as the period of a given wavelet increases it becomes more difficult to determine its exact "arrival time." Some of this difficulty arises from an inherent uncertainty of measuring the

time of arrival to an accuracy much greater than the time scale of a single cycle, but it seems likely that part of the problem lies with the analytical techniques. Because MEM can give vastly improved results over Fourier analysis for short segments of harmonic waves, it is appropriate to investigate whether or not it can provide better time resolution for the arrival of long periods over conventional techniques.

To test the performance of MEM on dispersed waves, we generated a synthetic signal that was linearly dispersive with a flat amplitude spectrum between 0.078 and 0.156 Hz. The spectrum was cosine-tapered over 20 Fourier harmonics outside that frequency interval. Various window lengths for MEM analysis were used, and the results are shown in Fig. 80. Over a fairly wide range of frequencies MEM gives results close to the theoretical line in the nontapered frequency range, between 0.078–0.156 Hz. The results of this analysis are encouraging, although the long period part of the spectrum still presents some problems. Further experimentation needs to be done using real data, with various window lengths.

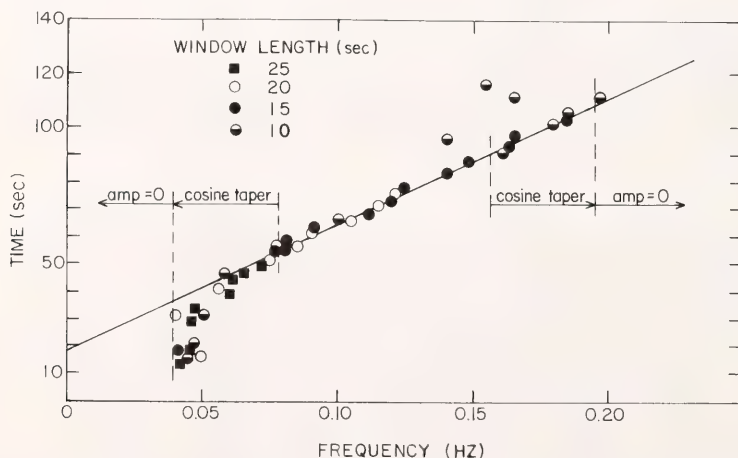


Fig. 80. Maximum entropy frequency analysis of synthetic dispersed wave train using a sliding window of varying length. Time is taken to be the center of the window. The synthetic signal is of constant amplitude over the frequency range 0.078–0.156 Hz, and its amplitude spectrum is cosine tapered to zero over the frequency range shown. Frequencies over which spectral amplitudes are zero are indicated. The solid sloping line through the points is the theoretical linear dispersion curve.

Concluding Remarks

Maximum entropy analysis of synthetic signals of geophysical interest suggests that this technique may be a powerful tool. These preliminary investigations indicate that, at least for the Brune model and the dispersed wave, MEM does not suffer from the signal truncation effects in the same manner as the Fourier transform. For the dispersed wave, MEM correctly obtains a linear dispersion curve over a fairly wide range of frequencies. The failure to find the curve at the upper and lower ends of the frequency range may be due to artificial tapering of the data. MEM does not seem to provide the desired results at the low frequency end of the spectrum of signals such as the sine wave convolved with instrument response or the double Brune pulse. It is not clear why MEM produces a nonzero plateau at the long-period end of the amplitude spectrum yet succeeds on simple sine waves and a few more complex signals such as the Brune pulse.

Acknowledgments

This research was supported in part by National Science Foundation Grant No. DES 72-01295A02.

References

- Akaike, H., Fitting autoregressive models for prediction, *Ann. Inst. Statist. Math.*, 21, 243–247, 1969.
- Akaike, H., Statistical predictor identification, *Ann. Inst. Statist. Math.*, 22, 203–217, 1970.
- Brune, J.N., Tectonic stress and the spectra of seismic shear waves from earthquakes, *J. Geophys. Res.*, 75, 4997–5009, 1970, erratum, 76, 502, 1971.
- Burg, J.P., Maximum entropy spectral analysis, paper presented at the 37th Annual International Meeting, Soc. of Explor. Geophys., Oklahoma City, Okla., Oct. 31, 1967.
- Burg, J.P., A new analysis technique for time series data, paper presented at Advanced Study Institute on Signal Processing, NATO, Enschede, Netherlands, 1968.
- Chen, W.Y., and G.R. Stegen, Experiments with maximum entropy power spectra of sinusoids, *J. Geophys. Res.*, 79, 3019–3022, 1974.
- Claerbout, J.F., *Fundamentals of Geophysical Data Processing*, McGraw-Hill, New York, 274 pp., 1976.
- Linde, Alan T. and I. Selwyn Sacks, Errors in the spectral analysis of long-period seismic body waves, *J. Geophys. Res.*, 76, 3326–3335, 1971.
- McGee, T.M., On Berg's method of spectral analysis, unpublished manuscript, Ven- ing Meinesz Laboratory, Utrecht, 1969.
- Seber, C., Maximum entropy spectral analysis with particular interest in applications to seismic waves, Unpublished LBA Thesis, Kalamazoo College, 1976.
- Shannon, C.E. and W. Weaver, *The Mathematical Theory of Communication*, University of Illinois Press, Urbana, 117 pp., 1949.
- Ulrych, Tad J., and Thomas N. Bishop, Maximum entropy spectral analysis and autoregressive decomposition, *Rev. Geophys. Space Phys.*, 13, 183–199, 1975.
- Ulrych, T.J., D. E. Smylie, O. G. Jensen, and G. K. C. Clarke, Predictive filtering and smoothing of short records by using maximum entropy, *J. Geophys. Res.*, 78, 183–200, 1973.

ATOMIC PHYSICS AND PROPERTIES OF MATERIALS

L. Brown, A. W. Hofmann, M. Magaritz, and G. H. Pepper

DIFFUSION IN SILICATE MELTS AND GLASSES

Albrecht W. Hofmann and Mordeckai Magaritz

Introduction

Our experimental work on cation diffusion in natural melts was originally

motivated by the need to know more about the length and time scales of chemical processes in a partially molten upper mantle (see Hofmann, *Year Book 73*, pp. 935–941, 1974; *Year Book 74*, pp. 183–189, 1975). For this purpose, calcium and strontium diffusion were investigated in a natural basalt

(olivine tholeiite). We have continued and expanded this work and report more complete diffusion data for strontium and data for barium and cobalt in the same basalt matrix. The results confirm that at temperatures of 1300°–1400°C, i.e., somewhat above the basalt liquidus at 1 atm. pressure, the diffusion coefficients of all divalent cations so far investigated lie in the range of 10^{-7} to 10^{-6} cm² s⁻¹.

In addition, we have started extensive diffusion studies on glass of granitic composition. This glass serves as a model for melts typical of those occurring in the earth's crust, and the results are of particular importance to the interpretation of Rb-Sr age measurements on partially molten crustal rocks, migmatites. We report results for Sr and Ba diffusion in this glass. We find that diffusive transport distances of strontium in granitic melts do not exceed a few tens of centimeters in 10^6 yr, so that the range of isotopic equilibration of Sr in migmatites is expected to be small also.

The measured diffusion coefficients for Ba and Sr in both basaltic and granitic melts (which have viscosity differences of several orders of magnitude) demonstrate that the mobility of these cations is not related in a simple way to the viscosity of the liquid as would be predicted by the Stokes-Einstein relation. Rather, ionic charge and ionic radius are shown to have a very strong effect on the mobility, especially in the lower temperature range of the obsidian measurements of 675°–890°C. Many ionic species such as Fe, Co, and Eu can be present in more than one oxidation state in the silicate melt, and the contrast in diffusivities can be used to determine the proportions, for example, of $\text{Co}^{+3}/\text{Co}^{+2}$ in the melt. The determination of oxidation state is particularly important for europium, whose partition coefficient in plagioclase melt systems depends on the relative abundance of the 2⁺ state. In this way it is advantageous to use *kinetic* measurements to determine equilibrium behavior. Because of its

importance to rare earth geochemistry, we plan to explore this prospect more fully in the future.

Diffusion in Basalt Melt

Tracer diffusion of ⁸⁵Sr and ¹³³Ba was determined by the thin-source technique explained in last year's report (Hofmann, *Year Book* 74, pp. 183–189, 1975). To overcome the effects of initial convective movement in the region of the tracer source, the charges (basalt-filled Pt tubes) were generally 2.0–2.5 cm long, and run durations were several days. The Ba-diffusion and Co-diffusion measurements were made in a new high-temperature furnace with a large (about 5-in diameter) heating chamber, MoSi₂ heating elements, and thermocouple (Pt₃₀Rh₆) controlled temperature regulation. The sectioning method was improved by using a bench micrometer capable of measuring lengths to about 1 μm.

Figure 81 shows the results of the measurements of the residual activity of ¹³³Ba after successive length reductions by grinding the basalt rod from the "hot" end. The residual activity for diffusion from a thin source into a semiinfinite medium is given by:

$$\frac{A_{\text{resid}}}{A_0} = \text{erfc } y$$

$$\text{where } y = x/2 \sqrt{Dt} \quad (1)$$

For convenience of data analysis the measured activities are converted (using Equation 1) to the dimensionless parameter y , which is then plotted as a function of length removed, x , or as a function of $x/2 \sqrt{t}$ where t is the duration of the diffusion experiment. The analytical data will define a straight line if the results conform to the initial and boundary conditions of one-dimensional Fick's Law diffusion with constant diffusion coefficient from a thin source into an infinite medium. A least-squares regression analysis determines the best line through the data, and the diffusion coefficient is given by the square of the slope of the

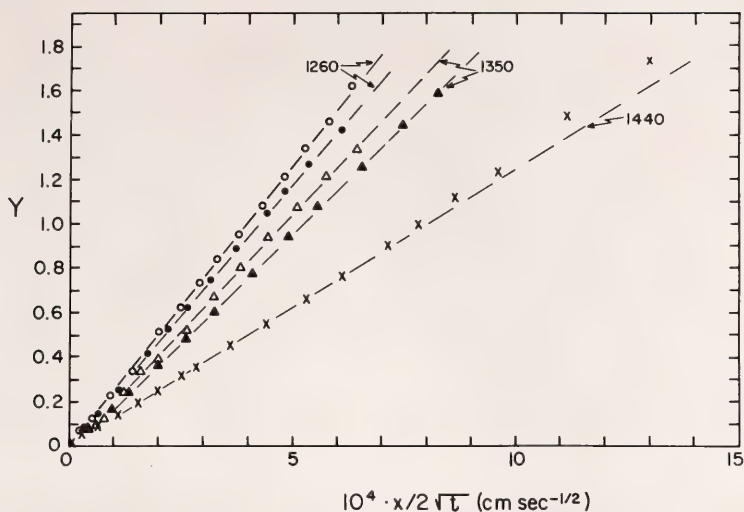


Fig. 81. Linearized plot of residual activity versus $x/2 \sqrt{t}$ for ^{133}Ba diffusion in olivine tholeiite basalt: x is the length removed from the cylinder; t , the derivation of the diffusion experiment; and Y is the dimensionless parameter calculated from the measured residual activity using Equation 1. Each symbol plotted represents a separate diffusion experiment; the numbers are the temperatures in degrees Celsius for each experiment.

line. Inspection of Fig. 81 shows that the data do in general define excellent straight lines. Significant deviations occur only in the region near the origin where convection appears to disturb the diffusion profiles and where the melt frequently forms a convex or concave meniscus against air so that the position for the origin itself is poorly defined. Occasionally, significant deviations are also found for large values of $x/2 \sqrt{t}$ where small errors in the background correction cause significant systematic deviations from the straight line.

Figure 82 is an Arrhenius plot (log diffusion coefficient versus the inverse absolute temperature) of the new Ba, Sr, and Co data. Also shown is the Arrhenius line for Ca diffusion previously reported (*Year Book 74*, pp. 183–189) and three additional measurements of Sr diffusion determined by the diffusion-couple method reported in *Year Book 73*, pp. 935–941. In that report the error for the two lower-temperature points had been estimated to be within a factor of 2, and that of the highest-temperature measurement had been judged less reliable because of

deformation of the diffusion couple during the run. These error estimates appear to have been realistic; the Arrhenius line is drawn on the basis of the new thin-source data alone; and the activation energy of 44 kcal/mol supersedes the previously given value of 114 kcal/mol. The extreme error in the original estimate of the activation energy is largely a result of the error introduced by the above-mentioned high-temperature point whose D value is too large by a factor of 3. The Arrhenius lines given in Fig. 82 are described by the equations: $D(\text{Ca}) = 0.535 \exp(-44.0 \times 10^3/RT)$, $D(\text{Sr}) = 0.278 \exp(-43.5 \times 10^3/RT)$, and $D(\text{Ba}) = 0.059 \exp(-39.4 \times 10^3/RT)$, where R is the gas constant and T is the absolute temperature.

Figure 82 shows that there is a small but significant decrease in D values as a function of increasing ionic radius ($\text{Ca}^{2+} = 0.99\text{\AA}$, $\text{Sr}^{2+} = 1.13\text{\AA}$, $\text{Ba}^{2+} = 1.35\text{\AA}$ Pauling radii). On the other hand, the activation energies for the three species (44, 44, and 39 kcal/mol) are not significantly different from one another. Also shown on Fig. 82 are a few results for cobalt diffusion. Under

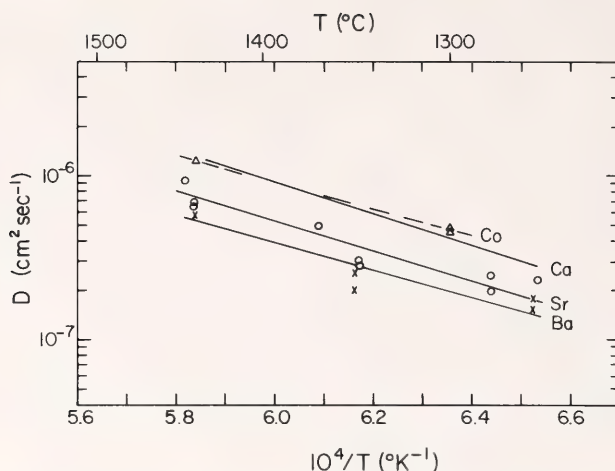


Fig. 82. $\log_{10} D$ versus $1/T$ (Arrhenius plot) for ^{133}Ba , ^{85}Sr , ^{45}Ca , ^{60}Co diffusion in olivine tholeiite basalt in air at 1 atm. Triangles = Co, circles = Sr, crosses = Ba. The line representing Ca diffusion is taken from Hofmann (1975).

the conditions of the experiment, dry heating in air, cobalt ions are expected to be primarily divalent at temperatures above 1000°C (Coons *et al.*, 1976), and the diffusivities are very close to those of calcium. These results conform roughly to the "compensation law" postulated by Winchell (1969), which states that the diffusion coefficient of all species is the same at some critical temperature. Winchell and Norman (1969) found that the critical values were $D \approx 10^{-6} \text{ cm}^2 \text{ s}^{-1}$ and $T = 1500^\circ\text{C}$. In detail, our results differ from this behavior in that the four Arrhenius lines are essentially parallel rather than intersecting at a single point. Nevertheless, estimates of diffusion coefficients using the compensation law appear to be much closer to the true values than those based on the Stokes-Einstein relation as done by Donaldson (1975). In the Stokes-Einstein relation the diffusion coefficient is proportional to the inverse of the viscosity of the liquid. As Donaldson showed, the estimated diffusion coefficients are within a factor of 10 or 20 of the correct value for basalt near its liquidus, but this agreement appears to be fortuitous, because as will be shown below, the Stokes-Einstein estimate of the diffusion coef-

ficient fails by many orders of magnitude when it is applied to high-viscosity silicate liquids such as granite melts.

When these data are compared with those given in the companion report by Hofmann and Brown, it appears that the diffusion coefficients for many cations in basalt in the temperature range of 1300°C to 1400°C are approximately $\log D = -6.5 \pm 0.9$. If the (unknown) effects of higher pressure and possible volatile content can be ignored, the characteristic transport distance by diffusion in a partially molten mantle can be estimated using the expression $\bar{x} = \sqrt{Dt}$, or about 1 km in 10^9 yr. This very limited chemical transport in the mantle provides some stringent restrictions on the choice of physically possible models for the chemical evolution of the mantle. Some of these have been discussed in previous reports (Hofmann, *Year Book* 73, pp. 935–941, 1974; and *Year Book* 74, pp. 183–189, 1975). The following may serve as an additional example of the consequences of the slow diffusion transport.

Kay (1975) proposed a model for the upper mantle "involving downward zone refining within a thickening lithosphere plate." The lithosphere is assumed to grow by downward solidifi-

cation of a partially molten mantle. "LIL(= large ion lithophile) elements and volatiles are largely excluded from the crystallizing solid phases and accumulate in a downward migrating zone at the base of the plate." The result is taken to be a zone of LIL element-enriched mantle that ultimately serves as the source material of oceanic islands. This model, like other zone refining processes, requires chemical transport and mixing in the molten zone. Without such transport the bulk composition of the solidifying liquid cannot change and no refining takes place. In the vicinity of the slowly advancing solidification front the melt fraction must be very small. This is required by the phase relations of thermodynamic systems that contain phases of continuously variable composition. As the melt fraction decreases toward the solidification front, the bulk viscosity of the material increases, thus inhibiting convection progressively toward the boundary. In addition, the zone refining mechanism requires that mixing occur on a scale that is small relative to thickness of the solidified material (so that a significant enrichment factor can be attained) but large enough so that the quantity of enriched material is of some geochemical significance. Thus, ideally the mixing zone below a 100-km-thick lithosphere should be on the order of 10 km thick. We must therefore consider a zone of increased viscosity (relative to the bulk of the partially molten mantle) and restricted size of convection cells (relative to "normal" mantle convection cells expected to have a characteristic size of 100–1000 km or more). Simple dimensional considerations show that the velocity in thermally driven free convection is proportional to $\rho\alpha g L^2 \Delta T / \mu$ (Bird *et al.*, 1960, Ch. 9), where ρ is the density, μ the viscosity, α the thermal expansion coefficient, g the gravitational acceleration potential, L a characteristic length, and ΔT the temperature difference. Consequently, if we allow a velocity of 10 cm/yr for large plate-driving convec-

tion cells with a minimum cell diameter of 100 km and if the bulk viscosity in the vicinity (i.e., within 10 km) of the solidification front increases by a minimum of a factor of 10, the maximum velocity in a hypothetical mixing cell of 10-km diameter would be on the order of 10^{-2} cm/yr or less—that is, at least an order of magnitude slower than the average rate of lithosphere growth (assumed to be 100 km/ 10^8 yr or 0.1 cm/yr). In view of this it seems reasonable to consider the case where chemical transport occurs predominantly by diffusion alone. This process will produce an LIL element-enriched zone in the vicinity of the solidification front. If the diffusion coefficient is 10^{-6} cm²sec⁻¹, and the velocity of the front is 0.1 cm/yr, a steady-state chemical gradient will evolve within about 10^5 years, after which the solidifying lithosphere will have a composition identical to that of the original partially molten asthenosphere. The width of the enrichment zone can be roughly estimated by the relation $x = D/V$, where D is the diffusion coefficient and V is the velocity of the solidification front (see Albarede and Bottinga, 1972). This yields a characteristic distance of 3 meters. It is unlikely that an enrichment zone of such minute thickness would be of any importance to the chemical evolution of the mantle, and Kay's model of downward zone refining is not expected to be effective. On the other hand, some degree of reenrichment of the asthenosphere as a whole cannot be excluded.

Diffusion in Obsidian Glass

An obsidian sample from Valles Caldera, New Mexico, was chosen as a model for granitic melts. Shaw (1963, 1974) had previously used this sample for measurements of viscosity and water diffusion. Cylinders were drilled from slabs of this glass, and radioactive tracer was loaded on the polished ends of the preannealed cylinders. Care was taken to avoid contamination of the sides of cylinders (1) by loading and drying only small drops of tracer solu-

tion near the center of cylinder face and (2) by annealing the loaded cylinder for about 60 min at 700°C to allow diffusion into a thin surface layer of the glass and subsequently dissolving the excess tracer salt from the surface by washing in dilute HCl. After this preliminary treatment the cylinders were annealed at temperatures between 675° and 950°C for periods of several days. The diffusion profiles were then determined by the same method of sectioning and residual-activity counting as previously explained for basalt.

Figure 83A shows two typical activity profiles for Sr and Ba at 850°C. Figure 83B shows the same data plotted as explained above for Fig. 81. Figure 84 is an Arrhenius plot of all the results for Sr and Ba. Judging from the fit of the data to the least-squares regression line, the precision is considerably better than was achieved in the basalts. We ascribe this to the absence of any convective movement in the case of the obsidian glass. In addition, the activation energy (proportional to the slope of the Arrhenius line) is more precisely defined because of the greater spread of measurements along the $1/T$ axis. The Arrhenius equations are: $D(\text{Sr}) = 0.09$

$\exp(-43.8 \times 10^3/RT)$ and $D(\text{Ba}) = 0.053 \exp(-45.8 \times 10^3/RT)$.

The results are relevant to the interpretation of Rb-Sr isochron measurements of migmatites (rocks of roughly granitic composition formed by partial melting of crustal rocks). Migmatites are typically inhomogeneous in composition and appear in layers of centimeters or tens of centimeters thickness. Thus it is immediately obvious that the high-grade metamorphic process that produced the migmatites did not cause chemical homogenization on a scale greater than a few tens of centimeters. On the other hand, isotopic homogenization is required (and frequently assumed to occur in high-grade metamorphism) in order for an Rb-Sr isochron to be "reset" by the metamorphism. The minimum distance of isotopic equilibration can be estimated assuming minimum values for temperature and duration of the metamorphism. Choosing values of $t = 10^6$ years for the duration of near-peak temperature and 700°C for the temperature itself, we obtain $D = 10^{-11} \text{ s}^{-1}$ and the characteristic transport distance of:

$$x = \sqrt{Dt} = 20 \text{ cm.}$$

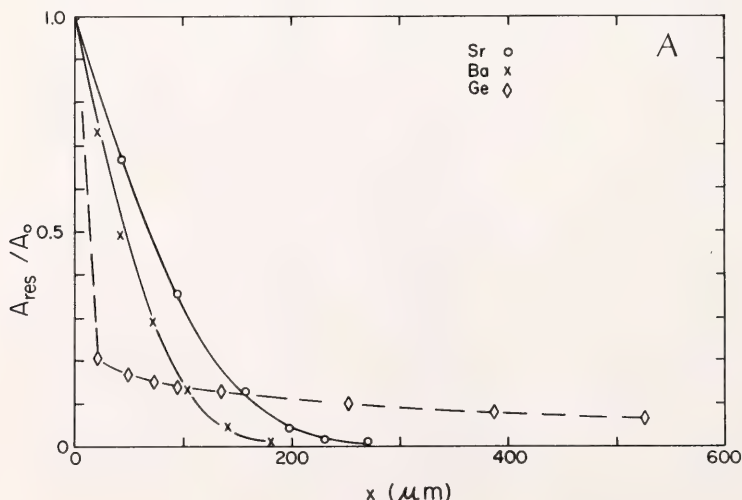


Fig. 83. Diffusion profiles in obsidian for Sr, Ba, and Ge at 850°C. (A) Plot of residual activity versus length of cylinder removed. The solid lines are ideal diffusion curves, Equation 1.

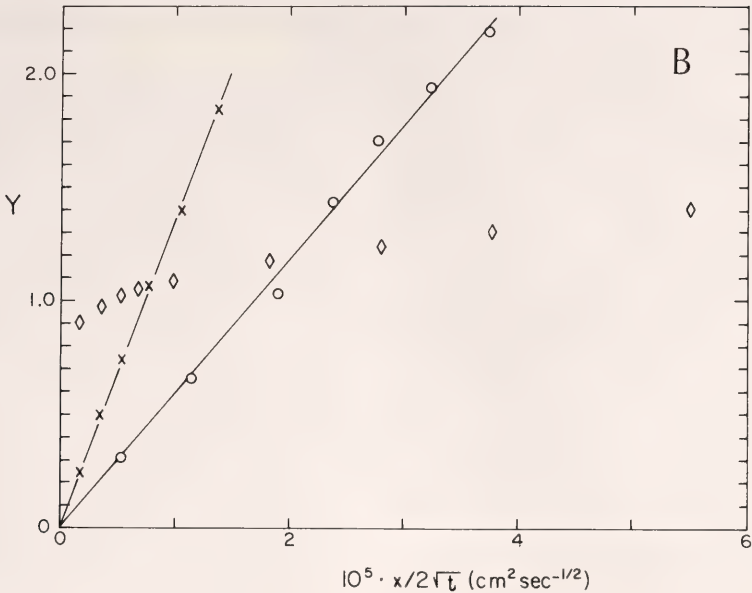


Fig. 83. (B) Linearized plot of the same data with Y calculated from Equation 1 (see also Fig. 81). These results show that diffusion of Sr and Ba can be described by a single constant diffusion coefficient, but that the Ge data either require a variable diffusion coefficient, or have more than one chemical species of Ge present.

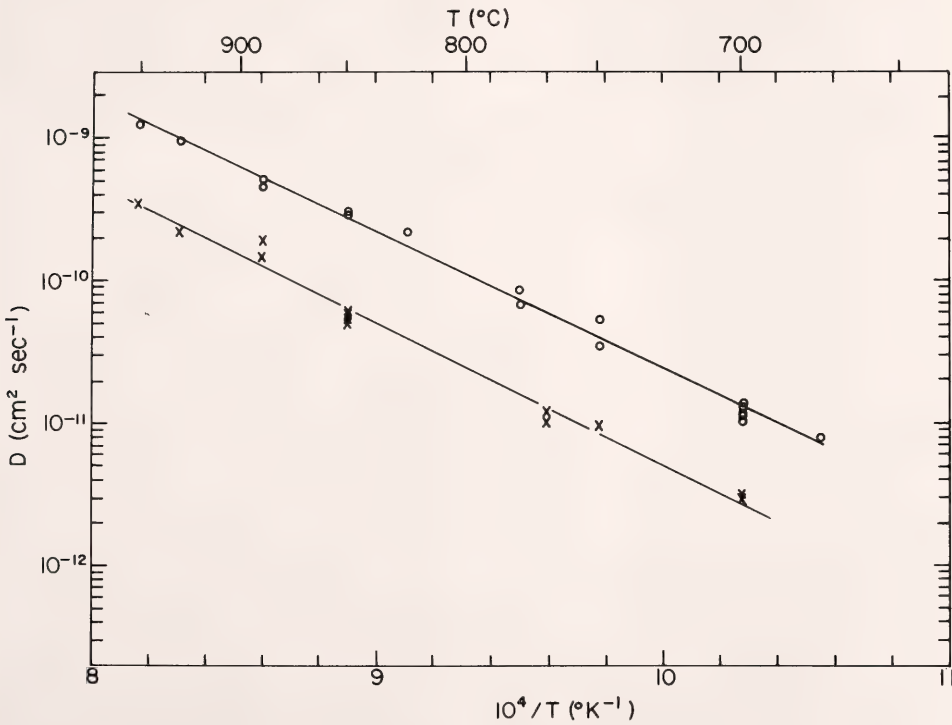


Fig. 84. Arrhenius plot for Sr (circles) and Ba (crosses) diffusion in obsidian (in air).

Such small transport distances must be considered when samples are taken for isochron measurements in order to determine the age of migmatization. For example, it is common practice to collect blocks of at least 20 cm diameter as individual samples and to space such samplings over meters or even kilometers. Isochron measurements on such suites of whole-rock samples are then frequently interpreted as determinations of the age of metamorphism. Although nondiffusive migration of aqueous pore fluids or melt may conceivably have accomplished such wide-ranging isotopic homogenization of strontium, that interpretation would need to be confirmed by small-scale sampling.

The similarity of inferred distance of Sr migration and major-element equilibrium leads to the rule of thumb that centimeter-scale sampling should be included for Rb-Sr age determinations of metamorphic rocks and that the range of major-element equilibrium in a rock should be used as a guide to the presumed range of isotopic equilibrium needed for the age measurements.

Some caution is in order for the geological interpretation of these diffusion data because the effect of water on these diffusivities is unknown. We are therefore preparing a new set of experiments to be conducted under hydrothermal conditions.

The determination of one of the fundamental properties of natural melts, ion mobility, has many applications in the earth and planetary sciences as well as in material science. These include such diverse problems as determination of quenching times and spatial configurations used in experimental petrology; interpretation of concentration gradients in natural terrestrial and lunar glasses; problems of crystallization kinetics, such as the development of oscillatory zoning in plagioclase (Bottinga *et al.*, 1966); determination of the structure of silicate melts; and measurement of oxidation state of ionic species in melts. We will discuss

briefly the latter two of these applications.

It is shown on Fig. 83 that the diffusion profile for Ge in obsidian is not compatible with a single constant diffusion coefficient. Similar results were obtained for Co diffusion. Both elements can be present in more than one oxidation state, and we have attempted to deconvolute the Ge profile into two components, each diffusing independently of the other. The solid symbols shown in Fig. 85 form approximately straight lines, which correspond to a diffusion coefficient of $D = 1.8 \times 10^{-8}$. This was calculated by subtracting from the measured profiles (open symbols) a slow-moving component, assuming this accounts for 90% of the total Ge activity and has a diffusion coefficient of $D = 3.8 \times 10^{-12} \text{ cm}^2 \text{ s}^{-1}$. Our interpretation that the two species involved are two oxidation states of Ge is subject to confirmation by experiment under controlled partial pressure of oxygen. This offers the possibility of measuring the proportions in which different oxidation states of the same chemical element are present in a melt. To our knowledge, other methods for determining this are not feasible for trace elements.

Figure 86 shows a compilation of our diffusion data. Also shown are tracer diffusion coefficients for alkalis in obsidian measured by Jambon and Carron (1973) on a single diagram. It is clear that extrapolation for the obsidian data to the temperature range of the basalt liquidus yields diffusion coefficients that differ from the various basalt diffusivities by factors of about 20 for barium and 2 for strontium. In contrast, the viscosity of these two melts varies by about three to four orders of magnitude (Murase and McBirney, 1973). From this it is evident that the Stokes-Einstein relation (which relates diffusivities to viscosity) is not applicable to liquids of this kind. Furthermore, the results are compatible with structure models that consider cation species such as Ca^2 , Sr^{2+} , and Ba^{2+}

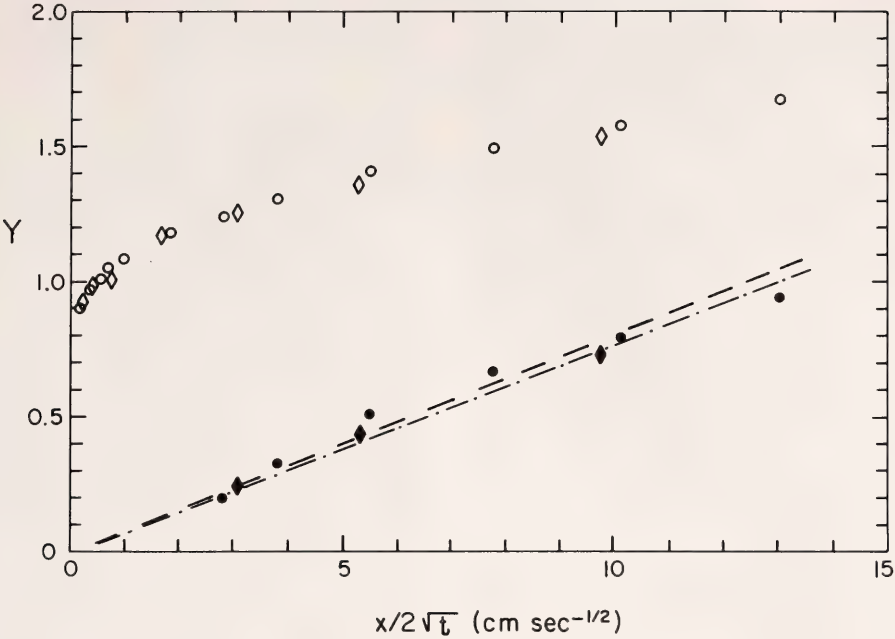


Fig. 85. Diffusion profiles for Ge in obsidian at 850°C. Open circles and open diamonds denote the results of the linearization procedure for two separate experiments as used in Figs. 81 and 83; the solid circles and solid diamonds were calculated by subtracting 90% of the total activity as the slow-moving Ge component ($D = 3.8 \times 10^{-12}$ cm² s⁻¹) in order to isolate the fast moving component which yields a straight line Y versus X relationship and a diffusion coefficient of $D = 1.8 \times 10^{-8}$ cm² s⁻¹.

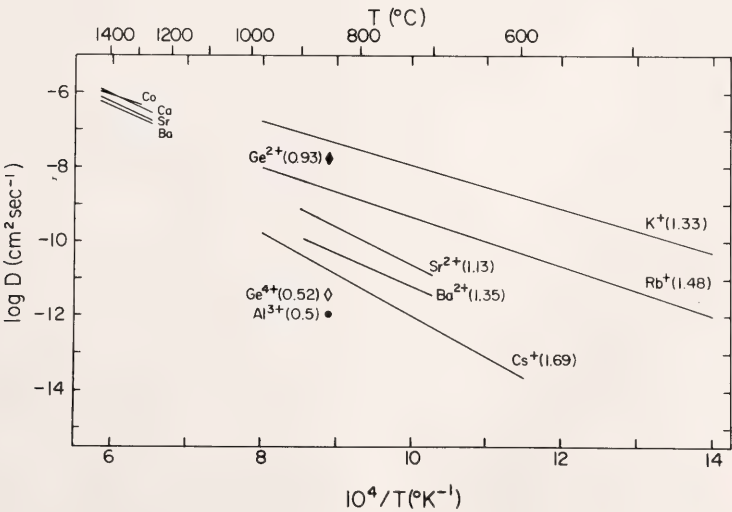


Fig. 86. Compilation of diffusion data in obsidian (at temperatures less than 1000°C) and basalt (at temperatures greater than 1250°C). The Arrhenius lines for K, Rb, and Cs are taken from Jambon and Carron (1973). The points for Ge are derived by using the deconvolution procedure shown in Fig. 85 and assuming that the slow and fast species involved are Ge⁴⁺ and Ge²⁺, respectively.

as single ions that migrate through the network of silica tetrahedra at a rate primarily dependent on ionic size and charge and nearly independent of the degree of polymerization of the silica tetrahedron. Figure 86 shows, for example, that Ba^{2+} and K^+ , which have similar ionic radii but different ionic charge, differ drastically in their mobility in obsidian. At 800°C the tracer diffusion coefficient for K^+ is greater by a factor of 10^3 than the coefficient for Ba^{2+} . In addition, it appears that the effect of ionic radius differences is more important for univalent ions than for divalent ions. Preliminary data for trivalent ions (Gd^{3+} and Al^{3+} , also shown on Fig. 86) give diffusion coefficients smaller than about $2 \times 10^{-12} \text{cm}^2 \text{s}^{-1}$ at 850°C in obsidian.

The above model for the structure of silicate liquids contrasts with models that propose the existence of larger complexes or "units of structure related to species or subspecies of minerals" (Yoder, 1973). These complexes are thought to mimic the composition of solid phases that would crystallize below the liquidus temperature. The presently available diffusion data are not compatible with such a model because the cations are evidently not sufficiently bound to the silica tetrahedra to form stable complexes.

Acknowledgments

We are grateful to Dr. H. S. Yoder, Jr., for supplying the basalt sample and for making the facilities of the Geophysical Laboratory available to us. We especially appreciate the use of a platinum-wound furnace at the Geophysical Laboratory. We also thank Dr. R. L. Smith, who kindly made the sample of obsidian available for this study. Financial support was given by the National Science Foundation, Grant No. GA-40250.

References

Albarede, F., and Y. Bottinga, Kinetic disequilibrium in trace element partitioning

- between phenocrysts and host lava, *Geochim. Cosmochim. Acta*, **36**, 141–156, 1972.
- Bird, R. B., W. E. Stewart, and E. N. Lightfoot, *Transport Phenomena*, John Wiley & Sons, New York, 1960.
- Bottinga, Y., A. Kudo, and D. Weill, Some observations on oscillatory zoning and crystallization of magmatic plagioclase, *Am. Mineral*, **51**, 792–806, 1966.
- Coons, W. E., J. R. Holloway, and A. Navrotsky, Co^{2+} as a chemical analogue for Fe^{2+} in high temperature experiments in basaltic systems, *Earth Planet. Sci. Lett.*, **30**, 303–308, 1976.
- Donaldson, C. H., Calculated diffusion coefficients and the growth rate of olivine in a basalt magma, *Lithos*, **8**, 163–174, 1975.
- Hofmann, A. W., Strontium diffusion in a basalt melt and implications for Sr isotope geochemistry and geochronology, in *Carnegie Inst. Wash. Year Book 73*, pp. 935–941, 1974.
- Hofmann, A. W., Diffusion of Ca and Sr in a basalt melt, in *Carnegie Inst. Wash. Year Book 74*, pp. 183–189, 1975.
- Jambon, A., and J. P. Carron, Étude expérimentale de la diffusion des éléments alcalins K, Rb, Cs dans une obsidienne granitique, *C.R. Acad. Sci. D*, **276**, 3069–3072, 1973.
- Kay, R., Chemical zonation of the oceanic mantle (Abstract), *EOS Trans. Am. Geophys. Union* **56**, 1077, 1975.
- Murase, T., and A. R. McBirney, Properties of some common igneous rocks and their melts at high temperatures, *Geol. Soc. Am. Bull.*, **84**, 3563–3592, 1973.
- Shaw, H. R., Obsidian- H_2O viscosities at 1000 and 2000 bars in the temperature range 700° to 900°C , *J. Geophys. Res.*, **68**, 6337–6343, 1963.
- Shaw, H. R. Diffusion of H_2O in granitic liquids: Part I, Experimental data; Part II, Mass transfer in magma chambers, in *Geochemical Transport and Kinetics*, A. W. Hofmann, B. J. Giletti, H. S. Yoder, and R. A. Yund, eds., *Carnegie Inst. Wash., Publ. 634*, pp. 139–170, 1974.
- Winchell, P., The compensation law for diffusion in silicates, *High Temp. Sci.*, **1**, 200–215, 1969.
- Winchell, P., and T. H. Norman, A study of the diffusion of radioactive nuclides in molten silicates at high temperatures, in *High Temperature Technology*, 3rd Intern. Symp., Asilomar 1967, pp. 479–492, 1969.
- Yoder, H. S., Jr., Contemporaneous basaltic

and rhyolitic magmas, *Am. Mineral.*, 58, 153–171, 1973.

DIFFUSION MEASUREMENTS USING FAST DEUTERONS FOR *in situ* PRODUCTION OF RADIOACTIVE TRACERS

A. W. Hofmann, and L. Brown

In connection with our program to measure diffusion in silicate melts we have carried out preliminary experiments to determine the feasibility of creating a sharply defined zone of radioactive tracers within a sample of quenched basalt glass. Such a technique has at least two potential advantages over the more conventional technique of applying a thin layer of tracer to the surface of the sample (see companion report by Hofmann and Magaritz): (1) Relatively volatile elements such as sodium can be easily contained within the sample; and (2) convective movement of the melt during initial heating of the sample may be less severe in the center than at the surface of the sample.

Sodium is quite volatile at temperatures of 1300° to 1400°C, and much of an externally applied sodium tracer would be expected to be lost by surface evaporation. In addition, the boundary conditions for the diffusion experiments would be uncertain and temperature dependent. This problem is eliminated if the sodium tracer is at the center of the sample and if the diffusion experiment is terminated before a significant amount of the tracer reaches the surface.

Convective mixing was found to cause significant errors in short-term diffusion experiments (less than one day) and it was believed that this convection may be confined to a relatively narrow zone near the open end of the platinum capillary tube that contains the melt (see Hofmann, *Year Book* 74, pp. 183–189, 1975). If this is correct, the problem of convective interference

could be circumvented by introducing the tracer in the center of the Pt tube and thus avoiding the near-surface convection. In addition, it is very difficult to prove conclusively that transport occurred primarily by volume diffusion rather than by some other process, perhaps resembling eddy diffusion, unless differential transport between different chemical species can be demonstrated.

Experimental Method

The basalt (olivine tholeiite, 1921 eruption of Kilauea) was contained as quenched glass in 2-mm Pt tubes. These were exposed to a collimated d beam of 40 MeV energy from the Lawrence Berkeley 88-in cyclotron which had passed through a 0.0025-cm Al foil and through 2 in of air before reaching the samples. A slotted 0.178-cm-thick brass plate was used for collimation. The width of the collimation slit was 1 mm in some experiments and 0.5 mm in others. The exposure varied between 5 and 40 $\mu\text{A}\cdot\text{min}$ per sample. In order to determine the initial distribution of activity within the sample, one basalt-filled tube was sectioned after irradiation, and the activity was measured using a 3×3 in NaI well detector with the sample placed in the well. Figure 87 shows this initial profile of the 0.847-MeV gamma peak, which is produced by ^{56}Co within the basalt. Also shown is the profile for the 0.099-MeV gamma peak combined with lower-energy Pt-x-ray peaks produced by ^{196}Au and ^{195}Au within the Pt tube. The gold isotopes are produced by deuteron interactions with platinum. The activity profiles in Fig. 87 show that the collimation is excellent and that the activity within the irradiated zone is uniform. The nonhorizontal slope on the right side is due to absorption effects during counting. The small tail beyond the 1-mm zone amounts to less than 2% of the total activity and is considered negligible for the purpose of these experiments.

A gamma-ray energy spectrum taken with the NaI detector showed

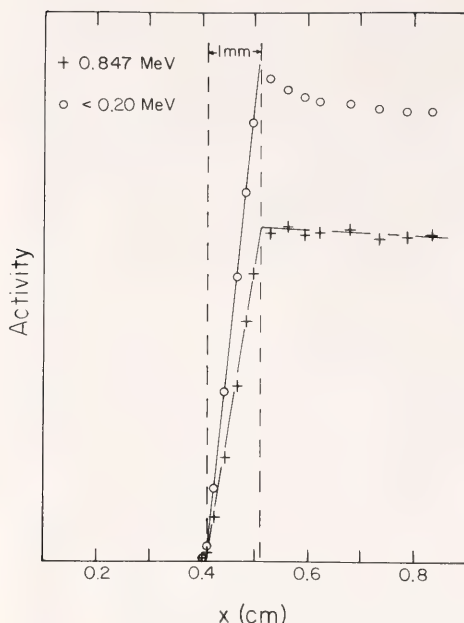


Fig. 87. Profile of residual activity (arbitrary scale) versus length (x) of cylinder after deuteron irradiation and before diffusion anneal. A conventional, well-type NaI detector was used for this profile only. The low-energy profile contains 0.099 MeV gamma and lower-energy Pt-x rays and shows the effects of absorption by the sample: The increase in apparent activity occurs as absorbing material near the "hot" zone is removed by successive sectioning. The absorption effect is much less pronounced in the 0.847-MeV profile for ^{56}Co . The actual width of the irradiation window is shown by the dashed vertical lines.

prominent peaks at 0.1, 0.35, 0.51, and 0.85 MeV, and a broadened peak at about 1.25 MeV. The only energies that were apparently associated with a single isotope were due to ^{196}Au and ^{56}Co . Fortunately, Dr. J. Rowe of the U.S. Geological Survey kindly made a Ge(Li) detector available for this study. This permitted us to obtain a high-resolution spectrum in which the following species were easily resolved: ^{22}Na , ^{46}Sc , ^{48}V , ^{54}Mn , ^{56}Co , ^{57}Co , ^{195}Au , ^{196}Au . The only overlap of spectral lines occurred between the 0.835-MeV and 0.847-MeV peaks of ^{54}Mn and ^{56}Co .

Five annealing experiments were made at a temperature of 1300°C with run durations varying between 17 min and 15.5 hr, using the equipment and

technique described in the companion report by Hofmann and Magaritz (this *Year Book*). The results of the 15.5-hr run are shown in Fig. 88. This clearly demonstrates the differential transport between the different chemical species. Two features argue strongly that this transport is primarily caused by volume diffusion rather than some other process such as convection: (1) the difference in transport distances between species, such as Na and V, and (2) the fit of the profiles to theoretical volume-diffusion profiles drawn as solid lines for Na ($D = 2.45 \times 10^{-6} \text{cm}^2 \text{s}^{-1}$), Co and Mn ($D = 4.58 \times 10^{-7} \text{cm}^2 \text{s}^{-1}$) and V ($D = 5.03 \times 10^{-8} \text{cm}^2 \text{s}^{-1}$). Only Sc does not fit such a diffusion profile. This may mean that there are two Sc (chemical) species present, perhaps with different oxidation states and with two different diffusion coefficients. These results show that any contribution by convective transport must have been smaller than the smallest total transport, that of vanadium. It has been our experience, however, that a small but significant convective contribution to the total transport is not necessarily detected as a significant deviation from the ideal diffusion profile. For example, if an infinitely thin source were spread out to a width of 1 mm by convection at the beginning of the annealing experiment, the resulting profiles after several hours of diffusion annealing would be essentially indistinguishable from profiles due to pure volume diffusion. Such convective contributions do, however, show up quite well when short-duration and long-duration anneals are compared (see Hofmann, *Year Book* 74, pp. 183–189, 1975). We believe therefore that isothermal time studies are indispensable in demonstrating the validity of any experimental technique concerned with diffusion.

The results of a series of five experiments at 1300°C for Na and Co transport are shown in Fig. 89, where the apparent diffusion coefficients are plotted against run duration. The total range of apparent D value is less than a

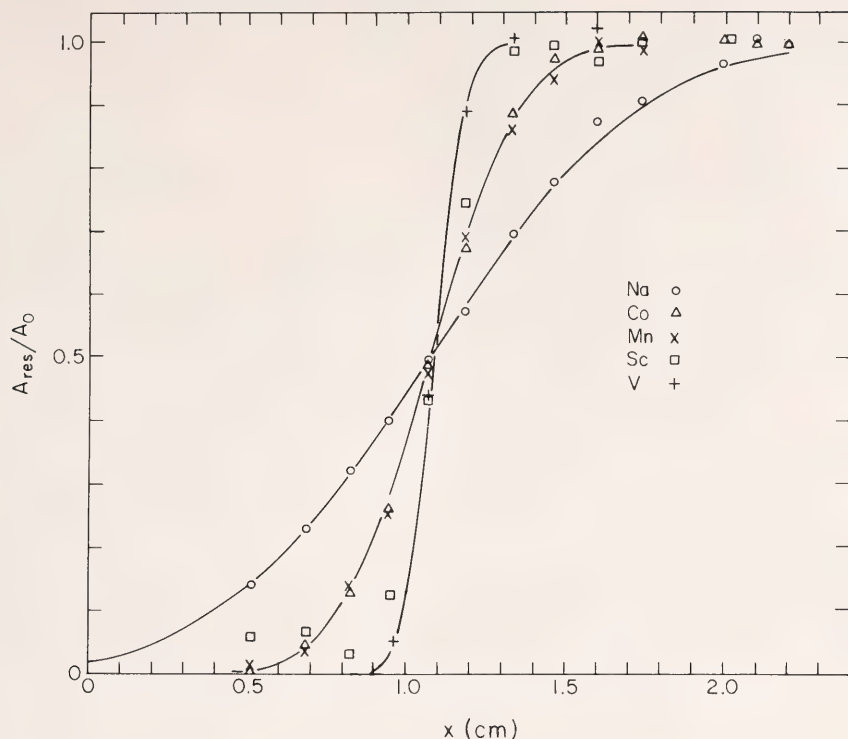


Fig. 88. Diffusion profiles (residual activity versus sample length) for five deuteron-activated species: ^{22}Na (1.275 MeV), ^{56}Co (0.847 and 1.238 MeV), ^{54}Mn (0.835 MeV), ^{46}Sc (0.889 and 1.121 MeV), and ^{48}V (0.983 and 1.312 MeV). The temperature was 1300°C , and the run duration was 15.5 hr. The solid curves are calculated diffusion profiles for $D = 2.45 \times 10^{-6}\text{cm}^2\text{s}^{-1}$ (^{22}Na), $D = 4.58 \times 10^{-7}\text{cm}^2\text{s}^{-1}$ (^{56}Co and ^{54}Mn), and $D = 5.03 \times 10^{-8}\text{cm}^2\text{s}^{-1}$ (^{48}V).

factor of 3 for Co and less than 1.5 for Na. In no case do the measured profiles deviate significantly from calculated volume diffusion profiles. The results indicate that some convective transport does occur in some of the experiments. However, the effect is much less pronounced than that found in a study of Ca diffusion reported last year (Hofmann, *Year Book* 74, pp. 183–189, 1975). In that study a thin source of ^{45}Ca was applied to the open surface of the melt at the end of the Pt tube. Also a Pt furnace with a vertical muffle tube was used in the Ca study, whereas we now use a furnace with a completely enclosed heating chamber, MoSi_2 -heating elements, and SCR-type temperature control.

We believe that convective movement occurs during heating-up time (which takes several minutes) and that

its magnitude depends on small differences in the heating schedule not yet under our control. In particular, we were surprised to find the apparent diffusion coefficients derived from the shortest (17-min) run to be identical within analytical error to the values derived from the longest run (15.5 hr). This indicates that there was a negligible amount of convective movement during this short run. This result and the comparatively small total range of apparent D values lead us to the estimate that the results obtained from the longest run (shown in Fig. 88) are correct within 20% for Na and 50% for Co and Mn. We are also encouraged by the excellent agreement obtained for Co diffusion at 1300°C between the conventional technique using a surficial thin source ($D_{\text{Co}} = 4.7 \times 10^{-7}\text{cm}^2\text{s}^{-1}$; see companion report by Hofmann and

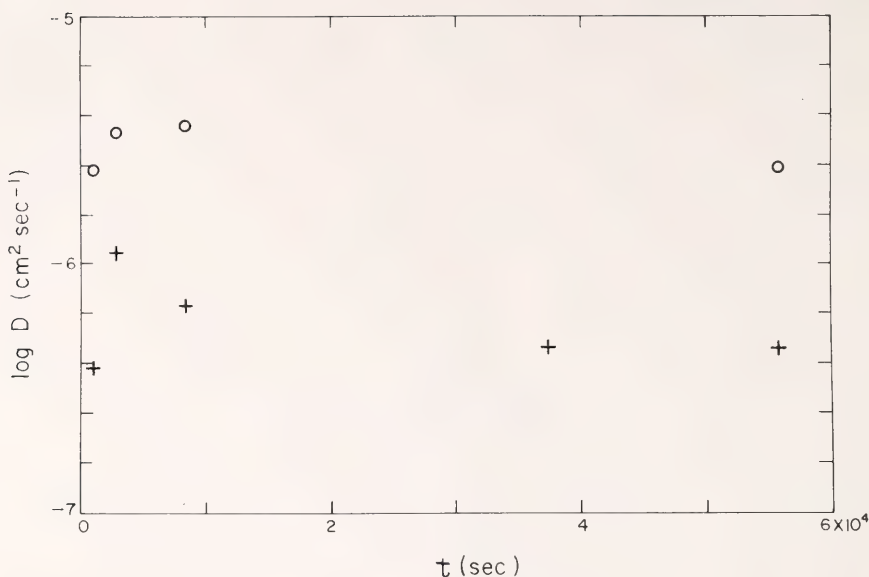


Fig. 89. Results of isothermal diffusion study for tholeiite basalt at 1300°C under atmospheric conditions. D is the apparent diffusion coefficient for Na (circles) and Co (crosses), and t is the run duration.

Magaritz) and the result of this study, $D_{\text{Co}} = 4.6 \times 10^{-7} \text{cm}^2 \text{s}^{-1}$.

Further improvement in accuracy should be easily obtainable by simply increasing the run duration. This was avoided in the current experiments in order to prevent the Na profile from reaching the ends of the cylinders (although this did occur inadvertently in one experiment for which no D value is plotted for Na; it also occurred marginally in the experiment shown in Fig. 88). We conclude that this is an excellent technique to study diffusion of certain chemical species, including the volatile species Na, and we expect that it will be applicable also to diffusion studies at high pressure for which the more conventional techniques are not suitable.

The results also show that the magnitude of the diffusion coefficient of cations is strongly dependent on ionic charge: Na ($D = 2.5 \times 10^{-6} \text{cm}^2 \text{s}^{-1}$) is monovalent, Mn and Co ($D = 4.6 \times 10^{-7}$) are divalent; Sc is generally believed to be trivalent (although the

shape of the diffusion profile might be taken to indicate the presence of some divalent Sc); and V (5.0×10^{-8}) is at least trivalent. This effect is even more pronounced at lower temperatures (see the companion report by Hofmann and Magaritz). We believe that the apparently very simple relationship between ionic charge and diffusivity will prove to be an extremely useful tool to determine the oxidation state of transition elements in natural melts.

Acknowledgments

We are grateful to Dr. H. E. Conzett and Ms. Ruth Mary Larimer of Lawrence Berkeley Laboratory for collaborating with us and carrying out the irradiations and to Dr. Jack J. Rowe of the U.S. Geological Survey in Reston, Va., for making available a Ge(Li) detector. We are also grateful to the National Science Foundation for providing financial support through Grant No. GA-40250.

OBSERVATION OF X RADIATION CHARACTERISTIC OF A UNITED ATOM

L. Brown and G. H. Pepper

Introduction

During the past year the Van de Graaff accelerator was used exclusively for the investigation of processes present in the collision of heavy ions at energies of a few MeV. Crucial to these studies, as well as serving as an incentive for them, was a newly purchased lithium-drifted silicon detector capable of resolving 800-eV spectral lines. This instrument, which is decidedly superior to the one we previously used through loan, has allowed us to examine regions of the x-ray spectrum that have disclosed two phenomena: One is the clearest manifestation yet observed of the formation of a united atom; the other is a selective transfer of an electron vacancy from a K shell to a single L subshell, a form of transfer not heretofore recognized.

When considering the collision of heavy ions wherein the electron shells of the two atoms interpenetrate, it is in some cases useful to consider them as having formed a united atom, i.e., an electronic system that has the nuclei of both target and projectile briefly forming a common center of attraction. This view, with its attendant idea of the formation of states in the united atom by way of the transformation from separated-atom levels through quasimolecular states, has difficulties, some of which were treated in last year's Annual Report, but it has certain elements of truth. When heavy ions collide, a continuum of x rays is observed (Macdonald *et al.*, 1973) that can result from neither nucleus-nucleus nor electron-nucleus bremsstrahlung. This continuum is generally interpreted as resulting from a transition of an electron to a vacancy in a molecular state formed during the collision. Since such states have energies that vary with time, these transitions

obviously form continua. However, transitions to orbitals terminating on a given united atom shell should have a limit given by the binding energy of that shell. This has not been observed for the K band. Instead, an exponential-shaped continuum is seen to extend well beyond the united atom limits.

The energies attainable with our accelerator do not allow an excitation of the K band sufficiently intense for study but do allow excitation of the L and M bands. These have been observed by others (Mokler *et al.*, 1975) and are more suggestive of a united atom than the K band, but these previous observations suffer from the interference of characteristic lines with the continuum and from few data showing the dependence of the continua on atomic number and projectile velocity. We have found a projectile-target combination that allows these two deficiencies to be removed and that shows continua, both of L and M bands, with easily recognized limits, which move exactly as predicted when the atomic number of the target is changed. Observations of the projectile velocity dependence of the continua show two obvious features: (1) Near the united-atom limit the cross section increases rapidly near the threshold and then levels off at high energies; (2) the continuum extends beyond the united-atom limit and its width increases with projectile velocity.

The lifetimes of united atoms could be estimated by dividing the radius of the shell in question by the projectile velocity. These lifetimes then give an upper limit to the uncertainties in the energies of the states through simple application of the Heisenberg uncertainty principle. It has been clear from the beginning that the observed extension of the spectrum beyond the united-atom limit follows from this, but previous attempts to explain K-band spectra theoretically (Macek and Briggs, 1974; Müller, 1976) have been in vain. Two circumstances combine to make interpretation difficult:

cause we had hoped that this simple manifestation would have the equally simple velocity dependence, i.e., a broadening proportional to velocity. A curious aspect of the matter is that the only theories now under serious consideration predict a square-root dependence but do so on the basis of assumptions that seem to us questionable. Since our data are the best verification of this dependence, our prejudices to the contrary notwithstanding, we are seeking to remove the weak elements of these theories or to find an acceptable alternate set of assumptions.

Vacancy Sharing in Heavy-Ion Collisions

The most striking phenomenon of heavy-ion collisions is the large probability for producing electron holes in the less tightly bound of two interpenetrating shells that have nearly equal binding energies, e.g., K shells of two atoms with $Z_1 \approx Z_2$. Conventional theory predicts a small probability, if applied strictly. The novel approach proposed here last year has found little acceptance because it predicts only the relative Z dependence (quite satisfactorily) and utilizes a mechanism not observed elsewhere. Whatever the details of its operation, molecular excitation depends in some way on the transformation of atomic into molecular wave functions, and its complete elucidation is the central problem of this field of research.

If one sets aside the mysterious manner in which vacancies appear in the more weakly bound shell and considers instead the method by which vacancies appear in the more strongly bound shell, then one finds things in a more satisfactory condition. Meyerhof (1973) demonstrated that, given the vacancy in a light K shell, he could calculate the probability of its transfer to the heavy K shell. The mechanism for this is radial coupling, which links molecular states of the same parity.

We set about to see if this process also coupled K and L shells and noted an unusual circumstance best illustrated with the raw data. In Fig. 92a is shown the spectrum of praseodymium produced by bombardment with 2-MeV Li^+ ; it is a normal example of Coulomb excitation, showing all the L lines that the detector is capable of resolving with intensities easily understood through conventional theory. In Fig. 92b is shown the spectrum of praseodymium when bombarded with 2-MeV K^+ ; the K lines of potassium are the most prominent feature and result from the molecular excitation discussed previously. L lines from praseodymium are also shown but are in marked contrast to the spectrum of Fig. 92a, as the total intensity is much less and the intensity ratio is entirely different; indeed only the L_α and $L_{\beta 2}$ lines are observed.

Reference to x-ray tables quickly discloses that these lines are transitions to vacancies in the $2p_{3/2}$ subshell and that transitions to the other L subshells, the $2p_{1/2}$ and $2s_{1/2}$, are absent within the observational limits imposed by the continuum radiation. The transfer of vacancies from the K shell of potassium, if the process is a transfer, is obviously selective. A study of the velocity dependence of the ratio of potassium K lines to praseodymium L lines shows values that lie along an exponential in $1/v$, which present interpretations would indicate as charge exchange.

Our tentative interpretation of the process can be understood by reference to Fig. 93a, which shows the manner by which the atomic energy levels transform through molecular orbitals into the energy levels of a united atom for the collision of $\text{K} + \text{Pr}$. One notices that the potassium K shell transforms by a $3d\sigma$ orbital which has the initial vacancy and the three praseodymium L subshells by a $2p\pi$, $2p\sigma$, and $2s\sigma$. Radial coupling proceeds between states of the same molecular parity, here between the $3d\sigma$ and the two orbitals $2p\sigma$ and $2s\sigma$. Rotational coupling between

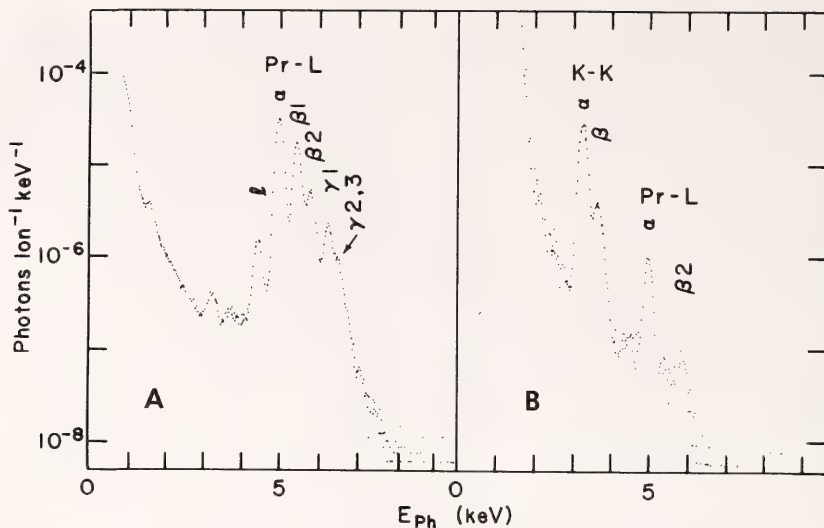


Fig. 92. The spectra of praseodymium L lines produced by (a) direct excitation with 2-MeV Li^+ and (b) vacancy sharing with 2-MeV K^+ . The identity of various praseodymium L lines capable of being resolved by the detector are indicated for both spectra with the location of the potassium K lines also shown for spectrum (b). Unmarked peaks are the result of target contaminants and a photon escape peak, an instrumental effect. The L lines of praseodymium in spectrum (b) are thought to result primarily from the transfer of vacancies from the potassium K shell to the praseodymium L III subshell ($2p_{3/2}$) through rotational coupling.

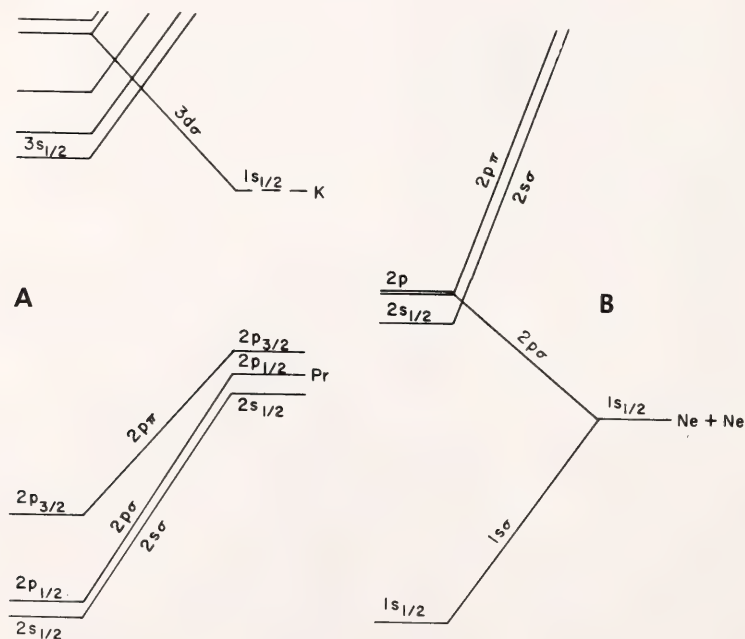


Fig. 93. Correlation diagrams for the collision of (a) $\text{K} + \text{Pr}$ and (b) $\text{Ne} + \text{Ne}$. In both diagrams the morphology of the transformation of separated-atom through molecular levels to united-atom energy states is shown. The vertical axis is proportional to the logarithm of the energy; the horizontal axis shows the internuclear distance schematically. The energy scales for (a) and (b) are different.

orbitals of opposite parity is also known to occur, but it has been observed only in collisions in which the exchanging orbitals attained nearly the same energy at small radii of separation, an example of which is shown in Fig. 93b. This shows the correlation of orbitals in the collision of neon and neon, a collision in which the transfer of a vacancy from the $2p$ shell of an incident ion is transferred by the $2p\sigma$ to the $2p\pi$ orbital. The theory of this transfer (Fastrup, 1976) agrees well with experiment. Except at very low velocities, the probability of transfer is nearly unity because the two orbitals have nearly the same energy at small values of internuclear radius.

Because of the different probability observed for $3d\sigma \rightarrow 2p\pi$ compared with $3d\sigma \rightarrow 2p\sigma$ and $2s\sigma$, we think that it must be a new manifestation of rotational coupling—a case of rotational coupling at large rather than small internuclear radius.

References

- Fastrup, B., Experimental studies of inner-shell excitation in slow ion-atom collisions, in *The Physics of Electronic and Atomic Collisions, Invited Papers of the IX ICPEAC*, p. 361, J. S. Risley and R. Geballe, ed., University of Washington Press, Seattle, 1976.
- Macdonald, J. R., M. D. Brown, and T. Chiao, Observation of a K x-ray band emitted by the transient C-C system formed at keV energies, *Phys. Rev. Lett.*, **30**, 471, 1973.
- Macek, J. H., and J. S. Briggs, Collision broadening and molecular orbital x-rays II, *J. Phys.*, **B7**, 1312, 1974.
- Meyerhof, W. E., K-vacancy sharing in near-asymmetric heavy-ion collisions, *Phys. Rev. Lett.*, **31**, 1341, 1973.
- Mokler, P. H., S. Hagmann, P. Armbruster, G. Kraft, H. J. Stein, K. Rashid, and B. Fricke, Superheavy quasimolecules, in *Atomic Physics*, **4**, G. zu Putlitz, E. W. Weber, and A. Winnacher, eds., Plenum Press, New York, 1975.
- Müller, B., Radiative processes in transient quasimolecules, in *The Physics of Electronic and Atomic Collisions, Invited Papers of the IX ICPEAC*, p. 481, J. S. Risley and R. Geballe, eds., University of Washington Press, Seattle, 1976.

BIBLIOGRAPHY

Publications listed below can be obtained at no charge from the Department of Terrestrial Magnetism, 5241 Broad Branch Rd., N.W., Washington, D.C. 20015. When ordering, please give reprint number(s). No reprints are available for titles marked with asterisks.

- Aldrich, L. T., *see* Ocola, L. C.
- Arculus, R. J., *see* Shimizu, N.
- Assousa, G. E., *see* Brown, L., and Warner, J. W.
- Boulter, D., *see* Wallace, D. G.
- Brooks, C., *see* James, D. E.
- 4415 Brown, L., G. E. Assousa, N. Thonnard, H. A. Van Rinsvelt, and C. K. Kumar, Characteristic and continuum x rays produced with potassium ions of a few MeV, *Phys. Rev., A12*, 425–433, 1975.
- Brown, L., *see* Pepper, G. H., and Rohrer, U.
- Cuyubamba, A., *see* James, D. E.
- Duggan, J. L., *see* McDaniel, F. D.
- Ford, W. K., Jr., *see* Rubin, V. C.
- Gardner, R. K., *see* McDaniel, F. D.
- Gettrust, J. F., *see* Ocola, L. C.
- Gray, T. J., *see* McDaniel, F. D.
- *4416 Hart, S. R., Basement rock synthesis: Geochemistry, petrology, physical properties, and paleomagnetism, in *Initial Reports of the Deep Sea Drilling Project, Vol. 34*, 814 pp., T. L. Vallier, ed., Washington, D.C., U.S. Government Printing Office, 1976.
- *4417 Hart, S. R., LIL-element geochemistry, Leg 34 basalts, in *Initial Reports of the Deep Sea Drilling Project, Vol. 34*, 814 pp., T. L. Vallier, ed., Washington, D.C., U.S. Government Printing Office, 1976.
- Hart, S. R., *see* Yeats, R. S.
- *4418 James, D. E., C. Brooks, and A. Cuyubamba, Andean Cenozoic volcanism: Magma genesis in the light of strontium isotopic composition and trace-element geochemistry, *Geol. Soc. Am. Bull.*, 87, 592–600, 1976.
- Kumar, C. K., *see* Brown, L.
- Kushiro, I., *see* Shimizu, N.
- Lear, R. D., *see* McDaniel, F. D.
- Light, G. M., *see* McDaniel, F. D.
- *4419 McDaniel, F. D., T. J. Gray, R. K. Gardner, G. M. Light, J. L. Duggan, H. A. Van Rinsvelt, R. D. Lear, G. H. Pepper, J. W. Nelson, and A. R. Zander, K-shell x-ray production cross sections of selected elements Ti to Sb for 1.0- to 5.0-MeV/amu ^7Li ions, *Phys. Rev., A12*, 1271–1280, 1975.
- Meyer, R. P., *see* Ocola, L. C.
- 4420 Mirabel, I. F., and K. C. Turner, An anomalous velocity neutral hydrogen structure near the galactic center, *Astrophys. Space Sci.*, 38, 381–394, 1975.
- Nelson, J. W., *see* McDaniel, F. D.
- 4421 Ocola, L. C., L. T. Aldrich, J. F. Gettrust, R. P. Meyer, and J. E. Ramirez, S. J., Project Narino I: Crustal structure under southern Colombia–northern Ecuador Andes from seismic refraction data, *Bull. Seis. Soc. Am.*, 65, 1681–1695, 1975.
- 4422 Pepper, G. H., and L. Brown, The $^{15}\text{N}(p,\alpha)^{12}\text{C}$ reaction with polarized protons from 0.34 to 1.21 MeV, *Nucl. Phys.*, A260, 163–171, 1976.
- Pepper, G. H., *see* McDaniel, F. D.
- Peterson, C. J., *see* Rubin, V. C.
- Ramirez, J. E., S. J., *see* Ocola, L. C.
- 4423 Rohrer, U., and L. Brown, The $^9\text{Be}(p,n)^9\text{B}$ reaction with polarized protons from 2.4 to 2.9 MeV, *Nucl. Phys.*, A261, 141–148, 1976.
- *4424 Rubin, V. C., W. K. Ford, Jr., and C. J. Peterson, Evidence for contraction in the nuclear ring of the barred spiral galaxy NGC 3351, *Astrophys. J.*, 199, 39–48, 1975.
- 4425 Rubin, V. C., N. Thonnard, and W. K. Ford, Jr., Observations of NGC 6764, a barred Seyfert galaxy, *Astrophys. J.*, 199, 31–38, 1975.
- Rubin, V. C., *see* Warner, J. W.
- 4426 Shimizu, N., Geochemistry of ultramafic inclusions from Salt Lake Crater, Hawaii, and from Southern African kimberlites, in *Physics and Chemistry of the Earth, Vol. 9*, pp. 655–669, L. H. Ahrens, J. B. Dawson, A. R. Duncan, and A. J. Erlank, eds., New York, Pergamon Press, 1975.
- 4427 Shimizu, N., and R. J. Arculus, Rare earth element concentrations in a suite of basanitoids and alkali olivine basalts from Grenada, Lesser Antilles, *Contrib. Mineral. Petrol.*, 50, 231–240, 1975.
- 4428 Shimizu, N., and I. Kushiro, The partitioning of rare earth elements between garnet and liquid at high pressures: Preliminary experiments, *Geophys. Res. Lett.*, 2, 413–416, 1975.
- 4429 Snoke, J. A., Archambeau's elastodynamical source-model solution and low-frequency spectral peaks in the far-field displacement amplitude, *Geophys. J. R. Astron. Soc.*, 44, 27–44, 1976.
- Thonnard, N., *see* Brown, L., and Rubin, V. C.
- Turner, K. C., *see* Mirabel, I. F.
- Van Rinsvelt, H. A., *see* Brown, L., and McDaniel, F. D.

- *4430 Wallace, D. G., Prediction of the secondary and tertiary structure of plastocyanin, *Biophys. Chem.*, 4, 123-130, 1976.
- *4431 Wallace, D. G., The sequence-immunology correlation among higher plant plastocyanins, *Immunochimistry*, in press.
- *4432 Wallace, D. G., and D. Boulter, Immunological comparisons of higher plant plastocyanins, *Phytochemistry*, 15, 137-141, 1976.
- 4433 Warner, J. W., G. E. Assousa, and others, Radio spectra of OH471 and OQ172, *Nature*, 249, 743-746, 1974.
- 4434 Warner, J. W., and V. C. Rubin, Physical conditions and structure in NGC 7293, "The Helix," *Astrophys. J.*, 198, 593-603, 1975.
- 4435 Wetherill, G. W., Late heavy bombardment of the moon and terrestrial planets, *Proc. 6th Lunar Sci. Conf.*, 2, 1539-1561, 1975.
- 4436 Wetherill, G. W., Radiometric chronology of the early solar system, in *Annual Review of Nuclear Science*, Vol. 25, pp. 283-328, E. Segre, J. R. Grover, and H. P. Noyes, eds., Annual Reviews, Inc., Palo Alto, California, 1975.
- *4437 Yeats, R. S., and S. R. Hart, Introduction and principal results, Leg 34, Deep Sea Drilling Project, in *Initial Reports of the Deep Sea Drilling Project*, Vol. 34, 814 pp., T. L. Valier, ed., Washington, D.C., U.S. Government Printing Office, 1976.
- Zander, A. R., see McDaniel, F. D.
- ity measurement (abstr.), *EOS Trans. Am. Geophys. Union*, 57, 286, 1976.
- King, G. C. P., see Evans, J. R.
- Linde, A. T., I. S. Sacks, and J. A. Snoke, A numerical model study of multiple rupture earthquakes (abstr.), *EOS Trans. Am. Geophys. Union*, 57, 154, 1976.
- Linde, A. T., see Sacks, I. S.
- Nicholls, I. A., see Whitford, D. J.
- Pepper, G. H. and L. Brown, An observation of the united-atom limit for the molecular orbital continuum (abstr.), *Bull. Am. Phys. Soc.*, 21, 649, 1976.
- Peterson, C. J., Rotation of the nuclear region of M31 (abstr.), *Bull. Am. Astron. Soc.*, 7, 254, 1975.
- Peterson, C. J., V. C. Rubin, and W. K. Ford, Jr., The peculiar galaxy NGC 1275 (abstr.), *Bull. Am. Astron. Soc.*, 8, 297, 1976.
- Peterson, C. J., V. C. Rubin, W. K. Ford, Jr., and N. Thonnard, Motions of the stars and excited gas in the barred spiral galaxy NGC 3351 (abstr.), *Bull. Am. Astron. Soc.*, 7, 538, 1975.
- Peterson, C. J., see Rubin, V. C.
- Roberts, M. S., see Rubin, V. C.
- Rodriguez B., A., see Sacks, I. S.
- Rubin, V. C., and W. K. Ford, Jr., The motion of our galaxy and the local group of galaxies (abstr.), *Bull. Am. Astron. Soc.*, 7, 253, 1975.
- Rubin, V. C., C. J. Peterson, and W. K. Ford, Jr., The rotation curve of the E7/S0 galaxy NGC 3115 (abstr.), *Bull. Am. Astron. Soc.*, 8, 297, 1976.
- Rubin, V. C., N. Thonnard, W. K. Ford, Jr., J. A. Graham, and M. S. Roberts, A galaxy of coefficients: $A_b, A_l, A_{ll}, A_{LC}, D_b$, and D_z (abstr.), *Bull. Am. Astron. Soc.*, 7, 531, 1975.
- Rubin, V. C., see Peterson, C. J.
- Sacks, I. S., and A. Snoke, Heterogeneous velocity structure at the base of the mantle (abstr.), *Trans. Am. Geophys. Union*, 57, 284, 1976.
- Sacks, I. S., J. A. Snoke, A. T. Linde, and A. Rodriguez B., Shallow seismicity in subduction zones (abstr.), 47th Annual Meeting of the Eastern Section of the Seismological Society of America held in St. Louis, Missouri, November 6-7, 1975.
- Sacks, I. S., see King, G. C. P., Linde, A. T., and Snoke, J. A.
- Snoke, J. A., Implications of moving boundaries in elastodynamics: Comments on "the pulse shapes and spectra of elastic waves generated when a cavity expands in an initial shear field" by Robert Burridge, *J. Geophys. Res.*, 81, 1035-1036, 1976.
- Snoke, J. A., and I. S. Sacks, Determination of the lithosphere-asthenosphere boundary using converted waves (abstr.), *EOS Trans. Am. Geophys. Union*, 57, 283, 1976.
- Snoke, J. A., see King, G. C. P., Linde, A. T., and Sacks, I. S.
- Thonnard, N., The 21-cm structure of WLM and its surroundings (abstr.), *Bull. Am. Astron. Soc.*, 7, 550, 1975.
- Thonnard, N., see Peterson, C. J., and Rubin, V.

ABSTRACTS AND MINOR PUBLICATIONS

- Ballard, G. S., see Evans, J. R.
- Beavan, R. J., see Evans, J. R., and King, G. C. P.
- Bilham, R. G., see Evans, J. R.
- Brooks, C., D. James, and S. R. Hart, Mantle isochrons and their implications for the isotopic composition of subcontinental lithosphere (abstr.), *EOS Trans. Am. Geophys. Union*, 57, 351, 1976.
- Evans, J. R., G. S. Ballard, R. J. Beavan, R. G. Bilham, G. John, and G. C. P. King, A tidal strain survey of Great Britain (abstr.), *EOS Trans. Am. Geophys. Union*, 57, 233, 1976.
- Evans, J. R., see King, G. C. P.
- Ford, W. K., Jr., see Peterson, C. J., and Rubin, V. C.
- Graham, J. A., see Rubin, V. C.
- Hart, S. R., see Brooks, C.
- James, D., see Brooks, C.
- John, G., see Evans, J. R.
- King, G. C. P., I. S. Sacks, J. R. Evans, R. J. Beavan, and A. Snoke, Single site phase veloc-

Wetherill, G. W., Total number of earth-crossing Apollo objects with radii larger than 500 meters (abstr.), *EOS Trans. Am. Geophys. Union*, 57, 275, 1976.

Whitford, D. J., and I. A. Nicholls, Potassium variation in quaternary lavas across the Sunda arc in Java and Bali (abstr.), *EOS, Trans. Am. Geophys. Union*, 57, 347, 1976.

PERSONNEL

Staff Members

L. Thomas Aldrich
George E. Assousa
Louis Brown
Dean B. Cowie¹
Scott E. Forbush, *Emeritus*
W. Kent Ford, Jr.
Stanley R. Hart²
Albrecht W. Hofmann
Bill H. Hoyer³

David E. James
Alan T. Linde
Nancy R. Rice⁴
Richard B. Roberts⁵
Vera C. Rubin
I. Selwyn Sacks
Norbert Thonnard
Kenneth C. Turner
George W. Wetherill, *Director*

Distinguished Service Member of Carnegie Institution

Merle A. Tuve

Research Associates (Staff)

Tom I. Bonner⁶
Mordeckai Magaritz⁷

J. Arthur Snoke
Kiyoshi Suyehiro⁸

Research Associates (Nonresident)

Mateo Casaverde, Instituto Geofísico del
Peru, Lima, Peru
Leonidas Ocola, Instituto Geofísico del
Peru, Lima, Peru

Hiromu Okada, Hokkaido University, Sapporo, Japan⁹
Anibal Rodriguez B., Universidad Nacional
de San Agustín, Arequipa, Peru

Shigeji Suyehiro, Japan Meteorological
Agency, Tokyo, Japan¹⁰

Carnegie Fellows (Postdoctoral)

John R. Evans¹¹
George H. Pepper
Charles J. Peterson

R. Sundar Rajan¹²
Stuart J. Weidenschilling¹³
David J. Whitford¹⁴

¹Institut Pasteur, Paris, France, from Jan. 20, 1975.

²Resigned Aug. 31, 1975.

³Resigned June 30, 1975.

⁴Resigned Feb. 15, 1976.

⁵Retired Dec. 31, 1975.

⁶Resigned Feb. 15, 1976.

⁷From Feb. 1, 1976.

⁸From April 1, 1976.

⁹Through Dec. 31, 1975.

¹⁰Through Dec. 31, 1975.

¹¹From Jan. 1, 1976.

¹²From Sept. 24, 1975.

¹³From Feb. 1, 1976.

¹⁴From Dec. 1, 1975.

Carnegie Fellows (Predoctoral)

John R. Bannister, University of Alberta,
Edmonton, Canada

Arturo Cuyubamba, McGill University,
Montreal, Canada¹⁵

Visiting Investigators

Claude Allégre, University of Paris, Paris,
France¹⁶

Montreal, Montreal, Canada¹⁷

Christopher Brooks, Université de

John R. Cleary, Australian National Uni-
versity, Canberra, Australia¹⁸

Trainee Fellows

Charles L. Bennett¹⁹

Antonio Flores²¹

Gregory S. DeWitt²⁰

Michael Schneider²²

Christine M. Seber²³

Collaborators

C. Aguirre B., Universidad Mayor de San
Andres, La Paz, Bolivia

S. del Pozo, Instituto Geofísico Boliviano,
La Paz, Bolivia

E. Arnal, Instituto Argentino de Radioas-
tronomía, Villa Elisa, Argentina

J. W. Erkes, State University of New York,
Albany, New York

L. G. Arnold, Ohio State University, Co-
lumbus, Ohio

A. J. Erlank, University of Capetown, Ron-
debosch, South Africa

E. Bajaja, Instituto Argentino de Radioas-
tronomía, Villa Elisa, Argentina

D. W. Evertson, University of Texas at
Austin, Texas

B. Balick, University of Washington, Seat-
tle, Washington

E. Filloy, Instituto Argentino de Radioas-
tronomía, Villa Elisa, Argentina

R. J. Beavan, Lamont Doherty Geological
Observatory, Palisades, New York

C. Garavito, Planetario Destrital, Bogota,
Colombia

E. Berg, University of Hawaii, Honolulu,
Hawaii

L. Gélinas, Génie Mineral, École Polytech-
nique, Montreal, Quebec, Canada

K. Bloomfield, Institute of Geological Sci-
ences, London, England

A. A. Giesecke, Instituto Geofísico del Peru,
Lima, Peru

M. Bracamonte, Trujillo, Peru

M. Gil, Instituto Argentino de Radioas-
tronomía, Villa Elisa, Argentina

B. F. Burke, Massachusetts Institute of
Technology, Cambridge, Massachusetts

Nicol Girardin, Institut de Physique du
Globe, Paris, France

R. Cabre, S. J., Observatorio San Calixto,
La Paz, Bolivia

M. Gordon, Instituto Argentino de Radioas-
tronomía, Villa Elisa, Argentina

G. N. Cohen, Institut Pasteur, Paris,
France

J. A. Graham, Cerro Tololo Interamerican
Observatory, La Serena, Chile

R. Colomb, Instituto Argentino de Radioas-
tronomía, Villa Elisa, Argentina

C. Heiles, University of California, Berke-
ley, California

H. E. Conzett, Lawrence Berkeley Labora-
tory, Berkeley, California

C. E. Helsley, University of Texas, Dallas,
Texas

G. L. Davis, Geophysical Laboratory, Car-
negie Institution of Washington, Wash-
ington, D. C.

D. Huaco, Instituto Geofísico del Peru,
Lima, Peru

¹⁵Through Dec. 31, 1975.

²⁰From June 1, 1976.

¹⁶From June 15, 1976.

²¹From May 1 to Aug. 31, 1975.

¹⁷Through Dec. 31, 1975.

²²From Sept. 29, 1975 to Mar. 3, 1976.

¹⁸From Sept. 15 to Dec. 31, 1975.

²³From Jan. 1 to Mar. 31, 1976.

¹⁹May 15–Aug. 15, 1975, and June 1–July 31,
1976.

- G. C. P. King, University of Cambridge, Cambridge, England
- C. K. Kumar, Howard University, Washington, D. C.
- I. Kushiro, Geophysical Laboratory, Carnegie Institution of Washington, Washington, D. C.
- Ruth M. Larimer, Lawrence Berkeley Laboratory, Berkeley, California
- R. P. Meyer, University of Wisconsin, Madison, Wisconsin
- I. Mirabel, Instituto Argentino de Radioastronomía, Villa Elisa, Argentina
- R. Morras, Instituto Argentino de Radioastronomía, Villa Elisa, Argentina
- Y. Motoya, Kamikineusu Seismological Observatory of Sapporo University, Hokkaido, Japan
- G. Olafsson, Akureyri, Iceland
- J. Oort, Sterrewacht, Leiden, The Netherlands
- R. W. Page, Bureau of Mineral Resources, Canberra, Australia
- E. Pimental, Cuzco University, Cuzco, Peru
- W. Pöppel, Instituto Argentino de Radioastronomía, Villa Elisa, Argentina
- G. Poupeau, Centre des Faibles Radioactivités, Gif-sur-Yvette, France
- J. E. Ramirez, S. J., Instituto Geofísico de los Andes Colombianos, Bogota, Colombia
- M. S. Roberts, National Radio Astronomy Observatory, Charlottesville, Virginia
- R. Rodriguez, Observatorio San Calixto, La Paz, Bolivia
- J. Rowe, U.S. Geological Survey, Reston, Virginia
- R. H. Sanders, National Radio Astronomy Observatory, Charlottesville, Virginia
- J. G. Schilling, Narragansett Marine Laboratory, University of Rhode Island, Kingston, Rhode Island
- D. W. Schwartzman, Howard University, Washington, D. C.
- R. G. Seyler, Ohio State University, Columbus, Ohio
- H. Sigtrygsson, Reykjavik, Iceland
- D. Simoni, Arequipa, Peru
- R. Stefansson, Reykjavik, Iceland
- L. Tamayo, Universidad Nacional de San Agustín, Arequipa, Peru
- J. L. Telleria, Planetario Destrital, Bogota, Colombia
- P. Truffa-Bachi, Institut Pasteur, Paris, France
- F. Volponi, Universidad Nacional de Cuyo, San Juan, Argentina
- R. E. White, Steward Observatory, University of Arizona, Tucson, Arizona
- J. G. Williams, Jet Propulsion Laboratory, Pasadena, California
- Y. Yamagishi, Matsushiro Seismological Observatory of Japan, Meteorological Agency, Matsushiro, Japan
- E. Zinner, McDonnell Center for Space Sciences, Washington University, St. Louis, Missouri

Supporting Staff

- | | |
|---|---|
| Caroline A. Busch, Typist, Fiscal Assistant ²⁴ | Janet C. Hunt, Secretary ²⁷ |
| R. Paul Busch, Caretaker (temporary) | Judith H. James, Typist ²⁸ |
| Louis S. Carter, Instrument Maker | Willis Kilgore, Jr., Caretaker |
| Gloria J. Counts, Clerk-Typist ²⁵ | Charles A. Little, Electronics Research Specialist |
| Dorothy B. Dillin, Librarian | Niels M. Pedersen, Fiscal Officer |
| John B. Doak, Electronics Research Specialist | Glenn R. Poe, Electronics Research Specialist |
| William N. Dove, Office Manager | Elliot M. Quade, Assistant Maintenance Foreman |
| Everett T. Ecklund, Design Engineer | Carl M. Rinehart, Instrument Maker |
| Mark Feigenson, Laboratory Assistant (temporary) | Michael Seemann, Design Engineer—Mechanical |
| Esther Gordon, Research Assistant | E. Lynn Smith, Typist, Fiscal Assistant ²⁹ |
| Bennie Harris, Caretaker | James E. Spicer, Maintenance Foreman |
| E. Kathleen Hill, Secretary ²⁶ | Milton T. Taylor, Instrument Maker |

²⁴From January 12, 1976.

²⁵From January 26, 1976.

²⁶Through February 15, 1976.

²⁷From May 6, 1976.

²⁸Through January 15, 1976.

²⁹Through September 30, 1975.

Hale Observatories

Operated by Carnegie Institution of Washington
and California Institute of Technology

Pasadena, California

Horace W. Babcock
Director

J. Beverley Oke
Associate Director

OBSERVATORY COMMITTEE

Horace W. Babcock, *Chairman*

J. Beverley Oke, *Vice-Chairman*

Jerome Kristian

Guido Münch

Allan Sandage

Wallace L. W. Sargent

Maarten Schmidt

Arthur H. Vaughan, Jr.

Contents

| | | | |
|--|-----|--|-----|
| Introduction | 277 | X-Ray Sources | 297 |
| Observing Conditions | 278 | Supernovae | 298 |
| Physics of the Sun | 279 | The Galaxy | 299 |
| Solar magnetic fields | 279 | Metal abundances in globular clusters .. | 299 |
| Large-scale velocity fields of the sun .. | 280 | Galaxies | 299 |
| Big Bear Solar Observatory | 280 | New redshifts for bright galaxies | 299 |
| Coronal holes | 280 | Distances to nearby galaxies derived | |
| Surge of 1971 | 281 | from brightest stars | 299 |
| X rays from solar flares | 281 | Supergiant cD galaxies | 300 |
| The lifetime and evolution of fibrils .. | 281 | Markarian galaxies | 300 |
| Macrospicules and microflares | 282 | Seyfert galaxies | 301 |
| Differential rotation | 282 | Infrared observations | 301 |
| Solar System Studies | 283 | Nuclear regions of M31 | 302 |
| Jupiter | 283 | Observational search for the | |
| Io | 283 | "missing mass" | 302 |
| Satellites and asteroids | 284 | Redshifts, magnitudes, and colors | |
| Stellar Spectroscopy | 284 | of a sample of galaxies | 302 |
| White dwarfs | 284 | Chemical history of galaxies | 303 |
| Studies of proper-motion stars | 287 | Large Magellanic Cloud | 303 |
| Rotation of B-type stars | 288 | Population synthesis | 304 |
| P- ³ He stars | 288 | Variable stars in the dwarf | |
| Braking of magnetic Ap stars | 288 | spheroidal galaxies | 304 |
| ³ He stars | 288 | Image processing of galaxy photographs | 305 |
| Circumstellar envelopes | 289 | Ejection from the spiral galaxy | |
| Stellar spectroscopy at 1 μ : R Aquarii .. | 289 | NGC 1097 | 305 |
| Stellar Chromospheres | 289 | Neighborhoods of galaxies | 306 |
| Absolute luminosities | 289 | M87 and its globular clusters | 308 |
| H and K fluxes in main-sequence stars .. | 289 | Clusters of Galaxies | 308 |
| Infrared and Millimeter-Band Photometry | 290 | Redshifts and magnitudes | 308 |
| Extragalactic objects | 290 | The Hubble diagram | 309 |
| Galactic center | 290 | Photometry and redshifts of first | |
| Nova Cygni 1975 | 290 | brightest cluster members | 310 |
| 1-mm photometry of compact | | Brightest cluster galaxies | 310 |
| extragalactic objects | 291 | The dynamics of galaxies and | |
| Globular Clusters | 291 | clusters of galaxies | 311 |
| Dynamical models | 291 | Equality of redshifts of E and S0 galaxies | |
| Interstellar Matter and Gaseous Nebulae | 292 | in the Virgo cluster | 311 |
| High-latitude reflection nebulosities | | A new nearby group | 311 |
| illuminated by stars of the | | X-ray clusters | 312 |
| galactic plane | 292 | Intergalactic hydrogen clouds | 312 |
| Interstellar matter | 294 | Radio Sources | 312 |
| Herbig-Haro object in the Orion Nebula | 294 | 3CR identifications | 312 |
| The H II region W3 | 295 | Perseus A | 312 |
| Infrared properties of OH masers | 295 | Quasars and Quasi-Stellar Objects | 312 |
| Dark clouds | 295 | Spectroscopic observations | 312 |
| Mapping of thermal emission from | | Quasar surveys | 313 |
| molecular clouds | 296 | Search for high-redshift QSOs | 313 |
| NGC 7538 | 296 | Absorption lines | 313 |
| Pulsars | 297 | Optical continuum | 315 |
| Search for the Hulse-Taylor binary | | Emission lines | 316 |
| pulsar | 297 | Observational Cosmology | 316 |
| | | The Hubble constant and | |
| | | deceleration parameter | 316 |

| | | | |
|---|-----|-------------------------------------|-----|
| Theoretical Studies | 317 | Guest Investigators | 322 |
| Gravitational radiation from pressureless nonaxisymmetric stellar collapse | 317 | | |
| Gravitational radiation from axisymmetric stellar collapse with pressure | 318 | | |
| Angular momentum of galaxies and tidal interaction | 318 | | |
| Instrumentation | 318 | Las Campanas Observatory | 334 |
| SIT acquisition and guiding system (SITEX) | 318 | 2.5-meter du Pont Telescope | 334 |
| Remote operation of Cassegrain ring rotation | 319 | Cassegrain camera | 335 |
| SIT-Vidicon digital spectrographs | 319 | Cassegrain spectrograph | 335 |
| Photon-Counting Image-Intensifier System | 319 | Television system | 335 |
| Charge-coupled devices | 320 | Infrared photometer | 336 |
| Photometry of stellar H and K lines | 320 | Coudé spectrograph | 336 |
| Infrared detection systems | 321 | Astronomers' Lodge | 336 |
| Astroelectronics Laboratory | 321 | Bibliography | 336 |
| | | Staff and Organization | 341 |
| | | Research Fellows and Students | 341 |

INTRODUCTION

New data on very faint sources far out in the Universe are beginning to accumulate at impressive rates. This situation, long worked for by observers, results from years of effort on the part of many individuals and groups to perfect digital or linear photoelectric devices capable of precise photometry on large numbers of picture elements within an optical image—in other words, to count incoming photons in the picture elements and to present the resulting large amount of information in a useful way. Such devices are equally important in the focal plane of a telescope or at the output end of a spectrograph that is attached to the telescope. But the photographic plate, especially when employing the most modern emulsions of high information content and optimum color sensitivity, continues to be invaluable, particularly for wide-angle recording.

Two groups at the Hale Observatories, Drs. Allan Sandage and Jerome Kristian, using the photographic method, and Drs. James E. Gunn and J. B. Oke, using an image tube, are reporting the discovery of impressive numbers of new faint clusters of galaxies. Such clusters are of importance because it is known that the brightest galaxy in a cluster (for reasons not yet understood) has a standard luminosity that is very nearly the same for any cluster. Thus the relative distances to such clusters can be derived, and if the redshifts of a number of the galaxies in each cluster can be measured with the spectrograph, new points in the Hubble diagram of redshift versus distance can be plotted.

Not only are dozens of distant clusters of galaxies being found, but the production of spectra and the measurement of redshifts of galaxies in them is proceeding at a record rate. For this work, Westphal, Kristian, and Sandage are using an SIT (silicon intensifier target) Vidicon on a prism

spectrograph at the 5-meter telescope, while Gunn and Oke are using the SIT-Vidicon with a grating spectrograph. Both of these SIT systems have been derived, with various technical improvements, from the system described in 1971 by Dr. Thomas B. McCord and Westphal (*Year Book* 71, p. 705). Most of the new redshifts being measured are greater than $z = 0.2$, and a substantial fraction have $z > 0.4$. These individual galaxies are of small angular extent, and most are much fainter than the uniform light of the sky (airglow and zodiacal light) that overlies them. Spectroscopy involves subtracting electronically the spectrum of the sky from that of the object plus sky. The principal limitation now is not measuring the spectra but finding faint candidates and positioning them on the slit. Observing depends upon low-level closed-circuit TV systems for these operations, which formerly involved the much more difficult technique of making blind offsets from nearby stars.

A significant new finding by Sandage further illuminates our understanding of the structure of the Galaxy. A photographic survey of the north and south galactic polar caps, in progress for several years, has not only resulted in discovery of many new remote clusters of galaxies, but has revealed, in our own Galaxy, faintly luminous nebulous regions, often in irregular connective patterns that extend over distances of degrees (see Fig. 4). The patterns display much local structure. Sandage's filter photography shows them to be reflection nebulae consisting of dust. The local surface brightness of the dust clouds that scatter illuminating radiation depends upon their optical thickness. Sandage shows that the observations are in good agreement with the hypothesis that the dust clouds are diffusely illuminated by general light of stars in the

galactic plane. The surface brightness of the denser reflection nebulae is predicted to be about 25.5 magnitudes per square arc second. The brightness of the clouds viewed as reflection nebulae is directly related to their extinction of the light of distant galaxies observed through them; this extinction can be as high as $\Delta m \simeq 0.3$ even in the direction of the pole of the Galaxy. Some parts of the north polar cap are free of detectable nebulosities to a level of 26 mag per square arc sec. Studies of the distribution and surface brightness of irregular reflection nebulosities in high galactic latitudes should produce detailed knowledge of the extinction, leading to more precise photometric corrections for the magnitudes of remote galaxies.

This year marks the completion of basic construction of the 2.5-meter Irénée du Pont Telescope of the Las Campanas Observatory in Chile. This project was initiated in December 1970 by a gift to the Carnegie Institution from Mr. and Mrs. Crawford H. Greenewalt. Design of the instrument by the staff of the Hale Observatories was begun soon thereafter, following a resolution by the Trustees that the Institution should augment the funds available to permit construction of a telescope of the 100-inch class. The telescope was constructed in the United States, shipped to Chile, and erected at the Observatory under the direction of Mr. Bruce H. Rule with the

collaboration of Las Campanas personnel. In May 1976, optics were installed and preliminary test photographs obtained. Staff members believe that the care taken in achieving near-perfection of the Cassegrain optical system of the telescope should permit the instrument to match the excellent quality of the natural observing conditions that prevail at the site.

The lengthy process of installing and adjusting the electronic control system and of perfecting all supplementary systems required for routine operation of the telescope is under way. Completion of these activities, together with the requirements for adjusting and testing the first series of auxiliary instruments for the telescope, is expected to require several additional months. Construction of the large coude spectrograph is a separate task that is expected to require three to four years.

It can now be made known that Miss Henrietta H. Swope was the donor of a very substantial gift to the Institution in 1967. This gift permitted development of the Las Campanas Observatory site, with its road and water system, as well as purchase of the 1-meter telescope that was installed in 1971. In accord with the wish of the donor, this gift remained anonymous for a number of years. It is evident that Miss Swope's generosity was of primary importance in the establishment of the new observatory.

OBSERVING CONDITIONS

The 2.5-meter Hooker Telescope at Mount Wilson was used for observations on 276 complete nights and 41 partial nights for a total of 2117 observing hours. Rainfall for the year was 551 mm, and total snowfall was 1066 mm.

The 5-meter Hale Telescope at Palomar Mountain was used for a total of 3489.8 hours, of which 3085.1 were nighttime hours, as shown in Table 1.

The difference represents twilight time that was used for infrared or planetary observations not requiring a dark sky. Total precipitation at Palomar was 596 mm, with 1168 mm of snow. The maximum temperature was 35.0°C in July; minima were -7.8°C in January and March.

Public visitors at the Palomar Observatory numbered 133,990 for the year.

TABLE 1. 5-Meter Observations

| Month | Complete Nights | Partial Nights | Zero Observation Nights | Total Hours Worked | Hours of Nighttime Observing |
|-----------|--------------------|-------------------|-------------------------------|--------------------------|------------------------------------|
| July | 25 | 5 | 1 | 261.5 | 239.6 |
| August | 29 | 1 | 1 | 303.3 | 255.9 |
| September | 29 | 1 | ... | 305.9 | 301.3 |
| October | 26 | 4 | 1 | 345.4 | 294.0 |
| November | 28 | 2 | 1 | 354.3 | 307.6 |
| December | 25 | 3 | 3 | 326.5 | 289.8 |
| January | 28 | 2 | 1 | 382.3 | 329.4 |
| February | 16 | 4 | 9 | 238.1 | 196.9 |
| March | 22 | 4 | 5 | 278.8 | 247.2 |
| April | 19 | 6 | 5 | 214.3 | 199.7 |
| May | 25 | 3 | 3 | 261.2 | 212.2 |
| June | 27 | ... | 3 | 218.2 | 211.5 |
| Totals | 299 | 35 | 33 | 3489.8 | 3085.1 |

PHYSICS OF THE SUN

Synoptic observations of the sun continue on Mount Wilson under the supervision of Howard. Between June 1, 1975, and May 31, 1976, the following observations were obtained:

| | |
|---|-----|
| Direct photographs | 334 |
| H α spectroheliograms, 9-meter focus | 621 |
| K2 spectroheliograms, 9-meter focus | 618 |
| Full-disk magnetograms | 341 |
| Integrated-light magnetic-field measurements | 317 |
| Sunspot drawings | 330 |
| Sunspot magnetic-field measurements | 327 |
| Solar observations were made on 341 days. | |

The daily magnetic-field plots are published monthly in the National Oceanic and Atmospheric Administration Bulletin *Solar Geophysical Data*. The magnetic synoptic charts are published in the *Quarterly Bulletin on Solar Activity* of the International Astronomical Union. Partial support for these observational programs comes from the National Aeronautics and Space Administration and the Office of Naval Research.

Solar Magnetic Fields

A study by Howard of magnetic-field measurements made on the same day with two different apertures shows a daily zero-level error in the setting of the Mount Wilson magnetograph of about 0.35 gauss (standard deviation). From the same observations, the scale (calibration) errors were found to be about 10%. On the size scale of the apertures used in this analysis (~10,000 km), the polarity mixing of magnetic elements varied from one portion of the period covered by these observations to the other. During the period of lower flux values, the polarities are more mixed. It is this mixing of polarities which, at least to some extent, is responsible for the lower flux measurements. Thus the difference in the measured total flux between activity maximum and minimum, which is only a factor of 2, is at least partially caused by a mixing of positive and negative elements within the aperture.

Howard, in collaboration with Z. Švestka, A. S. Krieger, and R. C. Chase of American Science and Engineering, Inc., has studied transequatorial co-

ronal loops seen in soft x rays from the A.S.&E. experiment on the Skylab mission. The loop system was probably born through reconnection within a few days after the birth of the second region. The loops could be seen in soft x rays for $2\frac{1}{2}$ days. Transient "sharpening" of the loops and a striking brightening of the whole loop system for about six hours seem to have been caused by changes in the magnetic-field configuration in one of the active regions. The electron temperature in the loops, equal to 2.1×10^6 K in the quiet phase, increased to 3.1×10^6 K during the brightening. At the same time, the loops became twisted while rising in the corona.

A study of the magnetic sector structure of the sun has been carried out by L. Svalgaard, J. M. Wilcox, and P. H. Scherrer at Stanford and by Howard. Using interplanetary magnetic-field data, 454 sector boundaries were identified, and the corresponding solar magnetic field configurations were mapped. The sector boundaries are clearly visible in the photospheric magnetic field as north-south polarity demarcation lines, extending to about 35° latitude on both sides of the equator.

Large-Scale Velocity Fields of the Sun

The study of the accumulated Mount Wilson solar velocity data continues by Howard and H. Yoshimura of the University of Tokyo. Evidence has been found in several instances for a large-scale boundary in the rotational velocity separating high and low velocity rates. The years preceding the solar activity minimum are characterized by an increase in the equatorial rotation rate, a striking decrease in the latitude gradient of the rotation rate at low latitudes ($\leq 40^\circ$), and a corresponding increase in the latitude gradient at high latitudes. The rotation of the polar latitudes remains unchanged. The rotation rate of the equatorial latitudes is now (May 1976) nearly up

to the sunspot rate ($2.9 \mu \text{ rad s}^{-1}$). This is the first time that such rotation changes have been observed, and it is the first time that such sensitive measurements have been available for this phase of the solar cycle, which is now very close to minimum.

Big Bear Solar Observatory

The 65-cm vacuum reflector was finally brought into proper alignment, and the coudé axis was aligned as well. Excellent photographs were obtained with a limiting resolution of $0.3''$, but it was found that only rarely did the atmosphere permit such good results. Drs. Alan Patterson and Kenneth Marsh are now resident at Big Bear to conduct the observational programs.

Coronal Holes

Zirin took part in the Skylab Coronal Hole Workshop, which met on several occasions in Boulder, Colorado, to combine the efforts of a number of people from different subdisciplines toward understanding the phenomena of coronal holes. Zirin devoted most of his efforts to trying to detect the presence of coronal holes in ordinary $H\alpha$ and K-line filtergrams. The results of this study were somewhat indeterminate; coronal holes clearly coincide with extensive areas where the chromosphere is quiet and relatively free of emission. It was found that if a hole is known to be present, it is fairly easy to draw in its boundaries from the $H\alpha$ and K-line pictures. However, given an $H\alpha$ or K-line picture, it is at present impossible to determine whether or not there is a coronal hole in it. One may thus conclude that the presence of a coronal hole has little effect on the underlying chromosphere, and that the chromospheric phenomena we see do not depend on conduction downward from the corona. (See also the report of William Adams on solar rotation near coronal holes.)

Surge of 1971

Zirin completed work on the analysis of a peculiar solar surge observed in 1971. This surge ejected a great mass of material that flew across the surface of the sun and formed a filament several hundred thousand kilometers away. The filament lasted for about 20 minutes, whereupon the material rose and returned to its origin. The significance of this most unusual event is not clear. It was possible to explain the radio emission from the surge with a simple thermal model at 200,000 °K. In addition, there is a hotter component of about 10% of the material at a temperature of several million degrees.

X Rays from Solar Flares

Zirin has made a study of nonthermal x rays from solar flares, comparing Big Bear data with data obtained by a number of different spacecraft. In every case (about 15 flares), the hard x-ray flux (greater than 20 keV) measures the time derivative of $H\alpha$ intensity. However, after the third hard x-ray burst ends, the $H\alpha$ intensity may continue near the maximum level if a thermal cloud is formed. This cloud is then responsible for the soft x-ray burst. The energy emitted in $H\alpha$ is often about 10% the energy of the nonthermal electrons, which typically have a hardness index of about 3. The radio spectrum produced by these electrons was then modeled, using the inferred density and spectrum from the hard x-ray burst and the observed $H\alpha$ area. It is possible to fit the observed radio-burst data in almost every case by appropriate use of synchrotron self-absorption and free-free absorption, but unfortunately there are many parameters and the results are not convincing. Typical values of magnetic field of several hundred gauss and density of 10^9 electrons in the nonthermal plasma are found. It is not possible to differentiate between the thin foil and thick foil models of hard x-ray bursts.

It was found that a clear distinction existed in $H\alpha$ between thermal and nonthermal x-ray bursts. The nonthermal bursts are invariably visible in offband $H\alpha$ (about 0.8 Å from line center), while the thermal bursts produce no emission offband. Thus the line width of $H\alpha$ excited by nonthermal particles is broad compared to that in a thermal x-ray flare. The profiles in impulsive x-ray bursts are consistent with the possible momentum transfer by hard electrons incident on protons. It is postulated that the initial energy input in a nonthermal flare occurs through acceleration of electrons according to a power-law spectrum, the entire input occurring in the first moments of the flare.

It was found that x-ray bursts with multiple spikes usually were related to optical flares with several stages, each new $H\alpha$ brightening or ejection corresponding to a new spike in the x-ray flux.

The Lifetime and Evolution of Fibrils

A detailed study has been made of the lifetimes and evolution of fibrils in McMath 12417, using high-resolution filtergrams in $H\alpha$ and Ca II K made at Big Bear Solar Observatory. It was found that when viewed near disk center the lifetime of a fibril is a monotonically increasing function of its maximum apparent length. This relationship, together with the form of the variation of fibril lengths as a function of time, suggests that fibrils result from material being impulsively injected into magnetic-field lines at approximately 30 km s⁻¹ and returning under gravity. The lifetimes and apparent lengths of fibrils are then a function of the inclination of the field lines only. A study of wavelength scans through the $H\alpha$ line confirms that the apparent extension and retraction of fibrils represent true mass motion.

Macrospicules and Microflares

From careful scrutiny of Big Bear full-disk $H\alpha$ time-lapse movies under high magnification, Tang has found a class of small flarelike events that occur in quiet regions at all latitudes, including the polar regions. These events are most noticeable at the limb, where they typically have the appearance of erupting loops or surges. They are smaller than a supergranule (heights, $5\text{--}15 \times 10^3$ km; widths, $1\text{--}15 \times 10^3$ km), last for 5 to 10 minutes, and rise at velocities up to about 100 km s^{-1} . In the polar regions, the larger of these eruptions are apparently the so-called polar-limb surges that have been observed in $H\alpha$ at several observatories since at least as long ago as 1957 (G. Godoli and F. Mazzucconi, *Astrophys. J.*, 147, 1131, 1967).

Small surgelike events, termed macrospicules, have been detected and studied on the polar limbs in *EUV* spectroheliograms from Skylab (J. D. Bohlin *et al.*, *Astrophys. J. [Lett.]*, 197, L133, 1975; P. L. Withbroe *et al.*, *Astrophys. J.*, 203, 528, 1976). The $H\alpha$ limb events are similar to the *EUV* macrospicules in shape, size, motion, and duration. On this basis, Moore and Tang (*Bull. Amer. Astron. Soc.*, 7, 423, 1975) proposed that the $H\alpha$ limb eruptions were the $H\alpha$ counterpart of the *EUV* macrospicules and named the $H\alpha$ events $H\alpha$ macrospicules.

Another discovery from Skylab was the observation of flare events in x-ray bright points (L. Golub *et al.*, *Astrophys. J. [Lett.]*, 189, L93, 1974). X-ray bright points are the x-ray images of ephemeral active regions: bipolar magnetic regions that are smaller than supergranules and with lifetimes usually less than a day. Since x-ray bright points occur at all latitudes and are the only observed centers of activity in the polar regions, Moore and Tang (*Bull. Amer. Astron. Soc.*, 7, 423, 1975) proposed that macrospicules are produced by flares in these ephemeral active regions. Because of their very

small size, these flares are appropriately termed microflares.

The above interpretations proposed by Moore and Tang were based on indirect evidence rather than on direct identification of $H\alpha$ events with either *EUV* macrospicules or flares in ephemeral active regions. However, more recently Moore, in collaboration with J. D. Bohlin at the Naval Research Laboratory and L. Golub at American Science & Engineering, has found several direct identifications of $H\alpha$ macrospicules with *EUV* macrospicules and with flares in x-ray bright points on the limb. Thus the identifications proposed by Moore and Tang have been confirmed.

Differential Rotation

Solar differential rotation measurements give a wide variety of results, depending upon the method of measurement employed, and it appears that the differences are genuine properties of the sun, i.e., different rotation tracers actually rotate at different rates. Long-lived filaments have long been used as such rotation tracers, but it is not at all clear that they are representative of filaments as a class (of which they compromise only about 5%). A study of short-lived filaments was therefore begun in the hope that the higher quality of the $H\alpha$ data currently available would make it possible to overcome the difficulties inherent in such an undertaking. The resulting measurements produced a rotation curve with a differential term approximately half the size of the corresponding term in the long-lived filament rotation curve.

A variation of the same measurement technique was then applied to a small sample of filaments bounding the unipolar magnetic region occupied by CH1, a large coronal hole observed by Skylab. This coronal hole had shown very little differential rotation during its several-month life span, and the ro-

tation of the underlying unipolar region was consequently of considerable interest. Inasmuch as filaments are known to form preferentially along field reversal lines, they furnish a possible tool for measuring the rotation of

the underlying unipolar region, and this provided the motivation for our measurements. The resulting rotation curve was in remarkably good agreement with that of the overlying coronal hole.

SOLAR SYSTEM STUDIES

Jupiter

The systematic observation of the variations in time of the intensity of the S1 and S0 lines of the (3, 0) band of H_2 over various regions of the Jupiter disk (*Year Book 73*, p. 131) was continued by Münch in collaboration with C. Pilcher of the University of Hawaii. For the purpose, the coudé interferometric scanner of the 2.5-meter Mount Wilson telescope was used, with a spectral resolution of 0.074 \AA and an angular resolution of $2''$. Similar measurements were also made on various regions of the Saturn disk.

Io

With the 150-mm aperture PEPSIOS spectrometer of the University of Wisconsin installed at the coudé focus of the 5-meter telescope, Münch, in collaboration with Drs. John Trauger and Fred Roesler of the University of Wisconsin, has studied the characteristics of the sodium emission associated with Io. The field optics ($f/40$) allowed use of a maximum entrance aperture $25''$ in diameter for a spectral resolving power of 150,000. A series of 60 profiles of the D_2 line was obtained when Io was near both its eastern and western elongations. The intensity-velocity distribution of the D_2 emission within $25''$ of Io was studied by line profiles obtained with a nested set of concentric annular quadrants of various radii. In addition, sample D_2 scans were obtained from regions $25''$ in diameter centered on the plane of Io's orbit, at distances of $69''$, $138''$, and $207''$ from Io in the direction away from Jupiter, and at a distance of $69''$ from Io toward Jupiter. The main

results of the observations can be summarized as follows:

1. The D_2 emission rate at a distance of $2.5''$ from Io has a value, near eastern elongation, of 80 kilorayleigh (KR), corresponding to a column density of $2 \times 10^{11} \text{ cm}^{-2}$. The emission rate decreases exponentially from this value, with a scale of $3''$, out to distances from Io of around $40''$. Farther out, the rate of decrease in surface brightness appears to be slower according to power law r^{-n} of the distance r from Io, with $n = 1.7$.

2. The line profiles for regions centered on Io are peaked at the value corresponding to the Io orbital radial velocity but are asymmetric, with a tail extending toward the larger velocities without regard to sign. This high-velocity tail extends beyond the velocity of escape from Jupiter. The degree of asymmetry of the profiles appears to increase with distance from Io.

3. At distances $\geq 69''$ from Io in the direction away from Jupiter, peak emission occurs at the Keplerian velocity around Jupiter; but at $r = 69''$ toward Jupiter, peak emission corresponds to the projected Io orbital velocity. It thus appears that the density of sodium atoms falls off sharply inside Io's orbit toward Jupiter.

4. The brightness distribution of D_2 line emission is not symmetric with respect to Io or to the trace of its orbital plane.

The presence of the $K I \lambda 7699$ line in the spectrum of the Io emission region was discovered by Münch, Roesler, and Trauger on August 28, 1975, also with the PEPSIOS spectrometer. Unlike the Na D_2 line, the profile of the K I line is

symmetrical, with a nearly gaussian form of 3.16 km s^{-1} dispersion. The measured emission rates imply a ratio of 20 between the column densities of sodium and potassium. The paths of line formation for both species are, however, different, as indicated by their different line shapes. Since the lifetime of the neutral K and Na atoms is determined by collisional ionization with thermal electrons in the Jupiter plasmasphere, and the cross section for this process is about twice as large for K as for Na, for a plasma temperature of 100 eV the abundance ratio Na/K will be less than the ratio of column densities, and depending on the results of model calculations under way, it may be closer to the value corresponding to the earth's crust (4:1) rather than the solar value (40:1).

The dependence on time of the shape of the Io emission cloud, expected from its interaction with the Jupiter magnetospheric plasma, has been studied by Münch in a series of spatial interferograms. The rings of a 40-mm aperture Fabry-Perot étalon were projected on the plane of the sky around Io by means of a collimator and then reimaged with an f/1.4 lens on a magnetically focused intensifier. The device was mounted on the coude spectrograph of the 1.5-meter Mount Wilson telescope in order to obtain a field of $110''$ diameter. The étalon spacer was chosen to make the rings of the D_2 and D_1 lines coincident at a central order of interference equal to 7945. Using a focal-plane occulting disk to block off the light of Io, it was possible to photograph rings of $35''$ diameter with an exposure of one hour. The limiting exposure, around two hours, was set by the amount of scattered continuum light from Jupiter. The interferograms obtained show clearly the strong concen-

tration of the Na emission toward Io and toward a plane close to but not coincident with Io's orbit. The emission cloud appears to be flattened to a degree increasing with distance from Io, and its form varies with the magnetic latitude of Io in the sense that the emission lines are weaker toward the Jupiter magnetic equator.

Satellites and Asteroids

Kowal, working under Sargent's general direction, continued his search for faint satellites of the outer planets and discovered a probable fourteenth satellite of Jupiter. The new object was photographed with the 1.2-meter Schmidt telescope on September 30, October 1, and October 2, 1975. Its visual magnitude is approximately 21, and it is estimated to be between 5 and 10 km in diameter. Not enough observations were obtained to allow the determination of an orbit for this object, but a heliocentric orbit has been ruled out. It is hoped that more observations can be obtained at the next opposition of Jupiter, in November 1976.

Plates of the outer satellites of Jupiter were also obtained for the U.S. Naval Observatory in a project to determine better ephemerides of those satellites.

A search was conducted for new satellites of Saturn, but none were found.

On December 27, 1975, Kowal discovered a new Apollo asteroid with the 46-cm Schmidt telescope. This object, designated 1975 YA, was found on a film taken for the supernova search and was moving across the sky at a rate of $21''$ per day when first sighted. The asteroid's orbit has the unusually high inclination of 64° and a perihelion distance of 0.9 A.U.

STELLAR SPECTROSCOPY

White Dwarfs

A deeper insight into the physical processes that separate the degenerate

stars with hydrogen from those with helium atmospheres has been obtained by Greenstein, largely with the multichannel spectrophotometer. With in-

creased numbers of helium stars, it became clear that convection to various depths must be episodic for degenerate stars in the range of temperature $25,000^{\circ}$ to $12,000^{\circ}\text{K}$. No helium-rich white dwarf atmosphere has been found hotter than $25,000^{\circ}$, where helium lines have their maximum strength. (Only one star, probably near $50,000^{\circ}$, has both ionized helium and hydrogen in its spectrum.) Among the cooler helium-atmosphere white dwarfs, two have been found in which the lines of ionized calcium appear. This extraordinary range of excitation is still compatible with a reduced abundance of calcium compared to the opacity-producing elements. Most cooler white dwarfs with metallic lines are extremely metal deficient. A working hypothesis is that degenerate stars start very hot, with or without hydrogen at the surface, but in any case, accrete interstellar matter of normal composition. In a relatively short time, the high gravity results in a very complete separation, with hydrogen at the top, helium below, and the metals still deeper. Near $25,000^{\circ}$ the stability of this molecular weight gradient is overturned by convection, and both helium and varying small amounts of metal dilute the accreted hydrogen for a time. The helium atmosphere with metals visible may represent a later stage as the molecular weight gradient reestablishes itself when convection stops. It is not obvious that this happens only once in the life of a white dwarf, nor that it requires the star to evolve in the direction mentioned. An alternate view is that convection may start at a lower temperature and because of the decrease of opacity result in a higher-temperature object that gradually cools again.

An important feature of the hydrogen white dwarfs has been discovered in collaboration with Drs. Alec Boksenberg, Robert Carswell, and Keith Shortridge of University College London. The Image Photon Counting System was used in the coudé spectrograph of the Hale reflector to study a

phenomenon discovered earlier by Greenstein in 40 Eridani B (Fig. 1) and Wolf 1346. Abnormally sharp cores exist at the center of the hydrogen lines $\text{H}\alpha$ and $\text{H}\beta$. The efficiency of the IPCS system permitted observation of ten hydrogen-atmosphere white dwarfs, with proof of the existence of sharp cores in $\text{H}\alpha$ or $\text{H}\beta$ for seven of them. Observations by Greenstein with the coudé image-tube spectrograph at 27 \AA mm^{-1} had already revealed the existence of sharp $\text{H}\alpha$ cores in five other white dwarfs of type DA. These cores arise from the large optical depth at the center of $\text{H}\alpha$ and the low boundary temperature of hydrogen atmospheres caused by Balmer and Lyman line blanketing. Greenstein and Deane Peterson of the State University of New York at Stony Brook predicted nonlocal thermodynamic-equilibrium profiles with cores essentially of thermal width (about 15 km s^{-1} , mean velocity). If the projected rotational velocity of a white dwarf is larger than this thermal velocity (30 or 40 km s^{-1}) the sharp core would be destroyed. It is now clear that very slow rotation, certainly less than 40 km s^{-1} and probably for some stars less than 10 km s^{-1} , is the rule for hydrogen white dwarfs. The implication is that during the red-giant phase considerable transfer of angular momentum between the center and envelope of the star must occur. The mass loss of the red giant should be accompanied by selective loss of matter of greater than average angular momentum per gram. The braking of the object, possibly by interaction of the stellar wind with the interstellar medium via magnetic fields, seems to be very successful. The core is finally exposed as a hot subdwarf and eventually a white dwarf of small specific angular momentum. If the sun were to shrink homologously to a white dwarf, the rotational velocities would be over 500 km s^{-1} . Since in many white dwarfs the mass lost is approximately three quarters of the star's initial mass, this mechanism is quite efficient.

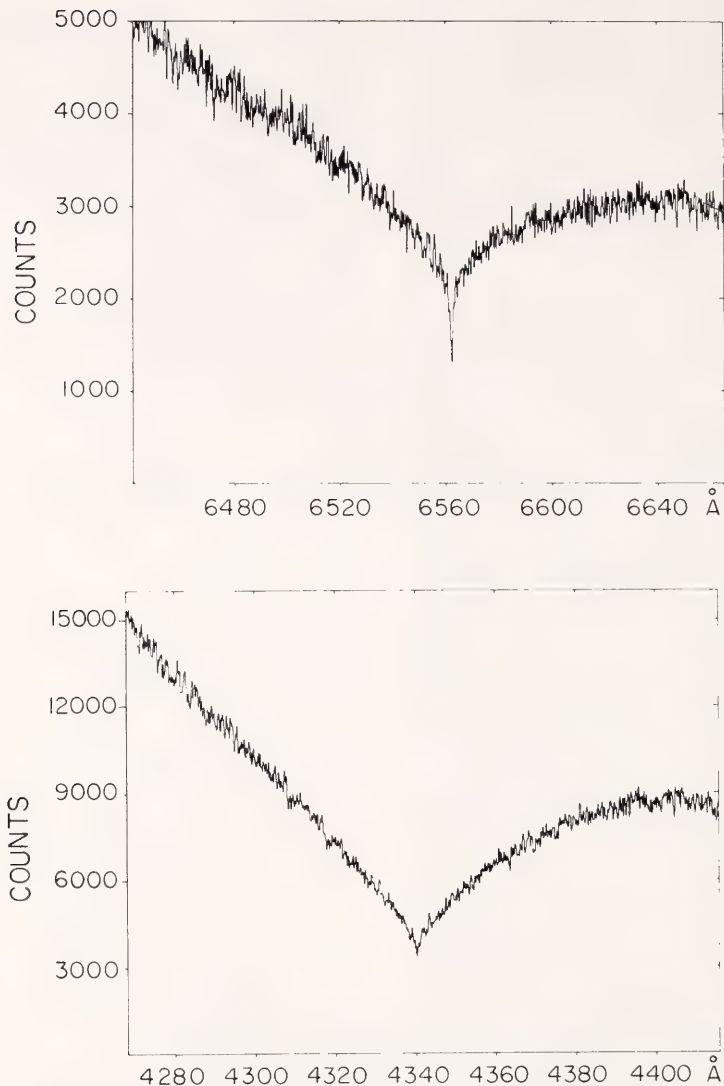


Fig. 1. The line profiles of hydrogen in the classical white dwarf 40 Eridani B. These were obtained with the Hale Telescope at Palomar, using the Image Photon Counting System developed by A. Boksenberg of University College London. The plots show the photon counts per picture element with this modern television system. The background slope is caused by the sensitivity changes within the entire system. Significant is the enormous width of the H γ line, caused by Stark broadening in the high-pressure atmosphere. The unusual feature of the H α line, however, is an extremely sharp deep core, less than 5 picture elements wide in toto. This deep core is produced at the top of the atmosphere where the pressure is so low that the Stark broadening is minimal. Part of the apparent width is instrumental in origin, in spite of the original dispersion of 15 \AA mm^{-1} . The deep core is produced by effects of nonlocal thermodynamic equilibrium. However, its sharpness proves that the white dwarf cannot be rotating rapidly, since rotation of as much as 30 km s^{-1} at the equator would blur the core out of existence. The estimated rotation is certainly less than 20 km s^{-1} and perhaps less than 10 km s^{-1} . Thus the period of rotation of the white dwarf must be longer than 30 min and possibly longer than 1 hr. Were the sun to contract without loss of angular momentum to the size of a white dwarf, its equatorial velocity would be about 300 km s^{-1} .

As a further result of the sharp line cores in the hydrogen-line white dwarfs, it has been possible to derive rather accurate radial velocities. The correlation between these and the prime-focus spectrograph results as measured by Virginia Trimble of the University of California at Irvine and Greenstein is fairly good, with 0.84 correlation coefficient and only small systematic difference. For the stars with sharp cores observed either with the coudé image tube or the IPCS, a mean K -term (i.e., a systematic expansion due to the gravitational redshift) of $+44 \text{ km s}^{-1}$ is derived. This is within the probable errors of the photographic value of Trimble and Greenstein, $+51 \text{ km s}^{-1}$. This confirms a mean mass of about 0.6 to 0.8 M_{\odot} for the white dwarfs.

Individual white dwarfs of special interest are being searched for by the multichannel spectrophotometric program. In studies made in collaboration with Boksenberg, the hot star Feige 7 seems almost certain to be a magnetic white dwarf, showing, without a Zeeman analyzer, resolved triplet patterns of $H\beta$ and $H\gamma$. The 12,000° helium-rich white dwarf G111-54 was found by Greenstein and Boksenberg to have only the strong, relatively sharp lines of ionized calcium. Several suspected late-type red degenerates were also studied for very weak metallic features. The difficulty of separating such metal-poor, helium-rich, cool degenerate stars from extremely high-velocity, metal-poor, hydrogen-rich G or K subdwarfs is extreme. Only parallax and proper motion will decide.

Greenstein has published data on 189 multichannel spectra observed for various types of degenerate stars, in the form of a number of monochromatic colors and magnitudes. Study of the correlation of colorimetric properties and luminosity for stars of known parallax indicates that the degenerate stars form a relatively narrow sequence with a spread of about ± 0.7 magnitude. These color-luminosity curves are presented in the *Astronomical Journal* (81, 323-338, 1976) and predict the ex-

pected photometric parallax to be compared with trigonometric parallaxes. A considerable number of cool degenerate stars exist with relatively large predicted parallax but have not yet been measured. The space motions are those of the old disk population, although some Population I and about 9% Population II degenerate stars exist. The number of cool ($< 7000^{\circ}$) degenerate stars has been doubled, but this is not enough for an elementary theory of cooling. The low number of red degenerates probably arises from the rapid drop in specific heat of the core below effective temperature 6000° .

There is evidence that Population II stars more than 1.5 mag subluminous are rare. When allowance is made for differential line blanketing, part of this discrepancy is eliminated. A large gap remains between the faintest red subluminous star and the faint red degenerates.

Studies of Proper-Motion Stars

A systematic program to improve the relation between luminosity and color for proper-motion stars has been continued by Greenstein with the multichannel spectrophotometer. About 100 stars of known parallax are included in this program, and another 300 of large proper motion. Preliminary indications are that a subluminous sequence approximately 1 mag below the main sequence exists in almost any color-luminosity plot of parallax stars. With a still insufficient number of parallaxes for late-type, very high-velocity stars, this difference seems to disappear at dm2 or dm3. The earlier high-velocity M stars are distinguished by a relatively greater ratio of hydride to oxide bands. At lower temperatures, the hydride bands weaken, and differential line blanketing may disappear. Alternatively, there may be few or no very high-velocity stars of late type and low luminosity. To illuminate the latter problem, basic for the existence of a possible galactic halo of low-mass M

dwarfs, a systematic program has been undertaken. The color-luminosity curves permit calibration of stars of known multichannel color. Greenstein's program will measure all Lowell stars with proper motion larger than $1''$ per year that are brighter than magnitude 16.4.

Rotation of B-Type Stars

Preston has used 20 \AA mm^{-1} spectrograms obtained with the Mount Wilson 2.5-meter telescope to estimate projected rotational velocities for 180 stars of types B1–B5. This study completes his survey of the rotational properties of the bright northern B-type stars. No new chemically peculiar stars were detected. Higher-dispersion (9 or 4.5 \AA mm^{-1}) spectrograms were subsequently obtained for some 40 of these stars with $v \sin i < 40 \text{ km s}^{-1}$ to better define the $v \sin i$ distribution near the origin and to lower the detection limits for chemical peculiarities. This effort led to the discovery of only one peculiar star, HR 7467, which exhibits enhanced lines of P II and P III and no detectable rotational broadening ($v \sin i \leq 5 \text{ km s}^{-1}$). As in the case of 3 Centauri A and ι Orionis B, positive wavelength shifts for the He I lines $\lambda\lambda$ 4921, 5015, and 6678 indicate a gross overabundance of ^3He ($^3\text{He}/^4\text{He} \sim 2$), but unlike 3 Cen A, HR 7467 does not exhibit lines of Ga II or Kr II that can be detected at 4 \AA mm^{-1} dispersion.

P– ^3He Stars

The companion of Rigel is a double-lined spectroscopic binary with a period of 10 days. Preston has found lines of P II and P III in the spectrum of the primary component and a $+0.25\text{-\AA}$ shift of He I λ 6678 that indicates a $^3\text{He}/^4\text{He}$ ratio comparable to those found for 3 Cen A, ι Ori B, and HR 7467. The P III/P II and Si III/Si II line ratios for Rigel B (primary) indicate a spectral type considerably earlier than B9, as estimated by Sanford, and more

nearly like that of 3 Cen A. Lines of Ga II and Kr II are not visible on 4 \AA mm^{-1} spectrograms. Instead, enhanced lines of A II are present, including the leading lines of RMT multiplets 1, 2, 6, 7, and 10. Thus, of the four P– ^3H stars known at present, no two are spectroscopically alike. Three, curiously, are members of visual binary systems in young stellar associations, while one, HR 7467, is an isolated field star with MK type (B5 II–III) and β , c indices that indicate a late stage of main-sequence evolution. All four are slow rotators, but the low incidence of such stars among slow rotators in the field sample suggests that slow rotation is not a sufficient condition for the production of the peculiarities of these objects.

Braking of Magnetic Ap Stars

Hartoog has completed a study of the rotation of Ap stars in clusters and associations to look for magnetic braking. No evidence for magnetic braking was found. Hot Ap stars seem to rotate more rapidly than cool Ap stars at all ages, so the observed decrease in average rotational velocity with decreasing temperature must not be an age effect. It would appear that most of the angular momentum is lost very early, probably before the star reaches the main sequence.

^3He Stars

Hartoog, using plates from the Hale Observatories' plate collection, has identified ^3He in α Sculptoris. The wavelengths of $\lambda\lambda$ 6678, 4387, and 5015 all indicate about 50% ^3He . Jugaku and Sargent (*Publ. Astron. Soc. Pacific*, 73, 249, 1961) describe this star as having underabundances of oxygen and helium and overabundances of strontium, chromium, and titanium. In this respect α Sculptoris is quite different from other ^3He stars.

Circumstellar Envelopes

The direct measurement of the angular diameter of the circumstellar envelope around α Orionis (M2 Ib) by A. P. Bernat and D. L. Lambert (*Astrophys. J. [Lett.]*, 201, L153, 1975) led Münch and S. Roesler and J. Trauger of the University of Wisconsin to attempt a similar measurement for the more luminous and distant star μ Cephei (M2 Ia). The observations were carried out at the coudé focus of the 5-meter telescope with the 150-mm PEPSIOS spectrometer. Using both an annular diaphragm with a central occulting disk of 2.7" diameter and the complementary aperture with the same diameter, scans of the K I λ 7699 and D_2 lines were obtained over a range of 75 km s^{-1} under excellent seeing conditions. By subtracting one scan from the other after normalizing them to the same continuum level, an excess of radiation was found in the scan corresponding to the annular diaphragm; this has been ascribed to emission of the circumstellar shell. The circumstellar D_2 -line emission has an apparent width at half maximum of 15 km s^{-1} and its peak intensity is 10% of the stellar continuum. Since μ Cep is at a distance of no less than 1 kpc, it follows

that the radius of its circumstellar envelope is of the order of 2000 A.U.

Stellar Spectroscopy at 1 μ : R Aquarii

In the course of reducing spectra taken in the 1-micron spectroscopy program, Zirin found that the variable star R Aqr, which had been identified as a source of radio emission by P. C. Gregory and E. R. Seaquist (*Nature*, 247, 532, 1974), also displayed the Fe XIII coronal line at 10747 Å. The coronal line was positively identified on two plates obtained in 1971 and 1972. A new plate obtained in 1976 did not show this line. On the basis of the coronal line identification, its intensity, and the absence of the companion 10798 Å line, it was possible to make a rough model of the coronal cloud that surrounds R Aqr. At a temperature of $1,000,000^\circ\text{K}$, the product of the cloud radius and electron density is 2×10^{18} , and the thermal radio flux at 3.5 cm is $1.44 \times 10^{-15} R_{\text{cor}} \text{ mJy}$. Thus, if the radius of the corona is less than $4 \times 10^{15} \text{ cm}$, the observed flux of 8 mJy can be obtained with a temperature of $2 \times 10^6 \text{ K}$.

STELLAR CHROMOSPHERES

Absolute Luminosities

Wilson has completed and published his work on the absolute magnitudes of over 700 late-type giants, subgiants, and supergiants from the widths of the chromospheric K-emission components.

H and K Fluxes in Main-Sequence Stars

The investigation of variations in flux of the chromospheric H and K

emission in main-sequence stars has continued. Several objects have completed about one cycle of variation, and several others appear close to completion. These cyclic variations are presumably the stellar analogs of the solar cycle. It is anticipated that this work will be published sometime in the coming calendar year.

INFRARED AND MILLIMETER-BAND PHOTOMETRY

Extragalactic Objects

This year marked the conclusion of a long-term infrared study of several extragalactic objects carried out by Neugebauer and Becklin to set limits on the source of infrared energy by studying the objects' time history. The 1967 and 1976 light curves for 3C273 and 3C345 are shown in Figs. 2 and 3. For 3C273 no significant variability greater than the uncertainties of about 10% is seen at either 2.2 or 3.5 μ . Since the infrared energy distribution of 3C273 appears to peak at 3.5 μ , it can be concluded that there is no evidence for infrared variability from this QSO. For 3C345, 2.2- μ variations of a factor of 3 are shown over the years; the variations appear to have the same phase and amplitude as visible variations. Changes by a factor of 2 within one month's time rule out a simple thermal source for the 2.2- μ radiation from 3C345.

2.5- μ spectra of several of the 2.2- μ point sources shown on the high-resolution maps of Becklin and Neugebauer (*Astrophys. J. [Lett.]*, 200, L71, 1975) have been made. Three of the sources, including the brightest, show strong carbon-oxide absorption at 2.3 μ , indicating that they are probably individual late-type giant or supergiant stars at the galactic center. Two sources do not show CO absorption; one is associated with the brightest 10- μ emission, while the other is near the nonthermal radio source found by B. Balick and R. L. Brown (*Astrophys. J.*, 194, 265, 1974).

Observations at 10 μ have been made by Willner. The major result is that the 10- μ silicate feature is shown to be mostly interstellar. Also, the Ne II line at 12.8 μ has been mapped at 5'' resolution; the results indicate that the 10- μ emission is not correlated closely with the ionized gas.

Galactic Center

During the past year much work has been done on the central 3-pc core of the center of the Galaxy by Becklin and Neugebauer. In particular, the 2.1 to

Nova Cygni 1975

During the past year extensive infrared observations of Nova Cygni

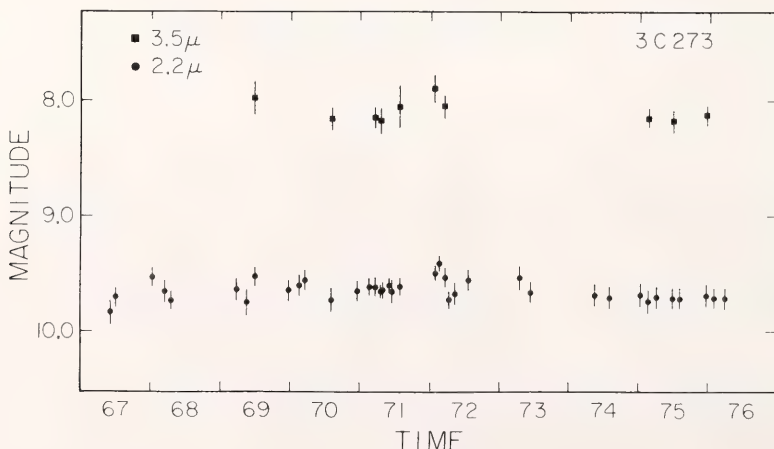


Fig. 2. Photometry of 3C 273 at 2.2 μ and 3.5 μ over the time period 1967–1976.

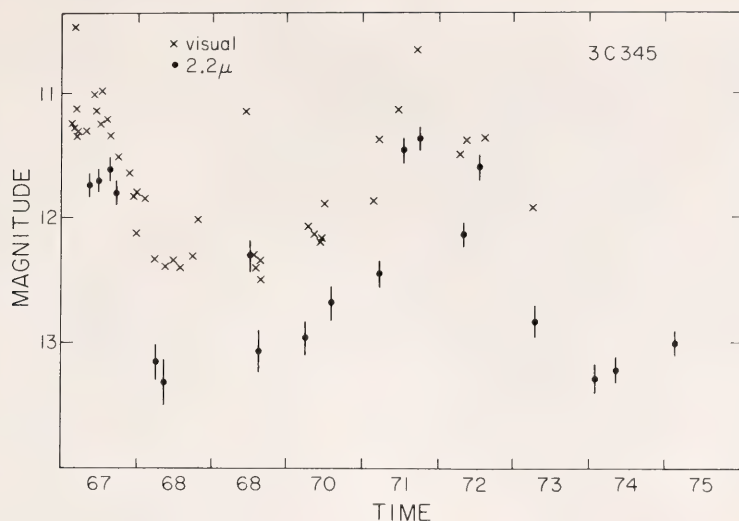


Fig. 3. Comparison of visual light and 2.2- μ variability of 3C 345 over the time period 1967–1975.

1975 have been made by Neugebauer, Becklin, and many members of the infrared group. The photometric results are in basic agreement with those of J. S. Gallagher and E. P. Ney (*Astrophys. J.*, 204, L35, 1976) but are much more extensive, particularly in the early and later phases of the nova. In addition, spectroscopy with 1% resolution was obtained in the 2.2- μ region. The observations are easily interpreted in terms of a uniformly expanding shell of ionized gas. The gas is initially optically thick at infrared wavelengths and shows a Rayleigh-Jeans spectrum and the Brackett γ line at 2.16 μ in absorption. After four days the gas becomes thin, the infrared spectrum becomes flat, and the Br γ line goes into emission. The flux decreased as t^{-2} until ~ 200 days, indicating that the gas is in a shell rather than uniformly filling an expanding volume. This dependence is now becoming closer to a t^{-3} function, which indicates that the shell has become more diffuse.

1-mm Photometry of Compact Extragalactic Objects

This program, headed by M. Werner, has resulted in the detection of five sources: 3C84, 3C120, 3C273, 3C279, and BL Lacertae. The derived fluxes lie in the range 5–20 janskys. Additionally, 3σ upper limits of ≤ 5 Jy have been set for a number of objects, including NGC 1068, NGC 4151, and M82. None of the sources detected show any significant 1-mm flux over what is expected from an extrapolation of the microwave spectrum. The latter limits are, however, just at the point where they are becoming significant in differentiating thermal from nonthermal origins for the large amount of infrared radiation present in these objects. Additionally, 3C273 has been monitored on a bimonthly basis from December 1973 to March 1976 and has shown no firm evidence for variation greater than $\sim 30\%$ of the mean flux, which is ~ 13 Jy.

GLOBAL CLUSTERS

Dynamical Models

Theoretical dynamical models of globular clusters incorporating veloc-

ity anisotropy and rotation have been constructed by Gunn to aid in interpretation of his and Dr. R. F. Griffin's (Cambridge Observatories, England)

radial-velocity data. The data for M3 will be analyzed first. The analysis is not quite complete as of this writing, but it is clear that models constructed from central-velocity dispersions alone are woefully inadequate to describe the true dynamical state of clusters. M3's light in its central regions, as elsewhere, is dominated by giants, and the radial-velocity data clearly indicate that there is a "cold" (low-velocity dispersion) population of giants in the nucleus. Conventional dynamical arguments for systems with relaxation times as short as those for globular clusters require that any such population have high mass, and it is possible

that these stars arise as the result of the evolution of close binaries, although no radial-velocity radiation survives to this epoch.

For M13, rotation is evident, and an exciting possibility exists of combining the radial-velocity data with the precision proper-motion measurements of Dr. Kyle M. Cudworth at Yerkes Observatory to find complete space motions for individual stars. This will not only give an almost completely unambiguous look at the dynamics but will also yield a distance for the cluster independent of all astrophysical assumptions (except perhaps for $1/r^2$ gravity and the Boltzmann equation).

INTERSTELLAR MATTER AND GASEOUS NEBULAE

High-Latitude Reflection Nebulosity Illuminated by Stars of the Galactic Plane

A new survey of the north and south galactic polar caps has been in progress for several years by Sandage, using the 1.2-meter Palomar Schmidt with fine-grain IIIaJ and 127-04 high-information-capacity plates. Its purpose is to find remote clusters of galaxies with which to extend the Hubble diagram in a program conducted jointly with Kristian and Westphal.

During the five years of the survey, there have been found occasional high-latitude fields that show bright nebulous regions, often in connective patterns that are correlated over distances of degrees.

A particularly interesting region occurs near the galaxies M81 and M82 at $l = 142^\circ$, $b = +41^\circ$, shown in the very high contrast print of Fig. 4. The filamentary nebula of highest surface brightness at $\alpha_{50} = 9^h48^m$, $\delta_{50} = +71^\circ 10'$ is almost due north of M81 and M82, which are shown as very overexposed images near the lower left border of the print.

The nebulosities over the print form only part of a very extensive network of

bright structures that extends over the adjacent *Sky Survey* field at $+72^\circ$, $9^h 4^m$; it can be seen on the original *Sky Survey* prints.

The fact that regions are nearly equally visible on the red and the blue prints, and especially that they are equally bright on a 103aD emulsion behind a Wratten-16 filter ($\lambda\lambda$ 5200–6000 Å) where no emission lines occur, is strong evidence that the structures are reflection nebulae. The source of illumination at these high-galactic latitudes is of much interest.

The observed surface brightness of the regions in Fig. 4 averages $SB \approx 25$ mag/□" for the brightest area. Calculations of the flux due to the light from the galactic plane show that the apparent magnitude of the plane at any height is $-6.7 V$ magnitude. The surface brightness of dust that scatters this light depends on the optical thickness of the structure. But if the same dust that obscures the background galaxies by Δm also scatters the light from the galactic plane, then the surface brightness of the nebulosities should be $SB_v \approx 24.2 - 2.5 \log \Delta m$ mag/□".

From galaxy counts on and off the brightest nebulosity in Fig. 4, and from

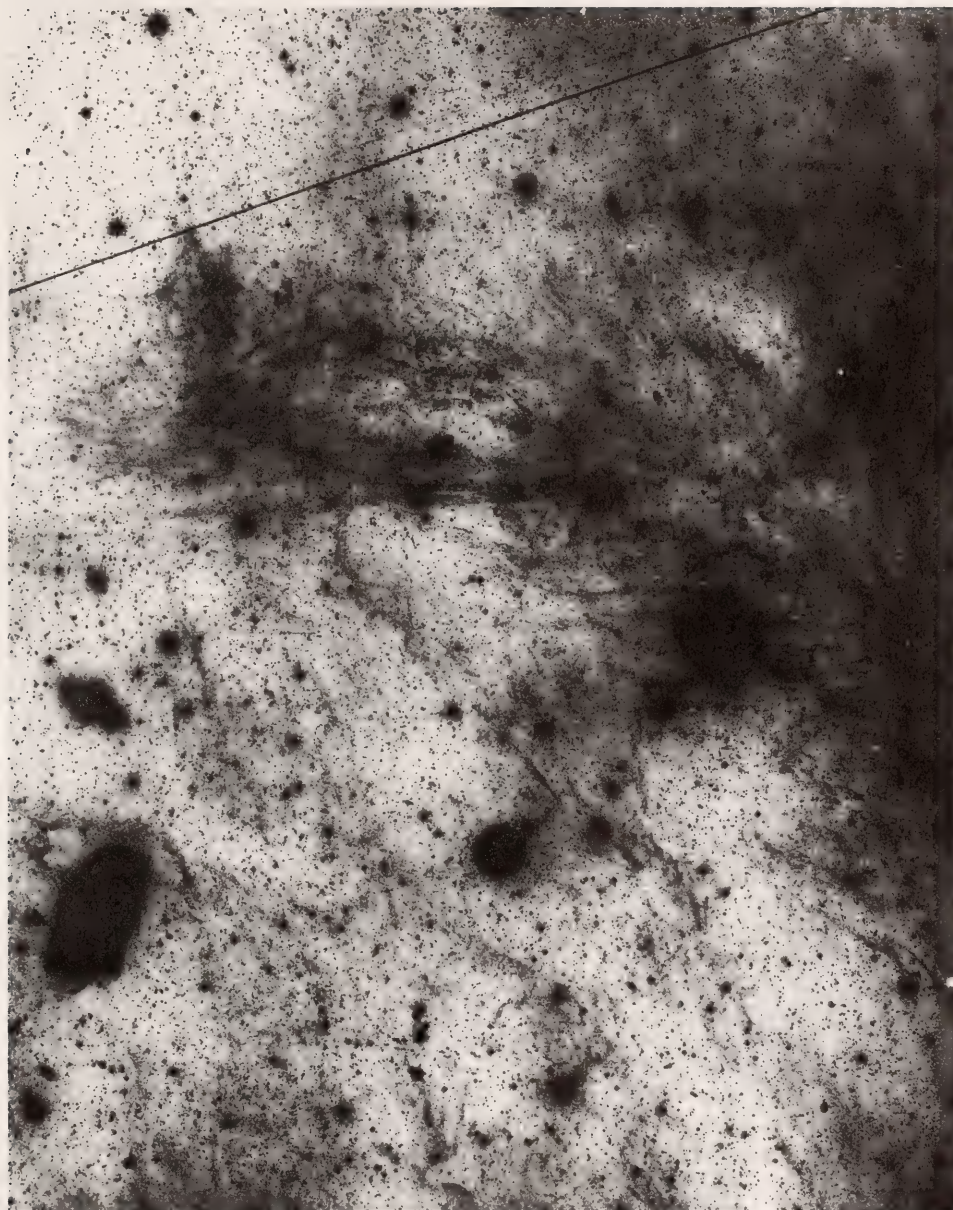


Fig. 4. A high-contrast print from part of a IIIa-J plate (+ Wratten 4 filter) of a high-latitude region ($\alpha_{50} = 9^{\text{h}}49^{\text{m}}$, $\delta_{50} = +71^{\circ}10'$, $l = 142^{\circ}$, $b = +42^{\circ}$) that contains varied reflection nebulae. Overexposed images of the galaxies M81 and M82 are in the lower third of the print near the left border. The surface brightness of the brightest reflection nebulae is $SB, \approx 25$ mag per square sec, which agrees with predicted values from a model in which the illumination of the high-latitude dust is provided by the galactic plane. The scale of the print is $2^{\circ}45'$ in width and $3^{\circ}32'$ in length.

the 21-cm column density of $N_{\text{H I}} = 5 \times 10^{20}$ atoms cm^{-2} in the same region, as measured by Heiles, it is estimated that $\Delta m = 0.3$ mag for the dense nebulae shown. Hence, if the galactic plane is the source of illumination, the surface brightness is predicted to be ~ 25.5 mag/ \square'' . This is in such good agreement with the observations as to suggest that the plane is in fact the illuminator.

Because the plane is always there, everywhere, the presence or absence of faint nebulosities at high latitudes that have SB less than or equal to ~ 25 mag/ \square'' should act as an indicator of dust clouds with extinction contrasts of $\Delta m \leq 0.3$ mag. Hence the presence or absence of reflection nebulae of this brightness should aid in new studies of the extinction through the halo in the polar directions.

The polar survey is not yet complete but is far enough along to note that although some fields do have many reflection nebulosities at this level and fainter, many parts of the north polar cap are free of detectable nebulosities to $SB_V \simeq 26$ mag/ \square'' , which means that the extinction is not lumpy on a scale of $\simeq 0.2$ mag in these regions. But, equally interesting, the presence of any reflection nebulae at high latitude shows the presence of dust above the galactic plane with optical depths that can be as high as $\tau \equiv 0.921 \Delta m \simeq 0.3$.

Interstellar Matter

The study of several cometary reflection nebulae by Greenstein had shown peculiarities in the form of differences in the spectrum between the reflection nebula and the central object. In collaboration with Dr. E. Ye. Khachikyan of the Byurakan Observatory, a study of Greenstein's spectra of R Monocerotis and NGC 2261 showed an outward acceleration, increasing negative velocities outward from the central object. There is also increasing strength of hydrogen and Ca II. The nebula is in general somewhat bluer than the central object and does not

show a steep upturn toward the infrared at 1μ . Greenstein and Oke have discovered anomalously high reflectivity near $\lambda 6500$ in the "Red Rectangle" centered on the star HD 44179. The dust grains in the Red Rectangle differ substantially in physical properties, therefore, from those in NGC 2261. HD 44179 has an enormous Balmer jump, requiring a temperature near 8000° , and surface gravity $\log g \approx 0$. No available model atmosphere fully explains the spectrum of HD 44179, although a circumstellar envelope of hydrogen can produce a large Balmer discontinuity.

Herbig-Haro Object in the Orion Nebula

Photographs of the Orion Nebula in radiation of the [O I] $\lambda 6300$ line show a nonstellar double object, $13''$ in p.a. 280° from the star Π 1782 (P. P. Parenago, *Trudy Sternberg Astron. Inst.*, 25, 1954), which does not appear on photographs in recombination lines. A series of spectra of this object at 29 \AA mm^{-1} dispersion was obtained by Münch with the f/1.5 camera of the 5-meter telescope coude spectrograph and an image intensifier. Guiding on the object was possible through the use of a two-stage electrostatically intensified eyepiece, filtered to cut down [O III] and $\text{H}\alpha$ light. The spectra obtained show the characteristics of classical Herbig-Haro (HH) objects; namely, great strength of [N I], [Fe II], [O I], and [S II] with respect to $\text{H}\alpha$. The most remarkable feature of the object, however, is that its spectral lines are distinctly double, with one component shifted by -250 km s^{-1} with respect to the other, which is intrinsically brighter in [O I] and which has nearly the same radial velocity as the mean of the Orion Nebula. It is conjectured that the two kinematically separated components correspond to the two distinct nuclei seen in the [O I] direct imagery. The large shift of the weaker line spectrum with respect to the nebula allows recognition of its [N II] and $\text{H}\alpha$ lines

within the greatly overexposed lines of the nebula. The intensity ratio between $[O\ I] \lambda\ 6300$ and $H\alpha$ in this high-velocity component is 1.5. The large relative shift between the two components of this HH object implies a time scale of only 50 years for its formation as a double. The violent nature of the phenomena involved in the evolution and formation of the HH objects is thus exhibited in a more striking fashion than heretofore.

The H II Region W3

Further observations of the region W3, a site of recent active star formation, have been carried out by S. Willner, a Caltech graduate student who discovered the presence of an emission line of Ar III at $8.99\ \mu$. He also measured more accurately the Ne II and S IV lines found previously. On the basis of the 8 to $13\text{-}\mu$ spectrophotometry and broadband measurements at 5 and $20\ \mu$, the compact sources in NGC 7538 and W3 can be divided into two classes. The first class, which includes NGC 7538, IRS-1, and W3-IRS-3, consists of compact sources whose emission from 5 to $20\ \mu$ can be described by a single dust temperature. The second class, which includes all the other sources in the two H II regions, consists of both compact and extended objects that exhibit a range of dust temperatures. The mass of the emitting dust can be derived for those objects with a single temperature; for the others, only a lower limit can be obtained. The mass of ionized gas can also be deduced for those objects that have been observed at radio wavelengths. NGC 7538-IRS-1 has a gas-to-dust ratio of 75; many of the other objects have upper limits below 1000. Other workers have found that the dust inside H II regions is depleted; little evidence for depletion has been found here.

Infrared Properties of OH Masers

The 1.5-meter telescope at Mount Wilson, which has recently become op-

erational as a good infrared telescope, was used by S. Beckwith, a graduate student at Caltech, in the continued program related to OH maser sources. The work was done in collaboration with N. Evans of Owens Valley Radio Observatory. Discovery of the infrared sources associated with OH 1821-12 (E. G. Hardebeck, *Astrophys. J.*, 172, 583, 1972) and OH 21.4-0.7 (Evans *et al.*, in preparation), as well as measurements of ON-4 at $10\ \mu$ and $20\ \mu$, concluded the observations of 1612 MHz, Type II OH maser emitters (W. J. Wilson, A. H. Barrett, and J. M. Moran, *Astrophys. J.*, 160, 545, 1971). The major results of the study are:

1. Of the eight OH maser sources included in the study, every one has an associated infrared source.

2. Of five sources followed for more than one year, four were found to vary both in the infrared ($2\text{--}20\ \mu$) and at 18 cm. In all cases the infrared and radio fluxes varied in the same sense.

3. One of the infrared sources, that associated with OH 30.2-0.3, is shown to have $2.4\text{-}\mu$ CO band, characteristic of stars with spectral type later than K.

4. Based on the observed flux at $3.4\ \mu$ and $12.5\ \mu$, infrared pumping of the 1612 MHz radio line is possible at $34\ \mu$ but not at $2.8\ \mu$.

Work continued on the properties of 1665 MHz OH masers with the discovery of two more infrared sources associated with the 1665 MHz masers OH 35.6 and OH 40.6 (Evans *et al.*, in preparation). The infrared sources are very weak and there appears to be no correlation between near-infrared flux and 1665 MHz line strength in all of the sources studied. No property characteristic of infrared sources associated with these masers has been found.

Dark Clouds

Scanning of dark clouds has continued by J. Elias, a Caltech graduate student. To date, three small cloud complexes have been scanned, those near IC 5146, NGC 7023, and Sharpless 239. In addition, scanning of the

two closest large complexes, in Taurus and Ophiuchus, has continued. Scanning of these regions is from half to two thirds completed.

The results to date demonstrate that the sources detected so far—about 10^3 in number—are for the most part background objects similar to those detected by earlier, lower-sensitivity surveys. Several interesting objects have been found. Some photometry and low-resolution spectrophotometry have been done on these, but the results are not yet fully analyzed, and definite conclusions cannot be drawn.

Mapping of Thermal Emission from Molecular Clouds

Maps with $1'$ resolution covering $\sim 5' \times 5'$ have been made by Werner and his collaborators of the 1-mm emission from four sources, W3, Sgr B2, W49, and M42 (OMC-1). In each case, the distribution of 1-mm surface brightness shows a sharp peak superposed on an extended background having $\lesssim 25\%$ of the peak brightness. The peak 1-mm flux density into the $1'$ beam is 35 Jy for W3, 90 Jy for W49, 215 Jy for OMC-1, and 310 Jy for Sgr B2. These fluxes are much too high to be due to free-free emission or unresolved molecular lines, and the 1-mm radiation is almost certainly due to thermal emission from dust. Thus it is noteworthy that the peaks are seen at the positions of compact H II regions and/or pointlike infrared sources, which are thought from other considerations to be the youngest and/or most dust-embedded objects in each of the regions mapped.

The data have been analyzed in terms of a simple model of a central object heating a surrounding dust cloud in which the dust density decreases radially outward as $\rho(r) \propto r^{-n}$. The best fits to the data are found for values of n between 1.5 and 2. This type of density gradient arises very generally in a variety of gravitational collapse calculations, so the steep density gradients inferred from the 1-mm

data may have been produced by the collapse process that led to the formation of the central luminosity source.

NGC 7538

The infrared group has continued its studies of the sites of recent star formation. One area studied is NGC 7538 (Sharpless 158), an object visible as a nebulosity on the *Palomar Sky Survey*. Aperture synthesis measurements at 21 cm (F. P. Israel, H. J. Habing, and T. de Jong, *Astron. Astrophys.*, 27, 143, 1973) show a large ($5'$ diameter) H II region associated with the nebulosity and a compact H II complex about $3'$ to the southeast. A $20\text{-}\mu$ map of this compact region shows three infrared sources within a region about $30''$ square, which higher-resolution radio observations (A.H.M. Martin, *Mon. Notic. R. Astron. Soc.*, 163, 141, 1973) show to be young H II regions. The most compact of these sources is IRS-1, which spectroscopy has shown to have a deep silicate feature.

During the past year, observations on NGC 7538, centered on the "infrared cluster," have been made simultaneously at 30, 50, and $100\text{ }\mu$ with $1'$ resolution from the NASA C-141 Airborne Telescope. An exciting aspect of these observations is the discovery of a new source not corresponding to any known radio or near-infrared feature, located about 1 arcminute to the southeast of the "infrared cluster," designated here NGC 7538 (East). The far-infrared color of this source is similar to that of the "infrared cluster," but its luminosity is about 5 times smaller.

Subsequently, a search at near-infrared wavelengths with the Mount Wilson 1.6-meter telescope has located this source, and broadband photometry shows its $1.6\text{--}13\text{ }\mu$ spectrum to be identical in shape and intensity to that of IRS-1. However, no radio emission is seen from this region down to 10 mJy at centimeter wavelengths (C.G. Wynn-Williams, private communication). Size measurements with the 5-meter telescope show that NGC 7538

(East) and IRS-1 are both less than $1''$ in size at $10\ \mu$.

Recently a 1-mm map of this region was constructed by Werner from observations made during twilight hours from the prime focus of the Hale 5-meter telescope. At 1 mm the maximum emission comes from the position of the "infrared cluster," but a significant extension is seen that includes both NGC 7538 (East) and a region about $1'$ to the south, which con-

tains an OH maser designated OH(S). The region around OH(S) shows significant $100\text{-}\mu$ flux but is not seen at 30 or $50\ \mu$, implying that it is extremely cold.

In summary, infrared observations of the region NGC 7538 between wavelengths of $1.6\ \mu$ and 1 mm have revealed a wealth of structures and varying conditions. Detailed analysis of these data should provide great insight into the evolution of young regions.

PULSARS

Search for the Hulse-Taylor Binary Pulsar

Kristian, Clardy, and Westphal have given the first results of a search for the optical counterpart of the binary pulsar PSR 1913+16, discovered by R. A. Hulse and J. H. Taylor. The 59 msec period of this pulsar is the shortest known except for the Crab pulsar. The frequency shows cyclic variations with an 8-hour period, due to an orbital motion about an undetected second body: The source is the radio analog of a single-line spectroscopic binary. It is the only pulsar known to occur in a binary system and is of considerable interest. Among other things, it offers the possibility of the direct determination of a pulsar mass and of a "laboratory" for a number of new tests of gravitational theories.

Early synchronous photoelectric measurements give a limit of $V > 23$

mag for visible pulsed radiation. This limit scaled against the Crab pulsar is roughly the fourth power of the period ratio. A recent improvement of the radio position accuracy to $0.2''$ offers the possibility of (1) a search for fainter visible pulsations and (2) detection of nonpulsed visible light, including that of the companion, at the pulsar position. The *Palomar Sky Survey* plates are empty at the radio position, which sets limits of $B \geq 21$ mag and $R \geq 20$ mag for any object, pulsating or not, associated with the pulsar. Rough estimates of the distance and absorption give a limit of $M \geq 3$ for the absolute magnitude of the pulsar and/or the companion. Deeper data taken with the SIT area photometer show two faint red objects $3''$ to $4''$ from the pulsar position. Further observations of these stars and a deeper search for pulsed radiation are anticipated during the 1976 observing season.

X-RAY SOURCES

Oke and Greenstein have made a study of the x-ray nova A0620-00, which appeared first as a strong x-ray source in August 1975. Observations between September 2, 1975, and March 20, 1976, were made with the multichannel spectrometer, the SIT digital spectrograph, or the Boksenberg camera in the coudé spectrograph. Infrared observations at 1.65 , 2.2 , and $3.5\ \mu$

were also obtained by Neugebauer and Becklin. The flux below $600\ \text{\AA}$ can be represented accurately by an energy distribution somewhere between that of a model atmosphere and a blackbody at $25,000^{\circ}$ – $30,000^{\circ}\text{K}$. This radiation appears to come from an accretion disk around the x-ray source. One possible source for the red and infrared radiation is a hot gas at 10^6K , also as-

sociated with the accretion disk; in this case, the density of the gas must be such that it becomes optically thick in the near infrared. A second possible source of the red and infrared radiation is a cool (4000°K) blackbody, which must be substantially larger than the binary system itself. The emission lines appear to come from the accretion disk. The derived reddening is consistent with $E_{B-V} = 0.39$ obtained from the Astronomical Netherlands Satellite *UV* observations. The distance is approximately 1200 pc. Using the observed data for September 2, 1975, it is found that the x-ray flux can be produced by a flow of 1.2×10^{18} gm s⁻¹ of matter into a neutron star. Using a simple accretion disk model, this same flow can generate the energy flux actually observed from the disk. The model predicts too small an energy release in the outer parts of the disk; this outer portion of the disk may be heated by the x rays themselves. The total mass in the disk is approximately 1.6×10^{23} gm, which is much more than the mass of optically thin gas in the disk and is of the right order to explain the characteristic times associated with variation in the optical and x-ray flux.

Oke has completed a study of the x-ray binary HZ Herculis (Her X-1),

using spectrophotometric observations around the 1.7-day eclipse cycle. Analysis of the data at minimum light yields $M/M_{\odot} = 2.60$, $L/L_{\odot} = 80.7$, and $R/R_{\odot} = 4.2$ for the large primary star, assuming the standard mass-luminosity law and conventional stellar evolution. Different but consistent results can be obtained, provided $\log g = 3.60$. The hot x-ray heated cap of the primary star has an angle of 26° and an effective temperature of 25,000°K. Analysis of the energy distributions at phases other than minimum suggests an accretion disk with a diameter of 2.1×10^{11} cm; its radiation is consistent with half of the visual flux coming from a plasma at 10⁶°K and $N_e = 10^{14}$ cm⁻² and the other half from an opaque body with a temperature of about 20,000°K.

Another x-ray source, A0535+26, which has an x-ray period of 104^s but no detected optical period, is being studied by Wade and Oke. Both multichannel observations and single-trailed SIT digital spectra were obtained around the 104^s period. The spectral energy distribution is nearly flat from 3300 to 10,000 Å. Balmer emission lines are seen and occasionally λ 5876 of He I. No periodicity has been found so far either in the continuum or in the emission lines.

SUPERNOVAE

Nine supernovae were discovered in the course of the Palomar supernova search during the report year, all with the 1.2-meter Schmidt telescope. Sargent decided to terminate this part of the search, which was mainly for statistical purposes, at the end of 1975. In all, 178 supernovae have been discovered with the 1.2-meter Schmidt since the systematic search was begun by Zwicky in 1959. The search on the 46-cm Schmidt is to go on in an ex-

panded form. The main aims will be to study the statistics of supernovae in Sc I galaxies and to maximize the chance of discovering a really bright supernova of Type II.

Kowal completed the work of setting up photoelectric *UBV* sequences in 20 of the 1.2-meter supernova fields. Work is now proceeding on measuring light curves for several supernovae observed during the 17 years of the search.

THE GALAXY

Metal Abundances in Globular Clusters

Searle is making a comparative study of the chemical history of the globular cluster systems of the Galaxy, of M31, and of the Magellanic Clouds. In this connection, Zinn and Searle are mapping the spatial distribution of clusters of different metal abundances within the Galaxy. A new method of determining the metal abundances in individual red giants belonging to a cluster has been developed. It is based upon measurements of the integrated metal-line absorption from spectrophotometric scans. This method is

much more sensitive than any previously used. The observations determine an intrinsic (reddening-free) index that varies by a full 1.5 mag over the abundance range between M71 and M92.

In this report year Searle and Zinn have calibrated the new system and have begun a program to determine the metal abundances of all globular clusters for which color-magnitude arrays are available. Particular emphasis has been placed on remote clusters and other stellar systems on the fringes of the Galaxy. So far in this program, abundances have been determined for 200 stars belonging to 25 systems.

GALAXIES

New Redshifts for Bright Galaxies

A long-range program to obtain redshifts for all (~ 1200) galaxies in the Shapley-Ames catalogue (whose limit is $m_{pg} \cong 13$) in both hemispheres is nearing completion by Sandage. During the report year, he prepared for publication new redshifts for 700 galaxies from 1100 plates taken between 1969 and 1975 with image-tube spectrograms on the Mount Stromlo 1.9-meter and the Hale 5-meter telescopes.

All but about 50 Shapley-Ames galaxies now have measured redshifts, either from literature sources or from the new data; so the redshift program begun in 1935 by Humason and Mayall is essentially complete.

Sandage and Dr. G. A. Tammann of the Astronomisches Institute der Universität Basel are preparing a redshift catalog for the complete Shapley-Ames list, where all available data will be combined. New two-dimensional morphological classifications of the same galaxies, using large-scale reflector plates from Mount Wilson, Palomar,

and Las Campanas, have also been completed, and these, combined with the redshift data, are expected to provide improved luminosity functions for the various Hubble-van den Bergh classes.

Distances to Nearby Galaxies Derived from Brightest Stars

Accurate photometric distances to nearby resolved galaxies just beyond the Local Group are still largely unknown. The brightest resolved stars provide the easiest fairly accurate method to find them, short of the very time-consuming search and photometry of Cepheid variables.

Sandage has begun a long-range program to use brightest stars to find distances to many of these resolved irregular dwarf systems whose distance moduli are less than $m - M \simeq 28$ ($D \lesssim 4$ Mpc).

The first phase of the program is a strengthening of the absolute magnitude calibration of the brightest stars. The color-magnitude diagram for

the Local Group irregular IC 1613 has been completed by Sandage and Katem. The galaxy is at the faint end of the calibration sample, with an integrated absolute magnitude of only $M_B = -14.4$. A special blink survey of 5-meter plates for the reddest stars shows that the brightest M-type supergiant has $M_V = -8.0$, $M_B = -6.0$, and the brightest blue supergiant has $M_V = -7.4$, $M_B = -7.6$, in agreement with previous studies of this galaxy reported in *Year Book 69* (p. 95).

Other calibrating galaxies, such as M33 and the Large and Small Magellanic Clouds, are currently being searched for the brightest stars on plates taken with the Mount Wilson 2.5-meter and the Las Campanas 1.0-meter reflectors.

The strengthening of the present calibration is expected to take several years, but the main program for the unknown galaxies has also begun, with the first results on the Wolf-Lundmark-Mellotte (WLM) system completed by Sandage and Katem. The color-magnitude diagram from 5-m plates shows the brightest three blue stars to have $\langle B(3) \rangle = 17.85$, $\langle V(3) \rangle = 18.00$. The brightest red supergiants have $\langle V \rangle = 18.20$. The previous calibration by Sandage and Tammann, done as a part of their steps toward the Hubble constant, gave, for luminosity class V galaxies, $M_{B(3)} = -7.99$ for the brightest blue supergiant, and $M_V(\text{red}) = -7.90$, with concordant moduli of $(m - M)_{AB} = 25.95$ and $(m - M)_{AV} = 26.10$, for a mean of 26.02 (or $D = 1.6$ Mpc). This puts the WLM system at the outer edge of the Local Group.

Plates in good seeing were obtained with the 5-meter telescope for the additional dwarf galaxies Pegasus A, Sextans A, Sextans B, Leo A, Leo B, GR 8, and Ho IX, which is the companion to M81. Photoelectric calibration of field stars to $V = 17$ was completed in each of these fields, using the Mount Wilson 2.5- and 1.5-meter reflectors. The sequences were extended to $V = 22$, using 5-m photographs that had sec-

ondary images 5 mag fainter, made with the Racine wedge calibrator in the converging prime-focus beam.

It is known that these very nearby dwarfs partake of the expansion (all have positive redshifts). The aim of the long-range program is to determine, from the distances, the deceleration effects of the Local Group, and hence to find its mass from deviations of the dwarf velocities from the global Hubble rate.

Supergiant cD Galaxies

Gunn and Thuan are using a new digital spectrograph with a cooled integrating SIT-Vidicon camera at the Cassegrain focus of the 5-meter Hale telescope to obtain velocity dispersions and rotation curves of cD galaxies in clusters. A synthesis of the total light of these intriguing systems will also be performed. This dynamical information, along with the light distributions obtained from plates taken by Thuan with the Schmidt camera, should permit construction of dynamical models of the supergiant galaxies.

Markarian Galaxies

Becklin, Neugebauer, Oke, and Searle have obtained slit spectra in the visible and spectrophotometric and infrared broadband observations of 18 Markarian galaxies with emission lines. Eight of the program galaxies can be classified as Seyfert galaxies. In general, thermal, nonthermal, and stellar radiation components are present. Broadly speaking, one group of Seyfert galaxies is characterized both by the presence of a high-density region of gas and by a continuum dominated by nonthermal radiation. The continua of the remaining program Seyferts that do not have a high-density region of gas are dominated by thermal radiation from dust and stellar continuum. The 10 galaxies that are not Seyfert galaxies are examples of extragalactic H II regions. There is

evidence for thermal emission at $10\ \mu$ from dust in four of these galaxies.

In a continuing study, Sulentic has completed a morphological study of Markarian galaxies 1 through 604, using the *Palomar Sky Survey*. The results have been correlated with radio-continuum measurements previously obtained with the National Radio Astronomy Observatory 300-foot telescope. It is found that useful coarse structural information can be obtained for most of the bright ($m \leq 15.5$) Markarian galaxies from the *Sky Survey*. The Markarian galaxies could be differentiated into spiral and irregular morphological types covering a wide range in absolute luminosity.

Previously Sulentic had suggested the existence of unusually high radio luminosities and radio detection fractions for a sample of multiple galaxy systems. In pursuing this idea, photometric and spectroscopic data are being obtained for a large sample of these systems. The correlation of these data with radio emission and structural morphology is in progress.

Seyfert Galaxies

Dr. Gregory A. Shields of the University of Texas at Austin and Oke have obtained and analyzed spectral-energy distributions for the two Zwicky compact galaxies ZW 2130+09 (II Zw 136) and Zw 0051+12 (I Zw 1), as well as for 3C273. All of these have strong Fe II lines in emission. The permitted line intensities are consistent with a filamentary emission region having $N_e \sim 10^9\ \text{cm}^{-3}$, $R \sim 1\ \text{pc}$, $M \sim 10^2\ M_\odot$, and $v \sim 3000\ \text{km s}^{-1}$. The observed H β intensities are smaller than expected on the basis of an extrapolation of the visual continua to ionizing frequencies, and this suggests that the emission-line region does not completely surround the continuum source or that the continuum slope becomes steeper for $\lambda < 3000\ \text{\AA}$. The Fe II line intensities can be explained by continuum fluorescence if the observed line widths result

from radial rather than circular motion. The derived column density is $\sim 10^{23} \pm 1\ \text{cm}^{-2}$, comparable with the value implied by the x-ray absorption in NGC 4151. The O I λ 8446 emission may result from continuum fluorescence; alternatively, it can be explained by Lyman- β fluorescence if a portion of the broad-line region has $\tau(\text{H}\alpha) > 100$ as a result of time-dependent ionization.

Infrared Observations

Persson, J. A. Frogel of the Cerro Tololo Inter-American Observatory, and M. J. Aaronson of Harvard College Observatory continued their studies of the stellar populations of elliptical galaxies by means of infrared photometry. The program of measuring the CO absorption at $2.2\ \mu$ was largely completed, and the results are being prepared for publication.

New observational programs were initiated to investigate further the infrared properties of galaxies with the 1.5-meter and 2.5-meter telescopes at Mount Wilson, the 5-meter telescope, and the 1-meter telescope at Las Campanas. The first program consists of measuring the depth of the $2.0\text{-}\mu\ \text{H}_2\text{O}$ band in spectra of galaxies and stars. The band-strength is quite sensitive to effective temperature in both giant and dwarf stars later than M2 and offers a means of studying the relative numbers of very late-type stars in galaxies. A preliminary result of this work is that the H_2O band is strong in galaxies and, hence, that a substantial fraction of the galaxy light at $2\ \mu$ is contributed by M stars. The effect of this parameter upon stellar synthesis models is under study.

A second program consists of determining accurate $V - [2.2\ \mu]$ colors for galaxies. Some preliminary results were reported by Frogel *et al.* (*Astrophys. J. [Lett.]*, 200, L123, 1975). The importance of these colors follows from an earlier finding that giant stars contribute much of the $2.2\text{-}\mu$ light of

elliptical galaxies. The $V - [2.2 \mu]$ color should thus depend to some extent upon the morphology of the composite giant branch through the effect of metal abundance on the luminosities and effective temperatures of the individual stars. A correlation between the line-blanketing-sensitive $U - B$ or $U - V$ colors and $V - [2.2 \mu]$ should therefore exist. The data for three samples of galaxies, Virgo (30 galaxies), Coma (12 galaxies), and the field (40 galaxies), show the effect in an unambiguous way: $\Delta(U - V)$ is approximately equal to $\Delta(V - 2.2 \mu)$. The $V - [2.2 \mu]$ color thus provides a means of studying metallicity, and perhaps also the relative distance moduli of clusters of galaxies.

Nuclear Regions of M31

Thuan and Oke have obtained spectrophotometric measurements of the nuclear region of M31 under conditions of excellent seeing and with M31 near the zenith. A round 3'6-diameter aperture was used for the nucleus measurements, while an annulus with a diameter of 3'8-9'9 was employed for the bulge observations. It is found that the nuclear region with $r \leq 1'8$ is only slightly redder and shows marginally stronger CN blends than the bulge from $r = 1'9$ to 4'9. The data can be interpreted in terms of an increase in heavy-element abundance toward the center of M31 by a factor substantially less than 2.

Observational Search for the "Missing Mass"

Thuan used the 1.2-meter telescope at Palomar to obtain plates of several edge-on galaxies. They will be used to test observationally the Ostriker-Peebles proposal that massive halos may exist around spiral galaxies and to study color-gradients in the halos of galaxies. Photoelectric data will also be obtained to supplement the photographic material.

Redshifts, Magnitudes, and Colors of a Sample of Galaxies

Thuan, in collaboration with G. R. Knapp of the Owens Valley Observatory and J. Huchra, has started a program to obtain redshifts, *UBVR* photometry and morphological data for a complete sample of about 1100 galaxies selected from the Zwicky catalogue of galaxies and groups of galaxies, such that $m_{pg} \leq 14^m$, $b^{11} \geq 40^\circ$, and $\delta \geq 0^\circ$. Since most of the galaxies ($\sim 90\%$) are spirals, the possibility exists of measuring their redshifts via their H I radio emission. Measurements of a large number of redshifts are being made quite accurately ($\sim 10 \text{ km s}^{-1}$) with the sensitive 21-cm system on the 300-foot telescope at the National Radio Astronomy Observatory. Redshifts of ellipticals, and the photometry, are being obtained with the Palomar 1.5-meter reflector and the Kitt Peak 91-cm reflector.

The investigations that can be carried out with these data are many, and all have important implications for cosmology and for the theories of formation and evolution of galaxies:

1. The study of systematic differences (if there are any) in properties, such as colors between cluster and noncluster galaxies.

2. The color-magnitude relation (Sandage, *Astrophys. J.*, 176, 21, 1972) for elliptical and S0 galaxies may be improved. If the tightness of the correlation holds, it may prove to be a very powerful cosmological tool.

3. The distributions of colors and absolute magnitudes of galaxies from a statistically complete sample could be compared with simple models of star formation in galaxies (Searle, Sargent, and Bagnuolo, *Astrophys. J.*, 179, 427, 1973).

4. By mapping the local velocity field, we can apply a "cosmic" virial theorem to deduce a local mean density and hope to make headway toward the outstanding problem of an open or closed universe.

5. In addition to the radial-velocity information, the H I data will provide virial masses and total H I content. Such a large sample should provide an interesting statistical study of H I content as a function of morphological type.

Chemical History of Galaxies

As part of an investigation into the comparative chemical histories of the Galaxy, of M31, and of the Magellanic Clouds, Searle has begun a program of classification of the integrated spectra of their globular clusters. In collaboration with A. Boksenberg of University College London, spectra were obtained of 12 globular clusters in M31. These spectra, obtained with the University College London image-photon-counting system, cover the range $\lambda\lambda$ 3500–5000 with a spectral resolution of 5 Å. Douglas Rabin, a Caltech graduate student, is collaborating with Searle and Boksenberg in the interpretation of these spectra. In a related investigation, Searle has obtained low-resolution spectrophotometric scans of 70 of the globular clusters in M31. So far, all of the observations obtained appear to be consistent with the idea that the M31 globular clusters differ from one another in one parameter only—presumably the metal abundance.

The situation is essentially different in the Magellanic Clouds. During the report year, Searle obtained five-color photometric observations of the integrated light of 30 Magellanic Cloud globular clusters at Las Campanas. These show that there are intrinsic differences between the globular clusters of M31 and of the Galaxy on the one hand and those of the Magellanic Clouds on the other. There are also intrinsic differences between the clusters of the Small and Large Clouds.

A possible explanation of the observations is that in the Galaxy and in M31 metal enrichment occurred suddenly, so that all globular clusters, of whatever composition, have closely

similar ages; whereas, in the Magellanic Clouds enrichment was slower and the metal-poor globular clusters in the Clouds have a substantial range of age.

Large Magellanic Cloud

The importance of the study of stellar populations in the Magellanic Clouds, and in particular of the old stellar component of the LMC disk, has been previously emphasized. Knowledge of the population structure of the LMC would make that galaxy, our closest neighbor, an ideal testing ground for some aspects of the kind of synthetic models that must be used with the unresolved, distant galaxies.

Hardy has studied a number of regions, 3'4 in diameter each, free of supergiants, and smooth in the distribution of stars, in and near the bar of the LMC. Observations were made photographically in *B* and *V* and photoelectrically in the integrated light of the *UBVR* and *DDO* systems. His main conclusions are:

The surface-brightness distribution shows the existence of an exponential disk of which the bar is a narrow axisymmetric perturbation. The blue-length scale for the exponential disk was found to be $\alpha_B^{-1} = 1.36 \pm 0.42$ kpc, while the central surface brightness was $\mu_B(0) = 21.93 \pm 0.22$ mag/□". There are no significant color gradients over the sampled baseline of 1.5 kpc, which roughly corresponds to one *e*-folding length over the surface brightness. But color asymmetries due to either population or reddening effects were detected when the bar was taken as an axis of symmetry.

Color-magnitude diagrams to $M_V = 0.5$ were constructed, and it was found that the observed giant branch resembles that of intermediate Population II clusters such as M4 or M75. The surface colors, which include new observations in the *R* region obtained at Las Campanas, are compatible with this interpretation. There are indications of

the existence of a horizontal branch of Population II, but an important contribution from intermediate-age stars cannot be ruled out only on the basis of the colors and the color-magnitude diagrams.

Luminosity functions were constructed by Hardy and then normalized to the total light contained in the area counted (count-brightness-ratios: CBR). A method was devised that involved comparison of the observed CBR in both V and B with those of known globular clusters of different metallicity to determine the fraction of the total light in Population II stars. It was found that if the giant branch is interpreted as belonging to an M4-M75 type of population, then Population II contributes $70\% \pm 10\%$ of the total light in V and $80\% \pm 20\%$ in B in the regions studied, thus leaving only a small fraction of the light to be accounted for by stars of the solar-neighborhood type that were too faint to be detected photographically.

The alternative, that the LMC disk is a scaled version of the galactic disk, was discussed. It was shown that the observed CBR in B light did not fit the CBR derived from the van Rhijn function for the solar neighborhood, and it was argued that this was not only an effect on the young stellar population but involved the old component as well.

Alternatives for the formation and evolution of the LMC disk were considered. Hardy concluded that the observed disk is likely to be as old as the galactic disk but, being more metal poor, resembles an enriched globular-cluster population rather than an M67-NGC 188 population, as in the galactic disk.

New data obtained with the 4-meter telescope at Cerro Tololo Inter-American Observatory in January 1976 are now being analyzed.

Population Synthesis

Turnrose has determined the stellar content of the nuclear regions of seven nearby Sc galaxies by means of popula-

tion syntheses, utilizing narrow-band spectrophotometry covering the wavelength range $\lambda\lambda 3300-10,400$. A linear-programming fitting technique was used in conjunction with simple models of star formation to provide physically consistent population models incorporating multiple generations of stars. Evidence is found for substantial intrinsic reddening in the nuclear regions studied. Upper-main-sequence stars are significant contributors to the light in most cases, and the lower main sequence contributes significantly in all cases. All available indicators are consistent with evolved-M-star dominance at the longest wavelengths and low photometric mass-to-light ratios ($0.3 \leq M/L_v \leq 10$). Using absolute measurements of the emission-line spectra of the nuclear regions, it is found that the O-B stars, which arise naturally in the population models, are just sufficient to provide the observed nuclear ionization in all cases except that of NGC 5194, which may be collisionally ionized. The inferred stellar populations are largely consistent with simple evolutionary models of star formation, using a "local" initial mass function and a variety of time dependences ranging from exponential decays with time constants $\sim 3-6$ billion years to constant rates. A possibly significant correlation between nuclear stellar content and overall dynamical properties among four of the program galaxies is pointed out.

Variable Stars in the Dwarf Spheroidal Galaxies

A rare class of variable stars that seem to occur preferentially in the dwarf spheroidal galaxies has been the subject of two investigations by Zinn in the current report year.

Together with Searle, he obtained spectrophotometric scans of five of these peculiar Cepheids in the Draco system. Comparing these with similar observations of RR Lyrae variables in this system, Zinn and Searle have

found that the masses of the anomalous Cepheids are from two to three times the masses of the RR Lyrae stars. This result, which was unexpected in an old stellar system whose evolved stars were believed to have the same mass, confirms the hypothesis put forward by J. Norris of Yale University and Mt. Stromlo-Siding Spring Observatory and Zinn on the basis of theoretical arguments. How the anomalous Cepheids acquired their large masses remains something of a puzzle, however. Either, as Norris and Zinn argued (see *Year Book* 74, p. 338), star formation occurred recently in Draco or, as suggested as an alternative by Zinn and Searle, the large masses were produced by the fusion of the components of close binary systems.

Until recently, the anomalous Cepheids had been found in only the dwarf spheroidal galaxies and the Small Magellanic Cloud. This past year Zinn and Conrad C. Dahn of the Naval Observatory showed that Variable 19 in the globular cluster NGC 5466 obeys the same period-luminosity law and has the same mass as the unusual Cepheids in the Draco system. The as yet unidentified characteristic of the dwarf spheroidal galaxies, the Small Cloud and NGC 5466 that distinguishes them from other systems is clearly a key to understanding the origin of these peculiar variables.

Image Processing of Galaxy Photographs

There has always been interest in extracting maximum information from astronomical photographs. In an experimental project that utilizes the capabilities of modern digital computers, Jean Lorre of the Jet Propulsion Laboratory's Image Processing Laboratory and Arp have collaborated in the analysis of a number of galaxy photographs. The photographs were made by Arp on fine-grain plates and under especially good observing conditions with the 4-meter reflector at Palomar. The plates have been scanned

with a PDS microphotometer and processed by a variety of mathematical algorithms by Lorre at JPL. Techniques have been demonstrated that (1) enhance the contrast and clarity of nebulous features, (2) detect previously invisible features, (3) moderately improve resolution (through partial seeing compensation), (4) add information from different plates to improve signal-to-noise ratios, and (5) compare response at different wavelengths in order to portray color differences.

In certain well-known and interesting groups of galaxies, new features were detected by these procedures. For example, in the region of NGC 7331 and Stephan's Quintet, luminous nebulous filaments were discovered (see *Astrophys. J.*, 210, No. 1, 1976, November 15). Additional detail is also revealed in some of the galaxies in Seyfert's Sextet. In one of the most striking results, a photograph of the famous jet in the spherical galaxy M87, taken with the 5-meter telescope on fine-grain emulsion, has been processed for maximum resolution. The deconvolution algorithm has reduced the smallest image sizes by about a factor of 2 and compressed the dynamic range so that the jet is seen in this picture as consisting of a very small well-spaced and well-aligned series of luminous points emerging from the nucleus of M87 (see Fig. 5a, b).

Ejection from the Spiral Galaxy NGC 1097

While cataloging peculiar southern galaxies in Edinburgh, using plates from the U.K. 1.2-meter Schmidt in Australia, Arp learned of the discovery by R. D. Wolstencroft and W. J. Zealey of luminous jets emerging from the bright southern spiral galaxy, NGC 1097. A few months later, with the new 4-meter telescope at Cerro Tololo in Chile, he obtained a series of deep plates on this object which reveal that it is one of the clearest examples of ejection from a galaxy that has so far been encountered. The 4-m plates show

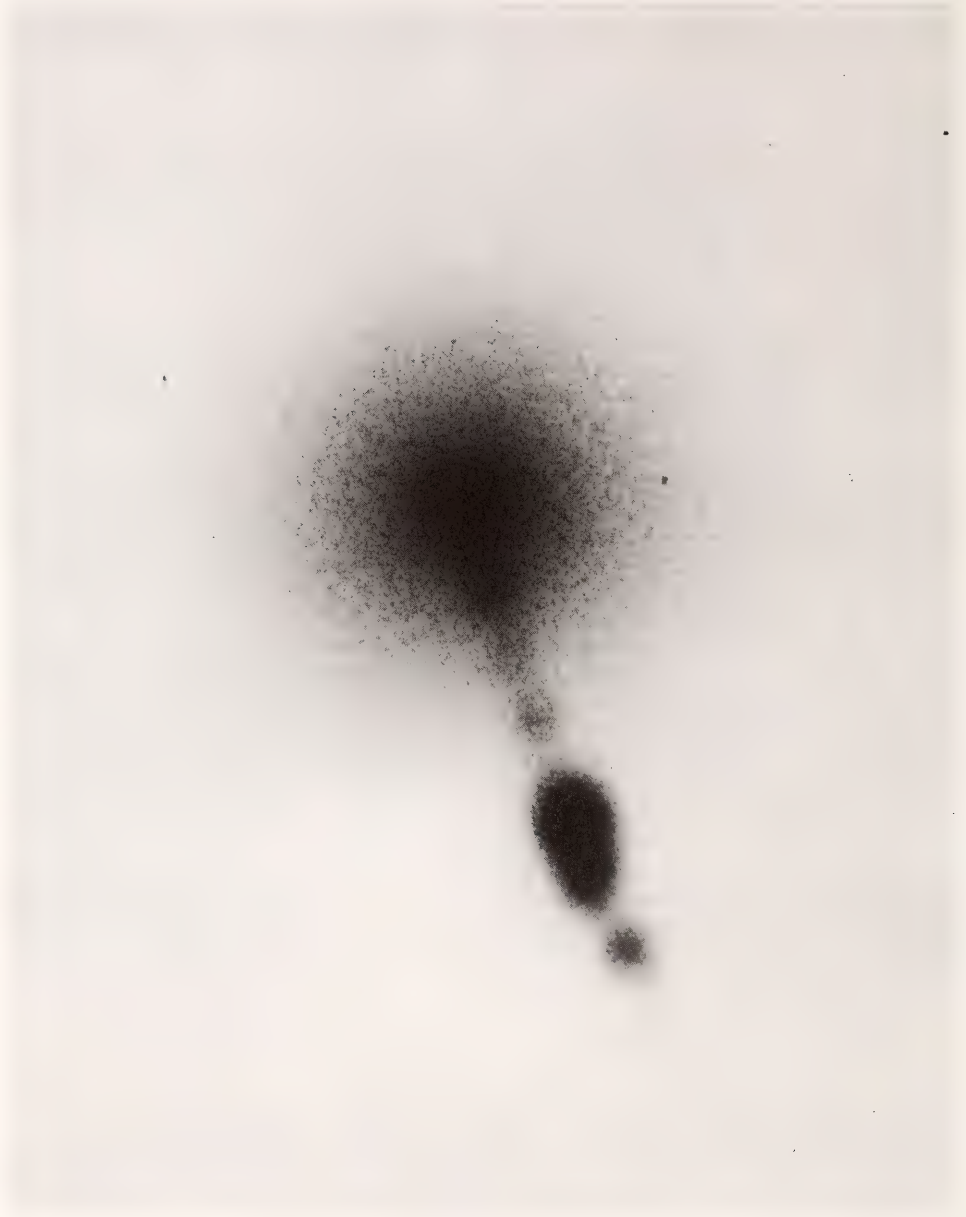


Fig. 5a. A photograph of the jet in M87 with the 5-meter telescope on fine-grain IIIa-J emulsion. This photograph has been subjected to an image deconvolution algorithm that improved the obtainable resolution by about a factor of 2 and increased the dynamic range.

that the three jets all point exactly back to the nucleus of the galaxy and suggest, therefore, that material has been ejected from the nucleus.

Neighborhoods of Galaxies

A two-year collaborative project was initiated by Arp with Francesco Ber-

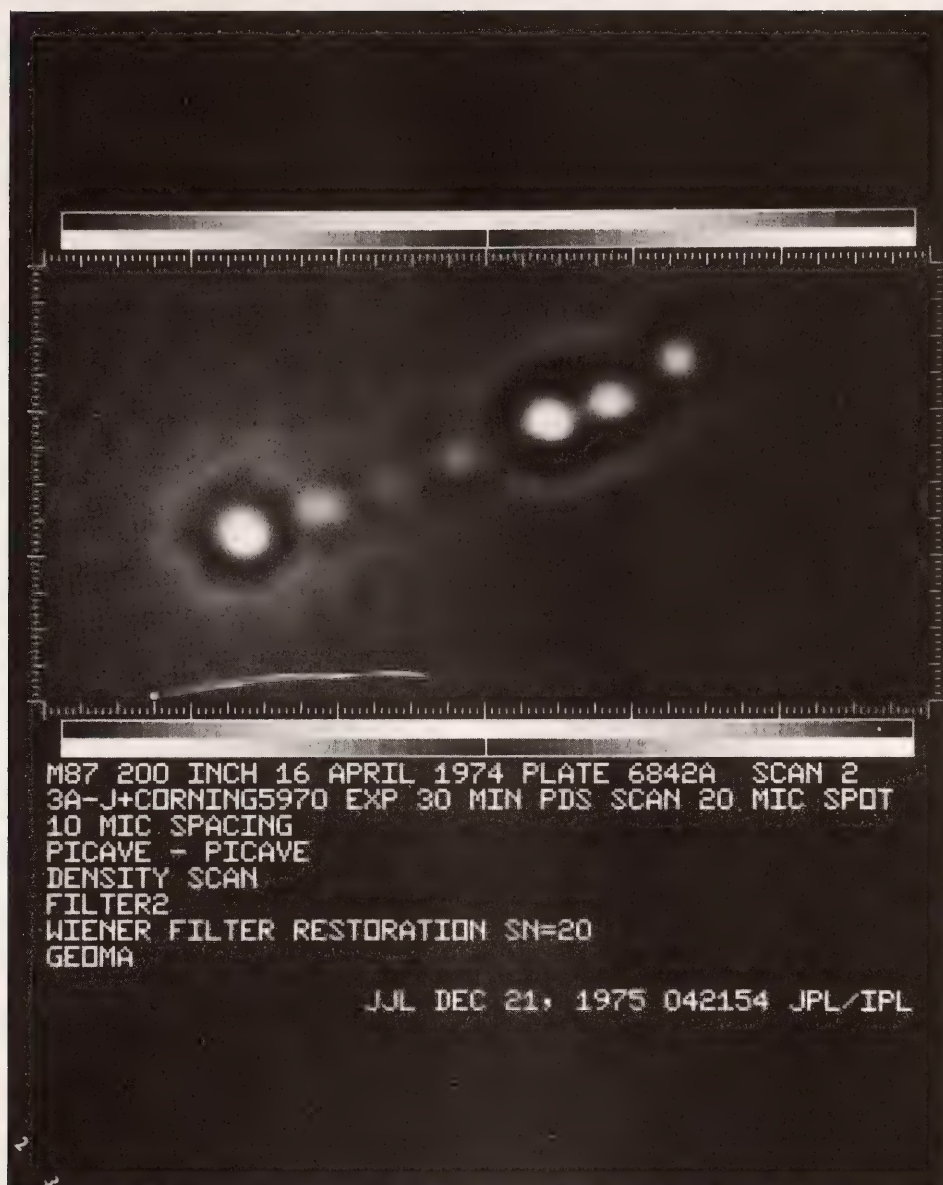


Fig. 5b. The resulting image-processed picture shows the well-known jet resolved into a series of evenly spaced, well-aligned points of light.

tola and Cesare Barbieri of Padova Observatory. Its purpose is to study the contents of fields in the vicinity of bright galaxies. Ninety-nine bright spiral galaxies between magnitudes 10 and 12 have been selected, as well as 99 control fields carefully chosen to be

more than 6° distant from any bright galaxies. The region within 1° of each of the spirals has been carefully studied in order to catalog companion galaxies and disturbed or nonequilibrium galaxies, including interacting double galaxies in which a quantita-

tive measure of relative separation may be recorded. Jack W. Sulentic, postdoctoral Hale Observatories Fellow, has completed the initial survey. The same kind of census has been completed for each of the associated control fields.

In May 1976, Dr. Graziella de Tullio of the Padova Observatory visited Pasadena to work on this same problem, comparing her independent cataloging of the fields with Sulentic's. Now a program is under way in both Pasadena and Padova to obtain photometric magnitudes, colors, spectroscopic classifications, and redshifts of these objects with the Palomar 1.5-meter and the Asiago 2.3-meter reflectors. A secondary phase of this program is to determine whether there are any photometric or spectroscopic differences that distinguish companions of the bright spirals from the background galaxies in the control fields.

With A. G. Willis and H. de Ruiter of Leiden Observatory, Arp has completed optical identifications of accurate Westerbork radio positions around a number of bright galaxies. Some of the more interesting identifications include a new 16.5–17.0 mag object of the BL Lacertae type very near the large spiral galaxy NGC 6503, a quasar that brightened almost 4 magnitudes in less than one month, and a number of quasars with redshifts greater than 2, including one with $z = 3.19$ (see *Year Book 74*, p. 333).

Sulentic and Arp have obtained U, B double-image plates of a number of their galaxy and control fields. These plates permit selection of ultraviolet excess stars that are quasar candidates and will allow an independent determination on the value of radio-quiet quasar numbers in the general field.

M87 and Its Globular Clusters

Sargent collaborated with C. R. Lynds of Kitt Peak National Observatory, F. D. A. Hartwick of the University of Victoria, and A. Boksenberg and R. F. Carswell of University College London in an attempt to measure the dispersion in velocity of the system of globular clusters around M87. The observations were made with Boksenberg's IPCS detector on Lynds' "Gold" spectrograph at the Cassegrain focus of the Kitt Peak 4-meter telescope. Because of indifferent seeing conditions, it proved possible to obtain a good spectrum of only one suspected cluster (IV-122 in an unpublished catalog by D. A. Hanes of David Dunlap Observatory). This object, which has $B = 20.6$ mag, proved to be a globular cluster (based on its redshift). Remarkably, IV-122 turns out to be more metal-rich than the galactic globular cluster M71, despite the fact that it is in the halo of M87, about 34 kpc from the center. This object was measured in a 3-hour exposure. It thus appears to be feasible to carry out the original project, given good seeing. A further attempt on the problem will be made on the Hale Telescope in 1977.

In view of the poor seeing during the run at Kitt Peak, the above team devoted a considerable effort to M87 itself. Lengthy exposures were made to determine the radial dependence of the velocity dispersion of the stars in M87 out to $150''$ from the center. Usable data were obtained despite the fact that at this radius M87 is about 1 mag fainter than the sky. They are now being analyzed. The ultimate aim of the observations of M87 and its clusters is to measure the total mass of the galaxy and its radial distribution.

CLUSTERS OF GALAXIES

Redshifts and Magnitudes

Kristian, Sandage, and Westphal are continuing a program to extend the Hubble diagram to redshifts greater

than 0.2. The main candidate lists in the first stage are (1) the fainter Abell clusters, (2) clusters found on a special high-latitude 1.2-meter deep survey with IIIa-J and 127–04 plates, and (3)

faint clusters associated with 3C radio sources. Redshifts are being measured with the SIT-prism digital spectrograph and *BVR* magnitudes with an S20 photomultiplier and the SIT area photometer. Redshifts have been measured for 80 clusters, including 60 with $z > 0.2$, 15 with $z > 0.3$, and 3 with $z > 0.5$ (3C330 at $z = 0.53$, 3C123 at $z = 0.63$, and 3C343.1 at $z = 0.75$ [preliminary]). With observations by Spinrad, using the image-dissector scanner at Lick Observatory, by Gunn and Oke, using the multichannel scanner, and those reported here, the 20-year-old "wall" at $z = 0.2$ has collapsed, and redshifts to $2\frac{1}{2}$ or 3 times larger distance are now routine. The principal limitation at present is not measuring the spectra but finding faint candidates and positioning them on the spectrograph slit. It now appears likely that about 100 clusters in the important range $z = 0.3$ – 0.5 can be measured in the next few years. Larger redshifts require rare nights of exceptionally good seeing and are likely to come more slowly.

Analysis of some early results in the range $z = 0.2$ to 0.3 shows several features: (1) In the absence of evolutionary corrections, the Friedmann models with $q_0 = 1$ continue to fit the data reasonably well. (2) The cosmic dispersion of 0.25 mag in the absolute magnitude of the brightest member and cluster richness found earlier by Sandage and Hardy is confirmed but is remarkably small over a large range of richness. This implies that if the magnitude of the brightest member is governed by a general luminosity function, then the slope of the function at the bright end must be very steep: $d \log f(M)/dM \geq 5$.

Preliminary analysis of 35 additional clusters to $z > 0.5$ supports the earlier conclusions and begins to show the expected turnover to bluer $B - V$ colors at large redshift, as the pass bands move into the ultraviolet regions of the galaxy rest spectrum. This color change is expected to be a useful discovery discriminant, and a program

has been started to use it to find extremely distant clusters.

The Hubble Diagram

The survey by Gunn and Oke with the 90-mm image tube and the 5-meter Hale Telescope now consists of 250–300 plates. On these plates approximately 60 faint clusters have been found. The south galactic hemisphere sample is essentially complete, but considerable work needs to be done on one or two of the spring fields, where progress has been slow due to bad weather. Since their first analysis of the Hubble diagram, an additional 38 galaxies in faint clusters have been observed, and redshifts and energy distributions now exist for most of these. A substantial fraction of these 38 objects have redshifts of 0.40 or more. The SIT spectrograph with on-line data handling and reduction system is now fully operational and is being used to obtain spectra of very faint galaxies; its expected speed advantage over the multichannel spectrometer is realized.

In their first analysis of the Hubble diagram, Gunn and Oke found that a significant uncertainty was introduced because of poor statistics for the relatively close clusters. This has been rectified by work with Thuan on a complete sample of nearby Abell clusters (all with distance class ≤ 4 , richness ≥ 1 , and $|b| > 30^\circ$, 102 in all). Photometry with an intermediate-band system, designed to be easily tied to the spectrophotometric system used for the distant objects with the 5-meter, has been carried out on the Palomar 1.5-meter telescope, and redshifts have been obtained, mostly with the image-tube spectrograph and more recently with the SIT digital spectrograph on the 5-meter telescope. This sample should provide very good statistics at the brighter end of the Hubble diagram. Since the sample is in some sense complete, it also allows more careful statistics to be done on systematic effects with richness and morphological type than have been possi-

ble before. Some of this work is being undertaken in collaboration with J. G. Hoessel, a graduate student doing thesis research with Gunn. It is clear that this sample is slightly brighter than the sample used in their last paper on the Hubble diagram and the deceleration parameter; this is not surprising since it is on average slightly richer, much more in accord with the mean richness of the distant sample. The change results in a *decrease* of the formal value of q_0 toward even more negative values.

The various kinds of systematic effects which must be guarded against point up the need to understand the evolutionary effects in galaxies much better. The observational work on galaxy synthesis by Gunn and B. Tinsley at Yale was finished last spring. It awaits resolution of some minor troubles with the photometric standards before the data can be finally put together in what they hope will be a definitive population synthesis for giant elliptical galaxies.

The study of the evolution of first-rank galaxies in faint clusters that is being made by Althea Wilkinson involves a sample of 36 galaxies measured with an aperture within 15% of a 32-kpc metric diameter, for which good absolute spectral energy distributions exist. Using the average of galaxies with redshifts between 0.10 and 0.20 as the standard galaxy spectrum, the comparisons with averaged galaxies in other redshift intervals show large scatter. Although the spectral resolution is poor (160 or 260Å), this scatter appears to be caused by known absorption features such as Mg-b λ 5175, the G-band, and the CN λ 4200 band. The resemblances of some of the individual galaxies are striking enough that an attempt to isolate a more homogeneous subsequence has been made, using the technique of cluster analysis. A significant sequence involving about half of the galaxies and roughly related to the redshift is found; this is mainly due to the decrease in strength of the absorption features mentioned above with in-

creasing distance. The sequence can be regarded as defining a mean giant elliptical spectrum, and the remainder of the spectra outline approximately the intrinsic scatter in the population at any given redshift. Both the changes with redshift and the means and dispersions of the populations will be much better defined when more and higher resolution SIT spectrograph observations are available. The rate of change of overall color with distance or lookback time is extremely small.

Photometry and Redshifts of First Brightest Cluster Members

Thuan and Gunn have obtained photometric data for all of a sample of 106 high-latitude Abell clusters (see *Year Book* 74, p. 339). The desired redshift data for some 40 clusters are still missing, but the program should be completed within the coming year.

Brightest Cluster Galaxies

P. Hickson, E. Turner, and Richstone discovered a correlation of the size of the largest galaxy in dense small groups with the mean intergalactic separation. They find that this correlation can be understood in terms of a simple theory of galaxy collisions.

In 1957, E. Scott at Berkeley proposed that the luminosity of the brightest galaxy in clusters of galaxies was determined by a statistical sampling of the same underlying luminosity function as the other galaxies. A minor controversy has recently developed over the validity of this model, inspired in part by its relevance to determining q_0 from the redshift magnitude diagram and to understanding the dynamics of clusters of galaxies. In the past, tests of the model have been based on an assumption of a specific universal underlying luminosity function. Scott Tremaine and Richstone have discovered a new class of tests of the model which does not depend on the form or universality of the underlying luminosity function. The application of

one of these tests to the magnitudes of first and second brightest cluster galaxies published by Sandage and Hardy yields a result that is inconsistent with any statistical sampling of any luminosity function. This result suggests that the luminosities of brightest cluster galaxies are determined by some physical process.

The Dynamics of Galaxies and Clusters of Galaxies

The new SIT-Vidicon spectrograph has been used by Gunn to obtain high-resolution spectra of several elliptical and early-type spiral galaxies in an attempt to elucidate the dynamical structure of these objects and, in particular, to study rotation and velocity dispersion far from the nucleus. If the M/L ratio of galaxies increases outward as markedly as studies of the dynamics of groups, clusters, and binary galaxies suggest, the effect should show up in these data at about the present level of sensitivity. Thuan and P. Schechter of the Institute for Advanced Study, Princeton, are collaborating on this project.

The same code that constructs models of globular clusters can be used to build model galaxies; elliptical galaxies with exterior massive halos have been constructed, and fits to the mass of luminous density with radius fully as satisfactory as earlier one-component models have been obtained. Dynamically, the models are quite different, with the halo models remaining quite hot all the way to the edge. Observations such as those being conducted with the SIT spectrograph now should be able to distinguish the two.

Equality of Redshifts of E and S0 Galaxies in the Virgo Cluster

From time to time it has been suggested that the elliptical and spiral galaxies in the Virgo cluster have different mean redshifts. The result, taken to be real, occasionally has been cited as evidence either for nonvelocity

redshifts or that the Virgo cluster is not a single dynamical unit (the spirals being more distant than the ellipticals). In either case, use of the Virgo cluster as a calibration step to the global value of H_0 could be questioned because the distance to the spirals (in both the radio and the optical methods) is used to determine the absolute magnitudes of the ellipticals.

Sandage has obtained new redshifts for 32 Shapley-Ames, E, S0, and spiral galaxies in the Virgo cluster for which no prior data exist, and with Tammann has combined these values with other new data from other sources to rediscuss the problem.

Redshifts now exist for 111 galaxies in the core of the cluster. All Shapley-Ames galaxies are in the sample. The extended material gives $\langle v_0 \rangle = 1105 \pm 120 \text{ km s}^{-1}$ for the spirals and $\langle v_0 \rangle = 1070 \pm 79 \text{ km s}^{-1}$ for E and S0 types, which are the same numbers to within 0.2σ of their combined errors. Equality of the two values supports the view that there is no nonvelocity redshift component that differs between E and S galaxies in this sample, that the Virgo E and S galaxies are members of the same dynamical unit, and that the Virgo cluster can be used with no special problems of this type in the determination of the expansion rate.

A New Nearby Group

During the reclassification of galaxies in the Shapley-Ames catalog, Sandage noticed that galaxies in the confused Ursa Major-Coma region could be separated into three distance groups on the basis of ease of resolution into stars. This separation also gave an almost unique separation into three velocity groups, one at $\langle v_0 \rangle = 285 \text{ km s}^{-1}$, another at $\langle v_0 \rangle = 750 \text{ km s}^{-1}$, and the third at $\langle v_0 \rangle \simeq 980 \text{ km s}^{-1}$. Galaxies in the low-velocity group are from a small area of about 15° radius on the sky, which contains the very well resolved late-type galaxies NGC 4144, 4214, 4244, 4395, and 4449. The brightest stars are very easy to resolve in these

systems, starting at about $B \sim 18$ mag, and the group has been put on the bright star program. Its importance is that it is as close as the M81-NGC 2403 and the South Polar Group, whose study is expected to provide the next steps in refining the extragalactic distance scale.

X-Ray Clusters

Sargent and graduate student Jorge Melnick used large-scale plates obtained at the Cassegrain focus of the Palomar 1.5-meter telescope to study the radial dependence of morphological type in several clusters of galaxies that are x-ray sources. It was found that in all cases the ratio of spiral to S0 galaxies increases outward. This is consistent with the notion that spirals are converted into S0s as they traverse

the hot gas thought to be responsible for the x-ray emission from the clusters' centers. It was also found that there is a good correlation between the velocity dispersion of the galaxies in a cluster and the overall proportion of S0s.

Intergalactic Hydrogen Clouds

A search for intergalactic neutral hydrogen clouds in nearby groups of galaxies was begun by Sargent and Dr. K. Y. Lo of the Owens Valley Radio Observatory. Extensive observations, principally of the M81 group, were made with the Hat Creek 85-foot dish and with the Owens Valley 130-foot dish. The idea is to search for intergalactic clouds that may be responsible for quasar absorption lines.

RADIO SOURCES

3CR Identifications

Katem, Kristian, and Sandage are continuing a program of identifications of 3CR radio sources to a uniform faint limit. The results of searches in 40 fields are being prepared for publication. Some of the new faint identifications are 3C13, 3C68.1, 3C123 ($z = 0.63$), 3C265, 3C325, and 3C437.

Perseus A

Dr. Gregory A. Shields of the University of Texas at Austin and Oke have analyzed absolute spectral-

energy distributions of NGC 1275 (Per A). The data are consistent with the heavy reddening discovered by Wampler. The line-emitting region has a characteristic density of about $3 \times 10^4 \text{ cm}^{-3}$, a mass of $3 \times 10^5 M_{\odot}$ and a volume-filling factor of 10^{-6} . The gas may be ionized by shock waves or by nonthermal or stellar radiation. It is again suggested, in the vein of Minkowski's original proposal, that the high-velocity emission-line knots described by Minkowski are H II regions in a galaxy or an intergalactic gas cloud seen in projection against NGC 1275.

QUASARS AND QUASI-STELLAR OBJECTS

Spectroscopic Observations

Schmidt has completed spectroscopic and spectrophotometric observations of a complete sample of quasi-stellar sources in the 6-cm National Radio Astronomy Observatory survey. The value of V/V_{max} , which measures the

position of an individual source within the available volume, appears to be correlated with the radio spectral index. Sources with steep radio spectra have a mean V/V_{max} around 0.7, similar to values found previously for quasars in the 3CR and 4C catalogs, most of which have steep radio spectra.

The space density of these quasars rises steeply with redshift (i.e., declines with cosmic time) by a factor of around 1000 to a redshift of 2.5. In contrast, quasars with flat or inverted radio spectra have a lower mean value of V/V_{max} , around 0.52 ± 0.05 (m.e.), consistent with a uniform distribution in space. It is not clear why flat-spectrum quasars would have a uniform space distribution; further work is needed to derive the optical and radio luminosity functions of these objects.

Quasar Surveys

Richard Green, a Caltech graduate student, is continuing his work on a Palomar 46-cm Schmidt survey, over an area of around 10,000 square degrees, designed to find bright quasars from their ultraviolet excess. He has determined *UBV* magnitudes for several stars each in the 300 survey fields, to allow calibration of the $U - B$ colors corresponding to the ultraviolet and blue images. Almost half of the films have been scanned and digitized with the PDS microdensitometer at the Image Processing Laboratory at the Jet Propulsion Laboratory. A reduction program has been designed that derives magnitudes and colors for all stars ($\sim 50,000$ on each film), selects *UV* excess objects, and supplies overlay finding charts to scale for the 46-cm film.

Dr. O. Ulfbeck, a Caltech Research Fellow, has reduced a two-color (U, B) 1.2-meter Schmidt plate of a field just north of M3. He has produced a list of 40 objects with a strong ultraviolet excess down to a magnitude of around 20. Schmidt and Richstone have observed most of these objects with the Gunn-Oke SIT-Vidicon spectrograph. About two thirds of the objects are quasars, most of which have redshifts between 1 and 2.5. Ulfbeck is extending the list to objects with less ultraviolet excess.

Search for High-Redshift QSOs

All of the five QSOs known to have redshifts $z_{\text{em}} \geq 3$ were discovered

through their radio emission, although at lower redshifts the radio-quiet QSOs vastly outnumber those that are radio sources. Sargent began an experimental program to try to find objects similar to OH471 that have no radiation beyond the Lyman limit. The idea is to photograph fields with the 1.2-meter Schmidt through three filters: one centered at λ 3800, one at λ 5200, and one at λ 6600. The plates are then scanned for objects in which the two long-wavelength images are roughly equal and in which the ultraviolet image is absent. It proved possible to isolate OH 471, which is in a rich star field, by a suitable choice of filters. At the end of the report year, no quasars had been found in two fields.

Absorption Lines

Sargent continued collaboration with A. Boksenberg and R. F. Carswell of University College London on spectroscopy of quasar absorption lines with the Image Photon Counting System (IPCS). The instrument was used for five nights in the fall and three and one half nights in the spring at the coudé focus of the Hale Telescope on high-resolution ($0.8\text{--}0.4 \text{ \AA}$) studies of relatively bright ($m \lesssim 17$) quasars with rich absorption spectra. It was also used for five nights in the fall on lower-resolution ($\sim 3 \text{ \AA}$) observations of fainter objects at the Cassegrain focus. Work continued on the reduction and analysis of these observations and of observations made in previous years.

The high-resolution observations were concentrated on three objects: Pks 0237-23 ($z_{\text{em}} = 2.22$), which had been studied in 1974 and 1973; 1225+31 ($z_{\text{cm}} = 2.2$, $m_p = 16$) was studied for the first time; and the "BL Lacertae" object Pks 0735+178, which has the Mg II λ 2800 doublet in absorption at a redshift of $z_{\text{abs}} = 0.424$. The major effort was put into observing particular spectral regions at as high a resolution and signal-to-noise ratio as possible in order to check the suggestion by Boksenberg and Sargent (*Astrophys. J.*,

198, 31, 1975) that absorption redshift systems tend to be split into close pairs separated by a "magic velocity" of 140 km s^{-1} . Preliminary work has shown that there is indeed no magic splitting, but that almost all redshift systems exhibit velocity structure on a scale of less than 200 km s^{-1} . It is not yet clear whether the distribution of these fine splittings is consistent with Bahcall's hypothesis (*Astrophys. J. [Lett.]*, 200, L1, 1975) that it results from clouds in the halos of intervening galaxies. A second aim was to try to resolve the individual lines; however, the lines in Pks 0734+178 were still unresolved at 25 km s^{-1} FWHM.

Sargent, Boroson, and Boksenberg completed a reanalysis of the spectrum of Pks 0237-23 based on the addition of three seasons' data covering the wavelength region $\lambda\lambda$ 3700-4300. The new data revealed the existence of many faint lines; the total number identified was 280. A large statistical excess of these lines could be identified with the C IV resonance doublet $\lambda\lambda$ 1548, 1550 at redshifts between $z_{\text{abs}} = 1.4$ and $z_{\text{abs}} = 1.75$. The fifty or so redshifts are not distributed uniformly in this interval but exhibit a pronounced peak centered on $z_{\text{abs}} = 1.65$. The half-width of the peak is $\Delta z_{\text{abs}} \sim 0.06$ or 7000 km s^{-1} . If these redshifts arise in intergalactic clouds, then the width of the peak is too large for them to be accounted for by a single cluster of galaxies; a structure such as a large cluster of clusters would be required. Moreover, it should be about 3° across on the plane of the sky. There is a high probability that a faint quasar with $z_{\text{abs}} \geq 1.65$ could be found in such a large area. A search for absorption redshifts with a similar peak in the distribution of z_{abs} as that found in Pks 0237-23 would be a direct test of the intergalactic hypothesis. It is planned to search for other QSOs around Pks 0237-23 in the coming season.

Several QSOs, for example Phl 957, have been found to have a large number of absorption lines shortward

of the Lyman- α emission line; C. R. Lynds has conjectured that these must be single Ly- α absorption lines. This hypothesis is strongly supported by the discovery of the many weak C IV doublets longward of the Ly- α emission line in Pks 0237-23. Boksenberg, Sargent, and Carswell obtained excellent high-resolution spectra of Phl 957 with the IPCS in 1974. As was mentioned in *Year Book 74* (p. 342), little progress was made in identifying the complex absorption spectrum. However, during 1976 it was found that several lines longward of the Ly- α emission line could be identified as C IV doublets. The experience with Pks 0237-23 suggests that these identifications are likely to be correct and gives a rationale for a renewed attempt to obtain better data on the spectrum of Phl 957.

Analysis of the high-resolution spectra of 1225+31 ($z_{\text{em}} = 2.2$) was only begun toward the end of the report year; however, it seems likely to be identifiable since, like Pks 0237-23, it contains clumps and groupings of strong lines. For example, there is a cluster of six lines near λ 4050 that are obviously three sets of C IV doublets at $z_{\text{abs}} = 1.62406, 1.62510, \text{ and } 1.62574$. A similar cluster of four C IV doublets near λ 4330 leads to four close redshifts, $z_{\text{abs}} = 1.79374, 1.79482, 1.79570, \text{ and } 1.79643$. The splittings between adjacent pairs of redshifts are 119, 73, 116, 95, and 79 km s^{-1} . These values are significantly less than the supposed "magic splitting" alluded to earlier.

The "BL Lac" object Pks 0735+178 is the brightest quasarlike object to show absorption lines. Sargent, Boksenberg, and Carswell were able to observe the Mg II double λ 2800 seen at $z_{\text{abs}} = 0.424$ in this object at a resolution of 0.35 \AA . It was found that each Mg II line splits into four components at this resolution. The components are separated by intervals of $50\text{--}70 \text{ km s}^{-1}$. Fits to theoretical profiles indicate that the individual clouds have Doppler parameters of about 5 km s^{-1} , very similar to

those found in galactic interstellar H I clouds.

The main effort in the low-resolution work went into a survey of a complete sample of QSOs with $1.90 < z_{\text{em}} < 2.20$ that were brighter than 18.5 mag and with R.A. from 22^h to 11^h. The spectral range $\lambda\lambda$ 3200–4500 was observed at a resolution of 3 Å in all the 19 objects in the above sample. Care was taken to accumulate the same number of continuum counts in all of the objects. It was found that 18 of the 19 QSOs showed certain absorption lines, with the remaining one being doubtful. The preliminary analysis shows that the mean number of clouds per object is about three and that the distribution is consistent with the Poisson distribution expected if the absorbing clouds are randomly distributed in space. This is contrary to earlier suppositions and means that an intergalactic nature for the clouds is not ruled out by this test.

Other low-resolution work was also done on the quasars OH471 ($z_{\text{em}} = 3.40$) and 0830+119 ($z_{\text{em}} = 2.98$). The observations of OH471 confirmed an earlier finding by Carswell *et al.* (*Astrophys. J.*, 195, 269, 1975) that the Lyman discontinuity is not at the wavelength corresponding to the emission redshift in this object. Several new redshifts were found in a detailed analysis of the spectrum.

In further work, Sargent and undergraduate Todd Boroson used the multichannel scanner on the Hale Telescope to search for evidence for emission from the absorbing regions of several high-redshift QSOs. It has been shown empirically in the case of OH471 that most of the ionizing radiation beyond the Lyman limit is absorbed in the clouds that produce the absorption lines and not in the region which gives rise to the broad emission lines. Simple arguments, based on a knowledge of an upper limit for the electron density in the clouds and their observed ionization states, show that they must be more than about 10 kpc from the QSO if they indeed provide

the source of ionizing radiation. At $z_{\text{em}} = 2.0$, a distance of 10 kpc corresponds to an angle of 1.5", 1.8", and 2.4" for $q_0 = 0, 0.1$, and 0.5, respectively. Sargent and Boroson searched for the extended, diffuse Ly- α emission from the absorbing clouds by measuring the equivalent width of Lyman- α through apertures of radius 1" and 7". No increase with aperture size was observed. If the clouds are much farther away from the QSO than 10 kpc, their masses and kinetic energies become implausibly large. The simplest conclusion, therefore, is that they are in intervening intergalactic space, unrelated to the QSO.

Optical Continuum

The large redshifts, variability, and power-law optical spectra of quasi-stellar objects indicate that they are nonthermal energy sources of immense volume emissivity. A natural mechanism for these sources, electron-synchrotron radiation, is implausible because of short energy-loss time scales for the electrons and huge predicted x- and γ -ray fluxes, which are ruled out observationally. A variety of other mechanisms have been proposed without wide acceptance. Delineating the optical spectral properties of these objects may provide the foundation for an eventual understanding of the energy-generation mechanism. With this in mind, Richstone has investigated the properties of 80 quasi-stellar objects observed with the multichannel spectrophotometer. Most of these objects come from Schmidt's complete samples of 4C and 5000 MHz radio quasars.

The continua of these sources are approximated by a power law of spectral index ranging from +0.3 to -3.0, with a median value of -0.7. Superimposed on the power law is a broad wave, which appears as a depression at 4500–4000 Å and as an excess at 3000 Å (rest wavelength). The strength of the depression is anticorrelated with the luminosity. This feature may result

from broad wings of the strong lines combined with unresolved weak lines and the Balmer continuum, but it seems more likely to be a property of the continuum. Richstone observed for the first time a dip in the continuum at 2100 Å. If it is due to dust grains similar to those in the Galaxy, then the dust-to-gas ratio in the line of sight to the quasar is very small. The absence of a correlation between the radio and optical spectral indices indicates that the optical photons are not radio photons that have scattered off their parent electrons.

Emission Lines

The systematics of the emission-line strengths are somewhat anomalous. If,

as is generally believed, the Balmer lines are formed in a region that is photoionized by the quasar, a strong anticorrelation should be observed between the Balmer-line equivalent widths and the optical spectral index of the quasar. This is not observed. The absence of such a correlation may result from a wide range in continuum optical depths in the gas responsible for the emission lines.

SIT-Vidicon spectra of 25 low-redshift quasars have been obtained at 7 Å resolution in the wavelength range 3700–6500 Å to study further the properties of the emission lines of these objects.

OBSERVATIONAL COSMOLOGY

The Hubble Constant and Deceleration Parameter

Sandage and Dr. G. A. Tammann of the Astronomisches Institut der Universität Basel have continued work on the rate of expansion of the universe, following the discovery of a new method by R. B. Tully and J. R. Fisher of the National Radio Astronomy Observatory. When these radio astronomers showed last year that the observed widths of the 21-cm line of neutral hydrogen in Sc, Sd, and Ir-Sm galaxies (corrected to edge-on inclination) were well correlated with absolute optical magnitude, the way was opened to test again the distance scale to very nearby galaxies. Distances to the M81-NGC 2403 and the M101 groups had been determined earlier by Sandage and Tammann from studies of the stellar content as the first step in their prior determination of the Hubble constant H_0 .

The result of the independent test is that the optical scale is confirmed to within $4\% \pm 8\%$ for the M81-NGC 2403 and to within $10\% \pm 17\%$ in the opposite direction from the M101

group. The radio distance moduli are $(M - M)_0 = 27.64 \pm 0.09$ and 29.08 ± 0.16 mag for the M81 and M101 groups, to be compared with the earlier optical values of 27.55 ± 0.15 and 29.30 ± 0.3 , respectively. (All these values are based on an assumed Hyades cluster modulus, which is the fundamental calibrator of $m - M = 3.03$.) The method was then applied to the Virgo cluster, with the result that $(m - M)_0 = 31.4 \pm 0.2$ from the radio data and $(m - M)_0 = 31.5 \pm 0.1$ from the optical data, based on the optical scales that had been previously adopted.

Taking the revised $m - M = 3.23$ for the Hyades gives $(m - M)_0$ for Virgo as 31.70 ± 0.1 (or $D = 21.9 \pm 1$ Mpc), from which the Hubble constant follows as

$$H_0 = 50.3 \pm 4.3 \sigma \text{ km s}^{-1} \text{ Mpc}^{-1}.$$

This is equal to the value derived earlier from the six-step optical procedure, taking account of the Hyades revision.

Sandage and Tammann state that the value is the *global* expansion rate independent of local deviations from a pure Hubble flow, no matter how large. This is because the calibrations via the Virgo cluster have been applied to a

sample of clusters at intermediate redshifts, where any local density anomalies have no effect.

This value of H_0 gives a Hubble time of $H_0^{-1} = (19.4 \pm 1.6) \times 10^9$ years. Comparison with the age of globular clusters, taking into account the collapse of our Galaxy from the pregalactic medium, shows that the time since the creation of the Universe at $T_0 \approx 16 \times 10^9$ years is so close to $H_0^{-1} = 19.4 \times 10^9$ years as to put significant limits on the deceleration parameter q_0 . With $H_0^{-1}/T_0 = 1.21 \pm 0.10$, it follows that $q_0 = 0.15 \pm 0.10$, which is well below the critical value of $\frac{1}{2}$ and in agreement with conclusions reached earlier from other methods. If the deceleration has been so mild, then the expansion is irreversible and the Universe has apparently happened only once.

Two general methods have been proposed to determine the cosmological density parameter $\Omega = 2q_0$ directly. One method involves adding up the mass per unit volume of all of the visible matter in a local volume of space. The second method involves an analysis of perturbations in the Hubble flow induced by density enhancements in the distribution of matter. Sargent and former graduate student Dr. E. L. Turner have devised a new method of

the second type. In this method, the distribution of galaxies in space is approximated by their distribution in a "redshift space" whose radial coordinate is cz/H_0 . Deviations from a smooth and uniform Hubble expansion, due either to perturbations arising from unbound density fluctuations in the distribution of galaxies or to virial motions in bound groups and clusters, cause characteristic distortions in this "redshift space." A method of detecting and measuring these distortions from the redshifts and relative positions on the sky of pairs of galaxies is proposed. Sargent and Turner have tried a simplified version of their general method on the available limited sample of data. They obtained $\Omega \sim 0.07$, which is consistent with other recent lines of evidence. They have also investigated the data requirements for a definitive application of their procedure. They estimate that redshifts for the 4000 brightest galaxies, accurate to $\pm 20 \text{ km s}^{-1}$, would be required. This is a formidable observational task but is not out of the question with the use of modern detectors and digital on-line analysis. Sargent, Turner, and Shectman are drawing up plans to pursue the above goal with the "Shectograph" detector when the du Pont Telescope comes into operation.

THEORETICAL STUDIES

Gravitational Radiation from Pressureless Nonaxisymmetric Stellar Collapse

Thuan and J. P. Ostriker of Princeton University Observatory (*Astrophys. J. [Lett.]*, 191, L105, 1974) have computed the amount of gravitational radiation emitted during a pressureless and axisymmetric stellar collapse, using Newtonian theory and the quadrupole-moment formalism. They are expanding the calculations to the case of nonaxisymmetric collapse. In particular, they are investigating

two possible situations: (1) If $t_f = |T_{\text{rot}}/W|_{\text{final}}$, the ratio of the final rotational energy to the final total binding energy is between 0.14 and 0.27, then the final state is secularly unstable and the star goes from an axisymmetric mode (Maclaurin sequence) to a nonaxisymmetric mode by conserving circulation. The star then follows the Dedekind sequence and loses angular momentum by emitting gravitational radiation to get back to the Maclaurin sequence. (2) If $t_f > 0.27$, the star is dynamically unstable and breaks up to form a binary, which in turn emits

gravitational radiation while losing angular momentum.

Gravitational Radiation from Axisymmetric Stellar Collapse with Pressure

Dr. I. D. Novikov of the Mathematical Institute, USSR Academy of Sciences, Moscow, has pointed out that by neglecting pressure the calculations by Thuan and Ostriker may have underestimated the amount of gravitational radiation emitted. The collapse of the star is likely to be stopped abruptly when neutron star densities ($\sim 10^{15}$ gm cm $^{-3}$) are reached, and the star will bounce. This abrupt deceleration will cause a substantial amount of gravitational radiation to be emitted. Thuan and Ostriker are extending their axisymmetric collapse calculation, including pressure, in order to follow the bounces a neutron star would undergo before reaching its final equilibrium. The competing effects of gravitational radiation and neutrino cooling are being taken into account.

Angular Momentum of Galaxies and Tidal Interaction

Hoyle and Peebles have argued that tidal interactions of protogalaxies, originally frozen in the Hubble flow at recombination and with a quadrupole moment of order unity, generate sufficient torques to give galaxies a typical angular momentum that agrees in order of magnitude with the observed values. Tidal interactions are especially appealing since they occur naturally in the gravitational instability theory of the formation of galaxies; therefore, extra sources of angular momentum, such as primordial turbulence, need not be invoked.

Thuan and J. R. Gott III of Princeton University have applied the tidal in-

teraction concept to the Local Group. They assume that the Galaxy and M31 derive their angular momentum from each other. This is supported by the observational fact that the two galaxies are nearly in a mutual plane. The theory predicts correctly that the rotation of M31 is counterclockwise as seen by us. M31 has 1.7 times the angular momentum of the Galaxy.

Since the tidal-interaction concept relies on statistical gravitational interactions, it can be used to predict more than just the rms angular momentum of galaxies. Thuan and Gott have used Monte Carlo calculations to predict the distribution of total angular momenta for galaxies of a given mass (or luminosity) from the tidal interaction picture and have compared the predictions with the observed distribution of ellipticities of elliptical galaxies as a function of absolute magnitude. They find a remarkable agreement, not only in the shapes of the individual distributions but also in the correlation of systematic properties with mass. The tidal theory predicts that the distribution of ellipticities in elliptical galaxies should be independent of absolute magnitude for $M \geq -20.7$, but that very bright galaxies ($M \leq -20.7$) should be systematically rounder than the others. The results are in excellent agreement with a dissipationless collapse picture for ellipticals in which star formation is essentially completed by the time of maximum collapse. Using the observed distribution of ellipticities, they are able to set rather severe limits on the amount of dissipation (if any) that can occur. They also discuss the predictions of the theory concerning the sizes of spiral galaxies; the tidal theory predicts many more disks of high surface brightness and small scale length compared to Freeman's observations.

INSTRUMENTATION

SIT Acquisition and Guiding System (SITEX)

A new system has been built for use at the Cassegrain focus of the Hale

Telescope. It is intended to be used in place of, and is functionally similar to, the system that has been in use since 1971. The earlier system has been ex-

tremely successful and has become indispensable for observing faint objects. The new system is adapted, in collaboration with Gunn and S. Knapp, from the Westphal-Kristian SIT photometer. The main differences are (1) the use of a SIT-Vidicon detector, which is less noisy and more rugged than the earlier SEC, and (2) a digital scan convertor, which is less noisy than the earlier analog devices and has a movable cursor whose position can be read to better than $1''$. This last feature is very useful for blind offsets. It is expected that the new system can be used to detect, acquire, and guide on appreciably fainter objects than the old system, and its first use at the telescope supports this expectation. It has been used to obtain the spectrum of a galaxy at $V = 20.8$ mag (preliminary $z = 0.75$); the exposure was guided on a substantially fainter object. With $20''$ integration times on fields with photoelectric sequences, stars of V magnitude 23 are seen.

Remote Operation of Cassegrain Ring Rotation

To facilitate remote operation at the Cassegrain focus of the 5-meter telescope, which now accounts for most of the operations at that station, Westphal has implemented remote control and readout of the orientation of the instrument mounting ring.

SIT-Vidicon Digital Spectrographs

There are now two such spectrographs for the 5-meter telescope, both based on the cooled SIT-Vidicon described by Westphal and McCord in *Year Book 71* (p. 705). The system used by Sandage, Kristian, and Westphal has been improved by addition of a unit that uses microprocessors to average the data on-line, do star-sky subtraction, and display the results in analog form, either on a digital scan convertor or an $x - y$ plotter. This detector is used on a prism instrument.

Another SIT-Vidicon spectrograph, this one using a grating, became fully

operational and has been used by Gunn, Oke, Shectman, Schmidt, and Arp to obtain data on a wide variety of problems. The interface and software have been refined by Knapp and Zimmerman and Oke so that real-time reduction of both spectroscopy and spectrophotometry is possible and is carried out routinely. The most serious lack to date has been the poor UV response; a new special vidicon with UV -transmitting fiber optics on the input has been obtained and will be tested soon. If the red response is satisfactory, the new tube will become standard.

Photon-Counting Image-Intensifier System

In July 1975, Shectman began the construction of a photon-counting image-intensifier system intended for high-resolution spectrophotometry at the Mount Wilson 2.5-meter and the Palomar 5-meter coude spectrographs. The instrument was successfully put into operation in May 1976 at Mount Wilson.

Individual photoelectrons from the first photocathode in a six-stage image intensifier generate bursts at the final phosphor which emit $\sim 10^8$ photons over an interval of several milliseconds. A fast transfer lens images these photon events onto a linear self-scanning diode-array image sensor. The complete row of 256 photodiodes is scanned in sequence every 0.5 millisecond. A sufficient change in the output of the sensor from one sweep to the next indicates the onset of a photon event at a particular location in the image.

The precise position of the center of each photon event is measured by an analog circuit, and a digital address corresponding to the event location is generated. This address is used by an on-line minicomputer to accumulate a tally of the number of photons detected at each wavelength in the spectrum. On a computer graphics terminal, the spectrum is constantly displayed as it is accumulated. The final result is recorded on magnetic tape.

The output of the photo-counting system is a spectrum of 1500 channels, each channel corresponding to a $10\text{-}\mu$ interval in the focal plane of the spectrograph. The FWHM resolution for spectral lines is consistently better than $40\text{ }\mu$. The advantages of this device lie in the high quantum efficiency of the photocathode, from 10 to 100 times that of photographic plates, and in the linearity and repeatability of its response. Corrections of sky background can be measured and accurately applied to the data. A thermoelectric cooling device lowers the thermal background of the image intensifier to a level at which it does not seriously compete with signals that take hours to accumulate. The use of a solid-state diode array results in a high degree of geometric stability. Compared to an earlier generation of single-channel photoelectric detectors, the ability to monitor all 1500 channels simultaneously for the arrival of photons results in vastly improved efficiency.

The minicomputer program allows the astronomer to monitor the progress of each observation and to control the system at each contingency. Data analysis and reduction are carried out, using the computing facility at the Santa Barbara Street offices. Both the data acquisition and reduction programs were developed by Ken Clardy.

During the coming year, several astronomers are scheduled to use the system for a variety of projects. Foremost among these are a program to measure the kinematical properties of the halo of our Galaxy, using as tracers Mira variables 3 mag fainter than have previously been practicable, and a program to observe the population of globular clusters in the Andromeda galaxy at resolutions unattainable with conventional detector systems.

Support for the development of this system was provided by a grant from the Sloan Foundation to the California Institute of Technology.

Charge-Coupled Devices

Using a grant from the President's Fund (Caltech), a program has been under way in collaboration with the Jet Propulsion Laboratory to build a CCD camera for both direct imaging and low-resolution spectroscopy. The work has been done by F. Landauer and L. Hovland of J.P.L. and Dennison and Oke of the Hale Observatories. The camera has been completed and used successfully with the digital spectrograph on the 5-meter Hale Telescope. The present detector is a 100×160 -element device with very high quantum efficiency; used at -73°C , the dark current is negligible. The camera electronics have been designed so that the camera is controlled by the PDP 11/40 computer, which also collects and processes the data, using the programs developed for SIT spectra reductions. In operation, the system performed well but there may be residual problems with charge transfer. The overall quantum efficiency also appears to be too low for reasons that are still being investigated. There are plans to replace the 100×160 array by a 400×400 array when it becomes available in the next few months.

Photometry of Stellar H and K Lines

The Carnegie Institution has received a grant of \$34,510 from the National Aeronautics and Space Administration to assist in the continuation of Olin Wilson's studies of cyclic variations in stellar chromospheres. Under the direction of Vaughan and Preston as principal investigators, the grant is being used in the construction of a special-purpose spectrometer that will measure photoelectrically the intensities of Ca II, H, and K line emission, which have been developed in Wilson's study as indices of stellar chromospheric activity. The new instrument is designed to make nearly simultaneous measurements of both H and K and the nearby continuum with a single detec-

tor, to yield precise ratios of these quantities with the necessary stability for the monitoring of variations over an interval of many years. The instrument will be used at the Cassegrain foci of the Mount Wilson 1.5-meter and 2.5-meter telescopes, replacing the coudé spectrograph of the 2.5-meter for this purpose once the new technique has been calibrated. Construction of the instrument is in progress and a new four-channel digital data recorder, incorporating a microprocessor with PROM storage of software logic controlling the system, has reached the testing stage at the Astroelectronics Laboratory.

Infrared Detection Systems

During the past year, two major instrumental developments were made

for use in the 1–40 μ ground-based program. First, a very sensitive indium-antimonide system was completed. It includes a 1.5–3.0 μ and a 3.0–6.0 μ 1% spectrometer. On the 5-meter telescope, spectra of 13-mag objects can easily be recorded at 2.0 μ . In the broadband colors at 1.65 and 2.2 μ , 17-mag objects can be observed. Second, improvements have been made on the wobbling secondary systems of the 1.5-meter at Mount Wilson and the 5-meter telescope at Palomar Mountain. At the present time, 2-hour integration on the 5-meter telescope reaches a 1 σ limit of approximately 0.003 Jy (10th magnitude). The latter number is 3–5 times smaller than any other reported 10- μ flux limit for a similar integration time.

ASTROELECTRONICS LABORATORY

The laboratory directed its major efforts this year toward completing the installation of the 2.5-meter Irénée du Pont Telescope control system and the design and construction of the local and remote control assemblies for the various auxiliary instruments that are to be used on the telescope. These included the Cassegrain rotating ring and the associated cable wrap-up, the auxiliary instrument mounting base and the offset guider, the plate camera, and the Cassegrain spectrograph.

The multiplexing technique was adopted for instrument control signals in a way similar to that in which data are multiplexed by the telescope's Microprocessor Automatic Control System (MACS). By using this method, instrumentation requirements for individual cable conductors on the telescope were reduced by a factor of 10.

Each auxiliary instrument now has its complete self-contained control system, designed for minimum power dissipation. In addition, each instrument will have a remote box with the neces-

sary switches and displays for control from the data room, using the proven MACS multiplexing system and hardware. A similar design philosophy has been followed for each of the auxiliary instruments, with standardization in circuitry and in mechanical design.

Another major project this year was the development of a new data system for the multichannel spectrometer (Multichannel II) to replace the existing counter assembly. Multichannel II is a self-contained, 64-channel pulse-counting system with integration times adjustable from 1 second to 2.78 hours. The system can operate as a stand-alone instrument or with a PDP 11 computer. All front panel controls and data entry are accessible from the computer. At the end of an integration, all data are transferred to the computer with full "handshake" action—the computer-to-printer signal that data is being transferred and the responding printer-to-computer signal acknowledging the data.

GUEST INVESTIGATORS

Dr. Saul J. Adelman of Boston University used the coudé spectrograph of the 2.5-meter telescope at Mount Wilson and the Cassegrain scanner with the 1.5-meter telescope at Palomar to continue his studies of sharp-lined magnetic Ap stars and suitable comparison main-sequence stars. He expects to complete shortly an abundance analysis of γ Herculis, B5IV, for which he has performed a line-identification study of ultraviolet scans, which were obtained with the Copernicus satellite.

Mr. Gonzalo Alcaïno of the European Southern Observatory has continued his photographic study of southern globular clusters. Work has been completed on NGC 362, NGC 1904, and NGC 4590.

Dr. T. B. Austin and Mr. K. L. Dixon of Oxford University used the 1.2-meter Schmidt to obtain plates in the fields of rich clusters of galaxies. In the context of the ongoing program of multicolor photographic photometry of clusters, the plates will be used for the study of the morphology, dynamics, and evolution of cluster galaxies. Plates were taken in five colors, the standard plate-filter combinations in U, B, V, and the combinations IIIa-J + Wratten 2C, and 127-04 + RG1. In excellent observing conditions, many good quality plates were obtained, including two clusters in all five colors. All plates were calibrated using a tube sensitometer built at Oxford along the lines of those described extensively in the A.A.S. *Photo Bulletins*. This sensitometer, which can be calibrated photoelectrically on site, produces 45 sensitometer spots over an intensity range of a factor 1000.

In October and November 1975, Dr. J. Bergstrahl of the Jet Propulsion Laboratory and Münch collaborated to image the neutral sodium cloud which surrounds Io (II) in the light of the D lines. The latter appear in emission due to resonant scattering of sunlight. A Fabry-Pérot étalon was set up in the

coudé spectrograph of the Mount Wilson 1.5-meter telescope; a camera lens imaged the étalon onto the photocathode of an intensified silicon vidicon (SIT). Since the Io sodium cloud is an extended discrete-line source, its image through the étalon appears as a series of partial circular fringes. By adjusting gas pressure in the étalon cell, it is possible to "scan" the fringes spatially. A sequence of images at different cell pressures thus recorded the entire D-line emitting portion of the sodium cloud. Drs. T. V. Johnson and D. L. Matson, also from the Jet Propulsion Laboratory, collaborated by making the vidicon system available and assisted in several observations. The data are being processed at the J.P.L. Image Processing Laboratory.

Dr. Howard E. Bond of Louisiana State University used the Hale Telescope to obtain coudé spectrograms of subgiant CH stars and extremely metal-deficient red giants. The subgiant CH stars are F- and G-type subgiants showing enhancements of CH and the s-process elements (H.E. Bond, *Astrophys. J.*, 204, 810, 1976) and can probably be interpreted as former red giants that returned to the vicinity of the main sequence following a partial-mixing event, possibly at the helium core ignition. Since these are weak-lined, relatively hot stars, they offer the most favorable known circumstances for the study of the s-process of nucleosynthesis. Excellent spectroscopic material was obtained for two subgiant CH stars, HD 216219 and HD 182274. Spectra of a bright, carbon-deficient red giant, HR 6791, were also obtained. Using objective-prism plates, several new members of the rare class of extremely metal-deficient red giants have been found, which are bright enough for coudé spectroscopy. Sufficient coudé material for abundance analysis was obtained with the Hale Telescope for two such stars, HD 2796 and HD 4306, located near the south

galactic pole. The analysis of these spectra is expected to be completed during 1977. The results should provide new information on element-producing processes occurring in the stars themselves or in previous generations of stars during the early evolution of the galaxy.

Drs. M. S. Burkhead and J. K. Kalinowski of Indiana University used the 1.2-meter Schmidt at Palomar to obtain multiple plates (127-04 emulsion and Wratten 23 filter) of M104, M94, NGC 2903, NGC 3379, and NGC 3628 in January 1976. All these plates have been digitized and initial contour maps produced at the Los Alamos Scientific Laboratory. The plates are quite deep and have been digitally added, and smooth background corrections have been applied. Together with photoelectric drift scans, these data will yield improved values for the sizes, shapes, and colors of any extended features. This work is a continuation of a project that will provide uniform data (UBVI) for a sample of galaxies ranging from E0 through Sc.

Drs. D. G. Currie, K. M. Liewer, and Mr. R. Braunstein of the University of Maryland and Dr. S. L. Knapp of the California Institute of Technology have continued the program of stellar diameter measurements using the Amplitude Interferometer. A summary of the observations conducted from 1972 to 1976 has recently been submitted for publication. This includes measurements of the effective diameters of 12 late-spectral-type stars (K0-M6), of which five have not been previously reported (ρ Persei, δ Ophiuchi, γ Herculis, γ Draconis, R Lyrae). These measurements were conducted at as many as 10 different wavelengths. The diameters range from 0.013" to 0.052". The internal precision of the more recent measurements ranges from 0.001" to 0.006", with accuracies of 0.002" to 0.006".

Test observations using the University of Maryland Array Photometer on

the 2.5- and 5-meter telescopes were conducted. This system, which will be a photon-counting array detector with a 100 by 100 array of channels, uses an Intensified Charge Coupled Device. This will be used both in a Direct Imaging mode, providing a very large dynamic range, and in the Multi-Aperture Amplitude Interferometer. The latter is the next generation Amplitude Interferometer, which has a data rate 8000 times greater than the current instrument.

Dr. Santo Catalano of the Astrophysical Observatory at Catania employed the coude scanner of the 2.5-meter telescope at Mount Wilson to obtain photoelectric scans of the H and K lines and the continuum near 3950 Å at a resolution of about 0.2 Å. Twenty main-sequence and giant stars later than F8 were observed. Four scans of the K line of the integrated light of the Sun through the Moon were also obtained. The profile at the center of the line shows considerable variations from one scan to another, while the wings appear to remain unchanged. Absolute fluxes of the integrated H and K lines will be obtained to study the behavior of stellar chromospheric emission in these lines. The ratio of the central intensity K_3/H_3 appears to be constant and equal to unity in giant stars, while it appears to become greater than unity with advancing spectral type of main-sequence stars, as already shown by Wilson.

Dr. Pierre Connes of the Observatoire de Meudon has continued to use his Fourier infrared spectrometer mounted in the lower coude spectrograph room of the 5-meter Hale Telescope. The previously detected O_2 emission on Mars has been analyzed by Carleton, Traub, and Noscon. In November 1975, four days and nights were used to produce high-resolution spectra of Mars with good spatial resolution. Since the O_2 emission is understood as a result of the photolysis of O_3 , and Mariner 9 showed O_3 to be far more abundant over the poles, the O_2 emis-

sion should appear much weaker along the equator. The new spectra fully confirm this prediction. In addition, spectra of Mars suitable for the detection of argon through pressure broadening of CO_2 lines were obtained. It has not been possible, however, to produce corresponding laboratory spectra of adequate quality due to the lack of a long-path-length cell connected to the interferometer. Much better spectra of Jupiter and Saturn have been secured in the $0.9\text{--}1.6\ \mu$ region; they are being analyzed by a group under Dr. D. Gautier. Spectra of the dark side of Venus were obtained under rather poor conditions. Surprisingly, intense O_2 emission was found but no OH emission was detected. This is the first evidence for non-blackbody emission in the visible and near infrared from the dark side of Venus.

The 1.2-meter Schmidt was used by Mr. P. M. Corben of the Royal Greenwich Observatory to obtain deep plates in the B , V , and I bands for two fields in the north galactic cap. These plates are now being measured on the "Galaxy" measuring machine at RGO. Photoelectric measures of stars in these fields have been obtained by Dr. D. H. P. Jones *et al.*, using the 1.5-meter telescope on Teneriffe. From these observations it is hoped to determine the number of faint red stars at the north galactic pole with a view to determining the absolute number of red dwarfs in the solar neighborhood.

Drs. Richard M. Crutcher and W. D. Watson of the University of Illinois employed the coudé scanner on the 2.5-meter Mount Wilson telescope to study interstellar lines. Searches were made for the previously undetected optical interstellar lines of OH (*Astrophys. J. [Lett.]*, 203, L123, 1976) and NH. The interstellar OH line $\lambda 3078$ has been measured toward α Persei and probably detected toward ζ Ophiuchi. This marks the first detection of the optical OH line in the interstellar medium and the first accurate abundance determination of OH in diffuse clouds. In current "ion-molecule"

schemes for gas reactions in diffuse clouds, OH formation is initiated by the $\text{H}^+ + \text{O}$ charge transfer. Assuming that the OH is produced by these processes, the rate coefficients for the charge-transfer reaction have been derived. An upper limit for the interstellar NH line $\lambda 3358$ toward α Per has been obtained which is a factor of 10 below the previous upper limit for diffuse clouds; the NH abundance is less than 1% of that of OH in the same direction. Since interstellar NH is expected to be produced at about the same rate per atom as OH if formation of NH occurs on grain surfaces, the absence of NH at the observed sensitivity is strong evidence in favor of pure gas phase formation for molecules other than H_2 in diffuse interstellar clouds.

Dr. S. J. Czyzak of Ohio State University and Dr. L. H. Aller of the University of California at Los Angeles mounted an image-tube camera designed by Mr. Holland Ford at the Cassegrain focus of the 1.5-meter telescope at Palomar to obtain monochromatic photographs in radiations of $\text{H}\alpha$, $\lambda 4686$ He II, $\lambda 6584$ [N II], $\lambda 3727$ and $\lambda 7330$ [O II], $\lambda 5007$ [O III], $\lambda 6717$ and $\lambda 6730$ [S II], and several continuum wavelengths. The following objects have been examined: NGC 40, 588, 604, 650, 2371-72, 2392, 3242, 4361, 6058, 6210, 6309, 6445, 6543, 6720, 6751, 6853, 6905, 7008, 7009, and IC1747. The monochromatic photographs for NGC 6720 have been published (L. H. Aller, H. W. Epps, and S. J. Czyzak, *Astrophys. J.*, 205, 798, 1976).

Dr. M. M. Dworetzky of University College London used the Palomar 50-cm telescope to obtain UBV photometry of approximately one hundred 8th to 10th visual magnitude ultraviolet objects found by the S2/68 experiment on the TD1 satellite. Most of these were also observed with the x-spectrograph on the 1.5-meter reflector at Mount Wilson at a dispersion of $42\ \text{\AA mm}^{-1}$. The spectrograms are being analyzed with the PDS microdensitometer at the Royal Greenwich

Observatory. Preliminary examination indicates that most *UV* objects are probably early B stars with very little reddening despite their large distances and low galactic latitudes. Two previously unreported hot subdwarfs and a probable new binary (K+B?), $-3^{\circ}5357$, were also found.

Observations of 78 known spectroscopic binaries and 30 standard stars were made by Dr. P. B. Etzel of San Diego State University and Lanning with the 2.5-meter telescope at Mount Wilson. A Varo image-tube system in the coudé spectrograph was used. Multiple spectra were obtained in most cases. The Li $\lambda 6707$ line strengths are being correlated with various orbital parameters such as period, eccentricity, semimajor axis, and mass function. In most cases the primaries are in the spectral range of G0 to M0 and at various stages of evolution from dwarfs to supergiants. Special attention is being given to previously published observations of chromospheric activity such as emission in the Ca II, H, and K lines. It has been pointed out by R. P. Kraft and O. C. Wilson (*Astrophys. J.*, 141, 829, 1965), and G. H. Herbig (*Astrophys. J.*, 141, 588, 1965) that for single stars there is a very strong correlation between the strengths of the Li line and the presence of Ca II emission. They also noted striking exceptions to the correlation for components of some visual binaries. The study of a large sample of spectroscopic binaries may provide some insight into these seemingly anomalous cases. The detection of H α emission features in several of the binary systems was an interesting byproduct of the project. It was discovered in the spectrum of the unique white dwarf-red dwarf eclipsing binary V471 Tau (BD +16° 516). This has ramifications for various models describing the observed period and light curve changes.

Dr. Neal J. Evans II of the University of Texas completed work on a project involving infrared sources associated with OH masers. Measurements from 2μ to 20μ were made of

each of the six new objects found during this program. The measurements, made during July 1975, followed closely measurements of the OH flux at Owens Valley Radio Observatory. These observations provide a comparison of OH flux and infrared flux at a fixed time, thereby allowing an evaluation of infrared pumping models. It was found that pumping by $35\text{-}\mu$ photons is consistent with the observations, but that $2.8\text{-}\mu$ pumping is very unlikely. Several of the sources had varied during the year following their discovery, some by a factor of ~ 4 . In addition to the OH project, further work was done on the project in an attempt to relate infrared sources to molecular clouds. Measurements at 20μ and through the $10\text{-}\mu$ silicate feature of S140 IR were made. This source is an unresolved, extremely red source at the peak of the molecular cloud in S140. Its luminosity exceeds $2 \times 10^3 L_{\odot}$, and it is an excellent candidate for studies of protostellar objects and for studies of the interaction of such objects with the surrounding molecular cloud. Combining the infrared data with molecular observations of CO and H₂CO has led to a model for the energetics of the molecular cloud and a prediction for the far-infrared emission. Similar work on other objects is under way to check whether the model developed for the S140 molecular cloud/infrared source is representative of other such regions.

During eight nights on the 1.2-meter Schmidt telescope, Drs. R. P. Fenkart and G. A. Tammann of the Basel Observatory obtained 45 RGU-plates of star fields in the galactic anticenter direction and around NGC 2420. The plates will be used to derive stellar density and absorption functions. This will be another step in W. Becker's program to investigate star distribution as a function of distance and of galactic longitude and latitude.

Dr. J. Frogel of the Cerro Tololo Inter-American Observatory, Persson, and Dr. Marc Aaronson of Harvard College Observatory have pursued a

number of infrared projects. They completed an initial survey of strong southern H II regions and molecular sources with the 1-meter telescope at Las Campanas. Twenty-three such sources have now been found to be strong 1–25 μ emitters. A survey in the J, H, and K photometric bands and measures of the strengths of CO and H₂O features in a selection of bright ellipticals has been nearly completed. The main results were known last year and were described in *Year Book 74* (p. 360). New observations of globular-cluster red giants have shown that the CO index is very metal sensitive for stars with metal abundances less than one-tenth solar. Combined with galaxy results, these observations suggest that at least out to $A/D(0) = 1.0$, the 2.2- μ light of ellipticals is dominated by stars at least as metal rich as the sun. They have begun a program at the Hale Observatories and at C.T.I.O. to obtain JHK photometry of a large sample of ellipticals in clusters and the field. Initial results, when combined with *UBVR* data, indicate the following: (a) The *U-K* index is twice as sensitive as *U-V* to galaxian absolute magnitude over a range of 8 magnitudes; (b) the relative distance moduli of the Virgo and Coma clusters obtained by *IR* photometry is the same as that obtained by visual methods alone; and (c) use of an absolute *K* magnitude rather than a *V* magnitude may further improve the sensitivity of the *U-K* or *V-K* color indices to luminosity.

Plates were taken with the 1.2-meter Schmidt telescope by Dr. T. Gehrels of the Lunar and Planetary Laboratory and sent to the Leiden Observatory for photometry of the outer satellites of Jupiter. In a similar program for asteroids, peculiar rotation statistics were found for the asteroids of about 1-kilometer radius in the sense that rotation periods are between 1½ and 5 hours, compared to typically 4–15 hour periods for the large asteroids. Apparently, the small ones are spun up by collisions. Shorter periods than 1½ hours are not found, however, presum-

ably because of low tensile strength of these small asteroids. Gehrels found his fifth comet at Palomar (1975o).

Dr. R. F. Griffin and Mr. G. A. Radford of the Cambridge Observatories, England, in collaboration with Dr. L. Hansen of Copenhagen University Observatory, undertook a large program of photometry in the north galactic pole field with the 50-centimeter and 1.5-meter telescopes on Palomar Mountain. Using the Copenhagen narrow-band system, they made observations that are expected to give estimates of temperature, absolute magnitude, and chemical abundance for all the late-type HD stars within 15° of the pole (about 700 stars) and for more than 100 fainter objects.

Griffin and Gunn continued their radial-velocity observations with the 5-meter telescope. Their four nights falling within this report year were in December, the principal objective being the Hyades. Bad weather greatly curtailed the observing program, but about 40 stars, including most of the particularly interesting ones, were measured. One unexpected result of the Hyades work has been the discovery that two of the four giants in the cluster, δ and θ^1 Tau are spectroscopic binaries. In the case of δ Tau, the orbit has already been established and is confirmed by published photographic observations going back to 1899.

Mr. Frank Holden of San Jose, California, used the 1-meter telescope at Las Campanas to measure visual double stars with a bifilar micrometer on loan from Lick Observatory. Some 200 measures of 80 pairs were obtained. These measures extended the series obtained during the previous year and again showed the suitability of the telescope for fine-resolution observations.

Drs. T. Johnson, D. Matson, and G. Veeder of the Jet Propulsion Laboratory have continued their study of the surface compositions of selected asteroids and satellites, using 0.3 to 2.5 μ spectrophotometry. The emphasis has been on obtaining accurate photometry

at 0.5, 1.65, and 2.2 μ . The data for 15 asteroids are being reduced at the present time. Preliminary results show that the reflectance of asteroids at 2.2 μ ranges at least from about 0.9 to greater than 1.7 (scaled relative to a value of 1.0 at 0.56 μ). This large range and the spread seen in the data for so-called S asteroids indicate that the classification scheme proposed on the basis of 0.3 to 1.1 μ spectral data is not adequate. Over the next year a better system of classification will be introduced. Results obtained for the Amor group Asteroid 433 Eros (nearly an Earth crosser) show a relatively bright reflectance at 1.65 and 2.2 μ . This suggests that a metallic phase is present in Eros's surface regolith layer (*Icarus*, 28, 79, 1976). The discovery of the new Apollo asteroid 1976 AA by Helin, Bus, and Pryor, using the 46-cm Schmidt at Palomar, provided a unique opportunity to observe this most unusual object. From the Mount Wilson 1.5-meter data, a 2.2- μ relative reflectance of 1.5 ± 0.3 was derived, indicating that 1976 AA has a silicate surface similar to all other Apollo-Amor objects for which surface composition data exist. From August 31, 1975, to September 3, 1975, the 2.5-meter telescope at Mount Wilson was used to observe Nova Cygnus 1975 (shortly after its discovery) with the Cassegrain scanner at 10 Å spectral resolution. The changes in emission lines from night to night were followed over the wavelength interval 0.38–1.1 μ .

Dr. R. P. Kirshner of Kitt Peak National Observatory worked with Dr. Keith Taylor using the Fabry-Pérot interferometer on the 1.5-meter telescope at Palomar. Their principal result is on the Cygnus Loop. By using very thin (70- μ) Mylar spacers in a single étalon, and pressure scanning with propane gas, a large free spectral range from -500 to +500 km s⁻¹ at H α was achieved. They observed regions of low surface brightness and found radial velocities of -300 km s⁻¹ in two locations near the center of the Loop. This is so much higher than Minkowski's value

(from slit spectra) of 116 km s⁻¹, that it requires a substantial revision of ideas about the age and physical state of that supernova remnant. In particular, it makes the presence of thermal x-rays at $2-3 \times 10^6$ K and coronal line emission from [Fe XIV] quite comprehensible. The higher velocity also implies that the Loop has an adiabatic shock, not a radiative one, and that it may be as young as 18,000 years rather than about 60,000 yr. However, the simultaneous presence of high velocities, such as those found here, and low ones, such as Minkowski found, requires that inhomogeneities play an important role in the appearance of the Loop and that the distance estimate made by comparing Hubble's proper-motion determination with Minkowski's largest velocity may be a serious overestimate.

Dr. John Kormendy of the University of California at Berkeley has continued a study, begun in a Caltech thesis, of lens and related components in galaxy brightness profiles. This includes disks like the one in NGC 2841, which have many short spiral features but no global spiral pattern. Like lenses, they have a shallow brightness gradient and a steep outer cutoff. However, both a lens and an NGC 2841-like disk appear in one object, NGC 2775, shown in the *Hubble Atlas*. Apparently these are distinct components. The present study aims to determine profiles and characteristic parameters for these components, and to investigate their differences and dynamical structure. Also under investigation is the intimate connection between bars and lenses, illustrated in the *Hubble Atlas*. The ultimate goal is a better understanding of the features that define Hubble types. Sixty-four surface photometry plates of 13 galaxies have been obtained with the 1.2-meter Schmidt telescope, mostly using IIIa-J emulsions with a Wratten 4 filter. Plate material is complete for nine objects. Lunar bright time was used to photograph galaxy centers, which are otherwise difficult to study on normal short exposures because the sky is un-

derexposed but not negligibly faint. Two peculiar galaxies, NGC 2685 and NGC 3077, were also photometered. All plates will be measured with the Berkeley PDS microdensitometer.

Speckle interferometry observations were carried out by Dr. A. Labeyrie and his collaborators of the Observatoire de Meudon in August 1975 and May 1976. During the May run, a new digital processor built at Meudon was used to analyze the data on-line. The processor correlates the photon-counting television signal and produces a three-dimensional display on which stellar morphology features such as duplicity, oblateness, or a resolved disk are visible. More than 100 objects were observed, up to visual magnitude 17, but usable signal levels were obtained only up to magnitude 14 with then prevailing seeing conditions. The spectroscopic binaries ξ Leonis, β Capricorni, δ Capricorni, η Pegasi, α Equulei, and σ Andromedae were resolved. Most of the previously resolved binaries were also confirmed, except in a few cases where orbital motion is believed to have decreased separations below $0''.02$. Mass determinations are under way. Among the supergiant stellar disks which were resolved are R Leonis, α Herculis, α Cygni (not certain), and β Pegasi. Determinations of size and limb-darkening in several colors, being made from these data, should benefit from the improved accuracy afforded by digital reduction. Certain objects have a resolved structure that is more difficult to interpret: β Lyrae is likely to have a shell, η Aquilae to be oblate or to be a barely resolved binary, and P Cygni to have a shell. Asteroids Ceres and Vesta are resolved but too large for precise size determinations. 3C 273, observed in $H\beta$ emission and in the continuum, is probably unresolved, although a refined analysis of the data is being pursued to evaluate the possible presence of nebulosity around the point source. Two Mira-type variables, σ Ceti and R Leonis, are well resolved and should easily yield information on their possi-

ble size or shape variations if observed at appropriate times of their cycles. Because of the operational simplicity of the speckle interferometer with digital readout, such observations and others could now be achieved by local astronomers more efficiently than is possible for groups based overseas.

During the last year Dr. J. D. Landstreet of the University of Western Ontario and Dr. E. F. Borra of the Université Laval at Quebec have continued to use the 1.5-meter telescopes at Palomar and Mount Wilson to search for and measure magnetic fields in peculiar A stars, using a Pockels-cell Cassegrain polarimeter with narrow-band interference filters. The technique is to measure the circular polarization induced in the wings of stellar $H\beta$ lines by the longitudinal Zeeman effect. Magnetic curves have been obtained by this method for 53 Camelopardalis, α^2 Canum Venaticorum, 78 Virginis, CS Virginis, HD 133029, β Coronae Borealis, HD 215441, and field geometry modeling is in progress. Fields have been discovered in θ Aurigae, CU Virginis, 3 Scorpii, φ Draconis, HD 170397, and HD 196178. The first results using this technique are presented in *Astrophys. J.*, 201, 624, 1975, and in the *Proceedings of International Astronomical Union Colloquium No. 32, Physics of Ap Stars* (Vienna, Austria, September 8–11, 1975).

Mr. Howard Lanning of Mount Wilson Observatory, using the Mount Wilson 1.5-meter telescope, continued his study of eclipse timings and *UBVR* photometry of the short period eclipsing white dwarf V471 Tau (BD+16°516). Significant changes in the light curves have been observed, as well as a continued rapid decrease in the period of the binary.

Of the twelve quasar fields to be studied in detail at the Anglo-Australian Telescope by MacKay, Madore, and Lynden-Bell, three now have photoelectric observations of sequence stars within 10 arc minutes of the quasar. These preliminary sequences

were established by Dr. B. F. Madore of Cambridge University, England, and Mr. MacKay on two nights in August 1975, using the Las Campanas 1-meter reflector. The *UBVR* sequences are needed for magnitude and color calibration of the SIT television system, which will be used to study these fields for underlying galaxies and clusters of galaxies. The remaining sequences will be established next season.

Dr. A. E. Martin of Rio Hondo College and Lanning used the 1.5-meter telescope at Mount Wilson to investigate A-type stars in several galactic clusters to look for Ap stars. Using the x-spectrograph, stars in NGC 6611, NGC 6910, NGC 6823, NGC 6531, NGC 6871, and the Coma cluster were observed, as was the binary star BD -3°5357.

Dr. D. H. McNamara of Brigham Young University, using the coude spectrograph of the 2.5-meter Mount Wilson telescope, obtained spectrograms of the dwarf Cepheid variables DE Lacertae and DY Pegasi. The spectrograms have been measured for radial velocities. These new data give much more precise information on the radial velocity variations of these two stars than obtained heretofore (*Publ. Astron. Soc. Pac.*, 88, 168, 1976). DE Lac was previously classified as a RRc variable, but it is apparently a RRs variable (dwarf Cepheid). Spectrograms of several A-F stars in the cluster NGC 2264 were also obtained. The radial velocity measurements of some of these stars indicate that they have velocities quite different from those of B stars; therefore, many of these A-F stars that had been thought to be cluster members in gravitational contraction are in reality foreground stars. Radial velocity studies have also been made of the RRc variables SS Piscium, and T Sextantis.

In August 1975, Dr. A. G. Millikan of the Eastman Kodak Company and Mr. W. C. Miller of the Hale Observatories used the 1.2-meter Schmidt telescope at Palomar to evaluate the utility of experimental plates which were slower

and finer grained than Kodak spectroscopic plate, type IIIa-J. The plates yielded an increase of approximately 0.5 magnitude in the limit of detection. This gain was at the expense of increased exposure time (requiring approximately 3½ hours to reach the sky limit on the f/2.5 Schmidt). Even with optimum nitrogen baking, the plates were judged to be sufficiently slow to exclude them from most observing programs. The gain in limit detection of 0"5 was somewhat less than that expected from laboratory experiments. This resulted from the fact that the image size in the exposure plane is seeing-limited (better-than-average seeing was encountered during the observations). Type IIIa-J plates are sufficiently fine grained so that the further reduction in grain size in the experimental plates did not significantly improve the limit of detection. The gain observed is attributed almost entirely to the higher contrast of the experimental plates.

Drs. S. C. Morris and G. Hill of the Dominion Astrophysical Observatory employed the 1.2-meter Schmidt to obtain plates to derive proper motions of faint stars, using the *Palomar Sky Survey* as a source of first-epoch material. Plates were centered on the *Sky Survey* fields and the same emulsion and filter (103a-E and red Plexiglas) were used. The fields covered were the Pleiades, the Hyades, Praesepe, and the Coma galactic clusters. For the first two regions, which overlap, a total of 19 plates were taken, while four plates were taken for each of the other fields. The 19 plates covering the fields of the Pleiades and Hyades were scanned against duplicate (and reject) first-epoch plates with Luyten's automated proper-motion machine. The data were subsequently processed on the University of Minnesota CDC 6600 computer. Preliminary results (by Luyten) indicate that about 35,000 real motions ($\geq 0".04/\text{year}$) have been detected. Proper motions of Hyades stars to the red plate limit (about 19 mag) have all been extracted from the com-

puter output, although they must still be confirmed by blinking. An examination of overlap measures of proper motion indicates errors of the motions of ≥ 0.007 annually. The Pleiades analysis will begin when the computer printouts and plate material (both epochs) arrive at the Dominion Astrophysical Observatory in the near future.

Drs. D. C. Morton and T. B. Williams of the Princeton University Department of Astrophysical Sciences used the multichannel spectrophotometer to obtain spectral-energy distributions and redshifts for the QSO III Zw 2 and two other galaxies in the group surrounding this quasar, and for the QSO PHL 1070. Using an occulting disk, they attempted to measure the spectral-energy distributions and redshifts of the nebulosities surrounding these quasars. Also with the same instrument, they attempted to detect the light of an extended halo around the spiral galaxy MK 10 and obtained spectral-energy distribution for supernova 1975 N in NGC 7723 and coude spectra of MK 79 and M31. The spectrum of M31 has been used to verify several interstellar lines previously detected by Morton and C. David Andereck.

The Palomar 1.5-meter telescope was used by Morton and Williams to test the use of the Princeton SEC-Vidicon television camera for direct imagery. They obtained sky-limiting exposures in *B* and *V* of the galaxies NGC 3115, 5194, 4594, 4472, and of the globular NGC 5272, and also narrow-band $H\alpha$ exposures of NGC 5194 and 4449.

As part of a continuing program of systematic observations of a complete and kinematically unbiased sample of late-type M dwarfs, Dr. Peter Pesch of Warner and Swasey Observatory obtained slit spectra of 24 stars from Sanduleak's catalog of probable dwarf stars of type M3 and later in the direction of the north galactic pole. The spectra, obtained with the image-tube spectrograph on the Palomar 1.5-meter telescope, cover a wavelength range $\lambda\lambda$

3800–7200 at a reciprocal dispersion of 285 \AA mm^{-1} . Although unsuitable for precise radial-velocity measurements, they were used for classification purposes. Photoelectric *BVRI* photometry of 40 stars from the same catalog was obtained with the Mount Wilson 1.5-meter telescope. These observations, combined with proper motions by Luyten, were used to derive absolute magnitudes, distances, and tangential motions. This sample of 40 stars out of 274 from Sanduleak's catalog, which was selected for bright apparent magnitude only, is characterized by a median *R-I* (Kron system) of ≈ 1.1 mag, median $M_c \approx 11$ mag, and a median $T \approx 35 \text{ km s}^{-1}$. Thus these stars are indeed primarily late, intrinsically faint, nearby dwarf M stars with moderate space velocities.

Dr. C. Pilcher of the University of Hawaii and Münch obtained data on the center-to-limb variation of the equivalent widths of the 3-0 S(1) quadrupole absorption line of H_2 on both Jupiter and Saturn, using the Fabry-Pérot coude scanner system of the 2.5-meter Mount Wilson telescope. The Jovian equivalent widths were generally constant across the disk, decreasing somewhat within 2–3 arc sec of the planetary limb. The Saturn data showed no apparent variation. The data for both planets are being analyzed, using anisotropically scattering, inhomogeneous atmospheric models.

Dr. M. W. Rayne of the Cambridge Observatories, England, devoted 10 nights on the 1-meter telescope to a study of the short-period variability of a small group of T Tauri stars, using photometry in the *U*, *B*, *V*, *R*, and $H\beta$ bands. The weather was very poor for most of the time, but variability was clearly observed in some of the T Tauri stars during the good nights. A preliminary analysis shows that during the run, changes of up to one magnitude in *V* occurred in RU and RY Lupi, the most active of the stars observed. Changes on a timescale of about one hour could be detected in RU

Lup. By contrast, the T Tauri stars in the ρ Ophiuchi dark cloud showed very little change. This is in agreement with the observations of Rydgren, Strom, and Strom (*Astrophys. J. Suppl.*, 30, 307, 1976), who regard the ρ Ophiuchi T Tauri stars as older, less active objects than the very extreme examples which show rapid variability, large ($U-B$) excesses, and strong spectral veiling.

Dr. Eugene M. Shoemaker and Mrs. Eleanor F. Helin of the California Institute of Technology continued the photographic search program for new planet-crossing asteroids, using the 46-cm Schmidt telescope at Palomar. Favorable weather conditions permitted 348 independent fields to be photographed. This sky coverage has led to the discovery of four new asteroids: 1975 TA, 1975 VA, 1975 VB, and 1976 AA. The object 1975 TA is a relatively bright eccentric main-belt asteroid. The second discovery, 1975 VA, is a Mars-crossing asteroid with a low inclination. 1975 VB is a bright Themis family asteroid. In January, 1976 AA, an Apollo asteroid, was discovered; it has an unprecedented orbit. It is the first known minor planet with an orbit smaller than that of the earth and a period of less than one year. It appears that 1976 AA presents an exceptionally favorable objective for a future space mission. Observations made over a period of several months have enabled the computation of well-defined orbits for these new discoveries. By supporting other observers, determinations of the orbits of other newly found fast-moving asteroids have been expedited. Based on the Palomar survey and two other surveys, initial estimates of the populations of Apollo, Amor, and Mars-crossing asteroids have been published.

Dr. S. M. Simkin of Michigan State University, using the 1.2-meter Schmidt telescope, obtained sky-limited plates in the U , G , and R spectral regions for the radio galaxies 3C33, 3C405, NGC 7385, and NGC 891. The faint outer structures of 3C33 and 3C405 have been analyzed, using

numerical mapping techniques and numerical methods for "cleaning" the data of star images. The intensity distributions of both galaxies are similar to those of the nonradio cD galaxies studied recently by Oemler. The position angle of the major axis for the outer isophotes of both objects changes with distance from the center and is not correlated with the inner plane of rotation in either galaxy. The plates of NGC 7385/86 and NGC 891 are being reduced, using similar techniques, and will be analyzed together with Westerbork radio continuum data. One noteworthy feature of the head-tail radio galaxy NGC 7385 is the presence of a very blue double structure in the nucleus that coincides with a compact double feature in the head of the radio source.

Drs. R. V. Stachnik and P. Nisenson of the Itek Corporation and Dr. D. M. Peterson of the State University of New York at Stony Brook collaborated in a test of the speckle imaging process at the Mount Wilson 2.5-meter telescope. Speckle imaging is a technique derived from speckle interferometry which permits recovery of telescope diffraction-limited images rather than image autocorrelations from sequences of short exposure photographs. To first order, the resulting images are unaffected by either atmospheric seeing or telescope aberrations. The technique involves recording the short exposure photographs in the same manner as in speckle interferometry, optically pre-processing each sequence of photographs to obtain an ensemble-average phase-coded Fourier transform, and digitally processing the mean phase-coded transform to obtain the final image. This procedure is an implementation of the algorithm proposed by Knox and Thompson (*Astrophys. J. [Lett.]*, 193, L45, 1975). In addition to observing close ($\rho < 0''.25$) binaries, which had already been studied using speckle interferometry, and suspected close binaries, a number of wide binaries were observed to measure the size of the isoplanatic region, over which the

effect of the atmosphere on different parts of the image is substantially the same. Images of the lunar limb and terminator region were the principal data collected to test the image reconstruction process, but observations were also obtained for Mars, Saturn, and Titan surface image processing, as well as Uranus limb-darkening measurements. Some observations were obtained for the quasar 3C 273.

The Palomar 1.5-meter telescope was employed by Dr. B. E. Turnrose, now of the NASA Johnson Space Center, to obtain calibrated photographic image-tube spectra of the nuclear regions of eight spiral galaxies at dispersions of 285 and 155 Å mm⁻¹. The observations were obtained to provide spectrophotometric and kinematical data for both barred and normal spirals. The spectra have been digitized with the PDS microdensitometer at the Johnson Space Center, and, upon complete reduction, the measured line strengths can be used in conjunction with the results of Turnrose's thesis to estimate stellar-population parameters in the galaxies observed. Particular emphasis was placed on the peculiar spiral NGC 1614 = Arp 186. A number of unwidened spectra obtained under conditions of good seeing indicate that the bright knot located in the western spiral arm 6 arcseconds from the nucleus is substantially bluer than the nucleus itself, with a strong early-type absorption spectrum. The strong emission-line spectrum seen in the nucleus, however, is absent from the spiral-arm condensation. The strength of the Ca II K-line in absorption is roughly equal in the nucleus and the western knot. The observed weakness of the higher Balmer-series lines in the absorption spectrum of the nucleus is likely due in part to emission-line fill-in, since net emission is visible down to at least H δ in the nucleus.

Dr. Sidney van den Bergh and Mr. Kamper of the David Dunlap Observatory have used prime-focus plates

taken with the Hale 5-meter reflector during the last 25 years to derive proper motions for more than 100 fast moving knots and for 30 quasi-stationary "flocculi" in the optical remnant of Cassiopeia A. These data yield a center of expansion for the system of fast moving knots at α (1950) = 23^h21^m12^s.0 \pm 0^s.1 and δ (1950) = +58°23'17".9 \pm 0".8 relative to the AGK3. An explosion date of 1667 \pm 3 A.D. is obtained from an expansion solution for all knots that remained visible for ten or more years. Knots that have appeared recently seem to be expanding less rapidly than predicted by the general expansion solution, whereas the knots that are located outside the shell are moving faster than expected. Explosion dates derived from the main shell of this supernova and from knots outside this shell are 1653 A.D. and 1671 A.D., respectively. The system of quasi-stationary "flocculi" is found to be expanding with a timescale of \sim 11,000 years. The origin of the velocity dispersion of \sim 3000 km s⁻¹ in filament No. 1 remains a mystery. Radial velocity observations extending over a four-year period rule out large present-day accelerations, whereas the small size of the filament militates against large accelerations that took place long ago. The space distribution of the knots in which [O III] is very much brighter than [S II] differs significantly from that for the knots in which this ratio is more nearly normal. Somewhat surprisingly, knots showing [O I] and [O III] but not [S II] seem to be lagging slightly behind the general expansion of the remnant. This contrasts with the behavior of "sulfur knots" in the jet that are expanding somewhat faster than would be expected from the general expansion solution. By stacking ten 5-meter red plates on the PDS microphotometer of the David Dunlap Observatory, it was found that any stellar remnant at the position of the center of expansion must now be fainter than $M_r = +8$. The magnitude limit on a stellar remnant moving

rapidly away from the center of expansion is $M_r \leq +5$.

Dr. P. C. van der Kruit and Mr. A. Bosma of the University of Groningen used the 1.2-meter Schmidt telescope to obtain deep exposures of a number of bright spiral galaxies in order to do relative surface photometry in the outer parts. Spectroscopic observations with the Cassegrain spectrograph on the 5-meter Hale Telescope were made for a few of these systems in order to derive rotation curves and orientation parameters. These data will be combined with H I 21-cm line observations with the Westerbork Synthesis Radio Telescope to derive detailed mass distribution, radial variation of the gas-to-local mass and mass-to-light ratio, and information on deviations from circular symmetry and from flat planes (warps). The data are being reduced.

Dr. G. Wallerstein of the University of Washington has started a program to obtain the carbon and oxygen abundances in extremely metal-poor stars. Spectrograms from $\lambda 6000$ to $\lambda 6600$ at a scale of 14.5 \AA mm^{-1} have been obtained at the 90-cm camera of the 5-meter coude using a 90-mm image tube. Spectra of various field stars and one plate of one star each in M13, M22, and M92 have been obtained. The O I line at $\lambda 6300$ is seen only in stars of moderate metal deficiencies. The presence of two lines of Ba II will permit the determination of the ratio of heavy s-process elements to iron-peak and lighter elements. Wallerstein has completed and submitted for publication a paper on the optical velocities of supergiants that show microwave maser emission. The stellar photospheric velocity for the supergiant maser sources was found to lie near the middle of the wide velocity pattern shown by the OH, 1612 mHz, lines. A special study was made of the M supergiants in η and χ Persei, using spectrograms taken many years ago by A. J. Deutsch and O. C. Wilson, and measured by Louise Lowen. The M supergiant velocity (including the master star S Per) is very

nearly the same as that of the A and B supergiants. Wallerstein has also found that Giclas 23-7, previously thought to be a dwarf with an extreme metal deficiency, is a subgiant that is deficient in metals by only a factor of about 10.

Dr. R. M. West of the European Southern Observatory, using the 1-meter telescope at Las Campanas, has made photographic observations on IIIa-J and 127-04 plates of about 35 galaxies found on ESO Schmidt plates for the Quick Blue Survey. As a result of a period of exceptionally good seeing, it was possible to achieve very high resolution, and it was found that a number of galaxies showed blue and red knots. Following these observations, image tube spectra were obtained with the ESO 1.5-meter telescope on La Silla, which showed that seven of the studied galaxies had strong emission lines (*Astron. Astrophys.*, 46, 327, 1976). Radial velocities and morphological descriptions of the remaining galaxies have been submitted and accepted for publication (*Astron. Astrophys.*, *Suppl. Ser.*, 1976). Spectra were obtained of approximately 35 galaxies from the ESO/Uppsala list of southern galaxies. Fourteen of these showed strong emission lines. Among these, it was found that NGC 2915 is a very close, fairly large intergalactic H II region and that 5 other galaxies showed comparatively broad emission lines ($\sim 500 \text{ km s}^{-1}$), although none were bona fide Seyfert galaxies. Three faint objects, recently found on red ESO Schmidt plates, were confirmed to be highly reddened planetary nebulae.

Dr. W. C. Wickes of Princeton University is commencing a program of double-star interferometry, using the Mount Wilson 1.5-meter telescope and a special interferometer developed by R. H. Dicke and Wickes. This telescope is ideal because of its excellent optics and the consistently good seeing conditions on Mount Wilson.

Dr. R. L. Younkin of the Jet Propulsion Laboratory has continued his spectrophotometric measurements of solar-system objects. The strengths of very strong methane bands of Titan have shown time variations, indicating the presence of weather on that satel-

lite. The program of monitoring the strengths of strong infrared methane bands of Uranus over an aspect-angle period is continuing. A new program to measure the strength and shape of asteroid absorption bands has been started.

LAS CAMPANAS OBSERVATORY

Observations were conducted with the 1-meter telescope on 154 nights by 18 different observers. Most of this time was scheduled during the dark of the moon.

Dr. Donald A. MacRae of the University of Toronto reported that the University's 61-cm telescope at Las Campanas was in use for 2700 hours, out of a possible 3500 hours; 2275 hours were of photometric quality.

2.5-Meter du Pont Telescope

The unaluminized primary mirror (together with the f/7.5 secondary) was installed for the first time in the telescope in March 1976, and preliminary cell support system adjustments were carried out. What may be regarded as "first light," consisting of visual observation of the star Sirius, was recorded by Brucato, Clark, Minnix, Poindexter, and Vaughan on the night of March 7. Further optical tests, final support adjustments, tracking and alignment tests were continued during May and were still in progress at the end of the report year. Preliminary assessment of optical performance was possible under excellent seeing conditions. Several conclusions could be drawn.

1. Notwithstanding lack of thermal equalization in the dome, excellent seeing was experienced, with star images of $\frac{1}{2}$ arc sec or better.

2. Photographic star images having a limiting diameter of about 0.7 arc seconds (as affected by seeing and by halation) were obtained, thus confirming substantially the performance anticipated on the basis of shop optical

tests. (In due course, Hartmann tests will be made to provide a definitive measure of performance independent of atmospheric effects.)

3. Knife-edge photographs of excellent quality were obtained. These results confirm the high quality of the optical figure.

4. The performance of the radial and axial support systems of the primary mirror are well within the desired tolerance limits. An engineering study is in progress concerning the rigidity of the focusing carriage of the secondary mirror, in which field tests have revealed excessive deflection; means for correcting this deflection are under consideration.

Optical polishing and figuring of the lightweight Ultra-Low-Expansion Fused Silica Cassegrain Secondary Mirror was completed by Mr. Don Loomis of Loomis Custom Optics in Tucson. Final acceptance of the mirror was made in November 1975. It was subsequently aluminized in Pasadena and shipped to Chile. The final shop tests, carried out in collaboration with Loomis, using a Hindle arrangement, knife edge, and Hartmann camera, showed that the performance of this mirror is within the tolerances established. The tests indicated an energy concentration of substantially 100% within $\frac{1}{3}$ arc sec diameter, and 70% within $\frac{1}{6}$ arc sec, if the mirror were employed with a perfect primary. These aberrations do not exceed those inherent in Bowen's geometric design of the Cassegrain system.

Progress on optical finishing of the coudé secondary and flat at Loomis

Custom Optics and of the wide-field Gascoigne corrector at the Santa Barbara Street Optical Shop continued throughout the report year. The coude secondary was essentially completed but not yet tested for acceptance in June of 1976.

Cassegrain Camera

The Cassegrain camera is nearing completion. As previously noted, it will use square photographic plates of the following sizes: 16 cm, 25 cm, 36 cm, and 51 cm (1.5°). Standard glass *UBVR* filters will be used for all plate sizes except the 51 cm, for which gelatin filters will be provided.

The camera is equipped with two guider systems on opposite sides of the instrument body. Each guider may be used either visually or with the television viewing system. Other features include an electric hoist for lifting the large plate holders from the handling cart to the camera, a vacuum system for bending the large plates to the curved focal surface, a spot sensitometer for plate calibration, and a degree of freedom to permit rotation of the plate through small angles for partial compensation of differential refraction.

Because long exposures will sometimes be made, a computer algorithm for automatic rotation of the plate holder and optimum translation of the guide heads has been written by Clardy. A control system for the three stepping motors, using a microprocessor, has been designed and will be provided as part of the automatic camera control. The camera may be operated remotely from the telescope control room. The remote control system was designed and built at the Astroelectronics Laboratory and will provide for control of the two guiders, camera rotation, dark slide, and vacuum system.

Darkroom equipment required for photographic processing has been provided. It includes a large oven for plate baking and a rotating rocker for developing. Equipment for hypersensiti-

zation of photographic emulsions by nitrogen baking will be installed soon.

Cassegrain Spectrograph

In 1975, Boller and Chivens delivered the Cassegrain spectrograph, a modified version of their standard design. Subsequent activity consisted of design and construction of a system for remote operation of the spectrograph and installation of the image-intensifier assembly. The control system is designed for operation by the observer from the telescope control room. The observer will be able to control the shutter, integrating exposure meter, slit decker, slit length, comparison sources, spectrum widener, and plate position. The image-tube assembly, built by Dr. Kent Ford, Jr., of the Department of Terrestrial Magnetism, was installed in January 1976. It consists of a two-stage magnetically focused image intensifier and a transfer lens to reimage the spectrum onto the photographic plate. The spectrograph, with four interchangeable gratings, provides dispersions ranging from 224 to 30 Å per millimeter over the range 3000–8000 Å. The camera is designed for acceptance of interchangeable detectors; at present the choice is either the image tube or a photographic plate holder.

Television System

The two-channel integrating television viewing system was tested and modified before acceptance in April 1976. It consists of two intensified SEC-Vidicon television cameras, two high-resolution image storage tubes with associated monitors and electronics. Each channel can be used for real-time viewing or in an integration mode in which the image is accumulated on the SEC target. The cameras will be mounted either on the two guiders of the Cassegrain camera or on the Cassegrain instrument mounting base—one camera for the offset guider, the other for aperture viewing.

Infrared Photometer

Together with K. Matthews, E. E. Becklin, and G. Neugebauer at Caltech, an infrared photometer for the du Pont Telescope was designed and is nearing completion. This device has the capability of simultaneous infrared and optical measurements, and very wide chopper spacing (5' on the plane of the sky). A modified and more flexible version of the near infrared In Sb system in use in California is also under construction.

Coudé Spectrograph

Structural engineering analysis of the coudé spectrograph frame was completed by structural engineering consultant H. Robert Hoggan with a view to support and stability requirements and earthquake safety. Preparation of detail drawings was initiated and is in progress in the telescope engineering office. Because of limited in-house facilities and manpower, it is anticipated that manufacturing of the frame and, in due course, of other major spectrograph components will be contracted to outside firms. The coudé spectrograph project is being supported in part by a grant from the National Science Foundation.

Dome

The contractor's work on the du Pont Telescope building was completed in June 1976. Observatory employees attended to many secondary require-

ments, including revision of the ventilation system, completion of the passenger elevator, revision of the dome shutter and wind screen, and installation of machine tools in the basement instrument shop.

Astronomers' Lodge

Basic work by the contractor is in the final stages, although much exterior masonry work and grading remains for the coming months. The total work force by the contractor on the Lodge complex as well as the du Pont Telescope building has averaged 38 people for the report year.

Observatory personnel are completing the interior of the common building of the Lodge and are coping effectively with the many operations involved in completion of observatory buildings and facilities. Chlorination equipment has been added to the water system, and the principal service well has been lined with 30 feet of 4-foot diameter steel pipe. Several improvements have been made in the equipment for generating electric power on the mountain. Access roads in the vicinity of the telescopes have been paved by Ecomac Ltda. to the extent of 7200 square meters, primarily for the purpose of allaying dust. The service area and office facilities on the mountain have been improved.

At the El Pino office of the observatory in La Serena, a 290-meter concrete-panel wall has been installed facing the city, and a new auto repair shop has been built.

BIBLIOGRAPHY

- Aaronson, M., *see* Frogel, J. A.
- Altschuler, Martin D., Dorothy E. Trotter, Gordon Newkirk, Jr., and Robert Howard, Tabulation of the harmonic coefficients of the solar magnetic fields, *Sol. Phys.*, in press, 1976.
- Ambartsumian, V. A., H. C. Arp, A. A. Hoag, and L. V. Mirzoyan, Some remarks on compact groups of compact galaxies, *Astrofizika*, 11, 193-206, 1975.
- Andreasian, N. K., *see* Arp, Halton.
- Angel, J. R. P., *see* Landstreet, J. D.; Woodgate, B. E.
- Arp, Halton, Photographs of 3C 120 and NGC 7603 compared to spectracon images, *Publ. Astron. Soc. Pac.*, 87, 545-549, 1975.

- Arp, Halton, E. Ye. Khachikian, and N. K. Andriasian, Markarian 459, a member of the triple system of galaxies, *Astrofizika*, 10, 625-627, 1974.
- Arp, Halton, Neil M. Pratt, and Jack W. Sulentic, Isophotal tracings of galaxies near quasars, *Astrophys. J.*, 199, 565-585, 1975.
- Arp, Halton, Roland Carpenter, Samuel Gulkis, and Michael Klein, The problems of spiral galaxies and satellite radio sources, *Astrophys. J.*, 205, 721-727, 1976.
- Arp, Halton C., *see also* Ambartsumian, V. A.
- Bahcall, John N., Neta A. Bahcall, Stephen Murray, and Maarten Schmidt, Optical studies of ten high galactic latitude x-ray sources, *Astrophys. J. (Lett.)*, 199, L9-L11, 1975.
- Bahcall, Neta, *see* Bahcall, John N.
- Becklin, E. E., and G. Neugebauer, High-resolution maps of the galactic center at 2.2 and 10 μ , *Astrophys. J. (Lett.)*, 200, L71-L74, 1975.
- Becklin, E. E., G. Neugebauer, J. B. Oke, and L. Searle, Optical and infrared spectrophotometry of Markarian galaxies, *Astrophys. J.*, 205, 29-43, 1976.
- Becklin, E. E., *see also* Frogel, J. A.; Neugebauer, G.; Westbrook, W. E.
- Beckwith, S., *see* Neugebauer, G.
- Boksenberg, A., R. F. Carswell, and J. B. Oke, 3C 68.1: a very red QSO with an intermediate redshift, *Astrophys. J. (Lett.)*, 206, L121-L123, 1976.
- Boksenberg, A., L. Searle, and R. P. Kirshner, Supernova in NGC 2487, *Int. Astron. Union Circ.*, 2874, December 3, 1975.
- Borra, Ermanno F., Optical activity and absorption lines in quasars, *Observatory*, 95, 141-143, 1975.
- Borra, Ermanno F., Photoelectric observations of the magnetic field of Sirius, *Astrophys. J.*, 202, 741-742, 1975.
- Borra, Ermanno F., and John D. Landstreet, Discovery of magnetic fields in four southern Ap stars, *Publ. Astron. Soc. Pac.*, 87, 961-963, 1975.
- Borra, Ermanno F., *see also* Landstreet, J. D.
- Carpenter, Roland, *see* Arp, Halton.
- Carswell, R. F., *see* Boksenberg, A.
- Clardy, K. D., *see* Kristian, J.
- Cragg, Thomas A., The classical Cepheid program, JD 2 441 000-2 442 000, *J. Amer. Assoc. Variable Star Observers*, 4, 68-77, 1976.
- Datlowe, Dayton W., *see* Moore, Ronald L.
- de Bruyn, A. G., *see* van der Kruit, P. C.
- Dennison, E. W., The Grant measuring engine, in *Image Processing Techniques in Astronomy*, pp. 199-208, C. de Jager and H. Nieuwenhuijzen, eds., D. Reidel Publishing Co., Dordrecht-Holland, 1975.
- Elias, J. H., *see* Werner, M. W.
- Fridenberg, Jerry T., J. A. Westphal, and Jerome Kristian, Microprocessors: a new alternative for automatic telescope control, in *Telescope Automation*, pp. 218-244, M. K. Huguenin and T. B. McCord, eds., Massachusetts Institute of Technology, Cambridge, Massachusetts, 1975.
- Frogel, J. A., S. E. Persson, M. Aaronson, E. E. Becklin, K. Matthews, and G. Neugebauer, The V - [2.2 μ] colors of elliptical galaxies, *Astrophys. J. (Lett.)*, 200, L123-L126, 1975.
- Frogel, J. A., S. E. Persson, M. Aaronson, E. E. Becklin, and K. Matthews, Infrared observations of the late-type stellar component of elliptical galaxies, *Roy. Greenwich Obs. Bull.*, No. 182, in press, 1976.
- Gezari, D. Y., *see* Werner, M. W.
- Glackin, David L., Emerging flux regions, *Solar Phys.*, 43, 317-326, 1975.
- Gott, J. Richard, III, and Trinh X. Thuan, On the formation of spiral and elliptical galaxies, *Astrophys. J.*, 204, 649-667, 1976.
- Gott, J. Richard, III, James E. Gunn, David M. Schramm, and Beatrice M. Tinsley, Will the universe expand forever? *Sci. Amer.*, 234, 62-79, 1976.
- Gott, J. Richard, III, *see also* Thuan, Trinh X.
- Green, Richard F., PG 2337+12, *Int. Astron. Union Circ.*, 2892, December 29, 1975.
- Greenstein, Jesse L., The role of LST in the astronomy of the 1980s, in *Large Space Telescope—A New Tool For Science*, pp. 15-17, F. P. Simmons, ed., American Institute of Aeronautics and Astronautics, Washington, D.C., 1974.
- Greenstein, Jesse L., Multichannel spectrophotometry and the luminosities of white dwarfs, *Astron. J.*, 81, 323-338, 1976.

- Greenstein, Jesse L., Subluminous stars: post-novae, white dwarfs, and hot subdwarfs, *Mém. Soc. Roy. Scis. Liège, IX*, 247-267, 1976.
- Greenstein, Jesse L., Forschung an den Grenzen der Astronomie, *UMSCHAU*, 76, 429-432, 1976.
- Greenstein, Jesse L., M. A. Kazarian, and E. Ye. Khachikian, On the electron density of cometary nebula (in Russian), *Soviet Astron. J. Lett.*, 1, 26-27, 1975.
- Greenstein, Jesse L., *see also* Oke, J. B.
- Gulkis, Michael, *see* Arp, Halton.
- Gunn, James E., On the mean mass density in the universe, *Annals New York Acad. Scis.*, 262, 21-29, 1975.
- Gunn, James E., Will the universe expand forever? *Mercury*, 4, 4-6, 1975.
- Gunn, James E., and Beatrice M. Tinsley, An accelerating universe? *Nature*, 257, 454-458, 1975.
- Gunn, James E., *see also* Gott, J. Richard, III; Thuan, Trinh X.; Tinsley, Beatrice M.
- Hart, M. H., *see* Thuan, Trinh X.
- Hauser, M. G., *see* Werner, M. W.
- Herbst, Elizabeth, *see* van den Bergh, Sidney.
- Hoag, A. A., *see* Ambartsumian, V. A.
- Howard, Robert, *see* Altschuler, Martin D.; Svalgaard, Leif.
- Huchra, John, Supernova in anonymous galaxy, *Int. Astron. Union Circ.*, 2825, August 29, 1975.
- Illing, R. M. E., *see* Landstreet, J. D.
- Kazarian, M. A., *see* Greenstein, Jesse L.
- Khachikian, E. Ye., *see* Arp, Halton; Greenstein, Jesse L.
- Kirshner, Robert P., and J. B. Oke, Supernova 1972e in NGC 5253, *Astrophys. J.*, 200, 574-581, 1975.
- Kirshner, Robert P., *see also* Boksenberg, A.; Woodgate, B. E.
- Klein, Michael, *see* Arp, Halton.
- Kowal, Charles T., Probable new satellite of Jupiter, *Int. Astron. Union Circ.*, 2845, October 3, 1975; 2855, October 23, 1975.
- Kowal, Charles T., Supernova in NGC 2487, *Int. Astron. Union Circ.*, 2874, December 3, 1975.
- Kowal, Charles T., Periodic comet Perrine-Mrkos, *Int. Astron. Union Circ.*, 2876, December 4, 1975.
- Kowal, Charles T., Supernova in NGC 3583, *Int. Astron. Union Circ.*, 2878, December 4, 1975.
- Kowal, Charles T., Comet Harlan (1976g), *Int. Astron. Union Circ.*, 2947, May 7, 1976; 2951, May 12, 1976.
- Kowal, Charles T., Fast moving object Kowal (1975 YA), *Int. Astron. Union Circ.*, 2893, December 31, 1975; 2897, January 7, 1976; 2902, January 13, 1976; 2903, January 16, 1976.
- Kowal, Charles T., *see also* van den Bergh, Sidney; Zwicky, Fritz.
- Kristian, Jerome, Cosmology (review), in *Science Year 1975*, pp. 254-255, Field Enterprises Education Corp., Chicago, Illinois, 1976.
- Kristian, Jerome, and R. Minkowski, Optical identification of 3CR sources (October 1972), Appendix to Chap. 6, in *Stars and Stellar Systems, Vol. IX, Galaxies and the Universe*, pp. 199-210, Allan Sandage, Mary Sandage, and Jerome Kristian, eds., University of Chicago Press, Chicago, Illinois, 1975.
- Kristian, Jerome, K. D. Clardy, and J. A. Westphal, Upper limits for the visible counterpart of the Hulse-Taylor binary pulsar, *Astrophys. J. (Lett.)*, 206, L143-L144, 1976.
- Kristian, Jerome, *see also* Fridenberg, Jerry T.; Sandage, Allan.
- LaBonte, Barry J., Solar activity on August 12, 1975, *Nature*, 261, 525, 1976.
- Landstreet, John D., Ermanno F. Borra, J. R. P. Angel, and R. M. E. Illing, A search for strong magnetic fields in rapidly rotating Ap stars, *Astrophys. J.*, 201, 624-629, 1975.
- Landstreet, John D., *see also* Borra, Ermanno F.
- Lanning, Howard H., Iris photometry of 3C273, *Publ. Astron. Soc. Pac.*, 88, 198-199, 1976.
- Massey, Philip L., Photometry of the cluster of compact ZwCl 0152+3337, *Astron. J.*, 80, 778-782, 1975.
- Matthews, K., *see* Frogel, J. A.; Neugebauer, G.
- Merrill, K. M., *see* Westbrook, W. E.
- Miller, William C., Summary of tests with spectroscopic plates baked in nitrogen, *Am. Astron. Soc. Photo-Bull.*, 9, 3-7, 1975.

- Minkowski, R., *see* Kristian, Jerome.
- Mirzoyan, L. V., *see* Ambartsumian, V. A.
- Moore, Ronald L., and Dayton W. Datlowe, Heating and cooling of the thermal x-ray plasma in solar flares, *Sol. Phys.*, **43**, 189-209, 1975.
- Münch, Guido, Highlights in planetary spectroscopy 1962-75, *Mém. Soc. Roy. Scis. Liège*, **IX**, 87-100, 1976.
- Murray, Stephen, *see* Bahcall, John N.
- Neugebauer, Gerry, Infrared capability with LST, in *Large Space Telescope—A New Tool for Science*, pp. 35-38, F. P. Simmons, ed., American Institute of Aeronautics and Astronautics, Washington, D.C., 1974.
- Neugebauer, Gerry, E. E. Becklin, S. Beckwith, K. Matthews, and C. G. Wynn-Williams, Late-type giants and supergiants in the galactic center, *Astrophys. J. (Lett.)*, **205**, L139-L141, 1976.
- Neugebauer, Gerry, *see also* Becklin, E. E.; Frogel, J. A.; Westbrook, W. E.
- Norris, John, and Robert Zinn, The Cepheid variables and the stellar populations of the dwarf spheroidal galaxies, *Astrophys. J.*, **202**, 335-345, 1975.
- Oke, J. B., and Jesse L. Greenstein, Nova Monocerotis 1975 (=0620-00), *Int. Astron. Union Circ.*, **2840**, September 25, 1975.
- Oke, J. B., *see also* Becklin, E. E.; Boksenberg, A.; Kirshner, Robert P.; Shields, G. A.; Thuan, Trinh X.
- Ostriker, J. P., and T. X. Thuan, Galactic evolution, II, Disk galaxies with massive halos, *Astrophys. J.*, **202**, 353-364, 1975.
- Ostriker, J. P., *see also* Thuan, Trinh X.
- Persson, S. E., *see* Frogel, J. A.
- Pratt, Neil M., *see* Arp, Halton.
- Roy, J-René, and Frances Tang, Slow x-ray bursts and chromospheric flares with filamentary disruption, *Sol. Phys.*, **42**, 425-439, 1975.
- Rule, Bruce H., Bending of large photographic plates, *Am. Astron. Soc. Photo-Bull.*, **8**, 20-21, 1975.
- Sandage, Allan, Cosmology with the LST, in *Large Space Telescope—A New Tool for Science*, pp. 19-22, F. P. Simmons, ed., American Institute of Aeronautics and Astronautics, Washington, D.C., 1974.
- Sandage, Allan, The redshift-distance relation, VIII, Magnitudes and redshifts of southern galaxies in groups: a further mapping of the local velocity field and an estimate of q_0 , *Astrophys. J.*, **202**, 563-582, 1975.
- Sandage, Allan, On the ratio of extinction to reddening for interstellar matter using galaxies, I, A limit on the neutral extinction from photometry of the 3C129 group, *Publ. Astron. Soc. Pac.*, **87**, 853-857, 1975.
- Sandage, Allan, The absolute magnitude of first-ranked cluster galaxies as a function of cluster richness, *Astrophys. J.*, **205**, 6-12, 1976.
- Sandage, Allan, Classification and stellar content of galaxies obtained from direct photography, in *Stars and Stellar Systems*, Vol. IX, *Galaxies and the Universe*, Chap. 1, pp. 1-3, Allan Sandage, Mary Sandage, and Jerome Kristian, eds., University of Chicago Press, Chicago, Illinois, 1975.
- Sandage, Allan, The redshift, in *Stars and Stellar Systems*, Vol. IX, *Galaxies and the Universe*, Chap. 19, pp. 761-785, Allan Sandage, Mary Sandage, and Jerome Kristian, eds., University of Chicago Press, Chicago, Illinois, 1975.
- Sandage, Allan, Jerome Kristian, and James A. Westphal, The extension of the Hubble diagram, I, New redshifts and BVR photometry of remote cluster galaxies: an improved richness correction, *Astrophys. J.*, **205**, 688-695, 1976.
- Sargent, Wallace L. W., Galaxies and their evolution, in *Structure and Evolution of Galaxies*, pp. 261-274, G. Setti, ed., D. Reidel Publishing Co., Dordrecht-Holland, 1975.
- Sargent, Wallace L. W., *see also* Zwicky, Fritz.
- Scherrer, John M., *see* Svalgaard, Leif.
- Schmidt, Maarten, The mass of the galactic halo derived from the luminosity function of high-velocity stars, *Astrophys. J.*, **202**, 22-29, 1975.
- Schmidt, Maarten, Problems associated with the M-dwarf population, in *Dynamics of Stellar Systems*, *Int. Astron. Union Symp.*, **69**, pp. 325-329, A. Hayli, ed., D. Reidel Publishing Co., Dordrecht-Holland, 1975.
- Schmidt, Maarten, Quasars, in *Stars and Stellar Systems*, Vol. IX, *Galaxies and the Universe*, Chap. 8, pp. 283-308, Allan Sandage, Mary Sandage, and Jerome Kristian, eds., University of Chicago Press, Chicago, Illinois, 1975.

- Schmidt, Maarten, *see also* Bahcall, John M.; Westbrook, W. E.
- Schramm, David N., *see* Gott, J. Richard, III.
- Searle, Leonard, Composition differences within and among galaxies, *Roy. Greenwich Obs. Bull. No. 182*, in press, 1976.
- Searle, Leonard, *see also* Becklin, E. E.; Boksenberg, A.
- Shields, G. A., and J. B. Oke, The spectral energy distribution of NGC 1275, *Publ. Astron. Soc. Pac.*, 87, 879-883, 1975.
- Sulentic, Jack W., *see* Arp, Halton.
- Svalgaard, Leif, John M. Wilcox, Philip H. Scherrer, and Robert Howard, The sun's magnetic sector structure, *Sol. Phys.*, 45, 83-91, 1975.
- Swings, Jean-Pierre, *see* White, Richard E.
- Tang, Frances, *see* Roy, J.-René.
- Thuan, Trinh X., and J. Richard Gott, III, Why there are no elliptical galaxies flatter than E7, *Nature*, 257, 774-776, 1975.
- Thuan, Trinh X., and J. B. Oke, Color gradients in the nuclear region of M31, *Astrophys. J.*, 205, 360-362, 1976.
- Thuan, Trinh X., M. H. Hart, and J. P. Ostriker, Galactic evolution, I, Single-zone models, *Astrophys. J.*, 201, 756-772, 1975.
- Thuan, Trinh X., J. B. Oke, and J. E. Gunn, Further observations of BL Lacertae, *Astrophys. J.*, 201, 45-49, 1975.
- Thuan, Trinh X., *see also* Gott, J. Richard, III; Ostriker, J. P.
- Tinsley, Beatrice M., and James E. Gunn, Evolutionary synthesis of the stellar population in elliptical galaxies, I, Ingredients, broad-band colors, and infrared features, *Astrophys. J.*, 203, 52-62, 1976.
- Tinsley, Beatrice M., and James E. Gunn, Luminosity functions and the evolution of low-mass Population I giants, *Astrophys. J.*, 206, 525-535, 1976.
- Tinsley, Beatrice M., *see also* Gott, J. Richard, III.
- van den Bergh, Sidney, Elizabeth Herbst, and Charles Kowal, Survey of bright variable stars in M33, *Astrophys. J., Suppl. Ser.*, 29, No. 287, 303-313, 1975.
- van der Kruit, P. C., The peculiar galaxy NGC 3310, II, The velocity field of the ionized gas, *Astron. Astrophys.*, 49, 161-171, 1976.
- van der Kruit, P. C., and A. G. de Bruyn, The peculiar spiral galaxy NGC 3310, I, General properties; far ultraviolet and radio continuum observations, *Astron. Astrophys.* 48, 373-382, 1976.
- Vaughan, Arthur H., *see* White, Richard E.
- Werner, M. W., J. H. Elias, D. Y. Gezari, M. G. Hauser, and W. E. Westbrook, Observations of 1-mm continuum radiation from the DR21 region, *Astrophys. J. (Lett.)*, 199, L185-L187, 1975.
- Westbrook, W. E., E. E. Becklin, K. M. Merrill, G. Neugebauer, M. Schmidt, S. P. Willner, and C. G. Wynn-Williams, Observations of an isolated compact source in Perseus, *Astrophys. J.*, 202, 353-364, 1975.
- Westbrook, W. E., *see also* Werner, M. J.
- Westphal, James E., *see* Fridenberg, Jerry T.; Kristian, Jerome; Sandage, Allan.
- White, Richard E., A. H. Vaughan, G. W. Preston, and J.-P. Swings, Isotopic abundances of Hg in mercury stars inferred from Hg II λ 3984, *Astrophys. J.*, 204, 131-140, 1975.
- Wilcox, John M., *see* Svalgaard, Leif.
- Williams, T. B., The rotation curve of NGC 3115, *Astrophys. J.*, 199, 586-590, 1975.
- Willner, S. P., 8 to 13 micron spectrophotometry of compact sources in NGC 7538, *Astrophys. J.*, 206, 728-734, 1976.
- Willner, S. P., *see* Westbrook, W. E.
- Wilson, Christopher P., Dynamical models of elliptical galaxies, in *Dynamics of Stellar Systems*, *Int. Astron. Union Symp.*, 69, pp. 207-208, A. Hayli, ed., D. Reidel Publishing Co., Dordrecht-Holland, 1975.
- Wilson, Olin C., Absolute magnitudes of stars from widths of chromospheric Ca II emission lines, *Astrophys. J.*, 205, 823-840, 1976.
- Woodgate, B. E., J. R. P. Angel, and R. P. Kirshner, Detection of the [Fe XIV] 5303 Å coronal line in the supernova remnant Vela X, *Astrophys. J.*, 200, 715-718, 1975.
- Wynn-Williams, C. G., *see* Neugebauer, Gerry; Westbrook, W. E.
- Yoshimura, Hirokazu, Solar cycle dynamo wave propagation, *Astrophys. J.*, 201, 740-748, 1975.
- Zinn, Robert, *see* Norris, John.

Zirin, Harold, The helium chromosphere, coronal holes, and stellar x-rays, *Astrophys. J. (Lett.)*, 199, L63-L66, 1975.

Zirin, Harold, The sun and man's environment, in *Souvenir—1975 on the Inauguration of Vedhshala's Udaipur Solar Observatory*, pp. 9-10, Naranpur, Ahmedabad, India, 1975.

Zirin, Harold, The Fe XIII line in R Aquarii, *Nature*, 259, 466-467, 1975.

Zwicky, Fritz, W. L. W. Sargent, and C. T. Kowal, An eighth list of compact galaxies, *Astron. J.*, 80, 545-558, 1975.

STAFF AND ORGANIZATION

The boards of trustees of the California Institute of Technology and of the Carnegie Institution of Washington resolved that the Las Campanas Observatory in Chile shall be accepted for unified operation as part of the Hale Observatories, together with the Mount Wilson Observatory and the Palomar Observatory.

Dr. George W. Preston was designated Assistant Director for the Mount Wilson Observatory.

Dr. Arthur H. Vaughan was named Assistant Director for the Las Campanas Observatory.

Mr. Bruce H. Rule retired after a 39-year association with the Obser-

vatories. He came to Caltech as electrical engineer on the 5-meter telescope project in 1937 and has since served the Observatories with distinction in several engineering and managerial capacities. He has been consulted on the design of practically every large telescope project throughout the world in the past 25 years. Since 1965, Rule has been a Staff Member and Chief Engineer of the Hale Observatories. During the construction of the Las Campanas Observatory, he served the Carnegie Institution as Chief Engineer and Project Officer of the 2.5-meter Irénée du Pont Telescope.

RESEARCH FELLOWS AND STUDENTS

The research work of Fellows and graduate students is reported in the body of this Report, together with that of Staff Members. In general, Fellows and students have much informal interaction with the staff, and frequently collaborate in research, in discussion of results, and in publication. They participate in the weekly astrophysics research conferences. Fellows are assigned nights on the telescopes in their own names for research programs that have been discussed with staff members and approved by the Observatory Committee. Graduate students in many instances assist staff members in their observing and in analysis of observations.

There were 28 student observers at the Observatories during the year.

These individuals are registered graduate students at the California Institute of Technology who are pursuing advanced degrees in astronomy and astrophysics.

Seventeen postdoctoral research fellows were in residence, of whom seven were Carnegie Fellows with grants from the Carnegie Institution. Two predoctoral Chilean students were holders of Carnegie-Chilean Fellowships, and both of these received the doctoral degree during the year; they are Eduardo Hardy from the University of Indiana and Maria Teresa Ruiz from Princeton University. Hardy's thesis was based on observations made by him at Las Campanas. His thesis advisor was Sandage. Following receipt of his degree, Hardy took up a postdoc-

toral appointment as Carnegie Fellow for one year.

Dr. Robert J. Zinn was advanced to become the first holder of a postdoctoral Las Campanas Fellowship. Although resident in Pasadena, his observing will be conducted largely with the facilities of the Las Campanas Observatory in Chile.

Research Division

Staff Members

Halton C. Arp
 Horace W. Babcock, *Director*
 Eric E. Becklin¹
 Edwin W. Dennison²
 Jesse L. Greenstein³
 James E. Gunn⁴
 Robert F. Howard
 Jerome Kristian
 Robert B. Leighton⁵
 Guido Münch¹
 Gerry Neugebauer⁶
 J. Beverley Oke, *Associate Director*⁴
 S. Eric Persson
 George W. Preston, *Assistant Director*,
Mount Wilson
 Bruce H. Rule, *Chief Engineer*⁷
 Allan R. Sandage
 Wallace L. W. Sargent⁸
 Maarten Schmidt⁵
 Leonard Searle
 Stephen A. Sheiman
 Arthur H. Vaughan, *Assistant Director*,
Las Campanas
 James A. Westphal⁹
 Harold Zirin¹⁰

¹Senior Research Fellow in Physics, California Institute of Technology.

²Resigned June 30, 1976.

³Lee A. DuBridge Professor of Astrophysics, California Institute of Technology.

⁴Professor of Astronomy, California Institute of Technology.

⁵Professor of Astronomy; Chairman of the Division of Physics, Mathematics, and Astronomy, California Institute of Technology.

⁶Professor of Physics, California Institute of Technology.

⁷Retired June 30, 1976.

⁸Professor of Astronomy; Executive Officer for Astronomy, California Institute of Technology.

Members Engaged in Postretirement Studies

Alexander Pogo
 Henrietta H. Swope
 Olin C. Wilson

Visiting Associate

Gustav A. Tammann

Staff Associates

Robert J. Brucato
 Michael W. Werner¹¹

Senior Research Fellow

Ronald Moore

Carnegie Fellows

A. Ger de Bruyn
 Eduardo Hardy
 Mark Hartoog
 François Schweizer¹²
 Christopher P. Wilson¹³
 Hirokazu Yoshimura¹⁴
 Robert J. Zinn

Research Fellows

William M. Adams
 Daniel Y. Gezari
 Gordon J. Hurford
 Stephen L. Knapp
 Kenneth A. Marsh
 Douglas O. Richstone
 Jack Sulentic
 Keith Taylor¹⁵
 Trinh X. Thuan
 Althea Wilkinson

Carnegie-Chilean Fellow

Maria Teresa Ruiz

⁹Associate Professor of Planetary Science, California Institute of Technology.

¹⁰Chief Astronomer, Big Bear Solar Observatory; Professor of Astrophysics, California Institute of Technology.

¹¹Assistant Professor of Physics, California Institute of Technology.

¹²Fellowship ended December 31, 1975.

¹³Fellowship ended August 31, 1975.

¹⁴Fellowship ended August 19, 1975.

¹⁵Fellowship ended January 31, 1976.

Librarians

Helen Z. Knudsen
Nan W. Schow

Senior Research Assistants

Grace V. Knox
Charles T. Kowal
A. Louise Lowen

Research Assistants

John M. Adkins
John E. Boyden
Ken D. Clardy
Thomas A. Cragg¹⁶
Thomas S. Gregory
Basil N. Katem
Margaret Katz
Peter N. Kupferman¹⁷
Frances Y. C. Tang

Student Observers

Steven V. W. Beckwith
Kirk Borne
Todd Boroson
France Cordova
David J. Diner
Jonathan H. Elias
Richard F. Green
John G. Hoessel
Paul Hickson¹⁸
John P. Huchra
Steven Kent
John Kormendy¹⁹
Barry J. Labonte
Philip Massey²⁰
Jorge Melnick
Daniel Nadeau
William C. Friedhorsky
Douglas M. Rabin
Russell O. Redman
Anneila I. Sargent
William L. Sebok
David Sholle
Richard J. Terrile
Edwin L. Turner²¹
Barry E. Turnrose²²
Richard Wade
Theodore B. Williams²³
Steven P. Willner²⁴

¹⁶Resigned June 30, 1976.

¹⁷Resigned February 6, 1976.

¹⁸Graduated March 16, 1976.

¹⁹Graduated April 9, 1976.

²⁰Graduated June 13, 1975.

Photographic Department

John R. Bedke, Photographer

Instrument Design and Construction

David A. Bell, Electronics Engineering Aide
Lawrence E. Blakée, Supervisor, Electronic Services
Maynard K. Clark, Electronics Operations Manager
John P. Cowley, Engineering Assistant²⁵
Barbara L. Dailey, Draftswoman
Lee B. Dennison, Design Draftsman
Stephen Doro, Machinist
Earle B. Emery, Research Engineer
Eugene B. Fair, Head Optician
Hannah Fox, Computing Analyst
Jerry T. Fridenberg, Head, Astroelectronics Laboratory; Chief Electronics Engineer
Robert D. Georgen, Machinist
Richard M. Goeden, Engineer
John G. Golson, Optician
Simon Groesz, Electronics Specialist
Fred H. Harris, Junior Electronics Technician
Melvin W. Johnson, Optician
Herman F. Kelderman, Research Engineer²⁵
Leroy M. Kimoto, Senior Electronics Specialist
Erich R. Koch, Senior Electronics Engineer
Wilfred H. Leckie, Senior Draftsman
William H. McLellan, Senior Engineer
Martin J. Olsiewski, Electronics Specialist²⁷
Frederick G. O'Neil, Shop Foreman
Richard A. Prout, Senior Engineer
Rudolf E. Ribbens, Design and Shop Superintendent²⁸
Juan M. Sanchez, Photographic Laboratory Technician
Orval A. Smith, Electronics Specialist
Sharon Soltesz, Administrative Secretary
Douglas Sprague, Senior Electronics Engineer

²¹Graduated September 13, 1975.

²²Graduated July 30, 1975.

²³Graduated October 20, 1975.

²⁴Graduated January 29, 1976.

²⁵Retired June 30, 1976.

²⁶Terminated June 30, 1976.

²⁷Resigned January 8, 1976.

²⁸Terminated June 30, 1976.

Robert G. Stiles, Optician²⁹
 Merle R. Sweet, Supervisor, Electronics
 Construction
 David F. Thompson, Technical Assistant
 Glenn A. Toennes, Electronics Techni-
 cian
 Timothy J. Tuler, Electrical Technician
 Virgil Z. Vaughan, Supervisor, Stock-
 room
 Felice Woodworth, Draftswoman

Maintenance and Operation

Mount Wilson Observatory and Offices

Robert A. Brenner, Mechanic
 Fern V. Borgen, Typist-Telephone
 Operator³⁰
 Clyde B. Bornhurst, Mountain Superin-
 tendent³¹
 Robert E. Cadman, Mountain Superin-
 tendent
 Herman E. Carpentier, Carpenter
 Linda Chaffee, Clerk-Typist
 Hugh T. Couch, Superintendent, Build-
 ings and Grounds
 Helen S. Czaplicki, Typist-Editor
 Bette DeSmet, Secretary
 Sue H. DeWitt, Secretary³²
 Raquel E. Ferrer, Secretary³³
 James Frazer, Night Assistant
 Hazel M. Fulton, Head Stewardess
 Eugene L. Hancock, Night Assistant
 Mary Hark, Stewardess
 Jeanne M. Knight, Bookkeeper
 Howard H. Lanning, Night Assistant
 Jose Lopez-Tiana, Purchasing Clerk
 Ernest O. Lorenz, Assistant Mountain
 Superintendent
 Ethel Marszalek, Custodian
 Delores Sahlin, Typist-Telephone
 Operator
 Glen Sanger, Senior Custodian
 William D. St. John, Chauffeur
 Frank Trylko, Custodian
 Frederick P. Woodson, Assistant to the
 Director

Palomar Observatory and Robinson Labo- ratory

Ranney G. Adams, Night Assistant
 Albert R. Andrews, Maintenance Me-
 chanic

Bradley N. Bailey, Relief Night Assistant
 and Junior Instrument Technician
 Ray L. Ballard, Senior Administrative
 Assistant
 Stephen A. Barry, Maintenance Me-
 chanic and Junior Night Assistant
 Donald C. Bates, Assistant Mountain
 Superintendent
 Jan Adriaan Bruinsma, Painter and
 General Maintenance
 Maria J. Bruinsma, Housekeeping Aide
 Juan R. Carrasco, Night Assistant and
 General Mechanic
 Lily D. Carrasco, Housekeeping Aide
 Philip E. Fain, Custodian³⁴
 Liselotte M. Hauck, Secretary
 Helen Holloway, Secretary
 Dorothy J. Howard, Administrative Sec-
 retary
 Kevin M. Jordan, Maintenance Mechanic
 and Junior Night Assistant
 Joyce E. Keeble, Secretary
 Taras Kiceniuk, Mountain Superinten-
 dent
 J. Luz Lara, Maintenance Mechanic
 Marilynne J. Rice, Secretary
 Irwin Teichman, Mechanic³⁵
 Elsa-Brita Titchenell, Secretary
 Gary M. Tuton, Senior Night Assistant
 Paul Van Ligten, Electrician
 Marion Warren, Secretary³⁶
 Ruth E. Weaver, Secretary
 David K. Williams, Relief Night Assis-
 tant and Maintenance Mechanic
 Dorothy Williams, Cook
 Mary R. Yates, Housekeeping Aide
 Barbara A. Zimmerman, Member, Pro-
 fessional Staff

Big Bear Solar Observatory

Alberta R. Altman, Clerk-Typist
 Jack R. Klemroth, Solar Observing As-
 sistant
 Eugene H. Longbrake, Superintendent
 Charles F. Mason, General Machinist
 Walter M. Nagao, Junior Mechanic
 Alan P. Patterson, Associate Scientist
 (Solar Scientist)

²⁹Resigned January 6, 1976.

³⁰Retired October 31, 1975.

³¹Resigned June 30, 1976.

³²Resigned June 15, 1976.

³³Resigned September 15, 1976.

³⁴Resigned September 3, 1975.

³⁵Terminated June 30, 1976.

³⁶Resigned March 22, 1976.

Las Campanas Observatory

Wilma J. Berkebile, Executive Secretary³⁷

S. Thomas Couch, Shipping and Receiving Clerk

Ljubomir Papic, Mountain Superintendent, *Las Campanas Observatory*

Manfred Wagner, Project Supervisor, *La Serena*

³⁷Retired June 30, 1976.

Irénée du Pont Telescope Project

Louis E. Beidler, Engineer

C. L. Friswold, Instrument Designer

Roger L. Minnix, Engineer

June A. Rains, Secretary³⁸

Bruce H. Rule, Chief Engineer and Project Officer⁶

Edward H. Snoddy, Engineer

³⁸Terminated June 30, 1976.

Department of Plant Biology

Stanford, California

Winslow R. Briggs

Director

Contents

| | |
|---|-----|
| Introduction (Briggs) | 351 |
| Sequence organization in pea DNA (Thompson) | 356 |
| DNA sequence comparisons in <i>Atriplex</i> (Belford and Thompson) | 362 |
| Plasmid modification associated with the loss and acquisition of virulence in <i>Agrobacterium tumefaciens</i> (Rogler and Thompson) | 367 |
| Blue light-induced absorbance changes in membrane fractions from <i>Neurospora crassa</i> (Brain and Briggs) | 372 |
| Blue light-induced absorbance changes in membrane fractions from <i>Zea mays</i> (Briggs, Freeberg, and Weiss) | 377 |
| An evaluation of markers for plasma membranes in membrane fractions from <i>Zea mays</i> (Cross and Briggs) | 379 |
| A multi-sample automatic monitoring device for the circadian rhythm of transmittance change in <i>Ulva</i> (Britz) | 383 |
| Two applications of a multi-sample automatic monitor for rhythmic transmittance changes in <i>Ulva</i> (Britz) | 392 |
| Measurements of auxin binding to solubilized receptor sites of corn seedling tissue (Dohrmann and Ray) | 395 |
| Comparison of the heat stability of photosynthesis, chloroplast membrane reactions, photosynthetic enzymes, and soluble protein in leaves of heat-adapted and cold-adapted C ₄ species (Björkman, Boynton, and Berry) | 400 |
| Genetic variation affecting metabolic phenotypes: an approach to analyzing photosynthetic carbon reduction in a C ₄ plant (Enama) | 407 |
| Molecular weight variation of phosphoenolpyruvate carboxylases from C ₄ plants (Enama) | 409 |
| Photosynthetic capacity of <i>in situ</i> Death Valley plants (Mooney, Björkman, Ehleringer, and Berry) | 410 |
| Leaf absorbance and photosynthesis as affected by pubescence in the genus <i>Encelia</i> (Ehleringer) | 413 |
| Carbon dioxide and temperature dependence of the quantum yield for CO ₂ uptake in C ₃ and C ₄ plants (Ehleringer and Björkman) | 418 |
| Hybridizations in <i>Atriplex</i> (Nobs) | 421 |
| Growth and photosynthesis of <i>Chlamydomonas reinhardtii</i> as a function of CO ₂ concentration (Berry, Boynton, Kaplan, and Badger) | 423 |
| Effects of temperature on respiration and uptake of Rb ⁺ ion by roots of barley and corn (Carey and Berry) | 433 |
| Possible use of hollow fiber hemodialysers in soil-plant water relations research (Mahall) | 438 |
| Enzyme polymorphism in the butterfly <i>Colias</i> : selection on metabolic phenotypes (Johnson) | 440 |

| | |
|---|-----|
| Characterization of electrophoretically hidden variation in the butterfly <i>Colias</i> (Johnson) | 449 |
| The effect of deuterium oxide on the gel-sieving behavior of proteins in electrophoresis (Johnson) | 456 |
| P700-chlorophyll <i>a</i> -protein complexes (Brown) | 460 |
| Temperature dependence of chlorophyll <i>a</i> fluorescence in algae and higher plants in relation to changes of state in the photosynthetic apparatus (Fork) | 465 |
| Correlation between growth temperature and heat-induced chlorophyll fluorescence changes in <i>Scenedesmus</i> <i>obliquus</i> (Schreiber) | 472 |
| Dark uptake of HCO_3^- by washed chloroplast grana (Stemler) | 477 |
| Bibliographic information retrieval (Brown) | 479 |
| Bibliography | 480 |
| Speeches | 481 |
| Personnel | 483 |

INTRODUCTION

On Friday, September 12, 1975, the Department of Plant Biology welcomed over 100 plant scientists to a brief symposium on the scientific programs of the department, followed by a reception and dinner. The purpose of the occasion was to celebrate the completion of construction and the beginning of normal scientific activity in the Department for the first time since the autumn of 1973. At that time, of course, we had no idea what constituted normal scientific activity, although we had made some guesses. One of these guesses is found in the introduction to last year's Report, in which I stated that we anticipated a total of about 15 scientific visitors at steady state. A brief glance at the section entitled "Personnel" at the end of this report will reveal how wide of the mark this estimate was. In addition to 11 postdoctoral visitors whom we were able to support with our fellowship funds, we had an additional 8 who came with their own support, and the steady-state level was 17 most of the time. There were in addition 15 students, both undergraduate and graduate, yielding an overall steady state of 32, over twice that predicted a year ago!

The principal reason for the large increase in the population of visitors doing science is the increased emphasis of the Department of Plant Biology on education below the postdoctoral level. Thus, three Stanford University undergraduates have been doing senior honors research with us, and five Stanford graduate students spent some or all of their research time at the Department. Four graduate students are finishing thesis work, having started it with a present faculty member while he was elsewhere, and two of our senior guests, with us on sabbatical leave, brought an additional three graduate students with them. These dry statistics should not hide the kinds of in-

teractions that have made the Department's contribution to predoctoral education remarkable: A single example will suffice. Dr. George Johnson, a senior visitor, brought two graduate students with him from Washington University of St. Louis, Mary Enama and William Curtis, both in the beginning stages. Curtis learned gas exchange measurement techniques from Professor Mooney of Stanford, another senior visitor; he learned about the genus *Viola* from Professor Solbrig of Harvard, a third senior visitor. Curtis, who has developed a sound thesis problem on this genus, will spend the rest of the summer of 1976 working with Professor Solbrig at Harvard. Enama began learning the kinds of powerful electrophoretic techniques that Johnson has used to uncover hidden genetic variability in insects, with the object of applying them to higher plant proteins. That they can be used effectively is indicated by what she has contributed to this Year Book. Both *Distichlis spicata* and *Atriplex lentiformis*, species that fix CO₂ by the C₄ pathway of photosynthesis, are elegantly adapted for such analysis. Enama also has found a sound thesis project. We expect to see both of these students again.

The Department made a number of formal teaching contributions to Stanford University. Dr. Briggs joined Professor Philip Hanawalt of the Department of Biological Sciences to offer a course in photobiology. Drs. Berry, Brown, Fork, and Stemler gave lectures in the series on photosynthesis in the course. In addition, Drs. Briggs and Berry participated in a series of lectures on photosynthesis for the Biochemistry Department at Stanford, and Drs. Fork, Briggs, Berry, and Thompson gave lectures in Professor Ray's plant physiology course. We fully expect this sort of teaching contribution to continue in the future.

Before considering some of the scientific accomplishments of the past year, a brief word about instrumentation is in order. The most important major addition is a Hewlett-Packard minicomputer the Department purchased last fall. It has analog-to-digital capability, and two spectrophotometers are already on line with it. Thus absorption or fluorescence spectra or kinetic data can be stored and manipulated. We anticipate putting more instruments on line in the near future. A fine library of programs has already been developed and is continually being augmented. For most applications at present, two people can work simultaneously at different terminals without interference. With ample core memory and double disc storage capacity (one disk is interchangeable in addition) we are far from reaching the full potential of the system.

I am gratified to report that the past year has been extremely productive scientifically. The large increase in the number of active workers makes the sorting out and summarizing of the year's accomplishments a very difficult task, however, and one that I undertake with some trepidation. Thompson's group, the newest in the Department, has made substantial progress in several directions. Rogler and Thompson have made a notable contribution to our knowledge of what is required for virulence in the crown gall bacterium *Agrobacterium tumefaciens*. They have been able to show, using restriction endonuclease, that only a relatively small portion of plasmid DNA from the bacterium is correlated with infectivity. Less than the entire plasmid is required. Thompson has continued and extended his careful analysis of the sequence organization of pea DNA. The pea genome shows a pattern much like that of the amphibian *Xenopus*, with single-copy DNA sequences less than 3000 nucleotides in length extensively interspersed with repetitive sequences. Belford and Thompson have successfully applied DNA-DNA hybridization techniques to

an analysis of the relationships between several species of the genus *At-riplex*, a genus already the subject of an enormous amount of physiological and ecological work in the Department. Preliminary results from hybridization of single-copy DNA from each species did not completely support the current evolutionary scheme for relationships between these species. Though further experimentation is obviously required, it is already clear that the technique is going to be useful in assessing evolutionary relationships within the genus, particularly with regard to the origin of C_4 photosynthesis within the genus and the DNA sequence homology distance between C_3 and C_4 species. These experiments are an important counterpart to the continuing interspecific hybridization studies in the genus *At-riplex* being carried out by Nobs.

Briggs' group also has progress to report on several fronts. Efforts have continued to isolate and identify the pigment system that serves as the photoreceptor for a large number of blue-ultraviolet sensitive processes both in higher plants and fungi. Brain, working with the mold *Neurospora*, and Freeberg and Weiss, working with corn, have isolated membrane fractions that respond to light by showing absorbance changes. In darkness the absorbance changes decay. The responses are caused by the reduction of a *b*-type cytochrome, and the actual photoreceptor is almost certainly a flavoprotein. The behavior of the system in vitro is strikingly similar to in vivo systems previously studied by others.

Cross has shown that the corn fraction contains a monovalent cation-dependent ATPase, and Brain has verified this result with *Neurospora*. Most recently Cross has used a fluorogenic reagent with an extremely short lifetime in water to attempt surface labeling of corn cells. The object was to determine which of the membrane fractions found in homogenates was the outermost one, the plasma membrane in intact cells. Preliminary experiments strongly suggest that the ac-

tive fractions in the experiments described briefly above are indeed plasma membrane. If these experiments are confirmed, then it follows that the plasma membrane contains some sort of cytochrome system. The implications, therefore, go beyond photoreception problems into the area of membrane regulation of ion movement.

In keeping with long Department tradition, Britz has developed some elegant instrumentation to use in his studies on the circadian movement of chloroplasts in the alga *Ulva lactuca*, sea lettuce. He has developed an automatic monitor that can handle 30 samples simultaneously, measuring transmittance of light through the samples once an hour. The measuring beam is dim enough to have no influence on the rhythm itself. Using the monitor he has been able to demonstrate antagonistic effects of the two inhibitors colchicine and cytochalasin B on chloroplast movement. Since the first is known to interact with microtubules and the second with microfilaments, the results suggest that these two contractile protein systems regulate chloroplast position by operating in opposing directions in a push-pull fashion. The data are sufficiently precise that extremely small perturbations of chloroplast movement are readily detected. For example, in less than two hours of a phase-shifting pulse of light there is a dramatic change in the course of chloroplast movement. Some progress has also been made in putting the data into the computer for normalization, averaging, and other manipulation, but the system is not yet on line.

In another kind of study with corn membrane fractions, Dohrmann and Professor Peter M. Ray of Stanford University have made some exciting progress in isolating and solubilizing a membrane-bound binding site for the plant growth hormone 2-indoleacetic acid. Though hormone receptors are by now well known in several animal systems, plant receptors have remained refractory despite strenuous efforts in a

number of laboratories. The Dohrmann and Ray results are extremely promising and could be a prelude to a major step forward in our knowledge of the action of this important plant hormone.

The Physiological Ecology group have continued and extended their series of studies on the ways in which plants adapted to extreme environments withstand stress, and on which systems are normally limiting. Thus Björkman, Boynton, and Berry have investigated a number of systems in two species, an extremely thermophilic species, *Tidestromia oblongifolia*, and a cool temperate species, *Atriplex sabulosa*, both C_4 species. They compared the effect of temperature on the quantum yield for photosynthesis by intact leaves with its effect on photosystem I and II activities; ribulose 1,5-diphosphate carboxylase activity (the C_3 enzyme for CO_2 fixation); phosphoenolpyruvate carboxylase activity (the C_4 enzyme for CO_2 fixation); and heat coagulability of soluble proteins as a measure of irreversible denaturation. It is clear that the best fit with thermal inhibition of photosynthesis in both cases is with system II activity. In addition, however, there were interesting differences in heat stability of the C_3 enzyme from the two species, suggesting that not just lipids but proteins may differ between high- and low-temperature-adapted plants. An additional finding, obtained in collaboration with Enama, was that the molecular weight of the C_4 enzyme from *Tidestromia* was almost twice that of the various *Atriplex* species, another oddity of this remarkable plant.

Mooney, Björkman, Ehleringer, and Berry have continued their seasonal studies of photosynthetic capacity of Death Valley plants. The creosote bush *Larrea divaricata* maintained an almost constant photosynthetic capacity under natural conditions all through the year. This homeostatic adjustment could be partially explained by changes in the temperature optimum for photosynthesis with the season, a response

shown by none of the other species. Of particular interest was the discovery that *Camissonia claviformis*, a C_3 winter annual, had a midday photosynthetic rate exceeding that of some of the best crop plants, such as corn and sugar cane.

Ehleringer completed quite a different kind of study on adaptation to high temperature in his work on leaf pubescence in the genus *Encelia*. Across a cline from cool and moist to hot and dry conditions there is a dramatic increase in leaf pubescence from species to species, within a single species along the cline, or with precipitation received during the growing season. Plants growing under the most extreme conditions of aridity and high temperature form a layer of pubescence that reflects more than 60% of the incident irradiation, substantially modifying the leaf energy balance and reducing the photosynthetic rate. However, the consequent reduction in heat load should be a considerable adaptive advantage to a desert plant.

Ehleringer and Björkman also looked carefully at the influence of both CO_2 concentration and temperature on the quantum yield for photosynthesis in the C_3 plant *Encelia californica* and the C_4 plant *Atriplex rosea*. Under atmospheric oxygen (21%) the quantum yield for the C_3 plant showed a sharp dependence upon CO_2 concentration, while at 2% O_2 it was independent of CO_2 concentration. In the C_4 plant, the quantum yield is independent of CO_2 concentration regardless of O_2 concentration. Thus the C_4 plant is clearly at a great advantage under extremely high light intensities in that its quantum efficiency is independent of intercellular CO_2 concentration. The quantum yield of the C_3 plant under normal atmospheric conditions declines with increasing temperature, while the yield of the C_4 plant does not. The crossover for the two is at about 30°C. Thus, at high temperature as well as at high light intensity the C_4 plant has the advantage.

Carey and Berry have investigated the influence of temperature on ion uptake and respiration in barley roots grown at two different temperatures and in corn roots. With barley roots grown at low temperature, respiration at any given temperature below 30°C is higher than for roots grown at higher temperature. The patterns for ion uptake, however, are different. For the cool-grown barley, the activation energy for rubidium uptake is inordinately high, suggesting that the ion accumulation mechanism is either damaged or incompletely developed during prolonged exposure to low temperature. There is no clear relationship between the influence of low temperature on ion uptake and its influence on respiration. In corn roots, however, the influence of temperature is parallel for both respiration and ion uptake. The corn response is what one would expect for roots that are generally chilling sensitive. The sharp effect of low temperature on ion uptake by barley roots at low temperature without much of an effect on respiration suggests that perhaps membranes associated with ion uptake are chilling sensitive, while those in the mitochondria are not.

In a sharp departure from studies involving desert plants in the desert or in the laboratory, Berry, Boynton, Kaplan, and Badger have carried out a detailed study of growth and photosynthesis of the unicellular motile alga *Chlamydomonas reinhardtii* as a function of CO_2 concentration. The CO_2 exchange kinetics are dramatically affected by growth conditions. For example, cells adapted to 5% CO_2 have a CO_2 requirement similar to that of C_3 species of higher plants, while those adapted to air levels (0.03%) are far more efficient. The difference is not in a change in CO_2 -fixation pathway, nor does it involve a change in the efficiency of the CO_2 -fixing enzyme ribulose 1,5-diphosphate carboxylase. Inhibitor studies suggested that the enzyme carbonic anhydrase played an essential role in the low- CO_2 adapted

cells and that there is a metabolic influx pump for HCO_3^- in these cells. The anhydrase would then be required to convert the HCO_3^- to CO_2 , the substrate for the fixation enzyme.

It may come as a surprise to find two papers in the Report of the Department of Plant Biology clearly devoted to studies of the butterfly *Colias*. Johnson has been collecting field and laboratory data on this insect for the past five years and has used his time in the Department partially to sort it out, analyze it, and prepare it for publication. The thrust of the work is, first, that there is a large amount of enzyme polymorphism across and between populations of *Colias* and, second, that this polymorphism is perhaps best viewed as adaptive strategy to match the flexibility of the metabolic phenotype with the heterogeneity of the environment. In the case of several key enzymes such as α -glycerophosphate dehydrogenase, the arguments are compelling ones. Enama's studies with *Distichlis* and *Atriplex* should provide an excellent botanical proving ground for this hypothesis.

Johnson also reports in detail on electrophoretic methods for detecting electrophoretically hidden variability—procedures involving using a series of gels of different porosities, allowing determination of net charge (divided by a constant), and determining a retardation coefficient by molecular weight and conformation. It is clear from his results that differences in electrophoretic mobility may exist between allelic proteins even when these proteins have the same molecular weight and charge. The mobility differences thus seem to arise exclusively from changes in the retardation coefficient.

Experiments with D_2O clearly eliminate variations in the hydration shell as accounting for the variation in retardation coefficient, but do not distinguish between a conformational change and a change in a subunit dissociation constant. Johnson is applying

a different kind of test to determine which of the two is responsible. However, careful analysis reveals that whichever the cause is, it has a genetic basis.

Brown has continued her studies on the isolation, purification, and characterization of the reaction center chlorophyll-protein complex from a variety of algae and from spinach chloroplasts. She discovered that a relatively modest decrease in the ratio of chlorophyll *a* to P700 yielded a large increase in a 695-nm fluorescence band at low temperature. A reasonable hypothesis is that the 695 band represents fluorescence from an oxidized form of P700 absorbing near 690 nm. Since the rise time for this fluorescence did not parallel the bleaching of P700 with illumination, the results suggested a two-step reaction involving a pair of associated P700 molecules. Studies with Fork on bleaching kinetics of the reaction center complex at room temperature revealed that the course of dark reduction after a saturating light flash depended upon the length of the initial light flash used to induce bleaching. With very short light exposures there is a far larger rapidly recovering component after photooxidation than there is with exposures more than 100 msec in length. The photobleaching and recovery kinetics support the hypothesis that the reaction center chlorophyll of photosystem I is a dimer and that the reaction proceeds by two steps.

In wide-ranging studies with a variety of algae and higher plants, Fork continued work initiated with Murata on fluorescence changes with changes in temperature. He also examined chloroplasts and a chlorophyll-protein reaction center complex. Although the curves obtained are extremely complex, some features were fairly consistent: a fluorescence maximum at a moderate temperature consistent with the temperature for a physical state change of membrane lipids, and a maximum (not seen in every case)

above which irreversible thermal damage occurred. The maximum for the chlorophyll-protein reaction center complex was very high, at 63°C, consistent with evidence from elsewhere that photosystem I is more resistant to high temperature than photosystem II. Parallel measurement of photochemical activity versus temperature with some of the organisms showed good correlation between change in fluorescence and change in photosynthetic activity.

Whereas Fork's studies involved relatively slow and steady temperature changes, Schreiber studied the effects both of slow heating and of a very rapid temperature jump (largely completed within 2 sec) on fluorescence kinetics with the alga *Scenedesmus obliquus*. He used cells grown at two different temperatures, and monitored fluorescence under two extreme conditions: with photosystem II reaction centers closed (high light intensity, electron transport blocked by an inhibitor) or with photosystem II reaction centers open (low light intensity, system kept aerobic). The fluorescence under the second condition, F_0 , shows a sharp rise between 46° and 52°C, while the fluorescence under the first, F_{\max} , showed a continuous decline with increasing temperatures, with a suggestion of a steeper decline above 46°C. The slope changes began a degree higher for cells grown at higher temperature. The kinetics for changes in F_0 and F_{\max} with a sharp temperature jump revealed an inverse relationship with an increase in F_0 paralleling a decrease in F_{\max} . Although the kinetics are complex, the relationship holds for jumps to temperatures below those causing irreversible damage. A working hypothesis is that temperature affects the distribution of energy be-

tween photosystems I and II, with higher temperatures favoring photosystem I, as monitored by the F_0 fluorescence. Schreiber also documented a role of preillumination in the expression of heat damage in fluorescence measurements. His studies, together with Brown's and Fork's, further underline the value of fluorescence studies in attempts to unravel the extreme complexities of photosynthesis.

Finally, Stemler has made some detailed studies of the binding of HCO_3^- to washed thylakoid membranes. He had previously demonstrated the importance of bicarbonate in activation of the O_2 -evolving system (entirely independent of its role as carbon donor). By careful binding studies, he has now shown that thylakoids have at least two classes of bicarbonate binding sites: a high affinity class, saturated by about 1 mM HCO_3^- , and a lower affinity class, saturated above 10 mM. The second class is more strongly implicated in the O_2 evolution role, since at least 10 mM bicarbonate is required to restore normal oxygen-evolving capacity to washed thylakoids.

The above summary can hardly do justice to this past productive year. It should, however, provide evidence for a viable and vigorous group of investigators working on fundamental problems of plant biology and making exciting progress on a number of fronts. As we inevitably must depend more and more on solar energy for food, fuel, and fiber, basic knowledge of solar energy conversion as practiced in photosynthesis, of the nature of adaptation to conditions permitting extremely rapid conversion in nature, and of the fundamental mechanisms of plant growth and development must assume high priority.

SEQUENCE ORGANIZATION IN PEA DNA

W. F. Thompson

In a majority of animal genomes so far studied, single-copy DNA sequences are extensively interspersed

with repetitive sequences. A variable but usually prominent fraction of the repetitive DNA in these genomes ap-

pears to be composed of elements some 200–400 nucleotides in length. Additional repetitive elements appear to be much longer (greater than about 1500 nucleotides). This pattern of sequence organization is often called the *Xenopus* pattern, in recognition of the extensive studies carried out on the DNA of this organism. Although different patterns have been found in *Drosophila* and honey bee DNA (Manning *et al.*, 1975; Davidson *et al.*, 1975a), the main features of the *Xenopus* pattern have been found to hold for a surprisingly wide variety of animal genomes (Goldberg *et al.*, 1975; Davidson *et al.*, 1975 a, b). Extensive interspersed of repetitive and single-copy DNA sequences has provided the basis for an attractive model of eukaryotic gene regulation (Davidson and Britten, 1973) which is consistent with a rather large body of experimental evidence from animal systems. Until recently, however, no information was available concerning interspersed of sequences in DNA of higher plants. Higher plants typically have much larger genomes, with much higher percentages of total repetitive sequence DNA, than most animals. Information on sequence organization in plant DNA will be of use in studies of molecular evolution and in experiments on gene regulation during development.

A recent study of the cotton genome (Walbot and Dure, 1976) shows that repetitive and single-copy sequences are interspersed in a fashion consistent with the *Xenopus* pattern, although both types of sequences are longer in cotton DNA, and the size distribution of repetitive elements is considerably more heterogeneous. The cotton genome (0.795 pg/cell, haploid) is considerably smaller and contains a smaller proportion of repetitive sequences (40%) than the genomes of many other higher plants. For example, Flavell *et al.* (1974) studied 23 species with DNA contents (1C) ranging from 0.75 to 49 pg per nucleus and found repetitive sequences accounted

for between 46% and 92% of the total DNA. Excluding polyploid species, the range of DNA content was from 0.75 to 31 pg, with the same range of repetitive sequence content. Thus, while the cotton genome data represent a significant advance in our understanding of plant DNA sequence organization, studies of plant species with more typical genome sizes and repetitive sequence contents are clearly required. We report here the results of some preliminary experiments on the garden pea (*Pisum sativum* L.), which has a haploid nuclear DNA content of 5 pg and about 75% repetitive DNA.

INTERSPERSION

Figure 1 depicts the reassociation of short fragments of pea DNA (350–400 nucleotides) in 4 M NaClO₄ (Hoyer and van de Velde, 1974). Almost two-thirds of the DNA reassociates by C_{0t} 5 (corresponding to approximately C_{0t} 18 in 0.12 M Na phosphate). The remaining

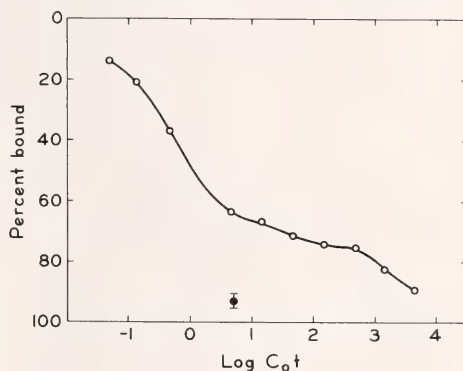


Fig. 1. Reassociation of pea DNA in 4 M NaClO₄-0.18 M Na phosphate buffer at T_m-25 . Open circles represent the reaction of short (350–400 nucleotide) fragments as measured by hydroxylapatite binding, while the solid circle shows the binding (standard deviation of 5 determinations) of 3200 nucleotide fragments reassociated to C_{0t} 5 under the same conditions. Samples were diluted into 0.12 M Na phosphate buffer and fractionated on columns equilibrated at 60°C; bound DNA was eluted with the same buffer by raising the temperature of the column to 97°–98°C. C_{0t} values are not corrected for the accelerating effect of NaClO₄ (about 3.5-fold, relative to 0.18 M Na+).

approximately one-third is composed of a small fraction of more slowly reassociating repetitive sequences and single-copy DNA. When DNA fragments 3200 nucleotides long are reassociated to $C_0t = 5$, about 93% bind to hydroxylapatite, indicating that the majority of slow repetitive and single-copy sequences are distributed in such a way that most fragments of 3200 nucleotides containing such sequences also contain repetitive DNA capable of forming duplexes by $C_0t\ 5$. Or, put another way, the slowly reacting sequences are mostly interspersed with rapidly reacting sequences, and there appear to be relatively few regions of slowly reacting DNA in excess of about 3000 nucleotides in length. Experiments in progress are designed to provide a more quantitative analysis of single-copy sequence lengths in pea DNA.

LENGTH OF REPETITIVE SEQUENCES

In most plant genomes, repetitive sequences account for 2–3 times as much DNA as do single-copy sequences. If all the repetitive DNA were present as 200–400 nucleotide elements separated by single-copy elements, the average length of single-copy sequences could only be of the order of 100–150 nucleotides. This length is less than that observed in other organisms—and smaller than a typical structural gene—by about an order of magnitude. Thus we would expect a priori that regions of repetitive DNA substantially longer than 200–400 nucleotides must exist in plant genomes, including pea genomes. Aggregation (or hyperpolymerization) during repetitive sequence reassociation with short DNA fragments from peas and other plants is probably related to the presence of such long repetitive sequence regions (Thompson, 1975, 1976).

However, several possibilities exist for the organization within a long repetitive region. On one extreme, an en-

tire region may be composed of a single long sequence (or a series of identical short sequences), repeated in its entirety at different sites in the genome. The other extreme would involve clustering of several smaller repetitive units. Clusters at different locations in the genome could involve different orders and/or combinations of short sequences, so that any given sequence would have different neighbors each time it occurred.

In beginning experiments on organization of repetitive sequences in pea DNA, we have tried to determine how much of this DNA is contained in long repetitive regions or tandem repeats. The experiments involve reassociating long fragments so that only repetitive sequences can react ($C_0t\ 5$ in 4 *M* NaClO₄ buffer). Single strands are then removed by digestion with the single strand-specific nuclease S1 (Ando, 1966; Britten *et al.*, 1974), and the size distribution of the remaining duplexes is determined. Long repetitive sequences or tandem repeats are expected to produce long S1-resistant duplexes, while short repeats occurring in different combinations or interspersed with single-copy sequences will yield short duplexes after S1 digestion.

Figure 2 shows the specificity of S1 nuclease for single strands under our digestion conditions. Native or denatured ³H-*E. coli* DNA was mixed with reassociated 3200-nucleotide fragments of pea DNA and subjected to S1 digestion. Digestion products passed through hydroxylapatite in 0.03 *M* Na phosphate at room temperature; essentially all the resistant DNA remained bound to the column at 60°C in 0.15 *M* Na phosphate and was eluted by raising the temperature to 97°C. Completely single-stranded DNA is digested rapidly, and there is little or no digestion of native DNA. Reassociated pea DNA is digested rapidly early in the reaction, presumably reflecting the removal of completely single-stranded regions. Subsequently the reaction is slow but significant, which may reflect

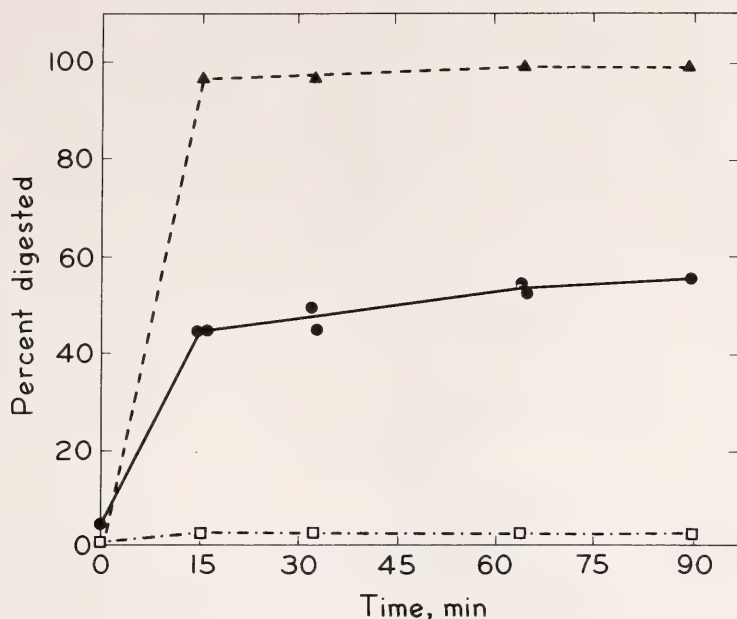


Fig. 2. Kinetics of S1 nuclease digestion. 3200 nucleotide fragments of pea DNA were reassociated to C_0t 5 in 4 M Na ClO₄-10 mM PIPES, pH 6.9, and then adjusted to 0.2 M NaClO₄, 0.1 M Na acetate, 0.5 mM PIPES, 0.1 M ZnSO₄, pH 4.5. Aliquots were mixed with native or denatured ³H-*E. coli* DNA and treated with 20 units of S1 nuclease per μ g of DNA for various times at 40°C. Aliquots were adjusted to 0.06 M Na phosphate, pH 6.8 and assayed on hydroxylapatite as described in the text. Filled circles, C_0t 5 pea DNA; filled triangles, denatured ³H-*E. coli* DNA; filled squares, native ³H-*E. coli* DNA.

slow digestion of DNA in regions of mismatched base pairs within otherwise duplex structures. To minimize this second process while ensuring complete digestion of single-stranded DNA, experimental treatments were carried out for 30 min. After correcting for the approximately 5% of A_{260} which failed to bind in 0.03 M NaPB without S1 treatment, about 58% of the pea DNA is resistant to digestion. This value is in reasonable agreement with the binding of short fragments to hydroxylapatite after reassociation to the same C_0t , and it therefore appears that these S1 conditions set approximately the same criterion for recognition of duplex structure as fractionation on hydroxylapatite at 60°C.

Nuclease-resistant duplexes were analyzed by chromatography on agarose (A50 m) gel filtration columns

in 0.12 M Na phosphate (Davidson *et al.*, 1974; Goldberg *et al.*, 1975). These columns are thought to exclude double-stranded DNA longer than about 1000-15000 nucleotide pairs. Fragments of pea DNA 3200 nucleotides long were reassociated and treated with S1 nuclease as above. The resistant duplexes were isolated by binding to hydroxylapatite and eluting with 0.4 M Na phosphate. This material was then mixed with marker ³H-*E. coli* DNA (400 nucleotide pairs) and applied to the column. The results are shown in Fig. 3A. About one-third of the sample was in the form of long duplexes in the exclusion peak. The remainder eluted as a broad band, indicating a heterogeneous distribution of lengths, although there is some suggestion of a peak in the region of 300-400 nucleotide pairs. These re-

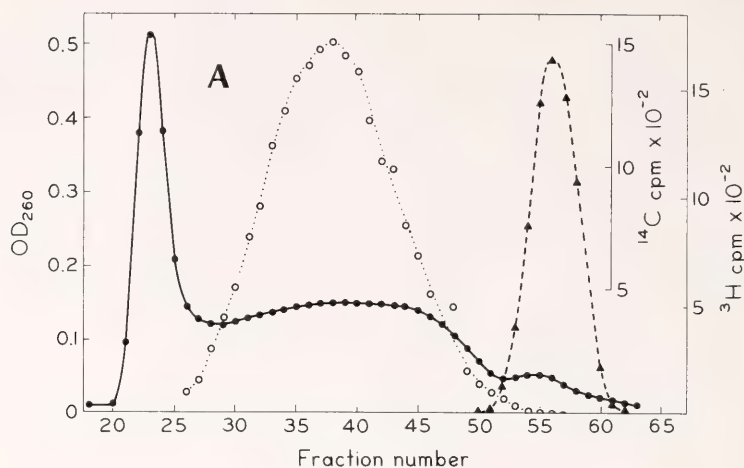


Fig. 3A. Agarose gel filtration of S1 nuclease-resistant duplexes. Pea DNA fragments (3200 nucleotides) were reassociated and treated with S1 nuclease for 30 min under the conditions of Fig. 2. Resistant duplexes were eluted from hydroxylapatite with 0.4 M Na phosphate buffer and mixed with trace amounts of sheared, native ³H-*E. coli* DNA (400 nucleotide pairs) and ¹⁴C-thymidine. The mixture was applied to a 1.2 × 45 cm column of Bio-Gel A50m equilibrated with 0.12 M Na phosphate buffer. Filled circles, pea DNA A₂₆₀; open circles, ³H-*E. coli* DNA; filled triangles, ¹⁴C-thymidine inclusion marker.

sults may underestimate the proportion of long duplexes which form by C_0t 5, since some 10%–15% of the S1-treated DNA could not be recovered from hydroxylapatite by salt elution, and we have observed in other experiments that hydroxylapatite fractionation reduces the size of long DNA fragments. In a preliminary experiment in which an S1 digest was analyzed without prior fractionation, about 60% of the DNA eluting prior to the void volume was in the excluded peak.

In alkaline sucrose gradients, most of the DNA from the excluded fraction sedimented as a relatively symmetrical peak around approximately 1500 nucleotides. Thus reassociation, S1 treatment, and HAP fractionation caused about a twofold reduction in the single-stranded length. Rice (1974) has found a similar reduction after S1 treatment of reassociated T-4 DNA, which is presumably caused by the failure of randomly sheared fragments to reassociate over their entire length. Smith *et al.* (1975) have recently de-

termined the average first collision overlap for randomly sheared simple DNA to be 0.55 of the single-stranded length. Thus, the data do not differ markedly from results predicted on the assumption that most of the DNA giving rise to the excluded fraction was composed of repetitive sequences as long as or longer than the 3200-nucleotide fragments used. Further analysis of the size distribution of long repetitive sequences will therefore require DNA fragments much longer than 3200 nucleotides. However, it is clear that individual repetitive sequences of substantial length are a prominent feature of the pea genome.

In several animal DNAs, including *Xenopus*, sea urchin, clam, and cow, it has been found that the longer repetitive sequences melt with a higher T_m than the short, interspersed repetitive sequence elements, even after correcting for the effect of duplex length on thermal stability (Davidson *et al.*, 1974; Davidson *et al.*, 1975a, 1975b; Goldberg *et al.*, 1975). This observation appears to hold also for pea DNA, as

shown in Fig. 3B. Duplexes eluting in the exclusion peak of agarose columns exhibit high thermal stability, with a T_m only about 1.5° lower than that of native DNA, but the T_m is rapidly reduced in later fractions. Length effects per se would be expected to result in only about a 2°–3° reduction in T_m for fragments in the range of 300 nucleotides in length (Britten *et al.*, 1974). Thus, most of the T_m reduction seen in short duplexes from the agarose column profile must be attributed to mismatched bases, and the short duplexes must therefore contain a larger fraction of mismatched bases than longer duplexes. While the significance of this observation is not understood, one may speculate that the shorter sequences are, on the average, evolutionarily older and more diverged than are longer repetitive sequences.

CONCLUSION

Although many details remain to be worked out, it is clear from the data so far that sequence organization in the

pea genome resembles the pattern for *Xenopus* and is distinctly different from that for *Drosophila*. Pea single-copy sequences are mostly less than 3000 nucleotides in length and are extensively interspersed with repetitive sequences, which is consistent with the *Xenopus* pattern but contrasts sharply with the very long (10,000 nucleotides or more) single-copy elements in the *Drosophila* genome (Manning *et al.*, 1975). Short (200–400 nucleotide) repetitive elements are less prominent—and longer repetitive sequences more prominent—in pea DNA than in the DNA of most animals (Goldberg *et al.*, 1975). However, the main features of the *Xenopus* pattern—extensive interspersion of single-copy DNA sequences and the presence of at least some short repetitive elements—are to be found in pea DNA as well. A more quantitative comparison must await more data.

We do not yet know whether all the short repetitive sequences in pea DNA are adjacent to single-copy sequences, as they appear to be in several animal

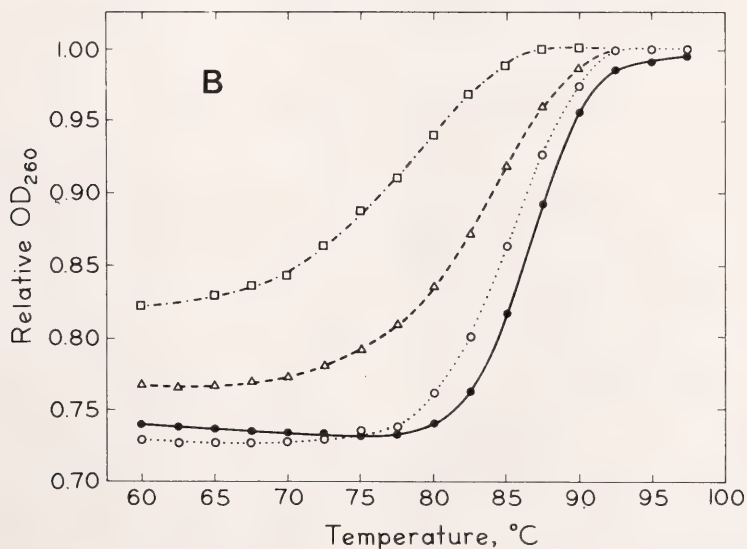


Fig. 3B. Melting profiles of native pea DNA and DNA from various fractions of the agarose profile shown in Fig. 3a. Samples in 0.12 M Na phosphate buffer were melted in a Gilford model 2527 Thermal Programmer cuvette. Solid circles, native DNA; open circles, fraction 22; open triangles, fraction 25; open squares, fraction 32. Absolute hypochromicity values for fraction 32 are unreliable, due to the low optical density of this fraction.

genomes. At present it is equally possible that some, or even most, of these short sequences might be arranged in variously ordered clusters, as in the "permuted tandem repetition" model proposed by Cech and Hearst (1976) for highly repetitive mouse main-band DNA. We hope that more information on this question can be obtained in future experiments.

References

- Ando, T., *Biochim. Biophys. Acta*, **114**, 158–168, 1966.
- Britten, R. J., D. E. Graham, and B. R. Neufeld, *Methods Enzymol.*, **29**, 363–418, 1974.
- Cech, T. R., and J. E. Hearst, *J. Mol. Biol.*, **100**, 227–256, 1976.
- Davidson, E. H., and R. J. Britten, *Q. Rev. Biol.*, **48**, 565–613, 1973.
- Davidson, E. H., G. A. Galau, R. C. Angerer, and R. J. Britten, *Carnegie Inst. Wash. Year Book 74*, pp. 673–678, 1975a.
- Davidson, E. H., G. A. Galau, R. C. Angerer, and R. J. Britten, *Chromosoma*, **51**, 253–259, 1975b.
- Davidson, E. H., D. E. Graham, B. R. Neufeld, M. E. Chamberlin, C. S. Amenson, B. R. Hough, and R. J. Britten, *Cold Spring Harbor Symp. Quant. Biol.*, **38**, 295–301, 1974.
- Flavell, R. B., M. D. Bennett, J. B. Smith, and D. B. Smith, *Biochem. Genet.*, **12**, 257–269, 1974.
- Goldberg, R. B., W. R. Crain, J. V. Rudderman, G. P. Moore, T. R. Barnett, R. C. Higgins, R. A. Gelfand, G. A. Galau, R. J. Britten, and E. H. Davidson, *Chromosoma*, **51**, 225–251, 1975.
- Hoyer, B. H., and N. W. van de Velde, *Carnegie Inst. Wash. Year Book 73*, pp. 1102–1104, 1974.
- Manning, S. E., C. W. Schmid, and N. Davidson, *Cell*, **4**, 141–155, 1975.
- Rice, N. R., *Carnegie Inst. Wash. Year Book 73*, pp. 1088–1098, 1974.
- Smith, M. J., R. J. Britten, and E. H. Davidson, *Proc. Nat. Acad. Sci. U.S.A.*, **72**, 4805 and 4809, 1975.
- Thompson, W. F., *Carnegie Inst. Wash. Year Book 74*, pp. 783–786, 1975.
- Thompson, W. F., *Plant Physiol.*, **57**, 617–622, 1976.
- Walbot, V., and L. S. Dure, *J. Mol. Biol.*, **101**, 503–536, 1976.

DNA SEQUENCE COMPARISONS IN *Atriplex*

Heather Strong Belford and W. F. Thompson

Last year (*Year Book 74*, pp. 780–791) we reported on the early stages of a project involving evolutionary studies of *Atriplex* DNA. Our objectives are to provide information on the phylogenetic relationships among the species in this genus which we hope will be of value in interpreting the evolution of C_4 photosynthesis and other adaptations, and (more generally) to characterize DNA changes associated with speciation and evolution in higher plants. This year, we report our first results from comparisons of single-copy DNA sequences in four species. While still preliminary, these results clearly demonstrate the applicability of the technique to *Atriplex* species and raise

some questions concerning previous phylogenetic interpretations. To our knowledge, this communication represents the first report of evolutionary comparisons carried out with single-copy DNA sequences from higher plants.

The use of single-copy DNA for evolutionary comparisons has several advantages, in spite of the fact that the experiments are technically more difficult than those using total DNA. In contrast to total DNA, in which rapid reassociation between related but nonidentical repetitive sequences occurs, single-copy sequences reassociate slowly and form precisely paired duplexes. Thus interspecific DNA hy-

bridizations may be carried out with purified single-copy tracer under conditions in which the reaction of tracer sequences with themselves is insignificant and in which virtually all the mispairing in interspecific duplexes can be attributed to evolutionary divergence between the species being compared (Kohne, 1970). In addition, the use of single-copy DNA avoids problems associated with possible addition or differential amplification of repetitive sequences in different species, with the result that measurements of single-copy DNA homology can be more simply related to evolutionary divergence time than measurements using total DNA.

Because these considerations simplify interpretation of data obtained from experiments with single-copy DNA (and because we are able to isolate a reasonable amount of single-copy DNA from *Atriplex*), we have chosen to focus our initial experiments on this fraction. We hope that experiments with single-copy DNA will yield useful phylogenetic information and provide a more solid foundation on which to base future studies of repetitive sequence evolution.

Table 1 shows the evolutionary relationships thought to exist among a variety of *Atriplex* species and indicates the four species chosen for initial investigation. We wished to determine the degree of DNA homology between representatives of closely related species groups as well as between species presumed to be much more distantly related. *Atriplex hortensis* and *A. triangularis* were therefore selected as representing groups closely related by morphological criteria. *A. serenana* should be distinctly different, since it is considered to represent a relatively high degree of advancement in a different subgenus. *A. sabulosa* was expected to be intermediate, although closer to *A. hortensis* than *A. serenana*.

Single-copy sequences were purified from *A. hortensis* DNA which had been sheared to about 350–400 base pairs in

a Vir-Tis "60" homogenizer (Britten *et al.*, 1974). It was heat denatured and allowed to reassociate at 25°C below the T_m of native DNA ($T_m - 25^\circ\text{C}$) in 4 M NaClO₄ containing 0.18 M Na phosphate buffer (Hoyer and van de Velde, 1974) to a C_0t of 100. (Under these conditions reassociation proceeds at about 3.5 times the rate in 0.12 M NaPB at 60° [Hoyer and van de Velde, 1974; our unpublished results] and thus the "equivalent C_0t " for this reaction is about 350.) After reassociation, the samples were diluted 30-fold in 0.12 M Na phosphate and fractionated on hydroxylapatite columns at 60° by standard techniques. About 70% of the total DNA bound to the column and was considered to be reassociated repetitive sequences. The 30% which failed to bind (containing unassociated single-copy DNA) was passed over a column of AG-50W \times 8 cation exchange resin (Bio Rad) to remove Ca⁺⁺ and any other residual basic impurities. It was then chromatographed on a column of agarose gel (A1.5 m, Bio Rad) to remove any degraded fragments, and the material eluting in the void volume (about 75% of the A_{260}) was used to prepare highly radioactive single-copy tracer by iodination.

Iodination was carried out for 10 min at 60° with Na¹²⁵I (Amersham, pH 8–11) following the technique of Orosz and Wetmur (Orosz and Wetmur, 1974), except that the buffer was 10 mM Na acetate, pH 5.2, and most of the unbound iodine was removed by chromatography on Sephadex G50 prior to the dialysis step.* The product had a specific activity of 5×10^5 – 6×10^5 cpm/ μg (approximately 5% of cytosine residues iodinated) and a mean fragment length of 250–300 bases. It was highly enriched in single-copy sequences, as shown in Fig. 4.

*These conditions were designed for iodination of single-stranded total DNA under conditions minimizing reassociation of repetitive sequences during the reaction.

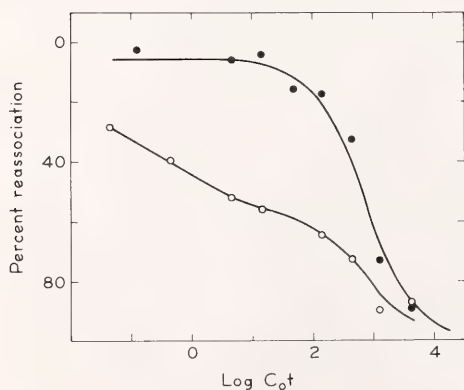
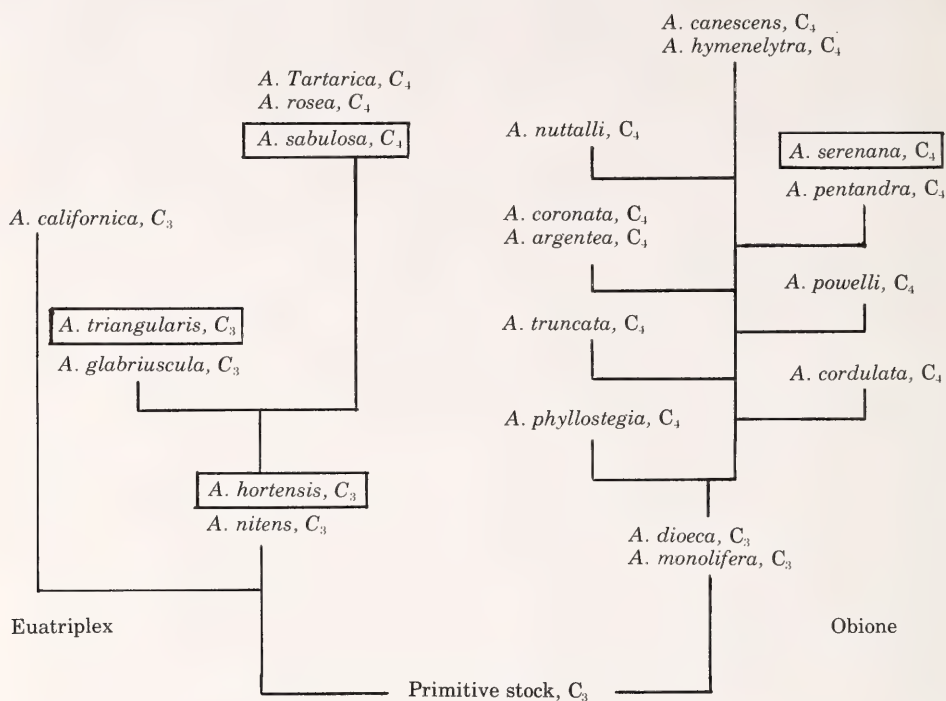
TABLE 1. Phylogenetic Scheme for the Genus *Atriplex* Based on Morphological Criteria

Fig. 4. Reassociation of ¹²⁵I single-copy tracer (filled circles) with a 3000-fold excess of unlabeled total *A. hortensis* DNA (open circles). Incubations were in 4 M NaClO₄-0.18 M Na phosphate buffer at *T_m*-25. Samples were diluted in 0.12 M Na phosphate and assayed on hydroxylapatite at 60°C. *C₀t* values have not been corrected for the accelerating effect of NaClO₄ (see text). The line through the tracer points represents a single theoretical second order component accounting for 95% of the reaction.

To measure sequence homology between this tracer and DNA from other species, aliquots of the tracer at low concentration (1.7 μg/ml) were mixed with a 3000-fold excess of total sheared DNA (5 mg/ml) from each of the four species. The mixtures were heat denatured and reassociated at *T_m*-25°C in NaClO₄ buffer. Under these conditions, the tracer is too dilute to reassociate significantly with itself (this was experimentally verified in control reactions containing only the tracer DNA), and the observed duplexes therefore result from reassociation between tracer and unlabeled DNA sequences. Since the high concentration of unlabeled DNA is required to drive the reaction, this DNA is often called "driver" DNA in the following discussion.

After dilution in 0.12 M NaPB, the reassociated mixtures were passed over hydroxylapatite at 60°C. The bound fraction, containing duplexes between

¹²⁵I-*A. hortensis* single-copy sequences and driver DNA from the various species, was then subjected to thermal elution with 0.12 M Na phosphate at increasing temperatures. The apparatus used consisted of multiple columns maintained in the same (rapidly stirred) water bath in order to assure temperature uniformity among the various samples. Results may be expressed both in terms of the extent of tracer reaction (cpm bound to HAP = total interspecific duplex) and the thermal stability of the hybrids.

Figure 5 shows the results of a thermal elution experiment using duplexes formed by incubation to a driver DNA *C*₀*t* of 1200 at *T*_m - 25°. The data are plotted in a differential form which allows simultaneous visualization of the amount of interspecific duplex and the distribution of this material in various thermal stability classes. In the control reaction, most of the tracer forms high-stability duplexes as expected for single-copy DNA. The shoulder at 70°C is consistent with the small contamination by repetitive sequences noted in the reassociation kinetics (Fig. 5), while most of the duplexes elute as a symmetrical peak around the *T*_m for native DNA (indicated by the arrow at 85°C).

In contrast, most products of the interspecific reactions show much reduced thermal stability, melting as broad peaks between 65° and 85°C. Data from this experiment are summarized in the left column of Table 2. Relative to the control, mean thermal stability of all three interspecific products is depressed to nearly the same ex-

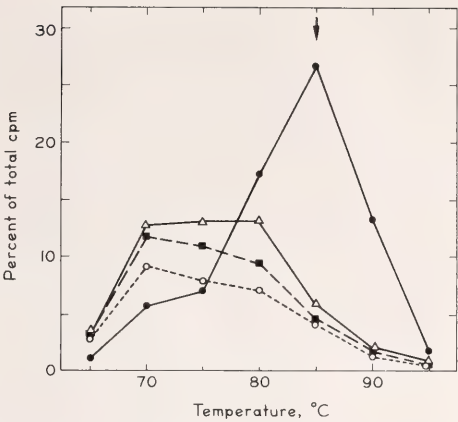


Fig. 5. Thermal elution profiles for duplexes formed between ¹²⁵I-*A. hortensis* single-copy DNA and unlabeled DNA from *A. hortensis* (filled circles), *A. triangularis* (open triangles), *A. sabulosa* (filled squares), and *A. serenana* (open circles). Incubations were as described in Fig. 4 to *C*₀*t* 1200. After dilution with 0.12 M Na phosphate buffer, samples were applied to hydroxylapatite at 60°C. The bound DNA was eluted with 0.12 M Na phosphate by raising the temperature in five increments. Each point represents the percentage of total ¹²⁵I counts in the reaction which eluted at the indicated temperature.

tent (7.3°-8°C), indicating that the duplexes formed involve sequences having nearly the same degree of evolutionary divergence from the *A. hortensis* single-copy sequences. Although estimates of the correlation between mismatching and thermal stability vary between 0.7° and 1.5°C per 1% mismatched base pairs, it is often assumed, as a convenient approximation, that a 1°*T*_m depression corresponds to 1% mismatch (Bonner *et al.*, 1973). Thus, these duplexes would be mismatched in 7%-8% of the bases.

TABLE 2. Reaction of ¹²⁵I Single-Copy DNA from *Atriplex hortensis* with Total Unlabeled DNA from *Atriplex* Species

| Unlabeled DNA | <i>T</i> _m - 25, <i>C</i> ₀ <i>t</i> = 1200 | | <i>T</i> _m - 25, <i>C</i> ₀ <i>t</i> = 5000 | | <i>T</i> _m - 35, <i>C</i> ₀ <i>t</i> = 1200 | |
|------------------------|---|------------------------------|---|--|---|------------------------------|
| | % Bound | Δ <i>T</i> _m (°C) | % Bound | | % Bound | Δ <i>T</i> _m (°C) |
| <i>A. hortensis</i> | 71 | ... | 89 | | 79 | ... |
| <i>A. triangularis</i> | 51 | 7.3 | 71 | | 55 | 8.0 |
| <i>A. sabulosa</i> | 43 | 8.0 | 50 | | 48 | 10.5 |
| <i>A. serenana</i> | 33 | 8.0 | 48 | | 48 | 9.8 |

The extent of tracer reaction at C_0t 1200, T_m -25° , decreases in the order expected for the relative relationships based on morphology. The most extensive cross-reaction is observed with *A. triangularis* and the least with *A. serenana*. However, these reactions are not complete at C_0t 1200, and the apparent differences could reflect different rates of heterologous reaction in different driver DNAs. This point is especially important because mismatched duplexes are known to form at a much reduced rate relative to well-matched sequences, especially at T_m -25° (Bonner *et al.*, 1973). Therefore, we have also measured the cross-reactivity of these DNAs after longer incubations (C_0t = 5000), and after reassociation at a lower temperature (T_m -35°). The lower temperature was used in an attempt to achieve a more favorable compromise between the rates of heterologous and homologous reactions. In both cases, no significant difference was observed between cross-reactions with *A. sabulosa* and *A. serenana* (Table 2). For the experiment at T_m -35° , thermal stability measurements showed a decrease in the relative thermal stability of interspecific duplexes. This decrease suggests that the more permissive reaction conditions allowed some sequences to react which would have been unstable at T_m -25°C . The decrease was most pronounced in *A. sabulosa* and *A. serenana*, the species showing the least homology with *A. hortensis* in the original experiment. Both T_m and cross-reactivity for these two species were virtually the same after reassociation at T_m -35°C .

The data so far are surprising in two respects when compared with the "classical" evolutionary scheme shown in Table 1. First, we did not expect to find such a large difference between *A. hortensis* and *A. triangularis*, two species considered to be fairly closely related. Second, the degree of homology between *A. hortensis* (subgenus *Euatriplex*) and *A. serenana* (subgenus *Obione*) was essentially the same as

that between *A. hortensis* and *A. sabulosa* (*Euatriplex*), and nearly as great as that between *A. hortensis* and *A. triangularis*. If evolution of single-copy DNA is assumed to proceed at a more or less constant rate, the time that has elapsed since any of these three species last shared a common ancestor with *A. hortensis* must be nearly the same. The possibility thus exists that the morphological distinction between the two subgenera (which is based principally on the position of the embryo on the seed) (Hall and Clements, 1923) may not reflect the actual phylogeny of the group. This consideration might have important implications with respect to the evolution of C_4 photosynthesis, since the conclusion that C_4 photosynthesis has arisen at least twice independently within *Atriplex* (Björkman *et al.*, 1973) is based largely on the idea that C_4 species evolved separately from C_3 progenitors in each subgenus. Clearly, the molecular hybridization data at present are inconsistent with the linear form of Table 1. On the other hand, both the molecular data and the results of an extensive series of attempted genetic hybridizations (Nobs, this *Year Book*) suggest that the main species groups of *Atriplex* are quite distinct from one another. It therefore seems possible that lines leading to the present-day C_4 species might have diverged more or less directly from the ancestral stock rather than from more recent C_3 progenitors. Molecular hybridization experiments using a greater variety of species and several different sources of tracer DNA will be required to clarify the situation. In particular, it will be of interest to examine the pattern of relationships obtained with *A. serenana* and *A. sabulosa* tracers, and to include additional *Obione* species in the comparisons.

References

- Björkman, O., J. Troughton, and M. Nobs, in *Brookhaven Symp. Biol.*, 25, 206-211, 1973.

- Bonner, T. I., D. J. Brenner, B. R. Neufeld, and R. J. Britten, *J. Mol. Biol.*, 81, 123-135, 1973.
- Britten, R. J., D. E. Graham, and B. R. Neufeld, *Methods in Enzymology*, 29, 363-418, 1974.
- Hall, H. M., and F. E. Clements, *Carnegie Inst. Wash. Publ.* 326, 1923.
- Hoyer, B. H., and N. W. van de Velde, *Carnegie Inst. Wash. Year Book* 73, pp. 1102-1104, 1974.
- Kohne, D. E., *Q. Rev. Biophys.*, 3, 327-375, 1970.
- Orosz, J. M., and J. G. Wetmur, *Biochemistry*, 13, 5467-5473, 1974.
- Strong, H. G., and W. F. Thompson, *Carnegie Inst. Wash. Year Book* 74, pp. 789-791, 1975.

PLASMID MODIFICATION ASSOCIATED WITH THE LOSS AND ACQUISITION OF VIRULENCE IN *Agrobacterium tumefaciens*

Charles E. Rogler and William F. Thompson

INTRODUCTION

Infection of wounded plant tissue with *Agrobacterium tumefaciens* results, under appropriate conditions, in the formation of tumors that have several physiological properties in common with mammalian cancer tumors. These properties include non-self-limiting growth on synthetic medium devoid of hormones required by normal cells and the inability to differentiate into organized, functional tissue in response to treatments causing such differentiation when applied to normal cultured cell lines. Crown gall tumor cells retain these properties when cultured in the absence of the inciting organism and, when grafted into healthy plants, produce tumorous overgrowths (Braun, 1972; Lippincott and Lippincott, 1975). The crown gall system is a useful model system for studies of tumorigenesis, since tumors are easily induced experimentally and the inciting organism (*Agrobacterium*) can be isolated and studied both biochemically and genetically. In addition, it seems likely that studies of the origin and maintenance of the tumor state may allow better understanding of the controls functioning in normal plant cells.

Recently it was discovered that all pathogenic strains of *Agrobacterium tumefaciens* contain one or more large plasmids, with molecular weights ranging from about $90-160 \times 10^6$ (Zaenen *et al.*, 1974). Curing experiments have shown that loss of the plasmid results in the loss of virulence (van Larebeke *et al.*, 1974; Watson *et al.*, 1975). On the other hand, transformation with plasmid DNA results in the acquisition of virulence by the strain acquiring the plasmid (personal communication with J. Schell). These two lines of evidence strongly support the conclusion that the plasmid is a necessary genetic element for virulence in *Agrobacterium*.

Our research has focused on characterizing changes which occur in plasmid DNA sequences in *Agrobacterium* during either the loss or the acquisition of virulence. In this report we will first discuss an instance in which a large deletion in the plasmid genome is associated with loss of virulence and the alteration of certain serological properties of the original pathogenic strain. We will then present evidence that acquisition of virulence may involve replacement of a pre-existing avirulent plasmid with a virulence plasmid derived from another strain of *Agrobacterium*.

*Correlation of Altered Serological
Properties with the Deletion of
Plasmid Sequences*

One approach to identifying the specific sequences on the *Agrobacterium* plasmid which code for pathogenicity is to obtain plasmid deletion mutants that have lost virulence. In these studies, we have used two non-pathogenic mutants of *Agrobacterium tumefaciens* obtained from Dr. James DeVay of the University of California at Davis. These mutants were of interest because DeVay and co-workers had observed that one (strain 210) had serological properties different from those of its parent strain (209), while the other (strain 226) remained serologically similar to the parent.

In view of the association of virulence with the presence of a large plasmid, we wished to determine whether or not the mutant strains still contained a plasmid and, if so, whether or not the nucleotide sequences had been altered. Dye buoyant density centrifugation in cesium chloride-ethidium bromide gradients revealed the presence of a plasmid in both mutant strains (210 and 226) as well as in the parent strain (209). We then determined the molecular weight of these plasmids by analysis of their contour length in the electron microscope (Fig. 6 and Table 3). It appears that the plasmid of strain 210 (abbreviated pAT 210) resulted from the deletion of sequences totaling 4.8×10^7 daltons from pAT 209 while no measurable loss of DNA occurred during the derivation of pAT 226. However, definitive proof that the lesions affecting virulence are

located on these plasmids will require that they be tested in a strain of *Agrobacterium* with a known permissive chromosomal background.

In strain 210 the loss of plasmid sequences can be correlated with changes in the serological properties of the strain. It seems likely that the antigenic determinant causing the precipitin bands close to the antigen well in strain 209, which are absent in the reaction with 210 antigen (Fig. 7), are coded by some of the plasmid sequences deleted from pAT 210. This conclusion is still speculative because we cannot eliminate the possibility of independent chromosomal mutations. However, transformation experiments with pAT 209 may answer this question. If chromosomal mutations have not occurred, strain 210 should regain both virulence and its original serological properties as a result of transformation with pAT 209 DNA. If so, these experiments will establish a new biochemical marker on the plasmid.

*The Acquisition of Plasmid DNA
Sequences Associated with the
Transformation to Virulence*

Many attempts have been made in the past to demonstrate virulence transfer between strains of *Agrobacterium* using standard methods of mating. These attempts have generally been unsuccessful. Recently, however, Alan Kerr reported successful transfer of virulence in *Agrobacterium* (Kerr, 1969, 1971). His experiments involved a novel system in which recipient strains are inoculated into a growing crown gall tumor that still contains the original inciting bacteria (donor strain). The donor and recipient strains carry appropriate chromosomal genetic markers which permit subsequent reisolation of recipients on selective media. After a period in which both strains grow together in the tumor, virulence transfer occurs and a high percentage (in many cases 50%) of the recipient bacteria reisolated from the tumor have acquired virulence. Details

TABLE 3. Molecular Weights of Plasmids from Pathogenic and Nonpathogenic Strains of *A. tumefaciens* as Determined by Contour Length Measurements Using Electron Microscopy

| Strain | Pathogenicity | Plasmid Molecular Weight |
|--------|---------------|---------------------------|
| 209 | + | $110 \pm 4.6 \times 10^6$ |
| 210 | - | $62 \pm 1.3 \times 10^6$ |
| 226 | - | $110 \pm 3.8 \times 10^6$ |

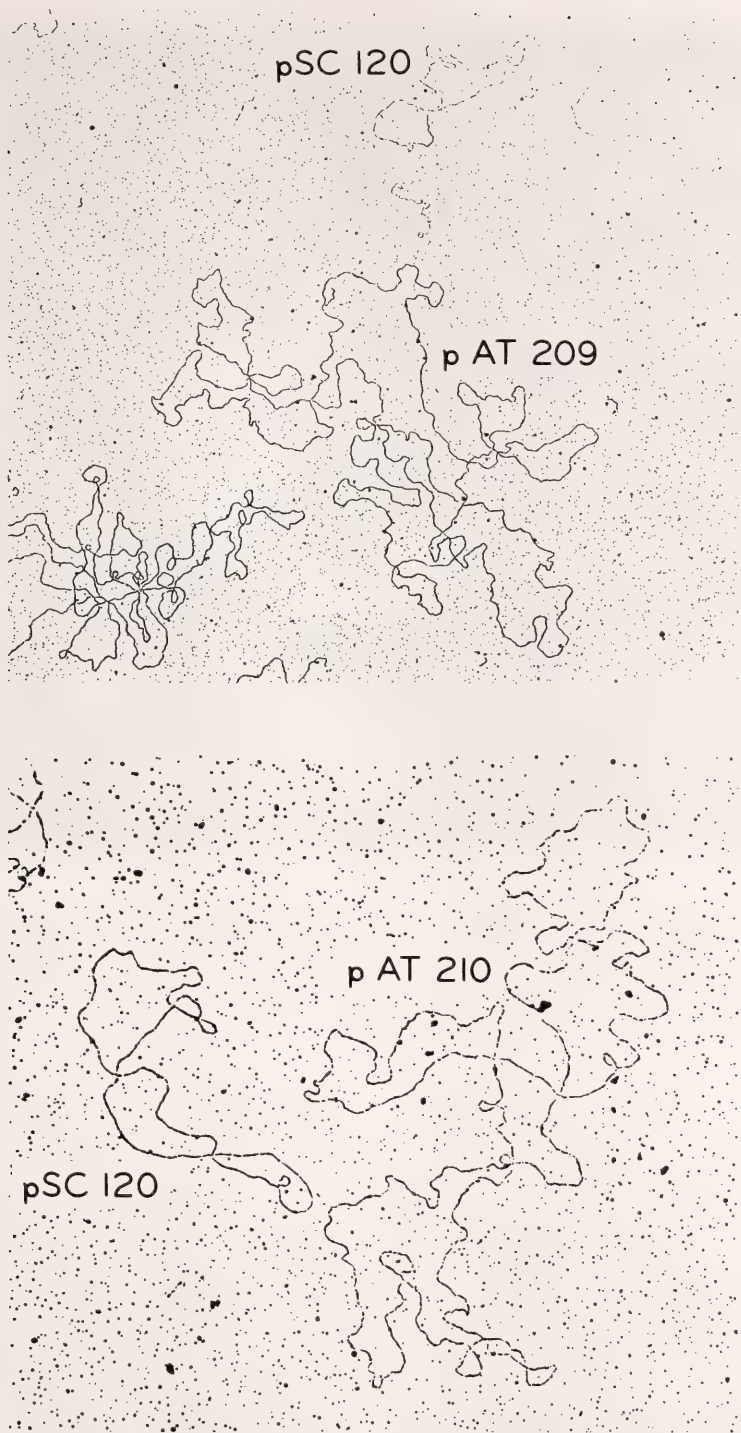


Fig. 6. Molecular weight determination by contour length analysis of *Agrobacterium* plasmids. Top: standard plasmid pSC 120, molecular weight = 18.7×10^6 , with *Agrobacterium* plasmid from strain 209 (pAT 209). Bottom: pSC 120 with nonpathogenic plasmid from strain 210 (pAT 210).

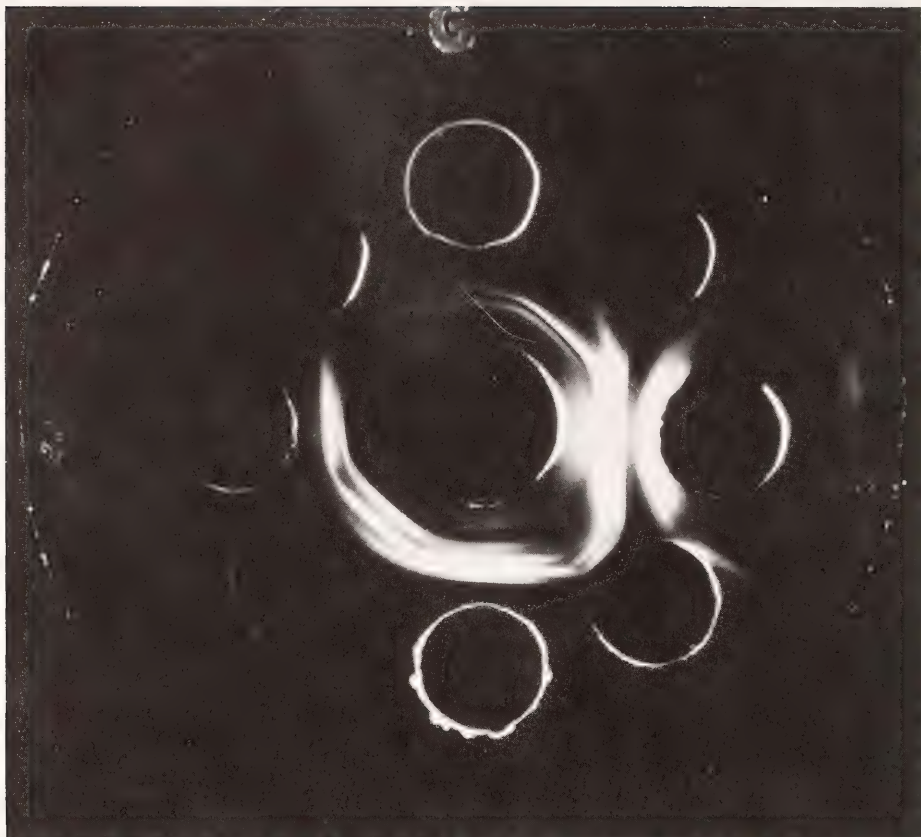


Fig. 7. Serological reaction of antigen preparations from strains 209 and 210 with antisera from strain 209. Center well: antisera to strain 209. Well at three o'clock: antigen from 209. Well at six o'clock: antigen from strain 210. Strain 210 was obtained by culture of strain 209 on high-glycine media and exhibits stable loss of virulence when transferred to nutrient agar. Strain 226, mentioned in text, was obtained by UV irradiation of strain 209. It also exhibits a stable loss of virulence. The strains and serological data were obtained from Dr. J. E. DeVay, University of California, Davis.

of the mechanism by which virulence transfer occurs in this system (commonly called a "Kerr cross") are unknown. However, several groups (Watson *et al.*, 1975; Van Larebeke *et al.*, 1975) have shown that the mechanism involves plasmid transfer from the donor pathogenic strain to the recipient strain. One specific case is the cross between pathogenic strain C-58 and nonpathogenic strain S1005. In this cross, virulence transfer was shown to be associated with the transfer of the C-58 plasmid to the initially plasmid-free recipient. The exconju-

gant contained the C-58 plasmid in an unaltered state, according to DNA-DNA hybridization criteria.

We were interested in studying plasmid transfer in several different crosses to determine if modification of the plasmid could occur during the process. The experiments to be reported were conducted with a set of donor, recipient, and exconjugant strains (K27, K18, and K18A, respectively) obtained from Alan Kerr. In this cross, the plasmid genes for nopaline utilization, agrocin 84 sensitivity, and virulence were transferred from the donor to the

exconjugant strain (Table 4; Roberts and Kerr, 1974).

Our initial experiments produced the unexpected result that both donor and recipient strains (K27 and K18, respectively) contained a plasmid. Therefore, this cross was significantly different from those previously reported in which the recipient strain did not contain a plasmid. The presence of a plasmid in both donor and recipient raised the possibility that both pAT K18 and pAT K27 plasmids would be present in the exconjugant strain K18A. However, closely related plasmids are often incompatible in the same cell (Falkow, 1975), and site-specific recombination of sequences between plasmids has been reported (Kopecko and Cohen, 1975). Thus it was also possible that a recombinational event had occurred and that only a single hybrid plasmid was present in strain K18A. Therefore, an experiment was carried out to distinguish between these two alternatives.

A sensitive method for comparing the DNA sequences of large plasmids is to compare the DNA fragments produced by restriction endonuclease digestion (Hedgepeth *et al.*, 1972). The fragments are separated according to molecular weight by agarose gel electrophoresis, and the pattern of fragments observed is analogous to a "fingerprint" analysis of the DNA sequences of the plasmid, reflecting the distribution of specific nuclease sensi-

tive sites in the molecule. This procedure was carried out for plasmid DNA preparations from strains K27, K18, and K18A, using the restriction endonuclease EcoRI. The patterns of fragments observed are diagramed in Fig. 8. Analysis of Fig. 8 enables one to make the following statements about the nature of the plasmids in these strains:

1. There are very few fragments common to pAT K27 (strain K27) and pAT K18 (Fig. 8, Δ). Therefore, the distribution of restriction endonuclease sites on each plasmid is different, and it may be inferred that these two plasmids differ significantly in their nucleotide sequences.

2. The pattern for the plasmid DNA of strain K18A is not merely the sum of those for pAT K27 and pAT K18. If both pAT K27 and pAT K18 were present in strain K18A, one would expect to find all the bands from each plasmid present in the plasmid fraction of strain K18A. This is clearly not the case, and we conclude that the entire plasmid of strain K18 is not present in strain K18A.

3. All the fragments of pAT K18A correspond in size to fragments present in pAT K27. (Fig. 8). This observation, together with item (2) above suggests that a plasmid from strain K27 was transferred to strain K18, and that the resident plasmid (pAT K18) was eliminated due to its incompatibility with the newly acquired plasmid.

TABLE 4. Genetic Markers on Kerr Cross Strains

| Strain | Plasmid Markers | | | | Chromosomal Markers | |
|------------------|-----------------|------------------|-----------------------------------|---|------------------------|-------------------------------------|
| | Pathogenicity | Plasmid Presence | Nopaline Utilization ¹ | Bacteriocin 84 Sensitivity ² | Growth on Shroth Media | Ketolactose Production ² |
| K27 donor | + | + | + | sensitive | - | - |
| K18 recipient | - | + | - | resistant | + | + |
| K18A exconjugant | + | + | + | sensitive | + | + |

¹Unpublished data.

²Roberts and Kerr, 1974.

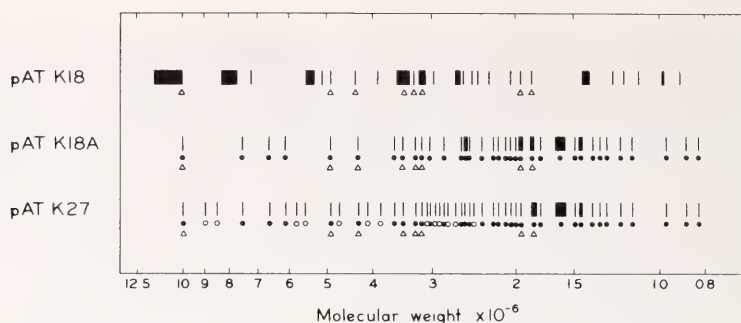


Fig. 8. Diagram representing profiles of DNA fragments obtained by EcoRI digestion of plasmid DNA from strains K18, K18A, and K27. Molecular weight of fragments greater than 3.4×10^6 d was determined from their mobility in 1.0% agarose gels and the molecular weight of fragments less than 3.4×10^6 d was determined from their mobility in 1.5% agarose gels. EcoRI fragments of R6-5 plasmid DNA run simultaneously in each gel were used as molecular weight standards. Solid circles: fragments common to pAT K18A and pAT K27 vir. Triangles: fragments common between pAT K18, pAT K18A and pAT K27 vir. Open circles: fragments present in pAT K27 and not represented in pAT 18A.

4. Plasmid pAT K27 has an additional set of fragments which are not present in pAT K18A (Fig. 8). These results are consistent with the report of Watson *et al.* (1975) in which strain K27 was shown to contain two plasmids. The additional fragments found in pAT K27 and not in pAT K18A can be inferred to represent the second plasmid in strain K27. The common fragments between pAT K27 and pAT K18A must therefore comprise the virulence plasmid which is transferred to strain K18.

These results provide indirect evidence for incompatibility between the virulence plasmid of strain K27 and the cryptic plasmid of strain K18. The stability of plasmid pAT K18 in strain K18 when it is grown in a crown gall tumor has not been directly tested, and it is therefore possible that strain K18 lost its plasmid before acquiring the virulence plasmid from strain K27. However, pAT K18 is stable in strain K18 under all in vitro growth conditions so far tested.

Although it appears that recombination did not occur between plasmids of strains K27 and K18, preliminary experiments indicate that recombinant plasmids may exist in two other, unrelated exconjugant strains. If recombination does occur, further studies of recombinant plasmids may help to identify portions of the plasmid genome re-

quired for virulence, since fragments containing virulence genes would be expected to be conserved in successive crosses.

A major question concerning the mechanism of crown gall tumorigenesis is whether or not the tumor induction process involves the transfer of genetic information from *Agrobacterium* to the plant cell. Specific fragments of DNA associated with the acquisition of virulence in several exconjugant strains would be likely candidates for transfer to the plant cell. The use of these specific fragments as probes in DNA-DNA hybridization experiments would enable one to test this possibility. Although some previous hybridization experiments with plasmid DNA have been unable to detect the presence of plasmid sequences in certain lines of plant tumor cells, a small fraction of the total plasmid genome might easily have been missed (Chilton *et al.*, 1974). On the other hand, evidence for plasmid sequences in a different plant tumor cell line has been obtained by hybridization with whole plasmid DNA (Matthysse, 1976). Experiments using only a selected portion of the plasmid DNA should provide a much more sensitive test and help to resolve the discrepancy between these two sets of results.

References

- Braun, A. C., in *Progress in Experimental Tumor Research: Plant Tumor Research*, Vol. 15, pp. 1-90, S. Karger, New York, 1972.
- Chilton, M. D., T. C. Currier, S. K. Far-
rand, A. J. Bendich, M. P. Gordon,
and E. W. Nester, *Proc. Nat. Acad. Sci. U.S.A.*, 71, 3672-3676, 1974.
- Falkow, S., *Infectious Multiple Drug Resistance*, Pion Ltd., pp. 1-85, 1975.
- Hedgepeth, J., H. M. Goodman, and H. W. Boyer, *Proc. Nat. Acad. Sci. U.S.A.*, 69, 3448-3452, 1972.
- Kerr, A., *Nature*, 223, 1175-1176, 1969.
- Kerr, A., *Phys. Plant Path.*, 1, 241-246, 1971.
- Kopecko, D. J., and S. N. Cohen, *Proc. Nat. Acad. Sci. U.S.A.*, 72, 1373-1377, 1975.
- Lippincott, J. A., and B. B. Lippincott, *Annu. Rev. Microbiol.*, 377-401, 1975.
- Matthysse, A., *J. Gen. Microbiol.*, in press, 1976.
- Roberts, W. P., and A. Kerr, *Phys. Plant Path.*, 4, 81-91, 1974.
- Van Larebeke, N., O. Engler, M. Holsters, S. van den Elsaker, I. Zaenen, R. A. Schilperoort, and J. Schell, *Nature*, 252, 169-170, 1974.
- Van Larebeke, N., Ch. Genetello, J. Schell, R. A. Schilperoort, A. K. Hermans, J. P. Hernalsteens, and M. Van Montagu, *Nature*, 255, 742-743, 1975.
- Watson, B., T. C. Currier, M. P. Gordon, M. D. Chilton, and E. W. Nester, *J. Bacteriol.*, 123, 255-264, 1975.
- Zaenan, I., N. van Larebeke, H. Teuchy, M. van Montagu, and J. Schell, *J. Mol. Biol.*, 85, 109-127, 1974.

BLUE LIGHT-INDUCED ABSORBANCE CHANGES IN MEMBRANE FRACTIONS FROM *Neurospora crassa*

Robert D. Brain and Winslow R. Briggs

The effects of blue light on phototropism, the biological clock, oxygen uptake, and a number of other biological processes have been known for some time (see Briggs, 1976). Only recently, however, has real progress been made in the possible identification of the blue light photoreceptor associated with these effects. Following the initial studies of Poff and Butler (1974) with *Dictyostelium* and *Phycomyces*, work by Muñoz and Butler (1975) implicated the flavin-mediated photoreduction of a *b*-type cytochrome as possibly a central element in the photoreception process in *Neurospora*. Since Muñoz and Butler worked with intact mycelium of *Neurospora*, it seemed appropriate to attempt isolation of a cell fraction that would show the same response.

A carotenoid-free albino mutant of *Neurospora crassa* (albino-timex) was used and treated in the following way: A liquid suspension (100 ml) was made

from a dark-grown five-day-old agar culture and poured into 1000 ml of a liquid medium (2% [v/v] Vogel's solution (1956), 0.5% [w/v] Difco Casamino acids, and 0.5% [w/v] dextrose). Liquid cultures were grown aerobically in the dark on a rotary shaker at 250 rpm for 24 hr at 30°C.

Approximately 40 g of mycelium were harvested by suction filtration, torn into small strips, and immersed in about 55 ml of extraction buffer (250 mM sucrose, 100 mM N-morpholinopropane sulfonic acid, 14 mM 2-mercaptoethanol, 3 mM ethylenediaminetetraacetate, and 0.1 mM MgSO₄, adjusted to pH 7.4 by titration with KOH). The strips of mycelium were broken by vigorous shaking with small glass beads in a mechanical homogenizer, and the homogenate was then centrifuged at 2000, 9000, 20,000, and 50,000 × *g* for 10, 15, 30, and 75 min, respectively, at 4°C. The pellets

are designated 2KP, 9KP, 20KP, and 50KP, and the final supernatant is designated 50KS. The 2KP, containing mostly broken walls and larger cell fragments, was discarded, and the $2000 \times g$ supernatant (2KS) served as a starting point for the assays to determine final yields in the subsequent fractions. The 9, 20, and 50KP's were resuspended in 4, 2, and 1 ml, respectively, in a buffer identical to that used in extraction except without 2-mercaptoethanol, and adjusted to pH 7.0 instead of 7.4. A 5-ml aliquot was kept from the 2KS and 50KS for the assays.

Measurements of light-induced absorbance changes were made with a Perkin-Elmer 365 dual wavelength spectrophotometer in the dual wavelength mode, with the beams set at 410 and 423 nm except during difference spectrum measurements. The readout was thus absorbance at 423 minus that at 410 in most cases. Actinic light was from a tungsten iodide source filtered through a Corning blue filter, 4-96. The intensity was 1.1×10^4 ergs $\text{cm}^{-2} \text{sec}^{-1}$. The assays for various organelle marker enzymes were those

used by Jesaitis *et al.* (1976) except for the monovalent cation-dependent ATPase. This assay was a slight modification of the procedure of Hedman (1964), that was used by Cross and Briggs (this Year Book).

We were unable to measure absorbance during actinic irradiation with our instrumentation and therefore could only look for changes following the end of the actinic exposure. Figure 9 shows the characteristic absorbance change seen after 60 sec of actinic illumination for the 20KP, following resuspension. The kinetics of decay for this signal (at room temperature) are very similar to those reported by Muñoz and Butler (1975), with half-lives of roughly 30 sec. Signal height was next measured as a function of length of actinic irradiation. A measurable signal occurs with as little as 1 sec; 10 sec yields half saturation; and full saturation is achieved by 60 sec. Hence, 60 sec was used in all subsequent assays for relative amount of photo-inducible absorbance change present.

A light-minus-dark difference spectrum for the resuspended 20KP was ob-

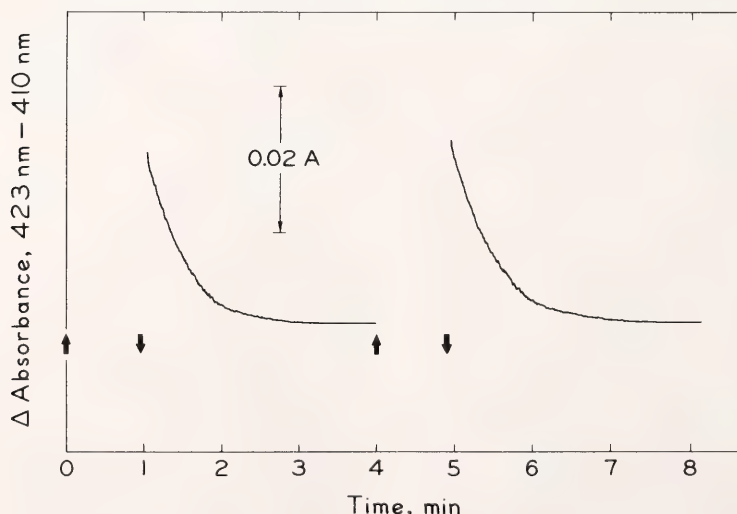


Fig. 9. Blue light-induced absorbance changes in a resuspended $20,000 \times g$ pellet from *Neurospora*. Upward arrow indicates light on, downward arrow, light off.

tained by setting one wavelength at 500 nm and varying the other from one actinic exposure to the next. Light induced a small decrease in absorbance near 410 nm, a sharp increase at 423 nm, and a sharp decrease at 450 nm. There was another small increase near 556 nm. These light-induced changes are very similar to those shown by Muñoz and Butler, and are indeed suggestive of a flavin-mediated reduction of a *b*-type cytochrome, as they proposed. Another important point of similarity between the signals reported here and those studied by Muñoz and Butler involves the intermediate redox state of the system required for actinic light to produce a signal. Muñoz and Butler had to wait with their sample in a cuvette until the normally reduced cytochromes became partially oxidized. In the 20KP preparation described here, the cytochromes are all completely oxidized at the start of an experiment. After a few irradiations during which little or no signal can be seen, the system begins spontaneously to become reduced. After two or three irradiations and about 10 min, it reaches a level of partial reduction, and then remains stable for as much as 8 hr, during which time it yields consistent signals like those in Fig. 9. Addition of dithionite reduces it completely, and a signal can no longer be obtained. Figure 10 shows absorption spectra of a 20KP in its initial oxidized state (A), its partially reduced state in which good signals are obtained (B), and in the presence of dithionite (C). The system will spontaneously go to the partially reduced state without the initial blue light irradiations, but the light treatment hastens the process. In the present case, the preparation goes from fully oxidized to partially reduced; in the Muñoz and Butler case, from completely reduced to partially oxidized; but the net result is the same intermediate redox state at which signals can be obtained.

Table 5 lists the distribution of the marker enzymes among the centrifugal fractions as well as the distribution of

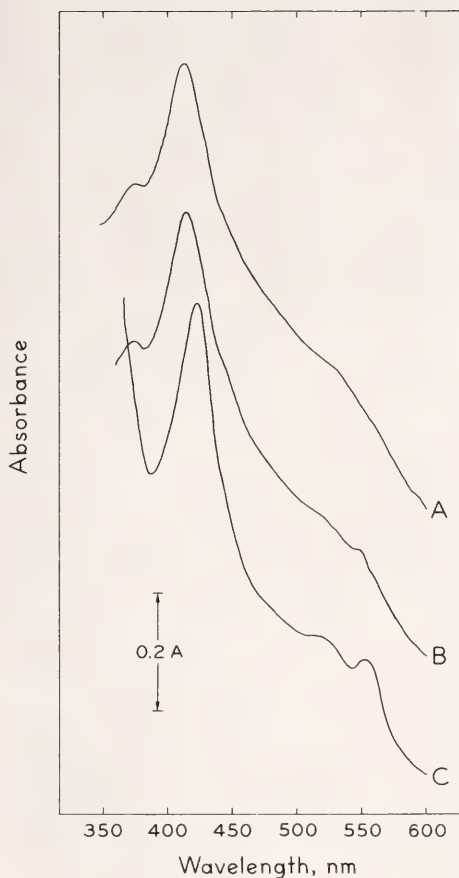


Fig. 10. Absorption spectra of a resuspended 20,000 \times g pellet from *Neurospora* (A) in its fully oxidized state, (B) in a stable partially reduced state during which light-induced cytochrome reduction can be demonstrated, and (C) fully reduced by dithionite. Curves vertically displaced for clarity. Excessive ultraviolet absorption in (C) caused by dithionite.

the potential for a light-induced absorbance change. Neither mitochondria (cytochrome *c* oxidase) nor endoplasmic reticulum (NADH-dependent cytochrome *c* reductase) has a distribution like that of the light-induced absorbance change. However, correspondence is excellent between the distribution of the signal and that of the Na-dependent ATPase. This correspondence could well indicate association of the pigment system with the plasma membrane, though definitive

TABLE 5. Distribution of Marker Enzymes and Light-Inducible Cytochrome in the Various Cell Fractions from *Neurospora crassa* (assays per mg protein)

| Fraction | Protein mg; ml ⁻¹ | Absorbance Change (Relative) | Na ⁺ -Dependent Adenosine Triphosphatase mM PO ₄ × min ⁻¹ × 10 ⁻³ | Cytochrome c Oxidase mM × sec ⁻¹ × 10 ⁻³ | NADH-Dependent Cytochrome c Reductase mM × sec ⁻¹ × 10 ⁻³ |
|----------|---------------------------------|------------------------------------|---|---|---|
| 2KS | 224 | 15.11 | 5.01 | 11.33 | 2.42 |
| 9KP | 185 | 48.96 (38)* | 11.26 (39) | 65.80 (207) | 0 (0) |
| 20KP | 169 | 130.07 (100) | 28.98 (100) | 31.82 (100) | 0.015 (100) |
| 50KP | 228 | 64.01 (49) | 14.41 (50) | 21.47 (67) | 6.380 (4.3 × 10 ⁴) |
| 50KS | 188 | 2.69 | 0.723 | 0.842 | 2.97 |

*Figures in parentheses represent amounts relative to the 20KP, normalized to 100.

evidence is still lacking. Calculations (not shown) indicate that recovery was close to 100% for all the markers and for the potential for a light-induced signal, based on what was initially present in the 2KS, except for the ATPase, which showed a loss of about 20%.

Preliminary studies have been initiated to determine more precisely which cytochromes might be involved in the process described above. The 20KP fraction from a *poky* mutant of *Neurospora* (Fungal Genetics Stock Center #3627-2) appears to give significantly smaller signals than the albino-timex mutant described here. Many studies have examined mitochondrial cytochrome deficiencies in *poky* mutants (Lambowitz and Bonner, 1974; Lambowitz *et al.*, 1972a,b), but there are as yet no studies on extra-mitochondrial cytochrome abnormalities. Preliminary reduced-minus-oxidized difference spectra show *poky* to be deficient in *b*-type cytochromes generally, as expected, but to be noticeably deficient in an NADH-reducible cytochrome in the 20KP and 50KP. Further studies are planned with low temperature and derivative spectra to analyze these deficiencies in detail. Studies are also under way to determine whether the *poky* mutant shows altered photosensitivity, measured either by suppression of expression of the circadian rhythm of conidia-

tion (Sargent and Briggs, 1967; Sargent, Woodward and Briggs, 1966) or by induction of carotenoid synthesis in mycelia grown in liquid culture (De Fabo, Harding and Shropshire, 1976; Zalokar, 1955).

In conclusion, the photoreduction measurements and light-minus-dark difference spectrum reported here for the 20KP are very similar to those reported by Muñoz and Butler for intact *Neurospora* mycelium. In both systems, an intermediate redox state is required for the signals to be obtained. It therefore seems reasonable that the same pigment system is involved in both cases. Hence the signals described by Muñoz and Butler appear to have their origin in a fraction that could be plasma membrane (and is clearly not mitochondria, endoplasmic reticulum, or the soluble fraction). However, it is still premature to state that this system is the photoreceptor complex for the various physiological blue light responses mentioned above. Such a conclusion would require evidence linking the behavior of this fraction to that of the physiological responses in question. The *poky* mutants seem promising objects for obtaining such evidence.

References

Briggs, W. R., in *Light and Plant Development*, H. Smith, ed., Butterworths, England, in press, 1976.

- De Fabo, E. C., R. W. Harding, and W. Shropshire, Jr., *Plant Physiol.*, **57**, 440–445, 1976.
- Hedman, S. H., Ph.D. thesis, Stanford University, 1964.
- Jesaitis, A. J., P. R. Heners, R. Hertel, and W. R. Briggs, *Plant Physiol.*, **58**, in press, 1976.
- Lambowitz, A. M., and W. D. Bonner, Jr., *J. Biol. Chem.*, **249**, 2886–2890, 1974.
- Lambowitz, A. M., C. W. Slayman, C. L. Slayman, and W. D. Bonner, Jr., *J. Biol. Chem.*, **247**, 1536–1545, 1972a.
- Lambowitz, A. M., E. W. Smith, and C. W. Slayman, *J. Biol. Chem.*, **247**, 4850–4858, 1972b.
- Muñoz, V., and W. L. Butler, *Plant Physiol.*, **55**, 421–426, 1975.
- Poff, K. L., and W. L. Butler, *Nature*, **248**, 799–801, 1974.
- Sargent, M. L., and W. R. Briggs, *Plant Physiol.*, **42**, 1504–1510, 1967.
- Sargent, M. L., W. R. Briggs, and D. O. Woodward, *Plant Physiol.*, **41**, 1343–1349, 1966.
- Vogel, H. J., *Microb. Genet. Bull.*, **13**, 42–43, 1956.
- Zalokar, M., *Arch. Biochem. Biophys.*, **56**, 318–325, 1955.

BLUE LIGHT-INDUCED ABSORBANCE CHANGES IN MEMBRANE FRACTIONS FROM *Zea mays*

Winslow R. Briggs, Jack Freeberg, and Charles V. Weiss

There is now a substantial amount of literature concerning light-induced absorbance changes in various fungi, and a detailed action spectrum for such a change in *Neurospora* mycelium is very similar to the action spectra for a host of blue light-induced physiological responses both in fungi and in higher plants (Muñoz and Butler, 1975). If such absorbance changes reflect a light reaction of the physiologically important blue light photoreceptor, one would expect to find similar changes in higher plants as well. Widell and Björn (1976) have indeed found light-induced absorbance changes in dark-grown wheat coleoptiles, but the light-minus-dark difference spectrum did not resemble that reported for the various fungi (see Briggs, 1976), and the action spectrum for the absorbance changes suggested that the cytochromes themselves were serving as photoreceptors, perhaps as in the *Dictyostelium* system described by Poff and Butler (1974). After eliminating spectral changes caused by blue-induced phytochrome photo-transformation and protochlorophyll photoconversion, Poff (personal com-

munication) also saw complex absorbance changes in corn coleoptiles. These changes did not resemble those described for the several fungi either. Thus, two studies with intact tissue of higher plant tissue failed to reveal a light-sensitive system with properties like those of *Neurospora* mycelium, and the evidence to date would suggest that the *Neurospora* system is not ubiquitous.

Brain and Briggs (this Year Book) report on the isolation of a membrane fraction from *Neurospora* which yields the characteristic light-induced absorbance changes described for *Neurospora* mycelium by Muñoz and Butler (1975). This report describes similar absorbance changes in a comparable membrane fraction isolated from corn coleoptiles.

Corn seeds (*Zea mays*, L. hybrid WF9 × Beo 38, Bear Hybrid Corn Co., Decatur, Ill.) were soaked overnight in running tap water and then grown in darkness in a constant temperature room at 25°C, 90% relative humidity for four days. The seedlings received 2 hr red light every night but the last for suppression of mesocotyl growth and

stimulation of coleoptile elongation. Coleoptiles were harvested directly into ice under dim green light as described by Hertel and Flory (1968).

Corn coleoptiles were harvested, homogenized, and the homogenate subjected to differential centrifugation as described elsewhere (*Year Book* 74, pp. 807–809). The pellet obtained following the $21,000 \times g$ centrifugation (21KP) was resuspended and used for the irradiation studies. For each 6 g of tissue homogenized, the final resuspension volume was 1 ml. This preparation is comparable to the *Neurospora* 20KP described by Brain and Briggs. The instrumentation and techniques for measuring absorbance changes on irradiation with blue light were also those of Brain and Briggs.

Figure 11 shows light-induced absorbance changes detected when absorbance at 410 nm is subtracted from that at 423 nm. The signal is clearly similar to that described by Brain and Briggs for the *Neurospora* fractions, with a half-life of about 30 sec. Under identical conditions of sample geometry and actinic light intensity,

the dose-response curve for the corn signal is also much like that for *Neurospora* preparations. Between 10 and 15 sec of the actinic blue light (1.1×10^4 ergs $\text{cm}^{-2} \text{sec}^{-1}$) yielded half-saturation, with 1 min close to complete saturation.

The corn preparations gave smaller signals than those from *Neurospora*, and were far less stable. Whereas from the fungal membranes one could obtain consistent signals repeatedly over a period of hours, the corn fractions rapidly lost the capacity to produce signals (sometimes within 15 min). For this reason, the only fraction examined was the 21KP.

Since it was not possible to obtain extensive data from any one preparation, a complete light-minus-dark difference spectrum could not be made. However, partial difference spectra were obtained on three different occasions. On each of these occasions, a maximum near 425 nm was found, with minima near 410, and on two occasions, 450 nm. Thus the light-minus-dark difference spectrum for corn appears similar to that described for intact *Neuro-*

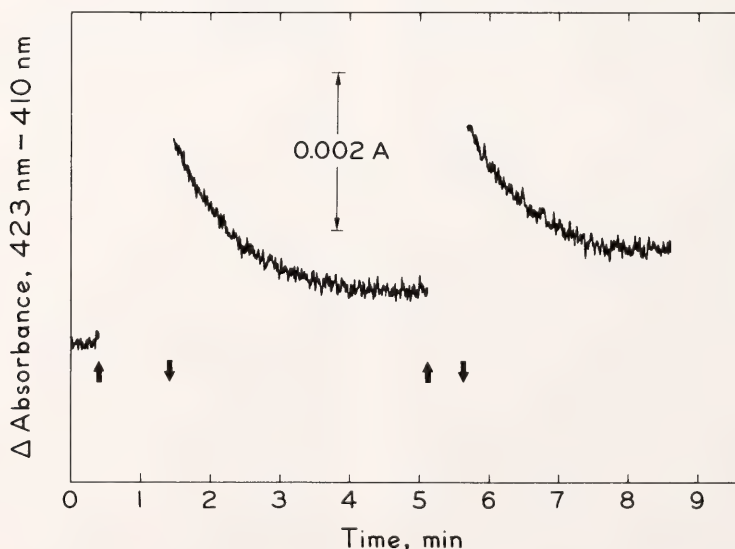


Fig. 11. Blue light-induced absorbance changes in a resuspended $21,000 \times g$ pellet from corn. Upward arrow indicates light on; downward arrow, light off. A 30-sec and a one-min radiation are shown.

spora mycelium (Muñoz and Butler, 1975) or *Neurospora* membrane preparations.

The corn preparations resembled those from *Neurospora* in another way. Signals could not be seen unless the system was poised with the cytochromes at an intermediate redox state. At the beginning of an experiment, the cytochromes were normally almost fully oxidized. Irradiation yielded either no signal or a slight decrease in the absorbancy difference between 423 nm and 410 nm. Following a series of 1-min irradiations, however, the cytochromes became partially reduced, as with *Neurospora*, and signals such as those shown in Fig. 11 could be observed. More fully reduced preparations no longer yielded signals, or showed light-induced oxidation of the cytochromes.

In conclusion, corn 21KP and *Neurospora* 20KP membrane preparations show very similar responses to blue light. The dose-response curves for the light-induced absorbance changes, the dark decay kinetics, and the light-minus-dark difference spectra re-

semble each other; and both preparations require an intermediate redox state to show the light responses. These similarities between the fungal and the higher plant systems support the hypothesis that they may indeed represent the physiologically active blue light photoreceptor. Future work will involve efforts to stabilize the corn preparations and determine the distribution of the potential for light-inducible absorbance change in the various fractions.

References

- Briggs, W. R., in *Light and Plant Development*, H. Smith, ed., Butterworths, England, in press, 1976.
 Hertel, R., and R. Flory, *Planta*, 82, 123-144, 1968.
 Muñoz, V., and W. L. Butler, *Plant Physiol.*, 55, 421-426, 1975.
 Poff, K. L., and W. L. Butler, *Photochem. Photobiol.*, 20, 241-244, 1974.
 Widell, S., and L. O. Björn, *Physiol. Plantarum*, 36, 305-309, 1976.

AN EVALUATION OF MARKERS FOR PLASMA MEMBRANES IN MEMBRANE FRACTIONS FROM *Zea mays*

John W. Cross and Winslow R. Briggs

The plasma membranes of plant cells are rapidly becoming the subject of increased research attention. This activity is partly because of the generally increasing interest of biologists in cell surfaces *per se*, and partly because these membranes are now suggested to be sites of biochemical activities that are uniquely vegetable, including blue light photoreception (Jesaitis *et al.*, 1976; Brain and Briggs, this Year Book) phytochrome action (Haupt, 1973; Yu, 1975), and auxin activity (Hertel *et al.*, 1972). In each of these cases the isolated membrane fractions involved have been identified as plasma membrane by means of enzymatic "markers" or from "specifi-

cally" stained electron micrographs. Of course this identification is valid only insofar as the "markers" are authentic. Unfortunately, the specificity of each of the various plasma membrane markers is subject to question.

Table 6 lists these "markers," and the basis for using each of them to identify the plasma membrane. They divide roughly into two groups, those expected on theoretical grounds to be associated with the cell surface, and those empirically selected (see Table 6). As can be seen, the "markers" in Class 1 are verified either by good correlation of their presence with PTA staining or with naphthylphthalamic acid (NPA) binding. NPA binding itself was

TABLE 6. "Markers" Used for Plasma Membranes of Higher Plants

| Marker | Grounds for Validity |
|--|--|
| Class 1 (chosen on theoretical grounds) | |
| Glucan synthetase, Mg^{++} independent | Thought to be involved in cell wall synthesis; correlation with NPA-binding activity in membrane fractions (VanDerWoude <i>et al.</i> , 1974). |
| ATPase (cation-dependent) | Thought to be involved in monovalent cation uptake by correlation of its kinetics with the kinetics of ion transport in roots (Leonard and Hodges, 1973); correlation with PTA staining (Hodges <i>et al.</i> , 1972). |
| Naphthylphthalamic acid (NPA) binding | An inhibitor of auxin transport; correlation with PTA staining (Hertel <i>et al.</i> , 1972). |
| Steroid content elevated | Analogy with animal cells, which have most steroids in the plasma membrane; correlation with NPA binding (Hartmann <i>et al.</i> , 1975). |
| Class 2 (empirically selected) | |
| PTA staining for electron microscopy (PTA = chromic-perchloris-phosphotungstic acid) | Thin sections of whole tissues or cells stain mainly at the plasma membrane (Roland, <i>et al.</i> , 1972). |

Note: Several well-known markers for the plasma membranes of animal cells are absent from plant cells (i.e., 5'-nucleotidase, Na^+ - K^+ -stimulated ATPase, adenyl cyclase, sphingomyelin, characteristic hexagonal protein complexes (Roland *et al.*, 1972).

verified by correlation with PTA staining (Hertel *et al.*, 1972), so the validity of each of these "markers" depends ultimately on the validity of this stain.

PTA staining was originally developed as a stain for plant plasma membrane by Roland *et al.* (1972) and subsequently improved (Leonard and VanDerWoude, 1976). It acts by oxidation and binding of complex membrane carbohydrates (Roland *et al.*, 1972). In thin sections of whole tissues, the stain definitely shows preference for the plasma membrane. However, its use as a selective stain with isolated membrane fractions seems more questionable. Since each membrane fraction is sectioned and stained separately, it is difficult to interpret light staining in one fraction and heavy staining in another, especially since the process of membrane fractionation itself might alter the intensity of staining. Is the observed variation in stain intensity caused by differences in staining or photography, or by actual specific differences in the binding of stain? Membrane fractions that are sedimented to

about 38% sucrose consistently stain most heavily, so the variation does not appear random (Hodges *et al.*, 1972; Leonard and VanDerWoude, 1976). However, considerable stain can be found in other fractions. Since the validity of all the other markers currently depends upon that of this stain it would seem best for caution to prevail.

Because of this situation we are attempting to verify the reliability of some of these "markers" for the plasma membrane and to develop new ones. Our initial work in this area centered on the monovalent cation-dependent ATPase. This enzyme activity has been correlated with the plasma membrane not only by coincidence with PTA staining of sucrose gradient fractions but by the similarity of Eadie-Hofstee plots of its kinetics with the plots for monovalent cation uptake in whole roots (Leonard and Hodges, 1973). This analysis assumes that only one such ATPase enzyme exists, and that it is present only in the plasma membrane.

We harvested the coleoptiles of dark-grown corn seedlings and

homogenized them at 0° in the light. The homogenates were then fractionated by differential sedimentation and by isopycnic sucrose density gradients. The highest specific activities of K⁺-stimulated ATPase were found in the 21,000 × *g* and 48,000 × *g* pellets (21KP and 48KP; (Table 7). This distribution was clearly distinct from basal ATPase (mostly in the 48,000 × *g* supernatant) and cytochrome *c* oxidase (mostly in the 9000 × *g* pellet (9KP). It is also distinct from the microsomal marker, NADH-cytochrome *c* oxidoreductase, which generally is enriched in the 48KP pellet (Jesaitis *et al.*, 1976; and data not shown). On isopycnic gradients (not shown) the K⁺-stimulated ATPase formed two distinct peaks of activity. The lighter was at 30% sucrose, distinctly denser than the microsomal marker, NADH-cytochrome *c* oxidoreductase (26% sucrose). This membrane fraction does not correspond to the density of any of the other plasma membrane "marker" enzymes. This peak was similar in density to the peak of Mg⁺⁺-dependent glucan synthetase activity (glucan synthetase

I, a golgi membrane marker [Ray *et al.*, 1969]), although the glucan synthetase has not as yet been tested on the same gradient with the ATPase.

The second peak occurred at higher density (38% sucrose), just above the peak of cytochrome *c* oxidase activity (40% sucrose), but not identical to it. It did not correspond to the peak of NPA binding activity, which was closely correlated with the cytochrome *c* oxidase peak. Thus it appears that NPA binding and K⁺-stimulated ATPase do not reside exclusively in common membrane fractions and therefore cannot represent markers for the same membrane. In addition, the NPA binding activity becomes equilibrated in close correspondence to cytochrome *c* oxidase and may in fact be bound to mitochondria rather than plasma membranes, although this possibility remains to be proven.

The two distinct bands for K⁺-stimulated ATPase could reflect the observation that plant cells contain two separate internal compartments of K⁺, believed to be protoplasm and vac-

TABLE 7. Basal and K⁺-Stimulated ATPase Activity from Maize Coleoptiles: Differential Sedimentation*

| Sample | ATPase Activity | | Cytochrome <i>c</i> Oxidase $\Delta A_{550} \text{ min}^{-1} \text{ mg protein}^{-1}$ |
|--|--|--|--|
| | nm P _i min ⁻¹ Basal | mg protein ⁻¹ K ⁺ -stimulated | |
| Crude homogenate | 206 | 8 | 0.94 |
| 500 × <i>g</i> _{max} 15 min pellet | 32 | 30 | 0.87 |
| 9 × 10 ³ × <i>g</i> _{max} 15 min pellet | 80 | 44 | 1.22 |
| 21 × 10 ³ × <i>g</i> _{max} 15 min pellet | 108 | 81 | 0.69 |
| 48 × 10 ³ × <i>g</i> _{max} 60 min pellet | 136 | 67 | 0.36 |
| 48 × 10 ³ × <i>g</i> _{max} supernatant | 261 | 9 | 206 |

*Coleoptiles (10 g) were chopped with a razor and ground in a mortar in 0.25 *M* sucrose, 50 *mM* tris-acetate (pH 8.0), 1 *mM* EDTA, 0.1 *mM* MgCl₂ and 14 *mM* 2-mercaptoethanol (2 vol buffer/g of tissue), filtered through 2 layers of cheese cloth and centrifuged as described in the Sorvall SS34 rotor. Operations were at 0–5°C. ATPase was assayed (Hodges *et al.*, 1972) in a 1 ml reaction mix with 30 *mM* Tris-MES (pH 6.0), 1.5 *mM* MgCl₂, 3 *mM* ATP·Tris (pH 6.0), and 0.050 ml of the washed membrane fraction resuspended in the grinding buffer at 0.5–2 mg protein per ml. Tests began by addition of ATP after 10 min preincubation and were continued for 15 min, when 0.4 ml 20% trichloroacetic acid was added. P_i in the centrifuged supernatant was determined by the method of Hedman (1964). Basal ATPase activity was corrected for ATP hydrolysis in the absence of enzyme, and K⁺-stimulated activity represents the activity at 50 *mM* KCl in the reaction minus basal activity. Cytochrome *c* oxidase was assayed by the method of Jesaitis *et al.* (1976).

uole, at different K^+ potentials (Davis and Higinbotham, 1976). The lighter K^+ -stimulated ATPase could reside in the tonoplast membrane (for which we do not as yet have a marker), and the denser activity in the plasma membrane, although other possibilities exist.

In order to resolve some of the problems mentioned above, we are attempting to label the plasma membrane of intact cells prior to homogenization and fractionation. Our initial experiments have made use of Fluorescamine (FLURAM), which reacts rapidly with primary amines to yield a fluorescent product. This reaction occurs with a $t_{1/2}$ of milliseconds (Udenfriend *et al.*, 1972), and excess reagent spontaneously hydrolyzes to nonfluorescent products within a few seconds. Since this rapid hydrolysis should prevent significant labeling within the cells, fluorescamine should be an ideal cell surface label. Indeed, it has recently been reported that fluorescamine can label surface-specific peptides of chick fibroblasts without labeling internal peptides (Hawkes *et al.*, 1976).

To test the utility of this reagent as a surface label, 2-mm segments of corn coleoptiles were briefly exposed to fluorescamine and then homogenized and fractionated by differential sedimentation (Table 8). The distribution of fluorescence in the fractions was quite similar to that reported above for K^+ -stimulated ATPase, with the greatest label bound to the 21KP and 145KP. In another experiment (not shown) it was found that homogenizing the tissue *before* adding fluorescamine resulted in a tenfold increase in the labeling of soluble amines with only a twofold increase in the labeling of membranes. From these results it appears that fluorescamine does primarily label the surface of intact cells unless the permeability barriers of the cell are first broken. The reasonable correspondence of fluorescamine labeling with the presence of K^+ -stimulated ATPase suggests that at least one of the ATPases may be present on the plasma membrane. Further experiments are now in progress to optimize the specificity of this label and to verify that it reacts with the cell surface.

TABLE 8. Fluorescamine Labeling of Maize Coleoptile Segments: Differential Sedimentation*

| Sample | Relative Fluorescence (per mg protein) | K^+ -Stimulated ATPase nmoles P_i min ⁻¹ mg protein ⁻¹ |
|---|---|---|
| Crude homogenate | 1.0 (0.33) [†] | 178 (0.46) |
| 500 × g_{max} 15 min pellet | 2.2 (0.73) | 0 (0) |
| 9 × 10 ³ × g_{max} 15 min pellet | 1.5 (0.50) | 164 (0.42) |
| 21 × 10 ³ × g_{max} 15 min pellet | 3.0 (1.00) | 390 (1.00) |
| 145 × 10 ³ × g_{max} 30 min pellet | 2.9 (0.97) | 364 (0.93) |
| 145 × 10 ³ × g_{max} supernatant | 0.7 (0.23) | 151 (0.39) |

*Dark-grown corn coleoptiles were collected on ice and weighed into two groups of 10 g each. These were chopped into 2-mm segments, and washed three times at room temperature in 10 mM sodium phosphate-pyrophosphate buffer, pH 7. The first two washes were accompanied by vacuum infiltration (5 min each). Washed segments were rinsed and suspended in 30 ml labeling buffer (0.25 M sucrose, 1 mM EDTA, 25 mM $Na_2P_2O_7$, brought to pH 8.5 with 25 mM NaH_2PO_4). The samples received either 0.30 ml of fluorescamine freshly dissolved in pure acetonitrile (10 mg/ml), or 0.30 ml of acetonitrile alone. After 1 min at 20° the solutions were aspirated and the samples rinsed three times in the same buffer at 0°, then rinsed and resuspended in 30 ml of grinding buffer (see Table 7). Coleoptile segments were then homogenized and fractionated as described in the legend to Table 7. To assay fluorescence, a 0.10 ml aliquot was removed from each fraction, diluted in 2.0 ml SDS (0.25%, w/v), and centrifuged at 1000 × g , 5 min. Fluorescence at 475 nm was excited at 390 nm. Half-band widths were 10 and 8 nm for emission and excitation, respectively. The fluorescence of each sample was corrected for protein content and for the auto-fluorescence of the corresponding unlabeled sample (which was at least tenfold lower than the labeled sample). K^+ -stimulated ATPase activity was assayed as described in the legend to Table 7.

[†]Figures in brackets represent amounts relative to the 21KP, normalized to 1.00.

References

- Davis, R. F., and N. Higinbotham, *Plant Physiol.*, 57, 129–136, 1976.
- Hartmann, M. A., G. Normand, and P. Benveniste, *Plant Sci. Lett.*, 5, 287–292, 1975.
- Haupt, W., *Bio. Sci.*, 23, 289–296, 1973.
- Hawkes, S. P., T. D. Meehan, and M. J. Bissell, *Biochem. Biophys. Res. Commun.*, 68, 1226–1233, 1976.
- Hedman, S. H., Ph.D. Thesis, Stanford University, 1964.
- Hertel, R., K.-S. Thompson, and V. E. A. Russo, *Planta*, 107, 325–340, 1972.
- Hodges, T. K., R. T. Leonard, C. E. Bracker, and T. W. Keenan, *Proc. Nat. Acad. Sci. U.S.A.*, 69, 3307–3311, 1972.
- Jesaitis, A. J., P. R. Heners, R. Hertel, and W. R. Briggs, *Plant Physiol.*, 58, in press, 1976.
- Leonard, R. T., and T. K. Hodges, *Plant Physiol.*, 52, 6–12, 1973.
- Leonard, R. T., and W. J. VanDerWoude, *Plant Physiol.*, 57, 105–114, 1976.
- Ray, P. M., T. L. Shining, and M. M. Ray, *Proc. Nat. Acad. Sci. U.S.A.*, 64, 605–612, 1969.
- Roland, J. C., C. A. Lembi, and D. J. Morre, *Stain Tech.*, 47, 195–200, 1972.
- Udenfriend, S., S. Stein, P. Böhlen, W. Dairman, W. Leimgruber, and M. Weigele, *Science*, 178, 871–872, 1972.
- VanDerWoude, W. J., C. A. Lembi, D. J. Morre, J. I. Kindinger, and L. Ordin, *Plant Physiol.*, 54, 333–340, 1974.
- Yu, R., *J. Exp. Bot.*, 26, 808–822, 1975.

A MULTI-SAMPLE AUTOMATIC MONITORING DEVICE FOR THE CIRCADIAN RHYTHM OF TRANSMITTANCE CHANGE IN *Ulva*

S. J. Britz

As discussed last year (*Year Book* 74, p. 794), a circadian rhythm of chloroplast movement in the green alga *Ulva lactuca* L. causes a differential sieve effect and results in a corresponding rhythm of visible light transmittance change (Britz and Briggs, 1976). The vegetative thallus of *Ulva* forms a flat sheet two cell layers thick, with each cell containing one large, cup-shaped chloroplast. In daily light-dark (LD) cycles the chloroplasts cover the outer cell face (face position) during most of the day, and the transmittance is low. Starting late in the day and continuing through most of the night, the chloroplasts move slowly down the side walls, expose the central portion of the cell (profile position) and greatly increase the transmittance (up to 200%). Movement back to face position begins before the end of the dark period and continues more rapidly with the onset of light. Rhythmic chloroplast movement continues during periods of con-

stant darkness (DD) or constant light (LL).

The relation between chloroplast position and thallus transmittance has been studied in detail by direct techniques and computer modeling (Britz, manuscript in preparation). The results of these studies show that within certain bounds, the correlation between chloroplast position and transmittance is excellent. For a given orientation change, the transmittance change depends mainly on the absorbance; the higher the absorbance, the greater the transmittance change and the better the correlation with chloroplast position. The correlation between position and transmittance is also better for rhythmic movement in DD than in LD; orientation during the light period appears to be accompanied by chloroplast shape changes. At wavelengths at which absorbance is low, the transmittance changes not only become much smaller but are in-

fluenced more by changes in other factors such as light scattering and reflectance. These features of chloroplast movement can be matched by a computer model (a preliminary version of which has been described; *Year Book 74*, p. 794) indicating the movement-related transmittance changes can be described quantitatively in terms of known and measurable parameters.

For various reasons (ease, objectivity, integration of the result over many cells), transmittance measurements are useful for the study of chloroplast orientation. Long-term, rhythmic transmittance changes in a single *Ulva* thallus have been monitored both by an automatic, continuously recording microphotometer and flow-through cuvette combination and by non-flow-through cuvettes measured manually (Britz *et al.*, 1976). The transmittance changes were large, highly regular, and persistent for many days. In both cases sampling noise was minimized because the thalli were kept in a constant geometry with respect to the measuring beam. Moreover, thalli were measured without disturbing the rhythm, something not possible with conventional techniques.

The following paper describes the design, construction, and operation of a practical system to monitor rhythmic transmittance changes automatically for multiple samples. This system is useful for the study of any type of slow transmittance change, such as that accompanying chloroplast movement.

DESIGN AND CONSTRUCTION

The basic unit of the monitor is the sample holder. It must be convenient in terms of size, manipulation, and amount of tissue and medium required (the latter, an important consideration in inhibitor experiments). While it is not necessary that the sample holder reproduce a "natural" environment, it must offer physiological conditions for long-term measurement. Moreover, the design should be simple and flexible.

Thus, it was decided to make the sample holder essentially a small dish in which the *Ulva* thallus would be held horizontally and for which the measuring beam would be vertical. This design is suitable for *in situ* light microscopy (particularly with an inverted microscope) or spectrophotometry. Experiments parallel to those in the monitor can be conducted on the physiological and biochemical properties of other samples maintained in small Petri dishes, a comparable environment.

The sample holder and dimensions are depicted in Fig. 12. The holder is constructed with a clear Plexiglas cylinder melded to a circular black Plexiglas base. The base has a large central hole over which a cover slip masked with black photographic tape is paraf-

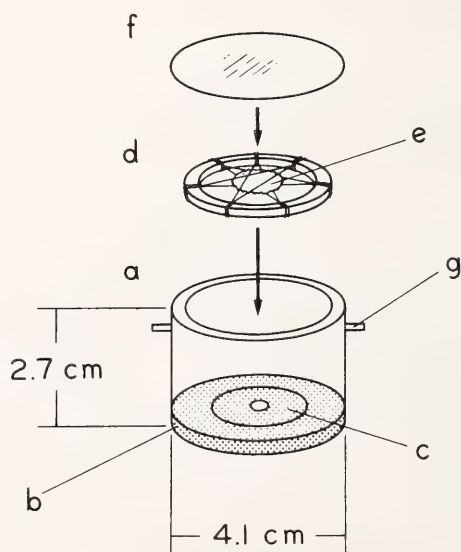


Fig. 12. Perspective view of the disassembled sample holder: a, clear Plexiglas cylinder (3 mm thick); b, black Plexiglas base (3 mm thick) with a 20-mm diameter central hole (not shown); c, 22-mm circular cover slip paraffined over the central hole and masked on the underside with black photographic tape with a window 4 mm in diameter; d, nylon filament-Plexiglas support ring (2 mm thick, 3 mm wide); e, 11.5-mm diameter *Ulva* thallus disc fastened between the crossed nylon filaments; f, clear plastic cover; g, orientation pin. The raised support ring fits snugly against the base, holding the *Ulva* about 1 mm off the bottom.

fined in place. The *Ulva* thallus can then be positioned flush against the cover slip by dialysis membrane or nylon mesh. Alternatively, as shown in Fig. 12, the thallus can be supported above the cover slip by a nylon filament and Plexiglas ring combination. The tape mask has a 4-mm diameter window such that when the *Ulva* thallus is positioned over the window only light passing through the sample is transmitted by the holder. In this configuration the sample should be illuminated by a measuring beam coming from above, thereby exposing the entire thallus and eliminating any possible effects of differential light treatment. An advantage of the cover slip is that the size of the window may be varied. The holder is covered by a clear polystyrene top and there is a small notch cut in the top of the cylinder to allow for gas exchange. There are no problems with evaporation or condensation on the clear cover, at least under the operating conditions described below. Pins extending from the holder anchor it reproducibly in the monitor.

The choice of lighting conditions for the monitor poses the next problem; obviously light must be used for transmittance measurements. Since the transmittance changes depend strongly on the absorbance, the optimal wavelength to monitor the rhythm should be about 436 nm, the absorbance maximum. However, there are several problems which urge caution. The period of circadian rhythms depends on the quality and quantity of ambient lighting. Both blue light and red light shift the phase of the *Ulva* rhythm (Britz, unpublished data), and continuous exposure to blue light (and presumably red) can decrease the free-running period (Britz *et al.*, 1976). For photosynthetically active organisms, light may supply energy and affect the amplitude of the rhythm. In addition, light may modify chloroplast shape, thus influencing transmittance (Britz, manuscript in preparation). Measurements made in higher intensity light run the risk of error due to bubble

formation in the measuring beam. Thus, the monitor should operate at light intensities approaching effective DD with the potential to operate under LL.

The requirement for minimal light (less than $1 \text{ erg cm}^{-2} \text{ sec}^{-1}$ continuous exposure of which from 5% to 20% would reach the photodetector; Britz *et al.*, 1976) eliminates at present the possibility of continuously illuminating an array of samples, each with its own inexpensive solid-state photodetector. A more sensitive light-detecting system is required, such as a single photomultiplier past which samples are moved sequentially. For this purpose a device like a fraction collector seems ideal. However, the transmittance signal is quite sensitive to sample position. When many samples must be measured, precise repositioning becomes a problem. Therefore, it was decided to have the monitor consist of 30 sample holders positioned along the rim of a constantly revolving wheel (one revolution per hour) such that the samples are swept through a dim, vertical measuring beam with the transmitted light measured by a photomultiplier beneath. The output from the photomultiplier, amplified and recorded on a strip chart recorder, constitutes a single channel of data on which the records of 30 samples appear in sequence every hour. This number of samples and measurements is reasonable and sufficient for most purposes. A schematic representation of the monitoring device is shown in Fig. 13.

The wheel consists of an aluminum frame and an outer circle of plywood with holes for the sample holders. Next to these holes are raised supports for the orientation pins. A small electric motor drives the wheel, which is connected to the drive shaft by cork pressure plates that allow optional manual rotation.

The entire apparatus (sample holders, wheel, light source, and photomultiplier) is enclosed in a temperature-controlled chamber, with the associated power supplies,

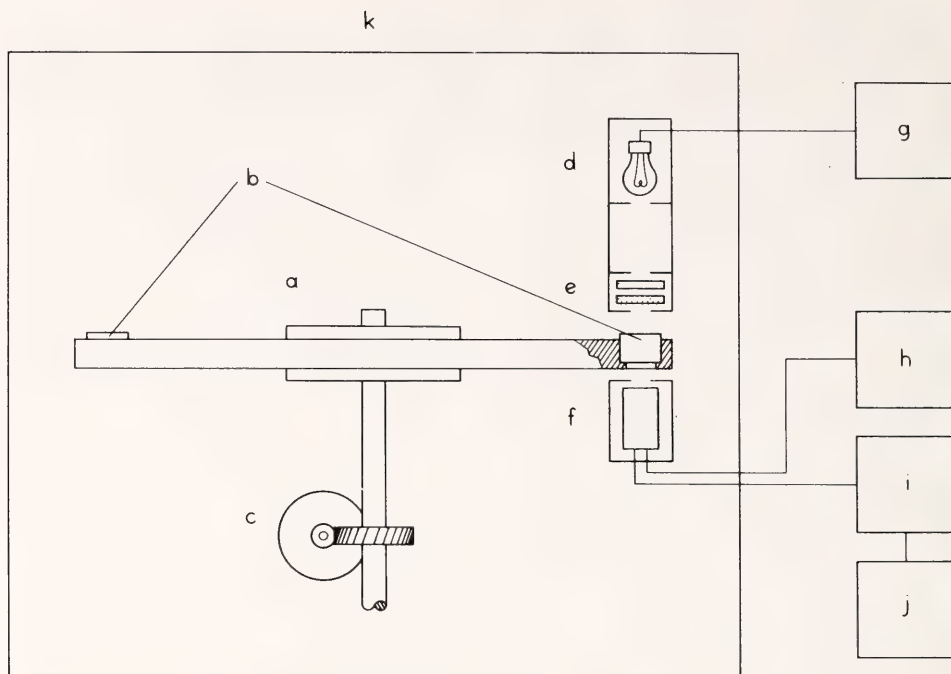


Fig. 13. Schematic representation of the automatic monitoring device: *a*, revolving (1 rph) sample holder wheel; *b*, sample holder, one of 30 positioned along rim of wheel; *c*, electric motor and worm gear to drive wheel; *d*, measuring beam lamp; *e*, interference and neutral density filters; *f*, end-on photomultiplier tube; *g*, measuring beam lamp regulated power supply, Dressen-Barnes Model 61-55; *h*, photomultiplier high-voltage power supply, Fluke Model 412B; *i*, amplifier, Keithley 150B Microvolt-ammeter with 100 mV output; *j*, strip chart recorder, E&K; *k*, constant temperature chamber, Percival Model E-54B. Additional details are discussed in text.

amplifier, and strip chart recorder located outside in a dimly lit room. The walls of the constant temperature chamber are black, and the measuring beam is shielded so that stray light is not a problem. Temperature control is necessary, not only for the samples but also for the lamp and photomultiplier whose characteristics are temperature sensitive.

The monitor could be modified to measure transmittance changes in LL by illuminating the surface with a homogeneous field of constant intensity and inserting suitable color, neutral density, and/or interference filters before and/or after the sample. With more rapid rotation of the wheel the monitor could be used for faster transmittance changes, and with modification of the LL measuring beam system (see Pfau *et al.*, 1974) the monitor

would be suitable for studies on light-induced chloroplast movement.

OPERATION

Ulva for these experiments was cultured in an aerated, enriched seawater nutrient medium on LD 16:8 (light intensity 150 fc from one 40-W cool-white fluorescent lamp) at 20°C. Except for aeration (by an aquarium pump) and illumination, the general growth and experimental conditions are as described elsewhere (Britz and Briggs, 1976; Britz *et al.*, 1976). After inoculation, the thalli go through a rapid phase of growth for two to three weeks, followed by several weeks of much slower growth. After five weeks the thalli are usually too wrinkled to be suitable for photometric measurements.

For a given experiment, a single large *Ulva* thallus is cut into discs (11.5 mm in diameter) with a cork borer; the discs are mounted in the sample holders, and the holders are filled with "aged" nutrient medium (i.e., the same medium in which the original large thallus had been cultured, refiltered in the meantime). The samples are then adapted for up to three days in normal LD cycles and loaded into the monitor at the end of a light period. Additional details of sample preparation are discussed below.

When monitored at constant temperature, circadian rhythms typically have periods that are almost temperature independent. However, rhythms are sensitive to changes in temperature, and even diurnal fluctuations as small as 1°C might suffice to synchronize the period of a rhythm to a 24-hr cycle. Thus, all experiments were at $20 \pm 0.25^\circ\text{C}$, the same temperature as culture. The temperature of the monitor chamber was recorded continuously (Partlow RFT, dry bulb thermometer). Within the limits of the temperature sensing system, no diurnal fluctuations were observed.

The monitor measuring beam wavelength is 436 nm isolated with an interference filter (Baird-Atomic; half-band width, 11 nm; blocked past 800 nm, and IR opaque as measured with a Corning 7-56 IR-transmitting filter and a thermopile) from a 6-V tungsten microscope illumination lamp operated at 4.5 V by a regulated power supply (stable to 0.01%). Neutral density filters are inserted in the beam to give a light intensity on the sample holders of approximately $0.1 \text{ erg cm}^{-2} \text{ sec}^{-1}$. Intermediate diaphragms delimit the beam to about 15 mm which, centered over the samples, is large enough to illuminate the thallus disc completely. The end-on photomultiplier tube, an RCA 6217 run at about 500 V, is mounted underneath the wheel.

Shown in Fig. 14 are typical strip chart recordings of the photomultiplier output for 1-hr periods corresponding

to times when the chloroplasts occupy profile (DD_5 to DD_6) and face ($\text{DD}_{14.75}$ to $\text{DD}_{15.75}$) positions. The results show a dark current base line when the measuring beam is occluded by the wheel with spikes of photocurrent occurring at 2-min intervals as the samples pass in and out of the measuring beam. Each sample is in the beam for about 1 min every hr. Spike height is linearly proportional to transmittance. The monitor is always run with one of the 30 samples as a reference. Note that while the reference remains constant, the sample transmittances decrease considerably in face position (Fig. 14).

The reference is used to assess instrument stability and to correct for drift, if desired. It contains a filter that gives it approximately the same transmittance as *Ulva* thalli with profile position chloroplasts. The absolute transmittance of the reference relative to sample holders alone is about 17.5%. With the above-mentioned instrument parameters, the reference gives an absolute photocurrent of about 7 nA. When monitoring constantly the reference photocurrent or the dark current, there is almost no short-term noise, and long-term drift over several days is less than 1%. Thus, the chamber presumably is keeping a constant temperature, and the lamp and instrumentation are stable. However, under normal operating conditions when the wheel is moving samples in and out of the measuring beam, there is substantial variability in the reference, short-term noise of a few tenths of a percent superimposed on a long-term drift of as much as 2%–3%. There are sometimes rapid shifts in the reference over a range of 1%–3%, but there may also be periods of relative stability.

Spike heights are measured directly by ruler at hourly or two-hourly intervals and sorted out by sample for analysis. The average values for a group of five samples all treated in the same way are plotted in Fig. 15 along with the individual values for the two most extreme samples in that group.

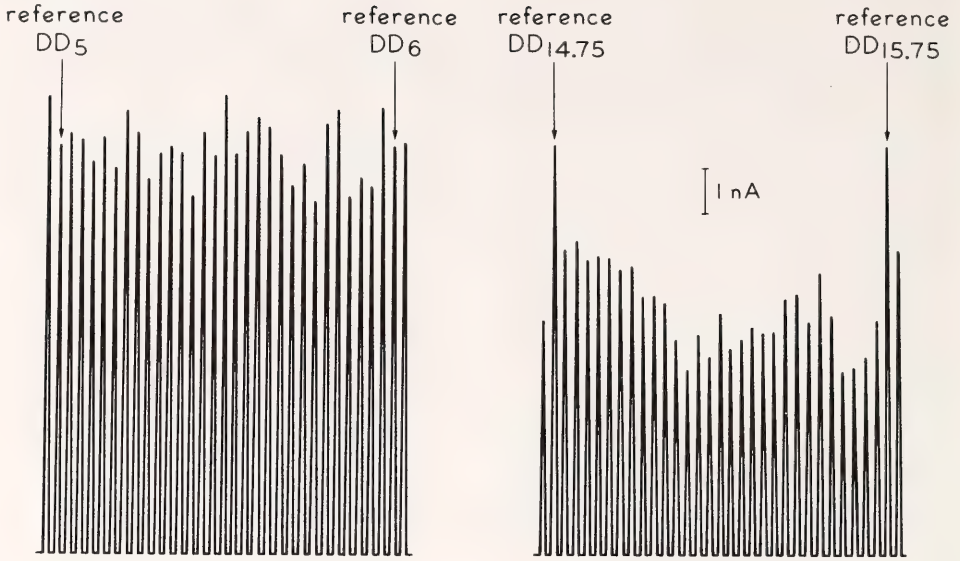


Fig. 14. Typical strip chart recordings of photomultiplier output at times when chloroplasts occupy profile (DD_5 to DD_6) and face ($DD_{14.75}$ to $DD_{15.75}$) positions. The bar represents approximately 1 nA. The spike height (nA) is proportional to transmittance. Note the change in sample transmittance with respect to the reference.

Also shown are the hourly values for the reference.

The individual samples present a regular and even pattern of transmittance change. Thus, one does not depend on sample averaging to relieve hidden noise. While there are obvious differences in the magnitude of transmittance and the amplitude of change, the patterns are remarkably similar to one another and to their average. Such repeatability within an experiment is typical and, on the basis of 16 monitor runs, the reproducibility between different experiments is almost as good.

Considering many experiments and expressing the transmittances as a percentage of the first transmittance maximum, one can state the value for the first transmittance minimum is usually 50%–60%, the second maximum is 80%–110%, and the second minimum is about 70%–80%. These results compare well with transmittance values obtained in parallel experiments that were correlated to direct microscope observation of chloroplast position (Britz, manuscript in prepara-

tion). For the first two maxima the chloroplasts are approximately in full profile position, and the highest transmittance values are measured. For the first transmittance minimum the chloroplasts are in full face position, and the lowest transmittance value is measured. At subsequent minima and maxima the chloroplasts fail to reach the extreme positions, and intermediate transmittance values are measured. The rhythm generally damps out with the chloroplasts in an intermediate-to-face position. With the monitor, rhythmic transmittance changes can be detected for at least six cycles, although the last cycles frequently become distorted by noise, at least part of which may be related to reference instability.

There is also excellent repeatability within one experiment for the times of transmittance maxima. The maxima for the five samples from Fig. 15 have been calculated by the parabola slope technique (Britz *et al.*, 1976) and are presented in Table 9. The phase alignment between different samples also

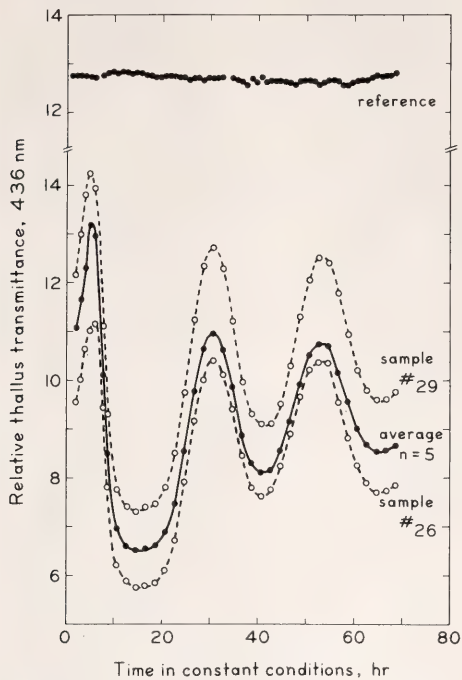


Fig. 15. Reproducibility of the *Ulva* transmittance change rhythm. The average values for five samples treated in the same way and the individual values for the two most extreme samples are plotted together. Also shown are the reference values. The ordinate is the spike height in cm.

shows that the averaging of samples does not “smear out” the peaks.

The free-running period of the *Ulva* transmittance change rhythm is usually observed to be about 24 hr, a value comparable to previous determinations (Britz *et al.*, 1976). Because the value is

so close to 24 hr, it is impossible to rule out diurnal synchronizing factors such as small temperature fluctuations. However, a major role for such factors is unlikely because it is possible to alter experimentally the length of the free-running period as well as to reset stably the phase of the rhythm.

While the above-mentioned sample differences in transmittance magnitude and amplitude of change are not important for rhythm studies per se, they present serious problems for quantitative application of the transmittance change measurements to chloroplast movement studies. However, the direct dependence of amplitude on the magnitude of transmittance suggests normalization as an empirical correction. This observation is surprising, since spectrophotometry studies determined the amplitude of transmittance change to be inversely proportional to the minimum (i.e., face position) transmittance (Britz, manuscript in preparation). The spectrophotometry studies were done with special attention to keeping the thalli flattened, but in the monitor sample holders the thalli may be more or less wrinkled. Because the sieve effect due to chloroplast orientation is very sensitive to the angle of incidence of the measuring beam, the wrinkling factor will decrease the maximum transmittance more than the minimum, thereby decreasing the amplitude of the change. In fact, maximum transmit-

TABLE 9. Phase Coincidence of *Ulva* Transmittance Change Rhythm Maxima*

| Sample | Maxima (hr after start of DD) | | |
|--------|-------------------------------|--------------|--------------|
| | First | Second | Third |
| 25 | 5.37 ± 0.51 | 30.72 ± 0.14 | 53.54 ± 0.12 |
| 26 | 5.5† | 30.96 ± 0.13 | 52.55 ± 0.28 |
| 27 | 4.99 ± 0.29 | 30.99 ± 0.14 | 53.33 ± 0.16 |
| 28 | 4.76 ± 0.36 | 30.8 ± 0.15 | 52.89 ± 0.16 |
| 29 | 5.27 ± 0.28 | 30.8 ± 0.17 | 53.28 ± 0.15 |

*The values are the zero slope times in hours ± 95% confidence limits of the estimate. The larger errors for the first maxima result from taking fewer points (5 vs. 7) over a shorter period of time (5 hr vs. 12 hr) than for the second and third maxima.

†This value is estimated because the fifth point is higher than the fourth (Fig. 15), which causes aberrant behavior of the parabola slope method.

tance values are less than expected. There is also a fair amount of variability, probably caused by the wrinkling.

The effects of normalization are shown in Fig. 16 where the average of the raw data from Fig. 15 plus standard errors of the mean are depicted along with the average of the same data after normalization to 1.0 at the estimated transmittance value for the first maximum. Normalization has reduced the standard errors to 25%–50% that of the raw data when expressed in terms of the transmittance change. Thus, the data within one experimental treatment can be made more compatible, and the data between different treatments can be made more comparable.

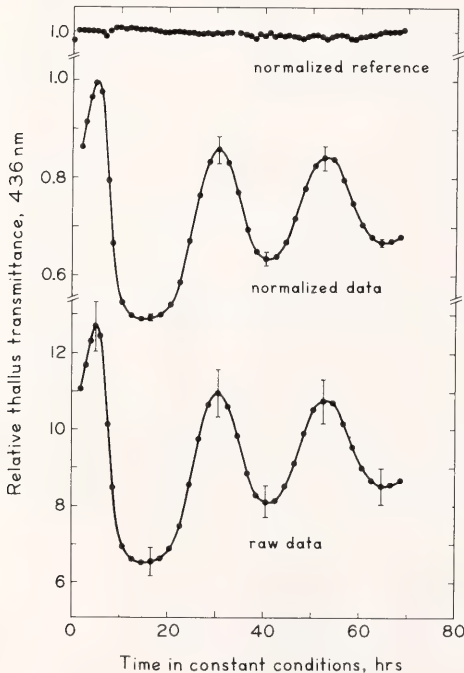


Fig. 16. Normalizing the *Ulva* transmittance change rhythm values. The upper curve shows the average values of five samples after each sample has been normalized to the estimated transmittance value of the first maximum. The lower curve shows the average values of the raw data (spike height in cm) expressed on a scale normalized to give the same amplitude as the upper cover. The bars represent one standard error of the mean. The data is the same as that presented in Fig. 15.

With this background, a brief survey was made to ascertain reasonable sample preparation methods for reproducible operation of the monitor. The first concern was the method of fastening *Ulva* in the sample holder. As mentioned above, samples could be held flush against the cover slip or supported slightly above the surface. Contact of the thallus with nutrient medium may be critical in terms of free-running period, amplitude, and damping characteristics (Britz *et al.*, 1976).

In the present study it has been observed for flush-mounted thalli that bottom cells not exposed to medium are about twice as large as top cells after a typical experimental protocol of three days' adaptation in LD cycles and six days in the monitor. The bottom cells are apparently inhibited from dividing but not from enlarging. This effect was not observed in samples mounted directly before the start of monitoring (i.e., without LD adaptation in cuvettes) and may therefore depend on events during adaptation. It is not known whether there is a differential movement rhythm between top and bottom cells, although the transmittance rhythm curves appeared "normal" (i.e., no peak splitting or broadening of the peaks was observed). The flush-mounted samples had rhythms with similar amplitude and damping characteristics but somewhat longer free-running periods than samples in the raised mounts (24 vs. 23 hr based on one trial with three samples for each treatment). No top–bottom cell size differential has been observed in samples adapted in support rings.

The raised support mode offers advantages for the removal of oxygen bubbles that form in bright light and become trapped under the thallus. However, thalli grow under these conditions, and with the raised support mode they can become wrinkled. Thus, it is necessary to rearrange the samples once during adaptation. The increased distance of the sample from the cover slip obviates the use of inverted

microscopy and requires a larger thallus disc to ensure that none of the measuring beam leaks past. The agreement between monitor studies and parallel spectrophotometric studies indicates this increased distance does not introduce complications caused by light scattering.

The amount of nutrient medium in the sample holder is important in terms of volume-to-surface ratio (gas exchange relies on diffusion) and volume-to-thallus area ratio. The smallest thallus disc that can be used reliably with the support ring is 11.5 mm in diameter, and the cuvette can conveniently hold up to 10 ml. This combination provides a volume-to-thallus area ratio about twice that in the growth flask. The use of either 7.5 or 10 ml of medium made no difference in the results.

Since the length of adaptation in the sample holders can affect the sample, this factor was also tested. Adaptation of one day or less consistently gave irregular rhythms with drastically skewed baselines, nonmonotonic damping patterns, and periods greater than 25 hr. However, no difference appeared between samples adapted 2½ and 3½ days.

In earlier work, *Ulva* from the "slowly growing" phase of culture was used, as it gave the longest-lasting rhythms (Britz and Briggs, 1976). The monitor was therefore used to compare the rhythm patterns of samples from rapidly growing and slowly growing phases of culture. The "younger" thalli were similar through three to four days of monitoring. Then in about 50% of the cases (out of 14 trials) the transmittance change rhythms appeared to become uncoupled from the clock and began to drift around in varying patterns. Control samples continued to give normal patterns. No systematic differences in the rhythms have been detected for *Ulva* from various times during the slowly growing phase of culture. Also, for a three-week-old culture it did not appear to matter from where in the thallus sample discs were cut.

The most perplexing matter has been that of pH control. Because of contamination problems the culture medium is unbuffered. During several weeks of growth under LD the pH can therefore rise to 9.0 or 9.5, conditions under which *Ulva* can still actively photosynthesize. During adaptation the medium in the sample holders becomes stabilized around 8.5 in the daytime and drops a few tenths of a pH unit at night. During constant darkness in the monitor the pH drops to about 8.0. Since certain studies require pH control, the effect on the rhythm of buffered medium was tested.

Five mM Tris buffer did not stabilize the pH except near 8.0 and, in any case, appeared to have no effect. Ten mM Tris had some distinct effects independent of pH (tested were pH 8.1 and 8.8 which bracketed the pH of the unbuffered controls); these included lengthening of the free-running period and some initial inhibition of the transmittance change. Ten mM HEPES had only a slight effect on the period (also lengthening it, apparently independently of the pH at 8.1 and 8.6) and no effect on the initial amplitude. The rhythm under both Tris and HEPES appeared to damp more rapidly and was noisier by the fifth cycle than the unbuffered controls; the Tris-treated samples were worse. The actual transmittance for the pH 8.1 samples under both Tris and HEPES was considerably lower than for the higher-pH buffered samples or the unbuffered controls. It was not clear whether this feature was caused by the chloroplasts being more in face position or, for example, by increased pigment.

On the basis of the above discussed results, a routine protocol was selected. Thallus discs 11.5 mm in diameter are cut from *Ulva* in the slowly growing phase, mounted in holders with raised support rings, filled with 9–10 ml of unbuffered culture medium per sample, and then allowed to adapt for 2½ days in LD cycles before loading in the monitor. With this protocol, samples mounted in the wheel and shielded

from the measuring beam for the first 72 hr of monitoring (DD_0 to DD_{72}) had rhythms from DD_{72} to DD_{114} identical in terms of amplitude and phase with those of the continuously monitored controls. The effects of the measuring beam are therefore negligible and the monitor may be assumed to offer conditions approaching DD.

DISCUSSION

The results of the present study show the *Ulva* transmittance change rhythm to be not only large and regular but also remarkably precise, quantitative, and reproducible, provided that certain methods of sample preparation and data handling are employed. For example, adaptation in sample holders seems to enhance reproducibility and may have been a factor in an earlier study where samples were not adapted and where substantial variability in rhythm patterns between samples was observed (Britz *et al.*, 1976).

It was not intended here to characterize different sample preparation methods exhaustively or to optimize monitoring conditions. Certainly, many details remain unresolved, such

as the role of pH control, temperature, and prior culture conditions. Nonetheless, a sufficient basis has been established to realize the advantages of multiple sample monitoring and to employ rhythmic *Ulva* transmittance changes as an experimental system for chloroplast movement and circadian rhythm studies.

ACKNOWLEDGMENTS

The author thanks Drs. J. Pfau, W. Nultsch, C. S. French, and W. R. Briggs for helpful discussions leading to the design of the monitoring device, and Mr. R. Hart for technical expertise in transforming these designs into reality.

References

- Britz, S. J., *Carnegie Inst. Wash. Year Book* 74, pp. 794–803, 1975.
- Britz, S. J., and W. R. Briggs, *Plant Physiol.*, 58, 22–27, 1976.
- Britz, S. J., J. Pfau, W. Nultsch, and W. R. Briggs, *Plant Physiol.*, 58, 17–21, 1976.
- Pfau, J., G. Throm, and W. Nultsch, *Z. Pflanzenphysiol.*, 71, 242–260, 1974.

TWO APPLICATIONS OF A MULTI-SAMPLE AUTOMATIC MONITOR FOR RHYTHMIC TRANSMITTANCE CHANGES IN *Ulva*

S. J. Britz

The completion of an automatic monitoring device for rhythmic changes in transmittance in *Ulva* offers expanded possibilities to study the underlying chloroplast movement, from the standpoints of the motility mechanism and the controlling circadian rhythm. This paper presents the results of two experiments that exemplify the quantitative application of the monitor in such studies.

Inhibitors have been applied to examine the mechanism of chloroplast movement. Experiments with the monitor have repeated and expanded upon preliminary work with conventional transmittance measuring tech-

niques (Britz, 1975). Several features of the monitor have aided in the experiments. The ability to measure the same sample in the same position repeatedly increases the accuracy. The ability to gather data at hourly intervals and to continue measurements for at least three to four days facilitates the determination of small effects and effects that do not become apparent until after the first cycle has passed. Moreover, it is easier to distinguish possible action on the clock from inhibition of movement mechanism.

Table 10 shows the effects of two common inhibitors of cellular movement, colchicine and cytochalasin B, on

TABLE 10. Cytochalasin B Reversal of Colchicine-Inhibited Rhythmic *Ulva* Chloroplast Movement*

| Treatment and Number of Samples (n) | Movement in the Direction from Profile to Face, Relative Thallus Transmittance Change | | |
|--|---|---------------|---------------|
| | First | Second | Third |
| Control (n = 4) | 0.437 ± 0.028 | 0.286 ± 0.036 | 0.185 ± 0.033 |
| 52 μM Cytochalasin B (n = 4) | 0.461 ± 0.014 | 0.260 ± 0.010 | 0.183 ± 0.044 |
| .1 mM colchicine (n = 4) | 0.421 ± 0.017 | 0.064 ± 0.022 | 0.024 ± 0.016 |
| 52 μM cytochalasin B + 1 mM colchicine (n = 3) | 0.385 ± 0.054 | 0.274 ± 0.018 | 0.192 ± 0.016 |

*Presented are the first three successive transitions in the direction from profile to face. Intervening face to profile movement is not shown. "First" refers to the movement from the first transmittance maximum to the first minimum in DD. Control exhibits normal damping. The extent of movement is measured by reference-corrected and normalized relative thallus transmittance changes ± 2 × S.E. Note that values are amplitudes and not absolute transmittances. All treatments were given starting at DD₆, immediately following the first transmittance maximum and point of normalization. Concentrated solutions of the drugs were added to nutrient medium, partially removed from the sample holders (cytochalasin B formed a flocculent upon addition and required a minute or two to dissolve), and then redistributed, to yield the above final concentrations. These treatments do not seem to disrupt greatly either the amplitude or phase characteristics of the rhythm. All treatments are 0.5% (v/v) dimethylsulfoxide (DMSO) which is used as a carrier for the cytochalasin B. DMSO by itself does have an effect upon both the rhythm and movement.

chloroplast movement in *Ulva*. Colchicine is a presumptive inhibitor of microtubule-related phenomena (Weisenberg *et al.*, 1968), and cytochalasin B is a presumptive inhibitor of microfilament-related phenomena (Wessells *et al.*, 1971). Microfilaments and microtubules are major candidates for the contractile, movement-generating forces with cells (Hepler and Palevitz, 1974). Both colchicine and cytochalasin B have side effects which limit their application as diagnostic tools for microtubules or microfilaments. However, the attempt here has been to dissect various aspects of the movement through the differential sensitivity of the two phases (face-to-profile and profile-to-face) to these drugs.

The data in Table 10 are amplitudes and therefore do not show the relative thallus transmittance relationships between treatments. Thus, Table 10 does not present a complete view of the action of these inhibitors. Nonetheless, it is clear that colchicine dramatically

inhibits the extent of movement after the passage of one cycle, while cytochalasin B alone has little or no effect. However, if both cytochalasin B and colchicine are added at the same time, the colchicine effect fails to develop. Cytochalasin B has in a sense reversed the action of colchicine.

The present experiment and others indicate that chloroplast movement involves the action of two different and opposing mechanisms (possibly microtubules vs. microfilaments) and that actual rhythmic movement may result from changes in the balance between these two systems.

Light-induced phase shifting experiments have also been undertaken with the monitoring device. Preliminary results are shown in Table 11. A 1-min light pulse was given at DD₆, the first transmittance maximum and, as previously determined, the time of maximum sensitivity to phase advances. The times of subsequent transmittance maxima were determined with the parabola slope tech-

TABLE 11. Light-Induced Phase Shifting of the *Ulva* Transmittance Change Rhythm*

| Sample | Maxima (hr after start of DD) | | |
|---|-------------------------------|------------------|------------------|
| | Second | Third | Fourth |
| 4 | 26.52 \pm 0.24 | 49.56 \pm 0.13 | 73.47 \pm 0.22 |
| 5 | 26.72 \pm 0.16 | 49.81 \pm 0.11 | 73.59 \pm 0.16 |
| 6 | 30.38 \pm 0.15 | 53.77 \pm 0.14 | 77.49 \pm 0.21 |
| 7 | 30.72 \pm 0.10 | 54.43 \pm 0.09 | 78.76 \pm 0.18 |
| 8 | 30.57 \pm 0.16 | 54.32 \pm 0.06 | 78.04 \pm 0.17 |
| average phase shift (hr) $\pm 2 \times$ S.E. | 3.94 \pm 0.16 | 4.49 \pm 0.28 | 4.57 \pm 0.47 |

*Samples 4 and 5 were given 1 min of white light (67 kerg cm⁻² sec⁻¹ from a 500-W tungsten projection lamp filtered through 3 cm of 1.4% CuSO₄, IR-opaque as judged by a Corning 7-56 IR-transmitting filter and a thermopile) at time DD₆. Samples 6, 7, and 8 received no treatment. Times of relative transmittance maxima and 95% confidence limits are calculated by the parabola slope technique (Britz *et al.*, 1976).

nique. The 1-min light treatment has resulted in a steady-state, 4 1/2-hr phase advance within two cycles. Dose-response characteristics have not yet been determined, but such a treatment is probably many times beyond saturation.

Four aspects of the analysis deserve emphasis. First, the parabola slope technique gives a very accurate estimate for the times of the maxima. Second, the behavior of the samples is very reproducible. Third, based on the first two points, it is possible to estimate the magnitude of the shift with great accuracy. Fourth, the treatment came to equilibrium quickly (i.e., minimal transient behavior). As a result it should be possible to get multiple estimates of the shift within one experiment.

The mechanics of measuring shifts is clearly well established. The ability to produce a shift with as little as one minute of light indicates that *Ulva* is considerably more sensitive to such treatments than other photosynthetic organisms (Cummings and Wagner,

1968). Since a shorter light exposure is less likely to influence processes other than the rhythm, *Ulva* should be an attractive organism for further phase shifting studies.

References

- Britz, S. J., *Carnegie Inst. Wash. Year Book* 74, pp. 803-805, 1975.
- Britz, S. J., J. Pfau, W. Nultsch, and W. R. Briggs, *Plant Physiol.*, 58, 17-21, 1976.
- Cummings, B. G., and E. Wagner, *Annu. Rev. Plant Physiol.*, 19, 381-416, 1968.
- Hepler, P. K., and B. A. Palevitz, *Annu. Rev. Plant Physiol.*, 25, 309-362, 1974.
- Weisenberg, R. C., G. G. Borisy, and E. Taylor, *Biochemistry*, 7, 4466-4479, 1968.
- Wessells, N. K., D. S. Spooner, J. F. Ash, M. O. Bradley, M. A. Ludueña, E. L. Taylor, J. T. Wrenn, and K. M. Yamada, *Science*, 171, 135-143, 1971.

MEASUREMENTS OF AUXIN BINDING TO SOLUBILIZED
RECEPTOR SITES OF CORN SEEDLING TISSUE*Ulrike Dohrmann¹ and Peter M. Ray²*

Kinetics and properties of membrane-associated binding sites for auxins have been studied with an *in vitro* system of homogenized and purified membrane preparations from corn coleoptiles; the physiochemical interaction between ligand and target unit was demonstrated by the pelletable binding of radioactive-labeled auxin (mostly ¹⁴C-naphthaleneacetic acid = NAA) to membrane vesicles, which are formed during extraction (Hertel *et al.*, 1972; Ray *et al.*, in preparation, 1976).

The binding can be considered specific, since it is a saturable, reversible process and is in agreement with the physiological characteristics of auxin action: Analogs compete according to their affinity in growth and transport tests; further, binding is mainly seen with hormone-sensitive tissues (Ray *et al.*, in preparation, 1976). Graphical analysis of the data indicates a single class of binding sites with a $K_{1/2}$ of $407 \times 10^{-7} M$ as being responsible for the specifically bound radioactivity; total binding is about 10% if a concentration of labeled NAA below the $K_{1/2}$ is mixed with the particles, whereas 6% is bound specifically. The receptor is expected to be a protein, but in its function may be dependent upon lipids: Pronase digestion, for example, only results in a significant loss of binding if it is preceded by an incubation with phospholipase C (Ray *et al.*, in preparation, 1976).

Binding studies on fractionated, subcellular membranes showed significant quantitative and certain qualitative differences of auxin binding properties within the three investigated classes of ER, golgi, and plasmamembrane vesicles (Ray *et al.*, in preparation, 1976; Dohrmann, 1975). In an isopycnicly centrifuged, linear sucrose density gradient, a sharp peak of specifically bound ¹⁴C-NAA is seen at 25% sucrose,

coinciding with the ER-marker enzyme NADH-cytochrome *c* reductase, while a minor amount of binding occurs at densities higher than 30% sucrose; these fractions should contain mainly golgi and plasmamembrane vesicles, as suggested by the simultaneously measured activity of the markers β -1,4- and β -1,3-glucansynthetase and ³H-naphthylphthalamic acid binding. By changing the binding assay conditions it has been possible selectively to demonstrate specific binding characteristics for each of these membrane types.

In order to get further information about the nature of the receptor site(s), we are presently attempting to isolate and identify the molecular binding component. The binding pattern of density-separated vesicles raises the question, whether there are chemically and kinetically different receptors present in those membranes or whether the sites may be basically similar but somewhat modified, for instance as a result of membrane flow sequences. Also, we hope to obtain data that will explain the function of the ligand-receptor complex.

Isolation and purification steps after membrane disruption have to be monitored by assaying for capacity to bind auxin, using a method other than the previously employed centrifugation assay, which is not applicable to a soluble receptor. Several possible approaches have been tried:

(a) Equilibrium dialysis did not turn out to be satisfactory; in the sedimentation assay, bound and unbound ligand (about 90%) are separated to a maximal extent, whereas in equilibrium dialysis the concentration of free

¹Carnegie Department of Plant Biology Fellow and Stanford University, Stanford, California.

²Stanford University, Stanford, California.

labeled auxin creates a very large background of radioactivity in contrast to the small amount of bound ligand, which therefore cannot be detected reliably.

(b) Ultrafiltration also is not an appropriate method to measure binding to solubilized receptors in the corn membrane system.

(c) A third possible method was to reduce the background of unbound radioactivity by absorption of free NAA; in this case the limiting factor will be the timing of dissociation of the ligand-receptor complex. However, exposure of ^{14}C -NAA-containing receptor suspensions (either unsolubilized or solubilized with Triton X-100) to Dowex-1 or charcoal, for instance, for only a few minutes resulted in a virtually complete removal of radioactivity; therefore, either the bound NAA dissociated completely from the receptor or the receptor itself was absorbed—in either event the assay failed.

Finally a gel filtration method was designed which yielded a successful assay for the NAA-binding activity of solubilized membrane components. This type of method has been used with animal tissues to demonstrate both ligand-protein (Hummel and Dreyer, 1962; Fairclough and Fruton, 1966; Henderson and Wang, 1972) and ligand-lipid (Jennings and Salomon, 1976) interactions. In the column chromatography binding test with corn coleoptile tissue, Sephadex G25 is used in a pasteur pipette with a bed volume from 0.5–1 ml. All steps of the experiment are done at 0° – 4°C . The column is equilibrated with the standard assay buffer (250 mM sucrose, 10 mM Na-citrate, 5 mM MgSO_4 , pH 5.5) to which 1% Triton X-100 and 5×10^{-8} – 10^{-7} M ^{14}C -NAA was added (these concentrations of radioactive auxin are below the affinity measured with the sedimentation test and therefore should not saturate all binding sites). Washed membrane pellets from 4-day-old homogenized corn seedling shoots are resuspended in the equilibration medium without detergent at a concen-

tration of 15–30 g fresh weight per ml (1 g fresh weight contains about 1 mg membrane protein). Aliquots of this suspension are assayed for binding conventionally by centrifugation at $133,000 \times g \times 20$ min. The remaining homogenate is incubated with 1% Triton X-100 for 30 min on ice; then membrane structures that remain unsolubilized are pelleted for 60 min at $133,000 \times g$. Since not more than 10% of the original binding activity is recovered in the small pellet obtained after this step, at least 90% of auxin binding receptor sites should be present in the solubilized form in the supernatant.

A typical gel filtration binding experiment is done as follows: 0.3 ml of the supernatant (which had been already mixed with labeled auxin) is added to the top of the column; before the run is started, the sample is overlaid without mixing with equilibration buffer, which then is continuously applied during the flow. A constant flow rate of about 5 ml/hr is provided by pumping out the effluent with a peristaltic pump; 0.1–0.2 ml fractions of the effluent are collected and assayed for radioactivity.

With regard to the principles of gel chromatography there are certain theoretical predictions: Since Sephadex G25 has a resolution range of 1000–5000 daltons molecular weight, proteins and other larger molecules of the sample should emerge with the excluded volume of the column. If they do bind auxin during their passage, the elution diagram of radioactivity should have a characteristic pattern; as the ligand-receptor complex comes out of the gel bed, the measured radioactivity should rise above the equilibrating level; in fractions corresponding to the included volume of the column, radioactivity should be decreased below the initial basal value because the solution within the gel has been depleted by free ligand during the flow of auxin-binding molecules; subsequently, radioactivity in the effluent should return to its initial value, which

is that of the equilibration and elution buffer. Peak and trough fractions can be separated by effluent fractions containing basal radioactivity if the column is long enough to separate excluded and included molecules well and if the amount of applied binding material is small in proportion to the bed volume. The area under the depletion trough should equal the area under the peak if the concentration of radioactive ligand is identical throughout the Sephadex beads, the elution buffer, and the sample; therefore either the surplus of radioactivity seen in the peak or the decrease expressed by the trough can give measure for the amount of bound ligand.

Figure 17A shows that this predicted elution pattern of ^{14}C -NAA activity is seen when solubilized membrane preparations from corn seedling shoots are applied to Sephadex G25; this result indicates that the auxin-binding capacity is not eliminated by the detergent treatment. A sharp increase in radioactivity is followed by a depletion area; peak and trough in this case are not separated by a plateau region because of the ratio between column length and

sample size. But since this method was not developed to separate molecules on a very sensitive scale, the normally recommended relationship between sample size, bed volume, and efficiency of resolution can be neglected to some extent; also, this test for binding is the only step within the whole program of receptor isolation and identification during which a loss of binding activity has to be expected, and for that reason it is necessary to reduce the time for these tests.

When the remaining resuspended pellet from the Triton supernatant used in the first experiment is passed through the column, data as plotted in Fig. 17B are obtained: No significant deviation from the basal activity is seen. Thus, the detergent treatment does result in an almost complete release of membrane-associated binding sites. If the assays are carried through as described, it can be noticed that the area under the peak is less than that in the trough region. This discrepancy can be explained by the fact that resuspension of the relatively large pellets (before solubilization) in the same (^{14}C -NAA-containing) buffer as used

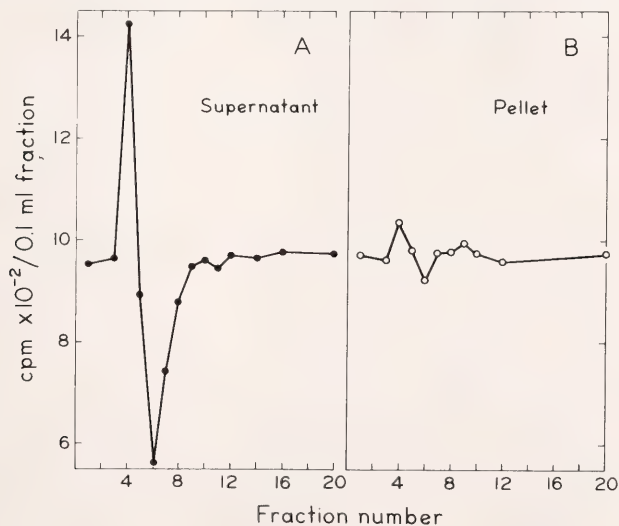


Fig. 17. A Triton-treated membrane homogenate was sedimented at $133,000 \times g \times 60$ min; supernatant and pellet were separated, and the pellet was resuspended in an equal volume of assay buffer with Triton X-100; 0.3-ml aliquots of the supernatant and the pellet suspension were assayed for binding activity by the column method.

for equilibration and elution causes a dilution of radioactivity in the suspension. Correcting calculations show that the difference in labeled auxin, which has to be bound to gain just the concentration of ^{14}C -NAA present in the Sephadex bed before additional ligand can be bound, is exactly reflected in the difference between trough and peak. Considering this, the amount of bound ^{14}C -NAA can be calculated as:

$$\% \text{ bound} = \frac{(\text{cpm}^1_{\text{peak}}) - (\text{cpm}^1_{\text{basal}}) \times 100}{(\text{cpm}^2_{\text{total}})}$$

where $(\text{cpm}^1) =$ amount of ^{14}C -NAA in cpm measured in all fractions which contain radioactivity exceeding the basal value, and $(\text{cpm}^2) =$ cpm per volume of column (sample before run).

The amount of bound ^{14}C -NAA is directly proportional to the amount of sample added to the column and is also dependent upon the concentration of unlabeled NAA used in the assay, as seen in Fig. 18. These data were ob-

tained from a series of column assays using increasing concentrations of nonradioactive NAA up to saturation of all specific receptor sites with ligand. The elution figures show gradually decreasing peaks and troughs and finally come close to zero deviation from the base line. For a clear illustration only the data with $5 \times 10^{-7} M$ NAA (in the range of half-saturation) and $10^{-4} M$ NAA (virtually all specific sites should be occupied by unlabeled NAA) are plotted. With the first NAA concentration the peak is reduced by about 50% ($\text{cpm}_{\text{peak}} = 2273$ with ^{14}C -NAA alone vs. 1230 when $5 \times 10^{-7} M$ NAA is added), whereas addition of $10^{-4} M$ NAA reduces the amount of bound radioactive NAA almost completely (144 cpm).

These data show that the column assay is a quantitative measure for the binding capacity of solubilized receptor sites for auxin. Differences in the binding properties between solubilized and membrane-associated receptor sites on the other hand may be expected, as

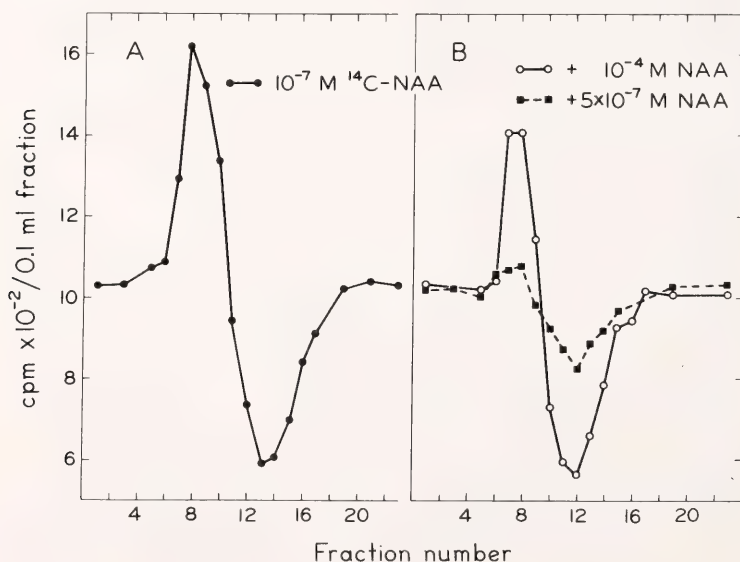


Fig. 18. Membrane suspensions were solubilized and centrifuged as described in the text. To equal amounts of the supernatant mixed with ^{14}C -NAA none, 5×10^{-7} or 10^{-4} unlabeled NAA was added; the samples were assayed with Sephadex G25 columns which had been equilibrated with the ^{14}C -NAA buffer to which in each case nonradioactive NAA was added to yield the same concentration as the sample.

further experiments indicate. Table 12 is a summary of assays done so far to compare the specific binding features. Addition of benzoic acid, structurally related to auxin but not growth promoting, at a concentration of 10^{-3} M, which only at this high concentration will affect ^{14}C -NAA binding to intact vesicles at all, competes to some extent when used in the column test. Differences are also seen with dithioerythritol (DTE): It has a strong inhibitory effect on the auxin binding to membranes, but it is less effective on solubilized preparations. Furthermore, data reflecting the heat sensitivity are included in Table 12. The samples were incubated at different temperatures for 60 min, before the binding tests were done at 4°C ; these results (see values for 50°C and 100°C) suggest that solubilized receptor sites have a reduced heat lability. Digestion with pronase or phospholipase C causes only partial inactivation of binding activity, both with vesicle suspensions and with solubilized binding sites. Although one has to account for differences in the binding properties of unsolubilized and detergent-treated particles, there is no

doubt that the Sephadex G25 test can be taken as a quantitative auxin binding test. Questions concerned with these discrepancies will be approached in the future, following the planned isolation of the component that is responsible for the binding.

Preliminary data from fractionation experiments using appropriate Sephadex or agarose gels for separation of larger molecular weight substances resulted in a pattern of binding activity not identical with the general protein profile.

References

- Dohrmann, U., Inaugural Dissertation, Freiburg, Germany, 1975.
 Fairclough, G. F., and J. S. Fruton, *Biochemistry*, 5, 673-683, 1966.
 Henderson, R., and J. H. Wang, *Biochemistry*, 11, 4565-4569, 1972.
 Hertel, R., K.-St. Thomson, and V. E. A. Russo, *Planta (Berl.)*, 107, 325-340, 1972.
 Hummel, J. P., and W. J. Dreyer, *Biochim. Biophys. Acta*, 63, 530-532, 1962.
 Jennings, M. L., and A. K. Salomon, *J. Gen. Physiol.*, 67, 381-397, 1976.

TABLE 12. ^{14}C -NAA Binding Assay on Membrane-Associated and Solubilized Receptor Sites

| Treatment | Binding Assay | |
|--|------------------|---------------------|
| | By Sedimentation | Sephadex G25 Column |
| 25°C (60 min) | 83* | 71* |
| 50°C (60 min) | 3.5 | 43 |
| 100°C (60 min) | ... | 4.6 |
| 3mM DTE (0°C, 120 min) | 16 | 49 |
| Pronase (18.5 mg/ml; 25°C, 60 min) | 45 | 43 |
| Phospholipase C (1.5 mg/ml; 25°C, 60 min) | 39 | 79 |
| 10^{-3}M Benzoic Acid | 88 | 43 |

*The numbers represent the relative specific binding (sedimentation) or the relative radioactivity over basal activity compared to the controls (= 100).

The original suspensions from washed membrane preparations were mixed with ^{14}C -NAA and divided in half. One portion was treated with 1% Triton X-100 and centrifuged for 60 min at $133,000 \times g$; the supernatant from this step and the original suspension with unsolubilized vesicles were incubated as indicated in the left column. Aliquots of each incubate were then assayed for binding: 0.1 ml particles/ml ^{14}C -NAA assay buffer $\pm 10^{-4}\text{M}$ NAA were pelleted at $133,000 \times g$ for 20 min; 0.3 ml supernatant was passed through a 0.5-ml Sephadex G25 column equilibrated with ^{14}C -NAA buffer.

COMPARISON OF THE HEAT STABILITY OF PHOTOSYNTHESIS, CHLOROPLAST MEMBRANE REACTIONS, PHOTOSYNTHETIC ENZYMES, AND SOLUBLE PROTEIN IN LEAVES OF HEAT-ADAPTED AND COLD-ADAPTED C_4 SPECIES

Olle Björkman, John Boynton, and Joseph Berry

During the year studies have been continued to determine the thermal stability of key components of the photosynthetic machinery responsible for the marked differences in temperature tolerances between thermophilic higher plant species such as *Tidestromia oblongifolia* and cool-temperate plants such as *Atriplex sabulosa*. As reported last year (*Year Book* 74, pp. 743-759), the two C_4 species differ in their high-temperature stability in several respects, including the maintenance of semipermeability of the cell membranes; respiratory activity, and photosynthetic activity. While onset of high-temperature damage differed by about 10°C in each case, photosynthesis was affected at considerably lower temperatures than either respiration or membrane semipermeability. Complete inhibition of photosynthesis occurred before other symptoms of high-temperature damage could be detected. Thus, the high-temperature inhibition of photosynthesis could not result from a general breakdown of the integrity of the cell.

Light-saturated photosynthesis was inhibited at 37°C and above in *A. sabulosa* (a C_4 plant native to cool oceanic habitats), but no signs of inhibition were evident in *T. oblongifolia* (a summer-active C_4 plant native to the floor of Death Valley) until the leaf temperature exceeded 47°C. It was unequivocally shown that the high-temperature inhibition of photosynthesis in *A. sabulosa* and *T. oblongifolia* was not even in part due to changes in the resistance to diffusive transport of CO_2 . This conclusion was valid for CO_2 transport through the stomata as well as inside the leaf parenchyma.

Our previous studies indicated that thermal inhibition occurred at very

similar temperatures for light-saturated and light-limited photosynthesis. Measurements of fluorescence kinetics on leaf discs and photochemical activities of chloroplasts isolated from heat-treated leaves pointed to the possibility that inactivation of photosystem II was primarily responsible for the observed high-temperature inhibition of the quantum yield of photosynthesis in intact leaves. Studies this year comparing the quantum yield for CO_2 uptake by intact leaves and the quantum yield for DCIP reduction by isolated chloroplasts, as a function of the temperature at which the leaves had been pretreated, provide strong evidence that inactivation of a component of photosystem II, or a breakdown of the integrity of the membranes with which this photosystem is associated, constitutes one of the sites most sensitive to high temperature.

As shown in Fig. 19A and 19B, the responses to the quantum yield of photosynthesis measured at a non-limiting temperature for intact leaves exposed to increasing pretreatment temperature closely matches changes in the relative quantum yield for DCIP reduction of chloroplasts isolated from pretreated leaves of each species. In both cases, *T. oblongifolia* is able to sustain a constant quantum yield at much higher temperatures than *A. sabulosa*. In contrast the quantum yield of electron transport driven by photosystem I (reduction of NADP using DCIP ascorbate as electron donor in the presence of DCMU) in chloroplasts isolated from similar heat-treated leaves, remains fully active at temperatures that cause nearly complete inactivation of both photosystem II and CO_2 fixation by intact leaves. This result agrees with our previous findings that the light-saturated rate

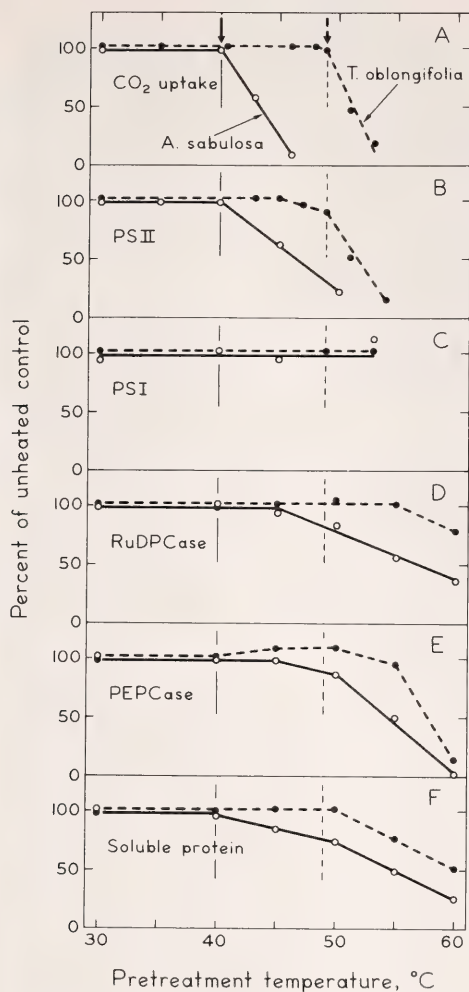


Fig. 19. Comparison of the heat stability in vivo of complete photosynthesis of *A. sabulosa* and *T. oblongifolia* with that of selected light and dark reaction components. Quantum yields for complete photosynthesis (A) and for photosystem I and II activities (B and C) of isolated chloroplasts together with activities of RuDP and PEP carboxylases (D and E) and extractability of total soluble protein (F) are shown for leaves treated at the temperatures indicated. The quantum yield of complete photosynthesis by attached leaves as influenced by pretreatment was measured at 30°C as described in *Year Book 74*, pp. 760–761. Chloroplasts were isolated as a 2000 \times g pellet from leaves after 5 min pretreatment, using media containing 0.33 M sucrose, 0.05 M Tricine, 15 mM KCl, 1 mM $MgCl_2$, 1 mM $MnCl_2$, pH 7.4. Photosystem I was assayed as NADP reduction at 340 nm and photosystem II as DCIP reduction at 600 nm in a Perkin-Elmer 356 spectrophotometer equipped with an actinic illumi-

nation attachment. The intensity of actinic illumination was varied by use of neutral density filters from a maximum intensity of 3 nE $cm^{-2} sec^{-1}$. The reaction mixtures contained: (1) for NADP reduction, media plus chloroplasts to 25 μg chlorophyll/ml 3×10^{-5} M DCIP, 10^{-2} M ascorbate, 2.5×10^{-4} M NADP and 50 μg /ml spinach ferridoxin; (2) for DCIP reduction, isolation media plus chloroplasts to 10 μg chlorophyll/ml, 3×10^{-5} M DCIP and 10^{-2} M NH_4Cl_2 . The light-dependence curves were linear, and since chlorophyll concentrations were identical, changes in the slopes of these curves with pretreatment were taken to indicate changes in the relative quantum yield of the reactions assayed. The chloroplasts used were derived predominantly from mesophyll cells. Leaves heat-treated for 10 min were extracted by grinding exhaustively with glass beads in a pre-chilled mortar followed by homogenization in a glass tissue grinder. Microscopic examination indicated nearly complete breakage of the bundle sheath cells. The supernatant after 40,000 \times g centrifugation was assayed for soluble protein by the Lowery Method; RuDP carboxylase was activated and assayed according to Lorimer *et al.* (1976), and PEP carboxylase was assayed according to Björkman and Gauhl (1969).

of photosystem I was highly heat stable (*Year Book 74*, pp. 743–759).

These studies substantiate the hypothesis that thermal damage to specific sites of the photochemical apparatus is a major factor limiting photosynthetic performance after exposure of intact tissue to damaging temperatures. Furthermore, substantial differences exist among plants in their resistance to such damage. While photosystem II is the most heat-sensitive photosynthetic component assayed, neither the mechanism responsible for the damage nor how specific this damage may be is clear. Several reports (Krause and Santarius, 1975; Mukohata *et al.*, 1973; Emmett and Walker, 1969) suggest that ATP formation by photophosphorylation is also sensitive to heat in isolated chloroplasts. Our studies indicate that chloroplasts damaged by pretreatment of intact leaves are also uncoupled. We feel that thermal damage is probably not specific to only one site or component in photosystem II but rather may be a secondary result of either ionic or pH changes in the chloroplast envi-

ronment or a modification of the organization of the lipid-protein membrane structure necessary for photosynthetic activity.

One factor known to play an important role in membrane function is the degree of unsaturation of the fatty acids of the membrane lipids. The fatty acids of the major chloroplast lipids—monogalactosyl diglycerides (MGDG), digalactosyl diglycerides (DGDG), and phosphatidyl glycerol (PG)—are somewhat more saturated in *Tidestromia* than in *A. sabulosa* or in *A. glabriuscula*, a C_3 species also from cool marine habitats (Table 13). However, this difference in extent of saturation of the glycolipids is small. In contrast, the relative difference in unsaturation of the fatty acids of phosphatidyl glycerol is much greater than that of the other chloroplast lipids. Anderson (1975) suggests that this lipid, because of its charge, may play a specific role in lipid-protein associations within the membrane. We are currently examining the hypothesis that changes in the unsaturation of fatty acids of this lipid might have specific effects upon the heat stability of chloroplast membranes.

While differences observed in the susceptibility of photosystem II activity to heat inactivation in the two species are sufficient to explain the observed high-temperature inhibition of the quantum yield for complete photosynthesis in intact leaves, one cannot rule out the possibility that other photosynthetic components, such as key enzymes of the carbon fixation and reduction process, have the same tem-

perature sensitivity and are being inactivated together with photosystem II. Inactivation of nonphotochemical components would not affect the quantum yield, but might have substantial effects upon the light-saturated photosynthetic capacity, which as previously noted (*Year Book* 74, pp. 748–751) is affected at lower temperatures than those which cause inhibition of the quantum yield.

This year systematic comparative studies of the heat susceptibility in vivo of a number of key photosynthetic enzymes have been initiated. To date we have examined the heat stability of the activity of the two carboxylation enzymes, ribulose-diphosphate carboxylase (RuDPCase) and phosphoenolpyruvate carboxylase (PEP-Case). In addition, we have followed the effect of heat treatment of intact leaves of denaturation of the bulk soluble protein.

As shown in Fig. 19D, RuDPCase is a remarkably heat-stable enzyme. In *T. oblongifolia* leaves, no inactivation was observed until the temperature exceeded 55°C and even after exposure of the leaves to 60°C for 10 min, 80% of the activity remained. In *A. sabulosa* leaves inactivation of this enzyme could be detected at about 10°C lower temperature. Yet this temperature is much higher than the temperature at which inhibition of light-saturated photosynthesis sets in. After heat treatment of the leaves at 47°C, which causes complete inhibition of photosynthesis in this species, at least 90% of the RuDPCase activity remained. Thus, even though a difference be-

TABLE 13. Comparison of the Extent of Unsaturation, Expressed as Double Bonds per Carbon Atom, of the Fatty Acids Separated by Gas Chromatography from the Chloroplast Lipids of *Tidestromia oblongifolia*, *Atriplex sabulosa*, and *A. glabriuscula**

| Lipid | Double Bonds Per Carbon Atom | | |
|----------------------------|------------------------------|--------------------|------------------------|
| | <i>T. oblongifolia</i> | <i>A. sabulosa</i> | <i>A. glabriuscula</i> |
| Monogalactosyl diglyceride | 0.150 | 0.151 | 0.161 |
| Digalactosyl diglyceride | 0.120 | 0.140 | 0.151 |
| Phosphatidyl glycerol | 0.052 | 0.086 | 0.092 |

*Data is from an undergraduate honors research thesis by Thomas H. Payne (1976).

tween the species in apparent heat stability of this enzyme *in vivo* was detected, the onset of heat denaturation was at a temperature 10°C higher than that required to inactivate complete photosynthesis. These results indicate that RuDPCase from both a cool- and a heat-adapted C_4 species is highly heat stable and that heat inactivation of this enzyme is not involved in high temperature inhibition of photosynthesis.

PEPCase (Fig. 19E) exhibits a considerably lower heat stability *in vivo* than RuDPCase, although marked differences again exist between the two species. However, inhibition of PEPCase activity in each species also occurs at considerably higher temperatures than inhibition of photosynthesis. In contrast, Phillips and McWilliam (1971) report that RuDPCase and PEPCase from *Atriplex nummularia*, a C_4 species, begin to show a temperature-dependent decline in activity at considerably lower temperatures when detached leaves are heat treated for several hours. These studies do not necessarily contradict our findings, since such long-term changes in activity may be due to factors other than heat-induced protein denaturation *per se*. The studies reported here are for short-term (10 min) heat exposure during which changes other than protein denaturation should be minimized.

As shown in Fig. 19F, one or several unidentified components of the soluble protein in the leaves evidently undergo heat denaturation and aggregation so that they are no longer soluble in the aqueous extraction buffers. The temperature at which this denaturation commences in each species is very close to the temperature at which heat inhibition of leaf photosynthesis can first be observed and is considerably lower than the corresponding temperatures for inactivation of the two carboxylases. Hence, high-temperature inhibition of photosynthesis may involve both inactivation of photosystem II, associated with the chloroplast

membranes, and denaturation of one or more soluble, non-membrane-bound enzymes which constitute a significant fraction of the bulk soluble protein. Studies are now being initiated to determine whether this denaturation involves other heat-labile photosynthetic enzymes in *A. sabulosa* and *T. oblongifolia*.

The heat stabilities of the various components of the photosynthetic apparatus observed *in vivo* for the two species might not necessarily reflect the intrinsic heat stabilities of the components. For example, heat inactivation of a certain component may be an indirect effect caused by a high-temperature-induced change in its immediate cellular environment, such as a change in pH or ionic composition, both of which are known to influence strongly the stability of proteins.

Therefore, differences in heat stability between the species could in part be due to factors determining the heat stability of the cells' partitioning membranes. Experiments reported last year (Year Book 74, pp. 751-759) showed that differences in the heat resistance to loss of semipermeability of the membrane which prevent leakage of solutes from immersed leaves into the surrounding aqueous media cannot account for the differences in heat stability of the photosynthetic apparatus. However, these results do not rule out the possibility that the heat stability of other partitioning membranes within the cell are involved.

Krause and Santarius (1975) have shown that chloroplasts isolated with their outer membranes intact are more resistant to thermal damage than are chloroplasts lacking this membrane. Presumably the only effect of the outer membrane on thermal stability of the photosynthetic membrane is to maintain a more favorable internal environment than that provided in the external medium. Within an intact leaf cell the possibilities of such interactions are manifold.

Therefore, we chose to compare the heat stabilities of the various photo-

synthetic components *in vitro* as well as *in vivo*. To date, our *in vitro* studies have been limited to comparisons of isolated and purified RuDP carboxylase from leaves of *A. glabriuscula* and of RuDP carboxylase and PEP carboxylase from leaves of *T. oblongifolia*. For this purpose, extracts containing all of the soluble leaf protein were applied to 38 ml 0.29–0.88 *M* linear sucrose density gradients (Boynton *et al.*, 1972). After centrifugation for approximately 40 hr at 25,000 rpm in an SW-27 rotor at 2°C, the gradients were fractionated and the distribution of protein, RuDPCase, and PEPCase activities determined. With most *C*₃ and *C*₄ species, in which Fraction I protein (RuDPCase) constitutes a large fraction of the total soluble protein, this technique provides an excellent yield of highly purified enzyme in a single-step procedure (Fig. 20A and B). With *T. oblongifolia*, in which RuDPCase constitutes only a small fraction of the total protein (Fig. 20C), prior enrichment using (NH₄)₂SO₄ fractionation is necessary to obtain adequate amounts and purity of the enzyme.

Preparations of RuDPCase from *A. glabriuscula* and *T. oblongifolia* appeared homogeneous as determined by sedimentation velocity centrifugation in the analytical ultracentrifuge and by polyacrylamide gel electrophoresis. No differences between RuDPCase in the two species in molecular weight (ca. 530,000 daltons), net charge, or specific activities (2.0 $\mu\text{mole CO}_2 \cdot \text{min}^{-1} \text{ mg protein}^{-1}$ at 30°C) could be resolved. Similar analyses are in progress on RuDPCase purified from *A. sabulosa*.

Heat inactivation of the proteins *in vitro* was assayed either as the time-dependent decline in catalytic activity in high-speed supernatants subjected to various temperatures or as the increase in absorbance at 285 nm of the purified enzyme. These two assay techniques gave very similar estimates of denaturation in our experiments. The heat stability of RuDPCase and PEPCase *in vitro* was strongly influ-

enced by pH during treatment of the proteins in 10 mM Mg⁺² and 5 mM dithiothreitol (omitted in the absorbance assays) in 0.1 *M* HEPES or MES buffers over the pH range of 5.5–8.5. Maximum heat stability for PEPCase was observed in pH range 5.5–6.0, and the rate of inactivation increased sharply as the pH was increased from 6 to 7. RuDPCase exhibited maximum heat stability at pH 7.0–7.6, and the rate of inactivation increased steeply below pH 6.8 and above pH 7.8. At their respective pH optima for maximum heat stability, appreciable inactivation of the *T. oblongifolia* PEPCase and RuDPCase was not detected until 48° and 57°C, respectively. This difference in high-temperature inactivation is similar to that found *in vivo*, suggesting that the two carboxylation enzymes have intrinsically different heat stability characteristics. Comparative data on the heat stability *in vivo* of RuDPCase and PEPCase from *A. sabulosa* remain to be obtained.

Preliminary results also indicate that the heat stability of RuDPCase *in vitro* is appreciably lower in *A. glabriuscula* than in *T. oblongifolia*, again resembling the situation *in vivo*. Further comparative studies of the heat stability of this enzyme isolated from *T. oblongifolia*, *A. sabulosa*, and other cold-adapted and heat-adapted species of higher plants, together with determinations of the relative hydrophobicities of the proteins should provide additional insight into a problem of considerable evolutionary and ecological interest.

It is also interesting from an evolutionary viewpoint that PEPCase shows a large difference in molecular weight between the two *C*₄ species *A. sabulosa* and *T. oblongifolia*, whereas RuDPCase does not. Clearly different peak positions for PEPCase activity are seen in Fig. 20B and 20C, with the *T. oblongifolia* enzyme position at higher density (greater molecular weight) than the *A. sabulosa* enzyme. This difference in molecular weight was con-

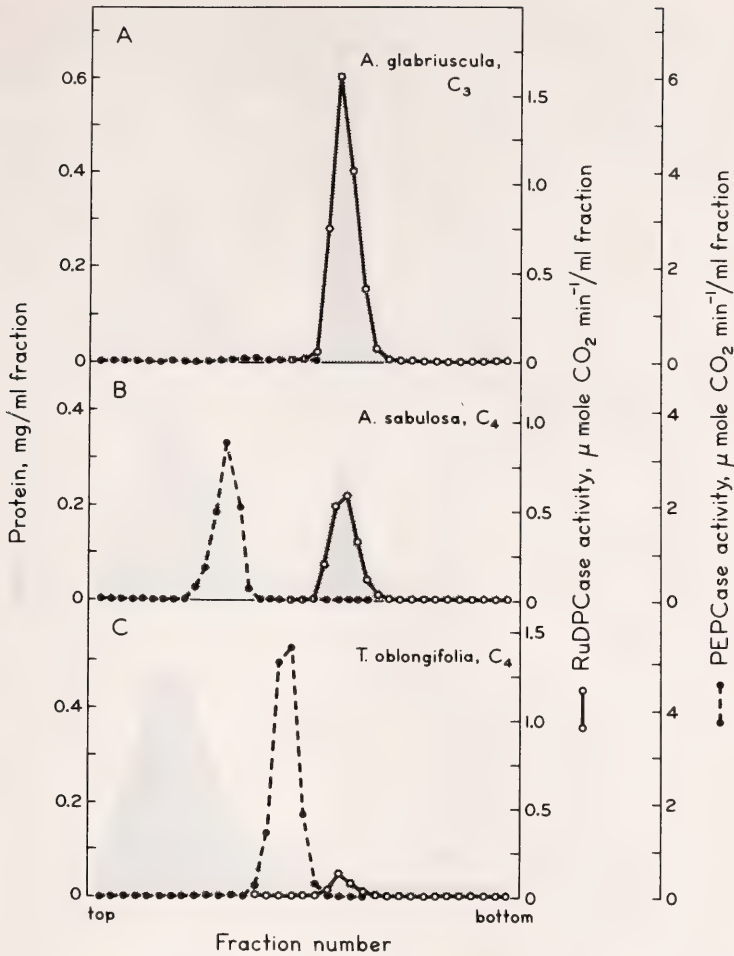


Fig. 20. Comparison of the distribution of total soluble protein with RuDP and PEP carboxylase activities in *A. glabriuscula*, *A. sabulosa*, and *T. oblongifolia*. 40,000 $\times g$ supernatant fractions prepared as in Fig. 19 were loaded on 38 ml 0.29–0.88 *M* sucrose gradients containing 25 mM Tris, pH 7.5, 25 mM MgCl_2 , 25 mM KCl, 5 mM Dithiothreitol (Boynton *et al.*, 1972) and centrifuged in an SW-27 rotor at 25,000 rpm, 2°C for 40 hr. PEPCase and RuDPCase activities were assayed on aliquots of 1 ml fractions as outlined in Fig. 19. Protein content was determined after TCA precipitation by the Lowery Method.

firmed by polyacrylamide gel electrophoresis with crude leaf extracts, followed by a staining procedure specific for PEPCase activity. The molecular weights estimated by this method were 170,000 and 340,000 for *A. sabulosa* and *T. oblongifolia* enzymes, respectively. We previously reported (Year Book 71, pp. 135–141) two electrophoretic forms of PEPCase in C_4 species of *Atriplex* and a third isozyme in C_3 species of this genus. A survey of

the molecular weights of PEP carboxylase in a number of related species, covering a very wide geographical and ecological range, has now been started to determine the extent and possible significance of this variation.

In addition to providing a convenient method for enzyme purification, sucrose density gradient centrifugation also permits an accurate, direct, and reasonably simple means of assessing the fraction of the total soluble leaf

protein that different plants allocate to a single major protein, RuDPCase, and how this allocation is influenced by environmental factors. As shown in Table 14, this enzyme accounts for 41%–46% of the total protein in *A. glabriuscula*, a value typical of those reported in the literature for C_3 plants. *A. sabulosa* (C_4), which like *A. glabriuscula* (C_3) is native to cool oceanic habitats, allocates one-fifth of its soluble protein to RuDPCase when grown under identical conditions (22°C day/15°C night). However, both species have similar growth and photosynthetic rates (Year Book 73, pp. 748–767; Year Book 74, pp. 743–748). The amount of total soluble protein is similar in the two species. In contrast, the thermophilic C_4 plant *T. oblongifolia* allocates less than 10% of its soluble protein to RuDPCase when grown under a 45°C day/32°C night regime, which is close to the optimum temperature for growth in this species. This low proportion of RuDPCase is not compensated for by a higher content of total soluble protein, since the soluble protein content is considerably lower than in the other species. The smaller amount of RuDPCase detected in this C_4 species is not a result of an incomplete breakage of the bundle-sheath cells, because special precautions were taken to make certain that complete breakage of all cells was obtained.

One might ask how *T. oblongifolia* is able to get by with a much smaller amount of RuDPCase than, for example, *A. sabulosa*, and yet is capable of at least as high photosynthetic rates at the optimum temperature. A simple answer to this question may be that at a temperature of 45°C, the total cata-

lytic activity of this amount of RuDPCase is as high as that of the larger amount of enzyme in *A. sabulosa* at 22°C.

Preliminary studies suggest that while total RuDPCase activity is not limiting photosynthesis in *T. oblongifolia* at 45°C, it may well be rate limiting at lower temperature. This suggestion could explain the rapid decline in photosynthetic rate with decreasing temperature (Year Book 70, pp. 511–520), and thus also the high optimum temperature for photosynthesis in high-temperature-grown plants of this species (Year Book 74, pp. 743–759). These early results further suggest that the amount of RuDPCase increases with decreasing growth temperature over a 25°C range, as does also the photosynthetic capacity at rate-limiting temperatures. Studies designed to test the validity of such a proposed temperature-controlled adjustment of RuDP carboxylase synthesis are planned.

This work was supported in part by NSF Grant No. BMS to O. Björkman. We thank Ms. Mary Enama, a CIW graduate student from the Department of Biology, Washington University, St. Louis, for carrying out the polyacrylamide gel electrophoresis experiments.

References

- Anderson, J. M., *Biochim. Biophys. Acta*, 416, 191–235, 1975.
- Björkman, O., and E. Gauhl, *Planta*, 88, 197–203, 1969.
- Boynton, J. E., N. W. Gillham, and J. F. Chabot, *J. Cell Sci.*, 10, 267–305, 1972.

TABLE 14. Comparison of the Total Leaf Protein, Total Soluble Protein, and Fraction I Protein (RuDPCase) in *A. glabriuscula*, *A. sabulosa*, and *T. oblongifolia*

| Species | Fraction I Protein, % of total soluble protein | Total Soluble Protein, mg/g dry wt | Total Leaf Protein, mg/g dry wt |
|--------------------------------|--|--|---------------------------------------|
| <i>A. glabriuscula</i> , C_3 | 41–46 | 130 | 260 |
| <i>A. sabulosa</i> , C_4 | 19–21 | 117 | 250 |
| <i>T. oblongifolia</i> , C_4 | 4–8 | 64 | 185 |

- Emmett, J. M., and D. A. Walker, *Biochim. Biophys. Acta*, 180, 424–425, 1969.
- Krause, G. H., and K. A. Santarius, *Planta*, 127, 285–299, 1975.
- Lorimer, G. H., M. R. Badger, and T. J. Andrews, *Biochemistry*, 15, 529–536, 1976.
- Mukohata, Y., T. Yagi, M. Higashida, K. Shinozaki, and A. Matsuno, *Plant Cell Physiol.*, 14, 111–118, 1973.
- Payne, T., Stanford University Undergraduate Honors Thesis, 1976.
- Phillips, P. J., and J. R. McWilliam, in *Photosynthesis and Photorespiration*, M. D. Hatch, C. B. Osmond, and R. O. Slayter, eds., pp. 97–104, Wiley-Interscience, New York, 1971.

GENETIC VARIATION AFFECTING METABOLIC PHENOTYPES: AN APPROACH TO ANALYZING PHOTOSYNTHETIC CARBON REDUCTION IN A C₄ PLANT

Mary Enama

The physiological processes of an organism depend on the action of many enzymes. Because the various pathways are coordinated, it has been argued that the associated allelic variation should show similar coordination, comprising a "metabolic phenotype." To date, there has been no reported study of genetic variation among the enzyme loci of a single physiologically important metabolic pathway in plants. This paper describes a series of investigations to provide this information for a C₄ plant.

A multi-locus study of evolutionary adaptation of a metabolic process should have the following characteristics in addition to those described for a single locus study:

- (1) The metabolic process should be of primary physiological importance.
- (2) The process should be well characterized biochemically.
- (3) The organism studied should be found in a variety of habitats in which individuals of one habitat are known to differ physiologically and genetically from those in other natural locations.
- (4) The organism should be easily grown and should produce a sufficient quantity of tissue to allow analysis of several enzymes from each individual.

In plants, such a metabolic process is photosynthetic carbon reduction. Gas-exchange analysis has shown it to be

influenced by and adapted to environmental parameters such as light, temperature, and water stress (Björkman *et al.*, 1975). The biochemical pathway is well known, and its various components are under intensive investigation in many laboratories. In addition, for a variety of plants, transplant studies have indicated the existence of ecotypes in which primary productivity varies in individuals of a given species transplanted between two natural habitats of the species (Björkman *et al.*, 1974). That is, the physiological plasticity of individual plants is genetically controlled and differs with site of origin. Thus, it would be very informative to do a multi-locus analysis of such ecotypes with regard to photosynthetic carbon fixation.

Two species that are likely candidates for such a study are *Distichlis spicata* and *Atriplex lentiformis*, both NAD-malic enzyme C₄ species. Both species grow naturally in desert and coastal habitats. Existing data indicate that a biochemical analysis might show interesting differences between ecotypes (Björkman *et al.*, 1974; Percy and Harrison, 1974).

The set of enzymes chosen for the analysis should include those thought to be of major regulatory importance for the metabolic process under consideration. For photosynthetic carbon re-

duction in a C_4 plant one might consider the following ten enzymes: phosphoenolpyruvate carboxylase (E.C. 4.1.1.38) [PEP carboxylase]; ribulose-1,5-diphosphate carboxylase (E.C. 4.1.1.39) [RuDP carboxylase]; glutamate-oxaloacetate transaminase (E.C. 2.6.1.1) [GOT]; NAD-malic enzyme (E.C. 1.1.1.39); phosphoglyceric acid kinase (E.C. 2.7.2.3); NADP glyceraldehyde-3-phosphate dehydrogenase (E.C. 3.1.3.11) [NADP G-3-PDH]; fructose-1, 6-diphosphatase (E.C. 3.1.3.11) [FDPase]; phosphoribulokinase (E.C. 2.7.1.19); pyruvate, p_i dikinase (E.C. 2.7.9.1); and adenylate kinase (E.C. 2.7.4.3) [AK]. Electrophoretic assays for some of these presently exist (Shaw and Prasad, 1970; Hatch *et al.*, 1972) and are being developed for the others.

Individuals of *Distichlis spicata* have been used as a trial system to test and develop assays. To date, electrophoretic assays for PEP carboxylase, RuDP carboxylase, GOT, NADP G-3-PDH, FDPase, and AK have been successful in a Tris-glycine electrophoretic system (Davis, 1964) using crude leaf extract. Of these six enzymes, three show multiple bands: four bands for GOT, two for FDPase, and two for AK. As the isozyme literature shows, these multiple bands may represent isozymes from different organelles, participating in separate metabolic functions (Scandalios *et al.*, 1975; Viswanathan and Krishnam, 1962). Since the interest of the proposed study is to characterize allelic variation in photosynthetic carbon reduction, it will be necessary to show by subcellular fractionation or other means which isozyme(s) are involved in the process under consideration.

The band which appears for NADP G-3-PDH seems to be NADP-specific, since no band appears if NAD is substituted in the stain. In the case of NAD-malic enzyme one has the problem of distinguishing malic enzyme from malate dehydrogenase. In animals and many plants malic enzyme is

NADP-specific, so the same basic assay can be used for both by adding NAD when assaying MDH or NADP for a malic enzyme assay. For some species NAD-malic enzyme requires Mn^{++} for activity (Hatch, Mau, and Kagawa, 1974). This information offers a possibility for distinguishing the various malate-utilizing enzymes since different bands do appear, depending on what combination of Mn^{++} , Mg^{++} , NAD, and NADP are used in the electrophoretic stain. Whether this approach is valid will have to be confirmed by an independent method.

Thus, the outline of the proposed study is to collect plants of the same species from two dissimilar habitats and to survey the suggested ten enzymes from each individual, using standardized Ferguson plots as described by Johnson elsewhere in this Report. It will be interesting to see if distinct arrays of structural alleles characterize the different ecotypes and if in vitro characteristics of the enzymes can reasonably be correlated with in vivo differences in photosynthesis.

References

- Björkman, O., M. Nobs, H. Mooney, J. Troughton, J. Berry, F. Nicholson, and W. Ward, *Carnegie Inst. Wash. Year Book* 73, p. 748, 1974.
- Björkman, O., H. A. Mooney, and J. Ehleringer, *Carnegie Inst. Wash. Year Book* 74, p. 743, 1975.
- Davis, B., *Ann. N.Y. Acad. Sci.*, 121, 404, 1964.
- Hatch, M. D., C. B. Osmond, J. Troughton, and O. Björkman, *Carnegie Inst. Wash. Year Book* 71, p. 135, 1972.
- Hatch, M. D., S.-L. Mau, and T. Kagawa, *Arch. Biochem. Biophys.*, 165, 188, 1974.
- Pearcy, R. W., and A. T. Harrison, *Ecology*, 55, 1104, 1974.
- Scandalios, J. G., J. C. Sorenson, and L. A. Ott, *Biochem. Genet.*, 13, 759, 1975.

Shaw, C., and R. Prasad, *Biochem. Genet.*, 4, 297, 1970.

Viswanathan, P. N., and P. S. Krishnam, *Nature*, 193, 166, 1962.

MOLECULAR WEIGHT VARIATION OF
PHOSPHOENOLPYRUVATE
CARBOXYLASES FROM C₄ PLANTS

Mary Enama

The phosphoenolpyruvate carboxylase reaction is the first step in photosynthetic carbon fixation in C₄ plants. As such, it plays an important role in metabolic regulation and is present and highly active in C₄ plants. In the course of purifying this enzyme by means of sucrose density gradient centrifugation it was noted that the enzyme from *Tidestromia oblongifolia* had a considerably larger molecular weight than that from *Atriplex sabulosa* (this *Year Book*). An electrophoretic Ferguson plot analysis is a quick means of measuring size and relative charge of proteins even from crude extracts when a specific stain is available.

A Ferguson plot analysis has been done for the phosphoenolpyruvate carboxylases from *T. oblongifolia*, *A. sabulosa*, *Atriplex hymenelytra*, and *Distichlis spicata*. Leaf tissue was prepared by grinding in 2–4 volumes of 0.1 M Tris, pH 7.8, 0.01 M MgCl₂, 2.5 × 10⁻⁴ M EDTA, 2% Na ascorbate, 5 mM DDT, and 4.5 mM diethyldithio carbamic acid at 4°C. The mixture was then centrifuged at 27,000 *g* for 30 minutes at 4°C. The supernatant was

run on 4%, 5%, 6%, 7%, 8%, and 9% polyacrylamide gels in a Tris-glycine electrophoretic system (Johnson, 1975). The gels were stained with 2 mM phosphoenolpyruvate, 1 mM NaHCO₃, 10 mM MgCl₂, 6.5 mM Fast Violet B Salt, and 2.5 × 10⁻⁴ M EDTA in a 0.1 M Tris buffer, pH. 7.8. A red band appears within 15 minutes at the location of the phosphoenolpyruvate carboxylase. Figure 21 shows the results of a sample run for each species. Replicate runs for each species yield similar results within experimental error.

The equation which describes the lines depicted in Fig. 21 is discussed elsewhere in this Report. The *y*-intercept is the free electrophoretic mobility (*M*₀) and the slope is the retardation coefficient (*K*_{*r*}), which can be correlated with molecular weight (Johnson, 1975). Table 15 shows the values of *K*_{*r*} and the estimated molecular weights for the phosphoenolpyruvate carboxylases of the four species tested and average values for the two internal standards used in every gel, hemoglobin and ferritin. These estimates indicate that the *Tidestromia*

TABLE 15. Values of *K_r* and Estimated Molecular Weight for Phosphoenolpyruvate Carboxylases of Four C₄ Species and Two Protein Standards from a Typical Run

| | <i>K_r</i> | Est. Mol. Wt.* | Actual MW |
|------------------------|----------------------|----------------|-----------|
| <i>A. sabulosa</i> | -0.094 ± 0.006 | 170,000 | |
| <i>A. hymenelytra</i> | -0.106 ± 0.006 | 190,000 | |
| <i>D. spicata</i> | -0.099 ± 0.005 | 180,000 | |
| <i>T. oblongifolia</i> | -0.142 ± 0.005 | 340,000 | |
| Hemoglobin | -0.049 ± 0.002 | 50,000 | 64,500 |
| Ferritin | -0.164 ± 0.009 | 440,000 | 450,000 |

*The molecular weight value shown was calculated from a standard curve (Johnson, 1975). As can be seen from the value for hemoglobin there can be up to 20% error in the values obtained. Thus, there is no significant difference between the estimated molecular weights from the first three species, but these values are significantly different from that for *T. oblongifolia*.

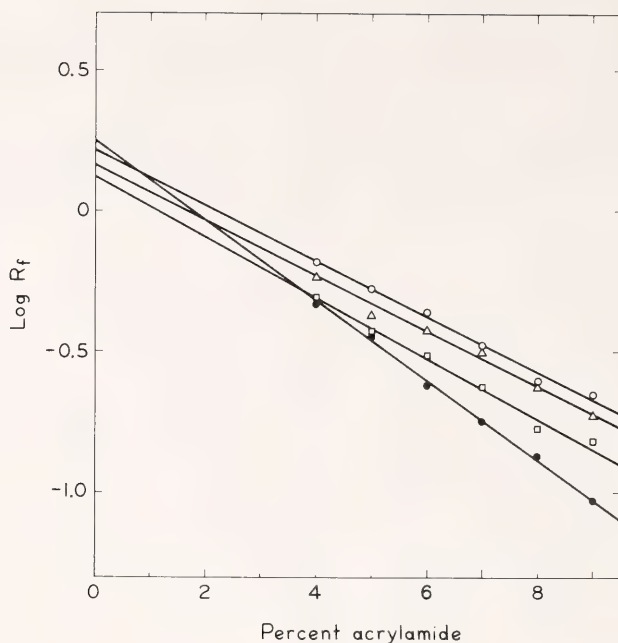


Fig. 21. Ferguson plots for phosphoenolpyruvate carboxylases from four C_4 species: open circles, *D. spicata*; open triangles, *A. sabulosa*; open squares, *A. hymenelytra*; filled circles, *T. oblongifolia*.

enzyme is about twice the molecular weight of the phosphoenolpyruvate carboxylases from the other three species. Whether or not the apparent size difference is an evolutionarily and structurally significant increase of the enzyme size is not yet known. The available information in the plant literature indicates a molecular weight of 350,000 for the phosphoenolpyruvate carboxylase from *Atriplex spongiosa* (Ting and Osmond, 1973).

Other C_4 plants, including *A. spongiosa* and plants in the Amaranthaceae

related to *Tidestromia*, will be tested to see if *Tidestromia* has a unique phosphoenolpyruvate carboxylase or if there are apparently two size classes of phosphoenolpyruvate carboxylase among C_4 plants.

References

- Johnson, G. B., *Biochem. Genet.*, 13, 833, 1975.
 Ting, I. P., and C. B. Osmond, *Plant Physiol.* 51, 439, 1973.

PHOTOSYNTHETIC CAPACITY OF *in situ* DEATH VALLEY PLANTS

H. A. Mooney, O. Björkman, J. Ehleringer, and J. Berry

As part of our long-term studies on the physiological ecology of plants we have been concentrating our efforts on the characteristics of components of the native flora of Death Valley, California. While Death Valley is often identified as one of the hottest and driest

environments on earth, these extremely high air temperatures (exceeding 50°C) occur only during the summer months (Fig. 22). In the winter months relatively cool temperatures (20°C) predominate, and in the spring and fall months air temperatures are

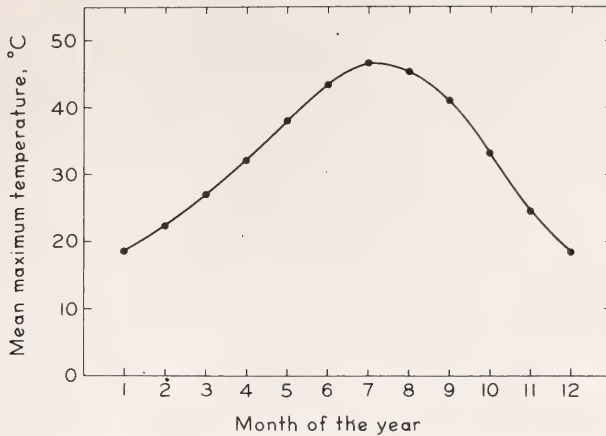


Fig. 22. The yearly course of mean maximum daily air temperatures on the floor of Death Valley, California.

often around 30°C. Consequently, Death Valley provides us with a broad variety of thermal environments and a unique opportunity to study the mechanisms plants possess to adapt to these seasonal thermal regimes.

We report here studies of the intrinsic photosynthetic capacities of several species in response to seasonal changes in thermal regimes of their natural habitat. The measurements were made on plants growing under natural conditions on the floor of Death Valley (*Year Book* 73, pp. 748–757).

Using the mobile laboratory, we measured the photosynthetic capacity of plants during the winter (January), spring (March), summer (late May), and fall (October) seasons. Plants studied included a winter annual (*Camissonia claviformis*), a summer-active, herbaceous perennial (*Tidestromia oblongifolia*), and two evergreen shrubs (*Larrea divaricata* and *Atriplex hymenelytra*).

Under natural conditions the two evergreen shrub species were photosynthetically active throughout the year, although their maximum photosynthetic rates were considerably below those of the two that hold their leaves for a short period (Fig. 23). The two herbaceous species *Tidestromia* (C_4) and *Camissonia* (C_3) possess extremely high maximum photosynthetic rates

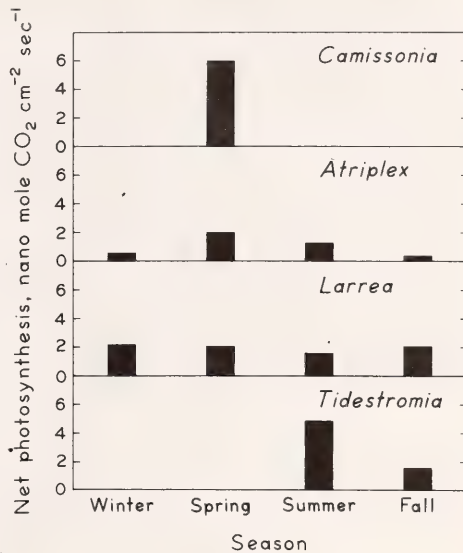


Fig. 23. Light-saturated rates of photosynthesis of four plant species native to the floor of Death Valley. Rates were measured on natural plants at leaf temperatures of 30°C, except *Tidestromia*, which was measured at 35°C. All measurements were made at 325 μ bar CO₂, 21% O₂, and a water vapor pressure deficit of less than 15 mbar.

(exceeding 5 nmol CO₂ cm⁻²sec⁻¹), yet their physiological activities are restricted for the most part to a single season during the year. There appears to be an inverse relationship between maximum photosynthetic rate and leaf longevity among the species in this

study. Of the species with the highest rates observed, the winter-active annual *Camissonia* is a C_3 plant, whereas the summer-active herbaceous species *Tidestromia* is a C_4 plant.

At the 30°C measurement temperature, *Larrea*, the C_3 evergreen species, maintained a relatively constant photosynthetic capacity under natural conditions at all times of the year. This homeostasis persisted in spite of widely disparate midday seasonal air temperatures (20° to 45°C) and leaf water potentials (−25 to −50 bars). The unusual homeostatic adjustment comes about, in part, because of changes in the photosynthetic thermal optimum (Fig. 24). These data were obtained with plants receiving irrigation to eliminate the effect of water stress. Although the photosynthetic rate was relatively constant at the various seasonal temperature optima (2.4–2.7 nmol CO_2 $cm^{-2}sec^{-1}$), the temperature optimum shifted from 20°C during the cool season to over 30°C in the fall.

Atriplex, the C_4 evergreen species, exhibited its highest photosynthetic rate under natural conditions in the spring with newly produced leaves. The photosynthetic rates were reduced during the other season coincident with changes in leaf reflectivity (Year

Book 73, pp. 846–852). Associated also with the lower photosynthetic rates were decreases in leaf water potential, leaf conductance, and leaf nitrogen. In contrast to *Larrea*, *Atriplex* showed little change in its temperature optimum for photosynthesis between seasons (data not shown). As shown in Fig. 25 the optimum temperature for photosynthesis was 30°C.

The summer-active C_4 plant *Tidestromia* is characterized by a very high photosynthetic rate during its principal growth period. In the summer months when *Tidestromia* is active, leaf temperatures may be in excess of 45°C. The optimum temperature for photosynthesis was similar (Year Book 74, pp. 743–751). Under spring and winter temperatures *Tidestromia* would have very low photosynthetic rates. The measured photosynthetic rates were lower in the fall, however, because of the onset of leaf senescence.

The C_3 winter-active annual *Camissonia* germinates following heavy winter rains and can, under certain conditions, complete its entire life cycle in six weeks. This short-lived species has a remarkable capacity to capture sunlight and fix carbon. *Camissonia* converted incident photosynthetically active radiation (400–700 nm) into

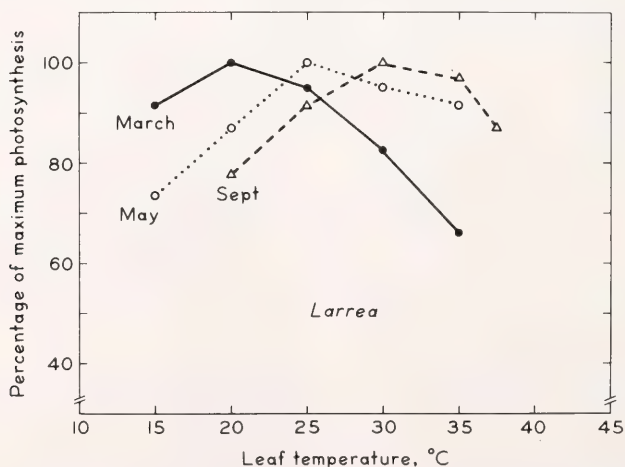


Fig. 24. Seasonal photosynthetic temperature responses of *Larrea* in Death Valley. These values were measured on irrigated plants under conditions of 170 nE $cm^{-2} s^{-1}$, an ambient CO_2 concentration of 325 μ bar, and a water vapor pressure deficit of less than 15 mbar.

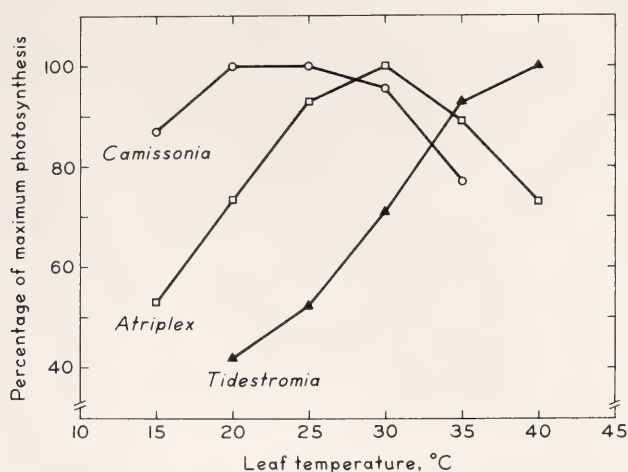


Fig. 25. Seasonal photosynthetic temperature responses of three plant species native to the floor of Death Valley. Measurement conditions as given in Fig. 24.

chemical energy with an efficiency of 8.5%. This is a consequence of the lack of light saturation at midday irradiances, a feature that is also characteristic of *Tidestromia* (Year Book 70, pp. 540–550). The *in situ* midday photosynthetic rate of *Camissonia* was nearly $6 \text{ nmol CO}_2 \text{ cm}^{-2} \text{ sec}^{-1}$, a rate that is higher than has been measured on such productive crop species as corn, sorghum, and sugar cane.

The thermal optimum of photosynthesis of the various species coincides with the prevailing temperatures during their principal growing period (Fig. 25). The winter-active C_3 *Camissonia* has a thermal optimum near 20°C and the summer-active C_4 *Tidestromia*, of

over 45°C . The C_3 plant *Larrea* can potentially grow throughout the year, except during midsummer. This plant shifts its thermal optimum in concert with the prevailing air temperatures. The C_4 plant *Atriplex* grows only during the winter and spring months and maintains a thermal optimum at 30°C .

The major results from these studies will be published elsewhere in greater detail along with a full analysis of the physiological components responsible for the changing seasonal photosynthetic responses of the plants.

This work was supported in part by the National Science Foundation. We thank the U.S. Park Service in Death Valley for their considerate assistance.

LEAF ABSORPTANCE AND PHOTOSYNTHESIS AS AFFECTED BY PUBESCENCE IN THE GENUS *Encelia*

James Ehleringer

Among higher plants there is a trend toward increasing leaf pubescence (presence of leaf hairs) along environmental gradients of decreasing precipitation (Schimper, 1903; Warming, 1909; Clausen, Keck, and Hiesey, 1940). These hairs, covering the surface of the

leaf, are generally considered to be an adaptive feature of plants occupying arid habitats. The reason is that pubescence can reduce the heat load of leaves by increasing the reflectance from the leaf surface, reducing the amount of radiation absorbed. The adaptive value

of a reduced heat load to plants growing in hot or arid climates is great because it can result in lower leaf temperatures and less transpirational losses.

In the southwestern United States and northern Mexico there are several species of the genus *Encelia* (Compositae), each species characteristically showing differences in its degree of pubescence and each occupying habitats differing in precipitation and temperature. Two extremes of leaf pubescence in *Encelia* are *E. farinosa*, a drought-deciduous shrub with white, densely pubescent leaves, and *E. californica*, also drought-deciduous, but with green nonpubescent leaves (Fig. 26). The two species are allopatric in their distributions: *E. californica* is restricted to the relatively moist coastal regions of southern California and

northern Baja California, and *E. farinosa* occurs in the dry desert areas of the southwestern United States and northern Mexico.

The absorption spectra of leaves from each of these two species were measured between 400 and 700 nm (visible light) to determine to what extent pubescence was modifying light absorption. The waveband between 400 and 700 nm was chosen because (1) it is these wavelengths that are useful for the photosynthetic process, and (2) some 80% of the sun's light that is normally absorbed by green nonpubescent leaves is in this waveband. Light absorbance of intact, metabolically active leaves was measured monochromatically using an Ulbricht sphere (Rabideau *et al.*, 1946). Solar absorption coefficients for the 400–700 nm spectral range were calculated from

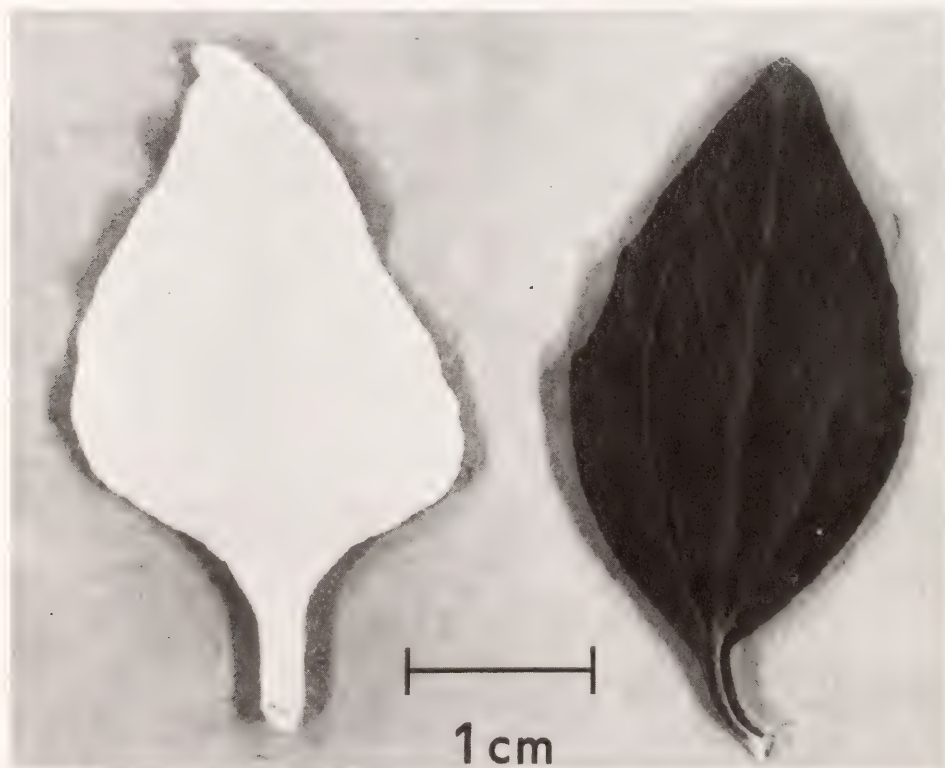


Fig. 26. Typical leaves of the white pubescent *Encelia farinosa* (left) and green nonpubescent *E. californica* (right).

the absorption spectra of the upper leaf surface in conjunction with the solar spectrum at the earth's surface. The solar absorption coefficients represent the integrated percentage of quanta absorbed by the leaf over the photosynthetically active wavelengths. The percentage of quanta absorbed is not necessarily equivalent to the percentage of energy absorbed, since quanta of different wavelengths contain different amounts of energy. Over the range 400–700 nm, however, the percentages were nearly identical for leaves of *Encelia*.

Absorption spectra for a nonpubescent *E. californica* and a very pubescent *E. farinosa* were measured and have been published elsewhere (Ehleringer *et al.*, 1976). The non-pubescent *E. californica* exhibited a spectrum typical of intact green leaves (Year Book 64, pp. 420–425; Gates *et al.*, 1965), but in the pubescent *E. farinosa*, the absorptance values were sharply reduced (Ehleringer *et al.*, 1976). The transmittance through the leaf hairs was less than 1%. This low transmittance and high reflectance at all wavelengths indicated that the pubescent layer was serving as a blanket reflector, decreasing the light absorbed by approximately 56% below the values of *E. californica* at all wavelengths. The differences between the two spectra were due only to differences in pubescence. The chlorophyll contents of leaves from both species were equivalent (about $40 \mu\text{g cm}^{-2}$), and the thickness of the epidermis and that of the mesophyll layers were similar. Solar absorption coefficients for the examples described were 84.8% and for *E. californica* and 29.0% for *E. farinosa*. The degree of pubescence appears most certainly to modify energy absorption by the leaf. In the example described the pubescent *E. farinosa* is absorbing only 29% of the incident radiation between 400 and 700 nm. This value represents only 34% of the radiation being absorbed by the nonpubescent *E. californica* leaf over the same waveband.

If this pubescence layer is indeed acting as a blanket reflector, removal of the pubescence from *E. farinosa* should yield a spectrum similar to that of *E. californica*. Figure 27 shows the absorption spectra for a leaf of *E. farinosa* with hairs intact, the same leaf after the pubescence has been removed, and, for comparison purposes, the absorption spectra of an intact *E. californica* leaf. As shown, once the pubescence of *E. farinosa* has been removed, it is not possible to distinguish the spectrum of that leaf from the spectrum of non-pubescent *E. californica*. This comparison provides conclusive evidence that between 400 and 700 nm the pubescence layer is serving as a blanket reflector and that it is not preferentially reflecting particular wavelengths.

In addition to variation in pubescence between species there are temporal or seasonal changes in absorptance among some of the pubescent species. To illustrate this, the seasonal course of solar absorption coefficients was measured in leaves of the pubescent *E. farinosa* and nonpubescent *E.*

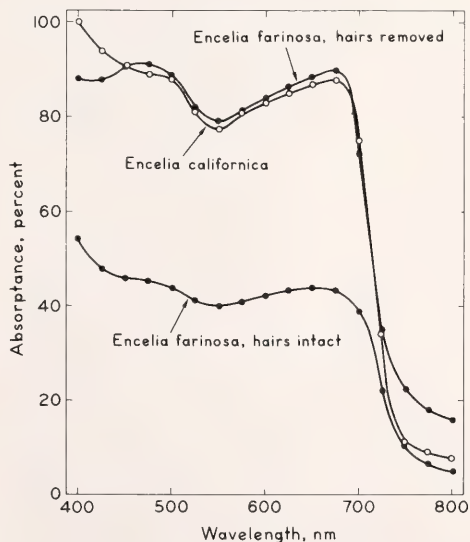


Fig. 27. Absorption spectra from 400 to 800 nm of intact leaves of *Encelia farinosa* with hairs intact and after hairs had been removed, compared to the spectrum of *E. californica*.

californica. Field observations of solar absorption coefficients for both species were made in December (1974), March (1975), and July (1975). *E. californica* was sampled at Point Mugu (362 mm mean annual precipitation) and San Diego (240 mm) in southern California. *Encelia farinosa* was sampled at Superior (433 mm), Tucson (270 mm), Tonopah (155 mm), and Ehrenberg (90 mm) in southwestern Arizona. Five representative samples were collected from each site. The means of all samples of a species at a given sampling time were reduced to a single value.

As shown in Fig. 28 the mean solar absorption coefficients for *E. californica* were 83.9%, 83.8%, and 82.4% and for *E. farinosa* 71.7%, 63.4%, and 52.5%, respectively, for sampling dates of December, March, and July. The range of values between sites averaged 2% for *E. californica* and 10% for *E. farinosa*, while the range within a site averaged 2% for both species. These field data clearly show that the solar absorption coefficient for *E. californica* remains higher than that for *E.*

farinosa at all times through the growing season. Additionally, whereas the solar absorption coefficients for *E. californica* remained constant through the season, the absorption coefficients for *E. farinosa* steadily declined as the season progressed. By July *E. farinosa* averaged 30% less visible light absorbed than *E. californica*. This decrease in leaf absorptance by *E. farinosa* through the season occurred in conjunction with an increase in mean maximum air temperatures. This correlation suggests a role for pubescence in modifying the leaf energy balance as the environment becomes harsher and reduces leaf temperatures. Cunningham and Strain (1969) have also shown that leaf size decreased through the season, further providing a more favorable energy balance.

If pubescence is adaptive for *E. farinosa*, then a positive correlation should exist between leaf absorptance and precipitation for sites occupied by this species. Solar absorption coefficients from each of the *E. farinosa* during March, the period of peak productivity, were plotted against the precipitation received up to the sampling date at the site during the current growing season (Fig. 29). These data reveal a strong correlation ($r^2 = 0.995$, $P < 0.01$) between the solar absorption coefficient and precipitation, suggesting, first, that the reduction in energy absorbed by pubescent leaves is directly dependent on the aridity of the environment and, second, that the degree of pubescence is a plastic response by the leaves to the amount of precipitation received. Since transmittance through pubescent leaves is quite small, there is also a strong correlation between the solar reflection coefficient and precipitation. It should be noted that it is the plastic response by pubescent leaves which is responsible for most of the variation in solar absorption coefficients between *E. farinosa* sample sites. The possible correlation between pubescence and aridity on a community basis rather than on a single

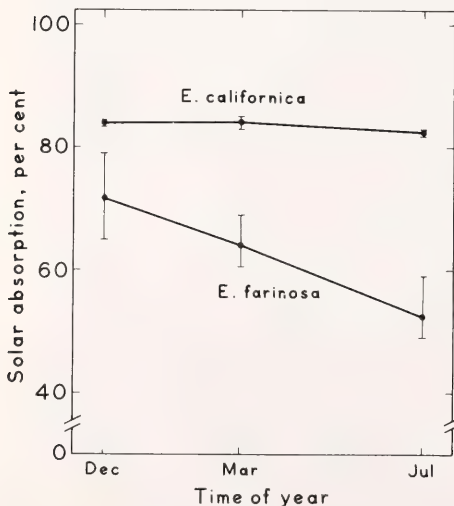


Fig. 28. Seasonal course of changes in the solar absorption coefficients in leaves of *Encelia californica* and *E. farinosa*. Points represent means of samples from different sites, and vertical bars represent the ranges of values between sites.

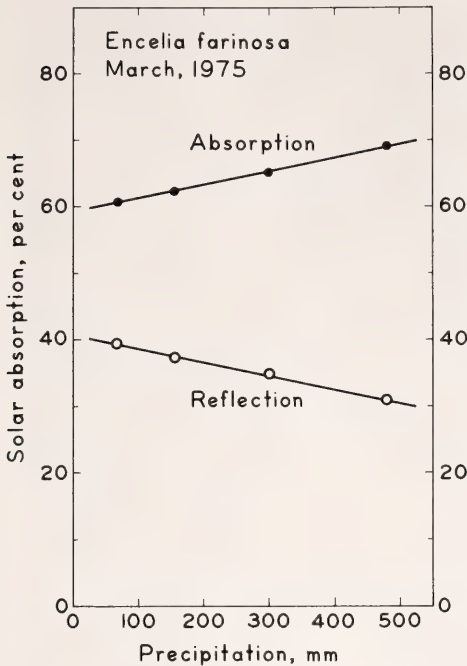


Fig. 29. Solar absorption coefficients for leaves of *Encelia farinosa* on several sites plotted as a function of the seasonal precipitation received at that site during current growing season.

species basis was discussed by Billings and Morris (1951), but solar absorption coefficients were not reported.

The decrease in light absorbed by pubescent *E. farinosa* leaves over the 400–700 nm waveband is sufficient to cause significant reduction in the heat load of leaves. This decreased radiation load should indeed be of selective advantage to *E. farinosa* in arid desert sites since nearly 50% of the solar radiation load on the leaf and approximately 80% of the radiation absorbed by typical green leaves is in the 400–700 nm range. Yet a reduction in the amount of light absorbed carries with it a great disadvantage because reduction in light absorption means less light is available for photosynthesis. To minimize these effects of pubescence on light-limited photosynthesis it is likely that there is an inverse relationship between the degree of pubescence and the water available to the plant, such

that as plants are less stressed the degree of pubescence is lowered. The strong correlation between solar absorption coefficients and precipitation (Fig. 29) serves as indirect evidence for such a relationship.

To determine to what degree the advantages of pubescence—in terms of reduced heat load on the leaf—may be offset by lower rates of carbon gain, photosynthetic rates were measured on individuals of *E. farinosa* differing in degree of pubescence. All plants were grown under conditions of sufficient water and nutrients and full sunlight in phytocells (Year Book 72, pp. 393–403). Simultaneous measurements of CO_2 and water vapor exchange were made on single attached leaves using a leaf chamber and gas-exchange system (Mooney *et al.*, 1971; Osmond and Björkman, 1975). All measurements were made in normal air, 325 μbars CO_2 , and 21% O_2 .

Photosynthesis–light response curves for leaves of *E. farinosa* with solar absorption coefficients of 53%, 65%, and 82% are shown in Fig. 30. Three significant features evident in these curves are: (1) The incident quantum yield (slope of linear part of curve between 0 and 30 $\text{nE cm}^{-2} \text{sec}^{-1}$) decreases as the pubescence increases; (2) the maximum rates decrease as pubescence increases; and (3) unlike most plants, net photosynthesis under all three pubescence conditions is not light saturated even at 200 $\text{nE cm}^{-2} \text{sec}^{-1}$, which is equivalent to full noon sunlight during the summer. Quantum yields on an incident light basis were 0.025, 0.033, and 0.041 for absorptances of 53%, 65%, and 82%, respectively. When calculated on an absorbed quanta basis, the quantum yields were 0.048, 0.050, and 0.050. These quantum yields, typical for higher plants (Year Book 74, pp. 760–761), indicate that although pubescence in *E. farinosa* increases light reflectance and reduces net photosynthesis, it does not affect the basic photosynthetic process (CO_2 fixed per

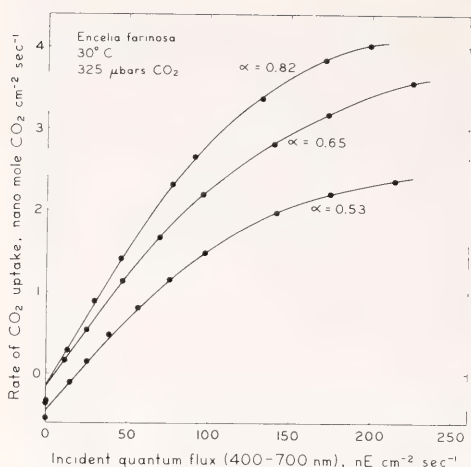


Fig. 30. Light dependence of net CO_2 uptake by single attached leaves of *Encelia farinosa* differing in their degree of pubescence. Rates were determined at a leaf temperature of 30°C , a CO_2 partial pressure of $325\ \mu\text{bar}$, an O_2 concentration of 21% by volume, and a water vapor pressure deficit of less than $10\ \mu\text{bar}$. α = absorption coefficient.

quantum absorbed). Net photosynthesis is so dramatically affected by pubescence that at a leaf absorptance of 53% the net photosynthetic rate is nearly linear with light intensity up to full sunlight. Stomatal conductances to water and CO_2 exchange were similar for the leaves at any given light intensity, suggesting that CO_2 diffusion limitations were not responsible for differences among the curves. When photosynthetic data from these three curves are plotted against absorbed rather than incident quanta, all data lie on a single curve, indicating that the principal differences among the curves were due primarily to decreases in light absorption due to pubescence and not to physiological differences.

Studies on the ecophysiology of the genus *Encelia* will continue in the oncoming year. Having documented the extraordinary capability of the pubes-

cence layer to reflect light and also to affect physiological processes, this coming year's work will focus on three main questions that have arisen during the past year: (1) What are the causes of the extremely high photosynthetic rates observed in leaves of *Encelia* species? (2) What other heat transfer or energy balance functions does the pubescence layer have? In particular, does the pubescence serve as an insulating layer between the metabolically active tissues and the hot, arid external environment? (3) What are the ecological relationships in the tradeoff between carbon gain and reduced heat load on the leaf in pubescent leaves along aridity gradients?

References

- Billings, W. D., and R. J. Morris, *Am. J. Bot.*, **38**, 327-331, 1951.
 Clausen, J. D., D. Keck, and W. M. Hiesey, *Carnegie Inst. Wash. Publ.* **520**, 1940.
 Cunningham, G., and B. R. Strain, *Ecology*, **50**, 400-408, 1969.
 Ehleringer, J., O. Björkman, and H. A. Mooney, *Science*, **192**, 376-377, 1976.
 Gates, D. M., H. J. Keegan, J. C. Schletter, and V. R. Weidner, *Appl. Opt.*, **4**, 11-20, 1965.
 Mooney, H. A., E. L. Dunn, A. T. Harrison, P. A. Morrow, B. Bartholomew, and R. L. Hays, *Photosynthetica*, **5**, 128-132, 1971.
 Osmond, C. B., and O. Björkman, *Aust. J. Plant Physiol.*, **2**, 155-162, 1975.
 Rabideau, G. S., C. S. French, and A. S. Holt, *Am. J. Bot.*, **33**, 769-777, 1946.
 Schimper, A. F. W., *Plant Geography upon a Physiological Basis*, Clarendon, Oxford, 1903.
 Warming, E., *Oecology of Plants: An Introduction to the Study of Plant Communities*, Oxford Univ. Press, London, 1909.

CARBON DIOXIDE AND TEMPERATURE DEPENDENCE OF THE QUANTUM YIELD FOR CO_2 UPTAKE IN C_3 AND C_4 PLANTS

James Ehleringer and Olle Björkman

Last year we reported that at a leaf temperature of about 30°C and in nor-

mal air the quantum yield for CO_2 uptake in plants possessing the C_3 path-

way was equivalent to that of plants possessing the C_4 pathway (Year Book 74, pp. 760–761). This seemed remarkable since it means that the decrease in the quantum yield of C_4 plants by its inherent higher energy requirement (2 additional ATP molecules per CO_2 fixed) offsets the decrease in the quantum yield of C_3 plants caused by oxygen inhibition under normal atmospheric conditions. This year we have extended this study to include the effects of changing CO_2 partial pressure and leaf temperature on the quantum yield of leaves to determine how these factors interact with the inhibitory effect of O_2 and if the quantum yields of C_3 and C_4 plants are indeed equivalent over a range of temperatures. All measurements were made at strictly rate-limiting light intensities on intact leaves attached to the plants. All plants were potted and grown under conditions of sufficient water and nutrients in growth cabinets.

The quantum yield for CO_2 uptake at normal atmospheric CO_2 concentration is markedly inhibited by 21% O_2 in C_3 plants, but it is unaffected by oxygen in C_4 plants (Björkman, 1966; Year Book 68, pp. 629–631; Year Book 70, pp. 522–524; Year Book 71, pp. 141–148; Year Book 74, pp. 760–761). Similarly, at normal atmospheric O_2 concentration the quantum yield is markedly CO_2 dependent in C_3 but not in C_4 plants (Year Book 70, pp. 522–524; Year Book 71, pp. 141–148). Figure 31 shows the quantum yield of the C_3 plant *Encelia californica* as a function of CO_2 concentration in low and normal O_2 concentration and 30°C leaf temperature. Over the range of intercellular CO_2 concentrations normally encountered by leaves (8–14 μM , equivalent to a partial pressure of 200–350 μbar) the quantum yield in 21% oxygen is markedly dependent on CO_2 concentration, ranging from 0.042 to 0.059 mol CO_2 /absorbed einstein over this span. Even at intercellular CO_2 pressures as high as 1500 μbar , the quantum yield is still measurably lowered by 21% oxygen. At low CO_2 intercellular pressures (less than 200 μbar) the oxy-

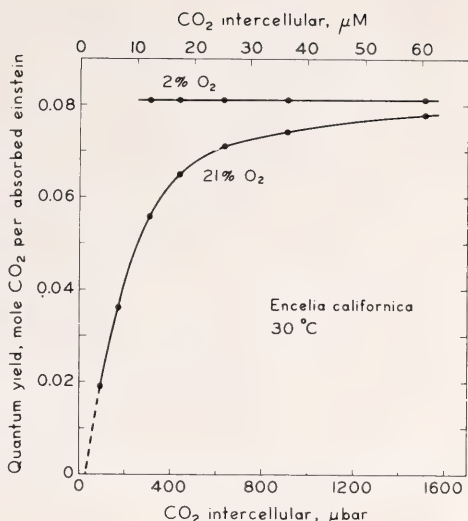


Fig. 31. Quantum yield for CO_2 uptake in *Encelia californica* (C_3) determined as a function of intercellular pressure in 21% and in 2% oxygen. Leaf temperature was 30°C.

gen inhibition is much greater than at normal CO_2 pressures and the quantum yield extrapolates to zero at the CO_2 compensation point. In contrast, under low oxygen the quantum yield of the C_3 plant *E. californica* is independent of CO_2 pressure. The absence of a CO_2 dependence of the quantum yield in low oxygen suggests that the carboxylase activity of RuDP carboxylase-oxygenase in vivo is saturated by 300 μbar CO_2 at rate-limiting light intensities. The presence of a strong CO_2 dependence of the quantum yield in C_3 plants at higher O_2 concentrations is consistent with the view that the O_2 inhibition of net CO_2 uptake is primarily caused by the oxygenase activity of RuDP carboxylase.

The steep dependence of the quantum yield in C_3 plants such as *E. californica* (and other C_3 species) on CO_2 concentration at normal atmospheric O_2 concentration and the independence of the quantum yield on CO_2 in C_4 plants such as *Atriplex rosea* point out one of the selective pressures favoring the evolution of the C_4 pathway. The ability of the C_4 pathway to concentrate CO_2 at the Calvin cycle

carboxylation sites effectively makes light-limited photosynthesis of C_4 plants independent of intercellular CO_2 pressure over a very wide range. However, in a primitive atmosphere of high CO_2 , or low O_2 concentrations, or both, selective pressures would strongly favor the C_3 pathway because of its lower intrinsic quantum requirement for CO_2 fixation.

Figure 32 compares the temperature dependence of the quantum yield for CO_2 uptake in the C_3 species *E. californica* with that of the C_4 species *Atriplex rosea* in normal air of 325 μ bar CO_2 and 21% O_2 (Fig. 32). These results show clearly that in normal air the quantum yield of the C_3 plant is superior to that of the C_4 plant at leaf temperatures below approximately 30°C, but at higher temperatures the quantum yield of the C_4 plant is superior to that of the C_3 plant. This change in the quantum yield in the C_3 species with temperature cannot be accounted for by changes in the liquid phase solubilities of CO_2 and O_2 over the temperature span, since corrections for changes in the solubilities of these gases fail to alter the observed quantum yields significantly. The change in

the quantum yield in C_3 plants such as *E. californica* with leaf temperature must therefore be due to a change in the degree of oxygen inhibition with temperature. Oxygen inhibition of the quantum yield increases exponentially as the temperature is increased from 10° to 40°C. In normal air the oxygen inhibition is only 14% at 14°C but increases to 47% at 38°C. Over this same temperature span there is no change in the absolute value of the quantum yield of *E. californica* when measured in low oxygen. The change in quantum yield due to inhibition by 21% O_2 in *E. californica* follows the Arrhenius equation, giving an activation energy approximately equivalent to -8 Kcal mol^{-1} . If the view is correct that the O_2 inhibition of the quantum yield is caused by the oxygenase activity of RuDP carboxylase, then the present results imply that oxygenase activity increases more steeply with temperature than does carboxylase activity. Experiments designed to determine if this is the case are being conducted with the purified enzyme by Dr. Murray Badger in this laboratory.

The distribution of C_3 and C_4 species in nature correlates generally with daylight temperature, i.e., C_4 species are more common in hot climates than in cool or cold climates. Since the rate of photosynthesis and primary production in many plant canopies is strongly light limited, the observed difference in quantum yield between C_3 and C_4 species as a function of leaf temperature may be an important factor in determining their distribution. Under conditions of sufficient soil moisture, a C_3 plant will have greater potential for carbon gain at low temperatures. Conversely, a C_4 plant will have greater potential for carbon gain at high temperatures with a crossover point at approximately 25°–30°C. This greater potential for carbon gain in C_3 plants at low temperatures would imply that C_4 photosynthesis would be at a disadvantage in cool, low-light habitats such as the floor of cool temperate forests and the arctic tundra. On the other hand,

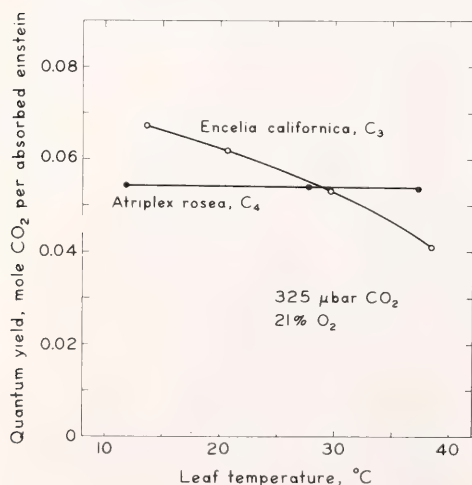


Fig. 32. Quantum yield for CO_2 uptake in *Encelia californica* (C_3) and *Atriplex rosea* (C_4) as a function of leaf temperature. The CO_2 pressure was held constant at 325 μ bar and the oxygen concentration was 21% by volume.

the C_4 pathway would be selectively more advantageous in shaded habitats of high temperature and in dense stands in high-light, high-temperature habitats such as tropical grasslands. C_4 photosynthesis would of course be particularly advantageous in hot, sun-baked desert habitats where little mutual shading of the leaves occurs within the plant stands. However, under these conditions the advantage of C_4 photosynthesis is largely due to the increased capacity for photosynthesis at high light intensities. Nevertheless, the higher quantum yield at high temperatures would also be ex-

pected to confer a significant advantage. It is apparent that both the increased capacity for photosynthesis at high light intensities and the higher quantum yield at high temperatures are the results of the same mechanism, namely the ability of the C_4 pathway to increase the concentration of CO_2 at the site of fixation by RuDP carboxylase.

References

- Björkman, O., *Physiol. Plant.*, 19, 618, 1966.

HYBRIDIZATIONS IN *Atriplex*

Malcolm A. Nobs

In 1968 the first hybrid between a species having the C_4 photosynthetic pathway and one with the C_3 pathway was successfully obtained. This F_1 hybrid, *Atriplex rosea* L. \times *A. triangularis* Wildenow (*A. patula* ssp. *hastata*, Hall and Clements), was a diploid with $2n = 18$. During the reduction division in this hybrid, only four pairs of chromosomes formed, resulting in less than 10% fertility. The progeny obtained in the second generation formed a series of polyploids ranging from triploid to above pentaploid, making a critical genetic analysis of the inheritance of the C_4 vs. the C_3 pathways impossible.

During the ensuing years, 22 additional intraspecific hybridizations have been attempted. These attempts were made for three basic reasons. The first was to obtain a hybrid combination between C_3 and C_4 species which would remain diploid and be sufficiently fertile for genetic analysis. The second was to obtain hybrid combinations between different C_4 species to determine whether in later generations there would be segregation within the C_4 characteristics. The third was to obtain data on the genetic relationships within the genus *Atriplex* which could supplement the studies by Thompson on DNA hybridization.

The crossing diagram (Fig. 33) summarizes these accumulated data. It is apparent that during the evolution of *Atriplex* the *Obione* subgenus diverged profoundly from the subgenus *Euatriples*. Only one hybrid combination out of eight attempts, *A. rosea* \times *argentea* ssp. *expansa*, has yielded hybrids; within *Euatriples*, by contrast, six of the eight attempts have yielded hybrid progeny, and within *Obione* two out of five have been successful.

Within *Euatriples* the species studied have become highly differentiated genetically. Table 16 summarizes the cytological data. In three of the combinations the hybrids were so weak that they never reached maturity. The remaining three form a progressive series from nearly sterile to partially fertile. The low fertility in the *rosea* \times *sabulosa* combination, both in the *rosea* group and believed by Hall and Clements (1923) to be very closely related, is in part due to chromosomal rearrangements. Bridges and fragments are commonly seen during the first anaphase of reduction division.

The one fertile hybrid, as judged by regular reduction division resulting in 98% normal pollen, is *A. fruticulosa* \times *A. serenana*. Both species are diploids in the pentandra group of *Obione*. It is

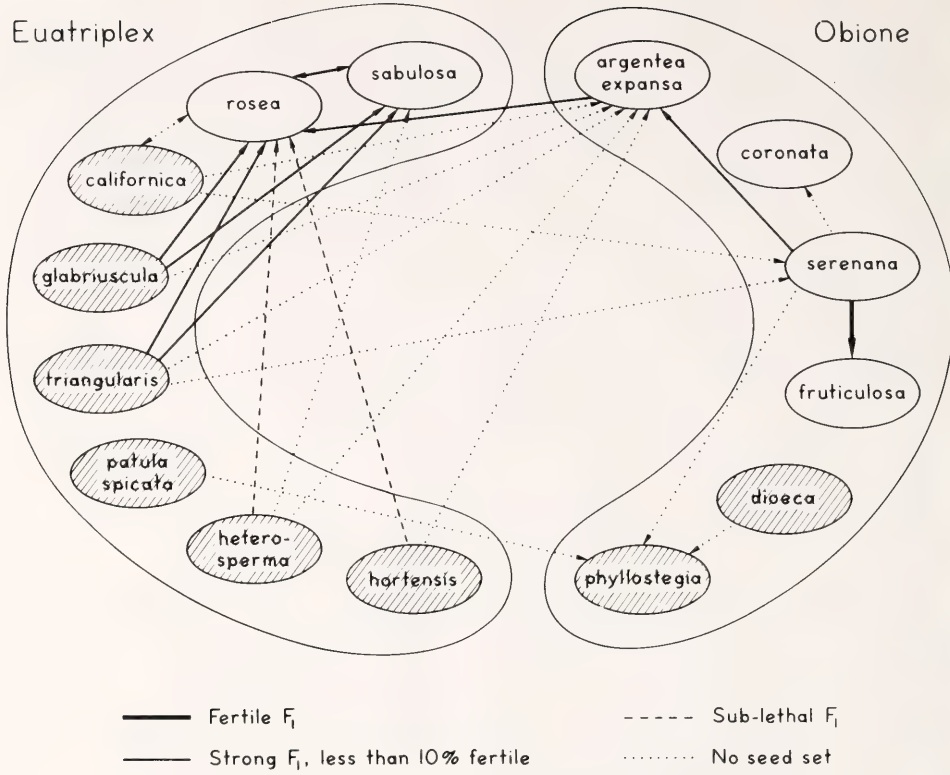


Fig. 33. Summary of crossings between species of *Atriplex*. Open ovals are species which possess C₄ photosynthesis. The shaded ovals possess the classic C₃ pathway.

TABLE 16. Cytological Characteristics of *Euatriplex* Hybrids.

| Combination | Chromosome Pairing | Normal Pollen |
|---------------------------------------|---------------------------------|---------------|
| <i>rosea</i> × <i>hortensis</i> | Sub lethal | ... |
| <i>rosea</i> × <i>heterosperma</i> | Sub lethal | ... |
| <i>sabulosa</i> × <i>triangularis</i> | Sub lethal | ... |
| <i>rosea</i> × <i>triangularis</i> | 4 ^{II} 10 ^I | 6%– 7% |
| <i>rosea</i> × <i>glabriuscula</i> | 6 ^{II} 6 ^I | 8%–10% |
| <i>rosea</i> × <i>sabulosa</i> | 8 ^{II} 2 ^I | 29% |
| | rarely, 9 ^{II} | |

a vigorous hybrid and is intermediate morphologically between the parents. It has regular Kranz-type leaf anatomy as do both of its parents. The second generation of this combination should yield valuable material for the study of the C₄ photosynthetic system.

The other successful hybrid combination within *Obione* is *A. serenana* ×

A. argentea ssp. *expansa*. The former is diploid while the later is tetraploid. The hybrid is triploid with 27 chromosomes. At first metaphase in reduction division frequently nine pairs of chromosomes are formed with nine univalents. As the *A. argentea* parent frequently has 1–3 multivalents at this stage, the observed pairing is pre-

sumed to be autopolyploidization between the chromosomes of the *argentea* parent.

A similar situation exists in the one hybrid between *Euatiriplex* and *Obione*, *A. rosea* (diploid) \times *A. argentea* ssp. *expansa* (tetraploid). This hybrid is also triploid, and has 27 chromosomes, with nine chromosome pairs at metaphase and nine univalents. If autopolyploidization does occur, it would form a physiologically sound genomic foundation which could accommodate foreign chromosomes. The lack of success in the attempted cross between *A. phyllostegia* and *A. dioeca* came as a surprise, since they are morphologically very similar. Both are diploid, possess the rudimentary perianth in the female flowers, have succulent leaves with classic C_3 anatomy, and have very similar inflorescences. In fact Hall and Clements (1923) consider them closely enough re-

lated that they might be united into one species. Apparently, however, they have diverged considerably genetically, for although aborted embryos were formed, no hybrid seed matured.

At the present time not all of our basic objectives have been fulfilled, for we have not achieved a diploid hybrid between a C_3 and a C_4 *Atriplex* which is sufficiently fertile to produce a second generation for genetic and physiological study. However, considerable progress has been made on our understanding of the genetic structure of the genus.

References

- Hall, H. M., and F. E. Clements, *Carnegie Inst. Wash. Publ. No. 326*, 1923.

GROWTH AND PHOTOSYNTHESIS OF *Chlamydomonas reinhardtii* AS A FUNCTION OF CO_2 CONCENTRATION

Joseph Berry, John Boynton, Aaron Kaplan, and Murray Badger

Earlier studies by Bowes and Berry (*Year Book 71*, pp. 148-157) showed that photosynthesis by cells of the green alga *Chlamydomonas reinhardtii* was competitively inhibited by O_2 and that a portion of the carbon fixed (depending upon the CO_2 and O_2 concentration) was excreted to the medium as glycolic acid. These effects were correlated with the effects of O_2 and CO_2 on ribulose 1-5 diphosphate (RuDP) carboxylase/oxygenase, the enzyme that catalyzes CO_2 fixation and appears to be the site of O_2 inhibition in species of higher plants having C_3 photosynthesis.

Experiments were initiated this year to investigate the effect of O_2 and CO_2 concentration upon the growth of *Chlamydomonas*. The initial objective was to find an appropriate combination of high O_2 and low CO_2 concentration which would inhibit growth of the wild type strain and serve as a positive selective method for mutant genotypes

with altered CO_2 requirements. We hypothesized that such mutant genotypes might result from changes in the properties of the RuDP carboxylase/oxygenase molecule which would affect its $K_m(O_2)$ or $K_m(CO_2)$. Selective screening of mutagenized haploid and diploid genotypes under this condition might permit the identification of nuclear or chloroplast gene loci, respectively (Lee *et al.*, 1973), coding for the peptides comprising the small and large subunits of the enzyme RuDP carboxylase/oxygenase (Wildman *et al.*, 1975).

In similar experiments with higher plants (*Year Book 70*, pp. 507-511), a controlled atmosphere of 60 ppm CO_2 and 21% O_2 was found to permit very little growth of the C_3 plant *Atriplex patula*, while the C_4 species *A. rosea* grew well under this condition. This growth regime was used to screen F_2 hybrid genotypes derived from a cross between *A. rosea* and *A. patula* for the

more efficient C_4 mechanism of CO_2 fixation.

In the present experiments, the wild type *C. reinhardtii* (haploid Strain 137C, Stock GB-126) was grown phototrophically in 300 ml shake cultures of HS culture media (Sueoka, 1960) aerated with different mixtures of O_2 and CO_2 . Light intensity was $50 \text{ nE cm}^{-2}\text{sec}^{-1}$ from VHO fluorescent lamps in the physiology and biochemistry experiments and $41 \text{ nE cm}^{-2}\text{sec}^{-1}$ from cool white fluorescent lamps in the growth experiments. The results of the growth experiments are presented in Table 17. Maximum growth rate (minimum doubling time) was obtained in air enriched with 3×10^4 ppm CO_2 . At this CO_2 concentration, growth rate was substantially inhibited by increasing the O_2 partial pressure to 97%. However, decreasing the CO_2 concentration from 3×10^4 to 350 ppm had little effect upon growth, suggesting that CO_2 uptake is nearly saturated at air levels of CO_2 under the light levels and cell densities used. Substantial but slow photosynthetic growth was obtained at less than 100 ppm. At both 65 and 33 ppm, growth rate was not significantly affected by changing the O_2 concentration dramatically. Since growth rate under the low CO_2 regimes appears to be linearly dependent upon

CO_2 concentration, the CO_2 compensation point for photosynthetic growth must be quite close to zero (or very low). These results are remarkably different from those obtained with C_3 species of higher plants, and indicate both a greater resistance of O_2 inhibition and a higher efficiency of CO_2 fixation at low CO_2 concentrations. Superficially, these algae would appear to use a mechanism of CO_2 assimilation which differs from that of normal C_3 species of higher plants and resembles C_4 photosynthesis in the sense that the organism can utilize very low exogenous CO_2 concentrations for photosynthetic growth.

PHOTOSYNTHETIC CO_2 FIXATION

The earlier studies by Bowes and Berry (*Year Book 71*, pp. 148–157) indicated that photosynthesis by cells of *C. reinhardtii* grown on air enriched with $2\text{--}3 \times 10^4$ ppm CO_2 was quite similar to C_3 photosynthesis of higher plants. They reported a $K_M(CO_2)$ of approximately $30 \mu M$ at pH 7.8 and low O_2 , incorporating $^{14}CO_2$ into acid stable products as the assay method. CO_2 fixation was competitively inhibited by increased O_2 concentrations. Very efficient CO_2 uptake has been reported for certain algal species. Whittingham

TABLE 17. Phototrophic Growth of *C. reinhardtii* in HS Media Aerated with Gas Mixtures of Differing O_2 and CO_2 Concentrations (balance N_2) at $25^\circ C$ and $41 \text{ nE cm}^{-2}\text{sec}^{-1}$ Cool White Fluorescent Light*

| Gas Mixture | | Growth | |
|-----------------|-----------|--------------------|---------------------------------------|
| CO_2 , ppm | O_2 , % | Doubling Time (hr) | Final Yield (cells/ml $\times 10^6$) |
| 3×10^4 | 21 | 9.1 | 14.4 |
| 3×10^4 | 97 | 25.3 | 11.9 |
| 350 | 21 | 9.9 | 15.2 |
| 350 | 97 | 14.6 | ... |
| 65 | 4 | 21.9 | 1.5 |
| 65 | 84 | 19.2 | 1.9 |
| 33 | 2 | 41 | 0.89 |
| 33 | 92 | 37 | 0.90 |
| 0 | 100 | ... | 0.29 |
| 0 | 0 | ... | 0.25 |

*Flow rates varied from 9 to 18 l/hr per flask. Cultures were inoculated at a density of 1×10^5 cells/ml from log phase phototrophic cultures pre-grown at 350 ppm CO_2 –21% O_2 . Cell density was followed daily by hemocytometer counts. Experiments were terminated when each culture reached stationary phase, and the doubling time was calculated for the linear portion of the growth curve.

(1952), Steemann-Neilsen (1955), and Brown and Tregunna (1967) have demonstrated that *Chlorella* species become CO_2 -saturated at CO_2 concentrations less than atmospheric. Brown and Tregunna (1967) and Steemann-Neilsen and Jensen (1958) have shown that this alga has a very low CO_2 compensation point, and Björkman (*Year Book 65*, pp. 446–454) reports that, in contrast to the findings of Tamiya and Huzisige (1949), photosynthesis of *Chlorella* is not inhibited by 21% O_2 . The growth experiments reported in Table 17 suggest that *Chlamydomonas* has photosynthetic characteristics similar to those discussed above for *Chlorella*.

The apparent contradiction of the growth studies with the photosynthetic properties reported by Bowes and Berry (*Year Book 71*, pp. 148–157) can be explained on the basis of different physiological states of the algae. An abundance of literature, starting with J. S. Turner (unpublished) and R. Howels (1940), reviewed by Briggs and Whittingham (1952), indicates that *Chlorella* can exist in two distinctly different states depending upon whether the cells were exposed to air (0.03% CO_2) or air enriched with 1%–5% CO_2 during growth. The alga may be induced to change from one state to the other by exposure to the appropriate CO_2 supply. Induction may take from $\frac{1}{2}$ hr to several hours depending upon the strain and direction of the transformation (Briggs and Whittingham, 1952; Graham and Whittingham, 1968; Steemann-Neilsen and Willemoes, 1966). Clearly, the physiological efficiency for use of CO_2 in photosynthesis differs dramatically for *Chlorella* induced to one state or the other. Such cells also differ in their metabolism of glycolic acid (Nelson and Tolbert, 1969) and their content of carbonic anhydrase (Graham *et al.*, 1971). A similar phenomenon has been documented in the blue-green alga *Coccochloris* (Ingle and Coleman, 1976), and *Chlamydomonas reinhardtii* (Nelson *et al.*, 1969; Graham *et al.*, 1971). Thus,

Chlamydomonas grown at low CO_2 might be expected to have quite different kinetics of CO_2 assimilation and interaction with O_2 than those reported by Bowes and Berry (*Year Book 71*, pp. 148–157), for cells adapted to higher CO_2 .

While the general features of this adaptive developmental differentiation by algae are known, the mechanism(s) responsible are not clear. Some workers assume the photosynthetic capabilities of high- CO_2 grown cells to be impaired (Österlund, 1950; Steemann-Neilsen, 1955; Steemann-Neilsen and Willemoes, 1966). Our interest in this topic was whetted by the indication (discussed previously) that high- CO_2 adapted cells have kinetics of CO_2 assimilation which resemble higher plant species with C_3 photosynthesis, and low- CO_2 adapted algae appear to be exceptional and are considerably more efficient in assimilating CO_2 . No comparable data of the kinetics of CO_2 exchange of high- and low- CO_2 adapted algae were available to evaluate this hypothesis, nor had the factors governing the kinetics of CO_2 assimilation in the respective states been investigated. For these reasons, a comparative study of *C. reinhardtii* adapted to low- and high- CO_2 concentration was initiated.

Photosynthesis was measured as O_2 production in a closed electrode chamber (Rank Brothers, Bottisham, Cambridge, England) modified for increased sensitivity as described previously (*Year Book 72*, pp. 405–407). After depletion of endogenous CO_2 (contained in the media, or as a pool within the cells) O_2 evolution was completely dependent upon addition of CO_2 or NaHCO_3 to the electrode chamber.

The dependence of photosynthesis (measured as O_2 evolution) upon added HCO_3^- concentration in 50 mM HEPES, pH 7.0, is shown in Fig. 34 for both low- and high- CO_2 grown cells. Similar maximum rates are achieved on a per-cell basis for cells cultured under both regimes, but the concentration dependence is dramatically different. The apparent K_M 's on a HCO_3^-

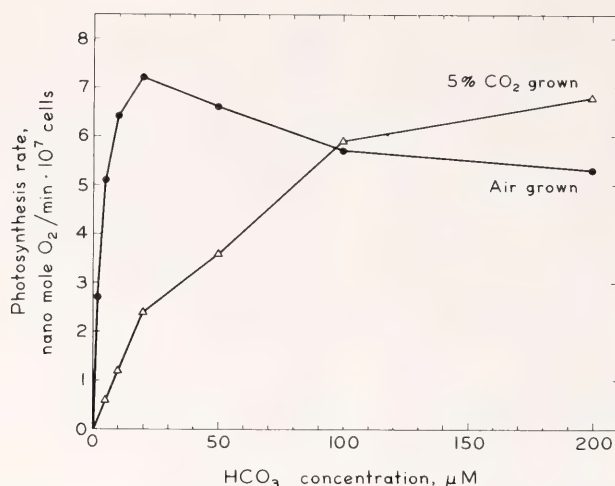


Fig. 34. Dependence of photosynthesis of low- and high- CO_2 -adapted cells of *C. reinhardtii* upon added HCO_3^- concentration in 50 mM HEPES buffer at pH 7.0. Saturating light of $70 \text{ nE cm}^{-2} \text{ sec}^{-1}$ was provided. Temperature was 20°C . O_2 increased with use of HCO_3^- and ranged from 5% to 15%. Data for low HCO_3^- concentrations were obtained at the lowest O_2 concentration measured. $\text{O}_2/\text{HCO}_3^-$ exchange ratios were between 0.9 and 1.0.

basis are $3.6 \pm \mu\text{M}$ and $64.4 \pm 10.8 \mu\text{M}$ for the low- CO_2 and high- CO_2 grown cells, respectively. The $K_M(\text{CO}_2)$ calculated for high- CO_2 grown cells at this pH is $15 \mu\text{M}$, which is quite similar to the apparent $K_M(\text{CO}_2)$ of C_3 species of higher plants and that reported earlier (Year Book 71, pp. 148–157) for high- CO_2 adapted *C. reinhardtii*. In contrast, cells grown at low CO_2 concentrations have nearly 20-fold greater affinity for CO_2 at this pH ($K_M(\text{CO}_2) = 0.83 \mu\text{M}$) than the high- CO_2 grown cells. The CO_2 requirement of low- CO_2 adapted *C. reinhardtii* is similar to that reported by Whittingham (1952) and Steemann-Neilsen and Jensen (1958) for low- CO_2 adapted *Chlorella*. These CO_2 requirement studies were made under low ($<15\%$) O_2 concentration, with the lowest HCO_3^- concentrations always at the lowest O_2 concentration, and the ratio of O_2 evolved/ CO_2 fixed was nearly one. As will be discussed later, this ratio falls below 1.0 at limiting CO_2 concentrations under high O_2 .

Chromatographic analysis of the acid stable products formed by low- CO_2 and high- CO_2 grown cells fed $^{14}\text{CO}_2$ at half-saturating concentrations for short periods did not indicate any sub-

stantial difference in the pathway of CO_2 assimilation (data not shown). Sugar phosphate and 3-PGA were major products, and only small quantities of label appeared in malate and aspartate.

Supernatant fractions from extracts of high- CO_2 and low- CO_2 grown cells were assayed for activities of RuDP carboxylase/oxygenase and PEP carboxylase. As shown in Table 18, there was little difference between cells grown under either condition. RuDP carboxylase is the predominant carboxylase in both cell types.

Kinetic properties of RuDP carboxylase isolated from *Chlamydomonas* grown at high- CO_2 and low- CO_2 concentrations were also studied using methods described by Lorimer *et al.* (1976). We found apparent $K_M(\text{CO}_2)$ of the activated form of this enzyme to be $57 \pm 5 \mu\text{M}$ for both high- and low- CO_2 grown cells. Purification of the cell extract by Sephadex G25 did not affect the apparent $K_M(\text{CO}_2)$. Our assays of RuDP carboxylase from the C_3 plant *Encelia californica* by the same method yielded a fourfold lower $K_M(\text{CO}_2)$ of $15 \mu\text{M}$. Since the *Chlamydomonas* RuDPCase was found

TABLE 18. Comparison of RuDP Carboxylase and PEP Carboxylase Activities in Cells of *C. reinhardtii* Grown at Low (Air) and High (5%) CO₂ Concentrations*

| | nmol CO ₂ (O ₂) fixed per min per 10 ⁷ cells | | |
|--------------------------|--|-------------------|-----------------|
| | RuDP Carboxylase | RuDP Oxygenase | PEP Carboxylase |
| Air grown | 17 | 1.5 | 1.6 |
| 5% CO ₂ grown | 26 | 1.8 | 2.0 |

*Cells were harvested by centrifugation and broken in the French press at 6000 psi in 0.1 M Tris, pH 8.0, 5 mM Dithiothreitol buffer at a density of 2×10^8 /ml. Enzyme assays were carried out on S₄₀ fractions for 2 min at 25°C in 0.1 M Tris buffer, pH 8.2. The RuDP carboxylase/oxygenase enzyme was activated, RuDP carboxylase was assayed at 25°C, 10 mM HCO₃⁻, and RuDP oxygenase assayed at 20°C and 0.251 mM O₂ at saturating RuDP concentrations according to the methods of Lorimer *et al.* (1976). PEP carboxylase was assayed as described by Björkman and Gauhl (1969). Chlorophyll content was 5.2 μg and 6.7 μg per 10⁷ air-grown and 5% CO₂-grown cells, respectively.

to become activated by preincubation with CO₂ and Mg²⁺ in a manner quite similar to the higher plant enzyme, the higher $K_{1/2}(\text{CO}_2)$ of the activated *Chlamydomonas* enzyme does not appear to be an artifact of our assay system. The significance of this higher $K_{1/2}(\text{CO}_2)$ of the *Chlamydomonas* enzyme is not clear. However, no evidence was obtained for a change in the properties of RuDP carboxylase with high-CO₂ or low-CO₂ adaptation.

We have compared high-CO₂ and low-CO₂ grown cells for their capacity to excrete glycolate and for their O₂/CO₂ exchange ratio. These studies were conducted in an oxygen electrode fitted with a syringe pump that permitted continuous injection of bicarbonate to the reaction compartment, and thus permitted indefinite maintenance of steady-state conditions at subsaturating rates of bicarbonate injection. Although the steady-state bicarbonate concentrations maintained in this system could not be determined directly, they could be inferred from comparisons of the photosynthetic rate obtained with the curve for the dependence of photosynthetic rate upon bicarbonate concentration for the same cell type, concentration, and pH. At saturating rates of HCO₃⁻ injection the concentration becomes undefined. Figure 35 summarizes the results of these experiments, conducted in the presence of 20%–25% O₂. The ratio of O₂/HCO₃⁻ was calculated from the ratio of the rate of O₂ evolution to HCO₃⁻ injection.

Glycolate was measured by the technique of Calkins (1943) on cell-free filtrate of the medium after 20 minutes of steady-state photosynthesis. The ratio of glycolate excreted to HCO₃⁻ assimilated increases when the HCO₃⁻ concentration is limiting. Similar data were obtained with high-CO₂ adapted algae (cf. Fig. 39, *Year Book* 71, p. 153). The data reported here illustrate that low-CO₂ adapted *C. reinhardtii* also excretes glycolate. This had not been detected before because much lower HCO₃⁻ concentrations are required in low-CO₂ adapted cells to induce glycolate excretion (1 μM HCO₃⁻ for the low CO₂ cells vs. 50 μM HCO₃⁻ for the higher CO₂ cells at pH 7.0). Nelson *et al.* (1969) reported that low-CO₂ adapted *C. reinhardtii* has an increased capacity to metabolize glycolate. While this could contribute to the difference in glycolate excretion, we believe that the difference in the affinity of the low-CO₂ and high-CO₂ grown cells for CO₂ is the reason that glycolate excretion is not normally observed in low-CO₂ adapted algae. This is supported by the finding (not shown) that 10 mM isonicotinic acid hydrazide did not affect glycolate excretion in low-CO₂ adapted cells of *C. reinhardtii* and the blue-green alga *Coccochloris* (Ingle and Coleman, 1976).

Since glycolate is more oxidized than carbohydrate, the normal product of photosynthesis, less O₂ should be evolved per CO₂ fixed when glycolate is a major product of photosynthesis. This

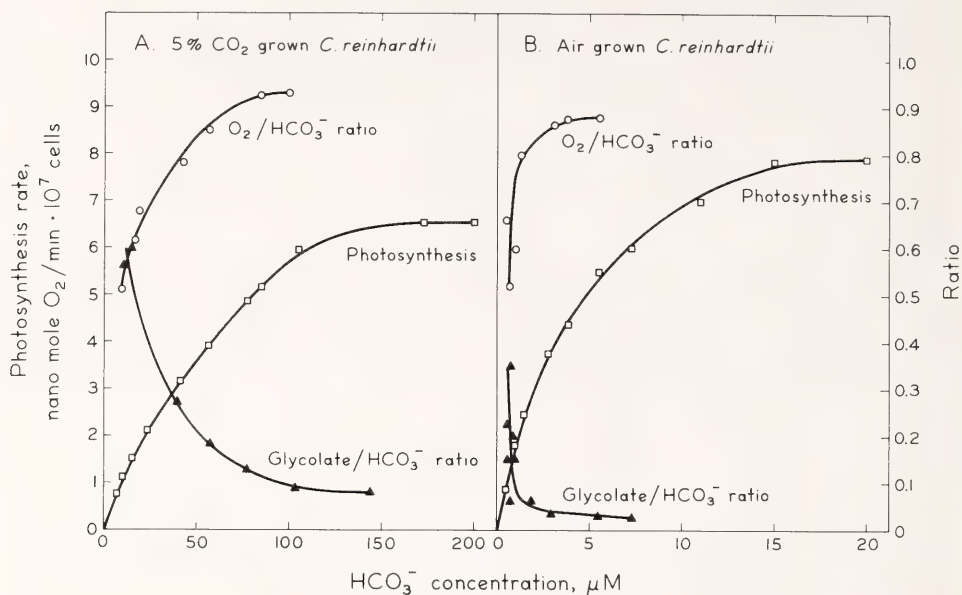


Fig. 35. Comparison of glycolate excretion, the $\text{O}_2/\text{HCO}_3^-$ ratio and O_2 evolution as influenced by the steady state HCO_3^- concentration for high- CO_2 adapted (A) and low- CO_2 adapted (B) cells of *C. reinhardtii*. Conditions were as described in Fig. 34 except that 10 mM phosphate buffer, pH 7.0, was used and O_2 was 20%–25%. Note that the scale of the bicarbonate axis differs by a factor of 10.

result is in fact obtained with both high- CO_2 and low- CO_2 grown cells. In experiments with several combinations of O_2 and HCO_3^- concentrations, we were able to account quantitatively for the changes in the measured $\text{O}_2/\text{HCO}_3^-$ ratio of high- CO_2 adapted cells by the amounts of glycolate formed (Fig. 36). In low- CO_2 adapted cells glycolate excretion followed the same trend but could not quantitatively explain the drop in the $\text{O}_2/\text{HCO}_3^-$ ratio. The significance of this difference is not clear. Under conditions of low O_2 (~1%–5%), neither cell types excreted detectable amounts of glycolate, and the $\text{O}_2/\text{HCO}_3^-$ ratio was very close to unity. Because glycolate formation alters the O_2/CO_2 exchange ratio, the effect of O_2 upon the kinetics of CO_2 assimilation cannot be assessed by measuring O_2 evolution with respirometers (cf. Tamiya and Huzisige, 1949), or by using the oxygen electrode system of these studies without also monitoring the exchange ratio. The reports that low- CO_2 adapted algae are resistant to

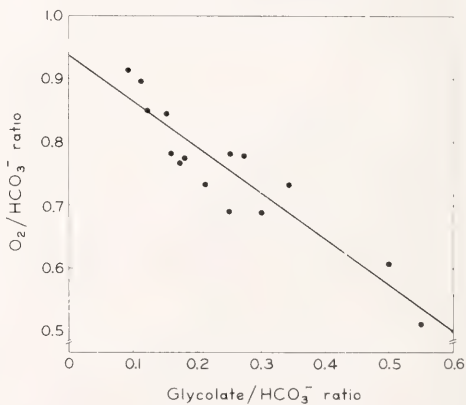


Fig. 36. A plot of the ratio of O_2 evolved to HCO_3^- assimilated vs. the ratio of glycolate/ HCO_3^- observed. The line drawn is a linear regression. Experiments were conducted with high- CO_2 adapted cells as in Fig. 35.

O_2 inhibition of photosynthesis should be reexamined in view of the observation reported here that effects of O_2 upon photosynthesis of low- CO_2 adapted *C. reinhardtii* are only evident at very low bicarbonate concentrations.

Several lines of evidence reported here including products of CO_2 fixation, studies of carboxylase enzyme levels and effects of O_2 upon photosynthesis suggest that RuDP carboxylase is the mechanism of initial CO_2 fixation utilized by both high- and low- CO_2 adapted cells. Studies of the kinetics of CO_2 assimilation by these cells indicate a very large difference in the quantitative requirement for CO_2 . The very low CO_2 requirement of low- CO_2 adapted cells verifies the hypothesis that *C. reinhardtii* can adapt to become substantially more photosynthetically efficient than C_3 species of higher plants. This also appears to be true of the green algae *Chlorella* and *Scenedesmus*, the blue-green alga *Coccochloris* (Ingle and Coleman, 1976), and perhaps many other algal species. Evidence presented indicates that, as in plants with C_4 photosynthesis, RuDP carboxylase is not more efficient in low- CO_2 adapted *C. reinhardtii* compared to C_3 plants. In contrast to C_4 plants, no evidence for an alternate initial carboxylation mechanism in *C. reinhardtii* was obtained either from studies of PEP carboxylase levels or studies of initial products of CO_2 fixation.

Reed and Graham (1968) have suggested that changes in the level of the enzyme carbonic anhydrase might explain the improved efficiency of low- CO_2 adapted *Chlorella*. Subsequently, carbonic anhydrase activity in low- CO_2 grown cells was found to be manyfold higher than in high- CO_2 grown cells (Graham and Reed, 1971; Graham *et al.*, 1971; Nelson *et al.*, 1969). Furthermore, Graham *et al.* (1971) showed that when high- CO_2 grown cells of either *Chlorella* or *C. reinhardtii* were transferred to low CO_2 , both carbonic anhydrase activity and O_2 evolution increased dramatically during the first 90 minutes without detectable changes in activity of the Calvin cycle or β -carboxylation enzymes. We question whether this increase in carbonic anhydrase activity is in itself sufficient to explain the more

efficient photosynthetic behavior of low- CO_2 adapted cells. Carbonic anhydrase catalyzes the equilibration of unhydrated CO_2 with HCO_3^- , but should not be able to alter the position of this equilibrium. Thus, in the presence of carbonic anhydrase alone, the affinity of the system for CO_2 should not exceed that of the carboxylating enzyme. Furthermore, C_3 species of higher plants have more carbonic anhydrase activity than either low- CO_2 adapted *C. reinhardtii* or C_4 plants (Graham *et al.*, 1971).

In order to explain the behavior of low- CO_2 adapted cells, we postulate that either (1) an unknown and undetected carboxylation enzyme with a greater affinity for CO_2 is present, or (2) a mechanism capable of enhancing the concentration of CO_2 at the site of fixation by RuDP carboxylase is operating. The requirement of such a concentrating mechanism for CO_2 , combined with glycolate excretion, may explain the $\text{O}_2/\text{HCO}_3^-$ ratio in low- CO_2 adapted cells.

Raven (1968, 1970, 1974) has provided experimental evidence and reviewed the work of others indicating that some algae are capable of assimilating HCO_3^- . In contrast to CO_2 assimilation, which appears to be via passive diffusion, HCO_3^- assimilation by the alga *Hydrodictyon africanum* appears to occur via a metabolic influx pump that operates across a cellular membrane. Raven (1970) has invoked this mechanism to explain the ability of certain algae to photosynthesize at alkaline pH. Since metabolic energy may be coupled to ion transport to effect large concentration gradients (Mitchell, 1966), there is no reason in principle why such a mechanism might not also be invoked to serve as a means of concentrating HCO_3^- or CO_2 within the cell under conditions of limiting CO_2 supply.

Findenegg (1974) has shown that low- CO_2 adapted cells of *Scenedesmus obliquus* possess a Cl^- influx pump that is absent in high- CO_2 adapted cells. The Cl^- uptake is inhibited by

HCO_3^- , and he suggests that the normal physiological substrate is HCO_3^- . Whether or not *Chlamydomonas* has the capacity for HCO_3^- uptake is not clear from the literature (see Raven, 1970). Therefore, experiments were conducted to determine if CO_2 or HCO_3^- is the form of carbon assimilated. Since the ratio of HCO_3^- to H_2CO_3 present in solution can be manipulated by changing the $p\text{H}$, one should be able to assess the effect of $p\text{H}$ on the total inorganic carbon requirement for photosynthesis in whole cells and infer which form (CO_2 or HCO_3^-) is actually utilized (see Raven, 1970).

We have determined Michaelis-Menten constants for photosynthesis in high- CO_2 and low- CO_2 grown cells calculated on the basis of CO_2 or HCO_3^- as a function of $p\text{H}$ (Table 19). Over the $p\text{H}$ range 7.0–8.0, the $K_{1/2}(\text{CO}_2)$ of the high- CO_2 grown cells is fairly constant (15–23 μM) while the $K_{1/2}(\text{HCO}_3^-)$ varies by a factor of more than 10. This result indicates that CO_2 is probably the form utilized in photosynthesis by the high- CO_2 grown cells. In the low- CO_2 grown cells, the $K_{1/2}(\text{CO}_2)$ falls and the $K_{1/2}(\text{HCO}_3^-)$ increases with increasing $p\text{H}$ over the range from $p\text{H}$ 7.0 to $p\text{H}$ 8.0. These data do not permit a clear decision as to which form of carbon is assimilated by the low- CO_2

adapted cells, but rather suggest that the cells are capable of utilizing variable proportions of CO_2 or HCO_3^- , depending upon the inorganic carbon concentration and $p\text{H}$. Regardless of the form of carbon present, the $K_{1/2}(\text{CO}_2)$ of low- CO_2 adapted cells of *C. reinhardtii* is much lower over the $p\text{H}$ range examined than for species of higher plants with C_3 photosynthesis. This contrasts with *Hydrodictyon africanum* (Raven, 1968) and *Scenedesmus* (Brown and Tregunna, 1967), which can utilize HCO_3^- at high $p\text{H}$ but do not appear to have enhanced CO_2 uptake at low $p\text{H}$. Either *C. reinhardtii* has a higher affinity for HCO_3^- and thus can utilize HCO_3^- at a lower $p\text{H}$, or its accumulating mechanism can utilize CO_2 as well as HCO_3^- , depending upon the form available.

Another insight into the question of how carbon is assimilated in *C. reinhardtii* is provided by studies with Diamox, an inhibitor of carbonic anhydrase in *Chlorella* (Graham and Reed, 1971; Graham *et al.*, 1971) and *Coccochloris* (Ingle and Coleman, 1976). We have found that Diamox alters the efficient response of low- CO_2 adapted cells to added HCO_3^- (Fig. 37) and shifts the concentration dependence toward that of high- CO_2 adapted cells. The effect of Diamox suggests

TABLE 19. The Influence of $p\text{H}$ upon the Apparent K_m (Total $\text{CO}_2 + \text{HCO}_3^-$) and K_m (HCO_3^-) or K_m (CO_2) of Photosynthetic O_2 Evolution by Cells of *C. reinhardtii* Adapted to High- or Low- CO_2 Concentrations*

| $p\text{H}$ | K_m (total) | K_m (HCO_3^-) μM | K_m (CO_2) | V_{\max} nmol O_2 $\text{min}^{-1}/10^7$ cells |
|--------------------------------|------------------|--|----------------------------|---|
| Low- CO_2 Grown Cells | | | | |
| 6.5 | 6.3 ± 0.5 | 3.6 | 2.7 | 12.3 ± 0.2 |
| 7.0 | 2.9 ± 0.1 | 2.4 | 0.5 | 20.0 ± 1.0 |
| 7.5 | 6.8 ± 0.5 | 6.3 | 0.5 | 13.7 ± 0.2 |
| 8.0 | 9.0 ± 1.0 | 8.8 | 0.2 | 12.6 ± 0.3 |
| High CO_2 Grown Cells | | | | |
| 6.5 | 61 ± 4 | 35 | 25.7 | 28.2 ± 0.6 |
| 7.0 | 149 ± 9 | 121 | 27.9 | 23.2 ± 0.4 |
| 7.5 | 504 ± 34 | 470 | 34.2 | 14.5 ± 0.4 |
| 8.0 | 1163 ± 64 | 1137 | 26.2 | 11.7 ± 0.2 |

* Conditions as in Fig. 34 except for $p\text{H}$. Kinetic constants were calculated according to Wilkinson (1961).

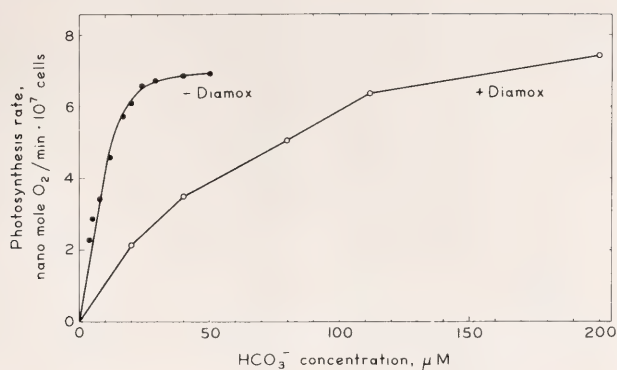


Fig. 37. The effect of Diamox upon the HCO_3^- dependence of photosynthesis of low- CO_2 adapted *C. reinhardtii*. Conditions are the same as for Fig. 34 except that phosphate buffer, pH 7.0, was used. Diamox was used at $4 \times 10^{-5} M$.

that carbonic anhydrase is essential for the mechanism of carbon assimilation by low- CO_2 adapted cells. High- CO_2 adapted cells of *C. reinhardtii* have only very low levels of carbonic anhydrase (Graham *et al.*, 1971; Nelson *et al.*, 1969).

We found that addition of carbonic anhydrase to the media of high- CO_2 adapted cells has no influence on the kinetics of photosynthesis. Thus the difference between low- and high- CO_2 adapted cells cannot be explained by the effect of carbonic anhydrase on the rate of CO_2 and HCO_3^- equilibration in the medium.

More than a single isozyme of carbonic anhydrase has been observed in 14 species of higher plants (Graham *et al.*, 1971), and Everson (1970) has shown that carbonic anhydrase is present both at the surface of and within spinach chloroplasts. Graham and Reed (1971) discuss several possible intracellular roles for carbonic anhydrase, none of which appears to explain the specific role of this enzyme in low- CO_2 adapted algal cells. Findenegg (1974) showed that adaptation of *Scenedesmus* to low- CO_2 concentration correlates with induction of carbonic anhydrase activity and a Cl^- (presumed HCO_3^-) influx pump. If HCO_3^- is the form of carbon entering the cell, it must be converted to CO_2 prior to fixation by RuDP carboxylase (Cooper

et al., 1969). Thus, both a bicarbonate influx pump and carbonic anhydrase should be required for the uptake mechanism of low- CO_2 adapted cells to enhance photosynthesis.

In summary, key components theoretically required for a CO_2 -accumulating mechanism based on an HCO_3^- influx pump have been individually characterized in various algae by a number of workers. However, in no single experimental system have these observations been integrated with one another or with studies of the kinetics of CO_2 assimilation. If this can be achieved, it may document yet another mechanism, in addition to the C_4 and CAM pathways evolved by green plants, to increase photosynthetic competence without altering the molecular properties of RuDP carboxylase.

Studies reported in this paper indicate that the CO_2 -exchange kinetics of *Chlamydomonas reinhardtii* are dramatically changed by the previous growth conditions of the algae. Cells adapted to 5% CO_2 during growth have a CO_2 requirement similar to C_3 species of higher plants, while cells adapted to air levels of CO_2 (0.03%) are substantially more efficient at low- CO_2 concentrations. We have shown that the improved efficiency of the CO_2 uptake cannot be attributed to a new pathway of CO_2 fixation or to induction of a more

efficient form of RuDP carboxylase. The increased efficiency of low- CO_2 adapted algae was abolished by the inhibitor Diamox. This suggests that carbonic anhydrase plays an essential role in the mechanism which improves the efficiency of CO_2 uptake. We suggest that HCO_3^- may be actively accumulated by a metabolic influx pump in low- CO_2 adapted cells. Carbonic anhydrase would be required to convert HCO_3^- to CO_2 , the substrate for carboxylation by RuDP carboxylase. A concentration gradient between the inside of the cells and their surroundings, established by the influx pump, could account for the increased efficiency of CO_2 uptake observed.

References

- Björkman, O., and E. Gauhl, *Planta*, **88**, 197–203, 1969.
- Briggs, G. F., and C. P. Whittingham, *New Phytol.*, **51**, 236–249, 1952.
- Brown, D. L., and E. B. Tregunna, *Can. J. Bot.*, **45**, 1135–1143, 1967.
- Calkins, V. P., *Anal. Chem.*, **15**, 762–763, 1943.
- Cooper, T. G., D. Filmer, M. Wishnick, and M. D. Lane, *J. Biol. Chem.*, **244**, 1081–1083, 1969.
- Everson, R. G., *Phytochemistry*, **9**, 25–32, 1970.
- Findenegg, G. R., *Planta*, **116**, 123–131, 1974.
- Graham, D., and C. P. Whittingham, *Z. Pflanzenphysiol.*, **58**, 418–427, 1968.
- Graham, D., C. A. Atkins, M. L. Reed, B. D. Patterson, and R. M. Smillie, "Carbonic anhydrase, photosynthesis and light-induced pH changes," in *Photosynthesis and Photorespiration*, pp. 267–274, M. D. Hatch, C. B. Osmond, and R. O. Slayter, eds., Wiley-Interscience, New York, 1971.
- Graham, D., and M. L. Reed, *Nature (London) New Biol.*, **231**, 81–83, 1971.
- Ingle, R. K., and B. Coleman, *Planta*, **128**, 217–223, 1976.
- Lee, R. W., N. W. Gillham, K. P. Van-Winkle, and J. F. Boynton, *Mol. Gen. Genet.*, **121**, 109–116, 1973.
- Lorimer, G. H., M. R. Badger, and T. J. Andrews, *Biochemistry*, **15**, 529–536, 1976.
- Mitchell, P., *Biol. Rev.*, **41**, 445–502, 1966.
- Nelson, E. B., A. Cenedella, and N. E. Tolbert, *Phytochemistry*, **8**, 2305–2306, 1969.
- Nelson, E. B., and N. E. Tolbert, *Biochem. Biophys. Acta*, **184**, 263–270, 1969.
- Österlund, S., *Physiol. Plant.*, **3**, 353–360, 1950.
- Raven, J. A., *J. Exp. Bot.*, **19**, 193–206, 1968.
- Raven, J. A., *Biol. Rev.*, **45**, 167–221, 1970.
- Raven, J. A., "Carbon dioxide fixation," in *Algal Physiology and Biochemistry*, Ch. 15, pp. 434–455, W. D. P. Stewart, ed., Univ. California Press, Berkeley, 1974.
- Reed, M. L., and D. Graham, *Plant. Physiol.*, **43**, S-29, 1968.
- Steemann-Nielsen, E., *Physiol. Plant.*, **8**, 317–335, 1955.
- Steemann-Nielsen, E., and P. K. Jensen, *Physiol. Plant.*, **11**, 170–180, 1958.
- Steemann-Nielsen, E., and M. Willemoes, *Physiol. Plant.*, **19**, 279–293, 1966.
- Sueoka, N., *Proc. Nat. Acad. Sci. U.S.A.*, **46**, 83–19, 1960.
- Tamiya, H., and H. Huzisige, *Acta Phytochim.*, **15**, 83–104, 1949.
- Whittingham, C. P., *Nature*, **170**, 1017–1018, 1952.
- Wildman, S. G., K. Chen, J. C. Gray, S. D. Kung, P. Kwanyuen, and K. Sakano, "Evolution of ferredoxin and Fraction I protein in the genus *Nicotiana*," in *Genetics and Biogenesis of Mitochondria and Chloroplasts*, Ch. 9, pp. 309–329, C. W. Birky, P. S. Perlman, and T. J. Byers, eds., Ohio State Univ. Press, Columbus, 1975.
- Wilkinson, G. N., *Biochem. J.*, **80**, 324–332, 1961.

EFFECTS OF TEMPERATURE ON RESPIRATION AND UPTAKE OF Rb^+ ION BY ROOTS OF BARLEY AND CORN*Richard Carey and Joseph Berry*

The root has received little emphasis in physiological interpretations of a plant's adaptation to different temperatures. Previous studies have measured the influence of the environmental temperature on various metabolic processes in the aerial portions of several plant species (Billings *et al.*, 1971; Björkman and Holmgren, 1961; Mooney and Billings, 1961). Grobelaar (1963) observed the virtual cessation of root growth in corn grown at 5°C. MacLean and Donovan (1973) and Porter and Moraghan (1975) have shown a differential response to low root temperatures by different cultivars of corn as well as a lower temperature limit for root growth that is above freezing. However, these studies have not examined the physiological mechanisms that determine the influence of temperature on root function. Chapin (1974) found that species of plants from cool soil regimes maintain a greater capacity for phosphate absorption than species native to warm regimes, regardless of whether the growth temperature was 5° or 20°C, but too few temperatures have been analyzed to determine the nature of the effect of temperature on ion uptake.

This paper will investigate how ion accumulation and respiration are influenced by short-term temperature variation and whether the rate of either process is modified by environmental growth temperatures. Uptake of rubidium was used because of its similarity to K^+ uptake and because of the desirable features of the tracer ^{86}Rb (Epstein, 1972).

MATERIALS AND METHODS

Barley seeds (*Hordeum vulgare* cv. Mariout Ferry Morse) and corn seeds (*Zea mays*, cv. WF9 × Bear 38) were weighed (10 g) and rinsed three times with fresh 0.5 mM CaSO_4 solution. The

seeds were spread onto acrylic-framed polyethylene-coated fiberglass mesh screens floating on 3 liters of aerated 0.5 mM CaSO_4 solution in polyethylene boxes. These boxes were placed in the dark either for 5 days at 28° ± 0.5°C (warm barley and corn) or for 14 days at 10° ± 0.5°C (cool barley). The seedlings were rinsed daily with deionized water and transferred to clean boxes with fresh CaSO_4 solution. At the end of the growth period the seedlings from the 10° or 28°C regimes were of comparable size. These were rinsed with CaSO_4 solution, and the terminal 10 cm of roots extending below the screen were excised for the experiments described below.

Oxygen consumption at various temperatures was measured on approximately 100 mg excised roots in the 5 ml vessel of a Rank Brothers' oxygen electrode. Oxygen consumption by the electrode was subtracted from the total oxygen consumed by the sample whenever the amount consumed by the electrode exceeded 2% of the total. After conditioning the roots for 15–20 min at each temperature in an aerated solution, respiration measurements were obtained. Data reported is on a fresh weight basis.

Rubidium uptake was measured from an 0.05 mM RbNO_3 solution (0.5 mM CaSO_4 added) labeled with $^{86}\text{RbCl}$ (approximately 1 $\mu\text{Ci}/300$ ml). This concentration is rate-saturating for the low concentration isotherm mechanism (Epstein *et al.*, 1963a). Roots with a fresh weight of 200–300 mg in a "tea bag" (Epstein *et al.*, 1963b) were conditioned for 20 min in a 0.5 mM CaSO_4 solution at the appropriate temperature. The "tea bags" were then transferred to 300 ml of labeled solution at the appropriate temperature for either 20 min below 15°C or 10 min above 15°C. After the uptake period, the roots

were immediately plunged into a (0° – 4°C) desorption solution (0.05 mM RbNO_3 and 0.5 mM CaSO_4) for 1 min and then transferred to a room temperature desorption solution of the same composition for about 30 min. The roots were then freeze-dried and dry weights obtained using an electro balance accurate to $3 \times 10^{-4}\text{ mg}$. The ^{86}Rb was counted on an LKB liquid scintillation counter by placing the root samples into vials and directly adding scintillation fluid toluene, Triton X-100, omnifluor, water, 1000 : 500 : 6.66 : 166).

RESULTS AND DISCUSSION

In Fig. 38 the rate of rubidium accumulation is plotted as a function of root temperature for barley grown at two temperatures. Warm-grown barley shows a temperature optimum above 30°C in contrast to the 20° – 25°C optimum of cool-grown barley. The maximal rate of rubidium accumulation for cool-grown barley is $5.0\text{ }\mu\text{moles g}^{-1}\text{hr}^{-1}$ and for warm-grown barley is $12.2\text{ }\mu\text{moles g}^{-1}\text{hr}^{-1}$. Even at 20°C the warm-grown barley has a rate of $9.7\text{ }\mu\text{moles g}^{-1}\text{hr}^{-1}$, twice the rate of cool-grown barley at the same temperature. This difference may indicate that pro-

longed exposure to low temperature inactivates portions of the ion accumulation mechanism. The change in rate from 5° to 30°C in warm-grown barley is from 1.8 to $12.2\text{ }\mu\text{moles g}^{-1}\text{hr}^{-1}$, giving a Q_{10} of 2.11 (5° – 30°C). A similar Q_{10} for barley roots was suggested by Epstein (1972) based on the difference between the rate at 4.5° and at 30°C . However, in warm-grown barley Q_{10} does not remain constant over the entire range of 5° – 30°C , indicating a changing activation energy.

The shape of the curve for warm-grown barley does not fit the monotonic exponential increase in rate normally associated with the increase in rate of a single enzymatic reaction with temperature. The very steep temperature dependence of ion uptake at low temperature lessens at temperatures between 15° and 30°C . This is seen more clearly in Fig. 39 where the natural logarithm of the rate for rubidium accumulation by barley roots is plotted as a function of the inverse of temperature (an Arrhenius plot). The data for warm-grown barley fit two different straight lines for the temperature

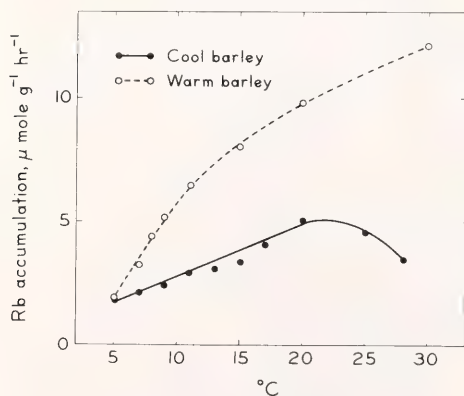


Fig. 38. Rubidium accumulation as a function of temperature by roots of warm (28°C) and cool (10°C) grown barley. Rubidium concentration was 0.05 mM in the solution. Each data point represents the average of at least four separate experiments. Rates are expressed on a gram fresh weight basis.

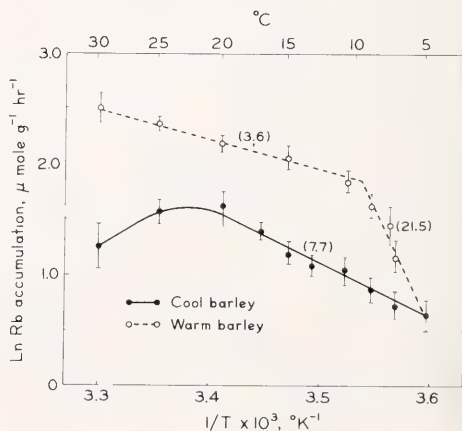


Fig. 39. Arrhenius plots for rubidium uptake by warm- and cool-grown barley roots shown in Fig. 38. Each data point represents the average and standard error of the mean (vertical bars) of at least four separate experiments. The numbers in parentheses equal the activation energy in $\text{kcal mol}^{-1}\text{deg}^{-1}$ calculated from the slope of the line.

ranges 11°–30°C and 5°–9°C. At temperatures from 11° to 30°C, apparent Arrhenius activation energy is 3.6 kcal mole⁻¹deg⁻¹, equivalent to a Q_{10} of 1.3, and indicates that ion uptake is little affected by temperatures above 10°C. Similarly, Holmern *et al.* (1974) have shown that sulfate accumulation in barley is little affected by temperatures from 20° to 30°C. Below 10°C (Fig. 39), small changes in temperature have a dramatic effect on the rate of Rb⁺ ion accumulation in the roots, with an apparent activation energy of 21.5 kcal mole⁻¹deg⁻¹ and a Q_{10} of 5.5. Such dramatic changes in Q_{10} do not occur in cool-grown barley. The reasons for this difference are not clear, but one possibility is that ion accumulation by the roots grown at high temperatures becomes limited by their respiratory capacity at low temperatures.

Temperature control of respiration was also measured. As shown in Fig. 40, the respiratory rate of cool-grown barley roots is in excess of the rate for warm-grown barley roots at temperatures below 30°C. Stimulation of respiratory capacity by cool growth temperature has also been shown by Billings *et al.* (1971). They reported that lower

environmental growth temperatures yielded higher dark respiration at a given temperature by leaves of *Oxyria digyna* adapted to arctic regimes than by those from warmer alpine regimes. Many other workers have found similar plant responses (Björkman and Holmgren, 1961; Chapin, 1974; and Mooney and Billings, 1961).

Respiration of barley roots grown at either temperature increases exponentially with temperature (Fig. 41), yielding an activation energy of 8.0 kcal mole⁻¹deg⁻¹ for warm-grown barley, and an activation energy of 10.6 kcal mole⁻¹deg⁻¹ or 8.7 kcal mole⁻¹deg⁻¹ for cool-grown barley, depending on the temperature range. Warm-grown barley does not show the same sharp change in activation energy for respiration as seen for ion uptake.

Cool-grown barley roots have more respiratory capacity than warm-grown barley and hence more energy available to the root tissue, yet they have a lower rate of ion uptake. Both the higher rate of ion accumulation and the sharp drop in rate below 10°C (Fig. 38) of warm-grown barley are distinct from the pattern in cool-grown barley. Because the rate of ion accumulation

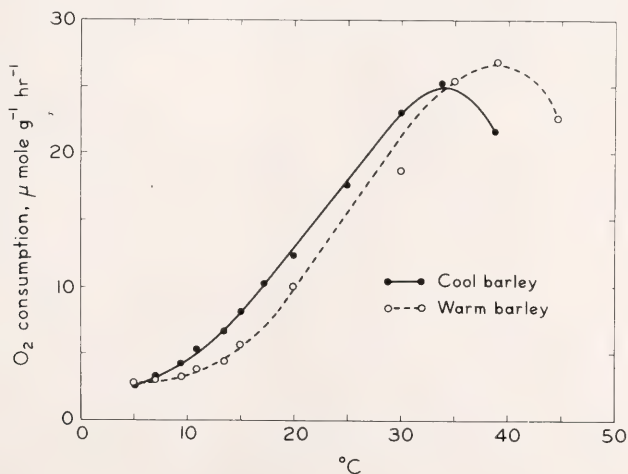


Fig. 40. Total respiration measured as oxygen consumption by warm and cool grown barley roots over the temperature range of 5° to 45°C. One root sample was used to examine a range of temperatures, either from the temperature optimum down or from the lowest temperature upward. No difference between upward or downward direction of temperature change was observed.

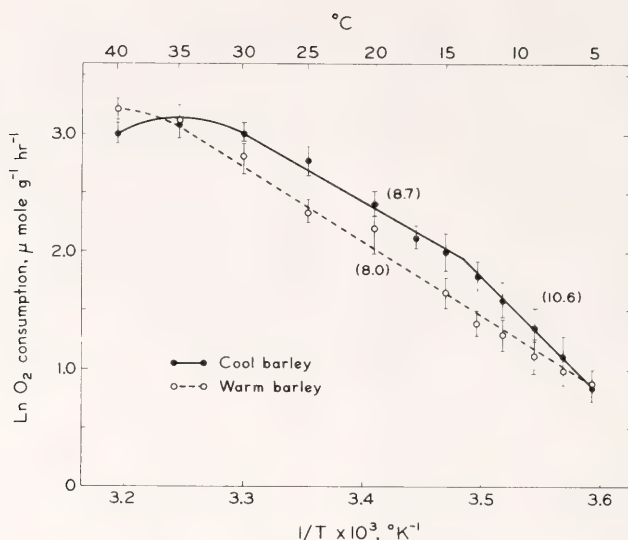


Fig. 41. Arrhenius plots for respiration by warm- and cool-grown barley roots shown in Fig. 40. The vertical bars are the S.E. of the mean obtained from each experiment. Stable rates were obtained 3–5 min after transfer into the electrode cell. Numbers in parentheses equal the activation energy in kcal mol⁻¹deg⁻¹ calculated from the slope of the line.

for roots grown at low temperature is much lower than the rate for roots that develop at normal temperatures, we suggest that development of the ion uptake mechanism may be abnormal at low temperature.

Ion accumulation in warm-grown barley is much more severely reduced (by 60%) than respiration (by 30%) as the temperature is reduced from 10° to 5°C. This suggests that respiratory limitation may not be solely responsible at low temperatures. We suggest that the effect of low temperature on ion uptake may be related to a temperature effect upon a cellular membrane. Such membrane-based temperature effects have been extensively studied in relation to chilling injury in chilling-sensitive plants such as corn, sweet potato, and tomato. Sharp changes at low temperature in the activation energy of some membrane-associated reactions and changes in the permeability of membranes have been related to chilling injury in these plants (Lyons and Raison, 1970; Raison, 1973). The temperature response of many membrane-associated activities, in-

cluding sugar uptake by bacteria (Linden *et al.*, 1973), also show such chilling-sensitive responses.

We have also examined the effect of temperature on respiration and Rb⁺ ion uptake by roots of corn, which is known to be chilling sensitive. In corn, in contrast to barley, rates of ion accumulation and respiration are closely correlated over the temperature range examined, and both have discontinuous Arrhenius plots with high activation energies at low temperatures (Fig. 42). The temperature response of corn root respiration is similar to that reported for isolated corn mitochondria (Raison, 1974). The sharp break in activation energy is taken to indicate a chilling-sensitive response. This author has shown that this type of discontinuity is caused by a change in state or phase of the membrane lipids. Later studies which considered the physical nature of membrane changes with temperature, using techniques such as electron spin resonance, indicated that the membrane phase change was dependent on the degree of saturation of fatty acids in the membrane lipids

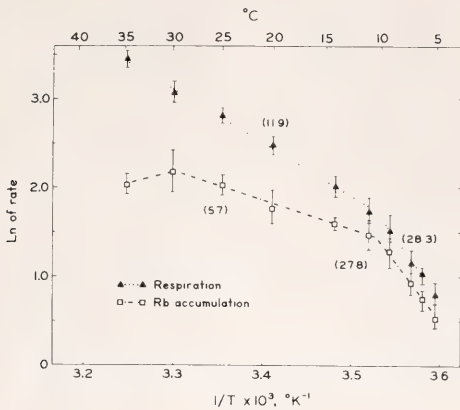


Fig. 42. Arrhenius plots of rubidium accumulation and oxygen consumption by excised corn roots over the temperature range of 5°–35°C. Rubidium concentration and method of analysis are similar to the barley roots. Numbers in parentheses equal the activation energy in kcal mol⁻¹deg⁻¹ calculated from the slope of the line.

(Raison, 1973). Organisms that lack chilling sensitivity were found to have a greater degree of unsaturation in their lipids and to lack the characteristic membrane phase transitions. Within one species, Kangaroo grass, chloroplast membranes from strains native to temperate regions have a phase change at 7°C, whereas the tropical strain had the transition at 14°C (Raison, 1974), indicating phenotypic or evolutionary adjustment to the environment.

However, since the activation energy for both ion accumulation and respiration are almost identical and respiration could limit ion uptake, it is not clear whether ion accumulation is also subject to chilling sensitivity in corn. The effect of low temperature on ion uptake by barley roots is similar to that observed with corn and may indicate an effect of low temperature on a membrane involved in ion uptake. If the response of ion uptake by barley to low temperature is caused by a phase change of the lipids of a membrane, that membrane would appear to have a different lipid composition than that of the mitochondria of barley grown at warm temperature.

Power *et al.* (1970) have shown that barley germinated at 25°C and then placed at 9°C does not grow for the first 3 weeks and subsequently has a lower maximum growth rate when compared to plants grown with 15.5° or 22°C. The plants grown at low temperatures, however, eventually equal the yields obtained by those grown at the highest temperatures. The sharp effect of low temperature (below 10°C) on growth of barley may be related to the effect of low temperature on the functioning or development of ion uptake capacity by barley roots described in the present study.

Chapin (1974) examined the degree to which plants native to warm and cool edaphic environments can maintain the capacity for phosphate uptake with severe alteration of their normal root temperatures. Data presented here indicate the need to examine these species over a range of temperatures (5°–30°C) to reveal the mechanisms responsible for limitation of ion uptake. Our studies also indicate a need to differentiate between chilling injury to the membranes functioning in ion uptake and the effect of temperature on the capacity for ion uptake or on the turnover of the ion uptake mechanisms.

In summary, we have shown phenotypic adjustment to low growth temperatures. Root respiration is clearly stimulated when barley is exposed to low root temperatures during growth. Activation energies for rubidium accumulation in corn and warm-grown barley indicate that uptake of this ion is not dramatically influenced by root temperature over the normal edaphic range (10°–30°C). A lower capacity for rubidium accumulation in cool-grown barley and a higher apparent activation energy may be caused by a damaged or incomplete ion accumulation mechanism due to prolonged exposure to low temperature. However, a phenological lag in development cannot be discounted. Unlike barley, corn exhibits a parallel pattern for the effect of low temperature on

both ion accumulation and respiration. The effect of low temperature on these activities indicates that both are involved in chilling sensitivity. A similar sharp effect of low temperature upon ion uptake by barley roots at temperatures below 10°C indicates that the ion uptake mechanism of barley may be subject to membrane-based chilling injury at low root temperatures.

References

- Billings, W. D., P. J. Godfrey, B. F. Chabot, and D. P. Bourque, *Arct. Alp. Res.*, **3**, 277–289, 1971.
- Björkman, O., and P. Holmgren, *Ann. R. Ag. Coll., Sweden*, **27**, 297–304, 1961.
- Chapin, F. S., *Science*, **183**, 521–523, 1974.
- Epstein, E., *Mineral Nutrition of Plants: Principles and Perspectives*, John Wiley and Sons, Inc., New York, p. 108, 1972.
- Epstein, E., D. W. Rains, and O. E. Elzam, *Proc. Nat. Acad. Sci. U.S.A.*, **49**, 684–692, 1963a.
- Epstein, E., W. E. Schmid, and D. W. Rains, *Plant Cell Physiol.*, **4**, 79–84, 1963b.
- Grobbelaar, W. P., *Meded. Landbouwhogeschool Wageningen*, **63**, 1–71, 1963.
- Holmern, K., M. S. Vange, and P. Nissen, *Physiol. Plant.*, **31**, 302–310, 1974.
- Linden, C. D., K. L. Wright, N. M. McConnell, and C. F. Fox, *Proc. Nat. Acad. Sci. U.S.A.*, **70**, 2271–2275, 1973.
- Lyons, J. M., and J. K. Raison, *Plant Physiol.*, **45**, 386–389, 1970.
- MacLean, A. J., and L. S. Donovan, *Can. J. Soil Sci.*, **53**, 128–129, 1973.
- Mooney, H. A., and W. D. Billings, *Ecol. Monogr.*, **31**, 1–29, 1961.
- Porter, O. A., and J. T. Moraghan, *Agron. J.*, **67**, 515–518, 1975.
- Power, J. F., D. L. Grunes, G. A. Reichman, and W. O. Willis, *Agron. J.*, **62**, 567–571, 1970.
- Raison, J. K., in *Membrane Structure and Mechanisms of Energy Transduction*, J. Avery, ed., 559–583, Plenum, 1973.
- Raison, J. K., *CSIRO Bull.*, **12**, 487–494, 1974.

POSSIBLE USE OF HOLLOW FIBER HEMODIALYSERS IN SOIL-PLANT WATER RELATIONS RESEARCH

Bruce E. Mahall¹

A major limitation of research in soil-plant water relations has been the inability to control the water potential in soil rooting media at moisture contents of less than field capacity. As pointed out long ago by Shantz (1925), the addition of small quantities of water to dry soil (less water than that necessary to reach field capacity throughout the soil volume) results in nonuniform water potential distributions with large moisture gradients. With such techniques the water potential around roots is unknown and uncontrollable at any particular time. It is also nearly impossible to control soil water potential accurately through time in the presence of a plant trans-

piring at variable rates. Recent attempts to control soil water content at levels below field capacity have not been successful (Kramer, 1974).

In studies of soil-plant water relations, hydroponic culture has become an important alternative to soil because it allows precise control of water potential uniformly distributed around roots, and the water potential may be easily altered through time. The artificiality of the hydroponic technique results in some important disadvantages, however. Solutes such as polyethylene

¹Current address: Department of Biological Sciences, University of California, Santa Barbara, California 93106.

glycol (PEG), used to maintain osmotic potentials, may be taken up by plants and may have direct physiological effects unrelated to osmotic effects (Leshem, 1966; Greenway *et al.*, 1968; Janes, 1974). Perhaps even more important is the unnatural (for most terrestrial plants) absence of gas space surrounding roots. It has been shown that this absence may affect root anatomy by a response to soil water content rather than directly to oxygen diffusion rates (Varade *et al.*, 1970, 1971). Moreover, Mexal *et al.* (1975) have demonstrated that availability of oxygen for root respiration may be severely limited in solutions of PEG of higher molecular weights.

The purpose of this note is to introduce the possibility that the problems of control of known water potentials through space and time, solute poisoning, and aeration may be greatly reduced by the use of hollow fiber hemodialyser units as root chambers. These units are now commonly used in artificial kidney machines and in routine laboratory dialysing operations. There are many models of hemodialysers commercially available, but because of their cost (~ \$25 each) and geometry, the Cordis-Dow C-DAK Models 4 and 5 appear to be most appropriate for soil-plant water relations research. These units consist of over 13,000 regenerated cellulose hollow fiber membranes aligned parallel to each other and extending 16–20 cm from one manifold to another. The fibers have an inside diameter of 200 μ , a wall thickness of 30 μ , and a collective surface area in excess of 1.3 m². Between the manifolds the fibers are enclosed by a polycarbonate jacket, closed off from the manifold chambers except by passage through the fiber walls. When in use as an artificial kidney, blood is pumped through the hollow fibers and dialysate is flushed through the jacket.

I have modified the jackets of such devices by adding a hole with a collar so that plants may be grown with their roots enclosed in the jackets among the

hollow fibers. A nutrient solution containing an osmotic solute too large to pass easily through the fiber membrane pores at the hydrostatic pressures present is pumped slowly through the fibers. Solutes as small as PEG 600 (average molecular weight) show no tendency to leak through these membranes under the small hydrostatic transmembrane pressure produced by a Buchler Polystaltic Pump. When transmembrane pressures exceeding 0.05 kg cm⁻² are produced by adding a solution to the jacket with an osmotic potential exceeding that inside the fibers, even PEG 6000 will slowly diffuse through the membranes. The rationale here is that the relatively small gas volume inside the jacket surrounding the fibers should quickly reach a water potential in equilibrium with the osmotic potential inside the fibers since water moves freely through the membranes. In addition, the physical contact between the fibers and the plant roots should result in a water film connection between the inside of the fibers and the roots through which inorganic nutrients may diffuse to the roots. Because the hollow fibers are cellulose, the root chamber must be maintained free of microorganisms capable of decomposing the fibers.

With this method, uniform distributions of accurately known water potentials around roots may be maintained and controlled precisely through short-term or long-term changes. Since the contact of the osmotic solute with roots will be restricted, the solute poisoning problem may be reduced to a large degree. Because the hollow fiber rooting medium is a composite of gas, liquid, and solid, it much more closely simulates the natural conditions than do hydroponic solutions, and oxygen around the roots may be controlled and made readily available. In fact, by connecting the root chamber to a gas analysis system, it should be possible to monitor root gas exchange.

Tests are now being conducted to determine rates of movement of various osmotic solutes and inorganic nu-

trients through the membranes and their uptake from the fibers into plants. Comparisons of plants growing hydroponically with those growing in hemodialyser-root chambers will be made with regard to nutrient and osmotic solute uptake, growth rates, and gas exchange.

References

- Greenway, H., R. G. Hiller, and T. Flowers, *Science*, 159, 984-985, 1968.
- Janes, B. E., *Plant Physiol.*, 54, 226-230, 1974.
- Kramer, P. J., *Plant Physiol.*, 54, 463-471, 1974.
- Leshem, B., *Plant Soil*, 24, 322-323, 1966.
- Mexal, J., J. T. Fisher, J. Osteryoung, and C. P. Patrick Reid, *Plant Physiol.*, 55, 20-24, 1975.
- Shantz, H. L., *J. Am. Soc. Agron.*, 17, 705-711, 1925.
- Varade, S. B., J. Letey, and L. H. Stolzy, *Calif. Agric.*, 24, 15, 1970.
- Varade, S. B., J. Letey, and L. H. Stolzy, *Plant Soil*, 34, 415-420, 1971.

ENZYME POLYMORPHISM IN THE BUTTERFLY *Colias*: SELECTION ON METABOLIC PHENOTYPES

George B. Johnson

INTRODUCTION

In the last decade it has become abundantly clear that levels of genetic variability detected by electrophoresis are very high in animal populations. However, the evolutionary significance of this variation is not clear. The difficulty is in understanding why there is so much of it. Most natural populations seem to be polymorphic at around a third of their enzyme loci, and over 10% of individuals are heterozygous at a typical enzyme locus. This is far more genetic variability than theory had led us to expect. The disparity from expectation is not unlike Diogenes searching for one honest man—and finding hundreds! Among population geneticists there has been a lively discussion concerning the possibility that these very high levels of polymorphism are simply "noise," with no adaptively important differences between alleles. Allozymes are viewed as reflecting small changes in protein structure large enough to change migration in electrophoresis, but too small to alter enzyme activity significantly. Because selection cannot differentiate between two alleles with the same activity, the polymorphism is spoken of as "selectively neutral."

Many workers, however, have not accepted this hypothesis; they argue instead that each of the polymorphic variants is functionally different in activity and that these activity differences affect fitness in such a way that the polymorphism is maintained by selection.

I will not review the history of this argument here. It has been treated in depth in a variety of recent articles representing a spectrum of opinion (Crow, 1972; Johnson, 1973; Selander and Johnson, 1973; Harris *et al.*, 1974; Lewontin, 1974). My personal judgment is that the weight of the evidence favors a selective view, but a clear and unambiguous general case has not yet been made.

EXPERIMENTAL APPROACH: A SINGLE LOCUS STUDY

To assess the adaptive significance of genetic variation is not a trivial matter. It is not enough to simply observe patterns of allele frequency which correlate with some aspect of the natural environment, as many factors other

than adaptation may generate such patterns: Migration, founder effect, genetic drift in small populations, linkage to other loci under selection, all may have important effects. What is required is a well-defined empirical question designed to contrast adaptive values directly. To study polymorphic variation at a single gene locus, an ideal system would involve at least five factors: (1) The organism should be typically polymorphic (e.g., heterozygosity at enzyme loci of between 10% and 20%). (2) The organism should lend itself to formal genetic analysis, so that the allelic nature of variants may be verified. (3) The chosen locus should be that of a single enzyme whose physiological function is clearly understood. (4) The chosen physiological function should be influenced by a discrete quantifiable habitat factor. (5) The organism should occur in natural populations where this habitat factor differs. The investigator may then directly ask whether different alleles function differently, whether the habitat variation affects that difference, and whether the functional difference may in any way be construed as an adaptive response to the habitat variation. An approach like this, although focused on only one locus, is very powerful because the investigator knows and can measure all the important experimental factors.

Such a single locus approach has been applied to lactate dehydrogenase in fish (Merritt, 1972), alcohol dehydrogenase in *Drosophila* (Day *et al.*, 1974; Clarke, 1975), and α -glycerophosphate dehydrogenase in *Colias* butterflies (Johnson, 1975a). The approaches and results of the three analyses are similar; I will describe the α -GPdH system in *Colias*, the subject of my work, as typical. I have collected experimental data on this system for five years, and over the course of the last year have analyzed these data and published them as CIW-DPB publication 559 (Johnson, 1976a; CIW-DPB publication 562 (Johnson, 1976b); and CIW-DPB publication 568 (Johnson, 1976c).

The α -GPdH system has all the properties of a good single-locus experimental system:

1. In five *Colias* species, mean heterozygosity varies from 11% to 24%, based upon examination of 14 loci in samples exceeding 100 individuals.

2. The function of α -GPdH is well understood in insects, where it plays much the same role that LdH does in vertebrates—It modulates cell redox potential $[(\text{NADH})/(\text{NAD}^+)]$ so as to regenerate NAD^+ during prolonged flight (Sacktor, 1970). Thus, null mutants for this enzyme locus in insects are flightless.

3. Formal genetic analysis of α -GPdH variants may be carried out routinely, if not conveniently. Variants segregate in crosses in a simple Mendelian fashion.

4. Flight in *Colias* is influenced by a discrete and measurable habitat factor, temperature. The interaction has been elegantly investigated by Watt (1968), who implanted thermistors in *Colias* butterflies and asked under what conditions they fly. They fly only within a narrow range of body temperature. Because this critical flight temperature is usually higher than ambient, the butterflies raise their body temperatures by solar heating. This behavior is unmistakable in the field. When a cloud covers the sun, all flying *Colias* drop to the ground; when the sun comes back out, they warm up again in a few minutes and resume flying. By recording solar flux with a pyrothermograph, one may quantitatively characterize a habitat in terms of available flight windows for *Colias*. Thus habitat temperature, particularly solar flux, seems a promising choice for an environmental factor importantly affecting the functioning of α -GPdH. Temperature has proven a fortunate choice, as the biochemical behavior of enzyme alleles of α -GPdH in *Colias* is indeed differently affected by reaction temperature (Johnson, 1976a). By marking the wings of live individuals, one may carry out mark-release-recapture studies in a straightforward manner,

and thus learn the size and genetic structure of natural populations.

5. Finally, the available habitats of the Colorado *Colias* encompass many very different thermal environments. The alpine species *C. meadii* is typically found on tundra, above timberline (>12,000 ft). The montane species *C. alexandra* occurs in montane open valleys at elevations of about 9500 ft. *C. scudderi* lives in montane habitats of 9000–11,000 ft in conjunction with willow (the other species are restricted to legumes). The lowland species complex *C. philodice*–*C. eurytheme* occurs as an agricultural pest in lowland farmland from 5000 to 8000 ft. Transitional populations occasionally occur in which populations of the lowland complex occupy montane meadows, or in which the alpine species occurs in montane habitat.

POLYMORPHISM AT THE α -GPdH
LOCUS IN
Colias (SUMMARY OF CIW-DPB
PUBLICATION 562)

Polymorphism at the α -GPdH locus was examined in 18 populations over a period of five years. Two variant forms were detected by analysis of population samples on 7% polyacrylamide gels (there is reason to believe that additional "hidden" alleles exist which are not detected by this approach). Chemical characterization of the two allozymes indicates that the same homologous alleles occur in each of the five species examined. The two alleles segregate in crosses in a Mendelian manner, and heterozygous individuals can be shown to possess three electrophoretic bands (the middle band being a heterodimer or hybrid molecule). The substrate-binding kinetics of the two forms are significantly different. In particular, the faster-migrating variant enzyme binds substrate more effectively at 10°C (has a lower $K_{1/2}$), while the slower-migrating variant is more effective at 30°C. As this corresponds roughly to the thermal range of the butterfly habitat dur-

ing the *Colias* flight season, this difference between the alleles is likely to be of adaptive significance.

When polymorphism for α -GPdH is compared for the 18 populations, a significant pattern is evident (Table 20): All nine montane populations are quite polymorphic (heterozygosity greater than 10%), while alpine or lowland populations are far less variable. This is true within species as well as between them. Thus alpine populations of *C. meadii* are not variable at this locus, while montane populations are. The result seems quite general over the five species: For 162 alpine individuals, heterozygosity was 35%; for 174 lowland agricultural individuals, average heterozygosity was 7%.

This pattern of genetic variability is consistent with what we know of the thermal nature of these habitats. While the montane valleys may get quite cold at night, they offer warmer habitats during the day than the wind-swept open tundra of the high alpine populations. It is in the colder high altitude populations that the fast allele predominates, and it is the fast allele which is the most effective binder of substrate at low temperature. Montane environments are consistently less predictable in their thermal extremes than are alpine areas, so that the pattern as well as the range of the two habitats differ.

The general results are thus quite consistent with the hypothesis that enzyme polymorphism at the α -GPdH locus reflects adaptation to a heterogeneous thermal environment. This hypothesis makes a clear and testable prediction: When single populations occupy diverse habitats, different portions of the population should experience very different selection. Thus, for example, a number of populations of *C. meadii* are known which occur right at timberline. Portions of these populations live in alpine habitats, while other portions extend down into the montane. The genetic structure of one such population (Mesa Seco) has been studied intensively by Watt and co-

TABLE 20. Patterns of α -Glycerophosphate Dehydrogenase Polymorphism in Several Species of *Colias*

| Species | Location (Altitude) | Habitat | No. of Individuals Analyzed | Heterozygosity of α -GPdH |
|---------------------|------------------------------|--------------|-----------------------------------|-------------------------------------|
| <i>C. meadii</i> | Cumberland Pass (12,000') | Alpine | 48 | 0.04 |
| | Uncompahgre Peak (12,500') | Alpine | 23 | 0.04 |
| | Mesa Seco (12,200') | Alpine | 30 | 0.17 |
| | Upper Cement Creek (12,000') | Alpine | 36 | 0.03 |
| | Upper Queen Basin (12,100') | Alpine | 18 | 0 |
| | Copper Creek (10,200') | Montane | 16 | 0.50 |
| | Los Pinos Pass (10,500') | Montane | 20 | 0.45 |
| <i>C. scudderi</i> | Upper Cement Creek (11,700') | Alpine | 7 | 0 |
| | Lower Cement Creek (9,800') | Montane | 21 | 0.24 |
| | Taylor Park (10,500') | Montane | 32 | 0.17 |
| <i>C. alexandra</i> | East River (9,500') | Montane | 76 | 0.42 |
| | Brush Creek (9,400') | Montane | 40 | 0.45 |
| <i>C. philodice</i> | Slate River (9,100') | Montane | 46 | 0.39 |
| | Lower Cement Creek (9,400') | Montane | 22 | 0.27 |
| | Hotchkiss (5,000') | Agricultural | 89 | 0.10 |
| | St. Louis, Mo. | Agricultural | 40 | 0.05 |
| <i>C. eurytheme</i> | Lower Cement Creek (9,200') | Montane | 19 | 0.21 |
| | Los Banos, Calif. (500') | Agricultural | 45 | 0.02 |

workers, and it is known from their mark-release-recapture studies that the population is genetically continuous, with at least a few individuals passing along its entire length each generation. Thus, migration within the population would be expected to render it genetically uniform—unless very strong differential selection were acting upon the two alleles.

When α -GPdH polymorphism is examined along a transect from alpine to montane within the Mesa Seco population, the transect is not uniform (Table 21). A pronounced cline in heterozygosity is seen: The alpine sites are essentially monomorphic for the fast allele, as observed previously, but the slow allele becomes increasingly more common as lower sites are examined. Only in the highly heterozygous lower sites are the two alleles in Hardy-Weinberg equilibrium; the higher sites show large deficiencies in the slow homozygote.

Again, this result seems quite general. When the same population was sampled again two years later, an iden-

tical cline was seen. Two other timberline populations, geographically quite distant, exhibit similar alpine-montane clines in α -GPdH heterozygosity.

Thus variation at this locus is in all respects consistent with an adaptive hypothesis. One cannot, of course, rule out the possibility that selection actually is occurring on some other locus that we don't know about, and that α -GPdH is simply linked to it. However, if linkage forms the basis for the observed α -GPdH polymorphism, it is remarkably fortunate that it has produced such a functionally suitable distribution of alleles!

VARIATION AT OTHER LOCI— THE MULTI-LOCUS PROBLEM

While a single-locus approach such as described above accounts reasonably well for the genetic polymorphism seen at the α -GPdH locus, the result need not be general. Species of the genus *Colias* exhibit high levels of genetic variability at many enzyme loci, and

TABLE 21. α -GPdH Polymorphism along a Transect through the Mesa Seco Population

| Year | Site No. | Altitude of Site | No. of Individuals Analyzed | Observed Frequency of α -GPdH Heterozygotes |
|------|----------|------------------|-----------------------------|--|
| 1971 | 13 | 12,200 | 21 | 0.19 |
| | 13a | 12,000 | 9 | 0.11 |
| | 12 | 11,500 | 24 | 0.21 |
| | 10 | 11,000 | 21 | 0.43 |
| | 9 | 10,800 | 5 | 0.80 |
| 1973 | 13 | 12,200 | 40 | 0.11 |
| | 12 | 11,500 | 40 | 0.21 |
| | 11 | 11,300 | 40 | 0.38 |
| | 10 | 11,000 | 40 | 0.43 |
| | 9 | 10,800 | 20 | 0.47 |

we have accounted for only one. What of the others?

To account for the generalized occurrence of enzyme polymorphism, one of two hypotheses is usually advanced. They are both fundamentally single-locus hypotheses. One is the hypothesis we have used to account for the α -GPdH variation: a heterogeneous environment selecting for different alleles under different circumstances. Similarly contrasting environmental influences are known to produce a polymorphism for sickle-cell hemoglobin in man and have been implicated in lactate dehydrogenase (AdH) polymorphism in *Drosophila*. However, if such single-locus explanations provide the basis for most of the polymorphic enzyme variation that is being reported, then we shall have to do a great deal of work to document this fact!

An alternative hypothesis is that of molecular overdominance: Hybrid enzyme molecules (formed from subunits of both parental types) are viewed as intrinsically more stable or kinetically superior. This functional superiority produces a direct heterosis, and because heterozygotes are always at an advantage, high levels of polymorphism result. This hypothesis has great difficulty, however, in accounting for polymorphisms at loci of monomeric enzymes without multiple subunit structures.

Thus, neither of these single-locus hypotheses is particularly satisfactory.

I believe that the reason for this situation lies less with the hypotheses than with the question they address. The key is in realizing that α -GPdH, LdH, AdH, and hemoglobin were selected for study because each involves a discrete physiological function directly affected by environmentally imposed reaction conditions; it is not unreasonable that a single-locus hypothesis would be satisfactory in these cases. However, this is true of few of the other polymorphic loci of *Colias*. Most of the polymorphic enzymes are intimately involved in intermediary metabolism, and a change in the activity of one may influence the functioning of many others. Thus a change in hexokinase, which generates glucose-6-phosphate, cannot help but affect the reactions of phosphoglucumutase, phosphoglucoisomerase, and glucose-6-phosphate dehydrogenase, all of which use glucose-6-phosphate as a substrate. It seems likely that only a multi-locus hypothesis will be able to account for variation among such loci. In this regard it is worth noting that polymorphic variation occurs primarily at regulatory (rate-limiting) steps in intermediary metabolism. This is a pattern one would expect only if selection were acting on the integrated metabolic phenotype rather than on individual loci *per se*.

One multi-locus hypothesis which seems to me very attractive is that enzyme polymorphism is selected at regu-

latory loci so as to buffer these reactions from environmental perturbation. To maintain metabolic integration in a variable environment is of major evolutionary importance, as many metabolic control systems are interrelated. Yet critical reactions may respond quite differently to changes in temperature, etc. It may be of significant adaptive advantage to be able to maintain a constant relationship among critical regulatory reactions.

It is easy to envision molecular mechanisms that would produce such a homeostasis. If the activities of two alleles respond differently to a habitat variable such as temperature (and such differences are well documented for tissue-specific isozymes), then the functional displacement with respect to temperature can buffer the coordination of metabolism from the effects of a temperature change. Any one allele of a regulatory enzyme can exhibit a low $K_{1/2}$ (e.g., bind substrate well) only over a relatively narrow temperature range. This thermal sensitivity is an inevitable result of the requirement that regulatory enzymes be structurally flexible enough to be sensitive to allosteric "effectors" (low molecular weight molecules such as ATP whose binding acts as a metabolic signal). Over a broad temperature range a regulatory reaction cannot maintain a constant affinity for substrate and a constant binding affinity for effector molecules. As a result, it is difficult to maintain coordinate regulation with respect to other pathways catalyzed by different proteins responding differently to the change. A heterozygous individual, however, has *two* allelic forms present in each cell. For alternative alleles α and β , the α allozyme may have the stronger binding affinity for substrate (lower $K_{1/2}$) at lower temperatures. When substrate concentrations are low, which is typically the case, only the α form will bind substrate at low temperature, and it will determine the reaction rate. Were it the only form present, the rate of binding would change at higher temperature. How-

ever, if there is a functional displacement of the β allele, the β allele has the lower $K_{1/2}$ at higher temperatures. As a result, in heterozygotes it is the form which binds the substrate at these temperatures—and the *realized* binding affinities have not changed over the broad range of temperatures!

This model suggests that heterozygotes are not overdominant so much as conditionally hemizygous, and that it is the very difference between the alleles which produces the adaptive advantage. Polymorphism is seen as a genetic strategy for maintaining metabolic integration in the face of environmental heterogeneity.

MULTIPLE LOCI IN *Colias*
(SUMMARY OF CIW-DPB
PUBLICATIONS 559 AND 568)

The highly coordinated nature of intermediary metabolism suggests that if polymorphic alleles at regulatory enzyme loci are functionally different, then the particular allele present at one locus will importantly affect the activity of many other reactions. Thus if an individual possesses a "low-temperature" allele at one locus rather than a "higher temperature" form, then it makes a difference which functional forms are present at other regulatory loci. If a network of related regulatory enzymes are all optimally suited to low temperature, then one may speak of a *metabolic phenotype* adapted to these conditions. It is at this level that selection would be most reasonably expected to act on the expressed phenotype of individuals rather than upon individual loci. Because the particular functional variant occurring at each regulatory locus influences the physiological state of the individual, *selection on metabolic phenotypes implies selection on allozymic genotypes*. To understand enzyme polymorphism, then, it will be necessary to characterize simultaneously a variety of loci in each sampled individual of a population.

Such a study is best carried out within a single population to eliminate the possibility that differences in allele frequencies arise from demographic complications. If different loci sampled from the same individuals exhibit different patterns of allele frequency, then the result may not be attributed simply to migration or habitat selection by mobile adults.

For such a genotypic comparison, 12 loci of *C. meadii* were characterized, each butterfly being tested for all 12 loci. The Mesa Seco population was selected for the study, and samples collected at each of five sites along a transect from alpine to montane: an alpine site (#13), timberline (#12), montane forest (#11), montane forest-meadow boundary (#10), and open montane meadow (#9). The total distance traversed by the transect was about 2 miles, and the elevational differences about 2000 ft. The population size was known from previous mark-release-recapture studies to exceed 1000 individuals (one generation per

year) and seemed to maintain approximately the same numbers from year to year. Individuals are seen to exchange between adjacent sites at a frequency of about 10%, although little or no exchange is seen between the more distal sites.

The general result of this survey is that despite extensive migration, a variety of different patterns of allele frequency are seen at different loci sampled from the same individuals. There is no way in which migration alone may be evoked to account for these results.

What then of the genotypes? The results from site #9 are typical. Of 20 individuals, fully nine appear to have highly organized genotypes: Five individuals have identical alleles at each of seven of the 12 loci; four others are identical at six loci. The odds that an individual would exhibit such coordination by chance are very low. For the first group, the common genotype and associated allele frequencies are:

| Locus | α -GPDH | EST-1 | EST-2 | AK-1 | AK-2 | G6PDH | HK-1 | HK-2 | ME | PGM | FUM | MdH-1 | MdH-2 | TPI |
|------------|----------------|-------|-------|------|------|-------|------|------|-----|-----|-----|-------|-------|------|
| Allele | B | A | C | A | C | A/B | A | B | A | A | A | A | A | B |
| (Genotype) | | | | | | | | | | | | | | |
| Allele | 0.79 | 1.0 | 0.50 | 1.0 | 0.84 | 0.80 | 0.25 | 0.37 | 1.0 | 1.0 | 1.0 | 1.0 | 1.0 | 0.61 |
| Frequency | | | | | | | | | | | | | | |

The joint probability that one individual will have this genotype is the product of the allele frequencies, $P = 0.02$. The probability that five individuals would possess this genotype by chance is only $(5^{20})p^5q^{15}$, or 3.66×10^{-5} !

Two such commonly recurring genotypes are apparent in the sample from site #9, one involving six loci and one involving seven. The implication is very strong that they reflect selection for particular constellations of alleles.

When the other sites are examined, similar results are obtained: Highly organized genotypes involving more than half the examined loci repeatedly occur at high frequency. However,

these genotypic combinations are different for each site! In the face of the observed adult migration, this is a remarkable result. None of the genotypic combinations common at one site are ever observed at any other. These results are summarized in Table 22. In this table, loci where more than one genotype occur among the group are symbolized by a dash.

The genotypic organization seen in the results of Table 22 clearly relates to the overall metabolic phenotype, as it involves almost exclusively regulatory as opposed to nonregulatory loci. Only those reactions which significantly affect the rate of intermediary

TABLE 22. Genotypic Combinations Specifying at least One Half of Examined Loci

| Site | Environmental | | | Regulatory | | | | Nonregulatory | | | | | Frequency |
|------|----------------|-------|---------------|--------------|-------|--------------|----|---------------|-----|-------|-------|-----|-----------|
| | α -GPdH | EST-1 | EST-2 & -3 | AK-1 & -2 | G6pDH | HK-1 & -2 | ME | PGM | FUM | MdH-1 | MdH-2 | TPI | |
| | | | | | | | | | | | | | |
| 13 | A | — | A/— | B,C | A/B | A,B | B | — | — | — | B | A | 0.25 |
| 12 | B | — | — | A,C | B | A,B | C | B | — | A | B | A | 0.33 |
| | C | — | A/C | B,C | A/B | A,B | A | — | — | A | — | B | 0.20 |
| 11 | A | C | B | A,C | A/B | A,B | B | B/— | — | — | — | — | 0.20 |
| 10 | C | — | — | —,C | A/B | A,B | C | A/— | — | — | — | — | 0.35 |
| | B | C | — | A,C | A/B | A,B | B | — | — | — | — | B | 0.20 |
| | C | C | — | —,C | A/B | A,B | D | — | — | — | — | — | 0.15 |
| 9 | B | — | C | —,C | A/B | A,— | B | — | — | — | A/— | B | 0.25 |
| | B | — | D | A/C | A/B | A,B | D | — | — | — | B | — | 0.20 |

metabolism seem to be included in the organized genotypes.

I have considered α -GPdH and the esterases separately, as their functions are individually relatable to habitat factors such as temperature or secondary plant compounds. The genotypes of these loci also appear highly correlated with the localized habitat.

The unavoidable conclusion one must draw from these results is that organized genotypes do exist in natural populations, apparently maintained by selection in the face of significant migration.

POLYMORPHISM AS GENETIC STRATEGY

The genotypic associations described above suggest rather strong selection. For the genotypes of site #9, the indicated fitness (expected genotypic frequency/observed) is about 0.10. This seems very strong selection, and it raises the question of how the genetic and population structure of *C. meadii* has evolved to cope with what appear to be stringent environmental constraints.

The observed properties of the *C. meadii* genetic system are: (1) It involves a very large number of small chromosomes ($2N = 62$). (2) Although each female will lay several hundred eggs during a yearly flight season, population sizes remain relatively constant (this suggests a mean zygotic fitness of the order of 0.005). (3) Mark-release-recapture studies indicate low adult mortality, suggesting that selection is primarily at the larval stage. (4) Mating appears to be panmictic within local populations. (5) Members of individual subpopulations appear to be quite sedentary; while some individuals may forage for several hundred meters, the distribution of most adult individuals appears localized to portions of the cline. (6) Unlike alpine populations of *C. meadii* studied at other localities (where there is little exchange between subpopulations), there is significant exchange between adjacent

subpopulations of the Mesa Seco population.

The observed genotypic associations may be maintained in such a genetic system by at least two very different genetic strategies. One strategy is that of linkage. If the key loci are tightly linked, then the observed high-linkage disequilibrium would be an inevitable result of the low recombination fraction between them. Such a hypothesis implies that the subpopulations along the cline must be genetically isolated from one another, despite migration. Otherwise genotypes common in one subpopulation would appear in adjacent ones. To maintain the observed genotypic discontinuities would require strong selection.

The alternative hypothesis is that the genetic system of *C. meadii* is analogous to that of the plants on which it feeds—that it utilizes the great segregational power of its high chromosome number to produce in each generation a wide array of genotypes. From this varied assortment a small fraction survive to become adults at any given site. Different sites might then select for different genotypes. Such a genetic strategy is highly flexible, being capable of reorganizing the genotypic constitution of a local subpopulation yearly. Such a strategy would constitute ideal adaptation to an unpredictably variable local habitat.

In this respect it is worth noting that efficient food processing is of paramount importance to *Colias* larvae, and that the regulatory loci of Table 22 encompass many of the key points of physiological regulation of intermediary metabolism.

Both segregation and linkage strategies imply a heterogeneous habitat and strong selection within the Mesa Seco population. It is possible to distinguish experimentally between them by reexamining these sites in subsequent years. The population subdivision suggested by a linkage strategy predicts temporal stability: The local genotypic combinations should recur

from year to year. In contrast to this, a segregational strategy implies temporal as well as spatial habitat variability: The local genotypic combinations may be quite different from year to year. The data are not yet available to distinguish between these two alternatives.

It is clear that a great deal remains to be done to understand these patterns of genetic variation. To me, the most attractive conceptual framework within which to organize the findings discussed above is to view the patterns of enzyme polymorphism seen within *Colias* butterflies as adaptive strategies, which in each case *match the flexibility of the metabolic phenotype to the heterogeneity of the environment*. The detailed information needed to evaluate this interpretation involves both biochemical study of the differential functioning of allozymes and far more extensive surveys of natural populations.

References

Clarke, B., *Genetics*, 79, 101–113, 1975.

- Crow, J., *J. Hered.*, 63, 306–316, 1972.
 Day, T., P. Hiller, and B. Clarke, *Biochem. Genet.*, 11, 155–165, 1974.
 Harris, H., D. Hopkinson, and E. Robson, *Ann. Hum. Genet., Lond.*, 37, 237–253, 1974.
 Johnson, G., *Annu. Rev. Ecol. Syst.*, 4, 93–116, 1973.
 Johnson, G., *Biochem. Genet.*, 14, 403–426, 1976a (CIW-DPB Publ. 562).
 Johnson, G., *Ann. Mo. Bot. Gard.*, 63, 1976b (CIW-DPB Publ. 559).
 Johnson, G., *Evolution*, in press, 1976c (CIW-DPB Publ. 568).
 Lewontin, R., *The Genetic Basis of Evolutionary Change*, Columbia Univ. Press, New York, 1974.
 Merritt, R., *Am. Nat.*, 106, 173–184, 1972.
 Sacktor, B., *Adv. Insect Physiol.*, 7, 267–347, 1970.
 Selander, R. K., and Johnson, W. E., *Ann. Rev. Ecol. Syst.*, 4, 75–92, 1973.
 Watt, W., *Evolution*, 22, 437–458, 1968.

CHARACTERIZATION OF ELECTROPHORETICALLY HIDDEN VARIATION IN THE BUTTERFLY *Colias*

George B. Johnson

Several lines of evidence have recently begun to suggest that allelic variants detected by electrophoresis may be heterogeneous—discrete electrophoretic variants actually representing a collection of alleles, each migrating to the same position on a gel. This paper describes a series of investigations carried out over the last six years employing gel-sieving analysis to detect and characterize electrophoretically “cryptic” variation. A method has been developed during the past year which permits characterization of such variation in natural populations. This approach is described in Carnegie Institution of Washington—Department of Plant Biology Publications 561 and 569, and implications of the results are discussed in Carnegie Institution of

Washington—Department of Plant Biology Publications 563, 572, and 573.

GEL-SIEVING ANALYSIS

Electrophoretic alleles of enzyme loci are typically detected and characterized by comparing their mobilities on starch or acrylamide gels. This has provided a particularly straightforward and convenient approach to detect genetic polymorphism, as mobility classes appear clearly discontinuous in most systems. In discussing electrophoretically detected enzyme polymorphism of this sort, differences between alleles are commonly ascribed to amino acid substitutions involving charged residues. The observed discon-

tinuities in gel mobility would be an integral property of such "charge state" variation.

From a theoretical point of view, such a model is overly simple. In ideal electrophoresis a protein migrates in a field at a rate (the free electrophoretic mobility) determined by its net charge. Gel electrophoresis does not conform to ideal conditions, however, as the gel and protein interact during the course of the protein's migration. Whether one visualizes the interaction as frictional (the protein "bumps into" fibers) or hydrodynamic (sheer forces are generated by the protein's movement past fibers), the shape and size of proteins should also affect their migration rates on gels.

The migration of proteins in polyacrylamide gels has been studied by physical chemists in some detail (the matter is reviewed in Chrambach and Rodbard, 1971). The theory describing how a protein migrates in polyacrylamide gel electrophoresis stems from the observation by Ferguson that a protein's mobility in gel electrophoresis is a *logarithmic* function of gel pore size (Ferguson, 1964). This suggests a straightforward theoretical description:

$$R_f = \frac{M_0}{U_f} e^{(K_r T)} \quad (1)$$

Where R_f = protein mobility relative to front; U_f = a buffer constant; M_0 = free electrophoretic mobility, a function of net charge; K_r = retardation coefficient, a function of molecular weight and protein conformation; and T = percentage of acrylamide, which determines pore size and is inversely proportional to it.

A considerable body of theory has been developed elaborating this simple model (Fawcett and Morris, 1966; Rodbard and Chrambach, 1970, 1971; Chrambach and Rodbard, 1971; Gonnenne and Lebowitz, 1975). In this model the rate of migration is seen to

vary not only as a function of net charge (expressed as free electrophoretic mobility, M_0 , corrected by a constant, U_f , for the buffer employed) but also, as suggested by Ferguson, as a logarithmic function of the gel pore size (expressed as percentage of acrylamide) and of the gel-protein interaction as the protein passes through these pores (expressed as the retardation coefficient, K_r).

The approach suggested by Equation 1 permits independent characterization of the contributions of charge and of interactive effects such as size or conformational differences to the electrophoretic behavior of a protein. These parameters may be empirically estimated by the simple expedient of taking the log of both sides of Equation 1, yielding a function of linear form:

$$\underbrace{\log R_f}_y = \underbrace{\log \frac{M_0}{U_f}}_{\text{intercept}} + \underbrace{K_r T}_{\text{slope} \times x} \quad (2)$$

One runs replicate samples of an individual in parallel on several gels of differing pore size (T), and determines for each gel the corresponding mobility (R_f), thus characterizing directly the degree to which reducing the pore size retards migration. Regressing $\log R_f$ on T , one obtains a linear plot with a slope of K_r and an intercept whose antilog is M_0 divided by a constant. A typical result is presented in Fig. 43.

One may standardize determinations of K_r and M_0 for an enzyme of an individual by expressing the values relative to the corresponding value of the (similar) internal standard determined from the same gels. Because the standard is evaluated many hundreds of times in population survey work, the procedure permits standardization of any error affecting both proteins. Details of such standardization procedures are given in CIW-DPB Publications 561 and 569.

In order to demonstrate that an enzyme characterized in one individual is

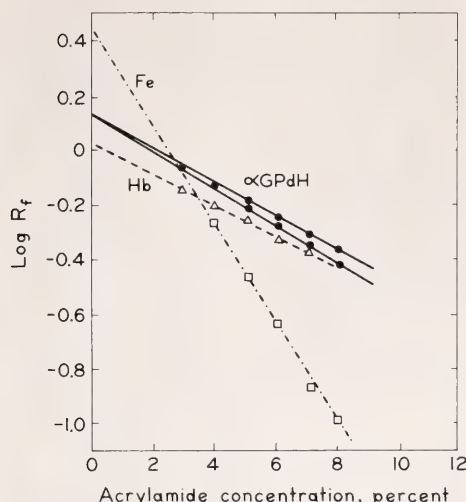


Fig. 43. Gel-sieving analysis of two alleles of α -glycerophosphate dehydrogenase (α -GPdH) with identical charge. Hemoglobin (Hb) and ferritin (Fe) are run in the same gels as internal standards, after Johnson, in press (a).

electrophoretically different from that characterized in another, it is necessary to demonstrate that K_r or M_0 or both differ significantly between the two forms. In comparing estimates of K_r and M_0 , it is important to note that K_r and M_0 pairs are determined from a single linear regression as slope and intercept, and that error in the estimation of an intercept is not independent of error in the estimation of the corresponding slope.

One simple approach to estimating the error associated with a mobility estimate independent of that associated with a corresponding K_r estimate is to express mobility in terms of the R_f observed at the mean value of T . A linear regression may be considered to rotate around such a midpoint as its slope varies, the midpoint remaining unchanged despite great changes in the y intercept. The error in the estimate of this parameter is independent of the error in the estimate of the slope K_r .

When sampling from a natural population, there will be an error variance in K_r and in mid- Y associated with each protein type present in the sam-

ple. To document the existence of multiple classes requires an independent estimate of experimental error. This estimate may be readily obtained from the internal standards run in the same gels. In plotting K_r , mid- Y estimates from a natural population, points reflecting homologous proteins should have a distribution no greater than that seen for the standard. A significantly greater distribution is evidence of heterogeneity.

VARIATION AT THE α GPdH LOCUS IN *Colias*¹

When gel-sieving analysis such as described above was carried out on individuals sampled from natural populations of butterflies, it was immediately apparent that the variation in mobility observed previously reflected more than simple charge differences. If the only source of difference is net charge (presumably produced by amino acid substitutions involving charged residues), then one would expect variants to have similar retardation coefficients, K_r , and to differ primarily in free electrophoretic mobility, M_0 . The range of variability in their K_r values would be expected to be limited to about that observed for the hemoglobin internal standard. In fact, the distribution of K_r values obtained is very much broader than the corresponding hemoglobin distribution. Noncharge differences clearly contribute to the differences seen in mobility on 7% acrylamide gels.

This proved an important result, as it provided the basis for understanding the apparently continuous variation in mobility consistently seen in samples of natural populations. The difficulty in analysis on 7% acrylamide gels is that charge and size/conformation *interact* in determining mobility, and these two protein properties prove to vary concordantly—As M_0 values increase, so do the absolute values of K_r (e.g. bigger or more asymmetric proteins have greater net charge). The re-

¹Summary of CIW-DPB Publication 561.

sult is that the mobility functions described by Equation 2 *intersect* at intermediate gel pore size. The nature of the mobility variation at the α -GPdH locus is now clear (Fig. 44): A survey conducted at 5% acrylamide (equivalent to 10%–11% starch) will not discriminate between variants and will reveal a single, uniform mobility type. Such a survey would classify this locus as uniformly homozygous. A survey conducted at 5% acrylamide, as were my previous surveys, would report two segregating alleles (*see*, for instance, Johnson, 1972, or Johnson, 1976b), with considerable variation in the exact mobility observed. This mobility variation reflects the fact that there is a minimum of *five* alleles segregating at this locus.

Gel-sieving analysis thus provides direct evidence of protein heterogeneity within electrophoretic classes. Note also that there are alleles that do not differ in net charge but only in K_r .

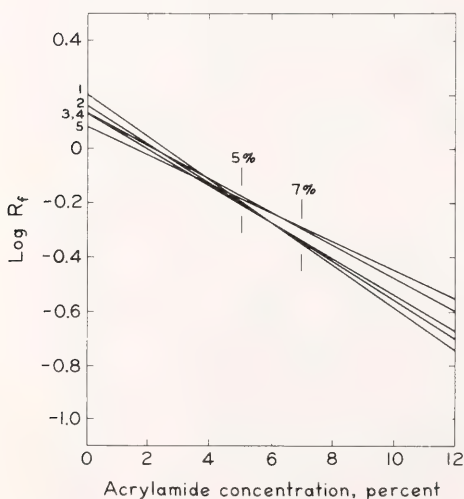


Fig. 44. Gel-sieving analysis of the five α -GPdH alleles in *Colias* (from Johnson, 1976a).

THE NATURE AND EXTENT OF HETEROGENEITY

The results reported above raise a variety of interesting questions concerning the nature and extent of elec-

trophoretically detectable protein variation. I will address myself here to four: (1) To what extent is the newly detected variation genetic? Particularly, does variation in K_r have a genetic basis? (2) Does such electrophoretically cryptic variation occur in other organisms than *Colias*? Do intensively studied groups such as *Drosophila* also exhibit this class of variation? (3) How much variation of this sort is there? Is it restricted to one or a few loci, or is it typical of most loci? What is the allele frequency distribution of these electrophoretically cryptic alleles? (4) Are the many newly detected variant proteins significantly different in how they function? Particularly important, does a heterogeneous electrophoretic class of uniform (5% T) R_f contain variant proteins with differing K_M or V_{max} values?

The Genetic Basis of Variation in K_r *

When variants of the five allelic classes shown in Fig. 44 are crossed and their progeny analyzed (CIW-DPB Publ. 571), the resulting ratios are consistent with normal Mendelian segregation, indicating that the variants represent true alleles (Table 23): When two individuals presumed homozygous for the same allele are crossed, the progeny exhibit K_r values for α -GPdH with standard errors of approximately 6% of the mean, very similar to the 5% standard error associated with the K_r values of hemoglobin determined from the same gels. In presumptive backcrosses, involving a homozygote and a presumed heterozygote, 1:1 segregation was observed. In the single dihybrid cross, the results were consistent with a 1:2:1 pattern of segregation. It should be noted here that the Class 4 of Table 23 has proven heterogeneous upon subsequent study; this will be discussed below.

When the progeny of a gravid female homozygous for a Class 4 variant of α -GPdH are analyzed, only three clas-

*CIW-DPB Publications 561, 563 and 569.

TABLE 23. Genetic Crosses of α -GPDH Variants of *Colias philodice**

| Phenotype Classes of Crosses | Numbers (Phenotype) of Progeny | | |
|------------------------------------|-----------------------------------|----------|----------|
| | a | a/b | b |
| ♀ × ♂ | | | |
| 2/3 2/3 | 18 (2/2) | 46 (2/3) | 12 (3/3) |
| 4/3 3/3 | 24 (3/3) | 19 (4/3) | 0 |
| 2/3 3/3 | 31 (3/3) | 27 (2/3) | 0 |
| 3/3 4/4 | 0 | 30 (3/4) | 0 |
| 4/4 3/3 | 0 | 13 (3/4) | 0 |
| 2/2 2/2 | 17 (2/2) | 0 | 0 |
| 3/3 3/3 | 62 (3/3) | 0 | 0 |

*After Johnson, 1976a.

ses of protein variant are seen among 20 progeny subjected to analysis (CIW-DPB Publ. 569): female parental type, heterodimer, and presumptive male parental type (8 progeny were single-banded, Class 4, while 12 were triple-banded). These results are consistent with segregation from an a/a × a/b mating. It is important for the discussion below to note that no other variant types were observed in the analysis of these progeny.

More powerful genetic analysis is available in *Drosophila* than in difficult-to-raise *Colias*. As discussed in the following section, *Drosophila* species also exhibit the heterogeneity described in *Colias*. Detailed genetic studies have been carried out on electrophoretically cryptic variants within the standard 1.00 allele class at the esterase-5 locus of *D. pseudoobscura* (the strain was kindly provided by R. L. Lewontin). Two variants are revealed by gel-sieving analysis. They differ only in K_r , having identical M_0 values. The results of crosses between these two variants support a genetic interpretation (CIW-DPB Publ. 563). When variant 0.76 is crossed with itself, only this variant type is found among the F_2 progeny. However, when the two variants are crossed with each other, both variant types segregate among the F_2 progeny.

Thus, a variety of studies indicate that electrophoretically cryptic variants are in fact alleles in the accepted

sense of the word, segregating in crosses just as electrophoretically distinct alleles do. This does not, of course, establish that all such variation need be allelic, but no evidence of post-translational or other nongenetic effects has been obtained to date. General verification of the allelic nature of electrophoretically cryptic variants will require more extensive genetic data.

*Heterogeneity in Drosophila**

To assess the degree to which commonly employed "homozygous" strains of *Drosophila* may also carry hidden heterogeneity, gel-sieving analysis has been carried out on several species.

Drosophila pseudoobscura. Gel-sieving analysis of the esterase-5 locus of *D. pseudoobscura* indicates that at least 14 variants are detected by gel-sieving analysis of seven presumably homozygous esterase-5 lines. These variants are not routinely detected by electrophoresis, as all analyzed individuals yield indistinguishable R_f values on 5% acrylamide gels. In all, seven allelic classes were examined, and all but one proved heterogeneous.

Drosophila aldrichi. Nineteen lines of *D. aldrichi*, representing five alleles of the esterase-C locus, were provided by Dr. R. H. Richardson, and their gel-sieving characteristics analyzed. Eleven distinct variants are observed, each presumptive allelic class proving heterogeneous. (Johnson, unpublished).

Drosophila mulleri. Twelve lines of *D. mulleri* were examined (again provided by R. H. Richardson), representing two alleles of the esterase-C locus. Five variants were detected. (Johnson, unpublished data).

Gel-sieving analysis thus appears to discriminate a significant amount of heterogeneity in each of the three *Drosophila* species examined to date. It seems quite likely that the finding of extensive electrophoretically cryptic variation will prove a general result in surveys of natural populations.

*CIW-DPB Publ. 563.

*Evaluating Patterns of Hidden
Heterogeneity**

The discovery of extensive variation among α -GPdH and esterase alleles raises the question of whether these two enzyme loci are typical in this respect. Certain loci, particularly esterases, typically exhibit far more electrophoretically detectable variation than others. Is the newly detected variation concentrated among a particular subset of enzyme loci? To address this question, gel-sieving analyses were carried out on 14 loci of the alpine but-

*CIW/DPB Publication 569.

terfly *Colias meadii*. For all loci but MdH, several common variants were detected (Table 24). Most of them would not have been detected in routine 7% acrylamide gels, as the associated values of R_f (7% T) indicate. At all loci, a number of unique variants occur clearly distinct from the common forms. A typical locus, G6PdH, is illustrated in Fig. 45.

The common variants. Among the 14 loci examined, 32 variants occur at frequencies of greater than 10%. Sixteen of the 32 variants would not have been distinguished on 7% acrylamide gels.

TABLE 24. Electrophoretic Characterization of Common Variants at
14 Enzyme Loci of *Colias meadii**

| Locus | R_f 7% | K_r | M^0 | Frequency |
|---|----------|--------|-------|-----------|
| Adenylate | 0.20 | -0.027 | 1.11 | 0.39 |
| Kinase-1 | 0.20 | -0.053 | 1.71 | 0.22 |
| Adenylate | 0.28 | -0.035 | 1.06 | 0.50 |
| Kinase-2 | 0.29 | -0.041 | 1.15 | 0.23 |
| Esterase-1 | 0.62 | -0.083 | 1.06 | 0.13 |
| | 0.57 | -0.082 | 1.15 | 0.26 |
| | 0.54 | -0.082 | 1.24 | 0.43 |
| Esterase-2 | 0.32 | -0.058 | 1.41 | 0.32 |
| | 0.20 | -0.057 | 1.83 | 0.16 |
| Fumarase | 1.6 | -0.32 | 4.67 | 0.16 |
| | 1.5 | -0.27 | 3.01 | 0.24 |
| | 1.3 | -0.22 | 2.04 | 0.28 |
| | 1.5 | -0.09 | 0.17 | 0.12 |
| Glucose-6-phosphate dehydrogenase | 0.60 | -0.086 | 1.16 | 0.54 |
| | 0.56 | -0.083 | 1.22 | 0.24 |
| α -glycerophosphate dehydrogenase | 0.33 | -0.065 | 1.52 | 0.24 |
| | 0.34 | -0.068 | 1.57 | 0.32 |
| | 0.34 | -0.071 | 1.63 | 0.29 |
| Hexokinase-1 | 0.21 | -0.052 | 1.64 | 0.44 |
| | 0.20 | -0.054 | 1.74 | 0.33 |
| Hexokinase-2 | 0.23 | -0.050 | 1.50 | 0.36 |
| | 0.23 | -0.054 | 1.62 | 0.36 |
| Malic enzyme | 0.73 | -0.148 | 2.31 | 0.50 |
| | 0.72 | -0.144 | 2.30 | 0.27 |
| Malate dehydrogenase-1 | 0.69 | -0.068 | 0.69 | 0.43 |
| Malate dehydrogenase-2 | 1.66 | -0.342 | 6.21 | 0.47 |
| Phosphoglu- comutase | 0.38 | -0.056 | 1.18 | 0.32 |
| | 0.36 | -0.056 | 1.24 | 0.25 |
| | 0.33 | -0.054 | 1.28 | 0.16 |
| Triose phosphate isomerase | 0.34 | -0.064 | 1.48 | 0.19 |
| | 0.35 | -0.068 | 1.50 | 0.21 |
| | 0.34 | -0.068 | 1.56 | 0.48 |

*The sample represents a single collection from one natural population (after Johnson).

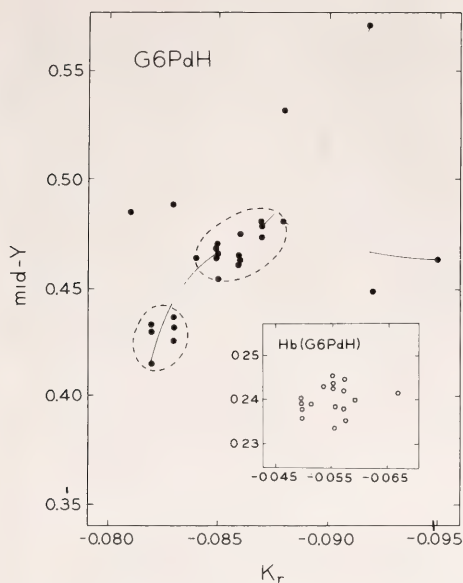


Fig. 45. Electrophoretic gel-sieving survey of glucose-6-phosphate dehydrogenase (G6PdH) in a natural population of *Colias meadii*. Values for hemoglobin (Hb) were determined from the same gels, after Johnson, in press (a).

Of the 32 common variants, 30% differ only in charge, 10% differ only in K_r , and 70% differ in both M_0 and K_r . Thus fully 80% of the common variants differ significantly in K_r . If differences in K_r reflect conformational differences, as seems likely (the matter is discussed below), then it seems quite unlikely that this widespread variation in shape does not affect the functioning of the enzymes.

The rare variants. Among the 14 loci, a total of 97 "rare" variants occur! In a sample of 20 individuals, 91 variants occur only once and 6 others occur twice. Fully 30% of the genes analyzed in this survey code for proteins that appear only once in the sample. Perhaps these variants all occur typically at frequencies of 5%; or, they may be unique alleles occurring only once. A larger sample is required to resolve this issue. The variants appear allelic: Note that Class 4 of α -GPdH discussed earlier is heterogeneous and composed of rare variants. Class 4 variants were observed to segregate in crosses in a Mendelian fashion.

All 14 loci exhibit rare variants. Fully 70% of the rare variants are not detected on 7% acrylamide gels.

Of the 97 rare variants, 34% differ solely in charge, 21% differ solely in K_r , and 45% involve differences in both M_0 and K_r . Thus fully two-thirds of the rare variants involve significant differences in K_r ; Again, conformational variation seems prevalent.

Other classes of variation. It seems likely that cryptic variation reported in the thermal stability of proteins is quite different from the sorts of variation reported here. These variants may well represent polymorphism for conservative (polar \rightarrow polar; nonpolar \rightarrow nonpolar) amino acid substitutions within the interior of the protein which alter hydrogen bonding and thus affect stability. It is unlikely that such variants would be detected by gel-sieving analysis.

The chances of detecting variation cryptic because of identical net charge (as described by the charge state model of electrophoretic mobility) are much better. A body of data indicate that the pK's of amino acids may be strongly influenced by an amino acid residue's position in a protein (the matter is discussed in detail in Johnson, 1975b). Two proteins with different amino acid substitutions but with the same net charge at one pH would be very unlikely to exhibit identical changes in net charge at a different pH. Thus serial analysis at two different pH's (in my laboratory, 7.0 and 8.9) should reveal any amino acid differences cryptic at one pH because of identical net charge. The finding of substantial microheterogeneity in isoelectric point within M_0 classes (Johnson, 1976a) reflects this same underlying heterogeneity.

Are Electrophoretic Classes Functionally Heterogeneous?

Extensive K_r variation, if conformational, suggests that biochemical comparisons of polymorphic alleles may be difficult to interpret unless the alleles

are demonstrably homogeneous. The extensive literature on functional variation within alleles of *D. melanogaster* alcohol dehydrogenase perhaps reflects to some degree undetected structural heterogeneity.

References

- Chrambach, A., and D. Rodbard, *Science*, 172, 440-451, 1971.
 Fawcett, J., and C. Morris, *Separation Science*, 1, 9-26, 1966.
 Ferguson, K., *Metabolism*, 13, 985-1002, 1964.
 Gonnene, A., and J. Lebowitz, *Anal. Biochem.* 64, 414-424, 1975.
 Johnson, G., Ph.D. thesis, Stanford University, Stanford, California, 1972.
 Johnson, G., *Genetics* 78, 771-776, 1975.
 Johnson, G., *Genetics* 86, 149-167, 1976a.
 Johnson, G., *Biochemical Genetics* 14, 403-426, 1976b.
 Johnson, G., *Genetics*, in press, (a).
 Johnson, G., *Genetics*, in press, (b).
 Rodbard, D., and A. Chrambach, *Proc. Nat. Acad. Sci. U.S.A.*, 65, 970-977, 1970.
 Rodbard, D., and A. Chrambach, *Anal. Biochem.* 40, 95-134, 1971.

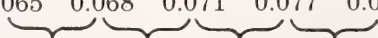
THE EFFECT OF DEUTERIUM OXIDE ON THE GEL-SIEVING BEHAVIOR OF PROTEINS IN ELECTROPHORESIS

George B. Johnson

In animal and plant populations extensive genetic variation occurs at enzyme loci. Several papers in this *Year Book* describe variation in the gel-sieving properties of proteins. This variation is too small in magnitude to be ascribed to different states of subunit aggregation, and appears heritable. It is usually discussed as reflecting allelic proteins which differ in conformation, although other interpretations are possible.

Any interpretation of variation in the "conformational" retardation coefficient, K_r , must account for at least three unexpected phenomena:

1. At a given locus, the spacing between the K_r values of the variants is unexpectedly uniform. For α -glycerophosphate dehydrogenase (α -GPdH) in *Colias*, for instance, the values obtained are:

| | | | | |
|---|-------|-------|-------|-------|
| 0.065 | 0.068 | 0.071 | 0.077 | 0.080 |
|  | | | | |
| .003 | .003 | .006 | .003 | |

2. The value of the step in K_r magnitude varies from one enzyme to another and is not a function of subunit molecular weight.

3. Hybrid dimer molecules seen in heterozygous individuals are not intermediate in K_r , but rather assume a K_r similar to one of the parental types.

There are three basic hypotheses that would entail genetically heritable variation in gel sieving behavior while at the same time accounting for these three phenomena:

A. Variation in K_r may reflect conformational differences. A variety of studies are consistent with this interpretation: (1) When α -chymotrypsin is made asymmetric, its K_r value changes significantly (Johnson, 1976).

(2) Fibrinogen is a molecule of 341,000 molecular weight which is known to be very asymmetric. Such a molecular weight would produce a K_r value of -0.14 for a symmetrical molecule, but the observed value is -0.065 , indicating that asymmetry is easily detected by this approach. However, because asymmetry may alter K_r , does not imply that all K_r variation is produced by asymmetry. Nor do conformational interpretations readily account for the uniform spacing seen between variants in the magnitude of K_r .

B. Variation in K_r may reflect changes in the hydration shells of the proteins. Much of the sieving behavior of proteins in electrophoresis may be hydrodynamic and could in principle be sensitive to the diameter of the hydration shell. If substituting a polar amino acid for a nonpolar one (or vice versa) on the surface of a protein altered the hydration shell diameter, then uniform spacing in K_r between variants may easily be explained. This hypothesis would require that single amino acid substitutions produce rather large changes in the volume of the hydration shell (up to 20%).

C. Variation in K_r may reflect alteration in the dissociation constant of dimers, $\alpha\alpha \rightleftharpoons 2\alpha$. If the rate is fast and the equilibrium towards dimer formation, then only one band (the dimer) will be seen in electrophoresis. A slight decrease in such a rate has the effect of lessening the fraction of time the protein molecules are in the dimer form. This will decrease the sieving retardation of the protein by the gel fibers in electrophoresis. The perceived result will be a K_r suggesting a smaller molecule. Uniform changes in K_r might reflect polar/nonpolar substitutions in the hydrophobic patch comprising the subunit binding site. This hypothesis would suggest that the magnitude of the uniform change in K_r between variants would be a function of the area of the hydrophobic subunit binding region, and therefore a function of subunit molecular weight.

It is possible to test the suitability of these alternative conceptualizations by altering the conditions of electrophoresis. This paper reports data that permit the rejection of the hydration shell hypothesis.

The hydration shell of a protein is produced largely by the hydrogen binding of uncharged polar surface amino acids with the polar solvent water. A significant increase in the polarity of the water solvent would be expected to contract the water envelope. Thus a protein in 99.8% D_2O rather than H_2O would exhibit a smaller hydration

shell. If the magnitude of K_r reflects the volume of the hydration shell, then electrophoresis in D_2O should alter K_r . More to the point, two proteins with similar molecular weights but with different K_r values ought to respond differently to D_2O , one exhibiting a greater K_r alteration than the other.

Two such similar protein pairs are bovine hemoglobin and *Drosophila pseudoobscura* esterase-5, or the same hemoglobin and *Colias meadii* α -glycerophosphate dehydrogenase. The subunit molecular weights are 64,500, about 66,000, and 65,000, respectively. For each pair the effect of D_2O was examined by running eight gels for each individual: 5%, 6%, 7%, and 8% acrylamide in H_2O , and 5%, 6%, 7%, and 8% acrylamide in 99.8% D_2O . For the D_2O runs, all gel reagents and running buffers were made up in 99.8% D_2O . The two sets of four gels were run in parallel simultaneously under controlled temperature (10°C), assayed, scanned, and K_r/M_0 values calculated for the matched treatments. Data for the two protein pairs are presented in Tables 25 and 26 (with the dissimilar standard protein ferritin).

In Table 27 the differences in K_r produced by D_2O are summarized. For both Hb/esterase and Hb/ α -GPdH, the responses of the two proteins to D_2O are precisely parallel, despite very different K_r values. This relationship is illustrated in Fig. 46 for Hb/ α -GPdH, where all points fall about the axis of symmetry. When the α -GPdH results are standardized to the hemoglobin run in the same gels (α GPdH) to reveal any pattern of difference from hemoglobin, very little difference is seen as a result of D_2O . These results are not consistent with the hypothesis that the K_r differences between the protein pairs reflect hydration shell differences.

It is important to note that changes in K_r do occur, both enzyme and hemoglobin standard exhibiting K_r values 10%–20% more negative. This result is consistent with a conformational interpretation if the initial differences in K_r are produced by strong

TABLE 25. The Retardation Coefficient of Esterase-5 from *Drosophila pseudoobscura* Determined in Parallel in H₂O and in 99.8% D₂O*

| No. | Hb Standard | Fe Standard | Esterase | EST |
|---------------------------|----------------|----------------|--------------|-------|
| $-K_r$ (H ₂ O) | | | | |
| 1 | 0.055 ± .019 | 0.203 ± .060 | 0.080 ± .023 | 0.081 |
| 2 | 0.050 ± .008 | 0.206 ± .055 | 0.075 ± .015 | 0.082 |
| 3 | 0.055 ± .016 | 0.210 ± .059 | 0.079 ± .021 | 0.081 |
| 4 | 0.054 ± .004 | 0.205 ± .022 | 0.078 ± .006 | 0.080 |
| 5 | 0.051 ± .008 | 0.201 ± .033 | 0.074 ± .004 | 0.079 |
| 6 | 0.055 ± .007 | 0.217 ± .046 | 0.076 ± .006 | 0.079 |
| $-K_r$ (D ₂ O) | | | | |
| 1 | 0.052 ± .011 | 0.201 ± .030 | 0.075 ± .018 | 0.080 |
| 2 | 0.050 ± .005 | 0.205 ± .024 | 0.072 ± .009 | 0.079 |
| 3 | 0.061 ± .001 | 0.212 ± .027 | 0.081 ± .009 | 0.078 |
| 4 | 0.060 ± .011 | 0.235 ± .098 | 0.083 ± .016 | 0.079 |
| 5 | 0.050 ± .008 | 0.219 ± .062 | 0.076 ± .007 | 0.080 |
| 6 | 0.060 ± .009 | 0.235 ± .090 | 0.085 ± .013 | 0.081 |

*Numbers represent different individuals. K_r values are determined from four gels of 5%, 6%, 7%, and 8% acrylamide. EST values represent point-to-point standardization of esterase to hemoglobin (this Year Book). Hb: Hemoglobin; Fe: Ferritin.

TABLE 26. The Retardation Coefficient of α -Glycerophosphate Dehydrogenase from *Colias meadii* Determined in Parallel in H₂O and in 99.8% D₂O*

| No. | Hb Standard | Fe Standard | α GPdH | α GPdH |
|---------------------------|------------------|------------------|------------------|---------------|
| $-K_r$ (H ₂ O) | | | | |
| 1 | 0.049 \pm .001 | 0.202 \pm .031 | 0.060 \pm .003 | 0.068 |
| 2 | 0.051 \pm .008 | 0.195 \pm .015 | 0.062 \pm .009 | 0.068 |
| 3 | 0.055 \pm .007 | 0.214 \pm .021 | 0.067 \pm .004 | 0.068 |
| 4 | 0.053 \pm .010 | 0.193 \pm .042 | 0.063 \pm .007 | 0.066 |
| 5 | 0.050 \pm .003 | 0.207 \pm .055 | 0.065 \pm .010 | 0.072 |
| 6 | 0.055 \pm .008 | 0.209 \pm .047 | 0.059 \pm .023 | 0.066 |
| | | | 0.066 \pm .010 | 0.068 |
| | | | 0.057 \pm .040 | 0.057 |
| $-K_r$ (D ₂ O) | | | | |
| | | | GPdH | GPdH |
| 1 | 0.063 \pm .004 | 0.245 \pm .089 | 0.073 \pm .016 | 0.067 |
| 2 | 0.055 \pm .005 | 0.224 \pm .083 | 0.068 \pm .016 | 0.071 |
| 3 | 0.061 \pm .008 | 0.231 \pm .061 | 0.075 \pm .016 | 0.071 |
| 4 | 0.060 \pm .011 | 0.231 \pm .059 | 0.071 \pm .010 | 0.068 |
| 5 | 0.060 \pm .003 | 0.236 \pm .086 | 0.069 \pm .004 | 0.067 |
| 6 | 0.057 \pm .008 | 0.232 \pm .067 | 0.070 \pm .031 | 0.067 |
| | | | 0.071 \pm .011 | 0.070 |
| | | | 0.070 \pm .035 | 0.070 |

*Numbers represent different individuals. K_r values are determined from four gels of 5%, 6%, 7%, and 8% acrylamide. EST values represent point-to-point standardization of esterase to hemoglobin (this Year Book). Hb: Hemoglobin; Fe: Ferritin.

TABLE 27. Effect of D₂O on Value of K_r*

| | Hb | Fe | | |
|---------------------------------|----------|----------|----------|---------------|
| No. | Standard | Standard | Esterase | EST |
| <i>Drosophila pseudoobscura</i> | | | | |
| 1 | -0.05 | -0.01 | -0.06 | -0.01 |
| 2 | 0 | -0.01 | -0.04 | -0.04 |
| 3 | 0.09 | 0.01 | 0.08 | -0.04 |
| 4 | 0.11 | 0.03 | 0.06 | -0.01 |
| 5 | -0.02 | -0.01 | 0.03 | -0.06 |
| 6 | 0.10 | 0.02 | 0.12 | -0.04 |
| <i>Colias meadii</i> | | | | α GPdH |
| 1 | 0.19 | 0.21 | 0.22 | 0.01 |
| 2 | 0.08 | 0.15 | 0.10 | 0.04 |
| 3 | 0.11 | 0.08 | 0.12 | 0.04 |
| 4 | 0.13 | 0.20 | 0.13 | 0.03 |
| 5 | 0.20 | 0.14 | 0.19 | 0.01 |
| 6 | 0.08 | 0.11 | 0.06 | 0.01 |
| | | | 0.08 | 0.03 |
| | | | 0.23 | 0.03 |

*Data are presented as the fractional difference ρ observed in K_r [e.g., K_r(H₂O) + K_r(H₂O) • ρ = K_r(D₂O)].

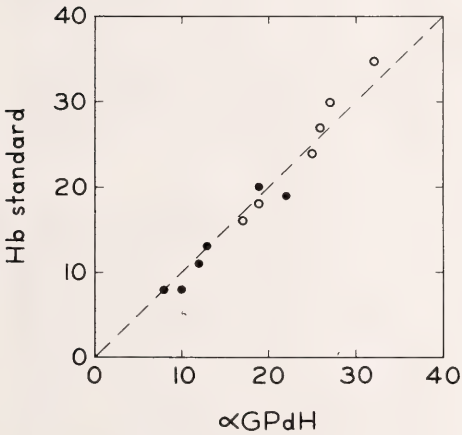


Fig. 46. A comparison of percentage differences in electrophoretic behavior of hemoglobin with *Colias meadii* α -GPdH produced by D₂O. Filled circles, K_r; open circles, M_i.

localized binding forces. It is also consistent with a subunit dissociation hypothesis: As mol wt's are similar, the size of the subunit binding sites should

also be similar and therefore equally sensitive to the polarity of the solvent.

The effect is variable from one *Colias* individual to another. This variability is of some interest because the standard hemoglobin also varies in its response to D₂O. When run alone (no extract), there is no significant variation in the effect of D₂O on hemoglobin. When run with *Colias* extracts, on the other hand, hemoglobin exhibits great variation in the magnitude of its response to D₂O. Clearly, some physiological variable is important in the D₂O effect.

Finally, D₂O is seen to produce large positive changes in M₀. Such a relationship is expected, as isotope effects alter hydrogen ion dissociation constants. The effect is to increase the net negative charge in alkaline buffer and thus to increase M₀. While hemoglobin and α -GPdH have different M₀ values, the effect of D₂O is the same for both molecules because D₂O acts on all charged residues and not simply on the small fraction that constitutes the net difference in charge.

These experiments with D₂O permit rejection of the hypothesis that variation in K_r reflects variation in the hydration shell of proteins. They do not, however, serve to distinguish between the conformational and subunit dissociation hypotheses. Entirely different lines of experimentation will be required to do this. The most obvious approach is to obtain purified protein from each of several K_r variants and to determine whether varying the protein concentration affects the magnitude of K_r. A subunit dissociation hypothesis would predict a significant dependence, while a conformational hypothesis would not. Such experiments are currently being initiated.

Reference

Johnson, G., *Genetics*, 38, 149-167, 1976.

P700-CHLOROPHYLL *a*-PROTEIN COMPLEXES

J. S. Brown

Studies of P700-chlorophyll-protein complexes have continued this year, and the results may be divided into two sections. The first describes some preliminary attempts to isolate these complexes from different kinds of algae. The second deals with fluorescence and light-induced absorbance changes of a highly enriched P700 complex from spinach chloroplasts and leads to a new interpretation of electron transfer through the photosystem I reaction center.

ISOLATION OF CHLOROPHYLL-PROTEIN COMPLEXES FROM DIVERSE ALGAE

Among the green algae, *Chlamydomonas* has been a frequent choice of study because it has a known sexual life-cycle which makes genetic analysis possible and because it is easily cultured and broken. CPI* has been isolated from this alga (Kan and Thornber, 1976) and appears to be similar to that from higher plant leaves. Chlorophyll-proteins enriched in P700 have also been isolated from various blue-green algae (Thornber, 1975).

In the present study, various microalgae were grown in liter batches under appropriate conditions, harvested by centrifugation, washed and broken with a French pressure cell. The fragments were washed to remove much of the soluble protein, pelleted, and stored in a freezer. If cells are harvested and frozen before breaking, phaeophytinization of some of the chlorophyll may occur during early steps of the following procedure and prevent recovery of the reaction center.

The method of Shiozawa *et al.* (1974) was followed for the preparation of CPI except that 20 mM sodium ascorbate was omitted from the washing solutions. A pellet containing a measured amount of chlorophyll was homogenized in sufficient 1% Triton X-100

to give a Triton-to-chlorophyll ratio of about 75 (w/w). CPI was eluted in 0.2 M sodium phosphate, pH 7.5, except for *Euglena* as noted below.

The yellow-green algae, which contain only chlorophyll *a* of the photosynthetic pigments, have been little studied. After some trial and error, we chose from this group two species that grow readily in batch culture and can be broken by one passage through a French pressure cell. These species are *Bumilleriopsis filiformis* (No. 309, Culture Collection of Algae, Indiana University) and *Botrydiopsis* sp. (AB-2a-ADN, kindly supplied by Professor Ralph Lewin, Scripps Institute of Oceanography, University of California at San Diego). Preliminary experiments with both of these species indicate that a fraction enriched in P700 can be eluted in 0.2 M phosphate. Thus far, the lowest molecular ratios of chlorophyll to P700 obtained were 41 for *Bumilleriopsis* and 80 for *Botrydiopsis*. It is to be expected that both these ratios can be lowered by further experimentation.

Considerable effort was spent in attempting to isolate a P700-chlorophyll *a*-protein from *Euglena gracilis* (No. 752, Culture Collection of Algae, Indiana University). Eventually it was discovered that the fraction most enriched in P700 is eluted from the hydroxylapatite column by the 10 mM phosphate normally used as a washing solution and is therefore gone by the time the 0.2 M phosphate is applied. This 10 mM phosphate fraction usually had a chlorophyll to P700 ratio of 60-70, but in one experiment this ratio was lowered to 46 by a repeated chromatography on hydroxylapatite.

A second result of the *Euglena* fractionation was the finding that the 0.2 M phosphate eluate contained another chlorophyll *a*-protein (CP_{a1}) having the unique absorption spectrum shown in *Year Book* 73, p. 703 (1974) and

*CPI = P700-chlorophyll *a*-protein.

without detectable P700. Not only is the appearance of a 684-nm absorption band unusual, but the steepness of the slope on the long wavelength side of this band is also remarkable. This year the corresponding fluorescence emission spectrum of this fraction was measured. The emission maximum is at 683–684 nm at 20°C and 687 nm at –196°C. At both temperatures this emission band is unusually narrow (half-band width ~ 12 nm at –196°C). This is about 60% as wide as emission bands in other comparable chlorophyll complexes *in vivo*. These unusual characteristics have been observed in CPa₁ preparations from at least five separate experiments and do not seem to have any obviously trivial explanation.

Previously Shiozawa *et al.* (1974) reported that P700 and cytochrome *f* were found in equimolar amounts in CPI prepared from tobacco leaves. However, this relationship does not mean that they are associated. Difference spectra between samples oxidized by ferricyanide and reduced by ascorbate have been measured from different eluates from *Euglena* chromatography and with CPI preparations from spinach chloroplasts. The amounts of cytochrome *f* and P700 can be calculated from the differences in absorption at 552 and 697 nm. Occasionally an equimolar amount of P700 and cytochrome *f* was observed in spinach CPI, but usually the proportion of P700 increased and cytochrome decreased following repeated chromatography. The *Euglena* CPI eluted in 10 mM phosphate did not show any evidence of a cytochrome in its difference spectrum. Furthermore, measurement of light-induced absorbance changes of a spinach CPI preparation (described below) gave no evidence of a change near 550 nm characteristic of a cytochrome coupled to P700 oxidation. All of this evidence suggests that cytochrome *f* is probably a contaminant in CPI preparations made according to Shiozawa *et al.* (1974) and is not bound closely to P700 as an electron donor.

ABSORPTION AND FLUORESCENCE OF CPI

Fluorescence emission spectra of spinach CPI were published in last year's Report (*Year Book* 74, p. 779). Even at that time, considerable variability had been encountered when measuring different preparations, particularly at low temperature. We now understand some of the reasons for that variability and have improved procedures for preparing CPI routinely with a chlorophyll *a* to P700 ratio of 30 to 35.

The main problem seems to have been the tendency of CPI to aggregate on the hydroxylapatite column, in solution and especially during freezing. Recently it has been found that this problem can be alleviated by making the 0.2 M phosphate eluting buffer 0.02% in Triton X-100. This small amount of detergent does not modify the spectral characteristics of the chlorophyll-protein complex itself.

Figure 47 shows the fluorescence emission and Fig. 48, the absorption at –196°C of CPI preparations having different ratios of chlorophyll to P700. All samples were dilutions of 0.2 M phosphate eluates from hydroxylapatite

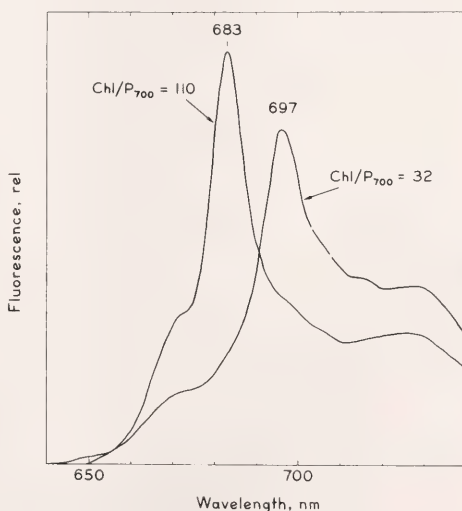


Fig. 47. Fluorescence emission spectra of spinach CPI preparations. Excitation at 438 nm, slit-width = 10 nm, emission slit-width = 3 nm, –196°C.

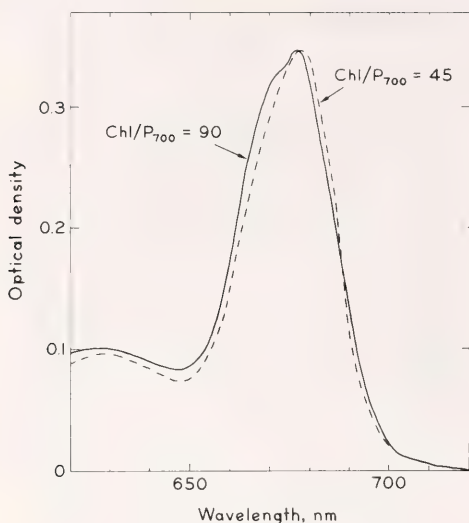


Fig. 48. Absorption spectra of spinach CPI preparations. Curves normalized at 677 nm, -190°C .

columns. The only difference between them was the proportion of light-harvesting or antenna chlorophyll *a* which had been removed from the reaction center complex by repeated chromatography. In numerous experiments CPI has been prepared from spinach chloroplasts and rechromatographed several times to give different chlorophyll to P700 ratios; so far 30 has been the lowest ratio observed.

Figure 47 illustrates the difference between CPI preparations as a function of their P700 concentration. As the chlorophyll to P700 ratio decreases from 100 to 30, a shoulder near 695 nm on the side of the 685 nm band increases until it becomes the maximum. Also, as the proportion of antenna chlorophylls to reaction centers decreases, the fluorescence yield also decreases because more of the actinic light energy is funneled directly to a reaction center.

The amount of fluorescence near 670 nm varies in different preparations and is thought to come from a small amount of highly fluorescent Triton-solubilized chlorophyll *a*. The longer wavelength bands around 720–730 nm

may be due to lower vibrational bands of the biological forms of chlorophyll *a*. It can be seen in Fig. 48 that there is a small redshift in chlorophyll absorption with increased P700 concentration. The amount of this shift does not vary consistently with a change in P700 concentration, but the shoulder near 670 nm always decreases as the proportion of antenna chlorophyll decreases. Therefore, the differences in relative proportion of the long wavelength emission bands (720–730 nm) may reflect changes in proportion of the 670-nm and 684-nm forms of chlorophyll *a*. We have not yet been able to do detailed curve analysis as in previous years because of a change in computer hardware at Stanford University.

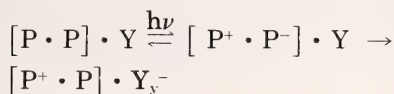
This rather detailed discussion of the differences in fluorescence and absorption spectra has been given to show why it is unlikely that the small differences in absorption that occur when the relative concentration of P700 is increased can account for the large increase in emission near 695 nm. It seems very probable that this emission is related in a direct way to P700. The difficulty, of course, is to determine how a pigment absorbing at 700 nm could fluoresce at shorter wavelengths.

One very reasonable explanation comes from the observation first made by Kok (1956) that the negative band near 700 nm in light-minus-dark difference spectra of various algae did not have the normal shape of an absorption band but was skewed, being steeper on the shorter wavelength side. If this band was made symmetrical and the experimental curve subtracted from it, a new absorption band with a lower extinction coefficient appeared at about 690 nm. This experiment has now been repeated with CPI, and the hypothetical absorption band occurs at 687 nm. Lozier and Butler (1974) and Visser and Rijgersberg (1975) have measured the light-minus-dark difference spectra of chloroplasts at -196°C . In both cases an increase in absorption near 690 nm was observed when P700 was photo-

oxidized. Therefore, it could be oxidized P700 absorbing near 690 nm that fluoresces near 695 nm.

If this were strictly true, one might expect to see a rise in 695-nm fluorescence that is kinetically identical to P700 bleaching. Ulrich Schreiber looked for such corresponding changes both at room and low temperature in CPI preparations. He did not see the predicted kinetic change in fluorescence but only the effect of the transmission change and reabsorption of fluorescence when P700 was bleached. It was therefore necessary to look further for an explanation of the 695-nm fluorescence.

A suggested explanation was found in the paper by Lozier and Butler (1974), who were attempting to explain both the positive absorbance change near 690 nm and the fact that only a part of the P700 absorbance change is reversible at low temperature. They proposed a formulation similar to the following:



where P is a chlorophyll molecule in a P700 dimer and Y is an electron acceptor. The species $[P^+ \cdot P^-]$ would be the candidate for the 690-nm absorption band and, in the present case, the source of 695-nm fluorescence. This scheme can account for the lack of fluorescence yield change in parallel with the light-induced bleaching and also for a low extinction coefficient of the 690 absorption band because one of the pair of chlorophylls is oxidized or bleached.

Recently Katz *et al.* (1976) found strong evidence from line-width studies of the EPR signal caused by the photooxidation of P700 that the reaction center must indeed be a dimer or, as they prefer to say, a "special pair" of chlorophyll molecules. They also suggest a formulation for the electron transfer from P700 to the acceptor Y that is almost identical to the above.

The only major difference is that the Argonne group believes there may be a water molecule bound between the chlorophyll molecules in the "special pair." However, an equally valid hypothesis is that it is the electron acceptor Y and the protein which serve to bind and orient the chlorophyll dimer in a particular way that is necessary to make the charge separation energetically feasible.

The natural electron acceptor is probably a type of bound ferredoxin or iron-sulfur protein (Malkin, 1975). Nelson *et al.* (1975) have also been studying the relationship between P700 and the iron-sulfur protein in reaction center complexes using EPR spectroscopy. They were able to measure the signal from P700 oxidation after the signal from the iron-sulfur protein had disappeared following special treatment. This experiment indicated that the iron-sulfur protein is not the primary electron acceptor. The above formulation also accounts for their results, since in this case one of the chlorophyll molecules is the primary acceptor.

ABSORPTION CHANGE KINETICS

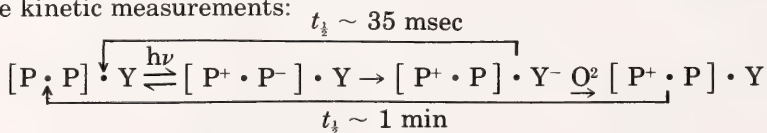
Absorption change kinetics in the millisecond time range were measured in a CPI sample having a chlorophyll to P700 ratio of about 40. These experiments were performed in collaboration with David Fork, using equipment described in *Year Book 71*, p. 183. We did not average a series of signals as we did last year because the dark reduction of the photooxidized P700 by ascorbate was very slow ($t_{1/2} \approx 1$ min). The change from a single flash was displayed on an oscilloscope and then transferred to an X-Y recorder.

A light-minus-dark difference spectrum was measured using a saturating actinic light of 1.4 sec duration and 2-min dark time between exposures. The sample contained approx. 30 mM sodium ascorbate but no other artificial electron donors or acceptors. The dif-

ference spectrum was similar to that reported last year (*Year Book* 74, pp. 779–783) with negative peaks at 700 and 430 nm, typical of P700. However, there was no shoulder near 420 nm or change near 550 nm that would have indicated the photooxidation of cytochrome *f* in this CPI preparation (see discussion of cytochrome *f* in *Euglena* section above).

While measuring the difference spectrum, we again noticed biphasic recovery kinetics that last year were attributed to some involvement of cytochrome *f*. However, further investigation has now revealed that the proportion of the rapid recovery phase ($t_{1/2} \sim 35$ msec) depends upon the length of the light exposure. The curves at the top of Fig. 49 show that after a 60-msec exposure, 82% of the P700 was reduced rapidly, whereas after 680 msec only 23% was reduced rapidly. The percentage of rapid recovery was measured for a number of different exposure times, and these results are plotted on the lower half of Fig. 49. It is apparent that after about 100 msec, the rapidly recovering component begins to disappear.

An extension of the same formulation shown above to explain the fluorescence results can also be used for these kinetic measurements:



We assume that in this CPI preparation the natural electron acceptor, Y^- can react back with P^+ with a half-time of about 35 msec. But during a longer exposure time, Y^- is oxidized by O_2 , and then P^+ can only be reduced by ascorbate. Malkin (1975) reported the light-dependent electron transfer from ascorbate to O_2 with the half-time of ~ 1 min by a similar CPI preparation.

This model formulation suggests several experiments to test the hypothesis further, e.g., to test the effect of anaerobiosis and viologen dyes upon the kinetics of the chlorophyll absorption changes. It also predicts that the

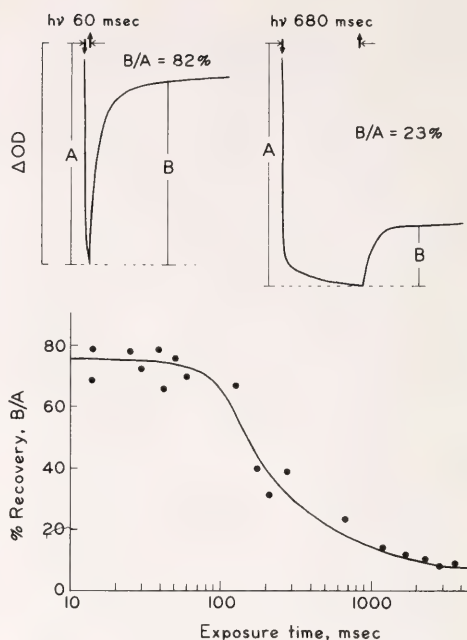


Fig. 49. Upper: absorbance change at 430 nm after 60 and 680 msec exposure to saturating red light; ΔOD after 680 msec = 5.4×10^{-3} , 5 mm light pathlength, $9.6 \mu M$ chlorophyll *a*. Lower: the percent recovery of the rapid component ($t_{1/2} \sim 35$ msec) as a function of the light exposure time.

light-dark difference spectrum measured after a flash too short for the transformation of $[P^+ \cdot P^-]$ to $[P^+ \cdot P]$ would show only the symmetrical band of bleached P700 and not be skewed by the 690 band.

The model that Lozier and Butler (1974) originally proposed accounts for the partial reversibility of the absorbance change at $-196^\circ C$ by the back reaction of P^+ and P^- . It would also be expected that the difference spectrum of the reversible change would show only the symmetrical bleached band, whereas the spectrum of the irreversible change would be skewed by the

formation of the 690 band. Such spectral differences were actually observed by Mayne and Rubinstein (1966) when they measured absorption changes in *Anacystis nidulans* at -196°C .

The new data presented here on the spectral characteristics of P700-chlorophyll *a*-protein, as well as the reinterpreted data of several other experimenters, provide strong support for the concept that the reaction center of photosystem I is a chlorophyll dimer. Light energy may effect a charge separation within this special pair of chlorophyll molecules; one becomes oxidized and the other reduced. The reduced chlorophyll may in turn reduce another electron acceptor that is probably a bound iron-sulfur protein. In vivo, the oxidized chlorophyll of the dimer is probably reduced by an electron from photosystem II passed through plastocyanin and cytochrome *f*, but in CPI preparations this electron must come from an artificial donor such as ascorbate.

References

- Kan, K.-S., and J. P. Thornber, *Plant Physiol.*, 57, 47-52, 1976.
 Katz, J. J., W. Oettmeier, and J. R. Norris, *Philos. Trans. R. Soc. London, Ser. B.*, 273, 227-253, 1976.
 Kok, B., *Biochim. Biophys. Acta*, 22, 399-401, 1956.
 Lozier, R. H., and W. L. Butler, *Biochim. Biophys. Acta*, 333, 465-480, 1974.
 Malkin, R., *Arch. Biochem. Biophys.*, 169, 77-83, 1975.
 Mayne, B. C., and D. Rubinstein, *Nature*, 210, 734-735, 1966.
 Nelson, N., C. Bengis, B. L. Silver, D. Getz, and M. C. W. Evans, *FEBS. Lett.*, 58, 363-365, 1975.
 Shiozawa, J. A., R. S. Alberte, and J. P. Thornber, *Arch. Biochem. Biophys.*, 165, 388-397, 1974.
 Thornber, J. P., *Annu. Rev. Plant Physiol.*, 26, 127-158, 1975.
 Visser, J. W. M., and C. P. Rijgersberg, in *Proc. 3rd Intern. Congr. Photosynthesis, I*, M. Avron, ed., pp. 399-408, 1975.

TEMPERATURE DEPENDENCE OF CHLOROPHYLL *a* FLUORESCENCE IN ALGAE AND HIGHER PLANTS IN RELATION TO CHANGES OF STATE IN THE PHOTOSYNTHETIC APPARATUS

David C. Fork

INTRODUCTION

Measurements made last year (Year Book 74, pp. 766-776; Murata *et al.*, 1975; Murata and Fork, 1975) of fluorescence as a function of temperature in the blue-green alga *Anacystis* treated with DCMU to eliminate the influence of photosynthetic photochemical reactions on the fluorescence yield revealed maxima in fluorescence yields that changed depending upon the temperature used to grow the algae. These maxima were found to reflect a change in the physical phase of the lipids in the photosynthetic membrane and occurred at approximately 13° or 24°C in

the organisms grown at 28° or 38°C , respectively. The activation energies of several photosynthetic reactions were found to change at the temperature of phase transition.

In this investigation fluorescence versus temperature curves were measured over a wide range of temperatures and for a number of algae and higher plants adapted both to warm and to cool growth conditions and for chloroplasts and a chlorophyll-protein preparation. The resulting curves were complex and varied widely, depending upon the growth temperature of the organism in question. Some parallel measurements of the photochemical

activity versus temperature were also made, and correlations could be seen between the changes of fluorescence yield and photosynthetic activities.

TEMPERATURE DEPENDENCE OF CHLOROPHYLL *a* FLUORESCENCE IN ALGAE

The thermophilic unicellular alga *Cyanidium caldarium* inhabits acidic hot springs where it has been found growing at temperatures up to 56°C. This organism grows best at a pH between 2 and 3. Although this alga contains the chromoprotein phycocyanin, as do the blue-green algae, it nevertheless has a morphological and cytoplasmic organization more like a red alga (Doemel and Brock, 1971).

Figure 50 shows the fluorescence versus temperature (*F-T*) curve measured for *Cyanidium* grown at 45°, 39°, and 21°C. In these and other measurements of the *F-T* curves, 10⁻⁵ M DCMU [(3-(3', 4'-dichlorophenyl)-1, 1-dimethylurea)] was added to prevent the effect of photosynthetic photochemical reactions on the fluorescence yield. For cells grown at 45°C, broad maxima were seen near 37.5° and 10°C upon lowering the temperature. These peaks were much more pronounced when the temperature was immediately increased after attaining 1°C and were separated by a clear minimum near 27.5°C. Increasing the temperature still further gave rise to a broad shoulder centered around 47°C and minima at 60° and 65°C, a small maximum near 63.5°C, and a large peak in fluorescence emission at 67°C. Above this temperature the fluorescence decreased sharply.

Upon lowering the temperature of *Cyanidium* grown at 39°C, a broad maximum was seen around 9°C; and upon increasing the temperature, conspicuous maxima appeared at 8°, 30°, 62°, and 67°C and minima at 21.5°, 57°, and 65°C. The *F-T* curve for cells grown at 21°C shows less distinct maxima around 2°, 22°, 55°, and 65°C and minima near 19° and 38°C, as well as at

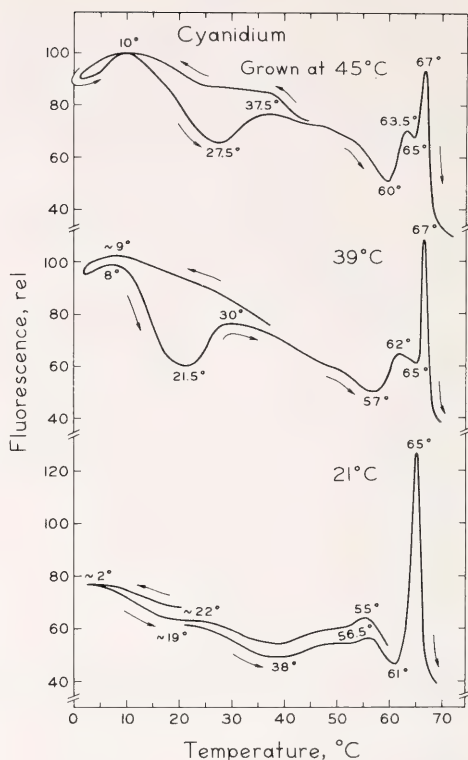


Fig. 50. Temperature dependence of chl *a* fluorescence in *Cyanidium caldarium* grown at 45°, 39°, and 21°C upon excitation of chl *a* with 440 nm actinic light (500 ergs cm⁻² sec⁻¹). Fluorescence at 685 nm was measured continuously as the temperature was decreased and increased at the rates of 0.5° and 1°C/min, respectively. The sample was held in a 5-mm thick brass cuvette whose top was covered by a Lucite window and bottom surface soldered to a 100 ml insulated brass container through which circulated 100 ml of coolant fluid DCMU, 10⁻⁵ M.

61°C. In this experiment two different samples were used; one was cooled from 20° to 5°C and then heated to 60°C, and another sample was heated from 20° to about 70°C. Maxima and minima at about these same temperatures were observed previously (Murata and Fork, 1975) in the *F-T* curve measured in the region from about 2° to 40°C for *Cyanidium* grown at 38°C. These and earlier observations show how the intensity of fluorescence varies with temperature and how the positions of these maxima and minima depend upon the growth temperature.

Heating cells above the high-temperature fluorescence peak leads to irreversible loss of fluorescence variations as a function of temperature. Figure 51 shows an example of this for *Cyanidium* grown at 39°C and heated to 67°C and then cooled immediately to 39°C. It can be noted that the *F-T* curve upon cooling lacks the previously seen maxima and minima.

The *F-T* curves for *Anacystis* grown at 39°C and 22°C are given in Fig. 52. Fluorescence maxima appeared near 13°C when the temperature was lowered and around 19°C when the temperature was raised. In the culture grown at 22°C the maximum appeared at 6°C upon lowering the temperature and 10°C upon increasing the temperature. Maxima appeared near 55°C for both cultures. Similar results were reported previously for *Anacystis* grown

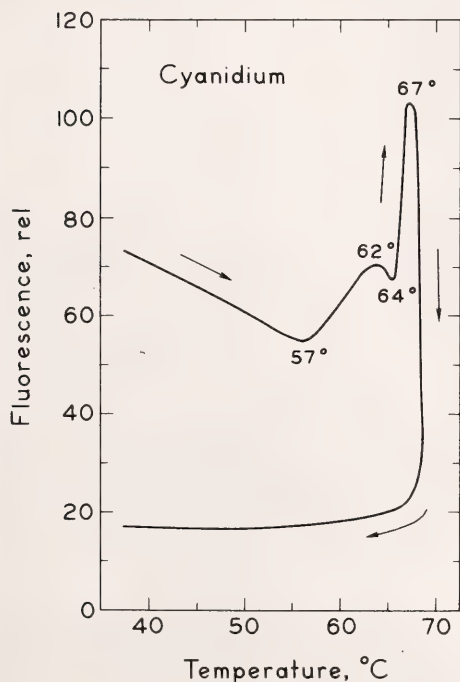


Fig. 51. The temperature dependence of chl *a* fluorescence in *Cyanidium* grown at 39°C and treated with 10^{-5} M DCMU. The cells were heated to 67°C and then cooled at once to 27°C. Fluorescence was measured as described in Fig. 50.

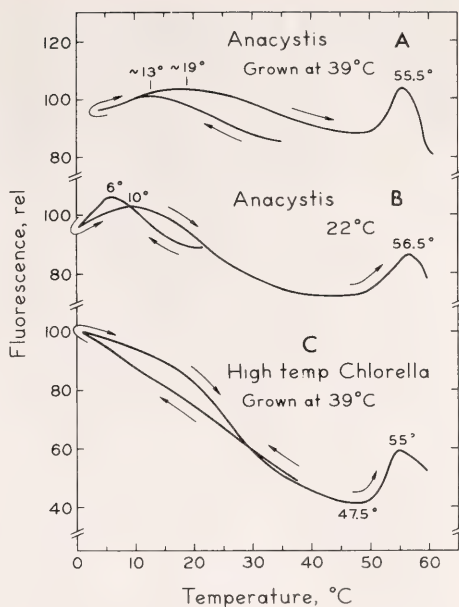


Fig. 52. The temperature dependence of chl *a* fluorescence for *Anacystis* grown at 39°C (A) and at 22°C (B) and for a high-temperature strain of *Chlorella* grown at 39°C (C) DCMU, 10^{-5} M. Fluorescence was measured as described previously (Murata *et al.*, 1975) with blue actinic light (440 nm, 500 ergs $\text{cm}^{-2} \text{sec}^{-1}$).

near these temperatures. (Year Book 74, pp. 766–776; Murata *et al.*, 1975).

The *F-T* curve of a high-temperature strain of *Chlorella* (Sorokin and Myers, 1953; Sorokin, 1967), which has its optimum temperature for growth near 39°C, showed a maximum, as did *Anacystis*, around 55°C (Fig. 52). Unlike *Anacystis*, however, it did not show maxima near 13° or 20°C. It seems that a fluorescence maximum will occur at temperatures somewhat below 0°C. Cells of the high-temperature strain of *Chlorella* that had been heated to 60°C and cooled again produced a flat fluorescence versus temperature curve with none of the previously seen maxima or minima.

A number of *F-T* curves were measured for intertidal marine algae. The red alga *Iridaea* had a complex curve with maxima at 37°, 46°, and 51.5°C and minima at 30°, 43.5°, and 48°C. The green alga *Ulva* did not show the complicated curve of *Iridaea* but had a

steep decline of fluorescence with increasing temperature, with a shoulder around 32°C. The brown alga *Laminaria* also showed a steep decline of fluorescence with increasing temperature, with an inflection near 38°C.

The red alga *Porphyra perforata* was used to compare the behavior of fluorescence and photosystem II activity. This alga inhabits the upper reaches of the tidal zone and undergoes repeated cycles of drying and rehydration with tidal changes. It was found previously (Year Book 72, pp. 384–388) that dried *Porphyra* lost its photosystem II activity upon drying but still retained measurable photosystem I activity (P700 oxidation). However, the photosystem II activity was restored immediately when the dried alga was rehydrated with seawater.

The ratio of variable fluorescence to maximum fluorescence yield (F_v/F_{\max}) was measured in *Porphyra* as a function of increasing temperature. This ratio has been proposed (Duysens and Sweers, 1963; Butler and Kitajima, 1975) to be a measure of the photochemical activity in photosystem II. Figure 53 shows a plot of F_v/F_{\max} and F_{\max} versus temperature in *Porphyra* treated with 10^{-5} M DCMU. The F_v/F_{\max} ratio (Fig. 53B) decreased with increasing temperature above 20°C. At temperatures above 37.5°C the F_v/F_{\max} ratio declined steeply and the F_{\max} curve (Fig. 53A) increased rapidly. The F_v/F_{\max} ratio reached zero when the F_{\max} curve had attained its maximum.

Figure 53 C illustrates that features of the F - T curve seen previously were lost when a dried thallus was measured. After reconstitution of the thallus with seawater, the F - T curve showed features noted previously (Fig. 53 D).

Temperature Dependence of Chlorophyll a Fluorescence in Higher Plants

The F - T curves measured for a number of higher plants leaves are presented in Fig. 54. A leaf from

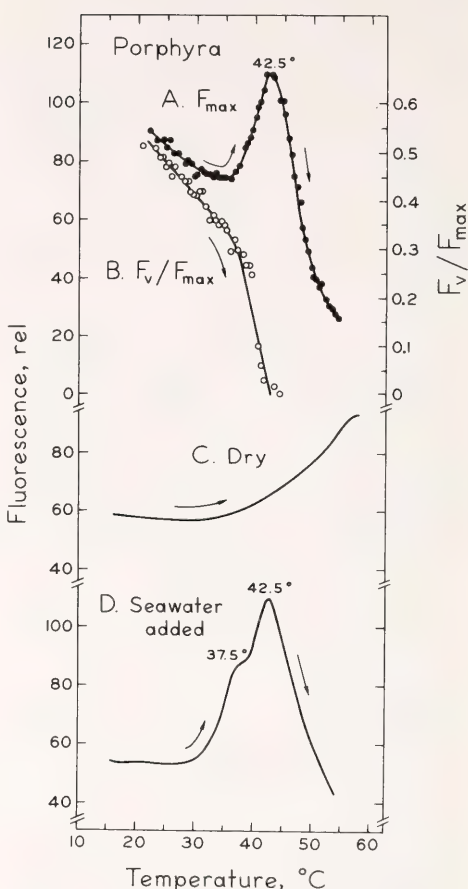


Fig. 53. The temperature dependence of chl *a* fluorescence in *Porphyra perforata* treated with 10^{-5} M DCMU. As the temperature was increased at the rate of 0.8°C/min, measurements were made of the time course of the fluorescence of chl *a* at 685 nm, using a broad band of green actinic light (140 ergs $\text{cm}^{-2} \text{sec}^{-1}$). (C), a piece of the thallus (not treated with DCMU) was exposed to the sun for 2 hr and air dried for an additional 9 hr, after which the F - T curve was measured. D, the temperature dependence of chl *a* fluorescence in *Porphyra* that had been dried as described in C above and reconstituted with seawater to which DCMU was added to a final concentration of 10^{-5} M.

"winter" spinach had minima at 31°C and a maximum at 42.5°C (Fig. 54A). Chloroplasts prepared from spinach leaves by contrast showed only an inflection at 31°C and a faint shoulder around 43°C (Fig. 54B). Chloroplasts prepared from winter spinach were used to measure the photochemical ac-

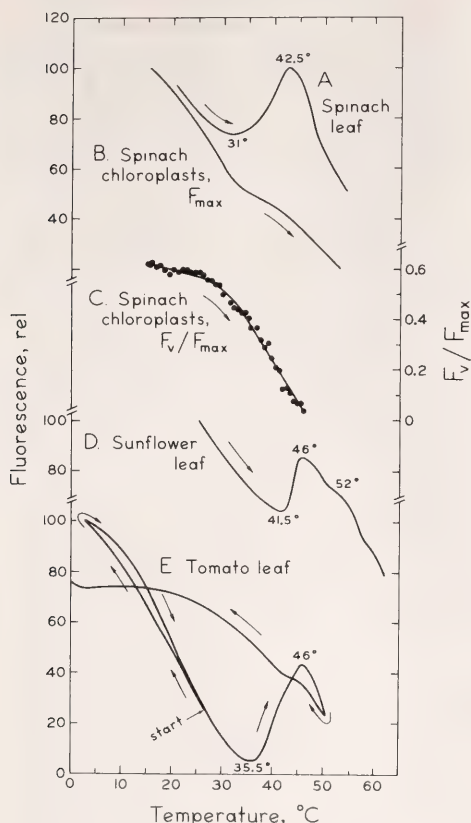


Fig. 54. The temperature dependence of chl *a* fluorescence in leaves of spinach (A), sunflower (D), and tomato (E) vacuum infiltrated with 10^{-5} M DCMU and for spinach chloroplasts (B) treated with 10^{-5} M DCMU. The spinach chloroplasts and leaves used were obtained from winter frost-hardy spinach plants. The chloroplasts were suspended in 0.4 M sucrose, 0.01 M NaCl, 0.05 M phosphate buffer, pH 7.4. The F_v/F_{max} ratio in spinach chloroplasts (C) was measured by the chl *a* fluorescence at 685 nm produced using 5.7-sec exposures to blue actinic light that was obtained by filtering white light through two Corning 9782 filters. Dark intervals between exposures = 40 sec. In E, a tomato leaf at 26°C was cooled to 5°C and then heated to 50°C and cooled again to 0°C.

tivity of photosystem II as a function of temperature from 10° to 46°C as the F_v/F_{max} ratio described above. The activity of photosystem II declined slowly with temperature to about 30°C and declined steeply thereafter. This decline corresponded to the beginning of the steep fluorescence increase with temperature of F_{max} (Fig. 54C). In

another experiment the ratio of F_v/F_{max} in a spinach leaf harvested in the spring after freezing conditions had ended showed an abrupt change of slope at a somewhat higher temperature (35°C).

In sunflower leaf (Fig. 54 D) the minimum appeared at 41.5° and a maximum at 46°C, with a small inflection around 52°C. In a pea leaf (not shown) an indistinct minimum was seen near 38°C and a peak near 46°C. In tomato (Fig. 54 E) fluorescence increased as the temperature was lowered to 5°C. Increasing the temperature from this point resulted in a decline of fluorescence to a minimum at 35.5°C and a subsequent increase to a maximum at 46°C. Cooling the leaf again after passing over the 46°C peak produced a fluorescence to temperature curve that increased with increasing temperatures and did not show the characteristic features seen previously. Although no low-temperature fluorescence maximum appeared in the tomato curve, it appears that a maximum could be seen at slightly lower temperatures, perhaps near or below 0°C.

Chlorophyll a Protein from Spinach

The temperature dependence of fluorescence was measured for a chlorophyll protein preparation made from spinach that contained a chlorophyll *a*/P700 ratio of about 50. Some characteristic properties of this preparation are described elsewhere in this Report. The temperature dependence of this preparation is shown in Fig. 55. Unlike spinach chloroplasts, it has a broad minimum near 40°C and a maximum around 63°C.

This survey of the variation of fluorescence as a function of temperature in a number of plants having distinct pigmentation and growing under different conditions reveals several common features.

The fluorescence maxima seen at 13°C upon decreasing and at 19°C upon

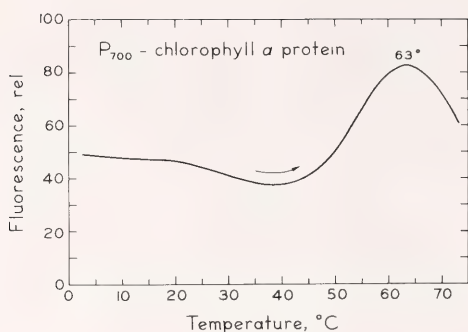


Fig. 55. The temperature dependence of chlorophyll *a* fluorescence in a P700-chlorophyll-protein complex isolated from spinach. No DCMU was added.

increasing the temperature in *Anacystis* grown at 22°C were attributed last year (Year Book 74, pp. 766–776; Murata *et al.*, 1975; Murata and Fork, 1975) to a thermal transition of the physical phase of membrane lipids. The maxima occurred near the temperatures where the transition of the phase of membrane lipids changed from the liquid crystalline to the mixed, solid-liquid crystalline states. In *Anacystis* we found that the Arrhenius plots of reduction rates of P700, of oxygen evolution, and of the configurational change of the thylakoid membrane that are related to the state 1 and state 2 shifts (Murata, 1969, 1970; Bonaventura and Myers, 1969) were composed of two straight lines with breaks near the phase transition temperatures as determined by electron spin resonance or by the appearance of fluorescence maxima. Activation energies were always lower above the transition temperature and higher below the transition point.

The fluorescence maxima seen in *Cyanidium* near 10°C for cells cultured at 45°C, and near 8°C for cells cultured at 39°C, and from 0° to 5°C in cells cultured at 21°C also appear to represent similar phase changes in this alga. As is the case with *Anacystis*, the lipid composition of *Cyanidium* changes with growth temperature. The ratio of unsaturated to saturated fatty acids has been found to decrease threefold

with increasing growth temperature. Cells cultured at 20°C contained 30% of their fatty acids as linoleic acid. This fatty acid was not found in cells grown at 55°C (Kleinschmidt and McMahon, 1970a, 1970b). Studies are in progress with *Cyanidium* to see if, as in *Anacystis*, fluorescence maxima represent lipid phase changes that can also be correlated to changes of photosynthetic reactions.

It was expected that the high temperature strain of *Chlorella* might show a phase change like those seen for *Anacystis* cultured at 39°C. Perhaps the phase change as detected by the appearance of a fluorescence maximum may occur at temperatures near or slightly below 0°C, and the lipid composition of *Chlorella* adapted to high temperatures will be found to be different from that of *Anacystis* or *Cyanidium*.

Most of the plants examined exhibited a high-temperature fluorescence maximum. At temperatures above this maximum irreversible effects were produced such that the previously observed variations of fluorescence with temperature were lost. Lavorel (1969) has observed similar maxima in fluorescence yield in the green algae *Chlorella* and *Scenedesmus* heated at a rate of 0.7°C/min. The rise began at about 42°C, peaked near 52°C, and then declined at higher temperatures.

The high-temperature fluorescence peak was not invariably seen, however. It could not be detected in *Ulva* and was seen only as a shoulder in *Laminaria*. It was likewise indistinct in pea leaf, and chloroplasts from spinach showed only a minor inflection where a peak was seen in the leaves. It may be, as discussed previously (Year Book 74, pp. 751–759), that the high-temperature fluorescence peak, particularly as seen in leaves, represents some alteration in the scattering or absorption properties produced by heat damage of cells and chloroplasts of the leaves. This explanation, however, does not explain the 55°C maximum

seen in the blue-green alga *Anacystis*. These organisms, like the bacteria, have a primitive cellular organization. They lack vacuoles and do not have lamellae organized into grana stacks as do higher plants but have them distributed throughout the entire cell. It may be that the fluorescence peak seen at high temperatures represents the irreversible denaturation of a pigment-protein complex. The disappearance of variations of fluorescence as a function of temperature after heating above the high-temperature fluorescence maximum is consistent with this idea. In addition, the system I chlorophyll-protein preparation that has only a trace of lipid (Thorner, personal communication) also showed a high-temperature fluorescence peak. The maximum at 63°C seen in this preparation is consistent with many observations that system I is more resistant to high temperatures than is system II.

The high-temperature fluorescence maximum did not change much with growth temperature in *Anacystis* or *Cyanidium*; however, the smaller satellite peak at temperatures below the high-temperature fluorescence peak did vary with growth temperature in *Cyanidium*.

Most of the leaves examined had a high-temperature peak around 46°C, as did leaves of *Atriplex sabulosa*, which is native to a cool habitat (Year Book 74, pp. 751-759). Exceptions to this observation were seen in winter spinach (maximum at 42.5°C) and in *Tidestromia oblongifolia* native to a hot habitat (peak near 57°C) (Year Book, 74, pp. 751-759).

In this study the loss of photosystem II activity as revealed by the steep drop in the F_v/F_{max} ratio in the red alga *Porphyra* and in spinach chloroplasts seemed to be correlated with the beginning of the steep rise of fluorescence to its high-temperature maximum. This was also seen earlier in a leaf of *Atriplex*; but in *Tidestromia*, damage to photosynthesis was seen already around 46°C, whereas the beginning of

the high-temperature fluorescence rise occurred near 53°C (Year Book 74, pp. 751-759).

A decline of photosynthetic activity with increasing temperature was observed by Mukohata *et al.* (1973), who showed that ferricyanide reduction in spinach chloroplasts was inhibited at temperatures higher than about 40°C. Krause and Santarius (1975) noted that the rate of rise of variable fluorescence in the light was slowed down by mild heat treatment. This rate dropped rapidly at temperatures above 40°C, as did the activity of cyclic photophosphorylation.

Santarius (1974) found seasonal changes in plant membrane stability to heat treatment. In thylakoid membranes isolated from frost-hardy spinach plants harvested in November, the decline of the Hill reaction measured as ferricyanide reduction began at temperatures above about 40°C. Surprisingly, the Hill reaction and cyclic photophosphorylation in thylakoid membranes isolated from summer spinach were found to be more sensitive to heat treatment, the decline in activity of both beginning around 30°, similar to that observed here for the F_v/F_{max} ratio.

ACKNOWLEDGMENT

The chlorophyll protein preparation used in this study was kindly provided by Dr. Jeanette S. Brown.

References

- Bonaventura, C., and J. Myers, *Biochim. Biophys. Acta*, 189, 366-383, 1969.
- Butler, W. A., and W. Kitajima, *Biochim. Biophys. Acta.*, 376, 116-125, 1975.
- Doemel, W. N., and Brock, T. D., *J. Gen. Microbiol.*, 67, 17-32, 1971.
- Duysens, L. N. M., and H. E. Sweers, in *Studies on Microalgae and Photosynthetic Bacteria*, Univ. Tokyo Press, pp. 353-372, 1963.

- Kleinschmidt, M. G., and V. A. McMahon, *Plant Physiol.*, **46**, 286–289, 1970a.
- Kleinschmidt, M. G., and V. A. McMahon, *Plant Physiol.*, **46**, 290–293, 1970b.
- Krause, G. H., and K. A. Santarius, *Planta*, **127**, 285–299, 1975.
- Lavorel, J., in *Progress in Photosynthesis Research*, H. Metzner, ed., International Union of Biological Sciences, Tübingen, Vol. 2, pp. 883–898, 1969.
- Murata, N., *Biochim. Biophys. Acta*, **172**, 242–251, 1969.
- Murata, N., *Biochim. Biophys. Acta*, **205**, 379–389, 1970.
- Murata, N., and D. C. Fork, *Plant Physiol.*, **56**, 791–796, 1975.
- Murata, N., J. Troughton, and D. C. Fork, *Plant Physiol.*, **56**, 508–517, 1975.
- Mukohata, Y., T. Yagi, M. Higashida, K. Shinozaki, and A. Matsuno, *Plant Cell Physiol.*, **14**, 111–118, 1973.
- Santarius, K. A., *Z. Pflanzenphysiol.*, **73**, 448–451, 1974.
- Sorokin, C., *Science*, **158**, 1204–1205, 1967.
- Sorokin, C., and J. Myers, *Science*, **117**, 330–331, 1953.

CORRELATION BETWEEN GROWTH TEMPERATURE AND HEAT-INDUCED CHLOROPHYLL FLUORESCENCE CHANGES IN *Scenedesmus obliquus*

Ulrich Schreiber

INTRODUCTION

Chlorophyll fluorescence is a sensitive intrinsic probe to determine the efficiency of quantum conversion in photosynthesis. The fluorescence yield in chloroplasts or algae is primarily determined by the rate of charge separation at photosystem II reaction centers. But substantial yield changes can also be effected by changes in other radiationless de-excitation processes, such as energy transfer, including that to photosystem I (spillover), quenching by molecular oxygen, and heat dissipation. Both PS II reaction centers and antenna pigments are embedded in the fluid mosaic of the thylakoid membrane. The properties that determine fluorescence yield are correlated with the state and intactness of this membrane. Murata *et al.* (1975) and Murata and Fork (1975) have demonstrated a correlation between maximum fluorescence yield in *Anacystis nidulans* and a thylakoid membrane fluidity change in the 10°–25°C region, adaptable to growth temperature. We have reported previously on large increases (up to 400%) in fluorescence yield with a

jump from room temperature to 45°–55°C in a variety of plants (Schreiber *et al.*, 1975; Schreiber *et al.*, 1976). In those studies, the heat-induced fluorescence increase was most pronounced in plants from a low-temperature environment, suggesting a correlation between heat stability and heat-induced fluorescence increase.

In the present study, a unicellular alga, *Scenedesmus obliquus*, was grown at 20° and 28°C. It was found that fluorescence properties at 45°–55°C are substantially altered by a change in growth temperature. Included are changes in fluorescence yield with slow heating and changes in fluorescence induction with a temperature jump (*T*-jump). It will be shown that there is a close correlation between these fluorescence changes monitored at high temperatures and heat damage in the vicinity of PS II centers, assayed after returning the algae to room temperatures.

METHODS

Scenedesmus obliquus (Indiana Culture Collection) was grown either at

20° or at 28°C. Samples were dark-adapted for 2 hr at room temperature (20°–23°C) before the experiments.

The apparatus for rapid temperature changes (95% of a 25°C change in 2 sec) and fluorescence measurements was essentially the same as described earlier (Schreiber *et al.*, 1976). The method was improved by using solenoid valves to regulate cold and hot water flow through the cuvette. Usually, very dilute cell suspensions were used with approximately 5×10^3 cells/ μ l. Fluorescence curves were corrected for stray excitation light reaching the photomultiplier.

RESULTS

Slow Heating Curves

Temperature and temperature adaptation can be expected to affect a great number of photosynthetic partial reactions, all of which will more or less directly determine fluorescence yield. In order to study the *direct* effect of temperature and temperature adaptation on the state of Chl *a* and PS II reaction centers in the thylakoid membrane via fluorescence measurements, it is necessary to eliminate the influence of photosynthetic dark reactions on fluorescence. Such influences are minimized in two extreme situations. The first is that of all PS II centers being closed, e.g. in the presence of DCMU in continuous strong light, with fluorescence displaying its maximum level, F_{\max} . The second is that of all PS II centers being open, e.g. in an extremely weak fluorescence measuring beam, yielding minimum fluorescence, F_0 .

In practice it is difficult to assure complete inhibition of fluorescence quenching in F_{\max} measurements. Even in the presence of DCMU there is fluorescence quenching via molecular oxygen, spillover, and the back-reaction at PS II reaction centers. It can be expected that these quenching mechanisms show some temperature dependency. For example, it is known

that the PS II back-reaction is stimulated substantially at higher temperatures (Bennoun, 1970). On the other hand, it becomes irreversibly blocked at 45°–55°C (see section below). To exclude this factor NH_2OH , which prevents the back-reaction, was added for F_{\max} measurements. In F_0 measurements it is difficult to keep Q fully oxidized with extended periods at elevated temperatures, where O_2 uptake is stimulated and an endogenous electron donor, possibly related to hydrogenase, is induced when conditions become anaerobic (Gaffron, 1944; Schreiber *et al.*, 1976). Use of extremely dilute algal suspensions retards the development of anaerobic conditions.

With these precautions, F_{\max} and F_0 changes with slow heating of *Scenedesmus* cells grown at 20° or 28°C are shown in Fig. 56. Both F_{\max} and F_0 curves display a correlation with growth temperature. The characteristic yield changes are shifted by approximately 1°C in the 28°C cells, relative to the 20°C cells. This shift is particularly clear in the F_0 curves, which have a main rise phase (at 46°–52°) well separated from a minor rise at $T < 46^\circ$ and a decay at $T > 52^\circ$. The F_{\max} curves show a less conspicuous main decay phase extending over the whole temperature region, with some characteristic slope changes. The significance of these slope changes will become clearer from an analysis of the F_{\max} T -jump curves to be shown below. It appears that the F_0 curves are a sensitive indicator for a dramatic change within a relatively narrow temperature interval of a parameter essential in regulating fluorescence yield. The same change causes an inverse effect on F_{\max} , but as far as slow-heating curves are concerned, the information from F_0 seems to be more specific.

The fact that F_0 and F_{\max} slow-heating curves are shifted with growth temperature indicates that beyond expected changes in the enzymatic dark reaction part of photosynthesis, temperature adaptation has also affected

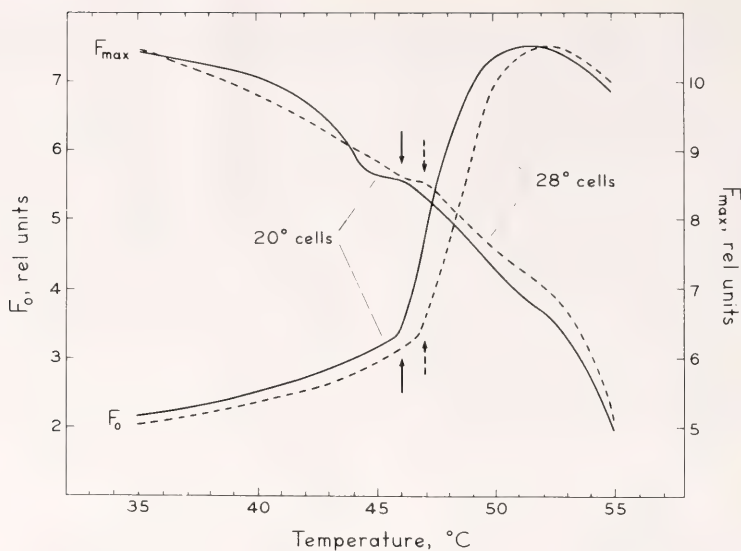


Fig. 56. Slow heating curves for F_0 and F_{\max} in cells grown at 20 and 28°C. For F_{\max} measurement $5 \times 10^{-5} M$ DCMU and $10^{-3} M$ NH_2OH was added; light intensity 5×10^4 erg/cm²s. Light intensity for F_0 , 2 erg/cm²s. Units for F_0 and F_{\max} are on the same relative scale normalized with respect to light intensities. Note the shifted scales for F_0 and F_{\max} . Rate of heating, approximately 1°C/min. Correlation between beginning of major rise phase in F_0 and corresponding decay in F_{\max} is indicated by full arrows for 20° cells (at 46°) and broken arrows for 28° cells (at 47°).

some parameter associated with the pigment system and PS II reaction centers. Slow-heating curves as such do not reveal which parameter is affected.

T-Jump Curves

With a T -jump the time course of the heat-induced fluorescence changes can be monitored, giving additional information on the nature of changes. Figure 57 shows T -jump curves of F_0 and F_{\max} for the 20° and 28° cells. As with the slow-heating curves, there is a clear correlation with growth temperature. Heat-induced changes are more pronounced in the 20° cells. Temperatures for roughly equivalent fluorescence time courses are shifted by approximately 1°C upward for the 28° cells. At a given temperature, 28° cells have to be heated about twice as long as 20° cells to give an equivalent fluorescence increase (e.g. compare curves for 47°C). The T -jump curves reveal several phases, suggesting that there are several mechanisms by which heat induces fluorescence changes. A

detailed analysis for F_0 curves has been presented elsewhere (Schreiber *et al.*, 1976). A new finding is the inverse relationship between the time courses of the F_0 and F_{\max} curves, particularly pronounced in the slower part of the curves. At present no definite explanation can be given for this phenomenon. However, it appears unlikely that it is based on changes in quenching at PS II centers or changes in de-excitation rate constants of Chl *a* in the pigment system. Such changes should affect F_0 and F_{\max} in the same direction. As a working hypothesis it may be proposed that the process that leads to the increase in F_0 and the decrease in F_{\max} affects the energy distribution favoring PS I in the F_0 state and PS II in the F_{\max} state. Any disturbance of such an active distribution mechanism would cause an increase in F_0 and a decrease in F_{\max} .

Reversibility of the Light-Induced Fluorescence Increase in the Presence of DCMU

In the sections above it was shown that *Scenedesmus* grown at different

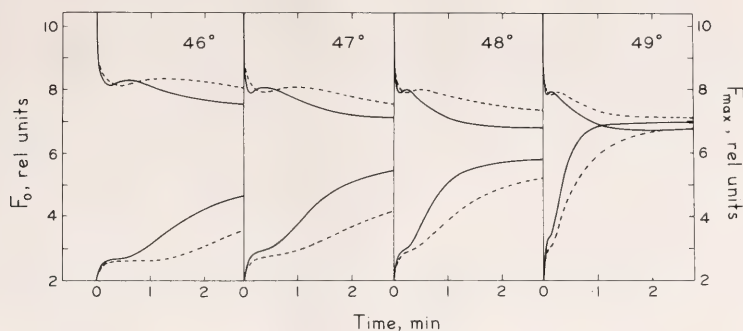


Fig. 57. T -jump fluorescence induction for F_0 and F_{\max} in 20° and 28° cells. T -jump from 30° to indicated temperatures. Solid lines, 20° cells; broken lines 28° cells. Conditions as in Fig. 56. Units for F_{\max} and F_0 are on the same relative scale, normalized with respect to light intensities.

temperatures displays consistent differences in heat-induced fluorescence changes. It remains to be shown that these differences relate to a difference in thermal stability. It has been shown previously that heat treatment inhibits the back reaction at PS II centers (Schreiber, 1971). When a sample is illuminated in the presence of DCMU, a high steady-state fluorescence yield reflects complete reduction of Q . In a following dark period Q normally becomes reoxidized, as indicated by a reproducible fluorescence rise curve with subsequent illumination. Heat treatment prevents this reoxidation. Figure 58 compares fluorescence rise curves in the presence of DCMU in a nonheated control and a sample heated for 1 min at 56°C . In Fig. 58A dark-adapted samples are compared; heating causes only a small increase in F_0 . Figure 58B demonstrates that there is no reoxidation of Q in the heat-treated sample following preillumination. The light-induced fluorescence rise in the presence of DCMU is irreversible. This behavior is identical to that in the presence of NH_2OH , which has been shown to inhibit the back-reaction at PS II centers by keeping the donor Z-reduced (Bennoun, 1970).

When a sample is only partially heat damaged, only part of the PS II reaction centers will be inactivated in their back-reaction, and part of the DCMU fluorescence rise is reversible. The de-

gree of irreversibility can be considered a measure of heat damage.

In Fig. 59 the term $(F_{\max} - F_0)/F_{\max}$ is plotted as an expression of still active centers versus heating temperature for the 20° and 28° cells. Inhibition of the back-reaction occurs in the same temperature region where slow-heating and T -jump curves showed characteristic fluorescence yield changes. The inhibition characteristic is shifted by about 1°C toward higher temperatures for the 28° cells.

Heat damage in higher plant chloroplasts has been correlated with changes in F_0/F_{\max} by Berry *et al.* in this laboratory (Year Book 74, p. 751, and elsewhere in this Report). New aspects suggested by the present study are the importance of controlled preillumination and the similarity of the heat damage to the action of NH_2OH . As with NH_2OH , heat damage does not block the PS II primary reaction as such, because without preillumination a close-to-normal fluorescence rise is observed (see Fig. 58). By analogy with the effect of NH_2OH , heat damage appears to prevent reoxidation of Q via electron transfer to Z^+ at the PS II donor side (Bennoun, 1970). To date, it is difficult to distinguish between two alternate hypotheses. Heat damage possibly causes the breakdown of a barrier that normally prevents reduction of Z^+ by endogenous electron donors. This barrier may be provided

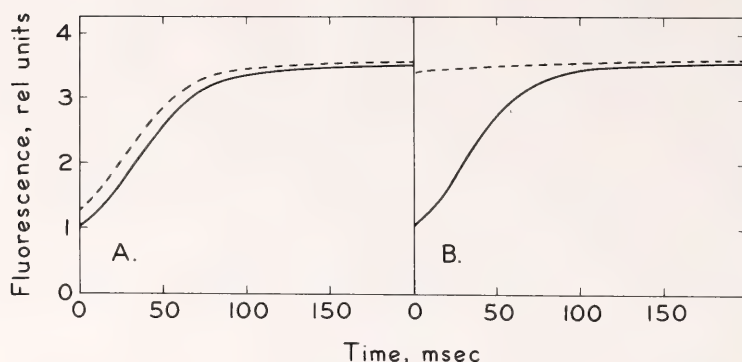


Fig. 58. Effect of heat treatment on reversibility of fluorescence rise-curve measured at 25°C in the presence of DCMU. Solid lines, unheated control; broken lines, sample heated 1 min at 56°C. A, samples before preillumination; B, samples preilluminated for 1 sec. Curves measured following subsequent 1 min dark time. $5 \times 10^{-6} M$ DCMU was added in the dark 2 min before measurement of curves (a). 20° cells; light intensity, 10^3 erg/cm²s.

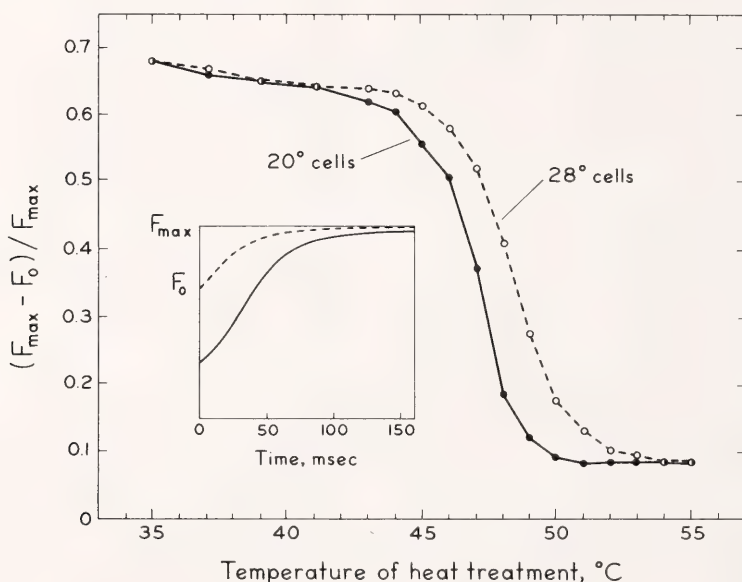


Fig. 59. Reversibility of DCMU rise-curve in dependency of heating temperature in 20° and 28° cells. Samples were heated for 1 min at given temperature; DCMU was added in the dark; after 2-min incubation, 1-sec preillumination was given; the DCMU rise-curve was measured after subsequent 1-min dark time; F_{\max} and F_0 values determined as indicated in the inset. The inset shows the remaining rise in 20° cells for 47°C treatment (broken line) as compared to a nonheated control (solid line). Conditions as in Fig. 58.

by an intact membrane. Alternatively, heat damage could cause denaturation of the water-splitting enzyme. Both hypotheses account for a block of the PS II back-reaction and a block of O₂ evolution.

There is close similarity between F_0 slow-heating curves (see Fig. 56) and

the deactivation curves in Fig. 59. One may conclude that irreversible heat damage and the F_0 increase measured at elevated temperatures are related. Deactivation of the PS II back-reaction or the water-splitting enzyme system as such should not cause the dramatic increase in F_0 . Both phenomena appear

to be caused by a common drastic change in the photosynthetic apparatus in a critical temperature region. This critical temperature region is higher in plants grown at higher temperatures, suggesting the capacity for partial adaptation. The common cause may be a fluidity change in the thylakoid membrane, affecting energy transfer and distribution as well as lipid-protein interaction. Adaptation to growth temperature could involve a change in the ratio of unsaturated to saturated fatty acids, as is known for blue-green algae (Holton *et al.*, 1964).

CONCLUSIONS

The above results demonstrate a correlation between growth temperature, heat damage, and heat-induced fluorescence changes in *Scenedesmus obliquus*. Similar experiments were carried out with other unicellular algae (*Chlorella pyrenoidosa* and *Anacystis nidulans*) and gave similar results. It can be concluded that these algae can partly adapt their photosynthetic apparatus to their thermal environment. Chlorophyll fluores-

cence, particularly in F_0 measurements, appears to be a sensitive indicator for heat-induced damage and, consequently, for assaying heat sensitivity in plants.

REFERENCES

- Bennoun, P., *Biochim. Biophys. Acta*, **216**, 357-363, 1970.
- Gaffron, H., *Biol. Rev.*, **19**, 1-20, 1944.
- Holton, R. W., H. H. Blecker, and M. Onore, *Phytochem.*, **3**, 595-602, 1964.
- Murata, N., and D. C. Fork, *Plant Physiol.*, **56**, 791-796, 1975.
- Murata, N., J. H. Troughton, and D. C. Fork, *Plant Physiol.*, **56**, 508-517, 1975.
- Schreiber, U., Dissertation, Rheinisch-Westfälische Technische Hochschule Aachen, West Germany, 1971.
- Schreiber, U., K. Colbow, and W. Vidaver, *Z. Naturforsch., Teil C.*, **30**, 689-690, 1975.
- Schreiber, U., K. Colbow, and W. Vidaver, *Biochim. Biophys. Acta*, **423**, 249-263, 1976.

DARK UPTAKE OF HCO_3^- BY WASHED CHLOROPLAST GRANA

Alan Stemler

Bicarbonate ions play an important role in both the light and the dark reactions in photosynthesis. Of the two light reactions, HCO_3^- is necessary for photosystem II activity. Evidence suggests (Stemler and Govindjee, 1973) that HCO_3^- is taken up by broken chloroplasts as a prior condition to activation of oxygen evolution during a Hill reaction. A quantitative estimate of HCO_3^- uptake by broken chloroplasts is therefore desirable to allow insight into possible modes of action of this ion. To obtain such an estimate, competitive binding studies were done using $\text{H}^{14}\text{CO}_3^-$ and maize chloroplast fragments.

Chloroplasts were isolated by a procedure described elsewhere (Stemler

and Govindjee, 1973). During isolation, they were subjected to an osmotic shock, after which they were washed, frozen, and then thawed before use. Such chloroplasts normally cannot assimilate CO_2 in the usual fashion and cannot evolve oxygen without an added Hill oxidant such as ferricyanide. Nevertheless, under certain conditions such chloroplast fragments can bind large amounts of HCO_3^- in the dark.

When grana are provided with $\text{H}^{14}\text{CO}_3^-$ and increasing concentrations of cold HCO_3^- , competition develops for a limited number of binding sites on or within the thylakoid membranes. After correction for "trapped" $\text{H}^{14}\text{CO}_3^-$ (i.e., unbound HCO_3^- associated with the chloroplasts because of their finite vol-

ume), results are expressed in a Scatchard plot (Scatchard, 1949) shown in Fig. 60. Where a single binding site is involved, a Scatchard plot will yield a straight line with the intercept of the abscissa indicating the concentration of the binding site. The plot in Fig. 60 shows instead a curved line, indicating the presence in chloroplast grana of more than one binding site for HCO_3^- . The sharp drop in the left portion of the curve shows a small pool of binding sites having a relatively high affinity for HCO_3^- . A rough estimate of the maximum size of this pool can be obtained by a line tangent to the upper section of the curve and intersecting the abscissa (Klotz and Hunston, 1971). The dashed line so drawn in Fig. 60 intersects the abscissa at $3.5 \mu\text{M}$, and this represents the upper limit of the concentration of this binding site (or sites, as the pool may be heterogeneous) when the chlorophyll concentration is 1.0 mM .

The long tail of the Scatchard plot (Fig. 60), which approaches the abscissa very obliquely, indicates that there also exists in grana another quite large pool of relatively low affinity HCO_3^- binding sites. The size of this pool is difficult to determine, since it

cannot be saturated on account of the limited solubility of $\text{HCO}_3^-/\text{CO}_2$ at the pH at which the experiment was done (6.5). However, the size must be greater than $160 \mu\text{M}$ when the chlorophyll concentration is 1.0 mM , since this amount was actually observed bound under a nonsaturating concentration of HCO_3^- . The conditions of this experiment, however, may not have been optimal for HCO_3^- binding, so conclusions concerning the actual number of both high- and low-affinity sites can only be tentative until other parameters such as temperature, illumination, and incubation time can be studied.

An example of a very critical factor controlling the amount of $\text{H}^{14}\text{CO}_3^-$ bound to grana is the pH of the suspension. This relationship is plain in Fig. 61. Chloroplasts take up very little $\text{H}^{14}\text{CO}_3^-$ above pH 7.0, but show nearly a tenfold increase in bound $\text{H}^{14}\text{CO}_3^-$ when the pH is lowered from 7.0 to 5.6. As other factors that may influence binding are examined, a better idea of the size and function of the binding sites should emerge.

With our present limited knowledge, we can only guess the significance of the two pools of bound HCO_3^- in grana.

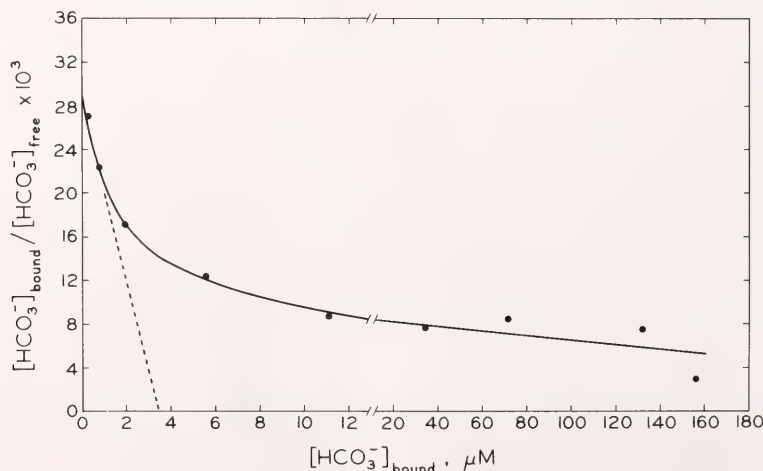


Fig. 60. Scatchard plot for the binding of HCO_3^- to chloroplast grana. The suspension contained $1.0 \text{ mg chlorophyll ml}^{-1}$ (i.e., 1.0 mM), $0.1 \text{ M Na phosphate}$, pH 6.5, 0.2 M NaCl , $1.2 \mu\text{Ci NaH}^{14}\text{CO}_3$. The concentration of unlabeled NaHCO_3 was varied from 0.0 to 50 mM . The grana were incubated for 5 min at 30°C after addition of $\text{H}^{14}\text{CO}_3^-$.

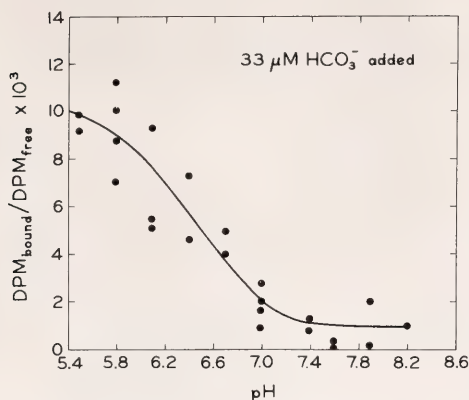


Fig. 61. Binding of $\text{H}^{14}\text{CO}_3^-$ to chloroplast grana as a function of pH. The suspension contained $384 \mu\text{g}$ chlorophyll ml^{-1} , 0.1 M Na phosphate, 0.2 M NaCl, $33 \mu\text{M}$ NaHCO_3 ($1.2 \mu\text{Ci ml}^{-1}$). The pH was varied by addition of appropriate amounts of NaOH.

We know, for instance, that depleting chloroplasts of HCO_3^- has two distinct effects (Stemler *et al.*, 1974): About half the photosystem II reaction centers become totally inactive, while those still able to evolve oxygen have dramati-

cally reduced recovery rates. Assuming both pools of bound HCO_3^- are indeed functional in photosystem II activity, each may control one of the above observed effects.

Of the two pools of bound HCO_3^- , the larger is already more strongly implicated in oxygen evolution. The small pool is saturated by addition of about 1 mM HCO_3^- while 10 mM HCO_3^- , a concentration needed to fill the larger pool substantially, is required to restore oxygen evolution fully in HCO_3^- depleted chloroplasts. Both pools, however, may be equally important, and will be studied in detail.

References

- Klotz, I. M., and D. L. Hunston, *Biochemistry*, **10**, 3065-3069, 1971.
 Scatchard, G., *Ann. N.Y. Acad. Sci.*, **51**, 660-672, 1949.
 Stemler, A., and Govindjee, *Plant Physiol.*, **52**, 119-123, 1973.
 Stemler, A., G. T. Babcock, and Govindjee, *Proc. Nat. Acad. Sci. U.S.A.*, **71**, 4679-4683, 1974.

BIBLIOGRAPHIC INFORMATION RETRIEVAL

J. S. Brown

In *Year Book 72*, p. 407, a computer-based system for the storage and retrieval of bibliographic information from the photosynthesis literature was described. Also, the Thesaurus (list of categories) under which the references in the "Plantbio" file are listed was printed out. Currently, the file size has increased to more than 6000 entries, and the following new categories have been added to the Thesaurus: C-3, ecological; C-4, solar energy; D-6, xanthophylls; G-14, temperature effects; G-15, oxidation/reduction; G-16, pH effects; H-14, superoxides; L-3, superoxide dismutase; R-6, N_2 fixation.

Unfortunately, the cost of storing the file in a way that makes on-line searching possible at any time has become prohibitive (about \$10.00 per day) unless justified by a large number of users. An attempt was made to form a

Users' Club by sending out information about the file to approximately 150 photosynthesis workers around the world. Many were interested, but few could support it financially.

Therefore, we now have a new procedure whereby we can unload the complete file on to tape and restore it again when we choose for about \$20.00. This means that we can search and update the file only during specified periods, but on-line storage costs are greatly reduced.

However, we have found another way in which the file can be useful. It is easily possible to search and print out all of the references in a particular category alphabetically by first author for a reasonable cost (\$5.00 for categories having less than 300 references). We have already sent several of these cat-

egory listings to other laboratories, and we shall be glad to provide more specific information such as category size

and costs upon request. Inquiries should be addressed to "The Librarian."

BIBLIOGRAPHY

- Anderson, J. M., *see* Boardman, N. K.
 Berry, J. A., *see* Mooney, H. A.
 Björkman, O., *see* Boardman, N. K.; Ehleringer, J. R.; Mooney, H. A.
- 558* Boardman, N. K., O. Björkman, J. M. Anderson, D. J. Goodchild, and S. W. Thorne, Photosynthetic adaptation of higher plants to light intensity: Relationship between chloroplast structure, composition of the photosystems and photosynthetic rates, *Proc. 3rd Int. Congr. Photosynthesis*, M. Avron, ed., Sept. 1974, Weizmann Inst. of Science, Rehovot, Israel, Elsevier Scientific Pub. Co., Amsterdam, The Netherlands, pp. 1809-1827, 1975.
- 567 Boardman, N. K., J. M. Anderson, O. Björkman, D. J. Goodchild, L. H. Grimme, and S. W. Thorne, Chloroplast differentiation in sun and shade plants; relationship between chlorophyll content, grana formation, photochemical activity and fractionation of the photosystems, *Port. Acta Biol., Ser. A*, 14 (1-2), 213-236, 1974.
- Briggs, W. R., *see* Britz, S. J.; Song, P.-S.
- 553 Briggs, W. R., H. O. Borthwick and S. B. Hendricks—Pioneers of Photomorphogenesis, Introduction in *Light and Plant Development*, H. Smith, ed., Butterworths, London, in press, 1976.
- 556 Briggs, W. R., Phytochrome: Plant light sensor and photoswitch, *An. Acad. Bras. Cienc.*, 45 (Suplemento: XX NOVAS TENDENCIAS EN FOTOBIOLOGIA, Proc. International Symposium, Rio de Janeiro, July), 85-92, 1973.
- 570 Briggs, W. R., The nature of the blue light photoreceptor in higher plants and fungi, Chap. 2 in *Light and Plant Development*, H. Smith, ed., Butterworths, London, in press. Proc. 22nd Easter School, Nottingham, England, 1976.
- 565 Britz, S. J., and W. R. Briggs, Studies on circadian rhythms of chloroplast orientation and photosynthetic capacity in *Ulva*, *Plant Physiol.*, in press, 1976.
- 566 Britz, S. J., J. Pfau, W. Nultsch, and W. R. Briggs, Automatic monitoring of a circadian rhythm of change in light transmittance in *Ulva*, *Plant Physiol.*, in press, 1976.
- Chae, Q., *see* Song, P.-S.
- 560 Ehleringer, J. R., O. Björkman, and H. A. Mooney, Leaf pubescence: Effects on absorbance and photosynthesis in a desert species, *Science*, 192, 376-377, 1976.
- Fork, D. C., *see* Murata, N.
- 557 Fork, D. C., Photosynthesis, Chap. 13 in *The Science of Photobiology*, K. C. Smith, ed., Plenum Press, New York, 1976, in press.
- Goodchild, D. J., *see* Boardman, N. K.
- Grimme, L. H., *see* Boardman, N. K.
- 559 Johnson, G. B., Enzyme polymorphism and adaptation in alpine butterflies, *Ann. Mo. Bot. Gard.*, 43, in press, 1976.
- 561 Johnson, G. B., Hidden alleles at the α -glycerophosphate dehydrogenase locus in *Colias* butterflies, *Genetics*, 83, 149-167, 1976.
- 562 Johnson, G. B., Polymorphism and predictability at the α -glycerophosphate dehydrogenase locus in *Colias* butterflies: Gradients in allele frequency within single populations, *Genetics*, in press, 1976.
- 563 Johnson, G. B., Evaluation of the stepwise mutation model of electrophoretic mobility: Comparison of the gel sieving behavior of alleles at the esterase-5 locus of *Drosophila pseudoobscura*, *Genetics*, in press, 1976.
- 568 Johnson, G. B., Microgeographic patterns of enzyme polymorphism within a single population of *Colias meadii*: selection of metabolic phenotypes, *Evolution*, in press, 1976.
- 569 Johnson, G. B., Characterization of electrophoretically cryptic variation in *Colias* butterflies, *Genetics*, in press, 1976.
- 572 Johnson, G. B., Hidden heterogeneity among the electrophoretically detected alleles of *Colias* butterflies, in *Measuring Selection in Natural Populations*, O. Barndorff-Nielsen, F. Christiansen, and T. Fenchel, eds., Univ. Aarhus Press, in press, 1976.
- 573 Johnson, G. B., Assessing electrophoretic similarity: The problem of hidden heterogeneity, *Annu. Rev. Ecol. Syst.*, 7, in press, 1976.
- Mackenzie, J. M., Jr., *see* Britz, S. J.
- 537 Mahall, B. E., and R. B. Park, The ecotone between *Spartina foliosa* Trin. and *Salicornia virginica* L. in salt marshes of northern San Francisco Bay. I. Biomass and productivity, *J. Ecol.*, 64 (2), in press, 1976.

*Department of Plant Biology publication number.

- 540 Mahall, B. E., and R. B. Park, The ecotone between *Spartina foliosa* Trin. and *Salicornia virginica* L. in salt marshes of northern San Francisco Bay. II. Soil water and salinity, *J. Ecol.*, 64 (3), in press, 1976.
- 541 Mahall, B. E., and R. B. Park, The ecotone between *Spartina foliosa* Trin. and *Salicornia virginica* L. in salt marshes of northern San Francisco Bay. III. Soil aeration and tidal immersion, *J. Ecol.*, 64 (3), in press, 1976.
- Mooney, H. A., see Ehleringer, J. R.
- 525 Mooney, H. A., O. Björkman, and J. A. Berry, Photosynthetic adaptations to high temperatures, in *Environmental Physiology of Desert Organisms*, Neil F. Hadley, ed., Halsted Press, pp. 138-151, 1975.
- 551 Murata, N., and D. C. Fork, Temperature dependence of chlorophyll *a* fluorescence in relation to the physical phase of membrane lipids in algae and higher plants, *Plant Physiol.*, 56, 791-796, 1975.
- Nultsch, W., see Britz, S. J.
- Park, R. B., see Mahall, B. E.
- 520 Percy, R. W., and J. H. Troughton, C₄ photosynthesis in tree form *Euphorbia* species from Hawaiian rainforest sites, *Plant Physiol.*, 55, 1975.
- Pfau, J., see Britz, S. J.
- Radmer, R., see Stemler, A.
- 564 Song, P.-S., Q. Chae, and W. R. Briggs, Temperature dependence of the fluorescence quantum yield of photochrome, Res. note in *Photochem. Photobiol.*, 22, 75-76, 1975.
- 555 Stemler, A., and R. Radmer, Source of photosynthetic oxygen in bicarbonate-stimulated Hill reaction, *Science*, 190, 457-458, 1975.
- Thorne, S. W., see Boardman, N. K.
- 548 Thompson, W. F. Aggregate formation from short fragments of plant DNA, *Plant Physiol.* 57, 617-622, 1976.
- Troughton, J. H., see Percy, R. W.

SPEECHES

- Berry, Joseph A., James Ehleringer and Harold A. Mooney, Death Valley Days. Meeting of the Bay Area Biosystematists, University of California Marine Laboratory, Bodega Bay, California, March 20, 1975.
- Boynton, John E., Mapping Chloroplast Genes in *Chlamydomonas*. Symposium on Non-chromosomal Inheritance, The Genetics Society of America, University of North Carolina, Chapel Hill, North Carolina, August 19, 1975.
- Boynton, John E., The Genetics of Chloroplast Ribosome Biogenesis. Stanford-Carnegie Plant Physiology Graduate Seminar, Department of Plant Biology, Carnegie Institution, Stanford, California, November 5, 1975.
- Boynton, John E., Transmission, Segregation and Recombination of Chloroplast Genes. Seminar, Plant Development Group, University of California, Davis, California, November 17, 1975.
- Boynton, John E., The Genetics of Chloroplast Ribosome Biogenesis. Seminar, Department of Biology, University of California, Davis, California, December 5, 1975.
- Boynton, John E., Transmission, Segregation and Recombination of Chloroplast Genes. Seminar, Department of Genetics, University of California, Davis, California, February 2, 1976.
- Boynton, John E., The Genetics of Chloroplast Ribosome Biogenesis. Seminar, Department of Biology, University of California, Los Angeles, California, May 17, 1976.
- Brain, R. D., J. Freeberg, C. V. Weiss, and W. R. Briggs, Light-Induced Cytochrome Reduction in Membrane Fractions from Corn and *Neurospora*. Meeting of the American Society of Plant Physiologists, New Orleans, Louisiana, May 31, 1976.
- Briggs, Winslow R., Studies on the Blue Light Photoreceptor in Corn and *Neurospora*. Seminar, Plant Research Laboratory, Michigan State University, East Lansing, Michigan, October 22, 1975.
- Briggs, Winslow R., Some Studies on the Action of Red Light on Plant Development. Seminar, Sigma Xi, Virginia Polytechnic Institute and State University, Blacksburg, Virginia, October 24, 1975.
- Briggs, Winslow R., Blue Light-Induced *b*-Type Cytochrome Reduction in Membrane Fractions of Corn and *Neurospora*. Symposium on Sensory Transduction in Microorganisms, Gordon Conference, Santa Barbara, California, December 30, 1975.
- Briggs, Winslow R., Recent Studies on a Blue-Light-Sensitive Pigment System in *Neurospora*. Biology Department Conference on Circadian Rhythms, University of California, San Diego, La Jolla, California, January 23, 1976.
- Briggs, Winslow R., Some Recent Studies on the Blue Light Photoreceptor in Higher Plants and Fungi. Seminar, Department of Botany, University of Illinois, Urbana, Illinois, April 16, 1976.
- Briggs, Winslow R., Studies on the Phototropic Photoreceptor. Seminar, Department of Biology, University of California, Los Angeles, California, May 10, 1976.
- Briggs, Winslow R., Blue Light Photoreceptor in Higher Plants and Fungi. Meeting of the

- American Society of Biological Sciences, San Francisco, California, June 8, 1976.
- Briggs, W. R., *see* Brain, R. D.
- Britz, S. J., Circadian Rhythm of Chloroplast Orientation in *Ulva*. Meeting of the American Society of Plant Physiologists, Corvallis, Oregon, August 21, 1975.
- Britz, S. J., Rhythmic and Light-Induced Chloroplast Orientation in Marine Algae. Meeting of the Western Society of Naturalists, San Francisco, California, December 30, 1975.
- Brown, Jeanette S., Studies of the P700-Chlorophyll *a*-Protein Complex. Meeting of the American Society of Plant Physiologists, Corvallis, Oregon, August 21, 1975.
- Brown, Jeanette S., Fluorescence Emission from the Oxidized Photosystem I Reaction Center, P700⁺. Meeting of the Brookhaven Symposium in Biology, Brookhaven National Laboratory, Upton, New York, June 8, 1976.
- Brown, Jeanette S., *see* Fork, David C.
- Cross, John, and Daniel McMahon, Temperature-Sensitive Mutants in Initiation of Protein Synthesis in *Chlamydomonas reinhardtii*. Meeting of the American Society of Plant Physiologists, New Orleans, Louisiana, June 1, 1976.
- DeVay, J. E., *see* Rogler, Charles.
- Dohrmann, Ulrike, *In vitro* Binding of Auxin to Membranes from Corn Coleoptiles and Membrane Receptors. Seminar, Department of Biology, San Diego State University, San Diego, California, May 31, 1976.
- Dohrmann, U., and P. M. Ray, An Assay for Auxin-Binding to Solubilized Receptor Sites of Corn Membranes. Meeting of the American Society of Plant Physiologists, New Orleans, Louisiana, May 31, 1976.
- Ehleringer, James, Effects of Pubescence on Energy Balance and Photosynthesis. Symposium on Biological Surfaces, Ecological Society of America, New Orleans, Louisiana, June 1, 1976.
- Ehleringer, James, *see* Berry, Joseph A.
- Fork, David C., Pigments and Energy Harvesting. Department of Biological Sciences, Stanford University, Stanford, California, October 13, 1975.
- Fork, David C., Photosynthesis. Stanford-Carnegie Plant Physiology Graduate Seminar, Department of Plant Biology, Carnegie Institution, Stanford, California, October 15, 1975.
- Fork, David C., Electron Transport in Photosynthesis. Stanford University, Department of Biological Sciences-Carnegie Institution of Washington, Course on Photobiology, March 4, 1976.
- Fork, David C., and Jeanette S. Brown, The Use of Rapid Light-Induced Absorbance Changes of Chlorophylls and Carotenoids to Distinguish between Algae of Different Pigment Composition (presented by Jeanette S. Brown). Meeting of the Phycological Society of America/AIBS, Corvallis, Oregon, August 18, 1975.
- Freeberg, J., *see* Brain, R. D.
- Johnson, George, Enzyme Polymorphism and Adaptation in Alpine Butterflies. Missouri Botanical Garden Symposium, St. Louis, Missouri, October 18, 1975.
- Johnson, George, Adaptive Strategies and Metabolic Organization. Seminar, Department of Biology, University of Colorado, Boulder, Colorado, October 24, 1975.
- Johnson, George, Enzyme Polymorphism in Alpine Butterflies. Seminar, Department of Biology, San Diego State University, San Diego, California, November 17, 1975.
- Johnson, George, Do Most Electrophoretically Detected Enzyme Polymorphisms Involve Differences in Charge? Seminar, Department of Biology, University of Indiana, Bloomington, Indiana, December 10, 1975.
- Johnson, George, Evaluation of Kimura and Ohta's Stepwise Mutation Model of Electrophoretic Mobility: Gel Sieving Analysis of Esterase-5 Alleles of *Drosophila pseudoobscura*. Seminar, Department of Biology, University of California, Santa Cruz, California, January 20, 1976.
- Johnson, George, The Use of Electrophoresis in Biosystematics. Seminar, Department of Botany, University of Wyoming, Laramie, Wyoming, February 27, 1976.
- Johnson, George, Molecular Studies of Enzyme Polymorphism: Cryptic Alleles in *Colias*. Seminar, Department of Evolutionary Biology and Ecology, University of Kansas, Lawrence, Kansas, March 3, 1976.
- Johnson, George, Selection on Metabolic Phenotypes in Alpine Butterflies. Seminar, Department of Genetics and Ecology, University of Aarhus, Denmark, May 10-14, 1976.
- Johnson, George, Selection on Integrated Metabolic Phenotypes. Seminar, Department of Genetics and Ecology, University of Aarhus, Denmark, May 12, 1976.
- Johnson, George, Characterization of Electrophoretically Cryptic Alleles in *Colias* Butterflies. Meeting of the AIBS/Evolution Society of America, New Orleans, Louisiana, June 1, 1976.
- Mackenzie, John, and L. H. Pratt, Immunocytochemical Localization of Pfr and Its Relation to the Destruction Reaction. Meeting of the American Society of Plant Physiologists, Corvallis, Oregon, August 21, 1975.
- Mooney, H. A., *see* Berry, Joseph A.
- Pratt, L. H., *see* Mackenzie, John.
- Rogler, Charles E., Characterization of Plasmid DNA from *Agrobacterium tumefaciens* and Its Role in Crown Gall Disease. Seminar, Department of Plant Sciences, University of California, Riverside, California, March 24, 1976.
- Rogler, Charles, W. F. Thompson, and J. E. DeVay, Correlation of Serological and Plasmid

- Characteristics in Pathogenic and Non-pathogenic Strains of *Agrobacterium tumefaciens*. Meeting of the American Society of Plant Physiologists, New Orleans, Louisiana, June 3, 1976.
- Solbrig, Otto T., The Evolution of Breeding Systems in Plants with Special Reference to the Genus *Leavenworthia*. Seminar, Department of Botany, University of Washington, Seattle, Washington, October 18, 1975.
- Solbrig, Otto T., The Evolution of Life Form in Desert Plants. Meeting of the California Botanical Society, Berkeley, California, January 15, 1976.
- Solbrig, Otto T., The Evolution of Breeding Systems in Plants. Seminar, Department of Biology, University of California, Santa Barbara, California, February 4, 1976.
- Solbrig, Otto T., The Population Biology of Dandelions. Seminar, Department of Botany, University of California, Berkeley, California, February 13, 1976.
- Solbrig, Otto T., The Population Biology of Dandelions. Seminar, Department of Ecology and Evolutionary Biology, University of Arizona, Tucson, Arizona, March 4, 1976.
- Stemler, Alan, Binding of Bicarbonate Ions to Chloroplast Grana. Meeting of the American Society of Plant Physiologists, New Orleans, Louisiana, June 2, 1976.
- Thompson, William F., Sequence Studies on Plant DNA. Seminar, Department of Botany, San Diego State University, San Diego, California, December 5, 1975.
- Thompson, W. F., *see* Rogler, Charles.
- Weiss, C. V., *see* Brain, R. D.

PERSONNEL

Research Staff

Joseph A. Berry
 Olle Björkman
 Winslow R. Briggs, Director
 Jeanette S. Brown
 David C. Fork
 C. Stacy French, Director Emeritus
 William M. Hiesey, Emeritus
 Malcolm A. Nobs
 William F. Thompson

Clerical and Technical Staff

Donna C. Atwood, Department Secretary
 Benny Catanzaro, Electronic Technician
 Ruth Fischer, Administrative Assistant-Accountant
 Glenn Ford, Laboratory Manager
 Edward G. Gausden, Technician
 Steven Graff, Technician
 Alan Grundmann,¹ Administrator
 Richard W. Hart, Mechanical Engineer
 James Johnson, Technician
 Kathleen Keller, Secretary
 Jan Kowalik,² Technician
 Fred Lakin, Technical Illustrator
 Frank Nicholson, Senior Technician
 Ernest Ramos, Technician
 Susan Reed, Technician
 Jonathan Walton,³ Technician
 Charles V. Weiss, Technician

¹Resigned April 15, 1976.

²Retired August 31, 1975.

³Resigned April 30, 1976.

Carnegie Institution of Washington Fellows

John Cross, Fellow
 Ulrike Dohrmann, Fellow
 Algirdas J. Jesaitis, Fellow⁴
 George Johnson, Senior Fellow, Washington University, St. Louis, Missouri
 Aaron Kaplan, Fellow
 Bruce E. Mahall, Fellow⁵
 Norio Murata, Senior Fellow, Tokyo University, Tokyo, Japan
 Michael Murray, Fellow
 Charles E. Rogler, Fellow
 Ulrich Schreiber, Fellow
 Alan Stemler, Fellow

Fellows

Murray Badger, Fellow, CSIRO, Canberra, Australia
 John Boynton, Senior Fellow, National Institutes of Health Research Development Award, Duke University, Durham, North Carolina
 Richard Carey, Senior Fellow, San Jose State University, San Jose, California
 Jack Freeberg, Senior Fellow, University of Massachusetts, Amherst, Massachusetts⁶

⁴To December 15, 1975.

⁵To September 1, 1975.

⁶To January 9, 1976.

Ulrich Knopf, Fellow, Stanford University School of Medicine and Swiss National Science Foundation

Harold A. Mooney, Senior Fellow, Stanford University, Stanford, California

Erich Schrott, Senior Fellow, Deutsche Forschungsgemeinschaft, Munich, Germany

Otto Solbrig, Senior Fellow, Harvard University, Cambridge, Massachusetts⁷

Students

Brian Anderson, Undergraduate, Stanford University, Stanford, California

Michael Blatt, Graduate, Stanford University, Stanford, California⁸

Robert D. Brain, Undergraduate, Stanford University, Stanford, California

Steven J. Britz, Graduate, Harvard University, Cambridge, Massachusetts⁸

James Collatz, Graduate, Stanford University, Stanford, California⁸

Daniel Cosgrove, Graduate, Stanford University, Stanford, California

William Curtis, Graduate, Washington University, St. Louis, Missouri

James Ehleringer, Graduate, Stanford University, Stanford, California⁹

Mary Enama, Graduate, Washington University, St. Louis, Missouri

John Mackenzie, Graduate, Harvard University, Cambridge, Massachusetts⁸

Thomas Payne, Undergraduate, Stanford University, Stanford, California

Richard Preisler, Graduate, Stanford University, Stanford, California

Diana Stein, Graduate, University of Massachusetts, Amherst, Massachusetts⁹

Heather Strong Belford, Graduate, University of Massachusetts, Amherst, Massachusetts¹⁰

Karen Swift, Graduate, Duke University, Durham, North Carolina

⁷To June 18, 1976.

⁸Carnegie Institution of Washington Predoctoral Fellows.

⁹To September 30, 1975.

¹⁰To August 31, 1975.

Geophysical Laboratory

Washington, District of Columbia

Hatten S. Yoder, Jr.

Director

Contents

| | | | |
|--|-----|---|-----|
| Director's Commentary and Review . . . | 491 | ilite in the Nyiragongo rocks (Sahama) | 585 |
| Experimental Studies Bearing on the Core-Mantle Boundary | 509 | Igneous Petrology: Experimental and Field | 592 |
| Compressibility and x-ray diffraction of the epsilon phase of metallic iron (ϵ -Fe) and periclase (MgO) to 0.9 Mbar pressure, with bearing on the earth's mantle-core boundary (Mao and Bell) | 509 | Liquid immiscibility in the system $KAlSi_3O_8$ - $NaAlSi_3O_8$ -FeO- Fe_2O_3 - SiO_2 and its application to natural mag- mas (Naslund) | 592 |
| Compressibility of magnesiowüstite ($Fe_{0.4}Mg_{0.6}O$) to 264 kbar (Rosen- hauer, Mao, and Woermann) | 513 | Metastable liquid immiscibility and MgO-FeO- SiO_2 fractionation pat- terns in the system Mg_2SiO_4 - Fe_2SiO_4 - $CaAl_2Si_2O_8$ - $KAlSi_3O_8$ - SiO_2 (Irvine) | 597 |
| High-pressure disproportionation study of iron in synthetic basalt glass (Bell, Mao, Weeks, and Van Valk- enburg) | 515 | Decrease in viscosity of some synthetic silicate melts at high pressures (Kushiro) | 611 |
| Ultramafic Rocks and Minerals | 521 | Viscosity of basaltic and andesitic liq- uids at high pressures (Kushiro, Yoder, and Mysen) | 614 |
| Inflected and noninflected geotherms (Boyd) | 521 | Infrared spectra of high-pressure quenched silicate liquids (B. Velde and Kushiro) | 618 |
| A noninflected geotherm for the Udach- naya kimberlite pipe, USSR (Boyd, Fujii, and Danchin) | 523 | Coordination changes of aluminum in silicate melts: evidence from data on carbon dioxide solubility in al- bite melt (Mysen) | 621 |
| Ultramafic nodules from the Premier kimberlite pipe, South Africa (Dan- chin and Boyd) | 531 | Composition of the partial melt of car- bonated peridotite in the system CaO - MgO - SiO_2 - CO_2 (Eggler) | 623 |
| A geotherm from megacrysts in the Sloan kimberlite pipes, Colorado (Eggler and McCallum) | 538 | The solubility of CO_2 in liquids on the join CaO - MgO - SiO_2 - CO_2 (Hollo- way, Mysen, and Eggler) | 626 |
| Clinopyroxene-ilmenite intergrowths from the Iron Mountain kimber- lite district, Wyoming (Smith, Mc- Callum, and Eggler) | 542 | Stability of carbonate minerals in a hy- drous mantle (Eggler, Kushiro, and Holloway) | 631 |
| Ultramafic nodules from the Kimber- ley pipes, South Africa (Boyd and Nixon) | 544 | Fluid-absent melting of peridotite con- taining phlogopite and dolomite (Holloway and Eggler) | 636 |
| Compositional variation of coexisting phases with degree of melting of peridotite under upper mantle con- ditions (Mysen and Kushiro) | 546 | Mineralogical variations in the upper part of the Skaergaard intrusion, quence (Ohashi) | 640 |
| Melting relations of ultramafic lavas (komatiites) at 1 atm and high pressure (Arndt) | 555 | Lattice energy of some silicate minerals and the effect of oxygen bridging in relation to crystallization se- hauer) | 644 |
| Phase relations of mafic layers in the Ronda peridotite (Obata and Dickey) | 562 | Effect of pressure on the melting en- thalpy of diopside under dry and H_2O -saturated conditions (Rosen- East Greenland (Naslund) | 648 |
| Solubility of Al_2O_3 in enstatite coexist- ing with forsterite and spinel (Fujii) | 566 | The adiabatic gradient and adiabatic compressibility (Rumble) | 651 |
| The partitioning of iron and magnesium between garnet and clinopyroxene (Wood) | 571 | Trace Element Partitioning | 656 |
| The chemical composition of melilite- bearing eruptive rocks (D. Velde and Yoder) | 574 | Rare earth partitioning between crys- tals and liquid in the upper mantle (Mysen) | 656 |
| Importance of alkali content of magma yielding melilite-bearing rocks (Yo- der and D. Velde) | 580 | Samarium distribution between garnet and liquid at high pressure (Wood) Nickel partitioning between upper man- | 659 |
| Composition of clinopyroxene and mel- | | | |

| | | | |
|---|-----|--|-----|
| tle crystals and partial melts as a function of pressure, temperature, and nickel concentration (Mysen) | 662 | and disordering in wollastonite (Ohashi and Finger) | 746 |
| Partitioning of Ni and Mg between olivine and silicate liquids (Irvine and Kushiro) | 668 | Electron paramagnetic resonance of two magnesiowüstites (Weeks, Mao, and Bell) | 753 |
| Rare earth fractionation with controlled partial melting of peridotite (Mysen and Holloway) | 675 | Gillespite at high pressure: results of a detailed Mössbauer study (Huggins, Mao, and Virgo) | 756 |
| Partitioning of iron, nickel, and magnesium between metal, oxide, and silicates in Allende meteorite as a function of f_{O_2} (Mysen and Kushiro) | 678 | Metasomatism | 759 |
| Experimental plutonium, thorium, and uranium partition coefficients with application to meteoritic assemblages (Benjamin, Burnett, and Seitz) | 684 | Metasomatic zoning resulting from intergranular diffusion: concentration profiles and the determination of complicated reaction paths in n -component systems (Frantz and Mao) | 759 |
| Petrology of Lunar Rocks and Meteorites | 688 | Fluid interaction between granite and sediment during metamorphism, south-central Maine (Ferry) | 764 |
| A study of the oxidation states of iron and titanium in synthetic glasses of lunar basalt composition (Bell, Mao, and Weeks) | 688 | Fugacity and activity coefficients of molecular species in fluids at high pressures and temperatures (Holloway) | 771 |
| Compositional variability of the lunar metallic phase (Mao and Bell) | 695 | Ca-amphibole composition as a function of temperature, fluid pressure, and oxygen fugacity in a basaltic system (Spear) | 775 |
| Optical spectra of thin metallic coatings with application to the spectra of lunar soil samples (Bell and Mao) | 699 | Statistical Petrology | 780 |
| Crystal-field spectra of fassaite from the Angra dos Reis meteorite (Bell and Mao) | 701 | Systematic Petrology | 780 |
| Mineralogy | 705 | Asymmetry in the distributions of SiO_2 , Al_2O_3 , CaO , and Fe in the products of Cenozoic volcanism (Chayes) | 780 |
| The crystal chemistry of melanites and schorlomite (Huggins, Virgo, and Huckenholz) | 705 | Distribution of oxygen in Cenozoic volcanic rocks (Chayes) | 781 |
| A reconnaissance study of the Ti-garnet stability field at defined oxygen fugacities (Huckenholz, Hözl, Huggins, and Virgo) | 711 | Characterizing the consistency of current usage of rock names by means of discriminant functions (Chayes) | 782 |
| Intrinsic oxygen fugacities of natural melanites and schorlomite and crystal-chemical implications (Virgo, Rosenhauer, and Huggins) | 720 | On the sampling variance of coefficients of principal components (Chayes and Trochimczyk) | 784 |
| Petrologic implications of intrinsic oxygen fugacity measurements on titanium-containing silicate garnets (Virgo, Huggins, and Rosenhauer) | 730 | Minimum SiO_2 requirement of the CIPW norm (Chayes and D. Velde) | 786 |
| Interpretation of ^{27}Al and ^{57}Fe nuclear quadrupole data in rare earth garnets (Hafner and Raymond) | 735 | Development of an Information System for Igneous Petrology | 787 |
| Interpretation of the ^{57}Fe nuclear quadrupole data for some silicate garnets (Hafner, Raymond, Virgo, and Huggins) | 739 | Design and construction of a world data base for petrology (Chayes) | 787 |
| On the stoichiometry of clinopyroxenes in the system CaO - MgO - Al_2O_3 - SiO_2 (Wood) | 741 | A revised structure for system reduction programs (Chayes) | 788 |
| The effect of Ca substitution on the structure of clinoenstatite (Ohashi and Finger) | 743 | Modification of existing programs (Chayes) | 790 |
| Stepwise cation ordering in bustamite | | New programs (Trochimczyk and Chayes) | 790 |
| | | Independent exploitation of the data base and reduction repertoire of the petrographic information system (Chayes) | 791 |
| | | Biogeochemistry | 792 |
| | | The formation and clay mineral reactions of melanoidin (Hedges) | 792 |

| | | | |
|---|-----|--|-----|
| Relative reaction rates and activation energies for some amino acid reactions (Hare) | 801 | A controllable thermocouple micro-heater for high-temperature microscopy (Ohashi and Hadidiacos) ... | 828 |
| Molecular fossils from the Precambrian Nonesuch shale (Hoering) | 806 | A new furnace assembly with a small temperature gradient in solid-media, high-pressure apparatus (Kushiro) | 832 |
| Geochronology | 813 | Accurate modal analysis of experimental run products (Mysen) | 833 |
| Response of U-Pb zircon and Rb-Sr total rock systems to low-grade regional metamorphism in Proterozoic igneous rocks, Mount Isa, Australia (Page) | 813 | Staff Activities | 835 |
| The ages of zircons from kimberlites from South Africa (Davis, Krogh, and Erlank) | 821 | Field Studies | 835 |
| New Techniques and Equipment | 824 | Petrologists' Club | 836 |
| The ultrahigh-pressure diamond cell: design applications for electrical measurements of mineral samples at 1.2 Mbar (Mao and Bell) | 824 | Washington Crystal Colloquium | 836 |
| High-pressure research: 1-Mbar pressure on the ruby pressure scale (Mao and Bell) | 827 | Seminar Series | 836 |
| | | Lectures | 837 |
| | | Bibliography | 840 |
| | | References Cited | 841 |
| | | Personnel | 857 |

DIRECTOR'S COMMENTARY AND REVIEW

The world population has recently passed four billion people and the per capita consumption of minerals is rising at an increasing rate. These facts alone are sufficient to warrant an accelerated effort in locating new mineral resources. No country can be completely independent in the acquisition of mineral resources; greater dependence on other nations for world supplies, restricted by the natural limitations of their geochemical concentrations in the earth, is inevitable. In addition, the United States is particularly vulnerable to the changing political alignments that have already led to one serious shortage of a vital mineral resource. Many other mineral resources that are obtained almost entirely from other nations may suddenly be cut off. The prudent nation will develop a set of alternatives to meet such catastrophes: one of several reasonable alternatives, and deterrents, is the establishment of domestic standby reserves that may or may not now be economical. First, however, it will be necessary to find and outline those mineral resources.

There is an urgent need, therefore, to rejuvenate and reorient that field of economic geology in which the techniques for exploration and discovery of ore deposits are developed. The principles of element concentration need to be established, and an understanding of the chemical transport mechanisms of specific elements must be gained. It is essential to know why elements accumulate in special environments. The problem demands an organized effort on the scale of the lunar-sample program or the JOIDES core studies. Recent discussions indicate that mechanisms for developing a national program are not clear; however, there are several laboratories where new efforts could be initiated.

The Geophysical Laboratory has been

dedicated since its beginning to developing basic research of the kind needed to resolve some of the problems of element concentration, in particular those involving the major elements of the earth's crust. Because of the great array and diversity of talent that will be required to resolve mineral resource problems, especially those for minor elements, new avenues of scientific training must be explored. The fellowship programs of a few small institutions, however, will not be adequate for training the required number of investigators. Universities and other organizations, whose economic geology staffs are generally at a low ebb now, will have to assemble their thermodynamicists skilled in irreversible processes, metallurgists, physical chemists, field geologists, experimental petrologists, geophysicists, solid state physicists, and spectral mineralogists under an institute arrangement, for example, to ensure the proper training of a new generation of scientists. As the nucleus groups grow through interaction and self-instruction, it would appear that a productive program could be operational and significant research directions defined within a relatively few years. Enlargement of the effort could be carried out through concerned government agencies, an enlightened mining industry, and the universities staffed with the new breed of scientists. The smaller institutions would continue to provide the highly innovative ideas and take the initiative—and the risks—in assessing the directions for major developments.

Facets of the required basic research are taking form at the Geophysical Laboratory under headings that do not even smack of economic geology. Current studies of trace element partitioning, metasomatism, ultramafic rocks, and others noted below include fundamental ideas that bear on the mineral resource

problems. In each case, the principal stimulus for the research has been the curiosity of the individual investigator—none was project-oriented research. It is still believed at the Geophysical Laboratory that the best research is carried out by talented people free to pursue their quest for knowledge. There is nothing like a fascinating idea backed by exciting preliminary results that attracts one's colleagues to the search. And with the nucleus of talent now at the Geophysical Laboratory, the ideas have come as will be seen in the pages that follow. What dedicated scientist can resist the opportunities presented by the diamond-anvil high-pressure apparatus, the new theory of infiltration, the analytical techniques sensitive to the parts-per-billion level, or the direct measurement of enthalpy of melting at high pressure?

*Experimental Studies Bearing on the
Core-Mantle Boundary*

A major advance in the capability of investigating experimentally the physical chemistry of the region near the postulated core-mantle boundary was recently achieved. Temperatures in excess of 3000°C at pressures close to 1.2 Mbar can now be sustained in a device developed by *Mao and Bell*. They have concluded a series of experiments from which they derived simultaneously the equation of state of MgO (periclase) and of pure Fe at 510, 670, 730, and 865 kbar. A ruby crystal contained in the sample was used to determine pressure by the fluorescence technique. The volumes of MgO and Fe determined independently at shock-wave pressures agree with the values based on ruby fluorescence. The compressibility values are the first obtained at static pressures above 300 kbar.

Rosenhauer, Mao, and Woermann measured the compressibility of magnesiowüstite in the range 1–270 kbar in an effort to determine its stoichiometry and its volume relative to other minerals that are predicted to occur in the

earth's mantle. The volume curve for magnesiowüstite ($\text{Mg}_{0.6}\text{Fe}_{0.4}\text{O}$) falls between those of MgO and wüstite, and thus magnesiowüstite also appears to be a possible mantle mineral, at least to a depth of 1000 km.

Reactions involving the chemical disproportionation of ferrous iron in minerals to produce assemblages in which ferric and metallic iron coexist were discovered to be of great importance at pressures above 100 kbar, corresponding to depths of 300 km or more in the earth. *Bell, Mao, Weeks, and Van Valkenburg* document the presence of ferric iron in their experimental products by electron paramagnetic resonance and Curie temperature methods. The confirmation lends weight to the idea that the core and mantle are in chemical equilibrium. The disproportionation process probably began as the pressure rose in the interior of the accreting earth. Melting of the metallic iron by radioactive heating and conversion of gravitational energy to heat is believed to have led to core formation. It is evident that this study is a major contribution to an understanding of the early stages of the formation of the earth.

Ultramafic Rocks and Minerals

The determination of fossil geotherms by *Boyd* using the compositions of pyroxenes coexisting with garnet has stimulated much new work on nodules from kimberlite pipes and alkali basalts. The inflections in some of the geotherms were at first believed by Boyd to result from the stress-heating of sheared nodules from the low-velocity zones. He now thinks it more likely that the inflections are due to convective movements in the mantle that preceded most major kimberlite eruptions. The point of inflection is about the same at a variety of widely separated localities and is perhaps related to a partially melted zone of low seismic velocity. Such a hypothesis, however, is not wholly supported by recent seismic studies, and other explanations are being sought.

A geotherm obtained by *Boyd, Fujii, and Danchin* from nodules in the Udachnaya kimberlite pipe in Siberia shows no inflection. The fact that both inflected and noninflected geotherms have been obtained from studies of nodule suites from kimberlite suggests that inflection is not likely to be an artifact of the method of estimating temperature and depth. The ultramafic nodules from Udachnaya and other Siberian pipes are very similar in texture and mineral chemistry to rocks from the mantle beneath southern Africa.

The unique Precambrian nodule suite from the Premier kimberlite pipe in the Republic of South Africa has been compared by *Danchin and Boyd* with the Late Cretaceous nodule suites from other South African pipes. They conclude that the chemical and thermal evolution of the African mantle was essentially complete at least 1115 m.y. ago, the time of formation of the Premier pipe. The source of the vast outpouring of Karroo basalts that covered southern Africa 150–190 m.y. ago may thus have been a section of mantle deeper than that sampled by the kimberlite eruptions (200 km). The nodule suite from the Premier pipe includes a previously undiscovered variety of harzburgite in which the compositions of garnet and chromite are identical with those found as inclusions in diamonds. Such harzburgites are believed by *Danchin and Boyd* to be the source rocks for most diamonds.

A group of kimberlite diatremes on the Colorado-Wyoming state line has received considerable attention recently because of the discovery by *Eggler and McCallum* of diamonds in a peridotite nodule from them. Their study, bearing on the mantle region from which the diamonds are believed to have come, included the determination of the fossil geotherm using megacryst assemblages from the Sloan pipes in Colorado. They found two assemblages, one Cr-rich, similar in composition to minerals from peridotite nodules, and the other Cr-poor, unlike those from nodules of pe-

ridotite. The latter group overlaps in composition part of the discrete nodule suite from Lesotho described by *Boyd and Nixon (1973)*. The geotherm is interpreted to have been partially inflected, perhaps by movement of a diapir into a depleted subcontinental section.

Nodules from dikes and one pipe of kimberlite in the newly discovered Iron Mountain, Wyoming, district were examined by *Smith, McCallum, and Eggler*. The nodules, principally peridotites and eclogites, are similar to nodules in pipes of the State Line district 70 km to the south (described by *Eggler and McCallum*). Some distinctive nodules are present, including clinopyroxene-ilmenite symplectic intergrowths. These intergrowths resemble those found in South African pipes (Monastery) but have apparently equilibrated in a lower temperature regime, on the basis of the two-pyroxene geothermometer.

The upper mantle nodules from the Kimberley, South Africa, pipes differ from a number of other well-studied nodule suites, according to *Boyd and Nixon*, in that they lack both high-temperature ($>1100^{\circ}\text{C}$) lherzolites and Fe-rich pyroxene-ilmenite intergrowths. Low-temperature ($<1100^{\circ}\text{C}$) lherzolites are little deformed in most occurrences, but at Kimberley some of them are intensely deformed. The differences in the kinds of nodules found in different areas appear to reveal heterogeneity in the upper mantle, whereas differences in deformation probably reflect variation in the tectonics of kimberlite eruption. The geotherm for the Kimberley pipes exhibits an inflection.

Among the nodules believed to come from the mantle are those composed of garnet peridotite, the most likely parental material for the formation of basaltic liquids by partial melting. Two natural garnet peridotites were melted at high pressures by *Mysen and Kushiro*, and the proportion of melt at each temperature was determined with the β -track mapping technique. They found that melting of volatile-free peridotite

can be described almost quantitatively by the phase relations in appropriate simple systems. The partial melts in equilibrium with two pyroxenes, olivine, and an aluminous phase have reaction relations with their residual phase assemblages similar to those proposed by Kushiro and Yoder (*Year Book* 73, pp. 266-269) in the simple system $\text{CaSiO}_3\text{-MgSiO}_3\text{-Al}_2\text{O}_3$. Mysen and Kushiro also found that melting of volatile-free spinel peridotite can yield alkali basalt, tholeiite, picrite, and peridotitic komatiite compositions, depending on the phase assemblage present.

A sample of the very olivine-rich lava komatiite from Munro Township in northeastern Ontario was melted at a series of temperatures by Arndt to ascertain its phase relations at 1 atm. A striking difference between the crystallization behavior of samples under experimental conditions and the apparent crystallization sequence of the lavas as they cooled after eruption was revealed. In the laboratory, olivine is the only silicate phase present through most of the melting interval at 1 atm; clinopyroxene appears only close to the solidus, and orthopyroxene is absent. By contrast, in many of the lavas clinopyroxene or orthopyroxene appears relatively early in the crystallization sequence, on the basis of textural evidence, and in some lavas is even the liquidus phase. A possible explanation is that the lavas were altered by either seawater interaction or low-grade metasomatism, with loss of CaO , SiO_2 , and alkali elements, and gain of MgO .

In another phase equilibrium study of an ultrabasic rock, a natural garnet-plagioclase pyroxenite from the Ronda massif of southern Spain, the experimental results led to three possible explanations of origin. In the light of their field studies, *Obata and Dickey* concluded that the pyroxenite could have formed by (1) partial fusion of peridotite without fractional crystallization at less than 8 kbar, (2) partial fusion of peridotite followed by olivine fractiona-

tion at less than 30 kbar, or (3) fractional crystallization of a mafic or ultramafic magma at 23-30 kbar.

The compositions of pyroxenes that occur in nodules and among the melting products of laboratory experiments on natural rocks can yield valuable temperature-pressure information if suitably calibrated. Some compositional parameters are especially sensitive to temperature, whereas others are sensitive to pressure. According to *Fujii*, it is now clear that the solubility of alumina in enstatite coexisting with forsterite and spinel is not highly sensitive to pressure but depends largely on temperature. It is proposed by *Fujii*, therefore, that the alumina content of orthopyroxene coexisting with spinel is a potential geothermometer. Preliminary experiments in analogous iron-bearing systems indicate that the geothermometer is applicable in more complex systems. Additional experiments in Cr_2O_3 -bearing systems are needed, however, before this geothermometer is applied to Cr_2O_3 -rich natural rocks.

The partitioning of iron and magnesium between garnet and clinopyroxene is also an extremely useful geothermometer for mafic and ultramafic rocks crystallized at high pressure. The influence of composition and pressure on the partition coefficient has been investigated by *Wood*. Garnet-clinopyroxene pairs from ultramafic rocks give partition coefficients similar to those of pairs crystallized from mafic compositions. It appears, however, that pressure has a larger effect on iron-magnesium partitioning for mafic than for ultramafic compositions. The probable reason for the difference lies in the dependence of the Ca content of garnet on pressure. In mafic compositions, the garnet becomes more calcic with increasing pressure, whereas in ultramafic compositions little pressure dependence is observed. Nonideal Ca-Mg-Fe interactions in garnet solid solutions serve to alter the overall partitioning relation-

ships as a function of Ca content of that phase.

Melilite, a relatively rare ultramafic mineral, occurs in rocks believed to have formed at low pressures, yet related in an as yet unknown way to magmas generated at great depths. The available analyses of melilite-bearing eruptive rocks were assembled from the literature by *D. Velde and Yoder*, who found that on the basis of bulk chemical composition there were two compositional groups. A high-alkali, low-magnesium group consists of rocks that commonly contain melilite phenocrysts; and a low-alkali, high-magnesium group includes lavas in which melilite is a groundmass phase. A comparison between the chemical composition of melilite-bearing igneous rocks and that of feldspar-free lavas indicates that melilite appears in silica-poor and alumina-poor liquids, that is, in lavas in which the molar aluminum content is seldom much greater than the molar sum of Na + K. These observations led them to reconsider the available experimental data, and they were able to show that the addition of alkalis (Na or K) to a nepheline composition will induce the crystallization of melilite. The nepheline-CaO-MgO-SiO₂ system considered by Bowen (1928) was further analyzed by *Yoder and D. Velde*, using the vast amount of new phase equilibrium data, and this analysis led them to the same conclusion, namely, that the alkali content of the magma is a most important factor in the generation of melilite-bearing rocks.

Sahama used the electron microprobe to obtain more detailed information on the composition of melilite and its co-existing clinopyroxene from lavas of the volcano Nyiragongo, Zaire. He found unusual sector zoning in both the melilite and the clinopyroxene, with the variability in the clinopyroxene almost equal to that in some of the lunar zoned clinopyroxenes. Sahama noted that the peg structure of melilite is probably just one stage in the eventual complete al-

teration of melilite by metasomatic processes.

Igneous Petrology: Experimental and Field

Liquid immiscibility was dismissed many years ago as being an unimportant factor in the generation of the diversity of igneous rocks. New discoveries, however, in iron-rich rocks from the moon and on earth have revived interest in the concept. Although direct observation of the products of immiscible liquids in rocks is confined to the later stages of magma evolution, the immiscibility fields are now believed to affect profoundly, albeit indirectly, the course of liquid fractionation. One senses a major concept evolving in the role of immiscibility regions in affecting magma equilibria.

A series of compositions in the system $\text{KAlSi}_3\text{O}_8\text{-FeO-Fe}_2\text{O}_3\text{-SiO}_2$ was studied by *Naslund* to determine the effect of f_{O_2} on the low-temperature immiscibility field of this system (*Roedder, 1951a*). Both the degree of liquid-liquid separation and the upper temperature limit of liquid immiscibility showed a progressive increase with increasing oxygen fugacity. A similar series of compositions in the system $\text{NaAlSi}_3\text{O}_8\text{-FeO-Fe}_2\text{O}_3\text{-SiO}_2$ showed no low-temperature immiscibility field under reducing conditions ($f_{\text{O}_2} = 10^{-12}$ atm), but at higher oxygen fugacities a low-temperature immiscibility field was observed that expanded with increasing f_{O_2} . *Naslund* suggests that, in natural magmas, liquid immiscibility would be most likely to occur in those systems in which the f_{O_2} is buffered to either the fayalite-magnetite-quartz or the magnetite-hematite-quartz univariant curves.

Liquid immiscibility in silicate melts can be expected to have important effects in magmas extending far beyond the compositional regions in which it actually occurs, according to *Irvine*. He has undertaken a detailed study of these effects in the system $\text{Mg}_2\text{SiO}_4\text{-Fe}_2\text{SiO}_4\text{-CaAl}_2\text{Si}_2\text{O}_8\text{-KAlSi}_3\text{O}_8\text{-SiO}_2$ (Fo-Fa-An

Or-Q). He has outlined experimentally extensive regions of metastable liquid immiscibility in the bounding joins Fo-Or-Q and Fa-Or-Q, extending from previously defined fields of stable immiscibility and detectable to temperatures as much as 600°C below the liquidus in some compositions. Particular attention was given to the relationship of Fe/Mg liquidus fractionation patterns to these regions. His data show that, in the absence of Or, melts crystallizing on the olivine-plagioclase and pyroxene-plagioclase cotectics do not change toward silica-rich compositions. He suggests that this is because of a barrier of high-silica activity associated with the immiscibility. The result is an iron-rich, silica-poor final liquid. With the introduction of substantial amounts of Or (or presumably of NaAlSi₃O₈, Ab) this barrier, however, is bypassed and a haplo-rhyolitic residual liquid develops.

Irvine concludes that immiscibility is such a fundamental feature of this type of system that the observed contrast in fractionation patterns is probably representative of the difference between the Skaergaard-type of differentiation trend toward extreme iron enrichment (the Fenner trend) and tholeiitic and calc-alkaline trends leading to rhyolitic or granitic end products (the Bowen trend). He notes, moreover, that all the major magmatic series extending from basic to acidic compositions apparently pass close to regions of immiscibility and that even if they did not intersect these regions, the magmas probably underwent a change in the structure of the liquid so fundamental that it could be reflected in almost any aspect of the chemistry of the series as well as in certain physical properties of the magmas, such as viscosity.

Kushiro determined the viscosity of melts of NaAlSi₂O₆, K₂MgSi₅O₁₂, and Na₂Si₃O₇ composition. He found that the viscosity of all three melts decreased isothermally with increasing pressure. The NaAlSi₂O₆ melt composition showed a particularly rapid drop in viscosity

between 5 and 10 kbar at 1350°C. Kushiro reasoned that because a coordination shift of Al^{IV} to Al^{VI} would effect a breakup of (Al,Si)-O-(Al,Si) bonds in tetrahedral polymers with a concomitant decrease in viscosity, the rather abrupt change in viscosity of the NaAlSi₂O₆ melt at 1350°C between 5 and 10 kbar probably resulted from a transformation of the type Al^{IV} → Al^{VI} in the melt. The other two melt compositions showed a continuous decrease in viscosity with increasing pressure. A similar continuous decrease was seen in the NaAlSi₂O₆ melt composition above 10 kbar and below 5 kbar. Kushiro therefore reasoned that cations such as K⁺, Na⁺, Mg²⁺, and Si⁴⁺ in silicate melts also change coordination with changing pressure. On the basis of these data, Kushiro argues that silicate magmas in the upper mantle probably are denser and more fluid than previously supposed.

To evaluate the proposed effects on natural magmas, Kushiro, Yoder, and Mysen selected the Kilauea 1921 olivine tholeiite and a Crater Lake, Oregon, andesite for viscosity measurements along the liquid up to 30 kbar pressure. The viscosity of tholeiite decreased from about 170 poise at 1 bar to 10 poise at 30 kbar. Similarly, the viscosity of a Crater Lake andesite decreased from about 5000 poise at 1 bar to about 1000 poise at 20 kbar. In addition, they found that the addition of about 4 wt % H₂O to the andesite melt lowered the viscosity about 2 orders of magnitude, probably as a result of breakup of tetrahedral polymers of H₂O. Kushiro, Yoder, and Mysen emphasize that the high fluidity of silicate melts has important effects on models of the separation and ascent of magma in the upper mantle. The viscosity data also place constraints on the rate of ascent of magmas carrying ultramafic nodules from the upper mantle. For example, a magma carrying garnet peridotite nodules 10 cm in diameter must have ascended from at least 100 km depth in less than about 55 hr to avoid settling-out of the nodules.

Infrared transmission spectra of quenched high-pressure silicate melts have been made by *B. Velde and Kushiro* in order to understand the structure of these melts. Hydrous and anhydrous $\text{Na}_2\text{O} \cdot 3\text{SiO}_2$ and jadeite compositions were studied. They deduce from the results that the addition of H_2O tends to depolymerize the melt. At pressures between 10 and 30 kbar, the anhydrous jadeite melt also seems to become less polymerized. It is possible that Al ions are regrouped into Al-O complexes at elevated pressures instead of being distributed in silica tetrahedral chains as they are in glass at 1 bar. The decrease in polymerization is presumed to result in a decrease in the viscosity of the melts.

Also using infrared spectroscopy, *Mysen* studied the proportions of molecular CO_2 and carbonate in silicate melts and found that the relative importance of CO_3^{2-} decreases isothermally with increasing polymerization of silicate melt as the pressure is increased. At 1450°C Mysen noticed that the proportion of carbonate relative to total amount of dissolved CO_2 in albite melt doubles between 20 and 30 kbar. He reasoned that this change reflects a coordination transformation of $\text{Al}^{\text{IV}} \rightarrow \text{Al}^{\text{VI}}$ in the $\text{NaAl-Si}_2\text{O}_6$ melt similar to that seen by *B. Velde and Kushiro* in quenched $\text{NaAl-Si}_2\text{O}_6$ melt. The somewhat higher pressure of the inferred transition in quenched melts compared to the transition deduced from *Kushiro's* viscosity data at higher pressure and temperature may be due to the overpressure required to preserve the transition in the quench experiment. Mysen speculated that crystal-liquid partition coefficients of transition metals probably decrease equally abruptly as a result of the octahedral transformation. Furthermore, he suggested that at constant temperature and f_{O_2} , the $\text{Fe}^{2+}/\text{Fe}^{3+}$ of silicate melts may increase as a result of such coordination changes.

The effects of CO_2 on the composition of liquid produced on the partial melt-

ing of peridotite have been found to be most important. *Eggler* had shown previously that in the system $\text{CaO-MgO-SiO}_2\text{-CO}_2$, at pressures above 29 kbar, dolomite is stable on the peridotite solidus. Near that pressure the solidus falls dramatically in temperature. He has now determined the composition of the liquid on that solidus at 30 kbar pressure and finds that the liquid is extremely silica-undersaturated. It is known that liquids formed at lower pressures and in the presence of H_2O are silica-saturated. One can now appreciate the conclusion that small changes in the depth of origin, in the concentrations of volatiles, and in the amount of melting can produce dramatic changes in compositions of primary magmas, particularly in suites of carbonatite-kimberlite-melilitite rocks.

Holloway, Mysen, and Eggler have made the first measurements of CO_2 solubility in highly larnite-normative liquids on the join CaO-MgO-SiO_2 . Their systematic investigations of the effect of liquid composition on CO_2 solubility lead to the conclusion that the primary factor in controlling CO_2 solubility is the ratio of network-modifying cations to the network-forming cations. That effect is exhibited on the join diopside-dolomite, along which there is a tenfold increase in CO_2 solubility, reaching values near 35 wt % in dolomite-rich compositions at 30 kbar pressure. Smaller variations in CO_2 solubility were found for the exchange of one network-modifying cation for another, the order from highest to lowest solubility being $\text{CaO} > \text{MgO} > \text{CoO}$ (CoO is an analogue for FeO). *Holloway, Mysen, and Eggler* conclude that CO_2 solubility will be less than 3 wt % in melts rich in olivine or hypersthene at pressures up to 35 kbar.

Because of the extensive effects of H_2O on the stability of carbonates, *Eggler, Kushiro, and Holloway* have investigated the carbonation of forsterite composition in the presence of fluids containing H_2O and CO_2 (20%–100%

CO₂). They have found that magnesite is almost as stable in these hydrous fluids as in pure CO₂. Carbonate minerals, therefore, could be stable mantle phases and might be present on or above the solidus of peridotite for a wide range of volatile compositions. They calculated the phase equilibrium relationships as well, using Holloway's modified Redlich-Kwong data on fugacity. Encouraged by the agreement between the calculated and the experimentally determined curves, they have calculated other decarbonation reactions that are important under conditions in the lower crust and upper mantle in the system CaO-MgO-SiO₂-CO₂.

Although the melting of peridotite has been previously studied in the absence of volatiles and in the presence of volatiles contained in a fluid phase, *Holloway and Eggler* have performed the first experiments on melting of peridotite containing CO₂ and H₂O entirely bound in crystalline phases (dolomite and phlogopite). They find that this assemblage melts isobarically (30 kbar) at a single temperature to a eutectic-like liquid, regardless of the ratio of H₂O to CO₂. For a wide range of volatile ratios, dolomite melts at the solidus, but phlogopite persists over a short supersolidus temperature interval. Over that interval, a wide compositional range of liquids can be produced whose trace element patterns will no doubt reflect partitioning with phlogopite. Above that interval, liquid will be in equilibrium with olivine and pyroxenes, but phlogopite will be absent.

From time to time classic field areas of petrologic interest are reexamined in the light of new theory and technique. The often investigated layered gabbroic intrusion of the Skaergaard, east Greenland, is now being studied again by a group formed from several organizations. *Naslund* participated in the field work and has made an electron microprobe study of silicate minerals from the upper part of the intrusion. His results confirm the general chemical trends

proposed by *Wager and Deer* (1939), but there appear to be systematic variations in different parts of the intrusion. These variations led to the interpretation that the Skaergaard magma was laterally inhomogeneous during the last stages of its crystallization and that local inhomogeneities existed during most of the differentiation process. It is also suggested by *Naslund* that there was a systematic difference in the conditions of crystallization between the upper border group and the layered series.

An alternative to direct observation of the crystallization sequence of minerals in igneous rocks is the determination of the sequence on the basis of the calculation of structural energies of the competing minerals. Precise atomic coordinates are available for many minerals, yet the exact calculation of structural energies is still a goal of the future. *Ohashi* has adopted Bertaut's Fourier series method to calculate electrostatic energies, as well as site energies, for the ions of various rock-forming minerals. He used a high-speed digital computer to obtain convergence of the Fourier series. With these values he was able to treat the degree of polymerization of the silicate tetrahedra more quantitatively, and he found that the oxygen bridging two tetrahedra has a lower energy than the apical oxygen by approximately 200 kcal/mole. Although the calculations are only at the beginning stages, it now appears possible to gain some insight into the energetics of crystallization of complex silicates.

The thermal effects associated with the melting or crystallization of silicates have considerable bearing on the generation and transport of magmas. Little is known about the pressure effect on the enthalpy of melting, particularly if volatiles such as H₂O and CO₂ are present. A modified DTA technique adapted by *Rosenhauer* has led to the direct determination of the pressure dependence of the enthalpy of melting of diopside. The principle of the method is to compare an accurately known amount of

heat generated inside the DTA capsule with the latent heat of the sample. The present preliminary results indicate an increase in the latent heat with pressure for the dry system consistent with theoretical estimations. Under H_2O -saturated conditions, however, the heat of melting is essentially independent of pressure between 1 and 4 kbar.

In theories of magma generation and ascent to the earth's surface the adiabatic gradient and adiabatic compressibility are important reference parameters. The thermodynamic equations for these quantities quoted by geophysicists, however, are oversimplified and formally valid only for a one-phase, one-component system. *Rumble* has derived thermodynamically valid equations for the adiabatic gradient and compressibility for a binary system containing two binary solutions. The method may be readily extended to treat still more complex phase equilibria. Multicomponent, multiphase equilibria have a number of effects on the adiabatic gradient, such as (1) changing phase composition and proportion affect the slope of the gradient and (2) passage from higher variance to lower variance phase assemblages introduces discontinuities in the slope of adiabats.

Trace Element Partitioning

The definition of a trace element is somewhat obscure because under some conditions an element may have the properties of an element in trace amounts or exhibit the characteristics of a major element, yet under other conditions obey Henry's law. Some investigators believe, however, that the partitioning of trace elements may be more sensitive to ambient conditions than that of major elements and therefore is more likely to yield detailed and independent information on the conditions of formation of mineral assemblages. The current experiments are contributing to a more rigorous definition of a trace element and are calibrating trace element parti-

tioning in terms of temperature, pressure, and bulk composition.

Mysen studied fractionation of the rare earth elements (REE) between olivine, orthopyroxene, and hydrous silicate liquid. Samarium was used as a representative REE, the content of Sm in the products being determined by counting β tracks generated by the decay of the samarium-151 source. He estimates that only about 1 ppm Sm can enter olivine and orthopyroxene before the activity coefficients of Sm^{3+} become compositionally dependent. He also noted that the concentration range of behavior according to Henry's law is about 25% greater in orthopyroxene than in olivine and increases in both minerals about 15%/100°C. The crystal-liquid partition coefficients of both minerals within the range of Henry's law increase with decreasing pressure. However, increasing temperature results in increasing K_{Sm}^{ol-liq} , whereas $K_{Sm}^{opx-liq}$ decreases. *Mysen* reasoned that because the Al content of orthopyroxene decreases rapidly with increasing temperature, the activity coefficient of Al probably changes, thus affecting the $K_{Sm}^{opx-liq}$. He also speculated that a similar effect may be expected in other alumina-bearing phases. Most mantle minerals contain less samarium and other REE than the limit of behavior according to Henry's law, and it is likely that the total REE content of a given phase affects the individual partition coefficients and perhaps changes them by as much as a factor of 2. Such effects must be considered when deducing the genesis of igneous rocks in light of their REE content.

The partitioning of samarium between garnet and liquid at high pressures was also studied by *Wood*. The REE content of igneous rocks is greatly affected by the presence or absence of garnet among the phases crystallizing from magmas during their ascent to the surface. *Wood* used the β -track mapping technique at concentrations of samarium present in nature. The partition coefficient $C_{Sm}^{garnet}/C_{Sm}^{liquid}$ was found to depend strongly

on temperature and bulk composition and to be less dependent on pressure. Because there are at least two mechanisms of Sm substitution into garnet, the partition coefficient at very low Sm concentrations is dependent on the total amount of samarium in the system as well as on major element composition. The values of the partition coefficient for basaltic liquids could aid in improving petrogenetic modeling of igneous processes.

Nickel has been a most important element in arguments concerning the depth of origin of igneous rocks. For example, a high nickel content of olivine is believed by some investigators to indicate a great depth of formation. *Mysen*, using the β -track mapping technique with ^{63}Ni as a source of β particles, found that the partition coefficient of nickel between olivine and liquid at 10–20 kbar and 1025°–1075°C varies between 12 and 18 as a function of physical conditions within the range of applicability of Henry's law. The olivine-liquid partition coefficient decreases slightly with increasing pressure and with increasing temperature. The effects of temperature and pressure on the orthopyroxene-liquid partition coefficient are less pronounced than for olivine-liquid. Nickel follows Henry's law in olivine up to about 1000 ppm. At higher concentrations, the partition coefficient decreases by a factor of 3–4 and reaches a minimum at about 5000 ppm in olivine, and then increases again as the Ni content is increased further. Orthopyroxene-liquid partition coefficients show that Ni solution in orthopyroxene behaves according to Henry's law until about 100 ppm is dissolved in the orthopyroxene. The lowest value of the olivine-liquid partition coefficient (≤ 5), according to *Mysen*, occurs near the Ni content of olivines from peridotite believed to have formed in the upper mantle. Olivine fractionation of magma derived from the mantle, therefore, will result in an increasing olivine-liquid partition coefficient of nickel as frac-

tionation proceeds and in rapid reduction of the Ni content of magma as olivine fractionation proceeds. The effect of the Ni content of other mantle minerals on the Ni content of partial melts is less pronounced because the partition coefficients are near unity.

Another long-standing problem in the olivine system, Mg_2SiO_4 - Ni_2SiO_4 , is that the liquid has a higher Ni/Mg than the crystals, whereas in basaltic and more acidic magmas, the reverse is true. Two explanations in particular have been advocated for the reversal: one, that it is related to the presence of iron in the natural magmas; the other, that it is due to crystal-field stabilization effects associated with the greater polymerization of the magmatic liquids owing to their higher contents of silica and alkalies and their lower temperatures. *Irvine and Kushiro* have tested these possibilities in two sets of experiments with simple systems. In one set, the partitioning was examined at 20 kbar in a composition lying approximately on the olivine join Mg_2SiO_4 - Fe_2SiO_4 - Ni_2SiO_4 . The results show that although Fe has some effect on shifting the partitioning of Ni in favor of olivine, the liquid continues to have a higher Ni/Mg. In the other experiments, carried out under 1-atm conditions, the partitioning was measured at stages during the fractional crystallization of compositions produced by combining Ni-bearing forsterite with SiO_2 and $\text{K}_2\text{O} \cdot 6\text{SiO}_2$. It was found that simply raising the level of silica to that of pyroxene composition was sufficient to cause the partitioning to switch so that the Ni/Mg was higher in olivine. The change became extreme with the high silica values achieved by the addition of the potassium silicate. The partitioning correlates strongly with temperature but also shows features that may be attributed to changes in melt structure.

Mysen and Holloway selected appropriate degrees of melting of one of the nodules studied by *Mysen and Kushiro* and determined experimentally the REE

fractionation patterns of the partial melts. They combined the REE data with the major element data of Mysen and Kushiro. Mysen and Holloway, using β -track mapping, chose cerium-141, samarium-151, and thulium-171 as representative elements for generating the experimental REE patterns. They found that only the patterns from the experimental melt of tholeiitic composition resemble those of natural tholeiite and concluded that only olivine tholeiite can be generated by partial melting of volatile-free peridotite.

The Ni-Fe-Mg distribution between metallic sulfide, oxides, and silicates in a partially molten sample of Allende type-3 carbonaceous chondrite was studied by *Mysen and Kushiro* as a function of oxygen fugacity at 1 atm. They found the Ni partitioning between sulfide and silicate (determined with β -track mapping) and the $Mg/(Mg + Fe)$ of silicates quite different from terrestrial averages but similar to values observed in lunar ferrobasalt when the f_{O_2} is kept within the stability field of metallic iron. Because the nickel partitioning between molten metal sulfide and olivine is about 2 orders of magnitude smaller than that of metallic sulfide phase and olivine in chondritic meteorite, separation of nickel between these two phases in chondrites must result from some other process. It is unlikely that a composition similar to Allende meteorite could be representative of the bulk composition of the earth.

Models of stellar nucleosynthesis and the relative contributions of the processes involved are constrained by the observed abundances of Pu, Th, and U in meteorites. An experimental study of the fractionation of ^{239}Pu , ^{230}Th , and ^{235}U between whitlockite $[\text{Ca}_3(\text{PO}_4)_2]$, apatite, and diopsidic clinopyroxene was required to determine the contributions of nucleosynthesis and crystal-chemical fractionation deduced from the meteoritic actinide (Pu, Th, U) element ratios. Fractionations determined experimentally by *Benjamin, Burnett, and Seitz*

are remarkably similar to those obtained in recent measurements on the primitive achondrite Angra dos Reis, suggesting that equilibrium was achieved. The strong fractionation of Pu relative to U implies an order of magnitude reduction in the observed meteoritic Pu/U for the Angra dos Reis achondrite source reservoir that excludes this meteorite from models of noncontinuous stellar nucleosynthesis. The experimental partition coefficients may be applied to meteorite data to calculate relative ages of objects formed in the early evolution of the solar system.

Petrology of Lunar Rocks and Meteorites

Optical spectra of the moon's surface obtained by telescope have been difficult to interpret because of a previously unrecognized spectral imprint caused by glass particles in the lunar soil. *Bell, Mao, and Weeks* report on the results of a comprehensive experimental study of the spectra of synthetic lunar basalt glasses of different compositions formed at specific temperatures and oxygen fugacity. From the spectra of these products they are able to deduce the concentrations and oxidation states of iron and titanium in lunar soil samples. The data can be used to interpret optical spectra of various parts of the moon's surface in terms of oxygen fugacity and certain compositional parameters.

Perhaps one of the most important assessments to be made of the lunar surface regolith is the contribution of meteorites to the surface layer. Although earlier investigators had thought that the composition of metallic particles could be used to determine whether the particles are of lunar or meteoritic origin, *Mao and Bell* have found complex relationships between metals, melts, and host anorthosite in an electron microscope study of rocks from the Apollo 16 site. The relationships illustrate the effects of melting processes on the surface where heating was apparently caused by meteorite impact. The metallic grains

have apparently changed composition during melting, and Mao and Bell have concluded that impact melting on the surface has severely contaminated rocks of the lunar highlands.

The fine, welded particles in lunar soils, thought to result from heat generated by the impact of micrometeorites striking the moon's surface in a continuous flux, contain finely divided metal grains less than $1\ \mu\text{m}$ in diameter. *Bell and Mao* have analyzed the absorption spectra of these particles by precipitating metal coatings of iron and carbon on mineral and glass powders and determining their spectral properties. It was discovered that the metal coatings transmit visible and near infrared radiation and that the resulting spectra can be used semiquantitatively to determine the agglutinate content of lunar soils.

Pyroxene crystals from the Angra dos Reis meteorite are found by *Bell and Mao* to have extraordinary optical absorption properties in the visible region; these properties apparently are related to complex electric and magnetic interactions of iron and titanium. These crystals are the first reported to have both electric and magnetic vectors; they have five absorption directions rather than the three directions normally observed in pyroxenes. A sixth direction in the Angra dos Reis pyroxene shows virtually no absorption in the visible spectrum. The Angra dos Reis pyroxenes have a unique transmission direction of visible light, for which the electric vector and propagation directions are defined. The optical properties were studied to determine the redox potential and its influence on the processes of formation of this ancient (8–10 b.y. old) meteorite.

Mineralogy

The characterization of a single mineral often requires a wide variety of talent and technique. A cooperative program involving *Huggins, Virgo, Huckenholz, and Rosenhauer* reached a rewarding climax this year in the study of

the petrology and crystal chemistry of natural titanium-bearing garnets. Their investigation generated many new insights into these complex garnets and brought to the fore a fundamentally different rationale for the petrogenesis of many alkalic, silica-undersaturated igneous rocks.

Huggins, Virgo, and Huckenholz re-examined the crystal chemistry of a suite of natural Ti-rich garnets, using electron microprobe analyses and ^{57}Fe Mössbauer spectroscopy. For the first time, it was demonstrated that such garnets can contain up to five distinct coordinations of iron cations: tetrahedral and octahedral ferric and tetrahedral, octahedral, and dodecahedral ferrous. Furthermore, small but significant concentrations of octahedrally coordinated Ti^{3+} are also inferred. On the basis of principles previously established for synthetic garnets, it was shown that during crystallization of natural garnets from a melt, all octahedral and tetrahedral Al, Fe, and Ti cations are involved in an exchange process. Extensive electron-hopping occurs between the Fe and Ti cations so that different oxidation states of Fe or Ti cannot be distinguished. During subsequent cooling, the electrons become localized on specific cations. Thus, the observed coexistence of Fe^{3+} and Ti^{3+} in the garnet structure at room temperature may result from an arrested electron-hopping equilibrium process.

Consistent with the low f_{O_2} conditions of formation that are inferred from the presence of octahedrally coordinated Fe^{2+} and Ti^{3+} in these garnets, *Huckenholz, Hölzl, Huggins, and Virgo* have determined the stability and phase relations of two natural and two synthetic Ti-garnets hydrothermally at 1 kbar over the temperature range from 600° to $\sim 1100^\circ\text{C}$ as a function of oxygen fugacity. In general, the stability field of the natural garnets occurs at a lower f_{O_2} than that of the synthetic garnet solid solution containing only Fe^{3+} and Ti^{4+} and extends to below the iron-quartz-fayalite buffer. The experimental

results indicate that at high oxygen fugacities and necessarily high temperatures, the stability field of natural Ti-rich garnets, having oxidation ratios calculated as $(\text{Fe}^{3+} + \text{Ti}^{4+})/\Sigma(\text{Fe} + \text{Ti})$ and approximately equal to 1.0, is rather restricted in terms of composition but can extend to f_{O_2} values of the order of 1 bar. With decreasing f_{O_2} , garnets with a wider range of oxidation ratio (0.80–0.95) are stable, but in general, the garnet solid solution becomes more reduced and thus less Si-deficient and may have crystallized at lower temperatures. Within this framework, the stability ranges of natural Ti-rich garnets from different geological environments are related to the f_{O_2} at the time of formation, as indicated by their oxidation ratios.

To provide quantitative data regarding the conditions of formation of specific Ti-rich garnets, *Virgo*, *Rosenhauer*, and *Huggins* have measured the 1-atm intrinsic oxygen fugacity as a function of temperature of six natural Ti-rich garnets using the solid-state, ZrO_2 electrolyte method. The results show that the values of the intrinsic f_{O_2} of the natural garnets plot in a restricted field that is confined between the Fe-Qtz-Fa and Fe-Wü buffer curves in a $\log f_{\text{O}_2}$ vs. $1/T$ diagram. Above a certain critical temperature, T_c , the oxygen fugacity increases rapidly and irreversibly. These data are interpreted as indicating that T_c and the associated f_{O_2} value reflect the oxygen fugacity prevailing at temperature T_c during crystallization of the garnet_{ss}. In fact, T_c is the maximum temperature at which the garnet could have crystallized.

Despite the predominance of the oxidized cations Ti^{4+} and Fe^{3+} in the garnet structure, the low f_{O_2} values emphasize the importance of the crystalline structure in controlling the relationship between f_{O_2} and cation oxidation states. The compatibility of the low f_{O_2} values and the crystal chemistry of the garnets is reconciled, however, because of the different valence states of iron and ti-

tanium at the tetrahedrally and octahedrally coordinated sites of the garnet structure.

The natural Ti-rich garnets appear to reflect the lowest oxygen fugacities in terms of the representative results for terrestrial igneous rocks. Such low f_{O_2} values, according to *Virgo*, *Huggins*, and *Rosenhauer*, however, are consistent with the strongly reducing conditions prevailing in deep-seated magma chambers. It is suggested by them that the f_{O_2} values for the natural garnets are consistent with the low f_{O_2} boundaries of the stability fields of other minerals from alkali-rich rocks and that the highly oxidized characteristics of the host rocks, e.g., $\text{Fe}_2\text{O}_3/\text{FeO} > 1$, may result from a strong degree of nonideality in the melt due to high alkali or volatile contents. They caution against the general application of previous experimental studies carried out under oxidizing conditions to questions concerning the petrogenesis of alkalic, SiO_2 -undersaturated rocks containing garnet.

The manner in which atoms are bonded together in a crystal structure is fundamentally important, according to *Hafner and Raymond*, because the chemical bonding controls the response of a crystal structure to different conditions of pressure and temperature. They have developed an ionic model of the electronic charge distribution that also includes the effect of oxygen polarization and overlap distortion to explain the nuclear quadrupole coupling tensors at the cationic sites in the garnet solid solution series $\text{Y}_3\text{Fe}_{5-x}\text{Al}_x\text{O}_{12}$ and related aluminates of the same structure type. The computed electric-field gradients in these rare earth garnets are predicted to be negative in accord with the experimentally determined values. The observed trends in the Fe^{3+} nuclear quadrupole coupling tensors at the cationic sites can be interpreted with the model principally in terms of the overlap distortion; the latter effect, however, does not account for the significant differences between the Al^{3+} and Fe^{3+} field

gradients of the different sites and in samples of the same composition. These electric-field gradient ratios are shown to be critically sensitive to the contribution provided by the dipole polarization of the oxygen ions.

Hafner, Raymond, Virgo, and Huggins also demonstrate that the model can be applied to the geologically important silicate garnets pyrope, spessartite, andradite, and grossular. The relative magnitudes and the sign of the electric-field gradients at the tetrahedral and octahedral sites are in agreement with experiment for these silicate garnets. The sign of the gradient at the octahedral sites is reversed compared with the rare earth garnets. The application of their chemical bonding model to members of the garnet family has demonstrated that purely geometrical considerations of the garnet crystal structure (e.g., polyhedral distortion, edge-sharing) are insufficient for interpreting a critical bonding parameter like the quadrupole coupling tensor.

It has been suggested that pyroxenes may exhibit a certain amount of solid solution toward Mg_2SiO_4 (in silica-undersaturated compositions) or toward SiO_2 (in silica-saturated compositions). *Wood* has found that in clinopyroxenes coexisting with quartz and liquid at high pressures and temperatures the extent of solid solution toward SiO_2 increased with increasing Al_2O_3 content of the pyroxene. The resulting nonstoichiometry appears to be linked to the presence of the component $\text{Ca}_{0.5}\text{AlSi}_2\text{O}_6$. The substitution of significant amounts of this component explains the observed discrepancy between the stability of $\text{CaAl}_2\text{SiO}_6$ -rich clinopyroxenes in quartz-bearing and quartz-free bulk compositions.

Simplicity in chemical composition of minerals does not always imply simple phase relationships; the polymorphs of enstatite, MgSiO_3 , are an example. The incorporation of a small amount of Ca in clinoenstatite has recently been found to stabilize the structure, and as a result a narrow field of pigeonite exists be-

tween protoenstatite and diopside. The lack of refined structures near the enstatite composition, however, has curtailed discussion of the structural changes associated with the Ca substitution. For this reason *Ohashi and Finger* investigated the effect of Ca on the clinoenstatite structure, using synthetic single crystals of iron-free clinopyroxenes. With addition of Ca, one cation polyhedron expands slightly, and this change, in turn, causes straightening of the chain of silicate tetrahedra. This relatively sharp change in the chain leads to the suggestion that the two different chains in enstatite become identical with the addition of 15–20 mole % CaSiO_3 , producing the augite structure.

Knowledge of not only the limits on bulk chemical composition but also the degree of intracrystalline order-disorder is essential for understanding solid solutions in mineralogy. As a part of their study of pyroxenoids, *Ohashi and Finger* refined crystal structures and cation site occupancies for three bustamites and two wollastonites in an attempt to elucidate differences in the way the solid solutions are formed in the two minerals. Although bustamite and wollastonite are both chain silicates with the formula $(\text{Ca}, \text{Mn}, \text{Fe}, \text{Mg})\text{SiO}_3$, the calcium content varies from 30% to 80% of the total octahedral cations in bustamite, whereas deviation from the ideal composition, CaSiO_3 , rarely exceeds a few mole % in wollastonite. *Ohashi and Finger* have found that the very wide field of solid solution in bustamite is mainly due to stepwise substitutions in two of the four cation sites. On the other hand, the three cation sites in wollastonite are found to be disordered, with the manganese or iron almost equally distributed.

Electron spin resonance measurements are especially helpful in ascertaining the presence of small amounts of ferric iron. *Weeks, Mao, and Bell* used the technique to record for the first time the spin components of ferric iron in syn-

thetic, iron-bearing spinels and magnesio-wüstites.

The striking red-blue color change in gillespite, $\text{BaFeSi}_4\text{O}_{10}$, at high pressure has been investigated with ^{57}Fe Mössbauer spectroscopy. In a synthetic sample the color was observed by *Huggins, Mao, and Virgo* to change from red to deep purplish blue at a pressure of 12 ± 1 kbar. The color change was not accompanied, however, by the appearance of extra peaks in the Mössbauer spectrum. The small changes in Mössbauer parameters across the transition appear to be compatible with the very slight distortion of the Fe^{2+} square-planar site responsible for the color change. On further increase of pressure, the color changed gradually from deep purplish blue to a paler greenish blue. The observation of a second Mössbauer doublet with octahedral parameters, as reported in *Year Book 74*, did not occur until the pressure exceeded 30 kbar. Above 70 kbar, this octahedral doublet dominated the Mössbauer spectrum, and the mineral became colorless. These results indicate that a second transition occurs in gillespite at about 70 kbar and that it is this transition, not the red-blue color change, that results in the observation of a second doublet in the Mössbauer spectrum.

Metasomatism

Reaction zones have great attraction for mineralogists because of the development of large masses of one or relatively few kinds of crystals, and for petrologists because the sequence of zones contains information on the conditions of formation. *Frantz and Mao* have developed a general theoretical model and a numerical technique useful in the calculation of metasomatic zones resulting from intergranular diffusion or infiltration, or both, of any number of components. Solution concentrations at noninvariant boundaries were found to be dependent on diffusion coefficients, zone thicknesses, and volume flux. After the fluid concentration profiles were cal-

culated, the growth of solids at each point was characterized and calculated. To illustrate the method, reaction paths resulting from ternary diffusion in the system $\text{CaO-MgO-SiO}_2\text{-H}_2\text{O-CO}_2$ have been calculated. Relationships between the various mobilities of the diffusing species and the sequence of biminerally and monomineralic reaction zones have been shown. The zone sequence was found to be entirely dependent upon the mobilities of the various diffusing species, and what often appears to be uphill diffusion was found to be the result of widely differing mobilities. The new theoretical model now provides a basis for calculating the conditions of formation of complex metasomatic rocks using the observed sequence of assemblages, the zone thicknesses, and the composition of minerals as well as the measured diffusion coefficients. In addition, the Frantz-Mao theory will be useful for the determination of the genesis of ore deposits that occur in skarns formed by metasomatic processes.

Skarns are often associated with the emplacement of igneous bodies. Extensive interaction between granites, for example, and the rocks they intrude is a most important process by which ore bodies are formed. Many investigators have tried to deduce the effects of fluids from the country rocks on the granites by observing the changes of stable isotopes in the vicinity of the contact. Utilizing a petrologic approach, *Ferry* has observed several effects of fluids active during the intrusion of granitic rocks and simultaneous metamorphism of sediments, on both the igneous rocks and the metasediments. Formation of zoisite in the carbonate sediments records an introduction of H_2O -rich fluids from the cooling granite. Alteration of feldspars in the granitic rock to calcite, epidote, muscovite, and quartz records an introduction of CO_2 derived from metamorphic decarbonation reactions in the sediments. The fluid composition in both the granite and the sediments has been estimated from mineral relations.

Mineral assemblages in the sediments and garnet-biotite pairs in the granitic rocks both record a common 520°C temperature that may represent the temperature at which fluid interaction between granite and sediment terminated. Feldspar and biotite alteration assemblages and feldspar pairs in the granites record a common 425°C temperature that may represent the temperature at which residual fluids within the granite were consumed by hydration reactions. It is evident that the simple observations of mineral composition and assemblage provide a sound basis for deducing direction of flow of various fluid components in metasomatic processes.

Thermodynamic calculation of reaction involving CO₂ or H₂O in the fluid phase requires accurate fugacity and activity coefficients for these species. *Holloway* has further modified a recently published modification of the Redlich-Kwong equation of state for mixtures of molecular gases. An evaluation of the accuracy of the resulting equation suggests that it can be used to calculate fugacities of pure H₂O, CO₂, H₂, and CH₄ with a relative accuracy of $\pm 5\%$ or better and to calculate activities of these species in mixtures with a relative accuracy of $\pm 20\%$ or better over the temperature range 450°–1600°C and the pressure range 0.5–35 kbar. *Holloway* uses the equation to calculate the molecular composition of C-O-H fluids in equilibrium with graphite at total pressures up to 30 kbar, thus opening the way for experiments in iron-bearing systems under known conditions of H₂O, CO₂, and O₂ fugacity.

As a result of the introduction of H₂O, basalts are commonly converted to amphibolites. *Spear* determined the compositions of amphiboles synthesized hydrothermally from a basalt over a range of temperature, fluid pressure, and oxygen fugacity. He found that amphiboles are enriched in K, Na, Ti, and Al at the expense of Si with increasing temperature and decreasing oxygen fugacity. Most of the compositional variation

could be described in terms of the substitutions (Na,K) (A site) + R³⁺ (VI) + 2Al (IV) = □ + R²⁺ (VI) + 2Si (IV) and Ti⁴⁺ (VI) + 2Al (IV) = R²⁺ (VI) + 2Si (IV). These substitutions are similar to those found in amphiboles from regionally metamorphosed amphibolites, and several heterogeneous reactions between amphiboles and coexisting phases are presented that can describe these variations. He suggested that the "pargasitic trend" displayed by amphiboles from natural amphibolites can be brought about by a change in either temperature or oxygen fugacity at a constant bulk rock composition or by a change in the activity of SiO₂ at constant metamorphic grade.

Statistical Petrology

Chayes has found that distributions of three of the major elements (Al, Ca, Fe) in Cenozoic volcanic rocks are negatively skewed and that the third moment about the mean (m_3) for each is comparable in absolute value to those of the positively skewed elements Mg, Na, K, and Ti. The net skew of cations would thus be strongly positive, for the absolute value of m_3 for Si is very much larger than that of any other element, and as shown in last year's report, the skew of Si is positive. Curiously, the distribution of the only essential anion, oxygen, calculated from the same data, shows very slight asymmetry.

The sampling variance of the coefficients of multivariate equations generated in discriminant function, principal component, and factor analysis is a source of experimental variation usually ignored in geologic applications of these increasingly popular procedures. Preliminary results of *Trochimczyk* suggest that the coefficients of functions that yield remarkably similar partitions of sample variance in random samples of the same body of data may differ widely. Even though the statistical interpretation of such coefficients may be clear and forthright, their sampling variance may render geological or geochemical inter-

pretation of them—as, for instance, when the coefficients of a principal component are used as coefficients in a mass-balance equation—exceedingly difficult and unclear.

By means of binary discriminant function analysis *Chayes* has been able to characterize numerically the chemical consistency of current usage of the commoner names of Cenozoic volcanic rocks. The work will provide a background against which inconsistencies inevitably introduced by proposed changes in the denotations of existing rock names can be evaluated.

Development of a standard form for use in building a world data base for petrology is still in its initial stage, but *Chayes* reports that the work already suggests that construction of such a base will be a much more demanding and time-consuming task than had been anticipated. It now seems apparent that the services of his existing information system, and of similar systems elsewhere, will be required for considerably longer than had been expected. Accordingly, he has restructured the system so that its increasingly complex file structure does not interfere with ready expansion of its program repertoire, and *Trochimczyk* has been expanding the program repertoire. They and *D. Velde* are collaborating in a substantial revision of the data base, scheduled for completion by the end of 1976.

Biogeochemistry

Sugars and amino acids readily condense to form polymers known as melanoidins that closely resemble natural humic substances. In a series of experiments *Hedges* reacted glucose with one of three amino acids: glutamic acid, valine, or lysine. The basic amino acid lysine was found to react with glucose at a much greater rate than either the neutral amino acid valine or the acidic amino acid glutamic acid. The polymers formed from these condensations have some chemical properties that closely resemble those of the amino acid from

which they were produced. These inherent properties are reflected by differences in the associative reactions of the individual melanoidins with kaolinite and montmorillonite clay minerals. Over a wide range of pH and melanoidin concentration, the polymer produced from glucose and lysine was removed from solution by both clays to a greater extent than were the valine and glutamic acid products. Montmorillonite removed more of each melanoidin than did kaolinite under most reaction conditions. The extent of uptake of all polymers by montmorillonite clays that were saturated with Na^+ , Ca^{2+} , or Fe^{3+} increased with increasing ionic potential of the exchangeable ions. Some of the observed associative trends appear to result from ion-exchange reactions. These studies suggest that sugar-amino acid condensation reactions may occur in seawater and marine sediments. Nitrogen-rich polymers formed from the more rapid reaction of basic amino acids have a great affinity for clay mineral surfaces and should be preferentially incorporated in fine-grained marine sediments.

The free amino acids found in ancient fossils have had a complex chemical history. These free amino acids arise from the hydrolytic splitting of a protein that was once part of a living organism. After formation, they can racemize and also decompose to non-amino acids. In order to apply amino-acid geochemistry to the paleothermometry and geochronology of fossils, knowledge of the relative rates and activation energies for hydrolysis, racemization, and decomposition is necessary. The rate of release of various amino acids during the hydrolysis of protein was found by *Hare* to follow a simple exponential law. The temperature dependence of the rates yields activation energies that average about 21–23 kcal/mole. Aspartic acid and glycine are released about an order of magnitude faster than valine or isoleucine, but the activation energies are similar. The rates of racemization of free amino acids also follow a simple first-order rate law but

have activation energies of about 30 kcal/mole, about 7–8 kcal greater than for hydrolysis. A mathematical treatment of the rate expressions shows that it is possible to deduce the age and mean temperature of fossils forming a closed system with both partially hydrolyzed proteins and partially racemized free amino acids.

Hoering has developed an analytical scheme for fractionating and identifying components of saturated hydrocarbon mixtures that occur in Precambrian rocks. The new computer-based data-handling system on the tandem gas chromatograph-mass spectrometer is a key part of the experiment. Hydrocarbons from the oil seep in the well-preserved billion-year-old Nonesuch shale of Michigan were examined for six classes of molecules that can be related to known precursors of living cells, the so-called molecular fossils. Four of the classes—normal, isoprenoid, 2-methyl and 3-methyl hydrocarbons—are present in appreciable concentrations. The other two, sterane and triterpane hydrocarbons, contribute less than 50 ppm to the material. The presence of the four classes indicates that a number of biochemical pathways existing today were operative at the time of deposition of the shale. The absence of appreciable sterane hydrocarbons is puzzling and raises questions about the state of cellular evolution at that time. *Hoering* points out that understanding of Precambrian life is directly tied to the state of knowledge about mechanisms of transformation and preservation of organic matter in rocks.

Geochronology

Proterozoic volcanic and intrusive rocks from Mount Isa, Australia, where field relationships are well known, have been studied by *Page*, using U-Pb ages of zircons. The detail of the geochronological control and its accord with the geology lead to simple conclusions about the petrogenesis of the igneous rocks encountered. Comparison of the U-Pb re-

sults, field constraints, and earlier determined Rb-Sr total-rock isochrons from these slightly altered acidic volcanic rocks and granites shows that the Rb-Sr ages in most of these rocks are about 100–200 m.y. less than the U-Pb ages. The Rb-Sr isochrons of these rocks (especially acidic lavas) portray all degrees of disturbed isotopic systems. Some of the isochrons are approximately linear; others are curved. Curved isochrons at low Rb/Sr yield higher apparent ages than samples with higher Rb/Sr. This comparative isotopic study conclusively demonstrates that such spurious Rb-Sr isochrons on low-grade metamorphosed acidic igneous rocks may not give dependable ages for either primary crystallization or metamorphism.

Uranium-lead ages were measured for the first time for zircons from kimberlites, using the hydrothermal decomposition technique and the ^{205}Pb tracer developed at this Laboratory. Zircons from kimberlite pipes located near the center of the African shield give ages close to 90 m.y., but zircons from the edge of the shield, where the lithosphere is thinner, crystallized 70 m.y. ago. These preliminary results of *Davis, Krogh, and Erlank* can be interpreted to indicate that the zircons crystallized from a magma only a few million years before the kimberlite erupted through overlying Cretaceous sediments.

New Techniques and Equipment

A major event in high-pressure research took place in December 1975—a pressure in excess of 1 Mbar was sustained in a laboratory device for 1 week. The diamond-anvil high-pressure apparatus of *Weir et al.* (1959) was greatly improved by *Mao and Bell* so that samples of geological interest could be held at pressures up to 1.2 Mbar and subjected to temperatures up to 3000°C with the use of a laser beam. At sustained high-pressure conditions it is now possible to monitor pressure continu-

ously by means of the spectral shift of the sharp fluorescent R lines of a ruby crystal situated in the sample cell and excited by a Cd-He gas-diffusion laser beam. The sample can be observed visually, and x-ray diffraction, infrared spectral, and Mössbauer spectral data can be taken. Mao and Bell succeeded in melting metallic iron at 1 Mbar in the first of many exciting experiments. It will now be possible to study routinely the properties of materials under conditions approximating those near the earth's core-mantle boundary.

In the study of melting and crystallization of minerals, it is highly desirable to observe the phenomena under the microscope. *Ohashi and Hadidiacos* have built a microheater in which the Pt-PtRh thermocouple has three functions: holding, heating, and measuring the temperature of the sample. Because of its small heat mass and fast thermal response, any changes in temperature are instantaneously measured and corrected, thus resulting in precise temperature control. The highest operating temperature is at present 1600°C, a useful maximum temperature for the melting of many common rock-forming sili-

cates. The new furnace may also be especially useful for determining the structure of crystals in the temperature region just below the melting point.

Kushiro designed a new furnace assembly of 3/4-in diameter for work at pressures up to 30 kbar with more than 0.5 g of rock powder in an individual sample. By tapering the ends of the graphite furnace, the temperature gradient along a 12-mm section of the furnace is kept within 15°C compared with the more than 50°C gradient in a normal untapered furnace with similar sample volume capacity.

Beta-track counting was employed by *Mysen* as a means of determining accurately the proportions of melts formed in experiments with natural rocks and simple synthetic systems. The technique is based on a tracer that preferentially enters the melt and does not affect the phase relations. About 50 ppm ^{14}C -spiked CO_2 was used as tracer to test the technique on melting experiments on a natural garnet peridotite. The β -track maps are also useful in studying the geometry of melt formation in rocks and in determining the volatile content of partial melts.

EXPERIMENTAL STUDIES BEARING ON THE CORE-MANTLE BOUNDARY

COMPRESSIBILITY AND X-RAY DIFFRACTION OF THE EPSILON PHASE OF METALLIC IRON (ϵ -Fe) AND PERICLASE (MgO) TO 0.9 MBAR PRESSURE, WITH BEARING ON THE EARTH'S MANTLE-CORE BOUNDARY

H. K. Mao and P. M. Bell

One of the first steps in developing a physical model of the earth's deep mantle and core is to obtain physical properties of the minerals and mineral assemblages that are considered likely to occur at the mantle-core boundary. Seismic and experimental data indicate that the minerals are close-packed oxides and metals (Mao, *Year Book* 73); thus

the phases MgO and ϵ -Fe were selected for the present study as possible representative phases. Both phases have been studied by shock-wave methods, and their equations of state are determined (McQueen and Marsh, 1960; Carter *et al.*, 1971). Compressibility of the two phases was measured experimentally in the present study to 0.9 Mbar, and it was found that no phase changes occurred above 130 kbar. The data serve to set volume- (and density-) pressure constraints on the potential mineral properties to an equivalent depth in the earth of 2000–2500 km. These are the first static high-pressure experiments

that can be used directly to set physical constraints at the mantle-core boundary.

Experimental Procedures

These experiments utilized a unique sample configuration in the diamond-anvil high-pressure cell. Crystals of ruby and powdered MgO of reagent grade were placed on both sides of a thin sheet (0.003 mm thick) of iron (99.999% Fe). The assemblage was placed between the diamonds. The crystals and powder were embedded in the iron sheet as pressure was applied. A pressure gradient existed in the sample, but the gradient could be mapped out accurately to a scale of 30 μm , as described below. A beam of MoK α x rays of 70 μm diameter was incident upon the central portion of the sample, and a precision x-ray film cassette attached to the pressure cell recorded the diffracted beam.

Within and surrounding the central 70- μm -diameter area intersected by the x-ray beam, five circular areas, each 30 μm in diameter, were sampled for pressure measurement using the ruby-fluorescence technique (Fig. 1). Pressure measurement was done by focusing a He-Cd laser beam in epi-illumination apparatus described last year (Bell and Mao, *Year Book* 74). The ruby R_1 fluorescent line was measured in each of the five areas, and an average pressure was calculated. This method offered an excellent opportunity to compare the ruby pressure scale with shock-wave data.

Pressure Calibration of the Compressibility of MgO

The five circular areas where pressure was measured by ruby fluorescence are shown in Fig. 1. The pressure distribution within the overall areas that included the five areas sampled was assumed to be parabolic, and a weighted average of $3/4 P_{\text{center}} + 1/4 P_{\text{rim}}$ was used to calculate the pressures listed in Table 1 (P_{ruby}).

Calibration of the pressure values determined by ruby fluorescence was done by measuring the volume of MgO by

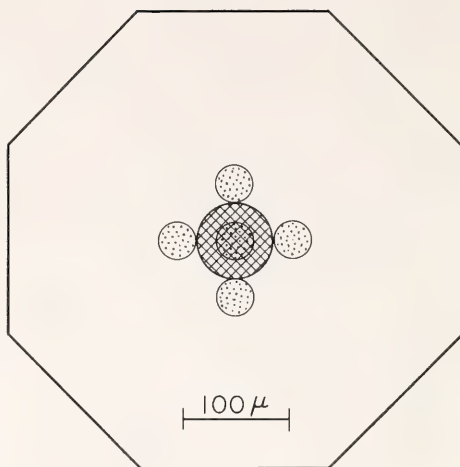


Fig. 1. Location of areas sampled for pressure measurement in the pressure cell (cross-hatched, x-ray beam; stippled, laser beam).

x-ray diffraction at the pressures at which the ruby fluorescence technique was employed. The volumes of MgO thus determined are compared with the volume-pressure curve for MgO of Carter *et al.* (1971) in Fig. 2, and the experimental pressures are listed in Table 1. On the basis of this calibration the pressures are plotted in Fig. 3 with a linear extension of the ruby fluorescence scale (Piermarini and Block, 1975). The ruby fluorescence scale appears to be linear to approximately 0.9 Mbar.

Compressibility of ϵ -Fe

The compressibility of ϵ -Fe determined simultaneously with that of MgO is listed at the calibrated pressures in Table 1. The experimental points are plotted in Fig. 4 with existing data on α -Fe to 150 kbar and ϵ -Fe to 300 kbar (Mao, Bassett, and Takahashi, 1967) and the shock-wave Hugoniot curve for ϵ -Fe of McQueen and Marsh (1960). The present data can be fitted to an isothermal Birch equation of state with $\xi = 0$:

$$P = 1.5B_0[(V/V_0)^{-7/3} - (V/V_0)^{-5/3}]$$

where $B_0 = 1.86$ Mbar and $V_0(\epsilon\text{-Fe}) = 6.72 \text{ cm}^3 \text{ mole}^{-1}$. The Hugoniot curve is

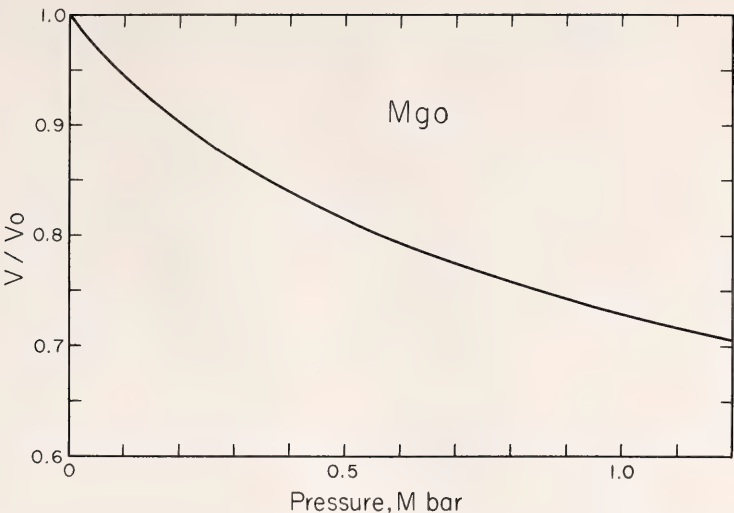


Fig. 2. Calibration curve for pressure versus volume of MgO (curve after Carter *et al.*, 1971).

uncorrected for temperature, and part or all of the differences between the Hugoniot and the present data may lie in the correction.

The present data show that no phase change occurs in ϵ -Fe to approximately 0.9 Mbar. Figure 5 shows a plot of the lattice parameter ratio (c/a) of ϵ -Fe as a function of pressure. This line $c/a = 1.607 - 0.018P$ (Mbar) fits the present data points and the points of Mao, Bassett, and Takahashi (1967). There is strong departure between both sets of data and the data of Clendenen and Drickamer (1966).

Discussion

The present data are the first direct measurements of compressibility of iron calibrated with the compressibility of MgO and can be used as primary physical constraints in geophysical models of the earth. The data carry no uncertainties regarding spherical and radial homogeneity in the mantle and core as do the theoretical derivations and calculations of the Adams-Williamson solution. Recent seismic observations by M. N. Töksoz (personal communication, 1976) suggest that the core is radially inhomogeneous and that the molar volume of

TABLE 1. Pressure and Compressibility Measurements

| Experiment No. | P_{ruby}^* (kbar) | | | MgO | | Fe | |
|----------------|----------------------------|------|----------|---------|-------------|-----------|-------|
| | Center | Rim† | Average‡ | V/V_0 | P (kbar)§ | $V/V_0 $ | c/a |
| 4C1 | 528 | 495 | 520 | 0.8120 | 510 | 0.7772 | 1.599 |
| 5C1 | 702 | 630 | 684 | 0.7802 | 670 | 0.7519 | 1.592 |
| 5C2 | 806 | 759 | 794 | 0.7696 | 730 | 0.7411 | 1.593 |
| 5C3 | 878 | 807 | 860 | 0.7473 | 865 | 0.7233 | 1.592 |

* Calculated on the basis of linear extrapolation of the calibration below 300 kbar (Piermarini and Block, 1975).

† Average of four measurements outside the rim of the x-rayed area.

‡ Weighed average of $\frac{1}{4} P_{\text{rim}} + \frac{3}{4} P_{\text{center}}$.

§ Based on the P - V relations determined by shock-wave technique (Carter *et al.*, 1971).

|| $V_{P,\epsilon\text{-Fe}}/V_{0,\alpha\text{-Fe}} = 7.093 \text{ cm}^3/\text{mole}$.

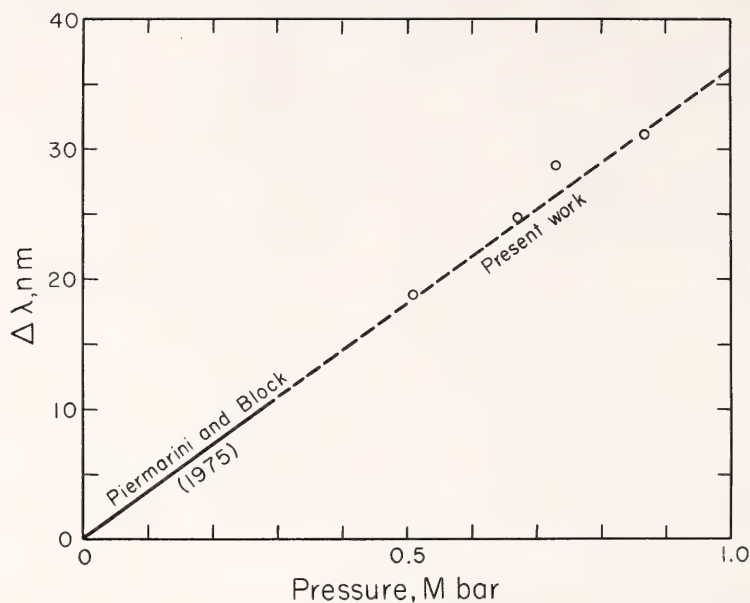


Fig. 3. Pressure of MgO (calibrated by shock-wave data) versus $\Delta\lambda$ (nm) of the ruby R_1 line (measured simultaneously with MgO compressibility). Solid curve, after Piermarini and Block (1975); dashed curve, linear extrapolation; circles, present data.

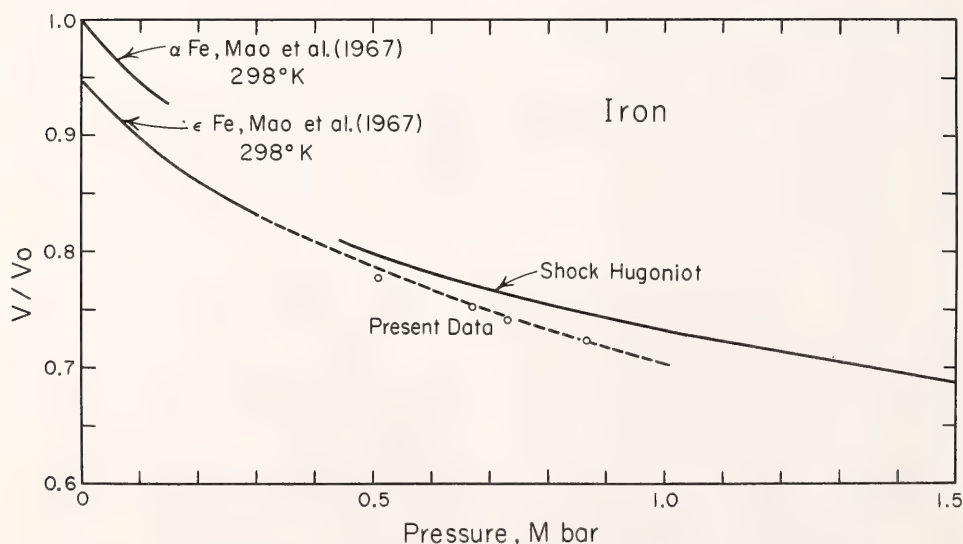


Fig. 4. Compressibility of ϵ -Fe. Circles and dashed curve, present data; α -Fe and ϵ -Fe curves, Mao, Bassett, and Takahashi (1967); shock Hugoniot curve, after McQueen and Marsh (1960).

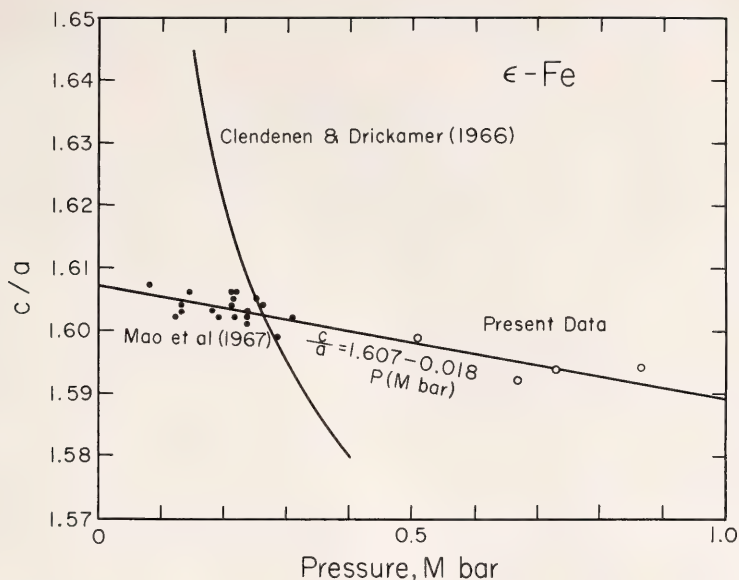


Fig. 5. Lattice parameter ratio (c/a) of ϵ -Fe as a function of pressure (curve and solid points, after Mao, Bassett, and Takahashi, 1967; curve, Clendenen and Drickamer, 1966; open circles, present data).

the outer core is at least 8%–10% higher than that of pure iron. With direct compressibility measurements of iron alloys it may be possible to resolve the question of the composition of the outer core. The present data on pure Fe are the limiting compositional values of compressibility and thus are the physical constraints on any model involving pressures of the order of 1 Mbar (cf. Anderson, Sammis, and Jordan, 1972).

COMPRESSIBILITY OF MAGNESIOWÜSTITE ($\text{Fe}_{0.4}\text{Mg}_{0.6}\text{O}$) TO 264 KBAR

*M. Rosenhauer, H. K. Mao,
and E. Woermann*

Magnesiowüstite is a stable phase in the system Mg-Fe-O. The density and electrical properties of the magnesiowüstites are considered appropriate for models of the earth's mantle (Mao, *Year Book* 73). The correlation of compressibility and stoichiometry of magnesiowüstite is crucial to the understanding of disproportionation processes (Mao, *Year Book* 74). In this study direct

measurements of molar volume data of a magnesiowüstite with well-characterized $\text{Fe}^{3+}/\text{Fe}^{2+}$ were obtained with the diamond-anvil high-pressure cell. These results are the first compressibility data on magnesiowüstite at pressures of 264 kbar calibrated with the sodium chloride internal standard.

Synthetic magnesiowüstite was prepared from mixtures of reagent-grade Fe_2O_3 and MgO . Ten-gram samples were ground and fired in air at 1000°C for 15 hr. The samples were reground and pressed into pellets (6 mm diameter, 6 mm thickness) and then placed in a CO_2 - H_2 gas mixing furnace at 1300°C for 24 hr. The gas mixture was adjusted to the richest hydrogen mixture at which metallic iron did not precipitate. Chemical analyses of the run products are given in Table 2. Lattice parameter measurements obtained by x-ray diffraction are plotted against composition in Fig. 6. The composition selected for this study was $\text{Fe}_{0.4}\text{Mg}_{0.6}\text{O}$, with a lattice parameter of 4.262 Å.

The magnesiowüstite was studied by

TABLE 2. Chemical Analyses of Magnesiowüstites Synthesized along the Join FeO-MgO

| Fe | | | | | | | | | Atomic Ratio ($O^{2-} = 1.0$) | | | Vacancies |
|-----------|------------|-------|-------------------|------------------|------------------|-----------------|--------|----------|---------------------------------|------------------|------------------|-----------|
| Fe + Mg | Fe | Fe | Weight Percentage | | | | | Σ | Fe ²⁺ | Fe ³⁺ | Mg ²⁺ | |
| (weighed) | (analyzed) | | Fe ²⁺ | Fe ³⁺ | Mg ²⁺ | O ²⁻ | | | | | | |
| 0.4 | 0.4021 | 41.82 | 40.32 | 1.50 | 27.08 | 30.01 | 98.91 | 0.3849 | 0.0143 | 0.5937 | 0.0 | |
| 0.6 | 0.6030 | 55.88 | 53.84 | 2.04 | 16.02 | 26.84 | 98.74 | 0.5747 | 0.0218 | 0.3927 | 0.0 | |
| 0.8 | 0.8006 | 68.06 | 63.46 | 4.60 | 7.38 | 25.01 | 100.45 | 0.7269 | 0.0527 | 0.1947 | 0.02 | |
| 1.0 | 1.0 | 77.07 | 68.81 | 8.26 | ... | 23.26 | 100.33 | 0.8475 | 0.1017 | ... | 0.05 | |

x-ray diffraction at nine pressures in the range 7–264 kbar; the data are given in Table 3. The pressures were determined by measuring the volume of NaCl as an internal standard, using the volume equation of state determined by Decker (1965). A plot of the data is given in Fig. 7.

A Birch equation of state (high-order terms truncated), $P = 1.5B_0 [(V/V_0)^{-1/3} - (V/V_0)^{-5/3}]$ was fitted to the data, and the B_0 was found to be

1.57 ± 0.1 Mbar. The pressure-volume curves for wüstite (Mao *et al.*, 1969) and periclase (Weaver, Takahashi, and Bassett, 1971) are also plotted on Fig. 7 for comparison.

Figure 7 shows the uniform self-consistency of the present measurements of compressibility of magnesiowüstite. One can approximate an intermediate value for compressibility between values for MgO and FeO in constructing physical models of the mantle, but it should be

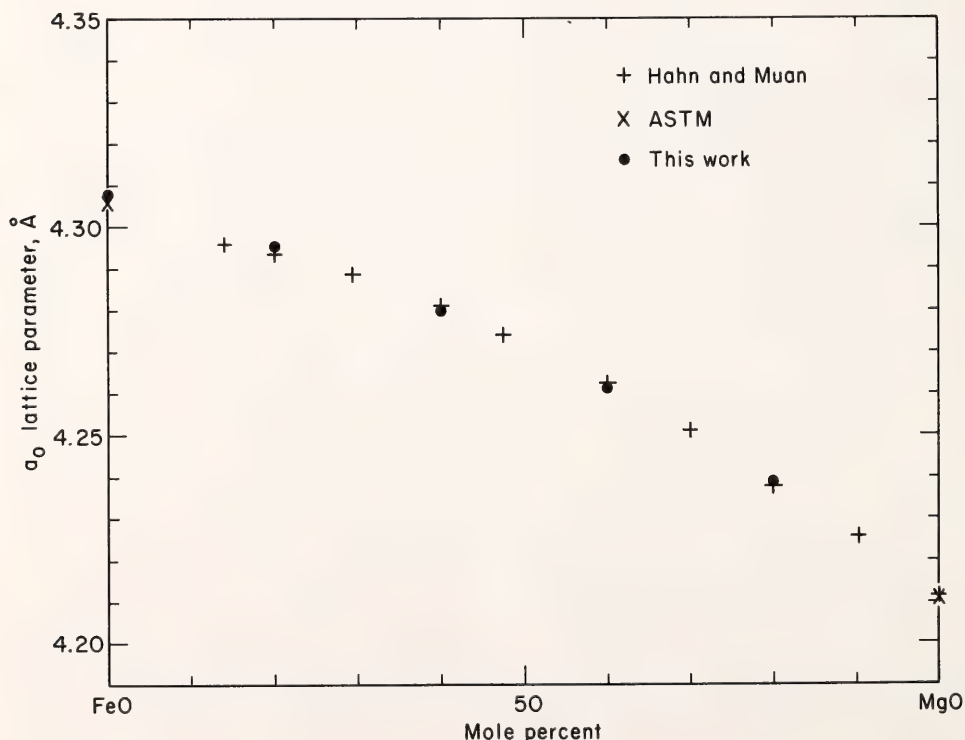


Fig. 6. Lattice parameters of magnesiowüstites along the join FeO-MgO.

TABLE 3. Effect of Pressure on the Lattice Parameter, a , and the Volume of Magnesio-wüstite, ($\text{Mg}_{0.6}\text{Fe}_{0.4}$)O

| Run No. | a_{NaCl} (Å) | P (kbar) | a_{MW} (Å) | $V/V_0 \text{ MW}$ |
|---------|-----------------------|------------|---------------------|--------------------|
| 15UP-3 | 5.585 | 7 | 4.249 | 0.991 |
| 15UP-4 | 5.499 | 21 | 4.248 | 0.990 |
| 1C-2 | 5.303 | 67 | 4.203 | 0.959 |
| 1C-3 | 5.106 | 140 | 4.153 | 0.926 |
| 15UP-7 | 5.070 | 158 | 4.140 | 0.916 |
| 15UP-9 | 5.051 | 168 | 4.130 | 0.910 |
| 1C-4 | 5.008 | 192 | 4.121 | 0.904 |
| 15UP-5 | 4.985 | 205 | 4.116 | 0.901 |
| 15UP-1 | 4.900 | 264 | 4.080 | 0.877 |

noted that the magnesio-wüstite is not stoichiometric: $\text{Fe}^{3+}/\text{Fe}^{2+} = 0.04$ (see Table 2).

The compressibility values for magnesio-wüstite are accurate representatives of the chemical series between FeO and MgO end members to 264 kbar. The pressures studied are equivalent to a depth range of approximately 10–900 km.

HIGH-PRESSURE DISPROPORTIONATION STUDY OF IRON IN SYNTHETIC BASALT GLASS

*P. M. Bell, H. K. Mao, R. A. Weeks,
and A. Van Valkenburg*

Oxide minerals produced at high pressure are postulated to form the mineralogical framework of the earth's mantle (Mao, *Year Book 73*). Because of the abundance of iron in the total composition of the earth, the production of iron oxide phases by chemical disproportionation reactions could thus be a predominant process if such disproportionation actually occurs. This study is part of an effort to explore the process itself and to determine its applicability to geochemical processes at high pressure.

The results of high-pressure experiments with spinel of fayalite composition (Fe_2SiO_4) constitute direct evidence that ferrous iron spinel disproportionates to stishovite plus nonstoichiometric wüstite (Mao and Bell, *Year Book 70*).

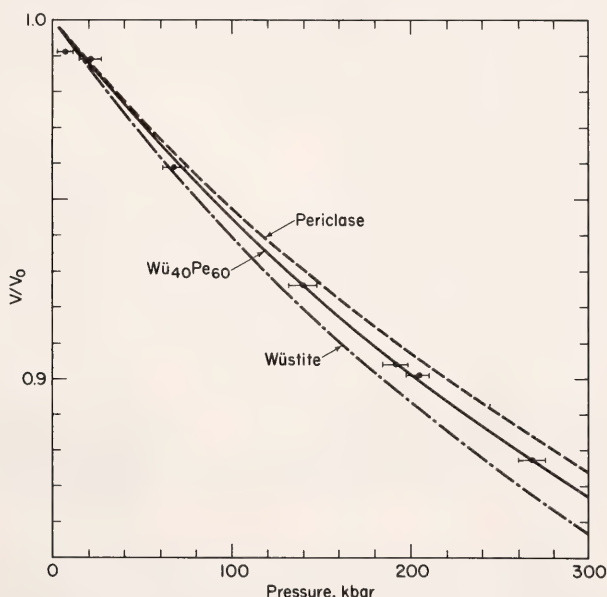


Fig. 7. Volume of magnesio-wüstites synthesized in this study versus pressure. Also shown are the volume of MgO (Weaver, Takahashi, and Bassett, 1971) and that of wüstite (Mao *et al.*, 1969).

The reaction is stabilized by high pressure (Mao, *Year Book* 73). Further experiments on a more complex system of basalt composition indicated that disproportionation may occur as well in common rock compositions (Mao and Bell, *Year Book* 74). The present results confirm the general nature of the process.

Experiments

A basalt glass studied previously (Bell and Mao, *Year Book* 74; glass F₃T₀, this Report) was used as starting material. The glass was first fused in air and then reduced chemically by a 6–8 hr treatment at 1400°C in an atmosphere of log $P_{O_2} = -9.1$. The reduced glass was then subjected to 150 kbar in the diamond-window high-pressure cell. At pressure, the glass was remelted at 2000°C by scanning a focused laser beam onto the sample. No pressure gasket was used, and thus a radial pressure gradient was developed in the cell, with pressures of approximately 100–150 kbar restricted to a central circular area 100 μm across. Figure 8 shows a view into the diamond cell while under pressure, after the laser beam has been scanned. The area of dark precipitates is the central portion. As the laser beam was scanned across the pressure gradient, formation of the dark material ceased at approximately 100 kbar and only clear glass that quenched along the scan into the low-pressure region was observed. Figure 9 shows a portion of the high-pressure zone after the pressure was released and the sample removed. Analysis by electron microscopy and x-ray diffraction showed that the dark zones contained a mixture of quenched garnet and metallic iron (Bell and Mao, *Year Book* 74).

These results are consistent with a disproportionation reaction but are incomplete because a mixture of ferric iron and metallic iron must be demonstrated to coexist. The metallic iron was observed, but analysis for ferric iron in these small samples required electron-spin resonance techniques, described below.

Electron Paramagnetic Resonance

The products of 60 experimental runs were combined into a sample sufficient for electron paramagnetic resonance (EPR). This technique was employed because it is sensitive to the presence of ferric and metallic iron but does not detect ferrous iron. The reaction that probably occurred in the experiments was $3\text{Fe}^{2+} \rightarrow 2\text{Fe}^{3+} + \text{Fe}^0$, so the EPR technique was ideally suited. There is no possibility of confusing the oxidation states of the starting material with those of the products. Figure 10 shows ferromagnetic resonance spectra for (a) the oxidized basalt glass, (b) the reduced basalt glass used as starting material, and (c) the 60 run products of reduced basalt glass that had been held at 150 kbar and melted at 2000°C. The strong resonance in the (a) and (c) spectra is caused by ferric iron. Asymmetry of the resonance in spectrum (c) is caused by the existence of metallic iron, crystal shape, and magnetic anisotropy. Figure 11 shows temperature dependence of the ferromagnetic resonance. (A plot of the line width of resonance versus temperature is given in comparison with other materials by Weeks, Mao, and Bell, this Report.)

Conclusions

The new data are a confirmation of preliminary observations of chemical disproportionation of iron in a complex basalt. The experiments above 100 kbar produced detectable reaction, and theoretically the amount of reaction should increase with increasing pressure. The temperature of these experiments (2000°C) was set sufficiently high to cause complete melting but was not intended to correlate with average temperatures at depths equivalent to 100 kbar. The conclusion drawn from these results is that at depths in the earth greater than approximately 350 km (equivalent to 100 kbar), ferrous iron-bearing compounds will disproportionate into phases containing ferric iron plus a metallic iron phase.

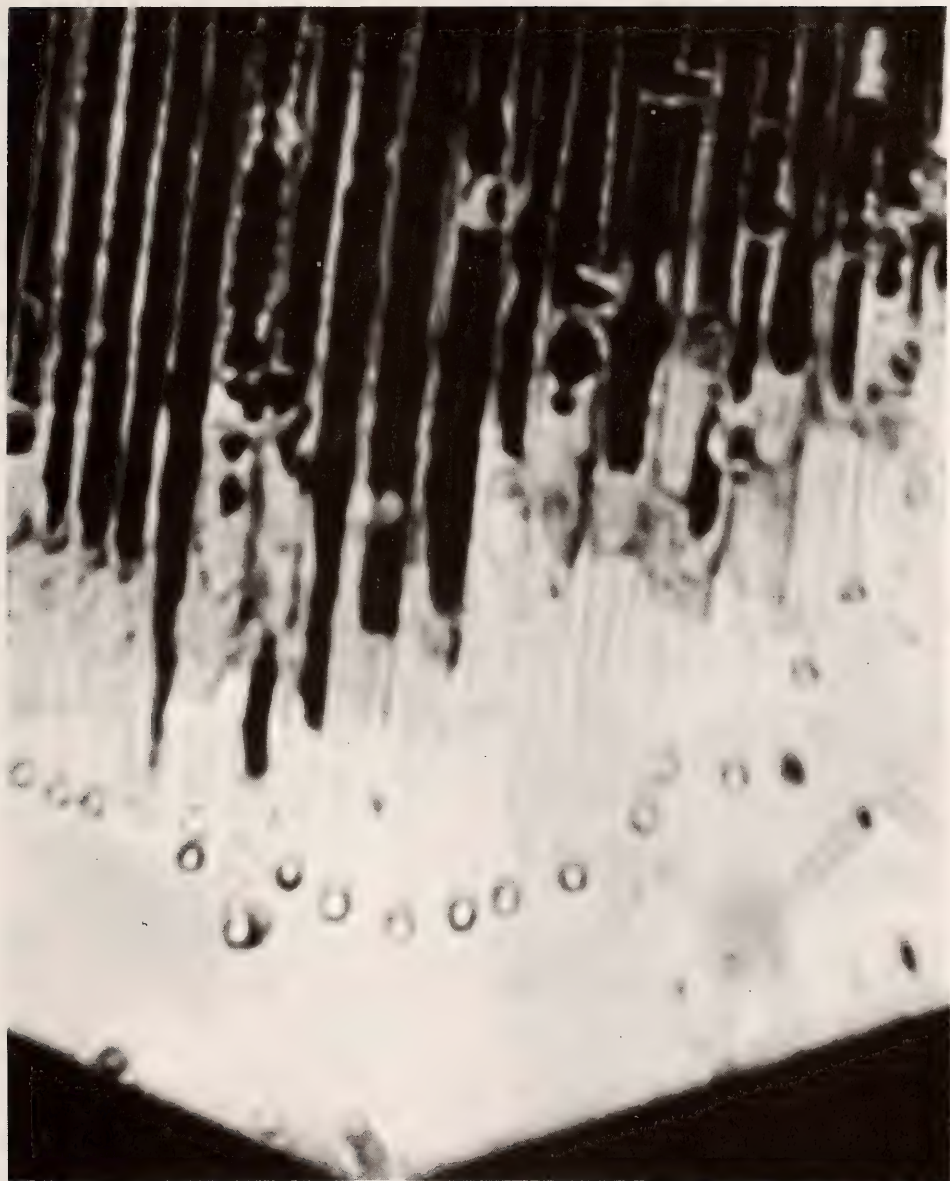


Fig. 8. View into the diamond cell of laser melting scans of basalt glass. Precipitate of metallic iron plus ferric iron-bearing phases occurs in the dark region where pressure exceeds 100 kbar; no precipitate is observed in the melted portion of the laser scan where pressure is less than 100 kbar. (Photomicrograph is slightly defocused by the diamond window; width of laser scan is 10 μm .)



Fig. 9. Photomicrograph of sample in Fig. 8 after removal from pressure cell (enlarged from Fig. 8 by a factor of 2).

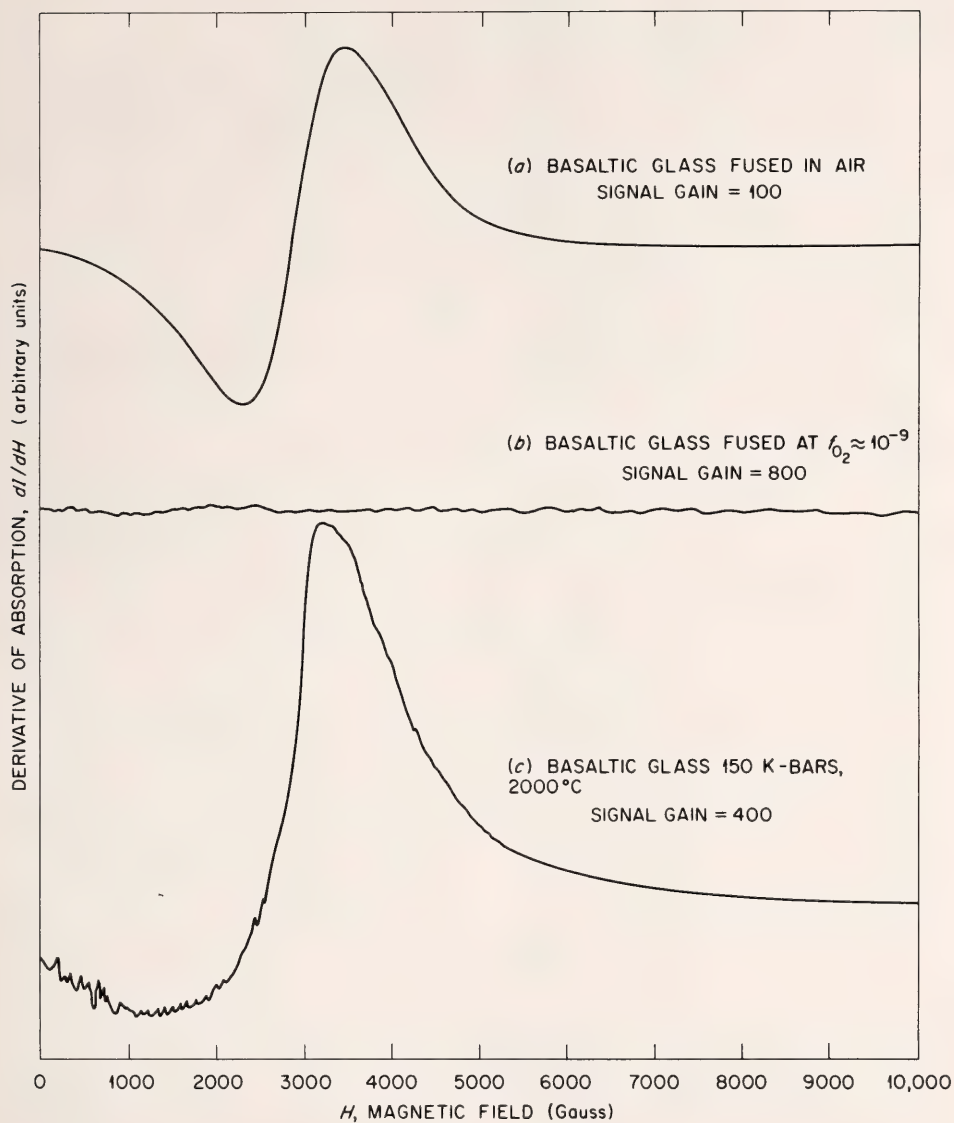


Fig. 10. Ferromagnetic resonance of (a) basalt glass fused in air, (b) basalt glass fused at $f_{O_2} \approx 10^{-9}$, (c) basalt glass run products, a sample of sixty experimental run products of reduced basalt glass (b), that had been melted at 150 kbar, 2000°C.

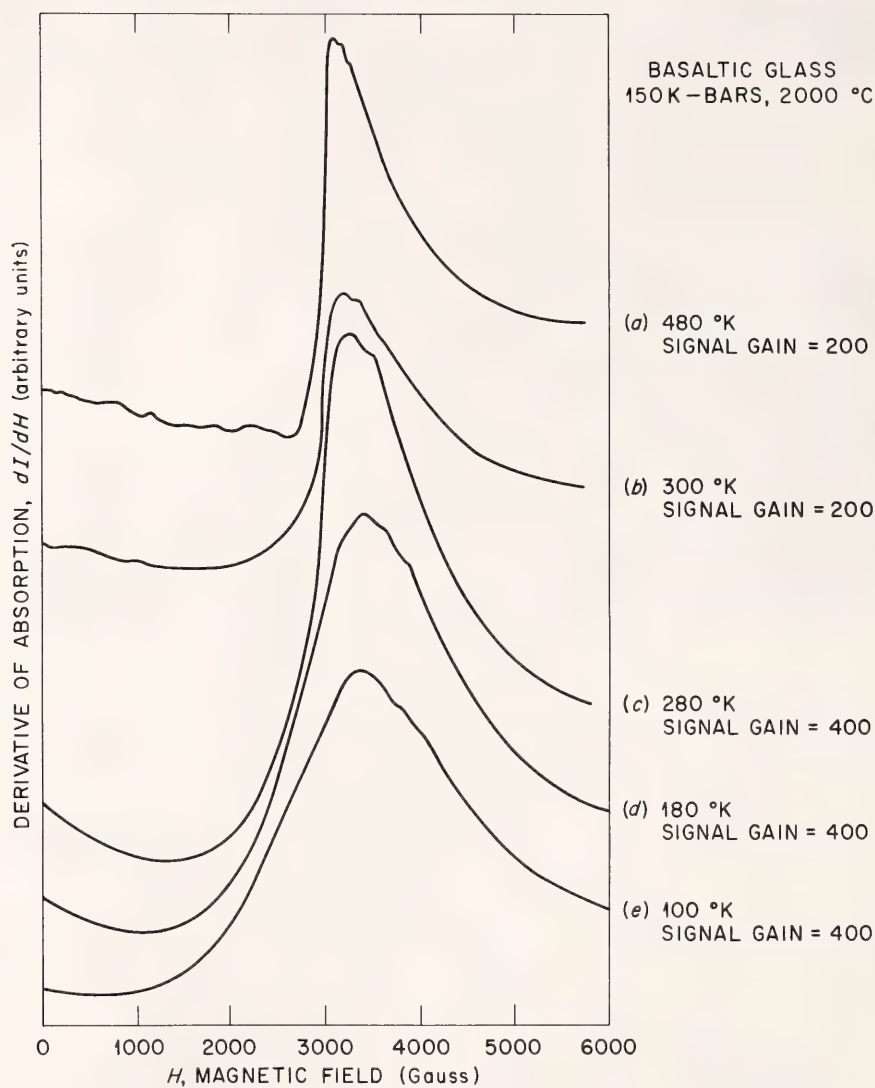


Fig. 11. Temperature dependence of ferromagnetic resonance of high-pressure fused basaltic glass.

ULTRAMAFIC ROCKS AND MINERALS

INFLECTED AND NONINFLECTED
GEOTHERMS*F. R. Boyd*

Inflected geotherms based on pyroxene geothermometry and geobarometry have now been obtained for a number of areas in southern Africa in addition to the original determination for northern Lesotho (Boyd and Nixon, 1975). These include Kimberley (Boyd and Nixon, this Report) and the Frank Smith pipe (Boyd, *Year Book* 73, p. 285) in the central portion of the Kaapvaal Craton and Farm Louwrencia in Southwest Africa (MacGregor, 1975). The Kimberley pipes and those in northern Lesotho have been dated at approximately 90 m.y., whereas those in Southwest Africa are significantly younger, about 70 m.y. (Davis, Krogh, and Erlank, this Report). Moreover, Danchin and Boyd (this Report) have obtained an inflected geotherm for the Precambrian Premier pipe, Transvaal, and this geotherm is very similar to the plots obtained for Late Cretaceous nodule suites.

Inflected geotherms thus appear to be the rule in southern Africa, regardless of age, and the data of Hearn and Boyd (1975) suggest a similar pattern for an Eocene diatreme in Montana. Nevertheless, not all geotherms based on pyroxene compositions are inflected. Boyd, Fujii, and Danchin (this Report) have determined a geotherm for the Udachnaya pipe (Late Paleozoic) in Siberia that shows no inflection whatsoever. Moreover, results obtained by McCallum and Eggler (1976) for the Sloan II diatreme (Devonian) in Colorado also suggest no inflection, although Eggler and McCallum (this Report) note that some enstatite discrete nodules from Sloan II appear to have equilibrated at temperatures above this geotherm. In view of the fact that inflections are sometimes present and sometimes not, it is suggested that the inflections based on pyroxene compositions are real and

are not an artifact of the method of estimation.

The nodule suites from most pipes in northern Lesotho show an approximately progressive increase in the degree of deformation with increasing depth of origin (e.g., Boyd and Nixon, 1975). This relationship led to the proposal that the inflection in the geotherm was caused by stress-heating during creep in the Low Velocity Zone (LVZ), and it was conjectured that the point of inflection marked the top of the LVZ. In this hypothesis the predominantly granular rocks that define the "normal" limb of the geotherm, that portion which is approximately parallel to the shield geotherm of Clark and Ringwood (1964), are interpreted to represent the base of a rigid, little-deformed lithosphere.

Subsequently, Mercier and Carter (1975) showed that creep in the LVZ was unlikely to be an adequate source of heat to produce a thermal anomaly that appears to be as large as 200°–300°C. Moreover, Goetze (1975) argued that the deformation textures exhibited by the high-temperature, sheared lherzolites were produced under conditions of high stress and strain rate and that they were produced in a short period of time ("minutes or days") prior to eruption. It thus appears that the deformation texture of these rocks may have been impressed on preexisting assemblages of minerals whose solid solutions have been largely unaffected by the deformation. Exceptions are the fine-grained groundmasses of some sheared peridotites from Kimberley that have been altered or reequilibrated or both during deformation (Boyd, *Year Book* 74, p. 525).

Some geologic evidence that has been obtained in the past several years also appears inconsistent with the stress-heating hypothesis. Lherzolite nodules with high equilibration temperatures from the Frank Smith pipe (Boyd, *Year Book* 73, p. 285) show wide variations

in degree of deformation, but they all appear to have originated at a common depth. Similar relations have been found for the nodule suite from the Sloan II pipe (McCallum and Eggler, 1976). The Kimberley lherzolites were deformed at lower temperatures (Boyd and Nixon, this Report), but here too intensely sheared rocks appear to have come from the same depth range as little-deformed rocks. Moreover Dawson, Gurney, and Lawless (1975) described wide variation in deformation in individual nodules from the Bultfontein Floors. The lherzolites with fluidal mosaic textures from Udachnaya (Boyd, Fujii, and Danchin, this Report) appear identical to intensely sheared nodules from Africa and North America, and they have equilibration temperatures near 1200°C. Nevertheless, they plot on a normal, noninflected geotherm. Clearly, these results do not support the concept of major stress-heating.

In most cases the deformation appears to have strongly affected only the most deep-seated rocks, those that had equilibrated near the maximum depths "sampled" by the kimberlite eruption. Presumably the deformation is in some way connected with the kimberlite eruption itself (e.g., Nicolas, 1975). Nevertheless in the eruption of the Kimberley pipes and possibly also at Matsoku (Harte, Cox, and Gurney, 1975) the eruptive tectonics differed in such a way that peridotites of shallower origin, with equilibration temperatures below 1100°C, have also been deformed.

It is possible that an inflected geotherm would result from convective movement of partially melted mantle. Parmentier and Turcotte (1974) have shown that an off-center thermal profile of a plume would have exactly the shape of the Lesotho geotherm. Green and Gueguen (1974) have argued that such a profile could be produced by a thermal section through the top of a diapir. Essentially what is required is that the convecting mass be sufficiently large not to cool and that it move sufficiently

slowly that there is continuous reequilibration between pyroxene and garnet, reflecting changes in depth. Unfortunately, there are insufficient diffusion data for one to be quantitative about these equilibration rates at this time.

A difficulty with the diapir hypothesis is that the depth to the point of inflection is approximately the same for northern Lesotho, Frank Smith, the Kimberley pipes, and the Premier pipe near Pretoria. In Southwest Africa this depth appears to be somewhat less (MacGregor, 1975). The Kimberley area is 400 km west of northern Lesotho, and Premier is 400 km to the north. Premier is Precambrian, whereas the kimberlites of northern Lesotho and the Kimberley area are Late Cretaceous (Allsopp, Burger, and Van Zyl, 1967; Davis, Krogh, and Erlank, this Report). Obviously the presence of a number of diapirs would have to be assumed, and if so, why is the point of inflection, which might be taken to be the top of the diapir, the same?

A Low Velocity Zone model overcomes this difficulty. Obviously it is possible to combine a diapir hypothesis with the assumed presence of a partially melted LVZ. It could be reasoned that diapirs rise through the asthenosphere and erupt as they impinge on the base of a rigid lithosphere. The fact that geotherms that are not inflected have been obtained from studies of nodule suites from Yakutia and possibly Colorado could be interpreted to mean that diapiric activity is not a prerequisite to kimberlite eruption.

A problem with a hypothesis that involves a postulated LVZ, however, is that recent seismic research suggests that differences between continental and oceanic mantles persist to depths as great as 400 km (e.g., Jordan, 1975). There is a well-defined LVZ in the oceanic mantle, but beneath the stable continental shields "this low velocity zone is weakly expressed and in some regions it may be nonexistent" (Jordan,

1975). The solution to this problem is not apparent at present.

A NONINFLECTED GEOTHERM FOR THE UDACHNAYA KIMBERLITE PIPE, USSR

F. R. Boyd, T. Fujii, and R. V. Danchin

Kimberlite pipes on the Siberian Platform are dispersed in clusters over an area that extends northward from Lake Baikal over 2000 km to the mouth of the Lena River on the Arctic Ocean. Those kimberlites that occur around the margins of the Platform are nondiamondiferous and are believed to be Late Mesozoic in age, whereas those in the central portion of the Platform are diamondiferous and are thought to be of Late Paleozoic age (Sobolev, 1974).

A group of six peridotite nodules from the diamondiferous Udachnaya kimberlite pipe are of special interest because they include both sheared lherzolites with high ($>1100^{\circ}\text{C}$) equilibration temperatures and granular peridotites with low ($<1100^{\circ}\text{C}$) equilibration temperatures. This relationship is precisely the same pattern of occurrence found for a number of localities in southern Africa and North America (Boyd, this Report). Temperature-depth estimates for five Udachnaya lherzolites, supplemented by estimates made on the basis of mineral analyses reported by Sobolev (1974), appear to define a geotherm that is *not inflected* (Fig. 12). In this respect the Udachnaya geotherm is possibly similar to that obtained for the Sloan II pipe, Colorado, by McCallum and Eggler (1976; Eggler and McCallum, this Report).

Two nodules from the nondiamondiferous Obnazhennaya pipe, described below, are not suitable for geotherm calculations because their clinopyroxenes exhibit very reduced solid solutions toward enstatite and have hence equilibrated below 900°C . However, points obtained for two granular lherzolites from an unidentified Yakutian kimberlite (which may be the Mir pipe) plot in

a temperature range distinctly lower than that defined by the Udachnaya granular xenoliths. This temperature difference of 75° – 100°C is comparable to the difference found to exist between the granular nodules from northern Lesotho (Boyd and Nixon, 1975) and the granular nodules from the Frank Smith Mine, 400 km to the west in South Africa (Boyd, *Year Book* 73, p. 285).

The fact that the Udachnaya sheared lherzolites have textures identical with those of the intensely deformed lherzolite nodules from southern Africa, yet plot on a normal, noninflected geotherm, strongly suggests that the stress-heating hypothesis proposed by Boyd (1973) is incorrect.

Udachnaya Suite

The three sheared lherzolites from the diamondiferous Udachnaya pipe show a considerable range in texture and degree of alteration. Specimens Uv-1111* and Uv-1 are very strongly serpentinized, but the original *fluidal mosaic* texture (Harte *et al.*, in preparation) can still be seen. Remnant grains of pyroxene and olivine have strained, undulate extinction. Rounded porphyroclasts of garnet with thin (0.2-mm) kelyphite rims are up to 6 mm in diameter. The serpentine in the groundmass preserves the original outlines of the olivine neoblasts, including some euhedral crystals. Dark lenticles of serpentine and magnetite (?), enveloping or trailing out from enstatite porphyroclasts, mark the original zones of disaggregated, fluidized enstatite.

Specimen UDA-1, on the other hand, is quite fresh. The texture is also mosaic, but the deformation was less intense, and there is only slight fluidization of enstatite. The rock is crowded with porphyroclasts of pyroxene and a few remaining coarse olivine grains. There are

*The specimen numbers used in this report are those that were attached to the specimens when they were received from Soviet colleagues.

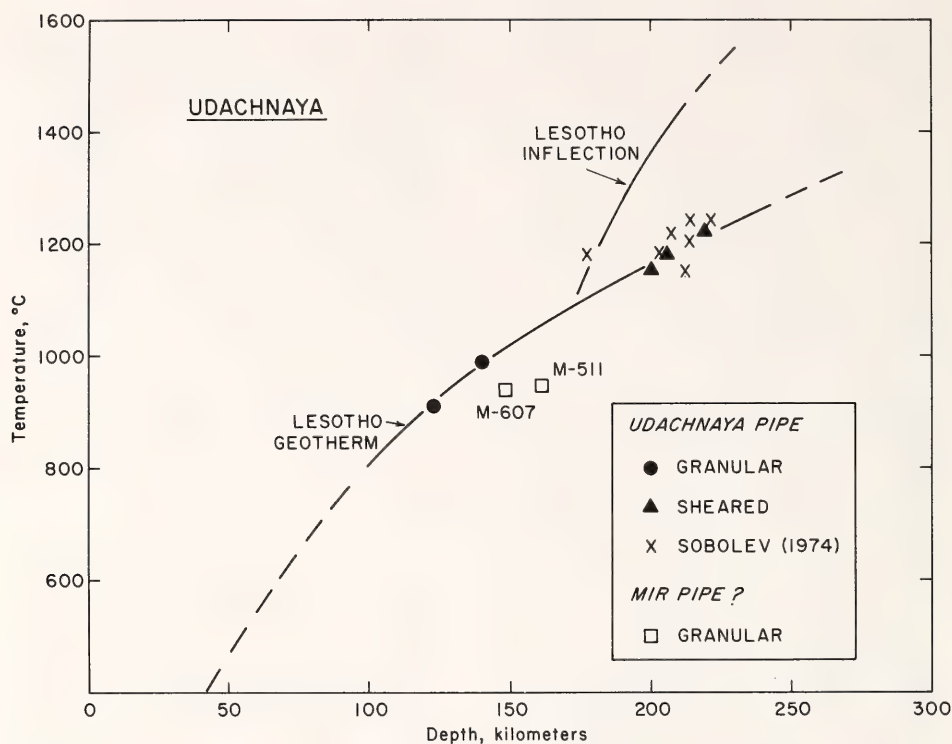


Fig. 12. Temperature-depth estimates for lherzolite nodules from the Udachnaya kimberlite pipe together with two points (M-511 and M-607) for nodules that are believed to have come from the Mir pipe. Solid and open points are calculated from analyses given in Tables 4-8. Points marked X are calculated from analyses given by Sobolev (1974). The latter are believed to be all sheared lherzolites, but this is not certain. An analysis for an enstatite in a granular lherzolite (Ud-111) given by Sobolev (1974) and quoted by Borley (1975) shows 0.33 wt % Al_2O_3 and is thus very discordant; no plot has been made for this rock. For purposes of comparison with the Lesotho geotherm (Boyd, 1973) the older phase studies of Davis and Boyd (1966) and MacGregor (1974) were used in calculating the temperature-depth points.

patches of olivine neoblasts that extinguish in near unison, marking the sites of what once were porphyroclasts. A few small, rounded garnets are up to 3 mm in size and have thick (0.5-mm) kelyphite rims.

Olivine neoblasts in these rocks have a grain size in the range 0.1–0.2 mm and are thus comparable to those found in the high-temperature ($>1100^\circ\text{C}$) sheared lherzolites from southern Africa. They are substantially coarser than neoblasts in the low-temperature ($<1100^\circ\text{C}$) sheared rocks from Kimberley (Boyd and Nixon, in preparation).

Two other lherzolites and a harzburgite from Udachnaya have coarse

granular textures (Harte *et al.*, in preparation), although these textures are somewhat obscured by extensive serpentinization. The grains are up to 6 mm in size. Some unserpentinized remnant grains of these minerals show slightly undulate extinction, and kink banding is locally present, but no second-generation olivine was observed. The garnets have very irregular, lobate and cusped boundaries with numerous inclusions of olivine. In this respect they contrast with the rounded garnets in the sheared lherzolites. Diopside is very sparse, and none at all was found in Uv-198/75.

Analytical data for the Udachnaya specimens (Tables 4, 5, and 6) reveal

many similarities to nodule suites from southern Africa. The granular Udachnaya nodules are strongly depleted, with $Mg/(Mg + Fe)$ for olivines grouping closely about an average value of 0.923. The Cr_2O_3 in the garnets is moderately rich, in the range 4–5 wt %, whereas TiO_2 is extremely low and is below the detectability level in all the minerals in two of the granular rocks (Uv-198/75, Table 4; Uv-244/75, Table 5). The garnet and enstatite in harzburgite Uv-198/75 appear saturated in Ca, despite the apparent absence of diopside.

The sheared lherzolites from Udachnaya are consistently more Fe-rich than

the granular rocks. The $Mg/(Mg + Fe)$ for the olivines show the range 0.872–0.914, with a mean value of 0.900. The average values of $Mg/(Mg + Fe)$ for olivines in the high-temperature sheared and low-temperature granular Udachnaya rocks are almost identical with those obtained for a variety of African nodule suites (Danchin and Boyd, this Report, Table 10).

In the pyroxenes and garnets from the sheared lherzolites, TiO_2 is uniformly present, in contrast to its virtual absence in the granular peridotites. This relationship exactly parallels the variations for TiO_2 found for lherzolite nodules

TABLE 4. Compositions of Minerals in Two Granular Peridotite Nodules from the Udachnaya Kimberlite Pipe, wt %

| | Uv-71/75 | | | | | | Uv-198/75 | | | |
|--------------------------------|----------|-----------|----------|-------|------------|------|-----------|-----------|------------|------|
| | Olivine | Enstatite | Diopside | | Garnet | | Olivine | Enstatite | Garnet | |
| SiO ₂ | 40.4 | 56.2 | 55.4 | 0.43* | 41.2 | 0.66 | 41.3 | 56.4 | 41.1 | 0.41 |
| TiO ₂ | <0.03 | <0.03 | <0.03 | | 0.05 | | <0.03 | <0.03 | <0.03 | |
| Al ₂ O ₃ | 0.04 | 1.04 | 2.19 | 0.17 | 20.5 | 0.26 | 0.04 | 1.07 | 19.7 | 0.19 |
| Cr ₂ O ₃ | <0.03 | 0.41 | 1.57 | 0.06 | 4.00 | 0.31 | <0.03 | 0.38 | 4.80 | 0.15 |
| FeO† | 7.72 | 4.86 | 1.44 | 0.06 | 8.11 | 0.35 | 7.28 | 4.69 | 7.93 | 0.13 |
| MnO | 0.10 | 0.13 | 0.08 | | 0.49 | 0.05 | 0.12 | 0.12 | 0.50 | 0.01 |
| MgO | 50.8 | 35.6 | 16.8 | 0.35 | 19.4 | 0.46 | 50.6 | 35.6 | 19.3 | 0.12 |
| CaO | <0.03 | 0.54 | 22.0 | 0.14 | 5.91 | 0.17 | <0.03 | 0.40 | 5.91 | 0.10 |
| Na ₂ O | n.d.‡ | 0.04 | 1.26 | 0.03 | <0.03 | | n.d. | 0.04 | <0.03 | |
| NiO | 0.42 | n.d. | n.d. | | n.d. | | 0.41 | n.d. | n.d. | |
| Totals | 99.5 | 98.8 | 100.7 | | 99.7 | | 99.8 | 98.7 | 99.2 | |
| | O = 4000 | O = 6000 | O = 6000 | | O = 12,000 | | O = 4000 | O = 6000 | O = 12,000 | |
| Si | 988 | 1954 | 1982 | | 2979 | | 1003 | 1961 | 2992 | |
| Ti | 0 | 0 | 0 | | 3 | | 0 | 0 | 0 | |
| Al | 1 | 43 | 92 | | 1745 | | 1 | 44 | 1689 | |
| Cr | 0 | 11 | 44 | | 229 | | 0 | 10 | 276 | |
| Fe | 158 | 141 | 43 | | 491 | | 148 | 136 | 483 | |
| Mn | 2 | 4 | 2 | | 30 | | 2 | 4 | 31 | |
| Mg | 1853 | 1843 | 897 | | 2096 | | 1833 | 1842 | 2093 | |
| Ca | 0 | 20 | 844 | | 458 | | 0 | 15 | 461 | |
| Na | n.d. | 3 | 87 | | 0 | | n.d. | 3 | 0 | |
| Ni | 8 | n.d. | n.d. | | n.d. | | 8 | n.d. | n.d. | |
| Totals | 3010 | 4019 | 3991 | | 8031 | | 2995 | 4015 | 8025 | |
| Ca/(Ca + Mg) | ... | 0.011 | 0.485 | | ... | | ... | 0.008 | ... | |
| Mg/(Mg + Fe) | 0.921 | 0.929 | 0.954 | | 0.810 | | 0.925 | 0.931 | 0.813 | |

* Values given in italics are for the standard deviation.

† Total Fe as FeO.

‡ Not determined.

TABLE 5. Compositions of Minerals in a Granular Lherzolite (Uv 244/75) and a Sheared Lherzolite (UDA-1) from the Udachnaya Kimberlite Pipe, wt %

| | Uv 244/75 | | | | UDA-1 | | | |
|--------------------------------|-----------|-----------|----------|------------|----------|-----------|----------|------------|
| | Olivine | Enstatite | Diopside | Garnet | Olivine | Enstatite | Diopside | Garnet |
| SiO ₂ | 41.9 | 57.7 | 55.6 | 41.9 | 40.3 | 57.3 | 54.7 | 42.5 |
| TiO ₂ | <0.03 | <0.03 | <0.03 | <0.03 | <0.03 | 0.13 | 0.26 | 0.54 |
| Al ₂ O ₃ | 0.04 | 0.97 | 1.87 | 20.0 | <0.03 | 0.57 | 1.69 | 20.0 |
| Cr ₂ O ₃ | <0.03 | 0.34 | 1.53 | 5.00 | <0.03 | 0.05 | 0.78 | 2.85 |
| FeO† | 7.39 | 4.66 | 1.47 | 7.93 | 12.4 | 7.48 | 4.78 | 9.51 |
| MnO† | 0.13 | 0.13 | 0.08 | 0.52 | 0.13 | 0.12 | 0.10 | 0.36 |
| MgO | 50.7 | 36.4 | 17.3 | 19.5 | 47.6 | 33.8 | 18.2 | 20.1 |
| CaO | <0.03 | 0.48 | 21.1 | 6.07 | <0.03 | 0.93 | 17.1 | 4.18 |
| Na ₂ O | n.d.‡ | 0.05 | 1.35 | <0.03 | <0.03 | 0.05 | 1.46 | 0.09 |
| NiO | 0.42 | n.d. | 0.07 | n.d. | 0.27 | 0.02 | <0.03 | <0.03 |
| Totals | 100.6 | 100.7 | 100.3 | 100.9 | 100.7 | 100.5 | 99.1 | 100.1 |
| | O = 4000 | O = 6000 | O = 6000 | O = 12,000 | O = 4000 | O = 6000 | O = 6000 | O = 12,000 |
| Si | 1009 | 1963 | 1995 | 2997 | 992 | 1978 | 1993 | 3046 |
| Ti | 0 | 0 | 0 | 0 | 0 | 3 | 6 | 26 |
| Al | 1 | 39 | 79 | 1687 | 0 | 23 | 71 | 1692 |
| Cr | 0 | 9 | 43 | 283 | 0 | 1 | 22 | 160 |
| Fe | 149 | 133 | 44 | 474 | 256 | 215 | 145 | 570 |
| Mn | 3 | 4 | 2 | 32 | 2 | 3 | 2 | 20 |
| Mg | 1820 | 1847 | 923 | 2079 | 1746 | 1737 | 987 | 2144 |
| Ca | 0 | 17 | 811 | 465 | 0 | 34 | 666 | 320 |
| Na | n.d. | 3 | 94 | 0 | 0 | 3 | 103 | 10 |
| Ni | 8 | n.d. | n.d. | n.d. | 5 | 0 | 0 | 0 |
| Totals | 2990 | 4015 | 3991 | 8017 | 3001 | 3997 | 3995 | 7988 |
| Ca/(Ca + Mg) | ... | 0.009 | 0.468 | ... | ... | 0.019 | 0.403 | ... |
| Mg/(Mg + Fe) | 0.924 | 0.933 | 0.954 | 0.814 | 0.872 | 0.890 | 0.872 | 0.790 |

* Values in italics are for the standard deviation.

† Total Fe as FeO.

‡ Not determined.

TABLE 6. Compositions of Minerals in Two Sheared Lherzolite Nodules from the Udachnaya Kimberlite Pipe, wt %

| | Uv-1 | | | | Uv-1111 | | | |
|--------------------------------|----------|-----------|----------|------------|----------|-----------|----------|------------|
| | Olivine | Enstatite | Diopside | Garnet | Olivine | Enstatite | Diopside | Garnet |
| SiO ₂ | 40.7 | 57.5 | 55.4 | 41.0 | 40.6 | 58.1 | 55.2 | 41.6 |
| TiO ₂ | <0.03 | 0.18 | 0.31 | 0.06 | <0.03 | 0.06 | 0.11 | 0.23 |
| Al ₂ O ₃ | <0.03 | 0.58 | 1.58 | 17.1 | <0.03 | 0.57 | 1.28 | 17.1 |
| Cr ₂ O ₃ | 0.04 | 0.28 | 1.23 | 7.87 | 0.19 | 0.30 | 0.07 | 0.88 |
| FeO† | 8.63 | 5.17 | 3.01 | 7.12 | 0.18 | 5.10 | 0.09 | 6.89 |
| MnO | 0.15 | 0.14 | 0.13 | 0.37 | 0.08 | 0.17 | 0.06 | 0.06 |
| MgO | 50.6 | 35.6 | 18.9 | 19.8 | 0.14 | 36.1 | 0.13 | 0.36 |
| CaO | 0.05 | 0.89 | 18.7 | 5.97 | 50.2 | 0.89 | 19.5 | 20.3 |
| Na ₂ O | n.d.‡ | 0.18 | 1.41 | 0.03 | 0.06 | 0.13 | 0.23 | 0.54 |
| NiO | n.d. | 0.11 | n.d. | n.d. | 0.35 | n.d. | 0.98 | 5.68 |
| Totals | 100.5 | 100.6 | 100.7 | 99.32 | 99.8 | 101.4 | 99.7 | 99.1 |
| | O = 4000 | O = 6000 | O = 6000 | O = 12,000 | O = 4000 | O = 6000 | O = 6000 | O = 12,000 |
| Si | 989 | 1966 | 1981 | 3001 | 992 | 1971 | 1988 | 3036 |
| Ti | 0 | 5 | 8 | 3 | 0 | 2 | 3 | 13 |
| Al | 0 | 23 | 67 | 1477 | 0 | 23 | 54 | 1469 |
| Cr | 1 | 8 | 35 | 456 | 1 | 8 | 28 | 397 |
| Fe | 175 | 148 | 90 | 436 | 173 | 145 | 86 | 423 |
| Mn | 3 | 4 | 4 | 23 | 3 | 5 | 4 | 22 |
| Mg | 1833 | 1818 | 1008 | 2161 | 1830 | 1823 | 1049 | 2212 |
| Ca | 1 | 33 | 717 | 469 | 2 | 32 | 721 | 444 |
| Na | n.d. | 12 | 98 | 4 | n.d. | 9 | 68 | 0 |
| Ni | 7 | 3 | n.d. | n.d. | 7 | n.d. | n.d. | n.d. |
| Totals | 3009 | 4020 | 4008 | 8030 | 3008 | 4018 | 4001 | 8016 |
| Ca/(Ca + Mg) | ... | 0.018 | 0.416 | ... | ... | 0.017 | 0.407 | ... |
| Mg/(Mg + Fe) | 0.913 | 0.925 | 0.918 | 0.832 | 0.914 | 0.927 | 0.925 | 0.839 |

* Values in italics are for the standard deviation.
† Total Fe as FeO.
‡ Not determined.

from northern Lesotho (Nixon and Boyd, 1973a) and from the Frank Smith pipe, South Africa (Boyd, *Year Book* 73, p. 285).

The Al_2O_3 content of the enstatites from the Udachnaya sheared lherzolites is about 0.6 wt %, a value markedly less than the 1.0% found for enstatites in the granular peridotites. This relationship is the exact *opposite* of the one that exists with nodule suites for which inflected geotherms are found.

The Cr_2O_3 content of the garnets from the sheared lherzolites is highly variable, ranging from 2.85 wt % (UDA-1, Table 5) to 7.87 wt % (Uv-1, Table 6). Moreover it tends to be inhomogeneous, as can be seen from the standard deviations given for the analyses. One garnet porphyroclast in UDA-1 was found to be zoned (Fig. 13), which is unusual for garnets in kimberlite nodules. Both Cr_2O_3 and Al_2O_3 are enriched in the core of the porphyroclast (Fig. 13), implying

a decrease in Fe_2O_3 , which may be reflected by the apparent increase in $\text{Mg}/(\text{Mg} + \text{Fe})$.

Obnazhennaya Nodules

One of the two nodules obtained from the nondiamondiferous Obnazhennaya pipe is an olivine-bearing garnet pyroxenite (OBJ-1) which is so rich in diopside and garnet as to appear transitional to eclogite. The texture is *coarse-granular* (Harte *et al.*, in preparation), with a grain size up to 7 mm. The garnet grains have irregular outlines and sometimes include or partially envelop pyroxene. The rock contains small (0.2–0.5 mm) grains of aluminous spinel (Table 7), which tend to be included in garnet, and there is a trace of pale phlogopite. Thin exsolution lamellae are present in both pyroxenes, and very thin plates of rutile were also observed in pyroxene and garnet. This pyroxenite is little altered; in particular the garnets have almost no kelyphite rims.

Pyroxenite OBJ-1 is magnesian (Table 7) with $\text{Mg}/(\text{Mg} + \text{Fe})$ for olivine of 0.916. Both TiO_2 and Cr_2O_3 are present in the pyroxene and garnet in low to moderate amounts. The diopside contains 23 mole % jadeite. The K_D for $(\text{Fe}/\text{Mg})_{\text{gt}}/(\text{Fe}/\text{Mg})_{\text{di}}$ is 4.283; application of the 30 kbar relation of Råheim and Green (1974) gives an equilibration temperature for OBJ-1 of 925°C. This estimate appears somewhat high in relation to the diopside solvus. Extrapolation of the solvus determination of Lindsley and Dixon (1975) indicates an equilibration temperature of ~700°C for a $\text{Ca}/(\text{Ca} + \text{Mg})$ of 0.49. Nevertheless, a low equilibration temperature, together with the fact that Al_2O_3 in the enstatite is 1.30 wt %, suggests a relatively shallow origin for OBJ-1.

The other Obnazhennaya nodule (OBJ-2) is a clinopyroxene megacryst, 4 cm in diameter, containing numerous coarse (0.5–3 mm) garnet lamellae oriented parallel to (110), (010), and (130) together with a small amount of exsolved orthopyroxene in lamellae and blebs.

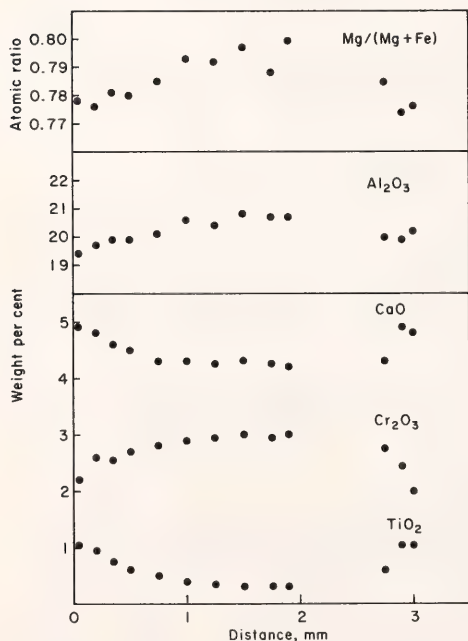


Fig. 13. Chemical variations in a scan across the full width of a garnet porphyroclast in a sheared lherzolite (UDA-1) from the Udachnaya kimberlite pipe.

TABLE 7. Compositions of Minerals in a Granular Garnet Pyroxenite (OBJ-1) and a Clinopyroxene Megacryst (OBJ-2) from the Obnazhennaya Kimberlite Pipe, wt %

| | OBJ-1 | | | | OBJ-2 | | | |
|--------------------------------|----------|-----------|----------|------------|----------|----------------|---------------|------------|
| | Olivine | Enstatite | Diopside | Garnet | Spinel | Orthopyroxene* | Clinopyroxene | Garnet* |
| SiO ₂ | 41.2 | 56.7 | 53.5 | 0.39† | 0.84 | 56.1 | 54.4 | 41.0 |
| TiO ₂ | <0.03 | 0.07 | 0.54 | 0.03 | 0.22 | 0.03 | 0.14 | 0.06 |
| Al ₂ O ₃ | <0.03 | 1.30 | 5.43 | 0.17 | 41.8 | 0.92 | 5.11 | 22.5 |
| Cr ₂ O ₃ | <0.03 | 0.32 | 2.05 | 0.07 | 26.6 | 0.06 | 0.38 | 0.36 |
| FeO‡ | 8.18 | 5.14 | 1.51 | 0.09 | 12.7 | 12.1 | 4.20 | 16.6 |
| MnO | 0.09 | 0.14 | 0.13 | 0.03 | 0.17 | 0.12 | 0.06 | 0.46 |
| MgO | 49.9 | 35.8 | 14.0 | 0.27 | 18.3 | 30.7 | 13.4 | 15.2 |
| CaO | <0.03 | 0.21 | 18.7 | 0.22 | 0.02 | 0.35 | 18.2 | 4.20 |
| Na ₂ O | <0.03 | <0.03 | 3.32 | 0.10 | <0.03 | <0.03 | 3.35 | <0.03 |
| NiO | 0.38 | <0.03 | <0.03 | 0.03 | 0.23 | 0.11 | 0.05 | <0.03 |
| Totals | 99.7 | 99.7 | 99.1 | 100.1 | 99.1 | 100.5 | 99.3 | 100.4 |
| | O = 4000 | O = 6000 | O = 6000 | O = 12,000 | O = 4000 | O = 6000 | O = 6000 | O = 12,000 |
| Si | 1004 | 1953 | 1940 | 3007 | 0 | 1977 | 1978 | 3000 |
| Ti | 0 | 1 | 14 | 2 | 4 | 0 | 3 | 2 |
| Al | 0 | 52 | 232 | 1826 | 1369 | 37 | 219 | 1940 |
| Cr | 0 | 8 | 58 | 122 | 583 | 1 | 10 | 18 |
| Fe | 167 | 147 | 45 | 545 | 294 | 356 | 127 | 1019 |
| Mn | 1 | 4 | 3 | 33 | 3 | 3 | 1 | 29 |
| Mg | 1815 | 1837 | 755 | 2124 | 756 | 1608 | 728 | 1662 |
| Ca | 0 | 7 | 727 | 348 | 0 | 12 | 708 | 328 |
| Na | 0 | 0 | 233 | 0 | 0 | 0 | 236 | 0 |
| Ni | 7 | 0 | 0 | 0 | 5 | 2 | 1 | 0 |
| Totals | 2994 | 4009 | 4007 | 8007 | 3014 | 3997 | 4009 | 7998 |
| Ca/(Ca + Mg) | ... | 0.004 | 0.491 | ... | ... | 0.007 | 0.493 | ... |
| Mg/(Mg + Fe) | 0.916 | 0.926 | 0.944 | 0.796 | 0.720 | 0.819 | 0.851 | 0.620 |

* Exsolved phase.

† Values given in italics are for the standard deviation.

‡ Total Fe as FeO.

TABLE 8. Compositions of Minerals in Two Yakutian Lherzolites, Specific Locality Unknown, wt %

| M-511 | | | | | | M-607 | | | | | | |
|------------------------------------|-------|-------|-------|--------|-------|-------|-------|-------|-------|--------|--------|------|
| | Ol | En | Di | Gt | | Ol | En | Di | Gt | | | |
| SiO ₂ | 40.9 | 57.6 | 0.36* | 0.30 | 41.9 | 0.19 | 40.7 | 0.13 | 57.4 | 0.34 | 41.8 | 0.17 |
| TiO ₂ | <0.03 | <0.03 | <0.03 | 0.04 | <0.03 | 0.25 | <0.03 | 0.03 | <0.03 | 0.02 | 0.04 | 0.23 |
| Al ₂ O ₃ | <0.03 | 0.56 | 0.04 | 0.04 | 22.2 | 0.25 | <0.03 | 0.08 | 2.64 | 0.02 | 22.5 | 0.07 |
| Cr ₂ O ₃ | <0.03 | 0.24 | 0.03 | 0.04 | 2.59 | 0.25 | <0.03 | 0.03 | 0.16 | 0.03 | 1.62 | 0.07 |
| FeO† | 6.85 | 4.07 | 0.03 | 0.03 | 7.20 | 0.17 | 8.32 | 0.05 | 5.04 | 0.04 | 8.39 | 0.18 |
| MnO | 0.06 | 0.11 | 0.05 | 0.05 | 0.41 | 0.01 | 0.07 | 0.12 | 0.05 | 0.05 | 0.39 | 0.05 |
| MgO | 51.4 | 37.4 | 0.28 | 0.13 | 21.1 | 0.08 | 50.2 | 0.22 | 36.8 | 0.07 | 20.6 | 0.33 |
| CaO | <0.03 | 0.30 | 0.20 | 0.22 | 4.80 | 0.07 | <0.03 | 0.18 | 20.9 | 0.06 | 4.68 | 0.06 |
| Na ₂ O | n.d.‡ | 0.03 | 0.03 | 0.03 | <0.03 | | n.d. | 2.06 | 0.04 | 0.05 | <0.03 | |
| NiO | 0.40 | n.d. | | n.d. | n.d. | | 0.43 | n.d. | n.d. | | n.d. | |
| Totals | 99.6 | 100.4 | 99.6 | 100.2 | 99.8 | 100.5 | 99.7 | 100.1 | 99.7 | | 100.1 | |
| Number of Cations for O = n × 1000 | | | | | | | | | | | | |
| Si | n = 4 | n = 6 | n = 6 | n = 12 | n = 4 | n = 6 | n = 6 | n = 6 | n = 6 | n = 12 | n = 12 | |
| Ti | 994 | 1963 | 1971 | 2976 | 995 | 1960 | 995 | 1977 | 1977 | 2980 | 2980 | |
| Al | 0 | 0 | 0 | 0 | 0 | 1 | 0 | 1 | 1 | 2 | 2 | |
| Cr | 1 | 22 | 91 | 1854 | 1 | 25 | 1 | 113 | 113 | 1888 | 1888 | |
| Fe | 0 | 6 | 56 | 145 | 0 | 4 | 0 | 35 | 35 | 91 | 91 | |
| Mn | 139 | 116 | 39 | 427 | 170 | 144 | 170 | 51 | 51 | 500 | 500 | |
| Mg | 1 | 3 | 2 | 25 | 1 | 3 | 1 | 2 | 2 | 24 | 24 | |
| Ca | 1863 | 1899 | 903 | 2233 | 1830 | 1873 | 1830 | 887 | 887 | 2188 | 2188 | |
| Na | 1 | 11 | 823 | 365 | 0 | 13 | 0 | 811 | 811 | 357 | 357 | |
| Ni | n.d. | 2 | 141 | 0 | n.d. | 3 | n.d. | 144 | 144 | 0 | 0 | |
| | 8 | n.d. | n.d. | n.d. | 8 | n.d. | 8 | n.d. | n.d. | n.d. | n.d. | |
| Totals | 3006 | 4023 | 4026 | 8025 | 3005 | 4026 | 3005 | 4020 | 4020 | 8029 | 8029 | |
| Mg/(Mg + Fe) | 0.930 | 0.942 | 0.958 | 0.839 | 0.915 | 0.929 | 0.915 | 0.946 | 0.946 | 0.814 | 0.814 | |
| Ca/(Ca + Mg) | ... | 0.005 | 0.477 | ... | ... | 0.007 | ... | 0.478 | 0.478 | ... | ... | |

*Values in italics are for the standard deviation.

† Total Fe as ferrous iron.

‡ Not determined.

The phases in OBJ-2 are homogeneous except for Na and Al in the host clinopyroxene; Na_2O varies in the range 2.6–3.9 wt %. The minerals in OBJ-2 are considerably more Fe-rich than those in OBJ-1 (Table 7), but their chemical features are otherwise similar. Presumably this megacryst originated by disruption of an ultracoarse pyroxenite.

Yakutian Nodules, Locality Unknown

Two coarse granular nodules studied in this investigation have specimen numbers (M-511 and M-607) suggesting that the nodules might have come from the Mir pipe, but this identification is uncertain. These rocks are somewhat richer in diopside and in rounded to irregular grains of garnet than are the Udachnaya granular nodules. Olivine and enstatite grains up to 5 mm in size show considerable strain with well-developed kink bands and undulate extinction. Fine exsolution lamellae are present in some grains of both pyroxenes and are probably responsible for the unusually high standard deviations for CaO in the enstatite analyses (Table 8).

These granular nodules are quite magnesian with $\text{Mg}/(\text{Mg} + \text{Fe})$ for olivine of 0.915 and 0.930. The TiO_2 content is extremely low in both rocks, but Cr_2O_3 is also rather low (e.g., 1.62 and 2.59 wt % in the garnets, Table 8). The Al_2O_3 content in the enstatites is 0.56 and 0.63 wt %, much lower than for enstatites in the Udachnaya granular rocks, and therefore their temperature-depth points do not fit the Udachnaya geotherm (Fig. 12).

ULTRAMAFIC NODULES FROM THE PREMIER KIMBERLITE PIPE, SOUTH AFRICA

R. V. Danchin and F. R. Boyd

Discovery of a large and varied suite of ultramafic nodules in the Precambrian Premier kimberlite pipe, near Pretoria, has provided an extraordinary opportunity to determine the chemical

characteristics and thermal structure of the African mantle as it existed over a billion years ago. Extensive studies of Late Cretaceous (70–90 m.y., Davis, Krogh, and Erlank, this Report) nodule suites in recent years have shown that the mantle beneath southern Africa is strongly depleted of basaltic constituents to a depth of the order of 150 km and somewhat depleted in the depth range 150–200 km. Many petrologists have wondered if this depletion was connected with the vast outpouring of Karroo basalts that covered southern Africa 150–190 m.y. ago (Fitch and Miller, 1971). Yet our preliminary studies of the Premier nodules show them to be extremely similar in mineral composition and texture to the Late Cretaceous nodules. Moreover, a geotherm obtained from Premier nodules (Fig. 14) is very similar to the inflected Late Cretaceous geotherms found for northern Lesotho and other areas in southern Africa (e.g., Boyd and Nixon, this Report).

The implications of this discovery are quite far-reaching. These data suggest that the chemical and thermal evolution of the upper 200 km of the African mantle was essentially complete by at least 1115 m.y. ago, the age of the Premier kimberlite (Allsopp, Burger, and Van Zyl, 1967; Barrett and Allsopp, 1973). The source of the Karroo basalts may thus have been a section of mantle deeper than that sampled by the kimberlite eruptions.

The Premier nodule suite resembles those from localities in northern Lesotho and South Africa in that it includes garnet lherzolites, garnet harzburgites, dunites, garnet-free chromite peridotites and harzburgites, and eclogites, as well as a suite of megacrysts consisting chiefly of garnet, diopside, enstatite, and ilmenite. The garnet lherzolites may be subdivided into two groups that differ markedly in both texture and mineral chemistry. The first category consists of coarse-grained granular and tabular rocks that are strongly depleted in basaltic constituents and are believed to

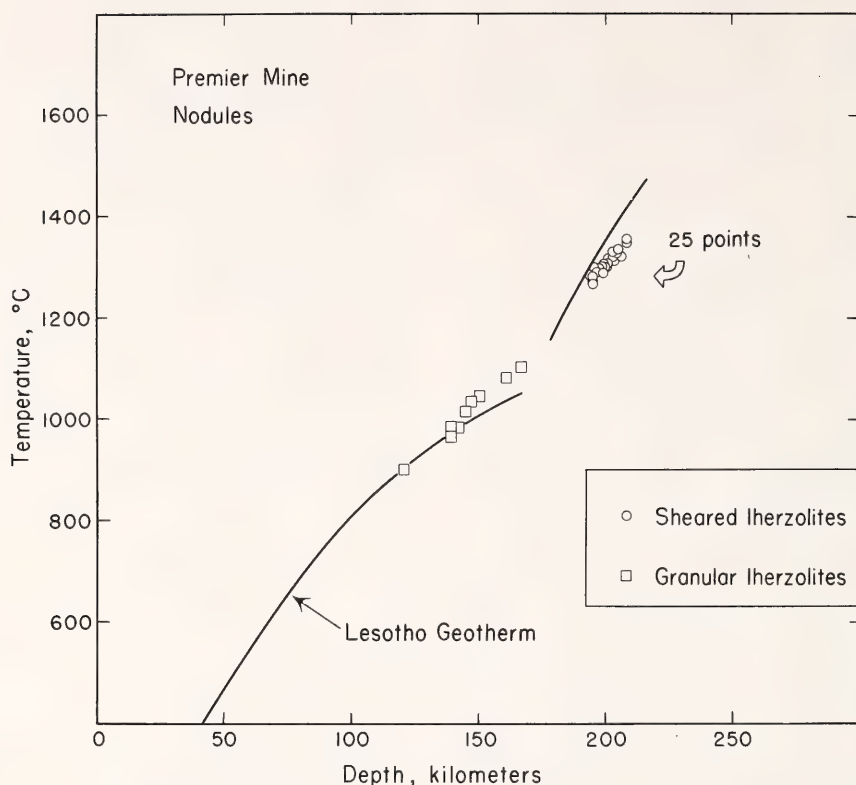


Fig. 14. Estimates of the temperatures and depths of equilibration of 34 garnet lherzolite nodules from the Premier Mine compared with the Lesotho geotherm (Boyd and Nixon, *Year Book 72*).

have originated at depths of 100–160 km (Fig. 14). The second group is represented by deformed, extensively recrystallized, garnet-rich lherzolites, whose textures vary from porphyroclastic to fluidal mosaic, that are believed to have been derived from depths of the order of 200 km. This pattern is precisely the same as that found for most Late Cretaceous pipes in southern Africa.

Variations in Cr_2O_3 and TiO_2 contents are most easily studied in the garnets and are of interest because Cr is thought to be concentrated in residual rocks, whereas Ti may be concentrated either by fractionation or metasomatism. The garnets in the sheared lherzolites are reddish brown and are characterized by unusually high titanium content—in several samples, values of almost 2%

TiO_2 were recorded (e.g., RVD 101, Table 9). The garnets in the granular lherzolites, by contrast, have a mauve color and an average TiO_2 content of 0.2%. The Na_2O content is likewise depleted in the latter garnets, and the two groups have average Na_2O contents of 0.10 and 0.05%, respectively. Chromium contents vary erratically in garnets from both groups, particularly in the granular rocks where strong zoning was observed in several instances. Representative analyses of minerals from both lherzolite types are given in Table 9.

Differences in the compositions of olivines and pyroxenes in the sheared and granular suites are also marked. In the sheared lherzolites both minerals are more iron-rich and have significantly higher Ti, Ca, and Al contents than

TABLE 9. Compositions of Minerals in Representative Sheared and Granular Lherzolites from the Premier Mine, wt %

| | RVD 106 | | | | RVD 101 | | | | RVD 181 | | | | RVD 155 | | | |
|------------------------------------|---------|-------|-------|--------|---------|-------|-------|--------|---------|-------|-------|--------|---------|-------|-------|--------|
| | Ol | En | Di | Gt | Ol | En | Di | Gt | Ol | En | Di | Gt | Ol | En | Di | Gt |
| SiO ₂ | 40.8 | 56.7 | 54.9 | 42.1 | 40.6 | 57.1 | 54.7 | 41.2 | 41.4 | 57.6 | 54.6 | 41.4 | 41.0 | 57.6 | 54.8 | 42.3 |
| TiO ₂ | <0.03 | 0.26 | 0.50 | 1.10 | 0.03 | 0.36 | 0.65 | 1.86 | <0.03 | 0.13 | 0.28 | 0.50 | <0.03 | <0.03 | <0.03 | <0.03 |
| Al ₂ O ₃ | 0.05 | 1.00 | 2.24 | 18.1 | 0.05 | 0.97 | 2.21 | 17.2 | 0.04 | 0.93 | 2.35 | 18.6 | <0.03 | 0.99 | 2.76 | 21.8 |
| Cr ₂ O ₃ | 0.08 | 0.40 | 1.36 | 5.22 | 0.07 | 0.42 | 1.37 | 5.74 | <0.03 | 0.43 | 2.21 | 6.21 | <0.03 | 0.24 | 1.34 | 2.16 |
| FeO* | 8.48 | 5.23 | 3.45 | 6.46 | 8.70 | 5.20 | 3.35 | 7.00 | 6.67 | 4.11 | 2.13 | 5.84 | 7.64 | 4.71 | 2.01 | 6.88 |
| MnO | 0.12 | 0.14 | 0.12 | 0.32 | 0.14 | 0.17 | 0.16 | 0.33 | 0.11 | 0.11 | 0.10 | 0.32 | 0.09 | 0.13 | 0.07 | 0.37 |
| MgO | 49.9 | 34.4 | 19.8 | 21.3 | 49.7 | 34.6 | 19.7 | 21.1 | 51.1 | 35.8 | 17.4 | 21.4 | 50.8 | 35.8 | 16.7 | 21.7 |
| CaO | 0.08 | 1.26 | 15.4 | 5.05 | 0.09 | 1.22 | 15.4 | 5.52 | 0.08 | 0.67 | 18.9 | 5.52 | 0.03 | 0.47 | 20.4 | 4.59 |
| Na ₂ O | n.d.† | 0.36 | 1.90 | 0.12 | n.d. | 0.37 | 1.85 | 0.14 | 1 | 0.19 | 2.01 | 0.11 | n.d. | 0.07 | 1.76 | <0.03 |
| NiO | 0.38 | n.d. | n.d. | n.d. | 0.38 | n.d. | n.d. | n.d. | 0.40 | n.d. | n.d. | n.d. | 0.42 | n.d. | n.d. | n.d. |
| Totals | 99.9 | 99.8 | 99.7 | 99.7 | 99.7 | 100.4 | 99.4 | 100.1 | 99.8 | 100.0 | 100.0 | 99.9 | 100.0 | 100.0 | 99.8 | 99.9 |
| Number of Cations for O = n × 1000 | | | | | | | | | | | | | | | | |
| Si | n = 4 | n = 6 | n = 6 | n = 12 | n = 4 | n = 6 | n = 6 | n = 12 | n = 4 | n = 6 | n = 6 | n = 12 | n = 4 | n = 6 | n = 6 | n = 12 |
| Ti | 997 | 1961 | 1971 | 3025 | 995 | 1961 | 1971 | 2979 | 1003 | 1970 | 1970 | 2976 | 996 | 1971 | 1978 | 3003 |
| Al | 0 | 7 | 14 | 59 | 1 | 9 | 18 | 101 | 0 | 3 | 8 | 27 | 0 | 0 | 0 | 0 |
| Cr | 1 | 41 | 95 | 1530 | 1 | 39 | 94 | 1463 | 1 | 38 | 100 | 1577 | 0 | 40 | 117 | 1824 |
| Fe* | 2 | 11 | 39 | 297 | 1 | 11 | 39 | 328 | 0 | 12 | 63 | 353 | 0 | 6 | 38 | 121 |
| Mn | 173 | 151 | 104 | 388 | 178 | 149 | 101 | 423 | 135 | 118 | 64 | 351 | 155 | 135 | 61 | 408 |
| Mg | 2 | 4 | 4 | 19 | 3 | 5 | 5 | 20 | 2 | 3 | 3 | 19 | 2 | 4 | 2 | 22 |
| Mg | 1816 | 1773 | 1062 | 2285 | 1815 | 1772 | 1059 | 2273 | 1845 | 1828 | 935 | 2295 | 1840 | 1829 | 898 | 2294 |
| Ca | 2 | 47 | 594 | 389 | 2 | 45 | 593 | 427 | 2 | 25 | 728 | 425 | 1 | 17 | 787 | 349 |
| Na | n.d. | 24 | 132 | 17 | n.d. | 25 | 129 | 20 | n.d. | 13 | 140 | 15 | n.d. | 5 | 123 | 3 |
| Ni | 7 | n.d. | n.d. | n.d. | 7 | n.d. | n.d. | n.d. | 8 | n.d. | n.d. | n.d. | 8 | n.d. | n.d. | n.d. |
| Totals | 3001 | 4018 | 4015 | 8010 | 3003 | 4017 | 4009 | 8034 | 2996 | 4008 | 4011 | 8039 | 3003 | 4008 | 4005 | 8025 |
| Mg/(Mg + Fe) | 0.913 | 0.921 | 0.911 | 0.855 | 0.911 | 0.922 | 0.913 | 0.843 | 0.932 | 0.940 | 0.936 | 0.867 | 0.922 | 0.931 | 0.937 | 0.849 |
| Ca/(Ca + Mg) | | 0.026 | 0.359 | | | 0.250 | 0.359 | | | 0.013 | 0.438 | | | 0.009 | 0.467 | |

* Total Fe as ferrous iron.

† Not determined.

RVD 106: sheared lherzolite; fluidal mosaic texture.

RVD 101: sheared lherzolite; porphyroclastic-mosaic.

RVD 181: coarse-granular lherzolite.

RVE 155: tabular lherzolite.

those in the granular lherzolites. Also, enstatites from the sheared rocks are enriched in Na compared with those from the granular suite.

Average olivine compositions for the two Premier lherzolite suites are given in Table 10, where they are compared with lherzolite olivines from four other southern African kimberlite suites. The $Mg/(Mg + Fe)$ of olivines from high-temperature ($>1100^{\circ}C$) lherzolites are tightly clustered about a mean value of 0.906 and are significantly lower than those for olivines in low-temperature ($<1100^{\circ}C$) lherzolites, which likewise exhibit only marginal deviation about a mean value of 0.926.

Estimates of temperatures and depths of equilibration of the Premier lherzolites are compared with the Lesotho geotherm of Boyd and Nixon (1975) in Fig. 14. Equilibration temperatures were calculated from the $Ca/(Ca + Mg)$ of the diopsides (Boyd, 1973), using the diopside solvus determined by Davis and Boyd (1966). Equilibration pressures were estimated from isopleths determined for the system $MgSiO_3-Al_2O_3$ by MacGregor (1974). The purpose of this plot is simply comparative, and for this reason more recent and improved phase studies were not used.

Garnet harzburgites included in the Premier nodule suite may be subdivided into three distinct groups that differ markedly from one another with respect

to both mineral chemistry and degree of deformation. Representative mineral analyses for rocks of each type are given in Table 11. Group I harzburgites have mosaic or fluidal mosaic textures and mineral compositions equivalent to those of the sheared lherzolites described above (e.g., RVD 146). Within the group the TiO_2 and Na_2O contents correlate closely with $Mg/(Mg + Fe)$ of each of the three major phases present. Group III rocks (e.g., RVD 183) have granular textures and mineral compositions comparable to those of the granular lherzolites. Group II harzburgites (e.g., RVD 127) are intermediate between these two extremes, notably with respect to the $Mg/(Mg + Fe)$ of the component minerals, the $Ca/(Ca + Mg)$ of the enstatites, and the TiO_2 contents of the garnets and enstatites. Also, these rocks are not so intensely deformed as those assigned to group I.

Figure 15 is a plot of CaO versus Cr_2O_3 for the garnets from lherzolites and harzburgites. The lherzolites and group I harzburgites exhibit a high degree of positive correlation characteristic of lherzolite sequences (Sobolev *et al.*, 1973). The group II and group III garnets, however, do not form a part of this trend and are enriched to varying degrees in chromium relative to calcium. Moreover, these garnets, particularly RVD 183, which contains 10.2% Cr_2O_3 and 3.9% CaO , plot within the field of garnets occurring as inclusions in natural diamonds (Sobolev *et al.*, 1969; Meyer and Boyd, 1972; Meyer and Svisero, 1975; Prinz *et al.*, 1975). Mauve garnet megacrysts from Premier Mine concentrate (Lawless, 1974) are likewise unassociated with the lherzolite trend and plot with the harzburgites in the diamond inclusion field.

Harzburgite RVD 183 was found to contain chromite whose composition, like the coexisting garnet, is identical to that of chromites found as inclusions in diamond (Sobolev *et al.*, 1969; Meyer and Boyd, 1972; Prinz *et al.*, 1975). One garnet-free harzburgite (RVD 182, Ta-

TABLE 10. Comparison of Average $Mg/(Mg + Fe)$ in Olivines of Five Garnet Lherzolite Nodule Suites from the Kimberlites of Southern Africa

| | High Temperature* ($>1100^{\circ}C$) | Low Temperature ($<1100^{\circ}C$) |
|------------------|---|---|
| Premier | 0.907 | 0.922 |
| Northern Lesotho | 0.905 | 0.930 |
| Kimberley | ... | 0.928 |
| Frank Smith | 0.907 | 0.929 |
| Angola | ... | 0.922 |

* Equilibration temperatures based on the diopside solvus.

TABLE 11. Minerals in Representative Garnet Harzburgites and a Granular Chromite-Spinel Harzburgite from the Premier Mine, wt %

| | Group I RVD 146 | | | | Group II RVD 127 | | | | Group III RVD 183 | | | | RVD 182 | | | |
|------------------------------------|--------------------|-------|--------|-------|---------------------|--------|-------|--------|----------------------|--------|-------|-------|---------|-------|-------|--|
| | Ol | En | Gt | | Ol | En | Gt | | Ol | En | Gt | Chr | Ol | En | Chr | |
| SiO ₂ | 40.7 | 57.0 | 41.2 | 41.1 | 57.3 | 41.2 | 41.5 | 41.4 | 57.7 | 41.4 | 41.4 | 0.20 | 41.4 | 58.0 | 0.24 | |
| TiO ₂ | 0.03 | 0.29 | 1.82 | <0.03 | 0.04 | 0.23 | <0.03 | <0.03 | <0.03 | <0.03 | <0.03 | 0.05 | <0.03 | <0.03 | <0.03 | |
| Al ₂ O ₃ | 0.05 | 0.95 | 16.4 | 0.03 | 0.86 | 18.8 | 0.03 | 16.5 | 0.85 | 16.5 | 8.58 | 8.58 | <0.03 | 0.21 | 4.07 | |
| Cr ₂ O ₃ | 0.08 | 0.51 | 6.44 | 0.06 | 0.38 | 5.89 | 0.06 | 10.2 | 0.67 | 10.2 | 62.2 | 62.2 | <0.03 | 0.14 | 66.9 | |
| Fe ₂ O ₃ | ... | ... | ... | ... | ... | ... | ... | ... | ... | ... | 3.60* | 3.60* | ... | ... | 1.44 | |
| FeO | 9.10† | 5.41 | 7.21 | 7.14 | 4.16 | 5.75 | 5.18 | 4.68 | 3.13 | 4.68 | 9.41 | 9.41 | 6.14 | 3.82 | 14.3 | |
| MnO | 0.15 | 0.13 | 0.32 | 0.10 | 0.11 | 0.30 | 0.08 | 0.30 | 0.06 | 0.30 | 0.28 | 0.28 | 0.10 | 0.09 | 0.46 | |
| MgO | 49.5 | 34.0 | 20.7 | 51.1 | 36.3 | 22.8 | 52.3 | 23.1 | 37.1 | 23.1 | 15.6 | 15.6 | 51.8 | 37.4 | 11.7 | |
| CaO | 0.11 | 1.26 | 5.41 | 0.06 | 0.82 | 4.26 | <0.03 | 3.93 | 0.45 | 3.93 | <0.03 | <0.03 | <0.03 | 0.08 | 0.04 | |
| Na ₂ O | n.d.‡ | 0.33 | 0.15 | n.d. | 0.08 | 0.03 | n.d. | <0.03 | 0.10 | <0.03 | n.d. | n.d. | n.d. | 0.04 | n.d. | |
| NiO | 0.36 | n.d. | n.d. | 0.38 | n.d. | n.d. | 0.42 | n.d. | n.d. | n.d. | 0.14 | 0.14 | 0.40 | n.d. | 0.10 | |
| Totals | 100.1 | 99.9 | 99.9 | 100.0 | 100.0 | 99.9 | 99.6 | 100.2 | 100.0 | 100.2 | 100.1 | 100.1 | 99.9 | 99.8 | 99.2 | |
| Number of Cations for O = n × 1000 | | | | | | | | | | | | | | | | |
| Si | n = 4 | n = 6 | n = 12 | n = 4 | n = 6 | n = 12 | n = 4 | n = 12 | n = 6 | n = 12 | n = 4 | n = 4 | n = 4 | n = 6 | n = 4 | |
| Ti | 996 | 1969 | 3001 | 997 | 1962 | 2994 | 1000 | 2978 | 1965 | 2978 | 6 | 6 | 1000 | 1980 | 8 | |
| Al | 1 | 8 | 100 | 0 | 1 | 12 | 0 | 1 | 0 | 1 | 1 | 1 | 0 | 0 | 1 | |
| Cr | 1 | 39 | 1407 | 1 | 35 | 1579 | 1 | 1400 | 34 | 1400 | 324 | 324 | 0 | 8 | 162 | |
| Cr | 2 | 14 | 371 | 1 | 10 | 333 | 1 | 578 | 18 | 578 | 1575 | 1575 | 0 | 4 | 1784 | |
| Fe ³⁺ | ... | ... | ... | ... | ... | ... | ... | ... | ... | ... | 87* | 87* | ... | ... | 37 | |
| Fe ²⁺ | 186 | 156 | 439 | 145 | 119 | 343 | 104 | 281 | 89 | 281 | 252 | 252 | 124 | 109 | 403 | |
| Mn | 3 | 4 | 20 | 2 | 3 | 18 | 2 | 18 | 2 | 18 | 8 | 8 | 2 | 3 | 13 | |
| Mg | 1803 | 1751 | 2242 | 1847 | 1851 | 2430 | 1881 | 2472 | 1881 | 2472 | 744 | 744 | 1865 | 1906 | 588 | |
| Ca | 3 | 47 | 422 | 2 | 30 | 326 | 1 | 303 | 16 | 303 | 1 | 1 | 0 | 3 | 1 | |
| Na | n.d. | 22 | 21 | n.d. | 5 | 4 | n.d. | 7 | n.d. | 7 | 3 | n.d. | n.d. | 3 | n.d. | |
| Ni | 7 | n.d. | n.d. | 7 | n.d. | n.d. | 8 | n.d. | n.d. | n.d. | 4 | 4 | 8 | n.d. | 3 | |
| Totals | 3002 | 4009 | 8021 | 3002 | 4017 | 8040 | 2999 | 8034 | 4012 | 8034 | 3000§ | 3000§ | 3000 | 4015 | 3000§ | |
| Mg/(Mg + Fe) | 0.906 | 0.918 | 0.836 | 0.927 | 0.940 | 0.876 | 0.947 | 0.898 | 0.955 | 0.898 | 0.747 | 0.747 | 0.938 | 0.946 | 0.593 | |
| Ca/(Ca + Mg) | ... | 0.026 | ... | ... | 0.016 | ... | ... | ... | 0.009 | ... | ... | ... | ... | 0.002 | ... | |

* Ferric iron calculated from mineral formula.

† Total Fe as ferrous iron.

‡ Not determined.

§ Cation total normalized in course of Fe²⁺ calculation.

RVD 146: garnet harzburgite; mosaic texture.
 RVD 127: porphyroclastic garnet harzburgite.
 RVD 183: coarse-granular garnet harzburgite.
 RVD 182: granular chromite-spinel harzburgite.

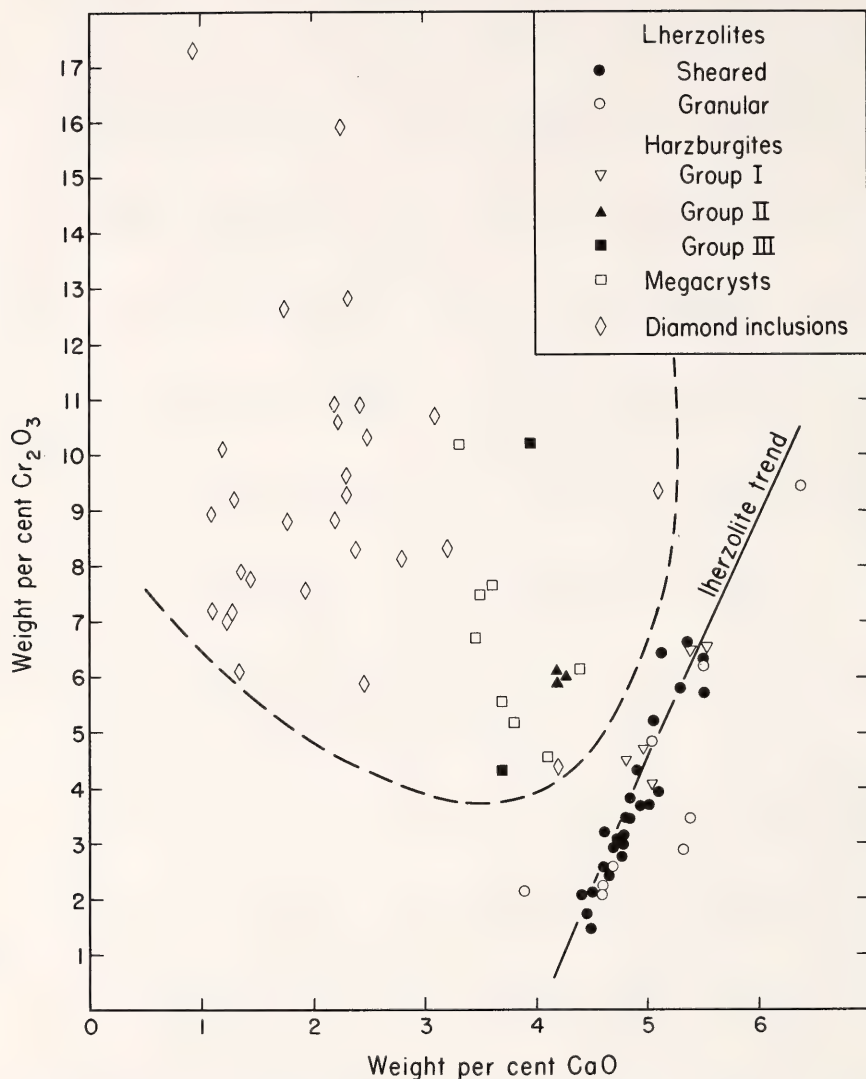


Fig. 15. Plot of CaO versus Cr_2O_3 (wt %) for Iherzolite and harzburgite garnets from Premier Mine compared with Iherzolite-type garnets included in diamond (Sobolev *et al.*, 1969; Meyer and Boyd, 1972; Meyer and Svisero, 1975; Prinz *et al.*, 1975) and mauve garnet megacrysts from Premier Mine concentrate (Lawless, 1974).

ble 11) is of interest in this context in that it contains 67% Cr_2O_3 and less than 0.03% TiO_2 , and is therefore also directly comparable with chromites included in natural diamond. The enstatites and olivines in each of these rocks are extremely magnesian, and $\text{Mg}/(\text{Mg} + \text{Fe})$ is 0.95 and 0.94, respectively.

Temperature-depth estimates for the nine garnet harzburgites (Fig. 16) depend on the assumption that the enstatites are saturated in Ca despite the apparent absence of diopside. The group II and group III garnets are obviously not saturated in Ca, but the fact that points for these rocks fit the Iherzolite

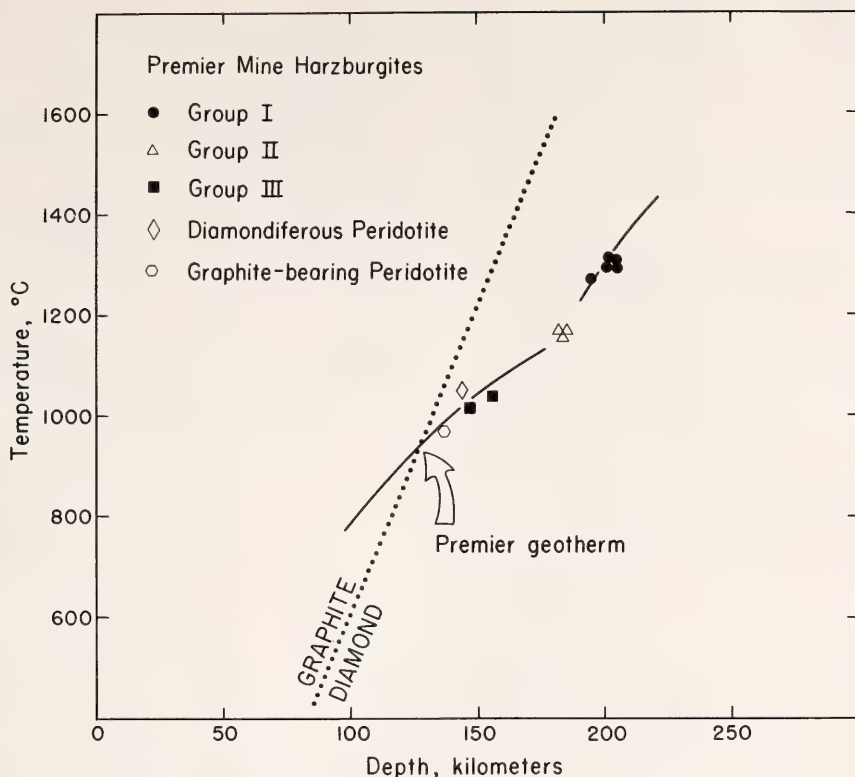


Fig. 16. Temperature-depth relations for harzburgites from the Premier Mine compared with the lherzolite geotherm (Fig. 14), a diamond-bearing peridotite (Dawson and Smith, 1975), and a graphite-bearing peridotite (Nixon and Boyd, 1973a; Boyd and Finger, *Year Book* 74).

geotherm (Fig. 16) suggests that the enstatites still are approximately Ca-saturated.

The group II and group III harzburgites thus appear to have equilibrated in the range 1000°–1200°C between 140 and 180 km, and it is significant that this range encompasses the P - T estimate for the only known diamond-bearing garnet lherzolite (Dawson and Smith, 1975). McCallum and Eggler (1976) show a point for their serpentinized diamond-bearing peridotite, based on data for lherzolites with similar textures, and it plots close to the Dawson and Smith point. The garnet in the nodule described by McCallum and Eggler is compositionally equivalent to those of the harzburgite association in that it

contains 12% Cr_2O_3 and 4.7% CaO (cf. RVD 183, Table 11). Also shown in Fig. 16 is a point for graphite-bearing nodule PHN 1569, in which the graphite occurs in ± 1 -mm primary-appearing flakes (Nixon and Boyd, 1973a; Boyd and Finger, *Year Book* 74, Table 21). The graphite peridotite point plots at slightly lower temperature and shallower depth than the diamond peridotite point (Fig. 16), and the two may constitute a bracket on the diamond/graphite equilibrium boundary. The discrepancy (Fig. 16) is well within the uncertainty of pyroxene barometry.

The compositional similarity between the garnets in these harzburgites and the most abundant type of garnet found as inclusions in diamond suggests that such

harzburgites may be a common source rock for diamond. It would thus appear that the rocks of deepest origin (Fig. 14) are not those in which diamonds have commonly formed. In fact the data in Fig. 16 suggest that many diamonds may have formed close to the boundary of the diamond stability field.

A GEOTHERM FROM MEGACRYSTS IN
THE SLOAN KIMBERLITE PIPES,
COLORADO*

David H. Eggler and M. E. McCallum

The discovery of diamonds in concentrates of kimberlites on the Colorado-Wyoming state line (McCallum and Mabarak, 1976) and the further discovery of diamonds in a peridotite nodule from one of these pipes (McCallum and Eggler, 1976) have attracted widespread attention to these Paleozoic diatremes. A fossil geotherm in the region from which these diamonds originated has been derived from studies of a limited number of peridotite nodules (McCallum and Eggler, 1976). To define this geotherm further, two assemblages of megacrysts have been examined, particularly orthopyroxene (opx) crystals from each suite, because orthopyroxenes from megacryst assemblages have been shown to be effective single-phase geobarometers and thermometers (Boyd and Nixon, 1973).

Two compositionally distinct groups of megacrysts (discrete nodules >2 cm in diameter) occur in all these pipes, but unaltered opx megacrysts amenable to geobarometry are preserved in only one diatreme, Sloan 2. In order to define the compositional limits of other megacryst phases that may have been in equilibrium with the opx, megacrysts from only this pipe and its close neighbor, Sloan 1, are described here, although megacrysts are found in all the diatremes on the state line (McCallum, Eggler, and

Burns, 1975) and in dikes in the Iron Mountain district (McCallum *et al.*, 1975; Smith, McCallum, and Eggler, this Report).

The ranges of chemical parameters of the two suites (Table 12) in general adjoin but do not significantly overlap. The compositions of the Cr-rich megacrysts are similar to those of minerals of lherzolites and harzburgites believed to be residual (depleted) and are particu-

TABLE 12. Ranges of Chemical Parameters of Minerals in Two Megacryst Assemblages and in Peridotites from the Sloan 2 Kimberlite Pipe, Colorado, wt %

| | Cr-Rich Mega- crysts | Cr-Poor Mega- crysts | Lherzo- lites and Harz- burgites |
|--------------------------------|----------------------------|----------------------------|---|
| Garnets | | | |
| | (n = 32) | (n = 11) | (n = 6) |
| TiO ₂ | 0.6-0.9 | 0.7-1.1 | 0.2-1.2 |
| Cr ₂ O ₃ | 6.5-12.7 | 1.4-4.3 | 5-15 |
| Na ₂ O | 0.00-0.06 | 0.04-0.12 | 0.01-0.10 |
| CaO | 7-9 | 4.4-5.1 | 5-9 |
| Mg/(Mg + Fe) | 82-84 | 78-83 | 82-84 |
| Inclusions | cpx, opx | opx | |
| Clinopyroxenes | | | |
| | (n = 18) | (n = 11) | (n = 5) |
| TiO ₂ | 0.1-0.2 | 0.2-0.4 | 0.1-0.4 |
| Cr ₂ O ₃ | 1.0-2.3 | 0.4-0.8 | 1.0-2.5 |
| Al ₂ O ₃ | 1.1-1.4 | 1.9-2.2 | 1.4-1.9 |
| Na ₂ O | 0.9-1.6 | 1.3-1.5 | 1.1-1.7 |
| Mg/(Mg + Fe) | 92-93 | 87-90 | 91-93 |
| Inclusions | none | none | |
| Orthopyroxenes | | | |
| | (n = 47) | (n = 12) | (n = 6) |
| Cr ₂ O ₃ | 0.4-0.6 | 0.1-0.3 | 0.3-0.8 |
| Mg/(Mg + Fe) | 92-93 | 88-91 | 92-93 |
| Inclusions | cpx | ilm | |
| Olivines | | | |
| | | (n = 2) | (n = 6) |
| Mg/(Mg + Fe) | | 88-90 | 91-92 |
| Ilmenites | | | |
| | | (n = 15) | |
| Cr ₂ O ₃ | | 0.4-3.5 | |
| Mg/(Mg + Fe) | | 44-55 | |
| | | ol, opx, cpx | |
| Inclusions | | | |

* Research partially supported by the National Science Foundation, Earth Sciences Section, grant DES 74-13098.

larly distinctive for their high Cr_2O_3 content and tightly grouped, relatively high $\text{Mg}/(\text{Mg} + \text{Fe})$. The grain size of the peridotites (whose textures vary from granular through tabular to porphyroclastic) is, however, considerably finer than that of the megacrysts. The second suite of megacrysts chiefly differs from the first suite and from peridotite nodules in its relative deficiency in Cr_2O_3 and higher, broader range of iron content. Ilmenite is exclusively associated with megacrysts of the Cr-poor suite, even though some ilmenites contain as much as 3.5 wt % Cr_2O_3 . Minerals of the Cr-poor suite have general chemical similarities (Tables 12 and 13) to dis-

crete nodules from Lesotho described by Boyd and Nixon (1973), but they differ in that high-temperature ($>1300^\circ\text{C}$) megacrysts found in Lesotho have not been found in Colorado and in that the Cr-poor megacrysts have slightly higher $\text{Mg}/(\text{Mg} + \text{Fe})$ and the garnet and clinopyroxene contain more Cr_2O_3 . The Lesotho pipes (Boyd and Nixon, 1973) and the Frank Smith Mine, South Africa (Boyd, *Year Book* 73, pp. 285–293), do not contain Cr-rich megacrysts.

Pressures and temperatures of equilibration of the enstatite megacrysts have been calculated in the following manner. Temperatures have been derived from the opx thermometer of Boyd and Nixon

TABLE 13. Representative Megacryst Analyses from the Sloan 2 Kimberlite Pipe, Colorado*

| | SD2-G15 | | | SD2-I16 | | | O4 | G151 |
|-------------------------|---------|-------|-------|---------|-------|-------|-------|--------|
| | Gt | Opx | Cpx | Ilm | Opx | Ol | Cpx | Gt |
| SiO_2 | 39.5 | 57.2 | 55.4 | 0.17 | 56.1 | 40.1 | 55.4 | 42.2 |
| TiO_2 | 0.74 | 0.13 | 0.19 | 52.9 | 0.28 | 0.04 | 0.22 | 0.72 |
| Al_2O_3 | 12.6 | 0.71 | 1.43 | 0.44 | 1.29 | 0.02 | 2.07 | 20.4 |
| Cr_2O_3 | 12.7 | 0.61 | 2.43 | 2.80 | 0.27 | 0.01 | 0.63 | 2.13 |
| Fe_2O_3 | ... | ... | ... | 7.5 | ... | ... | ... | ... |
| FeO | 6.7 | 4.9 | 2.88 | 21.5 | 6.8 | 12.0 | 4.1 | 8.3 |
| MnO | 0.38 | 0.14 | 0.12 | 0.25 | 0.15 | 0.16 | 0.14 | 0.32 |
| NiO | 0.10 | 0.11 | 0.06 | 0.05 | 0.07 | 0.20 | 0.08 | 0.00 |
| MgO | 17.6 | 35.3 | 18.4 | 14.2 | 34.2 | 48.2 | 20.0 | 21.4 |
| CaO | 8.9 | 0.95 | 17.8 | 0.02 | 0.75 | 0.04 | 16.3 | 4.9 |
| Na_2O | 0.03 | 0.20 | 1.55 | ... | 0.11 | 0.00 | 1.34 | 0.05 |
| K_2O | 0.00 | 0.00 | 0.04 | ... | 0.00 | 0.00 | 0.02 | 0.00 |
| Totals | 99.3 | 100.3 | 100.3 | 99.8 | 100.0 | 100.7 | 100.2 | 100.4 |
| Si | 2974 | 1964 | 1987 | 3 | 1945 | 986 | 1980 | 3006 |
| Ti | 40 | 3 | 4 | 11 | 7 | 0 | 5 | 38 |
| Al | 1119 | 28 | 60 | 905 | 52 | 0 | 87 | 1708 |
| Cr | 758 | 16 | 68 | 50 | 7 | 0 | 17 | 119 |
| Fe^{3+} | ... | ... | ... | 128 | ... | ... | ... | ... |
| Fe^{2+} | 422 | 141 | 86 | 410 | 195 | 246 | 123 | 493 |
| Mn | 22 | 4 | 3 | 4 | 4 | 2 | 4 | 19 |
| Ni | 4 | 2 | 1 | 0 | 2 | 3 | 2 | 0 |
| Mg | 1977 | 1809 | 986 | 480 | 1767 | 1769 | 1063 | 2267 |
| Ca | 714 | 34 | 685 | 0 | 27 | 0 | 623 | 374 |
| Na | 2 | 12 | 107 | ... | 7 | 0 | 92 | 6 |
| K | 0 | 0 | 1 | ... | 0 | 0 | 1 | 0 |
| Cations | 8032 | 4013 | 3988 | 2000 | 4012 | 3007 | 3997 | 8028 |
| Oxygens | 12,000 | 6000 | 6000 | 3000 | 6000 | 4000 | 6000 | 12,000 |

* Including ortho- and clinopyroxene inclusions in a Cr-rich garnet, intergrown olivine and Cr-poor orthopyroxene in an ilmenite, and separate Cr-poor clinopyroxene and garnet crystals.

Abbreviations: Gt, garnet; Opx, orthopyroxene; Cpx, clinopyroxene; Ilm, ilmenite; Ol, olivine.

(1973), assuming that these enstatites were equilibrated with clinopyroxene and garnet and that the Lesotho thermometer is applicable to these megacrysts. The first assumption is reasonable, because the pyroxenes are found in a few cases as inclusions within each other or within other phases (Table 12). The second assumption was tested by plotting the $\text{Ca}/(\text{Ca} + \text{Mg})$ molar content of coexisting pairs of pyroxenes from megacrysts and lherzolites; agreement with the Boyd and Nixon (1973) thermometer was reasonable. Pressures were calculated using the procedure of Wood (1974), with some modifications (see McCallum and Eggler, 1976). The $\text{Ca}/(\text{Ca} + \text{Mg} + \text{Fe})$ content of garnet assumed to be in equilibrium with pyroxenes was taken to be 0.20 for Cr-rich garnets and 0.12 for Cr-poor garnets, the average values from Fig. 17.

Five garnet lherzolite nodules and ten

garnet websterite nodules from the Sloan pipes that were equilibrated at depths of 50–180 km fall along a shield geotherm (McCallum and Eggler, 1976). The calculated equilibration conditions of the megacrysts, together with this geotherm, are plotted in Fig. 18. The majority of the megacryst points lie near the shield geotherm, but nine Cr-rich megacrysts and one Cr-poor megacryst lie about 100°C above the geotherm. This variability is far greater than can be accounted for by analytical error. Nor are the high-temperature megacrysts significantly different in composition from megacrysts on or near the geotherm. The array of points is interpreted as a partially disturbed geotherm. In contrast, the megacryst geotherms presented by Nixon and Boyd (1973b) for the Lesotho pipes and by Boyd (*Year Book 73*, pp. 285–293) for the Frank Smith Mine, South Africa, are distinctly kinked (to

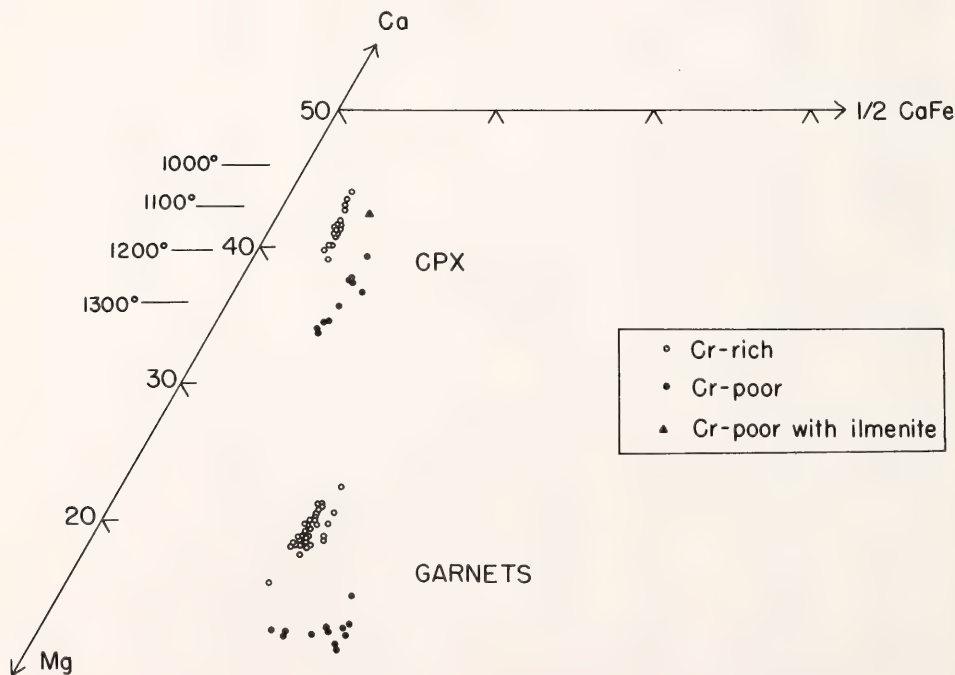


Fig. 17. Compositions of clinopyroxene and garnet megacrysts from the Sloan 2 kimberlite pipe, Colorado, plotted in mole % on a Ca-Mg-Fe projection. Temperatures are for points on the diopside solvus after Davis and Boyd (1966).

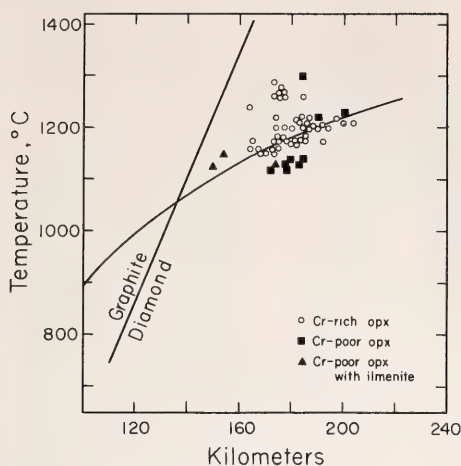


Fig. 18. Estimates of equilibration temperatures and depths for orthopyroxene megacrysts from the Sloan 2 kimberlite pipe, Colorado. The geotherm drawn is the shield geotherm of Clark and Ringwood (1964). Diamond-graphite equilibrium boundary after Bundy *et al.* (1961).

the high-temperature side) at depths below about 150 km.

Nixon and Boyd (1973b) suggested that the inflected limb of the Lesotho geotherm was caused by stress-heating in the low-velocity zone. This type of heating has been discounted by Green and Gueguen (1974) and Goetze (1975), and alternative models have been presented for heating by an upwelling diapir (Green and Gueguen, 1974) and by a mantle plume (Parmentier and Turcotte, 1974). Boyd (this Report) now considers that a diapir associated with convective overturn is a possible explanation of the inflected limb.

In the model of Green and Gueguen (1974) it is assumed that peridotite of the diapir was less depleted than the mantle through which it flowed, that the top of the diapir was at the same temperature as the undisturbed mantle, that the diapir partially melted, and that there was no low-velocity zone in that mantle region. This model adequately explains features of the Colorado megacryst-lherzolite suites if it is assumed that the diapir rose to a depth of about

160 km. Lherzolites at depths of 180 km would be above or very near the top of the diapir, and therefore equilibration temperatures could very well be undisturbed. Megacrysts, on the other hand, especially if they were part of the diapir, might be expected to show disturbed temperatures. The Cr-poor megacrysts could be interpreted to have crystallized in the presence of a partial melt of a diapir more fertile than the surrounding peridotite. The Cr-poor megacryst minerals are more Fe-rich than minerals in lherzolites (and differ in other chemical parameters as well), and they have many of the characteristics that led Boyd and Nixon (1973) to interpret that Lesotho discrete nodules grew in the presence of a fractionating liquid—they display a range in $Mg/(Mg + Fe)$, intergrowths among minerals are uncommon, and the grain size is ultracoarse. The principal difficulty with this theory is that the equilibration conditions of only one of the Cr-poor enstatites are in the disturbed group; most (nine) of the disturbed enstatites are Cr-rich. These Cr-rich enstatite megacrysts would not be thought to have been part of the diapir, inasmuch as their compositions are similar to those of enstatites of depleted lherzolites. On the other hand, the coarse size of the Cr-rich megacrysts may indicate that they crystallized in the presence of liquid.

In summary, orthopyroxenes from relatively Cr-rich and Cr-poor megacryst suites from the Sloan pipes define a partially disturbed geotherm. Chemical and physical characteristics of at least one and possibly both suites can be explained by crystal-liquid equilibria. The thermal disturbance and the production of liquid may be related to intrusion of mantle diapirs, and a low-velocity zone need not have been present. This interpretation is consistent with geophysical interpretations that the low-velocity layer beneath continental shields is ill-defined or absent (Knopoff, 1972).

CLINOPYROXENE-ILMENITE INTER-
GROWTHS FROM THE IRON MOUNTAIN
KIMBERLITE DISTRICT, WYOMING*

*C. B. Smith, M. E. McCallum,
and D. H. Eggler*

Pyroxene-ilmenite intergrowths have been found in a megacryst suite in the Iron Mountain kimberlite district, Wyoming. Nodules from this newly discovered kimberlite district are a fascinating supplement to the peridotite-megacryst suite of the State Line district 70 km to the south (McCallum, Eggler, and Burns, 1975; Eggler and McCallum, this Report). This area is only the second known source of such intergrowths in North America. The other locality is Riley County, Kansas, where one nodule containing fresh pyroxene and ilmenite (Gurney, Fesq, and Kable, 1973) and other nodules containing ilmenite and altered pyroxene (Brookins, 1971; McCallister, Meyer, and Brookins, 1975) have been found.

The Iron Mountain district, consisting of 57 kimberlite dikes and associated blows and pipes, has been described previously only briefly (McCallum *et al.*, 1975). The northeast-trending dike system intrudes Precambrian Sherman granite in the core of an eroded anticlinorium about 8 km wide. At the margins of the anticlinorium the granite and kimberlite are overlain unconformably by Pennsylvanian Casper limestone. Because one pipe contains Ordovician and Silurian sedimentary xenoliths, the kimberlite age must be from Late Silurian to Early Devonian, the same age inferred for the State Line district (McCallum and Eggler, 1971). Kimberlite composition, texture, and alteration are quite variable. Serpentine-rich varieties and carbonatitic varieties are most abundant, although transitional serpentine carbonate-rich phases and wall-rock-rich breccia phases are important locally.

* Research supported by the National Science Foundation, Earth Sciences Section, grant DES 74-13098.

Mantle-derived nodules found at Iron Mountain include eclogites, garnet and spinel lherzolites, websterites, and diopside-ilmenite intergrowths. There are also monomineralic xenocrysts of clinopyroxene, pyrope garnet, and ilmenite. Most xenoliths are physically and chemically similar to nodules found in the State Line district (Eggler and McCallum, *Year Book* 73, pp. 295-300). Attention is directed here to one class of xenocrysts, the Cr-poor megacrysts, and associated diopside-ilmenite intergrowths. Relatively Cr-rich megacrysts and associated smaller (<2-cm) xenocrysts of chrome diopside and garnet are also found; as in the State Line district (Eggler and McCallum, this Report), these Cr-rich megacrysts are compositionally similar to minerals of lherzolites. Unfortunately, at Iron Mountain these lherzolites have been intensely serpentinized, silicified, and carbonatized. No olivine or orthopyroxene crystals have survived this alteration. However, the compositions of relict diopside and garnet or spinel reveal the Cr-rich (hence presumably depleted) nature of the lherzolites. The textures appear to have been granular before alteration.

Twenty-six lamellar intergrowths of diopside and ilmenite have been collected. In most, the pyroxene is completely altered to serpentine, chlorite, and calcite. However, five of the intergrowths contain unaltered diopside. In these nodules the ilmenite rods and plates can be seen to be regularly distributed in a single-crystal diopside host. Analyses of a typical intergrowth are given in Table 14. Compositional variation of diopside and of ilmenite among the 26 intergrowths is very restricted. The one exception is ilmenite from a graphic intergrowth (a texture similar to that of sample BD-1374 reported from Monastery by Dawson and Reid [1970]), which is more Mg- and Mn-rich (Table 14). No unaltered pyroxene was found in the graphic intergrowth.

The compositions of intergrowth clinopyroxenes (Fig. 19) and of ilmenites

TABLE 14. Representative Analyses of Megacrysts and Intergrowths from Iron Mountain District, Wyoming, Kimberlite Dikes*

| | IM7-IC1 | | IM4-IC1 | IM20-G1 | | IM26-G17 | |
|--------------------------------|---------|-------|---------|---------|-------|----------|-------|
| | Cpx | Ilm | Ilm | Gt | Cpx | Gt | Ilm |
| SiO ₂ | 54.9 | 0.16 | 0.16 | 42.9 | 55.1 | 41.7 | 0.13 |
| TiO ₂ | 0.37 | 50.6 | 52.1 | 0.56 | 0.18 | 0.63 | 49.4 |
| Al ₂ O ₃ | 2.16 | 0.88 | 0.88 | 20.3 | 2.23 | 21.9 | 0.75 |
| Cr ₂ O ₃ | 0.10 | 0.43 | 0.56 | 2.61 | 0.73 | 0.07 | <0.03 |
| Fe ₂ O ₃ | ... | 10.4 | 4.0 | ... | ... | ... | 12.5 |
| FeO | 5.3 | 26.2 | 24.9 | 7.5 | 4.0 | 13.0 | 26.5 |
| MnO | 0.16 | 0.23 | 3.3 | 0.28 | 0.16 | 0.44 | 0.27 |
| NiO | 0.04 | 0.00 | 0.17 | 0.00 | 0.07 | <0.03 | 0.08 |
| MgO | 18.0 | 11.0 | 11.8 | 21.3 | 20.1 | 18.2 | 9.8 |
| CaO | 17.8 | <0.03 | <0.03 | 5.2 | 16.3 | 4.4 | <0.03 |
| Na ₂ O | 1.32 | <0.03 | 0.00 | 0.03 | 1.13 | 0.06 | <0.03 |
| K ₂ O | <0.03 | 0.00 | 0.00 | 0.00 | <0.03 | 0.00 | 0.00 |
| Totals | 100.2 | 100.0 | 97.9 | 100.7 | 100.0 | 100.4 | 99.5 |
| Si | 1981 | 3 | 3 | 3037 | 1976 | 3011 | 2 |
| Ti | 9 | 887 | 921 | 29 | 4 | 34 | 878 |
| Al | 91 | 24 | 24 | 1697 | 93 | 1863 | 20 |
| Cr | 2 | 7 | 10 | 145 | 20 | 2 | 0 |
| Fe ³⁺ | ... | 182 | 70 | ... | ... | ... | 222 |
| Fe ²⁺ | 160 | 510 | 489 | 442 | 120 | 781 | 524 |
| Mn | 4 | 4 | 65 | 17 | 4 | 25 | 4 |
| Ni | 0 | 0 | 3 | 0 | 1 | 0 | 1 |
| Mg | 970 | 380 | 413 | 2245 | 1073 | 1954 | 344 |
| Ca | 690 | 0 | 0 | 390 | 625 | 338 | 0 |
| Na | 92 | 0 | 0 | 4 | 78 | 8 | 2 |
| K | 0 | 0 | 0 | 0 | 1 | 0 | 0 |
| Cations | 3998 | 2000 | 2000 | 8005 | 3994 | 8017 | 2000 |
| Oxygens | 6000 | 3000 | 3000 | 12,000 | 6000 | 12,000 | 3000 |

* Including a clinopyroxene-ilmenite lamellar intergrowth, ilmenite from a pyroxene-ilmenite graphic intergrowth, a garnet megacryst and included clinopyroxene, and a garnet megacryst and included ilmenite.

fall within the range of compositions of the assemblage of Cr-poor megacrysts. This assemblage includes clinopyroxene, garnet, and ilmenite and may have included (before alteration) orthopyroxene and olivine, by analogy with the Sloan 2 pipe (State Line district) assemblage (Eggler and McCallum, this Report). The chemical compositions of the megacryst minerals vary considerably, as illustrated in the Ca-Mg-Fe projection (Fig. 19). In addition to the intergrowths, other pairs of coexisting minerals found include two clinopyroxene inclusions and one ilmenite inclusion in garnets (Table 14) and one clinopyroxene inclusion in ilmenite. The cor-

relations of chemical parameters among coexisting minerals are the same as those found by Boyd and Nixon (1973) for Lesotho discrete nodules. High-temperature pyroxenes and associated garnets (IM20-G1, Table 14) are more magnesian and more chromian than lower temperature pyroxenes and associated garnets, which are more iron-rich and chrome-poor and are associated with ilmenite (IM7-IC1 and IM26-G17). The intergrowths are a very restricted portion of the latter group.

Pyroxene-ilmenite intergrowths have been interpreted to have crystallized from liquid (e.g., Williams, 1932; Boyd and Dawson, *Year Book* 71, pp. 373-

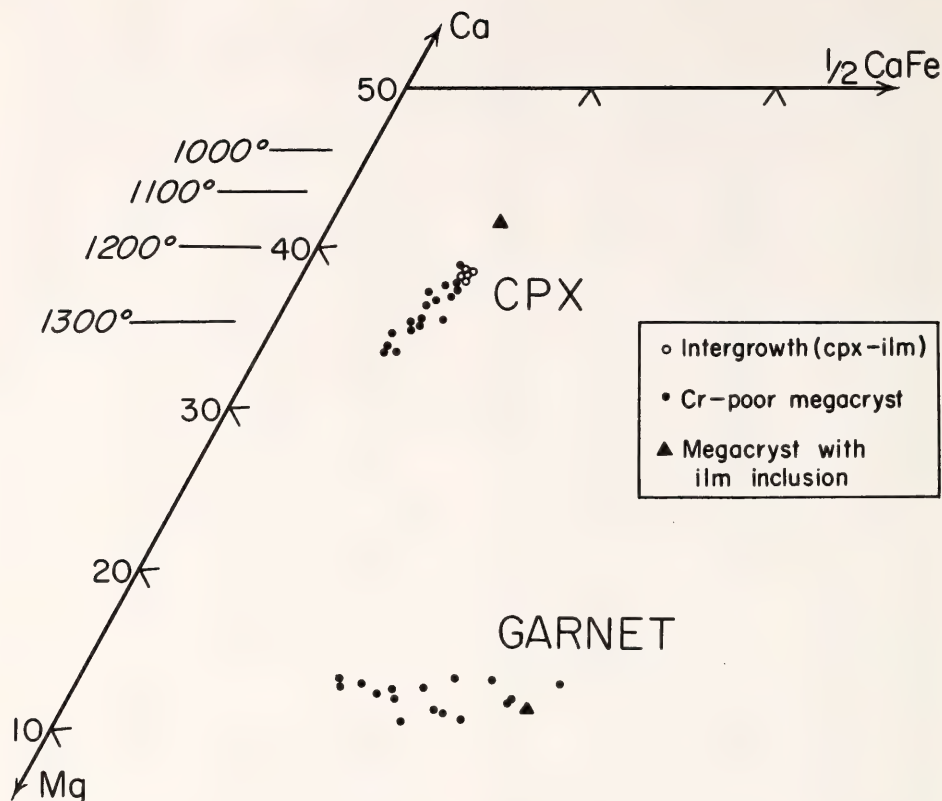


Fig. 19. Compositions of Cr-poor clinopyroxene and garnet megacrysts from the Iron Mountain kimberlite district, Wyoming, plotted in mole % on a Ca-Mg-Fe projection. Temperatures are for points on the diopside solvus after Davis and Boyd (1966).

378; Gurney, Fesq, and Kable, 1973), a process verified by experiment at 38-kbar pressure (Wyatt *et al.*, *Year Book* 74, pp. 536-539). Thus the presence of intergrowths is another indication that the State Line-Iron Mountain Cr-poor megacryst suite crystallized in the presence of liquid. Equilibration temperatures of the Iron Mountain intergrowths (on the assumption that orthopyroxene was another phase coexisting with the liquid) are 1150°-1165°C, corresponding to depths on the undisturbed State Line megacryst geotherm (Eggler and McCallum, this Report) of 167-175 km. These depths are within the range of megacrysts associated with ilmenite from the State Line district.

ULTRAMAFIC NODULES FROM THE KIMBERLEY PIPES, SOUTH AFRICA

F. R. Boyd and P. H. Nixon

Six large kimberlite diatremes clustered together at Kimberley have produced a considerable fraction of the world's supply of diamonds and a rich storehouse of ultramafic xenoliths from the upper mantle. Petrographic and electron microprobe study of these xenoliths shows that they differ from most xenolith suites from northern Lesotho and elsewhere in southern Africa in three important respects:

1. Sheared lherzolites with high equilibration temperatures (>1100°C) are not found in the Kimberley nodule suite,

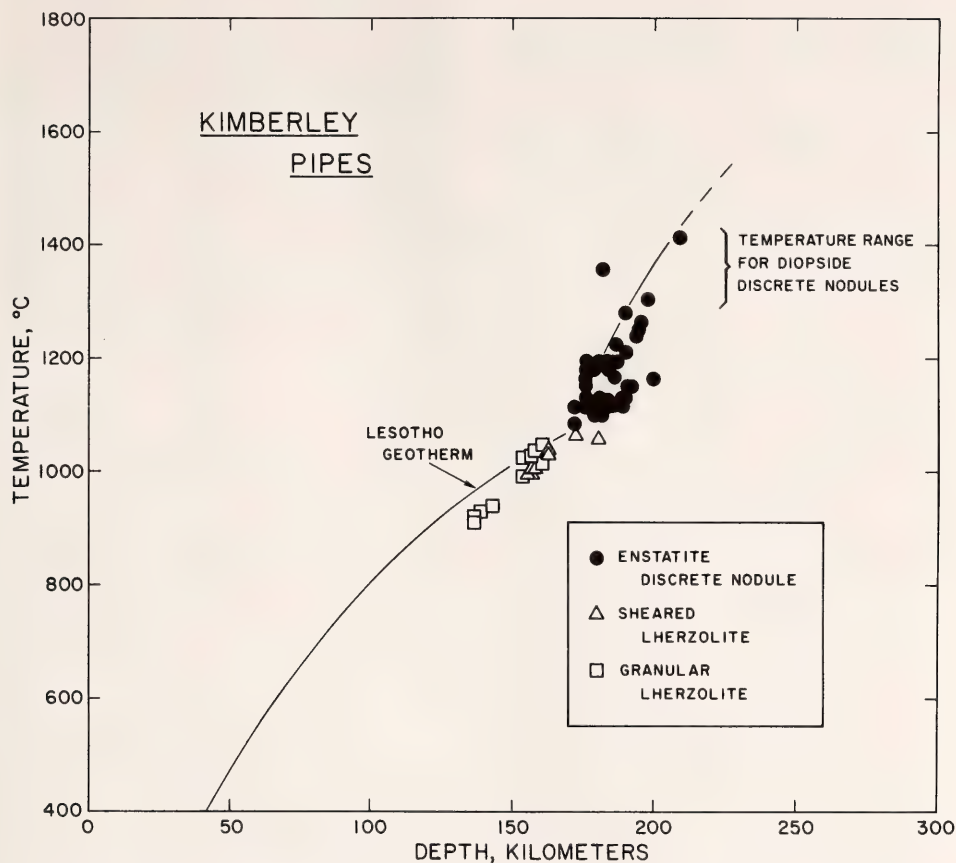


Fig. 20. Temperature-depth estimates for lherzolites and enstatite discrete nodules from the Kimberley pipes compared with the Lesotho geotherm (Boyd, 1973, Fig. 7A). Inasmuch as the purpose of this figure is solely comparative, the older phase studies used to calculate the Lesotho geotherm (Davis and Boyd, 1966; MacGregor, 1974) were also used to make the estimates for the Kimberley rocks.

although they are found in abundance in many kimberlites in northern Lesotho, as well as at the Monastery, Frank Smith, Premier, and Jagersfontein pipes in South Africa and in the Farm Louwrencia kimberlite in Southwest Africa (MacGregor, 1975). Instead, the high-temperature section at Kimberley, which equilibrated along the inflected limb of the geotherm, consists of discrete nodules like those found in Lesotho, possibly accompanied by sheared dunites.

2. The more Fe-rich discrete nodules, which in many kimberlites commonly

form lamellar intergrowths with ilmenite or form host-inclusion relations with ilmenite, have not been found at Kimberley.

3. The strongly depleted, low-temperature ($<1100^{\circ}\text{C}$) lherzolite and harzburgite nodules in the Kimberley pipes have textures ranging from coarse granular to fluidal and disrupted mosaic. In most nodule suites from southern Africa and elsewhere in the world, these low-temperature lherzolites are uniformly very little deformed. Exceptions, possibly analogous to Kimberley, are the low-temperature lherzolites from the

Matsoku pipe in Lesotho (Harte, Cox, and Gurney, 1975), which exhibit considerable deformation and recrystallization.

The differences in the kinds of nodules found in different areas appear to reveal heterogeneity in the upper mantle beneath southern Africa, whereas the differences in texture probably reflect variation in the tectonics of kimberlite eruption.

The Kimberley lherzolites (Fig. 20) appear to define a segment of a normal geotherm similar to the "granular" limb of the Lesotho geotherm but displaced to slightly lower temperatures. In this respect the pattern is very similar to that found for the Frank Smith pipe (Boyd, *Year Book* 73, p. 285), 60 km north of Kimberley.

Because of the absence of high-temperature lherzolites at Kimberley, it is necessary to use enstatite discrete nodules to define the high-temperature segment of the geotherm. This procedure is less precise (Boyd and Nixon, 1973), but estimates for the Kimberley enstatites appear to show an inflection (Fig. 20). The overall pattern is thus broadly similar to those found for northern Lesotho and Frank Smith.

A detailed petrographic study of these Kimberley xenoliths and a discussion of mineral compositional variations determined by nearly 200 mineral analyses will be published separately (Boyd and Nixon, in preparation).

COMPOSITIONAL VARIATION OF COEXISTING PHASES WITH DEGREE OF MELTING OF PERIDOTITE UNDER UPPER MANTLE CONDITIONS

Bjørn O. Mysen and Ikuo Kushiro

Genesis of magma by partial melting in the upper mantle has been discussed either in terms of phase equilibrium in appropriate model systems (e.g., Yoder and Tilley, 1962; O'Hara and Yoder, 1967; Kushiro, 1969b, 1972a) or simply in terms of varying degrees of partial

melting of peridotite with only subordinate concern for the phase equilibria involved (e.g., Green and Ringwood, 1967). Inasmuch as the same rules apply to both complex natural and simple model systems, one would expect that relevant model systems, with allowance for solid solutions, adequately describe melting of natural rocks. In an attempt to study quantitatively the phase equilibria of partial melting of natural peridotite, the degree of melting as a function of temperature and pressure has been determined.

The compositions of two natural garnet peridotite nodules used as starting material are shown in Table 15. Nodule 1611 is judged the least chemically depleted of the suite of Cretaceous garnet peridotite nodules in South African kimberlites (Nixon and Boyd, 1973a; Shimizu, *Year Book* 73, pp. 954-961) and is therefore used as a representative of the continental upper mantle. Nodule 66SAL-1 has been suggested as the least depleted of the suite of peridotite nodules found in Hawaiian nephelinite tuff (Jackson and Wright, 1970; Shaw and Jackson, 1973) and serves as an example of oceanic upper mantle in these experiments.

The rocks were spiked with about 50 ppm BaCO₃ containing radiogenic carbon-14 to be used for the determination of the degree of melting (Mysen, this Report). The rocks were crushed under acetone to <5 μ m grain size and run in high-pressure apparatus (Boyd and England, 1960) using furnace assemblies of 1/2-in diameter with Pyrex glass sleeves. Sealed capsules were used to avoid CO₂ loss from the samples. The Pt₉₅Au₅ capsule material dissolves iron, resulting in approximately 20% Fe loss from the samples at 20 kbar and about 1550°C. The Fe loss is higher at 35 kbar, owing to the increased diffusion rate of cations in silicate melt as pressure is increased (Kushiro, Yoder, and Mysen, this Report). The increased diffusion rates also result in crystallization of consealed Pt₉₅Au₅ capsules in solid-media,

TABLE 15. Composition of Starting Materials

| | 1611* | 66SAL-1† |
|--------------------------------|--------|----------|
| SiO ₂ | 43.70 | 44.82 |
| TiO ₂ | 0.25 | 0.52 |
| Al ₂ O ₃ | 2.75 | 8.21 |
| Fe ₂ O ₃ | 1.38 | 2.07 |
| FeO | 8.81 | 7.91 |
| MnO | 0.13 | 0.19 |
| MgO | 37.22 | 26.53 |
| CaO | 3.26 | 8.12 |
| Na ₂ O | 0.33 | 0.89 |
| K ₂ O | 0.14 | 0.03 |
| H ₂ O ⁻ | 0.05 | 0.11 |
| H ₂ O ⁺ | 1.94 | 0.15 |
| P ₂ O ₅ | tr. | 0.04 |
| Cr ₂ O ₃ | 0.28 | 0.20 |
| NiO | n.d. | 0.20 |
| Totals | 100.24 | 99.99 |

* Analysis from Nixon and Boyd (1973a).

† Analysis from Mysen and Boettcher (1975a).

Both analyses are of unfired samples. The analysis of 1611 corresponds to 1611 + 1.9 wt % H₂O in the text.

siderable amounts of quench minerals at the highest pressures (35 kbar).

Prior to addition of BaCO₃ both starting materials were fired at 1150°C with f_{O₂} similar to that of the QFM buffer for 12 hr and stored at 110°C until use. These samples are thus considered completely volatile-free. In addition, a split of sample 1611 was dried only at 110°C before use and therefore contained H₂O in an amount similar to that bound in hydrous minerals (1.94 wt % H₂O; Nixon and Boyd, 1973a).

Phase relations of anhydrous 1611 and 66SAL-1 at 20 kbar are plotted as degree of melting (X_{melt}) versus temperature (T) in Fig. 21. The X_{melt} versus T relation was also estimated for a composition in the system Mg₂SiO₄ (Fo)-CaMgSi₂O₆ (Di)-SiO₂ at 20 kbar (Kushiro, 1969b) to illustrate the melting behavior of a simple system at invariant points, along univariant curves, and within divariant fields in this type of diagram. The model composition Fo₅₅-En₃₀Di₁₅ (by weight) is close to that of typical peridotite.

The identification of phase fields as presented in the figures is based on optical data and confirmation by the electron microprobe. Whether spinel occurs together with olivine and two pyroxenes in sample 1611 (Fig. 21) is uncertain. A few apparently isotropic grains, ~1 μm across, may be spinel. This possibility could not be confirmed with the electron microprobe, however, and spinel is left off the figure. Clinopyroxene is called Ca-rich or Ca-poor on the basis of its chemical composition.

The melting ranges of these peridotites are divided into three fields (Fig. 21): olivine + 2 pyroxenes + liquid (+ spinel), olivine + orthopyroxene + liquid, and olivine + liquid. There is also a striking similarity between the melting patterns of the natural peridotites and the pattern of the composition Fo₅₅En₃₀Di₁₅ in the three-component system Fo-Di-SiO₂. Solid solutions involving Fe, Al, Cr, and Na in the natural samples do, of course, result in slightly different curvature of the melting curves of the natural samples compared with the simple system. The initial melting step (Ol + 2 Px + Sp + Liq) of both 1611 and 66SAL-1 closely resembles the isobaric, invariant melting interval of the synthetic composition (Fig. 21), suggesting that volatile-free melting of natural peridotite may approximate isobaric, invariant character. However, both melting curves of the rocks show an abrupt change close to the solidi without change of phase assemblages. Both nodules contain several tenths of a percent alkalis. Such cations (chain breakers or depolymerizers, Bottinga and Weill, 1972; Waff, 1975) may induce a small amount of melting at a considerably lower temperature than that at which the rock would melt in their absence. The melting of peridotite is obviously not invariant in this region.

Samples 1611 and 66SAL-1 are quantitatively different in terms of temperature and degree of melting where phase changes occur. In sample 66SAL-1 the degree of melting increases from 1.5%

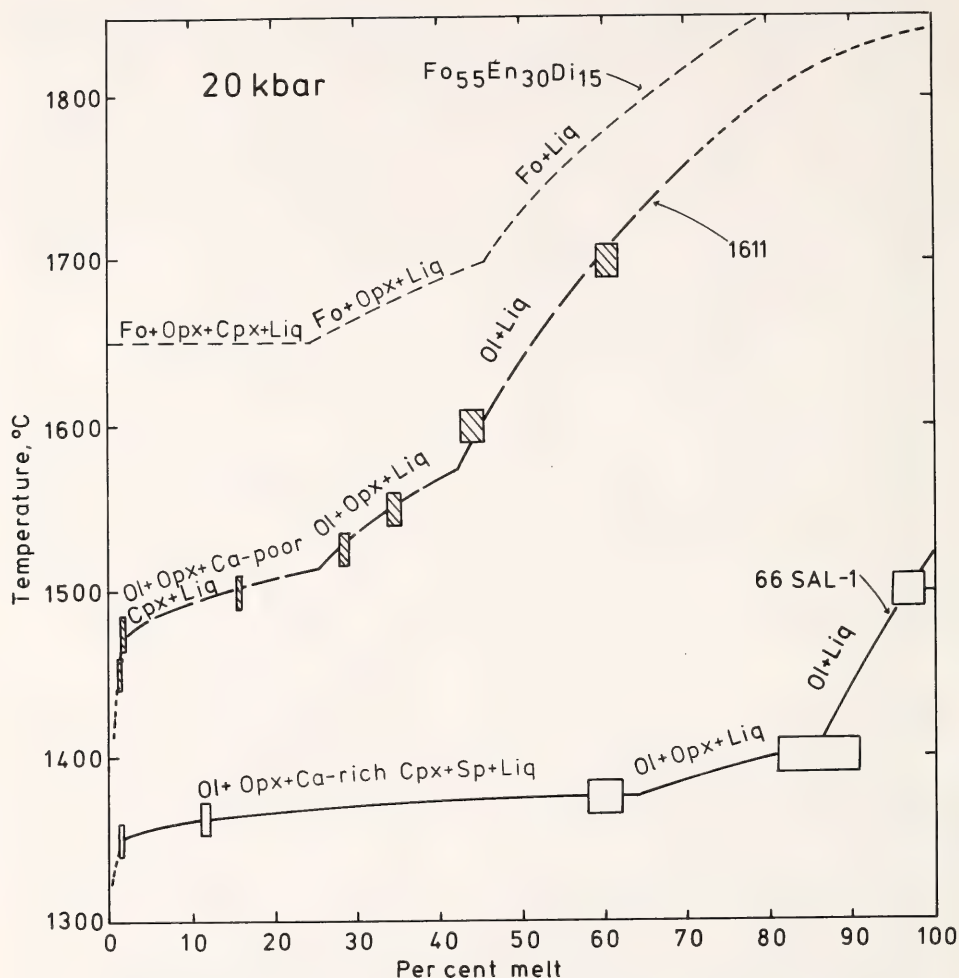


Fig. 21. Melting curves of nodules 1611 and 66SAL-1 at 20-kbar pressure (anhydrous). Size of symbols includes uncertainties in temperature ($\pm 10^\circ\text{C}$) and determination of percentage of liquid ($\pm 1\%$).

to 60% between 1350° and 1375°C without change of mineral assemblage. In comparison, only 25% melt can be extracted from nodule 1611 before clinopyroxene disappears.

The anhydrous and hydrous water-undersaturated (1.9 wt % H_2O) melting behavior of sample 1611 are shown in Fig. 22. When CO_2 is used as a tracer, the presence of H_2O vapor with a low degree of melting results in significant partitioning of CO_2 into the vapor. About 20 wt % H_2O dissolves in silicate melts

under these pressure conditions (Boettcher and Wyllie, 1969; Burnham and Davis, 1974). Consequently, with $X_{\text{melt}} \leq 10\%$, a separate vapor phase will exsolve, and the amounts of melt calculated from the CO_2 content of the melt become overestimates. The lowest degree of melting determined for 1611 + 1.9 wt % H_2O (6.1% melt, Fig. 22) is therefore probably an overestimate of the amount of melt. The hydrous melting curve is located at slightly lower temperatures than that determined for

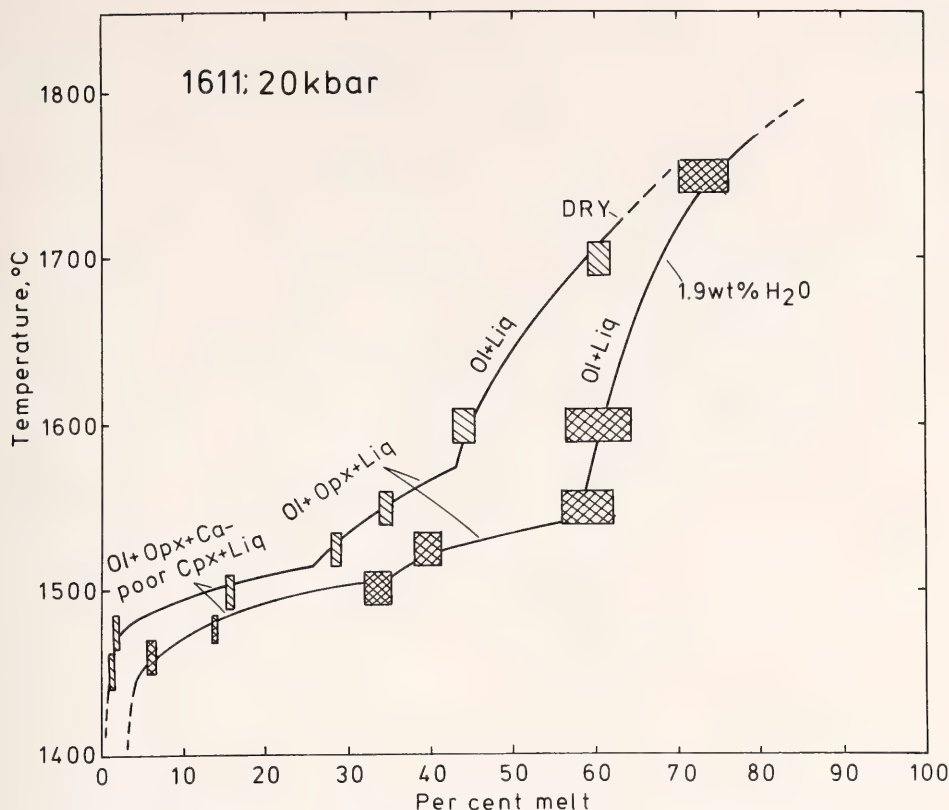


Fig. 22. Melting curves of anhydrous 1611 and 1611 + 1.9 wt % H₂O. Size of symbols as in Fig. 21.

anhydrous conditions. The temperature difference increases from 25°C within the olivine + 2 pyroxenes + liquid fields to more than 150°C at 60% melting. Because of the moderate slope of the melting curves, the absolute difference in the degree of melting at a given temperature could be as much as 25%.

The results for sample 1611 at 20 and 35 kbar are shown in Fig. 23. As at the lower pressure, the melting interval at 35 kbar can be subdivided into distinct regions. The highest temperature field in Fig. 23 was not determined. The stippled line and the bracketed "Ol + Liq" field are merely a suggestion constrained only by the 35-kbar melting curve remaining on the high-temperature side of the 20-kbar melting curve.

The phase assemblages at 35 kbar are

different from those at 20 kbar in two respects. First, garnet appears on the 35-kbar solidus and remains stable until about 25% melting. Apart from the abrupt change below 1% melting, the garnet stability melting range comprises 40°C. The degree of melting of nodule 1611 is the least temperature-dependent in this interval, and the melting of nodule 1611 therefore most closely resembles isobaric, invariant behavior. Second, pyroxene has a much wider stability interval at 35 kbar than at 20 kbar (to 60% and 45% melting at 35 and 20 kbar, respectively). Notably, the melting intervals at temperatures above the stability of garnet involve the same mineral assemblages as those at 20 kbar (Fig. 23).

Reliable chemical data on the phases

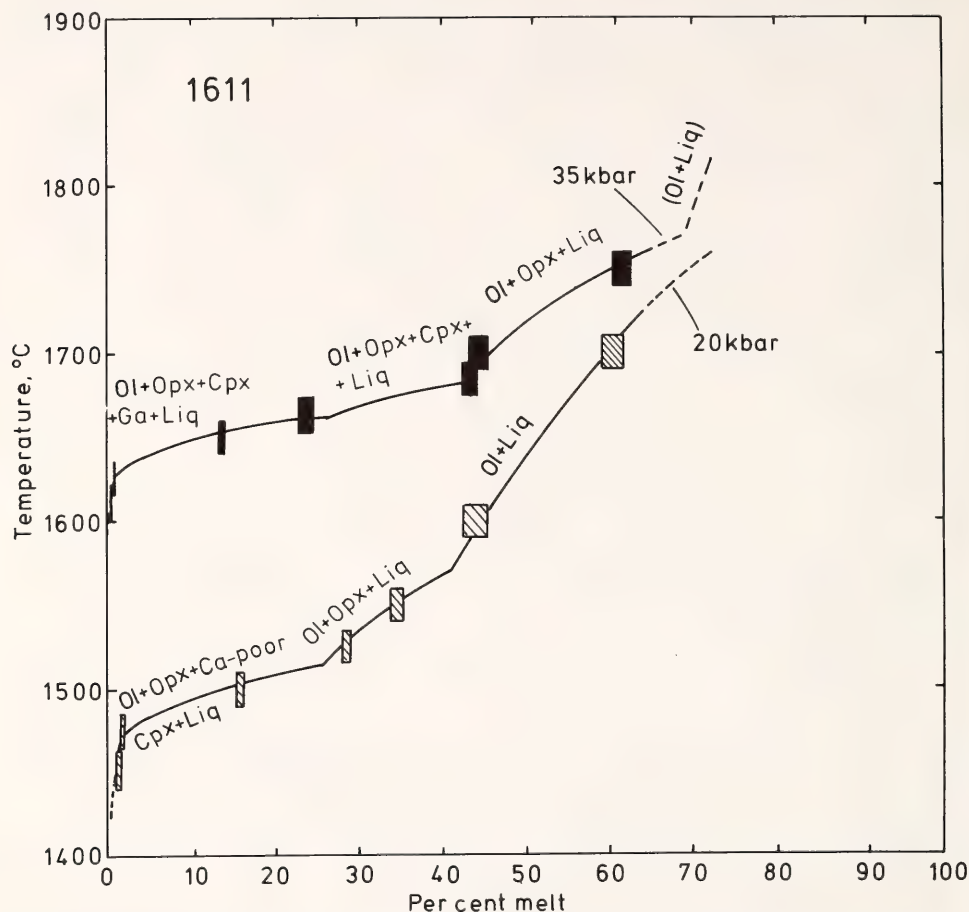


Fig. 23. Melting curves of anhydrous 1611 at 20- and 35-kbar pressure. Size of symbols as in Fig. 21.

present were obtained at 20 kbar, although quenching problems became increasingly cumbersome as temperature, H_2O , and alkali contents increased. The presence of significant amounts of quench clinopyroxene in 1611 + 1.9 wt % H_2O made it particularly difficult to obtain analyses of stable clinopyroxene from those experiments. All 35-kbar runs yielded very extensive crystallization of quench minerals, including both olivine and two pyroxenes, and therefore no attempts were made to obtain chemical data from 35-kbar runs.

All crystalline phases show a systematic increase of $Mg/(Mg + Fe)$ with

increasing melting, as exemplified by olivine in Fig. 24. The rate of increase is highest at the beginning of each melting interval. Minor constituents, such as Cr, Ni, and Na, also show systematic variations. Clinopyroxene, having the widest range of solid solutions, is used as an example in Fig. 25. There is an apparent difference between the clinopyroxenes from 1611 and 66SAL-1, as shown in Fig. 26. The clinopyroxenes from 1611 (high-temperature melting interval) have only about half the amount of wolastonite in solid solution compared with the clinopyroxenes from 66SAL-1 (low-temperature melting range). Further-

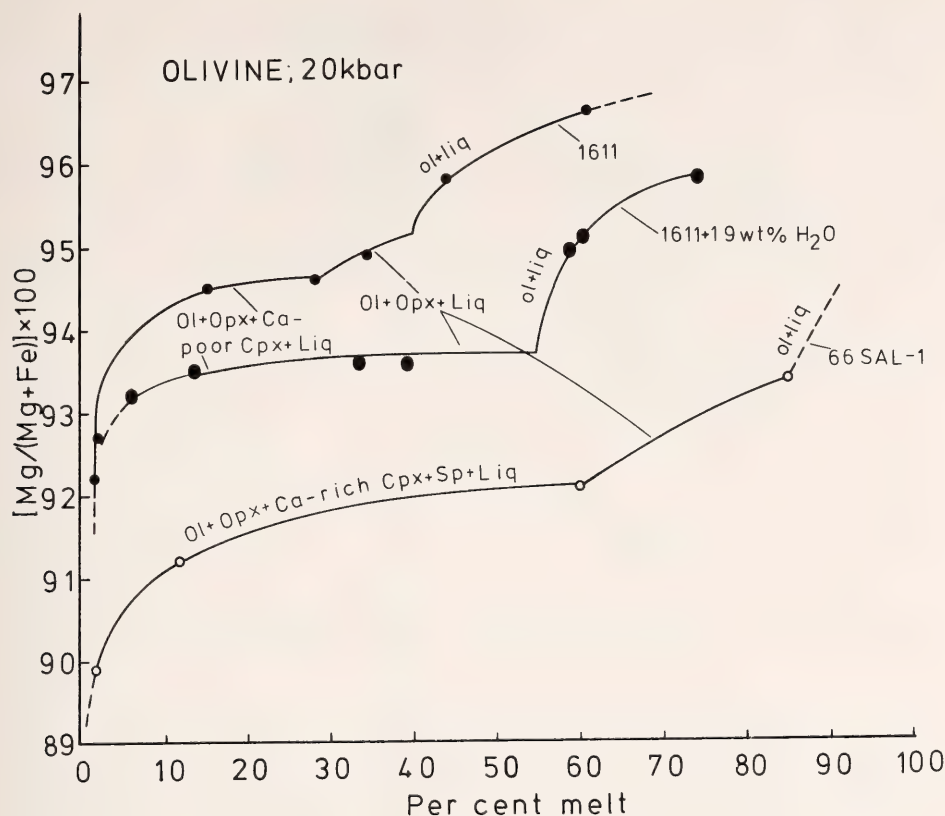


Fig. 24. Chemical trends in olivine as a function of degree of melting. Phase assemblages describe coexisting crystalline phases in the melting interval.

more, the clinopyroxenes from 1611 are more iron-rich than those from 66SAL-1 (Figs. 25 and 26) despite their higher temperatures of formation and more magnesian coexisting phases (Fig. 24). The Mg-Fe partitioning between Ca-poor clinopyroxene (pigeonite) and orthopyroxene is also in close agreement with the partitioning determined experimentally by Hensen (*Year Book* 72, pp. 527-535). It is therefore likely that the clinopyroxenes from nodule 1611 at 20 kbar are pigeonite.

Clinopyroxene analysis from 1611 + 1.9 wt % H₂O proved difficult because of interference from quench pyroxene. It is concluded from semiquantitative data that these clinopyroxenes are also pigeonite. In contrast, the clinopyrox-

enes from 66SAL-1 are diopsidic. The difference between these two samples is caused by the temperatures of the melting intervals (1450°-1500°C for 1611 and 1350°-1375°C for 66SAL-1). Kushiro and Yoder (*Year Book* 68, pp. 226-229) determined that the lower stability limit of iron-free pigeonite in the diopside-enstatite join was 1450°C at 20 kbar, in agreement with the data shown here.

Liquid compositions are given in Table 16. The liquids can be classified into three groups (excluding the composition of partial melts where the abrupt change of the melting curves occurs near the solidus). Partial melts coexisting with olivine + 2 pyroxenes + spinel are olivine tholeiitic, followed by picritic melt

CLINOPYROXENE; 20kbar

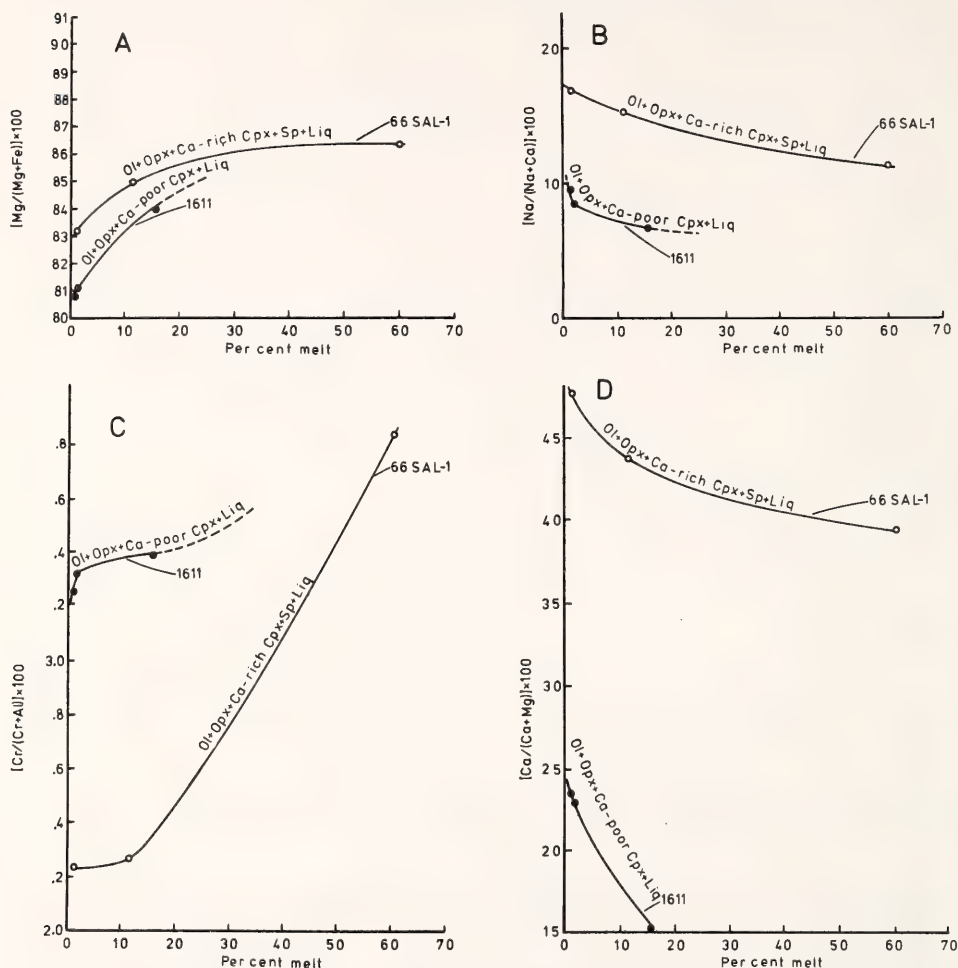


Fig. 25. Chemical trends of clinopyroxenes as a function of degree of melting. Phase assemblages describe coexisting phases in the melting intervals.

composition when olivine + orthopyroxene coexist, and finally peridotitic komatiite liquids coexisting with olivine alone. Melts of both 66SAL-1 and 1611 are nepheline normative where the abrupt change of the melting curves ($<2\%$ melt) occurs, with normative nepheline contents decreasing from 7.6% nepheline at 1.3% melt to 4.7% nepheline at 1.8% melt (Table 16).

Chemical analyses of liquids from 35-kbar runs proved unattainable be-

cause of quench problems. However, a few semiquantitative analyses of liquids coexisting with olivine + garnet + 2 pyroxenes suggest that the liquids resemble alkali picrite. The phase assemblages at successively higher temperatures are similar to those of 1611 at 20 kbar starting from the solidus (Fig. 23); this similarity leads to the suggestion that the liquids in these melting ranges at 35 kbar are similar to those at 20 kbar. In that case, the 35-kbar melting

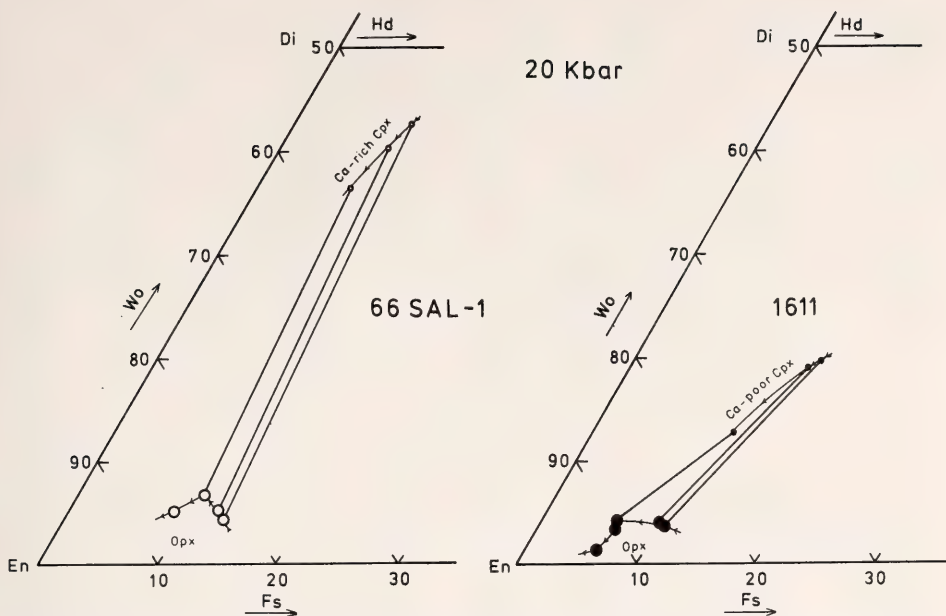


Fig. 26. Pyroxene quadrilateral showing coexisting pyroxenes of nodules 1611 and 66SAL-1 at 20 kbar (anhydrous).

range of nodule 1611 would produce four distinct types of melts. The first 25% melt is alkali picritic (in the presence of garnet), followed by olivine tholeiitic melt (in the presence of olivine + 2 pyroxenes) from 25% to 45% melting, followed by picritic melt from 45% to 75% melting (coexisting with olivine + orthopyroxene), and finally peridotitic komatiitic liquid coexisting with olivine alone.

Partial melting of volatile-free natural peridotite in the pressure range of the upper mantle is clearly quite systematic. Generally, the most important control of liquid composition is the presence of certain mineral assemblages, not the proportions of minerals or small chemical variations of the mineral composition. The peridotite melting interval can be subdivided into specific melting ranges defined by a given phase assemblage and rather constant liquid composition within each range. The width of the melting interval of a given phase assemblage, however, depends on the

peridotite itself, inasmuch as the bulk composition of peridotite controls the proportions of the individual minerals. Thus complex natural peridotite behaves similarly to simple model systems often used to describe melting of peridotite in the upper mantle.

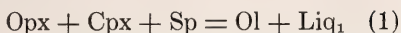
At pressures below the stability of garnet, the liquid composition from 1.5% melt to 25% melt resembles olivine tholeiite. This liquid composition (from both 1611 and 66SAL-1) cannot be described by its four coexisting phases. The melt contains 90% spinel + clinopyroxene and lies on the silica-rich side of the Cpx-Opx-Sp plane. Consequently, partial melts from both peridotites have a reaction relation to their spinel peridotite residue. On the basis of studies by Kushiro and Yoder (*Year Book* 73, pp. 266-269) in the system $\text{CaSiO}_3\text{-MgSiO}_3\text{-Al}_2\text{O}_3$, two reaction relations can be deduced for the melting of the two nodules. The lower temperature melting of 66SAL-1 generates a tholeiitic liquid by the reaction

TABLE 16. Compositions of Quenched Liquids

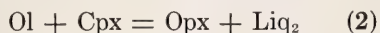
| Starting Material: Temperature (°C): | 1611 1450 | 1611 1475 | 1611 1500 | 1611 1525 | 1611 1550 | 1611 1600* | 1611 1700* | 66SAL-1 1360 | 66SAL-1 1375 |
|---|-----------------|-----------------------------------|-----------------------------------|-----------------------------------|-----------------------------------|-----------------------------------|------------------------------------|------------------------------------|-----------------------------------|
| SiO ₂ | 43.80 | 44.60 | 50.20 | 49.60 | 50.99 | 48.70 | 46.30 | 41.80 | 47.70 |
| TiO ₂ | 1.40 | 1.00 | 0.80 | 0.70 | 0.70 | 0.60 | 0.40 | 0.80 | 0.80 |
| Al ₂ O ₃ | 12.70 | 12.20 | 12.20 | 9.10 | 8.80 | 6.10 | 4.50 | 15.80 | 12.30 |
| FeO† | 13.70 | 12.50 | 9.60 | 9.70 | 12.20 | 17.80 | 14.60 | 9.80 | 7.90 |
| MnO | 0.30 | 0.20 | 0.30 | 0.20 | 0.10 | 0.10 | 0.10 | 0.20 | 0.20 |
| MgO | 12.00 | 14.30 | 13.80 | 19.60 | 15.70 | 18.50 | 27.40 | 19.90 | 17.80 |
| CaO | 13.70 | 13.20 | 10.70 | 9.20 | 9.3 | 7.20 | 5.30 | 10.10 | 12.10 |
| Na ₂ O | 1.40 | 1.10 | 1.50 | 0.90 | 1.3 | 0.70 | 0.50 | 0.90 | 0.80 |
| K ₂ O | 0.60 | 0.50 | 0.60 | 0.50 | 0.3 | 0.30 | 0.20 | 0.10 | 0.20 |
| Totals | 99.60 | 99.60 | 99.70 | 99.50 | 99.30 | 100.00 | 99.30 | 99.40 | 99.80 |
| Cationic norm | | | | | | | | | |
| Or | 1.81 | 2.94 | 3.51 | 2.89 | 1.59 | 1.77 | 1.14 | 0.40 | 0.98 |
| Ab | 0 | 1.94 | 13.32 | 7.89 | 12.08 | 6.26 | 4.33 | 1.70 | 6.83 |
| An | 26.70 | 26.73 | 24.52 | 18.86 | 17.05 | 12.58 | 9.11 | 37.60 | 28.75 |
| Ne | 7.57 | 4.73 | 0 | 0 | 0 | 0 | 0 | 3.72 | 0 |
| Lc | 1.40 | 0 | 0 | 0 | 0 | 0 | 0 | 0 | 0 |
| Cpx | 33.22 | 30.72 | 22.40 | 20.57 | 23.00 | 18.42 | 13.00 | 8.52 | 23.87 |
| Opx | 0 | 0 | 18.98 | 25.66 | 32.59 | 35.07 | 23.84 | 0 | 12.36 |
| Ol | 27.34 | 31.56 | 16.18 | 23.18 | 12.76 | 25.06 | 48.03 | 46.97 | 26.19 |
| Il | 1.96 | 1.39 | 1.10 | 0.95 | 0.94 | 0.83 | 0.54 | 1.08 | 1.02 |
| Starting Material: Temperature (°C): | 66SAL-1 1400 | 1611+ H ₂ O 1460 | 1611+ H ₂ O 1475 | 1611+ H ₂ O 1500 | 1611+ H ₂ O 1525 | 1611+ H ₂ O 1550 | 1611+ H ₂ O* 1550 | 1611+ H ₂ O* 1600 | 1611+ H ₂ O 1750 |
| SiO ₂ | 46.80 | 45.10 | 46.70 | 48.40 | 46.30 | 46.40 | 47.00 | 46.10 | 46.10 |
| TiO ₂ | 0.90 | 1.10 | 0.90 | 0.90 | 0.50 | 0.40 | 0.40 | 0.40 | 0.40 |
| Al ₂ O ₃ | 12.60 | 11.00 | 10.40 | 10.70 | 7.50 | 4.80 | 4.60 | 4.40 | 4.40 |
| FeO† | 8.80 | 13.60 | 13.40 | 12.00 | 12.20 | 13.90 | 13.80 | 13.70 | 13.70 |
| MnO | 0.20 | 0.30 | 0.20 | 0.20 | 0.30 | 0.10 | 0.20 | 0.10 | 0.10 |
| MgO | 16.30 | 13.70 | 16.00 | 13.30 | 23.40 | 27.60 | 28.00 | 29.50 | 29.50 |
| CaO | 12.60 | 13.40 | 9.90 | 12.70 | 8.00 | 5.40 | 5.40 | 5.10 | 5.10 |
| Na ₂ O | 1.20 | 1.10 | 1.50 | 1.30 | 0.90 | 0.60 | 0.60 | 0.50 | 0.50 |
| K ₂ O | 0.10 | 0.50 | 0.60 | 0.50 | 0.40 | 0.20 | 0.20 | 0.20 | 0.20 |
| Totals | 99.50 | 99.80 | 99.60 | 100.00 | 99.50 | 99.40 | 100.20 | 100.00 | 100.00 |
| Cationic norm | | | | | | | | | |
| Or | 0.58 | 3.19 | 3.39 | 2.89 | 2.46 | 1.36 | 1.30 | 1.23 | 1.23 |
| Ab | 10.56 | 2.77 | 13.50 | 11.45 | 8.07 | 5.00 | 4.87 | 4.51 | 4.51 |
| An | 28.15 | 23.51 | 19.63 | 21.92 | 14.51 | 9.40 | 8.87 | 8.51 | 8.51 |
| Ne | 0 | 4.21 | 0 | 0 | 0 | 0 | 0 | 0 | 0 |
| Lc | 0 | 0 | 0 | 0 | 0 | 0 | 0 | 0 | 0 |
| Cpx | 26.53 | 34.34 | 23.17 | 32.68 | 19.07 | 13.07 | 13.32 | 12.38 | 12.38 |
| Opx | 1.87 | 0 | 1.07 | 5.95 | 8.24 | 21.67 | 23.15 | 18.91 | 18.91 |
| Ol | 31.08 | 30.56 | 38.04 | 23.91 | 46.96 | 48.96 | 47.93 | 53.94 | 53.94 |
| Il | 1.23 | 1.42 | 1.20 | 1.21 | 0.70 | 0.70 | 0.56 | 0.52 | 0.52 |

* Liquid composition calculated from mass balance (proportions of olivine and coexisting liquid are known).

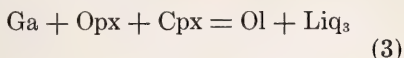
† Total iron as FeO.



In the higher temperature melting interval of sample 1611, the clinopyroxene is pigeonite, and the melting reaction is



Although liquid compositions could not be obtained from the 35-kbar experiments, the data of Kushiro and Yoder (*Year Book 73*, pp. 266-269) suggest that the reaction



describes the melting of sample 1611 within the stability interval of garnet.

The data summarized here strongly support the contention that partial melting of peridotite in the upper mantle is closely approximated by experiments in some simple systems such as $\text{CaSiO}_3\text{-MgSiO}_3\text{-Al}_2\text{O}_3$. The partial melts are thus compositionally controlled by their coexisting silicate minerals and not by the proportion of minerals, as sometimes suggested in developments of petrogenetic grids for partial melting in a peridotitic mantle (e.g., Green and Ringwood, 1967).

MELTING RELATIONS OF ULTRAMAFIC LAVAS (KOMATIITES) AT 1 ATM AND HIGH PRESSURE

N. T. Arndt

Viljoen and Viljoen (1969) presented evidence that certain ultramafic rocks in the Barberton Mountain Land, South Africa, were extrusive in origin. They called these rock types "komatiites" and proposed that many of them formed from magmas of ultrabasic composition. Critical to their interpretation are spinifex-textured lavas (Pyke, Naldrett, and Eckstrand, 1973), which contain large skeletal plates of olivine and are believed to have formed by rapid cooling of phenocryst-free ultrabasic liquids (Nesbitt, 1971; Donaldson, 1974). Komatiites have now been recognized in many other Archean shield areas, in-

cluding Australia (Williams, 1972), Canada (Pyke, Naldrett, and Eckstrand, 1973), India (Viswanathan, 1974), and South Africa (Bickle, Martin, and Nisbet, 1975), and also have been reported from the Paleozoic Rambler Group in Newfoundland (Gale, 1973). In an attempt to investigate their formation and differentiation, several samples of spinifex-textured peridotitic komatiite from Munro Township, Ontario (Arndt, 1975), and several synthesized mixtures of komatiitic composition were studied in a series of experiments at high temperatures and over a range of pressures.

The first sample studied (SA 3091, Table 17) is a split from drill core through an entire spinifex-textured portion of a peridotitic komatiite lava flow (Pyke, Naldrett, and Eckstrand, 1973). In this sample, large blades of skeletal olivine (up to 2 cm long but only 0.05 mm thick; 40%) occur in a groundmass of fine, skeletal subcalcic augite (45%) and devitrified glass (15%). Approximately 60% of the olivine is serpentinized, but the clinopyroxene is fresh, and the sample was presumed to have a composition similar to that of the original ultrabasic lava except for the addition of water. Comparison of the phase relations of this sample, as determined in the laboratory, with the order of appearance of crystalline phases in komatiitic lava flows, as judged from petrographic study, raised questions related to the temperature of appearance of clinopyroxene, which led to the investigation of two less mafic lavas (samples FC-1 and FSX) and several synthesized komatiites (samples SKIB, SKIE, and FSXA).

The crushed lava samples were heated at 900°C in nitrogen for 30 min to break down hydrous minerals and then were ground under alcohol to an average grain size of less than 10 μm . The oxide mixtures were ground to the same grain size.

High-pressure experiments were run in a solid-media apparatus of design similar

to that described by Boyd and England (1960), using the piston-out technique and no friction correction. Temperatures were measured with W3%Re/W25%Re thermocouples. Charges were enclosed in graphite capsules that were then welded inside platinum capsules. Because the double capsules are relatively long, temperatures at the center of the capsules were significantly higher than at the thermocouples. A series of measurements showed that the difference was 20°–30°C, so a correction of 25°C was applied to all high-pressure results.

The 1-atm runs were made in vertical quenching furnaces with oxygen fugacities controlled by gas mixing. Samples were suspended on loops of fine platinum wire, using a technique similar to that of Presnall and Brenner (1974). The ratio of CO₂ to H₂ was kept at a constant value such that oxygen fugacities were maintained within the wüstite field, approximately at a constant interval from the magnetite-wüstite buffer curve ($f_{O_2} = 10^{-12}$ and 10^{-9} bar at 1100° and 1400°C, respectively).

The phase relations of the peridotitic komatiite sample SA 3091 as determined

by the 1-atm and high-pressure studies are shown in Fig. 27. Although the relations resemble those of other types of peridotite (Ito and Kennedy, 1967; Kushiro, Syono, and Akimoto, 1968; Green, 1970; Green *et al.*, 1975; Mysen and Kushiro, this Report), there are significant differences. Olivine is the liquidus phase at all pressures studied but is joined at lower temperatures by a calcic pyroxene, not orthopyroxene as in the other peridotites. At 1 atm the pyroxene has a diopsidic composition with 19 wt % CaO and 4 wt % Al₂O₃ (Table 17). As the pressure increases, the CaO content first decreases to a minimum of 8–12 wt % at 20–30 kbar, then increases slightly to 12–15 wt % as garnet appears at pressures above 35 kbar. The Al₂O₃ content increases to a maximum of 6–8 wt % at 20 kbar, then decreases to 4–6 wt % at 40 kbar. Thus the pyroxenes have subcalcic augite compositions at pressures of 10 and 40 kbar and aluminous pigeonite compositions at pressures between 20 and 30 kbar. The compositions of these pyroxenes in any given run are uniform and their Mg/Fe matches those of coexisting olivine (Ta-

TABLE 17. Electron Microprobe Analyses of Starting Materials* and Run Products

| | 1 | 2 | 3 | 4 | 5 | 6 | 7 |
|--------------------------------|-------|------|-------|-------|-------|-------|-------|
| SiO ₂ | 45.4 | 47.6 | 50.4 | 50.0 | 48.3 | 53.3 | 51.4 |
| TiO ₂ | 0.39 | 0.50 | 0.57 | 0.69 | 0.57 | 0.52 | 0.47 |
| Al ₂ O ₃ | 7.5 | 11.0 | 10.5 | 11.7 | 11.2 | 8.7 | 9.8 |
| Cr ₂ O ₃ | 0.40 | 0.40 | 0.20 | 0.10 | 0.26 | 0.18 | 0.22 |
| FeO† | 12.9 | 13.5 | 11.7 | 8.4 | 12.7 | 9.4 | 9.6 |
| MnO | 0.28 | 0.29 | 0.22 | 0.18 | 0.0 | 0.22 | 0.0 |
| MgO | 25.1 | 15.4 | 16.1 | 11.1 | 14.9 | 14.0 | 12.7 |
| CaO | 7.4 | 10.2 | 8.2 | 18.1 | 10.9 | 11.8 | 15.4 |
| Na ₂ O | 0.73 | 0.56 | 1.99 | 0.16 | 1.25 | 1.86 | 0.36 |
| Totals | 100.1 | 99.4 | 99.9 | 100.4 | 100.1 | 99.9 | 100.0 |
| Cationic Norms | | | | | | | |
| Q | 0.0 | 0.0 | 0.0 | 0.0 | 0.0 | 0.0 | 0.72 |
| Ab | 6.3 | 5.0 | 17.6 | 1.4 | 11.1 | 16.7 | 3.2 |
| An | 16.3 | 27.6 | 19.4 | 31.3 | 24.8 | 15.4 | 25.3 |
| Cpx | 15.1 | 18.6 | 16.5 | 47.0 | 23.1 | 34.5 | 41.2 |
| Opx | 12.2 | 29.2 | 24.7 | 18.6 | 17.0 | 24.4 | 28.9 |
| Ol | 49.6 | 18.8 | 21.0 | 0.7 | 23.3 | 8.3 | 0.0 |
| Ilm | 0.52 | 0.70 | 0.78 | 0.96 | 0.79 | 0.72 | 0.66 |
| Totals | 100.0 | 99.9 | 100.0 | 100.0 | 100.1 | 100.0 | 100.0 |

TABLE 17 Continued. Electron Microprobe Analyses of Starting Materials* and Run Products

| | 8 | 9 | 10 | 11 | 12 | 13 | 14 |
|--------------------------------|-------|-------|-------|-------|-------|-------|-------|
| SiO ₂ | 39.3 | 50.8 | 51.1 | 50.8 | 0.44 | 0.94 | 42.3 |
| TiO ₂ | 0.00 | 0.38 | 0.21 | 0.17 | 0.34 | 0.21 | 0.30 |
| Al ₂ O ₃ | 0.18 | 4.37 | 6.06 | 7.41 | 25.1 | 51.5 | 21.6 |
| Cr ₂ O ₃ | 0.11 | 1.25 | 0.37 | 0.60 | 42.6 | 11.7 | 1.27 |
| Fe ₂ O ₃ | 19.7† | 6.33 | 9.1 | 10.2 | 2.3‡ | 2.9 | 10.6 |
| FeO | | | | | 12.9 | 13.9 | |
| MnO | 0.25 | 0.19 | 0.26 | 0.25 | 0.35 | 0.18 | 0.32 |
| MgO | 40.5 | 17.2 | 18.2 | 20.3 | 15.1 | 17.7 | 18.2 |
| CaO | 0.33 | 19.1 | 12.8 | 9.8 | 0.18 | 0.11 | 6.0 |
| Na ₂ O | 0.00 | 0.12 | 1.20 | 0.52 | 0.05 | 0.05 | 0.05 |
| Totals | 100.4 | 99.7 | 99.3 | 100.1 | 99.3 | 99.1 | 100.6 |
| Structural formulae | | | | | | | |
| O | 4 | 6 | 6 | 6 | 4 | 4 | 12 |
| Si | 1.004 | 1.867 | 1.873 | 1.841 | 0.013 | 0.025 | 3.033 |
| Ti | 0.000 | 0.009 | 0.005 | 0.003 | 0.007 | 0.004 | 0.015 |
| Al | 0.005 | 0.188 | 0.261 | 0.312 | 0.891 | 1.633 | 1.817 |
| Cr | 0.002 | 0.035 | 0.011 | 0.016 | 1.015 | 0.249 | 0.069 |
| Fe ³⁺ | | | | | 0.053 | 0.059 | |
| | 0.420 | 0.194 | 0.277 | 0.309 | | | 0.620 |
| Fe ²⁺ | | | | | 0.325 | 0.312 | |
| Mn | 0.005 | 0.005 | 0.007 | 0.007 | 0.009 | 0.004 | 0.018 |
| Mg | 1.541 | 0.943 | 0.996 | 1.093 | 0.678 | 0.710 | 1.944 |
| Ca | 0.008 | 0.752 | 0.502 | 0.381 | 0.005 | 0.003 | 0.454 |
| Na | 0.000 | 0.008 | 0.083 | 0.042 | 0.001 | 0.000 | 0.003 |
| Totals | 2.985 | 4.003 | 4.017 | 4.001 | 3.000 | 3.000 | 7.973 |

* Samples were melted and quenched, and the resultant glasses were analyzed with the electron microprobe.

† Total iron as FeO.

‡ Calculated from structural formula.

1. SA 3091: Peridotitic komatite, spinifex-textured lava from Munro Township.
2. Glass produced at 1350°C, 1 atm from SA 3091.
3. FSX: Pyroxene spinifex-textured flowtop of thick, layered flow, Munro Township.
4. FC-1: Pyroxene spinifex-textured flowtop of thick, layered flow, Alexo area.
5. SKIB: Synthesized mixture with composition matching the 1350°C, 1-atm glass from SA 3091.
6. FSXA: Sample FSX with additional CaO and SiO₂.
7. SKIE: Sample SKIB with additional CaO and SiO₂.
8. Olivine, SA 3091 at 1425°C, 20 kbar.
9. Calcic pyroxene, diopside, SA 3091 at 1165°C, 1 atm.
10. Calcic pyroxene, subcalcic augite, SA 3091 at 1350°C, 10 kbar.
11. Calcic pyroxene, aluminous pigeonite, SA 3091 at 1425°C, 20 kbar.
12. Spinel, chrome-rich, SA 3091 at 1425°C, 10 kbar.
13. Spinel, aluminum-rich, SA 3091 at 1425°C, 20 kbar.
14. Garnet, SA 3091, 1625°C, 40 kbar.

ble 17). Similar pyroxenes are formed in synthetic komatiite compositions, and there seems no doubt that they are stable, equilibrium phases and not quench products.

Aluminous phases appear only at temperatures close to the solidus. As the pressure increases, the dominant alumi-

nous phase changes from plagioclase at 1 atm, to spinel at 10–30 kbar, and to garnet at 40 kbar. Chromite coexists with plagioclase at 1 atm and also is present at high temperatures at 10–20 kbar, but as the temperature drops at these pressures the Al₂O₃ content of the spinel increases, the Cr₂O₃ content drops,

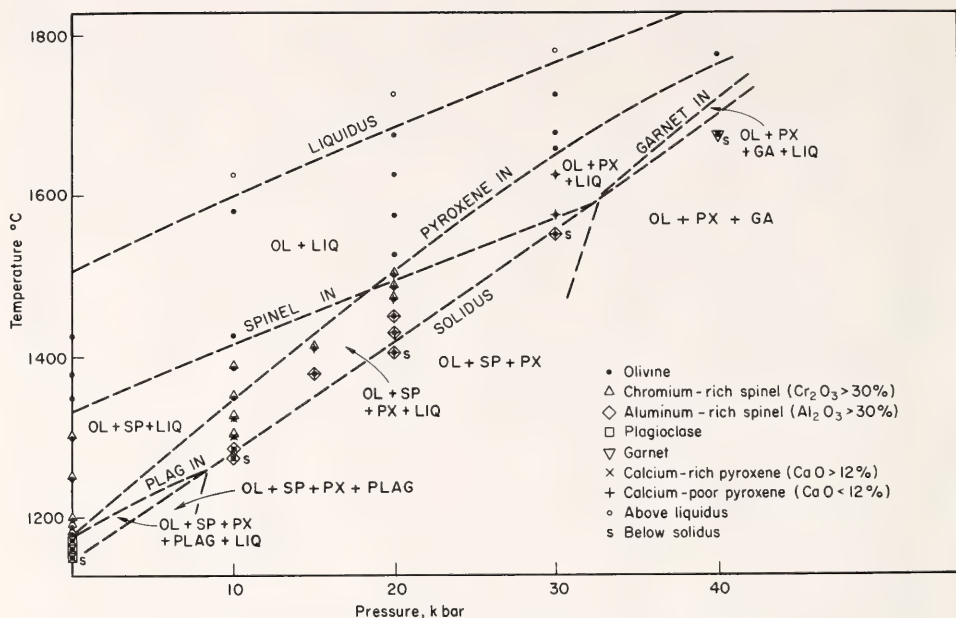


Fig. 27. Phase relations of peridotitic komatiite sample SA 3091.

and it becomes the major aluminous phase.

In Fig. 28 electron microprobe analyses of glasses in equilibrium with crystalline phases are projected into the ol-cpx-qtz plane of the ol-cpx-plag-qtz "system" (Irvine, 1970). Glasses produced at 1 atm and high pressure are included. The dominant trend of olivine subtraction extends from the starting composition (SA 3091) to the 1200°C, 1-atm glass composition, at which point olivine is joined by calcic pyroxene, and the two phases crystallize together to produce a trend away from the ol-cpx boundary. Phase boundaries deduced from this behavior agree with those outlined by Irvine (1970) from Yoder and Tilley's (1962) experimental data on basalts.

An important feature of Figs. 27 and 28 is the wide interval between the liquidus and the appearance of the second silicate phase. Not even at the highest pressure applied (40 kbar) did pyroxene or garnet crystallize close to the liquidus, indicating that this komatiitic liquid cannot have formed as a liquid at or

near the minimum melting temperature of source rock, down to depths of about 120 km. If the pyroxene and garnet liquidus curves are extrapolated to higher pressures (ca. 50–60 kbar), they do meet on the liquidus, and komatiites may be formed as minimum melting liquids under these conditions. However, alternative mechanisms involving a high degree of melting of normal mantle, or a lower degree of melting of mantle depleted in its low-melting fraction, may be more plausible.

In Fig. 29A, the electron microprobe analyses of glasses formed in 1-atm runs are plotted in terms of weight percentage of MgO, CaO, and Al_2O_3 . As was shown in Fig. 28, olivine is the only phase to crystallize in sample SA 3091 from the liquidus down to 1200°C. At lower temperatures clinopyroxene crystallizes with olivine or plagioclase, and the liquid compositions move away from the MgO-CaO boundary. The liquid in which clinopyroxene first appears contains about 9 wt % MgO.

In Fig. 29B, whole-rock compositions of noncumulate lavas from Munro

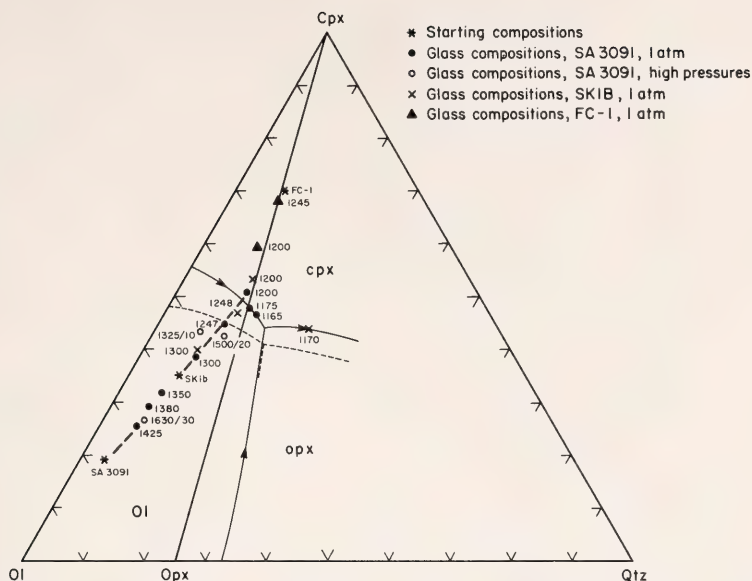


Fig. 28. Compositions of glasses produced by melting samples SA 3091, SKIB, and FC-1 at 1 atm and high pressure, projected into the ol-cpx-qtz plane of the ol-cpx-plag-qtz "system." Beside each point representing a glass composition is shown the run temperature for 1-atm experiments and the run temperature and pressure for high-pressure experiments. The phase boundaries shown by solid lines are deduced from the results of experiments on sample SA 3091; the phase boundaries shown by dashed lines are from Irvine (1970).

Township are plotted in the same type of diagram. These liquids form a series similar to that produced by the SA 3091 glasses, except that the corner in the curve corresponding to the appearance of clinopyroxene occurs at about 14 wt % MgO, not 9 wt %. Clinopyroxene apparently crystallizes in natural lavas with compositions similar to the composition of the 1300°C glass produced from SA 3091, i.e., at temperatures about 100°C higher than the clinopyroxene liquidus under experimental conditions.

To explore this discrepancy, melting experiments were carried out on the spinifex-textured mafic komatiite lavas FSX and FC-1 and the synthesized komatiites SKIB and SKIE (Table 17). As is shown in Fig. 29A, FSX and SKIB, which have compositions similar to the composition of the glass quenched from SA 3091 at 1350°C, have the same crystallization behavior as SA 3091: even though FSX contains both clinopyrox-

ene and orthopyroxene and is devoid of olivine, it crystallizes only olivine to temperatures as much as 120°C below its liquidus. Only FC-1 and SKIE, which have CaO/Al₂O₃ greater than 1.5, have clinopyroxene on the liquidus.

A number of explanations for the enhanced crystallization of pyroxene in the lavas were considered, and the more plausible of these were tested experimentally. In most cases the factors considered could be shown to have an effect opposite to what is required or to exert only minimal influence. For example, the presence of volatiles in the lavas could have enhanced pyroxene crystallization, but water would only inhibit orthopyroxene crystallization and would have little effect on clinopyroxene (Kushiro, 1969b), and carbon dioxide is so insoluble at low pressures that its effect would be negligible (Eggler, *Year Book* 73). Similarly, experiments at high oxygen fugacities produced abundant mag-

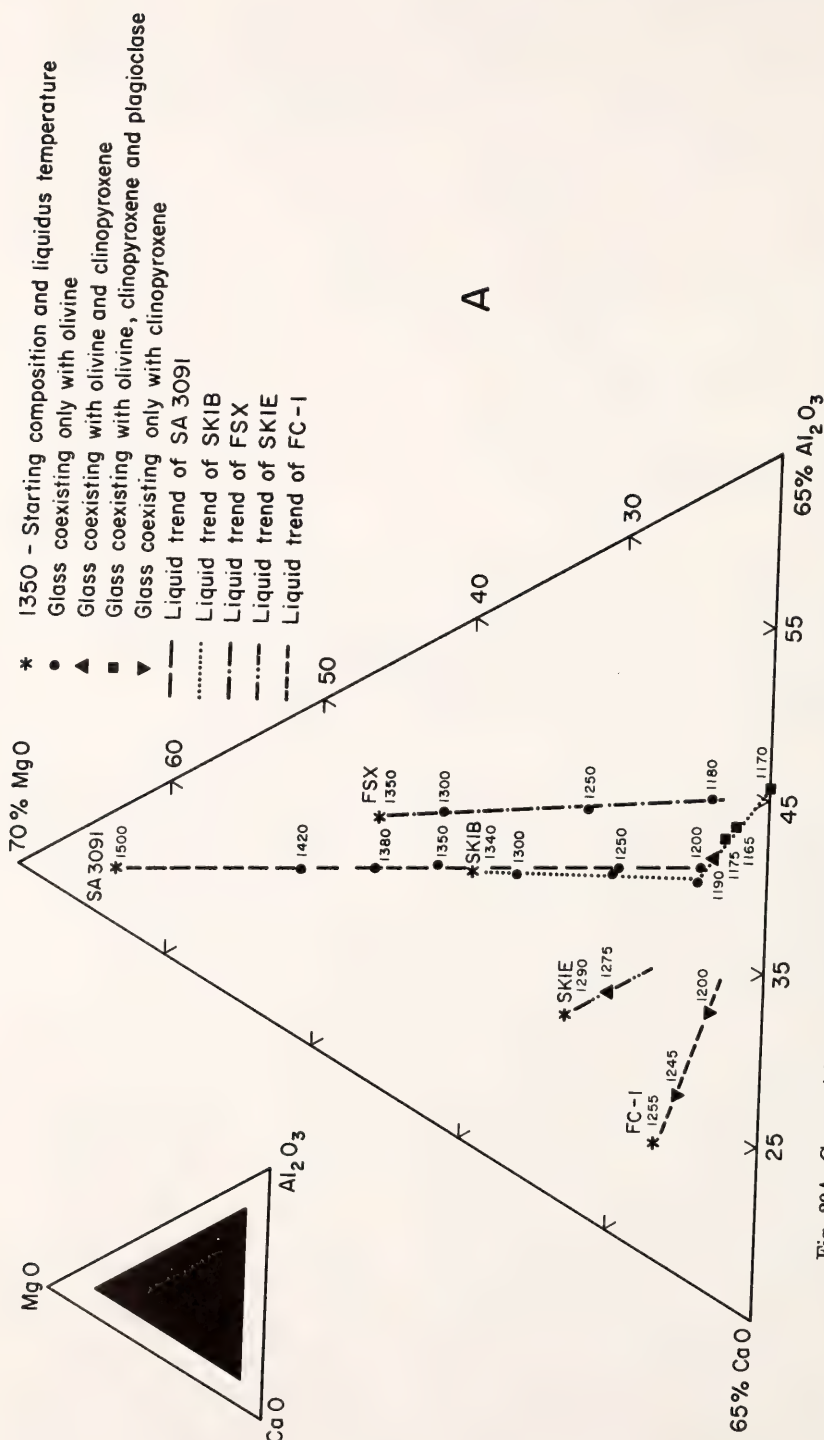


Fig. 29A. Compositions of glasses produced by melting natural and synthetic komatiite samples at 1 atm.

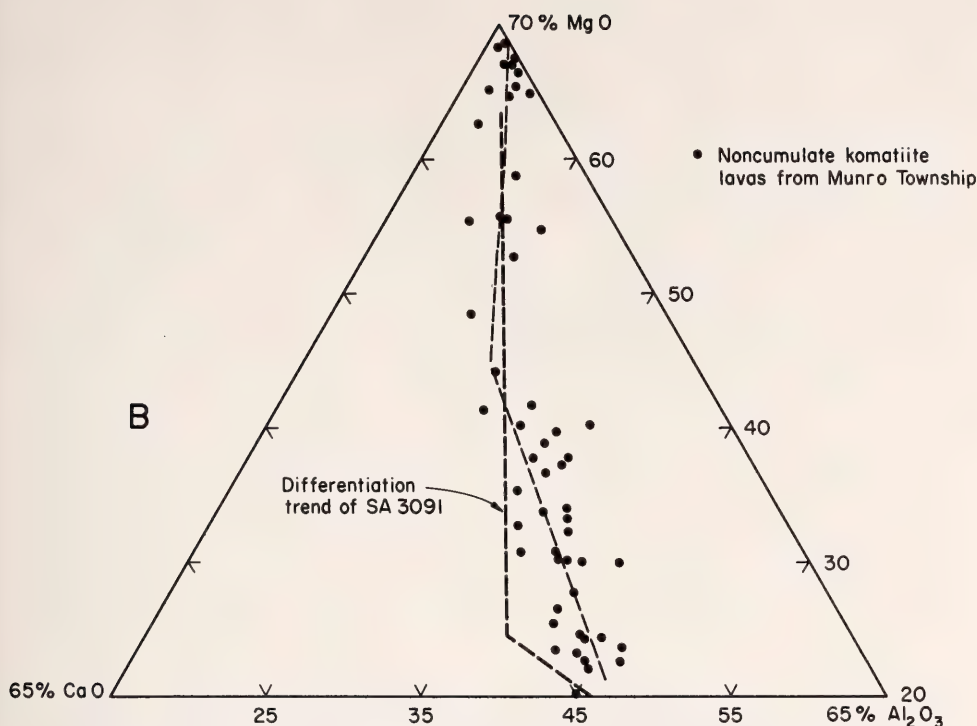


Fig. 29B. Compositions of noncumulate komatiitic lavas from Munro Township, Ontario.

netite but did not crystallize clinopyroxene at significantly higher temperatures. The appearance of clinopyroxene on the liquidus in sample SKIB at 20 kbar suggested that high-pressure differentiation could be important, but petrographic studies show that clinopyroxene and orthopyroxene are the first phases to crystallize, presumably at pressures close to 1 atm, in lavas of composition similar to that of SKIB. Finally, the rapid cooling required to produce spinifex texture (Nesbitt, 1971) probably inhibits clinopyroxene crystallization but only slightly suppresses olivine, according to experiments on SKIB and FSX and data of Donaldson (1974), Gibb (1974), and Walker *et al.* (1976).

The explanation that best fits the experimental results is that the Munro samples are altered and do not accurately represent the original lava compositions. Numerous studies (e.g., Hart,

1970; Shido, Miyashiro, and Ewing, 1974; Bischoff and Dickson, 1975) have shown that a fresh basalt subjected to seawater alteration or low-grade metamorphism loses CaO and SiO₂, gains MgO, and loses or gains alkali elements, depending on the type of alteration. Experiments on samples FC-1, the lava with high CaO/Al₂O₃, and SKIE, the synthesized komatiite with similar composition, show that higher CaO contents cause clinopyroxene to crystallize in more mafic compositions (Fig. 29A). Similarly, higher SiO₂ or alkali element contents would explain the presence of orthopyroxene in some lavas and its absence from experimental runs. However, an explanation requiring the loss of CaO and SiO₂ from the Munro komatiite samples is inconsistent with abundant field, petrographic, and chemical data, indicating that in Munro Township (Pyke, Naldrett, and Eckstrand, 1973;

Arndt, 1975) as well as in Western Australia (Williams, 1972; Nesbitt and Sun, 1976) and southern Africa (Bickle, Martin, and Nisbet, 1975), the freshest komatiites have $\text{CaO}/\text{Al}_2\text{O}_3$ close to 1.

PHASE RELATIONS OF MAFIC LAYERS IN THE RONDA PERIDOTITE

Masaaki Obata and John S. Dickey, Jr.

Five mineral assemblages had been recognized in magmatic-type mafic layers of the Ronda peridotite massif in Spain (Dickey, 1970). Recent extensive remapping of the massif and petrographic studies led to a redefinition of the layers and their distribution in the massif in terms of three mineral assemblage groups characterized by the presence or absence of garnet and olivine:

Group I. Garnet pyroxenites

- (a) Cpx + Gar + Plag
- (b) Cpx + Opx + Gar
- (c) Cpx + Gar
- (d) Cpx + Gar + Plag + Qz
- (e) Cpx + Opx + Gar + green Sp (ceylonite)

Group II. Pyroxenites

- (a) Cpx + Opx \pm green Sp
- (b) Cpx + Opx + green Sp + Plag
- (c) Cpx

Group III. Olivine gabbros

- (a) Cpx + Ol + Plag + Opx + brown Sp (picotite)
- (b) Cpx + Ol + Plag + Opx + opaque Sp (chromite)

Layers of the groups are distributed in the massif from west to east (Fig. 30), corresponding (with a few exceptions near the south contact) to an easterly decrease in pressure. Most of the layers have complex textures owing to incomplete subsolidus reactions: Garnets typically have kelyphite rims; pyroxenes reveal exsolution lamellae; and Al-rich pyroxenes are breaking down to fine-grained mixtures of olivine, plagioclase, spinel, and Al-poor pyroxenes. The present mineral assemblages do not represent the original conditions of crystallization

of magma (in contrast to the interpretation of Dickey, 1970) but simply reflect the metamorphic conditions of the massif.

Peridotites are predominantly harzburgite followed in abundance by lherzolite and dunite. Pyrope-rich garnet ($\text{Py}_{70}\text{Gross}_{12}\text{Alm}_{18}$) occurs locally in the lherzolite in the west of the massif (Fig. 30). Plagioclase surrounds spinel in the east.

A study has been made of the high-pressure phase relations of a plagioclase-garnet pyroxenite layer that occurs in spinel lherzolite in the massif. The experiments were conducted in graphite crucibles in a $\frac{1}{2}$ -in diameter, solid-media, high-pressure apparatus (Boyd and England, 1960), using the piston-out technique. Sealed $\text{Pt}_{95}\text{Au}_5$ crucibles were also used for long runs near solidus temperatures to avoid possible introduction of water by the dehydration of the assembly parts. The analyzed rock powder (Table 18), which contained garnet, plagioclase, and clinopyroxene ($10\ \mu\text{m}$), was used for liquidus runs. Glass prepared from the rock powder (by fusion in $\text{Pt}_{95}\text{Au}_5$ foil in N_2 gas at 1 atm and 1400°C), mixtures of 70 wt % glass and 30 wt % rock powder, or mixtures of 95 wt % glass and 5 wt % garnet that had been separated from the rock were used for subsolidus runs. Except for a few low-temperature runs in which the charge was slightly moistened (breathed on) before loading, the loaded capsules were dried by heating to glowing red with a gas torch for 30 sec immediately prior to the run. Run times ranged from 20 min to 12 hr. Run products were identified by optical, x-ray diffraction, and electron microprobe methods.

The experimental results are summarized in Fig. 31. At pressures up to 8 kbar, olivine (Fo_{85}), clinopyroxene, and plagioclase all crystallize within 25° of the liquidus, but above 8 kbar clinopyroxene is the sole liquidus phase. From 8 to 20 kbar, clinopyroxene is followed by plagioclase with decreasing temperature. Olivine is not stable above 9 kbar.

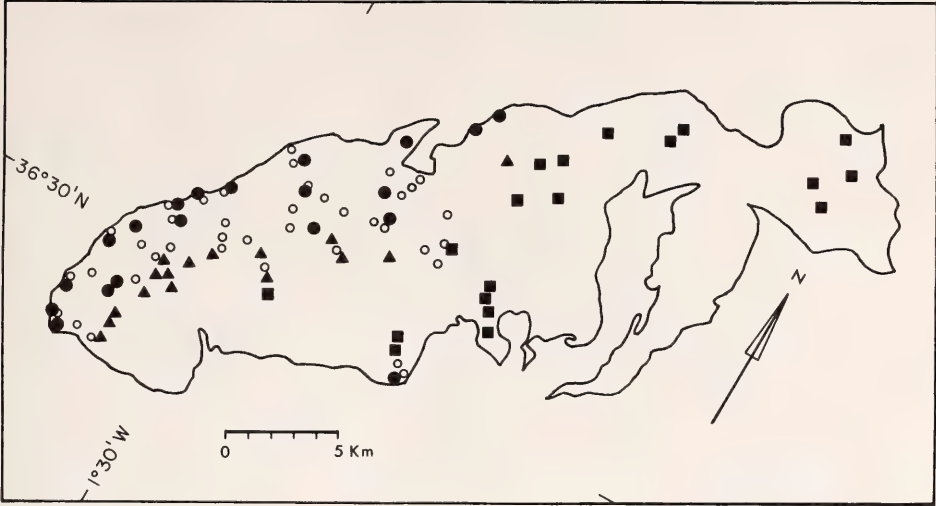


Fig. 30. Regional distribution of the three groups of the mafic layers and garnet peridotites. Open circles, garnet pyroxenites; triangles, pyroxenites; squares, olivine gabbro; solid circles, garnet peridotites.

Garnet first appears above the solidus at about 18 kbar and expands its field toward higher pressure. The plagioclase field decreases with increasing pressure and pinches out at 29 kbar.

Four different subsolidus assemblages

TABLE 18. Chemical Analysis and CIPW Norm of Plagioclase-Garnet Clinopyroxene R127*

| | | | |
|--------------------------------|-------|-------|-------|
| SiO ₂ | 47.73 | Or | ... |
| TiO ₂ | 0.73 | Ab | 15.76 |
| Al ₂ O ₃ | 16.16 | An | 35.61 |
| Cr ₂ O ₃ | 0.00 | Ne | 0.12 |
| Fe ₂ O ₃ | 0.94 | Di | 28.02 |
| FeO | 7.84 | Hy | ... |
| MnO | 0.15 | Ol | 17.19 |
| MgO | 9.88 | Mt | 1.36 |
| CaO | 14.15 | Chr | ... |
| Na ₂ O | 1.89 | Ilm | 1.39 |
| K ₂ O | 0.01 | Rest | 0.35 |
| H ₂ O ⁺ | 0.35 | | |
| H ₂ O ⁻ | 0.06 | Total | 99.82 |
| P ₂ O ₅ | 0.00 | | |
| NiO | 0.01 | | |
| SO ₄ | 0.00 | | |
| Total | 99.88 | | |

* Mode: 61% Cpx, 23% Plag, 5% Gar, 11% kelyphite (Dickey, 1970).

have been identified: clinopyroxene + plagioclase + olivine; clinopyroxene + plagioclase; clinopyroxene + plagioclase + garnet; and clinopyroxene + garnet + quartz. The olivine of the first assemblage disappears at the boundary A (Fig. 31) by reacting with plagioclase to form aluminous pyroxene components. Garnet appears at boundary B and increases in abundance with pressure toward the boundary C, where plagioclase disappears. Boundaries A and B are established on the basis of marked changes in the kind and abundance of phases. Boundary C was difficult to locate precisely because plagioclase is too sparse to be detected by x-ray powder diffraction and must be identified by optical and electron microprobe methods. Plagioclase (An 40-50) in addition to clinopyroxene and garnet was formed from glass up to 27 kbar at 1250°C. Trace amounts of quartz were identified by scanning electron microscopy in some of the runs beyond boundary C.

The mineral assemblage of the original rock, plagioclase + garnet + clinopyroxene, is apparently stable over a

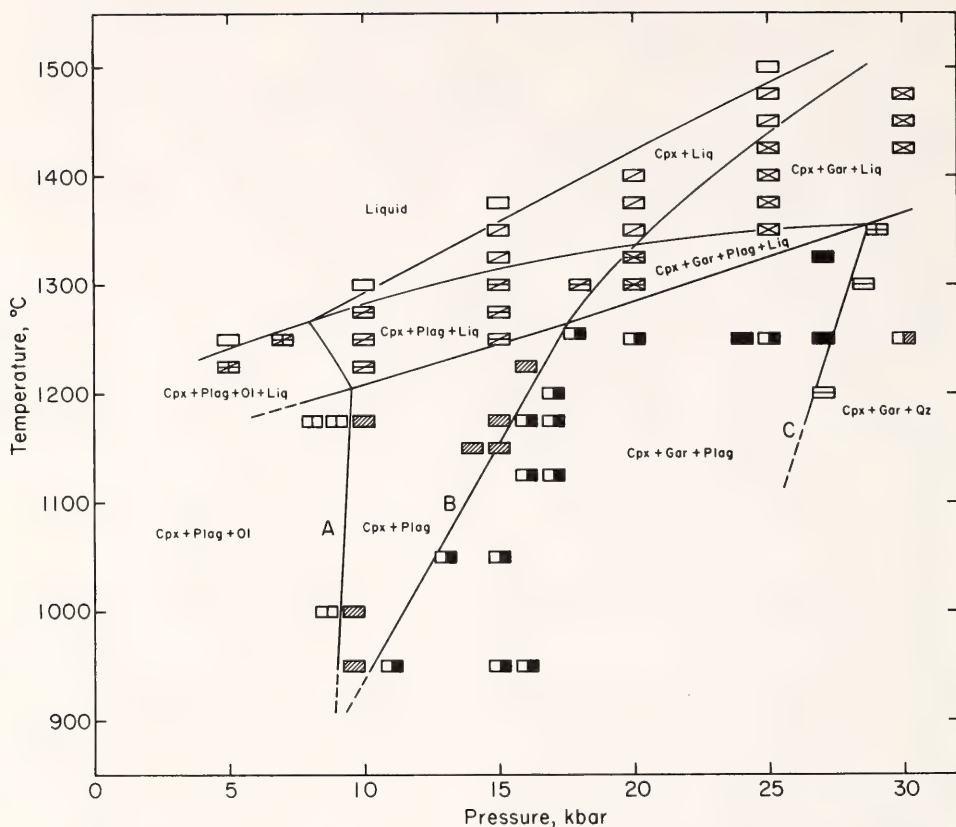


Fig. 31. Pressure-temperature diagram for the composition of plagioclase-garnet clinopyroxene R127. Symbols in the subsolidus region: open rectangles with vertical line, Cpx + Plag + Ol formed from glass when seeded with a small amount of rock powder; shaded rectangles, Cpx + Plag formed from glass when seeded with a small amount of rock powder; half-solid rectangles, Cpx + Gar + Plag formed from glass when seeded with a small amount of rock powder; solid rectangles, Cpx + Gar + Plag formed from glass; open rectangles with horizontal line, Cpx + Gar + Qz formed from glass; crossed open rectangles, Cpx + Gar + Qz formed from glass when seeded with a small amount of garnet; half-shaded rectangle, Cpx + Gar + Qz formed from glass when seeded with a small amount of rock powder.

broad P - T interval, and it would be expected that the phases would vary in composition through this field. However, because of the fine grain size of the subsolidus run products and their complex textural intergrowths, the phases could rarely be analyzed with the electron microprobe. As an alternative, the compositional changes have been monitored indirectly by x-ray diffraction methods by measuring the 2θ difference between the (221) peak of clinopyroxene and the (420) peak of garnet. The re-

sults (Fig. 32) indicate that this $\Delta 2\theta$ changes systematically over the temperature-pressure field of the assemblage and that the natural rock equilibrated at a temperature of 800°–900°C.

A successful electron microprobe analysis was obtained for a clinopyroxene formed with garnet at 1250°C and 30 kbar (5.7 hr), and the result is compared in Table 19 with an analysis of the pyroxene in the original rock. The synthetic pyroxene is exceptionally high in Al_2O_3 , and the sum of cations per 6

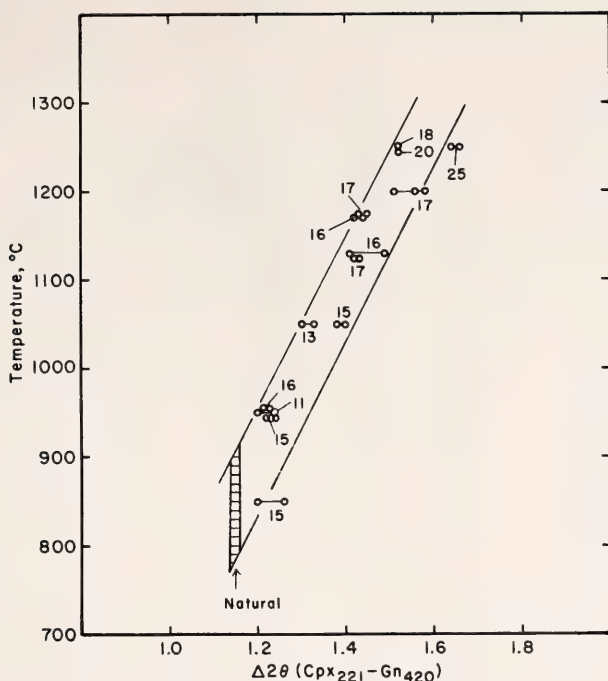


Fig. 32. Temperature versus $\Delta 2\theta$ ($\text{Cpx}_{221}\text{-Gn}_{420}$) diagram for garnets and clinopyroxenes coexisting with plagioclase in experimental run products synthesized from the composition of plagioclase-garnet clinopyroxenite R127. Numbers on data points are pressures in kilobars. Each point is a single measurement.

oxygens is unusually low. Expressed in terms of end-member components with all iron as FeO, the analysis shows 3.8 wt % excess silica. If any of the iron is ferric, the silica excess is even larger. Excess silica is not common in pyroxenes but has previously been reported in both natural and synthetic clinopyroxenes formed at high pressures (Sobolev, Kuznetsova, and Zyuzin, 1968; Kushiro, 1969a; Wood, this Report).

The experimental results give the following constraints of P - T conditions for three alternative hypotheses for the origin of the layer:

1. If the mafic layers were formed by partial fusion of peridotite without subsequent fractional crystallization, as suggested by Dickey (1970), the fusion must have occurred at less than 8 kbar (24 km), which is the maximum pressure at which olivine is a liquidus phase.

The liquid would crystallize initially to olivine gabbro but might be later metamorphosed, under increasing pressure, to the assemblage garnet + plagioclase + clinopyroxene.

2. If partial fusion of dry peridotite occurred at pressures greater than 8 kbar, it must have been followed by fractional crystallization of olivine from the melt at a pressure less than 30 kbar. Because of the reaction relationship of olivine with liquid below 30 kbar (Kushiro and Yoder, *Year Book* 73, pp. 266-268), the fractionated liquid could have been displaced from the olivine field.

3. Alternatively, the layers might have formed by fractional crystallization of a mafic or ultramafic magma at pressures between 23 and 30 kbar (from ~69 to 100 km), yielding peridotite and garnet pyroxenite cumulates. The plagioclase might then have formed by

TABLE 19. Clinopyroxene Compositions

| | a | b | c |
|--|-------------|-------|--------|
| SiO ₂ | 49.6 (0.8)* | 48.9 | 51.99 |
| TiO ₂ | 0.8 (0.04) | 1.3 | 0.28 |
| Al ₂ O ₃ | 15.8 (0.4) | 9.0 | 15.75 |
| Cr ₂ O ₃ | 0.1 | 0.1 | 0.03 |
| FeO† | 6.5 (0.5) | 6.6 | 1.98 |
| MnO | 0.1 | 0.1 | tr |
| MgO | 9.0 (0.2) | 12.0 | 10.72 |
| CaO | 15.5 (0.5) | 20.1 | 14.75 |
| Na ₂ O | 2.8 (0.1) | 1.3 | 4.22 |
| Totals | 100.0 | 99.8 | 100.09 |
| Si | 1.787 | 1.805 | 1.828 |
| Ti | 0.021 | 0.035 | 0.008 |
| Al | 0.669 | 0.389 | 0.654 |
| Cr | 0.002 | 0.002 | 0.001 |
| Fe ²⁺ | 0.202 | 0.212 | 0.059 |
| Mn | 0.003 | 0.004 | tr |
| Mg | 0.481 | 0.689 | 0.561 |
| Ca | 0.598 | 0.786 | 0.555 |
| Na | 0.193 | 0.080 | 0.287 |
| Totals | 3.956 | 4.001 | 3.961 |
| NaAlSi ₂ O ₆ | 18.0 | 7.3 | 27.5 |
| CaTiAl ₂ O ₆ | 2.3 | 4.3 | 0.9 |
| CaAl ₂ SiO ₆ | 21.9 | 11.8 | 18.2 |
| Ca ₂ Si ₂ O ₆ | 19.2 | 32.9 | 20.5 |
| Mg ₂ Si ₂ O ₆ | 22.3 | 31.0 | 26.7 |
| Fe ₂ Si ₂ O ₆ | 12.5 | 12.8 | 3.7 |
| SiO ₂ | 3.8 | 0.0‡ | 2.5 |

* Standard deviation of six averaged analyses.

† Total Fe calculated as FeO.

‡ With total Fe calculated as FeO this calculation shows a silica deficiency. Ferric iron is present, however (cf. Table 18), and the silica deficiency is artificial.

a. Clinopyroxene formed at 30 kbar, 1250°C.

b. Natural clinopyroxene in R127.

c. Natural clinopyroxene in kyanite eclogite, Z52, from a kimberlite pipe in Yakutia (Sobolev, Kuznetsova, and Zyuzin, 1968).

subsolidus reactions from jadeitic clinopyroxene during decompression. Plagioclase lamellae in clinopyroxene are common in the mafic layers at Ronda.

Although the presence of H₂O would extend the olivine liquidus to higher pressures (Kushiro, 1969b) and therefore complicate these possibilities, the pyroxenite layers are in fact anhydrous, and it seems unlikely that they ever contained much water.

SOLUBILITY OF AL₂O₃ IN ENSTATITE COEXISTING WITH FORSTERITE AND SPINEL

Toshitsugu Fujii

Solubility of alumina in orthopyroxene has been proposed as a potential geobarometer applicable to peridotite in both the garnet and the spinel stability region (e.g., O'Hara, 1967). Experiments (MacGregor, 1974) conducted to calibrate this geobarometer, however, are internally inconsistent in the spinel stability region, as discussed by Wood (1975), Obata (1975), and Fujii and Takahashi (1976). Therefore, it was necessary to reexamine the alumina content of orthopyroxene coexisting with olivine and spinel and determine whether it is useful as a geobarometer. In this report it is shown that alumina solubility in orthopyroxene is useful as a geothermometer rather than a geobarometer, mainly on the basis of experiments in the system MgO-Al₂O₃-SiO₂.

The data on alumina solubility were obtained from run products (forsterite, spinel, and aluminous enstatite) using a starting material that was a mixture of glass and crystals of the composition En(MgSiO₃)₄ Sp(MgAl₂O₄)₁ (mole %). The material, which was prepared by adding enstatite glass to amesite composition heated at 1580°C, yielded stout subidiomorphic enstatite crystals that contained a few rather large octahedral spinel inclusions.

Experiments were carried out in a 1/2-in. solid-media, high-pressure apparatus (Boyd and England, 1960) using the piston-out method. Graphite capsules were used for all the runs. The starting materials were moisturized by breathing on them except for the runs at 1400°C. Run time ranged from 4 to 45 hr.

Compositions of aluminous enstatite coexisting with forsterite and spinel are plotted in Fig. 33 as percentage of Al in the M1 site ($X_{Al}^{M1} \times 100$; $X_{Al}^{M1} = 2X_{Al}$). The Al content of enstatite is insensitive to pressure at constant tem-

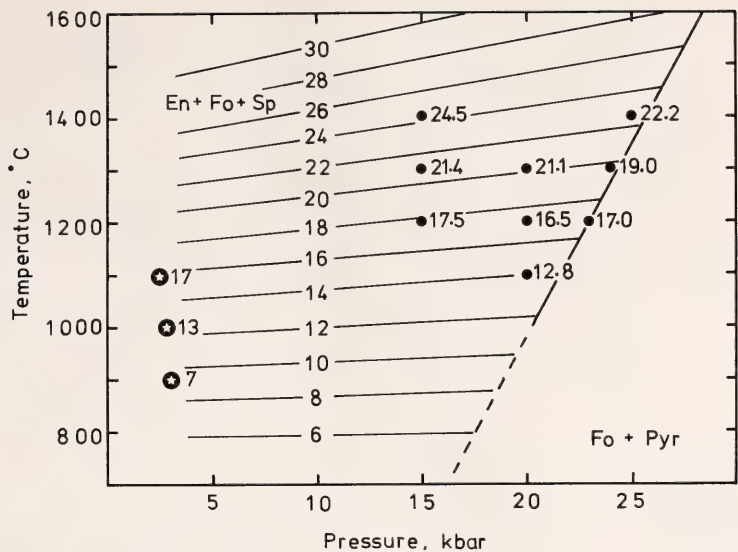
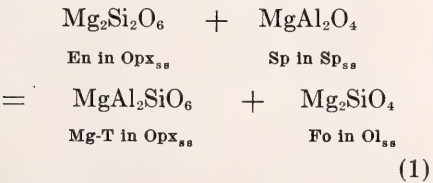


Fig. 33. Alumina solubility in orthopyroxene plotted as functions of pressure and temperature. Solid circles indicate results of this study. Stars indicate data of Anastasiou and Seifert (1972). Numbers beside symbols are percentage of Al in the M1 site of orthopyroxene. Light lines with numbers are calculated isopleths. Heavy line is univariant line delimiting the spinel stability region from the garnet stability region in the system MgO-Al₂O₃-SiO₂ (MacGregor, *Year Book* 63, p. 157; 1974).

perature but increases with increasing temperature at constant pressure. The analyses of coexisting spinel indicate that it does not form a solid solution toward corundum under these experimental conditions, differing from the results of Fawcett and Yoder (*Year Book* 62, pp. 143-145).

The solubility of alumina in enstatite coexisting with forsterite and spinel is expressed by the following reaction:



If the standard state of each component is taken as the pure phase at the pressure and temperature under consideration, the condition for equilibrium of Reaction 1 in the system MgO-Al₂O₃-SiO₂ is (see Table 20 for summary of notations)

$$(\Delta G^\circ)_{P,T} = -RT \ln \frac{a_{\text{MgAl}_2\text{SiO}_6}}{a_{\text{Mg}_2\text{Si}_2\text{O}_6}} \quad (2)$$

According to the two-site, simple-mixture model for orthopyroxene of Wood and Banno (1973), Equation 2 becomes

$$\begin{aligned} (\Delta G^\circ)_{P,T} = & -RT \ln \left(\frac{X_{\text{Al}}^{\text{M1}}}{X_{\text{Mg}}^{\text{M1}}} \right)_{\text{OpX}} \\ & - \int_1^P (\bar{V}_{\text{MgAl}_2\text{SiO}_6} - V^\circ_{\text{MgAl}_2\text{SiO}_6} \\ & - \bar{V}_{\text{Mg}_2\text{Si}_2\text{O}_6} + V^\circ_{\text{Mg}_2\text{Si}_2\text{O}_6}) dP \end{aligned} \quad (3)$$

Rearrangement of Equation 3 gives

$$\begin{aligned} (\Delta G^\circ)_{1,T} + \int_1^P & (V^\circ_{\text{MgAl}_2\text{SiO}_6} \\ & + V^\circ_{\text{Mg}_2\text{SiO}_4} - V^\circ_{\text{Mg}_2\text{Si}_2\text{O}_6} \\ & - V^\circ_{\text{MgAl}_2\text{O}_4}) dP \\ = & -RT \ln \left(\frac{X_{\text{Al}}^{\text{M1}}}{X_{\text{Mg}}^{\text{M1}}} \right)_{\text{OpX}} \\ & - \int_1^P (\bar{V}_{\text{MgAl}_2\text{SiO}_6} - V^\circ_{\text{MgAl}_2\text{SiO}_6} \\ & - \bar{V}_{\text{Mg}_2\text{Si}_2\text{O}_6} + V^\circ_{\text{Mg}_2\text{Si}_2\text{O}_6}) dP \end{aligned}$$

TABLE 20. Summary of Notations

| | |
|--------------------------|---|
| a_i | Activity of component i . |
| $(\Delta G^\circ)_{P,T}$ | Free-energy change in the standard state at P bar and $T^\circ\text{K}$. |
| ΔH° | Enthalpy change in the standard state at 1 bar. |
| ΔS° | Entropy change in the standard state at 1 bar. |
| $(X_m^n)_1$ | Atomic fraction of element m in the site n of phase 1. |
| \bar{V}_i | Partial molar volume of component i . |
| V°_i | Molar volume of component i . |

If the molar volume does not change with pressure, because the compressibility of silicate is very small, then the above equation becomes

$$\begin{aligned}
 &(\Delta G^\circ)_{1,T} = \\
 &-RT \ln \left(\frac{X_{\text{Al}}^{\text{M1}}}{X_{\text{Mg}}^{\text{M1}}} \right)_{\text{Opx}} - \\
 &(P-1) \Delta V
 \end{aligned} \quad (4)$$

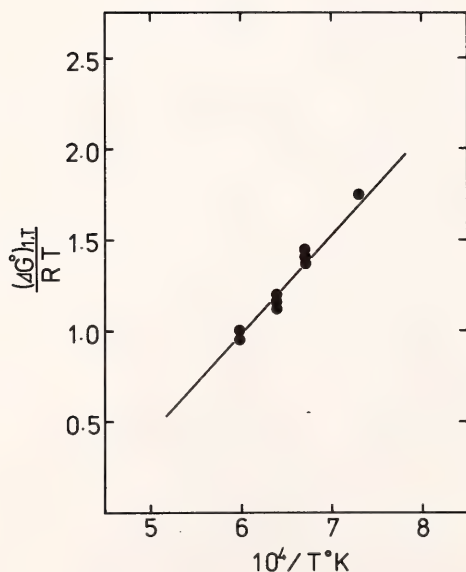


Fig. 34. Calculated free-energy changes for reaction 1 at 1 atm as a function of temperature using data of this study. Solid line is a least-squares fit.

where

$$\begin{aligned}
 \Delta V = &\bar{V}_{\text{MgAl}_2\text{SiO}_6} \\
 &- \bar{V}_{\text{Mg}_2\text{Si}_2\text{O}_6} + V^\circ_{\text{Mg}_2\text{SiO}_4} - V^\circ_{\text{MgAl}_2\text{O}_4}.
 \end{aligned} \quad (5)$$

Using Equation 12 of Wood and Banno (1973) and the molar volume data for spinel and forsterite (Robie and Wald- baum, 1968, p. 256), Equation 5 can be expressed as follows:

$$\begin{aligned}
 \Delta V = &4.07 - X_{\text{Mg}}^{\text{M1}} (7.52 \cdot X_{\text{Mg}}^{\text{M1}} - \\
 &3.24) + X_{\text{Al}}^{\text{M1}} (7.52 \cdot X_{\text{Al}}^{\text{M1}} - 4.28) \\
 (\text{cm}^3) = &7.52 \cdot X_{\text{Al}}^{\text{M1}} - 0.21 (\text{cm}^3) = \\
 &0.18 \cdot X_{\text{Al}}^{\text{M1}} - 0.005 (\text{cal/bar})
 \end{aligned}$$

Therefore, Equation 4 can be rearranged to

$$\begin{aligned}
 \frac{\Delta H^\circ}{RT} - \frac{\Delta S^\circ}{R} = &-\ln \left(\frac{X_{\text{Al}}^{\text{M1}}}{X_{\text{Mg}}^{\text{M1}}} \right)_{\text{Opx}} \\
 &- \frac{P-1}{RT} (0.18 \cdot X_{\text{Al}}^{\text{M1}} - 0.005)
 \end{aligned} \quad (6)$$

If the data are reliable, the calculated values of the right-hand side of Equation 6 should be on a straight line when plotted against $1/T$. As shown in Fig. 34, the points calculated using the experimental data of this study are almost on a straight line. A least-squares fit to these data yields

$$\begin{aligned}
 &\frac{10.4 \times 10^3}{RT} - \frac{4.3}{R} \\
 = &-\ln \left(\frac{X_{\text{Al}}^{\text{M1}}}{X_{\text{Mg}}^{\text{M1}}} \right)_{\text{Opx}} \\
 &- \frac{P-1}{RT} (0.18 X_{\text{Al}}^{\text{M1}} - 0.005)
 \end{aligned} \quad (7)$$

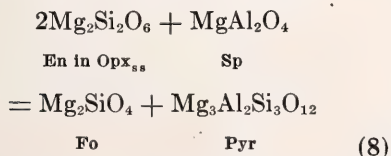
The isopleths of alumina solubility in orthopyroxene were calculated using this equation and are shown in Fig. 33. It is clear that the alumina solubility in enstatite in the spinel stability region is not sensitive to pressure, especially at temperatures lower than 1000°C . Thus, the alumina content of orthopyroxene coexisting with olivine and spinel may

be useful as a geothermometer but cannot be used as a geobarometer.

MacGregor's (1974) results show that the alumina content of orthopyroxene coexisting with olivine and spinel decreases greatly with increasing pressure at constant temperature. In order to explain his data, it is necessary to assume that the volume change in reaction 1 is larger by the order of 10–100 under the experimental conditions than at 1 atm and 298.15°K. Such a difference is unlikely because the compressibilities of silicates and spinel are very small (Birch, 1966). Moreover, the data of MacGregor (1974), when plotted on a diagram similar to Fig. 34, are scattered and do not lie on a straight line (Fig. 35). These considerations suggest that the results of MacGregor (1974) may not be correct.

The new results obtained here are supported by the hydrothermal experiments of Anastasiou and Seifert (1972). They examined the isobaric invariant points at which forsterite, enstatite, spinel, and cordierite or sapphirine exist. The alumina content of orthopyroxene at the above isobaric invariant points is 3.5 wt % at 3 kbar and 900°C, 6 wt % at 2.8 kbar and 1000°C, and 9 wt % at 2.7 kbar and 1100°C. These values correspond to $X_{Al}^{M1} = 0.07, 0.13,$ and 0.17 , respectively, and closely fit the calculated isopleths based on Equation 7 (Fig. 33).

Another check of the experimental data may be obtained by considering the univariant reaction curve in the $MgO-Al_2O_3-SiO_2$ system, defined as follows:



This equation is a linear combination of Equation 1 and the following equation, which delimits the solubility of alumina in the garnet stability region (Wood and Banno, 1973):

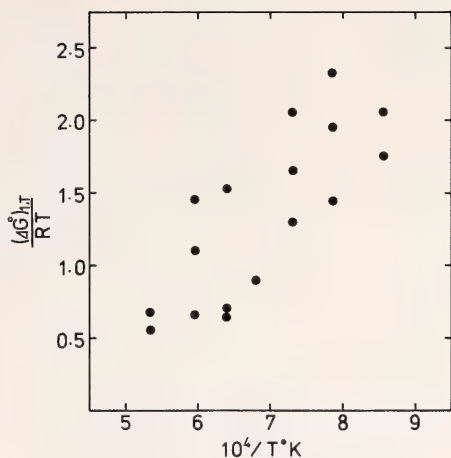
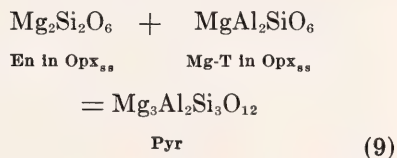


Fig. 35. Calculated free-energy changes for reaction 1 at 1 atm as a function of temperature using MacGregor's (1974) data.



Then the curve for reaction 8 can be calculated if the enthalpy and entropy changes for reactions 1 and 9 are known. The enthalpy and entropy changes for reaction 9 calculated from the results of MacGregor (1974) are 7.6 kcal and 4.4 cal/deg, respectively (Fujii and Takahashi, 1976); those for reaction 1 are calculated in this study (Equation 7). The calculated univariant curve on the P - T diagram is plotted in Fig. 36 together with the curve determined experimentally by MacGregor (*Year Book 63*, p. 157; 1964). As shown in Fig. 36, these two curves are in agreement within the error limits of MacGregor (1974). This agreement also means that the isopleths in the spinel stability region calculated in this report must agree with those in the garnet stability region (MacGregor, 1974) on the univariant curve.

Before applying the above results to natural rocks, it is necessary to consider the effects of other elements such as FeO , Fe_2O_3 , Cr_2O_3 , and CaO . If it is assumed

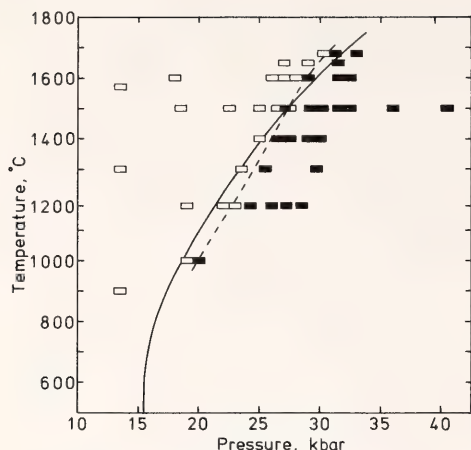


Fig. 36. The univariant reaction $\text{En} + \text{Sp} = \text{Fo} + \text{Pyr}$. Solid line is a calculated curve. Dashed line is MacGregor's (1974) preferred univariant reaction line based on his data (squares). Open squares represent the $\text{En} + \text{Sp} + \text{Fo}$ assemblage and solid squares, the $\text{Fo} + \text{Pyr}$ assemblage.

that olivine and spinel form ideal solid solutions, the activities of forsterite and Mg-Al spinel may be expressed as follows:

$$\begin{aligned} a_{\text{Mg}_2\text{SiO}_4} &= (X_{\text{Mg}}^{\text{M}2})_{\text{Ol}} \cdot (X_{\text{Mg}}^{\text{M}1})_{\text{Ol}} \\ a_{\text{MgAl}_2\text{O}_4} &= (X_{\text{Mg}}^{\text{A}})_{\text{Sp}} \cdot (X_{\text{Al}}^{\text{B}})_{\text{Sp}}^2 \end{aligned}$$

Then, in a multicomponent system, Equation 7 becomes

$$\begin{aligned} &\frac{10.4 \times 10^3}{RT} - \frac{4.3}{R} \\ &= -\ln \left\{ \left(\frac{X_{\text{Al}}^{\text{M}1}}{X_{\text{Mg}}^{\text{M}1}} \right)_{\text{Opx}} \right. \\ &\quad \left. \frac{(X_{\text{Mg}}^{\text{M}2})_{\text{Ol}} \cdot (X_{\text{Mg}}^{\text{M}1})_{\text{Ol}}}{(X_{\text{Mg}}^{\text{A}})_{\text{Sp}} \cdot (X_{\text{Al}}^{\text{B}})_{\text{Sp}}^2} \right\} - \frac{P-1}{RT} \Delta V \end{aligned} \quad (10)$$

To check the applicability of this equation two preliminary experiments were carried out on an iron-bearing system at 1200°C and 20 kbar.

Two starting materials were prepared by mixing glass of Fo_{30} composition with

heated amesite composition in different proportions. Graphite capsules were used to avoid loss of iron; in these capsules the oxygen fugacity is estimated to be in the wüstite stability field (Thompson and Kushiro, *Year Book* 71, pp. 615–616). The analyses show that ferric iron may be present in spinel produced in these runs, but the presence of ferric iron in pyroxene or olivine is uncertain. The Al_2O_3 content of orthopyroxene (En_{97}) coexisting with olivine (Fo_{98}) and spinel [$\text{Mg}/(\text{Mg} + \text{Fe}^{2+}) = 0.98$, $\text{Al}/(\text{Al} + \text{Fe}^{3+}) = 0.99$] is 8.2 wt %. The Al_2O_3 content of orthopyroxene (En_{91}) coexisting with olivine (Fo_{91}) and spinel [$\text{Mg}/(\text{Mg} + \text{Fe}^{2+}) = 0.90$, $\text{Al}/(\text{Al} + \text{Fe}^{3+}) = 0.97$] is 8.3 wt %. These values are only slightly lower than those of the simple system under the same conditions.

In the iron-bearing system it is necessary to consider the effects of site preference of cations. According to Virgo (*Year Book* 70, pp. 215–221), the intracrystalline Fe-Mg partition coefficient of orthopyroxene is about 0.3 at 1200°C (extrapolated value). Thus $X_{\text{Al}}^{\text{M}1}/X_{\text{Mg}}^{\text{M}1}$ should be smaller than it is when calculated neglecting the effects of site preference. Olivine becomes disordered in the distribution of Fe and Mg with increasing temperature, and completely disordered olivine occurs at temperatures above 1300°C (Finger and Virgo, *Year Book* 70, pp. 221–225). Then, at 1200°C it may be assumed that

$$\begin{aligned} (X_{\text{Mg}}^{\text{M}2})_{\text{Ol}} &= (X_{\text{Mg}}^{\text{M}1})_{\text{Ol}} \\ &= \left(\frac{\text{Mg}}{\text{Mg} + \text{Fe}} \right)_{\text{Ol}} \end{aligned}$$

Thus values of the apparent reaction constant,

$$\begin{aligned} K &= \left(\frac{X_{\text{Al}}^{\text{M}1}}{X_{\text{Mg}}^{\text{M}1}} \right)_{\text{Opx}} \cdot \\ &\quad \frac{(X_{\text{Mg}}^{\text{M}2})_{\text{Ol}} \cdot (X_{\text{Mg}}^{\text{M}1})_{\text{Ol}}}{(X_{\text{Mg}}^{\text{A}})_{\text{Sp}} \cdot (X_{\text{Al}}^{\text{B}})_{\text{Sp}}^2} \end{aligned}$$

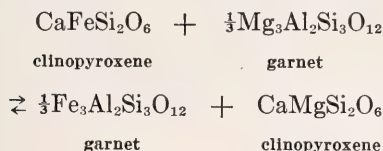
are 0.203 and 0.204. These values fit well with that in the simple system under the

same conditions (0.204). It is concluded that the geothermometer proposed here may also be useful in the iron-bearing system.

THE PARTITIONING OF IRON AND
MAGNESIUM BETWEEN GARNET
AND CLINOPYROXENE

B. J. Wood

The iron-magnesium exchange reaction involving garnet and clinopyroxene



is potentially an extremely useful geothermometer (e.g., Banno, 1970). Råheim and Green (1974) have measured the empirical distribution coefficient K_D ($= \text{Fe}^{\text{gt}} \cdot \text{Mg}^{\text{cpx}} / \text{Fe}^{\text{cpx}} \cdot \text{Mg}^{\text{gt}}$) for garnet-clinopyroxene pairs crystallized from glasses of basaltic composition at 30 kbar over a wide range of temperature. The temperature dependence of K_D , determined at 30 kbar, was combined with some results on the pressure dependence of K_D at 1100°C in an attempt to calibrate the garnet-clinopyroxene geothermometer.

Råheim and Green found that the effect of increasing pressure was to increase K_D , as expected from the negative ΔV obtained from the molar volumes of the end-member components of garnet and clinopyroxene. The magnitude of the pressure effect observed by these authors is, however, considerably larger than that predicted from molar volume data. Thus, although the pressure effect on K_D observed by Råheim and Green may be correct for the complex compositions studied by them, it cannot be applied to $\text{Ca}(\text{Mg},\text{Fe})\text{Si}_2\text{O}_6$ clinopyroxene coexisting with $(\text{Fe},\text{Mg})_3\text{Al}_2\text{Si}_3\text{O}_{12}$ garnet solid solution. One possible explanation of their results is that increasing pressure changes the composition of one of the two phases in such a way that the ac-

tivity coefficients for iron and magnesium components are considerably altered. In view of the marked nonideality of $\text{Mg}_3\text{Al}_2\text{Si}_3\text{O}_{12}$ - $\text{Ca}_3\text{Al}_2\text{Si}_3\text{O}_{12}$ garnet solid solution (Hensen, Schmid, and Wood, 1975), it is possible that a variation in the $\text{Ca}_3\text{Al}_2\text{Si}_3\text{O}_{12}$ content of garnet would produce a change in K_D at constant P and T . Råheim and Green have observed some apparent dependence of K_D on grossular content of garnet at 30 kbar and 1100°C. In addition, their experiments on basaltic compositions produced garnets of increasing grossular content with increasing pressure and increasing K_D .

The purpose of this study was to investigate the pressure dependence of K_D for garnet-clinopyroxene pairs in which the grossular content of garnet is not a function of pressure. Starting materials consisted of mixtures of a diopsidic clinopyroxene that was low in Al_2O_3 and a garnet containing about 12 mole % $\text{Ca}_3\text{Al}_2\text{Si}_3\text{O}_{12}$ component (Table 21); some experiments were performed on pyroxene-garnet mixtures that had been recrystallized at 30 kbar and 1250°C. The mineral mixes were ground together under alcohol to a grain size of 1–2 μm and run at temperatures of 1100°–1400°C in the pressure range 20–45 kbar. Experiments at 1100°C were performed in graphite capsules sealed, together with about 2% H_2O (to induce melting),

TABLE 21. Compositions of Starting Materials

| | Clinopyroxene | Garnet |
|-------------------------|---------------|--------|
| SiO_2 | 53.94 | 42.2 |
| Al_2O_3 | 0.66 | 20.88 |
| TiO_2 | 0.26 | 1.28 |
| CaO | 24.55 | 4.74 |
| MgO | 16.93 | 19.45 |
| FeO^* | 2.93 | 11.58 |
| Na_2O | 0.24 | 0.11 |
| Cr_2O_3 | 0.21 | 0.45 |
| MnO | 0.07 | 0.34 |
| Totals | 99.79 | 101.0 |

* All Fe as FeO .

TABLE 22. Compositions of Garnets and Clinopyroxenes

| Run Conditions: | | 20 kbar/1100°C, 51 hr | | | | 40 kbar/1100°C, 43 hr | | | | 40 kbar/1100°C, 43 hr | | | | 40 kbar/1100°C, 28 hr | | | | |
|--------------------------------|-------|-----------------------|----------|-------|----------|-----------------------|----------|-------|----------|-----------------------|----------|-------|----------|-----------------------|----------|------|----------|------|
| Initial K_D : | | 3.6 | | | | 3.6 | | | | 2.0 | | | | | | | | |
| No. of Analyses: | | 10 | | 10 | | 4 | | 9 | | 9 | | 9 | | 6 | | 4 | | |
| | | Cpx | σ | Gt | σ | Cpx | σ | Cpx | σ | Gt | σ | Cpx | σ | Gt | σ | Opx | σ | |
| SiO ₂ | 53.1 | 0.9 | 42.3 | 0.2 | 54.6 | 0.4 | 54.2 | 0.5 | 42.9 | 0.7 | 53.9 | 1.0 | 42.5 | 0.6 | 42.5 | 0.6 | 56.9 | 1.0 |
| Al ₂ O ₃ | 2.94 | 0.53 | 21.6 | 0.5 | 3.70 | 0.17 | 1.57 | 0.30 | 20.33 | 0.45 | 2.09 | 0.41 | 21.9 | 0.5 | 22.54 | 0.37 | 1.40 | 0.04 |
| TiO ₂ | 0.34 | 0.06 | 0.76 | 0.29 | 0.22 | 0.03 | 0.31 | 0.17 | 1.11 | 0.09 | 0.10 | 0.03 | 0.41 | 0.09 | 0.41 | 0.09 | 0.03 | 0.01 |
| CaO | 21.63 | 0.69 | 5.84 | 0.67 | 1.38 | 0.09 | 23.01 | 0.75 | 5.47 | 0.59 | 20.60 | 0.47 | 5.94 | 0.56 | 5.81 | 0.12 | 0.86 | 0.17 |
| MgO | 17.72 | 0.35 | 18.48 | 0.74 | 31.06 | 0.43 | 17.09 | 0.20 | 18.84 | 0.27 | 18.37 | 0.36 | 18.69 | 0.52 | 19.98 | 0.30 | 36.73 | 0.61 |
| FeO* | 4.26 | 0.09 | 11.26 | 0.36 | 8.93 | 0.13 | 3.35 | 0.23 | 10.97 | 0.21 | 3.00 | 0.26 | 8.80 | 0.43 | 8.41 | 0.26 | 2.71 | 0.34 |
| Na ₂ O | 0.14 | 0.07 | ... | ... | ... | ... | 0.24 | 0.03 | 0.06 | 0.05 | 0.14 | 0.05 | ... | ... | ... | ... | ... | ... |
| Cr ₂ O ₃ | 0.32 | 0.06 | 0.68 | 0.16 | 0.33 | 0.04 | 0.20 | 0.10 | 0.46 | 0.03 | 0.28 | 0.07 | 0.81 | 0.10 | 0.91 | 0.07 | 0.47 | 0.19 |
| MnO | 0.20 | 0.02 | 0.43 | 0.05 | 0.24 | 0.04 | 0.13 | 0.03 | 0.36 | 0.03 | 0.13 | 0.02 | 0.37 | 0.05 | 0.46 | 0.03 | 0.21 | 0.02 |
| Totals | 100.6 | | 101.3 | | 100.5 | | 100.1 | | 100.5 | | 98.6 | | 99.4 | | 101.0 | | 99.3 | |
| Fe/Mg | 0.134 | 0.005 | 0.342 | 0.008 | 0.161 | 0.000 | 0.109 | 0.008 | 0.327 | 0.007 | 0.091 | 0.008 | 0.264 | 0.019 | | | | |
| K_D | 2.55 | 0.11 | | | | | 3.00 | 0.23 | | | 2.90 | 0.34 | | | | | | |

| Run Conditions: | | 30 kbar/1250°C, 22½ hr | | | | 40 kbar/1300°C, 25 hr | | | | 45 kbar/1300°C, 31 hr | | | | 40 kbar/1400°C, 22 hr | | | |
|--------------------------------|-------|------------------------|----------|-------|----------|-----------------------|----------|-------|----------|-----------------------|----------|-------|----------|-----------------------|----------|-------|----------|
| Initial K_D : | | 3.6 | | | | 3.6 | | | | 3.6 | | | | 3.6 | | | |
| No. of Analyses: | | 8 | | 10 | | 10 | | 9 | | 13 | | 12 | | 9 | | 11 | |
| | | Cpx | σ | Gt | σ | Cpx | σ | Gt | σ | Cpx | σ | Gt | σ | Cpx | σ | Gt | σ |
| SiO ₂ | 52.9 | 0.5 | 42.6 | 0.5 | 53.4 | 0.5 | 43.3 | 0.9 | 43.8 | 0.5 | 55.3 | 0.4 | 43.8 | 52.6 | 0.4 | 41.5 | 0.4 |
| Al ₂ O ₃ | 2.64 | 0.12 | 22.3 | 0.6 | 4.69 | 0.40 | 21.9 | 0.6 | 22.0 | 0.6 | 2.73 | 0.24 | 22.0 | 2.22 | 0.25 | 22.1 | 0.6 |
| TiO ₂ | 0.29 | 0.06 | 0.49 | 0.15 | 0.30 | 0.05 | 0.48 | 0.008 | 0.39 | 0.08 | 0.18 | 0.03 | 0.39 | 0.18 | 0.02 | 0.50 | 0.12 |
| CaO | 18.71 | 0.42 | 6.02 | 0.29 | 18.71 | 0.46 | 6.71 | 0.41 | 6.19 | 0.40 | 18.06 | 0.75 | 6.19 | 21.00 | 0.47 | 6.88 | 0.46 |
| MgO | 19.42 | 0.30 | 19.53 | 0.38 | 18.30 | 0.32 | 18.98 | 0.33 | 19.17 | 0.19 | 18.87 | 0.27 | 19.17 | 17.80 | 0.25 | 17.67 | 0.33 |
| FeO* | 4.58 | 0.16 | 9.23 | 0.59 | 4.07 | 0.37 | 7.92 | 0.64 | 3.71 | 0.21 | 8.59 | 0.33 | 4.13 | 4.13 | 0.19 | 9.84 | 0.41 |
| Na ₂ O | 0.16 | 0.03 | ... | ... | 0.19 | 0.04 | ... | ... | 0.22 | 0.04 | ... | ... | ... | 0.32 | 0.04 | ... | ... |
| Cr ₂ O ₃ | 0.20 | 0.04 | 0.67 | 0.11 | 0.28 | 0.02 | 0.63 | 0.02 | 0.21 | 0.01 | 0.71 | 0.05 | 0.18 | 0.18 | 0.02 | 0.70 | 0.06 |
| MnO | 0.19 | 0.04 | 0.36 | 0.04 | 0.16 | 0.02 | 0.34 | 0.03 | 0.14 | 0.02 | 0.32 | 0.03 | 0.14 | 0.14 | 0.02 | 0.33 | 0.03 |
| Totals | 99.1 | | 101.2 | | 100.1 | | 100.3 | | 101.2 | | 99.4 | | 101.2 | 98.6 | | 99.5 | |
| Fe/Mg | 0.132 | 0.006 | 0.266 | 0.019 | 0.124 | 0.010 | 0.234 | 0.020 | 0.110 | 0.006 | 0.251 | 0.011 | 0.130 | 0.130 | 0.005 | 0.312 | 0.010 |
| K_D | 2.02 | 0.17 | | | 1.89 | 0.22 | | | 2.28 | 0.16 | | | | 2.40 | 0.12 | | |

* All Fe as FeO.

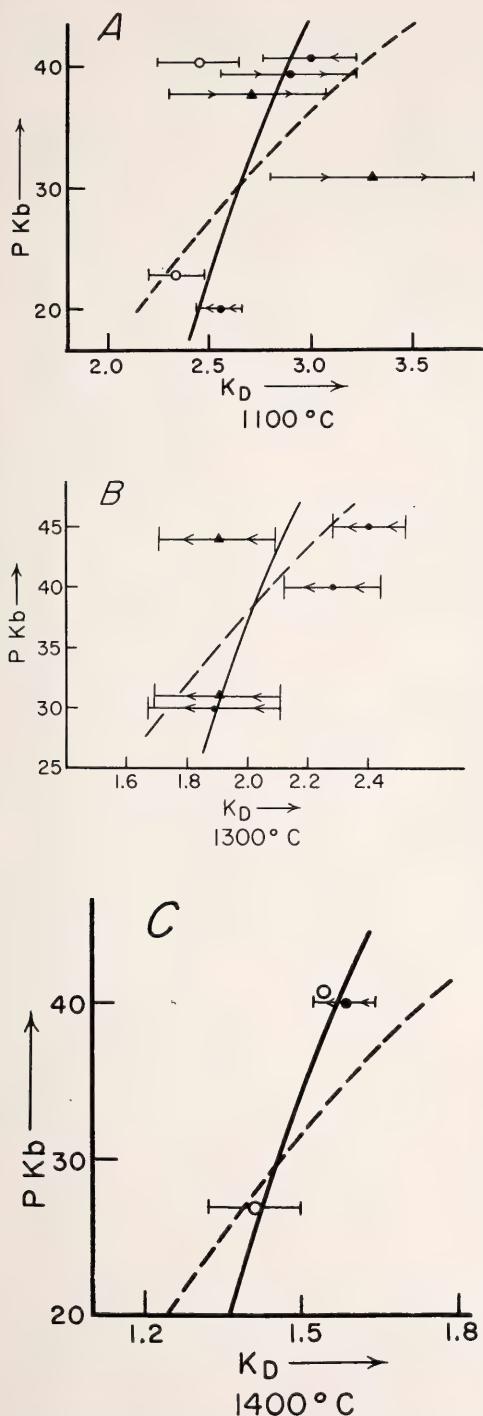


Fig. 37. K_D (garnet-clinopyroxene) as a function of pressure at 1100°C (A), 1300°C (B),

inside Pt capsules. Thermocouples of Pt/Pt90Rh10 were used. Runs at higher temperatures were performed essentially dry inside graphite capsules, and temperature control was achieved via W3Re97/W25Re75 thermocouples. Crystals of 10–20 μm diameter or larger were produced in almost all experiments, but the variable degree of partial melting occasionally resulted in the appearance of orthopyroxene or the loss of garnet, or both (Table 22).

The garnets and clinopyroxenes produced were analyzed using the electron microprobe. Results, given in Table 22, demonstrate that both phases are relatively unzoned, even in 1100°C runs. As may be seen from this table the calcium contents of product garnets are relatively independent of pressure and temperature, the range of $\text{Ca}_3\text{Al}_2\text{Si}_3\text{O}_{12}$ mole fractions being from 0.13 to 0.17. Any effect on K_D of variable calcium contents of the garnet should thus be very small. It should be noted that in calculating the averages and standard deviations the occasional analysis of obviously unequilibrated starting material (as crystal cores) has been omitted. The standard deviations of Fe/Mg of each of the two phases were computed from the sums and deviations of Fe/Mg of each analysis rather than by combining σ_{Fe} and σ_{Mg} .

The results of this study are compared with those of Hensen (*Year Book 72*, pp. 527–534), Akella and Boyd (*Year Book 73*, pp. 269–273), and Råheim and

and 1400°C (C). Dashed curves are from the data of Raheim and Green (1974). Solid curves are for the calculated pressure dependence of K_D based on the following assumptions (see text): K_D at 30 kbar and 1100°C is 2.65; K_D at 30 kbar and 1300°C is 1.90; K_D at 30 kbar and 1400°C is 1.46; ΔV is -1.0 cm^3 . Experimental data from this work are shown as solid circles with error bars equal to ± 1 standard deviation. Open circles are data from Hensen (*Year Book 72*, p. 527). Solid triangles are data from Akella and Boyd (*Year Book 73*, p. 267). Arrows indicate direction of approach to equilibrium, where known.

Green (1974) in Fig. 37 (A–C). All experiments on very magnesian compositions with approximately 15 mole % grossular in garnet (Hensen, Akella and Boyd, and this study) give similar results. The data also agree reasonably well with calculated values derived from the equation for K_D given by Råheim and Green, but as can be seen from Fig. 37 A and C, the pressure dependence of K_D appears to be less than that suggested by them. The solid line shown in Fig. 37 A–C is based on the 30-kbar data of Råheim and Green extrapolated to other pressures, using the molar volumes of the end-member minerals ($\Delta V = -1.0 \text{ cm}^3$). Thus, at 30 kbar and 1100° and 1400°C it appears that K_D s for ultramafic compositions are close to those obtained by Råheim and Green but that the pressure dependence of K_D is small. The 1300°C results (Fig. 37B) are more difficult to interpret, the best fit to the data being obtained by combining the volume change of reaction with an estimated K_D at 30 kbar and 1300°C of 1.9, a value slightly greater than that obtained by Råheim and Green (1.75).

In conclusion, it seems probable that the pressure dependence of K_D is smaller for ultramafic bulk compositions than for basaltic compositions. The differences could be due either to a variable excess volume of mixing in one of the phases or to large compositional dependence of activity coefficients in one of the solid solutions. It is concluded from the available molar volume data for garnet and clinopyroxene solid solutions (Chinner, Boyd, and England, *Year Book* 59, pp. 76–78; Turnock, Lindsley, and Grover, 1973) that excess volumes of mixing are very small. It is likely therefore that compositional dependence of K_D is due to varying activity coefficients of one or more of the components of interest. Although this study does not provide unequivocal proof of which compositional parameters affect K_D , the calcium content of garnet is probably of greatest importance.

THE CHEMICAL COMPOSITION OF MELILITE-BEARING ERUPTIVE ROCKS

D. Velde and H. S. Yoder, Jr.

The chemical composition of natural eruptive rocks appears to be an important but ill-defined factor controlling the crystallization of melilite. Moreover, variations in the composition of coexisting phases that have been reported (Yoder, 1973; El Goresy and Yoder, *Year Book* 73; Sahama, this Report) could be related to variations in bulk composition. A search of the literature produced 299 complete analyses of melilite-bearing eruptive rocks. The geographical origins of the analyzed samples are as follows: 135 from the African continent; 18 from Hawaii; 42 from France, Germany, and Spain; 21 from Italy; 33 from Czechoslovakia; 10 from the Atlantic Ocean islands; 26 from North America, Japan, Australia, and Java; 14 from Scandinavia and the USSR. Of these 299 analyses, 269 that contained less than 3% CO_2 and less than 5% H_2O were used for the computations to avoid initially carbonate-rich or excessively altered samples. Rocks described as hybrids or contaminated were not included. The computations were made using the NTRM version of the rock information system (Chayes, this Report).

Univariate and Bivariate Frequency Distribution of Major Oxides

Figure 38 A–G represents the frequency distributions of major oxides in the 269 melilite-bearing igneous rocks. Total iron, SiO_2 , CaO , and TiO_2 all show homogeneous distributions. However, Al_2O_3 and especially MgO , as well as the sum of alkalis, $\text{Na}_2\text{O} + \text{K}_2\text{O}$, strongly suggest the existence of two groups. Table 23 illustrates the bivariate nature of MgO versus $(\text{Na}_2\text{O} + \text{K}_2\text{O})$. One of the two groups can be defined as relatively alkali-poor (with total alkalis less than 7.25%) and MgO -rich (MgO greater than 7.50%); the other, as MgO -poor and alkali-rich. The former group

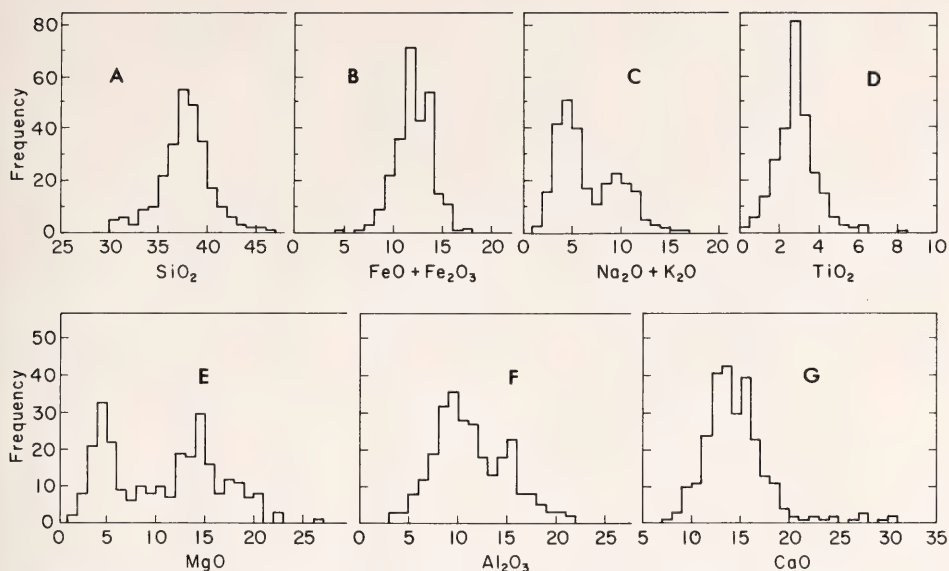


Fig. 38. Univariate frequency distribution of major constituent oxides (wt %) in 269 melilite-bearing eruptive rocks.

(mainly melilite ankaratrites) includes 173 analyses; the latter (corresponding mainly to lavas usually designated as melilite nephelinites) comprises 96 analyses.

Averages (Table 24, columns 1 and 2) were computed for these two groups of analyses, using the value $(\text{Na}_2\text{O} + \text{K}_2\text{O}) = 7.25\%$ as a discriminant. As could be expected, values for oxides showing a simple distribution are very close in both groups, and differences are very striking for those oxides that showed bimodal distributions. These differences are enhanced by computation of the CIPW norm for each of the group averages: The sum of Ne + Lc is 47.02% in the melilite nephelinites as opposed to 19.71% in the melilite ankaratrites, whereas the corresponding values of Ol are 5.63 and 19.95%.

Normative larnite (Ln) is absent from 19 of the 269 melilite-bearing lavas. It seems possible that the composition of some of these rocks was modified after the crystallization of melilite and that they are in some respect altered. The alterations can be of the

various types known to affect volcanic rocks in general, but another possible kind, the leaching of alkalies, is discussed below. A composition that is Ln normative is probably a necessary condition for the precipitation of melilite from a rock liquid, but it is not a sufficient one.

Mineralogical Composition of Melilite-Bearing Igneous Rocks

Such contrasted compositions must obviously reflect differences in mineralogical compositions: The alkali-rich group includes feldspathoid-rich rocks, whereas the other corresponds to olivine-clinopyroxene-rich lavas. There is no evidence that the melilite content differs much between the two groups, the range of normative larnite content being comparable and the composition of melilite similar.

Mineralogical differences may also be reflected in differences in the order of crystallization. To test this hypothesis, the nature of the phenocrysts and the presence or absence of key silicate phases were included on the data cards used in

TABLE 23. Joint Frequency Distribution of MgO and (Na₂O + K₂O) in 269 Melilite-Bearing Eruptive Rocks*

| | MgO | | | | | | | | | | | | | | | | | | | | | | | | |
|----|-----|---|---|---|---|---|---|---|---|----|----|----|----|----|----|----|----|----|----|----|----|----|----|----|----|
| | 1 | 2 | 3 | 4 | 5 | 6 | 7 | 8 | 9 | 10 | 11 | 12 | 13 | 14 | 15 | 16 | 17 | 18 | 19 | 20 | 21 | 22 | 23 | 24 | 25 |
| 18 | | | | | | | | | | | | | | | | | | | | | | | | | |
| 17 | | | | | | | | | | | | | | | | | | | | | | | | | |
| 16 | | | | | | | | | | | | | | | | | | | | | | | | | |
| 15 | | | | | | | | | | | | | | | | | | | | | | | | | |
| 14 | | | | | | | | | | | | | | | | | | | | | | | | | |
| 13 | | | | | | | | | | | | | | | | | | | | | | | | | |
| 12 | | | | | | | | | | | | | | | | | | | | | | | | | |
| 11 | | | | | | | | | | | | | | | | | | | | | | | | | |
| 10 | | | | | | | | | | | | | | | | | | | | | | | | | |
| 9 | | | | | | | | | | | | | | | | | | | | | | | | | |
| 8 | | | | | | | | | | | | | | | | | | | | | | | | | |
| 7 | | | | | | | | | | | | | | | | | | | | | | | | | |
| 6 | | | | | | | | | | | | | | | | | | | | | | | | | |
| 5 | | | | | | | | | | | | | | | | | | | | | | | | | |
| 4 | | | | | | | | | | | | | | | | | | | | | | | | | |
| 3 | | | | | | | | | | | | | | | | | | | | | | | | | |
| 2 | | | | | | | | | | | | | | | | | | | | | | | | | |
| 1 | | | | | | | | | | | | | | | | | | | | | | | | | |

* Origin = 0 and class width = 1 wt % for both variables. One analysis with 26.41% MgO lies outside the area of the plot.

TABLE 24. Average Compositions of Melilite-Bearing Eruptive Rocks

| No. of Analyses: | 1 (173) | 2 (96) | 3 (100) | 4 (64) |
|--------------------------------|---------|--------|---------|--------|
| SiO ₂ | 37.06 | 38.94 | 37.49 | 37.92 |
| Al ₂ O ₃ | 9.48 | 14.75 | 10.26 | 13.00 |
| Fe ₂ O ₃ | 5.56 | 5.18 | 5.52 | 5.71 |
| FeO | 6.79 | 6.21 | 6.86 | 6.22 |
| MgO | 14.13 | 5.07 | 13.52 | 6.96 |
| CaO | 15.31 | 13.47 | 14.39 | 14.19 |
| Na ₂ O | 2.78 | 4.85 | 3.05 | 4.54 |
| K ₂ O | 1.72 | 5.35 | 1.91 | 4.61 |
| TiO ₂ | 2.91 | 2.70 | 2.80 | 3.01 |
| P ₂ O ₅ | 1.03 | 1.17 | 1.09 | 1.21 |
| H ₂ O (total) | 2.34 | 1.40 | 2.40 | 1.67 |
| CIPW Norms | | | | |
| An | 8.31 | 2.68 | 8.66 | 1.48 |
| Lc | 7.97 | 24.79 | 8.85 | 21.36 |
| Ne | 12.74 | 22.23 | 13.98 | 20.81 |
| Di | 21.40 | 15.59 | 22.22 | 16.55 |
| Ol | 19.95 | 5.63 | 18.86 | 8.00 |
| Ln | 10.43 | 11.42 | 8.47 | 12.38 |
| Mt | 8.06 | 7.51 | 8.00 | 8.28 |
| Il | 5.53 | 5.13 | 5.32 | 5.72 |
| Ap | 2.39 | 2.71 | 2.53 | 2.80 |

1 and 2, average compositions of melilite-bearing rocks with (Na₂O + K₂O) less or greater than 7.25%; 3, average composition of lavas with melilite in the groundmass; 4, average composition of lavas with melilite phenocrysts.

the computations. Figure 39 shows the distribution of MgO: (A) in all rocks with (Na₂O + K₂O) less than 7.25%, (B) in all rocks with melilite in the

groundmass only, (C) in rocks with (Na₂O + K₂O) greater than 7.25%, (D) in all rocks with melilite phenocrysts. Excluded from this tally to avoid any ambiguity were rocks with no phenocrysts at all (i.e., aphanitic rocks, present in both groups) as well as rocks in which melilite was described as forming microphenocrysts.

In Fig. 39 the similarity between A and B and between C and D is obvious, and it is concluded that the two proposed groups of melilite-bearing rocks are not the result of crystallization sequence or melilite accumulation. Average compositions for the mineralogically defined groups were computed and appear in Table 23 as columns 3 and 4. The relation between chemical composition, particularly alkali content, and the order of appearance of the various phases was known experimentally (Yoder, 1973, Fig. 17) and could be predicted from results obtained in the system diopside-nepheline (Bowen, 1928).

A number of assumptions have to be made before these two compositions can be expressed in terms of a reasonably simplified system amenable to experimentation. The compositions found could correspond to two invariant points. The alkali-rich group would be represented in the Ab-Ak-Di-Ne tetrahedron at 40%

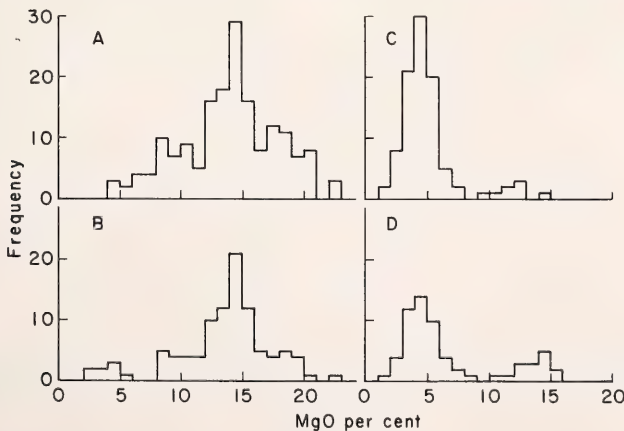


Fig. 39. MgO distribution in (A) all melilite-bearing eruptive rocks with (Na₂O + K₂O) < 7.25%, (B) all lavas with melilite in the groundmass only, (C) all melilite-bearing eruptive rocks with (Na₂O + K₂O) > 7.25%, (D) all lavas with melilite as a phenocryst phase.

nepheline, the respective proportions of the components Ab, Ak, and Di being 2:4.5:3.5. The MgO-rich group would correspond to a point situated in the Ak-Di-Ne-Fo tetrahedron at 25% nepheline, the relative proportions of Ak, Di, and Fo being approximately 3.5:3.5:3, respectively. This relationship is in keeping with Bowen's contention that the melilite field is drawn toward SiO_2 as more nepheline is added to the system CaO-MgO- SiO_2 (Bowen, 1928).

Comparison with Nonmelilite-Bearing Ankaratrites and Nephelinites

A useful comparison can be made with the nonmelilite-bearing, feldspar-free lavas, ankaratrites and nephelinites. The NTRM data base includes 214 such lavas, and univariate frequency distribution of major oxides and important normative minerals have been generated and compared with those obtained from melilite-bearing rocks.

More than a quarter of the ankaratrites and nephelinites (60 out of the 214 analyses) contain normative Ln. The appearance of Ln in the norm of feldspar-free lavas is readily explained by the equation $2\text{Di} + \text{Ts} = \text{An} + \text{Ol} + \text{Ln}$ (Chayes and Yoder, *Year Book* 70, p. 206), which shows that the normative equivalents of a clinopyroxene rich in Tschermak's molecule will, in feldspar-free lavas, include Ln.

Distributions of FeO, Fe_2O_3 , TiO_2 , Al_2O_3 , CaO, and MgO are similar in both groups, the nephelinites showing a small concentration at low MgO values. SiO_2 (Fig. 40A) is lower, however, and the total alkalis (particularly K_2O) are higher in the melilite-bearing rocks.

Another difference between melilite-bearing and nonmelilite-bearing igneous rocks can be seen in the range of normative anorthite content (Fig. 40B): the conclusion from this comparison is that melilite-bearing rocks are silica-poor, alumina-poor, and alkali-rich compared with other feldspar-free lavas. Only 3 out of 214 nephelinites and ankaratrites are acmite normative.

The Alumina Content of Melilite-Bearing Eruptive Rocks

Expressed in terms of normative components, the excess Al over the sum of Na + K leads to 2.68 and 8.31% normative anorthite (Table 24, columns 1 and 2), respectively, for the high- and low-alkali groups. Furthermore, 40 out of 269 melilite-bearing igneous rocks contain normative acmite. The presence of normative acmite in the norm of such basic rocks seems important in connection with both the mineralogical composition of melilite-bearing rocks and the possible genesis of melilite-bearing lavas.

As shown by El Goresy and Yoder

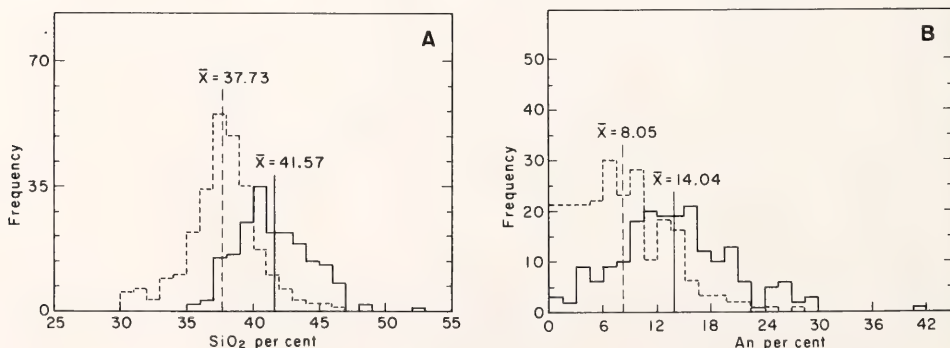


Fig. 40. Comparison between melilite-bearing eruptive rocks and feldspar-free nephelinites and ankaratrites: (A) SiO_2 frequency distribution, (B) normative anorthite frequency distribution. \bar{X} represents for each group the mean of all nonzero values. Broken line, melilite-bearing rocks; solid line, nephelinites and ankaratrites.

(*Year Book* 73, p. 361), there is always in natural melilites a molecular excess of alumina over sodium (and potassium) and even an indication that this excess becomes greater as the proportion of sodium melilite increases. Available clinopyroxene analyses (Sahama, this Report; Velde and Yoder, unpublished analyses) also show a large excess of molar Al over molar Na, the clinopyroxenes of melilite ankaratrites being particularly rich in Al_2O_3 . A number of melilite-bearing rocks must then contain alkali-rich, alumina-deficient phases.

The examination of a large selection of thin sections from widely distributed occurrences and electron microprobe analyses of a selected number of samples indeed confirms the presence of alkali minerals. One common phase is an alumina-poor (sometimes alumina-free) mica, similar to those reported by Nash (1972) in carbonatites. Acmitic clinopyroxenes have also been found.

The genetic importance of the alumina deficiency can be deduced from the experimental results published by Yagi (*Year Book* 62, pp. 133–134): The addition of acmite to the nepheline-diopside system brings melilite onto the liquidus. It has been conclusively demonstrated more recently by F. E. Hough (personal communication, 1973). She studied the melting behavior of two fragments of olivine-melilitite from the ashes of Chabachu Crater, Uganda. Both have the same mineralogy and contain melilite phenocrysts, but only one of them when melted and recrystallized would precipitate melilite. Hough found that if 10% K_2CO_3 , Na_2CO_3 , or CaCO_3 was added to the other, melilite would also crystallize from its melt. The addition of $(\text{NH}_3)_2\text{CO}_3$ did not produce any melilite, and this result serves to rule out the possibility that the appearance of melilite could be linked to the presence of CO_2 . She concluded that alkali cations had been leached from one of the fragments after the crystallization of melilite. The unpublished chemical analyses of these two samples are similar for most ele-

TABLE 25. Compositions of an Etindite and Melilite Nephelinite and Results of Melting Experiments* (from Tilley and Thompson, 1972)

| | 1 | 2 |
|------------------------------|-------|-------|
| SiO_2 | 40.54 | 39.64 |
| Al_2O_3 | 16.07 | 15.06 |
| Fe_2O_3 | 4.85 | 2.37 |
| FeO | 6.14 | 10.19 |
| MgO | 4.33 | 4.06 |
| CaO | 12.77 | 11.81 |
| Na_2O | 5.47 | 6.13 |
| K_2O | 3.70 | 5.67 |
| MnO | 0.28 | 0.29 |
| TiO_2 | 3.53 | 2.79 |
| P_2O_5 | 1.07 | 1.47 |
| H_2O (total) | 1.23 | 0.25 |
| CIPW Norms | | |
| An | 8.37 | |
| Lc | 17.15 | 26.27 |
| Ne | 25.07 | 24.86 |
| Ac | | 5.26 |
| Di | 26.94 | 1.43 |
| Wo | 2.61 | |
| Ol | | 17.51 |
| Ln | 2.39 | 14.64 |
| Mt | 7.03 | 0.80 |
| Il | 6.70 | 5.30 |
| Ap | 2.48 | 3.41 |

* 1: 1118°C (Cpx), 1085°C (Ne), 1064°C (Lc). 2: 1100°C (Ne + Mel), 1070°C (Ol).

ments, including Al_2O_3 and K_2O , but one contains 1.20% Na_2O and the other 2.74% Na_2O .

Experiments performed by Tilley and Thompson (1972) on two basic alkaline rocks whose compositions have been reproduced in Table 25 corroborate the role of alkali cations. The etindite (a nephelinite), column 1, is a clinopyroxene-nepheline-leucite-magnetite-apatite-perovskite-sphene lava (Tilley, 1953), whereas "Lava Lake," from Nyiragongo volcano, contains phenocrysts of melilite, nepheline, and magnetite in a glassy groundmass. A completely crystallized sample from the same volcano, with almost identical chemical composition, is described by Denaeyer (1972, pp. 40–41, analysis F1(24)) as composed of nepheline, melilite, and leucite phenocrysts in a groundmass of nepheline, greenish clinopyroxene apatite, and

opaque minerals. Similar assemblages were observed in experimental products (Tilley and Thompson, 1972), and more recently Thompson (1975) has reproduced them under conditions of controlled oxygen fugacities. It appears that the critical difference between these two lavas is the higher alkali content (and the hyperalkaline character) of the Lava Lake sample; addition of 0.8% Na₂O and 2.2% K₂O to the etindite induces the crystallization of melilite. The reaction taking place can be written: $\text{Cpx}_1 + \text{Ne} + \text{Lc} + (\text{Na}_2\text{O} + \text{K}_2\text{O}) = \text{Ne} + \text{Mel} + \text{Lc} + \text{Cpx}_2 + \text{Ol}$. One essential difference rests in the composition and the modal proportions of clinopyroxene according to the reaction $2\text{CaAl}_2\text{SiO}_6 + 5\text{CaMgSi}_2\text{O}_6 + 2\text{Na}_2\text{O} = 3\text{Ca}_2\text{MgSi}_2\text{O}_7 + \text{CaNaAlSi}_2\text{O}_7 + \text{Mg}_2\text{SiO}_4 + 3\text{NaAlSiO}_4$. Any excess diopside over the proportions required to balance the equation would survive the reaction. Olivine is not mentioned in the rock description cited above, but olivine is a common accessory phase in melilite-bearing nephelinites from Nyiragongo. Furthermore, Thompson (1975) found a field of $\text{Ne} + \text{Mel} + \text{Or} + \text{Lc} + \text{Cpx} + \text{Mt} + \text{L}$ when recrystallizing Lava Lake under controlled conditions of oxygen fugacity. If this interpretation is correct, the clinopyroxene in the etindite would be considerably richer in Tschermak's molecule than the clinopyroxene of the melilite-bearing lava. In this connection it may be noted that the Al + Ti content of clinopyroxenes in melilite-bearing rocks from Nyiragongo (Sahama, this Report, Fig. 46A) is smaller than it is in clinopyroxenes from olivine leucites and nephelinites from the same volcano. A similar reaction has been observed in a bergalite from Kaiserstuhl, in which alumina-rich clinopyroxene phenocrysts are replaced by melilite, nepheline, and magnesian biotite, an alumina-poor aegirine clinopyroxene being an abundant groundmass phase.

Such modifications of the alkali contents of the rocks conspicuously change the normative assemblage (Table 25,

columns 1 and 2). The effects will, of course, depend on the original composition, but in most cases Ln and Ol will increase at the expense of Di; the computation of aegirine will also result in higher percentages of the strongly undersaturated normative minerals. If An is present in the norm calculated from the original composition, the sum of Ne + Lc will increase, whereas if An is absent, the Kp content will be augmented at the expense of leucite.

It would seem from the experiments discussed above that the addition of alkalis to a nephelinite composition could produce a melilite-bearing lava. The extent to which this process could play a role in the genesis of melilite-bearing igneous rocks is difficult to evaluate, but it should be remembered that fenitization of the country rock is not an unknown process around melilite-bearing rocks, an example being the area around the Haystack intrusion of Montana (Buie, 1941).

IMPORTANCE OF ALKALI CONTENT OF MAGMA YIELDING MELILITE-BEARING ROCKS

H. S. Yoder, Jr., and D. Velde

Natural melilite-bearing rocks appear to have been formed from alkali-rich magmas according to D. Velde and Yoder (this Report). The same conclusion was deduced by Bowen (1928, pp. 262-266) on the basis of an analysis of the system nepheline-CaO-MgO-SiO₂ within which only the liquidus relations of the join nepheline (Ne)-diopside (Di) had been determined in a preliminary way. Relevant portions of Bowen's compositional tetrahedron have since been worked out in detail by various investigators, and a new analysis of the data has therefore been made.

The alkali basalts and basanites may be represented for the most part in the subtetrahedron forsterite (Fo)-diopside (Di)-albite (Ab)-nepheline (Ne) of the tetrahedron Fo-larnite (Ln)-Ne-Quartz (Qz) displayed in Fig. 41. Because the

melilite-bearing assemblages lie outside the alkali basalt subtetrahedron, it is important to ascertain whether melilite-bearing magmas can be derived by fractionation from a parental olivine nepheline (Di + Fo + Ne) or alkali basalt or whether they form independently from a different, as yet undefined, fractionation series.

The critical relations displayed by Bowen in planes of constant nepheline content (20, 40, 55 wt %) parallel to the CaO-MgO-SiO₂ base actually occur in the subtetrahedron Ab-Di-Ne-Wo (Fig.

41). The principal planes of this subtetrahedron are Ab-Ne-Wo (Foster, 1942), Ab-Di-Ne (Schairer and Yoder, 1960), Ab-Di-Wo (Yoshiki and Yoshida, 1952), and Di-Ne-Wo (Schairer and Yoder, *Year Book 63*, p. 71). The interior of the subtetrahedron is cut by part of the sections Ab-Ak-Ne (Schairer and Yoder, *Year Book 63*, p. 70), Ab-Ak-Di (Schairer and Yoder, *Year Book 63*, p. 69), Ab-Ak-Wo (Schairer and Yoder, *Year Book 63*, p. 68). The liquidus relations determined experimentally are displayed in Fig. 42 A, B, and C.

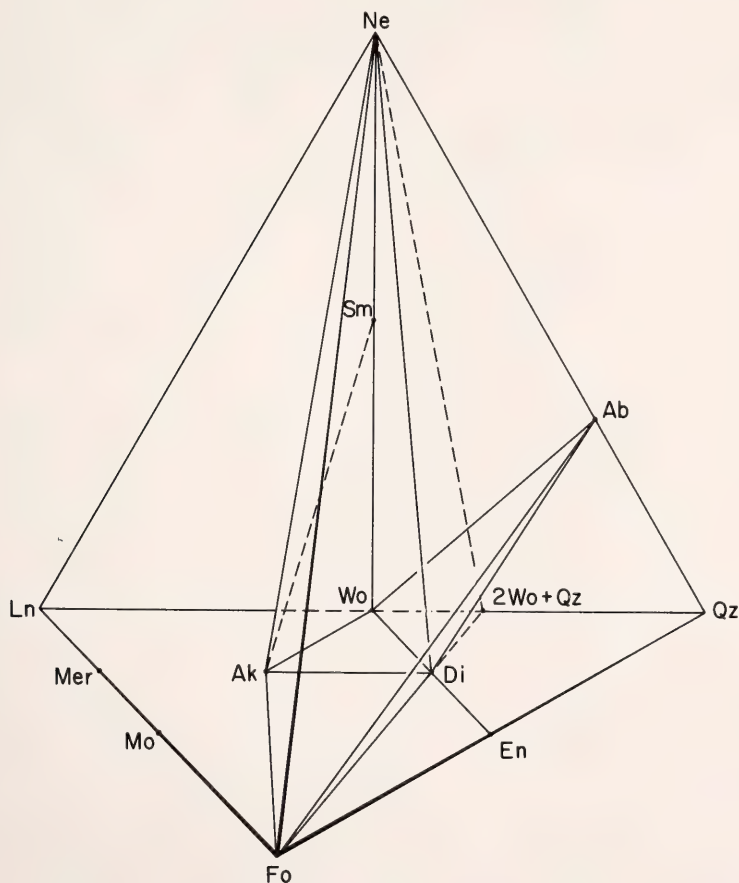
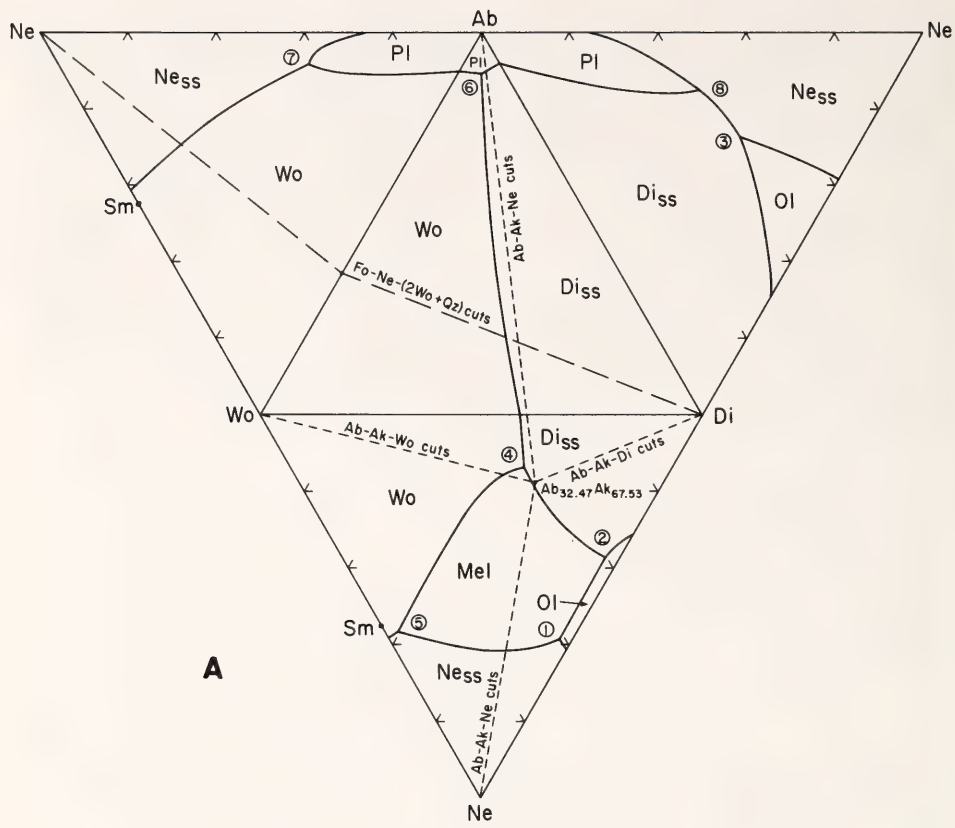
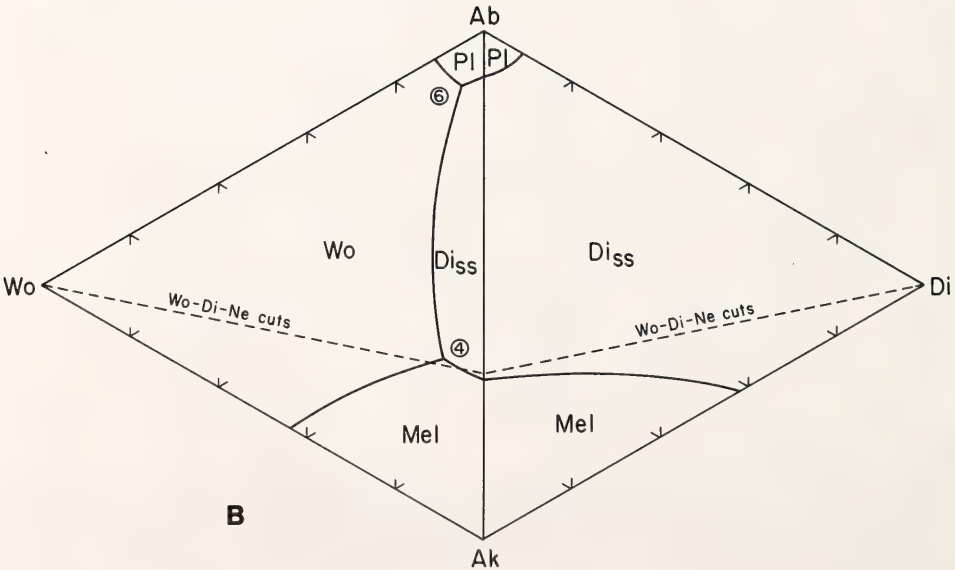


Fig. 41. A portion of the Ne-CaO-MgO-SiO₂ system of Bowen (1928) illustrating the location of the key subtetrahedron Ab-Di-Ne-Wo and the critical plane Fo-Ne-(2Wo + Qz) (mole %). Ab, albite; Ak, akermanite; Di, diopside; En, enstatite; Fo, forsterite; Ln, larnite; Mer, merwinite; Mo, monticellite; Ne, nepheline; Qz, quartz; Sm, soda melilite; Wo, wollastonite.



A



B

In view of the piercing points on the plane Di-Ne-Wo (Fig. 42A), it is evident that the pertinent "invariant" points lie in the Ab-Di-Ne-Wo subtetrahedron. Some liquids generated in the alkali basalt (Ab-Di-Fo-Ne) subtetrahedron will fractionate into this contiguous subtetrahedron because of the penetration of the field of forsterite through the plane Ab-Di-Ne. The penetration of a field of melilite into the plagioclase-bearing subtetrahedron through the plane Di-Ne-Wo was recognized by Schairer and Yoder (*Year Book 63*) as critical to the understanding of the incompatible relationship of the melilite- and plagioclase-bearing lavas, not uncommonly issuing at different times from the same volcano. The extent of the penetration of the melilite field was determined in part in the sections Ab-Ak-Wo (Fig. 42B) and Ab-Ak-Ne

(Fig. 42C). (There is no analogous penetration of the melilite field into the leucite-sanidine-Wo-Di system.) Note that one end-member of the melilites (soda melilite, Sm, $\text{CaNaAlSi}_2\text{O}_7$), stable only at elevated pressures, lies on one of the boundary joins. The composition of the common melilite in igneous rocks is about $\text{Ak}_{2/3}\text{Sm}_{1/3}$ (wt).

Three "invariant" points lie within Ab-Di-Ne-Wo involving the phases Di, Mel, Ne, Ol; Di, Mel, Ne, Wo; and Di, Ne, Pl, Wo as displayed in the flow sheet of Fig. 43. The points marked with encircled numbers correspond to those in Fig. 42. The exact positions of the "invariant" points have not been determined; however, the proximity of the associated piercing points constrains each "invariant" point to a specific region of the subtetrahedron. (The relationship of these three "invariant" points

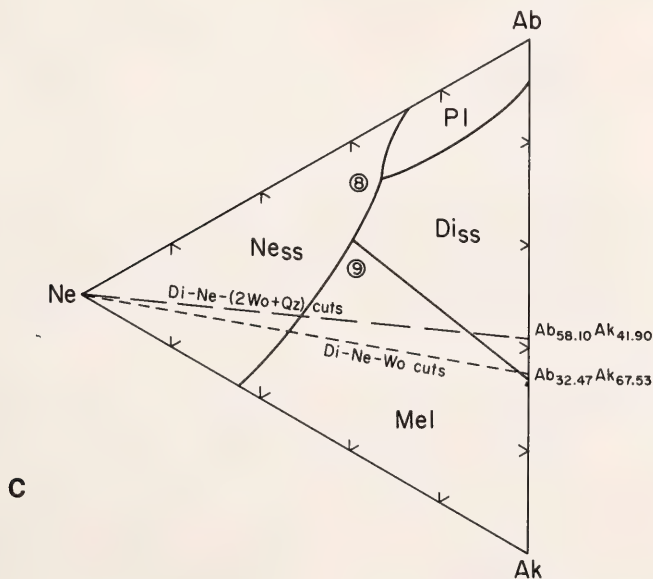


Fig. 42A. "Fold out" of the subtetrahedron Ab-Di-Ne-Wo shown in Fig. 41 with determined phase equilibria (wt %). Dashed lines show intersection of subsidiary sections with bounding ternary systems. Encircled numbers refer to piercing points used in the construction of Fig. 43. Abbreviations are given in Fig. 41, and references to data in bounding planes and subsidiary sections are given in the text. High-temperature polymorphs are neglected.

Fig. 42B. Phase equilibria of the subsidiary sections Ab-Ak-Di and Ab-Ak-Wo pertinent to the subtetrahedron Ab-Di-Ne-Wo (wt %).

Fig. 42C. Phase equilibria of the subsidiary section Ab-Ak-Ne pertinent to the subtetrahedron Ab-Di-Ne-Wo (wt %).

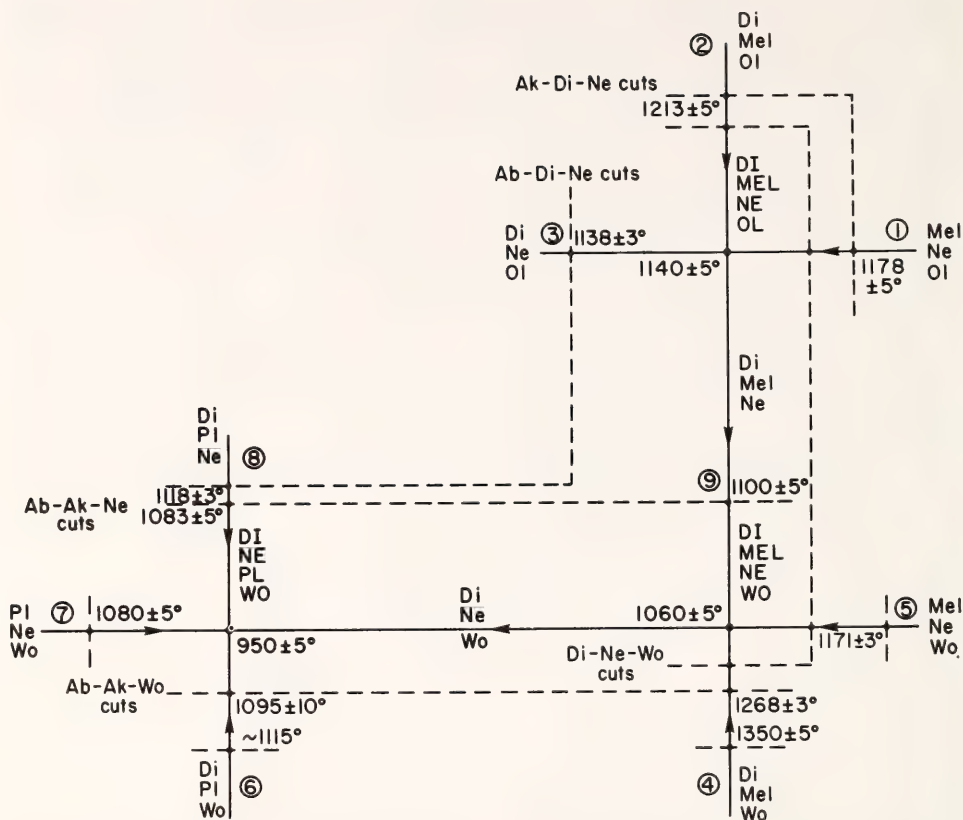


Fig. 43. Flow sheet for the subtetrahedron Ab-Di-Ne-Wo. Encircled numbers relate to piercing points in the bounding planes or subsidiary sections of Fig. 42A, B, and C. Dashed lines indicate planes or sections that cut "univariant" lines. Large dots are "invariant" points, and upper case abbreviations indicate assemblages stable with liquid at the "invariant" points. Solid solutions and high-temperature polymorphs are not indicated.

to the two compositional groups recognized by D. Velde and Yoder [this Report] cannot be determined without the phase equilibrium data for the leucite-bearing systems.)

Bowen's deduction can be visualized by examining the relations on the extension of the olivine nephelinite plane Di-Fo-Ne (cf. basalt tetrahedron of Yoder and Tilley [1962]). The extension intercepts Wo-Qz at the ratio 2:1 and Ab-Wo at 36.88 wt % Ab as shown in Figs. 41 and 42, respectively. The deduced liquidus relations on the plane Fo-Ne-(2 Wo + Qz) are shown in Fig. 44. It appears that extraction of olivine

from liquids generated at least in the ruled area would eventually yield melilite. Those magmas having less Ne than the ruled area would not necessarily yield melilite and probably would fractionate to plagioclase-bearing assemblages—the full range of compositions of appropriate parental material that will crystallize melilite has yet to be determined experimentally.

The determination by experiment of the composition of the Di, Fo, Mel, Ne "invariant" point would be helpful in outlining the limiting compositions of magmas from which melilite may form. Petrographic evidence for a melilite re-

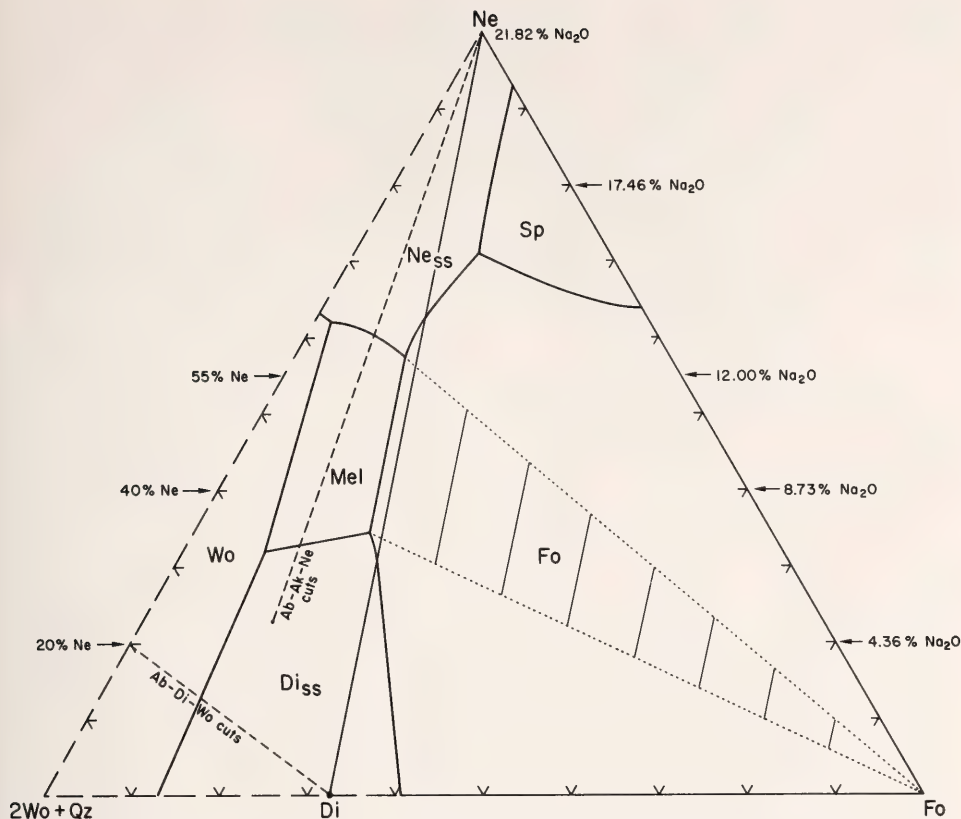


Fig. 44. Schematic planar extension of the determined system Ne-Di-Fo (Schairer and Yoder, *Year Book* 59, p. 70, Fig. 18) to include more siliceous compositions using the data in the bounding planes Ab-Ne-Wo and Ab-Di-Wo as well as that in the Ab-Ak-Ne section (wt %). High-temperature polymorphs are neglected. The dotted lines outline the maximum region of compositions of parental materials of relatively high soda content that will yield melilite on crystallization. The full extent of compositions of likely parental materials that form melilite has not as yet been determined.

action relation analogous to that suggested in Fig. 43 has not been found even after an examination of thin sections of almost 300 different melilite-bearing rocks.

It appears that the initial alkali content of the initial magma is important in determining whether melilite- or plagioclase-bearing lavas are produced as fractionation products. Confirmation of the relations in Fig. 44 is required before melilite can be considered a normal fractionation product of alkali-rich magmas. Those alkali-rich magmas could be the partial melt product of a suitable

parent with or without appropriate volatiles, or could result from the metasomatic effects of alkali-rich volatiles on already existing critically undersaturated magmas (Bailey, 1970).

COMPOSITION OF CLINOPYROXENE AND MELILITE IN THE NYIRAGONGO ROCKS

Th. G. Sahama

The active volcano Mt. Nyiragongo in the Virunga volcanic field, eastern Zaire, consists of all-feldspathoidal nephelinitic lavas. Although the general geology (Tazieff, 1966) and the chemistry and

petrology of the rocks (Denaeyer, Schellinck, and Coppez, 1965; Denaeyer, 1972) are determined, the few wet chemical analyses published of clinopyroxene and melilite are insufficient to characterize the compositions of these important constituents of the rock suite. Therefore, a series of electron microprobe analyses on the two minerals was undertaken using the computer-automated technique (Finger and Hadidia-cos, *Year Book 71*, pp. 598-600).

Summary of Rock Sequence

Beginning with the oldest lava beds accessible for study in the Nyiragongo upper crater, the rock succession is as follows (Sahama, 1962):

1. Brownish bergalite and nephelinite lavas and pyroclastics, which are rich in melilite and may or may not contain leucite, kalsilite, and calcite, are the oldest accessible rocks. In mineralogy and texture the lavas represent an unaltered, haüyne-free analogue to the type rock from Kaiserstuhl in southern Germany (Soelnner, 1913).

2. Leucitites and leucite-rich nephelinites, many with aggregates of leucite phenocrysts, in extreme cases reaching the size of a fist, are next. Melilite is subordinate or absent.

3. Nepheline aggregate lava, so named because of its characteristic aggregates of potassium-rich nepheline phenocrysts, is next in succession. This leucite melilite nephelinite lava covers the outer slopes of the main cone and is equivalent to the molten lava lake material and to the horizontal beds exposed in the walls of the inner pit of the crater.

4. Dikes petrographically representing all three rock groups cut the upper crater beds. The most conspicuous of these dikes, which cuts the uppermost bed of rock group 2, is named dike No. 6 and consists of leucite-rich nephelinite without melilite.

All these rocks also contain clinopyroxene, titanian magnetite, and apatite, and some contain small amounts of olivine and perovskite.

Clinopyroxene

Analyses of the Nyiragongo clinopyroxene display considerable compositional variation even within each rock group listed in the above summary. The variation of clinopyroxenes in the bergalite lavas (Table 26) is illustrated by the calculated average composition and high standard deviations. Although some variations in the bulk composition of the melt and its rapid, nonequilibrium consolidation may have had an effect, the variation in the clinopyroxene composition is largely caused by sectoral zoning, which is well developed both in the phenocrysts and in the groundmass crystals. In addition, large phenocrysts exhibit oscillatory zoning and banding parallel to the outer crystal faces of the sectors (Downes, 1974). Table 27 illustrates the differences in composition between two sectors of a sectorally zoned clinopyroxene crystal. The differences shown in the table are in accord with the general trend in sectorally zoned clinopyroxene grains from alkaline rocks summarized by Fleet (1975).

The principal differences between alternate sectors are in the Al and Ti contents. In thin section, it is not possible to tell which sector(s) the particular crystal exhibits or whether the section cuts it centrally or marginally, and the overall variations in the contents of these cations must be discussed statis-

TABLE 26. Composition of Clinopyroxene from Bergalite, Nyiragongo (wt %)*

| | | |
|--------------------------------|-------|-------|
| SiO ₂ | 48.4 | (3.3) |
| Al ₂ O ₃ | 5.40 | (2.8) |
| FeO† | 5.48 | (1.1) |
| MnO | 0.14 | |
| MgO | 13.6 | (1.5) |
| TiO ₂ | 2.40 | (1.1) |
| CaO | 23.9 | (0.5) |
| Na ₂ O | 0.45 | (0.2) |
| K ₂ O | 0.03 | |
| Total | 99.80 | |

* Average of 70 analyses made of 7 specimens. Standard deviations in parentheses.

† Total iron as FeO.

TABLE 27. Average Compositions of Two Sectors in a Sectorally Zoned Clinopyroxene Phenocryst from Leucite Nephelinite (Specimen VM. 168), Nyiragongo (wt %)*

| | (111) sector 11 analyses | | (100) sector 4 analyses | |
|--------------------------------|-----------------------------|-------|----------------------------|-------|
| SiO ₂ | 47.0 | (0.4) | 42.5 | (0.4) |
| Al ₂ O ₃ | 5.98 | (0.2) | 9.54 | (0.2) |
| FeO† | 6.17 | (0.1) | 6.90 | (0.4) |
| MnO | 0.16 | | 0.16 | |
| MgO | 12.9 | (0.2) | 11.2 | (0.1) |
| TiO ₂ | 2.89 | (0.1) | 4.82 | (0.2) |
| CaO | 24.1 | (0.4) | 23.7 | (0.2) |
| Na ₂ O | 0.43 | (0.1) | 0.45 | (0.1) |
| K ₂ O | 0.00 | | 0.01 | |
| Totals | 99.63 | | 99.28 | |

* Standard deviations in parentheses.
† Total iron as FeO.

tically. Figure 45 A, B illustrates the negative correlation between Ti and Al with Si. There is no difference in the range of Al/Si and Ti/Si between phenocrysts and groundmass crystals, with the exception of the anhedral clinopyroxene grains that fill the interstices between melilite, nepheline, and Ti-magnetite in some bergalites. These grains plot in the extreme right of Fig. 45B.

Instead of being plotted in terms of the pyroxene end-members En-Di-Hed-Fs, the Nyiragongo clinopyroxene compositions are presented in terms of Mg-(Al + Ti)-(Fe + Mn) in Fig. 46A and in terms of the cations (Al + Ti) and cationic ratio 100(Ca + Na)/(Ca + Na + Fe + Mn + Mg) in Fig. 47. These diagrams were chosen because the Ca content and Mg/Fe of the pyroxenes are relatively constant, whereas Al and Ti vary considerably. The (Al + Ti) contents extend to somewhat higher values in rock group 2 than in group 1, and Fe/Mg increases in the order group 1 → 2 → 3.

Melilite

Most melilites plot in the upper half of the double tetrahedron of Fig. 48. Only rarely are the alkalis in excess

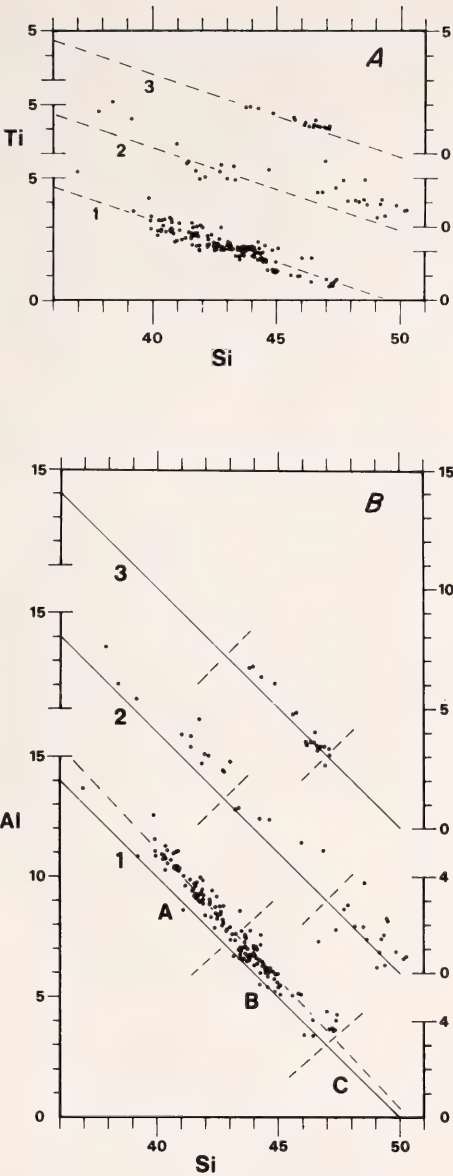


Fig. 45. (A) Nyiragongo clinopyroxene. Ti plotted against Si (cation %). (1) Phenocrysts. (2) Groundmass crystals. (3) Crystals in dike No. 6. Total 198 data points. (B) Nyiragongo clinopyroxene. Al plotted against Si (cation %). Approximate limits between clinopyroxene from peralkalic (A), alkalic (B), and tholeiitic (C) rocks in the Al-Si diagram according to Kushiro (1960) and LeBas (1962). Solid lines, Al + Si = 50. Broken lines, regression lines of the data points for phenocrysts.

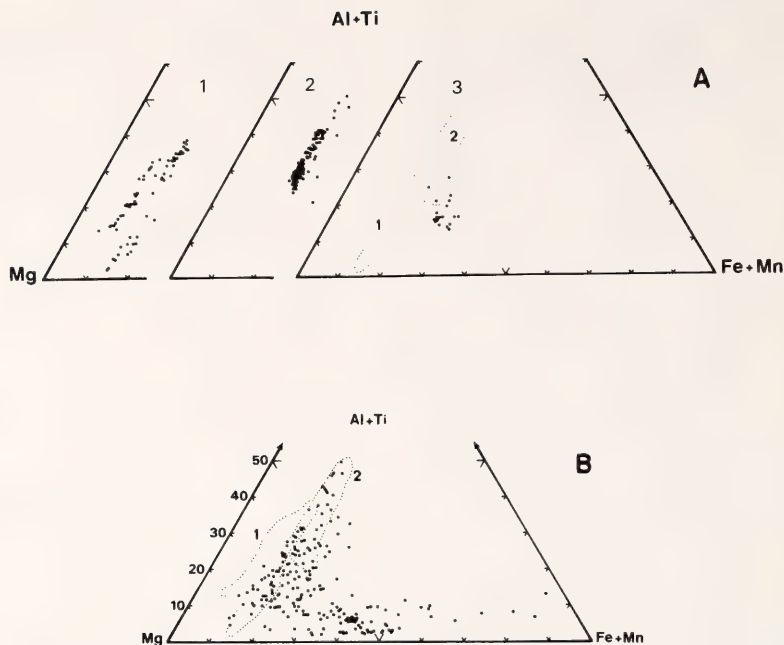


Fig. 46. Clinopyroxene compositions plotted in a Mg-(Al + Ti)-(Fe + Mn) triangle (atomic ratios). (A) Nyiragongo clinopyroxene from the bergalites (1); from the leucites, leucite (melilite) nephelinites, and nepheline aggregate lavas (2); from the dike No. 6 (3). Areas occupied by the data points in 1 and 2 marked with dotted lines, 198 data points. (B) 224 microprobe clinopyroxene analyses selected from the literature (the same analyses as in Fig. 47, part 2, with 27 additional analyses from Carmichael, 1967*b*); dotted lines from part 3 of Fig. 46A.

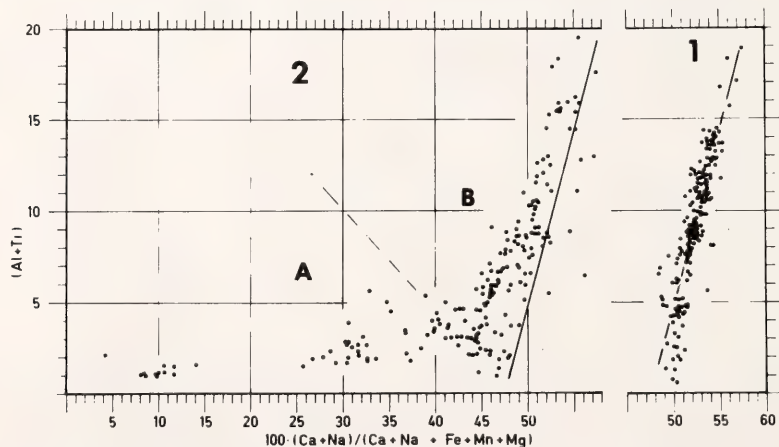


Fig. 47. Clinopyroxene compositions. (Al + Ti) (cation %) plotted against $100 \cdot (Ca + Na) / (Ca + Na + Fe + Mn + Mg)$. (1) 198 microprobe analyses from the Nyiragongo lavas with regression line of the data points. (2) 197 microprobe clinopyroxene analyses selected from the literature (Fodor, Keil, and Bunch, 1975; Gibb, 1973; Gramse, 1970; Hollister and Grancarz, 1971; James, 1971; Leung, 1974; Nakamura, 1973; Schorer, 1970; Wass, 1973; Ferguson, 1973); solid line indicates the regression line in 1; broken line illustrates roughly the boundary between clinopyroxene from tholeiitic (A) and alkalic (B) rocks.

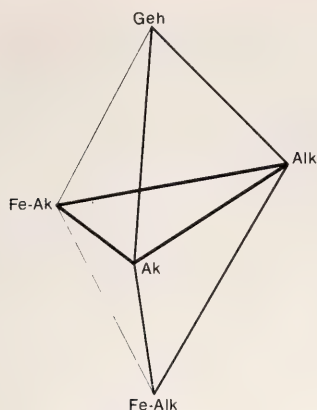


Fig. 48. The melilite double tetrahedron for plotting microprobe analyses. Alk, $\text{Ca}(\text{Na,K})\text{-AlSi}_2\text{O}_7$; Ak, $\text{Ca}_2\text{MgSi}_2\text{O}_7$; Fe-Ak, $\text{Ca}_2\text{FeSi}_2\text{O}_7 + \text{Ca}_2\text{Fe}_2\text{SiO}_7$; Geh, $\text{Ca}_2\text{Al}_2\text{SiO}_7$; Fe-Alk, $\text{Ca}(\text{Na,K})\text{FeSi}_2\text{O}_7$.

over Al, causing the mineral to plot in the lower half.

The compositions of the Nyiragongo melilites, excluding the narrow crystal margins and melilites of thermal metamorphic growth or post-extrusional

vesicle crystallization (Sahama, 1961, 1967), vary within narrow limits (Fig. 49, left). Melilite 3, from a nepheline aggregate lava, is slightly richer in Fe-Ak than are the bergalitic melilites, corresponding to higher $\text{Fe}/(\text{Fe} + \text{Mg})$ of the nepheline lavas. Fig. 49, right, illustrates the low Geh (or Fe-Alk) content of volcanic-subvolcanic melilites (Yoder, 1973).

Melilite microphenocrysts of many volcanic rocks show narrow margins with a birefringence higher than in the large crystal core. A higher birefringent zone is common in the melilite of the Nyiragongo bergalites and is not confined to the outer margins but occurs also around inclusions. The zone represents the last stages of magmatic melilite crystallization and should not be confused with the thermal metamorphic growth of the mineral found especially in some lavas of the central crater pit. The boundary between the low birefringent core and the higher birefringent margin is not sharp but gradual. The only notable differences in composition

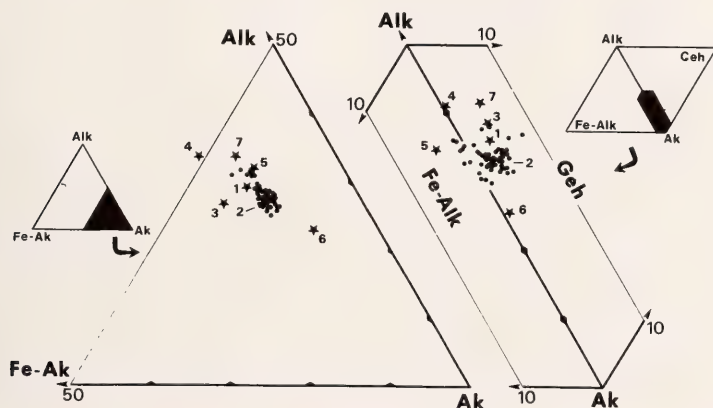


Fig. 49. Melilite compositions plotted in the Fe-Ak/Alk/Ak section and in the Fe-Alk/Alk/Ak or Geh/Alk/Ak faces of the melilite double tetrahedron (molecular ratios). Abbreviations as in Fig. 48. Solid circles: single melilite analyses from the Nyiragongo bergalites; total 57 analyses from 7 specimens. Stars: wet chemical analyses (melilites) from the literature. (1) Nyiragongo bergalite FEAE 83 (Sahama and Meyer, 1958, p. 77). (2) Nyiragongo bergalite VM. 569 (Sahama, 1961, p. 173; in the middle of the highest concentration of the solid circles, not shown). (3) Nyiragongo nepheline aggregate lava FEAE 93 (Sahama and Meyer, 1958, p. 77). (4-6) Sugar Load, Mt. Elgon, and Katunga, respectively (Neuvonen, 1955, p. 16). (7) Uvalde (Spencer, 1969, p. 286).

between crystal core and margin were found in the contents of FeO and Na₂O, both slightly higher in the margin (examples in Table 28).

Some melilite phenocrysts of the bergalites exhibit an hourglass structure in sections roughly parallel to the *c* axis. This structure results from sectoral zoning made visible by the very slightly higher birefringence of the (001) sector (facing the large basal plane) as compared with that of the (*hk*0) sector (facing the ends of the lath-shaped crystal). On two sectorally zoned crystals of bergalite VS. 260, the (001) sector was slightly enriched in Al(Al₂O₃ 6.5 ± 0.02 wt %; MgO 8.7 ± 0.04 wt %), and the (*hk*0) sector, slightly enriched in Mg (Al₂O₃ 6.1 ± 0.07 wt %; MgO 9.0 ± 0.06 wt %). The partitioning of Al and Mg between the two sectors is qualitatively analogous to that in sectorally zoned, long-prismatic clinopyroxene where Al is enriched in the sectors of the large prism faces and Mg is enriched in the sectors facing the narrow crystal ends.

Melilite Alteration

The alteration of the Nyiragongo melilite (peg structure; Stelzner, 1883; Gentil, 1894; Soellner, 1913) is well advanced in the bergalite beds that alternate with the pyroclastic strata in the main crater and in the bergalite dikes cutting these strata. When fresh, the melilite phenocrysts appear dark gray to almost black in a hand specimen. When the phenocrysts are heavily altered, the color is bright brownish yellow. When

viewed along the *c* axis, the crystals exhibit a silky luster.

Figure 50 illustrates that the formation of a single peg involves leaching out Ca and Mg and introducing K. The enrichment of Si, Al, and Fe in the peg largely may be passive. A number of analyses of the altered material of several melilite crystals from bergalites VS. 205 and VM. 555 indicate variable composition and confirm the qualitative trend of Fig. 50: The alteration product contains low MgO (~1½ wt %), and CaO (~1½ wt %), and high K₂O, ranging up to values higher than those for pure kalsilite. The strong mark instantly created by the electron beam on the specimen surface indicates a high water content resulting in low analysis totals. The silica-rich phase contained in a peg in melilite (bergalite VM. 567, Nyiragongo) reported by El Goresy and Yoder (*Year Book* 73, p. 363) seems to represent a material formed at an early stage of the alteration characterized mainly by removal of Ca and introduction of water. The melilite of that specimen shows only pegs, and not the more advanced alteration of the entire crystal. In some pegs El Goresy and Yoder also found small amounts of K-rich nepheline and (ferrian-barian) kalsilite. The alteration of melilite appears to be a complicated metasomatic process during which some spots may reach the composition of nepheline or kalsilite or both, and could even crystallize in structures of long-range order without necessarily originating as an exsolution product from the host melilite.

TABLE 28. Melilite from Bergalite, Nyiragongo: FeO and Na₂O Contents in Core and Margin of the Same Microphenocryst*

| Specimen No. | FeO† (wt %) | | | | Na ₂ O (wt %) | | | |
|--------------|-------------|--------|--------|--------|--------------------------|--------|--------|--------|
| | Core | | Margin | | Core | | Margin | |
| VM. 234 | 2.67 | (0.07) | 3.07 | (0.02) | 2.90 | (0.08) | 3.16 | (0.09) |
| VM. 233 | 2.85 | (0.06) | 3.55 | (0.18) | 2.93 | (0.15) | 3.42 | (0.05) |
| VM. 216 | 3.34 | (0.03) | 3.45 | (0.15) | 2.95 | (0.10) | 3.44 | (0.11) |

* Averages of 4-8 analyses. Standard deviations in parentheses.

† Total iron as FeO.

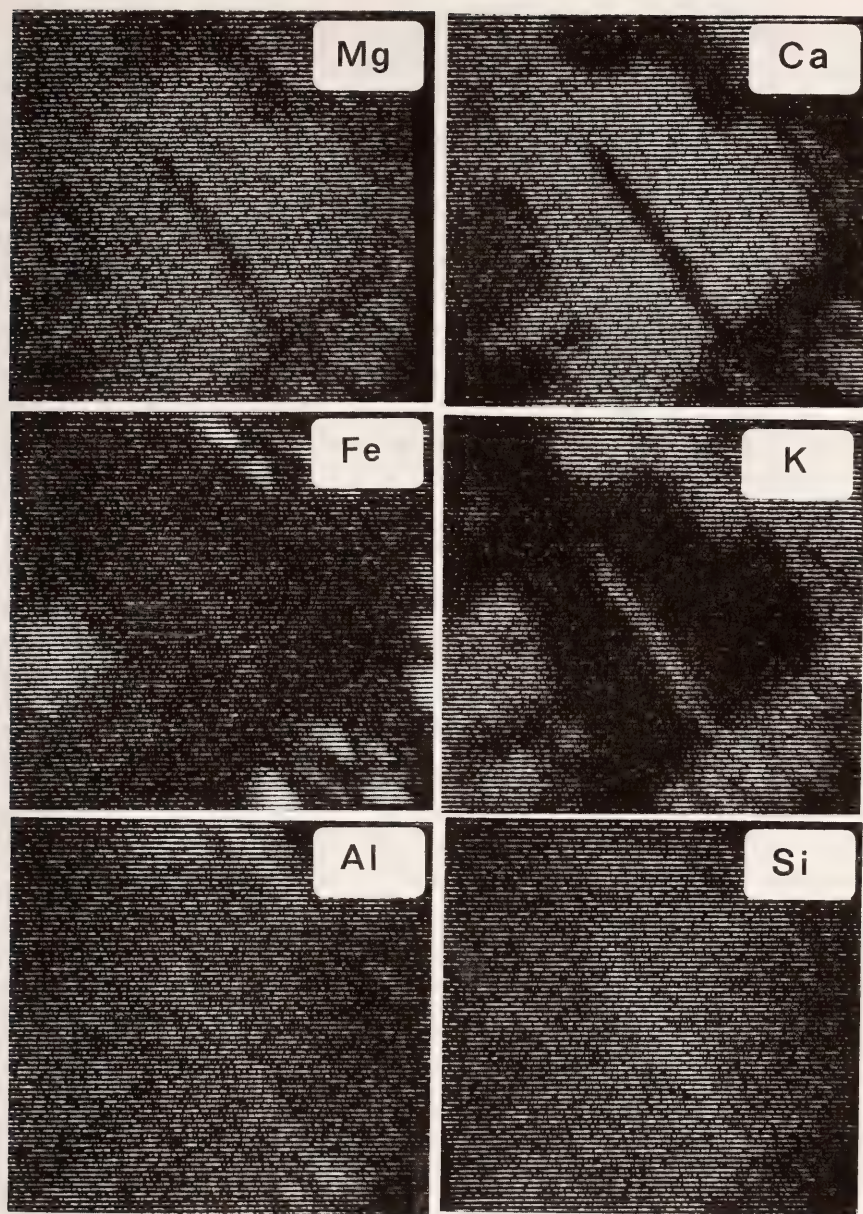


Fig. 50. X-ray scanning image photographs of a single peg in fresh melilite. Bergalite VS. 205, dike No. 2 cutting the pyroclastics of the Nyiragongo crater. Courtesy of Dr. J. Siivola of the Geological Survey of Finland. Na shows no marked difference between peg and fresh melilite and is not included.

IGNEOUS PETROLOGY: EXPERIMENTAL AND FIELD

LIQUID IMMISCIBILITY IN THE SYSTEM $\text{KAlSi}_3\text{O}_8\text{-NaAlSi}_3\text{O}_8\text{-FeO-Fe}_2\text{O}_3\text{-SiO}_2$ AND ITS APPLICATION TO NATURAL MAGMAS

*H. R. Nashund**

Greig (1927*a,b*) demonstrated that binary systems of SiO_2 with MgO , CaO , SrO , MnO , ZnO , FeO , NiO , CoO , and Fe_2O_3 contain fields of liquid immiscibility, and he showed that the addition of only small amounts of K_2O , Na_2O , or Al_2O_3 to any of these systems will suppress the immiscibility. In addition, he made the observation that the two-liquid field in these simple systems occurs at such high temperatures (in excess of 1650°C) and the immiscible liquids are of such extreme compositions that this type of immiscibility is of little direct importance to igneous petrogenesis.

Roedder (1951*a*) showed that the system leucite-fayalite-silica contains two fields of liquid immiscibility. One field, located along the fayalite-silica join at temperatures above 1690°C , is of the type described by Greig (1927*a,b*). The other field is located along the fayalite-tridymite boundary curve at temperatures between 1100° and 1270°C , and the immiscibility occurs through a range of temperatures common to magmas. In a simple way, the liquid compositions in the synthetic system approximate those of some natural magmatic liquids. Related systems, however, such as nepheline-fayalite-silica (Bowen and Schairer, 1938) and leucite-forsterite-silica (Schairer, 1954), do not show a low-temperature immiscibility field.

Recent discoveries of quenched immiscible liquids in lunar and terrestrial basalts (Roedder and Weiblen, 1970, 1971, 1972; De, 1974) and the discovery

of immiscibility in experimental Skaergaard liquids (McBirney and Nakamura, *Year Book* 73, pp. 348-352; McBirney, 1975) have generated renewed interest in liquid-liquid exsolution as a petrogenetic process. The system $\text{KAlSi}_3\text{O}_8\text{-NaAlSi}_3\text{O}_8\text{-FeO-Fe}_2\text{O}_3\text{-SiO}_2$ has therefore been investigated to gain a better understanding of the compositional factors that affect liquid immiscibility in silicate magmas. Particular attention has been given to the effects of Na_2O and Fe_2O_3 on the compositional and temperature ranges of the low-temperature immiscibility field.

Method

A series of compositions along the 30% FeO isopleth of the system $\text{KAlSi}_3\text{O}_8\text{-FeO-SiO}_2$ was prepared from mixtures of synthetic leucite, cristobalite, and synthetic fayalite. A similar series along the 30% FeO isopleth of the system $\text{NaAlSi}_3\text{O}_8\text{-FeO-SiO}_2$ was prepared from mixtures of synthetic nepheline, cristobalite, and synthetic fayalite. All starting materials were ground under acetone in an agate mortar for at least 1 hr and then dried overnight at 120°C .

Experimental charges were prepared by packing a small portion (0.020-0.030 g) of starting material into a 95Pt/5Au foil crucible ($0.5 \times 0.3 \times 0.3$ cm). A small platinum wire (0.01×1.25 cm) bent into a Y shape was inserted into the charge with the stem of the Y protruding, and the charge was then sintered for 10-15 min at a temperature $50^\circ\text{-}100^\circ\text{C}$ below its solidus. After sintering, the foil crucible was removed, and the charge was suspended by the stem of the Pt wire from a ceramic washer in a vertical 1-atm quenching furnace. Samples were quenched by dropping them into a mercury reservoir below the furnace.

Temperature measurements were made before and after each run with a Pt/

* Work carried out under a cooperative predoctoral fellowship program of the Geophysical Laboratory and the University of Oregon.

90Pt10Rh thermocouple and are believed to be accurate within 5°C. Oxygen fugacity was controlled by passing appropriate mixtures of either CO and CO₂ or H₂ and CO₂ through the furnace. The mixtures were calibrated in accordance with the data of Deines *et al.* (1974). Run times in the system KAlSi₃O₈-FeO-SiO₂ were 20–24 hr at temperatures below 1400°C and 8–10 hr at temperatures above 1400°C. In the system NaAlSi₃O₈-FeO-SiO₂ run times of 2–2½ hours below 1400°C and approximately 1 hr above 1400°C were used. Selected samples were analyzed with the electron microprobe.

To test rates of equilibration, a composition within the immiscibility field of the system KAlSi₃O₈-FeO-SiO₂ was run at a temperature of 1150°C and an oxygen fugacity (f_{O_2}) of 10⁻⁹ atm for 3, 6, 12, and 48 hr. Almost identical results were obtained in each run, indicating that equilibrium was reached in less than 3 hr. The same sample run at 1500°C in air showed consistent results after 1, 10, and 20 hr. In all runs, the loss of K₂O due to volatilization was between 3.0% and 5.0% of the amount present, the loss of Na₂O due to volatilization was between 5.0% and 10.0%, and the loss of FeO (as Fe to the Pt wire) was less than 5.0%.

Results

Compositions in the system KAlSi₃O₈-FeO-SiO₂ were run at oxygen fugacities of 10⁻¹², 10⁻⁹, 10⁻⁵, and 10^{-0.7} atm. Liquid immiscibility, in the form of spheres of an Fe-rich glass in a matrix of Si-rich glass, was observed at all four oxygen fugacities (Fig. 51). The compositional difference between the two liquids in this system increased progressively with increasing oxygen fugacity. The maximum extent of the immiscibility field, as measured by the maximum difference in the percentage of total iron (FeO + 0.9Fe₂O₃) between coexisting glasses, increased from 25% at an f_{O_2} of 10⁻¹² atm to more than 70% at an

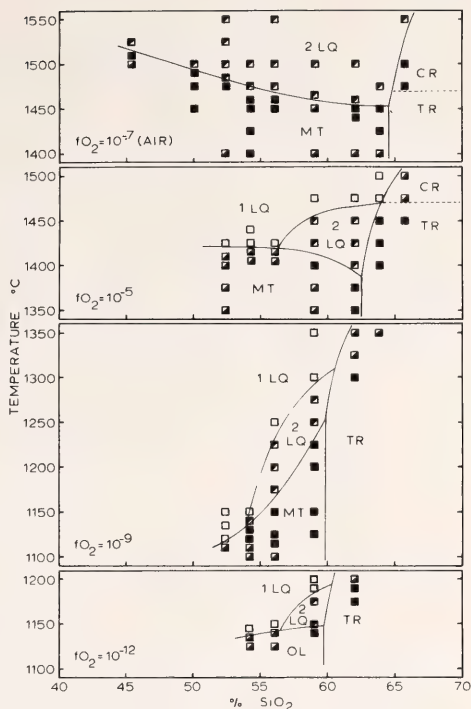


Fig. 51. Summary of experimental data along the join from 30% FeO, 70% SiO₂, to 30% FeO, 70% KAlSi₃O₈ (wt %). The stability fields where magnetite, olivine, tridymite, or cristobalite is the liquidus phase are indicated by MT, OL, TR, and CR, respectively. The stability fields for one liquid and two liquids in which no crystals are present are indicated by 1LQ and 2LQ. Symbols: open squares, one liquid; upper left half shaded, two liquids; lower right half shaded, one liquid + crystals; solid squares, two liquids + crystals.

f_{O_2} of 10^{-0.7} atm (Fig. 52). The temperatures at which immiscibility occurs also increased with increasing oxygen fugacity. The width of the immiscibility field and the total range of temperature over which immiscibility occurs decreased from 10⁻⁹ to 10⁻⁵ atm. This apparent anomaly in the general trend is the result of a rapid increase in the temperature of the magnetite liquidus over this fugacity range. Both Al₂O₃ and K₂O were enriched in the Si-rich glass and depleted in the Fe-rich glass, and the atomic ratio of K to Al, which was

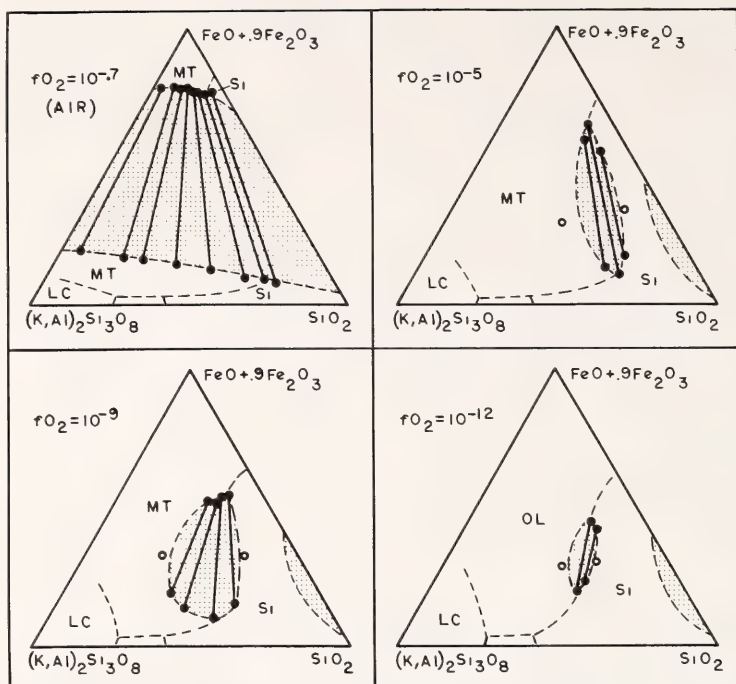


Fig. 52. Plot in weight percent of electron microprobe analyses of experimental glasses in the system $(K,Al)_2Si_3O_8$ -FeO-Fe₂O₃-SiO₂. Solid circles with tie lines indicate the compositions of coexisting quenched immiscible liquids in equilibrium with one or more crystal phases. Open circles indicate compositions in which no immiscibility was observed. The inferred phase boundaries, represented by dashed lines, are based partly on the work of Roedder (1951a) and Muan (1955). The stability fields with magnetite, silica (tridymite or cristobalite), olivine, or leucite as the liquidus phase are indicated by the symbols MT, Si, OL, and LC. The unlabeled field along the base of the diagrams is the field of K-feldspar. The fields of liquid immiscibility are shaded.

1.0 in the starting material, was less than 1.0 in the Fe-rich glass and greater than 1.0 in the Si-rich glass. Figure 52 is therefore not a true phase diagram for the system orthoclase-FeO-silica, but represents only the projection of one surface in the system K_2O -Al₂O₃-SiO₂-FeO-Fe₂O₃ onto the orthoclase-FeO-silica plane.

In the system $NaAlSi_3O_8$ -FeO-SiO₂, no low-temperature immiscibility was observed in runs at an f_{O_2} of 10^{-12} atm (Fig. 53). At oxygen fugacities of 10^{-9} , 10^{-5} , and $10^{-0.7}$ atm, a low-temperature immiscibility field, similar to that in the system $KAlSi_3O_8$ -FeO-SiO₂, expands

with increasing f_{O_2} . The maximum extent of the immiscibility field, measured by the maximum difference in the percentage of total iron, increased from 15% at an f_{O_2} of 10^{-9} atm to more than 60% at an f_{O_2} of $10^{-0.7}$ atm (Fig. 54). Both Al₂O₃ and Na₂O were enriched in the Si-rich glass, and the atomic ratio of Na to Al was greater than 1.0 in the Si-rich glass and less than 1.0 in the Fe-rich glass.

Discussion

Compositions within the system $KAlSi_3O_8$ - $NaAlSi_3O_8$ -FeO-Fe₂O₃-SiO₂

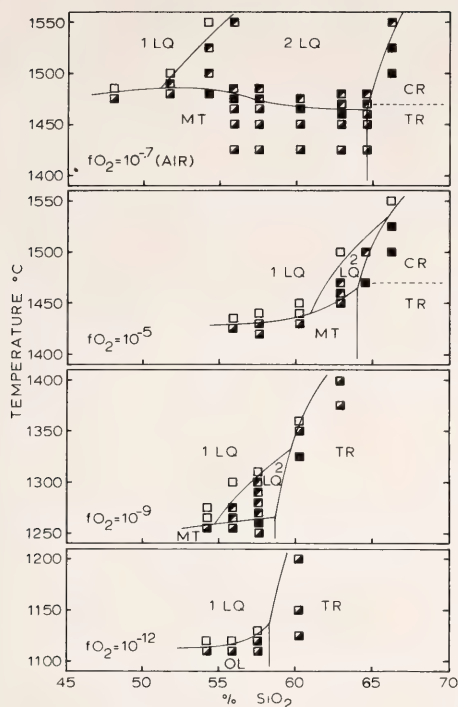


Fig. 53. Summary of experimental data along the join from 30% FeO, 70% SiO₂, to 30% FeO, 70% NaAlSi₃O₈ (wt %). See Fig. 51 for explanation of symbols.

are roughly analogous to some natural magmas. Although the system contains only six oxides, it includes most of the major cation types found in natural silicate liquids (i.e., network-forming cations, trivalent cations, divalent cations, and alkali cations; Watson, *Year Book* 74, pp. 500–504). Although the range of liquidus temperatures and oxygen fugacities is generally higher than those reported for natural magmas, all the experiments in this study lie between the buffer curves for iron-wüstite and magnetite-hematite (Fig. 55). It is assumed that the addition of more components to these artificial melts would lower the liquidus temperatures and therefore the f_{O_2} for a given ferrous/ferrie ratio and bring them within the ranges observed for similar natural melts.

It is apparent from Figs. 52 and 54

that the field of low-temperature immiscibility is elongated along the fayalite-tridymite and magnetite-tridymite boundary curves. These curves are the traces of a surface of silica saturation in the system $KAlSi_3O_8$ - $NaAlSi_3O_8$ - FeO - Fe_2O_3 - SiO_2 . It has been proposed by Holgate (1954) that the low-temperature immiscibility field in the system leucite-fayalite-silica represents the intersection of the fayalite-tridymite boundary curve with a subsolidus field of metastable immiscibility that extends over much of the system. A similar field of metastable immiscibility in the system $KAlSi_3O_8$ - $NaAlSi_3O_8$ - FeO - Fe_2O_3 - SiO_2 is intersected by the liquidus surface along the fayalite-tridymite and magnetite-tridymite boundary curves because they represent a local temperature minimum in the liquidus surface. Because the largest relative temperature minimums in the slope of the liquidus surface occur along the olivine-magnetite-tridymite and magnetite-hematite-tridymite univariant curves, the liquids most likely to develop immiscibility are those in equilibrium with olivine, magnetite, and silica (either tridymite or quartz) or in equilibrium with magnetite, hematite, and silica. In the system $KAlSi_3O_8$ - FeO - Fe_2O_3 - SiO_2 liquid immiscibility was best developed at f_{O_2} 's of 10^{-9} and $10^{-0.7}$ atm. An examination of the system FeO - Fe_2O_3 - SiO_2 (Muan, 1955) shows that of the four f_{O_2} 's investigated in the present study, those of 10^{-9} and $10^{-0.7}$ atm are the closest to the fayalite-magnetite-tridymite and the magnetite-hematite-tridymite curves, respectively.

In conclusion, it has been shown that (1) liquid immiscibility is present in the system $KAlSi_3O_8$ - $NaAlSi_3O_8$ - FeO - Fe_2O_3 - SiO_2 over a range of temperatures and f_{O_2} 's that are roughly analogous to many natural magmas; (2) the degree of separation in the immiscibility field of this system shows a progressive increase with increasing oxygen fugacity; (3) owing to the interaction between the immiscibility field and the liquidus surface, im-

miscibility is best developed along the olivine-magnetite-tridymite and magnetite-hematite-tridymite univariant curves; and (4) although liquid immiscibility is

best developed in the K_2O -rich portion of the system, a high K_2O to total alkali ratio is not crucial for the formation of immiscibility.

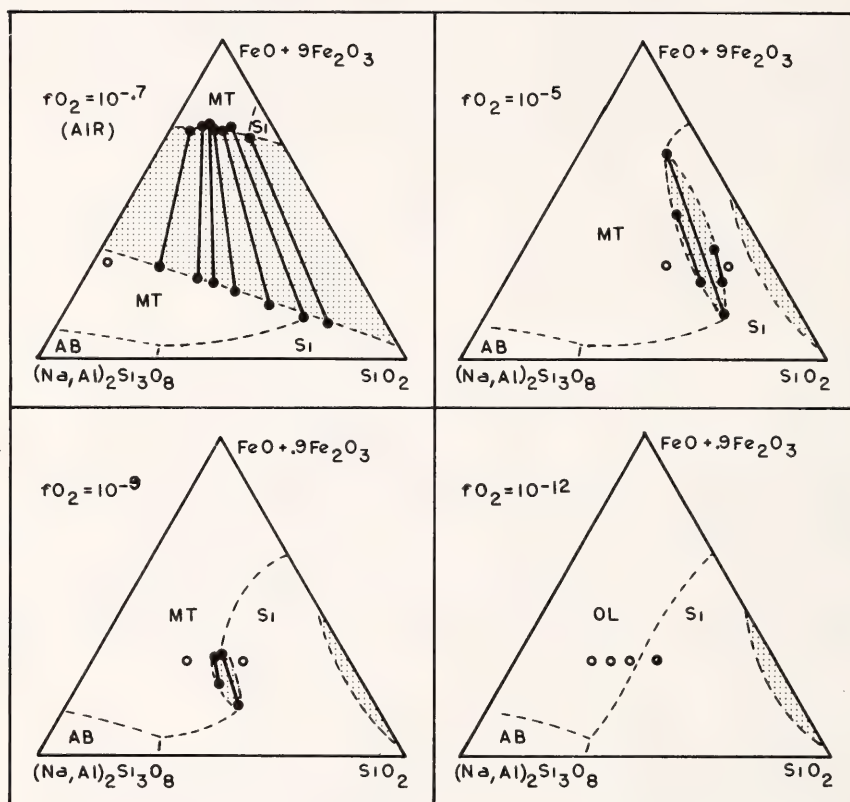


Fig. 54. Plot in weight percent of electron microprobe analyses of experimental glasses in the system $(Na,Al)_2Si_3O_8$ - FeO - Fe_2O_3 - SiO_2 . The inferred phase boundaries, represented by the dashed lines, are based partly on the work of Bowen and Schairer (1938) and Muan (1955). The stability fields with albite, olivine, magnetite, or silica (tridymite or cristobalite) as the liquidus phase are indicated by AB, OL, MT, and Si. See Fig. 52 for explanation of symbols.

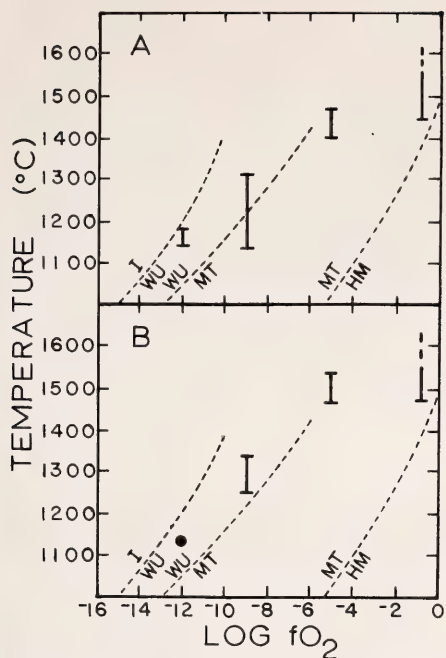


Fig. 55. (A) Plot of the range of temperatures (heavy vertical lines) over which liquid immiscibility was observed in the system $\text{KAlSi}_3\text{O}_8\text{-FeO-Fe}_2\text{O}_3\text{-SiO}_2$ at oxygen fugacities of 10^{-12} , 10^{-9} , 10^{-5} , and $10^{-0.7}$ atm. The lower temperature limit at each f_{O_2} represents the minimum temperature at which two crystal-free liquids are stable. The upper temperature limit for immiscibility was not reached for an f_{O_2} of $10^{-0.7}$ atm. The symbols I/WU, WU/MT, and MT/HM indicate the buffer curves (light dashed lines) of iron-wüstite, wüstite-magnetite, and magnetite-hematite. (B) Plot of the range of temperatures over which liquid immiscibility was observed in the system $\text{NaAlSi}_3\text{O}_8\text{-FeO-Fe}_2\text{O}_3\text{-SiO}_2$ at oxygen fugacities of 10^{-9} , 10^{-5} , and $10^{-0.7}$ atm. The upper temperature limit of immiscibility was not reached for an f_{O_2} of $10^{-0.7}$ atm. The dot at the f_{O_2} of 10^{-12} atm indicates the liquidus temperature at the intersection of the olivine-tridymite boundary curve with the 30% FeO contour.

METASTABLE LIQUID IMMISCIBILITY AND MgO-FeO-SiO_2 FRACTIONATION PATTERNS IN THE SYSTEM $\text{Mg}_2\text{SiO}_4\text{-Fe}_2\text{SiO}_4\text{-CaAl}_2\text{Si}_2\text{O}_8\text{-KAlSi}_3\text{O}_8\text{-SiO}_2$

T. N. Irvine

Attention was drawn in *Year Book 74* (pp. 484-492) to the fact that at liquidus temperatures at 1 atm silica melt

shows extensive immiscibility with the melts of most end-members of the mafic silicate and oxide minerals but is completely miscible with feldspar melts. It was shown that because of this contrast cotectic boundaries between plagioclase and the mafic and oxide minerals should tend to deflect away from and skirt the miscibility gaps, and it was demonstrated that such deflection is evident both in simple systems and in the chemical trends of volcanic rock series and is significant petrogenetically. The analysis also revealed that when alkali feldspar components are introduced into systems comprised of a mafic mineral, anorthite, and silica, the following major changes in phase relations are generally indicated to occur: The stable two-liquid solvus that in most cases overlies the silica minerals liquidus field* is suppressed, apparently becoming metastable; the silica minerals field shrinks dramatically, giving way to the fields of the mafic mineral and anorthite; and the liquidus of the mafic mineral appears to override the metastable two-liquid solvus. These changes suggest that in the absence of the alkali feldspar components the activity of silica in the melt solution is abnormally high—and hence the silica minerals field is relatively large—because of the nonideality manifest in the immiscibility. When the nonideality is suppressed by the modifying effect of the alkalis on the melt structure, the silica minerals field recedes, and the mafic mineral and anorthite can crystallize from more siliceous melts. In the present study, these features have been examined in more detail in the system $\text{Mg}_2\text{SiO}_4\text{-Fe}_2\text{SiO}_4\text{-CaAl}_2\text{Si}_2\text{O}_8\text{-KAlSi}_3\text{O}_8\text{-SiO}_2$ (Fo-Fa-An-Or-Q) on the possibility that they might significantly affect magma fractionation trends. It has been found that (1) large regions of metastable liquid immiscibil-

*The term "silica minerals liquidus field" is used here to refer to the combined liquidus of cristobalite and tridymite (and could also include the liquidus of quartz, were it relevant).

ity do indeed extend from the previously known fields of stable immiscibility to beneath the olivine and pyroxene liquidus fields, and (2) strongly contrasting liquid fractionation patterns are possible in terms of silica enrichment versus MgO/FeO variations, depending on the concentration of Or.

Experimental Methods Used to Determine Stable Phase Relations

Starting materials consisted of crystallized mixes of Fo, Fa, and An composition combined in various proportions with either silica (cristobalite) or a glass of $\text{Or}_{56}\text{Q}_{44}$ composition. The mixtures were ground to a maximum grain size of about 2 μm . Phase relations were determined by melting experiments in 1-atm quenching furnaces. Temperatures were controlled to about $\pm 2^\circ\text{C}$, and the values reported for individual runs are believed generally to be accurate to $\pm 5^\circ\text{C}$. Compositions containing no iron were melted in envelopes made from $\text{Pt}_{95}\text{Au}_5$ foil; those with iron were contained in capped iron capsules sealed in evacuated silica tubes. The iron-encapsulated charges were dried just before they were sealed in the silica tubes by heating them to a red glow under vacuum for a few seconds. Most runs were 18–22 hr long, and all charges were quenched in water, generally with no quench crystallization. Liquidus boundaries were located by bracketing the appearance and disappearance of phases as a function of temperature, but most of the data that appear on the diagrams presented here are based on phase compositions as determined by electron microprobe analysis and are plotted at the run temperatures.

In the course of using the iron capsules in silica tubes for the iron-bearing compositions, it became evident that oxygen slowly diffuses into the silica tube. After most runs, the inside of the tube was coated with a film of fayalite against the iron capsule, and in some runs the reaction was relatively extensive. Moreover, although the charges

rich in Fa typically show tiny globules of iron formed through the incongruent melting of fayalite, with increased Or and Q, and especially at high Fo/Fa, the melt analyses show systematic increases in iron oxide due to iron gain from the capsules (Figs. 59B and 61A). It would appear that there was some oxygen buffering according to either (depending on temperature) the reaction $\text{iron} + \text{silica} = \text{fayalite}$ or a melting reaction approximately represented by the iron-tridymite cotectic in the system $\text{FeO-Fe}_2\text{O}_3\text{-SiO}_2$ (cf. Muan and Osborn, 1965). This combination of reactions should yield f_{O_2} values ranging from about 10^{-15} atm at 1000°C to about 10^{-10} atm at 1400°C . If the melt gained iron, its f_{O_2} must have been below the buffer curves; if iron was precipitated, the buffer limit had presumably been reached. The gains and losses of iron were not themselves of any serious consequence inasmuch as the phase compositions were generally determined by analysis.

The $\text{Fe}_2\text{O}_3/\text{FeO}$ of the melts have not been determined, but from data of Bowen and Schairer (1935), Schairer (1942), and Roedder (1951a, 1952) for parts of the same system and adjoining systems (based on experiments in iron crucibles in nitrogen), it may be inferred that less than a tenth of the iron was ferric in most of the melts. In the diagrams, the iron has been treated entirely as FeO and is plotted as Fa.

Methods Used to Detect Metastable Liquid Immiscibility

The method used to produce metastable liquid immiscibility was to heat the charge to above its liquidus for a time period sufficient to ensure complete melting and homogenization, and then, by temporarily turning off the furnace, to supercool the melt to the temperature at which the immiscibility was suspected. That temperature was held for a time to allow some exsolution to occur, and the charge was quenched. For the join Fo-Or-Q, starting materials were

mixes prepared by Schairer (1954) in his study of liquidus relations in the more extensive system Mg_2SiO_4 - KAlSi_2O_6 - SiO_2 (Fo-Lc-Q). For Fa-Or-Q, only two compositions have been investigated; they were prepared by mixing fayalite with Lc-Q glasses made by Schairer and Bowen (1955). The time allowed for exsolution to occur was generally established by trial and failure as just less than the time in which the supercooled melt began to undergo appreciable crystallization. In Fo-Or-Q, compositions near the Or-Q join could be held for several hours, but the limit for the more magnesian compositions was

only a matter of minutes. In one mix it was evident that exsolution initiated crystallization: The melt was stable for 20–30 min just above the solvus boundary but for only a minute or so just below it.

The metastable immiscibility was relatively easy to detect but in some melts was difficult to prove. In a few compositions it could be distinguished by routine optical methods (Fig. 56 A, B), but more commonly the phase separation was too fine to be resolved. However, if the ordinarily colorless quenched melts in Fo-Or-Q were unmixed, they appeared megascopically milky and slightly opal-

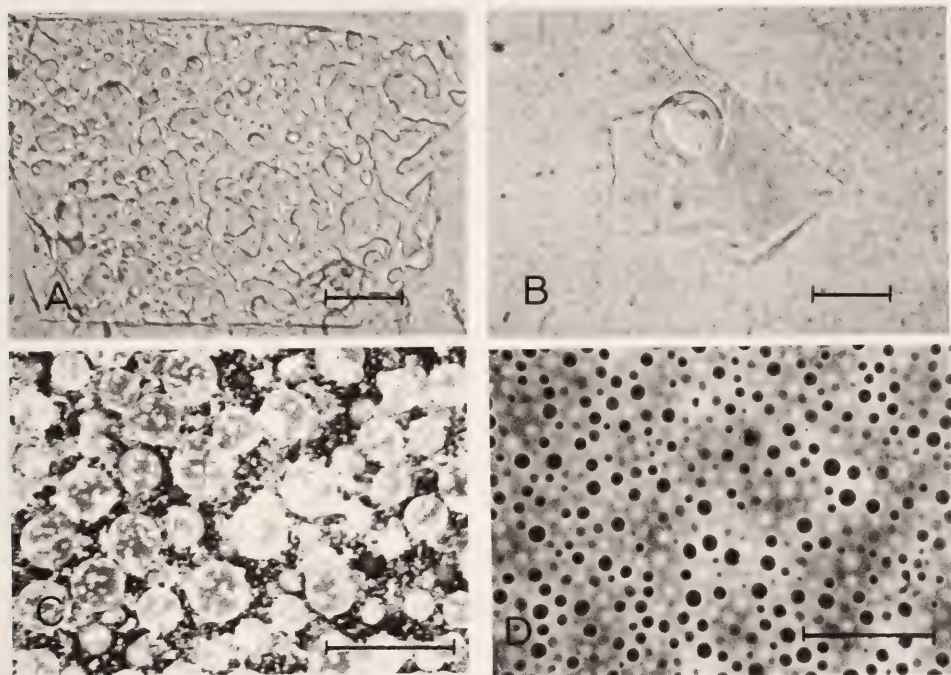


Fig. 56. (A) Photomicrograph of quenched immiscible liquids formed metastably in 1 hr at 1210°C in a charge of composition $\text{Fo}_{30}\text{Lc}_{20}\text{Q}_{50}$. This composition has protoenstatite on the liquidus at about 1497°C ; the upper limit of the immiscibility is 1255°C . (B) Photomicrograph of composition $\text{Fo}_{30}\text{Lc}_{10}\text{Q}_{60}$ showing a spherical growth of metastable immiscible liquids surrounded by finely exsolved liquids. Similar spheres in other parts of the charge contain rosettes of cristobalite (?) crystals. The charge was quenched from 1495°C ; the composition has cristobalite on the liquidus at about 1590°C ; the upper limit of the immiscibility is about 1510°C . (C) Scanning electron photomicrograph of the finely exsolved liquids in another charge of the composition (B). Tiny crystals, presumably of cristobalite, occur throughout. (D) Scanning electron photomicrograph of quenched immiscible liquids formed metastably in 10 min at 1050°C in a composition $\text{Fa}_{40.5}\text{Lc}_{35}\text{Q}_{12.5}$. The upper limit of immiscibility is about 1090°C ; the stable assemblage at 1100°C consists of a large proportion of fayalite, some leucite, and one liquid. Scale bars are $50\text{ }\mu\text{m}$.

escent and were microscopically brownish because of the light interference arising from the differences in refractive index between the contrasting glasses. In these circumstances, identification was most effectively confirmed with the scanning electron microscope (Fig. 56C), but a useful phase equilibrium technique, if the supercooled liquids were relatively stable, was to reverse the exsolution process metastably. The procedure was to supercool the melt to a temperature where the apparent immiscibility was known to occur reproducibly, and then, after an appropriate time, to raise the temperature to above the apparent solvus boundary (but still below the liquidus) for a comparable time. If the quenched melt was clear, the previously observed milkiness was almost certainly caused by exsolution; if it was caused by crystallization, the milkiness persisted (and usually became even more pronounced). Reversing the exsolution in this way at a temperature just above the limit of its occurrence also proves that the limit is an equilibrium boundary, not a spinodal.

With the two compositions in Fa-Or-Q, it was not possible to use iron capsules in silica tubes as containers because the supersolvus melts could not be quenched fast enough in them to avoid metastable exsolution. The experiments were performed therefore by suspending the charge on the looped end of a thin platinum wire in a gas mixing furnace in which f_{O_2} was controlled by mixing CO and CO₂ (see Naslund, this Report, for details of the method). The small droplets of melt formed in these experiments adhered to the platinum wire by surface tension and quenched satisfactorily in mercury. For one of the compositions, lying between the two fields of stable liquid immiscibility defined in the system by Roedder (1951a), charges were superheated for 1–2 hr at 1550°C at an f_{O_2} of 10^{-11} atm, and then were supercooled for 10–15 min. The upper limit of exsolution was roughly bracketed at 1350°C; the stable assemblage at that

temperature in the same gas mixture consists of a single liquid and a large proportion of tridymite. For the other composition, lying on the Or side of the low-temperature stable solvus, the charges were superheated for 20 hr at 1300°C at an f_{O_2} of 10^{-10} atm. The immiscibility is illustrated in a scanning electron photomicrograph in Fig. 56D; the caption describes the phase relations. For both compositions, the unexsolved melts were green and clear; those showing exsolution were brown and murky.

Phase Relations of the Metastable Two-Liquid Solvi

The thermodynamic relationship of a metastable two-liquid solvus to the liquidus above it is such that the liquidus should tend to flatten as it descends over the solvus and then steepen once the top has been cleared. The protoenstatite liquidus in the system Fo-Lc-Q features exceptional development of this type of sigmoidal profile (Fig. 57A); hence the system was a logical place to look for metastable immiscibility. The data obtained (Fig. 57B) demonstrate with reasonable certainty that the metastable solvus extends from the stable two-liquid region along the Fo-Q join to at least as far as the Fo-Or join, separating basic liquids of moderate Fo content from salic liquids just inside the Or-Q join. Of particular interest is the way in which the protoenstatite-silica minerals cotectic (boundary *bji*) skirts the high-temperature part of the solvus and then drops steeply down the Or-Q side. As seen in Fig. 58, the available information on immiscibility in Fa-Lc-Q can be interpreted as representing a solvus similar to that in Fo-Lc-Q with the fayalite-tridymite cotectic starting off on a course (*da*) comparable with that of the protoenstatite-cristobalite boundary. The main difference is that the fayalite-tridymite cotectic starts at such a low temperature that it does not clear the solvus; consequently there develops the low-temperature field of stable immiscibility discovered by Roedder (1951a).

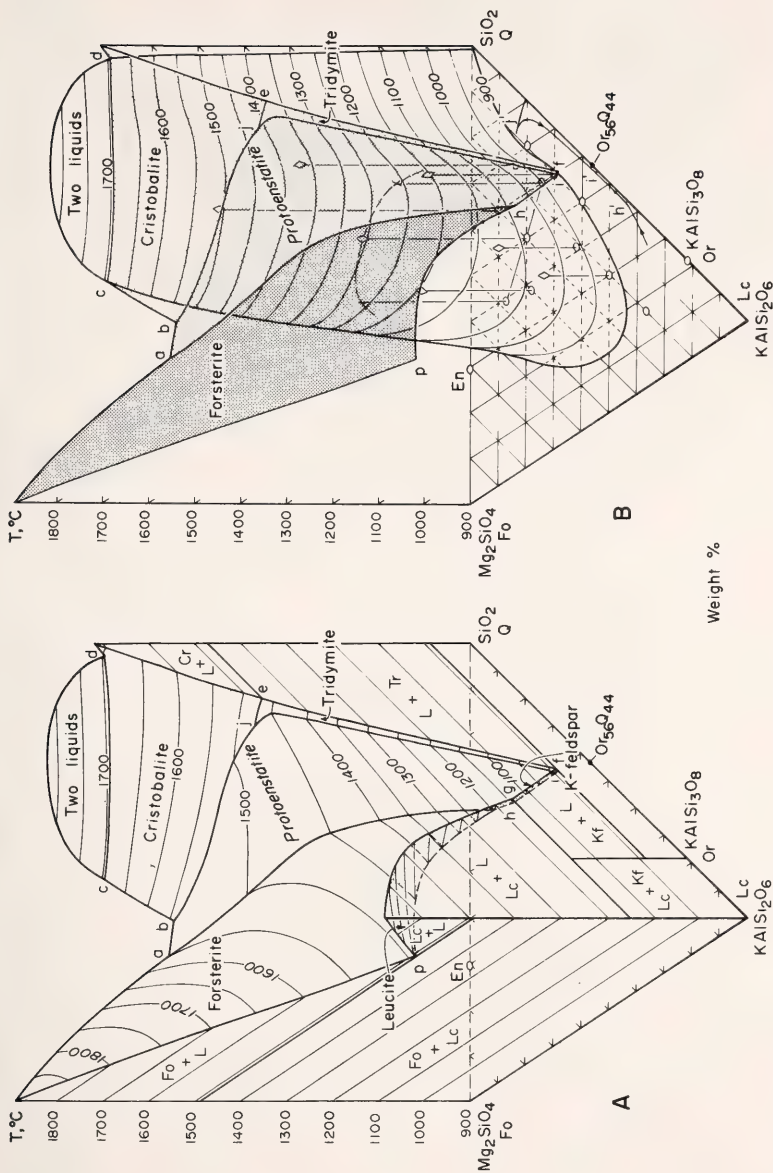


Fig. 57. (A) Liquidus and solvus relations in the system Fo-Lc-Q (which includes Fo-Or-Q), redrawn from Schairer (1954). The leucite and K-feldspar liquids are seen from the under side and so are shaded; solvus temperatures are inferred. (B) The same system with present information on the extent of metastable liquid immiscibility; leucite and K-feldspar liquids omitted for clarity. Circular symbols indicate the compositions that have been investigated for metastable immiscibility; diamonds indicate the temperatures at which the metastable solvus boundary has been bracketed, generally within $\pm 15^\circ C$; crosses represent the immiscible liquids in Fig. 56A as determined by analysis. Note the location of the composition $Or_{44}Q_{44}$, which is an "end-member" in subsequent figures.

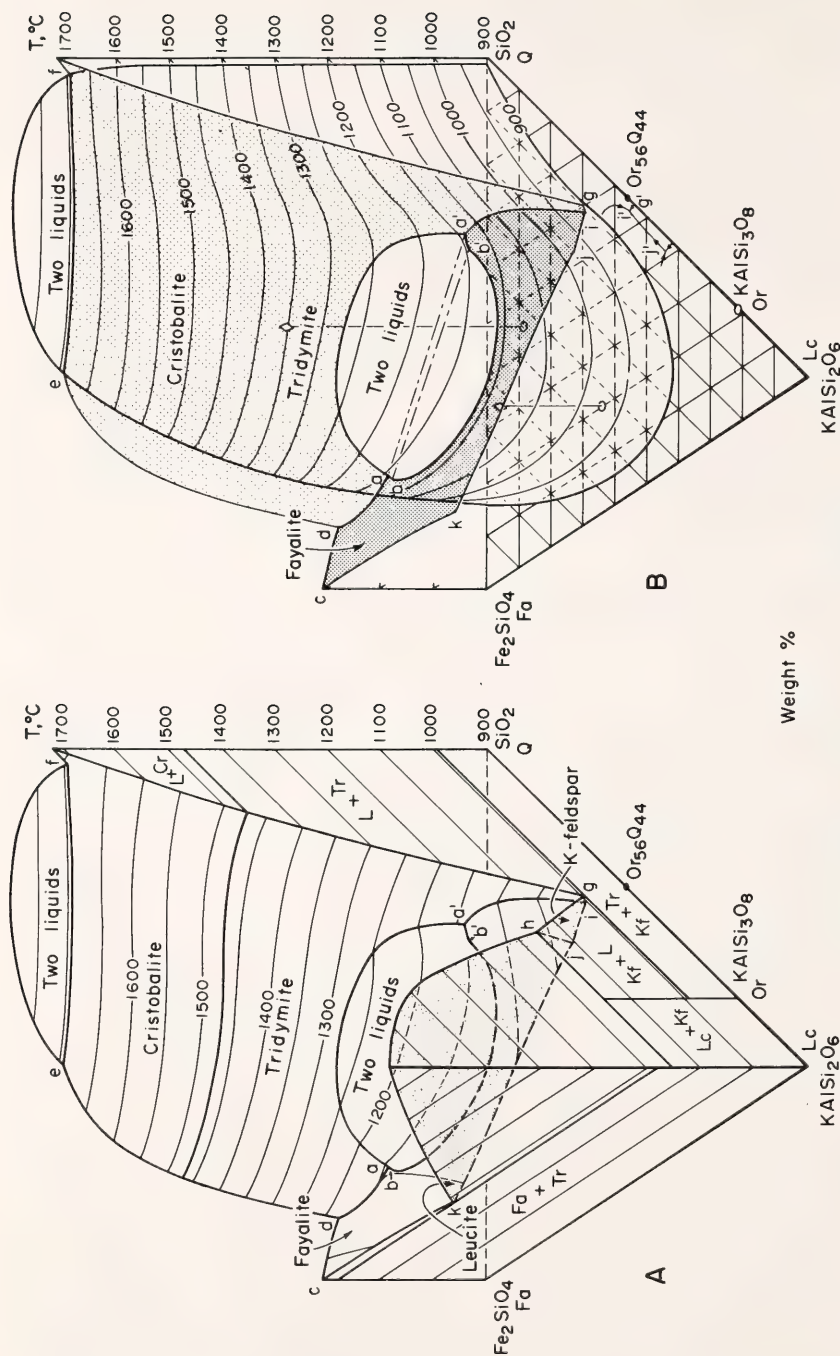


Fig. 58. (A) Approximate liquidus and solvus relations in the system Fa-Lc-Q (which includes Fa-Or-Q), based on a preliminary diagram by Roedder (1951a). The leucite and K-feldspar liquids are seen from the under side and so are shaded; temperatures of the upper solvus are inferred. (B) The same system showing the inferred extent of metastable liquid immiscibility; leucite and K-feldspar fields omitted for clarity. The two diamond symbols indicate points where the metastable solvus boundary has been bracketed (see text for details). Note the location of the composition $\text{Or}_{56}\text{Q}_{44}$ for reference in subsequent figures.

It is interesting also, by way of further comparison of the two systems, that the best phase separation observed for the liquids in Fo-Lc-Q (Fig. 56A) occurs in the same compositional region and temperature range as the stable low-temperature immiscibility in Fa-Lc-Q. A possible interpretation is that the excellence of the phase separation reflects a particularly favorable balance between the viscosities of the immiscible liquids along the crest of the solvus as the viscosities change in accordance with the opposing effects of decreasing silica and decreasing temperature. However, both solvi appear to bulge in this region, suggesting that there may also be a structural change in the liquids.

A possibly associated feature of the solvus in Fo-Lc-Q is the slight indentation in the Or-Q side near the composition $\text{Fo}_{10}\text{Lc}_{20}\text{Q}_{70}$. Confirmation of this indentation is needed, but a feature that suggests that it is real is its occurrence just where the protoenstatite-silica cotectic clears the solvus and begins to drop rapidly in temperature. The impression is that the indentation is a convenient place for the clearance. If the indentation is real, it too would suggest a change in melt structure in the Q-Or direction.

As the data stand, both solvi drop below 900°C at about the olivine-Or join, but the temperature profile of the forsterite-leucite cotectic in Fig. 57B suggests continued extensions into the Lc-normative region at lower temperatures. In the system $\text{Mg}_2\text{SiO}_4\text{-NaAlSiO}_4\text{-SiO}_2$ (Fo-Ne-Q), liquidus relations in the Q-rich region are virtually identical with those in Fig. 57A (cf. Schairer and Yoder, *Year Book 60*, p. 142), and the overall profile of the olivine liquidus suggests that a metastable solvus extends well into the Ne-normative region. The intersection of such a solvus in a somewhat more complex system with a "syenitic" cotectic akin to the low-temperature forsterite-nepheline-albite eutectic would give rise to a field of stable liquid immiscibility for alkaline magmas much

like that proposed by Ferguson and Currie (1971, Fig. 2).

Mg-Fe Fractionation Patterns and Silica Enrichment

In the study of liquid fractionation patterns in Fo-Fa-An-Or-Q, attention has been concentrated on the cotectics between the anorthite liquidus and the liquid of olivine and pyroxene on the premise that crystallization paths on these surfaces should most nearly approximate those of basaltic and intermediate magmas. The cotectics have been defined in two tetrahedral joins, Fo-Fa-An-Q and Fo-Fa-An- $\text{Or}_{56}\text{Q}_{44}$; their configurations in these joins, and the fractionation paths along them, are compared below, particularly in relation to the indicated regions of liquid immiscibility. The use of the composition $\text{Or}_{56}\text{Q}_{44}$ is continued from an introductory study (*Year Book 74*, pp. 492-500) in which it was chosen because it is a haplogranitic composition close to the K-feldspar-tridymite eutectic.

The liquidus relations in two critical bounding joins, Fo-An-Q and Fa-An-Q, are available from Andersen (1915) and Schairer (1942) (see *Year Book 74*, Figs. 61 and 59). Comparative data for Fo-An- $\text{Or}_{56}\text{Q}_{44}$ and Fa-An- $\text{Or}_{56}\text{Q}_{44}$ are presented in Fig. 59. It will be noted that Fo- $\text{Or}_{56}\text{Q}_{44}$ passes through the metastable two-liquid solvus in Fo-Lc-Q (Fig. 57B) and that Fa- $\text{Or}_{56}\text{Q}_{44}$ intersects the low-temperature stable portion of the solvus in Fa-Lc-Q (Fig. 58B). Comparison of the diagrams in Fig. 59 with those for Fo-An-Q and Fa-An-Q shows that the fields of spinel, olivine, and anorthite have all expanded to more siliceous compositions with the addition of Or, and that the protoenstatite field has shifted strongly in the same direction, all at the expense of the silica minerals field. The two-liquid solvus along Fo-Q has become metastable in Fig. 59A and is overridden by the olivine and pyroxene liquid; the solvus along Fa-Q has reemerged from metastability but above the fayalite liquidus rather than

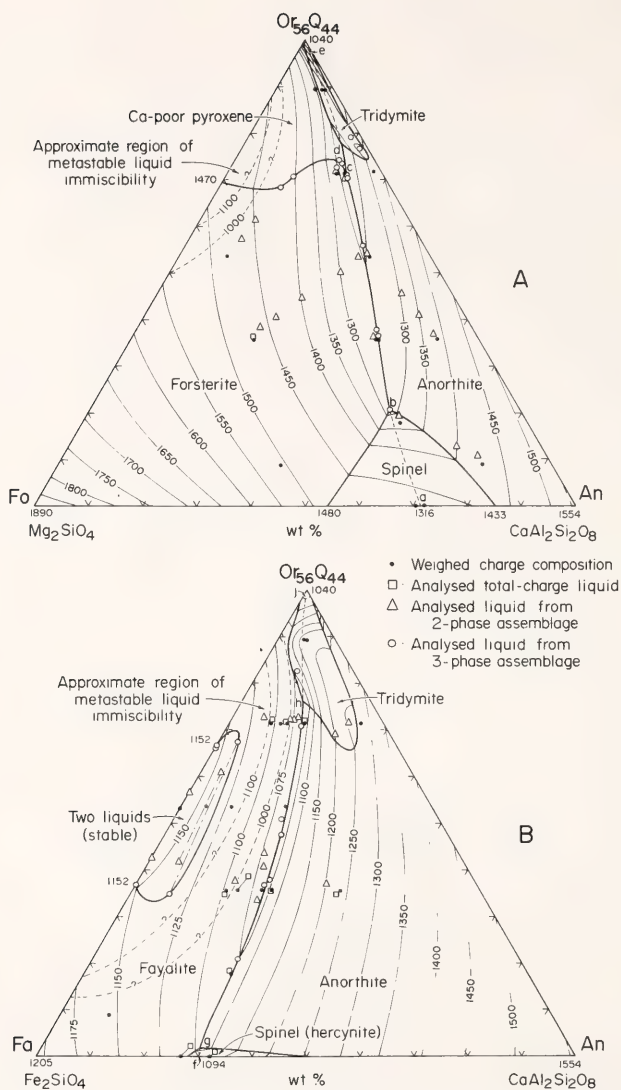


Fig. 59. Liquidus and approximate solvus relations in the joins $\text{Fo}-\text{An}-\text{Or}_{56}\text{Q}_{44}$ and $\text{Fa}-\text{An}-\text{Or}_{56}\text{Q}_{44}$. Relations along the edges of the diagrams are largely from the following sources: $\text{Fo}-\text{Or}_{56}\text{Q}_{44}$, Schairer (1954); $\text{Fa}-\text{Or}_{56}\text{Q}_{44}$, Roedder (1951a); $\text{An}-\text{Or}_{56}\text{Q}_{44}$, Schairer and Bowen (1947); $\text{Fo}-\text{An}$, Andersen (1915), Osborn and Tait (1952), Schairer and Yoder (*Year Book* 65, Fig. 2); $\text{Fa}-\text{An}$, Schairer (1942). The fields of forsterite, fayalite, and anorthite are effectively ternary, but all other fields are at least quaternary. Tridymite relations are provisional. The metastable solvus in (A) is based on Fig. 57B, but its extent within the triangle is inferred. In (B), the metastable solvus has been approximately defined in the mixes at 71%–72% $\text{Or}_{56}\text{Q}_{44}$ down to about 900°C beneath the fayalite-anorthite cotectic. Attempts to define its extent in more basic compositions were unsuccessful because the melts did not supercool. Points e in (A) and j in (B) represent the quaternary eutectic points between anorthite, K-feldspar, tridymite, and either protoenstatite or fayalite, respectively, projected into the compositional joins along lines parallel to $\text{Or}-\text{Q}$. Their exact locations are unknown, but they presumably lie within a few percentage points of the binary K-feldspar-tridymite eutectic located at $\text{Or}_{56}\text{Q}_{42}$ by Schairer and Bowen (1955).

the silica minerals field and with a further metastable extension toward An.

Figure 59 also shows that the cotectics between the anorthite liquidus and the olivine and pyroxene liquids are deflected or bowed away from the regions of liquid immiscibility in accord with theory presented in *Year Book 74* (pp. 484–492). In the magnesian join, the deflection is slight, but the immiscibility is metastable, and the cotectics are distant from it and at relatively high temperatures. On the other hand, the bowing of the fayalite-anorthite cotectic is marked, and the stable low-temperature solvus is bypassed at a temperature some 70°C below its lowest point.

The fields of tridymite in Fig. 59 are still provisional, but they are so unusual as to require comment. They extend to compositions far beyond, and to temperatures as much as 200°C above, the limits that might be anticipated from relations on the bounding joins. There seemed no doubt, however, that tridymite is stable in these regions—it grew in mixes containing the only alternative solids that might be stable and survived as the sole liquidus phase in runs of several days' duration. Moreover, the suggested relations, although unusual, are geometrically possible in terms of the tetrahedral joins Fo-An-Or-Q and Fa-An-Or-Q, the tridymite fields representing sections through deep, high-temperature clefts between the liquidus volume of anorthite and those of protoenstatite and fayalite. The fields would be expected to shrink rapidly if Or/Q were increased to the values obtaining at the quaternary eutectic with K-feldspar (points *e* and *j* in Fig. 59A and 59B, respectively), but in the compositional sections investigated, silica activity is apparently much higher where An is combined with Fo or Fa in cotectic melts than where they are separate along the bounding joins. This feature presumably relates to the proximity of the cotectics to the indicated regions of metastable immiscibility.

The cotectic surfaces at intermediate

Fo/Fa in the two investigated tetrahedral joins are illustrated in Figs. 60, 61, and 62. The temperature profiles for the surfaces in the Or-bearing join in Fig. 60 are complicated by the presence of the spinel and tridymite liquids, but the sigmoidal form characteristic of a liquidus above a metastable solvus is clearly indicated. The diagrams in Fig. 62 are comparable to the DI'-CI'-An (differentiation index-color index-anorthite) normative projection for natural rocks introduced in *Year Book 74* (Fig. 60).

The main point demonstrated by Figs. 61 and 62 is that without Or the liquids fractionate to a final composition (labeled *h'* in Figs. 61A and 62A) that is poor in silica and rich in iron, whereas with Or they trend to a highly siliceous composition. The end product in the latter case is the fayalite-anorthite-K-feldspar-tridymite eutectic, which is inferred to project to *j* in Figs. 61B and 62B. It has $\text{Fe}/(\text{Fe} + \text{Mg}) = 1$ but is essentially granitic or rhyolitic.

It is also evident in Figs. 61 and 62 (especially Fig. 62A) that without Or a trend to silica enrichment is effectively blocked by a barrier of high silica activity directly manifest in the large size of the silica minerals liquidus field and clearly associated with the indicated regions of liquid immiscibility. With the introduction of Or, the immiscibility is suppressed, the silica minerals field shrinks, and the liquids bypass the remaining barrier of nonideality by skirting it in composition (Fig. 62B) and overriding it in temperature (Fig. 60).

The substitution of $\text{NaAlSi}_3\text{O}_8$ (Ab) for Or would not be expected to change greatly the phase boundary relations in Figs. 59–62, on the basis of a comparison of bounding systems in which both components have been investigated. However, the fractionation paths would be considerably altered in detail because of extensive solid solution of the Ab and An (in contrast to the practically negligible solubility of Or in anorthite). The rate of silica enrichment as a function

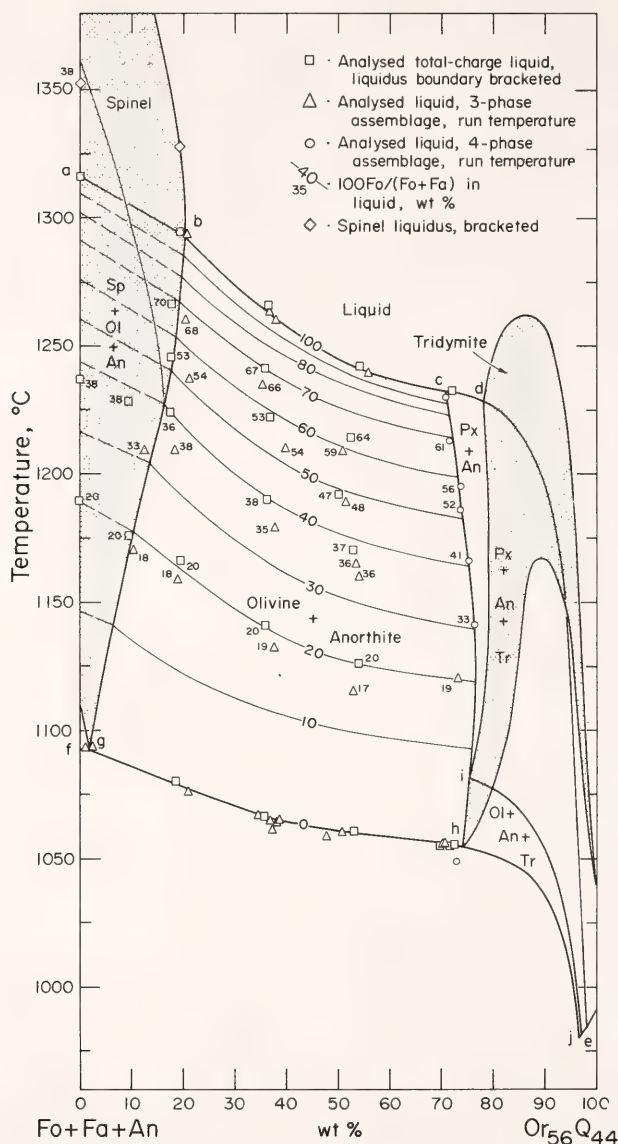


Fig. 60. Temperature profiles of the olivine-anorthite and pyroxene-anorthite cotectics in the join Fo-Fa-An-Or₅₆Q₄₄. These surfaces lie partly beneath the liquidus of spinel and tridymite. Points a-e are the same as in Fig. 57A; points f, g, h, and j are the same as in Fig. 57B.

of percentage of solidification would be reduced, and Ab/Q would not be constant when plagioclase crystallized.

An important question for which no definite answer is yet available is whether the transition from the one type of fractionation pattern to the other is

sharp or gradual. Indications are, however, that it may be relatively sharp. For example, in the join Fo-Or-Q (Fig. 57A), if a liquid in the olivine field has Or/Q greater than about 3/97, it can fractionate to highly siliceous compositions without precipitating a silica min-

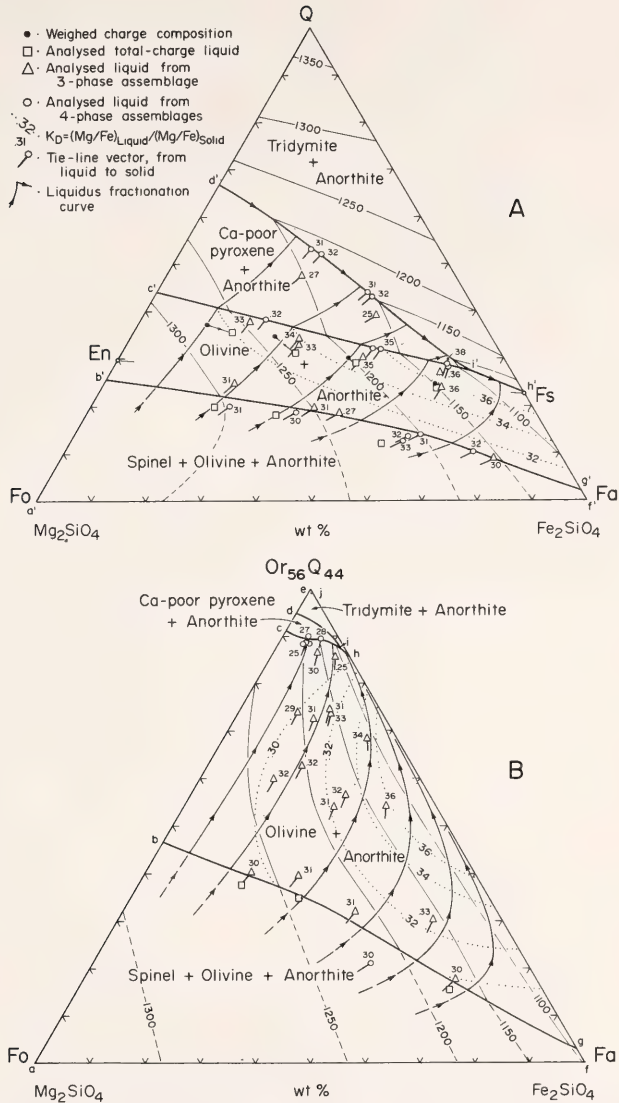


Fig. 61. (A) Liquidus relations and fractionation curves for the anorthite saturation surface of the join Fo-Fa-An-Q. The region of spinel crystallization is not quaternary, and the data points and tentative temperature contours within it pertain to the spinel-olivine-anorthite cotectic beneath the spinel liquidus volume. Points *a'*, *b'*, *c'*, and *d'* are from the system Fo-An-Q as revised from Andersen (1915) in *Year Book 74* (Fig. 61). Points *f'*, *g'*, and *h'* are from the system Fa-An-Q based on data by Schairer (1942; cf. *Year Book 74*, Fig. 59D). (B) Comparative diagram for the join Fo-An-Or₅₆Q₄₄. The olivine + anorthite field is effectively quaternary and can be read as in a ternary diagram, but the pyroxene + anorthite and tridymite + anorthite fields involve at least five components, and the spinel + olivine + anorthite field, at least six. Points *a-j* are the same as in Fig. 60. The fractionation curves are computed on the basis of the *K_D* values as fitted with the surfaces defined by the dotted-line contours.

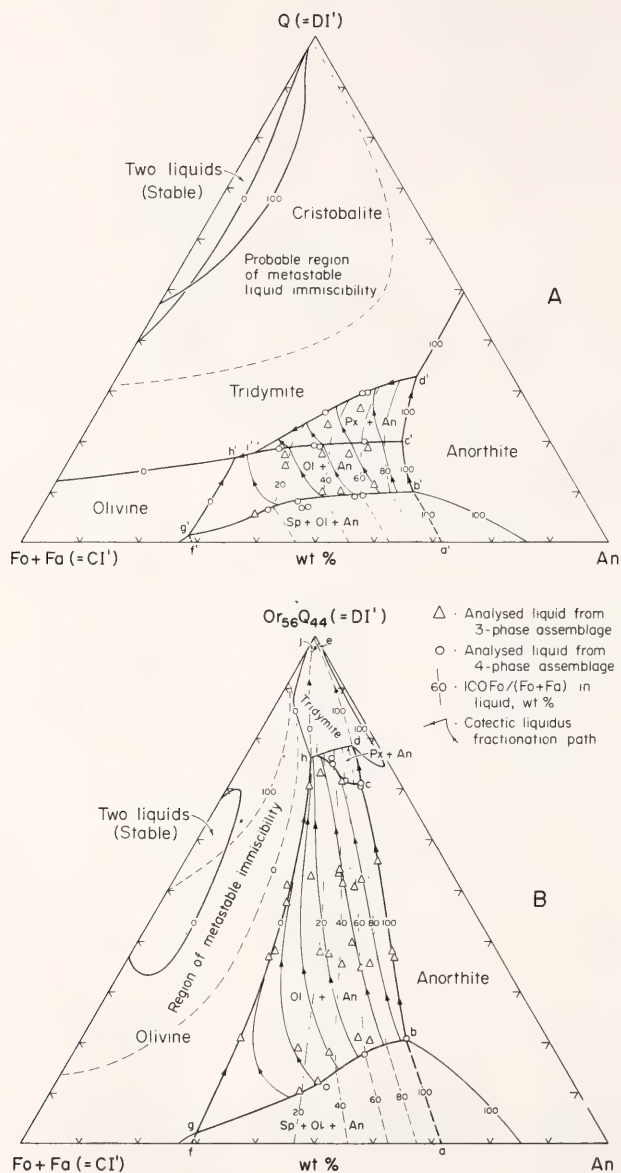


Fig. 62. Liquidus relations for the tetrahedral join Fo-Fa-An-Q projected parallel to the Fo-Fa edge. The cotectic surfaces between the anorthite liquidus volume and the olivine and pyroxene volumes are contoured according to the normative ratio $100\text{Fo}/(\text{Fo} + \text{Fa})$ in the liquid. Boundary curves labeled "100" are from Andersen (1915; cf. *Year Book 74*, Fig. 61); those labeled "0" are based on data by Schairer (1942; cf. *Year Book 74*, Fig. 59D). Points $a'-j$ are the same as in Fig. 61A. The fractionation curves are transferred (by projection) from Fig. 61A. (B) Comparative data for the join Fo-Fa-An-Or₅₆Q₄₄. Boundary curves labeled "100" are from Fig. 59A; those labeled "0" are from Fig. 59B. Points $a-j$ are the same as in Figs. 60 and 61B.

eral, but at only slightly lower Or/Q, tridymite crystallizes early. Similarly sharp divides obtain in Fo-Ne-Q (Schairer and Yoder, *Year Book* 60, p. 142) and Fa-Ne-Q (Bowen and Schairer, 1938). The transition in Di-Ne-Q (Schairer and Yoder, 1960) is gradual, however, and that in An-Lc-Q (Schairer and Bowen, 1947) is intermediate.

Implications and Applications

The direct petrologic significance of metastable liquid immiscibility is probably very limited. One may anticipate that it will eventually be identified in volcanic glasses, especially those of intermediate composition, and it may be responsible for some of the variole-type structures observed in volcanic rocks (cf. Fig. 56B). But the metastable exsolution process itself is such a short-lived phenomenon that it is not likely to have any major effects in igneous systems.

The indirect significance, however, is extremely broad. Holgate (1954) drew attention to sigmoidal liquidus profiles suggestive of metastable immiscibility in several ternary systems, and it now appears that such immiscibility probably obtains (even though it may not always be realizable experimentally) along most compositional lines from the Lc-Q and Ne-Q joins to the end-members of the common mafic silicate and oxide minerals and also to certain minor phases such as apatite, sphene, and zircon. If so, then there is an ever-present possibility in basic-to-intermediate magmas that through appropriate combination of these and other components the solvus might be sufficiently enhanced or the liquidus sufficiently depressed, or both, that stable immiscibility would develop and a second, salic liquid would evolve. The salic liquid would most probably be granitic but, as noted above, might be syenitic.

Opposing the development of stable immiscibility, however, are two major effects that may be expected to obtain in all basic-to-intermediate magmas: (1) the tendency of An to suppress im-

miscibility, and (2) the tendency of liquidus surfaces and boundaries—and particularly the cotectics between plagioclase and the mafic minerals—to deflect around regions of immiscibility. Both are evident in Fig. 59B. At present it appears that for these effects to be overcome, the crystallization path of the magma must reach some especially low-temperature cotectic for the mafic minerals, such as a joint cotectic for the iron-rich pyroxenes and olivine, magnetite, ilmenite, and apatite. The alkalis, as in Or and Ab, are like An in that they suppress immiscibility over a wide range of liquid compositions, but they are evidently essential to its development under magmatic conditions, both for the formation of the salic melt and for the suppression of the silica minerals liquidus so that melts crystallizing mafic minerals can have access to the solvus. The status of H₂O is less clear; it is known commonly to have effects on melts similar to those of the alkalis, but whether the balance is ever favorable for stable immiscibility is not known. Possibly CO₂ is more effective than H₂O in promoting immiscibility in that it increases the activity of silica in some basic melts.*

Probably of greater petrological significance, however, than the implications of metastable immiscibility with respect to stable immiscibility are the effects of the factors responsible for the former on the liquidus relations of magmas and their fractionation trends. The immiscibility is symptomatic of major structural changes in the melt solution and is *prima facie* evidence that the solution is thermodynamically highly nonideal. Thus, even if a magmatic liquid differentiating from basic to acidic compositions does not intersect a stable solvus, the liquid nevertheless will generally pass through a constitutional transition

* This effect is evident in the discovery by Eggler (*Year Book* 73, pp. 215-224) that the forsterite-enstatite liquidus boundary shifts away from silica with the introduction of CO₂.

so fundamental that it could be reflected in almost any aspect of the compositional variations of the liquid or of the rocks and minerals that crystallize from it. The tendency of the cotectic boundaries between plagioclase and the mafic minerals to deflect away from the regions of immiscibility is one manifestation of the effects of this transition; the contrast in MgO-FeO-SiO₂ fractionation patterns described above is another.

As a first approximation, the contrast between the fractionation pattern leading to an iron-rich residual liquid in Fo-Fa-An-Q and that leading to a salic liquid when Or is introduced appears to be representative of the difference between the Skaergaard trend of iron enrichment and the more common trend of tholeiitic and calc-alkaline magmas toward a rhyolitic end product. In fact, the association with liquid immiscibility appears so critical as to suggest that the main requirement for basic magmas to follow a trend of silica enrichment is that they have an appropriate composition—especially a sufficient proportion of alkalis and alumina at the stage when Mg/Fe is still relatively high—to bypass the immiscibility region and its aureole of high silica activity. Other factors, such as oxidation, may be contributory but appear secondary by comparison. For example, even if all the Fa in Fig. 62A were oxidized to magnetite + silica, the lowest temperature liquid would still be on the silica-poor side of the immiscibility region.

The experimentally defined pattern of iron enrichment is still far from simulating the Skaergaard differentiation in detail, but the differences are themselves informative in this regard. The outstanding difference is that the advance of the liquids in Figs. 61A and 62A toward silica is halted by the fractionation of tridymite, an event for which no evidence has been found in the Skaergaard intrusion. The failure of the Skaergaard liquid to advance toward silica is more reasonably attributed to the precipitation of two other phases—a Ca-poor py-

roxene (i.e., pigeonite) and an immiscible silica-rich liquid. The importance of the silica-rich liquid has been demonstrated by McBirney and Nakamura (*Year Book* 73, pp. 348–352) and McBirney (1975), but the role of the Ca-poor pyroxene does not appear to have been fully appreciated. It is implied in the reappearance of olivine as a cumulus phase in the Upper Zone of the layered series after it had given way to pigeonite in the Middle Zone owing to their reaction relationship in magnesian liquids. As noted by Wager and Deer (1939, p. 137) and Wager and Brown (1968, p. 71), fractional crystallization paths in the system MgO-FeO-SiO₂ that feature this sequence of events have been described by Bowen and Schairer (1935). A critical factor, however, that was not emphasized in relation to Skaergaard is that for olivine to reappear through fractional crystallization after having ceased to precipitate because of a reaction relation to Ca-poor pyroxene, the liquid must come to a part of the olivine-Ca-poor pyroxene phase boundary such that if the boundary is projected onto the join MgO-FeO-SiO₂ (or its subjoin Fo-Fa-Q as in Fig. 61A) from the composition points of any other phases that may be precipitating concurrently, it will fall on the *silica-poor side* of the pyroxene solid solution line (essentially the En-Fs join in Fig. 61A). This relationship obtains in the system MgO-FeO-SiO₂ for liquids on the olivine-pyroxene boundary at moderate to high FeO/MgO but with anorthite saturation of the liquids in Fo-Fa-An-Q (Fig. 61A), the projected olivine-pyroxene phase boundary is shifted in its entirety to the silica-rich side of the En-Fs join. Inasmuch as An was a major component of the Skaergaard liquid, it follows that the liquid must also have embodied components or constituents that were effective in shifting the boundary in the opposite direction. Of the major constituents known to occur in the Skaergaard liquid, TiO₂ and P₂O₅ appear especially pertinent in that they are effective in shift-

ing the forsterite-protonstatite liquidus junction away from silica when they are added to systems such as MgO-SiO_2 (cf. Kushiro, *Year Book* 73, pp. 497-502).^{*} By the same token, the alkali content of the Skaergaard liquid could not have been very high, in view of the pronounced effect of Or and Ab to shift the olivine-Ca-poor pyroxene liquidus boundary toward silica (e.g., Fig. 61). In fact, this argument for low alkali content is probably as compelling as any that has been advanced on the basis of chemical data on the Skaergaard rocks (e.g., Chayes, 1970) in that it is independent of sampling problems.

The above discussion in relation to Skaergaard differentiation can also be applied to the Bushveld complex, the Bushveld magma having reverted to olivine crystallization at high FeO/MgO after switching to orthopyroxene at an early stage (cf. Wager and Brown, 1968, Fig. 192). The possibility that some of the granophyric and other siliceous rocks at the top of the complex might represent immiscible silica-rich liquid exsolved from the basic magma appears also to warrant more consideration.

DECREASE IN VISCOSITY OF SOME SYNTHETIC SILICATE MELTS AT HIGH PRESSURES

I. Kushiro

The viscosity of a melt is closely related to its structure. To aid in understanding the structural changes of silicate melts with pressure, the viscosities of melts of three different compositions ($\text{NaAlSi}_2\text{O}_6$, $\text{Na}_2\text{Si}_3\text{O}_7$, and $\text{K}_2\text{MgSi}_5\text{O}_{12}$) have been determined at pressures between 5 and 24 kbar using the falling sphere method. The results of the pres-

ent experiments show that the viscosities of all the melts decrease with increasing pressure owing to structural changes, indicating that magmas are less viscous at greater depths.

Experiments were made in a solid-media, high-pressure apparatus with graphite capsules 10 mm long and 5 mm in inside diameter. To reduce the temperature gradient within the capsules, a specially designed graphite heater (Kushiro, this Report) was used. The temperature gradient within the capsules is less than 15°C . Starting materials were glasses of the compositions $\text{NaAlSi}_2\text{O}_6$ (jadeite), $\text{Na}_2\text{Si}_3\text{O}_7$ (more exactly, $\text{Na}_{2.0-\text{Si}_{2.9}\text{O}_{6.8}}$), and $\text{K}_2\text{MgSi}_5\text{O}_{12}$.

Spheres of platinum, made by melting platinum wires (0.33 and 0.20 mm in diameter) with a direct current arc welder, were used to measure the viscosities of the melts. The platinum spheres were placed at the top of the charges but covered with a thin film of the sample to avoid direct contact with the graphite cap. The heating and quenching procedures are described by Kushiro, Yoder, and Mysen (this Report).

NaAlSi₂O₆ (Jadeite) Composition

This composition was selected because of the possible structural change of the melt reflecting the solid-state phase change nepheline + albite = 2 jadeite. Viscosity measurements of melt of this composition were made at 1350°C and pressures between 5 and 24 kbar. The velocity of the sinking platinum sphere can be obtained by determining the relation between the time and the distance of sinking of the sphere. The results obtained at 15 kbar are shown in Fig. 63. The points lie along a straight line that projects to near zero on both axes, indicating that the platinum sphere begins to drop as soon as the planned temperature is reached. Because of the relationship shown in Fig. 63, the velocity of a sinking sphere at different pressures can be obtained on the basis of a single run at each pressure. The results of velocity

^{*}It is noted that both the silica minerals liquidus and the two-liquid solvus along the join MgO-SiO_2 also expand away from silica with the addition of TiO_2 and P_2O_5 (cf. Levin, Robbins, and McMurdie, 1964, Figs. 723 and 725). Evidently these oxides cause a substantial increase in the activity of silica in the melt solution.

measurements using platinum spheres 0.80–0.81 mm in diameter are shown in Fig. 64.

From these velocities, the viscosity of melt at different pressures was calculated by Stokes' law using the measured density of the glass (2.42–2.58 g/cm³ at pressures of 5–21 kbar) instead of the density of the melt, for which no data are available. The difference in density between melt and glass (less than 0.2 g/cm³, based on Dane, 1941) does not introduce a significant error (about 1%), because of the high density of platinum (21.45 g/cm³). The viscosity of the melt of NaAl₂SiO₆ composition as a function of pressure is given in Fig. 65 with the data at 1 atm by Riebling (1966). The viscosity of the melt decreases from 6.8×10^4 poise at 1 atm to 7.9×10^3 poise at 24 kbar.

The rate of decrease in viscosity is particularly high between 7.5 and 10 kbar. This result might be due to overestimation of the pressure below 10 kbar because of an inadequate pressure correction in the solid-media apparatus. To test this possibility a run was made at 5 kbar in a sealed Pt capsule with gas-media apparatus. The viscosity obtained in this run is also given in Fig. 65. The curve based on the measurement in the gas-media apparatus is shifted toward the low-pressure side; however, the rate of decrease in viscosity is still greater between 5 and 10 kbar.

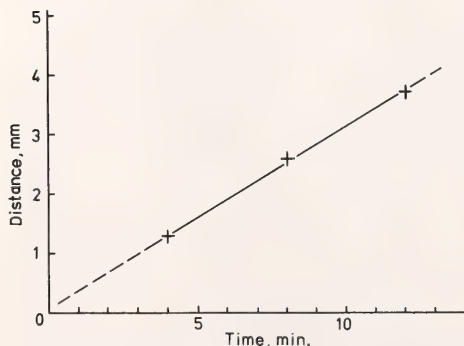


Fig. 63. Relations between run duration and distance of sinking of Pt spheres in the melt of jadeite composition at 15 kbar and 1350°C.

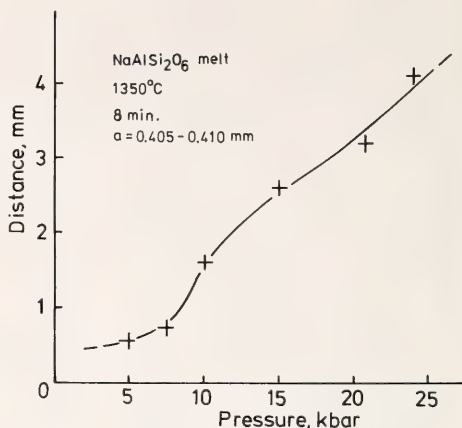


Fig. 64. Distance of sinking of Pt spheres as a function of pressure in the melt of jadeite composition. Temperature, 1350°C; time, 8 min (except the run at 5 kbar, 10 min); radius of spheres (a), 0.405–0.410 mm.

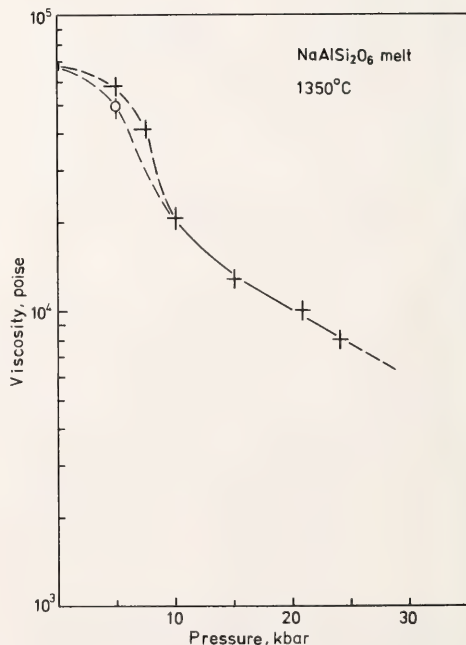


Fig. 65. Viscosity of the melt of jadeite composition as a function of pressure. Open circle indicates the viscosity obtained with a gas-media apparatus.

Na₂Si₃O₇ Composition

This composition was selected to compare with results on the NaAlSi₂O₆ composition, thereby elucidating the role of Al in the viscosity change of melt of the latter composition with pressure. The Na₂Si₃O₇ composition is near the minimum on the join Na₂O-SiO₂ and has a relatively low liquidus temperature even at high pressures. The method of measurement was the same as for the NaAlSi₂O₆ melt. Because melt of Na₂Si₃O₇ composition is less viscous than NaAlSi₂O₆ melt even at lower temperatures, smaller platinum spheres and shorter run durations were used. The temperature of the run was fixed at 1175°C. The viscosity of the melt of Na₂Si₃O₇ composition as a function of pressure is given in Fig. 66 with the value at 1 atm calculated from the data by Bockris, Mackenzie, and Kitchener (1955). The viscosity decreases by a factor of about 2.5 from 480 poise at 1 atm to 200 poise at 20 kbar.

K₂MgSi₅O₁₂ Composition

The forsterite-enstatite liquidus boundary in the system K₂O-MgO-SiO₂ shifts strongly with increasing pressure (Kushiro, 1975), and the shift of this boundary may be related to the change of polymerization of Si-O chains with pressure. Because the viscosity is closely related to the degree of polymerization of Si-O chains in the melt, the effect of pressure on the viscosity of a melt in this ternary system has been examined. The composition K₂O·MgO·5SiO₂ was selected because it is close to the extension of the forsterite-protoenstatite liquidus boundary at 1 atm (Roedder, 1951b). The method of measurement was the same as in the previous experiments. The melt of this composition is moderately viscous, and the relation between the time and the distance of sinking of the platinum spheres was first determined (Fig. 67). The lines connecting points obtained at 5 and 20 kbar extrapolate to near zero on the time axis, indi-

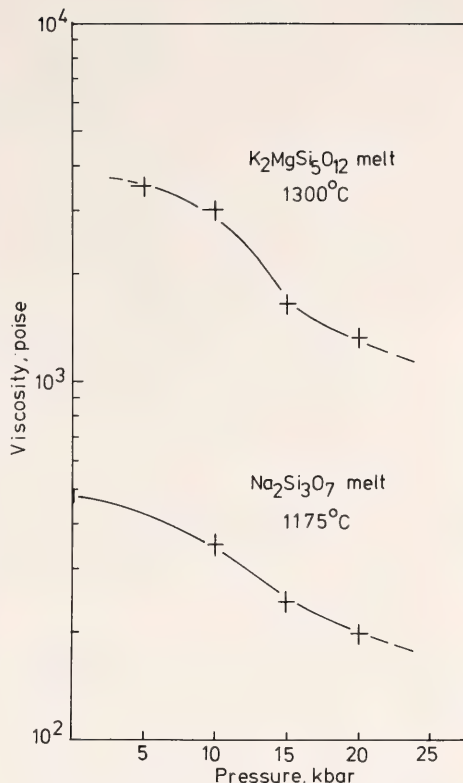


Fig. 66. Viscosities of the melts of Na₂Si₃O₇ (more exactly, Na₂Si_{2.8}O_{6.8}) and K₂MgSi₅O₁₂ compositions as a function of pressure.

cating that the platinum spheres begin to sink almost as soon as the temperature reaches 1300°C. The viscosity of the melt of K₂MgSi₅O₁₂ composition was determined at pressures between 5 and 20 kbar at 1300°C. The results are shown in Fig. 66. The viscosity decreases by a factor of about 3 from 3500 poise at 5 kbar to 1300 poise at 20 kbar.

Discussion

The viscosities of the melts of the three compositions studied decrease with increasing pressure at constant temperature. The rate of decrease is greater in the NaAlSi₂O₆ melt than in the Al-free melts. It is concluded from these results that Al plays an important role in the large viscosity drop in the melt of NaAlSi₂O₆ composition.

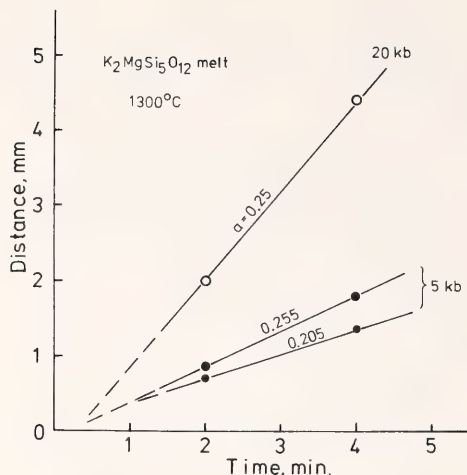


Fig. 67. Relations between run duration and distance of sinking of Pt spheres in the melt of $K_2MgSi_5O_{12}$ composition at 5 and 20 kbar. Numbers are radii (a) of Pt spheres.

By analogy with the phase transformation in the crystalline phases, it is likely that Al^{3+} shifts from 4-fold to 6-fold oxygen coordination in the $NaAlSi_2O_6$ melt at higher pressures. Waff (1975) suggested this possibility and calculated the decrease in viscosity of tholeiitic and andesitic magmas at high pressures on the basis of the model of Bottinga and Weill (1972). The rate of decrease in viscosity of the $NaAlSi_2O_6$ melt (a factor of 8) is much smaller than the rates calculated by Waff for tholeiitic and andesitic melts (factors of 14 and 47, respectively). Nevertheless, the shift of Al^{3+} from 4-fold to 6-fold coordination actually takes place in the melt of $NaAlSi_2O_6$ composition according to the infrared absorption spectra of the glasses quenched at high pressures (B. Velde and Kushiro, this Report). The transformation of Al^{3+} in the melt is gradual and begins at low pressures compared with the transition in the crystalline phases (i.e., nepheline + albite = 2 jadeite).

The decrease in the viscosity of the two Al-free melts with pressure must also be related to the structural change,

such as the coordination change of alkali ions, Mg^{2+} , and Si^{4+} in the melts. The viscosity of silicate melt is reduced most effectively by breaking the Si-O chains. The shift of part of Si^{4+} from 4-fold to 6-fold coordination in these melts would therefore explain the observed viscosity decrease in these Al-free melts with pressure. Although the transformation of Si to 6-fold coordination takes place at pressures higher than 100 kbar in crystalline silicates (e.g., stishovite), it may begin to take place at much lower pressures in silicate melts. The transformation of Al^{3+} in melt begins to take place at pressures much lower than in the crystalline phases, as illustrated by the melt of $NaAlSi_2O_6$ composition.

From the results of the present experiments it is suggested that magmas become less viscous with increasing depths in the upper mantle. The viscosity data on melts of basaltic and andesitic compositions at high pressures (Kushiro, Yoder, and Mysen, this Report) support this view. The transformation of Si^{4+} from 4-fold to 6-fold coordination in silicate melts may take place at a greater rate at pressures higher than 100 kbar, resulting in a drastic decrease in viscosity and increase in density of silicate melts. Magmas at depths greater than 300 km, if any, may be much more fluid and denser than those at shallower depths.

VISCOSITY OF BASALTIC AND ANDESITIC LIQUIDS AT HIGH PRESSURES

I. Kushiro, H. S. Yoder, Jr., and B. O. Mysen

A knowledge of the viscosity of magmatic liquids at high pressures is important to the understanding of igneous processes such as the ascent of magma from depth, fractionation of magmas by crystal settling, diffusion in magmas, and separation of magma from source areas in the upper mantle. In the present experiments, the viscosities of melts of an olivine tholeiite from the 1921 eruption of Kilauea, Hawaii (Yoder and

Tilley, 1962), and a calc-alkaline andesite from Crater Lake, Oregon, have been determined at pressures up to 30 and 20 kbar, respectively. The viscosities were determined by a falling sphere method in a solid-media, high-pressure apparatus. A specially designed furnace assembly (Kushiro, this Report) with a relatively small temperature gradient was used in the experiments. The data demonstrate that the viscosities of liquids of basaltic and andesitic composition decrease with increasing pressures along their liquid.

Kilauea 1921 Olivine Tholeiite

For the viscosity measurements of the olivine tholeiite liquid, spheres of chromian diopside were found to be the most suitable at pressures higher than 15 kbar. Spheres of Pt, Ag-Pd, chromite, and pyrope-rich garnet were tested, but they either settled too rapidly or reacted too rapidly with the basaltic melt to be usable. The chromian diopside spheres (density, 3.33 g/cm³) were made from angular fragments using a device designed by Bond (1951). The difference between the long and short diameters of most spheres was less than 20%. An "effective" diameter was obtained by averaging the lengths of the long and short axes and of the axis 90° to them.

The spheres were placed at the top of a charge before the experiment; afterward the side of the cylindrical charge was ground away until the spheres were exposed and was then polished. The distance the sphere had settled was measured with a microscale.

The heating process was the same for all experiments. Pressure was first raised to 2 kbar above the planned pressure, and the temperature of the charge was raised to slightly below its solidus and held for 2 min. The pressure was then adjusted to the desired value, and the temperature was raised to the desired value in exactly 1 min and held there for the planned duration of the experiment. The charge was quenched by turning off the power to the heater. The rate of

quenching was 70°–80°C/sec, and in most experiments the temperature fell to below the solidus in less than 5 sec.

The relationship between run time and settling distance of chromian diopside spheres is shown for some of the runs in Fig. 68. Three runs of different durations at 1400° and 1375°C and 20 kbar for spheres of similar diameters plot along nearly straight lines. From the slopes of these lines, the average settling velocity of the spheres can be obtained. When extrapolated to zero distance, the lines do not intersect the time axis at 0, but intersect it between 1.5 and 3 min. These time lags are believed to represent the time required for the starting material to melt.

The viscosity of the olivine tholeiite melt is calculated by Stokes' law, $v = 2a^2g\Delta\rho/9\eta$ (v , velocity of sinking sphere; a , radius of sphere; g , gravity constant; $\Delta\rho$, density difference between sphere and surrounding melt; η , viscosity). The density of the glass, as measured by the Berman (1939) method, was used in the calculation instead of the density of the melt. The density difference between glass and melt is about 0.1 g/cm³ at 1 atm (Dane, 1941), a difference that yields uncertainties of about 20% in the

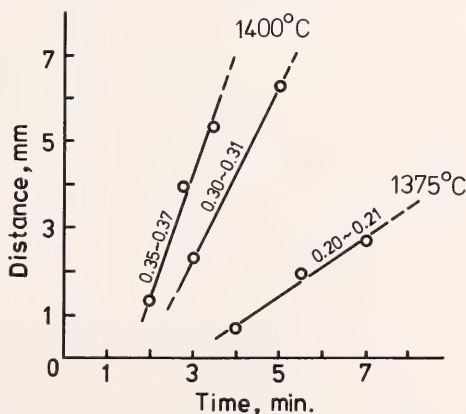


Fig. 68. Relations between run duration and distance of settling of chromian diopside spheres in melt of Kilauea 1921 olivine tholeiite at 20 kbar. Numbers are radii of the diopside spheres (mm).

viscosity data (the quenched glass is heavier than the liquid). The absolute correction for the high-pressure liquids is not known, however, and so the glass densities are used. The data obtained are summarized in Fig. 69 together with values for 1 atm calculated according to the method of Bottinga and Weill (1972). It is seen that the viscosity decreases with increasing temperature at constant pressure and that the viscosity decreases slightly with increasing pressure at constant temperature. The calculated 1-atm viscosities are slightly higher than those at high pressure for the same temperature. In total, the data show clearly that the viscosity of the olivine tholeiite melt decreases with increasing pressure along its liquidus. At 30 kbar, it is only about 10 poise, a value that compares with the viscosity of glycerin at 20°C and 1 atm.

Crater Lake Andesite

The anhydrous andesite melt was much more viscous than the tholeiite melt, and spheres of Pt were used to measure its viscosity. Almost perfect spheres can be made by melting the end of Pt wire (0.33 mm in diameter) simply by touching it on a direct current welder. The method of measuring the viscosity was the same as for the Kilauea 1921 olivine tholeiite.

The relationship between the run time and settling distance for the Pt spheres was first determined by making more than two runs of different duration for the same conditions using spheres of similar diameters. From the settling velocities obtained by these runs, the viscosity of the melt was calculated by Stokes' law for different pressure and temperature conditions. The results are shown in Fig. 70, together with the val-

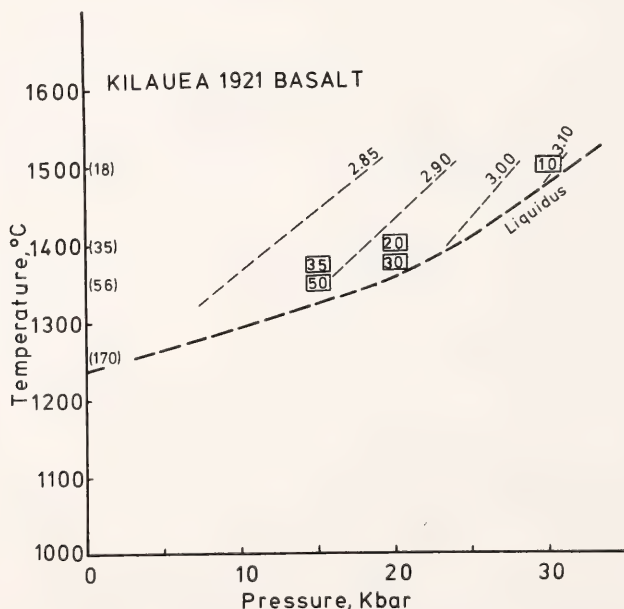


Fig. 69. Viscosity of Kilauea olivine tholeiite melt. Numbers in rectangles indicate measured values (poise): Those in parentheses are calculated for 1 atm according to the method of Bottinga and Weill (1972). The liquidus temperature curve is based on data of Tilley, Yoder, and Schairer (*Year Book 62*, pp. 77-84), Tilley and Yoder (*Year Book 63*, pp. 114-121), and B. J. Wood (personal communication). Dashed lines represent isodensity curves of glasses quenched at high pressure.

ues for 1 atm calculated by the method of Bottinga and Weill (1972).

The data show that the viscosity of the andesite melt decreases with increasing temperature at a constant pressure of 7.5 kbar and with increasing pressure at a constant temperature of 1350°C. At this temperature the measured viscosity at 20 kbar is higher than at 15 kbar, but the melt in the 20 kbar runs contained about 5% relic minerals, and the viscosity value for the liquid alone would probably be lower than that given in Fig. 70.

The viscosity of the same andesite melt, but with 4 wt % H_2O , has also been determined at 15 kbar and 1350°C, using sealed Pt capsules and spheres of chromian diopside. The value obtained is 45 ± 5 poise, which is lower by a factor of 25 than the viscosity under anhydrous conditions and comparable to the viscosity of anhydrous Kilauea olivine tholeiite.

Discussion and Applications

The decrease in the viscosity of olivine tholeiite and andesite melts with in-

creasing pressure must be the result of a structural change in the melts at high pressure. In a study of melt of NaAl-Si₂O₆ composition (Kushiro, this Report), it has been found that the viscosity drops markedly (by a factor of 9) from 1 atm to 24 kbar, probably because of a change of Al^{3+} from 4 to 6 coordination (Waff, 1975). A similar structural change may occur in the basalt and andesite melts. The rate of decrease in the viscosity of the basalt and andesite melts is much smaller than that of the jadeite melt, but this difference may be attributed to lower molecular concentrations of Al and Na in the basalt and andesite (1/2 to 2/3 and 1/5 to 1/3, respectively).

From the viscosity data for the olivine tholeiite melt at high pressure, rates of crystal settling at depth can be calculated, assuming that basalt magma behaves as a Newtonian liquid at liquidus temperatures. For the melt viscosity and glass density determined for olivine tholeiite melt at 30 kbar and 1500°C ($\eta = 10$ poise, $\rho = 3.08$), garnet crystals ($\rho = 3.5$, diameter = 2 mm) settle at a

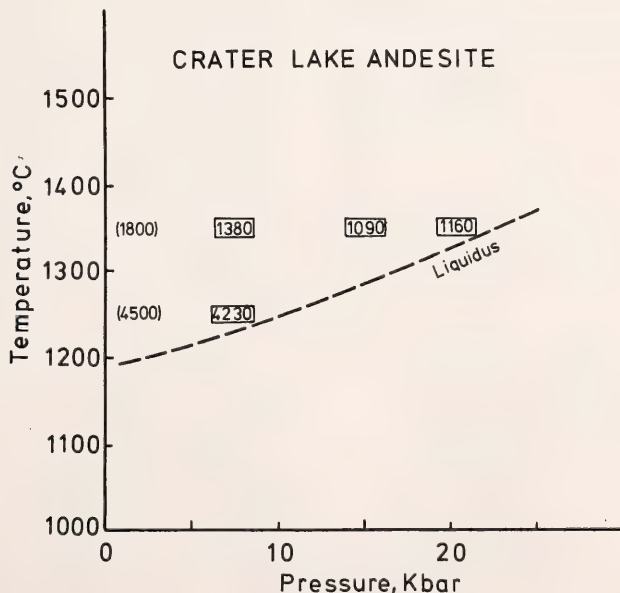


Fig. 70. Viscosity of melt of Crater Lake andesite. Symbols as in Fig. 69.

velocity of 0.093 cm/sec or 3.3 m/hr, and chromian diopside crystals ($\rho = 3.32$, diameter = 2 mm) sink at a rate of 0.056 cm/sec or 2.0 m/hr. At these large values, crystal fractionation in basaltic magma should be effective in the upper mantle.

From the present viscosity data, the minimum velocity of ascent of magmas carrying ultramafic inclusions can also be calculated. If the viscosity of basalt magma is assumed to be 50 poise, a peridotite inclusion ($\rho = 3.3$, diameter = 10 cm) sinks with a velocity of 44 cm/sec or 1.6 km/hr. With ascent of magma the viscosity decreases because of lower liquidus temperature and lower pressure. Near the surface, the viscosity of the olivine tholeiite magma is about 170 poise. The velocity of sinking of the same inclusion in magmas of this viscosity is 13.1 cm/sec or 470 m/hr. Assuming a log-linear increase in viscosity from 50 to 170 poise during the ascent of magma, the time for the ascent of the magma from the depth of 50 km to the surface must be less than 58 hr for nodules greater than 10 cm in diameter. The presence of H_2O in the magma reduces the viscosity, and alkali basalt magmas would have lower viscosity than tholeiitic magmas at high pressures because of lower SiO_2 and higher alkali content. The actual time of ascent of alkali basalt magmas carrying ultramafic inclusions, therefore, should be less than the above estimate. This estimate is consistent with the lack of appreciable reaction between orthopyroxene in nodules and nepheline-normative host magma.

INFRARED SPECTRA OF HIGH-PRESSURE QUENCHED SILICATE LIQUIDS

B. Velde and I. Kushiro

It has been demonstrated that pressure tends to reduce the viscosity of some simple silicate liquids (Kushiro, this Report). The viscosity of simple silicate liquids at 1 atm is also affected by alkali content (Morey and Bowen,

1925) and water content (e.g., Shaw, 1965; Scarfe, 1973; Kushiro, this Report). The chemical effects have been interpreted as the result of an interaction between the added ions and the basic silica-oxygen network such that the polymerization of the network is reduced (Hanna and Su, 1964; Fripiat, Leonard, and Barake, 1963).

Infrared spectra of silica glasses are relatively simple. They are characterized essentially by two broad bands, one near 1000 cm^{-1} and the other near 780 cm^{-1} , resulting from, respectively, Si-O stretching vibrations and Si-O-Si bending around bridging oxygens in the network. In pure silicon-oxygen compositions, a 1050 cm^{-1} (ν^3) vibration is attributed to movement along C_3 axes in the silicon-oxygen tetrahedra, and a 900 cm^{-1} vibration is attributed to apical oxygen-silicon stretching vibrations (Hanna and Su, 1964; Ferraro and Manghnani, 1972; Hanna, 1965). It is known that the addition of Na_2O and Al_2O_3 to silica decreases the frequency of the 1000 and 780 cm^{-1} bands (Day and Rindone, 1962; Hanna and Su, 1964), and a new band near 950 cm^{-1} appears at high (ca. 25 mole %) Na_2O contents. Addition of H_2O to SiO_2 - Al_2O_3 glasses also decreases the frequency of the 1000 cm^{-1} band (Fripiat, Leonard, and Barake, 1963). These effects are interpreted as the result of an interaction of the added cations with the oxygens in the network that weakens the Si-O bonds. A second effect of both alkalis and water is to decrease the intensity of the Si-O-Si band near 780 cm^{-1} . This effect is attributed to a decrease in the number of oxygens linking two silicon atoms in the melt or glass structure.

Finally, the effect of pressure (at $25^\circ C$) on glass is to increase the band frequencies in the 1000 - 700 cm^{-1} region at a rate of about $13\text{ cm}^{-1}/30\text{ kbar}$ (Ferraro and Manghnani, 1972). Thus, addition of Na_2O , Al_2O_3 , and H_2O decreases band frequencies, and application of pressure increases them. Addition of large amounts of alumina does not

produce any distinct new bands, nor does the presence of 6-fold coordinated hydrated aluminum produce any specific Al-O absorption bands (Day and Rindone, 1962; Fripiat, Leonard, and Barake, 1963). Apparently no specific bands appear as a result of aluminum-oxygen octahedra, even though these octahedra would be expected in a glass or quenched melt.

In the present study, the spectra of melts thermally quenched at high pressure have been investigated. Two anhydrous compositions, $\text{NaAlSi}_2\text{O}_6$ (jadeite) and $\text{Na}_2\text{Si}_3\text{O}_7$ (more exactly $\text{Na}_2\text{Si}_{2.9}\text{O}_{6.8}$), were subjected to high pressure at 1350°C (jadeite) and 1175°C ($\text{Na}_2\text{Si}_3\text{O}_7$). The melts were maintained at these temperatures for 3–12 min at pressures between 10 and 30 kbar and then were quenched essentially isobarically. The rate of quenching was $70^\circ\text{--}80^\circ\text{C sec}^{-1}$. The temperature dropped below the solidus within 3 sec.

The infrared spectra of the quenched sodium silicate melts showed little variation as a function of pressure (Fig. 71); the Si-O and Si-O-Si bands both retained the same frequencies and intensities. The spectra of the quenched melts of jadeite did change, however. In these spectra the frequency of the Si-O band position first decreased from 1010 cm^{-1} for the melt quenched at 1 atm to 985 cm^{-1} for the melt quenched at 21 kbar, and then increased to 1005 cm^{-1} for the melt quenched at 30 kbar. The Si-O-Si band gradually decreased in frequency with pressure, its intensity decreased, and the band broadened toward low frequencies.

In addition to the above experiments, charges of the above compositions with additions of about 10 wt % H_2O were melted at 15 kbar. In both experiments the spectra had a marked decrease in the intensity of the $700\text{--}800\text{ cm}^{-1}$ band, and this band was broader toward low frequencies for the quenched melt of jadeite composition as compared with the spectra of the anhydrous composi-

tion. The 1000 cm^{-1} band of the spectrum of the quenched sodium silicate melt split into 1060 and 1000 cm^{-1} components similar to those of silicate glasses with high sodium content. The spectrum of the hydrous jadeite composition had a higher Si-O stretching frequency (1020 cm^{-1} "wet" versus 995 cm^{-1} "dry" at 15 kbar, a new 870 cm^{-1} band that can be attributed to Al-O-H bending (Leonard *et al.*, 1964), and a very low intensity, broadened Si-O-Si bending band.

These experiments indicate that pressure has the effect of decreasing the polymerization of the silica-oxygen network when alumina is present in the melt. The decrease in the intensity of the $700\text{--}800\text{ cm}^{-1}$ band can be interpreted as the result of polymerization. At high pressure, water seems to associate with Al ions (indicated by the presence of an 870 cm^{-1} band). Water also seems to depolymerize the melt structure (indicated by the decrease in intensity of the $700\text{--}800\text{ cm}^{-1}$ band). In the spectra of the dry quenched melts of jadeite composition, the shift and broadening of the $700\text{--}800\text{ cm}^{-1}$ band might be attributed to the existence of Al-O octahedral coordination inasmuch as this type of spectrum is characteristic of β -alumina, which contains both 6- and 8-fold coordinated aluminum ions (Tarte, 1963). The shift in frequency of the Si-O stretching vibrational mode toward higher values at 20–25 kbar in the region of the metastable extension of the jadeite stability (22 kbar at 1350°C , Boettcher and Wyllie, 1968) suggests that the basic structure of (Si,Al)-O coordination in the melt is changing due to a new configuration of Al-O ions.

It is suggested that the structure of the quenched sodium silicate melts is modified by the presence of Al and H_2O at high pressures. It would appear that this modification results in a less polymerized melt structure. This interpretation accords with the viscosity measurements made by Kushiro (this Report).

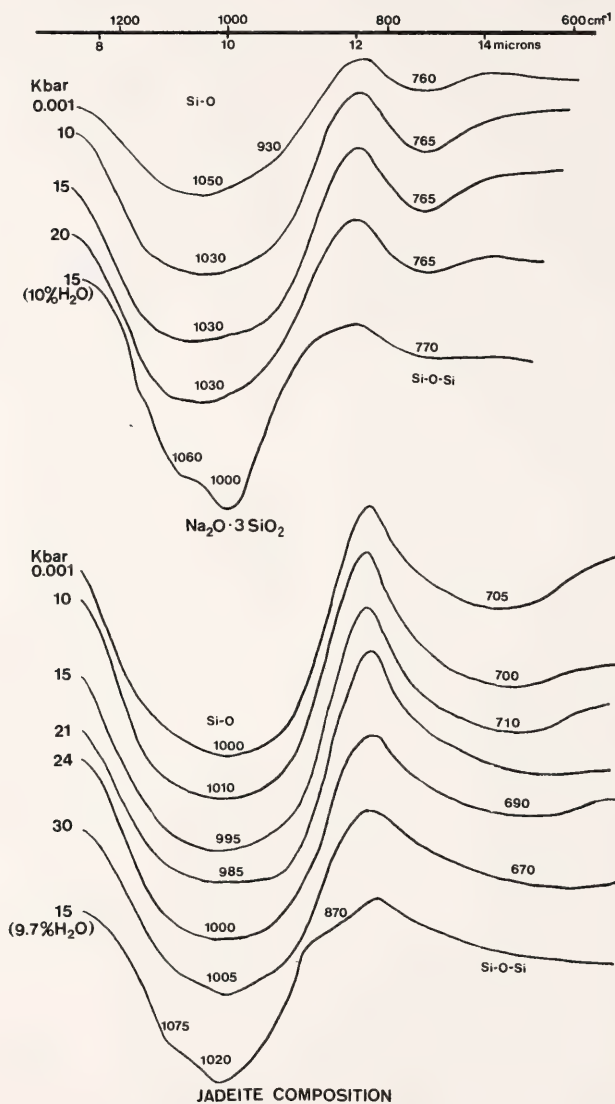


Fig. 71. Infrared transmission spectra of quenched glasses produced at various pressures. Transmission increases toward the top of the figure. Minimum values at 1000 cm^{-1} were at 10%–20% transmission; the maximum near 850 cm^{-1} is at 80%.

COORDINATION CHANGES OF ALUMINUM
IN SILICATE MELTS: EVIDENCE FROM
DATA ON CARBON DIOXIDE SOLUBILITY
IN ALBITE MELT

Bjørn O. Mysen

Coordination changes of the cations in silicate melts affect properties of the melt such as the solubility of volatiles, the viscosity, and the activity coefficient of elements in the melt. Direct evidence for termination of (Si,Al)-O-(Al,Si) bonds in melt of $\text{NaAlSi}_2\text{O}_6$ composition at high pressure is provided by infrared data (B. Velde and Kushiro, this Report) and is supported by viscosity data for similar melts (Kushiro, this Report). These data have led to the suggestion that the coordination of aluminum in $\text{NaAlSi}_2\text{O}_6$ melt changes rather abruptly from 4 to 6 as the pressure is increased above 10 kbar at 1350°C (for example, Kushiro, this Report).

Solubility models for carbon dioxide in silicate melts involve the activity of the oxygen ion ($a_{\text{O}^{2-}}[\text{melt}]$) inasmuch as a major proportion of the carbon dioxide is dissolved as carbonate (Egler, Mysen, and Seitz, *Year Book* 73, pp. 226-228; Mysen *et al.*, 1976). Provided no major change in the melt structure occurs with increasing P_{CO_2} , the fraction of carbon dioxide that dissolves as CO_3^{2-} * should follow a smooth isothermal, polybaric curve without inflections or discontinuities. In tetrahedral coordination, aluminum participates in polymerization of the melt. By changing to higher coordination, polymers are broken up, resulting in increased $a_{\text{O}^{2-}}(\text{melt})$ (Pearce, 1964). The stability of carbonate relative to molecular carbon dioxide may therefore be enhanced.

To test these possibilities, CO_2 -saturated albite glass was prepared at pressures ranging from 10 to 30 kbar and temperatures of 1450° and 1625°C . The carbon dioxide solubility experiments and the sample preparation methods used for the infrared studies are described by Mysen (*Year Book* 74, pp. 454-468). Infrared spectrometry was

used to determine the molecular combinations of carbon and oxygen in the quenched albite glass (Mysen *et al.*, 1976; Mysen, *Year Book* 74, pp. 454-468), and the measurements have been extended here to determine the relative proportions of CO_3^{2-} and CO_2 . The carbonate absorption peak is relatively broad and therefore amenable to analysis, but the CO_2 peak is quite narrow and unsuitable for this purpose. The carbonate peaks were calibrated relative to the peak from ΣCO_2 -saturated† albite glass quenched from 1625°C and 20 kbar. The amount of CO_3^{2-} in the other samples is simply the proportion of the areas of CO_3^{2-} absorption peaks of the unknown samples relative to the area of the peak in the standard. The amount of molecular CO_2 is the difference between ΣCO_2 and the calculated CO_3^{2-} content. The calculated $X^{\text{m}}_{\text{CO}_3^{2-}}$ values are therefore only relative, not absolute values.

The molar proportion, $X^{\text{m}}_{\text{CO}_3^{2-}}$, is plotted against pressure at 1450° and 1625°C in Fig. 72. The $X^{\text{m}}_{\text{CO}_3^{2-}}$ increases with increasing temperature (Fig. 72), suggesting that $a_{\text{O}^{2-}}(\text{melt})$ increases with increasing temperature. Such an interpretation accords with the discussions of Zachariasen (1932) and of Adam and Gibbs (1965), who suggested that silicate liquids become less polymerized with increasing temperature. It also agrees with the viscosity data of Kushiro (this Report) and Kushiro, Yoder, and Mysen (this Report), showing that the viscosity of silicate melts decreases with increasing temperature. The $X^{\text{m}}_{\text{CO}_3^{2-}}$ decreases with increasing pressure between 10 and 30 kbar at 1625°C and between 10 and 20 kbar at 1450°C . Kushiro (1975) suggested that silicate melts become more polymerized with increasing pressure, resulting in decreasing oxygen ion activity; hence decreased $X^{\text{m}}_{\text{CO}_3^{2-}}$ was expected. However, the molar pro-

* Defined as molar proportion: $X^{\text{m}}_{\text{CO}_3^{2-}} = \text{CO}_3^{2-}/(\text{CO}_2 + \text{CO}_3^{2-})$.

† ΣCO_2 = total amount of carbon determined in the glass calculated as CO_2 .

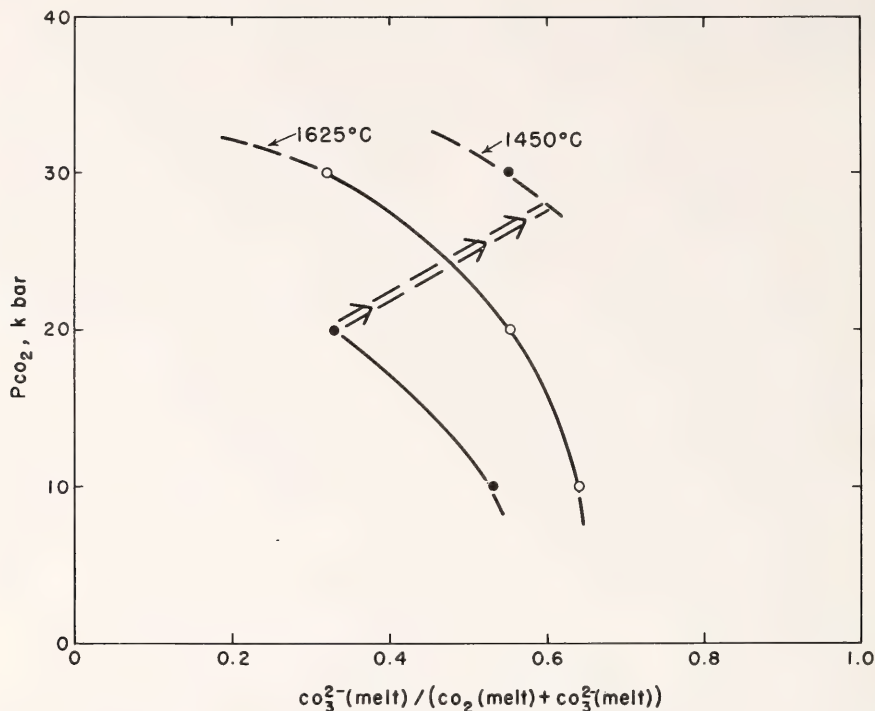


Fig. 72. Mole fraction of carbonate, $X^m_{CO_3^{2-}}$, of total carbon dioxide (ΣCO_2) in albite melt as a function of pressure at 1625° and 1450°C.

portion of carbonate in the melt increases by approximately 100% at 1450°C between 20 and 30 kbar. The reaction



extended metastably to 1450°C, occurs at about 31 kbar (Boettcher and Wyllie, 1969). Because of the similarity between the P - T coordinates of the metastable breakdown of albite to jadeite and quartz and those at which the value of $X^m_{CO_3^{2-}}$ doubles, it is suggested that a transition similar to that in crystalline $NaAlSi_3O_8$ also occurs in the silicate melt. An $Al^{IV} \rightarrow Al^{VI}$ transformation in the melt would be accompanied by breaking (Al,Si)-O-(Al,Si) bonds in the tetrahedral polymers. The result is an increase of $a_{O^{2-}}(\text{melt})$, and at fixed f_{CO_2} , increased $a_{O^{2-}}(\text{melt})$ yields higher $X^m_{CO_3^{2-}}$.

The higher pressure of the $Al^{IV} \rightarrow Al^{VI}$ transformation in $NaAlSi_3O_8$ melt as compared with $NaAlSi_2O_6$ melt (Kushiro, this Report) is in qualitative agreement with the lower pressure of the reaction (Boettcher and Wyllie, 1969)



compared with that of Equation 1, and with the lower temperature (1350°C) of the experiments with the $NaAlSi_2O_6$ melt by Kushiro (this Report). Velde and Kushiro (this Report), on the basis of infrared spectra of quenched jadeite glass, place the $Al^{IV} \rightarrow Al^{VI}$ transition of the $NaAlSi_2O_6$ composition near 20 kbar, in close agreement with the present data. However, both the present data and those of Velde and Kushiro (this Report) were obtained on quenched glasses, whereas the viscosity data of Kushiro (this Report) were obtained on

melts at high pressure and temperature. It is possible that the reason higher pressures of the inferred $\text{Al}^{\text{IV}} \rightarrow \text{Al}^{\text{VI}}$ transition were obtained on quenched material is that the equilibrium pressure must be exceeded to quench in the transition.

The abrupt decrease of viscosity of $\text{NaAlSi}_2\text{O}_6$ melt with increasing pressure was ascribed by Kushiro (this Report) to the change of aluminum to a high-coordination state. From the present result (Fig. 72), a similar isothermal decrease in viscosity would be expected in $\text{NaAlSi}_3\text{O}_8$ melt in the pressure range 20–30 kbar at 1450°C.

Waff (1975) pointed out that change of aluminum to higher coordination in silicate melts also increases their shear wave attenuation (Q_s) because of the drop in viscosity that accompanies such coordination changes (Walsh, 1969). The low-velocity channel in the mantle is generally at depths corresponding to pressures in excess of those required for the $\text{Al}^{\text{IV}} \rightarrow \text{Al}^{\text{VI}}$ transition in silicate melts. Thus, calculations of shear wave attenuation should be based on the viscosity of melt with aluminum in the high-coordination state. Such calculations, as pointed out by Waff (1975), would result in greater proportions of melt being required to produce the same attenuation that would be the case when calculating Q_s with aluminum in the low-coordination state.

Element partitioning between crystals and silicate depends on the activity coefficients of the elements in the melts as well as in the crystals. The activity coefficients depend therefore on the structure of the silicate melt. For example, Burns and Fyfe (1964, 1966) considered the effect of crystal-field stabilization energy (CFSE) on transition elements (Ni, Co) partitioning between olivine and melt. The partition coefficients of both nickel and cobalt between melt and crystal (defined as $C_i^{\text{melt}}/C_i^{\text{crystal}}$) should increase when the aluminum of the melt is transformed to its high-coordination state. In addition, the smaller CFSE of

Co^{2+} relative to Ni^{2+} in octahedral coordination would result in a larger increase of $K_{\text{Ni}^{\text{liq-ol}}}$ as compared with $K_{\text{Co}^{\text{liq-ol}}}$, yielding an increase of Ni/Co in a melt in equilibrium with olivine.

It is thus proposed that the coordination states of cations in silicate melts should be considered when oxidation states of elements in silicate melts are evaluated and when element partitioning between melts and crystals in the mantle are calculated.

COMPOSITION OF THE PARTIAL MELT OF CARBONATED PERIDOTITE IN THE SYSTEM $\text{CaO-MgO-SiO}_2\text{-CO}_2^*$

David H. Eggler

In the last year it has been shown that in the system $\text{CaO-MgO-SiO}_2\text{-CO}_2$ at pressures above about 29 kbar a peridotitic phase assemblage containing a small amount of CO_2 becomes carbonated at its solidus (i.e., the solidus assemblage is $\text{Di} + \text{En} + \text{Fo} + \text{Dol} + \text{L}$) (Eggler, *Year Book* 74, pp. 468–474; Eggler, 1976; Wyllie and Huang, 1975a,b). At pressures immediately below the carbonation reaction, the solidus falls dramatically in temperature, about 350°C in a 2-kbar pressure interval. Oceanic geotherms project across this bend in the solidus, and on this basis a new explanation was suggested for the low-velocity zone. In order to determine more closely the composition of the liquid formed by melting of carbonated peridotite, two more joins in the same system, $\text{Ca}_2\text{SiO}_4\text{-Mg}_2\text{SiO}_4\text{-CO}_2$ (Fig. 73) and $\text{CaMgSi}_2\text{O}_6\text{-CaMgO}_2\text{-CO}_2$ (Fig. 74), have been investigated at 30-kbar pressure.

Starting compositions were finely ground mechanical mixtures of SiO_2 (tridymite or cristobalite), MgO , calcite, synthetic and natural dolomite, and synthetic enstatite. Charges were sealed in Pt capsules and run in talc-boron nitride

* Research supported by the National Science Foundation, Earth Sciences Section, grant DES 73-00266A01.

the minimum is also consistent with phase relations on the join $\text{MgCO}_3\text{-CaCO}_3$ (Irving and Wyllie, 1975).

The topology in Fig. 75 differs from earlier versions of the same system (Eggler, *Year Book* 74, pp. 468-474; Eggler,

1976) on the silica-poor side of the join $\text{Mg}_2\text{SiO}_4\text{-Ca}_2\text{SiO}_4$. The earlier versions were inferred from the join Di-Fo-CO_2 and from preliminary results for the join La-Fo-CO_2 . It was known that the four-phase line Fo-En-L-V crossed the La-

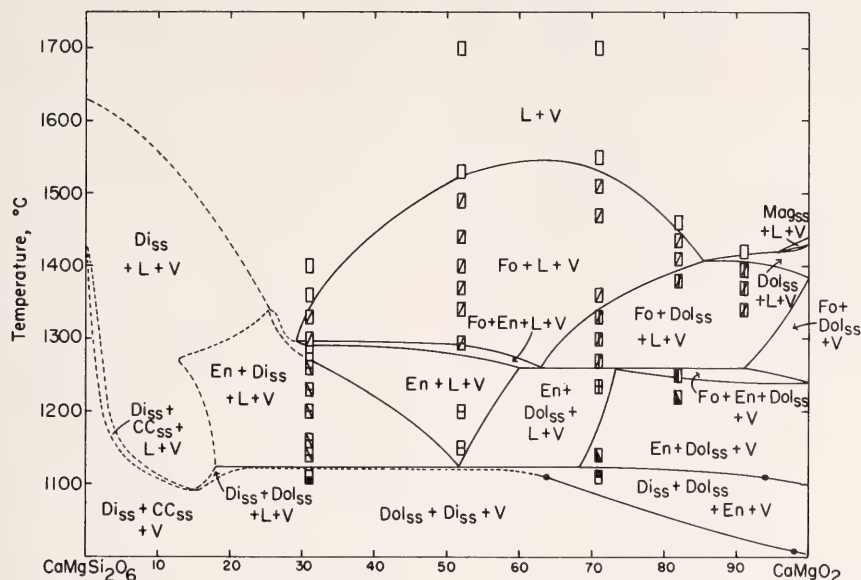


Fig. 74. Vapor-saturated phase relations on the join $\text{CaMgSi}_2\text{O}_6\text{-CaMgO}_2\text{-CO}_2$ at 30 kbar pressure. Dotted boundaries are inferred from the preceding figure. Liquidus phase relations involving magnesite (Mag) are inferred from data on the join $\text{CaCO}_3\text{-MgCO}_3$ by Irving and Wyllie (1975); no magnesite was found in the products of runs shown (on the basis of electron microprobe analyses).

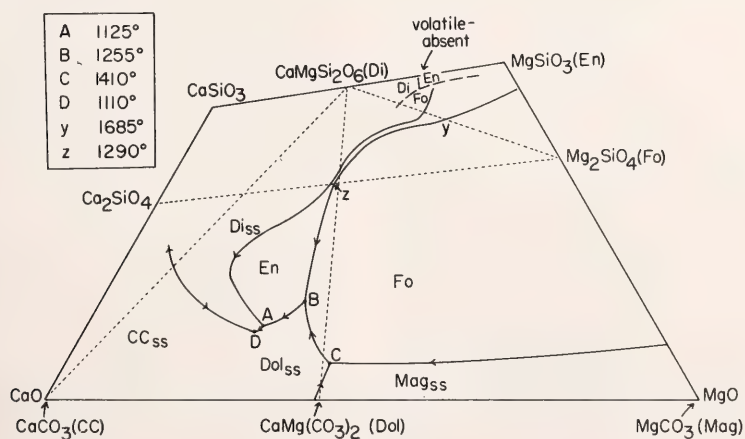


Fig. 75. Vapor-saturated liquidus phase relations in the system $\text{CaO-MgO-SiO}_2\text{-CO}_2$ at 30 kbar pressure, projected onto the volatile-free base. Relations on the joins Di-CaO-CO_2 and En-MgO-CO_2 are from Wyllie and Huang (1976); those on the join MgO-CaO-CO_2 are from Irving and Wyllie (1975).

Fo-CO₂ join at 1290°C and terminated at *B* at 1255°C; *B* was inferred to lie somewhat to the silica-poor side of the join La-Fo-CO₂. The four-phase line is now known to extend considerably farther toward the CaO-MgO-CO₂ sideline. Wyllie and Huang (1975a,b; 1976) have also determined positions for the reaction points represented by *A* and *B* on the basis of unpublished data on a number of joins, including Di-Dol and Di-CC. They place *B* at a volatile-free composition of 10% SiO₂, 29% MgO, 61% CaO, in contrast to 17% SiO₂, 31% MgO, 52% CaO in Fig. 75. The sequence of reactions between points *B* and *D* also differs from the relations proposed by Wyllie and Huang. In their diagram the minimum is placed between *A* and *B*, but such topology is inconsistent with the data presented here in that, for the composition La₅₅Fo₄₅, En precipitates at temperatures down to point *A* at 1125°C, where En reacts out.

The solubility of CO₂ in the liquids can be estimated from solubility data of Holloway, Mysen, and Eggler (this Report) on the joins Di-CaMgO₂-CO₂ and Fo-La-CO₂. In liquid *A*, CO₂ solubility is approximately 40 wt %; in liquid *B*, it is about 27 wt %.

From these new results, it is evident that liquids produced by fusion of carbonated peridotite at 30-kbar pressure (equivalent to 90-km depth) can be extremely silica-undersaturated and can fractionate to even more basic, carbonatitic (<10% SiO₂) liquids. If such liquids were produced in the low-velocity zone (Wyllie and Huang, 1975a; Eggler, *Year Book* 74, pp. 468-474), they might migrate upward and enrich the upper part of the zone in carbonate (Wyllie and Huang, 1976), and if CO₂ vapor were evolved, it might contribute to explosive kimberlite and carbonatite eruption (Wyllie and Huang, 1975a,b). It should be remembered, however, that natural kimberlite magmas originate at much greater depths than 90 km (Boyd, 1973), beneath stable continental shields

where a low-velocity zone probably does not exist (Knopoff, 1972).

Even though the experiments were not conducted at pressures directly applicable to kimberlite origin, an important principle is illustrated that applies to kimberlite and other highly undersaturated magmas. The principle is that the partial melts of carbonated peridotite can differ enormously in composition, depending on only relatively small changes in pressure, degree of melting, or volatile composition. For example, at 30 kbar, the first melt (*B*) for the assemblage Fo + Di + En + Dol has a silica content of only 17% (calculated volatile-free). But at only 4 kbar less pressure (26 kbar), the first melt in the presence of CO₂ lies on the Di-Fo join and has a silica content of about 50% (Eggler, 1976). With higher degrees of melting at 30 kbar, the liquid composition moves rapidly from *B* toward the volatile-free partial melt composition (Fig. 75), particularly if the source area contains only a small amount of CO₂ (e.g., 0.1-0.2 wt %). Previous work has established that increased CO₂/(CO₂ + H₂O) in the vapor phase changes the first melt composition from silica-poor to relatively silica-rich compositions (Mysen and Boettcher, 1975a; Eggler, 1975). The wide range in composition of kimberlite (Dawson, 1967) has previously been attributed to mixing of magmas (Boyd and Nixon, 1973) and to mixing of magma and ultramafic inclusions, but it may also reflect, in part, small variations in the depth and volatile content of the source regions.

THE SOLUBILITY OF CO₂ IN LIQUIDS ON THE JOIN CaO-MgO-SiO₂-CO₂*

John R. Holloway, Bjørn O. Mysen,
and David H. Eggler

Eggler (*Year Book* 72, pp. 457-467) demonstrated that silicate liquids can dissolve significant amounts of CO₂ and

* Research supported by the National Science Foundation, Earth Sciences Section, grant DES 73-00266A01.

that the magnitude of the solubility depends upon the composition of the liquid, including its H_2O content, and upon pressure. In recent detailed investigations (Mysen, 1976b; Mysen *et al.*, 1976) it has been shown that CO_2 dissolves in both molecular (CO_2) and ionic (CO_2^{2-}) forms and that the solubility of CO_2 is greater in basic than in acidic liquids. Mysen *et al.* (1976) also showed that in silica-saturated liquids the CO_2 species is dominantly molecular CO_2 , that CO_2 solubility is independent of the type of network-modifying cation in the liquid, and that the temperature dependence of solubility is positive. In this study the solubility of CO_2 in very silica-under-saturated liquids in the join $\text{CaO-MgO-SiO}_2\text{-CO}_2$ was investigated because these liquids are haplokimberlites and carbonatites. The dependence of CO_2 solubility on temperature and composition, in particular upon Si/O and the type of network-modifying cation, was considered to be critical to an understanding of the origin of these important rock types.

Starting materials were prepared in the manner described by Mysen *et al.* (1976); all CO_2 was introduced as Ca, CaMg, or Mg carbonate. The compositions studied are shown projected onto the CaO-MgO-SiO_2 plane in Fig. 76. All runs were made in Pt capsules in solid-media apparatus (Boyd and England, 1960) using the piston-out technique. Assemblies consisted of crushable alumina, boron nitride, tale, and a graphite furnace. Great care was taken to dry the

assemblies prior to use. Temperature was measured with Pt-Pt10Rh thermocouples.

Most runs were made at temperatures well above the liquidus because only runs that quench to clear glass are amenable to carbon analysis. (Even at superliquidus temperatures, composition DD3 [Fig. 80] quenched to a mixture of glass and crystals, and hence solubility measurements may be in error for that composition.) Run durations were 20 min at 1500°C , 10 min at 1600°C , and 5 min at 1700°C . In all runs semi-spherical depressions were found on the outer surfaces of quenched glasses. These depressions are evidence of a coexisting fluid phase at run conditions. That is, the system was saturated with CO_2 , and except for minor amounts (<2 mol %) of CO, H_2 , and H_2O , the CO_2 pressure was essentially equal to the total pressure. (Amounts of CO and H_2O are small because these species are produced by reduction of CO_2 by H_2 , and H_2 fugacity in the assemblies is very small [Eggler, Mysen, and Hoering, *Year Book* 73, pp. 228–232].)

Quenched glasses were analyzed using ^{14}C -produced β -particle tracks recorded in Ilford K-5 nuclear emulsions (Mysen and Seitz, 1975). Standards used were CaCO_3 spiked with known amounts of ^{14}C and crystallized to calcite at 1200°C and 20 kbar for 2 hr.

To extrapolate the solubility data measured at superliquidus temperatures to the near-solidus temperatures of interest in petrologic models, it is important to know the effect of temperature on CO_2 solubility. In previous investigations the temperature coefficient for CO_2 solubility ($\partial X/\partial T$) was found to be positive (Mysen, Arculus, and Eggler, 1975; Mysen *et al.*, 1976; Mysen, 1976b). From the data presented in Fig. 77A it can be seen that the behavior of $\partial X/\partial T$ is more complex for some of the compositions investigated in this study.

The features in Fig. 77A can be rationalized from two postulates. Consider an isobaric temperature-composition sec-

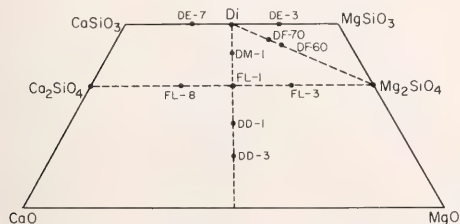


Fig. 76. Volatile-free compositions of starting materials used in this investigation, plotted in molar proportions in a portion of the join CaO-MgO-SiO_2 .

positions differ significantly in liquidus temperature or in degree of polymerization. Comparison of isothermal solubilities for the same composition at different pressures could also be misleading if the liquidus temperature is a strong function of pressure.

The effect of network-modifying cation composition on CO₂ solubility was evaluated in investigations along the

metasilicate join CaSiO₃-MgSiO₃ (Fig. 78) and along the orthosilicate join Ca₂SiO₄-Mg₂SiO₄ (Fig. 79). The solubility of CO₂ tends to decrease as Ca is replaced by Mg. There are large variations in liquidus temperatures across the joins, however, and hence large variations in intervals between liquidus and measurement temperatures. As discussed above, these variations cause difficulties

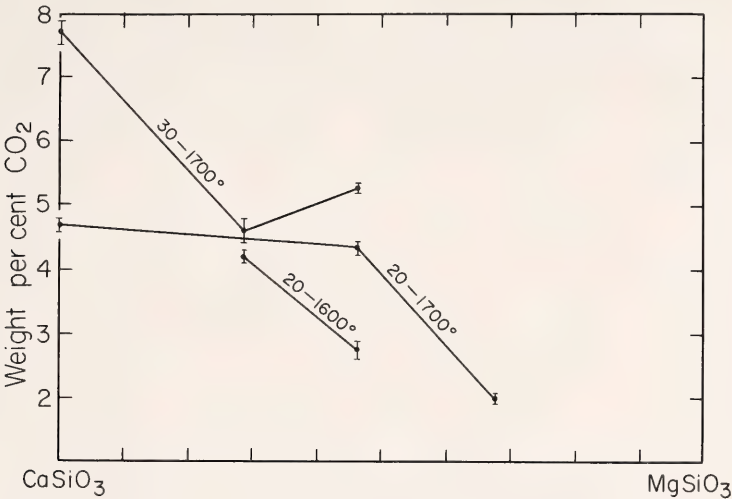


Fig. 78. Solubility of CO₂ in liquids on the join CaSiO₃-MgSiO₃ (wt %). Error bars indicate 2 standard deviations. The labels on the lines indicate pressure (kbar) and temperature (°C).

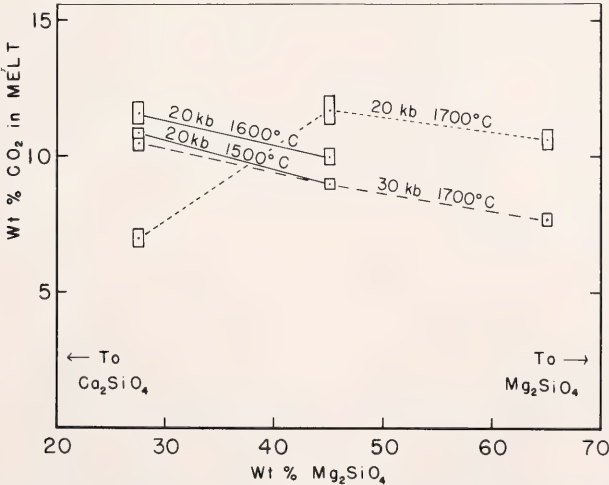


Fig. 79. Solubility of CO₂ in liquids on the join Ca₂SiO₄-Mg₂SiO₄. Rectangles indicate 2 standard deviations. The labels on the lines indicate pressure (kbar) and temperature (°C).

STABILITY OF CARBONATE MINERALS IN A HYDROUS MANTLE*

David H. Eggler, Ikuo Kushiro,
and John R. Holloway

The importance of carbonate minerals in the mantle has been realized in the past several years. Carbonate minerals are stable in peridotite assemblages (Newton and Sharp, 1975; Kushiro, Satake, and Akimoto, 1975; Huang and Wyllie, 1975; Eggler, *Year Book* 74, pp. 468-474) and are participant phases in the melting of peridotite at high pressures (Wyllie and Huang, 1976; Eggler, 1976). Another important volatile species in the mantle is H_2O , and in its presence stability fields of carbonates may be expected to decrease. In this study, the effect of H_2O upon one decarbonation reaction was investigated experimentally at 26-kbar pressure. The experimental results were then compared with those obtained by thermodynamic calculation. The differences were sufficiently small to warrant calculation of the important decarbonation reactions in the system $CaO-MgO-SiO_2-CO_2-H_2O$ over the pressure range 2-45 kbar.

The reaction $MgSiO_3$ (En) + $MgCO_3$ (Mag) = Mg_2SiO_4 (Fo) + CO_2 has been studied in the presence of a CO_2-H_2O fluid at 26-kbar pressure (Fig. 81). Weighed amounts of the mixtures (Fig. 81) and water were sealed in Pt capsules and run in talc-boron nitride furnace assemblies in solid-media, high-pressure apparatus (piston-out technique). The temperature determined for anhydrous decarbonation at 26 kbar, $1160^\circ \pm 10^\circ C$ (Fig. 81), agrees within $10^\circ C$ with the decarbonation curve of Newton and Sharp (1975). In the hydrous runs, the Fo + Mag + V field was delineated by observation of the presence or absence of discrete grains of enstatite and magnesite. Runs interpreted to be in the Fo + V field contained traces of intergranular carbonate, probably produced

either by solution of silica in the fluid or by back reaction upon the quench. The boundary between these fields was reversed (Fig. 81).

The upper curve in Fig. 81 can be used for thermodynamic calculation. Along this curve the fluid has the $CO_2/(CO_2 + H_2O)$ indicated on the abscissa, because immediately above the upper curve, no carbonate is present, and all CO_2 is present in the fluid. Below the upper curve, varying amounts of carbonate are present, and consequently the CO_2 content of the fluid is unknown. The lower curve is specific only for the bulk composition studied, but because it represents the onset of decarbonation of an En + Mag + V assemblage, it can be calculated from the upper curve.

The decarbonation curve (upper curve, Fig. 81) can also be calculated. The data of Newton and Sharp (1975) on the anhydrous decarbonation from 2 to 40 kbar were plotted on a $\ln K - 1/T$ diagram (Anderson [1970] method) for 26-kbar pressure, using molar volume data (Robie and Waldbaum, 1968) and modified Redlich-Kwong (MRK) CO_2 fugacities (Holloway, this Report). A linear fit is assumed (constant ΔH), but the data will not fit a line if there are inconsistencies in either the experimental points or the CO_2 fugacity values. The fit is in fact linear, demonstrating that the MRK fugacities are internally consistent. From this plot an isobaric decarbonation curve for a CO_2-H_2O fluid can be calculated by assuming ideal mixing of CO_2 and H_2O (Lewis and Randall rule), by assuming ideal gas behavior, or by using MRK activity coefficients (nonideal mixing). These curves are shown in Fig. 82 together with the experimental data. The curve calculated assuming ideal gas behavior ($f_{CO_2} = X_{CO_2} \cdot P_{total}$) does not fit the data. The other two models fit the data within about $50^\circ C$, but the nonideal mixing model provides the closest fit. To reproduce the nominal experimental curve (Fig. 81) at $X_{CO_2} = 0.3$, an activity coefficient of 1.92 is required, compared

* Research supported by the National Science Foundation, Earth Sciences Section, grant DES 73-00266A01.

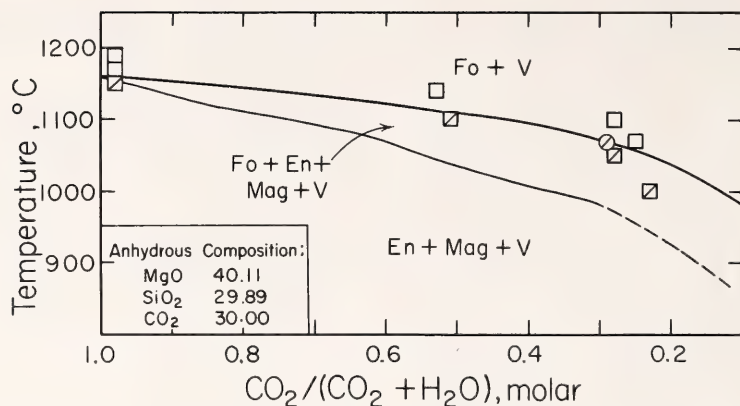


Fig. 81. Results of quenching experiments at 26 kbar pressure on the reaction $\text{En}(\text{MgSiO}_3) + \text{Mag}(\text{MgCO}_3) = \text{Fo}(\text{Mg}_2\text{SiO}_4) + \text{V}(\text{CO}_2)$ in a $\text{CO}_2\text{-H}_2\text{O}$ fluid. The abscissa is the molar $\text{CO}_2/(\text{CO}_2 + \text{H}_2\text{O})$ composition of the volatile portion of the bulk composition. Squares refer to a starting composition of finely mixed cristobalite, magnesite, and magnesia; circles, to a composition of forsterite and $\text{Ag}_2\text{C}_2\text{O}_4$. The lower curve is calculated from the upper curve.

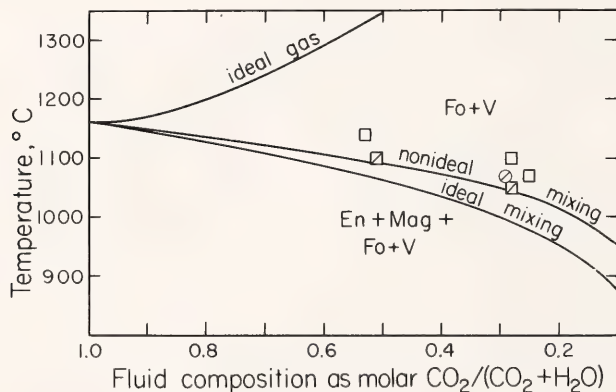


Fig. 82. Comparison of quenching experiments on the reaction $\text{En} + \text{Mag} = \text{Fo} + \text{V}$ with decarbonation curves calculated for an ideal gas model, for an ideal mixing model, and for nonideal mixing (MRK activity coefficients).

with the MRK value of 1.44. A variance in the coefficient of about 20% is possible, however, because of uncertainties in the temperature measurements. Therefore the agreement between experimental and calculated curves, within experimental error, is excellent.

Because the test of the MRK fugacity data was successful, two other sets of reactions were calculated. One set, the family of carbonation curves for peridotite in the presence of a $\text{CO}_2\text{-H}_2\text{O}$ fluid at various pressures, is discussed below.

The other set comprises the decarbonation reactions in the system $\text{CaO-MgO-SiO}_2\text{-CO}_2$ of importance with respect to peridotite, carbonatite, and kimberlite compositions at mantle pressures (Fig. 84). The reactions are for the simple system only and do not involve spinel or garnet, which are peridotite minerals, or alkali carbonates, which are important minerals in magmatic carbonatites. The calculations do not take into consideration the effects of solid solutions; however, at the temperatures of calcula-

tion, solid solutions of pyroxenes, dolomite, and magnesite are limited. Free energies calculated with appropriate activities of phases inserted in equilibrium constants differ by a maximum of 500 cal, an amount that, for a typical decarbonation reaction, corresponds to about 1.3 kbar in pressure or 28°C in temperature. Furthermore, errors due to activity terms tend to cancel because the calculated free energies are based on experiments involving solid solutions.

The decarbonation reactions at pressures greater than 2 kbar are listed in Table 29. Free energies of these reactions were derived in the following manner:

(a) The experimental data for reaction 1 of Newton and Sharp (1975) from 550° to 1300°C were fitted by Anderson's (1970) method using MRK fugacity data and molar volumes from Robie and Waldbaum (1968), and 1-bar free-energy values were calculated with the equation in Table 29.

(b) The free energy of reaction 2 at 1000°C was calculated from the well-determined experimental bracket of Kushiro, Satake, and Akimoto (1975), but the slope of the reaction was calculated from entropy data of Robie and Waldbaum (1968). The resulting line fit the other experimental points of Kushiro, Satake, and Akimoto (1975) well, and the free energies could then be simply derived.

(c) Reaction 5 was determined experimentally at 28–30 kbar pressure (Fig. 83b). This determination was not straightforward. Runs denoted by filled symbols (Fig. 83b) contained diopside and small (<5%) amounts of quartz and dolomite after the quench. Inasmuch as the amounts of quartz and dolomite were essentially constant (as measured by x-ray diffractograms) for runs at different temperatures and for runs with different starting materials, and inasmuch as run durations were long (18–22 hr) compared with normal procedures with similar highly reactive samples, the quartz and dolomite are considered to have formed by back reaction during the quench. In runs denoted by half-filled symbols, substantial amounts of both products and reactants were present. These runs are interpreted to be very close to the reaction boundary—slightly on the high-pressure side for diopside starting material and slightly on the low-pressure side for carbonate starting material. From the carbonate starting material no reaction to diopside was detected on the high-pressure side (unfilled symbol). If these interpretations of run products are correct, the reaction has been reversed. The reaction was extended to other temperatures and pressures with entropy data of Robie and Waldbaum (1968).

(d) Reaction 7 was calculated from the thermodynamic data of Skippen

TABLE 29. Free-Energy Data

| Reaction* | A(cal) | B(cal/°C) | ΔV_s (cal/bar) |
|--|--------|-----------|------------------------|
| 1. En + Mag = Fo + CO ₂ | 9600 | -40.50 | -0.3752 |
| 2. Mag + 1/2Di = En + 1/2Dol | -1245 | - 1.318 | +0.0617 |
| 3. 2En + 1/2Dol = 1/2Di + Fo + CO ₂ | 10,850 | -39.25 | -0.4368 |
| 4. Fo + Q = 2En | -5150 | 1.855 | |
| 5. 1/2Dol + Q = 1/2Di + CO ₂ | 5705 | -37.40 | -0.5214 |
| 6. Q + Mag = En + CO ₂ | 4450 | -38.65 | -0.4598 |
| 7. Di + Dol = 2En + 2Cc | 3068 | - 5.162 | +0.1525 |
| 8. 1/2Di + 1½Dol = Fo + 2Cc + CO ₂ | 13,917 | -44.41 | -0.2843 |

* En, enstatite; Fo, forsterite; Di, diopside; Dol, dolomite; Cc, calcite; Mag, magnesite; Q, quartz.

$$\Delta G^\circ_{T,1 \text{ bar}} = A + BT$$

$$\Delta G_{T,P} = \Delta G^\circ + RT \ln f_{\text{CO}_2} + (P - 1)\Delta V_s$$

(1971) at 2 kbar, the pressure at which his experiments were conducted. The P - T coordinates at higher pressures calculated from Skippen's data were topologically unsatisfactory, so the reaction was extended to higher pressures using the entropy data of Robie and Wald-
baum (1968).

From these four reactions all other reactions can be calculated at pressures above 2 kbar (Fig. 84). Two of the calculated reactions can be checked with experimental data. Reaction 3 lies approximately 70°C higher at 20 kbar than the position determined by Eggler (1976). Reaction 6 is consistent with

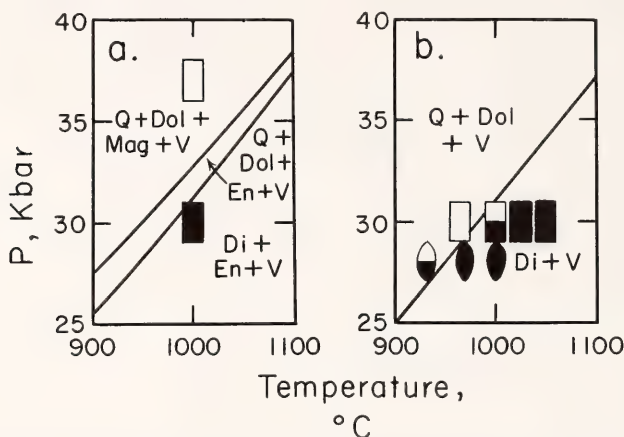


Fig. 83. Quenching experiments on the compositions (a) $\text{Di}_{60}\text{Fo}_{40} + 39 \text{ wt } \% \text{CO}_2$ and (b) $\text{Di} + 44 \text{ wt } \% \text{CO}_2$. In (b) boxes refer to runs on a starting material of quartz, MgO , CaCO_3 , and $\text{Ag}_2\text{C}_2\text{O}_4$, and ellipses, to runs on a starting material of crystalline diopside and $\text{Ag}_2\text{C}_2\text{O}_4$. Carbonation curves shown in (a) and (b) are calculated (see text).

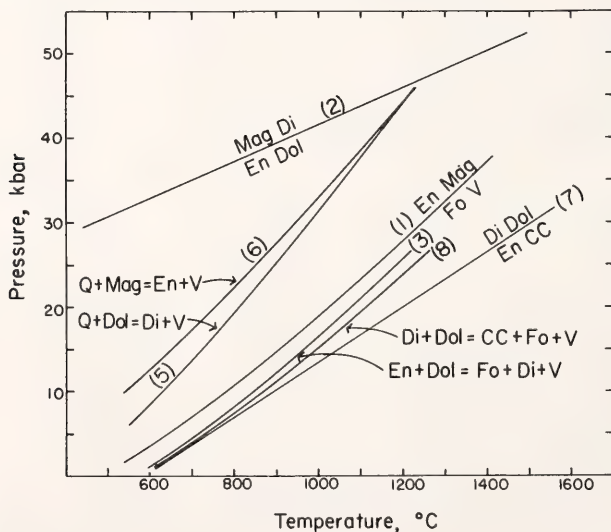


Fig. 84. Calculated decarbonation reactions in the system $\text{CaO-MgO-SiO}_2\text{-CO}_2$ applicable to peridotite, kimberlite, and carbonatite compositions. High-temperature parts of some of the reactions are metastable because of melting reactions. Reactions involving wollastonite or the high-temperature, low-pressure phases monticellite, akermanite, periclase, and spurrite have not been considered.

A set of decarbonation curves for peridotite in the presence of a $\text{CO}_2\text{-H}_2\text{O}$ fluid was also calculated. This set was calculated for reaction 3, it being the fundamental decarbonation reaction (Eggler, 1976). That is, at pressures below reaction 3, CO_2 vapor but no carbonate minerals can be present, whereas

The peridotite reaction curves (Fig. 85) show that decarbonation of peridotite in a mixed volatile fluid takes place

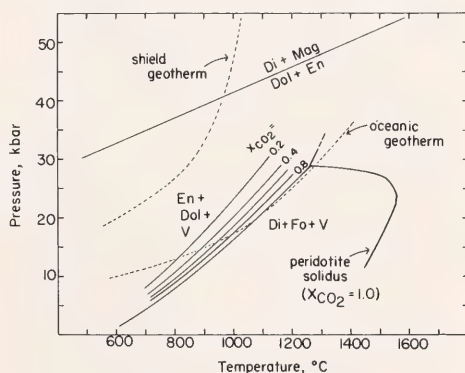


Fig. 85. Calculated decarbonation reactions in the system $\text{CaO-MgO-SiO}_2\text{-CO}_2\text{-H}_2\text{O}$ for peridotite compositions with small amounts ($<5\%$) of CO_2 . For the reaction $\text{En} + \text{Dol} = \text{Di} + \text{Fo} + \text{V}$, molar composition isopleths for $\text{CO}_2/(\text{CO}_2 + \text{H}_2\text{O})$ in the fluid are shown. Some of these curves over part of their length may be metastable because the appropriate compositions melt. Peridotite solidus (CO_2 -saturated) from Eggler (1976). Shield geotherm after Clark and Ringwood (1964); oceanic geotherm after Ringwood, MacGregor, and Boyd (*Year Book 63*, pp. 147-152).

well within the dolomite stability field. Along a shield geotherm, dolomite should be a stable phase in peridotite even at very high H_2O/CO_2 in the fluid. The paucity of carbonate reported from peridotite nodules may reflect two facts—that most nodules are brought to the surface along paths outside the carbonate stability field and that decarbonation reactions proceed very rapidly. The curves in Fig. 85 also demonstrate that carbonate minerals are stable to solidus temperatures and must therefore be considered in peridotite melting reactions.

FLUID-ABSENT MELTING OF PERIDOTITE CONTAINING PHLOGOPITE AND DOLOMITE*

John R. Holloway and David H. Eggler

The upper mantle is known to contain small amounts of CO_2 and H_2O (Roeder, 1965; Rubey, 1951), but there is a strong possibility, at pressures above 28 kbar, that no separate fluid phase is present—all H_2O is bound in phlogopite (Modreski and Boettcher, 1973; Kushiro, *Year Book* 68, pp. 245–247) and all CO_2 , in dolomite (Wyllie and Huang, 1976; Eggler, 1976). The dolomite and phlogopite presumably would be minor phases in garnet lherzolite. Phase equilibria of such a lherzolite were investigated at 30-kbar pressure to determine the nature of melting of dolomite and phlogopite because these phases would be expected to influence strongly the major element and trace element composition of liquids formed by small degrees of melting of the upper mantle.

Starting materials were prepared from mixtures of crystalline $CaSiO_3$, $CoSiO_3$, $CaMg(CO_3)_2$, $CaCO_3$, SiO_2 , Al_2O_3 , MgO , $Mg_3Al_2Si_3O_{12}$, and $KMg_3AlSi_3O_{10}(OH)_2$. Thus all CO_2 was introduced as carbonate and all H_2O as phlogopite. The starting mixes were ground for 1 hr under

acetone. The cobalt, which served as proxy for ferrous iron (Coons, Holloway, and Navrotsky, 1976), was used primarily because CoO/MgO could be used to distinguish stable and quench phlogopite. Materials were sealed in Pt capsules and run in solid-media, high-pressure apparatus (Boyd and England, 1960) using the piston-out technique. Furnace assemblies consisted of crushable alumina, Pyrex, and talc, and temperatures were measured with Pt-Pt10Rh thermocouples; reported pressures and temperatures are nominal values. To maintain cobalt in the divalent state and thus minimize its solution in the platinum capsules, the oxygen fugacity in the capsule must be at or above that of the hematite-magnetite buffer (Coons, Holloway, and Navrotsky, 1976). High f_{O_2} was maintained by carefully drying the furnace assembly and by surrounding the sample capsule with dry PtO_2 . At high temperatures, the PtO_2 decomposes to $Pt + O_2$ (Huckenholz and Yoder, *Year Book* 69, pp. 182–188), and the oxygen reacts with residual hydrogen in the furnace assembly, reducing diffusion of H_2 through the capsule wall into the charge.

Phases were identified by transmitted light microscopy, by scanning electron microscopy using energy-dispersive methods for qualitative elemental analysis, and by ^{14}C -produced β -particle maps recorded on Ilford K-5 nuclear emulsions. The last two techniques were especially useful in distinguishing between the quench and stable forms of carbonate and phlogopite. The liquid never quenched to glass; it always crystallized to a mixture of silicates and carbonates. Criteria to distinguish quench from stable forms were developed from repetitive examination of a series of runs. Quench phlogopite was distinguished on the basis of both texture and composition. It occurs as broad, thin, commonly ragged plates with irregular extinction, whereas the stable phlogopite occurs as small, nearly equant crystals that extinguish uniformly. The CoO/MgO of the

* Research supported by National Science Foundation, Earth Sciences Section, grant DES 73-00266A01.

quench phlogopite was typically about 5% higher than that of the stable phlogopite in the same charge. Quench carbonate occurs in two forms, as large grains filled with silicate inclusions and as fine-grained aggregates surrounding stable silicate crystals. The latter form can be distinguished on β -track maps. The stable carbonate contained very few silicate inclusions, and in β -track maps it is seen to occur as discrete grains.

Experimental determinations have been made of the beginning of melting of dolomite in H_2O -free peridotite systems (Wyllie and Huang, 1976; Eggler, 1976) and of phlogopite in CO_2 -free peridotite systems (Modreski and Boettcher, 1973; Bravo and O'Hara, 1975), indicating that the temperatures of melting of dolomite and phlogopite are within $35^\circ C$ of each other in garnet lherzolite assemblages (Fig. 86). Because fluid-absent melting of phlogopite in a CO_2 -

free garnet lherzolite assemblage had not previously been attempted, an initial set of experiments was performed on one composition (COMAN-2, Table 30) to determine the solidus temperature. This temperature is $1235^\circ \pm 15^\circ C$ at 30-kbar pressure, in agreement with the work of Modreski and Boettcher (1973) on similar compositions in simpler systems. In the system $CaO-MgO-Al_2O_3-SiO_2-K_2O-H_2O$, the assemblage $gar + cpx + opx + ol + ph + L$ is isobarically invariant, and so the phlogopite should completely melt at a fixed temperature. Phlogopite melted over a small interval in the present experiments, probably because CoO/MgO changes through the melting interval.

Dolomite-phlogopite melting experiments were carried out on the join shown in Fig. 87. This join is in turn part of a more inclusive join (inset, Fig. 87), at the corners of which are projected the compositions garnet lherzolite (LHZ), dolomite, and phlogopite. Two compositions on the join, COMAN-D and COMAN-DC (Table 30), were investigated. The solidus temperature determined for these compositions, $1125^\circ \pm 25^\circ C$, is also the solidus temperature for all other compositions on the join, because for all these compositions K_2O/H_2O is fixed in all phases (specifically phlogopite and liquid). Above the solidus LHZ minerals + phlogopite + dolomite coexist over a short temperature interval, above which either phlogopite or dolomite melts completely. The compositions studied (Fig. 87) had a rather large phlogopite melting interval. However, a bulk composition to their left (shown schematically as a composition with $ph/[ph + dol] = 0.5$ in Fig. 87) will melt to a liquid (plus LHZ minerals) over a temperature interval of less than $10^\circ C$, and hence the liquid is eutecticlike. (The $\sim 5^\circ C$ divariant melting interval reflects the presence of CoO . The CoO/MgO of phases will change slightly over that interval, but the composition of the eutecticlike liquid will not change significantly.)

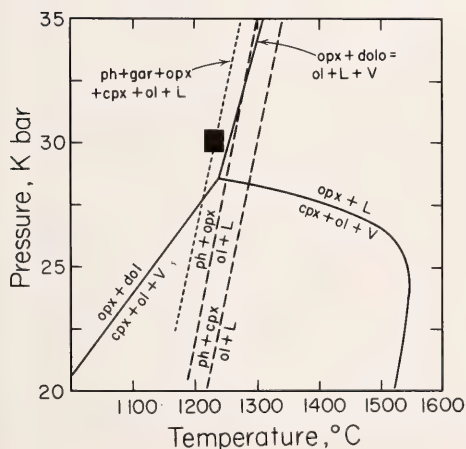


Fig. 86. P - T projection of equilibria involving dolomite or phlogopite. Solid curves are from Eggler (1976); dashed curves, from Modreski and Boettcher (1973). Dotted line is the solidus of the assemblage $gar + opx + cpx + ol + ph$ determined in this study at 30 kbar pressure (indicated by solid rectangle) and drawn parallel to the $ph + cpx = ol + L$ curve determined by Modreski and Boettcher (1973).

TABLE 30. Composition of Starting Materials, wt %

| | COMAN-1 | COMAN-2* | COMAN-D† | COMAN-DC‡ |
|---|---------|----------|----------|-----------|
| Oxides | | | | |
| SiO ₂ | 48.49 | 46.99 | 42.29 | 40.18 |
| Al ₂ O ₃ | 7.51 | 8.85 | 7.97 | 7.57 |
| CoO | 11.48 | 8.21 | 7.39 | 7.02 |
| MgO | 24.44 | 25.73 | 25.35 | 24.08 |
| CaO | 8.08 | 5.79 | 8.25 | 10.64 |
| K ₂ O | ... | 3.21 | 2.89 | 2.75 |
| H ₂ O | ... | 1.23 | 1.11 | 1.05 |
| CO ₂ | ... | ... | 4.77 | 6.73 |
| Totals | 100.00 | 100.01 | 100.02 | 100.02 |
| End-Member Minerals | | | | |
| M ₂ SiO ₄ § | 14.3 | 10 | 9 | 8.6 |
| CaMSi ₂ O ₆ | 28.6 | 20 | 18 | 22.5 |
| MSiO ₃ | 28.6 | 20 | 18 | 12.1 |
| M ₂ Al ₂ Si ₃ O ₁₂ | 28.6 | 20 | 18 | 17.1 |
| KM ₃ AlSi ₃ O ₁₀ (OH) ₂ | ... | 30 | 27 | 25.7 |
| CaMg(CO ₃) ₂ | ... | ... | 10 | 14.1 |
| Totals | 100.1 | 100 | 100 | 100.1 |
| Wt ratio ph/(ph + dol) | | 0.000 | 0.730 | 0.646 |

* Made by adding 30 wt % crystalline phlogopite to COMAN-1.

† Made by adding 10 wt % crystalline dolomite to COMAN-2.

‡ Made by adding 5 wt % calcite containing ¹⁴C to COMAN-D.

§ M represents Mg + Co.

The contents of H₂O and CO₂ in compositions on the join investigated (Fig. 87) are large compared with contents believed to be present in the upper mantle (probably less than 1%). A *T-X* section equivalent to Fig. 87, but appropriate to the upper mantle, would fall very close to the garnet lherzolite apex of the inset in Fig. 87. In such a section (Fig. 88), the solidus temperature will be the same as in Fig. 87, and the composition of the eutecticlike liquid will be essentially the same. Because the bulk compositions contain substantially less volatiles and hence less phlogopite and dolomite, the melting intervals of phlogopite or dolomite must be less.

Several conclusions pertinent to major element and trace element geochemistry of mantle-derived liquids can be reached from examination of Fig. 88:

(1) A fluid-absent garnet lherzolite containing dolomite and phlogopite will

begin to melt (at 30-kbar pressure) at a single temperature to a single liquid regardless of the ratio of phlogopite to dolomite.

(2) The eutecticlike liquid produced at the solidus will change very slightly in composition over a 5°–10°C interval in which dolomite and phlogopite co-exist. The composition of the liquid is not known precisely, but inasmuch as the liquid contains volatiles in a ratio H₂O/(H₂O + CO₂) ≈ 0.2, the liquid is estimated to be melilititic (Brey and Green, 1975).

(3) At higher temperatures above the solidus, phlogopite or dolomite will melt out over a temperature interval of 0°–100°C, and liquid compositions will quickly diversify from the eutecticlike liquid, depending on bulk composition. For bulk compositions containing volatiles in the molar ratio CO₂/(CO₂ + H₂O) ≈ 0.2–1.0, phlogopite is the phase

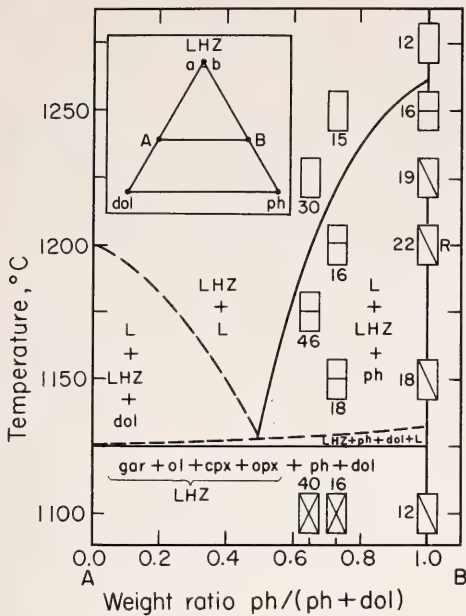


Fig. 87. Experimental results at 30 kbar pressure plotted on the temperature-composition section shown as line A-B in the inset. Runs are indicated by rectangles whose size represents the uncertainty in temperature and composition. A horizontal bar indicates the presence of liquid and stable phlogopite; a diagonal bar, the absence of liquid and presence of stable phlogopite. Numbers next to rectangles indicate run duration in hours. The run indicated by *R* was reversed (to verify the solidus determination) by holding it at 1350°C, 30 kbar, for 10 min and then reducing the temperature to 1200°C. The inset at the top of the figure shows a triangular diagram (in wt %) whose corners represent garnet lherzolite, dolomite, and phlogopite. Compositions used in this study lie along the line A-B.

that melts. The liquid in equilibrium with phlogopite can be expected to change composition with temperature increase. Because phlogopite releases K_2O and H_2O to the melt, the liquid will probably increase in K_2O content and in its degree of silica saturation (Mysen and Boettcher, 1975b). For the CO_2 -rich bulk compositions for which dolomite is the supersolidus phase, liquids will probably become less silica-satu-

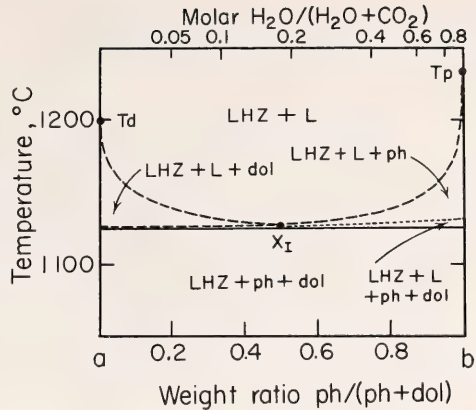


Fig. 88. A temperature-composition section depicting near-solidus phase relations for a garnet lherzolite composition containing small amounts of dolomite and phlogopite. The line *a-b* is shown in the inset in the preceding figure. The weight ratio phlogopite/(phlogopite + dolomite) is plotted along the bottom of the diagram. The molar ratio of $H_2O/(H_2O + CO_2)$ is plotted on the top of the diagram. The composition axes are valid only for the assemblages LHZ + *L* and LHZ + ph + dol. The symbols X_i , T_d , and T_p are taken from the preceding figure and represent the liquid composition at the beginning of melting, the highest temperature for the existence of dolomite, and the highest temperature for the existence of phlogopite, respectively. Except for those points, the section is largely schematic.

rated with increasing melting (Eggler, 1976).

(4) Over the supersolidus melting intervals of dolomite or phlogopite, trace element patterns will reflect partitioning with those phases.

(5) At temperatures above the dolomite or phlogopite melting intervals, liquid compositions will change much less because the ratio of volatiles in the liquid does not change, because the amount of volatiles in the liquid diminishes as more liquid is produced and because the liquids are in equilibrium (over an interval of at least 200°C) with a common garnet lherzolite assemblage (Mysen and Kushiro, this Report).

MINERALOGICAL VARIATIONS IN THE
UPPER PART OF THE SKAERGAARD
INTRUSION, EAST GREENLAND

*H. R. Naslund**

The Skaergaard intrusion is widely regarded as the type example of a strongly fractionated, layered gabbroic intrusion, and through the classic work of L. R. Wager and his co-workers (Wager and Deer, 1939; Wager and Brown, 1968; and numerous other publications) it has served as a standard of comparison for a wide variety of studies in igneous petrology. Owing to the extensive advances in analytical techniques and petrologic theory that have occurred since most of the original work was

done, however, a new investigation of the intrusion was initiated in 1971, with expeditions to the area in 1971 and 1974. The present account is a preliminary report on a study of the upper part of the intrusion and is based primarily on electron microprobe analyses of samples collected during the 1974 expedition.

The Skaergaard intrusion can be divided into three main structural units: a layered series that accumulated on the floor of the intrusion, an upper border group that solidified from the roof downward, and a marginal border group that crystallized from the sides inward (Fig. 89). The layered series can be subdivided into lower, middle, and upper zones based on the disappearance and then reappearance of olivine as a cumulus phase (i.e., the middle zone is olivine-free). The boundary between the upper zone and the upper border group is marked by a thin, discontinuous unit called the sandwich horizon that evidently represents the end product of the

* Work carried out under a cooperative pre-doctoral fellowship program of the Geophysical Laboratory and the University of Oregon. Field expenses for this study were provided by a GSA Penrose grant to H. R. Naslund and by National Science Foundation and National Geographic Society grants to A. R. McBirney.

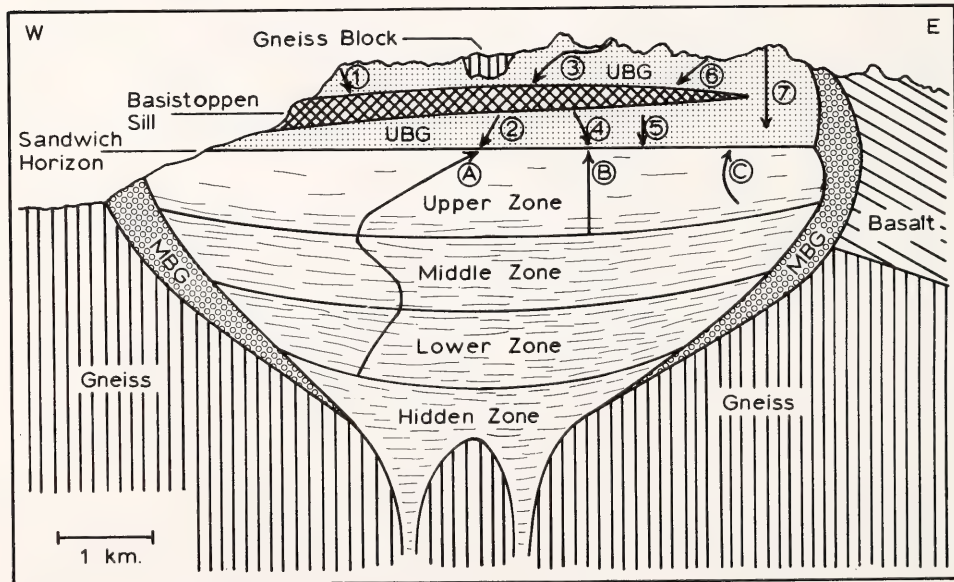


Fig. 89. Schematic west to east cross section of the Skaergaard intrusion showing the relationships between the major units. Arrows indicate the relative positions of traverses A-C and 1-7. Traverse arrows point in the direction of increasing differentiation. The symbols UBG and MBG refer to the upper border group and the marginal border group. The lower, middle, and upper zones are subdivisions of the exposed layered series, and the hidden zone is the unexposed base of the intrusion.

differentiation process because it contains the most Fe-rich olivine and the most Na-rich plagioclase in the intrusion. Stratigraphic relationships within the upper border group, which in many respects is a mirror image of the layered series, are complicated by the inclusion of numerous gneiss blocks and by the later intrusion of the Basistoppen sill. The upper border group has been subdivided (Wager and Brown, 1968) into α , β , and γ zones, which are roughly correlative to the lower, middle, and upper zones of the layered series, respectively. Although Wager and Brown regarded these subdivisions as tentative, owing to the ruggedness of the topography and the difficulty of distinguishing these units in the field, the present study has shown that the basic features are correct in that the upper portion of the upper

border group contains Mg-rich olivines, the middle portion is olivine-free, and the lower portion contains Fe-rich olivines.

Data from three traverses of the upper zone of the layered series, labeled *A*, *B*, and *C* from west to east, and seven traverses of the upper border group, labeled 1–7 from west to east, have been studied to determine whether there are any systematic lateral variations in the compositions of olivine, clinopyroxene, or plagioclase and whether there are any systematic differences between the mineral compositions in the upper border group and layered series. Data on the traverses of the layered series are mainly from Wager and Deer (1939), Douglas (1961), and Wager and Brown (1968).

It is apparent from Figs. 90, 91, and 92 that there are significant lateral vari-

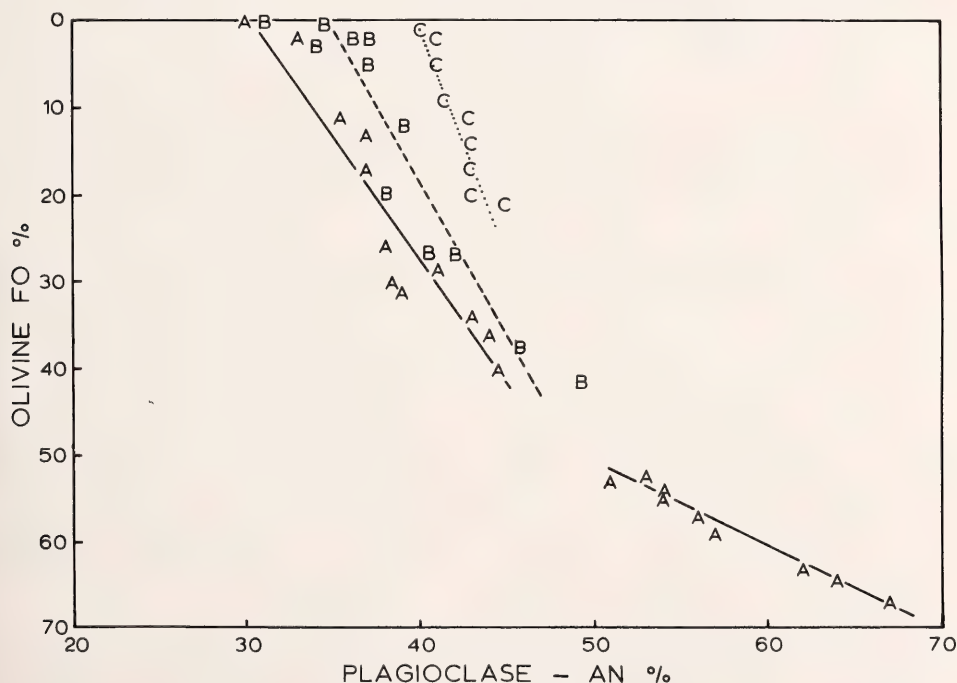


Fig. 90. Plot (in mole %) of forsterite in olivine versus anorthite in plagioclase for samples from traverses *A*, *B*, and *C* in the layered series. The solid line, the dashed line, and the dotted line indicate trends for traverses *A*, *B*, and *C*, respectively. The gap in the trend of traverse *A* reflects the olivine-free middle zone of the layered series. Data on traverse *A* are from Wager and Deer (1939) and Wager and Brown (1968). Data on traverses *B* and *C* are primarily from Douglas (1961), but traverse *B* also includes four analyses from the present study.

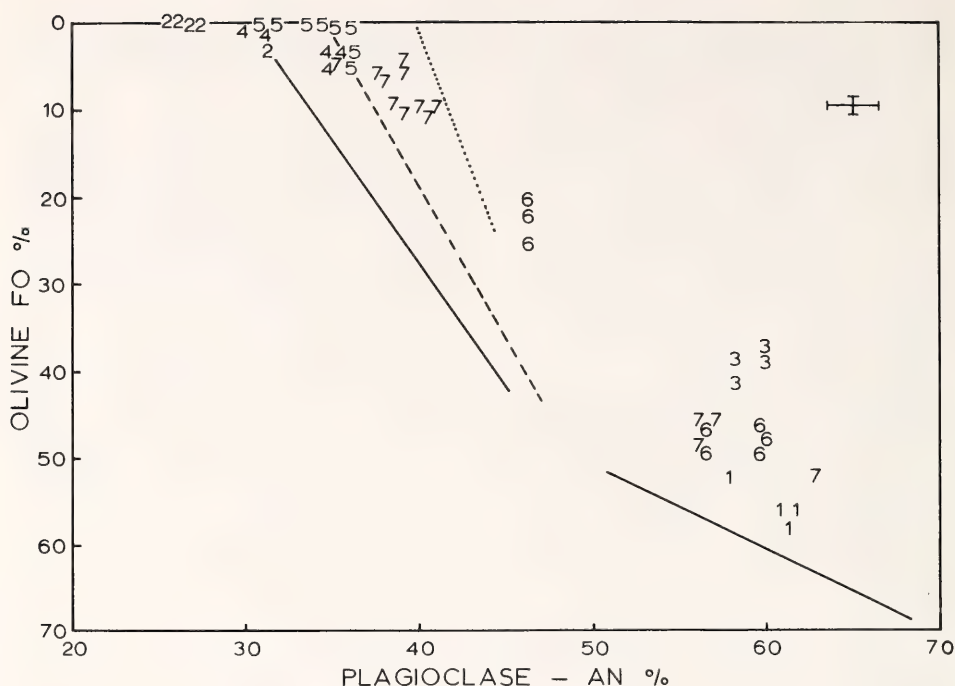
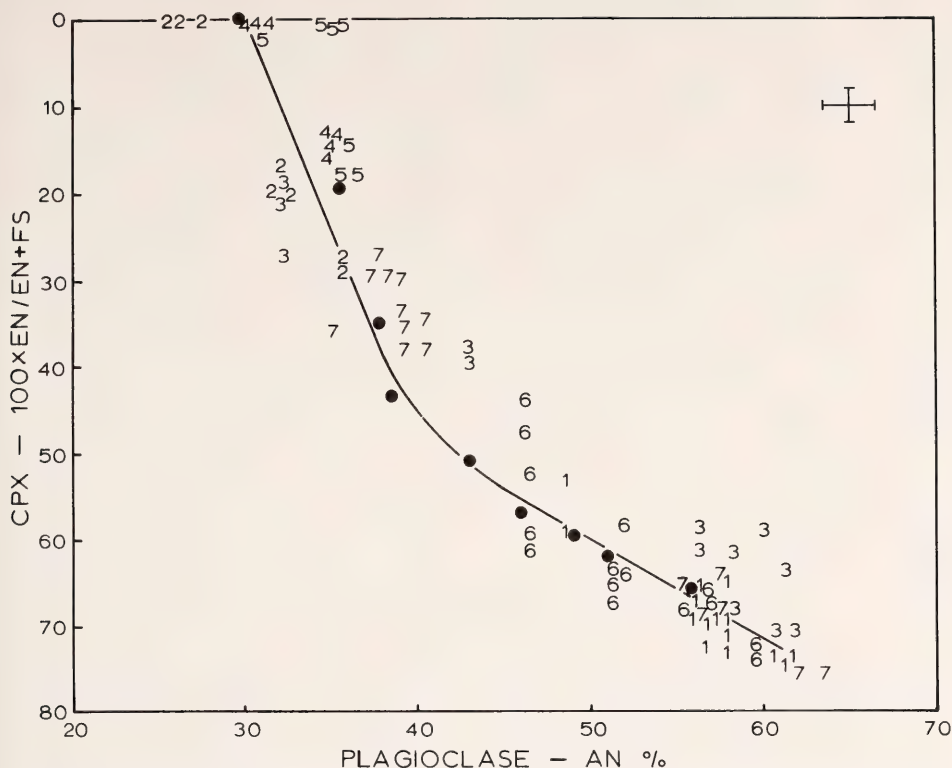


Fig. 91. Plot (in mole %) of forsterite in olivine versus anorthite in plagioclase for samples from traverses 1-7 in the upper border group. The trend lines from Fig. 90 are shown for comparison. Each symbol represents an average of at least three electron microprobe analyses. The approximate range of compositions represented by each symbol is indicated in the upper right.

ations in the rocks formed during the late stages of differentiation of the intrusion, as suggested by Douglas (1961). For any given Fe/Mg in the olivine or clinopyroxene from samples of the upper zone of the layered series or the lower part of the upper border group, the plagioclases become systematically richer in Ca toward the east side of the intrusion. This relationship is best seen in Fig. 90, where the data from traverses A, B, and C define three distinct trends for the upper zone of the layered series. The data from traverses 2, 4, and 5 through upper border group γ (Figs. 91 and 92) also show a progressive increase in the percentage of An for a given degree of iron enrichment, from west to east. The cause of this lateral variation is not known, but it may be related to the difference in country rock on the two sides of the intrusion at this level. The

country rock in the west is acidic gneiss; that in the east is basalt. The upper zone of the layered series and the lower part of the upper border group, which together represent the last 15% to 20% of the intrusion to crystallize (McBirney, 1975), lack the well-developed layering that characterizes most of the rest of the intrusion. Possibly the factors that caused the cessation of the layering during the late stages of differentiation also contributed to the formation of lateral inhomogeneity.

Systematic east-west variations are not apparent in traverses through the upper part of the upper border group (Figs. 91 and 92). In these traverses, which represent the earlier stages of differentiation of the intrusion, samples from near the center of the intrusion (traverse 3) have either more An-rich plagioclases or less Mg-rich olivines and



clinopyroxenes than samples from either the west side of the intrusion (traverse 1) or the east side (traverses 6 and 7). There are no significant differences in the country rock at this level of the intrusion, but possibly the variation is related to the distribution of gneiss inclusions within the upper border group.

A comparison of pyroxene-plagioclase pairs in samples from the upper border group and layered series indicates that although the minerals in the upper border group samples show compositional variation, they follow the same general differentiation trend as the minerals in the layered series samples (Fig. 92). A similar comparison of olivine-plagioclase pairs, however, indicates that the olivine of the upper border group is more

Fe-rich than the olivine of the layered series for any given An content in the plagioclase. The difference in degree of iron enrichment between the olivines and pyroxenes of the upper border group is shown in Fig. 93, where upper border group olivine-pyroxene pairs are obviously displaced from the general trend for the layered series. The layered series data in Fig. 93 are from Wager and Brown (1968) and are consistent with recent electron microprobe analyses (McBirney and Naslund, unpublished data). Because the compositions of pyroxene-plagioclase pairs are similar in the upper border group and in the layered series, the difference in olivine composition between these two units is possibly a function of factors other than a

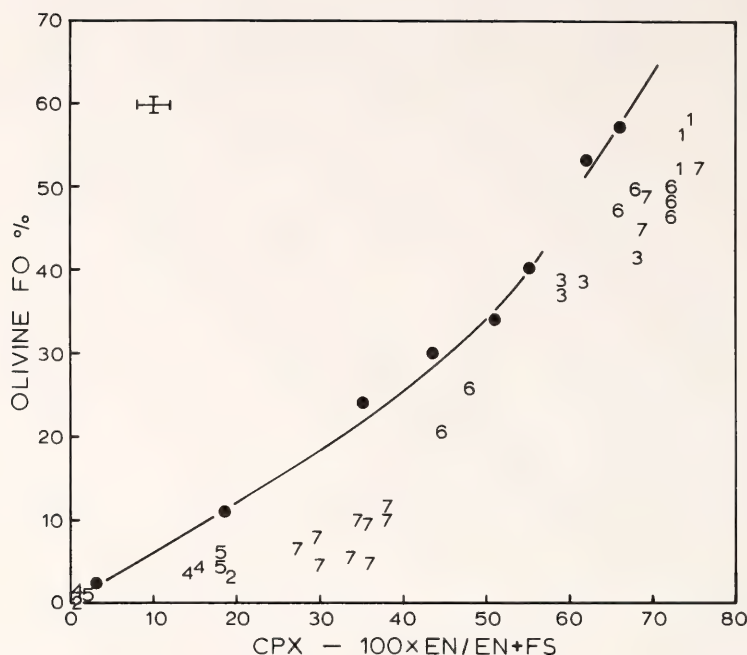


Fig. 93. Plot (in mole %) of forsterite in olivine versus the enstatite/(enstatite + ferrosilite) in clinopyroxene for samples from traverses 1-7 in the upper border group. The approximate range in composition represented by each symbol is shown in the upper left. The trend for the layered series (Wager and Brown, 1968) is indicated by the solid line and solid points.

difference in magma composition. Variations in the conditions of crystallization, such as the rate of cooling, the efficiency of fractionation (i.e., the separation of crystals from liquid), the volatile pressure, or the equilibration temperature (i.e., the temperature at which the crystals are effectively separated from the liquid) can affect the composition of the resulting mineral phases.

The results of this study have important implications in respect to fractionation mechanisms in the Skaergaard intrusion. The east-west variation in the mineral composition of samples from the lower part of the upper border group and the upper zone of the layered series suggests that the magma body was laterally inhomogeneous during the late stages of crystallization. This lateral inhomogeneity implies, perhaps, that convection did not operate during the late stages of differentiation or that it was restricted to small, partially iso-

lated cells. The differences in relative mineral compositions within the upper part of the upper border group suggest that local inhomogeneities were probably present during much of the differentiation process. The difference between the olivine-clinopyroxene pairs in the upper border group and those in the layered series probably reflects a systematic difference in the conditions of crystallization between these two parts of the intrusion.

LATTICE ENERGY OF SOME SILICATE MINERALS AND THE EFFECT OF OXYGEN BRIDGING IN RELATION TO CRYSTALLIZATION SEQUENCE

Y. Ohashi

One of the goals of crystal structure analysis, although still remote, is characterization of the chemical bond and evaluation of the lattice energies of

crystals. In principle, direct calculation of a lattice energy is possible if the nature of the chemical bonds and precise atomic positional parameters are known. Most theoretical calculations, however, have been limited to high-symmetry cases such as the NaCl structure (Tosi, 1964), and only in the last several years have such calculations been successfully extended to crystalline materials of mineralogical significance (Smyth and Smith, 1969; Raymond, *Year Book 70*, pp. 225-227; Whittaker, 1971; Ohashi and Burnham, 1972; Tokonami *et al.*, 1972; Fenn and Brown, 1975).

Among the several methods for evaluation of the slowly converging Coulomb interactions, the Ewald method and the Bertaut method are most widely used. In the present study, electrostatic energies have been calculated for a fully ionized model using the Bertaut formulae (Bertaut, 1952) with the correction factors of Templeton and Johnson (1961) for the termination effects of Fourier series. The results of the calculation are applied to discussions of (a) cation-site energies in clinoenstatite, (b) the effect of oxygen bridging in silicates, and (c) the relationship between the lattice energy and the crystallization sequence of silicate minerals.

The *site* energy is defined as the energy that would be required to move a particular ion from its equilibrium position in a structure to infinite distance. The *lattice* energy is that required to separate all ions in the crystal to infinite distance. Thus, the site energy is a constituent of the lattice energy. As shown below, the lattice energy may also be obtained from experimental values, but the site energy can be calculated only from an appropriate theoretical model.

The two-term (electrostatic and repulsive) approximation for the lattice energy gives, in general, reasonable agreement with the experimental value for the NaCl-type structure (Tosi, 1964). This approximation has been applied to the calculation of the site energies at the metal sites in pyroxenes

(Ohashi and Burnham, 1972), but the lattice energy could not be obtained because the repulsive parameters for Si-O were not known. The partially covalent nature of Si-O bonds still remains an unsolved problem in the direct calculation of the lattice energy in silicates; however, an approximate value of the repulsive energy for Si-O can be estimated from the difference between the theoretical and experimental lattice energies for quartz. As shown in Table 31, the repulsive energy for the Si atom in the tetrahedral site may be around 1500 kcal mole⁻¹ or 350-400 kcal mole⁻¹ for each Si-O bond. This value is also consistent with the similar difference calculated for clinoenstatite (Table 31).

In the study of site energies of the metal sites in pyroxenes, clinoenstatite was found to differ from other clinopyroxenes in site energy, and unremoved shearing stress in the structure was suggested as a possible explanation (Ohashi and Burnham, 1972, p. 5763). The results of the site-energy calculations (Table 32) obtained from the new structural data on clinoenstatite (Ohashi and Finger, this Report), however, are consistent with those for other pyroxenes (see Ohashi and Burnham, 1972, Table 3 and Fig. 1, for other data). Therefore, the Mueller hypothesis of energy equivalence (Mueller, 1962; Matsui and Banno, 1965) holds for all pyroxenes including clinoenstatite.

Linkage of the Silicate Tetrahedra

The most important structural feature in silicates is the way in which the silicate tetrahedra are linked together. The effect of bridging two tetrahedra can be analyzed by examining the site energy of oxygen anions in various silicate structures. Some examples of the oxygen site energies are shown in Fig. 94.

In the olivine structure, which consists of individual SiO₄ tetrahedra, the electrostatic site energy of the oxygen anions is about -1250 kcal mole⁻¹. When tetrahedra are linked by sharing oxygen anions, as in the pyroxene struc-

TABLE 31. Lattice Energies Obtained from the Born-Harber Cycle and the Electrostatic-Repulsive Potential Calculation (kcal mole⁻¹)

| Quartz, SiO ₂ | | | |
|---|--|--------------|------|
| SiO ₂ | → Si + O ₂ | -217.1 | (1)* |
| (Si) _{solid} | → (Si) _{vapor} | -106.0 | (1) |
| O ₂ | → 2O | -117.9 | (2) |
| Si | → Si ⁴⁺ + 4e | -2323.9 | (3) |
| 2(2e + O) | → 2O ²⁻ | +320 | (4) |
| SiO ₂ | → Si ⁴⁺ + 2O ²⁻ | -2446 | (a) |
| Electrostatic energy | | -3968 | (b) |
| Repulsive energy (Si-O) | | ? | (5) |
| $a - b = 1522 \text{ kcal mole}^{-1}$ | | | |
| Clinoenstatite, MgSiO ₃ | | | |
| MgSiO ₃ | → Mg + Si + 3/2 O ₂ | -370.1 | (1) |
| (Mg) _{solid} | → (Mg) _{vapor} | -32.6 | (1) |
| (Si) _{solid} | → (Si) _{vapor} | -106.0 | (1) |
| 3/2 O ₂ | → 3O | -176.9 | (2) |
| Mg | → Mg ²⁺ + 2e | -522.5 | (3) |
| Si | → Si ⁴⁺ + 4e | -2323.9 | (3) |
| 3(2e + O) | → 3O ²⁻ | +480 | (4) |
| MgSiO ₃ | → Mg ²⁺ + Si ⁴⁺ + 3O ²⁻ | -3052 | (a) |
| Electrostatic energy | | -4706.9 | (b) |
| Repulsive energy Mg(M1)-O | | -215.9 × 1/2 | (c) |
| Mg(M2)-O | | -193.1 × 1/2 | (d) |
| Si-O | | ? | (5) |
| $a - (b + c + d) = 1450 \text{ kcal mole}^{-1}$ | | | |

* Source of data: (1) Robie and Waldbaum, 1968; (2) *American Institute of Physics Handbook*, 1972, p. 179; (3) *International Critical Tables*, 1929, Vol. 6, pp. 71-72; (4) Huggins and Sakamoto, 1957, quoted by Raymond, *Year Book 70*, p. 227; (5) this study.

ture, the site energy for the bridging oxygen is lowered to -1400 kcal mole⁻¹. In clinoenstatite, the difference in site energy between the bridging oxygen,

TABLE 32. Electrostatic and Repulsive Site Energies for Clinoenstatite (kcal mole⁻¹)

| Site | Electrostatic | Repulsive* | Total |
|-------|---------------|------------|---------|
| M1 | -1242.1 | 215.9 | -1026.2 |
| M2 | -1135.2 | 193.1 | -942.1 |
| SiA | -4396.2 | | |
| SiB | -4353.7 | | |
| O1A | -1213.7 | | |
| O1B | -1215.9 | | |
| O2A | -1213.9 | | |
| O2B | -1221.4 | | |
| O3A | -1425.0 | | |
| O3B | -1410.1 | | |
| Total | -18827.2 | | |

Electrostatic lattice energy: $-18827.2 \times 1/2 = -9413.6$ per mole of Mg₂Si₂O₆

* The repulsive parameters used are $\lambda = 5.98 \times 10^{-10}$ erg and $\rho = 0.3785$ Å (Ohashi and Burnham, 1972, Table 1).

$\bar{O}3$, and the nonbridging oxygens, $\bar{O}1$ and $\bar{O}2$, is about 200 kcal mole⁻¹.

For amphibole, in which silicate tetrahedra form double chains, the electrostatic site energies of the bridging oxygen, $\bar{O}5$, $\bar{O}6$, and $\bar{O}7$, are lower than those of the nonbridging oxygens, $\bar{O}1$, $\bar{O}2$, and $\bar{O}4$. The oxygen anions, $\bar{O}2$ and $\bar{O}4$, in the amphibole structure are coordinated to the same Si atom in T2; thus they resemble $\bar{O}1$ and $\bar{O}2$ in the pyroxene structure, whereas $\bar{O}1$ in the amphibole structure is the only nonbridging oxygen in the T1 tetrahedron. The other three oxygens in T1 are all shared by the adjacent tetrahedra.

As the degree of tetrahedral linkage increases further, the stable silicate structure is a two-dimensional network or sheetlike structure like that of the micas. The only nonbridging oxygen in the mica structure is $\bar{O}3$, which is similar to $\bar{O}1$ in the amphibole structure in its coordination to the Si atom. In micas,

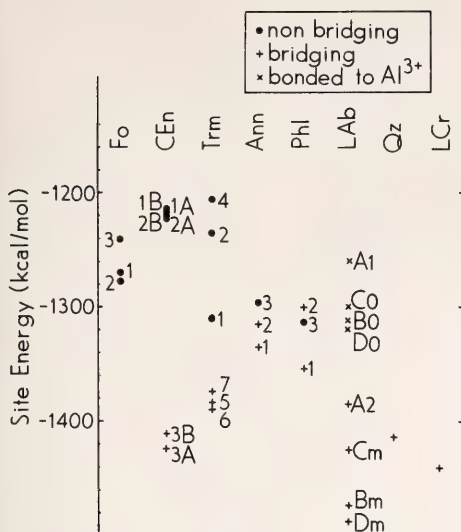


Fig. 94. Site energy of oxygens in various silicate minerals. The symbols associated with each point are atomic site nomenclature for oxygens (see references given in Table 32 for more detail). Abbreviations: Fo, forsterite; CEn, clinoenstatite; Trm, tremolite; Ann, annite; Phl, phlogopite; LAB, low albite; Qz, quartz; LCr, low cristobalite.

the bridging and nonbridging oxygens do not differ significantly in energy, but the reason is not clear.

Finally, the tetrahedra are linked at all four corners and form a three-dimensional framework. In low albite, the oxygens that are bonded to two Si cations have a lower site energy than do $\bar{O}A1$, $\bar{O}C0$, $\bar{O}B0$, and $\bar{O}D0$, which are coordinated to Al^{3+} in T10.

In summary, the electrostatic site energy is -1400 to ~ -1500 kcal mole⁻¹ for the bridging oxygen anion and -1200 to ~ -1300 kcal mole⁻¹ for the nonbridging oxygen anion. By bridging two tetrahedra, the oxygen site generally acquires an additional stabilization energy of approximately 150–200 kcal mole⁻¹ as compared with the nonbridging oxygen in the same structure.

Lattice Energy and Crystallization Sequence

During the course of crystallization of minerals from a silicate melt, the ar-

rangement of the silicate tetrahedra in the liquid plays an important role in controlling the type of phases that crystallize from the melt. A systematic shift of liquidus boundaries has been attributed to the effect of cations on polymerization of the silicate tetrahedra in the melt (Kushiro, 1975). A knowledge of the structure of silicate melt is essential for the discussion of crystallization, yet the structure has not been well characterized experimentally. The energies of solid phases will be considered here only in relation to the sequence of crystallization.

The enthalpy of melting, which is the energy difference between a solid and a liquid, has been discussed by Yoder (*Year Book* 74, pp. 515–519) for olivine, pyroxene, garnet, and feldspar. In this work, the electrostatic lattice energy has been computed for these minerals (Table 33). When corrected for repulsive energy, which is usually only 10%–15% of the electrostatic energy, these values represent the difference between the crystalline state and free ions in the gaseous state.

In order to compare the lattice energies of different minerals on the same basis, the energy values must be normalized to an appropriate structural unit. In Table 33, three values normalized to the same numbers of oxygens, cations, and tetrahedral cations are given for each mineral. It is apparent that the Bowen reaction series olivine \rightarrow pyroxene \rightarrow amphibole \rightarrow biotite can be rationalized on a structural basis as an increase in the degree of oxygen sharing between tetrahedra. The energy values normalized to either oxygens or cations do not show any simple relationship to the series. When normalized to the same number of tetrahedra, the series corresponds to a progressive decrease in the stability of the lattice as indicated by the progressively less negative values for the lattice energy per tetrahedral site. The earlier in the reaction series, the lower the lattice energy normalized to one tetrahedron.

TABLE 33. Electrostatic Lattice Energy for Some Silicate Minerals (kcal mole⁻¹)

| Mineral and Formula Unit | | Electrostatic Lattice Energy | | | |
|--|------|------------------------------|-------------------|-------------------|--------------------------------|
| | | per one formula unit | per one oxygen | per one cation | per one tetrahedral site |
| Grossular, Ca ₃ Al ₂ Si ₃ O ₁₂ | (1)* | -18735 | -1561 | -2341 | -6245 |
| Forsterite, Mg ₂ SiO ₄ | (2) | -5849 | -1462 | -1950 | -5849 |
| Fayalite, Fe ₂ SiO ₄ | (3) | -5661 | -1415 | -1887 | -5661 |
| Orthoenstatite, MgSiO ₃ | (4) | -4708 | -1569 | -2354 | -4708 |
| Orthoferrosilite, FeSiO ₃ | (5) | -4687 | -1562 | -2344 | -4687 |
| Clinoenstatite, MgSiO ₃ | (4) | -4708 | -1569 | -2354 | -4708 |
| Tremolite, Ca ₂ Mg ₅ Si ₈ O ₂₂ (OH) ₂ | (6) | -36070 | -1503 | -2405 | -4509 |
| Phlogopite, KMg ₃ Si ₃ AlO ₁₀ (OH) ₂ | (7) | -16653 | -1388 | -2082 | -4163 |
| Annite, KFe ₃ Si ₃ AlO ₁₀ (OH) ₂ | (7) | -16550 | -1379 | -2069 | -4138 |
| High albite, NaAlSi ₃ O ₈ | (8) | -13136 | -1642 | -2627 | -3284 |
| Low albite, NaAlSi ₃ O ₈ | (8) | -13505 | -1688 | -2701 | -3376 |
| Quartz, SiO ₂ | (9) | -3968 | -1984 | -3968 | -3968 |
| Low cristobalite, SiO ₂ | (10) | -3664 | -1832 | -3664 | -3664 |

* Source of crystal structural data: (1) Abrahams and Geller, 1958; (2) Smyth and Hazen, 1973; (3) Smyth, 1975; (4) this study; (5) Sueno, Cameron, and Prewitt, 1976; (6) Papike, Ross, and Clark, 1969; (7) Hazen and Burnham, 1973; (8) Wainwright, quoted by J. V. Smith, 1974, p. 86; (9) G. S. Smith and Alexander, 1963; (10) Dollase, 1965.

EFFECT OF PRESSURE ON THE MELTING ENTHALPY OF DIOPSIDE UNDER DRY AND H₂O-SATURATED CONDITIONS

M. Rosenhauer

The latent heat associated with melting of silicate liquids has important bearing on the depth and time required to generate basaltic liquid (Yoder, *Year Book* 74, pp. 515-519). A prerequisite to further delineation of the thermal history of magmas is quantitative knowledge of the pressure effect on the enthalpy of melting under dry conditions and in the presence of volatiles such as H₂O and CO₂. Unfortunately, these basic data cannot be obtained by standard calorimetric methods. Other methods for their direct measurement have not so far been used; therefore, attempts have been made to derive estimates of latent heats by indirect methods. Khitarov and Kadik (1973) concluded from thermodynamic estimates that there are large pressure effects on the enthalpy of melting of water-saturated silicate melts. Burnham and Davis (1974), on the other hand, derived from *PVT* data a mixing

enthalpy for albite-H₂O of the order of a few hundred calories per mole. The lack of direct measurements of melting enthalpy at pressure and the obvious discrepancy in the magnitude of the reported enthalpies made a direct measurement, under pressure and temperature, desirable.

This report summarizes preliminary results obtained on the enthalpy of melting of diopside under dry and water-saturated conditions. High-pressure differential thermal analysis (DTA), previously described by Rosenhauer and Eggler (*Year Book* 74, pp. 474-479), was utilized. Application of DTA to calorimetric measurements is common and is known as differential scanning calorimetry (DSC). Details of the method have been described by Rouquerol and Boivin (1972). Although with the DTA-based method the high accuracy of standard calorimetric measurements cannot be reached, the method is versatile and can be used in the study of reactions, such as nonquenchable phase transformations, that cannot be measured by calorimetry.

The underlying principle of the present method is a comparison of the DTA peak area resulting from melting of the sample with the area of an auxiliary peak generated under run conditions inside the DTA capsule. The auxiliary, artificial heat effect is produced by a small furnace for which the input heat can be determined very accurately by measurements of the current, the voltage, and the time during which power is applied to the furnace. It was found in all calibration experiments that under isothermal, isobaric conditions the input power is directly proportional to the peak area of the resulting auxiliary, artificial peak. Because of the symmetry in the arrangement of the sample and the auxiliary furnace (Fig. 95), there must also be a proportionality between the heat generated or absorbed in the sample and the resulting DTA peak.

Diopside used in this work was synthetic $\text{CaMgSi}_2\text{O}_6$ kindly provided by Dr. D. H. Eggler. DTA capsules were prepared from Pt tubing and contained two compartments to accommodate the sample and the auxiliary furnace assembly. The auxiliary furnace was approximately 5 mm long and consisted of 40 windings of 0.004-in Pt/Pt10Rh wire wound with 186 threads per inch on a four-hole ceramic capillary of 2-mm outside diameter. Approximate sizes and arrangement of the parts inside the DTA capsule are shown in Fig. 95. The assembled DTA capsule was loaded with 80-mg diopside and was welded shut. For each experiment a new capsule was prepared.

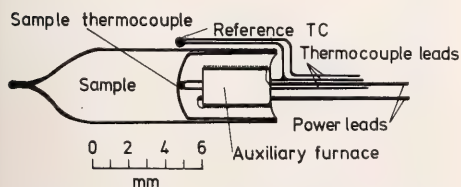


Fig. 95. The DTA capsule arrangement used in the present study. Dimensions are approximately to scale.

Enthalpy values were measured under isobaric conditions and involved determination of the input-output ratios (R) of the auxiliary furnace and measurement of the area under the DTA peak, representing the latent heat of the sample, on heating and on cooling. The ratio R is a relative number that is defined as the quotient of the input power of the auxiliary furnace and the resulting area of the output peak. During the experiment, R is determined in a series of measurements at various input energies above and below the melting point of the sample. A schematic sequence illustrating the variations of the parameters involved is depicted in Fig. 96. Although in theory this calibrating procedure could yield absolute enthalpy values, only the influence of pressure on the area of the DTA peak of the sample was evaluated. No assumptions on the absolute relationship between input power and resultant peak area were made, because the relationship will crucially depend on the geometry of the capsule arrangement and must be calibrated prior to the run with a sample of known heat content. In this study the relative enthalpy values obtained have been extrapolated to 1 atm; the enthalpy value at 1 atm was taken to be 85.5 cal/g.

Preliminary results obtained for the enthalpy of melting of diopside under dry and H_2O -saturated conditions are presented in Fig. 97. A significant difference in the effect of pressure under these conditions is apparent. The enthalpy of dry melting increases with pressure (curve *a*), whereas under H_2O -saturated conditions the latent heat drops within the first 1000 bars by about 18% to 70 cal/g and remains at that level, within experimental uncertainties, up to 4 kbar (curve *b*). Error bars show the maximum spread of at least two independent enthalpy determinations. Part of the dispersion in the measurements results from the calibration itself. Input-output ratios for samples above and below the melting point differ significantly in that under dry conditions R for the melted

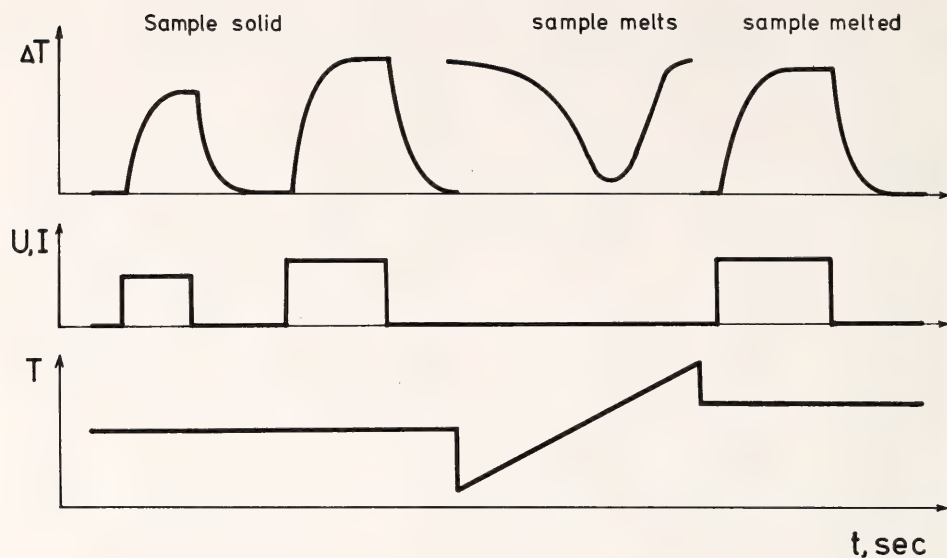


Fig. 96. Schematic sequence for enthalpy determination showing ΔT (T sample- T reference), power input of the auxiliary furnace (U , I), and T sample (T) as a function of time (t). Each determination involved at least four artificial DTA peaks above and four below the melting temperature, not all of which are shown, plus the DTA peak generated upon melting.

sample is always smaller than for the solid, whereas under H_2O -saturated conditions the opposite effect is found. Most likely this behavior is related to variation in the specific heat of the sample. Assuming that R is proportional to the heat capacity of the sample, the above results suggest that the heat capacity of the dry melt is larger than that of crystalline diopside, whereas the heat capacity of H_2O -saturated melt is smaller. The influence on R resulting from changes in thermal conductivity is thought to be small because of the homogeneous temperature distribution around the sample. No attempts have been made to overcome the problem of dispersion in measurements by averaging the results, a manipulation that would involve further assumptions. Experimentally this problem could be solved if the energy required to compensate the DTA effect of the sample could be generated continuously.

Although the uncertainties in the

present results do not make a detailed discussion desirable, it is useful to compare them with theoretically derived estimates. Using the data given by Yoder (*Year Book* 74, pp. 515-519), the pressure effect on the heat of melting of dry diopside may be calculated as 1.10 cal/g kbar. This value is consistent with the observed pressure dependency within the experimental uncertainties. Estimates of the effect of pressure for diopside under water-saturated conditions have been given by Khitarov and Kadik (1973), who concluded that the heat required to melt diopside under H_2O -saturated conditions at pressures between 1000 and 2000 bars is 25-40 cal/g, compared with 105 cal/g at 1 atm. The present experimental data are not in agreement with their estimates, and the differences are believed to be beyond the uncertainties of the method. It is likely, however, that part of the discrepancy may be accounted for in the extrapolation of their volume data.

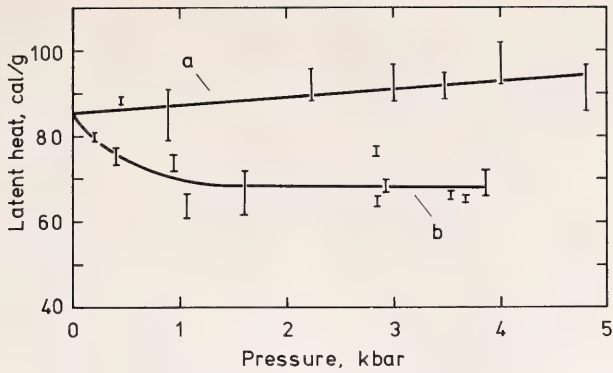


Fig. 97. Pressure effect on the enthalpy of melting of diopside under (a) dry and (b) H₂O-saturated conditions.

THE ADIABATIC GRADIENT AND
ADIABATIC COMPRESSIBILITY

Douglas Rumble

The adiabatic or isentropic gradient and the adiabatic compressibility of rocks and magmas are important reference parameters in geophysical studies of the earth's interior and in theories of magma ascent toward the earth's surface. The vertical temperature gradient necessary to initiate convection in the mantle is greater than the adiabatic gradient, but with prolonged convection it will tend to approach the adiabatic condition (Verhoogen, 1965). Estimates of the vertical distribution of density in the earth's interior using the Williamson-Adams equation (Williamson and Adams, 1923) make use of the inverse of the adiabatic compressibility, the adiabatic bulk modulus (Jeffreys, 1962, p. 159). Theories of magma generation by adiabatic ascent require that a parcel of magma or protomagma be thermally insulated from its surroundings for at least a part of the ascent in order to generate liquid and prevent its solidification. During such a process, the contents of the parcel undergo adiabatic decompression.

The usual equation for the adiabatic gradient given in geophysics textbooks (Jeffreys, 1962, p. 287, Eq. 5) and in textbooks on igneous petrology (Car-

michael, Turner, and Verhoogen, 1974, p. 349) is

$$\left(\frac{\partial T}{\partial P}\right)_s = \frac{\alpha_P T}{\rho \bar{C}_P} = \frac{\bar{V} \alpha_P T}{C_P}$$

where α_P is the isobaric thermal expansion coefficient, ρ is the density, (in moles/cm³), \bar{C}_P is the molar isobaric heat capacity, and \bar{V} is the molar volume of the substance in question. This equation is formally valid for a closed system consisting of but a single phase. The equation does not take into account thermodynamically the effect of the presence of different phases such as crystals, liquid, or vapor. Nor does it include the effects of changes in the chemical compositions and proportions of solid, liquid, or gaseous solutions subjected to adiabatic decompression. Measurement of the thermodynamic properties of solid, liquid, and gaseous phases of geological interest continues at an ever-increasing pace. Thus, the accumulation of data presents the opportunity to investigate the effects of multicomponent, multiphase equilibria on the previously used, simplified model of the adiabatic gradient.

The purpose of this report is (1) to present a thermodynamically rigorous derivation of equations for the adiabatic gradient and adiabatic compressibility in multicomponent, multiphase systems

and (2) to illustrate the nature of phase diagram effects on the adiabatic gradient, using data of Burnham and Davis (1971, 1974) on the system $\text{NaAlSi}_3\text{O}_8\text{-H}_2\text{O}$.

The derivation of equations for the adiabatic gradient and adiabatic compressibility is based on a method reviewed by Rumble (1974) yielding algebraic relationships between P , T , chemical potentials of phase components (μ_i), and chemical compositions of phases (X_{iA}), in multicomponent, multiphase systems. For present purposes, three additional variables are included: entropy of the chemical system (S_s), volume of the system (V_s), and bulk chemical composition of the system (X_{is}).

The goal of the analysis that follows is to obtain expressions for the partial derivatives $(\partial T/\partial P)$ and $(\partial V_s/\partial P)$ subject to the two constraints of constant entropy and constant bulk chemical composition of the system. For simplicity, the discussion will be limited to two-phase assemblages in a binary chemical system. The examples in this report together with the review of Rumble (1974) provide sufficient information to derive equations for more complicated systems. (Symbols are defined in Table 34.)

The variables S_s , V_s , and X_{is} may be introduced by considering the entropy and volume of a given chemical system as a function of P , T , phase composition, phase proportion, and system composition. For a binary chemical system consisting of two phases A and B ,

$$S_s = n_A \bar{S}_A + n_B \bar{S}_B$$

Dividing through by $(n_A + n_B)$ and rearranging gives

$$\bar{S}_s = X_{As} (\bar{S}_A - \bar{S}_B) + \bar{S}_B$$

and differentiation yields

$$d\bar{S}_s = d\bar{S}_B + X_{As} (d\bar{S}_A - d\bar{S}_B) + (\bar{S}_A - \bar{S}_B) dX_{As}$$

The term X_{As} may be expressed in terms

of X_{1A} , X_{1B} , and X_{1s} using the lever rule:

$$\frac{n_A}{n_B} = \frac{X_{1B} - X_{1s}}{X_{1s} - X_{1A}} = \frac{X_{As}}{1 - X_{As}}$$

or

$$X_{As} = (X_{1B} - X_{1s}) / (X_{1B} - X_{1A})$$

and differentiation yields

$$dX_{As} = [(X_{1B} - X_{1s})dX_{1A} + (X_{1s} - X_{1A})dX_{1B} + (X_{1A} - X_{1B})dX_{1s}] / (X_{1B} - X_{1A})^2$$

Finally, substituting the two equations

$$d\bar{S}_A = (\bar{C}_A^P/T)dT - (\bar{V}_A \alpha_A^P)dP + (\bar{S}_{1A} - \bar{S}_{2A})dX_{1A}$$

and

$$d\bar{S}_B = (\bar{C}_B^P/T)dT - (\bar{V}_B \alpha_B^P)dP + (\bar{S}_{1B} - \bar{S}_{2B})dX_{1B}$$

and the results obtained above gives

$$d\bar{S}_s = NdT - AdP + KdX_{1A} + MdX_{1B} + IdX_{1s} \quad (1)$$

A similar derivation yields an analogous equation for the volume of the system

$$d\bar{V}_s = AdT - BdP + CdX_{1A} + DdX_{1B} + EdX_{1s} \quad (2)$$

In addition to Equations 1 and 2, four other equations are required to describe the binary system of two phases. These include one Gibbs-Duhem equation for each phase

$$\bar{S}_A dT - \bar{V}_A dP + X_{1A} (d\mu_1 - d\mu_2) + d\mu_2 = 0 \quad (3)$$

$$\bar{S}_B dT - \bar{V}_B dP + X_{1B} (d\mu_1 - d\mu_2) + d\mu_2 = 0 \quad (4)$$

and one equation relating dP , dT , dX_{1A} , and another relating dP , dT , and dX_{1B} (Rumble, 1974, pp. 202-203)

$$-(\bar{S}_{1A} - \bar{S}_{2A})dT + (\bar{V}_{1A} - \bar{V}_{2A})dP - (d\mu_1 - d\mu_2) + \bar{G}_{11A}dX_{1A} = 0 \quad (5)$$

$$-(\bar{S}_{1B} - \bar{S}_{2B})dT + (\bar{V}_{1B} - \bar{V}_{2B})dP - (d\mu_1 - d\mu_2) + \bar{G}_{11B}dX_{1B} = 0 \quad (6)$$

In summary, there are six equations (1-6) for the nine unknowns dT , dP , $d\mu_1$, $d\mu_2$, dX_{1A} , dX_{1B} , dX_{1s} , $d\bar{S}_s$, and $d\bar{V}_s$. The expressions for $(\partial T/\partial P)_{\bar{S}_s, X_{1s}}$ and $(\partial \bar{V}_s/\partial P)_{\bar{S}_s, X_{1s}}$ are obtained by setting

$$\begin{aligned} \left(\frac{\partial T}{\partial P}\right)_{\bar{S}_s, X_{1s}} &= \frac{M\bar{G}_{11A}V_1 - K\bar{G}_{11B}V_2 + A\bar{G}_{11A}\bar{G}_{11B}(X_{1B}-X_{1A})}{M\bar{G}_{11A}S_1 - K\bar{G}_{11B}S_2 + N\bar{G}_{11A}\bar{G}_{11B}(X_{1B}-X_{1A})} \\ \left(\frac{\partial \bar{V}_s}{\partial P}\right)_{\bar{S}_s, X_{1s}} &= [\{(DK + MC)(\bar{S}_{1B} - \bar{S}_{2B}) + G_{11B}(NC - AK)\}V_2 \\ &\quad - \{(DK + CM)(\bar{S}_{2A} - \bar{S}_{1A}) - \bar{G}_{11A}(DN + AM)\}V_1 \\ &\quad + (BM - AD)\bar{G}_{11A}S_1 + (BK - AC)\bar{G}_{11B}S_2 \\ &\quad - (DK + CM)(\bar{S}_B - \bar{S}_A)(\bar{V}_{1B} - \bar{V}_{2B} - \bar{V}_{1A} + \bar{V}_{2A}) \\ &\quad + (A^2 - BN)\bar{G}_{11A}\bar{G}_{11B}(X_{1B} - X_{1A})]/[MG_{11A}S_1 \\ &\quad - K\bar{G}_{11B}S_2 + N\bar{G}_{11A}\bar{G}_{11B}(X_{1B} - X_{1A})] \end{aligned}$$

If only one of the phases (e.g., the liquid) is of variable composition, the equations simplify to

$$\left(\frac{\partial T}{\partial P}\right)_{\bar{S}_s, X_{1s}} = \frac{L(\bar{V}_A - \bar{V}_{2B}) + AX_{1B}\bar{G}_{11B}}{L(\bar{S}_A - \bar{S}_{2B}) + NX_{1B}\bar{G}_{11B}}$$

and

$$\left(\frac{\partial \bar{V}_s}{\partial P}\right)_{\bar{S}_s, X_{1s}} = \frac{(NJ - AL)(\bar{V}_A - \bar{V}_{2B}) + (BL - AJ)(\bar{S}_A - \bar{S}_{2B}) + X_{1B}\bar{G}_{11B}(A^2 - BN)}{L(\bar{S}_A - \bar{S}_{2B}) + NX_{1B}\bar{G}_{11B}}$$

The two sets of equations given above can be simplified and integrated by observing that in a divariant assemblage of phases, phase composition, X_{1A} and X_{1B} , is a function of P and T only. Thus, $(\partial T/\partial P)_{X_{1s}, \bar{S}_s}$ and $(\partial \bar{V}_s/\partial P)_{X_{1s}, \bar{S}_s}$ may be expressed as functions of P , T , and X_{1s} .

If the two phases both have fixed chemical composition, the equations simplify still more:

$$\left(\frac{\partial T}{\partial P}\right)_{\bar{S}_s, X_{1s}} = \frac{A}{N}$$

and

$$\left(\frac{\partial \bar{V}_s}{\partial P}\right)_{\bar{S}_s, X_{1s}} = \frac{A^2 - BN}{N}$$

The effects on adiabats of one-, two- and three-phase equilibria in the system $\text{NaAlSi}_3\text{O}_8\text{-H}_2\text{O}$ are illustrated in Fig. 98. Consider, for example, the path of adiabatic decompression along the adia-

$d\bar{S}_s = 0$ and $dX_{1s} = 0$, and by dividing through by dP . The resulting set of six inhomogeneous equations in six unknowns may be solved by Cramer's rule (Aitken, 1962, pp. 55-56).

bat labeled "98." At $P = 10$ kbar and $T = 950^\circ\text{C}$ and for a bulk composition of $X_{\text{H}_2\text{O},s} = 0.5$ (mole fraction), the system consists of 10% albite crystals and 90% liquid (i.e., melt). As adiabatic expansion proceeds, the remaining albite melts, until at approximately 3.5 kbar and 875°C the system contains liquid alone. The adiabat follows a steeper path through the one-phase field of melt. At 1.9 kbar and 860°C the liquid becomes saturated with vapor and adiabatic decompression accompanied by evolution of vapor proceeds along a less steep course. Crystals reappear as the univariant equilibrium, liquid = albite crystals + vapor, is reached at 1.5 kbar and 850°C . Adiabatic decompression continues along the univariant curve with a consequent temperature increase in the system until all the liquid is exhausted.

Isentropic paths of systems with lower water contents than those illustrated in

Fig. 98 are steeper (greater dP/dT) than those of Fig. 98. Moreover, with less H_2O , the one-phase field of melt and the two-phase field of melt + vapor are reduced in size.

The system $NaAlSi_3O_8-H_2O$ illustrates two contrasting styles of behavior in that adiabatic decompression along the univariant curve causes crystallization, whereas adiabatic decompression through the crystal + melt field (divariant equilibrium) results in melting. Thus, divariant adiabatic decompression is not an impediment to convection, whereas

univariant adiabatic decompression would tend to freeze rising convection currents.

The general features of the effects of multicomponent, multiphase equilibria on adiabatic decompression are as follows: (1) Within a given multiphase, multivariant P - T field, the slope of an adiabat depends not only on variation of α_P , and \bar{C}_P with P and T , but also on phase proportion and composition; (2) passage from higher to lower variance phase equilibria introduces discontinuities in the slope of adiabats.

TABLE 34. Explanation of Symbols

| | | | |
|--|--|-------|---|
| X_{1A} | mole fraction of component i in phase A . | A | $\equiv X_{As}\bar{V}_A\alpha_P^A + X_{Bs}\bar{V}_B\alpha_P^B$ |
| X_{1S} | mole fraction of total amount of component i in chemical system. | B | $\equiv -(X_{As}\bar{V}_A\beta_T^A + X_{Bs}\bar{V}_B\beta_T^B)$ |
| X_{As} | mole fraction of phase A in chemical system. | C | $\equiv X_{As}(\bar{V}_{1A} - \bar{V}_{2A}) + X_{As}(V_A - \bar{V}_B)/(X_{1B} - X_{1A})$ |
| \bar{V}_{1A} | partial molar volume of component i in phase A . | D | $\equiv X_{As}(\bar{V}_{1B} - \bar{V}_{2B}) - (\bar{V}_A - \bar{V}_B)(X_{1S} - X_{1A})/(X_{1B} - X_{1A})^2 - (\bar{V}_{1B} - \bar{V}_{2B})$ |
| \bar{V}_A | molar volume of phase A . | E | $\equiv (\bar{V}_B - \bar{V}_A)/(X_{1B} - X_{1A})$ |
| \bar{V}_s | total mean molar volume of chemical system. | N | $\equiv X_{As}\bar{C}_P^A/T + X_{Bs}\bar{C}_P^B/T$ |
| \bar{S}_{1A} | partial molar entropy of component i in phase A . | M | $\equiv X_{As}(\bar{S}_{1B} - \bar{S}_{2B}) + (\bar{S}_A - \bar{S}_B)(X_{1S} - X_{1A})/(X_{1B} - X_{1A})^2 + (\bar{S}_{1B} - \bar{S}_{2B})$ |
| \bar{S}_A | molar entropy of phase A . | K | $\equiv X_{As}(\bar{S}_{1A} - \bar{S}_{2A}) + X_{As}(\bar{S}_A - \bar{S}_B)/(X_{1B} - X_{1A})$ |
| \bar{S}_s | total mean molar entropy of chemical system. | I | $\equiv (\bar{S}_B - \bar{S}_A)/(X_{1B} - X_{1A})$ |
| μ_i | chemical potential of component i . | J | $\equiv X_{1s}(\bar{V}_A - \bar{V}_{2B})/(X_{1B})^2$ |
| \bar{G}_A | molar Gibbs free energy of phase A . | L | $\equiv X_{1s}(\bar{S}_A - \bar{S}_{2B})/X_{1B}^2$ |
| $\bar{G}_{11A} \equiv (\partial^2 \bar{G}_A / \partial X_{1A}^2)_{P,T}$ | | S_1 | $\equiv \bar{S}_A - \bar{S}_{2B} - X_{1A}(\bar{S}_{1B} - \bar{S}_{2B})$ |
| $\alpha_P^A \equiv ((\partial \bar{V}_A / \partial T)_{P,X_{1A}}) / \bar{V}_A$ | | S_2 | $\equiv \bar{S}_B - \bar{S}_{2A} - X_{1B}(\bar{S}_{1A} - \bar{S}_{2A})$ |
| $\beta_T^A \equiv -((\partial \bar{V}_A / \partial P)_{T,X_{1A}}) / \bar{V}_A$ | | V_1 | $\equiv \bar{V}_A - \bar{V}_{2B} - X_{1A}(\bar{V}_{1B} - \bar{V}_{2B})$ |
| $\bar{C}_P^A \equiv T(\partial \bar{S}_A / \partial T)_{P,X_{1A}}$ | | V_2 | $\equiv \bar{V}_B - \bar{V}_{2A} - X_{1B}(\bar{V}_{1A} - \bar{V}_{2A})$ |

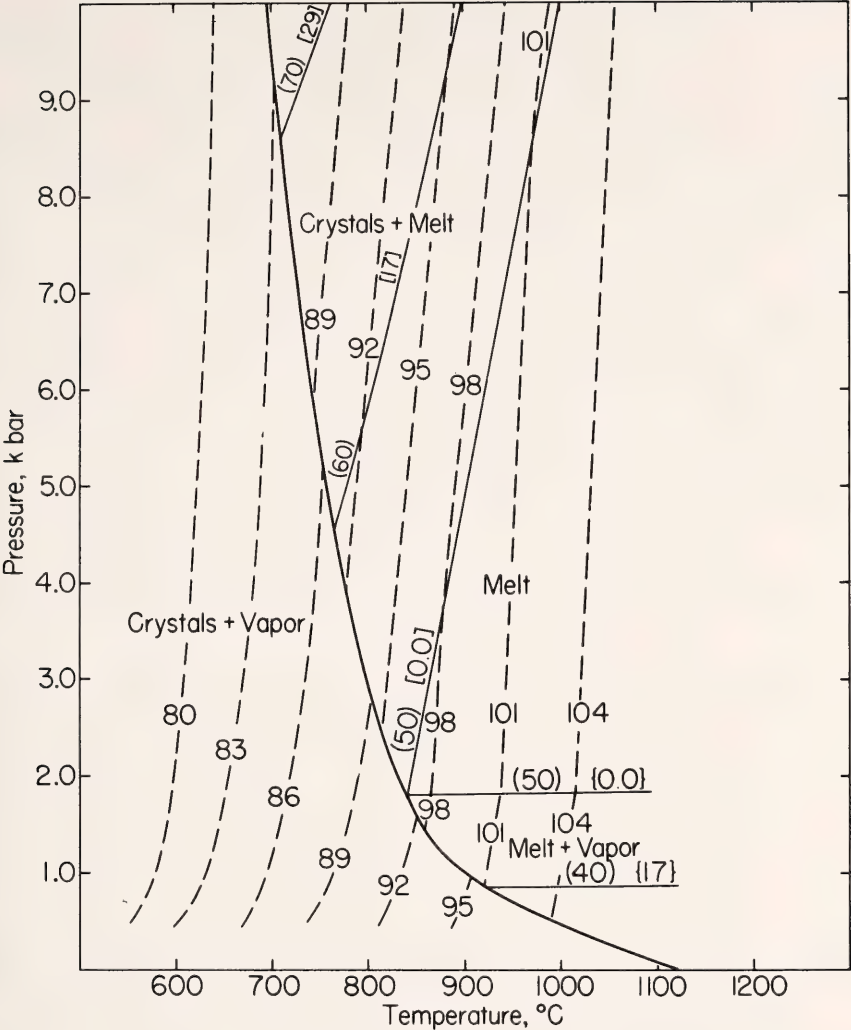


Fig. 98. Adiabats plotted on P - T diagram of the system $\text{NaAlSi}_3\text{O}_8\text{-H}_2\text{O}$ for bulk composition $X_{\text{H}_2\text{O}} = 0.5$ mole fraction. Dashed lines are adiabats and are labeled with numerical value of total mean molar entropy of system. Numbers in parentheses give mole percentage of H_2O in melt (i.e., liquid) in equilibrium with crystals (light solid lines with steep positive slope) or in equilibrium with vapor (light solid lines with gentle positive slope). Numbers in brackets give mole percentage of crystals in crystal + melt field. Numbers in braces give mole percentage of vapor in melt + vapor field. Systems containing less water than $X_{\text{H}_2\text{O}} = 0.5$ have steeper adiabats, and their one-phase fields of melt and their two-phase fields of melt + vapor are reduced in size.

TRACE ELEMENT PARTITIONING

RARE EARTH PARTITIONING BETWEEN
CRYSTALS AND LIQUID IN THE
UPPER MANTLE*Bjørn O. Mysen*

Rare earth elements (REE) are believed by some investigators to be indicators of conditions of formation of partial melts in the upper mantle (e.g., Gast, 1968; O'Nions and Clark, 1972; Mysen and Holloway, this Report). However, accurate determinations of REE partition coefficients between upper mantle minerals and silicate melts are scarce (Shimizu and Kushiro, 1975; Irving and Frey, 1976). Experiments by Irving and Frey (1976) indicate that REE partition coefficients depend on major element composition of both crystals and liquid. Data by Mysen (1976a) and Wood (this Report; personal communication, 1976) suggest that crystal-liquid partition coefficients also depend on the amount of REE present. In addition, in light of the structural incompatibility of REE with mantle minerals, it is possible that REE partition coefficients vary with pressure and temperature. In view of the importance assigned to rare earth fractionation during magma genesis, a detailed study of REE partitioning between crystals and liquids under upper mantle conditions has been initiated. Samarium, an REE of intermediate atomic number, was the first of this group of elements to be subjected to a detailed study.

The experiments were performed in a solid-media, high-pressure apparatus similar to the design of Boyd and England (1960), using the piston-out technique with no friction correction of the pressure. Sealed Pt capsules were used as containers. Temperatures were measured with Pt-Pt90Rh10 thermocouples and with no pressure correction on the emf output.

Starting material (PFS 5043) and major element compositions of phases present in experimental run products were

similar to those reported for the nickel partitioning experiments presented by Mysen (this Report). In all experiments, forsterite and aluminous enstatite coexist with hydrous silicate liquid of haplobasaltic composition. Radioactive samarium-151 was added in chloride solution together with sufficient H₂O to saturate the silicate melt (12 wt % H₂O in melt at 10 kbar and 17 wt % H₂O in melt at 20 kbar). The samarium content of the phases was determined with β -track counting (Mysen and Seitz, 1975) using K-5 and K-2 nuclear emulsions (supplied by Ilford Co., England). The K-2 emulsions are less sensitive than the K-5 and were used for high activity of samarium to increase exposure times and therefore decrease uncertainties. The uncertainty ($\pm 1\sigma$) of individual analyses is 2%–3% (relative), resulting in 4%–5% relative uncertainty in partition coefficients.* Samarium contents of the liquids were recalculated to an H₂O-free basis.

Samarium concentrations of olivine coexisting with hydrous silicate liquid at 10 and 20 kbar and 1025° and 1075°C appear in Fig. 99. For all compositions in this system (coexisting opx, ol, and liquid), $K_{\text{Sm}^{\text{ol-llq}}}$ remains constant to about 40 ppm Sm dissolved in the liquid. The $K_{\text{Sm}^{\text{ol-llq}}}$ is plotted against the Sm content of olivine in Fig. 100. It appears that (1) the $K_{\text{Sm}^{\text{ol-llq}}}$ increases with increasing temperature (0.25%/°C) within the samarium concentration range of constant $K_{\text{Sm}^{\text{ol-llq}}}$; (2) the partition coefficient increases with decreasing pressure (0.75%/kbar at 1075°C relative to the value at 20 kbar); (3) the concentration range of Sm in olivine with constant $K_{\text{Sm}^{\text{ol-llq}}}$ increases with increasing temperature (0.6 ppm Sm in olivine at

* Partition coefficient, $K_{i^{\alpha-\beta}} = \text{ppm of element } i \text{ in phase } \alpha / \text{ppm of element } i \text{ in phase } \beta$. Because of the low Sm contents used in these experiments and the similarity of major element compositions, the $K_{i^{\alpha-\beta}}$ is nearly proportional to Nernst's distribution coefficient.

20 kbar and 1025°C versus 0.9 ppm Sm in olivine at 20 kbar and 1075°C) and probably with decreasing pressure.

Samarium concentrations of coexisting orthopyroxene and hydrous silicate liquid are plotted in Fig. 101. As with the olivine-liquid pair, there is an upper limit of Sm content in the two phases

where the $K_{\text{Sm}}^{\text{opx-liq}}$ decreases with further increase of Sm content. For all pressures and temperatures investigated, this limit corresponds to about 20 ppm Sm in the liquid (slightly above 1 ppm Sm in orthopyroxene). The rate of decrease of $K_{\text{Sm}}^{\text{opx-liq}}$ with increasing Sm content is smaller the higher the tem-

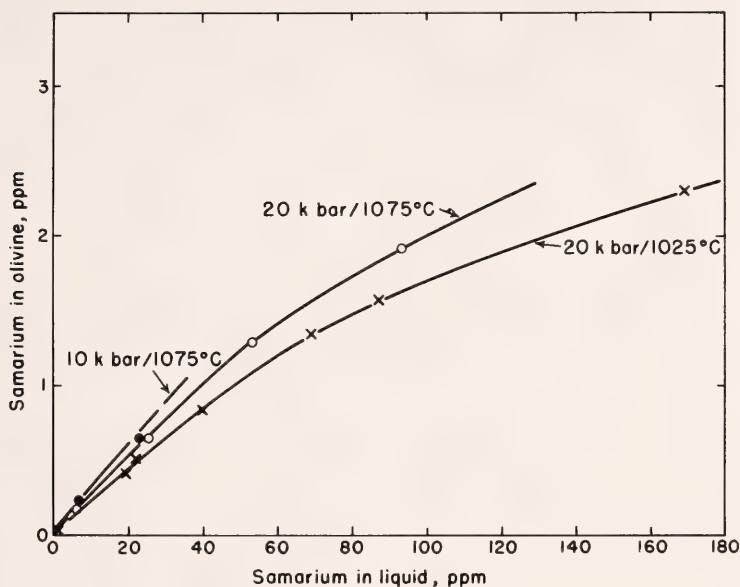


Fig. 99. Samarium in coexisting olivine and H_2O -saturated silicate liquid at 10 and 20 kbar, 1025° and 1075°C.

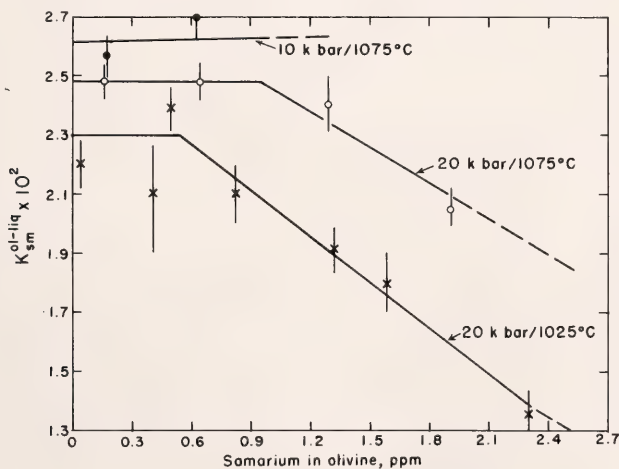


Fig. 100. Partition coefficient of samarium between olivine and hydrous silicate liquid versus samarium content of olivine at 10 and 20 kbar, 1025° and 1075°C. Length of error bars = 2σ .

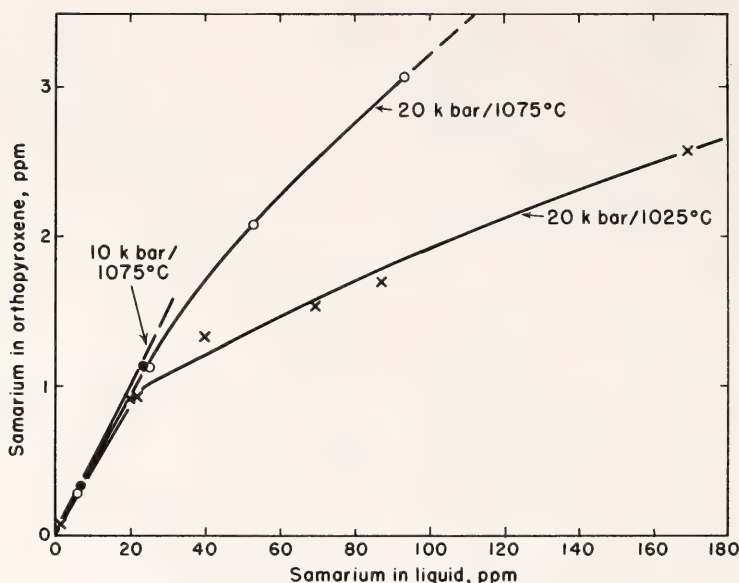


Fig. 101. Samarium in coexisting orthopyroxene and H_2O -saturated liquid at 10 and 20 kbar, 1025° and 1075°C.

perature (Fig. 102). As with the olivine-liquid pair, the Sm concentration of the crystalline phase (opx) where the $K_{Sm}^{opx-liq}$ becomes dependent on Sm content, increases with increasing temperature (1 ppm and 1.3 ppm at 1025° and 1075°C, respectively). In contrast to the olivine-liquid pair, the $K_{Sm}^{opx-liq}$ decreases with increasing temperature (0.2%/°C relative to the value at 1025°C). The $K_{Sm}^{opx-liq}$ increases by about 1%/kbar as the pressure is lowered.

Deviations from constant $K_{Sm}^{crystal-liquid}$ as a function of Sm content could relate to variations of the activity coefficient of samarium in crystals ($\gamma_{Sm}^{crystal}$), in liquid, or in both. In this system the Sm content of the liquid is 20 ppm where the $K_{Sm}^{opx-liq}$ begins to vary, whereas the concentration of Sm in liquid is 40 ppm before K_{Sm}^{ol-liq} becomes a variable dependent on Sm content. The variations of the partition coefficients result from the $\gamma_{Sm^{3+}}^{crystal}$ becoming a compositionally dependent variable, whereas the $\gamma_{Sm^{3+}}^{liquid}$ remains constant.

Cations of samarium, as well as other

REE, are large ($\sim 1\text{\AA}$) trivalent cations. Based on size considerations alone, the mixing properties of Sm^{3+} in olivine and orthopyroxene are probably far from ideal. In addition, substitution of Sm^{3+} must be electrically balanced, perhaps by an $MgSi \rightleftharpoons SmAl$ or an $MgSi \rightleftharpoons SmSm$ type substitution. The orthopyroxene from the experimental run products contains 3.5–5 wt % Al_2O_3 (Mysen, this Report) so that charge-balancing involving trivalent cations is not a problem in orthopyroxene. Aluminum substitution in olivine is only minor (< 0.05 wt % Al_2O_3), hence there are less favorable conditions for solid solution of Sm^{3+} in olivine, as also evidenced by the 100% larger $K_{Sm}^{opx-liq}$ than K_{Sm}^{ol-liq} . The similarity of the Sm contents of orthopyroxene and olivine where the partition coefficients become compositionally dependent suggests that the cationic radius plays a major role in substituting REE in both pyroxenes and olivine.

For the application of these data to magma genesis in the upper mantle, similar data are needed for the parti-

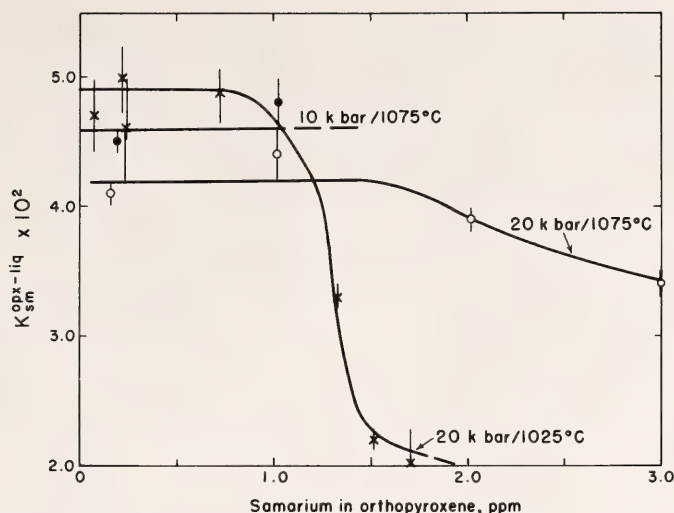


Fig. 102. Partition coefficient of samarium between orthopyroxene and hydrous silicate liquid versus samarium content of orthopyroxene at 10 and 20 kbar, 1025° and 1075°C. Length of error bars = 2σ .

tioning of samarium between liquid, clinopyroxene, and garnet. It is also necessary to know the effects of the presence of orthopyroxene, clinopyroxene, olivine, and garnet on the individual crystal-liquid partition coefficients. However, the principles developed here for simple systems most likely apply to complex natural rocks as well. The implications of these principles for the application of REE data to magma genesis are discussed below. Wood (personal communication; this Report) has shown that $K_{\text{Sm}}^{\text{cpx-liq}}$ and $K_{\text{Sm}}^{\text{ga-liq}}$ decrease with increasing temperature and increasing pressure. Furthermore, the partition coefficients remain constant to only several parts per million Sm in the crystals. Thus, the solution behavior of REE in garnet and clinopyroxene is similar to that in orthopyroxene and olivine, and probably also in a peridotite upper mantle.

Rare earth elements are chemically quite similar. Consequently, it is expected that REE other than samarium will partition between upper mantle crystals and partial melts in a way similar to that of Sm, and the individual

partition coefficients will remain constant to only a few parts per million of the individual element. Because the ionic radii of REE increase with increasing atomic number, the concentration ranges of behavior of the individual REE according to Henry's law most likely decrease with increasing atomic number. An added complexity of the chemical similarity of the REE is that the $K_{\text{REE}}^{\text{crystal-liquid}}$ probably will depend on the total REE content of the phase in a manner very similar to that seen for samarium here. Thus, even though individual REE contents of upper mantle phases rarely exceed 1–2 ppm, the total amount of REE does, and the partition coefficients of individual REE may change as a function of total REE content.

SAMARIUM DISTRIBUTION BETWEEN GARNET AND LIQUID AT HIGH PRESSURE

B. J. Wood

The rare earth element (REE) contents of volcanic rocks may, in principle, give considerable information about the origin and evolution of the melts con-

cerned (e.g., Gast, 1968). Although a number of attempts to model petrogenetic processes have been based on REE contents of volcanic rocks, these models generally depend on poorly constrained values of liquid-solid partition coefficients. It was the purpose of this study to determine experimentally the partition coefficient K_D for a typical rare earth element, Sm, between garnet of varying composition and liquid at high pressure.

The partitioning of Sm between garnet and liquid has been studied in the systems $\text{Mg}_3\text{Al}_2\text{Si}_3\text{O}_{12}\text{-H}_2\text{O}$ and $\text{CaMgSi}_2\text{O}_6\text{-Mg}_3\text{Al}_2\text{Si}_3\text{O}_{12}\text{-H}_2\text{O}$ and in complex garnets crystallized from Kilauea 1921 basalt. Experiments were performed in a solid-media, high-pressure apparatus using the piston-out technique with no correction for friction. Temperatures were measured with Pt/Pt90Rh10 thermocouples.

Radioactive ^{151}Sm in chloride solution was added to the glass and crystalline starting materials, and the mixtures were ground under acetone. At high samarium concentrations (>50 ppm) samarium in excess of 50 ppm was added as stable Sm_2O_3 . After each run the concentrations of ^{151}Sm tracer in garnet and liquid were measured by placing a polished section of the charge in contact with a nuclear emulsion (K-5 type, Ilford Co., England). The densities of β -particle tracks were then determined in the manner described by Mysen and Seitz (1975). $\text{NaAlSi}_3\text{O}_8$ glasses (Mysen, this Report) containing known amounts of ^{151}Sm were used as standards.

Garnet-Liquid Partitioning in the System $\text{Mg}_3\text{Al}_2\text{Si}_3\text{O}_{12}\text{-H}_2\text{O}$

Initial experiments were performed at 30 kbar and temperatures of $1200^\circ\text{--}1500^\circ\text{C}$ on a starting material consisting of cordierite, forsterite, spinel, and glass to which 10.3 ppm Sm had been added. The charges were sealed, together with small amounts of H_2O , in Pt capsules. All experiments were brought to the desired pressure and temperature and run for times of 1 hr (at 1500°C) to $12\frac{1}{2}$

hr (at 1200°C). In this system pure pyrope garnet coexists with H_2O -undersaturated melts, which from mass-balance considerations were calculated to contain between 24.2 (at 1200°C) and 3.31 (at 1500°C) wt % H_2O . Large (up to $50\text{ }\mu\text{m}$) quench orthopyroxenes were observed in all runs. Fortunately it was found that the Sm content of the quench crystals is exactly the same as that of the remaining glass. Hence quench crystals do not present any analytical problem if the β -track technique is used to measure Sm contents. Zoning of the garnets with respect to samarium was not observed, even in $40\text{-}\mu\text{m}$ -diameter crystals.

The partition coefficient $K_D (= C_{\text{Sm}}^{\text{gt}}/C_{\text{Sm}}^{\text{liq}}$ with concentration of Sm in ppm) was found to increase regularly from 0.079 at 1200°C and 30 kbar (1.46 ppm Sm in garnet) to 0.172 at 1500°C and 30 kbar (2.90 ppm Sm in garnet) (Fig. 103). This variation is due to changing temperature or changing liquid composition (variable H_2O content) or to a combination of these parameters. It is believed, however, that temperature is the dominant factor because an experiment at 40 kbar and 1500°C gave a value

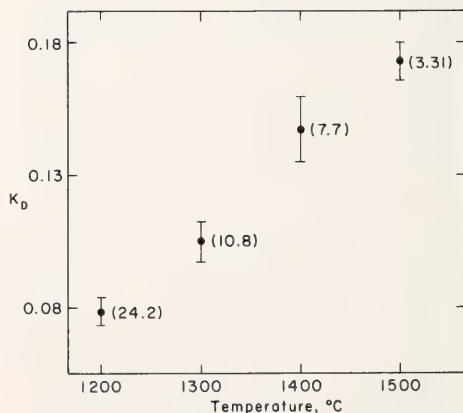


Fig. 103. $K_D (= \text{Sm}^{\text{gt}}/\text{Sm}^{\text{liq}})$ as a function of temperature in the system $\text{Mg}_3\text{Al}_2\text{Si}_3\text{O}_{12}\text{-H}_2\text{O}$ at 30 kbar. Vertical error bars refer to 1 standard deviation. Values in parentheses are H_2O contents (wt %) of the liquids. Estimated temperature uncertainty is $\pm 10^\circ\text{C}$.

of K_D (0.196), little different from that obtained at 30 kbar and 1500°C despite a considerable difference in liquid composition, 10.3% H_2O as opposed to 3.31% H_2O . A considerable amount of additional work will be needed before the effects on K_D of pressure, temperature, and liquid composition can be separated and fully characterized.

Experiments were performed at 30 kbar and 1500°C to determine the effect of varying the total samarium content of the system on the observed value of K_D . The results, shown in Fig. 104, indicate that at low Sm concentrations ($C_{Sm}^{gt} < 5$ ppm) the partition coefficient is strongly dependent on samarium content, whereas at higher concentrations K_D is constant. Drake and Weill (1975) obtained a result similar to the latter for plagioclase-liquid partitioning involving a substitution ($Sm^{3+} + Al^{3+}$ for $Ca^{2+} + Si^{4+}$) analogous to that under consideration here. The region of constant K_D ($C_{Sm}^{gt} > 5$ ppm) is tentatively ascribed to Henry's law of behavior of liquid and solid phases. The composition-dependent region shown in Fig. 104 may be due to two mechanisms of substitution of Sm into garnet. A small amount of Sm may enter defects in the garnet structure. At high concentrations, however, Sm substitution is almost certainly as charge-balanced $Sm_3Al_5O_{12}$ "molecule" with Sm occupying the eight-coordinated cubic

site. The former "defect" mechanism will have a large influence on K_D at low samarium concentrations, but its effect falls off with increasing Sm content of the garnet. To test the defect hypothesis an experiment was performed on a bulk composition containing 1.4 ppm Sm and 88 ppm of stable dysprosium. The garnet-liquid partition coefficient at 30 kbar and 1500°C was observed to drop from 0.193 ($\sigma = 0.015$) when Dy-free to 0.142 ($\sigma = 0.011$) in the presence of Dy. Because the small amount of Dy present is unlikely to alter the activity coefficient for the $Sm_3Al_5O_{12}$ component of the garnet, it seems probable that the dysprosium saturates the small number of defects present, forcing almost all Sm substitution to be in the cubic sites.

Garnet-Liquid Partition of Sm in Ca- and Fe-Bearing Systems

Addition of calcium to the $Mg_3Al_2Si_3O_{12}$ - H_2O system ought, in principle, to increase K_D for samarium because the Sm^{3+} ion is larger than Mg^{2+} and addition of Ca^{2+} to pyrope garnet increases the size of the cubic site. Thus, addition of Ca should produce a cubic site into which Sm^{3+} enters more readily than it does in the site present in pure pyrope.

Shimizu and Kushiro (1975) have determined the partition of Sm and other REE between garnet and H_2O -undersaturated melt in the system CaO - MgO - Al_2O_3 - SiO_2 at 30 kbar and 1275°C. Using the differential dissolution technique (DDT) and analysis by isotope dilution, these authors obtained a K_D of 0.217. This result has been checked by the β -track method, using the same starting material (glass of diopside₃₀pyrope₇₀ composition) as that used by Shimizu and Kushiro. For garnet of composition $(Ca_{0.10}Mg_{0.90})Al_2Si_3O_{12}$ and a bulk composition containing 11.2 ppm Sm, K_D was determined to be 0.197 ($\sigma = 0.013$). Agreement with the DDT result obtains and demonstrates that a relatively small change in bulk composition produces (at fixed pressure and temperature) a large change in K_D . In the $Mg_3Al_2Si_3O_{12}$ - H_2O

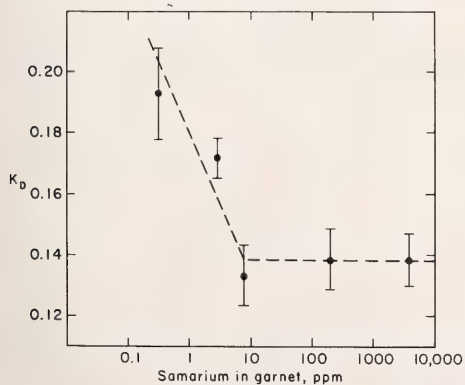


Fig. 104. K_D as a function of Sm content of garnet at 30 kbar and 1500°C. Uncertainties refer to ± 1 standard deviation.

system, K_D at 30 kbar/1275°C should, from Fig. 104, be approximately 0.095.

An experiment on Kilauea 1921 basalt produced a result similar to that obtained in the diopside-pyroxene system. At 30 kbar and 1240°C Kilauea 1921 basalt with 6.5% H_2O gives garnet of the approximate composition $(Ca_{0.22}Mg_{0.41}Fe_{0.37})Al_2Si_3O_{12}$, clinopyroxene, and liquid. With 14 ppm samarium in the system, K_D was found to be 0.215 ($\sigma = 0.013$). This value of K_D is over twice that found for the system $Mg_3Al_2Si_3O_{12}-H_2O$ (0.09) under the same physical conditions and with similar Sm content.

Conclusions

Experiments on systems approximating to natural basalts yield values of K_D close to 0.2 at 30 kbar and 1240°–1280°C. These results are in reasonable agreement with previous estimates based on natural phenocryst matrix partition data (Shimizu, 1975; Kay and Gast, 1973) and should facilitate modeling of petrogenetic processes for physicochemical conditions close to those of the experiments.

It has been found, however, that K_D is strongly dependent on both temperature and bulk composition of the system under consideration. Thus, the results obtained here cannot be used if large temperature, pressure, or compositional extrapolations are necessary. In the system $Mg_3Al_2Si_3O_{12}-H_2O$, K_D increases by a factor of 2 between 1200° and 1500°C at 30 kbar. In addition, partition coefficients in this system are smaller than those observed in systems containing calcium and iron. Apart from the influence of major element chemistry, it has been found that at low samarium concentrations ($C_{sm}^{gt} < 5$ ppm) the partition coefficient also depends on the Sm content of the garnet. This compositional dependence, which disappears at higher Sm contents or if a small amount of another REE is added, is probably due to the substitution of a small amount of Sm into defects in the garnet structure. The extent to which K_D in natural systems depends on Sm content is as yet unknown,

but it is likely that the presence of moderate concentrations of other REE in natural garnets suppresses the influence of any defects in a manner analogous to that described above. Thus K_D in natural systems should be independent of Sm content of the garnet.

NICKEL PARTITIONING BETWEEN UPPER MANTLE CRYSTALS AND PARTIAL MELTS AS A FUNCTION OF PRESSURE, TEMPERATURE, AND NICKEL CONCENTRATION

Bjørn O. Mysen

Models for magma generation can be evaluated by considering trace element partitioning between magma and possible coexisting crystalline phases. Such evaluation requires reliable trace element partition coefficients as a function of both intensive and extensive variables and knowledge of the melting reactions involved in the magma genesis. Melting reactions describing magma formation by partial melting of peridotite mantle have been discussed by Kushiro and Yoder (*Year Book 73*, pp. 266–269) and by Mysen and Kushiro (this Report); however, experimental data on trace element partitioning are scarce. The functions describing the dependence of partition coefficients on intensive and extensive variables are virtually unknown. Irvine and Kushiro (this Report) have shown effects of liquid composition on partition coefficients of nickel between silicate melts and olivine. This report discusses the behavior of nickel in a system with forsterite, aluminous enstatite, and hydrous silicate liquid (12–17 wt % H_2O) of haplobasaltic composition as coexisting phases. The bulk composition of the starting material is in the system Fo-Ab₅₀An₅₀-SiO₂-H₂O. The phase equilibria of the system relevant to the present study have been described by Kushiro (*Year Book 73*, pp. 244–248). A composition, PFS 5043 (plagioclase₅₀ [An₅₀Ab₅₀], forsterite₄₃silica₇), within the primary phase field of olivine at 10

and 20 kbar was selected as starting material. Sufficient H₂O was added to saturate the silicate liquid. The range of temperature of the experiments was 1025°–1075°C.

Starting material was a fine-grained oxide mixture of the silicate components. Nickel-63 was added in chloride solution. With more than 200 ppm Ni in the system, additional nonradiogenic nickel was added as NiO. All experiments were carried out in solid-media, high-pressure apparatus (Boyd and England, 1960) using sealed Pt₉₅Au₅ capsules as sample containers. Run durations were from 3 days at 1075°C to 5 days at 1025°C. The individual grains in a charge grew during the entire run, as evidenced by 5–15 μm grains after 24 hr, compared with more than 50 μm after 5 days. After 24 hr, the nickel is heterogeneously distributed between different grains and within individual crystals; however, such chemical heterogeneities disappeared after 3 days (at 1075°C) and 5 days (at 1025°C), indicating that the system equilibrated with respect to Ni distribution between the individual phases with these run durations.

Nickel contents were determined with β-track counting (Mysen and Seitz, 1975) using nickel-63 as the source of β tracks and K-5 nuclear emulsions supplied by Ilford Co., England, to detect the β activity. The data were corrected for collision loss in both liquids and crystals using techniques and data from Berger and Selzer (1964) and Mysen and Seitz (1975). The nickel contents of water-saturated liquids were recalculated to an H₂O-free basis using the H₂O solubility data of Boettcher and Wyllie (1969) and Burnham and Davis (1974).

Major element data for coexisting phases are shown in Table 35. Nickel partitioning data for olivine and liquid are shown in Fig. 105A, and those for coexisting orthopyroxene and liquid, in Fig. 105B. The olivine-liquid data at 20 kbar and 1075°C extended to about 10 wt % Ni in the olivine appear in Fig. 106. The data are plotted as K_{Ni}^{ol-liq} and $K_{Ni}^{opx-liq}$ versus nickel content of liquid in Fig. 107. It should be emphasized that the absolute values of the partition coefficients (defined as parts per million Ni in opx [or ol]/parts per million Ni in

TABLE 35. Major Element Compositions of Crystals and Liquids

| Phase: | 10 kbar, 1075°C | | | 20 kbar, 1075°C | | | 20 kbar, 1025°C | | |
|--------------------------------|-----------------|--------------------|-------|-----------------|--------------------|-------|-----------------|--------------------|-------|
| | Olivine | Ortho- pyroxene | Liq.* | Olivine | Ortho- pyroxene | Liq.† | Olivine | Ortho- pyroxene | Liq.‡ |
| SiO ₂ | 41.93 | 56.76 | 50.9 | 42.90 | 57.76 | 51.9 | 43.6 | 55.0 | 50.4 |
| Al ₂ O ₃ | 0.05 | 3.16 | 23.1 | 0.02 | 2.56 | 25.4 | ... | 6.4 | 25.8 |
| MgO | 56.07 | 37.69 | 12.7 | 56.40 | 38.41 | 10.1 | 56.0 | 37.4 | 9.2 |
| CaO | 0.10 | 0.64 | 10.2 | 0.05 | 0.53 | 9.5 | ... | 0.51 | 11.1 |
| Na ₂ O | 0.07 | 0.03 | 3.1 | ... | 0.06 | 3.0 | ... | 0.03 | 3.5 |
| Totals | 98.21 | 98.29 | 100.0 | 98.97 | 98.41 | 100.0 | 99.6 | 99.34 | 100.0 |
| | O = 4 | O = 6 | | O = 4 | O = 6 | | O = 4 | O = 6 | |
| Si | 1.000 | 1.934 | | 1.010 | 1.947 | | 1.022 | 1.854 | |
| Al ^{IV} | 0.001 | 0.066 | | ... | 0.053 | | ... | 0.146 | |
| Al ^{VI} | ... | 0.061 | | ... | 0.045 | | ... | 0.108 | |
| Mg | 1.993 | 1.914 | | 1.980 | 1.975 | | 1.956 | 1.890 | |
| Ca | 0.002 | 0.023 | | ... | 0.020 | | ... | 0.018 | |
| Na | 0.004 | 0.001 | | ... | 0.001 | | ... | ... | |

* Recalculated from oxide total = 88.0 wt % (H₂O content = 11.8 wt %).

† Recalculated from oxide total = 82.9 wt % (H₂O content = 17.2 wt %).

‡ Recalculated from oxide total = 81.0 wt % (H₂O content = 17.2 wt %).

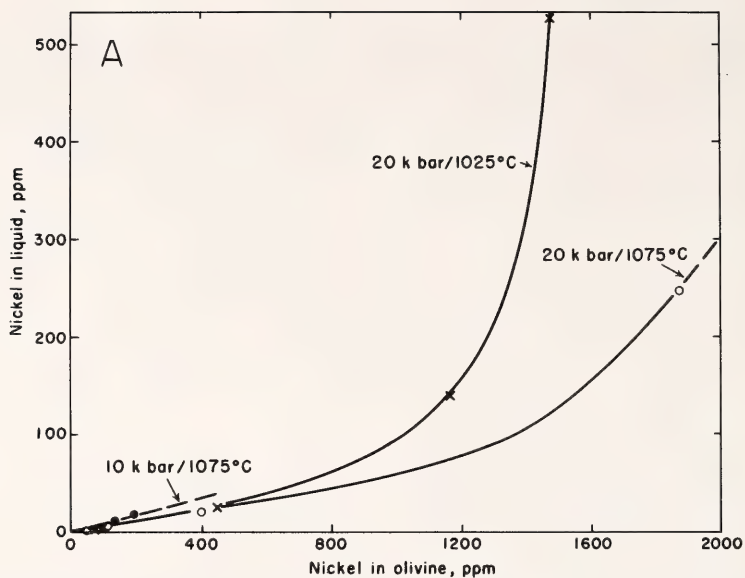


Fig. 105A. Nickel partitioning between olivine and hydrous silicate liquid at 10 and 20 kbar, 1025° and 1075°C.

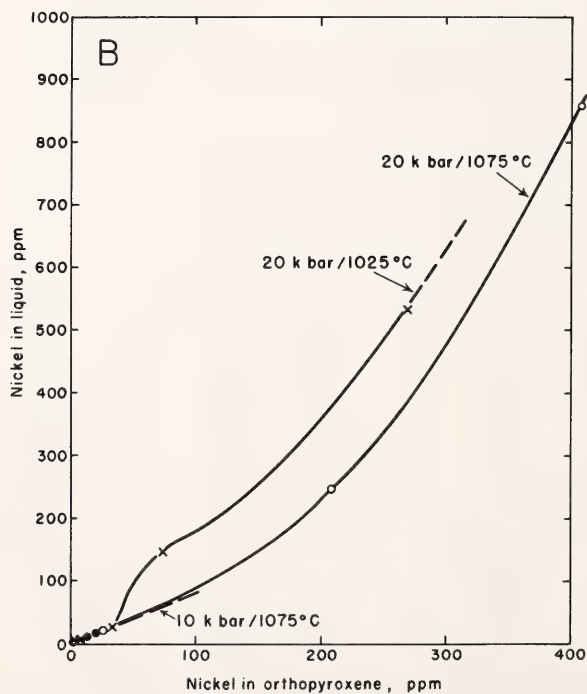


Fig. 105B. Nickel partitioning between orthopyroxene and hydrous silicate liquid at 10 and 20 kbar, 1025° and 1075°C.

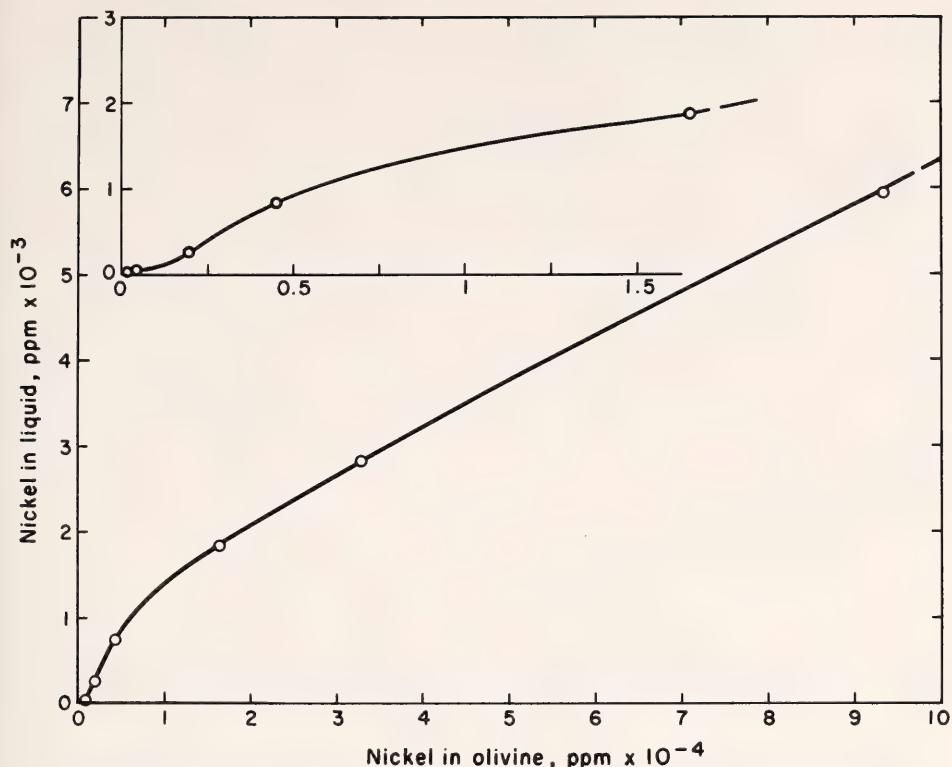


Fig. 106. Nickel partitioning between olivine and liquid to about 10 wt % Ni in olivine.

liquid) apply only to this particular system (coexisting opx, ol, and liquid) and should not be applied to more complex natural rock systems without information on the effects of other phases, the proportions of phases, and possible temperature and pressure effects. Four features of the data warrant comment. (1) The partition coefficient remains constant from the origin to about 50 ppm nickel dissolved in the liquid. (2) The nickel partition coefficients between olivine and liquid are slightly pressure and temperature dependent. Within the nickel concentration range of constant K_{Ni}^{ol-liq} , the partition coefficient is 15.5 ± 0.7 at 20 kbar and 1025°C , 14.1 ± 0.9 at 20 kbar and 1075°C , and 12.0 ± 0.4 at 10 kbar and 1075°C . (3) At least at 20 kbar and 1075°C , the partition coefficient K_{Ni}^{ol-liq} decreases and passes through a minimum with increasing Ni

content in the system. (4) The $K_{Ni}^{opx-liq}$ is near 1 but decreases to less than 1 with increasing nickel content of the system. The effects of pressure and temperature on the nickel partition coefficient between orthopyroxene and liquid at high pressure appear smaller than for the pair olivine-liquid.

The simple partition coefficient $K_i^{\alpha-\beta}$, as used here (parts per million of element i in phase α /parts per million of element i in phase β), is proportional to the Nernst distribution coefficient with low concentrations of element i , provided the ratio of activity coefficients, $\gamma_i^\alpha/\gamma_i^\beta$, is constant. Unless the ratio remains constant while the individual activity coefficients (γ_i^α and γ_i^β) vary (a very unlikely situation), the concentration range of element i where $K_i^{\alpha-\beta}$ is constant is also the concentration range where the solubility behavior of i in

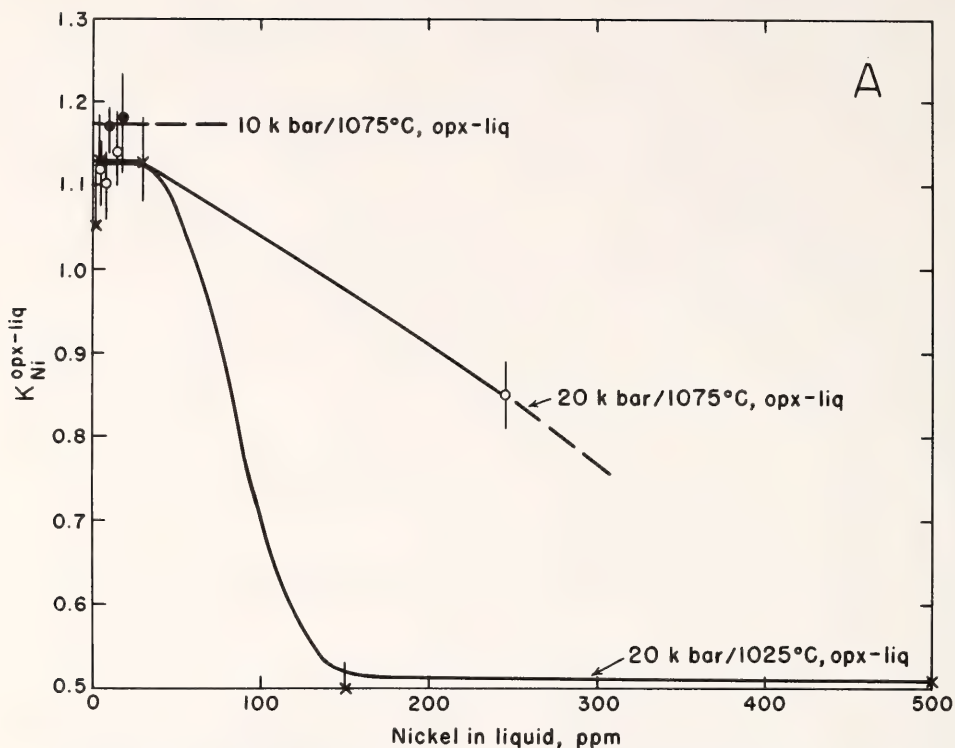


Fig. 107A. Partition coefficient, $K_{\text{Ni}}^{\text{opx-liq}}$, as a function of nickel content of liquid. Length of error bars = 2σ .

phases α and β obeys Henry's law. Thus, the data shown here (Figs. 105–107) indicate that below about 1000 ppm Ni in olivine (≤ 50 ppm Ni in liquid), the solution of nickel in both silicate liquid and olivine is according to Henry's law. Similarly, between 50 and 100 ppm Ni can enter aluminous enstatite before the partition coefficient, $K_{\text{Ni}}^{\text{opx-liq}}$, begins to decrease.

Mysen (this Report) suggests that $\gamma_{\text{REE}}^{\text{liq}}$ of hydrous silicate liquids remains constant to at least 40 ppm REE in the liquid. It is therefore unlikely that the $\gamma_{\text{Ni}}^{\text{liq}}$ of similar silicate liquids varies within a similar concentration interval of nickel. Under such circumstances, the variations of the partition coefficients between olivine and liquid and orthopyroxene and liquid shown here must reflect deviations from Henry's law in the crystalline phase. For (Ni,

Mg) solid solutions in olivine, the data of Matsui and Syono (1968), Huggins (1973), and Rajamani, Brown, and Pre-witt (1975) show clear preference of Ni for the M1 site and show a positive volume of mixing along the join Ni_2SiO_4 – Mg_2SiO_4 . These relations indicate that (Ni,Mg) solid solutions in olivine deviate from ideality. Thus, one would expect the partition coefficient of nickel between olivine and hydrous silicate liquid to change as the nickel content of the olivine is varied. Deviations from ideality of the (Ni,Mg) solid solutions would decrease with increasing temperature. The function $K_{\text{Ni}}^{\text{ol-liq}} = f(X_{\text{Ni}})$ would therefore show less extreme variations with increasing temperature. Such an explanation agrees well with the data for nickel partitioning between hydrous liquid and olivine shown here (Figs. 105–107).

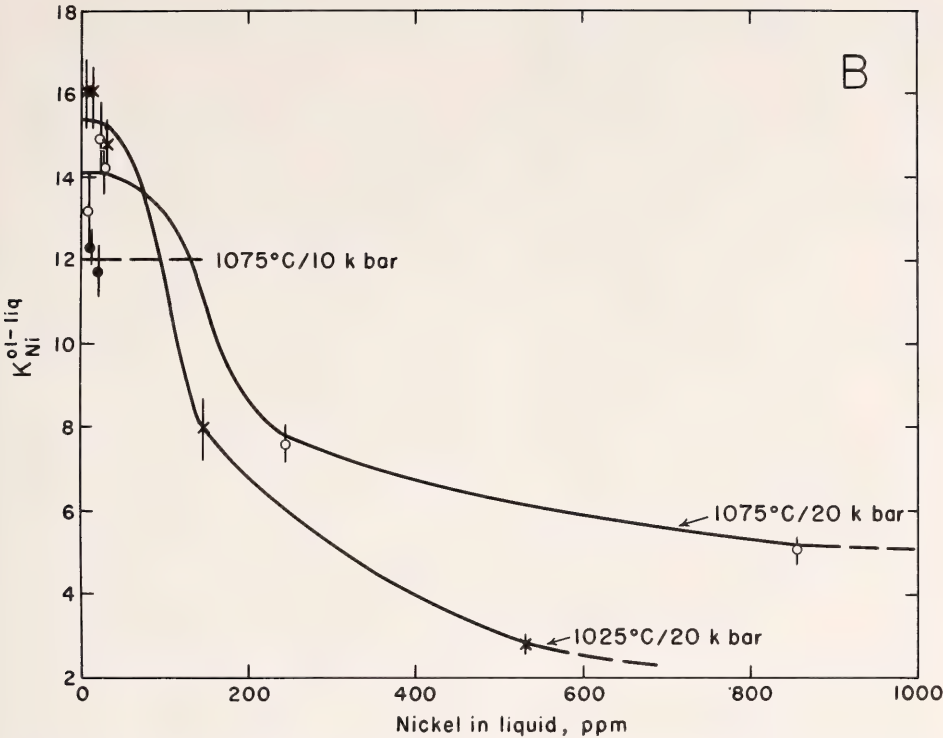


Fig. 107B. Partition coefficient K_{Ni}^{ol-liq} , as a function of nickel content of the liquid. Length of error bars = 2σ .

The function $K_{Ni}^{opx-liq} = g(X_{Ni})$ (Figs. 105 and 107) has the geometry expected for partitioning of an element between an ideal and a regular solution (Mueller, 1964; Saxena, 1969). Within the Ni concentration range of constant γ_{Ni}^{liq} , a similar effect is expected. It is thus proposed that nickel solution in aluminous enstatite is of the nature of a regular solid solution. With increasing temperature, the nonideality of the orthopyroxene becomes less pronounced.

It has been suggested that the K_{Ni}^{ol-liq} for olivine in equilibrium with natural basalt liquid is strongly temperature dependent (Leeman, 1974). Häkli and Wright (1967), using naturally occurring olivine-liquid pairs in the Hawaiian Makaopui lava lake, also suggested a significant temperature dependence of the K_{Ni}^{ol-liq} , although their proposed temperature dependence was signifi-

cantly less than that suggested by Leeman (1974). In both studies, however, temperature and $Mg/(Mg + Fe)$ are dependent variables. Irvine and Kushiro (this Report) have shown that the K_{Ni}^{ol-liq} decreases with increasing $Mg/(Mg + Fe)$ of the two phases. Because the $Mg/(Mg + Fe)$ of olivine and coexisting liquid in the two studies by Leeman (1974) and Häkli and Wright (1967) both decreased with decreasing temperature, their temperature dependences reflect the effects of both decreasing temperature and decreasing $Mg/(Mg + Fe)$. It can be seen from the present data that K_{Ni}^{ol-liq} changes by about 2.5 units/100°C, a factor of more than 2 less than the temperature dependence suggested by Leeman (1974). The experiments by Leeman (1974) were performed at 1 atm under dry conditions with up to several percent nickel

added to natural basalt compositions. The nickel contents in his experiments were far greater than the concentration range of Henry's law of behavior of Ni indicated by the present data. Compared with the present data, different partition coefficients and different temperature dependences of those partition coefficients would be expected.

The data by Häkli and Wright (1967) were obtained by measuring nickel contents of olivine phenocryst-basalt matrix pairs within the nickel concentration range of Henry's law as determined here. However, those experiments were also near 1 atm and under dry conditions. It is notable that there is close agreement between the partition coefficients of the natural olivine-basalt pairs of Häkli and Wright (1967) and those obtained under H_2O -saturated conditions and high pressure reported here. Rather than indicating that olivine phenocrysts in basalts were formed under high f_{H_2O} conditions, it is suggested that even though the activity coefficient of nickel in silicate liquid must depend on liquid composition, pressure, and water content, these effects do not produce large differences in partition coefficients of nickel between olivine and silicate liquid.

The minimum values of K_{Ni}^{ol-liq} occur in the concentration range 3000–4000 ppm Ni in the olivine. Such nickel contents are also found in olivine from mantle peridotite. Thus, during partial melting of a peridotite in the upper mantle, one would expect that olivine is less effective in retaining Ni in the crystalline residue than would be the case during a later stage of olivine fractionation from a basalt in a shallow magma chamber such as, for example, found in Hawaii. The absolute effects of variable partition coefficients between liquid and orthopyroxene, and probably clinopyroxene, on nickel concentrations in partial melts would be quite small compared with olivine because the K_{Ni}^{px-liq} is near 1.

PARTITIONING OF NI AND MG BETWEEN OLIVINE AND SILICATE LIQUIDS

T. N. Irvine and I. Kushiro

It has been well established for many years that Ni is more strongly fractionated into olivine than is Mg during crystallization differentiation of basaltic and other magmas (Vogt, 1923; Wager and Mitchell, 1951). Ringwood (1956) showed, however, that this relationship is opposite to that in the system Ni_2SiO_4 - Mg_2SiO_4 , where olivine has lower Ni/Mg than the liquid with which it is in equilibrium. Ringwood argued that the reversal in magmas is an effect of their iron content, on the basis that fayalite has a lower melting temperature than the Ni-Mg olivines. More recently, however, Burns and Fyfe (1964, 1967) and Burns (1970) interpreted the reversal as an effect of the large crystal-field stabilization energy of the Ni^{2+} ion and its resultant strong octahedral-site preference energy. They argued that basaltic liquid has a much smaller number of octahedral sites than olivine melts by virtue of its higher content of silica, alumina, and alkalies, and that consequently, the partitioning of Ni is preferentially shifted in favor of coexisting olivine.

The partitioning of Ni may be described in terms of either a partition coefficient, $D = (Ni \text{ in olivine}) / (Ni \text{ in liquid})$, or a distribution coefficient relative to Mg, $K_D = (Ni/Mg \text{ in olivine}) / (Ni/Mg \text{ in liquid})$. Burns and Fyfe (1964) predicted that these coefficients should increase as the liquid is enriched in silica and alkalies, and such variation has been recorded for D in basaltic liquids by Leeman (1973) and by Irvine (*Year Book* 73, Fig. 56), although Leeman emphasized correlation with decreasing temperature rather than composition. On the other hand, Sato (1976) has argued that although D is variable, K_D is relatively constant in basalt.

In the present study, an attempt has been made to test the effects of iron and of silica and alkalies in separate experi-

ments, using the simplest possible compositional systems. The results are interpreted as supporting a modified version of the thesis of Burns and Fyfe, but some basis is also indicated for each of the other proposals.

Effect of Iron

The starting material used to examine the effect of iron was a mix in the olivine join $\text{Mg}_2\text{SiO}_4\text{-Fe}_2\text{SiO}_4\text{-Ni}_2\text{SiO}_4$ of composition $\text{Fo}_{36}\text{Fa}_{57}\text{NiOl}_{13}$ prepared from synthetic Mg-Fe olivine and pyroxene, and NiO. There are major difficulties, however, in maintaining such a composition under experimental conditions. The Ni and Fe both tend to dissolve in noble metal containers, and if the oxygen fugacity (f_{O_2}) is too low, they may also precipitate as a metallic phase. If f_{O_2} is too high, the iron is oxidized to Fe_2O_3 . No satisfactory 1-atm method was found, and the melting experiments therefore were run at 15 kbar in graphite capsules in a solid-media, high-pressure apparatus. Experiments were performed at 1550° and 1600°C. The f_{O_2} imposed on the charge under these conditions is relatively low (approximately that of the iron-wüstite buffer; Thompson and Kushiro, *Year Book* 71), and a metallic phase (ca. $\text{Ni}_{80}\text{Fe}_{20}$, atomic %) did precipitate along with the new olivine formed in the melting process. There was also the problem that liquids near the olivine join do not quench to glass, but the melt was readily distinguishable in the run products as a matte of fine acicular quench crystals around the coarser, stable olivine grains. Composition relations were determined with the electron microprobe, the melt composition being derived from analyses of the quench-crystal matte made at many places in the charge with a broad (10–15 μm) electron beam. The data are summarized in Table 36, where it is seen that at both temperatures the olivine was somewhat richer in Ni than the liquid ($D > 1$), but the liquid nevertheless had the higher Ni-Mg ratios ($K_D < 1$).

Because of the formation of the metal-

lic phase, however, the liquid was enriched in silica as compared with the olivine join. In an attempt to compensate for this effect, a second starting mix was prepared, of the same composition but with an additional 7 wt % FeO, and it was melted at 1500°C and 15 kbar. The quench-crystal matte formed in this experiment was closer in composition to olivine, but the partitioning of Ni was about the same, the value for K_D being 0.51. For comparison, the value of K_D indicated by the Ringwood (1956) phase diagram for the system $\text{Ni}_2\text{SiO}_4\text{-Mg}_2\text{SiO}_4$ is about 0.4; a typical value for basaltic liquid is 2.3 (Sato, 1976).

Thus, although iron apparently has some effect in shifting the partitioning of Ni in favor of olivine, as believed by Ringwood (1956), and so is probably contributory to the D and K_D relationships observed in magmas, the effect is clearly small and not the complete explanation.

Effect of Silica and Alkalies

The effects of silica and alkalies were investigated along two compositional lines in the join $\text{Mg}_2\text{SiO}_4\text{-Ni}_2\text{SiO}_4\text{-K}_2\text{O-SiO}_2$. For the one line, denoted *A* in Fig. 108, starting materials consisted of 50:50 mixtures of a pure forsterite and an Ni-bearing forsterite (containing 4 wt % NiO as Ni_2SiO_4) combined in various proportions with a crystallized mix of $\text{K}_2\text{O} \cdot 6\text{SiO}_2$ composition. For the other line, *B* in Fig. 108, the mixes were combinations of Ni-bearing enstatite (containing 2 wt % NiO as NiSiO_3) and $\text{K}_2\text{O} \cdot 6\text{SiO}_2$. Along these lines, as was inferred from the system $\text{K}_2\text{O-MgO-SiO}_2$ (Fig. 108), olivine is the liquidus phase in compositions containing as much as 72 wt % SiO_2 and 16% K_2O . Charges of the mixes were partially melted in $\text{Pt}_{95}\text{Au}_5$ foil envelopes in a 1-atm quenching furnace at temperatures appropriate to yield olivine and a large proportion of liquid. Oxygen was passed through the furnace in an attempt to keep as much of the nickel as possible as NiO and thereby minimize losses to the envelopes.

TABLE 36. Compositional Relations of Olivine and Liquid in Melting Experiments at 15 kbar on a Composition in the Join $\text{Mg}_2\text{SiO}_4\text{-Fe}_2\text{SiO}_4\text{-Ni}_2\text{SiO}_4$

| Temperature (°C) | Phase | Mg | Fe | Ni | D Ni in Olivine Ni in Liquid | K_D Ni/Mg in Olivine Ni/Mg in Liquid |
|---------------------|---------|----------|------|-----|--------------------------------------|--|
| | | Atomic % | | | | |
| 1600 | Olivine | 70.8 | 26.6 | 2.6 | 1.73 | 0.61 |
| | Liquid | 24.9 | 73.7 | 1.5 | | |
| 1550 | Olivine | 66.2 | 30.7 | 3.1 | 1.35 | 0.49 |
| | Liquid | 24.3 | 73.4 | 2.3 | | |

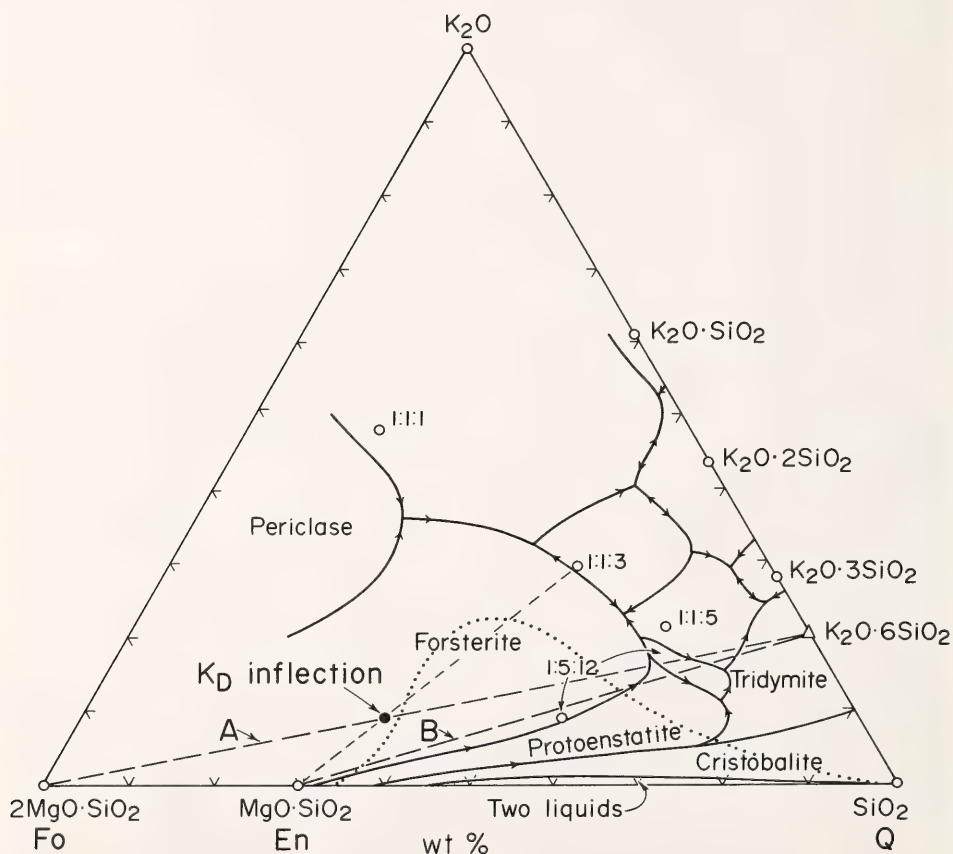


Fig. 108. Liquidus relations in the join $\text{Mg}_2\text{SiO}_4\text{-K}_2\text{O-SiO}_2$, redrawn from Roedder (1951b), showing the two composition lines along which mixes spiked with nickel were investigated in the present study. The K_D inflection is from Figs. 109A and 110. The dotted line represents the probable extent of the metastable part of the two-liquid solvus (see text). The ratios 1:1:1, etc., denote the composition points and liquidus fields of intermediate compounds in terms of the proportions of K_2O , MgO , and SiO_2 . Note that $\text{K}_2\text{O} \cdot 6\text{SiO}_2$ is not a compound.

Run times ranged from 30 min to 64 hr, depending on the temperature and apparent equilibration rates (see below). The melts quenched to glass in mercury in all experiments, although fringes of quench crystals formed around some of the olivine grains in runs at 1600°C and higher temperatures. The olivine ranged in habit from roughly equant crystals 5–20 μm on a side in the higher temperature runs, to thin blades 10–40 μm long and 0.5–3 μm thick at the lowest temperatures. The starting materials had been ground to less than 2 μm , hence it was evident that the run crystals were formed either by recrystallization of the two different kinds of olivine in the one set of mixes or through the incongruent melting of the Ni-bearing enstatite in the other set.

The electron microprobe was also used to analyze the olivine and glass in these experiments. The procedure was to analyze a crystal, usually in duplicate, and then to make from two to four analyses of the glass around it. The results were averaged, and the coefficients D and K_D and other compositional parameters were computed from the averages. Several crystal-glass pairs were analyzed in different parts of the charge, and the data for each pair have been plotted in Figs. 109 and 110. In the graphs, each cluster of points represents a run, and inasmuch as each point represents averages of several analyses, the spread of the cluster is believed to reflect the degree to which equilibrium was reached in the charge. Analyses of the foil from the Pt-Au envelopes indicate some loss of Ni, but no evidence was found that the loss significantly affected the equilibrium; for example, olivine-glass pairs next to the foil gave the same results as those well within the charge.

As seen in Fig. 109, D was greater than 1 in all experiments, including one on Ni-bearing enstatite only (i.e., a composition equivalent to olivine + silica with no alkalies). The relative partitioning of Ni and Mg was observed to reverse, K_D ranging from about 0.8 to 6.0. Both co-

efficients increase as the melt becomes richer in silica and alkalies, in accord with the prediction of Burns and Fyfe (1964), but the variation also bears a strong inverse relationship to temperature, a point in support of the approach by Leeman (1973). The coefficient K_D is relatively constant through a compositional range that compares with tholeiitic basalt in terms of silica saturation, whereas D is more variable, seemingly in accord with Sato's (1976) observation; but in a logarithmic comparison, the overall variations of the two coefficients are almost parallel. The values of D and K_D span those typically recorded for basalt ($D = 10\text{--}15$; $K_D = 2\text{--}3$).

In view of these relations, it seems clear that, effectively, silica and alkalies are largely responsible for the Ni-Mg partitioning observed between olivine and magmatic liquids, although other constituents (particularly alumina) are no doubt contributory.

Interpretation and Discussion

The plot of $\ln K_D$ versus $1000/T$ in Fig. 110 was made as a step toward separating the inverse temperature effect from effects that appear to relate more closely to composition.* The plot reveals a curvilinear relationship in the lower part of the temperature range and marked inflection just below 1600°C. A

* A common objective in making this type of plot is to demonstrate a correlation from which the enthalpy change (ΔH) of the exchange reaction represented in K_D can be estimated (on the assumption that K_D closely reflects the equilibrium constant of the reaction). However, no such estimate is possible in the present case—not even if a straight-line relationship had been found—because the liquid composition changes markedly with temperature in respects other than just Ni/Mg. It is emphasized also that because the liquid composition and temperature are related, their effects on K_D cannot really be isolated by any simple graphical method such as used here. However, the combination of plots versus composition in Fig. 109 appears to accentuate the effects of temperature, whereas the plot versus inverse temperature in Fig. 110 emphasizes features that are almost certainly strongly dependent on composition.

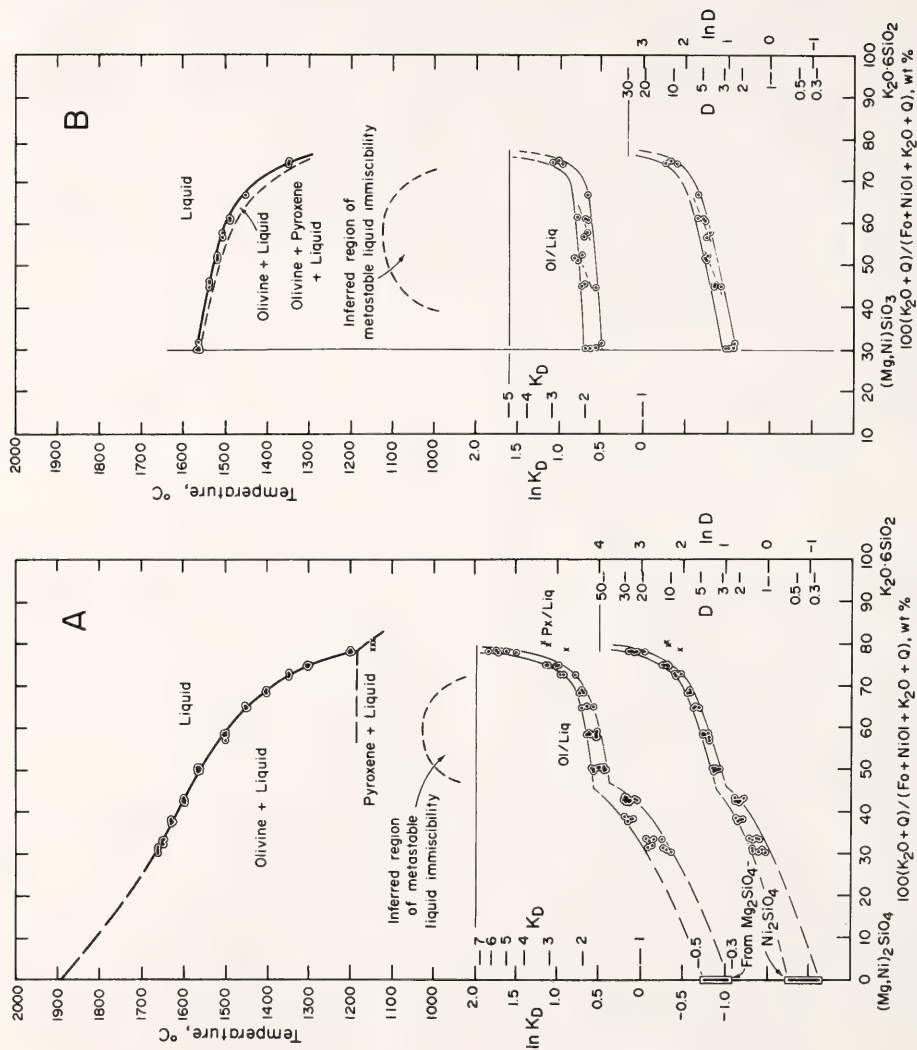


Fig. 109. Experimental data on the liquidus temperatures and Ni partitioning coefficients for the composition lines A and B in Fig. 108. The inflections in the K_D and D curves are based on Fig. 110. See text for details.

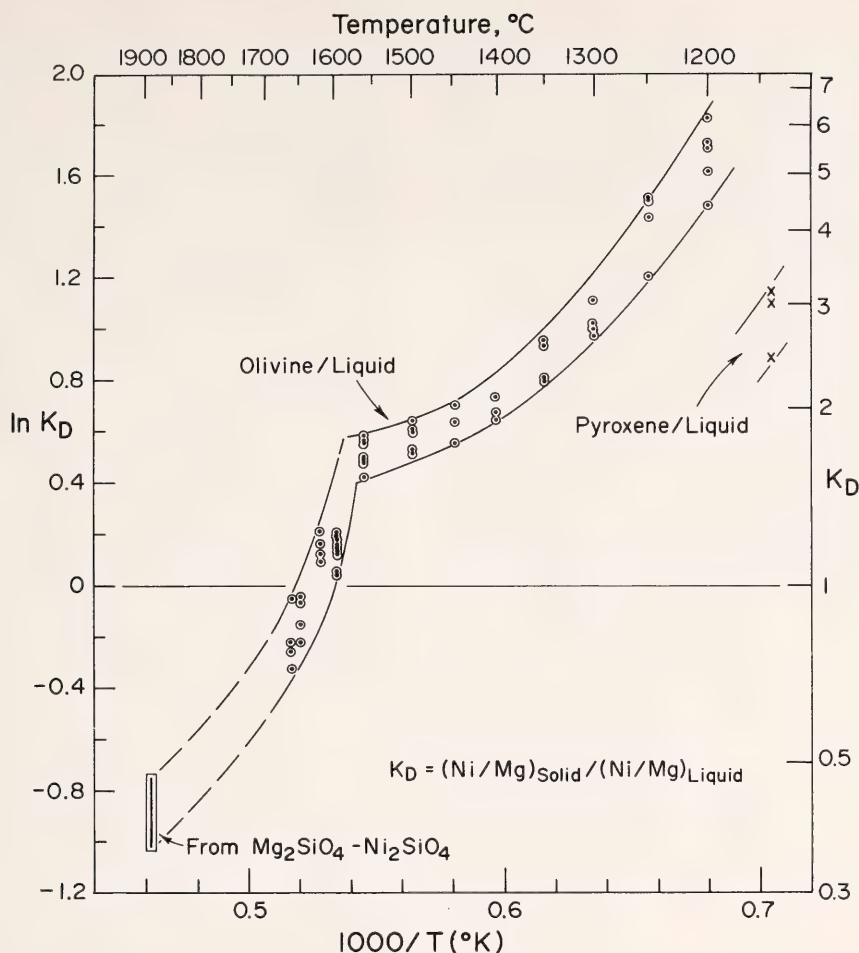


Fig. 110. Plot of $\ln K_D$ versus $1000/T(^{\circ}\text{K})$ for the composition line A from $(\text{Mg,Ni})_2\text{SiO}_4$ to $\text{K}_2\text{O} \cdot 6\text{SiO}_2$ in Fig. 108.

second curvilinear relationship is indicated at temperatures above the inflection on the basis of the K_D value estimated from the Ringwood (1956) phase diagram for the system Ni_2SiO_4 - Mg_2SiO_4 .

The evidence for the inflection is believed to be satisfactory, although there is a slight reservation in that the lower K_D values derive from experiments that were necessarily very short (only 20–30 min) because the temperatures were above the practical working limit of the furnace. However, there appeared also to be a distinct change in equilibration rates in the vicinity of the inflection. As

judged by the homogeneity of the distribution of Ni in the olivine and glass, the best equilibrated experiment was a 30-min run at 1600°C , but a 30-min run on the same mix at 1575°C was far from equilibrated, and at 1565°C , about 4 hr were required to obtain an acceptable result. It would seem therefore that a considerable change occurs in the system at 1575° – 1600°C , and in the absence of any known transition in olivine in that range, it is inferred that the change is in the structure of the melt.

In considering possible origins for the inflection and associated features, it is

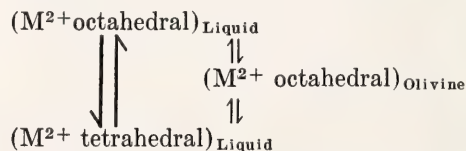
useful first to examine the liquidus profiles in Fig. 109. These profiles are typical of a liquidus above a metastable two-liquid solvus, and the overall relations in the join $\text{Mg}_2\text{SiO}_4\text{-K}_2\text{MgSi}_3\text{O}_8\text{-SiO}_2$ (Fig. 108) closely parallel those of the system $\text{Mg}_2\text{SiO}_4\text{-KAlSi}_3\text{O}_8\text{-SiO}_2$ in which extensive metastable liquid immiscibility has been detected by Irvine (this Report). Several attempts were made to detect metastable immiscibility along the composition line *B* (Fig. 109B), using methods described by Irvine, but without success—the melts could not be supercooled. For the present, therefore, approximate locations for the solvus have been inferred, using the relations in Fig. 108 as a base and the system $\text{Mg}_2\text{SiO}_4\text{-KAlSi}_3\text{O}_8\text{-SiO}_2$ as a model. There are large uncertainties as to the temperature and detailed shape of the solvus profiles, but the locations of their axes should be relatively accurate, and the profile for line *B* is undoubtedly at a higher temperature than that for line *A*.

The presence of a metastable two-liquid solvus also implies a change in the melt structure, a strong possibility in the present case being a transition from a structure in which the silicon-oxygen tetrahedra are loosely connected in chains like those in pyroxene to a linkage that is more akin to that of a framework silicate such as cristobalite. The question that immediately arises is whether the K_D inflection is related. The inflection appears, however, to lie distinctly to the silica-poor side of the solvus. This relationship is suggested in the profiles in Fig. 109 but is most definitely indicated in the fact that no inflection occurs along line *B* from the pyroxene composition (Mg,Ni) SiO_3 . The K_D variation along line *B* is like that on the silica-rich side of the inflection (Fig. 109), but the pyroxene composition undoubtedly lies on the silica-poor side of the stable part of the two-liquid solvus, as in the join $\text{Mg}_2\text{SiO}_4\text{-K}_2\text{O-SiO}_2$ (Fig. 108).

On the other hand, the temperature of the inflection is about that of the pyrox-

ene melting point (metastable at about 1560°C), and compositionally it lies on a line from pyroxene to $\text{K}_2\text{MgSi}_3\text{O}_8$ (1:1:3, Fig. 108) (which compares with the En-Or join in the equivalent alumina-bearing system). The following tentative interpretation of the inflection is therefore suggested. It is proposed that in the composition-temperature interval along line *A* from the olivine melting point to the inflection, the melt undergoes a gradual transition from a structure in which the SiO_4 tetrahedra are essentially isolated, as in an orthosilicate, to a structure in which they are extensively linked in chains, as in pyroxene. At the inflection, a new transition begins, from the chain structure to a structure more akin to that of a framework silicate. In a sense, the incompatibility of forsterite and the silica minerals extends into the melt.

As for the variations of K_D itself, it is noted that the Ni/Mg relations along line *B*, representing the join $\text{MgSiO}_3\text{-NiSiO}_3\text{-K}_2\text{O}\cdot 6\text{SiO}_2$, are analogous to the Cr/Mg relations along the chromite-forsterite cotectic in the join $\text{MgSiO}_3\text{-Cr}_2\text{O}_3\text{-K}_2\text{O}\cdot 6\text{SiO}_2$ as determined by Irvine (*Year Book* 73, pp. 306–311). Thus, inasmuch as Ni^{2+} and Cr^{3+} both have very large octahedral-site preference energies, it seems likely that this property is a dominant controlling factor in the Ni partitioning. However, the Burns and Fyfe (1964, 1967) explanation of the way in which the control is implemented appears to require modification. The basic equilibria can be represented in the manner proposed by Irvine (*Year Book* 73, p. 306)



where $\text{M}^{2+} = \text{Ni}^{2+}$ and Mg^{2+} , and the essential thesis of the Burns and Fyfe explanation seems still to be reasonable: namely, as the liquid becomes more siliceous, the equilibria for Ni^{2+} shift

strongly in favor of olivine, whereas some of the Mg^{2+} ions transfer from octahedral to tetrahedral sites in the liquid. However, it appears that for a given structural type of melt solution, the shifting of equilibria is primarily dependent on temperature, the relationship to melt composition deriving largely from the fact that the liquidus temperature of a melt is a function of its composition. The importance of temperature is indicated particularly in Fig. 109 in that K_D is almost constant along the relatively flat parts of the liquidus (in the case of line A, to the right of the inflection), despite large changes in composition, and then increases sharply as the liquidus temperature drops rapidly in the silica-rich region. It would seem also that the critical variable is not strictly the number or frequency of octahedral sites in the liquid, or even the ratio of octahedral to tetrahedral sites. This inference stems from the observation that K_D changes very little through the composition interval spanning the metastable two-liquid solvus, even though this interval would be expected to be a zone of rapid structural change, marked probably by a sharp decrease in the frequency of octahedral sites and a strong increase in tetrahedral sites. Possibly a more critical parameter is the ratio of octahedral sites to $(Ni + Mg)$ ions in the liquid. If this ratio decreased with temperature, there would be more competition for the octahedral sites, and consequently the site-preference energy of Ni^{2+} would become more significant.

RARE EARTH FRACTIONATION WITH CONTROLLED PARTIAL MELTING OF PERIDOTITE*

Bjørn O. Mysen and John R. Holloway

Models of basalt genesis in peridotitic upper mantle are often based on trace element abundances in the basalts (e.g.,

Gast, 1968; Schilling and Winchester, 1969; O'Nions and Clark, 1972). Mysen and Kushiro (this Report) have discussed the melting behavior of volatile-free peridotite mantle in the light of phase equilibria in model and natural peridotite systems. They find that the major element compositions of partial melts are controlled by the residual mineral assemblages and that similar melt compositions change little over extensive melting intervals, provided the co-existing mineral assemblage does not change. Trace element abundances, however, such as those of the rare earth elements (REE), may be sensitive to the degree of melting even within the individual melting intervals delineated by Mysen and Kushiro (this Report). Furthermore, the applicability to the genesis of basalts of data on major elements from melting experiments with mantle rocks would rely heavily on the extent to which experimentally derived trace element patterns are compatible with those of the natural rocks. Consequently, this report describes an attempt to combine experimental determinations of major and trace element data to partial melting of upper mantle peridotite.

Starting material was a sheared garnet peridotite nodule sample (1611) from a Lesotho kimberlite diatreme previously described by Nixon and Boyd (1973a) and Shimizu (*Year Book* 73, pp. 954-961). Experimental REE patterns were obtained by spiking one split of 1611 with 3.11-ppm cerium-141, another with 0.585-ppm samarium-151, and a third with 0.0173-ppm thulium-171. The starting material was fired for 12 hr at 1150°C with $f_{O_2} = 10^{-9}$ atm prior to the addition of trace elements to eliminate all chemically bound and adsorbed H_2O , CO_2 , and SO_2 . This heat treatment did not alter the mineralogy of the sample (Mysen and Kushiro, this Report). The radioactive isotopes were added in chloride solution, and the samples were dried and stored at 110°C before use. Run durations were from 4 hr at 1450°C to 1 hr at 1650°C.

* Research partially supported by the National Science Foundation, Earth Sciences Section, grant DES 73-00266A01.

The amount of radioactive isotope in the partial melts was determined by β -track counting (Mysen and Seitz, 1975). Standards were albite glass with known amounts of radioactive tracer added and equilibrated at 1600°C and 20 kbar for 30 min. With this technique, only the amount of radioactive spike in the partial melts can be determined. Shimizu (*Year Book 73*, pp. 954-961) has shown, however, that the REE of nodule 1611 (natural abundance) are essentially chondritic and about equal to the abundances in average chondrite. Consequently, enrichment of radioactive REE in experimental partial melts relative to the total amount of radioactive spike in 1611 is the same as the total amount of a given REE in the partial melt relative to chondritic abundance.

The experimental conditions were selected from the data of Mysen and Kushiro (this Report). The pressure was 20 kbar where the aluminous phase in 1611 is spinel. At 1450°C (1.3% melt) and 1500°C (15% melt), the coexisting minerals are clinopyroxene (pigeonite), orthopyroxene, olivine, and spinel. The liquid is alkali basaltic in composition at 1450°C and olivine tholeiitic in composition at 1500°C. The reasons for the differences in major element composition are discussed by Mysen and Kushiro (this Report). The partial melt composition remains olivine tholeiitic from about 2% to about 25% melting. At 1550°C, the assemblage is olivine + orthopyroxene + 35% picritic melt, and at 1650°C, the assemblage is olivine + 50% peridotitic komatiite melt. The proportions of melt were determined by Mysen and Kushiro (this Report) using a β -emitting tracer (carbon-14).

Results of the experiments are shown in Fig. 111. The enrichment factor equals parts per million of tracer in partial melt divided by the amount of tracer added to the starting material. As discussed above, the REE patterns thus derived for partial melts from this nodule are identical with the chondrite normalized REE pattern. The pattern for

Hawaiian alkali basalt is from Schilling and Winchester (1969), and the Baffin Bay tholeiite pattern, from O'Nions and Clark (1972). The rock names associated with the experimental runs are from Mysen and Kushiro (this Report) and are based on normative compositions of the partial melts.

The REE patterns from 1.3% and 15% melting are different despite the identical phase assemblages. The relatively large enrichment of REE in 1.3% melt relative to 15% melt is mostly a function of the differences in degree of melting. As can be seen from the data in Figs. 111 and 112, however, the 15% melting pattern is more enriched in the light REE than the 1.3% melting pattern.

The differences between REE patterns from 15% melting and those with larger proportions of melt are caused by the absence of clinopyroxene with more than 25% melting in these experiments, resulting in greatly decreased enrichment of light REE in 35% and 50% melting curves (Fig. 112). The difference between the patterns of the 35% and 50% melting curves is the absence of orthopyroxene in the residue of the latter. However, because of the small values of $K_{\text{REE}}^{\text{crystal-liquid}}$ for both olivine and orthopyroxene (Mysen, this Report), the geometry of the two curves is quite similar (Fig. 111). The larger total enrichment of REE in the 35% melt is caused by the larger proportion of crystals in those experiments.

The ratios of enrichment factors, Ce/Sm and Ce/Tm, in experimentally produced liquid of alkali basaltic composition are 1.07 and 1.32, respectively (Fig. 112). In contrast, natural alkali basalts have Ce/Sm and Ce/Tm in the ranges 1.5-3 and 2-10, respectively (Schilling and Winchester, 1969; Shimizu and Arculus, 1975). Thus, even though the major element composition of experimentally produced liquid from anhydrous peridotite resembles alkali basalt, the experimental trace element composition suggests that alkali basalts

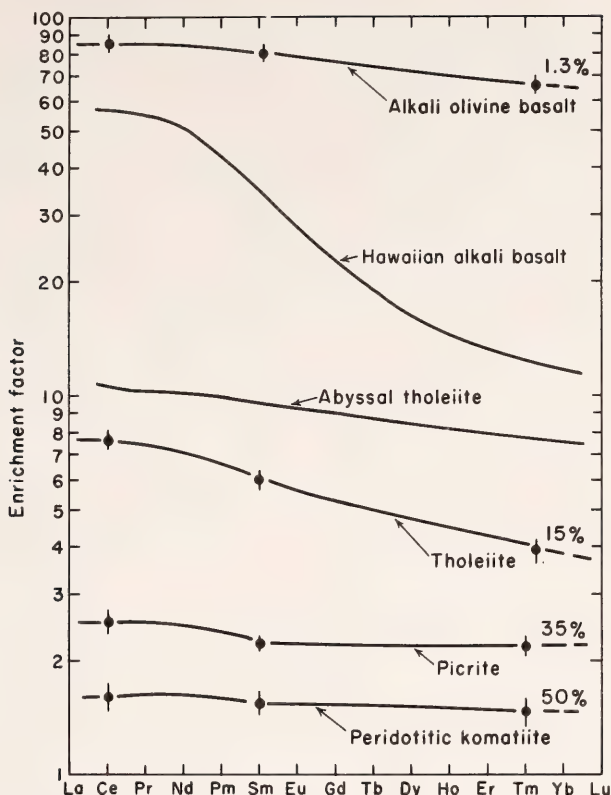


Fig. 111. Experimental rare earth element patterns from nodule 1611 at 20 kbar. Alkali basalt pattern is from Schilling and Winchester (1969); tholeiite, from O'Nions and Clark (1972). Length of error bars = 2σ .

are not formed in this way. Substitution of garnet for spinel as the aluminous phase may change the experimental REE patterns to approximate those of natural alkali basalt (Shimizu and Arculus, 1975), but under those circumstances, the major element composition of the liquid is that of an alkali picrite (Mysen and Kushiro, this Report).

The REE patterns of abyssal tholeiite (O'Nions and Clark, 1972) and those of liquids of olivine tholeiite composition produced by 15% melting of nodule 1611 at 20 kbar are rather similar, although the REE enrichment factor of the abyssal tholeiites (chondrite normalized REE patterns) is generally slightly higher. Provided nodule 1611 has a representative upper mantle REE content (flat REE pattern and REE content similar

to that of chondrite), abyssal tholeiites could be formed by somewhat less than 15% melting of volatile-free spinel peridotite.

Rare earth element patterns of picritic melts generally show a slight depletion of the light REE relative to chondrite (e.g., O'Nions and Clark, 1972). It is therefore unlikely, in light of the data in Fig. 111, that picrite is formed by direct partial melting of volatile-free peridotite. Rare earth element data for peridotite komatiite are scarce. The few that are becoming available (N. T. Arndt, personal communication, 1976), however, suggest a pattern somewhat similar to that of picrite. In that case, peridotitic komatiite cannot have been formed by direct partial melting of peridotite.

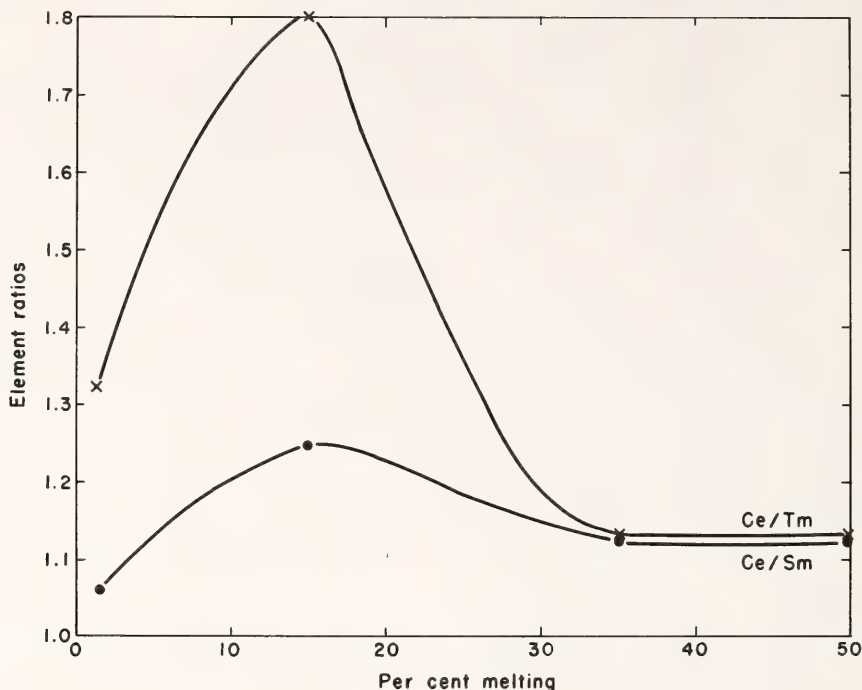


Fig. 112. Ratios of enrichment factors, Ce/Sm and Ce/Tm, of experimental partial melts as a function of degree of melting at 20 kbar pressure.

PARTITIONING OF IRON, NICKEL, AND
MAGNESIUM BETWEEN METAL, OXIDE,
AND SILICATES IN ALLENDE METEORITE
AS A FUNCTION OF f_{O_2}

Bjørn O. Mysen and Ikuo Kushiro

Carbonaceous chondrites appear to be the least differentiated condensed material in the solar system (Larimer and Anders, 1967; Wasson, 1974). If planets such as the earth were derived from a similar material, melting experiments on carbonaceous chondrites may shed light on events in the early, postaccretion evolution of the solar system.

Carbonaceous chondrites are rich in nickel and iron; both elements can occur in different oxidation states depending on the oxygen fugacity and the phases present. Consequently, experimental data on partitioning of iron and nickel between metal (+ sulfide), silicate crystals, silicate melt, and oxide in carbonaceous chondrite as a function of f_{O_2} are

important for the understanding of processes relating to the early evolution of the earth and of planets resembling the earth.

The experiments were carried out in a vertical quench furnace with CO/CO_2 gas mixtures to control the f_{O_2} . All experiments were made at 1275°C (within the silicate melting interval and above the metallic sulfide liquidus). One set of experiments was within the stability field of metallic iron in the system Fe-O ($f_{O_2} = 10^{-12}$ atm); one set was within the wüstite stability field ($f_{O_2} = 10^{-10.5}$ atm), and another set was inside the magnetite stability field ($f_{O_2} = 10^{-9}$ atm). A split of finely crushed bulk Allende meteorite (type-3 carbonaceous chondrite) was spiked with 101.3-ppm nickel-63 to facilitate nickel analysis using β -track counting (Mysen and Seitz, 1975). All phases except the metallic sulfide phase were also analyzed with the electron microprobe. Olivine

from the experiment with $f_{O_2} = 10^{-10.5}$ atm was analyzed with the electron microprobe and contains 0.56 ± 0.02 wt % NiO. This olivine was used as the standard for determination of nickel by β -track counting. Metallic sulfide liquid droplets were 2–5 μ m across. Surrounding silicates interfered with the electron microprobe analyses of the metallic sulfide liquid. Thus, using β -track counting, only the nickel content of the metallic sulfide phase was quantitatively determined. However, semiquantitative microprobe analyses of the sulfide phase revealed significant amounts of only Ni, Fe, and S. The appearance of small amounts (>1 wt %) of Si, Mg, Ca, and Al in the microprobe analyses was assumed to be caused by interference from the surrounding silicates.

The samples were suspended on a loop of Pt wire to minimize Fe and Ni loss. Run durations were 12–16 hr. The high temperatures and low oxygen fugacities resulted in alkali loss by volatilization. Although the bulk $Na_2O + K_2O$ content of the Allende meteorite is about 0.6 wt %, even the silicate partial melt in these experiments contained <0.2 wt % alkalis. No attempt was made to correct for this problem.

Experimental results are given in Table 37. At $f_{O_2} = 10^{-12}$ atm, the assemblage is nickel-iron sulfide melt (4.6 Ni, 75 Fe, 20 S, wt %), olivine ($Fe_{71.8}$), silicate liquid ($Mg/[Mg + Fe] = 0.459$), and traces of clinopyroxene. At $f_{O_2} = 10^{-10.5}$ atm, the assemblage is nickel-iron sulfide melt (30 Ni, 40 Fe, 30 S, wt %), nickel-rich aluminous spinel (7.2 wt % NiO), olivine ($Fe_{66.2}$), silicate liquid ($Mg/[Mg + Fe] = 0.352$), and traces of clinopyroxene. At the highest oxygen fugacity (10^{-9} atm) the phases are aluminous spinel, olivine ($Fe_{65.5}$), silicate liquid ($Mg/[Mg + \Sigma Fe] = 0.283$), and traces of clinopyroxene.

Element partitioning between the phases in the Allende meteorite depends on oxygen fugacity because the f_{O_2} controls the relative stabilities of Fe^0 , Fe^{2+} , Fe^{3+} , Ni^0 , and Ni^{2+} . The nickel content

of the metallic sulfide melt increases rapidly as the f_{O_2} is increased above 10^{-12} atm. This observation is expected because metallic nickel in the system Ni-O is stable to oxygen fugacities 5 orders of magnitude above that of metallic iron in the system Fe-O ($10^{-11.25}$ and 10^{-6} atm at 1275°C for Fe^0 and Ni^0 , respectively).

Nickel contents of spinel, olivine, and silicate liquid are plotted as a function of f_{O_2} in Fig. 113. The nickel content of the silicates increases with increasing f_{O_2} , whereas that of spinel decreases. The relative stabilities of NiO in spinel and silicates are f_{O_2} -dependent (Fig. 114). This dependence is illustrated in Fig. 114 by using a simple exchange reaction to define an exchange equilibrium constant for NiO and MgO,

$$K_{Ni-Mg}^{ol-\alpha} = \frac{[(X_{NiO}^{ol}) \times (X_{MgO}^{\alpha})]}{[(X_{MgO}^{ol}) \times (X_{NiO}^{\alpha})]} \quad (1)$$

where α is spinel or silicate melt, and X_{NiO}^{ol} , for example, is the mole fraction of oxide in a given phase. The data in Fig. 114 demonstrate that Ni^{2+}/Mg^{2+} in silicate melts (assuming negligible metallic nickel in silicates) increases more rapidly with increasing f_{O_2} than in olivine (the exchange equilibrium constant K_{Ni-Mg}^{ol-liq} decreases with increasing f_{O_2}). On the other hand, the K_{Ni-Mg}^{ol-sp} increases with increasing f_{O_2} , suggesting that Ni^{2+}/Mg^{2+} in olivine increases more rapidly than in spinel. Partitioning of nickel between metallic sulfide melt and silicates is controlled mainly by the relative stabilities of metallic iron and nickel as a function of f_{O_2} , resulting in an increase of $C_{Ni}^{metallic\ sulfide-olivine*}$ from about 15 at 10^{-12} atm to about 70 at $10^{-10.5}$ atm. Brett (1971) reported $C_{Ni}^{metal-silicate} \sim 2100$ in meteorite, and for core/mantle the ratio was calculated to be about 54. It thus appears that the mechanism of separation of nickel between the metallic sulfide phase and olivine in chondritic mete-

* $C_{i\alpha-\beta}$ = concentration of i in α /concentration of i in β .

TABLE 37. Results of Experiments with Allende Meteorite

| f_{O_2} (atm): | $10^{-10.5}$ | | | | 10^{-9} | | | | | |
|------------------------|---------------------|-------------|-------------------------|----------------|------------------|---------------|---------|---------------|--------|---------------|
| | metal, ol, liq, cpx | | metal, ol, liq, sp, cpx | | ol, liq, sp, cpx | | | | | |
| Coexisting phases: | Olivine | Liquid | Metal | Olivine | Spinel | Liquid | Metal | Olivine | Spinel | Liquid |
| Phase: | Olivine | Liquid | Metal | Olivine | Spinel | Liquid | Metal | Olivine | Spinel | Liquid |
| SiO_2 | 36.72 | 43.49 | | 35.75 | ... | 37.49 | | 36.59 | ... | 36.73 |
| TiO_2 | 0.04 | 0.49 | | 0.02 | 0.44 | 0.54 | | ... | 0.57 | 0.14 |
| Al_2O_3 | 0.28 | 11.99 | | 0.21 | 35.88 | 11.11 | | ... | 38.41 | 10.70 |
| FeO^* | 25.59 | 22.73 | | 29.91 | 26.86 | 29.26 | | 29.95 | 31.25 | 31.28 |
| MnO | | 0.30 | | 0.28 | 0.28 | 0.23 | | 0.25 | 0.28 | 0.64 |
| MgO | 36.53 | 10.81 | | 32.89 | 10.99 | 8.91 | | 31.86 | 9.97 | 6.94 |
| CaO | 0.33 | 8.72 | | 0.51 | ... | 10.11 | | 0.48 | ... | 10.66 |
| Na_2O | ... | 0.15 | | 0.05 | ... | 0.24 | | ... | ... | 0.12 |
| K_2O | ... | 0.02 | | ... | ... | ... | | ... | ... | ... |
| Cr_2O_3 | 0.51 | 0.48 | | 0.17 | 18.37 | 0.18 | | 0.15 | 15.45 | 0.10 |
| Totals | 100.19 | 99.15 | | 100.84 | 92.82 | 98.08 | | 99.51 | 95.95 | 97.28 |
| Ni(ppm) | 3000 \pm 60 | 166 \pm 4 | 45,600 \pm 1300 | 4400 \pm 100 | 56,400 | 1070 \pm 40 | 300,000 | 5960 \pm 40 | 15,400 | 1440 \pm 20 |
| $Mg/(Mg + Fe)^*$ | 0.718 | 0.459 | | 0.662 | 0.422 | 0.352 | | 0.655 | 0.363 | 0.283 |
| $C_{Ni}^{metal-ol}$ | 15.2 | | | 68 | | | | | | |
| C_{Ni}^{sp-ol} | ... | | | 3.6 | | | | ... | | |
| C_{Ni}^{ol-liq} | 18.1 | | | 4.1 | | | | 9.4 | | |
| K_{Ni-Mg}^{ol-liq} | 0.33 | | | 0.28 | | | | 4.1 | | |
| $K_{Fe^*-Mg}^{ol-liq}$ | 5.35 | | | 1.11 | | | | 0.21 | | |
| K_{Ni-Mg}^{ol-sp} | ... | | | 0.026 | | | | 0.90 | | |
| K_{Fe-Mg}^{sp-liq} | ... | | | 0.74 | | | | 0.121 | | |
| K_{Fe-Mg}^{ol-sp} | ... | | | 0.37 | | | | 0.70 | | |
| | | | | | | | | 0.30 | | |

*Total iron as FeO.

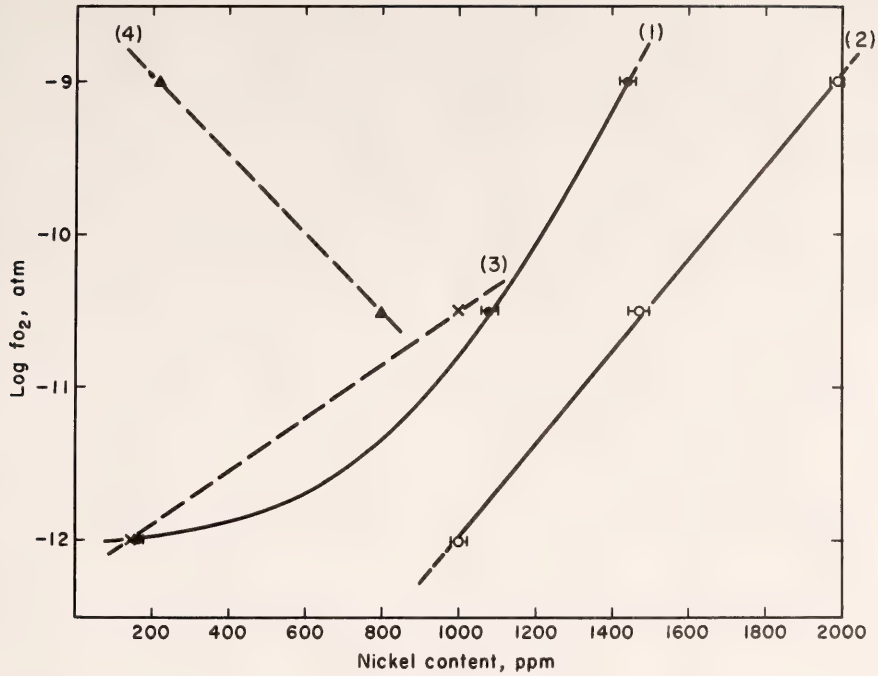


Fig. 113. Nickel content of silicates, spinel, and metal of Allende meteorite as a function of f_{O_2} at 1275°C. (1) Silicate liquid; error bar = 2σ . (2) Olivine/3; error bar = 2σ . (3) Metal/300. (4) Spinel/70. Errors of 3 and 4 are not estimated because the grains are too small for statistical treatment of β -track distribution.

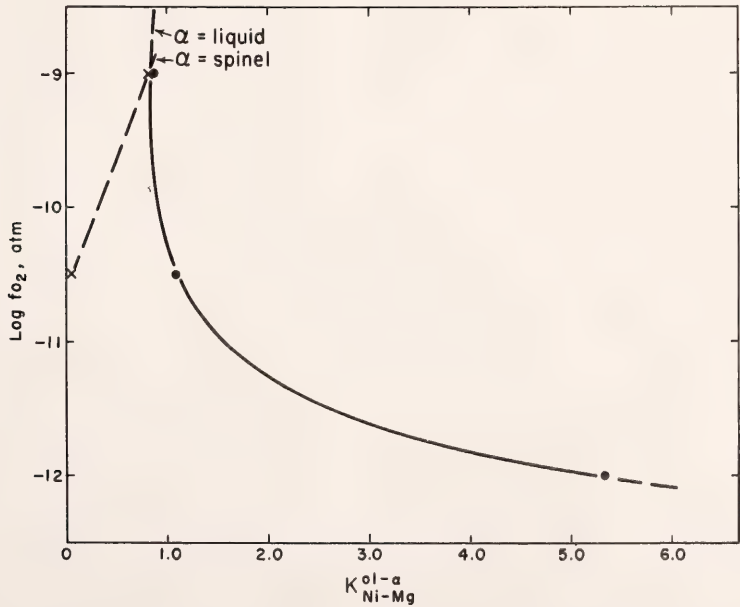


Fig. 114. K_{Ni-Mg}^{ol-sp} and K_{Ni-Mg}^{ol-liq} as a function of oxygen fugacity for Allende meteorite at 1275°C.

orites cannot be the same as that between the molten metal sulfide and silicate. However, the ratio of nickel between the mantle and the core of the earth is within the range of $C_{\text{Ni}}^{\text{metallic sulfide-olivine}}$ found here.

Iron behaves qualitatively much like nickel with respect to varying f_{O_2} . However, the partitioning of iron between the phases in the meteorite is complicated by the occurrence of iron as Fe^0 , Fe^{2+} , and Fe^{3+} . The $\text{Mg}/(\text{Mg} + \Sigma\text{Fe})$ of the spinel and silicate phases is plotted against oxygen fugacity in Fig. 115. The data show that all silicates and the spinel phase become enriched in iron relative to magnesium (calculated as FeO) with increasing f_{O_2} . An exchange reaction similar to Equation 1, substituting FeO for NiO , is used to separate the effects of oxidation of iron in silicate melt and spinel relative to olivine (olivine is assumed to contain only FeO). The results are shown in Fig. 116. The rapidly decreasing $K_{\Sigma\text{Fe-Mg}}^{\text{ol-liq}}$ and $K_{\Sigma\text{Fe-Mg}}^{\text{ol-sp}}$ suggest that the ferric iron content of liquid and spinel increases relative to that of olivine with increas-

ing f_{O_2} . Thus, even though ferrous oxide is chemically similar to NiO (e.g., probably entering spinel in preference to olivine), the oxidation of some Fe^{2+} to Fe^{3+} results in a decrease in $K_{\Sigma\text{Fe-Mg}}^{\text{ol-sp}}$ (total iron as FeO) with increasing f_{O_2} . Similarly, the $K_{\Sigma\text{Fe-Mg}}^{\text{ol-liq}}$ decreases with increasing f_{O_2} . For the pair olivine-liquid a consequence of this argument is that some ferric iron may appear in liquid even at $f_{\text{O}_2} = 10^{-10.5}$ atm (inside the wüstite stability field in the system Fe-O) or that some metallic iron is dissolved in silicate liquid at $f_{\text{O}_2} = 10^{-12}$ atm (Table 37). Similar observations were made by Mysen (1975) for $\Sigma\text{Fe-Mg}$ partitioning between olivine and liquid in a hydrous peridotite system at high pressure. The pair spinel-liquid can be treated analogously to olivine-liquid (Table 37), suggesting that ferric iron has a slight preference for spinel relative to liquid.

The bulk composition of the silicate melt obtained at 10^{-12} atm (Table 37) closely resembles that determined by Seitz and Kushiro (1974) at 20 kbar and 1350°C with f_{O_2} buffered by the graphite

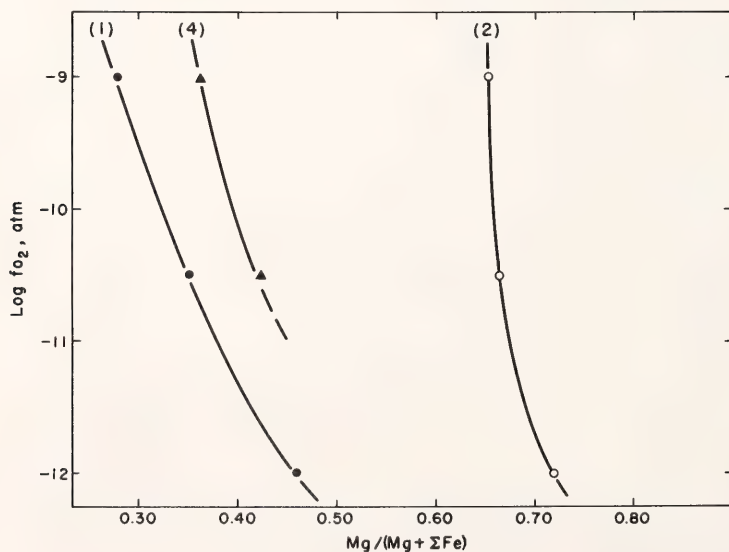


Fig. 115. $\text{Mg}/(\text{Mg} + \Sigma\text{Fe})$ of silicates and spinel as a function of oxygen fugacity for Allende meteorite at 1275°C . (ΣFe = total iron as FeO .) (1) Silicate liquid. (2) Olivine. (4) Spinel.

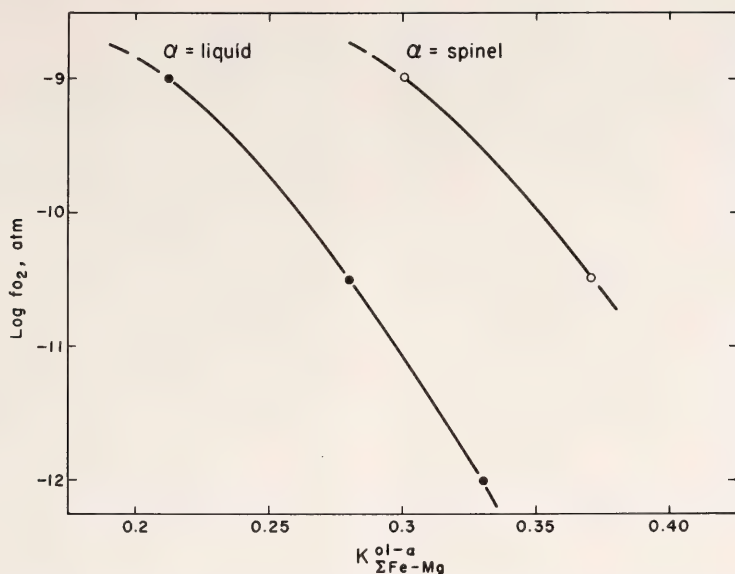


Fig. 116. $K_{\Sigma Fe-Mg}^{ol-sp}$ and $K_{\Sigma Fe-Mg}^{ol-liq}$ as a function of oxygen fugacity for Allende meteorite at 1275°C. (ΣFe = total iron as FeO .)

capsule (f_{O_2} in graphite capsule is 1–2 orders of magnitude higher than 10^{-12} at 1275°C and 1 atm). The liquid was called ferrobasalt by Seitz and Kushiro (1974). The nickel content of the ferrobasalt obtained at 1 atm is positively correlated with f_{O_2} and is too high for lunar ferrobasalt at f_{O_2} significantly higher than 10^{-12} atm. Thus, if carbonaceous chondrite is representative of the bulk composition of the moon, the f_{O_2} during partial melting cannot have exceeded about 10^{-12} atm. This f_{O_2} value is in close agreement with data on the oxygen fugacity of crystallization of lunar basalts obtained by Haggerty *et al.* (1970) and by Bell, El Goresy, and Mao (Year Book 73, pp. 464–467), lending credence to the suggestion that the bulk lunar composition may not be very different from that of carbonaceous chondrite.

It is more difficult to relate the melting behavior of the Allende meteorite to the formation of the earth. If the nickel partitioning coefficient between the core and the mantle is near 50 (Brett, 1971), the oxygen fugacity of the metal-olivine

equilibrium is near 10^{-11} atm. It has been suggested that the silicates break down to simple oxides in the lower mantle (Mao and Bell, Year Book 70, pp. 176–178; Ming and Bassett, 1974). If so, the metal/spinel data at $f_{O_2} = 10^{-10.5}$ atm may be used as a model, indicating $C_{Ni}^{metal-oxide} \sim 4$. Thus, partitioning of nickel between metal and oxide rather than between metal and silicate only results in a partition coefficient of Ni even more different from that of core/mantle. In other words, the melting of a composition similar to that of the Allende meteorite does not seem to generate a mantle and a core with the appropriate nickel contents.

Under the f_{O_2} conditions producing the most favorable nickel partitioning between metal and silicate, the olivine composition is Fo_{66} . However, the $Mg/(Mg + \Sigma Fe)$ of the mantle ranges between 0.8 and 0.95. In a simple oxide mixture, rather than silicates, the $Mg/(Mg + \Sigma Fe)$ may be even lower. Mao (Year Book 73, pp. 510–518) proposed that at pressures corresponding to the lower mantle FeO may disproportionate

to Fe^0 and Fe^{3+} . Such disproportionation may increase the $\text{Mg}/(\text{Mg} + \Sigma\text{Fe})$ of the mantle. In light of the data shown here, it appears, however, that carbonaceous chondrite may not be representative of the bulk composition of the earth.

EXPERIMENTAL PLUTONIUM, THORIUM,
AND URANIUM PARTITION COEFFICIENTS
WITH APPLICATION TO METEORITIC
ASSEMBLAGES

T. M. Benjamin, D. S. Burnett,†
and M. G. Seitz‡*

Measurements of Pu, Th, and U abundances in meteorites have resulted in estimates of the mean age of formation of the elements that comprise the solar system (Schramm and Wasserburg, 1970). Models of stellar nucleosynthesis and the relative contributions of each of the processes involved are constrained by the abundances of these long-lived radioisotopes at the end of nucleosynthesis.

Meteorites have retained these actinide (Pu, Th, U) abundances except for the radioactive decay during the interval between the end of nucleosynthesis and meteorite formation. Measurements of the actinide concentrations in meteoritic phases have yielded ratios of the post-nucleosynthesis actinide elements (Podosek, 1970; Keil *et al.*, 1976; Crozaz, 1974). Until recently the actinides (Pu, Th, U) were assumed to be nearly identical geochemically. Seitz, Burnett, and Bell (*Year Book 73*, pp. 451–454) demonstrated experimentally, however, that Pu, Th, and U differentially fractionate between crystals and silicate melts. Thus, the measured ratios of the meteoritic actinide elements may be different from the “initial” actinide ratios at the end

of nucleosynthesis as a result of chemical fractionation.

This report is a description of the preliminary experimentation to determine the precise values of actinide element partitioning between crystals and silicate melt and to assess the effect on this partitioning of variations in T , P , f_{O_2} , and bulk composition.

The techniques of crystal growth and trace element detection were described by Seitz (*Year Book 72*, pp. 581–586) and Seitz and Shimizu (*Year Book 72*, pp. 294–299). The bulk composition of the system is $\text{Di}_{50}\text{An}_{25}\text{Ab}_{25}$ with 15–25 wt % reagent grade $\text{Ca}_3(\text{PO}_4)_2$ or fluorapatite from Durango, Mexico, added to produce the appropriate liquidus phases. The plagioclase component is a stoichiometric glass (Kushiro, personal communication); the diopside is from Twin Lakes, California. Spikes of ^{235}U (17 ppm), ^{230}Th (24–54 ppm), or ^{239}Pu (8 ppm) were added to the charges. Runs were made in unsealed graphite capsules. The 1/2-in diameter furnace assemblies contain a boron nitride sleeve between the interior graphite heater (and sample capsule) and an outer talc sleeve. The boron nitride reduces access of H_2O , generated by dehydration of talc, to the sample area. The furnace assembly was dried for 30 min at 900°C under N_2 . The f_{O_2} in the graphite capsule is in the stability field of wüstite (Thompson and Kushiro, *Year Book 71*, pp. 615–616). Slow cooling (3.3°C/min) from above the liquidus aided crystal growth and suppressed chemical gradients in the melt that were observed at greater cooling rates (Seitz, *Year Book 73*, pp. 551–553). A JEOL scanning electron microscope was employed in track counting of the α - and fission-track detectors because the statistics obtainable on individual grains are limited by the small crystal size (20–50 μm). Heterogeneity on a millimeter scale in the glass is within 1 σ standard deviation, based on counting statistics.

Most runs were held at 1340°C for 1 hr at 20 kbar. In several extended runs

* Work carried out under a cooperative predoctoral fellowship program between the Geophysical Laboratory and the California Institute of Technology.

† California Institute of Technology, Pasadena, California.

‡ Argonne National Laboratory, Argonne, Illinois.

(40 hr) the presence of H₂O in the quenched glasses was detected by infra-red spectrophotometry. Microprobe analyses of these glasses yield 7–10 wt % H₂O by difference. The standard 1-hr runs, however, produce glasses with only ~0.01% of the absorption observed in the glasses from the 40-hr runs. More importantly, the microprobe analyses of the synthetic apatites yield the expected quantities of halogens for fluorapatite even for the longest runs, although the accuracy of the F analyses is not yet well established. Thus, it seems that the H₂O enters the system after crystallization has ceased, and there is little exchange between OH in the melt and F in the apatite. Runs in sealed Pt capsules are being carried out to ensure anhydrous conditions and to confirm the above conclusion.

The crystal-liquid partition coefficients, $K_{\text{Pu,Th,U}}^{\text{x1-liq}}$, for whitlockite, apatite, and diopside clinopyroxene are presented in Table 38. The data have been corrected assuming equilibrium Rayleigh fractionation except when the crystal-liquid partition coefficient is greater than 2 or when crystallization exceeds 50%, a value greater than any obtained in this study. ation (i.e., equilibrium only at the crystal-

liquid interface) during crystal growth that produces a concomitant change in actinide element concentrations in the melt. The corrected values are given in parentheses in Table 38. The validity of Rayleigh fractionation is based on the extremely low diffusion rates, relative to silicate melts, of Th and U in diopside and fluorapatite at 1340°C measured by Seitz (*Year Book* 73, pp. 586–588). The correction expression,

$$K^{\text{x1-liq}} = 1 - \frac{\ln[1 + S(K_A^{\text{x1-liq}} - 1)]}{\ln(1 - S)}$$

(Albarede and Bottinga, 1972) requires knowledge of $K_A^{\text{x1-liq}}$, the apparent partition coefficient based on the average concentration measured in the crystal, and S , the fraction crystallized. The modal compositions of the experimental charges were determined by mass-balance calculations based on microprobe analyses or by optical estimates. The magnitude of the correction is relatively insensitive to the modal composition of the charges

The zoning of the actinide elements in the crystals that is predicted by the Rayleigh fractionation model is not sufficiently large to have been detected conclusively in experiments to date. Superimposed on the zoning are the effects of

TABLE 38. Plutonium, Thorium, and Uranium Partitioning between Crystals and Melt at 20 kbar Pressure, 1340°C*

| | $K^{\text{Wh-11q}}$ | | $K^{\text{Ap-11q}}$ | | $K^{\text{Cpx-11q}}$ | |
|------|------------------------|----------------|---|-----------------------------|---|--------------------------------|
| Pu | 2.9 ± 0.1 2.8 ± 0.2 | (2.5) (2.6) | 1.20 ± 0.04 1.58 ± 0.09 1.99 ± 0.11 | (1.17) (1.46) (1.77)‡ | 0.17 ± 0.03 0.11 ± 0.03 | (0.19)† (0.12) |
| Mean | | | (1.47 ± 0.17) | | (0.16 ± 0.03) | |
| Th | 2.20 ± 0.07§ | (1.96)† | 0.52 ± 0.06 | (0.59) | 0.042 ± 0.006 | (0.047)† |
| U | 0.10 ± 0.03 | (0.12)† | 0.072 ± 0.012 0.061 ± 0.007 | (0.080)*¶ (0.068)*¶ | 0.013 ± 0.002 0.012 ± 0.003 0.008 ± 0.002 | (0.017) (0.012) (0.008)† |
| Mean | | | (0.074 ± 0.007) | | (0.012 ± 0.002) | |

* Errors in $K^{\text{x1-11q}}$ are 1σ based on counting statistics only. Errors of mean values either are 1σ based on the mean of the counting statistics/√N or are based on the error of the mean of the corrected values (in parentheses), whichever is larger.
† Correction based on optical estimate of S (fraction crystallized).
‡ Run held at 1340°C for 45 hr.
§ Recount of original 1-atm run of Seitz, Burnett, and Bell (*Year Book* 73).
|| Typographical error in *Year Book* 73; value should have been 0.6.
¶ Chlorapatite.

crystallization over a finite T interval and changes in bulk composition. Neither of these effects is included in the above equation. The absence of any pronounced zoning, however, indicates that these effects are small relative to the present statistical errors. As shown in Table 38, deleting the Rayleigh fractionation correction will only slightly alter the ratios in Tables 39 and 40 and will not significantly alter the discussion or conclusions that follow.

As seen from the data in Table 38, Pu is always fractionated into the crystals to a greater extent than is Th, whereas U is always excluded from the crystals relative to Pu and Th. The three actinides are preferentially incorporated in whitlockite [β - $\text{Ca}_3(\text{PO}_4)_2$] relative to apatite [$\text{Ca}_5(\text{PO}_4)_3(\text{F}, \text{Cl}, \text{OH})$] and clinopyroxene. Whitlockite has the largest Ca structural site; the diopsidic clinopyroxene contains the smallest site. The increasing size of the tetravalent actinide cations in the order $\text{Pu} < \text{Th} < \text{U}$ may be the fundamental property governing the above fractionation.

The variations of $K_{\text{Pu}}^{\text{Ap-liq}}$ in Table 38 may reflect variable amounts of oxida-

tion of Pu and U by H_2O or minor substitution of hydroxyl for halogens. The $K_{\text{Pu}}^{\text{Ap-liq}}$ for the 45-hr run (Table 38) varies only 35% from the mean of the two 1-hr runs, although the glass contains $\sim 7\%$ H_2O . Because of contamination from an unknown source, the apatites obtained in the U-spiked runs are chlorapatites (Table 38). Chlorine and fluorine occupy slightly different structural positions in apatite; thus fluorapatite and chlorapatite may have distinct $K^{\text{Ap-liq}}$. The difference should be small, however, as the actinides are presumably substituting for Ca.

Tables 39 and 40 contain concentration-independent ratios of the partitioning data as well as the data of Keil *et al.* (1976) on the Angra dos Reis achondrite for comparison. Both the synthetic and the meteoritic clinopyroxenes contain approximately 9 wt % Al_2O_3 . The agreement between the experimental data in Table 40 and the data on Angra dos Reis, a magmatic differentiate (Keil *et al.*, 1976), is remarkable. This agreement suggests that the experiments described in this report have simulated natural actinide element partitioning. Pellas and

TABLE 39. Ratios of Crystal-Melt Partition Coefficients for Actinides in Meteoritic Phases (i.e., $K_{\text{Pu}}^{\text{Wh-liq}}/K_{\text{U}}^{\text{Wh-liq}}$)*

| | Whitlockite | Apatite | Clinopyroxene | Reference |
|--|-------------|------------|---------------|-----------------------------|
| Pu/U | 22 ± 6 | 20 ± 4 | 13 ± 5 | This work |
| Th/U | 16 ± 5 | 8 ± 2 | 4 ± 1 | This work |
| Measured Actinide Element Ratios: Angra dos Reis | | | | (Keil <i>et al.</i> , 1976) |
| Pu/U | 0.0233 | | 0.0145 | |
| Th/U | 19 | | 4.0 | |

* Error based on those given in Table 38.

TABLE 40. Actinide Element Enrichment Factors (Crystal-Crystal Partition Coefficients) for Meteoritic Phases*

| | Plutonium | Thorium | Uranium | Reference |
|--------|------------------|------------------|------------------|---|
| Wh/Cpx | 16 ± 4 18 | 42 ± 7 49 | 10 ± 4 12 | This work Angra dos Reis (Keil <i>et al.</i> , 1976) |
| Ap/Cpx | 9 ± 3 | 13 ± 3 | 6 ± 2 | This work |

* Error based on those given in Table 38.

Storzer (1975) have measured the U contents of chlorapatite and whitlockite from equilibrated chondrites and obtained U^{Ap}/U^{Wh} ranging from 6 to 10 in contrast to the experimental ratio of 0.6 ± 0.4 . At present the reasons for this difference are not well understood.

Recent fission Xe measurements on meteorites of widely different chemical and physical compositions yield an apparent convergence at a Pu-U ratio of 0.015 that is inconsistent with models of continuous stellar nucleosynthesis. The examined meteorites include St. Severin, a highly reequilibrated ordinary chondrite (Podosek, 1970); an Allende coarse-grained, type-B (Grossman, 1975) white inclusion (Podosek, personal communication); and Angra dos Reis, a unique pyroxenitic meteorite (Keil *et al.*, 1976).

On the basis of the initial $^{87}\text{Sr}/^{86}\text{Sr}$ (Keil *et al.*, 1976), the Angra dos Reis meteorite is one of the most primitive objects studied to date; thus the similarity of Pu/U to that of St. Severin (which is believed to have had a long history of metamorphism) is surprising. It is conceivable that this agreement is fortuitous. If the Angra dos Reis meteorite is considered to be a cumulate rock, and if the experimental crystal-liquid partition coefficients presented in this report (Table 39) are applicable, then the Pu/U in the liquid from which Angra dos Reis separated is 0.0011 ± 0.0003 , an order of magnitude lower than that measured (Keil *et al.*, 1976). If ordinary chondrites contain the full "cosmic complement" of the actinide elements, the above result could mean that the Angra dos Reis meteorite may be 3×10^8 years younger than the St. Severin meteorite, but this conclusion is in disagreement with the initial $^{87}\text{Sr}/^{86}\text{Sr}$ data. Furthermore, by the same argument, the Th/U of the Angra dos

Reis parent liquid would be 1.1 ± 0.2 , a value much lower than the accepted solar system Th-U abundance ratio of approximately 4 (the Angra dos Reis whole-rock ratio, Table 39). Therefore, either the melt that coexisted with the Angra dos Reis meteorite was initially highly fractionated, or the amount of residual liquid following the accumulation of Angra dos Reis was very small. It is apparent that, being a cumulate rock, the Angra dos Reis may not contain abundances of Pu, Th, and U that are representative of the early solar system.

Further experimental studies of actinide element partitioning will be directed to the ordinary chondrites to determine whether or not the observed Pu-U ratios are products of chemical fractionation (as is found for Angra dos Reis). These results could help resolve the fundamental question of continuous or noncontinuous stellar nucleosynthesis.

Another application of the present experimental partitioning coefficients of the actinide elements is in the relative age-dating of ancient objects, meteoritic and lunar, by comparing actinide element ratios of any sample with those of an accurately dated meteorite as a reference point. The observed actinide element ratios for any of the phases (including glass) for which experimental data exist (whitlockite, apatite, diopside clinopyroxene, glass) can be corrected for chemical fractionation. The corrected Pu-U or Pu-Th ratios can be converted to an age, either younger or older, relative to the reference object. Internal consistency can be tested by the use of two or more phases. This precise dating of primitive objects is essential in addressing the major problems of understanding the time scales and processes involved in the early evolution of the solar system.

PETROLOGY OF LUNAR ROCKS AND METEORITES

A STUDY OF THE OXIDATION STATES OF
IRON AND TITANIUM IN SYNTHETIC
GLASSES OF LUNAR BASALT
COMPOSITION*P. M. Bell, H. K. Mao, and R. A. Weeks*

Lunar glasses quenched from liquids of rock composition contain chemical information on the oxidation states of iron and titanium that can be related by experiment to the temperature and oxygen fugacity of the melt. The redox characteristics have been preserved in the glasses, and it is possible to interpret them in terms of the chemical environment on the moon's surface at the time of quench. The oxidation states can be documented in crystal-field spectra by optical absorption features that have been observed, but not explained, in spectroscopic data obtained by earth-based telescope. The objective of the present study was to determine systematically the relationship of spectral features to oxygen fugacity, temperature, and composition.

Analytical and Experimental Methods

Transmission spectral measurements in the region 375–2500 nm were made of fragments of lunar glasses and of synthetic glasses whose compositions are described below (Table 41). The instrumental techniques employed in this study were described by Mao and Bell (1973) and by Bell, Mao, and Rossman (1975).

Table 42 shows compositions of the starting mixtures, the original glasses

quenched in air, and the glasses after treatment under controlled atmospheres more reducing than air. The procedure for changing the composition utilizes the process of diffusion of iron into the supporting Pt wire during melting at 1400°C. Depending on the wire thickness, P_{O_2} , temperature, and duration of the experiment, one can predict approximately the iron loss of the liquid to the Pt wire and thus produce a shift in composition toward lower iron values. The size of the experimental charge must be small (no greater than about 3 mm diameter) if it is to remain chemically homogeneous. The final composition must be determined and is reported in Table 42.

*Intermediate Iron-Titanium
Compositions (F_1T_3 to F_3T_1)*

Figure 117 shows spectra of starting composition F_3T_3 and gives the weight percentage of FeO for an initial TiO_2 content of 9.2 wt % at the various partial pressures of oxygen studied from $-\log P_{O_2} = 0.7$ (air) to $-\log P_{O_2} = 11.6$. The octahedral and tetrahedral Fe^{2+} bands are evident at 1000 and 1900 nm. What is significant in these spectra is the strong shoulder or slope in the spectral range 500–700 nm. This slope is the shoulder of a charge-transfer band caused by the $Fe^{2+}-Ti^{4+}$ coupled interaction. The slope was not observed in F_3T_0 and F_0T_3 compositions.

The 500–700 nm slope is a measure of the probability of the $Fe^{2+}-Ti^{4+}$ interaction, and its value is directly propor-

TABLE 41. Compositions of Synthetic Glasses

| | F_3T_3 | F_3T_0 | F_0T_3 | F_3T_1 | F_3T_2 | F_1T_3 | F_2T_3 |
|-----------|----------|----------|----------|----------|----------|----------|----------|
| FeO | 22.48 | 24.71 | 0 | 23.97 | 23.22 | 7.49 | 14.99 |
| TiO_2 | 9.04 | 0 | 11.66 | 3.01 | 6.03 | 10.79 | 9.91 |
| Al_2O_3 | 6.35 | 6.98 | 8.19 | 6.77 | 6.55 | 7.58 | 6.96 |
| CaO | 7.74 | 8.51 | 9.99 | 8.25 | 8.00 | 9.24 | 8.49 |
| MgO | 14.97 | 16.46 | 19.31 | 15.96 | 15.47 | 17.86 | 16.42 |
| SiO_2 | 39.42 | 43.34 | 50.85 | 42.03 | 40.73 | 47.04 | 43.23 |

TABLE 42. Compositions of Glasses Quenched at 1400°C

| Sample: | | F_3T_3 | | | | | |
|--------------------------------|------------------|-----------|--------|-------|--------|-------|-------|
| $-\log P_{O_2}$: | Starting mixture | 0.7 (air) | 6.6 | 7.5 | 9.1 | 10.0 | 11.6 |
| FeO* | 22.48 | 21.45 | 20.08 | 19.91 | 16.66 | 18.68 | 11.30 |
| TiO ₂ * | 9.04 | 9.05 | 9.35 | 9.54 | 9.27 | 8.95 | 10.56 |
| Al ₂ O ₃ | 6.35 | 6.36 | 6.55 | 7.05 | 6.93 | 6.68 | 7.22 |
| CaO | 7.74 | 7.91 | 8.17 | 8.57 | 8.55 | 8.05 | 9.06 |
| MgO | 14.97 | 14.79 | 15.44 | 13.46 | 16.39 | 15.66 | 17.16 |
| SiO ₂ | 39.42 | 39.76 | 40.74 | 40.82 | 42.76 | 41.13 | 44.16 |
| Totals | 100.00 | 99.31 | 100.33 | 99.36 | 100.57 | 99.15 | 99.47 |

| Sample: | F ₃ T ₂ | | F ₂ T ₃ | | F ₃ T ₁ | | F ₁ T ₃ | |
|-----------------------------------|-------------------------------|--------|-------------------------------|--------|-------------------------------|--------|-------------------------------|-------|
| −log P _{O₂} : | Starting mixture | 9.1 | Starting mixture | 9.1 | Starting mixture | 9.1 | Starting mixture | 9.1 |
| FeO* | 23.22 | 16.47 | 14.99 | 11.04 | 23.97 | 14.99 | 7.49 | 5.53 |
| TiO ₂ * | 6.03 | 6.45 | 9.91 | 10.27 | 3.01 | 3.33 | 10.79 | 11.00 |
| Al ₂ O ₃ | 6.55 | 7.33 | 6.96 | 7.29 | 6.77 | 7.61 | 7.58 | 7.71 |
| CaO | 8.00 | 8.90 | 8.49 | 9.00 | 8.25 | 9.24 | 9.24 | 9.43 |
| MgO | 15.47 | 16.66 | 16.42 | 16.68 | 15.96 | 17.30 | 17.86 | 18.02 |
| SiO ₂ | 40.73 | 44.61 | 43.23 | 46.01 | 42.03 | 48.17 | 47.04 | 48.25 |
| Totals | 100.00 | 100.42 | 100.00 | 100.28 | 100.00 | 100.64 | 100.00 | 99.94 |

| Sample: | | F_3T_0 | | | | | |
|--------------------------------|------------------|-----------|-------|-------|-------|-------|-------|
| $-\log P_{O_2}$: | Starting mixture | 0.7 (air) | 6.6 | 7.5 | 9.1 | 10.0 | 11.6 |
| FeO* | 24.71 | 22.95 | 21.32 | 21.37 | 19.97 | 19.11 | 7.73 |
| TiO ₂ * | 0 | 0 | 0 | 0 | 0 | 0 | 10.50 |
| Al ₂ O ₃ | 6.98 | 7.10 | 7.05 | 7.38 | 7.51 | 7.56 | 8.27 |
| CaO | 8.51 | 8.56 | 8.98 | 8.86 | 8.74 | 9.43 | 10.50 |
| MgO | 16.46 | 16.50 | 16.79 | 17.19 | 17.74 | 17.75 | 19.44 |
| SiO ₂ | 43.34 | 43.74 | 44.55 | 44.85 | 45.91 | 45.52 | 52.38 |
| Totals | 100.00 | 98.85 | 98.69 | 99.65 | 99.87 | 99.38 | 98.32 |

| Sample: | | F_0T_3 † | | |
|--------------------------------|------------------|------------|-------|-------|
| $-\log P_{O_2}$: | Starting mixture | 7.5 | 10.0 | 11.6 |
| FeO* | 0 | | | |
| TiO ₂ * | 11.66 | 11.56 | 11.75 | 9.54 |
| Al ₂ O ₃ | 8.19 | 8.03 | 8.10 | 8.45 |
| CaO | 9.99 | 10.05 | 10.22 | 10.11 |
| MgO | 19.31 | 18.74 | 18.45 | 19.34 |
| SiO ₂ | 50.85 | 50.86 | 50.92 | 51.93 |
| Totals | 100.00 | 99.30 | 99.48 | 99.43 |

* All Fe as FeO. All Ti as TiO₂.

† The compositions of F_0T_3 at $-\log P_{O_2}$ between 0.7 and 10.0 are the same as the starting material within detection limits.

tional to the algebraic product of the concentration of Fe^{2+} and Ti^{4+} . The influence of the 1000-nm crystal-field band on the charge-transfer slope causes a transmission "window" between the two absorption regions. For a given Fe^{2+}

concentration the height (absorption coefficient) and wavelengths of the window are approximately proportional to the Ti^{4+} concentration.

Figure 118 is a plot of the absorption slope at 20,000 wave numbers in absorp-

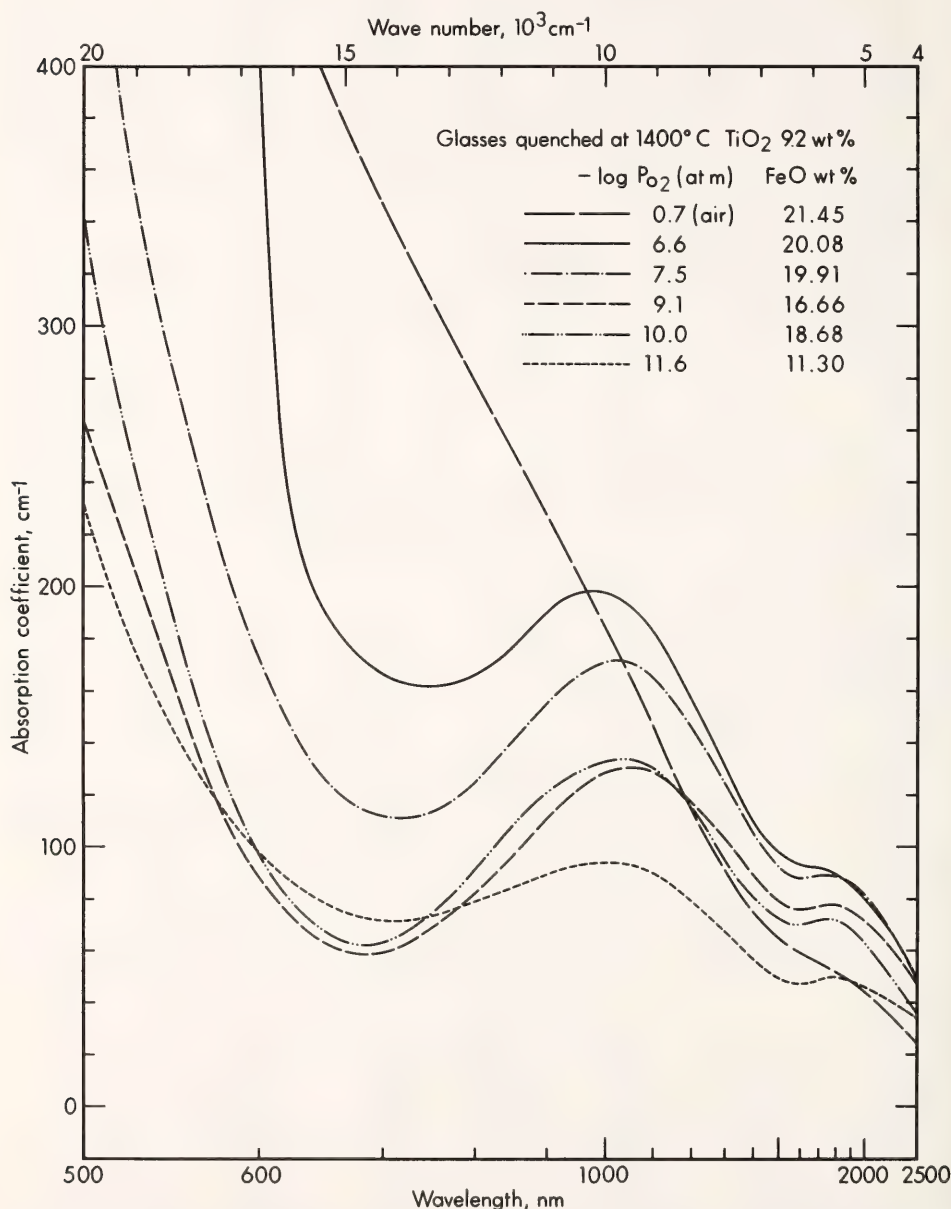


Fig. 117. Optical absorption spectra of glass F_3T_3 after treatment at 1400°C , and the various atmospheres at the oxygen fugacities indicated.

tion coefficient (cm^{-1}) per thousand wave numbers versus the algebraic product of the weight percentages of FeO and TiO_2 for the matrix of compositions. In each sample, the points plotted represent experimental products quenched at $-\log P_{\text{O}_2} = 9.1$ ($\text{CO}_2/\text{CO} = 1$), which is the approximate average oxygen fugacity (at 1400°C) of crystallization of most of the returned lunar samples. The excellent correlation of this plot makes it useful for calibration of telescope spectra, assuming no other interfering absorption. Figure 119 shows a plot of the spectral region from which the points on Fig. 117 were calculated. This plot (linear in wave number) tends to accentuate possible errors, but the con-

sistency of the algebraic relationship noted above is approximately continuous in this wavelength range.

Figure 120 shows a continuation of the observations plotted in Fig. 119 to 2500 nm (4000 wave numbers) in relatively compressed scale to show the wavelength shift of the transmission window. The shift is nonlinear and becomes small at high iron concentrations, as shown in the plot given in Fig. 121. This nonlinearity is a cause of scatter in the diagram in addition to that caused by varying $\text{Ti}^{3+}/\text{Ti}^{4+}$. Figure 122, which plots the absorption coefficient of the Fe^{2+} band at 1000 nm against weight percentage of FeO, indicates the correlation of this feature. In Fig. 117, in view

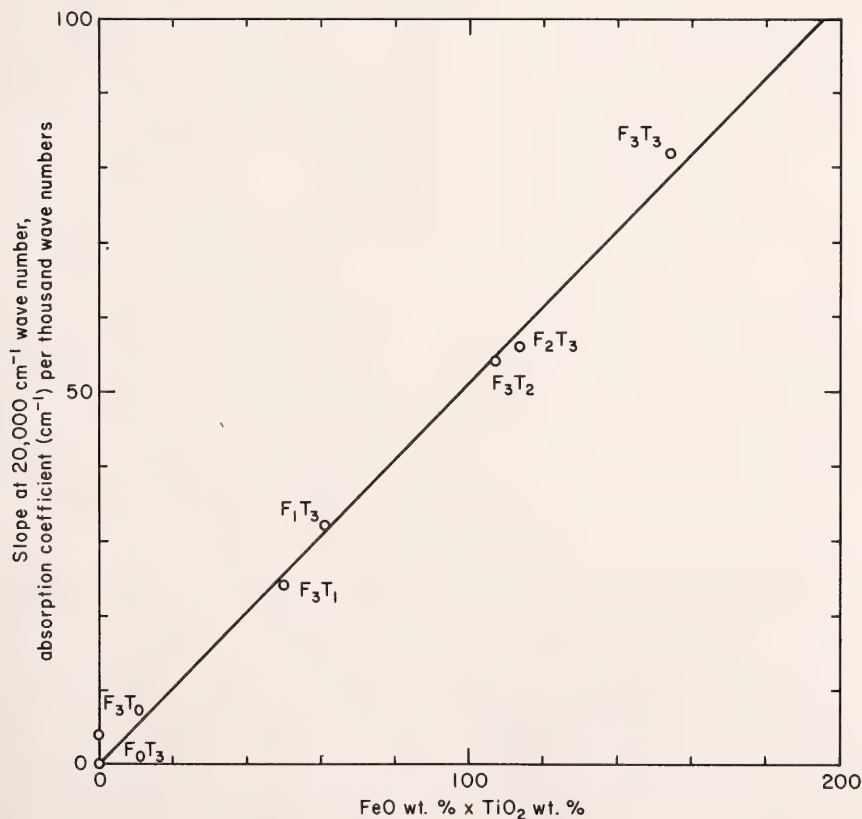


Fig. 118. Absorption slope at 20,000 wave numbers in absorption coefficient (cm^{-1}) per thousand wave numbers versus the algebraic product of the weight percentage of FeO and the weight percentage of TiO_2 of the seven compositions studied.

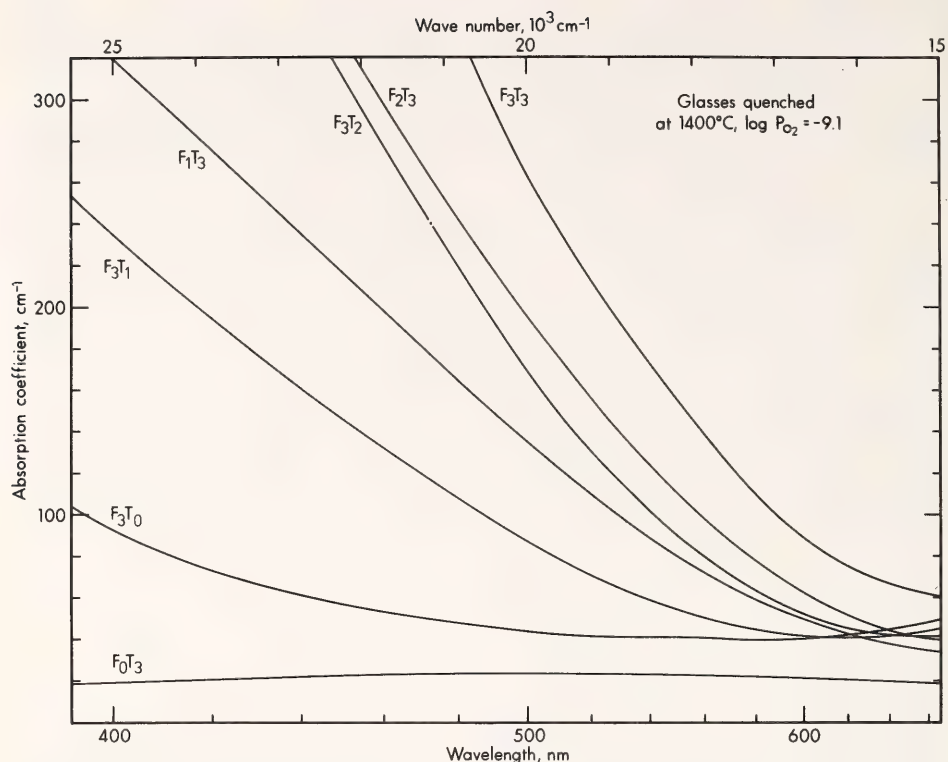


Fig. 119. Spectral region 400-660 nm for the glasses whose slope at 20,000 wave numbers is plotted in Fig. 118.

of the varying FeO content, it is seen that under increasingly reducing conditions the slope caused by Fe^{3+} diminishes as the 1000 and 1900 nm Fe^{2+} bands become stronger but is reestablished as the Fe^{2+} - Ti^{4+} transition occurs at lower oxygen fugacity.

Conclusions

All lunar soil samples returned from the Apollo and Luna projects contain glasses. The absorption properties of the glasses strongly influence the spectrum of the soil and hence the lunar surface. The spectral features are caused mainly by Fe^{2+} and Ti^{4+} , but also by Ti^{3+} , and they can be interpreted in terms of iron and titanium concentration and in terms of oxygen fugacity. The properties of the samples themselves, for example, the bright colors of lunar glasses, are indicative of the proc-

ess of their chemical formation. When the Ti^{4+} concentration dominates the Fe^{2+} concentration, as in synthetic glass compositions F_1T_3 and F_2T_3 , the glass is red in response to a shift in energy of the transmission window. Intermediate compositions give rise to colors of brown and orange, depending on oxygen fugacity at the quench.

Except for absorption effects that might be superimposed upon glass spectra (e.g., metallic coatings thin enough or particles small enough to transmit light; see Hapke and Wells, 1976), the spectra obtained in the present study can be used to document Fe^{2+} , Fe^{2+} - Ti^{4+} interaction, Fe^{3+} , and oxygen fugacity in the moon's surface from telescope spectra and in samples directly. The range of oxygen fugacity employed in the present study encompasses that observed in lunar samples. Examples of

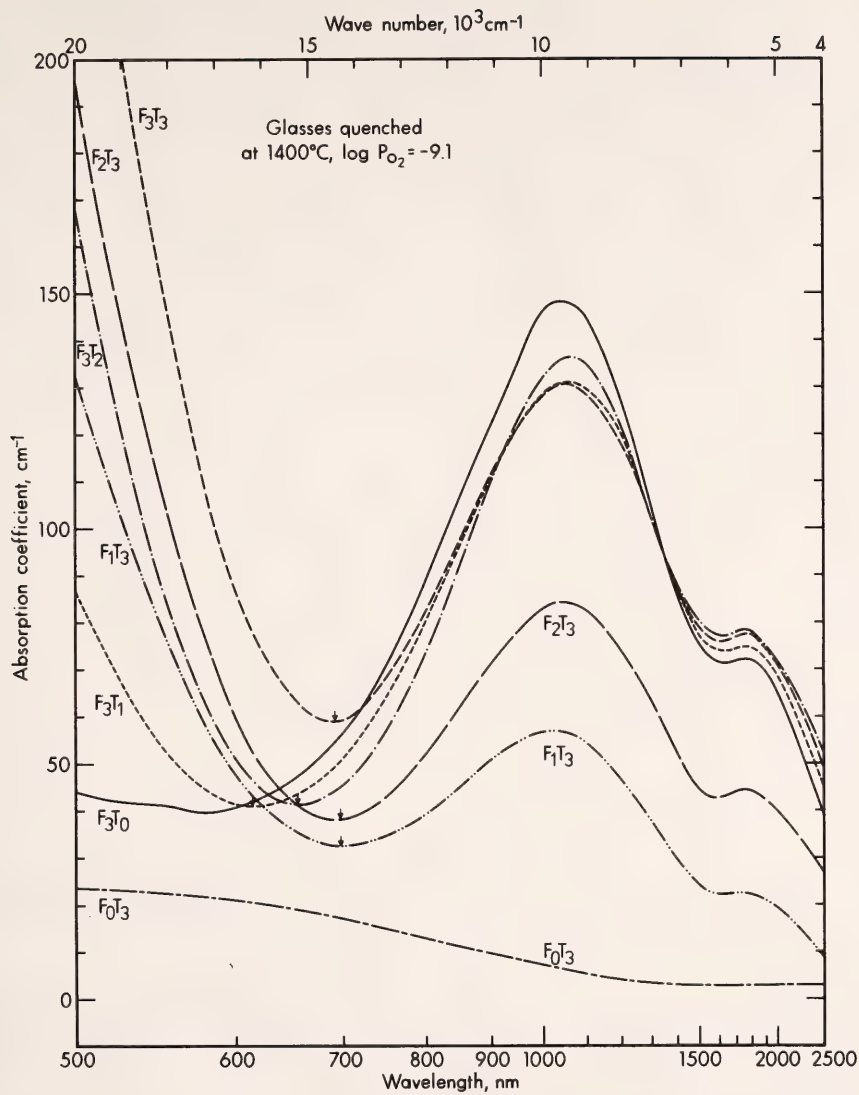


Fig. 120. Continuation of the observations plotted in Fig. 119 to 2500 nm (four wave numbers).

spectra of Apollo 14 and 15 and Luna 20 glasses are plotted in Figs. 121 and 122. In employing the present data, the spectral slope at 20,000 wave numbers can be used directly from Fig. 118. The plot in Fig. 122 compares the FeO content of synthetic glasses with that of glasses selected from Apollo 14 and 15 and Luna 20 soil samples, on the basis of the band intensity at 1000 nm, and

the high degree of accuracy is noteworthy. Application of the data in Fig. 121 requires further qualification. In Fig. 121 the wavelength minimum or "window" is plotted against weight percentage of TiO₂, and perhaps the most striking feature is the absence of points below a 45° boundary that isolates the lower right corner of the diagram. Because the data reflect oxidation

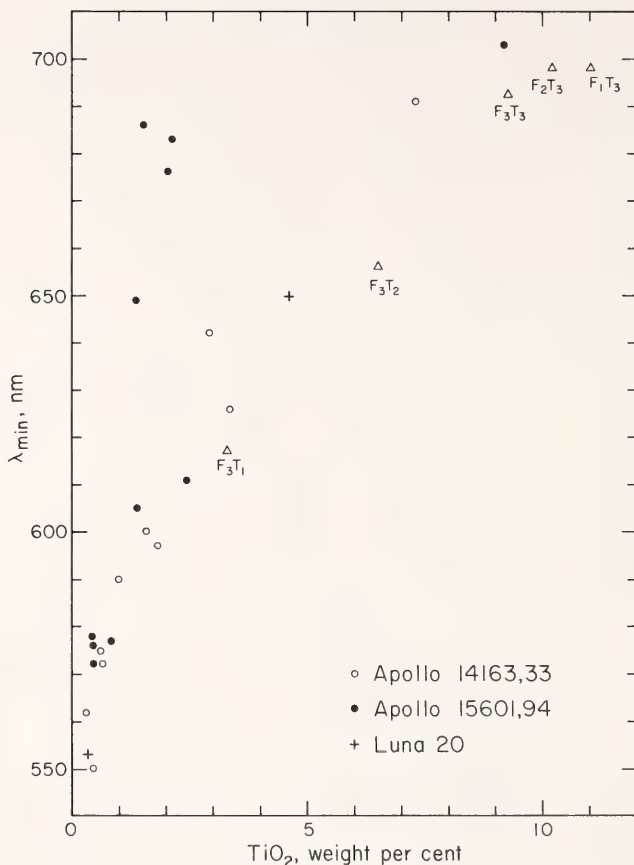


Fig. 121. Plot of the absorption "window" (λ_{\min}) of the glasses F_1T_3 , F_2T_3 , F_3T_3 against weight percentage of TiO_2 at $-\log P_{O_2} = 9.1$ compared with plots of glasses from Apollo 14 and 15 samples 14163,33 and 15601,94 and the Luna 20 sample.

states, the boundary approximates the limiting oxygen fugacity of the samples. Most of the Apollo and Luna data cluster about the experimental points, defining the average oxygen fugacity ($-\log P_{O_2} = 9.1$, $1400^\circ C$) as being close to the iron-wüstite buffer. Interpretation of strong departures from the boundary is more ambiguous. At the two ends (0 and 11 wt % TiO_2) of the compositional range, obvious nonlinearities exist. These are caused by the lack of sufficient TiO_2 to contribute to the Ti^{4+} - Fe^{2+} interaction and by the close proximity of the wavelength minimum to the steep slope of the Fe^{2+} crystal-field band centered at 1000 nm. If the TiO_2 content is less

than 2 wt %, an absorption shoulder, if it exists, is caused by Fe^{3+} , as described earlier. The Apollo 15 glasses whose wavelength minima at 1–2 wt % TiO_2 plot between 645 and 690 nm, appear to be less reduced by 1–1.5 orders of magnitude of oxygen fugacity on the basis of the data in Fig. 120. Clearly, the optimum range of titanium content in this diagram is 2–10 wt % TiO_2 . Compositions outside this range cause no error in interpretation but simply give insufficient useful information. The data plotted in Figs. 117–122 bracket the compositions and oxidation states of the lunar samples. The spectra of the lunar samples are characterized by glasses

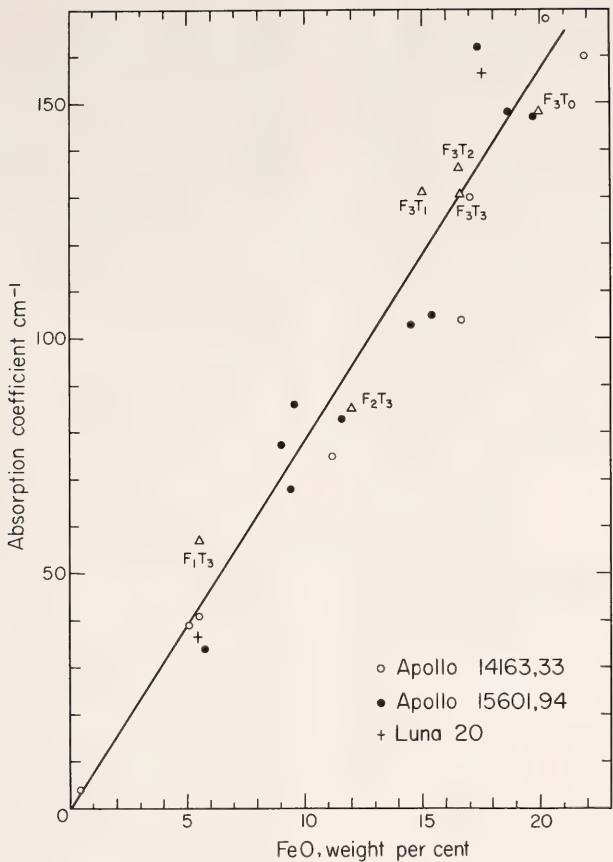


Fig. 122. Absorption maxima at 1000 nm of the glasses plotted in Fig. 121, plotted against weight percentage of FeO.

whose iron content is ferrous and ranges from 0 to 20 wt % FeO, and whose titanium content is a mixture of Ti^{3+} and Ti^{4+} and ranges from 0 to 20 wt % TiO_2 .

COMPOSITIONAL VARIABILITY OF THE LUNAR METALLIC PHASE

H. K. Mao and P. M. Bell

Many significant questions related to the state of equilibrium in the lunar crust depend on the interpretation of the metallic phase assemblage in the regolith. The questions range from those concerning the oxidation state of the outer portions of the moon to those regarding the metal contribution to the regolith from

meteoritic projectiles. If the iron-troilite association is observed and if contamination has not occurred, the eutectic relationship of Brett and Bell (1969) can be employed to define the minimum solidus. However, with the exception of homogeneous mare basalts, in which mineral homogeneity is great and evidence of contamination is lacking (if contamination occurred), most metal-bearing lunar samples of highland origin contain so-called lunar or meteoritic metal. The present study is an analytical approach to examine possible compositional evidence of metal origin.

Hewins and Goldstein (1975) have reviewed their extensive effort to distinguish between lunar and meteoritic metal

in lunar samples on the basis of composition alone. The parameters are the Fe-Ni-Co concentrations obtained by electron microprobe, although some workers (e.g., Gooley, Brett, and Warner, 1973; Misra and Taylor, 1975; Taylor, Misra, and Walker, 1976) consider such compositional evidence inadequate or invalid. In the present study metal grains in one of the rocks examined by Hewins and Goldstein (specimen 60015) was studied in great detail at high dimensional resolution for the following reasons:

1. Rock 60015 is an anorthosite that contains excellent textural and compositional evidence of having been quenched in the process of being melted. An anorthositic core grades in composition and texture to a mixed anorthositic-mafic zone (1 cm wide) and finally to a glassy rind of approximately basalt composition (1 cm wide) (see Selar and Bauer, 1974, for an analysis of the glassy rind and for a detailed description of rock 60015). The glassy rind contains molten rock from the regolith that has frozen at a stage where metal compositions in the anorthosite host, in the mixed zone, and in the outer melt zone can be used as indicators of reaction to a range of silicate hosts.

2. Metallic grains 10 μm in diameter or less have been quenched soon after forming and have not homogenized. Grains larger than 10 μm in diameter are relatively homogeneous in composition, giving the false impression that they represent an uncontaminated metal phase, possibly of meteoritic origin.

An objective of the study has been to examine an intermediate step in the process of chemical contamination by remelting of anorthosite in contact with mafic liquid, annealing, and melting in the regolith. An additional objective was to assess the dangers of assigning provenance to metals in lunar rocks solely on the basis of composition of the iron alloy. Rock 60015 is an anorthositic breccia coated with a dark rind of glassy quench product and, on the basis of analyses by

electron microprobe, is an example in which a liquid considerably more mafic than the anorthosite rock with which it is in contact has reacted in a narrow zone. Evidence of the reaction, indicated by the composition of the metallic phase in the several zones, was obtained in the present study.

Technique

A sample of 60015,4 was sectioned orthogonally, and the polished mounts were coated with standard Au-Pd alloy or with coatings of both C and Au-Pd. Metal particles of an average diameter of 10 μm or less were examined at 6000–25,000 \times magnification with a JEOL JSM35u scanning electron microscope. Analysis was performed with a Kevex nitrogen-cooled, lithium-drifted silicon detector whose resolution was measured to be 145 eV (MnK β). The nondispersive data were stored in a Nova-2 computer coupled with a Tracor TN-1700 multichannel analyzer (16K channels). Data analysis was done with a Digital Equipment PDP 11/05 computer, utilizing twin Digital Equipment disk storage units, and a Digital Equipment decwriter II.

Data reduction incorporated a program written by L. W. Finger and C. G. Hadidiacos (personal communication, 1976). To avoid the hazards of peak shift in digital-to-analogue conversion when least-squares stripping techniques are employed, the system employs total data analysis. Problems of take-off angle and particle geometry were essentially eliminated by using a flat sample with a fixed take-off angle of 45°.

Most metal grains of 0.1–0.2 μm diameter within the 10- μm host grains of silicate quench product were analyzed, and it was impossible to avoid totally sampling a small portion of the surrounding host matrix at 15 kV. By analyzing a sufficient number of grains, it was possible to reduce the uncertainty to 5–15 wt % of the amount present of a given element. Therefore, data reduction using only element ratios was appropriate, and no attempt was made to obtain quantita-

tive analyses. The elements Fe, S, P, and Ni were in sufficient abundance to make such an analysis meaningful, but generally the Co abundance was not sufficient (average 1 wt % or less), and it is not included in the reported data; S and P were analyzed for the purpose of identification of troilite and schreibersite.

In order to obtain the required constancy of the take-off angle, it was necessary to have a high degree of flatness in the polished surfaces of the mounts. Such a polish left most surfaces without apparent relief (except for occasional grooves not removed in polishing), and therefore the electron photomicrographs are secondary electron images, sensing chemical differences alone.

The analyses of individual grains showed variations within a grain, caused by zoned inhomogeneity, inclusions that had formed as eutectic or exsolved intergrowths (see Fig. 124), or perhaps lack of sample flatness at the 10- μ m diameter scale. This intragrain variability, in addition to the analytical uncertainty (5–15 wt % of the amount of a given element), made histogram plots of the data meaningless. The averages given in Table 43 were within the limits of analytical error. Each average included ten grains.

Textural Evidence for Two Liquids

Aside from chemical evidence, described below, of reaction of the metal phase with changing silicate melt compositions, there is extensive textural evidence that at least two liquids existed—the silicate melt and a metallic liquid. Along the edges of the metallic grains shown in Fig. 123 A,B, anorthite crystals

have grown, indenting what must have been a metallic liquid. Such relative indentation is caused by differences in the surface free energy between crystal and liquid. In Fig. 123A the anorthite crystals are surrounded by quenched silicate glass of more mafic composition.

Composition of the Metal Phase Assemblage

The metal phases consist of nearly pure metallic iron or an assemblage of iron-nickel-cobalt alloy and various amounts of troilite and schreibersite. The nickel content ranges in concentration between 0 and 30 wt %, depending on the silicate liquid composition with which it coexisted.

Figure 123A is a grain of Fe-Ni-Co alloy (Ni, 15 wt %) with a narrow rind of troilite and occasional inclusions of schreibersite. Figure 124 shows a sphere and an inner subsphere of iron-nickel (Ni, 10 wt %) with inclusions of troilite and schreibersite. The inner sphere is surrounded by an outer sphere of iron-nickel (Ni, 5 wt %) with numerous inclusions of troilite. Other grains are similar but have various amounts of Ni in the alloy. As listed in Table 43, metallic grains in unmelted anorthositic zones are essentially pure Fe metal.

Metallic grains, whose average compositions are listed in Table 43, occurred in all sections of 60015,4. Ten or more metallic grains were analyzed in each distinct zone: (1) glassy rind (1 cm wide), (2) intermediate reaction zone between mafic glass and anorthosite (0.5–1.0 cm wide), (3) partially melted zone adjacent to anorthosite (0.5–1.0 cm

TABLE 43. Average Fe/Ni Metal Compositions Determined by Nondispersive X-Ray Analysis*

| Grain Location | Fe | Ni | Other Phases Present |
|-------------------------|-----|----|-------------------------|
| Outer quench rind | 70 | 30 | None |
| Intermediate zone | 85 | 15 | Troilite, schreibersite |
| Zone adjacent anorthite | 95 | 5 | Troilite, schreibersite |
| Anorthite | 100 | 0 | None |

* The analysis is uncertain by 5%–15% of the amount of Fe and Ni present. Co was detected at levels of 1 wt % or less and is not listed.



A



B

Fig. 123. (A) Metallic grain contains troilite rim and inclusions of troilite and schreibersite. Note plagioclase crystals indenting spherical metallic surface (maximum grain diameter 10 μm). (B) Nickel-rich metallic grain showing indentation of anorthite crystals (maximum grain diameter 10 μm). Scanning electron photomicrograph.

wide), (4) unmelted anorthite (interior of rock). The compositions fell into the following categories (corresponding to the zones): (1) high nickel (30 wt % Ni, maximum); (2) intermediate nickel

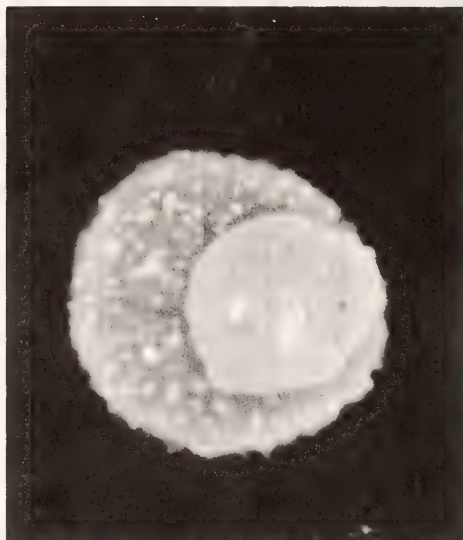


Fig. 124. Sphere and subsphere of iron-nickel alloy with inclusions of troilite and schreibersite (maximum grain diameter 10 μm). Scanning electron photomicrograph.

(10–15 wt % Ni); (3) low nickel (1–5 wt % Ni); (4) minor nickel. An apparent further variation in nickel content was noted in each zone (except unmelted anorthosite) where the range, high or low nickel, could be roughly correlated with the presence or the approximate amount of troilite and schreibersite.

The range in composition is compatible with the positions of zones of mafic melt, melt mixture of mafic and anorthositic compositions, and anorthosite host. The host shows recrystallization evidence of having been heated but not melted because no glass or quench textures were observed. The highest nickel concentrations are found in small grains near the outer portions of the rind. The system can be considered a hypothetical three-component system of silicate liquid, Fe, and trace Ni. The tie lines in such a system would fan out from the silicate component, and crystallization would first result in high nickel enrichment. Longer cooling times would have resulted in greater grain growth, homogenization, and a shift in composition toward the Fe-silicate join, approaching the bulk

equilibrium composition, as has apparently occurred in metal grains $>10\text{ }\mu\text{m}$ in diameter. Quenching has frozen the early nickel-rich disequilibrium stage in the smaller grains.

Grading toward the anorthosite core, very small grains ($0.01\text{--}0.03\text{ }\mu\text{m}$ diameter) show nickel enrichment, but larger grains (up to $10\text{ }\mu\text{m}$ diameter) show less, probably reflecting less available nickel in the anorthosite. The apparent variation of nickel in metallic grains within a zone correlates with troilite (and schreibersite for P) as follows. Sulfur-poor metallic melts extract sulfur from the silicate melt and selectively from troilite, causing a relative enrichment of nickel in the alloy. The reverse could also occur.

Metallic grains within the anorthosite host contained no troilite or schreibersite and rarely, detectable nickel or cobalt. These grains apparently exsolved from the anorthosite during heating and simply were out of contact with the melt system.

Summary

The measurement of composition of metallic grains demonstrates that they are not uniform and, furthermore, that their variation in composition has resulted from reaction with the liquids. The melting process was quenched at a stage where the metallic grains had not reached equilibrium, thereby providing evidence of the reactions. The process of contamination by a melt of meteorite composition or of composition other than that of the host rock is widespread in Apollo 16 rocks, and the process tends to mask the original constituents of the anorthosite. It is apparent that all the metallic phases in zones 1, 2, and 3 of 60015 were produced in this melting and contamination process. The variability in metal composition renders invalid an assignment of meteoritic or other origin based on composition. Meteoritic metal, if it had been present initially, has lost its chemical identity. The range in metal composition is an indicator of the

quenched-melt process and is clear evidence of compositional change in response to reaction with silicate liquids.

OPTICAL SPECTRA OF THIN METALLIC COATINGS WITH APPLICATION TO THE SPECTRA OF LUNAR SOIL SAMPLES

P. M. Bell and H. K. Mao

Apollo soil samples of the lunar regolith contain minute (approximate diameter: $1\text{--}200\text{ }\mu\text{m}$) glass-welded particles that form continuously from impacts of micrometeorites. The particles are agglutinates in a process that involves a surprising chemical fractionation on a submicrometer scale (Rhodes *et al.*, 1975). The agglutinate fractions of the soils sampled during the Apollo are enriched, relative to the bulk soils, in the ferromagnesian elements (Fe, Ti, Mg, Mn, Cr, Sc) and lithophile elements (K, La, Ce, Sm, Yb, Lu, Hf, Th, Ta). The agglutinate fractions are depleted in elements that readily enter plagioclase (Ca, Na, Al, En). In the more "mature" or exposed soils, the agglutinates can comprise over 50% of the soil, so the process of chemical fractionation is recognized to change significantly the chemical character of the lunar regolith.

The formation of agglutinates is accompanied by the precipitation of iron particles of submicrometer size that may have precipitated in a chemical disproportionation process, on the basis of their optical absorption spectra (Mao, Bell, and Adams, *Year Book* 74). Whether or not disproportionation actually occurred is determined with difficulty because of the limitations of analysis of particles of submicrometer size; however the spectral properties of agglutinates contribute supporting evidence. Moreover, identification of the spectral dependence on agglutinate properties is of considerable importance in the interpretation of bulk soil spectra and of spectral reflectance curves obtained from earth-based telescopes. In the present study spectral data in the range $0.3\text{--}2.5\text{ }\mu\text{m}$ were obtained on sam-

ples of glass coated with thin films (10–100 Å) of carbon, iron, and gold palladium alloy. The spectra were compared with that of lunar agglutinate sample 67701. In this report data are presented that demonstrate that metal coatings, if thin enough, produce spectral features, some of which are similar to those of agglutinates.

Metallic Coatings

Samples of powdered silica glass were placed in a vacuum evaporator and then coated by evaporating carbon, iron, or gold palladium. The powders were removed, ground, and replaced for a total of three treatments. Silica glass slides (1-mm thickness) were also coated.

The samples were stored in vacuo after removal from the evaporator. For spectral analysis, they were promptly placed into the sample part of a Cary 17I crystal-field spectrometer. It should be noted that even under the procedures followed, oxidation of the metallic coatings could occur, and because the coating thicknesses are in the angstrom range, oxidized metal could contribute to an observed spectrum. However, the spectrum of metallic iron did not show characteristic bands of the ferric (Fe^{3+}) ion that would have indicated that oxidation took place. On the other hand, ferric iron bands tend to be broad, and low concentrations may not be detected. The experimental samples have been subjected to less atmospheric exposure than the lunar samples that contain metal both as coatings and as particles and droplets protected in glass. Thus the experimental values may approach those of the returned lunar samples.

Spectra

The spectra of metallic iron, carbon, and gold-palladium alloy coatings on silica glass are shown in Fig. 125. Several features are apparent. Both iron and carbon coatings absorb in the near ultraviolet regions and their spectra appear as steep shoulders between 950 and 350 nm. Iron shows an additional fea-

ture in that its absorption spectrum is a two-component curve. In the range 950–3000 nm, the slope is gentle; in the range 350–950 nm, the slope is steep. The cause of the slope, a possible background imprint of ferric iron absorption, could not be determined. The gold-palladium alloy coating causes a darkening effect, which is realized as a nearly constant background level. No steep slope such as those observed with iron and carbon occurs.

The agglutinate sample studied was 67701,38, whose features were described last year (Mao, Bell, and Adams, *Year Book* 74). A portion of the agglutinate that contained glass and fine metallic droplets and that had a characteristic brown color caused by submicroscopic inclusions was selected for spectral analysis. The spectra in Fig. 125 show marked similarities to that of the synthetically produced iron coating. It should be pointed out, however, that the agglutinate sample is not coated; the metallic grains are completely isolated within glass.

The findings of this study can be summarized as follows. Metals that are normally opaque produce spectral absorption features from transmitted radiation if the metals are thin (10–100 Å). The features are, in some cases, merely an increase in background throughout the wavelength region studied (350–3000 nm); however, iron produces a steep two-component absorption shoulder.

The absorption shoulder of the iron-coating nodules approximates the absorption curve of agglutinate particle 67701,38, suggesting that both spectra arise from the same cause. The two-component slope of the spectra may be caused by a mixture of ferric and metallic iron. If this interpretation is correct, the theory of a disproportion reaction in agglutinate that produces ferric and metallic iron would be supported. Possible oxidation of both experimental and lunar specimens as a result of atmospheric exposure would lead to the same interpretation.

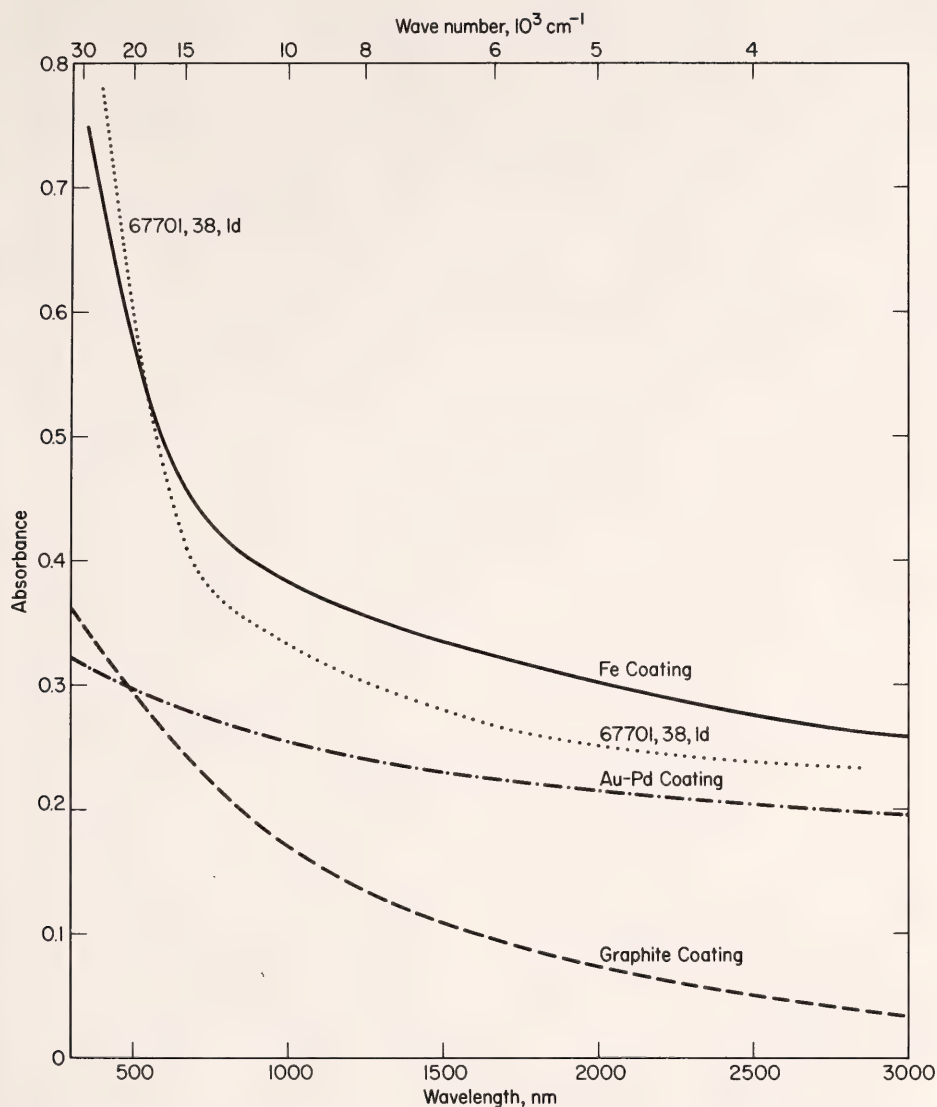


Fig. 125. Optical spectra of Fe, Au-Pd alloy, and graphite coatings on silica glass, and the optical spectra of agglutinate specimen 6770I,38,Id.

CRYSTAL-FIELD SPECTRA OF FASSAITE FROM THE ANGRA DOS REIS METEORITE

P. M. Bell and H. K. Mao

The Allende fassaite (Mao and Bell, *Year Book 73*) is unique in that it contains the Ti^{3+} ion but is iron-free. The Angra dos Reis fassaite of the present study may also contain Ti^{3+} but con-

tains abundant ferrous iron as well. Crystal-field spectra of the fassaites show the absorption bands of the titanium and iron ions; the band energies are related to transition energies, some of which are subject to crystal-field splitting. One of the fassaites was evidently more strongly reduced and the other more strongly oxidized than lunar

pyroxenes, as judged from the crystal-field spectra. Few lunar pyroxenes show absorption at energies appropriate for the Ti^{3+} crystal-field transition. The Angra dos Reis fassaite is close to lunar pyroxenes in composition, and its ferric iron content is believed to reflect more oxidizing conditions of formation.

The Crystals

The crystals of fassaite were selected from a sample of the Angra dos Reis meteorite supplied by Dr. M. Gaffey (see Gaffey, 1976). The meteorite is composed predominantly of pyroxene, with minor olivine and accessories. There is a rich complement of rare earth elements whose contribution to the optical spectra could be significant but is as yet unevaluated. Compositions of the fassaite are given in Table 44 (Keil *et al.*, 1976).

The crystals were oriented and mounted polished on parallel sides. Polarized spectra were made at maximum and minimum absorption directions.

Complex Optical Absorption Properties

During orienting of the fassaite crystals, it became evident that the directions of maximum and minimum absorption in plane polarized light did not coincide with crystallographic (except *b*) or optical (indicatrix) axes. Such a relationship is possible with monoclinic or triclinic symmetry, but the absorption

(pleochioism) in these crystals follows no simple laws. The minimum absorption can be observed in a single direction only when the optic plane is aligned with the polarization direction. Rotation of the crystals about the axis where minimum absorption occurs causes maximum absorption in all directions.

Attempts to distinguish electric transition vectors or magnetic transition vectors in the above observations could not be made unless both electric and magnetic processes were active simultaneously. Obviously, the types of electric vector (dipole and quadrupole) could not be distinguished either. The transitions may or may not be as complex as they now appear.

The optical orientation of Angra dos Reis fassaite is shown in Fig. 126. The optic plane is oriented normal to the *b* axis (β is the optic normal). The direction normal to the *c* axis, *n*, is the unique direction of minimum absorption. Note the radiation-source orientation diagram for the light propagation vector (\vec{L}), the electric vector (\vec{E}), and the magnetic vector (\vec{H}).

Figure 127 shows the absorption spectra. There are five directions instead of the usual three (α , β , γ) for the absorption at 480 nm. The absorption maxima are not of constant intensity (absorption coefficient, cm^{-1}), and the differences are not yet explained. The *n* direction is unique for the following reasons. Minimum absorption occurs only when \vec{E} is parallel to *n*, with \vec{L} parallel to the *c* axis. If \vec{E} remains parallel to *n*, but \vec{L} is rotated away from parallelism with *c*, minimum absorption disappears.

The absorption band close to 1000 nm appears to be typical of the d^6 band of octahedral Fe^{2+} in pyroxene (Bell and Mao, *Year Book 71*), but the ferrous iron content is low, and thus the resolution is relatively poor (see Table 44).

Conclusions

The Angra dos Reis fassaite has complex absorption properties and strong polarized absorption spectra. The prop-

TABLE 44. Composition of Angra dos Reis Clinopyroxene (Fassaite) Obtained by Electron Microprobe Analysis

| | |
|----------------------------------|--------|
| SiO ₂ | 45.9 |
| TiO ₂ | 2.16 |
| Al ₂ O ₃ | 10.0 |
| Cr ₂ O ₃ | 0.21 |
| Fe ₂ O ₃ * | 2.89 |
| FeO* | 4.1 |
| MnO | 0.06 |
| MgO | 10.6 |
| CaO | 24.1 |
| Total | 100.02 |

* Ferrous and ferric iron are in a proportion to satisfy the total oxygen content calculated by difference.

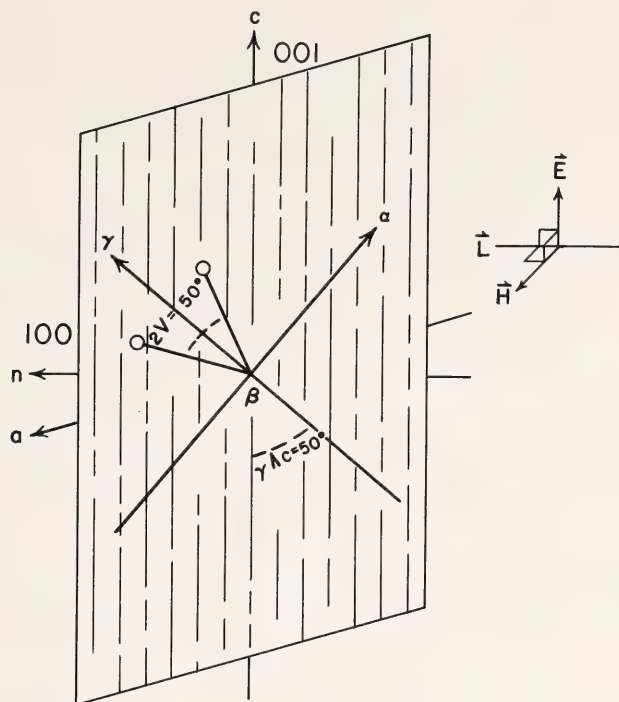
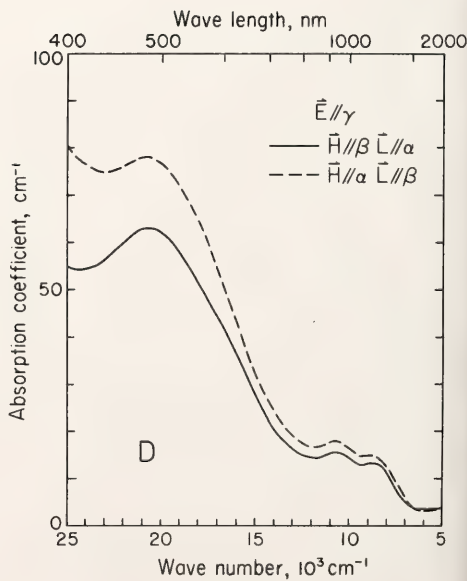
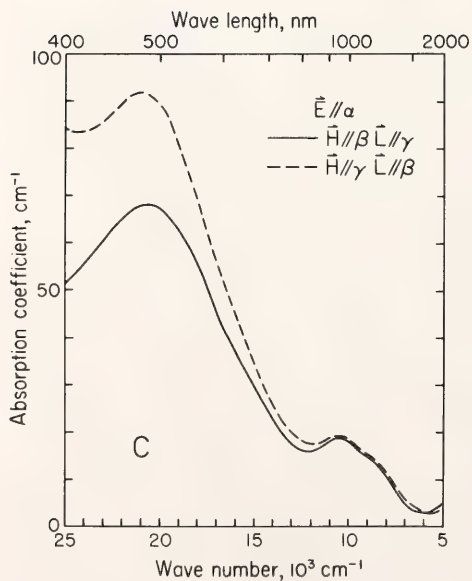
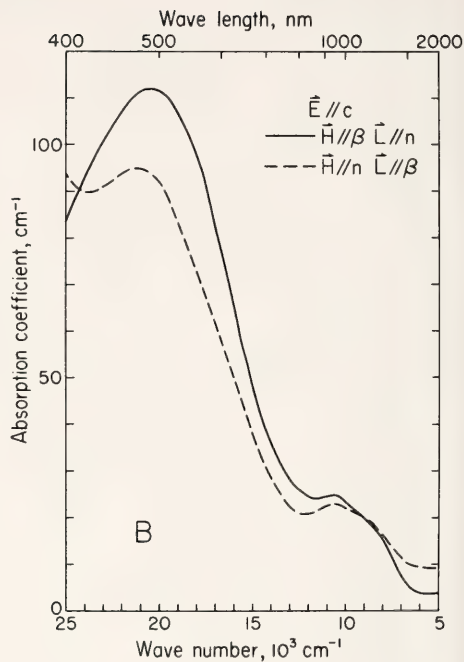
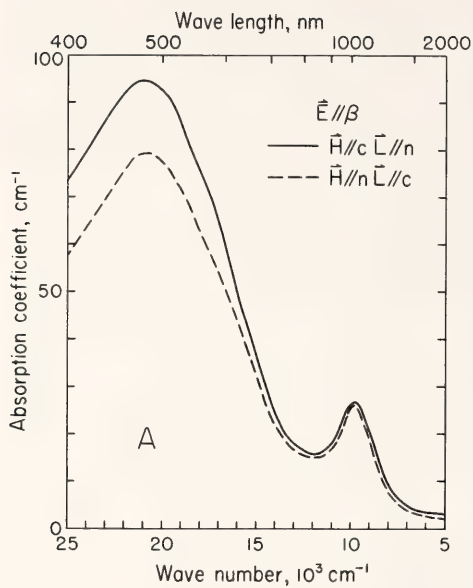


Fig. 126. Orientation of Angra dos Reis fassaite (note also vector diagram for \vec{L} , direction of light propagation; \vec{H} , direction of magnetic vector; \vec{E} , direction of electric vector).

erties are not understood at this time, but the following conclusions can be drawn. The absorption band at 1000 (and 2000) nm is caused by octahedral Fe^{2+} , and the band at 500 nm is probably caused by Fe^{3+} , although probably not by a simple electronic transition. Comparison of the spectra with those of the Allende fassaite, lunar pyroxenes, and synthetic glasses suggests that the Angra dos Reis fassaite is less reduced. The intensity of the 500-nm band is significantly greater than that of the 500-nm band normally observed in Fe^{3+} -bearing pyroxene and dominates the spectra. The Angra dos Reis meteorite consists mostly of fassaite; thus the 500-nm band also dominates the spectra of the entire meteorite. This dominance should be noted in interpret-

ing telescope spectra of objects in space.

The unique property of the Angra dos Reis fassaite is that it absorbs light at 480-nm wavelength in all directions except one (n) in which light in the visible region is not absorbed in a band. Near 1000 nm in the near infrared, Fe^{2+} absorption bands occur, evidently unaffected by the absorption in the visible. In plane polarized visible light the crystal is deep pink, except in the minimum absorption direction, where it is nearly colorless. The observed absorption behavior cannot be explained by conventional electric or magnetic dipole vectors. It would appear that the Angra dos Reis fassaite either has absorption caused by both vectors being nearly aligned or absorbs because of some yet undiscovered process.



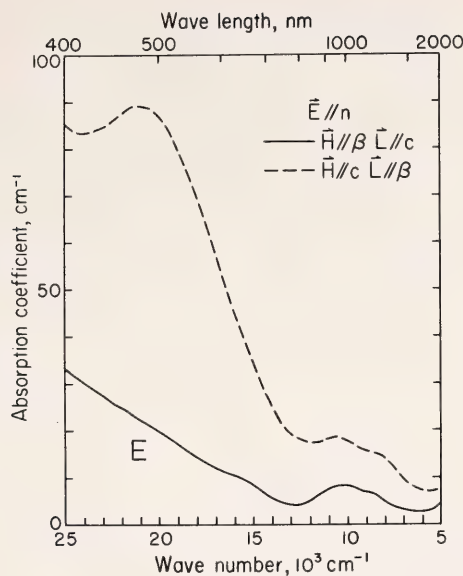


Fig. 127. Polarized absorption spectra of Angra dos Reis fassaite. (A) \vec{E} parallel to β ; (B) \vec{E} parallel to c ; (C) \vec{E} parallel to α ; (D) \vec{E} parallel to γ ; (E) \vec{E} parallel to n .

MINERALOGY

THE CRYSTAL CHEMISTRY OF MELANITES AND SCHORLOMITES

F. E. Huggins, D. Virgo, and H. G. Huckenholz

The crystal chemistry of natural melanite and schorlomite garnets has been a source of controversy for many years. Two main problems have been identified: (1) What are the relative site preferences of Al, Fe, and Ti for the tetrahedral site? (2) What are the oxidation states of iron and titanium in these garnets? Present interest in these garnets arises from the fact that answers to these two questions may show that such garnets are indicators of thermal history, based on the distribution of elements between distinct crystallographic sites, and also of oxygen-fugacity conditions at the time of formation, as a result of elements in more than one oxidation state in the garnet structure. In view of the occurrence of such garnets in alkalic igneous rocks, often in association with carbonatite complexes, constraints on the thermal history and oxygen-fugacity

conditions at the time of formation of the garnets will also apply to alkaline igneous rocks containing such garnets and possibly to carbonatite complexes as well.

In the present study, a detailed interpretation of the crystal chemistry of melanites and schorlomites is given that includes answers to the two questions discussed above. The techniques of electron microprobe analysis and Mössbauer spectroscopy in conjunction with the cation distribution scheme established for synthetic titanium silicate garnets (Huggins *et al.*, *Year Book* 74, pp. 579–585; Huggins, Virgo, and Huckenholz, 1976a) were used to resolve these outstanding crystal-chemical problems.

Eleven melanite and schorlomite garnets* were investigated in detail in the course of this study; their location, petro-

* The generosity of Drs. R. A. Howie, Th. G. Sahama, S. O. Agrell, and J. S. White, Jr., who supplied specimens of melanites and schorlomites for this study, is gratefully acknowledged.

TABLE 45. Locations, Petrologic Occurrences, and Symbols for Garnet Samples

| Symbol | Description |
|--------|--|
| O | Ijolite from Oka carbonatite complex, Quebec. Rock supplied by M. Rosenhauer. |
| F | Calc-silicate bomb in pyroclastic sediments, Alban Hills, Frascati, Italy. |
| LB | Nepheline syenite from Loch Borolan, Scotland. Coarse grains supplied by R. A. Howie. |
| SB | Serpentinized peridotite from Dallas gem mine, San Benito County, California. USNM R15546-5, supplied by J. S. White, Jr. |
| OL | Volcanic ash from Oldoinyo Lengai, Tanzania. Magnetic separate of ash supplied by Th. G. Sahama. |
| DW | From skarn near Dirbat Well, Red Sea Hills, Sudan. Coarse powder supplied by R. A. Howie. |
| K | Phonolite dike from Oberrotweil, Kaiserstuhl, West Germany. |
| Iv | Pegmatoid in ijolite, from Iivaara alkaline igneous complex, Finland. Massive single crystal supplied by Th. G. Sahama. |
| ML | Melteigite from Iivaara alkaline igneous complex, Finland. Rock supplied by Th. G. Sahama. |
| R | Agglomerate from Rusinga Island, Uganda. USNM 107272, supplied by J. S. White, Jr. |
| Ar | Schorlomite-wollastonite-titanaugite vein in pegmatitic pyroxenite from Ardnamurchan, Scotland. Rock section supplied by S. O. Agrell. |

logic occurrence, and symbols are described in Table 45. All the garnets were black or very dark brown macroscopically; however, their colors in grain mounts varied from yellow to an almost opaque smoky red.

Results

The electron microprobe analyses were carried out in the manner described by Finger and Hadidiacos (*Year Book* 71, pp. 598–600). Seven elements were found to constitute the quantitative analysis (Table 46); however, an additional 14 elements were sought on a qualitative basis to rule out the possibility of other

elements contributing significantly to the garnet analysis. The lower half of Table 46 shows the formulae of the garnets calculated on the basis of the cation: anion ratio of 8:12. From such calculations estimates of $[\text{Fe}^{2+}]/\Sigma\text{Fe}$ were obtained; it should be noted, however, that this calculation could also be carried out in terms of reducing Ti^{4+} to Ti^{3+} and therefore does not distinguish between Ti^{3+} and Fe^{2+} but rather yields the total number of cations of reduced charge. Hence $[\text{Fe}^{2+}]$ includes not only Fe^{2+} cations but also the charge reduction due to Ti^{3+} , if present.

The ^{57}Fe Mössbauer spectra were obtained in the manner described previously (*Virgo, Year Book* 71, pp. 607–608), and results were evaluated as described by Weber, Virgo, and Huggins (*Year Book* 74, pp. 575–579). The spectra were taken at 77°K to improve the resolution of the ferrous peaks and to eliminate differences in recoil-free fractions between Fe^{2+} and Fe^{3+} absorptions in garnets, which have been found to be significantly different at room temperature (Amthauer, Annersten, and Hafner, 1976; Whipple, 1973). In order to accommodate the ferrous absorptions as well as the ferric absorptions, it was necessary to fit the spectra with up to six peaks (Fig. 128). As indicated in Fig. 128, the spectra are interpreted as consisting of up to five doublets: tetrahedral and octahedral ferric and tetrahedral, octahedral, and dodecahedral ferrous. The relative areas of the different absorptions for the 11 garnet samples are listed in Table 47.

Discussion

A comparison of $[\text{Fe}^{2+}]/\Sigma\text{Fe}$ as determined by Mössbauer spectroscopy and by calculation from the electron microprobe analyses or wet chemical analyses, if available, is shown in Fig. 129 for the eleven garnets and for four others reported by Whipple (1973) and Dowty (1971). With the latter two techniques, Fe^{2+} cannot be distinguished from Ti^{3+} , so $[\text{Fe}^{2+}]/\Sigma\text{Fe}$ includes con-

TABLE 46. Chemical Analyses and Formulae of Garnets

| | O | F | LB | SB* | OL | DW | K | Iv | ML | R | Ar |
|--|-------|-------|--------|-------|--------|-------|-------|-------|-------|-------|-------|
| (a) Analyses, wt % | | | | | | | | | | | |
| SiO ₂ | 34.77 | 35.49 | 34.57 | 33.44 | 30.89 | 27.14 | 28.70 | 28.38 | 28.95 | 28.17 | 26.15 |
| TiO ₂ | 2.48 | 2.53 | 3.56 | 8.57 | 10.84 | 12.37 | 12.72 | 13.18 | 13.20 | 14.34 | 16.46 |
| Al ₂ O ₃ | 4.68 | 6.57 | 2.69 | 1.55 | 0.70 | 5.23 | 2.24 | 0.93 | 1.02 | 1.05 | 3.51 |
| Fe ₂ O ₃ † | 23.17 | 20.62 | 25.43 | 20.58 | 24.36 | 20.44 | 22.19 | 23.42 | 22.84 | 22.04 | 21.15 |
| MgO | 0.45 | 0.57 | 0.40 | 0.71 | 0.47 | 0.86 | 0.89 | 0.85 | 0.96 | 0.89 | 0.52 |
| MnO | 0.99 | 0.28 | 0.64 | 0.13 | 0.40 | 0.09 | 0.41 | 0.20 | 0.25 | 0.33 | 0.38 |
| CaO | 32.58 | 33.01 | 33.36 | 33.66 | 32.64 | 30.66 | 31.43 | 31.54 | 31.77 | 31.65 | 31.18 |
| Totals | 99.12 | 99.07 | 100.65 | 98.64 | 100.30 | 99.79 | 98.58 | 98.50 | 98.12 | 98.47 | 99.35 |
| (b) Formulae, assuming 8:12 cation:anion ratio | | | | | | | | | | | |
| Si | 2.900 | 2.924 | 2.868 | 2.834 | 2.623 | 2.276 | 2.470 | 2.472 | 2.492 | 2.442 | 2.250 |
| Ti | 0.154 | 0.157 | 0.222 | 0.546 | 0.692 | 0.780 | 0.823 | 0.863 | 0.854 | 0.935 | 1.065 |
| Al | 0.458 | 0.638 | 0.263 | 0.155 | 0.070 | 0.517 | 0.227 | 0.101 | 0.103 | 0.107 | 0.353 |
| Fe ³⁺ | 1.433 | 1.201 | 1.557 | 1.083 | 1.299 | 1.290 | 1.186 | 1.228 | 1.204 | 1.140 | 1.017 |
| "Fe ²⁺ " | 0.020 | 0.077 | 0.030 | 0.229 | 0.257 | 0.000 | 0.251 | 0.268 | 0.275 | 0.298 | 0.351 |
| Mg | 0.054 | 0.070 | 0.049 | 0.090 | 0.059 | 0.107 | 0.114 | 0.120 | 0.123 | 0.115 | 0.065 |
| Mn | 0.069 | 0.020 | 0.045 | 0.009 | 0.029 | 0.006 | 0.030 | 0.016 | 0.018 | 0.024 | 0.025 |
| Ca | 2.912 | 2.914 | 2.965 | 3.055 | 2.970 | 3.024 | 2.898 | 2.932 | 2.930 | 2.939 | 2.874 |
| ΣFe | 1.453 | 1.278 | 1.587 | 1.312 | 1.566 | 1.290 | 1.437 | 1.496 | 1.479 | 1.438 | 1.368 |
| "Fe ²⁺ "/ΣFe | 0.015 | 0.06 | 0.02 | 0.17 | 0.17 | 0.00‡ | 0.17 | 0.18 | 0.19 | 0.21 | 0.26 |

* SB is an average of all zones (cf. Huggins, Virgo, and Huckenholz, 1976b).

† All iron as Fe₂O₃.

‡ Σ oxygen = 11.96.

tributions to the reduced state from both cations. Therefore, the excess "Fe²⁺"/ΣFe indicated by the chemical methods over the Mössbauer calculation can be attributed to Ti³⁺ because titanium is the only other major element in the garnet that exhibits variable valency. In Fig. 129, the presence of Ti³⁺ is indicated by the deviation of the data points to the right of the 1:1 line. Except for samples SB and possibly GN4, Ti³⁺/ΣTi is not found to exceed 0.10. For SB, Ti³⁺/ΣTi reaches 0.25, an exceptionally high value, but agrees in principle with the findings of Manning and Harris (1970) on a sample from the same locality. These authors concluded that most of the titanium was Ti³⁺ in their particular garnet on the basis of the optical absorption spectrum.

By combining the Mössbauer and electron microprobe data, the crystallographic location of nearly all the cations can be ascertained (Table 48). It is not possible, however, to determine

directly the distribution of Al and Ti between the octahedral and tetrahedral sites and, for some samples, the distribution of Fe²⁺ and Mg between the octahedral and dodecahedral sites.

By comparing the distribution of ferric iron in these garnets with that obtained for the synthetic garnets, a number of important conclusions, including the probable distribution of Al and Ti between the octahedral and tetrahedral sites in the natural garnets, can be reached. The comparison of the ferric distribution data is shown in Fig. 130. The curves for the synthetic samples are calculated from the values of the distribution coefficients found for Al-Fe and Ti-Fe exchange at about 1225°C (Huggins, Virgo, and Huckenholz, 1976a). Based on the order of tetrahedral site preference, Al > Fe > Ti, these curves are not expected to change greatly with decreasing temperature and therefore provide a suitable framework with which to compare the various ratios for the natural garnets. It

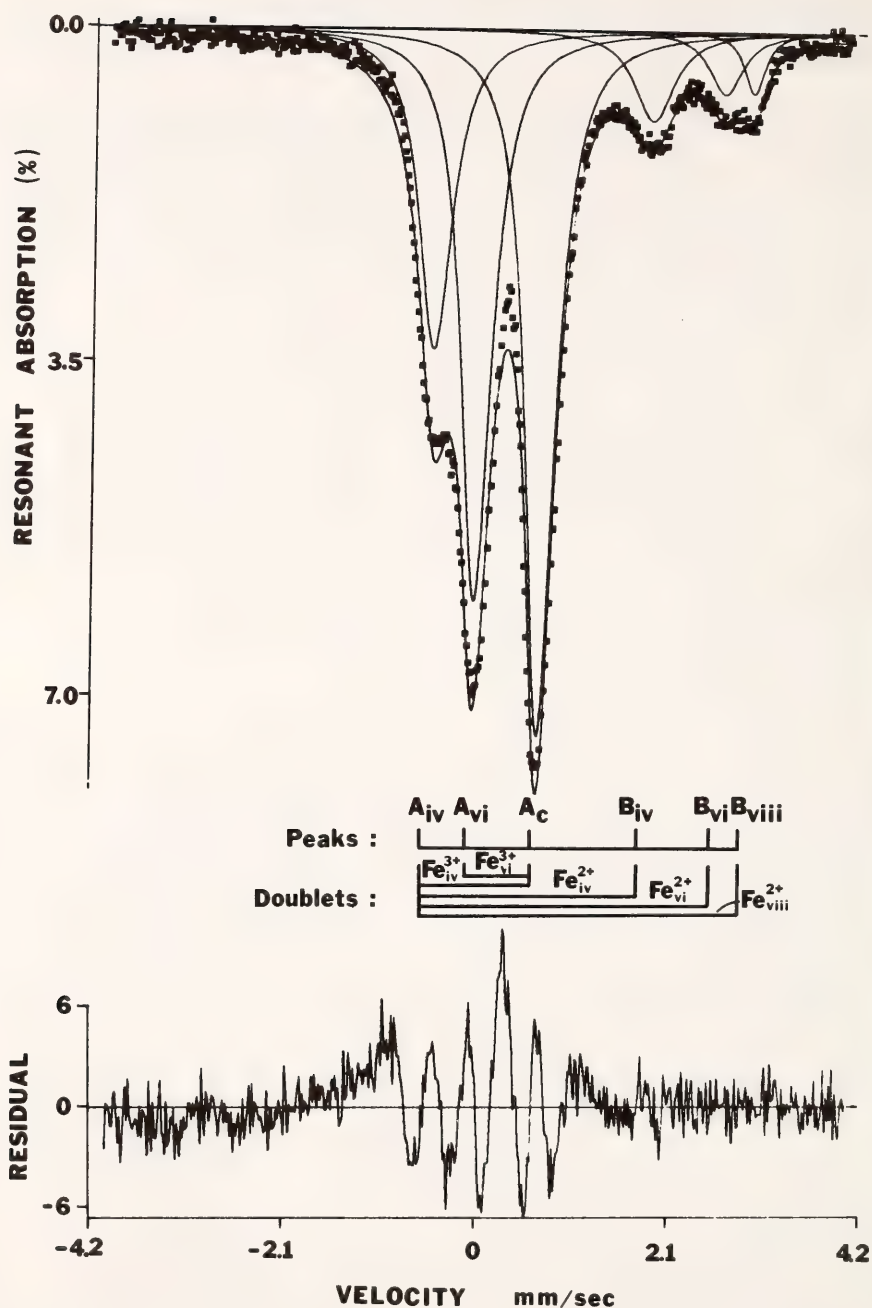


Fig. 128. Mössbauer spectrum of schorlomite from Ardnamurchan, Scotland, sample Ar. Spectrum is fitted to six peaks. Also shown are the labeling scheme for the peaks and the definitions of the doublets for the five distinct types of iron cations.

TABLE 47. Area Ratios for the Distinct Kinds of Iron Cations in the Mössbauer Spectra

| | O | F | LB | SB | OL | DW | K | Iv | ML | R | Ar |
|----------------------------------|------|------|--------|------|------|------|-------|------|------|------|------|
| "Fe ²⁺ "/ΣFe | 0.03 | 0.05 | ~0.03 | 0.07 | 0.19 | 0.00 | 0.16 | 0.14 | 0.16 | 0.19 | 0.26 |
| Fe ³⁺ _{IV} | 2.6 | 3.6 | 7.8 | 0.0 | 7.8 | 27.6 | 14.1 | 15.0 | 10.2 | 17.8 | 12.2 |
| Fe ³⁺ _{VI} | 94.0 | 91.6 | 89.2 | 93.0 | 73.4 | 72.4 | 70.0 | 71.0 | 73.8 | 64.4 | 61.8 |
| Fe ²⁺ _{IV} | 0.0 | 0.0 | ~1.0* | 3.6 | 9.0 | 0.0 | 5.4 | 9.2 | 10.4 | 9.4 | 13.2 |
| Fe ²⁺ _{VI} | 0.0 | 0.0 | | 3.4 | 9.8 | 0.0 | | | | | 7.6 |
| | | | ~2.0*† | | | | 10.6† | 4.8† | 5.6† | 8.4† | |
| Fe ²⁺ _{VIII} | 3.4 | 4.8 | | 0.0 | 0.0 | 0.0 | | | | | 5.2 |

* Estimated visually.
† Fe²⁺_{VI} and Fe²⁺_{VIII} contributions not resolvable.
See Huggins, Virgo, and Huckenholz (1976*b*) for more detailed tabulation of Mössbauer data.

is immediately apparent that Fe³⁺_{VI}/ (ΣFe³⁺ + Fe²⁺_{IV}) is in best agreement with the synthetic curves. Hence, for the natural garnets to have a distribution consistent with the synthetic garnets, the amount of tetrahedral Fe²⁺ should not be considered distinct from that of tetrahedral Fe³⁺ for the purposes of cation exchange. This observation implies that upon crystallization at temperatures

where cation exchange might be taking place reasonably rapidly, electron-hopping occurs much faster, so that the distinction between Fe²⁺_{IV} and Fe³⁺_{IV} (and presumably between Fe²⁺_{VI} and Fe³⁺_{VI} and between Ti³⁺_{VI} and Ti⁴⁺_{VI} as well) cannot be made. Evidence for electron-hopping is given by (1) the dark colors and intense charge-transfer features in the optical absorption spectra

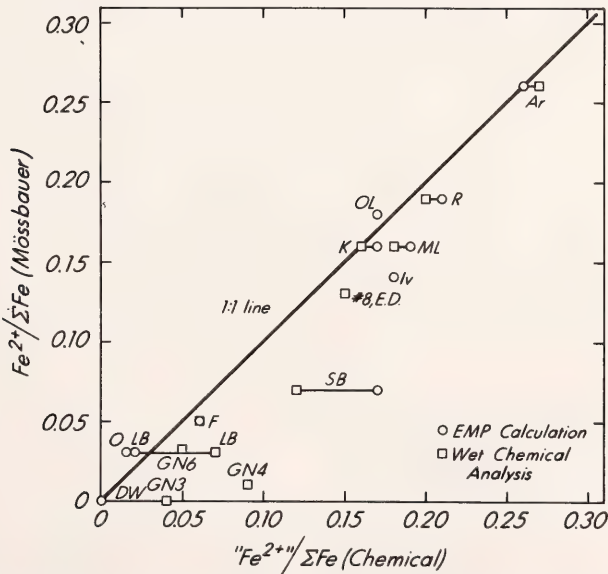


Fig. 129. Comparison of "Fe²⁺"/ΣFe as determined by Mössbauer spectroscopy and by chemical methods for melanite and schorlomite garnets. Significant deviation to the right of the 1:1 line indicates the presence of Ti³⁺. Data for samples GN3, GN4, and GN6 are from Whipple (1973) ; data for 8 E.D., from Dowty (1971).

TABLE 48. Location of Cations at Crystallographic Positions in Natural Melanite and Schorlomite Garnets

| | O | F | SB | OL | DW | K | Iv | ML | R | Ar |
|-----------------------|-------|-------|-------|-------|-------|---------|---------|---------|---------|-------|
| Tetrahedral cations: | | | | | | | | | | |
| Si | 2.900 | 2.924 | 2.834 | 2.623 | 2.276 | 2.470 | 2.472 | 2.492 | 2.442 | 2.250 |
| Fe ³⁺ | 0.038 | 0.046 | 0.000 | 0.121 | 0.356 | 0.203 | 0.224 | 0.151 | 0.223 | 0.167 |
| Fe ²⁺ | 0.000 | 0.000 | 0.047 | 0.140 | 0.000 | 0.078 | 0.138 | 0.154 | 0.121 | 0.181 |
| Al + Ti | 0.062 | 0.030 | 0.119 | 0.116 | 0.368 | 0.250 | 0.166 | 0.203 | 0.214 | 0.402 |
| Octahedral cations: | | | | | | | | | | |
| Ti ³⁺ | 0.000 | 0.015 | 0.131 | 0.000 | 0.000 | 0.022 | 0.060 | 0.044 | 0.029 | 0.000 |
| Fe ³⁺ | 1.366 | 1.171 | 1.220 | 1.142 | 0.934 | 1.006 | 1.062 | 1.092 | 0.943 | 0.845 |
| Al + Ti | 0.550 | 0.749 | 0.450 | 0.647 | 0.929 | 0.775 | 0.738 | 0.710 | 0.798 | 1.016 |
| Fe ²⁺ | 0.000 | 0.000 | 0.045 | 0.152 | 0.000 | } 0.197 | } 0.140 | } 0.154 | } 0.230 | 0.104 |
| Mg | 0.054 | 0.065 | 0.090 | 0.059 | 0.107 | | | | | 0.035 |
| Mn | 0.030 | 0.000 | 0.009 | 0.000 | 0.006 | 0.000 | 0.000 | 0.000 | 0.000 | 0.000 |
| Ca | 0.000 | 0.000 | 0.055 | 0.000 | 0.024 | 0.000 | 0.000 | 0.000 | 0.000 | 0.000 |
| Dodecahedral cations: | | | | | | | | | | |
| Mg | 0.000 | 0.005 | 0.000 | 0.000 | 0.000 | } 0.072 | } 0.052 | } 0.052 | } 0.037 | 0.030 |
| Fe ²⁺ | 0.049 | 0.061 | 0.000 | 0.001 | 0.000 | | | | | 0.071 |
| Mn | 0.039 | 0.020 | 0.000 | 0.029 | 0.000 | 0.030 | 0.016 | 0.018 | 0.024 | 0.025 |
| Ca | 2.912 | 2.914 | 3.000 | 2.970 | 3.000 | 2.898 | 2.932 | 2.930 | 2.939 | 2.874 |

Garnet specimen LB not included as small amounts of Fe²⁺ cannot be measured accurately.

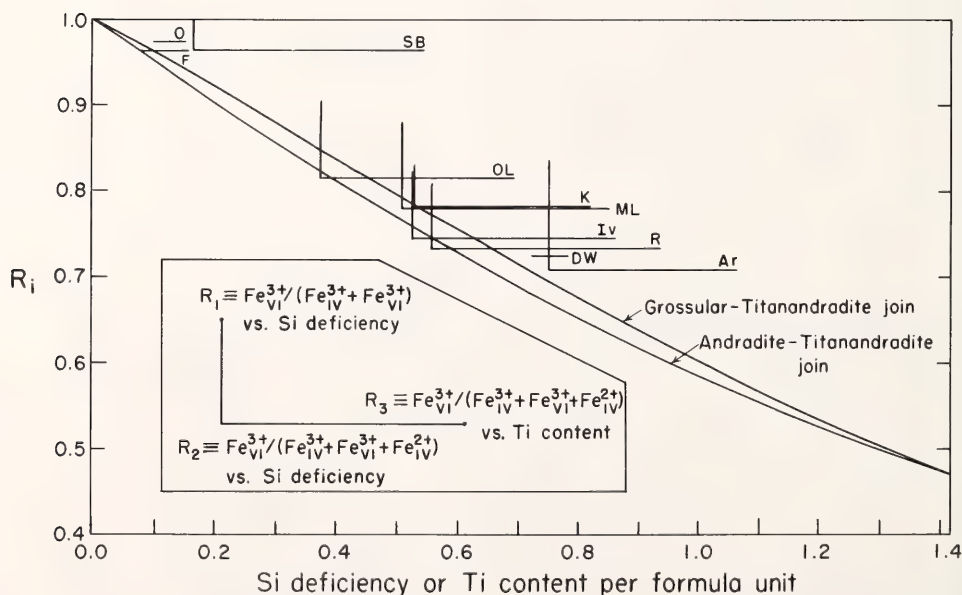


Fig. 130. Comparison of three different ferric distribution parameters for the natural samples with the distribution trends established for synthetic garnets synthesized above 1200°C (Huggins, Virgo, and Huckenholz, 1976a).

of the melanites and schorlomites (Moore and White, 1971) and (2) the unusually low isomer-shift value for the $\text{Fe}^{2+}_{\text{IV}}$ absorption (Huggins, Virgo, and Huckenholz, 1976b). Both phenomena can be best explained by the presence of labile electrons.

This result implies that *all* Al, Fe, and Ti cations take part in the exchange reactions between the octahedral and tetrahedral sites, that the order of tetrahedral site preference, $\text{Al} > \text{Fe} > \text{Ti}$, found for the synthetic garnets (Huggins, Virgo, and Huckenholz, 1976a) also applies to natural garnets, and that electron-hopping among iron and titanium cations occurs considerably more rapidly than the cation-exchange reactions.

At room temperature, both electron-hopping and cation-exchange reactions are probably quenched-in, so that the observation of $\text{Fe}^{2+}_{\text{IV}}$ in the garnets represents an electron trapped at a $\text{Fe}^{3+}_{\text{IV}}$ site. As a result, the substitution mechanism proposed by Dowty (1971), $2\text{Ti}^{4+}_{\text{VI}} + \text{Fe}^{2+}_{\text{IV}} \rightleftharpoons 2\text{M}^{3+}_{\text{VI}} + \text{Si}^{4+}_{\text{IV}}$, is no longer necessary. Rather, the mechanisms needed to account for Ti in the garnet are primarily $\text{Ti}^{4+} \rightleftharpoons \text{Si}^{4+}$ (followed by Al, Fe, Ti order-disorder between sites), $\text{M}^{2+} + \text{Ti}^{4+} \rightleftharpoons 2\text{M}^{3+}$ (followed by electron-hopping when $\text{M}^{2+} = \text{Fe}^{2+}$), and possibly $\text{Ti}^{3+} \rightleftharpoons \text{M}^{3+}$. It is apparent from the fact that the titanium content always exceeds the silicon deficiency that no one mechanism is responsible for introducing all the titanium into the garnet structure.

In conclusion, the crystal chemistry of natural titanium-containing garnets results from two phenomena: (1) the cation-exchange reactions between octahedral and tetrahedral sites involving all Al, Fe, and Ti cations, and (2) electron-hopping among iron and titanium cations. The complexity of the crystal chemistry of melanites and schorlomites reflects not only the phenomena themselves, but also the quenched-in nature of the phenomena present in room temperature observations.

A RECONNAISSANCE STUDY OF THE Ti-GARNET STABILITY FIELD AT DEFINED OXYGEN FUGACITIES

*H. Huckenholz, E. Hölzl, F. E. Huggins,
and D. Virgo*

In a previous article, Huggins, Virgo, and Huckenholz (this Report) showed that Ti-garnets have an unusual crystal chemistry with respect to the distribution of Fe^{2+} and Fe^{3+} . It was found that in natural Ti-bearing garnets different valence states of iron and titanium occur at both the tetrahedrally and octahedrally coordinated sites of the garnet structure. These results are considered significant from a petrological point of view because they suggest that the crystallization of the natural Ti-garnets occurred at lower oxygen fugacities than the low f_{O_2} limit of the stability field of pure andradite. Gustafson (1974) showed that pure andradite is stable in 2-kbar experiments only at higher f_{O_2} values than a T - f_{O_2} line approximately between the QFM and IM, IW buffers below $\sim 800^\circ\text{C}$.

Thus a reconnaissance study at defined oxygen fugacities was conducted at a total pressure of 1 kbar in order to elucidate the stability and phase relations of synthetic and natural Ti-garnet solid solutions. Four Ti-garnets with variable titanium content were selected for the (isobaric) temperature versus oxygen-fugacity experiments. Chemical compositions of the samples are listed in Table 49. Samples AS 2 and GTA 7 are synthetic titangrandites that were crystallized from glasses of appropriate compositions at temperatures of 1100° and 1050°C , respectively, and at a total pressure of 1 atm (Huckenholz, 1969; Hölzl and Huckenholz, in preparation). The sample labeled GHG 1 consists of hand-picked crystals from calc-silicate bombs occurring in pyroclastics of the Alban Hill volcano, near Frascati, Italy, and sample GHG 2 consists of euhedral crystals weathered from a phonolite dike near Oberrotweil, Kaiserstuhl volcanic area, Germany.

TABLE 49. Microprobe Analyses of Titangrandites Used in This Study

| | AS 2 | GTA 7 | HGH 1A | HGH 1B | HGH 1C | HGH 2A | HGH 2B |
|------------------------------------|--------|--------|---------|--------|--------|---------|--------|
| SiO ₂ | 22.75 | 26.64 | 35.49 | 34.60 | 36.20 | 28.70 | 29.00 |
| TiO ₂ | 15.14 | 12.67 | 2.53 | 4.06 | 1.62 | 12.72 | 13.10 |
| Al ₂ O ₃ | ... | 9.05 | 6.57 | 5.57 | 5.78 | 2.24 | 2.02 |
| Fe ₂ O ₃ | 30.03 | 17.62 | { 20.62 | 20.27 | 20.83 | { 22.19 | 19.44 |
| FeO* | 0.20 | 0.22 | | 1.20 | 1.23 | | 3.20 |
| MgO | ... | ... | 0.57 | 0.68 | 0.46 | 0.89 | 0.93 |
| MnO | ... | ... | 0.28 | 0.24 | 0.33 | 0.41 | 0.40 |
| CaO | 31.86 | 33.78 | 33.01 | 33.30 | 33.70 | 31.43 | 32.00 |
| Na ₂ O | ... | ... | ... | ... | ... | ... | 0.10 |
| Totals | 99.98 | 99.98 | 99.07 | 99.92 | 100.15 | 98.58 | 100.19 |
| Si | 2.000 | 2.210 | 2.924 | 2.839 | 2.955 | 2.470 | 2.449 |
| Ti ⁴⁺ | 1.000 | 0.790 | 0.142 | 0.249 | 0.100 | 0.801 | 0.831 |
| Ti ³⁺ † | ... | ... | 0.015 | ... | ... | 0.022 | ... |
| Al | ... | 0.886 | 0.638 | 0.549 | 0.558 | 0.227 | 0.201 |
| Fe ³⁺ | 1.986 | 1.098 | 1.201 | 1.251 | 1.281 | 1.186 | 1.234 |
| Fe ²⁺ | 0.014* | 0.015* | 0.077‡ | 0.084* | 0.083* | 0.251‡ | 0.228* |
| Mg | ... | ... | 0.070 | 0.083 | 0.055 | 0.114 | 0.117 |
| Mn | ... | ... | 0.020 | 0.017 | 0.022 | 0.030 | 0.030 |
| Ca | 3.000 | 3.000 | 2.914 | 2.928 | 2.946 | 2.898 | 2.895 |
| Na | ... | ... | ... | ... | ... | ... | 0.015 |
| Cations | 8.000 | 7.999 | 8.000 | 8.000 | 8.000 | 8.000 | 8.000 |
| Oxygens | 11.993 | 11.991 | 12.000 | 11.989 | 11.975 | 12.000 | 12.000 |
| Ti ⁴⁺ +Fe ³⁺ | 0.995 | 0.992 | 0.936 | 0.947 | 0.962 | 0.879 | 0.899 |
| total Ti+Fe | | | | | | | |

* FeO determined by wet-chemical methods.

† Ti³⁺ is obtained indirectly by assigning 8.000 cations (including Fe²⁺) to 12.000 oxygens.

‡ FeO determined by Mössbauer analyses.

AS 2: Starting composition of a titangrandite crystallized from a glass at 1100°C and 1 atm. FeO determined after crystallization procedure (Huckenholz, 1969).

GTA 7: Starting composition of a titangrandite crystallized from a glass at 1050°C and 1 atm (Hölzl and Huckenholz, in preparation). FeO determined after crystallization procedure by Gisela Cammann, Munich.

HGH 1: Melanite from a calc-silicate bomb occurring in the pyroclastics of the Alban Hill volcano near Frascati, Italy. Several euhedral crystals up to 20 mm across. HGH 1A: Microprobe analysis of a single, unzoned crystal (Huggins, Virgo, and Huckenholz, this Report). HGH 1B (core) and HGH 1C (rim): Microprobe analyses of a zoned crystal by Th. Frisch (unpublished). FeO determined by Gisela Cammann, Munich.

HGH 2: Schorlomite from a phonolite dike near Oberrotweil, Kaiserstuhl volcanic area. Several euhedral crystals up to 5 mm across. HGH 2A: Microprobe analysis of a single crystal (Huggins, Virgo, and Huckenholz, this Report). HGH 2B: Microprobe analysis of a single crystal by Th. Frisch (unpublished). FeO determined by Gisela Cammann, Munich.

The crystal chemistry of the synthetic and natural garnets has been considered previously (Virgo and Huckenholz, *Year Book 73*, p. 426; Huggins, Virgo, Hölzl, and Huckenholz, *Year Book 74*, p. 579; Huggins, Virgo and Huckenholz, this Report). It is noteworthy, however, that the chemical analyses of the synthetic samples AS 2 and GTA 7, when recalculated on the basis of 8.0 cations and 12 oxygens per formula unit, reveal a sili-

con deficiency equal to the amount of the total titanium, i.e., Si + Ti = 3 per formula unit (Table 49). In contrast, the natural garnet samples are characterized by Si + Ti > 3.0 per formula unit and furthermore the amount of oxygen assigned to the mineral formula based on 8 cations is greater than 12. Thus it is necessary to consider part of the iron and titanium as Fe²⁺ and Ti³⁺, respectively.

From the cation proportions, titan-grandite end-member compositions can be calculated. In this way, and neglecting minor components such as almandite, spessartite, Na-melanite, Mg-melanite, and the grossularite components of GTA 7, Frascati, and Kaiserstuhl, the four selected titangrandites will, as a first approximation, plot in the CaTi-CaSi-CaTiSi-Fe portion of the Ca-Ti-Fe-Si(-O-H) system according to their cation proportions (Fig. 131).

Hydrothermal experiments at 1 kbar H_2O pressure and temperatures below $800^\circ C$ were conducted in cold-seal, high-pressure vessels. An internally heated, gas-media apparatus was used for temperatures above $800^\circ C$. Oxygen fugaci-

ties were controlled with solid-state oxygen buffers (PtO₂-Pt, Huckenholz and Yoder, 1971; Fe₃O₄-Fe₂O₃, Ernst, 1960; Ni-NiO, Eugster and Wones, 1962; Fe₂SiO₄-Fe₃O₄-SiO₂, Ernst, 1960; Fe_{1-x}O-Fe₃O₄, Ernst, 1960; Fe-Fe_{1-x}O, Eugster and Wones, 1962; Fe-SiO₂-Fe₂SiO₄, Eugster and Wones, 1962). Sample and buffer were exposed to temperatures of 600° – $1100^\circ C$ for durations within the operational limits of the buffer.

Experimental Results and Discussion

The experimental results obtained on the stability and phase relations of the four titangrandites are depicted in a series of isobaric (1 kbar) temperature versus oxygen-fugacity plots (Fig. 132

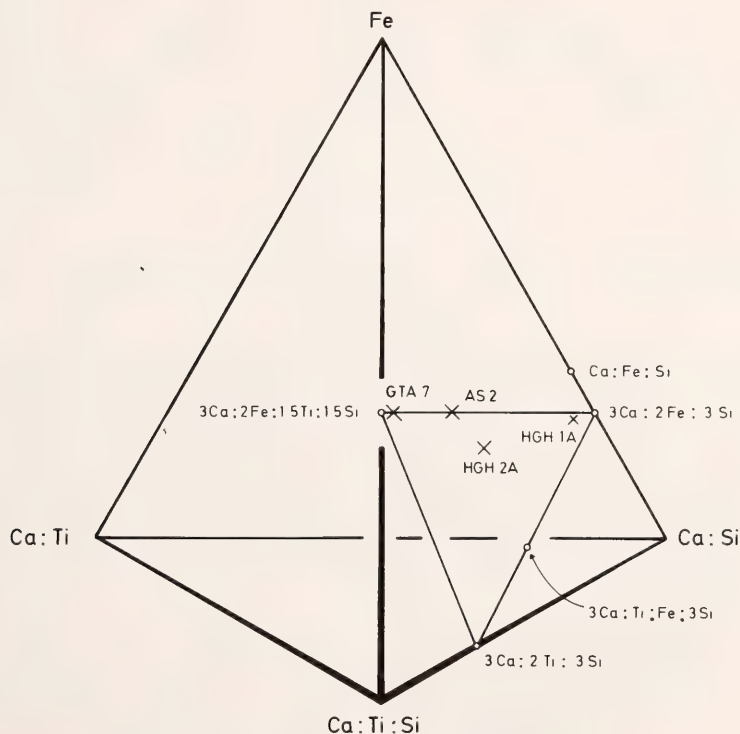


Fig. 131. Ca:Ti-Ca:Si-Ca:Ti:Si-Fe portion of the Ca-Ti-Fe-Si system at excess H_2O and variable oxygen content. (Approximate) cation proportions neglecting Mg and Al refer to phases produced from the reduced and oxidized breakdown of garnets AS 2, GTA 7, HGH 1A (Frascati), and HGH 2A (Kaiserstuhl). Cation proportions are Fe, hematite, magnetite, iron; Ca:Ti, perovskite; Ca:Si, wollastonite; Ca:Ti:Si, sphene; Ca:Fe:Si, kirschsteinite; 3Ca:2Fe:3Si, andradite; 3Ca:2Fe:1.5Ti:1.5Si, titanandradite; 3Ca:Fe:Ti:Si, Fe-melanite; 3Ca:2Ti:3Si, Ca₂Ti⁸⁺Si₃O₁₂.

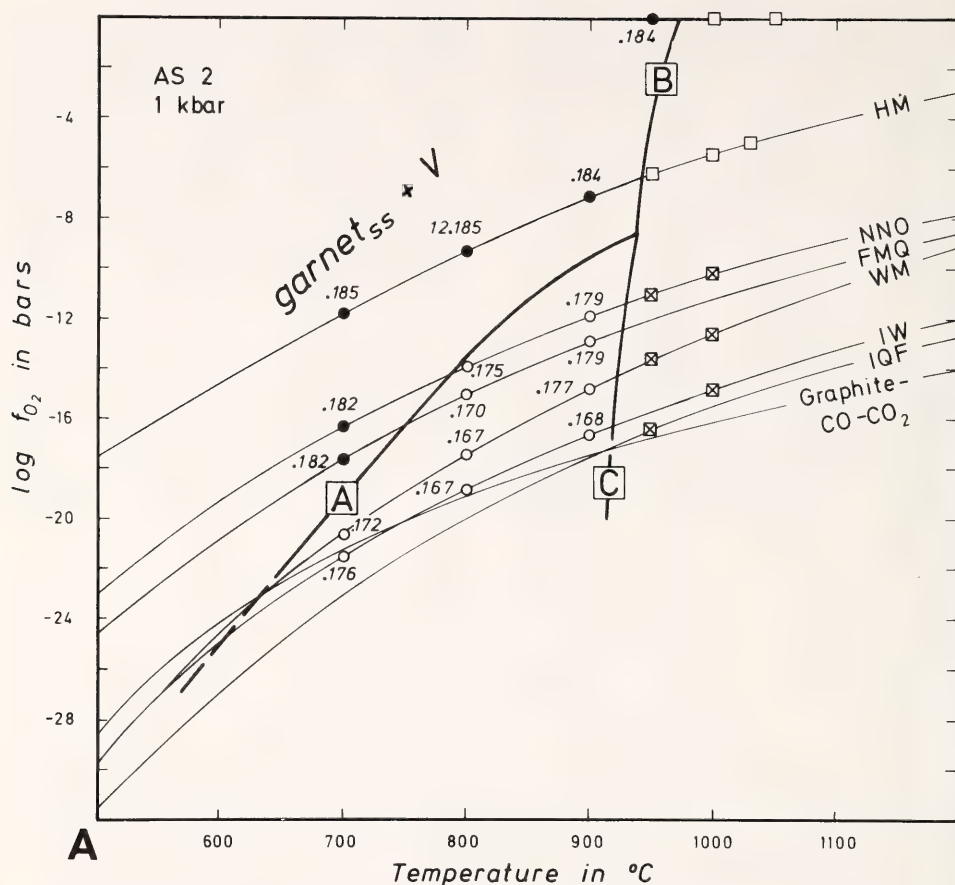


Fig. 132A. Isobaric (1 kbar_{H₂O}) temperature versus oxygen-fugacity plot of data for titan-grandite AS 2. Phase assemblages are garnet_{ss} + V (solid circles), garnet_{ss} + wollastonite + kirschsteinite_{ss} + magnetite_{ss} + V (open circles), garnet_{ss} + liquid + wollastonite + kirschsteinite_{ss} + V (squares with crosses), and garnet_{ss} + liquid + wollastonite + magnetite_{ss} + V (open squares). Numbers at open and solid circles refer to the fraction of garnet unit-cell parameters that is larger than 12 Å. Solid-state buffer curves are HM (hematite-magnetite), NNO (nickel-nickel oxide), FMQ (fayalite-magnetite-quartz), WM (wüstite-magnetite), IW (iron-wüstite), and IQF (iron-quartz-fayalite). The platinum-dioxide dissociation is plotted at 1 bar. For comparison the graphite-CO-CO₂ buffer curve is also shown. Curve labeled A refers to the reduced subsolidus breakdown of garnet_{ss} + V; curves B and C are the beginning of melting.

A-D). Individual ranges of temperature versus f_{O_2} stabilities are displayed for the four titan-grandites studied. Each phase diagram in Fig. 132 A-D is actually a unique section through an (isobaric) temperature versus f_{O_2} versus composition hyperspace. Composition might be expressed by $(Ti^{4+} + Fe^{3+}) / (total\ Ti + Fe)$. This ratio indicates the degree of oxidation and, indirectly, the

degree of silicon deficiency. Samples AS 2 and GTA 7 have ratios close to 1.000 in which $Ti + Si = 3.000$. Their stability fields (Fig. 132 A and B) are bounded by curves A and B. Because of the fine-grained nature of the garnets and the small amounts of their breakdown products, attempts to determine the phase boundaries through observation of contiguous phase assemblages

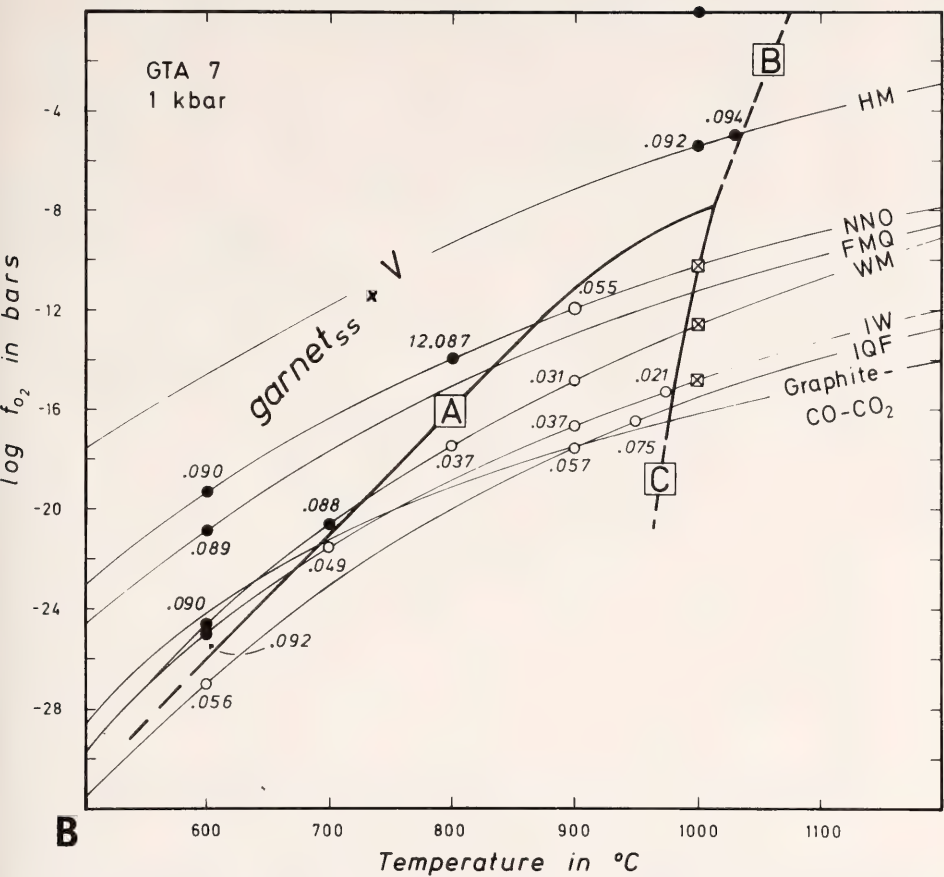


Fig. 132B. Isobaric (1 kbar_{H₂O}) temperature versus oxygen-fugacity plot of data for titan-grandite GTA 7. Phase assemblages, symbols, numbers, and abbreviations as in Fig. 132A.

proved to be unsatisfactory. Better results were obtained when the individual unit-cell parameters of garnets coexisting in the various phase assemblages were considered. Unit-cell parameters remain constant (within the limits of error) for the assemblage garnet_{ss} + V. They change abruptly to smaller values for garnets coexisting with wollastonite + kirschsteinite_{ss} (rich in Ca₂SiO₄ component) + magnetite_{ss} + V below curve A. The decrease of the unit-cell dimensions may be associated with the garnet_{ss} becoming less Si-deficient, and thus silicon-undersaturated or silicon-free phases (kirschsteinite_{ss} and magnetite_{ss}) occur as breakdown products.

In both samples it can be seen that an increase in temperature tends to decrease the stability of the garnets. At 600 $^{\circ}C$ samples AS 2 and GTA 7 are stable at higher f_{O_2} than those defined by the IW buffer or between the IW and IQF buffers. Garnets AS 2 and GTA 7 decompose at 940 $^{\circ}$ and 1010 $^{\circ}C$, respectively, at oxygen fugacities defined by the NNO and HM buffers. The larger T - f_{O_2} stability field of GTA 7 compared with AS 2 might be attributed to differences in bulk composition. Garnet AS 2, consisting of 33.3 mole % andradite and 66.7% titanandradite, has a Ti/Fe of 0.5, whereas GTA 7 is made up of 52.7% titanandradite, 3.1% andradite, and

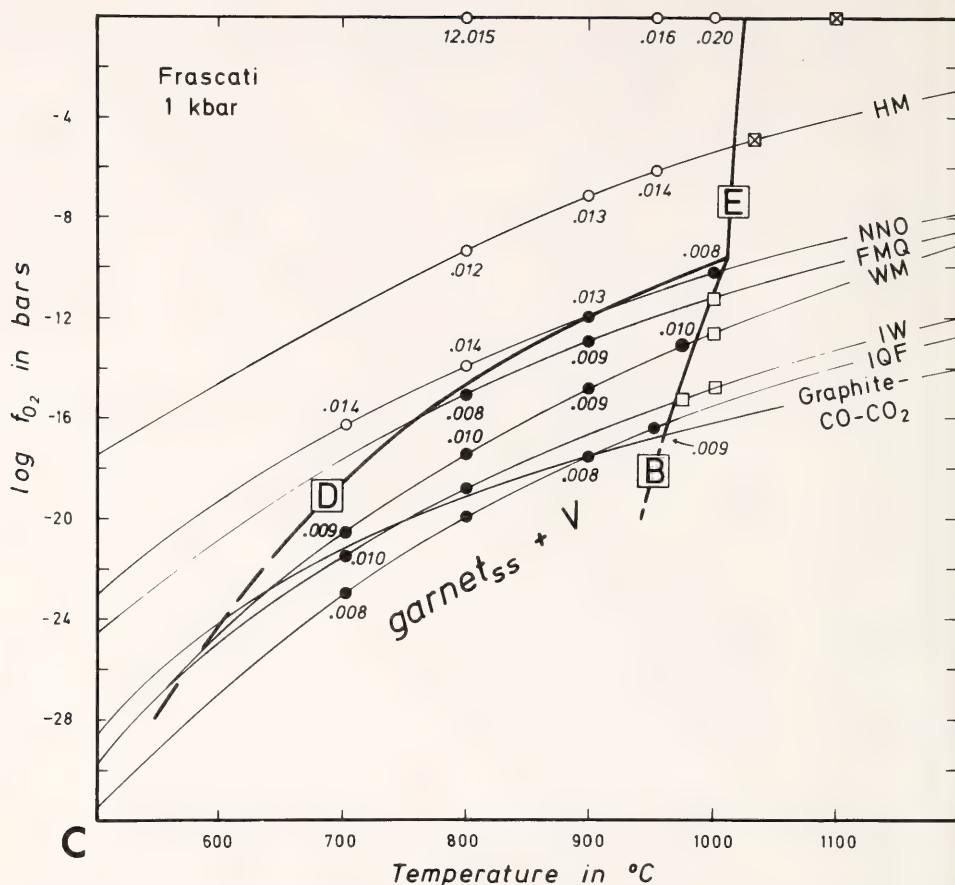


Fig. 132C. Isobaric (1 kbar_{H₂O}) temperature versus oxygen-fugacity plot of data for the Frascati titangrandite HG1A. Phase assemblages are garnet_{ss} + V (solid circles), garnet_{ss} + wollastonite + sphene + quartz + V (open circles), garnet_{ss} + liquid + wollastonite + magnetite_{ss} + V (open squares), and garnet_{ss} + liquid + wollastonite + V (squares with crosses). Numbers and abbreviations as in Fig. 132A. Curve labeled *D* refers to the oxidized subsolidus breakdown of garnet_{ss} + V; curves *B* and *E* are the beginning of melting.

44.2% grossularite with Ti/Fe = 0.71. Apparently, increasing amounts of Ti (and Al) over Fe might stabilize the iron as Fe³⁺ within the garnet structure, and the garnet will persist as a stable phase to a lower f_{O_2} . Curves *B* and *C* for AS 2 exhibit the beginning of melting of the Ca-Fe-Ti-Si-O-H system at a total pressure of 1 kbar. Compositional differences, that is, the presence of Al and a higher Ti/Fe have shifted curves *B* and *C* for GTA 7 to higher temperature. The products of incongruent melting are liquid + garnet_{ss} +

wollastonite + magnetite + V above curve *B*. They are liquid + garnet_{ss} + wollastonite + kirschsteinite_{ss} + V above curve *C*. The intersection of curves *A*, *B*, and *C* might denote an (isobaric) invariant point containing four solids (garnet_{ss} + wollastonite + kirschsteinite_{ss} + magnetite_{ss}) + liquid + V in equilibrium. It appears to be degenerate owing to the solid-solutions' participating in the equilibrium or to the opaque phase magnetite_{ss} that consists of two indistinguishable phases.

The Frascati and Kaiserstuhl samples,

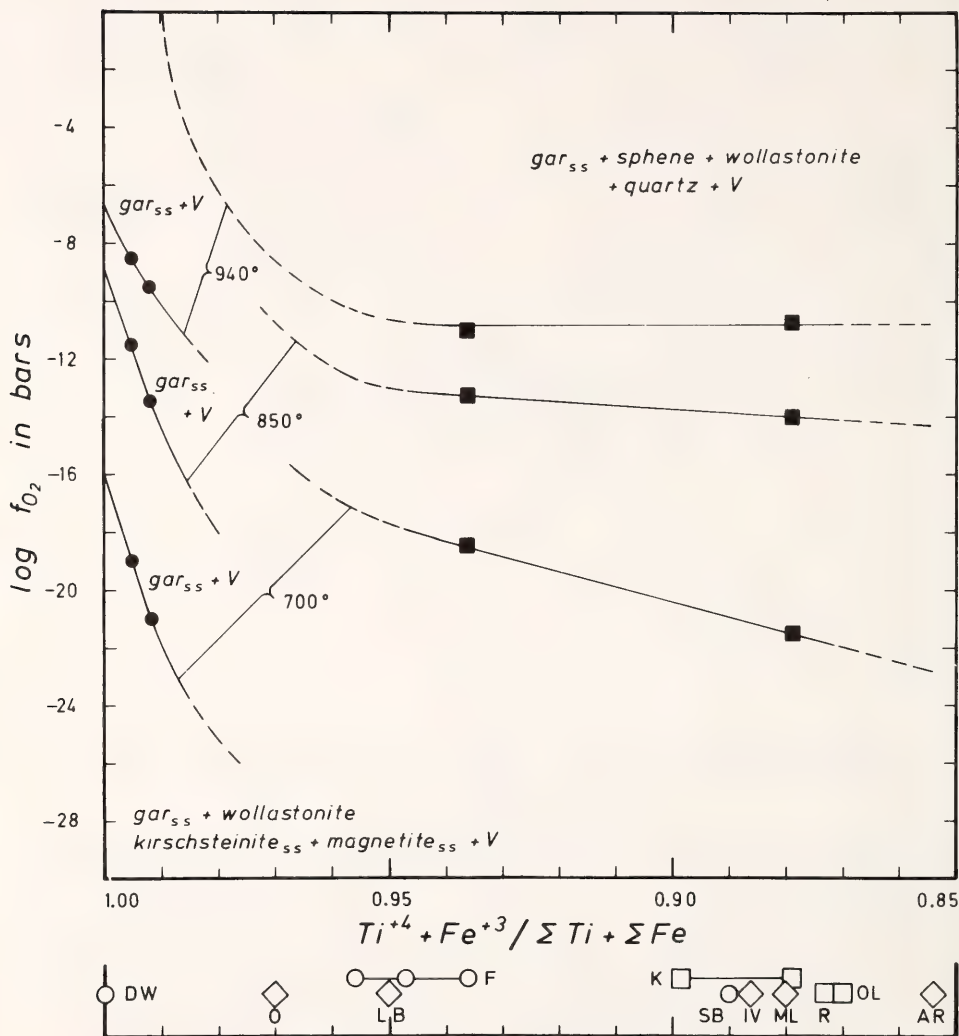


Fig. 133. Oxygen fugacity versus composition (expressed as $[\text{Ti}^{4+} + \text{Fe}^{3+}]/[\text{total Ti} + \text{Fe}]$) plot of data at temperatures of 940°, 850°, and 700°C and at a total pressure of 1 kbar_{H₂O}. Solid squares refer to the oxidized breakdown of the two natural garnets_{ss} (= gar_{ss}) from the Frascati (HGH 1A) and Kaiserstuhl (HGH 2A) areas. Solid circles represent the reduced breakdown of the two synthetic garnets AS 2 and GTA 7. Ratios plotted below the abscissa are from natural titangrandites analyzed by Huggins, Virgo, and Huckenholz, this Report) and Th. Frisch (unpublished). DW, skarn rock, Dirbat Well, Sudan; O, ijolite, Oka Complex, Quebec; F, dolomitic limestone block in pyroclastics, Frascati; LB, nepheline syenite, Loch Borolan, Scotland; IV, ijolite, Iivaara; ML, melteigite, Iivaara; R, nephelinite, Rusinga Island, Kenya; OL, volcanic ash, Oldoinyo Lengai, Tanzania; AR, pegmatitic pyroxenite, Ardnamurchan, Scotland. Open squares refer to volcanic rocks; open diamonds refer to plutonic rocks; and open circles refer to the San Benito, Frascati, and Dirbat Well samples.

ples AS 2 and GTA 7, mapping of sub-solidus phase boundaries was conducted by observing the change in unit-cell parameters, which deviate from 12.009(2) Å for the Frascati garnet and 12.120(2) Å for the Kaiserstuhl garnet within the oxidized decomposition products.

In comparison with the corresponding changes in the cell dimensions of the synthetic garnet_{ss}, it is suggested that the natural garnets in the breakdown assemblages became more and more silicon-deficient with increasing f_{O_2} , and thus quartz occurs as a separate phase.

Curves *B* and *E* denote the beginning of melting in the natural (multicomponent) system. The assemblage garnet_{ss} + *V* gives way to garnet_{ss} + wollastonite + magnetite_{ss} + liquid + *V* above curve *B*, whereas the assemblage garnet_{ss} + wollastonite + sphene + quartz + *V* changes to garnet_{ss} + wollastonite + liquid + *V* above curve *E*. The intersection of the curves *D*, *B*, and *E* resembles isobaric (degenerate) invariant conditions with five solids (garnet_{ss} + wollastonite + sphene + quartz + magnetite_{ss}) + liquid + *V*.

Petrogenetic Conclusions

With the data at hand, an isobaric and isothermal composition (expressed as $[Ti^{4+} + Fe^{3+}]/[total\ Ti + Fe]$) versus f_{O_2} plot can be constructed summarizing the experimental results obtained on the four titanium-bearing garnets studied (Fig. 133). Two sets of isotherms for each temperature at 940°, 850°, and 700°C bound the upper (oxidized) and lower (reduced) garnet stability range. At high oxygen fugacities and large $(Ti^{4+} + Fe^{3+})/(total\ Ti + Fe)$ the stability range of titangrandites is rather restricted but extends to f_{O_2} on the order of 1 bar. With the decrease of f_{O_2} , the oxidation ratios decrease likewise, and the garnet becomes more reduced and thus less silicon-deficient. No reduced breakdown of the garnet will occur at oxygen fugacities as low as those defined by the IQF buffer.

The oxidation ratio calibrated against

oxygen fugacity can be used to suggest the stability range of titangrandites under which they might have formed. A sequence of natural melanites, schlorlornites, and iivaarites of various origins (Huggins, Virgo, and Huckenholz, this Report) is plotted below the abscissa of Fig. 133. Garnets from igneous volcanic rocks plot close together with their oxidation ratios, covering the range from 0.900 to 0.870. They are from a phonolite dike of the Kaiserstuhl volcanic area, Germany, from volcanic ash of Oldoinyo Lengai, Tanzania, and from melanite agglomerates in a nephelinite of Kenya. Igneous plutonic rocks such as nepheline syenites, ijolites, melteigites and pegmatites have a wide range of $(Ti^{4+} + Fe^{3+})/(total\ Ti + Fe)$. A schlorlornite from a garnet-wollastonite-titanaugite vein in a pegmatitic pyroxenite of Ardnamurchan, Scotland, has a ratio of 0.854, showing the possibility of an origin at a low oxygen fugacity when crystallized under magmatic conditions. A ratio of 0.970 is revealed for a melanite from ijolite of the Oka carbonate complex, Quebec. The other plutonic garnets occur in a nepheline syenite (Loch Borolan, Scotland), ijolite and melteigite (Iivaara, Finland). Their oxidation ratios are intermediate between those from Oka and Ardnamurchan. Also plotted in Fig. 133 are the San Benito, Dirbat Well, and Frascati garnets, which together show a wide range of $(Ti^{4+} + Fe^{3+})/(total\ Ti + Fe)$. The petrogenesis of these samples is ambiguous, and some constraints on their origin are discussed elsewhere (Virgo, Rosenhauer, and Huggins, this Report).

The foregoing experiments indicate stability ranges of natural titangrandites depending on f_{O_2} that might be expressed as $(Ti^{4+} + Fe^{3+})/(total\ Ti + Fe)$ or by the degree of silicon deficiency. Although the formation of these garnets under a very low oxygen fugacity (Virgo, Rosenhauer, and Huggins, this Report) indicates an upper mantle origin, their stability under magmatic conditions extends the range of oxygen fu-

gacities close to those of basalts and their derivatives (Carmichael and Nicholls, 1967).

INTRINSIC OXYGEN FUGACITIES OF NATURAL MELANITES AND SCHORLOMITES AND CRYSTAL-CHEMICAL IMPLICATIONS

D. Virgo, M. Rosenhauer, and F. E. Huggins

In a previous article and on the basis of hydrothermal phase-equilibrium studies of natural and synthetic Ti-garnets, Huckenholz, Hölzl, Huggins, and Virgo (this Report) have suggested that a complete range of Ti-garnets_{ss} could be stable from air to very reduced conditions of oxygen fugacity consistent with concomitant changes in the redox equilibria involving the different valence states of iron and titanium. The possibility exists, therefore, that Ti-garnets from different geological environments might be used as petrogenetic indicators of oxygen fugacity.

To provide data pertaining to the crystallization conditions of Ti-garnets, measurements of the intrinsic oxygen fugacity as a function of temperature for Ti-garnets selected from the suite of samples discussed by Huggins, Virgo, and Huckenholz (this Report) were made using the solid-state ZrO_2 electrolyte method of Sato (1971). The $\log f_{\text{O}_2}$ values are plotted against the reciprocal temperature for six natural Ti-garnets and a synthetic Ti-andradite ($\text{Ca}_3\text{Fe}_2\text{Si}_{1.58}\text{Ti}_{1.42}\text{O}_{12}$) in Figs. 134–139. In these figures the solid lines are visually drawn through the loci of points obtained in the replicate heating and cooling cycles. The numbered arrows refer to the sequence of heating and cooling cycles. The anticipated intrinsic $\log f_{\text{O}_2} - 1/T$ relationship depends on the geometry of the f_{O_2} isobars in a temperature-composition plot and therefore need not be linear. The criterion for reliable intrinsic oxygen-fugacity measurements on stable phases was reproducibility better than 0.3 log unit during replicate cycles.

The data for the Frascati and Howie No. 9 samples (Fig. 134) show that the

$\log f_{\text{O}_2} - 1/T$ plots obtained in the first heating cycle are respectively higher and lower than those from the data collected in subsequent cycles. These initial results are interpreted in terms of disequilibrium at low temperatures in view of the results of the subsequent cooling and heating cycles. The ^{57}Fe Mössbauer spectra of the Frascati garnet cooled from the cell is unchanged from the starting material (Fig. 140), and this result indicates the stable nature of the garnet during the oxygen-fugacity measurements.

In contrast, the synthetic Ti-andradite (Fig. 135) gives reproducible, approximately linear data over the range 850°–1150°C during three distinct heating cycles. The equilibrium f_{O_2} values are much higher, however, compared with those of the natural garnets discussed above, and the results compare closely with the 1-atm data for the quartz-fayalite-magnetite buffer reaction. Significantly, the sample after cooling from 1150°C is black, compared with the yellow color of the starting material. In fact, from the x-ray diffraction profile, the garnet sample consists almost entirely of magnetite + perovskite + wollastonite. This observation explains the similarity of the data to those for the synthetic quartz-fayalite-magnetite buffer curve. The instability of the synthetic Ti-garnet at these f_{O_2} 's and under subsolidus conditions is consistent with the hydrothermal phase-equilibrium studies of Huckenholz, Hölzl, Virgo, and Huggins (this Report).

The data for the Rusinga (Fig. 136), Kaiserstuhl (Fig. 137), melteigite 9/54 (Fig. 138), and San Benito (Fig. 139) samples reveal distinctly different behavior at high temperature compared with the Frascati and Howie No. 9 garnets. The intrinsic oxygen-fugacity measurements for the Rusinga sample have been made extensively over a temperature range from ~700 to 1150°C (Fig. 136). Data for two aliquots, labeled *a* and *b*, are given. Initially sample *a* was heated at ~1050°C and held at that temperature for 2 hr, after which it was

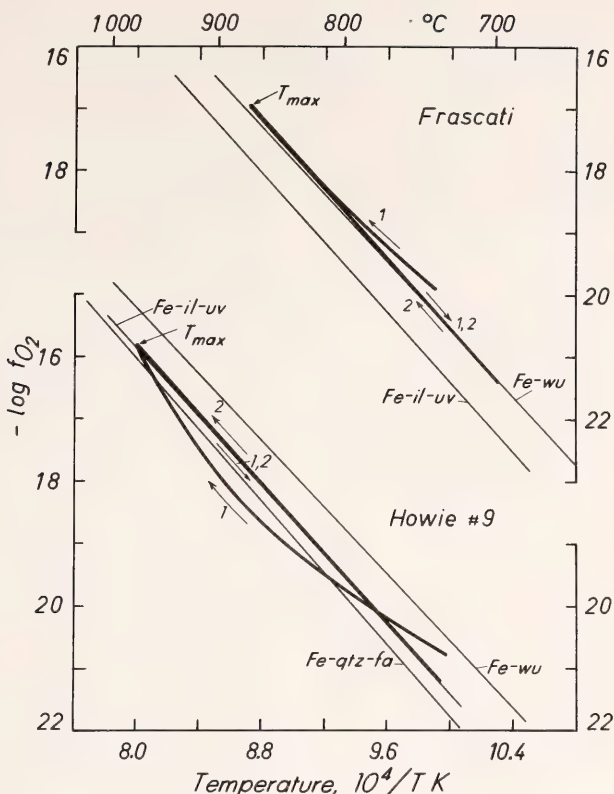


Fig. 134. The measured $\log f_{O_2}$ values of the Frascati (upper) and Howie No. 9 (lower) garnets plotted as a function of temperature. Numbered arrows refer to the sequence of heating and cooling cycles. The data are compared with the iron-wüstite (Fe-wü), iron-ilmenite-ulvospinel (Fe-il-uv), and iron-quartz-fayalite (Fe-qtz-fa) synthetic buffer reactions. T_{\max} corresponds to the maximum temperature attained in the electrochemical cell.

cooled to $\sim 800^\circ\text{C}$ in steps of $\sim 40^\circ\text{C}$. Subsequent heating and cooling cycles were extended to $\sim 1130^\circ\text{C}$. The resultant plot has a break in slope at $\sim 1067^\circ\text{C}$, however, indicating a steeper $\log f_{O_2} - 1/T$ relationship at the higher temperatures. In subsequent cycles (data not plotted), the $T-f_{O_2}$ data define approximately subparallel lines but at progressively lower f_{O_2} values, depending on the $T-f_{O_2}$ coordinates at which cooling was commenced. The sample after removal from the cell had partially melted. On the other hand, replicate heating and cooling experiments on the second aliquot (b), in which the heating cycle was started at $\sim 700^\circ\text{C}$, gave much lower f_{O_2} values, which showed an approxi-

mately linear increase in f_{O_2} up to $\sim 930^\circ\text{C}$. At higher temperatures there was again a rapid increase in f_{O_2} . Furthermore, at any given $\log f_{O_2} - 1/T$ value in this high-temperature region the sample can be cooled, and f_{O_2} values will decrease linearly with temperature, and the plot will be approximately parallel to the initial results (e.g., the third cooling and fourth heating cycle for aliquot b in Fig. 140).

The results for the Kaiserstuhl, melteigite 9/54, and San Benito samples exhibit behavior similar to that described above (cf. Figs. 137, 138, 139). It is suggested, then, that the equilibrium intrinsic $\log f_{O_2} - 1/T$ relationship can be measured, but at temperatures higher than certain

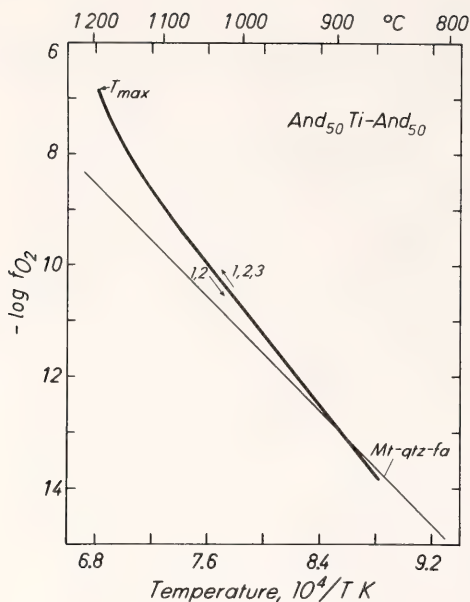


Fig. 135. The measured $\log f_{O_2}$ values of the synthetic Ti-andradite ($Ca_3Fe_2Si_{1.58}Ti_{1.42}O_{12}$) plotted as a function of temperature. The data are compared to the magnetite-quartz-fayalite (Mt-qtz-fa) synthetic buffer reaction. T_{max} corresponds to the maximum temperature attained in the electrochemical cell.

critical temperatures, a rapid, irreversible increase in oxygen fugacity occurs.

The irreversible behavior observed for the Kaiserstuhl, San Benito, Rusinga, and melteigite garnets above certain critical temperatures requires further explanation to support the inference that the equilibrium intrinsic oxygen fugacities of these samples have been determined. The ^{57}Fe Mössbauer spectra at 77°K of the Rusinga (aliquot *b*, Fig. 136) and San Benito (Fig. 139) samples cooled from the cell are compared with the natural untreated samples in Figs. 141 and 142, respectively. Both comparative plots show significant changes in the iron oxidation states in the garnets cooled from the cell compared with the starting materials. For the Rusinga garnet, there is a dramatic increase in $Fe^{2+}/\Sigma Fe$. This effect can be seen from the increase in the intensity of the positive velocity absorption peaks labeled B_{IV} , B_{VI} , and

B_{VIII} , corresponding to Fe^{2+} in the 4-, 6-, and 8-fold coordinated sites, respectively. The increase in $Fe^{2+}/\Sigma Fe$ determined from the spectra now exceeds the maximum reducing capacity of the crystals as determined from the electron microprobe analysis (Huggins, Virgo, and Huckenholz, this Report, Table 47). These changes in the crystal chemistry of the garnet might be explained to some extent by cation exchange processes at high temperature to achieve charge balance and stoichiometric requirements or the possibility of some degree of non-stoichiometry in the Ti-garnet structure, or both. It was shown from mineral stability experiments that at 1050°C, a temperature slightly in excess of the critical temperature for the Rusinga and Kaiserstuhl garnets (Figs. 136 and 137), the natural garnets were unstable. In view of these results, the irreversible behavior observed in the oxygen-fugacity measurements results from incipient breakdown of the garnet structure. On the other hand, the San Benito sample cooled from the cell (Fig. 139a) is completely oxidized (cf. Fig. 142), but there is also a dramatic change in the color of the cooled sample (yellow, translucent crystals) compared with the opaque starting material. In this case, the change in the crystal chemistry could be simply explained by concomitant changes in the redox states of iron and titanium. Garnet breakdown at temperatures slightly in excess of the critical temperature suggests that the rapid increase in oxygen fugacity above the critical temperature is probably associated with the instability of the garnet structure.

The above results show that the intrinsic f_{O_2} 's of the natural garnets studied plot in a restricted field that is confined between the Fe-ilrn-ru and Fe-wü buffer curves in a $\log f_{O_2} - 1/T$ diagram. However, at temperatures above a critical value, T_c , the oxygen fugacity increases rapidly and returns on cooling irreversibly along a T - f_{O_2} path subparallel to the initial heating cycle but shifted to higher oxygen fugacities. In

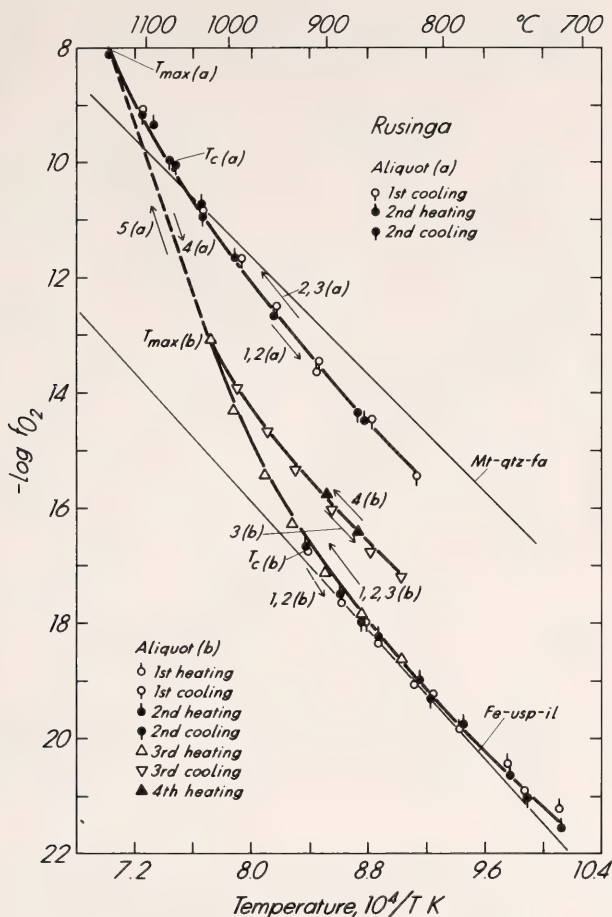


Fig. 136. The measured $\log f_{O_2}$ values of the Rusinga garnet plotted as a function of temperature. Data for two separate aliquots (a and b) are plotted in the upper and lower parts of the figure. The data are compared with the magnetite-quartz-fayalite (Mt-qtz-fa) and the iron-ulvospinel-ilmenite synthetic buffer reactions. T_{max} corresponds to the maximum temperature attained in the electrochemical cell, and the interpretation of the critical temperature T_c is discussed in the text.

subsequent heating cycles not exceeding a new T_c , the oxygen fugacity values are reversible. These findings are believed to have geological significance in that T_c and the associated f_{O_2} value are interpreted to reflect the oxygen fugacity that prevailed at the temperature T_c in the host melt. The important inference, of course, is that the natural garnets have never undergone more oxidizing conditions at higher temperatures, as shown for example by the irreversible behavior above the critical

temperature, T_c . Hence T_c is the maximum temperature at which the garnet could have crystallized.

The equilibrium $\log f_{O_2} - 1/T$ relationships for the natural garnets, inferred from Figs. 134–139, are replotted in Fig. 143 of Virgo, Huggins, and Rosenhauer (this Report), where the results are compared with the Fe-wü, Fe-qtz-fa, and Fe-ilrn-rut synthetic buffer reactions for 1-atm total pressure. These data are within the 1-kbar stability fields determined for the Kaiserstuhl and Frascati

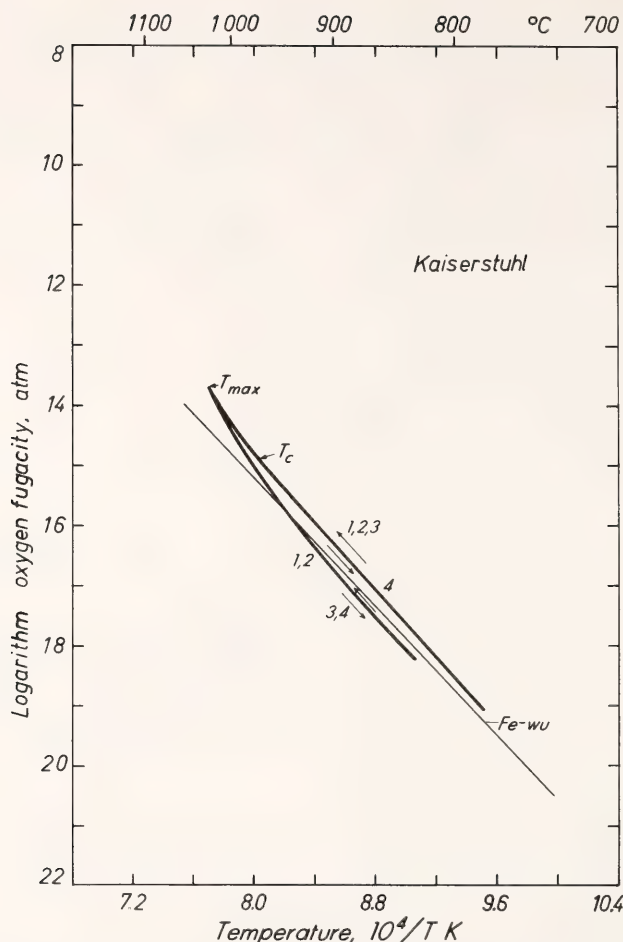


Fig. 137. The measured $\log f_{O_2}$ values of the Kaiserstuhl garnet plotted as a function of temperature. The data are compared with the iron-wüstite (Fe-wü) synthetic buffer reactions. T_{max} and T_c are explained in the caption of Fig. 136.

garnets (Huckenholz, Hölzl, Huggins, and Virgo, this Report).

The above results are in apparent conflict with previous crystal-chemical principles in view of the presence of predominantly oxidized cations such as Fe^{3+} and Ti^{4+} in the garnet structure. For iron-bearing systems, the trend of iron oxidation states with oxygen fugacity is well known from the hydrothermal buffer systems initiated by Eugster (1959). There is no quantitative relationship, however, because the atomic ratio, Fe^{2+}/Fe^{3+} , or the chemical potential ratio,

$\mu Fe^{2+}/\mu Fe^{3+}$, depends on f_{O_2} differently for different phases. Extreme examples of the latter effect are the stability fields of predominantly ferric-rich minerals that extend over a wide range of oxygen fugacities, e.g., andradite (Gustafson, 1974), magnesioriebeckite (Ernst, 1960), ferriannite (Wones, 1963). The results of this study demonstrate for the first time that mineral phases composed of predominantly oxidized cations have crystallized at very low oxygen fugacities.

The occurrences of reduced oxidation

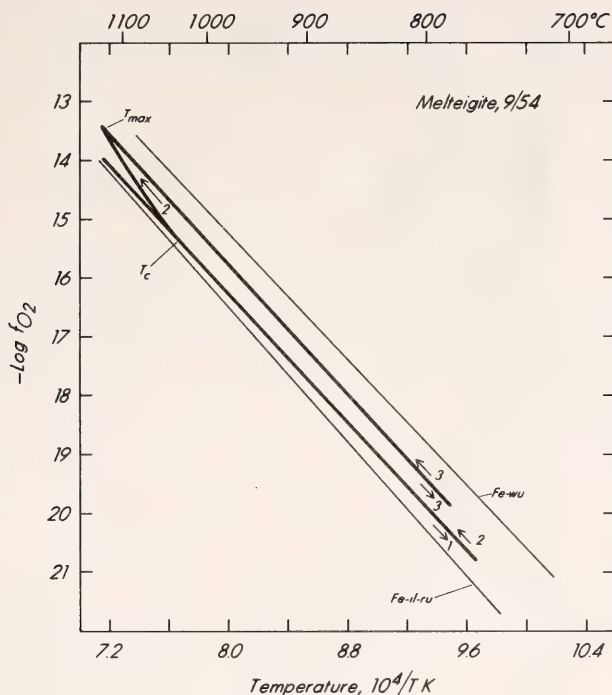


Fig. 138. The measured $\log f_{O_2}$ values of the melteigite 9/54 garnet plotted as a function of temperature. The data are compared with the iron-wüstite (Fe-wü) and iron-ilmenite-rutile (Fe-il-ru) synthetic buffer reactions. T_{max} and T_c are explained in the caption of Fig. 136.

states of titanium are rare in terrestrial rocks, but Ti^{3+} is an established component of extraterrestrial minerals. Trivalent Ti is the dominant oxidation state in iron-free pyroxenes in the Allende meteorite (Dowty and Clark, 1973) and in the chondritic sulfide heideite (Keil and Brett, 1974). Also, Ti^{3+} is an established component of Fe^{2+} -rich lunar minerals such as armalcolite (Wechsler, Prewitt, and Papike, 1976), ilmenite (Bayer *et al.*, 1972), and clinopyroxenes (Burns *et al.*, 1973). In fact, the intrinsic oxygen fugacities for lunar rocks (Sato, Hickling, and McLane, 1973) are in general compatible with the results of this study. However, it might be anticipated that the crystallization processes of lunar minerals occurred at somewhat lower oxygen fugacities than those of the Ti-garnets because of the effect of different

total pressures (Virgo, Huggins, and Rosenhauer, this Report).

The results on natural Ti-garnets emphasize the importance of the relationship between the crystalline structure, oxygen fugacity, and cation oxidation states. The present results can be rationalized in terms of their crystal-chemical properties because of the presence of the mixed valence states of iron and titanium at the tetrahedral and octahedral sites. This compatibility is also consistent with the restricted stability field of synthetic garnet analogues containing only Fe and Ti in trivalent and tetravalent states (cf. Fig. 135), with the lower stability field of andradite (Gustafson, 1974), and with the hydrothermal stability fields at 1 kbar determined for the Kaiserstuhl and Frascati garnets (Huckenholz, Hölzl, Huggins, and Virgo, this Report).

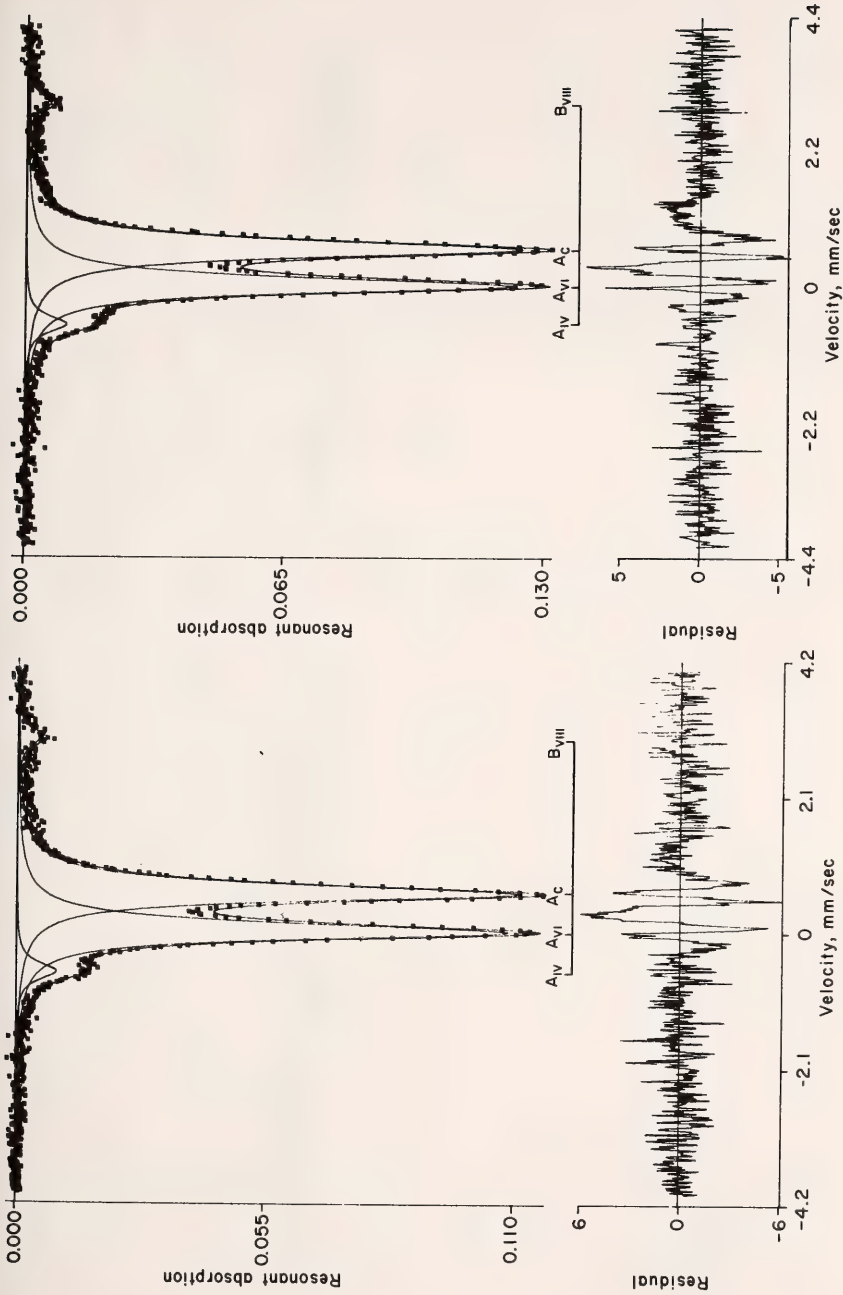


Fig. 140. ^{57}Fe Mössbauer spectra at 77°K of the natural (left) and quenched (right) Frascati garnet after treatment in the ZrO_2 electrochemical cell. The absorption data were fitted to four lines of Lorentzian shape consisting of two Fe^{3+} absorption doublets $A_{\text{IV}}-A_{\text{C}}$ and $A_{\text{VI}}-A_{\text{C}}$, corresponding to Fe^{3+} in the tetrahedral and octahedral sites, respectively, and the positive velocity component of an Fe^{2+} doublet corresponding to Fe^{2+} in the dodecahedrally coordinated site B_{VIII} . The low-velocity component of the Fe^{2+} doublet occurs beneath the peak labeled A_{IV} .

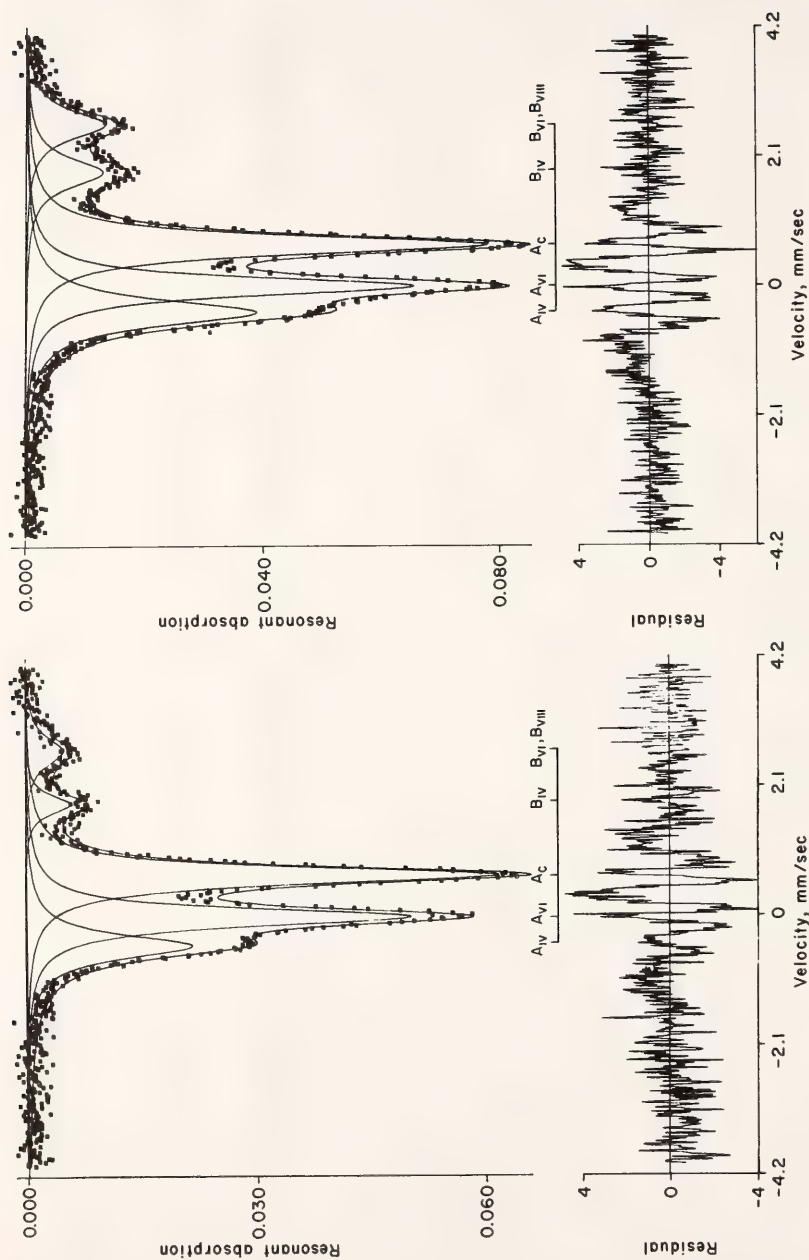


Fig. 141. ^{57}Fe Mössbauer spectra at 77°K of the natural (left) and quenched (right) Rusinga garnet after treatment in the ZrO_2 electrochemical cell. The absorption data were fitted to five lines of Lorentzian shape consisting of two Fe^{3+} absorption doublets ($A_{IV}-A_C$, $A_{VI}-A_C$) corresponding to Fe^{3+} in the tetrahedral and octahedral sites, respectively, and the positive velocity components of two Fe^{2+} doublets corresponding to Fe^{2+} in the tetrahedral site (B_{IV}) and a composite peak corresponding to Fe^{2+} in the octahedral and dodecahedrally coordinated sites (B_{VI} , B_{VIII}), respectively. The low-velocity components of the Fe^{2+} doublets occur beneath the peak labeled A_{IV} (cf. Huggins, Virgo, and Huckenholz, 1976a). The f_0 data on the heated sample (aliquot b) are plotted in Fig. 136.

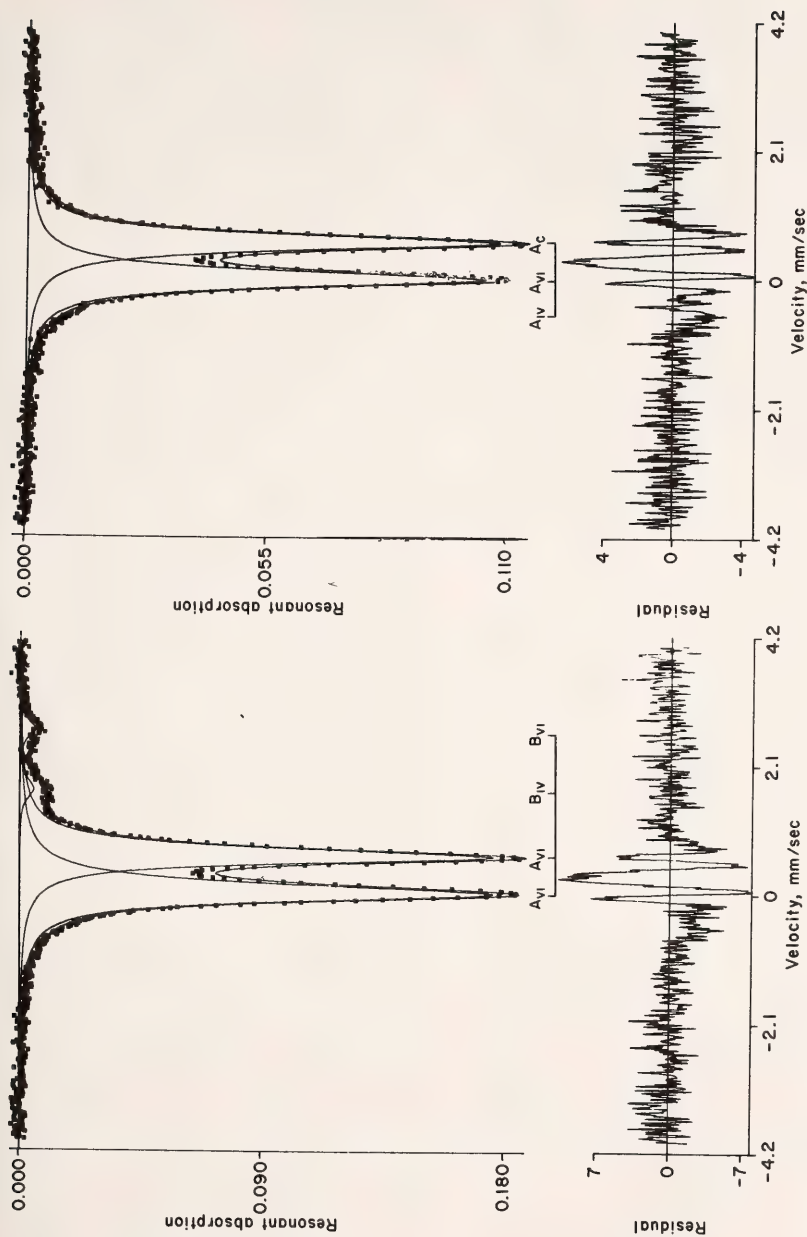


Fig. 142. ^{57}Fe Mössbauer spectra at 77°K of the natural (left) and quenched (right) San Benito garnet after treatment in the ZrO_2 electrochemical cell. The absorption data were fitted to four lines of Lorentzian shape consisting of a Fe^{3+} doublet ($A_{\text{VI}}-A_{\text{IV}}$) corresponding to Fe^{3+} in the octahedral site and the positive velocity component of two Fe^{3+} doublets corresponding to Fe^{3+} in the tetrahedral (B_{IV}) and octahedral sites (B_{VI}). The low-velocity components of the Fe^{3+} doublets were not fitted to the data. The f_0 data of the treated sample are plotted in Fig. 139 (a); Fe^{3+} in the tetrahedral site (A_{IV}) for this sample is inferred from the larger degree of absorption of this velocity position and the larger asymmetry of the Fe^{3+} absorption doublet compared with the natural garnet.

PETROLOGIC IMPLICATIONS OF INTRINSIC
OXYGEN FUGACITY MEASUREMENTS ON
TITANIUM-CONTAINING SILICATE
GARNETS

D. Virgo, F. E. Huggins, and M. Rosenhauer

Previous studies of the phase equilibria of synthetic systems (e.g., Bailey and Schairer, 1966) and pyroxene and garnet stability experiments (e.g., Nolan and Edgar, 1963; Nolan, 1969; Yagi and Onuma, 1969; Flower, 1974; Huckenholz, 1969; Huckenholz and Yoder, 1971) pertinent to questions concerning the petrogenesis of alkalic, SiO_2 -undersaturated rocks have been carried out under oxidizing conditions. The rationale for these studies stems principally from the oxidation ratio of the rocks (e.g., $\text{Fe}_2\text{O}_3/\text{FeO} \geq 1$), from considerations of the crystal chemistry of the constituent mineral phases, and in particular, from the predominance of oxidized cations such as trivalent iron and tetravalent titanium.

In previous reports concerning the crystal chemistry, phase equilibria, and intrinsic oxygen-fugacity measurements of a representative suite of natural Ti-garnets, it was emphasized that the crystalline structure is important in any consideration of the relationship between cation oxidation states and oxygen fugacity. In this report, petrological considerations of the oxygen fugacity results for the Ti-garnets are reviewed in the framework established by previous measurements of oxygen fugacities of other igneous rocks. Because of the very low oxygen fugacities determined for the natural garnets, necessary constraints on the conditions of formation of other alkaline rock minerals and consequently on the host rocks are also discussed.

Of the six natural Ti-garnets discussed in a previous section (Huggins, Virgo, and Huckenholz, this Report), the Rusinga and Kaiserstuhl garnets are of undisputed volcanic origin and the

Iivaara garnet is of plutonic igneous origin. The Frascati garnet crystals, however, are from calc-silicate bombs occurring in the pyroclastics of the Alban hill volcano, Italy, and as such may be mantle derived. The San Benito crystals are found in a chlorite matrix within blocks of serpentinized peridotite within the Franciscan formation, California. As pointed out by Switzer, Melson, and Thompson (1971), however, the occurrence of a Ti-garnet in such an environment is quite unlike the usual metasomatism of ultrabasic rocks to produce "rodingite" in which hydrogrossular is the dominant garnet phase. A garnet of similar composition and in the same geological environment occurs in dredged material from the Mid-Atlantic Ridge. The sample referred to as Howie No. 9 is a monomineralic vein within a massive skarn formation that is part of the Precambrian basement complex, northern Red Sea hills, Sudan.

Previous estimates of the oxygen fugacities in igneous rocks have been determined by one of four methods: (1) measurements of the intrinsic oxygen fugacities (Sato, 1971) on mineral separates, bulk rocks, and volcanic gases; (2) measurements of the magnetite-ilmenite equilibria using the method of Buddington and Lindsley (1964); (3) synthetic f_{O_2} reequilibration at near-liquidus temperatures of atomic ratios such as $\text{Fe}^{2+}/\text{Fe}^{3+}$ (Fudali, 1965); and (4) determination of f_{O_2} from a comparison of the melting behavior of rocks as a function of f_{O_2} with the observed constituent phenocrysts (Thompson, 1975). Data on f_{O_2} in various terrestrial basaltic lavas and plutonic rocks are summarized in Fig. 143 and show that for a variety of compositions the log f_{O_2} - T relationships vary by at least 10 orders of magnitude of log f_{O_2} at a given temperature. Despite the overall variation, the results appear to fall into three distinct groups:

1. "Subaerial" basalts and volcanic gases that approximate or are more oxi-

dizing than the mt-qtz-fa synthetic buffer.*

2. Rocks from the slowly cooled plutonic Stillwater and Bushveld complexes in which equilibrium intrinsic oxygen fugacities for specific mineral equilibria are approximately between the 1-atm Fe-wü and mt-qtz-fa buffers.

3. Phenocrysts of deep-seated origin such as the olivine phenocrysts in the glassy matrix of the crust of a Hawaiian tholeiitic pillow lava that approximate to the Fe-wü buffer. However, the T - f_{O_2} coordinates for the coexistence and last equilibration of perovskite, olivine, and magnetite in the Oka carbonatite conform to the mt-qtz-fa buffer at $\sim 700^\circ\text{C}$.

The equilibrium intrinsic f_{O_2} data for the natural garnets appear to reflect the lowest oxygen fugacities of the representative results for terrestrial igneous rocks plotted in Fig. 143. Sato (1972) interpreted the low oxygen fugacity for the olivine phenocrysts in the submarine tholeiite in terms of strongly reducing conditions prevailing in a deep magma reservoir considering the predicted depth of origin of the magma (Moore, 1965). It is also likely that these results on the olivine phenocrysts are primordial values in view of the improbable loss or gain of oxygen by diffusion. Moore and Fabbi (1971) and Anderson (1974) argued that submarine pillow lavas have retained their primordial H_2O and S

contents in comparison with subaerial basalts because of rapid quenching.

It has been suggested that the oxidized nature of the subaerial basalts and volcanic gases can be explained by H_2 loss in near-surface magma chambers and during magma extrusion (Sato, 1972) because of the ease with which H_2 can diffuse compared with other gas species. By way of comparison, Gerlach and Nordlie (1975b), from their calculations based on natural volcanic gas compositions, demonstrated that H_2 diffusion and sulfur loss from a gas are two of the most efficient mechanisms for altering the oxidative capacity of a magnetic gas. As pointed out by the latter authors, however, the overall effect in a magma-gas equilibrium depends to some extent on the degree of equilibrium in such a system, and the total effect may be minimized because of reequilibration and material exchange within the magma.

Viewed in this framework, the low oxygen-fugacity values for the Ti-garnets are suggestive of crystallization of the garnet phenocrysts at high pressure. The influence of pressure on intrinsic oxygen fugacities has been ignored up to this point in the present discussion. Inasmuch as only low total pressures are considered, the pressure effect results in only a small correction of the 1-atm f_{O_2} measurements. At higher pressures, however, the influence on the oxygen fugacity can become significant. For example, the major effect of pressure on the synthetic hydrothermal buffers (Eugster and Wones, 1962; Heubner, 1971) can be calculated from the volume changes of the solids involved in the reaction. This effect amounts to an increase in f_{O_2} of several orders of magnitude at 50 kbar and at a given temperature, but the absolute change also depends on the specific buffer being considered. The pressure effect on the intrinsic oxygen fugacity of a nonstoichiometric phase, however, is given by integration of the partial molar volumes of the constituent components. Such

* Not plotted in Fig. 143 are the results of Carmichael (1967a) and Carmichael and Nicholls (1967), who determined a range of T - f_{O_2} coordinates for the equilibration of magnetite and ilmenite phenocrysts in a variety of salic volcanic rocks, Icelandic volcanic rocks, and Cascadian andesites. These results spread over the temperature range $800^\circ\text{--}1100^\circ\text{C}$, and f_{O_2} data at a given temperature vary from the mt-qtz-fa buffer to ~ 4 orders of magnitude higher log f_{O_2} values. Also not plotted in Fig. 143 are the results of Gerlach and Nordlie (1975a,b,c) using the measured atomic compositions of natural volcanic gases normalized to the C-O-H-S system. The latter authors showed that under conditions of closed-system cooling the equilibrium oxygen fugacities are within the range defined by the synthetic NNO and QFM buffers at 1000°C and 1-atm pressure.

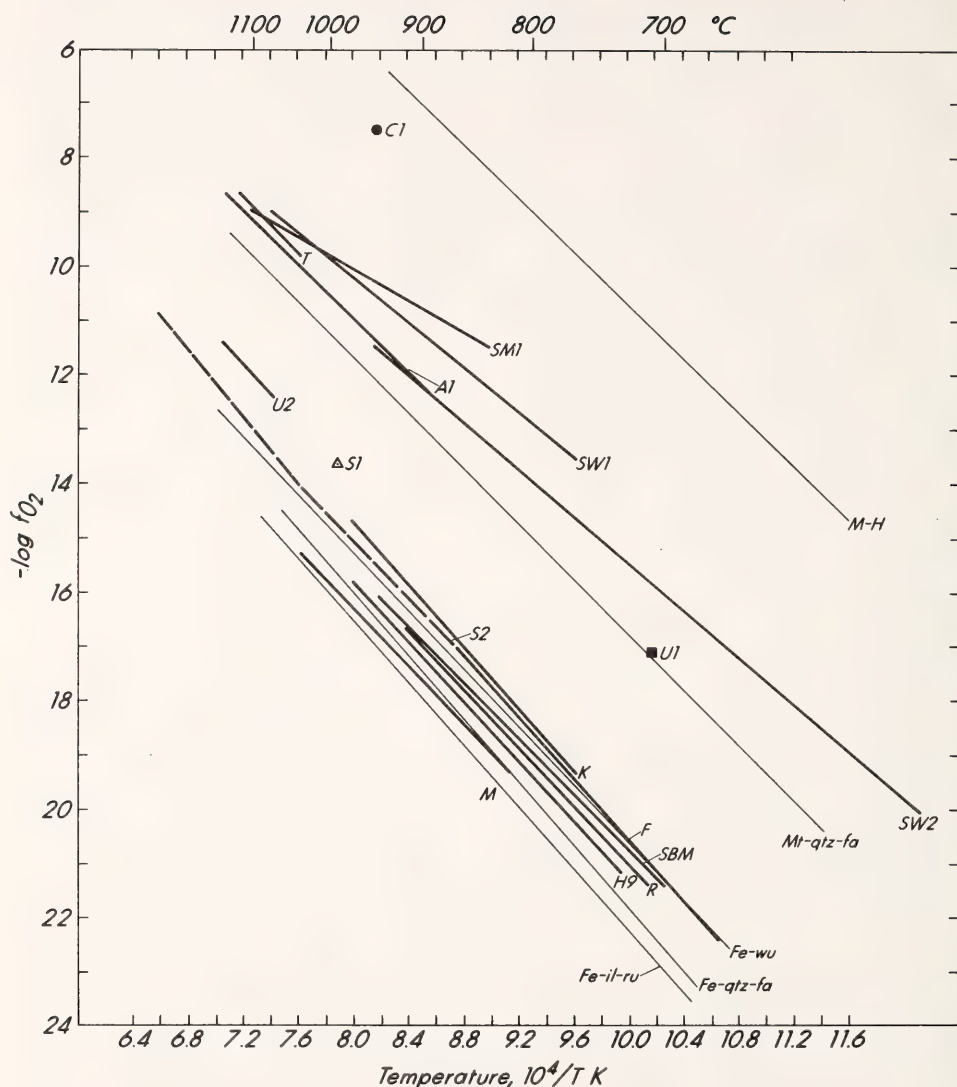


Fig. 143. The equilibrium $\log f_{O_2}-1/T$ relationships of the natural garnets are compared with synthetic buffer reactions and published data for mineral equilibria in igneous rocks and volcanic gases. Plotted are data for the following garnets: Kaiserstuhl (*K*); Frascati (*F*); San Benito, sample supplied by Dr. P. G. Manning (*SBM*); Rusinga (*R*); Howie No. 9 (*H9*); melteigite 9/54 (*M*). *S2* corresponds to olivine phenocrysts in a submarine tholeiite (Sato, 1972); *S1*, *U2*, and *U1*, respectively, refer to mineral equilibria in the Bushveld (Ulmer *et al.*, 1976), Stillwater (Sato, 1972), and Oka carbonatite (Friel and Ulmer, 1974). Other symbols refer to subaerial basalt and volcanic gas data as follows: *SW2* and *SW1*, Sato and Wright (1966); *A1*, Anderson (1968); *T*, Thompson (1975); *SM1*, Sato and Moore (1973), *C1*, Carmichael and Nicholls (1967).

values cannot at present be calculated for garnets. Nevertheless, the effect of pressure on the hydrothermal buffer curves might be useful in placing some constraints on the intrinsic oxygen fugacities of phases such as magnetite and fayalite, which are confined between the H-Mt and Mt-Wü and the Fa-qtz-mt and Fe-qtz-fa buffers, respectively, at all pressures. Extrapolating this method to higher pressures is meaningful only if the participating phases do not change. For example, wüstite is known to become stoichiometric under high pressure. A wüstite sample quenched under high pressure in equilibrium with magnetite will have a high activity of divalent iron. If this sample is now used to determine 1-atm intrinsic f_{O_2} 's, the fugacity values probably would resemble those for Fe-wü because the high Fe^{2+} activity of the quenched high-pressure phase cannot be accommodated by the wüstite structure at 1 atm and metallic iron must therefore precipitate. This behavior is inherent in all non-stoichiometric phases that tend to become more stoichiometric with increasing pressure. Consequently, care must be exercised in relating intrinsic f_{O_2} measurements on minerals derived from possible high-pressure environments to 1-atm buffer curves and in using these measurements for comparative purposes with other oxygen fugacity measurements. Nevertheless, it is not anticipated that the effect of pressure will account for the total spread of data for different igneous rocks depicted in Fig. 143.

In terms of the above hypothesis for the low intrinsic oxygen-fugacity measurements on the natural garnets, it is of interest to speculate whether the rapid irreversible increase in f_{O_2} above specific critical temperatures, T_c , is in response to the 1-atm instability of the garnet phenocrysts. In this respect, the results on the Rusinga garnet (Virgo, Rosenhauer, and Huggins, this Report, Fig. 136), may eventually be significant insofar as the f_{O_2} changes over 200°C by almost 10 orders of magnitude of log f_{O_2}

values. Significant deviations from the linear equilibrium log f_{O_2} - $1/T$ plots reflect cation rearrangement, or changes in the redox behavior of the natural garnets or both, in response to the 1-atm conditions. By way of comparison, similar rapid increases in f_{O_2} are also observed for olivine megacrysts within the matrix of kimberlite rocks (M. Rosenhauer, G. C. Ulmer, personal communications). The above suggestion is noteworthy because such a mechanism may provide an alternative explanation for the high oxygen fugacities of subaerial basalts (cf. Fig. 143).

In view of the very low f_{O_2} values determined for the natural Ti-garnets and the rationalization of these results in terms of their crystal-chemical properties (Virgo, Rosenhauer, and Huggins, this Report), it is of importance to consider the conditions of formation of other alkaline rock minerals. As previously mentioned, most experimental studies pertaining to the stability of pyroxene and garnet constituents of SiO_2 -undersaturated rocks have been made under highly oxidizing conditions. The rationale for these studies stems from the predominance of oxidized cations such as Fe^{3+} and Ti^{4+} . In view of the results of this study, however, the experimental observation that pure acmite is stable at low oxygen fugacities (in equilibrium with metallic iron) and to high pressures (Gilbert, 1969) may also have important geological significance because acmitic pyroxenes are common constituents in alkalic rocks and certainly are present in rocks containing Ti-garnets. In fact, preliminary intrinsic oxygen-fugacity data on the acmitic pyroxene in the melteigite sample 9/54 are compatible with the data for the coexisting garnet. The stability of Fe^{3+} -rich aenigmatite solid solutions at significantly lower oxygen fugacities than the Ti end-member compositions containing only divalent iron (cf. Hodges and Barker, *Year Book* 72, pp. 578-581), should also be noted because aenigmatite is a common accessory mineral in

SiO₂-undersaturated peralkaline rocks. The inferred low f_{O_2} conditions for Ti-rich magnetite_{ss} and coexisting Fe³⁺-rich pyroxenes in the alkaline Ilimausag intrusion, South Greenland (Larsen, 1976), is also pointed out. It is suggested that the above observations in conjunction with the results of this study establish a basis for the reconsideration of the conditions of formation of alkaline rock minerals.

In contrast, the inferred low oxygen fugacities for the host rocks, and in particular rocks of the ijolite series containing principally Ti-garnet, pyroxene, and nepheline (e.g., the melteigite sample 9/54), despite their oxidized nature, inferred from the chemical analyses ($Fe_2O_3/FeO > 1$), are at variance with the available experimental results on synthetic systems. In the range of oxygen fugacities that overlap the stability field of metallic iron it is known from previous experimental studies that Fe^{3+}/Fe^{2+} is comparatively low in moderately iron-rich melts (e.g., Bowen and Schairer, 1932; lunar melts). Under similar f_{O_2} conditions, the presence of Ti³⁺ in a melt can be expected, as shown by Bell, Mao, and Weeks (*Year Book* 73, pp. 492–496), and the presence of Ti³⁺ in lunar minerals has also been previously noted. These experimental results appear to reflect the following equilibria in a melt: $Fe^{3+}_{liq} + Ti^{3+}_{liq} \rightleftharpoons Ti^{4+}_{liq} + Fe^{2+}_{liq}$. They suggest that the equilibrium constant for such a reaction is comparatively large at low oxygen fugacities consistent with the greater stability of the higher valence states of titanium oxides compared with iron, i.e., $Ti^{4+}/Ti^{3+} > Fe^{3+}/Fe^{2+}$. In the absence of measurements of the equilibrium constant for the above reaction in systems with different bulk composition, it is suggested that the influence of alkalis in such a melt is important to enhancing the Fe_2O_3 content. This suggestion is based on indications from chemically simple systems that high alkali contents in glasses dramatically increase Fe^{3+}/Fe^{2+} (Paul and Douglas,

1965). It is also possible that the high volatile content of such melts has a similar effect (Kogarko, 1974). Underlying these considerations is the fact that the Fe^{3+} concentration in the host magma may be considerable at low f_{O_2} values owing to a low activity coefficient for Fe^{3+} that results from the strong degree of nonideality of components in the melt.

In the above discussion an attempt has been made to rationalize the low oxygen fugacities determined for the natural Ti-garnets in terms of available experimental data for other alkaline rock minerals and the bulk chemistry of the host rocks. Finally, some obvious constraints on the low f_{O_2} conditions during crystallization of igneous rocks can be pointed out. These constraints must, of course, follow from the absence of metallic iron in most terrestrial igneous rocks except in a few isolated occurrences (e.g., the Josephine peridotite, the Disco Island basalts). The anomaly suggested from the compatibility of experimentally determined $\log f_{O_2}$ – $1/T$ relationships for the Ti-garnets reported in this study and for olivine phenocrysts in submarine basalts as measured by Sato (1972) to synthetic buffering systems involving metallic iron (Fig. 143) therefore requires some explanation. Although the activity of metallic iron in a melt increases with decreasing f_{O_2} at a given temperature, the apparent discordancy, mentioned above, results because the stability field of metallic iron can vary over approximately 2 orders of magnitude in $\log f_{O_2}$ values in systems of different bulk composition. The more reduced values are associated with bulk compositions containing TiO₂ (cf. Fig. 143).

Further constraints on the low oxygen fugacities for mantle-derived phenocrysts are apparent from discussions of core-mantle equilibrium (Ringwood, 1966; Mao, *Year Book* 73, pp. 510–518). Although these authors differ in their viewpoint of the core-mantle equilibrium, it is inferred from both studies

that the prevailing oxygen fugacities during crystallization of the upper-mantle Mg-rich silicates have not overlapped the stability field of metallic iron. Certainly, the low oxygen fugacities determined for the olivine phenocrysts in a submarine tholeiite (Sato, 1972) must be somewhat higher than the conditions necessary for equilibration of metallic iron and silicates with $\text{Mg}/(\text{Mg} + \text{Fe})$ approaching those determined for primitive mantle olivines (Nitsan, 1974). On this basis it can be suggested that the absolute values of 1-atm intrinsic oxygen fugacities for the Ti-garnets approach the lower limits likely for magmas derived from upper mantle magma chambers.

Whereas the above discussion raises a number of unresolved questions, the overall indications strongly suggest caution against the general applications of previous experimental studies carried out under oxidizing conditions to questions concerning the petrogenesis of alkaline SiO_2 -undersaturated rocks.

INTERPRETATION OF ^{27}Al AND ^{57}Fe NUCLEAR QUADRUPOLE DATA IN RARE EARTH GARNETS

S. S. Hafner and M. Raymond

The quadrupole-split doublet of ^{57}Fe in Mössbauer spectra has been used to identify the oxidation state and location of iron in crystal structures of silicate garnets. The assignment of the Fe^{2+} and Fe^{3+} doublets to the cation positions in garnets has been obtained so far on an empirical basis. The ^{57}Fe spectra of andradite, $\text{Ca}_3\text{Fe}_2\text{Si}_3\text{O}_{12}$, and kimzeyite, $\text{Ca}_3\text{Zr}_2\text{FeSi}_2\text{O}_{12}$, have been used to specify the Fe^{3+} splittings at the octahedrally and tetrahedrally coordinated positions, and the spectrum of almandine has yielded the characteristics of the Fe^{2+} doublet at the eight-fold coordinated position. In this way, the spectra of the geologically important iron-bearing garnet solid solution (including almandine, andradite, grossular, and pyrope) have revealed a remarkably

consistent pattern. No attempt has been made, however, to interpret the observed trends in the splittings in terms of the crystal structures. In natural silicate crystals the trends may, of course, be complicated by multiple cation substitutions at the crystallographic positions due to complex chemical compositions.

A simple model is proposed in which the observed nuclear quadrupole splittings of Fe^{3+} ions in terms of the crystal structure are interpreted. The model is then used to predict the trends of the splitting in rare earth garnet solid solutions. The cation Fe^{3+} is especially interesting because it may occur in tetrahedrally as well as octahedrally coordinated positions. In addition, the Fe^{3+} splitting at both sites shows a dependence on the chemical composition of the garnet. Garnets of the solid solution series $\text{Y}_3\text{Fe}_{5-x}\text{Al}_x\text{O}_{12}$ are suitable examples to test the proposed model because their crystal structures are well refined and the ^{57}Fe quadrupole splitting may be compared with ^{27}Al data obtained from nuclear magnetic resonance. Hafner, Raymond, Virgo, and Huggins (this Report) consider the ^{57}Fe splittings in silicate garnets using the conclusions reached from the $\text{Y}_3\text{Fe}_{5-x}\text{Al}_x\text{O}_{12}$ series.

From the experimentally determined quadrupole splittings of ^{57}Fe , ΔE_Q (Tables 50 and 51), the electric field gradient V_{zz} , at the nuclear site is obtained using the equation

$$\Delta E_Q = 1/2 eQ_1 V_{zz}. \quad (1)$$

Similarly, V_{zz} at the site of ^{27}Al is obtained from the ^{27}Al quadrupole coupling constant C , where

$$C = eQ_2 V_{zz}/h. \quad (2)$$

Here, Q_1 and Q_2 are the nuclear quadrupole moments of ^{57}Fe (first excited state) and ^{27}Al (ground state), respectively; e is the electronic charge; h is Planck's constant; and Z is the direction of the maximum eigen-value of the second rank tensor, which is in the direction of the $\bar{3}$ axis at the octa-

TABLE 50. $Y_3Fe_{5-x}Al_xO_{12}$: Electric Field Gradient at Octahedral Position

| V_{zz}^* | α^\dagger | $x =$ 0 | $x =$ 0.99 | $x =$ 1.97 | $x =$ 2.97 | $x =$ 3.97 | $x =$ 5 | $x =$ 5 |
|-------------------------------------|------------------|------------|---------------|---------------|---------------|---------------|--------------------------|--------------------------|
| | | Fe^{3+} | Fe^{3+} | Fe^{3+} | Fe^{3+} | Fe^{3+} | Fe^{3+} | Al^{3+} |
| Point charge | | | | | | | | |
| $(1-\gamma_\infty)(V_{zz}^p)$ | 0 | -13.22 | -10.51 | -9.77 | -8.13 | -7.31 | -5.76 | -1.92 |
| Point charge | | | | | | | | |
| and dipole ‡ | 0.5 | -7.40 | -4.75 | -4.19 | -2.66 | -1.76 | -0.26 | -0.09 |
| $(1-V_\infty)(V_{zz}^p + V_{zz}^d)$ | 1.0 | -3.32 | -1.10 | -0.36 | +1.15 | +2.09 | +3.56 | +1.19 |
| Overlap $§$ | 0 | -12.75 | -11.00 | -10.59 | -9.60 | -9.19 | -8.20 | -1.98 |
| $[(1-R)V_{zz}^{overlap}]$ | 0.5 | -11.31 | -9.62 | -9.19 | -8.19 | -7.73 | -6.74 | -1.62 |
| | 1.0 | -10.31 | -8.66 | -8.22 | -7.22 | -6.71 | -5.73 | -1.38 |
| Total | 0 | -25.97 | -21.51 | -20.37 | -17.73 | -17.49 | -13.96 | -3.90 |
| V_{zz} | 0.5 | -18.71 | -14.36 | -13.38 | -10.85 | -9.50 | -7.00 | -1.71 |
| | 1.0 | -13.63 | -9.76 | -8.58 | -6.06 | -4.62 | -2.18 | -0.19 |
| Experimental $ $ | | -8.19 $¶$ | -8.0** | -7.5** | -6.8** | -5.7** | (-5.0) †† | 0.585 ‡† |

* Negative field gradient (maximum eigen-value of the positive second derivative of the electrostatic potential) in units of 10^{14} esu.

† Dipole polarizability of O^{2-} .

‡ Using $\gamma_\infty(Fe^{3+}) = -9.19$ (Ray *et al.*, 1975), $R(Fe^{3+}) = +0.059$ (Gupta and Sen, 1973), $\gamma_\infty(Al^{3+}) = -2.4$, $R = -0.063$ (Sternheimer and Peierls, 1971), and crystal structure data of Euler and Bruce (1965).

$§$ Using the wave functions of Clementi (1965) for Fe^{3+} and Al^{3+} and of Pantelides, Mickish, and Kunz (1974) for O^{2-} .

$||$ Using $Q(^{57}Fe) = 0.18$ and $Q(^{27}Al) = 0.140$ (Sternheimer and Peierls, 1971).

$¶$ Housley and Grant (1972).

** Czerlinsky and MacMillan (1970).

†† Extrapolated from Czerlinsky and MacMillan (1976).

‡† Brog, Jones, and Verber (1966).

TABLE 51. $Y_3Fe_{5-x}Al_xO_{12}$: Electric Field Gradient at Tetrahedral Position

| V_{zz}^* | α^\dagger | $x =$ 0 | $x =$ 0.99 | $x =$ 1.97 | $x =$ 2.97 | $x =$ 3.97 | $x =$ 5 | $x =$ 5 |
|-------------------------------------|------------------|------------|---------------|---------------|---------------|---------------|---------------------------|--------------------------|
| | | Fe^{3+} | Fe^{3+} | Fe^{3+} | Fe^{3+} | Fe^{3+} | Fe^{3+} | Al^{3+} |
| Point charge | | | | | | | | |
| $(1-\gamma_\infty)(V_{zz}^p)$ | 0 | -6.34 | -5.87 | -6.27 | -5.68 | -5.40 | -5.36 | -1.79 |
| Point charge | | | | | | | | |
| and dipole ‡ | 0.5 | -8.46 | -8.43 | -9.08 | -8.81 | -8.79 | -8.91 | -2.97 |
| $(1-V_\infty)(V_{zz}^p + V_{zz}^d)$ | 1.0 | -11.18 | -11.58 | -12.47 | -12.52 | -12.76 | -11.81 | -3.94 |
| Overlap $§$ | 0 | -14.84 | -15.27 | -16.18 | -16.26 | -16.58 | -17.36 | -4.23 |
| $[(1-R)V_{zz}^{overlap}]$ | 0.5 | -16.00 | -17.49 | -17.56 | -17.76 | -18.27 | -19.16 | -4.90 |
| | 1.0 | -17.40 | -18.08 | -19.15 | -19.59 | -20.02 | -21.20 | -5.33 |
| Total | 0 | -21.18 | -21.14 | -22.45 | -21.94 | -21.99 | -22.72 | -6.02 |
| V_{zz} | 0.5 | -24.46 | -25.03 | -26.64 | -26.57 | -27.06 | -28.67 | -7.87 |
| | 1.0 | -28.58 | -29.67 | -31.62 | -32.12 | -32.78 | -33.01 | -9.47 |
| Experimental $ $ | | -18.33 $¶$ | -16.9** | -17.3** | -17.6** | -17.3** | (-17.3) †† | 5.571 ‡† |

Footnotes as in Table 50.

hedral position and the $\bar{4}$ axis at the tetrahedral position. The electric field gradient V_{zz} is the second derivative of the electrostatic potential at the nucleus, i.e., the negative gradient of the electrostatic field.

In predominantly ionic crystals, the

total electric field gradient at the nucleus can be calculated from

$$V_{zz} = (1-\gamma_\infty)V_{zz}^o + (1-R)V_{zz}^{overlap} \quad (3)$$

where

$$V_{zz}^o = V_{zz}^p + V_{zz}^d + \dots \quad (4)$$

and γ_∞ and R are the Sternheimer factors of the free ion; V°_{zz} is the electric field gradient produced by the ionic charges of all neighboring ions in the crystal, and V_{zz}^{overlap} is the electric field gradient produced by the overlap between the orbitals of the cation in question and those of the ligands. The term V^P_{zz} is the electric field gradient due to the net charges of all neighboring ions (point-charge contribution) and V^D_{zz} is the electric field gradient due to the electronic dipole moments induced in the electron density distribution of the ions (contribution of ionic polarization). Higher-order terms in Equation 4 will be neglected. The terms V^P and V^D may be obtained from lattice summations (Raymond, 1971).

The overlap contribution V_{zz}^{overlap} has been calculated by Taylor (1968), Sawatzky and Hupkes (1970), Sharma (1970, 1972), and Raymond (*Year Book* 73, pp. 576–578). Housley and Grant (1972) suggested that the effect of electrostatically induced distortion of the ligand wave functions should be included. This effect has been accounted for by calculating the valence shell displacements from the electronic dipoles of the oxygen ion. The overlap was then calculated on the basis of the local approximation that neglects the effect on the electric field gradient of the overlap distortions of the anion orbitals. Its contribution to the electric field gradient is (Sharma, 1972; Raymond, *Year Book* 73, pp. 576–586)

$$V_{zz}^{\text{overlap}} = \frac{4}{5} e < r^{-3} > \sum S_K^2 (3 \cos^2 \theta_K - 1) \quad (5)$$

where K denotes the cation orbital (2p, 3p, 3d), $< 1/r_K^{-3} >$ is the expected value of r^{-3} of orbital K ; S is the overlap integral between the cation and anion orbitals, and θ_K is the angle between the direction from the cation (K) to the anion (Z). All other overlaps are either zero or neglected.

Unfortunately, field gradients computed from Equations 3 and 4 exhibit large errors, mainly because the nuclear

quadrupole moments for ^{57}Fe and ^{27}Al , the Sternheimer factors γ_∞ and R for Fe^{3+} and Al^{3+} , and the dipole polarizability α of the oxygen ion are not well known. Moreover, accurate wave functions for the free oxygen ion are not available, so the computed overlap integrals will not be precise.

A test of the proposed model can be made, however, using the trends of the electric field gradient in different garnet solid solutions because the nuclear quadrupole moments will be the same, and γ_∞ , R , and α are expected to be very similar in garnets.

The results of the present calculations are compared with the experimental data in Tables 50, 51, and 52. The magnitude of the electric field gradients cannot be accurately predicted from the present model at the distinct cationic sites, but the ratios between samples correctly reflect an increase with increasing aluminum concentration (x). In particular, the decreasing magnitude of the octahedral Fe^{3+} electric field gradient across the solid solution series $\text{Y}_3\text{Fe}_{5-x}\text{Al}_x\text{O}_{12}$ with increasing x is qualitatively in accord with the experimental observations. All three contributions to V_{zz} , namely, point charge, dipole, and overlap distortion, exhibit a regular decrease.

The nearly invariant value of the tetrahedral Fe^{3+} electric field gradient is also consistent with the experimental data. The small decrease in the point-charge term with increasing x is almost canceled by the opposite trend in the dipole term. The dipoles also produce a displacement of the oxygen orbitals, resulting in a small increase in the overlap contribution.

From the proposed model, it is also possible to predict the sign of the electric field gradient. From experiments, the sign for the rare earth garnet series is known to be negative at both the octahedral and tetrahedral positions (Housley and Grant, 1972; Czerlinsky and MacMillan, 1970). In fact, the signs of the point-charge and overlap contributions at both distinct crystal sites are

TABLE 52. Electric Field Gradient at Al^{3+} Positions in Garnets

| V_{zz}^* | α^\dagger | $\text{Y}_3\text{Al}_5\text{O}_{12}$ | | $\text{Tm}_3\text{Al}_5\text{O}_{12}$ | | $\text{Yb}_3\text{Al}_5\text{O}_{12}$ | |
|---|------------------|--------------------------------------|--------|---------------------------------------|---------|---------------------------------------|---------|
| | | Oct. | Tetr. | Oct. | Tetr. | Oct. | Tetr. |
| Point charge ($1-\gamma_\infty$)(V^P_{zz}) | 0 | -1.92 | -1.79 | -2.12 | -2.15 | -2.80 | -2.06 |
| Point charge and dipole‡ | 0.5 | -0.09 | -2.97 | -0.20 | -3.46 | -0.76 | -3.27 |
| ($1-V_\infty$)($V^P_{zz}+V^D_{zz}$) | 1.0 | +1.19 | -3.94 | +1.13 | -4.96 | +0.64 | -4.70 |
| Overlap§ | 0 | -1.98 | -4.23 | -2.10 | -4.54 | -2.51 | -4.39 |
| [($1-R$) V_{zz}^{overlap}] | 0.5 | -1.62 | -4.90 | -1.73 | -5.00 | -2.11 | -4.83 |
| | 1.0 | -1.38 | -5.53 | -1.48 | -5.52 | -1.84 | -5.33 |
| Total | 0 | -3.90 | -6.02 | -4.22 | -6.69 | -5.31 | -6.45 |
| V_{zz} | 0.5 | -1.71 | -7.87 | -1.93 | -8.46 | -2.88 | -8.10 |
| | 1.0 | -0.19 | -9.47 | -0.35 | -10.48 | -1.20 | -10.03 |
| Experimental | | 0.585¶ | 5.571¶ | 0.892** | 6.065** | 1.038†† | 6.208†† |

*—|| Footnotes as in Table 50.

¶ Brog, Jones, and Verber (1966).

** Schmidt and Jones (1970).

†† Edmonds and Lindop (1968).

negative (Tables 50 and 51). The electric field gradients for the aluminate garnets of Tm and Yb (Table 52) are also predicted to be negative. A negative value of the field gradients, however, is not general; the electric field gradient at the octahedral position in silicate garnets is indeed positive (Hafner, Raymond, Virgo, and Huggins, this Report).

The importance of the dipole term, V^D_{zz} , in the calculations is also evident from Tables 50 and 51 (cf. Sharma, 1972). In particular, the difference of a factor of ~ 2.0 between the experimental Fe^{3+} field gradients at the octahedral and tetrahedral sites of $\text{Y}_3\text{Fe}_5\text{O}_{12}$ cannot easily be explained in terms of the point-charge and overlap contributions. The difference can be explained, however, from the dipole contribution, V^D_{zz} , which is positive at the octahedral position and negative at the tetrahedral position, and also partly from the change of V_{zz}^{overlap} due to the dipole-displaced orbitals of O^{2-} . Both effects reduce the electric field gradient at the octahedral sites and enhance it at the tetrahedral sites.

It is also of interest to compare the Al^{3+} and Fe^{3+} electric field gradients in

$\text{Y}_3\text{Al}_5\text{O}_{12}$. The observed Al^{3+} gradient at the octahedral sites is almost ten times smaller than the corresponding gradient at the tetrahedral sites, whereas the respective values of the Fe^{3+} gradients in that compound differ only by a factor of ~ 3.5 . This difference is remarkable. The generally smaller Al^{3+} gradients result, of course, primarily from the smaller Sternheimer factor, γ_∞ , and the smaller overlap term, V_{zz}^{overlap} , of the Al^{3+} ion, which are indeed about three and four times smaller, respectively. Because all three contributions to V_{zz} (point charge, dipole, and overlap) have *negative* signs at the tetrahedral position, the computed total Al^{3+} electric field gradient is in fact about three times smaller than that of Fe^{3+} . Yet, V^D_{zz} is *positive* and cancels most of V_{zz}^{overlap} of Al^{3+} at the octahedral position. An exceptionally small field gradient for Al^{3+} is therefore predicted at that position, as observed.

On the basis of the model, the ratio of the observed Al^{3+} and Fe^{3+} field gradients at the octahedral position in $\text{Y}_3\text{Al}_5\text{O}_{12}$ can be used to determine the dipole polarizability α of O^{2-} : The calculated value is $\alpha = 0.9 \text{ \AA}^3$. Here, the effect of local distortion of the Al^{3+} positions by

Fe^{3+} in $\text{Y}_3\text{Al}_5\text{O}_{12}$ is neglected. The ratio of the octahedral to tetrahedral Al^{3+} gradient yields $\alpha = 0.73 \text{ \AA}^3$. About the same value for α is also obtained from the ratios in $\text{TmAl}_5\text{O}_{12}$ and $\text{Yb}_3\text{Al}_5\text{O}_{12}$ (cf. Table 52). Moreover, the predicted trend in the gradient ratios is consistent with the experimental data.

Alternatively, the ratio of the octahedral to tetrahedral Fe^{3+} gradient in $\text{Y}_3\text{Fe}_5\text{O}_{12}$ is indicative of a somewhat higher α value: $\alpha = 1.1 \text{ \AA}^3$. This value is in agreement with the comparatively high refractive index of $\text{Y}_3\text{Fe}_5\text{O}_{12}$. (E. C. T. Chao, U.S. Geological Survey, determined the refractive index and found the value to be 2.99 ± 0.07 .) Using the Lorentz relationship, the molar polarizability α_m for $\text{Y}_3\text{Fe}_5\text{O}_{12}$ obtained from refractive index determinations (Tessman, Kahn, and Shockley, 1953) is found to be significantly higher than α_m for $\text{Y}_3\text{Al}_5\text{O}_{12}$. Thus, α of O^{2-} must be higher in $\text{Y}_3\text{Fe}_5\text{O}_{12}$.

It is concluded that the observed trends in the nuclear quadrupole coupling tensors at the cationic sites in yttrium iron garnets and related aluminates of the same structure type can be interpreted, on a qualitative basis, in terms of an ionic model that includes the effect of oxygen polarization and overlap distortion. Overlap distortion alone would apparently account for the trends of the observed Fe^{3+} gradients. It would not account for the ratio of the Fe^{3+} to Al^{3+} field gradients in $\text{Y}_3\text{Al}_5\text{O}_{12}$ or the octahedral to tetrahedral Al^{3+} gradient ratios in the other rare earth aluminates. These ratios are critically sensitive to the dipole polarization of the oxygen ion. Because of the necessity of including the contributions of the overlap distortion and the dipole polarization terms to the total electric field gradients, it is apparent that purely geometrical considerations of the crystal structures (e.g., polyhedral distortion, edge sharing) are insufficient for interpreting a critical bonding parameter like the quadrupole coupling tensor.

INTERPRETATION OF THE ^{57}Fe NUCLEAR QUADRUPOLE DATA FOR SOME SILICATE GARNETS

*S. S. Hafner, M. Raymond, D. Virgo,
and F. E. Huggins*

Hafner and Raymond (this Report) propose an ionic model of the electronic charge distribution that includes the effects of overlap distortion and oxygen polarization to explain differences in the nuclear quadrupole coupling tensors at the cationic sites in some rare earth garnet structures. In this report, the applicability of the model to the geologically important garnet end-members—pyrope, spessartine, andradite, and grossular—is examined.

The results of the calculated and experimentally determined electric field gradients are summarized in Tables 53 and 54. In general, the calculated ^{57}Fe octahedral quadrupole splitting increases in the series pyrope, spessartine, andradite, and grossular (Table 53) consistent with the experimental data. The field gradient at the tetrahedral site is considerably larger than at the octahedral site, thus lending support to the suggestion that the electron density distribution of the tetrahedrally coordinated polyhedron in andradite and grossular should be considered strongly distorted. Although a similar distinction is also observed in yttrium iron garnet, the difference between the octahedral and tetrahedral field gradient is enhanced in the silicate garnets.

Whereas the field gradient at the octahedral position in the $\text{Y}_3\text{Fe}_{5-x}\text{Al}_x\text{O}_{12}$ solid solution series is *negative*, it is generally *positive* in silicate garnets. This interesting distinction is primarily due to the large positive contribution of the O^{2-} dipoles. The point-charge and dipole terms (Table 53) have the same signs as in $\text{Y}_3\text{Fe}_{5-x}\text{Al}_x\text{O}_{12}$, but they are in different proportion. Also, the contribution of overlap distortion may be positive or negative, depending on the crystal structure of the garnet and consequently on the degree of displacement of the ligand

TABLE 53. Silicate Garnets: Electric Field Gradient at Octahedral Position

| V_{zz}^* | α^\dagger | Pyrope Fe^{3+} | Spessartine Fe^{3+} | Andradite Fe^{3+} | Grossular | |
|--|------------------|----------------------------|---------------------------------|-------------------------------|------------------|------------------|
| | | | | | Fe^{3+} | Al^{3+} |
| Point charge ($1-\gamma_\infty$)(V_{zz}^p) | 0 | -12.38 | -6.81 | -0.85 | -0.27 | -0.09 |
| Point charge and dipole‡ ($1-V_\infty$)($V_{zz}^p+V_{zz}^d$) | 0.5 | +6.91 | +9.90 | +11.80 | +12.95 | +4.32 |
| | 1.0 | +19.95 | +21.46 | +19.36 | +22.37 | +7.46 |
| Overlap§ | 0 | -5.89 | -1.40 | +2.20 | +3.70 | +0.89 |
| [($1-R$) V_{zz}^{overlap}] | 0.5 | -0.97 | +2.71 | +4.64 | +6.71 | +1.62 |
| | 1.0 | +2.13 | +5.31 | +6.20 | +8.65 | +2.08 |
| Total | 0 | -18.27 | -8.20 | +1.36 | +3.43 | +0.80 |
| V_{zz} | 0.5 | +5.94 | +12.61 | +16.44 | +19.66 | +5.94 |
| | 1.0 | +22.08 | +26.77 | +25.56 | +31.02 | +9.54 |
| Experimental | | 4.63¶ | 5.87¶ | +9.79¶ | 10.7** | 3.56†† |

*—|| Footnotes as in Table 50.

¶ Amthauer, Annersten, and Hafner (1976).

** Extrapolated from Huggins, Virgo, and Huckenholz (1976a); cf. Whipple (1973).

†† Derighetti and Ghose (1969).

TABLE 54. Electric Field Gradient at Tetrahedral Position for Andradite and Grossular

| V_{zz}^* | α^\dagger | Andradite Fe^{3+} | Grossular Fe^{3+} |
|--|------------------|-------------------------------|-------------------------------|
| | | | |
| Point charge ($1-\gamma_\infty$)(V_{zz}^p) | 0 | -8.63 | -7.86 |
| Point charge and dipole‡ ($1-V_\infty$)($V_{zz}^p+V_{zz}^d$) | 0.5 | -14.98 | -12.00 |
| | 1.0 | -21.96 | -17.28 |
| Overlap§ | 0 | -16.45 | -16.59 |
| [($1-R$) V_{zz}^{overlap}] | 0.5 | -19.11 | -19.14 |
| | 1.0 | -22.44 | -22.30 |
| Total | 0 | -25.08 | -24.45 |
| V_{zz} | 0.5 | -34.10 | -31.14 |
| | 1.0 | -44.40 | -39.59 |
| Experimental | | 21.18¶ | 22.6** |

Footnotes as in Table 53.

orbitals due to ionic polarization. The sign of the total gradient, however, is not reversed by the overlap term. In general, then, the simple model shows that the sign is generally positive in silicate garnets, in accord with the ^{57}Fe quadrupole splitting at the octahedral Fe^{3+} position in andradite that was recently found to be positive in an applied magnetic field (Amthauer, Annersten, and Hafner, 1976).

At the tetrahedrally coordinated site,

the calculations based on the model yield a negative electric field gradient, as in the $\text{Y}_3\text{Fe}_{5-x}\text{Al}_x\text{O}_{12}$ series (Table 54). Whereas the sign in the yttrium iron garnet is known to be negative from experiment (Housley and Grant, 1972), the sign in andradite and grossular has not been determined experimentally.

From the magnitudes of the computed and experimental octahedral field gradients, it is suggested that an oxygen polarizability of $\alpha = 0.3\text{--}0.5 \text{ \AA}^3$ provides

the closest agreement. The predicted smaller values for the oxygen polarizability in silicate garnets (cf. Hafner and Raymond, this Report) are in agreement with the smaller molar polarizability α_m obtained from refractive indices of silicate garnets compared with α_m of $\text{Y}_3\text{Fe}_5\text{O}_5$ (Tessman, Kahn, and Shockley, 1953).

As in $\text{Y}_3\text{Al}_5\text{O}_{12}$ (Hafner and Raymond, this Report) the ^{27}Al and ^{57}Fe data in grossular can be directly compared with the experimental and calculated ratio of the octahedral Al^{3+} and Fe^{3+} electric field gradients. Because both computations are based on the same atomic coordinates (Novak and Gibbs, 1971), the differences in the Al^{3+} and Fe^{3+} electric field gradient ratios are due solely to the differences in the Sternheimer factors γ_∞ and R and the different overlap terms for Al^{3+} and Fe^{3+} . The predominant terms, V_{zz}^D and V_{zz}^{overlap} , have the same sign, and the ratio of the Al^{3+} and Fe^{3+} electric field gradients is predicted to be between ~ 3 (ratio of the respective γ_∞ factors) and ~ 4 (ratio of the respective overlap contributions). The point-charge contribution, which has opposite sign, is small and may be neglected. The predicted ratio of the Al^{3+} and Fe^{3+} gradients is in agreement with the experimental data (Table 53), as concluded previously for yttrium aluminate (Hafner and Raymond, this Report).

It is expected that the nuclear quadrupole splitting would reflect the geometrical distortion of the specific coordination polyhedra and the type of its edge-sharing with adjacent polyhedra. It is apparent, however, that there is no direct correlation between the results of this study (Table 53) and the systematic variations of the geometrical distortions in the garnet structure (Novak and Gibbs, 1971) that were based on nine crystal-structure refinements of silicate garnets. For example, the magnitudes of the quadrupole splittings in pyrope and spessartine are in direct contrast with the larger octahedral distortion in pyrope compared with that in spessartine (No-

vak and Gibbs, 1971, Table 13). In addition, silicate garnets generally possess relatively smaller octahedral distortions than yttrium iron garnet, which is also in contradistinction with the experimentally determined electric field gradients.

The overlap distortion is, of course, directly correlated to the geometrical deformation of the oxygen polyhedron. If the oxygen octahedron is elongated along the $\bar{3}$ axis, as observed in pyrope, the overlap distortion is negative, whereas if it is flattened along the $\bar{3}$ axis, as in grossular, the distortion is positive. The dipole contribution to the electric field gradient is, however, not correlated. Also, the displacements of the ligand orbitals caused by dipole polarization may produce an overlap distortion with opposite sign and as a result may cancel the overlap distortion based on the positional coordinates of the oxygen nucleus (cf. data for pyrope and spessartine in Table 53). The magnitude of the dipole contribution to the electric field gradient accounts for the lack of correlation between the quadrupole splitting and the distortion of the octahedra.

It is evident from the relative magnitudes and the signs of the electric field gradients at the crystal sites that the structures of the cubic silicate garnets can be rationalized only in terms of a model in which the ions have lower than spherical symmetry (cf. Novak and Gibbs, 1971).

ON THE STOICHIOMETRY OF CLINOPROXENES IN THE SYSTEM $\text{CaO-MgO-}\text{Al}_2\text{O}_3\text{-SiO}_2$

B. J. Wood

Several investigators have suggested that clinopyroxenes containing large amounts of alumina deviate from the expected stoichiometry of four cations to six oxygens. In particular, the subsolidus experiments of Kushiro (1969a) indicated that aluminous clinopyroxenes crystallized from quartz-saturated compositions

contain silica in apparent excess of the amounts requisite for "ideal" clinopyroxenes. The presence of excess silica (probably as the molecule $\text{Ca}_{0.5}\text{AlSi}_2\text{O}_6$) should result in a cation sum, to six oxygens, of less than four. A recent experimental study of subsolidus clinopyroxene-anorthite-quartz assemblages in which the pyroxenes were analyzed with an electron microscope microanalyzer (Wood, 1976) also suggested the presence of excess silica in those clinopyroxenes with high alumina content. Cawthorn and Collerson (1974) have found that published analyses of natural clinopyroxenes also show decreasing cation sums as Al^{VI} increases. The purpose of the present study was to investigate, using the electron microprobe, the stoichiometry of clinopyroxenes crystallized in the system $\text{CaO-MgO-Al}_2\text{O}_3\text{-SiO}_2$ at high pressures. The electron microprobe yields analyses that are considerably more accurate than those obtained by the electron microscope technique used previously (Wood, 1976).

High-pressure experiments were carried out in solid-media, high-pressure apparatus in the pressure and temperature ranges 20–30 kbar and 1275°C–1430°C. Glass and crystalline starting materials together with 2–6 wt % water were sealed in Pt capsules and run for 1–5 hr. Bulk compositions and run conditions were chosen so that clinopyroxene and quartz coexisted with H_2O -undersaturated melts.

Alumina-free mixtures of crystalline diopside and quartz readily recrystallized between 1300°C and 1400°C (20–25 kbar) to give large clinopyroxene crystals ($\sim 30\ \mu\text{m}$) that could be easily analyzed. From eight to twelve electron microprobe analyses of the product clinopyroxenes were performed on each charge. The analyses indicate that little, if any, excess silica is soluble in alumina-free clinopyroxenes under the physical conditions of these experiments. The lowest observed cation total was from a run at 20 kbar and 1400°C that gave 3.982 ($\sigma = 0.009$) cations to six oxygens; the

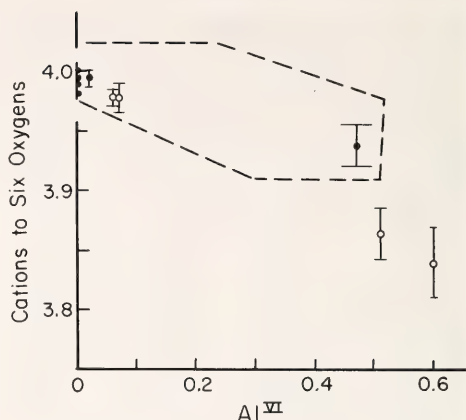


Fig. 144. Cation sums of synthetic clinopyroxenes as a function of Al^{VI} . Bars denote ± 1 standard deviation. Open circles, glass starting material; solid circles, crystalline starting material (diopside and quartz in Al-free system; Cpx, ~ 3 mole % $\text{CaAl}_2\text{SiO}_6$, anorthite, quartz in Al-bearing systems). Outlined area is approximate range of stoichiometry of natural clinopyroxenes from Cawthorn and Collerson (1974).

highest cation sum, at 25 kbar and 1300°C, was 3.999 ($\sigma = 0.008$).

Addition of Al_2O_3 to the system CaO-MgO-SiO_2 has a profound effect on the size of the product clinopyroxenes. Only six of the eighteen experiments performed on Al_2O_3 -bearing compositions produced some pyroxenes of lengths greater than $10\ \mu\text{m}$, and in two of these ($\text{Al}^{\text{VI}} = 0.46$ and 0.597 , Fig. 144), only four analyses were possible. The results shown in the figure demonstrate, however, that there is indeed a correlation between the alumina content of clinopyroxenes coexisting with quartz and their stoichiometry. The magnitudes of deviations from "ideal" stoichiometry are similar to those found by Cawthorn and Collerson (1974) for natural clinopyroxenes of a wide range of paragenesis. It is of interest to note that an extrapolation of these results to pure calcium Tschermak's (nominally $\text{CaAl}_2\text{SiO}_6$) clinopyroxene coexisting with quartz implies that the composition of such a pyroxene would be similar to that of anorthite ($\text{Ca}_{0.75}\text{Al}_{1.5}\text{Si}_{1.5}\text{O}_6$).

THE EFFECT OF CA SUBSTITUTION ON THE STRUCTURE OF CLINOENSTATITE

Y. Ohashi and L. W. Finger

The phase relationships on the join between enstatite and diopside have been extensively studied; only recently, however, Kushiro (1972b) and Yang and Foster (1972) have shown a stability field for iron-free pigeonite at 1 atm. At the enstatite end member there are at least three polymorphs, but a small amount of Ca in solid solution has the effect of stabilizing the pigeonite form. The present study was undertaken to delineate the structural changes associated with changes in composition. In the Fe-Ca clinopyroxenes, Ohashi, Burnham, and Finger (1975) found that pigeonite with the composition $\text{Fs}_{85}\text{Wo}_{15}$ * differed from clinoferrosilite in the kinking of the silicate chain. From this result they concluded that a relatively large change in the silicate chain configuration took place between $\text{Fs}_{100}\text{Wo}_0$ and $\text{Fs}_{85}\text{Wo}_{15}$.

The end-member clinopyroxenes on the join have different symmetry, $P2_1/c$ for clinoenstatite (Morimoto, Appleman, and Evans, 1960) and $C2/c$ for diopside (Clark, Appleman, and Papike, 1969). There are two crystallographically distinct silicate chains in the clinoenstatite structure but only one in diopside. This difference in the chain configuration is mainly the result of the cation occupancy in the M2 site (e.g., Ohashi, Burnham, and Finger, 1975). With the addition of Ca, the difference between the two chains in Ca-poor clinopyroxenes decreases until they become identical at some critical composition.

Synthetic crystals of iron-free clinopyroxenes used in the present study are $\text{En}_{100}\text{Wo}_0$ (supplied by Dr. J. Ito), $\text{En}_{94.4}\text{Wo}_{5.6}$ (supplied by Dr. Y. Nakamura), and $\text{En}_{91.6}\text{Wo}_{8.4}$ (synthesized by Dr. R. Schwab and supplied by Dr. M. Rosenhauer). The diffraction symmetry

* Compositions are in mole percentage of Fs (FeSiO_3), En (MgSiO_3), and Wo (CaSiO_3).

of the three crystals studied is consistent with space group $P2_1/c$. Unit-cell parameters, obtained from least-squares refinement of twelve reflections centered on a four-circle diffractometer, are given in Table 55. X-ray intensities of all unique reflections with 2θ less than 65° ($\text{En}_{94.4}\text{Wo}_{5.6}$ and $\text{En}_{91.6}\text{Wo}_{8.4}$) and 70° (En_{100}) for MoK α radiation were measured using an automated four-circle diffractometer. Corrections were made for the Lorentz, polarization, and absorption effects. Atomic coordinates, anisotropic temperature factors, and the extinction coefficient were refined using computer program RFINE2 (Finger and Prince, 1975). The final residual factor R for observed reflections is 3.1%, 5.5%, and 6.3%, respectively, for $\text{En}_{100}\text{Wo}_0$, $\text{En}_{94.4}\text{Wo}_{5.6}$, and $\text{En}_{91.6}\text{Wo}_{8.4}$. The refined atomic coordinates and equivalent isotropic temperature factors are given in Table 56.

Cation Sites

The M1 site was assumed to be fully occupied by Mg, and the site occupancy for M2 was fixed according to the bulk composition of the crystals. These cation assignments have been verified by M-O interatomic distances (Table 57) and also by isotropic temperature factors (Table 56). The average of the six shortest M1-O distances varies only from 2.078 to 2.084 Å. In contrast, the average of the six shortest M2-O distances changes from 2.142 to 2.198 Å as the composition changes from $\text{En}_{100}\text{Wo}_0$ to $\text{En}_{91.6}\text{Wo}_{8.4}$.

In the structural refinement of a pigeonite $\text{Mg}_{0.39}\text{Fe}_{0.52}\text{Ca}_{0.09}\text{SiO}_3$ from

TABLE 55. Unit-Cell Parameters for Mg-Ca Clinopyroxenes

| | $\text{En}_{100}\text{Wo}_0$ | $\text{En}_{94.4}\text{Wo}_{5.6}$ | $\text{En}_{91.6}\text{Wo}_{8.4}$ |
|-----------------------|------------------------------|-----------------------------------|-----------------------------------|
| a (Å) | 9.605(1) | 9.639(1) | 9.657(1) |
| b | 8.813(1) | 8.835(1) | 8.846(2) |
| c | 5.166(1) | 5.192(1) | 5.208(1) |
| β (deg.) | 108.46(1) | 108.39(1) | 108.34(1) |
| V (Å ³) | 415.1(1) | 419.6(1) | 422.3(1) |

TABLE 56. Atomic Coordinates and Equivalent Isotropic Temperature Factors (\AA^2) for Mg-Ca Clinopyroxenes

| | | En ₁₀₀ Wo ₀ | En _{94.4} Wo _{5.6} | En _{91.6} Wo _{8.4} |
|-----|----------|-----------------------------------|--------------------------------------|--------------------------------------|
| M1 | <i>x</i> | 0.2510(1) | 0.2508(3) | 0.2496(4) |
| | <i>y</i> | 0.6533(1) | 0.6535(3) | 0.6539(3) |
| | <i>z</i> | 0.2177(1) | 0.2219(5) | 0.2238(6) |
| | <i>B</i> | 0.43(1) | 0.50(3) | 0.66(4) |
| M2 | <i>x</i> | 0.2558(1) | 0.2558(3) | 0.2557(4) |
| | <i>y</i> | 0.0130(1) | 0.0165(3) | 0.0194(3) |
| | <i>z</i> | 0.2146(1) | 0.2205(5) | 0.2240(6) |
| | <i>B</i> | 0.56(1) | 0.89(4) | 1.11(4) |
| SiA | <i>x</i> | 0.0433(1) | 0.0427(2) | 0.0418(2) |
| | <i>y</i> | 0.3409(1) | 0.3414(3) | 0.3413(3) |
| | <i>z</i> | 0.2944(1) | 0.2888(3) | 0.2839(4) |
| | <i>B</i> | 0.31(1) | 0.36(3) | 0.55(4) |
| SiB | <i>x</i> | 0.5533(1) | 0.5515(2) | 0.5506(2) |
| | <i>y</i> | 0.8372(1) | 0.8374(3) | 0.8379(3) |
| | <i>z</i> | 0.2300(1) | 0.2326(3) | 0.2338(4) |
| | <i>B</i> | 0.32(1) | 0.42(3) | 0.51(4) |
| O1A | <i>x</i> | 0.8666(1) | 0.8672(5) | 0.8676(5) |
| | <i>y</i> | 0.3398(1) | 0.3400(6) | 0.3394(7) |
| | <i>z</i> | 0.1850(2) | 0.1800(8) | 0.1788(11) |
| | <i>B</i> | 0.39(2) | 0.52(7) | 0.58(8) |
| O2A | <i>x</i> | 0.1228(1) | 0.1221(6) | 0.1219(7) |
| | <i>y</i> | 0.5010(1) | 0.5013(5) | 0.5025(7) |
| | <i>z</i> | 0.3215(3) | 0.3215(9) | 0.3247(12) |
| | <i>B</i> | 0.49(2) | 0.56(7) | 0.96(10) |
| O3A | <i>x</i> | 0.1067(1) | 0.1056(5) | 0.1048(6) |
| | <i>y</i> | 0.2795(1) | 0.2764(5) | 0.2733(6) |
| | <i>z</i> | 0.6153(3) | 0.6049(9) | 0.5959(12) |
| | <i>B</i> | 0.50(2) | 0.64(7) | 1.00(10) |
| O1B | <i>x</i> | 0.3761(1) | 0.3744(5) | 0.3738(6) |
| | <i>y</i> | 0.8400(1) | 0.8392(6) | 0.8405(8) |
| | <i>z</i> | 0.1246(2) | 0.1263(8) | 0.1259(11) |
| | <i>B</i> | 0.41(2) | 0.53(6) | 0.89(9) |
| O2B | <i>x</i> | 0.6338(1) | 0.6320(5) | 0.6287(7) |
| | <i>y</i> | 0.9827(1) | 0.9834(9) | 0.9849(7) |
| | <i>z</i> | 0.3892(3) | 0.3843(5) | 0.3746(13) |
| | <i>B</i> | 0.52(2) | 0.73(8) | 1.13(10) |
| O3B | <i>x</i> | 0.6052(1) | 0.6049(5) | 0.6047(6) |
| | <i>y</i> | 0.6942(1) | 0.6994(6) | 0.7036(6) |
| | <i>z</i> | 0.4539(3) | 0.4630(9) | 0.4670(11) |
| | <i>B</i> | 0.47(2) | 0.81(8) | 0.94(9) |

Mull, Scotland, Morimoto and Güven (1970) reported a seven-coordinated M2 polyhedron. The seventh M2-O interatomic distance in En_{91.6}Wo_{8.4}, however, is over 3 Å, and the M2 coordination can still be regarded as six in En_{91.6}Wo_{8.4}. The temperature factor is abnormally

large for M2 in En_{91.6}Wo_{8.4}, indicating a positional fluctuation of Ca and Mg in the site. The similar tendency of large apparent temperature factors has been observed in many intermediate compositions (see Ohashi and Finger, *Year Book* 73, p. 528, Fig. 204).

TABLE 57. M-O Interatomic Distances (Å) for Mg-Ca Clinopyroxenes

| | En ₁₀₀ Wo ₀ | En _{94.4} Wo _{5.6} | En _{91.6} Wo _{8.4} |
|--------|-----------------------------------|--------------------------------------|--------------------------------------|
| M1-O1A | 2.142(1) | 2.152(6) | 2.144(7) |
| -O1A | 2.032(1) | 2.038(5) | 2.046(6) |
| -O2A | 2.006(1) | 2.005(6) | 2.000(7) |
| -O1B | 2.178(1) | 2.175(6) | 2.193(7) |
| -O1B | 2.067(1) | 2.063(5) | 2.060(6) |
| -O2B | 2.042(1) | 2.058(5) | 2.063(7) |
| Mean | 2.078 | 2.081 | 2.084 |
| M2-O1A | 2.090(1) | 2.119(6) | 2.142(7) |
| -O2A | 2.034(1) | 2.072(5) | 2.084(7) |
| -O3A | 2.279(1) | 2.292(5) | 2.306(7) |
| -O1B | 2.053(1) | 2.086(6) | 2.106(7) |
| -O2B | 1.987(1) | 1.995(5) | 2.037(7) |
| -O3B | 2.412(1) | 2.475(5) | 2.512(7) |
| Mean | 2.142 | 2.173 | 2.198 |

Tetrahedral Chain Angle

One of the important parameters that characterize the silicate chain configuration is the tetrahedral chain angle, O3-O3-O3. The importance of the kinking direction in comparison with the octahedral arrangement has been emphasized by Thompson (1970) in his study of the idealized stacking topologies in chain silicates. A comparison of ideal chain configuration and real pyroxene structures has been made by Papike *et al.* (1973). Ohashi and Finger (*Year Book 73*, pp. 522-525) have analyzed the correlation between the tetrahedral chain angle and the site of cation coordination polyhedra.

The tetrahedral chain angle is plotted in Fig. 145 as a function of Ca content for clinopyroxenes on the joins enstatite-diopside and ferrosilite-hedenbergite. Both chains in clinoenstatite show a larger deviation from the fully extended chain angle (180°) than do the corresponding chains in clinoferrosilite. In contrast, the chain angle is not very different in diopside and hedenbergite, in both of which the M2 site is occupied by Ca. This result is consistent with the earlier observation for intermediate pyroxenes that chains are kinked to a greater degree when the cations in M2 are smaller (Papike *et al.*, 1973; Ohashi

and Finger, *Year Book 73*, pp. 522-525).

As Ca substitutes for Mg or Fe, both the *A* and *B* chains become extended. At a particular temperature, there is a composition where the space group changes from *P2₁/c* to *C2/c*. In the latter space group the two chains are identical. At room temperature in the Fe-Ca clinopyroxenes, this change occurs between *Fs*₈₅*Wo*₁₅ and *Fs*₈₀*Wo*₂₀ (Ohashi, Burnham, and Finger, 1975). If the silicate chain angle in Mg-Ca clinopyroxenes changes in the same manner as that in Fe-Ca clinopyroxenes, this phase transition would be expected to take place on the join enstatite-diopside at a more Ca-rich composition, probably around *En*₈₀*Wo*₂₀, because both the *A* and *B* chains in clinoenstatite must be more extended than those in clinoferrosilite in order to become equivalent.

In the pigeonite region of Fig. 145 the rate of change in chain angle with the wollastonite component increases as the composition becomes more Ca-rich, as is often found in cooperative phenomena. Therefore the effect of Ca substitution on the Ca-poor clinopyroxene structure is expected to be more significant, for example, in the range of the *En*₉₀*Wo*₁₀-*En*₈₀*Wo*₂₀ than in the range of *En*₁₀₀*Wo*₀-*En*₉₀*Wo*₁₀.

In conclusion, the major structural

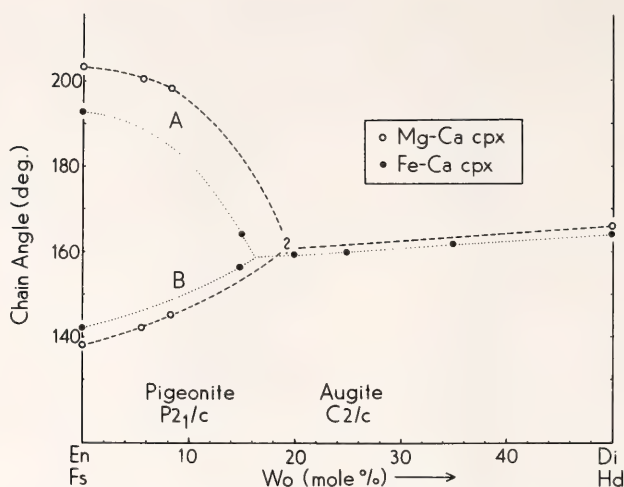


Fig. 145. Variation of the tetrahedral chain angle, O3-O3. If the angle is greater than 180° , the chain is of *S* rotation (Thompson, 1970). Sources of data: Burnham (*Year Book 65*, pp. 285-290); Cameron *et al.* (1973); Clark, Appleman, and Papike (1969); Ohashi, Burnham, and Finger (1975); this study. Standard errors are smaller than the radii of the circles.

changes in the Ca-poor clinopyroxene structure with increasing wollastonite component, are expansion of the M2 coordination polyhedron and extension of the two silicate chains. The difference in the chain angle between the A and B chains decreases as the composition becomes more Ca-rich. Increases of Ca (Fig. 145) and temperature (Sueno, Cameron, and Prewitt, 1976, p. 49, Fig. 7) both seem to have a similar effect on the silicate chain angle.

STEPWISE CATION ORDERING IN BUSTAMITE AND DISORDERING IN WOLLASTONITE

Y. Ohashi and L. W. Finger

Bustamite and wollastonite, both single chain silicates, are of interest because of the great difference in the extent of their solid solutions. Bustamite has the widest compositional range of the pyroxenoid minerals, its CaSiO_3 content ranging from approximately 30 mole % to more than 80 mole % (Mason, 1973, 1975; Hodgson, 1975; Shimazaki and Yamana, 1973; Matsueda, 1973). In contrast, the composition of wollastonite is

often close to the ideal composition, CaSiO_3 ; other components, such as MnSiO_3 and FeSiO_3 , rarely exceed a few mole percent in this mineral. The present study has been undertaken to analyze crystal structural factors that might control the compositional limits and intracrystalline cation distribution in the two minerals.

In their study of an intermediate Ca-Mn bustamite containing 54 mole % CaSiO_3 , Peacor and Buerger (1962), using a difference Fourier map, suggested that Ca occupies the M2 and M4 sites and that M1 and M3 contain Mn with a small amount of excess Ca in M1. This cation ordering scheme for intermediate compositions has been confirmed in a synthetic iron analogue, ferrobustamite ($\text{Ca}_{0.5}\text{Fe}_{0.5}\text{SiO}_3$), by Rapoport and Burnham (1973).

Their study, however, was inconclusive with regard to cation ordering in a Ca-rich ferrobustamite ($\text{Ca}_{0.79}\text{Fe}_{0.19}\text{Mn}_{0.02}\text{SiO}_3$) owing to difficulties caused by twinning. For Ca-rich ferrobustamite, which has sometimes been improperly described as iron wollastonite in spite of its bustamite structure, Yamanaka, Ta-

keuchi, and Shimazaki (Y. Takeuchi, personal communication) have found that the iron atoms are concentrated in the M3 site, in agreement with their prediction (Shimazaki and Yamanaka, 1973) based on the upper limit of CaSiO_3 in natural ferrobustamite.

In this study, three different compositions of bustamite and two of wollastonite have been chosen to represent the range of chemical compositions of the minerals. The crystal chemical data for these samples are given in Table 58. The Mn-rich bustamite sample was kindly supplied by Dr. A. Kato; the intermediate and Ca-rich bustamite samples, by Dr. M. Nambu; the Mn-wollastonite of Dr. Hodgson's specimen, by Dr. B. Mason; and the Fe-wollastonite, by Dr. D. E. Appleman.

Because of their triclinic symmetry, several different unit-cell settings are

possible for bustamite and wollastonite. The setting used in this study is as follows: The tetrahedral chain direction is chosen as the c axis, and the oxygen close-packed layers are parallel to the (100) plane. In the study of rhodonite and pyroxmangite (Ohashi and Finger, *Year Book* 74, pp. 564-569) a similar setting was adopted for direct comparison of pyroxenes and pyroxenoids. The projections of the bustamite and wollastonite structures, shown in Fig. 146, correspond to a similar projection for rhodonite and pyroxmangite (*Year Book* 74, p. 567, Fig. 96).

Experimental

The x-ray intensities for all the pyroxenoid crystals used in this study were measured on the automated four-circle diffractometer, employing an ω - 2θ variable scanning-rate technique (Finger,

TABLE 58. Chemical Composition and Unit Cell Parameters for Bustamites and Wollastonites

| Specimen: | Mn-Bs | Bs | Ca-Bs | Mn-Wo | Fe-Wo |
|---------------------------------------|---|------------------------------|--|------------------------------|---------------------------|
| Locality: | Mitsuka, Gifu, Japan | Hijikuzu, Iwate, Japan | Hijikuzu, Iwate, Japan | Broken Hill, Australia | Scawt Hill, Ireland |
| Composition (mole fraction) | | | | | |
| CaSiO_3 | 0.314 | 0.500 | 0.783 | 0.961 | 0.949 |
| MnSiO_3 | 0.600 | 0.370 | 0.122 | 0.034 | 0.005 |
| FeSiO_3 | 0.043 | 0.120 | 0.075 | 0.005 | 0.036 |
| MgSiO_3 | 0.043 | 0.009 | 0.020 | 0.000 | 0.010 |
| Space group | | | | | |
| a (Å) | $I\bar{1}$ 9.807(4) | $I\bar{1}$ 9.864(3) | $I\bar{1}$ 9.994(3) | $C\bar{1}$ 10.121(2) | $C\bar{1}$ 10.104(1) |
| b | 10.680(4) | 10.790(5) | 10.946(3) | 11.070(1) | 11.054(1) |
| c | 7.091(2) | 7.139(3) | 7.231(3) | 7.312(1) | 7.305(1) |
| α (deg.) | 99.58(2) | 99.53(4) | 99.53(4) | 99.51(1) | 99.53(1) |
| β | 99.99(3) | 99.71(3) | 100.56(3) | 100.51(1) | 100.56(1) |
| γ | 83.79(3) | 83.83(3) | 83.29(2) | 83.43(1) | 83.44(1) |
| Unit-cell volume (Å ³) | | | | | |
| Z based on MSiO_3 | 718.8(4) | 736.1(5) | 764.3(4) | 791.5(2) | 788.0(1) |
| Transformation matrix T^* | | | | | |
| | 12 | 12 | 12 | 12 | 12 |
| | $\begin{pmatrix} -\frac{1}{2} & -\frac{1}{2} & -\frac{1}{2} \\ 0 & 0 & 1 \\ -1 & 1 & 0 \end{pmatrix}$ | | $\begin{pmatrix} \frac{1}{2} & \frac{1}{2} & 0 \\ 0 & 0 & 1 \\ \frac{1}{2} & -\frac{1}{2} & 0 \end{pmatrix}$ | | |

* In the form of $A'=TA$ where A is the base vector set for the $I\bar{1}$ cell (bustamite) or $C\bar{1}$ cell (wollastonite); and A' for the $A\bar{1}$ cell (bustamite) or $P\bar{1}$ cell (wollastonite) used by Peacor and Prewitt (1963).

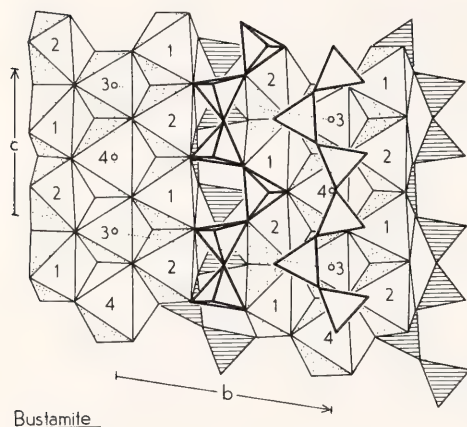
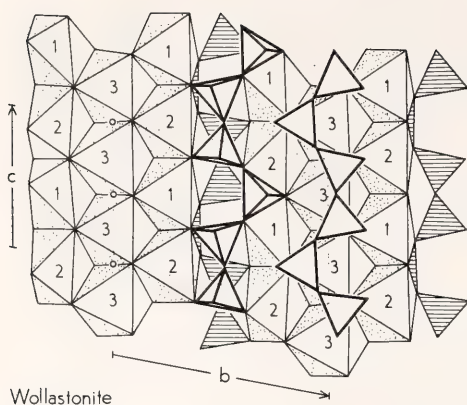


Fig. 146. Portions of the bustamite and wollastonite structures projected onto the plane parallel to the oxygen close-packed layer. Note that the tetrahedral chains above and below the octahedral layer are related by the body-centering translation in bustamite and by the C -centering translation in wollastonite for the unit-cell setting used in this study.

Hadidiacos, and Ohashi, *Year Book* 72, pp. 694–699), with Nb-filtered $\text{MoK}\alpha$ radiation. Integrated intensities were corrected for Lorentz and polarization effects, and absorption corrections were computed by numerical integration (Burnham, 1966).

The atomic coordinates of bustamite reported by Rapoport and Burnham

(1973) and those of wollastonite given by Buerger and Prewitt (1961) were taken as initial values for subsequent least-squares refinements using a computer program RFINE2 (Finger and Prince, 1975). The atomic scattering factors and dispersion corrections are from Cromer and Mann (1968) and Cromer (1965), respectively. The refined atomic coordinates and isotropic temperature factors are given in Table 59. The final residual factor, R , for observed reflections of all of the specimens ranges from 3.6% to 5.2%.

Structural Difference between Bustamite and Wollastonite

Peacor and Prewitt (1963) have discussed in detail the crystal structures of bustamite and wollastonite, and only a few features relevant to the cation ordering will be mentioned here. Although bustamite and wollastonite are commonly classified as chain silicates, the minerals also have a layered character—alternating layers of octahedral and tetrahedral cations parallel to (100) at the unit-cell setting of this study (Fig. 146).

The octahedral layer, consisting of an infinite band with a width of three octahedra, is topologically similar in both minerals but symmetrically distinct. In bustamite, centers of inversion are located at the M3 and M4 positions, whereas in wollastonite they are on the oxygen-oxygen edge shared by adjacent M3 sites. As a result, the arrangement of octahedral cations in the central portion of the three-octahedra-wide bands is -M3-M3-M3-M3- in wollastonite and -M3-M4-M3-M4- in bustamite.

Because of this difference, the M3 and M4 sites in bustamite, both of which correspond to M3 in wollastonite, may be different in cation occupancy. In addition, the two closest equivalent layers (e.g., the two tetrahedral layers above and below a given octahedral layer) are related by the $(a + b)/2$ translation in wollastonite and the $(a + b + c)/2$ translation in bustamite. As will be

shown later, this difference in the translation produces a variety of different arrangements of tetrahedra around some octahedral positions in the two minerals.

Cation Distribution

The occupancies in the octahedral sites have been refined with the constraint of total composition. The refined values (Table 60) show that M3 and M4 in bustamite can be regarded as essentially invariant—M3 is the site for smaller cations such as Mn or Fe, whereas M4 is the site for Ca. The occupancy in M1 and M2 is variable de-

pending on the bulk composition of bustamite. On the subcalcic side of the 1:1 composition, Ca(Mn,Fe,Mg)Si₂O₆, M2 shows the most significant change in occupancy (Fig. 147), whereas on the Ca-rich side, M1 changes its cation occupancy. Figure 148 demonstrates three different cation distributions found for bustamite.

The present study thus indicates that cation substitution in bustamite is a two-step process. The smaller cations such as Mn or Fe occupy the M3 and part of the M1 site if there is any excess. This scheme continues until the smaller

TABLE 59. Atomic Coordinates and Isotropic Temperature Factors (Å²) for Bustamites and Wollastonites

| | | Mn-Bs | Bs | Ca-Bs | Mn-Wo | Fe-Wo |
|-----|----------|--------|--------|----------|----------|---------|
| M1 | <i>x</i> | 0.0241 | 0.0245 | 0.0223 | 0.0208 | 0.0212 |
| | <i>y</i> | 0.2713 | 0.2721 | 0.2771 | 0.2807 | 0.2800 |
| | <i>z</i> | 0.3227 | 0.3257 | 0.3179 | 0.0772 | 0.0772 |
| | <i>B</i> | 0.96 | 0.67 | 0.64 | 0.58 | 0.71 |
| M2 | <i>x</i> | 0.0225 | 0.0231 | 0.0247 | 0.0171 | 0.0180 |
| | <i>y</i> | 0.2753 | 0.2783 | 0.2766 | 0.2806 | 0.2803 |
| | <i>z</i> | 0.8387 | 0.8410 | 0.8333 | 0.5709 | 0.5712 |
| | <i>B</i> | 0.93 | 0.72 | 0.71 | 0.58 | 0.73 |
| M3* | <i>B</i> | 0.73 | 0.55 | 0.64 | —0.0144 | —0.0137 |
| | | | | <i>x</i> | 0.0115 | 0.0111 |
| M4* | <i>B</i> | 0.74 | 0.65 | 0.64 | <i>z</i> | 0.7496 |
| | | | | <i>B</i> | 0.54 | 0.67 |
| Si1 | <i>x</i> | 0.2195 | 0.2226 | 0.2267 | 0.2265 | 0.2265 |
| | <i>y</i> | 0.4565 | 0.4566 | 0.4640 | 0.4583 | 0.4585 |
| | <i>z</i> | 0.1435 | 0.1473 | 0.1395 | 0.8877 | 0.8876 |
| | <i>B</i> | 0.54 | 0.48 | 0.51 | 0.42 | 0.53 |
| Si2 | <i>x</i> | 0.2223 | 0.2235 | 0.2296 | 0.2267 | 0.2266 |
| | <i>y</i> | 0.4517 | 0.4534 | 0.4573 | 0.4577 | 0.4576 |
| | <i>z</i> | 0.6967 | 0.6978 | 0.6983 | 0.4537 | 0.4540 |
| | <i>B</i> | 0.53 | 0.50 | 0.50 | 0.44 | 0.54 |
| Si3 | <i>x</i> | 0.2184 | 0.2201 | 0.2209 | 0.2264 | 0.2260 |
| | <i>y</i> | 0.6764 | 0.6757 | 0.6755 | 0.6707 | 0.6711 |
| | <i>z</i> | 0.4778 | 0.4801 | 0.4727 | 0.2236 | 0.2237 |
| | <i>B</i> | 0.52 | 0.48 | 0.51 | 0.42 | 0.52 |
| O41 | <i>x</i> | 0.1200 | 0.1178 | 0.1169 | 0.1163 | 0.1164 |
| | <i>y</i> | 0.0802 | 0.0803 | 0.0747 | 0.0797 | 0.0786 |
| | <i>z</i> | 0.2766 | 0.2757 | 0.2748 | 0.0381 | 0.0381 |
| | <i>B</i> | 1.12 | 0.77 | 0.86 | 0.76 | 1.00 |
| O42 | <i>x</i> | 0.1141 | 0.1139 | 0.1109 | 0.1169 | 0.1168 |
| | <i>y</i> | 0.0767 | 0.0730 | 0.0733 | 0.0814 | 0.0807 |
| | <i>z</i> | 0.8174 | 0.8170 | 0.8200 | 0.5611 | 0.5612 |
| | <i>B</i> | 1.21 | 0.84 | 0.77 | 0.76 | 0.98 |

* On inversion centers; M3 at (0,0,0) and M4 at (0,0, $\frac{1}{2}$).

TABLE 59 Continued. Atomic Coordinates and Isotropic Temperature Factors (\AA^2) for Bustamites and Wollastonites

| | | Mn-Bs | Bs | Ca-Bs | Mn-Wo | Fe-Wo |
|-----|----------|--------|--------|--------|--------|--------|
| OA3 | <i>x</i> | 0.1085 | 0.1095 | 0.1084 | 0.1152 | 0.1147 |
| | <i>y</i> | 0.7977 | 0.7961 | 0.7925 | 0.7864 | 0.7874 |
| | <i>z</i> | 0.4846 | 0.4849 | 0.4772 | 0.2267 | 0.2271 |
| | <i>B</i> | 0.82 | 0.75 | 0.72 | 0.56 | 0.67 |
| OA4 | <i>x</i> | 0.1171 | 0.1164 | 0.1177 | 0.1149 | 0.1149 |
| | <i>y</i> | 0.8137 | 0.8136 | 0.8132 | 0.8141 | 0.8142 |
| | <i>z</i> | 0.9776 | 0.9744 | 0.9804 | 0.7307 | 0.7305 |
| | <i>B</i> | 0.78 | 0.72 | 0.76 | 0.68 | 0.81 |
| OB1 | <i>x</i> | 0.1106 | 0.1133 | 0.1192 | 0.1239 | 0.1235 |
| | <i>y</i> | 0.3568 | 0.3587 | 0.3659 | 0.3584 | 0.3577 |
| | <i>z</i> | 0.1399 | 0.1491 | 0.1264 | 0.8745 | 0.8750 |
| | <i>B</i> | 1.84 | 1.18 | 1.19 | 0.81 | 1.05 |
| OB2 | <i>x</i> | 0.1297 | 0.1328 | 0.1353 | 0.1230 | 0.1239 |
| | <i>y</i> | 0.3379 | 0.3402 | 0.3483 | 0.3577 | 0.3567 |
| | <i>z</i> | 0.6026 | 0.6010 | 0.6135 | 0.3669 | 0.3657 |
| | <i>B</i> | 1.67 | 1.09 | 0.99 | 0.88 | 1.13 |
| OC1 | <i>x</i> | 0.2111 | 0.2105 | 0.2280 | 0.2211 | 0.2201 |
| | <i>y</i> | 0.4799 | 0.4787 | 0.4927 | 0.4963 | 0.4955 |
| | <i>z</i> | 0.9241 | 0.9259 | 0.9257 | 0.6785 | 0.6780 |
| | <i>B</i> | 2.45 | 1.46 | 1.26 | 1.02 | 1.29 |
| OC2 | <i>x</i> | 0.1678 | 0.1687 | 0.1747 | 0.1820 | 0.1811 |
| | <i>y</i> | 0.5876 | 0.5887 | 0.5880 | 0.5886 | 0.5887 |
| | <i>z</i> | 0.6206 | 0.6221 | 0.6141 | 0.3704 | 0.3703 |
| | <i>B</i> | 0.99 | 0.81 | 0.81 | 0.70 | 0.85 |
| OC3 | <i>x</i> | 0.1738 | 0.1787 | 0.1787 | 0.1827 | 0.1823 |
| | <i>y</i> | 0.5974 | 0.5966 | 0.5988 | 0.5907 | 0.5912 |
| | <i>z</i> | 0.2575 | 0.2605 | 0.2560 | 0.0121 | 0.0119 |
| | <i>B</i> | 0.97 | 0.80 | 0.83 | 0.73 | 0.84 |

Estimated Standard Errors

| | M | Si | O |
|----------|-----------|-----------|-----------|
| <i>x</i> | 0.0001 | 0.0001 | 0.0004 |
| <i>y</i> | 0.0001 | 0.0001 | 0.0004 |
| <i>z</i> | 0.0001 | 0.0002 | 0.0005 |
| <i>B</i> | 0.01-0.03 | 0.01-0.02 | 0.04-0.07 |

* On inversion centers; M3 at (0,0,0) and M4 at (0,0, $\frac{1}{2}$).

cations completely fill up M1. When the total amount of the smaller cations exceeds that of Ca, then the M2 site begins to accommodate these smaller cations. A similar stepwise substitution of Ca and Fe is also found in the M1 and M2 sites in the olivine solid solution between Ca_2SiO_4 and Fe_2SiO_4 (Smith, Majumdar, and Ordway, 1965).

Energetically, this procedure can be

considered in terms of the energy difference between ordered and anti-ordered states, i.e., $[\text{Ca}(\text{M2}) + \text{Mn}(\text{M1})]$ versus $[\text{Ca}(\text{M1}) + \text{Mn}(\text{M2})]$, which must be so large that in a practical temperature range, the disordering process between the M1 and M2 sites does not occur in bustamite. Thus, the anti-ordered state in bustamite resembles $[\text{Ca}(\text{M1}) + \text{Fe,Mg}(\text{M2})]$ in clinopyroxenes, a

TABLE 60. Cation Site Occupancies* in Bustamites and Wollastonites

| | Mn-Bs | | Bs | | Ca-Bs | |
|-----------|-------|---------|-------|---------|-------|---------|
| | Ca | Mn | Ca | Mn | Ca | Mn |
| M1 (1.0)† | 0.08 | 0.92(1) | 0.13 | 0.87(1) | 0.93 | 0.07(1) |
| M2 (1.0) | 0.49 | 0.51(1) | 0.93 | 0.07(1) | 0.95 | 0.05(1) |
| M3 (0.5) | 0.19 | 0.81(2) | −0.05 | 1.05(1) | 0.12 | 0.88(2) |
| M4 (0.5) | 0.83 | 0.17 | 0.99 | 0.01 | 1.00 | 0.00 |
| | | | Mn-Wo | | Fe-Wo | |
| | | | Ca | Mn | Ca | Fe |
| M1 (1.0) | | | 0.95 | 0.05(1) | 0.97 | 0.03(1) |
| M2 (1.0) | | | 0.97 | 0.03(1) | 0.97 | 0.03(1) |
| M3 (1.0) | | | 0.96 | 0.04 | 0.93 | 0.07 |

* The Fe ion can be treated as Mn, and Mg effectively increases the apparent Ca occupancy factor.

† Equipoint fraction.

state that is not observed (e.g., Ohashi, Burnham, and Finger, 1975).

The two wollastonite specimens studied contain approximately 4 mole % MnSiO₃ or FeSiO₃. By analogy from the cation ordering scheme in bustamite, the Mn and Fe atoms had been expected to show some ordering among the three cation sites in the wollastonite structure. The results of occupancy refinements, however, show that the Mn or Fe atoms are distributed over the three sites. The M3 site in Fe wollastonite is slightly richer in iron but there is little difference in occupancy for the other octahedral sites.

Arrangement of Tetrahedra
around Octahedron

Probably the most critical constraint on the cation substitution at a particular coordination polyhedron is its size. In the present case, the flexibility of oxygen atom positions around the possible position for octahedral cations is most critical for determining the size. The flexibility or rigidity of the oxygen positions is controlled by the other part of the structure, particularly neighboring coordination polyhedra.

Thus, it is important to analyze the arrangement of tetrahedra around the octahedral site in order to obtain a crystal structural explanation for the observed cation occupancy. When viewed normal to one of the triangle faces, the octahedra have three oxygens in both upper and lower adjacent tetrahedral levels. Coordination of the three oxygens on each level can be analyzed in terms of the linkages with the rest of the structure.

In bustamite and wollastonite, there are five types of tetrahedral-octahedral links (Fig. 149). Because the octahedron is sandwiched between the two tetrahedral layers, two types of linkages must

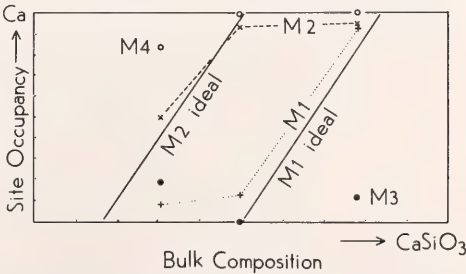


Fig. 147. Variation of the cation-site occupancy in bustamite.

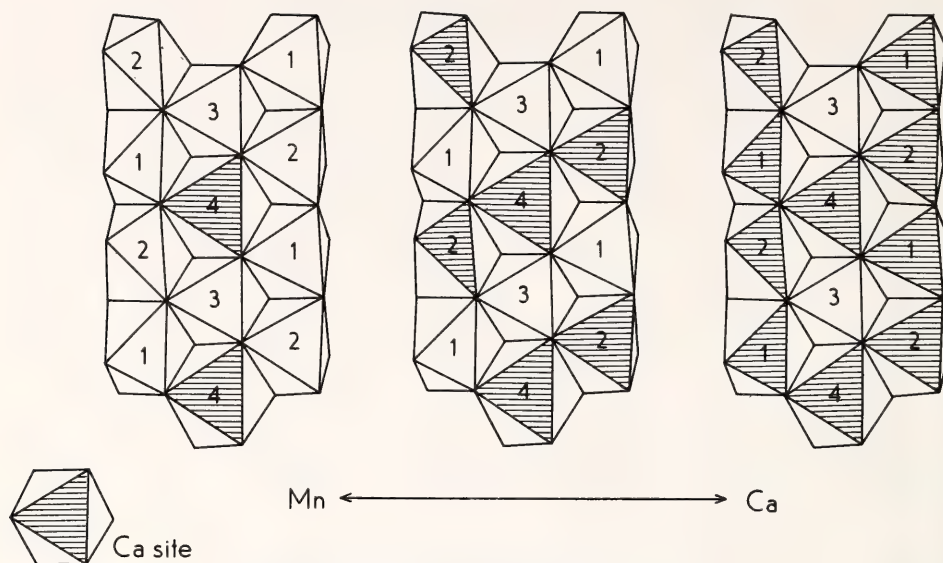


Fig. 148. Three schemes of Ca ordering in bustamite.

be specified for each octahedron. $M1_B$ and $M1_W$, for example, are both characterized by a combination of types 1 and 3, the subscripts B and W denoting bustamite and wollastonite, respectively. It is found that type 4-4 of $M4_B$ is suitable to accept the larger Ca atom and that type 5-5 of $M3_B$ provides a smaller octahedron for Mn or Fe. Interestingly, $M3_W$ is of type 4-5, a hybrid of $M3_B$ and $M4_B$. The M1 and M2 octahedra in the two minerals each share one edge with a tetrahedron but are different in the second link.

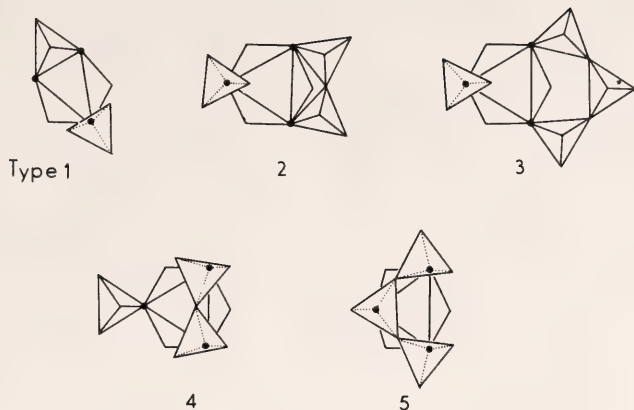
In conclusion, the wide compositional range of the bustamite solid solution is explained by the fact that both M1 and M2 sites can change their occupancy in a sequential, stepwise fashion. Analysis of the geometrical relationships between the tetrahedra and octahedra indicates that M3 and M4 are quite different in bustamite, probably resulting in the occupancy being essentially fixed. This nearly complete ordering of small ca-

tions in M3 and Ca in M4 results in more flexibility in the range of size of the M1 and M2 crystallographic sites.

On the other hand, none of the three sites in wollastonite, with its M3 intermediate to M3 and M4 of bustamite, discriminates against smaller cations. All three sites can accommodate some Mn, Fe, or Mg, and this nearly disordered distribution in turn places a limit on how far they can substitute for Ca in each site.

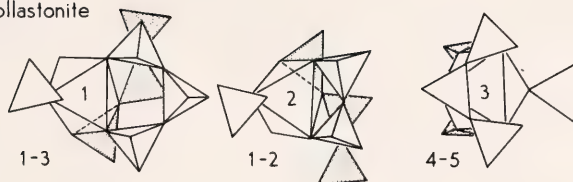
When a mineral shows a relatively wide but incomplete solid solution between components and a large difference in cation size, it probably means structurally that there are two kinds of cation sites—"soft" sites of variable size and occupancies and "hard" sites having a strong preference for certain ions. The sites M1 and M2 in bustamite, M5 in rhodonite, and M5 and M7 in pyroxmangite are examples of soft sites. The sites in wollastonite, however, do not fit such a simplistic model.

(A)



(B)

Wollastonite



Bustamite

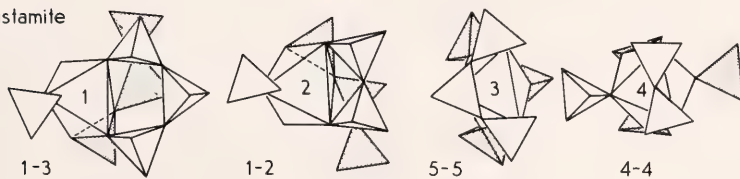


Fig. 149. (A) Five types of octahedral-tetrahedral linkages found in bustamite and wollastonite. (B) Arrangements of tetrahedra around octahedra in bustamite and wollastonite.

ELECTRON PARAMAGNETIC RESONANCE OF TWO MAGNESIOWÜSTITES

R. A. Weeks, H. K. Mao, and P. M. Bell

Magnesiowüstite is a mineral whose properties may be representative of those of minerals in the earth's mantle (Mao, *Year Book* 72). Its compositional range is in the system Fe-Mg-O, and its density range is 3.6–5.3 g/cm³. It is produced from decomposition and disproportionation reactions of silicate minerals. Magnesiowüstites are typically

nonstoichiometric, and they contain mixed valence states of iron. As part of an effort to characterize the properties of magnesiowüstite for its eventual consideration as a mineral phase in models of the earth's deep mantle, the present observations of its electron paramagnetic resonance (EPR) were made on one of the same materials, (FeO)_{0.40}(MgO)_{0.60}, whose compressibility was determined (Rosenhauer, Mao, and Woermann, this Report). A second magnesiowüstite, (FeO)_{0.22}(MgO)_{0.78}, whose

electrical conductivity and optical spectra were determined as functions of pressure and temperature (Mao, *Year Book 72*), was also studied. The two magnesio-wüstites are characterized as a result of the detection of coordinated ferric ions in the ferromagnetic resonance spectrum.

Samples

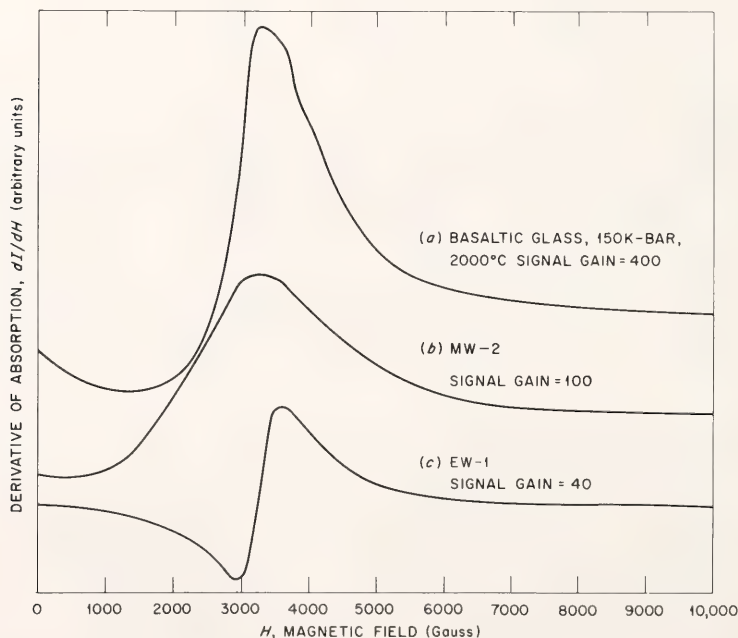
The sample (MW-2) of composition $(\text{FeO})_{0.22}(\text{MgO})_{0.78}$ was synthesized by Mao (*Year Book 72*). The other sample (EW-1), of composition $(\text{FeO})_{0.40}(\text{MgO})_{0.60}$, was synthesized by E. Woermann (see Rosenhauer, Mao, and Woermann, this Report, for wet chemical analysis). Also described in this study are two synthetic lunar basaltic glasses, one containing disproportionated iron (Bell, Mao, Weeks, and Van Valkenburg, this Report); the other, a greatly

reduced sample, synthesized by G. W. Pearce.

Electron Paramagnetic Resonance (EPR)

Samples MW-2 and EW-1 were studied by EPR to characterize their ferromagnetic resonance spectra. Figure 150 shows room-temperature EPR spectra for both samples and for an experimentally disproportionated basalt glass (see Bell, this Report). The resonance is sensitive to the presence of ferric ions and to metallic iron, but not to ferrous iron. The signal line width (ΔH , gauss) is characteristic of the ferric iron crystal site or of the shape of metallic iron particles.

A study of the EPR of the magnesio-wüstite phases down to cryogenic temperatures was made to determine the



Ferromagnetic Resonance of Three Iron Containing Materials at 300 K.

Fig. 150. Ferromagnetic resonance of three iron-containing materials at 300°K. *a*, experimentally disproportionated basalt glass; *b*, magnesio-wüstite, MW-2; *c*, magnesio-wüstite, EW-1; note instrument signal values on figure.

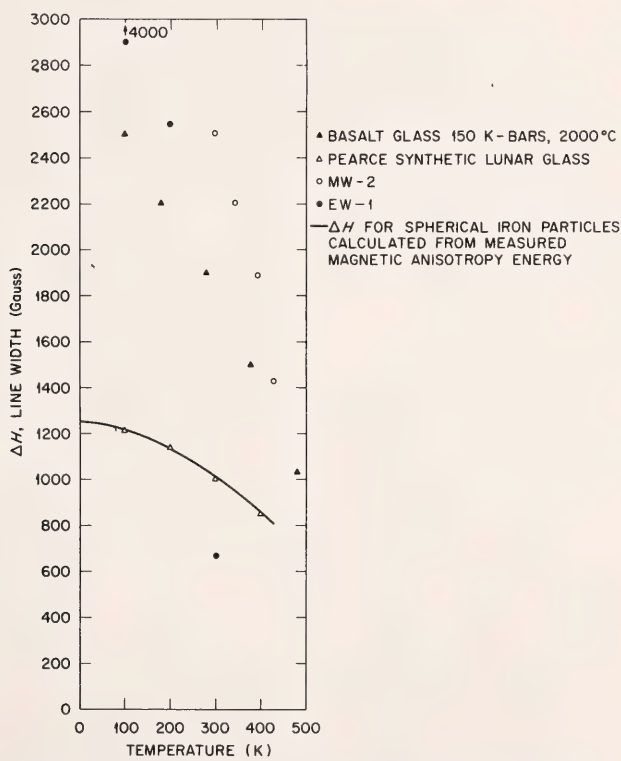
temperature dependence of line width (Fig. 151). The data on basalt glass plot in a region and at a trajectory similar to those of the magnesiowüstite data, suggesting that ferric iron is in similar crystalline sites in the samples. These similarities of the temperature dependence of line width are remarkable for data of this type.

Also plotted are data for a synthetic lunar glass of basalt composition that was prepared under sufficiently reducing conditions to cause the precipitation of submicroscopic particles of metallic iron. The line width is relatively insensitive to temperature compared with that of the materials containing ferric ions. A calculated line-width curve for iron par-

ticles of spherical shape plots in close agreement with the measured points.

Summary

The EPR spectra of two magnesio-wüstites and a disproportionated synthetic lunar glass contain distinctive ferromagnetic resonance absorption caused by coordinated ferric ions. The slope for temperature dependence versus line width is steep and of similar position for the three materials, but the slope is gentle for a synthetic lunar glass that contains submicroscopic spherical iron particles. These are some of the first EPR measurements made on minerals and glass of this composition. The disproportionated basaltic glass and the two mag-



Temperature Dependence of Line Width of Ferromagnetic Resonance Absorption in Glasses and Compounds.

Fig. 151. Temperature dependence of line width of ferromagnetic resonance absorption in glasses and compounds. Solid triangles, basalt glass run products; open triangles, Pearce synthetic lunar glass; solid circles, sample EW-1; open circles, sample MW-2; solid line for spherical iron particles calculated from measured magnetic antisotropy energy.

nesiowüstites apparently contain ferric ions in the same or similar crystalline sites.

GILLESPIE AT HIGH PRESSURE:
RESULTS OF A DETAILED MÖSSBAUER
STUDY

F. E. Huggins, H. K. Mao, and D. Virgo

The mineralogical rarity gillespite ($\text{BaFeSi}_4\text{O}_{10}$) has been the subject of a number of studies, out of all proportion to its abundance, because of the dramatic color change that occurs under high-pressure and room-temperature conditions. Originally, this transition was reported as a change from red to colorless, occurring at 26 kbar (Strens, 1966, 1969). The interpretation of this transition as a high-spin to low-spin transition in Fe^{2+} generated considerable interest because of the ramifications that such spin-pairing transitions in ferrous silicates and oxides may have for the mineralogy of the lower mantle. Subsequent investigations (Abu-Eid, Mao, and Burns, *Year Book 72*, pp. 564–567; Hazen and Burnham, 1974; Abu-Eid, 1975), however, have shown that the color change is from red to blue and that a structural rearrangement rather than a change in spin-state is probably responsible for the color change. In addition, a recent theoretical study (Tossell, 1976) predicts that spin-pairing will not occur in gillespite at any pressure.

Hence, the evidence currently indicates that the dramatic color change is due simply to crystallographic rearrangement at high pressure. However, preliminary ^{57}Fe Mössbauer studies (D. J. Vaughan and J. A. Tossell, unpublished data; see also Tossell, 1976; Huggins, Mao, and Virgo, *Year Book 74*, pp. 405–410) did not appear to be consistent with the crystallographic rearrangement proposed for the transition. In particular, these studies indicated that two distinct ferrous species coexisted above the transition, in contrast to the crystallographic investigation (Hazen and Burn-

ham, 1974), which showed that the transition from the red to blue phase is abrupt. The present study is therefore an extension of the preliminary results reported last year (Huggins, Mao, and Virgo, *Year Book 74*) and is designed to resolve the differences between the previous studies.

The gillespite sample used in this study is the same synthetic, ^{57}Fe -enriched sample described and used for the preliminary study. As before, the sample was contained in the diamond-anvil high-pressure cell in a nickel gasket, filled with a 4:1 methanol-ethanol mixture to ensure that the sample was in a hydrostatic environment. The high-pressure Mössbauer experimentation is basically the same as that described previously (Huggins, Mao, and Virgo, *Year Book 74*); in this study, however, the count-rate was maximized by aligning the source, sample, and detector with a rate meter, and the pressure was measured with an accuracy of $\pm 3\%$ by using the fluorescence of the R_1 line of ruby (Piermarini *et al.*, 1975; Bell and Mao, *Year Book 74*, pp. 399–402). Unlike the previous study in which only one spectrum was taken at a pressure well above the red-blue transition, spectra were taken at a number of different pressures. In addition, close attention was paid to the color of the mineral as a function of pressure.

Results

The pressure at the abrupt red-blue transition was found to be 12 ± 1 kbar for the gillespite sample investigated in this study. This pressure is considerably lower than the pressure of 26 kbar reported by Strens (1966) and subsequently assumed by most investigators. This difference may be real and reflect the effect of subtle compositional differences between the synthetic and natural samples; it may reflect an error in pressure calibration in the earlier study, or it may be related to hysteresis effects in the single-crystal samples (Abu-Eid, 1975). As indicated in Fig. 152, as the

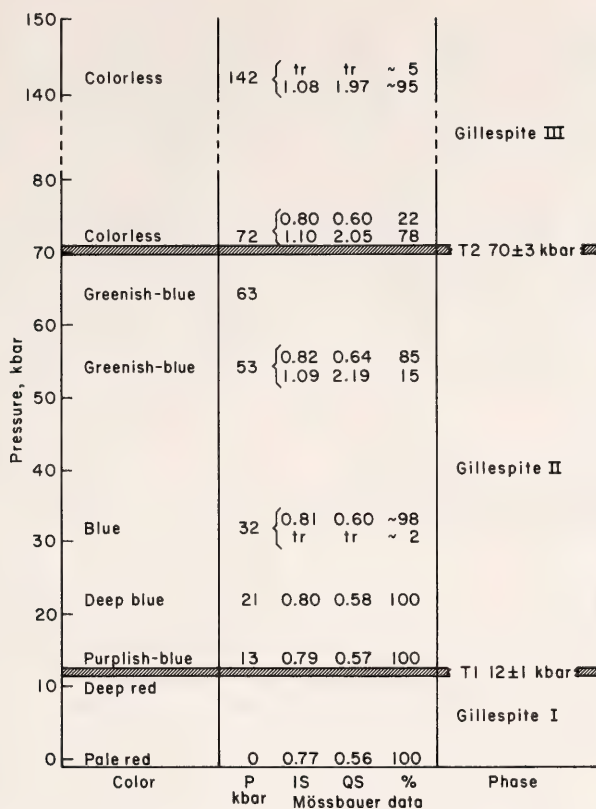


Fig. 152. Summary of changes in color and Mössbauer parameters of gillespite as a result of pressure. Abrupt changes in color are observed at the two transitions, T1 and T2.

pressure was further increased, the color changed gradually from deep purplish blue at 13 kbar to greenish blue at about 70 kbar. A second, abrupt color change from greenish blue to colorless was then observed at 70 ± 3 kbar.

Mössbauer spectra of gillespite were taken at 13, 21, 32, 53, 73, and 142 kbar; the changes in the Mössbauer spectra and hyperfine parameters with pressure are documented in Fig. 152. Except for small increases in the Mössbauer hyperfine parameters, the spectra of gillespite above the red-blue transition at 13 and 21 kbar were very similar to that at 0 kbar (Year Book 74, p. 408, Fig. 7) and showed only a single Fe^{2+} doublet. Only in spectra of gillespite at 53 kbar was a second absorption doublet of sufficient intensity to be reliably fitted, although a

trace of this doublet was also observed for gillespite at 32 kbar. Hence, the appearance of the second doublet with much larger values of the isomer shift and quadrupole splitting is *not* associated with the red-blue color change.

The Mössbauer spectra of gillespite at pressures above the blue-colorless transition at 70 kbar are significantly altered. At 72 kbar, the second Fe^{2+} doublet now dominates the spectrum, and the original doublet is much reduced in intensity (Fig. 153). The parameters of the two doublets are not significantly different from those found for gillespite at 53 kbar, except possibly for the quadrupole splitting of the larger split doublet, which decreases somewhat with increasing pressure. The spectrum of gillespite at 142 kbar is very similar to

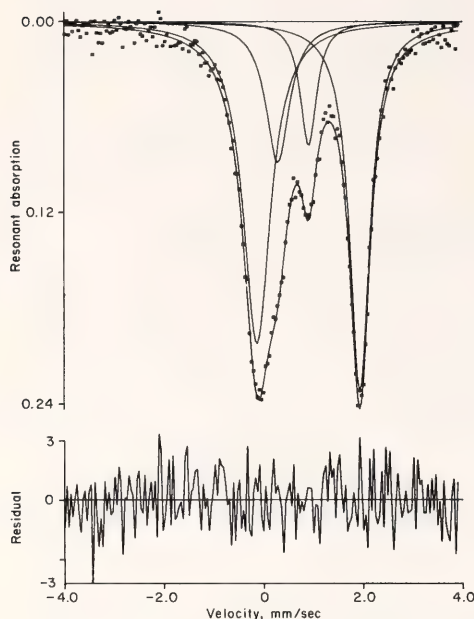


Fig. 153. Mössbauer spectrum of gillespite at a pressure of 72 kbar. The larger, outer doublet is the absorption feature due to Fe^{2+} in the highest pressure phase, whereas the smaller, inner doublet corresponds to Fe^{3+} in the lower pressure phases (compare Fig. 7, *Year Book* 74). The spectrum is fitted to four Lorentzian peaks without constraints.

that at 72 kbar, except that only a trace of the original doublet remains.

Interpretation

The present study shows that there are at least two distinct high-pressure transitions in gillespite: one at 12 kbar, associated with the red-blue color change; the other at 70 kbar, associated with a color change from blue to colorless. Whereas the lower pressure transition is not obviously associated with significant changes in the Mössbauer spectrum, the higher pressure transition is associated with marked changes in the Mössbauer spectrum.

The minor changes in the parameters of the doublet in the Mössbauer spectra at the 12-kbar transition are quite consistent with the slight puckering of the

Fe^{2+} square planar site reported by Hazen and Burnham (1974). It appears unlikely that such a minor structural rearrangement of this site could cause a greatly different Mössbauer spectrum, as may have been implied by the preliminary Mössbauer studies. Hence, it is concluded that the second doublet is not associated with the 12-kbar transition but rather with the 70-kbar transition. The exact nature of this higher pressure transition can only be speculated about at this time, but it must involve a much more drastic rearrangement of the Fe^{2+} site. The isomer shift of the larger doublet above 70 kbar is intermediate between that expected for octahedral and tetrahedral Fe^{2+} ; however, by allowing for the effect of pressure on the isomer shift of ferrous minerals (Huggins, 1974), it is more probable that the Fe^{2+} site is octahedral. It should be noted that the parameters for the doublet are not consistent with low-spin Fe^{2+} , so that the possibility that this higher pressure transition in gillespite may result from spin-pairing is unlikely. The coexistence of two types of iron cations over a range of pressure is a feature shared by a number of electronic transitions found in organo-iron compounds (Drickamer and Frank, 1973), hence the possibility that the 70-kbar transition involves an electronic transition in Fe^{2+} cannot be completely eliminated.

In conclusion, the results of this study of the response of gillespite to pressure have shown that the changes in the Mössbauer spectrum at the red-blue transition do appear to be quite compatible with the single-crystal x-ray and optical absorption studies. However, a second transition at about 70 kbar, which must involve a much more drastic rearrangement of the Fe^{2+} site, has been found. It is this higher pressure transition that gives rise to the coexistence of two ferrous absorptions and caused the apparent disagreement between the preliminary Mössbauer studies and other studies.

METASOMATISM

METASOMATIC ZONING RESULTING FROM INTERGRANULAR DIFFUSION: CONCENTRATION PROFILES AND THE DETERMINATION OF COMPLICATED REACTION PATHS IN n -COMPONENT SYSTEMS*J. D. Frantz and H. K. Mao*

The identification of transport mechanisms and the determination of their controlling parameters are fundamental to the understanding of such metasomatic rock systems as skarns and associated porphyry copper deposits. In complicated columns involving sequences of multimineralic reaction zones, the number of measurable variables (i.e., zone sequences, mineralogies, modes, and thicknesses) normally exceeds the number of controlling parameters (diffusion coefficients, volume flux, and solution compositions). This deficiency is especially evident in systems in which three or more components are transported. To aid in the interpretation of such metasomatic columns, a general n -component transport model has been developed in which material transfer through an aqueous grain boundary film that is in equilibrium with neighboring solids is assumed. Comparison of natural metasomatic sequences with columns calculated using the above model and various combinations of input parameters promises to yield new insights into the petrogenesis of nonisochemical rock systems.

Frantz and Mao (*Year Book* 74, pp. 418–419) derived sets of differential equations describing the growth or disappearance of solid phases both at zone boundaries and within zones. A method of calculation was presented in which changes in the solution concentration profiles, calculated first, were related to the growth or disappearance of the solid phases. A simple example was presented showing the growth by ternary diffusion or infiltration, or both, of a single bi-mineralic reaction zone bounded by two *invariant* boundaries. The solution con-

centration profiles were calculated using a single linear mass-balance equation and two mass-action expressions. Several serious problems exist, however, in the calculation of more complicated reaction paths. In binary diffusion (Frantz and Mao, *Year Book* 73) the solution concentrations at zone boundaries are always invariant. In ternary diffusion, however, the boundaries may be univariant; thus calculation of their paths necessitates the simultaneous solution of many linear mass-balance equations and nonlinear mass-action equations. Another aspect of binary diffusion is that the zone sequence is independent of porosity, diffusion coefficients, and volume flux, whereas in ternary diffusion, zone sequences are dependent upon these parameters and therefore must be determined. A general computational scheme by which complicated reaction paths can be predicted is presented in this report.

General Theoretical Considerations

The general growth equations for p coexisting phases in an n -component system are of the form (tensor notation, repeated subscript implies summation):

$$a_{ik}N_k = \Delta J_i \quad i = 1, n; k = 1, p \quad (1)$$

where a_{ik} is the stoichiometric coefficient of the i th component in the k th solid phase, and ΔJ_i is the net accumulation of the i th component into the solid phases. The term N_k refers to the growth rate of the k th solid.

A general set of mass-balance equations can be derived from the above growth equations (provided the region is not invariant, i.e., $n - p > 0$) by eliminating the variables N_k :

$$b_{ki}\Delta J_i = 0 \quad i = 1, n; k = 1, n - p \quad (2)$$

where b_{ki} is a $p \times p$ matrix with elements a_{ik} .

In the present model, transport of material is assumed to be solely the result

of intergranular diffusion, or infiltration, or both, within a grain boundary fluid,

$$\Delta J_i = D_i \Delta \nabla c_i - \beta (\partial c_i / \partial t) \Delta x \quad (3)$$

where D_i is the diffusion coefficient of the i th species; c_i is the concentration of the i th species; v is the volume flux of the fluid; β is the porosity, Δx is the change in the space coordinate, and t is time. The profiles of solution concentration resulting from transport must be continuous; otherwise, infinite diffusion gradients would exist.

The general mass-balance equations can be expressed in terms of concentration by substituting Equation 3 into Equation 2. Within a reaction zone, the concentration profiles are smooth (∇c_i is continuous), and Equation 2 becomes

$$b_{ki}(D_i \nabla^2 c_i - v \nabla c_i - \beta \partial c_i / \partial t) = 0 \quad (4)$$

For steady-state concentration profiles ($\beta \ll 1$; $c_i \ll 1$),

$$b_{ki}(D_i \nabla^2 c_i - v \nabla c_i) = 0 \quad (5)$$

At zone boundaries, the concentration profiles often have kinks (∇c_i is discontinuous; $\nabla^2 c_i$ does not exist). The $n - p$ mass-balance equations are of the form

$$b_{ki} D_i \Delta \nabla c_i = 0 \quad (6)$$

At each point in the reaction column, p mass-action equations exist:

$$a_{ik} \ln c_i = \ln K_k \quad (7)$$

Computational Schemes

As stated by Frantz and Mao (Year Book 73, p. 419), the preceding sets of equations can be solved by first determining the solution concentration profiles and subsequently using the general growth equations (1) to evaluate the growth rates of the solids at each point. The profiles of solid and solution concentration can then be evaluated as functions of time. The key step in this process lies in the determination of the

profiles of solution concentration. As stated in the introduction, calculation of solution profiles for systems with three or more diffusing solutes often involves the simultaneous solution of several reaction zones that are separated from one another by noninvariant boundaries. As described in Frantz and Mao (1976), the concentration profiles within a reaction zone can be calculated provided the concentrations at the zone boundaries are known. Thus, the following method has been adopted: (1) The entire reaction column is grouped into sections, each bounded by boundaries of known composition (invariant boundaries or infinitely thick end zones); (2) the solution concentrations of all noninvariant boundaries that lie between sets of invariant boundaries are calculated; (3) the solution profiles within individual zones are then computed using only the concentrations of the boundaries bordering each zone.

Calculation of Solution Compositions at Noninvariant Boundaries

Consider a section with m intermediate noninvariant boundaries. Each boundary j with p_j coexisting phases has $n - p_j$ mass-balance equations of the form of Equation 6:

$$b_{ki} D_i (\nabla c_i^{j+1} - \nabla c_i^j) = 0 \\ i = 1, n; k = 1, n - p_j \quad (8)$$

where subscript j refers to boundary j and superscript j refers to a point in zone j . Zone j is bounded by boundaries $j - 1$ and j , and boundary j is between zone j and zone $j + 1$. The index j indicates a particular set of variables associated with a given zone or zone boundary and thus is not summed according to conventional tensor notation.

For zone j , Equation 5 can be written:

$$b_{ki} D_i \nabla^2 c_i^j = 0 \\ i = 1, n; k = 1, n - p_j \quad (9)$$

where b_{ki} in Equation 9 is identical with

the respective b_{ki_j} in Equation 8 even though zone j may not have all p_j phases of the boundary j . Integration of Equation 9 with respect to x yields the following relations for zones j and $j + 1$, respectively:

$$b_{ki_j} D_i \nabla c_i^j = \frac{1}{L^j} b_{ki_j} D_i (c_{i_j} - c_{i_{j-1}}) \quad (10)$$

$$b_{ki_j} D_i \nabla c_i^{j+1} = \frac{1}{L^{j+1}} b_{ki_j} D_i (c_{i_{j+1}} - c_{i_j}) \quad (11)$$

where L^j is the thickness of the j th zone. Combining Equations 6, 10, and 11:

$$\begin{aligned} \frac{1}{L^{j+1}} b_{ki_j} D_i (c_{i_{j+1}} - c_{i_j}) - \\ \frac{1}{L^j} b_{ki_j} D_i (c_{i_j} - c_{i_{j-1}}) = 0 \end{aligned} \quad (12)$$

Notice that for each boundary there are $n - p$ such mass-balance equations involving only the *solution concentrations at the boundaries*.

In diffusion with infiltration, Equation 12 becomes (all diffusion coefficients considered equal):

$$\begin{aligned} \left(\frac{v e^{\frac{v}{D}} L^j}{e^{\frac{v}{D}} - 1} \right) b_{ki_j} D (c_{i_{j+1}} - c_{i_j}) - \\ \left(\frac{v}{e^{\frac{v}{D}} L^{j+1} - 1} \right) b_{ki_j} D (c_{i_j} - c_{i_{j+1}}) = 0 \end{aligned} \quad (13)$$

where D is the diffusion coefficient for all components.

Combining all mass-balance equations of the m intermediate boundaries in the section, there are $m \times n - \sum_{j=1}^m p_j$ linear equations for $m \times n$ unknown values of c_{i_j} . These, together with $\sum_{j=1}^m p_j$ mass-action expressions (7), provide $m \times n$ equations for $m \times n$ unknown c_{i_j} 's in a

section. This set of linear log-linear equations is identical with the typical form of linear mass-balance and log-linear mass-action equations found in chemical equilibrium computations. Numerous computational schemes have been developed and perfected for solving sets of equations of this type (Van Zeggeren and Storey, 1970). The authors utilize a modified Newton-Raphson technique developed by I and Nancollas (1972).

After the solution concentrations at the univariant boundaries have been determined, the concentration profiles within the individual reaction zones and the growth rates of the solid phases can be calculated in a manner similar to that described by Frantz and Mao (*Year Book 74*, p. 421).

Calculations for Ternary Diffusion in the System MgO-CaO-SiO₂-H₂O-CO₂

A computer program based on the principles of the preceding sections has been developed to model the growth of multiple reaction zones resulting from diffusion or infiltration, or both, of three aqueous species. Test calculations have been made using the schematic solution compositions for the system MgO-CaO-SiO₂-H₂O-CO₂ shown by Frantz and Mao (*Year Book 74*, pp. 417-424). Since the diffusion coefficients in the system are unknown at the present time, the diffusion coefficient of silicon is set at unity, with the units of thickness, time, and other diffusion coefficients defined accordingly. In the future when diffusion coefficients are determined, the present results need only be multiplied by a constant factor in order to be converted into conventional units. The relative thickness and time need not be changed, however.

Calculations of columns with all reaction zones of zero thicknesses at time zero cannot be accomplished unless the stable zone sequence is known. As previously stated, the zone sequences are dependent upon porosity, diffusion coefficients, and volume flux. At zero thick-

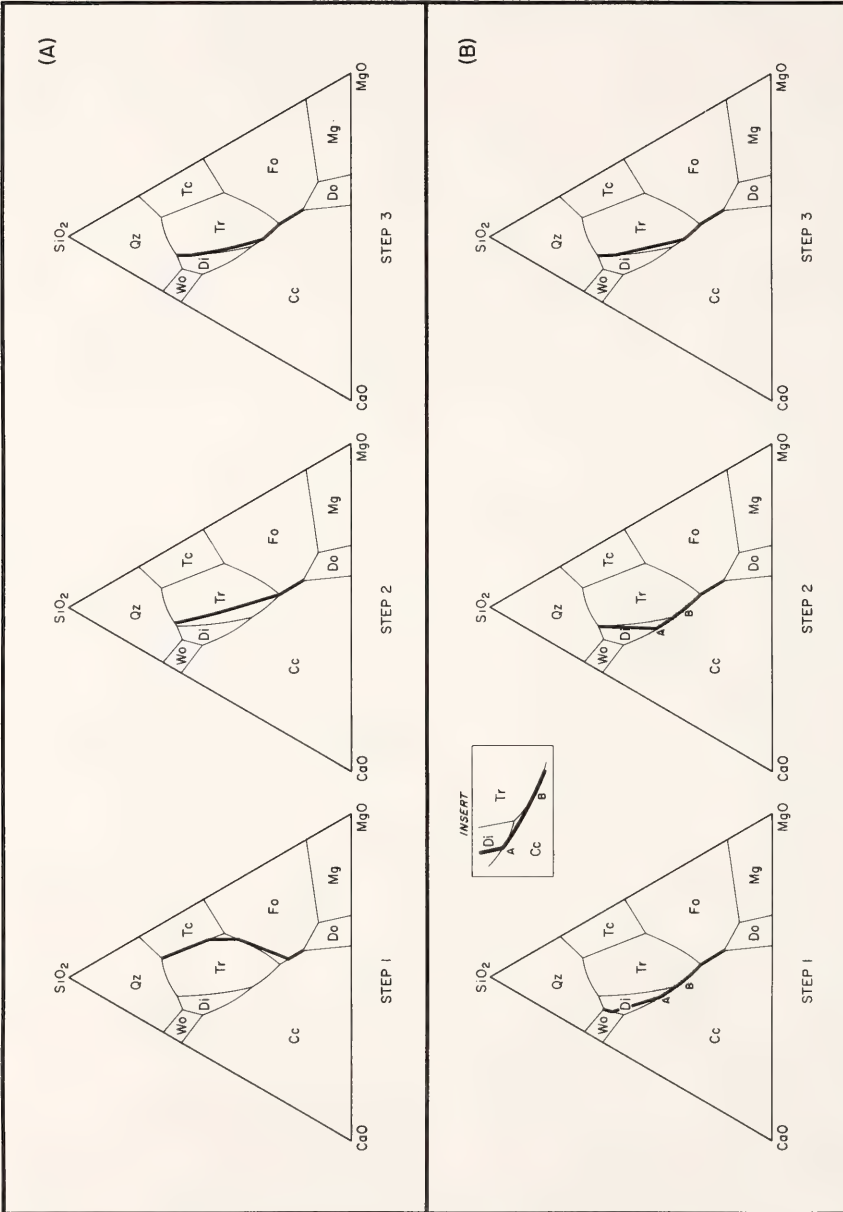


Fig. 154. Computation of stable metasomatic sequence between thick quartz and dolomite zones with all diffusion coefficients equaling unity. (A) Initial sequence quartz/talc/forsterite/dolomite. (B) Initial sequence quartz/wollastonite/calcite/dolomite. Heavy curves indicate solution path. Qz, quartz; Wo, wollastonite; Di, diopside; Tr, tremolite; Tc, talc; Fo, forsterite; Cc, calcite; Do, dolomite; Mg, magnesite.

ness, concentration gradients are infinite and give little useful information for the prediction of the correct reaction path. Therefore, a set of very thin, thermodynamically compatible reaction zones that do not necessarily correspond to the stable zone sequence are chosen to begin the computation. The correct reaction path is then calculated from the trial sequence. In Fig. 154, the stable reaction path corresponding to all diffusion coefficients equaling unity was computed using two different initial paths. In the first case (A), the sequence quartz/talc/forsterite/dolomite was chosen;

in the second case (B), the zone sequence quartz/wollastonite/calcite/dolomite was used. In both cases, the end zones were very thick (10^{20}) compared with the two thin reaction zones (10^{-1}). The resulting stable path (quartz/diopside + tremolite/tremolite/tremolite + calcite/calcite + forsterite/dolomite) was identical in both cases. Furthermore, the thicknesses and modes of the zones in both cases approached one another as time progressed. The correct reaction path was found in a relatively short time.

As seen in Fig. 155 and Table 61 (all

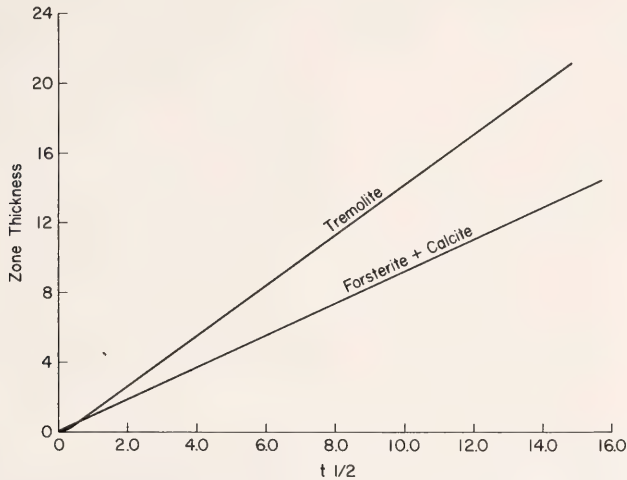


Fig. 155. Plot of zone thickness versus the square root of time for reaction zones tremolite and calcite + forsterite (all diffusion coefficients equal).

TABLE 61. Growth of Metasomatic Column Quartz/Diopside + Tremolite/Tremolite/Tremolite + Calcite/Forsterite + Calcite/Dolomite after Stable Path Is Achieved

| Time | Zone Thicknesses | | | | Modes | | | |
|-----------|------------------|--------|---------|---------|-------------|-----|-------------|-------------|
| | Di + Tr | Tr | Tr + Cc | Fo + Cc | Di + Tr | Tr | Tr + Cc | Fo + Cc |
| 0.0076 | 0.155 | 0.0109 | 0.101 | 0.101 | 0.709-0.291 | 1.0 | 0.978-0.022 | 0.720-0.280 |
| 0.0819 | 0.274 | 0.1890 | 0.246 | 0.273 | 0.582-0.418 | 1.0 | 0.753-0.247 | 0.713-0.287 |
| 0.1470 | 0.318 | 0.3080 | 0.312 | 0.362 | 0.584-0.416 | 1.0 | 0.735-0.265 | 0.713-0.287 |
| 0.6090 | 0.458 | 0.8560 | 0.569 | 0.729 | 0.632-0.368 | 1.0 | 0.725-0.275 | 0.713-0.287 |
| 3.280 | 0.778 | 2.350 | 1.220 | 1.69 | 0.703-0.297 | 1.0 | 0.732-0.268 | 0.713-0.287 |
| 23.20 | 1.710 | 6.740 | 3.120 | 4.49 | 0.749-0.251 | 1.0 | 0.740-0.260 | 0.713-0.287 |
| 218.0 | 4.770 | 21.20 | 9.390 | 13.70 | 0.766-0.234 | 1.0 | 0.744-0.256 | 0.713-0.287 |
| 1,540.0 | 12.30 | 56.90 | 24.90 | 36.60 | 0.771-0.229 | 1.0 | 0.745-0.255 | 0.713-0.287 |
| 19,100.0 | 42.90 | 201.0 | 87.30 | 129.0 | 0.773-0.227 | 1.0 | 0.746-0.254 | 0.713-0.287 |
| 722,000.0 | 263.0 | 1240.0 | 537.0 | 796.0 | 0.773-0.227 | 1.0 | 0.746-0.254 | 0.713-0.287 |

Abbreviations as in Fig. 154.

diffusion coefficients equal) parabolic growth, after the stable reaction path was found, was approached with increasing time. Note also that the bulk modes of the individual stable zones appear to be quite insensitive to changing time.

In order to test the sensitivity of reaction paths to changes in diffusion coefficients, the diffusion coefficient of calcium was made six orders of magnitude smaller than those of silicon and magnesium. The resulting sequence was quartz/talc + tremolite/tremolite/calcite + tremolite/calcite + forsterite/dolomite (Fig. 156a). When the diffusion coefficient

of magnesium was set six orders of magnitude lower than calcium and silicon, a different path was produced: quartz/wollastonite/diopside/tremolite/forsterite/forsterite + calcite/dolomite (Fig. 156b).

From the above calculations, it is evident that the identities, thicknesses, and modes of the zones in metasomatic reaction sequences are unique functions of mobilities of the different species and the topology of the solution phase diagram. In natural metasomatic zoning, measurement of the thickness and the mode of each zone is an independent parameter that can be used to reconstruct the conditions of formation. In comparison with the conventional method of determining the conditions of formation by the identity of the equilibrium phase assemblage, the transport model yields more parameters and also produces a continuous monitor of the pressure-temperature-composition conditions of formation. The present scheme of calculation can be applied to any number of components, and thus the formational processes of complex metasomatic deposits, such as the porphyry coppers, are amenable to this new method of analysis.

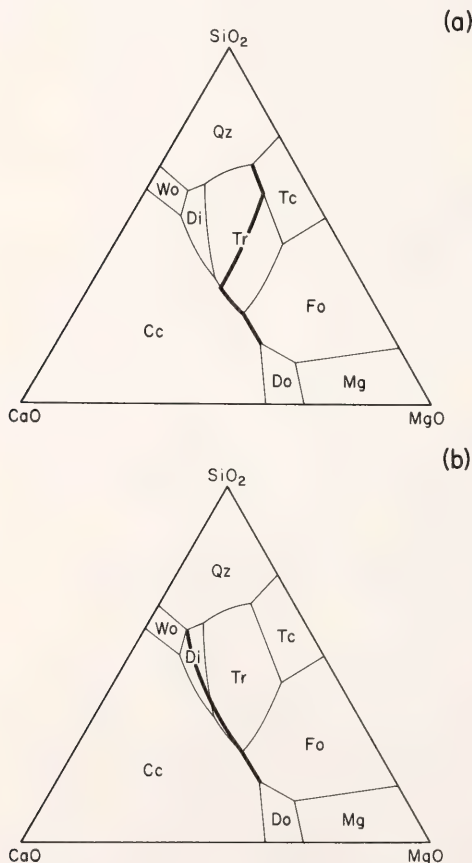


Fig. 156. Dependence of reaction path on relative diffusion coefficients. (a) D_{Ca} much smaller than D_{Si} and D_{Mg} . D_{Mg} much smaller than D_{Si} and D_{Ca} . Abbreviations as in Fig. 154.

FLUID INTERACTION BETWEEN GRANITE AND SEDIMENT DURING METAMORPHISM, SOUTH-CENTRAL MAINE

J. M. Ferry

When granitic bodies intrude sediments and cool, hydrothermal convection cells develop that circulate fluids between granites and the rocks they intrude. Most information about this phenomenon has been obtained from studies of stable isotopes (Taylor, 1974; Shieh, Schwarcz, and Shaw, 1976). Isotopic data, however, characterize only a very limited part of granitic rocks. Several questions remain about the fluid circulation that cannot be answered from isotopic data alone: (1) Do the circulating fluids react chemically with the granite? (2) How does the fluid circulation affect

the metamorphism of the rocks that the granite intrudes? (3) What is the chemical composition of the fluids? (4) How and why does the fluid circulation cease? (5) What are the sources of the fluids? (6) Can the subsolidus temperatures recorded by geothermometers in response to the presence of the circulating fluids be related to distinct geologic events during the cooling of the granites? This report presents both mineralogical and petrological evidence for granite-sediment-fluid interaction associated with the emplacement of three stocks near Augusta, Maine, and information bearing on these six questions.

Two of the stocks are muscovite-biotite-garnet quartz monzonite, and the third is biotite-garnet granodiorite with

and without hornblende. They intrude metamorphosed Silurian and Siluro-Devonian sediments (Fig. 157). The lithology, modal mineralogy, and field aspects of the stocks have been reported by Goodspeed (1962), Barker (1964), and Osberg (1968). The stocks are probably of Devonian age (Osberg, 1968). Osberg (1968) believes that the metamorphism postdates the intrusion of the granites, but Barker (1964) found that field evidence strongly suggests that the granites have not been metamorphosed. The configurations of the isograds mapped by Ferry (1976a) are strong arguments that the metamorphism, metasomatism, and emplacement of the granitic rocks were contemporaneous events.

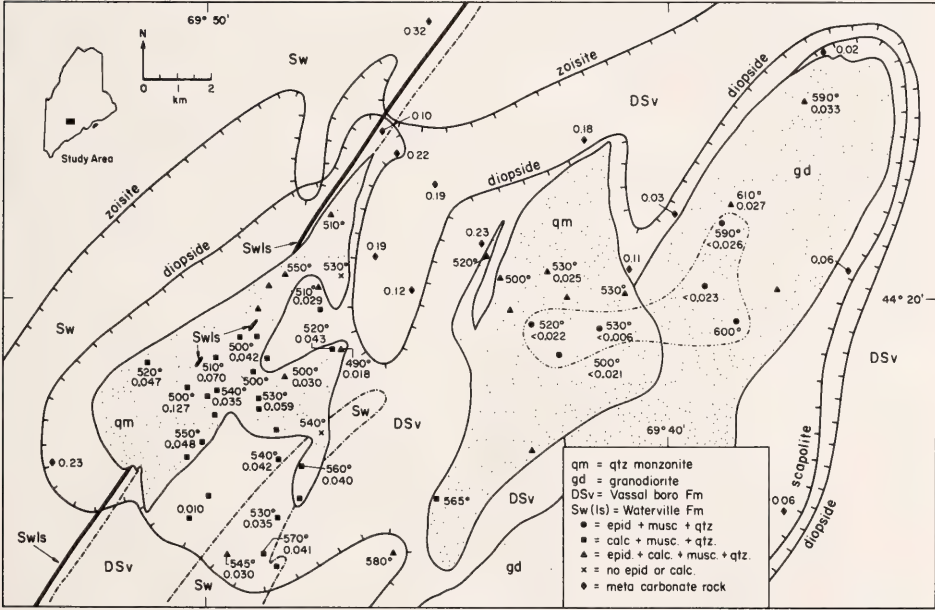


Fig. 157. Geologic sketch map of the granitic rocks (stippled area) near Augusta, Maine. Swls = marble unit within the Waterville Formation. Solid hachured lines are isograds mapped from minerals in the metacarbonate rocks. Solid lines are granite-sediment contacts. Dash-dot line is the stratigraphic boundary between the Waterville and Vassalboro Formations. Dash-double dot line is explained in the text. Symbols outside mapped bodies of granitic rock are samples from granitic dikes or small satellite bodies in metasediment. Numbers by squares, triangles, circles, and crosses are biotite-garnet temperatures and X_{Co_2} values recorded by mineral assemblages associated with alteration of the feldspars. Numbers by diamonds are X_{Co_2} values recorded by plagioclase + calcite + zoisite in metacarbonate rocks. Data from Osberg (1968), Goodspeed (1962), Barker (1964), and Ferry (1976a,b; this study).

Minimum Crystallization Temperature and Pressure of the Granitic Rocks

To evaluate the effect of circulating fluids on the granites, the crystallization conditions of the granitic rocks must first be determined. The bulk composition of the quartz monzonite is very similar to the composition of the Westerly, Rhode Island, granite (Barker, 1964); the H_2O -saturated solidus of the Westerly granite was determined experimentally by Tuttle and Bowen (1958). The H_2O -saturated solidus of natural granites does not appear to be particularly sensitive to bulk rock composition (Tuttle and Bowen, 1958; Piwinski, 1968; Whitney, 1975). The experimentally determined solidus of the Westerly granite, therefore, closely approximates the minimum P - T conditions under which the granitic rocks near Augusta could have been partly molten. Several samples of quartz monzonite from near Augusta contain the texturally primary assemblage muscovite + quartz + sillimanite + K-feldspar. Following the scheme of Ferry (1976b), it can be demonstrated that the conditions for equilibrium between these four minerals (with compositions determined by electron microprobe from the rocks near Augusta) and an H_2O vapor depart negligibly from the equilibrium curve for muscovite + quartz + sillimanite + sanidine + H_2O determined by Chatterjee and Johannes (1974) in the system K_2O - Al_2O_3 - SiO_2 - H_2O . The P - T conditions for the equilibrium of muscovite, quartz, sillimanite, K-feldspar, H_2O vapor, and a solidus silicate liquid (with compositions of minerals and solidus liquid appropriate for the granitic rocks near Augusta) are $650^\circ \pm 10^\circ C$, $P_{total} = p_{H_2O} = 3500 \pm 300$ bars (intersection of the solidus curve for the Westerly granite with the muscovite + quartz + sillimanite + sanidine + H_2O curve). For conditions of $p_{H_2O} < P_{total}$, the equilibrium conditions are shifted to both higher temperatures and higher pressures (Kerrick, 1972). The minerals in the granitic rocks near Augusta, there-

fore, could not have crystallized from a granitic liquid below $650^\circ \pm 10^\circ C$.

Ferry (1976b) has estimated from mineral assemblages in the metamorphic rocks adjacent to the granites that lithostatic pressure was 3500 ± 300 bars during metamorphism near Augusta. Quartz grains from the granitic rocks contain abundant fluid inclusions. The fluid inclusions and the estimate of pressure during metamorphism are evidence that the granitic rocks crystallized under vapor-saturated conditions ($p_{H_2O} \sim P_{total}$) and that the lowest temperature at which a silicate liquid was present during crystallization of the granitic rocks near Augusta was, in fact, $650^\circ \pm 10^\circ C$.

Effects of Fluids on the Granitic Rocks: Cation-Exchange Equilibria

The measured fractionations of Fe and Mg between coexisting biotite and garnet and of K, Ca, and Na between coexisting plagioclase and alkali feldspars indicate temperatures lower than $650^\circ C$. The average compositions of 35 biotite-garnet pairs were determined by electron microprobe, and the Fe-Mg fractionation temperature was calculated from the calibration of Goldman and Albee (1976); results are presented in Fig. 157. The mean garnet-biotite fractionation temperature for the western quartz monzonite body is $528^\circ C$ with a standard deviation (σ) of 20° ; the mean garnet-biotite temperature for the eastern quartz monzonite body is $522^\circ C$, $\sigma = 29^\circ$; the mean garnet-biotite temperature for the granodiorite body is $599^\circ C$, $\sigma = 11^\circ$. These temperatures are significantly less than $650^\circ C$, the minimum temperature at which the biotite and garnet initially crystallized. Ferry (1976b) has determined that the last temperature recorded by metamorphosed carbonate rocks adjacent to the quartz monzonite stocks is $520^\circ \pm 30^\circ C$. The scapolite isograd mapped in metacarbonate rocks (Fig. 157; Ferry, 1976a) indicates a hotter metamorphic environment around the granodiorite stock, and

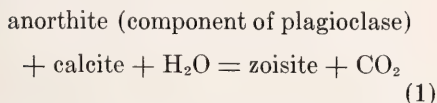
this is complemented by significantly higher garnet-biotite temperatures from the granodiorite than from the quartz monzonite stocks. Biotite-garnet Fe-Mg fractionation from the granitic rocks perhaps records temperatures close to the peak metamorphic conditions in the Augusta area.

The compositions of 37 plagioclase-alkali feldspar pairs were determined by electron microprobe, and the Ca-K-Na fractionation temperatures were calculated from the calibration of Stormer (1975). Two-feldspar temperatures are similar from all three stocks, with a mean of 391°C and σ of 22°. The feldspar temperatures do not represent crystallization conditions but may be correlated with a subsolidus event of hydrothermal alteration of the feldspars.

In agreement with the mineralogical data on biotite, garnet, and feldspars, the measured fractionation of ^{18}O and ^{16}O between different minerals in granitic rocks commonly indicates subsolidus temperatures, which may be attributed to the presence of fluids through which minerals exchange both isotopes and chemical elements as they cool.

Effects of Fluid Interaction on the Metamorphosed Sediments

The zoisite isograd mapped by Ferry (1976a) in argillaceous carbonate rocks intruded by these granitic stocks is based on the reaction

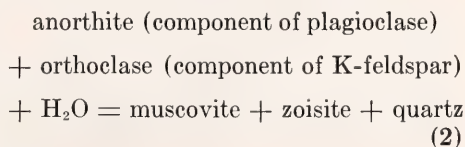


which is observed to proceed from left to right with increasing proximity to the stocks. Ferry (1976b) has measured a monotonic increase in temperature recorded by minerals in metacarbonate rocks with increasing proximity to the stocks. Experimental data indicate, however, that at a fixed $f_{\text{CO}_2}/f_{\text{H}_2\text{O}}$ ($X_{\text{CO}_2} = p_{\text{CO}_2}/[p_{\text{CO}_2} + p_{\text{H}_2\text{O}}]$), anorthite + calcite, not zoisite, is the high-temperature

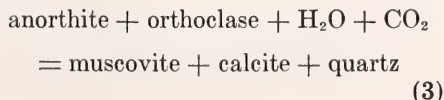
side of reaction 1. The zoisite isograd, therefore, cannot be explained in terms of a mineral reaction favored by increasing temperature. From the stoichiometric coefficients of H_2O and CO_2 in reaction 1, it is evident that the formation of zoisite can be explained only by a significant increase in $f_{\text{H}_2\text{O}}/f_{\text{CO}_2}$ (decrease in X_{CO_2}) in the metacarbonate rocks close to the granitic stocks. Calculated results of Ferry (1976b), combined with the configuration of the zoisite isograd, suggest that the isograd records the introduction of an H_2O -rich fluid into the metacarbonate rocks from the intruding granitic stocks. The distance of the zoisite isograd from the stocks is an estimate of the minimum distance that H_2O migrated from the granites into the sediments, approximately 1500 m.

Effects of Fluid Interaction on the Granitic Rocks: Alteration of the Feldspars

The phase petrology of the granitic rocks near Augusta indicates that the granites reacted after crystallization with circulating fluids that altered the original chemical composition of the rocks. Between 1% and 10% of the feldspars in practically all samples of granitic rock from the study area are altered to the assemblage muscovite + calcite + quartz, epidote + calcite + quartz, or epidote + calcite + muscovite + quartz. The geographic distribution of these three assemblages is plotted in Fig. 157. Textural evidence indicates that the feldspars were altered by one or both of the idealized reactions



and



The compositions of epidote + plagioclase + K-feldspar + muscovite + quartz from eight samples were determined with the electron microprobe, and the temperatures of equilibration of these five minerals with an H_2O fluid under conditions of $p_{H_2O} = P_{total} = 3500$ bars were calculated following the scheme of Ferry (1976b, appendix 2, relations 6 and 9). The mean temperature was $417^\circ C$, $\sigma = 17^\circ$. Four of the eight samples contain calcite, and an X_{CO_2} of 0.027–0.033 was calculated from the assemblage plagioclase + epidote + calcite at the previously determined muscovite + epidote + quartz + plagioclase + K-feldspar temperatures. Evidently the initial assumption of $p_{H_2O} = P_{total}$ was not unreasonable. The fluid in equilibrium with the epidote-bearing, calcite-free samples must have been characterized by an $X_{CO_2} < 0.026$, the X_{CO_2} of a fluid in equilibrium with plagioclase + calcite + epidote. Feldspar alteration in reaction 3 probably proceeded at the same temperature as that calculated for reaction 2; X_{CO_2} was calculated at this temperature from mineral compositions of the assemblage muscovite + calcite + quartz + plagioclase + K-feldspar in equilibrium with a CO_2 - H_2O fluid in which $p_{H_2O} + p_{CO_2} = P_{total} = 3500$ bars. For calcite-bearing, epidote-free samples, $X_{CO_2} = 0.035$ –0.127. Results of all the X_{CO_2} calculations are presented in Fig. 157.

The alteration of the feldspars correlates with the observation that granites frequently react after crystallization with fluids that alter the original isotopic composition of the rocks.

The geographic distribution of the assemblages muscovite + calcite + quartz and muscovite + epidote + quartz in Fig. 157 gives additional information about the fluid interaction between granite and sediment during metamorphism. The epidote-bearing, calcite-free assemblages are limited to the eastern two granitic stocks; calcite-bearing, epidote-free assemblages are primarily located in the western stock. This pattern may

be caused by three possible factors: plagioclase composition, f_{O_2} , or X_{CO_2} in the fluid that altered the feldspars. Plagioclase composition and f_{O_2} , recorded by compositions of minerals from the granitic stocks, however, are not significantly different between the epidote-bearing and epidote-free rocks.

Figure 158 illustrates that the distribution of the mineral assemblages associated with alteration of the feldspars could be caused by more H_2O -rich fluids in the eastern two stocks and more CO_2 -rich fluids in the western stock. For instance, path 1 would correspond to alteration in the western quartz monzonite body; path 2, to alteration in the two eastern bodies. Calculated X_{CO_2} values (Fig. 157) in both granitic rocks and metacarbonates support this hypothesis. The difference in X_{CO_2} may be due to a difference in primary volatile content of the three granitic magmas, but the explanation does not account for the zonation pattern of calcite-free assemblages at the core and calcite + epidote assemblages at the margins of the eastern stocks. A more plausible explanation is based on the observation that the Swls marble unit (Fig. 157) strikes directly into and forms recognizable inclusions in the western quartz monzonite body. Metamorphism of the Swls unit would produce more CO_2 than metamorphism of the Vassalboro Formation, which contains less carbonate rock. A possible explanation of the variation in X_{CO_2} values of fluids that altered the feldspars is that the fluids contained a significant amount of CO_2 that was derived from metamorphic decarbonation reactions and migrated from the metasediments into the granitic rocks during metamorphism. Decarbonation reactions in Swls sediments yielded more CO_2 than those in Vassalboro sediments. The CO_2 migration further accounts for the calcite-free alteration assemblages in the cores of the eastern two stocks; CO_2 was not able to penetrate to the cores of these stocks. The distance of the dash-double dot line in Fig. 157 from the mar-

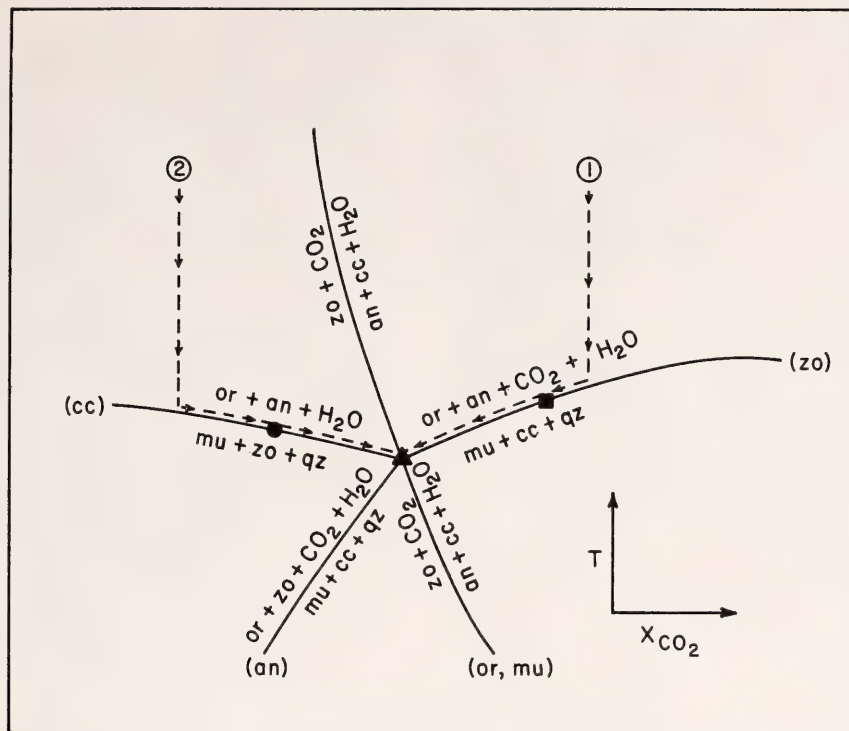


Fig. 158. Qualitative T - X_{CO_2} diagram for phases with the compositions $\text{KAl}_3\text{Si}_3\text{O}_{10}(\text{OH})_2$ (mu), KAlSi_3O_8 (or), $\text{CaAl}_2\text{Si}_2\text{O}_8$ (an), $\text{Ca}_2\text{Al}_2\text{Si}_2\text{O}_{12}(\text{OH})$ (zo), and CaCO_3 (cc). $X_{\text{H}_2\text{O}} = 1 - X_{\text{CO}_2}$. Topologies of curves are from Hewitt (1975). Paths 1 and 2 are explained in the text; symbols are the same as in Fig. 157.

gins of the stocks is an estimate of the minimum distance that CO_2 migrated into the granites from the sediments, approximately 800 m.

The reactions represented in Fig. 158 probably terminate granite-sediment-fluid interaction. The small amount of alteration of the feldspars suggests a small fluid/rock ratio during the final cooling of the granitic rocks. A sample of granitic rock from near Augusta with a fixed amount of fluid (less than 0.072 mole $\text{CO}_2 + \text{H}_2\text{O}/100 \text{ cm}^3$ granite) cooling along path 1 or 2 (Fig. 158) will consume the fluid by reaction along the (zo) or (cc) curve or at the invariant point. Reaction at the invariant point will proceed at constant temperature until K-feldspar, plagioclase, or fluid is consumed. Because the granitic rocks near Augusta contain both plagioclase

and K-feldspar, the invariant point represents the minimum temperature at which the residual fluid was present in the rock. Fluid interaction between granite and sediment may have been terminated by the consumption of residual fluids by reactions 2 and 3. The temperature recorded by K-Na-Ca fractionation between plagioclase and K-feldspar and by the assemblage muscovite + epidote + quartz + plagioclase + K-feldspar is $405^\circ \pm 15^\circ\text{C}$. The temperature may record the termination of the alteration of the feldspars and K-Ca-Na exchange between plagioclase and K-feldspar caused by the final consumption of residual fluids.

In summary, cation partitioning between coexisting minerals in the granitic rocks records temperatures well below the conditions under which they crys-

tallized from the granitic melts. The partitioning of Fe and Mg between garnet and biotite may record peak conditions of metamorphism associated with the emplacement of the granites. The partitioning of Ca, K, and Na between plagioclase and K-feldspar probably records the temperature of the consumption of residual fluids within the granites by chemical reactions that altered the feldspars and consumed CO_2 and H_2O . The formation of zoisite in metacarbonate rocks and the assemblages produced by alteration of the feldspars in the granite indicate significant chemical reaction between granite, sediment, and CO_2 - H_2O fluids migrating between the sediments and granitic rocks. The fluids were probably derived partially from metamorphic reactions. In addition, mineral relations record that the fluids were characterized by X_{CO_2} values of

< 0.026 – 0.127 in the granites and of 0.06 – 0.32 in the metasediments. The conclusions reached in investigations of stable isotopes in granitic intrusions agree with those reached in this study. Evidence for granite-sediment-fluid interaction is summarized in Fig. 159, which illustrates the kind of hydrothermal convection cell deduced from studies of oxygen isotopes in granitic intrusions (Sheppard, Nielsen, and Taylor, 1969; Taylor, 1974). Because of the hydrothermal cell illustrated in Fig. 159, metamorphism associated with the intrusion of granitic bodies is probably not simply a process of increasing temperature and concomitant dehydration with increasing proximity to the granite. Circulating hydrothermal fluids may actually hydrate the sediments and minimize the temperature gradient around the granitic bodies. The convection cell

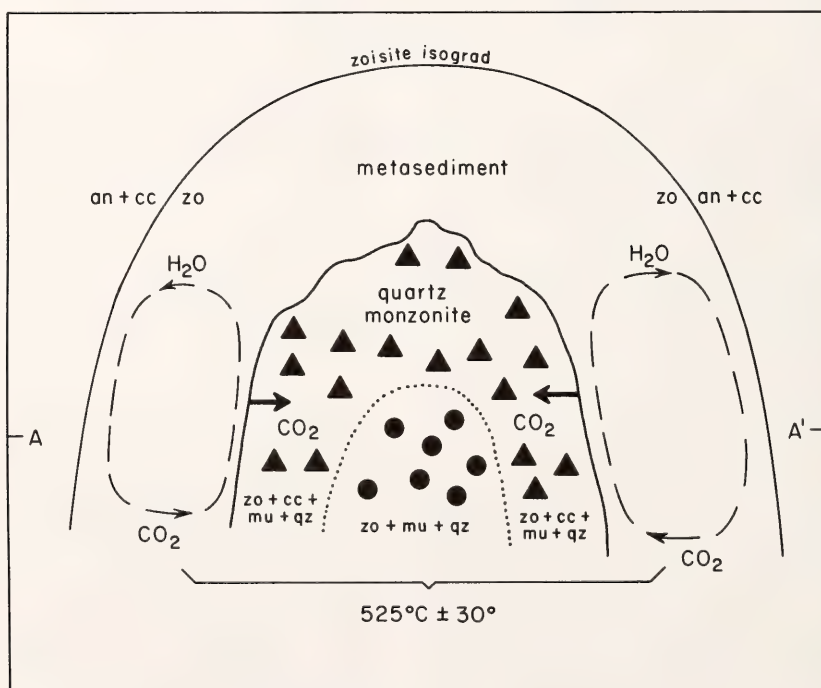


Fig. 159. Schematic cross section through the eastern quartz monzonite stock in Fig. 157. The illustration is based on similar diagrams in Taylor (1974) and Sheppard, Nielsen, and Taylor (1969) and summarizes the evidence for granite-sediment-fluid interaction in the Augusta area. Mineral symbols are the same as in Fig. 158. A-A' is the present level of exposure. For scale, the width of the diagram corresponds roughly to 15 km.

in Fig. 159 is a mechanism by which H_2O could have been transferred from the cooling granitic rocks into the sediments. The μ_{CO_2} gradient required to transfer CO_2 from the metasediments into the granites was established under conditions of $p_{\text{CO}_2} \sim 0$ in the granites, whereas $p_{\text{CO}_2} = 0.10\text{--}0.32 P_{\text{total}}$ in the metacarbonate rocks (Fig. 157). As the hydrothermal cell developed, the porosity increased in both the metamorphic rocks (owing to the negative $\Delta\bar{V}_{\text{solids}}$ of metamorphic reactions) and the granitic rocks (possibly by hydrofracturing). The increase in porosity would further aid in fluid transfer between granite and sediment. Chemical reactions that altered the feldspars and consumed CO_2 and H_2O terminated the circulation of hydrothermal fluids.

FUGACITY AND ACTIVITY COEFFICIENTS OF MOLECULAR SPECIES IN FLUIDS AT HIGH PRESSURES AND TEMPERATURES*

John R. Holloway

Many reactions that occur in metamorphic and igneous systems involve fluids containing more than one volatile species. The thermodynamic calculation of reactions, the thermodynamic interpretation of experimental results, and the accurate determination of fluid compositions recorded by natural assemblages require knowledge of the mixing properties (partial molar volume, activity coefficient) of geologically important fluid-phase species such as H_2 , H_2O , CO , CO_2 , and CH_4 . Accurate experimental determinations of these properties have been limited to pressures below 1 kbar and temperatures below 700°C .

The experimental determination of mixing properties can be greatly extended by the use of an equation of state whose accuracy can be verified by a few experiments. Such an equation should have a sound theoretical basis so that it

can be extrapolated with confidence. An equation that closely fits these requirements is the Redlich-Kwong equation (Redlich and Kwong, 1949) as modified by de Santis, Breedvelde, and Prausnitz (1974) (hereafter referred to as the MRK). The form of the equation for one-component fluids is

$$P = \frac{RT}{v-b} - \frac{a(T)}{T^{1/2}v(v+b)}$$

in which v is the molar volume and b is a constant similar to the excluded volume in the van der Waals equation. The constant a is a function of temperature for complex molecules with hydrogen bonds, dipoles, or quadrupoles, but is independent of temperature for simple nonpolar molecules with spherical symmetry. For simple molecules, a and b can be derived from corresponding state theory, but for complex molecules the constants must be derived from measured quantities (de Santis, Breedvelde, and Prausnitz, 1974).

A set of FORTRAN IV routines was written to solve the MRK following the method proposed by Edmister (1968). The MRK was first tested by comparing calculated values with measured fugacities for the pure species: H_2 (Presnall, 1969; Shaw and Wones, 1964), CO_2 (C. W. Burnham and V. J. Wall, personal communication, 1974), and H_2O (Burnham, Holloway, and Davis, 1969). Agreement with the data for H_2 is within $\pm 2\%$ relative using values of a and b calculated from effective critical constants as described by Newton (1935). The fit with the data for CO_2 is within the $\pm 5\%$ relative error quoted by Burnham and Wall. The agreement with H_2O was not satisfactory using the temperature coefficients for a given by de Santis, Breedvelde, and Prausnitz (1974), so a new equation for a was obtained by fitting the data from Burnham, Holloway, and Davis (1969). The new equation employs data from 400° to 1300°C ; because it is linear in temperature above 800°C , it is probably valid to much higher temperatures. The equation

*Research supported by National Science Foundation, Earth Sciences Section, grant DES 73-00266A01.

is $a = 166.8 - 0.19308T - 1.864 \times 10^{-4}T^2 - 7.1288 \times 10^{-8}T^3$ or $a = 140.0 - 0.05T$ ($T > 1200^\circ\text{C}$), where T is in degrees celsius. Deviations between the MRK (with the new equation for a) and the data of Burnham, Holloway, and Davis (1969) average 1.3% relative over the range of available data. It should be noted that the MRK fits the H_2O data using only five adjustable parameters, none of which is a function of pressure. The close agreement of the MRK with measured values for pure H_2O and CO_2 at pressures up to 10 kbar, together with the fact that the analytical form of the MRK is reduced to a limiting law at very high pressures, suggests that it may be extrapolated to pressures of 10–50 kbar with considerable confidence. In the case of H_2O , this conclusion is supported by the close agreement between volumes and fugacities calculated by the MRK and those calculated by linear extrapolation of isochors (Holloway, unpublished data), and between fugacities calculated using the MRK and those calculated from an experimental determination of brucite dehydration by Irving, Huang, and Wyllie (1976) to pressures of 33 kbar.

A mixing model for two or more molecular species is described by Redlich and Kwong (1949). The original equation was modified by de Santis, Breedvelde, and Prausnitz (1974, Equations 12 and 13) to include complex formation between H_2O and CO_2 . Very few experimental data are available to test the mixing model for compositions, pressures, and temperatures of petrologic interest. Shaw (1963) reported activity-composition relations for H_2 - H_2O mixtures at 800 bars and 700°C . The MRK yields activities that are systematically lower than those calculated from Shaw's (1967) equation, but the curve calculated using the MRK falls within the probable error of his experiments (Shaw, 1963). Pressure-volume-temperature measurements of CO_2 - H_2O mixtures have been made by Greenwood (1969) up to 800°C and 500 bars, and by Franck

and Tödheide (1959) to 750°C and 2 kbar. Values of the compressibility factor calculated using the MRK fit the Franck-Tödheide data with an average deviation of 6% relative. Activity coefficients calculated from the MRK fit those calculated by Greenwood (1973) to within $\pm 5\%$ relative. Calculations made using the MRK also predict a topology for the two-phase region in the H_2O - CO_2 system that is in qualitative agreement with the topology depicted by Tödheide and Franck (1963). Eggler, Kushiro, and Holloway (this Report) show that MRK fugacities provide a much better fit to the experimentally determined decarbonation reaction enstatite + magnesite = forsterite + CO_2 at 25 kbar (H_2O - CO_2 fluid) than does the ideal mixing model.

The available data suggest that the MRK can be used to estimate the fugacity of CO_2 , H_2O , H_2 , and probably CO and CH_4 in multispecies fluids at temperatures above about 450° to 1800°C and at pressures from 0.5 to about 40 kbar. Figure 160 shows activity-composition relations for binary mixtures of H_2O and CO_2 for several pressures at 700°C . Note that although the deviations from ideality increase with increasing pressure, they approach an asymptotic limit at very high pressure. The behavior on other isotherms is similar, although at constant pressure non-ideality becomes more pronounced at lower temperatures. The curves for 100 kbar are shown in Fig. 160 to demonstrate that activity values calculated using the MRK approach an asymptotic limit. It is not suggested that these values are accurate. It is important to note that the method of calculation is based on the assumption that there is no change in the formula units of the molecular species regardless of pressure and temperature. The only exception is the provision for complex formation between H_2O and CO_2 , which is assumed to depend only on temperature (de Santis, Breedvelde, and Prausnitz, 1974).

Large positive deviations of H_2O and

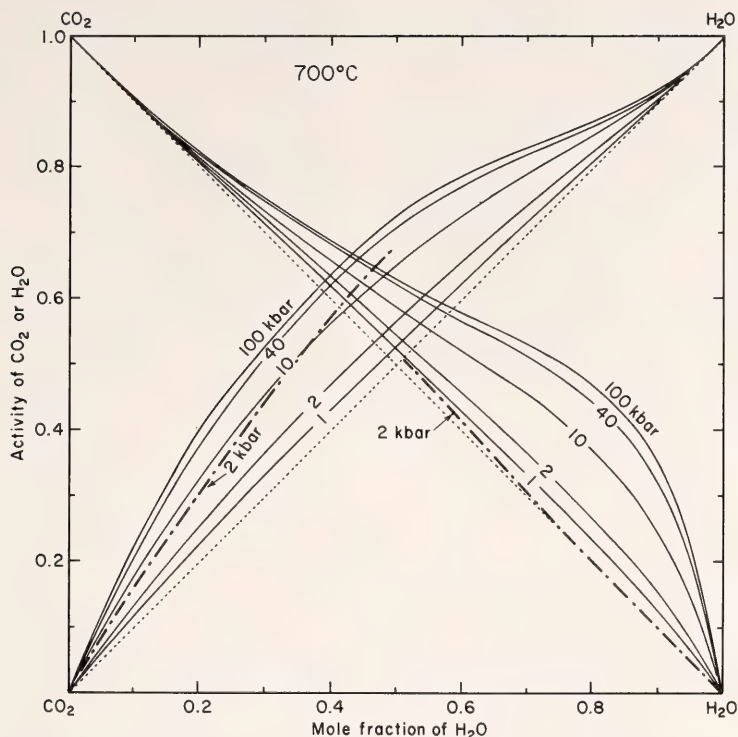


Fig. 160. Activity-composition relations for binary mixtures of H_2O and CO_2 at 700°C for pressures of 1, 2, 10, 40, and 100 kbar, calculated according to the MRK equation. Ideal mixing is shown by light dotted lines, and values for binary mixtures of H_2O and CO_2 , by solid lines. Ternary mixtures of H_2O , CO_2 , and CH_4 with the mole fraction of CH_4 held constant at 0.50 are shown as dot-dash lines for a total pressure of 2 kbar.

CO_2 from ideality at small mole fractions will have a considerable effect on calculated equilibria involving dehydration-decarbonation reactions. The reaction tremolite + 3 calcite + 2 quartz = 5 diopside + 3 CO_2 + H_2O will serve as an example (Skippen, 1971, Fig. 9). In an isobaric temperature-fluid composition projection, the stability of the tremolite + calcite + quartz assemblage is expanded to higher mole fractions of both CO_2 and H_2O if activity values for H_2O and CO_2 are calculated using the MRK instead of an ideal mixing model. This expansion is a general phenomenon for those reactions in which H_2O and CO_2 appear together on the same side of the reaction. For those reactions in which H_2O and CO_2 appear on opposite

sides, the effect of nonideal mixing cannot be so easily predicted and should be calculated for specific cases.

The effect of dilution of H_2O - CO_2 mixtures by a third species is also shown in Fig. 160 for a fluid at a total pressure of 2 kbar containing 50 mole % CH_4 . Note that addition of methane causes CO_2 to behave more ideally and H_2O much less ideally because CH_4 is chemically very similar to CO_2 but quite dissimilar to H_2O . Consequently, for a geological system in the two-phase field of aqueous liquid and CO_2 -rich vapor, methane would partition strongly into the vapor.

To illustrate the effect of nonideal mixing in fluids of geological interest, the fluid composition in equilibrium with

graphite in the C-O-H system was calculated using the equations derived by French (1966). Calculations were carried out for three cases: (1) ideal gas behavior, the assumption used by French (1966); (2) ideal mixing (also known as the Lewis and Randall rule), the assumption used by Eugster and Skippen (1967) and by Holloway and Reese (1974); (3) nonideal mixing based on the MRK equation. Results for the three cases are shown in Fig. 161 for a total pressure of 2 kbar. The general appearance of plots at other pressures is quite similar. It can be seen that at tempera-

tures above about 600°C, there are only small differences between the ideal mixing and the MRK calculations. Calculations at other pressures and hydrogen fugacities suggest that if the hydrogen fugacity is lower than that fixed by the assemblage quartz + fayalite + magnetite + H_2O (QFM[OH]), methane will be an abundant species only at pressures below 2 kbar and at temperatures of 400°–600°C. If hydrogen fugacity is only slightly greater than QFM(OH), however, methane becomes very abundant over a wide range of pressure and temperature.

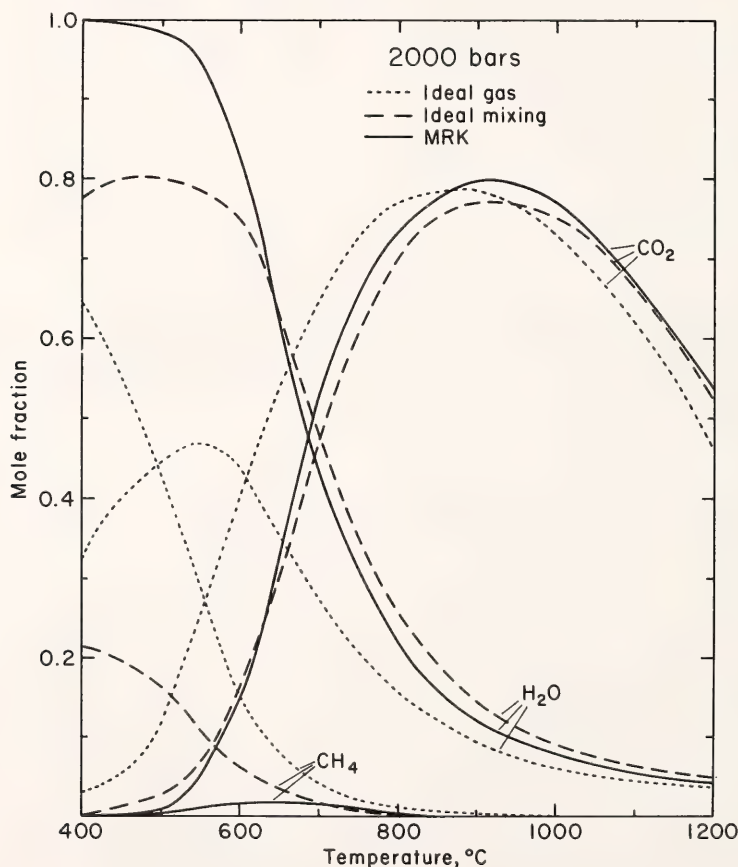


Fig. 161. Mole fractions of species in a fluid phase in equilibrium with graphite in which the hydrogen fugacity is externally fixed by the quartz + fayalite + magnetite + H_2O (QFM[OH]) assemblage. Dotted lines were calculated assuming ideal gas behavior, dashed lines assuming ideal mixing, and solid lines assuming nonideal mixing as calculated by the modified Redlich-Kwong equation.

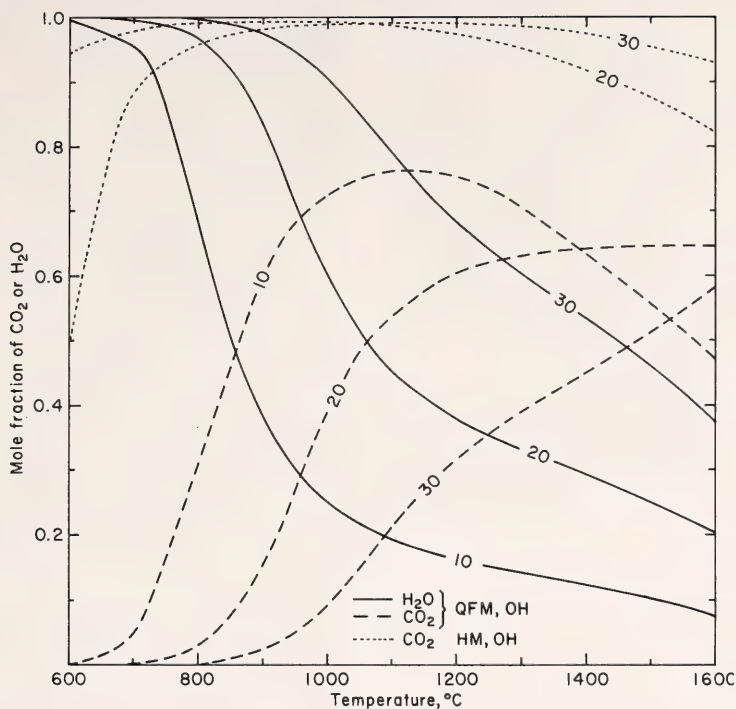


Fig. 162. Mole fractions of species in a fluid phase in equilibrium with graphite. Numbers on curves indicate total pressure in kilobars. Solid and dashed lines are for a fluid in which hydrogen fugacity is externally controlled by the assemblage QFM(OH). Solid lines represent H_2O and dashed lines, CO_2 . The dotted lines represent CO_2 in a fluid in which hydrogen fugacity is externally controlled by the assemblage hematite + magnetite + H_2O .

The fugacities of CO_2 , H_2O , and O_2 are fixed in a C-O-H fluid in equilibrium with graphite and a fixed external hydrogen fugacity (Eugster and Skippen, 1967), a configuration used in many phase-equilibrium experiments. Calculation of fluid-species activities with the MRK will result in increased accuracy of data obtained in such hydrothermal experiments. For example, the mole fractions of H_2O and CO_2 for fluids in equilibrium with graphite are shown for various pressures in Fig. 162. It is noteworthy that the fluid will be nearly pure CO_2 if the hydrogen fugacity is kept at the hematite-magnetite- H_2O value. Under these conditions, oxygen fugacity in the C-O-H fluid will be about that of the QFM buffer.

CA-AMPHIBOLE COMPOSITION AS A FUNCTION OF TEMPERATURE, FLUID PRESSURE, AND OXYGEN FUGACITY IN A BASALTIC SYSTEM

Frank S. Spear

Investigations conducted on the paragenetic relationships of metamorphosed basaltic rocks (e.g., Binns, 1965; Cooper and Lovering, 1970; Engel and Engel, 1962; Ernst, 1972) have led to generalizations regarding the variability of calcic amphibole composition with metamorphic grade (summarized by Leake, 1965): (1) The amphibole chemistry is largely a function of bulk rock composition; (2) where a Ti-bearing phase such as rutile, sphene, or ilmenite is present, the Ti content of the amphibole in-

creases with increasing grade; and (3) K, Na, Al(IV), and Al(VI) tend to increase with increasing grade, whereas Si decreases. In natural systems, however, the effects of bulk rock composition are difficult to distinguish from changes in intensive parameters of metamorphism. An effort was made, therefore, to test experimentally the generalizations cited above and to quantify Ca-amphibole compositional variability as a function of T , P_{fluid} , and f_{O_2} of formation for a single mafic composition.

*Experimental and Phase Relations**

Cold-seal hydrothermal apparatus and crystalline buffers of oxygen fugacity were used for all experiments. The starting material was a crystalline mid-oceanic ridge olivine tholeiite.†

Pertinent features of the phase equilibria are: (1) On the HM buffer, amphibole begins to break down incongruently to clinopyroxene at $725^\circ \pm 8^\circ\text{C}$ and $P_{\text{fluid}} = 1$ kbar and at $740^\circ \pm 9^\circ\text{C}$ and $P_{\text{fluid}} = 3$ kbar. Below the temperature of the first appearance of clinopyroxene, amphibole coexists with plagioclase + titanohematite + sphene with or without quartz. Above this temperature the assemblage is amphibole + plagioclase + clinopyroxene + titanohematite + sphene with or without quartz. (2) On the QFM buffer amphibole begins to break down incongruently to clinopyroxene + orthopyroxene at $765^\circ \pm 8^\circ\text{C}$ and $P_{\text{fluid}} = 1$ kbar and at $785^\circ \pm 12^\circ\text{C}$ and $P_{\text{fluid}} = 3$ kbar. Below the temperature of the pyroxene-in reaction, amphibole coexists with plagioclase + ilmenite with or without sphene, and above this temperature the assemblage is amphibole + clinopyroxene + orthopy-

roxene + plagioclase + ilmenite with or without sphene. Equilibrium was demonstrated by reversing the pyroxene-in reactions, monitoring the composition of amphibole as a function of time, and reversing the amphibole composition at fixed temperature and fluid pressure by changing the oxygen fugacity.

Analytical Procedures and Results of Amphibole Analyses

The procedure outlined by White (1964) for the analysis of microparticles on the electron microprobe was adopted for this study because the grain size of the synthetic amphiboles (1–10 μm) prohibited the analysis of flat polished surfaces of the phases. Replicate analyses of microparticles of amphiboles, pyroxenes, and olivines, the compositions of which were determined by electron microprobe analysis of large specimens of the same material, indicate that a precision of $\pm 5\%$ of the amount present of major elements and $\pm 10\%$ of the amount present of minor elements is possible using this technique. Samples were prepared by disaggregating in an ultrasonic cleanser, dispersing on a diamond substrate, and carbon coating. From five to twenty amphibole grains were analyzed from each experiment using an accelerating potential of 15 kV and a sample current of 40–60 nA with a defocused beam. A working-curve correction, based on analyses of standards, was applied to the unknowns.

The amphibole analyses were normalized on an anhydrous basis to 23 oxygens, and cations were assigned to structural sites using the following scheme: (1) tetrahedral site—Si and sufficient Al to sum to 8.0; (2) M1, M2, and M3 sites—remaining Al, then, in the following order, Ti, Fe^{3+} , Mg, Fe^{2+} , and Mn to sum to 5.0; (3) M4 site—Ca, then remaining Fe^{2+} , Mn, and sufficient Na to sum to 2.0; (4) A site—remaining Na and K.

The $\text{Fe}^{3+}/\text{Fe}^{2+}$ in the amphiboles was measured directly on the products of three experiments run at different buffers

*The experimental part of this study was conducted at the University of California, Los Angeles, with the support of National Science Foundation grant GA-37157X (to W. G. Ernst).

†Analyzed specimen supplied to the author by A. Miyashiro. Analysis unpublished but similar to that of specimen A150-RD7-AM1 in Miyashiro, Shido, and Ewing (1969).

using Mössbauer spectroscopy.* The spectra were complicated by the presence of ilmenite in the WM- and QFM-buffered experiments and hematite in the HM-buffered experiment, but peaks due to these phases were resolved and their effect subtracted from the amphibole spectra. The measured ferric iron contents of amphiboles synthesized on the WM, QFM, and HM buffers, respectively, are $11.4 \pm 1\%$, $12.5 \pm 1.2\%$, and $40.0 \pm 4\%$ of the total Fe. These ferric iron contents were used in the recalculation of all amphiboles synthesized at the respective buffers.

It is of interest to compare the measured $\text{Fe}^{3+}/\text{Fe}^{2+}$ in the amphiboles with the ferric iron content calculated using different procedures described in the literature. The method proposed by Stout (1972), based on stoichiometric constraints, places the following lower and upper limits on the percentage of ferric iron: 0.0–98.1%, 0.0–77.1%, and 0.0–100.0% of the total Fe for amphiboles synthesized, respectively, on the WM, QFM, and HM buffers. In each case the calculated ferric iron content brackets the measured ferric iron content; the brackets are so broad, however, that the important difference in ferric iron content between amphiboles equilibrated at the QFM and WM buffers and at the HM buffer is obscured. Normalizing the amphibole analyses such that $0.3 \text{ Al(IV)} = A$ site occupancy (justification for this procedure is given in Robinson, Ross, and Jaffe, 1971) yields ferric iron contents of 13.5%, 13.3%, and 47.7% of the total iron for amphiboles synthesized, respectively, at the WM, QFM, and HM buffers. These numbers are close to the measured values and provide a reasonable estimate of the observed ferric iron content.

Figure 163 is a plot of some of the measured amphibole cation numbers versus temperature at 3 kbar P_{fluid} . The

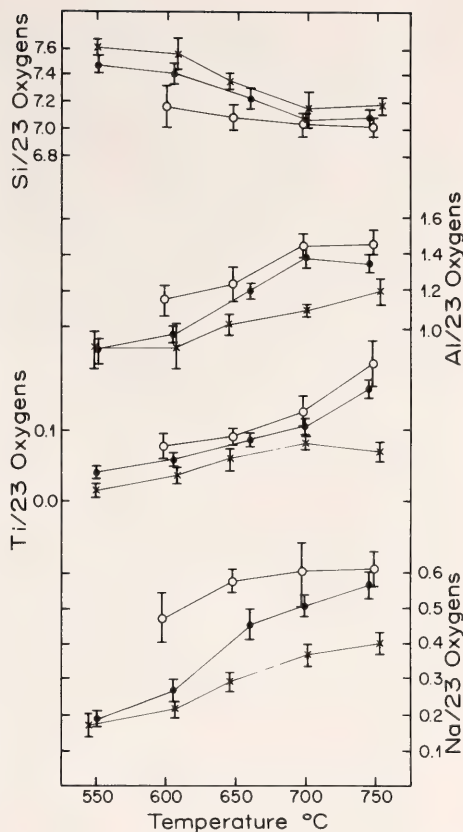


Fig. 163. Plot of Si, Al, Na, and Ti (per 23 anhydrous oxygens) versus $T^{\circ}\text{C}$ for Ca-amphiboles synthesized on the WM, QFM, and HM buffers (3000 bars $P_{\text{H}_2\text{O}}$): crosses, HM buffer; closed circles, QFM buffer; open circles, WM buffer. Error bars are 2 standard deviations of the mean of 5–20 analyses per run product.

cations that show the largest temperature dependence are Na, Ti, and Al, which increase with increasing temperature, and Si, which decreases with increasing temperature. Similar trends are observed at 1 kbar P_{fluid} . Little or no temperature dependence is displayed by Ca and Mg, whereas Fe_{total} decreases slightly with increasing temperature. Also apparent in Fig. 163 is a systematic shift in composition with oxygen fugacity. With increasing f_{O_2} of formation, Ti, Na, and Al all decrease, whereas Si increases. There is also a suggestion that

* Mössbauer spectra were collected at the Geophysical Laboratory with the assistance of F. Huggins and D. Virgo.

the temperature dependence of Ti is stronger in run products produced with the WM and QFM buffers than with the HM buffer. The $Fe_{total}/(Fe_{total} + Mg)$ of the amphibole, although insensitive to temperature, changes from 0.38 to 0.19 between the QFM and HM buffers. The cations that display significant dependence on fluid pressure are Al and Si, with Al increasing and Si decreasing with increasing pressure.

A plot of Al(IV) versus *A* site occupancy is presented in Fig. 164. This plot reveals that the pargasite substitution, $Na(A) + Al(VI) + 2Al(IV) = \square(A) + Mg(VI) + 2Si(IV)$, can account for the observed variability in the *A* site occupancy. The intercept on this plot at a value of approximately 0.45 Al(IV) indicates that there are additional substitutions involving Al(IV) not accounted for by the pargasite substitution. Figure 165 is a plot of Al(IV) versus *A* site occupancy + 2Ti + Al(VI) + Fe^{3+} . If all Al(IV) were compensated for by substitutions of the type

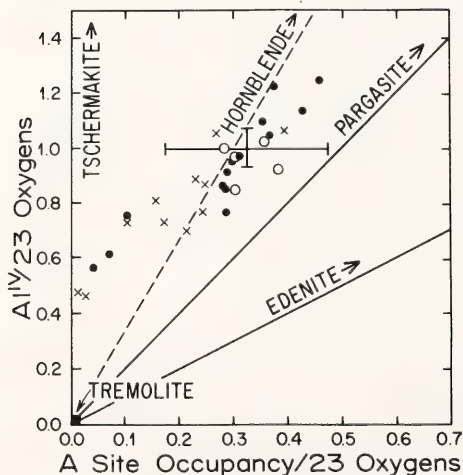


Fig. 164. Plot of Al^{IV} versus *A* site occupancy in Ca-amphiboles: crosses, HM buffer; closed circles, QFM buffer; open circles, WM buffer. Maximum errors were calculated using 2 standard deviations of the mean of 5–20 analyses per run product propagated through the recalculation procedure. The error bar plotted is the average of these maximum errors. The dashed line is the trace of the compositional join actinolite-hornblende.

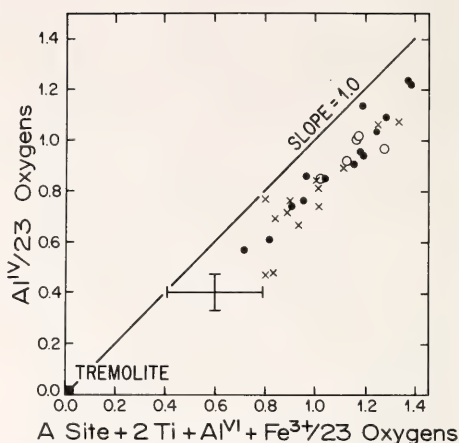


Fig. 165. Plot of Al^{IV} versus *A* site occupancy + 2Ti + Al^{VI} + Fe^{3+} in Ca-amphiboles: crosses, HM buffer; closed circles, QFM buffer; open circles, WM buffer. Error bar calculated as in Fig. 164.

$R^{1+}(A) + R^{3+}(VI) + 2Al(IV) = \square(A) + R^{2+}(VI) + 2Si(IV)$ (pargasite or hastingsite) or $R^{4+}(VI) + 2Al(IV) = R^{2+}(VI) + 2Si(IV)$ (Tischermakite), then the data would fall on a line passing through the origin with a slope of 1.0. As can be seen from Fig. 165, the intercept on the abscissa is approximately 0.2, indicating that a small amount of Fe^{3+} , Al(VI), Ti, or *A* site cations is compensated for by the substitution glaucophane, $Na(M4) + Al(VI) = Ca(M4) + Mg(VI)$; riebeckite, $Na(M4) + Fe^{3+}(VI) = Ca(M4) + Mg(VI)$; or richterite, $Na(A) + Na(M4) = \square(A) + Ca(M4)$; or by a substitution such as $2Na(M4) + Ti(VI) = 2Ca(M4) + Mg(VI)$. No correlation is observed between Na(M4) and *A* site occupancy or Na(M4) and Ti, whereas Na(M4) and Al(VI) display reasonable correlation with a slope of 1.0. This relationship indicates that the glaucophane substitution is active in these amphiboles.

It should be emphasized that the changes in amphibole chemistry in response to changes in experimental conditions are accompanied by changes in the chemistry and proportions of phases

coexisting with amphibole. For example, the Ti content of the amphibole is largely controlled by heterogeneous equilibria involving sphene, as is evidenced by the inverse relationship between the modal proportion of sphene and the Ti content of the amphibole. In a similar fashion the alkali and Al contents of the amphibole are controlled by equilibria involving plagioclase.

The presence of free quartz in experiments run at the HM buffer is the result of the breakdown of the ferrotremolite component in the amphibole by a reaction such as $\text{Ca}_2\text{Fe}_5\text{Si}_8\text{O}_{22}(\text{OH})_2 + 7/4\text{O}_2 + 2\text{FeTiO}_3 = 2\text{CaTiSiO}_5 + 7/2\text{Fe}_2\text{O}_3 + 6\text{SiO}_2 + \text{H}_2\text{O}$. Quartz liberated by this reaction is in part consumed by reactions such as $\text{NaCa}_2\text{Fe}_3\text{Al}_5\text{Si}_5\text{O}_{22}(\text{OH})_2 + 3/4\text{O}_2 + 2\text{SiO}_2 = 3/2\text{Fe}_2\text{O}_3 + 3(\text{Na}_{0.33}\text{Ca}_{0.66})\text{Al}_{1.66}\text{Si}_{2.33}\text{O}_8 + \text{H}_2\text{O}$ and $\text{NaCa}_2\text{Fe}_4\text{TiAl}_3\text{Si}_5\text{O}_{22}(\text{OH})_2 + \text{O}_2 + \text{SiO}_2 = \text{CaTiSiO}_5 + 2\text{Fe}_2\text{O}_3 + 2(\text{Na}_{0.5}\text{Ca}_{0.5})\text{Al}_{1.5}\text{Si}_{2.5}\text{O}_8 + \text{H}_2\text{O}$. The net result of the concurrent operation of these three end-member reactions with increasing oxidation is the production of sphene, hematite, and quartz, an increase in modal plagioclase, a decrease in modal amphibole, and a change in amphibole composition toward more Mg-rich and Ti- and pargasite-poor compositions.

Discussion

Robinson, Ross, and Jaffe (1971) have postulated the existence of a solid solution series between actinolite, $\text{Ca}_2(\text{FM})_5\text{Si}_8\text{O}_{22}(\text{OH})_2$, and hornblende with the ideal formula $\text{Na}_{0.6}\text{Ca}_2(\text{FM})_{3.6}(\text{Fe}^{3+}, \text{Al})_{1.4}\text{Al}_2\text{Si}_6\text{O}_{22}(\text{OH})_2$ for Ca-amphiboles from regionally metamorphosed metabasites. The trend of the data from the present study falls across this composition join but does not parallel it exactly (see Fig. 164). The discrepancy may reflect compositional differences

between the amphiboles surveyed by Robinson, Ross, and Jaffe and the amphiboles from the present study. Alternatively, the discrepancy may be the result of accumulated errors in the calculation of A site occupancy (see error bar in Fig. 164) or systematic differences in $\text{Fe}^{3+}/\text{Fe}^{2+}$ between amphiboles from this study that have low Al(IV) content and those with high Al(IV) content. It is also possible that the data of Robinson, Ross, and Jaffe, compiled from various sources in the literature, contain errors in Fe_2O_3 or H_2O determinations. In view of the possible sources of error, the data from the present study tend to support the existence of the postulated solid solution series, although determination of the compositions of the end-members of the series will require additional careful analytical work.

The amphiboles encountered in this study are progressively enriched in Na, K, Ti, and Al at the expense of Si with increasing temperature or decreasing oxygen fugacity. Much of this compositional change can be described in terms of pargasite and Ti-tschermakite substitutions, and the general trend is toward enrichment in these components with increasing T and decreasing f_{O_2} . Similar trends toward increasingly pargasitic and Ti-rich compositions have been observed in Ca-amphiboles from regionally metamorphosed terrains (Binns, 1965; Cooper and Lovering, 1970; Engel and Engel, 1962; Ernst, 1972; Graham, 1974). The conclusion to be drawn from the present study is that these compositional trends can be brought about by either an increase in temperature or a decrease in oxygen fugacity. Estimates of differences in metamorphic grade based on amphibole chemistry cannot, therefore, be made without an independent estimate of differences in oxygen fugacity.

STATISTICAL PETROLOGY

SYSTEMATIC PETROLOGY

ASYMMETRY IN THE DISTRIBUTIONS OF
SiO₂, Al₂O₃, CaO, AND Fe IN THE
PRODUCTS OF CENOZOIC VOLCANISM*Felix Chayes*

The distribution of SiO₂ in Cenozoic volcanic rocks—as sampled by the data base of system NTRM—is characterized by strong positive skew. The bearing of this finding on the suggestion (Richardson and Sneesby, 1922, 1923) that SiO₂ is bimodally distributed in igneous rocks as a whole was discussed at some length in last year's report (*Year Book* 74, p. 542 ff.). From time to time it is

suggested either that the major elements may in fact be lognormally distributed in the lithosphere or that the log transformation, by reducing asymmetry of minor or trace element distributions, might facilitate statistical analysis and evaluation of some geochemical data. Apart from the early work of Richardson and Sneesby, however, the actual distribution of major elements in the lithosphere as a whole has been little studied.

In particular, no one seems to have suggested that other major elements may be *negatively* skewed; yet in the products of Cenozoic volcanism that is

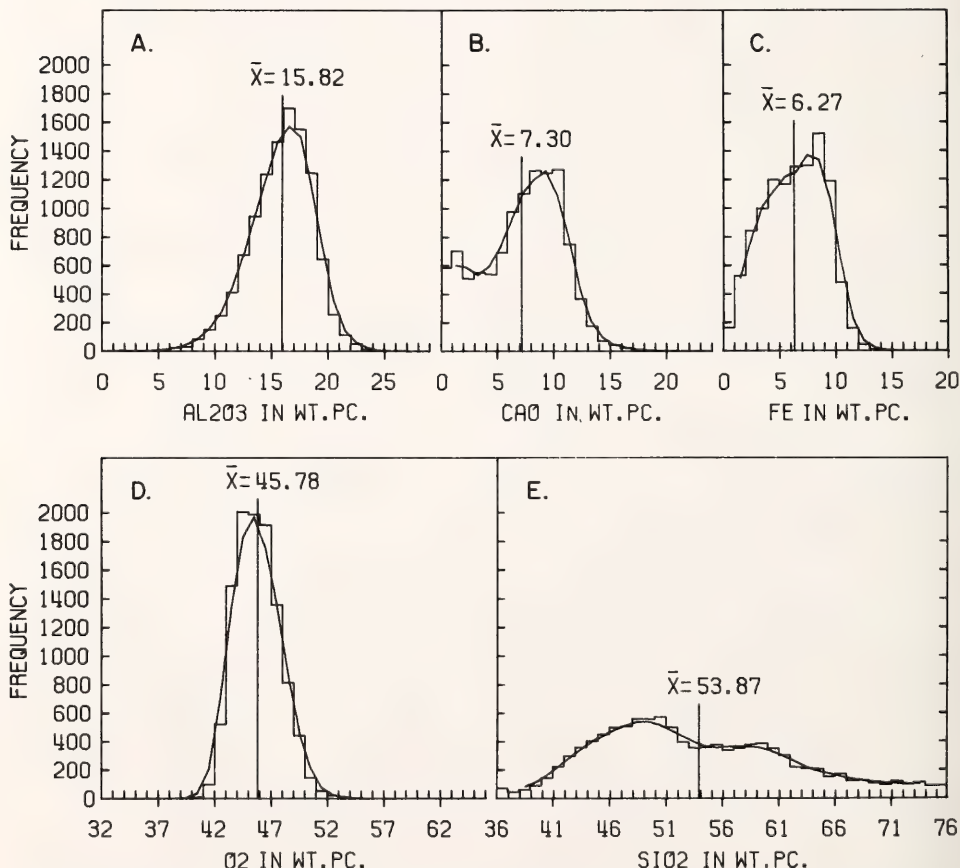


Fig. 166. Frequency distributions of Al₂O₃, CaO, Fe, SiO₂, and O₂ in 10869 analyses of Cenozoic volcanic rocks.

clearly the case for Al, Ca, and total Fe. Distributions of these and SiO_2 are shown in A, B, C and E of Fig. 166, in which, in order to facilitate visual comparison, the same grouping interval and frequency scale are used throughout. (The choice is a compromise; it is not optimum for any one of the variables.) The mean and a moving average are plotted in each diagram.

The variables Al_2O_3 , CaO , and Fe are negatively correlated with SiO_2 , the latter two strongly so. It is thus likely that if the distribution of SiO_2 were strongly enough skewed in one sense, the distributions of the others would have some tendency toward a skew of opposite sign. That this tendency finds such clear expression in all three, however, suggests an underlying nonrandom association controlled by constraints on mineral compositions and associations found in volcanic rocks, and perhaps also on the compositions of the liquids that give rise to them. It is to be noted, however, that Mg is markedly skewed in a positive sense, in this respect resembling Na, Ti, and K more than Al, Fe, and Ca.

DISTRIBUTION OF OXYGEN IN CENOZOIC VOLCANIC ROCKS

Felix Chayes

Goldschmidt (1928) pointed out that in a substance having the composition of H. S. Washington's average for the lithosphere, 46.59% of the atoms by weight, 62.46% by number, and 91.77% by volume would be oxygen. From the data of C. P. Merrill he computed analogous average oxygen values of 58.76 by number and 90.81 by volume for the silicate phase of stony meteorites. The lithosphere, he concluded, is in effect an "oxy-sphere."

Oxygen is by a very large margin the major elemental constituent of igneous rocks, and Goldschmidt's calculations for these limiting cases suggest that it is also one of the least variable. In view of both properties, Barth (1948a,b) pro-

posed an approximate "standard cell" for igneous rocks, based on 160 oxygen atoms. The calculation scheme he developed for the purpose of recasting analyses in this fashion has never been widely used, perhaps chiefly because the choice of 160 atoms is unsupported by any satisfying theoretical argument, but also because until recently no direct determinations of the oxygen content of silicate rocks were made. The oxygen content calculated from a conventional complete analysis receives contributions from all the "direct" determinations reported as oxides, and so too must its error. But just what these various error components are is never known with any assurance.

The computed amount of oxygen is nevertheless a statistic of much interest even though the individual estimates on which it is based are subject to variable, unknown, and probably sometimes rather large analytical uncertainty. In particular, for instance, one cannot help wondering whether the skews found for individual oxides—and hence for individual cations—in the Cenozoic volcanic rocks are reflected in the distribution of oxygen itself. On the average, as may be seen in Table 62, the number of cations whose distributions are positively skewed is more than twice as large as the number whose distributions are negatively skewed, and the absolute value of the largest negative skew is much smaller than the smallest positive skew; yet the positive skew of calculated oxygen is very small indeed, as may be seen from Fig. 166D or Table 62.

The examination of skewness is usually carried through with the dimensionless statistic $\beta_3 = m_3/s^3$, where m_3 is the third moment about the mean and s is the standard deviation. When the question at issue is how objects of various kinds fill space and the distributions are all plotted in the same units and on the same scale, however, the third moment itself seems in some respects more informative. Both statistics are included in Table 62. In terms of 3d moments, the

TABLE 62. Weight Percentage Means (\bar{x}), Standard Deviations (s), Coefficients of Variation ($C=s/\bar{x}$) and Skewness ($\beta_3=m_3/s^3$), Third Moments (m_3), and Relative Numbers of Atoms (P_n) of Essential Elements in Cenozoic Volcanic Rocks

| Element | \bar{x} | s | C | β_3 | m_3 | P_n |
|--|-----------|------|-------|-----------|-------|-------|
| A. 10867 analyses in which $\text{SiO}_2 > 30\%$ | | | | | | |
| O | 45.78 | 1.97 | 0.043 | 0.14 | 1.04 | 61.73 |
| Si | 25.18 | 4.14 | 0.164 | 0.50 | 35.5 | 19.34 |
| Al | 8.37 | 1.45 | 0.173 | -0.46 | -1.40 | 6.69 |
| Fe | 6.27 | 2.68 | 0.427 | -0.12 | -2.31 | 2.42 |
| Ca | 5.21 | 2.56 | 0.491 | -0.22 | -3.69 | 2.80 |
| Mg | 2.93 | 2.41 | 0.821 | 1.57 | 2.20 | 3.00 |
| Na | 2.73 | 1.17 | 0.428 | 1.39 | 2.23 | 2.56 |
| K | 1.90 | 1.48 | 0.778 | 1.40 | 3.23 | 1.05 |
| Ti | 0.91 | 0.68 | 0.746 | 0.93 | 0.29 | 0.41 |
| B. 7614 analyses in which $\text{SiO}_2 > 30\%$, $\text{H}_2\text{O} < 2\%$ and $\text{Fe}^{3+} < \text{Fe}^{2+}$ | | | | | | |
| O | 45.35 | 1.83 | 0.040 | 0.11 | 0.67 | 61.55 |
| Si | 24.76 | 3.66 | 0.148 | 0.78 | 38.2 | 19.14 |
| Al | 8.39 | 1.40 | 0.167 | -0.50 | -1.37 | 6.75 |
| Fe | 6.91 | 2.42 | 0.351 | -0.36 | -5.10 | 2.69 |
| Ca | 5.82 | 2.17 | 0.372 | -0.62 | -6.33 | 3.15 |
| Mg | 3.38 | 2.36 | 0.696 | 1.53 | 2.01 | 3.02 |
| Na | 2.55 | 0.96 | 0.387 | 1.23 | 1.09 | 2.42 |
| K | 1.49 | 1.23 | 0.825 | 1.97 | 3.67 | 0.83 |
| Ti | 0.99 | 0.68 | 0.688 | 0.84 | 0.26 | 0.45 |

negative skews of Al, Ca, and Fe are comparable in size to the positive skews of Mg, Na, and K. Yet the skew of oxygen is smaller than that of any of these six and seems in no way influenced by the overriding positive skew of Si.

In comparing the lithosphere with what is to be expected either in the earth's interior or on the surfaces of other planets or the moon, it is clearly a matter of major importance that rock chemistry is basically an oxygen chemistry. In distinguishing igneous rocks from each other and characterizing their interrelations, however, cation content and variation are far more useful than calculated oxygen content, for the latter in fact varies very little.

CHARACTERIZING THE CONSISTENCY OF CURRENT USAGE OF ROCK NAMES BY MEANS OF DISCRIMINANT FUNCTIONS

Felix Chayes

After a long period of disinterest and neglect, the vexing question of the classification of igneous rocks is once more

attracting the attention and concern of petrologists. It seems unlikely that any new petrographic system, however admirable in other respects, will be widely adopted unless it finds a way to preserve most of the commonly used rock names and groupings of names. Redefinition of the more important of these terms will be required, however, for if they were already unambiguously defined and consistently used, the problem of arranging them in some suitably hierarchical taxonomic structure would almost certainly be trivial. And everyone who has attempted it knows that this is very far from the case.

Accordingly, there is pressing need for a reasonably objective procedure by which to determine whether proposed modifications of the denotations of terms that are already in the public domain would be in the public interest. A major initial effect of such modifications will be to generate differences between current and proposed or future usage. This will always be bothersome, but whether it is bearable will depend on whether, in the long run, the modifications would

tend to increase the consistency and reduce the ambiguity with which the terms in question are used. The first requirement would thus appear to be some means of characterizing the consistency of *current* usage of the commoner rock names, those that will almost certainly be carried over, with or without redefinition, into any new classification.

Development of a widely acceptable general measure of the actual consistency of current and recent practice would be a formidable task and might prove impossible. For a very important class of rocks, however, it is not difficult to specify by discriminant functions based on chemical composition, the highest level of consistency that *might* be attained if it were possible to codify existing usage with a minimum of ambiguity. The only requirements are that (1) chemical compositions be of major importance in the naming of the rocks in question, and (2) paired names and chemical analyses be available for a large collection of such rocks.

The commoner Cenozoic volcanic rocks satisfy both requirements. Results of an extensive study of the consistency of current usage in the naming of these rocks, recently undertaken in connection with the work of the IUGS subcommission on Systematic Petrology, will be published in full elsewhere. Here the testing procedure is summarized, and attention is directed to the unexpectedly large sampling variances of the coefficients of discriminant functions that may nevertheless yield remarkably similar partitions in randomly chosen samples of the same sets of data.

A discriminant function calculated from chemical analyses of specimens denoted by any two names (or sets of names) can be used as a classifying device either on the data from which it is computed or on a new sample. The results of the classification operation may be cast in a 2×2 table in which the elements of the leading diagonal are the frequencies of rocks to each of which the discriminant function assigns the

name applied in the source reference. The proportion of such "consistent" classifications is a convenient measure of the optimum consistency of current usage of the pair of names (or of sets of names) in question.

Multivariate calculations of this sort are now more or less routine, and one's first impulse is simply to compute the discriminant from as large a sample as possible. This is unwise in at least three respects: (1) for large samples the calculation is still rather expensive, (2) the amount of information (numbers of analyses) available for different rocks varies widely, and (3) if all available data are used in construction of the function, no independent test of it is possible. The force of objections (1) and (3) is evident. The effect of (2) is to generate results of very uneven quality; a basalt-andesite discriminant will be based on large amounts of information about both rocks, for instance, but a basalt-tephrite discriminant will be based largely on information about basalt for the reason that rocks called tephrite are in fact quite uncommon.

Reduction and equalization of sample sizes by random sampling would eliminate all three objections if data sets were very large and sampling of them were carried through without replacement. If the first of these criteria is unsatisfied, however, the second will soon bring the operation to a halt. The data sets in question differ widely in size, and unfortunately some are so small that sampling of them without replacement is impractical. As a compromise, sampling was performed with replacement throughout, each test cycle consisting of the calculation of the function from a sample of approximately the desired size selected randomly from the available data, followed by a test of the function on a second such sample. Each sample is generated by a scan of the entire array of available data, and the probability that an analysis is actually used in a sample is unaffected by whether or not it has been used in earlier samplings.

TABLE 63. Means (\bar{m}) and Standard Deviations (s) of the Coefficients of Discriminant Functions (λ) Calculated from Random Samples of About 100 Specimens, and of the Proportions of Specimens Consistently Classified by Them (P_c) in Similar Random Samples*

| | λ | | | | | | | | | |
|--|------------------|--------------------------------|--------------------------------|-----|-----|-----|-------------------|------------------|------------------|----------------|
| | SiO ₂ | Al ₂ O ₃ | Fe ₂ O ₃ | FeO | MgO | CaO | Na ₂ O | K ₂ O | TiO ₂ | P _o |
| A. For 10 functions calculated from 229 specimens of trachybasalt and 231 specimens of trachyandesite. | | | | | | | | | | |
| \bar{m} | 3 | 9 | 0.3 | 35 | 18 | 52 | 72 | 8 | 84 | 84 |
| s | 14 | 21 | 45 | 23 | 23 | 23 | 30 | 30 | 16 | 2 |
| B. For 10 functions calculated from 447 specimens of phonolite and 338 specimens of basanite. | | | | | | | | | | |
| \bar{m} | -23 | 12 | 15 | 89 | 31 | 72 | -46 | -57 | 58 | 97 |
| s | 19 | 28 | 28 | 21 | 23 | 24 | 34 | 27 | 53 | 1 |

* All entries multiplied by 100 to eliminate decimal points.

In view of the piety with which multivariate functions of this sort are now sometimes viewed in practical statistical work in earth sciences, the results are, to say the least, surprising. It turns out that the taxonomic behavior of the functions varies very little from cycle to cycle although the functions themselves differ enormously. Two examples are summarized in Table 63, entries in which have been multiplied by 100 to eliminate decimal points. In each example the random sampling was designed to select samples of approximately 100 analyses of each nominal rock type. In the first example, the rocks involved are trachyandesite and trachybasalt, chosen because earlier work indicated that the consistency of this partition would be mediocre; the rocks involved in the second, phonolite and basanite, were known to yield a highly consistent partition.

All coefficients lie in the range $-1 \leq \lambda_i \leq 1$, and the proportion of consistent classifications is in the range $0.5^* \leq P_c \leq 1$, so the scale of variation of these statistics is in the ratio 4:1. In the first example, however, no coefficient is subject to a standard deviation less than seven times as large as that of P_c ; in the

second, the smallest standard deviation attached to a coefficient is 18 times as large as that of P_c . The square root of the mean of s^2 in the first example is 0.26 as compared to a standard deviation of 0.02 for P_c . Analogous figures for the second example are 0.30 and 0.01.

These findings are entirely compatible with the results of less extensive numerical experimentation on 43 other binary discriminations examined in connection with the work on the nomenclature and taxonomy of Cenozoic volcanic rocks noted above. Evidently the statistical behavior of a discriminant function as a taxonomic device may be quite reliable and reproducible even though the coefficients of the function are subject to such large sampling variance that the function itself may have no readily interpretable petrological significance.

ON THE SAMPLING VARIANCE OF COEFFICIENTS OF PRINCIPAL COMPONENTS

Felix Chayes and Juergen Trochimczyk

The availability of electronic computers has made possible the widespread application of three powerful multivariate data reduction techniques—discriminant function, principal component, and factor analysis—whose theoretical de-

* This lower limit is an expectation; presumably smaller observed values are not impossible, but so far none has occurred.

velopment dates from the interbellum period. In all three procedures the original or "raw" variables are replaced by a smaller, usually a much smaller, number of transformed variables. The transformed variables are always linear combinations of the raw variables, and the major computational problem is to find the coefficients of these combinations.

The most extreme reduction in the number of variables occurs in discriminant function analyses. In every such analysis the variable count is reduced by $(n-1)$, whatever the value of n ; a discriminant function always replaces a multivariate array by a univariate one. The linear combinations called principal components, on the other hand, are exactly as numerous as the raw variables, and the sum of their sample variances is exactly equal to the sum of the variances of the original variables. It is in this sense, at least initially, that the components are said to "account for" or "explain" or "contain" the variation of the raw data. Often, however, the bulk of the variance attaches to a few of the components and the remainder are dropped, the variance associated with them being recorded as "unexplained" or dismissed as noise. Sample description and interpretation are then continued in terms of the small number of components with which the bulk of the variance is associated.

The sampling variation of the coefficients of the components usually receives no attention in practical work in the earth sciences. The results noted in the preceding section suggest, however, that the subject deserves close attention, for the calculation of principal components is of the same general type as that of the discriminant function. If coefficients of the latter are commonly subject to large sampling variation, it seems very likely that this will be true also of those of the former.

Numerical experimentation with principal components, like that described above for discriminant functions, indicates that this is in fact the case. For the

work with principal components the approximate size of the random samples was 100, and 10 such samples were processed as before, but the reservoir of analyses from which the samples were drawn consisted of 1358 subalkaline basalts collected from the literature (see *Year Book* 74, pp. 547-549). Computation of components from the correlation rather than covariance matrix assured that the absolute values of the coefficients of the components would be ≤ 1 . Scaling of the eigenvalues as proportions rather than percentages also yielded values in the same range. The means and standard deviation of the coefficients of the first three components (κ) and their associated eigenvalues (V) are shown in Table 64. (All entries in the table have been multiplied by 100 to eliminate decimal points.)

The object of the exercise is to select components whose associated V 's are large. From inspection of the table it is clear that the coefficients of the factors vary much more widely than the eigenvalues. Like discriminant functions, principal components seem to perform quite consistently even though their coefficients may be subject to such large sampling variance that meaningful petrological interpretation is difficult or impossible. The coefficients of both types of function are generated from covariance or correlation matrices, so it is not surprising, though apparently not previously noted in earth science applications, that even in rather large samples they are subject to large sampling variance. It does seem surprising, however, that both functions nevertheless perform with such admirable consistency. This striking juxtaposition suggests that appropriate statistical application of the methods is well warranted but that over-detailed substantive interpretation of the results—as, for instance, when coefficients of a component based on a small sample are used as coefficients in a mass balance equation—is to be avoided or handled with extreme caution.

TABLE 64. Means (\bar{m}) and Standard Deviations (s) of the Coefficients of the First Three Components (κ), and of Their Associated Eigen-values (V), for Ten Sets of Principal Components Calculated from Approximately 100 Items Each, Selected Simply at Random with Replacement, from 1358 Analyses of Cenozoic Subalkaline Basalt*

| | κ | | | | | | | | | | |
|----------------|------------------|--------------------------------|--------------------------------|-----|-----|------|-------------------|------------------|------------------|-----|------------|
| | SiO ₂ | Al ₂ O ₃ | Fe ₂ O ₃ | FeO | MgO | CaO | Na ₂ O | K ₂ O | TiO ₂ | V | ΣV |
| Component I | | | | | | | | | | | |
| \overline{m} | −149 | −127 | −27 | 129 | 129 | 70 | −162 | −149 | 72 | 335 | |
| s | 669 | 671 | 205 | 673 | 722 | 470 | 648 | 649 | 477 | 27 | |
| Component II | | | | | | | | | | | |
| \overline{m} | −33 | −215 | 120 | −7 | 220 | −278 | 144 | 159 | 222 | 207 | 542 |
| s | 349 | 496 | 538 | 354 | 414 | 583 | 374 | 451 | 541 | 21 | 34 |
| Component III | | | | | | | | | | | |
| \overline{m} | 55 | 89 | −23 | −62 | 10 | 92 | −151 | −103 | −173 | 160 | 700 |
| s | 473 | 317 | 715 | 481 | 258 | 402 | 282 | 197 | 294 | 9 | 35 |

* All entries have been multiplied by 1000.

MINIMUM SiO₂ REQUIREMENT OF THE CIPW NORM

Felix Chayes and Danielle Velde

With so much normative calculation now being done electronically, it is easy to overlook the fact that in every petrographic system such calculation is subject to materials balance constraints that, except as they may reflect inadequacies in the definitions of the normative parameters or in the analysis for which a norm is being computed, are basically algebraic rather than petrological. An interesting example, in which negative lc was reported in certain norms, has recently been encountered in the CIPW system in the course of routine operation of version NTRM of the rock information system RKNFSYS.

Normative parameters of the CIPW system are by definition nonnegative, and in a calculation schedule so widely used and thoroughly tested the emergence of a negative norm "molecule" is a reliable index of error in either the subroutine that performs the calculation or the data it receives. A number of coding and transcription errors have been detected in this fashion, and the

present case is not entirely exceptional. The analyses in question proved to have been transcribed correctly from the source references, but two minor coding errors were detected in the subroutine in which the calculation is performed. These errors deflected control around a trap designed to catch certain analyses for which, for the reason described immediately below, the standard CIPW combining conventions do indeed lead to impossible results. It is perhaps indicative of how often this particular trap is needed that its very existence had been forgotten.*

* Readers who have used any version of RKNFSYS to generate work files containing normative parameters calculated from analyses of rocks known or thought to be melilite-bearing should resubmit; occasional analyses of this type should have found their way to the trap but did not. Instead of rejecting these analyses, the system work-file builder will have generated and stored faulty norms from them, but the errors will probably have escaped detection unless individual values of the normative parameters were printed in some subsequent data reduction. That extreme deficiency of silica is a fertile source of error in normative calculations is hardly novel; for a recent example, see Mysen, Arculus, and Eggler (1976).

The standard normative calculation cannot be completed unless the molar amount of SiO_2 available after formation of *an* is at least equal to $R_2\text{O} + (R^*\text{O})/2$, where *R* denotes alkalies and *R** denotes bivalent metals other than those complexed in *an*, *mt*, and *il*. Such massive silica deficiency is exceedingly rare in Cenozoic volcanic rocks. The current data base of version NTRM of RKNFSYS contains only one example in 11,977 analyses; a collection of 303 analyses of melilitic and mafic alkalic volcanic rocks now being prepared for insertion in the next edition of the base contains another three.

It is well known that CIPW norms of volcanic rocks are often abmodal in the sense that normative assemblages differ qualitatively from modal ones. Astonishingly few volcanic rocks, however, are abnormative in the sense that their analyses cannot be successfully recast according to the standard CIPW combining conventions. The examples cited above, incidentally, are of altered, hydrated materials, and it seems quite possible that silica deficiency of this magnitude simply does not occur in lavas still liquid or freshly frozen.* Indeed, the development of such a lava by solid-liquid interactions of the sort usually invoked would imply either the existence of strange and as yet unknown phases in the parent material or their generation during the formative process. (Although norms of rock-forming silicates are almost by definition abmodal, the compositions of these minerals are very rarely abnormative, the only exception currently known to us being rhönite.)

*A caveat should perhaps be entered with respect to carbonatites. Until quite recently, CO_2 was never more than a very minor constituent of any rock considered igneous, and the CIPW conventions for handling it are, accordingly, fragmentary and simplistic. It is quite possible that extensive application of standard normative calculation to carbonatite analyses would yield some rather odd results. Even now, however, very few carbonatites are known or thought to be lavas.

DEVELOPMENT OF AN INFORMATION SYSTEM FOR IGNEOUS PETROLOGY

DESIGN AND CONSTRUCTION OF A WORLD DATA BASE FOR PETROLOGY

Felix Chayes

Even in some of the smaller natural sciences the amount of published information has for some time been so vast that diligent application of conventional scholarly procedures no longer provides the level of awareness and control of subject matter expected of competent naturalists a few decades ago. Unless this situation is relieved, the long-range consequence must be either a further burst of specialization in fields already overspecialized or a general decline of standards, or both.

In the storage, referencing, and retrieval of data, however, the world of scholarship is approaching a divide not unlike that it passed across with the invention of the printing press. For most descriptive sciences, relief could now be found in judicious application of electronic data processing, and preliminary steps in this direction are being taken, with varying degrees of energy and success, in many of these fields. The urgency of the problem, like that of the steps being taken to solve it, varies widely among the sciences. In some there seems to be no sense of emergency at all. In others, particularly the newer aspects of geophysics, data accumulate at such a rate that currently available techniques of electronic storage are thoroughly inadequate, and in a recent report Savit (1976) warns that unless facilities are expanded and technology is improved "data centers will increasingly become repositories for data that are effectively inaccessible to the majority of potential users."

The position of igneous petrology in this spectrum of impending disaster is perhaps particularly favorable. The published corpus of the subject has indeed grown to the point at which its mastery by conventional nonelectronic referencing techniques is thoroughly impractical

and, for most practitioners, simply impossible. Yet the volume of data to be "recaptured" from the printed page is such that its collection is probably well within the capacity of intelligent cooperative action by the profession and is certainly not such that its storage, retrieval, and reduction by electronic means would in any way tax the capacity or capability of existing large computers and storage devices.

The first step in the computerization of published petrological data is the preparation of a form that will provide reasonably compact nonelectronic storage of data extracted from the literature pending their conversion to punched card or other machine-readable mode. The start of an experiment whose objective is to test and improve such a data form was announced in last year's report (*Year Book 74*, p. 549). It has proved much more demanding than was anticipated and is still in progress. One very important result has matured. It is now evident that rather large vocabularies for mineral names and petrographic descriptors will be necessary, but that very few elements of either will be required in any single specimen description. The key-number system of referencing will therefore be preferable to the key-bit system. This choice, of critical importance in the design of the new data base and system, is now considered final.

In other respects, however, the results of the experiment have been far less decisive. So many modifications of the data form have been suggested by contributors that it seems the better part of valor to repeat the experiment, using a revised form incorporating as many of these suggestions as possible. Participants are also agreed that extraction of nonnumerical data from the texts of published petrographic descriptions is considerably more time-consuming than transcribing numerical data from the tables that ordinarily accompany such descriptions. Earlier estimates of the rate at which the new base could be built were necessarily based largely on

experience with the latter and now seem rather unrealistic.

In accord with these early estimates, version NTRM of RKNFSYS (see *Year Book 74*, p. 550) was initially intended to serve only as a very temporary standby; at this time a year ago further systematic expansion of its data base was not contemplated, and only such extension of its program repertoire as would contribute directly and immediately to the development of a far more sophisticated successor system was to be undertaken. It now seems likely, however, that the services of NTRM (and similar systems elsewhere) will be required for a considerable period. Accordingly, in recent months NTRM has been put on a much firmer footing. It has been equipped with a new, much improved base generator, and most of the remainder of this report describes modifications of or additions to its program repertoire.

A REVISED STRUCTURE FOR SYSTEM REDUCTION PROGRAMS

Felix Chayes

Version NTRM provides extensive simplification of input format for system reduction and retrieval programs. Conveniences of this sort extended to the user must of course be compensated for by considerable internal complication of the programs he uses. Such complication proved particularly bothersome with regard to extension of the program repertoire of the system, and finally prompted a complete redesign of the structure of system programs. The new structure will be used *ab initio* in all new programs and introduced into older ones whenever extensive editing of them seems advisable on other grounds. Although ultimate users will be unaware of the structural modification except perhaps as it facilitates more rapid expansion of the program repertoire of the system, the changes will be of interest to all readers involved in work of this type.

Every system program must read, interpret, and store a set of instructions it receives at operation time and then apply the set in a scan either of a work file previously generated from the system data base or of the base itself. These operations are most efficiently performed by in-line coding, but when, as is now the case, extensive reorganization of communications received from the user must precede execution, the computational efficiency of in-line coding is purchased at considerable loss of programming facility. The preparation of new programs becomes an onerous chore that is fraught with possibilities for clerical error, requires close familiarity with the file structure of the system, and leads to long programs that are in large part identical, however different their objectives.

The obvious alternative is to perform all system-specific functions in standard system subroutines. Ideally, all processing requiring knowledge of the file structure of the system, the grammar and syntax of system specification lists, the ways in which these lists are converted into machine-usable instructions, the names of the variables in which they are stored, or the manner in which they are applied in the course of the data scan should be performed in such subroutines. Each main program would then receive and process only data required by calculations specific to it. In fact, this goal is very nearly attainable.

Although in version NTRM a small part of system-specific work, namely, the initial interpretation of specification lists and communication between core and mass storage files, has always been performed by subroutines, most of it has been programmed individually in each main program. In the new structure virtually all processing of instructions and data except that specific to particular main programs will be handled by system subroutines. As its first activity a main program will call a new system subroutine, *READER*, that reads all specification lists, obtains interpreta-

tions of them from a second system subroutine, *LSTNKD*, stores and prints all interpreted instructions, and returns control to the main program, together with a variable whose value is the number of physical records to be scanned. The main program then enters a loop with this number as upper parameter; at each cycle of the loop it passes the current value of the loop index, which is also the index number of the current record, to an entry of *READER* named *SCREEN*. *SCREEN*, in turn, finds the record address and passes it to the system file reader (*RANDW*, see Finger, *Year Book 70*, p. 201), which brings the data record into core. *SCREEN* then processes the record in accordance with its stored instructions, extracting from it, and returning to the main program in a single block, all appropriate data it contains. Depending on the nature of the computation and the structure of the main program, this information may be either processed on receipt or stored for subsequent processing, following which another pass through the loop is initiated, etc. Thus neither the main program nor the programmer constructing it need be concerned with the now rather involved vocabulary, grammar, syntax, and file structure of the system. The loss of computational efficiency in the new scheme will usually be trifling, since subroutine *READER* scans data in blocks of exactly the size contained in system work files. If such a file is blocked into, say, n physical records, its scan by most existing system programs requires $(n+1)$ subroutine calls, whereas in the new system $(2n+1)$ will be required. The current system limit of n is 150, and values larger than 50 are rare.

The new program structure has already proved convenient, but its major benefits will accrue as the vocabulary, grammar, and logic of the system are expanded to permit inclusion and manipulation of qualitative data such as mineral assemblages, petrographic descriptors, etc. The necessary changes in the reading, interpretation, storing, and

execution of instructions will then be both drastic and basic, but only the sub-routines *READER* and *LSTNKD* will require revision; the main programs of the repertoire will be unaffected.

MODIFICATION OF EXISTING PROGRAMS

Felix Chayes

The system two-group discriminant function program *TUGPNT* has been completely rewritten. In the new version the groups need not be either resident in the same work file or subject to the same directory, and a random number generator may be used in the final screening of the data to generate test groups of approximately the same size from raw data groupings that may differ sharply in size. All the changes are useful and some are indispensable in a continuing study of consistency in rock classification, some results of which are described in an earlier section of this report.

Retrieval of data from work files in the form of punched cards or "card-image" tape, as described in the section following the next, is accomplished by a modification of system program *DSPLNT*, originally designed to yield printed retrievals only.

NEW PROGRAMS

Juergen Trochimczyk and Felix Chayes

UVPLNT, a routine that plots histograms from data placed in a mass storage file by program *UVFRNT*, has been added to the system. The user specifies at operation time whether he wants a bar or a step diagram, the number of labeled ticks to be used on the abscissa, the largest frequency anticipated, the units of measurement to be included in the abscissa caption, whether a moving average is to be plotted, and if so, its width in classes. Figure 166 of this report has been assembled from output of *UVPLNT*.

PRKMNT, a principal components

program in which the components may be calculated from either the covariance or the correlation matrix and are printed out with their individual and cumulated variances, has been added to the system. It is the first element of the system repertoire using subroutine *READER* and the new program structure described in the preceding section.

An entirely new principal components and factor analysis program is now being tested. On request, it calculates principal components from either the covariance or the correlation matrix, or the factors from a correlation matrix in which the diagonal elements are replaced by the vector of squared multiple correlations, D , as initial communalities (Harman, 1964, pp. 87-91). The j th element of D is calculated as $1 - 1/r^{jj}$, where r^{jj} is the j th diagonal element of the inverse of the correlation matrix.

The correlation matrix, R , the product matrix, $R^+ = AA'$, where A is the matrix of principal components or common factors, and the residual matrix, $R^- = R - R^+$, are printed out. An option provides an approximate test (Lawley and Maxwell, 1963) of whether a sufficient number of factors have been generated. Specifically, χ^2 is estimated by

$$n' \sum_{i < j} \frac{r^{-ij^2}}{r^{-ii} \cdot r^{-jj}},$$

where the adjusted sample size (n') is $n' = n - 1/6 (2p + 5) - 2/3k$, and the approximate number of degrees of freedom (f) available for the test is $f = \frac{1}{2} [(p-k)^2 - (p+k)]$, n being the initial sample size, p the number of variables, and k the number of factors generated.

A second option permits rotation of the factor matrix approximating "simple structure" (Thurstone, 1969, p. 335) with orthogonal rotations based on the normal varimax criterion of Kaiser (1959). The matrix of rotated factors is printed out.

Finally, an option allows calculation

of factor scores, \hat{P} , for either unrotated or rotated factors, or both, from $\hat{P} = A' R^{-1} Z$, where Z is the matrix of raw variables.

INDEPENDENT EXPLOITATION OF THE
DATA BASE AND REDUCTION REPERTOIRE
OF THE PETROGRAPHIC
INFORMATION SYSTEM

Felix Chayes

Many forms of data reduction and summary needed by students of igneous rocks can now be obtained by routine operation of system programs: A publicly accessible system of this type would thus obviate much of the need for extensive data retrievals and the annoying storage and maintenance problems they create. It is obvious, however, that no system can anticipate all the data-processing needs of petrologists. Many users may wish to process raw data from the system data base, or system-generated restatements of such data, in ways not provided for by the program repertoire of the system. Conversely, some may wish to use various elements of the system program repertoire in the processing of data not contained in its base. In the report year steps have been taken to meet the needs of both groups.

A system program, DSPLNT, now provides retrieval, in print or on punched cards, of the contents of any system-generated work file. The work file rather than the data base was chosen as the starting point for retrieval because it permits the user to obtain not only raw data but current values of calculated quantities such as molar proportions, normative molecules, and optional expressions of considerable complexity. Each data card of an output deck con-

tains information derived from an analysis whose location in the system data base is recorded in the first two fields of the card. Each deck includes also a caption card and a card containing an array that may be used as a Fortran IV Format statement under which the data cards can be read. The program thus permits ready extraction of data from the base in a form easily processed either at other sites or in ways not facilitated by the program repertoire of the system.

The opposite situation, in which the user desires to apply system reduction procedures to data not included in the system data base, is rather more difficult to handle. If the user can prepare, either manually or electronically, a card deck or the image of a card deck that can be used as input to the system base builder, however, it becomes a simple matter to generate a private base that can be read by system programs. (Work files, incidentally, can be extended at will from any base that satisfies system requirements; in this fashion data drawn from the system base can be either compared or pooled with private data.)

In the course of the report year the system has been used in both ways described above. Retrieval of data from the data base for external reduction is now simple and routine; it is offered as a regular system service, provided neither infringement of copyright nor excessive clerical obligation is involved. There has also been intensive application of system reduction facility to private data (see, for instance, Velde and Yoder, this Report). At present, however, this latter service and the plotting routine are available only to users in residence at the Laboratory.

BIOGEOCHEMISTRY

THE FORMATION AND CLAY MINERAL REACTIONS OF MELANOIDIN

John Hedges

Brown acidic polymers known as humic substances often account for over one half of the biogenetic material that is dissolved in natural waters or entrapped in fine-grained sediments. Since the early work of Maillard (1913), evidence has accumulated suggesting that natural humic substances may be produced by nonbiological condensations of sugars with amino acids (Enders and Theis, 1938; Abelson and Hare, *Year Book* 69, pp. 327-334). Much of this evidence is based upon chemical similarities between natural humic substances and sugar-amino acid condensation products (melanoidins) produced in the laboratory (Hoering, *Year Book* 72, pp. 682-690). The effects of reactants and reaction conditions upon the chemical properties of melanoidin polymers, however, have not been studied systematically.

Reported here is an investigation of the chemical properties of melanoidins produced from the reaction of glucose with amino acids of contrasting compositions. Model laboratory experiments were designed to determine (a) which amino acids most readily react with glucose to form melanoidins, (b) what relationships exist between the chemical compositions of the melanoidins and their component amino acids, and (c) how inherent chemical compositions control melanoidin-clay mineral association reactions in aqueous solutions. The model studies provide guidelines and establish some boundary conditions for the possible formation and transportation of melanoidins in natural environments.

Experimental

Reaction rate studies. Relative rates of melanoidin formation were calculated from characteristic absorbances by the

polymers of ultraviolet light (290 nm). All reaction solutions were 0.01 *M* in glucose and amino acid (if present). Phosphate buffers (0.10 *M*), made by adding H_3PO_4 to Na_2HPO_4 , were used throughout. Reactions were carried out at 80°C in closed quartz cells within a spectrophotometer. Reaction rates were determined over a region of linearly increasing absorbance that characteristically followed an initial lag period and a brief episode of rapid chromophore production.

Chemical compositions of the standard melanoidins. A set of nine standard melanoidins was prepared by reacting D-glucose with glutamic acid, valine, or lysine at sugar to amino acid concentration ratios of 9/1, 1/1, and 1/9. The reactions were carried out in closed glass bottles that were heated at 100°C for 1 week. Sodium carbonate was added to retard the buildup of CO_2 .

Melanoidin polymers of molecular weight greater than 6000 were isolated by dialysis and freeze-dried. The percentages by weight of carbon, nitrogen, and hydrogen in the melanoidins were determined with a commercial analyzer. Cation-exchange capacities were calculated from the ash contents of the melanoidins and from x-ray fluorescence analyses of the ashes. Oxygen compositions were determined by difference on an ash-free basis.

Association reactions. The kaolinite and montmorillonite clay minerals used in this study have been described (Hedges, *Year Book* 74, pp. 604-609). The montmorillonite clay was also prepared in Na^+ , Ca^{2+} , and Fe^{3+} -saturated forms.

Association reactions were carried out as described in the previous reference. The extent of melanoidin uptake was calculated from the absorbances (275 nm) of clay supernatant and control solutions after 24 hr of reaction. Background absorbances by unsedimented crystals were determined from a corre-

sponding melanoidin-free suspension. Percentages of melanoidin uptake determined by direct carbon analyses agreed well with values obtained by absorbance differences (Table 65).

Results and Discussion

Reaction rate studies. Glutamic acid, valine, and lysine were chosen to represent, respectively, acidic, neutral, and basic amino acids found in living organisms. The three amino acids vary essentially in the number of carboxyl and amino groups that they contain.

The relative rates at which the three representative amino acids react with glucose vary widely (Table 66, Fig. 167). At pH's of 6, 7, and 8 the order of relative reaction rates is the same: lysine >> valine > glutamic acid > glucose alone. The rate of polymer formation increases with increasing pH in all four systems. Glucose polymerizes with itself at an appreciable rate only at pH 8. At this pH a significant amount of the

TABLE 65. Percentage of Uptake of Melanoidin by Two Different Measurements*

| Method | Uptake (%) | |
|--------------------------------|------------|-----------------|
| | Kaolinite | Montmorillonite |
| Absorbance at 275 nm | 5.8 | 56 |
| Carbon in freeze-dried residue | 5.4 | 54 |

* Comparisons were carried out using the 1/1 glucose-lysine melanoidin at initial concentrations near 1000 mg/l in a sodium phosphate buffer at pH 6. The suspensions contained 25 mg clay/10 ml solution.

polymer formed in the glucose-amino acid systems may also result from glucose-glucose condensations.

The rate studies suggest that melanoidins may form more readily in seawater or in marine sediments (pH about 8) than in terrestrial waters or soils, which are generally more acidic (Beck-

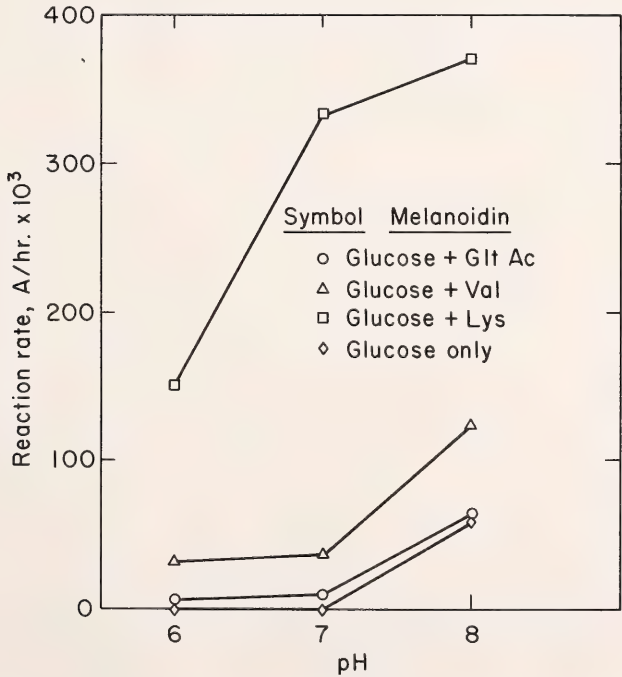


Fig. 167. Rates of color formation in four different glucose systems at pH 6, 7, and 8.

TABLE 66. Rates of Melanoidin Formation at Three Different pH's

| Reactants | Rate (absorbance units/hr × 1000) | | |
|-------------------------|---|------|------|
| | pH 6 | pH 7 | pH 8 |
| Glucose + glutamic acid | 5.8 | 9.0 | 63 |
| Glucose + valine | 31 | 36 | 123 |
| Glucose + lysine | 150 | 333 | 370 |
| Glucose only | 0 | 0 | 59 |

ing, Kaplan, and Moore, 1960). If sugars react with a mixture of amino acids, basic amino acids should condense most readily.

Chemical compositions of the standard melanoidins. The weights, elemental compositions, and cation-exchange capacities of the nine standard melanoidins are listed in Table 67. The recovered weights of melanoidin were directly proportional to the concentrations of glucose in the reaction systems. This relationship results because amino acids do not polymerize with themselves under these reaction conditions. Lysine-glucose reaction solutions consistently produced more polymer than the corresponding glutamic acid and valine solutions.

The elemental compositions of the nine melanoidins correspond to the type and relative concentrations of amino acid in the reaction solutions. These trends are reflected by the nitrogen contents of the polymers. At all three reactant ratios, lysine (two nitrogen atoms/molecule) combines with glucose to form melanoidins that contain approximately twice the nitrogen of the corresponding polymers derived from valine or glutamic acid (1 N/molecule). In all three amino acid systems the nitrogen content of the melanoidins increases with an increase in the relative concentration of amino acid in the reaction solutions.

The nitrogen concentrations of the standard melanoidins can be used to estimate the relative abundances of glu-

cose and amino acid units within the polymers. Figure 168 shows three lines indicating the percentages by weight of nitrogen that would result if glucose and each representative amino acid were combined at various molar ratios to form melanoidin polymers. The calculations were made with the assumptions that all glucose residues in the polymers are dehydrated once and that all amino acids are conservatively incorporated (Hodge, 1953).

The percentages by weight of nitrogen in the nine standard melanoidins (Table 67) are plotted on the theoretical composition lines in Fig. 168. Melanoidins formed from the reaction of glutamic acid or valine with an excess of sugar (9/1 solutions) apparently contain approximately 20 mole % amino acid and therefore are composed of about four sugar residues for each amino acid unit. Polymers formed in an excess of the same amino acids (1/9 solutions), however, contain nearly equal amounts of glucose and amino acid units. The lysine-glucose products exhibit similar trends, but the ratios of amino acid to sugar residues within the polymers are consistently larger and greater than 1 for the melanoidin formed in the 1/9 reaction solution.

The compositional trends and rate studies are both consistent with a model of two competing reactions: glucose-glucose condensations and glucose-amino acid condensations. The relative contributions from each pathway depend upon the type and concentration of amino acid in the reaction solution. High sugar to amino acid ratios and unreactive amino acids favor glucose-glucose polymerizations at the basic pH's that were used. High amino acid concentrations and reactive amino acids favor glucose-amino acid condensations. The nearly equal concentrations of sugar and amino acid residues in melanoidins produced in an excess of amino acid suggests that the polymers are composed primarily of reactive intermediates that are formed in a rate-determining step by the con-

TABLE 67. Chemical Compositions of the Nine Standard Melanoidins

| Melanoidin | Molar Ratio (G/AA)* | Weight product (mg) | Acidity (meq/g) | Elemental Analysis (wt %) | | | | | Mole % Amino Acid in Melanoidin† |
|-------------------------|---------------------|---------------------|-----------------|---------------------------|-----|-----|------|-----|----------------------------------|
| | | | | C | H | N | O | C/N | |
| Glucose + glutamic acid | 9/1 | 114 | 3.5 | 46.4 | 5.2 | 1.7 | 46.7 | 25 | 20 |
| | 1/1 | 45 | 5.3 | 46.0 | 3.6 | 3.5 | 46.9 | 13 | 40 |
| | 1/9 | 19 | 6.5 | 42.6 | 2.9 | 4.4 | 50.1 | 9.7 | 50 |
| Glucose + valine | 9/1 | 121 | 2.3 | 51.8 | 6.1 | 1.8 | 40.3 | 29 | 20 |
| | 1/1 | 61 | 3.4 | 53.3 | 3.7 | 3.8 | 39.2 | 14 | 40 |
| | 1/9 | 11 | 4.7 | 52.1 | 5.1 | 5.0 | 37.8 | 10 | 49 |
| Glucose + lysine | 9/1 | 239 | 1.1 | 54.1 | 5.8 | 5.2 | 34.9 | 10 | 31 |
| | 1/1 | 185 | 1.3 | 54.4 | 7.4 | 8.0 | 30.2 | 6.8 | 49 |
| | 1/9 | 25 | 1.5 | 50.6 | 9.4 | 9.7 | 30.3 | 5.2 | 60 |

*Moles glucose/moles amino acid in original reaction solution.

† Calculated from Fig. 168.

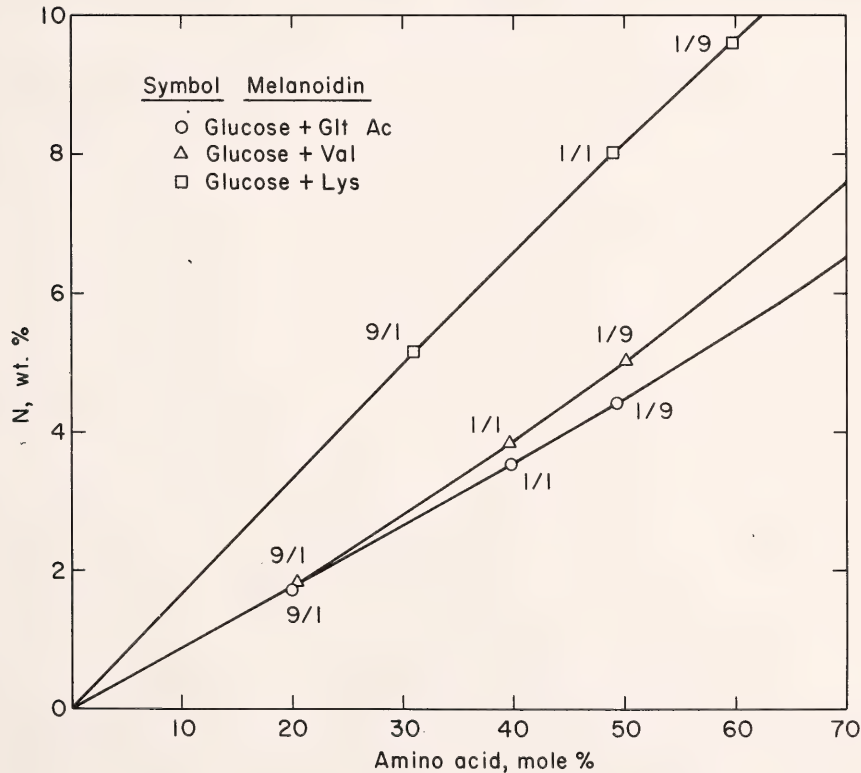


Fig. 168. Locations of percentages by weight of nitrogen in the nine standard melanoidins along lines indicating the calculated percentages of nitrogen in hypothetical polymers formed by the combination of dehydrated glucose and amino acid at various molar ratios. The ratios 9/1, 1/1, and 1/9 indicate the glucose to amino acid molar ratios in the reaction solutions in which the melanoidins were formed.

densation of one sugar and one amino acid molecule (Hodge, 1953).

The relative acidities of the nine melanoidins, as indicated by their cation-exchange capacities (Table 67), also reflect the amino acid compositions of the solutions in which they are formed. Glutamic acid produces polymers of greater acidity than does valine or lysine under equivalent conditions. Melanoidins produced by all three amino acids become more acidic as the relative concentrations of the respective amino acids are increased in the reaction solutions. Apparently, a major component of the total acidity of the melanoidins is contributed by carboxyl groups in amino acid residues.

Association reactions. The three 1/1 melanoidins (Table 67) were reacted

with kaolinite and montmorillonite clay minerals to determine whether chemical properties inherited by the polymers from their component amino acids might cause differences in clay mineral affinity. The montmorillonite clay has more than ten times the surface area and cation-exchange capacity of the kaolinite (Hedges, *Year Book* 74, pp. 604-609).

Melanoidin-clay mineral associations were investigated as a function of pH because changes in pH are known to affect a wide variety of organic-clay interactions (Theng, 1974). Partition coefficients of the three melanoidins (50 mg/l) by the two clays (100 mg/10 ml) are illustrated in Fig. 169. Commercial buffers (0.05 M , K salts) of pH 2, 4, 6, 8, and 10 were used.

The clay minerals removed more mel-

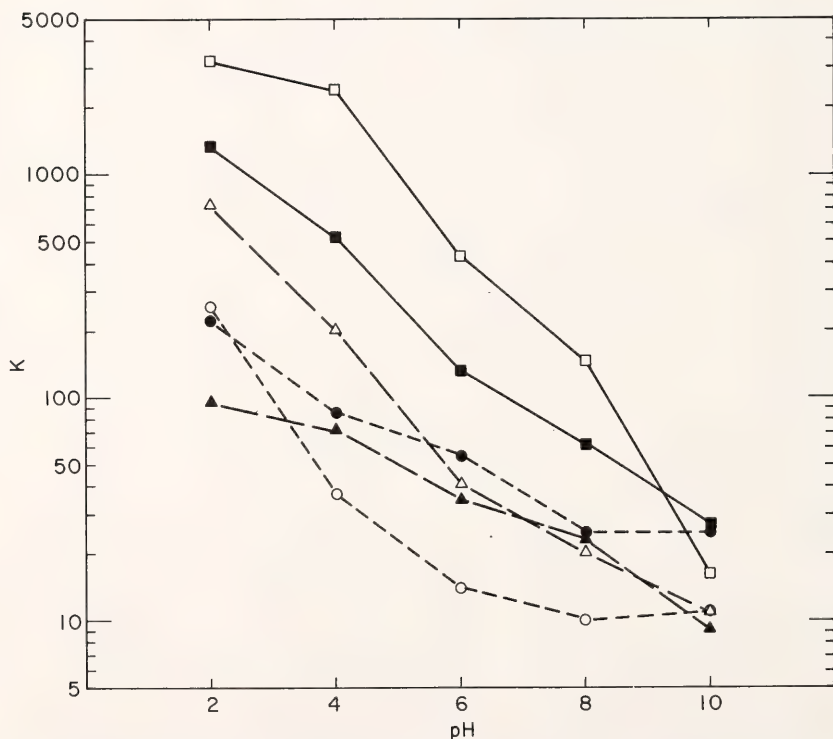


Fig. 169. Plot of the partition coefficient (K) against pH for six clay-melanoidin systems. Systems with glutamic acid melanoidins are denoted by circles; valine melanoidin systems, by triangles; and lysine melanoidin systems, by squares. Solid symbols indicate kaolinite systems, and open symbols indicate montmorillonite systems.

anoidin in more acidic solutions. At all pH's except 10, the lysine melanoidin is taken up by both clay minerals to a greater extent than are melanoidins formed from glutamic acid or valine. The relative affinities of kaolinite and montmorillonite minerals for dissolved melanoidins vary with pH. At low pH's montmorillonite removes more of each melanoidin than does kaolinite. In more basic solutions the order is eventually reversed. The crossover points occur at progressively higher pH's for melanoidins formed from more basic amino acids.

The general decrease in uptake at higher pH's results primarily from an increase in the solubilities of the melanoidins. As indicated by the fine structure in Fig. 169, however, a component of the total uptake may result from ion-exchange reactions that are controlled by the different amino acid residues within the three polymers.

At a pH of 2 the amino acid residues should all carry a net positive charge (*Handbook of Chemistry and Physics*, 1961, p. 1761) that will largely determine the charges on the corresponding melanoidins. Under these conditions, montmorillonite should remove more melanoidin than kaolinite because the montmorillonite crystals have a higher density of negative charge. When suspension pH's are increased, all three melanoidins will be eventually converted to negatively charged molecules, and electrostatic forces will then favor uptake by kaolinite crystals. The observed crossover points of the glutamic acid, valine, and lysine melanoidins at progressively higher pH values support this model.

Adsorption isotherms were determined at 25°C for the previously described clay-melanoidin systems (Fig. 170). Initial concentrations of melanoidin were varied from about 10 to 1000 mg/l in suspensions that contained 25 mg of clay in 10 ml of solution at pH 6. Polymers formed from basic and neutral amino acids were more efficiently removed from

solution by montmorillonite than by kaolinite. The glutamic acid melanoidin was adsorbed in small and nearly equal amounts by both clays. The percentages by weight of lysine melanoidin bound to montmorillonite were approximately an order of magnitude greater than those obtained in any other system at comparable concentrations.

The montmorillonite clays from this experiment were washed with an excess of distilled water to remove reversibly bound melanoidin and were analyzed with an x-ray diffractometer. Only the lysine melanoidin caused a significant increase in the interbasal spacing of the clay crystals (Fig. 171). Studies with natural humic substances (Schnitzer and Kodama, 1966) and proteins (Albert and Harter, 1973) indicate that these polymers are adsorbed on the basal surfaces of sodium montmorillonite crystals as organic cations and suggest that the bound lysine melanoidin may also be positively charged.

The three 1/1 melanoidins and a polymer formed from glucose alone (50 mg/l) were reacted (in distilled water) at pH 6 with the natural montmorillonite and its Na⁺-, Ca²⁺-, and Fe³⁺-saturated forms (100 mg/10 ml). The partition coefficients of the natural montmorillonite and its Na⁺-saturated counterpart were nearly identical (Fig. 172). This result is to be expected because the Belle Fourche montmorillonite is essentially a sodium clay (American Petroleum Institute, 1951).

The differences in association observed between the various homoionic clays, however, were dramatic. In all systems the extent of uptake increased with increasing ionic potential of the exchangeable ions. The sodium-saturated clay bound relatively small quantities of all the melanoidins except the lysine product. The Ca²⁺ and Fe³⁺ clays efficiently removed all four polymers from solution.

The previously described experiments were repeated using the three 1/1 melanoidins at initial concentrations of about 1000 mg/l. The reacted clays were re-

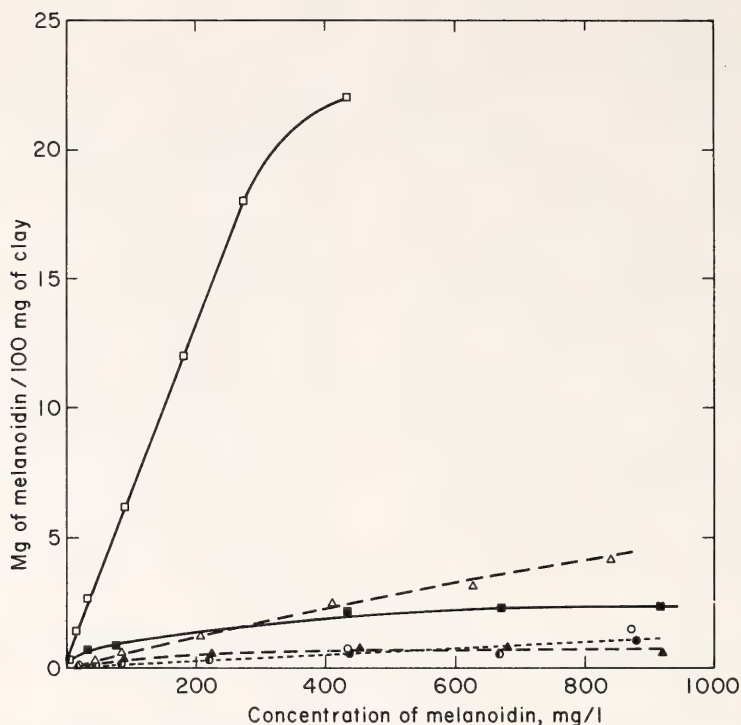


Fig. 170. Adsorption isotherms for six clay-melanoidin systems. Plotted concentrations are at steady state. Symbols as in Fig. 169.

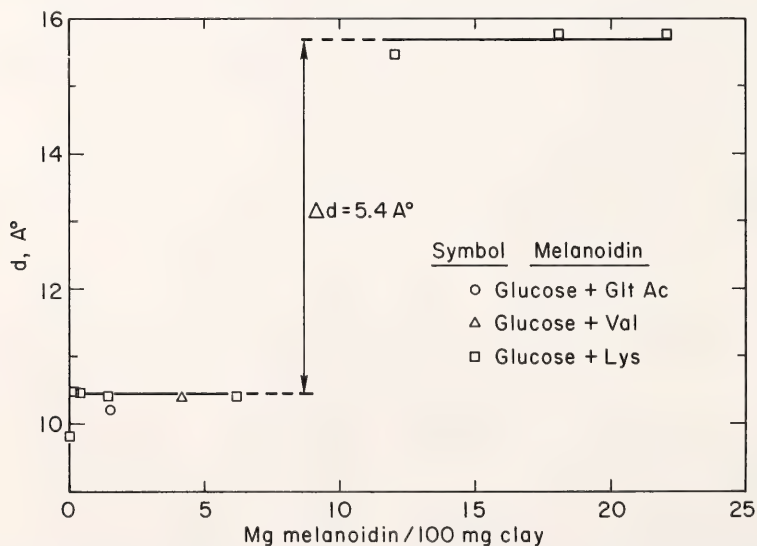


Fig. 171. Interbasal distances of washed montmorillonites from the adsorption isotherm experiments. Only the maximum melanoidin concentrations and corresponding spacings are given for clays reacted with glutamic acid and valine melanoidins. The percentages by weight of melanoidin on the clays are calculated values for unwashed clays.

equilibrated with distilled water so that the reversibility of the association reactions could be measured by comparing actual and theoretical wash losses. Systems with large partition coefficients exhibited irreversible uptake reactions (Table 68). The dependence of associa-

tion upon exchangeable ion and melanoidin acidity was similar to that observed at 50 mg/l. Only the lysine melanoidin intercalated the sodium clay, whereas all three melanoidins increased the interbasal spacing of the Fe³⁺ montmorillonite.

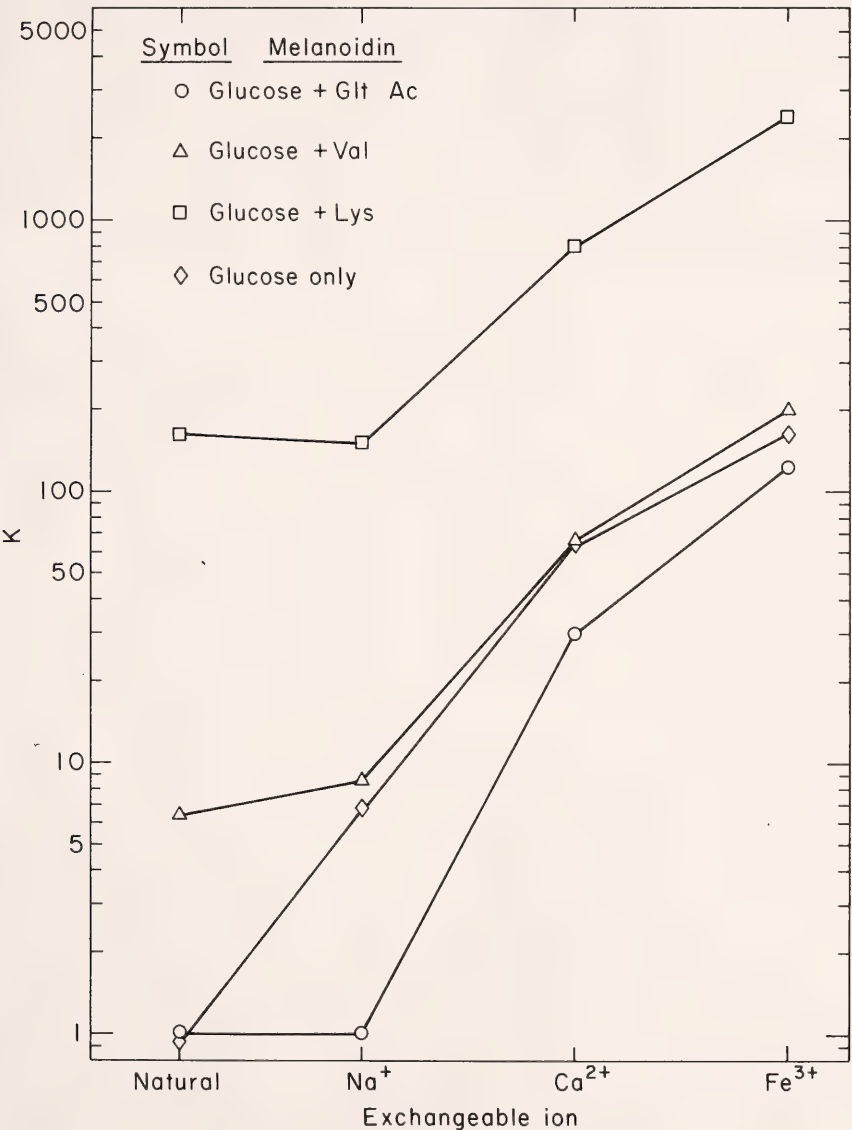


Fig. 172. Plots of partition coefficients (*K*) for melanoidins reacted with Na⁺-, Ca²⁺-, and Fe³⁺-saturated montmorillonites.

TABLE 68. Association of Na^+ , Ca^{2+} , and Fe^{3+} -Saturated Montmorillonites with Three Melanoidins

| Melanoidin | Ion | Melanoidin Concentrations at Steady State | | <i>K</i> | Theoretical Wash Loss (mg/100 mg clay) | Actual Wash Loss (mg/100 mg clay) | <i>d</i> (Å) |
|----------------------------|------------------|--|------|----------|---|--|-----------------|
| | | mg/100 mg clay | mg/l | | | | |
| Glucose + glutamic acid | Na^+ | 1.8 | 860 | 21 | 1.7 | 1.7 | 11.2 |
| | Ca^{2+} | 2.0 | 860 | 26 | 1.9 | 2.0 | 11.1 |
| | Fe^{3+} | 9.1 | 680 | 130 | 6.8 | 3.2 | 11.9 |
| Glucose + valine | Na^+ | 1.8 | 890 | 20 | 1.7 | 1.9 | 11.3 |
| | Ca^{2+} | 6.8 | 770 | 88 | 5.6 | 2.9 | 11.5 |
| | Fe^{3+} | 18 | 510 | 340 | 9.7 | 4.6 | 12.4 |
| Glucose + lysine | Na^+ | 14 | 620 | 230 | 9.0 | 2.8 | 15.6 |
| | Ca^{2+} | 24 | 380 | 630 | 9.4 | 3.1 | 13.6 |
| | Fe^{3+} | 30 | 220 | 1300 | 6.9 | 1.8 | 13.7 |

Abbreviations: *K*, partition coefficient; *d*, interbasal distance in Ångströms.

The mechanisms by which the melanoidins are bound to the various clays cannot be determined from the data at hand. Uptake of the polymer made from glucose only, however, indicates that nitrogen, and thus a center of positive charge, is not necessary for association of the melanoidins with Ca^{2+} and Fe^{3+} montmorillonites. Apparently, even negatively charged melanoidins can intercalate unit layers if exchangeable polyvalent cations are present (Theng and Scharpenseel, 1976).

The model studies indicate that 100- to 1000-fold concentrations of dissolved melanoidins on clay crystals are possible, especially when nitrogen-rich polymers or montmorillonites saturated with polyvalent cations are present. In natural environments under similar conditions, clay minerals could effectively collect and physically transport melanoidin polymers. Polymers bound between clay crystals would be exposed to a unique chemical environment in which reactions not obtained in the surrounding medium might occur.

It has yet to be proved conclusively that melanoidins are formed in any natural environment. It is known, however,

that marine humic substances exhibit high nitrogen contents (Nissenbaum and Kaplan, 1972), low aromaticity (Stuerner and Harvey, 1974), and low cation-exchange capacities (Rashid and King, 1970) in comparison to terrestrial humic substances. These chemical properties resemble those of melanoidins prepared in the laboratory (Hoering, *Year Book* 72, pp. 682-690; this study) and suggest that marine humic substances, in particular, may have a large melanoidin component. The low lignin concentrations (Hedges, *Year Book* 73, pp. 581-590) and high *pH*'s characteristic of ocean waters and sediments should also favor greater melanoidin concentrations.

If melanoidins are formed in the sea, the model experiments suggest that basic amino acids should preferentially combine with sugars to form nitrogen-rich polymers with a great affinity for clay minerals. These melanoidins could be extracted with ease from fine-grained sediments and isolated from more acidic polymers by electrophoresis. The polymers should bear a strong chemical resemblance to artificial melanoidins prepared by reacting sugars with a mixture of amino acids.

RELATIVE REACTION RATES AND
ACTIVATION ENERGIES FOR SOME
AMINO ACID REACTIONS*P. E. Hare*

Proteins in living organisms are composed of amino acids bonded by peptide linkages. Proteins that escape rapid microbial degradation are subject to a number of slow chemical changes during fossilization. These changes are of potential interest in the study of the diagenetic history of fossils. The reactions are directly influenced by several environmental factors, such as temperature, relative amount of H_2O present, pH , and eH . In this report data are presented on the relative rates of release of several amino acids from the hydrolysis of a soluble protein (gelatin) at temperatures from 25° to $150^\circ C$. These rates of release are compared with the rates of racemization and decomposition reactions of some of the same amino acids under the same conditions.

The Arrhenius equation relates the reaction rate to the temperature of a reaction. By observing the change in the rate constant with changes in temperature it is possible to use the Arrhenius equation to calculate the activation energy for the reaction. In this report the activation energies for release of amino acids during protein hydrolysis are compared with the activation energies for racemization and decomposition.

Methods

A solution of gelatin (Nutritional Biochemical Corporation) in 6 *N* HCl was prepared at a concentration of 500 mg per liter, and cysteic acid was added as an internal standard. From this stock solution (stored at $-20^\circ C$) 100 μ l aliquots were transferred to glass vials with Teflon-lined screw caps. The vials were flushed with nitrogen before capping. After incubation at the desired temperature ($\pm 1/2^\circ$) for a measured time the vials were attached to a rotary evaporator, and the excess HCl was evaporated. The gelatin was dissolved

in 6 *N* HCl in order to keep the pH constant during the course of the reactions and to accelerate the hydrolysis reactions so that they could be studied at relatively low temperatures. The residue was dissolved in 100 μ l of buffer at pH 2, and a 10 μ l aliquot was taken for amino acid analysis. Another aliquot was reacted with (+)-2-butanol and trifluoroacetic anhydride for gas chromatography of the *D,L* amino acid isomers (Hare and Hoering, *Year Book* 72, p. 690). The stock solution of gelatin in 6 *N* HCl showed a free amino acid content of less than 1 part in 300 after the evaporation and diluting steps. The unhydrolyzed protein was washed through the column with the basic buffer and did not interfere in any way with the determination of the free amino acids. At each selected temperature several samples were taken at various times to determine the rate of reaction for that temperature.

Results

The hydrolysis reactions yield measurable amounts of free amino acids at $25^\circ C$ within a few days. In 2 min of heating at $100^\circ C$ nearly 4% of the glycine in the gelatin is hydrolyzed to free glycine. Table 69 shows the results for a series of samples run at $100^\circ C$ for time periods of 2 min–1 hr. A series of samples incubated at $150^\circ C$ for increasing lengths of time to ensure complete hydrolysis and to account for labile amino acids was used to determine the composition of the gelatin.

The release of free amino acids during the hydrolysis of gelatin in 6 *N* HCl follows an apparent first-order rate law for most of the amino acids with (H+) and water activity held constant. Aspartic acid and glutamic acid are exceptions. The reaction rate of each amino acid released during hydrolysis has been found to be proportional to the fraction of that amino acid still peptide-bound. In Equation 1, the amount of a particular free amino acid, X , and the amount of that amino acid still peptide-bound, P (as determined by complete hydroly-

TABLE 69. Data from Gelatin Hydrolysis Series at 100°C from 2.5 to 60 Min*

| | Min at 100°C | | | | | | <i>k</i> (hr ⁻¹) | <i>t</i> _{1/e} (hr) | <i>t</i> _{1/2} (hr) |
|---------------|--------------|------|------|------|------|------|---------------------------------|---------------------------------|---------------------------------|
| | 2.5 | 5 | 10 | 20 | 30 | 60 | | | |
| Aspartic | 0.95 | 0.89 | 0.82 | 0.73 | 0.65 | 0.48 | 1.39 | 0.72 | 0.50 |
| Threonine | 0.98 | 0.95 | 0.93 | 0.88 | 0.83 | 0.69 | 0.38 | 2.72 | 1.88 |
| Serine | 0.96 | 0.92 | 0.87 | 0.77 | 0.70 | 0.48 | 0.73 | 1.37 | 0.95 |
| Glutamic | 0.97 | 0.93 | 0.87 | 0.77 | 0.70 | 0.50 | 0.71 | 1.4 | 0.97 |
| Glycine | 0.96 | 0.90 | 0.82 | 0.66 | 0.56 | 0.29 | 1.23 | 0.82 | 0.57 |
| Alanine | 0.96 | 0.91 | 0.84 | 0.69 | 0.63 | 0.39 | 0.93 | 1.07 | 0.74 |
| Valine | ... | ... | ... | ... | 0.95 | ... | 0.16 | 6.20 | 4.30 |
| Isoleucine | ... | ... | ... | ... | 0.94 | 0.85 | 0.17 | 5.95 | 4.12 |
| Leucine | ... | ... | 0.87 | ... | 0.79 | 0.52 | 0.64 | 1.58 | 1.09 |
| Phenylalanine | ... | ... | ... | ... | 0.72 | 0.48 | 0.69 | 1.44 | 1.0 |
| Lysine | ... | ... | ... | ... | 0.68 | 0.49 | 0.62 | 1.6 | 1.11 |
| Arginine | ... | ... | ... | ... | 0.71 | 0.54 | 0.61 | 1.64 | 1.14 |

* Fraction remaining as peptide bound. Calculated values of reaction rate constant, *k*, the 1/*e* life, *t*_{1/e}, and the half-life, *t*_{1/2}.

sis), are related to the specific rate constant *k* and time *t*:

$$\ln \frac{P_1 - X_1}{P_1} = -k_1 t. \quad (1)$$

In Equation 1, when

$$\frac{P - X}{P} = \frac{1}{e},$$

$$\ln \frac{1}{e} = -1 = -k \cdot t_{1/e}$$

$$t_{1/e} = \frac{1}{R}.$$

As the protein hydrolyzes, smaller peptides become prevalent, and it is likely that the rates of hydrolysis of the smaller units will be different from those for the intact protein. It is during the early stages of hydrolysis that the rates of release of the various amino acids would be expected to follow a simple rate law. Figure 173 shows the results for glycine at 90° and 100°C. The slopes are equal to the reaction rate constants *k* and are just the reciprocal of the 1/*e* life or *t*_{1/e}, the time for the concentration of peptide-bound amino acid to drop from 1 to 1/*e* or 0.37. The half-life *t*_{1/2} is equal to 0.693/*k*.

There is nearly an order of magnitude

difference in the release rates of the various amino acids during gelatin hydrolysis in 6 *N* HCl. Initially, aspartic acid has the fastest rate, but the rate slows down after about 20% of the aspartic acid has been released. At the various reaction temperatures, glycine was an order of magnitude faster in rate than was valine, the amino acid with the slowest release rate. The results of a number of studies on peptide-bond stability indicate that peptide bonds adjacent to valine and isoleucine are much more stable than bonds adjacent to glycine and serine (Hill, 1965).

Temperature Effects

The Arrhenius equation relates the reaction rate constant *k* to the temperature

$$k = Ze^{-E_a/RT} \quad (2)$$

where *k* = the rate constant; *E*_a = the activation energy; *R* = the gas constant, 1.987 cal deg⁻¹ mole⁻¹; *T* = the absolute temperature; *Z* = the Arrhenius frequency factor.

Equation 1 can be written

$$k = \frac{1}{t} \ln \frac{P}{P - X} \quad (1a)$$

Combining with Equation 2,

$$k = \left(\frac{1}{t}\right) \left(\ln \frac{P}{P-X}\right) = Ze^{-E_a/RT}$$

or

$$t = \frac{1}{Z} e^{-E_a/RT} \left(\ln \frac{P}{P-X}\right) \tag{3}$$

The time for any specific extent of reaction can be used instead of *k*. If the 1/*e* life *t*_{1/*e*} is used, Equation 3 becomes

$$t_{1/e} = \frac{1}{Z} e^{E_a/RT} \tag{4}$$

or

$$\ln t_{1/e} = (E_a/RT) - \ln Z \tag{4a}$$

or

$$\log t_{1/e} = (E_a/2.303RT) - \log Z \tag{4b}$$

A graph of log *t*_{1/*e*} against 1/*T* will give a line whose slope is *E*_{*a*}/2.303*R* if the Arrhenius equation is applicable.

Figure 174 shows the Arrhenius plot of log *t*_{1/*e*} versus 1/*T* for the release of the various amino acids. The Arrhenius equation relates the temperature and rate constant reasonably well for a change in the rate constant of over 5 orders of magnitude. Although there are significant differences in reaction rates among the various amino acids, there are no significant differences in their activation energies. The activation energies for hydrolysis are about 22–23 kcal/mole, although valine and isoleucine appear to have slightly higher activation energies than do the other amino acids.

The Arrhenius frequency factor *Z* for glycine, as calculated from the graph, is 10¹³. For glycine released during the

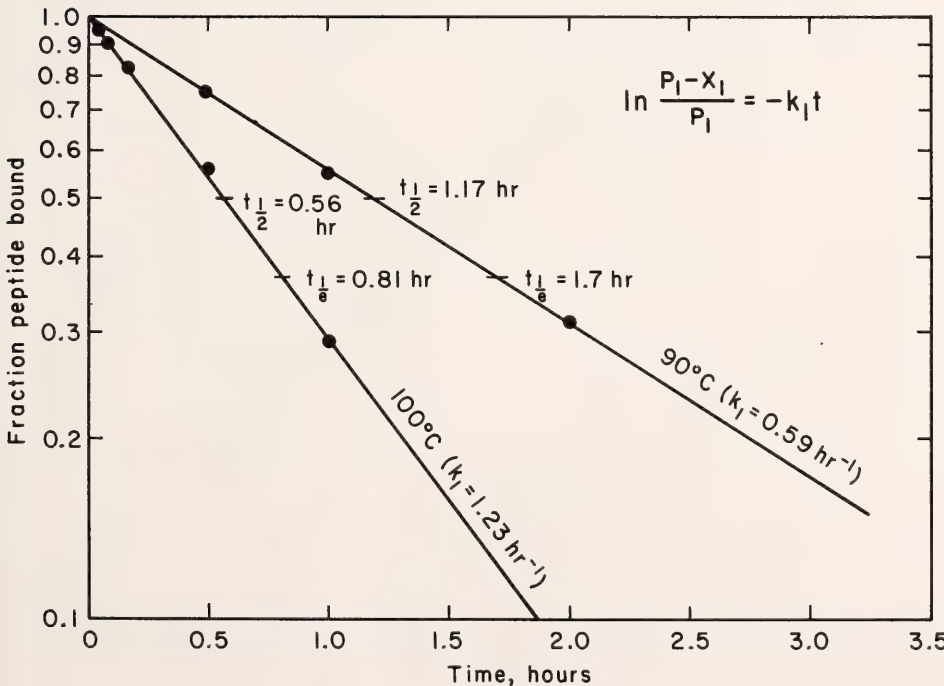


Fig. 173. Release of glycine during gelatin hydrolysis in 6 N HCl at 90° and 100°C. Slope of each curve equals the specific rate constant, *k*, for that temperature.

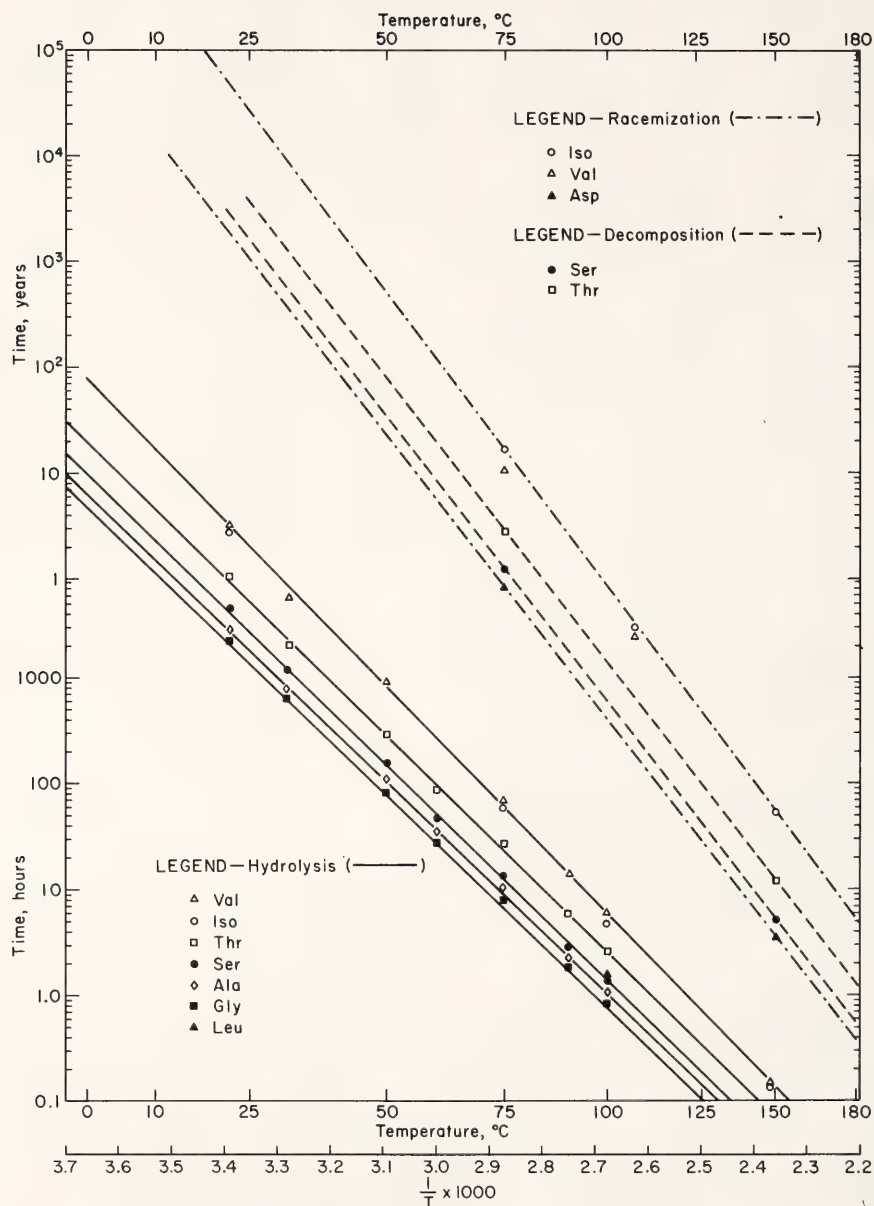


Fig. 174. Arrhenius plot of hydrolysis reactions of gelatin yielding various free amino acids. Also shown is a plot of aspartic acid racemization, isoleucine epimerization, and threonine and serine decomposition.

hydrolysis of gelatin in 6 *N* HCl, Equation 3 can be written

$$t_{1/e} \text{ (hr)} = 10^{-13} e^{11,080/T}$$

or

$$\log t_{1/e} \text{ (gly)} = 4810/T - 13 \quad (4c)$$

This equation accurately represents the experimental data obtained for glycine at various temperatures. Figure 174 also shows the Arrhenius plots for some of the racemization and decomposition reactions for threonine and serine. The activation energies for racemization of the various amino acids are significantly higher than for hydrolysis. Again there appears to be little difference in the activation energies for aspartic acid and isoleucine, the amino acids with the fastest and slowest rates of racemization. The activation energies for racemization are about 29–30 kcal/mole, about 7–8 kcal higher than for hydrolysis. The Arrhenius frequency factors are nearly an order of magnitude higher than for hydrolysis: 8.92×10^{13} for isoleucine and 4.36×10^{14} for aspartic acid.

The decomposition of threonine and of serine both follow a first-order rate equation and have activation energies of about 29,500 cal/mole. The frequency factor for serine is 3.19×10^{14} and for threonine, 1.22×10^{14} .

A reaction with an activation energy of 23.0 kcal/mole will have a rate constant approximately 4 or 5 times *slower* (depending on the temperature) than a reaction with an activation energy of 22.0 kcal/mole if both reactions have the same frequency factors. An increase in the frequency factor causes a proportional increase in the rate constant, as can be seen from Equation 2. The frequency factor can be interpreted in terms of an entropy of activation and a temperature-dependent function (Frost and Pearson, 1961), but in the temperature range 0°–150°C, of interest for geochemical and biochemical applications, the frequency factor can be considered a constant.

The data in this report are useful in evaluating the effects of sample preparation and treatment because 6 *N* HCl is used in dissolving fossil samples and hydrolyzing the remaining peptides. The extent of laboratory-induced changes is now readily evaluated. Appreciable hydrolysis can occur during the sample-preparation step unless it is done quickly at low temperatures.

The data presented here are also useful in estimating the rate of hydrolysis of proteins at various temperatures and in accurately determining the amount of degradation and racemization that accompanies this hydrolysis. This study has led to the routine adoption of a procedure for sample preparation that hydrolyzes a protein or peptide for 10–20 min at 155°C instead of the traditional 20–24 hr at 110°C used in most biochemical laboratories for protein hydrolysates.

Another procedure, generally requiring several days or a week, can be shortened to a few hours to determine the amino acid composition of a protein. When accurate compositional data are necessary for a protein, a series of samples is hydrolyzed for increasing lengths of time, generally up to 72 hr or longer. Slowly hydrolyzed peptide bonds such as those adjacent to isoleucine and valine are completely hydrolyzed only after several days of heating at 110°C. Labile amino acid residues such as threonine and serine are decomposed slowly and decrease in concentration. By plotting a graph of the composition of the protein at each hydrolysis time it is possible to extrapolate back to zero time for labile components like threonine and serine and to determine at the longer hydrolysis times the maximum concentrations of the slowly released residues such as isoleucine and valine. Hydrolysis at 155°C gives equivalent information and accuracy in a few hours instead of nearly a week. By reference to the Arrhenius plot, any equivalent combination of time and temperature can readily be determined for a given degree

of hydrolysis, racemization, and decomposition.

Comparison of reaction rates in 6 *N* HCl with reaction rates in neutral or slightly basic solutions and in fossils shows that although hydrolysis reactions proceed significantly faster in 6 *N* HCl, there is no significant difference in the activation energies for hydrolysis regardless of the environmental medium as long as water is present in excess for the reaction to proceed. The rate of acid hydrolysis is directly proportional to the hydrogen ion concentration (or activity) (Lawrence and Moore, 1951).

The activation energies for racemization and decomposition also appear to be independent of the environment. The activation energy for racemization is apparently the same in 6 *N* HCl as it is in shells and bone even though the rates of reaction vary considerably from one system to another. Therefore, for natural systems, activation energies determined from laboratory experiments should be applicable, and frequency factors and reaction rates need only to be determined for the natural environment.

Because it has been shown that reactions of significantly different activation energies proceed simultaneously in fossils, it should be possible to use these two general types of reactions to calculate both an effective temperature and a time for a fossil's diagenetic history. Before these measurements can be accomplished, the degree of departure from a closed system model will need to be evaluated.

MOLECULAR FOSSILS FROM THE PRECAMBRIAN NONESUCH SHALE

Thomas C. Hoering

Organic geochemistry has played an important role in describing the life that existed on earth before the onset of an abundant fossil record at the start of the Paleozoic era. A significant part of the work has been the discovery of ancient molecules that can be related to pre-

cursors found in living organisms (McKirdy, 1974); these organic compounds have been called "molecular fossils." Recent advances in experimental techniques and in the understanding of the diagenesis of organic molecules over long periods of time now make it possible to search for molecular fossils in Precambrian rocks with more certainty.

Well-preserved organic matter as old as the Precambrian is rare because most sedimentary rocks have been extensively metamorphosed; however, the Nonesuch shale exposed in the White Pine copper mine, White Pine, Michigan, is an exception (White and Wright, 1966). This highly carbonaceous, fine-grained shale contains mixed-layer minerals derived from clays and an aluminous serpentine. Although the upper temperature limit for the stability of these minerals is not known exactly, the evidence indicates that the rock has not been heated above 200°C. Radiometric dating of associated igneous rocks has shown that the shale is between 1.0 and 1.1 b.y. old. The Nonesuch shale is a sedimentary copper deposit, and the ore exists as sulfide minerals and native copper. The ore is not associated with hydrothermal activity or with faulting. A petroleum seep occurs within the copper mineralization, and the rock matrix contains well-preserved kerogen. Some features of the organic matter in this shale have been studied. It is highly probable that the petroleum originated in the shale and has not migrated from younger formations (Barghoorn, Meinschein, and Schopf, 1965; Eglinton *et al.*, 1966; Hoering, 1967). The petroleum is worthy of detailed examination because it represents the remains of life dating back one-fourth of geological time. Large quantities of it are available for study, and problems due to contamination by younger organic matter appear to be minimal.

Saturated hydrocarbons are very stable and represent the best classes of compounds to study for evidence of Precambrian life. The petroleum seep in the

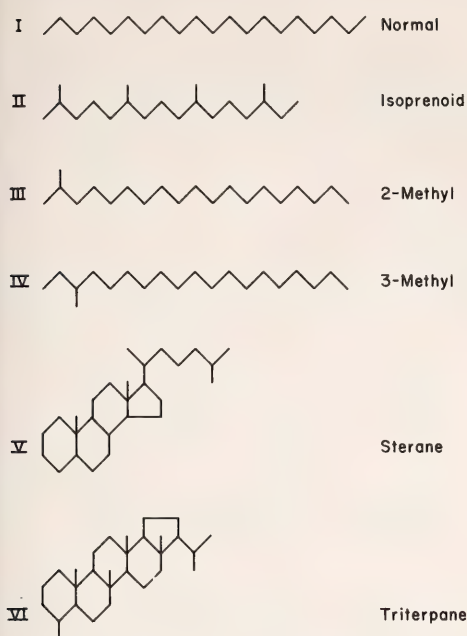


Fig. 175. Molecular structure of six saturated hydrocarbon molecular fossils. The probable sources of these compound types are as follows. (I) Normal: fatty acids and alcohols common to most microorganisms. (II) Isoprenoid (with 20 or less carbon atoms): phytol side chain of chlorophyll. (III, IV) 2- and 3-methyl substituted: bacterial lipids. (V) Sterane: sterols of eucaryotic organisms. (VI) Triterpane: minor triterpenoid constituents of photosynthetic microorganisms.

Nonesuch shale contains 61 wt % saturated hydrocarbons. Figure 175 gives the molecular structure of six of the best understood types and their biological precursors. The exact mechanism by which the precursors have been transformed into hydrocarbons is not known; in every case, however, a few plausible chemical reactions would be sufficient.

The mixture of molecules found in petroleum is one of the most complex in all of chemistry. An extensive separation is needed before pure compounds can be isolated and identified. Many methods for fractionating saturated hydrocarbons and identifying them are known, and two recent developments have made the present study possible. Hydrocar-

bons are chemically inert, but separation into classes based on molecular shape and size is possible by exclusion chromatography. Tandem gas chromatography-mass spectrometry is one of the most powerful tools available to the organic geochemist for identifying components of mixtures. In complex systems, however, the amount of data that is collected is too large for manual handling. It is possible, by means of computer-based data systems, to collect and store mass spectra continuously during a gas-chromatographic run. To use the data efficiently, programs for recalling the spectra and presenting them in numerical or graphical forms are employed.

Figure 176 outlines the separation scheme that was used on the petroleum seep. A large quantity (13.7 g) of the crude oil was collected by rinsing it from specimens of the wall rock with benzene and subsequently evaporating the solvent. The general strategy of the separation is as follows. The saturated hydrocarbons are isolated by silica gel chromatography and separated into four major classes on the basis of molecular shape and size by inclusion into crystals of synthetic zeolite, urea, and thiourea (adduct formation). Each of these classes is further fractionated into six or more subgroups by exclusion chromatography on a 3 m by 15 mm column of Sephadex LH-20 expanded in benzene-methanol. The separations are monitored at each step by gas-liquid chromatography. When necessary, an additional step of exclusion chromatography on an alumina column is made to simplify the mixtures. If the subgroups are still too complex to give unambiguous mass spectra, individual pure compounds are isolated by multiple, preparative gas chromatography on a series of substrates.

As the separation proceeded, it became evident that over half of the fractions were too complex to be resolved by existing techniques. The only practical course was to focus on the fractions that would contain the six classes of hydrocarbons shown in Fig. 175.

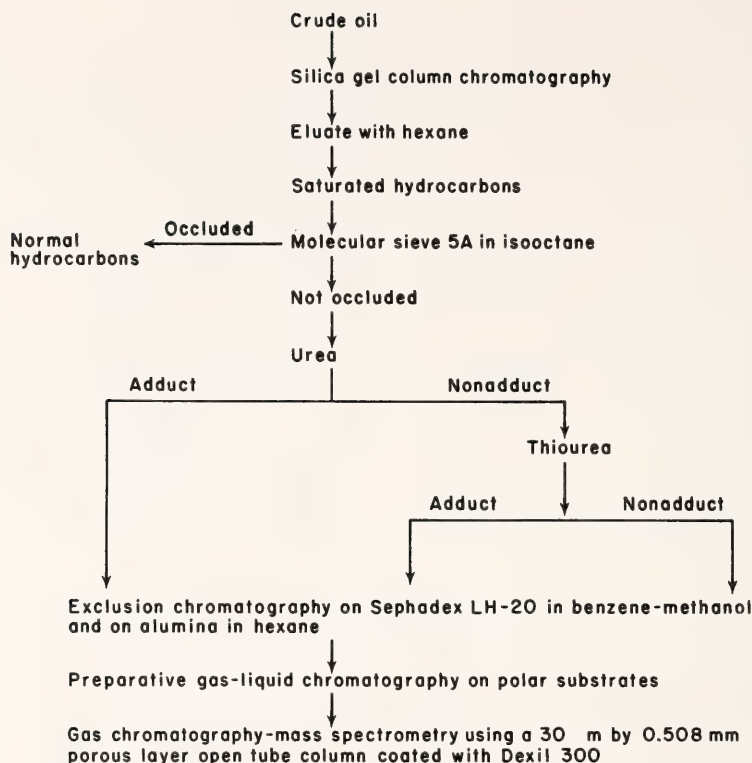


Fig. 176. Separation scheme used to fractionate saturated hydrocarbons.

Some results are illustrated by the gas chromatograms of Figs. 177 to 181. Figure 177 shows a chromatogram of the total hydrocarbons isolated from the petroleum by silica gel chromatography. It is dominated by peaks due to the normal alkanes (I of Fig. 175), which constitute 21 wt %. The normal alkanes were easily removed by occlusion into molecular sieve 5A, a synthetic zeolite. The remaining compounds gave the exceedingly complex chromatogram shown in Fig. 178. When this mixture was exposed to urea crystallizing from a benzene-methanol solution, 27 wt % of the initial hydrocarbons were precipitated. This adduct is known to contain linear molecules having a small amount of branching, such as III and IV of Fig. 175. The urea adduct was fractionated by exclusion chromatography, and fraction 4, which amounted to 8.6 wt % of

the initial hydrocarbons, was isolated. It gave the chromatogram shown in Fig. 179. After additional separation on alumina and preparative gas chromatography of selected peaks, the identifications shown in the figure were made.

The remaining mixture was then exposed to thiourea crystallizing from a chloroform-methanol solution, and 7.2 wt % of the initial hydrocarbons were precipitated. This operation is known to separate isoprenoid hydrocarbons and certain sterane hydrocarbons (structures II and V of Fig. 175). The thiourea adduct was recovered and fractionated by exclusion chromatography. Fraction 8, having 1.2 wt % of the initial hydrocarbons, was isolated. The calibration of the exclusion column with pure compounds showed that both isoprenoid and sterane hydrocarbons, if present, would be concentrated in it. The gas chromat-

ogram of Fig. 180 and accompanying identifications show that a homologous series of isoprenoid hydrocarbons is present, but no trace of steranes could be detected. The identification of the

isoprenoids was verified by the coinjection technique. Pure synthetic isoprenoid hydrocarbons are not available for comparison. The homologous series that exists in the Green River shale has been

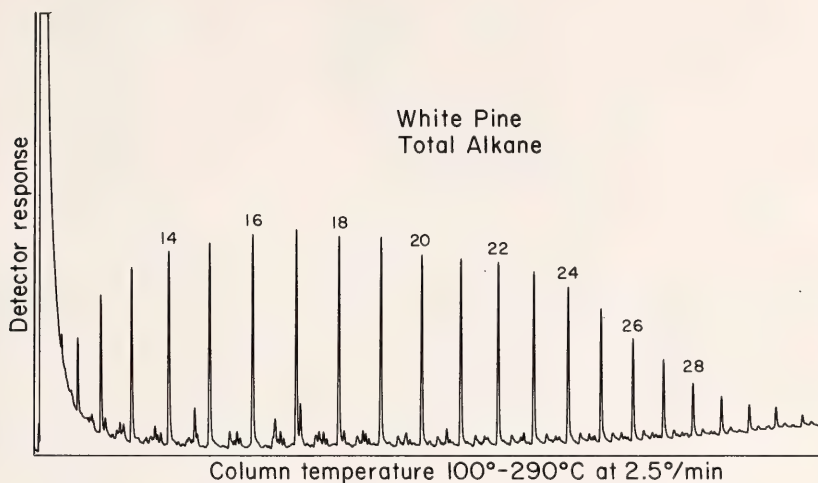


Fig. 177. Gas chromatogram of total saturated hydrocarbon fraction from oil seep in None-such shale at the White Pine locality. The chromatograms in Figs. 176-180 were made with a 90 m by 0.75 mm i.d. glass, porous-layer, open-tube capillary column coated with SE-30. A short precolumn of 0.160 mm i.d. packed with 3% SE-30 was used. No stream splitting was employed. The helium flow rate was 8 cc per min. The column temperature was programmed linearly from 100° to 290°C at a rate of 2.5°/min and held isothermally at the upper limit for 20 min. The prominent peaks are due to normal hydrocarbons with carbon numbers as indicated on the chromatogram.

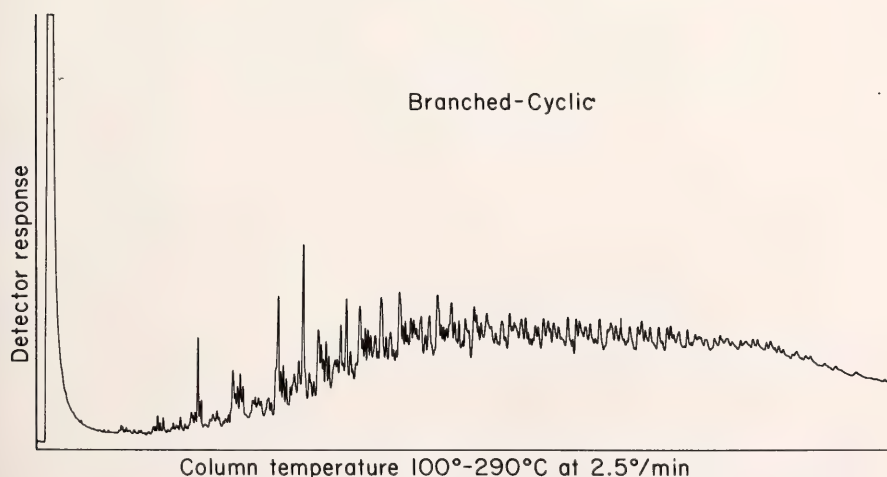


Fig. 178. Gas chromatogram of saturated hydrocarbons after treatment with molecular sieve 5A to remove normal hydrocarbons.

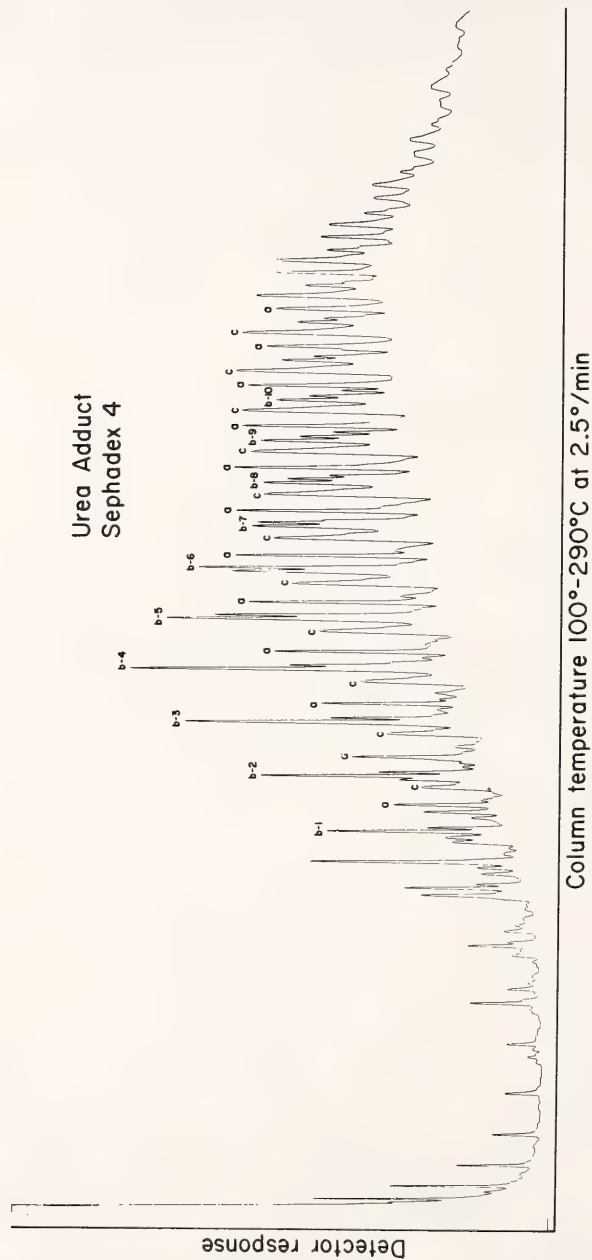


Fig. 179. Gas chromatogram of hydrocarbons that formed an adduct with urea and were eluted in fraction 4 from the Sephadex column. Peaks labeled with *a* are due to normal hydrocarbons not completely removed by molecular sieve 5A. The labeled peaks run from $C_{16}H_{34}$ to $C_{30}H_{62}$. The sets of two peaks designated *b-1* to *b-10* are due to 2-methyl and 3-methyl substituted hydrocarbons and run from $C_{17}H_{36}$ to $C_{31}H_{64}$. The broad peaks labeled *c* are due to unresolvable mixtures of monomethyl and dimethyl substituted linear hydrocarbons with the branching points in interior positions of the carbon chain.

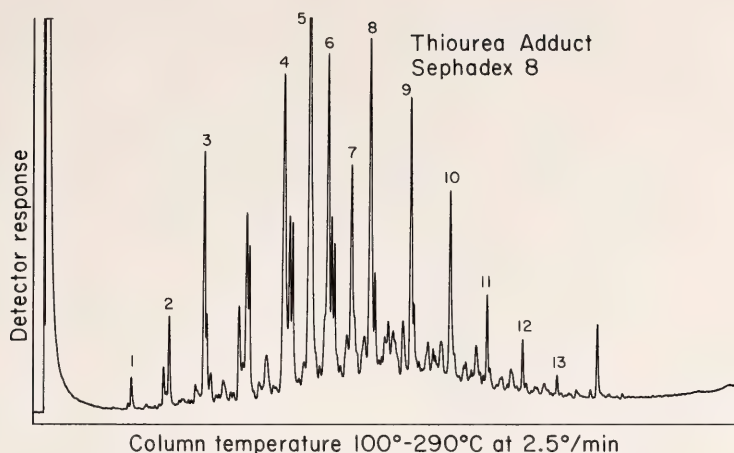


Fig. 180. Gas chromatogram of hydrocarbons that formed a thiourea adduct and were eluted in fraction 8 from the Sephadex column. Identifications of peaks are as follows. Isoprenoid hydrocarbons: (1) 3,8,13 trimethyl undecane; (2) 3,8,13 trimethyl dodecane (farnesane); (3) 3,8,13 trimethyl tridecane; (4) 3,8,13 trimethyl pentadecane; (5) 3,8,13,18 tetramethyl pentadecane (pristane); (7) 3,8,13,18 tetramethyl hexadecane (phytane). Alkyl cyclohexanes: (6) *n*-undecyl cyclohexane; (8) *n*-dodecyl cyclohexane; (9) *n*-tridecyl cyclohexane; (10) *n*-tetradecyl cyclohexane; (11) *n*-pentadecyl cyclohexane; (12) *n*-hexadecyl cyclohexane; (13) *n*-heptadecyl cyclohexane.

studied intensively, however, and the structures of its members are known. A sample was isolated from the Green River shale and injected simultaneously into the gas chromatograph with a portion of fraction 8 from the Nonesuch petroleum seep. The isoprenoid components of the two sets eluted at exactly the same time and gave identical mass spectra.

The remaining hydrocarbons that did not form a stable adduct were extremely complex and did not yield appreciably simpler fractions when separated by exclusion chromatography. Figure 181 shows the gas chromatogram of one of the fractions. This mixture is too complex to be resolved.

There was no indication in any of the fractions studied of the presence of sterane and triterpane hydrocarbons. A more careful search was made using mass chromatography. In this technique, the mass spectrometer is used as a very specific and sensitive detector to monitor the output of the gas chromatographic column. The spectrometer is set

to detect a specific ion that is characteristic for a class of compounds. Ions at mass 217 and 191 are prominent and unique features of the mass spectra of steranes and triterpanes, respectively. Although nanogram quantities of these compounds are detectable by this technique, no trace of them was found in any of the fractions at gas chromatographic retention times where they are expected to elute. It can be concluded that they constitute less than 50 ppm of the hydrocarbons in the Nonesuch oil seep.

The molecular fossil concept is powerful for studying paleobiochemical processes. Organic molecules can exist in many arrangements (isomers), but biological processes are very selective and only a few of the possible arrangements are actually used. On the other hand, diagenetic alteration of organic matter over long periods of time is relatively nonselective and produces a complex suite of isomers. There is a marked selectivity in the structures of some hydrocarbon isomers preserved in the

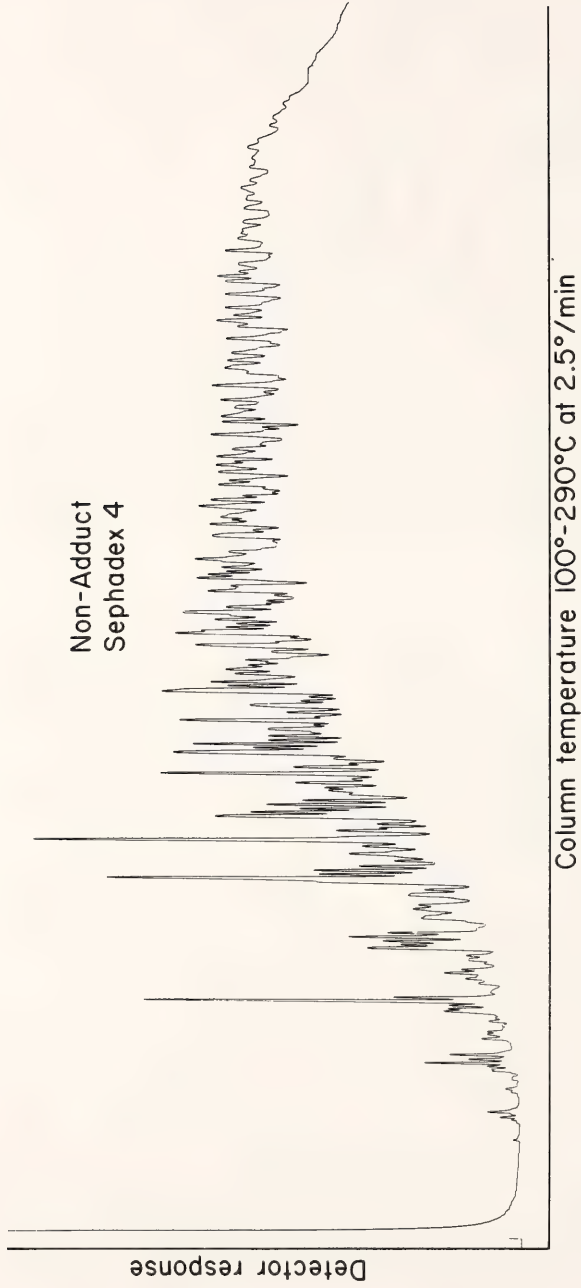


Fig. 181. Gas chromatogram of hydrocarbons not forming a stable adduct and eluting in fraction 4 from the Sephadex column.

Nonesuch shale. For example, there are over 2 million possible isomers with the formula $C_{20}H_{42}$, yet only four of them (normal, isoprenoid, 2-methyl, and 3-methyl) have an appreciable concentration. These compounds are all molecular fossils. Other fractions are very complex and seem to have been diagenetically altered. The fossil record has been obscured.

The presence of an abundant amount of normal hydrocarbons indicates that lipid synthesis was prevalent a billion years ago and had many of the same properties it has had subsequently. Isoprenoid hydrocarbons with less than 20 carbon atoms point clearly to the widespread use of chlorophyll as a photosynthetic pigment. The preponderance of 2-methyl and 3-methyl substituted hydrocarbons in the urea adduct over all of the other possible positional isomers suggests, but does not prove, a large contribution of bacterial lipids. The uncertainty arises because the mechanism of the diagenesis of organic matter is not well understood. Although it is believed that nonbiological transformations would not preferentially produce this pair of isomers, the hypothesis is not well documented.

There are limitations at present on the use of hydrocarbons as molecular fossils. Even though an extensive separation scheme was used in this study, only a minor fraction of the hydrocarbons could be identified. The mixtures were extremely complex, and pure synthetic standard compounds are lacking. Some

major classes of compounds were identified (the internally branched hydrocarbons in Fig. 179 and the cycloalkanes in Fig. 180) but could not be related to known biological precursors. Possibly their source lies in nonbiological transformation during diagenesis.

The low concentration of sterane hydrocarbons is puzzling. Such compounds are fairly common in rocks of more recent geological age, and they have probably been derived from sterols known to exist in unicellular organisms. The chemical stability of steranes over long periods of time under geological conditions is not well established. Possibly they have been dehydrogenated into aromatic hydrocarbons, and a search through this fraction of the petroleum seep may give a clue. Sterols are interesting compounds for evolutionary studies in the Precambrian. They require molecular oxygen for their synthesis and are indicators for aerobic metabolism. However, the geochemistry of sterols and corresponding sterane hydrocarbons is not well enough known for speculations on the nature of the Precambrian atmosphere based on these studies alone.

The organic matter in the Nonesuch shale represents a unique opportunity for Precambrian studies and forms a baseline with which to compare results obtained on older rocks that have not been so well preserved. It is evident that a number of questions must be answered before the molecular fossil concept can be extended to earlier parts of the earth's history.

GEOCHRONOLOGY

RESPONSE OF U-Pb ZIRCON AND Rb-Sr TOTAL ROCK SYSTEMS TO LOW-GRADE REGIONAL METAMORPHISM IN PROTEROZOIC IGNEOUS ROCKS, MOUNT ISA, AUSTRALIA

R. W. Page

Many geochronological studies have employed comparative isotopic dating techniques in both magmatic and high-

grade metamorphic terrains as a means of testing the significance and behavior of the Rb-Sr, U-Pb, and K-Ar methods. In contrast the present test involves a very common Proterozoic setting in which low-grade regional metamorphism has affected a sequence of volcanic rocks and intrusive granites. The U-Pb zircon work undertaken during the past year and Rb-Sr data acquired earlier, together

with earlier published K-Ar ages (Richards, Cooper, and Webb, 1963), are evaluated to determine which system(s) can record geologically meaningful ages in the low-grade metamorphic environment.

The approach using Rb-Sr total rock isochrons is based on the widely demonstrated realization that a collinear array of isotopic data on a $^{87}\text{Rb}/^{86}\text{Sr}$ versus $^{87}\text{Sr}/^{86}\text{Sr}$ plot can be interpreted to provide the age of crystallization of co-genetic samples from an intrusive or volcanic suite. A long-standing problem, described by several workers (Fairbairn *et al.*, 1966; Compston, Crawford, and Bofinger, 1966; Lanphere, 1968; Fairbairn and Hurley, 1969; Cormier, 1969; Hart and Davis, 1969; Zartman and Marvin, 1971; Peterman *et al.*, 1972; Charlot, 1976; Bickford and Mose, 1976), is the application of the technique to slightly altered Precambrian igneous rocks, especially acid volcanic rocks, in regions where no obvious post-crystallizational metamorphic disturbances are found. Burial metamorphism or other low-grade metamorphism produces only minor mineralogical changes in acid rocks, and in the absence of independent evidence these changes can just as well be ascribed to devitrification or deuteric alteration. This petrographic ambiguity, together with the fact that finer grained acid rocks are peculiarly susceptible to drastic isotopic disturbance, could lead to the determination and interpretation of Rb-Sr isochron ages that are considerably younger than actual ages of igneous crystallization.

Geological field relationships of low-grade meta-acid volcanic rocks and granites at Mount Isa, northwest Queensland, Australia, and Rb-Sr total rock measurements made on those rocks at the joint Australian National University-Bureau of Mineral Resources isotope laboratory in Canberra had revealed a number of spurious isochrons with large and unrealistic age spreads, as well as conflicts with unequivocal stratigraphic evidence and high and

variable initial $^{87}\text{Sr}/^{86}\text{Sr}$ values. These difficulties, evidently due to partial open-system behavior of Rb-Sr total rock systems, led to the present U-Pb zircon work, aimed at determining ages of volcanism and intrusion. The definitive stratigraphic order established (see below), especially in the basement volcanic succession (Derrick, Wilson, and Hill, 1976), affords a unique opportunity to test the geological validity of high-precision U-Pb zircon measurements. If this independent age control is successful, a more adequate petrogenetic interpretation of the high initial $^{87}\text{Sr}/^{86}\text{Sr}$ values and other unusual features associated with the Rb-Sr data will be possible.

Geological Background

Proterozoic rocks in the Mount Isa region lie in a north-south structural belt that is part of the eastern margin of the Australian Precambrian shield. The oldest known rocks occur in a central basement volcanic sequence cut by early granites, which in turn are overlain unconformably by eastern and western sedimentary-volcanic successions that are cut by later granites (Carter, Brooks, and Walker, 1961). The Mount Isa group, containing the well-known Mount Isa Ag-Pb-Zn deposit, is part of the western succession. Within the 5000-m-thick basement sequence (Fig. 182) there exist an older (Leichhardt metamorphics) and a younger (Argylla formation) acid volcanic suite, separated from each other by extrusive metabasalts (Magna Lynn metabasalt). The older acid volcanic unit is intruded by a multiphase, largely concordant batholith (Kalkadoon granite), which is considered to be unconformably overlain by the Magna Lynn metabasalt. The sedimentary and volcanic successions (about 7000 m thick) that unconformably overlie these basement units are intruded in parts by several later granitic bodies, one of which (Wonga granite) is examined in this work. In the upper part of the western geosynclinal succession is

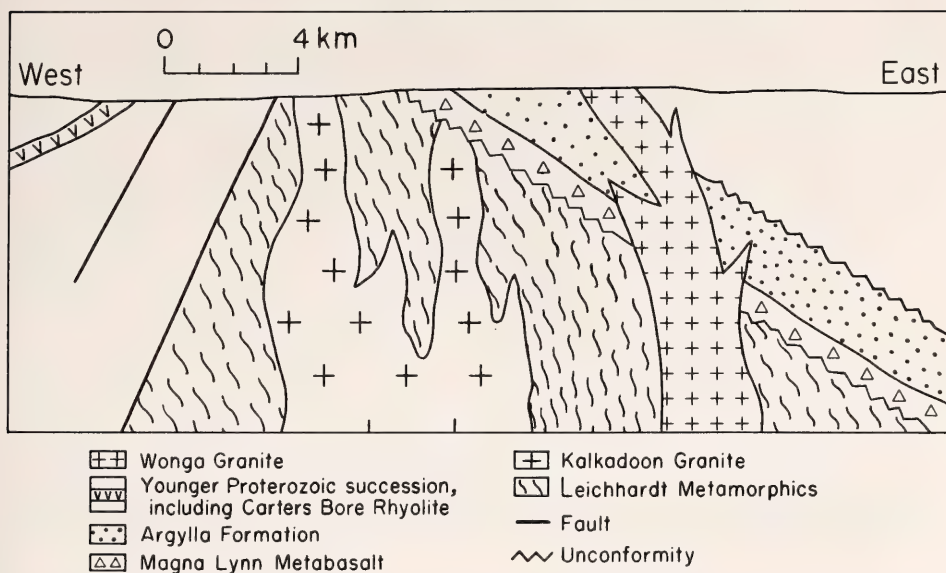


Fig. 182. Schematic E-W cross section (looking north) of the geological relationships within the Mount Isa basement sequence, the younger Proterozoic succession, and intrusive granites.

a third important acid volcanic horizon (Carters Bore rhyolite), stratigraphically the youngest unit now investigated. The K-Ar mica ages (Richards, Cooper, and Webb, 1963) determined on some of the granites and schists all lie close to 1400 m.y., irrespective of stratigraphic position, thus providing a minimum age for the regional metamorphism. The general metamorphic grade is low- to middle-greenschist facies.

Rb-Sr Data

A summary of the Rb-Sr data obtained in Canberra is as follows. Ages were calculated with the 1.39×10^{-11} yr⁻¹ decay constant of ⁸⁷Rb. At each outcrop site clustered sampling was employed so that individual total rock isochrons were obtained for several sites within each unit. For rhyodacites and dacites (some of which may be partly pyroclastic) from the Leichhardt metamorphics (the example given in Fig. 183) the apparent isochron ages at each site range from 1840 to 1690 m.y., with younger isochrons having higher extrapolated initial ⁸⁷Sr/⁸⁶Sr intercepts of up

to 0.72. Treating all the data together, a regression like that of McIntyre *et al.* (1966) gives an indicated age of 1750 ± 40 m.y. with an initial ⁸⁷Sr/⁸⁶Sr of 0.7105 ± 0.0016 (95% confidence limits), but even visual inspection of these pooled data (Fig. 183) makes it clear that the analyses do not fit a single isochron.

With respect to an 1843-m.y. reference isochron, equivalent to the oldest indicated age from one site, an apparent downward curvature of the data points with increasing Rb/Sr is seen. Model ages for each total rock sample are clearly dependent on Rb/Sr and also show correlation with Sr content; samples with Sr concentrations greater than 100 ppm are relatively less disturbed than those with lower Sr concentrations. There is no similar correlation with Rb and no apparent relationship between the extent of isotopic disturbance and the degree of petrographically visible alteration.

Several phases of the Kalkadoon granite yielded individual Rb-Sr total rock isochron ages between 1860 and

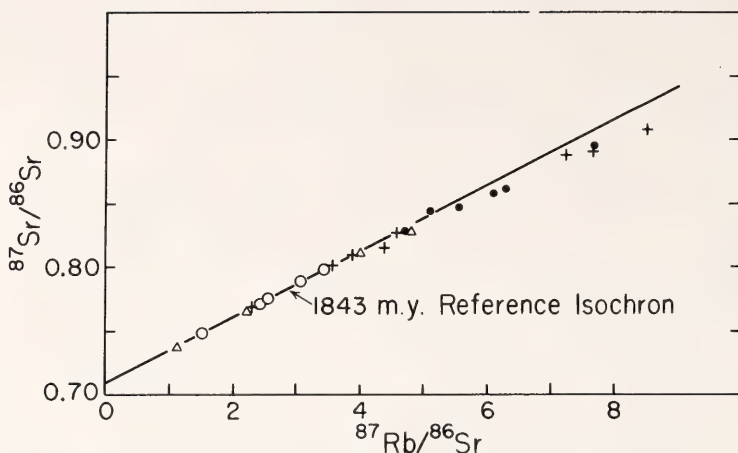


Fig. 183. Rb-Sr isochron plot of 23 acid volcanic total rock samples from the Leichhardt metamorphics. Four outcrop sites are represented by the four different types of data points. The 1843 m.y. reference slope is the fitted isochron of McIntyre *et al.* (1966) only to the five data points marked by open circles.

1680 m.y., again with generally high and variable initial $^{87}\text{Sr}/^{86}\text{Sr}$ (0.710–0.730). Disturbed Rb-Sr rock systems are again manifest as the data points associated with each result do not fulfill basic isochron assumptions. For the Argylla formation acid volcanic rocks, the next youngest suite, it was found that the total rock Rb-Sr results are similar in pattern to that for the Leichhardt metamorphics. Two pooled isochron ages of 1575 ± 33 m.y. (initial $^{87}\text{Sr}/^{86}\text{Sr} = 0.714 \pm 0.005$) and 1610 ± 35 m.y. (0.720 ± 0.005) are found in the Argylla lavas, but partly curved or rotated isochrons are again evident on close examination of the data from each site. The Wonga granite that intrudes the Argylla formation volcanic rocks yields a Rb-Sr isochron age of 1665 ± 16 m.y. with a high initial $^{87}\text{Sr}/^{86}\text{Sr}$ of 0.731 ± 0.006 ; at another site this granite gives a somewhat older but poorly defined isochron age of about 1740 m.y. Both ages are in conflict with the Argylla formation ages.

Other relevant Rb-Sr data apply to the youngest acid volcanic unit, the Carters Bore rhyolite. Fresh samples of this unit are known at only one locality, and as rocks from this site give no dis-

persion in Rb/Sr ($^{87}\text{Rb}/^{86}\text{Sr} = 64$), only a model (maximum) age of 1585 m.y. could be determined.

U-Pb Zircon Geochronology

Some of the same outcrops examined in the Rb-Sr dating were resampled for U-Pb zircon work. The hydrothermal dissolution and chemical techniques of Krogh (1973) and two-bottle reagent stills of Mattinson (1972) were employed. Single Re filament Pb analyses, using silica-gel as an activator with H_3PO_4 , and U analyses, using Ta_2O_5 with H_3PO_4 , were performed on the 9-in NIMA mass spectrometer at the Department of Terrestrial Magnetism. Replicate analyses of the National Bureau of Standards Equal Atom Lead Isotopic Standard 982 showed a downward mass discrimination of 0.09% per mass unit relative to the certified value. This deviation is essentially the same as that reported for the same instrument by Krogh and Davis (*Year Book* 73, p. 569). In most of the analyses, 0.001–0.002 g of zircon was used per dissolution, but smaller quantities, as low as 0.00007 g (giving uncorrected $^{206}\text{Pb}/^{204}\text{Pb}$ of 1230), were analyzed. Measured total Pb processing blanks (includ-

ing column chemistry) were from 0.1 to 0.2×10^{-9} g, and two Pb loading blank determinations were 0.006 and 0.007×10^{-9} g. The U-Pb ages are calculated with the decay constants of Jaffey *et al.* (1971). Most of the measured $^{207}\text{Pb}/^{235}\text{U}$ values have a 2σ error of better than 0.015% , and the U/Pb values, about 0.5% .

Zircons from three volcanic rocks from the oldest unit in the Mount Isa basement sequence, the Leichhardt metamorphics, were separated into fractions according to size and magnetic susceptibility; analyses of these fractions are plotted on the U-Pb concordia diagram (Fig. 184). Zircons from these three separate rocks show distinct but varying

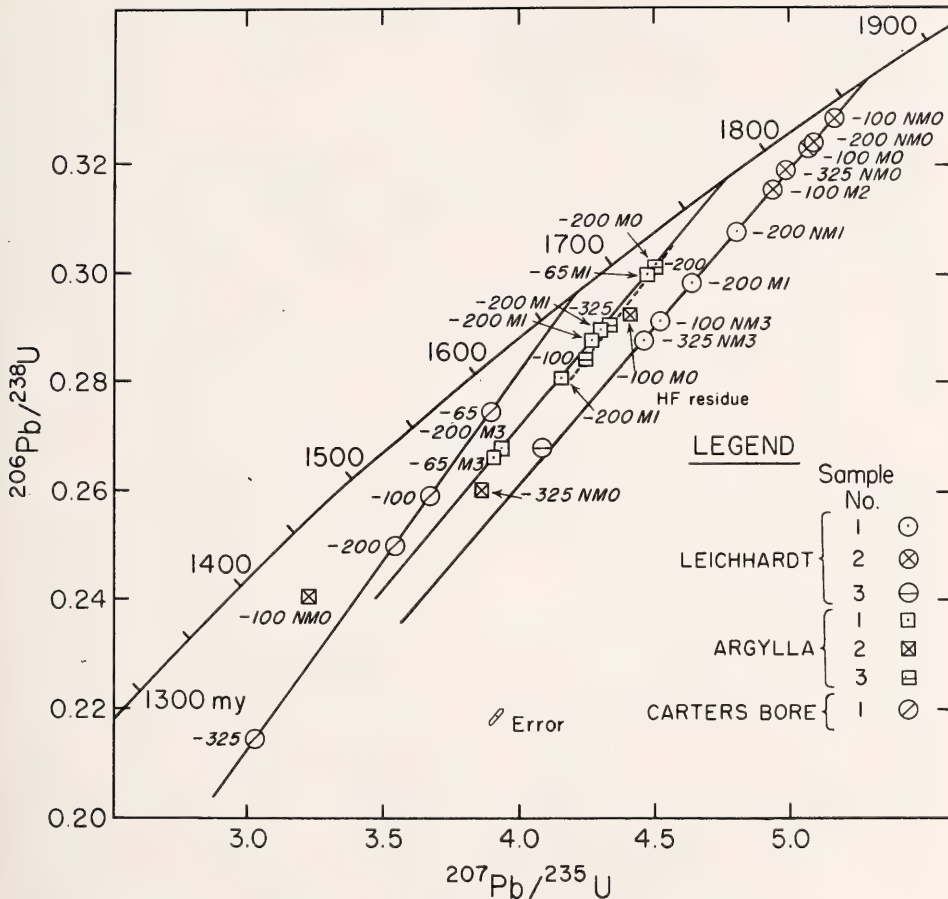


Fig. 184. U-Pb concordia diagram for zircons from three acid volcanic sequences at Mount Isa. Symbols used relate to the three different rocks from each of the Leichhardt metamorphics and Argylla formation and the single rock from Carters Bore rhyolite. The numbers -65, -100, etc., are the mesh size of each zircon fraction; size fractions of -65 + 100, -100 + 200, -200 + 325 are designated -65, -100, -200, respectively. Magnetic (M) and non-magnetic (NM) splits are indicated after each size fraction, together with the tilt angle (0° , 1° , 2° , 3°) of the Frantz isodynamic separator. Where magnetic properties are not specified, the least magnetic fraction is implied. Solid lines are straight linear regressions of the data from each sequence; the broken line is for the three zircons from Argylla sample 3.

degrees of lead loss, and pooled together these data give a discordia array with an upper intercept of 1865 m.y., interpreted as the age of crystallization of the zircon. It is geologically reasonable that the discordia age intercept of 1870 m.y. given by the five fractions from sample 2 (about 1500 m stratigraphically below sample 1) is truly distinct from the sample 1 discordia that has an upper intercept of 1858 m.y. The inferred 12 m.y. age difference is analytically reasonable, but would be best substantiated by at least one more independent discordia age from the same sequence. Of overriding importance at present, however, is the fact that the pooled zircon results point to an age of Leichhardt volcanism of 1865 m.y. with an analytical error probably less than 5 m.y. This age is more than 100 m.y. older than the pooled Rb-Sr isochron age but is experimentally indistinguishable from the 1840 ± 36 m.y. indicated by the steepest (low Rb/Sr) sector of the Leichhardt Rb-Sr isochron (Fig. 183). As the zircons themselves are euhedral and generally show a pattern of euhedral internal zonation, there is little possibility that the upper intercept age of the size and magnetic fractions reflects other than the time of primary magmatic crystallization. The one zircon analysis of Leichhardt sample 3 (from the Blockade area 20 km south of samples 1 and 2) is entirely consistent with 1865 m.y. pooled discordia age, demonstrating that the volcanic rocks in this region are coeval with those in the type section to the north.

U-Pb data from sized and magnetically split zircon fractions from four Kalkadoon granite samples are shown in Fig. 185. A limiting factor to interpretation of these data is that not more than two fractions from each rock have been analyzed. Nevertheless, the approximate collinearity of the five fractions from samples 3, 5, and 6 points to a simple zircon chord having an upper intersection age of 1861 m.y. The two fractions from sample 2 are more dis-

cordant than any of the others and cannot be adequately interpreted; the two-point chord joining them has an upper intersection equivalent to 1877 m.y., but it is just as likely that they may have a younger age, defined by a chord subparallel to the 1861 m.y. discordia. No detailed conclusions can be drawn about the relative ages of the analyzed Kalkadoon granite zircons, but their general linear distribution is indicative of an age of crystallization close to 1860 m.y.

Attempts were made to find zircon in samples from the Magna Lynn metabasalt that unconformably overlies the Kalkadoon granite, but none was found in the two samples so far examined. Porphyritic rhyolites and rhyodacites in the next youngest acid volcanic unit, the Argylla formation, yielded euhedral, elongate zircon crystals generally free of inclusions with characteristic internal magmatic zoning. The best-fit chord through the seven U-Pb data points of sample 1 (Fig. 184) has an upper intersection with concordia at 1777 m.y. Linearity of the points for the size and magnetic fractions indicates that the error in this age intercept (visually estimated) is a few million years at the most. The igneous character of these rocks, their low-grade metamorphism, and the systematic lead-loss pattern described by the discordia are again evidence that only one primary igneous population of zircon is present. This result, considered to be the age of volcanism and zircon crystallization, is in accord with the other U-Pb ages and the known geological relationships, but as found with the Leichhardt data, the Argylla U-Pb zircon age is about 10% higher than the Rb-Sr isochron ages. A similar but less precisely determined U-Pb age of 1772 m.y. is given by the three-point zircon chord for another of the Argylla lavas (sample 3). This sample has more than 10% secondary biotite, almost certainly crystallized at the time of regional metamorphism, the minimum age of which is 1400 m.y. As with the other examples, the zircon lead-

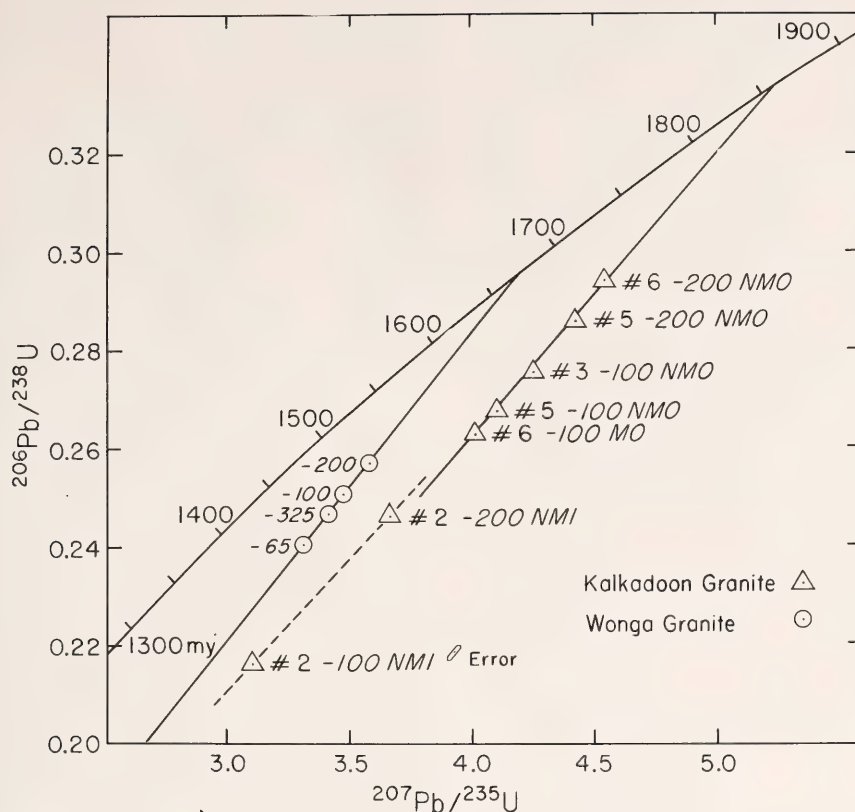


Fig. 185. U-Pb concordia diagram for zircons from the Kalkadoon granite and Wonga granite, Mount Isa. The sample numbers of the four Kalkadoon granite rocks (2, 3, 5, 6) are shown; other symbols are same as in Fig. 184. An average 2σ error box is indicated.

loss trajectories show no indication of this late Proterozoic metamorphic disturbance.

The foliated Wonga granite mass that postdates the Argylla formation lavas yields plentiful zircons whose morphology is similar in most respects to that of the Wonga zircons described by Joplin, Rudowski, and Abbott (1962). Unlike the euhedral Kalkadoon granite zircons, most Wonga granite zircons have rounded-off terminations suggestive of magmatic resorption. The U-Pb analyses of four size fractions of the least magnetic varieties are shown in Fig. 185. The linear distribution of these data and the resultant chord, the upper

intercept being 1671 m.y., points to an interpretation of a simple primary crystallization age. This result is entirely consistent with the geological relationships between the Wonga granite and the 1780-m.y. Argylla formation lavas and is close to the well-defined Rb-Sr total-rock isochron age of 1665 ± 16 m.y., which had a high initial $^{87}\text{Sr}/^{86}\text{Sr}$ of 0.731. The total rock sample from which the zircon was extracted, however, is from the second site, which gave the poorly defined 1740-m.y. Rb-Sr isochron. If the latter result is substantiated, an argument could be made that the Rb-Sr system is preserving an inheritance of an earlier differentiation

and cooling episode some 70 m.y. prior to the 1670-m.y. zircon crystallization age. This interpretation accords well with the most likely explanation of the high initial Sr isotope ratio of 0.731 found for the 1665-m.y. isochron. Such an initial ratio could have been obtained by a 1665-m.y. remobilization and Sr isotopic homogenization of a mass, with the same high average $^{87}\text{Rb}/^{86}\text{Sr}$ of 27, that had initially differentiated and cooled 70–80 m.y. earlier.

The final unit examined is the youngest stratigraphically mapped acid lava, the Carters Bore rhyolite. Its relationship to the Wonga granite is, however, not known. Four least magnetic size fractions from the same total rock samples used in the Rb-Sr work give a well-defined discordia (Fig. 184) having an upper intercept of 1678 m.y., some 100 m.y. older than the model Rb-Sr age. It appears that the same phenomenon of disturbed strontium total rock systems observed from the data for Leichhardt and Argylla acid lavas is operative in the case of the Carters Bore rhyolite.

Conclusions

The U-Pb zircon results from various low-grade metamorphosed volcanic suites and intrusions in the Mount Isa area are consistent with geological constraints, and for this reason the zircon data are considered to indicate ages of primary magmatic crystallization. These results contribute greatly to knowledge of the geological history of the region. In the Wonga granite, comparison of U-Pb zircon and two different Rb-Sr total-rock isochron ages suggests that two stages of magmatic differentiation and cooling, about 70 m.y. apart, were responsible for the observed isotopic disparities. Rb-Sr isochron data for the Kalkadoon granite and for three acid volcanic units show high and variable initial $^{87}\text{Sr}/^{86}\text{Sr}$ values and ages that are considerably younger by 100–200 m.y. than the respective U-Pb zircon ages, which are considered the true crystalli-

zation ages. Disturbed Sr systems are evident especially in the acid volcanic isochrons. This younger offset of the Rb-Sr results does not bear any relation to the postulated 1400-m.y. Mount Isa metamorphism. It is also difficult to suggest that the younger Rb-Sr isochron data merely represent incomplete response to the 1400-m.y. event, as the linearity or sublinearity of points defining isochrons requires a mechanism that affects all the samples in a somewhat regular fashion. It appears necessary to invoke some regional but nonsynchronous (continuous) alteration to which the acid volcanic suites are most susceptible, because of some existing conditions, for some 100–200 m.y. after the age of primary igneous activity. As circulating groundwater solutions were almost certainly present among this submarine extruded acid volcanic pile, it is considered that open-system behavior of the total rock systems could well be maintained while such percolating aqueous solutions merely exchanged Sr (and to a lesser degree, Rb) under these conditions. Stable isotope studies suggest that the temperature of alteration in such environments need not be more than 50°–100°C (Wenner and Taylor, 1976). The "events" dated by the sub-linear arrays of Rb-Sr isotopic data would approximately correspond to the different times of cessation of the mild hydrothermal leaching and exchange within the various units considered. The Leichhardt and Argylla Rb-Sr data suggest that a quantitative loss of Sr from the total rocks has occurred. In this manner lower Sr (high Rb/Sr) total rock systems would be more readily modified than rocks that contain more common Sr, and curvature of the resultant isochrons may result. Thus, prolonged diagenetic processes, including feldspar unmixing and devitrification of glassy portions of the rocks, are considered likely causes of the spurious Rb-Sr total rock systematics encountered in this and many other weakly metamor-

phosed Proterozoic acid igneous sequences.

The individual discordant arrays of U-Pb zircon data seen in this study may have some bearing on the significance of the lower discordia intercepts with concordia. It might have been predicted from an episodic lead-loss model (Wetherill, 1956) that the minimum age for the Mount Isa metamorphism of 1400 m.y. (as given by mica K-Ar ages) would be reflected in the lower discordia intercepts. This is not the case, as all the lower intercept "ages" are 500 m.y. or less, and no Lower Paleozoic geological events are known. The errors in extrapolating the data toward the lower intercept are obviously large, but if taken at face value the pooled zircon data from the Leichhardt zircon data would cut concordia at 370 m.y., and essentially the same lower intercepts are obtained from the Kalkadoon, Argylla, and Wonga zircon data. These observations would be consistent with the Goldich and Mudrey (1972) uplift-dilatancy model to explain zircon discordancy, and its implications of a lower Paleozoic uplift would also be geologically reasonable. As well, these approximate lower intercepts would have been predicted by a simple lead-loss line, as given by the continuous diffusion model of Tilton (1960). However, serious ambiguities arise and cast some doubt on the applicability of any such model when it is considered that one of the volcanic units (Carters Bore rhyolite) has a much lower intercept of 70 m.y. Also, separate treatment of the two possible Leichhardt discordias (samples 1 and 2) and two possible Argylla discordias (samples 1 and 3) give uninterpretable lower intercepts of 240 and 510 m.y. (Leichhardt 1 and 2), and 360 and 70 m.y. (Argylla 1 and 3). Use of any of the possible lead-loss models bears no relation to, and does not change, the conclusions from the upper intercept ages as determined by linear regression of all the data points.

THE AGES OF ZIRCONS FROM KIMBERLITES FROM SOUTH AFRICA

Gordon L. Davis, Thomas E. Krogh,
and A. J. Erlank†*

Kimberlite and its ultramafic inclusions are believed to provide a sample of the mantle lying beneath the pipes and diatremes that are formed at the surface. Studies of the mineral assemblages in the inclusions have led to an evaluation of the conditions of temperature and pressure that may have existed in the source regions (Boyd, 1973). In an attempt to understand the sequence of events involved in the formation and eruption of kimberlites, a study has been initiated to measure the ages of zircon, one of the minerals sometimes found in kimberlite. Zircon, because it incorporates uranium in its structure at the time of crystallization, is uniquely suited for the determination of radiometric ages by measurement of the uranium-lead ratios. The uranium-lead ages presented here are the first to be reported for zircons from kimberlites. The measurements were made possible by the development at this Laboratory of the low-contamination hydrothermal method for decomposing zircons (Krogh, 1973).

Zircons are concentrated during the processing of kimberlite for the recovery of diamonds. In the diamond-bearing kimberlites, zircons are rarer than diamonds. They also occur in nondiamondiferous pipes and show up in the heavy mineral concentrates that result from prospecting and evaluation. In general, all these zircons are large, from 2 to 20 mm in diameter, and are usually rounded, but some show crystal faces. They range from colorless to light brown, and are commonly coated with a chalky layer of zirconium oxide. The concentrations of uranium and lead are very low. Because radiation damage is slight, the crystals are very difficult to

* Department of Geology, Royal Ontario Museum, Toronto, Ontario, Canada.

† University of Cape Town, Cape Town, Republic of South Africa.

TABLE 70. Zircons from South African Kimberlites

| Name | Location | U (ppm) | Pb (rad.) (ppm) | 206/238 age (m.y.) |
|-----------------------|------------------------|------------|--------------------|-----------------------|
| Bultfontein | Kimberley | 12.2 | 0.184 | 91.2 |
| De Beers | Kimberley | 28.2 | 0.399 | 92.0 |
| Wesselton | Kimberley | 18.4 | 0.259 | 90.3 |
| Monastery | Orange Free State | 6.1 | 0.080 | 90.4 |
| Mothae | Lesotho | 8.6 | 0.118 | 87.1 |
| Orapa | Botswana | 14.4 | 0.201 | 93.1 |
| Rietfontein | Northern Cape Province | 25.2 | 0.270 | 71.9 |
| Rietfontein* | | 23.4 | 0.249 | 71.7 |
| Bokputs Camp | Namaqualand | 97.9 | 3.871 | 67.9 |
| Bakwanga (Mbuji Mayi) | Zaire | 38.0 | 0.422 | 71.3 |

* Washed with 48% HF.

Decay constants: $^{238}\text{U} = 0.15513 \times 10^{-9} \text{ yr}^{-1}$; $^{235}\text{U} = 0.98485 \times 10^{-9} \text{ yr}^{-1}$.

decompose, even using the hydrothermal method.

The results of the analyses of nine zircons are shown in Table 70. The samples were provided by Erlank and by F. R. Boyd of this Laboratory. Isotope ratios were measured using the 9-in mass spectrometer at the Department of Terrestrial Magnetism. The concentrations of lead and uranium were determined by the method of isotope dilution, using either a tracer of ^{208}Pb and ^{235}U or the new tracer of ^{205}Pb and ^{235}U (Krogh and Davis, *Year Book* 74, pp. 416–417). The ages appear to be grouped about 90 ± 1 m.y. for pipes in the vicinity of Kimberley and about 70 m.y. for outlying occurrences. Duplicate analyses for one zircon indicate an age sensitivity of 200,000 years for a 71-m.y.-old crystal. Phlogopite micas from nodules from the Kimberley area have been dated at 90 ± 20 m.y. by Allsopp and Barrett (1975) using the rubidium-strontium method.

Figure 186 is a concordia diagram on which are plotted the uranium-lead ratios. Except for two samples, the diagram shows that the ages are concordant. The two zircons that show horizontal spread, Mothae and Monastery, have the lowest concentrations of uranium and lead. This spread is a result of the experimental difficulty in correcting the ^{207}Pb for the amount of that isotope contributed by common lead. The cor-

rection for ^{206}Pb is much smaller, so for minerals having young ages the 206/238 age is most reliable. In Fig. 187 the vertical spread is small and illustrates clearly the grouping of 206/238 ages.

The mid-Cretaceous age of these South African zircons can be interpreted, at least in Zaire where the kimberlites are contemporaneous with upper Cretaceous sediments, as indicating that the magma from which the zircons crystallized had a brief existence after crystallization before breaking through the surface sediments—brief in terms of a few million years. This magma could have been the kimberlite itself. Alternatively the zircons could have been part of a discrete nodule assemblage. In either case, the age values measured for the zircons mark the time that has elapsed since ^{206}Pb and ^{207}Pb , the stable products of the radioactive decay of ^{238}U and ^{235}U , began to accumulate in the crystals. Previous to this time, the zircons were in an environment where the temperature was high enough that the stable and intermediate daughter products diffused out of the crystals. Boyd and Nixon (1973) have hypothesized that the discrete nodules are phenocrysts from crystal-mush magmas in the outer portions of the low-velocity zone (1000° – 1250°C), carried to the surface by the erupting kimberlite magma.

The locations and ages of the South African kimberlites from which the zir-

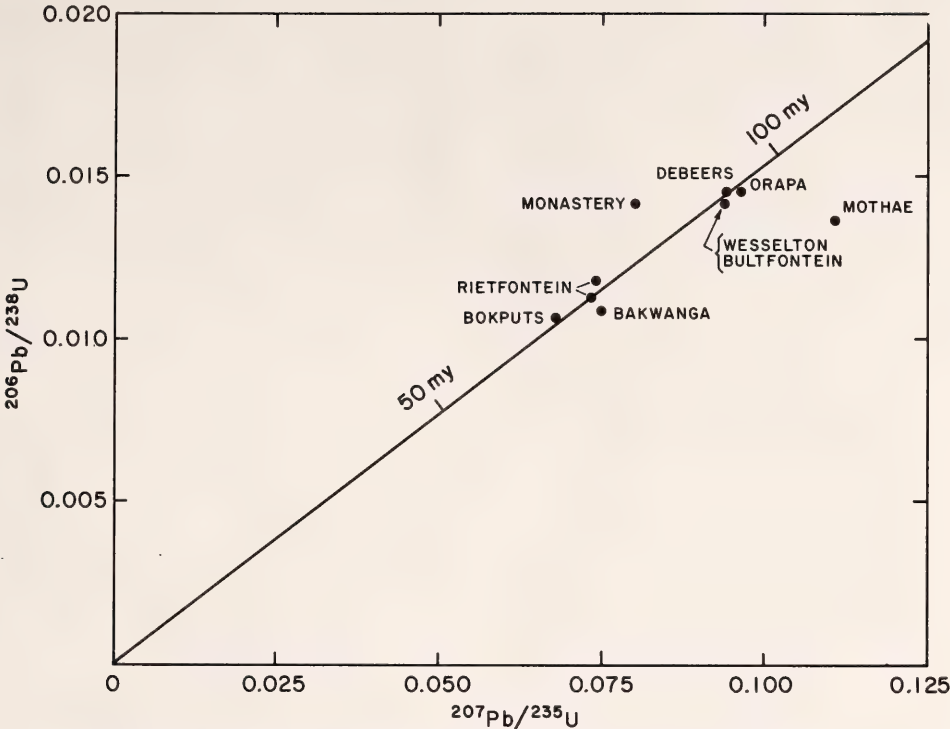


Fig. 186. Concordia diagram for zircons from kimberlites from southern Africa.

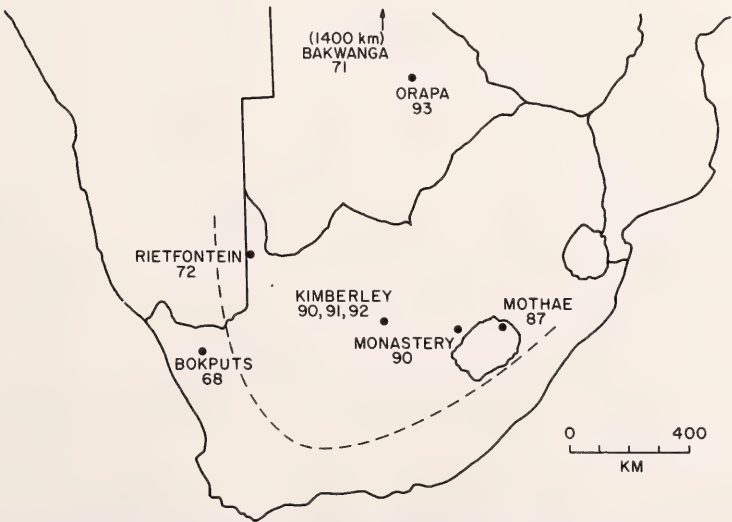


Fig. 187. Map of southern Africa showing the location of the kimberlite pipes and the ages in million years of zircons from the kimberlites.

cons were obtained are shown in Fig. 187. Although the data are few, the age pattern does not conflict with the hypothesis that the base of the lithosphere is at progressively shallower depths moving east or west from Kimberley. The regional thinning of the lithosphere parallels other changes, such as the decrease in the number of diamonds in kimberlite and the systematic increase of alkali basalt and carbonatite over

kimberlite from Kimberley westward. The dashed line roughly separates the central part of the shield, where diamond-bearing kimberlites have been found, from an outer zone that is non-diamondiferous. More zircons from the outer zone pipes are being studied to determine whether this apparent relationship between younger ages and depth to the bottom of the lithosphere will be substantiated.

NEW TECHNIQUES AND EQUIPMENT

THE ULTRAHIGH-PRESSURE DIAMOND CELL: DESIGN APPLICATIONS FOR ELECTRICAL MEASUREMENTS OF MINERAL SAMPLES AT 1.2 MBAR

H. K. Mao and P. M. Bell

The success of producing approximately 1-Mbar pressures in the diamond-anvil high-pressure cell resulted from an improvement in design over that described last year (Mao and Bell, *Year Book 74*). The apparatus based on the new design not only can produce a megabar in pressure but also is routinely operational, lending itself to physical measurements of the sample at the highest pressures. Designs for heating of the sample by a laser beam, for obtaining x-ray diffraction data measuring crystal-field spectra, and for measuring ^{57}Fe Mössbauer spectra have already been described (Bell and Mao, and Huggins, Mao, and Virgo, *Year Book 74*). The present report describes design improvements that extend the pressure from 0.5 to 1.2 Mbar and the techniques of obtaining electrical measurements in this pressure range.

The Megabar Cell

Simplified diagrams of the modified cell were given last year (Mao and Bell, *Year Book 74*), and reference to the diagrams can be made in conjunction with the pressure cylinder shown in Fig. 188. The design is made to eliminate differential strains, and therefore, alignment and dimensional precision of

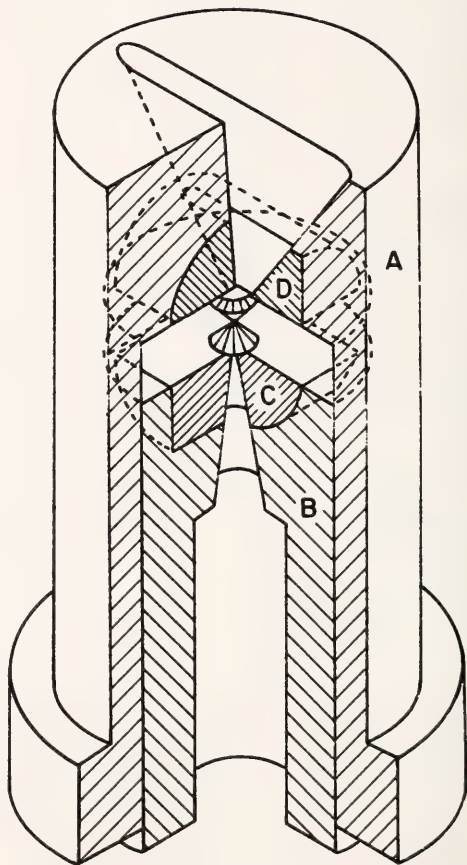


Fig. 188. Details of the pressure cylinder (see Mao and Bell, *Year Book 74*, for amplified diagrams of the entire apparatus). A, outer cylinder, slotted for exit of diffracted x-ray beam (outer diameter, 2 inches). B, inner piston, tapered port for entry of primary x-ray beam. C and D, tungsten carbide half-cylinder or "rocker" upon which the diamond surfaces are in contact.

greater than $5.0\text{ }\mu\text{m}$ are essential. The cylindrical seats for the tungsten carbide half-cylinders upon which the diamonds rest are machined using a precision spark-erosion (Elox) technique. Figure 188 shows the upper half-cylinder support containing a slotted hole for exit of the diffracted beam during x-ray studies. Rotation and translation of these half-cylinders (sometimes referred to as "rockers") during the first stages of an experiment provide the excellent alignment required to avoid damage to the diamonds.

The forces applied to the diamonds and then to the sample are obtained by a 5:1 lever designed for linear motion (see Mao and Bell, *Year Book* 74). With careful alignment and uniform application of pressure one can maintain electrical contact with parts of the sample employing fine wires in the procedure described below.

Electrical Measurement

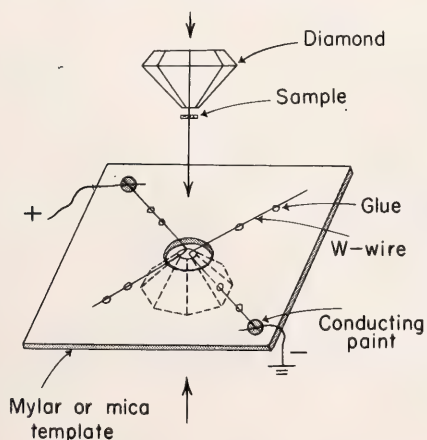
Electrical conductivity of minerals at high pressure ranges from 10^{-12} to $10\text{ ohm}^{-1}\text{ cm}^{-1}$ (these values are for olivine at 1 atm to 350 kbar, Mao, *Year Book* 72), which spans the insulator,

semiconductor, and conductor regions. In efforts to obtain conductivity measurements in the pressure range 0.5–1 Mbar, a technique for introducing electrical leads to the sample has been devised for the ultrahigh-pressure cell described above.

The wires are usually tungsten, or thermocouple alloy (chromel-alumel, Pt-Pt10Rh, or W3Re-W25Re) of $10\text{ }\mu\text{m}$ diameter. The wires are first glued to a template made of Mylar or mica sheet (0.2-mm thickness) and aligned by hand under a binocular microscope at a hole in the template ($600\text{-}\mu\text{m}$ diameter). The template with wires is then set in place on one of the diamonds and mounted with wax. Figure 189A shows the template arrangement, and Fig. 189B shows an alternative arrangement for which a template is not needed.

Various configurations of the electrical leads are shown in Fig. 190. Electrical resistance and temperature can be measured simultaneously. The closest point of a pair of leads is located in the central portion, because in these experiments a metal gasket is not employed, and a pressure gradient is developed in the samples. If electrical conductivity

(A) Template arrangement



(B) Parallel wire arrangement

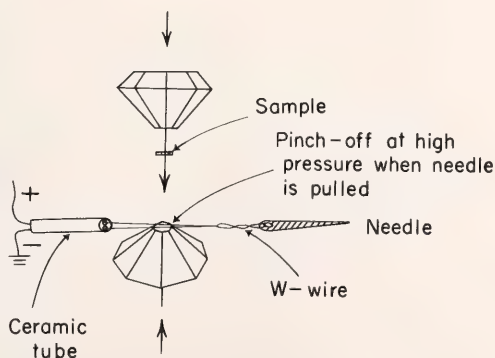


Fig. 189. (A) Template arrangement for positioning electrical leads. (B) Parallel wire arrangement. Size of diamonds, 0.33 carat; sample diameter, $300\text{ }\mu\text{m}$. Used for externally heating experiment when temperature is expected to rise above the usable range of template.

does not increase greatly with pressure or when conductivity decreases with pressure (e.g., as in KCl), an insulator gasket is needed. Figure 191 shows a

ample in the central portion of the diamond face. In these experiments MgO powder is pressed into a disk shape and then drilled. The drilled portion is filled with sample and repressed between the

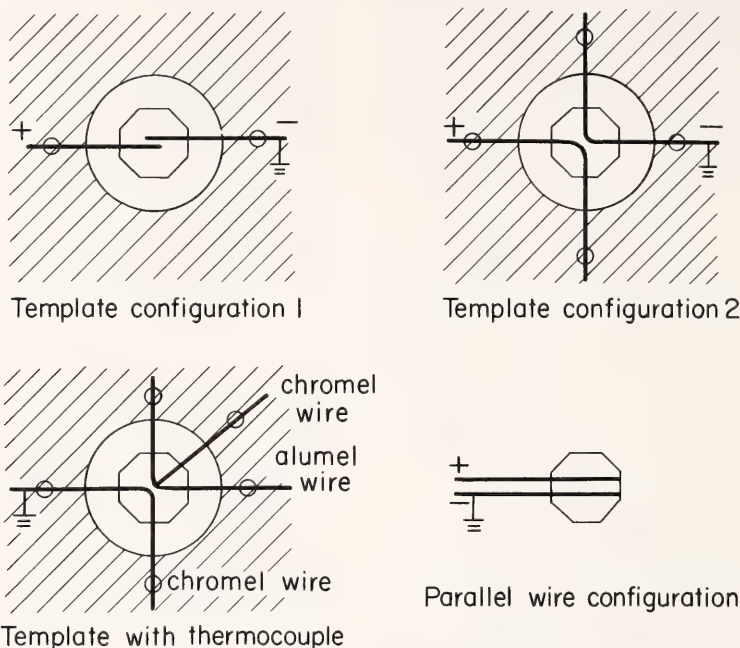


Fig. 190. Various configurations for electrical leads; octagonal form is the trace of the diamond pressure face that is approximately $300\text{ }\mu\text{m}$ maximum diameter. (A) Template configuration 1; (B) template configuration 2; (C) template with thermocouple; (D) parallel wire configuration.

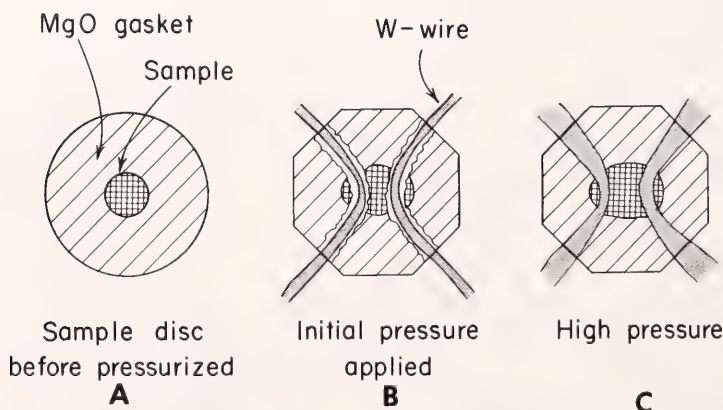


Fig. 191. Placement of electrical leads in magnesia gasket. (A) Sample disc before being pressurized; (B) sample disc after initial pressure was applied; (C) sample disc under high pressure.

diamond faces before the electrical leads are introduced. The magnesia gasket causes minor sample distortion and relatively uniform sample distribution.

This apparatus has been employed successfully with mineral samples whose electrical conductivity changes range between 10^{-12} and $10 \text{ ohm}^{-1} \text{ cm}^{-1}$ in the pressure range 1 bar to 300 kbar (Mao, *Year Book* 72).

HIGH-PRESSURE RESEARCH: 1-MBAR PRESSURE ON THE RUBY PRESSURE SCALE

H. K. Mao and P. M. Bell

The design of apparatus to produce static pressures of 0.5 Mbar reported last year (Mao and Bell, *Year Book* 74) was developed further to produce pressures of 1.2 Mbar. This pressure appears to be the highest ever reported for a sustained static experiment in which an internal calibration was employed (the pressure was kept constant for two weeks and could have been held indefinitely).

Calibration of the pressure was obtained by using the spectral shift with pressure of the ruby R_1 fluorescence line. During each experiment ruby crystals were subjected to pressure in the diamond-window cell, and fluorescence was excited by impingement of an He-Cd gas-laser beam at 441 nm and monitored by the spectrophotometer apparatus described by Bell and Mao (*Year Book* 74). It was thus possible to monitor the pressure during the experiment.

In other experiments (Mao and Bell, this Report), a linear shift of the ruby R lines with pressure was assumed, and correlation of pressure with shock-wave data was obtained. Before the present experiments were done the sodium chloride B1-B2 (NaCl-CsCl structure types) transition was observed at 291 kbar, and the wavelengths of the R ruby lines were simultaneously measured. A single ruby fragment was monitored each time an experiment was done. The observed

spectral shift of the R_1 ruby line in a typical experiment and the corresponding pressures from a linear extension of the National Bureau of Standards scale (Piermarini and Block, 1975) are listed in Table 71. Figure 192 shows the observed spectral curves corresponding to data listed in Table 71. Departure from hydrostatic pressure was caused by line-broadening, and the intensity of the R_1 ruby line appeared to diminish as the pressure was increased to the megabar range.

No sign of mechanical failure was observed in the diamonds, and with improved support it should be possible to increase the pressure to at least 1.5 Mbar. Pressures of 1.2 Mbar have been produced repeatedly with diamond anvils whose faces were 0.2, 0.35, 0.45, and 0.55 mm in diameter.

The capability of routinely experimenting at pressures in the megabar range has far-reaching applications. It will be possible to study insulator-metal transitions and numerous other proposed physical and chemical changes in materials at high pressures. With the accessibility of this pressure range coupled with high temperatures (Bell and Mao,

TABLE 71. Observed Spectral Shift ($\Delta\lambda$) of the R_1 Line of a Ruby Crystal at High Pressure*

| $\Delta\lambda$ (Å) | Pressure (kbar) |
|------------------------|--------------------|
| 30 | 83 |
| 75 | 206 |
| <i>106</i> | <i>291</i> |
| 180 | 495 |
| 225 | 619 |
| 290 | 797 |
| 310 | 823 |
| 320 | 880 |
| 370 | 1018 |

* The shift of 106 Å (values in italics) corresponds to the B1-B2 transition in NaCl. Pressures below 291 kbar were determined from the National Bureau of Standards calibration curve. Pressures above 291 kbar were determined from a linear extension of the NBS curve.

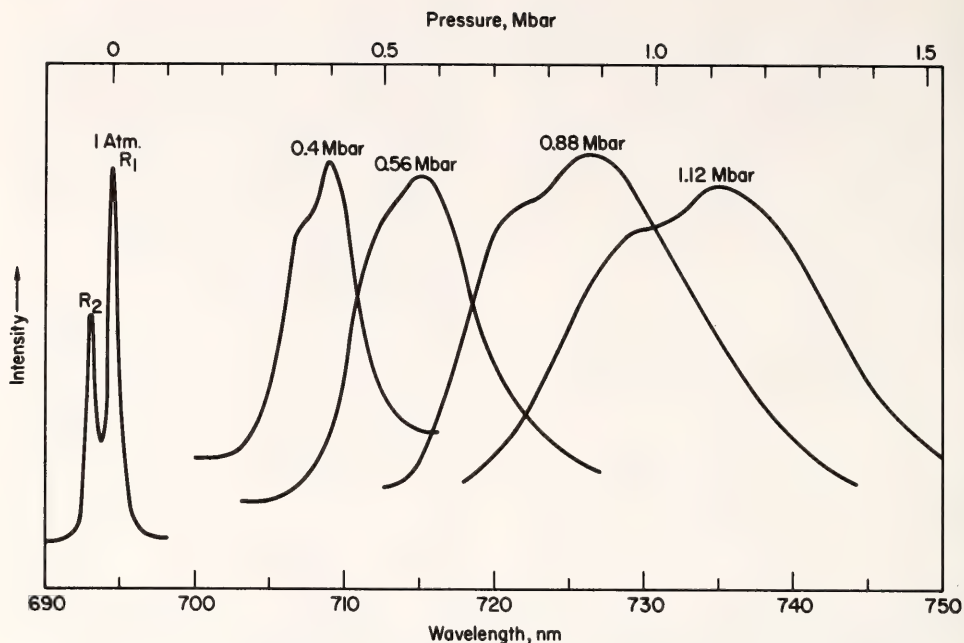


Fig. 192. Spectra of the ruby R_1 fluorescent line at various pressures. (Note: intensity scale is arbitrary; the line intensity decreases at high pressure. The observed splitting of the R_1 and R_2 lines is consistent with the crystal-field transition ${}^4A_2 \rightarrow {}^2E$ in Cr^{3+} .)

Year Book 74) it is now possible to experiment directly at the approximate conditions of the boundary of the earth's core (equivalent pressure, approximately 1–1.5 Mbar).

A CONTROLLABLE THERMOCOUPLE MICROHEATER FOR HIGH-TEMPERATURE MICROSCOPY

Y. Ohashi and C. G. Hadjidiacos

The phenomena of crystallization and melting are of fundamental importance in studies of the genesis of minerals in igneous rocks. It is highly desirable to observe these phenomena with the petrographic microscope under precisely controlled conditions of temperature and atmosphere. The temperature required for the study of silicate melting, however, is generally very high ($<1700^\circ\text{C}$), and the most important consideration is the accuracy of the temperature determination. Measurement of the specimen

temperature with very fine thermocouple wires does not provide satisfactory results because of heat loss in the wires by conduction. If the heater is relatively small, the problem of heat conduction is particularly critical. A wire-wound resistance furnace is bulky and requires a cooling system to protect the microscope. A method that overcomes these difficulties is one in which the thermocouple itself is both heating element and sample support.

The design of a thermocouple circuit used to achieve concurrently both heating and temperature measurement is complex electronically. One such scheme utilizes high-frequency heating (Ordway, 1952), where the frequency is filtered out leaving only the dc component of the generated emf. Another method, described by Welch (1954), utilizes a switching relay where one contact applies power and the other measures the thermocouple emf. This method has been

used with reasonable success for heating and temperature measurement; however, its weakness lies in the lack of reliability of the relay.

Circuit Design

The circuit shown in Fig. 193 employs half-cycle heating using a silicon-controlled rectifier (SCR). Heating takes

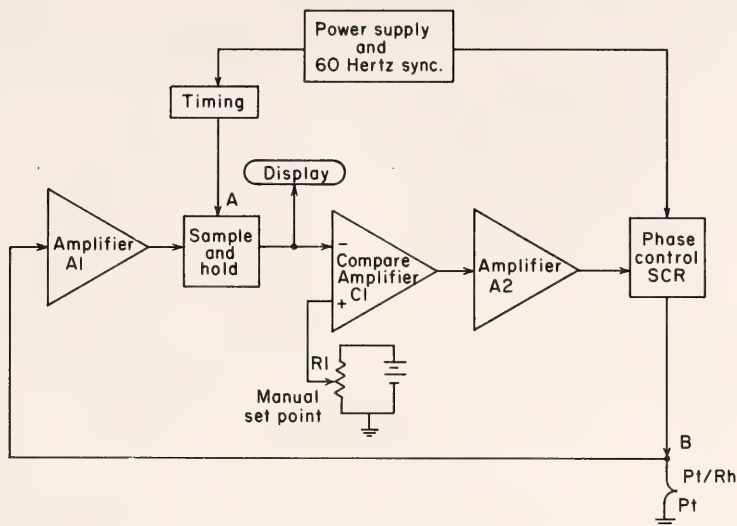


Fig. 193. The composite microheater control circuitry.

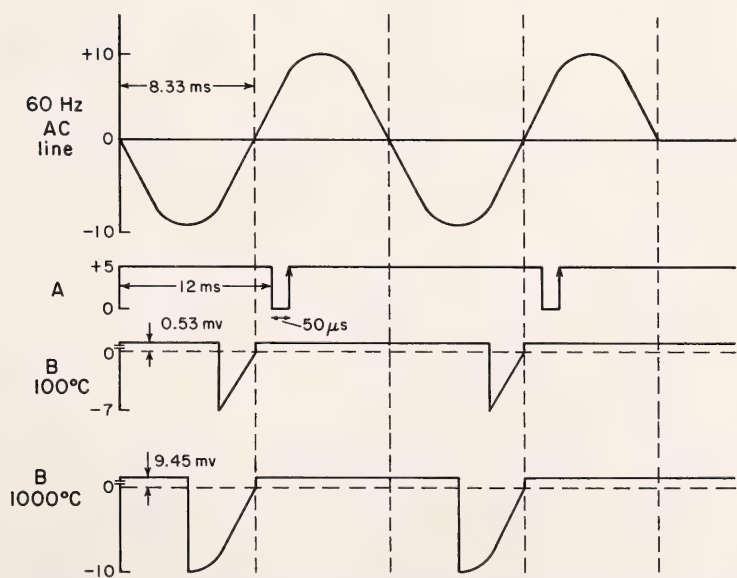


Fig. 194. Timing and control signals applied to the microheater. Temperatures referenced to room temperature.

place during the first half of each 60-Hz power-line cycle. The thermocouple emf is measured during the second half-cycle. The power applied for heating is controlled by changing the phase conduction angle of the SCR (General Electric Company, 1964); in this way proportional control of the heating cycle is achieved. During the measurement cycle, the heating current is interrupted by the reverse bias characteristics of the rectifier. The 2N697 SCR used in this design has a reverse current leakage of 30×10^{-19} A at 10 V. The net effect of this leakage in the thermocouple measurement circuit is 0.06 μ V, less than 0.1°C.

As shown in Fig. 193, as the manual setpoint R1 is increased, the voltage output of the comparator amplifier C1 is amplified by A2 and applied to the phase control circuitry. The higher the applied potential, the greater is the applied power to the thermocouple heater. As the thermocouple heats, the generated emf and the applied voltage are amplified by A1. Owing to the internal clamping and high-frequency characteristics, A1 is able to recover from saturation for accurate amplification of the thermocouple emf. Both heating and measurement potentials are still present at the output of A1. A sample-and-hold circuit is provided to select only the measurement portion of the potentials. The sample-and-hold circuit is triggered only during the amplified emf signal by the control signal at point A. The timing circuitry is synchronized with the measurement cycle; therefore, at each cycle, temperature measurement is resumed and held through the next heating cycle, as outlined in line B in Fig. 194. The emf output of the thermocouple is displayed by a digital voltmeter as well as being applied to the comparator amplifier C1. As the emf increases, the proportion of emf to the reference potential decreases, resulting in less applied heater power. This closed-loop servo maintains a constant monitor of emf and applied and thermocouple response are nearly

instantaneous, and thus very precise temperature control is possible.

Microheater Assembly

The overall size of the heater assembly is approximately 45 mm wide, 70 mm long, and 13 mm thick (Fig. 195). A cell (a) was machined from a solid heating power. The temperature increase

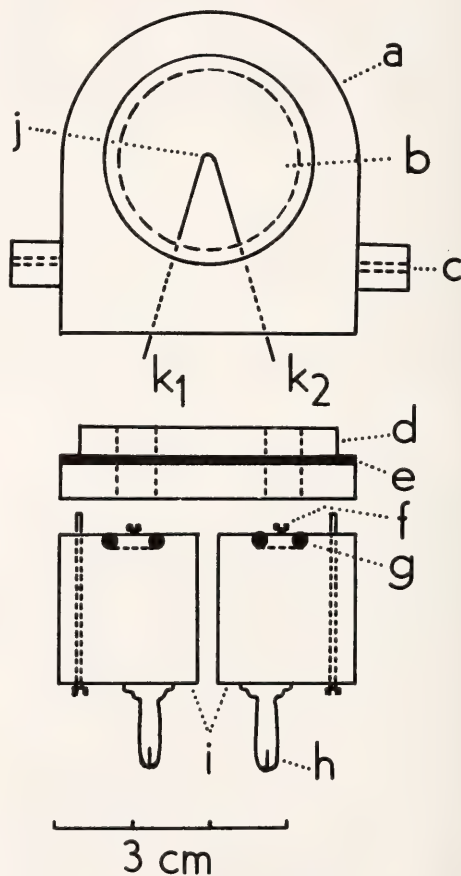


Fig. 195. Microheater assembly for high-temperature microscope. (a) Brass cell, (b) glass windows (top and bottom), (c) gas inlet and outlet, (d) Bakelite base, (e) neoprene gasket, (f) thermocouple mounting screws, (g) neoprene O-rings, (h) Pt-PtRh thermocouple extension wire, (i) brass blocks, (j) thermocouple junction, (k_1) Pt 0.013-in wire, and (k_2) Pt90Rh10 0.013-in wire.

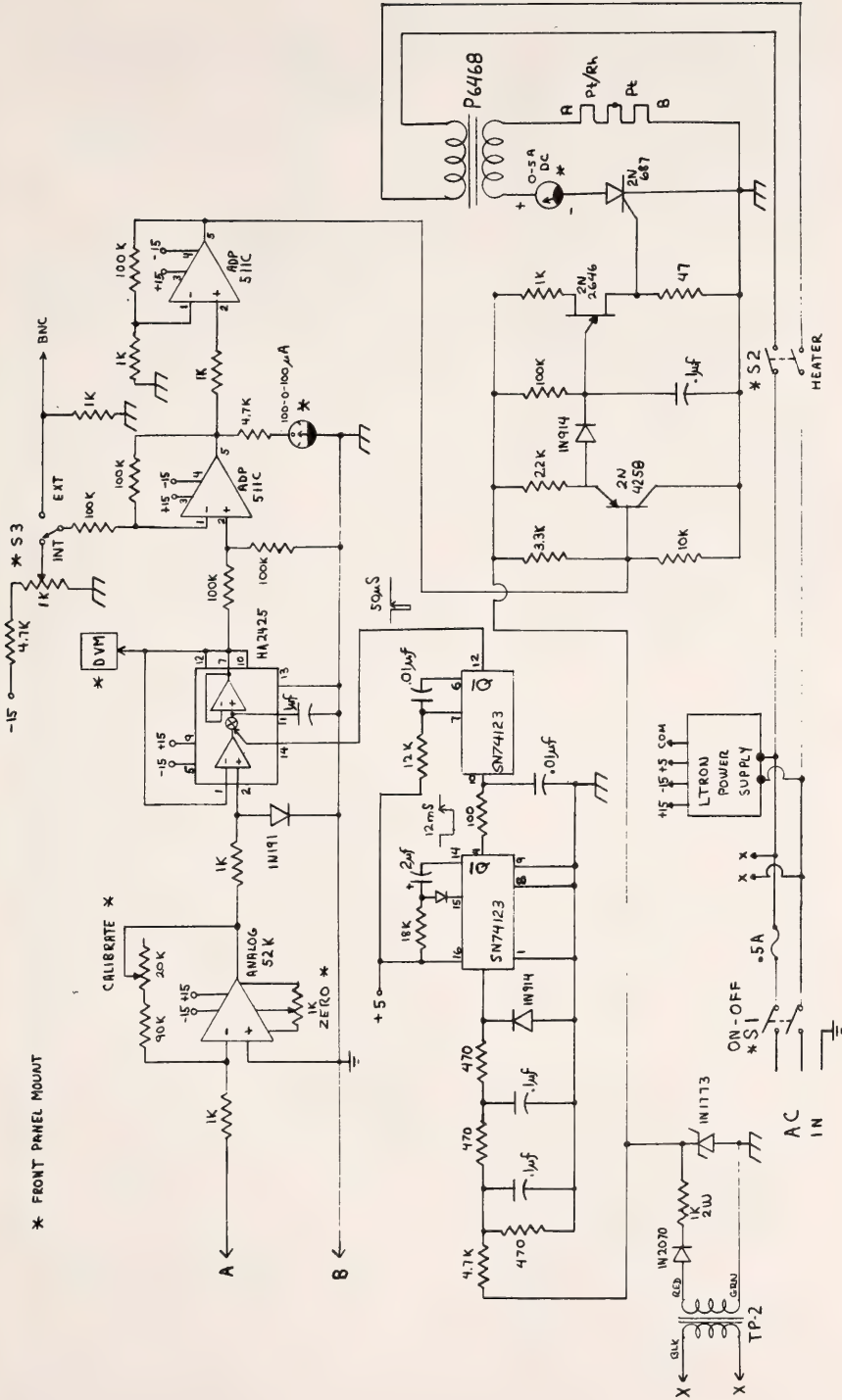


Fig. 196. The circuit diagram implemented for simultaneously heating and measuring the generated emf from a thermocouple. The manufacturers cited are for reference only.

brass block to give a wall $3/32$ in thick and two holes for glass windows (b) of 1 in diameter. The atmosphere inside the cell can be controlled by either evacuating or letting an inert gas or a gas mixture flow through small tubes (c). The cell is insulated by a Bakelite base (d) from two brass blocks (i) to which the thermocouple wires are connected.

For better support, the 0.013-in Pt and Pt90Rh10 wires (k_1 and k_2) are reinforced by five additional wires of the same size from the brass blocks for $2/3$ or $3/4$ of their entire length, leaving approximately 1 cm of the single 0.013-in wire on each side of the thermocouple junction (j). The junction can be made V-shaped to obtain a very localized hot spot or a small loop to introduce a slight temperature gradient from the wire to the center of the loop. The latter geometry is particularly suitable for growing a single crystal (Welch, 1954, p. 461).

Thermocouple compensation leads connect the brass blocks (Fig. 196) to the measurement circuit (Fig. 193), where a room-temperature reference function is made. The brass blocks are designed to avoid the introduction of error in thermocouple emf, even if the blocks are heated as high as 50°C .

The temperature difference of the blocks is negligible, and the system (Fig. 196) controls the microheater temperature to $\pm 2^\circ\text{C}$. This control is possible because of the fast thermal response of the thermocouple/heater.

The highest operating temperature is at present 1700°C , at a power consumption of 30 W, using a Pt/Pt90Rh10 thermocouple and 2150°C using an Ir-IrRh thermocouple (Gutt, 1964). The heater and control are simple to construct; the parts cost about \$400. The microheater can be modified for x-ray diffraction experiments under automatic temperature control through an automated diffractometer system (Finger, Hadidiacos, and Ohashi, *Year Book* 72, pp. 694-699).

A NEW FURNACE ASSEMBLY WITH A SMALL TEMPERATURE GRADIENT IN SOLID-MEDIA, HIGH-PRESSURE APPARATUS

I. Kushiro

Large volume containers in solid-media, high-pressure apparatus have been used for experiments under controlled oxygen fugacity or for synthesis of starting materials at high pressures; however, large temperature gradients have limited their use. During measurements of the viscosities of melts at high pressures (Kushiro *et al.*, this Report), a large volume container with a small temperature gradient was highly desirable because of the sensitive change of viscosity with temperature. A new furnace assembly with a $3/4$ -in o.d. has therefore been developed by changing the design of the graphite heater. Because the thinner part of the graphite heater has a greater electrical resistance and produces higher temperatures, the thickness of the graphite heater was varied to reduce the temperature gradient.

The conventional straight-wall graphite heater generates a parabolic temperature distribution along the axis of the furnace with the hottest point near the center. The thickness of the graphite heater was therefore gradually reduced from the center toward both ends. Several different angles of taper were tested; however, the best design among those tested has an internal taper of 3° from each end of the graphite heater (12.6 mm o.d.), as shown in Fig. 197. The thickness of the graphite heater is 0.055 in (1.40 mm) at the center and 0.025 in (0.64 mm) at both ends. The axial temperature gradient along the 10-mm-long capsule in this new furnace is 15°C at temperatures between 1200° and 1400°C and at 20 kbar (Fig. 197). The temperature gradient within the graphite capsule itself is about 10°C , which is acceptable for the viscosity measurements. The radial temperature gradient was not measured. The temperature gradient in

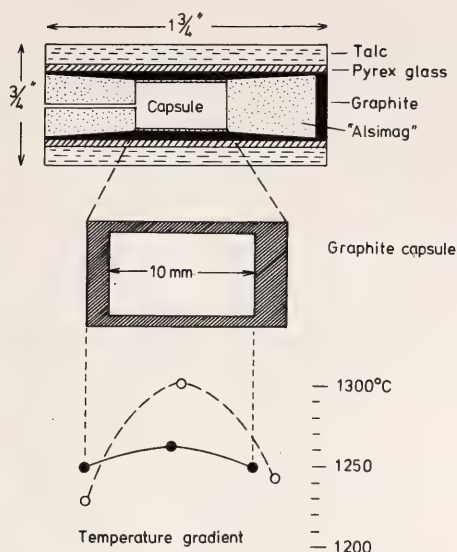


Fig. 197. Furnace assembly with graphite heater having a 3° internal taper, and results of measurements of the temperature gradient. Solid circles show the temperature gradient within the tapered graphite heater, and open circles show the gradient within the conventional straight-wall graphite heater.

the conventional $\frac{3}{4}$ -in furnace assembly with a graphite heater having a straight internal wall, measured by Dr. Y. Nakamura, is about 75°C in the same temperature range (Fig. 197). It is theoretically possible to eliminate entirely the temperature gradient along the capsule by changing the angle of the taper and the thickness of the graphite heater.

This new furnace assembly may have many useful applications, such as making multiple runs with different charges in a single experiment and measuring physical properties of crystals and liquids at high pressures and temperatures.

ACCURATE MODAL ANALYSIS OF EXPERIMENTAL RUN PRODUCTS

Bjørn O. Mysen

Accurate analysis of the modal composition of experimental run products is an important aid in experimental studies

of phase equilibria of both simple and natural systems. Conventional modal analysis frequently results in large uncertainties. One alternative is a mass-balance calculation utilizing least-squares fitting techniques (Bryan, Finger, and Chayes, *Year Book 67*, pp. 243-244). This technique, however, requires high-quality, time-consuming chemical analysis of all phases present, and such data are not always attainable. Another approach makes use of a tracer (element or compound) that enters only the phase(s) whose mode is to be determined. The modal proportion of the phase is then directly related to the concentration of the tracer in the phase. The procedure yields a modal proportion with the same accuracy as the analysis itself. Although the method is applicable to any number of phases, proportions of liquid in experimental charges are most frequently sought, and the technique will be described here for the liquid phase as an example.

In adding a tracer to an experimental charge, three requirements must be met before the tracer can be used in the proposed manner: (1) The presence of the tracer should not affect the phase relations of the system; (2) the concentration of the tracer in the experimental charge should be easily determinable; and (3) the tracer distribution within the phase to be determined should not be affected by nonequilibrium growth (quench crystals). The first requirement can be met by keeping the concentration of tracer low (a few ppm). In situ analysis of elements or compounds in trace amounts is attainable with the β -track technique by labeling the element or compound with a radioactive isotope (activity range: 10^{-7} – 10^{-3} Ci/g) (Mysen and Seitz, 1975), thus meeting the second requirement. Less than 1 mg of sample is needed for such analysis. When analyzing quenched liquids, growth of quench crystals may change the tracer content of liquid as analyzed after the quenching of an experiment. Fortunately, incompatible elements or

compounds in trace amounts are not expelled from crystals growing during the few seconds needed to quench an experiment. The homogeneity of β -track maps over regions of quenched liquid that contain quench crystals indicates that the third requirement is met.

The selection of a tracer depends on the phase or phases to be determined. The method has been tested for liquids in equilibrium with crystals using carbon-14-spiked CO_2 as a tracer. Carbon dioxide is advantageous because it is a gas that dissolves in amounts of a few percent in silicate melts at high pressures (Mysen, Arculus, and Eggler, 1975), and the run durations required for equilibrium amounts of CO_2 to dissolve in silicates have been studied in some detail (Mysen and Seitz, 1975). Furthermore, the partition coefficient, $K_{\text{CO}_2}^{\text{silicate liquid-crystal}}$, is known (~ 0.0008 ; Eggler, Mysen, and Seitz, *Year Book* 73, pp. 226-228). Thus, for all practical purposes, all CO_2 in a crystal-liquid system enters the liquid. By using a completely melted starting material spiked with tracer as standard, the modal proportion of liquid in an experimental charge (wt %) is % liquid = [(wt % CO_2 in 100% melt)/(wt % CO_2 in partial melt)] $\times 100$.

The carbon dioxide contents of liquid can be determined routinely at levels below 1 ppm with $<2\%$ uncertainty. This uncertainty in individual analyses results in an uncertainty of the proportion of liquid in an experimental run that is less than 3%. The detection limit of liquid is controlled by the geometry of the phase (a minimum area is required for counting β tracks) and by the β -track counting method. With an optical microscope, the lower limit is usually 0.5%–1.0% melt depending on the accuracy required. This limit can be lowered further by using the scanning electron microscope (SEM) to facilitate track counting in smaller regions and by using higher track density. With SEM counting, the saturation limit of the nuclear emulsions used for recording the tracks

is determined by the grain size of the emulsion itself ($\sim 0.2 \mu\text{m}$), resulting in about 10^8 tracks/ cm^2 . On an optical scale, the saturation limit of the nuclear emulsion is about 5×10^7 tracks/ cm^2 (Mysen and Seitz, 1975).

This technique can also be applied to studies of solubility of an element or a compound in one or more phases in the system. The principle is illustrated in Fig. 198, using H_2O solubility in silicate liquid at high pressure as an example and carbon-14-spiked CO_2 as a tracer. Only 10–20 ppm CO_2 is required. Water depresses silicate liquids and solids. The degree of melting of a system increases as the amount of H_2O added to the system is increased. As a result, the CO_2 content of liquid decreases slowly as a function of degree of melting until vapor evolves. At the saturation point, however, a separate vapor phase forms (point A, Fig. 198). Because at high pressures CO_2 partitions into the vapor (Eggler, *Year Book* 72, pp. 457–467), at point A the CO_2 content of the liquid drops dramatically. Point A in Fig. 198 therefore is the saturation point of H_2O in the partial melt. By determining the amount of melt with a H_2O content just below that corresponding to point A,

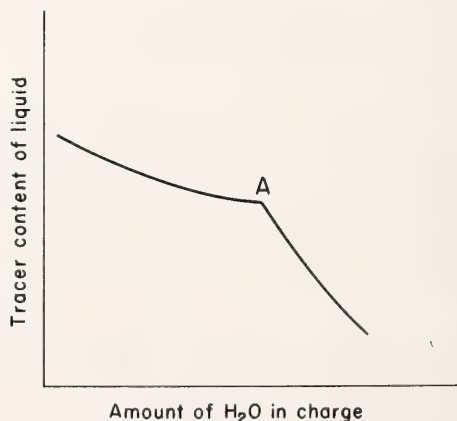


Fig. 198. Amount of tracer in a partial melt as a function of H_2O content of an experimental charge.

the saturation concentration of H_2O in the partial melt can be calculated to be equal to the amount of H_2O in the experimental charge divided by the proportion of liquid. The inflection of the curve in Fig. 198 becomes less pro-

nounced the smaller the partition coefficient, $K_{CO_2}^{vapor-liquid}$. As long as there is significant partitioning of CO_2 between vapor and liquid, however, an inflection will occur, and the solubility of a volatile can be determined.

STAFF ACTIVITIES

Field Studies

Bell used his 40-ft sloop to obtain samples from two seamounts off Bermuda. The New England Seamount Chain and the Bermuda Rise, near the eastern coast of the United States, consist of over 1000 seamounts that were uncharted until 1969. The composition of the seamounts is of considerable interest to students of the plate tectonics of the Atlantic. *Bell* retrieved samples of titanium-rich basalt using a modern version of the reliable "pipe dredge."

Boyd visited kimberlite localities in the Republic of South Africa and Lesotho during July. Large peridotite nodules, suitable for bulk chemical analysis, were obtained from the Frank Smith pipe. *Boyd* also went underground at the De Beers Mine, the Letseng-la-Terai Mine, and the Sover-Doornkloof Mine, to study flow structures in kimberlites. Specimens collected during these visits will form the basis of an electron microprobe study of the kimberlite groundmass.

Eggler, accompanied by M. E. McCallum of Colorado State University and the U.S. Geological Survey, examined and collected nodule suites from kimberlite pipes in Colorado and Wyoming. Of particular interest were the several pipes in the State Line district that have been found to contain diamonds and some newly discovered dikes in the Iron Mountain district.

Ferry continued his field studies near Augusta, Maine, collecting samples from three granitic stocks for petrologic investigations and mapping granite-metasediment contacts. He also led a field trip focused on the metamorphism of pelites and carbonates in the Augusta

area for Geophysical Laboratory staff members and others (see below).

Fujii participated, as a representative for Japan, in Leg 45 of the International Phase of Ocean Drilling (IOPD). Leg 45 was devoted to drilling oceanic crust near the Mid-Atlantic Ridge, and drill core samples of abyssal basalt and peridotite were obtained from penetration depths as great as 580 m.

Irvine spent two months in the field in north-central British Columbia. He completed the mapping of the Axelgold layered gabbro intrusion and a cluster of about a dozen Alaskan-type ultramafic bodies while working with a helicopter-supported operation of the Geological Survey of Canada. Descriptions of the field results of this work are given in the *Geological Survey of Canada Report of Activities, Paper 76-1A* (pp. 75-81, 1976).

Rumble completed field work in New Hampshire on a project in collaboration with Gerhard Oertel of the University of California, Los Angeles. The objective of the project was to integrate structural and petrologic studies to obtain estimates of the energy budget of metamorphism. Quantitative data on the strain that occurs during deformation will be combined with data on the pressures, temperatures, and energy requirements of dehydration reactions.

Rumble continued field research on other aspects of the regional geology and metamorphic petrology of western New Hampshire. Among the problems studied were the stratigraphy of the pre-Silurian rocks, the nature of amphibolite mineral assemblages in a variety of metamorphic grades, and the fossilization process of clam-like Paleozoic shells

that have been converted by metamorphism to grossularite-calcite-quartz assemblages.

Rumble also organized a one-week field trip for Geophysical Laboratory staff to examine a variety of igneous and metamorphic rocks in New England. The group consisted of J. M. Ferry, B. Harte, T. C. Hoering, R. Page, and D. Rumble from the Laboratory; C. W. Burnham, K. Shay, A. B. Thompson, and J. B. Thompson, Jr., from Harvard University; J. Creasy from Bates College; and C. Graham from the University of Edinburgh. Professor J. B. Thompson, Jr., led a one-day trip on metamorphic rocks in southeastern Vermont; Rumble led a two-day trip on metamorphic rocks in western New Hampshire; Creasy led a two-day trip on igneous rocks of the White Mountain batholith; and Ferry led a one-day trip on metamorphic rocks in central Maine.

Osborn visited the Hawaiian Volcanic Observatory in August 1975 and made a two-day trip to points of geological interest on the island of Hawaii. In October, he participated in a Geological Society of America field trip to examine volcanic features and structures in the western Grand Canyon and along the margin of the Colorado Plateau and Basin and Range province.

Petrologists' Club

Five meetings were held during the sixty-fifth year of the Petrologists' Club. The lectures presented were:

"Petrogenesis of Andean calc-alkaline magmas," by David James (Department of Terrestrial Magnetism), November 18, 1975.

"Petrology and geochemistry of basalt glasses from the project FAMOUS area, Mid-Atlantic Ridge," by W. F. Bryan (Woods Hole Oceanographic Institution), December 16, 1975.

"Sneesby revisited, or does silica skew?" by Felix Chayes (Geophysical Laboratory), January 20, 1976.

"Experimental study and geometric analysis of metastability as applied to

the problem of nucleation during cooling," by R. J. Williams (Johnson Spacecraft Center), February 17, 1976.

"Geothermal studies in Long Valley, California," by Roy Bailey (U.S. Geological Survey), March 23, 1976.

Washington Crystal Colloquium

The Washington Crystal Colloquium, an informal monthly assembly of crystallographers from the Washington area, met seven times during the report year. The following lectures were presented:

"Structures of some organic derivative metal-oxide complexes," by Carl Quicksall (Georgetown University), October 17, 1975.

"Experiences in the nonroutine solution of the structures of four medium size (mole wt ~ 500) organic molecules," by J. V. Silverton (National Institutes of Health), November 21, 1975.

"Terrestrial low tridymite, determination and refinement of a 240-atom structure related to glasses," by J. H. Konnert (Naval Research Laboratory) and "Mineralogical implications of the structure of tridymite," by D. E. Appleman (Smithsonian Institution), January 9, 1976.

"X-ray '76, a bicentennial issue," by J. M. Stewart (University of Maryland), February 13, 1976.

"Novel minerals, shattuckite, plancheite, and sherwoodite," by H. T. Evans, Jr. (U.S. Geological Survey), March 26, 1976.

"Structure of hemerythrins: non-heme oxygen carrying proteins," by W. A. Hendrickson and K. B. Ward (Naval Research Laboratory), April 23, 1976.

"Relationships between crystal structure and liquid crystal behavior," by R. F. Bryan (University of Virginia), May 21, 1976.

Seminar Series

The seminar series met eleven times during the report year. The following lectures were presented:

"A new, easily loaded information

system for igneous petrology," by F. Chayes (Geophysical Laboratory), October 2, 1975.

"Modeling the behavior of crystal structures," by R. Strens (Newcastle-upon-Tyne), October 14, 1975.

"Physical properties of mixtures," by R. Strens (Newcastle-upon-Tyne), October 15, 1975.

"Experimental studies of pyroxene phase equilibria at high temperature and pressure, and applications to *P-T* estimates of peridotites," by T. Mori (Australian National University), October 21, 1975.

"Geologic significance of some deep crustal nodules in South African kimberlites," by P. H. Nixon (University of Leeds), November 13, 1975.

"Crystallography of Fe^{3+} in forsterite," by S. S. Hafner (University of Marburg), November 26, 1975.

"Phase transitions in the lower mantle," by L. Liu (Australian National University), December 18, 1975.

"Response of Rb-Sr total rock and U-Pb zircon systems to low-grade regional metamorphism in the Mount Isa Precambrian block, Australia," by R. W. Page (Bureau of Mineral Resources, Canberra), March 25, 1976.

"Noncubic silicate garnets," by Y. Takéuchi (Mineralogical Institute, University of Tokyo), March 29, 1976.

"The use of fluid inclusions in geothermometry-geobarometry: analytical, experimental, and theoretical approach," by A. Weisbrod (University of Nancy, France), April 9, 1976.

"Metamorphosed carbonate rocks of the Nashobu formation, eastern Massachusetts," by Larry P. Cook (Solid State Chemistry Section, National Bureau of Standards), April 22, 1976.

Lectures

During the report year Staff Members and Fellows were invited to present lectures and participate in symposia and other extracurricular activities as follows:

P. M. Bell lectured to the Geological

Society of Washington on "Experiments on the electrical properties of the earth's deep mantle" and on "Crystal field effects in minerals" at the Department of Geology, Brooklyn College. He served as chairman of the Facilities Subcommittee at the Space Science Directorate, Johnson Spacecraft Center, Houston, and was a member of the Lunar Polar Orbiter Mission Advisory Panel, NASA Headquarters, Washington, D.C.

F. R. Boyd, Jr., delivered an invited lecture on "The mantle sample from kimberlites" at the Department of Geology, Yale University. He participated in a kimberlite symposium sponsored by the De Beers Corporation and held at St. Johns College, Cambridge, England, and is serving as co-convenor of the Second International Kimberlite Conference to be held in the U.S.A. in September 1977.

F. Chayes attended the meetings of the International Association for Volcanology in Grenoble, France, and participated in the concurrent sessions of the IUGS Subcommittee on Systematic Petrology during the first week of September.

D. H. Eggler lectured on petrologic interpretations of the low-velocity zone at the Department of Geological Sciences, Cornell University; and on plate tectonic theory as it affects the kimberlite study project south of Laramie, Wyoming, at a meeting of the Mineralogical Society of the District of Columbia. He is serving on the Organizing Committee of the Second International Kimberlite Conference.

J. M. Ferry presented an invited lecture on "Metamorphism of calcareous sediments in the Waterville-Vassalboro area, south-central Maine" at the U.S. Geological Survey, Reston, Virginia, in November.

P. E. Hare gave an invited lecture at a symposium on chronological techniques at the annual meeting of the Archaeological Institute of America. He served as chairman of a symposium on high performance liquid chromatography

sponsored by the National Institutes of Health.

J. I. Hedges addressed the Departments of Geology at the University of Pennsylvania and the University of California at Los Angeles; the Department of Geosciences at Purdue University; the Department of Oceanography at the University of Washington; and the Continental Oil Company at Ponca City, Oklahoma.

T. C. Hoering gave invited lectures on "Stable isotopes of hydrogen in Precambrian organic matter" at a Symposium on Chemical Evolution at the University of Maryland and on "The geochemistry of organic substances" at the Department of Geology, University of Alberta, Edmonton, Canada. He served as visiting investigator at the Marine Science Institute, University of Texas, Port Aransas, in August 1975 and lectured on "Biogeochemistry of the stable hydrogen isotopes." He also served on the Graduate Examination Committee, Department of Chemistry, University of Maryland.

J. R. Holloway lectured at the Geology Departments of the University of North Carolina, The Virginia Polytechnic Institute and State University, and the Johns Hopkins University, and at the Experimental Petrology Branch of the U.S. Geological Survey, Reston.

F. E. Huggins presented talks on "Mössbauer resonance spectroscopy of iron minerals under high pressures" as an invited participant in a symposium on minerals and rocks under high pressures at the Geological Society of America annual meeting at Salt Lake City; "Cation distributions in minerals and its application to the thermal history of rock" at the Research Division of Phillips Petroleum Company, Bartlesville, Oklahoma; "Mössbauer spectroscopy and its applications in earth sciences" at a geochemistry seminar series at the Department of Chemistry, University of Maryland; and "The crystal chemistry of titanium silicate garnets and its petrological implications" at the De-

partment of Geology, Washington University, St. Louis, and at the Basic Research Division of U.S. Steel Research, Monroeville, Pennsylvania.

T. N. Irvine and H. R. Naslund participated in the Geological Society of America Penrose Conference on "Magmatic sulfides and mafic plutons" held at Ely, Minnesota, on September 14-19, 1975. Irvine spoke on "Muskox intrusion, magma contamination, and magmatic ores"; Naslund talked on "The role of oxygen and sulfur in crystallization of the Skaergaard Intrusion."

I. Kushiro gave lectures at the Summer School of the University of Paris, held at Corsica, and at the Department of Geology, University of Oregon.

H. K. Mao lectured at the Departments of Geological Sciences at Cornell University and the University of Rochester. He also presented a paper at the U.S. Army Symposium on Ultra-High Pressure Phenomena at Rensselaerville, N.Y.

B. O. Mysen participated in the Geological Society of America Penrose Conference on "The Lithosphere-Asthenosphere Boundary" at Vail, Colorado, and presented an invited lecture on "Chemical characteristics of deep-seated rocks." He also gave invited lectures at Princeton University on "The effect of volatiles on partial melting in the upper mantle" and at the Lamont-Doherty Geological Observatory of Columbia University on "Volatiles in the mantle."

Y. Ohashi participated in the Conference on Computer Simulation for Materials Applications at the National Bureau of Standards, and gave lectures at the University of Pennsylvania, the Lunar Science Institute, the State University of New York at Stony Brook, and the State University of New York at Albany.

E. F. Osborn presented addresses on "The role of research and development in the world energy and mineral resource situation" at an International Symposium, sponsored by the National Acad-

emy of Sciences, Republic of Korea, commemorating the 30th Anniversary of the Korean Liberation at Seoul, Korea; "The mineral shortage and what can be done about it" at the AIME All-Institute Session on Materials, Energy, and Society at Las Vegas, Nevada; "The May 2, 1972, Sunshine Mine disaster and rescue effort" at the annual meeting of the Pittsburgh Section, American Ceramic Society; "Phase diagrams and refractories" at the annual meeting of the American Ceramic Society at Cincinnati, Ohio. He presented O. Frank Tuttle for the Roebling Medal of the Mineralogical Society of America at the MSA Luncheon at the annual meeting of the Society at Salt Lake City, Utah. Dr. Osborn served as chairman of the Board on Mineral Resources of the National Research Council; chairman of the U.S. National Committee on Geology, operating under the aegis of the Department of the Interior and the National Academy of Sciences. He attended meetings as a member of the Commission on Natural Resources of the National Research Council and as a member of the Materials Advisory Committee, Office of Technology Assessment, Congress of the United States, and chaired the panel on Mineral Accessibility on Federal Lands. Osborn served on the Visiting Advisory Committee on Mineral Science and Engineering, Michigan Technological University; the Steering Committee for the National Academy of Engineering/National Academy of Sciences Forum on "Materials and the Development of Nations"; a Workshop on Resource Identification and Development (chairman); the Geosciences Advisory Panel, Los Alamos Scientific Laboratory, Energy Research and Development Administration; the Pennsylvania Science and Engineering Foundation Board (Commonwealth of Pennsylvania, Harrisburg); the Pennsylvania Research Corporation Board of Directors (Pennsylvania State University); the Geisinger Medical Center Board of Directors, Danville, Pennsylvania; the

Board of Directors of the Institute for Medical Education and Research at Geisinger Medical Center; and the College of Engineering Advisory Board at the University of California at Berkeley. On March 5, 1976, Dr. Osborn received the Albert Victor Bleining Memorial Award for "distinguished achievement in the field of ceramics" at the annual meeting of the Pittsburgh Section of the American Ceramic Society.

D. Rumble III addressed a seminar at the Department of Earth and Space Sciences, State University of New York at Stony Brook; delivered two lectures at the Department of Geosciences, Purdue University; and presented a lecture series on Schreinemaker's analysis at Manchester University, England. He was chairman of the Mineralogical Society of America Management Committee and convenor of the MSA Short Course on Rock-Forming Minerals.

A. Van Valkenburg presented a paper at the U.S. Army Symposium on Ultra-High Pressure Phenomena at Rensselaerville, N.Y.

B. Velde lectured on "Partition coefficients for exchange cations in synthetic montmorillonites" at the School of Agronomy, Purdue University.

H. S. Yoder, Jr., attended a White House Conference on Earth Sciences sponsored by the American Geological Institute on 21 July 1976. Its purpose was to present the concerns of the geological community before the leaders of federal agencies dealing with minerals and energy. Dr. Yoder spoke on the urgent need for expanding the knowledge base to meet energy and mineral resource problems. Dr. Yoder also gave presentations before the U.S. National Committee on Geochemistry, Geophysics Research Board, Committee on Science and Public Policy, U.S. Geodynamics Committee, and the Assembly for Mathematical and Physical Sciences to bring attention to the critical need for basic research in the principles of element concentration.

Dr. Yoder presented two lectures at

the Lunar Science Institute on January 29 and 30, 1976, on the "Parental material for magma generation" and "Tectonophysics of melting in the mantle." Two lectures on magma generation were also presented at the Virginia Polytechnic Institute and State University, Blacksburg, Virginia. His address before the Annual Meeting of the Carnegie Institution of Washington was entitled "Molten rocks from the depths."

Dr. Yoder served on the U.S. National Committee for Geology, the U.S. National Committee on Geochemistry, the National Academy of Sciences Committee on Science and Public Policy, the National Academy of Sciences Auditing Committee, Geophysics Research

Board Review Committee, the Executive Committee of the Assembly of Mathematical and Physical Sciences, the National Research Council Earth Sciences Advisory Board, the Geosciences Advisory Panel at the Los Alamos Scientific Laboratory, and the Working Group on Long-Range Planning for Geodynamics. He completed his three-year term as chairman of the Geology Section of the National Academy of Sciences. In addition, Dr. Yoder was a member of the thesis defense committee of Frank Luther at Lehigh University on September 24, 1975, and he served on the Visiting Committee of Brown University at Providence, Rhode Island, on September 25-26, 1975.

BIBLIOGRAPHY

- Arculus, R. J., *see* Mysen, B. O.
- Bell, P. M., H. K. Mao, E. Roedder, and P. W. Weiblen, The problem of the origin of symplectites in olivine-bearing lunar rocks, in *Proc. Sixth Lunar Sci. Conf., Geochim. Cosmochim. Acta*, Suppl. 6, Vol. 1, Pergamon Press, New York, pp. 231-248, 1975 (G. L. Paper 1670).
- Bell, P. M., *see also* Mao, H. K.
- Boyd, F. R., and P. H. Nixon, Origins of the ultramafic nodules from some kimberlites of northern Lesotho and the Monastery Mine, South Africa, *Phys. Chem. Earth*, 9, 431-454, 1975 (G. L. Paper, 1648).
- Chayes, F., On the need, design, and prospects for an electronic information system serving igneous petrology, *J. Int. Assoc. Math. Geol.*, 7, 363-371, 1975 (G. L. Paper 1666).
- Eggler, D. H., CO₂ as a volatile component of the mantle: the system Mg₂SiO₄-SiO₂-H₂O-CO₂, *Phys. Chem. Earth*, 9, 869-881, 1975 (G. L. Paper 1642).
- Eggler, D. H., Does CO₂ cause partial melting in the low-velocity layer of the mantle? *Geology*, 4, 69-72, 1976 (G. L. Paper 1684).
- Eggler, D. H., and B. O. Mysen, The role of CO₂ in the genesis of olivine melilitite: discussion, *Contrib. Mineral. Petrol.*, 55, 231-236, 1976 (G. L. Paper 1678).
- Eggler, D. H., *see also* McCallum, M. E.; Mysen, B. O.
- Finger, L. W., and Y. Ohashi, The thermal expansion of diopside to 800°C and a refinement of the crystal structure at 700°C, *Am. Mineral.*, 61, 303-310, 1976 (G. L. Paper 1674).
- Hare, P. E., Amino acid composition by column chromatography, in *Protein Sequence Determination*, 2d rev. ed., S. B. Needleman, ed., Springer-Verlag, New York, pp. 204-231, 1975 (G. L. Paper 1676).
- Holloway, J. R., *see* Mysen, B. O.
- Huckenholz, H. G., Uvarovite stability in the CaSiO₃-Cr₂O₃ join up to 10 kbar, *Neues Jahrb. Mineral., Monatsch.*, 337-360, 1975 (G. L. Paper 1668).
- Mao, H. K., Charge-transfer processes at high pressure, in *The Physics and Chemistry of Minerals and Rocks*, R. G. J. Strens, ed., John Wiley and Sons, Inc., New York, pp. 573-581, 1976 (G. L. Paper 1673).
- Mao, H. K., and P. M. Bell, High-pressure physics: the 1-megabar mark on the ruby R₁ static pressure scale, *Science*, 191, 851-852, 1976 (G. L. Paper 1680).
- Mao, H. K., *see also* Bell, P. M.
- McCallum, M. E., and D. H. Eggler, Diamonds in an upper mantle peridotite nodule from kimberlite in southern Wyoming, *Science*, 192, 253-256, 1976 (G. L. Paper 1682).
- Muehlenbachs, K., Oxygen-isotope geochemistry of DSDP Leg 34 basalts, in *Initial Reports of the Deep Sea Drilling Project*, U.S. Government Printing Office, Washington, D.C., Vol. 34, Chap. 20, pp. 337-339, 1976 (G. L. Paper 1685).
- Mysen, B. O., Partitioning of iron and magnesium between crystals and partial melts in peridotite upper mantle, *Contrib. Mineral. Petrol.*, 52, 69-76, 1975 (G. L. Paper 1669).
- Mysen, B. O., Partitioning of samarium and nickel between olivine, orthopyroxene, and liquid; preliminary data at 20 kbar and 1025°C, *Earth Planet. Sci. Lett.*, 31, 1-7, 1976 (G. L. Paper 1681).
- Mysen, B. O., R. J. Arculus, and D. H. Eggler,

- Solubility of carbon dioxide in melts of andesite, tholeiite, and olivine nephelinite composition to 30 kbar pressure, *Contrib. Mineral. Petrol.*, **53**, 227–239, 1975 (G. L. Paper 1671).
- Mysen, B. O., D. H. Eggler, M. G. Seitz, and J. R. Holloway, Carbon dioxide in silicate melts and crystals, Part I, Solubility measurements, *Am. J. Sci.*, **276**, 455–479, 1976 (G. L. Paper 1679).
- Mysen, B. O., *see also* Eggler, D. H.
- Nixon, P. H., *see* Boyd, F. R.
- Ohashi, Y., *see* Finger, L. W.
- Osborn, E. F., The role of research and development in the world energy and mineral resource situation, in *Proceedings, International Symposium Commemorating the 30th Anniversary of Korean Liberation, August 11–20, 1975*, National Academy of Sciences, Republic of Korea, pp. 505–514, 1975 (G. L. Paper 1677).
- Roedder, E., *see* Bell, P. M.
- Seitz, M. G., *see* Mysen, B. O.
- Weiblen, P. W., *see* Bell, P. M.
- Yoder, H. S., Jr., Relationship of melilite-bearing rocks to kimberlite: a preliminary report on the system akermanite- CO_2 , *Phys. Chem. Earth*, **9**, 883–894, 1975 (G. L. Paper 1641).

REFERENCES CITED

- Abrahams, S. C., and S. Geller, Refinement of the structure of a grossularite garnet, *Acta Crystallogr.*, **11**, 437–441, 1958.
- Abu-Eid, R. M., Absorption spectra and phase transformation of minerals at pressures up to 200 kilobars, Ph.D. thesis, Massachusetts Institute of Technology, 1975.
- Adam, G., and J. H. Gibbs, On the temperature dependence of cooperative relaxation properties in glass-forming liquids, *J. Chem. Phys.*, **43**, 139–146, 1965.
- Aitken, A. C., *Determinants and Matrices*, 9th ed., Oliver and Boyd Ltd., Edinburgh, 1962.
- Albarede, F., and Y. Bottinga, Kinetic disequilibrium in trace element partitioning between phenocrysts and host lava, *Geochim. Cosmochim. Acta*, **36**, 141–156, 1972.
- Albert, J. T., and R. D. Harter, Adsorption of lysozyme and ovalbumin by clay: effect of clay suspension pH and clay mineral type, *J. Soil Sci.*, **116**, 130–136, 1973.
- Allsopp, H. L., and D. R. Barrett, Rb-Sr age determinations on South African kimberlite pipes, *Phys. Chem. Earth*, **9**, 605–617, 1975.
- Allsopp, H. L., A. J. Burger, and C. Van Zyl, A minimum age for the Premier kimberlite pipe yielded by biotite Rb-Sr measurements, with related galena isotopic data, *Earth Planet. Sci. Lett.*, **3**, 161–166, 1967.
- American Petroleum Institute, *American Petroleum Institute Research Project No. 49 (Clay Mineral Standards)*, Columbia University, New York, 1951.
- Amthauer, G., H. Annersten, and S. S. Hafner, The Mössbauer spectrum of ^{57}Fe in silicate garnets, *Z. Kristallogr.*, in press, 1976.
- Anastasiou, P., and F. Seifert, Solid solubility of Al_2O_3 in enstatite at high temperatures and 1–5 kb water pressure, *Contrib. Mineral. Petrol.*, **34**, 272–287, 1972.
- Andersen, O., The system anorthite-forsterite-silica, *Am. J. Sci.*, **39**, 407–454, 1915.
- Anderson, A. T., The oxygen fugacity of alkaline basalt and related magmas, Tristan da Cunha, *Am. J. Sci.*, **266**, 704–727, 1968.
- Anderson, A. T., Chlorine, sulfur and water in magmas and oceans, *Geol. Soc. Am. Bull.*, **85**, 1485–1495, 1974.
- Anderson, D. L., C. Sammis, and T. Jordan, Composition of the mantle and core, in *The Nature of the Solid Earth*, E. C. Robertson, ed., McGraw-Hill Book Company, New York, pp. 41–66, 1972.
- Anderson, G. M., Some thermodynamics of dehydration equilibria, *Am. J. Sci.*, **269**, 392–401, 1970.
- Arndt, N. T., Ultramafic rocks of Munro Township and their volcanic setting, Ph.D. thesis, University of Toronto, 1975.
- Bailey, D. K., Volatile flux, heat-focusing and the generation of magma, in *Mechanism of Igneous Intrusion*, G. Newall and N. Rast, eds., Gallery Press, Liverpool, pp. 177–186, 1970.
- Bailey, D. K., and J. F. Schairer, The system $\text{Na}_2\text{O}-\text{Al}_2\text{O}_3-\text{Fe}_2\text{O}_3-\text{SiO}_2$ at 1 atmosphere and the petrogenesis of alkaline rocks, *J. Petrol.*, **7**, 114–170, 1966.
- Banno, S., Classification of eclogites in terms of physical conditions of their origin, *Phys. Earth Planet. Inter.*, **3**, 405–421, 1970.
- Barghoorn, E. S., W. G. Meinschein, and J. W. Schopf, Paleobiology of a Precambrian shale, *Science*, **148**, 461–472, 1965.
- Barker, D. S., The Hallowell granite, south-central Maine, *Am. J. Sci.*, **262**, 592–613, 1964.
- Barrett, D. R., and H. L. Allsopp, Rubidium-strontium age determinations on South African kimberlite pipes, in *International Conference on Kimberlites, Extended Abstracts*, University of Cape Town, Rondebosch, South Africa, pp. 23–26, 1973.
- Barth, T. F. W., The distribution of oxygen in the lithosphere, *J. Geol.*, **56**, 41–50, 1948a.
- Barth, T. F. W., Oxygen in rocks: a basis for petrographic calculations, *J. Geol.*, **56**, 50–61, 1948b.
- Bayer, G., J. Felsche, H. Schulz, and P. Rüeggsegger, X-ray study and Mössbauer spectroscopy on lunar ilmenites (Apollo 11), *Earth Planet. Sci. Lett.*, **16**, 273–274, 1972.
- Becking, L. G. M. B., I. R. Kaplan, and D.

- Moore, Limits of the natural environment in terms of pH and oxidation-reduction potentials, *J. Geol.*, **68**, 243-284, 1960.
- Bell, P. M., H. K. Mao, and G. R. Rossman, Absorption spectroscopy of ionic and molecular units in crystals and glasses, in *Infrared and Raman Spectroscopy of Lunar and Terrestrial Minerals*, C. Karr, Jr., ed., Academic Press, New York, pp. 1-38, 1975.
- Berger, M. J., and S. M. Selzer, Tables of energy losses and ranges of electrons and positrons, *NAS-NRC Publ.*, **1133**, 205-268, 1964.
- Berman, H., A torsion microbalance for the determination of minerals, *Am. Mineral.*, **24**, 434-440, 1939.
- Bertaut, F., L'énergie électrostatique de Réseaux ioniques, *J. Phys. Radium*, **13**, 499-505, 1952.
- Bickford, M. E., and D. G. Mose, Geochronology of Precambrian rocks in the St. Francois Mountains, southeastern Missouri, *Geol. Soc. Am. Spec. Pap.*, **165**, 1976.
- Bickle, M. J., A. Martin, and E. G. Nisbet, Basaltic and peridotitic komatiites and stromatolites above a basal unconformity in the Belingwe greenstone belt, Rhodesia, *Earth Planet. Sci. Lett.*, **27**, 155-162, 1975.
- Binns, R. A., Hornblendes from some basic hornfels in the New England region, New South Wales, *Mineral. Mag.*, **34**, 52-65, 1965.
- Birch, F., Compressibility; elastic constants, in "Handbook of Physical Constants," S. P. Clark, ed., *Geol. Soc. Am. Spec. Pap.*, **97**, 97-173, 1966.
- Bischoff, J. L., and F. W. Dickson, Seawater basalt interaction at 200°C and 500 bars: implications for origin of sea-floor heavy metal deposits and regulation of seawater chemistry, *Earth Planet. Sci. Lett.*, **25**, 385-397, 1975.
- Bockris, J. O'M., J. D. Mackenzie, and J. A. Kitchen, Viscous flow in silica and binary liquid silicates, *Trans. Faraday Soc.*, **51**, 1734-1748, 1955.
- Boettcher, A. J., and P. J. Wyllie, Jadeite stability measured in the presence of silicate liquids in the system NaAlSiO₄-SiO₂-H₂O, *Geochim. Cosmochim. Acta*, **32**, 999-1012, 1968.
- Boettcher, A. L., and P. J. Wyllie, Phase relationships in the system NaAlSiO₄-SiO₂-H₂O to 35 kilobars pressure, *Am. J. Sci.*, **267**, 875-909, 1969.
- Bond, W. L., Making small spheres, *Rev. Sci. Instrum.*, **22**, 344-345, 1951.
- Borley, G. D., Mantle deformation beneath the South African and Siberian platforms, *Nature (London)*, **254**, 489-491, 1975.
- Bottinga, Y., and D. F. Weill, The viscosity of magmatic silicate liquids: a model for calculation, *Am. J. Sci.*, **272**, 438-475, 1972.
- Bowen, N. L., *The Evolution of the Igneous Rocks*, Princeton University Press, Princeton, N.J., 1928.
- Bowen, N. L., and J. F. Schairer, The system, FeO-SiO₂, *Am. J. Sci.*, **24**, 177-213, 1932.
- Bowen, N. L., and J. F. Schairer, The system, MgO-FeO-SiO₂, *Am. J. Sci.*, **29**, 151-217, 1935.
- Bowen, N. L., and J. F. Schairer, Crystallization equilibrium in nepheline-albite-silica mixtures with fayalite, *J. Geol.*, **46**, 397-411, 1938.
- Boyd, F. R., A pyroxene geotherm, *Geochim. Cosmochim. Acta*, **37**, 2533-2546, 1973.
- Boyd, F. R., and J. L. England, Apparatus for phase-equilibrium measurements at pressures up to 50 kb and temperatures up to 1750°C, *J. Geophys. Res.*, **65**, 741-748, 1960.
- Boyd, F. R., and P. H. Nixon, Origin of the ilmenite-silicate nodules in kimberlites from Lesotho and South Africa, in *Lesotho Kimberlites*, P. H. Nixon, ed., Lesotho National Development Corporation, Maseru, Lesotho, pp. 254-268, 1973.
- Boyd, F. R., and P. H. Nixon, Origins of the ultramafic nodules from some kimberlites of northern Lesotho and the Monastery Mine, South Africa, *Phys. Chem. Earth*, **9**, 431-454, 1975.
- Bravo, M. S., and M. J. O'Hara, Partial melting of phlogopite-bearing synthetic spinel and garnet-ilherzolites, *Phys. Chem. Earth*, **9**, 845-854, 1975.
- Brett, R., The earth's core: speculations on its chemical equilibrium with the mantle, *Geochim. Cosmochim. Acta*, **35**, 203-221, 1971.
- Brett, R., and P. M. Bell, Melting relations in the Fe-rich portion of the system Fe-FeS at 30 kb pressure, *Earth Planet. Sci. Lett.*, **6**, 479-482, 1969.
- Brey, G., and D. H. Green, The role of CO₂ in the genesis of olivine melilitite, *Contrib. Mineral. Petrol.*, **49**, 93-103, 1975.
- Brog, K. C., W. H. Jones, Jr., and C. M. Verber, ²⁷Al and ²⁹Al nuclear magnetic resonance in yttrium-aluminum garnet, *Phys. Lett.*, **20**, 258-260, 1966.
- Brookins, D. G., Ilmenite-(serpentinized) pyroxene nodules from the Stockdale kimberlite pipe, Riley County, Kansas (abstract), *Abstr. with Programs (Geol. Soc. Am.)*, **3**, 233, 1971.
- Buddington, A. F., and D. H. Lindsley, Iron-titanium oxide minerals and synthetic equivalents, *J. Petrol.*, **5**, 310-357, 1964.
- Buerger, M. J., and C. T. Prewitt, The crystal structures of wollastonite and pectolite, *Proc. Natl. Acad. Sci. U.S.A.*, **47**, 1884-1888, 1961.
- Buie, B. F., Igneous rocks of the Highwood Mountains, Montana, *Geol. Soc. Am. Bull.*, **52**, 1753-1808, 1941.
- Bundy, F. P., H. P. Bovenkerk, H. M. Strong, and R. H. Wentorf, Jr., Diamond-graphite equilibrium line from growth and graphitization of diamond, *J. Chem. Phys.*, **35**, 383-391, 1961.
- Burnham, C. W., Computation of absorption

- correction and the significance of end effect, *Am. Mineral.*, **51**, 159-167, 1966.
- Burnham, C. W., Thermodynamics of melting in experimental silicate-volatile systems, *Geochim. Cosmochim. Acta*, **39**, 1077-1084, 1975.
- Burnham, C. W., and N. F. Davis, The role of H₂O in silicate melts, I, *P-V-T* relations in the system NaAlSi₃O₈-H₂O to 10 kilobars and 1000°C, *Am. J. Sci.*, **270**, 54-79, 1971.
- Burnham, C. W., and N. F. Davis, The role of H₂O in silicate melts, II, Thermodynamic and phase relations in the system NaAlSi₃O₈-H₂O to 10 kilobars, 700°C to 1100°C, *Am. J. Sci.*, **274**, 902-940, 1974.
- Burnham, C. W., J. R. Holloway, and N. F. Davis, Thermodynamic properties of water to 1,000°C and 10,000 bars, *Geol. Soc. Am. Spec. Pap.*, **132**, 96 pp., 1969.
- Burns, R. G., *Mineralogical Applications of Crystal Field Theory*, Cambridge University Press, Cambridge, 1970.
- Burns, R. G., and W. S. Fyfe, Site preference energy and selective uptake of transition metal ions during magmatic crystallization, *Science*, **144**, 1001-1003, 1964.
- Burns, R. G., and W. S. Fyfe, Distribution of elements in geologic processes, *Chem. Geol.*, **1**, 49-56, 1966.
- Burns, R. G., and W. S. Fyfe, Crystal-field theory and the geochemistry of transition elements, in *Researches in Geochemistry*, Vol. 2, P. H. Abelson, ed., John Wiley and Sons, Inc., New York, pp. 259-285, 1967.
- Burns, R. G., D. J. Vaughan, R. M. Abu-Eid, and M. Witner, Spectral evidence for Cr³⁺, Ti³⁺, and Fe²⁺ rather than Cr²⁺ and Fe³⁺ in lunar ferromagnesian silicates, in *Proc. Fourth Lunar Sci. Conf.*, *Geochim. Cosmochim. Acta*, Suppl. 4, Vol. 1, Pergamon Press, New York, pp. 983-994, 1973.
- Cameron, M., S. Sueno, C. T. Prewitt, and J. J. Papike, High-temperature crystal chemistry of actinolite, diopside, hedenbergite, jadeite, spodumene, and ureyite, *Am. Mineral.*, **58**, 594-618, 1973.
- Carmichael, I. S. E., The iron-titanium oxides of salic volcanic rocks and their associated ferromagnesian silicates, *Contrib. Mineral. Petrol.*, **14**, 36-64, 1967a.
- Carmichael, I. S. E., The mineralogy of Thingmuli, a Tertiary volcano in eastern Iceland, *Am. Mineral.*, **52**, 1815-1841, 1967b.
- Carmichael, I. S. E., and J. Nicholls, Iron-titanium oxides and oxygen fugacities in volcanic rocks, *J. Geophys. Res.*, **72**, 4665-4687, 1967.
- Carmichael, I. S. E., F. J. Turner, and J. Verhoogen, *Igneous Petrology*, McGraw-Hill Book Company, New York, 1974.
- Carter, E. K., J. H. Brooks, and K. R. Walker, The Precambrian mineral belt of northwestern Queensland, *Bur. Miner. Resour. Aust. Bull.*, **51**, 344 pp., 1961.
- Carter, W. J., S. P. Marsh, J. N. Fritz, and R. G. McQueen, The equation of state of selected materials for high-pressure references, *Natl. Bur. Stand. (U.S.) Spec. Publ.*, **326**, 147-158, 1971.
- Cawthorn, R. G., and K. D. Collerson, The recalculation of pyroxene end-member parameters and the estimation of ferrous and ferric iron content from electron microprobe analyses, *Am. Mineral.*, **59**, 1203-1208, 1974.
- Charlot, R., The Precambrian of the Anti-Atlas (Morocco); a geochronological synthesis, *Precambrian Res.*, **3**, 273-299, 1976.
- Chatterjee, N. D., and W. Johannes, Thermal stability and standard thermodynamic properties of synthetic 2M₁-muscovite, KAl₂[AlSi₃O₁₀(OH)₂], *Contrib. Mineral. Petrol.*, **48**, 89-114, 1974.
- Chayes, F., On estimating the magnitude of the hidden zone and the compositions of the residual liquids of the Skaergaard layered series, *J. Petrol.*, **11**, 1-14, 1970.
- Clark, J. R., D. E. Appleman, and J. J. Papike, Crystal-chemical characterization of clinopyroxenes based on eight new structure refinements, *Mineral. Soc. Am. Spec. Pap.*, **2**, 31-50, 1969.
- Clark, S. P., Jr., and A. E. Ringwood, Density distribution and constitution of the mantle, *Rev. Geophys.*, **2**, 35-88, 1964.
- Clementi, E., Ab initio computations in atoms and molecules, *IBM J. Res. Dev.*, **9**, 2-19, 1965.
- Clendenen, R. L., and H. G. Drickamer, Lattice parameters of nine oxides and sulfides as a function of pressure, *J. Chem. Phys.*, **44**, 4223-4228, 1966.
- Compston, W., A. R. Crawford, and V. M. Bofinger, A radiometric estimate of the duration of sedimentation in the Adelaide geosyncline, South Australia, *J. Geol. Soc. Aust.*, **13**, 229-276, 1966.
- Coons, W. E., J. R. Holloway, and A. Navrotsky, Co²⁺ as a chemical analogue for Fe²⁺ in high temperature experiments in basaltic systems, *Earth Planet. Sci. Lett.*, in press, 1976.
- Cooper, A. F., and J. F. Lovering, Greenschist amphiboles from Haast River, New Zealand, *Contrib. Mineral. Petrol.*, **27**, 11-24, 1970.
- Cormier, R. F., Radiometric dating of the Coldbrook group of southern New Brunswick, Canada, *Can. J. Earth Sci.*, **6**, 393-398, 1969.
- Cromer, D. T., Anomalous dispersion corrections computed from self-consistent field relativistic Dirac-Slater wave functions, *Acta Crystallogr.*, **18**, 17-23, 1965.
- Cromer, D. T., and J. B. Mann, X-ray scattering factors computed from numerical Hartree-Fock wave functions, *Acta Crystallogr., Sect. A*, **24**, 321-324, 1968.

- Crozaz, G., U, Th, and extinct ^{244}Pu in the phosphates of the St. Severin meteorite, *Earth Planet. Sci. Lett.*, **23**, 164–169, 1974.
- Czerlinsky, E. R., and R. A. MacMillan, Cation distribution in aluminum-substituted yttrium iron garnets by Mössbauer effect spectroscopy, *Phys. Status Solidi*, **41**, 333–341, 1970.
- Dane, E. B., Jr., Densities of molten rocks and minerals, *Am. J. Sci.*, **239**, 809–818, 1941.
- Davis, B. T. C., and F. R. Boyd, The join $\text{Mg}_2\text{Si}_2\text{O}_6\text{--CaMgSi}_2\text{O}_6$ at 30 kilobars pressure and its application to pyroxenes from kimberlites, *J. Geophys. Res.*, **71**, 3567–3576, 1966.
- Dawson, J. B., Geochemistry and origin of kimberlite, in *Ultramafic and Related Rocks*, P. J. Wyllie, ed., John Wiley and Sons, Inc., New York, pp. 269–278, 1967.
- Dawson, J. B., J. J. Gurney, and P. J. Lawless, Paleogeothermal gradients derived from xenoliths in kimberlite, *Nature (London)*, **257**, 299–300, 1975.
- Dawson, J. B., and A. M. Reid, A pyroxene-ilmenite intergrowth from the Monastery Mine, South Africa, *Contrib. Mineral. Petrol.*, **26**, 296–301, 1970.
- Dawson, J. B., and J. V. Smith, Occurrence of diamond in a mica-garnet lherzolite xenolith from kimberlite, *Nature (London)*, **254**, 580–581, 1975.
- Day, D. E., and G. E. Rindone, Properties of soda aluminosilicate glasses: I, Refractive index, density, molar refractivity, and infrared absorption spectra, *J. Am. Ceram. Soc.*, **45**, 489–496, 1962.
- De, A., Silicate liquid immiscibility in the Deccan traps and its petrogenetic significance, *Geol. Soc. Am. Bull.*, **85**, 471–474, 1974.
- Decker, D. L., Equation of state of NaCl and its use as a pressure gauge in high-pressure research, *J. Appl. Phys.*, **36**, 157–161, 1965.
- Deines, P., R. H. Nafziger, G. C. Ulmer, and E. Woermann, Temperature-oxygen fugacity tables for selected gas mixtures in the system C-H-O at one atmosphere total pressure, *Pa. State Univ. Earth Miner. Sci. Exp. Stn. Bull.*, **28**, 1974.
- Denaeyer, M.-E., Les laves du fossé tectonique de l'Afrique Centrale (Kivu, Rwanda, Toro-Ankole), I, Supplément au recueil d'analyses de 1965, II, Magmatologie, III, Magmatogenèse, *Mus. R. Afr. Cent. Belg. Ann. Ser. Octavo Sci. Geol.*, No. 72, 1972.
- Denaeyer, M.-E., F. Schellinck, and A. Coppez, Recueil d'analyses des laves du fossé tectonique de l'Afrique Centrale (Kivu, Rwanda, Toro-Ankole), *Mus. R. Afr. Cent. Belg. Ann. Ser. Octavo Sci. Geol.*, No. 49, 1965.
- Derighetti, B., and S. Ghose, Nuclear magnetic resonance of ^{27}Al in the garnet grossularite, *Phys. Lett. A*, **28**, 523–524, 1969.
- Derrick, G. M., I. H. Wilson, and R. M. Hill, Revision of stratigraphic nomenclature in the Precambrian of northwestern Queensland, I, Tewinga group, *Queensl. Gov. Min. J.*, March 1976.
- de Santis, R., G. F. J. Breedvelde, and J. M. Prausnitz, Thermodynamic properties of aqueous gas mixtures at advanced pressures, *Ind. Eng. Chem., Process Des. Dev.*, **13**, 374–377, 1974.
- Dickey, J. S., Jr., Partial fusion products in alpine-type peridotites: Serrania de la Ronda and other examples, *Mineral. Soc. Am. Spec. Pap.*, **3**, 33–49, 1970.
- Dollase, W. A., Reinvestigation of the structure of low cristobalite, *Z. Kristallogr.*, **121**, 369–377, 1965.
- Donaldson, C. H., Olivine morphology in the Tertiary harrisites of Rhum and in some Archean spinifex rocks, *Geol. Soc. Am. Bull.*, **18**, 22–28, 1974.
- Douglas, J. A. V., A further petrological and chemical investigation of the upper part of the Skaergaard intrusion, East Greenland, unpublished Ph.D. thesis, University of Oxford, 1961.
- Downes, M. J., Sector and oscillatory zoning in calcic augites from Mt. Etna, Sicily, *Contrib. Mineral. Petrol.*, **47**, 187–196, 1974.
- Dowty, E., Crystal chemistry of titanian and zirconian garnet: I, Review and spectral studies, *Am. Mineral.*, **56**, 1983–2009, 1971.
- Dowty, E., and J. R. Clark, Crystal structure refinement and optical properties of a Ti^{3+} fassaite from the Allende meteorite, *Am. Mineral.*, **58**, 230–242, 1973.
- Drake, M. J., and D. F. Weill, Partition of Sr, Ba, Ca, Y, Eu^{2+} , Eu^{3+} and other REE between plagioclase, feldspar and magmatic liquid: an experimental study, *Geochim. Cosmochim. Acta*, **39**, 689–712, 1975.
- Drickamer, H. G., and C. W. Frank, *Electronic Transitions and the High Pressure Chemistry and Physics of Solids*, Chapman and Hall, Ltd., London, 1973.
- Edmister, W. C., Applied hydrocarbon thermodynamics, Part 32, Compressibility factors and fugacity coefficients from the Redlich-Kwong equation of state, *Hydrocarbon Process.*, **47**, 239–244, 1968.
- Edmonds, D. T., and A. J. Lindop, Quadrupole splittings and paramagnetic shifts in the NMR of ^{27}Al in rare earth aluminum garnets, *J. Appl. Phys.*, **39**, 1008–1009, 1968.
- Eggler, D. H., CO_2 as a volatile component of the mantle: the system $\text{Mg}_2\text{SiO}_4\text{--SiO}_2\text{--H}_2\text{O--CO}_2$, *Phys. Chem. Earth*, **9**, 869–881, 1975.
- Eggler, D. H., Does CO_2 cause partial melting in the low-velocity layer of the mantle? *Geology*, **4**, 69–72, 1976.
- Eglinton, G., P. M. Scott, T. Belsky, A. L. Burlingame, W. Richter, and M. Calvin, Occurrence of isoprenoid alkanes in a Precambrian sediment, in *Advances in Organic Geochemistry*, 1964, G. D. Hobson and M. C.

- Louis, eds., Pergamon Press, Oxford, pp. 41-77, 1966.
- Enders, C., and K. Theis, Die Melanoidine und ihre Beziehung zu de Huminsäuren, *Brennst.-Chem.*, 19, 402-407, 1938.
- Engel, A. E. J., and C. E. Engel, Hornblendes formed during progressive metamorphism of amphibolites, northwest Adirondack Mountains, New York, *Geol. Soc. Am. Bull.*, 73, 1499-1515, 1962.
- Ernst, W. G., The stability relations of magnesioriebeckite, *Geochim. Cosmochim. Acta*, 19, 10-40, 1960.
- Ernst, W. G., Ca-amphibole, paragenesis in the Shirataki District, Central Shikoku, Japan, *Geol. Soc. Am. Mem.*, 135, 73-94, 1972.
- Eugster, H. P., Reduction and oxidation in metamorphism, in *Researches in Geochemistry*, Vol. 1, P. H. Abelson, ed., John Wiley and Sons, Inc., New York, pp. 397-426, 1959.
- Eugster, H. P., and G. B. Skippen, Igneous and metamorphic reactions involving gas equilibria, in *Researches in Geochemistry*, Vol. 2, P. H. Abelson, ed., John Wiley and Sons, Inc., New York, pp. 492-520, 1967.
- Eugster, H. P., and D. R. Wones, Stability relations of the ferruginous biotite, annite, *J. Petrol.*, 3, 82-125, 1962.
- Euler, F., and J. A. Bruce, Oxygen coordinates of compounds with garnet structure, *Acta Crystallogr.*, 19, 971-978, 1965.
- Fairbairn, H. W., M. L. Bottino, W. H. Pinson, and P. M. Hurley, Whole-rock age and initial $\text{Sr}^{87}/\text{Sr}^{86}$ of volcanics underlying fossiliferous lower Cambrian in the Atlantic provinces of Canada, *Can. J. Earth Sci.*, 3, 509-521, 1966.
- Fairbairn, H. W., and P. M. Hurley, Northern Appalachian geochronology as a model for interpreting ages in older orogens, *Mass. Inst. Technol. 17th Ann. Prog. Rep. to USAEC*, 11-17, 1969.
- Fenn, P. M., and G. E. Brown, Energetics of the alkali site in K-Na feldspars (abstract), *Abstr. with Programs (Geol. Soc. Am.)*, 7, 1071-1072, 1975.
- Ferguson, A. K., On hour-glass sector zoning in clinopyroxene, *Mineral. Mag.*, 39, 321-325, 1973.
- Ferguson, J., and K. L. Currie, Evidence of liquid immiscibility in alkaline ultrabasic dikes at Callander Bay, Ontario, *J. Petrol.*, 12, 561-585, 1971.
- Ferraro, J. R., and M. H. Manghnani, Infrared absorption spectra of sodium silicate glasses at high pressures, *J. Appl. Phys.*, 43, 4595-4599, 1972.
- Ferry, J. M., Metamorphism of calcareous sediments in the Waterville-Vassalboro area, south-central Maine: mineral reactions and graphical analysis, *Am. J. Sci.*, in press, 1976a.
- Ferry, J. M., P , T , f_{CO_2} , and $f_{\text{H}_2\text{O}}$ during metamorphism of calcareous sediments in the Waterville-Vassalboro area, south-central Maine, *Contrib. Mineral. Petrol.*, in press, 1976b.
- Finger, L. W., and E. Prince, A system of Fortran IV computer programs for crystal structure computations, *Natl. Bur. Stand. (U.S.) Tech. Note*, 854, 133 pp., 1975.
- Fitch, F. J., and J. A. Miller, Potassium-argon radioages of Karroo volcanic rocks from Lesotho, *Bull. Volcanol.*, 35, 64-84, 1971.
- Fleet, M. E., Growth habits of clinopyroxene, *Can. Mineral.*, 13, 336-341, 1975.
- Flower, M. F. J., Phase relations of titanacmite in the system $\text{Na}_2\text{O}-\text{Fe}_2\text{O}_3-\text{Al}_2\text{O}_3-\text{TiO}_2-\text{SiO}_2$ at 1000 bars total water pressure, *Am. Mineral.*, 59, 536-548, 1974.
- Fodor, R. V., K. Keil, and T. E. Bunch, Contributions to the mineral chemistry of Hawaiian rocks, IV, Pyroxenes in rocks from Haleakala and West Maui volcanoes, Maui, Hawaii, *Contrib. Mineral. Petrol.*, 50, 173-195, 1975.
- Foster, W. R., The system $\text{NaAlSi}_3\text{O}_8-\text{CaSiO}_3-\text{NaAlSiO}_4$, *J. Geol.*, 50, 152-173, 1942.
- Franck, E. U., and K. Tödheide, Thermische Eigenschaften überkritischer Mischungen von Kohlendioxyd und Wasser bis zu 750°C und 2000 Atm., *Z. Phys. Chem.*, 37, 232-243, 1959.
- Frantz, J., and H. K. Mao, Metasomatic zoning resulting from intergranular diffusion: I, A theoretical model for monomineralic reaction zone sequences, *Am. J. Sci.*, 276, in press, 1976.
- French, B. M., Some geological implications of equilibrium between graphite and a C-H-O gas at high temperatures and pressures, *Rev. Geophys.*, 4, 223-253, 1966.
- Friel, J. J., and G. C. Ulmer, Oxygen fugacity thermometry of the Oka carbonatite, *Am. Mineral.*, 59, 314-318, 1974.
- Fripiat, J. J., A. Leonard, and N. Barake, Relation entre la structure et la texture des gels de silice, *Bull. Soc. Chim. Fr.*, 23, 123-140, 1963.
- Frost, A. A., and R. G. Pearson, *Kinetics and Mechanism*, John Wiley and Sons, Inc., New York, 1961.
- Fudali, R. F., Oxygen fugacities of basaltic and andesitic magmas, *Geochim. Cosmochim. Acta*, 29, 1063-1075, 1965.
- Fujii, T., and E. Takahashi, On the solubility of alumina in orthopyroxene coexisting with olivine and spinel in the system $\text{MgO}-\text{Al}_2\text{O}_3-\text{SiO}_2$, *Mineral. J.*, 8, 122-128, 1976.
- Gaffey, M. J., Spectral reflectance characteristics of the meteorite classes, *J. Geophys. Res.*, 81, 905-920, 1976.
- Gale, G. H., Paleozoic basaltic komatiite and ocean-floor basalts from northeastern Newfoundland, *Earth Planet. Sci. Lett.*, 18, 22-28, 1973.
- Gast, P. W., Trace element fractionation and the origin of tholeiitic and alkaline magma types, *Geochim. Cosmochim. Acta*, 32, 1057-1086, 1968.

- General Electric Company, *Silicon-Controlled Rectifier Manual*, 1964.
- Gentil, L., Sur la microstructure de la mélilité, *Bull. Soc. Fr. Mineral.*, 17, 108-119, 1894.
- Gerlach, T. M., and B. E. Nordlie, The C-O-H-S gaseous system, Part I, Composition limits and trends in basaltic gases, *Am. J. Sci.*, 275, 353-376, 1975a.
- Gerlach, T. M., and B. E. Nordlie, The C-O-H-S gaseous system, Part II, Temperature, atomic composition, and molecular equilibria in volcanic gases, *Am. J. Sci.*, 275, 377-394, 1975b.
- Gerlach, T. M., and B. E. Nordlie, The C-O-H-S gaseous system, Part III, Magmatic gases compatible with oxides and sulfides in basaltic magmas, *Am. J. Sci.*, 275, 395-410, 1975c.
- Gibb, F. G. F., The zoned clinopyroxenes of the Shiant Isles Sill, Scotland, *J. Petrol.*, 14, 203-230, 1973.
- Gibb, F. G. F., Supercooling and the crystallization of plagioclase from a basaltic magma, *Mineral. Mag.*, 39, 641-653, 1974.
- Gilbert, M. C., High-pressure stability of acmite, *Am. J. Sci.*, Schairer Vol., 267A, 145-159, 1969.
- Goetze, C., Sheared lherzolites: from the point of view of rock mechanics, *Geology*, 3, 172-173, 1975.
- Goldich, S. S., and M. G. Mudrey, Jr., Dilatancy model for discordant U-Pb zircon ages, in *Contributions to Recent Geochemistry and Analytical Chemistry*, A. I. Tugarinov, ed., Nauka Publishing Office, Moscow, pp. 415-418, 1972.
- Goldman, D. S., and A. L. Albee, Correlation of Mg/Fe partitioning between garnet and biotite with O^{18}/O^{16} partitioning between quartz and magnetite, *Am. Mineral.*, in press, 1976.
- Goldschmidt, V. M., Über die Raumerfüllung der Atomen (Ionen) in Kristallen und über das Wesen der Lithosphäre, *Neues Jahrb. Mineral., Beil. Band, Abt. A*, 57, 1119-1130, 1928.
- Goodspeed, R. M., The petrology of the Togus plutonic complex, south-central Maine, M.S. thesis, University of Maine, 109 pp., 1962.
- Gooley, R. C., R. Brett, and J. L. Warner, Crystallization history of metal particles in Apollo 16 rake samples, in *Proc. Fourth Lunar Sci. Conf.*, *Geochim. Cosmochim. Acta*, Suppl. 4, Vol. 1, Pergamon Press, New York, pp. 799-810, 1973.
- Graham, C. M., Metabasite amphiboles of the Scottish Dalradian, *Contrib. Mineral. Petrol.*, 47, 165-185, 1974.
- Gramse, M., Quantitative Untersuchungen mit der Elektronen-Mikrosonde an Pyroxenen aus Basalten und Peridotit-Einschlüssen, *Contrib. Mineral. Petrol.*, 29, 43-74, 1970.
- Green, D. H., The origin of basaltic and nephelinitic magmas, *Trans. Leicester Lit. Philos. Soc.*, 64, 28-54, 1970.
- Green, D. H., I. A. Nicholls, M. Viljoen, and R. Viljoen, Experimental demonstration of the existence of peridotitic liquids in earliest Archean magmatism, *Geology*, 3, 11-15, 1975.
- Green, D. H., and A. E. Ringwood, The genesis of basaltic magmas, *Contrib. Mineral. Petrol.*, 15, 103-190, 1967.
- Green, H. W., II, and Y. Gueguen, Origin of kimberlite pipes by diapiric upwelling in the upper mantle, *Nature (London)*, 249, 617-620, 1974.
- Greenwood, H. J., The compressibility of gaseous mixtures of carbon dioxide and water between 0 and 500 bars and 450° and 800° Centigrade, *Am. J. Sci.*, Schairer Vol., 267A, 191-208, 1969.
- Greenwood, H. J., Thermodynamic properties of gaseous mixtures of H_2O and CO_2 between 450° and 800°C and 0 to 500 bars, *Am. J. Sci.*, 273, 561-571, 1973.
- Greig, J. W., Immiscibility in silicate melts, *Am. J. Sci.*, 13, 1-44, 133-154, 1927a.
- Greig, J. W., On liquid immiscibility in the system $FeO-Fe_2O_3-Al_2O_3-SiO_2$, *Am. J. Sci.*, 14, 473-484, 1927b.
- Grossman, L., Petrography and mineral chemistry of Ca-rich inclusions in the Allende meteorite, *Geochim. Cosmochim. Acta*, 39, 433-454, 1975.
- Gupta, R. P., and S. K. Sen, Sternheimer shielding-antishielding, II, *Phys. Rev. A*, 8, 1169-1172, 1973.
- Gurney, J. J., H. W. Fesq, and E. J. D. Kable, Clinopyroxene-ilmenite intergrowths from kimberlite: a re-appraisal, in *Lesotho Kimberlites*, P. H. Nixon, ed., Lesotho National Development Corporation, Maseru, Lesotho, pp. 238-253, 1973.
- Gustafson, W. I., The stability of andradite, hedenbergite, and related minerals in the system Ca-Fe-Si-O-M, *J. Petrol.*, 15, 455-496, 1974.
- Gutt, W., A microfurnace for high temperature microscopy and X-ray analysis up to 2150°C, *J. Sci. Instrum.*, 41, 393-394, 1964.
- Haggerty, S. E., F. R. Boyd, P. M. Bell, L. W. Finger, and W. B. Bryan, Iron-titanium oxides and olivine from 10020 and 10071, *Science*, 167, 613-615, 1970.
- Hahn, W., and A. Muan, Activity measurements in oxide solid solutions: the system $FeO-MgO$ in the temperature interval 1100° to 1300°, *Trans. AIME*, 224, 416-420, 1962.
- Häkli, T. A., and T. L. Wright, The fractionation of nickel between olivine and augite as a geothermometer, *Geochim. Cosmochim. Acta*, 31, 877-884, 1967.
- Handbook of Chemistry and Physics*, 43rd ed., C. D. Hodgman, ed., Chemical Rubber Publishing Company, Cleveland, Ohio, 1961.
- Hanna, R., Infrared spectrum of silicon dioxide, *J. Am. Ceram. Soc.*, 48, 595-599, 1965.
- Hanna, R., and G.-J. Su, Infrared absorption

- spectra of sodium silicate glasses from 4 to 30 μ , *J. Am. Ceram. Soc.*, **47**, 597-601, 1964.
- Hapke, B., and E. Wells, Lunar bi-directional reflectance spectroscopy, in *Lunar Science VII*, Lunar Science Institute, Houston, pp. 345-347, 1976.
- Harman, H. H., *Modern Factor Analysis*, The University of Chicago Press, Chicago, Ill., 1964.
- Hart, R., Chemical exchange between sea water and deep ocean basalts, *Earth Planet. Sci. Lett.*, **9**, 269-279, 1970.
- Hart, S. R., and G. L. Davis, Zircon U-Pb and whole-rock Rb-Sr ages and early crustal development near Rainy Lake, Ontario, *Geol. Soc. Am. Bull.*, **80**, 595-616, 1969.
- Harte, B., K. G. Cox, and J. J. Gurney, Petrography and geological history of upper mantle xenoliths from the Matsoku kimberlite pipe, *Phys. Chem. Earth*, **9**, 447-506, 1975.
- Hazen, R. M., and C. W. Burnham, The crystal structures of one-layer phlogopite and annite, *Am. Mineral.*, **58**, 889-900, 1973.
- Hazen, R. M., and C. W. Burnham, The crystal structure of gillespite I and II: a structure determination at high pressure, *Am. Mineral.*, **59**, 1166-1176, 1974.
- Hearn, B. C., Jr., and F. R. Boyd, Garnet peridotite xenoliths in a Montana, U.S.A., kimberlite, *Phys. Chem. Earth*, **9**, 247-255, 1975.
- Hensen, B. J., R. Schmid, and B. J. Wood, Activity-composition relationships for pyrope-grossular garnet, *Contrib. Mineral. Petrol.*, **51**, 161-166, 1975.
- Heubner, J. S., Buffering techniques for hydrostatic systems at elevated pressures, in *Research Techniques for High Pressure and High Temperature*, G. C. Ulmer, ed., Springer-Verlag, New York, pp. 123-177, 1971.
- Hewins, R. H., and J. I. Goldstein, The provenance of metal in anorthosite rocks, in *Proc. Sixth Lunar Sci. Conf.*, *Geochim. Cosmochim. Acta*, Suppl. 6, Vol. 1, Pergamon Press, New York, pp. 343-362, 1975.
- Hewitt, D. A., Stability of the assemblage phlogopite-calcite-quartz, *Am. Mineral.*, **60**, 391-397, 1975.
- Hill, R. L., Hydrolysis of proteins, *Adv. Protein Chem.*, **20**, 37-107, 1965.
- Hodge, J. E., Chemistry of browning reactions in model systems, *Agric. Food Chem.*, **1**, 928-943, 1953.
- Hodgson, C. J., The geology and geological development of the Broken Hill lode, in the New Broken Hill Consolidated Mine, Australia, Part II, Mineralogy, *J. Geol. Soc. Aust.*, **22**, 33-50, 1975.
- Hoering, T. C., The organic geochemistry of Precambrian rocks in *Researches in Geochemistry*, Vol. 2, P. H. Abelson, ed., John Wiley and Sons, Inc., New York, pp. 89-111, 1967.
- Holgate, N., The role of liquid immiscibility in igneous petrogenesis, *J. Geol.*, **62**, 439-480, 1954.
- Hollister, L. S., and A. J. Gancarz, Compositional sector-zoning in clinopyroxene from the Narce area, Italy, *Am. Mineral.*, **56**, 959-979, 1971.
- Holloway, J. R., and R. L. Reese, The generation of N_2 - CO_2 - H_2O fluids for use in hydrothermal experimentation, I, Experimental method and equilibrium calculations in the C-O-H-N system, *Am. Mineral.*, **59**, 587-597, 1974.
- Housley, R. M., and R. W. Grant, Electrostatic forces, molecular-orbital theory, and the electric field gradient in yttrium iron garnet, *Phys. Rev. Lett.*, **29**, 203-206, 1972.
- Huang, W. L., and P. J. Wyllie, Influence of mantle CO_2 in the generation of carbonatites and kimberlites, *Nature (London)*, **257**, 297-299, 1975.
- Huang, W. L., and P. J. Wyllie, Melting relationships in the systems CaO - CO_2 and MgO - CO_2 to 33 kilobars, *Geochim. Cosmochim. Acta*, **40**, 129-132, 1976.
- Huckenholz, H. G., Synthesis and stability of Ti-andradite, *Am. J. Sci.*, *Schairer Vol.*, **267A**, 209-232, 1969.
- Huckenholz, H. G., and H. S. Yoder, Jr., Andradite stability relations in the $CaSiO_3$ - Fe_2O_3 join up to 30 kb, *Neues Jahrb. Mineral., Abh.*, **114**, 246-280, 1971.
- Huggins, F. E., Cation order in olivines: evidence from vibrational spectra, *Chem. Geol.*, **11**, 99-109, 1973.
- Huggins, F. E., Mössbauer studies of iron minerals under pressures of up to 200 kilobars, Ph.D. thesis, Massachusetts Institute of Technology, 1974.
- Huggins, F. E., D. Virgo, and H. G. Huckenholz, Titanium-containing silicate garnets, I, The distribution of Al, Fe^{3+} and Ti^{4+} between octahedral and tetrahedral sites, *Am. Mineral.*, **61**, in press, 1976a.
- Huggins, F. E., D. Virgo, and H. G. Huckenholz, Titanium-containing silicate garnets, II, The crystal chemistry of melanites and schorlomites, *Am. Mineral.*, **61**, in press, 1976b.
- Huggins, M. L., and Y. Sakamoto, Lattice energies and other properties of alkaline earth chalcogenites, *J. Phys. Soc. Jpn.*, **12**, 241-251, 1957.
- I, Ting-Po, and G. H. Nancollas, EQUIL—a general computational method for the calculation of solution equilibria, *Anal. Chem.*, **44**, 1940-1951, 1972.
- Irvine, T. N., Crystallization sequences in the Muskox intrusion and other layered intrusions, 1, Olivine-pyroxene-plagioclase relations, *Geol. Soc. S. Afr. Spec. Publ.*, **1**, 441-476, 1970.
- Irving, A. J., and F. A. Frey, Effects of composition on the partitioning of rare earth

- elements, Hf, Sc and Co between garnet and liquid; experimental and natural evidence (abstract), *Eos*, 57, 339, 1976.
- Irving, A. J., W. L. Huang, and P. J. Wyllie, Phase relations of portlandite, $\text{Ca}(\text{OH})_2$, and brucite, $\text{Mg}(\text{OH})_2$, to 33 kilobars, *Am. J. Sci.*, in press, 1976.
- Irving, A. J., and P. J. Wyllie, Subsolidus and melting relationships for calcite, magnesite, and the join $\text{CaCO}_3\text{-MgCO}_3$ to 36 kilobars, *Geochim. Cosmochim. Acta*, 39, 35-53, 1975.
- Ito, K., and G. C. Kennedy, Melting and phase relations in a natural peridotite to 40 kilobars, *Am. J. Sci.*, 265, 519-538, 1967.
- Jackson, E. D., and T. L. Wright, Xenoliths in the Honolulu volcanic series, Hawaii, *J. Petrol.*, 11, 405-430, 1970.
- Jaffey, A. H., K. F. Flynn, L. E. Glendenin, W. C. Bentley, and A. M. Essling, Precision measurement of the half-lives and specific activities of U^{235} and U^{238} , *Phys. Rev. C*, 4, 1889-1906, 1971.
- James, O. B., Origin and emplacement of the ultramafic rocks of the Emigrant Cap area, California, *J. Petrol.*, 12, 523-560, 1971.
- Jeffreys, H., *The Earth*, 4th ed., Cambridge University Press, Cambridge, 1962.
- Joplin, G. A., R. Rudowski, and M. Abbott, Zircon in some granites from north-western Queensland, *Proc. R. Soc. N.S.W.*, 96, 9-13, 1962.
- Jordan, T. H., Lateral heterogeneity and mantle dynamics, *Nature (London)*, 257, 745-750, 1975.
- Kaiser, H. F., Computer program for varimax rotation in factor analysis, *Educ. Psychol. Meas.*, 19, 413-420, 1959.
- Kay, R. W., and P. W. Gast, The rare earth content and origin of alkali-rich basalts, *J. Geol.*, 81, 653-682, 1973.
- Keil, K., and R. Brett, Heideite, $(\text{Fe,Cr})_{1-2}\text{-}(\text{Ti,Fe})_2\text{Si}_4$, a new mineral in the Bustee enstatite achondrite, *Am. Mineral.*, 59, 465-470, 1974.
- Keil, K., et al., Progress by the consorts of Angra dos Reis (abstract), in *Lunar Science VII*, Lunar Science Institute, Houston, pp. 443-445, 1976.
- Kerrick, D. M., Experimental determination of muscovite + quartz stability with $P_{\text{H}_2\text{O}} < P_{\text{total}}$, *Am. J. Sci.*, 272, 946-958, 1972.
- Khitrov, N. I., and A. A. Kadik, Water and carbon dioxide in magmatic melts and peculiarities of the melting process, *Contrib. Mineral. Petrol.*, 41, 205-215, 1973.
- Knopoff, L., Observation and inversion of surface-wave dispersion, *Tectonophysics*, 13, 497-519, 1972.
- Kogarko, L. N., Role of volatiles, in *The Alkaline Rocks*, H. Sørensen, ed., John Wiley and Sons, Inc., New York, pp. 474-487, 1974.
- Krogh, T. E., A low-contamination method for hydrothermal decomposition of zircon and extraction of U and Pb for isotopic age determination, *Geochim. Cosmochim. Acta*, 37, 485-494, 1973.
- Kushiro, I., Si-Al relation in clinopyroxenes from igneous rocks, *Am. J. Sci.*, 258, 548-554, 1960.
- Kushiro, I., Clinopyroxene solid solutions formed by reactions between diopside and plagioclase at high pressures, *Mineral. Soc. Am. Spec. Pap.*, 2, 179-191, 1969a.
- Kushiro, I., The system forsterite-diopside-silica with and without water at high pressures, *Am. J. Sci.*, Schairer Vol., 267A, 269-294, 1969b.
- Kushiro, I., Effect of water on the composition of magmas formed at high pressures, *J. Petrol.*, 13, 311-334, 1972a.
- Kushiro, I., Determination of liquidus relations in synthetic silicate systems with electron probe analysis: the system forsterite-diopside-silica at 1 atmosphere, *Am. Mineral.*, 57, 1260-1271, 1972b.
- Kushiro, I., On the nature of silicate melt and its significance in magma genesis: regularities in the shift of the liquidus boundaries involving olivine, pyroxene, and silica minerals, *Am. J. Sci.*, 275, 411-431, 1975.
- Kushiro, I., H. Satake, and S. Akimoto, Carbonate-silicate reactions at high pressures and possible presence of dolomite and magnesite in the upper mantle, *Earth Planet. Sci. Lett.*, 28, 116-120, 1975.
- Kushiro, I., Y. Syono, and S. Akimoto, Melting of a peridotite nodule at high pressures and high water pressures, *J. Geophys. Res.*, 73, 6023-6029, 1968.
- Lanphere, M. A., Geochronology of the Yavapai series of central Arizona, *Can. J. Earth Sci.*, 5, 757-762, 1968.
- Larimer, J. W., and E. Anders, Chemical fractionations in meteorites, II, Abundance patterns and their interpretation, *Geochim. Cosmochim. Acta*, 31, 1239-1270, 1967.
- Larsen, L. M., Clinopyroxenes and coexisting mafic minerals from the alkaline Ilimaussag intrusion, South Greenland, *J. Petrol.*, 17, 258-290, 1976.
- Lawless, P. J., Some aspects of the geochemistry of kimberlite xenocrysts, unpublished M.Sc. thesis, University of Cape Town, 1974.
- Lawley, D. N., and A. E. Maxwell, *Factor Analysis as a Statistical Method*, Butterworth and Co., London, 1963.
- Lawrence, L., and W. J. Moore, Kinetics of the hydrolysis of simple glycine peptides, *J. Am. Chem. Soc.*, 73, 3973-3977, 1951.
- Leake, B. E., The relationship between composition of calciferous amphibole and grade of metamorphism, in *Controls of Metamorphism*, W. S. Pitcher and G. W. Flinn, eds., John Wiley and Sons, Inc., New York, pp. 299-318, 1965.

- LeBas, M. J., The role of aluminum in igneous clinopyroxenes with relation to their parentage, *Am. J. Sci.*, **260**, 267-288, 1962.
- Leeman, W. P., Partitioning of Ni and Co between olivine and basaltic liquid: an experimental study (abstract), *Eos*, **54**, 1222-1223, 1973.
- Leeman, W. P., Experimental determination of partitioning of divalent cations between olivine and basaltic liquid, part 2 of unpublished Ph.D. thesis, University of Oregon, 1974.
- Leonard, A., S. Suzuki, J. J. Fripiat, and C. DeKimpe, Structure and properties of amorphous silico-aluminas, I, Structure from x-ray fluorescence spectroscopy and infrared spectroscopy, *J. Phys. Chem.*, **68**, 2608-2617, 1964.
- Leung, I. S., Sector-zoned titanagmites: morphology, crystal chemistry, and growth, *Am. Mineral.*, **59**, 127-138, 1974.
- Levin, E. M., C. R. Robbins, and H. F. McMurdie, *Phase Diagrams for Ceramists*, American Ceramic Society, Inc., Columbus, Ohio, 1964.
- Lindsley, D. H., and S. S. Dixon, Coexisting diopside and enstatite at 20 kbar and 900-1200°C (abstract), *Abstr. with Programs (Geol. Soc. Am.)*, **7**, 1171, 1975.
- Lofgren, G., An experimental study of plagioclase crystal morphology: isothermal crystallization, *Am. J. Sci.*, **274**, 243-273, 1974.
- MacGregor, I. D., The system $MgO-Al_2O_3-SiO_2$: solubility of Al_2O_3 in enstatite for spinel and garnet peridotite compositions, *Am. Mineral.*, **59**, 110-119, 1974.
- MacGregor, I. D., Petrologic and thermal structure of the upper mantle beneath South Africa in the Cretaceous, *Phys. Chem. Earth*, **9**, 455-466, 1975.
- Maillard, L. C., Formation de matières humiques par action de polypeptides sur sucres, *C. R. Acad. Sci.*, **156**, 148-149, 1913.
- Manning, P. G., and D. C. Harris, Optical-absorption and electron-microprobe studies of some high-Ti andradites, *Can. Mineral.*, **10**, 260-271, 1970.
- Mao, H. K., W. A. Bassett, and T. Takahashi, Effect of pressure on crystal structure and lattice parameters of iron up to 300 kbar, *J. Appl. Phys.*, **38**, 272-276, 1967.
- Mao, H. K., and P. M. Bell, Polarized crystal-field spectra of micro particles of the moon, *Am. Soc. Test. Mater. Spec. Tech. Publ.*, **539**, 100-119, 1973.
- Mao, H. K., T. Takahashi, W. A. Bassett, and J. S. Weaver, Effect of pressure and temperature on the molar volumes of wüstite and of three $(Fe,Mg)_2SiO_4$ spinel solid solutions, *J. Geophys. Res.*, **74**, 1061-1069, 1969.
- Mason, B., Manganese silicate minerals from Broken Hill, New South Wales, *J. Geol. Soc. Aust.*, **20**, 397-404, 1973.
- Mason, B., Compositional limits of wollastonite and bustamite, *Am. Mineral.*, **60**, 209-212, 1975.
- Matsueda, H., Iron-wollastonite from the Sampo Mine showing properties distinct from those of wollastonite, *Mineral. J.*, **7**, 180-201, 1973.
- Matsui, Y., and S. Banno, Intracrystalline exchange equilibrium in silicate solid solutions, *Proc. Jpn. Acad.*, **41**, 461-466, 1965.
- Matsui, Y., and Y. Syono, Unit cell dimensions of some synthetic olivine group solid solutions, *Geochem. J.*, **2**, 51-59, 1968.
- Mattinson, J. M., Preparation of hydrofluoric, hydrochloric, and nitric acids at ultralow lead levels, *Anal. Chem.*, **44**, 1715-1716, 1972.
- McBirney, A. R., Differentiation of the Skaergaard intrusion, *Nature (London)*, **253**, 691-694, 1975.
- McCallister, R. H., H. O. A. Meyer, and D. G. Brookins, "Pyroxene"-ilmenite xenoliths from the Stockdale pipe, Kansas: chemistry, crystallography, and origin, *Phys. Chem. Earth*, **9**, 287-293, 1975.
- McCallum, M. E., and D. H. Eggler, Mineralogy of the Sloan diatreme, a kimberlite pipe in northern Larimer County, Colorado, *Am. Mineral.*, **56**, 1735-1749, 1971.
- McCallum, M. E., and D. H. Eggler, Diamonds in an upper mantle peridotite nodule from kimberlite in southern Wyoming, *Science*, **192**, 253-256, 1976.
- McCallum, M. E., D. H. Eggler, and L. K. Burns, Kimberlitic diatremes in northern Colorado and southern Wyoming, *Phys. Chem. Earth*, **9**, 149-161, 1975.
- McCallum, M. E., and C. D. Mabarak, Diamond from kimberlite diatremes in northern Colorado and southern Wyoming (abstract), *Abstr. with Programs (Geol. Soc. Am.)*, **8**, 609, 1976.
- McCallum, M. E., C. B. Smith, L. K. Burns, D. H. Eggler, and W. A. Braddock, Kimberlitic diatremes and dikes in the Iron Mountain area, southern Laramie Range, Wyoming (abstract), *Abstr. with Programs (Geol. Soc. Am.)*, **7**, 628, 1975.
- McGetchin, T. R., Y. S. Nikhanj, and A. A. Chodos, Carbonatite-kimberlite relations in the Cane Valley diatreme, San Juan County, Utah, *J. Geophys. Res.*, **78**, 1854-1869, 1973.
- McIntyre, G. A., C. Brooks, W. Compston, and A. Turek, The statistical assessment of Rb-Sr isochrons, *J. Geophys. Res.*, **71**, 5459-5468, 1966.
- McKirdy, D. M., Organic geochemistry in Precambrian research, *Precambrian Res.*, **1**, 75-137, 1974.
- McQueen, R. G., and S. P. Marsh, Equation of state for nineteen metallic elements from shock-wave measurements to two megabars, *J. Appl. Phys.*, **31**, 1253-1269, 1960.
- Mercier, J. C., and N. L. Carter, Pyroxene geotherms, *J. Geophys. Res.*, **80**, 3349-3362, 1975.

- Meyer, H. O. A., and F. R. Boyd, Composition and origin of crystalline inclusions in natural diamonds, *Geochim. Cosmochim. Acta*, **36**, 1255-1273, 1972.
- Meyer, H. O. A., and D. P. Svisero, Mineral inclusions in Brazilian diamonds, *Phys. Chem. Earth*, **9**, 785-795, 1975.
- Ming, L. C., and W. A. Bassett, Post-spinel phases in $\text{Mg}_2\text{SiO}_4\text{-Fe}_2\text{SiO}_4$ system up to 80% Fe_2SiO_4 (abstract), *Eos*, **55**, 416-417, 1974.
- Misra, K. C., and L. A. Taylor, Characteristics of metal particles in Apollo 16 rocks, in *Proc. Sixth Lunar Sci. Conf., Geochim. Cosmochim. Acta*, Suppl. 6, Vol. 1, Pergamon Press, New York, pp. 615-639, 1975.
- Miyashiro, A., F. Shido, and M. Ewing, Diversity and origin of abyssal tholeiite from the Mid-Atlantic Ridge near 24° and 30° north latitude, *Contrib. Mineral. Petrol.*, **23**, 38-52, 1969.
- Modreski, P. J., and A. L. Boettcher, Phase relations of phlogopite in the system $\text{K}_2\text{O-MgO-CaO-Al}_2\text{O}_3\text{-SiO}_2\text{-H}_2\text{O}$ to 35 kilobars: a better model for micas in the interior of the earth, *Am. J. Sci.*, **273**, 385-414, 1973.
- Moore, J. G., Petrology of deep-sea basalt near Hawaii, *Am. J. Sci.*, **263**, 40-52, 1965.
- Moore, J. G., and B. P. Fabbri, An estimate of the juvenile sulfur content of basalt, *Contrib. Mineral. Petrol.*, **33**, 118-127, 1971.
- Moore, R. K., and W. B. White, Intervalence electron transfer effects in the spectra of the melanite garnets, *Am. Mineral.*, **56**, 826-840, 1971.
- Morey, G. W., and N. L. Bowen, The melting relations of the soda-lime-silica glasses, *Trans. Soc. Glass Technol.*, **9**, 226-264, 1925.
- Morimoto, N., D. E. Appleman, and H. T. Evans, The crystal structures of clinoenstatite and pigeonite, *Z. Kristallogr.*, **114**, 120-147, 1960.
- Morimoto, N., and N. Güven, Refinement of the crystal structure of pigeonite, *Am. Mineral.*, **55**, 1195-1209, 1970.
- Muan, A., Phase equilibria in the system $\text{FeO-Fe}_2\text{O}_3\text{-SiO}_2$, *Trans. AIME*, **203**, 965-976, 1955.
- Muan, A., and E. F. Osborn, *Phase Equilibria among Oxides in Steelmaking*, Addison-Wesley, Inc., Reading, Massachusetts, 1965.
- Mueller, R. F., Energetics of certain silicate solid solutions, *Geochim. Cosmochim. Acta*, **26**, 581-598, 1962.
- Mueller, R. F., Theory of immiscibility in mineral systems, *Mineral. Mag.*, **33**, 1015-1023, 1964.
- Mysen, B. O., Partitioning of iron and magnesium between crystals and partial melts in peridotite upper mantle, *Contrib. Mineral. Petrol.*, **52**, 69-76, 1975.
- Mysen, B. O., Partitioning of samarium and nickel between olivine, orthopyroxene and liquid; preliminary data at 20 kbar and 1025°C, *Earth Planet. Sci. Lett.*, in press, 1976a.
- Mysen, B. O., The role of volatiles in silicate melts: solubility of carbon dioxide and water in feldspar, pyroxene, and feldspathoid melts to 30 kb and 1625°C, *Am. J. Sci.*, in press, 1976b.
- Mysen, B. O., R. J. Arculus, and D. H. Eggler, Solubility of carbon dioxide in melts of andesite, tholeiite, and olivine nephelinite composition to 30 kbar pressure, *Contrib. Mineral. Petrol.*, **53**, 227-239, 1975.
- Mysen, B. O., and A. L. Boettcher, Melting in a hydrous mantle, I, Phase relations of natural peridotite at high pressures and temperatures with controlled activities of water, carbon dioxide and hydrogen, *J. Petrol.*, **16**, 520-548, 1975a.
- Mysen, B. O., and A. L. Boettcher, Melting of a hydrous mantle: II, Geochemistry of crystals and liquids formed by anatexis of mantle peridotite at high pressures and high temperatures as a function of controlled activities of water, hydrogen and carbon dioxide, *J. Petrol.*, **16**, 549-593, 1975b.
- Mysen, B. O., D. H. Eggler, M. G. Seitz, and J. R. Holloway, Carbon dioxide in silicate melts and crystals, I, Solubility measurements, *Am. J. Sci.*, **276**, 455-479, 1976.
- Mysen, B. O., and M. G. Seitz, Trace element partitioning determined by beta track mapping: an experimental study using carbon and samarium as examples, *J. Geophys. Res.*, **80**, 2627-2635, 1975.
- Nakamura, Y., Origin of sector-zoning in igneous clinopyroxenes, *Am. Mineral.*, **58**, 986-990, 1973.
- Nash, W. P., Mineralogy and petrology of the Iron Hill Carbonatite Complex, Colorado, *Geol. Soc. Am. Bull.*, **83**, 1361-1382, 1972.
- Nesbitt, R. W., Skeletal crystal forms in the ultramafic rocks of the Yilgarn Block, Western Australia: evidence for an Archean ultramafic liquid, *Geol. Soc. Aust., Spec. Publ.*, **3**, 331-348, 1971.
- Nesbitt, R. W., and S. S. Sun, Geochemistry of Archean spinifex-textured peridotites and magnesian and low-magnesian tholeiites, *Earth Planet. Sci. Lett.*, in press, 1976.
- Neuvonen, K. J., On the composition of natural melilites, *Bull. Comm. Geol. Finl.*, **168**, 13-26, 1955.
- Newton, R. C., and W. E. Sharp, Stability of forsterite CO_2 and its bearing on the role of CO_2 in the mantle, *Earth Planet. Sci. Lett.*, **26**, 239-244, 1975.
- Newton, R. H., Activity coefficients of gases, *Ind. Eng. Chem.*, **27**, 302-306, 1935.
- Nicolas, A., Structural and petrological comparison of peridotites from Alpine massifs, basalt and kimberlite xenoliths (abstract), in *Volume of Abstracts, Kimberlite Symposium*, Cambridge, England, p. 56, 1975.

- Nissenbaum, A., and I. R. Kaplan, Chemical and isotopic evidence for the *in situ* origin of marine humic substances, *Limnol. Oceanogr.*, **17**, 570-582, 1972.
- Nitsan, U., Stability field of olivine with respect to oxidation and reduction, *J. Geophys. Res.*, **79**, 706-711, 1974.
- Nixon, P. H., and F. R. Boyd, Petrogenesis of the granular and sheared ultrabasic nodule suite in kimberlites, in *Lesotho Kimberlites*, P. H. Nixon, ed., Lesotho National Development Corporation, Maseru, Lesotho, pp. 48-56, 1973a.
- Nixon, P. H., and F. R. Boyd, The discrete nodule association in kimberlites from northern Lesotho, in *Lesotho Kimberlites*, P. H. Nixon, ed., Lesotho National Development Corporation, Maseru, Lesotho, pp. 67-75, 1973b.
- Nolan, J., Physical properties of synthetic and natural pyroxenes in the system diopside-hedenbergite-aegirine, *Mineral. Mag.*, **36**, 5-21, 1969.
- Nolan, J., and A. D. Edgar, An X-ray investigation of synthetic pyroxenes in the system aegirine-diopside-water at 1000 kg/cm² water vapor pressure, *Mineral. Mag.*, **33**, 625-634, 1963.
- Novak, G. A., and G. V. Gibbs, The crystal chemistry of the silicate garnets, *Am. Mineral.*, **56**, 791-825, 1971.
- Obata, M., The solubility of Al₂O₃ in orthopyroxenes in spinel and plagioclase peridotites and spinel pyroxenite (abstract), *International Conference on Geothermometry and Geobarometry*, Pennsylvania State University, 1975.
- O'Hara, M. J., Mineral parageneses in ultrabasic rocks, in *Ultramafic and Related Rocks*, P. J. Wyllie, ed., John Wiley and Sons, Inc., New York, pp. 393-403, 1967.
- O'Hara, M. J., and H. S. Yoder, Jr., Formation and fractionation of magmas at high pressures, *Scott. J. Geol.*, **3**, 67-117, 1967.
- Ohashi, Y., and C. W. Burnham, Electrostatic and repulsive energies of the M1 and M2 cation sites in pyroxenes, *J. Geophys. Res.*, **77**, 5761-5766, 1972.
- Ohashi, Y., C. W. Burnham, and L. W. Finger, The effect of Ca-Fe substitution on the clinopyroxene crystal structure, *Am. Mineral.*, **60**, 423-434, 1975.
- O'Nions, R. K., and D. B. Clark, Comparative trace element geochemistry of Tertiary basalts from Baffin Bay, *Earth Planet. Sci. Lett.*, **15**, 436-447, 1972.
- Ordway, F., Techniques for growing and mounting small single crystals of refractory compounds, *J. Res. Natl. Bur. Stand.*, **48**, 152-158, 1952.
- Osberg, P. H., Stratigraphy, structural geology, and metamorphism of the Waterville-Vassalboro area, Maine, *Maine Geol. Surv. Bull.*, **20**, 1968.
- Osborn, E. F., and D. B. Tait, The system diopside-forsterite-anorthite, *Am. J. Sci., Bowen Vol.*, 413-433, 1952.
- Pantelides, S. T., D. J. Mickish, and A. B. Kunz, Electronic structure and properties of magnesium oxide, *Phys. Rev. B*, **10**, 5203-5212, 1974.
- Papike, J. J., C. T. Prewitt, S. Sueno, and M. Cameron, Pyroxenes: comparisons of real and ideal structural topologies, *Z. Kristallogr.*, **138**, 254-273, 1973.
- Papike, J. J., M. Ross, and J. R. Clark, Crystal-chemical characterization of clinopyroxenes based on five new structure refinements, *Mineral. Soc. Am. Spec. Pap.*, **2**, 117-136, 1969.
- Parmentier, E. M., and D. L. Turcotte, An explanation of the pyroxene geotherm based on plume convection in the upper mantle, *Earth Planet. Sci. Lett.*, **24**, 209-212, 1974.
- Paul, A., and R. W. Douglas, Ferrous-ferric equilibrium in binary alkali silicate glasses, *Phys. Chem. Glasses*, **6**, 207-211, 1965.
- Peacor, D. R., and M. J. Buerger, Determination and refinement of the structure of bustamite, CaMnSi₂O₆, *Z. Kristallogr.*, **117**, 331-343, 1962.
- Peacor, D. R., and C. T. Prewitt, Comparison of the crystal structures of bustamite and wollastonite, *Am. Mineral.*, **48**, 588-596, 1963.
- Pearce, M. L., Solubility of carbon dioxide and variation of oxygen ion activity in soda-silicate melts, *J. Am. Ceram. Soc.*, **47**, 342-347, 1964.
- Pellas, P., and D. Storzer, Uranium and plutonium in chondritic phosphates (abstract), *Meteoritics*, **10**, 471-473, 1975.
- Peterman, Z. E., S. S. Goldich, C. E. Hedge, and D. H. Yardley, Geochronology of the Rainy Lake region, Minnesota-Ontario, *Geol. Soc. Am. Mem.*, **135**, 193-215, 1972.
- Piermarini, G. J., and S. Block, An ultrahigh pressure diamond-anvil cell and several semiconductor phase transition pressures in relation to the fixed point pressure scale, *Rev. Sci. Instrum.*, **46**, 973-979, 1975.
- Piermarini, G. J., S. Block, J. D. Barnett, and R. A. Forman, Calibration of the pressure dependence of the R₁ ruby fluorescence line to 195 kbar, *J. Appl. Phys.*, **46**, 2774-2780, 1975.
- Piwnicki, A. J., Experimental studies of igneous rock series, central Sierra Nevada batholith, California, *J. Geol.*, **76**, 548-570, 1968.
- Podosek, F. A., The abundance of ²⁴⁴Pu in the early solar system, *Earth Planet. Sci. Lett.*, **8**, 183-187, 1970.
- Presnall, D. C., Pressure-volume-temperature measurements on hydrogen from 200° to 600°C and up to 1800 atmospheres, *J. Geophys. Res.*, **74**, 6026-6033, 1969.

- Presnall, D. C., and N. L. Brenner, A method for studying iron silicate liquids under reducing conditions with negligible iron loss, *Geochim. Cosmochim. Acta*, **38**, 1785-1788, 1974.
- Prinz, M., D. V. Manson, P. F. Hlava, and K. Keil, Inclusions in diamonds: garnet lherzolite and eclogite assemblages, *Phys. Chem. Earth*, **9**, 797-815, 1975.
- Pyke, D. R., A. J. Naldrett, and A. R. Eckstrand, Archean ultramafic flows in Munro Township, Ontario, *Geol. Soc. Am. Bull.*, **84**, 955-978, 1973.
- Råheim, A., and D. H. Green, Experimental determination of the temperature and pressure dependence of the Fe-Mg partition coefficient for coexisting garnet and clinopyroxene, *Contrib. Mineral. Petrol.*, **48**, 179-203, 1974.
- Rajamani, V., G. E. Brown, and C. T. Prewitt, Cation ordering in Ni-Mg olivine, *Am. Mineral.*, **60**, 292-300, 1975.
- Rapoport, P. A., and C. W. Burnham, Ferrobustamite: the crystal structures of two Ca,Fe bustamite-type pyroxenoids, *Z. Kristallogr.*, **138**, 419-438, 1973.
- Rashid, M. A., and L. H. King, Major oxygen containing functional groups present in humic and fulvic acid functions isolated from contrasting marine environments, *Geochim. Cosmochim. Acta*, **34**, 193-201, 1970.
- Ray, S. N., T. Lee, T. P. Das, R. M. Sternheimer, R. P. Gupta, and S. K. Sen, Role of consistency effects on the antishielding of nuclear quadrupole moments: comparison between diagrammatic and differential-equation approaches for the ferric ion, *Phys. Rev. A*, **11**, 1804-1809, 1975.
- Raymond, M., Electric-field gradient calculations in the aluminum silicates (Al_2SiO_5), *Phys. Rev. B*, **3**, 3692-3702, 1971.
- Redlich, O., and J. N. S. Kwong, On the thermodynamics of solutions, V, An equation of state: fugacities of gaseous solutions, *Chem. Rev.*, **44**, 233-244, 1949.
- Rhodes, J. M., J. B. Adams, D. P. Blanchard, M. P. Charette, K. V. Rodgers, J. W. Jacobs, J. C. Brannon, and L. A. Haskin, Chemistry of agglutinate fractions in lunar soils, in *Proc. Sixth Lunar Sci. Conf.*, *Geochim. Cosmochim. Acta*, Suppl. 6, Vol. 3, Pergamon Press, New York, pp. 2291-2307, 1975.
- Richards, J. R., J. A. Cooper, and A. W. Webb, Potassium-argon ages on micas from the Precambrian region of north-western Queensland, *J. Geol. Soc. Aust.*, **10**, 299-312, 1963.
- Richardson, W. A., and G. Sneesby, The frequency-distribution of igneous rocks, I, Frequency-distribution of the major oxides in analyses of igneous rocks, *Mineral. Mag.*, **19**, 304-313, 1922.
- Richardson, W. A., and G. Sneesby, The frequency-distribution of igneous rocks, II, The laws of distribution in relation to petrogenic theories, *Mineral. Mag.*, **20**, 2-20, 1923.
- Riebling, E. F., Structure of sodium aluminosilicate melts containing at least 50 mole % SiO_2 at 1500°C, *J. Chem. Phys.*, **44**, 2857-2865, 1966.
- Ringwood, A. E., Melting relationships of Ni-Mg olivines and some geochemical implications, *Geochim. Cosmochim. Acta*, **10**, 297-303, 1956.
- Ringwood, A. E., Chemical evolution of the terrestrial planets, *Geochim. Cosmochim. Acta*, **30**, 41-104, 1966.
- Robie, R. A., and D. R. Waldbaum, Thermodynamic properties of minerals and related substances at 298.15°K (25.0°C) and one atmosphere (1.013 bars) pressure and at higher temperatures, *U.S. Geol. Surv. Bull.*, **1259**, 1968.
- Robinson, P., M. Ross, and H. W. Jaffe, Composition of the anthophyllite-gedrite series, comparisons of gedrite and hornblende, and the anthophyllite-gedrite solvus, *Am. Mineral.*, **56**, 1005-1041, 1971.
- Roedder, E., Low-temperature liquid immiscibility in the system $\text{K}_2\text{O}-\text{FeO}-\text{Al}_2\text{O}_3-\text{SiO}_2$, *Am. Mineral.*, **36**, 282-286, 1951a.
- Roedder, E., The system $\text{K}_2\text{O}-\text{MgO}-\text{SiO}_2$, *Am. J. Sci.*, **249**, 81-130, 1951b.
- Roedder, E., A reconnaissance of liquidus relations in the system $\text{K}_2\text{O}-2\text{SiO}_2-\text{FeO}-\text{SiO}_2$, *Am. J. Sci.*, *Boven Vol.*, **435-456**, 1952.
- Roedder, E., Liquid CO_2 inclusions in olivine-bearing nodules and phenocrysts from basalts, *Am. Mineral.*, **50**, 1746-1782, 1965.
- Roedder, E., and P. W. Weiblen, Lunar petrology of silicate melt inclusions, Apollo 11 rocks, in *Proc. Apollo 11 Lunar Sci. Conf.*, *Geochim. Cosmochim. Acta*, Suppl. 1, Vol. 1, Pergamon Press, New York, pp. 801-837, 1970.
- Roedder, E., and P. W. Weiblen, Petrology of silicate melt inclusions, Apollo 11 and Apollo 12 and terrestrial equivalents, in *Proc. Second Lunar Sci. Conf.*, *Geochim. Cosmochim. Acta*, Suppl. 2, Vol. 1, The MIT Press, Cambridge, pp. 507-528, 1971.
- Roedder, E., and P. W. Weiblen, Silicate melt inclusions and glasses in lunar soil fragments from the Luna 16 core sample, *Earth Planet. Sci. Lett.*, **13**, 272-285, 1972.
- Rouquerol, J., and P. Boivinnet, Calorimetric measurements, in *Differential Thermal Analysis*, Vol. 2, R. C. Mackenzie, ed., Academic Press, New York, pp. 23-46, 1972.
- Rubey, W. W., Geologic history of seawater, *Geol. Soc. Am. Bull.*, **62**, 1111-1148, 1951.
- Rumble, D., III, Gibbs phase rule and its application in geochemistry, *J. Wash. Acad. Sci.*, **64**, 199-208, 1974.
- Sahama, Th. G., Thermal metamorphism of the volcanic rocks of Mt. Nyiragongo (eastern Congo), *C. R. Soc. Geol. Finl.*, **33**, 151-174, 1961.

- Sahama, Th. G., Petrology of Mt. Nyiragongo, *Trans. Edinburgh Geol. Soc.*, 19, 1-28, 1962.
- Sahama, Th. G., Iron content of melilite, *C. R. Soc. Geol. Finl.*, 39, 17-28, 1967.
- Sahama, Th. G., and A. Meyer, Study of the volcano Nyiragongo, a progress report, *Inst. Parc Nationaux Congo, Explor. Parc Natl. Albert*, No. 2, 1958.
- Sato, H., Nickel content of magma and olivine as a measure of the degree of early-stage fractional crystallization of basaltic magmas, *Contrib. Mineral. Petrol.*, in press, 1976.
- Sato, M., Electrochemical measurement and control of oxygen fugacity and other gaseous fugacities with solid electrolyte sensors, in *Research Techniques for High Pressure and High Temperature*, G. C. Ulmer, ed., Springer-Verlag, New York, pp. 43-99, 1971.
- Sato, M., Intrinsic oxygen fugacities of iron-bearing oxide and silicate minerals under low total pressure, *Geol. Soc. Am. Mem.*, 135, 289-307, 1972.
- Sato, M., L. Hickling, and J. E. McLane, Oxygen fugacity values of Apollo 12, 14, and 15 lunar samples and reduced state of lunar magmas, in *Proc. Fourth Lunar Sci. Conf., Geochim. Cosmochim. Acta*, Suppl. 4, Vol. 1, Pergamon Press, New York, pp. 1061-1079, 1973.
- Sato, M., and J. G. Moore, Oxygen and sulphur fugacities of magmatic gases directly measured in active vents of Mount Etna, *Philos. Trans. R. Soc. London, Ser. A*, 274, 137-146, 1973.
- Sato, M., and T. L. Wright, Oxygen fugacities directly measured in magmatic gases, *Science*, 153, 1103-1105, 1966.
- Savit, C. A., *Geophysical Data Centers: Impact of Data Intensive Programs*, Geophysics Research Board, National Research Council, Washington, D.C., 1976.
- Sawatzky, G. A., and J. Hupkes, Redetermination of nuclear quadrupole moments from hyperfine interactions in compounds, *Phys. Rev. Lett.*, 25, 100-101, 1970.
- Saxena, S. K., Silicate solid solutions and geothermometry, 2, Distribution of Fe^{2+} and Mg^{2+} between coexisting olivine and pyroxene, *Contrib. Mineral. Petrol.*, 22, 147-156, 1969.
- Scarfe, C. M., Viscosity of basic magmas at varying pressure, *Nature (London)*, 241, 101-102, 1973.
- Schairer, J. F., The system of $\text{CaO-FeO-Al}_2\text{O}_3\text{-SiO}_2$: I, Results of quenching experiments on five joins, *J. Am. Ceram. Soc.*, 25, 241-274, 1942.
- Schairer, J. F., The system $\text{K}_2\text{O-MgO-Al}_2\text{O}_3\text{-SiO}_2$: 1, The results of quenching experiments on four joins in the tetrahedron cordierite-forsterite-leucite-silica and on the join cordierite-mullite-potash feldspar, *J. Am. Ceram. Soc.*, 37, 501-533, 1954.
- Schairer, J. F., and N. L. Bowen, The system anorthite-leucite-silica, *Bull. Soc. Geol. Finl.*, 20, 67-87, 1947.
- Schairer, J. F., and N. L. Bowen, The system $\text{K}_2\text{O-Al}_2\text{O}_3\text{-SiO}_2$, *Am. J. Sci.*, 253, 681-746, 1955.
- Schairer, J. F., and H. S. Yoder, Jr., The nature of residual liquids from crystallization, with data on the system nepheline-diopside-silica, *Am. J. Sci., Bradley Vol.*, 253A, 273-283, 1960.
- Schilling, J.-G., and J. W. Winchester, Rare earth contribution to the origin of Hawaiian lavas, *Contrib. Mineral. Petrol.*, 23, 27-37, 1969.
- Schmidt, V. H., and E. D. Jones, Nuclear-magnetic-resonance study of thulium aluminum garnet, *Phys. Rev. B*, 1, 1978-1986, 1970.
- Schnitzer, M., and H. Kodama, Montmorillonite: effect of pH on its adsorption of a soil humic compound, *Science*, 153, 70-71, 1966.
- Schorer, G., Sanduhrbau und Optik von Titanagiten alkali-basaltischer Gesteine des Vogelsberges, *Neues Jahrb. Mineral. Monatsh.*, 310-325, 1970.
- Schramm, D. N., and G. J. Wasserburg, Nucleochronologies and the mean age of the elements, *Astrophys. J.*, 162, 57-69, 1970.
- Sclar, C. B., and J. F. Bauer, Shock-induced melting in anorthositic rock 60015 and a fragment of anorthositic breccia from the "picking pot" (70052), in *Proc. Fifth Lunar Sci. Conf., Geochim. Cosmochim. Acta*, Suppl. 5, Vol. 1, Pergamon Press, New York, pp. 319-336, 1974.
- Seitz, M. G., and I. Kushiro, Melting relations of the Allende meteorite, *Science*, 183, 954-957, 1974.
- Sharma, R. R., Nuclear quadrupole moment of Al^{27} in Al_2O_3 , *Phys. Rev. Lett.*, 25, 1622-1623, 1970.
- Sharma, R. R., Nuclear quadrupole interactions in several rare-earth iron garnets, *Phys. Rev. B*, 6, 4310-4323, 1972.
- Shaw, H. R., Hydrogen-water vapor mixtures: control of hydrothermal atmospheres by hydrogen osmosis, *Science*, 139, 1220-1222, 1963.
- Shaw, H. R., Comments on viscosity, crystal settling and convection in granitic magmas, *Am. J. Sci.*, 263, 120-152, 1965.
- Shaw, H. R., Hydrogen osmosis in hydrothermal experiments, in *Researches in Geochemistry*, Vol. 2, P. H. Abelson, ed., John Wiley and Sons, Inc., New York, pp. 521-541, 1967.
- Shaw, H. R., and E. D. Jackson, Linear island chains in the Pacific; results of thermal plumes or gravitational anchors? *J. Geophys. Res.*, 78, 8634-8652, 1973.
- Shaw, H. R., and D. R. Wones, Fugacity coefficients for hydrogen gas between 0° and 1000°C, for pressures to 3000 atm, *Am. J. Sci.*, 262, 918-929, 1964.
- Sheppard, S. M. F., R. L. Nielsen, and H. P.

- Taylor, Jr., Oxygen and hydrogen isotope ratios of clay minerals from porphyry copper deposits, *Econ. Geol.*, **64**, 755-777, 1969.
- Shido, F., A. Miyashiro, and M. Ewing, Compositional variation in pillow lavas from the Mid-Atlantic Ridge, *Mar. Geol.*, **16**, 177-190, 1974.
- Shieh, Y.-N., H. P. Schwarcz, and D. M. Shaw, An oxygen isotope study of the Loon Lake pluton and the Apsley gneiss, Ontario, *Contrib. Mineral. Petrol.*, **54**, 1-16, 1976.
- Shimazaki, H., and T. Yamanaka, Iron-wollastonite from skarns and its stability relation in the $\text{CaSiO}_3\text{-CaFeSi}_2\text{O}_6$ join, *Geochem. J.*, **7**, 67-79, 1973.
- Shimizu, N., Rare earth elements in garnets and clinopyroxenes from garnet lherzolite inclusions in kimberlites, *Earth Planet. Sci. Lett.*, **25**, 26-32, 1975.
- Shimizu, N., and R. J. Arculus, Rare earth element concentrations in a suite of basanoids and alkali olivine basalts from Grenada, Lesser Antilles, *Contrib. Mineral. Petrol.*, **50**, 231-240, 1975.
- Shimizu, N., and I. Kushiro, The partitioning of rare-earth elements between garnet and liquid at high pressures: preliminary experiments, *Geophys. Res. Lett.*, **2**, 413-416, 1975.
- Skippen, G. B., Experimental data for reactions in siliceous marbles, *J. Geol.*, **79**, 457-481, 1971.
- Smith, D. K., A. Majumdar, and F. Ordway, The crystal structure of γ -dicalcium silicate, *Acta Crystallogr.*, **18**, 787-795, 1965.
- Smith, G. S., and L. E. Alexander, Refinement of the atomic parameters of α -quartz, *Acta Crystallogr.*, **16**, 462-471, 1963.
- Smith, J. V., *Feldspar Minerals*, Vol. 1, Springer-Verlag, New York, 1974.
- Smyth, J. R., High temperature crystal chemistry of fayalite, *Am. Mineral.*, **60**, 1092-1097, 1975.
- Smyth, J. R., and R. M. Hazen, The crystal structures of forsterite and hortonolite at several temperatures up to 900°C, *Am. Mineral.*, **58**, 588-593, 1973.
- Smyth, J. R., and J. V. Smith, Electrostatic energies for ion clustering in intermediate plagioclase feldspar, *Mineral. Mag.*, **37**, 181-184, 1969.
- Sobolev, N. V., *The Deep Seated Inclusions in Kimberlites and the Problem of the Upper Mantle Composition* (in Russian), Nauka, Novosibirsk, 1974.
- Sobolev, N. R., Jr., I. K. Kuznetsova, and N. I. Zyuzin, The petrology of groszpydite xenoliths from the Zagadochnaya kimberlite pipe in Yakutia, *J. Petrol.*, **9**, 253-280, 1968.
- Sobolev, N. V., Yu. G. Lavrent'ev, N. P. Pokhilenko, and L. V. Usova, Chrome-rich garnets from the kimberlites of Yakutia and their parageneses, *Contrib. Mineral. Petrol.*, **40**, 39-52, 1973.
- Sobolev, N. V., Yu. G. Lavrent'ev, L. I. Pospe-lova, and V. S. Sobolev, Chrome pyrope in diamonds from Yakutia, *Dokl. Akad. Nauk SSSR*, **189**, 162-165, 1969.
- Soellner, J., Über Bergalith, ein neues melilith-reiches Gestein aus dem Kaiserstuhl, *Mitt. Bad. Geol. Landesanst.*, **7** (2), 413-466, 1913.
- Spencer, A. B., Alkaline igneous rocks of the Balcones Province, Texas, *J. Petrol.*, **10**, 272-306, 1969.
- Stelzner, A., Über Melilith und Melilithbasalte, *Neues Jahrb. Mineral., Beil. Band II*, 369-439, 1883.
- Sternheimer, R. M., and R. F. Peierls, Calculation of fine-structure splittings and quadrupole antishielding factors for atomic states, *Phys. Rev. A*, **4**, 1722-1728, 1971.
- Stormer, J. C., A practical two-feldspar geothermometer, *Am. Mineral.*, **60**, 667-674, 1975.
- Stout, J. H., Phase petrology and mineral chemistry of coexisting amphiboles from Telemark, Norway, *J. Petrol.*, **13**, 99-145, 1972.
- Strens, R. G. J., Pressure-induced spin-pairing in gillespite, $\text{BaFe(II)Si}_6\text{O}_{10}$, *Chem. Commun.*, **21**, 777-778, 1966.
- Strens, R. G. J., The nature and geophysical importance of spin-pairing in minerals of iron (II), in *The Application of Modern Physics to the Earth and Planetary Interiors*, S. K. Runcorn, ed., John Wiley and Sons, Inc., New York, pp. 213-220, 1969.
- Stuermer, D. H., and G. R. Harvey, Humic substances from seawater, *Nature (London)*, **250**, 480-481, 1974.
- Sueno, S., M. Cameron, and C. T. Prewitt, Orthoferrosilite: high temperature crystal chemistry, *Am. Mineral.*, **61**, 38-53, 1976.
- Switzer, G., W. G. Melson, and G. Thompson, Garnet from the Mid-Atlantic Ridge near 43°N latitude, *Geol. Soc. Am. Bull.*, **81**, 895-898, 1971.
- Tarte, P., Applications nouvelles de la spectrométrie infrarouge à des problèmes de cristalochimie, *Silic. Ind.*, **28**, 345-354, 1963.
- Taylor, D. R., Overlap contribution to the electric field gradient in an ionic complex, *J. Chem. Phys.*, **48**, 536-537, 1968.
- Taylor, H. P., Jr., The application of oxygen and hydrogen isotope studies to problems of hydrothermal alteration and ore deposition, *Econ. Geol.*, **69**, 843-883, 1974.
- Taylor, L. A., K. C. Misra, and B. M. Walker, Experimental subsolidus annealing of selected Apollo 16 rocks: reequilibration of native FeNi metal and schreibersite (abstract), in *Lunar Science VII*, Lunar Science Institute, Houston, pp. 852-854, 1976.
- Tazieff, H., État actuel des connaissances sur le volcan Nyiragongo (République démocratique du Congo), *Bull. Soc. Geol. Fr.*, **8**, 176-200, 1966.
- Templeton, D. H., and Q. C. Johnson, Computation of Madelung sum and crystal energies,

- in *Computing Methods and the Phase Problems in X-Ray Crystal Analysis*, R. Pepinsky and J. M. Robertson, eds., Pergamon Press, New York, pp. 150-153, 1961.
- Tessman, J. R., A. H. Kahn, and W. Shockley, Electronic polarizabilities of ions in crystals, *Phys. Rev.*, **92**, 890-895, 1953.
- Theng, B. K. G., *The Chemistry of Clay-Organic Reactions*, John Wiley and Sons, Inc., New York, 1974.
- Theng, B. K. G., and H. W. Scharpenseel, The adsorption of ¹⁴C-labelled humic acid by montmorillonite, in *Proceedings of the International Clay Conference 1975*, S. W. Bailey, ed., Applied Publishing, Wilmette, Illinois, pp. 643-653, 1976.
- Thompson, J. B., Jr., Geometrical possibilities for amphibole structures, *Am. Mineral.*, **55**, 292-293, 1970.
- Thompson, R. N., The 1-atmosphere liquidus oxygen fugacities of some tholeiitic intermediate, alkalic and ultra-alkalic lavas, *Am. J. Sci.*, **275**, 1049-1072, 1975.
- Thurstone, L. L., *Multiple-Factor Analysis*, 8th ed., The University of Chicago Press, Chicago, Ill., 1969.
- Tilley, C. E., The nephelinite of Etinde, Cameroons, West Africa, *Geol. Mag.*, **90**, 145-151, 1953.
- Tilley, C. E., and R. N. Thompson, Melting relations of some ultra alkali volcanics, *Geol. J.*, **8**, 65-70, 1972.
- Tilton, G. R., Volume diffusion as a mechanism for discordant lead ages, *J. Geophys. Res.*, **65**, 2933-2945, 1960.
- Tödheide, K., and E. U. Franck, Das Zweiphasengebiet und die Kritische Kurve im System Kohlendioxid-Wasser bis zu Drucken von 3500 bar, *Z. Phys. Chem.*, **37**, 387-401, 1963.
- Tokonomi, M., N. Morimoto, S. Akimoto, Y. Syono, and H. Takeda, Stability relations between olivine, spinel and modified spinel, *Earth Planet. Sci. Lett.*, **14**, 65-69, 1972.
- Tosi, M. P., Cohesion of ionic solids in the Born model, *Solid State Phys.*, **16**, 1-120, 1964.
- Tossell, J. A., Electronic structures of iron-bearing oxide minerals at high pressures, *Am. Mineral.*, **61**, 130-144, 1976.
- Turnock, A. C., D. H. Lindsley, and J. E. Grover, Synthesis and unit cell parameters of Ca-Mg-Fe pyroxenes, *Am. Mineral.*, **58**, 50-59, 1973.
- Tuttle, O. F., and N. L. Bowen, Origin of granite in the light of experimental studies in the system NaAlSi₃O₈-KAlSi₃O₈-SiO₂-H₂O, *Geol. Soc. Am. Mem.*, **74**, 153 pp., 1958.
- Ulmer, G., M. Rosenhauer, E. Woermann, J. Gröner, A. Dröry-Wolff, and P. Wasilewski, Applicability of electrochemical oxygen fugacity measurements to geothermometry, *Am. Mineral.*, in press, 1976.
- Van Zeggeren, F., and S. H. Storey, *The Computation of Chemical Equilibria*, Cambridge University Press, Cambridge, 1970.
- Verhoogen, J., Phase changes and convection in the earth's mantle, in *A Symposium on Continental Drift*, P. M. S. Blackett et al., eds., Royal Society of London, pp. 276-283, 1965.
- Viljoen, M. J., and R. P. Viljoen, The geology and geochemistry of the lower ultramafic unit of the Onverwacht Group, and a proposed new class of igneous rock, *Geol. Soc. S. Afr., Spec. Publ.*, **2**, 221-244, 1969.
- Viswanathan, S., Basaltic komatiite occurrences in the Kolar gold field of India, *Geol. Mag.*, **111**, 353-354, 1974.
- Vogt, J. H. L., On the content of nickel in igneous rocks, *Econ. Geol.*, **18**, 307-352, 1923.
- Waff, H. S., Pressure-induced coordination changes in magmatic liquids, *Geophys. Res. Lett.*, **2**, 193-196, 1975.
- Wager, L. R., and G. M. Brown, *Layered Igneous Rocks*, Oliver and Boyd, Ltd., Edinburgh, 1968.
- Wager, L. R., and W. A. Deer, Geological investigations in East Greenland, Part III, The petrology of the Skaergaard intrusion, Kangerdlugssuaq, East Greenland, *Medd. Grönl.*, **105**, No. 4, 352 pp., 1939 (reissued 1962).
- Wager, L. R., and R. L. Mitchell, The distribution of trace elements during strong fractionation of basic magma, *Geochim. Cosmochim. Acta*, **1**, 129-208, 1951.
- Walker, D., R. P. Kirkpatrick, J. Longhi, and J. F. Hays, Crystallization history of lunar picritic basalt 12002: phase-equilibria and cooling-rate studies, *Geol. Soc. Am. Bull.*, **87**, 646-656, 1976.
- Walsh, J. B., New analysis of attenuation in partially melted rock, *J. Geophys. Res.*, **74**, 4333-4337, 1969.
- Wass, S. Y., The origin and petrogenetic significance of hour-glass zoning in titaniferous clinopyroxenes, *Mineral. Mag.*, **39**, 133-144, 1973.
- Wasson, J. T., *Meteorites*, Springer-Verlag, New York, 1974.
- Weaver, J. S., T. Takahashi, and W. A. Bassett, Calculation of the P-V relation for sodium chloride up to 300 kilobars at 25°C, *Natl. Bur. Stand. (U.S.) Spec. Publ.*, **326**, 189-199, 1971.
- Wechsler, B. A., C. T. Prewitt, and J. J. Papike, Chemistry and structure of lunar and synthetic armalcolite, *Earth Planet. Sci. Lett.*, **29**, 91-103, 1976.
- Weir, C. E., E. R. Lippincott, A. Van Valkenburg, and E. N. Bunting, Infrared studies in the 1- to 15-micron region to 30,000 atm, *J. Res. Natl. Bur. Stand., Sect. A*, **63**, 55-62, 1959.

- Welch, J. H., A simple microscope attachment for observing high-temperature phenomena, *J. Sci. Instrum.*, **31**, 458-462, 1954.
- Wenner, D. B., and H. P. Taylor, Jr., Oxygen and hydrogen isotope studies of a Precambrian granite-rhyolite terrane, St. Francois Mountains, S.E. Missouri, *Geochim. Cosmochim. Acta*, in press, 1976.
- Wetherill, G. W., Discordant uranium-lead ages, I, *Trans. Am. Geophys. Union*, **37**, 320-326, 1956.
- Whipple, E. R., Quantitative Mössbauer spectra and chemistry of iron, Ph.D. thesis, Massachusetts Institute of Technology, 1973.
- White, E. W., Microprobe technique for the analysis of multiphase microcrystalline powders, *Am. Mineral.*, **49**, 196-197, 1964.
- White, W. S., and J. C. Wright, Sulfide mineral zoning in the basal Nonesuch shale, northern Michigan, *Econ. Geol.*, **61**, 1171-1190, 1966.
- Whitney, J. A., The effects of pressure, temperature and X_{H_2O} on phase assemblage in four synthetic rock compositions, *J. Geol.*, **83**, 1-27, 1975.
- Whittaker, E. J. W., Madelung energies and site preferences in amphiboles, I, *Am. Mineral.*, **56**, 980-996, 1971.
- Williams, A. F., *The Genesis of the Diamond*, 2 vol., E. Benn, Ltd., London, 1932.
- Williams, D. A. C., Archaean ultramafic, mafic and associated rocks, Mt. Monger, Western Australia, *J. Geol. Soc. Aust.*, **19**, 163-188, 1972.
- Wones, D. R., Phase equilibria of "ferriannite," $KFe^{2+}_3Fe^{3+}_3Si_3O_{10}(OH)_2$, *Am. J. Sci.*, **261**, 581-596, 1963.
- Wood, B. J., The solubility of alumina in orthopyroxene coexisting with garnet, *Contrib. Mineral. Petrol.*, **46**, 1-15, 1974.
- Wood, B. J., The application of thermodynamics to some subsolidus equilibria involving solid solutions, *Fortschr. Mineral.*, **52**, Spec. Issue, 21-45, 1975.
- Wood, B. J., Mixing properties of tschermakitic clinopyroxenes, *Am. Mineral.*, in press, 1976.
- Wood, B. J., and S. Banno, Garnet-orthopyroxene and orthopyroxene-clinopyroxene relationships in simple and complex systems, *Contrib. Mineral. Petrol.*, **42**, 109-124, 1973.
- Wyllie, P. J., and W. L. Huang, Influence of mantle CO_2 in the generation of carbonatites and kimberlites, *Nature (London)*, **257**, 297-299, 1975a.
- Wyllie, P. J., and W. L. Huang, Peridotite, kimberlite, and carbonatite explained in the system $CaO-MgO-SiO_2-CO_2$, *Geology*, **3**, 621-624, 1975b.
- Wyllie, P. J., and W. L. Huang, Carbonation and melting reactions in the system $CaO-MgO-SiO_2-CO_2$ at mantle pressures with geophysical and petrological applications, *Contrib. Mineral. Petrol.*, **54**, 79-107, 1976.
- Yagi, K., and K. Onuma, An experimental study on the role of titanium in alkalic basalts in light of the system diopside-akermanite-nepheline- $CaTiAl_2O_6$, *Am. J. Sci.*, *Schairer Vol.*, **267A**, 509-549, 1969.
- Yang, H.-Y., and W. R. Foster, Stability of iron-free pigeonite at atmospheric pressure, *Am. Mineral.*, **57**, 1232-1241, 1972.
- Yoder, H. S., Jr., Melilite stability and paragenesis, *Fortschr. Mineral.*, **50**, 140-173, 1973.
- Yoder, H. S., Jr., and C. E. Tilley, Origin of basalt magmas: an experimental study of natural and synthetic rock systems, *J. Petrol.*, **3**, 342-532, 1962.
- Yoshiki, B., and R. Yoshida, Composition of low-alkali glass, *J. Am. Ceram. Soc.*, **35**, 166-169, 1952.
- Zachariasen, W., The atomic arrangement in glass, *J. Am. Chem. Soc.*, **54**, 3841-3851, 1932.
- Zartman, R. E., and R. F. Marvin, Radiometric age (Late Ordovician) of the Quincy, Cape Ann, and Peabody granites from eastern Massachusetts, *Geol. Soc. Am. Bull.*, **82**, 937-957, 1971.

PERSONNEL

Scientific Staff

Director: H. S. Yoder, Jr., *Petrologist*
Emeritus Research Associate: E. G. Zies,
Chemist

Distinguished Professor, CIW: E. F. Osborn,
Petrologist

Systematic Petrologist: F. Chayes

Petrologists: F. R. Boyd, Jr., D. H. Eggler,
 T. N. Irvine, I. Kushiro,¹ D. Rumble III

Physical Chemists: J. D. Frantz, T. C.
 Hoering

Geophysicists: P. M. Bell, H. K. Mao

Organic Geochemists: J. R. Cronin,² P. E.
 Hare

Crystallographers: L. W. Finger,³ Y. Ohashi⁴

Isotope Geochemists: G. L. Davis, T. E.
 Krogh⁵

Solid-State Geochemist: D. Virgo

Postdoctoral Fellows: R. J. Arculus, Durham
 University, England;⁶ N. T. Arndt, Uni-
 versity of Toronto;⁷ J. M. Ferry, Harvard
 University;⁸ A. A. Finnerty, University of
 California at Los Angeles;⁹ T. Fujii, Uni-
 versity of Tokyo, Japan;¹⁰ J. I. Hedges,
 Marine Science Institute, University of
 Texas at Port Aransas; F. E. Huggins,
 Massachusetts Institute of Technology;¹¹

G. H. Miller, University of Colorado;¹²
 B. O. Mysen, Pennsylvania State Univer-
 sity; J. Trochimezyk, University of Mainz,
 Germany;¹³ Rosemary J. Vidale, State
 University of New York at Binghamton;¹⁴
 B. J. Wood, University of Manchester,
 England¹⁵

Predoctoral Fellows: T. M. Benjamin, Cali-
 fornia Institute of Technology;¹⁶ H. R.
 Naslund, University of Oregon; F. S.
 Spear, University of California at Los
 Angeles;¹⁶ E. B. Watson, Massachusetts
 Institute of Technology¹⁷

Fellowship Trainees: Julia A. Dill, Yale Uni-
 versity;¹⁸ Dora Y. Lee, Princeton Univer-
 sity;¹⁹ Catherine A. McCammon, Massa-
 chusetts Institute of Technology²⁰

Guest Investigators: J. Akella, NASA John-
 son Space Center; J. D. Bass, Lehigh Uni-
 versity; D. S. Burnett, California Institute
 of Technology; Robert V. Danchin, Anglo
 American Research Laboratories, Johannes-
 burg, South Africa; J. Friel, Lehigh Uni-
 versity; Stefan S. Hafner, University of
 Marburg, Germany; B. Harte, University
 of Edinburgh, Scotland; Alice Hoersch,
 Johns Hopkins University; John R. Hollo-
 way, Arizona State University; H. G.
 Huckenholz, University of Munich, Ger-
 many; Lin-gun Liu, Australian National
 University, Canberra; G. H. Miller, Uni-
 versity of Colorado; Jim Myers, Johns
 Hopkins University; Saki Olsen, Johns
 Hopkins University; R. W. Page, Aus-
 tralian Bureau of Mineral Resources, Geol-
 ogy, and Geophysics, Canberra; Craig
 Rithgmyer, Johns Hopkins University; M.
 Rosenhauer, University of Frankfurt, Ger-
 many; A. K. Saha, Presidential College,
 Calcutta, India; Th. G. Sahama, Univer-
 sity of Helsinki, Finland; Bruce Simonson,
 Johns Hopkins University; Craig B. Smith,

¹ On leave of absence at University of Tokyo,
 Japan, from July 1 through September 30, 1975,
 and from April 16, 1976.

² Temporary appointment terminated Sep-
 tember 15, 1975, to return to Arizona State
 University.

³ On leave of absence from September 1, 1975,
 through June 30, 1976, as Visiting Professor at
 the State University of New York at Stony
 Brook.

⁴ Temporary appointment from July 1, 1975,
 terminated June 30, 1976, to accept position as
 Lecturer at Department of Geology, University
 of Pennsylvania.

⁵ Resigned August 31, 1975, to accept position
 as Director, Geochronology Laboratory, Royal
 Ontario Museum, Toronto, Canada.

⁶ Appointment terminated August 31, 1975,
 to accept position as Assistant Professor, De-
 partment of Geology, Rice University, Houston,
 Texas.

⁷ Appointment from September 1, 1975.

⁸ Appointment from July 1, 1975.

⁹ Appointment from April 1, 1976.

¹⁰ Appointment from January 16, 1976.

¹¹ Appointment terminated June 30, 1976, to
 accept position as Visiting Scientist, Physics
 Division, U.S. Steel Research, Monroeville, Pa.

¹² Appointment terminated September 30,
 1975, to return to University of Colorado.

¹³ Appointment from January 1, 1976.

¹⁴ Appointment terminated August 31, 1975,
 to accept position as Staff Scientist at Los
 Alamos Scientific Laboratory, New Mexico.

¹⁵ Appointment from September 1, 1975,
 through February 29, 1976.

¹⁶ Appointment from October 1, 1975.

¹⁷ Appointment terminated December 31, 1975.

¹⁸ Appointment from June 15, 1976.

¹⁹ Appointment from June 21, 1976.

²⁰ Appointment from June 1, 1976.

Colorado State University; Anthony Torres, National Cancer Institute, National Institutes of Health; A. Van Valkenburg, U.S. Bureau of Mines (retired); Bruce Velde, University of Paris, France; Danielle Velde, University of Paris, France; H. P. Weber, Lamont-Doherty Geological Observatory

Operating and Maintenance Staff

Executive Officer: A. D. Singer

Accountant and Purchasing Agent: C. B. Petry

Editor and Librarian: Dolores M. Thomas

Stenographers: Marjorie E. Imlay, Mabel B. Mattingly

Typist-Clerk: Barbara B. Jones²¹

²¹ Temporary appointment through August 6, 1975, and from September 8, 1975.

Clerk and Technician: H. J. Lutz

Electronics Technicians: D. J. George,²² C. G. Hadidiacos

Acting Shop Foreman: W. Roos²³

Laboratory Technician and Instrument Maker: G. E. Speicher

Instrument Makers: C. A. Batten, C. Brown,²⁴ J. W. Schwartz²⁵

Machinist: P. M. Vacchio¹⁷

Building Engineer: H. L. Moore

Custodian and Painter: M. Ferguson

Custodian and Thin-Section Technician: D. Ratliff, Jr.

Custodian and Mechanic: L. B. Patrick

²² Appointment from August 25, 1975.

²³ Temporary appointment from October 31, 1975, through June 30, 1976.

²⁴ Temporary appointment from November 10, 1975.

²⁵ Temporary appointment from January 5, 1976.

Developmental Biology Research Group

*Pasadena, California
and Kerckhoff Marine Laboratory,
Corona Del Mar, California*

Roy J. Britten
Senior Research Fellow

Eric H. Davidson
Professor, California Institute of Technology

Contents

| | |
|---|-----|
| Introduction | 861 |
| DNA Sequence Arrangement | 861 |
| DNA sequence organization in the lepidopteran <i>Antheraea pernyi</i> | 861 |
| Absence of short-period interspersion of repetitive and nonrepetitive sequences in the DNA of <i>Drosophila melanogaster</i> | 870 |
| Contrasting patterns of DNA sequence arrangement in <i>Apis mellifera</i> (honeybee) and <i>Musca domestica</i> (housefly) | 883 |
| DNA Sequence Expression Studied by Transcription into RNA | 890 |
| Structural gene sets active in embryos and adult tissues of the sea urchin | 890 |
| Sequence complexity of the RNA accumulated in oocytes of <i>Arbacia punctulata</i> | 918 |
| Nucleic Acid Evolution | 925 |
| Evolutionary divergence and length of repetitive sequences in sea urchin DNA | 925 |
| Single-copy DNA and structural gene sequence relationships among four sea urchin species | 944 |
| Acknowledgments | 955 |
| References Cited | 955 |
| Recent Publications | 958 |
| Staff | 959 |

INTRODUCTION

The work of this group continues as it has in past years to concentrate on four major areas: DNA sequence arrangement and its phyletic generality; studies of transcription in relation to DNA sequence arrangement; examination of the mechanisms of DNA reassociation and hybridization; and the evolutionary changes in DNA. While a considerable number of measurements have been made of DNA reassociation kinetics in relation to the mechanism of reassociation, none of the recent work is sufficiently complete for description in this report and will be deferred to next year. Great effort is being expended on the preparation of specific fragments of sea urchin DNA by means of recombinants with bacterial plasmids. The intention is to isolate specific regions that are likely to be informative about sequence organization and the control of gene expression. These projects are not advanced enough for description in this year's report.

The studies of DNA sequence organization described this year are for three insect species chosen because of the observation (Manning *et al.*, 1975) that *Drosophila* DNA appears to have a

quite different pattern than that of most other species. The DNA of all organisms except a few insects has a short-period interspersion pattern similar to that first examined in detail for *Xenopus laevis*. The characteristic feature of the *Xenopus* or short-period pattern is that most of the repetitive DNA occurs in sequences about 300 nucleotides long, alternating with single-copy sequences from 1000 to several thousand nucleotides long. Most of the single-copy DNA is interspersed in this way. However, *Drosophila* and a few other insects appear to lack short repetitive sequences spaced by recognizable single-copy sequences. The work described this year includes the surprising observation that *Musca domestica* (housefly) DNA shows the short-period or *Xenopus* pattern in contrast to the long-period or *Drosophila* pattern shown by other diptera. A lepidopteran (*Antheraea pernyi*) is also shown to exhibit the short-period interspersion, while honeybee shows the long-period pattern. Large-scale changes in genome arrangement and loss or gain of large quantities of highly organized DNA sequences must have occurred during insect evolution.

DNA SEQUENCE ARRANGEMENT

DNA SEQUENCE ORGANIZATION IN THE LEPIDOPTERAN *Antheraea pernyi*

A. Efstratiadis,* W. R. Crain, R. J. Britten,
E. H. Davidson, and F. C. Kafatos*

Recent studies have shown that repetitive and nonrepetitive sequences are extensively interspersed in the genomes of several eukaryotes. Studies of this kind have been reported for calf (Britten and Smith, 1970), rat (Bonner *et al.*, 1974), *Xenopus* (Davidson *et al.*, 1973),

sea urchin (Graham *et al.*, 1974), *Aplysia*, a mollusc (Angerer *et al.*, 1975), a slime mold (Firtel and Kindle, 1975), and six other invertebrate species from diverse phylogenetic groups (Goldberg *et al.*, 1975; Davidson *et al.*, 1975a). It was shown that in these organisms the major fraction of the DNA is organized in a pattern described first in detail for *Xenopus* DNA ("Xenopus pattern"). This pattern of DNA sequence organization has the following characteristics: (a) The majority of the repetitive sequences are short (with an average

*The Biological Laboratories, Harvard University, Cambridge, Mass. 02138

length of 300 nucleotides), and these alternate with single-copy sequences; (b) the majority of the single-copy sequences extend for less than about 1500 nucleotides before terminating in repetitive-sequence elements; (c) a fraction of the single-copy sequences are longer, up to several thousand nucleotides in length, but are also interspersed with repetitive sequences.

A strikingly different pattern of DNA sequence organization has been found in two insects, *Drosophila melanogaster*, a dipteran (Manning *et al.*, 1975; Crain *et al.*, 1976a) and in the honeybee, a hymenopteran (described in a later section of this report). The *Drosophila* genome contains a few short repetitive sequences interspersed with single-copy regions (Manning *et al.*, 1975; Crain *et al.*, 1976a). The electron micrographic studies of Manning, Schmid, and Davidson, 1975, indicate that the repetitive sequence regions range from a few hundred to more than 10,000 nucleotides in length. Manning *et al.* were unable to measure the length of the single-copy sequences, but they estimated that there were about 2800 repetitive regions, which would have an average spacing of 30,000 nucleotides of single-copy DNA if they were generally distributed throughout the DNA. Recent measurements (Finnegan, Rubin, and Hogness, personal communication) with cloned *Drosophila* DNA sequences show that in some cases a small fraction of a repetitive region has a sequence in common with a small fraction of another region. This suggests that there is another level of sequence organization of the repeated sequence still to be revealed.

The widespread occurrence of the *Xenopus* pattern of DNA organization (Goldberg *et al.*, 1975; Davidson *et al.*, 1975a) suggests that the short interspersed repetitive sequence might play an important role in chromosome function. It was postulated that they are involved in the regulation of genetic activity (Davidson and Britten, 1973). This notion was indirectly supported by

the observation that the sea urchin DNA single-copy sequences contiguous to interspersed repetitive elements include most or all of the structural genes that are active in embryogenesis (Davidson *et al.*, 1975b). It is important, therefore, to determine whether or not the *Drosophila* and honeybee exceptions are characteristic of DNA sequence arrangement in insects. As we report here, silkmoth DNA sequence organization belongs to the more general *Xenopus* pattern. In addition, knowledge of the general features of genome organization in the silkmoth provides a necessary background for ongoing studies of chorion genes and their organization in this species.

Reassociation Kinetics of 250-Nucleotide DNA Fragments

The reassociation kinetics of 250-nucleotide-long DNA fragments are shown in Fig. 1a. Because of the wide range of kinetic components it was necessary to determine independently the rate of single-copy DNA reassociation. The open triangles show measurements of the reassociation of single-copy tracer with an excess of total 250-nucleotide-long DNA driver. The least-squares solution for a single second-order component for these data gives a rate constant of $1.05 \times 10^{-3} M^{-1} \text{ sec}^{-1}$. This is the rate constant expected for the genome size of 1 pg, which was estimated in preliminary experiments by measuring photometrically the amount of DNA in Feulgen-stained nuclei of testis squashes, with *Drosophila* testis squashes as standard, and also by measuring the DNA content of counted sperm samples by diphenylamine. The circles in Fig. 1a show the reassociation of 250-nucleotide-long fragments of total *A. pernyi* DNA, and the solid line drawn through them is the least-squares solution for three second-order components, assuming only that the rate of the single-copy component is $1.05 \times 10^{-3} M^{-1} \text{ sec}^{-1}$. The reassociation of these three individual components is portrayed by the dashed

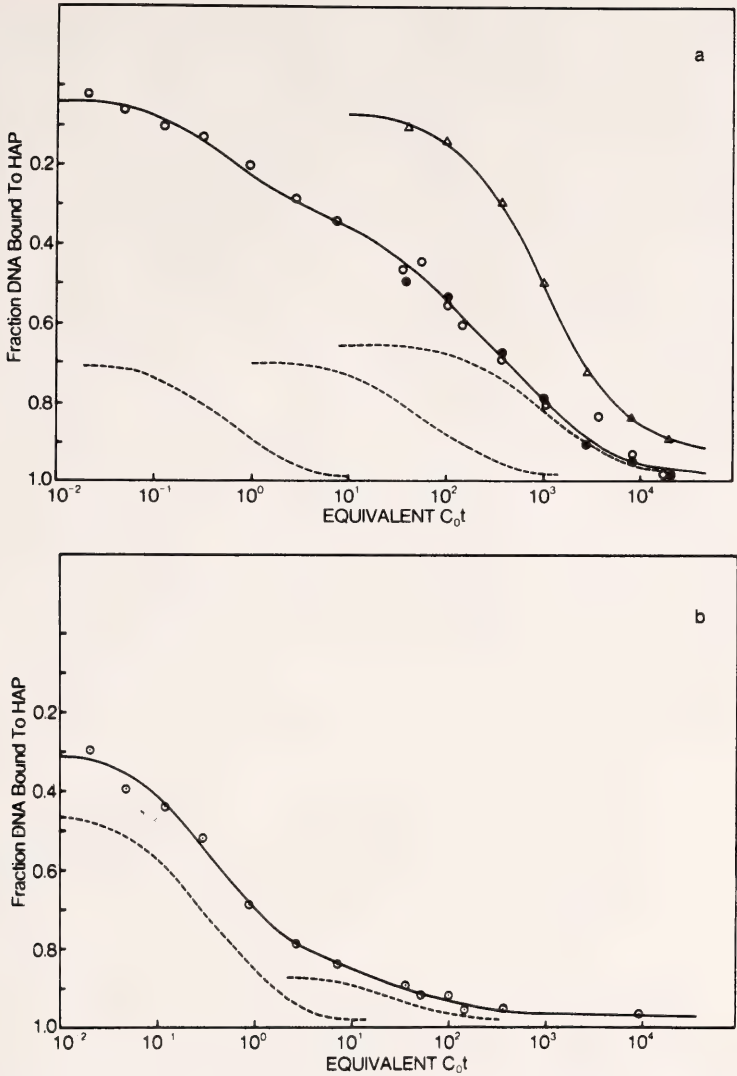


Fig. 1. Reassociation kinetics of *A. pernyi* DNA at fragment lengths of 250 nucleotides and 2200 nucleotides. DNA was reassociated at 0.35 mg/ml in 0.12 M PB at 60° ($C_0t < 0.5$) or at 7 mg/ml in 0.4 M PB at 66° ($C_0t > 0.5$). Data for reassociation in 0.4 M PB are corrected to the equivalent C_0t in 0.12 M PB. The fraction of the DNA fragments containing duplex regions was estimated by HAP binding. Fractions were eluted with 0.12 M PB at 60° (single stranded, unbound) and 98° (duplex-containing, bound). Fig. 1a shows the reassociation of 250-nucleotide fragments of unlabeled total moth DNA (open circles). The reassociation was followed by monitoring A_{260} in the HAP column eluates. The rate of reassociation of isolated single-copy sequences is also shown (open triangles). For this analysis, a fraction of 250-nucleotide tracer not bound to HAP at C_0t 3000 was reassociated together with a 75-fold mass excess of total unlabeled 250-nucleotide driver DNA (filled circles). Fig. 1b shows the reassociation of 3H -labeled 2200-nucleotide tracer DNA in the presence of a 360-fold excess of 250-nucleotide unlabeled DNA. The solid curves in both Fig. 1a and Fig. 1b represent the solutions of a least-squares computer analysis of the data yielding the second order components indicated by the dotted lines.

lines in Fig. 1a, and the rate constants and fraction of DNA fragments given by the least-squares solution are listed in Table 1. There is no deviation which suggests the presence of other components. Furthermore it is clear from the fact that the principal part of the reassociation is initiated at about C_0t 0.05 that there is a major fast component that is half reassociated at about C_0t 0.5. However, there is no way from these measurements to decide whether several other components exist or even a continuum of components with repetition frequencies ranging from a few thousand copies to less than ten. We use in our analysis the minimum number of repetitive components that the reassociation kinetic measurements require and term these the very fast or foldback fraction, and the fast and slow repetitive components; the latter two components are present in about 1600 and 15 copies, respectively. These components may

represent classes of repeated sequences with a range of repetition frequencies.

Determination of the quantities of repetitive sequences from the magnitude of the kinetic components measured by hydroxyapatite binding is of course affected by their interspersions. Our estimate of the fraction of the genome actually present in the repetitive and single-copy sequences is also shown on Table 1. The measured components may be described as: fragments containing only single-copy sequences; fragments containing slow sequences but not more rapidly reassociating sequences; fragments containing fast sequences but not very fast or foldback; and finally, those containing very fast or foldback sequences. Each fraction is bound to HAP as a result of the reassociation of the most rapidly reassociating sequence present and may include significant quantities of those components which reassociate more slowly.

TABLE 1. Reassociation Analysis of *A. pernyi* DNA at Two Fragment Lengths*

| Fragment Length (nucleotides) | Fragments Bearing Exclusively Single-Copy Sequences (single-copy) | | Fragments Bearing Repetitive Sequences of Only the Slowly Reassociating Type (slow) | | Fragments Bearing Repetitive Sequences of the Rapidly Reassociating Type (fast) | | Fragments Bearing Foldbacks and/or Very Rapidly Reassociating Repetitive Sequences (very fast) |
|---|---|---|---|---|---|---|--|
| | Fraction of Total | Rate constant ($M^{-1} \text{ sec}^{-1}$) | Fraction of Total | Rate constant ($M^{-1} \text{ sec}^{-1}$) | Fraction of Total | Rate constant ($M^{-1} \text{ sec}^{-1}$) | Fraction of Total |
| 250 | 0.35 | 1.05×10^{-3} | 0.30 | 1.53×10^{-2} | 0.30 | 1.69 | 0.05 |
| 2200 | <0.03 | | 0.12 | 2.99×10^{-2} | 0.54 | 2.63 | 0.31 |
| Estimate of fraction of genome in sequence class* | 0.56 | | 0.30 | | 0.10 | | 0.04 |

* These estimates are approximate and have been made in the following way: The single-copy fraction is the remainder after all of the repetitive classes have been calculated. For the slow repetitive sequences we use the fraction of fragments observed in the kinetics of reassociation of 250-nucleotide fragments, since we do not know the slow repetitive sequence organization. For estimating the quantity of the very fast fraction, we have reduced slightly the quantity observed with 250-nucleotide fragments by analogy to the results for the DNA of other species. The estimate for the fast fraction was obtained from the sum of fast plus very fast fractions as calculated in the text, after subtraction of the value listed in this table for the very fast fraction.

Reassociation Kinetics of 2200-Nucleotide DNA Fragments

^3H -labeled 2200-nucleotide fragments were incubated to various C_0t values with an excess of unlabeled 250-nucleotide driver DNA (tracer: driver, 1:360), and the fraction of the labeled DNA bound to HAP was measured. Fig. 1b shows the results, together with the least-squares solution for two unrestricted second-order components. Table 1 lists the characteristics of the two kinetic components resolved by the computer.

It is immediately clear that the long DNA fragments reassociate very rapidly with the short driver fragments. For example, the fraction of the 2200-nucleotide fragments which have not reassociated with short fragments by C_0t 10 is only one seventh of the corresponding value for 250-nucleotide fragments themselves. The rapid reaction cannot be accounted for by the effect of length on the reassociation rate (Wetmur and Davidson, 1968) and is indicative of DNA sequence interspersions (Davidson *et al.*, 1973; Graham *et al.*, 1974).

The apparent reassociation constants for the slow and fast repetitive components of our solution for the 2200-nucleotide fragments are in reasonable agreement with the corresponding values at 250 nucleotides. The rate constants for both components are somewhat greater for the 2200-nucleotide fragments. This effect is not significant for the slow component since there is too little present in the 2200-nucleotide case for an accurate least-squares solution. For the fast component the apparent 50% acceleration could result from inaccuracy or from the fact that the full length of the repetitive-sequence element is likely to be present on the 2200-nucleotide fragments, while on the short fragments the sequences are most often broken as the fragments are sheared to 250-nucleotide length.

In any case, the major difference between the 2200-nucleotide and 250-

nucleotide solutions is in the proportions of fragments which appear to carry each class of sequence. Fragments carrying exclusively single-copy DNA account for one third of the 250-nucleotide DNA (see Fig. 1a) but are undetectable at a length of 2200 nucleotides. Clearly, single-copy sequences are extensively interspersed with repetitive sequences in the *A. pernyi* genome. The large quantity of 2200-nucleotide fragments that carry fast repetitive sequences indicates that these sequences are widely dispersed in the genome. The decrease in the proportion of fragments which appear to be carrying slow repetitive sequences is clearly due to the interspersions of this class with the fast repetitive sequences.

Therefore, we know that both single-copy and slow repetitive sequences are interspersed with fast repetitive sequences. However, we do not know to what extent slow and single-copy sequences are interspersed with each other. It is also unresolved whether the 12% slow kinetic component in the 2200-nucleotide curve contains some linked single-copy sequences. Future measurements would be required to illuminate this aspect of the interspersions pattern. This point is emphasized here because it relates to the following measurements of the spacing between repetitive sequences.

Measurement of Length and Amount of Repetitive DNA Sequences using S1 Nuclease

If reassociated DNA is digested with a single-strand-specific nuclease under carefully controlled conditions, the duplex regions may be separated from the unreassociated single-strand regions (Britten *et al.*, in press). To study the characteristics of repetitive DNA sequences, *A. pernyi* DNA fragments of about 1800 nucleotides were incubated to C_0t 10 and digested with S1 nuclease under standard conditions (Britten *et al.*, in press; Davidson *et al.*, 1974)

which leave duplex regions intact even if they contain as much as 20% mismatch. The duplexes were then separated from the partially digested single-stranded fragments by binding to HAP. The HAP-bound fraction was chromatographed on agarose A-50 (Fig. 2). Approximately 75% (18% of the starting DNA) eluted almost coincidentally with a 300-nucleotide marker. The single-strand length was shown by subsequent alkaline sucrose gradient centrifugation to be about 230 nucleotides. The remainder of the S1-nuclease-resistant material (6% of the starting DNA) was excluded from the agarose column and was polydispersed in alkaline sucrose gradients, varying from a few hundred to a few thousand nucleotides in single-strand length.

Figure 3 and Table 2 show spectrophotometric melting measurements on fractions obtained in the chromatograph of Fig. 2. The T_m of the long duplex fraction (33) is actually slightly higher than that of native DNA, indicating the presence of long repetitive sequences relatively high in GC content. The T_m of the

short duplexes is about 74°. About 3° reduction in T_m is expected to result from the short length of these fragments. Thus we estimate a reduction in T_m of about 7° due to mismatch. It follows that the short interspersed repeated sequences show greater evolutionary divergence than do the long repeated sequences. A similar result has been observed for all of the other species that have been examined in this way, including sea urchin (see later section of this report), *Xenopus* (Davidson and Britten, 1973; Davidson *et al.*, 1974), calf (unpublished data, Britten), *Spisula* (Goldberg *et al.*, 1975), and sea hare (unpublished data, Angerer and Britten).

The fraction of the DNA which is resistant to S1 nuclease under these conditions (24%) permits an estimate of the actual fraction of the DNA which is in repetitive sequences. Approximately 10% of the S1-resistant material might be single-strand tails, as suggested by the reduced hyperchromicity (see Table 2). Therefore, the repetitive sequences reassociated at C_0t 10 are approximately

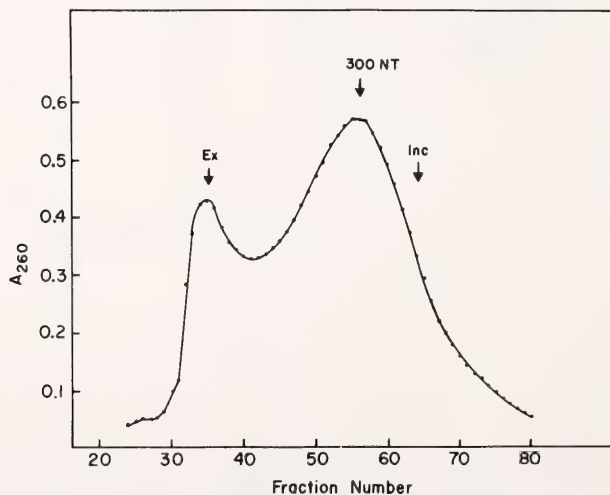


Fig. 2. Size distribution of S1-resistant repetitive DNA sequences. Total DNA of 1800-nucleotide fragment length was reassociated to C_0t 10 and treated with S1 nuclease. The enzyme-resistant duplexes were passed over HAP and eluted with 0.4 M PB. They were then chromatographed on a calibrated agarose A-50 column in 0.12 M PB. The arrows show the elution positions of an exclusion marker (*Ex*, long native DNA); an inclusion marker (*Inc*, $^{32}\text{PO}_4^{3-}$); and a 300-nucleotide-long DNA marker.

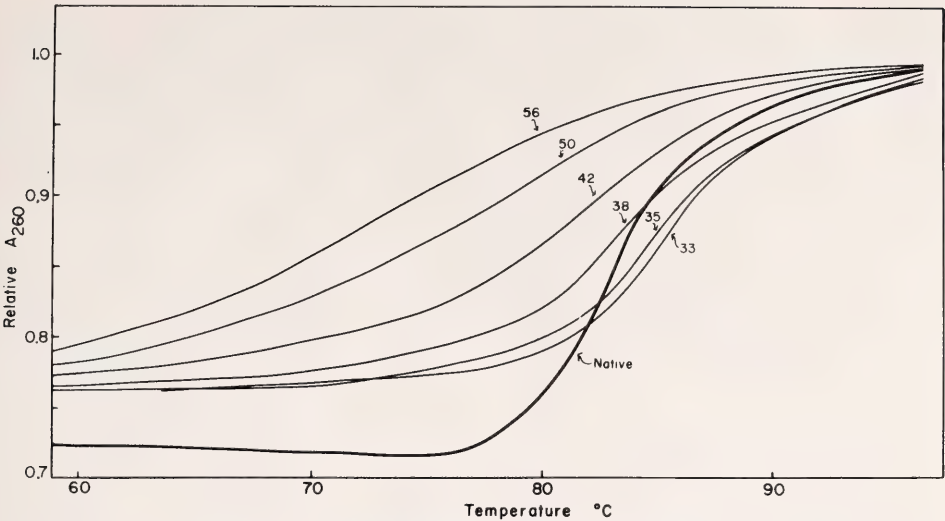


Fig. 3. Thermal stability and hyperchromicity of repetitive sequences as a function of their elution position from the A-50 column. Individual fractions (identified by number) from the A-50 column shown in Fig. 2 were melted in a water-jacketed cell in a spectrophotometer, and the A_{260} was measured. The solvent was the 0.12 M PB column eluant.

22% of the total DNA. At C_0t 10 the fast fraction would have been completely reassociated while the slow fraction would only be about 25% reassociated

TABLE 2. Thermal Stability of S1-Resistant Repetitive Sequences

| Fraction of the A-50 Column (Fig. 2) | Hyperchromicity* | T_m (°C) |
|--------------------------------------|------------------|------------|
| 33 | .23 | 85.7 |
| 35 | .23 | 85.0 |
| 38 | .23 | 84.0 |
| 42 | .22 | 81.2 |
| 50 | .21 | 77.2 |
| 56 | .20 | 74.2 |
| Native DNA | .27 | 84.0 |

* Hyperchromicity is calculated as $(A_{260} \text{ at } 98^\circ - A_{260} \text{ at } 60^\circ)/A_{260} \text{ at } 98^\circ\text{C}$. As can be seen from Fig. 2 the agarose column contributes an unknown small UV-absorbing background, and these figures are probably too low by about 5% or 10% of their values. The average hyperchromicity of the S1-resistant material compared to that of fully paired DNA suggests the existence of 15% to 20% single-stranded sequence. Approximately half of this is due to mismatch according to the T_m measurements, suggesting that the other half is single-strand tails.

(Table 1). Therefore, the maximum amount of slow repeated DNA in the nuclease-resistant fraction is one fourth of 30%, or about 8%, of the genome. The fast and very fast fractions are completely reassociated at C_0t 10 and correspond to about 14% of the genome.

The Spacing of Repeated Sequences as Estimated from the Increase with Length of the Fraction of Fragments Containing Repeated Sequences

Tracer fragments of various defined lengths were obtained from sheared DNA fractionated on a preparative alkaline sucrose gradient. Each fraction was reassociated with a 400-fold excess of 250-nucleotide unlabeled driver DNA, at driver C_0t 20, and the fraction of tracer fragments containing reassociated sequences was assayed by HAP chromatography. At C_0t 20, the fast fraction is completely reassociated, and the single-copy fraction is unreassociated. The slow fraction is partially reassociated. Thus, the HAP binding of the tracer fragments is due principally to the reassociation of the fast fraction with some

contribution from the slow sequences and none from the single-copy sequences. As a result of interspersion of different sequence classes with each other, the length of the single-stranded regions linked to the reassociated sequences increases with fragment length.

Figure 4 shows our best estimate of R , the fraction of fragments which contains repeated sequences as a function of tracer fragment length. See references (Davidson *et al.*, 1973, and Graham *et al.*, 1974) for analyses of sequence interspersion by this method. For this estimate a correction has been made for the increase in binding at $C_0t\ 5 \times 10^{-4}$ due to foldback and very fast repeated sequences (Davidson *et al.*, 1973; Graham *et al.*, 1974) using the formula $R = F - Z/1-Z$, where F is the fraction of tracer fragment bound to HAP at $C_0t\ 20$ and Z is the fraction of fragments bound at $C_0t\ 5 \times 10^{-4}$.

The solid line of Fig. 4 represents the least-squares solution of these measurements by the method described by Graham *et al.*, 1974. This curve extrapolates to 14% for very short fragment lengths. This is surely too low an estimate of the total amount of repetitive sequences re-

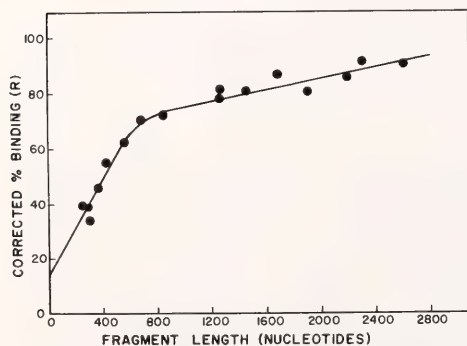


Fig. 4. The fraction of DNA fragments containing repetitive sequence elements as a function of fragment size. Tracer fragments of the indicated length were reassociated together with a 400-fold excess of 250-nucleotide-long driver, at driver $C_0t\ 20$. R represents the fraction of tracer bound, after correction for the binding that occurred at $C_0t\ 5 \times 10^{-4}$. The line is an unrestricted computer least-squares fit. For further details, see the text.

associated by $C_0t\ 20$. The solution is obviously affected by scatter in the data at short fragment lengths. Many other solutions are possible, and the differences between them are unimportant in their effect on the interpretation of the major features of the curve in Fig. 4. All solutions show a strong decrease in slope at about 800 nucleotides and a relatively small slope at long fragment lengths. The interpretation of such R curves previously described (Davidson *et al.*, 1973; Graham *et al.*, 1974) indicates that there are many repetitive-sequence elements spaced by about 800 nucleotides of DNA that was not reassociated at $C_0t\ 20$. In addition, there is another class of repetitive sequences that are spaced much farther apart. Since no curvature is evident in the data at long lengths, we conclude that most of the longer spacings are greater than 2400 nucleotides.

Thus we conclude that there are two broad classes of repetitive-sequence spacing in *A. pernyi* DNA which can be termed long-period and short-period interspersion. We can also conclude that almost all of the single-copy DNA sequences are included in this interspersion pattern. We presume that many of these single-copy sequences have a length of about 800 nucleotides and that another class is longer, by analogy to the situation in the DNA of other species. However, this pattern is not directly demonstrated for *A. pernyi* DNA because of the presence of substantial amounts of slow repetitive component, which is only partially reassociated at $C_0t\ 20$ in these measurements. The slow repetitive sequences could also be interspersed with fast repetitive sequences, and thus the 800-nucleotide lengths may include slow sequences in addition to single-copy sequences. For this reason it is impossible to derive an accurate conclusion about the preponderant length of the interspersed single-copy sequences. The principal part of the DNA that is reassociated at $C_0t\ 20$ is the fast repetitive fraction, and most of the 800-nucleotide-long spaces separate fast repeti-

tive sequences. Nevertheless, the main conclusions of this work are that most single-copy sequences in *A. pernyi* DNA are interspersed with repetitive DNA sequences, and that the repetitive DNA sequences are typically 200–300 nucleotides in length.

Conclusion

The reassociation kinetic measurements of *A. pernyi* DNA made at a fragment length of 250 nucleotides are summarized in Table 1. The fraction of DNA in the several kinetic components does not reflect accurately their abundance in the genome because of sequence interspersion. Our best estimate of the amount of DNA in the various sequence classes is also given in Table 1, as derived from measurements of S1-nuclease resistance. The kinetics of reassociation of 2200-nucleotide-long labeled fragments with short driver DNA indicate that almost all of the single-copy DNA sequence and most of the slow repeated DNA sequence are interspersed with fast repetitive sequences. In fact, more than 85% of 2200-nucleotide fragments contain repetitive sequences that have reassociated by C_0t 10.

The length and melting characteristics of S1-nuclease-resistant duplexes show a striking similarity to those for many other species. The short repetitive sequence duplexes account for about three-fourths of the total enzyme-resistant repetitive DNA at C_0t 10, and have a mode length between 200 and 300 nucleotides. About 25% of the S1-resistant duplexes (6% of the genome) are excluded from agarose A-50, and many of these are reassociation products from longer repetitive regions in the genome. They appear to be polydispersed in alkaline sucrose sedimentation measurements and little can yet be said about their actual sequence organization.

The measurements shown in Fig. 4 of the fraction of fragments that contain repeated sequences as a function of length show that the sequence organiza-

tion of *A. pernyi* is similar to that of *Xenopus laevis*. A very large fraction of the single-copy DNA is interspersed with repetitive sequences. The possibility exists that the slow, fast, and single-copy sequences are all interspersed with each other and this prevents a direct conclusion from the R curve measurements of the length of the single-copy sequences. However, it is clear that most of the fast repetitive sequences are short (200–300 nucleotides) and spaced by about 800 nucleotides, partially if not exclusively with single-copy DNA sequences.

In conclusion, we have shown that the *A. pernyi* genome is organized in a pattern quantitatively similar to the patterns of DNA sequence organization in *Xenopus laevis*, *Strongylocentrotus purpuratus*, and *Aplysia californica*. Therefore, the widespread *Xenopus* pattern occurs even among insects. After this study was completed, we showed that the *Xenopus* pattern also occurs in another insect, *Musca domestica*, a dipteran (see section after next). The *Drosophila* pattern thus seems exceptional, as it has been observed in only two insects, the honeybee and *Drosophila* itself (Manning *et al.*, 1975; Crain *et al.*, 1976b; see next section). The functional and evolutionary implications of this unusual sequence organization are as yet unclear. The pattern of sequence organization revealed by these studies in the genome of *A. pernyi*, the first lepidopteran to be studied, is of very general occurrence throughout the animal kingdom as well as in some plants. We attribute the general occurrence and evolutionary conservatism of this pattern to some as yet unknown crucial function in the genome.

Experimental Procedures

Preparation of DNA. DNA was extracted from nondeveloping pupae of *Antheraea pernyi* obtained commercially and stored at 2°. For each preparation 60 pupae were shredded for 1 min

(Waring Blender, full speed, in 0.1 M NaCl, 0.01 M EDTA, 0.05 M Tris, pH 8.7). The homogenate was filtered (Nitetex, 153 and 56 μ m mesh) and spun for 10 min at $4000 \times g$. The pellet was resuspended in the same buffer containing 1 M NaClO₄ and made 2% in NaDodSO₄. After 1 hr at 37° an equal volume of Sevag solution (chloroform:isomyl alcohol, 24:1, v/v) was added. The suspension was shaken for 15 min and centrifuged. An equal volume of phenol was added to the aqueous phase and, after shaking, a volume of Sevag solution. The aqueous phase was reextracted with phenol-Sevag solution (1:1) twice. The DNA was precipitated with 0.5 volume of cold isopropanol, wound, dissolved overnight in 1 mM EDTA, pH 7, and digested for 1 hr at 37° with 50 μ g/ml RNase A (preheated for 10 min at 80°). The solution was digested with 200 μ g/ml pronase for 1 hr at 37° (preincubated for 2 hr at 37°) and extracted with phenol-Sevag solution. The DNA was precipitated with 2 volumes of ethanol and dissolved in 1 mM EDTA, pH 7. To remove contaminating polysaccharides, the solution was spun for 30 min at $150,000 \times g$.

³H-labeled DNA was synthesized by ovarian follicles (stages from germarium to degeneration of the nurse cells), in organ culture for 8 hr in 1.5 ml Grace's medium containing 1 mCi [³H-methyl]-thymidine (specific activity 50.8 Ci/mmole). The DNA was extracted from nuclei and showed a specific activity of about 2×10^4 cpm/ μ g.

The hyperchromicity of all DNA preparations was about 27% of the optical density after full denaturation at 98°. Melting profiles and analytical equilibrium density ultracentrifugation in CsCl gradients did not distinguish such DNA preparations from the DNA of pupal testes, which are rich in spermatocytes. Relative to a phage SPO1 DNA marker, the DNA had a buoyant density of 1.694 g/cc, corresponding (Mendel *et al.*, 1968) to 35% G+C.

Fragmentation of DNA. DNA frag-

ments of desired lengths were generated by shearing in a Virtis-60K homogenizer (Britten *et al.*, 1974) or were selected from sheared DNA fractionated in preparative alkaline sucrose gradients. Single-stranded DNA lengths were determined by sedimentation in isokinetic alkaline sucrose gradients (Noll, 1967) as described previously (Angerer *et al.*, 1975; Goldberg *et al.*, 1973).

ABSENCE OF SHORT-PERIOD INTERSPER- SION OF REPETITIVE AND NONREPETI- TIVE SEQUENCES IN THE DNA OF *Drosophila melanogaster*

William R. Crain, Francine C. Eden,*
William R. Pearson, Eric H. Davidson,
and Roy J. Britten

Interspersion of short repetitive sequences with single-copy sequences of one to a few thousand nucleotides appears to be a very widespread—even nearly universal—feature of higher animal genomes. DNAs of 15 organisms widely distributed on the phylogenetic tree have now been examined. In the typical case a majority of the genome consists of short (300 nucleotide pairs) repeated sequences adjacent to longer (1000–2000 nucleotide pairs) single-copy sequences (recently reviewed by Davidson *et al.*, 1975a). *Drosophila melanogaster* DNA does not share this pattern of sequence organization (Manning *et al.*, 1975), and at this time two other exceptions have been found among the insects. These differences are of conceptual importance, since DNA sequence organization probably has significant implications for the functional organization of the genome and for genetic regulation (Britten and Davidson, 1969, 1971; Davidson and Britten, 1973). Previous studies of the *Drosophila* genome (Manning *et al.*, 1975) were done principally by electron microscopy of reassociated DNA, while most of the data obtained on more typical genomes have

* Department of Zoology, Indiana University, Bloomington, Indiana 47401

been derived from other methods such as hydroxyapatite assay of reassociation of short and long fragments and S1 nuclease resistance. The question obviously arises as to whether the differences between *Drosophila* DNA and other DNAs are more apparent than real; that is, a result of differences in experimental approach. Studies of sequence arrangement in the *Xenopus* genome by electron microscopy (Chamberlin *et al.*, 1975) have yielded results which are entirely consistent with those obtained by other methods. *Xenopus* DNA has a typical pattern of short-period sequence interspersion and is the type organism, since its DNA was the first to be studied in detail (Davidson *et al.*, 1973). An additional effort to determine sequence organization in the *Drosophila* genome by several methods other than electron microscopy appeared justified to us. Not only is *Drosophila* an important experimental species, but the application of other methods might conceivably uncover short repeated sequences missed in the electron microscopic measurements. In addition, earlier measurements on *Drosophila* DNA (Wu *et al.*, 1972) had been differently interpreted. In this paper we report a search for short repeated sequences in the *Drosophila* genome by a combination of five methods.

Manning *et al.* (1975) concluded that the number average length of the repeated sequences in *Drosophila* DNA is about 5500 nucleotides and that these are probably terminated by single-copy sequences. They estimated that there are 3000 repeats in the genome. From these results we may estimate the quantity of single-copy sequence expected to be linked to repeated sequences by a calculation described in the Conclusion. If there were a significant number of previously unobserved, short interspersed repetitive sequences, the measurements reported here would show a larger fraction of single-copy DNA linked to repetitive sequences than suggested by Manning *et al.* The conclusions from our measurements are in

substantial agreement with those of Manning *et al.* (1975).

Reassociation Kinetics of Drosophila DNA

Figure 5 shows the reassociation kinetics of two different fragment sizes of *Drosophila melanogaster* DNA assayed by binding to hydroxyapatite. The curves show that *Drosophila melanogaster* has a relatively small quantity of middle repetitive DNA, as previously observed (Laird, 1971; Wu *et al.*, 1972; Schachat and Hogness, 1974; Manning *et al.*, 1975). The kinetic curves are dominated by the single-copy DNA reassociation. About 10% of *Drosophila* DNA binds at very early times to hydroxyapatite. This is probably composed of satellites and inverted repeats (Gall *et al.*, 1971; Peacock *et al.*, 1973; Wilson and Thomas, 1974; Manning *et al.*, 1975; Schmid *et al.*, 1975). We have not investigated this fraction in the present work.

The fraction of the DNA fragments containing middle repetitive sequences or only single-copy sequences was determined by least-squares analysis. These quantities and the most likely rate constant are shown in the legend to Fig. 5. The reassociation of the fragments averaging 1830 nucleotides is somewhat faster than that of the 360-nucleotide fragments. Such a result is expected for the following reasons. First, for those fragments which are purely repetitive or purely single copy, the rate of reassociation is increased approximately in proportion to the square root of the fragment size (Wetmur and Davidson, 1968; Wetmur, in press). Some of the fragments from interspersed regions contain both repetitive and single-copy sequences linked together. These fragments are bound to hydroxyapatite when the repetitive regions are reassociated, and therefore when longer fragments are used a greater fraction of the single-copy DNA is bound at a given C_0t . This process supplies one of the major meth-

ods for the detection and measurement of short-period interspersed of repeated and single-copy sequences. The rate of reassociation of long and short frag-

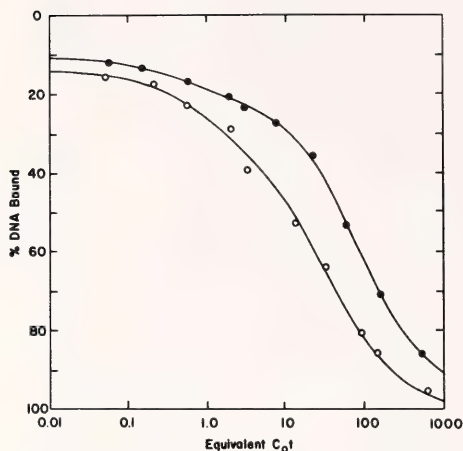


Fig. 5. Reassociation kinetics of *Drosophila* DNA. *Drosophila* DNA fragments of 360 (filled circles) and 1830 (open circles) nucleotides were prepared by mixing unlabeled DNA from syncytium stage eggs with ^3H -labeled DNA from *Drosophila* tissue culture cells (mass ratios of 1500/1 and 750/1, respectively). These mixtures were sheared in the Virtis homogenizer (Britten *et al.*, 1974). Reassociation and assay of the fraction of fragments containing double-stranded regions was carried out by binding to hydroxyapatite (see Experimental Procedures). The least-squares solution of the data yielded components with the following fraction of the genome (Q) and rate constants (k): For the 360-nucleotide fragments, very highly repetitive sequences, and foldback, $Q = 0.12$, k cannot be clearly defined; middle repetitive sequences, $Q = 0.108$, $k = 2.1 \text{ M}^{-1} \text{ sec}^{-1}$; single-copy sequences, $Q = 0.751$, $k = 0.0121 \text{ M}^{-1} \text{ sec}^{-1}$. Least-squares analysis on the 1830-nucleotide fragment data was carried out with the rate constant for single-copy sequence fixed to a value of $0.0273 \text{ M}^{-1} \text{ sec}^{-1}$. This value was obtained by adjusting the k for single-copy sequence from that measured with 360-nucleotide fragments. Thus

$$k_{1830} = k_{360} \left(\frac{1830}{360} \right)^{1/2} = 0.0273.$$

The values for the components in the 1830-nucleotide curve are as follows: very highly repetitive and foldback, $Q = 0.15$, k not defined; middle repetitive, $Q = 0.22$, $k = 0.94 \text{ M}^{-1} \text{ sec}^{-1}$; single-copy, $Q = 0.64$, $k = 0.0273 \text{ M}^{-1} \text{ sec}^{-1}$.

ments has been measured for the DNA of a number of species (Davidson *et al.*, 1973; Goldberg *et al.*, 1975; Davidson *et al.*, 1975a; Angerer *et al.*, 1975). In each case in which other methods show the presence of short-period interspersed, the reassociation rate of fragments a few thousand nucleotides long is observed to be strikingly faster than that of fragments a few hundred nucleotides long. However, for *Drosophila melanogaster* DNA the effect of increased fragment length is relatively modest. The rate of reassociation of the 1830-nucleotide fragments is faster than that of the 360-nucleotide fragments by a factor only slightly larger than the ratio of the square roots of the fragment lengths. This is true for both the repetitive and the single-copy parts of the reaction. It follows that only a small fraction of the 1830-nucleotide-long fragments are made up of linked repetitive and single-copy sequences. We do not yet know whether the rate of reassociation is exactly proportional to the square root of length for fragments as short as 360 nucleotides, and thus a quantitative examination of such measurements is limited in accuracy. The accuracy of this method is not sufficient to detect a small amount of relatively short interspersed repetitive sequences if they exist.

Reassociation of Long Labeled Fragments with an Excess of Short Fragments

The reassociation of long labeled fragments with an excess of short fragments was the first method used to demonstrate repetitive-sequence interspersed (Britten and Smith, 1970), and it has been used for the measurements of the length of the interspersed single-copy sequences in the DNA of several species (e.g., Davidson *et al.*, 1973; Graham *et al.*, 1974; Angerer *et al.*, 1975; Efstradiatis *et al.*, 1976). Figure 6 shows the kinetics of reassociation of labeled 2200-nucleotide-long *Drosophila* DNA fragments with excess 390-nucleotide un-

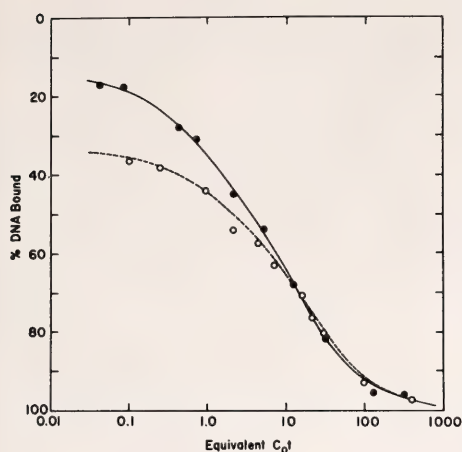


Fig. 6. Reassociation kinetics of 2200-nucleotide labeled fragments in the presence of an excess of 390-nucleotide DNA fragments. The upper curve (filled circles) shows the binding of the labeled fragments to hydroxyapatite at 60°C in 0.12 *M* phosphate buffer after incubation under the same conditions. The lower curve (open circles) shows the binding to hydroxyapatite at 50°C in 0.12 *M* phosphate buffer after incubation under these conditions. Least-squares analysis was performed on the data at 60°C and 50°C yielding the following components. 60°C: very highly repetitive and foldback, $Q = 0.17$, k not defined; middle repetitive, $Q = 0.27$, $k = 1.66 \text{ M}^{-1} \text{ sec}^{-1}$; single copy, $Q = 0.584$, $k = 0.074 \text{ M}^{-1} \text{ sec}^{-1}$. 50°C: very highly repetitive and foldback, $Q = 0.34$, k not defined; middle repetitive, $Q = 0.166$, $k = 1.06 \text{ M}^{-1} \text{ sec}^{-1}$; single copy, $Q = 0.497$, $k = 0.048 \text{ M}^{-1} \text{ sec}^{-1}$.

labeled fragments. As above, the rate of reassociation of the long fragments is affected by their length, so that a small amount of sequence interspersion is difficult to detect. Previous measurements with bacterial DNA fragments (Davidson *et al.*, 1973) indicated that the rate of reassociation of long labeled fragments with an excess of short fragments is directly proportional to the length of the long fragments. The least-squares solutions for the rates and quantities of the repetitive and single-copy components are shown in the legend to Fig. 6. The single-copy rate is in fact accelerated by just the ratio of the lengths (2200/390). Thus the majority of the

single-copy sequences are not linked to repetitive sequences on fragments of 2200 average nucleotide length.

In Fig. 5 the quantity of the repetitive component appears somewhat larger for the 2200-nucleotide-labeled fragments than for the 360-nucleotide fragments. This is in part caused by linkage of single-copy sequences to the ends of long repetitive sequences. However, the accuracy of these measurements is not sufficient to determine whether the quantity is greater than that expected from the electron microscopic measurements of Manning *et al.* (1975; see Conclusion).

It is possible that short interspersed repetitive sequences exist but are either very short or very divergent and thus cannot be bound to hydroxyapatite at the standard criterion. If this were true it might be possible to detect these less stable sequences by lowering the criterion of reassociation. To test this possibility the incubations and hydroxyapatite assays were done in 0.12 *M* phosphate buffer at 50°C—10° C lower than the standard criterion. Under these conditions more divergent or shorter repeats would reassociate and bind to hydroxyapatite than at the 60°C criterion used in the preceding experiments. The lower curve of Fig. 6 shows the result. Additional binding occurred at very low C_0t , but no substantial change is observed in the middle repetitive and single-copy regions of the kinetics. The implication of the low C_0t binding is that under these conditions a greater amount of DNA was associated with foldback or satellite sequences. Since in *Drosophila* (Schmid *et al.*, 1975) and other species the foldback or palindrome (Wilson and Thomas, 1974) sequences are interspersed throughout much of the genome, it is likely, though not proved here, that we are seeing the effect of a larger class of such interspersed sequences. There is, however, no sign of an increased amount of middle repetitive sequences. Thus no evidence for unusually divergent or short interspersed mid-

dle repetitive sequences can be obtained by lowering the criterion 10°C .

The Size of S1-Nuclease-Resistant Reassociated Repetitive Sequences

Under appropriate conditions (Britten, Graham, Eden, Painchaud, and Davidson, in press) the single-strand-specific nuclease S1 from *Aspergillus* (Ando, 1966; Vogt, 1973; Sutton, 1971) is useful for determining the length of repetitive sequences. With a carefully controlled digestion, single strands can be effectively removed without the enzyme attacking duplexes containing even 10%–20% mismatched base pairs. The following procedure has been developed to measure the length distribution of short repetitive sequences: (a) reassociation of approximately 2000-nucleotide-long fragments to a C_0t at which few single-copy sequences are reassociated; (b) limited digestion with S1 nuclease to cleave single strands from duplexes; (c) binding to hydroxyapatite (0.12 M phosphate buffer, 60°C) to separate duplexes from undigested single strands; (d) gel filtration analysis of the S1-resistant duplexes on agarose A-50 columns. This method has been applied to the DNA of a number of species that possess typical short interspersed repetitive sequences. In every case the resistant duplexes separate into two size classes: a long-fragment class, which is excluded from the agarose column; and a short-fragment class with a mode size of about 300 nucleotide pairs (Goldberg *et al.*, 1975; Britten, Graham, Eden, Painchaud and Davidson, in press). The fraction of the repeats that fall in the short repetitive sequence class varies from 35% to 85%, depending on the species (Davidson *et al.*, 1975a).

In order to achieve greater sensitivity the *Drosophila* DNA fragments were partially separated into a very rapidly reassociating fraction and a middle repetitive fraction. For this purpose the 2400-nucleotide-long fragments were incubated to C_0t 0.05 and passed over

hydroxyapatite. The bound fraction was eluted with 0.4 M phosphate buffer. The unbound fraction was reincubated to C_0t 3. Both fractions were digested with S1 nuclease, and the size of the resistant duplex structure measured by gel filtration on agarose A-50. Details of the procedure and the yield of DNA in each fraction are given in Experimental Procedures. The size distributions of the S1-resistant duplexes are shown in Fig. 7 along with a control (labeled sea urchin DNA). Identical patterns were obtained for the sea urchin DNA in both runs. The yield of the short fragments of sea urchin DNA is a little less than the amount expected, but the S1 digestion was clearly effective. The C_0t 0.05 bound fraction of the *Drosophila* DNA shows no measurable quantity of short S1-resistant duplexes. The middle repetitive fraction (C_0t 0.05–3) appears to show a small quantity of short resistant duplexes. About 25% of the DNA has a k_{av} greater than 0.3, or a size less than 1000 nucleotide pairs. This result is consistent with the pattern of long repetitive sequences measured by the electron micrographic measurements of Manning *et al.* (1975).

The Hyperchromicity of Reassociated Repetitive Fragments

When DNA fragments containing both repetitive and single-copy sequences are reassociated to low C_0t , the single copy regions remain unpaired. The quantity of these unpaired regions can be measured by collecting all the fragments containing paired regions on hydroxyapatite and measuring their hyperchromicity.

The amount of single-copy DNA linked to repetitive sequences on such fragments depends on the sequence interspersion pattern. If there are many short interspersed repeats, there will be many single-copy sequences linked to them and a low hyperchromicity will be observed. The amount of hyperchromicity decreases as the length of the fragments increases. This effect has been

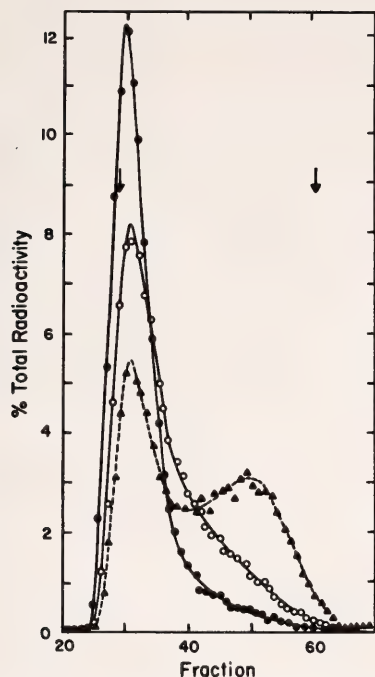


Fig. 7. Length of S1-resistant duplexes formed by renaturing highly repetitive and middle repetitive *Drosophila* DNA. Highly repetitive and middle repetitive DNA sequences were prepared from 2400-nucleotide fragments as described in text and treated with S1 nuclease sufficient to remove single strands without digesting mismatched regions. 436 μ g of highly repetitive and 600 μ g of middle repetitive DNA were digested under the following conditions: 0.15 M NaCl, 0.005 M PIPES, 0.025 M Na acetate, pH 4.3, 0.1 mM ZnSO₄, 37°C, 45 min. The resistant duplex fraction was collected on hydroxyapatite and chromatographed on agarose A-50 in 0.12 M phosphate buffer. Sea urchin DNA (2000 nucleotides) reassociated to *Cot* 4 was added to the *Drosophila* DNA before S1 digestion as a control. The arrows indicate the positions of exclusions and inclusion markers; filled circles represent *Drosophila* satellite DNA (*Cot* 0.05, bound); open circles are *Drosophila* middle repetitive DNA (*Cot* 0.05–3.0); and triangles are sea urchin repetitive DNA.

demonstrated in measurements of the hyperchromicity of partially reassociated DNA fragments in several species that display typical interspersion of short repetitive sequences (Davidson *et*

al., 1974; Graham *et al.*, 1974; Goldberg *et al.*, 1975; Angerer *et al.*, 1975).

The results for the middle repetitive fraction of *Drosophila* are listed on the lower part of Table 3. The upper parts of this table show the incubations and hydroxyapatite fractionation steps used in purifying the appropriate middle repetitive fraction of *Drosophila* DNA. The reassociated fragments that are 300 nucleotides long at the end of the procedure have about 95% of the hyperchromicity of native DNA, indicating that very little single-copy sequence is linked to them. Even the longer fragments (1000 and 1660 nucleotides) show hyperchromicities of 83% and 79% of native DNA. These values suggest that some single-copy DNA is linked to repeats in fragments of this size, and indeed, some is expected if the average repetitive sequence is 5000 nucleotides long (Manning *et al.*, 1975).

Kinetic Assay for Single-Copy DNA Sequences Linked to Repetitive Sequences

The following is probably the most direct and most sensitive of the methods reported in this paper to determine the amount of single-copy DNA sequences that are linked to repetitive DNA sequences. Long labeled DNA fragments that contain repetitive sequences were selected. These fragments were sheared and reassociated with an excess of total *Drosophila* DNA fragments. The reassociation kinetics were analyzed for evidence of fragments bearing only single-copy sequences. The sensitivity of this experiment is such that a few percent of single-copy DNA can be detected.

The first step was to isolate a large quantity of short repetitive DNA fragments to be used to select the long labeled fragments containing repeats. The frequency with which middle repetitive sequences occur in the *Drosophila* genome is relatively low, about 30 copies of each sequence. This agrees well with the previously reported repetition fre-

TABLE 3. Hyperchromicity of Middle Repetitive DNA Sequence after Reassociation

| Initial Average Fragment Length (nucleotides) | 350 | 1600 | 3200 |
|---|-------|-------|-------|
| Preparation of Middle Repetitive DNA Fraction | | | |
| First Incubation | | | |
| <i>C₀t</i> | 3 | 3 | 3 |
| Fraction bound | 0.24 | 0.31 | 0.32 |
| Fraction of total DNA | 0.24 | 0.31 | 0.32 |
| Second Incubation | | | |
| <i>C₀t</i> | 0.012 | 0.016 | 0.016 |
| Fraction unbound | 0.41 | 0.55 | 0.56 |
| Fraction of total DNA | 0.096 | 0.17 | 0.18 |
| Third Incubation | | | |
| <i>C₀t</i> | 0.29 | 0.51 | 0.54 |
| Fraction bound | 0.44 | 0.30 | 0.22 |
| Fraction of total DNA | 0.042 | 0.05 | 0.039 |
| Hyperchromicity Determination | | | |
| Fourth Incubation (for spectrophotometric melt) | | | |
| <i>C₀t</i> | 12.6 | 15.3 | 11.7 |
| Final fragment size (nucleotides) | 300 | 1000 | 1600 |
| Hyperchromicity | 0.22 | 0.20 | 0.19 |
| Fraction of native DNA hyperchromicity | 0.95 | 0.83 | 0.79 |
| <i>T_m</i> (°C) | 78.1 | 83.5 | 84.5 |

quency of the middle repetitive component (Wu *et al.*, 1972; Schachat and Hogness, 1974; Manning *et al.*, 1975). This makes it difficult to separate single-copy from repetitive DNA, and a single fractionation step does not suffice. Table 5 shows the fractionation steps and yield at each stage in comparison with that expected from our best estimates of the repetitive frequency components of *Drosophila* DNA (Table 4). Twenty mg of *Drosophila* DNA were sheared to 300 nucleotides, and 14% was recovered as the repetitive fraction. This should consist of 34% highly repetitive, 66% middle repetitive, and 0.2% single-copy DNA, were there no sequence interspersion in this genome. The reassociation kinetics of this fraction were measured in the spectrophotometer by optical hyperchromicity. The results were consistent with the expected components, and the reassociation went to completion (final optical density = 0.75 of the initial denatured A_{260}). No single-copy component could be observed in the reassociation kinetics.

The second step was to prepare long labeled fragments. ^3H -labeled DNA was

sheared to 1800 nucleotide pairs, denatured, incubated to C_0t 0.005, and passed through hydroxyapatite to remove the zero time binding or foldback fraction. This step was repeated, and a total of 10.2% of the fragments were removed. The remaining fragments were incubated with a 50-fold excess of the short repetitive fragments (described above) to C_0t 3.2. The sample was then passed over hydroxyapatite in 0.12 M phosphate buffer at 60°C. Twenty-seven percent of the long labeled fragments and 79% of the short driver fragments were bound. The bound fragments were eluted at 98°C, and the tracer recovered was 1225 nucleotides long, as assayed by alkaline sucrose sedimentation. These fragments were sheared to 375 nucleotides and incubated with a fivefold excess of total *Drosophila* DNA. The kinetics of the reassociation are shown in Fig. 8. It is clear that the principal portion of the labeled fragments is made up of repetitive DNA sequences. Least-squares analyses were carried out to determine the best estimates of the fraction of the sheared tracer fragments which contained only single-copy sequence. For

TABLE 4. Estimates from Reassociation Kinetics of the Components of *Drosophila* DNA

| Component | Single Copy | Middle Repetitive | Fast |
|---|-----------------------|--------------------|------|
| Quantity | 0.74 | 0.09 | 0.14 |
| Repetition frequency | 1.0 | 30 | ... |
| Complexity | 6.7×10^7 NTP | 3.14×10^6 | ... |
| Rate constant in whole DNA | 0.0121 ^a | 0.35 ^b | ... |
| Rate constant if pure | 0.0164 | 3.89 | ... |
| Data of Manning <i>et al.</i> , 1975 ^c | | | |
| Quantity | 0.70 | 0.12 | 0.12 |
| Repetition frequency | 1 | 70 | ... |
| Rate constant in whole DNA | 0.0069 | 0.5 | ... |

^a In the fit described here, the single-copy rate constant was fixed to agree with that of the free fit for the 360-nucleotide fragment reassociation curve.

^b For this fit the rate constant for the middle repetitive component in the 1830- and 2200-nucleotide curves were corrected to their predicted value for 360-nucleotide fragments, and the average rate constant was determined. This average middle repetitive rate constant was then fixed in the least-squares fit of the 360-nucleotide fragment reassociation curve. The predicted rate constants for 360-nucleotide fragments from the two longer fragment size curves were calculated as follows: For 1830-nucleotide fragments, where $0.936 M^{-1} \text{ sec}^{-1}$ is the rate observed for the middle repetitive sequences in the experiments of Fig. 5,

$$k = 0.936 \left(\frac{360}{1830} \right)^{1/2} = 0.45$$

For 2200 nucleotide fragments driven by 390 nucleotide fragments, where $1.66 M^{-1} \text{ sec}^{-1}$ is the rate observed for the middle repetitive sequences in the experiment of Fig. 6,

$$k = 1.66 \left(\frac{390}{2200} \right) \left(\frac{360}{390} \right)^{1/2} = 0.283$$

The average of these two rate constants is $0.35 M^{-1} \text{ sec}^{-1}$.

^c Fits of data from Manning *et al.* (1975) for *Drosophila* DNA fragments of 400 nucleotides length.

TABLE 5. Fractionation of *Drosophila* Repetitive DNA

| C_0t | Fraction Bound to Hydroxy- apatite | Fraction Unbound | Predicted* Fraction Bound | Predicted* Fraction Unbound |
|--------|--|------------------|------------------------------|--------------------------------|
| 40 | 0.47 | | 0.47 | |
| 20 | 0.63 | | 0.54 | |
| 0.005 | | 0.724 | | 0.63 |
| 5 | 0.74 | | | 0.73 |

* The fraction of the DNA bound to hydroxyapatite at the different steps in the fractionation was ascertained by calculating the theoretical fraction reassociated for each component according to the equation

$$\frac{C}{C_0} = \frac{1}{1 + kC_0t}$$

where C is the concentration of totally single-stranded fragments, C_0 is the total DNA nucleotide concentration, t is time, and k is the second-order rate constant. The predicted recoveries for the individual components were added to give the predicted total fractions bound or unbound. The rate constants of each component were adjusted according to the new concentration in the remaining DNA in order to calculate the recovery in the next step, using the components arrived at from these data: 14% zero time binding and highly repetitive DNA; 9% middle repetitive sequences with a rate constant of $0.35 M^{-1} \text{ sec}^{-1}$, and 74% single copy with a rate constant at $0.0121 M^{-1} \text{ sec}^{-1}$. The rate constants were adjusted to their values for 290-nucleotide-length fragments, and a rate constant of $100 M^{-1} \text{ sec}^{-1}$ was estimated for the fast component.

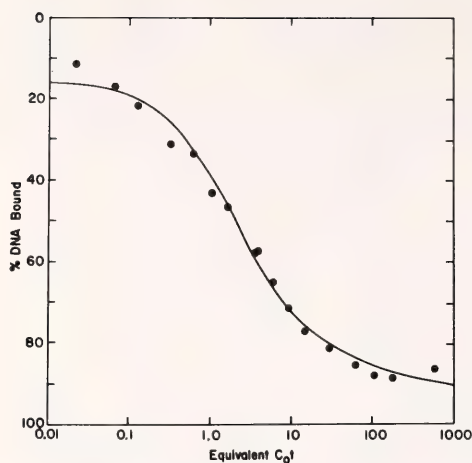


Fig. 8. Reassociation of sheared, selected repetitive DNA in the presence of excess whole DNA. Tritium-labeled *Drosophila* DNA (tracer) fragments which had been stripped of zero time binding sequences were reassociated to C_0t 3.1 in the presence of a 50-fold excess of 290-nucleotide purified *Drosophila* repetitive DNA (driver). The tracer that had reassociated with the repetitive driver was collected by hydroxyapatite chromatography. The single-strand size of the tracer after elution from hydroxyapatite was 1225 nucleotides. The DNA that bound to hydroxyapatite was recovered and sheared, reducing the tracer length to 375 nucleotides. The sheared material was mixed with 290-nucleotide whole *Drosophila* DNA in a ratio of 1 to 5 and reassociated to various C_0t values. The fraction of fragments containing duplexed regions was measured on hydroxyapatite. The curve represents a least-squares fit to the data with the rate constant for the single-copy component fixed at $0.012 M^{-1} \text{ sec}^{-1}$ according to the following description. The rate of the single-copy component for the 375-nucleotide fragment tracer in this curve was obtained by adjusting the rate for 360-nucleotide fragments as follows:

$$k_{290} = k_{360} \left(\frac{290}{360} \right)^{1/2} \left(\frac{375}{290} \right) = 0.014 M^{-1} \text{ sec}^{-1}$$

This rate constant was further adjusted to allow for the dilution of the single-copy sequences when whole DNA driver was mixed with purified repeat driver. Assuming that the repeat driver contained no single-copy sequences the single-copy sequences would be diluted by a factor of 0.833. The resulting rate constant for single-copy sequences is, thus, $0.833 (0.014) = 0.012 M^{-1} \text{ sec}^{-1}$.

this purpose the rate constant for the single-copy component was fixed at $0.012 M^{-1} \text{ sec}^{-1}$, the rate constant of single-copy sequence in the driver DNA. All of the other parameters were allowed to remain free. The solution indicates that 9% of the labeled fragments are single-copy sequences. We have also made a least-squares analysis with the middle repetitive as well as the single-copy rate constants fixed at the values shown in Table 4 (corrected for the additional repetitive sequences present in this mixture). With these restrictions the calculated fraction of fragments bearing only single-copy sequences is 14%.

Conclusion

Our purpose here is to calculate the expected amount of single-copy sequence linked to repetitive sequences and to examine the quantitative conclusions from the five types of measurements. In this calculation G is the genome size in nucleotide pairs, and L is the fragment length. For a particular set of repetitive sequences (indicated by the subscript 1) S_1 is the length of the interspersed single-copy sequences; Q_1 , the fraction of the genome in these single-copy sequences; and F_1 , the number of interspersed repetitive or single-copy sequences in this set. Figure 9 shows for an ideal case the increase with fragment length of the fraction of fragments containing single-copy DNA linked to repeated sequences. The slope (for $L < S_1$) in Fig. 9 is $dR/dL = Q_1/S_1$. Since $Q_1 = F_1 S_1/G$, the slope can be written:

$$dR/dL = F_1/G \quad (1)$$

This simple relationship is for a particular set of interspersed sequences, and we may add up the contribution to the slope of each such set as long as the fragment length is less than the length of the single-copy sequences. Thus for $L < S$ the total initial slope of the curve for the fraction of fragments containing single-copy DNA linked to repetitive sequence is:

$$(dR/dL)_{\text{initial}} = (F_1 + F_2 + F_3 + \dots F_n)/G = N/G \quad (2)$$

where F_1 , F_2 , etc., are the numbers of single-copy (or repetitive) sequence elements in each interspersed set and N is the total number of interspersed sequences in the genome. For L less than S , the fraction of the genome which is in single-copy sequences linked to repetitive sequences (Y) follows directly:

$$Y = L (dR/dL) = L N/G \quad (3)$$

Manning *et al.* (1975) take the genome size of *Drosophila melanogaster* to be 1.3×10^8 nucleotide pairs (Fristrom and Yund, 1973) and estimate that there are 2800 interspersed repeated sequences with an average length of 5500 nucleotides. If we assume that all of

these are interspersed with single-copy sequences that are more than a few thousand nucleotides long, then for a 1000-nucleotide fragment length: $Y = 1000 \times 2800 / 1.3 \times 10^8 = 0.0215$. Therefore we expect to find about 2% of the genome (2.8×10^6 nucleotide pairs) as single-copy sequences linked to fragments 1000 nucleotides long which contain middle repetitive sequences. From Table 4 the amount of middle repetitive DNA is 9% of the genome or 11.7×10^6 nucleotide pairs. Therefore 1000-nucleotide-long fragments of middle repetitive DNA would contain 19% ($2.8 \times 10^6 / 2.8 \times 10^6 + 11.7 \times 10^6$) single-copy DNA. We take this to be the best estimate from the electron micrographic measurements of Manning *et al.* For calculations involving other fragment lengths, the quantity of linked single-copy DNA is simply proportional to the fragment length as long as the length of typical single-copy sequence is not exceeded.

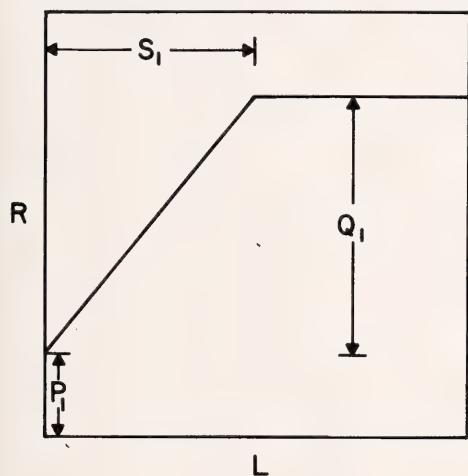


Fig. 9. The contribution of one element of a sequence interspersion pattern to hydroxyapatite binding. Shown as a function of fragment length (L) is R , the amount of DNA in fragments that contain one set of repeated sequences spaced by single-copy sequences of length S_1 . The total quantity of single-copy DNA interspersed with this set is Q_1 and the quantity of repeated DNA is P_1 . For short fragments, little single-copy DNA is linked to the repeats, and in the limit only the repetitive DNA (P_1) would be included. The amount of single-copy DNA increases in proportion to the fragment length until the length of the single-copy sequences is reached (plus enough length to recognize the succeeding repeat). The slope of the linear rising portion is S_1/Q_1 .

Calculations from the Kinetics of Reassociation (Parts 1 and 2)

Table 6 shows the expected fraction of the single-copy DNA calculated as above from the number of middle repetitive sequences (2800) estimated by Manning *et al.* (1975). We have subtracted this estimate from the least-squares estimates of the fraction of DNA in the middle repetitive kinetic components. If the number of interspersed middle repetitive sequences were significantly greater than 2800 we would observe, after this subtraction, an increase in the middle repetitive fraction with fragment length. Though small, such an effect is seen in Table 6, and it is this uncertain result which led us to attempt corroboration with other, more sensitive methods.

Measurement of the Size of the S_1 -Nuclease-Resistant Fragments

The size distribution of S_1 -resistant middle repetitive duplexes is shown on Fig. 7 as open circles. The great ma-

TABLE 6. Fraction of middle repetitive and single copy sequences in *Drosophila* genome

| Fragment Size | Middle Repetitive Component | | | Single-Copy Component | | |
|------------------|---|---|---|------------------------------------|---|---|
| | Fraction of Fragments Observed ^a | Fraction of Genome That Is Single Copy Attached to Repeats ^b | Corrected Fraction of Genome in Middle Repetitive Sequence ^c | Fraction of Fragments ^a | Fraction of Genome That Is Single Copy Attached to Repeats ^b | Corrected Fraction of Genome in Single-Copy Sequence ^c |
| 360 nucleotides | 0.091 | 0.008 | 0.083 | 0.739 | 0.008 | 0.747 |
| 1830 nucleotides | 0.221 | 0.039 | 0.182 | 0.637 | 0.039 | 0.676 |
| 2200 nucleotides | 0.267 | 0.047 | 0.220 | 0.584 | 0.047 | 0.631 |

^a Quantities of components determined from least-squares fit of reassociation data at given fragment length (from Figs. 5 and 6 and Table 4).

^b Fraction of genome that is single-copy sequences attached to repeated sequences at the various fragment lengths. Calculation as described in text.

^c Fraction of genome composed of component after correction for fraction of DNA which is single copy linked to repeats at the fragment lengths used.

jority of the fragments are excluded from agarose and are therefore greater than 2000 nucleotides in length. A small fraction, perhaps 15% of the mass of DNA, has a k_{av} greater than about 0.4, and thus their length is less than 400 or 500 nucleotide pairs. This represents the best estimate by this method of the fraction of the middle repeats of about 300-nucleotide average length. While this is a simple and direct method, the following calculation shows that it is not a sensitive way to detect a small number of short repetitive sequences. If there were, for example, as many 300-nucleotide repetitive duplexes as all others combined, we would expect $300/5600 = 5\%$ of the total DNA in this region of the A-50 chromatogram. We obviously cannot rule out such a possibility from this measurement. In fact, the data suggest a potentially larger number of short repeats. However, there are a variety of artifactual possibilities which could give rise to short fragments, for example, shear breakage and internal nicking by the S1 nuclease. We prefer to draw no conclusion from the tail of short fragments shown in Fig. 7. In any case, it is clear from this measurement that most of the middle repetitive sequences are long.

Hyperchromicity of Reassociated Repetitive Fragments

The results of fractionating *Drosophila* DNA fragments of various sizes are shown on Table 3 along with the hyperchromicity of the purified middle repetitive fractions. The fractionation indicates that only a small increase in single-copy DNA linked to middle repetitive DNA occurs with fragment size. The three final fragment lengths are 300, 1000, and 1600 nucleotides. The hyperchromicity data for these three fragment lengths imply that 5%, 16.5%, and 21%, respectively, were made up of linked single-copy DNA. The calculation described above, assuming that there are just 2800 interspersed middle repetitive sequences in the genome, yields 5%, 14%, and 21% for the three lengths. This agreement is surprisingly good, considering the possible sources of error in these measurements.

Direct Kinetic Assay for Single-Copy Sequences Linked to Middle Repeats

The least-squares solutions of the data shown in Fig. 8 indicate that 9%–14% of the selected 1225-nucleotide-long fragments are made up of linked single-copy DNA sequences. The calculation

described above yields 17% for this fragment length. This agreement is certainly within error. This measurement is the only one of all of the approaches we have applied to *Drosophila* DNA which directly implies that single-copy DNA is interspersed with the repeats at any length. The other measurements have relied, for example, on the increase with length of the fraction of the genome associated with middle repeats or on the fact that the linked DNA was single stranded. In every case it was a reasonable but unproved assumption that the linked DNA is actually single-copy sequence. The electron micrographic measurements of Manning *et al.* are subject to the same proviso. However, the least-squares solution of the data of Fig. 8 includes a component with the kinetics of single-copy DNA which is of about the quantity expected if there are 2800 repetitive sequences interspersed with single-copy sequences.

Some of the fragments of *Drosophila* DNA that have been "cloned" and examined by Wensink *et al.* (1974) contain both single-copy and repetitive sequences. In addition, all the cloned middle repetitive sequences so far examined are several thousand nucleotides or more in length. The data shown in Fig. 8 give the best direct estimate of the number of places in the *Drosophila* genome at which repeated sequences are linked to single-copy sequences. The actual number of such transitions in the DNA sequence is, of course, just twice the number of interspersed repetitive and single-copy sequences.

Each of the measurements described gives a result that is consistent, within error, with the conclusion that about 2800 relatively long middle repetitive sequences are interspersed with single-copy sequences in the *Drosophila* genome. We may ask how many more interspersed repetitive sequences could be added to the 2800 used in the calculations above without creating an unacceptable deviation from the observed measurements.

It seems very unlikely that a doubling of the number would be acceptable. While this would not introduce a problem of interpretation for the kinetics and S1-resistance methods, serious deviations would be revealed by the last two methods described. The hyperchromic shift in one set of measurements and the amount of single-copy DNA in the other would have to be in error by a factor of 2. We do not believe this is at all likely and conclude that a twofold greater number of interspersed repeats is ruled out. Of course, smaller deviations are possible.

Experimental Procedures

DNA preparation. Unlabeled DNA was prepared from syncytium stage eggs that had been stored at -70°C . The eggs were dechorionated by suspension in 50% Clorox for 2 min at room temperature (2–3 ml/g tissue). They were then caught on a Nitex screen and washed sequentially with distilled H_2O , 70% EtOH, and H_2O . The eggs were gently removed from the screen and allowed to settle three times in ice-cold saline Triton (0.9% NaCl, 0.1% Triton—100:10 ml/g tissue). The dechorionated eggs (Elgin and Hood, 1973) sink in this mix. The eggs that did not sink were washed again with distilled H_2O . The saline Triton-washed eggs were then washed once more with H_2O (10 ml/g tissue) and suspended in 0.05 *M* Tris-maleate buffer, pH 7.4; 0.005 *M* MgCl_2 (5 ml/g tissue). The eggs were homogenized with two strokes in a Dounce homogenizer and the homogenate filtered through two layers of Miracloth. The material that was trapped on the Miracloth was resuspended in a small volume of Tris-maleate buffer, rehomogenized in the Dounce homogenizer and filtered through Miracloth again. The filtered material was centrifuged at 2000 rpm for 10 min through a $\frac{1}{3}$ volume sucrose cushion (0.2 *M* sucrose in Tris-maleate buffer) to pellet the nuclei. The pellet was resuspended in one half

the original volume of Tris-maleate buffer plus 0.1% Triton, and centrifuged a second time through a sucrose cushion. The nuclear pellet was resuspended in 0.1 M Tris, 0.1 M EDTA, pH 8.0 (1 ml buffer to 1 g starting material) and the nuclei lysed in 1% SDS. The sample was treated with 100 μ g/ml predigested pronase (B grade, Calbiochem) for 2 hr at room temperature. The mixture was brought to 1.0 M NaClO₄ and extracted with an equal volume of phenol: IAC (1:1) and IAC (24:1 chloroform:isoamyl alcohol). The DNA was spooled after precipitation with two volumes of 95% EtOH and redissolved in 0.015 M NaCl, 0.05 M Tris, 0.01 M EDTA, pH 7.6. The DNA was further purified by treatment with 50 μ g/ml RNase A (chromatographically pure, Worthington Biochemical Co.) for 1 hr at 37°C. The solution was adjusted to 0.1 M NaCl and incubated with 200 μ g/ml predigested pronase at 37°C for 1.5 hr. After digestion the mixture was extracted with an equal volume of IAC and reprecipitated with ethanol. The yield of DNA was approximately 300 μ g/g eggs. As an additional purification step, sheared DNA was bound to hydroxyapatite at 60°C and washed with 0.12 M phosphate buffer followed by elution with 0.4 M phosphate buffer.

Tritium-labeled *Drosophila* DNA purified from tissue culture cells was generously provided to us by Drs. Ray White and David Hogness. A 60-ml suspension of cells that had been grown in the presence of ³H-thymidine was centrifuged and the cells washed in medium without serum. The pellet was suspended in 0.5 ml medium without serum and brought to 10.5 ml with 0.5 M EDTA, pH 9.55; 2.5% sarcosyl, followed by incubation at 60°C. After 2 hr 11 ml of 0.1 M EDTA containing 1 mg/ml proteinase K (EM Laboratories) was added, and the mixture was incubated at 37°C for 7 hr. CsCl was added (1.21 g/ml), and the samples were centrifuged at 33,000 rpm for 3 days at 15°C in a Spinco-40 rotor. The fractions

containing the tritium counts were pooled and dialyzed extensively against 0.1 M NaAcetate. The ³H label was shown to be greater than 97% sensitive to DNase and completely resistant to RNase. All sheared tracer preparations were subjected to one further purification step by binding to and elution from hydroxyapatite. The purified tracer melted with an optical hyperchromicity of 95% of that expected for pure DNA. Its specific activity was determined to be 1×10^5 cpm/ μ g.

Preparation of DNA fragments. DNA fragments of desired lengths were obtained by shearing in a Virtis-60K homogenizer as previously described (Britten *et al.*, 1974).

Sizing of DNA fragments. The single-strand length of the DNA fragments was determined on isokinetic alkaline sucrose gradients as described by Noll (1967). The parameters were as follows: $V_{\text{mix}} = 9.84$ ml, $C_{\text{res}} = 43\%$ w/v, $C_{\text{flask}} = 16\%$ w/v in 0.1 M NaOH. The gradients were centrifuged at 41,000 rpm for 20–24 hr at 20°C in the Spinco-SW41 rotor. The weight average fragment length was determined according to the equations of Studier (1965), relative to markers sized by electron microscopy.

DNA reassociation. Unless otherwise indicated, the DNA was reassociated in 0.12 M phosphate buffer at 60°C or 0.4 M phosphate buffer at 66°C C_0t values determined in the higher salt were corrected to "equivalent" C_0t by multiplying by 4.9. All buffers and DNA solutions were passed through BioRad Chelex 100 equilibrated in the desired buffer. The fraction of DNA molecules containing double-strand regions was assayed by hydroxyapatite chromatography (Britten *et al.*, 1974).

The reassociation of DNA was monitored in some experiments by measuring the hypochromicity of denatured DNA samples at 260 nm in 0.12 M phosphate buffer in a water-jacketed cuvette in a Beckman ACTA Mark III spectrophotometer.

S1-nuclease digestion and sizing of re-

sistant regions. Reassociated DNA was adjusted to 0.15 M NaCl, 0.025 M Na-Acetate, 0.005 M PIPES, 0.1 mM ZnSO₄, 0.005 M β -mercaptoethanol, pH 4.4, and digested for 45 min at 37°C with enough single-strand-specific S1 nuclease to digest all single-strand regions (Ando, 1966). The reaction was terminated by addition of phosphate buffer to a final concentration of 0.12 M, and S1-resistant duplex regions were collected on hydroxyapatite at 60°C. ¹⁴C-labeled sea urchin DNA incubated to appropriate *C₀t* was included as an internal control in each S1 digestion experiment. After elution from hydroxyapatite with 0.4 M phosphate buffer, the resistant regions were chromatographed on a BioRad Biogel A-50 column (1.5 × 110 cm) in 0.12 M phosphate buffer. The column was poured around a support of 6-mm glass beads. An exclusion marker of long native DNA and an inclusion marker of ³²PO₃ were used to calibrate the column.

CONTRASTING PATTERNS OF DNA
SEQUENCE ARRANGEMENT IN *Apis
mellifera* (HONEYBEE) AND *Musca
domestica* (HOUSEFLY)

W. R. Crain, E. H. Davidson,
and R. J. Britten

Here we report measurements of the patterns of sequence organization of the genomes of two insects which were chosen to provide insight into the phylogenetic distribution of the two patterns. The surprising results are that the DNA of a dipteran (housefly) has short-period interspersions similar to that of *Xenopus* and that the DNA of a hymenopteran (honeybee) lacks short-period interspersions as does *Drosophila*. These results suggest that the pattern of sequence organization has undergone remarkable change in the course of insect evolution.

Reassociation Kinetics of Honeybee
DNA Assayed by Hydroxyapatite

Honeybee DNA fragments 330 or 2200 nucleotides long were reassociated, and

the fragments remaining single stranded at different *C₀t* values were assayed by hydroxyapatite chromatography. The results of this kinetic analysis are shown in Fig. 10. The least-squares solution for each set of data yields a single second-order component which accounts for 85% of the reassociation. Table 7 lists the quantities and rate constants of the components for each solution. The rate of reassociation of DNA fragments not exhibiting sequence interspersions is proportional to the square root of the fragment length (Wetmur and Davidson, 1968). Thus, the rate constant expected for the reassociation of 2200-nucleotide-long single-copy honeybee DNA fragments calculated from the observed rate for 330-nucleotide fragments is

$$0.0038 \times \left(\frac{2200}{330} \right)^{1/2} = 0.010.$$

This value is in close agreement with that observed for the 90% component of the 2200-nucleotide curve (0.013), suggesting that this component represents the reassociation of fragments consisting entirely of single-copy sequences. The observation that the quantity of the single-copy component at a fragment length of 2200 nucleotides is not signifi-

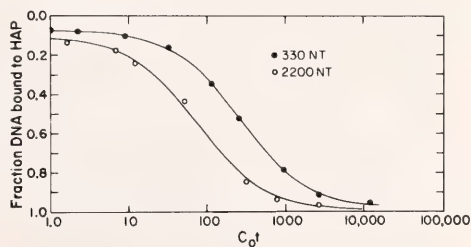


Fig. 10. Reassociation of honeybee DNA. Honeybee DNA fragments 330-nucleotides (filled circles) and 2230 nucleotides (open circles) were reassociated in 0.12 M PB at 60°C. The fraction of fragments containing double-strand regions was assayed by hydroxyapatite chromatography in 0.12 M PB at 60°C. The curves represent a least-squares solution to the data for one second-order component in each case (see Table 7).

TABLE 7. Kinetic Analysis of *Apis mellifera* DNA

| Fragment Length | Component | Fraction of Fragments | K^a | $C_0t_{1/2}$ | RMS Deviation (%) |
|-----------------|--------------------------------------|-----------------------|--------|--------------|-------------------|
| 330 nucleotide | zero-time and repeats single copy | 0.07 | 0.0038 | 263 | 0.7 |
| | | 0.917 ^b | | | |
| 2200 nucleotide | zero-time and repeats single copy | 0.103 | 0.0132 | 76 | 1.3 |
| | | 0.897 | | | |

^a Rate constant in whole DNA, $M^{-1} \text{ sec}^{-1}$.

^b Jordan and Brosemer (1974) also observed approximately 90% single copy sequences in the genome of *Apis mellifera*.

cantly decreased over that at 330 nucleotides shows that no detectable portion of the 2200-nucleotide fragments consists of both repeated and single-copy sequences.

This result shows that the principal part of the single-copy sequences occurs in long stretches rarely interrupted by repetitive sequences. Regions where the repetitive sequences occur contain little if any single-copy sequences. Therefore, it is likely that both the repetitive and the nonrepetitive sequences are long compared to the 2200-nucleotide fragments. We could not rule out an arrangement in which short repeats are interspersed with still shorter single-copy sequences in such a way that the majority of the length of these regions is repetitive. There is, however, no evidence for such a pattern, and as yet we know nothing of sequence arrangement within the repetitive regions of honeybee DNA.

Optical Reassociation Kinetics of Honeybee Repeated Sequences

Based on the data in Fig. 10, it appears that no more than 10% of honeybee DNA consists of repeated sequences. In order to estimate the amount of repeated sequences, DNA fragments 330 nucleotides long were reassociated to C_0t 2. The fragments containing double-stranded regions were collected on hydroxyapatite, eluted with 0.4 *M* PB, and dialyzed into 0.12 *M* PB. The reassocia-

tion kinetics of this fraction (7.8% of the original DNA) were assayed by optical hypochromicity as shown in Fig. 11. A large initial drop in optical density is observed before the first measured point at about C_0t 0.01. This presumably results from a combination of foldback DNA and, possibly, very rapidly reassociating fractions. After C_0t 0.01 reassociation typical of repetitive sequences is observed which may not be complete by C_0t 20. At least 40% of this C_0t 2 hydroxyapatite-bound fraction (3% total DNA) consists of repetitive sequences since this much reassociation was directly observed. It is possible that there is a highly repetitive component, although no direct evidence for it exists. Therefore, most of the C_0t 2 fraction could be repetitive DNA (about 8% of the genome). The reassociation kinetics appear to be heterogeneous, with a midpoint at about C_0t 0.3 for the part of the reaction measured. The rate of reassociation measured optically is half that measured with hydroxyapatite (Britten and Kohne, 1968), and the component could have been enriched by a factor of 10 in the isolated repetitive fraction. Therefore, we estimate the half reassociation C_0t in total honeybee DNA to be about 1.5 or greater. Since the preparative fractionation was done at C_0t 2, we probably recovered 60% or less of the repetitive DNA and surely would have recovered less of the more slowly reassociating fractions. Therefore we estimate that 6%–10% of the honeybee

genome consists of sequences repeated a hundred or more times.

Reassociation Kinetics of Housefly DNA

Housefly DNA fragments 250 or 2000 nucleotides long were self-reassociated and the fraction of single-strand fragments assayed by hydroxyapatite chromatography. Figure 12 shows that reassociation of the 250-nucleotide fragments occurs over at least seven decades of C_0t . The result of a least-squares solution with three second-order components is described in Table 8. The reassociation rate constant of the slowest

component is 0.00095, which is very close to 0.00093, the expected value for single-copy sequences in a genome of 0.89 pg (Bier and Müller, 1969). Reassociation of 2000-nucleotide fragments, as seen in Fig. 12, is completed at much lower C_0t values than reassociation of the 250-nucleotide fragments. A least-squares solution for two second-order components is described in Table 8. Fragments 2000 nucleotides long containing only single-copy sequences would be expected to reassociate with $k = 0.00095(2000/250)^{1/2} = 0.0026 \text{ M}^{-1} \text{ sec}^{-1}$. It can be seen that no significant amount of reassociation occurs in this appropriate range of C_0t . Most, if not all, of the single-copy sequences had been bound much earlier. They are therefore present on fragments containing repetitive sequences that had previously reassociated. This is a direct indication that a high percentage of the single-copy sequences alternates with repeated sequences at some distance less than 2000 nucleotides. Reassociation of fragments of each of these lengths goes to only about 85% completion. We believe that the 85% observed reassociation reasonably represents all the kinetic classes present.

The least-squares solution for each fragment length yields a fast and a slow repetitive component (Table 8). The fast component increases from 23% to 32% of the DNA. The slow component increases from 22% to 40% of the DNA. These increases show that large quantities of single-copy sequences are interspersed with both of these components. The total increase ($9 + 18 = 27\%$) is almost equal to the total single-copy component (34%) observed for the 250-nucleotide curve. This is consistent with the lack of an observed single-copy component in the 2000-nucleotide curve.

Size and Sequence Divergence of Reassociated Repeated Sequences in Housefly DNA

In order to determine the size of the repetitive sequence elements of housefly

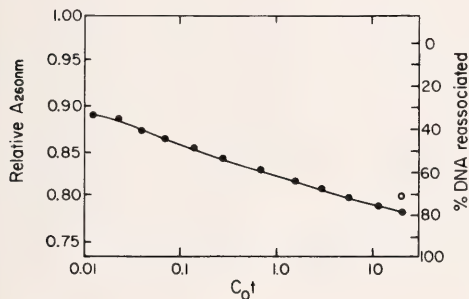


Fig. 11. Reassociation of honeybee repeated DNA monitored by optical hyperchromicity. Honeybee DNA fragments 330 nucleotides were reassociated to C_0t 2.3. The fragments containing duplexed regions were collected on hydroxyapatite and eluted with 0.4 M PB (7.8% of the DNA). This fraction was dialyzed into 0.12 M PB, melted, and allowed to reassociate at 60°C, while the A_{260} was monitored in the Acta,III recording spectrophotometer (left vertical axis). The hyperchromicity (H) at each point is calculated as $\frac{A_{260}(98^\circ\text{C}) - A_{260}(T)}{A_{260}(98^\circ\text{C})}$.

The percentage of DNA reassociated is calculated as follows: $\% \text{ reassociated} = \frac{H - 0.03}{0.24}$

$\times 100$ and is shown on the right vertical axis. The solid circles represent the data points, calculating the hyperchromicity as the denatured A_{260} in the original melt of the DNA before reassociation. After reassociation for approximately 48 hr the renatured DNA was remelted giving a T_m of 81°C which is within 1°–2°C of the native T_m . The denatured A_{260} at this point was slightly lower than during the first melt. The fraction DNA reassociated using this lowered denatured A_{260} is shown for C_0t 20 (open circles).

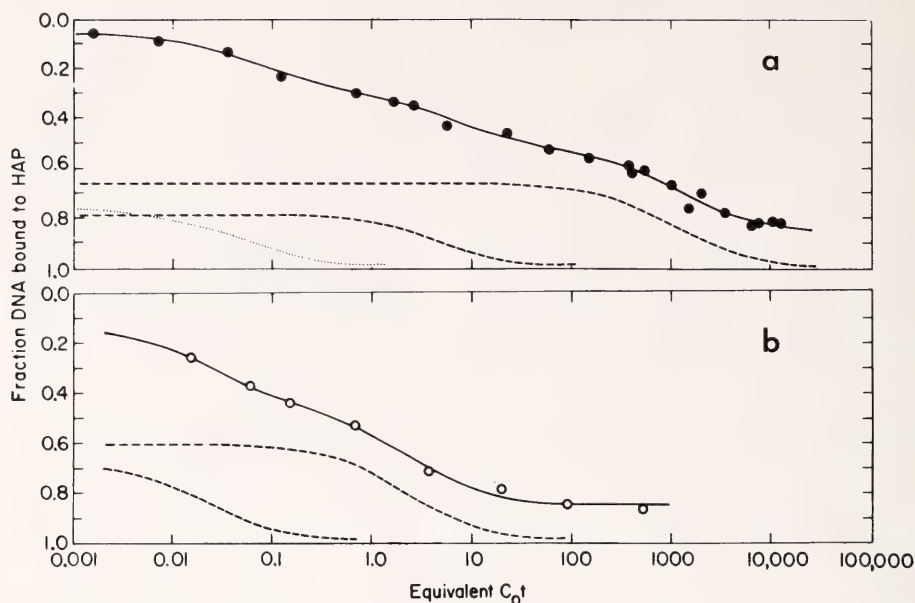


Fig. 12. Reassociation of housefly DNA. 12a. The solid circles represent the reassociation of tritium-labeled housefly DNA fragments 250 nucleotides long. The solid line represents a least-squares solution of the data with three second-order components. The dashed lines show the three components as described in Table 8. In Fig. 12b, the open circles represent the reassociation of unlabeled housefly DNA fragments 2000 nucleotides long. The solid line represents a least-squares solution of the data with two second-order components. The dashed lines show the two components as described in Table 8. In both cases the fragments were allowed to reassociate in either 0.12 *M* PB at 60°C or 0.4 *M* PB at 66°C. The fraction of fragments containing double-strand regions was assayed by hydroxyapatite chromatography in 0.12 *M* PB at 60°C.

TABLE 8. Kinetic Analysis of *Musca domestica* DNA

| Fragment Length | Component | Fraction of Fragments | K^a | $C_0t_{1/2}$ | Average Repetition Frequency | RMS Deviation (%) |
|-----------------|-------------|-----------------------|----------------------|--------------|------------------------------|-------------------|
| 250 nucleotide | fast | 0.23 | 17.2 | 0.058 | 18,000 | 1.8 |
| | slow | 0.22 | 0.192 | 5.21 | 200 | |
| | single copy | 0.34 | 0.00095 ^b | 1050.0 | 1 | |
| 2000 nucleotide | fast | 0.32 | 42.9 ^c | 0.023 | | 1.3 |
| | slow | 0.40 | 0.44 ^c | 2.27 | | |

^a Rate constant in whole DNA, $M^{-1} \text{ sec}^{-1}$.

^b This single-copy rate constant agrees well with the predicted rate constant of 0.00093 based on a measurement of genome size of 0.89 pg (Bier and Müller, 1969). This rate is very close to that for *S. purpuratus* (0.88 pg) and thus the expected rate constant for 450-nucleotide fragments is 0.00125 and for 250-nucleotide fragments is $(250/450)^{1/2} \times 0.00125 = 0.00093$.

^c These components are those generated by an unrestricted least-squares analysis of the data for two components. A fit of the data in which the rates of the repetitive components in the 250-nucleotide fragment curve are imposed directly on the 2000-nucleotide fragment curve gives a fit with no significant changes in the RMS. Since it is not clear how the fragment size affects the reassociation rate for interspersed elements it is not possible to define the repetitive components in the 2000-nucleotide fragment curve more precisely.

DNA, fragments 2000 nucleotides long were reassociated to *Cot* 9 and digested with a light treatment of the single-strand-specific nuclease S1. Our estimate is that under these digestion conditions 80% of single strand DNA be included on a G100 column (DIG = 80%, Britten *et al.*, in press). After S1 digestion, 34.4% of the DNA bound as double strands to hydroxyapatite. The S1-resistant double-stranded fragments were eluted from HAP with 0.4 M PB and chromatographed on an agarose A-50 column. As is seen in Fig. 13, the S1-resistant reassociated repeats gave a bimodal distribution; those excluded from the column, which are about 1500 nucleotides or greater, and those which gave a broad distribution with a peak around 300 nucleotides. This profile is qualitatively quite similar to that of all other organisms previously studied which show a short interspersion pattern (Goldberg *et al.*, 1975; Efstratiadis *et al.*, 1976).

When various DNA fractions were melted in a spectrophotometer, a direct

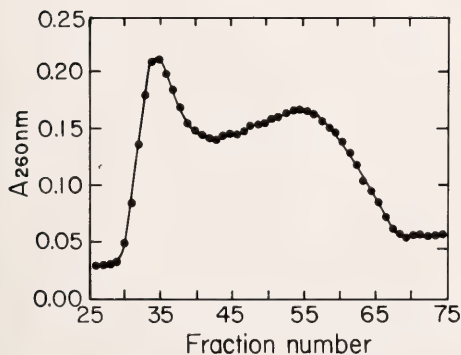


Fig. 13. Agarose A-50 profile of S1-resistant reassociated repeated sequences of housefly DNA. Housefly DNA fragments 2000 nucleotides long were reassociated to *Cot* 9 and then digested (DIG = 80%) with S1 nuclease (0.15 M NaCl, 0.005 M PIPES, 0.025 M Na acetate, pH 4.3, 0.1 mM ZnSO₄, 37°C, 45 min). Duplexes were collected on hydroxyapatite (34.4% of the DNA was bound to HAP in 0.12 M PB) and then chromatographed on an agarose A-50 column.

correlation was observed between the length of the repeats and their T_m (Table 9). A difference in T_m of 9°C was observed between the long and short repeated sequences; this reduces to about 7°C when correction is made for effect

of length on T_m ($\Delta T_m = \frac{650}{L}$). This cor-

relation has been observed in the DNA of sea urchin (Graham *et al.*, 1974), *Xenopus* (Davidson *et al.*, 1973), *Spisula* (Goldberg *et al.*, 1975) and silk moth (Efstratiadis *et al.*, 1976) and is a result of the greater sequence divergence of the shorter repeats.

The T_m of DNA from the excluded peak is 5°C below that of native housefly DNA. In the DNA of the other organisms examined in this manner, the T_m of the excluded peak is within 1° or 2°C of the native T_m . Whether or not the difference in T_m of the long repeated sequences with respect to native DNA represents a real divergence of these sequences is not clear. In order to better understand this observation, the following experiment was done. Fractions 30–38 (excluded peak) and 51–61 (~300 nucleotide pairs) were pooled from the A-50 column and redigested more heavily with S1 (DIG = 95%, Britten *et al.*, in press). The S1-resistant DNA was concentrated on hydroxyapatite and chromatographed on an A-50 column and melted. The redigested long repeats were 86% S1 resistant, and the resistant duplexes chromatographed as a single excluded peak on A-50. The redigested short repeats, which were 85% S1 resistant, chromatographed as a single peak with an average size of about 300 nucleotides. It is seen in Table 9 that when DNA from the two peaks was melted in 0.12 M PB, their T_m s differed by about 11°C. When corrected for the effect of length this difference was about 9°C. The T_m of the excluded peak (long repeats) was just 1°C below that of native DNA, a result consistent with the other organisms studied.

TABLE 9. Thermal Stability of S1-Resistant Repetitive Sequences of *Musca domestica*

| Enzyme Treatment | Fraction from A-50 Column | Hyperchromicity ^a | T_m (°C) ^b |
|------------------------|----------------------------|------------------------------|-------------------------|
| DIG = 80% ^c | Excluded peak ^d | 0.235 | 79.5 |
| | Valley ^e | 0.213 | 76.0 |
| | Included peak ^f | 0.22 | 70.5 |
| DIG = 95% ^g | Excluded peak ^h | 0.175 | 83.5 |
| | Included peak ⁱ | 0.21 | 72.0 |
| | Native DNA | 0.269 | 84.5 |

^a Hyperchromicity is calculated as A_{260} at 98° - A_{260} at 60°/ A_{260} at 98°.

^b T_m is not corrected for length.

^c Enzyme treatment at which 80% of single-stranded DNA would be included on a G-100 column (Britten *et al.*, in press).

^d Fraction 35 from A-50 column in Fig. 13.

^e Fraction 42 from A-50 column in Fig. 13.

^f Fraction 55 from A-50 column in Fig. 13.

^g Enzyme treatment at which 95% of single-stranded DNA would be included on a G-100 column (Britten *et al.*, in press).

^h Fractions 30-38 of A-50 column in Fig. 13 were pooled, dialyzed into 0.15 M NaCl, 0.005 M PIPES, 0.025 M acetic acid, 1 mM ZnSO₄, and digested with an enzyme treatment equivalent to DIG = 95% (Britten *et al.*, in press). The resistant material was concentrated on HAP and rechromatographed on agarose A-50. The excluded material was pooled, concentrated on HAP, dialyzed into 0.12 M PB, and melted.

ⁱ Fractions 51-61 of the A-50 column in Fig. 13 were pooled and treated as described in *h*. The included material was pooled, concentrated on HAP, dialyzed into 0.12 M PB, and melted.

Conclusion

These analyses of sequence arrangement in the DNA of the housefly (Diptera) and the honeybee (Hymenoptera) were designed to extend our knowledge of the occurrence of long-period and short-period patterns of DNA sequence interspersions.

The DNA of the honeybee shows only long-period interspersions and contains no detectable amount of linked single-copy and repetitive DNA on fragments 2200 nucleotides long. This conclusion is drawn from the observation that the small fraction of the genome that reassociates as repeated sequences by hydroxyapatite assay is virtually the same for 330- and 2200-nucleotide-long fragments. For housefly DNA, on the other hand, most fragments 2000 nucleotides long reassociate at repetitive *Cot* by hydroxyapatite assay. Since more than half of housefly DNA is probably made up of single-copy sequences, most of the single-copy sequences must be linked

closely to repetitive sequences and are less than a few thousand nucleotides long.

Our present knowledge of insect DNA sequence organization can be summarized as follows. Insect genomes in which short-period interspersions have been identified are *Musca* (Diptera) and *Antheraea* (Lepidoptera) (Efstratiadis *et al.*, 1976). The genomes of *Drosophila*, *Chironomus* (Diptera), and *Apis* (Hymenoptera) lack detectable short-period interspersions (Manning *et al.*, 1975; Crain *et al.*, 1976a). Another arthropod, *Limulus* (Goldberg *et al.*, 1975), and all other animal and plant species yet studied show the short-period pattern.

The short-period pattern is clearly the most widespread; except for insects, it is universally observed (so far). Moreover, the short-period pattern occurs in some insect species (silk moth) and even within the Diptera, as shown by these measurements on housefly DNA. The presence of the short-period pattern in

the housefly, which has polytene chromosomes, suggests that no correlation exists between the sequence arrangement pattern and polytenization of chromosomes. As our knowledge grows we are likely to learn of more subtle variations in the patterns of DNA sequence organization. However, at the moment, the stark contrast between the long- and short-period patterns stands out. It is not easy to visualize how an evolutionary transition could occur between two so apparently different patterns. Yet this may have occurred more than once in the course of insect evolution. Only one transition would have been needed in the event that one branch of the Diptera, including the housefly, were evolutionarily more closely related to the Hymenoptera than it is to other Diptera such as *Chironomus* and *Drosophila*.

The probable occurrence of evolutionary transitions between long-period and short-period interspersed patterns suggests that they share some fundamental similarity which is obscured by our sensitivity to the differences. In every case of the short-period interspersed pattern that has been examined, the repetitive sequence lengths are distributed around a mode value of about 300 nucleotides. *Drosophila* DNA shows an average repetitive sequence length of 5600 nucleotides. In *Chironomus* the mean repeat length is also long, about 4300 nucleotides (Wells *et al.*, in press), but there is as yet no measurement of this for *Apis*. In the case of one long repetitive sequence of *Drosophila* that has been examined as a recombinant clone (Finnegan, Rubin, and Hogness, 1976, personal communication), it appears that the long repetitive sequence is made up of shorter repetitive sequences. Perhaps individual repetitive sequences are similar in length, and one difference between the short- and long-pattern genomes is the presence or absence of interspersed single-copy sequences.

Another similarity exists between genomes with and without short-period

interspersed sequences. Both types of genome contain similar percentages of relatively long repeated sequences. In all of the short-period interspersed species that have been studied, a small part of the genome is made up of repetitive sequences that are longer than about 2000 nucleotides which, when reassociated, have high thermal stability. The observations described above (Table 9) for housefly DNA are typical. In every case the long sequences have been observed to be relatively precisely repeated. For two long-pattern genomes, *Drosophila* (Crain *et al.*, 1976a) and honeybee (see above), the melting temperatures of reassociated long repetitive sequences have been measured and both are near that of native DNA, indicating relatively precise repetition in these cases as well.

An important point is that the three insect species in which short-period interspersed sequences are apparently lacking all have small genome sizes. *Drosophila* has a genome size of about 0.1 pg (Fristrom and Yund, 1973); *Chironomus*, 0.2 pg (Wells *et al.*, in press); and *Apis*, about 0.35 pg (determined kinetically, above, and Jordan and Brosemer, 1974). This correlation is at least consistent with the concept of DNA loss in an evolutionary transition from the short- to the long-interspersed pattern. Other metazoan species have genome sizes in this range, but their DNA sequence organization has not yet been determined. All of the metazoan species whose DNA is known to have a short-period interspersed pattern have genome sizes greater than 0.7 pg (Davidson *et al.*, 1975b). The slime mold *Dictyostelium* apparently has short-pattern sequence organization and a genome size of about 0.1 pg (Firtel and Kindle, 1975), but it is so distant from other studied species that no evolutionary implication can be drawn from this observation. All three insects without short-period interspersed sequences also have a small fraction of the genome as repetitive DNA compared to the 20%–40% observed in typical metazoan genomes. Since the genome sizes of these three

insects are also small, the absolute quantity of repetitive sequences is very small, on the average less than 2×10^7 nucleotide pairs.

Since the significance of these observations depends on the functional role of

the repetitive DNA and this is not known, we cannot appreciate the meaning of these correlations. Nor can we guess whether they will hold up as more patterns of sequence organization are studied.

DNA SEQUENCE EXPRESSION STUDIED BY TRANSCRIPTION INTO RNA

STRUCTURAL GENE SETS ACTIVE IN EMBRYOS AND ADULT TISSUES OF THE SEA URCHIN

Glenn A. Galau, William H. Klein,
Mark M. Davis, Barbara J. Wold,
Roy J. Britten, and Eric H. Davidson

The amount of difference in the sets of genes expressed in the various cell types of a complex animal is not yet known. The special functions of each cell type may be generated by a small fraction of the total number of active structural genes, and in this case a large majority of the messenger RNAs would be shared by all or most of the tissues. Genes whose mRNAs are ubiquitous have been termed "housekeeping genes," the implication being that their role is to program the basic life functions necessary to all cells. Alternatively, housekeeping genes could represent a minor fraction of the expressed structural genes, so that in many cases the sets of genes active in diverse tissues will be largely distinct.

In this paper we report direct measurements of the amount of sequence overlap in the mRNA populations in several stages of sea urchin embryo and in various adult tissues. We have compared the set of structural genes whose transcripts are active in gastrula stage embryos to those active in the other states of differentiation investigated. Structural genes are here defined experimentally as single copy DNA sequences which hybridize with mRNA released from purified polysomes. Previous work has provided considerable quantitative information about the gastrula mRNA

set. The structural genes transcribed at this stage are almost all nonrepetitive sequences (Goldberg *et al.*, 1973; McColl and Aronson, 1974). According to our recent measurements (Galau *et al.*, 1974), the complexity (i.e., total length in nucleotide pairs of DNA sequences represented in the RNA) of the gastrula mRNA is about 17×10^6 nucleotide pairs. This is equivalent to about $1\text{--}1.5 \times 10^4$ diverse structural genes.

A few structural genes are far more extensively represented in polysomal messenger RNA than are most. Galau *et al.* (1974) found that about 90% of the polysomal mRNA in gastrula, the "prevalent message class," consists of fewer than several hundred species, while the other 10% is made up of the $1\text{--}1.5 \times 10^4$ species mentioned above. We term the latter fraction of the message population the "complex class." Each mRNA in the complex class is present only 1–10 times per gastrula cell, and prevalent class messages are probably present at least 100 times more frequently. Prevalent and complex message classes are not peculiar to sea urchin embryos but have been identified in most of the other tissues and cell types so far investigated. These include Friend cells (Birnie *et al.*, 1974), mouse fibroblasts (Williams and Penman, 1975), HeLa cells (Bishop *et al.*, 1974), *Drosophila* embryos (Levy and McCarthy, 1975), and several mouse organs and cell types (Ryffel and McCarthy, 1975).

The experiments described in this report concern only the complex class of messages. The prevalent message class represents so small a fraction of the to-

tal active set that its pattern of expression is not detectable by our present methods. However, previous measurements have demonstrated striking alterations in the activity of structural genes coding for highly prevalent messenger RNAs in other animal tissues. Among many possible examples might be mentioned studies on the activity of the genes coding for hemoglobin (e.g., Axel *et al.*, 1973; Hunt, 1974); ovalbumin (e.g., Chan *et al.*, 1973; Palmiter, 1973; Rhoads *et al.*, 1973; Harris *et al.*, 1975); cocoonase (Kafatos, 1972); and chorion proteins (Paul *et al.*, 1972). Several groups have prepared cDNA against total cytoplasmic poly(A) RNA of given tissue types and reacted this cDNA with poly(A) RNA of other tissues (Levy and McCarthy, 1975; Ryffel and McCarthy, 1975; Williams and Penman, 1975). Most of the cDNA represents messages of the prevalent class. In some of these experiments differences in the amount and rate of the cDNA reaction with the other poly(A) RNAs were observed. Such results suggest that at least in some cases there may be significant differences in the sets of structural genes active in the various tissues.

The experimental rationale is as follows. When labeled single-copy DNA is hybridized to termination with mRNA from gastrulae at ratios such that even messages of the complex class are in considerable sequence excess, only about 1.35% of the DNA reacts. This is too small a fraction of the total single-copy DNA to permit much resolution in comparing diverse mRNA populations. For example, if the messages of another sea urchin cell type differed from the gastrula message set by as much as 20%, a change in hybrid content equal to only 0.27% of the total DNA would result. Such a small difference, though difficult to measure convincingly, could obviously be important, since it would represent the addition or subtraction of 2000–3000 sequences from the expressed structural gene set. To increase sensitivity we have prepared a single-copy DNA frac-

tion, the majority of which is complementary to the gastrula mRNA. We report here the purification of this set of DNA sequences by a factor of about 50, by a modification of the procedure described by Galau *et al.* (1974). About 63% of the reactable DNA in the partially purified preparation hybridizes with gastrula message compared to the original 1.35%, which provides more than an order of magnitude increase in sensitivity to differences in sequence content when hybridization reactions are carried out with other mRNAs. We refer to the single-copy DNA fraction representing gastrula messages as *mDNA*. A single-copy DNA fraction depleted of the sequences represented in gastrula mRNA was also prepared and is termed *null mDNA*. Reaction of a nongastrula mRNA preparation with *mDNA* measures the fraction of the structural genes expressed in gastrula, which is also represented in the test messenger RNA population. Reaction with *null mDNA*, on the other hand, measures the number of structural genes represented in mRNA, which are different from those represented in gastrula mRNA.

Characterization of Single-Copy 3H-DNA Labeled in Vitro

The RNA-driven hybridization reactions on which our measurements are based require single-copy DNA tracer of high specific activity. This is necessary so that the hybridizations can be carried out with moderate amounts of mRNA and at ^3H -DNA concentrations sufficiently low to prohibit appreciable DNA self-reaction. The highest specific activities so far obtained by labeling sea urchin embryos *in vivo* are in the range $1\text{--}3 \times 10^5$ cpm/ μg (e.g., Galau *et al.*, 1974). Since this specific activity is inadequate for our present purposes, an *in vitro* labeling method was required. The procedure we have used is a modification of the "nick-translation" method of Schachat and Hogness (1974). The single-copy DNA fraction was first isolated

and then labeled in vitro with DNA polymerase I. Whole sea urchin DNA was first sheared to a mean length of about 250 nucleotides, and the single-copy sequences were purified by conventional hydroxyapatite fractionation methods (see Experimental Procedures). The single-copy DNA was then reassociated to C_0t 20,000, about 40 times the $C_0t_{1/2}$ for this kinetic fraction. At this point most of the DNA is present in large hyperpolymers (Graham, Eden, Davidson, and Britten, in preparation; Davidson, 1975c).

We find that these structures serve as excellent templates for DNA polymerase. It is therefore unnecessary to use DNAase to introduce nicks, as was done by Schachat and Hogness (1974) in labeling double-stranded DNA. The polymerase apparently initiates at single-stranded gaps between individual frag-

ments in the hyperpolymers, and then proceeds along the DNA chain, displacing one strand and replacing it with a newly synthesized strand containing radioactive nucleotides. The single-copy DNA preparation used for the experiments reported here was labeled by this method to a specific activity of 6×10^6 cpm/ μ g. This is equivalent to 20% nucleotide substitution in vitro. By the end of the purification and labeling procedures the single-strand length of the labeled fragments had decreased slightly from the starting value to a mean of about 200–250 nucleotides. We refer to this ^3H -DNA preparation as the parental tracer.

The labeled single-copy DNA reacts with unlabeled 450-nucleotide sea urchin DNA driver as shown in Fig. 14. The dashed line describes the reassociation of the driver DNA, based on a large

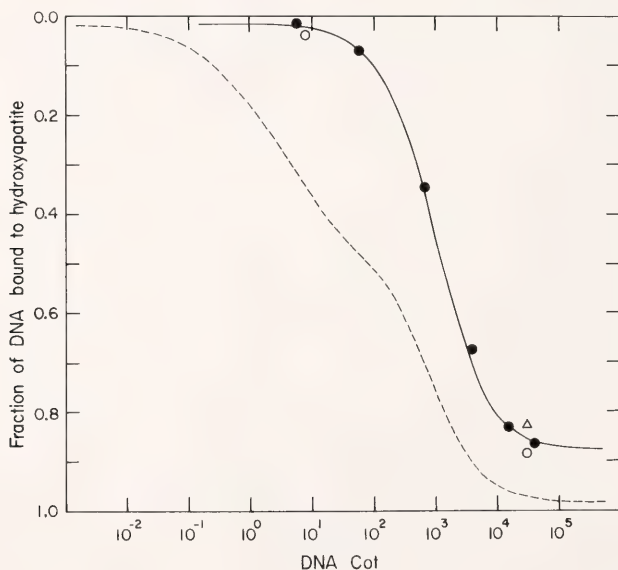


Fig. 14. Reactivity of single-copy ^3H -DNA, gastrula mRNA, and null mRNA with sea urchin DNA. 250-nucleotide-long single-copy ^3H -DNA (filled circles), mRNA (open circles), and null mRNA (open triangles) were incubated with a large excess of unfractionated 450-nucleotide-long sea urchin DNA in 0.12–0.41 M phosphate buffer at 60°C and analyzed by hydroxyapatite. The dashed curve is the reassociation of carrier DNA reproduced from Galau *et al.*, 1974; these data are not shown here. The solid curve is a least-squares fit to the single-copy ^3H -DNA data, yielding a rate constant of $1.0 \times 10^{-3} M^{-1} \text{sec}^{-1}$. The reassociation rate constant of single-copy DNA in 450-nucleotide-long DNA carrier is $1.31 \times 10^{-3} M^{-1} \text{sec}^{-1}$ based on extensive data shown by Galau *et al.*, 1974.

number of previous observations not reproduced here (Graham *et al.*, 1974; Smith *et al.*, 1974). Closed circles show the reassociation of trace quantities of the labeled DNA with the 450-nucleotide driver. The least-squares fit illustrated indicates that the rate constant for the reaction of labeled fragments with the driver DNA is $1.0 \times 10^{-3} M^{-1} \text{sec}^{-1}$, i.e., within about 25% of that expected for the single-copy fraction in whole DNA. There is no detectable contamination with repetitive sequences, and about 88% of the labeled DNA is reactable. In our experience this compares favorably with single-copy DNA preparations labeled *in vivo* (e.g., Galau *et al.*, 1974). In the absence of driver DNA less than 0.2% of the ^3H -DNA binds to hydroxyapatite after denaturation and incubation to C_0t s below 1. The reactivity of the *in vitro* labeled DNA with both DNA and RNA decreases slowly with time. The preparation used for the experiments presented in this paper decreased in reactivity from 90% to about 60% over a 6-month period, based on reactions with whole sea urchin DNA similar to those illustrated in Fig. 14. This unexplained slow loss in reactivity is a particular characteristic of DNA labeled to very high specific activity by this polymerase translation procedure. Some evidence suggests that the loss in activity is associated with strand scissions, which would be likely to have a noticeable effect on tracers of the short single-strand length used in these experiments.

The internal location of the radioactive nucleotides was shown as follows. The DNA was renatured to C_0t 85,000 and treated with single-strand-specific S1 nuclease. At this point about 85% of the single-copy DNA that binds to hydroxyapatite is expected to be resistant to S1-nuclease digestion (Smith *et al.*, 1975). One portion of the reaction mixture was passed over an hydroxyapatite column directly, and the other portion was treated with S1 nuclease under conditions promoting complete digestion of

single-stranded regions (Smith *et al.*, 1975). It was then bound to the hydroxyapatite column. About 77% of the ^3H -DNA which bound without digestion could still be bound after S1-nuclease treatment—or approximately 90% of the expected value. The small difference is probably due to the short chain length of the tracer, which is only about half the size of the shortest DNAs studied by Smith *et al.* (1975). It is evident in any case that almost all of the nucleotides incorporated into the hyperpolymers are located within single-copy DNA sequences and could not reside, for example, in noncomplementary external "tails."

*Oocyte RNA and Intestine mRNA
Complexities Measured with Total
Single-Copy Tracer*

The single-copy tracer was used to measure the overall sequence complexities of two RNA preparations relative to that of gastrula mRNA, as shown in Fig. 15. The mRNAs employed in these experiments were isolated by puromycin release from polysomes of gastrulae (Goldberg *et al.*, 1973; Galau *et al.*, 1974) and adult sea urchin intestine. The other RNA used was total RNA extracted from mature unfertilized oocytes. These measurements were designed mainly as controls to provide terminal hybridization values for comparison with those obtained with the mDNA and null mDNA tracers. All data in Fig. 15 were derived with the particular single-copy DNA tracer preparation from which the mDNA and null mDNA were prepared. At the time the experiments of Fig. 15 were carried out, however, the parental tracer reactivity had decreased. Initially the parental tracer reacted with gastrula message to the extent of 1.2%, yielding a complexity for this mRNA which agrees with that reported by Galau *et al.* (1974): 17×10^6 nucleotides. At the time of the measurements shown in Fig. 15, about 0.67% of the tracer reacts with the gastrula message

at termination. This amount of reaction is thus taken to represent a complexity of 17×10^6 nucleotides. On this basis, Fig. 15 shows the complexity of the oocyte RNA to be about $37 \pm 4 \times 10^6$ nucleotides. This result is in close agreement with more extensive measurements of oocyte RNA complexity carried out in this laboratory using different tracer DNA preparations (data to be reported in a separate communication, in connection with other studies). The complexity obtained from Fig. 15 for the intestine message preparation is $6.0 \pm 0.2 \times 10^6$ nucleotides, about one third that of the gastrula mRNA. The data plotted in Fig. 15 and the hybridization rate constants and terminal values estimated from least-squares fits are listed in Table 10. The errors given represent 1 standard deviation (see Experimental Procedures).

When only a small fraction of the total tracer reacts with the message, as in the experiments of Fig. 15, the ^3H -DNA-DNA duplex formed by tracer self-reaction must be quantitated with as much accuracy as possible. Table 10 shows that the ^3H -DNA-DNA duplex content in these experimental samples amounts to a significant fraction of the total duplex formed during the hybridization reactions. The methods used in the present study to measure DNA-RNA and DNA-DNA duplex content provide a high degree of reproducibility and are derived with only slight modification from those described by Galau *et al.* (1974). Exact methods are detailed in Experimental Procedures. Briefly, the reaction mixture is divided into two equal aliquots, one of which is treated with RNAase A in a low-salt medium (0.075 M Na^+) to destroy RNA-DNA

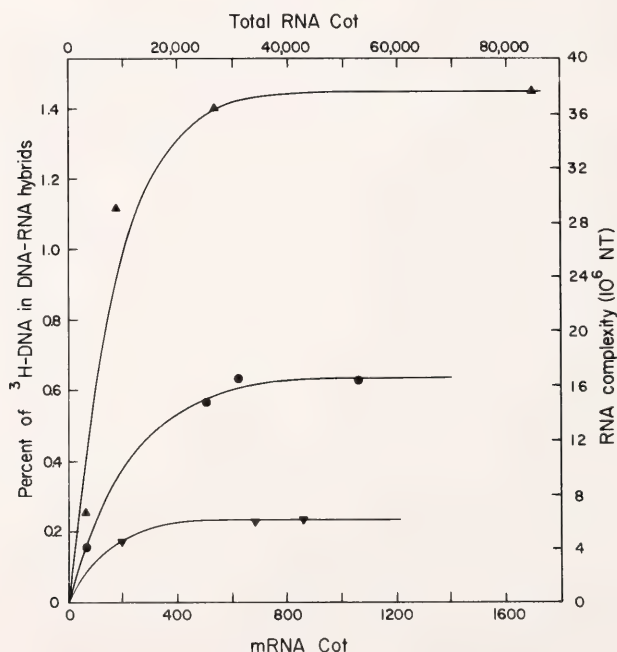


Fig. 15. Hybridization of single-copy ^3H -DNA with sea urchin RNAs. Data presented here are listed in Table 10. Each curve represents a least-squares fit, assuming a single pseudo-first-order hybridization reaction, with the additional assumption that the ordinate intercept is zero. The parameters obtained from these fits are shown in Table 10. Gastrula mRNA are represented by filled circles; total oocyte RNA, upright triangles; and intestine mRNA, upside-down triangles.

TABLE 10. Hybridization of Single-Copy ³H-DNA with Various Sea Urchin RNAs^a

| RNA | RNA Prepa- ration | <i>Cot</i> | | ³ H-DNA in Duplex (%) | | | Com- plexity ^b (10 ⁶ NT) |
|------------------|-------------------------|------------|--------------------|----------------------------------|-------------|---|--|
| | | RNA | ³ H-DNA | Total | DNA- DNA | DNA-RNA | |
| Gastrula mRNA | 1 | 75 | 0.25 | 0.31 | 0.15 | 0.16 | |
| | | 500 | 1.67 | 0.82 | 0.24 | 0.58 | |
| | | 624 | 1.56 | 1.06 | 0.41 | 0.65 | |
| | | 1063 | 3.54 | 1.27 | 0.63 | 0.64 | |
| Terminal value | | | | | | 0.67 ± 0.03 | 17° |
| Rate constant | | | | | | 4.2 ± 0.8 × 10 ⁻³ M ⁻¹ sec ⁻¹ | |
| Intestine mRNA | 1 | 202 | 1.44 | 0.63 | 0.45 | 0.18 | |
| | | 681 | 4.86 | 1.22 | 0.99 | 0.23 | |
| | | 857 | 6.12 | 1.00 | 0.76 | 0.24 | |
| Terminal value | | | | | | 0.24 ± 0.01 | 6.0 ± 0.3 |
| Rate constant | | | | | | 7.1 ± 0.7 × 10 ⁻³ M ⁻¹ sec ⁻¹ | |
| Oocyte total RNA | 2 | 3360 | 0.17 | 0.59 | 0.33 | 0.26 | |
| | | 8800 | 0.44 | 6.29 | 5.17 | 1.12 | |
| | | 26,900 | 1.35 | 2.66 | 1.25 | 1.41 | |
| | | 85,000 | 4.25 | 4.21 | 2.75 | 1.46 | |
| Terminal value | | | | | | 1.47 ± 0.15 | 37 ± 4 |
| Rate constant | | | | | | 1.2 ± 0.5 × 10 ⁻⁴ M ⁻¹ sec ⁻¹ | |

^a Errors listed represent ±1 standard deviation. Kinetics of the reactions were analyzed on the basis of the assumption of a single kinetic component with an ordinate intercept of 0, at 0 RNA *Cot*. See Experimental Procedures for discussion of this method and interpretation of the error estimates. Terminal values and errors thereon are essentially independent of kinetic assumptions in any case.

^b Complexity is calculated in the following way:

complexity = $\frac{17 \times \text{terminal fraction of } ^3\text{H-DNA in hybrid}}{0.67}$

^c 17 × 10⁶ nucleotides was obtained by Galau *et al.* (1974) for the polysomal mRNA of the gastrula.

hybrids while leaving DNA-DNA duplex unaffected. The other aliquot is treated with RNAase A in high salt (0.36 M Na⁺). Under these conditions mRNA-DNA hybrids are not digested, although nonhybridized RNA is totally destroyed (Galau *et al.*, 1974). The two samples are deproteinized and passed over hydroxyapatite columns. The RNA-DNA hybrid content is calculated from the total duplex bound to hydroxyapatite by subtraction of the DNA-DNA duplex content (Table 10). In the experiments described in this paper, the

two-column procedure was used to analyze samples reacted with unfractionated single-copy DNA and with null mDNA.

Galau *et al.* (1974) deduced from gastrula mRNA hybridization kinetics similar to those in Fig. 15 that the sequences driving the reaction constitute only about 10% of the total mRNA mass. This is the complex class of the message population referred to in the Introduction. The method of calculating the driver RNA fraction from the pseudo-first-order reaction kinetics is

detailed in Galau *et al.* (1974). Given the measured complexity of the RNA, the calculation is essentially a comparison of the hybridization rate observed with the rate expected, if all of the RNA present were driving the reaction. The expected hybridization rates can be calculated directly from DNA-DNA renaturation kinetics since there is no significant difference between RNA-DNA nucleation rates and DNA-DNA nucleation rates in RNA excess reactions (Galau, Smith, Klein, Britten, and Davidson, in preparation; Hutton and Wetmur, 1973). In Fig. 15, a single observable kinetic component beginning at zero is assumed for the intestine mRNA hybridization reaction, as for the other reactions analyzed in this paper. Where sufficient low C_0t kinetic data exist, this assumption is found to be justified (Galau *et al.*, 1974). The rate constant for the reaction of intestine messenger RNA, $7.1 \times 10^{-3} M^{-1} \text{ sec}^{-1}$, is about 1.7 times that for the gastrula message, $4.2 \times 10^{-3} M^{-1} \text{ sec}^{-1}$, close to expectation, since the complexity is about one third that of gastrula message. It follows that the high complexity class of mRNA amounts to less than 10% of the total mRNA in the intestine cells of the adult sea urchin, as well as in the gastrula. The data are not sufficient to fix the rate of either reaction in Fig. 15 within a range of 10%–20% (i.e., one standard deviation; see Experimental Procedures) even with the assumptions noted above. However, this degree of error does not alter the conclusion that a minor fraction of the intestine mRNA mass is the source of most of its sequence complexity.

Preparation and Characterization of Gastrula mRNA and Null mRNA

The preparation of these DNA fractions is described in detail in Experimental Procedures. In outline the procedure used was as follows: Single-copy ^3H -DNA was reacted with gastrula mRNA to mRNA C_0t 400, and RNA-

DNA hybrids plus DNA-DNA duplexes were bound to hydroxyapatite. About 1.1% of the parental single-copy tracer reacted with the gastrula messages. At the time the mRNA preparation was carried out, 88% of the ^3H -DNA was reactable (Fig. 14), and the maximum expected hybridization was 1.19% (i.e., 1.35% of reactable tracer). The amount of reaction expected at C_0t 400 was 1.05%. The single-stranded DNA was eluted from the hydroxyapatite column at 60°C in 0.12 *M* phosphate buffer and used to prepare the null mRNA preparation. The duplex fraction was denatured and then reacted a second time with gastrula mRNA. The duplex fraction was again separated on hydroxyapatite and was treated with KOH to hydrolyze the RNA. This DNA fraction was the gastrula mRNA used in the subsequent experiments. The single-stranded DNA from the first hydroxyapatite column was reacted an additional time with gastrula mRNA to achieve further purification. The fraction remaining single stranded was separated on hydroxyapatite, and this constituted the null mRNA preparation.

Goldberg *et al.* (1973) showed that the messenger RNAs of sea urchin gastrulae are almost completely transcribed from single-copy sequences. In accord with this, Galau *et al.* (1974) found that the DNA isolated from gastrula mRNA excess hybrids reacts with whole DNA with exactly the kinetics expected for single-copy sequence. Nonetheless, since the gastrula mRNA represents only about 1.2% of the total ^3H -DNA, it was considered necessary to assay its repetitive sequence content, if any. Figure 14 shows that when reacted with unfractionated sea urchin DNA driver, less than 5% of the gastrula mRNA has reacted by C_0t 40, when most of the repetitive sequence of the driver DNA is already in duplex form. In addition, the extensive fractionations involved in preparing the mRNA and null mRNA did not affect their reactivity. It can be seen in Fig. 14 that both DNA preparations

react to about 90% with the whole DNA driver, the same as does the parental single-copy tracer.

Experiments which establish that the mDNA and null mDNA fractions have been satisfactorily purified are shown in Fig. 16. Both tracers were reacted with aliquots of the same gastrula mRNA preparation used in their isolation, as well as with other gastrula mRNA preparations. Data for the individual reactions and results of the least-squares fits to these data are listed in Table 11. The gastrula mDNA reacts with gastrula mRNA at a rate of $5.8 \times 10^{-3} M^{-1} \text{ sec}^{-1}$, very similar to that obtained in the less extensive experiments of Fig. 15 using the parental single-copy ^3H -DNA tracer (i.e., $4.2 \times 10^{-3} M^{-1} \text{ sec}^{-1}$). Therefore, as expected, the same complex class mRNAs that react with unfractionated single-copy ^3H -DNA react with the ^3H -mDNA.

The final extent of the reaction of gastrula mRNA with mDNA is $57\% \pm 2\%$ of the total radioactive ^3H -DNA, or about 63% of the reactable mDNA sequence (Fig. 16, Table 11). Since 1.35%

of reactable single-copy ^3H -DNA is complementary to gastrula mRNA, a 46-fold purification has been achieved in the preparation of the mDNA. The maximum possible purification could have been 74-fold. The fraction of the mDNA which does not react with messenger RNA is 43% of the total radioactive ^3H -DNA, or 37% of the reactable tracer. Very possibly this DNA contains sequences, complementary to gastrula message, which have become too short to form stable hydroxyapatite binding duplexes. The total quantity of this contaminant amounts to less than 0.5% of the starting single-copy ^3H -DNA. Reactions of this single-copy contaminant, either with itself or with the various messenger RNAs, are insignificant in the experiments described below, compared to the reactions with the sequences complementary to the gastrula message.

Hybridization reactions with four separate gastrula messenger RNA preparations are included in Fig. 16 and Table 11. These were extracted over a two-year period by different investigators. As is demonstrated graphically in Fig.

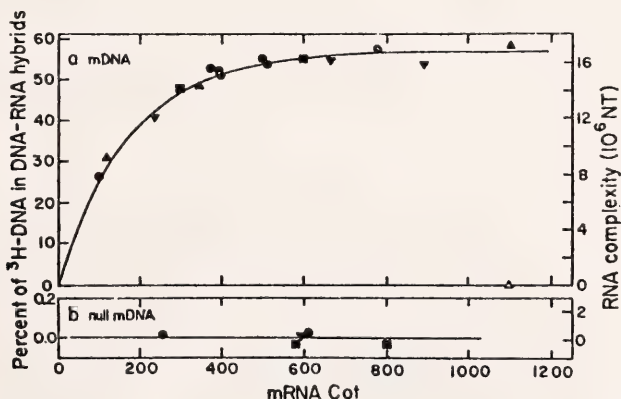


Fig. 16. Hybridization of gastrula mDNA and null mDNA with four different gastrula mRNA preparations. The line drawn through the data of 16a is a least-squares fit of a pseudo-first-order hybridization reaction with the assumption that the ordinate intercept is zero. Data and parameters obtained for this fit are shown in Table 11. Gastrula mRNA preparations are 1 (circles), 2 (upright filled triangles), 3 (upside-down filled triangles), and 4 (filled squares) (see Experimental Procedures for details of each preparation). Preparation 4 was prepared by EDTA (rather than puromycin) release. Also shown is a reaction mixture using preparation 2 mRNA (open triangle) which was treated with RNAase to destroy DNA-RNA hybrids before assay.

TABLE 11. Hybridization of Gastrula mRNA and Null mRNA with Gastrula mRNAs

| mRNA Preparation | mDNA | | | Null mDNA | | | | |
|-----------------------------|-----------------------|--------------------|---|-----------------------|--------------------|-------------------------------------|------|-------|
| | <i>C_{ot}</i> | | ³ H-DNA in Hybrid (%) | <i>C_{ot}</i> | | ³ H-DNA in Duplex (%) | | |
| | RNA | ³ H-DNA | | RNA | ³ H-DNA | Total | DNA- | DNA- |
| | | | | | | | DNA | RNA |
| 1 | 100 | 0.006 | 26.7 | 250 | 2.94 | 0.77 | 0.74 | 0.03 |
| | 371 | 0.028 | 53.2 | 600 | 3.00 | 0.83 | 0.80 | 0.03 |
| | 392 | 0.029 | 52.6 | | | | | |
| | 392 | 0.029 | 51.4 | | | | | |
| | 496 | 0.037 | 55.8 ^a | | | | | |
| | 507 | 0.019 | 54.0 ^b | | | | | |
| | 775 | 0.047 | 57.9 | | | | | |
| 2 | 116 | 0.009 | 31.5 | | | | | |
| | 341 | 0.026 | 48.8 | | | | | |
| | 1100 | 0.084 | 58.8 | | | | | |
| | 1100 | 0.084 | ≤0.5 ^c | | | | | |
| 3 | 233 | 0.014 | 40.8 | 598 | 1.19 | 0.89 | 0.87 | 0.02 |
| | 660 | 0.040 | 55.0 | | | | | |
| | 905 | 0.054 | 54.0 | | | | | |
| 4 | 295 | 0.022 | 47.9 ^b | 573 | 0.96 | 0.47 | 0.50 | —0.03 |
| | 597 | 0.045 | 55.7 ^b | 795 | 1.32 | 0.85 | 0.88 | —0.03 |
| Terminal value ^d | | | 56.9 ± 1.6 ^e | | | | | ≤0.03 |
| Rate constant ^d | | | 5.8 ± 0.7 × 10 ⁻³ M ⁻¹ sec ⁻¹ | | | | | ... |

^a Reaction mixture was incubated at 68°C, 0.5 *M* phosphate buffer, equivalent to 0.12 *M* phosphate buffer, 60°C, and analyzed as usual in 0.12 *M* phosphate buffer, 60°C.

^b Assayed by hydroxyapatite at 50°C in 0.12 *M* phosphate buffer. This criterion is approximately the same as 60°C, 0.5 *M* phosphate buffer.

^c Treated with RNAase A to destroy DNA-RNA hybrids.

^d Errors listed represent ±1 standard deviation. Assumptions applied to the kinetic analysis are discussed in footnote *a* of Table 10, and in Experimental Procedures.

^e Since 90% of the ³H-mDNA is reactable (Fig. 14), the plateau value represents 63% of the reactable mDNA.

16a, the data from the four preparations are completely coherent. One preparation was isolated by EDTA rather than puromycin release, a change which was without any effect on either the rate or the terminal value of the hybridization reaction. Thus either procedure, when carried out on previously isolated polyosomes, suffices to separate the messenger from any remaining hnRNA contaminants. Figure 16a also shows that binding of the reacted gastrula mRNA-mDNA hybrids to hydroxyapatite is totally abolished by the low-salt RNAase treatment. All of the duplex scored is thus mRNA-DNA hybrid. No additional

hybrids were formed when the reaction temperature was increased to 68°C or the assay temperature was lowered to 50°C, indicating that the amount or rate of the reaction is not dependent on the conditions we have used. We conclude from these experiments that the terminal value of the gastrula mRNA-mDNA reaction is constant for the various mRNA preparations examined, is not criterion limited, and represents only mRNA-single-copy DNA hybrids. The fraction of the ³H-mDNA hybridized by gastrula mRNA, 56.9% (63% of reactable ³H-mDNA), is therefore taken to be the sequence complexity of the gastrula

message, 17×10^6 nucleotides (Galau *et al.*, 1974). Terminal reaction values of gastrula mDNA with any heterologous RNA will thus provide a direct measurement of the complexity of those sequences found both in the gastrula message and in the heterologous RNA.

Figure 16b shows the absence of detectable reaction between the null mDNA and the gastrula mRNA. As described in the previous section, these reaction mixtures were divided into equal aliquots, and one aliquot was used to measure RNA-DNA hybrids plus DNA-DNA duplexes, while the other was analyzed for DNA-DNA duplexes. The difference represents the fraction of gastrula null mDNA in RNA-DNA hybrid. However, Fig. 16b and Table 11 show that essentially no mRNA-DNA duplex existed in these samples. Various gastrula mRNA preparations gave values ranging from -0.03% to $+0.03\%$ for the amount of hybrid formed. This result shows that the structural gene sequences whose transcripts are present in the gastrula have been successfully removed during the preparation of null

mDNA. The null mDNA has excellent reactivity with DNA, as demonstrated in Fig. 14, and it is shown below that the null mDNA reacts well with RNAs from sources other than gastrula. In the experiments which follow, the absolute complexity represented by heterologous mRNA-null mDNA reactions is calculated from the reactivity of the null mDNA with unfractionated DNA, measured as in Fig. 14 at 86%.

Reaction of Gastrula mDNA and Null mDNA with Adult Nonreproductive Tissue mRNAs

Messenger RNA preparations were derived from three nonreproductive tissues of adult sea urchins as described in Experimental Procedures. These were intestine (excluding the esophageal region), coelomocytes, and tubefeet. Reactions of the adult tissue mRNAs with gastrula mDNA and null mDNA are shown in Fig. 17, and the data from individual reactions, plus the results of least-squares analyses, are listed in Table 12. The reaction of gastrula mDNA

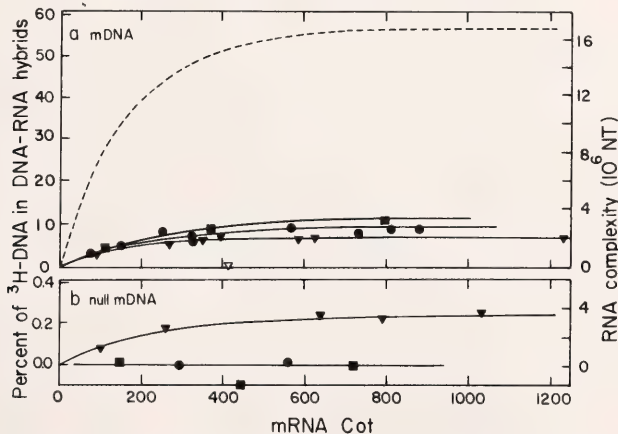


Fig. 17. Hybridization of gastrula mDNA and null mDNA with adult nonreproductive tissue mRNAs. The dashed line of 17a is the hybridization reaction of gastrula mRNA with gastrula mDNA from Fig. 16. The solid lines of 17a and 17b, where detectable hybridization is observed, are least-squares fits of pseudo-first-order hybridization reactions, assuming in each case that the ordinate intercept is zero. Data and parameters obtained from these fits are shown in Table 12. Intestine mRNA (filled triangles), tubefoot mRNA (filled circles) and coelomocyte mRNA (filled squares). ^3H -DNA binding to hydroxyapatite after RNAase treatment of intestine mRNA-mDNA hybrid (open triangle).

TABLE 12. Hybridization of Gastrula mRNA and Null mRNA with Adult Nonreproductive Tissue mRNAs^a

| Adult Tissue | mRNA Preparation | mDNA | | | | Null mDNA | | | | | Total Com-plexity (10 ⁶ NT) |
|---------------------------------|------------------|-----------------|--------|--|----------------------|-----------------|----------------------|---------|---|-----------|--|
| | | C _{ot} | | Com-plexity ^b (10 ⁶ NT) | 3H-DNA in Duplex (%) | C _{ot} | 3H-DNA in Duplex (%) | | Com-plexity ^c (10 ⁶ NT) | | |
| | | RNA | 3H-DNA | | | | DNA | DNA-RNA | | | |
| | | | | | | | | | | RNA | |
| Intestine | 1 | 88 | 0.006 | 2.9 | | 99 | 0.33 | 0.39 | 0.31 | 0.08 | |
| | | 263 | 0.017 | 5.4 | | 640 | 2.10 | 0.70 | 0.46 | 0.24 | |
| | | 405 | 0.026 | ≤1.2 ^a | | 1027 | 3.40 | 0.90 | 0.64 | 0.26 | |
| | | 621 | 0.041 | 7.0 | | | | | | | |
| | | 1230 | 0.080 | 6.0 | | | | | | | |
| 2 | | 389 | 0.039 | 7.4 ^e | | 255 | 1.70 | 0.71 | 0.53 | 0.18 | |
| | | 583 | 0.058 | 6.3 | | 788 | 2.63 | 0.81 | 0.58 | 0.23 | |
| 3 | | 325 | 0.008 | 6.2 | | | | | | | |
| | | 325 | 0.008 | 5.2 ^f | | | | | | | |
| Terminal value Rate constant | | | | 7.2 ± 0.4 | | 2.1 ± 0.1 | | | | | 5.8 ± 0.2 |
| | | | | 6.5 ± 1.8 × 10 ⁻³ M ⁻¹ sec ⁻¹ | | | | | 0.26 ± 0.01 | 3.7 ± 0.1 | |
| Tubefoot | 1 | | | | | | | | | | 4.4 ± 0.8 × 10 ⁻³ M ⁻¹ sec ⁻¹ |
| | | 130 | 0.025 | 5.0 | | | | | | | |
| | | 322 | 0.061 | 7.5 | | | | | | | |
| | | 730 | 0.138 | 8.1 | | | | | | | |
| | | 880 | 0.166 | 9.0 | | | | | | | |
| 2 | | 77 | 0.015 | 3.5 | | | | | | | |
| | | 565 | 0.107 | 9.6 | | | | | | | |
| 3 | | 250 | 0.019 | 8.5 | | | | | | | |
| | | 329 | 0.049 | 5.8 | | | | | | | |
| 4 | | 813 | 0.044 | 9.1 | | | | | | | |
| | | | | 9.3 ± 0.7 | | 2.7 ± 0.2 | | | | | |
| Terminal value Rate constant | | | | 5.3 ± 1.5 × 10 ⁻³ M ⁻¹ sec ⁻¹ | | | | | | | 0-0.4 |
| | | | | | | | | | | | 2.5-3.3 |

with its homologous mRNA, from Fig. 16, is indicated by the dashed line in Fig. 17a. It is immediately evident that only a small fraction of the mRNA sequences present on the gastrula polyosomes is represented in the messenger RNA populations of these adult tissues. Thus Table 12 shows that the complexities of the coelomocyte, tubefoot, and intestine mRNAs which react with gastrula mDNA are $3.5 \pm 0.4 \times 10^6$ nucleotides, representing 21% of the gastrula mRNA sequences; $2.7 \pm 0.2 \times 10^6$ nucleotides, representing 16% of the gastrula mRNA sequences; and $2.1 \pm 0.1 \times 10^6$ nucleotides, representing 12% of the gastrula mRNA sequences, respectively. To ensure that the relatively low amount of reaction with the adult tissue RNAs is due to RNA-DNA hybridization rather than to reaction between mDNA and cellular DNA which could have contaminated the RNA preparations, one reaction mixture was analyzed after low-salt RNAase treatment, which destroys RNA-DNA hybrids. Thus, in the case of an intestine mRNA-mDNA reaction, the amount of ^3H -mDNA present in duplex is reduced by this RNAase treatment from about 7% to $\leq 1.2\%$ (Table 12).

The small differences in extent of reaction among the mRNAs of the three tissues appear to be reproducible. Three different intestine mRNA preparations give the same extent of reaction, and this is also the case with four different preparations of tubefoot mRNA (Fig. 17; Table 12). An additional control experiment is also displayed in Table 12. The purpose of this was to test the possibility that the relatively low saturation values were caused by degradation of either mRNA or mDNA during the course of the reaction. A mixture containing intestine mRNA and the gastrula mDNA was reacted to mRNA C_0t 325, then heat-denatured and reincubated to C_0t 325. If a significant fraction of the reactable mRNA or mDNA had been destroyed during the first incubation, far less hybrid would have

formed the second time. Instead, about the same hybrid content was measured in the reincubated sample, i.e., 5.2% of the mDNA on the second reaction, compared to 6.2% in the control at C_0t 325.

Since the extent of these mDNA reactions was relatively low, precise determination of the hybridization kinetics would have been difficult to achieve as well as costly in mDNA. The experiments of Fig. 17 were mainly intended to measure the plateau values. If we make the reasonable assumption of a single kinetic component beginning at zero hybrid formation, as discussed above, the kinetics of these mDNA reactions all appear similar. The best-fit rate constants fall within a factor of 1.6 of the rate constant for the gastrula mRNA-mDNA reaction illustrated in Fig. 16a, and the rate of the intestine mRNA-mDNA reaction is almost exactly the same as that of the intestine mRNA-single-copy DNA reaction (Table 10). As stated above, this implies that the complex class is a minor fraction of the total message in all of the adult tissues studied here.

The complexities listed in Table 12 for the adult tissue messenger RNAs which hybridize with mDNA show that this set of sequences includes $1.5\text{--}3 \times 10^3$ diverse messengers. To determine whether the sequences reacting with mDNA are the same in all three tissues, combinations of the various adult mRNAs were reacted with mDNA. If the sequences shared with gastrula were a distinct or partially distinct set in each adult tissue, an increase in the amount of gastrula mDNA reacted would be observed when the mRNAs are mixed. Three experiments of this kind are shown in Table 13. In Experiment 1, where intestine and tubefoot mRNA are combined, about 16.5% of the gastrula ^3H -mDNA would be hybridized at termination if the sequences are distinct, while about 9.3% of the mDNA would be hybridized if the intestine mRNA sequences are a subset of the tubefoot mRNA sequences. The observed value is

TABLE 13. Hybridization of Gastrula mRNA with Combinations of Adult Tissue mRNAs*

| Experiment | mRNA in Mixture | mRNA Preparation | <i>C_{ot}</i> | | ³ H-mDNA in Hybrid (%) |
|------------|--------------------|---------------------|-----------------------|--------------------|--------------------------------------|
| | | | RNA | ³ H-DNA | |
| 1 | Intestine | 2 | 376 | | |
| | Tubefoot | 4 | 275 | 0.021 | 8.8 |
| 2 | Intestine | 3 | 335 | | |
| | Coelomocyte | 1 | 335 | 0.052 | 10.7 |
| 3 | Intestine | 3 | 389 | | |
| | Tubefoot | 3 + 4 | 282 | | |
| | Coelomocyte | 2 | 389 | 0.027 | 8.9 |

* Terminal values for hybridization with mRNA of these mRNA preparations are intestine, 7.2 ± 0.4%; coelomocyte, 11.8 ± 1.3%; tubefoot, 9.3 ± 0.7%.

8.8%, demonstrating that the same sequences shared by intestine with gastrula are shared by tubefoot as well. Similar results are obtained with intestine and coelomocyte mRNAs. Complete additivity of these sequence sets would result in hybridization of 19% of the mRNA at termination, while if the intestine sequences were a subset of the coelomocyte sequence set, about 11.8% of the mRNA would be hybridized. The value obtained is 10.7%. A triple mixture of all three adult mRNAs yields the same conclusion. Thus the experiments of Table 13 show that within the limits of detection the same subset of gastrula polysomal mRNA sequences is present in all three adult tissues. We conclude that there is a class of about 1000–1500 messenger RNAs that is common to all of these very distinct cell populations.

Hybridization of the adult tissue mRNAs with gastrula null mRNA is shown in Fig. 17b. The null mRNA appears to react with intestine mRNA with the usual pseudo-first-order kinetics, to a terminal value representing a complexity of $3.7 \pm 0.1 \times 10^6$ nucleotides (Table 12). This is the complexity of those mRNA sequences which are not present on the gastrula polysomes. The total complexity of intestine mRNA is thus about $5.8 \pm 0.2 \times 10^6$ nucleotides (Table 12). The most important conclusion is that about 36% of the messenger RNA species of the intestine cell

polysomes are also found in gastrula polysomes, while the other 64% are not. We note that the total complexity determined from the mRNA and null mRNA reactions is in excellent agreement with that obtained by using unfractionated single-copy ³H-DNA, as shown in Fig. 15 and Table 10. Those experiments indicated a total complexity of $6.0 \pm 0.2 \times 10^6$ nucleotides for intestine mRNA. Since the rate of the null mRNA reaction with intestine mRNA is close to that calculated in Fig. 16 for the reaction of mRNA with this message preparation, the sequences not shared with gastrula are present in roughly the same number per cell as those which are shared with gastrula.

No significant reaction between the gastrula null mRNA and either coelomocyte or tubefoot mRNAs could be detected. However, the sensitivity of these reactions is limited in the lower range by the need to subtract DNA-DNA duplex from total duplex. Thus both the tubefoot and coelomocyte could include a relatively small set of mRNAs other than those present on gastrula polysomes. A rough estimate of the maximal mRNA complexity which could have escaped detection in the null mRNA experiments (see Table 12) is about 1.4×10^6 nucleotides for the coelomocyte reactions and about 0.4×10^6 nucleotides for the tubefoot reactions. Probably the accuracy is better than these estimates.

These values, of course, might represent over 1000 distinct messenger RNAs, although when the experiments were carried out the values amounted to less than 0.1% of the total ^3H -null mRNA. In any case, it can be concluded that the set of messenger RNAs shared with gastrula by all three adult nonreproductive tissues represents a significant fraction of the set of structural genes active in these tissues. For the intestine this fraction is about one third, and for the tube-feet and coelomocytes, at least three fourths.

Reaction of Gastrula mRNA and Null mRNA with Mature Oocyte RNA and Adult Ovary mRNA

Polysomes were extracted from minced whole sea urchin ovaries after removal of the mature oocytes. A significant number of immature oocytes remained in the preparation, and an unknown fraction of the polysomes derived from these cells. Reactions of the ovary mRNA with gastrula mRNA and null mRNA are shown in Fig. 18, and the data from these experiments are listed in Table 14. The hybridization kinetics for both the mRNA (Fig. 18a) and the null mRNA (Fig. 18b) reactions with ovary polysomal mRNA are similar to those observed with gastrula mRNA. Table 14 lists the rate constant for the ovary mRNA-mDNA reaction as about $6.3 \times 10^{-3} \text{ M}^{-1} \text{ sec}^{-1}$ and that for the null mRNA reaction as about $3.1 \times 10^{-3} \text{ M}^{-1} \text{ sec}^{-1}$, which can be compared to $5.8 \times 10^{-3} \text{ M}^{-1} \text{ sec}^{-1}$ for the gastrula mRNA-mDNA reaction (Table 11). Thus, like the gastrula, the ovary clearly includes a complex set of messages. The amount of hybridization with mRNA is about 80% of that obtained with the gastrula mRNA (dashed line in Fig. 18a). There is evidently a large overlap between the set of mRNA sequences present on the ovary polysomes and the set present on the polysomes of the gastrula. However, these mRNA populations are clearly distinct, both quantitatively and

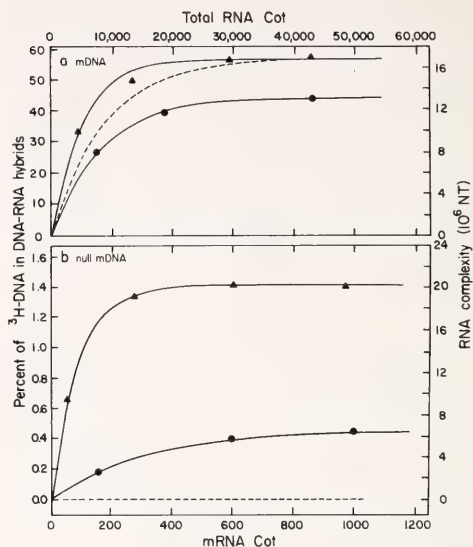


Fig. 18. Hybridization of gastrula mRNA and null mRNA with total oocyte RNA and ovary mRNA. The data presented here are listed in Table 14. The dashed lines of 18a and 18b are the hybridization reaction of gastrula mRNA with gastrula mRNA and null mRNA, respectively, from Fig. 16. The solid lines of 18a and 18b are least-squares fits of pseudo-first-order hybridization reactions, assuming an ordinate intercept of zero for each case. Data and parameters obtained from these fits are shown in Table 14. Total oocyte RNA, (filled triangles); ovary mRNA, (filled circles).

qualitatively. About 20% of the gastrula mRNA sequences are not present on the ovary polysomes, and Fig. 18b shows that a relatively large set of messenger RNAs that is absent from gastrula polysomes exists in the ovary. The complexity of this sequence set is $6.7 \pm 0.1 \times 10^6$ nucleotides. Since the complexity of the sequences shared with gastrula is $13 \pm 1 \times 10^6$ nucleotides (Table 14), the total complexity of ovary polysomal message is around 20×10^6 nucleotides. This is about 120% of the complexity of the gastrula message set, and thus the ovary polysomes include as many as $1.2\text{--}1.7 \times 10^4$ diverse messenger RNA species. The complexity of the ovary messenger RNA population is manifold greater than that of the adult nonrepro-

TABLE 14. Hybridization of Gastrula mRNA and Null mRNA with Ovary mRNA and Oocyte RNA*

| mDNA | | | | | Null mRNA | | | | | | |
|------------------|-------------|------------------------------------|----------------------------------|--|----------------------------------|--------------------------|----------------------|----------------------|----------------------|--|-----------|
| RNA | Preparation | C ₀ t | | 3H-DNA in Hybrid (%) | Com-plexity (10 ⁶ NT) | 3H-DNA in Duplex (%) | | | | | |
| | | RNA | 3H-DNA | | | C ₀ t | | | | | |
| | | | | | | RNA | 3H-DNA | Total | DNA-DNA | DNA-RNA | |
| Ovary mRNA | 1 | 144 376 855 | 0.011 0.029 0.064 | 2.69 40.5 44.9 | | 160 600 1015 | 0.80 3.00 5.07 | 1.04 1.94 2.36 | 0.86 1.54 1.91 | 0.18 0.40 0.45 | |
| Terminal value | | | | 45.0 ± 2.9 | 13 ± 1 | | | | | 0.47 ± 0.01 | 20 ± 1 |
| Rate constant | | | | 6.3 ± 0.2 × 10 ⁻³ M ⁻¹ sec ⁻¹ | | | | | | 3.1 ± 0.2 × 10 ⁻³ M ⁻¹ sec ⁻¹ | 6.7 ± 0.1 |
| Oocyte total RNA | 1 | 4000 13,000 29,000 42,500 | 0.002 0.007 0.006 0.021 | 34.0 50.2 57.5 59.3 | | 30000 | 3.00 | 2.05 | 0.64 | 1.41 | |
| | 2 | | | | | 2860 13,600 48,140 | 0.05 0.25 0.88 | 0.86 2.06 2.95 | 0.20 0.70 1.53 | 0.66 1.36 1.42 | |
| Terminal value | | | | 57.5 ± 2.0 | 17 ± 1 | | | | | 1.42 ± 0.01 | 20 ± 1 |
| Rate constant | | | | 2.1 ± 0.3 × 10 ⁻⁴ M ⁻¹ sec ⁻¹ | | | | | | 2.2 ± 0.1 × 10 ⁻⁴ M ⁻¹ sec ⁻¹ | 37 ± 1 |

* Errors listed represent ±1 standard deviation. Assumptions applied to kinetic analysis are discussed in footnote a of Table 10 and Experimental Procedures. Complexities are calculated as described in footnotes b and c of Table 12.

ductive tissues examined in the preceding experiments.

The mature sea urchin oocyte contains few polysomes (Epel, 1967; Infante and Nemer, 1967). Much evidence demonstrates that the sea urchin oocyte contains large amounts of maternal message that is translated following fertilization but in mature oocytes is not loaded on polysomes. The data presented in Fig. 18 and Table 14 represent the reactions of gastrula mDNA and null mDNA with the *total* oocyte RNA, and a priori it cannot be stated what fraction of this RNA is maternal message. The upper abscissa in Fig. 18 is the total RNA C_{ot} , as in Fig. 15. A surprising and significant result shown in Fig. 18a and Table 14 is that all of the mRNA sequences of the gastrula polysomes are already present in mature oocyte RNA. That is, as much gastrula mDNA reacts with mature oocyte RNA as with gastrula mRNA. The reaction with gastrula null mDNA shown in Fig. 18b demonstrates the presence of a large additional set of RNA sequences in the oocyte. Their complexity is measured at $20 \pm 1 \times 10^6$ nucleotides, yielding a total complexity for this RNA of about $37 \pm 1 \times 10^6$ nucleotides. This value conforms well with the oocyte RNA complexity measured with the total single-copy ^3H -DNA tracer in the experiments shown in Fig. 15, where a complexity of $37 \pm 4 \times 10^6$ nucleotides was found. It is clear that the total oocyte RNA is significantly different from the ovarian messenger RNA population, both in total complexity and in the specific sets of sequences present. The overall complexity of the oocyte RNA far exceeds that of any of the mRNA preparations studied in this work.

Since 45% of the oocyte RNA sequence set reacts with mDNA, we may conclude that these are structural gene transcripts, either maternal messenger RNAs or the immediate precursors thereof. An argument that the remaining 55% of the set of complex oocyte RNAs may also be stored message can

be derived from the kinetics of the null mDNA-oocyte RNA reaction. Table 14 shows that according to the least-squares fits the rate of this reaction ($2.2 \times 10^{-4} M^{-1} \text{ sec}^{-1}$) is the same as that of the mDNA reaction ($2.1 \times 10^{-4} M^{-1} \text{ sec}^{-1}$). Thus the RNA molecules reacting with the null mDNA are present about the same number of times per oocyte as are the maternal message sequences reacting with mDNA. An additional point is that the frequency of occurrence of these RNA molecules is only slightly larger than the frequency of occurrence of complex mRNAs in the gastrula. Approximately 1% of the total oocyte RNA drives the hybridization reactions, while 0.1% of the total RNA of the gastrula reacts with the mDNA. The complexity of the oocyte RNA is about twice that of the gastrula mRNA. Therefore the number of oocyte RNA molecules representing each mDNA sequence is only five times the number of copies of each sequence represented in the gastrula polysomes.

Reaction of Gastrula mDNA and Null mDNA with the mRNAs of Other Embryonic Stages

Polysomal mRNAs derived from mesenchyme blastulae and plutei were reacted with gastrula mDNA and null mDNA. At the stages used, the blastulae contain about 450 cells and the plutei about 1000–1500 cells, while the gastrulae contain 600 cells. In addition we studied mRNAs extracted from a developmentally abnormal form well known in sea urchin embryos, the exogastrula (Çzihak, 1971). The hybridization reactions are illustrated in Fig. 19 and the data obtained in these experiments are listed in Table 15. All the reactions display similar kinetics (Fig. 19), and the values of the rate constants shown in Table 15 indicate that the concentrations of the complex mRNA sequences are about the same for all the embryonic stages studied as for the gastrula.

Figure 19a shows that about 70% of

the mRNA sequences found in the gastrula polysomes are also present on blastula polysomes. These mRNA sequences have a complexity of $12 \pm 1 \times 10^6$ nucleotides (Table 15). The blastulae from which the mRNA was isolated are only 12 hr earlier in development than the early gastrulae used to prepare the mDNA. Nevertheless, all three blastula mRNA preparations, irrespective of the methods of extraction (see Experimental Procedures), display the same qualitative distinction from gastrula mRNA. A real difference thus exists between the mRNA populations of these developmental stages: Some 30% of the gastrula message set is absent from the blastula polysomes. This distinction is further demonstrated in the hybridization reactions of blastula mRNA with gastrula null mDNA (Fig. 19b, Table 15). The blastula contains a set of mRNAs not present on gastrula

polysomes, the complexity of which is $15 \pm 1 \times 10^6$ nucleotides. These sequences must be degraded by the time gastrulation occurs. The total sequence complexity of the blastula mRNA is $27 \pm 1 \times 10^6$ nucleotides, or about 160% of the complexity found in gastrula. It is not yet clear whether the additional mRNA sequences found in the blastula are a subset of those stored in the mature oocyte.

A different picture derives from the experiments with pluteus mRNA shown in Fig. 19. About 82% of the gastrula mRNA sequences are still present on the pluteus polysomes 54 hr later. The complexity of these shared sequences is $14 \pm 1 \times 10^6$ nucleotides (Table 15). However, few additional sequences are represented in pluteus mRNA, since no null mDNA reaction can be detected (see Fig. 19b). In this case we estimate that the largest amount of null mDNA reaction that could have escaped detection is equivalent to a complexity of only 0.6×10^6 nucleotides. The total sequence complexity of the pluteus mRNA thus cannot be very much greater than 15×10^6 nucleotides. These results mean that virtually all of the pluteus mRNA sequences must already be present on the gastrula polysomes. Furthermore, these sequences are apparently all represented in the RNA of the mature oocyte, since this is true of the gastrula mRNA sequences. Figure 19 and Table 15 also show that the overall complexity of the exogastrula mRNA is about 14×10^6 nucleotides, or 82% of the gastrular mRNA complexity. Few additional mRNA sequences, if any, are present in this aberrant embryo form since there is no detectable null mDNA reaction (Figure 19b). Therefore, the exogastrula appears to lack a set of mRNAs present in normal gastrulae, the complexity of which is about 3×10^6 nucleotides. This would imply that the absence of as many as 2000 species of messenger RNA is correlated with the failure to form a normal archenteron and the associated developmental abnormalities.

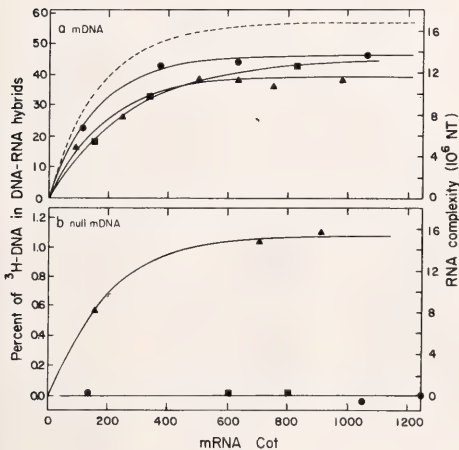


Fig. 19. Hybridization of gastrula mDNA and null mDNA with other embryo mRNAs. The dashed line of 19a is the hybridization reaction of gastrula mRNA with gastrula mDNA from Fig. 16. The solid lines of 18a and 18b are least-squares fits of pseudo-first-order hybridization reactions, assuming in each case an ordinate intercept of zero. Data and parameters obtained from these fits are shown in Table 15. Exogastrula mRNA, filled circles; blastula mRNA, filled triangles; and pluteus mRNA, filled squares.

TABLE 15. Hybridization of Gastrula mDNA and Null mDNA with Other Embryo mRNAs^a

| Embryo mRNA | Preparation | mDNA | | | Null mDNA | | | | | | |
|---------------------------------|-------------|------------------|-------------------|---|------------------|---|---------------------|-------------|---------|--|--|
| | | C ₀ t | | Com- plexity (10 ⁶ NT) | C ₀ t | | H-DNA in Duplex (%) | | | | |
| | | RNA | H-DNA | | RNA | H-DNA | Total | DNA- DNA | DNA-RNA | | |
| | | | | | | | | | | | |
| Blastula | 1 | 505 | 0.008 | 39.8 | 155 | 0.08 | 1.11 | 0.51 | 0.60 | | |
| | | | | | | | | | | | |
| | 2 | 92 | 0.003 | 16.2 | 706 | 0.73 | 1.30 | 0.29 | 1.01 | | |
| | | | | | | | | | | | |
| | | | | | | | | | | | |
| Terminal value Rate constant | 3 | 752 | 0.011 | 36.8 | 912 | 0.49 | 1.82 | 0.74 | 1.08 | | |
| | | | | | | | | | | | |
| | 1 | 155 | 0.012 | 39.3 ± 1.7 | 600 | 3.00 | 0.67 | 0.64 | 0.03 | | |
| | | | | | | | | | | | |
| | | | | | | | | | | | |
| Pluteus | 1 | 338 | 0.025 | 32.6 | 800 | 1.33 | 0.26 | 0.22 | 0.04 | | |
| | | | | | | | | | | | |
| | 1520 | 0.049 | ≤0.5 ^c | 1.06 ± 0.03 | 15 ± 1 | 5.2 ± 0.7 × 10 ⁻³ M ⁻¹ sec ⁻¹ | 0.03 | 0.04 | | | |
| | | | | | | | | | | | |
| | | | | | | | | | | | |
| Terminal value Rate constant | 1 | 155 | 0.012 | 18.3 | 600 | 3.00 | 0.67 | 0.64 | 0.03 | | |
| | | | | | | | | | | | |
| | 1 | 830 | 0.033 | 43.3 | 1520 | 0.049 | ≤0.5 ^c | 1.06 ± 0.03 | 15 ± 1 | | |
| | | | | | | | | | | | |
| | | | | | | | | | | | |
| Exogastrula | 1, 2, 3 | 114 | 0.002 | 22.5 | 134 | 0.27 | 0.13 | 0.11 | 0.02 | | |
| | | | | | | | | | | | |
| | 1, 2, 3 | 371 | 0.028 | 43.2 | 1050 | 2.10 | 0.52 | 0.54 | -0.02 | | |
| | | | | | | | | | | | |
| | | | | | | | | | | | |
| Terminal value Rate constant | 1, 2, 3 | 630 | 0.010 | 44.4 | 1250 | 2.52 | 0.73 | 0.72 | 0.01 | | |
| | | | | | | | | | | | |
| | 1, 2, 3 | 1063 | 0.025 | 47.0 | 134 | 0.27 | 0.13 | 0.11 | 0.02 | | |
| | | | | | | | | | | | |
| | | | | | | | | | | | |
| Terminal value Rate constant | 1, 2, 3 | 114 | 0.002 | 22.5 | 134 | 0.27 | 0.13 | 0.11 | 0.02 | | |
| | | | | | | | | | | | |
| | 1, 2, 3 | 371 | 0.028 | 43.2 | 1050 | 2.10 | 0.52 | 0.54 | -0.02 | | |
| | | | | | | | | | | | |
| | | | | | | | | | | | |
| Terminal value Rate constant | 1, 2, 3 | 630 | 0.010 | 44.4 | 1250 | 2.52 | 0.73 | 0.72 | 0.01 | | |
| | | | | | | | | | | | |
| | 1, 2, 3 | 1063 | 0.025 | 47.0 | 134 | 0.27 | 0.13 | 0.11 | 0.02 | | |
| | | | | | | | | | | | |
| | | | | | | | | | | | |
| Terminal value Rate constant | 1, 2, 3 | 114 | 0.002 | 22.5 | 134 | 0.27 | 0.13 | 0.11 | 0.02 | | |
| | | | | | | | | | | | |
| | 1, 2, 3 | 371 | 0.028 | 43.2 | 1050 | 2.10 | 0.52 | 0.54 | -0.02 | | |
| | | | | | | | | | | | |
| | | | | | | | | | | | |
| Terminal value Rate constant | 1, 2, 3 | 630 | 0.010 | 44.4 | 1250 | 2.52 | 0.73 | 0.72 | 0.01 | | |
| | | | | | | | | | | | |
| | 1, 2, 3 | 1063 | 0.025 | 47.0 | 134 | 0.27 | 0.13 | 0.11 | 0.02 | | |
| | | | | | | | | | | | |
| | | | | | | | | | | | |
| Terminal value Rate constant | 1, 2, 3 | 114 | 0.002 | 22.5 | 134 | 0.27 | 0.13 | 0.11 | 0.02 | | |
| | | | | | | | | | | | |
| | 1, 2, 3 | 371 | 0.028 | 43.2 | 1050 | 2.10 | 0.52 | 0.54 | -0.02 | | |
| | | | | | | | | | | | |
| | | | | | | | | | | | |
| Terminal value Rate constant | 1, 2, 3 | 630 | 0.010 | 44.4 | 1250 | 2.52 | 0.73 | 0.72 | 0.01 | | |
| | | | | | | | | | | | |
| | 1, 2, 3 | 1063 | 0.025 | 47.0 | 134 | 0.27 | 0.13 | 0.11 | 0.02 | | |
| | | | | | | | | | | | |
| | | | | | | | | | | | |
| Terminal value Rate constant | 1, 2, 3 | 114 | 0.002 | 22.5 | 134 | 0.27 | 0.13 | 0.11 | 0.02 | | |
| | | | | | | | | | | | |
| | 1, 2, 3 | 371 | 0.028 | 43.2 | 1050 | 2.10 | 0.52 | 0.54 | -0.02 | | |
| | | | | | | | | | | | |
| | | | | | | | | | | | |
| Terminal value Rate constant | 1, 2, 3 | 630 | 0.010 | 44.4 | 1250 | 2.52 | 0.73 | 0.72 | 0.01 | | |
| | | | | | | | | | | | |
| | 1, 2, 3 | 1063 | 0.025 | 47.0 | 134 | 0.27 | 0.13 | 0.11 | 0.02 | | |
| | | | | | | | | | | | |
| | | | | | | | | | | | |
| Terminal value Rate constant | 1, 2, 3 | 114 | 0.002 | 22.5 | 134 | 0.27 | 0.13 | 0.11 | 0.02 | | |
| | | | | | | | | | | | |
| | 1, 2, 3 | 371 | 0.028 | 43.2 | 1050 | 2.10 | 0.52 | 0.54 | -0.02 | | |
| | | | | | | | | | | | |
| | | | | | | | | | | | |
| Terminal value Rate constant | 1, 2, 3 | 630 | 0.010 | 44.4 | 1250 | 2.52 | 0.73 | 0.72 | 0.01 | | |
| | | | | | | | | | | | |
| | 1, 2, 3 | 1063 | 0.025 | 47.0 | 134 | 0.27 | 0.13 | 0.11 | 0.02 | | |
| | | | | | | | | | | | |
| | | | | | | | | | | | |
| Terminal value Rate constant | 1, 2, 3 | 114 | 0.002 | 22.5 | 134 | 0.27 | 0.13 | 0.11 | 0.02 | | |
| | | | | | | | | | | | |
| | 1, 2, 3 | 371 | 0.028 | 43.2 | 1050 | 2.10 | 0.52 | 0.54 | -0.02 | | |
| | | | | | | | | | | | |
| | | | | | | | | | | | |
| Terminal value Rate constant | 1, 2, 3 | 630 | 0.010 | 44.4 | 1250 | 2.52 | 0.73 | 0.72 | 0.01 | | |
| | | | | | | | | | | | |
| | 1, 2, 3 | 1063 | 0.025 | 47.0 | 134 | 0.27 | 0.13 | 0.11 | 0.02 | | |
| | | | | | | | | | | | |
| | | | | | | | | | | | |
| Terminal value Rate constant | 1, 2, 3 | 114 | 0.002 | 22.5 | 134 | 0.27 | 0.13 | 0.11 | 0.02 | | |
| | | | | | | | | | | | |
| | 1, 2, 3 | 371 | 0.028 | 43.2 | 1050 | 2.10 | 0.52 | 0.54 | -0.02 | | |
| | | | | | | | | | | | |
| | | | | | | | | | | | |
| Terminal value Rate constant | 1, 2, 3 | 630 | 0.010 | 44.4 | 1250 | 2.52 | 0.73 | 0.72 | 0.01 | | |
| | | | | | | | | | | | |
| | 1, 2, 3 | 1063 | 0.025 | 47.0 | 134 | 0.27 | 0.13 | 0.11 | 0.02 | | |
| | | | | | | | | | | | |
| | | | | | | | | | | | |
| Terminal value Rate constant | 1, 2, 3 | 114 | 0.002 | 22.5 | 134 | 0.27 | 0.13 | 0.11 | 0.02 | | |
| | | | | | | | | | | | |
| | 1, 2, 3 | 371 | 0.028 | 43.2 | 1050 | 2.10 | 0.52 | 0.54 | -0.02 | | |
| | | | | | | | | | | | |
| | | | | | | | | | | | |
| Terminal value Rate constant | 1, 2, 3 | 630 | 0.010 | 44.4 | 1250 | 2.52 | 0.73 | 0.72 | 0.01 | | |
| | | | | | | | | | | | |
| | 1, 2, 3 | 1063 | 0.025 | 47.0 | 134 | 0.27 | 0.13 | 0.11 | 0.02 | | |
| | | | | | | | | | | | |
| | | | | | | | | | | | |
| Terminal value Rate constant | 1, 2, 3 | 114 | 0.002 | 22.5 | 134 | 0.27 | 0.13 | 0.11 | 0.02 | | |
| | | | | | | | | | | | |
| | 1, 2, 3 | 371 | 0.028 | 43.2 | 1050 | 2.10 | 0.52 | 0.54 | -0.02 | | |
| | | | | | | | | | | | |
| | | | | | | | | | | | |
| Terminal value Rate constant | 1, 2, 3 | 630 | 0.010 | 44.4 | 1250 | 2.52 | 0.73 | 0.72 | 0.01 | | |
| | | | | | | | | | | | |
| | 1, 2, 3 | 1063 | 0.025 | 47.0 | 134 | 0.27 | 0.13 | 0.11 | 0.02 | | |
| | | | | | | | | | | | |
| | | | | | | | | | | | |
| Terminal value Rate constant | 1, 2, 3 | 114 | 0.002 | 22.5 | 134 | 0.27 | 0.13 | 0.11 | 0.02 | | |
| | | | | | | | | | | | |
| | 1, 2, 3 | 371 | 0.028 | 43.2 | 1050 | 2.10 | 0.52 | 0.54 | -0.02 | | |
| | | | | | | | | | | | |
| | | | | | | | | | | | |
| Terminal value Rate constant | 1, 2, 3 | 630 | 0.010 | 44.4 | 1250 | 2.52 | 0.73 | 0.72 | 0.01 | | |
| | | | | | | | | | | | |
| | 1, 2, 3 | 1063 | 0.025 | 47.0 | 134 | 0.27 | 0.13 | 0.11 | 0.02 | | |
| | | | | | | | | | | | |
| | | | | | | | | | | | |
| Terminal value Rate constant | 1, 2, 3 | 114 | 0.002 | 22.5 | 134 | 0.27 | 0.13 | 0.11 | 0.02 | | |
| | | | | | | | | | | | |
| | 1, 2, 3 | 371 | 0.028 | 43.2 | 1050 | 2.10 | 0.52 | 0.54 | -0.02 | | |
| | | | | | | | | | | | |
| | | | | | | | | | | | |
| Terminal value Rate constant | 1, 2, 3 | 630 | 0.010 | 44.4 | 1250 | 2.52 | 0.73 | 0.72 | 0.01 | | |
| | | | | | | | | | | | |
| | 1, 2, 3 | 1063 | 0.025 | 47.0 | 134 | 0.27 | 0.13 | 0.11 | 0.02 | | |
| | | | | | | | | | | | |
| | | | | | | | | | | | |
| Terminal value Rate constant | 1, 2, 3 | 114 | 0.002 | 22.5 | 134 | 0.27 | 0.13 | 0.11 | 0.02 | | |
| | | | | | | | | | | | |
| | 1, 2, 3 | 371 | 0.028 | 43.2 | 1050 | 2.10 | 0.52 | 0.54 | -0.02 | | |
| | | | | | | | | | | | |
| | | | | | | | | | | | |
| Terminal value Rate constant | 1, 2, 3 | 630 | 0.010 | 44.4 | 1250 | 2.52 | 0.73 | 0.72 | 0.01 | | |
| | | | | | | | | | | | |
| | 1, 2, 3 | 1063 | 0.025 | 47.0 | 134 | 0.27 | 0.13 | 0.11 | 0.02 | | |
| | | | | | | | | | | | |
| | | | | | | | | | | | |
| Terminal value Rate constant | 1, 2, 3 | 114 | 0.002 | 22.5 | 134 | 0.27 | 0.13 | 0.11 | 0.02 | | |
| | | | | | | | | | | | |
| | 1, 2, 3 | 371 | 0.028 | 43.2 | 1050 | 2.10 | 0.52 | 0.54 | -0.02 | | |
| | | | | | | | | | | | |
| | | | | | | | | | | | |
| Terminal value Rate constant | 1, 2, 3 | 630 | 0.010 | 44.4 | 1250 | 2.52 | 0.73 | 0.72 | 0.01 | | |
| | | | | | | | | | | | |
| | 1, 2, 3 | 1063 | 0.025 | 47.0 | 134 | 0.27 | 0.13 | 0.11 | 0.02 | | |
| | | | | | | | | | | | |
| | | | | | | | | | | | |
| Terminal value Rate constant | 1, 2, 3 | 114 | 0.002 | 22.5 | 134 | 0.27 | 0.13 | 0.11 | 0.02 | | |
| | | | | | | | | | | | |
| | 1, 2, 3 | 371 | 0.028 | 43.2 | 1050 | 2.10 | 0.52 | 0.54 | -0.02 | | |
| | | | | | | | | | | | |
| | | | | | | | | | | | |
| Terminal value Rate constant | 1, 2, 3 | 630 | 0.010 | 44.4 | 1250 | 2.52 | 0.73 | 0.72 | 0.01 | | |
| | | | | | | | | | | | |
| | 1, 2, 3 | 1063 | 0.025 | 47.0 | 134 | 0.27 | 0.13 | 0.11 | 0.02 | | |
| | | | | | | | | | | | |
| | | | | | | | | | | | |
| Terminal value Rate constant | 1, 2, 3 | 114 | 0.002 | 22.5 | 134 | 0.27 | 0.13 | 0.11 | 0.02 | | |
| | | | | | | | | | | | |
| | 1, 2, 3 | 371 | 0.028 | 43.2 | 1050 | 2.10 | 0.52 | 0.54 | -0.02 | | |
| | | | | | | | | | | | |
| | | | | | | | | | | | |
| Terminal value Rate constant | 1, 2, 3 | 630 | 0.010 | 44.4 | 1250 | 2.52 | 0.73 | 0.72 | 0.01 | | |
| | | | | | | | | | | | |
| | 1, 2, 3 | 1063 | 0.025 | 47.0 | 134 | 0.27 | 0.13 | 0.11 | 0.02 | | |
| | | | | | | | | | | | |
| | | | | | | | | | | | |
| Terminal value Rate constant | 1, 2, 3 | 114 | 0.002 | 22.5 | 134 | 0.27 | 0.13 | 0.11 | 0.02 | | |
| | | | | | | | | | | | |
| | 1, 2, 3 | 371 | 0.028 | 43.2 | 1050 | 2.10 | 0.52 | 0.54 | -0.02 | | |
| | | | | | | | | | | | |
| | | | | | | | | | | | |
| Terminal value Rate constant | 1, 2, 3 | 630 | 0.010 | 44.4 | 1250 | 2.52 | 0.73 | 0.72 | 0.01 | | |
| | | | | | | | | | | | |
| | 1, 2, 3 | 1063 | 0.025 | 47.0 | 134 | 0.27 | 0.13 | 0.11 | 0.02 | | |
| | | | | | | | | | | | |
| | | | | | | | | | | | |
| Terminal value Rate constant | 1, 2, 3 | 114 | 0.002 | 22.5 | 134 | 0.27 | 0.13 | 0.11 | 0.02 | | |
| | | | | | | | | | | | |
| | 1, 2, 3 | 371 | 0.028 | 43.2 | 1050 | 2.10 | 0.52 | 0.54 | -0.02 | | |
| | | | | | | | | | | | |
| | | | | | | | | | | | |
| Terminal value Rate constant | 1, 2, 3 | 630 | 0.010 | 44.4 | 1250 | 2.52 | 0.73 | 0.72 | 0.01 | | |
| | | | | | | | | | | | |
| | 1, 2, 3 | 1063 | 0.025 | 47.0 | 134 | 0.27 | 0.13 | 0.11 | 0.02 | | |
| | | | | | | | | | | | |
| | | | | | | | | | | | |
| Terminal value Rate constant | 1, 2, 3 | 114 | 0.002 | 22.5 | 134 | 0.27 | 0.13 | 0.11 | 0.02 | | |
| | | | | | | | | | | | |
| | 1, 2, 3 | 371 | 0.028 | 43.2 | 1050 | 2.10 | 0.52 | 0.54 | -0.02 | | |
| | | | | | | | | | | | |
| | | | | | | | | | | | |
| Terminal value Rate constant | 1, 2, 3 | 630 | 0.010 | 44.4 | 1250 | 2.52 | 0.73 | 0.72 | 0.01 | | |
| | | | | | | | | | | | |
| | 1, 2, 3 | 1063 | 0.025 | 47.0 | 134 | 0.27 | 0.13 | 0.11 | 0.02 | | |
| | | | | | | | | | | | |
| | | | | | | | | | | | |
| Terminal value Rate constant | 1, 2, 3 | 114 | 0.002 | 22.5 | 134 | 0.27 | 0.13 | 0.11 | 0.02 | | |
| | | | | | | | | | | | |
| | 1, 2, 3 | 371 | 0.028 | 43.2 | 1050 | 2.10 | 0.52 | 0.54 | -0.02 | | |
| | | | | | | | | | | | |
| | | | | | | | | | | | |
| Terminal value Rate constant | 1, 2, 3 | 630 | 0.010 | 44.4 | 1250 | 2.52 | 0.73 | 0.72 | 0.01 | | |
| | | | | | | | | | | | |

*Unique Sets of Structural Genes
Expressed in Diverse Cell Types*

The measurements described provide quantitative comparisons of the sets of structural genes expressed in various states of differentiation. Though each set includes thousands of individual sequences, the fraction of the total single-copy sequence represented is only a small percentage of the total. This fact necessitated the use of two partially purified DNA fractions representing and excluding the active gene sequences of a reference mRNA population, that of gastrula. The excess mRNA hybridization reactions carried out with these DNA fractions have enabled us to measure distinctions in the patterns of structural gene expression with far greater resolution than in any previous studies. The results of the measurements are summarized in Fig. 20. Here the solid

portion of each bar shows the complexity of those structural gene sets represented in the mRNAs of various tissues and cell types which are also represented in gastrula mRNA. Similarly, the open portion of each bar gives the complexity of the structural gene sets represented in each tissue which are excluded from the gastrula gene set. The overall height of each bar indicates the total complexity of the mRNAs in each tissue. Complexity is expressed in three ways in Fig. 20. The left ordinate shows the total length of single-copy nucleotide sequence, and the two right ordinates show the percentage of gastrula mRNA complexity and the percentage of total single-copy sequence. Figure 20 shows clearly that each of the tissues we have investigated contains a different, though partially overlapping, set of structural gene transcripts. Before proceeding to a discussion of the biological implications

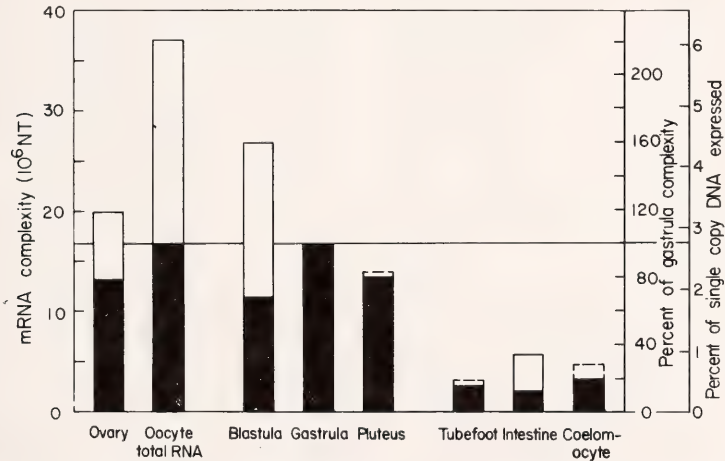


Fig. 20. Sets of structural genes active in sea urchin embryos and adult tissues. The solid portion of each bar indicates the amount of single-copy sequence shared between gastrula mRNA and the RNA preparations listed along the abscissa. These data are obtained from the mDNA reactions described in the text. The open portions show the amount of single-copy sequence present in the various RNAs studied but absent from gastrula mRNA. These data derive from the null mDNA reactions described in the text. Dashed lines indicate the maximum amount of null mDNA reaction which could have been present and escaped detection, in terms of complexity, for cases where no apparent null mDNA reaction was observed (see Tables 12 and 15). The total complexity of each RNA is indicated by the overall height of each bar. Complexity is calibrated in three ways along the three ordinates shown. From left to right these are: in nucleotides of single-copy sequence; as percentage of gastrula mRNA complexity; as percentage of total single-copy sequence.

of these data, however, we wish to consider the general significance of the messenger RNA subclass we have dealt with in this work.

Significance of the Complex Class of Messenger RNAs

As pointed out earlier in this paper our studies have necessarily focused on the complex class of mRNAs, since we are concerned with measuring the size and overlap of the active sets of structural genes. The complex class represents messages which may be present on the average as seldom as one copy per cell. The limit calculation yielding this low value is based on the experiments of Galau *et al.* (1974) with sea urchin gastrula mRNA and assumes that all 600 cells of the gastrula are perfectly equivalent in the sets of mRNA species present. Uncertainties in this calculation permit a lower limit estimate ranging up to five copies per cell. If, as is not unlikely in view of present results, the various embryonic anlagen contain partially distinct sets of complex class mRNAs, the number of occurrences per cell for many species of complex class messages could be greater. Nonetheless it is clear that the mRNAs driving the hybridization reactions described in this paper belong to a rare sequence class in which relatively few copies of each mRNA species are present per cell. The issue we wish to consider is whether this mRNA class is functionally significant. An alternative proposition might be that the complex mRNA class simply derives from "leakage" of repressed genes, similar to that known for inducible prokaryote systems in the repressed state.

Figure 20 shows that each state of differentiation investigated in the sea urchin is associated with a specific set of the complex mRNAs. These differ from each other by millions of nucleotides of sequence complexity, representing the transcripts of thousands of structural genes. Thus the putative "leakage" process would have to be tis-

sue- and cell-type specific. Since only a small fraction of the total single-copy sequence is represented in each mRNA set (Fig. 20), most of the single-copy DNA and, at least in some cases, most of the structural genes are repressed so effectively that their transcripts cannot be detected at all. We estimate that in the experiments presented in this work any significant number of additional polysomal mRNA sequences, if present at all, occur at least 2 orders of magnitude below the concentrations of the complex mRNA sequence class studied here. In other words, many DNA sequences, including structural gene sequences, are repressed in sea urchin cells to a far greater extent than are those represented by the complex class messages. This is, of course, true only with respect to the presence of their transcripts on cytoplasmic polysomes, as the data we discuss here do not concern nuclear RNAs. These considerations show that the mRNAs of the complex class are specifically selected, since they represent a highly restricted set of transcripts and are arranged in sets correlated with the functional state of the cell.

A further argument, and one which we find convincing, comes from examination of some known proteins of mammalian liver. Mouse liver is among the tissues in which a complex mRNA sequence class has been identified. From the data of Ryffel and McCarthy (1975) we calculate that there are an average of 20 copies of complex class mRNAs per cell. For a number of liver enzymes, sufficient information exists that by assuming typical rates of translation (see Kafatos, 1972), the approximate number of mRNAs needed to maintain the steady-state enzyme concentrations can be calculated. The data required are the amount of enzyme per cell, the rate of turnover of the enzyme, and the molecular weight of the enzyme subunits (Details of the calculations will be presented elsewhere [Galau, Ph.D. Thesis, 1976]). Some enzymes require large numbers of mRNAs for maintenance of their steady-

state concentrations. However, in a non-exhaustive search of the literature we have found several examples of enzymes whose function is clearly important to the liver in physiological terms but which appear to require for maintenance only 1–10 mRNA molecules per liver cell. Four such enzymes are acetyl CoA carboxylase, alanine aminotransferase, xanthine oxidase, and NAD glycohydrolase. It appears, therefore, that some complex class mRNAs play a functional role in liver. Although we cannot exclude the “leakage” hypothesis, the evidence summarized here appears to us to render it rather unlikely. Complex class messages are a ubiquitous feature of animal mRNA populations, since they have been identified in all the mRNA populations studied in somatic tissues. (See references.) Of course, by far the largest majority of active structural genes produce mRNAs that belong to the complex class. Our view at present is that these mRNAs play physiologically functional roles in differentiated cells. Regulation of their expression is therefore a basic aspect of cell differentiation.

Biological Significance of the mDNA and Null mDNA Hybridization Results

The number of structural genes needed for early development. To a first approximation our data cover one phase of the sea urchin life cycle, that extending from oogenesis to feeding pluteus (Fig. 20). The oocyte RNA may include most of the sequences in blastula message reacting with null mDNA, and we have shown here that the oocyte RNA includes all of the gastrula mRNA sequences. Thus, as a crude maximum estimate, the complexity of oocyte RNA approximates the structural gene information needed to program and carry out development from oogenesis to the feeding pluteus stage. This amounts to about 6% of the total single-copy sequence, some 37×10^6 nucleotides, or 20,000–30,000 diverse structural genes.

The concept of “housekeeping genes.” Our observations on the three adult non-

reproductive tissues provide an indication that the housekeeping gene concept may be a valid one. We find that gastrula, tubefoot, coelomocyte, and intestine all share a common subset of mRNAs. Housekeeping gene transcripts are supposed to be ubiquitous and obligatory in diverse cell types, and the shared subset of mRNAs demonstrated in the experiments of Table 13 so far conforms to this definition. According to our experiments such genes represent only about 0.3% of the single-copy DNA sequence. The number of such genes in the sea urchin genome is no more than 1000–1500.

Distinction between embryonic cells and adult nonreproductive tissues. The adult tissues we have studied consist of several different cell types, each present in significant concentration. In addition there may be rare cell types whose specific mRNA populations do not contribute significantly to the total complexities measured. Nonetheless, the structural gene sets active in the adult nonreproductive tissues are clearly severalfold smaller than those represented in reproductive cells and embryos. The complexity of the mRNA populations in these three adult nonreproductive tissues ranges from about 15% to 35% of that of gastrula mRNA. We cannot be certain that the measured complexities represent the true complexity of the mRNAs in the complete organ or tissue, e.g., the whole intestine, because of the unknown potential contribution of rare cell types. However, Fig. 17 shows that the amount of hybridization increases relatively little beyond RNA *C₀t* 400. Therefore there are few very rare sequences deriving from either rare cell types or infrequent transcription in major cell types. We conclude that there are differentiated adult tissue cell types, if not complete organs, which require less than about 5000 structural genes to operate. This statement refers to the usual circumstances of tissue maintenance and to messengers present at a frequency within 1–2 orders of magnitude of the typical

complex sequence class mRNAs. In comparison, the process of embryonic differentiation can be seen to be very expensive in terms of the number of structural genes and the number of complex class mRNA species required.

We can now take up the issue raised in the text. Figure 20 shows that it is unlikely that very small fractions of the active structural gene sets are responsible for the functional diversity of the various tissues. Generally the differences observed are quite large. For example, 56% of the mRNAs on the polyosomes of blastula stage embryos are distinct from those of gastrulae, and 44% are homologous. Similarly, 64% of the mRNAs of the intestine are distinct from those of gastrulae, and 36% are homologous. These differences amount to many thousands of individual structural genes whose transcripts are present at detectable levels in one set of cell types and are absent in another. Some adult nonreproductive tissues, such as coelomocytes and tubefeet, require a large fraction of their total structural gene activity as housekeeping genes. This is not the case for other adult tissues, e.g., intestine or ovary, and for differentiating embryos.

Relation between oocyte RNAs and embryo mRNAs. Among the most surprising and significant findings in this work is that virtually all of the polyosomal gastrula mRNA sequences are found to be represented in mature oocyte RNA. This claim has been made earlier (Whiteley *et al.*, 1966, 1970), but unfortunately these experiments are without relevance to most messenger RNA sequences, since nonrepetitive sequence transcripts could not have been detected. We show here as well that a large fraction of the gastrula message species are present in pluteus, blastula, and an abnormal form, the exogastrula. Each of the latter embryonic stages has a specific subset of the gastrula message set loaded on its polyosomes. A possible paradox is posed by these discoveries. It appears that the mass of the gastrula mRNA

can be accounted for by newly synthesized messages, while the oocyte RNA includes the complex class gastrula mRNA sequences and all subsets thereof. This statement follows from new measurements of mRNA content, turnover, and synthesis rates to be presented elsewhere (Galau, Britten, and Davidson, in preparation; see also Nemer, *et al.*, 1975; Nemer, 1975). However, the latter data refer to the bulk of the mRNA and not specifically to the complex message class. According to our results, sufficient RNAs of each of the complex class gastrula sequences are stored in the mature oocyte to supply the embryo polyosomes. Therefore, we cannot yet exclude the possibility that the complex mRNA sequences present on these polyosomes are all maternal messages, right up to the pluteus stage, while it is the prevalent message class that is newly transcribed. However, if it is found that complex class messages are synthesized and turn over with the same kinetics as the bulk of the mRNA, an interesting conclusion will follow. This is that the embryo inherits a program for structural gene transcription similar to that controlling transcription during oogenesis, as well as maternal messenger RNA molecules which are used early in development. The specific subsets of the gastrula mRNA set present in the pluteus, blastula, and exogastrula thus would represent stage specific modulations in the embryonic transcriptional program, rather than in the sets of preserved maternal messages being translated.

It is informative to compare the total complexity of blastula, gastrula, and pluteus mRNAs (Fig. 20). The diversity of the structural gene transcripts being translated in the embryo gradually decreases as development proceeds. Furthermore, little or no additional mRNA sequence is found in the pluteus, compared to gastrula. Therefore, many of the proteins needed to construct the much more complex structures of the pluteus must be synthesized during the gastrula stage or even earlier, and simi-

larly, proteins needed by gastrulae must be synthesized in all the pregastrula stages. These data suggest that there are important post-translational assembly mechanisms operating in embryonic morphogenesis.

Structural gene regulation. Our experiments provide an estimate of the dimensions of the process of structural gene regulation. It is clear that many thousands of structural genes are specifically required for the construction of the differentiating embryo. Thus large-scale changes in the sets of structural genes active must occur during development. An understanding of structural gene regulation requires an explanation of the coordinate activation of the many genes whose function is specifically required in differentiating cells.

Experimental Procedures

Growth of sea urchin embryos. Eggs of *Strongylocentrotus purpuratus* were collected, fertilized, and cultured at 15°C by standard methods (e.g., Smith *et al.*, 1974). The embryos were grown at $2-4 \times 10^4$ /ml in 30 units/ml penicillin G, 50 µg/ml streptomycin, with constant stirring and aeration. The developmental stages relevant to the experiments in this paper can be summarized briefly as follows: At 17–19 hr after fertilization the blastulae hatch and begin to swim. The mesenchyme blastulae from which the blastula mRNA used in these experiments is extracted are harvested at 24–25 hr. At this stage the embryos have well-defined primary mesenchyme cells. At 36 hr, the time at which gastrula mRNA was prepared, the embryos have initiated gastrulation, and skeletal formation has begun. Exogastrulae were obtained from cultures exposed to a contaminated air supply. The active airborne agent inducing exogastrulation is unknown, but the cultures were nearly homogeneous, classical exogastrulae at 50 hr. Exogastrula mRNA was extracted from such cultures at 36 hr. At this stage the embryos displayed regressive archenterons, a slightly enlarged oblate

shape, and a noticeable external posterior accumulation of cells. Normal plutei were harvested at 90 hr. *S. purpuratus* embryos can begin ingesting algae at about 70–80 hr. For this paper, mRNA extracted from unfed plutei was used. These are relatively well-differentiated larvae containing complete digestive tracts and well-formed, brachiated skeletons.

Isolation of mRNA

General mRNA extraction procedures.

The mRNA preparations used in these experiments include polysomal rRNA as well as mRNA, but have been extensively purified of nonpolysomal RNAs, particularly nuclear RNAs. The basic procedure we have used here is similar to that described by Galau *et al.* (1974) with occasional modifications as noted below. Embryos were washed in 1.5 M glucose and were pelleted by centrifugation. They were resuspended in 50 mM PIPES (pH 6.5), 500 mM KCl, 12 mM MgCl₂, containing 500 µg/ml PVS (polyvinyl sulfate), 5 mg/ml bentonite (PKM-PVS-bentonite); and the cells lysed by homogenization in a 40-ml glass, size-B Dounce homogenizer. The nuclei and cell debris were removed from the homogenate by low-speed centrifugation, and the resultant supernatant was brought to 1% Triton X-100 and 0.5% sodium deoxycholate, to release membrane-bound polyribosomes. Following a further centrifugation at 25,000 *g* to clarify the supernatant, the polysomes were pelleted by high-speed centrifugation; resuspended in 10 mM PIPES (pH 6.5), 2 mM MgCl₂, 500 mM KCl, and 25 µg/ml PVS; and layered on exponential sucrose gradients (5%–40%) made up in the same buffer. In some cases the sucrose gradients contained 5 mM MgCl₂. With some preparations, as noted below, the polyribosomes were not pelleted, but the 25,000 *g* supernatant was layered directly onto sucrose gradients. This was possible in preparations where the original lysate volume was small because no concentra-

tion step was necessary. Because of occasional difficulties in resuspending the polyribosomal pellet in the adult tissue mRNA preparations, the omission of the pelleting step generally improved the final yield. Polysomes sedimenting at $>100S$ were collected and pelleted by ultracentrifugation. The pellet was resuspended in 50 mM Tris (pH 7.4), 500 mM KCl, 2 mM $MgCl_2$, 25 $\mu g/ml$ PVS, and incubated with 2 mM puromycin for 30 min at 4°C and 30 min at 37°C to disaggregate the polyribosomes (Blobel, 1971). The mixture was then layered on sucrose gradients as described above, and the material sedimenting at $<80S$ was collected, made 5 mM in $MgCl_2$, and precipitated with ethanol. Total polysomal RNA was extracted from the ethanol precipitate by dissolving the pellet in 10 mM sodium acetate (pH 6.5), 100 mM NaCl, 1 mM EDTA, 1% SDS, and deproteinizing at room temperature with an equal volume of phenol:chloroform:isoamyl alcohol (50:48:2). The RNA was twice precipitated from 0.3 M sodium acetate with ethanol and dissolved in either water or 0.5 M phosphate buffer, 0.2% SDS, at total RNA concentrations of 10–25 mg/ml.

mRNA preparations from gastrula, exogastrula, and pluteus. Gastrula mRNA Preparations 1, 2, 3; exogastrula mRNA; and pluteus mRNA were all prepared in the manner just described. Gastrula mRNA Preparation 4 was extracted with the following modifications. The 25,000 g supernatant was layered directly on sucrose gradients. The sucrose gradients were centrifuged as described above, and the $>100S$ material was pelleted, resuspended in 50 mM Tris (pH 7.5), 500 mM KCl, 25 $\mu g/ml$ PVS, and the solution brought to 0.1 M EDTA (pH 6.8) at 4°C to disaggregate the polyribosomes. Isolation of the $<80S$ material was then carried out as described above.

mRNA preparations from blastula. Homogenization as described above caused significant nuclear lysis with blastula stage embryos. This problem

was avoided by the following procedures: The embryos used for mRNA Preparation 1 were washed in 1.5 M glucose and the cells lysed in 50 mM PIPES (pH 6.5), 200 mM KCl, 12 mM $MgCl_2$, 25 $\mu g/ml$ PVS and 2.5 mg/ml bentonite. The remainder of the procedure was as described above except that the 25,000 g supernatant was layered directly onto sucrose gradients with no prior concentration. Blastula mRNA Preparations 2 and 3 were prepared essentially as in the section above except that the polysomes were concentrated by centrifugation into a 2 M sucrose cushion followed by dialysis.

Ovary mRNA preparation. Ovarian tissue was dissected from 20 female urchins after the mature eggs had been shed by injection of 0.5 M KCl into the coelomic cavity. After disrupting the tissue into small pieces and shaking for several minutes in 15°C seawater, the tissue was inspected by light microscopy and judged to be almost entirely free of mature eggs. The tissue was then finely minced, washed in 1.5 M glucose and homogenized in 100 ml of PKM-PVS-bentonite buffer in a size-B Dounce homogenizer. The remainder of the isolation procedure was as described above.

Tube foot mRNA preparation. Extended tube feet were cut from adult sea urchins with scissors. A typical amount of starting material was 20–40 cc of tube foot tissue. Preparations 1, 2, and 3 were homogenized for 60 sec in a Waring blender with 200 ml of PKM-PVS-bentonite buffer per 40 cc of tissue. The remainder of the isolation was as described above. Preparation 4 was isolated as above, except that the 25,000 g supernatant was layered directly onto sucrose gradients and brought to 0.1 M EDTA (pH 6.8) to disaggregate the polyribosomes. We found that polysomal RNA prepared in this manner had trace amounts of RNAase activity associated with it. Therefore, the RNA was dissolved in 1% SDS, 1 mM EDTA, and 20 mM Tris (pH 8), and incubated with 10 $\mu g/ml$ proteinase K (EM Labora-

tories) for 1 hr at 4°C and 1 hr at 37°C. The RNA was then deproteinized with chloroform:isoamyl alcohol (24:1) and precipitated with ethanol.

Intestine mRNA preparation. Intestine tissue was dissected from about 50 sea urchins for each of the three mRNA preparations. For Preparation 1, after washing in cold seawater, the tissue was placed directly into a Waring blender with 200 ml of PKM-PVS-bentonite and homogenized for 60 sec. For mRNA Preparations 2 and 3, the tissue was minced and then homogenized in a size-B Dounce homogenizer with 200 ml of PKM-PVS-bentonite. The extraction of mRNA from the lysate was as described above.

Coelomocyte mRNA preparation. For each mRNA preparation 2-3 liters of coelomic fluid were obtained by opening the animal around the peristomal membrane and pouring the fluid contents into 250 ml of 0.25 M EGTA (pH 7.0) at 1°C to a final EGTA concentration of 0.25 M. The EGTA prevents coagulation of the coelomocytes. The cells (about 20 cc of packed cells per 1 coelomic fluid) were pelleted by centrifugation. From five to ten ml of packed cells were resuspended in 40 ml of PKM-PVS-bentonite. They were lysed by homogenization with a size-B Dounce homogenizer. In both mRNA preparations utilized in this report, the 25,000 g supernatant was layered directly onto sucrose gradients. In Preparation 1, 0.1 M EDTA (pH 6.5) at 4°C was used to disaggregate the polysomes. Other procedures were as above.

Total oocyte RNA. Two different RNA preparations were utilized for the hybridization reactions. For the first, 5×10^7 mature oocytes were washed in 1.5 M glucose and resuspended in 200 ml of 100 mM Tris (pH 7.4), 200 mM NaCl, 1 mM EDTA, 0.5% SDS, containing 10 µg/ml PVS. The eggs were lysed in a size-B Dounce homogenizer, and an equal volume of phenol:chloroform:isoamyl alcohol (50:48:2) was added. The aqueous solution was ex-

tracted two times at room temperature and precipitated with 2 vol of ethanol. The precipitate was taken up in 10 mM PIPES (pH 6.5), 5 mM MgCl₂, and DNAase I was added to 75 µg/ml. After incubation for 2 hr at room temperature the solution was deproteinized with an equal volume of phenol:chloroform:isoamyl alcohol (50:48:2), followed by ethanol precipitation. The RNA precipitate was taken up in 0.3 M sodium acetate (pH 6.5) and placed over a Sephadex G-200 column. The RNA in the excluded volume of the column was precipitated with ethanol and stored at -20°C in water at 23 mg/ml. For the second preparation 4×10^6 eggs were lysed in 80 ml of 50 mM sodium acetate (pH 5.1), 10 mM EDTA, 0.5% SDS, 10 µg/ml PVS, 7 M urea, and 1 mg/ml bentonite, in a size-B Dounce homogenizer at room temperature. Following lysis, an additional 130 ml of buffer was added, and the RNA was deproteinized at room temperature with phenol:m cresol:8-hydroxyquinoline (Kirby, 1965) and chloroform:isoamyl alcohol (24:1) and precipitated with ethanol. To ensure complete removal of any contaminating nucleases, the precipitate was dissolved in 20 mM Tris (pH 8.0), 0.5% SDS, 50 mM EDTA, and incubated with 10 µg/ml of proteinase K for 1½ hr at 37°C. The solution was deproteinized with chloroform:isoamyl alcohol (24:1) and precipitated with ethanol.

Preparation of Labeled Single-Copy 3H-DNA

Unlabeled DNA was isolated from frozen *S. purpuratus* sperm by standard techniques (Britten *et al.*, 1974). It was dissolved at 0.7 mg/ml in 30 ml 3.3 mM sodium acetate (pH 6.5), 67% glycerol, and sheared to a mean single-strand length of 250 nucleotides in a Virtis-60 homogenizer, using the large blade. Shearing was carried out at 50,000 rpm for 30 min in a 100-ml vessel cooled in a dry ice-ethanol bath. Single-copy DNA was isolated by denaturing and reassociating the DNA in 0.12 M phosphate

buffer (pH 6.8; an equimolar mixture of basic and dibasic sodium phosphate) at 60°C to a C_0t (moles nucleotide L^{-1} sec) of 600. The unreassociated DNA was recovered by hydroxyapatite chromatography and again reacted in 0.12 *M* phosphate buffer at 60°C, this time to C_0t 350. The DNA remaining single stranded was isolated by hydroxyapatite chromatography and was then incubated to C_0t 5000 in 0.12 *M* phosphate buffer at 60°C. DNA which had renatured at this point was harvested by hydroxyapatite chromatography.

Single-copy DNA was labeled in vitro by modification of the method of Schachat and Hogness (1974) for long double-stranded DNA, in which DNAase I is used to introduce single-strand nicks that serve as initiation sites for *E. coli* DNA polymerase I. The structures formed by extensively reassociating short DNA fragments are substrates for polymerase I in the absence of DNAase. We have used this method to label 1–20 μ g of reassociated 250–300 nucleotide long *E. coli* DNA or single-copy sea urchin DNA to a specific activity of 3×10^6 cpm/ μ g. Little or no change in the single-strand fragment length occurs. To prepare sea urchin single-copy DNA tracer, the unlabeled single-copy DNA was reassociated to a C_0t of 20,000 and labeled at 15–35 μ g/ml in 0.05 *M* phosphate buffer (pH 7.6), 0.01 *M* $MgCl_2$, 1 *mM* EDTA, containing 2×10^{-5} *M* dATP, dGTP, dCTP and $1\text{--}2 \times 10^{-5}$ *M* 3H -dTTP (55 Ci/mmol, 0.6–1 mCi/ml reaction mixture; Schwarz-Mann). Five units of *E. coli* DNA polymerase I (Boehringer Mannheim, grade 1) per μ g DNA were added, and the reaction mixture was incubated at 11–12°C for 27–48 hr. The rate of 3H -dTTP incorporation gradually declined with time but was still high at 30 hr. As much as 30%–40% of the 3H -dTTP was incorporated.

With the polymerase preparation used here, 20%–30% of the incorporated radioactivity was in DNA fragments containing self-complementary or foldback

regions. Along with unincorporated precursor, this was simply removed by passage over a hydroxyapatite column. The reaction mixture was adjusted to 0.03 *M* phosphate buffer (pH 7.6), 0.135 *M* NaCl, and 10 *mM* EDTA; heated to 100°C for 3–5 min; incubated at 50°C for 1 min; and passed over hydroxyapatite at 50°C in 0.03 *M* phosphate buffer, 0.135 *M* NaCl. The precursor eluted gradually from the column in two peaks with extensive washing with 0.03 *M* phosphate buffer, 0.135 *M* NaCl at 50°C. Single-strand DNA containing no foldback duplexes recognizable by hydroxyapatite at 50°C was washed from the column with 0.12 *M* phosphate buffer at 50°C and saved. Duplex-containing fragments were removed with 0.5 *M* phosphate buffer at 50°C or 0.12 *M* phosphate buffer at 98°C. Final recovery of foldback-free, labeled DNA has averaged 75%–80% of input DNA mass.

Preparation of Gastrula mDNA and Null mDNA

On a pilot scale gastrula mDNA and null mDNA were prepared previously by Galau *et al.* (1974). In that study RNAase A was used to liberate mDNA from single-copy DNA-mRNA hybrids in greater than 60%–70% purity. Subsequently, we have had difficulty completely removing this nuclease, which is obviously an absolute requirement. An alternate method was developed which relies instead on successive reactions with mRNA to enrich for mDNA sequences. Gastrula mRNA Preparation 1 (see above) was mixed with nonrepetitive 3H -DNA, denatured, and incubated in 0.41 *M* phosphate buffer, 0.2% SDS, at 60°C to an mRNA C_0t of 400 and a 3H -DNA C_0t of 27. All reaction mixtures were diluted to less than 100 μ g/ml total RNA in 0.12 *M* phosphate buffer, 0.2% SDS, for passage over the 60°C hydroxyapatite columns. Less than 100 μ g total RNA was loaded per cc hydroxyapatite. The material failing to bind to hydroxyapatite was passed over another column to completely recover

all duplexes. The single-strand material remaining after this additional passage was saved for the preparation of null mDNA. Duplex-containing ^3H -DNA was recovered from the columns with 0.5 M phosphate buffer, 0.2% SDS, at 60°C and pooled. This fraction was then denatured and reacted with additional mRNA to an equivalent (new) mRNA C_0t of 200 (total mRNA C_0t 500) and ^3H -DNA C_0t 0.8 in 0.41 M phosphate buffer, 0.2% SDS, at 60°C. The reaction mixture was diluted as above and passed over a single hydroxyapatite column, and the bound material was eluted with 0.5 M phosphate buffer, 0.2% SDS, at 60°C. Foldback-containing DNA was removed by denaturing the duplexes in 0.12 M phosphate buffer, 0.2% SDS, incubating 1 min at 60°C to a very low ^3H -DNA C_0t , and again placing the mixture over hydroxyapatite. The material that failed to bind was treated 45 min in 0.3 M KOH at 37°C to hydrolyze the residual gastrula mRNA, neutralized with acetic acid, and passed over a Sephadex G-100 column. The excluded DNA was the gastrula mDNA.

Preparation of null mDNA from the single-stranded fraction obtained in the first mRNA hybridization continued as follows. A second reaction mixture with additional mRNA was incubated to an equivalent mRNA C_0t of 200 and ^3H -DNA C_0t of 47 in 0.52 M phosphate buffer, 0.2% SDS, at 60°C. Considering carryover of mRNA from the first incubation, the total mRNA C_0t was approximately 250. The reaction mixture was diluted and passed over a single hydroxyapatite column. The single-stranded ^3H -DNA not bound was the null mDNA. When denatured in 0.12 M phosphate buffer, 0.2% SDS, and incubated 1 min at 60°C, less than 0.4% of the mDNA and less than 0.15% of the null mDNA bind to hydroxyapatite.

Hybridization of ^3H -DNAs with RNA and Analysis of Hybrid Content

Single-copy ^3H -DNA, null mDNA, and mDNA were incubated with RNA

in 0.50 M phosphate buffer, 0.2% SDS, at 60°C as described in the tables. From 100 to 500 cpm of ^3H -mDNA was used per reaction mixture. The input null mDNA and single-copy DNA were adjusted to yield 20–400 cpm (average 100 cpm) of DNA-DNA duplex per hydroxyapatite column. The mRNA C_0t is calculated for mRNA preparations, assuming 2% of the polysomal RNA is mRNA (Humphreys, 1971; Galau *et al.*, 1974). The RNA C_0t for the oocyte RNA is calculated for the total RNA. All mRNA C_0ts referred to in this paper are equivalent mRNA C_0ts ; that is, they have been corrected for accelerations in rate due to Na^+ concentration (Britten *et al.*, 1974) relative to the rate in 0.12 M phosphate buffer at 60°C. All DNA C_0ts referred to are also equivalent DNA C_0ts . After denaturation for 1–2 min at 98°C, hybridization samples were incubated from 3 hr to as long as 160 hr to the indicated mRNA or total RNA C_0ts . The majority of the reactions were incubated 24–48 hr, and only rarely did the time exceed 92 hr.

Control experiments described earlier (Fig. 16 and Table 11) indicate that RNA-driven reactions with mDNA contain essentially no DNA-DNA duplex. The reactions were analyzed by placing them directly over hydroxyapatite in 0.12 M phosphate buffer, 0.2% SDS, at 60°C. Single-stranded ^3H -DNA was washed through the column with the same buffer. Hybridized ^3H -DNA bound to the column was eluted at 98°C in the same buffer. Fractions from the column were assayed for radioactivity by direct counting in scintillation fluid. Where noted, low-salt RNAase treatment (see below) was used to destroy RNA-mDNA hybrids before hydroxyapatite assay.

Reaction mixtures containing total single-copy ^3H -DNA and null mDNA were analyzed as follows by a method modified slightly from the procedures used by Galau *et al.* (1974). The hybridization reactions were diluted to 100–150 μl with 0.05 M phosphate buffer and placed over a 0.3×20 cm Sephadex

G-100 column in 0.05 M phosphate buffer to remove the SDS. The excluded ^3H -DNA and RNA were diluted to 2 ml with 0.05 M phosphate buffer and divided into two equal parts. The first aliquot was used to assay total duplex content. This was brought to 0.25 M phosphate buffer and 10 $\mu\text{g}/\text{ml}$ RNAase A, incubated 1 hr at room temperature, and then stored at -20°C . Control experiments reported by Galau *et al.* (1974) indicate that gastrula mRNA-DNA hybrids are unaffected by this treatment. The second aliquot was used to assay DNA-DNA duplex content. This was incubated 12–20 hr in 0.05 M phosphate buffer, 10 $\mu\text{g}/\text{ml}$ RNAase A at 37°C in order to completely digest the RNA of RNA-DNA hybrids. This sample was then cooled to room temperature, brought to 0.25 M phosphate buffer, stored at room temperature 1 hr and then frozen at -20°C . For hydroxyapatite assay, the two samples were rapidly thawed, diluted 1:2 with 0.0025 M phosphate buffer and immediately deproteinized by shaking with 2 ml chloroform:isoamyl alcohol (24:1). The aqueous phase was recovered by centrifugation and brought to 0.2% SDS. The samples were then placed over hydroxyapatite as described above except that the single-strand ^3H -DNA was extensively washed from the column before elution of the bound ^3H -DNA. This included repeatedly stirring the column bed in small aliquots of buffer and blowing the bed completely dry with air pressure.

Data Reduction

Pseudo-first-order rate constants and terminal extents of the hybridization reactions were derived from the data by least-squares analysis with the aid of a computer. Errors calculated for each of these parameters are listed in the tables. These errors represent one standard deviation (not including systematic errors) around the best-fit parameter values. Data were fitted to the expression $D/D_0 = \exp[-C_0 t k]$ where D/D_0 is

the fraction of ^3H -DNA remaining single stranded at time t ; C_0 is the mRNA or (for oocyte RNA) the total RNA concentration; and k , the pseudo-first-order rate constant. See Galau *et al.* (1974) for calculations using this equation and further discussion. The only restrictions used in the curves fitted here were that there is a single kinetic component in each reaction and that no significant amount of hybrid forms at very low RNA $C_0 t$; i.e., the ordinate intercept is zero. These conditions conform to what was observed for gastrular mRNA-driven reactions with total single-copy ^3H -DNA, the kinetics of which were studied in great detail by Galau *et al.* (1974). Terminal values and the size of the standard deviations calculated for the terminal values change insignificantly if these restrictions are not applied. Where no low $C_0 t$ kinetic data exist, the rates are poorly determined by the data, and for these examples the assumption of zero ordinate intercept affects the rate significantly. However, this is a reasonable assumption, as in no case for which sufficient data exist do we find that non-zero ordinate intercepts appear. The least-squares computer program used to fit the hybridization data provides estimates of the standard deviation for each parameter. We wish to stress that these standard deviations describe the variability of the data, assuming that a single kinetic component exists. If more than one component is present or if other systematic errors intervene, the standard deviations no longer represent the actual errors in each set of measurements.

SEQUENCE COMPLEXITY OF THE RNA ACCUMULATED IN OOCYTES OF *Arbacia punctulata*

David M. Anderson,* Glenn A. Galau,
Roy J. Britten, and Eric H. Davidson

Maternal messenger RNAs are now known to be very important in early de-

* Department of Biological Sciences, Purdue University, West Lafayette, Ind. 47907

velopment. This has been demonstrated most extensively in sea urchin embryos (e.g., Gross *et al.*, 1973; Humphreys, 1971). Maternal messenger RNA and possibly other RNA species not yet identified are stored in the RNA of the mature oocyte. Measurement of the complexity of oocyte RNA, that is, the total length of nonrepetitive DNA sequence represented in the RNA, provides a molecular index of the magnitude of the developmental program stored in the RNA. Although complexity estimates exist for the oocyte RNAs of several species (Davidson and Hough, 1971; Davis, 1975; Roshash *et al.*, 1974), so far no measurements have been reported for sea urchin oocyte RNA. We report here a determination of the complexity of *Arbacia punctulata* oocyte RNA. Excess oocyte RNA was hybridized with *Arbacia* single-copy DNA tracer, and the complexity was estimated from the fraction of the single-copy DNA found to be complementary to total oocyte RNA. The results indicate the complexity of this RNA to be about 3.0×10^7 nucleotides.

Isolation and Characterization of Single-Copy ^3H -DNA

Figure 21 (closed circles) shows the reassociation kinetics of 300-nucleotide-long *Arbacia* sperm DNA, monitored by hydroxyapatite chromatography. The solid curve was obtained by least-squares analysis, assuming second-order renaturation kinetics (Britten *et al.*, 1974). To obtain the fit shown, the rate constant of the most slowly reassociating class of fragments, those containing only single-copy sequence (dotted line), was fixed at $1.3 \times 10^{-3} \text{ l} \cdot \text{mole}^{-1} \cdot \text{sec}^{-1}$. This is the rate constant expected for the fragment length used and the genome size of this organism. The genome size was measured at 0.76–0.79 pg by Hinegardner (1974) and Marshak and Marshak (1953). About 60% of the DNA fragments fall in this class. Insufficient low C_0t data were obtained to permit a quan-

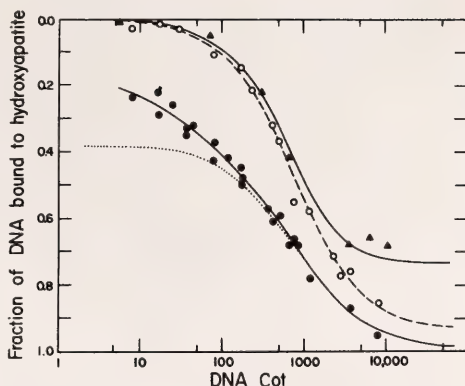


Fig. 21. Reassociation of various *Arbacia* DNA fractions. All incubations were at a concentration of 10 mg DNA/ml in 0.41 M phosphate buffer, 0.5% sodium dodecyl sulfate, at 67°C. Reassociation was monitored by binding to hydroxyapatite. Closed circles show data for the reassociation of 300-nucleotide-long fragments of total *Arbacia* DNA. The solid curve was obtained by least-squares analysis of the data (Britten *et al.*, 1974) with the single-copy component rate constant fixed at $1.3 \times 10^{-3} \text{ l} \cdot \text{mole}^{-1} \cdot \text{sec}^{-1}$, the theoretical rate for a genome of 0.76–0.79 pg, assuming 300-nucleotide-long DNA fragments. The dotted line represents the reassociation of the single-copy component. The size of this component (60%) is essentially independent of the number of repetitive components assumed. Open circles indicate the reassociation of isolated 300-nucleotide-long single-copy ^3H -DNA with a 2000-fold excess of total 300-nucleotide-long DNA. The least-squares solution (dashed line) gives a rate constant of $1.4 \times 10^{-3} \text{ l} \cdot \text{mole}^{-1} \cdot \text{sec}^{-1}$. Closed triangles show the reassociation of DNA isolated from DNA-RNA hybrids with a 20,000-fold excess of total 300-nucleotide-long DNA. The curve is a least-squares fit to the data with a rate constant of $1.8 \times 10^{-3} \text{ l} \cdot \text{mole}^{-1} \cdot \text{sec}^{-1}$.

titative description of the repetitive sequence components.

Due to the interspersed nature of single-copy DNA with repetitive DNA sequence (reviewed in Davidson and Britten, 1973, and Davidson *et al.*, 1975a), hydroxyapatite assay of reassociated DNA underestimates the amount of single-copy sequence in the genome. Some single-copy sequence is present as single-stranded "tails" on the duplexes bound to hydroxyapatite after incubation to low C_0t . Using a nuclease specific for

single-strand DNA to assay reassociation, Skoultschi and Gross (1973) observed 80%–85% of the nucleotides of short *Arbacia* DNA fragments reassociating at the rate expected for single-copy DNA. The sequence arrangement in another sea urchin DNA, that of *Strongylocentrotus purpuratus*, has been studied in detail (Graham *et al.*, 1974). By a variety of techniques, including the use of single-strand-specific nucleases, it is shown that 75% of the genome is single-copy sequence. Due to the interspersed nature of this sequence with repetitive DNA, however, only 50% of 450-nucleotide-long *Strongylocentrotus* DNA fragments are entirely single copy as assayed by hydroxyapatite binding. The data of Skoultschi and Gross (1973) and Fig. 21 for *Arbacia* DNA thus indicate that about 80% of the *Arbacia* genome is probably single-copy sequence.

Arbacia embryos were labeled with ^3H -thymidine, and the DNA was extracted and subjected to successive low C_0t incubations followed by hydroxyapatite fractionation to remove the reassociated repetitive sequences. The procedures used are described in Experimental Procedures.

To assay its purity, the resulting single-copy ^3H -DNA preparation was reassociated with an excess of 300-nucleotide-long total *Arbacia* DNA, and the results are presented in Fig. 21 (open circles). The least-squares solution for the reassociation of the single-copy DNA with total DNA (dashed line) gives a rate constant of $1.4 \times 10^{-3} \text{ l} \cdot \text{mole}^{-1} \cdot \text{sec}^{-1}$. This is in good agreement with that expected for this size genome. Figure 21 shows that the tracer contains no detectable repetitive DNA; the tracer displayed excellent reactivity (about 90%) when the experiments shown in Fig. 21 were carried out. Later the reactivity of the ^3H -DNA tracer declined to about 70%. A similar phenomenon has been reported by Galau *et al.* (1976a). In any case, the above results establish the labeled single-copy DNA

preparation as suitable for the hybridization experiments which follow.

Hybridization of ^3H -Single-Copy DNA to Oocyte RNA

Experiments in which small amounts of single-copy ^3H -DNA were reacted with a 4000-fold excess of unlabeled oocyte RNA are displayed in Table 16 and Fig. 22. The DNA-RNA reaction mixtures were incubated to various RNA

TABLE 16. Hybridization of Oocyte RNA to Single-Copy ^3H -DNA*

| Total RNA C_0t | Total Duplex (%) | DNA-DNA Duplex (%) | RNA-DNA Duplex (%) |
|---------------------|---------------------|-----------------------|-----------------------|
| 200 | 0.20 | (0) | 0.20 |
| 790 | 0.35 | 0 | 0.35 |
| 1,000 | 0.50 | (0) | 0.50 |
| 1,900 | 0.75 | (0) | 0.75 |
| 3,200 | 1.15 | 0.05 | 1.10 |
| 3,500 | 1.38 | (0.08) | 1.30 |
| 4,000 | 1.38 | 0.10 | 1.28 |
| 5,300 | 1.75 | (0.20) | 1.55 |
| 5,700 | 1.75 | (0.22) | 1.53 |
| 6,000 | 2.10 | (0.25) | 1.85 |
| 7,300 | 2.13 | 0.33 | 1.80 |
| 9,400 | 2.34 | 0.49 | 1.85 |
| 10,300 | 2.36 | (0.58) | 1.78 |
| 11,700 | 2.58 | 0.67 | 1.91 |
| 11,800 | 2.48 | (0.68) | 1.80 |
| 12,000 | 2.64 | (0.69) | 1.95 |
| 12,600 | 2.51 | 0.71 | 1.80 |
| 14,000 | 2.72 | (0.82) | 1.90 |
| 14,900 | 2.74 | 0.89 | 1.85 |
| 16,000 | 2.87 | 0.97 | 1.90 |
| 20,500 | 3.28 | (1.30) | 1.98 |
| 23,700 | 3.35 | (1.50) | 1.85 |
| 24,000 | 3.45 | 1.52 | 1.93 |

* The amount of RNA-DNA duplex was determined by subtracting the DNA-DNA value for each data point from the total amount of DNA in hydroxyapatite-bindable duplex as detailed in Galau *et al.* (1974). The DNA-DNA value was determined for a portion of each reaction mixture after RNase treatment to destroy RNA-DNA hybrids. The DNA-DNA duplex values in parentheses were not determined directly but were interpolated from the other self-reassociation data. All incubations were at 18–20 mg RNA/ml and contained 5 μg ^3H -DNA/ml in 0.41 M phosphate buffer, 0.5% sodium dodecyl sulfate. The reactions were carried out at 67°C.

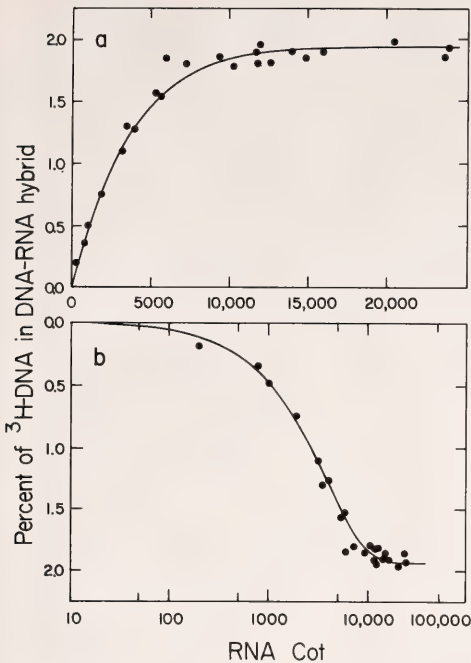


Fig. 22. Hybridization of oocyte RNA to single-copy ^3H -DNA. Two methods for presenting the data in Table 16 are shown in 22a and 22b. The solid line represents the best least-squares solution of the data according to the pseudo-first-order equation $D/D_0 = e^{-C_0t k}$, where D is the concentration of unreacted DNA; D_0 and C_0 are the initial concentrations of DNA and RNA, respectively; t is the time of incubation in seconds; and k is the pseudo-first-order rate constant (see Galau *et al.*, 1974 for discussion of pseudo-first-order hybridization kinetics). The rate constant obtained for this fit is $3.0 \times 10^{-4} \text{ l} \cdot \text{mole}^{-1} \cdot \text{sec}^{-1}$, and the terminal value is 1.93% of the ^3H -DNA in hybrid.

C_0t values, and the fraction of the DNA in RNA-DNA hybrid was determined by hydroxyapatite fractionation, as described by Galau *et al.* (1974). Briefly, part of each reaction mixture was assayed for total duplex and for DNA-DNA duplex remaining after a low-salt RNAase treatment which destroys RNA-DNA hybrids. The amount of ^3H -DNA in RNA-DNA hybrid is calculated as the difference between these two numbers.

The data are fitted well by a single

first-order kinetic component. The homogeneity of the reaction suggests that the species driving the reaction are each present in essentially the same concentration. The overall reaction has an RNA $C_0t_{1/2}$ of 2300 (rate constant $= 3.0 \times 10^{-4} \text{ l} \cdot \text{mole}^{-1} \cdot \text{sec}^{-1}$) and approaches completion at RNA C_0t 10,000. The best least-squares fit to the data places the DNA saturation value at 1.93% of the total DNA.

It is unlikely that this termination value is caused by nucleic acid degradation during the incubations. The absence of nucleic acid degradation in the hybridization mixtures was shown directly by Sephadex G-100 chromatography of reaction mixtures after incubation to RNA C_0ts as high as 20,000. All the RNA was excluded from the Sephadex column in these tests. Also, to prove that no more DNA is reactable with RNA after RNA C_0t 10,000, the DNA not in hybrid was isolated by hydroxyapatite and reincubated with additional RNA to a new RNA C_0t of 20,000. No detectable hybridization of this selected DNA with additional RNA occurred.

Demonstration That the ^3H -DNA in Hybrid Is Single-Copy DNA

It is desirable to determine the repetitive-sequence content, if any, in the hybridized ^3H -DNA. Any hybridization to repetitive ^3H -DNA in the samples could have contributed a large amount of hybrid while representing only a very small RNA complexity. The hybridization reactions we have described were carried out with total oocyte RNA, and in sea urchins this RNA is known to include substantial amounts of heterogeneous repetitive sequence transcript (Hynes and Gross, 1972; Whiteley *et al.*, 1966).

Oocyte RNA was incubated with single-copy ^3H -DNA to an RNA C_0t of 10,000, and the DNA that was in an RNA-DNA hybrid was isolated as described in Galau *et al.* (1974) by first isolating the total duplexes and then re-

covering the ^3H -DNA liberated from RNA-DNA hybrids with RNAase treatment. To prove that the selected ^3H -DNA was in fact complementary to oocyte RNA, a portion of this ^3H -DNA was incubated with a 4000:1 excess of oocyte RNA to an RNA C_0t of 2400, and the fraction of the ^3H -DNA in hybrid was determined as usual by binding to hydroxyapatite. This experiment showed that 30% of the ^3H -DNA was in RNA-DNA hybrid. However, the reaction is only 44% complete at RNA C_0t 2400 (Fig. 22), and as shown in Fig. 21 (closed triangles), the reactivity of the tracer had by then declined to 74%. Therefore, about 90% of the reactable ^3H -DNA tracer obtained from the hybrid fraction was complementary to oocyte RNA. To assay its repetitive sequence content, the selected ^3H -DNA was mixed with excess unlabeled whole 300-nucleotide-long *Arbacia* DNA. The DNA was heat denatured, incubated at 67°C in 0.41 M phosphate buffer, and the reassociation kinetics were followed by hydroxyapatite. The results are shown in Fig. 21 (closed triangles, solid line). Least-squares analysis yielded a second-order rate constant of 1.8×10^{-3} l·mole $^{-1}$ ·sec $^{-1}$ for this reaction, a value which agrees with the reaction rate constants noted earlier in this report for the single-copy sequences in the *Arbacia* genome. Figure 21 shows that there is no detectable repetitive sequence component in the recovered ^3H -DNA. These data indicate clearly that the oocyte RNA has indeed hybridized with single-copy ^3H -DNA sequences. The saturation value obtained can therefore be used to calculate the complexity of the oocyte RNA.

Calculation of Oocyte RNA Complexity and RNA Sequence Concentration

The calculation of RNA sequence complexity by these saturation techniques requires knowledge of the total single-copy DNA sequence complexity in the genome, and the fraction of the

reactive single-copy ^3H -DNA that is complementary to the RNA. As noted above, the size of the haploid *Arbacia* genome is approximately 7.2×10^8 nucleotide pairs, about 80% of which are nonrepetitive. As judged by reaction with whole DNA, about 74% of the ^3H -DNA remained reactable when the experiments shown in Fig. 22 were carried out. At termination 1.93% of the ^3H -DNA was hybridized with the oocyte RNA (Fig. 22). Assuming asymmetric transcription, this represents approximately 5.2% of the single-copy complexity, or about 3.0×10^7 nucleotides of diverse sequence. It is to be noted that this value is subject to several uncertainties. Among these are the size of the genome of *Arbacia punctulata*, the actual content of single-copy DNA in the *Arbacia* genome, and the range of hybridization results which would have been obtained had several RNA preparations rather than only one been used. We judge that these uncertainties are unlikely to affect the complexity by more than 20%–30% at most.

The concentration of the RNA sequences driving the reaction of Fig. 22 can be calculated from the RNA complexity and the rate constant of hybridization by reference to a standard reaction. With similar hybridization conditions, the pseudo-first-order rate constant for the reassociation of 300-nucleotide-long ϕX DNA with excess 360-nucleotide-long ϕX RNA (complexity of 5500 nucleotides) is 170 l·mole $^{-1}$ ·sec $^{-1}$ (Galau *et al.*, in preparation). The rate constant expected for a hybridization reaction driven by a purified RNA of 3.0×10^7 nucleotide complexity is thus about 3.1×10^{-2} l·mole $^{-1}$ ·sec $^{-1}$. This assumes that the reacting RNAs are about 360 nucleotides long. Although not measured in this study, the size of the oocyte RNAs during the hybridization reaction is likely to be larger than 360 nucleotides, which would decrease the expected hybridization rate. However, the rate reduction would not be more than a factor of two if the hy-

bridizing RNA were as long as 2000 nucleotides (Galau *et al.*, in preparation). The observed rate constant in Fig. 22 is $3.0 \times 10^{-4} \text{ l} \cdot \text{mole}^{-1} \cdot \text{sec}^{-1}$. We conclude, therefore, that 1%–2% of the oocyte RNA is driving the hybridization reaction with single-copy DNA (see Galau *et al.*, 1974, for discussion of this type of calculation).

Conclusion

The complexity of the *Arbacia* oocyte RNA measured in this report, 3.0×10^7 nucleotides, is very similar to that measured for several other oocytes. The complexity of the oocyte RNA of the sea urchin *Strongylocentrotus purpuratus* is about 3.7×10^7 nucleotides as measured by the same techniques used here (Galau *et al.*, 1976a). From similar data of Davis (1975) on oocyte RNA of the echinoid worm *Urechis caupo* we calculate the complexity of this RNA to fall in the range $3.1\text{--}4.7 \times 10^7$ nucleotides. The measurements of Davidson and Hough (1971), together with current knowledge of sequence organization in the *Xenopus* genome, yield a value in the range $2.7\text{--}4.0 \times 10^7$ nucleotides for the complexity of *Xenopus* oocyte RNA. In addition, it appears that the complex sequences are included in around 1% of the RNA in the oocytes of all these species.

The majority of these oocyte RNA sequences are probably maternal mRNAs. This is suggested by the observations that the polyadenylated RNAs of *Xenopus* oocytes have about the same complexity measured for the total RNA (Rosbash *et al.*, 1974). Furthermore, the polyadenylated RNAs are of the size characteristic of mRNAs in *Xenopus* cells (Rosbash and Ford, 1974). In the sea urchin *S. purpuratus*, polyadenylated oocyte RNAs can be translated in an *in vitro* system with good efficiency (Jenkins *et al.*, 1973). Direct measurements indicate that 45% of the RNA sequences present in *S. purpuratus* oocytes are also represented in the polysomal

mRNA of gastrula stage embryos alone (Galau *et al.*, 1976a). If the oocyte RNA of the complexity measured here is all maternal mRNA, its diversity is sufficient to code for $1.5\text{--}3 \times 10^4$ different proteins.

Experimental Procedures

Preparation of total unlabeled DNA.

DNA was extracted from sea urchin sperm by a modified Marmur (1961) procedure as reported in Britten *et al.* (1974). The purified DNA was ethanol precipitated, resuspended in 0.02 M sodium acetate (pH 6.8), and sheared to 300-nucleotide-long fragments by Virtis homogenization (50,000 rpm, 30 min) as described by Britten *et al.* (1974). The sodium acetate concentration was raised to 0.2 M, and the DNA was ethanol-precipitated. DNA was resuspended in 0.41 M phosphate buffer (equimolar Na_2HPO_4 and NaH_2PO_4), passed over Chelex (BioRad) to remove divalent cations (Davidson and Hough, 1971), and stored at 4°C over chloroform.

Preparation of single-copy ^3H -DNA.

Arbacia eggs were collected, washed, and fertilized by standard procedures. A total of 2×10^7 embryos were grown in culture at a concentration of 2×10^5 embryos/ml of seawater. At the four-cell stage, ^3H -thymidine (60 Ci/mole, Nuclear Dynamics) was added to 10 $\mu\text{Ci/ml}$. Embryos were grown to the mesenchyme blastula stage (12 hr) with additions of ^3H -thymidine to 10 $\mu\text{Ci/ml}$ at 3.5 hr and 7 hr after the first addition of isotope. Nuclei were prepared by standard procedures (Aronson *et al.*, 1972), and the ^3H -DNA was isolated by the method of Sinclair and Brown (1971). The yield was 1.7 mg ^3H -DNA at a specific activity of 8.9×10^4 cpm/ μg . The ^3H -DNA was sheared to a mean length of 300 nucleotides and passed over Chelex as described above.

Single-copy ^3H -DNA was prepared in the following manner: The ^3H -DNA was heat-denatured and incubated at 67°C in 0.41 M phosphate buffer, 0.5%

sodium dodecyl sulfate, to an equivalent C_0t of 20,000. C_0t is the concentration of DNA in moles of nucleotide per liter times the time of incubation in seconds. In this report, all C_0t values are equivalent C_0t s corrected for the acceleration of reactions in salt concentrations higher than the standard 0.12 *M* phosphate buffer (Britten *et al.*, 1974). The ^3H -DNA was adjusted to 0.12 *M* phosphate buffer and then slowly passed through an hydroxyapatite column maintained at 60°C. The column was then washed with 5 volumes of 0.12 *M* phosphate buffer. Under these conditions, single-stranded ^3H -DNA passes through the column, and double-stranded DNA is bound. The reassociated ^3H -DNA was then eluted from the column with 0.41 *M* phosphate buffer. This was denatured and reincubated to C_0t 200 in 0.41 *M* phosphate buffer at 60°C and passed over hydroxyapatite. The unbound fraction was collected, dialyzed against 0.2 *M* sodium acetate, precipitated with ethanol, and resuspended in 0.12 *M* phosphate buffer. The ^3H -DNA was again incubated at 60°C to C_0t 200 and again passed over hydroxyapatite. This procedure strips the preparation of repetitive sequences, which are all reassociated by a C_0t of 200 (Fig. 21). The unbound fraction from the final C_0t 200 incubation was the single-copy DNA preparation used in the following experiments.

Isolation of oocyte RNA. *Arbacia* oocytes were collected and washed by standard procedures. Eggs were pelleted and resuspended in 0.2 *M* NaCl, 0.001 *M* EDTA, 0.1 *M* Tris, 0.5% sodium dodecyl sulfate (*pH* 7.4), at a concentration of 1 cc of packed eggs per 20 ml of buffer. Eggs were lysed in a Dounce homogenizer and the lysate extracted for 20 min at room temperature with an equal volume of phenol. The lysate was centrifuged for 5 min at 4000 *g* and the aqueous phase was stored at 4°C. An equal volume of fresh buffer was then added to the phenol layer and interface,

and the extraction was continued for 10 min at 60°C. The mixture was again centrifuged, and the two aqueous phases were combined. The combined aqueous phases were then extracted repeatedly with chloroform:isoamyl alcohol (24:1, v/v); the aqueous layer was removed, and the RNA precipitated with 2 volumes of ethanol. The RNA was resuspended and treated with DNase I (Worthington) at 50 $\mu\text{g}/\text{ml}$ in 0.1 *M* sodium acetate (*pH* 5.0), 5 mM MgCl_2 at 22°C for 20 min. The RNA was extensively reextracted with chloroform and the aqueous phase passed over Sephadex G-100. The red *Arbacia* pigment was retarded by the column, while the RNA was excluded in the void volume. The RNA was precipitated with ethanol, resuspended in 0.41 *M* phosphate buffer containing 0.5% sodium dodecyl sulfate, passed over Chelex (Bio-Rad), and stored at -20°C.

DNA-DNA and DNA-RNA reassociation. DNA or RNA was resuspended in 0.41 *M* phosphate buffer, denatured and incubated at 67°C to various C_0t values. The extent of DNA reassociation was assayed by hydroxyapatite chromatography. The samples were adjusted to 0.12 *M* phosphate buffer, and the DNA was passed slowly over hydroxyapatite at 60°C in 0.12 *M* phosphate buffer. The single-stranded DNA was washed from the column with 0.12 *M* phosphate buffer, and the duplex-containing fragments bound in 0.12 *M* phosphate buffer were eluted with 0.41 *M* phosphate buffer. The amount of DNA in each fraction was determined either by its absorbance at 260 nm or by scintillation counting. RNA excess-DNA-RNA reassociation reaction mixtures included 0.5% SDS, and DNA-DNA and DNA-RNA duplexes were assayed by hydroxyapatite by the methods of Galau *et al.* (1974). RNA excess hybridization reactions follow pseudo-first-order kinetics, and the reaction kinetics observed were analyzed accordingly, as described by Galau *et al.* (1974).

NUCLEIC ACID EVOLUTION

EVOLUTIONARY DIVERGENCE AND
LENGTH OF REPETITIVE SEQUENCES
IN SEA URCHIN DNA

Roy J. Britten, Dale E. Graham,*
Francine C. Eden,† Denise M. Painchaud,
and Eric H. Davidson

Recent measurements have shown that short-period interspersions of repetitive and single-copy DNA sequences is the typical pattern of organization of the majority of the DNAs of most species. Short-period interspersions refers specifically to a pattern of repetitive sequences of a few hundred nucleotides alternating with single-copy sequences ranging in length from less than a thousand nucleotides. This pattern is characteristic of the majority of the DNAs of each of 17 animal species which have now been studied (Davidson *et al.*, 1975a), including the human (Schmid and Deininger, 1975). The quantity of DNA involved in this short-period pattern ranges from 50% to 80% of the total DNA (Goldberg *et al.*, 1975; Angerer *et al.*, 1975; Graham *et al.*, 1974; Davidson *et al.*, 1973, 1974, 1975a; Chamberlin *et al.*, 1975; Bonner *et al.*, 1974; Britten and Smith, 1970). *Drosophila* (Manning *et al.*, 1975) and certain other insects (Crain *et al.*, 1976b; Manning, personal communication) contain little or no short repeated sequences, and the majority of their single-copy sequences are probably very long. The dominant pattern of short-period interspersions of repeated and single-copy sequences therefore occurs very generally but not universally in higher-organism genomes. It seems likely that the interspersed repeated sequences carry out important functions in the cell (Britten and Davidson, 1969, 1971; Davidson and Britten, 1971). It has recently been shown that expressed single-copy structural genes

are nearly always next to interspersed repetitive sequences (Davidson *et al.*, 1975b).

The length of the repetitive sequences is clearly a significant aspect of DNA sequence interspersions. Chamberlin *et al.* (1975) showed by electron microscopy of DNA renaturation products that a major fraction of the repetitive sequence elements in *Xenopus* DNA are distributed sharply around a mean value of 345 nucleotides. Similar studies have not been carried out for sea urchin DNA, but in *Xenopus*, sea urchin, and many other DNAs, digestion of renaturation products with S1 nuclease has revealed approximately 300-nucleotide repetitive-sequence elements (e.g., Goldberg *et al.*, 1975; Davidson *et al.*, 1974). The *Xenopus* sequence organization studies are of particular significance for the work described in the present paper. Since no nuclease treatment was used in the electron microscope study of Chamberlin *et al.* (1975), and yet the same average repetitive sequence length was obtained for *Xenopus* DNA as in S1 nuclease experiments (Davidson *et al.*, 1973), it is clear that this enzyme does not often cut within repetitive sequences. This comment refers to the particular high-salt conditions for S1 nuclease applied in this laboratory in studies of repetitive sequence length (see Experimental Procedures) and to repetitive sequences with a base sequence divergence similar to that of *Xenopus* repetitive DNA. When renatured, the repetitive sequences of the sea urchin genome melt about the same number of degrees below long native DNA as do those of the *Xenopus* genome (see below) and thus are divergent to an approximately similar degree. In organisms displaying the *Xenopus* type of sequence organization, repetitive sequences much longer than 300 nucleotides are always present as well. In this paper all stretches of repeated sequences that are longer than 1000 nucleotides are considered to be

* Department of Biology, Purdue University, Lafayette, Indiana 47907

† Department of Biology, University of Indiana, Bloomington, Indiana 47401

part of the "long" repeat class. These have not yet been studied extensively by electron microscopy, and their actual lengths are not yet known.

In this paper we describe further detailed measurements of the length distribution of repetitive sequences in the sea urchin genome, using the single-strand-specific nuclease S1. Within bounds set by the specificity of the enzyme and the length of the original fragments, the length of the resistant duplexes is a measure of the length of the repetitive sequences in the genome. We have investigated the action of the enzyme and find that at appropriately high salt concentrations, the rate of nicking of imperfectly paired reassociated regions can be reduced to low levels. This was also the conclusion reached by Rice (1974a), who studied the effect of S1 nuclease on duplexes formed from denatured DNA of the bacteriophage T4. We have also found that early in the reaction, S1 acts as an endonuclease, making spaced cuts in single strands and thus detaching the repetitive duplexes from most of the single-strand regions. Limited digestion under high-salt conditions effectively prevents nicks within mismatched duplex regions, even though with very extensive digestion (Shenk *et al.*, 1975) or very low NaCl concentration (Wiegand *et al.*, 1975) S1 cuts DNA at single base mismatches.

The thermal stability of the reassociated short and long repetitive sequences isolated by S1-nuclease digestion has been examined in several genomes. We reported earlier that the long regions typically have high thermal stability, similar to that of perfectly paired DNA (Davidson *et al.*, 1973; Goldberg *et al.*, 1975). The short repetitive sequences show a broad range of thermal stabilities, with melting temperatures from a few degrees to as much as 15 degrees below that of native DNA of the same length. Thus there is an apparent correlation between length of repetitive sequence and the amount of divergence within homologous families of repeated

sequence. The validity of this correlation is examined in this paper. The amount of sequence divergence provides a significant insight into the possible evolutionary history of these sequences.

Kinetics and Mode of Action of S1 Nuclease on Eukaryotic DNA

The kinetics of S1 digestion were studied with partially reassociated 2000-nucleotide-long sea urchin DNA fragments since such a DNA preparation was used for the sequence-length measurements reported below. The kinetics of reassociation of sheared sea urchin DNA are well known (Graham *et al.*, 1974), and we estimate that 2000-long fragments reassociated to C_0t 20 will have about 90% of the repetitive sequences and 3% of the single-copy sequences in duplex. Digestion of such DNA with a single-strand-specific nuclease is expected to leave about 25% of the DNA as resistant duplexes. The progress of the digestion was assayed by gel filtration, using Sephadex G-100. Figure 23 shows the results of this experiment. There is an initial very rapid digestion of about 20% of the single strands, followed by a somewhat slower digestion terminating when only about 25% of the DNA remains in relatively large fragments. The resistant DNA fraction has been examined by melting in a spectrophotometer, and its hyperchromicity is within 2%–3% as great as that of native double-stranded DNA. This result shows that the resistant DNA fraction contains at least 90% duplex DNA.

Figure 24 shows the importance of the method of assay in the interpretation of the action of S1 nuclease. Three different methods have been used for these measurements. The abscissa for Fig. 24 is the logarithm of the product of incubation time and the ratio of the quantity of enzyme to the quantity of DNA (units of μ l enzyme min/mg) (see Experimental Procedures). The logarithmic scale is necessary to show the wide range

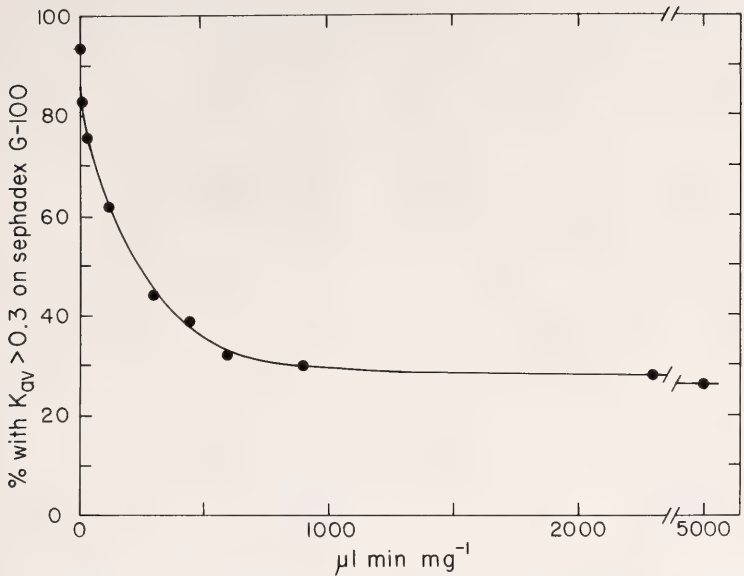


Fig. 23. Kinetics of S1 nuclease digestion of 2000-nucleotide-long sea urchin DNA reassociated to *Cot* 20. Digestions were performed under the standard conditions listed in the methods. The percentage of the DNA which elutes from Sephadex G-100 at $K_{av} < 0.3$ (ordinate) is plotted as a function of the product of enzyme concentration times digestion time divided by DNA concentration (abscissa). Units are μl of enzyme stock (see Experimental Procedures for comparative quantitation) \times min per mg of DNA. DNA concentration was 250 $\mu\text{g/ml}$. The first two points were 2 min and 6 min at 5.7 $\mu\text{l/mg}$. The next 5 points were 6, 15, 22.5, 30, and 135 min at 20 $\mu\text{l/mg}$; and the final point was 50 min at 100 $\mu\text{l/mg}$.

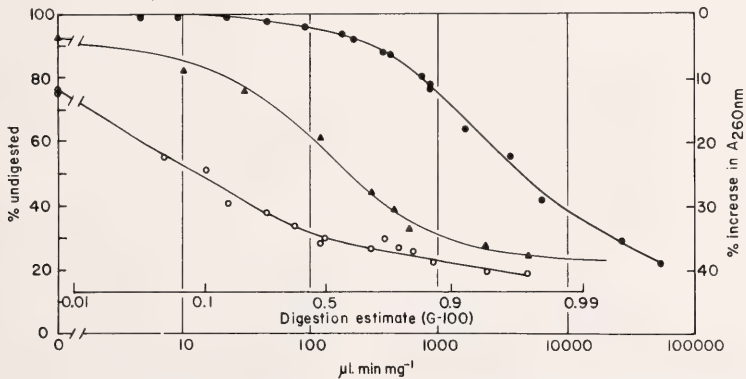


Fig. 24. Kinetics of S1 digestion of 2000 nucleotide long (*Cot* 20) sea urchin DNA assayed by three methods. The center curve (filled triangles) is the G-100 assay data of Fig. 23. The left curve (open circles) shows the percentage of the DNA that is bound to hydroxyapatite. The right curve (filled circles) is the result of two measurements of the optical density at 260 nm of digestion mixtures incubated at 37°C in the spectrophotometer cuvette. The ordinate on the right is the percentage increase in optical density, corrected by the factor 1.33 since only 75% of the DNA is single stranded and digested during the measurements. This scale is useful for DNA quantitation by optical density during extensive digestions. The abscissa is μl of enzyme stock \times min per mg of DNA, as described in Experimental Procedures and in the caption to Fig. 23. Also shown are values of the digestion estimate (DIG) described in the text.

of measurements. The parameter ($\mu\text{l min mg}^{-1}$) is convenient and practical and is justified over the range of enzyme and DNA concentrations used here. It would be inapplicable at very low concentrations or at very different enzyme-to-substrate ratios.

The center curve on Fig. 24 shows the results of the Sephadex assay using the data shown on Fig. 23. This assay depends on the conversion of single-strand DNA to short oligonucleotides. These results should be comparable to those of the commonly used TCA precipitation assay (Sutton, 1971; Vogt, 1973; Schenk *et al.*, 1975) even though DNA fragments can penetrate G-100 beyond $K_{av} = 0.3$, which is probably somewhat larger than the TCA precipitation limit of 10–20 nucleotides.

The right curve shows the increase in optical density at 260 nm for a similar DNA preparation plotted on a scale chosen for comparison with the other curves. This hyperchromic shift is measured at 37°C in the enzyme buffer and results from the destruction of the secondary structure of the single-strand fragments. Two-strand duplexes are not involved. In this low temperature environment the hyperchromicity depends on the fraction of single-strand DNA that has been digested to very small fragments or mononucleotides. By the stage at which most fragments are included (i.e., beyond $K_{av} = 0.3$) on Sephadex G-100, only about 10% or 20% of the ultimate hyperchromic shift has occurred.

The left curve on Fig. 24 shows the reduction in hydroxyapatite binding of DNA originally present as 2000-nucleotide-long fragments incubated to C_0t 20. At the start of the S1 digestion a major part of this DNA preparation consists, of course, of short repetitive duplexes with covalently linked single-strand tails. The single-strand regions make up a majority of these structures, and their average length is $(2000 - 300)/2 = 850$ nucleotides. The reduction in binding to hydroxyapatite is a result of endonu-

cleolytic cuts in the single-strand tails which very rapidly unlink most of the single-copy DNA from the duplex regions. As Fig. 24 shows, this assay measures a reaction which progresses more than 10 times as rapidly as that measured by the G-100 assay.

The relationship between the results of these three assays is qualitatively that expected from independent endonucleolytic scissions occurring throughout the single-strand DNA regions. The reduction in hydroxyapatite binding should be very much faster than the reduction in G-100 exclusion, since one cut every few hundred nucleotides would sharply reduce the length of single-strand tails. One cut every few tens of nucleotides would probably reduce the size far enough for the G-100 chromatography limit we are using. The hyperchromic shift assay reflects a very small fragment size resulting from a much larger number of strand scissions.

To obtain some quantitative insight into these expectations a simple model calculation was made for the scission process. A series of random numbers between 1 and 10,000 were generated in a computer and considered to be the locations of cuts in 10,000 nucleotides of DNA. As the calculation proceeded, the lengths of the surviving uncut fragments were scored and gave the results shown in Fig. 25. The left curve is the fraction of fragments greater than 200 long, while the center curve is for fragments greater than 20 long. The fraction of fragments 200 nucleotides or longer decays at about 10 times the rate of the fraction of fragments greater than 20 nucleotides long. Thus the calculation is consistent with the qualitative expectation. In addition the left and the center calculated curves on Fig. 25 are examples of the kinetics expected for a single-strand scission process. There is an approximately exponential decay of the number of fragments greater than 200 nucleotides or 20 nucleotides with the form of pseudo-first-order reactions. These reactions are essentially com-

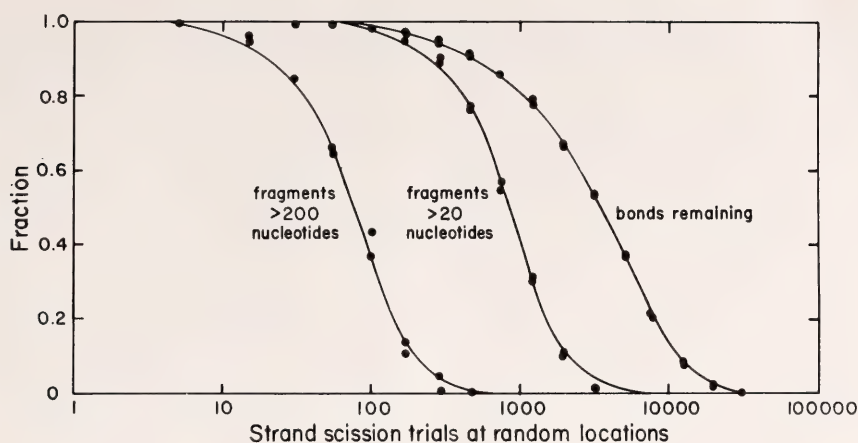


Fig. 25. Results of a model calculation of endonucleolytic digestion using a Monte Carlo method with a computer (see text). The left and center curves show the fraction of fragments remaining greater than 200 and 20 nucleotides as a function of the number of strand-scission trials at random locations per 10,000 nucleotides. The right curve shows the fraction of bonds remaining.

pleted (10%–90%) within about a factor of 10. However, the measurements of the digestion of single-stranded DNA shown on Fig. 24 require more than two decades for completion. We draw the conclusion that the measured S1-nuclease digestion is made up of more than one process; i.e., that the reaction cannot be described with a single rate constant. Thus the reaction appears to be heterogeneous in rate. Furthermore, there are good reasons to believe that more than one digestion mechanism is involved.

The choice of a unit for the quantitation of S1-nuclease activity is made difficult by the apparent heterogeneity of the rate of reaction at various stages and by the great dependence of the result on the method of assay. We have avoided the definition of a unit of S1-nuclease activity by describing each digestion in terms of an arbitrary quantity which depends on the concentration of enzyme in our particular batch (i.e., $\mu\text{l min mg}^{-1}$).

As mentioned, the kinetics of digestion are complex and cannot be described in terms of a single process. However, an estimate of the fraction of single-strand

DNA digested is useful for interpreting and planning measurements with S1-nuclease and for quantitative comparison with results in other laboratories. To arrive at an estimate of the extent of digestion we make use of the half-reaction point by G-100 assay in units of $\mu\text{l min mg}^{-1}$. A convenient empirical equation for the calculation of the estimated extent of digestion (DIG) at any given value of $\mu\text{l min mg}^{-1}$ is $\text{DIG} = 1 - (1 + \mu\text{l min mg}^{-1}/H)^{-1}$ where H is the value of $\mu\text{l min mg}^{-1}$ for half digestion. For our conditions, enzyme batch, and DNA, H is $135 \mu\text{l min mg}^{-1}$. As an example we calculate the DIG at $10 \mu\text{l min mg}^{-1}$, which is about half reaction by hydroxyapatite assay on Fig. 24. The DIG is $1 - (1 + 10/135)^{-1} = 0.07$. The G-100 assay measurements show about 10% digestion at this stage, which is in reasonable agreement. Under certain conditions, such as extreme enzyme-to-DNA ratio, the DIG calculation might be expected to yield a poor approximation, and it would be better to perform a G-100 assay at or near the actual digestion conditions.

The digestion of single strands is nearly complete (G-100 assay) by 1000

$\mu\text{l min mg}^{-1}$ ($\text{DIG} = 0.88$), and the curves for G-100 assay and hydroxyapatite assay show only a small slope on Fig. 24. However, the quantity of resistant DNA differs between the two assays. To investigate this difference 2000-long C_{ot} 20 reassociated sea urchin DNA was digested to $5000 \mu\text{l min mg}^{-1}$, and the fraction of the DNA that eluted from a Sephadex G-100 column at $K_{av} < 0.3$ was passed over hydroxyapatite. To confirm the reality of this fraction, the hydroxyapatite-unbound DNA was again passed over G-100 and hydroxyapatite. About 5% of the total original DNA was recovered, and this sample was melted in the spectrophotometer to determine the amount of duplex present. This fraction exhibited a low melting temperature of 70°C and a hyperchromicity of 9% or about one third that of native DNA. Thus perhaps one third of this DNA (i.e., 1.5% of the total starting DNA) is resistant repetitive duplexes which do not bind to hydroxyapatite. We have not further characterized this S1-resistant DNA.

The length of single-strand DNA fragments remaining undigested at various stages of the reaction has been studied to further elucidate the mechanism

of S1 digestion. These fragments are longer than would be expected as a result of endonucleolytic strand scissions at random locations. Since the fraction bound to hydroxyapatite is less than the fraction which elutes from G-100 at $K_{av} < 0.3$, purely single-strand fragments are present in the undigested fraction measured by the Sephadex assay. Therefore a hydroxyapatite binding step is now included in the purification of S1-resistant duplexes and is very important for light S1 digestion studies (less than $1000 \mu\text{l min mg}^{-1}$). The single-strand DNA fragments recovered from the G-100 columns after $450 \mu\text{l min mg}^{-1}$ ($\text{DIG} = 0.77$) digestion has a mode length of about 300 nucleotides, as assayed on alkaline sucrose gradients.

The more extensive observations described in Table 17 show that the mode size of single-strand DNA fragments decreases very slowly. Both *E. coli* and sea urchin DNAs were studied. The right column on Table 17 shows that after very little digestion the single-strand fragment length has been reduced to 400 nucleotides. Increasing the amount of enzyme increases the digestion but gives only a moderate reduction in single-strand fragment size. Therefore, the

TABLE 17. Length of Single Strands after 5 min S1 Digestion

| | Enzyme ^b $\mu\text{l min mg}^{-1}$ | DNA eluting at $K_{av} < 0.3^c$ (%) | Single-Strand Length ^d (nucleotides) |
|--|--|---|---|
| 2800 nucleotide | 0 | 95 | 2700 |
| Urchin DNA ($C_{ot} \approx 0.01$) ^{a, e} | 50 | 96 | 407 |
| | 150 | 76 | 305 |
| | 500 | 42 | 220 |
| 1600 nucleotide <i>E. coli</i> ^{a, e} | 0 | 99 | 1508 |
| | 100 | 65 | 270 |
| | 500 | 38 | 214 |

^a Alkaline sucrose measurements before denaturation.

^b Digestion under standard conditions.

^c Chromatographed on Sephadex G-100 in 0.12 M phosphate buffer, pH 6.8.

^d Alkaline sucrose measurements of fragments recovered from G-100 columns.

^e Sea urchin DNA at $112 \mu\text{g/ml}$ or *E. coli* DNA at $43 \mu\text{g/ml}$ was denatured in a sealed capillary tube at 100°C for 1 min, then blown out into 1 ml buffer at 27°C containing single-strand calf carrier DNA at $50 \mu\text{g/ml}$ and S1 nuclease. Less than 1% of the *E. coli* and less than 10% of the sea urchin DNA could have reassociated.

number of endonucleolytic scissions does not increase in proportion to the ratio of S1 nuclease to DNA. Line 3 of Table 17 shows 25% of the DNA digested (G-100 assay) while the mode size of the excluded fragments is 305 nucleotides. If the action of the enzyme were solely a result of random endonucleolytic scissions we would expect (after one fourth of the DNA had been reduced to less than 10 or 20 nucleotides) that a smaller mode size than 305 nucleotides would be observed. For example, a model calculation for randomly located strand scissions (Fig. 25) gives a mode size of about 25 nucleotides when 25% of the DNA has been reduced to fragments less than 20 nucleotides. We visualize that the digestion proceeds by means of a limited number of initial endonucleolytic strand scissions followed by dominantly exonucleolytic digestion. The measurements with *E. coli* DNA (Table 17) show that this is not a specific property of sea urchin or higher organism DNA. It is not clear that the endonucleolytic and exonucleolytic activities are present on the same enzyme molecule. A second batch of enzyme prepared in the same way as the one used here shows a somewhat greater ratio of reaction rate assayed by hydroxyapatite to the rate assayed by G-100, i.e., relatively greater endonucleolytic activity. The early endonucleolytic activity is useful for our purposes since at very limited enzyme digestion most of the single strands are cleaved from contiguous duplexes. At this early stage no measurable strand scissions take place within the mispaired duplexes under our conditions of reduced temperature and high salt concentration.

Repetitive DNA Duplexes after Limited Enzyme Digestion

The size distribution of repetitive S1-nuclease-resistant duplexes after very limited enzyme digestion is shown in Fig. 26. For this measurement sea urchin DNA was sheared to 2000 nucleotides, denatured, incubated to equivalent C_0t

20, and digested for 45 min with 5 μ l/mg S1 nuclease under standard conditions. Such a light digestion (DIG = 0.63) yields many single-strand fragments of a few hundred nucleotides length which are not linked to duplex regions (cf. Table 17). The duplex-containing fragments were isolated by diluting the sample into a large volume of 0.12 M phosphate buffer (PB) and passing it over hydroxyapatite at 60°C. About 26% of the DNA was bound to hydroxyapatite while 51% eluted from the Sephadex at $K_{av} < 0.3$ in a parallel assay. The duplex-containing fraction was eluted from the hydroxyapatite with 0.4 M PB and analyzed on a Biogel agarose A-50 column. The lower curves of Fig. 24 are a composite from an immediately previous calibration of the column using very long ^3H -labeled sea urchin DNA as an exclusion marker, $^{32}\text{PO}_4$ as an inclusion marker, and sheared native DNA to mark the position of 300 nucleotide duplexes.

Figure 26 shows a bimodal distribution of lengths consisting of structures which are 2000 nucleotide pairs and longer in the exclusion region and a broad distribution of shorter lengths included by the column, with a mode value near 300 nucleotide pairs. The length of the fragments in the exclusion region is presumably limited by the length of the initial DNA fragments. However, the following arguments indicate that the length of the shorter fragments recovered from an agarose A-50 column gives a good representation of the length of short repetitive sequences in the sea urchin genome. Much of the single-strand DNA remains a few hundred nucleotides long after this light digestion (Table 17), showing that the number of endonucleolytic cuts is relatively small even in purely single-strand regions. Furthermore, the rate of attack on mismatched duplexes is very low compared with the rate for single strands. Very few cuts can have been made in mismatched duplexes. Therefore, after the light enzyme digestion (DIG = 0.63)

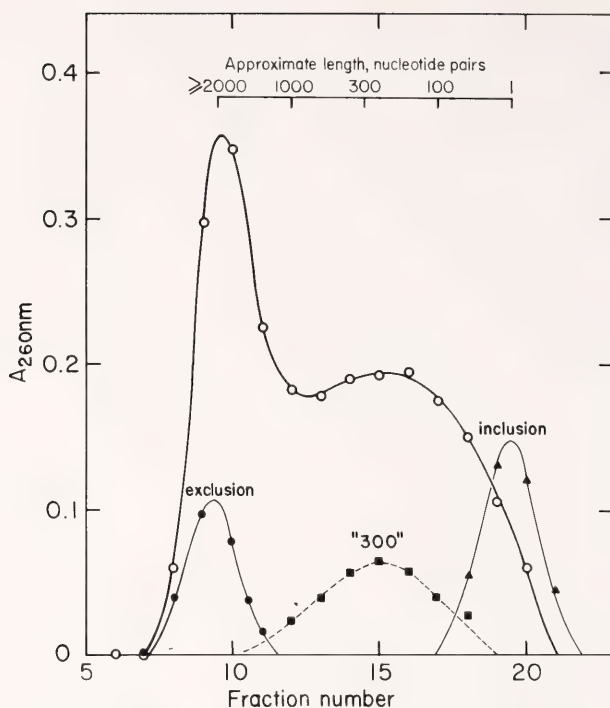


Fig. 26. Agarose A-50 fractionation of 2000-nucleotide-long sea urchin DNA fragments reassociated to *Cot* 20. The DNA was digested under standard conditions for 45 min at 5 μ l/mg and passed over hydroxyapatite (see Experimental Procedures). The three calibration markers shown in the lower part of the figure are from an immediately previous run with the same column and are very long native DNA, 300-long sheared duplex fragments, and radioactive orthophosphate. Each fraction corresponds to about 5 ml. The scale at the top shows an estimate from other agarose A-50 calibration runs of the expected elution positions for duplexes of various lengths.

the duplex length distribution cannot have been significantly reduced below that of the repetitive regions. The duplex lengths are somewhat overestimated because single-strand ends presumably remained attached to some of the duplex regions. However, the hyperchromicity of the fragments shows that they are principally duplex. We estimate that the single-strand tails amount to less than 25% of the short fragments, by mass.

The thermal stability and hyperchromicity were measured by melting in a spectrophotometer. The melting curves of each of the fractions is shown in Fig. 27 along with those of long native DNA and purely single-strand DNA for comparison. The hyperchromicity of the long

fragments (Fractions 9, 10, and 11) is greater than 90% of pure duplex while that of the 300-nucleotide peak fragments (Fractions 14, 15, and 16) is about 75% of that of pure duplex. Figure 27 also shows the correlation between thermal stability or sequence mismatch and length which will be examined in detail below. The low thermal stability of short fragments suggests that their hyperchromicity is reduced by internal mispaired bases, as well as by unpaired DNA at the ends of the two strands.

The Length of the Component Single Strands of the Repetitive Duplexes

In order to measure the length of the repetitive duplexes by an independent

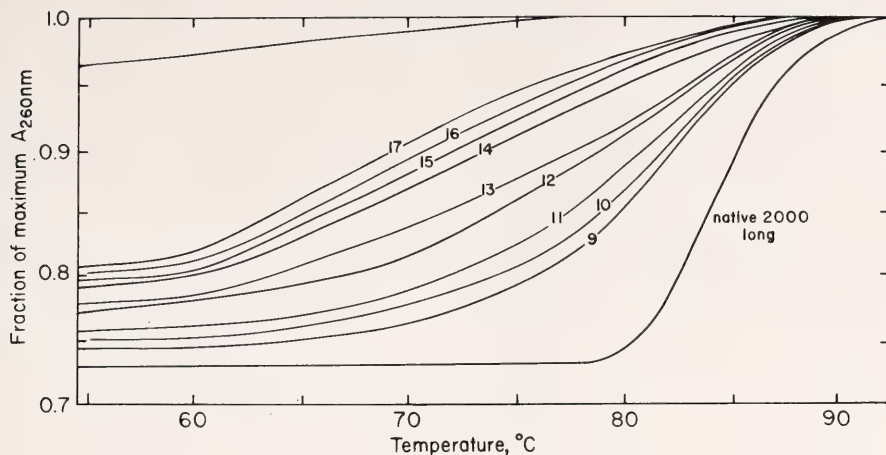


Fig. 27. Spectrophotometric melting curves of the fractions from Fig. 26. In order to determine the hyperchromicity the column effluent from Fractions 6 and 7 ($OD = 0.071$) and from Fractions 23 and 24 ($OD = 0.071$ and 0.066) of Fig. 26 was used to estimate the solution blank. Samples were melted in a spectrophotometer with paper tape recording and computer averaging to improve precision. The native 2000-long DNA was also sea urchin DNA.

method and to determine whether the S1 nuclease had created nicks within these duplexes, the length of the component single strands was determined by alkaline sucrose gradient sedimentation. This experiment showed the mode length of the single strands of the short interspersed repetitive sequences to be about 300 nucleotides, as expected. The details of the experiment are as follows. Two thousand-nucleotide-long fragments of 3H -thymidine-labeled DNA were reassociated to C_0t 4 and digested with 10 μ /mg of S1 nuclease for 45 min under standard conditions. The sample was brought to 0.12 M PB and passed over hydroxyapatite at 60°C. The binding is less than that shown on Fig. 24 because the incubation was to C_0t 4 rather than C_0t 20. Eighteen percent of the labeled DNA was bound, and this fraction was assayed on agarose A-50 (Fig. 28). Fractions 50–66, as indicated on Fig. 28, were combined and concentrated, and the single-strand fragment length was determined by alkaline sucrose sedimentation. Figure 29 shows the alkaline sucrose profile. A rather sharp peak is seen, indicating a narrow distribution of

lengths around a mode value of 328 nucleotides (311 in another measurement). Thus this measurement shows that S1 nuclease did not create any appreciable number of single-strand nicks in the imperfectly paired reassociated regions. A narrow distribution of lengths around 300 nucleotides has been observed for similar fractions of S1-nuclease-resistant DNA from a number of other organisms (Goldberg *et al.*, 1975; Davidson *et al.*, 1974; Chamberlin *et al.*, 1975).

The length of the component single strands of the long repetitive duplexes excluded on an agarose A-50 column was also determined by alkaline sucrose sedimentation. The results were 9.8 and 10.2 S, yielding an average single-strand length of 1460 nucleotides. This value is somewhat shorter than the starting fragment size of about 2000 nucleotides. It indicates that during denaturation, reassociation, hydroxyapatite chromatography, S1 treatment, and agarose A-50 chromatography, a small single-strand length reduction occurred, perhaps one nick in every other 2000-nucleotide strand. This result shows that the long reassociated DNA was almost entirely

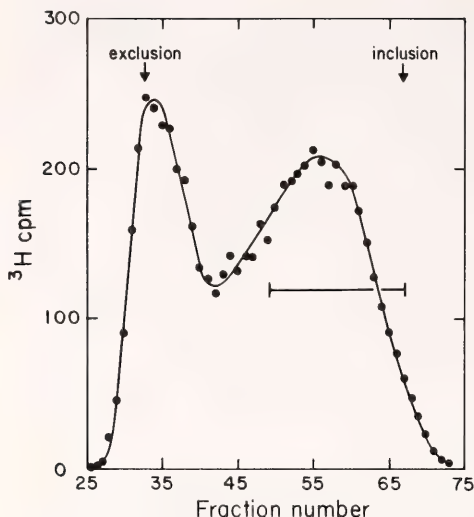


Fig. 28. Agarose A-50 fractionation of ^3H -labeled sea urchin 2000-long fragments incubated to C_{ot} 4 and digested for 45 min under standard conditions with 10 μl S1 nuclease per mg DNA ($\text{DIG} = 0.77$). The positions of exclusion and inclusion markers are shown by arrows. The fractions indicated were pooled and concentrated, and DNA single-strand size was determined by alkaline sucrose as shown in Fig. 29.

in duplex. There are apparently few S1-nuclease-sensitive single-stranded regions in the reassociated long repetitive DNA. Therefore in the genome the long repetitive sequences are longer than the fragment size of 2000 nucleotides. A similar conclusion can be drawn from the near native hyperchromicity of the excluded DNA fragments shown in Fig. 27. Were the long repetitive sequences interspersed with single-copy sequences at a 2000-nucleotide length, a fraction of the single-copy sequence would have remained attached, and the hyperchromicity of the excluded fractions would have been reduced significantly below the 25% observed in Fig. 27.

Repetitive Duplexes after Extensive S1 Digestion

The result of a more extensive digestion of reassociated DNA with S1 nu-

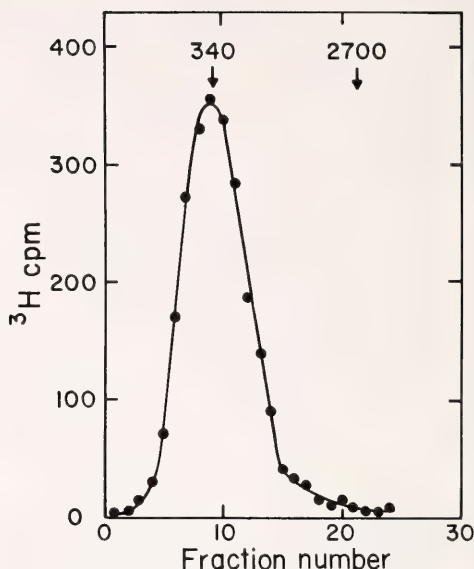


Fig. 29. Alkaline sucrose gradient profile of the pooled fractions from the agarose A-50 analysis shown on Fig. 28. The positions of two unlabeled markers of 340 and 2700 nucleotides are shown. The mode size of the pooled samples is 328 nucleotides, and the width is reasonably narrow.

lease is shown in Figs. 30 and 31. Two-thousand-nucleotide DNA fragments were denatured, reassociated to C_{ot} 20, and digested with 100 $\mu\text{l}/\text{mg}$ for 45 min under standard conditions ($\text{DIG} = 0.97$). In this measurement ^3H -thymidine-labeled sea urchin embryo DNA was mixed with a large quantity of sperm DNA. The quantities of DNA shown in Fig. 30 are based on the optical density of the fractions eluted from agarose A-50 column. The radioactivity was also assayed, and the long DNA fragments showed a slightly greater specific activity (^3H cpm/optical density at 260 nm) than did the short fragment region.

Our purpose here is to compare the results of the extensive digestion with those for the limited digestion described earlier. The quantity of enzyme per mg of DNA used for the measurement of Figs. 30 and 31 is the same as that used in the digestion kinetics measurement of

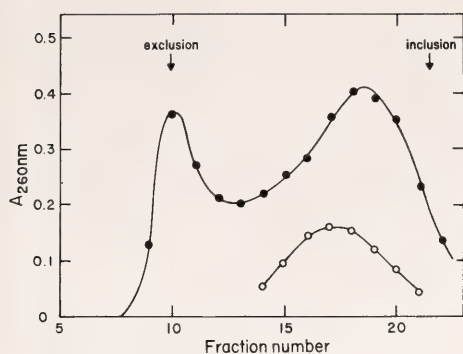


Fig. 30. Agarose A-50 analysis of 2000-nucleotide-long sea urchin DNA reassociated to *Cot* 20 and extensively digested with S1 nuclease at 100 $\mu\text{l}/\text{mg}$ DNA for 45 min (4500 $\mu\text{l min mg}^{-1}$ DNA, DIG = 0.97). The lower curve represents a 300-nucleotide-long duplex DNA marker.

Fig. 23 and 20 times that used in the measurements of Figs. 26 and 27. Qualitatively the results of this extensive digestion (DIG = 0.97) are similar to those of the limited digestions (DIG = 0.63 and 0.77) shown in Figs. 26, 27, and 28. In all cases an exclusion peak made up of long enzyme-resistant duplexes is seen as well as a short duplex peak with a mode size of about 300 nucleotides. However, quantitatively the effect of more extensive digestion is clearly visi-

ble. The long fragments account for a smaller fraction of the DNA as the digestion is increased (Table 18). In addition, there appears to be a slight reduction in the mode size of the short fragments. Some differences are also present in the melting curves of Fig. 31 (DIG = 0.97) compared to those of Fig. 27 (DIG = 0.63). The long duplex fractions such as 10 and 11 show an even higher melting temperature and hyperchromicity after the more extensive digestion. It appears that a low melting fraction has been removed from the long repetitive-sequence region. We interpret this to mean that there is a class of large reassociated structures made up of somewhat divergent repetitive sequences. These structures include mispaired or unpaired regions that can be digested or cut after extensive treatment with S1 nuclease. Since the total quantity of S1-resistant DNA does not appear to decrease very much, the products of the extensive digestion probably appear as short duplexes. Table 18 shows that after light digestion about half of the resistant DNA is in large structures (K_{av} less than 0.3), while after extensive digestion only about a third remains large. Therefore, about one sixth of the S1-resistant reassociated DNA is in structures which

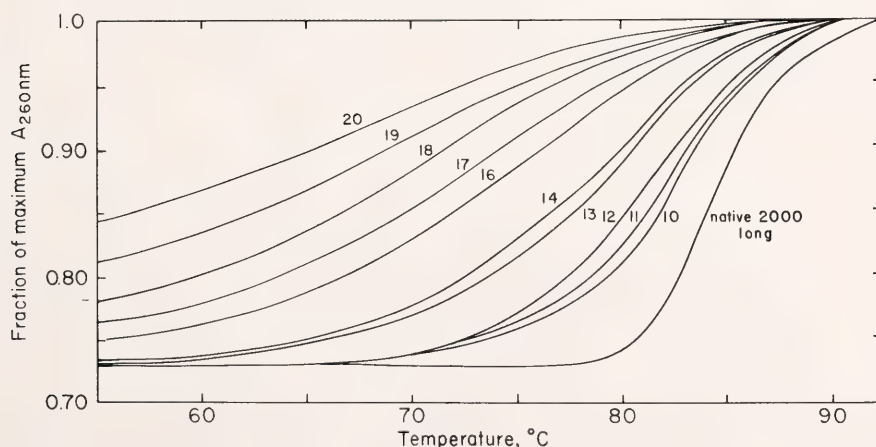


Fig. 31. Spectrophotometric melting curves of the fractions from Fig. 30. See caption of Fig. 27 for details.

TABLE 18. Fraction of DNA in Long and Short Duplexes after 45-min S1 Digestion of 2000-Nucleotide Reassociated Fragments

| Experiment | 1 | 2 | 3 |
|---|--------|--------|--------|
| Equivalent <i>Cot</i> | 20 | 4 | 10 |
| Enzyme/DNA (μ l/mg) | 5 | 10 | 100 |
| Digestion estimate (DIG) | 0.63 | 0.77 | 0.97 |
| S1-resistant DNA associated with duplex; hydroxyapatite binding (%) | 26 | 18 | 20 |
| Fragments longer than 1000 nucleotides; K_{av} less than 0.3 (%) | 47 | 40 | 30 |
| Figures showing results | 26, 27 | 28, 29 | 30, 31 |

are large after light digestion and are reduced to less than about 1000 nucleotide pairs by extensive digestion (K_{av} greater than 0.3). This amounts to about 4% of the genome, since about 25% of the DNA is in S1-resistant repetitive sequences reassociated by *Cot* 20.

Correlation between Precision of Repetition and Length

The melting curves shown in Figs. 27 and 31 exhibit a very striking effect. The short S1-resistant duplexes (Fractions 16–18) melt as much as 10°–15°C below the long repetitive duplexes (Fractions 9 and 10). Furthermore, there is a correlation between duplex length, as determined by agarose A-50 chromatography, and T_m over the whole range, from the exclusion peak to the smallest duplex that could be adequately measured. The data of Fig. 31 show this effect very clearly for DNA which had been extensively digested (DIG = 0.97). However, even with limited S1 digestion (DIG = 0.63) this correlation is clearly evident, as shown in Fig. 27. Part of the variation of T_m with length results from sequence divergence, and part results from the length of the fragments. The direct effect of length may be estimated from measurements of the thermal stability of perfectly matched DNA duplexes of

various lengths (Crothers *et al.*, 1965; Hayes *et al.*, 1970). These and other results have been reviewed by Britten *et al.* (1974), and under the conditions used here the differences in melting temperature between long DNA and fragments of length L (in nucleotides) is best estimated as $650/L$. On this basis, for a length of 300 nucleotides the expected melting temperature decrease is about 2°C. The length effect could be slightly greater for mismatched duplexes, but it is clear that only a minor fraction of the 10°–15°C difference is directly due to the length of the duplexes. The reduction in thermal stability therefore must be caused principally by sequence mismatch resulting from divergence of the repetitive-sequence classes. We estimate that the degree of divergence ranges from 0%–2% for the long DNA fractions to 10% or 15% for the short duplex class. These estimates are somewhat uncertain as a result of inaccuracy with which the relation between T_m reduction and percentage of mismatch is known. We have used a factor of 1% mismatch per 1°C reduction in T_m (Britten *et al.*, 1974; Wetmur, in press).

It is known that under certain conditions S1 nuclease will digest mispaired regions (Sutton, 1971). The proposition might be made that the correlation between length and precision is an artifact of the nuclease. That is, there might be a higher probability of an S1-nuclease cut occurring in more divergent duplexes, thus reducing their length relative to more precisely paired fragments. This proposition is inconsistent with three kinds of evidence which will be examined in the remainder of this section.

First, in the case of *Xenopus laevis* DNA the length of the short repeated sequences has been measured in the electron microscope without the use of enzyme digestion (Chamberlin *et al.*, 1975). These measurements, based on a total of 575 repetitive duplex regions for which both terminations could be observed, yielded a mean length of 345 nucleotides. The same result was obtained

from S1-nuclease measurements on re-natured *Xenopus* DNA (Davidson *et al.*, 1974) made in the manner described here.

Second, the measurements with sea urchin DNA have been repeated using the single-strand exonuclease Exo-7, which degrades single-strand DNA from both 3' and 5' ends but does not attack duplex regions (Chase and Richardson, 1974) even if they are mispaired. This measurement was done by incubating 800-nucleotide sea urchin DNA to C_0t 7 and digesting with 10 units of Exo-7/ μ g of DNA. The digestion products were passed over hydroxyapatite, and 16% of the DNA was bound. The bound fraction was analyzed on an agarose A-50 column. Since Exo-7 requires free single-strand ends, the digestion was incomplete. Due to the short initial fragments the long and short repeated regions were not so well resolved in this experiment. Nevertheless, the correlation between length and precision of pairing was observed. Measured by hydroxyapatite thermal chromatography the longer enzyme-resistant fractions had a T_m only 5°C below 2000-nucleotide native DNA fragments, while the shorter fractions melted 14°C below the native sea urchin DNA.

In a third approach the correlation between precision of base pairing and length of repeated regions has been directly demonstrated, without the aid of any nuclease, by means of hydroxyapatite thermal chromatography. The preparation of high and low thermal stability repetitive fractions from 2500-nucleotide-long DNA fragments is detailed in Table 19. Included with the repetitive sequence fractions are covalently linked single-copy sequences. The earlier steps remove the zero-time binding fraction (steps 1-2), and the single-copy DNA that is not linked to repeated sequences (steps 3-5). This is important since self-reassociated single-copy DNA would also appear in the high thermal stability fraction. Step 7 is the principal thermal fractionation procedure. It is

followed by a preparative alkaline sucrose step to assure that the high and low thermal stability fractions examined have the starting fragment length. It was found that little degradation had occurred and most of each fraction was recovered as long fragments. At this point the labeled fractions were sheared to separate most of the linked single-copy DNA from repetitive sequences. The kinetics of reassociation of the fractions were measured in the presence of a great excess of total sheared sea urchin DNA. Figure 32 shows the reassociation kinetics for the high and low thermal stability fractions. The difference between these two curves is principally due to the presence of a large single-copy component in the 60°-70°C fraction which is absent in the 80°-90°C fraction. The rate of reassociation of single-copy sequences in the presence of total sea urchin DNA is well known for this fragment size (Graham *et al.*, 1974; Davidson *et al.*, 1975b). Therefore, in the analysis of the kinetics shown in Fig. 32 the rate of the single-copy component was fixed ($k = 0.00125 M^{-1} \text{ sec}^{-1}$). Least-squares analysis showed that the single-copy component amounted to 53% of the 60°-70°C fraction. We conclude that this fraction is derived from the interspersed regions of the genome and that the repeated sequences are typical divergent short sequences about 300 nucleotides long. Least-squares analysis of the kinetics of the 80°-90°C fraction showed only a 5% single-copy component. Due to scatter in the data there remains an uncertainty of 5%-10% as to the quantity of single-copy sequences present in this fraction, and none might really exist. Since the quantity of single-copy sequences is small or nil, the high thermal stability fraction must have been derived from long repeated-sequence regions which were not interspersed with single-copy sequences on a length scale of about 2000 nucleotides. This observation directly demonstrates the correlation between the precision of repetition

TABLE 19. Measurement of Linkage of Single-Copy DNA to Sea Urchin Repetitive Fractions vs. Sequence Divergence

| Starting Material | 30 μg 2500-Nucleotide-Long Sea Urchin Labeled DNA | | | | |
|---|---|-----------------------------------|------|-------------|---------------|
| 1. Denature and incubate to | <i>C_{ot}</i> 6 × 10 ⁻⁴ | | | | |
| 2. Hydroxyapatite fractionation | unbound 89% bound 11% (discard) | | | | |
| 3. Add 1.5 mg 500-nucleotide-long driver DNA (a 50-fold excess) | | | | | |
| 4. Denature and incubate to | <i>C_{ot}</i> 49 | | | | |
| 5. Hydroxyapatite fractionation | unbound (discard) | bound 72% of tracer 40% of driver | | | |
| 6. Denature and incubate to | <i>C_{ot}</i> 20 | | | | |
| 7. Hydroxyapatite thermal chromatogram | Fraction eluted at | | | | |
| % labeled DNA loaded | 60°C | 70°C | 80°C | 90°C | 98°C |
| % original total labeled DNA | 44 (discard) | 18 | 30 | 18 | 0.6 (discard) |
| 8. Alkaline sucrose to eliminate small fragment contamination | | | | | |
| 9. Shear to | 477 | 311 | 444 | nucleotides | |
| 10. Add unfractionated 500-long driver DNA (600-fold excess over previously added driver) | | | | | |
| 11. Reassociation kinetic curve for each fraction by hydroxyapatite assay | | | | | |
| 12. Least-squares analysis, fixing the single-copy rate as 0.00125 (M ⁻¹ sec ⁻¹), the single-copy rate in total sea urchin DNA | | | | | |
| Fraction of labeled DNA which is single copy | 53% | 35% | 5% | | |

* The 53% single-copy sequence observed in the low thermal stability fraction suggests that the fragments had been somewhat reduced in size by this stage, as expected in a fractionation procedure involving this many steps. Long fragments of purely interspersed DNA would contain about 75% single-copy DNA (Graham *et al.*, 1974) and fragments of about 700-nucleotide length would contain about 55% single-copy DNA.

and the length of the repeated sequences by an independent route.

Conclusion

Both long and short repetitive sequences have been found in sea urchin DNA. Other briefly reported measurements indicate that this pattern is of general occurrence in eukaryotic DNA. Table 20 summarizes the results for the DNAs of the five species for which measurements of the type reported here have been completed, including thermal stability measurements of the long and

short repeated sequences. Each of these DNAs exhibits properties very similar to those of sea urchin DNA. The mode length of the short repeated sequences is almost identical (see references listed on Table 20), and the degree of sequence divergence of the families of short sequences is very similar. Calf and silk moth long repeated sequences show higher thermal stability than does native DNA, presumably as a result of the special nucleotide composition of satellites present in the long sequence fraction. Calf DNA is known to have high GC satellites (Britten and Smith, 1971).

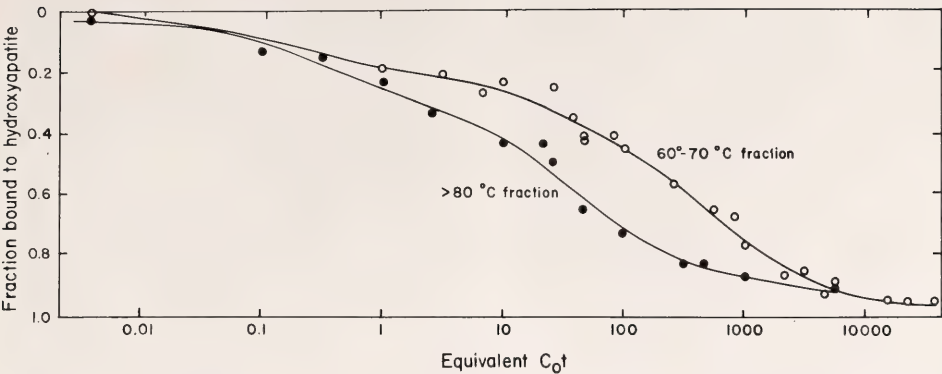


Fig. 32. Reassociation kinetics assayed by hydroxyapatite (60°C, 0.12 M PB) of high and low thermal stability fractions from the experiment described in Table 19. The labeled fractions eluted at 70°C and 90°C were sheared and mixed with a 600-fold excess of total unlabeled DNA (see Table 19). The curves shown are the result of least-squares analysis of the kinetics of reassociation for three second-order components. The driver DNA showed the expected reassociation kinetics for 450-nucleotide-long fragments (Graham *et al.*, 1974), including single-copy component half reassociation at *C*₀*t* 800.

The DNA of oyster, horseshoe crab, the jellyfish *Aurelia*, and the nemertean worm *Cerebratulus* (Goldberg *et al.*, 1975) have been reassociated to repetitive *C*₀*t*, digested with S1, and analyzed on agarose A-50 columns, although the thermal stabilities were not measured.

In each case both long and short repetitive sequences were observed, and the mode length of the short sequences appears to be about 300 nucleotides. Thus, not only are long and short repetitive sequences observed in the DNA of many species, but the details of their sequence

TABLE 20. Thermal Stabilities of Long and Short Repetitive Regions of Eukaryotic DNA*

| Organism | Melting Temperature of Duplexes Relative to Long Native DNA, Corrected for Duplex Length ^b (°C) | | Reference |
|--|---|---------------------------------------|--|
| | Long Repeats (>1500 nucleotides) | Short Repeats (300 nucleotides) | |
| <i>Spisula</i> (clam) | -1 | -8 | Goldberg <i>et al.</i> , 1975. Fig. 31. |
| <i>Strongylocentrotus</i> (sea urchin) | -2 | -9 | |
| <i>Xenopus</i> (clawed toad) | -2 | -12 | Davidson and Britten, 1973. |
| <i>Antheraea pernyi</i> (wild silk moth) | +1 | -10 | Efstratiadis <i>et al.</i> , in press. |
| <i>Bos</i> (cow) | +3 | -12 | Britten, unpublished. |

* 2000-4000 nucleotide long DNA was reassociated to a *C*₀*t* sufficient for the reassociation of most of the repetitive DNA and treated with S1 nuclease. Long and short duplexes were isolated by chromatography on agarose A-50 and melted in a spectrophotometer. The melting temperature of the excluded peak is compared to that of the mode of the short region which was about 300 nucleotides in each case.

^b Melting temperature depression due to duplex length was taken to be 650 divided by the duplex length in nucleotides.

organization are, at least in some respects, very similar. Many further observations will be required for a functional interpretation of these generally occurring patterns. However, their generality and the nonrandom distribution of both repetitive and nonrepetitive sequence element lengths indicates that the interspersal patterns have been selectively preserved during the evolution of higher organism genomes. This implies a functional significance.

The sequence organization of the long repetitive regions is as yet unknown. Probably these regions consist of a mixture of tandemly repeated short or simple sequences such as satellites and longer sequences which do not show internal repetition in short distances. The long repeated sequences have complexity and a range of repetition frequencies similar to the short repetitive sequences (Eden *et al.*, in preparation).

Evolutionary Implications

The correlation between precision and length of repeated sequences may have useful implications for understanding the evolution of both classes of repetitive sequence. Knowledge of repetitive sequence function is very limited except for some long repeated sequences that are clustered structural genes for tRNA, ribosomal RNA, and histones. In addition, there are probably other as yet unidentified clustered repeated genes (Galau *et al.*, 1976a; Goldberg *et al.*, 1973). It has been argued (Galau *et al.*, 1976b) that such clustered repetitive genes could account for a significant fraction, perhaps a majority, of the long repetitive regions.

Currently available evidence on the evolution of repetitive sequences has recently been reviewed (Britten and Davidson, in press), including the correlation between precision of repetition and sequence length. Here we limit discussion to two propositions which can be best supported: (1) The divergence of the short repeated sequences shows that

they have been present for extended periods of evolution; (2) the precisely repeated long sequence regions are relatively recent additions to the genome even though they may be multiple copies of preexisting sequences rather than totally new sequences.

We may estimate a lower limit for the evolutionary age of the long and short repetitive sequences from their degree of sequence divergence. Only limited measurements of evolutionary rates of change of DNA sequence are available, and these differ depending on the group of organisms. For example, the rate of nucleotide substitution in single-copy DNA during much of higher primate evolution has been measured to be about 0.1% per million years (Kohne *et al.*, 1970; Hoyer, *et al.*, 1972; Britten and Davidson, in press). In rodents this rate may be as much as five times greater (Rice, 1974b). Britten and Davidson (in press) argue that the rate of nucleotide substitution observed in the majority of single-copy DNA is not greatly affected by selection pressure. This observation was based on evidence suggesting that much of the single-copy DNA is probably not structural gene DNA and on the fact that in primates the most rapidly changing protein coding sequences evolve at the same rate as the majority of the single-copy DNA. Typical short repetitive sequences show about 10% average divergence. If the rate of substitution of the repeats were the same as that of primate single-copy DNA, 50 million years would be required to reach 10% average sequence divergence. Therefore we estimate that many of the short repetitive sequences have been present in primate genomes for at least 50 million years. If the rate of divergence of the repetitive sequences were reduced by selection pressure then the sequences could be much older. In other taxons the rates of divergence are higher and the minimum sequence age correspondingly lower. According to Table 20 the reassociated short repeats have an average reduction in T_m of 8°–12°C for all five species, and thus a se-

quence divergence of about 10%. The similarity in the degree of divergence within the short repetitive sequence families in DNAs from such phylogenetically diverse organisms poses a significant question. Perhaps it is due to common function and the resulting similarity in selection pressure. Whatever the cause, members of the short classes of repeated sequences survive for extensive evolutionary periods. It is an important conclusion that the evolutionary lifetime of most short repetitive-sequence families is far longer than the length of time during which typical species and even genera persist.

In principle the lack of divergence of the long repetitive regions could result either from their recent addition to the genome or from strong selection pressure which maintains these sequences unchanged and thus maintains the precision of repetition. In the latter case one would expect that related species would share the long, precisely related sequences and that little sequence divergence would be observed between the sets in the related genomes. A number of measurements have been made which, for the bulk of the precisely repetitive sequences, appear inconsistent with this alternative. Rice (1972) measured by hydroxyapatite thermal chromatography the thermal stabilities of hybrids between the repetitive DNAs among a number of rodents. Very few high thermal stability repetitive DNA hybrids were observed in these intergeneric comparisons. For example, no hybrids are formed between rat and mouse repetitive DNAs that display thermal stabilities within 10°C of that of perfectly paired DNA. On the other hand, studies of DNA sequence relationships between *Xenopus laevis* and *X. borealis* do show high thermal stability repetitive DNA hybrids (Galau *et al.*, 1976b). A conclusion from the rodent experiments of Rice (1972) is that the precise relationships observed among the long repeats are due to the recent multiplication of these DNA regions in the genome of each spe-

cies or genus. The generality of this conclusion has yet to be established.

A few structural genes are known to be arranged in long repetitive regions, and their evolutionary relationships are being explored. Examples are the histone genes and the genes for 5S, 18S, and 28S ribosomal RNA. In the case of the ribosomal RNA cistrons it is clear that the structural genes are highly conserved in evolution. However, there exist spacer sequences that are not conserved and that differ in nucleotide sequence between species of the same genus (Brown and Sugimoto, 1974). Nevertheless, the spacers are relatively precisely repeated sequences even though the individual spacers differ in length (Brownlee *et al.*, 1974; Wellauer *et al.*, 1974). The ribosomal gene spacers are therefore analogous to the bulk of the long repetitive regions in both their intragenomic precision of repetition and their intraspecies divergence. This similarity suggests that parallel processes may be involved in the evolution of all of the long repeated sequences. Their evolution apparently involves multiplication of particular sequences and loss of other precisely repeated sequences, either through divergence or deletion. The mechanism for this complicated process remains obscure although arguments have been advanced (Smith, 1974) that it is the result of unequal crossover in tandem repeated regions. The ribosomal gene regions are tandemly repeated, and some of the other long repetitive regions have been identified as satellites which are tandem repeats of very short sequences. The long repetitive regions studied here include very complex sequences, however, and current observations suggest that only a fraction of them are tandemly repeated (Eden *et al.*, in preparation).

When repetitive DNAs from species belonging to related genera are reassociated with each other, it is usually observed that there are many shared sequences showing low thermal stability. The existence of these shared sequences supports the concept that the short, im-

precisely repeated sequences are evolutionarily ancient in origin. Since long repeated sequences are currently being added to the genomes while the short ones have been present for longer periods, it is natural to consider whether the two classes are evolutionarily related. Perhaps the short repeats derive from long repeated-sequence regions by means of sequence rearrangement and nucleotide substitution (Britten and Kohne, 1966; Britten and Davidson, 1971). No direct evidence as yet exists for this concept.

Experimental Procedures

Preparation of DNA. DNA was extracted from sea urchin sperm as described in Graham *et al.*, 1974. Calf thymus DNA was purchased from Sigma.

Shearing of DNA. DNAs were sheared using a Virtis-60K homogenizer with 2.5-cm diameter blades. DNA 300 nucleotides long was prepared by shearing in a solution of 0.01 M NaAc, 66% glycerol, in a dry ice-ethanol bath at 50,000 rpm for 20 min (Britten *et al.*, 1974). DNA 2000 nucleotides long was prepared by shearing in 0.12 M PB in an ice-water bath at 10,000 rpm for 20 min.

Determination of fragment lengths. Isokinetic alkaline sucrose gradients (Noll, 1967; $V_{\text{mix}} = 9.84$ ml, $C_{\text{res}} = 43\%$ w/v, $C_{\text{flask}} = 16\%$ w/v in 0.1 M NaOH) were used for all DNA fragment length measurements. All measurements were made at least in duplicate with markers in each tube. The markers consisted of sheared preparations of labeled and unlabeled DNA calibrated against each other and ultimately calibrated by measurement of Kleinschmid preparations in the electron microscope and referred to the length of $\phi\chi$ replicative form double strand circles.

Conditions of reassociation. DNA to be digested with S1 nuclease was incubated at 60°C in 0.3 M NaCl, 0.01 M PIPES (Sigma), pH 6.7. For other pur-

poses, such as hydroxyapatite fractionation, incubation was in 0.12 M PB, pH 6.8. The ratio of the rates of reassociation in these two media was taken to be 2.5 (Britten *et al.*, 1974) for equivalent C_0t calculations. Equivalent C_0t is the C_0t ($M \times \text{sec/L}$) multiplied by the ratio of the rate in the medium to that in 0.12 M PB.

Preparation of S1 nuclease. We utilized a partially purified preparation, as described by Vogt (1973; personal communication). Five grams of crude alpha amylase type IV (*Aspergillus oryzae*) were dissolved at 4° for 1 hr in 0.02 M sodium acetate, pH 4.6, 5% glycerol, and then centrifuged. The pH of the supernatant was then readjusted down to 5.0 by the addition of acetic acid, and the supernatant was heated to 70° in an 80° waterbath. Following centrifugation, the supernatant had ammonium sulfate added to 3.8 M. It was stirred for 1 hr at 4° and was centrifuged again. Ammonium sulfate was added additionally to the supernatant to 0.6 M. The precipitate was collected by centrifugation, dissolved in 0.02 M Tris, pH 7.5, 5% glycerol, and then loaded on an 80-ml column of DE-52 (Whatman) equilibrated with the Tris buffer. The column was rinsed with 400 ml of buffer and eluted with a NaCl gradient from 0.0 to 0.4 M in the same buffer. The peak cuts of activity were combined; an equal volume of glycerol was added and the preparation stored at -20°C.

Conditions of digestion. The following standard digestion condition was established after studies showed that a significant fraction of reassociated repeated sequences was digested with lower salt and higher temperature conditions. Mercaptoethanol (MSH) is included because measurements showed that the enzyme lost a significant fraction of its single-strand activity within an hour in the absence of mercaptoethanol, while in the presence of mercaptoethanol the activity was very much more stable. For digestion, 1 vol of reassociation buffer (0.3 M NaCl, 0.01 M PIPES, pH 6.7)

was added to 1 vol of 0.05 M Na acetate, pH 4.4, containing 2×10^{-4} M ZnSO_4 . Then 0.05 ml per ml of final volume of 0.5 M MSH and the requisite volume of enzyme stock were added. The temperature was raised to 37°C for 45 min, and the digestion was terminated by chilling on ice and adjusting the sample to 0.12 M PB.

Removal of digestion products. For some purposes the reaction mixture was passed over Sephadex G-100 and the excluded region taken as the enzyme-resistant fraction. With light enzyme digestion (see text) fairly long single-strand fragments were present in the excluded fraction, and under these conditions the digestion mixture was diluted to several ml of 0.12 M PB and passed over hydroxypatite at 60°C to separate structures containing duplex regions.

Enzyme quantitation. The apparent rate of activity of S1 nuclease depends on a number of parameters such as salt concentration (Sutton, 1971) and temperature, as well as the method of assay. The presence of MSH may also affect the rate. Under the conditions we used, the ratio of quantity of enzyme to quantity of DNA almost totally controls the rate of digestion of single strands while the actual enzyme concentration has little effect on the rate. Since the rate of digestion is strongly dependent on the method of assay and since there is evidence that the reaction is heterogeneous in mechanism and rate, we have avoided the use of a unit of enzyme activity. Each of our digestions is described in terms of the quantity of a particular enzyme preparation used throughout this work in the units $\mu\text{l min mg}^{-1}$ DNA. For comparison with other work we also calculate a digestion estimate (DIG) based on the $\mu\text{l min mg}^{-1}$ required for 50% digestion with G-100 assay: $\text{DIG} = 1 - (1 + \mu\text{l min mg}^{-1}/135)^{-1}$. From this formula we may approximate the initial rate of digestion by G-100 assay as 7.4 μg of DNA per min per μl of our enzyme stock. Because of the heterogeneity in mechanism the initial rate is

actually somewhat greater. A Sutton unit (Sutton, 1971), under his conditions, converts 0.025 μg of DNA per minute to TCA solubility; thus 1 μl of our preparation works, under our conditions, at the rate that about 300 Sutton units would work under his conditions.

Shenk *et al.* (1975) define a unit as the amount of S1 nuclease that with their conditions and substrate will release "1 nanomole of nucleotides" per min. We take this to mean release of TCA-soluble oligonucleotides and compare it with the G-100 assay ($K_{av} = 0.3$). In these terms 7.4 μg is 22 nmol per min per μl . Shenk *et al.* use 135 of their units per μg for 30 min in a typical digestion. This corresponds to $135 \times 1000 \times 30/22 = 1.8 \times 10^5 \mu\text{l min mg}^{-1}$ or $\text{DIG} = 0.9993$. By this comparison their typical digestion was about 1000 times that used for Figs. 26 and 27 in this work. If their definition is taken literally as release of nucleotides it would be better to compare it with the hyperchromicity assay and the ratio would be more than a factor of 10 greater. This comparison is somewhat uncertain since Shenk *et al.* presumably depend on the initial rate of digestion, and we are estimating the rate from the half digestion point by G-100 assay.

Agarose fractionation. Agarose A-50 (BioRad), 100-200 mesh, columns were prepared with glass beads to prevent compression of the gel and to permit reproducible high flow rates. Coarser grade gel gave very poor or no resolution. Columns were washed and run in 0.12 M PB for duplex DNA analysis. Measurements showed that these columns absorb small amounts of double- or single-strand DNA and therefore high specific activity tracer preparations were analyzed in the presence of 50 μg of heterologous DNA fragments. For analysis of single-strand DNA, columns were run in the presence of 0.6% formaldehyde. DNA samples were denatured in the absence of formaldehyde to avoid cross-linking; 0.6% formaldehyde was added, and the sample was immediately cooled.

SINGLE-COPY DNA AND STRUCTURAL
GENE SEQUENCE RELATIONSHIPS
AMONG FOUR SEA URCHIN SPECIES

Robert C. Angerer, Eric H. Davidson,
and Roy J. Britten

Comparison of single-copy DNA sequences in the genomes of related species provides insight into the processes of evolution. Such measurements require incubating labeled DNA of one species with an excess of DNA from a second species and isolating the reassociated DNA fragments on hydroxyapatite. However, even though a number of such measurements have been made, this subject is still relatively undeveloped. Here we present a preliminary study of four sea urchin species, three belonging to the genus *Strongylocentrotus* and the fourth to the genus *Lytechinus*, which is in a different order. The evolutionary relationships of these species are dis-

played in Fig. 33, which is constructed in accordance with the phylogeny presented by Durham (1966). The two orders represented, *Temnopleuroida* and *Echinoida*, diverged approximately 175 million years ago. Within the order *Echinoida*, the family *Strongylocentrotidae* is represented in the fossil record from the early Miocene, about 20 million years ago. Exact divergence times for the three *Strongylocentrotus* species are not available because of the sparse fossil record. However, these species were morphologically distinct 7 million years ago, and this represents their minimum divergence time (Fig. 33; Durham, personal communication). Based on their morphology, *S. purpuratus* and *S. dröbachiensis* are the more closely related species. *S. franciscanus* appears slightly earlier in the fossil record and is morphologically less closely related to *S. purpuratus* than is *S. dröbachiensis*.

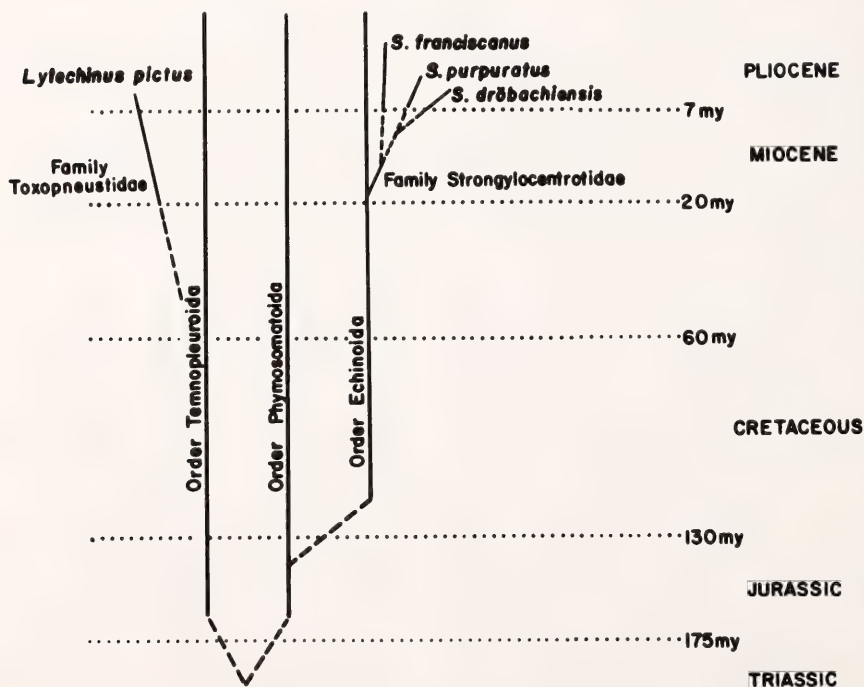


Fig. 33. Phylogeny of the sea urchin species studied. After Durham (1966). Dashed lines indicate uncertainty in the time of origin of the indicated taxa. my = million years.

Reassociation of Sea Urchin DNAs

DNA reassociation kinetics for *Strongylocentrotus purpuratus*, *S. franciscanus*, and *Lytechinus pictus* are presented in Fig. 34. For this analysis 450 nucleotide fragments of unfractionated DNA were reassociated to the indicated C_0t (see Experimental Procedures). The fraction of fragments containing duplex was determined by hydroxyapatite chromatography. The kinetics of reassociation appear quite similar for these three genomes. The solid line of Fig. 34 shows the best least-squares fit for *S. purpuratus*

DNA, using one repetitive and one single-copy kinetic component; the dashed and dotted lines show the best solutions for *S. franciscanus* and *L. pictus* DNAs, respectively. The genome sizes of these species are: *S. purpuratus*, 0.89 pg; *S. franciscanus*, 0.83 pg; and *L. pictus*, 0.97 pg (Hinegardner, 1974). Thus, the rates of reassociation of the single copy-components are expected to be indistinguishable. As Fig. 34 shows, the renaturation rate constants for the single-copy components obtained by least-squares procedures are close to $1 \times 10^{-3} M^{-1} \text{ sec}^{-1}$ for all three DNAs.

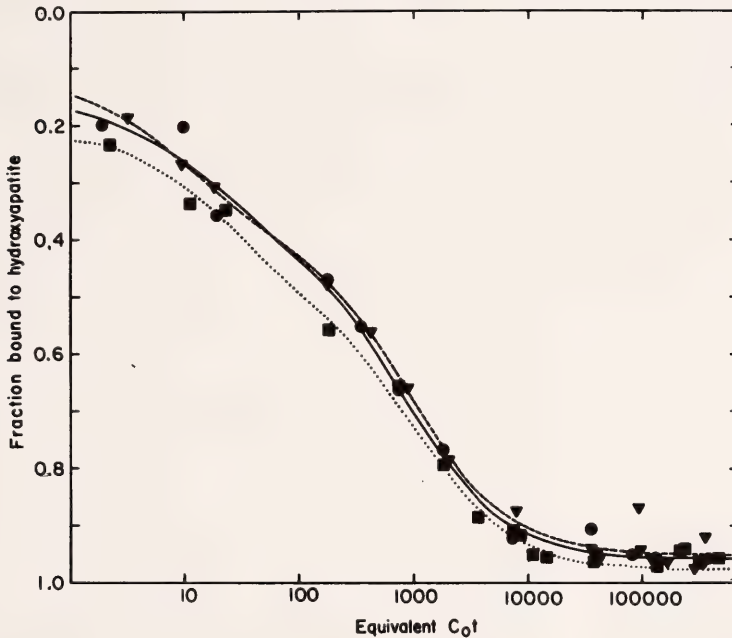


Fig. 34. Reassociation of unfractionated DNA from three sea urchin species. DNA fragments 450 nucleotides long were reassociated in 1 M NaCl buffer at 70°C at 7.5 mg/ml for C_0t values of 175 M-sec or greater. For C_0t values less than 175 M-sec incubation was at 250 $\mu\text{g/ml}$ in 0.12 M PB at 60°C. After incubation the samples (250 μg) were adjusted to 0.12 M PB, and the fraction of molecules containing duplex regions was determined by chromatography on 1 ml beds of hydroxyapatite at 60°C. Bound duplex material was subsequently eluted at 98°C in 0.12 M PB. Values of C_0t in 1 M NaCl buffer are corrected to the equivalent rate in 0.12 M PB, using a rate acceleration factor of 25. The solid line is a computer fit to the *S. purpuratus* data with two components: single copy component 55% with rate constant $k = 1.2 \times 10^{-3} M^{-1} \text{ sec}^{-1}$; repetitive component 25% with $k = 6.65 \times 10^{-2} M^{-1} \text{ sec}^{-1}$. The dashed line is a fit to the *S. franciscanus* data: single copy component 55% with $k = 1.1 \times 10^{-3} M^{-1} \text{ sec}^{-1}$; repetitive component 29% with $k = 0.103 M^{-1} \text{ sec}^{-1}$. The dotted line is a fit to the *L. pictus* data: single copy component 47% with $k = 9.6 \times 10^{-4} M^{-1} \text{ sec}^{-1}$; repetitive component 29% with $k = 4.7 \times 10^{-2} M^{-1} \text{ sec}^{-1}$. *S. purpuratus*, circles; *S. franciscanus*, triangles; *L. pictus*, squares.

The quantities of single-copy DNA in the *S. franciscanus* and *L. pictus* genomes are also quite similar to that in *S. purpuratus*, as are the amounts of intermediate frequency repetitive DNA. We do not have sufficient low C_0t data to determine whether the total distributions of repetition frequencies are similar.

Divergence of Total Single-Copy DNA Sequence

We have determined the extent of sequence relatedness between *S. purpuratus* single-copy DNA and the single-copy DNA of each of the other species. These measurements are made by reassociating tracer amounts of radioactively labeled single-copy DNA from *S. purpuratus* with a large excess of homologous or heterologous unfractionated driver DNA. Two quantities can then be measured as an indication of the sequence relatedness of the *S. purpuratus* tracer DNA to the driver DNA of another species. First, the extent of reaction of the tracer with heterologous driver measures the fraction of single-copy DNA fragments that include regions of sufficiently homologous sequence to form stable duplexes. Second, the thermal stability of the duplexes formed with heterologous DNA can be measured by thermal chromatography on hydroxyapatite. The difference in the midpoint of the thermal transition (T_m) for tracer reassociated with homologous and with heterologous DNA is termed ΔT_m . This quantity is directly related to the degree of base mispairing in the duplexes, and hence to the degree of sequence divergence between the single-copy DNAs of the two species (Laird *et al.*, 1969; Britten *et al.*, 1974). In most cases the extent of reaction is dependent on the reassociation criterion. The criterion imposes a lower limit on the T_m of mismatched duplexes, since the sequences included in the measurement are only those which form stable duplexes, and more distantly related sequences are ex-

cluded. Where the reassociation is incomplete for this reason, the measured ΔT_m underestimates the divergence between the DNA sequences of the two species. In these measurements this difficulty is accentuated by the short length of the tracer DNA preparation. The T_m of homologous tracer-driver duplexes is at least 8°C below that of long native urchin DNA (see Fig. 36).

The preparation of *S. purpuratus* single-copy DNA is described in Experimental Procedures. DNA labeled in vivo and fractionated to remove repetitive sequences was used in some measurements as single-copy tracer. Alternatively, unlabeled DNA was fractionated and the final single-stranded fraction was reassociated to high C_0t and labeled in vitro with ^3H -TTP, using *E. coli* DNA polymerase I. The length of the tracer fragments labeled in this way was about 230 nucleotides. The kinetics of reassociation of both types of tracer in the presence of a large excess of *S. purpuratus* DNA driver are shown in Fig. 35 (open and closed circles). The line drawn through the points represents the least-squares solution to the combined data using two kinetic components. The tracers are both 90% reactable with driver DNA, and 80% of each reacts as a single-copy component. About 8% of each of the tracers reacts as a repetitive contaminant. The rate constant for the reassociation of these tracers is less than that for the single-copy component of Fig. 34 because of the smaller fragment size of the tracer. These data show that there is no observable difference in the reassociation kinetics of tracers labeled in vivo and in vitro.

The kinetics of reassociation of *S. purpuratus* single-copy tracer with *S. franciscanus* and *L. pictus* DNAs are also presented in Fig. 35. A marked difference in the extent of reaction of *S. purpuratus* single-copy sequences with the DNAs of these two species can be seen in Fig. 35a. The reaction of the *S. purpuratus* tracer with *S. franciscanus*

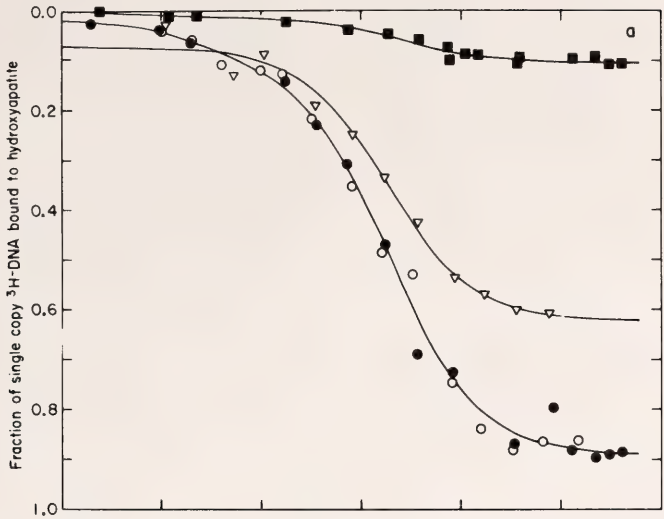


Fig. 35a. *S. purpuratus* single copy tracers labeled in vivo (open symbols) or in vitro (filled symbols) were combined with a 10^5 - or 2×10^4 -fold excess, respectively of *S. purpuratus* (open and filled circles), *S. franciscanus* (open triangles), or *L. pictus* (filled squares) driver DNA. The reassociation conditions were as indicated in the legend to Fig. 34. The data for reaction with *L. pictus* driver has been corrected for self-reassociation of the tracer (maximum 2.2% at $Cot\ 10^6$). The lines through the points represent best least-squares computer fits to the data using a single-copy and one repetitive component: *S. purpuratus* driver 89% final reaction, 79% single copy with $k = 5.1 \times 10^{-4}\ M^{-1}\ sec^{-1}$ and 9% repetitive; *S. franciscanus* driver 62% reaction, 55% single copy with $k = 5.6 \times 10^{-4}\ M^{-1}\ sec^{-1}$ and insufficient data to specify a repetitive component; *L. pictus* driver 10.5% final reaction, 8.8% single copy with $k = 3.7 \times 10^{-4}\ M^{-1}\ sec^{-1}$ and 1.8% repetitive.

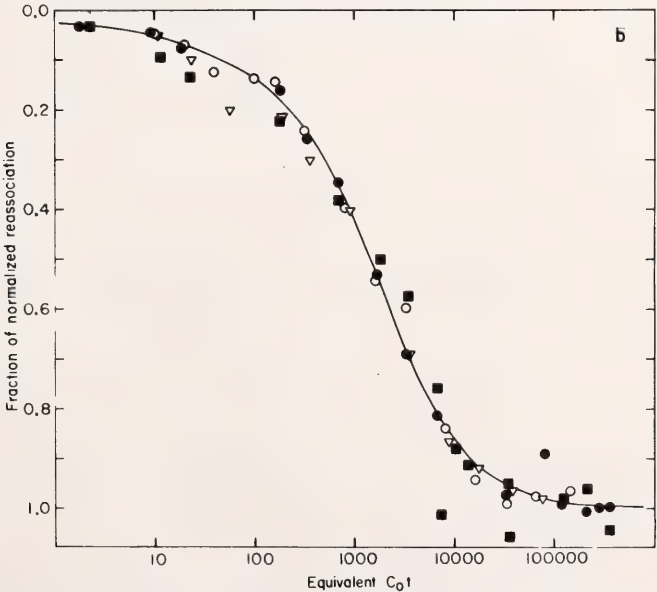


Fig. 35b. The data of 35a are shown normalized to 100% final reaction for each DNA driver. The solid line is the computer fit to the *S. purpuratus*-driven data from 35a, normalized to 100%.

DNA driver is 70% of the homologous reaction ($0.62 \times 100/0.89$), and with *L. pictus* DNA driver the reaction is only 11.8% of the homologous reaction ($0.105 \times 100/0.89$). In Fig. 35b these reactions are normalized to 100% to facilitate comparison of the rates of reassociation. The line drawn through the points is the least-squares solution to the data for the *S. purpuratus* DNA reaction.

It is evident that although the extents of reassociation of the *S. purpuratus* tracer with the heterologous DNAs are lower, the rates of the reactions are quite similar. The least-squares solution for the reaction of the *S. purpuratus* tracer with *S. franciscanus* DNA yields a rate constant equal to that for homologous driver. The reaction of the same tracer with *L. pictus* DNA gives a 30% lower rate constant. The similarity of

the heterologous and homologous rates is expected. Measurements described below show that the thermal stability of the products of the heterologous reactions is only 2.5°–7.5°C below that of the homologous reaction. The data of Bonner *et al.* (1973) suggest a rate reduction of a factor of only 2 per 10°C reduction in thermal stability.

Additional cross-reaction data are summarized in Table 21. The first three rows shows the cross-reaction of 250-nucleotide-long *S. purpuratus* single-copy tracers with whole DNA of the other three species at the 70°C criterion. The normalized cross-reaction values given in the last column are consistent with the evolutionary relationship of these species as outlined in the text: The two *Strongylocentrotus* species are most closely related to *S. purpuratus*, and *S. dröbachiensis* shares more single-copy

TABLE 21. Homology of *S. purpuratus* Single-Copy DNA Sequences to the DNA of Other Sea Urchin Species

| Driver ^a | Criterion ^b (°C) | % Reasso- ciated ^c (average) | % Reactable | Maximum % Self-Reaction ^e | Normalized Cross- Reaction ^h |
|-------------------------|--------------------------------|---|-------------------|---|---|
| <i>S. dröbachiensis</i> | 70 | 49.5, 57.1 (53.3) | 77.3 ^e | 2.7 | 67.8 |
| <i>S. franciscanus</i> | 70 | 41.5, 42.6, 40.8, 39.2 (41.0) | 77.3 ^e | 2.7 | 51.3 |
| <i>L. pictus</i> | 70 | (11.6) ^d | 89.0 ^f | 2.2 | 11.5 |
| <i>S. franciscanus</i> | 60 | 67.0, 63.1, 67.2 (65.8) | 85.1 ^e | 2.2 | 76.7 |

^a Whole-genome DNA sheared to 400-nucleotide fragments at a minimum driver mass excess of 1700.

^b Incubations in 1 M NaCl buffer at the indicated temperature.

^c Percentage of reassociation was determined as the percentage of the tracer fragments bound to hydroxyapatite in 0.12 M PB at 60°C (for incubations at 70°C) or 50°C (for incubations at 60°C) at equivalent *C*₀*t*s between 35,000 and 105,000. The tracers used were 230–260 nucleotides long.

^d Value determined from the data of Fig. 35.

^e Average percentage of reassociation of this tracer preparation to homologous DNA at the indicated criterion. Individual determinations were 75.5, 75.6, and 80.8 at 70°C, and 84.3 and 85.9 at 60°C.

^f Percentage of reassociation of this tracer to homologous DNA from the data in Fig. 35.

^g Percentage of the tracer in duplex after incubation under identical conditions but without driver DNA. Each number is the average of three determinations.

^h Computed as $\frac{\% \text{ reassociated} - \% \text{ self-reaction}}{\% \text{ reactable} - \% \text{ self-reaction}} \times 100$.

This normalization does not correct for the fraction of the cross-reaction caused by the small repetitive sequence contaminant in the *S. purpuratus* single-copy tracer (see Fig. 35). However this correction has no significant effect on the percentage of cross-reaction calculated for the single-copy component.

sequences in common with *S. purpuratus* than does *S. franciscanus*. *L. pictus* shows only a very small cross-reaction with *S. purpuratus* single-copy sequences.

The extent of the reaction of *S. purpuratus* single-copy tracer with *S. franciscanus* DNA presented in Table 21 is lower than that of Fig. 35a (51% vs. 69%). This effect is probably caused by differences in the fragment length distributions of the tracers used for the two measurements. The data of Table 21 were obtained with in vitro-labeled tracers of a mean length of 230 nucleotides, while for Fig. 35a a somewhat longer tracer which had been prepared from 450-nucleotide fragments was used. Our experience indicates that longer tracer preparations commonly have higher normalized reactivities to heterologous DNAs as assayed by hydroxyapatite binding. The fourth row in Table 21 shows a measurement of the extent of cross-reaction of *S. purpuratus* 230-nucleotide tracer with *S. franciscanus* DNA at a less stringent criterion. A 10°C decrease in incubation temperature results in a 50% increase in the extent of cross-reaction. This observation shows that the criterion of incubation has selected the better-matched fraction of the heterologous reassociation products from a population with a wide range of divergence.

The thermal stabilities of the duplexes formed between *S. purpuratus* single-copy tracer and homologous and heterologous DNAs are presented in Fig. 36. The T_m of *S. purpuratus* tracer reassociated with homologous driver is approximately 8°C below that of 500-nucleotide native *S. purpuratus* DNA. This decrease is largely attributable to the short fragment length of the tracer (reviewed in Britten *et al.*, 1974).

The values of ΔT_m for cross-reacting single-copy sequences are consistent with the relationships of these species based on the taxonomy presented in Fig. 33. The decrease in T_m of the heterologous duplexes ranges from 2.5° to 7.5°C and parallels the extents of reaction (Table

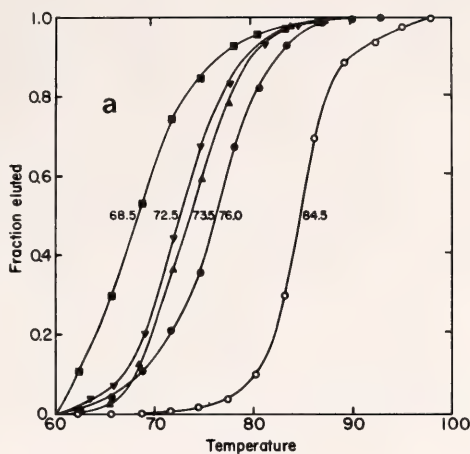
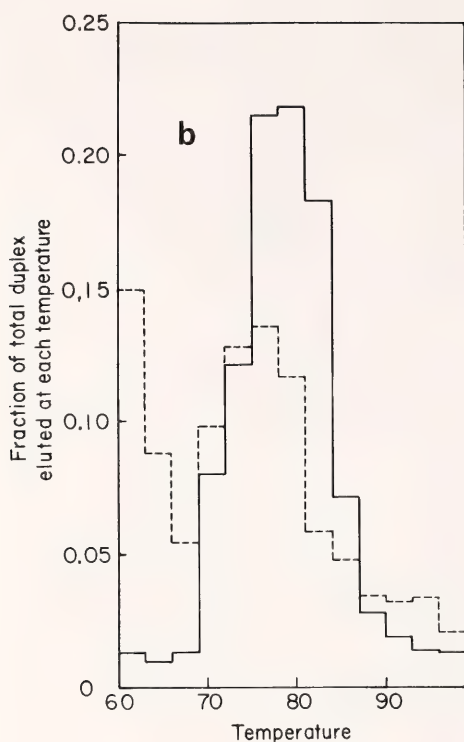


Fig. 36. Hydroxyapatite thermal chromatograms of *S. purpuratus* single-copy duplexes formed with homologous and heterologous driver DNAs. 36a. *S. purpuratus* single-copy ^3H -DNA tracers were reassociated with 400-nucleotide homologous and heterologous driver DNAs to equivalent C_0t_s of 42,000–88,000 in 1 M NaCl buffer at 70°C at the indicated mass excess of driver. The samples were diluted to 0.12 M PB at 60°C and applied to hydroxyapatite at 60°C. The temperature was increased in approximately 3°C increments, and the DNA fragments rendered completely single stranded at each temperature were eluted with 0.12 M PB. A given curve is for the reassociation products of one of the two tracers used (see Experimental Procedures); these tracers gave identical thermal chromatograms for duplexes formed with *S. purpuratus* driver DNA. The percentage of the tracer reassociated to each driver is given in parentheses: open circles, *S. purpuratus* native DNA, 500 nucleotide fragments; filled circles, *S. purpuratus* driver, 100,000 (89.8%); upside-down filled triangles, *S. franciscanus* driver 3,400 (40.8%); filled triangles, *S. dröbachiensis* driver 1,767 (57.1%); filled squares, *L. pictus* driver 100,000 (11.5%). Numbers given beside the curves represent the temperature at which 50% of the bound DNA is eluted from the column (T_m).

21). The divergence of the sequences observed to cross-react in these measurements is so small that little effect on the rate of reassociation is expected, as noted above. A particularly interesting result is the thermal elution profile of the duplexes formed between *S. purpuratus* tracer and *L. pictus* driver. Although 88% of the single-copy DNA of these



36b. The data for the *S. purpuratus* and *L. pictus* driven duplexes is presented in differential form: *S. purpuratus*, solid lines; *L. pictus*, broken lines.

two species has diverged beyond recognition at the 70°C criterion, the 12% that does react shows a decrease in T_m of only 7.5°C. This result is emphasized when the thermal elution data are plotted in differential form as in Fig. 36b. Approximately two thirds of the duplexes formed with *L. pictus* DNA have thermal stabilities in the range of those of the homologous reaction. This measurement shows that a small fraction of the sequences of these urchins has been relatively conserved in evolution. However, in order to evaluate the extent of this conservation we would need to know the base composition or native melting temperature of these particular sequences. If the GC content of the conserved sequences is the same as in the total single-copy DNA, then about 12% of these genomes show approximately 7.5% sequence divergence. However, it remains

possible, as implied by Fig. 36b, that a smaller fraction, say 5%, of these genomes shows almost no sequence divergence. Further measurements are required to establish which view is correct.

Divergence of Structural Gene Sequences

Structural gene sequences expressed at gastrula were selected from *S. purpuratus* single-copy DNA by hybridizing the DNA with purified gastrula polysomal RNA (Galau *et al.*, 1976a). DNA was recovered from the DNA-RNA hybrids and further selected by a second round of hybridization with the polysomal RNA. Details of the purification procedure are given in Galau *et al.* (1976a). The gastrula messenger RNA population contains transcripts of approximately 14,000 genes active in *S. purpuratus* gastrulae and thus represents a large sample of structural genes (Galau *et al.*, 1974). The final preparation of message complementary DNA (mDNA) reacted to about 57% with gastrula messenger RNA and 90% with excess DNA. This represents about a 50-fold purification.

The results of reassociation of these mDNA sequences with a large excess of *L. pictus* or *S. franciscanus* DNA are presented in Table 22. The reaction of *S. purpuratus* mDNA sequences with *S. franciscanus* DNA at the 60°C criterion (Table 22) shows that 85.4%–91.2% of these sequences have complements in the *S. franciscanus* genome (see footnotes e and f of Table 22). In fact, the normalized cross-reaction may be greater than 90% because the reactivity of the mDNA tracer in heterologous reactions is probably overestimated by using its reactivity with homologous DNA. By comparison, 77% of the total single-copy DNA is complementary at this criterion. We conclude that for these more closely related species, structural gene sequences are diverging at a lower rate than is the bulk of the single-copy DNA sequences. A similar conclusion was drawn by Rosbash *et al.* (1975) from experiments in

which cDNA transcribed from rat myoblast messenger RNA was reacted with rat and mouse DNA. The reaction of mDNA with *L. pictus* DNA (Table 22) shows that only 14% of the *S. purpuratus* structural gene sequences are sufficiently similar to their homologues in the *L. pictus* genome to reassociate at the 70°C criterion. The comparable reaction between the total single-copy DNAs of these two species is 12% (Table 21 and Fig. 35). Thus, we observe no specific conservation of structural gene coding sequences at very great evolutionary distance (i.e., the 175 million years separating *S. purpuratus* from *L. pictus*) but do see such conservation for the more closely related pair of species. Such an observation is consistent with extensive amino acid sequence conservation represented by the *L. pictus*-*S. purpuratus* comparison, even at this great evolutionary distance. Because of codon degeneracy one might expect that after considerable evolutionary time many third bases would differ even if the coded amino acid sequence were identical. After a very long time the steady-state condition of such highly conserved genes would probably yield 20%-30% DNA sequence divergence. This amount would be increased by the additional changes where amino acids could be substituted. The sum of these changes would almost certainly lead to a degree of divergence that would prevent the reassociation of structural gene single-copy DNA at the criterion used in these measurements.

Conclusion

The measurements of the degree of single-copy DNA sequence relatedness among these four species are qualitatively consistent with the species' phylogenetic relationships. The closest relative of *Strongylocentrotus purpuratus* on morphological and fossil grounds is *S. dröbachiensis*, and the DNA of this species reacts to the greatest extent with *S. purpuratus* single-copy DNA and forms the most stable heteroduplexes. *S.*

franciscanus, a member of the same genus, is less closely related to *S. purpuratus* on the basis of morphology, and the DNA sequences show greater divergence. Only a very small amount of single-copy sequence homology is seen between the DNAs of *S. purpuratus* and *L. pictus* which are members of different orders with lines of descent that have been separate for at least 175 million years.

One major purpose of measurements of this type is to establish the degree of DNA sequence relatedness among species. An appropriate quantitative description would include precise tabulation of the amount of DNA sequence shared at any particular degree of sequence divergence. For a number of reasons we cannot yet reach this goal. First, we have not examined the relationships at a low criterion of precision and therefore have not measured the widely divergent sequences. Second, adequate measurements are not yet available for the repeated sequence relationships among these species. The interpretation of such measurements is somewhat uncertain since we do not accurately know the conversion factor relating the thermal stability of duplexes and the degree of divergence, nor do we know the exact effects of shared sequence length on this factor. Finally, questions can be raised about the extent of completion of the reaction between more distantly related species. The fragments used in this study were about 230 nucleotides long, and the melting temperature of duplexes formed between the *S. purpuratus* tracer and homologous DNA was 8°C below that of long native DNA. For these reasons the results obtained were probably affected by the fact that the criterion incubation temperature 60°C (or equivalent) was only about 16°C below the T_m of the homologous tracer reaction. However, these difficulties refer mainly to the more distantly related species pairs.

We may estimate the average rate of change of single-copy DNA sequences during the evolution of these urchin spe-

TABLE 22. Homology of *S. purpuratus* Gastrula Polysomal Message Sequences to the DNAs of Other Sea Urchin Species

| Driver ^a | Criterion ^b (°C) | Reassociated ^c (average) (%) | Reactable ^d (%) | Normalized ^e Cross- Reaction (%) | Corrected ^f Cross- Reaction (%) |
|------------------------|--------------------------------|---|-------------------------------|--|---|
| <i>L. pictus</i> | 70 | 10.7, 12.7 (11.7) | 90.0 | 13.0 | 14.0 |
| <i>S. franciscanus</i> | 60 | 65.8, 70.1 (68.0) | 79.6 | 85.4 | 91.2 |

^a Whole-genome DNA sheared to 400-nucleotide fragments at a driver mass excess of 2.5×10^6 .

^b Incubations in 1 M NaCl buffer at the indicated temperature.

^c Percentage of reassociation was determined as the percentage of the tracer fragments bound to hydroxyapatite in 0.12 M PB at 60°C (for incubations at 70°C) or 50°C (for incubations at 60°C) at equivalent *C₀t*s between 70,000 and 250,000.

^d Percentage of reassociation of the tracer to homologous DNA at the indicated criterion. The percentage of reactable decreased with time due to decrease in fragment size of the tracer.

^e $\frac{\% \text{ reassociated}}{\% \text{ reactable}} \times 100$. This normalization assumes that the mRNA tracer consists entirely of sequences complementary to gastrula mRNA.

^f Corrected for the composition of the mRNA preparation, which consists of 60% sequences complementary to *S. purpuratus* gastrula messenger RNA and 40% (presumably random) single-copy sequences. The reaction with mRNA sequences is computed as reaction with mRNA sequences =

$$\frac{\text{normalized cross-reaction} - 0.4 (\text{single-copy cross-reaction from Table 21})}{0.6}$$

This normalization takes into account the possibility that 40% of the mRNA tracer consists of random single-copy sequences.

cies. In spite of the caveats mentioned above, the largest uncertainty in these estimates is in the time of divergence of the species as judged from the fossil record. For these estimates we assume that 1% sequence divergence reduces the melting temperature of the duplexes by 1°C (Laird *et al.*, 1969; Britten *et al.*, 1974). The extent of reassociation and thermal stability of the products are highest for the reactions between *S. purpuratus* tracer and *S. dröbachiensis* or *S. franciscanus* DNA, and there is the least ambiguity due to criterion limitation. The ΔT_m for reassociation with *S. dröbachiensis* DNA is 2.5°C, which indicates a base sequence divergence of about 2.5% between the DNAs of these two species. The paleontological evidence indicates that these species diverged no less than 7 nor more than 20 million years ago (Durham, personal communication). The rate of single-copy sequence divergence in the line leading

to each species is therefore between 0.06% and 0.25% per million years. Similar calculations for *S. franciscanus* vs. *S. purpuratus* give values of 0.08%–0.35% per million years. These estimates are not greatly different from the estimate for primates, using the data of Kohne (1970), of about 0.7% per million years and that for two *Xenopus* species of 0.2% per million years (Galau *et al.*, 1976b).

In the case of the relationship between *L. pictus* and *S. purpuratus* we observe only 12% sequence homology and therefore can make no estimate of the average rate of divergence. This small fraction of the single-copy DNA appears to be highly conserved. As indicated in Fig. 36b and discussed above, the degree of divergence of these sequences is only 7.5% or less. The measurement made with the DNA sequences expressed in gastrula messages (mDNA) shows that these conserved sequences are probably

not principally structural genes. Structural genes for even highly conserved proteins would not necessarily be expected to appear in the class of highly conserved sequences because of the number of changes that could occur in the third position of degenerate codons. This highly conserved fraction of the single-copy DNA could either be a residue of sequences that have by chance shown only a small percentage of substitution in evolution or sequences that could have been conserved by selection pressure. However, it seems unlikely that the sequences have survived by chance. Thus there may exist a set of single-copy DNA sequences of unknown role which are highly conserved by selection pressure resulting from important sequence-specific functions.

Experimental Procedures

Animals. Specimens of *Strongylocentrotus purpuratus*, *S. franciscanus* and *Lytechinus pictus* were collected locally. Sperm was collected from *S. dröbachienensis* in Seattle, Washington, by Dr. Carol Paschl and kindly shipped to us frozen on dry ice.

DNA extraction. Unlabeled DNA was isolated from fresh or frozen sperm by the modified Marmur method described in Table 2 of Britten *et al.* (1974), with the following modifications: NaClO_4 was omitted; after the initial deproteinization and precipitation steps, the DNA was dissolved in 0.1 M NaCl, 0.05 M ethylenediaminetetraacetate (EDTA), pH 8.0, and digested with 25 $\mu\text{g}/\text{ml}$ RNase (Worthington) at 37°C for 30 min. The pronase digestion, deproteinization, and precipitation steps were then repeated. RNase treatment was omitted for some samples which showed 26% or greater hyperchromicity [$(A_{260} \text{ at } 98^\circ\text{C} - A_{260} \text{ at } 60^\circ\text{C})/A_{260} \text{ at } 60^\circ\text{C} \times 100$] in 0.12 M PB (sodium phosphate buffer, pH 6.8) after the initial purification steps.

For the preparation of radioactively labeled DNA, *S. purpuratus* embryos

were raised to the 4-cell stage as described by Hinegardner (1967). Five mCi of ^3H -thymidine was then added to 1.5×10^7 embryos in 150 ml of seawater containing penicillin and streptomycin, and the embryos were incubated overnight to approximately hatching blastula stage. Embryos were frozen with dry ice, ground with powdered dry ice in a Waring blender and used for DNA isolation as described above. Specific activities for the two preparations used were 160,000 and 59,000 cpm/ μg under our counting conditions.

Preparation and sizing of DNA fragments. DNA fragments of the indicated sizes were produced by homogenization in a Virtis-60K homogenizer as previously described (Britten *et al.*, 1974). In some cases 450-nucleotide fragments were produced by passing the DNA twice through a press at 50,000 psi (Britten *et al.*, 1974).

The single-strand fragment length of DNA preparations was determined by centrifugation through isokinetic alkaline sucrose gradients (Noll, 1967); $V_{\text{mix}} = 9.84 \text{ ml}$, $C_{\text{res}} = 43\% \text{ w/v}$, $C_{\text{flask}} = 16\% \text{ w/v}$ in 0.1 N NaOH. Gradients were centrifuged at 41,000 rpm for 20–24 hr at 20°C in the Beckman SW-41 rotor. The weight average fragment length was determined in duplicate measurements with reference to known markers, using the equations of Studier (1965).

Reassociation conditions. Prior to reassociation, DNA samples were passed over Chelex 100 (BioRad) to remove heavy metal contaminants. Reassociations were carried out in 1 M NaCl, 0.01 M PB, 0.001 M EDTA, pH 6.8 (1 M NaCl buffer), at either 70°C or 60°C. The former condition is equivalent to a criterion of 0.12 M PB at 60°C. Values of C_0t in this buffer are corrected to the equivalent C_0t in 0.12 M PB, using a rate acceleration factor of 25. This factor was experimentally determined from comparison of the rate of reassociation of the single-copy component in whole *S. purpuratus* 450-nucleotide DNA in 1

M NaCl buffer at 70°C to the known rate in 0.12 M PB at 60°C. All values of C_0t quoted in this paper are corrected to be equivalent to that in 0.12 M PB, 60°C.

Hydroxyapatite chromatography. The fraction of DNA fragments in molecules containing duplex after reassociation was determined by chromatography on hydroxyapatite (BioRad, DNA Grade Lot #13412). Samples were diluted to 0.12 M PB and applied to water-jacketed hydroxyapatite columns at either 60°C or 50°C for incubations performed at 70°C or 60°C, respectively. Unbound material was removed by washing with at least 5 bed vol of 0.12 M PB. Duplex material was subsequently eluted by raising the temperature of the column to 98°C. DNA loads were less than 250 µg of DNA per cc (0.4 g) of packed hydroxyapatite.

The stability of reassociated DNA duplexes was determined by thermal chromatography from hydroxyapatite. Samples of reassociated DNA were applied to the columns as indicated. The temperature was then increased in 3°C increments, and the DNA fragments rendered completely single-stranded at each temperature were eluted from the column. As an internal standard, ^{14}C -labeled 500-nucleotide-long native DNA fragments were mixed with the sample.

Counting methods. Radioactive samples were counted in mixtures of 0.06 M PB and Instagel (Packard) in the proportions 1:1.25 or in 0.12 M PB in toluene-based scintillation fluid containing 20% (v/v) Scintisol (Isolab) in the proportion 1:5.

Preparation of *S. purpuratus* single-copy DNA. *S. purpuratus* single-copy tracer DNA was prepared either from DNA labeled in vivo with ^3H -thymidine (see above), or from unlabeled DNA that was subsequently labeled with ^3H -TTP using *E. coli* DNA polymerase I (see below).

DNA fragments 300–450 nucleotides long were reassociated in 1 M NaCl buffer to equivalent C_0t 700, and the unreassociated fragments separated by hy-

droxyapatite chromatography. The DNA was concentrated by ethanol precipitation and again reassociated to equivalent C_0t 700 and fractionated on hydroxyapatite. The unbound fraction was used as single-copy tracer for in vivo-labeled DNA. When DNA was to be labeled in vitro with *E. coli* DNA polymerase I, the unbound fraction was concentrated and reassociated to equivalent C_0t 18,000, and the duplex material was collected on hydroxyapatite and eluted with 0.5 M PB. This duplex material was used as template for the in vitro labeling procedure. From 18% to 21% of the input DNA was isolated as the single-copy fraction.

In vitro labeling of *S. purpuratus* single-copy DNA. Reassociated *S. purpuratus* single-copy DNA was dialyzed into 0.05 M sodium phosphate buffer, pH 7.53. This DNA was used as substrate for *E. coli* DNA polymerase I in a modification of the procedure developed by Schachat and Hogness (1974). The reaction mixture contained 1×10^{-4} M each dCTP and dATP, 1×10^{-3} M dGTP, 0.75 mCi/ml ^3H -TTP (35 Ci/mmol, Nuclear Dynamics Lot #335), 0.05 M sodium phosphate, pH 7.53, 0.01 M MgCl_2 , 5.7 µg/ml DNA template, and 100 units/ml of commercially obtained *E. coli* DNA polymerase I (Boehringer Mannheim, Grade 1). The sample was incubated at 11°C for 22 hr. The unincorporated nucleotides were removed by chromatography on Sephadex G-200 in 0.12 M PB. Self-complementary fold-back sequences were removed by denaturing the DNA in 0.12 M PB, incubating briefly at 50°C, and binding the "instantaneously renaturing" DNA sequences to hydroxyapatite (22% of the radioactivity in DNA). The specific activity of the DNA estimated from 10% TCA precipitation of an aliquot of the reaction mixture was 1.9×10^6 cpm/µg. The resulting DNA was 230 nucleotides long as determined on alkaline sucrose gradients.

Isolation of DNA complements to polysomal RNA of *S. purpuratus* gas-

trulae (mDNA). *S. purpuratus* single-copy DNA labeled in vitro was hybridized with RNA isolated from the polysomes of *S. purpuratus* gastrulae by a puromycin-release procedure. DNA recovered from these hybrids was further purified by a second round of hybridization to the polysomal RNA. De-

tails of this procedure and characterization of the mDNA preparations used here can be found in the report of Galau *et al.* (1976a). The final mDNA preparation reacted to about 60% with gastrula polysomal RNA, compared to the 1.2% reaction obtained with unfractionated single-copy tracer.

ACKNOWLEDGMENTS

Support for the research reported here was furnished by the National Institutes of Health (NIH), grant nos. HD-05753 and GM-20927; a National Science Foundation Grant, no. BMS75-07359; and NIH Training Grant, no. HD 00014, to the Woods Hole Marine Biological Laboratory's Embryology Course. F. C. Kafatos was supported by the National Science Foundation, grant no. BMS72-02336, and the National Institutes of Health, grant no. 2ROI-HD04701-06. D. E. Graham was supported by fellowship grants from the Damon Runyon-Walter Winchell Cancer Fund and the Carnegie Institution of Washington. W. R. Crain holds a postdoctoral fellowship from the National Institutes of Health,

no. GM-55726. R. C. Angerer holds a postdoctoral fellowship from the American Cancer Society, grant no. PF-925, and from the American Cancer Society, California Division, grant no. J-309. F. C. Eden held a postdoctoral fellowship from the American Cancer Society, grant no. PF-955. W. R. Pearson is a predoctoral fellow on a National Institutes of Health Training Grant, no. GM-00086. G. A. Galau and M. M. Davis are predoctoral fellows on a National Institutes of Health Training Grant, and B. J. Wold is a predoctoral fellow on a National Science Foundation Graduate Fellowship Grant. W. H. Klein held a postdoctoral fellowship from the Damon Runyon-Walter Winchell Cancer Fund.

REFERENCES CITED

- Ando, T., *Biochim. Biophys. Acta* (Amst.), 114, 158, 1966.
- Angerer, R. C., E. H. Davidson, and R. J. Britten, *Cell*, 6, 29, 1975.
- Aronson, A. I., F. H. Wilt, and J. Wartiovaara, *Exp. Cell Res.*, 72, 309, 1972.
- Axel, R., H. Cedar, and G. Felsenfield., *Proc. Nat. Acad. Sci., U.S.A.*, 70, 2029, 1973.
- Bier, Von K., and W. Müller, *Biol. Zb. L'viv. Derzh. Univ.*, 88, 425, 1969.
- Birnie, G. D., E. MacPhail, B. D. Young, M. J. Getz, and J. Paul, *Cell Differ.*, 3, 221, 1974.
- Bishop, J. O., J. G. Morton, M. Rosbash, and M. Richardson, *Nature*, 250, 199, 1974.
- Blobel, G., *Proc. Nat. Acad. Sci., U.S.A.*, 68, 832, 1971.
- Bonner, T. I., D. J. Brenner, B. R. Neufeld, and R. J. Britten, *J. Mol. Biol.*, 81, 123, 1973.
- Bonner, J., W. T. Garrard, J. Gottesfeld, D. S. Holmes, J. S. Sevall, and M. M. Wilkes, *Cold Spring Harbor Symp. Quant. Biol.*, 38, 303, 1974.
- Britten, R. J., and E. H. Davidson, *Science*, 165, 349, 1969.
- Britten, R. J., and E. H. Davidson, *Quart. Rev. Biol.*, 46, 111, 1971.
- Britten, R. J., and E. H. Davidson, *FASEB*, 35, 2151, 1976.
- Britten, R. J., and D. E. Kohne, *Carnegie Inst. Wash. Year Book* 65, p. 78, 1966.
- Britten, R. J., and D. Kohne, *Science*, 161, 529, 1968.
- Britten, R. J., and J. F. Smith, *Carnegie Inst. Wash. Year Book* 68, p. 378, 1970.
- Britten, R. J., and J. F. Smith, *Carnegie Inst. Wash. Year Book* 69, p. 506, 1971.
- Britten, R. J., D. E. Graham, and B. R. Neufeld, in *Methods in Enzymology*, L.

- Grossman and K. Moldave, eds., Vol 29, Part E, Academic Press, New York, p. 363, 1974.
- Britten, R. J., D. E. Graham, F. C. Eden, D. M. Painchaud, and E. H. Davidson, *J. Mol. Evol.*, in press.
- Brown, D. D., and K. Sugimoto, *Cold Spring Harbor Symp. Quant. Biol.*, 38, 501, 1974.
- Brownlee, G. G., E. Cartwright, and D. D. Brown, *J. Mol. Biol.*, 89, 703, 1974.
- Chamberlin, M. E., R. J. Britten, and E. H. Davidson, *J. Mol. Biol.*, 96, 317, 1975.
- Chan, L., A. R. Means, and B. W. O'Malley, *Proc. Nat. Acad. Sci., U.S.A.*, 70, 1870, 1973.
- Chase, J. W., and C. C. Richardson, *J. Biol. Chem.*, 249, 4553, 1974.
- Crain, W. R., F. C. Eden, W. R. Pearson, E. H. Davidson, and R. J. Britten, *Chromosoma* (Berl.), 56, 309, 1976a.
- Crain, W. R., E. H. Davidson, and R. J. Britten, *Chromosoma* (Berl.), in press, 1976b.
- Crothers, D. M., N. R. Jallenback, and B. H. Zimm, *J. Mol. Biol.*, 11, 802, 1965.
- Czihak, G., in *Experimental Embryology of Marine and Fresh-Water Invertebrates*, G. Reverberi, ed., North-Holland, Amsterdam, p. 363, 1971.
- Davidson, E. H., and R. J. Britten, *J. Theor. Biol.*, 32, 123, 1971.
- Davidson, E. H., and R. J. Britten, *Quart. Rev. Biol.*, 48, 565, 1973.
- Davidson, E. H., and B. Hough, *J. Mol. Biol.*, 56, 491, 1971.
- Davidson, E. H., B. R. Hough, C. S. Amenson, and R. J. Britten, *J. Mol. Biol.*, 77, 1, 1973.
- Davidson, E. H., D. E. Graham, B. R. Neufeld, M. E. Chamberlin, C. S. Amenson, B. R. Hough, and R. J. Britten, *Cold Spring Harbor Symp. Quant. Biol.*, 38, 295, 1974.
- Davidson, E. H., G. A. Galau, R. C. Angerer, and R. J. Britten, *Chromosoma* (Berl.), 51, 253, 1975a.
- Davidson, E. H., B. R. Hough, W. H. Klein, and R. J. Britten, *Cell*, 4, 217, 1975b.
- Davidson, E. H., B. R. Hough, M. J. Smith, D. E. Graham, W. H. Klein, G. A. Galau, M. E. Chamberlin, and R. J. Britten, in *The Eukaryote Chromosome*, W. J. Peacock and R. D. Brock, eds., p. 61, Australian National University Press, Canberra, 1975c.
- Davis, F. C., *Biochim. Biophys. Acta*, 390, 33, 1975.
- Durham, J. W., in *Treatise on Invertebrate Paleontology (U) Echinodermata*, Vol. 3, Part 1, The Geological Society of America and the University of Kansas Press, New York, p. 270, 1966.
- Efstratiadis, A., W. R. Crain, R. J. Britten, E. H. Davidson, and F. C. Kafatos, *Proc. Nat. Acad. Sci., U.S.A.*, 73, 2289, 1976.
- Elgin, S. C. R., and L. E. Hood, *Biochemistry*, 12, 4984, 1973.
- Epel, D., *Proc. Nat. Acad. Sci., U.S.A.*, 57, 899, 1967.
- Firtel, R. A., and K. Kindle, *Cell*, 5, 401, 1975.
- Fristrom, J. W., and M. A. Yund, *Crit. Rev. Biochem.*, 1, 537, 1973.
- Galau, G. A., R. Britten, and E. H. Davidson, *Cell*, 2, 9, 1974.
- Galau, G. A., W. H. Klein, M. M. Davis, B. J. Wold, R. J. Britten, and E. H. Davidson, *Cell*, 7, 487, 1976a.
- Galau, G. A., M. E. Chamberlin, B. R. Hough, R. J. Britten, and E. H. Davidson, in *Molecular Evolution*, F. J. Ayala, ed., Sinauer Press, Sunderland, Massachusetts, p. 200, 1976b.
- Galau, G. A., Ph.D. Thesis, 1976, California Institute of Technology.
- Gall, J. G., E. H. Cohen, and M. L. Polan, *Chromosoma* (Berl.), 33, 319, 1971.
- Goldberg, R. B., G. A. Galau, R. J. Britten, and E. H. Davidson, *Proc. Nat. Acad. Sci., U.S.A.*, 70, 3516, 1973.
- Goldberg, R. B., W. R. Crain, J. V. Ruderman, G. P. Moore, T. R. Barnett, R. C. Higgins, R. A. Gelfand, G. A. Galau, R. J. Britten, and E. H. Davidson, *Chromosoma* (Berl.), 51, 225, 1975.
- Graham, D. E., B. R. Neufeld, E. H. Davidson, and R. J. Britten, *Cell*, 1, 127, 1974.
- Gross, K., M. Jacobs-Lorena, C. Baglioni, and P. Gross, *Proc. Nat. Acad. Sci., U.S.A.*, 70, 2614, 1973.
- Harris, S. E., J. M. Rosen, A. R. Means, and B. W. O'Malley, *Biochemistry*, 14, 2072, 1975.
- Hayes, F. N., E. H. Lilly, R. L. Ratliff, D. A. Smith, and D. L. Williams, *Biopolymers*, 9, 1105, 1970.
- Hinegardner, R., in *Methods in Developmental Biology*, F. H. Wilt and N. K. Wessells, eds., Thomas Y. Crowell Co., New York, p. 139, 1967.
- Hinegardner, R., *Comp. Biochem. Physiol.*, 49B, 219, 1974.
- Hoyer, B. H., N. W. van de Velde, M. Goodman, and R. B. Roberts, *Carnegie Inst. Wash. Year Book* 71, p. 260, 1972.
- Humphreys, T., *Dev. Biol.*, 26, 201, 1971.

- Hunt, J. A., *Biochem. J.*, **138**, 499, 1974.
- Hutton, J. R., and J. G. Wetmur, *J. Mol. Biol.*, **77**, 495, 1973.
- Hynes, R., and P. Gross, *Biochim. Biophys. Acta*, **259**, 104, 1972.
- Infante, A. A., and M. Nemer, *Proc. Nat. Acad. Sci., U.S.A.*, **58**, 681, 1967.
- Jenkins, N., M. W. Taylor, and R. A. Raff, *Proc. Nat. Acad. Sci., U.S.A.*, **70**, 3287, 1973.
- Jordan, R. A., and R. W. Brosemer, *J. Insect. Physiol.*, **20**, 2513, 1974.
- Kafatos, F. C., *Curr. Top. Dev. Biol.*, **7**, 125, 1972.
- Kirby, K. S., *Biochem. J.*, **96**, 266, 1965.
- Kohne, D. E., *Quart. Rev. Biophys.*, **33**, 327, 1970.
- Kohne, D. E., J. A. Chiscon, and B. H. Hoyer, *Carnegie Inst. Wash. Year Book* **69**, p. 488, 1970.
- Laird, C. D., *Chromosoma* (Berl.), **32**, 378, 1971.
- Laird, C. D., B. L. McConaughy, and B. J. McCarthy, *Nature* (Lond.), **224**, 149, 1969.
- Levy, W. B., and B. J. McCarthy, *Biochemistry*, **14**, 2440, 1975.
- Manning, J. E., C. W. Schmid, and N. Davidson, *Cell*, **4**, 141, 1975.
- Mandel, M., C. L. Schildkraut, and J. Marmur, in *Methods in Enzymology*, L. Grossman and K. Moldave, eds., Vol. 12B, Academic Press, New York, p. 184, 1968.
- Marmur, J., *J. Mol. Biol.*, **3**, 208, 1961.
- Marshak, A., and C. Marshak, *Exp. Cell Res.*, **5**, 288, 1953.
- McColl, R. S., and A. I. Aronson, *Biochem. Biophys. Res. Commun.*, **56**, 47, 1974.
- Nemer, M., *Cell*, **6**, 559, 1975.
- Nemer, M., L. M. Dubroff, and M. Graham, *Cell*, **6**, 171, 1975.
- Noll, H., *Nature*, **215**, 360, 1967.
- Palmiter, R. D., *J. Biol. Chem.*, **248**, 8260, 1973.
- Paul, M., M. R. Goldsmith, J. R. Hunsley, and F. C. Kafatos, *J. Cell Biol.*, **55**, 653, 1972.
- Peacock, W. J., D. Brutlag, E. Goldring, R. Appels, C. W. Hinton, and D. L. Lindsley, *Cold Spring Harbor Symp. Quant. Biol.*, **38**, 405, 1973.
- Rhoads, R. E., G. S. McKnight, and R. T. Schimke, *J. Biol. Chem.*, **248**, 2031, 1973.
- Rice, N., in *Evolution of Genetic Systems*, Brookhaven Symp. No. 23, H. H. Smith, ed., Gordon and Breach, New York, p. 44, 1972.
- Rice, N. R., *Carnegie Inst. Wash. Year Book* **73**, p. 1094, 1974a.
- Rice, N. R., *Carnegie Inst. Wash. Year Book* **73**, p. 1098, 1974b.
- Rosbash, M., and P. J. Ford, *J. Mol. Biol.*, **85**, 87, 1974.
- Rosbash, M., P. J. Ford, and J. O. Bishop, *Proc. Nat. Acad. Sci., U.S.A.*, **71**, 3746, 1974.
- Rosbash, M., M. S. Campo, and K. S. Gummerson, *Nature* (Lond.), **258**, 682, 1975.
- Ryffel, G. U., and B. J. McCarthy, *Biochemistry*, **14**, 1379, 1975.
- Schachat, F. H., and D. S. Hogness, *Cold Spring Harbor Symp. Quant. Biol.*, **38**, 371, 1974.
- Schmid, C. W., and P. L. Deininger, *Cell*, **6**, 345, 1975.
- Schmid, C. W., J. E. Manning, and N. Davidson, *Cell*, **5**, 159, 1975.
- Shenk, T. E., C. Rhodes, P. W. J. Rigby, and P. Berg, *Proc. Nat. Acad. Sci., U.S.A.*, **72**, 989, 1975.
- Sinclair, J. H., and D. D. Brown, *Biochemistry*, **10**, 2761, 1971.
- Skoultschi, R., and P. R. Gross, *Proc. Nat. Acad. Sci., U.S.A.*, **70**, 2840, 1973.
- Smith, G., *Cold Spring Harbor Symp. Quant. Biol.*, **38**, 507, 1974.
- Smith, M. J., B. R. Hough, M. E. Chamberlin, and E. H. Davidson, *J. Mol. Biol.*, **85**, 103, 1974.
- Smith, M. J., R. J. Britten, and E. H. Davidson, *Proc. Nat. Acad. Sci., U.S.A.*, **72**, 4805, 1975.
- Studier, F. W., *J. Molec. Biol.*, **11**, 373, 1965.
- Sutton, W. D., *Biochim. Biophys. Acta*, **240**, 522, 1971.
- Vogt, V. M., *Eur. J. Biochem.*, **33**, 192, 1973.
- Wellauer, P. K., R. H. Reeder, D. Carroll, D. D. Brown, A. Deutch, T. Higashinakagawa, and I. B. Dawid, *Proc. Nat. Acad. Sci., U.S.A.*, **71**, 2823, 1974.
- Wells, R., H. D. Royer, and C. P. Hollenberg, in press.
- Wensink, P. C., D. J. Finnegan, J. E. Donelson, and D. S. Hogness, *Cell*, **3**, 315, 1974.
- Wetmur, J. G., *Annu. Rev. Biophys. Bioeng.*, **5**, in press.
- Wetmur, J. G., and N. Davidson, *J. Mol. Biol.*, **31**, 349, 1968.
- Whiteley, A. H., B. J. McCarthy, and H. R. Whiteley, *Proc. Nat. Acad. Sci., U.S.A.*, **55**, 519, 1966.
- Whiteley, H. R., B. J. McCarthy, and A. H. Whiteley, *Dev. Biol.*, **21**, 216, 1970.

- Wiegand, R. C., G. N. Godson, and C. M. Radding. *J. Biol. Chem.*, 250, 8848, 1975.
- Williams, J. G., and S. Penman, *Cell*, 6, 197, 1975.
- Wilson, D. A., and C. A. Thomas, Jr., *J. Mol. Biol.*, 84, 115, 1974.
- Wu, J.-R., J. Hurn, and J. Bonner, *J. Mol. Biol.*, 64, 211, 1972.

RECENT PUBLICATIONS

- Anderson, D. M., G. A. Galau, R. J. Britten, and E. H. Davidson, Sequence complexity of the RNA accumulated in oocytes of *Arbacia punctulata*, *Dev. Biol.*, 51, 138-145, 1976.
- Angerer, R. C., E. H. Davidson, and R. J. Britten, DNA sequence organization in the mollusc *Aplysia californica*, *Cell*, 6, 29-39, 1975.
- Angerer, R. C., E. H. Davidson, and R. J. Britten, Single copy DNA and structural gene sequence relationships among four sea urchin species, *Chromosoma*, 56, 213-226, 1976.
- Angerer, R. C., and B. R. Hough-Evans, Sequence organization of eukaryotic DNA, in *Hormone Action. 1. Steroid Hormone Receptors*, B. W. O'Malley and L. Birnbaumer, eds., Academic Press, in press.
- Britten, R. J., and E. H. Davidson, DNA sequence arrangement and preliminary evidence on its evolution, *Fed. Proc.*, 35, 2151-2157, 1976.
- Britten, R. J., and E. H. Davidson, Studies on nucleic acid reassociation kinetics: Empirical equations describing DNA reassociation, *Proc. Nat. Acad. Sci., U.S.A.*, 73, 415-419, 1976.
- Britten, R. J., D. E. Graham, F. C. Eden, D. M. Painchaud, and E. H. Davidson, Evolutionary divergence and length of repetitive sequences in sea urchin DNA, *J. Mol. Evol.*, in press.
- Chamberlin, M. E., R. J. Britten, and E. H. Davidson, Sequence organization in *Xenopus* DNA studied by the electron microscope, *J. Mol. Biol.*, 96, 317-333, 1975.
- Crain, W. R., E. H. Davidson, and R. J. Britten, Contrasting patterns of DNA sequence arrangement in *Apis mellifera* (honeybee) and *Musca domestica* (housefly), *Chromosoma*, in press.
- Crain, W. R., F. C. Eden, W. R. Pearson, E. H. Davidson, and R. J. Britten, Absence of short period interspersions of repetitive and nonrepetitive sequences in the DNA of *Drosophila melanogaster*, *Chromosoma*, in press.
- Davidson, E. H., *Gene Action in Early Development*, 2nd Ed., Academic Press, in press.
- Davidson, E. H., G. A. Galau, R. C. Angerer, and R. J. Britten, Comparative aspects of DNA organization in metazoa, *Chromosoma*, 51, 253-259, 1975.
- Davidson, E. H., W. H. Klein, and R. J. Britten, Sequence organization in animal DNA and an interpretation of hnRNA as a coordinate regulatory transcript, *Dev. Biol.*, submitted, 1976.
- Eden, F. C., D. E. Graham, D. M. Painchaud, E. H. Davidson, and R. J. Britten, Exploration of long and short repetitive sequence relationships in the sea urchin genome, in preparation.
- Efstathiadis, A., W. R. Crain, R. J. Britten, E. H. Davidson, and F. C. Kafatos, DNA sequence organization in the lepidopteran *Antheraea pernyi*, *Proc. Nat. Acad. Sci., U.S.A.*, in press.
- Galau, G. A., R. J. Britten, and E. H. Davidson, Synthesis and degradation of polyosomal messenger RNA and ribosomal RNA in sea urchin gastrula embryos, in preparation.
- Galau, G. A., M. E. Chamberlin, B. R. Hough-Evans, R. J. Britten, and E. H. Davidson, Evolution of repetitive and non-repetitive DNA, in *Molecular Evolution*, F. J. Ayala, ed., Sinauer Associates, pp. 200-224, 1976.
- Galau, G. A., W. H. Klein, R. J. Britten, and E. H. Davidson, Functional significance of mRNA sequences in the least abundant concentration class, in preparation.
- Galau, G. A., W. H. Klein, M. M. Davis, B. J. Wold, R. J. Britten, and E. H. Davidson, Structural gene sets active in embryos and adult tissues of the sea urchin, *Cell*, 7, 487-505, 1976.
- Goldberg, R. N., W. R. Crain, J. V. Ruderman, G. P. Moore, T. R. Barnett, R. C. Higgins, R. A. Gelfand, G. A. Galau, R. J. Britten, and E. H. Davidson, DNA sequence organization in the genomes of five marine invertebrates, *Chromosoma*, 51, 225-251, 1975.

- Hough-Evans, B. R., *Quart. Rev. Biol.*, 51, 111 (Book Review), 1976.
- Lee, A. S., F. Costantini, R. J. Britten, and E. H. Davidson, Initial studies of sea urchin DNA sequence organization by molecular cloning, in *Molecular Mechanisms in the Control of Gene Expression*, D. P. Nierlich, W. J. Rutter and C. F. Fox, eds., Vol. 5 (ICN-UCLA Symposia on Molecular and Cellular Biology), Academic Press, New York, in press.
- Smith, M. J., R. J. Britten, and E. H. Davidson, Studies on nucleic acid reassociation kinetics: Reactivity of single-stranded tails in DNA-DNA renaturation, *Proc. Nat. Acad. Sci., U.S.A.*, 72, 4805-4809, 1976.
- Thomas, T. L., DNA sequence organization in higher organisms, *New Scientist*, in press.

STAFF

- Roy J. Britten, *Senior Research Associate*
 Eric H. Davidson, *Professor*
 Barbara R. Hough-Evans, *Senior Research Fellow*
 William H. Klein, *Senior Research Fellow—Damon Runyon Fellowship and California Division, American Cancer Society, Lievre Fellowship*
 Michael J. Smith, *Senior Research Fellow*
 Robert C. Angerer, *Research Fellow—California Division, American Cancer Society Fellowship*
 William R. Crain, *Research Fellow—National Institutes of Health Fellowship*
 Francine C. Eden, *Research Fellow—American Cancer Society Fellowship*
 Susan G. Ernst, *Research Fellow—The National Foundation—March of Dimes Fellowship*
 Amy Shiu Lee, *Research Fellow—California Division, American Cancer Society Fellowship*
 Terry L. Thomas, *Research Fellow—National Institutes of Health Fellowship*
 Ted Tutschulte, *Research Fellow*
 Frank Costantini, *Graduate Research Assistant*
 Mark M. Davis, *Graduate Research Assistant*
 Glenn A. Galau, *Graduate Research Assistant*
 Barbara J. Wold, *Graduate Research Assistant*
 Margaret E. Chamberlin, *Senior Research Assistant*
 Jane Rigg, *Senior Research Assistant*
 Peggy R. Bierer, *Research Assistant*
 Doris Finch, *Research Assistant*
 Patrick S. Leahy, *Research Assistant*
 Denise M. Painchaud, *Research Assistant*
 Michael R. Kozlowski, *Undergraduate Assistant*
 Lee Venolia, *Undergraduate Assistant*
 John Mamin, *Undergraduate Assistant*
 Dennis B. Cochran, *Laboratory Assistant*
 Charles F. Collett, *Laboratory Assistant*

Bibliography

July 1, 1975–June 30, 1976

PUBLICATIONS OF THE INSTITUTION

Carnegie Institution of Washington Year Book 74. Octavo, vii + 35 + 860 pages, 365 figures. December 1975.

Algal Culture: From Laboratory to Pilot Plant. Edited by John S. Burlew. Publication 600. Octavo, ix + 357 pages, 91 figures. Reprint. May 1976.

Ceramics for the Archaeologist. Anna O. Shepard. Publication 609. Octavo, xxvi + 414 pages, 59 figures. Reprint. May 1976.

Carnegie Institution of Washington Catalogue 1976–1977. Octavo, 83 pages, 21 figures. June 1976.

Carnegie Institution of Washington Newsletter. Issued in July, November, and April.

PUBLICATIONS BY THE PRESIDENT OF THE INSTITUTION

Philip H. Abelson

International geophysics: science dominates politics, *Science*, 190, 34–35, 1975.

Editing *Science*, Faculty Club Forum, Rice University, Houston, Texas, 4 pp., October 6, 1975.

Environment: a delicate balance of costs and benefits (see *Year Book* 71, p. 736), reprinted in *Energy and Man: Technical and Social Aspects of Energy*, M. Granger Morgan, ed., pp. 134–138, IEEE Press, New York, 1975.

Arthur Louis Day (1869–1960), *Biographical Memoirs*, Vol. XLVII, pp. 26–47, National Academy of Sciences of the United States, Washington, D.C., 1975.

William Walden Rubey (1898–1974), *Year Book of The American Philosophical Society*, pp. 157–163, Philadelphia, Pennsylvania, 1975.

Foreword to *Food: Politics, Economics, Nutrition and Research* (editor), p. v, American

Association for the Advancement of Science, 1975.

Creating and applying knowledge, in *Criteria on Science Policy*, pp. 31–38, Proceedings of International Meeting on the Organization of Science, Madrid, April 11–14, 1973. Consejo Superior de Investigaciones Científicas, Madrid, 1975.

Spain—another Japan? (Editorial, *Science*; see *Year Book* 72, p. 735), reprinted in *Criteria on Science Policy*, pp. 270–271, Consejo Superior de Investigaciones Científicas, Madrid, 1975.

[Prospects for world energy.] Rip van Winkle Jrs. describe 1985, *New York Times*, p. 57, International Economic Survey Section, January 25, 1976.

The new world of materials [with Allen L. Hammond], *Science*, 191, 633–636.

Editorials in *Science*

Volume 189:

Absence of U.S. energy leadership, July 4, 1975, p. 11; Control of sulfur dioxide emissions from coal, July 25, 1975, p. 253; Energy alternatives for Brazil, August 8, 1975, p. 417.

Volume 190:

Federal intervention in universities, October 17, 1975, p. 221; Detlev Bronk [with Neva M. Abelson], December 5, 1975, p. 941.

Volume 191:

Enough of pessimism, January 9, 1976, p. 29; Renewable and nonrenewable resources, February 20, 1976, p. 631; A global rush toward nuclear energy, March 5, 1976; Energy from biomass, March 26, 1976, p. 1221.

Volume 192:

Energy diplomacy, April 30, 1976; Cost-effective health care, May 14, 1976, p. 619; Adjusting to change, June 18, 1976, p. 1187; More laws, more complexity, June 25, 1976, p. 1291.

Administrative Reports

Report of the Executive Committee

To the Trustees of the Carnegie Institution of Washington

In accordance with the provisions of the By-Laws, the Executive Committee submits this report to the Annual Meeting of the Board of Trustees.

During the fiscal year ending June 30, 1976, the Executive Committee held four meetings. Printed accounts of these meetings have been or will be mailed to each Trustee.

The estimate of expenditures for the fiscal year beginning July 1, 1976, has been reviewed by the Executive Committee.

Two vacancies exist in the membership of the Board of Trustees, resulting from the resignation of Patrick E. Haggerty in June 1975, and the death of William I. Myers in January 1976.

The terms of the Vice-Chairman and Secretary of the Board, all Committee Chairmen, and the following members of Committees also expire on April 30, 1976:

Executive Committee

Henry S. Morgan

Finance Committee

William T. Golden

Henry S. Morgan

Nominating Committee

William R. Hewlett

Auditing Committee

Juan T. Trippe

Frank Stanton, *Chairman*

April 30, 1976

Abstract of Minutes

of the Seventy-Eighth Meeting of the Board of Trustees

The annual meeting of the Board of Trustees was held in the Board Room of the Administration Building on Friday, April 30, 1976. The meeting was called to order by Chairman William McChesney Martin, Jr.

The following Trustees were present: John T. Connor, John Diebold, Michael Ference, Jr., Carl J. Gilbert, William T. Golden, Hanna H. Gray, Crawford H. Greenewalt, William C. Greenough, Caryl P. Haskins, William McChesney Martin, Jr., Henry S. Morgan, Walter H. Page, Robert M. Pennoyer, Richard S. Perkins, Robert C. Seamans, Jr., Frank Stanton, Charles H. Townes, Juan T. Trippe, and James N. White. Garrison Norton, Trustee Emeritus, and the President, Philip H. Abelson, were also in attendance.

The minutes of the Seventy-Seventh Meeting was approved.

The Chairman notified the Trustees of the death of William I. Myers, Trustee, and of Alfred L. Loomis and Keith S. McHugh, Trustees Emeriti. He read a memorial statement in tribute to Dr. Myers and the following resolution was unanimously adopted:

Be It Therefore Resolved, That the Board of Trustees of the Carnegie Institution of Washington hereby records its deep sense of loss at the death of William Irving Myers.

And Be It Further Resolved, That this resolution be entered on the minutes of the Board of Trustees and that a copy be sent to the family of Dr. Myers.

Dr. Haskins read a memorial statement in tribute to Dr. Loomis and the following resolution was unanimously adopted:

Be It Therefore Resolved, That the Board of Trustees of the Carnegie Institution of Washington hereby records its deep sense of loss at the death of Alfred Lee Loomis.

And Be It Further Resolved, That this resolution be entered on the minutes of the Board of Trustees and that a copy be sent to Mrs. Loomis.

Mr. Page read a memorial statement in tribute to Mr. McHugh and the following resolution was unanimously adopted:

Be It Therefore Resolved, That the Board of Trustees of the Carnegie Institution of Washington hereby records its deep sense of loss at the death of Keith Stratton McHugh.

And Be It Further Resolved, That this resolution be entered on the minutes of the Board of Trustees and that a copy be sent to Mrs. McHugh.

The reports of the Executive Committee, the Finance Committee, the Retirement Committee, and the Auditing Committee were accepted. On recommendation of the latter, it was resolved that Arthur Andersen & Co. be reappointed as public accountants for the fiscal year beginning July 1, 1976.

On the recommendation of the Nominating Committee, Robert O. Anderson and J. Paul Austin were elected members of the Board of Trustees.

Frank Stanton was elected Vice-Chairman of the Board and William T. Golden was elected Secretary of the Board, both for terms ending in 1979.

The following were elected for one year terms: Frank Stanton, as Chairman of the Executive Committee; Richard S. Perkins, as Chairman of the Finance Committee; Juan T. Trippe, as Chairman of the Auditing Committee; Robert M. Pennoyer, as Chairman of the Nominating Committee; and Carl J. Gilbert, as Chairman of the Retirement Committee.

Vacancies in Standing Committees, with terms ending in 1979, were filled as follows: Henry S. Morgan was elected a member of the Executive Committee; William T. Golden and Henry S. Morgan were elected members of the Finance Committee; Juan T. Trippe was elected a member of the Auditing Committee; and John Diebold was elected a member of the Nominating Committee.

The annual report of the President was accepted.

To provide for the operation of the Institution for the fiscal year beginning July 1, 1976, and upon recommendation of the Executive Committee, the sum of \$7,369,400 was appropriated.

An Ad Hoc Committee on Finance was established and the Chairman appointed the following Trustees to serve on the Committee: Frank Stanton (Chairman), John Diebold, Carl Gilbert, William T. Golden, and William C. Greenough.

Article V, Sections 1, 8, 13, and 14 of the By-Laws were amended to read as follows:

ARTICLE V

Committees

1. There shall be the following Standing Committees, *viz.* an Executive Committee, a Finance Committee, an Auditing Committee, a Nominating Committee, and an Employee Benefits Committee.

Finance Committee

8. The Finance Committee shall have custody of the securities of the Institution and general charge of its investments and invested funds and shall care for and dispose of the same subject to the directions of the Board of Trustees. It shall have power to authorize the purchase, sale, exchange, or transfer of securities and to delegate this power. So long as the Institution is the trustee under any retirement or other benefit plan for the staff members and employees of the Institution, it shall be responsible for supervision of matters relating to investments thereunder and for the appointment or removal of any investment manager or advisor. It shall also be responsible for reviewing the financial status and arrangements of any employee benefit

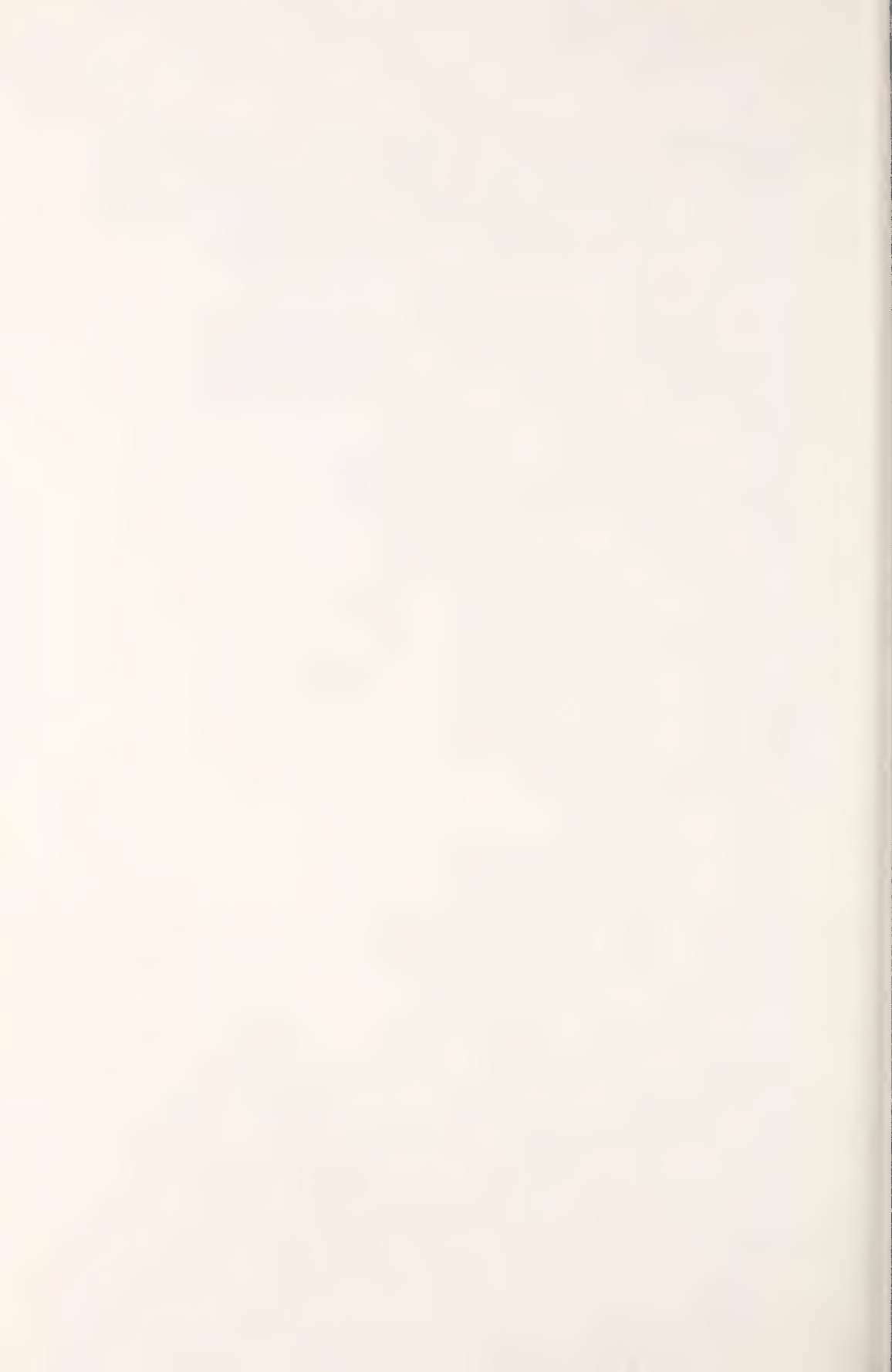
plan for which the Institution is not the trustee and for appointment or removal of any plan trustee or insurance carrier. It shall consider and recommend to the Board from time to time such measures as in its opinion will promote the financial interests of the Institution and improve the management of investments under any retirement or other benefit plan. The Committee shall make a report at the annual meeting of the Board.

Employee Benefits Committee

13. The Employee Benefits Committee shall consist of three members to be elected by the Board of Trustees by ballot for a term of three years, who shall be eligible for re-election, and the Chairman of the Finance Committee *ex officio*. Any member elected to fill a vacancy shall serve for the remainder of his predecessor's term.

14. The Employee Benefits Committee shall, subject to the directions of the Board of Trustees, be responsible for supervision of the activities of the administrator or administrators of any retirement or other benefit plan for staff members and employees of the Institution, except that any matter relating to investments or to the appointment or removal of any trustee or insurance carrier under any such plan shall be the responsibility of the Finance Committee. It shall receive reports from the administrator or administrators of the employee benefit plans with respect to administration, benefit structure, operation, and funding. It shall consider and recommend to the Board from time to time such measures as in its opinion will improve such plans and the administration thereof. The Committee shall submit a report to the Board at the annual meeting of the Board.

The members of the previous Retirement Committee were elected as members of the Employee Benefits Committee with the term of the Chairman and members of the Committee to continue.



Financial Statement

for the year ended June 30, 1976

CARNEGIE INSTITUTION OF WASHINGTON
TEN-YEAR FINANCIAL SUMMARY, 1967-1976
All Figures are Thousands of Dollars

| <i>Fiscal Year Ended June 30</i> | 1976* | 1975* | 1974* | 1973 | 1972 | 1971 | 1970 | 1969 | 1968 | 1967 |
|---|----------|------------|----------|-----------|-----------|-----------|----------|-----------|-----------|-----------|
| <i>Income</i> | | | | | | | | | | |
| Realized capital gain or loss, net. | \$ 4,365 | (\$ 1,369) | \$ 4,762 | \$ 6,576 | \$ 2,328 | \$ 2,924 | (\$ 117) | \$ 360 | \$ 581 | (\$ 307) |
| Interest and dividends | 3,958 | 3,295 | 3,356 | 3,647 | 3,863 | 4,127 | 4,077 | 4,213 | 4,092 | 4,091 |
| Other | 126 | 83 | 60 | 58 | 65 | 90 | 45 | 59 | 53 | 41 |
| Total | 8,449 | 2,009 | 8,178 | 10,281 | 6,256 | 7,141 | 4,005 | 4,632 | 4,726 | 3,825 |
| <i>Expenditures (Includes Plant Fund)</i> | | | | | | | | | | |
| Terrestrial Magnetism | 1,046 | 1,188 | 1,025 | 1,022 | 937 | 909 | 801 | 844 | 845 | 839 |
| Mount Wilson Observatory | 1,085 | 1,027 | 1,051 | 1,016 | 992 | 930 | 1,154 | 762 | 781 | 688 |
| Las Campanas Observatory | 1,753 | 2,138 | 2,572 | 2,559 | 1,075 | 1,184 | 466 | 126 | — | — |
| Geophysical Laboratory | 1,032 | 1,136 | 964 | 984 | 770 | 779 | 768 | 761 | 762 | 727 |
| Embryology | 816 | 851 | 791 | 718 | 699 | 668 | 613 | 618 | 562 | 557 |
| Plant Biology | 620 | 1,270 | 673 | 330 | 271 | 252 | 244 | 253 | 221 | 221 |
| Genetics Research Units | 22 | 24 | 70 | 65 | 68 | 165 | 151 | 142 | 147 | 166 |
| Research Projects, etc. | 89 | 51 | 98 | 29 | 22 | 61 | 63 | 86 | 118 | 151 |
| Office of Administration | 500 | 571 | 520 | 592 | 583 | 559 | 469 | 433 | 455 | 410 |
| General publications | 66 | 78 | 57 | 79 | 58 | 98 | 111 | 45 | 70 | 95 |
| Consulting fees, insurance, taxes . . | 158 | 134 | 95 | 62 | 67 | 75 | 44 | 80 | 38 | 78 |
| Employee benefits, special | 102 | 81 | 89 | 97 | 78 | 77 | 71 | 77 | 78 | 82 |
| Financial advisory services | 205 | 213 | 199 | 195 | 108 | 66 | 70 | 74 | 71 | 72 |
| Total | 7,494 | 8,762 | 8,204 | 7,748 | 5,728 | 5,823 | 5,025 | 4,301 | 4,171 | 4,086 |
| <i>Restricted Grants</i> | | | | | | | | | | |
| Grants received | 1,202 | 815 | 505 | 544 | 444 | 483 | 437 | 678 | 464 | 417 |
| Expenditures | 772 | 447 | 484 | 554 | 470 | 517 | 517 | 566 | 576 | 458 |
| <i>Gifts received</i> | 41 | 146 | 330 | 377 | 354 | 611 | 5 | 66 | 38 | 660 |
| <i>Endowment and Special Funds</i> | | | | | | | | | | |
| Endowment Fund | 76,054 | 75,048 | 79,852 | 79,322 | 76,863 | 76,649 | 75,641 | 76,157 | 76,542 | 76,019 |
| Special Funds | 1,294 | 1,188 | 1,049 | 1,007 | 947 | 934 | 893 | 888 | 1,505 | 1,453 |
| Total | 77,348 | 76,236 | 80,901 | 80,329 | 77,810 | 77,583 | 76,534 | 77,045 | 78,047 | 77,472 |
| Total market value of investments | \$92,215 | \$93,719 | \$98,200 | \$124,770 | \$128,826 | \$113,042 | \$89,000 | \$109,262 | \$114,796 | \$109,188 |

*Accrual Basis; prior years are stated on a Cash Basis.

ARTHUR ANDERSEN & Co.

1666 K STREET, N.W.
WASHINGTON, D. C. 20006

(202) 785-9510

September 3, 1976

REPORT OF INDEPENDENT PUBLIC ACCOUNTANTS

To the Auditing Committee of
Carnegie Institution of Washington:

We have examined the statement of assets, liabilities and funds of CARNEGIE INSTITUTION OF WASHINGTON (a non-profit corporation chartered by Act of the United States Congress) as of June 30, 1976, and June 30, 1975, the related summary statement of changes in funds for the year ended June 30, 1976, and the supporting exhibits and schedules, all of which are set forth on the thirteen immediately following pages. Our examination was made in accordance with generally accepted auditing standards, and accordingly included such tests of the accounting records and such other auditing procedures as we considered necessary in the circumstances.

In our opinion, the financial statements and supporting exhibits and schedules referred to above present fairly the assets, liabilities and funds of Carnegie Institution of Washington as of June 30, 1976, and June 30, 1975, and the changes in funds for the year ended June 30, 1976, in conformity with generally accepted accounting principles consistently applied during the periods.

Basis of Accounting

The financial statements of the Institution are prepared on the accrual basis of accounting. The Institution follows a policy of reporting all commitments outstanding at year-end as liabilities for financial statement purposes.

Land, Buildings and Equipment

The Institution capitalizes expenditures for land, buildings, telescopes and other significant equipment, and construction projects in progress. Expenditures for other equipment are charged to current operations as incurred, and the cost of such equipment is not capitalized. The Institution follows the policy of not depreciating its buildings, telescopes and significant equipment.

Retirement Plan

The Institution has a noncontributory retirement plan in which all regularly employed United States personnel are eligible to participate. Voluntary contributions may also be made by employees. Actuarially determined contributions are funded currently by the Institution, and there are no unfunded past service costs. The total contributions made by the Institution were \$476,656 in 1976 and \$453,684 in 1975. Benefits under the plan upon retirement are dependent upon the investment performance of the Institution's Retirement Trust. After four years' participation, benefits are fully vested.

During 1975, the plan was modified in order to comply with the Employees Retirement Income Security Act of 1974. The modifications were generally of a technical nature and had no significant impact on the plan.

CARNEGIE INSTITUTION OF WASHINGTON
STATEMENT OF ASSETS, LIABILITIES AND FUNDS
JUNE 30, 1976 AND 1975

ASSETS

| | 1976 | 1975 |
|----------------------------------|---------------------|---------------------|
| Cash | \$ 347,637 | \$ 145,588 |
| Accrued interest | 512,734 | 403,145 |
| Grants receivable | 651,228 | 428,509 |
| Advances | 73,275 | 47,227 |
| Investments (cost),* Schedule 2: | | |
| Governmental bonds | 12,541,263 | 5,047,113 |
| Nongovernmental bonds | 22,982,709 | 23,487,483 |
| Common stocks | 43,096,495 | 49,286,443 |
| Total investments | <u>78,620,467</u> | <u>77,821,039</u> |
| Land | 854,088 | 766,402 |
| Buildings | 4,756,290 | 4,603,555 |
| Equipment | 10,104,439 | 8,211,486 |
| Total assets | <u>\$95,920,158</u> | <u>\$92,426,951</u> |

LIABILITIES AND FUNDS

Appropriated funds:

| | | |
|--|---------------------|---------------------|
| Accounts payable and accrued expenses— | | |
| Operating Fund | \$ 440,232 | \$ 528,950 |
| Restricted Grants | 95,733 | 73,786 |
| Total liabilities | <u>535,965</u> | <u>602,736</u> |
| Operating Fund, Exhibit 1 | 1,487,321 | 1,603,090 |
| Restricted Grants, Exhibit 2 | 834,147 | 403,922 |
| Unappropriated Funds, Exhibit 3 | 77,347,908 | 76,235,760 |
| Plant Fund | 15,714,817 | 13,581,443 |
| Total liabilities and funds | <u>\$95,920,158</u> | <u>\$92,426,951</u> |

*Approximate market value on June 30, 1976: \$92,215,278; on June 30, 1975: \$93,719,359.

CARNEGIE INSTITUTION OF WASHINGTON
SUMMARY STATEMENT OF CHANGES IN FUNDS
FOR THE YEAR ENDED JUNE 30, 1976

| | <i>Appropriated Funds</i> | | <i>Unappropriated Funds (Exhibit 3)</i> | <i>Plant Fund</i> | <i>Total</i> |
|--|-----------------------------------|--------------------------------------|---|-------------------|--------------|
| | <i>Operating Fund (Exhibit 1)</i> | <i>Restricted Grants (Exhibit 2)</i> | | | |
| Balance, July 1, 1975 | \$1,603,090 | \$ 403,922 | \$76,235,760 | \$13,581,443 | \$91,824,215 |
| <i>Additions</i> | | | | | |
| Realized capital gain, net | — | — | — | — | 4,365,345 |
| Investment income | — | — | — | — | 2,414,093 |
| Interest | — | — | — | — | 1,543,794 |
| Dividends | — | — | — | — | 41,375 |
| Gifts | — | — | — | — | 125,669 |
| Other income | — | — | — | — | — |
| Land, buildings and equipment, capitalized | — | — | — | — | — |
| Current year | — | — | — | 1,332,274 | 1,332,274 |
| Prior years | — | — | — | 801,100 | 801,100 |
| <i>Appropriations</i> | | | | | |
| Budget | 6,454,715 | — | (6,454,715) | — | — |
| Las Campanas Observatory | 906,203 | — | (906,203) | — | — |
| Special Opportunities Fund | 15,000 | — | (15,000) | — | — |
| Bush Gift | 1,800 | — | (1,800) | — | — |
| Hale Relief Fund | 410 | — | (410) | — | — |
| Restricted grants | — | 1,202,478 | — | — | 1,202,478 |
| | 7,378,128 | 1,202,478 | 1,112,148 | 2,133,374 | 11,826,128 |
| <i>Deductions</i> | | | | | |
| Expenditures | 7,493,897 | 772,253 | — | — | 8,266,150 |
| Net change during year | (115,769) | 430,225 | 1,112,148 | 2,133,374 | 3,559,978 |
| Balance, June 30, 1976 | \$1,487,321 | \$ 834,147 | \$77,347,908 | \$15,714,817 | \$95,384,193 |

CARNEGIE INSTITUTION OF WASHINGTON

EXHIBIT 1

APPROPRIATED FUNDS

CHANGES IN OPERATING FUND FOR THE YEAR ENDED JUNE 30, 1976

| | |
|-----------------------------|-------------|
| Balance, July 1, 1975 | \$1,603,090 |
|-----------------------------|-------------|

Appropriations

| | | |
|---|-------------|-----------|
| Budget, July 1, 1975 to June 30, 1976 | \$6,454,715 | |
| Las Campanas Observatory | | |
| Unrestricted Capital Fund | 906,203 | |
| Special Opportunities Fund | 15,000 | |
| Bush Gift | 1,800 | |
| Hale Relief Fund | 410 | 7,378,128 |
| | | <hr/> |
| Total available for expenditures | | 8,981,218 |

Expenditures

| | | |
|---|-------------|-----------|
| Salaries | \$3,049,817 | |
| Employee benefits | 646,290 | |
| Building maintenance | 430,612 | |
| Educational and research supplies | 379,795 | |
| Equipment | 313,686 | |
| Administrative | 236,907 | |
| Financial advisory services | 205,397 | |
| Taxes | 196,430 | |
| Fellowship grants | 169,046 | |
| Insurance | 142,565 | |
| Travel | 109,918 | |
| Publications | 101,684 | |
| Consulting fees | 39,428 | |
| Awards | 37,799 | |
| Commissary | 32,977 | |
| Shop | 23,472 | |
| Rent | 21,771 | |
| Entertainment | 15,235 | |
| Fellowship travel | 8,794 | 6,161,623 |
| | | <hr/> |

Transfers to Plant Fund

| | | |
|---------------------------|---------|-----------|
| Construction in progress: | | |
| Equipment | 843,607 | |
| Salaries | 199,352 | |
| Building | 147,053 | |
| Employee benefits | 38,030 | |
| Taxes | 11,164 | |
| Land (improvements) | 87,686 | |
| Buildings | 5,382 | 1,332,274 |
| | | <hr/> |

| | |
|--------------------------|-----------|
| Total expenditures | 7,493,897 |
|--------------------------|-----------|

| | |
|------------------------------|-------------|
| Balance, June 30, 1976 | \$1,487,321 |
|------------------------------|-------------|

CARNEGIE INSTITUTION OF WASHINGTON

EXHIBIT 2

APPROPRIATED FUNDS

CHANGES IN RESTRICTED GRANTS
FOR THE YEAR ENDED JUNE 30, 1976

| | <i>Balance July 1, 1975</i> | <i>Grants</i> | <i>Expenditures</i> | | <i>Balance June 30, 1976</i> |
|---|---------------------------------|--------------------|---------------------|------------------|----------------------------------|
| | | | <i>Salaries</i> | <i>Other</i> | |
| Carnegie Corporation of New York | \$ 194 | \$ 80,000 | — | \$ 79,384 | \$ 810 |
| Max C. Fleischmann Foundation . . | — | 250,000 | — | 13,935 | 236,065 |
| Jet Propulsion Laboratory | 37 | (37) | — | — | — |
| Massachusetts Institute of Technology | — | 66,606 | \$ 17,054 | 48,571 | 981 |
| Moseley Gift | 1,199 | — | — | 64 | 1,135 |
| Muscular Dystrophy Association . . | — | 25,476 | — | 12,488 | 12,988 |
| National Academy of Sciences | 23,198 | 35,000 | — | 14,781 | 43,417 |
| National Aeronautics & Space Administration | 18,551 | 129,510 | 38,767 | 56,562 | 52,732 |
| National Cystic Fibrosis Research Foundation | 25,000 | (6,000) | — | 15,375 | 3,625 |
| National Science Foundation | 311,978 | 327,900 | 74,208 | 204,132 | 361,538 |
| Office of Naval Research | — | 20,550 | 14,800 | 5,750 | — |
| Preston Gift | — | 300 | — | 300 | — |
| Public Health Service | — | 243,085 | 28,357 | 114,220 | 100,508 |
| Whitehall Foundation | 8,852 | 35,000 | — | 23,504 | 20,348 |
| Wistar Institute | 14,913 | (4,912) | 7,950 | 2,051 | — |
| Total | <u>\$403,922</u> | <u>\$1,202,478</u> | <u>\$181,136</u> | <u>\$591,117</u> | <u>\$834,147</u> |

CARNEGIE INSTITUTION OF WASHINGTON

CHANGES IN UNAPPROPRIATED FUNDS
FOR THE YEAR ENDED JUNE 30, 1976

EXHIBIT 3

| | Balance July 1, 1975 | Investment Income | Gifts and Other Income | Realized Capital Gain, net | Appropriations | Transfers | Balance June 30, 1976 |
|----------------------------------|-------------------------|----------------------|------------------------------|----------------------------------|----------------|-----------|--------------------------|
| <i>Endowment Fund</i> | | | | | | | |
| Gift | | | | | | | |
| Andrew Carnegie | \$22,000,000 | — | — | — | — | — | \$22,000,000 |
| Realized capital gain, net | 31,197,753 | — | — | \$3,122,236 | — | — | 34,319,989 |
| Unrestricted Capital Fund | | | | | | | |
| Carnegie Corporation of New York | 10,000,000 | — | — | — | — | — | 10,000,000 |
| Other gifts | — | — | \$ 525 | — | 525 | — | — |
| Realized capital gain, net | 11,850,164 | — | — | 1,181,860 | 3,298,163 | — | 9,733,861 |
| Working Capital Fund | | | | | | | |
| Income | — | \$3,903,106 | — | — | 4,028,013 | \$124,907 | — |
| Sales | | | | | | | |
| Assets | — | — | 27,239 | — | — | (27,239) | — |
| Optical services | — | — | 6,101 | — | — | (6,101) | — |
| Indirect costs awards | — | — | 37,476 | — | — | (37,476) | — |
| Royalties | — | — | 22,730 | — | — | (22,730) | — |
| University of Toronto | — | — | 20,000 | — | — | (20,000) | — |
| Refunds | — | — | 5,801 | — | — | (5,801) | — |
| Rent | — | — | 3,723 | — | — | (3,723) | — |
| Miscellaneous | — | — | 1,837 | — | — | (1,837) | — |
| <i>Special Funds</i> | | | | | | | |
| Bush Bequest | 102,155 | 6,458 | — | 7,187 | — | — | 115,800 |
| Bush Gift | 27,822 | 2,098 | — | 2,337 | 1,800 | — | 30,457 |
| Colburn | 222,863 | 11,578 | — | 12,885 | 9,060 | — | 238,266 |
| Hale Relief | 6,507 | 214 | 762 | 217 | 608 | — | 7,092 |
| Harkavy | 10,895 | 506 | — | 563 | 396 | — | 11,568 |
| Lundmark | 43,778 | 1,859 | — | 2,069 | 1,500 | — | 46,206 |
| Martin | 26,327 | 1,474 | — | 1,641 | — | — | 29,442 |
| Morgenroth | 37,797 | 1,357 | — | 1,511 | 1,063 | — | 39,602 |
| Special Instrumentation | 97,290 | 3,821 | — | 4,252 | — | — | 105,363 |
| Special Opportunities | — | 821 | 40,850 | 1,216 | 15,000 | — | 27,887 |
| Wood | 612,409 | 24,595 | — | 27,371 | 22,000 | — | 642,375 |
| Total | \$76,235,760 | \$3,957,887 | \$167,044 | \$4,365,345 | \$7,378,128 | \$ — | \$77,347,908 |

CARNEGIE INSTITUTION OF WASHINGTON

SCHEDULE 1

APPROPRIATED FUNDS

BUDGET SUMMARY OF OPERATING FUND
FOR THE YEAR ENDED JUNE 30, 1976

| | <i>Unexpended Appropriations July 1, 1975</i> | <i>Appropriations</i> | <i>Transfers and Allotments</i> | <i>Total Expenditures</i> | <i>Unexpended Appropriations June 30, 1976</i> |
|---|---|-----------------------|---|-------------------------------|--|
| Terrestrial Magnetism | — | \$1,097,670 | (\$ 22,174) | \$1,045,700 | \$ 29,796 |
| Mount Wilson Observatory | \$ 43,065 | 1,044,955 | (2,284) | 1,085,103 | 633 |
| Las Campanas Observatory | 151,745 | 1,395,953 | 321,268 | 1,753,103 | 115,863 |
| Geophysical Laboratory | 12,424 | 1,043,555 | (16,571) | 1,032,151 | 7,257 |
| Embryology | 4,264 | 867,120 | (10,906) | 815,477 | 45,001 |
| Plant Biology | 74,268 | 537,540 | 7,826 | 619,634 | — |
| Genetics Research Unit | — | 21,500 | 529 | 22,029 | — |
| Research Projects, etc. | 69,009 | 104,025 | (19,535) | 89,155 | 64,344 |
| Office of Administration | — | 528,400 | (28,263) | 500,137 | — |
| General publications | 10,769 | 55,000 | 367 | 66,136 | — |
| Consulting fees, insurance, taxes | — | 99,000 | 58,792 | 157,792 | — |
| Employee benefits, retirees | 73,800 | 77,000 | 31,743 | 96,343 | 86,200 |
| Employee benefits, special | — | 6,410 | (670) | 5,740 | — |
| Financial advisory services | — | 200,000 | 5,397 | 205,397 | — |
| Contingent operating fund | 37,606 | 300,000 | (337,606) | — | — |
| Unallocated appropriations | 1,126,140 | — | 12,087 | — | 1,138,227 |
| Total | \$1,603,090 | \$7,378,128 | \$ — | \$7,493,897 | \$1,487,321 |

CARNEGIE INSTITUTION OF WASHINGTON

SCHEDULE 2

INVESTMENTS, JUNE 30, 1976

| <i>Description</i> | <i>Par</i> | <i>Cost</i> | <i>Approximate Market</i> |
|---|-------------|-------------------|-------------------------------|
| Federal Agency Bonds | | | |
| Federal Home Loan Banks, Cons., 7.80s, 1976 | \$1,000,000 | \$ 992,656 | \$ 1,001,250 |
| Federal Home Loan Banks, Cons., 9.50s, 1979 | 200,000 | 199,925 | 210,750 |
| Federal Home Loan Banks, Cons., 8.15s, 1979 | 500,000 | 502,344 | 508,750 |
| Federal Home Loan Banks, Cons., 7.80s, 1980 | 500,000 | 501,719 | 500,625 |
| Federal Home Loan Banks, Cons., 7.30s, 1983 | 1,000,000 | 999,375 | 965,000 |
| Federal National Mortgage Association, 6 ¾ s, 1977 | 600,000 | 602,437 | 597,000 |
| Federal National Mortgage Association, 9.80s, 1979 | 200,000 | 200,000 | 211,000 |
| Federal National Mortgage Association, 8s, 1980 | 500,000 | 497,656 | 504,375 |
| Federal National Mortgage Association, 8.40s, 1983 | 1,000,000 | 1,000,000 | 1,018,750 |
| Federal National Mortgage Association, 8.20s, 1984 | 600,000 | 599,063 | 603,750 |
| Federal National Mortgage Association, 7.95s, 1984 | 500,000 | 496,250 | 497,500 |
| Twelve Federal Land Banks, Cons., 6.40s, 1978 | 500,000 | 497,031 | 489,375 |
| Twelve Federal Land Banks, Cons., 7.30s, 1982 | 500,000 | 500,000 | 485,000 |
| Twelve Federal Land Banks, Cons., 8.20s, 1983 | 800,000 | 800,000 | 811,000 |
| United States of America Treasury, Notes, 6 ¾ s, 1978 | 500,000 | 499,609 | 496,715 |
| United States of America Treasury, Notes, 7 ¾ s, 1981 | 1,000,000 | 998,920 | 993,120 |
| United States of America Treasury, Notes, 8s, 1982 | 1,150,000 | 1,157,188 | 1,168,688 |
| United States of America Treasury, Notes, 7 ¾ s, 1982 | 1,000,000 | 997,090 | 1,008,750 |
| United States of America Treasury, Notes, 7 ¾ s, 1986 | 500,000 | 500,000 | 500,465 |
| Total | | <u>12,541,263</u> | <u>12,571,863</u> |
| Foreign Bonds | | | |
| Alcan Aluminum Corporation, Prom. Notes, 4 ¾ s, 1984 | 543,000 | 543,000 | 454,763 |
| Aluminum Co. of Canada, Ltd., S. F. Deb., 9 ½ s, 1995 | 500,000 | 517,267 | 495,000 |
| Churchill Falls (Labrador) Corp., Ltd., 1st Mtg. Series A, 7 ¾ s, 2007 | 800,000 | 800,000 | 676,000 |
| IAC, Ltd., Sec. Note Series Z, 5 ¼ s, 1982 | 750,000 | 750,000 | 583,125 |

CARNEGIE INSTITUTION OF WASHINGTON

INVESTMENTS—*Continued*

| <i>Description</i> | <i>Par</i> | <i>Cost</i> | <i>Approximate Market</i> |
|--|------------|-------------|-------------------------------|
| Foreign Bonds | | | |
| <i>—Continued</i> | | | |
| Quebec Hydro-Electric Commission, S. F. Deb., 5s, 1988 | \$ 618,000 | \$ 606,083 | \$ 458,865 |
| Quebec Hydro-Electric Commission, Deb., Series BN, 9 ¼ s, 1995 | 500,000 | 504,126 | 490,000 |
| Total | | 3,720,476 | 3,157,753 |
| Public Utility Bonds | | | |
| American Telephone & Telegraph Company, Deb., 8 ¾ s, 2000 | 375,000 | 375,500 | 386,719 |
| American Telephone & Telegraph Company, Deb., 8.70s, 2002 | 925,000 | 925,000 | 935,406 |
| National Rural Utilities Co-op Finance Corp., 9 ½ s, 1985 | 750,000 | 754,300 | 780,000 |
| Pacific Gas & Electric Co., 1st & Ref. Mtg. Series BB, 5s, 1989 | 250,000 | 251,050 | 175,000 |
| Pacific Power & Light Co., 1st Mtg., 4 ¾ s, 1986 | 250,000 | 251,551 | 175,625 |
| Potomac Electric Power Co., Deb., 4 ¾ s, 1982 | 210,000 | 212,225 | 172,463 |
| Washington Water Power Co., 1st Mtg. 4 ¾ s, 1987 | 300,000 | 300,000 | 223,125 |
| Total | | 3,069,626 | 2,848,338 |
| Industrial and Miscellaneous Bonds and Notes | | | |
| American Express Credit Corporation, Sr. Notes, 9 ½ s, 1982 | 500,000 | 500,000 | 527,500 |
| American Hoechst Corp., Notes, 5 ¾ s, 1986 | 736,000 | 736,000 | 634,800 |
| Arco Pipe Line Co., Notes, 8s, 1982 | 300,000 | 298,500 | 301,125 |
| Atlantic Richfield Company, Demand Note | 445,000 | 445,000 | 445,000 |
| Boeing Co., Notes, 6 ¾ s, 1986 | 584,000 | 584,000 | 467,200 |
| Columbia Broadcasting System, Inc., Prom. Note, 5 ½ s, 1991 | 680,000 | 680,000 | 549,100 |
| Crown Zellerbach Corp., Prom. Note, 4 ¾ s, 1981 | 150,000 | 150,000 | 134,250 |
| Crown Zellerbach Corp., S. F. Deb., 8 ¾ s, 2000 | 1,000,000 | 1,026,929 | 1,000,000 |
| Erie Mining Company, 1st Mtg. Series B, 4 ½ s, 1983 | 259,000 | 251,458 | 190,365 |
| First International Bancshares, Inc., Notes, 9s, 1983 | 450,000 | 450,000 | 463,500 |
| Four Corners Pipe Line Co., Sec. Note, 5s, 1982 | 62,000 | 62,000 | 55,645 |

CARNEGIE INSTITUTION OF WASHINGTON

INVESTMENTS—*Continued*

| <i>Description</i> | <i>Par</i> | <i>Cost</i> | <i>Approximate Market</i> |
|--|------------|--------------|-------------------------------|
| Industrial and Miscellaneous Bonds — <i>Continued</i> | | | |
| General Electric Co., Demand Note | \$ 300,000 | \$ 300,000 | \$ 300,000 |
| General Electric Credit Corp., Notes, 8.60s, 1985 | 500,000 | 500,500 | 515,625 |
| General Motors Acceptance Corp., Demand Note | 900,000 | 900,000 | 900,000 |
| General Motors Acceptance Corp., Deb., 5s, 1977 | 200,000 | 195,000 | 196,000 |
| General Motors Acceptance Corp., Deb., 5s, 1981 | 200,000 | 199,000 | 176,000 |
| General Motors Acceptance Corp., 4 ½ s, 1982 | 480,000 | 390,912 | 404,400 |
| Inter-American Development Bank, Notes, 8 ½ s, 1985 | 500,000 | 502,500 | 495,000 |
| International Bank for Reconstruction & Development, Notes, 8.15s, 1985 | 400,000 | 400,000 | 395,000 |
| Kaiser Aluminum & Chemical Corp., 1st Mtg., 5 ½ s, 1987 | 164,000 | 164,000 | 128,740 |
| Kresge (S. S.) Company, Prom. Note, 4 ½ s, 1983 | 513,333 | 513,333 | 419,650 |
| Mercantile Stores Co., Inc., S. F. Deb., 8.70s, 1995 | 500,000 | 500,000 | 472,500 |
| Montgomery Ward Credit Corp., Deb., 4 ¾ s, 1980 | 200,000 | 199,000 | 175,500 |
| NCNB Corp., S. F. Deb., 8.40s, 1995 | 500,000 | 497,500 | 462,500 |
| Revlon, Inc., Notes, 8.45s, 1985 | 500,000 | 501,375 | 507,500 |
| Searle (G. D.) & Co., Notes, 8s, 1981 | 800,000 | 794,000 | 809,000 |
| Sears, Roebuck Acceptance Corp., Sub. Deb., 4 ½ s, 1977 | 525,000 | 511,505 | 521,063 |
| Sears, Roebuck Acceptance Corp., Sub., 8 ¾ s, 1986 | 400,000 | 399,200 | 406,500 |
| Sears, Roebuck & Co., 7 ¾ s, 1985 | 500,000 | 491,250 | 496,250 |
| Shell Funding Corp., Collat. Tr. Series B, 4 ¾ s, 1985 | 584,000 | 584,000 | 492,020 |
| Union Carbide Corp., 8 ½ s, 2005 | 1,000,000 | 987,500 | 1,000,000 |
| United Air Lines, Inc., Notes, 5s, 1984 | 560,000 | 560,000 | 443,800 |
| Weyerhaeuser Co., Notes, 8s, 1985 | 500,000 | 498,750 | 505,000 |
| Woolworth (F. W.) Company, Prom. Note, 5s, 1981 | 419,395 | 419,395 | 352,291 |
| Total | | 16,192,607 | 15,342,824 |
| Bonds, funds invested | | \$35,523,972 | \$33,920,778 |

CARNEGIE INSTITUTION OF WASHINGTON

INVESTMENTS—Continued

| <i>Description</i> | <i>Shares</i> | <i>Cost</i> | <i>Approximate Market</i> |
|---|---------------|-------------|-------------------------------|
| Common Stocks | | | |
| Air Products & Chemicals, Inc. | 8,000 | \$ 382,109 | \$ 612,000 |
| Alcon Laboratories, Inc. | 5,000 | 164,318 | 113,750 |
| American Express Company | 20,000 | 644,375 | 730,000 |
| American Home Products Corp. | 15,000 | 606,581 | 513,750 |
| American Standard Inc. | 20,000 | 492,595 | 497,500 |
| AMP Incorporated | 12,000 | 261,089 | 399,000 |
| Automatic Data Processing Inc. | 2,500 | 68,006 | 168,125 |
| Boeing Company | 15,000 | 531,825 | 611,250 |
| Cameron Iron Works, Inc. | 1,200 | 139,500 | 174,000 |
| Caterpillar Tractor Co. | 15,000 | 922,034 | 1,366,875 |
| Central Telephone & Utilities Corp. | 40,000 | 596,511 | 880,000 |
| Charles River Breeding Labs, Inc. | 5,000 | 189,898 | 95,000 |
| Chemed Corporation | 5,000 | 171,062 | 102,500 |
| Chesebrough-Pond's, Inc. | 30,000 | 571,373 | 866,250 |
| Christiana Securities Company | 5,000 | 684,542 | 627,500 |
| Citicorp | 30,000 | 537,857 | 1,083,750 |
| Coca-Cola Company (The) | 10,000 | 160,455 | 841,250 |
| Colt Industries Inc. | 10,000 | 493,350 | 535,000 |
| Connecticut General Insurance Corp. | 14,000 | 740,500 | 696,500 |
| Cross (A. T.) Co. | 3,000 | 178,500 | 91,500 |
| Data General Corp. | 3,000 | 93,504 | 163,875 |
| Disney (Walt) Productions | 10,000 | 335,740 | 566,250 |
| Dow Chemical Co. | 30,000 | 887,086 | 1,447,500 |
| Eastman Kodak Company | 18,000 | 296,043 | 1,802,250 |
| Engelhard Minerals & Chemicals Corp. | 15,000 | 526,700 | 513,750 |
| Exxon Corporation | 20,000 | 652,115 | 2,092,500 |
| Ford Motor Co. | 14,000 | 602,055 | 819,000 |
| General Electric Company | 30,000 | 581,734 | 1,713,750 |
| General Motors Corporation | 30,000 | 900,794 | 2,055,000 |
| General Tire & Rubber Company (The) | 30,000 | 680,702 | 675,000 |
| Genuine Parts Co. | 15,000 | 433,428 | 568,125 |
| Gilbert Associates, Inc. | 7,000 | 265,737 | 131,250 |
| Goodyear Tire & Rubber Co. | 40,000 | 557,439 | 920,000 |
| Halliburton Company | 15,000 | 655,000 | 954,375 |
| Harland (John H.) Company | 5,000 | 130,137 | 87,500 |
| Hewlett-Packard Co. | 4,000 | 249,135 | 459,000 |
| Illinois Power Company | 20,000 | 518,728 | 500,000 |
| INCO Limited | 29,000 | 960,560 | 1,036,750 |
| Interco, Incorporated | 15,000 | 646,402 | 637,500 |
| International Business Machines Corp. | 13,000 | 318,426 | 3,597,750 |
| International Paper Co. | 10,000 | 427,500 | 730,000 |
| International Telephone & Telegraph Corp. | 25,000 | 718,086 | 709,375 |
| Interpace Corporation | 5,000 | 104,036 | 148,125 |
| Johnson & Johnson | 5,000 | 96,998 | 420,000 |

CARNEGIE INSTITUTION OF WASHINGTON

INVESTMENTS—*Continued*

| <i>Description</i> | <i>Shares</i> | <i>Cost</i> | <i>Approximate Market</i> |
|--|---------------|--------------|-------------------------------|
| <i>Common Stocks</i> | | | |
| <i>—Continued</i> | | | |
| Kaiser Aluminum & Chemical Corp. | 25,000 | \$ 781,075 | \$ 946,875 |
| Kresge (S. S.) Co. | 30,000 | 1,026,743 | 1,065,000 |
| Lawter Chemicals, Incorporated | 10,500 | 191,719 | 118,125 |
| Mary Kay Cosmetics, Inc. | 4,000 | 63,438 | 72,000 |
| Mead Corporation (The) | 30,000 | 603,304 | 622,500 |
| Merck & Co., Inc. | 12,000 | 210,517 | 864,000 |
| Middle South Utilities, Incorporated | 30,000 | 444,600 | 438,750 |
| Minnesota Mining & Manufacturing Company | 20,000 | 1,014,578 | 1,112,500 |
| Monsanto Company | 8,000 | 773,465 | 746,000 |
| Ocean Drilling & Exploration Company | 2,000 | 84,200 | 68,000 |
| Owens-Corning Fiberglas Corporation | 12,000 | 545,263 | 618,000 |
| Owens-Illinois, Inc. | 10,000 | 594,200 | 605,000 |
| Penney (J. C.) Company, Inc. | 15,000 | 843,031 | 783,750 |
| Perkin Elmer Corporation (The) | 20,000 | 479,635 | 470,000 |
| Petrie Stores Corporation | 2,000 | 136,781 | 142,750 |
| Phelps Dodge Corporation | 12,000 | 508,800 | 513,000 |
| Philip Morris, Inc. | 10,000 | 645,150 | 512,500 |
| Pittston Company (The) | 20,000 | 731,800 | 915,000 |
| Potlatch Corp. | 19,000 | 759,658 | 1,206,500 |
| Procter & Gamble Co. | 10,000 | 993,643 | 948,750 |
| Public Service Company of Indiana, Inc. | 18,000 | 472,500 | 459,000 |
| Ralston Purina Co. | 15,000 | 658,107 | 774,375 |
| Reynolds (R. J.) Industries | 10,000 | 579,500 | 563,750 |
| Sabine Royalty Corp. | 4,000 | 162,373 | 182,000 |
| Schering-Plough Corp. | 10,000 | 784,017 | 537,500 |
| Schlumberger Limited | 15,000 | 298,086 | 1,305,000 |
| Sears, Roebuck and Company | 15,000 | 1,578,576 | 971,250 |
| Snap-on Tools Corp. | 3,000 | 161,725 | 100,500 |
| Squibb Corp. | 20,000 | 930,667 | 657,500 |
| Standard Oil Company of California | 25,000 | 993,544 | 950,000 |
| Standard Oil Company (The) (Ohio) | 10,000 | 699,057 | 727,500 |
| UAL, Inc. | 20,000 | 560,550 | 555,000 |
| Union Camp Corp. | 12,000 | 529,428 | 765,000 |
| Union Carbide Corp. | 10,000 | 627,500 | 676,250 |
| Union Pacific Corporation | 6,000 | 533,651 | 554,250 |
| United States Steel Corporation | 15,000 | 682,500 | 813,750 |
| West Point-Pepperell, Inc. | 15,000 | 524,692 | 562,500 |
| Xerox Corporation | 10,000 | 713,857 | 616,250 |
| Common stocks, funds invested | | 43,096,495 | 58,294,500 |
| Aggregate investments | | \$78,620,467 | \$92,215,278 |

SCHEDULE 3

CARNEGIE INSTITUTION OF WASHINGTON
SUMMARY OF INVESTMENT TRANSACTIONS
FOR THE YEAR ENDED JUNE 30, 1976

Cash awaiting investment, July 1, 1975 \$ 1,427

Sales and Redemptions

| | <i>Capital</i> | | |
|----------------------------------|---------------------------|---------------------------|-------------------|
| | <i>Gain</i> | <i>Loss</i> | <i>Book Value</i> |
| Bonds | \$ 2,796 | \$ 102,246 | \$31,613,949 |
| Common stocks | 8,244,826 | 3,780,031 | 19,590,712 |
| | <u>8,247,622</u> | <u>3,882,277</u> | <u>51,204,661</u> |
| Realized capital gain, net . . . | <u>—</u> | <u>4,365,345</u> | <u>4,365,345</u> |
| | <u><u>\$8,247,622</u></u> | <u><u>\$8,247,622</u></u> | |

| | |
|--|--------------------|
| Total sales and redemptions | 55,570,006 |
| Gift of security recorded at fair market value | 9,506 |
| Cash transferred to Operating Fund | <u>(3,580,000)</u> |
| Total | 52,000,939 |

Acquisitions

| | |
|-------------------------|--------------|
| Bonds | \$38,603,325 |
| Common stocks | 13,400,764 |

| | |
|------------------------------|-------------------|
| Total acquisitions | <u>52,004,089</u> |
|------------------------------|-------------------|

| | |
|---|--------------------------|
| Cash awaiting investment, June 30, 1976 | <u><u>(\$ 3,150)</u></u> |
|---|--------------------------|



Articles of Incorporation

Fifty-eighth Congress of the United States of America;

At the Second Session,

Begun and held at the City of Washington on Monday, the seventh day of December, one thousand nine hundred and three.

AN ACT

To incorporate the Carnegie Institution of Washington.

Be it enacted by the Senate and House of Representatives of the United States of America in Congress assembled, That the persons following, being persons who are now trustees of the Carnegie Institution, namely, Alexander Agassiz, John S. Billings, John L. Cadwalader, Cleveland H. Dodge, William N. Frew, Lyman J. Gage, Daniel C. Gilman, John Hay, Henry L. Higginson, William Wirt Howe, Charles L. Hutchinson, Samuel P. Langley, William Lindsay, Seth Low, Wayne MacVeagh, Darius O. Mills, S. Weir Mitchell, William W. Morrow, Ethan A. Hitchcock, Elihu Root, John C. Spooner, Andrew D. White, Charles D. Walcott, Carroll D. Wright, their associates and successors, duly chosen, are hereby incorporated and declared to be a body corporate by the name of the Carnegie Institution of Washington and by that name shall be known and have perpetual succession, with the powers, limitations, and restrictions herein contained.

SEC. 2. That the objects of the corporation shall be to encourage, in the broadest and most liberal manner, investigation, research, and discovery, and the application of knowledge to the improvement of mankind; and in particular—

(a) To conduct, endow, and assist investigation in any department of science, literature, or art, and to this end to cooperate with governments, universities, colleges, technical schools, learned societies, and individuals.

(b) To appoint committees of experts to direct special lines of research.

(c) To publish and distribute documents.

(d) To conduct lectures, hold meetings, and acquire and maintain a library.

(e) To purchase such property, real or personal, and construct such building or buildings as may be necessary to carry on the work of the corporation.

(f) In general, to do and perform all things necessary to promote the objects of the institution, with full power, however, to the trustees hereinafter appointed and their successors from time to time to modify the conditions and regulations under which the work shall be carried on, so as to secure the application of the funds in the manner best adapted to the conditions of the time, provided that the objects of the corporation shall at all times be among the foregoing or kindred thereto.

SEC. 3. That the direction and management of the affairs of the corporation and the control and disposal of its property and funds shall be vested in a board of trustees, twenty-two in number, to be composed of the following individuals: Alexander Agassiz, John S. Billings, John L. Cadwalader, Cleveland H. Dodge, William N. Frew, Lyman J. Gage, Daniel C. Gilman, John Hay, Henry L. Higginson, William Wirt Howe, Charles L. Hutchinson, Samuel P. Langley, William Lindsay, Seth Low, Wayne MacVeagh, Darius O. Mills, S. Weir Mitchell, William W. Morrow, Ethan A. Hitchcock, Elihu Root, John C. Spooner, Andrew D. White, Charles D. Walcott, Carroll D. Wright, who shall constitute the first board of trustees. The board of trustees shall have power from time to time to increase its membership to not more than twenty-seven members. Vacancies occasioned by death, resignation, or otherwise shall be filled by the remaining trustees in such manner as the by-laws shall prescribe; and the persons so elected shall thereupon become trustees and also members of the said corporation. The principal place of business of the said corporation shall be the city of Washington, in the District of Columbia.

SEC. 4. That such board of trustees shall be entitled to take, hold and administer the securities, funds, and property so transferred by said Andrew Carnegie to the trustees of the Carnegie Institution and such other funds or property as may at any time be given, devised, or bequeathed to them, or to such corporation, for the purposes of the trust; and with full power from time to time to adopt a common seal, to appoint such officers, members of the board of trustees or otherwise, and such employees as may be deemed necessary in carrying on the business of the corporation, at such salaries or with such remuneration as they may deem proper; and with full power to adopt by-laws from time to time and such rules or regulations as may be necessary to secure the safe and convenient transaction of the business of the corporation; and with full power and discretion to deal with and expend the income of the corporation in such manner as in their judgment will best promote the objects herein set forth and in general to have and use all powers and authority necessary to promote such objects and carry out the purposes of the donor. The said trustees shall have further power from time

to time to hold as investments the securities hereinabove referred to so transferred by Andrew Carnegie, and any property which has been or may be transferred to them or such corporation by Andrew Carnegie or by any other person, persons, or corporation, and to invest any sums or amounts from time to time in such securities and in such form and manner as are permitted to trustees or to charitable or literary corporations for investment, according to the laws of the States of New York, Pennsylvania, or Massachusetts, or in such securities as are authorized for investment by the said deed of trust so executed by Andrew Carnegie, or by any deed of gift or last will and testament to be hereafter made or executed.

SEC. 5. That the said corporation may take and hold any additional donations, grants, devises, or bequests which may be made in further support of the purposes of the said corporation, and may include in the expenses thereof the personal expenses which the trustees may incur in attending meetings or otherwise in carrying out the business of the trust, but the services of the trustees as such shall be gratuitous.

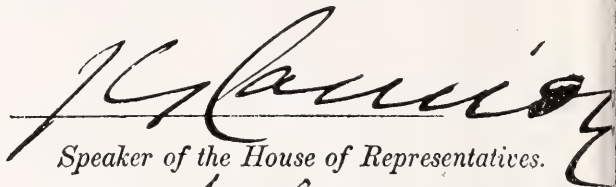
SEC. 6. That as soon as may be possible after the passage of this Act a meeting of the trustees hereinbefore named shall be called by Daniel C. Gilman, John S. Billings, Charles D. Walcott, S. Weir Mitchell, John Hay, Elihu Root, and Carroll D. Wright, or any four of them, at the city of Washington, in the District of Columbia, by notice served in person or by mail addressed to each trustee at his place of residence; and the said trustees, or a majority thereof, being assembled, shall organize and proceed to adopt by-laws, to elect officers and appoint committees, and generally to organize the said corporation; and said trustees herein named, on behalf of the corporation hereby incorporated, shall thereupon receive, take over, and enter into possession, custody, and management of all property, real or personal, of the corporation heretofore known as the Carnegie Institution, incorporated, as hereinbefore set forth under "An Act to establish a Code of Law for the District of Columbia, January fourth, nineteen hundred and two," and to all its rights, contracts, claims, and property of any kind or nature; and the several officers of such corporation, or any other person having charge of any of the securities, funds, real or personal, books or property thereof, shall, on demand, deliver the same to the said trustees appointed by this Act or to the persons appointed by them to receive the same; and the trustees of the existing corporation and the trustees herein named shall and may take such other steps as shall be necessary to carry out the purposes of this Act.

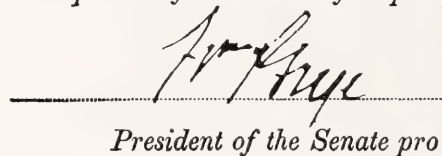
SEC. 7. That the rights of the creditors of the said existing corporation known as the Carnegie Institution shall not in any manner be impaired by the

passage of this Act, or the transfer of the property hereinbefore mentioned, nor shall any liability or obligation for the payment of any sums due or to become due, or any claim or demand, in any manner or for any cause existing against the said existing corporation, be released or impaired; but such corporation hereby incorporated is declared to succeed to the obligations and liabilities and to be held liable to pay and discharge all of the debts, liabilities, and contracts of the said corporation so existing to the same effect as if such new corporation had itself incurred the obligation or liability to pay such debt or damages, and no such action or proceeding before any court or tribunal shall be deemed to have abated or been discontinued by reason of the passage of this Act.

SEC. 8. That Congress may from time to time alter, repeal, or modify this Act of incorporation, but no contract or individual right made or acquired shall thereby be divested or impaired.

SEC. 9. That this Act shall take effect immediately.


Speaker of the House of Representatives.


President of the Senate pro tempore.

Approved.

April 28, 1904.

Theodore Roosevelt

By-Laws of the Institution

Adopted December 13, 1904. Amended December 13, 1910, December 13, 1912, December 10, 1937, December 15, 1939, December 13, 1940, December 18, 1942, December 12, 1947, December 10, 1954, October 24, 1957, May 8, 1959, May 13, 1960, May 10, 1963, May 15, 1964, March 6, 1967, May 3, 1968, May 14, 1971, August 31, 1972, May 9, 1974, and April 30, 1976.

ARTICLE I

The Trustees

1. The Board of Trustees shall consist of twenty-four members with power to increase its membership to not more than twenty-seven members. The Trustees shall hold office continuously and not for a stated term.

2. In case any Trustee shall fail to attend three successive annual meetings of the Board he shall thereupon cease to be a Trustee.

3. No Trustee shall receive any compensation for his services as such.

4. All vacancies in the Board of Trustees shall be filled by the Trustees by ballot at an annual meeting, but no person shall be declared elected unless he receives the votes of two-thirds of the Trustees present.

5. If, at any time during an emergency period, there be no surviving Trustee capable of acting, the President, the Director of each existing Department, and the Executive Officer, or such of them as shall then be surviving and capable of acting, shall constitute a Board of Trustees *pro tem*, with full powers under the provisions of the Articles of Incorporation and these By-Laws. Should neither the President, nor any such Director, nor the Executive Officer be capable of acting, the senior surviving Staff Member of each existing Department shall be a Trustee *pro tem* with full powers of a Trustee under the Articles of Incorporation and these By-Laws. It shall be incumbent on the Trustees *pro tem* to reconstitute the Board with permanent members within a reasonable time after the emergency has passed, at which time the Trustees *pro tem* shall cease to hold office. A list of Staff Member seniority, as designated annually by the President, shall be kept in the Institution's records.

6. A Trustee who resigns after having served at least five years and having reached age seventy shall be eligible for designation by the Board as a Trustee Emeritus. A Trustee Emeritus shall be entitled to attend the annual meeting of the Board but shall have no vote and shall not be counted for purposes of ascertaining the presence of a quorum. A Trustee Emeritus may be invited to serve in an advisory capacity on any committee of the Board of Trustees except the Executive Committee.

ARTICLE II

Officers of the Board

1. The officers of the Board shall be a Chairman of the Board, a Vice-Chairman, and a Secretary, who shall be elected by the Trustees, from the members of the Board, by ballot to serve for a term of three years. All vacancies shall be filled by the Board for the unexpired term; provided, however, that the Executive Committee shall have power to fill a vacancy in the office of Secretary to serve until the next meeting of the Board of Trustees.

2. The Chairman shall preside at all meetings and shall have the usual powers of a presiding officer.

3. The Vice-Chairman, in the absence or disability of the Chairman, shall perform the duties of the Chairman.

4. The Secretary shall issue notices of meetings of the Board, record its transactions, and conduct that part of the correspondence relating to the Board and to his duties.

ARTICLE III

Executive Administration

The President

1. There shall be a President who shall be elected by ballot by, and hold office during the pleasure of, the Board, who shall be the chief executive officer of the Institution. The President, subject to the control of the Board and the Executive Committee, shall have general charge of all matters of administration and supervision of all arrangements for research and other work undertaken by the Institution or with its funds. He shall prepare and submit to the Board of Trustees and to the Executive Committee plans and suggestions for the work of the Institution, shall conduct its general correspondence and the correspondence with applicants for grants and with the special advisers of the Committee, and shall present his recommendations in each case to the Executive Committee for decision. All proposals and requests for grants shall be referred to the President for consideration and report. He shall have power to remove, appoint, and, within the scope of funds made available by the Trustees, provide for compensation of subordinate employees and to fix the compensation of such employees within the limits of a maximum rate of compensation to be established from time to time by the Executive Committee. He shall be *ex officio* a member of the Executive Committee.

2. He shall be the legal custodian of the seal and of all property of the Institution whose custody is not otherwise provided for. He shall sign and execute on behalf of the corporation all contracts and instruments necessary in authorized administrative and research matters and affix the corporate seal thereto when necessary, and may delegate the performance of such acts and other administrative duties in his absence to the Executive Officer. He may execute all other contracts, deeds, and instruments on behalf of the corporation and affix the seal thereto when expressly authorized by the Board of Trustees or Executive Committee. He may, within the limits of his own authorization, delegate to the Executive Officer authority to act as custodian of and affix the corporate seal. He shall be responsible for the expenditure and disbursement of all funds of the Institution in accordance with the directions of the Board and of the Executive Committee, and shall keep accurate accounts of all receipts and disbursements. Following approval by the Executive Committee he shall transmit to the Board of Trustees before its annual meeting a written report of the operations and business of the Institution for the preceding fiscal year with his recommendations for work and appropriations for the succeeding fiscal year.

3. He shall attend all meetings of the Board of Trustees.

4. There shall be an officer designated Executive Officer who shall be appointed by and hold office at the pleasure of the President, subject to the approval of the Executive Committee. His duties shall be to assist and act for the President as the latter may duly authorize and direct.

5. The President shall retire from office at the end of the fiscal year in which he becomes sixty-five years of age.

ARTICLE IV

Meetings and Voting

1. The annual meeting of the Board of Trustees shall be held in the City of Washington, in the District of Columbia, in May of each year on a date fixed by the Executive Committee, or at such other time or such other place as may be designated by the Executive Committee, or if not so designated prior to May 1 of such year, by the

Chairman of the Board of Trustees, or if he is absent or is unable or refuses to act, by any Trustee with the written consent of the majority of the Trustees then holding office.

2. Special meetings of the Board of Trustees may be called, and the time and place of meeting designated, by the Chairman, or by the Executive Committee, or by any Trustee with the written consent of the majority of the Trustees then holding office. Upon the written request of seven members of the Board, the Chairman shall call a special meeting.

3. Notices of meetings shall be given ten days prior to the date thereof. Notice may be given to any Trustee personally, or by mail or by telegram sent to the usual address of such Trustee. Notices of adjourned meetings need not be given except when the adjournment is for ten days or more.

4. The presence of a majority of the Trustees holding office shall constitute a quorum for the transaction of business at any meeting. An act of the majority of the Trustees present at a meeting at which a quorum is present shall be the act of the Board except as otherwise provided in these By-Laws. If, at a duly called meeting, less than a quorum is present, a majority of those present may adjourn the meeting from time to time until a quorum is present. Trustees present at a duly called or held meeting at which a quorum is present may continue to do business until adjournment notwithstanding the withdrawal of enough Trustees to leave less than a quorum.

5. The transactions of any meeting, however called and noticed, shall be as valid as though carried out at a meeting duly held after regular call and notice, if a quorum is present and if, either before or after the meeting, each of the Trustees not present in person signs a written waiver of notice, or consent to the holding of such meeting, or approval of the minutes thereof. All such waivers, consents, or approvals shall be filed with the corporate records or made a part of the minutes of the meeting.

6. Any action which, under law or these By-Laws, is authorized to be taken at a meeting of the Board of Trustees may be taken without a meeting if authorized in a document or documents in writing signed by all the Trustees then holding office and filed with the Secretary.

7. During an emergency period the term "Trustees holding office" shall, for purposes of this Article, mean the surviving members of the Board who have not been rendered incapable of acting for any reason including difficulty of transportation to a place of meeting or of communication with other surviving members of the Board.

ARTICLE V

Committees

1. There shall be the following Standing Committees, viz. an Executive Committee, a Finance Committee, an Auditing Committee, a Nominating Committee, and an Employee Benefits Committee.

2. All vacancies in the Standing Committees shall be filled by the Board of Trustees at the next annual meeting of the Board and may be filled at a special meeting of the Board. A vacancy in the Executive Committee and, upon request of the remaining members of any other Standing Committee, a vacancy in such other Committee may be filled by the Executive Committee by temporary appointment to serve until the next meeting of the Board.

3. The terms of all officers and of all members of Committees, as provided for herein, shall continue until their successors are elected or appointed.

Executive Committee

4. The Executive Committee shall consist of the Chairman, Vice-Chairman, and Secretary of the Board of Trustees, the President of the Institution *ex officio*, and, in addition, not less than five or more than eight Trustees to be elected by the Board by ballot for a term of three years, who shall be eligible for re-election. Any member elected

to fill a vacancy shall serve for the remainder of his predecessor's term. The presence of four members of the Committee shall constitute a quorum for the transaction of business at any meeting.

5. The Executive Committee shall, when the Board is not in session and has not given specific directions, have general control of the administration of the affairs of the corporation and general supervision of all arrangements for administration, research, and other matters undertaken or promoted by the Institution. It shall also submit to the Board of Trustees a printed or typewritten report of each of its meetings, and at the annual meeting shall submit to the Board a report for publication.

6. The Executive Committee shall have power to authorize the purchase, sale, exchange, or transfer of real estate.

Finance Committee

7. The Finance Committee shall consist of not less than five and not more than six members to be elected by the Board of Trustees by ballot for a term of three years, who shall be eligible for re-election. The presence of three members of the Committee shall constitute a quorum for the transaction of business at any meeting.

8. The Finance Committee shall have custody of the securities of the Institution and general charge of its investments and invested funds and shall care for and dispose of the same subject to the directions of the Board of Trustees. It shall have power to authorize the purchase, sale, exchange, or transfer of securities and to delegate this power. So long as the Institution is the trustee under any retirement or other benefit plan for the staff members and employees of the Institution, it shall be responsible for supervision of matters relating to investments thereunder and for the appointment or removal of any investment manager or advisor. It shall also be responsible for reviewing the financial status and arrangements of any employee benefit plan for which the Institution is not the trustee and for appointment or removal of any plan trustee or insurance carrier. It shall consider and recommend to the Board from time to time such measures as in its opinion will promote the financial interests of the Institution and improve the management of investments under any retirement or other benefit plan. The Committee shall make a report at the annual meeting of the Board.

Auditing Committee

9. The Auditing Committee shall consist of three members to be elected by the Board of Trustees by ballot for a term of three years.

10. Before each annual meeting of the Board of Trustees, the Auditing Committee shall cause the accounts of the Institution for the preceding fiscal year to be audited by public accountants. The accountants shall report to the Committee, and the Committee shall present said report at the ensuing annual meeting of the Board with such recommendations as the Committee may deem appropriate.

Nominating Committee

11. The Nominating Committee shall consist of the Chairman of the Board of Trustees *ex officio* and, in addition, three Trustees to be elected by the Board by ballot for a term of three years, who shall not be eligible for re-election until after the lapse of one year. Any member elected to fill a vacancy shall serve for the remainder of his predecessor's term, provided that of the Nominating Committee first elected after adoption of this By-Law one member shall serve for one year, one member shall serve for two years, and one member shall serve for three years, the Committee to determine the respective terms by lot.

12. Sixty days prior to an annual meeting of the Board the Nominating Committee shall notify the Trustees by mail of the vacancies to be filled in membership of the Board. Each Trustee may submit nominations for such vacancies. Nominations so submitted shall be considered by the Nominating Committee, and ten days prior to the annual meeting the Nominating Committee shall submit to members of the Board by mail a list of the persons so nominated, with its recommendations for filling existing vacancies on the Board and its Standing Committees. No other nominations shall be received by the Board at the annual meeting except with the unanimous consent of the Trustees present.

Employee Benefits Committee

13. The Employee Benefits Committee shall consist of three members to be elected by the Board of Trustees by ballot for a term of three years, who shall be eligible for re-election and the Chairman of the Finance Committee *ex officio*. Any member elected to fill a vacancy shall serve for the remainder of his predecessor's term.

14. The Employee Benefits Committee shall, subject to the directions of the Board of Trustees, be responsible for supervision of the activities of the administrator or administrators of any retirement or other benefit plan for staff members and employees of the Institution, except that any matter relating to investments or to the appointment or removal of any trustee or insurance carrier under any such plan shall be the responsibility of the Finance Committee. It shall receive reports from the administrator or administrators of the employee benefit plans with respect to administration, benefit structure, operation, and funding. It shall consider and recommend to the Board from time to time such measures as in its opinion will improve such plans and the administration thereof. The Committee shall submit a report to the Board at the annual meeting of the Board.

ARTICLE VI

Financial Administration

1. No expenditure shall be authorized or made except in pursuance of a previous appropriation by the Board of Trustees, or as provided in Article V, paragraph 8, hereof.

2. The fiscal year of the Institution shall commence on the first day of July in each year.

3. The Executive Committee shall submit to the annual meeting of the Board a full statement of the finances and work of the Institution for the preceding fiscal year and a detailed estimate of the expenditures of the succeeding fiscal year.

4. The Board of Trustees, at the annual meeting in each year, shall make general appropriations for the ensuing fiscal year; but nothing contained herein shall prevent the Board of Trustees from making special appropriations at any meeting.

5. The Executive Committee shall have general charge and control of all appropriations made by the Board. Following the annual meeting, the Executive Committee may allocate these appropriations for the succeeding fiscal year. The Committee shall have full authority to reallocate available funds, as needed, and to transfer balances.

6. The securities of the Institution and evidences of property, and funds invested and to be invested, shall be deposited in such safe depository or in the custody of such trust company and under such safeguards as the Finance Committee shall designate, subject to directions of the Board of Trustees. Income of the Institution available for expenditure shall be deposited in such banks or depositories as may from time to time be designated by the Executive Committee.

7. Any trust company entrusted with the custody of securities by the Finance Committee may, by resolution of the Board of Trustees, be made Fiscal Agent of the Institution, upon an agreed compensation, for the transaction of the business coming within the authority of the Finance Committee.

8. The property of the Institution is irrevocably dedicated to charitable purposes, and in the event of dissolution its property shall be used for and distributed to those charitable purposes as are specified by the Congress of the United States in the Articles of Incorporation, Public Law No. 260, approved April 28, 1904, as the same may be amended from time to time.

ARTICLE VII

Amendment of By-Laws

1. These By-Laws may be amended at any annual or special meeting of the Board of Trustees by a two-thirds vote of the members present, provided written notice of the proposed amendment shall have been served personally upon, or mailed to the usual address of, each member of the Board twenty days prior to the meeting.

Index of Names

- Aaronson, M. J., 301, 325
publications, 337
- Abelson, P. H., v, vii, 98, 792, 967
Report of the President, 1-34
- Adams, W. M., 346
- Adelman, S. J., 322
- Adkins, J. M., 347
- Adler, W. H., 104
publications, 102
- Agassiz, A., vi, 989, 990
- Aguirre B., C., 149, 271
- Akella, A., 573, 574, 857
- Alcaino, G., 322
- Aldrich, L. T., 29, 34, 149, 270
publications, 268
- Allègre, C., 191, 201, 202, 270
- Aller, L. H., 324
- Anderson, B., 33, 484
publications, 480
- Anderson, D. M.
publications, 958
studies, 918-924
- Anderson, R. O., v, 27, 28, 968
- Angerer, R. C., 362, 861, 866, 870, 875, 925, 956, 959
publications, 958
studies, 944-955
- Arculus, R. J., 31, 676, 677, 786, 850, 857
publications, 840
- Arnal, E., 148, 271
- Arndt, N. T., 31, 494, 562, 677, 841, 857
studies, 555
- Arnold, L. G., 16, 271
- Arp, H. C., 32, 305, 307, 319, 346
publications, 336, 337
- Asch, E., 104
studies, 52-53
- Ashby, E., vi
- Assousa, G. E., 34, 112, 118, 136, 137, 139, 270
publications, 268
studies, 136-139, 139-141
- Austin, J. P., v, 27, 28, 968
- Austin, T. B., 322
- Babcock, G. T., 479
- Babcock, H. W., 31, 346
report of the Director, Hale Observatories, 273-346
- Badger, M., 354, 420, 432, 483
studies, 423
- Bagnuolo, W. G., 302
- Bajaja, E., 147, 148, 271
- Baldwin, G. J., vi
- Balick, B., 118, 136, 137, 139, 271, 290
- Bannister, J. R., 34, 149, 271
- Barbour, T., vi
- Barry, A., 98
- Bass, J. D., 857
- Beavan, R. J., 149, 243, 270
publications, 269
studies, 240-243
- Becklin, E. E., 32, 290, 291, 297, 300, 340, 346
publications, 337, 339, 340
- Beckwith, S. V. W., 32, 347
publications, 337, 339
- Belford, H. G. S., 33, 352, 384
studies, 362-367
- Bell, J. F., vi
- Bell, P. M., 9, 13, 29, 31, 492, 501, 502, 504, 508, 683, 684, 734, 835, 837, 841, 842, 846, 849
publications, 840
studies, 509-513, 515-520, 688-695, 695-699, 699-701, 701-705, 753-756, 824-827, 827-828
- Benjamin, T. M., 31, 501, 857
studies, 684-687
- Bennett, C. L., 34, 270
- Berg, E., 271
- Bergstrahl, J., 322
- Berry, J. A., 19, 33, 351, 353, 354, 408, 423, 424, 425, 481, 482, 483
publications, 480
studies, 400-407, 410-413, 413-438
- Bierer, P. R., 959
- Billings, J. S., vi, 989, 990, 991
- Björkman, O., 19, 33, 354, 366, 367, 368, 425, 432, 433, 438, 483
publications, 480
studies, 400-407, 410-413, 418-421
- Blatt, M., 33, 484
- Bliss, R. W., vi
- Bloomfield, K., 115, 149, 207, 212, 271
studies, 207-213
- Bohlin, J. D., 282
- Boise, J. W., vii
- Bokhon'ko, A.
publications, 102
studies, 23, 23-24, 27-28
- Boksenberg, A., 285, 287, 297, 303, 308, 313, 314
publications, 337
- Bolton, E. T., vii, 10
- Bond, H. E., 322
- Bonner, T. I., 34, 270, 925, 948, 955
- Borne, K., 32, 347
- Boroson, T., 32, 314, 315, 347

- Borra, E. F., 328
publications, 337, 338
- Bosma, A., 333
- Botchan, P., 22, 30, 11, 103
studies, 20-22
- Böving, B. G., 103
- Bowes, G., 423, 424, 425
- Bowen, I. S., 7
- Bowen, N. L., 496, 577, 578, 580, 581, 584, 592, 596, 598, 599, 604, 610, 618, 647, 734, 766, 842, 850, 853, 855
- Boyd, F. R., Jr., 9, 13, 31, 185, 202, 270, 492, 493, 539, 540, 541, 543, 547, 556, 562, 566, 573, 574, 577, 626, 627, 635, 636, 656, 663, 675, 821, 822, 835, 836, 857
publications, 840
studies, 521-522, 523-530, 531-538, 544-546
- Boyden, J. E., 347
- Boynton, J. E., 353, 354, 481, 483
studies, 400-407
- Bracamonte, M., 149, 271
- Bradford, A. H., vi
- Bradford, L., vi
- Bradley, O. N., vi
- Brain, R. D., 33, 352, 379, 481, 482, 484
studies, 373-377
- Branscomb, L., 5
- Braunstein, R., 323
- Briggs, W. R., 5, 6, 33, 352, 386, 391, 392, 394, 425, 432, 481, 482, 483
report of the Director, Department of Plant Biology, 447-484
publications, 480, 481
studies, 373-377, 377-379, 379-383
- Britten, R. J., vii, 18, 361, 362, 367, 955, 956, 959
publications, 958, 959
report of the Developmental Biology Research Group, 859-959
studies, 861-870, 870-883, 883-890, 890-918, 918-924, 925-943, 944-955
- Britz, S. J., 33, 353, 482, 484
publications, 480
studies, 383-393, 393-394
- Brookings, R. S., vi
- Brooks, C., 115, 149, 212, 271
publications, 268, 269
studies, 176-207, 213-216
- Brown, D. D., 11, 22, 24, 25, 28, 29, 30, 1, 8, 10, 11, 103, 923, 941, 956, 957
publications, 102, 103
studies, 12, 12-14
- Brown, J. S., 18, 33, 351, 355, 356, 482, 483
studies, 460-465, 479-480
- Brown, L., 34, 117, 118, 249, 270
publications, 268, 269
studies, 259-263, 263-267
- Brown, R. D., 14
publications, 102
- Brown, R. L., 290
- Brownlee, G., 14, 104, 114, 170
- Brucato, R. J., 32, 334, 346
- Burke, B. F., 271
studies, 118-119
- Burkhead, M. S., 323
- Burnett, D. S., 501, 857
studies, 684-687
- Bush, V., vi, 27, 29
- Cabre, R., 149, 271
- Cadwalader, J. L., vi, 989, 990
- Campbell, W. W., vi
- Carbonetto, S. T., 30, 11, 101, 103
studies, 76-78, 88-90, 90
- Card, D., 30, 11, 103
studies, 76-78, 83-84, 84-85
- Carey, R., 354, 483
studies, 433-438
- Carnegie, A., 990, 991
- Carswell, R., 285, 308, 313, 314, 315
publications, 337
- Carty, J. J., vi
- Casaverde, M., 270
- Catalano, S., 323
- Chamberlin, M. E., 871, 925, 933, 956, 957, 959
publications, 958
- Chase, J. W., 104
- Chase, R. C., 279
- Chayes, F., 9, 31, 506, 507, 578, 611, 833, 836, 837, 843, 857
publications, 840
studies, 780-781, 781-782, 782-784, 784-786, 786, 787-788, 788-790, 790, 790-791, 791
- Chen, H.-W., 104
studies, 76-78
- Clardy, K. D., 297, 347
publications, 338
- Cleary, J. R., 149, 184, 203, 271
- Cochran, D. B., 959
- Cohen, G. N., 271
- Cole, W. R., vi
- Collatz, J., 33, 484
- Collett, C. F., 959
- Colomb, R., 148, 271
- Connes, P., 323
- Connor, J. T., v, 967
- Constantini, F., 959
- Conzett, H. E., 271
- Coon, H. G., 8, 104
- Corben, P. M., 324
- Cordova, F., 32, 347
- Corner, G. W., 7, 98
- Cosgrove, D., 33, 484
- Cowie, D. B., 34, 270
- Cragg, T. A., 347
publications, 337
- Crain, W. R., 925, 955, 956, 959
publications, 958
studies, 861-870, 870-883, 883-890
- Cronin, J. R., 31, 857
- Cross, J. W., 33, 352, 482, 483
studies, 379-383
- Crutcher, R. M., 324
- Currie, D. G., 323
- Curtis, W., 34, 351, 484

- Cuyubamba, A., *34*, 149, 204, 213, 216, 271
 publications, 268
- Czyzak, S. J., 324
- Dahn, C., 305
- Danchin, R. V., 493, 521, 522, 857
 studies, 523-530, 531-538
- Davidson, E. H., 362, 955, 956, 957, 959
 publications, 958, 959
 report of the Developmental Biology Research Group, 859-959
 studies, 861-870, 870-883, 883-890, 890-918, 918-924, 925-943, 944-955
- Davignon, R., 98
- Davis, G. L., *31*, 149, 271, 508, 521, 522, 531, 534, 545, 548, 648, 771, 772, 816, 842, 844, 847, 857
 studies, 821-824
- Davis, M. M., 919, 923, 955, 956, 959
 publications, 958
 studies, 890-918
- Dawid, I. B., *22*, *23*, *24*, *25*, *30*, 8, 11, 103, 957
 publications, 102, 103
 studies, 20-22, 28-30, 30-36, 45-46, 46, 46-48, 48, 49-50
- de Bruyn, A., *30*, 346
 publications, 340
- de Caponi, M. Z., 147
- DeHaan, R. L., 9, 103
- Delano, F. A., vi
- del Pozo, S., 149, 271
- Dennison, E. W., *32*, 320, 346
 publications, 337
- de Ruiter, H., 308
- DeVay, J. E., 482
- Devreotes, P., *21*, *25*, *30*, 9, 104
 publications, 102
 studies, 76-78, 78-81, 81-82
- DeWitt, G. S., *34*, 271
- Dickey, J. S., Jr., 494
 studies, 562-566
- Dickes, R. H., 333
- Diebold, J., v, 967, 968
- Dill, J. A., *31*, 857
- Diner, D. J., *32*, 347
- Dixon, K. L., 322
- Dodge, C. H., vi, 989, 990
- Dodge, W. E., vi
- Doering, J., *22*, *30*, 11, 103
 studies, 12, 14-15
- Dohrmann, U., *33*, 353, 482, 483
 studies, 395-399
- Dubner, G., 148
- Duncan, D.
 studies, 52-53
- Duncan, W. H., 104
 studies, 52-53, 61-66, 76-78
- Dworetzky, M. M., 324
- bryology, 3-104
 studies, 73-76
- Ecklund, E. T., 113, 118, 272
 studies, 143-144
- Eden, F. C., 892, 955, 956, 959
 publications, 958
 studies, 870-883, 925-943
- Edidin, M., 104
- Efstratiadis, A., 872, 887, 888, 939, 956
 publications, 958
 studies, 861-870
- Eggler, D. H., *31*, 493, 497, 498, 523, 524, 559, 621, 648, 649, 786, 834, 835, 837, 844, 849, 850
 publications, 840
 studies, 521-522, 538-541, 542-544, 623-626, 626-631, 631-636, 636-640
- Ehleringer, J., *19*, *33*, 353, 354, 408, 482, 484
 publications, 480
 studies, 410-413, 413-418, 418-421
- Elias, J. H., *32*, 295, 347
 publications, 340
- England, J. L., 9
- Emmons, S., *22*, *30*, 11, 103
 studies, 12, 14-15, 15-16, 16-17
- Enama, M., *34*, 351, 353, 354, 355, 406, 484
 studies, 407-410
- Erkes, J. W., 118, 136, 137, 139, 271
- Erlank, A. J., 271, 521, 522, 531
 publications, 268
 studies, 821-824
- Ernst, S. G., 959
- Etzel, P. B., 325
- Evans, J. R., *34*, 117, 149, 243, 271
 publications, 269
 studies, 240-243
- Evans, N. J., 294, 325
- Evertson, D. W., *10*, 149, 271
- Fambrough, D. M., *21*, *24*, *25*, *30*, 8, 9, 11, 103
 publications, 102, 103
 studies, 76-78, 81-82, 85-87
- Fedoroff, N., *22*, *30*, 11, 103
 studies, 12, 17-20
- Feigenson, M., 149
- Fenkart, R. P., 325
- Fenner, C. P., vi
- Ference, M., Jr., v, 967
- Ferguson, H. L., vi
- Ferry, J. M., *31*, 505, 835, 836, 837, 845, 857
 studies, 764-771
- Fillooy, E., 271
- Finch, D., 959
- Finger, L. W., *31*, 504, 537, 570, 696, 706, 743, 744, 745, 746, 747, 748, 751, 789, 832, 833, 845, 846, 851, 857
 publications, 840
 studies, 538-541, 743-746
- Finnerty, A. A., 857
- Flexner, S., vi
- Flores, A., *34*, 149, 271
- Forbes, W. C., vi
- Ebert, J. D., *11*, *20*, *21*, *24*, *27*, *28*, *30*, 8, 9, 98, 103
 publications, 102
 report of the Director, Department of Em-

- Forbush, S. E., *34*, 176, 270
studies, 176
- Ford, W. K., Jr., *16*, *34*, 111, 112, 113, 120, 142, 270, 335
publications, 268, 269
studies, 118–119, 122–127, 127–130, 133–134, 139–141, 145–148
- Fork, D. C., *33*, 351, 356, 463, 477, 482, 483
publications, 480, 481
studies, 465–472
- Forrestal, J., vi
- Franco, M., 148
- Frantz, J. D., *31*, 505, 845, 857
studies, 759–764
- Freeberg, J., 352, 481, 482, 483
studies, 377–379
- French, C. S., *5*, *6*, *33*, 483
- Frew, W. N., vi, 989, 990
- Friel, J., 845, 857
- Frogel, J. A., 301, 325
publications, 337
- Fujii, T., *31*, 493, 494, 521, 522, 835, 845, 857
studies, 523–530, 566–570
- Gage, L. J., vi, 989, 990
- Gage, P., *25*
- Galau, G. A., 362, 940, 941, 950, 952, 955, 956, 959
publications, 957
studies, 890–918, 918–924
- Garavito, C., 271
- Gardner, E., 103
publications, 102
studies, 97–99
- Gardner, J., *30*, 104
- Gautier, D., 324
- Gehrels, T., 326
- Gélinas, L., 149, 271
- Gergely, T. E., 147, 148
- Geshelin, P., *30*, 11, 103
studies, 36, 36–37, 37
- Gezari, D. Y., 346
publications, 340
- Giesecke, A. A., 149, 271
- Gifford, W. S., vi
- Gil, M., 271
- Gilbert, C., vi
- Gilbert, C. J., v, 967, 968
- Gillett, F. H., vi
- Gilman, D. C., vi, 989, 990, 991
- Girardin, N., 149, 271
- Giza, P., 104
studies, 36, 36–37, 38–45
- Godwin, E. A., *30*, 11, 103
studies, 45–46
- Goldberg, R. N., 861, 862, 866, 870, 874, 875, 887, 888, 890, 893, 925, 926, 933, 939, 940, 956
publications, 958
- Golden, W. T., v, *29*, 965, 967, 968
- Gordon, M., 271
- Gott, J. R., III, 318
publications, 337, 340
- Graham, D. E., 861, 865, 868, 872, 874, 875, 887, 892, 893, 920, 955, 956
publications, 958
studies, 925–943
- Graham, J. A., 118, 119, 120, 271
- Gray, H. H., v, 967
- Green, R. F., *32*, 313, 347
publications, 337
- Greenewalt, C. H., v, *7*, *29*, 967
- Greenough, W. C., v, 967, 968
- Greenstein, J. L., *29*, 284, 285, 287, 288, 294, 297, 346
publications, 337, 338, 339
- Gregory, T. S., 347
- Griffin, R. F., 326
- Gunn, J. E., *17*, *29*, *32*, 277, 291, 300, 309, 310, 319, 330, 346
publications, 337, 338, 340
- Gurdon, J., *25*, 7
- Hadidiacos, C. G., 509, 696, 706, 748
studies, 828–832
- Hafner, S. S., 503, 504, 837, 841, 857
studies, 735–739, 739–741
- Haggerty, P. E., vi, 965
- Hanawalt, P., 351
- Hansen, L., 326
- Haraburda, J. M. S., vii
- Hardy, E., *32*, 311, 346
- Hare, P. E., *31*, 507, 801, 837, 857
publications, 840
studies, 801–806
- Harris, J. W. S., 104
- Hart, S. R., *10*, *34*, 115, 149, 270
publications, 268, 269
studies, 176–207
- Harte, B., 522, 523, 524, 528, 546, 561, 836, 847, 857
- Hartog, M., *32*, 288, 346
- Hartwick, F. D. A., 308
- Haskins, C. P., v, vi, *24*, 967
- Hatch, M. D., 408
- Hay, J., vi, 989, 990, 991
- Hedges, J. I., *31*, 507, 838, 857
studies, 792–800
- Heiles, C., 148, 271
- Helin, E. F., 331
- Helsley, C. E., 271
- Henard, K. R., vii
- Henry, B. McK., vi
- Herbig, G. H., 325
- Herrick, M. T., vi
- Hertig, A. T., 98, 103
- Hewitt, A. S., vi
- Hewitt, R. E., vii
- Hewlett, W. R., v, *5*, 965
- Hickson, P., *32*, 310, 347
- Hiesey, W. M., *33*, 413, 483
- Higashinakagawa, T., 957
studies, 28–30
- Higginson, H. L., vi, 989, 990
- Hill, G., 329

- Hitchcock, E. A., vi, 989, 990
 Hitchcock, H., vi
 Hoering, T. C., 31, 508, 627, 792, 800, 801, 836, 838, 847, 857
 studies, 806-813
 Hoersch, A., 857
 Hoessel, J. G., 32
 Hofmann, A. W., 34, 115, 117, 149, 270
 studies, 176-207, 249-259, 259-263
 Hogan, M. E., 104
 studies, 23, 24-25
 Hoggan, H. R., 336
 Hogness, D., 882
 Holden, F., 326
 Holloway, J. R., 497, 498, 500, 501, 626, 631, 656, 771, 774, 838, 843, 847, 850, 857
 studies, 636-640, 675-678, 771-775
 Hölzl, E., 502
 studies, 711-720
 Hoover, H., vi
 Hornblower, M., vii
 Hough-Evans, B. R., 919, 923, 956, 957, 959
 publications, 958, 959
 Hough, F. E., 579
 Hovland, L., 320
 Howard, R. F., 32, 279, 280, 346
 Howe, W. W., vi, 989, 990
 Hoyer, B. H., 270, 362, 363, 367, 940, 956, 957
 Huaco, D., 271
 Huang, L., 21, 30, 9, 11, 103
 publications, 102
 studies, 52-53, 53-57, 57-61, 67-73
 Huchra, J. P., 32, 302, 347
 publications, 338
 Huckenholz, H. G., 502, 636, 724, 725, 730, 847, 857
 publications, 840
 studies, 705-711, 711-720
 Huggins, F. E., 31, 502, 503, 504, 505, 706, 707, 709, 710, 738, 824, 838, 847, 857
 studies, 711-720, 720-730, 730-735, 756-758
 Hurford, G. J., 346
 Hutchinson, C. L., vi, 989, 990

 Irvine, T. N., 31, 495, 500, 558, 662, 667, 835, 838, 847, 857
 studies, 597-610, 668-677

 Jacq, C., 14
 James, D. E., 34, 115, 116, 117, 149, 211, 233, 270
 publications, 268, 269
 studies, 176-207, 213-216, 243-249
 Jesaitis, A. J., 33, 483
 Jessup, W. A., vi
 Jewett, F. B., vi
 Johnson, G., 33, 351, 355, 482, 483
 publications, 480
 studies, 440-449, 449-456, 456-459
 Johnson, T. V., 330, 326
 Jones, D. H. P., 324
 Jordan, E. D., 104
 studies, 12, 12-14

 Kafatos, F. C., 891, 910, 955, 956
 publications, 958
 studies, 861-870
 Kalinowski, J. K., 323
 Kamper, K., 332
 Kaplan, A., 33, 354, 483
 studies, 423
 Katem, B. N., 300, 312, 347
 Katz, M., 347
 Kaufmann, B. P., 26
 Kaushagen, C., 30, 104
 Kent, S., 32, 347
 King, G. C. P., 149, 272
 publications, 269
 studies, 240-243
 Kirshner, R. P., 327
 publications, 337, 338, 340
 Klein, W. H., 955, 956, 959
 publications, 958
 studies, 890-918
 Klukas, C. K.
 studies, 45-46, 49-50
 Knapp, S. L., 300, 319, 323, 346
 Knopf, U., 484
 Knox, G. V., 347
 Konigsberg, I. R., 7, 8, 103
 Kormendy, J., 32, 327, 347
 Kowal, C. T., 284, 298, 347
 publications, 338, 340, 341
 Kozlowski, M. R., 959
 Kraft, R. P., 325
 Krieger, A. S., 279
 Kristian, J., 17, 32, 277, 292, 297, 308, 312, 319, 346
 publications, 337, 338
 Krogh, T. E., 31, 508, 521, 522, 531, 816, 848, 857
 studies, 821-824
 Kumar, C. J., 118, 272
 publications, 268
 Kupferman, P. N., 347
 Kushiro, I., 31, 272, 493, 494, 496, 497, 500, 501, 509, 556, 559, 565, 566, 570, 621, 622, 623, 647, 656, 661, 662, 667, 741, 743, 832, 838, 848, 854, 857
 publications, 268
 studies, 546-555, 611-614, 614-618, 618-620, 631-636, 636-644, 668-678, 678-684

 Labeyrie, A., 328
 Labonte, B. J., 32, 347
 publications, 338
 Landauer, F., 320
 Landstreet, J. D., 328
 publications, 338
 Langley, S. P., vi, 989, 990
 Lanning, H., 328, 329
 publications, 338
 Larimer, R., 272
 Lawrence, E. O., vi
 Leahy, P. S., 959
 Lee, Amy Shiu, 959
 Lee, D. Y., 31, 857

- Leighton, R. B., 346
 Lewis, M. R., 7
 Lewis, W. H., 7
 Liewer, K. M., 324
 Lindbergh, C. A., vi
 Linde, A. T., 34, 116, 117, 149, 270
 publications, 269
 studies, 216–223, 229–233, 243–249
 Lindsay, W., vi, 989, 990
 Little, C. A., 113, 118, 272
 studies, 143–144
 Liu, L., 837, 857
 Lo, K. Y., 312
 Lodge, H. C., vi
 Lorre, J., 305
 Loomis, A. L., v, vi, 967
 Lovett, R. A., vi
 Low, S., vi, 989, 990
 Lowen, A. L., 347
 Lynds, B., 308, 314

 Mabin, A., 104
 studies, 76–78
 Mackenzie, J., 482, 484
 MacVeagh, W., vi, 989, 990
 MacRae, D. A., 338
 Madore, B. F., 328, 329
 Magaritz, M., 34, 117, 149, 200, 270
 studies, 249–259
 Mahall, B. E., 33, 483
 publications, 480
 studies, 438–440
 Mamin, J., 959
 Mao, H. K., 9, 13, 14, 31, 492, 501, 502, 504, 505,
 508, 682, 734, 838, 842, 845, 849, 857
 publications, 840
 studies, 509–513, 513–515, 515–520, 688–695,
 695–699, 699–701, 701–705, 753–756, 756–
 758, 759–764, 824–827, 827–828
 Marr, A. G., 98
 Marsh, K. A., 280, 346
 Martin, A. E., 329
 Martin, W. McC., Jr., v, 29, 967
 Massey, P., 32, 347
 publications, 338
 Matson, D. L., 322, 326
 Matthews, K., 336
 publications, 339
 McCallum, M. E., 493, 521, 522, 523, 537, 849
 publications, 840
 studies, 538–541, 542–544
 McCammon, C. A., 31, 857
 McClintock, B., vii
 McCord, T. B., 277
 McGough, S. A., vii
 McHugh, K. S., vi, 967
 McMahan, U. J., 104
 McMahan, D., 482
 McNamara, D. H., 329
 Mellon, A. W., vi
 Melnick, J., 32, 312, 347
 Merriam, J. C., vi

 Meyer, D. B., 98
 Meyer, J. C., 29
 Meyer, R. P., 272
 publications, 268
 Migeon, B.
 studies, 22–23
 Miller, G. H., 31, 531, 857
 Miller, M. C., vi
 Miller, O. L., Jr.
 studies, 28–30
 Miller, R., vi
 Miller, W. C., 329
 publications, 338
 Millikan, A. G., 329
 Mills, D. O., vi, 989, 990
 Minkowski, R., 25
 Mirabel, I., 148, 272
 Mitchell, S. W., vi, 989, 990, 991
 Montague, A. J., vi
 Mooney, H. A., 19, 351, 353, 408, 418, 433, 435,
 482, 484
 publications, 480, 481
 studies, 410–413
 Moore, R., 282, 346
 publications, 339
 Morgan, H. S., v, 29, 965, 967, 968
 Morras, R., 148, 272
 Morris, S. C., 325
 Morrow, W. W., vi, 989, 990
 Morton, D. C., 330
 Motoya, Y., 149, 272
 Mudd, S. G., vi
 Muller, F., 98
 Muller, K. J., 21, 22, 30, 10, 11, 103
 studies, 90, 90–95, 95–97
 Münch, G., 32, 283, 289, 322, 330, 346
 publications, 339
 Murata, N., 33, 470, 472, 477, 483
 publications, 481
 Murray, M., 33, 483
 Myers, J., 857
 Myers, W. I., vi, 25, 26, 965, 967
 Mysen, B. O., 31, 202, 493, 494, 496, 497, 499,
 500, 501, 509, 556, 639, 838, 850, 857
 publications, 840, 841
 studies, 546–555, 614–618, 620–623, 626–631,
 656–662, 662–668, 675–678, 678–684, 833–835

 Nadeau, D., 32, 347
 Naslund, H. R., 31, 495, 498, 600, 838, 857
 studies, 592–597, 640–644
 Neugebauer, G., 32, 290, 291, 297, 300, 336, 346
 publications, 337, 339, 340
 Nicholson, F., 408
 Nisenson, P., 331
 Nixon, P. H., 202, 493, 521, 523, 524, 528, 531,
 534, 537, 539, 540, 541, 543, 547, 626, 675, 822,
 837, 842, 846, 850
 publications, 841
 studies, 544–546
 Nobs, M. A., 33, 408, 483
 studies, 421–423

- Norris, J., 305
publications, 339
- Norton, G., v, 967
- Noyce, R. N., 4
- Ocola, L., 149, 270
publications, 268
- Ohashi, Y., 31, 498, 504, 509, 644, 645, 646, 747, 748, 751, 838, 851, 857
publications, 840
studies, 743-746, 828-832
- Ohi, S.
studies, 45-46, 48
- Ohshima, Y., 23, 30, 11, 103
studies, 36, 36-37, 37-38
- Okada, H., 149, 212, 216, 217, 218, 219, 222, 223, 240, 270
- Oke, J. B., 17, 31, 277, 297, 298, 300, 301, 302, 309, 319, 321, 346
publications, 337, 338, 339, 340
- Olafsson, G., 149, 272
- Olsen, S., 857
- Oort, J., 118, 272
- O'Rahilly, R., 103
publications, 102
studies, 97-99
- Osborn, E. F., 30, 838, 839, 857
publications, 841
- Osborn, W. C., vi, 29
- Osmond, C. B., 408, 410, 418
- Ostriker, J. P., 317, 318
publications, 339, 340
- Ozato, K., 21, 30, 9, 11, 103
publications, 102
studies, 52-53, 53-57, 57-61, 66-67, 73-76
- Pagano, R. E., 21, 30, 9, 11, 103
publications, 102
studies, 52-53, 53-57, 57-61, 61-66, 66-67, 76-78, 85-87
- Page, R. W., 836, 837, 857
studies, 813-821
- Page, R. W., 149, 272
- Page, W. H., v, 29, 967
- Painchaud, D. M., 874, 956, 959
publications, 958
studies, 925-943
- Parmelee, J., vi
- Parsons, W. B., vi
- Paschl, C., 953
- Paton, S., vi
- Patterson, A., 280
- Payne, T., 34, 484
- Pearson, W. R., 955
publications, 958
studies, 870-883
- Pennoyer, R. M., v, 967, 968
- Pepper, G. W., vi
- Pepper, G. H., 34, 118, 249, 263, 270
publications, 268, 269
- Perkins, R. S., v, 967, 968
- Pershing, J. J., vi
- Persson, S. E., 32, 301, 346
publications, 337
- Pesch, P., 330
- Peterson, C. J., 16, 34, 111, 112, 118, 270
publications, 268, 269
studies, 122-127, 127-130, 133-134, 134-136, 139-141
- Peterson, D. M., 285, 331
- Pilcher, C., 283, 331
- Pimental, E., 272
- Pollock, H. E. D., vii
- Pöppel, W., 148, 272
- Poupeau, G., 114, 149, 272
studies, 170-175
- Pratt, L. H., 482
- Preisler, R., 34, 484
- Preston, G. W., 29, 32, 288, 346
publications, 340
- Prentis, H. W., Jr., vi
- Priedhorsky, W. C., 33, 347
- Pritchard, W. R., 98
- Pritchett, H. S., vi
- Proskouriakoff, T., vii
- Rabin, D. M., 33, 303, 347
- Radford, G. A., 327
- Rajan, R. S., 34, 114, 149, 170, 175, 270
studies, 170-175
- Ramirez, J. E., 272
publications, 268
- Ramirez, J. L., 30, 104
studies, 45-46, 46, 46-48
- Ramsey, E. M., 98, 103
- Ray, P. M., 353, 383, 482
studies, 395-399
- Raymond, M., 503, 504, 645, 852
studies, 735-739, 739-741
- Rayne, M. W., 330
- Rebbert, M. L., 104
studies, 30-36, 45-46, 46
- Redman, R. O., 33, 347
- Reeder, R. H., 22, 24, 25, 30, 11, 103, 957
publications, 102, 103
studies, 20-22, 23, 23-24, 24-27, 28-30
- Rentschler, G. S., vi
- Rice, N. R., 34, 270, 926, 940, 957
- Richstone, D. O., 310, 315, 316, 346
- Rigg, J., 959
- Ritchie, A. K., 30, 103
publications, 103
studies, 67-73
- Rithgmyer, C., 857
- Roberts, R. B., 270, 956
- Roberts, M. S., 34, 118, 119, 120, 272
- Rockefeller, D., vi
- Rogler, C. E., 19, 33, 352, 482, 483
publications, 482
studies, 367-373
- Rodriguez B., A., 116, 149, 270
publications, 269
- Rodriguez, R., 272
studies, 229-233

- Roesler, F., 283, 289
 Root, E., vi, 989, 990, 991
 Root, E., Jr., vi
 Rosenhauer, M., 492, 498, 502, 503, 648, 719, 720, 743, 753, 754, 855
 studies, 513-515, 720-730, 730-735
 Rosenwald, J., vi
 Roth, W. M., v
 Rowe, J., 272
 Rubey, W. W., vi, 8
 Rubin, V. C., 16, 34, 111, 112, 142, 145, 270
 publications, 268, 269
 studies, 118-119, 119-120, 122-127, 127-130, 133-134, 139-141
 Ruiz, M. T., 32, 346
 Rule, B. H., 7, 32, 278, 346
 publications, 339
 Rumble, D., III, 31, 499, 835, 836, 838, 839, 852, 857
 studies, 651-655
 Ruysschaert, R. M., 104
 studies, 66-67
 Ryerson, M. A., vi
- Sacks, I. S., 10, 16, 34, 116, 117, 149, 206, 212, 246, 249, 270
 publications, 269
 studies, 216-223, 223-229, 229-233, 233-239, 240-243
 Saha, A. K., 857
 Sahama, Th. G., 495, 574, 578, 580, 852, 853, 857
 studies, 585-592
 Sandage, A. R., 17, 18, 32, 277, 292, 299, 300, 302, 308, 310, 312, 316, 319, 346
 publications, 339
 Sanders, R. H., 272
 Sandra, A., 30, 11, 103
 Sargent, A. I., 33, 284, 304, 312, 313, 314, 315, 317, 347
 publications, 341
 Sargent, W. L. W., 32, 288, 308, 347
 publications, 339
 Schairer, J. F., 581, 583, 592, 596, 598, 599, 601, 603, 604, 610, 734, 842, 853
 Schechter, P., 311, 346
 Scherrer, P. H., 280
 publications, 340
 Schilling, J. G., 206, 207, 272
 Schmidt, M., 18, 32, 319, 346
 publications, 339, 340
 Schneider, M., 34, 149, 271
 Schreiber, U., 33, 356, 463, 483
 studies, 472-477
 Schrott, E., 484
 Schwartzman, D. W., 272
 Schweizer, F., 32, 346
 Seamans, R. C., Jr., v, 967
 Searle, L., 18, 32, 299, 300, 302, 303, 304, 346
 publications, 337, 340
 Seber, C. M., 34, 149, 271
 studies, 243-249
 Sebok, W. L., 347
- Seitz, M. G., 621, 626, 656, 660, 663, 676, 682, 683, 833, 834, 850, 853
 publications, 841
 studies, 684-687
 Seyler, R. G., 272
 Shectman, S. A., 32, 317, 319, 346
 Shepley, H. R., vi
 Shields, G. A., 33, 301, 312
 publications, 340
 Shimizu, N., 546, 656, 661, 662, 675, 676, 677, 684
 Shoemaker, E. M., 331
 Sholle, D., 33, 347
 Shortridge, K., 285
 Sigtrygsson, R., 272
 Simkin, S. M., 331
 Simoni, D., 149, 272
 Simonson, B., 857
 Smith, C. B., 493, 537, 538, 857
 studies, 542-544
 Smith, M. J., 893, 913, 925, 938, 941, 956, 957, 959
 publications, 959
 Smith, T., vi
 Snoke, J. A., 16, 34, 116, 117, 149, 270
 publications, 268, 269
 studies, 216-223, 223-229, 229-233, 233-239, 240-243, 243-249
 Solbrig, O., 351, 483, 484
 Somerville, D. V., 104
 studies, 52-53
 Spear, F. S., 31, 506, 857
 studies, 775-779
 Spinrad, H., 309
 Spooner, J. C., vi, 989, 990
 Stachnik, R. V., 331
 Stanton, F., v, 965, 967, 968
 Stefansson, R., 149, 272
 Stein, D., 33, 484
 Stemler, A., 33, 351, 483
 publications, 481
 studies, 477-479
 Stone, G., 98
 Storey, W. B., vi
 Strauss, F., 98
 Strong, R. P., vi
 Sulentic, J., 300, 308, 346
 publications, 337
 Suyehiro, K., 34, 149, 270
 Suyehiro, S., 149, 270
 Suzuki, Y., 22, 23, 24, 25, 30, 8, 11, 103
 publications, 103
 studies, 36, 36-37, 37-38, 38-45
 Swift, K., 34, 484
 Swope, H. H., 7, 147, 278, 346
 Svalgaard, L., 280
 publications, 340
 Svetska, Z., 279
- Taft, C. P., v
 Taft, W. H., vi
 Takeichi, M., 30, 10, 103
 studies, 52-53, 61-66

- Tamayo, L., 149, 272
 Tammann, G. A., 297, 300, 316, 325
 Tang, F. Y. C., 282, 347
 publications, 339
 Tartof, K. D.
 studies, 30-36
 Taylor, K., 327, 346
 Telleria, J. L., 272
 Tepperman, K., 30, 11, 103
 studies, 76-78, 87-88
 Terrile, R. J., 33, 347
 Thayer, W. S., vi
 Thomas, B.
 studies, 95-97
 Thomas, C., 104
 publications, 103
 Thomas, T. L., 959
 publications, 959
 Thompson, W. F., 18, 19, 33, 351, 352, 483
 publications, 482
 studies, 356-362, 362-367, 367-373
 Townes, C. H., v, 5, 967
 Thonnard, N., 34, 111, 112, 113, 118, 142, 146, 270
 publications, 268, 269
 studies, 118-119, 119-120, 127-130, 130-132, 143-144, 144-145
 Thuan, T. X., 300, 302, 310, 311, 317, 318, 346
 publications, 337, 339, 341
 Tinsley, B. M.
 publications, 338, 339, 340
 Torres, A., 858
 Trauger, J., 283, 287
 Trimble, V., 287
 Trippe, J. T., v, 965, 967, 968
 Trochimczyk, J., 31, 507, 857
 studies, 784-786, 790-791
 Troughton, J., 408, 477
 publications, 481
 Truffa-Bachi, P., 272
 Truman, O. H., 29
 Tupper, C. J., 98
 Turner, E. L., 33, 310, 317, 347
 Turner, K. C., 34, 113, 118, 270
 studies, 121-122, 143-144, 144-145
 Turnrose, B. E., 33, 332, 347
 Tutschulte, T., 959
 Tuve, M. A., 9, 10, 34, 118, 270

 Ulfbeck, O., 313
 Upholt, W. B.
 studies, 45-46, 46, 48, 50-51

 van de Velde, N. W., 362, 367
 van den Bergh, S., 332
 publications, 340
 van der Kruit, P. C., 333
 publications, 340
 Van Valkenburg, A., 492, 754, 839, 855, 858
 studies, 515-520
 Vaughan, A. H., 32, 334, 346
 publications, 340

 Veeder, G., 326
 Velde, B., 497, 507, 584, 621, 622, 791, 839, 858
 studies, 574-580, 618-620, 786
 Velde, D., 495, 858
 studies, 580-584
 Venolia, L., 959
 Vidale, R. J., 31, 857
 Vieira, E. R., 148
 Virgo, D., 31, 502, 503, 504, 505, 570, 712, 717, 718, 719, 738, 824, 847, 857
 studies, 705-711, 711-720, 720-730, 730-735, 739-741, 756-758
 Volponi, F., 270

 Wade, R., 33, 298, 347
 Wadsworth, J. W., vi
 Wahn, H. L., 30, 11, 103
 studies, 23, 23-24, 24-27
 Walburn, M. H., vii
 Walcott, C. D., vi, 989, 990, 991
 Walcott, F. C., vi
 Walcott, H. P., vi
 Wallerstein, G., 333
 Ward, W., 408
 Watson, E. B., 31, 392, 857
 Watson, W. D., 324
 Weber, H. P., 706, 858
 Weed, L. H., vi
 Weeks, R. A., 492, 500, 504, 734
 studies, 515-520, 688-695, 753-756
 Weidenschilling, S. J., 34, 113, 152, 169, 270
 studies, 149-151
 Weiss, C. V., 352, 481, 483
 studies, 377-379
 Welch, W. H., vi
 Wellauer, P. K., 22, 25, 30, 11, 103, 941, 957
 publications, 103
 studies, 28-30, 30-36
 Werner, M. W., 32, 291, 296, 346
 publications, 340
 West, R. M., 333
 Westphal, J. A., 17, 32, 277, 292, 297, 308, 319, 346
 publications, 337, 338
 Wetherill, G. W., 10, 15, 34, 114, 152, 157, 163, 165, 166, 169, 270
 publications, 269, 270
 report of the Director, Department of Terrestrial Magnetism, 105-272
 studies, 151-169
 White, A. D., vi, 989, 990
 White, E. D., vi
 White, H., vi
 White, J. N., v, 967
 White, R., 882
 White, R. E., 118, 207, 272
 Whitford, D. J., 34, 115, 149, 201, 209, 211, 213, 270
 publications, 270
 studies, 207-213
 Wickersham, G. W., vi

- Wickes, W. C., 333
Wilcox, J. M., 280
Wilkinson, A., 310, 346
Williams, J. G., 149, 151, 166, 169, 272
Williams, T. B., 33, 330, 347
 publications, 340
Willis, A. G., 308
Willner, S. P., 33, 290, 295, 347
 publications, 340
Wilson, C. P., 32, 289, 346
 publications, 340
Wilson, O. C., 320, 325, 346
 publications, 340
Wilson, R. E., vi
Woermann, E., 492, 753, 754, 855
 studies, 513-515
Wold, B. J., 955, 956, 959
 publications, 958
 studies, 890-918
Wood, B. J., 31, 494, 498, 540, 565, 566, 568, 569,
 656, 856, 857
 studies, 570-575, 659-662, 741-743
Woodward, R. S., vi
Wozniak, W., 104
Wright, C. D., vi, 989, 990, 991
Yamagishi, Y., 149, 272
Yoder, H. S., Jr., 9, 30, 198, 207, 258, 494, 495,
 496, 546, 551, 553, 558, 565, 566, 590, 603,
 604, 609, 636, 647, 650, 662, 713, 791, 839,
 840, 851, 853, 856, 857
 publications, 841
 report of the Director, Geophysical Labora-
 tory, 485-858
 studies, 574-580, 580-584, 614-618
Yoshimura, H., 32, 280, 346
 publications, 340
Younkin, R. L., 334
Zies, E. G., 31, 857
Zimmerman, B. A., 319, 344
Zinn, R., 18, 32, 299, 304, 305, 346
 publications, 239
Zinner, E., 149, 170, 175, 272
Zirin, H., 32, 280, 281, 289, 346
 publications, 341

